

ENCYCLOPEDIA
of PALEOCLIMATOLOGY
AND ANCIENT
ENVIRONMENTS

Edited by
Vivien Gornitz

 Springer

ENCYCLOPEDIA *of*
PALEOCLIMATOLOGY AND
ANCIENT ENVIRONMENTS

Encyclopedia of Earth Sciences Series

ENCYCLOPEDIA OF PALEOCLIMATOLOGY AND ANCIENT ENVIRONMENTS

Volume Editor

Vivien Gornitz is a Senior Research Scientist, Center for Climate Systems Research, Columbia University and NASA Goddard Institute for Space Studies. She holds a B.A. from Barnard College and a Ph.D. from Columbia University. Her research interests include global sea level rise—past, present, and future, coastal hazards, climatic implications of land cover transformations, and planetary geology, including Mars. In addition to numerous scientific publications, she has edited *Geology of the Planet Mars* (Benchmark Papers in Geology, v. 48, Dowden, Hutchinson & Ross, Inc., 1979) and has contributed articles to several of the encyclopedias in the Earth Sciences Series. She was a Contributing Author for the IPCC in 1990, 1995, 2001, and 2007.

Advisory Board

Caspar Ammann
Climate and Global Dynamics Division—Paleoclimatology
National Center for Atmospheric Research (NCAR)
Boulder, CO 80307
USA

Joseph Ortiz
Department of Geology
Kent State University
Kent, Ohio 44242-0001
USA

Mark A. Chandler
5018 Woodburn Drive
Madison, WI 53711
USA
and
Goddard Institute for Space Studies
2880 Broadway
New York, NY 10025
USA

Linda Sohl
Goddard Institute for Space Studies
2880 Broadway
New York, NY 10025
USA

Anthony Hallam
School of Earth Sciences
University of Birmingham
Edgbaston
Birmingham B15 2TT
UK

James D. Wright
Department of Geological Sciences
Wright-Reiman Laboratories
Rutgers University
610 Taylor Road, Piscataway
NJ 08854-8066
USA

Aims of the Series

The *Encyclopedia of Earth Sciences Series* provides comprehensive and authoritative coverage of all the main areas in the Earth Sciences. Each volume comprises a focused and carefully chosen collection of contributions from leading names in the subject, with copious illustrations and reference lists.

These books represent one of the world's leading resources for the Earth Sciences community. Previous volumes are being updated and new works published so that the volumes will continue to be essential reading for all professional earth scientists, geologists, geophysicists, climatologists, and oceanographers as well as for teachers and students. See the back of this volume for a current list of titles in the *Encyclopedia of Earth Sciences Series*. Go to <http://www.springerlink.com/reference-works/> to visit the "Earth Sciences Series" on-line.

About the Series Editor

Professor Charles W. Finkl has edited and/or contributed to more than 8 volumes in the *Encyclopedia of Earth Sciences Series*. For the past 25 years he has been the Executive Director of the Coastal Education & Research Foundation and Editor-in-Chief of the international *Journal of Coastal Research*. In addition to these duties, he is Principal Marine Geologist with Coastal Planning & Engineering, Inc. and Research Professor at Florida Atlantic University in Boca Raton, Florida, USA. He is a graduate of the University of Western Australia (Perth) and previously worked for a wholly owned Australian subsidiary of the International Nickel Company of Canada (INCO). During his career, he acquired field experience in Australia; the Caribbean; South America; SW Pacific islands; Southern Africa; Western Europe; and the Pacific Northwest, Midwest, and Southeast USA.

Founding Series Editor

Professor Rhodes W. Fairbridge (deceased) has edited more than 24 Encyclopedias in the Earth Sciences Series. During his career he has worked as a petroleum geologist in the Middle East, been a WW II intelligence officer in the SW Pacific and led expeditions to the Sahara, Arctic Canada, Arctic Scandinavia, Brazil and New Guinea. He was Emeritus Professor of Geology at Columbia University and was affiliated with the Goddard Institute for Space Studies.

ENCYCLOPEDIA OF EARTH SCIENCES SERIES

ENCYCLOPEDIA
of PALEOCLIMATOLOGY
AND ANCIENT
ENVIRONMENTS

edited by

VIVIEN GORNITZ

Goddard Institute for Space Studies

and

Columbia University

New York

USA

 Springer

Library of Congress Control Number: 2008934597

ISBN: 978-1-4020-4551-6

This publication is available also as:

Electronic publication under ISBN 978-1-4020-4411-3 and

Print and electronic bundle under ISBN 978-1-4020-5197-5

Published by Springer

PO Box 17, 3300 AA Dordrecht, The Netherlands

Printed on acid-free paper

Cover photo: Landforms – Heart of the Colorado Plateau: The Story Behind the Scenery
(KC Publications, 1995). Photo reproduced courtesy of G. Ladd

Every effort has been made to contact the copyright holders of the figures and tables which have been reproduced from other sources. Anyone who has not been properly credited is requested to contact the publishers, so that due acknowledgement may be made in subsequent editions.

All Rights Reserved for Contributions on *Coal Beds, Origin and Climate; Glendonite/Ikaite and Ostracodes*

© 2009 Springer Science+Business Media B.V.

No part of this work may be reproduced, stored in a retrieval system, or transmitted in any form or by any means, electronic, mechanical, photocopying, microfilming, recording or otherwise, without written permission from the Publisher, with the exception of any material supplied specifically for the purpose of being entered and executed on a computer system, for exclusive use by the purchaser of the work.

Contents

List of Contributors	xi	Astronomical Theory of Climate Change	51
Preface	xxv	<i>André Berger</i>	
Acknowledgements	xxvii	Atmospheric Circulation During the Last Glacial Maximum	57
Aerosol (Mineral)	1	<i>David Rind</i>	
<i>Ina Tegen</i>			
Albedo Feedbacks	2	Atmospheric Evolution, Earth	61
<i>Andrew A. Lacis</i>		<i>James Farquhar</i>	
Alkenones	4	Atmospheric Evolution, Mars	66
<i>Mark Pagani</i>		<i>David C. Catling</i>	
Ancient Cultures and Climate Change	6	Atmospheric Evolution, Venus	75
<i>Vivien Gornitz</i>		<i>Bruce Fegley, Jr.</i>	
Animal Proxies, Invertebrates	10	Banded Iron Formations and the Early Atmosphere	85
<i>Robert R. Gaines and Mary L. Droser</i>		<i>Bruce M. Simonson and Alan J. Kaufman</i>	
Animal Proxies – Vertebrates	13	Basal Ice	89
<i>Thomas H. Rich and Patricia Vickers-Rich</i>		<i>Peter G. Knight</i>	
Antarctic Bottom Water and Climate Change	16	Beachrock	89
<i>Stan Jacobs</i>		<i>Ian D. Goodwin</i>	
Antarctic Cold Reversal	22	Beetles as Quaternary and Late Tertiary Climate Indicators	90
<i>Vincent I. Morgan</i>		<i>G. Russell Coope</i>	
Antarctic Glaciation History	24	Beryllium-10	92
<i>Kathy Licht</i>		<i>Jürg Beer</i>	
Antarctic Sea Ice History, Late Quaternary	31	Binge-Purge Cycles of Ice Sheet Dynamics	94
<i>Xavier Crosta</i>		<i>Martin J. Siegert</i>	
Archean Environments	34	Bolide Impacts and Climate	96
<i>William H. Peck and John W. Valley</i>		<i>Michael R. Rampino</i>	
Arctic Sea Ice	38	Bølling-Allerød Interstadial	100
<i>Anne de Vernal</i>		<i>Wim Z. Hoek</i>	
Arid Climates and Indicators	45		
<i>Andrew Goudie</i>			

Borehole Climatology <i>Hugo Beltrami and Daniela Nitoiu</i>	103	Cordilleran Ice Sheet <i>John J. Clague</i>	206
Carbon Cycle <i>Abraham Lerman</i>	107	Cosmogenic Radionuclides <i>Jürg Beer</i>	211
Carbon Dioxide and Methane, Quaternary Variations <i>Bernhard Stauffer</i>	118	Cretaceous Warm Climates <i>Erle G. Kauffman and Claudia C. Johnson</i>	213
Carbon Dioxide, Dissolved (Ocean) <i>Richard E. Zeebe and Dieter A. Wolf-Gladrow</i>	123	Cretaceous/Tertiary (K-T) Boundary Impact, Climate Effects <i>Elisabetta Pierazzo</i>	217
Carbon Isotope Variations Over Geologic Time <i>Ján Veizer</i>	128	Cryosphere <i>Philippe Huybrechts</i>	221
Carbon Isotopes, Stable <i>Steven W. Leavitt</i>	133	Cyclic Sedimentation (Cyclothem) <i>Allen W. Archer</i>	226
Carbonate Compensation Depth <i>Torsten Bickert</i>	136	Dansgaard-Oeschger Cycles <i>Irene A. Mogensén</i>	229
Carbonates, Cool Water <i>Jonathan Clarke</i>	138	Dating, Amino Acid Geochronology <i>Gifford H. Miller</i>	233
Carbonates, Warm Water <i>Dan Bosence</i>	143	Dating, Biostratigraphic Methods <i>Peter M. Sadler</i>	237
Cenozoic Climate Change <i>James D. Wright</i>	148	Dating, Dendrochronology <i>Brendan M. Buckley</i>	239
Cirques <i>Peter G. Knight</i>	155	Dating, Fission-Tracks <i>John I. Garver</i>	247
CLAMP <i>Robert A. Spicer</i>	156	Dating, Luminescence Techniques <i>Glenn W. Berger</i>	249
CLIMAP <i>James D. Hays</i>	158	Dating, Magnetostratigraphy <i>Wout Krijgsman and C. G. Langereis</i>	252
Climate Change, Causes <i>Thomas J. Crowley</i>	164	Dating, Radiometric Methods <i>Chris M. Hall</i>	255
Climate Forcing <i>Andrew A. Lacis</i>	174	Deep Sea Drilling Project (DSDP) <i>William W. Hay</i>	260
Climate Variability and Change, Last 1,000 Years <i>Michael E. Mann</i>	178	Deltaic Sediments, Climate Records <i>Steven L. Goodbred, Jr.</i>	265
Coal Beds, Origin and Climate <i>C. Blaine Cecil and Sandra G. Neuzil</i>	181	Dendroclimatology <i>Brendan M. Buckley</i>	269
Coastal Environments <i>Robert W. Dalrymple and Kyungsik Choi</i>	183	Desert Varnish as a Paleoclimate Proxy <i>Ronald I. Dorn</i>	275
Coccoliths <i>Jeremy R. Young</i>	187	Deuterium, Deuterium Excess <i>Gilles Delaygue</i>	278
COHMAP <i>Thompson Webb III</i>	188	Diamicton <i>John Menzies</i>	278
Continental Sediments <i>Marc S. Hendrix</i>	192	Diatoms <i>Amy Leventer</i>	279
Corals and Coral Reefs <i>John E. N. Veron</i>	198	Dinoflagellates <i>Anne de Vernal</i>	280

Dole Effect <i>Georg Hoffmann</i>	282	Glacial Isostasy <i>Kurt Lambeck</i>	374
Drumlins <i>Peter G. Knight</i>	284	Glacial Megalakes <i>Victor R. Baker</i>	380
Duricrusts <i>David J. Nash</i>	284	Glacial Sediments <i>Douglas I. Benn</i>	382
Dust Transport, Quaternary <i>Karen E. Kohfeld and Ina Tegen</i>	286	Glaciations, Pre-Quaternary <i>Emmanuelle Arnaud and I. Peter Martini</i>	384
Early Paleozoic Climates (Cambrian-Devonian) <i>Arthur J. Boucot</i>	291	Glaciations, Quaternary <i>Shawn J. Marshall</i>	389
Earth Laws and Paleoclimatology <i>Rhodes W. Fairbridge (deceased)</i> <i>and Vivien Gornitz</i>	294	Glaciofluvial Sediments <i>Douglas I. Benn</i>	394
Eccentricity <i>Marie-France Loutre</i>	301	Glaciomarine Sediments <i>Kathy Licht</i>	395
Eemian (Sangamonian) Interglacial <i>Ulrich C. Müller</i>	302	Glendonite/Ikaite <i>Ian P. Swainson</i>	396
Electrical Conductivity <i>Kendrick Taylor</i>	308	“Greenhouse” (Warm) Climates <i>Darren R. Gröcke</i>	397
Eolian Dust, Marine Sediments <i>David K. Rea</i>	308	Heat Transport, Oceanic and Atmospheric <i>Dan Seidov</i>	407
Eolian Sediments and Processes <i>Daniel R. Muhs</i>	312	Heinrich Events <i>Sidney Hemming</i>	409
Eolianite <i>David B. Loope</i>	319	History of Paleoclimatology <i>Rhodes W. Fairbridge (deceased)</i>	414
Eskers <i>Peter G. Knight</i>	320	History of Paleoclimatology – Biographies <i>Rhodes W. Fairbridge (deceased)</i> <i>and Vivien Gornitz</i>	428
Evaporites <i>Stefano Lugli</i>	321	Holocene Climates <i>Neil Roberts</i>	438
Evolution and Climate Change <i>David A. T. Harper</i>	325	Holocene Treeline Fluctuations <i>Mel A. Reasoner and Willy Tinner</i>	442
Faint Young Sun Paradox <i>James Farquhar</i>	333	Human Evolution and Climate Change <i>Gail M. Ashley</i>	446
Flood Basalts: Climatic Implications <i>Andrew D. Saunders</i>	335	Hypsithermal <i>Rhodes W. Fairbridge (deceased)</i>	451
Foraminifera <i>Harry J. Dowsett</i>	338	Ice Cores, Antarctica and Greenland <i>Dominique Raynaud and Frédéric Parrenin</i>	453
Geochemical Proxies (Non-Isotopic) <i>Matthew J. Higginson</i>	341	Ice Cores, Mountain Glaciers <i>Lonnie G. Thompson</i>	457
Glacial Erratics <i>Patrick M. Colgan</i>	354	“Icehouse” (Cold) Climates <i>Paul K. Link</i>	463
Glacial Eustasy <i>Stephen F. Pekar</i>	354	Ice-Rafted Debris (IRD) <i>Julian A. Dowdeswell</i>	471

Integrated Ocean Drilling Program (IODP) <i>Manik Talwani</i>	473	Maunder Minimum <i>Drew T. Shindell</i>	550
Interstadials <i>Wim Z. Hoek</i>	477	Medieval Warm Period <i>Rhodes W. Fairbridge</i> (deceased)	551
Iron and Climate Change <i>David Archer</i>	478	Mesozoic Climates <i>Gregory D. Price</i>	554
Isotope Fractionation <i>Dieter A. Wolf-Gladrow and Richard E. Zeebe</i>	479	Messinian Salinity Crisis <i>Stefano Lugli</i>	559
Kames <i>Peter G. Knight</i>	483	Methane Hydrates, Carbon Cycling, and Environmental Change	560
Kettles <i>Peter G. Knight</i>	483	<i>Gerard R. Dickens and Clayton Forswall</i>	
Lacustrine Sediments <i>Bernd Zolitschka and Dirk Enters</i>	485	Mid-Pliocene Warming <i>Mark A. Chandler</i>	566
Lake-Level Fluctuations <i>Mark B. Abbott and Lesleigh Anderson</i>	489	Millennial Climate Variability <i>Gerard Bond (deceased)</i>	568
Last Glacial Maximum <i>David Q. Bowen</i>	493	Mineral Indicators of Past Climates <i>Vivien Gornitz</i>	573
Last Glacial Termination <i>Didier Paillard</i>	495	Monsoons: Pre-Quaternary <i>Pinxian Wang and Qianyu Li</i>	583
Late Paleozoic Paleoclimates <i>Anne Raymond and Christopher R. Scotese</i>	498	Monsoons, Quaternary <i>Anil K. Gupta</i>	589
Late Quaternary Megafloods <i>Victor R. Baker</i>	504	Moraines <i>Peter G. Knight</i>	594
Late Quaternary-Holocene Vegetation Modeling <i>Jed O. Kaplan</i>	507	Mountain Glaciers <i>Lonnie G. Thompson</i>	595
Laterite <i>Michael Widdowson</i>	514	Mountain Uplift and Climate Change <i>Douglas W. Burbank</i>	596
Laurentide Ice Sheet <i>Arthur S. Dyke</i>	517	Nearest-Living-Relative Method <i>Volker Mosbrugger</i>	607
Little Ice Age <i>Drew T. Shindell</i>	520	Neogene Climates <i>Carin Andersson</i>	609
Loess Deposits <i>Konstantin G. Dlussky</i>	522	Nitrogen Isotopes <i>Julian P. Sachs</i>	612
Marine Biogenic Sediments <i>Wolfgang H. Berger and Gerold Wefer</i>	525	North Atlantic Deep Water and Climate Change <i>Thomas M. Marchitto, Jr.</i>	614
Marine Carbon Geochemistry <i>David Archer</i>	533	North Atlantic Oscillation (NAO) Records <i>Heidi M. Cullen</i>	619
Marine Clay Minerals <i>Alastair Ruffell</i>	539	Obliquity <i>Marie-France Loutre</i>	625
Mars: Water and Past Climates <i>Phillip R. Christensen</i>	540	Ocean Anoxic Events <i>Bradley Sageman</i>	626
Mass Extinctions: Role of Climate <i>Garland R. Upchurch, Jr.</i>	547	Ocean Drilling Program (ODP) <i>Joanne C. Reuss</i>	630

Ocean Paleocirculation <i>Roger Francois</i>	634	Paleosols, Quaternary <i>Tatiana D. Morozova and Andrei A. Velichko</i>	752
Ocean Paleoproductivity <i>Adina Paytan</i>	644	Paleotemperatures and Proxy Reconstructions <i>Thomas M. Cronin</i>	757
Ocean Paleotemperatures <i>Mara Weinelt</i>	651	Paleotempestology, the Sedimentary Record of Intense Hurricanes <i>Jeffrey P. Donnelly</i>	763
Organic Geochemical Proxies <i>Philip A. Meyers</i>	659	Palynology <i>Margaret Kneller and Sarah Fowell</i>	766
Ostracodes <i>Thomas M. Cronin</i>	663	Patterned Ground <i>Matthew R. Bennett</i>	768
Outwash Plains <i>Peter G. Knight</i>	665	Periglacial Geomorphology <i>Brigitte Van Vliet-Lanoë</i>	770
Oxygen Isotopes <i>Gilles Delaygue</i>	666	Phosphorite <i>Yehoshua Kolodny</i>	775
PAGES <i>Keith Alverson and Christoph Kull</i>	675	Phosphorus Cycle <i>Gabriel M. Filippelli</i>	780
Paleobotany <i>Elizabeth A. Kowalski and David L. Dilcher</i>	679	Pingos <i>Matthew R. Bennett</i>	783
Paleocean Modeling <i>Matthew Huber</i>	683	Plate Tectonics and Climate Change <i>Robert M. DeConto</i>	784
Paleoceanography <i>Katrin J. Meissner, Alvaro Montenegro, and Chris Avis</i>	690	Pleistocene Climates <i>David Q. Bowen</i>	798
Paleocene-Eocene Thermal Maximum <i>Gavin A. Schmidt</i>	696	Pliocene Climates <i>Alan M. Haywood</i>	804
Paleoclimate Modeling, Pre-Quaternary <i>Christopher J. Poulsen</i>	700	PMIP <i>Vivien Gornitz</i>	813
Paleoclimate Modeling, Quaternary <i>Robert J. Oglesby and Kirk A. Maasch</i>	709	Pollen Analysis <i>Margaret Kneller</i>	815
Paleoclimate Proxies, an Introduction <i>Vivien Gornitz</i>	716	Potassium-Argon/Argon-Argon Dating <i>Chris M. Hall</i>	823
Paleo-El Niño-Southern Oscillation (ENSO) Records <i>Michael K. Gagan</i>	721	Precession, Climatic <i>Marie-France Loutre</i>	825
Paleogene Climates <i>Donald R. Prothero</i>	728	Pre-Quaternary Milankovitch Cycles and Climate Variability <i>Paul E. Olsen and Jessica H. Whiteside</i>	826
Paleohydrology <i>Françoise Gasse</i>	733	Proglacial Lacustrine Sediments <i>Wibjörn Karlén</i>	835
Paleolimnology <i>Philip Barker</i>	738	Proterozoic Climates <i>Grant M. Young</i>	836
Paleo-Ocean pH <i>Martin R. Palmer</i>	743	Quaternary Climate Transitions and Cycles <i>Mark Maslin</i>	841
Paleo-Precipitation Indicators <i>Paul A. Baker</i>	746	Quaternary Vegetation Distribution <i>John Jack W. Williams</i>	856
Paleosols, Pre-Quaternary <i>Steven G. Driese</i>	748	Radiocarbon Dating <i>R. Ervin Taylor</i>	863

Radiolaria <i>Adolfo Molina-Cruz (deceased) and Kjell R. Bjørklund</i>	869	Sun-Climate Connections <i>Peter F. Almasi and Gerard Bond (deceased)</i>	929
Red Beds <i>Nathan D. Sheldon</i>	871	Tephrochronology <i>Andrew J. Dugmore and Anthony Newton</i>	937
Roches Moutonnées <i>Matthew R. Bennett</i>	873	The 8,200-Year BP Event <i>Allegra N. LeGrande</i>	938
Sapropels <i>Kay-Christian Emeis</i>	875	Thermohaline Circulation <i>Andrew J. Weaver and Oleg A. Saenko</i>	943
Scandinavian Ice Sheet <i>Jan Mangerud</i>	877	Tills and Tillites <i>Douglas I. Benn</i>	948
Sea Level Change, Last 250 Million Years <i>Kenneth G. Miller</i>	879	Time-Series Analysis of Paleoclimate Data <i>David J. Thomson</i>	949
Sea Level Change, Post-Glacial <i>Vivien Gornitz</i>	887	Transfer Functions <i>Stephen Juggins</i>	959
Sea Level Change, Quaternary <i>John M. Chappell</i>	893	Triassic-Jurassic Climates <i>Gregory J. Retallack</i>	962
Sea Level Indicators <i>Michael S. Kearney</i>	899	Uranium-Series Dating <i>Yemane Asmerom</i>	969
Sedimentary Indicators of Climate Change <i>Joseph P. Smoot</i>	902	Varved Sediments <i>Matti Saarnisto and Antti E. K. Ojala</i>	973
Snowball Earth Hypothesis <i>Grant M. Young</i>	907	Volcanic Eruptions and Climate Change <i>Richard B. Stothers</i>	976
SPECMAP <i>Franck C. Bassinot</i>	911	Weathering and Climate <i>Louis A. Derry</i>	981
Speleothems <i>Yemane Asmerom</i>	916	Wisconsinan (Weichselian, Würm) Glaciation <i>John T. Andrews</i>	986
Stable Isotope Analysis <i>Germán Mora</i>	918	Younger Dryas <i>Dorothy M. Peteet</i>	993
Strontium Isotopes <i>Ján Veizer</i>	923	Author Index	997
Sulfur Isotopes <i>Harald Strauss and Ján Veizer</i>	926	Subject Index	999
		Appendix	1049

Contributors

Mark B. Abbott
Department of Geology and Planetary Sciences
University of Pittsburgh
4107 O'Hara Street
Pittsburgh PA 15260-3332
USA
mabbott1@pitt.edu

Peter F. Almasi
Lamont-Doherty Earth Observatory (LDEO)
102 Core Lab
61 Route 9W
Palisades NY 10964
USA
palmasi@ldeo.columbia.edu

Keith Alverson
Global Ocean Observing System (GOOS)
IOC/UNESCO
1 rue Miollis
75732 Paris Cedex 15
France
k.alverson@unesco.org

Lesleigh Anderson
U.S. Geological Survey
Denver Federal Center
Box 25046
Denver CO 80225
USA
land@usgs.gov

Carin Andersson
Bjerknes Centre for Climate Research
Allégaten 55
5007 Bergen
Norway
carin.andersson@bjerknes.uib.no

John T. Andrews
Institute for Arctic and Alpine Research
University of Colorado
Boulder CO 80309-0450
USA
John.T.Andrews@colorado.edu

Allen W. Archer
Department of Geology
Kansas State University
108 Thompson Hall
Manhattan KS 66506-3201
USA
aarcher@ksu.edu

David Archer
Department of the Geophysical Sciences
University of Chicago
5734 South Ellis Avenue
HGS 419
Chicago IL 60637
USA
d-archer@uchicago.edu

Emmanuelle Arnaud
Department of Land Resource Science
University of Guelph
Guelph ON N1G 2W1
Canada
earnaud@uoguelph.ca

Gail M. Ashley
Department of Geological Sciences
Rutgers University
610 Taylor Road
Piscataway NJ 08854
USA
gmashley@rci.rutgers.edu

Yemane Asmerom
Department of Earth and Planetary Sciences
University of New Mexico
200 Yale Blvd. NE
Albuquerque NM 87131
USA
asmerom@unm.edu

Chris Avis
School of Earth and Ocean Sciences
University of Victoria
Petch Building 168, 3800 Finnerty Road (Ring Road)
Victoria BC V8W 3P6
Canada
caavis@uvic.ca

Victor R. Baker
Department of Hydrology and Water Resources
University of Arizona
1133 James E. Rogers Way
Tucson AZ 85721-0011
USA
baker@hwr.arizona.edu

Paul Baker
Division of Earth and Ocean Sciences
Duke University
Box 90227
Durham NC 27705-0227
USA
pbaker@duke.edu

Philip A. Barker
Lancaster Environment Centre
Lancaster University
Bailrigg
Lancaster LA1 4YQ
UK
p.barker@lancaster.ac.uk

Franck Bassinot
LSCE
CNRS/CEA/UVSQ
Domaine du CNRS (bat. 12)
91198 Gif-sur-Yvette
France
Franck.Bassinot@lsce.ipsl.fr

Jürg Beer
Surface Waters
Eawag
PO Box 611
8600 Dübendorf
Switzerland
beer@eawag.ch

Hugo Beltrami
Environmental Sciences Research Centre
St. Francis Xavier University
1 West Street
Antigonish NS B2G 2W5
Canada
hugo@stfx.ca

Douglas I. Benn
School of Geography and Geosciences
University of St. Andrews, Fife
Scotland KY16 9AL
UK
doug@st-andrews.ac.uk

Matthew R. Bennett
School of Conservation Sciences
Bournemouth University
Talbot Campus, Fern Barrow
Poole BH12 5BB
UK
mbennett@bournemouth.ac.uk

André Berger
Université Catholique de Louvain
Institut d'Astronomie et de Géophysique G. Lemaitre
2 Chemin du Cyclotron
1348 Louvain-la-Neuve
Belgium
berger@astr.ucl.ac.be

Glenn W. Berger
Division of Earth and Ecosystem Sciences
Desert Research Institute
2215 Raggio Parkway
Reno NV 89512
USA
glenn.berger@dri.edu

Wolfgang H. Berger
Scripps Institution of Oceanography
University of California, San Diego
La Jolla, CA 92093-0244
USA
wberger@ucsd.edu

Torsten Bickert
MARUM (Centre for Marine Environmental Sciences)
University of Bremen
Leobener Str. 2
28359 Bremen
Germany
bickert@uni-bremen.de

Kjell R. Bjørklund
Natural History Museum (Geology)
University of Oslo
P.O. Box 1172 Blindern
0318 Oslo
Norway
k.r.bjorklund@nhm.uio.no

Gerard Bond (deceased)

Dan Bosence
Department of Geology
Royal Holloway University of London
Egham Surrey TW20 0EX
UK
d.bosence@gl.rhul.ac.uk

Arthur J. Boucot
Department of Zoology
Oregon State University
Corvallis OR 97331-2914
USA

boucota@science.oregonstate.edu

David Q. Bowen
School of Earth and Ocean Sciences
Cardiff University
Cardiff Wales CF10 3YE
UK

bowendq@cardiff.ac.uk

Brendan Buckley
Lamont-Doherty Earth Observatory
61 Route 9W - PO Box 1000
Palisades NY 10964-8000
USA

bmb@ldeo.columbia.edu

Douglas W. Burbank
Department of Geological Sciences
University of California, Santa Barbara
Webb Hall 1031
Santa Barbara CA 93106-9630
USA

burbank@crustal.ucsb.edu

David C. Catling
Department of Atmospheric Sciences
University of Washington
Box 351640
Seattle WA 98195-1640
USA

davidc@atmos.washington.edu

C. Blaine Cecil
U.S. Geological Survey
12201 Sunrise Valley Drive Mail Stop 956
Reston VA 20192-0002
USA

bcecil@usgs.gov

Mark A. Chandler
NASA Goddard Institute for Space Studies
Columbia University
2880 Broadway
New York NY 10025
USA

mchandler@giss.nasa.gov

John M. Chappell
Research School of Earth Sciences
The Australian National University
Canberra ACT 200
Australia

john.chappell@anu.edu.au

Kyungsik Choi
Faculty of Earth Systems and Environmental Sciences
Chonnam National University
300 Yongbong-dong, Buk-gu

Gwangju 500-757
Korea
tidalchoi@hotmail.com

Phillip R. Christensen
Mars Space Flight Facility, School of Earth and Space
Exploration
Arizona State University
Box 876305
Tempe AZ 85287-6305
USA

phil.christensen@asu.edu

John Clague
Department of Earth Sciences
Simon Fraser University
8888 University Dr.
Burnaby BC V5A 1S6
Canada

jclague@sfu.ca

Jonathan Clarke
Geoscience Australia
P.O. Box 378
Canberra ACT 2601
Australia

jon.clarke@ga.gov.au

Patrick M. Colgan
Department of Geology
Grand Valley State University
Padnos Hall of Science
Allendale MI 49401
USA

colganp@gvsu.edu

G. Russell Coope
Department of Geography
Royal Holloway
University of London
Egham Surrey TW20 0EX
UK

coope@foss5.freereserve.co.uk

Thomas M. Cronin
U.S. Geological Survey
12201 Sunrise Valley Dr., Mail Stop 926A
Reston VA 20192-0002
USA

tcronin@usgs.gov

Xavier Crosta
UMR-CNRS 5805 EPOC
Université Bordeaux 1
Avenue des Facultés
33405 Talence Cedex
France

x.crosta@epoc.u-bordeaux1.fr

Thomas J. Crowley
Grant Institute, School of Geosciences
University of Edinburgh
King's Buildings
Edinburgh N/A EH9 3JW
UK
thomas.crowley@ed.ac.uk

Heidi M. Cullen
Climate Expert
The Weather Channel
300 Interstate North Parkway
Atlanta GA 30339
USA
hcullen@weather.com

Robert W. Dalrymple
Department of Geological Sciences and Geological Engineering
Queen's University
Kingston ON K7L 3N6
Canada
dalrymple@geol.queensu.ca

Anne de Vernal
Département des Sciences de la Terre et de l'Atmosphère
Université du Québec à Montréal
Québec QC H3C 3P8
Canada
devernal.anne@uqam.ca

Robert M. DeConto
Department of Geosciences
University of Massachusetts
Morrill Science Center
Amherst MA 1002
USA
deconto@geo.umass.edu

Gilles Delaygue
CEREGE
Aix-Marseille Université
Europôle de l'Arbois BP80
13545 Aix-en-Provence
France
delaygue@cerege.fr

Louis A. Derry
Department of Earth and Atmospheric Sciences
Cornell University
4142 Snee Hall
Ithaca NY 14853
USA
lad9@cornell.edu

Gerard R. Dickens
Department of Earth Sciences
Rice University
6100 Main Street
Houston TX 77005
USA
jerry@rice.edu

David Dilcher
Florida Museum of Natural History
University of Florida
254 Dickinson Hall
Museum Road & Newell Drive
Gainesville FL 32611
USA
dilcher@flmnh.ufl.edu

Konstantin G. Dlussky
AXYS Environmental Consulting Ltd.
4208-97 St., Suite 203
Edmonton AB T6E 5Z9
Canada
kdlusskiy@axys.net

Jeffrey P. Donnelly
Geology and Geophysics Department
Woods Hole Oceanographic Institution
MS 22
Woods Hole MA 02543
USA
jdonnelly@whoi.edu

Ronald I. Dorn
School of Geographical Sciences
Arizona State University
Tempe AZ 85287
USA
ronald.dorn@asu.edu

Julian A. Dowdeswell
Scott Polar Research Institute
Cambridge University
Lensfield Road
Cambridge CB2 1ER
UK
jd16@cam.ac.uk

Harry J. Dowsett
Eastern Earth Surface Processes
U.S. Geological Survey
926A National Center
Reston VA 22192
USA
hdowsett@usgs.gov

Steven G. Driese
Department of Geology
Baylor University
One Bear Place # 97354
Waco TX 76798
USA
steven_driese@baylor.edu

Mary L. Droser
Department of Earth Sciences
University of California
900 University Avenue
Riverside CA 92521
USA
mary.droser@ucr.edu

Andrew J. Dugmore
Institute of Geography, School of Geosciences
University of Edinburgh
Drummond Street
Edinburgh Scotland EH8 9XP
UK
andrew.dugmore@ed.ac.uk

Arthur S. Dyke
Geological Society of Canada
601 Booth Street
Ottawa ON K1A 0E8
Canada
adyke@nrcan.gc.ca

Kay Christian Emeis
Institut für Biogeochemie und Meereschemie
Universität Hamburg
Bundesstr. 55
20146 Hamburg
Germany
emeis@geowiss.uni-hamburg.de

Dirk Enters
Environnements Dynamiques et Territoires de Montagne
(EDYTEM)
Université de Savoie
Technolac
77376 Le Bourget du Lac
France
dirk.enters@univ-savoie.fr

Rhodes W. Fairbridge (deceased)

James Farquhar
ESSIC and Dept. of Geology
University of Maryland
College Park MD 20742
USA
jfarquha@geol.umd.edu

Bruce Fegley, Jr.
Department of Earth and Planetary Sciences
Washington University
Campus Box 1169
St. Louis MO 63130
USA
bfegley@wustl.edu

Gabriel Filippelli
Earth Sciences
Indiana University – Purdue University Indianapolis (IUPUI)
723 W. Michigan St.
Indianapolis IN 46202–5132
USA
gfilippe@iupui.edu

Clayton Forswall
aci consulting
1001 Mopac Circle, Suite 100
Austin TX 78746
USA
cforswall@aci-group.net

Sarah Fowell
Department of Geology and Geophysics
University of Alaska
Box 755780
Fairbanks AK 99775–5780
USA
ffsjf@uaf.edu

Roger Francois
Department of Earth and Ocean Sciences
University of British Columbia
6339 Stores Road
Vancouver BC V6T 1Z4
Canada
rfrancois@eos.ubc.ca

Michael K. Gagan
Research School of Earth Sciences
The Australian National University
Bldg 61, Mills Road
Canberra, ACT 0200
Australia
michael.gagan@anu.edu.au

Robert R. Gaines
Geology Department
Pomona College
185 East 6th Street
Claremont CA 91711
USA
Robert.Gaines@pomona.edu

John I. Garver
Department of Geology
Union College
807 Union Ave
Schenectady NY 12308–2311
USA
garverj@union.edu

Françoise Gasse
CEREGE
Université d'Aix-Marseille III
BP 80
13545 Aix-en-Provence
France
gasse@cerege.fr

Steven L. Goodbred, Jr.
Department of Earth and Environmental Sciences
Vanderbilt University
VU Station B 351805
Nashville TN 37235
USA
steven.goodbred@vanderbilt.edu

Ian D. Goodwin
Climate Risk CoRE
Department of Physical Geography
Building E7A
Macquarie University NSW 2109
Australia
igoodwin@els.mq.edu.au

Vivien Gornitz
NASA Goddard Institute for Space Studies
Columbia University
2880 Broadway
New York NY 10025
USA
vgornitz@giss.nasa.gov

Andrew Goudie
St Cross College
Oxford University
St Giles
Oxford OX1 3LZ
UK
andrew.goudie@stx.ox.ac.uk

Darren Gröcke
Department of Earth Sciences
Durham University
Durham DH1 3LE
UK
d.r.grocke@durham.ac.uk

Anil K. Gupta
Department of Geology & Geophysics
Indian Institute of Technology
IIT Campus
Kharagpur – 721302 W.B.
India
anilg@gg.iitkgp.ernet.in

Chris M. Hall
Department of Geological Sciences
University of Michigan
1100 North University Av.
Ann Arbor MI 48109–1005
USA
cmhall@umich.edu

David A. T. Harper
Natural History Museum (Geological Museum)
University of Copenhagen
Øster Voldgade 5–7
1350 Copenhagen
Denmark
DHarper@snm.ku.dk

William W. Hay
Department of Geological Sciences
University of Colorado at Boulder
2200 Colorado Ave.
Boulder CO 80309–0399
USA
whay@gmx.de

James D. Hays
Lamont-Doherty Earth Observatory
61 Route 9W – PO Box 1000
Palisades NY 10964–8000
USA
jimhays@ldeo.columbia.edu

Alan M. Haywood
British Antarctic Survey
Geological Sciences Division, High Cross
Madingley Road
Cambridge CB3 0ET
UK
ahay@bas.ac.uk

Sidney Hemming
Lamont-Doherty Earth Observatory
61 Route 9W - PO Box 1000
Palisades NY 10964–8000
USA
sidney@ldeo.columbia.edu

Marc S. Hendrix
Department of Geosciences
The University of Montana
32 Campus Drive
Missoula MT 59812
USA
marc.hendrix@umontana.edu

Matthew J. Higginson
LGC Forensics
F5 Culham Science Centre
Abingdon OX14 3ED
UK
matthew.higginson@lgcforensics.com

Wim Z. Hoek
Department of Physical Geography
University of Utrecht
Heidelberglaan 2
3584 CS Utrecht
The Netherlands
w.hoek@geog.uu.nl

Georg Hoffmann
Laboratoire des Sciences du Climat et de l'Environnement
l'Ormes des Merisiers, Commissariat à l'Énergie Atomique
Saclay
91191 Gif sur Yvette Cedex
France
Georg.Hoffmann@cea.fr

Matthew Huber
Department of Earth and Atmospheric Science
Purdue University
550 Stadium Mall Dr.
West Lafayette IN 47907
USA
huberm@purdue.edu

Philippe Huybrechts
Departement Geografie
Vrije Universiteit Brussel
Pleinlaan 2
1050 Brussel
Belgium
phuybrec@vub.ac.be

Stan Jacobs
Lamont-Doherty Earth Observatory
Columbia University
Route 9W
Palisades NY 10964
USA
sjacobs@ldeo.columbia.edu

Claudia C. Johnson
Department of Geological Sciences
Indiana University
1001 E. 10th St.
Bloomington IN 47405-1405
USA
claudia@indiana.edu

Stephen Juggins
School of Geography
University of Newcastle upon Tyne
Room: 4.14b, Daysh Building
Newcastle upon Tyne NE1 7RU
UK
stephen.juggins@ncl.ac.uk

Jed Kaplan
EPFL-ENAC-ECOS
Station 2
1015 Lausanne
Switzerland
jed.kaplan@epfl.ch

Wibjörn Karlén
Department of Social and Economic Geography
Uppsala University
Box 513
75 120 Uppsala
Sweden
wibjorn.karlen@kultgeog.uu.se

Erle G. Kauffman
Department of Geological Sciences
Indiana University
1001 E. 10th St.
Bloomington IN 47405-1403
USA
kauffman@indiana.edu

Alan J. Kaufman
Department of Geology
University of Maryland
GEOL #237
College Park MD 20742-4211
USA
kaufman@geol.umd.edu

Michael Kearney
Department of Geography
University of Maryland
College Park MD 20742
USA
mk11@uemail.umd.edu
kearney@glue.umd.edu

Margaret Kneller
John Cabot University
Via della Lungara 233
Rome 00165
Italy
mkneller@john.cabot.edu

Peter G. Knight
School of Physical and Geographical Sciences
Keele University
William Smith Building
Keele Staffordshire ST5 5BG
UK
p.g.knight@esci.keele.ac.uk

Karen E. Kohfeld
School of Earth and Environmental Sciences
Queens College
65-30 Kissena Blvd.
Flushing NY 11367
USA
karen@kohfeld.com

Yehoshua Kolodny
The Institute of Earth Sciences
Edmond Safra Campus, Givat Ram
The Hebrew University
91904 Jerusalem
Israel
kolodny@vms.huji.ac.il

Elizabeth A. Kowalski
Department of Geology and Geological Engineering
South Dakota School of Mines and Technology
501 E Saint Joseph Street
Rapid City, SD 57701
USA
ekowalsk@umich.edu
kowalski@flmnh.ufl.edu

Wout Krijgsman
Paleomagnetic Laboratory, Faculty of Earth Sciences
Utrecht University
Budapestlaan 17
3584 CD Utrecht
The Netherlands
krijgsma@geo.uu.nl

Christoph Kull
OeCC (Swiss advisory body on climate change)
Schwarztorstrasse 9
3007 Bern
Switzerland
christoph.kull@scnat.ch

Andrew A. Lacis
NASA Goddard Institute for Space Studies
Columbia University
2880 Broadway
New York NY 10025
USA
alacis@giss.nasa.gov

Kurt Lambeck
Research School of Earth Sciences
The Australian National University
Canberra ACT 0200
Australia
Kurt.Lambeck@anu.edu.au

C. G. Langereis
Paleomagnetic Laboratory 'Fort Hoofddijk'
Utrecht University
Budapestlaan 4
3584 CD Utrecht
The Netherlands
langer@geo.uu.nl

Steven W. Leavitt
Laboratory of Tree Ring Research
University of Arizona
Tucson AZ 85721
USA
sleavitt@ltr.arizona.edu

Allegra LeGrande
NASA Goddard Institute for Space Studies
Columbia University
2880 Broadway
New York NY 10025
USA
allegra.n.legrande@nasa.gov

Abraham Lerman
Department of Earth and Planetary Sciences
Northwestern University
1850 Campus Dr.
Evanston IL 60208
USA
alerman@northwestern.edu

Amy Leventer
Department of Geology
Colgate University
13 Oak Dr.
Hamilton NY 13346
USA
aleventer@mail.colgate.edu

Qianyu Li
School of Ocean and Earth Sciences
Tongji University
Siping Rd. 1239
Shanghai 200092
China
qli01@mail.tongji.edu.cn
qianyu.li@adelaide.edu.au

Kathy Licht
Department of Earth Sciences
Indiana University-Purdue University Indianapolis
723 West Michigan Street
Indianapolis IN 46202-5132
USA
klicht@iupui.edu

Paul K. Link
Department of Geosciences
Idaho State University
921 S. 8th Avenue, Stop 8072
Pocatello ID 83209
USA
linkpaul@isu.edu

David B. Loope
Department of Geosciences
University of Nebraska
214 Bessey Hall
Lincoln NE 68588
USA
dloope1@unl.edu

Marie-France Loutre
Institut d'Astronomie et de Géophysique G. Lemaître
Université Catholique de Louvain
2 chemin du Cyclotron
1348 Louvain-la-Neuve
Belgium
marie-france.loutre@uclouvain.be

Stefano Lugli
Dipartimento di Scienze della Terra
Università degli Studi di Modena e Reggio Emilia
Largo S. Eufemia 19
41100-Modena
Italy
lugli.stefano@unimore.it

Kirk A. Maasch
Climate Change Institute
University of Maine
5790 BGSC
Orono ME 04469-5790
USA
kirk.maasch@maine.edu

Jan Mangerud
Department of Geoscience and Bjerknes Centre for Climate
Research
University of Bergen
Allégt. 41
5007 Bergen
Norway
Jan.Mangerud@geo.uib.no

Michael E. Mann
Department of Meteorology
Pennsylvania State University
523 Walker Bldg.
University Park PA 16802
USA
mann@meteo.psu.edu

Thomas M. Marchitto, Jr.
INSTAAR and Department of Geological Sciences
University of Colorado
Campus Box 450
Boulder CO 80309
USA
tom.marchitto@colorado.edu

Shawn J. Marshall
Department of Geography
University of Calgary
2500 University Dr. N.W.
Calgary AB T2N 1N4
Canada
shawn.marshall@ucalgary.ca

I. Peter Martini
Department of Land Resource Science
University of Guelph
Guelph ON N1G 2W1
Canada
pmartini@uoguelph.ca

Mark Maslin
Department of Geography
University College London
Pearson Building
Gower Street
London WC1E 6BT
UK
mmaslin@geog.ucl.ac.uk

Katrin J. Meissner
School of Earth and Ocean Sciences
University of Victoria
P.O. Box 3055, Stn CSC
Victoria BC V8W 3P6
Canada
katrinm@ocean.seos.uvic.ca

John Menzies
Department of Earth Sciences and Geography
Brock University
500 Glenridge Avenue
St. Catharines ON L2S 3A1
Canada
jmenzies@brocku.ca

Philip Meyers
Geological Sciences
The University of Michigan
1100 North University Avenue
Ann Arbor MI 48109-1005
USA
pameyers@umich.edu

Gifford H. Miller
INSTAAR and Dept. of Geological Sciences
University of Colorado
Boulder CO 80309-0450
USA
gmiller@colorado.edu

Kenneth Miller
Department of Geological Sciences
Wright Geological Laboratory
Rutgers University
610 Taylor Road
Piscataway NJ 8854
USA
kgm@rci.rutgers.edu

Irene A. Mogensen
Sortemosevej 207
2730 Herlev
Denmark
iamb@mailme.dk
Danish Meteorological Institute
Lyngbyvej 100
2100 Copenhagen
Denmark
iam@dmi.dk
mas@dmi.dk

A. Molina-Cruz (deceased)

Álvaro Montenegro
School of Earth and Ocean Sciences
University of Victoria
Petch Building 168, 3800 Finnerty Road (Ring Road)
Victoria BC V8W 3P6
Canada
alvaro@ocean.seos.uvic.ca

German Mora
Department of Geological and Atmospheric Sciences
Iowa State University
12 Science I
Ames IA 50011
USA
gmora@iastate.edu

Vincent I. Morgan
Antarctic Cooperative Research Centre (CRC)
University of Tasmania
Private Bag 80
Hobart Tasmania 7001
Australia
vin.morgan@utas.edu.au

Tatiana Morozova
Laboratory of Evolutionary Geography
Russian Academy of Sciences
Staromonetny 29
119017 Moscow
Russia
paleo_igras@mail.ru

Volker Mosbrugger
Senckenberg Research Institute and Natural History Museum
Senckenberganlage 25
60325 Frankfurt
Germany
volker.mosbrugger@senckenberg.de
vmosbrugger@senckenberg.de

Daniel R. Muhs
U.S. Geological Survey
Denver Federal Center
MS 980, Box 25046
Denver CO 80225-0046
USA
dmuhs@usgs.gov

Ulrich C. Müller
Institute of Geology and Paleontology
Johann Wolfgang Goethe University-Frankfurt
Senckenberganlage 32–34
60054 Frankfurt
Germany
ulrich.mueller@em.uni-frankfurt.de

David J. Nash
School of Environment and Technology
University of Brighton
Lewes Road
Brighton BN2 4GJ
UK
d.j.nash@bton.ac.uk

Sandra G. Neuzil
U.S. Geological Survey
12201 Sunrise Valley Dr., MS 956
Reston VA 20192
USA
sneuzil@usgs.gov

Anthony Newton
Institute of Geography, School of Geosciences
University of Edinburgh
Drummond Street
Edinburgh Scotland EH8 9XP
UK
ajd@geo.ed.ac.uk
anthony.newton@ed.ac.uk

Daniela Nitoiu
Institute of Geodynamics of the Romanian Academy
19–21 Jean-Louis Calderon St.
020032 Bucharest–37
Romania
nitoiu@geodin.ro

Robert Oglesby
Department of Geosciences
University of Nebraska Lincoln
214 Bessey Hall
PO Box 880340
Lincoln NE 68588–0340
USA
roglesby2@unl.edu

Antti Ojala
Geological Survey of Finland
P.O. Box 96
2150 Espoo
Finland
antti.ojala@gtk.fi

Paul E. Olsen
Lamont-Doherty Earth Observatory
61 Route 9W
Palisades NY 10964
USA
polsen@ldeo.columbia.edu

Mark Pagani
Department of Geology and Geophysics
Yale University
P.O. Box 208109
New Haven CT 06520–8109
USA
mark.pagani@yale.edu

Didier Paillard
Laboratoire des Sciences du Climat et de l'Environnement
CEA-CNRS
Centre d'Etudes de Saclay
Orme des Merisiers
91191 Gif-sur-Yvette
France
didier.paillard@cea.fr

Martin R. Palmer
Southampton Oceanography Centre
University of Southampton
European Way
Southampton SO14 32H
UK
pmrp@soc.soton.ac.uk

Frédéric Parrenin
Laboratoire de Glaciologie et de Géophysique de l'Environnement
CNRS BP 96
38402 Grenoble, St. Martin d'Hères Cedex
France
parrenin@lgge.obs.ujf-grenoble.fr

Adina Paytan
Institute of Marine Sciences
Earth & Marine Sciences Build.
University of California Santa Cruz
1156 High St.
Santa Cruz CA 95064
USA
apaytan@ucsc.edu

William H. Peck
Department of Geology
Colgate University
13 Oak Dr.
Hamilton NY 13346
USA
wpeck@mail.colgate.edu

Stephen F. Pekar
Queens College
School of Earth and Environmental Sciences
65–30 Kissena Blvd.
Flushing, NY 11367
USA
stephen.pekar@qc.cuny.edu

Dorothy M. Peteet
NASA Goddard Institute for Space Studies
Columbia University
2880 Broadway
New York NY 10025
USA
dpeteet@giss.nasa.gov
peteet@ldeo.columbia.edu

Elisabetta Pierazzo
Planetary Science Institute
1700 E. Ft. Lowell, Suite 106
Tucson AZ 85719
USA
betty@psi.edu

Christopher J. Poulsen
Department of Geological Sciences
University of Michigan
1100 North University Ave.
Ann Arbor MI 48109
USA
poulsen@umich.edu

Gregory D. Price
Department of Geology
University of Plymouth
Drake Circus
Plymouth PL4 8AA
UK
g.price@plymouth.ac.uk

Donald R. Prothero
Department of Geology
Occidental College
1600 Campus Road
Los Angeles CA 90041
USA
prothero@oxy.edu

Michael Rampino
Earth and Environmental Science Program
New York University
1009 Silver Center
100 Washington Square East
New York NY 10003-6688
USA
mmr1@nyu.edu

Anne Raymond
Department of Geology and Geophysics
Texas A and M University
College Station TX 77843-3115
USA
raymond@geo.tamu.edu

Dominique Raynaud
Laboratoire de Glaciologie et de Géophysique
de l'Environnement CNRS BP 96
38402 Grenoble, St. Martin d'Hères Cedex
France
raynaud@lgge.obs.ujf-grenoble.fr

David K. Rea
1232 Regency Court
Las Cruces NM 88007
USA
davidrea@umich.edu

Mel A. Reasoner
(no address)

Gregory J. Retallack
Department of Geological Sciences
University of Oregon
1260 Franklin Boulevard
Eugene OR 97403-1272
USA
gregr@uoregon.edu

JoAnne Reuss
IODP Interim Planning Committee, Department of Geological
Sciences
University of Michigan
425 E. University Ave.
Ann Arbor MI 48109-1063
USA
jor@umich.edu

Thomas H. Rich
Curator of Vertebrate Paleontology
Museum Victoria
P.O. Box 666
Melbourne Victoria 3001
Australia
trich@museum.vic.gov.au

David H. Rind
NASA Goddard Institute for Space Studies
2880 Broadway
New York NY 10025
USA
david.h.rind@nasa.gov

Neil Roberts
School of Geography
University of Plymouth
Drake Circus
Plymouth PL4 8AA
UK
c.n.roberts@plymouth.ac.uk

Alastair Ruffell
School of Geosciences, School of Geography, Archaeology and
Palaeoecology
Queens University
Belfast Northern Ireland BT7 1NN
UK
a.ruffell@qub.ac.uk

Matti Saarnisto
Suomalainen Tiedeakatemia
Finnish Academy of Science and Letters
Pääsihteeri, Secretary General
Mariankatu 5
00170 Helsinki
Finland
matti.saarnisto@acadsci.fi

Julian Sachs
School of Oceanography & The Program on Climate Change
University of Washington
Ocean Sciences Building, Room 521
Box 355351
Seattle WA 98195-5351
USA
jsachs@u.washington.edu

Peter Sadler
Department of Earth Sciences
University of California
Riverside CA 92521
USA
peter.sadler@ucr.edu

Oleg A. Saenko
Canadian Centre for Climate Modelling and Analysis
University of Victoria
P.O. Box 3055
Victoria BC V8W 3P6
Canada
oleg.saenko@ec.gc.ca

Bradley Sageman
Earth and Planetary Sciences
Northwestern University
1850 Campus Drive
Evanston IL 60208
USA
brad@earth.northwestern.edu

Andrew D. Saunders
Department of Geology
University of Leicester
Leicester LE1 7RH
UK
ads@le.ac.uk

Gavin A. Schmidt
NASA Goddard Institute for Space Studies
2880 Broadway
New York NY 10025
USA
gschmidt@giss.nasa.gov

Christopher R. Scotese
Department of Geology
University of Texas
Arlington TX 76012
USA
cscotese@uta.edu

Dan Seidov
NOAA NODC/Ocean Climate Laboratory
SSMC-III, E/OC5, Room 4326
1315 East-West Highway
Silver Spring, MD 20910
USA
dan.seidov@noaa.gov

Nathan D. Sheldon
Department of Geology
Royal Holloway University of London
Egham, Surrey TW20 0EX
UK
n.sheldon@gl.rhul.ac.uk

Drew T. Shindell
NASA Goddard Institute for Space Studies
2880 Broadway
New York NY 10025
USA
drew.t.shindell@nasa.gov

Martin J. Siegert
School of Geosciences, Grant Institute
University of Edinburgh
West Mains Road
Edinburgh EH9 3JW
UK
m.j.siegert@ed.ac.uk

Bruce M. Simonson
Geology Department
Oberlin College
52 West Lorain Street
Oberlin OH 44074-1052
USA
bruce.simonson@oberlin.edu

Joseph P. Smoot
U.S. Geological Survey
12201 Sunrise Valley Drive MS 926A
Reston VA 20192
USA
jpsmoot@usgs.gov

Robert A. Spicer
Department of Earth Sciences
The Open University
Walton Hall
Milton Keynes MK7 6AA
UK
r.a.spicer@open.ac.uk

Bernhard Stauffer
Climate and Environmental Physics Department,
Physics Institute
University of Bern
Sidlerstrasse 5
3012 Bern
Switzerland
stauffer@climate.unibe.ch

Richard Stothers
NASA Goddard Institute for Space Studies
2880 Broadway
New York NY 10025
USA
rstothers@giss.nasa.gov

Harald Strauss
Geologisch-Paläontologisches Institut und Museum
Westfälischen Wilhelms-Universität Münster
Corrensstraße 24
48149 Münster
Germany
hstrauss@uni-muenster.de

Ian P. Swainson
Canadian Neutron Beam Centre
Stacie Institute for Molecular Sciences
National Research Council of Canada
Chalk River Laboratories
Chalk River ON K0J 1J0
Canada
ian.swainson@nrc.gc.ca

Manik Talwani
IODP-MI, Inc.
#210, 815 Connecticut Av., NW
Washington DC 20006
USA
mtalwani@iodp.org

Kendrick Taylor
Desert Research Institute
2215 Raggio Parkway
Reno NV 89512
USA
kendrick@dri.edu

R. Ervin Taylor
Radiocarbon Laboratory, Department of Anthropology
University of California at Riverside
Watkins Hall 1303 A
Riverside CA 92521-0423
USA
ervin.taylor@ucr.edu
retaylor@ucr.edu

Ina Tegen
Institute for Tropospheric Research
Permoserstrasse 15
04318 Leipzig
Germany
itegen@tropos.de

Lonnie G. Thompson
Department of Geological Sciences, School of Earth Sciences
Ohio State University
275 Mendenhall Laboratory, 125 S. Oval Mall
Columbus OH 43210-1002
USA
thompson.3@osu.edu

David J. Thomson
Mathematics and Statistics
Queen's University
411 Jeffery Hall
Kingston ON K7L 3N6
Canada
djt@mast.queensu.ca

Willy Tinner
Institute of Plant Sciences and Oeschger Centre for Climate
Change Research (OCCR)
University of Bern
Altenbergrain 21
3013 Bern
Switzerland
willy.tinner@ips.unibe.ch

Garland R. Upchurch, Jr.
Department of Biology
Texas State University
601 University Drive
San Marcos TX 78666
USA
gu01@txstate.edu

John W. Valley
Department of Geology and Geophysics
University of Wisconsin
1215 W Dayton St.
Madison WI 53706
USA
valley@geology.wisc.edu

Brigitte Van Vliet-Lanoë
UMR 6538 CNRS, Domaines Océaniques
IUEM
29280 Plouzané
France
brigitte.vanvlietlanoë@univ-brest.fr

Ján Veizer
Department of Earth Sciences
University of Ottawa
Ottawa ON K1N 6N5
Canada
jveizer@uottawa.ca

Andrei A. Velichko
Laboratory of Evolutionary Geography
Russian Academy of Sciences
Staromonetny 29
119017 Moscow
Russia
Paleo_igras@mail.ru

John E. N. Veron
Australian Institute of Marine Science
PMB 3
Townsville Queensland 4810
Australia
jveron@aims.gov.au
or
Coral Reef Research
10 Benalla Road
Oak Valley
Townsville Queensland 4811
Australia
j.veron@coralreefresearch.com

Patricia Vickers-Rich
School of Geosciences
Monash University
Clayton Victoria 3800
Australia
pat.rich@sci.monash.edu.au

Pinxian Wang
School of Ocean and Earth Sciences
Tongji University
Siping Rd. 1239
Shanghai 200092
China
pxwang@online.sh.cn

Andrew J. Weaver
School of Earth and Ocean Sciences
University of Victoria
P.O. Box 3055
Victoria BC V8W 3P6
Canada
weaver@uvic.ca

Thompson Webb III
Department of Geological Sciences
Brown University
324 Brook Street, Box 1846
Providence RI 2912
USA
Thompson_Webb_III@brown.edu

Gerold Wefer
General Geology – Marine Geology
University of Bremen
Marum, Leobener Straße
28359 Bremen
Germany
gwefer@rcom-bremen.de

Mara Weinelt
Institut für Geowissenschaften
University of Kiel
Ludwig Meyn Strasse 14
24118 Kiel
Germany
mw@gpi.uni-kiel.de

Jessica H. Whiteside
Geological Sciences
Brown University
324 Brook Street
Box 1846
Providence RI 02912
USA
Jessica_Whiteside@brown.edu

Michael Widdowson
Department of Earth and Environmental Sciences
The Open University
Walton Hall

Milton Keynes MK7 6AA
UK
m.widdowson@open.ac.uk

John W. Williams
Department of Geography
University of Wisconsin-Madison
Rooms 421 or 213 Science Hall
550 North Park St.
Madison WI 53706–1404
USA
jww@geography.wisc.edu

Dieter A. Wolf-Gladrow
Alfred Wegener Institut für Polar und Meeresforschung (AWI)
Am Handelshafen 12
27570 Bremerhaven
Germany
Dieter.Wolf-Gladrow@awi.de

James D. Wright
Department of Geological Sciences
Rutgers University, Wright-Reiman Labs
610 Taylor Rd.
Piscataway NJ 08854–8066
USA
jdwright@rci.rutgers.edu

Grant M. Young
Department of Earth Sciences
University of Western Ontario
London ON N6A 5B7
Canada
rokchip@rogers.com

Jeremy R. Young
Palaeontology Department
The Natural History Museum
Cromwell Road
London SW7 5BD
UK
j.young@nhm.ac.uk

Richard E. Zeebe
School of Ocean and Earth Science and Technology
Department of Oceanography
University of Hawaii, Manoa
1000 Pope Road MSB 504
Honolulu HI 96822
USA
zeebe@soest.hawaii.edu

Bernd Zolitschka
GEOPOLAR, Institute of Geography
University of Bremen
Celciusstrasse FVG-M
28359 Bremen
Germany
zoli@uni-bremen.de

Preface

The growing levels of atmospheric greenhouse gases generated by anthropogenic activities are already beginning to affect the Earth's climate, according to the latest report by the Intergovernmental Panel on Climate Change, and concern is mounting over potential adverse consequences to society. However, Earth's climate has shifted dramatically and frequently during the last few million years, alternating between ice ages, when vast glaciers covered Northern Europe and much of North America, and interglacials—warm periods much like today. Farther back in geologic time, climates have differed even more from the present. Could human actions push the Earth's climate system into an unstable mode, beyond the relatively mild oscillations of the last few millennia? To fully understand the unusual changes of the 20th century and possible future trends, these need to be placed in a longer-term context extending well beyond the period of instrumental records. Paleoclimatology—the study of climates of the past—may provide us with insights into the workings of the modern climate system. By reconstructing ancient climates using natural “archives” of environmental change recorded in trees, corals, cave deposits, ice cores, lake and ocean sediments, and running computer models, paleoclimatologists can place bounds on past climate variability and help us anticipate possible future changes.

The *Encyclopedia of Paleoclimatology and Ancient Environments*, a companion volume to the recently-published

Encyclopedia of World Climatology, provides the reader with an entry point to the rapidly expanding field of paleoclimatology. Highly interdisciplinary, paleoclimatology integrates information from a broad array of disciplines in the geosciences, spanning across stratigraphy, geomorphology, glaciology, paleoecology, paleobotany, isotope geochemistry, geochronology, and geophysics, among others. The encyclopedia covers the entire span of the Earth's climate history from the early Precambrian to the Little Ice Age, and also offers an interplanetary comparison with the contrasting climates of Mars and Venus in 230 informative articles written by over 200 well known international experts. The climates of the past were the product of closely inter-connected processes that shaped the Earth's atmosphere, lithosphere, and biosphere. Therefore, the separation between topics is somewhat arbitrary and a certain degree of overlap is inevitable. However, since authors often approach similar topics from differing perspectives, these differences can provide a fuller picture overall. The volume is abundantly illustrated with line-drawings, black-white and color photographs. Articles are arranged alphabetically, with extensive bibliographies and cross-references.

March 2008
Vivien Gornitz

Acknowledgements

This volume is offered in tribute to the memory of Rhodes W. Fairbridge, Senior Editor of the Encyclopedia of Earth Sciences Series, who sadly passed away before this encyclopedia could be completed. It was upon his recommendation and inspiration that this project was undertaken. Rhodes Fairbridge took a keen interest in paleoclimatology, which ties together many aspects of the geosciences. He wrote several articles especially for this encyclopedia, including a detailed history of paleoclimatology and “Earth Laws and Paleoclimatology”, which summarizes many of the ideas he had covered in his long and distinguished career. He was way ahead of his time in his early acceptance of Wegener’s theory of continental drift, the role of orbital cycles in climate change (i.e., the Milankovitch theory), solar influences on climate, and recognition of general aridity during glacial periods. He was among the first to report the twentieth century rise in global sea level in the 1960s. One of the recurrent themes in Rhodes’ many publications is the role of cyclical phenomena on all timescales. A 1961 symposium that he organized at Columbia University was among the earliest to explore the connections between Earth cycles and paleoclimates. With his

colleagues, he investigated planetary alignments, their possible effects on solar activity, and ultimately on Earth’s paleoclimates. While still controversial, a growing body of literature points to some solar influence on climate and one of the articles in this volume addresses this particular issue. His ability to see beyond the minutiae of narrow specialties combined with an amazing memory served him well as senior series editor. He will be sorely missed and fondly remembered.

I thank the contributing authors for their efforts in bringing this Encyclopedia to fruition. Thanks are also extended to the members of the Editorial Advisory Board for their helpful suggestions and recommendations. Appreciation is also expressed to Ms. Eden Licardo, for her secretarial assistance, to Mr. José Mendoza for graphics support, and to Dr. Cynthia Rosenzweig, Head, Center for Climate Systems Research, Columbia University and NASA Goddard Institute for Space Studies, New York, for her encouragement and understanding during this lengthy undertaking.

Vivien Gornitz

A

AEROSOL (MINERAL)

General

Wind-blown mineral aerosol consists of micrometer-sized airborne soil dust particles. Estimates of modern global dust emissions range from 1,000 to 3,000 Mt yr⁻¹ (Houghton et al., 2001). Dust aerosol has a high spatial and temporal variability; large uncertainties exist in quantitative estimates of large-scale dust loads. Modern global dust distribution and properties can be characterized by satellite retrievals and concentration measurements at surface stations. Dust deposition data from ice cores, marine sediments, and terrestrial sites provide information on dust in modern and past climate periods (Kohfeld and Harrison, 2001). Such records show that dustiness was increased 2- to 20-fold during glacial periods compared with interglacials, as a consequence of increased aridity, reduced vegetation, increased availability of fine, loose sediment, and more vigorous surface wind speeds in glacial climates.

Dust sources

Mineral aerosol is generated in arid and semi-arid continental regions. Major dust sources include the Saharan/Sahelian region, the Arabian Peninsula, the Gobi and Taklamakan Deserts in Asia, and the Australian Desert (Duce, 1995). Dust emission occurs when the surface wind stress exceeds a threshold value, which is a function of surface properties like roughness elements, grain size, and soil moisture. Theoretical considerations and wind tunnel experiments show a dependence of dust emissions on the surface wind stress to the third or fourth power (Gillette and Passi, 1988; Shao et al., 1993). Fine soil particles that can be transported over large distances are released when larger wind-blown sand impacts on the soil, mobilizing smaller particles (saltation). Dust emissions occur preferentially in areas that contain fine, loose sediment. Prospero et al. (2002) find a good agreement of satellite-observed dust emission maxima with the location of topographic depressions, where fine sediment can accumulate. Rough surfaces containing structural elements like rocks or vegetation

increase the threshold velocity required for dust emission (Marticorena and Bergametti, 1995) since wind energy is partly absorbed by the obstacles. Crusting of soil surfaces can reduce the possible dust release from a source region. Dust deflation can decrease over time due to loss of available fine soil material. Surface disturbance and disruption of the vegetation cover can lead to increased dust emissions, for example during the “dust bowl” events in the United States in the 1930s and 1950s following cultivation of the soils in dry regions.

Dust cycle

Dust injected into upper levels of the atmosphere can be transported over thousands of kilometers by strong wind systems. Most prominently, Saharan dust is transported across the North Atlantic to North and Central America, and is found as far downwind as the Amazon Basin. Dust from Asia is transported over the North Pacific towards mid-Pacific islands and North America.

Dust is removed from the atmosphere by precipitation (wet deposition) or through gravitational settling and turbulent mixing at the surface (dry deposition). Close to the source regions, gravitational sedimentation is responsible for most dust deposition, while wet deposition determines the removal rate of far-traveled dust particles over remote ocean areas. Unless removed by precipitation, the length of time that dust aerosols remain in the atmosphere depends on the deposition velocities of the different particle sizes. Atmospheric lifetimes of dust range from a few hours for particles larger than 10 μm to 10–15 days for submicron particles (Ginoux et al., 2001).

Properties

The particle size of mineral aerosols determines their atmospheric lifetime and thus the distance that the particles can travel. Close to source regions the median dust particle radii are around 30–50 μm. Dust that has been transported away from the sources has a median radius around 1 μm (e.g., Duce, 1995).

The mineral composition of dust particles reflects the mineralogy of the rocks at the Earth’s surface; some main constituents are quartz, feldspars, carbonates and clays. Dust particles from different source regions have specific mineralogical

compositions and as a consequence, different refractive indices determining their optical properties. For example, Saharan dust is richer in iron and therefore darker and redder than Asian dust. Refractive indices for different minerals span a wide range for solar and thermal wavelengths (Sokolik and Toon, 1999). Data on dust refractive indices are currently limited to only a few regions.

Dust effects on climate

Dust can influence the climate in several ways. Aerosols significantly impact on the climate system by changing the energy balance of solar and thermal radiation (Houghton et al., 2001). Dust not only scatters but also partly absorbs incoming solar radiation, and also absorbs and emits outgoing long-wave radiation. Any changes in atmospheric dust loads, like the increase in dust during glacial periods, would cause a change in the radiation balance and consequentially, in surface temperatures. The magnitude and even the sign of the direct radiative dust forcing is uncertain; it depends on the optical properties of the dust, cloud cover, and the albedo of the underlying surface (Liao and Seinfeld, 1998).

The presence of dust may alter cloud optical properties by changing the number of cloud condensation nuclei. The efficiency of dust particles in forming nuclei for water clouds may alter during transport due to mixing with soluble aerosol species. This can influence both the brightness of clouds and the formation of rainfall. Dust particles can potentially change chemical reactions in the atmosphere because of their large surface areas, and therefore have a significant impact on the ozone and nitrogen cycles. Micronutrients (e.g., Fe) deposited with dust aerosol possibly impact the productivity of marine and terrestrial ecosystems, thus influencing the carbon cycle and potentially changing the atmospheric greenhouse gas content. The impacts of these indirect dust effects on climate are uncertain, since the underlying processes are not yet fully understood.

Ina Tegen

Bibliography

- Duce, R.A., 1995. Sources, distributions, and fluxes of mineral aerosols and their relationship to climate. In Charlson, R.J., and Heintzenberg, J. (eds.), *Aerosol Forcing of Climate: Report of the Dahlem Workshop on Aerosol Forcing of Climate*, Berlin 1994, April 24–29, Chichester: Wiley. pp. 43–72.
- Gillette, D.A., and Passi, R., 1988. Modeling dust emission caused by wind erosion. *J. Geophys. Res.*, **93**, 14,233–14,242.
- Ginoux, P., Chin, M., Tegen, I., Prospero, J.M., Holben, B., Dubovik, O., and Lin, S.-J., 2001. Sources and distributions of dust aerosols simulated with the GOCART model. *J. Geophys. Res.*, **106**, 20255–20273.
- Houghton, J.T., Ding, Y., Griggs, D.J., Noguera, M., van der Linden, P.J., Dai, X., Maskell, K., and Johnson, C.A. (eds.), 2001. *Climate Change*. New York, NY: Cambridge University Press.
- Kohfeld, K.E., and Harrison, S.P., 2001. DIRTMAP: The geological record of dust. *Earth-Sci. Rev.*, **54**, 81–114.
- Liao, H., and Seinfeld, J.H., 1998. Radiative forcing by mineral dust aerosols: Sensitivity to key variables. *J. Geophys. Res.*, **103**, 31637–31645.
- Marticorena, B., and Bergametti, G., 1995. Modeling the atmospheric dust cycle 1. Design of a soil-derived dust emission scheme. *J. Geophys. Res.*, **100**, 16415–16430.
- Prospero, J.M., Ginoux, P., and Torres, O., 2002. Environmental characterization of global sources of atmospheric soil dust identified with the NIMBUS-7 TOMS absorbing aerosol product. *Rev. Geophys.* doi:10.1029/2000RG000095.
- Shao, Y., Raupach, M.R., and Findlater, P.A., 1993. Effect of saltation bombardment on the entrainment of dust by wind. *J. Geophys. Res.*, **98**, 12,719–12,726.

- Sokolik, I.N., and Toon, O.B., 1999. Incorporation of mineralogical composition into models of the radiative properties of mineral aerosol from UV to IR wavelengths. *J. Geophys. Res.*, **104**, 9423–9444.

Cross-references

Climate Forcing
 Dust Transport, Quaternary
 Eolian Dust, Marine Sediments
 Eolian Sediments and Processes
 Iron and Climate Change

ALBEDO FEEDBACKS

Technically, the term albedo refers to the reflecting power of a body, or a surface area, and is the fraction of light reflected by the body relative to the total light that is incident on the body, or surface. Thus, a perfect absorber has an albedo of zero while a perfect reflector has an albedo of unity. In general, the albedo of a given surface is a function of wavelength. It is also dependent on the angle at which the incident light strikes the reflecting surface. This leads to more specialized terminology such as “spectral albedo” and “plane albedo,” which refer to the wavelength and solar zenith angle dependence of the reflected radiation, respectively. Reflected radiation that has been averaged over all possible angles of incidence is called “spherical albedo.” It is also referred to as the Bond albedo, which is the ratio of the total light reflected by a spherical body, such as a planet, to the total radiation that is incident on the planet.

In the context of terrestrial climate where interest is primarily directed toward describing the radiative energy balance of the Earth, there is an implicit assumption that the spectral albedo of the Earth is then directly related to the solar energy that is available to drive atmospheric dynamics and for maintaining the temperature of the Earth-atmosphere system. It is also useful to differentiate between “surface albedo,” which is the reflectivity of the bare ground and ocean surface without including atmospheric scattering effects, and “planetary albedo,” which includes all atmospheric and surface scattering contributions and refers to the outgoing solar radiation at the top of the atmosphere that is reflected back to space.

Figure A1 shows the zonally averaged annual mean surface albedo (*dashed line*) and planetary albedo (*solid line*) of the Earth as computed with a general circulation climate model. Characteristically, the ocean and land are areas of low reflectivity with typical albedos in the 6–12% range. Substantially higher surface albedos due to snow and ice are evident in the polar regions where the albedo of fresh snow may exceed 90%. Globally averaged, the surface albedo of the Earth is about 12%. The planetary albedo is generally larger than the surface albedo due primarily to the high reflectivity of clouds. As in the case of fresh snow, the albedo of optically thick clouds can sometimes exceed 90%. However, because of absorption by atmospheric gases and multiple scattering effects between the atmosphere and ground surface, the planetary albedo in the polar regions is frequently lower than that of the highly reflecting snow surface. Globally averaged, the planetary albedo of the Earth, also called the global albedo, is approximately 30%. Thus, about 70% of the solar

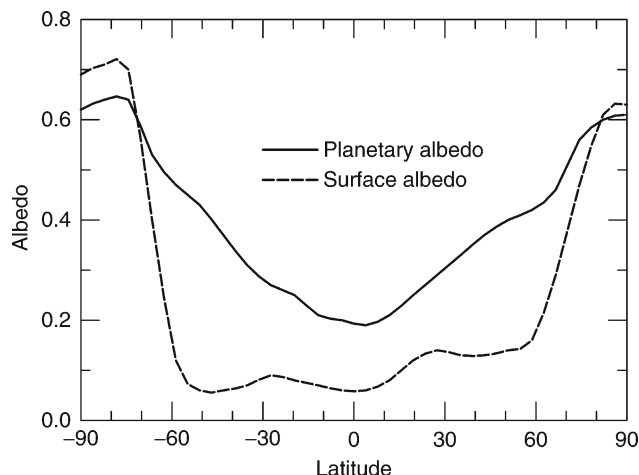


Figure A1 Zonally averaged annual mean surface albedo (*dashed line*) and planetary albedo (*solid line*) of the Earth as computed with a general circulation climate model.

radiation that falls on the Earth is absorbed by the Earth-atmosphere system, with most of the solar energy being absorbed at low latitudes and relatively little within the polar regions. This serves to establish the characteristic equator-to-pole temperature gradient and the corresponding atmospheric and oceanic circulation patterns that work to redistribute the absorbed solar energy more evenly.

Despite the high surface albedo at high latitudes, the atmospheric contribution to the global albedo exceeds that of the ground surface by about a factor of 2.5, with clouds being the single largest contributor. Smaller contributions to the global albedo are made by atmospheric aerosols and by Rayleigh scattering due to air molecules. Rayleigh scattering, which accounts for about 5% to the global albedo, is essentially a constant offset factor in climate considerations since it is not significantly affected by changes in atmospheric conditions. Snow, ice, and clouds on the other hand have specific temperature and humidity thresholds at which they form and dissipate. The large albedo contrast that occurs when snow, ice, and cloud amounts change strongly affects the amount of solar radiation that is absorbed by the Earth-atmosphere system. This in turn affects the atmospheric temperature distribution, leading to mutual interactions between regions of snow, ice, and cloud fields and the local surface and atmospheric temperature distributions. These physical interactions comprise the basic climate “feedback” effects whereby a given change in temperature directly or indirectly induces a change in snow, ice or cloud amount, which in turn affects the amount of solar energy that is absorbed, thus magnifying the original temperature perturbation.

Albedo feedbacks associated with changes in snow and ice cover are generally positive. This is because for an initial increase in temperature, ΔT_o , due to whatever cause, the expected result is the melting of a certain amount of snow and ice with a corresponding decrease in local albedo, which leads to increased absorption of solar energy and a subsequent increase in temperature. This results in a geometric series of temperature increments that converges to some equilibrium temperature that is ΔT_{eq} higher than the initial reference temperature. The ratio, $f = \Delta T_{eq}/\Delta T_o$, is called the feedback factor by which the initial forcing is magnified. Accordingly, if f is

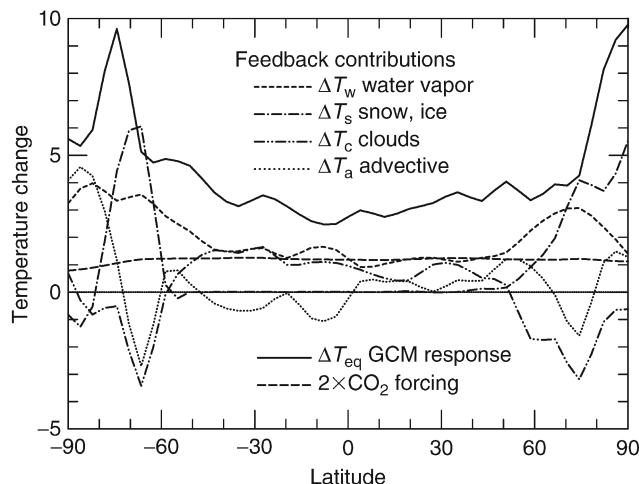


Figure A2 Annually averaged zonal-mean GCM surface temperature response for doubled CO_2 (*heavy solid line*) and temperature forcing due to doubled CO_2 (*heavy dashed line*). The other curves depict other feedback contributions as indicated.

greater than unity the feedback is positive, and if f is less than unity the feedback is negative.

The relative strengths of different climate feedback effects can be evaluated with the help of a general circulation climate model (GCM) and its radiative transfer model. The GCM is assumed to incorporate appropriate mathematical formulations for all of the necessary physical process to model the climate system, such as the evaporation, transport, and condensation of water vapor, precipitation, the freezing and melting of ice, the diurnal and seasonal changes in solar heating and thermal cooling, including the appropriate heat capacities for the ocean, land, and atmosphere. In typical GCM experiments of climate forcing, the GCM is first run to its reference equilibrium state, at which point the global distributions of water vapor, surface albedo, clouds, and temperature are recorded. A radiative perturbation, such as doubling the CO_2 amount, is then applied and the GCM is run to its new equilibrium state whereupon the changes in the distributions of water vapor, surface albedo, cloud, and temperature are again recorded and analyzed.

The principal results for a doubled CO_2 experiment are summarized in **Figure A2** by the heavy solid line which depicts the latitudinal dependence of the total annual-mean equilibrium temperature change, including albedo feedbacks which globally averaged, yields $\Delta T_{eq} = 3.9^\circ\text{C}$, and by the heavy dashed line which represents the applied forcing due to doubled CO_2 alone, which, globally averaged and expressed as a temperature change, yields $\Delta T_o = 1.2^\circ\text{C}$ (**Table A1**). The difference between the externally imposed temperature change ΔT_o , and the actual temperature change ΔT_{eq} that is realized as the model reaches its new thermal equilibrium, is the feedback contribution, which produces both a reduction of the planetary albedo of the Earth, and an enhancement of its atmospheric greenhouse strength.

Specific information regarding the relative magnitude of individual feedback contributions can be obtained by inserting the recorded cloud, water vapor, surface albedo differences between the perturbed and reference model results into the GCM one at a time, and by running the model to equilibrium with all physical process interactions turned off, except for only local

Table A1 Doubled CO₂ feedback contributions

Process	ΔT	Feedback gain	Feedback factor
2 × CO ₂ forcing	$\Delta T_o = 1.2$		
Water vapor	$\Delta T_w = 1.7$	$g_w = 0.44$	$f_w = 1.77$
Snow, ice	$\Delta T_s = 0.5$	$g_s = 0.13$	$f_s = 1.15$
Clouds	$\Delta T_c = 0.5$	$g_c = 0.13$	$f_c = 1.15$
Total	$\Delta T_{eq} = 3.9$	$g = 0.69$	$f = 3.25$

surface and atmospheric temperatures that are allowed to adjust. The resulting temperature differences define the strength of each feedback contribution relative to the total equilibrium temperature change ΔT_{eq} that may be considered as the driving force behind each feedback process. The relative strengths of different feedbacks can be readily compared when expressed as feedback gain factors ($g = \Delta T / \Delta T_{eq}$). Globally averaged, these are tabulated in [Table A1](#) for the principal feedback processes.

The surface albedo feedback, due primarily to changes in sea ice in the polar regions, and its latitudinal dependence, is shown by the heavy broken line in [Figure A2](#). The feedback effect of cloud changes is seen to be positive within low to middle latitudes, but is negative in the polar regions. About 60% of cloud feedback is the result a decrease in global albedo caused by a reduction in cloud fraction, while about 40% is attributable to greenhouse enhancement due to an increase in cloud altitude. Water vapor makes the largest individual feedback contribution with about 80% in the form of greenhouse enhancement, while 20% comes in the form of reduced planetary albedo due to increased absorption of solar radiation by water vapor. Overall, about 40% of the 2.7 °C global feedback effect in response to doubled CO₂, is the result of global albedo reduction, and about 60% is due to greenhouse enhancement. The *dotted line* in [Figure A2](#) refers to advective feedbacks that arise from changes in atmospheric circulation which act to redistribute energy latitudinally, but which, when globally averaged, must add to zero.

The feedback gain factors in [Table A1](#) combine linearly in the form $g = g_w + g_s + g_c$ to yield the total climate system feedback gain factor. Feedback factors, on the other hand, which determine the ratio by which the initial temperature perturbation will be magnified when the climate system reaches equilibrium, combine non-linearly and are evaluated as $f = (1 - g)^{-1}$. Acting alone, the snow-ice albedo feedback magnifies a given temperature perturbation by only a factor of $f_s = 1.15$. But, acting together with water vapor and cloud feedbacks, with $f_{wc} = 2.33$, it raises the combined feedback factor to $f_{wcs} = 3.25$. During the past glacial maximum when the global snow-ice cover was more extensive, the snow-ice feedback is estimated to have been about twice as strong as it is in current climate. This would have produce a combined feedback gain factor of 0.82, or a feedback factor of $f_{wcs} = 5.55$. For ice-age CO₂ amounts that were about half of those for current climate, the CO₂ radiative forcing of about $\Delta T_o = -1$ °C, would maintain a global-mean temperature 5–6 °C colder than the global-mean temperature of current climate.

Additional albedo feedback effects can arise from changes in vegetation cover. However circumstances regarding vegetation albedo feedback are more complicated than the relatively simple temperature dependence for snow and ice formation. This is because vegetation cover is more directly coupled to precipitation and drought conditions which are driven by changes in atmospheric circulation patterns rather than by changes in temperature.

Ultimately, of course, atmospheric circulation is driven by the distribution of solar heat energy, but the relationship between absorbed solar energy and vegetation albedo is somewhat indirect, making it more problematic to establish whether the vegetation albedo feedback is positive or negative. Typically, since vegetation tends to be less reflecting than the bare ground that would replace it, a decrease in vegetation cover would tend to increase the planetary albedo.

Andrew A. Lacis

Bibliography

- Hansen, J., Lacis, A., Rind, D., Russell, G., Stone, P., Fung, I., Ruedy, R., and Lerner, J., 1984. Climate sensitivity: Analysis of feedback mechanisms. In Hansen, J.E., and Takahashi, T. (eds.), *Climate Processes and Climate Sensitivity. Geophysical Monograph* 29. Washington, DC: American Geophysical Union, pp. 130–163.
- Hansen, J., Sato, M., and Ruedy, R., 1997. Radiative forcings and climate response. *J. Geophys. Res.* **102**, 6831–6864.
- Lacis, A.A., and Mishchenko, M.I., 1995. Climate forcing, climate sensitivity, and climate response: a radiative modeling perspective on atmospheric aerosols. In Charlson, R.J., and Heintzenberg, J. (eds.), *Aerosol Forcing of Climate*. New York: Wiley, pp. 11–42.

Cross-references

- [Arctic Sea Ice](#)
[Climate Forcing](#)
[Cryosphere](#)
[Paleoclimate Modeling, Quaternary](#)

ALKENONES

Alkenones are long-chained (C₃₆-C₃₉) *di*-, *tri*- and *tetra*-unsaturated ethyl and methyl ketones synthesized by a few species of Haptophyte algae in the modern ocean (Volkman et al., 1980; Conte et al., 1994). The cosmopolitan coccolithophorid *Emiliania huxleyi* is the most important contemporary source of alkenones, followed by substantial regional contributions from *Gephyrocapsa oceanica*. Other noncalcifying Haptophytes, including *Isochrysis* spp. and *Chrysothila lamellosa*, produce alkenones but are restricted to coastal marine environments (Ziveri and Broerse, 1997). *Emiliania huxleyi* evolved in the Late Pleistocene (Thierstein et al., 1977) and *G. oceanica* in the Pliocene (Hay, 1977), however, the geological range of alkenones extends to the early Cretaceous (Farrimond et al., 1986). The distribution of alkenones in Mesozoic and Cenozoic sediments reflects, in part, their refractory nature attributed to an unusual *trans* configuration – a molecular architecture that may inhibit bacterial biodegradation (Rechka and Maxwell, 1987). Examination of older sediments containing both alkenones and nannofossils has narrowed the probable source of alkenones to microalgae within the family Noelaerhabdaceae (Volkman, 2000).

Original aspirations that alkenones represented unambiguous biomarkers for coccolithophorids were surpassed by their capacity to record sea-surface temperatures at the time of biosynthesis. A relationship between the degree of alkenone unsaturation with temperature was first observed in Haptophyte cultures (Marlowe et al., 1984). This behavior, assumed to

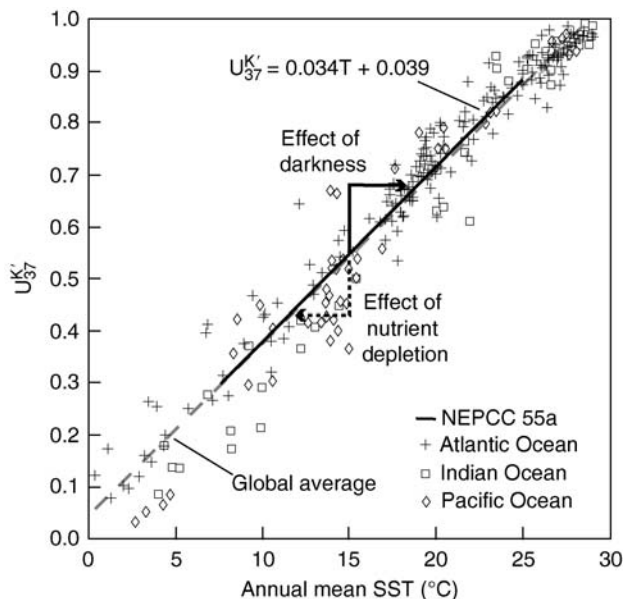


Figure A3 Relationship between U_{37}^K from surface sediments and mean annual surface temperature. Modified from Müller et al. (1998) and published in Prah1 et al. (2003).

reflect a biochemical response to maintain the integrity and permeability of its cell membrane, follows a pattern of increasing unsaturation with decreasing growth temperature. Brassell et al. (1986) pioneered the application of alkenone unsaturation in the interpretation of ancient sea surface temperatures and defined the alkenone unsaturation indices U_{37}^K and $U_{37}^{K'}$:

$$U_{37}^K = \frac{[37:2] - [37:4]}{[37:2] + [37:3] + [37:4]} \text{ and } U_{37}^{K'} = \frac{[37:2]}{[37:2] + [37:3]}$$

where [37:2], [37:3], and [37:4] represent the relative concentrations of C_{37} di-, tri-, and tetra-unsaturated alkenones respectively. Subsequent experiments using a Pacific strain of *E. huxleyi* (Prah1 and Wakeham, 1987; Prah1 et al., 1988) demonstrated a linear response of U_{37}^K and $U_{37}^{K'}$ with growth temperature between 8° and 25 °C. These critical experiments provided a calibration of $U_{37}^{K'}$ versus temperature widely applied in subsequent paleoceanographic studies. The calibration of Prah1 et al. (1988),

$$U_{37}^{K'} = 0.034T(^{\circ}\text{C}) + 0.039$$

is identical to field-based results derived from extensive surface sediment $U_{37}^{K'}$ values and mean annual sea surface temperatures at 0 m depth (Figure A3) (Müller et al., 1998). This agreement is remarkable in light of the observation that calibration differences exist between Haptophyte strains and species (Sikes and Volkman, 1993; Conte et al., 1998), as well as growth conditions (Epstein et al., 1998; Prah1 et al., 2003).

While alkenone unsaturation is useful in assessing sea surface temperatures, the stable carbon-isotope composition of these molecules contains information relevant to the concentration of dissolved carbon dioxide during algal production (Bidigare et al., 1997, 1999). Consequently, alkenone $\delta^{13}\text{C}$ values have been applied to evaluate equatorial Pacific paleoceanographic dynamics and surface-water $[\text{CO}_{2\text{aq}}]$ during the

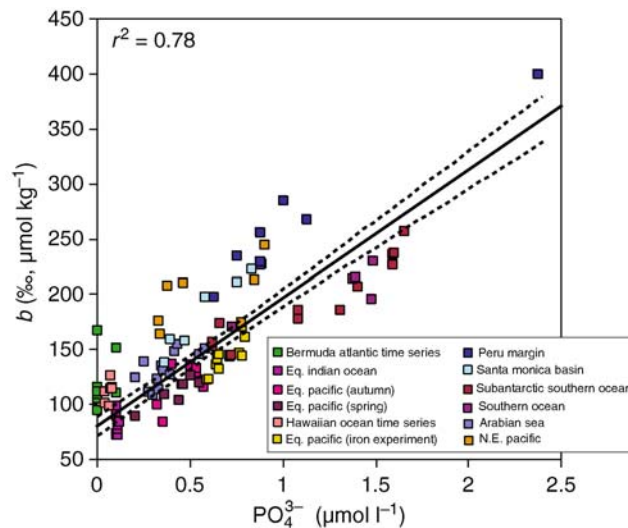


Figure A4 Compilation of “*b*” versus soluble phosphate for natural haptophyte populations (modified from Laws et al., 2001). Values for “*b*” are calculated using a value of 25‰ for ϵ_f . Solid line represents geometric mean regression. Dotted lines reflect 95% confidence intervals.

Pleistocene (Jasper et al., 1994), Late Quaternary surface-water CO_2 (Jasper and Hayes, 1990; Andersen et al., 1999), and global $p\text{CO}_2$ trends during the Miocene (Pagani et al., 1999). In addition to $[\text{CO}_2]$, other factors including cellular growth rate (Rau et al., 1992; Bidigare et al., 1997), cell geometry (Popp et al., 1998) strongly affect the stable carbon isotopic compositions of algae by influencing the magnitude of carbon isotope fractionation that occurs during carbon fixation (ϵ_p). For field-based research the expression for ϵ_p is simplified to

$$\epsilon_p = \epsilon_f - \frac{b}{C_c}$$

where ϵ_f is the carbon isotope fractionation associated with carbon fixation, C_c is the concentration of extracellular $\text{CO}_{2\text{aq}}$, and “*b*” represents the sum of physiological factors affecting the total carbon discrimination such as growth rate and cell geometry. Measurements of natural Haptophyte populations (see Laws et al., 2001) provide evidence for a robust relationship between the physiological-dependent term “*b*” and the concentration of reactive soluble phosphate (Figure A4). Although phosphate is a major limiting nutrient, it is unlikely that $[\text{PO}_4^{3-}]$ alone is responsible for the variability in growth rate inferred from variation in “*b*.” Instead, it is assumed that the availability of one or more trace element that display phosphate-like distributions in the ocean (i.e., Se, Co, Ni) influence the growth characteristics of these algae (see Bidigare et al., 1997; Laws et al., 2001 and references therein). Despite these uncertainties, the empirical relationship between the term “*b*” and $[\text{PO}_4^{3-}]$ in the modern ocean allows ϵ_p to be cast in terms of $[\text{PO}_4^{3-}]$ and $[\text{CO}_{2\text{aq}}]$, providing a proxy for evaluating paleo- $[\text{CO}_{2\text{aq}}]$ if ancient ϵ_p values are reconstructed and phosphate concentrations are constrained (Pagani et al., 1999, 2002).

Mark Pagani

Bibliography

- Andersen, N., Müller, P.J., Kirst, G., and Schneider, R.R., 1999. The $\delta^{13}\text{C}$ signal in C_{37-2} alkenones as a proxy for reconstructing Late Quaternary PCO_2 in surface waters from the South Atlantic. In Fischer, G., and Wefer, G. (eds.), *Proxies in Paleocyanography: Examples from the South Atlantic*. New York: Springer-Verlag, pp. 469–488.
- Bidigare, R.R., Fluegge, A., Freeman, K.H., Hanson, D.L., Hayes, J.M., Hollander, D., Jasper, J.P., King, L.L., Laws, E.A., Milder, J., Millero, F.J., Pancost, R., Popp, B.N., Steinberg, P.A., and Wakeham, S.G., 1997. Consistent fractionation of ^{13}C in nature and in the laboratory: Growth-rate effects in some haptophyte algae. *Global Biogeochem. Cycles*, **11**, 279–292.
- Bidigare, R.R., Fluegge, A., Freeman, K.H., Hanson, D.L., Hayes, J.M., Hollander, D., Jasper, J.P., King, L.L., Laws, E.A., Milder, J., Millero, F.J., Pancost, R., Popp, B.N., Steinberg, P.A., and Wakeham, S.G., 1999. Consistent fractionation of ^{13}C in nature and in the laboratory: Growth-rate effects in some haptophyte algae. *Global Biogeochem. Cycles*, **13**, 251.
- Brassell, S.C., Eglinton, G., Marlowe, I.T., Pflaumann, U., and Sarnthein, M., 1986. Molecular stratigraphy: A new tool for climatic assessment. *Nature*, **320**, 129–133.
- Conte, M.H., Volkman, J.K., and Eglinton, G., 1994. Lipid biomarkers of the Haptophyta. In Green, J.C., and Leadbeater, B.S.C. (eds.), *The Haptophyte Algae*. Oxford: Clarendon Press, pp. 351–377.
- Conte, M.H., Thompson, A., Lesley, D., and Harris, R.P., 1998. Genetic and physiological influences on the alkenone/alkenonate versus growth temperature relationship in *Emiliania huxleyi* and *Gephyrocapsa oceanica*. *Geochim. Cosmochim. Acta*, **62**, 51–68.
- Epstein, B.L., D'Hondt, S., Quinn, J.G., and Zhang, J., 1998. An effect of dissolved nutrient concentrations on alkenone-based temperature estimates. *Paleoceanography*, **13**, 122–126.
- Farrimond, P., Eglinton, G., and Brassell, S.C., 1986. Alkenones in Cretaceous black shales, Blake-Bahama Basin, western North Atlantic. *Org. Geochem.*, **10**, 897–903.
- Hay, W.W., 1977. Calcareous Nannofossils. In Ramsay, A.T.S. (eds.), *Oceanic Micropaleontology*. New York: Academic Press, pp. 1055–1200.
- Jasper, J.P., and Hayes, J.M., 1990. A carbon isotope record of CO_2 levels during the late Quaternary. *Nature*, **347**, 462–464.
- Jasper, J.P., Mix, A.C., Prahl, F.G., and Hayes, J.M., 1994. Photosynthetic fractionation of ^{13}C and concentrations of dissolved CO_2 in the central equatorial Pacific during the last 255,000 years. *Paleoceanography*, **6**, 781–798.
- Laws, E.A., Popp, B.N., and Bidigare, R.R., 2001. Controls on the molecular distribution and carbon isotopic composition of alkenones in certain haptophyte algae. *Geochim. Geophys. Geosyst.*, **2** doi: 2000GC000057.
- Marlowe, I.T., Green, J.C., Neal, A.C., Brassell, S.C., Eglinton, G., and Course, P.A., 1984. Long chain (n-C37-C39) alkenones in the Prymnesiophyceae: Distribution of alkenones and other lipids and their taxonomic significance. *Br. Phycol. J.*, **19**, 203–216.
- Müller, P.J., Kirst, G., Ruhland, G., von Storch, I., and Rosell-Melè, A., 1998. Calibration of the alkenone paleotemperature index U_{37}^{K} based on core-tops from the eastern South Atlantic and the global ocean (60°N – 60°S). *Geochim. Cosmochim. Acta*, **62**, 1757–1772.
- Pagani, M., Arthur, M.A., and Freeman, K.H., 1999. The Miocene evolution of atmospheric carbon dioxide. *Paleoceanography*, **14**, 273–292.
- Pagani, M., Freeman, K.H., Ohkouchi, N., and Caldeira, K., 2002. Comparison of water column $[\text{CO}_{2\text{aq}}]$ with sedimentary alkenone-based estimates: A test of the alkenone- CO_2 proxy. *Paleoceanography*, **17**: 1069 doi: 10.1029/2002PA000756.
- Popp, B.N., Laws, E.A., Bidigare, R.R., Dore, J.E., Hanson, K.L., and Wakeham, S.G., 1998. Effect of phytoplankton cell geometry on carbon isotopic fractionation. *Geochim. Cosmochim. Acta*, **62**, 69–77.
- Prahl, F.G., and Wakeham, S.G., 1987. Calibration of unsaturation patterns in long-chain ketone compositions for paleotemperature assessment. *Nature*, **330**, pp. 367–369.
- Prahl, F.G., Muehlhausen, L.A., and Zahnle, D.L., 1988. Further evaluation of long-chain alkenones as indicators of paleoceanographic conditions. *Geochim. Cosmochim. Acta*, **52**, 2303–2310.
- Prahl, F.G., Wolfé, G.V., and Sparrow, M.A., 2003. Physiological impacts on alkenone paleothermometry. *Paleoceanography*, **18** doi: 2002PA000803.
- Rau, G.H., Takahashi, T., Des Marais, D.J., Repeta, D.J., and Martin, J.H., 1992. The relationship between $\delta^{13}\text{C}$ of organic matter and $[\text{CO}_2(\text{aq})]$ in ocean surface water: Data from a JGOFS site in the northeast Atlantic Ocean and a model. *Geochim. Cosmochim. Acta*, **56**, 1413–1419.
- Rechka, J.A., and Maxwell, J.R., 1987. Characterization of alkenone temperature indicators in sediments and organisms. *Org. Geochem.*, **13**, 727–734.
- Sikes, E.L., and Volkman, 1993. Calibration of alkenone unsaturation ratios (U_{37}^{K}) for paleotemperature estimation in cold polar waters. *Geochim. Cosmochim. Acta*, **57**, 1883–1889.
- Thierstein, H.R., Geitzenauer, K.R., Molfino, B., and Shackleton, N.J., 1977. Global synchronicity of late Quaternary coccolith datum levels: Validation by oxygen isotope. *Geology*, **5**, 400–404.
- Volkman, J.K., 2000. Ecological and environmental factors affecting alkenone distributions in seawater and sediments. *Geochim. Geophys. Geosyst.*, **1** doi: 2000GC000061.
- Volkman, J.K., Eglinton, G., Corner, E.D., and Sargent, J.R. 1980. Novel unsaturated straight-chain C37-C39 methyl and ethyl ketones in marine sediments and a coccolithophore *Emiliania huxleyi*. In Douglas, A.G., and Maxwell, J.R. (eds.), *Advances in Organic Geochemistry 1979; Proceedings of the Ninth International Meeting on Organic Geochemistry, University of Newcastle-Upon-Tyne, U.K., September 1979*. UK: Pergamon Press, pp. 219–227.
- Ziveri, P., and Broerse, A., 1997. Coccolithophores in traps: Global coccolith flux data. *J. Nanoplankton Res.*, **19**, 11–13.

Cross-references

Carbon Isotopes, Stable
Coccoliths
Geochemical Proxies (Non-Isotopic)
Ocean Paleotemperatures
Organic Geochemical Proxies

ANCIENT CULTURES AND CLIMATE CHANGE

The Earth's climate warmed abruptly, starting around 11,500 years ago after the final stages of the last glaciation. The Holocene climatic amelioration following the last ice age coincided with a major transition in human history – from the hunting-gathering lifestyle of our ancestors to the onset of agriculture, permanent settlements, and the beginnings of civilization. Early populations depended on hunting, fishing, and foraging for wild plants. The abundances of these resources were strongly influenced by seasonal cycles and multi-decadal climate trends. Even after the development of agriculture, ancient societies were probably more vulnerable to the impacts of sudden climate change than modern societies, since they were predominantly agrarian and dependent on weather-sensitive crops.

The post-glacial warming trend reached its peak in the Hypsithermal during the early to mid-Holocene, between ~8,300 and 5,000 yBP. Although the Holocene has generally been regarded as a period of climate stability, relative to the sharp climate fluctuations of the Pleistocene, accumulating evidence demonstrates considerable climate variability (see *Holocene climates*). The Hypsithermal marked a time of improved climate, and also of significant population shifts and growing cultural sophistication in many parts of the world: the development of complex agricultural societies, irrigation systems, and cities, the invention of writing and metallurgy, i.e., the roots of civilization (e.g., Sandweiss et al., 1999). Stronger monsoons and a northward shift of tropical rainfall belts between ~9,000 and 7,000 yBP created a savannah-like environment in the eastern Sahara that encouraged cattle herders to settle in villages west of the Nile River, in an area that is now desert. The region was abandoned after the onset of arid conditions,

starting approximately 6,000 years ago. The migrations resulting from this dry phase may have led to the emergence of the pharaonic civilization in Egypt (Kuper and Kröpelin, 2006). Around this time, major construction of temples began in the Nile Valley. A trend toward cooler (and in some regions, drier) climates in the following millennia may have stimulated further cultural changes in many areas. Lengthy droughts in western Asia at around 8,200, 5,200, and 4,200 yBP may have triggered demographic shifts that resulted in depopulation of early settlements, relocation to more favorable areas, and re-colonization upon climatic amelioration (Staubwasser and Weiss, 2006). In China, cities grew after ~5,800 yBP and in Japan, a more complex society emerged (Sandweiss et al., 1999). The onset of a period of greater El Niño activity after 5,800 yBP, following a lull, correlated with the start of temple building along the Peruvian coast (Sandweiss et al., 2001).

Many authors have pointed out apparent relationships between the rise and fall of ancient civilizations and climate change (e.g., Ladirie, 1971; Lamb, 1977, 1995; Wigley et al., 1981; Fagan, 1999, 2004; Gill, 2000). However, changes in those societies could have also been instigated by the interaction of a number of other factors, including economic and/or political instability, diseases, human migrations, wars, cultural innovations, and environmental degradation (e.g., Kirch, 2005; Morrison, 2006), which may have been only indirectly related to climate, if at all. While it is probably an over-simplification to assume that climate change was the sole or dominant cause of sudden societal dislocations, a growing body of evidence lends support to the idea of a relationship between rapid alterations in settlement patterns, growth or abandonment of cities, with cultural discontinuities on the one hand and climate fluctuations on the other. Climate change by itself may not have been enough to initiate major population shifts or topple an otherwise stable civilization; however, it could have provided the final straw in environmentally marginal regions or in conjunction with one of the other destabilizing influences listed above. Some examples of possible connections between abrupt transitions in ancient civilizations and climate change are discussed below.

Eastern Hemisphere

The Black Sea, a freshwater lake during the last glaciation, subsequently expanded, fed by meltwater from retreating glaciers, but then dwindled to a brackish lake during the Younger Dryas, ~12,000 years ago. According to Ryan and his colleagues (Ryan et al., 1997; Ryan and Pitman, 1999), by ~7,500 yBP the global sea level had reached a point where a catastrophic flood of water from the Aegean Sea broke through the Bosphorus Strait and gushed into the Black Sea. Evidence for this event is shown by the first appearance of salt-tolerant Mediterranean mollusks. They further speculate that this event may have provided the basis for the biblical account of Noah's flood. Such a massive flood may also have triggered migration of people away from the region, west and north into Europe and south into the Middle East. Signs of a flooded settlement 95 m beneath the modern northern coast of Turkey (Ballard et al., 2000) lend further support to this hypothesis. However, this hypothesis has been challenged by Aksu et al. (2002) who instead suggest that the Black Sea, at a much lower level during the late glacial, began to rise by 11,000–10,000 yBP, fed by water from the Danube, Dniester, Dnieper, Don, southern Bug, and on occasion, Volta Rivers. A now-drowned 10–9 ka delta lobe at the southern exit of the Bosphorus Strait provides

evidence for early and strong Black Sea outflow. Sediments were deposited away from the delta across the Marmara Sea. No indication exists for erosion of these sediments by strong currents from the proposed catastrophic flood at 7,500 yBP. By ~8000 years, the sea level had risen to the point where the Marmara Sea overtopped the sills in the Bosphorus, introducing saline Mediterranean water into the Black Sea for the first time. Rather than a catastrophic flood, Aksu et al. (2002) propose instead a gradual establishment of a two-way flow in the Bosphorus. Paleo-hydrometeorological modeling of the Black Sea Basin (Georgievski and Stanev, 2006) suggests an arid period and Black Sea lowstand peaking at 11,500 yBP. Rising sea levels reached the Black Sea between 8,800 and 7,400 yBP, making a flood event possible. However, the exact timing and nature of the marine re-connection depends on several variables, such as sill depth and precipitation minus evaporation balance, which are not yet tightly constrained by the data.

The transition from hunting-gathering to agriculture in southwest Asia may have begun as early as 12,000 ago, during the Younger Dryas period, when the region became cooler and drier. The reduction in availability of wild food resources, on which Natufian groups depended, may have stimulated them to experiment with cultivation rather than depend entirely on gathering (Weiss and Bradley, 2001). During a global cold period ~8,200 yBP (see *The 8,200 ybp event*), a lengthy drought gripped the Middle East, at which time a number of early agricultural settlements appear to have been abandoned in northern and central Mesopotamia (Weiss and Bradley, 2001; Staubwasser and Weiss, 2006). This episode may have contributed to the development of irrigation agriculture in southern Mesopotamia. Another arid period ~5,200 yBP, associated with reduced Anatolian precipitation and lowered Tigris-Euphrates streamflow, may have led to the collapse of the Late Uruk culture in Mesopotamia (Staubwasser and Weiss, 2006).

Between 4,300 and 4,200 yBP, the Akkadian empire prospered in northern Mesopotamia. Yet, by ~4,200 yBP, the empire had collapsed. It has been suggested that the collapse was linked to a period of greater regional aridity and erosion in the Near East (Weiss et al., 1993; Cullen et al., 2000; deMenocal, 2001; Staubwasser and Weiss, 2006). Growing problems with salinization may have also led to declining crop yields (Roberts, 1998). A marked increase in eolian grains from a marine core in the Gulf of Oman ~4,000 years ago may be linked to the collapse. These grains were derived from adjacent terrigenous sources. A close geochemical match between volcanic shards found in the core and in a layer immediately above the Akkadian ruins suggests that Akkadian collapse and aridification were synchronous (Cullen et al., 2000). On the other hand, Tainter (2000) questions whether the extended period of drought at 4,200 yBP was the real cause of the Akkadian collapse. He points out that during an earlier period of drought, instead of a decline in population or sociopolitical complexity, the opposite had occurred – a stable state had emerged. Thus, why would adverse climate destroy a society at one time, but lead to societal advance at another?

Paleoclimate records, including geochemical data from speleothems in Israel and lacustrine sediments in Turkey and elsewhere, however, suggest that the 4,200 yBP drought was of regional extent (Cullen et al., 2000; Staubwasser and Weiss, 2006). The termination of the Harappan civilization in the Indus Valley at around 4,200 yBP may have also been related to this drought (Staubwasser et al., 2003). Dead Sea lake levels fell sharply beginning around 2,300–2,200 BC, reaching a minimum at around 1,400 BC (Enzel et al., 2003). Data from several

independent paleoclimate proxies in an Italian speleothem, interpreted as indicating an arid regime, have been accurately dated at ~4,100 yBP (Drysdale et al., 2006). This age is consistent within error limits with the timing of the southwest Asian drought. The drought may have extended as far as southern Europe, across the Middle East, northwest India and Pakistan, and into Tibet and south China (Staubwasser and Weiss, 2006).

The 10,000-year record of Dead Sea lake levels show several other fluctuations that appear to be associated with cultural transitions in the Near East (Enzel et al., 2003; Bookman et al., 2004; Migowski et al., 2006). Modern meteorological data show a high degree of correlation between rainfall in Jerusalem and many other stations in the region, including Jordan and Lebanon. Thus, variations in Dead Sea lake levels can serve as a proxy for Near East paleoprecipitation. In addition to a drop in lake level ~2,200 BC, at around the time of the collapse of the Akkadian empire mentioned above, Enzel et al. (2003) associate a drop in lake level between the late fifth and late eighth centuries with the decline of the Byzantine empire in the Near East and Arab expansion out of Saudi Arabia. Conversely, high lake levels of the second and first centuries BC and fourth century CE have been related to expansion of Roman and Byzantine presence, respectively, in the region and the Crusader period in the eleventh and twelfth century CE (Bookman et al., 2004). Examining Dead Sea lake level variations further back in time, Migowski et al. (2006) link the ~8,100–8,200 yBP drought with the decline of the earliest Jericho township. Climatic amelioration around 5,100 yBP paralleled the growth of Early Bronze Age Arad at the northeastern edge of the Negev desert. Jericho was resettled during this wetter period, but declined once more during the 4,200 yBP drought. Migowski et al. (2006) point out several other examples of growth and decline of Canaanite city-states coinciding with climatic changes.

One frequently cited example of an adverse impact of climate change is the demise of the Norse settlements in Greenland (Lamb, 1977, 1995). The failure of the settlements has also been blamed on an inability of the Vikings to adapt their agrarian economy to the hunting and fishing lifestyle of the native Inuit population as the climate grew colder, or to overgrazing and soil erosion, disease, hostilities, and declining demand for walrus ivory or furs. According to the sagas, Icelandic settlers led by Erik the Red colonized the southwest coast of Greenland c. AD 985, followed by a second settlement on the west coast. However, by around AD 1,450, the colonies had been abandoned. Foraminifera and lithologic proxies from marine cores in Nansen Fjord, eastern Greenland, as well as oxygen isotope data from Greenland ice cores suggest that warmer conditions prevailed from AD 700 to around AD 1,300, corresponding to the Medieval Warm Period (Ogilvie et al., 2000). The lithologic data, in particular, point to less sea ice and more open water, which would have been favorable for seafaring. The 1,300s were marked instead by more frequent occurrences of sea ice and colder temperatures. As the climate deteriorated, the Norse settlers relied less on cattle and increased their dietary intake of seafood (Arneborg et al., 2002). While seal, walrus, caribou, and wild birds had always been part of the Norse Greenlanders' diet, McGovern (2000) suggests that their inability to develop Inuit-style harpooning technology may have prevented them from hunting seals in winter, at times when other food resources were especially scarce. However, archeological remains do not show evidence for sudden disease, starvation, or warfare (although one medieval record blames the demise of the Western Settlement in the 1,360s on the "skraelings" [a derogatory term for native people]).

Trade with Norway and Iceland declined over time, as increased sea ice and storminess in the fourteenth century made ocean voyages riskier, with a greater likelihood of ships lost at sea. Although largely self-sufficient, the Norse Greenland economy would have declined as exports of luxury goods, such as walrus ivory and fur, and imports of metal tools and other non-locally produced goods would have ceased. Climatic cooling was undeniably an important factor in the decline of the Viking settlements in Greenland, yet a full explanation for their disappearance remains enigmatic. The Western Settlement was abandoned by ~1,360, followed by the Eastern Settlement ~1,450. It is still uncertain whether the last inhabitants emigrated to Iceland or died in Greenland.

Western hemisphere

The collapse of the Classic Maya civilization c. AD 750–950 is another example where the fall has been attributed to lengthy drought. Paleoclimate records inferred from lake sediments in central Yucatan, Mexico point to periods of peak aridity centered around AD 800 and AD 1,020 (Hodell et al., 1995, 2001). High-resolution geochemical data from a marine core in the Cariaco Basin off northern Venezuela provide additional evidence of regional drought (Haug et al., 2003). Bulk titanium content has been used as a proxy for terrigenous sediment flux into the Cariaco Basin during the regional rainy season (summer-fall), when the Intertropical Convergence Zone (ITCZ) is at its northernmost position in the southern Caribbean, including Central America and southern Mexico. The higher the rainfall, the greater the deposition of Ti-bearing terrigenous sediments, and vice-versa (i.e., low rainfall = low Ti content). Variations in titanium concentrations parallel periods of late Holocene climate change. For example, Ti levels were low ~200–500 yBP, corresponding to the Little Ice Age, but higher between 1,070 and 850 yBP during the Medieval Warm Period. Other dry periods lasted from 1,750 to 1,650 years ago and again between 1,300 and 1,100 years ago (Haug et al., 2003). This latter period was marked by several severe multi-year droughts, during which time many densely populated Mayan cities were completely abandoned, leading to the end of the Classic Maya civilization. Haug et al. (2003) suggest that the Maya population had expanded rapidly in preceding, wetter years until reaching the carrying capacity of the land, which left the society vulnerable to extreme climate events. For example, soil erosion and nutrient depletion, resulting from deforestation and land clearance, (Roberts, 1998) may have contributed to crop declines. However, the dry conditions affecting the Yucatan Peninsula may have been regional in scope, possibly extending into western South America (see below).

The Tiwanaku civilization on the Bolivian-Peruvian altiplano surrounding Lake Titicaca emerged around 400 BC and lasted until ~AD 1,100, when Tiwanaku was abandoned. Sediment cores from the Rio Catari Basin near Lake Titicaca and Quelccaya (Peru) ice core data reveal a long history of regional climate variation (Binford et al., 1997). The onset of agriculture and complex societies began during a more humid phase starting around 1,500 BC. Several dry episodes occurred subsequently, although lake levels remained relatively high for several centuries prior to the abandonment of Tiwanaku and dropped abruptly at AD 1,100. Snow accumulation in the Quelccaya ice core decreased, starting around AD 950, which was roughly contemporaneous with the Classic Mayan drought. Dust levels in the Quelccaya ice core peaked slightly earlier, at around AD 900. While there had been several earlier dry periods, the

impacts of the AD 1,100 drought were probably greater, since the population had become dependent on raised-field agriculture that required an abundant supply of water. On the other hand, major ENSO-related flood events at AD 690 and AD 1,300 on the Rio Moquegua, southwest of Lake Titicaca in southern Peru, did not lead to valley abandonment (Magilligan and Goldstein, 2001). However, evidence for severe drought at AD ~1,100 is absent from the river records. While negative consequences of prolonged drought cannot be ruled out, Magilligan and Goldstein believe instead that non-climatic factors, such as social instability, were the main drivers of the Tiwanaku collapse.

The Mochica civilization, noted for its exquisite pottery, refined metallurgy, and monumental architecture, developed along the northern coastline of Peru, between AD 300 and 500. Moche, the capital, and nearby coastal cities, were abruptly abandoned around AD 600, and resettlement took place farther inland at the foothills of the Andes, where river runoff was more reliable, between AD 600 and 750 (deMenocal, 2001). Agricultural fields and irrigation systems were overlain by desert dunes at the time of the abandonment. The Quelccaya ice core shows low ice accumulation rates and increased eolian dust in the period from AD 563 to 594. Other population shifts between coastal and highland cultures in Peru and Ecuador have also been associated with climate change. Much earlier, the start of temple construction along the Peruvian coast after 5,800 yBP coincided with the onset of El Niño events, following a period of low activity. However, regional abandonment of major temples after 3.2–2.8 yBP correlates with an increase in El Niño frequency (Sandweiss et al., 2001; *Paleo-El Niño-Southern Oscillation (ENSO) records*).

Climate reconstructions based on long-term tree-ring chronologies show that the American Southwest has experienced a number of extensive droughts (Cook et al., 2004; Benson et al., 2006a, b). A 400-year long dry spell persisted between AD 900 to 1,300, during which period particularly severe drought episodes were centered in AD 1,034, ~1,090, 1,150, 1,253, and 1,280. A number of independent proxies of long-term aridity changes from surrounding states bolster the tree-ring records. The 1,150 and 1,280 droughts affected much of the western U.S. (Benson et al., 2006a, b). The decline and abandonment of Chaco Canyon, Anasazi settlements in northern New Mexico, between AD 1,130 and 1,180, may have been related to the 1,150s drought. The abandonment of Mesa Verde, Colorado may have been spurred by the late thirteenth century droughts. In a marginal environment such as the Four Corners area of the U.S. Southwest, even the sophisticated water catchment systems developed by the Anasazi would have been insufficient to cope with minor precipitation shortfalls or changes in seasonal rainfall patterns. Skeptics argue that other causes, such as social disintegration, incursion by hostile tribes, deforestation, or disease may have contributed to the population decline. A major volcanic eruption in AD 1,258, the largest during the Holocene in terms of aerosol loading, may have caused temporary global cooling and a shortened growing season, perhaps reinforcing the effects of the drought (see *Volcanic eruptions and climate change*). Cook et al. (2004) speculate that higher temperatures, coinciding with the Medieval Warm Period, may have contributed to the more frequent and persistent droughts. Benson et al. (2006a, b) find that the 1,150 and 1,280 droughts appear to have been associated with minima in the Pacific Decadal Oscillation and a positive phase of the Atlantic Multidecadal Oscillation (see *Teleconnections*, Encyclopedia of World Climatology).

The cases outlined above illustrate examples of apparent correlations between episodes of abrupt cultural change and

documented climate fluctuations. While cultural and climatic events may closely match in time, this in itself does not prove causality. Minor climatic perturbations could have provided the last straw to societies already stressed to the brink by socio-economic and political instability, or environmental degradation. A careful analysis of archeological and paleoclimatological records, along with written documents wherever feasible, is necessary to determine the actual causes of major cultural transitions.

Vivien Gornitz

Bibliography

- Aksu, A.E., Mudie, P.J., Rochon, A., Kaminski, M.A., Abrajano, T., and Yasar, D., 2002. Persistent Holocene outflow from the Black Sea to the eastern Mediterranean contradicts Noah's Flood hypothesis. *GSA Today*, **12**, 4–10.
- Arneborg, J., Heinemeier, J., Lynnerup, N., Nielsen, H.L., Rud, N., and Sveinbjörnsdóttir, A.E., 2002. C-14 dating and the disappearance of Norsemen from Greenland. *Europhys. News*, **33**(3): 8pp.
- Ballard, R.D., Coleman, D.F., and Rosenberg, G.D., 2000. Further evidence of abrupt Holocene drowning of the Black Sea shelf. *Mar. Geol.*, **170**, 253–261.
- Benson, L.V., Berry, M.S., Jolie, E.A., Spangler, J.D., Stahle, D.W., and Hattori, E.M., 2006a. Possible impacts of early-11th, middle-12th-, and late-13th-century droughts on western Native Americans and the Mississippian Cahokians. *Quaternary Sci. Rev.* doi:10.1016/j.quascirev.2006.08.001.
- Benson, L., Peterson, K., and Stein, J., 2006b. Anasazi (pre-Columbian Native-American) migrations during the middle-12th and late-13th centuries—were they drought induced? *Climatic Change*. doi:10.1007/s10584-006-9065-y.
- Binford, M.W., Kolata, A.L., Brenner, M., Janusek, J.W., Seddon, M.T., Abbott, M., and Curtis, J.H., 1997. Climate variation and the rise and fall of an Andean civilization. *Quaternary Res.*, **47**, 235–248.
- Bookman, R., Enzel, Y., Agnon, A., and Stein, M., 2004. Late Holocene lake levels of the Dead Sea. *GSA Bull.*, **116**, 555–571.
- Cook, E.R., Woodhouse, C.A., Eakin, C.M., Meko, D.M., and Stahle, D.W., 2004. Long-term aridity changes in the western United States. *Science*, **306**, 1015–1018.
- Cullen, H.M., deMenocal, P.B., Hemming, S., Hemming, G., Brown, F.H., Guilderson, T., and Sirocko, F., 2000. Climate change and the collapse of the Akkadian empire: Evidence from the deep sea. *Geology*, **28**, 379–383.
- deMenocal, P.B., 2001. Cultural responses to climate change during the late Holocene. *Science*, **292**, 667–673.
- Drysdale, R., Zanchetta, G., Hellstrom, J., Maas, R., Fallick, A., Pickett, M., Cartwright, I., and Piccini, L., 2006. Late Holocene drought responsible for the collapse of Old World civilizations is recorded in an Italian cave flowstone. *Geology*, **34**, 101–104.
- Enzel, Y., Bookman, R., Sharon, D., Gvirtzman, H., Dayan, U., Ziv, B., and Stein, M., 2003. Late Holocene climates of the Near East deduced from Dead Sea level variations and modern regional winter rainfall. *Quaternary Res.*, **60**, 263–273.
- Fagan, B., 1999. *Floods, Famines, and Emperors; El Niño and the Fate of Civilizations*. New York, NY: Basic Books, 284pp.
- Fagan, B., 2004. *The Long Summer: How Climate Changed Civilization*. New York, NY: Basic Book, 284pp.
- Georgievski, G., and Stanev, E.V., 2006. Paleo-evolution of the Black Sea watershed: Sea level and water transport through the Bosphorus Straits as an indicator of the Lateglacial-Holocene transition. *Climate Dyn.*, **26**, 631–644.
- Gill, R.B., 2000. *The Great Maya Droughts: Water, Life, and Death*. Albuquerque: University of New Mexico Press, 464pp.
- Haug, G.H., Günther, D., Peterson, L.C., Sigman, D.M., Hughen, K.A., and Aeschlimann, B., 2003. Climate and the collapse of Maya civilization. *Science*, **299**, 1731–1735.
- Hodell, D.A., Curtis, J.H., and Brenner, M., 1995. Possible role of climate in the collapse of Classic Maya civilization. *Nature*, **375**, 391–394.
- Hodell, D.A., Brenner, M., Curtis, J.H., and Guilderson, T., 2001. Solar forcing of drought frequency in the Maya lowlands. *Science*, **292**, 1367–1370.

- Kirch, P.V., 2005. Archeology and global change: the Holocene record. *Annu. Rev. Environ. Resour.*, **30**, 409–440.
- Kuper, R., and Kröpelin, S., 2006. Climate-controlled Holocene occupation in the Sahara: Motor of Africa's evolution. *Science*, **313**, 803–807.
- Ladurie, Le Roy E., 1971. *Times of Feast, Times of Famine: A History of Climate Since the Year 1000*. Garden City, NY: Doubleday.
- Lamb, H.H., 1977. *Climate: Present, Past and Future*, vol. 2. Methuen, London.
- Lamb, L.H., 1995. *Climate, History, and the Modern World*, 2nd ed. Routledge, London
- Magilligan, F.J., and Goldstein, P.S., 2001. El Niño floods and culture change: A late Holocene flood history for the Rio Moquegua, southern Peru. *Geology*, **29**, 431–434.
- McGovern, T.H., 2000. The demise of Norse Greenland. In Fitzhugh, W.W., and Ward, E.I. (eds.), *Vikings: The North Atlantic Saga*. Washington, D.C.: Smithsonian Institution Press and National Museum of Natural History, pp. 327–339.
- Migowski, C., Stein, M., Prasad, S., Negendank, J.F.W., and Agnon, A., 2006. Holocene climate variability and cultural evolution in the Near East from the Dead Sea sedimentary record. *Quaternary Res.*, **66**, 421–431.
- Morrison, K.D., 2006. Failure and how to avoid it. *Nature*, **440**, 752–754.
- Ogilvie, A.E.J., Barlow, L.K., and Jennings, A.E., 2000. North Atlantic climate c. AD 1000: Millennial reflections on the Viking discoveries of Iceland, Greenland and North America. *Weather*, **55**, 34–45.
- Roberts, N., 1998. *The Holocene, an Environmental History*, 2nd ed. Malden, MA, Oxford, UK: Blackwell, 316pp.
- Ryan, W.B.F., and Pitman III, W.C., 1999. *Noah's Flood: The New Scientific Discoveries About the Event that Changed History*. New York: Simon & Schuster, 319pp.
- Ryan, W.B.F., Pitman III, W.C., Major, C.O., Shimkus, K., Maskalenko, V., Jones, G.A., Dimitrov, P., Görür, N., Sakinc, M., and Yüce, H., 1997. An abrupt drowning of the Black Sea shelf. *Mar. Geol.*, **138**, 119–126.
- Sandweiss, D.H., Maasch, K.A., and Anderson, D.G., 1999. Transitions in the mid-Holocene. *Science*, **283**, 499–500.
- Sandweiss, D.H., Maasch, K.A., Burger, R.L., Richardson, J.B., Rollins, H.B., and Clement, A., 2001. Variation in Holocene El Niño frequencies: Climate records and cultural consequences in ancient Peru. *Geology*, **29**, 603–606.
- Staubwasser, M., and Weiss, H., 2006. Holocene climate and cultural evolution in late-prehistoric–early historic West Asia. *Quaternary Res.*, **66**, 372–387.
- Staubwasser, M., Sirocko, F., Grootes, P.M., and Segl, M., 2003. Climate change at the 4.2 ka BP termination of the Indus valley civilization and Holocene south Asian monsoon variability. *Geophys. Res. Lett.*, **30**(8): 1425. doi:10.1029/2002GL016822.
- Tainter, J.A., 2000. Chap. 12: Global Change, History, and Sustainability. In McKintosh, R.J., Tainter, J.A., and McIntosh, S.K. (eds.), *The Way the Wind Blows: Climate, History, and Human Action*. New York: Columbia University Press.
- Weiss, H., and Bradley, R.S., 2001. What drives societal collapse? *Science*, **291**, 609–610.
- Weiss, H., Courty, M.-A., Wetterstrom, W., Guichard, F., Senior, L., Meadow, R., and Curnow, A., 1993. The genesis and collapse of third millennium North Mesopotamian civilization. *Science*, **261**, 995–1004.
- Wigley, T.M.L., Ingram, M.J., and Farmer, G., 1981. *Climate and History: Studies in Past Climates and their Impact on Man*. Cambridge, UK: Cambridge University Press.

Cross-references

[Dendroclimatology](#)
[Holocene Climates](#)
[Hypsithermal](#)
[Ice Cores, Mountain Glaciers](#)
[Lake Level Fluctuations](#)
[Little Ice Age](#)
[Medieval Warm Period](#)
[Paleo-El Niño-Southern Oscillation \(ENSO\) Records](#)
[Teleconnections, in Encyclopedia of World Climatology](#)
[The 8,200 ybp Event](#)
[Volcanic Eruptions and Climate Change](#)

ANIMAL PROXIES – INVERTEBRATES

Invertebrates are the most common constituents of the metazoan fossil record, and since they are abundant in Phanerozoic marine sedimentary rocks worldwide, they are of great utility in reconstructing ancient climates and environments. Here, we review two aspects of this record. First, we discuss the utility of invertebrate marine fossil assemblages in interpreting ancient climates and environments, and second, we explore the ways in which shell chemistry may be used to further address these issues.

Interpreting ancient climates

In modern environments, marine diversity is greatest at equatorial latitudes, and declines towards higher latitudes. In general, data from the fossil record is in accord with this observation, showing a similar pattern throughout the Phanerozoic (Hallam, 1994; Parrish, 1998). Although the primary factor governing this pattern is a subject of some debate, many environmental factors other than temperature are clearly important. These include availability of nutrients, decreased environmental stability at high latitudes (increasing seasonality with latitude) (Sanders, 1968), dominance of r-selected trophic generalists in resource-limited high latitude regions as opposed to high niche partitioning observed in resource-rich low latitude regions, possibly resulting from the effects of seasonality (Valentine, 1973), and variation in light incidence across latitudinal gradients (Ziegler et al., 1984). Additionally hypersalinity in restricted environments and brackish water (hyposalinity) in estuarine or deltaic environments significantly limit diversity of marine organisms (Heckel, 1972).

Two types of approaches have been used in understanding the relationship of fossil assemblages to ancient climates. The first utilizes the distributions of extant species and/or genera, and interprets the paleoclimatological settings of fossil assemblages that contain some of the same taxa. This approach carries the underlying assumption that organisms maintain a consistent climate range throughout their history. This approach is limited in temporal scope, but has been successfully applied to Tertiary and Quaternary deposits. The second approach incorporates paleogeographic data (typically paleomagnetic data, which provides an estimate of paleolatitude) in faunal assemblage analysis, permitting examination of ancient climate zones and latitudinal diversity patterns. Examples of each type of approach are discussed below.

One of the most influential examples of the first approach is Addicott's (1969) classic analysis of shallow water Tertiary molluscan faunas of the northeastern Pacific. In this study, Addicott used water temperature affinities of extant bivalves and gastropods along the western coast of Mexico and the United States to erect a latitudinal zonation of tropical (Panamic), subtropical (Surian), and warm-temperate (Californian) molluscan provinces. Through analysis of the distributions of selected warm-water genera across the Tertiary fossil record of this region, Addicott demonstrated a southerly retreat of warm-water genera from the Oligocene to Pleistocene, indicating an overall cooling trend across the Tertiary. The data, however, showed a pronounced northward migration of warm water taxa during the Miocene, indicating that tropical water conditions extended as far north as Washington, and revealing a striking Miocene warming event. Following this warming

event, a gradual southerly migration of warm water taxa from the Late Miocene through the Pleistocene was observed, indicating a re-establishment of the cooling trend following this thermal maximum.

This type of approach may also be used at a finer scale to identify either localized or shorter-term fluctuations in climate or ocean temperature, or shifts in paleoceanographic conditions. Roy et al. (1996) reviewed the response of the Pleistocene molluscan fauna of the eastern Pacific to recently discovered millennial-scale climate perturbations. Since species response to climate change is individualistic, high-amplitude climatic variations were found to produce short-lived, novel associations of species, unlike modern assemblages. Some such associations were interpreted as the result of time averaging in the fossil record, as the temporal scale of climate change closely approaches the limit of stratigraphic resolution; however, some novel assemblages clearly represent community associations resulting from rapid climate change. Nakashima (2002) analyzed the spatio-temporal distribution of the Miocene–Pliocene bivalve *Fortipecten* in the northwestern Pacific to identify a potential short term and/or localized cooling event in the Mid-Pliocene. Gladenkov et al. (2002) timed the opening of the Bering Strait at 5.32 Ma using the incursion of a North Atlantic molluscan fauna into the Northern Pacific. The increasing use of these types of localized studies will certainly yield an enhanced integrated perspective of Cenozoic climate change and the response of marine communities.

Studies of ancient paleoclimates using fossil assemblages are generally hindered by the paucity of extant genera in the fossil record. Additionally, many unique paleoclimatological problems are posed by past conditions such as the ice-free greenhouse world of the Cretaceous, or the existence of a single super-continent throughout much of the Mesozoic. Due to the lack of available comparisons with living taxa, interpretations of ancient climates typically rely much more on incontrovertible climate indicators, such as reef faunas, which occur under exclusively tropical conditions, or faunas associated with glacial deposits. Importantly, independent estimates of paleolatitude (from paleomagnetic data) are available for many ages and localities, facilitating study of latitudinal trends in biodiversity for ancient assemblages.

Brachiopods are a particularly useful group for Paleozoic strata, as they were abundant members of most marine communities across this era, and exhibit a relatively high degree of provincialism. In general, times of global cooling result in high latitudinal temperature gradients and are marked by the presence of several distinguishable latitudinal assemblages. In contrast, warmer eras exhibit a lower pole-equator temperature gradient, and, in the Paleozoic, tend to be characterized by cosmopolitan brachiopod faunas at low and mid latitudes, which are distinct from low-diversity, high latitude faunas (Harper and Sandy, 2001). For example, during the cool climate of the late Ordovician, at least three latitudinally controlled brachiopod assemblages are recognized, whereas only two are present in the warmer Silurian. A low-diversity (at times monospecific) brachiopod fauna, dominated by the genus *Clarkeia*, characterized high-latitude nearshore marine assemblages of the Silurian, while a higher-diversity cosmopolitan fauna existed at low and mid latitudes (Cocks and Fortey, 1990). Later in the Paleozoic, during the Carboniferous, northward shifts of northern range boundaries of many brachiopod genera in the late Viséan stage has been interpreted to represent warming at high latitudes. In the subsequent early Namurian stage,

a southward shift in northern range boundary of many genera is coincident with a northward shift of many southern range boundaries. Together, these trends were interpreted as indicative of high latitude cooling accompanied by equatorial warming (Raymond et al., 1989; Kelley et al., 1990).

The end of the Paleozoic Era is punctuated by the end-Permian mass extinction and the coincident shift in dominance of marine invertebrate assemblages from brachiopods to mollusks. Thus, bivalves and gastropods are of greatest use to biogeographic/paleoclimatologic studies in the Mesozoic and Cenozoic. In general, bivalve thickness and size is inversely correlated with latitude, as is ornamentation of gastropod shells (Vermeij, 1978). Additionally, bivalves (primarily rudistids, but also lithiotids), were the primary framework builders of Mesozoic reefs, which were confined to tropical seas and are thus of utility as paleoclimate indicators.

Fossil assemblages as paleoenvironmental indicators

While global-scale fossil assemblage data are needed to interpret paleoclimates or latitudinal gradients, on a local or regional scale, these assemblages provide excellent indicators of paleoenvironmental conditions, including attributes of paleobathymetry and paleo-oxygen levels. For a given latitude, the distribution of marine organisms from nearshore habitats to basinal ones is controlled largely by physical factors, such as current energy, substrate type and consistency, light and/or nutrient availability, etc. Thus, faunal assemblages show strong associations with sedimentary regimes, facilitating the recognition of biofacies (consistent associations of fossil assemblages and physical sedimentological properties).

In lower Paleozoic strata, trilobite assemblages are abundant and show a pronounced onshore-offshore gradient. Fortey (1975) demonstrated that, during part of the Ordovician period, each part of the shelf environment was dominated by different taxonomic groups of trilobites: inner shelf assemblages were dominated by ilaenids and cheirurids, the middle shelf by nileids, and the outer shelf by olenids. Fortey also noted that outer shelf trilobites tended to be cosmopolitan in distribution, while inner shelf trilobites showed a high degree of endemism. An implication of both of these studies is that open water forms were able to cross some ocean basins, while shallow water forms were not. Cook and Taylor (1975) found that Cambro-Ordovician trilobite assemblages the western United States and southern China shared deep-water trilobite faunas, but contained unique shelfal faunas. Through comparison with modern arthropod distributions, these authors concluded that a pronounced thermocline prevented migration of shelfal faunas, whereas deep-water trilobites lived in sub-thermocline habitats and were thus able to migrate. Biofacies models have been utilized throughout the Phanerozoic (e.g., Patzkowsky, 1995: Ordovician brachiopods; Webber, 2002: Ordovician whole-faunas; Johnson, 1974: Devonian brachiopods; Harper and Jeffrey, 1996: Carboniferous brachiopods; Sandy, 1995: Triassic–Jurassic brachiopods; Sageman and Bina, 1997: Cretaceous whole-faunas).

The marine trace-fossil record, overwhelmingly the product of invertebrate bioturbation, is of great utility in interpreting ancient benthic oxygen levels. An oxygen-deficient marine biofacies model, developed through actualistic study in modern environments, correlates trace fossils and depth and extent of bioturbation to the amount of dissolved oxygen present in bottom waters (Savrda et al., 1984). This model can be used to

infer relative degree of bottom water oxygenation in marine strata across much of the Phanerozoic. Using this model, Savrda and Bottjer (1987) identified a new marine biofacies, termed the exaerobic zone, which occurs at the boundary between anoxic and dysoxic bottom waters. In the rock record, exaerobic environments are characterized by high-density occurrences of a single species through narrow stratigraphic intervals, at the transition from unbioturbated to weakly bioturbated strata. Exaerobic taxa include some species of brachiopods and some “flat-clam”-type bivalves which apparently derived energy from sulfur-oxidizing chemolithoautotrophic bacteria, instead of from a phototrophic-based food web (Savrda and Bottjer, 1987). Trophic decoupling of whole ecosystems from photosynthetic primary productivity occurs also at hydrothermal vents and hydrocarbon seeps: vent and seep assemblages are also recognizable in the fossil record.

Shell chemistry as a proxy for paleoclimate

Whereas species presence/absence, assemblage content, diversity and distribution may be used to address the types of paleoclimatological questions outlined above, specific chemical signals contained within the shells or skeletons of invertebrates can provide highly sensitive proxies for paleotemperature and related climatic or environmental parameters. Of primary use to geochemical studies are mollusks, brachiopods and corals, all of which secrete calcareous skeletons and, importantly, possess a diagnostic original microstructure. As carbonate minerals are easily altered or recrystallized during post-burial diagenesis, care must be taken to sample only specimens which retain the original microstructure in order to assure that the geochemical signals attained are representative of the organism’s living environment, and not the diagenetic environment.

Stable isotope ratios of oxygen ($\delta^{18}\text{O}$ – $^{18}\text{O}/^{16}\text{O}$) and, to a lesser extent, carbon ($\delta^{13}\text{C}$ – $^{13}\text{C}/^{12}\text{C}$) from invertebrate shells and skeletons have proven particularly valuable for paleoclimate reconstructions. In general, cool waters are enriched in ^{18}O and warm waters are relatively depleted. For any given time in the past, however, the average $\delta^{18}\text{O}$ value of the ocean reservoir is determined primarily by planetary ice volume, as light isotopes are preferentially removed from the ocean by evaporation and stored in ice, leaving the ocean reservoir isotopically heavy. The carbon cycle is driven by biologic productivity; organisms selectively take up the light isotope, leaving productive surface waters isotopically heavy, and bottom waters isotopically light with respect to $\delta^{13}\text{C}$. Both carbon and oxygen in seawater are incorporated into the carbonate shells and skeletons of marine animals. Brachiopods and mollusks secrete their shells in isotopic equilibrium with seawater, but corals typically do not (Hudson and Anderson, 1989). While brachiopods secrete stable calcite shells, most mollusks secrete shells composed of aragonite, which is geologically less stable, and tends to re-crystallize to calcite, thereby acquiring the isotopic signal of the diagenetic environment. Therefore isotopic studies of mollusks, by far the most common carbonate-secreting members of fossil marine assemblages since the Mesozoic, must focus on rare original aragonitic shell material which has survived, or on mollusks which secrete an originally calcitic shell or portion of the shell, such as oysters, rudist and inoceramid bivalves, or belemnites (Hudson and Anderson, 1989).

Isotopic studies using marine invertebrates have focused on two primary goals. One objective has been to understand global trends in $\delta^{18}\text{O}$ and/or $\delta^{13}\text{C}$ of the marine reservoir as a whole

through a specific time interval of interest, in order to interpret climate, global ice volume and glacial history or changes in primary productivity, particularly those associated with biotic radiations or crises. The second approach involves more localized, fine scale isotopic study of marine assemblages in order to interpret local or regional paleoclimate or paleoceanographic conditions.

Hudson and Anderson (1989) compiled a data set of Paleozoic $\delta^{18}\text{O}$ values from brachiopods, marine cements, and other fossil organisms to interpret large-scale climate trends across that era, using $\delta^{18}\text{O}$ as a proxy for sea temperature. These authors found an overall decline in sea temperature across the Paleozoic, punctuated by significant highs in the Middle Ordovician and Late Devonian-Early Carboniferous, and lows in the Late Ordovician and Middle Carboniferous.

Lowenstam (1964) assessed latitudinal paleotemperature gradients for multiple stages of the Cretaceous period. Lowenstam collected $\delta^{18}\text{O}$ data from mollusks from multiple paleolatitudes across several discrete intervals of Cretaceous time, which, when plotted for each period, show greatest high-low latitude temperature gradients in the Maestrichtian and Albian stages, and also indicate that significantly greater temperature gradients existed in all stages of the Cretaceous than in the recent. The results of this study, conducted nearly four decades ago, are still significant today (Parrish, 1998).

At a more localized scale, stable isotope studies have revealed new insights into paleoceanographic conditions. By extracting $\delta^{18}\text{O}$ and $\delta^{13}\text{C}$ signals from mollusks of the Jurassic Oxford Clay (United Kingdom), Anderson et al. (1994) were able to assess temperature gradients and degree of mixing within the water column. These authors used animals which inhabited different parts of the water column including benthic bivalves and nektonic cephalopods, and found a pronounced $\delta^{18}\text{O}$ gradient, indicating a significant ($\sim 5^\circ\text{C}$) difference between bottom water temperature (cooler) and upper water column temperature (warmer). The authors found no significant differences in $\delta^{13}\text{C}$ composition among the groups studied, however, a finding that they interpreted to indicate a well-mixed water column. Allmon et al. (1996) used isotopic evidence to support the interpretation that upwelling conditions occurred on the west coast of Florida during the Pliocene. Using microsampling techniques, Allmon et al. (1996) captured seasonal variations in isotopic composition across individual bivalve and gastropod shells, and interpreted this signal as the result of seasonally strengthened upwelling, which would have brought nutrient-rich (low $\delta^{13}\text{C}$) cool waters (high $\delta^{18}\text{O}$) to the shallow shelf. The ready availability of mass spectrometers (used to conduct isotopic analysis) and the development of new techniques requiring ever-smaller quantities of sample will continue to stimulate higher-resolution isotopic investigations in the future.

Robert R. Gaines and Mary L. Droser

Bibliography

- Addicott, W.O., 1969. Tertiary climatic change in the marginal northeastern Pacific Ocean. *Science*, **165**, 583–586.
- Allmon, W.D., Emslie, S.D., Jones, D.S., and Morgan, G.S., 1996. Late Neogene oceanographic change along Florida’s west coast: evidence and mechanisms. *J Geol*, **104**, 143–162.
- Anderson, T.F., Popp, B.N., Williams, A.C., Ho, L.-Z., and Hudson, J.D., 1994. The stable isotopic record of fossils from the Peterborough Member, Oxford Clay Formation (Jurassic), UK: paleoenvironmental implications. *J Geol Soc Lond*, **151**, 125–138.

- Cocks, L.R.M., and Fortey, R.A., 1990. Biogeography of Ordovician and Silurian faunas. In McKerrow, W.S., and Scotese, C.R. (eds.), *Palaeo-zoic Palaeogeography and Biogeography*. Geological Society of London Memoir 12, pp. 97–104.
- Cook, H.E., and Taylor, M.E., 1975. Early Paleozoic continental margin sedimentation, trilobite biofacies, and the thermocline, western United States. *Geology*, **3**, 559–562.
- Fortey, R.A., 1975. Early Ordovician trilobite communities. *Fossils Strata*, **4**, 339–360.
- Gladenkov, A.Y., Oleinik, A.E., Marincovich, L. Jr., and Barinov, K.B., 2002. A refined age for the earliest opening of Bering Strait. *Palaeo-geography, Palaeoclimatology, Palaeoecology*, **183**, 321–328.
- Hallam, A., 1994. An outline of Phanerozoic biogeography, *Oxford Biogeography Series*, **10**.
- Harper, D.A.T., and Jeffrey, A.L., 1996. Mid-Dinantian brachiopod Biofacies from western Ireland. In Strogon, P., Somerville, I.D., and Jones, G.L. (eds.), *Recent advances in Lower Carboniferous geology*. vol. 107, London: Geological Society Special Publication, pp. 427–436.
- Harper, D.A.T., and Sandy, M.R., 2001. Paleozoic brachiopod biogeography. *Paleontol Soc. (Special Paper)*, **7**, 207–222.
- Heckel, P.H., 1972. Recognition of ancient shallow marine environments. *SEPM, (Special Publication)*, **16**, 226–286.
- Hudson, J.D., and Anderson, T.F., 1989. Ocean temperatures and isotopic compositions through time. *Trans R Soc Edinb*, **80**, 183–192.
- Johnson, J.G., 1974. Early Devonian brachiopod biofacies of western and Arctic North America. *J Paleontol*, **48**, 809–819.
- Kelley, P.H., Raymond, A., and Lutken, C.B., 1990. Carboniferous brachiopod migration and latitudinal diversity: a new paleoclimatic method. In McKerrow, W.S., and Scotese, C.R. (eds.), *Palaeo-zoic Palaeogeography and Biogeography*. Geological Society of London Memoir 12, pp. 325–332.
- Lowenstam, H.A., 1964. Palaeotemperatures of the Permian and Cretaceous periods. In Nairn, A.E.M. (ed.), *Problems in Paleoclimatology*. London: Wiley, pp. 227–248.
- Nakashima, R., 2002. Geographic distribution of the late Cenozoic bivalve *Fortipecten* in the northwestern Pacific. *Palaeoogeogr; Palaeoclimatol, Palaeoecol*, **186**, 261–274.
- Parrish, J.T., 1998. *Interpreting Pre-Quaternary Climate from the Geologic Record*. New York: Columbia University Press.
- Patzkowsky, M.E., 1995. Gradient analysis of Middle Ordovician brachiopod biofacies; biostratigraphic, biogeographic, and macroevolutionary implications. *Palaios*, **10**, 154–179.
- Raymond, A., Kelley, P.H., and Lutken, C.B., 1989. Polar glaciers and life at the equator: the history of Dinantian and Namurian (Carboniferous) climate. *Geology*, **17**, 408–411.
- Roy, K., Valentine, J.W., Jablonski, D., and Kidwell, S.M., 1996. Scales of climatic variability and time averaging in Pleistocene biotas: implications for ecology and evolution. *Trends Ecol Evol*, **11**, 458–463.
- Sageman, B.B., and Bina, C., 1997. Diversity and species abundance patterns in Late Cenomanian black shale Biofacies: Western Interior. *U.S. Palaios*, **12**, 449–466.
- Sanders, H.L., 1968. Marine benthic diversity: a comparative study. *Am Nat*, **102**, 243–282.
- Sandy, M.R., 1995. Early Mesozoic (Late Triassic–Upper Jurassic) Tethyan brachiopod Biofacies; possible evolution intra-phylum niche replacement within the Brachiopoda. *Paleobiology*, **21**, 479–495.
- Savrdra, C.E., and Bottjer, D.J., 1987. The exaerobic zone, a new oxygen-deficient marine Biofacies. *Nature*, **327**, 54–56.
- Savrdra, C.E., Bottjer, D.J., and Gorsline, D.S., 1984. Development of a comprehensive oxygen-deficient marine biofacies model: evidence from Santa Monica, San Pedro, and Santa Barbara Basins, California continental borderland. *AAPG Bull*, **68**, 1179–1192.
- Valentine, J.W., 1973. *Evolutionary Paleocology of the Marine Biosphere*. New Jersey: Prentice Hall.
- Vermeij, G.J., 1978. *Biogeography and Adaptation*. Cambridge, MA: Harvard University Press.
- Webber, A.J., 2002. Use of high-resolution faunal gradient analysis to assess the causes of meter-scale cyclicity in the type Cincinnati Series (Upper Ordovician). *Palaios*, **17**, 545–555.
- Ziegler, A.M., Hulver, M.L., Lottes, A.L., and Schmachtenberg, W.F., 1984. Uniformitarianism and paleoclimates: inferences from the distribution of carbonate rocks. In Brenchley, P.J. (ed.), *Fossils and Climate*. Chichester: Wiley, pp. 3–25.

Cross-references

Carbon Isotopes, Stable
 Coral and Coral Reefs
 Evolution and Climate Change
 Nearest-Living-Relative Method
 Oxygen Isotopes

ANIMAL PROXIES, VERTEBRATES

Nearest living relative

The most obvious way to make inferences about the paleoenvironment and paleoclimate using vertebrate fossils is to note the modern environments and climate associated with their nearest living relatives. The presence in the fossil record of one or a few specimens of a single genus or species has been used in this way. Based on such evidence, Vucetich and Verzi (2002) asserted that during the Pleistocene there were warm pulses that enabled tropical forms now known only from Brazil to extend their ranges more than 1,200 km south to the area of Buenos Aires.

Instead of considering only one taxon, it is a more common practice to compare the paleoenvironmental and paleoclimatic preferences for the nearest living relatives of all taxa represented in a fossil assemblage. Using this method with modern small mammals, Antoñanzas and Bescós (2002) inferred that during the Early to Middle Pleistocene at Atapuerca, Burgos, Spain there were several cycles of fluctuation between glacial conditions when the environment was steppe-like and interglacials, which were warmer. During transitions between these conditions, the fauna of small mammals was more species-rich, having elements of both extremes. It is rarely, if ever, the case that an extensive faunal list from a fossil site, even a Late Quaternary one, is identical to a living mammalian community. These disharmonious associations where taxa are found together as fossils but exist in separate modern communities or *visa versa*, such as the United States Late Quaternary mammal faunas as compared with those of Late Holocene and modern faunas, are thought to have been caused by a change from a more patchy environment in the Late Quaternary to a more uniform one in the Holocene (FAUNMAP Working Group, 1996). Thus, experience has shown that it is unlikely that an exact modern analog to a fossil vertebrate assemblage will be found except in sediments deposited during the last 4,000 years.

An inverse correlation between the number of modern species of arvicolid rodents in a fauna and mean annual temperature was established empirically by Montuire et al. (1997). This was done by determining the number of species of these rodents in 253 modern faunas, each covering an area between 100 and 10,000 km², and noting the mean annual temperature for the area. The mean annual temperature range for any one particular species in a fauna was found to be about 12 °C. This relationship was then applied to two Late Pleistocene fossil assemblages, with one giving a result that seemed plausible to the authors and the second less satisfactory owing to uncertainty in the correlation between various sites regarded as part of the same fossil assemblage.

Use of the nearest living relative of fossil vertebrates for making paleoenvironmental and paleoclimatic inferences is not restricted to the late Cenozoic. A mean annual temperature of 14 °C for Axel Heiberg Island during the Late Cretaceous,

then, as now, in the High Arctic, was based on the presence of champsosaurs. The temperature estimate was inferred from the tolerances of their nearest living relatives and analogs (crocodilians and large lizards; Tarduno et al., 1998).

Taphonomy

Taphonomy is the study of the processes by which an organism becomes a fossil. It is particularly focused on attempts to reconstruct otherwise missing data about organisms and the ecosystem of which they were a part. In carrying out such studies, reconstruction of the paleoenvironment is a vital part of the process. In a taphonomic analysis of a Late Cretaceous accumulation of small vertebrates at Naskal in India, Khajuria and Prasad (1998) reconstructed the environment of deposition of the fossils as, "... a distal flood plain, which served as a natural death trap, on whose banks terrestrial and other animals might have gathered in search of food and water during a prolonged drought and perished subsequently due to the desiccation of the lake." This interpretation was based both on the nature of the fossils, particularly the corroded surface of many of the specimens, and a detailed geological analysis of the site.

Analysis of a fossil assemblage may provide environmental information about the area that surrounded the site where the specimens accumulated independently of any other evidence. However, sometimes the data may yield ambiguous or contradictory results. For example, Alberdi et al. (2001) analyzed three Plio-Pleistocene mammal assemblages from the Guadix-Baza Basin, Spain. On the basis of the geology, they inferred that the immediate environment where the fossils were found in each case was a lake margin. However, solely considering the composition of the different assemblages, they reconstructed the paleoenvironments surrounding these ancient lakes in two quite different ways. The presence of a great diversity of artiodactyls, particularly browsers, at one site was regarded as, "... indicative of wooded or bushy areas. . .," while nearby, "... a high diversity of sub-aquatic forms and a smaller variety of artiodactyls species. . .," was interpreted as indicative of, "... an open, sparsely forested environment susceptible to seasonal drought."

The distribution of fossil vertebrates within a deposit can provide paleoclimatic information. The complete excavation of the sediment accumulated in what during the Plio-Pleistocene was a lake about 1 ha in area, yielded approximately 40 skeletons of three species of kangaroos near Morwell, Victoria, Australia. The specimens were at different stratigraphic levels, indicating that the fossils accumulated over a significant period of time rather than as a consequence of a single catastrophic event. In similar lakes today when a kangaroo drowns, its body first sinks, then bloats and floats to the surface. Eventually the body cavity containing the gas ruptures and the body sinks permanently to the bottom of the lake. While on the surface, a corpse is most often found near the lee margin of the lake. In the Morwell Plio-Pleistocene lake deposit, most of the specimens occurred in the southeast part of the paleolake, indicating that the prevailing direction of the wind was then from the northwest (T. Rich, personal observation).

Functional analysis

Corroboration of paleoenvironmental and paleoclimatic hypotheses based on other evidence can be found in the functional interpretation of fossil vertebrates. *Leaellynasaura amicagraphica*, a small ornithischian dinosaur, has been hypothesized

to be active all year around in a frigid polar setting in what is now southeastern Australia (Constantine et al., 1998). This was based on two independent lines of evidence. Taken together, the consequences of the evidence are to be expected in an animal that lived in such a manner under those conditions. Enlarged optic lobes were visible on the dorsal surface of the brain, which suggested the animal had enhanced ability to see under the low light conditions of a polar winter (Rich and Rich, 1989). Histological cross-sections of the bone of this same animal showed that it lacked lines of arrested growth (LAGs), which would be expected if for any reason, such as hibernation, its level of metabolic activity had decreased markedly during its lifetime. However, another dinosaur, an ornithomimosaur from the same site as *L. amicagraphica*, had LAGs (Chinsamy et al., 1998).

Stable isotopes

Chemists studying modern animals have been able to relate stable isotope ratios of the same element to a number of environmental factors. The variation in isotopic ratios is due to the fact that physical and chemical processes proceed more slowly for molecules that weigh more. For example, the rate of evaporation for a molecule of water with an oxygen atom with two additional neutrons, ^{18}O , is less than that of a molecule of water with the more common oxygen isotope, ^{16}O . As the temperature of the water increases, the difference in the rate of evaporation increases, leaving liquid water with proportionately heavier water molecules left behind. An animal that ingests that liquid water at a particular temperature will form molecules of body tissue with a ratio of ^{18}O to ^{16}O reflecting that temperature. However, the ratio incorporated in the body of the animal will not be exactly the same as that of the water it ingested. This is because fractionation, or a further segregation, of the two oxygen isotopes takes place during metabolic processes that occur within the animal as it deposits oxygen in bone, dentine, or enamel, for example. The correlation between the two isotopes deposited in the animal's tissue and the temperature of the water ingested has to be established empirically. Other factors affecting the ratio of the two isotopes come into play as well, such as the humidity of the environment. Thus, it is not always straightforward even in the case of modern animals to determine "environmental proxies" from isotopic ratio studies.

Because of the success of isotopic ratio investigations in modern animals, applying similar techniques to fossil vertebrates in order to try to determine past climatic and environmental factors has been underway for the past few decades. A major point of contention in isotopic research is whether the fossil material retains the isotopic ratios of the once living organism or if there is significant post-mortem chemical alteration (Kohn and Cerling, 2002). While there is considerable doubt about how long the isotopic integrity of a fossil bone remains, there is less reason to question the chemical stability of enamel. This is in part because enamel is more dense, has lower organic content, forms larger crystals than is the case in bone or dentine, and when it is chemically altered from hydroxyapatite, it changes to fluorapatite, which can be detected. For these reasons, much of the recent stable isotope work on fossil vertebrates has focused on tooth enamel.

The area where isotopic techniques has been applied most successfully are investigations of the ratio of the carbon isotopes ^{13}C and ^{12}C . This ratio is different in C_3 and C_4 plants. C_3 plants are, "... most leafy, woody, and other soft plants

(browse) and cool growing season or aquatic grasses, whereas C_4 plants include most tropical and temperate grasses” (MacFadden et al., 1999). The difference in the ratios of ^{13}C to ^{12}C in these two categories of plants is related to the fact that they have different photosynthetic pathways. C_3 plants, which use the Calvin Cycle as their photosynthetic pathway, concentrate less ^{13}C relative to ^{12}C than is the case with C_4 plants, which use the Hatch-Slack photosynthetic pathway.

In mammalian herbivores, there is a consistent difference in the ^{13}C to ^{12}C ratio of the tooth enamel between those that primarily feed on C_3 plants (browsers) and those that primarily feed on C_4 plants (grazers). Those that are mixed feeders have intermediate ratios. However, the values measured in the tooth enamel are not exactly the same as in the plants themselves. Rather, it has been established empirically that in all cases the tooth enamel is enriched in ^{13}C relative to the plants on which the animal feeds. The degree of this enrichment appears to be size dependent, with mouse-sized animals having one fractionation value and larger animals having a different, larger fractionation value. However, despite this variation, modern herbivores that feed exclusively on C_3 plants can be distinguished from those animals that feed solely on C_4 plants by analyzing their $^{13}C/^{12}C$ ratio in tooth enamel. Mixed feeders range in between the C_3 and C_4 endpoints. Making the assumption that this difference was also the case with fossil mammalian herbivores is the basis for interpreting diets of the extinct forms.

Using carbon isotope data together with wear facet analysis from the teeth of six different 5 million year old horses from Bone Valley Florida, MacFadden et al. (1999) were able to reconstruct their dietary preferences; ranging from browsers to mixed feeders to grazers. Wear facet analysis corroborated the isotopic results. This was surprising because on the basis of the high crowned nature of the horse teeth alone, they all would have been considered grazers. This result is concordant with paleoenvironmental, “. . .reconstructions of central Florida at 5 Ma [which] indicate low-elevation floodplain and estuarine environments with a mosaic of local close-canopy forests, woodlands, and open-country grasslands” (MacFadden et al., 1999). In this instance, isotopic ratios of vertebrate fossils were utilized to corroborate a paleoenvironmental reconstruction made from other lines of evidence and to caution against the use of a single indicator of dietary preference, such as crown height.

The other most common isotope system to be investigated in fossil vertebrates is that of oxygen, despite the complicating factors mentioned above. The ratio of ^{18}O to ^{16}O in vertebrates is sensitive to temperature, humidity and diet (Kohn and Cerling, 2002). In one recent study using fossil taxa, measurements of the oxygen isotope ratio in both terrestrial mammals and gar in the Big Horn Basin of Wyoming were interpreted as indicating that a rapid increase in mean annual temperature occurred at the end of the Paleocene and beginning of the Eocene (Fricke et al., 1998). This study circumvented the problem of variation in diet affecting the oxygen isotope ratio by sampling the same genera through the period of time under investigation.

Because mammalian molars generally grow from the tip of the cusps to the base of the roots, by measuring the ratio of ^{18}O to ^{16}O at different heights of the enamel of a horse molar it was possible for Bryant et al. (1996) to observe the $^{18}O/^{16}O$ ratio through the time that the tooth formed instead of taking an average for the entire tooth. The changes they observed were regarded as due to seasonal temperature changes through that period. Because molars develop consecutively, with the first molar forming, then the second, and finally

the third molar, it was possible for Bryant et al. (1996) to correlate between molars and estimate the seasonal fluctuations in temperature over the entire period that formation of the molars took place. An excellent, more technical summary of this topic is summarized in Parrish (1998, pp. 84–88 and 154–161).

Thomas H. Rich and Patricia Vickers-Rich

Bibliography

- Alberdi, M.T., Alonso, M.A., Azanza, B., Hoyos, A., and Morales, J., 2001. Vertebrate taphonomy in circum-lake environments: Three cases in Guadix-Baza Basin (Granada, Spain). *Palaeogeogr. Palaeoclimatol. Palaeoecol.*, **165**, 1–26.
- Antoñanzas, R.L., and Bescós, G.C., 2002. The Gran Dolina site (Lower to Middle Pleistocene, Atapuerca, Burgos, Spain): New palaeoenvironmental data based on the distribution of small mammals. *Palaeogeogr. Palaeoclimatol. Palaeoecol.*, **186**, 311–334.
- Bryant, J.D., Froelich, P.N., Showers, W.J., and Genna, B.J., 1996. Biological and climatic signals in the oxygen isotopic composition of Eocene-Oligocene equid enamel phosphate. *Palaeogeogr. Palaeoclimatol. Palaeoecol.*, **126**, 75–89.
- Chinsamy, A., Rich, T.H., and Vickers-Rich, P., 1998. Polar dinosaur bone histology. *J. Vertebr. Palaeontol.*, **18**, 385–390.
- Constantine, A., Chinsamy, A., Vickers-Rich, P., and Rich, T.H., 1998. Periglacial environments and polar dinosaurs. *S. Afr. J. Sci.*, **94**, 137–141.
- FAUNMAP Working Group 1996. Spatial response of mammals to Late Quaternary environmental fluctuations. *Science*, **272**, 1601–1606.
- Fricke, H.C., Clyde, W.C., O’Neill, J.R., and Gingerich, P.D., 1998. Evidence for rapid climate change in North America during the latest Paleocene thermal maximum: Oxygen isotope compositions of biogenic phosphate from the Bighorn Basin (Wyoming). *Earth Planet. Sci. Lett.*, **160**, 193–208.
- Khajuria, C.K., and Prasad, G.V.R., 1998. Taphonomy of a Late Cretaceous mammal-bearing microvertebrate assemblage from the Deccan inter-trappean beds of Naskal, peninsular India. *Palaeogeogr. Palaeoclimatol. Palaeoecol.*, **137**, 153–172.
- Kohn, M.J., and Cerling, T.E., 2002. Stable isotope compositions of biological apatite. In Kohn, M.J., Rakovan, J., and Hughes, J.M. (eds.), 2002. Phosphates. *Geochemical, Geobiological, and Materials Importance. Reviews in Mineralogy and Geochemistry v. 48*. Washington, D.C.: Mineralogical Society of America, pp. 455–488.
- MacFadden, B.J., Solounias, N., and Cerling, T.E., 1999. Ancient Diets, Ecology, and Extinction of 5-Million-Year-Old Horses from Florida. *Science*, **283**, 824–827.
- Montuire, S., Michaux J., Legendre, S., and Aguilar, J.-P., 1997. Rodents and climate. 1. A model for estimating past temperatures using arvicolid (Mammalia: Rodentia). *Palaeogeogr. Palaeoclimatol. Palaeoecol.*, **128**, 187–206.
- Parrish, J.T., 1998. *Interpreting Pre-Quaternary Climate from the Geologic Record*. New York: Columbia University Press, 338pp.
- Rich, T.H., and Rich, P.V., 1989. Polar dinosaurs and biotas of the early Cretaceous of southeastern Australia. *Natl. Geogr. Soc. Res. Rep.*, **5**, 15–53.
- Tarduno, J.A., Brinkman, D.B., Renne, P.R., Cottrell, R.D., Scher, H., and Castillo, P., 1998. Evidence for extreme climatic warmth from Late Cretaceous Arctic vertebrates. *Science*, **282**, 2241–2244.
- Vucetich, M.G., and Verzi, D.H., 2002. First record of Dasyproctidae (Rodentia) in the Pleistocene of Argentina. Paleoclimatic implication. *Palaeogeogr. Palaeoclimatol. Palaeoecol.*, **178**, 67–73.

Cross-references

[Carbon Isotopes, Stable](#)
[Cretaceous Warm Climates](#)
[Isotope Fractionation](#)
[Nearest-Living-Relative Method](#)
[Oxygen Isotopes](#)
[Paleotemperatures and Proxy Reconstructions](#)
[Pleistocene Climates](#)

ANTARCTIC BOTTOM WATER AND CLIMATE CHANGE

Background

The production and spreading of Antarctic Bottom Water (AABW) in the modern ocean is understood in general terms, if not in detail. Abyssal regions of the global ocean are filled by cold, dense bottom waters that originate in the Southern Ocean and saltier, less-dense deep water (NADW) formed in the North Atlantic. From the distribution of thermohaline properties near the sea floor, it has long been known that AABW influence extends everywhere except the northernmost Atlantic and Arctic Ocean (Mantyla and Reid, 1983). Production uncertainties result from a variety of formation scenarios, mixing recipes, source regions, bottom water definitions, and inferences from local expeditions extrapolated over wider regions. AABW properties vary spatially from the coldest, freshest waters on the Antarctic continental slope to trace amounts of Antarctic origin in the northern oceans. A brief outline of bottom water formation mechanisms and a discussion of formation regions and rates are presented here. A note about ongoing efforts to redefine AABW is followed by consideration of temporal variability over recent decades and implications for AABW generation during glacial periods. A review of present-day bottom water formation, with additional figures and references, appears in Jacobs (2004).

AABW formation mechanisms

Bottom waters are produced where cooling, salinization, and uptake of atmospheric gases “ventilate” and provide negative buoyancy to surface and shelf waters, enabling them to mix with “older” Circumpolar Deep Waters (CDW) along the Antarctic continental margin. Gill (1973) demonstrated that bottom water properties in the Weddell Sea appeared to be accounted for by a mixture of cold, salty shelf water and warmer, fresher water above the deep water salinity and temperature maxima over the continental slope (Figure A5). The shelf water results from sea ice formation and export from the continental shelf, but is denser and mostly located well south of the continental shelf break. Gill also showed a V-shaped double-sided frontal region over the continental slope, marking the convergence of a variety of shelf, surface and deep waters (Figure A6). A fresh, westward-flowing “river” imbedded in the center of this Antarctic Slope Front (ASF; Jacobs, 1991; Whitworth et al., 1998) has properties that reflect upstream melting, freezing and mixing processes. Sinking along the ASF is enhanced by non-linearities in the seawater equation of state, which introduce isopycnal curvatures that can increase seawater density during mixing (Figure A7). Density is also enhanced by thermobaricity, the pressure dependence of the thermal compressibility of seawater. Regionally higher tidal energy near the shelf break facilitates mixing and reduces local sea ice concentrations. Melting icebergs entrained into the rapid slope current increase vertical convection and create openings in the sea ice field that amplify the impacts of winter atmospheric forcing.

Another factor in modern AABW formation is the “ice shelf water” that results from melting and freezing in the large, deep sub-ice shelf cavities (Jacobs et al., 1970; Foldvik et al., 1985). While positively buoyant relative to the denser shelf waters from which it forms, and for which it provides another sink, the very

cold ice shelf water can augment thermobaric effects over the continental slope in the Weddell and Ross Seas (Figure A8). With salinities that are intermediate between shelf and surface waters, ice shelf water is also well positioned to mix isopycnally with CDW (Figure A5). The amount of AABW produced directly from ice shelf water is probably limited to ~ 3 Sv ($1 \text{ Sv} = 10^6 \text{ m}^3 \text{ s}^{-1}$), since more of the circumpolar ice shelf and iceberg meltwater, some resulting from CDW sources, upwells into the near-surface layers. A portion of that lighter product will be incorporated into the fresh slope current that eventually contributes to AABW.

Some AABW in the global ocean starts out as deep water that is ventilated by mixing and interleaving along the continental margin (Carmack and Killworth, 1978) or by “open ocean” deep convection. An example of the latter is the remnant “chimney” structure observed downstream from a prominent rise in the sea floor, in conjunction with the large Weddell Polynya of 1974–1976, showing that $>3,000$ m of the water column had been perturbed by winter air-sea interaction (Figure A9). The number, frequency and geographic limits of such features is unknown, but the accompanying polynya has not reappeared in the same form, and the associated deep water formation rate may again have been no greater than ~ 3 Sv. With limited spatial resolution, most global scale general circulation models have until recently formed AABW from this type of deep convection. Deep convective eddies may also develop along the continental margin and move seaward, resulting in similar relict features. Another process that can produce AABW is simple advection off the continental shelf, as evidenced by the properties of waters along the Weddell-Scotia Confluence, and trapped within the deep basins of the Bransfield Strait.

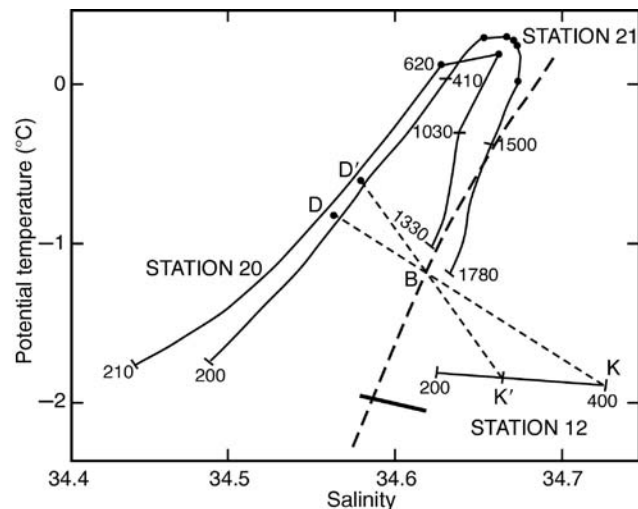


Figure A5 A “T/S diagram” of vertical profiles on the southern Weddell Sea continental shelf (12) and slope (20 and 21), with measurement depths in meters. Modified from Gill (1973), who observed that the properties of bottom water at B appeared to be a mixture of K–K’ shelf water and D–D’ slope water. The *short solid line* is the range of ice shelf water properties near the mouth of Filchner Trough, from Foldvik et al. (1985), and the *heavy dashed line* is an isopycnal (line of constant density). These additions show that bottom water can form more readily from ice shelf water and slope water below the salinity maximum.

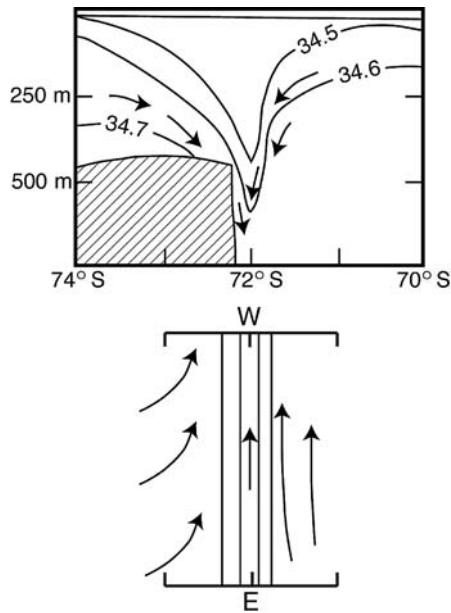


Figure A6 Suggested vertical and horizontal (400 m) circulation patterns near the continental shelf break at 50° W, 72° S in the Weddell Sea, modified from Gill (1973). The upper panel shows isohaline contours from several 1968 stations, including two of the three in Figure A5.

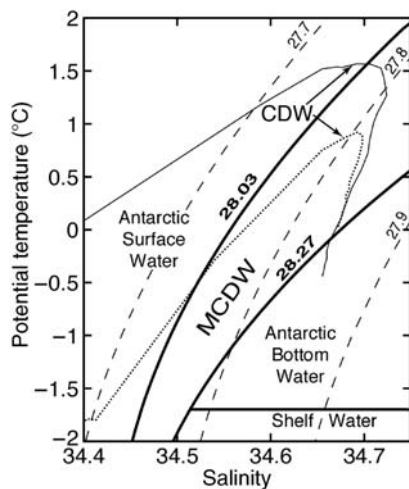


Figure A7 The T/S relationship of water masses near the Antarctic continental margin, modified from Whitworth et al. (1998). The solid curves labeled 28.27 and 28.03 are neutral density surfaces and the dashed curves from 27.7 to 27.9 are potential density. Dotted lines are from two reference stations, with arrows to the CDW temperature maxima. MCDW is modified Circumpolar Deep Water (CDW).

AABW formation regions

It is still widely believed that most AABW is produced in the Weddell Sea, where each of the formation mechanisms outlined above were initially identified. Most of those processes are not site specific, however, and other regions have similar water

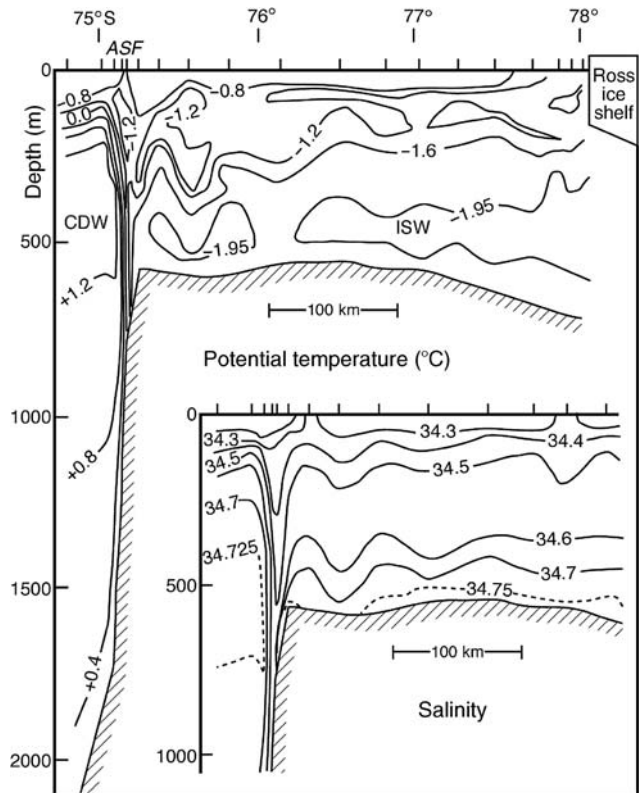


Figure A8 Vertical temperature and salinity (inset) sections across the continental shelf near 175° W in the Ross Sea, from February 1984 measurements at the indicated locations. Ice shelf water (ISW), with temperatures colder than the sea surface freezing point ($\sim -1.9^\circ\text{C}$) that formed from net melting into higher salinity water under the ice shelf, mixes with warmer Circumpolar Deep Water (CDW) and fresher waters along the Antarctic Slope Front (ASF) to form AABW.

masses, persistent winter coastal polynyas and sea ice export, ice shelves and an ASF. An historical focus on thermohaline properties in the Weddell sector influenced AABW definitions, which have typically been based on potential temperature. That is the temperature that would be reached by seawater raised adiabatically to the sea surface. For seawater with a salinity near 35 parts per thousand, a potential temperature of 0.0°C , the common upper boundary for AABW, represents a cooling of $\sim 0.2^\circ\text{C}$ for a 3,000 m decompression.

The Ross Sea physical regime is very similar to that of the Weddell Sea, and serves to illustrate the arbitrary nature of the $<0.0^\circ\text{C}$ and related definitions of AABW. CDW over the continental slope in the Ross is roughly a degree warmer than its counterpart in the Weddell. Since bottom water is a mixture of near-surface, shelf and deep waters, warmer varieties of bottom water can be produced in the Ross Sea, as shown by temperatures near the sea floor in the Southeast Pacific Basin (Obers et al., 1992, plate 54). The salinity range of newly formed AABW in the Ross Sea (Jacobs et al., 1970) is also wider than the high salinity type usually portrayed in volumetric analyses. In addition, some of the bottom water produced in the Ross Sea flows into the Australian Antarctic Basin (Gordon and Tchernia, 1972), and its properties will vary over time, e.g., in response to changing shelf water salinity (Jacobs, 2004).

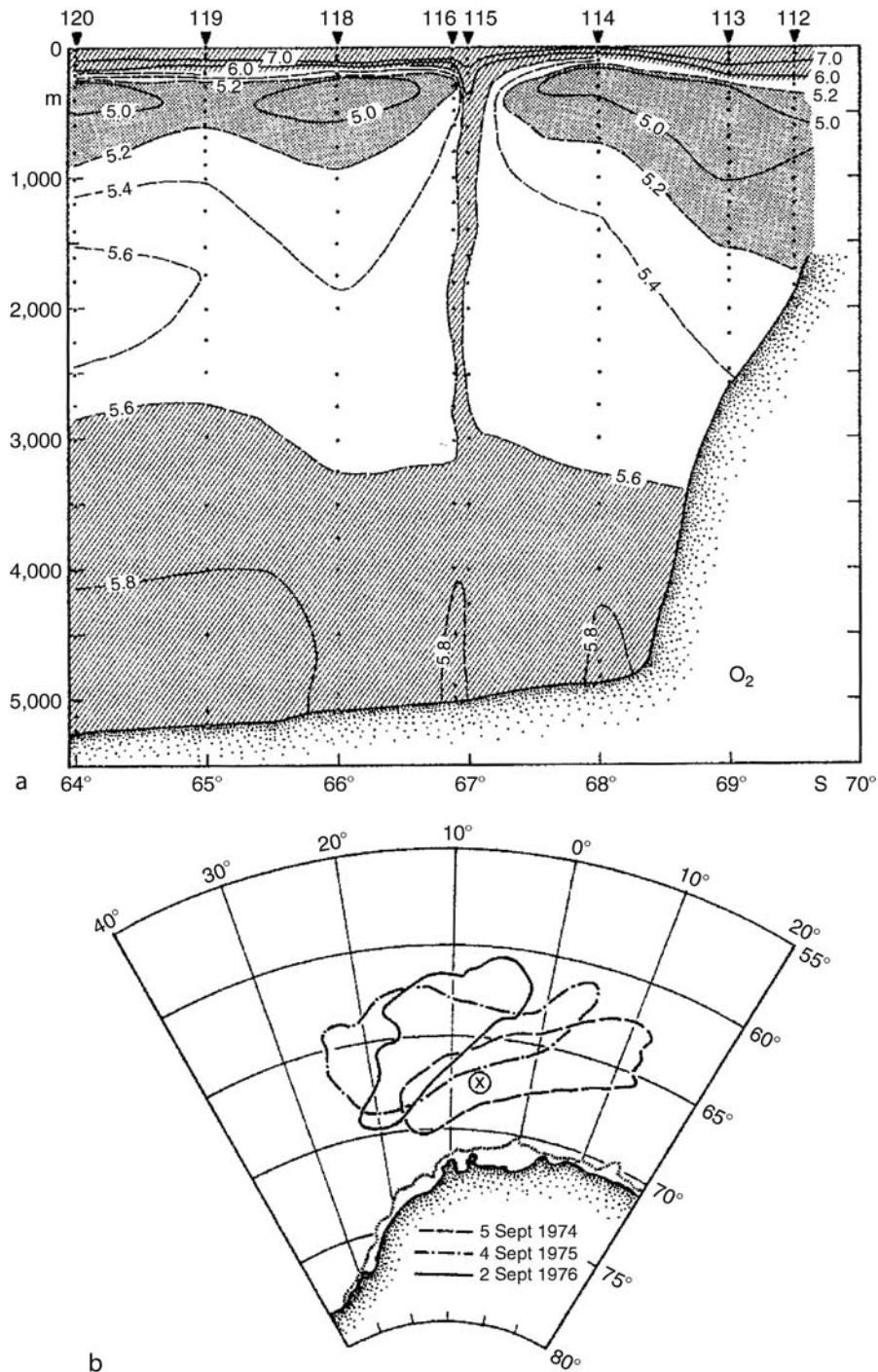


Figure A9 (a) Dissolved oxygen along a February 1977 NW–SE section near 8° W in the Weddell Sea displays a relict structure that resulted from an “open ocean” deep convection event, most likely associated with (b) the Weddell Polynya of 1974–1976, with its late winter limits defined by satellite-derived sea ice concentration maps. After Gordon (1978), where perturbations of the temperature, salinity and density field are also displayed. AMS copyright.

Neither thermohaline properties nor measurement location can thus be relied on to determine bottom water provenance.

The idea that all AABW of consequence to the deep ocean circulation is produced in the Weddell Sea was based mainly on early

temperature and dissolved oxygen measurements (Deacon, 1937; Stommel and Arons, 1960). More recent assessments show a substantially smaller Weddell sector contribution (Figure A10). The Ross Sea/Pacific percentage has increased to ~20% in those

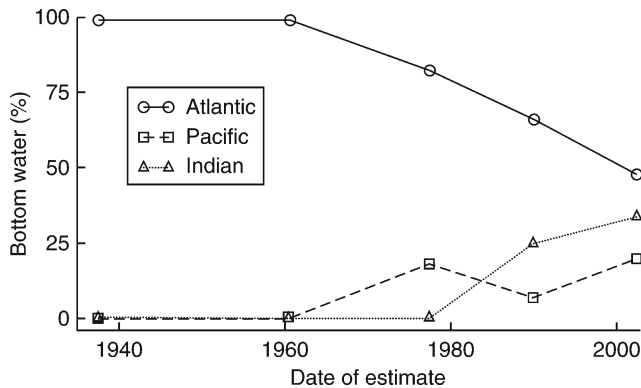


Figure A10 Changing estimates of bottom water source regions around Antarctica, with Atlantic representing the Weddell Sea, Pacific the Ross Sea and Indian typically only George V Coast (details and references in Jacobs, 2004).

analyses, not including its contribution to the Indian sector, where estimates have risen above 30%. While there are good reasons to doubt many of the estimates of origin, models are now able to resolve smaller-scale processes along the continental margin, and observations show substantial AABW production in the Pacific and Indian Ocean regions (Jacobs, 2004). Some of that production enters the Enderby Basin and diffuse eastern end of the Weddell Gyre from the east, evolving into deep and bottom water before being exported from the Weddell Sea.

AABW formation rates

Most investigations of the rate of AABW formation have also targeted the Weddell Sea, where the majority of estimates fall between 2 and 5 Sv (Figure A11). Values are for sustained annual production, although most observations have been made during the summer, and both rates and properties vary seasonally. Circumpolar rates cover a much wider range, but in both cases the high variability results in part from different definitions and study areas, along with different techniques, including boundary current transports, heat, salt, mass and geochemical budgets, numerical and inverse models. Global ocean circulation models typically call for about 20 Sv of new AABW production, and recent calculations tend to hover around this enduring estimate.

Whitworth et al. (1998) and Orsi et al. (1999, 2002) have utilized neutral density surfaces and the anthropogenic chloro-fluorocarbon (CFC) tracer to redefine bottom water and better constrain its present-day formation rate. Taking pure AABW to be heavier than the deepest isopycnal in the Drake Passage, and mapping the distribution of neutral density near the sea floor throughout the global ocean (Figure A12) revealed spreading patterns consistent with earlier work (e.g., Mantyla and Reid, 1983). Integrating the concentrations of CFC-11 within broader density bands along six N–S transects in the Atlantic, Pacific and Indian sectors indicated that the deep global ocean is currently being renewed from southern sources at a rate of ~ 17.5 Sv. This preliminary estimate of new production is comprised of $\sim 60\%$ partially ventilated near surface and shelf waters, and $\sim 40\%$ much older lower CDW. Analyses of additional CFC data sets may resolve questions about representative sections, water mass mixing and normalization, as the CFC source function and seawater saturation levels have varied over the

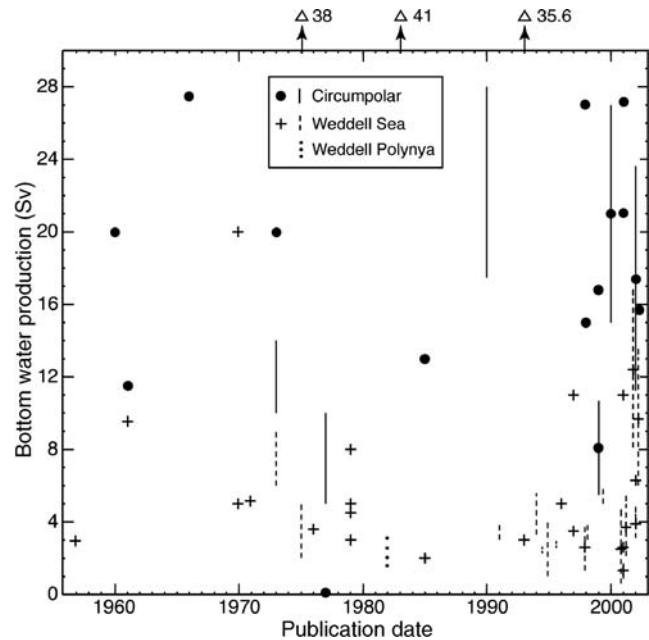


Figure A11 More than four decades of bottom water production estimates for the Weddell Sea and circumpolar Southern Ocean. 1 Sv = 1 Sverdrup = $10^6 \text{ m}^3 \text{ s}^{-1}$ (Jacobs, 2004).

measurement period. However, the revised definitions and CFC findings are consistent with inverse modeling of the World Ocean Circulation Experiment data set (Ganachaud and Wunsch, 2000), and with the venerable concept that AABW and NADW formation rates are roughly equal in the modern ocean.

AABW property variability

Interannual to multidecadal variability in AABW temperatures has been reported for many years, largest near the Antarctic continental margin. Moorings and repeat ocean stations seaward of the Filchner Trough and in the northwest Weddell Sea have displayed fluctuations and short term trends in temperature and salinity, consistent with changes in the overlying deep water (Fahrbach et al., 2004). Weddell deep water has warmed by $\sim 0.1^\circ \text{C}$ per decade since the early 1970s, due to changes in CDW inflow, processes within the Weddell Gyre or on the adjacent continental shelf (Robertson et al., 2002). Farther north, decadal temperature variability has been observed in and near the Vema Channel, although locations of restricted flow between basins are subject to strong mixing and countercurrents that complicate “choke point” monitoring and transport estimates.

Changes in salinity and other bottom water properties have also been reported at longer than seasonal time scales, and in other regions of the Southern Ocean (e.g., Foster and Middleton, 1979; Jacobs, 2004). The importance of salinity variability where bottom waters are formed is that a decrease of 0.01‰ lowers the density more than twice that of a warming of 0.10°C . Also, near-surface temperatures remain near the freezing point for much of the year in the polar oceans, whereas salinity ranges more widely, reflecting changes in precipitation, melting and sea ice volume, all elements of the hydrological cycle that are sensitive to climate change. Some salinity decreases observed over recent decades in the Southern

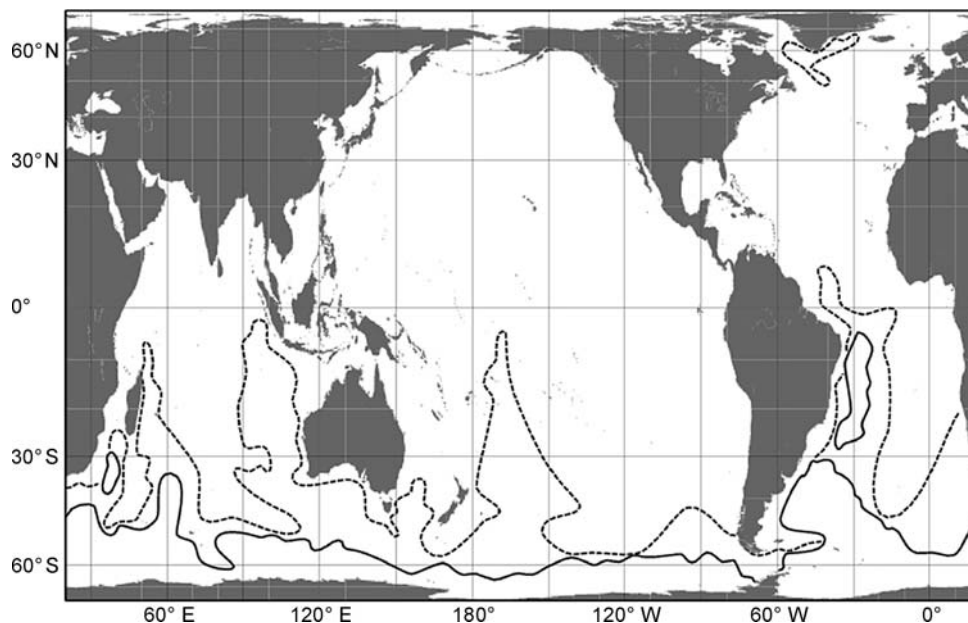


Figure A12 Distribution of neutral density near bottom in the world ocean, adapted from Orsi et al. (1999). The densest water lies south of the solid line, and an intermediate density class is limited by the dashed line.

Ocean are comparable to the “Great Salinity Anomaly” of the North Atlantic (Jacobs, 2004), albeit much less than models often require to significantly damp the strength of the thermohaline circulation.

AABW and past climate change

Analyses of the deep ocean circulation during glacial periods such as the Last Glacial Maximum (LGM) often indicate that AABW production increased as NADW formation waned (Boyle and Keigwin, 1987; Duplessy et al., 1988). Complete shutdown of the meridional ocean circulation cell that includes NADW is thought to require a very large perturbation of the hydrological cycle, such as the massive and rapid runoff of glacial meltwater. Models and observations show short term and less extreme sensitivity of the thermohaline circulation to smaller forcing changes that may apply in the Antarctic where vertical stability is low, but most work has been concentrated in the North Atlantic (Andrews, 2001; Clark et al., 2002). One attempt to consider a possible response of deep and bottom water formation to millennial scale climate change focused on the low production rates in the Weddell Sea (Figure A11). Along with its reputation as the primary source, this led to a hypothesis that the formation rate had recently slowed in the Southern Ocean (Broecker et al., 1999). However, the large rate uncertainties at present preclude reliable inferences about temporal variability, and that idea could not be reconciled with available evidence on water properties, mixing between young and old components, and other documented source regions.

Some models suggest more than one mode of stability in the thermohaline circulation, with sensitivity to winds and sea ice extent in addition to freshwater (e.g., Keeling, 2002). It is also possible that a shift in deep water formation sites may accompany changing climatic conditions without major modifications in the interior abyssal circulation. Depending on the associated property changes, this could be consistent with some chemical evidence,

and with early ocean circulation theory that focused on the main ocean thermocline but suggested deep water source locations are more or less a “climatological accident” (Stommel and Arons, 1960). In any case, glacial AABW would have been saltier than modern AABW by up to 1.5 psu, in proportion to the volume of freshwater residing in larger grounded ice sheets at that time. Its temperatures would have been lower in response to less or colder NADW inflow to the Southern Ocean, if not more extensive fields of sea ice. Such changes would have produced denser AABW than at present, but shallower waters were probably also denser at the LGM.

Several aspects of modern bottom water theory present problems for continued or enhanced AABW production at the LGM, or vice versa. These include the generation of high salinity shelf water, wide continental shelves for its accumulation and storage, and large ice shelves beneath which its properties are modified. With the Antarctic continental shelf largely filled with grounded glacial ice at the LGM (Denton and Hughes, 1981), most of the shelf area now accessible to the ocean, along with its ice shelves and their associated basal melting would have been eliminated. Kellogg (1987) postulated that AABW production could have been maintained at the LGM by a shift to the “open ocean” deep convection mode. Speculation at the time that open ocean deep convection might now be the dominant mode of deep and bottom water formation, and a suggestion that the Weddell Polynya existed during the LGM, encouraged the idea. However, thicker sea ice and colder CDW at that time would have made it more difficult to maintain sensible heat polynyas over the “open ocean,” although deep-reaching eddies might have occurred near the continental margin, or farther north if the sea ice edge were then near the Polar Front.

From the formation mechanisms outlined above, it can be inferred that a large continental shelf region, high salinity shelf water and ice shelves are helpful but not essential to AABW

generation. Nonetheless, the glacial ocean may have had access to the winter atmosphere in a region of strong sea ice formation, at or near a location where deep convection can take place. Since LGM grounded ice did not reach the shelf break in the Ross Sea (Conway et al., 1999), AABW production could have continued wherever similar conditions prevailed over the continental slope, and would have been strengthened by the more severe climate at that time (Figure A13). A larger ice sheet grounded on the outer continental shelf would have had steeper surface slopes, increasing the velocity of katabatic winds that now maintain coastal polynyas at various sites along the Antarctic coastline. If the coastline was then much closer to or directly above the continental slope, and less “warm” NADW was available, the stronger forcing would have injected more brine directly into colder

CDW. Lacking enough meltwater to provide vertical stability, a circumpolar band combining an ice front, winter polynyas and a continental slope could have experienced nearly continuous deep convection. More and colder AABW could thus have formed at the LGM, and during millennial scale coolings, along presently active and inactive portions of the continental margin. For considerations of the AABW response to climatic variability on longer time scales, see Hay (2001) and references therein.

Stan Jacobs

Bibliography

- Andrews, J.T., 2001. Millennial scale climate variability. In Steele, J.H., Thorpe, S.A., and Turekian, K.K. (eds.), *Encyclopedia of Ocean Sciences*. Orlando: Academic Press, pp. 1814–1821.
- Boyle, E.A., and Keigwin, L., 1987. North Atlantic thermohaline circulation during the past 20,000 years linked to high-latitude surface temperature. *Nature*, **330**, 35–40.
- Broecker, W.S., Sutherland, S., and Peng, T.-H., 1999. A possible 20th century slowdown of Southern Ocean Deep Water formation. *Science*, **286**, 1132–1135.
- Carmack, E.C., and Killworth, P.D., 1978. Formation and interleaving of abyssal water masses off Wilkes Land, Antarctica. *Deep Sea Res.*, **25**, 357–369.
- Clark, P.U., Pisias, N.G., Stocker, T.F., and Weaver, A.J., 2002. The role of the thermohaline circulation in abrupt climate change. *Nature*, **415**, 863–869.
- Conway, H., Hall, B.L., Denton, G.H., Gades, A.M., and Waddington, E.D., 1999. Past and future grounding – line retreat of the West Antarctic Ice Sheet. *Science*, **286**, 280–283.
- Deacon, G.E.R., 1937. The hydrology of the Southern Ocean. *Discov. Rep.*, **15**, 124.
- Denton, G.H., and Hughes, T.J. (eds.), 1981. *The Last Great Ice Sheets*. New York, Wiley, 484pp.
- Duplessy, J.-C., Shackleton, N.J., Fairbanks, R.G., Labeyrie, L., Oppo, D., and Kallel, N., 1988. Deep water source variations during the last climatic cycle and their impact on the global deep water circulation. *Paleoceanography*, **3**, 343–360.
- Fahrbach, E., Hoppema, M., Rohardt, G., Schröder, M., and Wisotzki, A., 2004. Decadal-scale variations of water mass properties in the deep Weddell Sea. *Ocean Dyn.*, **54**, 77–91.
- Foldvik, A., Gammelsrod, T., and Torresen, T., 1985. Circulation and water masses on the southern Weddell Sea Shelf. In Jacobs, S.S. (ed.), *Oceanology of the Antarctic Continental Shelf*. Washington, D.C: American Geophysical Union, Antarctic Research Series, No. 43, pp. 5–20.
- Foster, T.D., and Middleton, J.H., 1979. Variability in the bottom water of the Weddell Sea. *Deep Sea Res.*, **26A**, 743–762.
- Ganachaud, A., and Wunsch, C., 2000. Improved estimates of global ocean circulation, heat transport and mixing from hydrographic data. *Nature*, **408**, 453–457.
- Gill, A.E., 1973. Circulation and bottom water production in the Weddell Sea. *Deep Sea Res.*, **20**, 111–140.
- Gordon, A.L., 1978. Deep Antarctic convection west of Maud Rise. *J. Phys. Ocean.*, **8**, 600–612.
- Gordon, A.L., and Tchernia, P., 1972. Waters of the continental margin off Adelie Coast, Antarctica. In Hayes, D.E. (ed.), *Antarctic Oceanology II*. Washington, D.C: American Geophysical Union, Antarctic Research Series, No. 19, pp. 59–69.
- Hay, W.W., 2001. Climate models in paleoceanography. In Steele, J.H., Thorpe, S.A., and Turekian, K.K. (eds.), *Encyclopedia of Ocean Sciences*. Orlando: Academic Press, pp. 2082–2089.
- Jacobs, S.S., 1991. On the nature and significance of the Antarctic Slope Front. *Mar. Chem.*, **35**, 9–24.
- Jacobs, S.S., 2004. Bottom water production and its links with the thermohaline circulation. *Antarct. Sci.*, **16**(4), 427–437.
- Jacobs, S.S., Amos, A.F., and Bruchhausen, P.M., 1970. Ross Sea oceanography and Antarctic Bottom Water formation. *Deep Sea Res.*, **17**, 935–962.
- Keeling, R.F., 2002. On the freshwater forcing of the thermohaline circulation in the limit of low diapycnal mixing. *J. Geophys. Res.*, **107**, C7 (doi: 10.1029/2000JC000685).

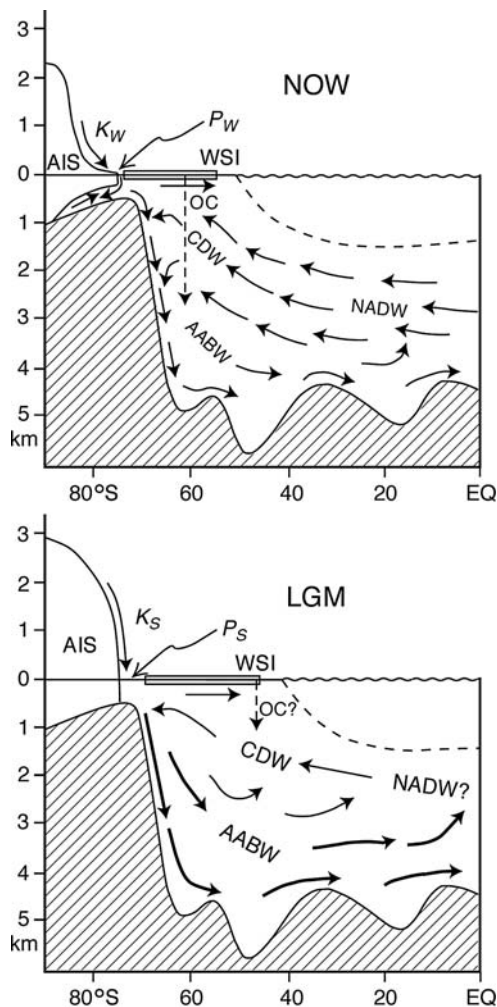


Figure A13 A schematic illustration of deep (NADW, CDW) and bottom (AABW) water circulation in the Atlantic sector of the Southern Hemisphere now and at the LGM, modified from Kellogg (1987). The Antarctic Ice Sheet currently supports ice shelves with net basal melting, along with weak katabatic winds and coastal polynyas (K_w and P_w). Grounded near the shelf break during glacial periods, the larger ice sheet could have supported stronger winds and polynyas (K_s and P_s) and more intense AABW formation. Intermittent open ocean convection (OC) at present may have occurred near the more northern winter sea ice edge (WSI) at the LGM. Weaker NADW or a shallower “glacial intermediate water” may also have prevailed at that time (Andrews, 2001).

- Kellogg, T.B., 1987. Glacial-interglacial changes in global deepwater circulation. *Paleoceanography*, **2**, 259–271.
- Mantyla, A.W., and Reid, J.L., 1983. Abyssal characteristics of the world ocean waters. *Deep Sea Res.*, **30**, 805–833.
- Olbers, D., Gouretski, V., Seib, G., and Schroter, J., 1992. Hydrographic Atlas of the Southern Ocean. Bremerhaven, Bremen, Germany: Alfred Wegener Institute, 17 pages and 82 plates.
- Orsi, A.H., Johnson, G.C., and Bullister, J.L., 1999. Circulation, mixing, and the production of Antarctic Bottom Water. *Progr. Oceanog.*, **43**, 55–109.
- Orsi, A.H., Smethie, W.M. Jr., and Bullister, J.L., 2002. On the total input of Antarctic waters to the deep ocean: A preliminary estimate from chlorofluorocarbon measurements. *J. Geophys. Res.*, **107** (doi: 10.1029/2001JC000976).
- Robertson, R., Visbeck, M., Gordon, A.L., and Fahrbach, E., 2002. Long-term temperature trends in the deep waters of the Weddell Sea. *Deep Sea Res. II*, **49**, 4791–4806.
- Stommel, H., and Arons, A.B., 1960. On the abyssal circulation of the world ocean – II. An idealized model of the circulation pattern and amplitude in oceanic basins. *Deep Sea Res.*, **6**, 217–233.
- Whitworth T., III, Orsi, A.H., Kim, S.-J., and Nowlin, W.D. Jr., 1998. Water masses and mixing near the Antarctic Slope Front. In Jacobs, S.S., and Weiss, R.F. (eds.), *Ocean, Ice and Atmosphere: Interactions at the Antarctic Continental Margin*. Washington, DC: American Geophysical Union, Antarctic Research Series, No. 75, pp. 1–27.

Cross-references

[Antarctic Glaciation History](#)
[Last Glacial Maximum](#)
[North Atlantic Deep Water and Climate Change](#)
[Ocean Paleocirculation](#)
[Ocean Paleotemperatures](#)
[Thermohaline Circulation](#)

ANTARCTIC COLD REVERSAL

The Antarctic Cold Reversal (ACR) is an event seen in Antarctic ice core proxy climate records in which the warming that occurred between 20,000 and 10,000 years ago, as the Earth emerged from the last glacial period into the present Holocene interglacial, was interrupted by a temporary cooling lasting about 1,500 years between 14,500 and 13,000 yBP.

The transition between the last glacial period and the Holocene is the most recent of a series of major changes in climate that have occurred throughout the Quaternary as the Earth cycled between glacial and interglacial conditions. These cycles, often referred to as Milankovitch cycles after Milutin Milankovitch, the Serbian mathematician who first showed that climate cycles are synchronized with cycles in the Earth's orbit, are characterized by a sawtooth pattern in which temperature decreases to a minimum over a period of about 90,000 years and then rises to warm or interglacial values within about 10,000 years. Milankovitch cycles are the Earth's response to variations in the distribution of the solar radiation that reaches its surface. The radiation varies in a complicated but regular manner due to variations in the Earth's elliptical orbit and to changes in the inclination of the Earth's spin axis.

The climate change that occurred in the transition between the last glacial episode and the Holocene was very large compared with changes that have occurred since then in the Holocene. Global temperatures rose by as much as 10 °C in some places and sea level increased by 120 m, principally as a result of the melting of the Laurentide and Fennoscandian

Ice Sheets that covered large parts of North America and northern Europe, respectively, throughout the glacial period. Proxy records of climatic temperature from sources such as marine sediments and ice cores show differing patterns of warming in different places, but the main contrast appears between records from the Northern and Southern Hemispheres. In Northern Hemisphere records, particularly those from around the North Atlantic Ocean, a slow warming starting at about 20,000 BP is followed by a large jump in temperature at 14,500 BP known as the Bølling Transition (or Interstadial). After the Bølling Transition there is a slow then more rapid cooling, ending with temperatures nearly as cold as those at the glacial maximum. This cold period, known as the Younger Dryas because it was first identified by the pollen of a flower, *Dryas Octopetala*, which grows in cold climates, starts at 12,700 BP and ends with another large jump at 11,600 BP to temperatures almost as warm as those of today (Figure A14).

Antarctic records also show a period when warming reverses, but the shape of the southern record is different from that in the north. In the south, the cooling period is considerably smaller in amplitude than the Younger Dryas and shows no rapid jumps. When the Antarctic cooling was first observed in ice core records, dating was uncertain, and it was seen as a possible Southern Hemisphere expression of the Younger Dryas. Later work, however, showed that the Antarctic cooling, first referred to as the Antarctic Cold Reversal (ACR) by Jouzel and others in 1995, preceded the Younger Dryas by at least 1,000 years.

Milankovitch cycles account for the long-term cycles of climatic change. However, the radiation variations are too small to account for the large temperature changes, and the forcing at the 100,000-year principal period of climate change (corresponding to the eccentricity period) is considerably weaker than that at the precession period (23,000 years) or the obliquity period (41,000 years). The magnitude of the climate change between glacials and interglacials, the dominance of the 100,000-year cycle in the long-term record, and the existence of rapid temperature jumps and reversals in the transitions all point to powerful feedbacks and thresholds in the Earth's climate system. One of the most important of these is ocean circulation. Ocean currents transport large amounts of heat and thus have large effects on regional climate. The best known is the Atlantic conveyor, which transports warm water from the tropics and the Southern Ocean to the North Atlantic, where it heats the atmosphere and ameliorates the climate of North America and Europe. The Atlantic circulation is maintained by evaporation and cooling in the north, which increases the salinity and density of the water, causing it to sink (thermohaline circulation). This only happens in the northern Atlantic Ocean because the northern part of the Pacific Ocean, although cold, is not saline enough to sink and the absence of any blocking land mass in the Southern Hemisphere results in flow around Antarctica and minimal North-South heat transport.

Computer model experiments suggest that the ocean circulation is sensitive to changes in evaporation and injections of fresh water. In today's interglacial climate, ice volume (and climate) is stable; however, during the glacial and transition periods, ice sheet fluctuations injected large quantities of fresh water into the oceans, resulting in large changes in circulation. Model simulations indicate that Atlantic Ocean circulation can take three general forms: an interglacial mode, such as exists today, in which warm water flow extends to the north of the shallow sill between Scotland and Iceland before sinking (the

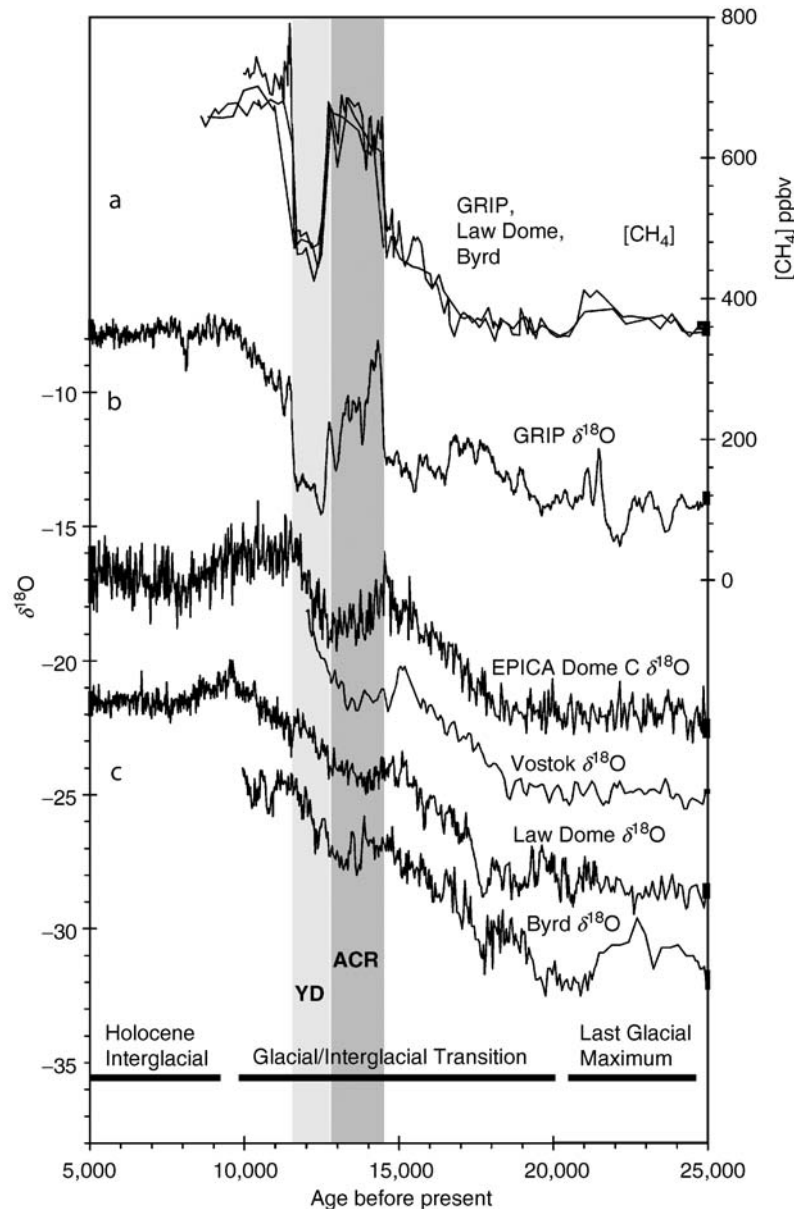


Figure A14 Ice core records showing principal features of the global warming through the glacial-interglacial transition. The period of the Antarctic Cold Reversal (ACR) is shaded. YD stands for Younger Dryas. (a) The overlaid plots are of atmospheric methane concentrations obtained from trapped air in the GRIP, Law Dome and Byrd cores. The large and rapid changes associated with the Bølling Transition and the Younger Dryas are used to synchronize the timing of the ice core records. (b) The stable isotope ratio ($\delta^{18}\text{O}$) record from the GRIP (Greenland Icecore Project) core. $\delta^{18}\text{O}$ is a proxy for climatic temperature. The record shows the characteristic Northern Hemisphere pattern of a rapid rise at the Bølling transition, a decline into the Younger Dryas, a rapid jump out of the YD and a subsequent rise to Holocene temperature. (c) Antarctic ice core records: EPICA and Dome C in inland East Antarctica, Vostok in central East Antarctica, Law Dome in coastal East Antarctic site, and Byrd in West Antarctica. GRIP, Byrd and Vostok data, including original references, are available at IGBP PAGES/World Data Center-A for Paleoclimatology, NOAA/NGDC Paleoclimatology Program, Boulder CO, USA. <http://www.ngdc.noaa.gov/paleo/icecore.html>

Atlantic Conveyor); a glacial mode, where the flow sinks to the south of the sill; and a third mode in which the flow is essentially cut off (see *North Atlantic Deep Water and climate change; Thermohaline Circulation*). These three modes are reasonably successful in describing two types of rapid change climate events seen in records from around the North Atlantic Ocean: Dansgaard-Oeschger events (named after the ice core

paleoclimatologists Willi Dansgaard and Hans Oeschger) and Heinrich events (named after the German paleoceanographer Hartmut Heinrich). In Dansgaard-Oeschger events, cold glacial conditions are interrupted by an abrupt (10–100 year) warming, which is followed by a slow cooling back to glacial conditions over some 1,000 years. It is surmised that the glacial mode of circulation, in which warm water sinks before

reaching very far north, is abruptly enhanced, leading to an interglacial mode of circulation and hence warmer climate in the far north. Under glacial conditions, however, this mode is not stable, so it gradually reverts to the glacial mode. Dansgaard-Oeschger events produce warming in the North and, because of the enhanced transport of heat; cooling in the south (the Atlantic Conveyor does not just carry warm tropical water north but also water from the Southern Ocean). Heinrich events operate in the opposite manner and enhance cooling in northern mid-latitudes. Heinrich events presumably occur when surges of the Laurentide Ice Sheet inject low-density freshwater into the North Atlantic, reducing circulation from glacial levels to the cutoff state. Heinrich events lead to the coldest conditions in the northern records, but the Heinrich mode in which Atlantic circulation is switched off is also unstable and circulation reverts to a normal glacial mode after a few centuries. Dansgaard-Oeschger and Heinrich events are observed throughout the late glacial and the glacial/Holocene transition, but not in the Holocene. The Bølling Transition in the Northern Hemisphere, the start of the Antarctic Cold Reversal at around 14,500 BP, and the end of the Younger Dryas at 11,500 BP are the second to last and last Dansgaard-Oeschger events before the warmer Holocene conditions led to the present-day stable interglacial ocean circulation pattern.

A significant advance in our understanding of the climate system came when air trapped in ice cores was used to synchronize records from Greenland (representing the Northern Hemisphere) and Antarctica (in the Southern Hemisphere). The ice-core trapped-air synchronization method relies on the fact that the atmosphere is well mixed on timescales of more than a few years so that changes in the atmosphere can serve as global time markers. The method is complicated, however, because the air is not sampled when the snow is deposited on the ice sheet surface, but is gradually trapped at a depth of about 70 m when pores in between snow crystals are closed by the weight of overlying snow. This produces two effects. The first is that the trapped air is younger than the surrounding ice (the ice that provides the proxy climate record) and the second is that the trapped air does not represent a sample taken at a single point in time. Typically, the age of the air is a few hundred years younger in the Holocene and up to several thousand years younger in glacial periods when snow accumulation rates were much lower. The corresponding errors in the age are likely to be around 100 and 1,000 years. Sites with higher accumulation rates, where the ice is younger at depth, have correspondingly smaller age uncertainties.

Using trapped air, Blunier and Brook (2001) showed that the large millennial scale Dansgaard-Oeschger fluctuations seen in Greenland records were synchronized with Antarctic records in a distinct pattern; Antarctic temperature varied smoothly, warming for a few thousand years and then cooling for a similar period. Greenland temperatures showed no increase while Antarctica warmed, but exhibited a large temperature jump around the time when the Antarctic went from warming to cooling (Figure A14). A similar pattern occurs throughout the glacial period and ends with the two events in the glacial-Holocene transition: the Bølling Transition and the jump at the end of the Younger Dryas (see *Bølling-Allerød Interstadial*; *Younger Dryas*).

Although the idea of one hemisphere driving the other in climate has now largely been discarded in favor of the concept of a coupled feedback system, the timing and order of events is important in determining cause and effect. Trapped air synchronization using a high accumulation record from Law Dome

on the coast of East Antarctica has shown that, in the transition, the start of the ACR is not exactly synchronous with the Bølling Transition but leads it by about 200 years (Figure A14 shows the sequence of events). Two hundred years is a relatively short time and this figure is still subject to some uncertainty, but the fact that the ACR occurs before the Northern Hemisphere cooling makes it difficult to ascribe a simple Northern Hemisphere driver. A possible mechanism that might explain the observed events comes from model simulations by Weaver and others (2003). They find that injection of a large amount of freshwater into the Southern Ocean by a surge of the Antarctic Ice Sheet would enhance the flow of the Atlantic Conveyor. The effect is similar but opposite in effect to the surges of the Laurentide Ice Sheet that result in Heinrich events. Just as a surge of the Laurentide Ice Sheet can slow or stop the Atlantic conveyor, a large amount of freshwater injected into the Southern Ocean enhances the conveyor flow and hence the transport of heat from the south to the north. The effect on climate would be a cooling in the south at the same time or slightly preceding a warming in the north.

Vincent I. Morgan

Bibliography

- Blunier, T., and Brook, E., 2001. Timing of millennial-scale climate change in Antarctica during the last glacial period. *Science*, **291**, 109–112.
- Jouzel, J., Vaikmae, R., Petit, J.R., Martin, M., Duclos, Y., Stievenard, M., Lorius, C., Toots, M., Mélières, M.A., Burckle, L.H., Barkov, N.I., and Kotlyakov, V.M., 1995. The two step shape and timing of the last deglaciation in Antarctica. *Clim. Dyn.*, **11**, 151–161.
- Weaver, A.J., Saenko, O.A., Clark, P.U., and Mitrovica, J.X., 2003. Meltwater pulse 1A from Antarctica as a trigger of the Bølling-Allerød warm interval. *Science*, **299**, 1709–1713.

Cross-references

[Antarctic Bottom Water and Climate Change](#)
[Astronomical Theory of Climate Change](#)
[Bølling-Allerød Interstadial](#)
[Climate Change, Causes](#)
[Dansgaard-Oeschger Cycles](#)
[Heinrich Events](#)
[Ice Cores, Antarctica and Greenland](#)
[North Atlantic Deep Water and Climate Change](#)
[Quaternary Climate Transitions and Cycles](#)
[Thermohaline Circulation](#)
[Younger Dryas](#)

ANTARCTIC GLACIATION HISTORY

The continent of Antarctica is currently 98% covered by two connected continental-scale ice sheets plus smaller ice caps and glaciers of the Antarctic Peninsula. The history and behavior of the two large ice sheets, the East Antarctic Ice Sheet (EAIS) and the West Antarctic Ice Sheet (WAIS) (Figure A15) have had a major influence on Earth's past climate. The waxing and waning of Antarctica's ice sheets are strongly tied to global sea levels and climate change, ocean circulation patterns, Earth's albedo and life on the planet.

Antarctica's glaciation history is partially a function of its sub-ice topography. Underlying the EAIS are cratonic rocks and mountain ranges that would be exposed subaerially if the ice sheet

was removed (Figure A16) and that served as a foundation for ice sheet inception. Exceptions include the Wilkes, Pensacola and Aurora Subglacial Basins and the Amery Basin, which all lie below sea level. In contrast, much of the bed beneath the WAIS lies below sea level (Figure A16), reaching depths $>2,000$ m in the Byrd Subglacial Basin and Bentley Subglacial Trench. The WAIS occupies a rift-related basin that is bounded by the Transantarctic Mountains (TAM) to the south and the mountain ranges of Marie

Byrd Land, Ellsworth Land and the Antarctic Peninsula to the north. These mountain ranges have influenced regional atmospheric circulation and also served as nucleation points for glaciation. In these tectonically active regions, the isostatic changes to the crust associated with ice sheet evolution is complicated by the complex tectonic history. The uplift of the Transantarctic Mountains, which reached their present height by ~ 34 Ma, played a particularly important role in ice sheet development. Overall, the fundamental differences in bed elevation between the EAIS and WAIS translate into different histories and ice flow characteristics.

Another major factor that affected ice sheet development was the opening of gateways, such as the Drake Passage and the Tasmanian Seaway, which allowed thermal isolation of the Antarctic continent after the breakup of Gondwana. Antarctica moved into a polar position in the Cretaceous; however, the complete opening of these rift-related gateways did not occur until the early Cenozoic. Both gateways appear to have opened near the Eocene-Oligocene boundary (34 Ma) (e.g., Lawver et al., 1992; Shipboard Scientific Party, 2000; Latimer and Filippelli, 2002). These openings allowed the development of the Antarctic Circumpolar Current (ACC), which prevents the delivery of warm surface water to the Antarctic continent. The details of the timing and influence of ACC onset on the development of continental scale Antarctic ice are not well constrained (Barker and Thomas, 2003). Alternatively, DeConto and Pollard (2003) argued that the opening of gateways was secondary to falling atmospheric CO_2 levels in causing Antarctic ice sheet development. From model simulations, they suggest that snowline lowering associated with falling CO_2 permitted glacier growth.

Proxy records of ice volume changes can be derived from the oxygen isotopic composition of deep-sea benthic foraminifera.

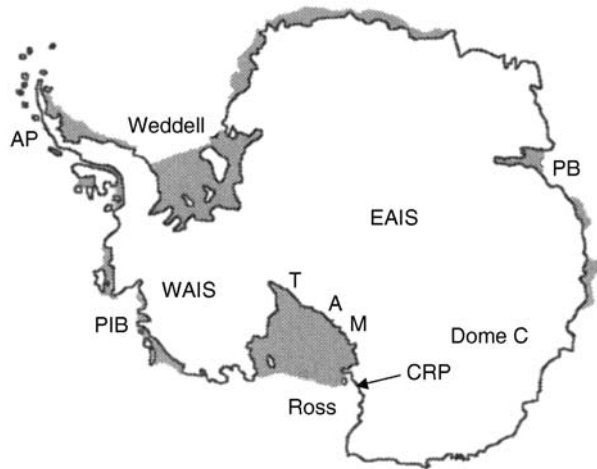


Figure A15 Antarctic place names along with ice shelves shown in gray. WAIS, West Antarctic Ice Sheet; EAIS, East Antarctic Ice Sheet; AP, Antarctic Peninsula; PB, Prydz Bay; TAM, Transantarctic Mountains; CRP, Cape Roberts Project site; PIB, Pine Island Bay.

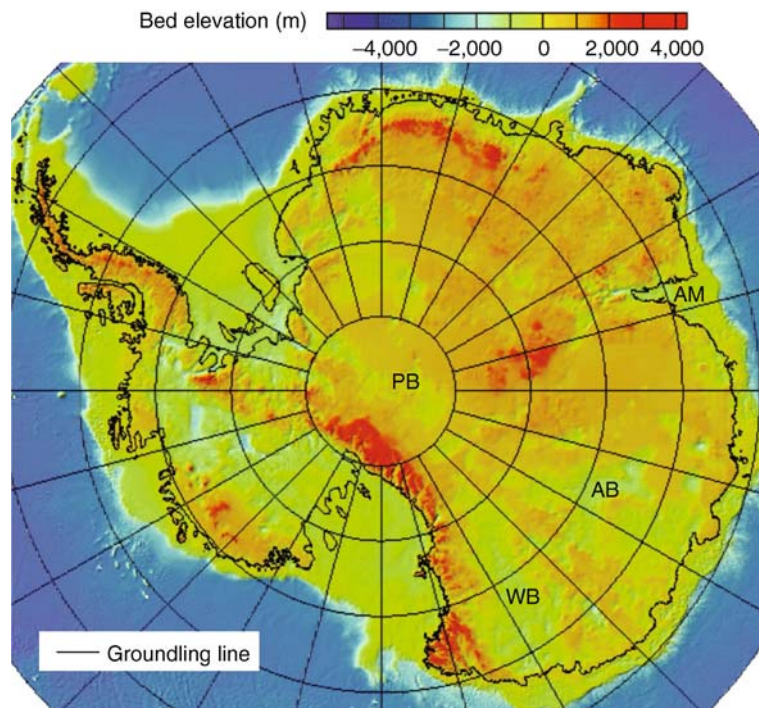


Figure A16 Antarctic sub-ice topography and bathymetry. WB, Wilkes Basin; AB, Aurora Basin; PB, Pensacola Basin; AM, Amery Basin. (Modified from Lythe et al., 2000.)

Positive $\delta^{18}\text{O}$ isotopic excursions can be interpreted as ice volume increases and/or bottom water temperature decreases (Figure A17). Assuming that the temperature effect on $\delta^{18}\text{O}$ is accurately accounted for, the benthic foram oxygen isotopic data indicate Antarctic ice sheet development at the Eocene-Oligocene boundary (34 Ma) (Shackleton and Kennett, 1975; Zachos et al., 2001). The isotopic data also indicate persistence of this ice until about 26 Ma when the $\delta^{18}\text{O}$ decreased $>1\%$. Zachos et al. (2001) interpreted part of this decrease as a reduction in Antarctic ice volume. The mid-Miocene increase in $\delta^{18}\text{O}$ is interpreted to represent the regrowth of the EAIS, followed several million years later by development of the WAIS (Figure A17). The lag in WAIS development is attributed to the bed elevation differences between East and West Antarctica. Since much of the bed beneath the WAIS is well below sea level (>700 m) (Figure A16), the ice had to become thick enough to overcome buoyancy effects in order to ground on the seafloor.

Southern Ocean records of ice-rafted debris (IRD) provide some of the earliest sedimentological evidence of Antarctic glaciation. Deep Sea Drilling Project (DSDP) and Ocean Drilling Program (ODP) sites in the Southern Ocean show a wide variety of dates for onset of ice rafting and range from the latest Cretaceous to the Pliocene (Anderson, 1999). Minor occurrences of IRD are found at several sites around the continent

in the late Eocene and early Oligocene, and the majority of sites show either minor or significant IRD content during the Miocene. One limitation of IRD records is that ice sheet volume cannot be determined; IRD only indicates that glaciers were calving from Antarctica and the icebergs reached the Southern Ocean.

Ice sheet evolution studies from the Antarctic continental margin draw upon marine seismic surveys, drill cores, and gravity cores. A number of DSDP and ODP cores have been collected around the Antarctic margin as well as the Southern Ocean, yielding volumes of data. Continental shelf sites that have targeted Cenozoic records of Antarctic glaciation include DSDP sites 270–273 in the Ross Sea, ODP sites 739–742 and 1,166 in Prydz Bay, and sites 1,098–1,100, 1,102 and 1,103 from the western Antarctic Peninsula. Few cores have been drilled on the continental shelves, in part because of the poor recovery that is common from these sites. For instance, ODP sites 1,100, 1,102 and 1,003 on the outer continental shelf averaged $<14\%$ recovery when trying to core through diamict (Shipboard Scientific Party, 1999).

The eastern Ross Sea DSDP sites contain Mid-Late Eocene to Early Oligocene glacial and glacial marine sediment (Hayes and Frakes, 1975; Hambrey, 1993). In these cores, a clear glacial sedimentary signal appears in the late Oligocene to early

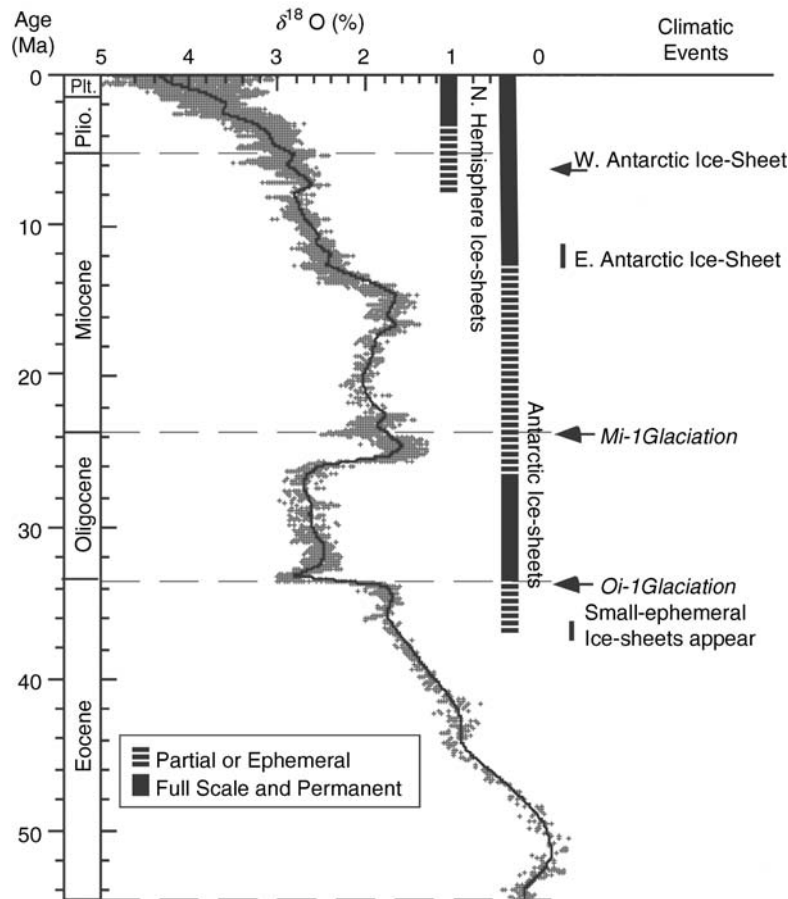


Figure A17 Composite oxygen isotopic curve from benthic foraminifera showing interpretation of Antarctic ice sheet evolution. (Modified from Zachos et al., 2001.)

Miocene with extensive ice throughout the early Miocene. More recently, cores drilled in the western Ross Sea for the Cape Roberts Project (Figure A15) contain a nearly complete record of Antarctic history from about 34 to 17 Ma and provide an excellent regional record of ice sheet evolution. The cores were drilled from a sea ice platform and around 1,500 m of Cenozoic sediments were recovered from three closely spaced sites. As in the eastern Ross Sea, these Oligocene sediments on the flanks of the Transantarctic Mountains record a glacial marine setting from 34 to 24 Ma, indicated by the presence of ice-rafted debris. From 24 to 17 Ma, grounded ice became more extensive under a cooler climate (Cape Roberts Science Team, 1999). In total, the Cape Roberts cores provide evidence of at least 22 cycles of glacial advance and retreat in the Oligocene and early Miocene.

In the Leg 188 synthesis of Prydz Bay cores, Cooper and O'Brien (2004) reported that glacial sediments first appeared on the continental shelf near the Eocene-Oligocene boundary, similar to the Ross Sea records. Prydz Bay Miocene sediments record a transition from a meltwater-rich setting to an IRD-dominated setting, reflecting a temperate to cold climate transition and buildup of ice in East Antarctica. Uplifted Miocene glacial marine sediments of the Pagodroma Group are exposed in the Prince Charles Mountains south of Prydz Bay (Hambrey and McKelvey, 2000). These strata support observations from the marine record, although the exact timing of the transition from temperate to polar conditions is not well constrained.

Marine seismic surveys provide a regional context for core data and are therefore valuable records of past ice sheet fluctuations. Major ice sheet advances are indicated by widespread erosional events, which produce strong seismic reflections that truncate underlying strata and that have a distinctive progradational geometry. The number of such erosional surfaces on a continental shelf represents a minimum number of ice sheet advances because evidence for some advances may be erased by subsequent ice sheet erosion of the shelf. Because of limited core recovery on the shelves, many seismic records lack age control on the glacial unconformities. The age of nearshore unconformities has been linked to Southern Ocean IRD records; however, increases in IRD abundance have been ascribed to both ice sheet maxima and minima (Anderson, 1999), thus clouding the issue of the timing of glacial fluctuations. Even considering these limitations, marine seismic records provide clear evidence of numerous major ice sheet fluctuations across the continental shelf since the Oligocene.

The Ross Sea has been extensively characterized by seismic surveys and a recent compilation of eastern Ross Sea seismic data is interpreted to show the presence of localized West Antarctic ice caps in the Early Oligocene (De Santis et al., 1995). Bart (2003) reported at least two episodes of Ross Sea glaciation to the outer continental shelf during the early mid-Miocene and suggested that it was a WAIS-dominated expansion. This reconstruction requires the WAIS expansion to precede the major EAIS regrowth after 14 Ma (Figure A17). Bart (2003) discussed the contradictions with $\delta^{18}\text{O}$ Antarctic ice sheet evolution, which suggest full WAIS development in the late Miocene (Zachos et al., 2001). Bart (2003) argued that possibly the bed of the WAIS was above sea level or that ocean and atmospheric temperatures in West Antarctica were cooler than previously thought. Marine seismic records around the East Antarctic perimeter also show major erosional events beginning in the Oligocene and continuing throughout the Miocene (Anderson, 1999).

The Pliocene ice sheet configuration has been the subject of vigorous debate and two contradictory reconstructions have been proposed. One model suggests that the EAIS has remained a stable continental-scale ice sheet since the Miocene whereas the other reconstruction suggests that the size of the EAIS was dramatically reduced from the late Miocene to mid-Pliocene, allowing marine incursion into the Wilkes-Pensacola Basins (Figure A16). Part of the debate stems from alternative explanations for the presence of marine diatoms in Sirius Formation glacial deposits that outcrop in the TAM at elevations from 1,750 to 2,500 m. Webb et al. (1984) suggested that these marine diatoms reflect airborne transport and subsequent deposition, and movement of sediment by glacial ice following a major deglaciation of East Antarctica. Others have suggested that the marine diatoms were transported to the Sirius Formation directly by eolian processes (e.g., Sugden et al., 1993). Additionally, Sugden et al. (1995) reported the presence of Miocene-age glacial ice in the East Antarctic Dry Valleys, indicating stable polar conditions for at least the past 8 million years. However, cosmogenic ^3He isotope data from depth profiles of till deposits in the region indicate high ablation rates, which is inconsistent with the presence of Miocene ice (Ng et al., 2005). The Pliocene climatic conditions and ice sheet configuration remain unresolved.

The marine evidence for Pliocene ice sheet fluctuations is less controversial but does not necessarily resolve the disparate terrestrial reconstructions. Combining DSDP and ODP core data with seismic data from the eastern Ross Sea, Antarctic Peninsula, and Prydz Bay, Bart (2001) estimated that all regions of Antarctica experienced one major ice sheet advance during the early Pliocene (5–3.5 Ma) and that the Antarctic Peninsula dataset shows at least six glacial erosional unconformities during this time. Using ice volume estimates from Southern Ocean $\delta^{18}\text{O}$ records and the seismic data, Bart (2001) suggested that, at times, the Pliocene ice sheet volume might have exceeded the Last Glacial Maximum (LGM) ice volume.

Pleistocene ice sheet reconstructions benefit from the data obtained from numerous ice cores that have been drilled in East and West Antarctica. These cores provide a nearly continuous record of environmental conditions both in the ice sheet interior and near the margin. All long ice core records show clear glacial-interglacial cycles, but details vary by site. For instance, the Siple Dome core shows an abrupt 6 °C increase in temperature at 22 ka (Taylor et al., 2004). This rapid warming has not been observed in other Antarctic ice cores. Climate records from the Dome C ice core now extend back over 700,000 years (Figure A18) (EPICA community members, 2004) and provide vital information about Earth's past greenhouse gas levels, as well as local paleotemperature estimates. Preliminary isotopic data from this record indicate that the variability in EAIS surface elevation since the mid-Pleistocene is similar to the variability over the past 40 kyr (EPICA community members, 2004).

Pre-LGM ice core records and glacial geological records cannot yet be unambiguously linked because of problems with chronology and lack of sediment cores that recover pre-LGM deposits. There is some evidence of a smaller Pleistocene WAIS in the Ross Sea. Scherer et al. (1998) reported evidence for major WAIS size reduction based on the presence of Quaternary diatoms in till collected from beneath Ice Stream B (Whillans Ice Stream) in the Ross Sea sector of the WAIS.

The evolution of the Antarctic Ice Sheet during and since the LGM has been studied extensively. The marine records

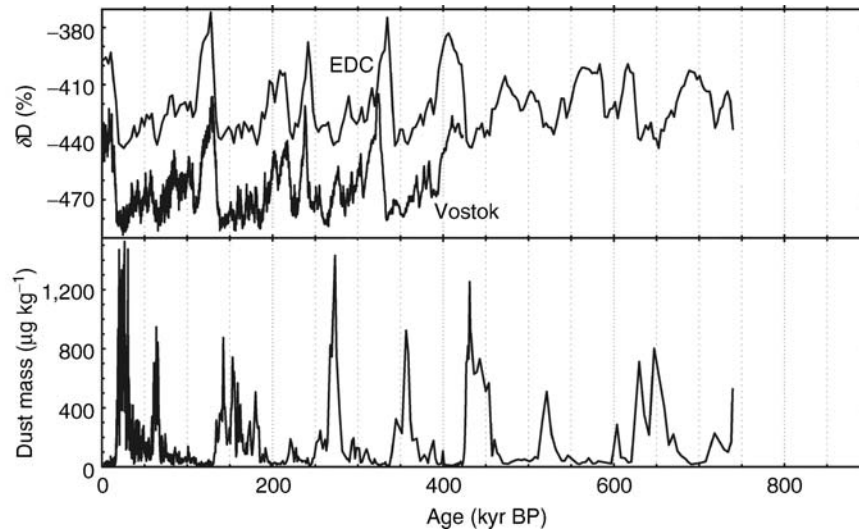


Figure A18 Dome C ice core data. δD is a temperature proxy and the Dome C data (EDC) show strong similarity to the shorter Vostok record. (Modified from EPICA community members, 2004.)

of the late Pleistocene have been accessed through piston coring, high-resolution seismic surveys and swath bathymetric surveys of the seafloor. On land, raised beaches, lacustrine sediments and moraines also provide important constraints on ice sheet history. The detailed LGM ice sheet reconstructions provide important limits for modeling exercises whose ultimate goal is predicting the fate of Antarctic ice under various climatic conditions. The chronological resolution of most continental margin records is limited by challenges with radiocarbon dating and is substantially lower than the equivalent deposits of the Northern Hemisphere. The ocean reservoir correction is well-known for carbonates (1,200–1,300 years) (Gordon and Harkness, 1992; Berkman and Forman, 1996); however, little carbonate material is preserved in the shelf sediments. The alternative of dating the acid-insoluble bulk organic fraction of marine sediments produces ages older than expected. Andrews et al. (1999) discussed strategies to correct these dates.

The timing of ice sheet advance around the continent is not well constrained for the LGM and therefore cannot provide information on the synchronicity of the behavior of the WAIS and EAIS. In the Ross Embayment, the LGM ice sheet grounded in McMurdo Sound (south of Cape Roberts) and blocked the mouths of the Dry Valleys after 26.9 ^{14}C ka and remained in that position until 12.7 ^{14}C ka (Denton and Marchant, 2000). Radiocarbon dates from central Ross Sea till show a somewhat later advance in this region, with ice reaching its maximum position as late as ~ 14 ^{14}C ka (Licht and Andrews, 2002). These data, however, do not provide the spatial resolution needed to characterize the WAIS and EAIS advances separately. The timing of ice advance across the Antarctic Peninsula, Weddell Sea and East Antarctic continental shelves is effectively unknown.

Ice-sheet size reconstructions for the LGM are constrained by terrestrial and marine geological records, which show that the WAIS and EAIS did not achieve an equilibrium thickness or position. Supporting evidence includes the observation that grounded ice did not reach the continental shelf break in many places around the perimeter, that ice of the East Antarctic interior

did not thicken substantially (Denton et al., 1989), and that ice may have only remained at its furthest extent for 2–3 kyr. Numerical models confirm that this is not an equilibrium position (e.g., Steig et al., 2001). Summaries of Antarctica's LGM ice extent and deglaciation can be found in Ingólfsson et al. (1998) and Bentley (1999) for terrestrial records, and Anderson et al. (2002) for marine records. The largest area with sparse data on ice extent and chronology is the Weddell Sea.

The characteristics of the LGM ice sheet, such as velocity, thickness and flow directions, provide important information on ice sheet dynamics. Marine geophysical studies of seafloor morphology and geometry of the strata around the Antarctic margin have been used to identify the signature of paleo ice streams. Evidence of past ice streams typically includes glacial lineations developed in deformable till (Figure A19). These features range in age from Miocene to LGM and have been reported for Prydz Bay (e.g., O'Brien and Harris, 1996), the Ross Sea (e.g., Shipp et al., 1999) and the Antarctic Peninsula (e.g., Canals et al., 2000). Past ice flow paths have been constrained for the Ross Embayment using till provenance. Recent studies have shown that till from TAM outlet glaciers and from beneath West Antarctic ice streams have unique isotopic and sand petrographic signatures that can be identified in Ross Sea till (Farmer et al., 2006; Licht et al., 2005). The central Ross Sea was identified as the zone of convergent flow from the EAIS and WAIS, which requires substantial reorganization of the West Antarctic ice streams between the LGM and today.

The timing of deglaciation from the maximum grounded ice extent was, in most places around the Antarctic margin, later than the eustatic sea level minimum at 18 ^{14}C ka, as reported by Fairbanks (1989) and subsequently confirmed at additional sites. Most records from Prydz Bay and the adjacent East Antarctic margin show evidence of initial deglaciation between 11 and 10 ^{14}C ka (summarized in Ingólfsson et al., 1998). Similarly, initial ice sheet retreat from the Antarctic Peninsula LGM positions occurred ~ 12 –11 ^{14}C ka (e.g., Domack et al., 1991; Pudsey et al., 1994). The oldest dates on raised marine deposits along the

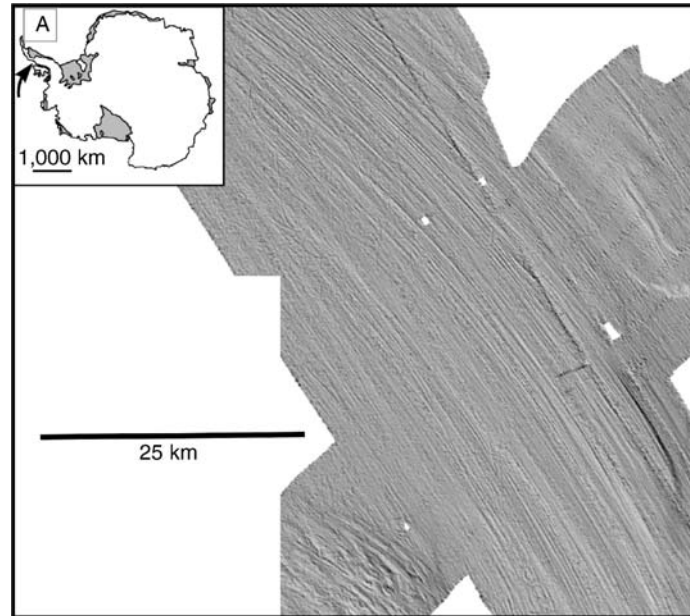


Figure A19 Glacial lineations in Marguerite Bay imaged with swath bathymetry. (Modified from Dowdeswell et al., 2004.)

Antarctic Peninsula, which indicate ice retreat onshore, range from 8.4 to 6 ^{14}C ka (Ingólfsson et al., 1998). The timing of ice sheet retreat is well constrained for the western Ross Sea, but more uncertain for the central and eastern Ross Sea (e.g., Licht and Andrews, 2002). Ice sheet retreat from the western Ross Sea began at ~ 12 ka (Domack et al., 1999), reached the Drygalski Trough at ~ 9 ka, and Ross Island at ~ 7 ka (Licht et al., 1996). The timing of ice sheet retreat from the western Ross Embayment was also estimated from a postglacial rebound curve created for the Scott Coast (west of Ross Island) (Hall and Denton, 1999). Unloading of the crust from ice sheet retreat led to coastal uplift of 8–31 m. Rapid uplift began at about 6.5 ^{14}C ka, indicating that ice sheet retreated shortly before this time. The timing of ice sheet retreat inferred from these coastal deposits agrees closely with the marine record of ice sheet retreat from the McMurdo Sound region (Licht et al., 1996). The Ross Embayment retreat chronology provides no evidence of rapid or catastrophic deglaciation (e.g., Conway et al., 1999). It is unclear whether the ice in the Weddell Sea sector of the continent behaved in lockstep with Ross Embayment ice because the deglaciation chronology is effectively unknown (Anderson et al., 2002).

The sources of rapid rises in sea level ($2\text{--}5\text{ cm yr}^{-1}$) during the latest Pleistocene, called meltwater pulse (mwp) 1A and 1B (Fairbanks, 1989), have been controversial and Antarctica has been implicated as a primary source for mwp-1A at ~ 12.5 ^{14}C ka (Clark et al., 1996). However, Antarctic deglaciation chronologies show that much of the ice retreat occurred after mwp-1A and that the ice volume reduction was too small to account for the observed rise (Licht, 2004).

More recently an increase in mean annual surface air temperature of $2.5\text{ }^{\circ}\text{C}$ has been measured at Faraday Station on the Antarctic Peninsula since 1945. This warming, plus an increase in ocean temperatures has been blamed for the recent disintegration of ice shelves on the eastern side of the Antarctic Peninsula (Rott et al., 1996) and in Pine Island Bay (Rignot, 1998). However, most of the continent is not warming and

if remains uncertain how Antarctic ice will respond to future global change and rising sea level.

Kathy Licht

Bibliography

- Anderson, J.B., 1999. *Antarctic Marine Geology*. Cambridge, UK: Cambridge University Press, 289pp.
- Anderson, J.B., Shipp, S.S., Lowe, A.L., Smith Wellner, J., and Mosola, A., 2002. The Antarctic Ice Sheet during the Last Glacial Maximum and its subsequent retreat history: A review. *Quaternary Sci. Rev.*, **21**, 49–70.
- Andrews, J.T., Domack, E.W., Cunningham, W.L., Leventer, A., Licht, K.J., Jull, A.J.T., DeMaster, D.J., and Jennings, A.E., 1999. Problems and possible solutions concerning radiocarbon dating of surface marine sediments, Ross Sea, Antarctica. *Quaternary Res.*, **52**, 206–216.
- Barker, P.F., and Thomas, E., 2003. Origin, signature and palaeoclimatic influence of the Antarctic Circumpolar Current. *Earth-Sci. Rev.*, **66**, 143–162.
- Bart, P.J., 2001. Did the Antarctic Ice Sheets expand during the early Pliocene? *Geology*, **29**, 67–70.
- Bart, P.J., 2003. Were West Antarctic Ice Sheet grounding events in the Ross Sea a consequence of East Antarctic Ice Sheet expansion during the middle Miocene? *Earth and Planetary Sci. Lett.*, **216**, 93–107.
- Bentley, M.J., 1999. Volume of the Antarctic ice at the last glacial maximum, and its impact on global sea level change. *Quaternary Sci. Rev.*, **18**, 1569–1595.
- Berkman, P.A. and Forman, S.L., 1996. Pre-bomb radiocarbon and the reservoir correction for calcareous marine species in the Southern Ocean. *Geophys. Res. Lett.*, **23**, 363–366.
- Canals, M., Urgeles, R., and Calafat, A.M., 2000. Deep sea-floor evidence of past ice streams off the Antarctic Peninsula. *Geology*, **28**, 31–34.
- Cape Roberts Science Team, 1999. Initial report on CRP-2/2A, Cape Roberts Drilling Project, Antarctica. *Terra Antarctica*, **6**(1/2), 173.
- Clark, P.U., Alley, R.B., Keigwin, L.D., Licciardi, J.M., Johnsen, S.J., and Wang, H., 1996. Origin of the first global meltwater pulse following the last glacial maximum. *Paleoceanography*, **11**, 563–577.
- Conway, H.W., Hall, B.L., Denton, G.H., Gades, A.M., and Waddington, E.D., 1999. Past and future grounding-line retreat of the West Antarctic Ice Sheet. *Science*, **286**, 280–286.

- Cooper, A.D., and O'Brien, P.E., 2004. Leg 188 Synthesis: Transitions in the glacial history of the Prydz Bay region, East Antarctica, from ODP drilling. In Cooper, A.K., O'Brien, P.E., and Richter C. (eds.), *Proceedings of the Ocean Drilling Program, Scientific Results*, **188**, http://www.odp.tamu.edu/publications/188_SR/synth/synth.htm.
- DeConto, R.M., and Pollard, D., 2003. Rapid Cenozoic glaciation of Antarctica induced by declining atmospheric CO₂. *Nature*, **421**, 245–249.
- Denton, G.H., and Marchant, D.R., 2000. The Geologic Basis for a Reconstruction of a Grounded Ice Sheet in McMurdo Sound, Antarctica, at the Last Glacial Maximum. *Geografiska Annaler, A* **82**, 167–211.
- Denton, G. H., Bockheim, J. G., Wilson, S. C., and Stuiver, M., 1989. Late Wisconsin and Early Holocene Glacial History, Inner Ross Embayment, Antarctica. *Quaternary Res.*, **31**, 151–182.
- De Santis, L., Anderson, J.B., Brancolini, G., and Zayatz, I., 1995. Seismic record of late Oligocene through Miocene glaciation on the central and eastern continental shelf of the Ross Sea. In Cooper, A.K., Barker, P.F., and Brancolini, G. (eds.), *Geology and Seismic Stratigraphy of the Antarctic Margin*, Antarctic Research Series 68. Washington, D.C.: American Geophysical Union, pp. 235–260.
- Domack, E.W., Jull, A.J.T., and Donahue, D.J., 1991. Holocene chronology for the unconsolidated sediments at Hole 740A: Prydz Bay, East Antarctica. In Barron, J., Larsen, B., et al. (eds.), *Proceedings of the Ocean Drilling Program Scientific Results*, **119**, 1–7.
- Domack, E.W., Jacobsen, E.A., Shipp, S.S., and Anderson, J.B., 1999. Late Pleistocene-Holocene retreat of the West Antarctic Ice-Sheet system in the Ross Sea: A new perspective. Part 2: Sedimentologic and stratigraphic signature. *Geological Soc. Am. Bull.*, **111**, 1517–1536.
- Dowdeswell, J.A., Ó Cofaigh, C., and Pudsey, C., 2004. Thickness and extent of the subglacial till layer beneath an Antarctic paleo-ice stream. *Geology*, **32**, 13–16.
- EPICA community members, 2004. Eight glacial cycles from an Antarctic ice core. *Nature*, **429**, 623–628.
- Fairbanks, R.G., 1989. A 17,000-year glacio-eustatic sea level record: Influence of glacial melting rates on the Younger Dryas even and deep-ocean circulation. *Nature*, **342**, 637–642.
- Farmer, G.L., Licht, K., Andrews, J.T., and Swope, R.J., 2006. Isotopic constraints on the provenance of five-grained sediment in LGM till from the Ross Embayment, Antarctica. *Earth and Planetary Science Letters*, v. 249, pp. 90–107.
- Gordon, J.E., and Harkness, D.D., 1992. Magnitude and geographic variation of the radiocarbon content in Antarctic marine life: Implications for reservoir corrections in radiocarbon dating. *Quaternary Sci. Rev.*, **11**, 697–708.
- Hall, B.L., and Denton, G.H., 1999. New relative sea-level curves for the southern Scott Coast, Antarctica: Evidence for Holocene deglaciation of the western Ross Sea. *J. Quaternary Sci.*, **14**, 641–650.
- Hambrey, M.J., 1993. Cenozoic sedimentary and climatic record, Ross Sea region, Antarctica. In Kennett J.P., and Warnke, D.A. (eds.), *The Antarctic Paleoenvironment: A Perspective on Global Change II*. Washington, D.C.: American Geophysical Union, pp. 91–124. Antarctic Research Series 60.
- Hambrey, M.J., and McKelvey, B.C., 2000. Major Neogene fluctuations of the east Antarctic Ice Sheet: Stratigraphic evidence from the Lambert Glacier region. *Geology*, **28**, 887–890.
- Hayes, D.E., and Frakes, L.A., 1975. General Synthesis, Deep Sea Drilling Project 28. In Hays, D.E., and Frakes, L.A. (eds.), *Initial Rep. Deep Sea Drilling Proj.*, **28**, 919–942.
- Ingólfsson, Ó., Hjort, C., Berkman, P.A., Björk, S., Colhoun, E., Goodwin, I., Hall, B., Hirakawa, K., Melles, M., Möller, P., and Prentice, M., 1998. Antarctic glacial history since the Last Glacial Maximum: An overview of the record on land. *Antarct. Sci.*, **10**, 326–244.
- Latimer, J.C., and Filippelli, G.M., 2002. Eocene to Miocene terrigenous inputs and export production: Geochemical evidence from ODP Leg 177, Site 1090. *Palaeogeogr., Palaeoclimatol., Palaeoecol.*, **182**, 151–164.
- Lawver, L.A., Gahagan, L.M., and Coffin, M.F., 1992. The development of paleoseaways around Antarctica. In Kennett J.P., and Warnke, D.A. (eds.), *The Antarctic Paleoenvironment: A Perspective on Global Change*. Antarctic Research Series 60. Washington, D.C.: American Geophysical Union, pp. 7–30.
- Licht, K.J., 2004. Antarctica's contribution to eustatic sea level during meltwater pulse – 1A. *Sediment. Geol.*, **165**, 343–353.
- Licht, K.J., and Andrews, J.T., 2002. The ¹⁴C Record of Late Pleistocene ice advance and retreat in the central Ross Sea, Antarctica. *Arctic, Antarctic, Alpine Res.*, **34**, 324–333.
- Licht, K.J., Jennings, A.E., Andrews, J.T., and Williams, K.M., 1996. Chronology of late Wisconsin ice retreat from the western Ross Sea, Antarctica. *Geology*, **24**, 223–226.
- Licht, K.J., Lederer, J.R., and Swope, R.J., 2005. Provenance of LGM Glacial Till (sand fraction) across the Ross Embayment, Antarctica. *Quaternary Sci. Rev.*, **24**, 1499–1520.
- Lythe, M.B., Vaughan, D.G., and the BEDMAP Consortium. 2000. BEDMAP – bed topography of the Antarctic, 1:10,000,000 scale map. BAS (Misc) 9. Cambridge, UK: British Antarctic Survey.
- Ng, F., Hallet, B., Sletten, R., and Stone, J.O., 2005. Fast-growing till over ancient ice in Beacon Valley, Antarctica. *Geology*, **33**, 121–134.
- O'Brien, P.E., and Harris, P.T., 1996. Patterns of glacial erosion and deposition in Prydz Bay and the past behavior of the Lambert Glacier. *R. Soc. Tasmania Pap. Proc.*, **130**, 79–86.
- Pudsey, C.J., Barker, P.F., and Larter, R.D., 1994. Ice sheet retreat from the Antarctic Peninsula Shelf. *Continental Shelf Res.*, **14**, 1647–1675.
- Rignot, E.J., 1998. Fast Recession of a West Antarctic Glacier. *Science*, **281**, 549–551.
- Rott, H., Skvarca, P., and Nagler, T., 1996. Rapid collapse of the Larsen Ice Shelf, Antarctica. *Science*, **271**, 788–792.
- Scherer, R.P., Aldahan, A., Tulaczyk, S., Possnert, G., Engelhardt, H., and Kamb, B., 1998. Pleistocene collapse of the West Antarctic Ice Sheet. *Science*, **281**, 82–85.
- Shackleton, N.J., and Kennett, J.P., 1975. Paleotemperature history of the Cainozoic and the initiation of Antarctic glaciation: Oxygen and carbon analyses in DSDP sites 277, 279, and 281. *Initial Rep. Deep Sea Drilling Proj.*, **29**, 743–755.
- Shipboard Scientific Party, 1999. Leg 178 Summary. *Proc. Ocean Drilling Program, Initial Rep.* **178**, 1–60.
- Shipboard Scientific Party, 2000. Leg 189 Preliminary Report: The Tasmanian Seaway between Australia and Antarctica – Paleoclimate and paleoceanography. ODP Preliminary Report 89 (online).
- Shipp, S.S., Anderson, J.B., and Domack, E.W., 1999. Late Pleistocene – Holocene retreat of the West Antarctic Ice-Sheet system in the Ross Sea: A new perspective. Part 1: Geophysical results. *Geological Soc. Am. Bull.*, **111**, 1486–1516.
- Steig, E.J., Fastook, J.L., Zweck, C., Goodwin, I.D., Licht, K.J., White, J.W.C., and Ackert, Jr., R.P., 2001. West Antarctic Ice Sheet elevation changes. In Alley, R.B., and Bindschadler, R.A. (eds.), *The West Antarctic Ice Sheet: Behavior and Environment*. Antarctic Research Series. Washington, DC: American Geophysical Union, **77**, 75–90.
- Sugden, D.E., Marchant, D.R., and Denton, G.H. (eds.) 1993. The case for a stable East Antarctic Ice Sheet. *Geografiska Annaler*, **75A**, 151–351.
- Sugden, D.E., Marchant, D.R., Potter, N. Jr., Souchez, R.A., Denton G.H., Swisher, C.C., and Tison, J.-L., 1995. Preservation of Miocene glacier ice in East Antarctica. *Nature*, **376**, 412–414.
- Taylor, K.C., White, J.W.C., Severinghaus, J.P., Brook, D.J., Mayewski, P.A., Alley, R.B., Steig, E.J., Spencer, M.K., Meyerson, E., Meese, D.A., Lamorey, G.W., Grachev, A., Gow, A.J., and Barnett, B.A., 2004. Abrupt climate change around 22 ka on the Siple Coast of Antarctica. *Quaternary Sci. Rev.*, **23**, 7–15.
- Webb, P.N., Harwood, D.M., McKelvey, B.C., Mercer, J.H., and Stott, L.D., 1984. Cenozoic marine sedimentation and ice-volume variation on the East Antarctic craton. *Geology*, **12**, 287–291.
- Zachos, J., Pagani, M., Sloan, L., Thomas, E., and Billups, K., 2001. Trends, Rhythms, and Aberrations in Global Climate 65 Ma to present. *Science*, **292**, 686–693.

Cross-references

Antarctic Sea Ice History, Late Quaternary
 Cenozoic Climate Change
 Deep Sea Drilling Project (DSDP)
 Glacial Sediments
 Glaciations, Quaternary
 Ice-Rafted Debris (IRD)
 Last Glacial Maximum
 Ocean Drilling Program (ODP)
 Oxygen Isotopes
 Plate Tectonics and Climate Change
 Radiocarbon Dating
 Sea Level Change, Post-Glacial

ANTARCTIC SEA ICE HISTORY, LATE QUATERNARY

Introduction

Sea ice results from the freezing of surface sea water. In the Southern Ocean, sea ice surrounds the Antarctic continent and it today covers 20×10^6 km² in winter and only 4×10^6 km² in summer (Gloersen et al., 1992). This pronounced seasonal cycle strongly affects the climate of the Southern Hemisphere through its impacts on the energy and gas budget, atmospheric circulation, the hydrological cycle, and biological productivity (Figure A20). Sea ice also modulates the climate of remote places through its impact on deep and intermediate oceanic circulations. More details about sea ice formation, its seasonal cycle and its importance in the climate and ocean systems can be found in the entry on *Arctic sea ice*, this volume.

Sea ice is a very reactive component of the cryosphere. It has experienced drastic changes through time. Whaling ship records (de la Mare, 1997), satellite measurements (Cavalieri et al., 2003), and ice core data (Curran et al., 2003) indicate that Antarctic sea ice underwent a dramatic decrease in maximum extent since the 1950s. Such a reduction may accelerate in the near future because of global warming, and this will in turn have important feedbacks on future climate. However, sea ice is still not well-computed in climate models because of its complicated relationship with climate change over a large range of timescales. One way to ameliorate our understanding of such relationship is to reconstruct sea ice extent over long time periods and certain key periods for which the global climate is reasonably well-known. These reconstructions, which started in the early 1980s, are still very sparse in numbers and coverage because of the scarcity of good sediment sequences in the Southern Ocean.

Three long records from the Atlantic and Indian sectors of the Southern Ocean are presented here to give an idea of sea ice dynamics over the last two climatic cycles. A map of winter and summer sea ice extent at the Last Glacial Maximum (LGM) is also shown to illustrate sea ice distribution under a very different climatic state from the present.

Long records

Long records of sea ice extent result almost exclusively from the investigation of fossil diatom assemblages preserved in deep-sea sediments. Diatoms are the most abundant photosynthetic micro-algae in Southern Ocean surface waters. The cell is surrounded by a test of biogenic silica that is generally well preserved in sediments subsequent to the organism's death. Some diatom species thriving in Antarctic waters present a strong affinity to sea ice (Horner, 1985) and are therefore most useful to estimate sea ice cover in the past.

Fossil sea ice diatoms can be used qualitatively to estimate past seasonal sea ice extent. Abundances greater than 3% of *Fragilariopsis curta* and *F. cylindrus* denote a recurrent presence of seasonal winter sea ice while abundance greater than 3% of *F. obliquicostata* marks the returning presence of summer sea ice at the core location (Gersonde and Zielinski, 2000). Increasing abundances of these taxa indicate greater sea ice cover. Fossil diatoms can also be used quantitatively, based on a statistical treatment of 30 diatom species including sea ice taxa and open ocean taxa (Crosta et al., 1998a). In this statistical method, called the Modern Analog Technique or MAT, open ocean taxa are essential in constraining the seasonal sea ice edge. The MAT compares the fossil diatom assemblages to a set of core-top diatom assemblages with known modern surface conditions that are subsequently used to attribute an estimate of sea ice duration in number of months per year to the fossil sample.

Long records of Antarctic sea ice extent are very rare and are restricted to the Atlantic and Indian sectors to date. Three records from the east Indian sector (core SO136-111, *black curve* in Figure A21), and the Atlantic sector (core TNO57-13PC4, *dark blue curve* in Figure A21; and core PS1768-8, *light blue curve* in Figure A21) are shown. Sea ice conditions at the first two core locations were estimated by MAT (Hodell et al., 2000; Shemesh et al., 2002; Crosta et al., 2004), while winter sea ice conditions at the third core site were documented by relative abundances of *F. curta* + *cylindrus* (Gersonde and Zielinski, 2000).

The three records give a very coherent picture of sea ice advance and retreat around Antarctica during the Late

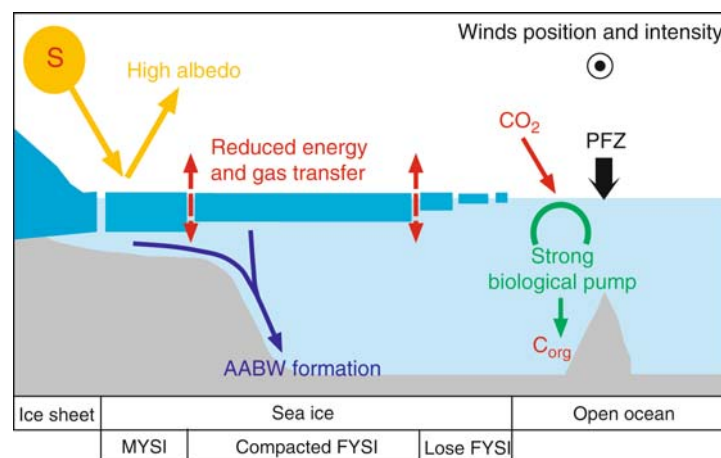


Figure A20 Schematic illustration of sea ice impacts on the Southern Hemisphere climatic system. AABW: Antarctic Bottom Water; MYSI: Multi-Year Sea Ice; FYSI: First-Year Sea Ice that freezes and melts every year. FYSI can be separated in consolidated ice (concentration above 40%) and unconsolidated ice (concentration below 40%).

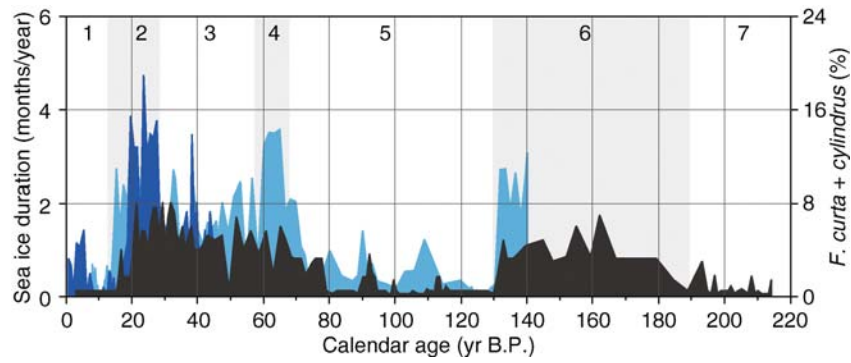


Figure A21 Sea ice history over the last 220 kyr BP. Sea ice duration was estimated by MAT in core SO136-111 from the east Indian sector of the Southern Ocean (black curve) and in core TNO57-13PC4 from the Atlantic Sector of the Southern Ocean (dark blue curve). Sea ice duration is compared to relative abundances of *F. curta* + *cylindrus* proxy of sea ice presence in core PS1768-8 (light blue curve). Core SO136-111 covers the last 220 kyr BP, core TNO57-13PC4 covers the last 40 kyr BP, and core PS1768-8 covers the last 140 kyr BP. Odd numbers and white areas represent interglacial stages while even numbers and shaded areas represent glacial stages.

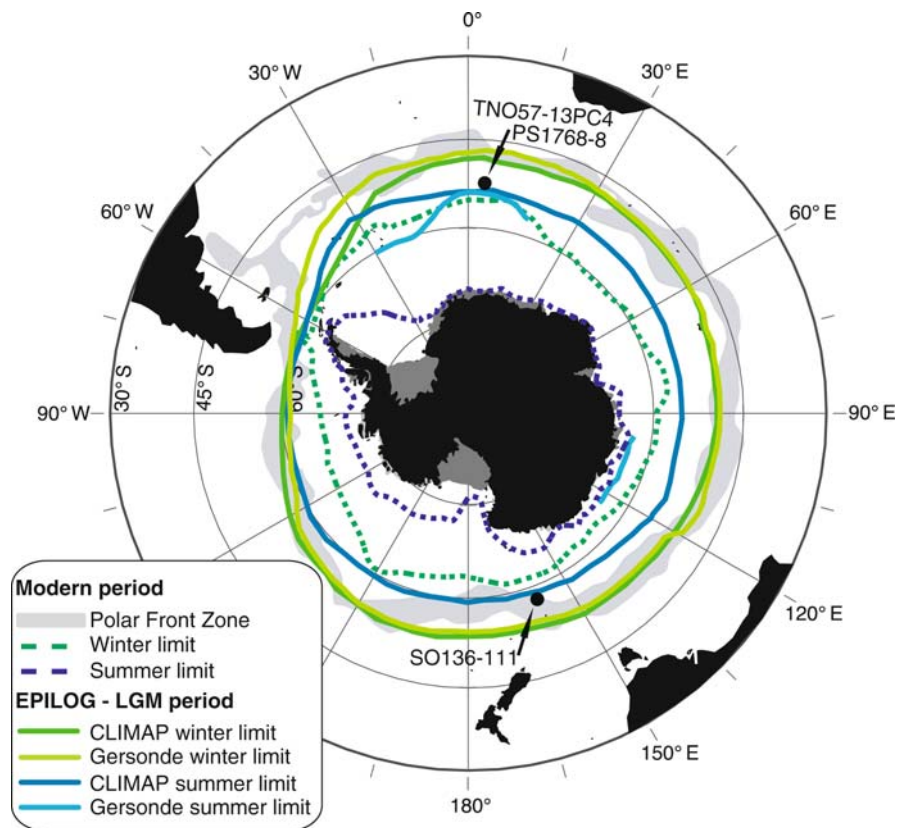


Figure A22 Comparison of LGM winter and summer sea ice edge reconstructions by CLIMAP (1981) and Gersonde et al. (2005) with modern winter and summer sea ice edges (Schweitzer, 1995).

Quaternary, although the amplitude of sea ice changes are more important in the Atlantic sector (Figure A21) in relation to the presence of the Weddell Gyre promoting northward ice transport. Today the cores are a few degrees latitude northward of the winter sea ice edge (Figure A22), and were similarly ice

free during other warm periods such as Marine Isotopic Stages 5 and 7 (MIS 5 and MIS 7 respectively). Winter sea ice extent during these periods was certainly very comparable to that of today. At interglacial-glacial transitions, sea ice advanced very rapidly to reach its full glacial extent within a few thousand

years (Figure A21). The two longest records indicate that sea ice conditions were certainly comparable during every glacial stage of the last 220 kyr. During glacial-interglacial transitions, sea ice retreats back very rapidly to its modern position within a few thousand years.

Sea ice advance and retreat are initiated by atmospheric and oceanic temperature changes but, due to the very reactive nature of sea ice, it reaches full glacial or full interglacial condition before the completion of the temperature change (Bianchi and Gersonde, 2002). Conversely, variations in sea ice cover during full glacial conditions are linked to feedback processes of wind stress and atmospheric temperatures.

Last glacial maximum

In the early 1980s, a tremendous effort was applied to reconstruct global conditions of the Earth at the Last Glacial Maximum (LGM), (CLIMAP, 1981). For the Southern Ocean, the reconstruction was based on estimates of sea-surface temperatures via a radiolarian-based transfer function and winter and summer sea ice limits via a combination of micropaleontological and lithological tracers. According to CLIMAP (1981), winter sea ice edge was 5–10° latitude northward of its modern position, overlying the modern Antarctic Polar Front (Figure A22), due to colder air and sea-surface temperatures and more intense winds. The winter sea ice cover at the LGM was therefore twice that of the modern surface. Similarly, the LGM summer sea ice edge was projected northward of its modern position, overlying the modern winter sea ice margin (Figure A22). The summer sea ice cover was thus 5–6 times greater than its modern counterpart is. A permanently covered area of around 20×10^6 km² was estimated, strongly affecting the Southern Hemisphere climate. For example, paleoclimatic models attribute a 70 ppm impact on atmospheric CO₂ to the Southern Ocean, out of the 80 ppm drop observed on the glacial-interglacial timescale when CLIMAP sea ice limits are introduced as boundary conditions (Stephens and Keeling, 2000).

Soon after the CLIMAP (1981) report, summer sea ice extent was found to actually represent spring sea ice extent (Burckle et al., 1982). However, no proxy was calibrated to document summer sea ice cover until the development of diatom-based transfer functions in the late 1990s that crystallized the relationships between diatoms and surface conditions (Zielinski and Gersonde, 1997; Crosta et al., 1998a). Diatom assemblages confirm a doubling of the winter sea ice cover at the LGM mainly due to the progression of the compacted sea ice (Burckle and Mortlock, 1998; Crosta et al., 1998b). Conversely, diatom assemblages argue for a more restricted summer sea ice cover than previously estimated (Figure A22). In the Atlantic sector, off the Weddell Sea, the glacial summer sea ice margin was certainly displaced northward to overlie the modern Antarctic Polar Front (Armand and Leventer, 2003). A similar situation probably prevailed in the western Pacific off the Ross Sea. In the Indian and the eastern Pacific, however, glacial summer sea ice cover was more comparable to modern conditions prevailing in these sectors. In the Northern Hemisphere, similarly, LGM winter sea ice cover was greatly expanded, while summer sea ice cover was comparable to today (de Vernal and Hillaire-Marcel, 2000). Paleoclimatic models estimate a 5–30 ppm impact of Antarctic sea ice cover on the glacial atmospheric CO₂ drop when sea ice extent and concentration data in agreement with diatom-based reconstructions are used as boundary conditions (Morales-Maqueda and Rahmstorf,

2002; Bopp et al., 2003). Although Antarctic sea ice, and more globally the Southern Ocean, is certainly a key component in regulating atmospheric CO₂ variations through albedo feedback, and therefore climate changes, it alone cannot explain glacial-interglacial changes in pCO₂ that are dependant upon feedbacks involving several components of the internal climate system.

Conclusion

Despite its importance in global climate change, Antarctic sea ice extent during the Late Quaternary has been weakly documented, in part because few proxies have been developed that can document past sea ice conditions and, in part, because of the lack of good sediment records. Early reconstructions of sea ice extent focused on the Last Glacial Maximum. Such reconstructions were still recently used in modeling. However, the evolution of paleoclimate models requires long records of sea ice cover to confront its dynamic response to climate changes. Very few such records exist, but they all argue for very rapid waxing and waning at climate transitions, leading to Antarctic sea ice cover doubling or halving in a few thousand years. Such variations in ice cover have deep impacts on the global climate through the albedo, the hydrological and wind systems, the deep and intermediate oceanic circulations, the transfer of gas and energy at the ocean-atmosphere interface, and the biological pump.

Xavier Crosta

Bibliography

- Armand, L., and Leventer, A., 2003. Palaeo sea ice distribution. In Thomas, D.N., and Dieckmann, G.S. (eds.), *Sea Ice: An Introduction to its Physics, Chemistry, Biology and Geology*. Oxford: Blackwell, pp. 333–372.
- Bianchi, C., and Gersonde, R., 2002. The Southern Ocean surface between Marine Isotope Stages 6 and 5d: shape and timing of climate changes. *Palaeogeogr. Palaeoclimatol. Palaeoecol.*, **187**, 151–177.
- Bopp, L., Kohfeld, K.E., Quéré, C.L., and Aumont, O., 2003. Dust impact on marine biota and atmospheric CO₂ during glacial periods. *Paleoceanography*, **18**(2), 1046. doi: 10.1029/2002PA000810, 24.1–24.17.
- Burckle, L.H., and Mortlock, R., 1998. Sea ice extent in the Southern Ocean during the last glacial maximum: Another approach to the problem. *Ann. Glaciol.*, **27**, 302–304.
- Burckle, L.H., Robinson, D., and Cooke, D., 1982. Reappraisal of sea-ice distribution in Atlantic and Pacific sectors of the Southern Ocean. *Nature*, **299**, 435–437.
- Cavaliere, D.J., Parkinson, P.L., and Vinnikov, K.Y., 2003. 30-year satellite record reveals contrasting Arctic and Antarctic decadal sea ice variability. *Geophys. Res. Lett.*, **30**(18), 1970 (doi: 10.1029/2003GL018031), 4.1–4.4.
- CLIMAP (Climate: Long range Investigation, Mapping, and Prediction), 1981. Seasonal reconstructions of the Earth's surface at the last Glacial maximum. Map series, Technical Report MC-36, Boulder, Colorado, Geological Society of America.
- Crosta, X., Pichon, J.J., and Burckle, L.H., 1998a. Application of modern analog technique to marine Antarctic diatoms: Reconstruction of the maximum sea ice extent at the last glacial maximum. *Paleoceanography*, **13**(3), 284–297.
- Crosta, X., Pichon, J.J., and Burckle, L.H., 1998b. Reappraisal of seasonal Antarctic sea-ice extent at the last glacial maximum. *Geophys. Res. Lett.*, **25**(14), 2703–2706.
- Crosta, X., Sturm, A., Armand, L., and Pichon, J.J., 2004. Late Quaternary sea ice history in the Indian sector of the Southern Ocean as recorded by diatom assemblages. *Mar. Micropaleontol.*, **50**, 209–223.
- Curran, M.A.J., Ommen, T.D.V., Morgan, V.L., Phillips, K.L., and Palmer, A.S., 2003. Ice core evidence for Antarctic sea ice decline since the 1950s. *Science*, **302**, 1203–1206.

- de la Mare, W.K., 1997. Abrupt mid-twentieth-century decline in Antarctic sea ice extent from whaling records. *Nature*, **389**, 57–60.
- de Vernal, A., and Hillaire-Marcel, C., 2000. Sea-ice cover, sea-surface salinity and halo-/thermocline structure of the northwest North Atlantic: Modern versus full glacial conditions. *Quat. Sci. Rev.*, **19**, 65–85.
- Gersonde, R., and Zielinski, U., 2000. The reconstruction of late quaternary antarctic sea-ice distribution – The use of diatoms as a proxy for sea-ice. *Palaeogeogr. Palaeoclimatol. Palaeoecol.*, **162**, 263–286.
- Gersonde, R., Crosta, X., Abelmann, A., and Armand, L.K., 2005. Sea surface temperature and sea ice distribution of the last glacial. Southern Ocean – A circum-Antarctic view based on siliceous microfossil records. *Quat. Sci. Rev.*, **24**, 869–896.
- Gloersen, P., Campbell, W.J., Cavalieri, D.J., Comiso, J.C., Parkinson, C.L., and Zwally, H.J., 1992. Arctic and Antarctic sea ice, 1978–1987: Satellite passive-microwave observations and analysis. *NASA Spec. Publ. SP-511*, National Aeronautics and Space Administration, Washington D.C., pp. 290.
- Hodell, D.A., Shemesh, A., Kanfoush, S., Crosta, X., Charles, C.D., and Guilderson, T., 2000. Abrupt cooling of Antarctic surface waters and sea ice expansion in the South Atlantic sector of the Southern Ocean at 5000 cal yr bp. *Quatern. Res.*, **56**, 191–198.
- Horner, R.A., 1985. Ecology of sea ice microalgae. In Horner, R.H. (ed.), *Sea Ice Biota*. Boca Raton, Florida: CRC Press, pp. 83–104.
- Morales-Maqueda, M.A., and Rahmstorf, S., 2002. Did Antarctic sea-ice expansion cause glacial CO₂ decline? *Geophys. Res. Lett.*, **29**(1): 1011. doi: 10.1029/2001GL013240.
- Schweitzer, P.N., 1995. *Monthly Averaged Polar Sea-Ice Concentration*. Virginia: U.S. Geological Survey Digital Data Series.
- Shemesh, A., Hodell, D.A., Crosta, X., Kanfoush, S., Charles, C.D., and Guilderson, T., 2002. Sequence of events during the last deglaciation in Southern Ocean sediments and Antarctic ice cores. *Paleoceanography*, **17**(4): 1056. doi: 10.1029/2000PA000599.
- Stephens, B.B., and Keeling, R.F., 2000. The influence of Antarctic sea ice on glacial-interglacial CO₂ variations. *Nature*, **404**, 171–174.
- Zielinski, U., and Gersonde, R., 1997. Diatom distribution in Southern Ocean surface sediments (Atlantic sector): Implications for paleoenvironmental reconstructions. *Palaeogeogr. Palaeoclimatol. Palaeoecol.*, **129**, 213–250.

Cross-references

Albedo Feedbacks
 Antarctic Glaciation History
 Arctic Sea Ice
 CLIMAP
 Cryosphere
 Diatoms
 Last Glacial Maximum
 Marine Biogenic Sediments
 Paleoclimate Modeling, Quaternary
 Radiolaria
 Transfer Functions

ARCHEAN ENVIRONMENTS

A primary research objective in the study of Archean rocks (>2.5 Ga) has been to determine conditions on the surface of the Earth during the first two billion years of its history. Recent advances in isotope geochemistry and geochemical microanalysis have allowed new insights into the earliest few hundred million years of Earth's history, and have pushed back the time at which the first life could have emerged.

The earliest subdivision of the Archean Eon beginning with Earth's accretion at 4.56 Ga and extending to ca. 4.0–3.8 Ga, has been called both the Priscoan (“previous time”) Era and Hadean (“Hell-like”) Era. These divisions of geologic time are based on the inherent bias of the rock record, making

distinctions in part based on whether or not rocks have survived. The term “Hadean” is also based on the preconception that Earth was so hot from formation and bombardment by meteorites that the atmosphere was dominated by steam and rock debris, and solid material would have been pulverized or melted (Cloud, 1972). Detrital zircon crystals (ZrSiO₄) from this period challenge this preconception (Compston and Pidgeon, 1986; Mojzsis et al., 2001; Peck et al., 2001; Wilde et al., 2001; Valley et al., 2002; Cavosie et al., 2004, 2005), and provide evidence for proto-continental crust and low temperatures at the surface of the Earth during the period 4.4–4.0 Ga.

4.57 to 4.45 Ga: the hot early earth

The most widely-cited age of the Earth is ca. 4.55 Ga as determined by Claire Patterson from lead isotopes in primitive meteorites and terrestrial sediments (Patterson, 1956). This is the age of condensation of solid material from the solar nebula (since revised to 4.56–4.57 Ga), and dates the origin of the material from which Earth began to accrete.

There are no recognized terrestrial samples from the first 150 Myr of Earth's history, thus constraints on surface conditions are inferred from isotopic data and the geologic history of the Moon. The currently accepted model of Moon formation calls for impact of the Earth with a planet-sized bolide, causing separation of the Moon from Earth's mantle (Canup and Righter, 2000). This model explains the orbit of the Moon and its geochemical similarity to Earth. The oldest Moon rocks have ages ca. 4.49 Ga, constraining the age of the catastrophic impact (Canup and Righter, 2000) and in agreement with W isotopes, which suggest formation of the Moon within 30 Myr of the Earth's accretion (Halliday, 2000).

Heat from meteorite impacts, residual heat from the Earth's accretion and core formation, and high heat production from radioactive elements likely made the surface unsuitable for the formation of oceans and continents during the beginning of Earth's history. For example, estimates of heat production from the early Earth's store of radioactive elements are on the order of 3–6 times that of today (Pollock, 1997). Conditions on the surface may have been extreme enough to form magma oceans until the waning of large impacts and the dissipation of heat into space (cf. Jones and Palme, 2000). Dissipation of heat could have resulted in rapid and turbulent mantle convection well into the Archean (Pollock, 1997). The last large terrestrial impact could have caused the resetting (and presumably planet-scale mixing) of xenon and other isotope systems at 4.45 ± 0.05 Ga (Zhang, 2002). It is possible that a slightly older impact formed the Moon. No terrestrial materials appear to have survived this last catastrophic event.

The cool early earth: evidence from 4.40 to 4.00 Ga detrital zircons

In the early 1980s newly developed ion microprobe technology was used to identify individual zircon crystals older than 4.0 Ga (Froude et al., 1983; Compston and Pidgeon, 1986). These crystals were eroded from their original host rocks, transported by water ca. 3 Ga, and are now found in metasedimentary rocks of the Narryer Gneiss Complex (Western Australia). The original ≥4.0 Ga igneous rocks are not known to have survived erosion and recycling. These Zircon crystals provide the only direct evidence for conditions at the surface of the Earth ≥4.0 Ga, as no other samples of solid material are known from this time period.

Recently, a crystal dated at 4.4 Ga was discovered (Wilde et al., 2001), providing a glimpse of conditions within 160 Myr of the Earth's accretion.

Zircons from Western Australia are evidence for 4.4–4.0 Ga rocks similar to modern continental crust. Mineral inclusions in the 4.4 Ga zircon include SiO_2 (Peck et al., 2001; Wilde et al., 2001; Cavosie et al., 2004), indicating crystallization from an evolved, silica-saturated magma. Similar conditions have been inferred for other Archean magmas based on inclusions from other 4.2–4.0 Ga zircons (Maas et al., 1992). Trace element compositions (including rare earth elements) of these zircons are also elevated relative to the mantle, consistent with crystallization from an evolved magma (Maas et al., 1992; Peck et al., 2001). All of these lines of evidence suggest the existence of igneous rocks similar to those of modern continental crust.

Isotopic analysis of these 4.4–4.0 Ga crystals has provided new constraints on surface conditions of the Earth (Peck et al., 2000, 2001; Mojzsis et al., 2001; Wilde et al., 2001; Cavosie et al., 2005). Oxygen isotope ratios ($^{18}\text{O}/^{16}\text{O}$) of these crystals are elevated relative to the primitive ratios of the Earth's mantle and the Moon (Valley, 2003). Elevated oxygen isotope ratios in terrestrial materials are most typically caused by low-temperature interaction between rocks and water at the surface of the Earth (i.e., hydrothermal alteration or low-temperature mineral formation). Magmas with elevated oxygen isotope ratios are formed by melting or assimilation of this material. The possible presence of liquid water calls into question some widely assumed conditions of the “hell-like” nature of the early Earth (Valley et al., 2002).

Emergence of continental crust

The first igneous rocks on Earth were most likely basaltic or komatiitic, with similarities to modern oceanic crust (e.g., Taylor, 1992). Lack of preservation of this crust may be due to melting and recycling back into the mantle. The timing and development of *continental* crust is a fundamental question as to surface conditions of the early Earth. The oldest recognized continental crust is 4.03 Ga granitic gneiss preserved in the Acasta Gneiss Complex, Northwest Territories, Canada. These strongly deformed rocks constitute $<20 \text{ km}^2$ of the 4.0–2.6 Ga Slave Craton. Other remnants of early (≥ 3.8 Ga) crust are limited to a few thousand square kilometers in the Uivak gneisses of Labrador, the Qianxi and Anshan Complexes in China, the Napier Complex of Antarctica, and the Isaq Gneiss Complex and Aasivik Terrane of southwestern Greenland (Figure A23). Sedimentary rocks ca. 3.5–3.0 Ga in age contain some of the oldest recognized terrestrial material: 4.4–3.2 Ga detrital zircons in the Narryer Gneiss Complex, detrital zircons as old as 4.0 Ga from the Wyoming Province, USA, and detrital zircons as old as 3.85 Ga from metasediments in the Qianxi complex (see Nutman et al., 2001). The Archean rock record is more complete for rocks ca. 3.5 Ga and younger.

The small amount of early Archean crust can either be interpreted as the surviving pieces of once extensive continental crust *or* as a reflection of the low rate of continental crust production in the early Archean. This dichotomy is reflected in different crustal growth models developed over the last 30 years: some propose rapid generation of Archean crust (most of which would be recycled), while others call for initially slow growth. Studies of middle Archean sediments support this latter view (e.g., Nutman et al., 2001), as recycled early Archean rocks constitute a minor component. This contrasts with geochemical signatures from the Acasta Gneiss, the Isaq

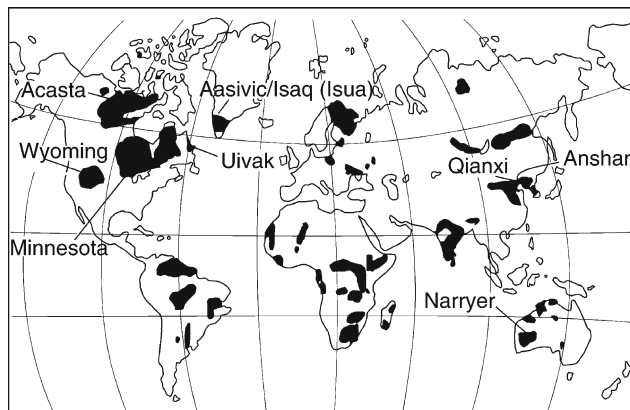


Figure A23 Preserved Archean crust (≥ 2.5 Ga), (after Bowring and Housh, 1995) and localities >3.8 , mentioned in text.

Gneiss Complex, and ≥ 4.0 Ga detrital zircons that show derivation from a mantle which had already produced crust earlier in its history (≥ 4.3 Ga; see Jacobsen, 2003 and references therein). Taken with the continental affinities of the Jack Hills detrital zircons, there is now ample evidence for continental crust between 4.4 and 4.0 Ga. Most of this original crust was eroded and/or recycled back into the mantle, perhaps aided by meteorite bombardment of the early Earth.

Timing of meteorite bombardment

Meteorite bombardment of the Earth during the period 4.4–3.8 Ga is known from the cratering record of other bodies in the inner solar system, but the terrestrial record has been erased by plate tectonics and erosion. On the Moon (where impact events have been dated) the time-integrated flux of impacts is estimated through crater density, addition of material to lunar crust, and the extent of impact stirring (Arrhenius and Lepland, 2000; Hartmann et al., 2000).

The terrestrial meteorite flux over time is controversial and has not been uniquely determined. Presumably meteorite bombardment would have been at its peak early in the Solar System's history, during and preceding extraction of the moon at ca. 4.5 Ga. The waning of impacts is not well constrained, although many lunar samples of impact glass yield a grouping of ~ 3.9 Ga ages called the “late heavy bombardment” (e.g., Cohen et al., 2000). If the rate of impacts has decreased steadily through time, then the high rate of impacting at 3.9 Ga suggests even more impacts earlier.

However, recent dating of lunar impact glasses supports an alternate hypothesis: that the cluster of 3.9 Ga ages represents a renewal of impact intensity caused by deflection of materials from the outer Solar System (Cohen et al., 2000). If the Earth was subjected to a spike of meteorite bombardment ca. 3.9 Ga, then the 4.4–4.0 Ga interval might have been relatively tranquil, consistent with cooler surface temperatures inferred from zircons crystallized during this period (see Valley et al., 2002).

The terrestrial record of bombardment is equivocal. There are no reported descriptions of shock features in 4.4–3.8 Ga zircons or rocks, as would be expected if they had been involved in large impacts. Metasedimentary rocks from southwestern Greenland (3.8–3.7 Ga) do not contain impact-related sedimentary structures (i.e., surge deposits, see Arrhenius and Lepland, 2000), nor has measurable extraterrestrial iridium

been found. However, evidence has been presented for an elevated extraterrestrial tungsten isotope signature in Isua metasediments of Greenland (Schoenberg et al., 2002), similar to evidence for extraterrestrial chromium isotopes associated with ~3.2 Ga South African beds of impact glass (Kyte et al., 2003).

The timing of the early bombardment of Earth is poorly constrained and limited by the rocks available for study. However, indirect geologic and geochemical evidence for liquid water during this period argues for at least transient periods of quiescence during bombardment. It is possible that tranquil periods allowed the precipitation of oceans between ~4.4 (the first evidence for continental crust) and 3.9 Ga (the late heavy bombardment).

Oceans

A critical parameter for evaluating surface conditions on Earth is whether or not liquid water is a stable phase, a function of both temperature and vapor pressure of the atmosphere. Supracrustal rocks in the Itsaq Gneiss Complex (the Isua and Akilia Island localities) are the earliest known rocks deposited in water: 3.8–3.7 Ga pillow lavas and chemical sediments (Myers and Crowley, 2000). The age and ultimate origin of rocks of the Akilia Island locality are controversial, but the Isua lithologies are widely accepted as having formed under submarine conditions (below wave base according to Fedo et al., 2001). The next oldest unequivocal evidence for submarine deposition, although indirect, is the abundance of metasediments ≤ 3.5 Ga worldwide. Volcanogenic massive sulfide deposits are also common in rocks ≤ 3.4 Ga and could have formed at a variety of ocean depths (including deep water $>1,000$ m; Rasmussen, 2000).

There are critical gaps in the rock record from ≥ 3.8 Ga and between 3.7 and 3.5 Ga, a period during which life is believed to have originated. A proxy for the presence of water is the geochemical signature of water-rock interaction associated with Archean detrital zircons (Peck et al., 2001; Mojzsis et al., 2001; Wilde et al., 2001; Valley et al., 2002; Cavosie et al., 2005). The elevated oxygen isotope ratios in these 4.4–4.0 Ga zircons are consistent with low-temperature exchange between rocks and water. On the modern seafloor, hydrothermal alteration \leq ca. 250 °C produces similar oxygen isotope ratios, but there is more uncertainty as to the conditions of water-rock interaction during the Archean. Lower temperature estimates are plausible if: (a) oxygen isotope ratios of the oceans have slowly risen over time (e.g., Perry, 1967), (b) meteoric waters instead of seawater were involved in Archean water-rock interaction, or (c) hydrothermal alteration was less efficient than today (Valley et al., 2002). Steam and liquid water could have coexisted at temperatures ≤ 250 °C, especially given the likelihood of periodic meteorite impacts. However, steam alone is an inefficient mechanism for exchange between water and rocks and a steam atmosphere the size of modern oceans would require temperatures outside of the oxygen isotope constraints from the detrital zircons (Valley et al., 2002).

The oxygen isotope record from zircons records the compositions of magmas from 4.4 Ga to the present (Figure A24). This record includes 4.4–4.0 and 3.6–3.2 Ga detrital zircons, and zircons in igneous rocks from ≤ 3.6 Ga. The Archean zircons came from igneous rocks that had oxygen isotope ratios ranging from mantle-like to elevated values, similar to Phanerozoic rocks but with a more limited spread (Valley, 2003). These similarities would not be expected if older rocks had formed in the absence of water and only younger ones had interacted with water (see also Campbell and Taylor, 1983).

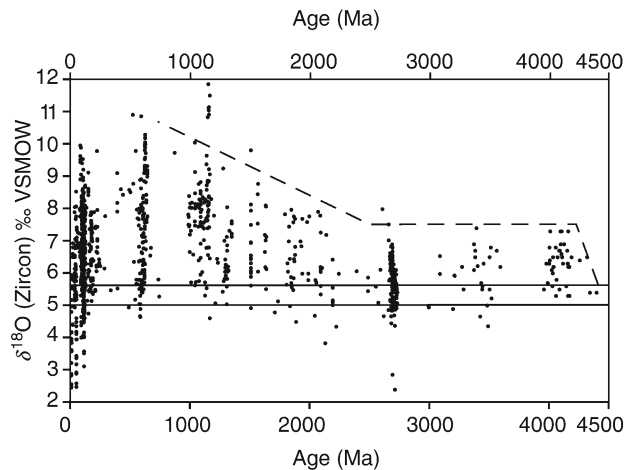


Figure A24 Oxygen isotope ratio of zircon through time (after Valley et al., 2005). Oxygen isotope ratios $\geq 6\%$ are indicative of interaction between liquid water and rocks at the surface of the Earth. Note that the signature of a liquid hydrosphere extends to samples as old as 4.4 Ga.

The constancy of isotope ratios suggests that surface temperatures from 4.4 to 4.0 Ga were similar to those of the later Archean. The increase in values starting at the Archean-Proterozoic boundary marks an increased involvement of mature supracrustal rocks (with a water-rock interaction signature) in the genesis of igneous rocks, but it is not certain if this indicates increased rates of recycling or more highly evolved compositions (Peck et al., 2000).

The temperature of Archean oceans has been controversial because 3.8–2.5 Ga chemical sediments have low oxygen isotope ratios compared to younger rocks (see Perry, 1967; Perry and Lefticaru, 2003). This has been taken to indicate any (and all combinations) of the following factors: (a) Archean ocean water temperatures of up to 80 °C, (b) lower oxygen isotope ratios of Archean ocean water, and (c) later alteration of original isotope ratios in ancient samples. The oxygen isotope ratio of the ocean seems to have been buffered at or near present levels since at least 3.6 Ga, as predicted by models and observed in hydrothermally altered rocks (see Muehlenbachs, 1998). In addition, careful sampling in ~3.5 Ga rocks has constrained the influence of post-depositional alteration. Although the oxygen isotope ratio of the ocean has certainly fluctuated within a relatively small range and some chemical sediments may have been altered, the overall evidence points towards ocean temperatures up to ca. 40 °C higher than those today as late as ~3.5 Ga (Knauth and Lowe, 2003; Perry and Lefticaru, 2003).

What was the thermal history of the hydrosphere during the Archean? During the period of accretion and heaviest bombardment of the Earth (≥ 4.5 Ga) all water must have been vapor or dissolved in silicate melts. Oxygen isotope evidence from 4.2 to 4.0 Ga zircons indicates a liquid or liquid-steam hydrosphere ≤ 250 °C. This is consistent with predictions of rapid cooling of the surface of the Earth (1–10 Myr) shortly after accretion and during waning bombardment (Pollack, 1997; Zahnle et al., 1988; Sleep et al., 2001). Late heavy bombardment of Earth at ~3.9 Ga could have vaporized Earth's oceans, but beginning at 3.6–3.8 Ga there is good geological evidence for a stable hydrosphere. It has been suggested that in order for oceans to remain liquid rather than freezing, the lower luminosity of the Sun during the Archean may have been offset by high levels

of greenhouse gases (Sagan and Chyba, 1997), or that oceans may have been partially covered by ice and warmed by submarine volcanism and periodic impacts (Bada et al., 1994).

Evidence and controversy for early life

The need to understand the timing of and conditions for the origin of life is one of the principle motivations for assessing the early Archean environment. The primary requirements for evolution of life are organic molecules, a source of energy, and liquid water. Organic molecules could have been delivered to Earth by carbonaceous meteorites and comets, and energy was available from the Sun and terrestrial volcanism. The precipitation of liquid water from an early steam-rich atmosphere was thus the final ingredient for an environment where life could have evolved during the period 4.4–4.0 Ga, perhaps to be extinguished by large bolide impacts or during the late heavy bombardment at 3.9 Ga. Theoretical limits of the habitability of the early Earth are thoroughly discussed elsewhere (see Nisbet and Sleep, 2001), but here we focus on evidence for early life from the rock record.

The earliest evidence for life is a distinctive carbon isotope signature from metamorphosed sedimentary rocks of southwestern Greenland. Low carbon isotope ratios ($^{13}\text{C}/^{12}\text{C}$) in reduced sedimentary carbon are commonly the result of isotope fractionation by biological pathways, and thus are taken as a “fingerprint” of ancient life even in the absence of preserved fossils (Schidlowski, 2001). While some studies have been controversial, the best evidence for early life comes from southwest Greenland: low carbon isotope ratios of graphite particles in clastic sedimentary rocks from 3.8 to 3.7 Ga rocks at Isua (Rosing, 1999). These rocks are preserved in low-strain zones, were clearly waterlain, and the graphite may represent original organic detritus.

The earliest fossil evidence for life are ~ 3.5 Ga microscopic structures in the Apex chert of Australia as well as numerous occurrences of stromatolites (mounds produced by photosynthetic microbes). These microstructures are interpreted as being the remains of various Archean microbes (Schopf, 1993). This claim of diversity of life has been challenged by Brasier et al. (2002), based on morphology of the features as well as a hydrothermal origin of the host-rock. However, the kero-gen-like Raman spectra and low carbon isotope ratios are strong evidence of biologic activity (Schopf et al., 2002). Furthermore, abundant stromatolites are found in associated rocks. The association of microfossils with seafloor hydrothermal systems has been recognized in rocks as old as 3.5 Ga (Van Kranendonk, 2001), supporting the hypothesis that life originally evolved near submarine vents or springs in early Archean oceans (e.g., Nisbet and Sleep, 2001).

William H. Peck and John W. Valley

Bibliography

Arrhenius, G., and Lepland, A., 2000. Accretion of moon and earth and the emergence of life. *Chem. Geol.*, **169**, 69–82.

Bada, J.L., Bigham, C., and Miller, S.L., 1994. Impact melting of frozen oceans on the early earth: Implications for the origin of life. *Proceedings of the National Academic Science*, **91**, 1248–1250.

Bowring, S.A., and Housh, T., 1995. The earth's early evolution. *Science*, **269**, 1535–1540.

Brasier, M.D., Green, O.R., Jephcoat, A.P., Kleppe, A.K., Van Kranendonk, M.J., Lindsay, J.F., Steele, A., and Grassineau, N.V., 2002. Questioning the evidence for earth's oldest fossils. *Nature*, **416**, 76–81.

Campbell, I.H., and Taylor, S.R., 1983. No water, no granites – no oceans, no continents. *Geoph. Res. Lett.*, **10**, 1061–1064.

Canup, R.M., and Righter, K., 2000. *Origin of the Earth and Moon*. Tucson: University of Arizona Press, 555p.

Cavosie, A.J., Wilde, S.A., Liu, D., Valley, J.W., and Weiblen, P.W., 2004. Internal zoning and U-Th-Pb chemistry of the Jack Hills detrital zircons: a mineral record of early Archean to mesoproterozoic magmatism. *Precam. Res.*, **135**, 251–279.

Cavosie, A.J., Valley, J.W., Wilde, S.A., and EIMF, 2005. Magmatic $\delta^{18}\text{O}$ in 4400–3900 Ma detrital zircons: A record of the alteration and recycling of crust in the early Archean. *Ear. Plan. Sci. Lett.* **235**, 663–681.

Cloud, P., 1972. A working model of the primitive earth. *Am. J. Sci.*, **272**, 537–548.

Cohen, B.A., Swindle, T.D., and Kring, D.A., 2000. Support for the lunar cataclysm hypothesis from lunar meteorite impact melt ages. *Science*, **290**, 1754–1756.

Compston, W., and Pidgeon, R.T., 1986. Jack Hills, Evidence of more very old detrital zircons in Western Australia. *Nature*, **321**, 766–769.

Fedo, C.M., Myers, J.S., and Appel, P.W.U., 2001. Depositional setting and paleogeographic implications of earth's oldest supracrustal rocks, the >3.7 Ga Isua greenstone belt, West Greenland. *Sed. Geol.*, **141/142**, 61–77.

Froude, D.O., Ireland, T.R., Kinny, P.D., Williams, I.S., Compston, W., Williams, I.R., and Myers, J.S., 1983. Ion microprobe identification of 4,100–4,200-Myr-old terrestrial zircons. *Nature*, **304**, 616–618.

Halliday, A.N., 2000. Terrestrial accretion rates and the origin of the moon. *Ear. Plan. Sci. Lett.*, **176**, 17–30.

Hartmann, W.K., Ryder, G., Dones, L., and Grinspoon, D., 2000. The time-dependent intense bombardment of the primordial earth/moon system. In: Canup, R.M., and Righter, K. (eds.), *Origin of the Earth and Moon*. Tucson: University of Arizona Press, pp. 493–512.

Jacobsen, S.B., 2003. Lost terrains of early Earth. *Nature*, **421**, 901–903.

Jones, J.H., and Palme, H., 2000. Geochemical constraints on the origin of the Earth and Moon. In: Canup, R.M., and Righter, K. (eds.), *Origin of the Earth and Moon*. Tucson: University of Arizona Press, pp. 197–216.

Knauth, L.P., and Lowe, D.R., 2003. High Archean climatic temperature inferred from oxygen isotope geochemistry of cherts in the 3.5 Ga Swaziland Supergroup, South Africa. *Geol. Soc. Am. Bull.*, **115**, 566–580.

Kyte, F.T., Shukolyukov, A., Lugmair, G.W., Lowe, D.R., and Byerly, G.R., 2003. Early Archean spherule beds: Chromium isotopes confirm origin through multiple impacts of projectiles of carbonaceous chondrite type. *Geology*, **31**, 283–286.

Maas, R., Kinny, P.D., Williams, I.S., Froude, D.O., and Compston, W., 1992. The earth's oldest known crust: A geochronological and geochemical study of 3900–4200 Ma old detrital zircons from Mt. Narryer and Jack Hills, Western Australia. *Geochim. Cosmochim. Acta*, **56**, 1281–1300.

Mojzsis, S.J., Harrison, T.M., and Pidgeon, R.T., 2001. Oxygen-isotope evidence from ancient zircons for liquid water at the earth's surface 4,300 Myr ago. *Nature*, **409**, 178–181.

Muehlenbachs, K., 1998. The oxygen isotopic composition of the oceans, sediments and the seafloor. *Chem. Geol.*, **145**, 263–273.

Myers, J.S., and Crowley, J.L., 2000. Vestiges of life in the oldest Greenland rocks? A review of early Archean geology in the Godthabsfjord region, and reappraisal of field evidence for >3850 Ma life on Akilia. *Precam. Res.*, **103**, 101–124.

Nisbet, E.G., and Sleep, N.H., 2001. The habitat and nature of early life. *Nature*, **409**, 1083–1091.

Nutman, A.P., Friend, C.R.L., and Bennett, V.C., 2001. Review of the oldest (4400–3600 Ma) geological and mineralogical record: Glimpses of the beginning. *Episodes*, **24**, 93–101.

Patterson, C.C., 1956. Age of meteorites and the earth. *Geochim. Cosmochim. Acta*, **19**, 157–159.

Peck, W.H., King, E.M., and Valley, J.W., 2000. Oxygen isotope perspective on Precambrian crustal growth and maturation. *Geology*, **28**, 363–366.

Peck, W.H., Valley, J.W., Wilde, S.A., and Graham, C.M., 2001. Oxygen isotope ratios and rare earth elements in 3.3 to 4.4 Ga Zircons: Ion microprobe evidence for high $\delta^{18}\text{O}$ continental crust in the early Archean. *Geochim. Cosmochim. Acta*, **65**, 4215–4229.

Perry, E.C. Jr., 1967. The oxygen isotope chemistry of ancient cherts. *Earth Planet. Sci. Lett.*, **3**, 62–66.

Perry, E.C., and Lefcicariu, L., 2003. Formation and geochemistry of Precambrian cherts. In: Holland, H., and Turekian, K. (eds.), *Treatise on Geochemistry*. Amsterdam: Elsevier, pp. 99–113.

- Pollock, H.N., 1997. Thermal characteristics of the Archaean. In: deWit, M., and Ashwal, L. (eds.), *Greenstone Belts*. Oxford: Oxford University Press, pp. 223–232.
- Rasmussen, B., 2000. Filamentous microfossils in a 3,235-million-year-old volcanogenic massive sulfide. *Nature*, **405**, 676–679.
- Rosing, M.T., 1999. ^{13}C -depleted carbon microparticles in >3700-Ma sea-floor sedimentary rocks from West Greenland. *Science*, **283**, 674–676.
- Sagan, C., and Chyba, C.F., 1997. The early faint Sun paradox: Organic shielding of ultraviolet-labile greenhouse gases. *Science*, **276**, 1217–1221.
- Schidlowski, M., 2001. Carbon isotopes as biogeochemical recorders of life over 3.8 Ga of earth history: Evolution of a concept. *Precam. Res.*, **106**, 117–134.
- Schoenberg, R., Kamber, B.S., Collerson, K.D., and Moorbath, S., 2002. Tungsten isotope evidence from approximately 3.8-Gyr metamorphosed sediments for early meteorite bombardment of the Earth. *Nature*, **418**, 403–405.
- Schopf, J.W., 1993. Microfossils of the early Archean Apex Chert: New evidence of the antiquity of life. *Science*, **260**, 640–646.
- Schopf, J.W., Kudryavtsev, A.B., Agresti, D.G., Wdowiak, T.J., and Czaja, A.D., 2002. Laser-Raman imagery of Earth's earliest fossils. *Nature*, **416**, 73–76.
- Sleep, N.H., Zahnle, K., and Neuhoff, P.S., 2001. Initiation of clement surface conditions on the earliest earth. *Proceedings of the National Academy of Science*, **98**, 3666–3672.
- Taylor, S.R., 1992. *Solar system evolution: A new perspective*. New York: Cambridge University Press, 307pp.
- Valley, J.W., 2003. Oxygen isotopes in zircon. In *Zircon* (eds. Hanchar, J., and Hoskins, P). *Rev. Miner. Geochem.*, **53**, 343–385.
- Valley, J.W., Peck, W.H., King, E.M., and Wilde, S.A., 2002. A cool early earth. *Geology*, **30**, 351–354.
- Valley, J.W., Lackey, J.S., Cavosie, A.J., Clechenko, C., Spicuzza, M.J., Basei, M.A.S., Bindeman, I.N., Ferreira, V.P., Sial, A.N., King, E.M., Peck, W.H., Sinha, A.K., Wei, C.S., 2005. 4.4 Billion Years of Crustal Maturation: Oxygen Isotope Ratios of Magmatic Zircon.
- Van Kranendonk, M.J., 2001. Volcanic degassing, hydrothermal circulation and the flourishing of early life on Earth: new evidence from the c. 3460 Ma Warrawoona Group, Pilbara, Western Australia. *Earth System Processes Programmes with Abstracts*, 91–92.
- Wilde, S.A., Valley, J.W., Peck, W.H., and Graham, C.M., 2001. Evidence from detrital zircons for the existence of continental crust and oceans on the earth 4.4 gyr ago. *Nature*, **409**, 175–178.
- Zahnle, K.J., Kasting, J.F., and Pollack, J.B., 1988. Evolution of a steam atmosphere during earth's accretion. *Icarus*, **74**, 62–97.
- Zhang, Y., 2002. The age and accretion of the earth. *Earth Sci. Rev.*, **59**, 235–263.

Cross-references

Atmospheric Evolution, Earth
 Bolide Impacts and Climate
 Carbon Isotopes, Stable
 Dating, Radiometric Methods
 Faint Young Sun Paradox
 Isotope Fractionation
 Oxygen Isotopes
 Stable Isotope Analysis

ARCTIC SEA ICE

Introduction

Sea ice occupies a large part of the world ocean (about 7%) and covers most of the Arctic Ocean (Figure A25), where it averages about three meters in thickness. Sea ice undergoes very large seasonal variations in its areal extent in response to changes in solar insolation. In circumpolar regions of the Northern Hemisphere, its coverage rises from approximately 7 to 15 million km² from summer to winter (see Figure A26). Sea ice is an extremely important component of the climate

system because its reflectivity plays a role in the energy budget at the Earth's surface and because it forms a barrier between the atmosphere and the ocean, thus reducing the exchange of heat, moisture and gases. Moreover, a portion of the Arctic sea ice is exported to the North Atlantic Ocean, where it becomes a source of freshwater that can interfere with deep water formation and thus with the thermohaline circulation pattern. Recent data on Arctic sea ice derived from direct observations and satellite imagery indicate large interannual variations and suggest a decreasing trend in both area and thickness during the last decades of the twentieth century. Longer-term data on a time scale ranging from 10² to 10⁶ years available from historical archives and from deep-sea sedimentary records reveal large fluctuations in the average extent of sea ice during the Quaternary, from more reduced to much more extended covers than at present, generally as a result of hemispheric-scale climate changes. For example, historical information indicates that sea ice expanded in the subpolar North Atlantic from the Medieval Warm Period to the Little Ice Age. At another time scale, biological and sedimentary tracers of sea ice demonstrate that it was significantly more widespread than at present in both the North Atlantic and North Pacific during the Last Glacial Maximum, whereas the middle Holocene warm episode seems to have been marked by reduced sea ice cover in the Arctic Ocean and circumpolar seas. The age of initial formation of the sea ice cover in the Northern Hemisphere during the late Cenozoic remains an open question, but the development of quasi-permanent pack ice in the Arctic Ocean probably occurred during the late Miocene.

Sea ice formation

Sea ice is a general term that comprises several types of ice originating from the freezing of marine waters, which occurs at a water temperature of about -1.8°C , depending upon salt content. The term “sea ice” excludes icebergs, which are massive pieces of floating freshwater ice that were calved from the front of continental glaciers. The freezing process of marine water differs from that of freshwater because it involves downward migration of brines resulting from the segregation of sea salts and ice crystals composed of almost pure water. It is a relatively complex process from a thermodynamic viewpoint since ice crystal formation induces an increase in the salt content of the surrounding seawater, thus increasing the density and decreasing the freezing point of this water.

Sea ice formation is a consequence of the cooling of marine water in response to low air temperatures. It also depends upon the structure of the water masses, since the vertical density gradient actually determines the depth of the mixed surface layer, which must cool before the surface can reach the freezing point (e.g., Barry et al., 1993). A shallow stratification in the upper water column and the presence of a low-salinity (thus, density) surface water layer are important parameters for the formation of sea ice. In the Arctic Ocean, a mixed layer with salinities often below 30‰ at the surface, overlies a generally warmer and more saline (>34.5‰) water layer originating from the Atlantic. The low salinity of the mixed layer in the Arctic Ocean results from freshwater inputs, notably from Eurasian rivers (Yenessei, Ob, Lena, Kolyma; $\sim 1,700 \text{ km}^3 \text{ yr}^{-1}$) and the Mackenzie River ($\sim 260 \text{ km}^3 \text{ yr}^{-1}$) (Carmack, 1998).

In the Arctic Ocean, a large part of the sea ice formation occurs over shallow continental shelves surrounding the basin (Figure A25), notably in the Siberian and Laptev Seas, where the shelf is particularly wide and sea surface salinity is



Figure A25 Map of the Arctic Ocean and adjacent subpolar seas. The bathymetry is indicated by 200 and 1000 meter isolines. The Arctic Ocean represents an area of approximately 9.5×10^6 km². About one third consists of shallow shelves that are roughly delimited by the 200-m isobath. A large part of sea ice formation takes place on the shelves, notably in the East Siberian and Laptev Seas.

relatively low because of large freshwater discharges from Eurasian rivers. South of the Arctic Circle, in subarctic seas and even in some mid-latitude epicontinental seas such as the Gulf of St. Lawrence in Eastern Canada, sea ice also develops seasonally at the result of a low saline, shallow (30–50 m depth) mixed layer, which fosters low thermal inertia and rapid cooling in winter.

New ice versus multiyear pack ice

When surface water reaches the freezing point, it first forms frazil ice (floating needle-shaped ice crystals) that is transformed gradually into grease ice (a slushy mixture of seawater and frazil ice) and then into floating ice. Floating ice may consist of small, circular meter-large pieces called pancake ice. It may also develop into more or less continuous fields known as pack ice, which can form a meter-thick layer of frozen ice solidly.

Sea ice develops annually, during winter. A large part of it melts during summer, but a large portion remains frozen. Sea ice that survives at least one melt season is called multiyear ice, and is distinguished from the new ice (annual sea ice and first year ice). Multiyear pack ice is typically 3–5 m thick, whereas annual ice rarely exceeds 2 m in thickness.

In general, the minimum extent of marine ice within the annual cycle corresponds to the multiyear pack ice distribution, and occurs in September. Annual ice that develops in winter

leads to a maximum coverage of about 15.0×10^6 km² in March (Figure A26), when sea ice extends southward along the East Coast of Canada and Eurasia.

The Arctic ice cap, summer pack ice, and ice motion

In the central Arctic Ocean, about 6 million km² are occupied by multiyear pack ice that remains frozen all year long. This massive Arctic pack ice is also known as the Arctic or polar ice cap and slowly rotates as a unit. Surrounding the polar ice cap, broken pieces of multiyear ice are separated by leads, which are linear fields of open water or thin ice. These pieces of multiyear ice form the summer pack ice, which never completely melts. In the Northern Hemisphere in summer, multiyear sea ice, including both the Arctic pack ice and the summer pack ice, covers a surface area of approximately 7.5×10^6 km² (see Figure A26).

A large part of the multiyear pack ice in the central Arctic originates from sea ice production over the Eurasian Shelf; from there it spreads northward toward the central Arctic Ocean to contribute to the multiyear pack ice. Depending upon the winds and surface currents, sea ice is in constant motion within the Arctic basin, and is eventually exported into the North Atlantic. The two main paths for pack ice drift are: (a) the Beaufort Gyre, which is a clockwise movement centered in the Canadian Basin, and (b) the Trans Polar Drift, which deflects ice away from the Siberian coasts across the Arctic

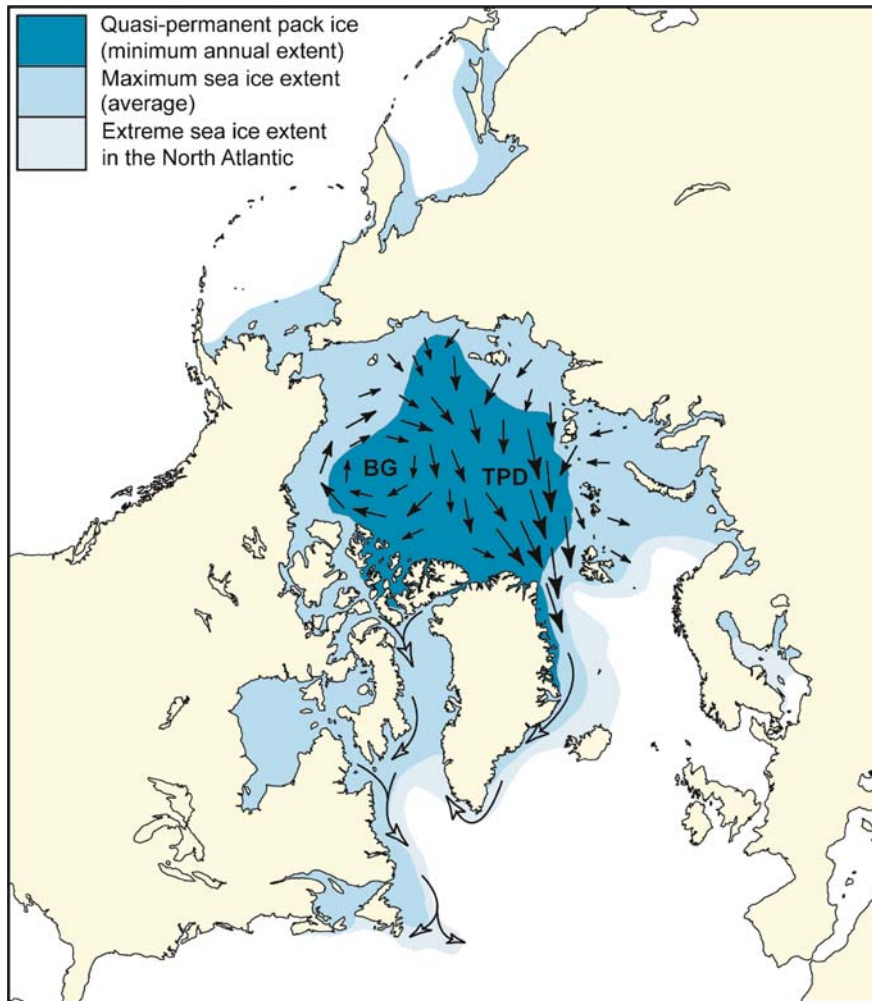


Figure A26 Map of maximum (March) and minimum (September) sea ice extent over the Northern Hemisphere. The main paths of sea ice drift, the Beaufort Gyre (*BG*) and the Trans Polar Drift (*TPD*) are schematically shown by *black arrows*. The main surface currents carrying Arctic sea ice melt waters toward the North Atlantic are illustrated by *open-end arrows*.

and toward the Atlantic Ocean (see Figure A26). The ice drift velocity ranges generally from 1 to 10 cm s^{-1} , with lower values in the Beaufort Gyre and higher values at the outlet of the Trans Polar Drift in Fram Strait. The times required for ice to make a revolution in the Beaufort Gyre and to traverse the Trans Polar Drift have been estimated to be 5–10 years, and about 3 years, respectively (e.g., Barry et al., 1993).

Biogenic productivity associated with sea ice and polynyas

Sea ice itself is a habitat for a specific food web that includes bacteria, viruses, and unicellular algae (notably diatoms) that form filaments and colonies as well as small invertebrates circulating within the brine network. The biomass in the pack ice, however, is very sparse, and the planktonic productivity below the permanent Arctic ice cap is extremely low because of much-reduced light penetration restricting photosynthetic activity and thus primary production. Higher production occurs along ice-marginal zones, which include mostly the annual sea ice that melts seasonally and also the summer ice pack. Many

unicellular algae species live within or beneath sea ice and reach a very high productivity in the ice-marginal zones. Other unicellular organisms adapted to complete their life cycle during a short ice-free season also appear to have high productivity in the ice-marginal zones, which can sustain large populations of zooplankton and animals.

Within the ice-marginal zones, areas of open water surrounded by sea ice, called polynyas, are maintained free of ice for at least several months a year through several processes, including currents, upwelling and winds. Polynyas are often characterized by a huge biological production, with fishes, mammals (seals, whales, polar bears, etc.) and birds. In the Arctic, there are several polynyas ranging from several km^2 to 50,000 km^2 .

The importance of Arctic sea ice in the climate and ocean systems

Sea ice and air temperature

Sea ice is a major component of the climate system, especially because of its high albedo or reflectance (up to about 80%), which reduces the fraction of incoming solar radiations

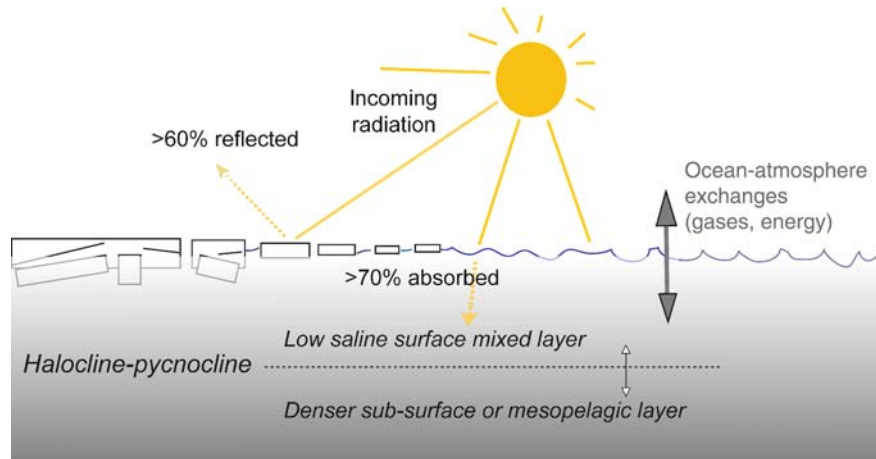


Figure A27 Schematic illustration of the role of sea ice in the climate system.

absorbed at the ocean's surface (Figure A27). The presence of sea ice therefore has an intrinsic cooling effect and its large coverage in high latitudes of both hemispheres modulates the energy budget at the Earth's surface.

Sea ice also plays a role in climate since it constitutes a barrier that restricts the heat and gas exchanges between the ocean and the atmosphere. As a consequence of sea ice, heat gain in the ocean during summer is suppressed, and heat release from the ocean to the atmosphere is also suppressed, thus further contributing to the cooling of the air during winter. In the last few decades, instrumental measurements in the Arctic indeed show an inverse correlation between sea ice cover and surface temperatures, with a spatial scope in temperature anomalies usually extending beyond sea ice boundaries (Comiso, 2002).

Beyond its cooling feedback effect, sea ice no doubt plays a role in large-scale climate conditions and atmospheric circulation pattern since it determines the surface pressure gradients.

Sea ice and thermohaline characteristics of marine waters

Freeze and thaw processes accompanying the development of seasonal sea ice determine the sea surface salinity, and therefore play a determinant role in the density and stratification of water masses. When freezing, at the bottom of the newly formed ice, seawater releases salt and brines, which sink and increase the density of underlying waters. Sea ice itself consists of almost fresh water and has a salinity ranging from 0 to 6‰. Arctic sea ice therefore is a low saline water reservoir, corresponding to a mean freshwater volume of about 17,300 km³ (Carmack, 2000). Annual sea ice melting in summer results in a low-saline buoyant surface water layer overlying a much denser water mass. As a consequence, the occurrence of seasonal sea ice is generally accompanied by the development of a strong stratification of water masses with a sharp gradient of salinity and density between a shallow surface or mixed layer and the sub-surface layer (or mesopelagic) layer.

Arctic sea ice and thermohaline circulation

A significant portion of Arctic sea ice drifts to be exported southward into the North Atlantic Ocean. The main routes for southward sea ice drift are determined by surface ocean

currents and follow the Trans Polar Drift and the eastern continental margins of Greenland and eastern Canada (Figure A26). The amount of fresh water exported from the Arctic Ocean to the North Atlantic Ocean as a result of melting of annual or summer multiyear sea ice is considerable, with a volume of approximately 3,500 and 900 km³ per year through Fram Strait and the Canadian Arctic Archipelago, respectively (Aagaard and Carmack, 1989). As a consequence, freshwater fluxes from the Arctic sea ice reservoir may play a significant role in the density of surface water in the northern North Atlantic Ocean, and thus in stratification in its water column. Because the main centers of convection and deep water formation in the North Atlantic Ocean are located in the Greenland and Labrador seas, the routes and intensity of Arctic sea ice export might prove to be critical parameters for determining the strength and pattern of the North Atlantic thermohaline circulation (e.g., Haak et al., 2003).

The instrumental record of Arctic sea ice variations

Instrumental data on Arctic sea ice have existed only for a few decades. From the nineteenth century to the middle part of the twentieth century, climatological archives and shipboard observations provide some indications on sea ice cover. After about 1953, an increasing volume of ship data, coupled with aircraft observations permitted the development of regional charts of sea ice extent and concentration. These charts combined with satellite observations starting in 1972, were used to produce comprehensive records of sea ice in the Northern Hemisphere for the last century on multidecadal time scales.

The composite instrumental record established by Walsh and Chapman (2000) suggests approximately constant year-to-year sea ice conditions during the first half of the twentieth century. It also indicates a decrease in the summer minimum sea ice cover extent starting from the mid-century, whereas winter sea ice remained unchanged until the 1970s, when the winter maximum extent started to diminish. According to Walsh and Chapman (2001), the observed decrease in both multiyear and annual sea ice covers recorded accounts for about 10% of the total coverage recorded by the beginning of the twentieth century. Other estimates also suggest that the decline in Arctic sea ice has been particularly significant during the last two decades of the twentieth century, with regard to both its extent (up to

14% according to Johannessen et al., 1999) and its thickness (up to 1–2 m locally; Rothrock et al., 2000).

Recent changes in the coverage of Arctic sea ice seem to be beyond dispute. However, the actual rate of decline in sea ice cover is difficult to evaluate quantitatively because of interannual-to-interdecadal variations (e.g., Mysak and Power, 1992; Yi et al., 1999; Comiso, 2002; Moritz et al., 2002) that obscure the longer-term trend. Moreover, the changes in ice cover extent have not been spatially uniform through space from one region to another. According to recent compilations, the largest decrease in sea ice cover has been recorded in the Western Arctic, notably in the Chukchi and East Siberian Seas (Comiso, 2002), whereas sea ice cover seems to be more extensive in the western Labrador Sea (Hill, 1998).

The linkages between Arctic sea ice and climate oscillations

Recent studies based on modeling or observations tend to illustrate linkages between high-frequency variations in Arctic sea ice and the dominant Northern Hemisphere climate oscillations, known as the Arctic (AO) and North Atlantic (NAO) oscillations (Thompson and Wallace, 1998; Greatbatch, 2000). These linkages are particularly apparent because the positive AO and NAO patterns correlate together, especially in winter (Rogers and McHugh, 2002), and correspond to intensified storm tracks through the Nordic seas, enhanced latitudinal and moisture heat fluxes toward high latitudes, and thus higher surface temperatures and a lesser extent of sea ice in the Eurasian Arctic (Dickson et al., 2000; Moritz et al., 2002). The positive AO-NAO situation also appears to be associated with an enhanced Trans Polar Drift resulting in a higher rate of Arctic sea ice export through Fram Strait toward the North Atlantic (Dickson et al., 2000; Moritz et al., 2002). Based on the record of the last 20 years of the twentieth century, the AO is considered to account to a large extent for the recent warming of the Eurasian Arctic together with a cooling over Labrador (Moritz et al., 2002).

In addition to linkages with AO-NAO, a coupling of sea ice with the thermohaline circulation in the North Atlantic may be cited. For example, particularly large freshwater outflow from the Arctic through Fram Strait in the 1960s was the source of a “great salinity anomaly” in the northern North Atlantic that apparently caused disruption of North Atlantic deep water formation through the early 1980s (Dickson et al., 1988).

The historical record of Arctic sea ice

Past records of sea ice extent in the northwestern North Atlantic are available from the accounts of voyages by Irish

monk-explorers in remote waters and Vikings who established settlements in Iceland and in southwest Greenland before the end of the first millennium (Lamb, 1977). Until AD 1200, sea ice was only occasionally reported to have caused difficulty in sailing, and all historical data suggest minimum sea ice extent around Iceland and off Greenland during the medieval warm episode, which was characterized by conditions favorable for navigation across the North Atlantic and the development of remote human settlements. Navigation reports and other historical archives show that the spread of seasonal sea ice became more and more extensive in the northern North Atlantic after AD 1250 (Figure A28). During the decade from AD 1340 to 1350, the increasing spread of Arctic sea ice around Greenland even led to the abandonment of the old sailing routes along the 65° N parallel, which caused the decline of the Viking settlements in southern Greenland.

Sedimentary tracers of sea ice changes

Remains related directly or indirectly to sea ice are found in marine sediments, permitting the reconstruction of past variations in the extent of sea ice cover or drift patterns.

Some of the proxies for sea ice are directly related to sedimentary processes. These include grain size. The coarse material (coarse silt and fine sand fractions) can be incorporated into sea ice during formation on the shelf, and thus provide indirect evidence for sea ice presence (e.g., Pfirman et al., 1990). The coarse material is entrained and transported by sea ice before it is released through melting at the sea ice margin (e.g., Hebbeln and Wefer, 1991). They also include mineralogical or geochemical analyses that permit the identification of source rocks for the detrital particles incorporated into the ice on the shallow shelves, thus allowing interpretations in terms of ice drift patterns (e.g., Bischof and Darby, 1997; Darby, 2003).

Most other sea ice proxies currently used in paleoceanography are related to biological activity, especially planktonic production in the photic zone, which is severely constrained by sea ice. Sea ice is indeed a determinant component of the ecosystem inasmuch as it influences light penetration and photosynthesis. Thus, close relationships exist between the sea ice cover and the phytoplanktonic populations. Sediments accumulated below the permanent multiyear pack ice are often devoid of biological remains whereas the sediments accumulated below the ice-marginal zone may contain abundant microfossils.

Amongst the microfossils used as sea ice proxy, diatoms are most useful because they include species specific to the ice-marginal zone. Many studies conducted in the Arctic and subarctic use diatom assemblages, which led to qualitative reconstruction of changes in sea ice cover extent during the late

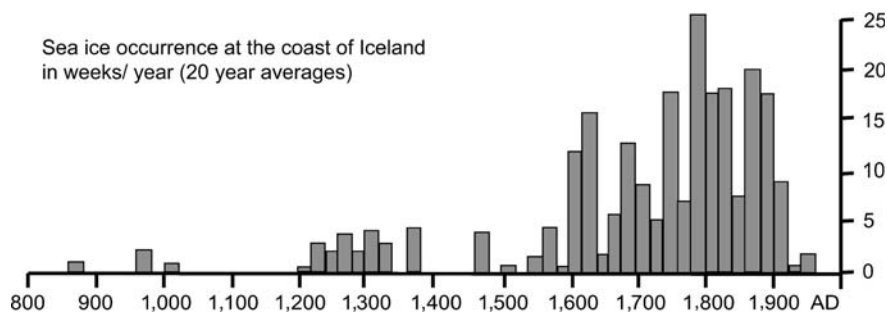


Figure A28 Historical record of sea ice occurrence around Iceland (modified from Lamb, 1977).

Quaternary in the northernmost Pacific (e.g., Sancetta, 1981, 1983), the Nordic seas (Koç et al., 1993), and the Russian Arctic seas (e.g., Bauch and Polyakova, 2000). However, because diatoms are composed of opal, which is susceptible to dissolution in marine waters unsaturated in dissolved silica, their preservation in sediment is often very poor. Other proxies of sea ice include the cysts of dinoflagellates, which yield relatively diversified and abundant organic-walled microfossils in the sea ice-marginal zone. The distribution of dinoflagellate cysts appears to depend upon the duration of the ice-free season during which the life cycle, including sexual reproduction and cyst formation, must be completed. It permitted the development of transfer functions for the quantitative reconstruction of changes in sea ice cover as expressed in number of months per year with sea ice cover (e.g., de Vernal and Hillaire-Marcel, 2000). In addition to diatoms and dinoflagellate cysts, the occurrence of a number of biological indicators, including coccoliths and foraminifera, can be used as proxies for sea ice-free conditions, at least seasonally. Biomarkers such as alkenones are also occasionally used as indicators for ice-free conditions since they rely on biogenic production of coccoliths.

Another indicator of past sea ice can be found in the continental ice cores, which may contain marine brine compounds as a result of sea ice free conditions. For example, sea salt variations in ice cores from Devon Island and Greenland have been interpreted as indices of sea ice cover changes in the adjacent marine environment (e.g., Mayewski and White, 2002).

The late Quaternary record of Arctic sea ice changes

Based on the above-mentioned proxies, there are time series that report sea ice cover variations, qualitatively (presence or absence) or quantitatively (e.g., in number of months per year; Figure A29). However, these time series have a regional value, and only very few data sets are available to develop scientifically reliable scenarios of Arctic sea ice cover during the geological past.

The interval that has been the most studied from this point of view is the Last Glacial Maximum, dated around 21,000 yBP. Maps of sea ice extent were developed at the scales of the World Ocean (CLIMAP, 1981), the circum-Antarctic oceans (Crosta et al., 1998), and the North Atlantic (de Vernal et al., 2000). These reconstructions of the LGM sea ice cover indicate that it was much more extensive than at present, in both the southern and northern hemispheres (see Figure A30). Climate modeling experiments of the LGM tend to demonstrate that such an extensive sea ice cover played a role as an important mechanism or feedback loop in the cooling recorded globally during the ice ages (e.g., Gildor and Tziperman, 2000; Hewitt et al., 2001).

Another interval in the recent geological past that has received much attention with respect to Arctic sea ice is the thermal optimum of the early- and mid-Holocene. Regional data sets illustrate reduced extent of sea ice cover as compared to present in the Nordic seas notably (Figure A31; Koç et al., 1993). In the case of the early Holocene, climate modeling also suggests that reduced sea ice may have played an amplifier role in the Northern Hemisphere warming due to high insolation (Smith et al., 2003).

The Cenozoic development of Arctic sea ice

The timing and processes at the origin of the sea ice cover in the Arctic Ocean are not accurately known or perfectly

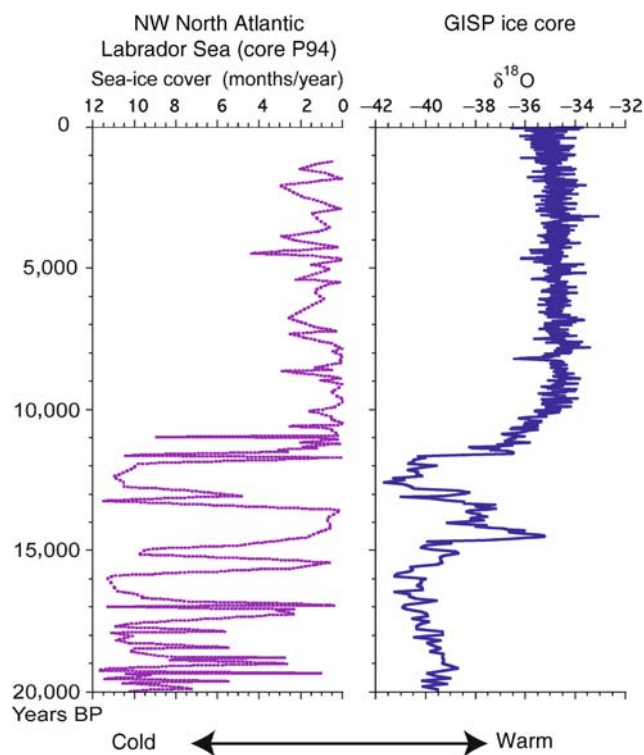


Figure A29 Example of reconstructed sea ice cover records for the last 20 kyr. The sea ice estimates (left) from a core collected in the Labrador Sea are based on dinocyst assemblages (de Vernal et al. 2000). They are compared to the GISP 2 isotopic record (right; cf. Grootes and Stuiver, 1997) on Greenland, which provides an independent record of climate.

understood. Nevertheless, the overall geological record suggests that pack ice developed during the mid-Cenozoic, after the Arctic Ocean had reached its polar, isolated position, and a bipolar glacial mode was established in the climate system (e.g., Clark, 1982; Bleil and Thiede, 1990).

During the Cretaceous and Paleocene, temperate conditions prevailed in the Arctic regions, where an ice-free ocean no doubt played a determinant role in poleward heat fluxes and the relatively uniform climates from low to high latitudes. The Arctic Ocean ice cover probably developed during the mid-Cenozoic, concomitantly with the general decrease in ocean temperatures, which is recorded worldwide on the basis of isotopic or micropaleontological data. In the Arctic Ocean, sea ice formation was likely fostered by salinity stratification due to freshwater river flows from the Eurasian continent combined with the isolation of the western Arctic from the Pacific, thus restricting exchange with oceanic waters (e.g., Clark, 1982).

The oldest sedimentary or micropaleontological indications of Arctic pack ice are Miocene in age. The development of a permanent ice cover over the Arctic Ocean may possibly date from the Late Miocene, but open ocean conditions have prevailed episodically during the Pliocene and Pleistocene according to microfossil data from Arctic cores (e.g., Clark, 1990).

In addition to sea ice cover in its strict sense, a floating ice sheet of about 1 km in thickness may have covered vast areas

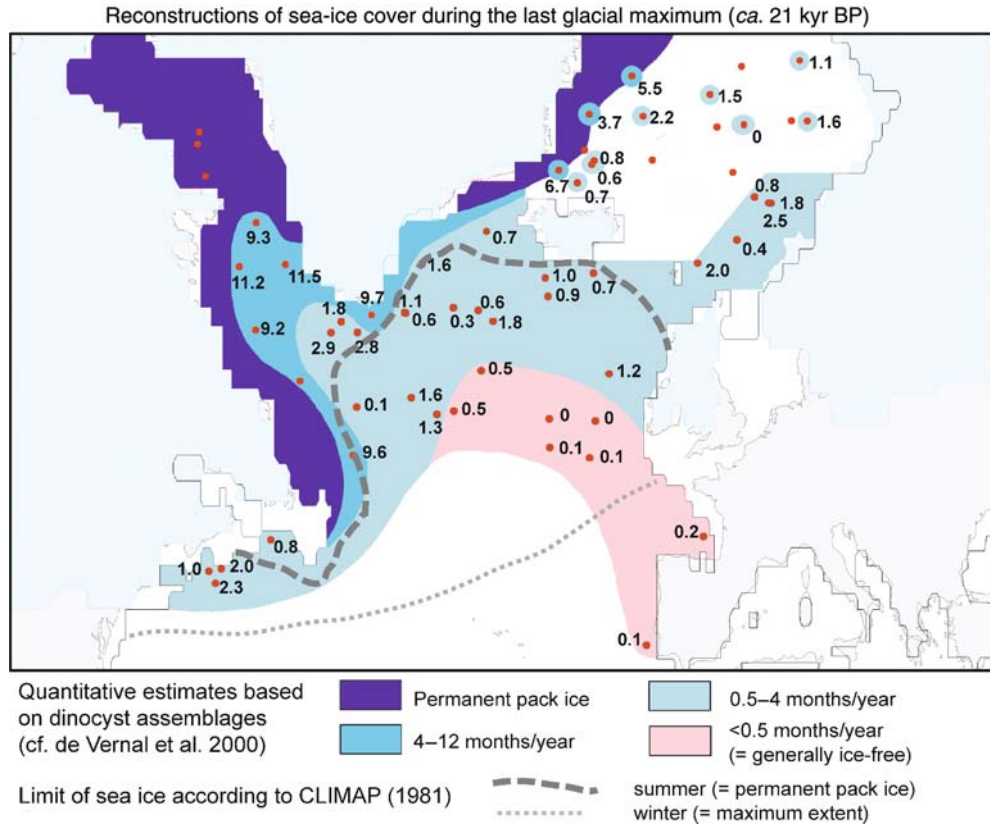


Figure A30 Map showing the reconstructed extent of sea ice cover in the northern North Atlantic during the Last Glacial Maximum. The CLIMAP estimates for the limits of sea ice are qualitatively based on indirect evidence, notably the occurrence of coccoliths and foraminifers. The quantitative estimates of sea ice occurrence in number of months per year by de Vernal et al. (2000) rely on the best analogue transfer function technique applied to dinoflagellate cyst assemblages.

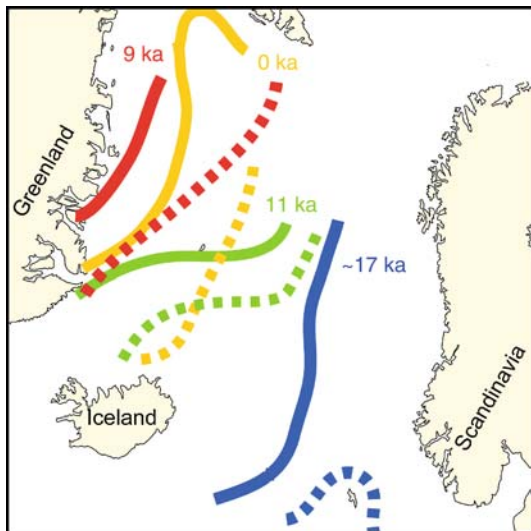


Figure A31 Map showing the variations of the sea ice limits in the Nordic seas since the Last Glacial Maximum based on diatom assemblages (Koç et al. 1993). The *full lines* represent the limit of the pack ice, whereas the *dashed lines* represent the position of the Arctic Front, which corresponds to extreme limit of the annual sea ice. The time intervals are expressed in thousand of calendar years (ka) before present.

of the Arctic Ocean during the early or mid-Pleistocene, as indicated by submarine imagery of the bottom topography showing iceberg scouring (Polyak et al., 2001).

Anne de Vernal

Bibliography

- Aagaard, K., and Carmack, E.C., 1989. The role of sea ice and other fresh waters in the Arctic circulation. *J. Geophys. Res.*, **94**, 14485–14498.
- Barry, R.G., Serreze, M.C., Maslanik, J.A., and Preller, R.H., 1993. The Arctic sea ice-climate system: Observations and modeling. *Rev. Geophys.*, **31**, 397–422.
- Bauch, H.A., and Polyakova, Y.I., 2000. Late Holocene variations in Arctic shelf hydrology and sea-ice regime: Evidence from north of the Lena Delta. *Intern. J. Earth Sci.*, **89**, 569–577.
- Bischof, J.A., and Darby, D.A., 1997. Mid to Late Pleistocene ice drift in the western Arctic Ocean: Evidence for a different circulation in the past. *Science*, **277**, 74–78.
- Bleil, U., and Thiede, J., 1990. Geological history of the Polar Oceans: Arctic versus Antarctic – An introduction. In Bleil, U., Thiede, J. (eds.), *Geological history of the Polar Oceans: Arctic Versus Antarctic*. Dordrecht: Kluwer Academic, pp. 1–8.
- Carmack, E.C., 2000. The Arctic Ocean's freshwater budget: Sources, storage and export. In Lewis, E.L., Jones, P.E., Lemke, P., Prowse, T.D., and Wadhams, P. (eds.), *The Freshwater Budget of the Arctic Ocean*. Dordrecht: Kluwer Academic, pp. 91–126.

- Clark, D.L., 1982. The Arctic Ocean and post-Jurassic paleoclimatology. In Berger, W.H., and Crowell, J.C. (eds.), *Climate in Earth History*. Washington: National Academy Press, pp. 133–138.
- Clark, D.L., 1990. Stability of the Arctic Ocean ice-cover and Pleistocene warming events: Outlining the problem. In Bleil, U., Thiede, J. (eds.), *Geological History of the Polar Oceans: Arctic Versus Antarctic*. Dordrecht: Kluwer Academic, pp. 273–287.
- CLIMAP Project Members 1981. Seasonal reconstructions of the earth's surface at the Last Glacial Maximum. *Geological Society of America Map and Chart Series MC-56*.
- Comiso, J.C., 2002. Correlation and trend studies of the sea-ice cover and surface temperatures in the Arctic. *Ann. Glaciol.*, **34**, 420–428.
- Crosta, X., Pichon, J.-J., and Burckle, L.H., 1998. Application of modern analog technique to marine Antarctic diatoms: Reconstruction of maximum sea-ice extent at the Last Glacial Maximum. *Paleoceanography*, **13**, 284–297.
- Darby, D.A., 2003. Sources of sediment found in sea ice from the western Arctic Ocean – New insights into processes of entrainments and drift patterns. *J. Geophys. Res.*, **108**, 3257.
- de Vernal, A., and Hillaire-Marcel, C., 2000. Sea ice, sea-surface salinity and the halo/thermocline structure in the northern North Atlantic: Modern versus full glacial conditions. *Quat. Sci. Rev.*, **19**, 65–85.
- de Vernal, A., Hillaire-Marcel, C., Turon, J.L., and Matthiessen, J., 2000. Sea-surface conditions in middle to high latitudes of the North Atlantic during the last glacial maximum (LGM): The cold paradigm revisited. *Can. J. Earth Sci.*, **37**, 725–750.
- Dickson, R.R., Meincke, J., Malmberg, S.A., and Lee, A.J., 1988. The “great salinity anomaly” in the North Atlantic, 1968–1982. *Progr. Oceanogr.*, **20**, 103–151.
- Dickson, R.R., Osborn, T.J., Hurrell, J.W., Meincke, J., Blindheim, J., Adlandsvik, B., Vinje, T., Alekseev, G., and Maslowski, W., 2000. The Arctic Ocean response to the North Atlantic Oscillation. *J. Climate*, **13**, 2671–2696.
- Gildor, H., and Tziperman, E., 2000. Sea ice as the glacial cycles' climate switch: Role of seasonal and orbital forcing. *Paleoceanography*, **15**, 605–615.
- Greatbatch, R.J., 2000. The North Atlantic Oscillation. *Stochastic. Env. Res. Risk assess.*, **14**, 213–242.
- Grootes, P.M., and Stuiver, M., 1997. Oxygen 18/16 variability in Greenland snow and ice with 10^{-3} to 10^5 -year time resolution. *J. Geophys. Res.*, **102**, 455–470.
- Haak, H., Jungclauss, J., Mikolajewicz, U., and Latif, M., 2003. Formation and propagation of the great salinity anomalies. *Geophys. Res. Lett.*, **30**, 26/1–26/4.
- Hebbeln, D., and Wefer, G., 1991. Effects of ice coverage and ice-rafted material on sedimentation in the Fram Strait. *Nature*, **350**, 409–411.
- Hewitt, C.D., Senior, C.A., and Mitchell, J.F.B., 2001. The impact of dynamic sea-ice on the climatology and climate sensitivity of a GCM: A study of past, present, and future climates. *Climate Dynamics*, **17**, 655–668.
- Hill, B., 1998. Historical record of sea ice and iceberg distribution around Newfoundland and Labrador, *Proceedings of the ACSYS Workshop on Sea Ice Charts of the Arctic*, Seattle, WA, pp. 5–7.
- Johannessen, O.L., Shalina, E.V., and Miles, M.W., 1999. Satellite evidence for an Arctic sea ice cover transformation. *Science*, **286**, 1937–1939.
- Koç, N., Jansen, E., and Hafliadason, H., 1993. Paleoceanographic reconstruction of surface ocean conditions in the Greenland, Iceland, and Norwegian seas through the last 14,000 years based on diatoms. *Quat. Sci. Rev.*, **12**, 115–140.
- Lamb, H.H., 1977. *Climate—Present, Past and Future*, volume 2: *Climate History and the Future*. London: Methuen & Co., 835pp.
- Mayewski, P.A., and White, F., 2002. *The ice chronicles: The quest to understand global climate change*. Hanover: University Press of New England, 233pp.
- Moritz, R.E., Bitz, C.M., and Steig, E.J., 2002. Dynamics of recent climate change in the Arctic. *Science*, **297**, 1497–1501.
- Mysak, L.A., and Power, S.B., 1992. Sea-ice anomalies in the western Arctic and Greenland-Iceland sea and their relation to an interdecadal climate cycle. *Climatol. Bull.*, **26**, 147–176.
- Pfirman, S., Lange, M.A., Wollenburg, I., and Schlosser, P., 1990. Sea ice characteristics and the role of sediment inclusions in deep-sea deposition: Arctic – Antarctic comparison. In Bleil, U., Thiede, J. (eds.), *Geological history of the Polar Oceans: Arctic Versus Antarctic*. Dordrecht: Kluwer Academic, pp. 187–211.
- Polyak, L., Edwards, M.H., Coakley, B.J., and Jakobsson, M., 2001. Ice shelves in the Pleistocene Arctic Ocean inferred from glaciogenic deep-sea bedforms. *Nature*, **410**, 453–457.
- Rogers, J.C., and McHugh, M.J., 2002. On the separability of the North Atlantic oscillation and Arctic oscillation. *Climate, Dynamics*, **19**, 599–608.
- Rothrock, D.D., Yu, Y., and Maykut, G.A., 2000. Thinning of sea ice cover. *Geophys. Res. Lett.*, **26**, 3469–3472.
- Sancetta, C., 1981. Oceanographic and ecologic significance of diatoms in surface sediments of the Bering and Okhotsk seas. *Deep-Sea Res.*, **28**, 789–817.
- Sancetta, C., 1983. Effect of Pleistocene glaciation upon oceanographic characteristics of the North Pacific Ocean and Bering Sea. *Deep-Sea Res.*, **30**, 851–869.
- Smith, L.M., Miller, G.H., Otto-Bliesner, B., and Shin, S.-I., 2003. Sensitivity of the Northern Hemisphere climate system to extreme changes in Holocene Arctic sea ice. *Quat. Sci. Rev.*, **22**, 645–658.
- Thompson, D.W.J., and Wallace, J.M., 1998. The Arctic Oscillation signature in the winter time geopotential height and temperature fields. *Geophys. Res. Lett.*, **25**, 1297–1300.
- Walsh, J.E., and Chapman, W.L., 2001. Twentieth-century sea-ice variations from observational data. *Ann. Glaciology*, **33**, 444–448.
- Yi, D., Mysak, L.A., and Venegas, S.A., 1999. Decadal-to-interdecadal fluctuations of Arctic sea-ice cover and the atmospheric circulation during 1954–1994. *Atmosphere-Ocean*, **37**, 389–415.

Cross-references

Albedo Feedbacks
 Alkenones
 Antarctic Sea Ice History, Late Quaternary
 Cenozoic Climate Change
 CLIMAP
 Coccoliths
 Diatoms
 Dinoflagellates
 Foraminifera
 Ice Cores, Antarctica and Greenland
 Last Glacial Maximum
 Little Ice Age
 Marine Biogenic Sediments
 Medieval Warm Period
 North Atlantic Deep Water and Climate Change
 North Atlantic Oscillation (NAO) records
 Thermohaline Circulation

ARID CLIMATES AND INDICATORS

The nature of aridity

Arid lands cover about a third of the Earth's land surface and occur in every continent including Antarctica (Goudie, 2002). They are areas where there is a severe shortage of moisture, predominantly because precipitation levels are low. In some years they may even receive no rain at all. In some deserts, aridity is in part also the result of high temperatures, which means that evaporation rates are great (Manguet, 1999).

Definitions of aridity relate to the water balance concept. This is a relationship that exists between the input of water in precipitation (P), the losses arising from evaporation and transpiration (evapotranspiration) (E), and any changes that may occur in storage (soil moisture, groundwater, etc.). In arid regions there is an overall deficit in water balance over a year, and the size of that deficit determines the degree of aridity. The actual amount of evapotranspiration (AE) that occurs varies according to whether there is available water to evaporate;

climatologists have therefore devised the concept of potential evapotranspiration (PE_i). This is a measure of the evapotranspiration that would take place from a standardized surface never short of water. The volume of PE_i will vary according to four climatic factors: radiation, humidity, temperature, and wind. Thornthwaite (1948) developed a general aridity index based on PE_i :

When $P = PE_i$ throughout the year, the index is 0.

When $P = 0$ throughout the year, the index is -100 .

When P greatly exceeds PE_i throughout the year, the index is $+100$.

Areas with values below -40 are regarded as arid, those with values between -20 and -40 as semi-arid, and those with values between 0 and -20 as sub-humid (Meigs, 1953). The arid category can be further subdivided into arid and extreme arid, with extreme aridity being defined as the condition in any locality where at least 12 consecutive months without any rainfall have been recorded, and in which there is not a regular seasonal rhythm of rainfall.

Extremely arid areas, such as occur in the Atacama, Namib, and the central and eastern Sahara, cover about 4% of the Earth's surface, arid about 15%, and semi-arid about 14.6%. In addition, deserts can be classified on the basis of their proximity to the oceans. Coastal deserts, such as the Namib or the Atacama have very different temperatures and humidity characteristics from the deserts of continental interiors. They have relatively modest diurnal and seasonal temperature ranges and are subject to frequent fogs. They are also very dry. In addition to the coastal and inland deserts of middle and low latitudes, there are also the cold polar deserts. Precipitation in the Arctic regions can be as low as 100 mm per annum and at Vostok in Antarctica can be less than 50 mm.

The causes of aridity

Most of the world's deserts derive their character from the fact that they receive little rainfall. This is because they tend to occur in zones where there is subsiding air, relative atmospheric stability and divergent air flows at low altitudes, associated with the presence of great high-pressure cells around latitude 30° . Such areas are seldom subjected to precipitation-bearing disturbances and depressions either from the Intertropical Convergence Zone (ITCZ) of the tropics or from the belt of mid-latitude depressions associated with the circumpolar westerlies. The trade winds that blow across these zones are evaporating winds, and, because of the trade-wind inversion, they tend to be areas of subsidence and stability.

The subtropical highs are the major cause of aridity, though deserts are not always continuous around the earth at 30° N. For instance, the Asian monsoon gives large quantities of rain over northern India, and elsewhere the high-pressure cells are disrupted into a series of local cells, notably over the oceans, where air moving clockwise around the equatorial side of the cell brings moisture-laden air to the eastern margins of the continents.

The global tendencies produced by the subtropical highs are often reinforced by local factors. Of these, *continentality* is a dominant one and plays a part in the location and characteristics of the deserts in areas like central Asia. The *rain-shadow* produced by great mountain ranges can create arid areas in their lee, as in Patagonia, where the Andes play this role. Other deserts are associated with the presence of cold currents offshore. In the case of the Namib and the Atacama, for example, any winds that do blow onshore tend to do so across cold

currents produced by the movement of water from high latitudes to low and are associated with zones of upwelling of cold waters from the depths of the oceans. Such winds are stable because they are cooled from beneath and have a relatively small moisture-bearing capacity. They reinforce the stability produced by the dominance of subsiding air in desert areas.

Indicators of aridity

Indicators of aridity can be grouped into three main categories: geomorphological, sedimentological and biological (Table A2). These indicators have demonstrated that arid conditions have been both greater and less than today and have shown frequent and substantial changes through time.

In present desert environments, indicators of higher levels of precipitation (pluvials) in the past include: high lake levels marked by ancient shorelines that are now dry, salty, closed basins; expanses of fossil soils of humid type, including laterites and other types indicative of very marked chemical changes under conditions of humidity; great spreads of spring-deposited *tufa*; river systems that are currently inactive and blocked by dune fields; and animal and plant remains, together with evidence of former human habitation, in areas now too dry for people to survive.

The evidence for formerly drier conditions includes the presence of degraded, stable sand dunes in areas that are now too wet for sand movement to occur.

Some of the more important indicators will now be considered in more detail (summarized in Table A2).

Table A2 Evidence for paleoenvironmental reconstruction in drylands

Evidence	Inference
<i>Geomorphological</i>	
Fossil dune systems	Past aridity
Breaching of dunes by rivers	Increased humidity
Discordant dune trends	Changed wind direction
Lake shorelines	Balance of hydrological inputs and outputs
Old drainage lines	Integrated hydrological network
Fluvial aggradation and siltation	Desiccation
Colluvial deposition	Reduced vegetation cover and stream flushing
Karstic (e.g., cave) phenomena	Increased hydrological activity
Frost screes	Paleotemperature
<i>Sedimentological</i>	
Lake floor sediments	Degree of salinity, etc.
Lee dune (lunette) stratigraphy	Hydrological status of lake basin
Spring deposits and tufas	Groundwater activity
Duricrusts and paleosols	Chemical weathering under humid conditions
Dust and river sediments in ocean cores	Amount of eolian and fluvial transport
Loess profiles and paleosols	Aridity and stability
<i>Biological and miscellaneous</i>	
Macro-plant remains, including charcoal (e.g., in pack-rat middens)	Vegetation cover
Pollen analysis of sediments	Vegetation cover
Faunal remains	Biome
Disjunct faunas	Biomes
Isotopic composition of groundwater and speleothems	Paleotemperature and recharge rates
Distribution of archeological sites	Availability of water
Drought and famine record	Aridity

Eolian sediments and landforms

The existence of large tracts of dunes provides unequivocal evidence of aridity, so that the existence of heavily vegetated, deeply weathered, gullied and degraded dunes indicates that there has been a shift towards more humid conditions (Tchakerian, 1999). There is some dispute about the precise precipitation thresholds that control major dune development. Undoubtedly wind strength and the nature of the vegetation cover have to be considered, but systems of palpably inactive dunes are today widespread in areas of relatively high precipitation. Dunes may also provide evidence for multiple periods of sand movement because of the presence of paleosols in them. Furthermore, comparison of modern winds and potential sandflows with those indicated by fixed dunes may suggest that there have been changes in wind regimes and atmospheric circulation.

Dunes developed from lake basins by deposition of material deflated from their beds on lee sides (lunettes) may indicate the nature of changing hydrological conditions. Dunes composed of clay pellets tend to form from desiccated saline surfaces, and those with a predominance of quartzose and sand-size material tend to form from lake beaches developed at times of higher lake levels (Bowler, 1973).

The interrelationships of dunes and rivers may indicate the alternating significance of eolian (dry) and fluvial (wet) conditions, as is made evident by consideration of the courses of some tropical rivers, which have in their histories been ponded up or blocked by dunes.

Other eolian features that have paleoclimatic significance are loess sheets. These are the product of deflation from relatively unvegetated surfaces. Within loess profiles there may be multiple paleosols that resulted from stabilization of land surfaces. A detailed treatment of the significance of such fine-grained eolian materials is provided by Pye and Sherwin (1999). In recent years, luminescence techniques have greatly facilitated the dating of aeolian sediments.

Paleolakes

The identification of high shorelines around closed lake basins and the study of deposits from cores put down through lake floors provide evidence for hydrological changes. These may be related to estimates of former higher precipitation and/or evaporation. There are problems in assessing the relative importance of temperature and precipitation in determining the water balance of a lake and some changes result from non-climatic factors (e.g., anthropogenic activity, tectonic disturbance, etc.). Nonetheless, correlations of dated shorelines and deposits have done much to improve knowledge of the extent and duration of humid phases in the Quaternary (Street and Grove, 1979).

Changes in effective precipitation may be reflected in the frequency and range of floods in desert rivers and in their load: discharge ratios. In particular, in sensitive piedmont zones, marked alternations may occur between planation and incision.

Although phases of fan aggradation and entrenchment may be a response to changes in precipitation, they can also result from tectonic changes, from changes in sediment supply resulting from changes in the operation of such temperature-controlled processes as frost-shattering, or from the inherent instability of fan surfaces.

Less contentious are the remains of fluvial systems in areas where flow is either very localized or non-existent under present conditions. For example, large wadi systems, traced by

the presence of both paleochannels and associated coarse gravel deposits, occur in hyper-arid areas such as the southeastern Sahara (Pachur and Kröpelin, 1987; Brookes, 2001).

Caves, karst, tufas and groundwaters

Solutional attack on limestones to produce karstic phenomena (e.g., major cave systems) requires water, therefore such phenomena may give some indication of past humidity. However, of more significance is that caves are major sites for deposition. Their speleothems often provide a record of environmental change that can be studied by sedimentological and isotopic means. Other sediments that may be preserved in cave systems are roof spall deposits produced by particular weathering processes.

Also of significance for environmental reconstruction are limestone precipitates that occur on the margins of limestone areas in the form of tufas (travertines). These may contain plant and animal remains, paleosols, etc., which may yield environmental information. The tufas themselves may be indicative of formerly more active groundwater and fluvial systems (Nicoll et al., 2001).

The isotopic dating of groundwater reserves has provided information on when groundwater was being recharged and when it was not. For example, Sonntag and collaborators (1980) have indicated that limited groundwater recharge in the Sahara occurred during the last glacial maximum (20,000–14,000 BP), confirming that this was a period of relative aridity.

Miscellaneous geomorphological indicators

Geomorphological indicators are often suggestive of significant change in environmental conditions, but it is often difficult to be precise about the degree of change involved, and to separate the role of climate from other influences.

In some arid areas there are weathering crusts and paleosols that exist outside what are thought to be their normal formative climatic ranges, and their current state of breakdown may indicate that they are out of equilibrium with the present climate. Examples of this are the iron-rich or silica-rich duricrusts of the southern margins of the Sahara and arid Central Australia.

Elsewhere, slope deposits provide evidence of changes in precipitation. For example, slumping along the escarpment of the plateaus of Colorado has been attributed to cooler and wetter conditions, which caused shales to become saturated and unstable. Ancient landslides are also widespread in the central Sahara (Busche, 1998). Likewise, in southern and central Africa, there are sheets of colluvium, which have infilled old drainage lines, and which may have formed when steep slopes behind the pediments on which the colluvium was deposited were destabilized by vegetation sparsity under arid conditions, providing more sediment supply than could be removed by pediment and through flowing stream systems (Price-Williams et al., 1982). The presence of extensive relict frost scree has also been seen as having climatic significance, having been produced under colder, but probably moist, conditions.

Faunal and floral remains

Pollen analysis provides evidence of past vegetation conditions, from which past climatic circumstances may, with care, be unraveled. Particular care has to be taken in assessing the significance of any pollen type that is known to be produced in large quantities and that can be preferentially transported and deposited over large distances by wind or other mechanisms.

Other evidence of past vegetation conditions is provided by charcoal, which, with the help of scanning electron microscopy, can enable the identification of woody plants, sometimes to the species level.

Inferences of paleoclimate may also be drawn from faunal remains and knowledge about their modern habitat preferences. For example, the relative proportions of grazers and browsers may indicate the importance of grassland or predominantly bushy vegetation respectively (Klein, 1980). Caves may preserve the remains of small rodents and insectivores, many of which are the result of deposition of regurgitated pellet material by birds such as owls. These can indicate environment both through their species composition and through the size of bones, which may be related to paleotemperature (Avery, 1982). In the southwestern USA there are some remarkable deposits that were accumulated by pack rats – a rodent of the genus *Neotoma*. Their middens contain extensive plant debris, and those sheltered in caves or overhangs may remain intact for tens of thousands of years (Wells, 1976).

Historical and archaeological evidence

The changing distributions and fortunes of human groups have been used to infer changes in the suitability of deserts for human habitation. The absence of human habitation has been used to infer increased aridity, while their existence in hyper-arid areas has been used to infer the existence of more humid conditions. Considerable care needs to be exercised in attributing the rise and fall of particular cultures to climatic stimuli of this type, given the range of other factors that could be important, but there are some instances where the evidence is relatively unambiguous. For example, in the hyper-arid Libyan Desert of Egypt, artefactual materials occur in areas that are far too dry for human habitation today (Wendorf et al., 1976). In historical times, attempts have been made to reconstruct African climates on the basis of famine and drought chronologies, and geographical and climatic descriptions in travelers' reports and diaries (Nicholson, 1996).

The evidence from the oceans

One of the most important developments in environmental reconstruction over the past four decades has been the use of deep-sea cores. Information derived from deep-sea cores covers long time spans. Such information is also less fragmented by past erosion and diagenesis than most terrestrial evidence.

Ocean floors off the world's major deserts have been depositories for sediments derived by aeolian and fluvial inputs from neighboring landmasses (Sirocko and Lange, 1991). These sediments contain a range of information for environmental reconstruction, and have the advantage that they may be susceptible to relatively accurate dating. They record the relative importance of fluvial and aeolian inputs, the degree of weathering of river-borne feldspars, the pollen and phytolith rain, the salinity of the ocean or sea, the intensity of monsoonal winds and of upwelling activity (Prell et al., 1980), and the temperature of offshore waters recorded by oxygen isotope ratios in foraminiferal tests.

The age of deserts

Although in the late nineteenth century and the first half of the twentieth century many deserts were regarded to be a result of post-glacial progressive desiccation, it is now clear that many

of our present desert areas are of considerable antiquity. This applies particularly in the case of the Namib and the Atacama coastal deserts. The development of their climate was closely related to plate tectonics and sea-floor spreading in that the degree of aridity must have been controlled to a considerable extent by the opening up of the seaways of the Southern Ocean, the location of Antarctica with respect to the South Pole, and the development of the cold offshore Benguela and Peruvian Currents. Arid conditions appear to have existed in the Namib for some tens of millions of years, as is made evident by such remarkable phenomena as the Tertiary Tsonab Sandstone – a lithified erg (Ward, 1988). Likewise, the Atacama appears to have been predominantly arid since at least the late Eocene, with hyper-aridity since the middle to late Miocene. The uplift of the Andes during the Oligocene and early Miocene produced a rain-shadow effect while the development of cold Antarctic bottom waters 15–13 million years ago created another crucial ingredient for aridity.

In India and Australia, the latitudinal shifts associated with sea-floor spreading caused moist conditions during much of the Tertiary, but they entered latitudes where conditions were more conducive to aridity in late Tertiary times. Isotopic studies in the Siwalik Foothills of Pakistan illustrate increasing aridity in the late Miocene. In China, Miocene uplift and a transformation of the monsoonal circulation caused the development of aridity. The eolian deposits (red clays and loess) of China may have started to form around 7.2–8.5 million years ago (Qiang et al., 2001). Indeed, it is possible that the uplift of mountains and plateaus in Tibet and North America caused a more general change in precipitation in the Late Miocene, as is made evident by the great expansion of C4 grasses in many parts of the world (Pagani et al., 1999).

With regard to the Sahara, sediment cores from the Atlantic contain eolian material that indicates that a well-developed arid area existed in North Africa in the early Miocene, around 20 million years ago (Diester-Haass and Schrader, 1979). It is possible that uplift of the Tibetan Plateau played a role, by creating a strong counter-clockwise spiral of winds that drove hot, dry air out of the interior of Asia and across Arabia and northern African (Ruddiman, 2001).

Pleistocene accentuation of aridity

Although deserts may have existed before the Pleistocene, there is evidence that aridity was intensified in many regions in the late Pliocene and Pleistocene. It appears to have become a prominent feature of the Sahara in the late Cenozoic, partly because of the cooling of the oceans and partly because the buildup of ice caps created a steeper temperature gradient between the Equator and the Poles. This in turn led to an increase in trade-wind velocities and in their ability to mobilize dust and sand. DeMenocal (1995) recognized a great acceleration in dust loadings in ocean cores off the Sahara and Arabia after 2.8 Ma, and attributed these to a decrease in sea surface temperatures associated with the initiation of extensive Northern Hemisphere glaciation. Likewise, loess deposition became more intense in China after around 2.5 Ma ago and eolian activity in the American High Plains dates back beyond 1.4 million ybp. The study of sediments from the central parts of the North Pacific suggest that eolian processes (dust deposition) became more important in the late Tertiary, accelerating greatly between 7 and 3 Ma (Leinen and Heath, 1981). It was around 2.5 Ma ago that the most dramatic increase in eolian sedimentation occurred – an increase that accompanied the onset of Northern Hemisphere glaciation. In Arabia, humid

conditions in the late Tertiary caused deep weathering and fluvial incision of lava flows dated to 3.5 Ma. Such signs are absent in early Pleistocene flows (Hötzl et al., 1978).

Environmental fluctuations within the Pleistocene

All deserts show the impact of Pleistocene climatic changes; no deserts were immune. On the one hand, the deserts expanded from time to time, covering areas that are now wooded and forested. As a consequence, stabilized sand seas occur in areas where rainfall levels are currently in excess of 800 mm. A large tract of dead ergs occurs on the south side of the Sahara from Senegal in the west to Sudan in the east, while in southern Africa the Mega-Kalahari extended into Angola, Zambia, Zimbabwe and the Congo Basin. Relict dunes are also present in various parts of South America, including the Llanos in the north and the Pampas in the south. The High Plains of America also have extensive areas of stabilized dunes. In North West India, the dunes of the Mega-Thar can be traced southwards into Gujarat and eastwards towards Delhi, while in Australia large linear dunes can be traced in the tropical north. Changes in the extent of sand seas (e.g., Sarnthein, 1978) may partly be the result of changes in precipitation, but it is also possible that high glacial trade wind velocities played a role (Ruddiman, 1997). These may also have had a marked influence on deflation and dust storm activity. There is clear evidence for increased dust inputs into the oceans at the time of the Last Glacial Maximum. Dust fluxes appear to have been 2–4 times higher than at present (Grousset et al., 1998). Studies of wind-transported materials (including diatoms deflated from desiccated lakes) have been made to plot wind strength changes over extended periods (e.g., Shi et al., 2001).

Conversely, at other times, large freshwater lakes occupied the Altiplano basins of South America, the many depressions of the Basin and Range Province in the USA (notably Lahontan and Bonneville), the Aral-Caspian of Central Asia, the Chad-Bodélé Depression in the Sahara, the Dead Sea in the Middle East and the Lake Eyre basin in Australia. Even in the hyper-arid heart of the Sahara and the Libyan Deserts, there are lake deposits, tufas, old drainage lines and other evidence of enhanced hydrological activity (Rognon, 1963).

Although some of the evidence for pluvial conditions can be explained by reduced rates of moisture loss under cooler conditions, this is by no means an adequate or universal explanation, not least for the many areas that were moist during interglacial times. It appears that inputs of precipitation were substantially increased. For example, studies of the Altiplano lakes in South America suggest that rainfall may have been 400–600 mm in areas that today receive just 200 mm (Clayton and Clapperton, 1997). Likewise, it has been estimated that, in the early Holocene, parts of the Nubian Desert, which now effectively are completely arid, received as much as 700 mm of rainfall (Hoelzmann et al., 2001).

The frequency of climatic change

In addition to being severe, climatic changes in deserts were frequent in the Quaternary. This is indicated by high-resolution studies of ocean and lake cores and because of the increasing availability of high-resolution luminescence dates for aeolian sediments. The multiple glaciations and deglaciations of high latitudes and the multiple climatic flickers within glacial and interglacials all indicate the instability of Quaternary climates. They were all associated with major changes in the oceans,

pressure systems and wind belts, which in turn impacted on deserts. Lake level fluctuations in arid basins may indicate short-lived fluctuations that correlate with Heinrich events (Benson et al., 1998) and Dansgaard-Oeschger cycles (Lin et al., 1998), while the Younger Dryas also seems to have its counterparts in arid regions (e.g., Zhou et al., 2001). Dunes were repeatedly reactivated and stabilized, both in the Pleistocene and the Holocene, lakes rose and fell over short spans of time, and pulses of dust were deposited in the world's oceans. The timing and correlation of these events is controversial, and there are reasons why climatic tendencies would have differed between temperate and tropical deserts and between northern and southern hemispheres, but a coherent pattern is starting to emerge. Dry conditions during and just after the Late Glacial Maximum and humid conditions during part of the early to mid-Holocene appear to have been characteristic of tropical deserts, though not of the southwest USA (Street and Grove, 1979).

The climatic context of change

Pluvials were not in phase in all areas and in both hemispheres (Spaulding, 1991). In a mid-latitude situation like the southwestern United States, there was greatly increased effective moisture at the time of the Last Glacial Maximum, as recognized by Smith and Street-Perrott (1983). This was partly caused by decreased rates of evaporation, but also by intensified zonal circulation and equatorward displacement of mid-latitude westerlies and associated rain-bearing depressions, particularly in winter.

Lower latitudes were much less influenced by the displaced westerlies during the full glacial, and they experienced relatively dry conditions at that time. They experienced major pluvials in early to mid-Holocene times (Grove and Goudie, 1971). Under warmer conditions monsoonal circulation was intensified, and in the Northern Hemisphere the ITCZ would have shifted northwards, bringing rainfall into areas like West Africa, Ethiopia, Arabia and Northwest India. The basis for this change may have been increased summer insolation associated with the 23,000 year rhythm of orbital precession, for at around 9,000 YBP, Milankovitch-forcing led to Northern Hemisphere summers with almost 8% more insolation than today (Kutzbach and Street-Perrott, 1985). Higher insolation caused greater heating of the land, stronger rising motion, more inflow of moist air and more summer monsoonal rainfall. In contrast, weaker insolation maxima around 35,000 and 60,000 years ago would have created weaker monsoons (Ruddiman, 2001).

Changes in insolation receipts at 9,000 BP can help to explain the Northern Hemisphere low latitude pluvial, but they have less direct relevance to the Southern Hemisphere (Tyson and Preston-Whyte, 2000). Also important in determining the spatial and temporal patterning of precipitation change are sea surface temperature conditions associated with the build-up and disintegration of the great ice-sheets (Shi et al., 2000). For example, the presence of a vigorous cold current off the Canary Islands and Northwest Africa, related to glacial meltwater and iceberg discharge into the North Atlantic, might account for arid conditions in the Late Glacial Maximum at a time when the presence of westerly winds might have been expected to produce moister conditions (Rognon and Coudé-Gaussen, 1996). Also important may have been the effects that changes in snow and ice cover over Asia, including Tibet and the Himalayas, could have had on the monsoon circulation (Zonneveld et al., 1997).

The Holocene may have experienced a series of abrupt and relatively brief climatic episodes, which have caused, for example, dune mobilization in the American High Plains (Arbogast,

1996) and alternations of pluvials and intense arid phases in tropical Africa. The Holocene in low latitudes was far from stable and benign, and it is possible that a climatic deterioration around 4,000 years ago could be involved in the mysterious collapse or eclipse of advanced civilization in Egypt, Mesopotamia, and Northwest India (Dalfes et al., 1997). These events cannot be readily accounted for by solar radiation changes, so other mechanisms need to be considered, including changes in the thermohaline circulation in the oceans, or in land surface conditions (Gasse and van Campo, 1994).

What is apparent is that the mechanisms causing changes in atmospheric circulation have been both numerous and complex, and that there will have been lagged responses to change (e.g., slow decay of ice-masses, etc.), it is also apparent that there will have been differing hemispheric and regional responses to change (deMenocal and Rind, 1993). For example, Arabia and Northeast Africa may have been especially sensitive to changes in North Atlantic sea surface temperatures, while monsoonal Asia may have been especially affected by snow and ice conditions in its high mountains and plateaux.

Andrew Goudie

Bibliography

- Arbogast, A.F., 1996. Stratigraphic evidence for late-Holocene eolian sand mobilisation and soil formation in south-central Kansas, USA. *J. Arid Environ.*, **34**, 403–414.
- Avery, D.M., 1982. Micromammals as palaeoenvironmental indicators and an interpretation of the Late Quaternary in the Southern Cape Province, South Africa. *Ann. S. Afr. Mus.*, **85**, 183–374.
- Benson, L., Lund, S.P., Burdett, J.W., Kashgarian, M., Rose, T.P., Smoot, J.P., and Schwartz, M., 1998. Correlation of Late-Pleistocene Lake-Level oscillations in Mono Lake, California, with North Atlantic climate events. *Quaternary Res.*, **49**, 1–10.
- Bowler, J.M., 1973. Clay dunes: Their occurrence, formation and environmental significance. *Earth-Sci. Rev.*, **9**, 315–338.
- Brookes, I.A., 2001. Possible Miocene catastrophic flooding in Egypt's Western Desert. *J. Afr. Earth Sci.*, **32**, 325–333.
- Busche, D., 1998. Die Zentrale Sahara. Gotha: Justus Perthes Verlag.
- Clayton, J.D., and Clapperton, C.M., 1997. Broad synchrony of a late-glacial advance and the highstand of palaeolake Tauca in the Bolivian Altiplano. *J. Quaternary Sci.*, **12**(3), 169–182.
- Dalfes, H.N., Kukla, G., and Weiss, H. (eds.), 1997 *Third Millennium bc Climate Change and Old World Collapse*. Berlin: Springer Verlag.
- DeMenocal, P.B., 1995. Plio-Pleistocene African climate. *Science*, **270**, 53–59.
- DeMenocal, P.B., and Rind, D., 1993. Sensitivity of Asian and African Climate to variations in seasonal insolation, glacial ice cover, sea surface temperature and Asian orography. *J. Geophys. Res.*, **98**(D4), 7265–7287.
- Diester-Haass, L., and Schrader, H.J., 1979. Neogene coastal upwelling history off north-west and south-west Africa. *Mar. Geol.*, **29**, 39–53.
- Gasse, F., and Van Campo, E., 1994. Abrupt post-glacial climate events in west Africa and North Africa monsoon domains. *Earth Planet. Sci. Lett.*, **126**, 435–456.
- Goudie, A.S., 2002. Great warm deserts of the world: Landscape and evolution. Oxford: Oxford University Press.
- Grousset, F.E., Parra, M., Bory, A., Martinez, P., Bertrand, P., Shimmield, G., and Ellam, R.M., 1998. Saharan wind regimes traces by the Sr-Nd isotopic composition of subtropical Atlantic sediments: Last Glacial Maximum versus today. *Quaternary Sci. Rev.*, **17**, 395–409.
- Grove, A.T., and Goudie, A.S., 1971. Late Quaternary Lake Levels in the Rift Valley of Southern Ethiopia and elsewhere in Tropical Africa. *Nature*, **234**, 403–405.
- Hoelzmann, P., Keding, B., Berke, H., Kropelin, S., and Kruse H.-J., 2001. Environmental change and archaeology: Lake evolution and human occupation in the Eastern Sahara during the Holocene. *Palaeogeogr. Palaeoclimatol. Palaeoecol.*, **169**, 193–217.
- Hötzl, J., Kramer, F., and Maurin, V., 1978. Quaternary sediments. In Al-Sayari, S., and Zötl, J.G. (eds.), *Quaternary Period in Saudi Arabia*. Vienna: Springer Verlag, pp. 264–311.
- Klein, R.G., 1980. Environmental and ecological implications of large mammals from Upper Pleistocene and Holocene sites in Southern Africa. *Ann. S. Afr. Mus.*, **81**, 223–83.
- Kutzbach, J., and Street-Perrott, F.A., 1985. Milankovitch forcing of fluctuations in the level of tropical lakes from 18 to 0 kyr BP. *Nature*, **317**, 130–134.
- Leinen, M., and Heath, G.R., 1981. Sedimentary indicators of atmospheric activity in the northern hemisphere during the Cenozoic. *Palaeogeogr. Palaeoclimatol. Palaeoecol.*, **36**, 1–21.
- Lin, J.C., Broecker, W.S., Hemming, S.R., Hajdas, I., Anderson, R.S., Smith, G.L., Kelley, M., and Bonani, G., 1998. A reassessment of U-Th and ¹⁴C ages for Late-Glacial High-Frequency hydrological events at Searles Lake, California. *Quaternary Res.*, **49**, 11–23.
- Manguet, M., 1999. Aridity, Droughts and Human Development. Heidelberg: Springer.
- Meigs, P., 1953. World distribution of arid and semi-arid homoclimate. *UNESCO Arid Zone Res. Ser.*, **1**, 203–209.
- Nicholson, S.E., 1996. Environmental change within the historical period. In Adams, W.M., Goudie, A.S., and Orme, A.R. (eds.), *The Physical Geography of Africa*. Oxford: Oxford University Press, pp. 60–87.
- Nicoll, K., Giegengack, R., and Kleindienst, M., 2001. Petrogenesis of artifact-bearing fossil-spring tufa deposits from Kharga Oasis, Egypt. *Geoarchaeology*, **14**, 849–863.
- Pachur, H.J., and Kropelin, S., 1987. Wadi Hower: Paleoclimatic evidence from an extinct river system in the southeastern Sahara. *Science*, **237**, 298–300.
- Pagani, M., Freeman, K.H., and Arthur, M.A., 1999. Late Miocene atmospheric CO₂ concentrations and the expansion of C₄ grasses. *Science*, **285**, 876–879.
- Prell, W.L., Hutson, W.H., Williams, D.F., Be, A.W.H., Geitzenauer, K., and Molino, B., 1980. Surface circulation of the Indian Ocean during the last glacial maximum, approximately 18,000 BP. *Quaternary Res.*, **14**, 309–336.
- Price-Williams, D., Watson, A., and Goudie, A.S., 1982. Quaternary colluvial stratigraphy, archaeological sequences and palaeoenvironments in Swaziland, Southern Africa. *Geogr. J.*, **148**, 50–67.
- Pye, K., and Sherwin, D., 1999. Loess. In Goudie, A.S., Livingstone, I., and Stokes, S. (eds.), *Aeolian Environments, Sediments and Landforms*. Chichester: Wiley, pp. 214–38.
- Qiang, X.K., Li, Z.X., Powell, C., and McA., Zheng, H. B., 2001. Magnetostratigraphic record of the Late Miocene onset of the East Asian monsoon, and Pliocene uplift of northern Tibet. *Earth Planet. Sci. Lett.*, **187**, 83–93.
- Rognon, P., 1963. L'Evolution des formes de relief dans l'Atakor (Hoggar Central). *Travaux Institut Recherches Sahariennes*, **22**, 61–78.
- Rognon, P., and Coudé-Gaussen, G., 1996. Paleoclimates off Northwest Africa (28°–35° N) about 18,000 yr BP based on continental Aeolian deposits. *Quaternary Res.*, **46**, 118–126.
- Ruddiman, W.F., 1997. Tropical Atlantic terrigenous fluxes since 25,000 yBP. *Mar. Geol.*, **136**, 189–207.
- Ruddiman, W.F., 2001. *Earth's Climate: Past and Future*. New York: W.H. Freeman and Company.
- Sarnthein, M., 1978. Sand deserts during the last glacial maximum and climatic optimum. *Nature*, **272**, 43–46.
- Shi, N., Dupont, L.M., Beug, H.-J., and Schneider, R., 2000. Correlation between vegetation in Southwest Africa and oceanic upwelling in the past 21,000 years. *Quaternary Res.*, **54**, 72–80.
- Shi, N., Schneider, R., Beug, H.-J., and Dupont, L.M., 2001. Southeast trade wind variations during the last 135 kyr: Evidence from pollen spectra in eastern South Atlantic sediments. *Earth Planet. Sci. Lett.*, **187**, 311–321.
- Sirocko, F., and Lange H., 1991. Clay mineral accumulation rates in the Arabian Sea during the later Quaternary. *Mar. Geol.*, **97**, 105–119.
- Smith, G.I., and Street-Perrott, F.A., 1983. Pluvial lakes of the western United States. In Porter, S.C. (ed.), *Late Quaternary Environments of the United States: The Late Pleistocene*. London: Longman, pp. 190–212.
- Sonntag, C., Thorweite, R.J., Lohner, E.P., Junghans, C., Munnick, K.O., Klitzsch, E., El Shazly, E.M., and Swailem, F.M., 1980. Isotopic identification of Saharan groundwater – groundwater formation in the past. *Palaeoecol. Afr.*, **12**, 159–171.

- Spaulding, W.G., 1991. Pluvial climatic episodes in North America and North Africa: Types and correlation with global climate. *Palaeogeogr. Palaeoclimatol. Palaeoecol.*, **84**, 217–229.
- Street, F.A., and Grove, A.T., 1979. Global maps of lake-level fluctuations since 30,000, yr BP. *Quaternary Res.*, **12**, 83–118.
- Tchakerian, V.P., 1999. Dune palaeoenvironments. In Goudie, A.S., Livingstone, I., and Stokes S. (eds.), *Aeolian Environments, Sediments and Landforms*. Chichester: Wiley, pp 261–292.
- Thornthwaite, C.W., 1948. An approach towards a rational classification of climate. *Geogr. Rev.*, **38**, 55–94.
- Tyson, P.D., and Preston-Whyte, R.A., 2000. *The Weather and Climate of Southern Africa*. Cape Town: Oxford University Press.
- Ward, J.D., 1998. Eolian, fluvial and pan (playa) facies of the Tertiary Tsondad Sandstone Formation in the Central Namib Desert, Namibia. *Sediment. Geol.*, **55**, 143–162.
- Wells, P.V., 1976. Macrofossil analysis of woodrat (*Neotoma*) middens as a key to the Quaternary vegetational history of arid America. *Quaternary Res.*, **6**, 223–248.
- Wendorf, F., Schild, R., Said, R., Haynes, C.V., Gautier, A., and Kobusiewicz, P., 1976. The prehistory of the Egyptian Sahara. *Science*, **193**, 103–116.
- Zhou, W., Head, M.J., An, Z., De Deckker, P., Liu, Z., Liu, X., Li, X., Donahue, D., Jull, A.J.T., and Beck, W.W., 2001. Terrestrial evidence for a spatial structure of tropical-polar interconnections during the Younger Dryas episode. *Earth Planet. Sci. Lett.*, **191**, 231–239.
- Zonneveld, K.A.F., Ganssen, G., Troelma, S., Versteegh, G.J.M., and Visser, H., 1997. Mechanisms forcing abrupt fluctuations of the Indian Ocean Summer Monsoon during the last deglaciation. *Quaternary Sci. Rev.*, **16**, 187–201.

Cross-references

Arid Climates, in *Encyclopedia of World Climatology*
 Aridity Indexes, in *Encyclopedia of World Climatology*
 Duricrusts
 Dust Transport, Quaternary
 Eolian Dust, Marine Sediments
 Eolian Sediments and Processes
 Evaporites
 Holocene Climates
 Lake Level Fluctuations
 Loess Deposits
 Millennial Climate Variability
 Paleoclimate Proxies, an Introduction
 Paleolimnology
 Paleo-Precipitation Indicators
 Plate Tectonics and Climate Change
 Pleistocene Climates
 Sedimentary Indicators of Climate Change

ASTRONOMICAL THEORY OF CLIMATE CHANGE

Abstract

The astronomical theory of paleoclimates aims to explain the climatic variations occurring with quasi-periodicities lying between tens and hundreds of thousands of years. Such variations are recorded in deep-sea sediments, in ice sheets, and in continental archives. The origin of these quasi-cycles lies in the astronomically driven changes in the latitudinal and seasonal distributions of energy that the Earth receives from the Sun. These changes are then amplified by feedback mechanisms which characterize the natural behavior of the climate system like those involving the albedo-, the water vapor-, and the vegetation-temperature relationships. Climate models of different complexities are used to explain the chain of processes which finally link the long-term variations of three

astronomical parameters to the long-term climatic variations at time scale of tens to hundreds of thousands of years.

Past climates at astronomical time scales

Our Ice Age, which the Earth entered 2–3 Ma ago is called the Quaternary Ice Age and is composed of the Pleistocene and the Holocene. Its last 1 Ma is characterized by multiple switches of the global climate between glacial (with extensive ice sheets) and interglacials (with a climate similar to or warmer than today). These past climates are reconstructed from analysis of proxy data taken from deep-sea cores, ice cores, and land records (e.g., Alverson et al., 2003). Throughout this last 1 million years, the glacial-interglacial cycles have occurred with a dominant quasi-periodicity of 100 ka. The astronomical theory of paleoclimates aims to explain the recurrence of these cycles. The last one goes from the Eemian interglacial, centered roughly 125 ka BP, to the current Holocene interglacial which peaked 6 ka BP, and also includes the Last Glacial Maximum (LGM) which occurred 21 ka BP.

The LGM was documented in great detail by the Climate Long-Range Investigation Mapping and Prediction group (CLIMAP, 1976; Schneider et al., 2000). In the Northern Hemisphere, the LGM world differed strikingly from the present in the huge land-based ice sheets, which reached approximately 2–3 km in thickness. Sea level was lower by at least 115 m which represents roughly $50 \times 10^6 \text{ km}^3$ more ice than now. Aerosol loading was higher than present and CO_2 levels were about 200 ppmv (much less than the 280 ppmv of the Pre-Industrial Revolution and than the 370 ppmv of AD 2000) but the global average surface air temperature was only 5°C below present (Petit et al., 1999).

In the glacial world, climate shifts occurred also over periods as short as a few decades to millennia (e.g., Heinrich, Dansgaard-Oeschger-Bond events; Bard, 2002). During the deglaciation, between the LGM and the onset of the Holocene, at about 10 ka BP, climate underwent another series of abrupt events with global impacts (e.g., the Bølling-Allerød-Dryas oscillation). This kind of millennium-scale climatic variability probably does not occur in direct response to the insolation forcing.

The astronomical theory of paleoclimates, an historical point of view

Over the last 1 million years the waxing and waning of ice sheets occurred in a more or less regular way. In Figure A32, one can recognize a saw tooth shape with a 100-ka quasi-cycle which is far from being constant and over which shorter quasi-cycles of roughly 41 and 21 ka are superimposed. These kinds of broad climatic features can be explained by the astronomical theory of paleoclimates (Berger, 1978). This astronomical theory is the oldest explanation of the existence of glacial periods found in the geological record of the Quaternary Ice Age. Through the Milankovitch approach, it is currently the most popular. In broad terms, proponents of this theory claim that the changes in three Earth's orbital and rotational parameters have been sufficiently large as to induce significant changes in the seasonal and latitudinal distributions of irradiation received from the Sun and so, to force glacial and interglacials to recur as seen in geological records.

Climatic variations at similar time scales also occurred during non-Ice Age periods and can also be explained by the astronomical theory (Shackleton et al., 1999).

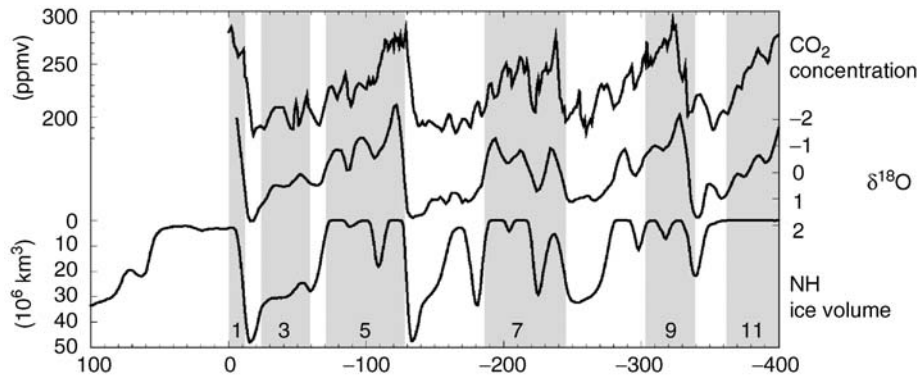


Figure A32 Long-term variations over the last 400 ka of the atmospheric CO_2 from Vostok (Petit et al., 1999), of the $\delta^{18}\text{O}$ recorded from the oceanic core MD900963 (Bassinot et al., 1994), and of the Northern Hemisphere continental ice volume simulated by the LLN 2-D NH model (Loutre, 2003).

Pioneers of the astronomical theory

Only a few years after the address delivered by L. Agassiz in 1837 (Agassiz, 1838) at the opening of the Helvetic Natural History Society at Neuchatel, "Upon Glaciers, Moraines and Erratic Blocks," Adh mar (1842) published his book explaining Agassiz's hypothesis on the existence of ice ages on the basis of the known precession of the equinoxes. An astronomer in Paris, Urbain Le Verrier (1855), famed for discovering the orbital anomalies of Uranus which led to the discovery of Neptune, immediately calculated the planetary orbital changes of the Earth over the last 10^5 years.

Within the next few decades, largely because of the discovery of the repetitive aspect of global glaciation, for example in the Vosges, in Wales, and in the American records of the Illinoian deposits, glacial geology became strongly tied to astronomy. In the mid nineteenth century, James Croll initiated a series of important works that would continue to bear much fruit into modern times. Three major astronomical factors were recognized in his model: axial tilt, orbital eccentricity and precession (Croll, 1875). A specific characteristic of his model essentially lies in his hypothesis that the critical season for the initiation of a glacial is Northern Hemisphere winter. He argued that a decrease in the amount of sunlight received during the winter favors the accumulation of snow and that any small initial increase in the size of the area covered by snow would be amplified by the snowfields themselves (positive feedback). After having determined which astronomical factors control the amount of sunlight received during the winter, he concluded that the precession of the equinoxes must play a decisive role. He also showed that changes in the shape of the orbit determine how effective the precessional wobble is in changing the intensity of the seasons. Croll's first theory predicts that one hemisphere or the other will experience an ice age whenever two conditions occur simultaneously: a markedly elongate orbit and a winter solstice that occurs far from the Sun. Later, Croll hypothesized that an ice age would be more likely to occur during periods when the axis is closer to vertical, for then the polar regions receive a smaller amount of heat.

As time went on, many geologists in Europe and America became more and more dissatisfied with Croll's theory, finding it at variance with new evidence about the last ice age.

Milankovitch era

It is only during the first decades of the twentieth century that Spitaler (1921) rejected Croll's theory. He adopted the opposite view, first put forward by Murphy (1876), that a long, cool summer and a short, mild winter are the most favorable. This diminution of heat during the summer half year was later recognized by Br ckner, K ppen, and Wegener (Br ckner et al., 1925) as the decisive factor in glaciation. However, it is Milankovitch who was the first to complete a full astronomical theory of Pleistocene ice ages, computing the orbital elements and the subsequent changes in the insolation and climate.

Milutin Milankovitch was a Yugoslavian engineer – geophysist – astronomer who was born in Dalj in 1879 and died in Beograd in 1958 (Milankovitch, 1995). He was a contemporary of Alfred Wegener (1880–1930), with whom he became acquainted through Vladimir K ppen (1846–1940), Wegener's father-in-law (Schwarzbach, 1985).

Milankovitch's first book (written in French) dates from 1920, but his massive Special Publication of the Royal Serbian Academy of Science was published in German in 1941. It was translated into English in 1969, which edition was re-edited in 1998. His theory actually requires that the summer in northern high latitudes must be cold enough to prevent the winter snow from melting. This allows a positive value in the annual budget of snow and ice, which initiates a positive feedback cooling of the Earth through a further extension of the snow cover and a subsequent increase of the surface albedo. On the assumption of a perfectly transparent atmosphere and of the northern high latitudes being the most sensitive to insolation changes, that hypothesis requires a minimum in the Northern Hemisphere summer insolation at high latitudes. This is why the essential product of the Milankovitch theory is his curve showing how the intensity of summer irradiation varied over the past 600,000 years at 65°N . It is on this curve that he identified the four European ice ages reconstructed 15 years earlier by Albrecht Penck and Eduard Br ckner (Penck and Br ckner, 1909).

Milankovitch debate

Until roughly 1970 the Milankovitch theory was largely disputed because the discussions were based on fragmentary geological sedimentary records and on inaccurate time scales

and because the climate was considered too resilient to react to “such small changes” in the Milankovitch summer half-year caloric insolation. Moreover, the accuracy of the astronomical solution for the Earth’s orbit and rotation and of the related insolation (namely in polar latitudes) had also to be verified.

The first criteria to test the astronomical theory used a visual or statistical relationship between minima and maxima of geological and insolation curves (e.g., Brouwer, 1950). The Milankovitch summer radiation curve for 65° N was used more frequently because of the more extensive nature of Pleistocene glaciation in the Northern Hemisphere. These qualitative coincidences will, however, remain somewhat illusory until the ambiguities stemming from a priori assumptions about sensitive latitudes and response mechanisms are resolved. As an attempt to solve this problem, many insolation values for different seasons and latitudes were used up to the late 1970s (e.g., Broecker, 1966; Kukla, 1972).

In the meantime, climatologists (Budyko, 1969; Sellers, 1970; Saltzman and Vernekar, 1971) started to analyze the problem theoretically, but they found that the climatic response to orbital change was too small to account for the succession of Pleistocene ice ages. However, these early numerical experiments were also open to question because the models used much too simple parameterizations of important physical processes.

Milankovitch renaissance

In the late 1960s, judicious use of radioactive dating and other techniques gradually clarified the details of the time scale and better instrumental methods came on the scene for reconstructing past climatic variations (Shackleton and Opdyke, 1973). At the same time, atmospheric general circulation models and more realistic climate models became available (Alyea, 1972).

Owing to these improvements, Hays et al. (1976) showed for the first time that quasi-periods of 100, 41, 23 and 19 ka are significantly present in proxy records of the past climate. Independently, these periods were being found in the long term variations of the eccentricity, obliquity and climatic precession using a new more accurate solution of the planetary system (Berger, 1978). These results were definitely at the origin of a revival of the astronomical theory of paleoclimates. New results were going being initiated in all four main steps of any astronomical theory, namely, (a) the computation of the astronomical elements, (b) the computation of the appropriate insolation parameters, (c) the development of suitable climate models, and (d) the analysis of geological data in the time and frequency domains (Imbrie et al., 1984) in order to investigate the physical mechanisms which are responsible for the long-term climatic variations and to calibrate and validate the climate models.

Long-term variations of the astronomical parameters

As here we are primarily interested by the glacial-interglacial cycles, we will focus only on the long-term variations of the energy received by the Earth from the Sun (here called the insolation) at time scales of tens to hundreds of thousands of years.

The incoming solar radiation changes from day to day due to the annual revolution of the Earth around the Sun. But there are other changes of interest related to the planetary system and the Sun’s interior. In particular, the solar output (the so-called solar constant) and the opacity of the interplanetary medium

are changing, but their effects remain difficult to prove at our time scales. More directly related to our problem, the seasonal and latitudinal distributions of insolation have long-term variations which are related to the orbit of the Earth around the Sun and to the inclination of its axis of rotation. These involved three well-defined astronomical parameters: the eccentricity, e (a measure of the shape of the Earth’s orbit around the Sun), the obliquity, ε (the tilt of the equator with respect to the plane of the Earth’s orbit), and the climatic precession, $e \sin \tilde{\omega}$, a measure of the Earth-Sun distance at the summer solstice ($\tilde{\omega}$, the longitude of the perihelion, being a measure of the angular distance between the perihelion and the vernal equinox that are both in motion). The present-day value of e is 0.016. As a consequence, although the Earth’s orbit is very close to a circle, the Earth-Sun distance, and consequently the insolation, varies by as much as 3.2 and 6.4% respectively over the course of 1 year. The obliquity, which defines our tropical latitudes and polar circles, is presently 23°27′. The longitude of the perihelion is 102°, which means that the Northern Hemisphere winter occurs when the Earth is almost closest to the Sun.

Celestial mechanics allows precession, obliquity and eccentricity to be expressed in trigonometrical form as quasi-periodic functions of time:

$$e \sin \tilde{\omega} = \Sigma P_i \sin(\alpha_i t + \eta_i) \quad (1)$$

$$\varepsilon = \varepsilon^* + \Sigma A_i \cos(\gamma_i t + \zeta_i) \quad (2)$$

$$e = e^* + \Sigma E_i \cos(\lambda_i t + \phi_i) \quad (3)$$

where the amplitudes P_i , A_i , E_i , the frequencies α_i , γ_i , λ_i and phases η_i , ζ_i , ϕ_i have been recomputed by Berger in 1978. They can be used over a few millions of years (Berger and Loutre, 1992) but for more remote times numerical solutions are necessary (Laskar, 1999).

These formulae show that ε and e vary quasi-periodically only around the constant values ε^* (23.32°) and e^* (0.0287). This implies that, in the estimation of the order of magnitude of the terms in insolation formulae where ε and e occur, they must be considered as a constant in a first approximation. Moreover, the amplitude of $\sin \tilde{\omega}$ is modulated by eccentricity in the term $e \sin \tilde{\omega}$. The envelope of $e \sin \tilde{\omega}$ is therefore given exactly by e , the frequencies of e originating strictly from combinations of the frequencies of $\tilde{\omega}$; for example: $\lambda_1 = \alpha_2 - \alpha_1$, $\lambda_2 = \alpha_3 - \alpha_1$, $\lambda_3 = \alpha_3 - \alpha_2$, $\lambda_4 = \alpha_4 - \alpha_1$, $\lambda_5 = \alpha_4 - \alpha_2$, and $\lambda_6 = \alpha_3 - \alpha_4$ (Berger and Loutre, 1990). This leads to conclude that the periods characterizing the expansion of e are non-linear combinations of the precessional periods and, in particular, that the eccentricity periods close to 100,000 years originate from the precession periods close to 23,000 and 19,000 years.

Over the past 3 million years, the orbit varied between near circularity ($e = 0$) and slight ellipticity ($e = 0.07$) with a quasi-period of about 400 ka over which a period of about 100 ka is superimposed. The tilt of the Earth’s axis varied between about 22° and 25° at a period of nearly 41 ka. As far as precession is concerned, two phenomena must be considered. The first is the axial precession. The second is related to the counterclockwise absolute motion of the perihelion whose period, measured relative to the fixed stars, is about 100 ka (the same as for the eccentricity). The two effects together result in what is known as the climatic precession of the equinoxes. This motion is mathematically described by $\tilde{\omega}$, the equinoxes and solstices shifting slowly around the Earth’s orbit, relative to the

perihelion, with a mean period of 21 ka. This period results actually from the existence in equation (1) of four periods which are close to 23 and 19 ka.

Figure A33 gives the long-term variations of these three astronomical parameters over the past 200,000 years and into the future for the next 100,000 years. It shows in particular that the 100-ka period is not stable in time (Berger et al., 1998) being remarkably shorter over the present time. It can also be shown that the most important theoretical period of eccentricity, 400 ka, is weak before 1 Ma BP, but becomes particularly strong over the next 400 ka, with the strength of the components in the 100-ka band varying in opposite ways. It is worth pointing out that this weakening of the 100-ka period started about 900 ka ago when this period began to be very strong in paleoclimate records. This implies that the 100 ka period found in paleoclimatic records can not, by any means, be considered to be linearly related to the eccentricity.

While today the Northern Hemisphere winter solstice occurs near perihelion, at the end of the deglaciation, roughly 10 ka BP, it occurred near aphelion. Moreover, because the length of the seasons varies in time according to Kepler's second law, the solstices and equinoxes occur at different calendar dates during the geological past and in the future. Presently in the Northern Hemisphere, the longest seasons are spring (92.8 days) and summer (93.6 days), while autumn (89.8 days) and winter (89 days) are notably shorter. In AD 1250, spring and summer had the same length (as did autumn and winter) because the winter solstice was occurring at perihelion. About 4,500 years into the future,

the northern hemisphere spring and winter will have the same short length and consequently summer and fall will be equally long. But we are now approaching a minimum of e at the 400-ka time scale and 27 ka from today, the Earth's orbit will be circular.

Daily irradiation

Let us call daily insolation, \bar{W} (in W m^{-2}), the energy received at the Earth's surface over a unit area divided by 24 hours without caring about the atmosphere. This value usually referred to as "at the top of the atmosphere" can be calculated exactly. It depends upon the solar constant, the distance from the Earth to the Sun, r , and the length of the day, L . For a given ecliptical longitude – it means for more or less a given day – the long term variations of r are a function of precession only and those of L are a function of ε only. The mathematical expression of \bar{W} show clearly (Berger et al., 1993) that (a) it is principally affected by variations in precession, although the obliquity plays an important role at high latitudes, mainly in the winter hemisphere; (b) at the equinoxes, insolation for each latitude is only a function of precession; (c) at the solstices, both precession and obliquity influence insolation, although precession is dominant at most latitudes. However, the total energy received during one particular season at a given latitude is only a function of ε as a consequence of Kepler's second law.

These behaviors differ from those of the caloric insulations introduced by Milankovitch. Indeed, he defined the caloric seasons as being exactly half a year long to avoid the variations

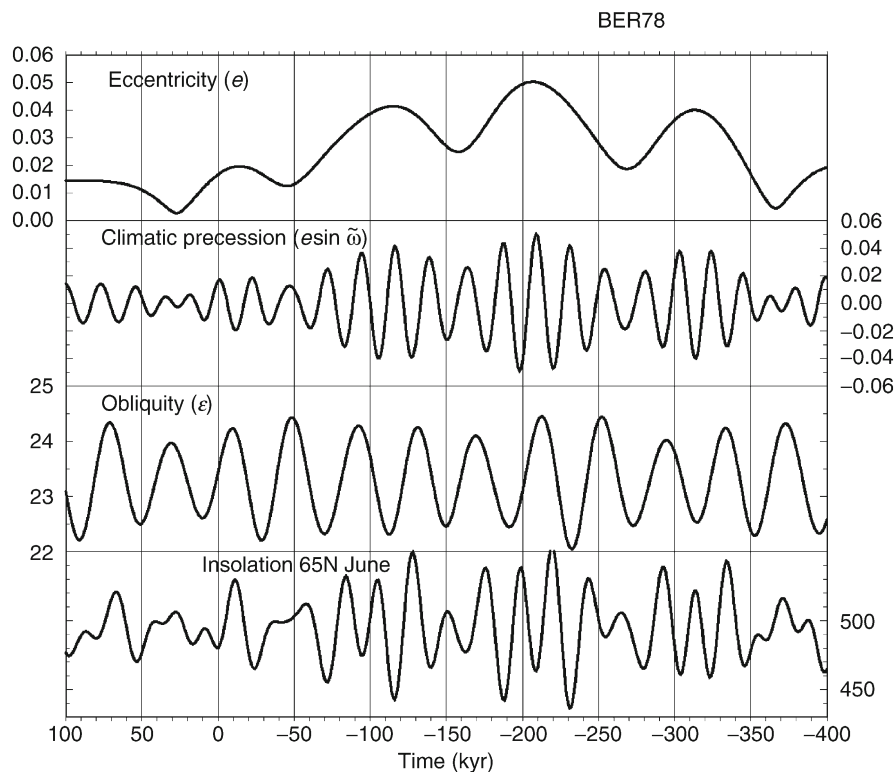


Figure A33 Long-term variations over the last 400 ka and the next 100 ka of eccentricity, climatic precession, obliquity and 65° N insolation at the summer solstice in W m^{-2} (Berger, 1978).

in length of the astronomical ones. The summer half-year comprises actually all the days receiving, each, more irradiation than any of the winter half-year. The resulting caloric insolutions (i.e., the total irradiation received during a half-year caloric season) are mainly a function of precession in low latitudes and of obliquity at high latitudes. We must stress that this is far from solving the difficulty of having to deal both with the total energy received during one season and with its length. The caloric seasons as defined by Milankovitch indeed raise two problems: first, their beginnings change with time; second, it is difficult to define them in the equatorial regions where the seasonal march of insolation has two maxima and two minima. Nevertheless the daily irradiation and the caloric insolutions are different approaches to the problem and they may be considered as complementary.

The geometry of the insolation problem allows one to calculate the insolation changes due to changes in obliquity and precession. Changes in incoming solar radiation due to changes in tilt are the same in both hemispheres during the same local season: an increase of ϵ leads to an increase of insolation in the summer hemisphere and a decrease in the winter hemisphere (Figure A34). As the strength of the effect is small in the tropics and maximum at the poles, an obliquity increase amplifies the seasonal cycle in the high latitudes of both hemispheres simultaneously. The precession effect can cause warm winters and cool summers in one hemisphere while causing the opposite effect in the other hemisphere. As shown

in Figure A34, going from a summer solstice occurring at aphelion to occurring at perihelion increases the energy received on Earth from the spring equinox to the fall equinox.

It must be stressed finally that the pattern of solar irradiation at the top of the atmosphere differs significantly from the pattern of radiation absorbed by the Earth's surface, particularly in high latitudes where the surface albedo is large (Tricot and Berger, 1988). This remark must be kept in mind when using directly the astronomical insolation for trying to explain the climatic variations reconstructed from proxy data.

Astronomical impact on climate

In order to test the possible climatic influence of the long-term variations of insolation, a climate model of intermediate complexity has been built (Gallée et al., 1991). It has been used for many different climatic situations covering the last 3 Ma. In particular, an atmospheric CO₂ concentration decreasing linearly from 320 ppmv at 3 Ma BP (Late Pliocene) to 200 ppmv at the Last Glacial Maximum was used to force this model in addition to the insolation. Under such conditions, the model simulates the entrance into our Ice Age, 2.75 Ma ago, the Late Pliocene – Early Pleistocene 41-ka cycle, the emergence of the 100-ka cycle around 850 ka BP and glacial-interglacial cycles over the last 600 ka (Berger et al., 1998). Sensitivity tests have also shown the importance of all the feedbacks related to the planetary albedo, water vapor, height and continentality of the inlandsis and the isostatic response of the lithosphere. They also confirmed that,

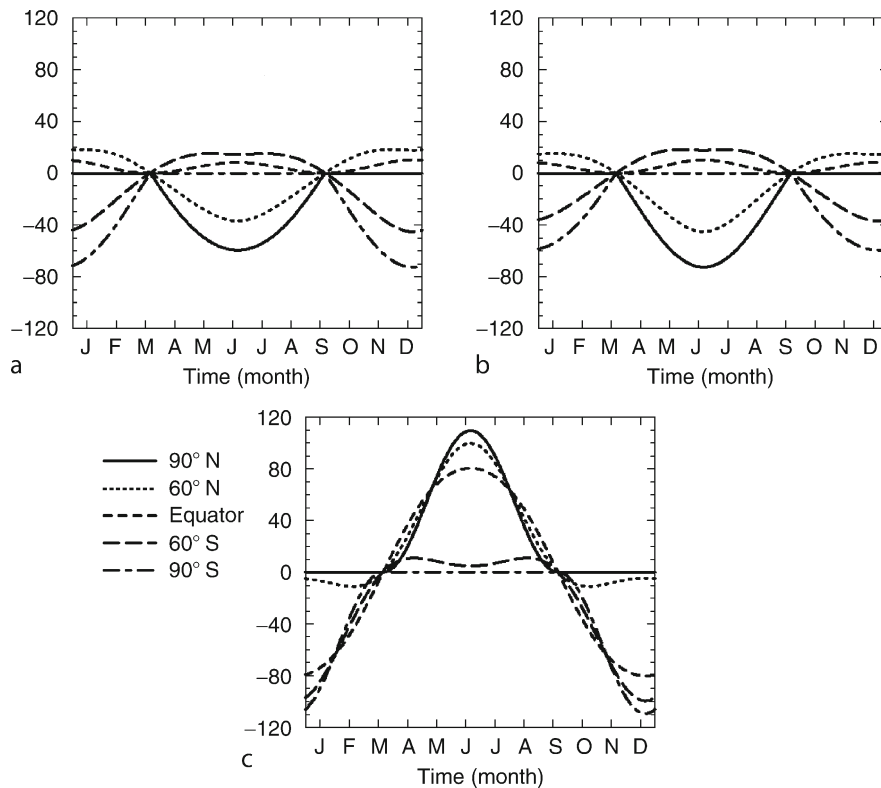


Figure A34 Changes in $W m^{-2}$ along the year of the daily insolation at 90° N, 60° N, the equator, 60° S and 90° S (1) for obliquity changing from 25° to 22°: (a) summer solstice at aphelion; (b) summer solstice at perihelion and (2) for summer solstice changing from aphelion to perihelion, with obliquity being kept at 23.445°. (c). In all figures, $e = 0.05$.

in our model, the astronomical forcing alone can generate glacial-interglacial cycles, but only if the atmospheric CO₂-concentration is lower than 230 ppmv. On the contrary, if the astronomical forcing is kept constant, the CO₂ variations cannot reproduce the ice volume variations characteristic of the glacial-interglacial cycles. Using both the long term variations of insolation and of CO₂ deduced from the Vostok ice cores (Petit et al., 1999) allows one finally to reproduce the glacial-interglacial cycles of the last 400 ka, in broad agreement with the reconstructions of the ice volume from proxy records. These simulations have also shown that the Marine Isotopic Stage 11–400 ka ago – is a much better analog of our Holocene than the Eemian, at least from the astronomical point of view. This result has led to a tentative projection of the future climate over the next tens of thousands of years. Under natural conditions, our interglacial would last exceptionally long (up to 50 ka AP) and man's activities might create a super-interglacial over the next millennia with a complete melting of the Greenland ice sheet from 10 to 20 thousands years into the future (Berger and Loutre, 2002).

Conclusions

It is now more and more accepted that the astronomically induced insolation variations are the pace-maker of the climatic variations over the Quaternary at time scale going from tens to hundreds of thousands of years. The feedback mechanisms related to the planetary albedo, greenhouse gases and ice sheets, are all necessary for amplifying the astronomical signal and to simulate glacial-interglacial cycles in agreement with reconstructions obtained from proxy records. Modeling past climatic variations, through the astronomical theory in particular, allows not only to better understand how the climate system works, but also to attempt modeling our future climate. This is why, in addition to acquiring proxy records for past climate reconstructions, models of diverse complexities must be constructed to test the reliability of the results described in this paper.

André Berger

Bibliography

- Adhémar, J.A., 1842. Révolution des mers, Déluges périodiques. Paris: Publication privée.
- Agassiz, L., 1838. Upon glaciers, moraines, and erratic blocks. *New Philosophical J.*, **24**(48), 364–383.
- Alverson, K.D., Bradley, R.S., and Pedersen Th.F. (eds.), 2003. *Paleoclimates, Global Change and the Future*. Berlin: Springer, 221pp.
- Alyea, F.N., 1972. Numerical simulation of an Ice Age paleoclimate. Atmospheric Science Paper No. 193, Department of Atmospheric Science, Colorado State University, Ft. Collins.
- Bard, E., 2002. Climate shock: Abrupt changes over Millennial Time Scales. *Phys. Today*, **55**(12), 32–38.
- Bassinot, F.C., Labeyrie, L.D., Vincent, E., Quidelleur, X., Shackleton, N.J., and Lancelot, Y., 1994. The astronomical theory of climate and the age of the Brunhes-Matuyama magnetic reversal. *Earth Planet. Sci. Lett.*, **126** (1–3), 91–108.
- Berger, A., 1978. Long-term variations of daily insolation and Quaternary climatic changes. *J. Atmos. Sci.*, **35**(12), 2362–2367.
- Berger, A., and Loutre, M.F., 1990. Origine des fréquences des éléments astronomiques intervenant dans le calcul de l'insolation. *Bull. Class. Sci.* **1**(1–3), 45–106.
- Berger, A., and Loutre, M.F., 1992. Astronomical solutions for paleoclimate studies over the last 3 million years. *Earth Plan. Sci. Lett.*, **111** (2/4), 369–382.
- Berger, A., and Loutre, M.F., 2002. An exceptionally long interglacial ahead? *Science*, **297**, 1287–1288.
- Berger, A., Loutre, M.F., and Tricot, C., 1993. Insolation and Earth's orbital periods. *J. Geophys. Res.*, **98**(D6), 10,341–10,362.
- Berger, A., Loutre, M.F., and Gallée, H., 1998. Sensitivity of the LLN climate model to the astronomical and CO₂ forcings over the last 200 ka. *Clim. Dyn.*, **14**(9), 615–629.
- Broecker, W.S., 1966. Absolute dating and the astronomical theory of glaciation. *Science*, **151**, 299–304.
- Brouwer, D., 1950. Vormen de Stralingcurven van Milankovitch een bruikbare grondslag van de indwelling van het Pleistocène. *Geol. Mynbouw*, **12**(1), 9–11.
- Brückner, E., Köppen, W., and Wegener, A., 1925. Über die Klimate der geologischen Vorzeit. *Zeitschrift für Gletscherkunde*, vol. 14.
- Budyko, M.I., 1969. Effect of solar radiation variations on the climate of Earth. *Tellus*, **21**(5), 611–620.
- CLIMAP Project Members, 1976. The surface of the Ice-Age Earth. *Science*, **191**, 1131–1136.
- Croll, J., 1875. Climate and Time in their Geological Relations. London, NY: Appleton, 577pp.
- Gallée, H., van Ypersele, J.P., Fichet, Th., Tricot, C., and Berger, A., 1991. Simulation of the last glacial cycle by a coupled sectorially averaged climate – ice-sheet model. I. The Climate Model. *J. Geophys. Res.*, **96**, 13,139–13,161.
- Hays, J.D., Imbrie, J., and Shackleton, N.J., 1976. Variations in the earth's orbit: Pacemaker of the ice ages. *Sciences*, **194**, 1121–1132.
- Imbrie, J., Hays, J., Martinson, D.G., Mcintyre, A., Mix, A.C., Morley, J.J., Piasias, N.G., Prell, W.L., and Shackleton, N.J., 1984. The orbital theory of Pleistocene climate: Support from a revised chronology of the marine ¹⁸O record. In: Berger, A. et al., (eds), *Milankovitch and Climate*, D. Reidel: Hingham, MA., pp. 269–305.
- Kukla, G., 1972. Insolation and glacial. *Boreas*, **1**(1), 63–96.
- Laskar, J., 1999. The limits of Earth orbital calculations for geological time scale use. In Shackleton, N.J., McCave, I.N., and Weedon, G.P. (eds.), *Astronomical (Milankovitch) calibrations of the geological time scale*. *Phil. Trans. R. Soc. Lond., Ser. A*, 357, 1735–1759.
- Le Verrier, U.J.J., 1855. *Recherches astronomiques*. Ann. Obs. Imp. Paris II.
- Loutre, M.F., 2003. Clues from MIS 11 to predict the future climate – a modeling point of view. *Earth Planet. Sci. Lett.*, **212**, 213–224.
- Milankovitch, M., 1941. *Kanon der Erdbestrahlung und seine Anwendung auf des Eiszeitenproblem*. Royal Serbian Sciences, Spec. pub. 132, section of Mathematical and natural Sciences, vol. 33, pp. 633, Belgrade. (“Canon of Insolation and the Ice Age Problem”, English Translation by Israël Program for the U.S. Department of Commerce and the National Science Foundation, Washington D.C., 1969, and by Zavod za Udzbenike I nastavna Sredstva in cooperation with Muzej nauke I tehnike Srpske akademije nauka I umetnosti, Beograd, 1998).
- Milankovitch, V., 1995. *Milutin Milankovic 1879–1958, from his autobiography with comments by his son, Vasko, and a preface by André Berger*. Katlenburg-Lindau, FRG: European Geophysical Society, 181pp.
- Murphy, J.J., 1876. The glacial climate and the polar ice-cap. *Q. J. Geol. Soc. Lond.*, **32**, 400–406.
- Penck, A., and Brückner, E., 1909. Die Alpen in Eiszeitalter. Leipzig: Tauchnitz.
- Petit, J.R., Jouzel, J., Raynaud, D., Barkov, N.I., Barnola, J.M., Basile, I., Bender, M., Chappellaz, J., Davis, M., Delaygue, G., Delmotte, M., Kotlyakov, V.M., Legrand, M., Lipenkov, V.Y., Lorius, C., Pépin, L., Ritz, C., Saltzman, E., and Stievenard, M., 1999. Climate and atmospheric history of the past 420,000 years from Vostok ice core, Antarctica. *Nature*, **399**(6735), 429–436.
- Saltzman, B., and Vernekar, A.D., 1971. Note on the effect of Earth orbital radiation variations on climate. *J. Geophys. Res.*, **76**(18), 4195–4198.
- Schneider, R.R., Bard, E., and Mix, A.C., 2000. Last Ice Age global ocean and land surface temperatures: The EPILOG initiative. *Global Change Newsletter*, **43**, 4–7.
- Schwarzbach, 1885. Wegener, le Père de la Dérive des Continents. Paris: Bélin.
- Sellers, W.D., 1970. The effect of changes in the Earth's obliquity on the distribution of mean annual sea-level temperatures. *J. Appl. Meteorol.*, **9**, 960–961.
- Shackleton, N.J., and Opdyke, N.D., 1973. Oxygen isotope and palaeomagnetic stratigraphy of equatorial Pacific core V28–238: Oxygen isotope

temperatures and ice volumes on a 10^5 and 10^6 year scale. *Quat. Res.*, **3**, 39–55.

Shackleton, N.J., McCave, I.N., and Weedon, G.P., 1999. Astronomical (Milankovitch) calibration of the geological time scale. *Philosophical Transactions of the Royal Society. Math. Phys. Eng. Sci.*, **357**(1757), 1731–2007.

Spitaler, R., 1921. *Das Klima des Eiszeitalters*. Prague: Selbstverl.

Tricot, C., and Berger, A., 1988. Sensitivity of present-day climate to astronomical forcing. In: Wanner, H., and Siegenthaler, U. (eds.), *Long and Short-Term Variability of Climate, Earth Sciences Series* (Springer Verlag, Berlin) pp. 132–152.

Cross-references

[CLIMAP](#)

[Climate Forcing](#)

[Eccentricity](#)

[History of Paleoclimatology–Biographies](#)

[Last Glacial Maximum](#)

[Quaternary Climate Transitions and Cycles](#)

[Precession, Climatic](#)

[Pre-Quaternary Milankovitch Cycles and Climate Variability](#)

ATMOSPHERIC CIRCULATION DURING THE LAST GLACIAL MAXIMUM

Introduction

The Last Glacial Maximum (LGM) offers us an opportunity to assess how the atmospheric circulation changes when in a different climate regime, one characterized by much colder temperatures ($\sim 5^\circ\text{C}$, globally), and different effective topography (i.e., the presence of large ice sheets on land at upper mid-latitudes). Yet, there are many aspects of the circulation that are known imperfectly. The evidence, to the extent that it exists, is generally indirect, especially for wind changes. Moisture and temperature changes are generally better known, and from these we have an indication of how the circulation may have been altered. Even with these parameters, however, there are major uncertainties, in particular associated with temperature changes in the tropics and subtropics.

An alternate line of evidence comes from General Circulation Model (GCM) studies of this time period. Here too, however, there is uncertainty, associated both with the LGM boundary conditions (e.g., sea surface temperatures [SSTs], and ice sheet topography) and with the models themselves. While model studies often give similar temperature change results (when forced with the same boundary conditions), circulation changes can differ, especially on the regional scale.

A third line of evidence comes from theoretical considerations. Basic quasi-geostrophic theory as applied in the extratropics suggests how the atmospheric circulation should respond in a climate change situation, associated, for example, with changes in the latitudinal temperature gradient. Of course, once again, our understanding of the latitudinal temperature gradient for the LGM is only as good as the paleoclimate evidence.

Given this state of affairs, a likely indication of some aspects of the circulation of the LGM can be offered. As more data is obtained, and model and theory improved, the assessment should become more refined.

The following will discuss circulation with respect to its latitudinal and altitude distribution in the extratropics and tropics.

The analysis will be reviewed with respect to the three tools noted above: GCMs (which allow the most direct assessments of circulation changes), observations, and theoretical considerations.

GCM analysis of circulation changes

Various general circulation models have been run with specified or calculated LGM boundary conditions, such as SSTs (a partial list includes the simulations of Gates, 1976; Hansen et al., 1984; Manabe and Broccoli, 1985; Rind and Peteet, 1985; Kutzbach and Guetter, 1986; Rind, 1987; COHMAP, 1988; Hall et al., 1996; Bonfils et al., 1998; Kageyama et al., 1999; Pinot et al., 1999a; and Hewitt et al., 2003). The specified SSTs were generally derived by the CLIMAP (Climate Long-Range Investigation Mapping and Prediction, 1981) reconstruction, although a few of the earlier analyses used colder tropical SSTs than CLIMAP generated, and a few later simulations have added arbitrary cooling to the CLIMAP tropical values (e.g., Toracinta et al., 2004). The calculated SSTs in models have been derived either from analyses using a mixed layer or slab ocean with specified ocean heat transports (e.g., Webb et al., 1997), or with truly coupled dynamical atmosphere-ocean models (e.g., Shin et al., 2003). The calculated SSTs have been almost uniformly colder than the CLIMAP reconstructions in the tropics. Controversy still exists over the proper tropical SST values. The degree of tropical temperature change strongly affects our understanding of LGM dynamics because of its influence on latitudinal temperature gradients and low latitude circulation.

Models have also used several different land ice sheet topographies, chiefly the Denton and Hughes (1981) reconstruction that was part of the CLIMAP LGM reconstruction, but more recently the topography set generated by Peltier (1994). The latter estimate, produced by a model of glacial isostatic adjustment, gives considerably lower (of order 1 km) ice sheet topography estimates, and is not consistent with the dynamics of ice sheet models (Clark et al., 2001). An alternative is to derive the topography from an ice sheet model (e.g., Fastook and Prentice (1994)), which restores the higher altitude (Toracinta et al., 2004). This too makes a difference in LGM dynamics, in particular by altering the magnitude by which the big ice sheets over North America influence the flow field and atmospheric waves.

Unfortunately, the uncertainties in important boundary conditions that influence the depiction of the general circulation in GCMs and atmospheric dynamics of the LGM can seriously impact our understanding. This must be borne in mind in the subsequent discussion. In particular, with calculated SSTs, and greater tropical cooling, the shifts in storm generation in the extratropics are more muted, and the Northern Hemisphere Hadley Cell change is larger. With reduced height of the ice sheets, the associated anticyclone is weaker (Ramstein and Joussaume, 1999; Bromwich et al., 2004).

Extratropics

With the previous caveats in mind, we can now describe the circulation in the LGM extratropics as depicted by GCMs. The sea level pressure field featured big high-pressure sheets over the Laurentide Ice Sheet region (primarily in winter) and the Scandinavian Ice Sheet (primarily in summer); in some models, storms were directed over the Laurentide Ice Sheet in summer, providing precipitation for snow cover. The high

pressure was generated by cooling over the ice sheet – a function of its height, in that with greater altitude of the land surface there is less atmosphere above and hence less greenhouse gas concentration (primarily water vapor) to reduce outward radiative fluxes. The albedo of these ice sheets, a very uncertain parameter, played a role in keeping the region cooler in summer, along with the difficulty of raising the surface air temperature above freezing, given the mass of snow and ice to melt. Winds around these features provided a greater west wind flow at the surface over the Arctic than currently exists, with weaker westerly winds to the south, helping the eastern and central United States to have a “more continental” climate (e.g., Kutzbach and Guetter, 1986). In a higher resolution model, strong katabatic winds came off the Laurentide Ice Sheet. There was a tendency towards some degree of warming south of the ice sheets, due to subsidence or altered advection (Rind 1987; Feltzer et al., 1996).

Storm systems and baroclinicity also underwent strong shifts in locations. Currently baroclinicity is highest over eastern Asia and North America. The presence of the cold Laurentide Ice Sheet produced a strong temperature gradient over North America that led to increased storm generation over land. At the same time, the strong gradient between warm air to the south, over the North Atlantic, and cold air in the vicinity of the southward-displaced sea ice edge led to increased baroclinic generation extending to the eastern North Atlantic. Hence, storms and storm tracks occurred across eastern North America all the way to western Europe (Hall et al., 1996; Kageyama et al., 1999; Bromwich et al., 2004). The stronger latitudinal temperature gradient also intensified the jet stream in its subtropical position, both coming across the Pacific and extending from the eastern Atlantic across southern Europe; hence, storms followed these altered paths. The main ocean low-pressure systems were thus displaced southward from their current locations. With a split flow in the jet stream (see below), storms also increased to the north of the ice sheets, along coastal Alaska and into the Arctic (Bromwich et al., 2004).

As to the intensity of the storms, there is little consistent indication of strengthening, despite the increased baroclinicity. Nor is there any agreement on the nature of the change between standing and transient wave energy. While the added topography would suggest greater stationary wave energy, the increased latitudinal temperature gradient aided transient energy generation. As these processes can work against one another, via poleward transport of heat, different models favor one over the other (e.g., in the study of Rind et al., 2001, standing wave energy actually decreased despite the big ice sheets). Surface winds also did not increase greatly in intensity – on the order of 10% in some models (Crowley, 1988).

At higher levels, the position of the standing wave troughs, which are currently over eastern North America, eastern Asia and eastern Europe in winter, appeared to undergo no major change, although there was amplification in some models (e.g., Felzer et al., 1996). In addition to the southward shift of the jet stream, some models produce a “split-jet” around the Laurentide Ice Sheet, bringing Pacific air over the Arctic, and intensifying flow south of the ice. There is no agreement on this feature, however, which varies in intensity from model to model and it is completely missing in some. Bromwich et al. (2004) show that it can be affected by the model resolution, as well as the presumed height of the ice sheet topography.

While most model simulations did not specifically address the vertical profiles of climate change, cooling undoubtedly occurred throughout the troposphere, associated with colder surface conditions, reduced atmospheric carbon dioxide, and reduced water vapor (from reduced evaporation) (Hansen et al., 1984; Rind et al., 2001). There was also a likely reduction in high-level cloudiness, associated with decreased convection. The most likely response of tropical and subtropical cooling is that the temperature was reduced in the tropical upper troposphere even more than at the surface. In the extratropics, maximum cooling would have been at heights just above the ice sheets. The resulting increased temperature gradient at low altitudes, and decreased temperature gradient at high altitudes, would likely have led to increasing west winds in the low-to-middle troposphere at mid-latitudes, with decreased west winds at higher levels. In the Northern Hemisphere polar regions, the latitudinal temperature gradient was actually reversed – colder conditions now occurred south of the Arctic Circle, so stronger east winds were likely at the highest latitudes. In the North Atlantic, the southward shift of the storm track in most models resulted in a more negative North Atlantic Oscillation phase, although in the study of Bromwich et al. (2004), the northern branch of the split jet stream maintained a vigorous westerly circulation (positive NAO phase). Considering all longitudes, a more negative Arctic Oscillation (AO) phase would have maximized at the surface, and diminished with altitude within the troposphere.

The tropopause was likely at a lower altitude in the colder climate, although its temperature change is uncertain. In at least one study (Rind et al., 2001) its temperature was unchanged. While the troposphere was cooling, the stratosphere was warming (due to reduced CO₂). Total stratospheric ozone would have increased due to the expanded stratosphere. HO_x and NO_x would have decreased because of lower concentrations of methane, tropospheric water vapor and N₂O, further increasing ozone. However, the warmer stratosphere would have favored less ozone photochemically, although this effect was unlikely to have offset the other gains. The stratospheric polar vortex was likely weaker in the stratosphere (again the negative AO phase) (Rind et al., 2001), due in part to increased planetary wave activity propagating up from the troposphere. Hence the stratospheric winds during winter were likely weaker. Gravity wave drag, which acts to decelerate the stratospheric winds, could also have been greater if the ice sheets had a sufficiently corrugated topography to generate them.

The summer time circulation had many current winter-like features, although weaker in intensity, due to the presence of the cold air masses produced by the ice sheets. In addition to the higher pressure over eastern Canada and western Europe in some models, the North American and North Atlantic troughs were amplified (Broccoli and Manabe, 1987; Felzer et al., 1996), with more storms over the North Atlantic, as the land/ocean temperature contrast was altered with respect to current conditions. As noted previously, a subset of models produced storm tracks up onto the Laurentide Ice Sheet during this season.

In the Southern Hemisphere, the consensus is that storms shifted poleward due to greater temperature gradients at higher latitudes, with a more equatorward extension of the sea ice field; major increases occurred in particular in the Indian Ocean sector. The “split-jet” seen in the Pacific therefore weakened or disappeared altogether (Hall et al., 1996).

Tropics/Subtropics

The major question concerning the LGM circulation in the tropics is the extent to which the Hadley Cell changed, both in terms of its magnitude and in terms of its latitudinal extent. Models, usually using CLIMAP SSTs, generally indicate that the July Hadley circulation, with rising air in the northern subtropics and descending air in the Southern Hemisphere, decreased in intensity. This was associated with cooler conditions over land, particularly over Asia. The most obvious expression was a weakened Indian monsoon, although a weaker monsoon in North America has also been noted (Hall et al., 1996).

The features of the Hadley Cell change are affected by the SST field used for the tropics and subtropics. Hall et al. (1996) found that the Hadley Cell moved north of the equator and strengthened in December to February, associated with the warm subtropical Pacific SSTs in the CLIMAP reconstruction. Felzer et al. (1996) found that the Northern Hemisphere portion of the Hadley Cell intensified in both seasons, with the major decrease during June to August occurring in the Southern Hemisphere component. Rind and Perlwitz (2004) found that, when using the CLIMAP SSTs, the December-February Hadley Cell intensified by some 10%, while the June-August intensity was some 20% lower; when using calculated (and colder) SSTs, the December-February change was similar, but June-August intensified by close to 70%. This latter result was due to a $\sim 70\%$ increase in the SST gradient between 27° N and 27° S, and emphasizes how closely related the Hadley Cell strength is to the SST gradient (also noted by Toracinta et al., 2004, especially for the Indian monsoon region). In these analyses, the poleward extent during December-February increased by some 5° of latitude, associated with dynamical processes involving the ice sheets; Ramstein et al. (1998) obtained a similar result.

Models have not yet been used to assess significant changes in El Niño-Southern Oscillation (ENSO) events during the LGM. The specified SST reconstructions of CLIMAP led to increased precipitation in the eastern tropical Pacific relative to the west (Joussame, 1999), implying a weakening of the Walker circulation. With calculated SSTs there was little systematic change.

An additional factor concerns the possible occurrence of hurricanes during the LGM. Hobgood and Cerveny (1988) used output from a GCM that used the CLIMAP SSTs and found that weak hurricanes were still possible, factoring in possible reductions in outgoing thermal radiation associated with the colder climate. Full-fledged hurricanes would presumably be less likely if colder SST values were to be employed.

Observational analysis of circulation changes

Given the uncertainties in the modeling results based on uncertainties in the boundary conditions used to force the models, can we use observations to imply what dynamical changes occurred? While most observational parameters are directly related to the paleodata (temperature, precipitation), we can potentially infer circulation responses by observing the pattern of these changes.

Extratropics

In the extratropics, wetter conditions in the southwestern U.S. and drier conditions in the northwestern U.S. are consistent with a southward shift of the jet stream and storm tracks. The model responses tend to be much smaller than observations imply

(Bromwich et al., 2004), for reasons that are not apparent. In addition, comparison of model and observed conditions for the LGM in southern Europe indicate that the models produced temperatures that were too high there, undoubtedly influenced by the CLIMAP SSTs but also with computed SSTs (Pinot et al., 1999b). This may imply circulation features that are not properly simulated in models, in particular cold air advection from regions further north; this suggests in turn a more active polar front jet stream relative to the subtropical jet (and hence cooler tropical temperatures, which would weaken the subtropical jet). Additional feedbacks, such as those associated with vegetation feedback, may also contribute (e.g., Levis et al., 1999).

Another intriguing feature was the CLIMAP reconstruction showing little additional ice growth in Alaska, which would be consistent with more southerly flow into the region, associated with a southeastward displacement of the Aleutian Low that has been seen in some models and the split-jet stream influence on storm tracks (Bromwich et al., 2004). However, Hall et al. (1996) found that drainage off the ice sheets actually kept Alaska cold in their model simulation.

Observations imply stronger surface winds, on the order of 20–40% (Crowley, 1988). This contrasts with a much smaller increase in model-generated surface winds (and storm intensities).

Tropics/Subtropics

At low latitudes, the Hadley Cell response is indicated by changes in soil moisture in the tropics and subtropics. High lake levels in northwestern Sahara, the Mediterranean region and sites in the Middle East (Farrera et al., 1999) may imply an increase in precipitation minus evaporation for this region of the subtropics. Markgraf (1989) and Colinvaux (1991) find similar subtropical moistening in southern and northern subtropical regions of the Americas (see also Street-Perrott et al., 1989), but changes of this nature are not uniformly recorded throughout the subtropics. In the tropics themselves, from Central America to western Africa, drier conditions prevailed, with only eastern Africa becoming wetter. There is thus some indication that the Hadley Cell weakened, with less subsidence in the subtropics and less rising air in the tropics, but the data is not definitive. Models often reproduce the nature of the change but not the magnitude, underestimating the extent of drying with and without CLIMAP-specified SSTs (although colder tropical/subtropical SSTs can lead to better qualitative agreement (Toracinta et al., 2004)). No moisture records are available from the Indian subcontinent to ascertain the extent to which reduced monsoons really occurred in this region (Farrera et al., 1999). Chylek et al. (2001) suggested that enhancement of dust source areas during past glacial periods implied a contraction of the Hadley Cell of some 3° of latitude.

Some reconstructed SSTs in the tropical Pacific suggest a relaxation of tropical temperature gradients, weakened Hadley and Walker circulation, southward shift of the Intertropical Convergence Zone, and a persistent El Niño-like pattern in the tropical Pacific (Koutavas et al., 2002). In contrast, Trend-Staid and Prell (2002) concluded that SSTs in the western tropical Pacific were relatively unaffected, while the eastern tropical Atlantic cooled substantially. Hence, it is not possible to determine what the circulation was like in this region; model simulations that use a particular SST depiction will produce a Walker circulation consistent with them (Joussame, 1999).

Theoretical considerations of circulation changes

Extratropics

The increased latitudinal temperature gradient driven by the existence of cold ice sheets at upper mid-latitudes likely increased the baroclinic generation of storms. Over the ice sheets themselves, and in the downstream areas to the east, large high-pressure systems, generated by radiative cooling from the high-altitude ice surface, would have dominated the circulation, with storms moving less poleward and more eastward at mid-latitudes. This would correspond, in effect, to the negative phase of the Arctic Oscillation and the North Atlantic Oscillation, although if the downstream trough in the North Atlantic were to be sufficiently amplified, a more positive phase would be possible (Bromwich et al., 2004). While the existence of the added topography features associated with the ice sheets would have seemed likely to generate greater standing wave energy, in some studies this failed to materialize as the increase in latitudinal temperature gradient resulted in a large increase in transient wave energy, which dominated the energy cycle change. This distinction would help determine whether the paleorecord would feature a more longitudinally uniform response of precipitation changes, or not.

The polar front jet stream was clearly further south, associated with the ice sheets, and this jet may have split to the north and south of the ice sheets, although different GCMs produce somewhat different results (which in turn would affect the air arriving at the Greenland Ice Sheet, and consequently the interpretation of isotope changes within the ice cores). The change in the subtropical jet is likewise somewhat uncertain. With relatively warm subtropics, it may have increased in intensity, while with the more likely cooler tropics and subtropics it may well have diminished in general. The change in frequency of El Niños would also affect this result, at least periodically.

Given the greater baroclinicity, stronger storms would have been expected, with substantial increases in surface winds at mid-latitudes, especially at locations featuring the contrast between the cold high-pressure cells off the ice sheets and storms propagating across North America. The model results indicating no marked strengthening of either storms or surface winds are surprising; presumably other limiting factors come into play (including perhaps the model resolution). In the vicinity of the big high pressure cells themselves, covering upper mid-latitudes, surface winds would have been weaker.

Tropics/Subtropics

The Hadley Cell during December-February is quite sensitive to the latitudinal gradient in SSTs. With the CLIMAP reconstruction, there is a tendency for increased circulation north of the equator and decreases to the south due to the warm subtropical SSTs. On the other hand, that distribution is not particularly conducive to drying out the tropics, for the warm subtropics provides plenty of moisture for tropical condensation, despite any reduced upwelling associated with the Hadley Cell decrease. Colder conditions in both the tropics and subtropics (but more so in the tropics) favor equatorial drying, although the impact on the Hadley Cell would be less and wetter conditions in the subtropics more problematical. None of the models produced these effects even when calculating their own SSTs. Hence, the extent to which the Hadley Cell was actually reduced during the LGM is not well known, although a reduction, associated with a decrease in the global hydrologic cycle, is probable.

Concerning the change in the poleward extent of the Hadley Cell, all else being equal, an increase in the equator to pole temperature gradient would have led to an expansion of the latitudinal extent (Held and Hou, 1980). However, a reduced tropopause height and increase baroclinicity in the extratropics would have affected the result.

Had the Hadley Cell intensity been reduced, the trade winds would have been weaker, probably resulting in weaker El Niño/La Niña oscillations (although perhaps locking into a more permanent El Niño state). What actually happened to the ENSO oscillation would have depended upon the temperature of the upwelling water as well, in response to ocean circulation changes (e.g., North Atlantic Deep Water and Intermediate Water changes).

Other aspects of the tropical circulation also depend on the actual SSTs. The occurrence of easterly waves is presumably associated with active convection. If the tropical SSTs were actually considerably colder, convection also would likely have been reduced. The tropical low-level jet, which may promote wave formation via barotropic instability, depends on the temperature gradient between the deep tropics and the warmer subtropics. If the Hadley Cell weakened, and this gradient reduced, the amplitude of the easterly jet would have been reduced as well.

Finally, the existence of hurricanes depends on the SSTs. Hurricanes derive their energy primarily from the latent heat release associated with moisture supplied by evaporation, largely in the subtropics. With substantial cooling in the subtropics, this source would have been less available, and without abundant convection the easterly waves that convert to hurricane vortices would have been less prevalent. Hurricanes, therefore, would likely have decreased.

Summary

Utilizing these three different approaches, can we reach any consensus on how the circulation of the LGM compared to that of the present day climate? The following is a summary of the main points.

- Cold high pressure systems built over the ice sheets, especially over North America during winter.
- Increased baroclinicity generated storms over a broader longitudinal area than currently.
- The jet stream probably shifted southward over North America and the North Atlantic, perhaps elsewhere during winter.
- Reduced Hadley Cell upwelling was likely over Asia in July.
- Hurricanes were likely weaker or non-existent.

More definitive results await a better understanding of LGM tropical SSTs, ice sheet topography, and perhaps increased model resolution.

David Rind

Bibliography

- Bonfils, C., Lewden, D., and Taylor, K., 1998. A summary documentation of the PMIP models. Web address: <http://www.pcmdi.llnl.gov/pmip>
- Broccoli, A.J., and Manabe, S., 1987. The influence of continental ice, atmospheric CO₂, and land albedo on the climate of the last glacial maximum. *Climate Dyn.*, **1**, 87–99.
- Bromwich, D.H., Toracinta, E.R., Wei, H., Oglesby, R.J., Fastook, J.L., and Hughes, T.H., 2004. Polar MM5 simulations of the winter climate of the Laurentide Ice Sheet. *J. Climate*, **17**, 3415–3433.

- Chylek, P., Lseins, L., and Lohmann, U., 2001. Enhancement of dust source area during past glacial periods due to changes of the Hadley circulation. *J. Geophys. Res.*, **106**, 18477–18485.
- Clark, P.U., Mix, A.C., and Bard, E., 2001. Ice sheets and sea level of the Last Glacial Maximum. *EOS*, **82**, 241–247.
- CLIMAP Project Members, 1981. Seasonal reconstruction of the earth's surface at the Last Glacial Maximum. Geological Society of America Map and Chart Series, MC-36.
- COHMAP Members, 1988. Climatic changes of the last 18,000 years: Observations and model simulations. *Science*, **241**, 1043–1052.
- Colinvaux, P., 1991. Paleocological Background: Neotropics. *Climatic Change*, **18**.
- Crowley, T.J., 1988. Paleoclimate Modeling. In Schlesinger, M.E. (eds.), *Physically-Based Modeling and simulations of Climate and Climate Change: Part II*. Kluwer, Dordrecht: pp. 883–949.
- Denton, G.H., and Hughes, T.J., 1981. *The Last Great Ice Sheets*. New York: Wiley, 484pp.
- Farrera, I., et al., 1999. Tropical climates at the Last Glacial Maximum: A new synthesis of terrestrial palaeoclimate data. 1 Vegetation, lake-levels and geochemistry. *Climate Dyn.*, **15**, 823–856.
- Fastook, J.L., and Prentice, M., 1994. A finite-element model of Antarctica: Sensitivity test for meteorological mass balance relationship. *J. Glaciol.*, **40**, 167–175.
- Felzer, B., Oglesby, R.J., Webb T., and III Hyman, D.E., 1996. Sensitivity of a general circulation model to changes in northern hemisphere ice sheets. *J. Geophys. Res.*, **101**, 19077–19092.
- Gates, W.L., 1976. The numerical simulation of ice-age climate with a global general circulation model. *J. Atm. Sci.*, **33**, 1844–1873.
- Hall, N.M., Dong B., and Valdes, P.J., 1996. The maintenance of the last great ice sheets: A UGAMP GCM study. *J. Climate*, **9**, 1004–1019.
- Hansen, J., Lacis, A., Rind, D., Russell, G., Stone, P., Fung, I., Ruedy, R., and Lerner, J., 1984. Climate sensitivity: Analysis of feedback mechanisms. In Hansen, J.E., and Takahashi, T. (eds.), *Climate Processes and Climate Sensitivity*. Washington, DC: American Geophysical Union, pp. 130–163.
- Held, I.M., and Hou, A.Y., 1980. Nonlinear axially symmetric circulations in a nearly inviscid atmosphere. *J. Atmos. Sci.*, **37**, 515–533.
- Hewitt, C.D., Stouffer, R.J., Broccoli, A.J., Mitchell, J.F.B., and Valdes, P.J., 2003. The effect of ocean dynamics in a coupled GCM simulation of the Last Glacial Maximum. *Climate Dyn.*, **20**, 203–218.
- Hobgood, J.S., and Cerverny, R.S., 1988. Ice-age hurricanes and tropical storms. *Nature*, **333**, 243–245.
- Joussaume, S., 1999. Modeling extreme climates of the past 20,000 years with general circulation models. In Holland, W.R., Joussaume, S., and David, F. (eds.), *Modeling the Earth's climate and its Variability*. Amsterdam, The Netherlands: Elsevier Science B.V., pp. 527–565.
- Kageyama, M., Valdes, P.J., Ramstein, G., Hewitt, C., and Wyputta, U., 1999. Northern Hemisphere storm tracks in present day and Last Glacial Maximum climate simulations: A comparison of the European PMIP models. *J. Climate*, **12**, 742–760.
- Koutavas, A., Lynch-Stieglitz, J., Marchitto, T.M. Jr., Sachs, J.P., 2002. El Niño-like pattern in ice age tropical Pacific sea surface temperature. *Science*, **297**, 202–203.
- Kutzbach, J.E., and Guetter, P.J., 1986. The influence of changing orbital parameters and surface boundary conditions on climate simulations for the past 18,000 years. *J. Atmos. Sci.*, **43**.
- Levis, S., Foley, J.A., and Pollard, D., 1999. Climate-vegetation feedbacks at the Last Glacial Maximum. *J. Geophys. Res.*, **104**, 31191–31198.
- Manabe, S., and Broccoli, A.J., 1985. The influence of continental ice sheets on the climate of an ice age. *J. Geophys. Res.*, **90**, 2167–2190.
- Markgraf, V., 1989. Palaeoclimates in Central and South America since 18,000 BP based on pollen and lake-level records. *Quart. Sci. Rev.*, **8**, 1–24.
- Peltier, W., 1994. Ice age paleotopography. *Science*, **265**, 185–201.
- Pinot, S., Ramstein, G., Harrison, S.P., Prentice, I.C., Guiot, J., Stute, M., and Joussaume, S., 1999a. Tropical paleoclimates at the Last Glacial Maximum: Comparison of Paleoclimate Modeling Intercomparison Project (PMIP) simulations and paleodata. *Climate Dyn.*, **15**, 857–874.
- Pinot, S., Ramstein, G., Marsiat, I., de Vernal, A., Peyron, O., Duplessy J.C., and Weinelt, M., 1999b. Sensitivity of the European LGM climate to North Atlantic sea-surface temperature. *Geophys. Res. Lett.*, **26**, 1893–1896.
- Ramstein, G., and Joussaume, S., 1999. Sensitivity experiments to sea surface temperatures, sea-ice extent and ice-sheet reconstructions, for the last glacial maximum. *Ann. Glaciol.*, **21**, 343–347.
- Ramstein, G., Serfaini-Le Treut, Y., Le Treut, H., Forichon, M., and Joussaume, S., 1998. Cloud processes associated with past and future climate changes. *Clim. Dyn.*, **14**, 233–247.
- Rind, D., 1987. Components of the ice age circulation. *J. Geophys. Res.*, **92**, 4241–4281.
- Rind, D., and Peteet, D., 1985. Terrestrial conditions at the last glacial maximum and CLIMAP sea-surface temperature estimates: Are they consistent? *Quat. Res.*, **24**, 1–22.
- Rind, D., and Perlwitz, J., 2004. The response of the Hadley Circulation to climate changes, past and future. In Diaz, H.F., and Bradley R.S. (eds.), *The Hadley Circulation: Present, Past and Future, vol. 21: Advances in Global Climate Change Research*, Berlin: Springer.
- Rind, D., Chandler, M., Lonergan, P., and Lerner, J., 2001. Climate change and the middle atmosphere: 5. Paleostratosphere in cold and warm climates. *J. Geophys. Res.*, **106**, 20195–20212.
- Shin, S.-I., Liu, Z., Otto-Bliesner, B., Brady, E.C., Kutzbach, J.E., and Harrison, S.P., 2003. A simulation of the Last Glacial Maximum climate using the NCAR-CCSM. *Clim. Dyn.*, **20**, 127–151.
- Street-Perrott, F.A., Marchand, D.S., Roberts, N., Harrison, S.P., 1989. Global lake-level variations from 18,000 to 0 years ago: A palaeoclimate analysis. US DOES/ER/60304-H1 TR046, US Dept. of Energy.
- Toracinta, E.R., Oglesby, R.J., and Bromwich, D.H., 2004. Atmospheric response to modified CLIMAP ocean boundary conditions during the last glacial maximum. *J. Clim.*, **17**, 504–522.
- Trend-Staid, M., and Prell, W.L., 2002. Sea surface temperature at the Last Glacial Maximum: A reconstruction using the modern analog technique. *Paleoceanography*, **17**, 1065
- Webb, A., Rind, D., Lehman, S., Healy, R., and Sigman, D., 1997. Influence of ocean heat transport on the climate of the Last Glacial Maximum. *Nature*, **385**, 695–699.

Cross-references

[Carbon Dioxide and Methane, Quaternary Variations](#)
[CLIMAP](#)
[COHMAP](#)
[Last Glacial Maximum](#)
[North Atlantic Deep Water and Climate Change](#)
[North Atlantic Oscillation \(NAO\) Records](#)
[Ocean Paleocirculation](#)
[Ocean Paleotemperatures](#)
[Paleoclimate Modeling, Quaternary](#)
[Paleo-El Niño-Southern Oscillation \(ENSO\) Records](#)

ATMOSPHERIC EVOLUTION, EARTH

Today's atmosphere plays a critical role in making Earth a habitable planet. It warms the surface with a greenhouse effect, and it blocks ultraviolet radiation that is harmful to life. The properties depend strongly on the concentrations of gases and aerosols in Earth's atmosphere that are in turn determined by a steady state balance between the amounts of gases, solids, and liquids that are added to, removed from, and interconverted by unidirectional chemical reactions. Terrestrial life has, in turn, had an impact on the composition of today's atmosphere. Dry air includes approximately 78% molecular nitrogen and 21% molecular oxygen that largely reflect the role of biological nitrogen fixation and oxygenic photosynthesis.

Many of the parameters that controlled atmospheric composition in the geologic past are the same as those that determine it today. Solar radiation drives atmospheric chemical reactions and sets the boundary conditions for Earth's greenhouse.

Biological activity and geological processes are responsible for significant addition and removal of gases such as oxygen, nitrogen, and carbon dioxide from the atmosphere. In addition to changes in the addition and removal of gases from the atmosphere (sources and sinks), interactions between gases and other elements of the Earth system (feedbacks) also impact atmospheric composition. A distinction is often made between short and long term controls on atmospheric composition. Short term variations of atmospheric composition are attributed to factors such as biological productivity and anthropogenic emissions. Longer term changes in atmospheric composition have been attributed to geological factors that change weathering sinks and volcanic sources, evolutionary events such as the evolution of oxygenic photosynthesis and the colonization of land by plants, in addition to changes in solar radiation through time.

The question of the origin of Earth's atmosphere is at its heart a complex one. Earth's primordial atmosphere is thought to have been lost as a result of atmospheric escape processes (Pepin, 1991), with this early atmosphere replaced by a secondary atmosphere whose origin was attributed initially to degassing of Earth's interior, but more recent thinking attributes much of this secondary atmosphere to extraterrestrial sources (Kasting and Catling, 2003). In the following discussion we will trace the evolution of greenhouse gases and the evolution of oxygen in this secondary atmosphere as well as one of the fundamental feedbacks that has controlled atmospheric composition and the surface temperature conditions of the Earth through time, known as the CO₂-weathering feedback loop (Walker et al., 1981).

Greenhouse gases in the precambrian atmosphere (4400–543 million years ago)

Evidence for liquid water at the surface of the Earth is present in the geologic record beginning 4.4 billion years ago (Mojzsis et al., 2001; Wilde et al., 2001). These observations have been interpreted to indicate that the concentrations of greenhouse gases in Earth's early atmosphere and throughout geologic history have been sufficient to maintain surface temperatures near those dictated by the stability field of liquid water (0–100 °C).

The factors that determine Earth's surface temperature include incoming and outgoing radiation, planetary albedo, and the greenhouse effect. The blackbody temperature for Earth is presently 255 K and matches the balance of incoming radiation from the Sun. The average surface temperature is considerably higher (289 K), however, because infrared active (greenhouse) gases in Earth's atmosphere trap outgoing radiation in the lower atmosphere. A large part of the greenhouse effect in today's atmosphere can be attributed to the role of water and carbon dioxide. In many cases, greenhouse gases occur only in trace concentrations (<1%) in today's atmosphere, but their strong absorption of infrared radiation makes their impact on Earth's surface temperature significant. In the Earth's early atmosphere, these gases also would have played a role in the greenhouse effect.

Standard models for solar evolution (Gilliland, 1989) indicate that the amount of radiation from the solar disk (solar luminosity) changes over time. At the time that Earth formed, 4.6 billion years ago, the amount of solar radiation is thought to have been as much as 25% lower than present-day values. A number of modeling studies indicate that Earth's climate would not have supported the presence of liquid water without higher concentrations of greenhouse gases in the early

atmosphere to compensate for reduced solar luminosity (Sagan and Mullen, 1972).

Studies of the 2.7 billion year old Mount Roe paleosol have used the presence of siderite (an iron carbonate mineral) and greenalite (an iron-bearing phyllosilicate mineral) to place upper limits on the concentration of CO₂ (100 times present atmospheric levels, PAL) in the atmosphere at this time (Rye et al., 1995). Energy balance models using these limits, and constraints imposed by reduced solar luminosity at 2.7 billion years ago, have been used to place limits on the amounts of a second major greenhouse gas (in addition to carbon dioxide) that would have been required to prevent global glaciations. Methane is presently the best candidate for this second greenhouse gas because it is not destroyed by the deep ultraviolet radiation that is thought to have penetrated Earth's early atmosphere.

A recent study presents an alternative solution that does not require enhanced greenhouse gas concentrations, but instead relies on significant changes in Earth's obliquity (tilt of the rotational axis) to inhibit icehouse conditions (Jenkins, 2000). According to this hypothesis, liquid water could have persisted on Earth if obliquity remained high throughout much of Earth's history, and low latitude glaciations would be possible when landmasses occupied equatorial positions. Evidence in the geologic record of Paleoproterozoic rocks of 2.4–2.2 billion years ago and Neoproterozoic rocks from between 750 and 500 million years ago shows a series of widespread, low-latitude glaciations (Hoffman et al., 1998; Bekker et al., 2001) and has been interpreted to reflect collapse of Earth's early greenhouse states, assuming an Earth with low obliquity. The first series of these events, termed "snowball Earth" events, consisted of at least three glacial cycles and is thought to represent the collapse of the Earth's early carbon dioxide plus methane greenhouse as a result of changes in the oxygen content of the Earth's atmosphere. The second series of events has been attributed to several causes including a similar reduction in atmospheric methane concentrations (Pavlov et al., 2003) or a runaway carbon dioxide sink that was associated with silicate mineral weathering reactions that occurred because all continental landmasses were situated at the equator.

In contrast to the inferred collapse of Earth's greenhouse that accompanies snowball Earth events, there have been periods when enhanced greenhouse states have been proposed. These include warm periods 500–400 and 150–55 million years ago and extreme greenhouse events (hothouse events) that have been suggested to have immediately followed Neoproterozoic snowball Earth events. Carbon dioxide levels suggested for these hothouse events are up to 350 times the present atmospheric level and are thought to have built up as a result of limited carbon dioxide sinks due to weathering during the immediately preceding snowball Earth episodes. These levels are, however, strongly dependent on the model simulations of conditions that would be required to overcome snowball-Earth conditions (Hoffman et al., 1998).

Greenhouse gases in the phanerozoic atmosphere (543 million years ago – present)

Estimates of atmospheric carbon dioxide in the past 543 million years have been made using a variety of techniques (Royer et al., 2001). Measurements of the carbon isotopic composition of soil carbonates (pedogenic carbonates) and carbonate associated with the iron oxy-hydroxide mineral goethite have been

combined with physical models of soil-atmosphere carbon dioxide exchange to constrain atmospheric carbon dioxide concentrations at the time of soil carbonate formation (Cerling, 1991; Yapp and Poths, 1992). A second technique uses measurements of carbon isotope ratios in marine organic matter and marine carbonate. These measurements are evaluated in the context of biosynthetic isotope fractionations that depend on the partial pressure of carbon dioxide in ocean water. Atmospheric carbon dioxide is then determined from estimates of oceanic carbon dioxide content. Recently, measurements of the density of stomatal openings observed in fossil leaves have been used to constrain paleo-carbon dioxide levels. An empirical relationship between stomatal density and atmospheric carbon dioxide concentrations was calibrated using modern plants and formed the basis for these methods. A fourth method relies on the boron isotope ratio of biogenic carbonate to determine the pH and $p\text{CO}_2$ of paleo-seawater. Reconstructions of atmospheric carbon dioxide made on the basis of these methods indicate that high levels of carbon dioxide (>20 times PAL) occurred 500 million years ago and decreased to near present-day values by about 300 million years ago. Carbon dioxide levels rose again by about 200 million years ago to a peak at eight times PAL at 150 Ma. Since 150 Ma, atmospheric CO_2 concentrations have decreased to values near present-day values. Smaller magnitude oscillations in atmospheric carbon dioxide concentrations (from levels near 180 to 240 ppm) have been documented for glacial and interglacial cycles over the last 430,000 years (Petit et al., 1999). Recent changes in greenhouse gas concentrations as a result of human activity have been documented and include introduction of greenhouse gases for which there are few or no natural sources (e.g., halocarbons) as well as significant increases in other greenhouse gases (e.g., CO_2 , CH_4 , N_2O , O_3) (Houghton et al., 2001).

Oxygen in the precambrian atmosphere (4400–543 million years ago)

The abundance of molecular nitrogen and molecular oxygen in Earth's atmosphere is much higher than in the atmospheres of Venus and Mars, our two nearest neighbors, and reflects the significant influence of biology on their sources and sinks (photosynthesis, respiration, and nitrogen fixation). Nitrogen in Earth's early atmosphere is thought to have existed predominantly as molecular N_2 because of its stability compared with more reduced and oxidized atmospheric nitrogen compounds such as NH_3 and NO (Kasting and Catling, 2003). Photochemistry involving oxygen produces atomic oxygen that reacts to form oxidized species like ozone (O_3), hydrogen peroxide (H_2O_2), and the hydroxyl radical (OH^*). In the present atmosphere, these species are abundant enough to determine the atmospheric lifetimes of reduced atmospheric species such as methane and carbon monoxide. In Earth's early atmosphere, the concentrations of these oxidized species may not have been high enough to determine the lifetimes of reduced atmospheric species.

Early in Earth's history, the abundance of oxygen is thought to have been considerably lower than it is today, and at some point in Earth's history the atmosphere is thought to have been reduced. The reduced state of the early atmosphere has been inferred because the materials that accreted to form Earth contained abundant hydrogen. Preston Cloud (1972) and Heinrich D. Holland (1984) argued on the basis of evidence from paleosols, iron formations, and the presence of detrital uraninite (UO_2) and pyrite (FeS_2), that the oxidation of Earth's atmosphere occurred just after the Archean-Proterozoic boundary

between 2.5 and 2.2 billion years ago. Under low oxygen conditions iron is leached from soils as Fe^{2+} , in aqueous phase; however, in oxygen-rich conditions Fe^{3+} remains in the soil as hematite Fe_2O_3 . Rye and Holland (1998) argue that Fe depletions in soil profiles developed before 2.2 billion years ago indicate reduced environments and are consistent with a low oxygen atmosphere. Banded iron formations peak in frequency about 2.5 billion years ago and, except for a few occurrences, are largely absent from the geologic record since 1.8 billion years ago. The presence of these sedimentary rocks is thought to reflect a change in ocean chemistry and oxidation state, namely the oxidation of oceanic Fe^{2+} (Canfield, 1998), and also to reflect a change in atmospheric oxidation state. The observation of uraninite and pyrite of detrital origin in Archean sediments (older than 2.5 billion years) has been interpreted as an indication that oxidative weathering was suppressed. In oxidized environments, uraninite (UO_2) oxidizes to UO_2^{2+} which is soluble in water, and pyrite (FeS_2) oxidizes to Fe_2O_3 and SO_4^{2-} . The arguments of Cloud and Holland have not been uncontested, and alternate interpretations that do not hinge on changes in atmospheric oxidation state have been suggested (Ohmoto et al., 1993). However, the arguments that call for a change in atmospheric oxygen content between 2.0 and 2.5 billion years ago have been largely accepted by the geological community.

Recent sulfur isotope measurements of sediments and metamorphosed sedimentary rocks have provided a new way to evaluate the abundance of oxygen in Earth's early atmosphere and the timing of atmospheric oxidation. A large anomalous sulfur isotope signature is present in samples of sediments and metamorphosed sedimentary rocks that are older than 2.45 billion years old, but not in younger rocks (Figure A35). This signature can be represented by the quantity $\Delta^{33}\text{S}$, which is the parts per thousand enrichment of the $^{33}\text{S}/^{32}\text{S}$ of a sample relative to that of a reference that follows the terrestrial mass fractionation array. The terrestrial mass fractionation array is a grand average of the variations of $^{33}\text{S}/^{32}\text{S}$, $^{34}\text{S}/^{32}\text{S}$, and $^{36}\text{S}/^{32}\text{S}$ that are produced by biological and geological chemical and physical processes. The widespread and global nature of this signature in Archean rocks has been interpreted to indicate that oxidative and reductive cycling of sulfur similar to that operating today was suppressed. Sulfur isotope signatures of this type are thought to be exclusively of atmospheric origin. Pavlov and Kasting used a one-dimensional model of atmospheric chemistry to determine that the presence of this signature in the rock record also requires efficient transfer of atmospheric sulfur and sulfate to Earth's surface. A second exit channel opens so that $\text{S} \rightarrow \text{S}_2 \rightarrow \text{S}_4 \rightarrow \text{S}_8$ chemistry can occur when oxygen levels drop below 10^{-5} of present atmospheric oxygen levels (PAL), making the sulfur isotope evidence the strongest argument in favor of a reduced Archean atmosphere (Pavlov and Kasting, 2002). The timing of the transition near 2.45 billion years ago has been interpreted to reflect the time when oxygen levels in the atmosphere first rose.

The rise in atmospheric oxygen that occurred ~ 2.45 billion years ago is thought to have been a step function, or a series of step functions, rather than a gradual rise in atmospheric oxygen (Walker et al., 1983). Archean oxygen levels were thought to have been maintained at levels $<10^{-12}$ PAL because oxygen sink reactions associated with volcanic outgassing out-competed source reactions. Once sources exceeded these sinks, oxygen levels rose until the point at which the next sink reaction would balance the sources. In the present atmosphere, these sink reactions are related to the oxidative weathering of Fe-bearing minerals on the continents. Intermediate oxygen sinks

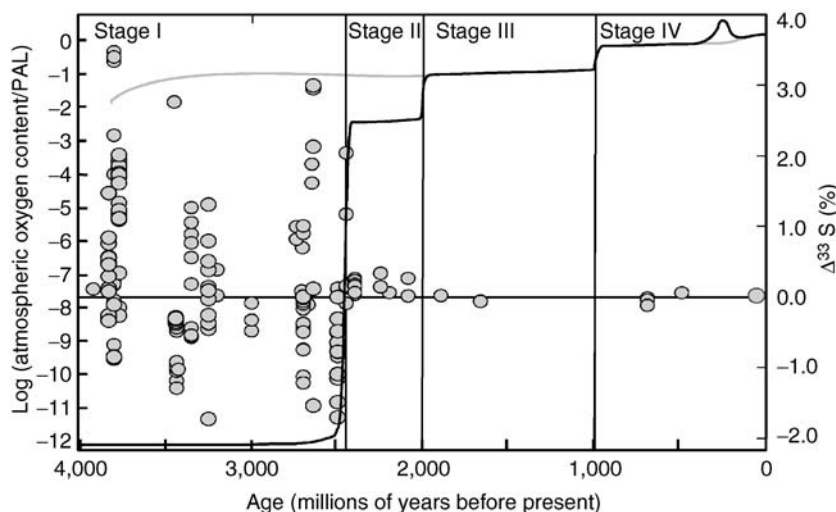


Figure A35 Schematic illustration of the evolution of atmospheric oxygen (*dark line*) with bounds provided by alternate interpretations (*gray line*) (e.g., Ohmoto, 1993). Data points are sulfur isotope data, plotted as $\Delta^{33}\text{S}$, that are used to infer the early evolution of oxygen and to divide the history into stages I (large positive and negative $\Delta^{33}\text{S}$), II (small positive $\Delta^{33}\text{S}$), III (near zero $\Delta^{33}\text{S}$, and $<40\%$ range for $\delta^{34}\text{S}$), and IV (near zero $\Delta^{33}\text{S}$, and $>40\%$ range for $\delta^{34}\text{S}$). The transition between stage I to stage II is marked by the disappearance of large positive and negative $\Delta^{33}\text{S}$ and the transition between stage II and stage III is marked by the disappearance of small $\Delta^{33}\text{S}$ that have been attributed to mass-independent chemistry (Farquhar et al., 2000). The transition between stages III and IV is marked by a change in the range of $^{34}\text{S}/^{32}\text{S}$ fractionations, described by Canfield and Teske (1996).

associated with ocean chemistry involving dissolved species such as Fe^{2+} and sulfide can also act as sinks and stabilize oxygen at intermediate levels (Walker et al., 1983). Arguments about the timing of changes in ocean chemistry associated with sulfide chemistry that are made on the basis of the magnitude of sulfur isotope variations for $^{34}\text{S}/^{32}\text{S}$ have been used to argue that oxygen levels in the atmosphere rose to near present levels sometime between 1 billion and 800 million years ago (Canfield and Teske, 1996).

An unresolved question in studies of atmospheric evolution is why the evidence for oxygenic photosynthesis predates geochemical evidence for an oxidized atmosphere by more than 200 million years. It has been recognized that photosynthesis produces both oxygen and reduced organic matter, and unless the reduced material is removed, no net long-term oxidation of the atmosphere or crust will occur. A number of hypotheses have been presented to account for the removal of reduced material from the atmosphere-crust-ocean system. These include burial of reduced organic matter in sediments, cycling of reduced material to the mantle, and loss of hydrogen to space. Catling et al. (2001) have recently argued that photodissociation of CH_4 in the upper atmosphere, followed by hydrogen escape, was the main loss process for reduced material from the atmosphere, and the reason that the atmosphere-ocean-crust system became oxidized ~ 2.45 billion years ago. Others have argued for changes in mantle redox state, changes in volcanic gases, or that the lag represents the time that it took for photosynthetic bacteria to flourish (Kasting and Siefert, 2002).

Oxygen in the phanerozoic atmosphere (543 million years ago – present)

Berner (2001) and others have investigated the geological evolution of oxygen over the past 543 million years using a variety

of techniques that include building a model that is based on carbon isotope and sulfur isotope variations in the geological record. They reconstruct the mass balance of the amounts of reduced and oxidized carbon and sulfur from their respective isotopic records. This can be done because the most significant carbon and sulfur isotope fractionations are introduced by oxidation/reduction reactions – photosynthesis in the case of carbon isotopes and bacterial sulfate reduction in the case of sulfur isotopes. From this information they have been able to quantify two of the largest source and sink terms for atmospheric oxygen, and in turn, to reconstruct the history of atmospheric oxygen over the past 543 million years. The most recent reconstructions of paleoatmospheric oxygen levels by Berner and colleagues indicate that oxygen levels may have been 25–50% PAL between 543 and 400 million years ago, but rose to 175% PAL by about 300 million years ago during the Permo-Carboniferous, a time when abundant organic rich carbon (coal was buried), vertebrates invaded land, and giant insects (dragonflies) lived. The high oxygen levels of the Permo-Carboniferous reconstructions have not been universally accepted (Lenton, 2001) because it is thought by some detractors that runaway fires would have obliterated forests, yet evidence for trees and vegetation exists.

On shorter timescales, variations in oxygen levels are thought to be strongly dependent on changes in bioproductivity. Variations in the isotopic composition of oxygen gas trapped in ice cores have been used to reconstruct variability of oxygen on orbital timescales associated with the $\sim 20,000$ year precession (wobble) of Earth's orbit (Petit et al., 1999). These variations are thought to reflect changes in biomass and carbon burial that were caused by orbitally-induced changes in solar insolation. Variations in the abundance and isotopic composition of molecular oxygen have also been found to vary on daily to yearly timescales as a result of

variations in biological activity (Bender et al., 1998). These variations point to the strong control of atmospheric oxygen content by bioproductivity in the short term.

In spite of their critical role in determining the lifetime of many trace atmospheric species, the abundances of species such as ozone, hydrogen peroxide, and the hydroxyl radical are much more difficult to constrain from the geological record. The abundance of these gases is linked to oxygen content in the atmosphere, but is also dependent on other factors. We have discussed sulfur isotope evidence (mass-independent fractionations, see above) that can be used to place upper limits on the concentrations of ozone during the first 2 billion years of Earth's history (Farquhar et al., 2001). More recent studies of the oxygen isotopic composition of sulfate in the ice core record using similar isotopic techniques (measurement of ^{16}O , ^{17}O , and ^{18}O) suggest that changes in oxidation pathways for sulfate over Antarctica have occurred over the course of the last glacial cycle (Alexander et al., 2002). Measurements of ozone concentrations made over the last 50 years have documented a decrease in stratospheric ozone that is attributed to chemistry involving chlorine and an increase in tropospheric ozone that is attributed to chemistry involving hydrocarbons (Houghton et al., 2001).

Our understanding of the evolution of Earth's atmosphere is only as good as the physical and chemical modeling studies and interpretations of geological and geochemical evidence upon which it has been constructed. Some of the tools used to study atmospheric evolution have only recently been developed. Future studies that provide new data and test underlying assumptions will undoubtedly refine and possibly provide unanticipated changes in our understanding of atmospheric evolution.

James Farquhar

Bibliography

- Alexander, B., Savarino, J., Barkov, N.I., Delmas, R.J., and Thiemens, M.H., 2002. Climate driven changes in the oxidation pathways of atmospheric sulfur. *Geophys. Res. Lett.*, **29**(14):1685.
- Bekker, A., Kaufman, A.J., Karhu, J.A., Beukes, N.J., Swart, Q.D., Coetzee, L.L., and Eriksson, K.A., 2001. Chemostratigraphy of the paleoproterozoic Duitschland Formation, South Africa: Implications for coupled climate change and carbon cycling. *Am. J. Sci.*, **301**(3), 261–285.
- Bender, M.L., Battle, M., and Keeling, R.F., 1998. The O^{-2} balance of the atmosphere: A tool for studying the fate of fossil-fuel CO_2 . *Ann. Rev. Energy Environ.*, **23**, 207–223.
- Berner, R.A., 2001. Modeling atmospheric O_2 over Phanerozoic time. *Geochimica Et Cosmochimica Acta*, **65**(5), 685–694.
- Canfield, D.E., 1998. A new model for Proterozoic ocean chemistry. *Nature*, **396**(6710), 450–453.
- Canfield, D.E., and Teske, A., 1996. Late Proterozoic rise in atmospheric oxygen concentration inferred from phylogenetic and sulphur-isotope studies. *Nature*, **382**(6587), 127–132.
- Catling, D.C., Zahnle, K.J., and McKay, C.P., 2001. Biogenic methane, hydrogen escape, and the irreversible oxidation of early Earth. *Science*, **293**(5531), 839–843.
- Cerling, T.E., 1991. Carbon-Dioxide in the atmosphere - evidence from cenozoic and mesozoic paleosols. *Am. J. Sci.*, **291**(4), 377–400.
- Cloud, P., 1972. Working model of primitive earth. *Am. J. Sci.*, **272**(6), 537–548.
- Farquhar, J., Savarino, J., Airieau, S., and Thiemens, M.H., 2001. Observation of wavelength-sensitive mass-independent sulfur isotope effects during SO_2 photolysis: Implications for the early atmosphere. *J. Geophys. Res. Planet.*, **106**(E12), 32829–32839.
- Gilliland, R.L., 1989. Solar evolution. In Barron, E.J. vol. 1, 1–2, *The Long Term Stability of the Earth System; Papers Presented at the Annual Workshop in Earth System Science*. Amsterdam: Elsevier, pp. 35–55.
- Hoffman, P.F., Kaufman, A.J., Halverson, G.P., and Schrag, D.P., 1998. A Neoproterozoic snowball Earth. *Science*, **281**(5381), 1342–1346.
- Holland, H.D., 1984. *The Chemical Evolution of the Atmosphere and Oceans*, Princeton, NJ: Princeton University Press.
- Houghton, J.T., et al., 2001. *Climate Change 2001: The Scientific Basis: Contribution of Working Group I to the Third Assessment Report of the Intergovernmental Panel on Climate Change*, Cambridge, UK: Cambridge University Press.
- Jenkins, G.S., 2000. Global climate model high-obliquity solutions to the ancient climate puzzles of the Faint-Young Sun Paradox and low-altitude Proterozoic glaciation. *J. Geophys. Res. Atmos.*, **105**(D6), 7357–7370.
- Kasting, J.F., and Siefert, J.L., 2002. Life and the evolution of Earth's atmosphere. *Science*, **296**(5570), 1066–1068.
- Kasting, J.F., and Catling, D., 2003. Evolution of habitable planet. *Annu. Rev. Astron. Astrophys.*, **41**, 429–463.
- Lenton, T.M., 2001. The role of land plants, phosphorus weathering and fire in the rise and regulation of atmospheric oxygen. *Glob. Chang. Biol.*, **7**(6), 613–629.
- Mojzsis, S.J., Harrison, T.M., and Pidgeon, R.T., 2001. Oxygen-isotope evidence from ancient zircons for liquid water at the Earth's surface 4,300 Myr ago. *Nature*, **409**(6817), 178–181.
- Ohmoto, H., Kakegawa, T., and Lowe, D.R., 1993. 3.4-Billion-year-old biogenic pyrites from Barberton, South Africa - sulfur isotope evidence. *Science*, **262**(5133), 555–557.
- Pavlov, A., Hurtgen, M.T., Kasting, J.F., and Arthur, M.A., 2003. Methane-rich Proterozoic atmosphere? *Geology*, **31**(1), 87–90.
- Pavlov, A.A., and Kasting, J.F., 2002. Mass-independent fractionation of sulfur isotopes in Archean sediments: Strong evidence for an anoxic Archean atmosphere. *Astrobiology*, **2**(1), 27–41.
- Pepin, R.O., 1991. On the origin and early evolution of terrestrial planetary atmospheres and meteoritic volatiles. *Icarus*, **92**, 2–79.
- Petit, J.R., Jouzel, J., Raynaud, D., Barkov, N.I., Barnola, J.M., Basile, I., Bender, M., Chappellaz, J., Davis, M., Delaygue, G., Delmotte, M., Kotlyakov, V.M., Legrand, M., Lipenkov, V.Y., Lorius, C., Pepin, L., Ritz, C., Saltzman, E., and Steievenard, M., 1999. Climate and atmospheric history of the past 420,000 years from the Vostok ice core, Antarctica. *Nature*, **399**(6735), 429–436.
- Royer, D.L., Berner, R.A., and Beerling, D.J., 2001. Phanerozoic atmospheric CO_2 change: Evaluating geochemical and paleobiological approaches. *Earth Sci. Rev.*, **54**(4), 349–392.
- Rye, R., and Holland, H.D., 1998. Paleosols and the evolution of atmospheric oxygen: A critical review. *Am. J. Sci.*, **298**(8), 621–672.
- Rye, R., Kuo, P.H., and Holland, H.D., 1995. Atmospheric carbon-dioxide concentrations before 2.2-billion years ago. *Nature*, **378**(6557), 603–605.
- Sagan, C., and Mullen, G., 1972. Earth and Mars: Evolution of atmospheres and surface temperatures. *Science*, **177**(4043), 52–56.
- Walker, J.C.G., Hays, P.B., and Kasting, J.F., 1981. A negative feedback mechanism for the long-term stabilization of Earth's surface temperature. *J. Geophys. Res. Oceans Atmos.*, **86**(NC10), 9776–9782.
- Walker, J.C.G., Klein, C., Schidlowski, M., Schopf, J.W., Stevenson, D.J., and Walter, M.R., 1983. Environmental evolution of the Archean-early Proterozoic Earth. In Schopf, J.W. (ed.), *Earth's Earliest Biosphere: Its Origin and Evolution*. Princeton: Princeton University Press, pp. 260–290.
- Wilde, S.A., Valley, J.W., Peck, W.H., and Graham, C.M., 2001. Evidence from detrital zircons for the existence of continental crust and oceans on the Earth 4.4 Gyr ago. *Nature*, **409**(6817), 175–178.
- Yapp, C.J., and Poths, H., 1992. Ancient atmospheric CO_2 pressures inferred from natural goethites. *Nature*, **355**(6358), 342–344.

Cross-references

- [Banded Iron Formations and the Early Atmosphere](#)
- [Carbon Isotope Variations Over Geologic Time](#)
- [Faint Young Sun Paradox](#)
- [Greenhouse Effect and Greenhouse Gases \(Encyclopedia of World Climatology\)](#)
- ["Greenhouse" \(Warm\) Climates](#)
- [Iron and Climate Change](#)
- [Obliquity](#)
- [Paleoclimate Proxies, an Introduction](#)
- [Snowball Earth Hypothesis](#)
- [Sulfur Isotopes](#)

ATMOSPHERIC EVOLUTION, MARS

Introduction

Today, Mars is a cold, dry global desert. However, there is considerable evidence that Mars' climate and its inventory of volatiles (substances that tend to form gases or vapor) have changed greatly during the planet's history. The evidence comes from a variety of sources, including the geomorphology and mineralogy of the surface, the atmospheric composition, and the nature of subsurface materials inferred from the analysis of Martian meteorites reviewed by Kieffer et al. (1992) and Carr (2006). In general, geochemical observations suggest that a once much greater volatile inventory was mostly lost very early in Martian history. We discuss below how isotopic data, in particular, suggests that as much as 99% of the original nitrogen and carbon atmospheric inventory of Mars was lost before about 3.8 Ga, $\sim 0.9\%$ has been lost since, and perhaps only $\sim 0.1\%$ remains. The geomorphology suggests a period of early Martian history when liquid water was present on the surface, although perhaps only sporadically. This period is largely coincident with the time before ~ 3.8 Ga when Mars was undergoing heavy bombardment from asteroid and comet impacts. Taken as a whole, the evidence suggests that Mars has likely been cold and dry for much of the last 4 Gyr. During this time, the surface of Mars has been altered by the effect of atmospheric sedimentation of dust and ice, and wind erosion. The climatic effects of quasi-periodic "ice ages" driven by changes in orbital parameters have probably been an important influence. During such times, polar ice, including both carbon dioxide and water ice, has extended down to much lower latitudes than today.

In discussing how the atmosphere has evolved, we use the geologic timescale for Mars. This timescale is divided up into three periods of increasing age: the Amazonian, the Hesperian, and the Noachian. Surfaces on Mars are categorized into these periods according to the density of superimposed impact craters. Older surfaces are those that have accumulated more impact craters. A Noachian surface is defined as one where an area of 10^6 km² has accumulated at least 200 impact craters with diameters larger than 5 km and 25 craters larger than 16 km. Over the same area, a Hesperian surface will have accumulated at least 67 larger impact craters larger than 5 km and 400 craters larger than 2 km, but not enough craters to be classified as Noachian. Amazonian surfaces have insufficient craters to be Hesperian. The absolute ages corresponding to these cratering intensities are poorly constrained. However, the impact cratering record of the Moon has been radiometrically dated using samples returned by the Apollo missions, and lunar cratering rates have been extrapolated to Mars via models to estimate absolute ages of cratered Martian surfaces. In this way, the Noachian is determined to end around 3.7 Ga, while the Hesperian-Amazonian boundary is estimated to be around 2.9–3.3 Ga (Hartmann and Neukum, 2001).

The present-day atmosphere and surface environment

The thin, present-day atmosphere of Mars exerts a spatial and annual average surface pressure of only ~ 600 Pa compared to Earth's sea-level pressure of 10^5 Pa. According to mass spectrometry measurements made by the Viking probes in the 1970s, the atmosphere is well mixed up to 120 km altitude

and is principally composed of carbon dioxide (95.3% by volume), with minor components of nitrogen (2.7%), argon (1.6%) and trace gases (Table A3). Mars is about 50% farther from the Sun than Earth, so on average the solar flux is 43% less. Were the atmosphere to be absent, the mean global temperature on Mars would be 210 K. However, the thin, dry Martian atmosphere provides a modest greenhouse warming of ~ 5 –8 K, which raises the mean global temperature to around 215–218 K. Temperatures and pressures are too low for liquid water to be in equilibrium with the atmosphere, and water persists at the surface only as vapor or ice. Water vapor is seasonally and geographically variable but typically exerts a partial pressure of only ~ 0.1 Pa. Consequently, the absolute abundance of water vapor is $\sim 10^3$ – 10^4 times less than in the Earth's atmosphere. Mars is also cold enough that the main constituent of the atmosphere condenses at the poles each winter, forming 1–2 m thick CO₂ ice deposits. During northern summer, CO₂ ice entirely sublimates away from the north polar cap to reveal underlying water ice. The southern cap is partially covered year round with CO₂ ice, although water ice is known to lie beneath. Measurements of the energy spectrum of neutrons emanating from Mars into space suggest that water ice also exists in the shallow subsurface in certain areas. Cosmic rays enter the subsurface and cause neutrons to be ejected with a variety of energies that can be related to the distribution of elements in the subsurface to a depth of ~ 1 meter. Hydrogen serves as a proxy for water and hydrated minerals. At latitudes greater than about 55° in each hemisphere, water ice is inferred to exist within 1 m of the surface at an average mass abundance of 50%. Hydrogen is also found to be relatively abundant (2–10% by mass) in certain low-latitude locations, such as Valles Marineris and Arabia Terra (Feldman et al., 2004). This may indicate either buried relic ice from ancient climate regimes or, more probably, hydrated minerals.

There is much interest in the possibility of life on Mars but the contemporary surface environment that we just described is hostile to life for several reasons. First, there is a lack of liquid water, which is thermodynamically unstable. Second, Mars has no ozone layer. Thus, ultraviolet (UV) light with wavelengths down to about 200 nm (below which CO₂ absorbs) reaches

Table A3 Basic planetary parameters for Mars and current atmospheric composition

Parameter	Value on Mars
Mean surface pressure (bar)	0.006
Mean global surface temperature (K)	215–218
Mass relative to Earth's mass of 5.97×10^{24} kg	$0.107 \approx 1/9$
Mean radius relative to Earth's mean radius of 6371 km.	$0.532 \approx 1/2$
Composition of the atmosphere (by volume) below 120 km	CO ₂ 95.32% N ₂ 2.7% Ar 1.6% O ₂ 0.13% CO 0.08% H ₂ O 0.03% (varies) NO ~ 100 ppm Ne 2.5 ppm Kr 0.3 ppm Xe 0.08 ppm O ₃ 0.04–0.2 ppm (varies)
Column dust content of the atmosphere	0.3–5 visible optical depth

the surface and sterilizes the soil. Third, photochemistry in the lower atmosphere produces peroxides, such as hydrogen peroxide (H_2O_2), that oxidize and destroy organic material in the soil. As a result, most hopes for extant life on Mars reside in the possibility that a primitive biota exists in the deep subsurface where geothermal heat might support aquifers. There is also much speculation about past life on early Mars when the ancient surface environment may have been less hostile.

Recently, methane (CH_4) has been spectroscopically detected in the Martian atmosphere at an average abundance of ~ 10 ppb (Formisano et al., 2004). Currently, a range of methane values have been reported and differences have yet to be reconciled. Methane only has a lifetime in the atmosphere of a few hundred years because photochemistry converts it to carbon dioxide and water. To maintain 10 ppb requires significant sources to replenish it, which at present are a matter of speculation. On Earth, methane production is dominated by biology. Biogenic methane production from subsurface life cannot be ruled out for Mars, but abiotic production from geothermal activity and photochemical reactions must be considered more probable at present if the methane detection is real.

Geological and geochemical inferences of past climates

Evidence for past liquid water from geomorphology

The present Martian climate contrasts sharply with a warmer, wetter ancient climate that has been commonly inferred from several types of eroded geological features seen on the Martian surface (Carr, 1996).

Dendritic valley networks are observed in the Noachian highlands (Figure A36). Valleys are typically a few kilometers wide, 100–200 m deep, with flat floors and steep walls. They often have some tributaries but generally with a much lower areal density than terrestrial river valleys. How the valleys were formed is debatable, but majority opinion holds that the process was gradual and required liquid water to flow at or near the surface. Various erosive valley formation mechanisms have been suggested, including runoff from rainfall, groundwater sapping (i.e., subsurface flow of water accompanied by collapse of overlying ground), and discharge from hot springs. Low drainage densities, rounded alcove-like termini, and relatively rectangular U-shaped cross-sections (unlike V-shaped valleys commonly seen on Earth) generally favor a sapping origin. However, valley networks are not uniform. Some valley morphologies are more consistent with formation from surface runoff and some valleys that originate at crater rim crests are incompatible with formation from sapping. Certain valleys also are associated with distributary fans. Figure A37 shows such a fan-like feature where the general pattern of the channels and low topographic slopes provide strong circumstantial evidence for a delta, i.e., a deposit made when a river or stream enters a body of water.

Noachian craters often have degraded rims and infilling, which suggests a more erosive Noachian climate. Rates of Noachian erosion, however, are still only comparable to those in drier regions on Earth. On post-Noachian surfaces, estimated erosion rates drop by a factor of about 10^3 . This strongly suggests a causal link between the heavy bombardment and the relatively higher ancient erosion rates. Some crater degradation models suggest that the erosion was in part caused by fluvial activity. However, the image data suggests that craters were also degraded or obscured by impacts, eolian transport, and mass wasting.



Figure A36 Nanedi Vallis (5.5° N, 48.4° W) imaged by the Mars Orbiter Camera (MOC) on NASA's Mars Global Surveyor (MGS) spacecraft. At the top of the image, the sinuous path of this valley is suggestive of river meanders. In the upper third of the image, a central channel is observed and large benches also indicate earlier river terraces. These features suggest that this valley was formed by sustained fluid flow (the inset in the figure shows a lower-resolution Viking Orbiter image for regional context; portion of image MOC-8704, NASA/Malin Space Science Systems).

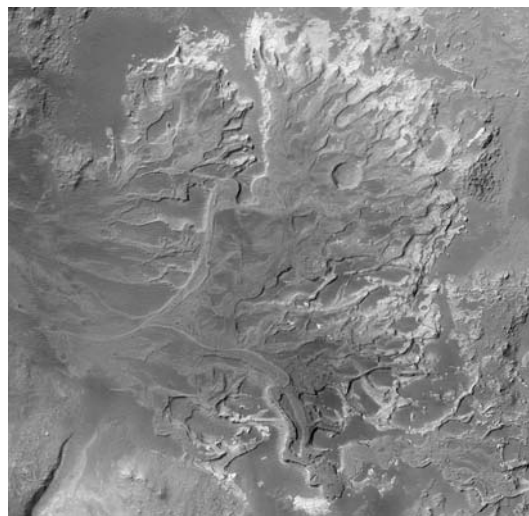


Figure A37 A 14 km by 13.3 km mosaic of high-resolution images taken by the camera on NASA's MGS spacecraft. North is up and the scene is illuminated by sunlight from the left. The picture shows a remnant distributary fan in a 64 km diameter crater northeast of Holden Crater. The floors of channels in the fan stand out in relief because of differential erosion. Presumably the material deposited in valley floors was more resistant to erosion than surrounding material (image MOC2-543a, NASA/Malin Space Science Systems).

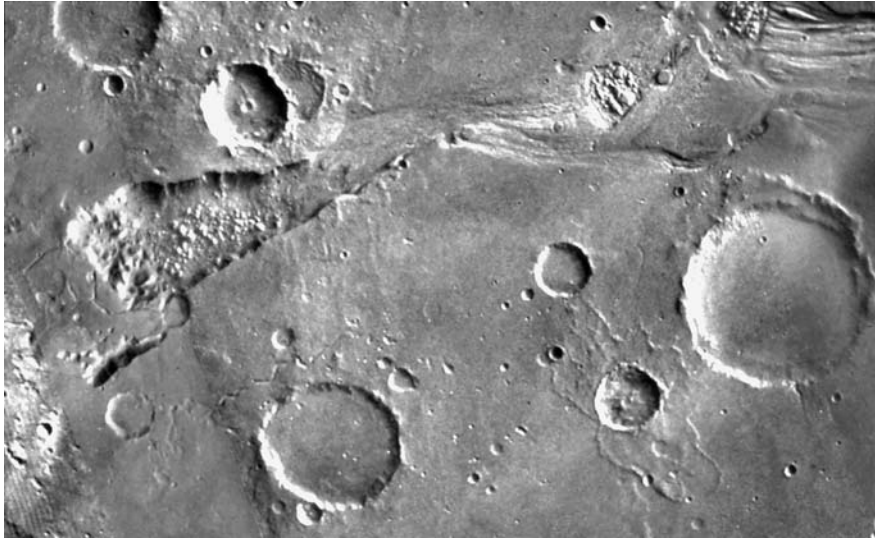


Figure A38 A mosaic of Viking Orbiter images showing the 300 km long head of the channel Ravi Vallis. The source region for the channel on the left is in an area of chaotic terrain. Ravi Vallis feeds into a system of channels that flow northward into Chryse Basin in the northern lowlands of Mars (NASA/Lunar and Planetary Institute).

Outflow channels are a further type of feature generally thought to have a fluvial origin (Baker, 2001). Such channels are 20–100 km wide and can extend for thousands of kilometers (Figure A38). The outflow channel interiors are generally not heavily cratered, and so the channels are inferred to be less ancient than the valley networks. Because the source of outflow channels often originates in chaotic terrain (areas where the ground is collapsed and broken), the expulsion of groundwater in floods is widely held to have been responsible for channel genesis. Such floods could conceivably have occurred in a cold environment similar to that of today, initiated by geothermal heating of subsurface ice or hydrated salts (Montgomery and Gillespie, 2005). Other workers have emphasized that wind and ice may have widened outflow channels over geologic time (Cutts and Blasius, 1981). Liquid CO₂ has also been suggested as a possible agent of erosion. However, CO₂ is unable to discharge as a liquid under present Martian conditions (it would turn into vapor under any plausible conditions) and also there is no well-defined mechanism for recharging CO₂ “aquifers.” Outflow channels drain into the northern lowlands on Mars, where possible shoreline features have been identified, which some interpret as the boundaries of a past ocean (Carr and Head, 2003). The shoreline features remain controversial because high-resolution images do not reveal distinctive geomorphology (Malin and Edgett, 1999) and “shorelines” have also been interpreted as tectonically-derived wrinkle ridges (Withers and Neumann, 2001).

Other intriguing geological features on Mars include gullies on the sidewalls of impact craters and valleys (Figure A39). These features are geologically recent because they lack superimposed small craters and sometimes have debris that overlies sand dunes. Such gullies are found preferentially on poleward-facing slopes at latitudes higher than 30° in both hemispheres. Longevity of ice is favored on such poleward-facing slopes. Consequently, it is possible that snowpack or ice formed in past



Figure A39 Gully-like features on the sidewall of a crater near 33.3° S, 267.1° W. The arrow indicates a light-toned material, probably rich in ice. This layer appears to be genetically associated with the gullies, given that the tops of the gullies originate from the same level as the top of the light-toned layer. The picture is about 2.8 km by 5.8 km, a portion of MOC image M09–02875 (NASA/JPL/Malin Space Science Systems).

orbital-driven climate regimes melted at its base, causing the formation of the gullies (Figure A39) (Christensen, 2003). However, the exact formation mechanism for gullies is currently uncertain.

Evidence for past liquid water from surface geochemistry and sedimentology

Although the surface of Mars is dominated by igneous rock (Christensen et al., 2001), infrared spectroscopy from NASA's Mars Global Surveyor orbiter indicates spectral absorption features consistent with the presence of coarse-grained crystalline hematite (Fe_2O_3) in a few unique locations on Mars where it outcrops from exhumed layered terrain. In 2004, NASA's Mars Exploration Rover B, or "Opportunity" rover, landed in Meridiani Planum to examine the hematite there (Squyres et al., 2006). The hematite is found in small spheres (with $>50\%$ Fe_2O_3 as hematite) uniformly distributed in laminated sulfate-rich sandstones. The sandstone is crumbling away due to wind erosion, and the hematite spherules, which are more resistant to erosion, are falling out. Hematite spherules or their broken fragments litter the plains of Meridiani and represent leftovers of several hundred thousand square kilometers of erosion. The spherules are concretions that form when water carries dissolved minerals through soft sediments or porous rock and minerals precipitate radially or concentrically, incorporating or replacing surrounding sediment. Although the Meridiani rocks are mostly wind-deposited sandstones, some upper sandstone beds show sinuous-crested ripples of a few centimeters height characteristic of sand that was subject to flow in shallow water. Overall, the geologic history in Meridiani Planum is inferred to have gone through three stages: (a) Basalt was altered by acid sulfate to produce sand grains consisting of sulfates and a residue of aluminum-rich amorphous silica. (b) Grains were eroded and re-deposited as sandstone by the wind. (c) Subsequently, groundwater penetrated the sandstone and even pooled at the surface in some areas. The groundwater produced hematite concretions and dissolved some soluble components in the rock. Because only wind has subsequently modified the sandstone, water has likely been scarce at Meridiani for the past several billion years.

Sulfates are an important component of the Martian surface according to many spacecraft observations. A companion rover to Opportunity, named Spirit, found sulfate-rich rocks in the Columbia Hills region, near Gusev Crater, while measurements by NASA's Mars Pathfinder and Viking landers showed that sulfur is a substantial component of soil ($\sim 7\text{--}8\%$ by mass) and surface rocks. Hydrated sulfate deposits have also been identified in numerous deposits, some the size of mountains, in the Martian tropics from near-infrared spectra obtained by the European Space Agency's Mars Express spacecraft. Observed sulfate minerals include gypsum ($\text{CaSO}_4 \cdot 2\text{H}_2\text{O}$) and kieserite ($\text{MgSO}_4 \cdot \text{H}_2\text{O}$), while jarosite has been found by Opportunity (jarosite is $\text{XFe}_3(\text{SO}_4)_2(\text{OH})_6$, where "X" is a singly charged species such as Na^+ , K^+ , or hydronium (H_3O^+)). Anhydrous sulfates, such as anhydrite (CaSO_4), may also be present but would give no signature in the spectral region studied by Mars Express. In general, the sulfates are thought to have formed from alteration of basaltic rocks by sulfuric acid.

Mars Express has also discovered clays in a few locations in the oldest exhumed Noachian terrain (Poulet et al., 2005). These clays incorporate Fe^{3+} and Fe^{2+} . Such clays generally form when basaltic rocks are altered by water. Given that clays often deposit in alkaline or near-neutral conditions, it has been proposed that they formed in a different environment from the acid sulfates found elsewhere. In addition, surface and orbital measurements have found silica (SiO_2) deposits, which is expected from the aqueous alteration of basaltic minerals.

Climate implications

Because liquid water is widely thought to have been the erosive agent that sculpted the ancient valley networks and produced the various hydrated minerals described above, it is often assumed that Mars must have had a persistently warmer and wetter climate in the Noachian than it does today. However, there are several problems with this hypothesis. First, the solar luminosity was about 30% lower 4 Gyr ago compared to today, which requires a very thick CO_2 atmosphere (up to ~ 5 bar surface pressure) to generate enough greenhouse warming to maintain a warm, wet climate at that time (Pollack et al., 1987). Such thick atmospheres on Mars are not physically plausible because at ~ 1 bar, CO_2 condenses into clouds and the CO_2 ice particles rain out (Kasting, 1991). Although there has been speculation that CO_2 ice clouds themselves could act as a greenhouse blanket, recent models suggest that they could not warm the surface above freezing because such warming is self-limiting: by heating the air, the clouds cause themselves to dissipate (Colaprete and Toon, 2003). Other significant greenhouse gases such as CH_4 and SO_2 are problematic. Enough CH_4 could only be sustained if there were a global microbial biosphere comparable to Earth's. Volcanic SO_2 would quickly dissolve and rain out if Mars had been warm enough for a hydrological cycle. Moreover, the net effect of sulfur dioxide on Earth and Venus is cooling through sulfate aerosols that reflect sunlight. There is no geochemical evidence that a thicker CO_2 atmosphere persisted long because under warm, wet conditions atmospheric CO_2 would weather rocks and make abundant carbonate sediments. No carbonate outcrops have been observed spectroscopically at the 100 m scale, despite a global search from spacecraft. Atmospheric dust particles contain a few percent carbonate but carbonate weathering of dust may have occurred in the prevailing cold dry climate and the total amount of carbonate may be small, depending on the global average depth of dust. Upon reflection, it is not surprising that carbonate outcrops are absent whereas sulfate deposits are relatively widespread. In the presence of abundant sulfuric acid, carbonate would be converted to sulfate with release of CO_2 to the atmosphere where CO_2 would be subject to various loss processes discussed below.

Atmospheric origin

Volatiles important to the origin of Mars' atmosphere include water, carbon and nitrogen. The depletion of noble gases on Mars relative to solar abundance indicate that when Mars formed it did not accrete gases directly from the solar nebula. Instead, volatiles must have been acquired as solids. For example, water would have been acquired as water ice or the water of hydration bound in silicate minerals, and carbon would have been acquired as solid hydrocarbons or perhaps carbonates. Mars acquired volatiles either during planetary accretion or during subsequent bombardment by impacting asteroids or comets. Computer simulations of the formation of planets suggest that Earth acquired much of its crustal and surface water from large "planetary embryos" that grew in the asteroid belt between the orbits of Mars and Jupiter before they were ejected by the gravitational influence of Jupiter towards Earth or outward from the Sun. Comets are ruled out as the source of Earth's oceans on isotopic and dynamical grounds (Zahnle, 1998). In contrast, to explain the smallness of Mars requires that it suffered essentially no giant collisions from planetary

embryos and that it grew through smaller asteroidal bodies that accreted later. This means that Mars could have started out with a much smaller fraction of the volatiles than the Earth (Lunine et al., 2003). However, an alternative school of thought argues that Mars and Earth acquired volatiles from local planetesimals in a cold nebula, which would argue for a similar volatile fraction on Earth and Mars (Drake and Righter, 2002).

Atmospheric loss: impact erosion, hydrodynamic escape, sputtering, and surface sinks

Today, the Martian atmosphere has little carbon and nitrogen, which suggests considerable atmospheric loss. The Earth is estimated to have the equivalent of 60–90 bar of CO₂ locked up in carbonate rocks, such that if it were all released, Earth's atmosphere would be similar to that of Venus. Mars, scaling by its relative mass, presumably had an original inventory of no more than 10 bar of CO₂, if we conservatively assume that Mars' volatile fraction had been similar to Earth's. However, there is no evidence for a large CO₂ inventory today. With an area of 88 km² and a thickness between 1 and 100 m, the residual southern cap contains no more than 0.6–60% as much CO₂ as the atmosphere. The regolith on Mars contains an unknown amount of adsorbed CO₂, but probably <0.04 bar (Kieffer and Zent, 1992). Martian meteorites contain <0.5% carbonate salts by volume, which scaled to the crust provide <0.25 bar CO₂ equivalent per kilometer depth. Thus, the current CO₂ inventory of Mars is perhaps a few times 0.1 bar, which, to the nearest order of magnitude, is ~0.1% of the original estimated inventory. This depletion is consistent with isotopic constraints discussed below. Similarly, the current atmospheric N₂ inventory is merely 1.6×10^{-4} bar, compared to 0.78 bar and 3.3 bar N₂ in the atmospheres of Earth and Venus, respectively. Nitrogen could perhaps exist on Mars as nitrate minerals, but the lack of nitrates in Martian meteorites and the absence of spectral evidence for nitrates on the surface do not support such speculation.

Impact erosion

One efficient mechanism for atmospheric loss is impact erosion. Impact erosion occurs when the hot vapor plume from a large asteroid or comet impact imparts sufficient kinetic energy as heat for atmospheric molecules to escape en masse. The impact velocity must be large enough to create a plume that expands faster than the planet's escape velocity. Consequently, Mars, with its small escape velocity, is much more prone to atmospheric impact erosion than Earth or Venus. Modeling based on the estimated cratering rate on early Mars suggests that the early atmosphere was reduced in mass by a factor of ~100 (Figure A40) (Melosh and Vickery, 1989). Thus, if Mars started with a 5 bar atmosphere after accretion, it would have had a 0.05 bar atmosphere by ~3.8–3.5 Ga, when bombardment had subsided, assuming that the CO₂ was in the atmosphere and subject to escape rather than locked up as carbonates in the surface.

Hydrodynamic escape

Another atmospheric loss process that is thought to have operated very early in Martian history is hydrodynamic escape. This escape mechanism applies to a hydrogen-rich primitive atmosphere, which may have existed from 4.5 Ga to roughly about 4.2 Ga. The source of hydrogen would have been volcanism generated by a much more radioactive mantle than today.

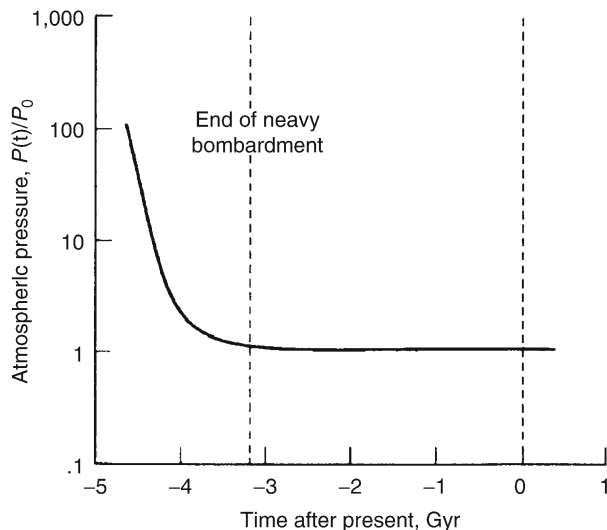


Figure A40 The effect of impact erosion on the surface atmospheric pressure $P(t)$ as a function of time, normalized to present surface pressure, P_0 (from Melosh and Vickery, 1989).

During this early time, the upper atmosphere was heated by high fluxes of extreme ultraviolet radiation (EUV) from the young sun. (Although the young sun was fainter than today overall, astronomical observations and theory show that young stars have much greater output of EUV). Hydrodynamic escape occurs when the typical thermal energy of hydrogen in the upper atmosphere becomes comparable to the gravitational binding energy. As a result, the atmosphere expands into the surrounding vacuum of space. The same process currently happens to the solar atmosphere and results in the solar wind. By analogy, hydrodynamic escape of a planetary atmosphere is termed a *planetary wind*. The escape rate is so rapid that the outward speed of the atmosphere at high altitudes reaches and then exceeds the speed of sound. Heavy atoms get dragged along when collisions with hydrogen push the heavy atoms upward faster than gravity can pull them back. This leads to loss of heavy gases and mass fractionation between different isotopes of the same element. The noble gases on Mars display isotopic patterns consistent with fractionation by early hydrodynamic hydrogen escape (see below). Consequently, bulk gases, such as CO₂ and N₂, should have also been lost through hydrodynamic escape.

Sputtering and nonthermal escape

A further atmospheric loss mechanism is sputtering, also known as solar wind stripping of the atmosphere. Ions in the upper atmosphere are “picked up” by magnetic fields generated by the flow of the solar wind around the planet. The ions undergo charge exchange, which is the process where a fast ion passes its charge to a neutral atom through collision and becomes a fast neutral atom. The large energy is then imparted to surrounding particles through further collisions. Fast, upward-directed particles generated in this process can escape. Today Mars has no global dipole field, but solar wind stripping would have been prevented by the presence of a substantial global magnetic field on early Mars, which would have forced the solar wind to flow around the planet at a greater distance, without significant atmospheric interaction. Mars is known to

have once had a global field because the planet has regions of large remnant magnetization, where new volcanic rocks crystallized in the presence of a magnetic field. Thus, sputtering would have only been important after Mars lost its magnetic field. The timing of the shut-off of the global magnetic field is uncertain. However, there are clues. Unlike much of the other ancient terrain, the Hellas impact basin and surrounding areas lack any magnetic signature. This is most easily explained if the Hellas impact, which is at least 4 Gyr old (based on its size), occurred when Mars no longer possessed a global magnetic field. Thus stripping of the atmosphere by the solar wind would have occurred since about ~ 4 Ga, but not before. Models suggest that solar wind stripping may have removed up to 90% of the post-4 Ga atmosphere. Such atmospheric losses are cumulative. For example, if impacts and hydrodynamic escape removed 99% of the earliest atmosphere and sputtering removed a further 90% of the remainder, the total loss would be 99.9%.

Atmospheric escape is happening today by sputtering and other means. Escape occurs from the base of the Martian exosphere, which is at about 230 km altitude. In the exosphere, the probability of collisions is so small that particles with sufficient upward velocities escape from the planet. The most important species that escape today are hydrogen, oxygen, nitrogen, and carbon. Hydrogen and oxygen loss are coupled. Water vapor photolysis in the lower atmosphere produces H_2 . Above ~ 120 km altitude, hydrogen diffuses upwards and gets converted to atomic hydrogen by photochemical reactions. Atomic hydrogen possesses enough thermal energy to escape to space, so the rate of escape is limited by slow diffusion through the upper atmosphere, and, in turn, by supply of hydrogen-bearing species from the lower atmosphere. Although oxygen produced from water vapor photolysis is too heavy to escape to space through its thermal motion alone, another mechanism exists for oxygen loss. Ionized oxygen molecules (O_2^+) in the ionosphere combine with electrons in “dissociative recombination.” Recombination dissociates the molecules into O atoms with enough kinetic energy to escape ($O_2^+ + e^- \rightarrow O + O$). On Mars, it has been hypothesized that the oxygen escape flux adjusts itself so that it balances the hydrogen escape flux in a 2:1 ratio, i.e., effectively, water escapes (McElroy and Donahue, 1972). However, recent estimates of O escape suggest that the H:O escape ratio is $\sim 20:1$, implying a surface sink for oxygen (Lammer et al., 2003).

Isotopic ratios of D/H and $^{18}O/^{16}O$ in the atmosphere and in Martian meteorites provide weak constraints on the amount of water that has escaped over Martian history. Upper bounds on the estimates of water loss range up to 30–50 m of equivalent global ocean (Krasnopolsky, 2002). These amounts are roughly

comparable to estimates of the inventory in the current polar caps and regolith. Nitrogen and carbon are also able to escape via dissociative recombination. Such loss mechanisms have probably been important for the last 4 Gyr of Martian history and can account for observed C and N isotopic ratios on Mars (see below).

Surface sinks

A final possible atmospheric loss mechanism is to the surface. In the presence of liquid water, CO_2 will dissolve to form carbonic acid and react with the surface through chemical weathering. Carbonic acid reacts with silicate minerals in igneous rocks to release cations (such as Mg^{2+} , Ca^{2+} , Fe^{2+} , K^+ , and Na^+), bicarbonate (HCO_3^-) and other anions, and silica. The ions so released would be expected to precipitate in sediments producing abundant carbonates such as siderite ($FeCO_3$), calcite ($CaCO_3$) and magnesite ($MgCO_3$). Weathering and deposition thus produce overall reaction of the type $CO_2 + CaSiO_3 = CaCO_3 + SiO_2$. The weathering lifetime of a massive CO_2 atmosphere is geologically so short ($\sim 1.5 \times 10^7$ years) that a recycling mechanism such as thermal decomposition by volcanism must be hypothesized to maintain the CO_2 (Pollack et al., 1987). A 1 bar CO_2 atmosphere, if it were all eventually converted to calcite, would generate a global layer of calcite about 200 m thick. But there is no evidence from remote spectroscopy for even a single carbonate outcrop. If Mars started out with abundant CO_2 , the most likely loss appears to have been to space and not to the surface. Noble gas constraints strongly support this idea.

Inferences from noble gases and the isotopic composition of the atmosphere

The isotopic composition of the atmosphere of Mars was measured directly on the surface of Mars by mass spectrometers on two Viking lander spacecraft in the 1970s. For noble gases, more precise measurements have become available from gases trapped within Martian meteorites (Table A4). Atmospheric gases were incorporated into these meteorites when they were melted under the shock of impact that ejected them from Mars. The compositional and isotopic similarity of such meteorite gases to the Viking measurements is convincing evidence that such meteorites come from Mars. Isotopic measurements of gases in the shergottite meteorite sub-class of Martian meteorites have proved particularly valuable because the shergottites originated from shallow depths on Mars so that they are not generally contaminated with gases that have emanated from the Martian interior.

The isotopic composition of volatiles on Mars points to loss of the early atmosphere. Both $^{40}Ar/^{36}Ar$ and $^{129}Xe/^{132}Xe$ noble

Table A4 The isotopic composition of the atmosphere of Mars as measured by the Viking lander spacecraft and in trapped gas bubbles in Martian shergottite meteorites (Owen, 1992; Bogard et al., 2001)

Isotopic ratio	Martian atmosphere (Viking)	Martian atmosphere (Shergottites)	Earth's atmosphere	Martian isotope ratio relative to terrestrial
D/H	$(9 \pm 4) \times 10^{-4}$	6.9×10^{-4}	1.56×10^{-4}	$\sim 4.4\text{--}5$
$^{12}C/^{13}C$	90 ± 5	not reported	89	~ 1
$^{14}N/^{15}N$	170 ± 15	>181	272	>0.6
$^{20}Ne/^{22}Ne$	not measured	~ 10	9.8	~ 1
$^{16}O/^{18}O$	490 ± 25	~ 490	489	~ 1
$^{40}Ar/^{36}Ar$	3000 ± 500	1800 ± 100	296	~ 6
$^{36}Ar/^{38}Ar$	5.5 ± 1.5	≤ 3.9	5.3	<0.7
$^{129}Xe/^{132}Xe$	2.5^{+2}_{-1}	2.4–2.6	0.97	~ 2.5

gas ratios are considerably larger than terrestrial values (Table A4). The “radiogenic isotopes,” ^{40}Ar and ^{129}Xe , result from the decay of radioactive ^{40}K and ^{129}I , respectively. In contrast, the “primordial isotopes,” ^{36}Ar and ^{132}Xe , are not radioactive decay products and were assimilated when Mars formed. The relative enrichment of the radiogenic isotopes suggests that the primordial isotopes were lost. ^{40}K has a ~ 1.28 Gyr half-life, while ^{129}I has a half-life of only ~ 16 Myr, which suggests that most of the ^{132}Xe was lost from Mars very early. A plausible loss mechanism for the primordial isotopes is intense impact erosion in the early Noachian.

Isotopic measurements also indicate that hydrogen, argon, carbon, nitrogen and oxygen have escaped from Mars by gradual processes that continue to operate today. As a result, the light isotopes are depleted relative to the heavy ones; for example, ^{14}N relative to ^{15}N (Table A4). This isotopic fractionation arises because above 120 km altitude, gases separate diffusively according to mass and the heavier isotopes decrease in abundance more rapidly than light isotopes. Consequently, more light isotopes are available for removal at the base of the exosphere. Thus, the atmosphere below becomes enriched in heavy isotopes. This enrichment indicates a loss of 50–90% of the atmospheric species to space (Jakosky and Jones, 1997; Jakosky and Phillips, 2001).

Hydrodynamic escape can reasonably account for the isotopic fractionation of some of the noble gases found in the Martian atmosphere: argon, neon and xenon. Hydrodynamic escape has been invoked to explain the Martian $^{36}\text{Ar}/^{38}\text{Ar}$ ratio of < 3.9 , which is isotopically heavy compared with a terrestrial ratio of 5.32 and the average carbonaceous chondrite value of ~ 5.3 (thought to be representative of the material from which Mars formed). However, if argon escapes and fractionates, neon must also fractionate because it is lighter. Martian atmospheric $^{20}\text{Ne}/^{22}\text{Ne}$ appears to be ~ 10 , similar to the terrestrial atmospheric ratio but smaller than a chondritic value, ~ 13.7 . If the original Martian ratios of $^{36}\text{Ar}/^{38}\text{Ar}$ and $^{20}\text{Ne}/^{22}\text{Ne}$ were 5.35 and 13.7, respectively, hydrodynamic escape models produce a $^{20}\text{Ne}/^{22}\text{Ne}$ ratio no greater than 9.5 ± 1.3 , similar to observation. Interpretation of xenon isotopes is complicated by virtue of its nine stable isotopes, several of which have been affected by the decay of extinct radionuclides. However, fractionation of non-radiogenic xenon isotopes can plausibly be explained by mass fractionation during hydrodynamic escape of hydrogen (Pepin, 1991). Xenon, in particular, is too heavy to escape by means such as sputtering or thermal escape, so early hydrodynamic escape would seem to be required.

Atmospheric loss has also left an imprint on the overall abundance of volatiles. The stable and most abundant isotope

of krypton, ^{84}Kr , is probably the best volatile tracer of atmospheric loss because it should not be subject to fractionation by gradual atmospheric escape of the kind that occurs today for hydrogen, nitrogen, carbon and oxygen. Thus, krypton has probably been retained ever since the end of heavy bombardment around 3.8 Ga. The ratio $\text{C}/^{84}\text{Kr}$ is $\approx 4 \times 10^7$ for Earth and Venus but $\approx (4.4\text{--}6) \times 10^6$ on Mars. This suggests that the amount of CO_2 that Mars had when heavy bombardment and impact erosion ended was 10 times greater (i.e., a 90% loss, consistent with isotopic fractionation of nitrogen). Given that Mars has ~ 6 mbar CO_2 now, the atmosphere may have had ~ 60 mbar CO_2 at around 3.8 Ga. In addition, ^{84}Kr per kg on Mars is only about 1% of that on Earth. This implies a factor of ~ 100 depletion (of both krypton and carbon) due to early impact erosion before 3.8 Ga, which is consistent with the predictions of impact erosion models. A primordial inventory of ≥ 6 bar CO_2 would be inferred, consistent with inferences about Mars’ original endowment of volatiles.

Taken together, we see that the isotopic and abundance evidence suggests that Mars may have lost $\sim 99\%$ of its atmospheric volatiles by the end of heavy bombardment and has perhaps since lost a further $\sim 90\%$ of what remained at that time. This conclusion is tempered by the knowledge that some volatiles, like water, readily form solids in the subsurface, which affords protection against loss to space.

Martian Milankovitch cycles, chaotic obliquity fluctuations, and quasi-periodic climate change.

Mars has very large variations in its orbital elements compared to the Earth (Table A5; Figure A41). Today, the eccentricity of the Martian orbit is 0.093, about 5 times greater than for the Earth, which means that Mars receives about 40% more insolation at perihelion than aphelion. Mars’ rotation rate and obliquity (the angle between its spin axis and the normal to the orbital plane) are similar to Earth’s. Consequently, daily and seasonal changes are analogous. Today, the obliquity of Mars, 25.2° , is close to its mean value over the last 10 Myr but obliquity has varied considerably during that time. Moreover, the spin dynamics are chaotic, with an exponential divergence timescale of 3–4 million years, so that for timescales longer than 10^7 years, the obliquity could have varied between 0° and 60° . The average obliquity for Mars over geologic time was $< 40^\circ$, and sometimes the obliquity may have reached as high as 80° (Laskar et al., 2004). In recent history, eccentricity and obliquity have oscillated with a primary period of $\sim 10^5$ years, modulated on timescales of 2.4 and 1.2 Myr, respectively (Figure A41). In addition, the spin axis orientation (which determines the season of perihelion) has precessed with a 51,000-year period.

Table A5 The orbital elements of Mars and the Earth and their variability

Parameter	Present mars	Martian variability		Present Earth	Terrestrial variability	
		Range	Cycle (years)		Range	Cycle (years)
Obliquity ($^\circ$)	25.19	$\sim 12\text{--}47^{\text{a}}$	120,000 ^b	23.45	22–24	41,000
Eccentricity ^c	0.093	0–0.12	120,000 ^d	0.017	0.01–0.04	100,000
Longitude of perihelion ($^\circ$)	250	0–360	51,000	285	0–360	21,000

^aFor times older than about 10 Ma, obliquity variations are chaotic and would have varied between 0 and 60° (Touma and Wisdom, 1993).

^bThe amplitude of obliquity oscillation is modulated with a ~ 1.2 Myr period envelope.

^cEccentricity, e , is defined by $e = (1 - (b/a)^2)^{0.5}$ where a is the semi-major axis and b is the semi-minor axis of the ellipse traced by the planet’s orbit around the Sun.

^dThe amplitude of eccentricity oscillation is modulated with a ~ 2.4 Myr period envelope.

Of the three parameters (season of perihelion, eccentricity and obliquity), obliquity exerts the largest influence on the climate because changes in obliquity alter the latitudinal distribution of sunlight. Indeed, above 54° obliquity, the poles receive more annual average insolation than the equator. However, the global annual mean surface temperature is calculated to drop at high obliquity because of the increased extent of the bright seasonal CO_2 ice caps. The larger caps would also cause the mean annual surface pressure to be somewhat lower at high obliquity, assuming that the amount of exchangeable CO_2 desorbed from polar regolith is small. If the obliquity were 45° (with other orbital parameters the same as today's), the southern winter cap would reach the equator of Mars during southern winter (Haberle et al., 2003). Consequently, polar ice may have reached the equator even in the last 10 Myr.

Probable evidence for orbital-driven climate change can be found in geologic features on Mars. Both polar regions have extensive layered terrain, which is ~ 10 Myr old based on the

lack of craters. The polar layered terrain consists of multiple layers, each meters to tens of meters thick, with variable brightness. One possible explanation for the origin of layered terrains is that quasi-periodic oscillations in Mars' orbital parameters cause the climate to oscillate. In particular, the shuffling of the climate regimes causes cyclic changes in ice and dust deposition over time. For example, higher (or lower) eccentricity will mean more (or less) dust transport, modulated with $\sim 10^6$ year cyclicity. The short period obliquity and precession cycles will also modulate deposition and erosion over 10^5 years. The two spatial frequencies observed in the polar-layered terrain may be related to these two temporal frequencies (Figure A42).

A thin, patchy mantle of material, apparently consisting of cemented dust, has also been observed within a $30\text{--}60^\circ$ latitude band in each hemisphere (Figure A43). The material is interpreted to be an atmospherically deposited ice-dust mixture

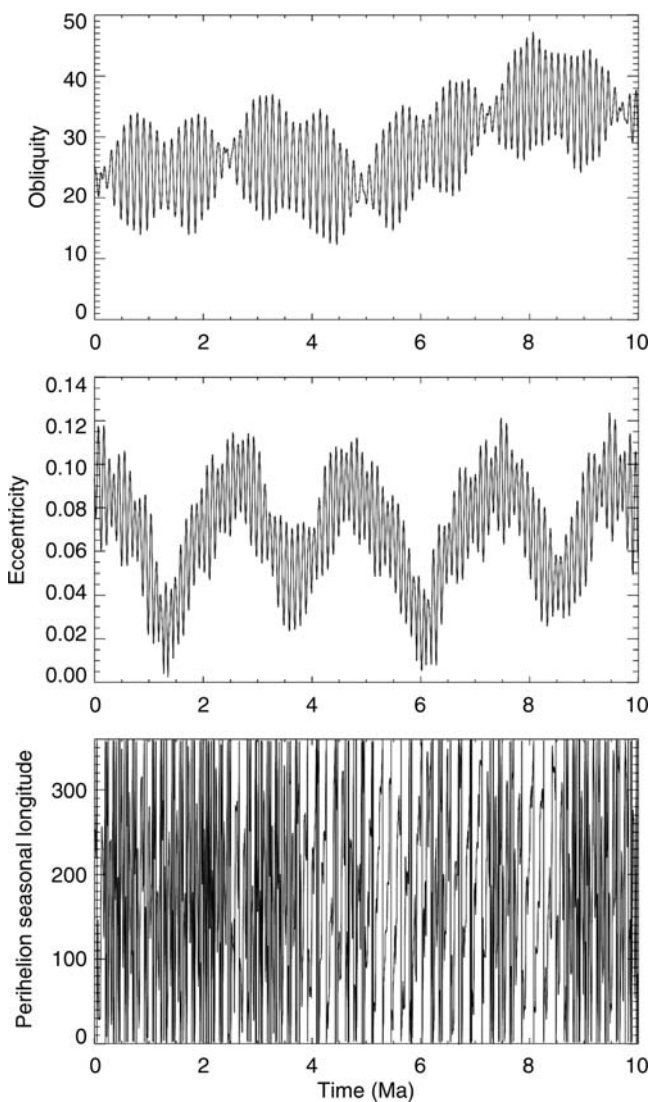


Figure A41 Simulated variations of Martian orbital elements over the last 10 Myr (data courtesy of J. Armstrong).

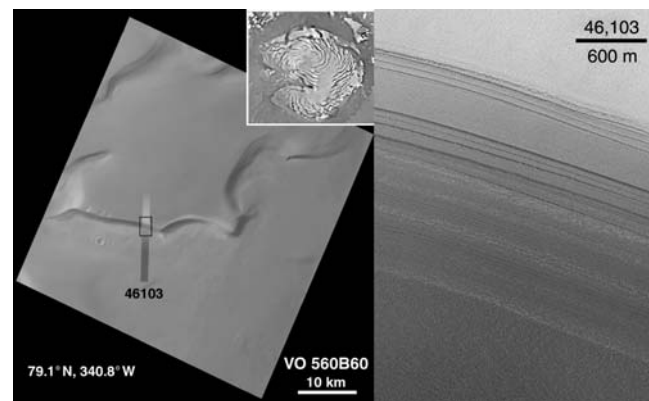


Figure A42 Polar layered deposits. Top inset shows a picture of the north polar cap. Left is a blow-up of the edge of the permanent north polar cap in a Viking Orbiter image (VO 560B60). This image shows a box, which is magnified further in the right-hand MOC image from the MGS spacecraft (portion of image number SP2-46103 near 79.1° N, 340° W). The high-resolution image shows that the polar cap is made up of many layers with thicknesses tens of meters in scale or less. Layers that are ~ 100 m thick have many discrete layers within them (images MOC2-70A-70B, NASA/JPL/Malin Space Science Systems).

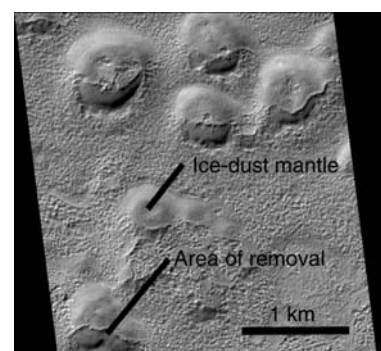


Figure A43 Ice-dust mantling material located at 43.7° S, 239.6° W. The material is being removed, typically on equator-facing slopes. In areas where the material is completely removed, the surface is rough and dissected at this scale (portion of MOC image FHA01450 NASA/JPL/Malin Space Science Systems).

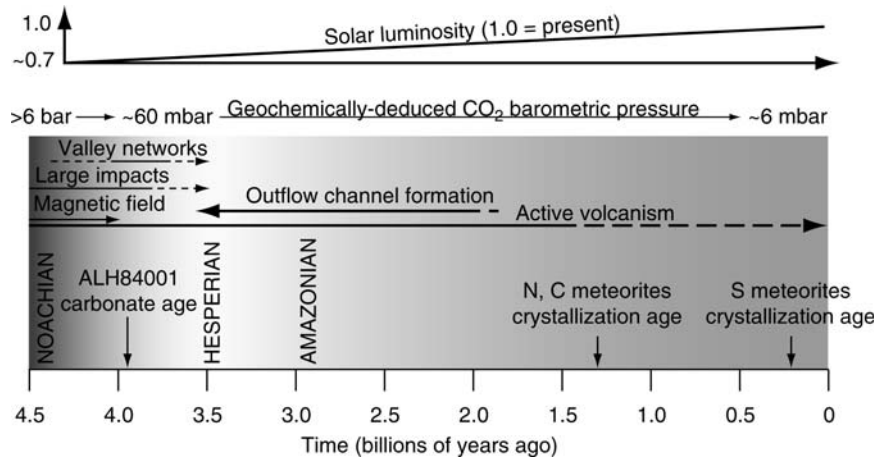


Figure A44 A schematic overview of the history of Mars, showing three periods: the Noachian, Hesperian and Amazonian. The igneous crystallization ages of Martian meteorites are shown, which indicate that Mars has been volcanically active throughout its history (N: nahklites; C: Chassigny; S: shergottites). The oldest meteorite, ALH84001, has a crystallization age of about 4.5 Ga, but contains carbonate salts of 3.9 Ga age. In the Noachian, the planet had a magnetic field and suffered heavy impact bombardment. Valley networks formed mainly in the Noachian. Later, the large outflow channels formed. As Mars aged, the Sun's brightness increased. Also the Martian atmosphere grew thinner, mostly in the Noachian.

from which the ice has sublimated, leaving behind a loosely cemented material. Such residue would be susceptible to wind erosion, which would account for its patchy nature. Today, near-surface ground ice is stable poleward of $\pm 60^\circ$ latitude (Feldman et al., 2004), whereas the two latitude bands where the mantling material is observed correspond to places where the stability of near-surface ice has occurred over the last few million years due to orbital changes. Viscous flow features and gullies, which are probably associated with ice from past climate regimes, are also found within these same latitude bands (Milliken et al., 2003). In addition, some geologic features at low latitudes resemble dust-covered glaciers or rock glaciers (Head et al., 2005).

Long-term atmospheric evolution: a synthesis of evidence and theory

The history of the Martian atmosphere is clearly subject to different interpretations because of uncertainty about the climate conditions under which various geological features were formed. However, certain geochemical indicators, such as inferences from the isotopic composition of the atmosphere, are less ambiguous.

Taken together, geochemical data and models support the view that most of the original CO_2 and nitrogen volatile inventory was lost very early by impact erosion and hydrodynamic escape. Models of impact erosion and the absolute abundance of volatiles like nitrogen and krypton suggest that as much as 99% of the original inventory may have been lost by 3.8 Ga. Before this time, however, large impacts would have provided sufficient heat to decompose carbonates and vaporize subsurface volatiles, such as water and CO_2 ice. Consequently, impacts could have generated temporary ($\sim 10^2$ – 10^3 years) warm, wet climates (Segura et al., 2002). During such episodes, rainwater would erode valley networks or recharge aquifers, producing conditions that allowed groundwater flow and sapping. During such warm episodes, SO_2 would be washed from the atmosphere and react with the surface to make sulfates. Such a scenario

would explain the apparent coincidence between the end of heavy bombardment and the large drop in erosion rates. It would also explain why valley networks are largely confined to heavily cratered Noachian terrains. During quiescent periods, and after heavy bombardment, water and carbon dioxide would be lost from the atmosphere to polar caps, to the subsurface, and to space. The disappearance of the global dipole field some time before 4.0 Ga allowed the solar wind to strip the upper atmosphere of Mars. As a result of solar wind stripping, as well as thermal and other nonthermal escape processes, another 50–90% of the Mars' volatile inventory of carbon and nitrogen was probably lost after 3.8 Ga. This is most clearly reflected today in the ratios of the stable isotopes of nitrogen and argon. In addition, the ratio of $\text{C}/^{84}\text{Kr}$, when compared to Earth and Venus, indicates loss of carbon that is consistent with calculations of escape to space. Outflow channels presumably formed as a result of geothermal activity that melted ground ice (perhaps accumulated near the equator during high obliquity or an ancient time when the pole was at a different location (Schultz, 1985)). Alternatively, hydrous salts were dehydrated. However, the huge size of outflow channels remains enigmatic. In recent epochs, the variation of the orbital elements of Mars in Milankovitch-type cycles has almost certainly caused ice to be stable at lower latitudes than today. As the ice has retreated, it has left behind a variety of telltale features including remnant loess from desiccated dust-ice mixtures, gullies, and perhaps remnant polar terrain at low latitudes. However, none of these features require an atmosphere that is substantially different from that of today (Figure A44).

David C. Catling

Bibliography

- Baker, V.R., 2001. Water and the martian landscape. *Nature*, **412**, 228–236.
 Bogard, D.D., Clayton, R.N., Marti, K., Owen, T., and Turner, G., 2001. Martian volatiles: Isotopic composition, origin, and evolution. *Space Sci. Rev.*, **96**, 425–458.

- Carr, M.H., 1996. *Water on Mars*. New York, NY: Oxford University Press, 229pp.
- Carr, M.H., 2006. *The Surface of Mars*. New York, NY: Cambridge University Press, 323pp.
- Carr, M.H., and Head, J.W., 2003. Oceans on Mars: An assessment of the observational evidence and possible fate. *J. Geophys. Res.*, **108**, 8–1.
- Christensen, P.R., 2003. Formation of recent martian gullies through melting of extensive water-rich snow deposits. *Nature*, **422**, 45–48.
- Christensen, P.R., et al., 2001. Mars global surveyor thermal emission spectrometer experiment: Investigation description and surface science results. *J. Geophys. Res.*, **106**, 23823–23871.
- Colaprete, A., and Toon, O.B., 2003. Carbon dioxide clouds in an early dense Martian atmosphere. *J. Geophys. Res.*, **108**, 6–1.
- Cutts, J.A., and Blasius, K.R., 1981. Origin of Martian outflow channels - The eolian hypothesis. *J. Geophys. Res.*, **86**, 5075–5102.
- Drake M.J., and Righter, K., 2002. Determining the composition of the Earth. *Nature*, **416**, 39–44.
- Feldman, W.C., et al., 2004. The global distribution of near-surface hydrogen on Mars. *J. Geophys. Res.*, **109**, doi:10.1029/2003JE002160.
- Formisano, V., Atreya, S., Encrenaz, T., Ignatiev, N., and Giuranna, M., 2004. Detection of methane in the atmosphere of Mars. *Science*, **306**, 1758–1761.
- Haberle, R.M., Murphy, J.R., and Schaeffer, J., 2003. Orbital change experiments with a Mars general circulation model. *Icarus*, **161**, 66–89.
- Hartmann, W.K., and Neukum, G., 2001. Cratering chronology and the evolution of Mars. *Space Sci. Rev.*, **96**, 165–194.
- Head, J.W., et al., 2005. Tropical to mid-latitude snow and ice accumulation, flow and glaciation on Mars. *Nature*, **434**, 346–351.
- Jakosky, B.M., and Jones, J.H., 1997. The history of Martian volatiles. *Rev. Geophys.*, **35**, 1–16.
- Jakosky, B.M., and Phillips, R.J., 2001. Mars' volatile and climate history. *Nature*, **412**, 237–244.
- Kasting, J.F., 1991. CO₂ condensation and the climate of early Mars. *Icarus*, **94**, 1–13.
- Kieffer, H.-H., and Zent, A.-P., 1992. Quasi-periodic change on Mars. In Kieffer, H.H., Jakosky, B.M., Snyder, C.W., and Matthews, M.S. (eds.), *Mars*. Tucson, AZ: University of Arizona Press, pp. 1180–1218.
- Kieffer, H.H., Jakosky, B.M., Snyder, C.W., and Matthews, M.S., (eds.), 1992. *Mars*. Tucson, AZ: University of Arizona Press.
- Krasnopolsky, V.A., 2002. Mars' upper atmosphere and ionosphere at low, medium, and high solar activities: Implications for evolution of water. *J. Geophys. Res.*, **107**, doi:10.1029/2001JE001809.
- Lammer, H., et al., 2003. Loss of water from Mars: Implications for the oxidation of the soil. *Icarus*, **165**, 9–25.
- Laskar, J., et al., 2004. Long term evolution and chaotic diffusion of the insolation quantities of Mars. *Icarus*, **170**, 343–364.
- Lunine, J.I., Chambers, J., Morbidelli, A., and Leshin, L.A., 2003. The origin of water on Mars. *Icarus*, **165**, 1–8.
- Malin, M.C., and Edgett, K.S., 1999. Oceans or seas in the Martian northern lowlands: High resolution imaging tests of proposed coastlines. *Geophys. Res. Lett.*, **26**, 3049–3052.
- McElroy, M.B., and Donahue, T.M., 1972. Stability of the Martian atmosphere. *Science*, **177**, 986–988.
- Melosh, H.J., and Vickery, A.M., 1989. Impact erosion of the primordial atmosphere of Mars. *Nature*, **338**, 487–489.
- Milliken, R.E., Mustard, J.F., and Goldsby, D.L., 2003. Viscous flow features on the surface of Mars: Observations from high-resolution Mars Orbiter Camera (MOC) images. *J. Geophys. Res.*, **108**, 11–1.
- Montgomery, D.R., and Gillespie, A., 2005. Formation of outflow channels by catastrophic dewatering of evaporite deposits. *Geology*, **33**, 625–628.
- Owen, -T., 1992. The composition and early history of the atmosphere of Mars. In Kieffer, H.H., Jakosky, B.M., Snyder, C.W., and Matthews, M.S. (eds.), *Mars*. Tucson, AZ: University of Arizona Press, pp. 818–834.
- Pepin, R.O., 1991. On the origin and evolution of terrestrial planet atmospheres and meteoritic volatiles. *Icarus*, **92**, 2–79.
- Pollack, J.B., Kasting, J.F., Richardson, S.M., and Poliakov, K., 1987. The case for a wet, warm climate on early Mars. *Icarus*, **71**, 203–224.
- Poulet, F., et al., 2005. Phyllosilicates on Mars and implications for early martian climate. *Nature*, **438**, 623–627.
- Schultz, P.H., 1985. Polar wandering on Mars. *Sci. Am.*, **253**, 94–102.
- Segura, T.L., Toon, O.B., Colaprete, A., and Zahnle, K., 2002. Environmental effects of large impacts on Mars. *Science*, **298**, 1977–1980.
- Squyres, S.W., et al., 2006. Two years at Meridiani Planum: Results from the opportunity Rover. *Science*, **313**, 1403–1407.
- Touma, J., and Wisdom, J., 1993. The chaotic obliquity of Mars. *Science*, **259**, 1294–1297.
- Withers, P., and Neumann, G.A., 2001. Enigmatic northern plains of Mars. *Nature*, **410**, 651.
- Zahnle, K., 1998. Origins of Atmospheres' In Woodward, C.E., Shull, J.M., and Thronson, H. (eds.), *San Francisco CA. Astron. Soc. Pacific Conf. Series*, vol. 148, *Origins*. pp. 364–391.

Cross-references

Astronomical Theory of Climate Change
 Atmospheric Evolution, Earth
 Atmospheric Evolution, Venus
 Faint Young Sun Paradox
 Mars: Water and Past Climates

ATMOSPHERIC EVOLUTION, VENUS

Overview

Venus and Earth are generally regarded as sister planets because Venus is the planet with mass, size, and mean density closest to that of the Earth (see [Table A6](#)). Cosmochemical and geochemical models also suggest that Venus' bulk composition is similar to that of the Earth (Lodders and Fegley, 1998; Tables 5.8 and 5.9). Despite these broad similarities, Venus' atmosphere is dramatically different from that of the Earth. These differences are primarily due to Venus' depletion in water relative to the Earth. As discussed below, Venus may either have formed “dry,” or may have formed “wet” and subsequently lost most of its water. A choice between these two alternatives is impossible at present and there are arguments for and against both models (Lewis and Prinn, 1984; Yung and DeMore, 1999).

Atmospheric evolution on Venus has probably been different than the evolution of the terrestrial atmosphere. However, before discussing this somewhat speculative topic it makes sense to review basic properties of Venus' atmosphere, and to compare its atmosphere to that of the Earth. This article is based on Fegley (2004), Prinn and Fegley (1987), and Warneck (1988). Readers seeking more information about Venus should consult the following sources. *The Encyclopedia of Planetary Sciences* (Shirley and Fairbridge, 1997) has several articles about Venus' atmosphere, geology, and geophysics. Brief reviews are given by Fegley (2004) and Lodders and Fegley (1998). Book-length treatments of results from Soviet missions are given by Barsukov et al. (1992), of *Pioneer Venus* results by Hunten et al. (1983), of *Magellan* results by Bougher et al. (1997), and atmospheric chemistry on Venus and Mars by Krasnopolsky (1986). Three recommended monographs about different aspects of the chemistry and physics of planetary atmospheres are Chamberlain and Hunten (1987), Lewis and Prinn (1984), and Yung and DeMore (1999).

Venus' present day atmosphere

Venus' atmosphere is mainly CO₂ (96.5% by volume) and N₂ (3.5%), with smaller amounts of noble gases (He, Ne, Ar, Kr, Xe), and chemically reactive trace gases (SO₂, H₂O, CO, OCS, H₂S, HCl, SO, HF, and elemental sulfur vapor). The average temperature and pressure at Venus' surface are 740 K

Table A6 Some properties of Venus and Earth (after Lodders and Fegley, 1998)

Property	Venus	Earth
Semi-major axis (10^6 km)	108.21	149.60
(A.U.)	0.7233	1.00
Average radius (km)	6051.4	6371.0
Mass (10^{24} kg)	4.8685	5.9736
Density (kg m^{-3})	5,243	5,515
Volume (10^{10} km ³)	92.84	108.3
Lithospheric mass (10^{24} kg)	3.14 (64.5%)	4.03 (67.5%)
Core mass (10^{24} kg)	1.73 (35.5%)	1.94 (32.5%)
Lithospheric volume (10^{10} km ³)	78.2 (84.2%)	90.6 (83.7%)
Core volume (10^{10} km ³)	14.6 (15.8%)	17.7 (16.3%)
Escape velocity (km s^{-1})	10.361	11.186
Sidereal orbital period (days)	224.70	365.26
Average length of day	116.75	1.0
Mean gravitational acceleration (m s^{-2})	8.870	9.820
Solar constant (W m^{-2})	2613.9	1367.6
Geometric albedo	0.76	0.30
Absorbed solar energy (W m^{-2})	166	243
Mean surface temperature (K)	740	288
Black body temperature (K)	240	250
Mean surface pressure (bar)	95.6	1.0
Scale height at surface (km)	15.90	8.42
Atmospheric lapse rate at surface (K km^{-1})	8.0	6.5
Dry adiabatic lapse rate at surface (K km^{-1})	7.8	9.8
Atmospheric composition of dry gas	CO ₂ (96.5%), N ₂ (3.5%), SO ₂ (0.015%)	N ₂ (78.1%), O ₂ (20.9%), Ar (0.93%), CO ₂ (0.036%)
Atmospheric mean formula weight (g mol^{-1})	43.45	28.97
Atmospheric mass (10^{18} kg)	495	5.28
Atmospheric water vapor ^a	0.003%	1–4%
Cloud composition and coverage (%)	H ₂ SO ₄ (100%)	H ₂ O (50%)
Important greenhouse gases	CO ₂ , SO ₂ , H ₂ O	CO ₂ , H ₂ O, CH ₄ , N ₂ O, CFCs ^b

^aTropospheric values. Water vapor is only a few ppmv in Earth's stratosphere and above Venus' clouds.

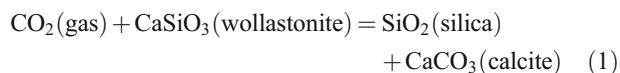
^bCFC gases are chlorofluorocarbon gases such as CF₂Cl₂, CFCl₃, and CF₄.

and 95.6 bar, respectively, at the modal radius (6051.4 km). The temperature gradient throughout Venus' troposphere (0–60 km altitude) is very close to the dry adiabatic gradient for a mixture of CO₂ (96.5%) and N₂ (3.5%). A global cloud layer composed of aqueous sulfuric acid droplets (H₂SO₄·2 H₂O) at ~45 to ~70 km altitude continuously shrouds Venus' surface from our view. The clouds also play a key role in Venus' current climate. They reflect about 75% of incident solar radiation back to space. Thus Venus absorbs only ~66% as much solar energy (160 W m^{-2}) as Earth (243 W m^{-2}) even though the incident solar radiation is ~1.9 times larger than at Earth. In addition, ~70% of the sunlight absorbed by Venus is deposited in the upper atmosphere and clouds, in sharp contrast with Earth, where ~66% of solar energy is absorbed at the surface. A cloud-free Venus would have a much different climate than Venus does today.

The abundances of CO₂, N₂ and the noble gases are apparently constant throughout much of Venus' atmosphere (0–100 km). However, many trace gas abundances vary with altitude, time, and location. These variations are due to photochemical reactions (including photochemical oxidation of SO₂ to aqueous sulfuric acid cloud droplets) that primarily occur in the upper atmosphere and clouds, and to thermochemical reactions that primarily occur in the hot, dense atmosphere below the clouds. Surprisingly, the *Pioneer Venus* gas chromatograph reported an altitude-dependent N₂ abundance below the clouds in the 22–52 km region (see below). Microwave spectroscopy from Earth, the *Pioneer Venus*, and *Magellan* spacecraft indicates that H₂SO₄ vapor is present below the

clouds with an abundance of about 12 parts per million by volume (ppmv). Sulfur trioxide vapor, which has not yet been observed, is expected to be present below the cloud layer in equilibrium with H₂SO₄ gas and water vapor. Both H₂SO₄ and SO₃ have several infrared (IR) absorption bands in the 2–20 μm region and are potentially important greenhouse gases, although at larger concentrations than probably exist in Venus' atmosphere today. Photochemical models predict potentially observable amounts of Cl, Cl₂, ClO, and O₂ in Venus' upper atmosphere (Yung and DeMore, 1999). Tables A6 and A7 summarize chemical and physical data about Venus' atmosphere.

The large abundance of CO₂ in Venus' atmosphere is equivalent to a global layer of calcium carbonate (CaCO₃) 0.88 km thick. This is about twice Earth's crustal carbon inventory, which corresponds to a global CaCO₃ layer 0.44 km thick. Volcanic outgassing is probably the major CO₂ source on Venus. The two major CO₂ sinks are solar UV photolysis to CO and O₂ in the upper atmosphere and carbonate formation on Venus' surface. The latter sink is exemplified by the Urey reaction



but other carbonates and carbonate-bearing minerals such as scapolite may also be involved. (Scapolite is a solid solution between marialite Na₄[Al₃Si₉O₂₄]Cl and meionite Ca₄[Al₆Si₆O₂₄]CO₃. Sulfate and OH anions may also substitute for the chloride and carbonate anions.)

Several arguments suggest that Venus' surface and interior contain carbonates. Degassing of ^{40}Ar on Venus is incomplete and the atmosphere contains only $24 \pm 10\%$ of the ^{40}Ar from radioactive decay (Kaula, 1999). The argon data imply that degassing of CO_2 is also incomplete because argon is degassed more easily than CO_2 (Ar is less soluble in silicate melts than is CO_2). Mass deficits in elemental analyses made by X-ray fluorescence (XRF) spectroscopy at the *Venera 13*, *14*, and *Vega 2* landing sites can be attributed to carbonates, as with the *Viking* XRF data for Mars. Calculated carbonate abundances are about

4–10% CaCO_3 (Kargel et al., 1994). Geochemical interpretations of the elemental analyses suggest that Venus' mantle contains more CO_2 than the terrestrial mantle (Kargel et al., 1993). Finally, some flow features in *Magellan* radar images may result from carbonatite magmas that have water-like rheologies.

The N_2 abundance in Venus' atmosphere is $3.5 \pm 0.8\%$ (see Table A7). Consequently the CO_2 abundance is also uncertain by $\pm 0.8\%$. The uncertainty reflects disagreements between N_2 abundances measured by mass spectrometers on *Pioneer Venus* and *Venera 11–12* and gas chromatographs on the same

Table A7 Chemical composition of Venus' atmosphere^a

Gas	Abundance	Source(s)	Sink(s)	Comments
CO_2	$96.5 \pm 0.8\%$	Outgassing	Solar UV photolysis, carbonate formation	Major greenhouse gas 2.7, 4.3, 15 μm bands
N_2	$3.5 \pm 0.8\%$	Outgassing	NO_x formation by lightning	Altitude-dependent mixing ratio needs confirmation
SO_2^b	0.01–1 ppmv (cloud top)	Outgassing, and oxidation of OCS and H_2S	Photochemical oxidation to H_2SO_4 cloud droplets, reaction with Ca-bearing minerals on Venus' surface to form anhydrite (CaSO_4), reduction to OCS and H_2S	Most abundant sulfur gas, important greenhouse gas 7.3, 8.7, 19.3 μm bands
	150 ± 30 ppmv (22–42 km)			
	25–150 ppmv (12–22 km)			
H_2O^b	30 ± 15 ppmv (0–45 km)	Outgassing, and cometary impacts	Hydrogen escape to space, and oxidation of ferrous iron minerals	Most abundant hydrogen gas, important greenhouse gas 0.9, 2.7, 6.3 μm bands
^{40}Ar	31^{+20}_{-10} ppmv	Outgassing (^{40}K decay)		About 3–4 times less ^{40}Ar than on Earth (g/g basis)
^{36}Ar	30^{+20}_{-10} ppmv	Outgassing (primordial)		About 70 times more ^{36}Ar than on Earth (g/g basis)
CO^b	45 ± 10 ppmv (cloud top)	CO_2 photolysis, and outgassing	Photochemical oxidation to CO_2 via catalytic cycles. Also consumed by thermochemical reactions with sulfur gases and ferric iron minerals	4.66 μm fundamental, potentially important greenhouse gas, involved in Venus atmospheric sulfur cycle
	30 ± 18 ppmv (42 km)			
	28 ± 7 ppmv (36–42 km)			
	20 ± 3 ppmv (22 km)			
	17 ± 1 ppmv (12 km)			
$^4\text{He}^c$	0.6–12 ppmv	Outgassing (U, Th decay)	Escape to space	
Ne	7 ± 3 ppmv	Outgassing (primordial)		About 20 times more Ne than on Earth (g/g basis)
^{38}Ar	5.5 ppmv	Outgassing (primordial)		
OCS ^b	4.4 ± 1 ppmv (33 km)	Outgassing, sulfide weathering	Conversion to SO_2	4.8, 11.6, 19.1 μm bands
H_2S^b	3 ± 2 ppmv (<20 km)	Outgassing, sulfide weathering	Conversion to SO_2	3.8, 4.2, 8.5 μm bands
HDO ^b	1.3 ± 0.2 ppmv (sub-cloud)	Outgassing	Hydrogen escape to space	
HCl	0.6 ± 0.12 ppmv (cloud top)	Outgassing	Formation of Cl-bearing minerals	3.46 μm fundamental
	0.5 ppmv (35–45 km)			
^{84}Kr	25^{+13}_{-18} ppbv	Outgassing (primordial)		
SO^b	20 ± 10 ppbv (cloud top)	Photochemistry	Photochemistry	
S^b_{1-8}	20 ppbv (<50 km)	Sulfide weathering, outgassing	Conversion to SO_2	
HF	$5^{+5}_{-2.5}$ ppbv (cloud top)	Outgassing	Formation of F-bearing minerals	2.52 μm fundamental
	4.5 ppbv (35–45 km)			
^{132}Xe	<10 ppbv	Outgassing (primordial)		
^{129}Xe	<9.5 ppbv	Outgassing (^{129}I decay)		

Modified from Fegley (2004).

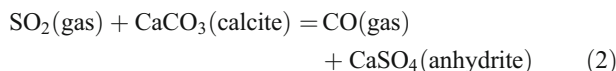
^aAbundance by volume, ppm = parts per million by volume, ppb = parts per billion by volume.

^bThe abundances of these gases are altitude-dependent.

^cThe He abundance has only been measured above the homopause where diffusive separation occurs. This value is 12^{+24}_{-6} ppm by volume (von Zahn et al., 1983). The value listed above is a model-dependent extrapolation below the homopause.

spacecraft. Volcanic outgassing is probably the major N_2 source on Venus and the formation of nitrogen oxides (NO_x) by lightning may be a N_2 sink. The chemical lifetime of N_2 in Venus' atmosphere is possibly very long ($\sim 10^9$ years). In any case, the apparent dependence of the N_2 abundance on altitude is hard to understand and new measurements are required to resolve this issue.

Sulfur dioxide is the major sulfur gas in Venus' atmosphere, the third most abundant gas overall, and one of the three most important greenhouse gases. It is intimately involved in the formation of the global sulfuric acid clouds, the energy budget and greenhouse effect in Venus' lower atmosphere, and atmosphere-lithosphere interactions such as volcanism and chemical weathering. *In situ* and Earth-based measurements of the SO_2 abundance in Venus' lower atmosphere give an average abundance of about 150 ppmv (22–42 km), which decreases at higher and lower altitudes (Krasnopolsky, 1986; Bézard et al., 1993). At higher altitudes photochemical oxidation converts SO_2 into aqueous sulfuric acid cloud droplets and efficiently removes it from Venus' upper atmosphere, which contains about 15,000 times less SO_2 (10 ppbv above the clouds vs. 150 ppmv below them). At lower altitudes gas phase thermochemistry reduces SO_2 to OCS. On a longer time-scale of ~ 1.9 million years, thermochemical reactions with CaO-bearing minerals on Venus' surface convert SO_2 into anhydrite ($CaSO_4$)



irreversibly removing SO_2 and the sulfuric acid clouds formed from it. The SO_2 lost from the atmosphere must be replenished by volcanism to maintain the global cloud cover. We return to this topic when we discuss volcanic outgassing and climate change.

Water vapor has an average abundance of about 30 ppmv below Venus' clouds. It is even less abundant above the clouds where only a few parts per million of water vapor are observed. Water reacts with H_2SO_4 to form hydronium (H_3O^+) and bisulfate (HSO_4^-) ions. Thus the concentration of "free" H_2O in concentrated sulfuric acid is very small. As a result, the H_2O partial pressure over the cloud droplets is less than that over water ice at the same temperature. The atmospheric H_2O abundance varies spatially and temporally (above and below the clouds). Although a trace gas, H_2O is the major hydrogen reservoir in Venus' atmosphere and is one of the three most important greenhouse gases. It is also involved in gas-solid reactions that regulate, or buffer, atmospheric HCl and HF. These reactions apparently equilibrate rapidly because HCl and HF concentrations above the clouds are the same, within error, as those below the clouds measured about 20 years later. Over a much longer time scale (10^8 – 10^9 years), water loss via H escape to space and oxidation of ferrous iron minerals in Venus' lithosphere regulate the oxidation state of Venus' atmosphere and surface. Volcanism and possibly cometary impacts replenish atmospheric water vapor. The H_2O abundance in Venus' atmosphere is equivalent to a global layer of water one cm thick. However, liquid water is unstable on Venus' hot surface. We consider the isotopic composition of Venusian water when we discuss atmospheric evolution.

The strong infrared nightglow of O_2 at 1.27 μm and the Herzberg II nightglow at 400–800 nm show that molecular oxygen is a trace species in the 100–130 km region of Venus'

upper atmosphere (Krasnopolsky, 1986). The spectroscopic upper limit for O_2 in Venus' lower atmosphere below ~ 100 km is less than 0.3 ppmv. For comparison, the Martian atmosphere contains 1300 ppmv O_2 , which is also produced by solar UV photolysis of CO_2 . The extremely small O_2 abundance on Venus shows that the catalytic recombination of $O + CO$ produced by solar UV photolysis of CO_2 is very efficient because the O_2 abundance is at least 4,300 times smaller than on Mars although the solar flux is about four times larger than on Mars. Yung and DeMore (1999) describe the CO_2 photochemical cycles on Mars and Venus.

Comparisons to Earth's atmosphere

Earth is an interesting and informative contrast to Venus. Oxygen makes up about 21% of dry air in Earth's atmosphere, with the balance being mainly N_2 (78%), Ar (9340 ppmv), and CO_2 (387 ppmv). The average surface temperature and pressure at sea level are 288 K and one atmosphere. The temperature gradient in the terrestrial troposphere (0–12 km) is an average of the dry and wet adiabatic gradients. Earth is about 50% covered by water clouds at any time. The H_2O abundance in the troposphere ranges from 1 to 4% and is highest near the equator and lowest near the poles. The H_2O concentration in tropospheric air decreases with altitude and roughly corresponds to 50% relative humidity at any level. The stratosphere contains much less water than the troposphere, about 2–7 ppmv. This is about the same as expected (5 ppmv) from the vapor pressure over water ice at 195 K, the temperature of the tropical tropopause. Some stratospheric water is mixed upward through the tropical tropopause while the rest is produced from CH_4 oxidation by OH radicals. Most of the water at Earth's surface is in the oceans, which are equivalent to a global layer about 2.7 km thick. There is about 270,000 times as much observable water on Earth as on Venus.

In contrast to Venus (and Mars), CO_2 is a trace gas in Earth's atmosphere with an abundance of ~ 387 ppmv. About 25% of this is anthropogenic and biological sources account for most of the rest. Volcanism is only a minor source of CO_2 in Earth's atmosphere. Most of the carbon at Earth's surface is in the crust (6×10^{19} kg), with carbonates making up 80% of this and organic carbon the remainder. Earth's crustal carbon reservoir is much larger than the oceanic (3.8×10^{16} kg), biospheric (3.7×10^{15} kg), or atmospheric (7.6×10^{14} kg) reservoirs.

Several of the reactive trace gases observed in Venus' atmosphere are also present in Earth's atmosphere, but at much lower abundances. The sources and sinks of these reactive trace gases are also generally different on Venus and Earth. For example, SO_2 has an abundance < 1 ppmv in the terrestrial troposphere and is mainly due to anthropogenic emissions and to a lesser extent volcanic outgassing. Carbonyl sulfide is present at about 0.5 ppbv in Earth's troposphere (versus ~ 4400 ppbv on Venus) and is mainly due to biogenic emissions (instead of volcanic outgassing and sulfide chemical weathering on Venus). Most of the sulfur at the surface of the Earth is in sedimentary deposits of gypsum $CaSO_4 \cdot 2H_2O$ (28%) and pyrite FeS_2 (57%), or as sulfate dissolved in the oceans (15%). Hydrogen chloride (~ 1 ppbv) and HF (~ 0.03 ppbv) are virtually absent from Earth's troposphere. Methyl chloride (CH_3Cl) present at ~ 0.5 ppbv and the chlorofluorocarbon (CFC) gases are the major Cl and F gases. The two major CFC gases are CF_2Cl_2 (~ 0.4 ppbv) and $CFCI_3$ (~ 0.2 ppbv). Methyl chloride results

from biogenic emissions but the CFC gases are produced industrially and have no natural sources. The atmospheric inventories of F and Cl are negligible in comparison to the oceanic and crustal inventories. About 75% of all Cl at Earth's surface is Cl^- dissolved in the oceans and essentially all F is found in the crust (Lodders and Fegley, 1997). However, the crustal (or oceanic) inventories of S, Cl, and F on Earth are much larger than the atmospheric inventories of these elements on Venus. Assuming that Venus and Earth have a similar bulk chemical composition, this suggests that significant amounts of S, Cl, and F remain in Venus' lithosphere instead of being completely degassed into its atmosphere.

The Earth's atmosphere contains over 10,000 times more O_2 than Venus' atmosphere and $\sim 15,000$ times more O_2 than the Martian atmosphere. Photosynthesis is the major source of O_2 in the terrestrial atmosphere and accounts for the large disparities between O_2 on Earth and on Venus and Mars.

The major differences between Venus' atmosphere and the terrestrial atmosphere are as follows:

1. Venus' atmosphere contains large amounts of C, S, Cl, and F relative to the atmospheric inventories on Earth. The high temperatures on Venus promote the outgassing of these rock-forming elements into its atmosphere.
2. The large amounts of CO_2 and SO_2 driven into Venus' atmosphere maintain a super-greenhouse effect and a surface temperature over 3 times higher than the blackbody temperature.
3. Venus' atmosphere is much drier than Earth's atmosphere. However the tiny amount of atmospheric water vapor on Venus also helps to maintain the super-greenhouse.
4. Venus' atmosphere contains only trace amounts of O_2 , which is the second most abundant gas on Earth because of the presence of life.

As mentioned earlier, Venus' lack of water is primarily responsible for all these differences.

Origin of Venus' volatile inventory

The Sun and all the planets in our solar system formed about 4.56 billion years ago from a cloud of gas and dust known as the solar nebula. The elemental abundances in the solar nebula were the same as those in the Sun when it formed and are known as solar system abundances (Lodders, 2003). Figure A45 shows a comparison of the abundances of chemically reactive volatile elements (e.g., H, C, N, S, Cl, F) and chemically inert volatile elements (Ne, Ar, Kr, Xe) on Venus and Earth relative to their solar system abundances. The volatile elements H, C, and N are plotted as H_2O , CO_2 , and N_2 in Figure A45, which are the major gases of these elements in the atmospheres of Venus and Earth. They are depleted relative to their solar system abundances because Venus and Earth captured only part of the solar system abundance of each volatile during their formation. However, the chemically reactive volatiles are not as depleted as the noble gases. For example, Venus contains about 10^{-9} of the Ne solar system abundance but has about 10^{-5} of the N solar system abundance. Nitrogen and neon have similar atomic weights (14.007 vs. 20.183) and have similar solar system abundances (1.95×10^6 atoms vs. 2.15×10^6 atoms). However, nitrogen forms minerals such as osbornite (TiN), sinoite ($\text{Si}_2\text{N}_2\text{O}$), and carlsbergite (CrN), while neon is inert and does not. Likewise Earth contains about 2×10^{-9} of the argon solar system abundance and about 7×10^{-5} of the sulfur solar system

abundance. Sulfur and argon also have similar atomic weights (32.06 vs. 36.32 for primordial argon) and similar solar system abundances (4.45×10^5 atoms vs. 1.02×10^5 atoms). Sulfur occurs in troilite (FeS) and other minerals, but argon does not form minerals. The larger depletions of noble gases and the smaller depletions of chemically reactive volatiles suggest that the atmospheres of Earth (e.g., Brown, 1949) and Venus primarily formed from volatile-bearing solids that outgassed during and after planetary accretion. The occurrence of volatile-bearing minerals in chondritic meteorites, which are relatively unaltered samples of nebular material, supports this argument.

Two observations suggest that Venus and Earth may have captured some nebular gas during their formation. Recent work on hafnium-tungsten (Hf–W) dating of meteorites indicates rapid accretion and early core formation for the terrestrial planets within the first 30 million years of solar system history (Yin et al., 2002; Kleine et al., 2002). In Cameron's (1995) model of the solar nebula, the loss of nebular gas, which is the last stage of nebular evolution, takes 3–30 million years. A possible implication of the Hf–W dating is that the terrestrial planets accreted in the presence of residual nebular gas and captured some of it. However, the nebular lifetime is uncertain and the recent Hf–W results are somewhat controversial. The second observation is that ^3He is currently degassing from the Earth's mantle. This discovery led to a large amount of work on the isotopic composition of other noble gases released from Earth's mantle. There is some evidence for degassing of Ne with solar isotopic ratios (primordial Ne), but there is little or no evidence for degassing of primordial Ar, Kr, or Xe from Earth's mantle (Ozima and Podosek, 2002). Pepin and Porcelli (2002) discuss the origin of noble gases on Venus, Earth, and Mars in some detail.

Dry versus wet accretion of Venus

Figure A45 graphically shows Venus' depletion in water relative to the Earth (about a factor of 270,000). As mentioned earlier, Venus may have formed "dry," or may have formed "wet" and subsequently lost most of its water. An initially "dry" Venus is predicted by the equilibrium condensation model. This model predicts the chemical composition of gas and grains in the solar nebula as a function of temperature and pressure, which vary as a function of radial distance from the Sun. The equilibrium condensation model predicts that Venus formed "dry" and that Earth formed "wet" because hydrous minerals were unstable where Venus formed but stable where Earth formed. Venus' meager water inventory is the result of cometary impacts over time (Lewis, 1974). The equilibrium condensation model explains the density difference between Venus and Earth, first order trends in planetary bulk compositions, and many chemical and mineralogical features of chondritic meteorites (Lewis and Prinn, 1984; Kerridge and Matthews, 1988).

However, persuasive arguments can be made against an initially "dry" Venus. Dynamical models of planetary accretion predict significant overlap of accretion zones for Venus and Earth (Weidenschilling, 1976). The overlap would lead to similar water inventories on the two planets. A second argument is that hydrous mineral formation is probably impossibly slow at the cooler temperatures where hydrous minerals are thermodynamically stable in the solar nebula (Fegley, 2000). This would lead to both planets accreting "dry" rock with water being supplied by subsequent impacts of icy planetesimals and comets

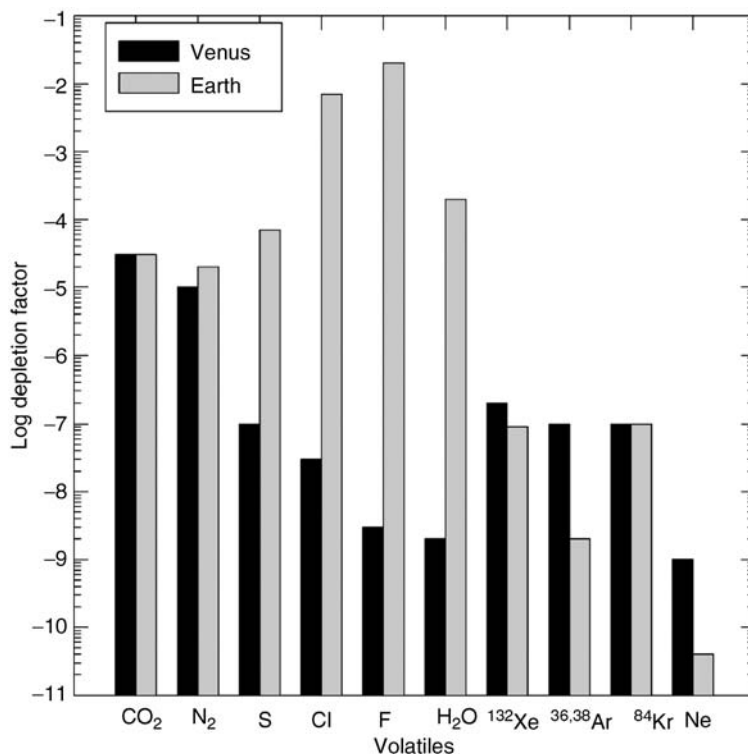


Figure A45 Depletions of chemically reactive volatiles and noble gases on Venus and Earth relative to their solar system abundances.

that are gravitationally scattered into the inner solar system by the outer planets.

We now consider the alternative that Venus formed “wet” and subsequently lost most of its water. Chondritic meteorites are often used as analogs for the types of material accreted by the terrestrial planets during their formation. Water contents of chondritic meteorites range from 9.5 to 10.8% (by mass) in the volatile-rich CM and CI carbonaceous chondrites, to 0.3–1.1% in the ordinary (H, L, LL) chondrites (Lodders and Fegley, 1998; Tables 16.10 and 16.11). For comparison, Earth’s hydrosphere corresponds to a water content of about 0.03%. As discussed elsewhere (Lodders and Fegley, 1997), Venus, Earth, and Mars each apparently formed from a mixture of chondritic material. In this case, formation of either an initially “moist” or “wet” Venus seems unavoidable. For example, the four-component meteorite model of Morgan and Anders (1980) predicts 0.03% water in Venus, which is comparable to Earth’s inventory.

The deuterium (D) to hydrogen (H) atomic ratio in Venusian water is 0.025 ± 0.005 , which is about 160 ± 32 times larger than the terrestrial D/H ratio of 1.558×10^{-4} in standard mean ocean water (SMOW). The high D/H ratio strongly suggests Venus originally had more H₂O (equivalent to 4–530 meters of liquid water) and lost most of it over time (Donahue et al., 1997). This interpretation assumes that Venusian water started with a D/H ratio like that of terrestrial ocean water. However, some chondritic meteorites, comets, and interplanetary dust particles have D/H ratios ranging up to 50 times the terrestrial value (Irvine et al., 2000; Table III). It is possible that Venus formed with a higher D/H ratio than the Earth. If so, Venus

may have had less water than if it formed with an Earth-like D/H ratio.

Even though the high D/H ratio is a good indicator, it is only indirect proof that Venus was initially “wet.” However, if Venus once had water, hydrous minerals, such as amphiboles, should have formed. Amphiboles are common on Earth and are found in metamorphic and igneous rocks. Experimental studies show that tremolite, one of the most common amphiboles, decomposes very slowly at Venus surface temperatures. Extrapolation of laboratory data shows that 50% decomposition of μm -size grains takes 2.7 billion years, and complete decomposition about 10 times longer. These data indicate tremolite and other amphiboles that formed on Venus during a wetter era in the past could still exist on Venus today and provide evidence that Venus was wet (Johnson and Fegley, 2003).

Venus’ accretionary atmosphere

The terrestrial planets probably formed by the accretion of smaller planetesimals (Wetherill, 1980). Impact devolatilization of sufficiently large planetesimals probably generated accretionary atmospheres containing N₂, CO₂, H₂O, and other volatiles once Venus (or Earth) reached about 10% of their present mass (Ahrens, 1993). Such accretionary atmospheres are called “steam” atmospheres, although H₂O is not necessarily the most abundant gas. Significant amounts of H₂, generated by the water gas reaction



or by the oxidation of Fe metal



to FeO-bearing minerals, may have been present in the “steam” atmospheres. Carbon, nitrogen, and sulfur gases such as CO_2 , CO , CH_4 , N_2 , NH_3 , SO_2 , H_2S , and OCS were probably also present in the “steam” atmospheres, with relative abundances dependent upon temperature, pressure, and oxidation state at a given time during planetary formation.

Matsui and Abe (1986) modeled the formation and properties of “steam” atmospheres on Venus and Earth. They found that accretion of planetesimals containing $\sim 0.1\%$ water, similar to that in some ordinary chondrites, led to development of a massive “steam” atmosphere on Venus. The greenhouse effect of this atmosphere trapped so much heat that Venus melted (at ~ 1500 K) once it reached about 40% of its current radius. The mass of Venus’ “steam” atmosphere reached about 10^{21} kg ($P \approx 100$ bar), comparable to that of Earth’s present hydrosphere, and was controlled by the solubility of water in molten silicate magma. However, Matsui and Abe’s (1986) conclusions are somewhat model dependent, and the existence and fate of a “steam” atmosphere on Venus remain unclear (Pollack, 1991).

After Venus had formed, its “steam” atmosphere may have rained out to form hot oceans or all the water may have remained in the atmosphere if the surface temperature remained above the critical point of water (647 K). Some of the water dissolved in the silicate magma may have crystallized as kaersutite, hornblende, or other igneous amphiboles. But, whether or not Venus ever had a “steam” atmosphere, the evolution of Venus’ water inventory is closely connected to the origin of the runaway greenhouse.

Origin of the runaway greenhouse and water loss

Models by Ingersoll (1969) and Rasool and deBergh (1970) qualitatively showed that Venus has a runaway greenhouse effect while Earth does not because Venus formed closer to the Sun. Once some H_2O or CO_2 was in Venus’ atmosphere, greenhouse warming led to sufficiently high surface temperatures to vaporize water and thermally decompose carbonates. Rasool and deBergh (1970) also suggest that reaction (1) and its analogs may have regulated the increasing CO_2 pressure as a function of temperature.

In both models, UV sunlight decomposed H_2O to its constituent elements with hydrogen loss to space. The hydrogen loss rates on Venus and Earth today (and presumably in the past) are controlled by the total H-atom mixing ratio ($f_{\Sigma\text{H}}$) at the homopause (above which diffusive separation of gases occurs)

$$f_{\Sigma\text{H}} = f_{\text{H}} + 2f_{\text{H}_2} + 2f_{\text{H}_2\text{O}} + f_{\text{HCl}} + f_{\text{HF}} \quad (5)$$

Venus’ hydrogen loss rate is currently $\sim 10^7$ H $\text{cm}^{-2} \text{s}^{-1}$, which could remove a global water layer only 21 cm thick over the age of the solar system. Loss rates $\sim 10^5$ times larger are required to remove an ocean’s worth of water in a geologically short time. These occur during hydrodynamic escape, which could have been driven by the significantly higher extreme UV flux that is expected to have been produced from the early Sun. A hydrodynamic flux of $\sim 10^{12}$ H $\text{cm}^{-2} \text{s}^{-1}$ could remove ~ 470 meters of water from Venus in 100 million years and produce the elevated D/H ratio observed on Venus today (e.g., Donahue et al., 1997).

However, astrophysical models predict that the early Sun’s visible solar flux was about 25–30% less than today. Because

of the lower solar flux, the runaway greenhouse (and water loss) may have happened some time after Venus formed, rather than right away (Pollack, 1991). Hydrodynamic escape of hydrogen is not viable once the solar extreme UV flux has declined. Instead, hydrogen loss occurs ~ 100 times slower via other non-thermal processes that remove much less water from Venus over time (~ 47 meters per 10^9 years). An initially “moist” Venus may be more likely than an initially “wet” Venus.

Huge amounts of residual O_2 are left after losing an ocean’s worth of hydrogen. For example, the loss of 2.7 km of water from Venus, equivalent to Earth’s oceans, would leave behind 1.1×10^{21} kg of O_2 , about 35 times the total amount of O_2 produced by photosynthesis on Earth over time. Loss of 470 meters of water leaves behind 1.9×10^{20} kg of O_2 , about 6 times Earth’s total photosynthetic oxygen. The disposal of so much oxygen is a formidable problem. One possibility is oxygen loss to space. This occurs on Venus today at a rate that would leave behind $\sim 30\%$ of the oxygen in water. However, if oxygen was not lost to space, all of it had to be consumed by chemical reactions.

On Earth about 96% of all O_2 produced over time was consumed by oxidation of reduced carbon, iron, and sulfur compounds and only 4% resides in the atmosphere. Currently, the major O_2 sinks on Earth are oxidation of organic carbon to CO_2 (1.6×10^{11} kg yr^{-1}), ferrous to ferric iron (4.7×10^{10} kg yr^{-1}), and sulfides to sulfate (6.2×10^{10} kg yr^{-1}), summing to 2.69×10^{11} kg $\text{O}_2 \text{ yr}^{-1}$ (Warneck, 1988). Oxidation of reduced carbon accreted by Venus plausibly happened during impact devolatilization. This leaves oxidation of reduced iron and sulfur in Venus’ lithosphere as possible O_2 sinks. The XRF elemental analyses of Venus’ surface found iron (8–9% “FeO”) and sulfur (0.9–4.7% SO_3), whose abundances are conventionally reported as oxides although their chemical form is unknown. The sulfur content of Venus’ lithosphere is probably closer to that in Earth’s mantle (0.04%) or oceanic crust (0.1%) than that found on the surface because reaction (2) adds sulfur by chemical weathering. If Venus’ lithosphere initially contained 10% “FeO,” which is oxidized to hematite (Fe_2O_3) or magnetite (Fe_3O_4), 1.9×10^{20} kg of O_2 would have to react with 0.5–0.8% of the lithosphere to be consumed. Removal of all this O_2 over 100 million years while water is lost requires a volcanic eruption rate of ~ 140 $\text{km}^3 \text{ yr}^{-1}$ to expose this much lithosphere to the atmosphere. For comparison, Earth’s volcanism rate is ~ 20 $\text{km}^3 \text{ yr}^{-1}$, and the estimated rate on Venus is $1 \text{ km}^3 \text{ yr}^{-1}$ (see below). A 100 million year removal rate also corresponds to a sink of $\sim 1.9 \times 10^{12}$ kg $\text{O}_2 \text{ yr}^{-1}$, which is ~ 7 times larger than the current O_2 loss rate on Earth. It is difficult to see how so much O_2 could be lost so rapidly on Venus or how so much lithosphere could be exposed so rapidly. It again seems that an initially “moist” Venus is more plausible than an initially “wet” Venus.

Volcanic outgassing and climate change

As mentioned earlier, CO_2 , SO_2 , and H_2O are the three most important greenhouse gases in Venus’ atmosphere. All three gases are common constituents of terrestrial volcanic gases and volcanism is a probable source for all three gases on Venus. Furthermore, all three gases are probably involved in atmosphere-lithosphere reactions on Venus. These and other arguments suggest that atmospheric chemistry and physics,

climate, and volcanism are closely linked on Venus (e.g., Bullock and Grinspoon, 2001).

The relative abundances of SO₂, OCS, H₂S, and elemental sulfur vapor (dominantly S₂) in Venusian volcanic gases are unknown. Sulfur dioxide is generally the major sulfur compound in basaltic volcanic gases on Earth, followed by H₂S, OCS, and elemental sulfur vapor. Venusian basalts probably erupt at higher or similar temperatures as terrestrial basalts. If Venusian volcanic gases are as oxidized as (or more oxidized than) terrestrial volcanic gases, SO₂ should be the major sulfur gas. More oxidized gases may also contain up to ~200 ppmv SO₃, which may provide an observational test for water loss and O₂ consumption on Venus. The large CO₂ and very low H₂O abundances in Venus' atmosphere imply that S₂ and OCS should be more abundant than H₂S in Venusian volcanic gases. For comparison, SO₂ and S₂ are the two major species in volcanic gases on Io, which has apparently lost all or most of its hydrogen and carbon.

As discussed earlier, reaction (2) would remove all SO₂ (and thus the sulfuric acid clouds) from Venus' atmosphere in ~1.9 million years in the absence of a volcanic source. Sulfur dioxide undergoes similar reactions with other calcium-bearing silicate minerals such as anorthite, diopside, and wollastonite, forming anhydrite (CaSO₄) by reactions analogous to equation 2. The measured Ca/S ratios are greater than unity at the *Venera 13*, *14*, and *Vega 2* sites. These ratios are larger than one, which is the expected value if all Ca were combined with S in anhydrite. Thus, loss of atmospheric SO₂ via chemical weathering of Ca-bearing minerals on Venus' surface is probably an ongoing process.

Maintenance of atmospheric SO₂ at current levels requires eruption of ~1 km³ yr⁻¹ of lava with the average composition of the *Venera 13*, *14*, and *Vega 2* landing sites. This volcanism rate is the same as the average rate of subaerial volcanism on Earth and is about 5% of the total volcanism rate of ~20 km³ yr⁻¹. The required sulfur eruption rate to maintain SO₂ on Venus at steady state is ~2.8 × 10¹⁰ kg yr⁻¹. This is similar to the SO₂ emission rates of 9 × 10⁹ kg yr⁻¹ (subaerial), 1.9 × 10¹⁰ kg yr⁻¹ (submarine), and 2.8 × 10¹⁰ kg yr⁻¹ (total) from terrestrial volcanism (Charlson et al., 1992).

Volcanism on Earth and on Io is episodic. By analogy, Venusian volcanism should be episodic, which may be one reason why active volcanism has not yet been seen on Venus. However, a volcanic source for SO₂ is required at present. What may happen if the volcanic source and anhydrite sink for SO₂ are not balanced? If less SO₂ is erupted than is lost by anhydrite formation, less SO₂ will be left in the atmosphere, less H₂SO₄ will be produced, and fewer clouds will form. Temperatures in Venus' atmosphere and at the surface may decrease because SO₂ as well as other volcanic volatiles such as CO₂ and H₂O are greenhouse gases, all of which are needed for the Venusian supergreenhouse state. As temperatures drop, the carbonates magnesite (MgCO₃) and dolomite (CaMg(CO₃)₂) may become stable and consume atmospheric CO₂ as they form. Conversely, if more SO₂ is erupted than is lost by anhydrite formation, more SO₂ will be added to the atmosphere, more H₂SO₄ will be produced, and more clouds will form. In this case, atmospheric and surface temperatures may rise as more greenhouse gases enter the atmosphere. Minerals now stable at 740 K on Venus' surface may decompose as temperatures increase, releasing more volatiles into the atmosphere (e.g., HCl, HF, elemental sulfur vapor). Some of these effects, which could operate in the future and may have done

so in the past, have been studied in climate models that incorporate variations of SO₂ and H₂O abundances on the clouds and temperatures on Venus (e.g., Bullock and Grinspoon, 2001). In particular, large temperature changes are predicted to result from the putative global resurfacing of Venus 500 ± 200 million years ago.

Bruce Fegley, Jr.

Bibliography

- Ahrens, T.J., 1993. Impact erosion of terrestrial planetary atmospheres. *Annu. Rev. Earth Planet. Sci.*, **21**, 525–555.
- Barsukov, V.L., Basilevsky, A.T., Volkov, V.P., and Zharkov, V.N. (eds.), 1992. *Venus Geology, Geochemistry, and Geophysics*. Tucson, AZ: University of Arizona Press, 421pp.
- Bézar, B., DeBergh, C., Fegley, B., Maillard, J.P., Crisp, D., Owen, T., Pollack, J.B., and Grinspoon, D., 1993. The abundance of sulfur dioxide below the clouds of Venus. *Geophys. Res. Lett.*, **20**, 1587–1590.
- Bougher, S.W., Hunten, D.M., and Phillips, R.J. (eds.), 1997. *Venus II*. Tucson, AZ: University of Arizona Press, 1362pp.
- Brown, H., 1949. Rare gases and the formation of the Earth's atmosphere. In Kuiper, G.P. (ed.), *The Atmospheres of the Earth and Planets*. Chicago, IL: University of Chicago Press, pp. 260–268.
- Bullock, M.A., and Grinspoon, D.H., 2001. The recent evolution of climate on Venus. *Icarus*, **150**, 19–37.
- Cameron, A.G.W., 1995. The first ten million years in the solar nebula. *Meteoritics*, **30**, 133–161.
- Chamberlain, J.W., and Hunten, D.M., 1987. *Theory of Planetary Atmospheres*. San Diego, CA: Academic Press, 481pp.
- Charlson, R.J., Anderson, T.L., and McDuff, R.E., 1992. The sulfur cycle. In Butcher, S.S., Charlson, R.J., Orians, G.H., and Wolfe, G.V. (eds.), *Global Biogeochemical Cycles*. San Diego, CA: Academic Press, pp. 285–300.
- Donahue, T.M., Grinspoon, D.H., Hartle, R.E., and Hodges, R.R. Jr., 1997. Ion/neutral escape of hydrogen and deuterium: Evolution of water. In Bougher, S.W., Hunten, D.M., and Phillips, R.J. (eds.), *Venus II*, Tucson, AZ: University of Arizona Press, pp. 385–414.
- Fegley, B. Jr., 2000. Kinetics of gas-grain reactions in the solar nebula. *Space Sci. Rev.*, **92**, 177–200.
- Fegley, B. Jr., 2004. Venus, In Davis, A.M. (ed.), *Meteorites, Comets, and Planets*. Holland, H.D., and Turekian, K.K. (eds.), *Treatise on Geochemistry*, vol. 1, Oxford, England: Elsevier-Perгамon, pp. 487–507.
- Hunten, D.M., Colin, L., Donahue, T.M., and Moroz, V.I. (eds.), 1983. *Venus*. Tucson, AZ: University of Arizona Press, 1143pp.
- Ingersoll, A.P., 1969. The runaway greenhouse: A history of water on Venus. *J. Atmos. Sci.*, **26**, 1191–1198.
- Irvine, W.M., Schloerb, F.P., Crovisier, J., Fegley, B. Jr., and Mumma, M.J., 2000. Comets: A link between interstellar and nebular chemistry. In Mannings, V., Boss, A.P., and Russell, S.S. (eds.), *Protostars and Planets IV*. Tucson, AZ: University of Arizona Press, pp. 1159–1200.
- Johnson, N.M., and Fegley, B. Jr., 2003. Tremolite decomposition on Venus II. Products, kinetics, mechanism. *Icarus*, **164**, 317–333.
- Kargel, J.S., Komatsu, G., Baker, V.R., and Strom, R.G., 1993. The volcanology of Venera and VEGA landing sites and the geochemistry of Venus. *Icarus*, **103**, 253–275.
- Kargel, J.S., Kirk, R.L., Fegley, B. Jr., and Treiman, A., 1994. Carbonate-sulfate volcanism on Venus? *Icarus*, **112**, 219–252.
- Kaula, W.M., 1999. Constraints on Venus evolution from radiogenic argon. *Icarus*, **139**, 32–39.
- Kerridge, J., and Matthews, M.S. (eds.), 1988. *Meteorites and the Early Solar System*. Tucson, AZ: University of Arizona Press, 1269pp.
- Kleine, T., Münker, C., Mezger, K., and Palme, H., 2002. Rapid accretion and early core formation on asteroids and terrestrial planets from Hf-W chronometry. *Nature*, **418**, 952–955.
- Krasnopolsky, V.A., 1986. Photochemistry of the Atmospheres of Mars and Venus. Berlin, Germany: Springer-Verlag, 334pp.
- Lewis, J.S., 1974. Volatile element influx on Venus from cometary impacts. *Earth Planet. Sci. Lett.*, **22**, 239–244.
- Lewis, J.S., and Prinn, R.G., 1984. *Planets and Their Atmospheres: Origin and Evolution*. New York, NY: Academic Press, 470pp.

- Lodders, K., 2003. Solar system abundances and condensation temperatures of the elements. *Astrophys. J.*, **591**, 1220–1247.
- Lodders, K., and Fegley, B. Jr., 1997. An oxygen isotope model for the composition of Mars. *Icarus*, **126**, 373–394.
- Lodders, K., and Fegley, B. Jr., 1998. *The Planetary Scientist's Companion*. New York, NY: Oxford University Press, 371pp.
- Matsui, T., and Abe, Y., 1986. Impact-induced atmospheres and oceans on Earth and Venus. *Nature*, **322**, 526–528.
- Morgan, J.W., and Anders, E., 1980. Chemical composition of the Earth, Venus, and Mercury. *Proc. Natl. Acad. Sci.*, **77**, 6973–6977.
- Ozima, M., and Podosek, F.A., 2002. *Noble Gas Geochemistry*, 2nd ed. Cambridge, England: Cambridge University Press, 286pp.
- Pepin, R.O., and Porcelli, D., 2002. Origin of noble gases in the terrestrial planets. In Porcelli, D., Ballentine, C.J., and Wieler, R. (eds.), *Noble Gases in Geochemistry and Cosmochemistry*, Washington, D.C.: Mineralogical Society of America, pp. 191–246.
- Pollack, J.B., 1991. Kuiper Prize Lecture: Present and past climates of the terrestrial planets. *Icarus*, **91**, 173–198.
- Prinn, R.G., and Fegley, B. Jr., 1987. The atmospheres of Venus, Earth, and Mars: A critical comparison. *Annu. Rev. Earth Planet. Sci.*, **15**, 171–212.
- Rasool, S.I., and DeBergh, C., 1970. The runaway greenhouse and the accumulation of CO₂ in the Venus atmosphere. *Nature*, **226**, 1037–1039.
- Shirley, J.H., and Fairbridge, R.W. (eds.), 1997 *Encyclopedia of Planetary Sciences*. London, England: Chapman & Hall, 990 pp.
- von Zahn, V., Kumar, S., Niemann, H., and Prinn, R., 1983. Composition of the Venus atmosphere. In Hunten, D.M., Colin, L., Donahue, T.M., and Moroz, V.I. (eds.), *Venus*. Tucson: University of Arizona Press, pp. 299–430.
- Warneck, P., 1988. *Chemistry of the Natural Atmosphere*. San Diego, CA: Academic Press, 757pp.
- Weidenschilling, S.J., 1976. Accretion of the terrestrial planets II. *Icarus*, **27**, 161–170.
- Wetherill, G.W., 1980. Formation of the terrestrial planets. *Annu. Rev. Astron. Astrophys.*, **18**, 77–113.
- Yin, Q., Jacobsen, S.B., Yamashita, K., Blichert-Toft, J., Télouk, P., and Albarède, F., 2002. A short timescale for terrestrial planet formation from Hf-W chronometry of meteorites. *Nature*, **418**, 949–952.
- Yung, Y.L., and DeMore, W.B., 1999. *Photochemistry of Planetary Atmospheres*. New York, NY: Oxford University Press, 456pp.

Cross-references

[Atmospheric Evolution, Earth](#)
[Atmospheric Evolution, Mars](#)
[Carbon Cycle](#)
[Deuterium, Deuterium Excess](#)
[“Greenhouse” \(Warm\) Climates](#)
[Volcanic Eruptions and Climate Change](#)
[Weathering and Climate](#)

B

BANDED IRON FORMATIONS AND THE EARLY ATMOSPHERE

IRON FORMATIONS, a class of chemical sediments comparable to evaporites or phosphorites, occur on all continental cratons and represent the largest repositories of iron ever precipitated from Earth's hydrosphere (Trendall and Morris, 1983; Clout and Simonson, 2005). Iron formations reveal much about the composition of the atmosphere because of the redox sensitivity of iron in solution, and because of the dramatic change in the way iron was deposited through geologic time. The first-order observations are that Precambrian iron-rich sediments (known as *iron formations*) are generally cherty, thinly laminated (or banded), and widespread, whereas Phanerozoic iron-rich sediments (known as *IRONSTONES*) generally lack chert and are richer in aluminum (reflecting clastic contamination), not laminated, and smaller in areal extent. In order to make correct inferences about temporal changes in Earth's atmosphere, iron formations must first be understood as chemical sediments.

Sedimentary characteristics of iron formations

Many iron formations have well-preserved sedimentary features, which permit them to be subdivided into banded and granular varieties. *BANDED IRON FORMATIONS* (BIFs) are by far the more abundant of the two. The present minerals in the least-altered BIFs are remarkably fine-grained and uniform, and although recrystallized, it is likely they have been largely derived from the primary precipitates. Layers rich in iron and chert generally alternate on a scale of millimeters to centimeters (Figure B1a), and many BIFs exhibit cyclic alternations of iron-rich and iron-poor minerals or of BIF and fine shaly or volcanoclastic strata (Trendall and Blockley, 1970; Ewers and Morris, 1981; Beukes, 1984). Based on these characteristics, BIF minerals (or their precursors) are inferred to have formed in the water column and precipitated to the seafloor below storm wave base in waters that were not in direct connection with the atmosphere.

In contrast to BIFs, *GRANULAR IRON FORMATIONS* (GIFs) consist largely of well-sorted sand-size clasts referred to as "granules" that were transported in high-energy environments where ocean waters mixed much more freely with atmospheric gases. Most of the clasts appear to be reworked fragments of BIF precursor muds (Figure B1b) but some GIFs are also rich in concentrically laminated ooids that grew on the seafloor. GIFs have dune-scale cross-bedding that is more irregular than the banding of BIFs and shows complex paleocurrent patterns typical of shallow marine sands (Ojakangas, 1983; Simonson, 1985). Flat pebble conglomerates and stromatolites are locally abundant. GIFs also contain an abundance of intergranular cement that consists largely of void-filling chalcedony and drusy quartz (Simonson, 1987) and were emplaced so rapidly that some GIFs show virtually no compaction. The presence of gelatinous silica also led to the formation of intra- and intergranular syneresis cracks (Gross, 1972; Beukes, 1984). Early silica cementation helped to preserve primary iron-rich phases with minimal alteration, as well as some of the best early Precambrian microbiotas (Walter and Hofmann, 1983).

Mineralogically, iron formations consist of one or more iron-rich minerals admixed with quartz-rich layers interpreted as recrystallized cherts (Maliva et al., 2005). The main iron minerals fall into four groups that James (1954) defined as the "facies" of iron formation. His groups were oxide, silicate, carbonate, and sulfide, but most iron formations are hybrid mixtures with iron minerals from two or even three of these groups. In unaltered iron formations lacking clastic contamination, the dominant iron minerals are magnetite and hematite in the oxide facies; greenalite in the silicate facies; siderite, ankerite or ferroan dolomite in the carbonate facies; and pyrite in the sulfide facies. Detailed petrographic and isotopic studies of finely-laminated BIFs and GIFs rich in early cement suggest that chert, greenalite, siderite and hematite (or more poorly-ordered precursors of similar composition) are the minerals most likely to have formed as primary precipitates. All other phases are viewed as diagenetic or metamorphic overprints (Klein, 1983; Kaufman et al., 1990).

Temporal variation in stratigraphic and environmental patterns

Pure GIF (i.e., high-energy iron formation) rarely occurs in layers thicker than a few meters as it is usually interbedded with BIF on a scale of meters to tens of meters. In contrast, BIFs (i.e., low-energy iron formation) commonly contain no discernible GIF and range up to hundreds of meters in thickness. The lateral dimensions of iron formation likewise vary dramatically from thin layers sandwiched between other lithologies (e.g., volcanoclastic turbidites) to units hundreds of meters thick of nearly pure iron formation persisting laterally for hundreds of kilometers with little change (Trendall and Blockley, 1970; Beukes, 1983; Fralick and Barrett, 1995).

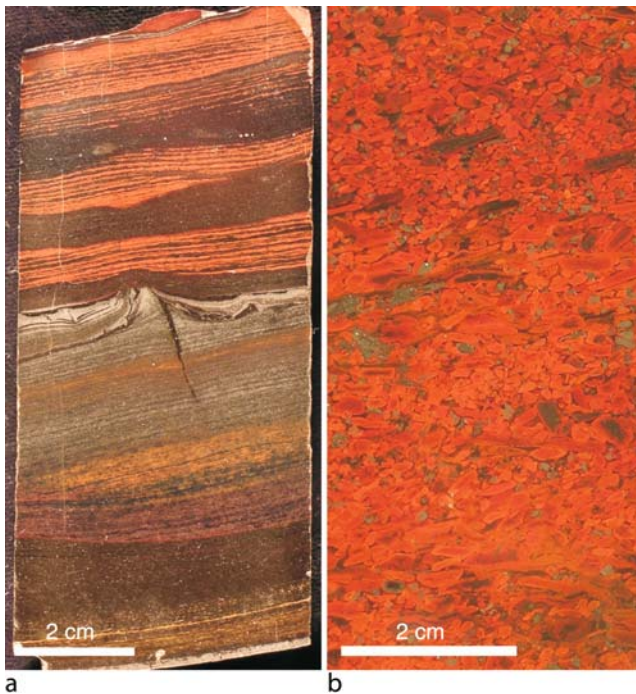


Figure B1 Sawed surfaces of iron formation samples. (a) Drill core of Dales Gorge banded iron formation (BIF, Hamersley Basin) consisting mainly of iron oxides (*silver to dark*) and hematitic chert (*reddish*). (b) Hand sample of granular iron formation from Sokoman Formation (GIF, New Quebec Orogen) consisting of unusually large intraclasts of hematitic chert and iron oxides; intergranular pores are filled with transparent chalcedonic cement.

The key to interpreting atmospheric evolution is to understand why the size, composition, and context of iron formations changed through time. Characterizing iron formations on their genetic associations as well as their sedimentary characteristics (i.e., BIF vs. GIF), Gross (1965, 1983) encapsulated the most important temporal changes by subdividing iron formations into two main categories. The category he called *Algoma-type iron formation* is a common component of Archean greenstone belts which range in age from ca. 2.7 Ga (billion years old) back to the oldest supracrustal rocks on Earth (Figure B2). By definition, Algoma-type iron formations are small and intimately associated with volcanic rocks. In addition, virtually all Algoma-type iron formations are BIFs (rather than GIFs), include significant thicknesses of all four of James' mineral facies, and are closely associated with deeper-water deposits consisting of volcanic rock, shale, and turbidites. The other category he called *Superior-type iron formation*, and these are much more massive accumulations of iron and silica that dominate the Neoproterozoic and Paleoproterozoic eras (about 2.7–1.8 Ga). Not only are Superior-type iron formations younger than most Algoma-type BIFs, they were deposited during marine transgressions on continental margins and therefore are thicker, laterally extensive, and generally associated with carbonate and siliciclastic strata (Simonson and Hassler, 1996). BIFs are the main constituent of many Superior-type iron formations, but many also contain substantial thicknesses of GIF. Moreover, Superior-type BIFs (like the Algoma-type iron formations) show the full spectrum of James' facies, whereas cherty Superior-type GIFs are rich in iron oxides and to a lesser extent iron silicates. Iron carbonates are scarce in GIFs with one notable exception, the Griquatown Iron Formation of South Africa (Beukes, 1984), which is one of the oldest of all Superior-type iron formations. In addition, BIF-rich Superior-type iron formations are associated with deep water shale and turbidites, whereas those with abundant GIFs are associated with shallow water deposits such as stromatolitic dolomites and quartzarenites (Simonson, 1985; Simonson and Hassler, 1996).

The distinction between Algoma- and Superior-type iron formations involves more than just a simple changeover at one point in time. For example, Algoma-type iron formations are not restricted to the Archean. Smaller iron-bearing volcanogenic deposits that meet the definition of Algoma-type BIFs persist into the later part of the Precambrian, and arguably even into the Phanerozoic. Moreover, Superior-type iron formations appear to be distributed unevenly in time between 2.7 and 1.8 Ga (Figure B2), possibly coinciding with discrete mantle plume events, which released voluminous iron through

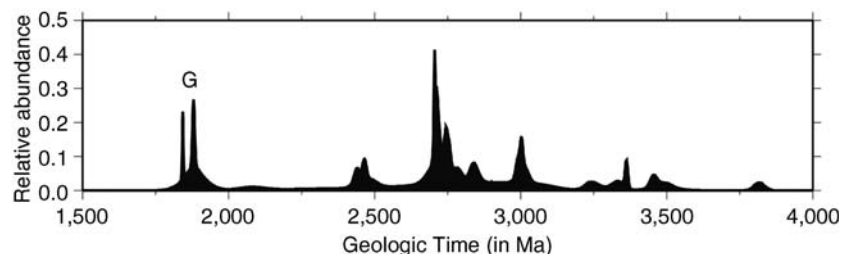


Figure B2 Time series of occurrences of iron formations in terms of numbers (but not sizes) through most of Precambrian calculated by summing Gaussian distributions of published age dates compiled by Isley and Abbott (1999); peaks under letter "G" include most of the GIFs; graph courtesy of Dr. Dallas Abbott.

hydrothermal activity (Isley and Abbott, 1999). It also appears that no BIFs were deposited during Earth's earliest glacial period (between 2.2 and 2.4 Ga) when continental glaciers and extensive sea ice covered the planet on at least three separate occasions. The deposition of large Superior-type iron formations ceased entirely around 1.8 Ga (Klein and Beukes, 1992; Simonson, 2003).

After a billion year hiatus, a remarkable, albeit brief, episode of global sedimentary iron accumulation took place in the Neoproterozoic. Iron-rich rocks that look much like BIF and meet the strict definition of iron formation were deposited in intimate association with glaciogenic sediments on several continents (Young, 1988; Derry et al., 1992). These late Precambrian iron formations tend to be richer in iron and have a simple mineralogy dominated by hematite, although both fine laminations similar to BIF and clastic textures similar to GIF are present locally (Klein and Ladeira, 2004). They also carry the geochemical signatures of a hydrothermal origin (Young, 1988; Klein and Beukes, 1993).

Implications for atmospheric history

The waxing and waning of iron formations early in Earth's long history must be linked to co-evolution of the atmosphere, hydrosphere, biosphere, and lithosphere. The sedimentary characteristics summarized above make it clear that iron formations were primary precipitates deposited mostly in open marine settings (Beukes, 1983; Ojakangas, 1983; Simonson, 1985). Cloud (1973) first suggested that dissolved ferrous iron was ubiquitous in the early ocean and that iron formations formed where photosynthesizing microbes produced free oxygen, causing iron oxides to precipitate. This hypothesis was elegant for its time, but it cannot explain the diversity of iron minerals in iron formations, nor the fact that contemporaneous carbonate sediments are depleted in iron relative to Phanerozoic carbonates (Veizer et al., 1990, 1992). To accommodate these observations, new theories evolved.

Most researchers now believe that large-scale hydrothermal activity and a stratified world ocean were important factors in the deposition of large iron formations (Klein and Beukes, 1992; Isley and Abbott, 1999). All iron formations record geochemical signatures of hydrothermal sources, and iron-rich plumes were probably capable of traveling from deep-sea sources to distant depocenters, provided that the early oceans were stratified (Isley, 1995). The need for a stratified water column mainly stems from the fact that, even though normal marine surface waters were clearly not well oxygenated in the early Precambrian, they were still too oxic to carry much dissolved ferrous iron (Trendall, 2002). Given a world ocean with a surface layer lacking dissolved iron, a deep reservoir of ferrous iron, and high concentrations of silica throughout, precipitating iron oxides and silicates such as hematite and greenalite (or suitable precursors) along a chemocline between the water masses presents no problem. Petrographic and isotopic observations also require primary precipitation of siderite (Kaufman et al., 1990; Kaufman, 1996). We attribute the siderite to a rain of calcium carbonate from shallow water environments that was dissolved as it encountered deeper and more acidic hydrothermal solutions rich in ferrous iron, as sideritic carbonate is notably less soluble than its calcium-rich counterpart (Kaufman, 1999). Exsolution or uptake of CO₂ (and iron)-rich hydrothermal solutions along a chemocline between reduced and oxidized water masses would have had a similar effect. Anomalously high variability in the isotopic composition of iron in

iron formations has been attributed to microbial involvement in their precipitation (Beard et al., 1999), but inorganic causes have also been proposed (Rouxel et al., 2005). This scenario of precipitate raining down from a chemocline explains why iron formations occurred in many different tectonic settings, associated with diverse rock types (Gross, 1983; Fralick and Barrett, 1995), and how iron accumulated essentially undiluted by other types of clastic and/or chemical sediment.

The transition from small Algoma-type to large Superior-type iron formations in the Neoproterozoic is generally attributed to the first appearance of extensive continental shelf environments rather than atmospheric evolution. Superior-type iron formations appeared at the same time and in the same basins as the first laterally extensive stable shelf deposits, e.g., platform carbonates (Grotzinger, 1994). The areal expansion of continental shelves offered larger, more uniform repositories than volcanic terrains, and presumably reflected a Neoproterozoic surge in the growth of continental crust and associated rise in sea levels (Lowe, 1992; Groves et al., 2005). "Cratonization" of shields was a highly diachronous process (Eriksson and Donaldson, 1986), which could account for the deposition of large iron formations on different continents at different times.

In contrast, the abrupt disappearance of iron formations around 1.8 billion years ago is generally attributed to a rise in the oxygen content of the atmosphere (e.g., figure 6 in Canfield, 2005). The key to terminating iron formations was to reduce the mobility of dissolved iron in the deep ocean. Although attributed to oxygenation, the first dramatic rise in atmospheric oxygen appears to have taken place much earlier, at around 2.4 Ga (Canfield, 2005). This event is generally associated with early Paleoproterozoic glaciation and the first strongly positive carbon isotope excursion recorded in marine carbonates (Bekker et al., 2001). Such excursions are indicative of the burial of a higher proportion of reduced carbon, so oxidants (like O₂) could have built up in the atmosphere at the time. Notably, the last of the Paleoproterozoic $\delta^{13}\text{C}$ excursions took place some 200–300 million years *before* iron formation deposition ended around 1.8 Ga. Given the lack of an oxidative signal, some now favor an alternative model of BIF cessation invoking increased levels of dissolved sulfide to limit iron solubility in the deep mid-Proterozoic ocean (Anbar and Knoll, 2002; Arnold et al., 2004). Whatever the change was, it clearly prevented the deep ocean from storing and transporting dissolved iron over long distances, thereby severing the connection between seafloor hydrothermal systems and continental shelf environments and putting a stop to the deposition of iron formations.

The temporal changes in Superior-type iron formations may also reflect changes in Earth's atmosphere. Most notably, the fact that the last Superior-type iron formations, the ones formed just before their abrupt disappearance around 1.8 Ga, show the greatest abundance of both GIF (Figure B2) and oxide minerals may reflect increasing concentrations of oxygen in the ocean's surface layer. Moreover, large iron formations occurred before and after, but not during, the 200 million year interval of Paleoproterozoic glaciation. Such variations are likely to record Neoproterozoic to Paleoproterozoic oscillations in both hydrothermal inputs and atmospheric oxygenation. These may have been coupled in the world ocean through the photosynthetic production of oxygen, which is stimulated by the availability of soluble iron, a known biolimiting nutrient (Coale et al., 1996). The recurrence of iron formation and iron-cemented glacial diamictites near the end of the Proterozoic suggests a brief return of localized oceanic anoxia, similarly associated with tectonic

rifting and hydrothermal delivery of iron to the oceans (Asmerom et al., 1991). Insofar as long-term nutrient-driven cycles of primary productivity may have drawn down greenhouse gases (Kaufman et al., 1997), the Neoproterozoic return of BIFs may have contributed to the widespread low latitude "snowball Earth" glaciations (Hoffman et al., 1998).

Bruce M. Simonson and Alan J. Kaufman

Bibliography

- Anbar, A.D., and Knoll, A.H., 2002. Proterozoic ocean chemistry and evolution: A bioinorganic bridge? *Science*, **297**, 1137–1192.
- Arnold, G.L., Anbar, A.D., Barling, J., and Lyons, T.W., 2004. Molybdenum isotope evidence for widespread anoxia in mid-Proterozoic oceans. *Science*, **304**, 87–90.
- Asmerom, Y., Jacobsen, S.B., Knoll, A.H., Butterfield, N.J., and Swett, K., 1991. Strontium isotopic variations of Neoproterozoic seawater; implications for crustal evolution. *Geochimica et Cosmochimica Acta*, **55**, 2883–2894.
- Beard, B.L., Johnson, C.M., Cox, L., Sun, H., Neelson, K.H., and Aguilar, C., 1999. Iron isotope biosignatures. *Science*, **285**, 1889–1892.
- Bekker, A., Kaufman, A.J., Karhu, J.A., Beukes, N.J., Swart, Q.D., Coetzee, L.L., and Eriksson, K.A., 2001. Chemostratigraphy of the Paleoproterozoic Duitschland Formation, South Africa: Implications for coupled climate change and carbon cycling. *Am. J. Sci.*, **301**, 261–285.
- Beukes, N.J., 1983. Palaeoenvironmental setting of iron-formations in the depositional basin of the Transvaal Supergroup, South Africa. In Trendall and Morris (eds.), *Iron Formations: Facts and Problems*. Amsterdam: Elsevier, pp. 131–209.
- Beukes, N.J., 1984. Sedimentology of the Kuruman and Griquatown Iron-formations, Transvaal Supergroup, Griqualand West, South Africa. *Precambrian Res.*, **24**, 47–84.
- Canfield, D.E., 2005. The early history of atmospheric oxygen. *Annu. Rev. Earth and Planetary Sci.*, **33**, 1–36.
- Cloud, P., 1973. Paleocological significance of the banded iron-formation. *Econ. Geol.*, **68**, 1135–1143.
- Clout, J.M.F., and Simonson, B.M., 2005. Precambrian iron formations and iron formation-hosted iron ore deposits. In Hedenquist, J.W., Thompson, J.F.H., Goldfarb, R.J., Richards, J.P. (eds.), *Economic Geology - 100th Anniversary Volume*. Littleton, Colorado: Society of Economic Geologists, pp. 643–680.
- Coale, K.H., Johnson, K.S., Fitzwater, S.E., Gordon, R.M., and Tanner, S., et al., 1996. A massive phytoplankton bloom induced by an ecosystem-scale iron fertilization experiment in the equatorial Pacific Ocean. *Nature*, **383**, 495–501.
- Derry, L.A., Kaufman, A.J., and Jacobsen, S.B., 1992. Sedimentary cycling and environmental change in the Late Proterozoic: Evidence from stable and radiogenic isotopes. *Geochimica et Cosmochimica Acta*, **56**, 1317–1329.
- Eriksson, K.A., and Donaldson, J.A., 1986. Basinal and shelf sedimentation in relation to the Archaean-Proterozoic boundary. *Precambrian Res.*, **33**, 103–121.
- Ewers, W.E., and Morris, R.C., 1981. Studies of the Dales Gorge Member of the Brockman Iron Formation, Western Australia. *Econ. Geol.*, **76**, 1929–1953.
- Fralick, P.W., and Barrett, T.J., 1995. Depositional controls on iron formation associations in Canada. In Plint, A.G. (ed.), *Sedimentary Facies Analysis*. International Association of Sedimentologists, Special Publication, **22**, pp. 137–156.
- Gross, G.A., 1965. Geology of Iron Deposits of Canada, vol. I: General Geology and Evaluation of Iron Deposits. Ottawa: Geological Survey of Canada, Economic Geology Report 22.
- Gross, G.A., 1972. Primary features in cherty iron formations. *Sediment. Geol.*, **2**, 241–261.
- Gross, G.A., 1983. Tectonic systems and the deposition of iron-formation. *Precambrian Res.*, **20**, 171–187.
- Grotzinger, J.P., 1994. Trends in Precambrian carbonate sediments and their implications for understanding evolution. In Bengtson, S. (ed.), *Early Life on Earth. Nobel Symposium, 84*. New York: Columbia University Press, pp. 245–258.
- Groves, D.I., Condie, K.C., Goldfarb, R.J., Hronsky, J.M.A., and Vielreicher, R.M., 2005. Secular changes in global tectonic processes and their influence on the temporal distribution of gold-bearing mineral deposits. *Econ. Geol.*, **100**, 203–224.
- Hoffman, P.F., Kaufman, A.J., Halverson, G.P., and Schrag, D.P., 1998. A Neoproterozoic snowball Earth. *Science*, **281**, 1342–1346.
- Isley, A.E., 1995. Hydrothermal plumes and the delivery of iron to banded iron formation. *J. Geol.*, **103**, 169–185.
- Isley, A.E., and Abbott, D.H., 1999. Plume-related mafic volcanism and the deposition of banded iron formation. *J. Geophys. Res.*, **104**, 15,461–15,477.
- James, H.L., 1954. Sedimentary facies of iron-formation. *Econ. Geol.*, **49**, 235–293.
- Kaufman, A.J., 1996. Geochemical and mineralogic effects of contact metamorphism on banded iron formation: an example from the Transvaal Basin, South Africa. *Precambrian Res.*, **79**, 171–194.
- Kaufman, A.J., 1999. The genesis of siderite in Archean and Paleoproterozoic oceans. In *Ninth Annual V.M. Goldschmidt Conference Abstracts with Program*. Houston: Lunar and Planetary Institute, Lunar and Planetary Institute Contribution No. 971, p. 146.
- Kaufman, A.J., Hayes, J.M., and Klein, C., 1990. Primary and diagenetic controls of isotopic compositions of iron-formation carbonates. *Econ. Geol.*, **54**, 3461–3473.
- Kaufman, A.J., Knoll, A.H., and Narbonne, G.M., 1997. Isotopes, ice ages, and terminal Proterozoic earth history. *Proc. Natl. Acad. Sci.*, **94**, 6600–6605.
- Klein, C., 1983. Diagenesis and metamorphism of banded iron-formations. In Trendall and Morris (eds.), *Iron-formations: Facts and Problems*. Amsterdam: Elsevier, pp. 417–469.
- Klein, C., and Beukes, N.J., 1992. Proterozoic iron formations. In Condie, K.C. (ed.), *Proterozoic Crustal Evolution*. Amsterdam: Elsevier, pp. 383–418.
- Klein, C., and Beukes, N.J., 1993. Sedimentology and geochemistry of the glaciogenic Late Proterozoic Rapitan iron-formation in Canada. *Econ. Geol.*, **88**, 542–565.
- Klein, C., and Ladeira, E.A., 2004. Geochemistry and mineralogy of Neoproterozoic banded iron-formations and some selected, siliceous manganese formations from the Urucum District, Mato Grosso do Sul, Brazil. *Econ. Geol.*, **99**, 1233–1244.
- Lowe, D.R., 1992. Major events in the geological development of the Precambrian earth. In Schopf, J.W., and Klein, C. (eds.), *The Proterozoic Biosphere - A Multidisciplinary Study*. New York: Cambridge University Press, pp. 67–75.
- Maliva, R.G., Knoll, A.H., and Simonson, B.M., 2005. Secular change in the Precambrian silica cycle: Insights from chert petrology. *Geol. Soc. Am. Bull.*, **117**, 835–845.
- Ojakangas, R.W., 1983. Tidal deposits in the early Proterozoic basin of the Lake Superior region - the Palms and Pokegama Formations: Evidence for subtidal shelf deposition of Superior-type banded iron-formation. In Medaris, L.G. Jr. (ed.), *Early Proterozoic Geology of the Great Lakes Region*. Geological Society of America Memoir, **60**, pp. 49–66.
- Rouxel, O.J., Bekker, A., and Edwards, K.J., 2005. Iron isotope constraints on the Archean and Paleoproterozoic ocean redox state. *Science*, **307**, 1088–1091.
- Simonson, B.M., 1985. Sedimentological constraints on the origins of Precambrian iron-formations. *Geol. Soc. Am. Bull.*, **96**, 244–252.
- Simonson, B.M., 1987. Early silica cementation and subsequent diagenesis in arenites from four early Proterozoic iron formations of North America. *J. Sediment. Petrol.*, **57**, 494–511.
- Simonson, B.M., 2003. Origin and evolution of large Precambrian iron formations. In Chan, M., and Archer, A. (eds.), *Extreme Depositional Environments: Mega End Members in Geologic Time*. Geological Society of America, Special Paper, **370**, pp. 231–244.
- Simonson, B.M., and Hassler, S.W., 1996. Was the deposition of large Precambrian iron formations linked to major marine transgression? *J. Geol.*, **104**, 665–676.
- Trendall, A.F., 2002. The significance of iron-formation in the Precambrian stratigraphic record. In Altermann, W., and Corcoran, P.L. (eds.), *Precambrian Sedimentary Environments: A Modern Approach to Ancient Depositional Systems*. International Association of Sedimentologists, Special Publication, **33**, pp. 33–66.
- Trendall, A.F., and Blockley, J.G., 1970. *The Iron Formations of the Precambrian Hamersley Group, Western Australia*. Perth: Geological Survey of Western Australia, Bulletin, 119.

- Trendall, A.F., and Morris, R.C. (eds.), 1983. *Iron-Formation: Facts and Problems*. Amsterdam: Elsevier.
- Veizer, J., Clayton, R.H., Hinton, R.W., von Brunn, V., Mason, T.R., Buck, S.G., and Hoefs, J., 1990. Geochemistry of Precambrian carbonates: 3 - shelf seas and non-marine environments of the Archean. *Geochimica Cosmochimica Acta*, **54**, 2717–2729.
- Veizer, J., Clayton, R.H., and Hinton, R.W., 1992. Geochemistry of Precambrian carbonates: IV - Early Paleoproterozoic (2.25–0.25 Ga) seawater. *Geochimica Cosmochimica Acta*, **56**, 875–885.
- Walter, M.R., and Hofmann, H.J., 1983. The palaeontology and palaeoecology of Precambrian iron-formations. In Trendall and Morris (eds.), *Proterozoic Iron-Formations: Facts and Problems*, pp. 373–400.
- Young, G.M., 1988. Proterozoic plate tectonics, glaciation and iron-formations. *Sediment. Geol.*, **58**, 127–144.

Cross-references

Archean Environments
 Atmospheric Evolution, Earth
 Mineral Indicators of Past Climates
 Ocean Anoxic Events
 Proterozoic Climates
 Sedimentary Indicators of Climate Change
 Snowball Earth Hypothesis

BASAL ICE

Basal ice is the ice close to the base of a glacier or ice sheet that has been affected by processes operating at the glacier bed (Hubbard and Sharp, 1989; Knight, 1997). Most of the ice in glaciers and ice sheets is formed by the accumulation of snow at the glacier surface, but basal ice is created, or substantially modified, by processes at the bed. Basal ice provides information about processes that operate in the inaccessible subglacial zone, it influences glacier dynamics, it contributes directly to glacier sedimentation, and it represents a barrier to the downward extension of the climate record to the bottom of deep ice cores. The presence of debris in the basal ice, and the processes by which it is entrained and released, are crucial to processes of glacial erosion and deposition. The basal layer is fundamental to realistically formulated models of ice sheet behavior and of the development of glacial landscapes.

Basal ice may be several tens of meters thick and comprises a variety of facies of ice and debris. Ice may be entrained from beneath the glacier, or may be derived from the glacier surface but modified by thermal, strain, and hydraulic conditions close to the bed. The characteristics of the basal ice vary widely between sites because of varying glaciological controls on basal ice formation and survival. The chemistry, physical structure, and debris content of the basal ice are different from the englacial ice above because of its interaction with the bed, and the high debris content of the basal ice affects its rheological properties and its geomorphic potential. Two key issues in the description and interpretation of the basal layer are the processes by which the ice is formed and the processes by which rock debris from the bed is entrained into the ice. Processes by which basal ice can be formed can be divided into: (a) formation and accretion of new ice at the base of the glacier and (b) metamorphic alteration of existing ice close to the bed. Entrainment of debris at the bed occurs by a variety of processes including regelation, congelation, flow of water through the vein system, shearing, and folding. The basal layer is accessible via boreholes drilled through the glacier to the bed in subglacial cavities and locations where it is exposed at the

glacier margin. Debris from the basal ice is a major source of material for glacial sedimentation, and the characteristics of the basal ice, and hence former subglacial conditions, can be reconstructed from the characteristics of basal ice debris in glacial deposits (Knight et al., 2000).

Peter G. Knight

Bibliography

- Hubbard, B., and Sharp, M.J., 1989. Basal ice formation and deformation: A review. *Prog. Phys. Geogr.*, **13**, 529–558.
- Knight, P.G., 1997. The basal ice layer of glaciers and ice sheets. *Quaternary Sci. Rev.*, **16**, 975–993.
- Knight, P.G., Patterson, C.J., Waller, R.I., Jones, A.P., and Robinson, Z.P., 2000. Preservation of basal-ice sediment texture in ice sheet moraines. *Quaternary Sci. Rev.*, **19**, 1255–1258.

Cross-references

Binge-Purge Cycles of Ice Sheet Dynamics
 Glacial Geomorphology

BEACHROCK

Occurrence and sedimentology

Beachrock comprises sediments deposited in the intertidal zone on the beach face, beach berm, upper shoreface, and on tidal flats that have been cemented in situ to form an indurated sedimentary rock. Beachrock outcrops are ubiquitous along modern tropical and subtropical shorelines bounded by 35° N and 35° S (Scoffin and Stoddart, 1983) (Figure B3). Beachrock forms pavements and can comprise sand to shingle size clasts forming a sandstone or conglomerate, but predominantly comprises carbonate sands. The physical sedimentology of beachrock is similar to that for cay sandstone that forms in the supratidal zone (Kuenen, 1950), submerged dune calcarenite and emerged reef rock (Hopley, 1986), although the characteristic cements of each of these rock types are distinguishable. The internal stratigraphy of beach and upper shoreface deposits is preserved during the formation of beachrock, and is often recognized by seaward dipping planar beds outcropping on the beach. Beachrock is generally friable to brittle and the outer surface is case hardened (Scoffin and Stoddart, 1983). It is subject to mechanical, biological and chemical erosion following exhumation.

Beachrock cementation: mineralogy and origin

Beach sand grain or shingle clasts are cemented by aragonite or magnesium-calcite in a marine-phreatic environment. Depending upon location, beach sands or shingle are cemented within an intertidal sediment package, through physicochemical precipitation of calcium carbonate (Ginsberg, 1953), microbial activity (Webb et al., 1999), or a combination of both. The physicochemical precipitation of carbonate cement results from the evaporation of seawater and seaward-flowing groundwaters within the beach deposits, and by CO₂ degassing of this water through wave agitation and tidal pumping (Hanor, 1978; Meyers, 1986), particularly on windward beaches (Gischler and Lomando, 1997). The form of the cement is characteristic of the diagenetic environment and includes: (a) isopachous fringes of needle cement (usually aragonite), (b) micritic, peloidal and bladed cement (often magnesium-calcite; Gischler and



Figure B3 Late Holocene beachrock outcrop on south coast Upolu Island, Samoa, following beach erosion (photograph, Ian D. Goodwin).

Lomando, 1997) in marine-phreatic (below the water table) environments where water fills the pore spaces between grains, and (c) microcrystalline rinds, laminated crusts, and needle fiber cements in meteoric-vadose (above the water table) environments where the pore spaces are filled with cement (Gischler and Lomando, 1997).

Beachrock as an indicator of former sea level

Emerged or submerged beachrock has been used in many studies as an indicator of former sea level (Hopley, 1986; Pirazzoli, 1996). Specific examples are the Bahamas (Kindler and Bain, 1993), South Africa (Cooper, 1991), and Bangladesh (Chowdhury et al., 1995). However, the application of beachrock outcrops as an indicator of former sea level requires caution (Hopley, 1986). The water level control on the upper level of cementation must be identified with respect to Mean High Water Spring Tide and Highest Astronomical Tide. The mineralogy, form and fabric of the cements must be determined and the diagenetic environment identified as marine-phreatic. The beachrock stratigraphy should be horizontal and dipping seaward. The stratigraphic relationships to overlying dune calcarenites and to coral reef below the beachrock support the reconstruction of former sea level. Dating the age of beachrock deposition has been problematic, although modern radiometric techniques using micro-samples such as accelerator mass spectrometry or thermal ionizing mass spectrometry allow the dating of cements or microfossils embedded within the beachrock. Whilst the use of beachrock as a sea level indicator has not been routine in studies, its ubiquitous nature is important in paleoenvironmental reconstructions. Since beachrock forms within the phreatic zone of beach deposits, its exposure on the surface of modern beaches is indicative of recent beach erosion on many of the Earth's tropical and subtropical beaches.

Ian D. Goodwin

Bibliography

Chowdhury, S.Q., Fazlul Haq, A.T.M., and Hasan, K., 1995. Beachrock in St. Martin's Island, Bangladesh: Implications of sea level changes on beachrock cementation. *Mar. Geol.*, **20**, 89–104.

- Cooper, J.A.G., 1991. Beachrock formation in low latitudes: Implications for coastal evolutionary models. *Mar. Geol.*, **98**, 145–154.
- Ginsberg, R.N., 1953. Beachrock in south Florida. *J. Sediment. Petrol.*, **23**, 85–92.
- Gischler, E., and Lomando, A.J., 1997. Holocene cemented beach deposits in Belize. *Sediment. Geol.*, **110**, 277–297.
- Hanor, J., 1978. Precipitation of beachrock cements: Mixing of marine and meteoric waters vs CO₂ – degassing. *J. Sediment. Petrol.*, **48**(2), 489–501.
- Hopley, D., 1986. Beachrock as a sea-level indicator. In van de Plassche, O. (ed.), *Sea-Level Research*. Great Yarmouth, UK: Galliard Printers, pp. 157–173.
- Kindler, P., and Bain, R.J., 1993. Submerged upper Holocene beachrock on San Salvador Island, Bahamas: Implications for recent sea-level history. *Geol. Rundsch.*, **82**, 241–247.
- Kuenen, P.H., 1950. *Marine Geology*. New York, USA: Wiley, 568pp.
- Meyers, J.H., 1986. Marine vadose beachrock cementation by cryptocrystalline magnesian calcite, Maui, Hawaii. *J. Sediment. Petrol.*, **57**(3), 558–570.
- Pirazzoli, P.A., 1996. *Sea-Level Changes, the Last 20000 Years*. Chichester, UK: Wiley, 212pp.
- Scoffin, T.P., and Stoddart, D.R., 1983. Beachrock and intertidal cements. In Goudie, A.S., and Pye, K. (eds.), *Chemical Sediments and Geomorphology*. London, UK: Academic Press, pp. 401–425.
- Webb, G.E., Jell, J.S., and Baker, J.C., 1999. Cryptic intertidal microbialites in beachrock, Heron Island, Great Barrier Reef: Implications for the origin of microcrystalline beachrock cement. *Sediment. Geol.*, **126**, 317–334.

Cross-references

- [Sea Level Change, Last 250 Million Years](#)
- [Sea Level Change, Post-Glacial](#)
- [Sea Level Change, Quaternary](#)
- [Sea Level Indicators](#)
- [Sedimentary Indicators of Climate Change](#)

BEETLES AS QUATERNARY AND LATE TERTIARY CLIMATE INDICATORS

Insect remains are particularly abundant in freshwater sediments that have remained waterlogged since their deposition. Most of the remains are of beetles (Coleoptera) because of their

robust exoskeletons, but many other orders of insect are also preserved. Beetle species from the Quaternary and late Tertiary can be shown to be identical to their present day representatives. Most past assemblages of beetles can be shown to resemble modern communities closely. It can therefore be safely assumed that physiological stability accompanied their demonstrable morphological constancy. Thus, paleoecological and paleoclimatic inferences can be made on the basis of the past presence of particular beetle species. Many beetle species have changed their geographical ranges by thousands of kilometers even within the limited timespan of the last glacial/interglacial cycle. For instance the most abundant dung beetle in the British Isles during the middle Weichselian (Wisconsin) glaciation is now restricted to the high plateau of Tibet.

Quantification of climatic (particularly thermal) parameters may be made from these range changes. In the past, climatic interpretations were based on the overlap of the modern geographical ranges of species or the fit of the distributional margins to some isotherm, thereby inferring the paleoclimate (Coope, 1959). This method has problems that arise from the vagaries of space and time that determine geographical distributions; a species may not fulfill its total range potential for reasons other than climate.

To avoid these geographical problems, the distribution of a species can be plotted on a climate-space chart, where the mean temperature of the warmest month (TMax) is plotted on the x-axis and the difference between the mean temperature of the warmest and coldest months (TRange) on the y-axis. These figures are measured in meteorological stations. These coordinates subsume most of the important thermal constraints that determine the gross distribution of a beetle species. Assuming a simple sinusoidal relationship between the mean monthly temperatures, it is then a simple matter to infer the mean temperature of the coldest month (TMin) or any other mean monthly temperature. In this way, a ragged geographical distribution map frequently condenses into a compact grouping (Coope, 1986) and new occurrences of a species often fall within the body of the group. When plotted in terms of geographical space, new records often involve repeated redrawing of the distribution maps. Once a temperature envelope has been constructed for each species, it is much more stable and can be stored electronically in a database. As of 2003, the database included 436 species.

In order to obtain figures that are independent of those derived from the plant data, only carnivorous or scavenging species were used in these paleoclimatic calculations. Quantitative climatic estimates were made by overlapping the thermal envelopes for each species in a fossil assemblage and determining values from the coordinates of the area of greatest of mutual overlap (usually 100%). This method has been termed the mutual climatic range (MCR) method (Atkinson et al., 1987). In order to check the effectiveness of this method, present day beetle assemblages from a geographically widespread area of Eurasia were treated in the same way as fossil assemblages and the reconstructed thermal regime was compared with that measured at nearby meteorological stations. The correspondence between the MCR estimates and the measured values were generally very close but there was a slight tendency for MCR to over-estimate both summer and winter temperatures at "cold" sites. An equation has been devised that may be applied to the raw MCR data to correct this minor deviation (Coope et al., 1998).

Quantitative estimates of the thermal paleoclimate of both glacial and interglacials using the MCR method on sub-fossil beetle assemblages have now become standard practice in

Britain. The results are not always compatible with the traditional paleoclimatic interpretation of the paleobotanical (chiefly pollen analytical) records. Thus, the climates of treeless interstadials can at times be shown to be temperate and oceanic, rather than indicative of tundra coldness (Coope et al., 1997; Coope, 2000). During the late glacial period, the climate of Britain warmed to present-day levels at the beginning of the Bølling-Allerød Interstadial before there was any response from the trees. The beetles show that this climatic warming from glacial to interglacial conditions took place within the timespan of one human lifetime. The Younger Dryas cold period saw a return to fully glacial conditions. During "cold" periods, the climate of the British Isles was often of Siberian continentality with mean July temperatures at or below 10 °C and mean January/February temperatures at or below -15 °C. (Coope, 2002).

Recently the MCR method has been applied to Quaternary beetle assemblages from North America (Elias, 2000). There the record has been extended back to the latest Miocene faunas, where the presence of extant beetle species has permitted valid paleoclimatic interpretations to be made (Elias and Matthews, 2002).

G. Russell Coope

Bibliography

- Atkinson, T.C., Briffa, K.R., and Coope, G.R., 1987. Seasonal temperatures in Britain during the past 22,000 years, reconstructed using beetle remains. *Nature* **325**, 587–592.
- Coope, G.R., 1959. A Late Pleistocene insect fauna from Chelford, Cheshire. *Proc. R. Soc. London*, **B151**, 70–86.
- Coope, G.R., 1986. The invasion and colonisation of the North Atlantic islands: A palaeoecological solution to a biogeographic problem. *Philos. Trans. R. Soc. London*, **B314**, 619–635.
- Coope, G.R., 2000. Middle Devensian (Weichselian) coleopteran assemblages from Earith, Cambridgeshire (UK) and their bearing on the interpretation of "Full glacial" floras and faunas. *J. Quaternary Sci.*, **15**, 779–788.
- Coope, G.R., 2002. Changes in thermal climate in northwestern Europe during Marine Oxygen Isotope Stage 3, estimated from fossil insect assemblages. *Quaternary Res.*, **57**, 401–409.
- Coope, G.R., Gibbard, P.L., Hall, R.C., Preece, R.C., Robinson, J.E., and Sutcliffe, A.J., 1997. Climatic and environmental reconstructions based on fossil assemblages from Middle Devensian (Weichselian) deposits of the River Thames at South Kensington, Central London. *Quaternary Sci. Rev.*, **16**, 1163–1195.
- Coope, G.R., Lemdahl, G., Lowe, J.J., and Walkling, A., 1998. Temperature gradients in Northern Europe during the last glacial-transition (14–9, ¹⁴C kyr BP) interpreted from coleopteran remains. *J. Quaternary Sci.*, **13**, 418–433.
- Elias, S.A., 2000. Mutual climatic range reconstructions of seasonal temperatures based on late Pleistocene fossil beetle assemblages in Eastern Beringia. *Quaternary Sci. Rev.*, **20**, 77–91.
- Elias, S.A., and Matthews, J.V. Jr., 2002. Arctic North-American seasonal temperatures from the latest Miocene to the Early Pleistocene based on mutual climatic range analysis of fossil beetle assemblages. *Can. J. Earth Sci.*, **39**, 911–920.

Cross-references

[Animal Proxies, Invertebrates](#)
[Bølling-Allerød Interstadial](#)
[Paleoclimate Proxies, an Introduction](#)
[Paleotemperatures and Proxy Reconstructions](#)
[Pleistocene Climates](#)
[Pollen Analysis](#)
[Quaternary Climate Transitions and Cycles](#)
[Wisconsinan \(Weichselian, Würm\) Glaciation](#)
[Younger Dryas](#)

BERYLLIUM-10

Beryllium is a lithophile element concentrated in the residual phases of magmatic systems. Due to its special properties as a metal (stiffness, light weight, dimensional stability), it is used in high-tech applications. Several radioactive isotopes exist beside the stable isotope of mass 9. However, only ^7Be and ^{10}Be have half-lives longer than a few seconds (Table B1).

^{10}Be production

^{10}Be is produced almost exclusively by the interaction of galactic cosmic rays with the atmosphere and other matter on the Earth's surface. In the atmosphere, neutron-induced spallation reactions with nitrogen contribute 75% of the total mean global production rate of $0.018 \text{ atoms cm}^{-2} \text{ s}^{-1}$ (Masarik and Beer, 1999). The production rate is variable in space and time. The magnetic fields originating from the Sun and Earth reduce the intensity of the galactic cosmic rays approaching the atmosphere from space.

At the Earth's surface, oxygen is the main target element in matter from which ^{10}Be is produced. The production rate is lower than in the atmosphere due to the attenuation of cosmic rays crossing the atmosphere. It decreases exponentially with increasing depth.

Temporal variability of ^{10}Be production can be caused by:

1. Supernova explosions within our galaxy that are in close proximity to Earth and enhance the galactic cosmic ray flux.
2. Solar wind streaming out of the Sun's coronal holes and affecting the propagation of cosmic ray particles through the heliosphere. High solar activity means strong shielding and low production rate. This effect is latitude dependent (Figure B4).
3. The geomagnetic field preventing cosmic ray particles with too low a rigidity (momentum per charge) entering the Earth's atmosphere.

Figure B5 shows the dependence of the mean global ^{10}Be production rate (in relative units) on solar activity, expressed by the solar activity parameter Φ , and on the geomagnetic dipole field, expressed in units relative to the present field. The range between low production (high solar activity, strong magnetic field) and high production (low solar activity, no geomagnetic field) is almost one order of magnitude.

Other production mechanisms beside spallation, such as neutron activation of ^9Be , are not important and in most cases can be neglected.

The ^{10}Be system

After it is produced in the atmosphere, ^{10}Be becomes attached to aerosols and follows their pathways. Within 1–2 years, ^{10}Be is removed from the atmosphere, mainly by wet precipitation. After deposition, several different processes are responsible for further transport and dispersion of ^{10}Be (McHargue and Damon, 1991). Figure B6 shows a schematic overview of the

main reservoirs and the corresponding ^{10}Be fluxes. The given numbers are still preliminary and to be used with caution.

Some reservoirs have residence times of many centuries or millennia. If ^{10}Be is stored in a reservoir in a stratigraphically undisturbed manner, this reservoir can be considered to be an archive. Provided a time scale is available, archives become the basis for the reconstruction of the history of production and transport of ^{10}Be . In contrast to ^{14}C , which is homogeneously mixed with ^{12}C within the carbon cycle, ^{10}Be and ^9Be are only partly mixed and therefore the isotopic $^{10}\text{Be}/^9\text{Be}$ ratio is only of limited value.

Applications

The range of applications of ^{10}Be depends strongly on the sensitivity of the analytical measuring technique. ^{10}Be was first detected by decay counting in a deep-sea sediment (Arnold, 1956). Due to the long half-life of ^{10}Be , decay counting is not very sensitive. The development of accelerator mass spectrometry (AMS) increased the detection limit by about 6 orders of magnitude, which opened up a large variety of new

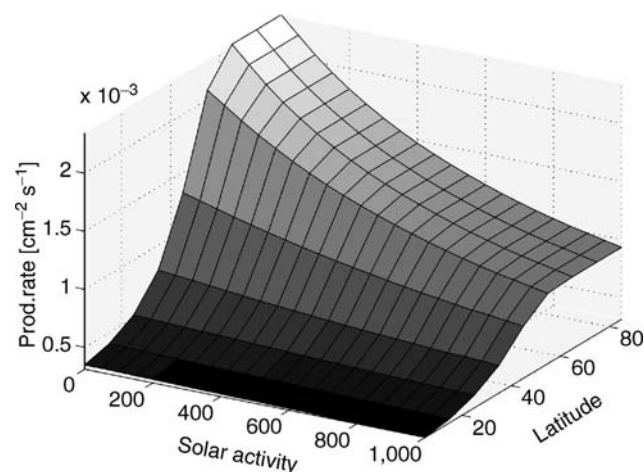


Figure B4 Dependence of the ^{10}Be production rate on latitude and solar activity.

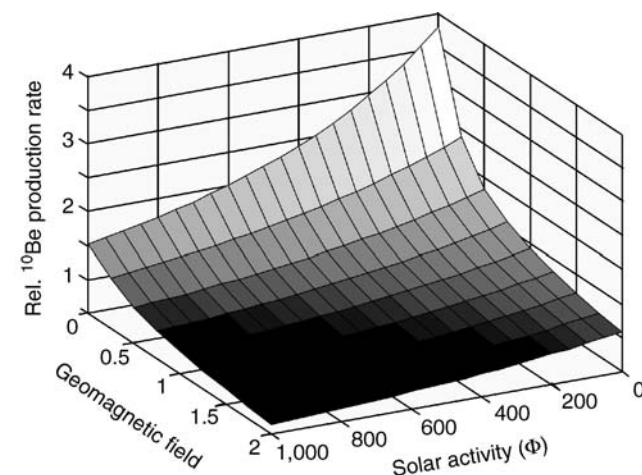


Figure B5 Dependence of the ^{10}Be production rate on solar activity (Φ) and magnetic field strength.

Table B1 Half-lives of ^7Be and ^{10}Be

	$T_{1/2}$	Product
^7Be	53.4 d	^7Li
^{10}Be	$1.51 \pm 0.06 \text{ My}$	^{10}B

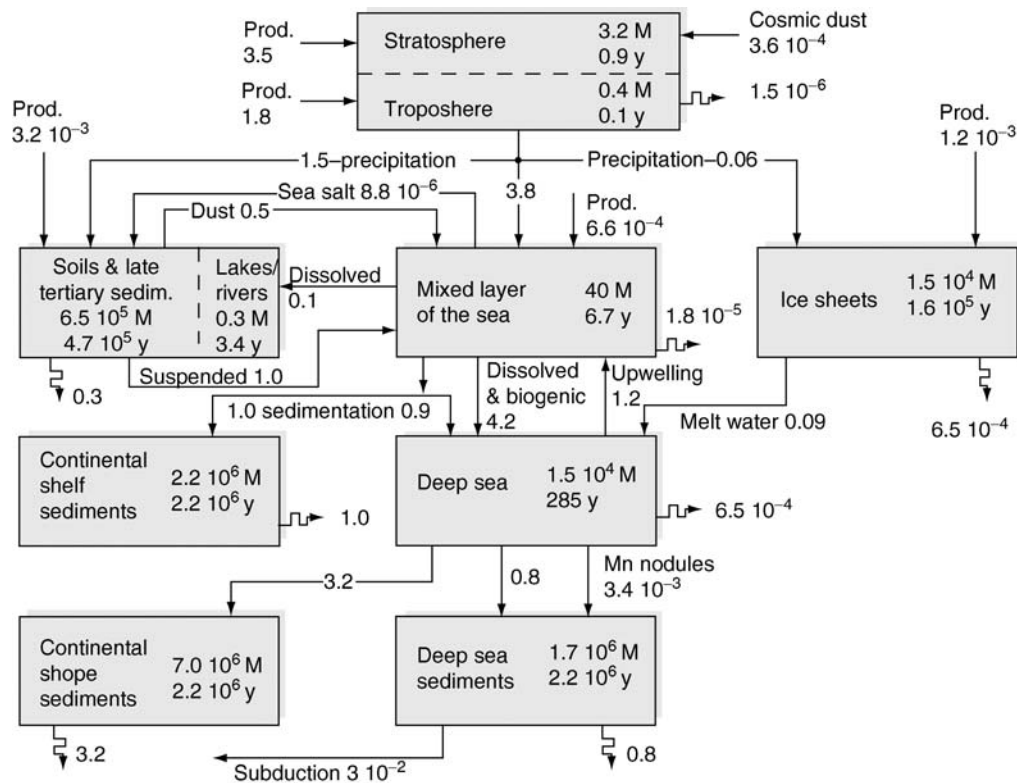


Figure B6 The ^{10}Be system. The inventories of the reservoirs are given in moles and the fluxes between the reservoirs in moles per year. (Modified after McHargue and Damon, 1991).

applications (Lal, 2000). The applications can be divided into three categories, related to production, transport and dating:

Production

All the applications in this category are based on the fact that changes in cosmic ray intensity or in the energy spectrum lead to changes in the production rate of ^{10}Be . So far, no significant fluctuations in the galactic cosmic rays outside the heliosphere have been detected. However, a supernova explosion in our galaxy could significantly increase the cosmic ray intensity.

The solar modulation effect offers the unique opportunity to trace solar activity back in time over many millennia and discover cycles and periods of reduced (e.g., Maunder Minimum) or enhanced activity. Satellite-based measurements show that solar irradiance (solar constant) and solar activity are related. This opens up the possibility of using a ^{10}Be record to estimate the effect of solar variability on the climate and establishing a long-term solar forcing function (Beer et al., 2000).

Using the known relationship between ^{10}Be production rate and the geomagnetic field (Figure B5), the field intensity can be reconstructed. Results from ice cores clearly show magnetic excursions such as the Laschamp event 40,000 years ago. ^{10}Be records from sediments can also be used but are more difficult to interpret.

Transport

All the different processes shown in Figure B6 can potentially be studied using ^{10}Be as a tracer. A short summary of some typical applications is given in the following.

Mixing within the atmosphere and exchange between stratosphere and troposphere occurs on short time scales of weeks to 1–2 years that can be investigated by using the $^{10}\text{Be}/^{7}\text{Be}$ ratio.

^{10}Be deposited on land becomes adsorbed to particles depending on the pH. In arid areas such as deserts, some of the fine dust particles are picked up and transported over long distances to other areas, forming loess deposits. Their accumulation rate can be derived from the total ^{10}Be flux, composed of the eolian and the local atmospheric components. In humid areas, soil erosion removes some of the deposited ^{10}Be . The erosion rate can be derived by analyzing either the total inventory of ^{10}Be or the ^{10}Be depth profile. ^{10}Be transport in aquatic systems occurs in either soluble form or bound to organic matter with too low a density to sediment. The insoluble part of ^{10}Be entering the oceans is finally scavenged into the sediments. The sediment is transported slowly with the oceanic plates, and at the continental margin a small part may become subducted and incorporated into the magma of a volcano.

Dating

An important aspect of ^{10}Be and other radionuclides is dating. There are different ways to use ^{10}Be as a dating tool: (a) characteristic features such as peaks caused by geomagnetic excursions (e.g., Laschamp event, 40,000 BP) or periods of reduced solar activity can be used as time markers to synchronize different records; (b) The decreasing concentration of ^{10}Be with increasing depth in a sediment can be attributed to the radioactive decay, which reveals an age scale; (c) A rock or mineral (e.g., quartz) that is shielded by ice, water or other matter basically contains

no ^{10}Be . If the shielding is removed and the rock is exposed to cosmic rays, ^{10}Be production occurs. From this known production rate and the measured ^{10}Be concentration, the exposure time can be calculated, assuming a certain erosion rate of the rock surface. Combining several different cosmogenic radionuclides enables determination of both the exposure age and the erosion rate (Bierman, 1994).

Jürg Beer

Bibliography

- Arnold, J.R., 1956. Beryllium-10 produced by cosmic rays. *Science*, **124**, 584–585.
- Beer, J., Mende, W., and Stellmacher, R., 2000. The role of the Sun in climate forcing. *Quat. Sci. Rev.*, **19**, 403–415.
- Bierman, P.R., 1994. Using in situ produced cosmogenic isotopes to estimate rates of landscape evolution: A review from the geomorphic perspective. *J. Geophys. Res.*, **99**, 13,885–13,896.
- Lal, D., 2000. Cosmogenic ^{10}Be : A critical view on its widespread domination in geosciences. *Proc. Indian Acad. Sci.*, **109**, 181–186.
- Masarik, J., and Beer, J., 1999. Simulation of particle fluxes and cosmogenic nuclide production in the Earth's atmosphere. *J. Geophys. Res.*, **104**, 12,099–12,111.
- McHargue, L.R., and Damon, P.E., 1991. The global Beryllium 10 cycle. *Rev. Geophys.*, **29**, 141–158.

Cross-references

[Cosmogenic Radionuclides](#)
[Maunder Minimum](#)
[Sun-Climate Connections](#)

BINGE-PURGE CYCLES OF ICE SHEET DYNAMICS

Background

Binge-purge cycles of ice sheets are based on a hypothesis that ice sheets may exhibit short periods of enhanced ice flow (the purge phase) followed by longer spells of much slower flow (the binge phase). This behavior is thought to be controlled by internal ice sheet dynamics and, hence, may occur under stable environmental conditions. The main application of this hypothesis has been to the Laurentide Ice Sheet, which lay across much of North America during the last ice age (e.g., Siebert, 2001).

Binge-purge cycles and the Laurentide ice sheet

Marine sedimentological investigations have revealed a series of ice rafted debris deposits across the North Atlantic, corresponding to the 7,000 year periodic production of huge volumes of icebergs, named Heinrich layers (Heinrich, 1988; Bond et al., 1992). The cause of Heinrich layers is still debated. However, a commonly held view is that they were formed by periodic unstable flow of the Laurentide Ice Sheet during the last glaciation; the so-called “binge-purge” theory (MacAyeal, 1993a, b). The explanation of this theory is as follows (Figure B7). From a relatively stable configuration, the ice sheet slowly builds up over an essentially frozen base (the binge phase). Heat supplied to the ice sheet base is, initially, from geothermal sources, which have a background value of around 50 mW m^{-2} . The ice sheet becomes larger and subglacial temperatures rise as a consequence of: (a) extra insulation from the cold air on the

ice surface and (b) extra heating induced by the deformation of ice, which is proportional to ice thickness to the power 4. The heat supplied through ice deformation to the ice base enhances that from the Earth such that the total heat received at the ice sheet base is significantly greater than the background geothermal value (up to twice as much). Eventually the basal temperatures reach the pressure melting value that initiates rapid basal motion (the purge phase). As the ice base becomes wet, subglacial sliding and the deformation of subglacial sediments can occur, which may contribute even more heat, from friction, to the ice base. For the Laurentide Ice Sheet, during the purge, ice is lost through iceberg calving, and the ice sheet thins as a consequence. Much of the ice is drained through a single outlet, the Hudson Strait, which becomes the focal point for iceberg release to the North Atlantic. The drainage of so much ice depletes the reserves in the parent ice sheet and it becomes thinner. As it does so, heat is lost from the ice sheet base (i.e., the insulating effect of the ice cover is reduced) and, eventually the ice becomes refrozen to the base, at which time the flux of ice to the ice margin is decreased. The end of the purge phase results in the reduction of ice passing into the Hudson Strait and the shutdown of iceberg calving. Once enhanced ice velocities have been curtailed, the cycle of binge-purge is completed, and re-growth occurs as the first stage of the purge phase.

Modeling binge-purge cycles in ice sheets

The binge-purge of an ice sheet (with implication to the Laurentide Ice Sheet) was modeled by MacAyeal (1993a, b) by considering heat conduction within and beneath an ice sheet and initial thermal conditions in accord with atmospheric temperature. The results of the numerical analysis showed that binge-purge oscillations had a cycle of around 7,260 years duration, a remarkably similar periodicity to that measured from IRD in the North Atlantic. The purge (surging) phase was predicted to last for only a short time (around 700 years).

While MacAyeal's model was original, it lacked a detailed analysis of the interplay between ice dynamics and the thermal regime. To solve this, Payne (1995) and Payne and Donglemans (1997) showed how the build-up and decay of ice sheets strongly controls the subglacial thermal regime. Under relatively stable external forcing conditions, an ice sheet may oscillate between periods of ice growth, when the ice is cold-based, and ice decay caused by the attainment of warm-based thermal conditions and the consequent initiation of rapid basal motion. By utilizing a thermo-coupled time-dependent ice sheet model, Payne (1995) highlighted the importance of basal sliding to the oscillatory behavior of ice sheets. In his model, Payne showed how the accumulation rate of ice governed the periodicity of ice sheet oscillations. For low accumulation rates, such as those experienced over the Laurentide Ice Sheet, periods of between 6,000 and 7,000 years were predicted, in support of MacAyeal's earlier work.

Binge-purge cycles and iceberg rafted debris

One problem associated with the notion of binge-purge oscillations being responsible for Heinrich layers is the method of entrainment of material within the ice sheet during the surge phase, when most icebergs are produced. The problem is that a surge-type situation will involve the ice sheet being effectively decoupled from the glacier bed, which may not allow the take-up of material into the basal ice layers. However, Alley and MacAyeal (1994) established a method that allows both

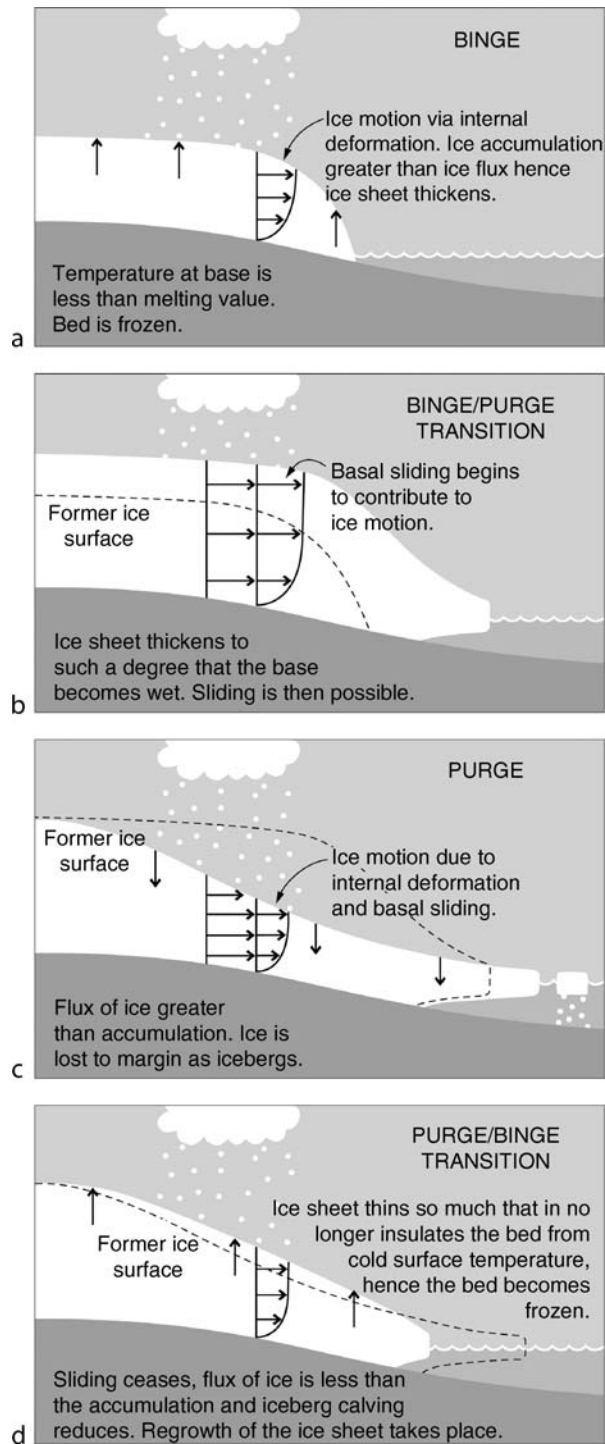


Figure B7 Binge-purge cycles of an ice sheet. (a) The binge phase. Ice sheet growth occurs as a result of ice accumulation exceeding the flux of ice to the margin. Basal temperatures are cold as the only heat supply is from geothermal sources. (b) The binge/purge transition. As ice sheet growth continues, the base of the ice sheet warms due to enhanced heating from ice deformation and extra insulation from the ice above, until a critical threshold is reached at which point the base becomes wet. (c) The purge phase. Once the subglacial conditions are warm, basal sliding takes place (and this supplies more heat to the ice

entrainment and surging to take place, which results in the production of sediment-laden icebergs. The model assumes that the start of the purge phase involves enough frictional heat to melt the ice base, lubricating the sediments and causing them to deform. As this happens, however, the ice stream begins to thin, which results in colder temperatures at the ice base and so water and sediment freeze onto the base of the ice stream. Beneath the refrozen basal ice the sediment is still warm and water-saturated, however, and so the ice stream remains active and fast flowing. When all the water-soaked sediment has frozen onto the ice stream base it becomes “cold-based” and the purge phase ends. This soft-bed model produces, in theory, a volume of sediment within the ice sheet that is larger than required to account for the Heinrich layers. However, a hard-bed model would produce far less. So, the presence of both hard and soft bed conditions would seem to make the model fit the measurements. Although this model remains unproven, Alley and MacAyeal (1994) suggest a number of good reasons as to why alternative entrainment mechanisms are less likely. For example, if the process of sediment entrainment was through ice-tectonics such as folding and cavitation, a rate of uptake of material far in excess of that calculated and measured in modern ice sheets and glaciers would be required to form the Heinrich layers. Further, a pressure-induced basal freezing process results in 2 orders of magnitude less sediment than is required. Therefore, the soft-bed freezing model appears a likely mechanism to explain the incorporation of material into the ice sheet during the latter period of the binge-purge cycle.

Dowdeswell et al. (1995) revealed that the thickness distributions of Heinrich layers one and two (at 14.5 ka and 21.1 ka) are similar. This similarity suggests that the volume and size of icebergs responsible for their formation, the proportion of sediment within these icebergs and the ocean currents were similar on both occasions. In addition, Dowdeswell et al. (1999) showed that there appeared to be a lack of correlation between Heinrich events and IRD features from the Fennoscandian Ice Sheet. This suggests that the cause of Heinrich events was particular to the Laurentide Ice Sheet, which reduces the likelihood of a climate-induced mechanism that would affect all ice sheets in the Northern Hemisphere. Thus, there seems to be a balance of sedimentary data in support of the oscillatory binge-purge internal ice sheet dynamics mechanism for Heinrich layers. Indeed, MacAyeal (1993a) demonstrated through numerical modeling that climate-induced changes would not result in periodic ice sheet variations as temperature perturbations are attenuated with depth in an ice sheet.

Binge-purge cycles and climate change

Although MacAyeal (1993a) showed it unlikely that Heinrich layers are caused by climate change, he also predicted that the product of the Laurentide Ice Sheet binge-purge cycle, namely a huge release of icebergs to the North Atlantic, would have forced climate change. MacAyeal (1993b) calculated that an ice sheet with a surface area of 10,000,000 km² would

base), which leads to more ice transported to the margin than is replaced by falling snow and, hence, the ice sheet thins. (d) The purge/binge transition. As the ice sheet thins, the insulation effect of the ice diminishes and the base becomes cold. Once freezing conditions are reintroduced, sliding is no longer possible and the purge phase ends. As the accumulation of ice is once again greater than the flux of ice, the ice sheet begins to thicken and the binge phase begins again.

produce about 1,250,000 km³ of icebergs. As these icebergs melted, the freshwater produced may have been large enough to slow the thermohaline-driven ocean-circulation. Thus, heat transport northward from the mid-Atlantic would have been reduced, lowering ocean and air temperatures in the North Atlantic and surrounding regions.

The interplay between ice dynamics and ice-sheet thermal regime, as hypothesized for the Laurentide Ice Sheet, is relevant to contemporary ice masses. In particular, the possibility that ice sheets can undergo rapid change as a consequence of their interior dynamics rather than through external forcing has caused some to speculate about the stability of the West Antarctic Ice Sheet.

Martin J. Siegert

Bibliography

- Alley, R.B., and MacAyeal, D., 1994. Ice-rafted debris associated with binge/purge oscillations of the Laurentide Ice Sheet. *Paleoceanography*, **9**, 503–511.
- Bond, G., Heinrich, H., Broecker, W., Labeyrie, L., McManus, J., Andrews, J., Huon, S., Jantschik, R., Clasen, S., Simec, C., Tedesco, K., Klas, M., Bonani, G., and Ivy, S., 1992. Evidence for massive discharges of icebergs into the North Atlantic ocean during the last glacial period. *Nature*, **360**, 245–249.
- Dowdeswell, J.A., Maslin, M.A., Andrews, J.T., and McCave, I.N., 1995. Iceberg production, debris rafting and extent and thickness of Heinrich layers (H-1, H-2) in North Atlantic sediments. *Geology*, **23**, 301–304.
- Dowdeswell, J.A., Elverhøi, A., Andrews, J.T., and Hebbeln, D., 1999. Asynchronous deposition of ice-rafted layers in the Nordic seas and North Atlantic Ocean. *Nature*, **400**, 348–351.
- Heinrich, H., 1988. Origin and consequences of cyclic ice rafting in the Northeast Atlantic Ocean during the past 130,000 years. *Quat. Res.*, **29**, 143–152.
- MacAyeal, D.R., 1993a. A low-order model of the Heinrich event cycle. *Paleoceanography*, **8**, 767–773.
- MacAyeal, D.R., 1993b. Binge-purge oscillations of the Laurentide Ice Sheet as a cause of the North Atlantic's Heinrich events. *Paleoceanography*, **8**, 775–784.
- Payne, A.J., 1995. Limit cycles and the basal thermal regime of ice sheets. *J. Geophys. Res.*, **100**, 4249–4263.
- Payne, A.J., and Dongelmans, P.W., 1997. Self organisation in the thermo-mechanical flow of ice sheets. *J. Geophys. Res.*, **102**, 12,219–12,234.
- Siegert, M.J., 2001. *Ice Sheets and Late Quaternary Environmental Change*. New York: Wiley, 231pp.

Cross-references

Basal Ice
 Glaciations, Quaternary
 Heinrich Events
 Ice-Rafted Debris (IRD)
 Laurentide Ice Sheet

BOLIDE IMPACTS AND CLIMATE

The coincidence of a large asteroid or comet (bolide) impact with the mass extinction of life that occurred at the Cretaceous/Tertiary (K/T) boundary (65 million years ago) suggests that the extinctions were caused by climatic and environmental changes triggered by the impact event (Alvarez et al., 1980; Toon et al., 1997). A number of possible mechanisms of impact-induced climatic change have been proposed, including the direct effects of: atmospheric dust produced by the impact;

soot from wildfires triggered by the initial blast and by ejecta re-entering the atmosphere; water vapor injected into the upper atmosphere by oceanic impacts; the creation of NO and HNO₃ acid rain; sulfuric acid aerosols derived from anhydrite deposits in the target rocks; and carbon dioxide released from limestone in the target. Indirect effects on climate could come from major perturbations of the global carbon and sulfur cycles generated by the mass extinctions, and related ecological perturbations (Rampino, 1995; Toon et al., 1997).

Effects of a global dust cloud

Alvarez et al. (1980) originally suggested that the large amount of fine ejecta distributed worldwide by the K/T boundary impact would have created a dense global atmospheric dust cloud. They proposed that the darkness and short-term surface cooling beneath such a cloud led to cessation of photosynthesis and frigid conditions (impact winter), resulting in the observed mass extinctions. Calculations and experiments suggest that even a few months of such darkness would have been sufficient to produce the severe extinction seen among photosynthetic plankton at the K/T boundary. This would have led to a collapse of marine and terrestrial food chains.

The energy release of a 10 km diameter asteroid (such as the object that hit the Earth 65 million years ago) traveling at about 20 km s⁻¹ is estimated to be equivalent to the explosion of 10⁸ Mt of TNT. In such an impact, it is estimated that more than 10¹⁹ g of excavated rock and vaporized asteroid could be lofted to high altitude. Most of the ejecta would be in the form of relatively large particles (0.1–1 mm in diameter) with an atmospheric residence time of a few hours to a few days. Toon et al. (1997) calculated that a mass equal to about 30% of the bolide mass (0.1% of the pulverized ejecta) reaches the stratosphere as sub-micron dust with a residence time of a few months. For a 10¹⁸ g impactor, this atmospheric dust load, roughly equal to about 3 × 10¹⁶ g, would produce a very high atmospheric optical depth of up to 10³–10⁴, and consequent reduced atmospheric transmission of solar radiation. Impacts with energies greater than 5 × 10⁶ Mt would lower light levels below those required for photosynthesis, and impacts larger than 10⁷ Mt could lead to light levels well below those needed for human vision (Figure B8).

Study of the climatic effects of a dense impact dust cloud using a one-dimensional model of aerosol physics and a one-dimensional radiative/convective climate model suggested that light levels would have remained too low for visibility for up to 6 months, and too low for photosynthesis for up to 1 year after the impact. Calculations of surface cooling showed decreases in continental temperatures to below freezing for up to 2 years, whereas ocean-surface temperatures fell only a few degrees C (Figure B9; Toon et al., 1997).

Possible changes in atmospheric thermal structure were also investigated. In normal conditions, solar energy is absorbed by the ground, and the infrared emission back to space comes largely from the upper troposphere. At times of heavy dust loading, however, both the level of solar energy deposition and the infrared emission level of the atmosphere are controlled by the dust, and both lie within the stratosphere. Earth's surface no longer receives any solar radiation, and has a net energy deficit. Under these conditions, one-dimensional models predict land-surface temperature decreases of about 30 °C in the first 1–2 months after impact of a 10 km diameter body (Figure B9).

Covey et al. (1994) utilized a more sophisticated three-dimensional global climate model (GCM) to study the effects

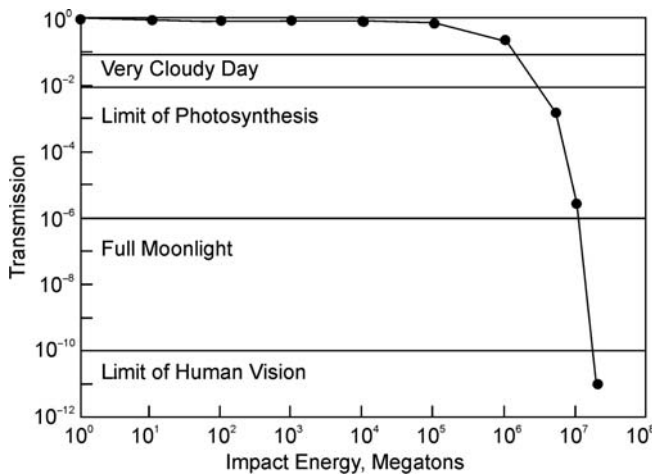


Figure B8 Estimate of the reduction in light transmission through the atmosphere as a result of submicron dust in clouds from impacts of various sizes (in megatons of TNT equivalent) (after Toon et al., 1997).

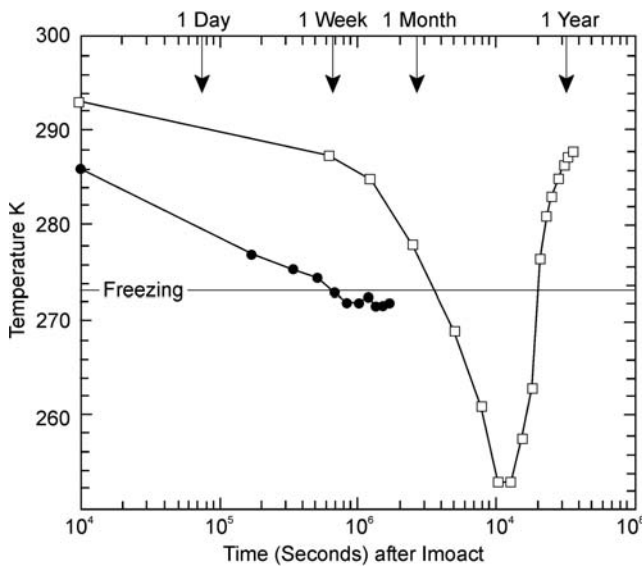


Figure B9 Estimates of the global cooling resulting from the fine dust produced by the impact of a 10 km diameter asteroid using the 1-D radiative convective model (*open squares*) of Toon et al. (1997) and the 3-D Global Climate Model (*filled diamonds*) of Covey et al. (1994).

of an impact-induced global dust cloud on climate. For a dust-loading equivalent to an optical depth (τ) of 10^4 (decaying to $\tau = 1$ after 400 days) after a 10 km diameter impact (in May of the model year), land-surface temperatures fell below freezing in less than a week (decreases of about 15°C), with partial recovery as summer approached in the Northern Hemisphere (Figure B9). Significant cooling was maintained for a year despite the gradual removal of the dust. Land-surface cooling was somewhat mitigated by the heat capacity of the oceans, and by atmospheric circulation patterns (created by the dust cloud) that transported additional heat from the oceans to land areas. In this simulation, however, fixed sea-surface temperatures somewhat exaggerated the oceanic heat reservoir.

GCM studies also suggest an almost complete collapse of the global hydrologic cycle after the modeled impact, with world-wide drought. The GCM model results indicated that impacts of smaller objects (approximately 1 km diameter asteroids or 10^6 Mt impacts) could cause less severe, but still quite significant drops in temperature (about 5°C) over the continents within 20 days of impact. Such rapid and severe decreases in temperatures could have devastated global vegetation.

By contrast, Pope (2002) proposed that most of the globally distributed ejecta from the K/T event were deposited as condensation droplets from the impact vapor plume. He estimated that less than 10^{12} kg of the distal ejecta was sub-micrometer dust. This smaller amount of dust would be insufficient by 2 or 3 orders of magnitude to cause a shutdown of photosynthesis, and would have had much smaller climatic effects (but see Kring and Durda, 2002).

Effects of injection of water vapor into the atmosphere

In the case of an oceanic impact, water would probably comprise a significant fraction of the ejecta lofted to high altitudes. For a 10 km impactor hitting the ocean, it is estimated that the expansion of the impact-related steam bubble would drive a plume of mixed impactor vapor, debris, and water vapor more than a hundred kilometers above Earth's surface. Condensation of the cloud of water vapor and meteoroid vapor could produce a combination of dust and ice particles in the upper atmosphere. McKay and Thomas (1982) considered the consequences of enhanced water vapor concentrations on the middle atmosphere (50–100 km) chemistry and heat budget. They estimated that the increased mixing ratio of hydrogen would have caused a decrease in ozone concentration above 60 km. The ozone reduction would lead to a lowering of the average height of the mesopause, and lowering of average temperature. These conditions were predicted to produce a long-lived (possibly 10^5 – 10^6 years) global layer of mesospheric ice clouds.

An increase in global albedo of up to several percent was predicted, but the net climatic effect (cooling or warming) would depend upon how much infrared radiation from below is also trapped by the clouds. This is a function of the mean size of the ice crystals in the clouds. The size of the dust and ice grains produced in the atmosphere is also critical to the mean lifetime of the dust and ice clouds – if the grains are large, rapid fallout would occur, and long-term darkness and climatic effects would be less likely. A measure of the initial grain-size distribution of material in the K/T boundary fallout layer would help in constraining these effects.

The water vapor would have locally supersaturated the stratosphere, and thus much of the vapor might have rapidly re-condensed and precipitated out of the atmosphere. If the coagulation time of the water vapor was similar to that of the dust as calculated by Toon et al. (1997), then most of the water would have left the atmosphere within weeks to months. However, during this time, an enhanced greenhouse effect and reduction of stratospheric ozone could have caused sudden global heating. A permanent increase in stratospheric water vapor by a factor of 25 would lead to an 8°C increase in average global surface temperatures.

Effects of the formation of NO_x and acid rain

The shock waves from the K/T impact and the transfer of energy from the fine ejecta to the atmosphere ($\sim 40\%$ of the energy transferred to the atmosphere) would have heated the

global atmosphere. Calculations suggest that, for a large 10^7 – 10^8 Mt impact, this could have produced an immediate heat pulse with a global average temperature increase of $\geq 15^\circ\text{C}$, and ocean-surface temperature increases of about 5°C (Toon et al., 1997).

The high-temperature shock waves produced by the passage of the impactor through the atmosphere and interaction of the high velocity plume of ejecta with the atmosphere could have created large amounts of NO (Toon et al., 1997), estimated to be as high as 3×10^{17} mol of NO, corresponding to $>0.2\%$ NO by volume. This amount of NO_x is enough to poison plants and animals, but it could have also produced destructive nitric acid rain with a pH of about 1. About 3×10^{14} mol of HNO_3 could lower the pH of ocean surface water sufficiently to dissolve calcite.

The large amount of fixed nitrogen deposited on Earth's surface after an impact might have denitrified to produce N_2O and NO. Smog reactions, involving the oxidation of CH_4 produced by anaerobically decaying organic matter, might then have led to significant amounts of ozone in the troposphere. Production of N_2O (along with CO_2 , HNO_3 and CH_4) could have resulted in an enhanced greenhouse effect over the approximately 150-year lifetime of N_2O in the atmosphere. The N_2O could have also interacted with the stratospheric ozone layer, depleting it within a decade.

In other studies, a much smaller total NO production (about 10^{14} mol) from a 10 km diameter impactor (10^8 Mt) was calculated. In these models, most of the global NO production came not from the initial shock wave or plume, but from the dispersed ejecta re-entering Earth's atmosphere.

According to some calculations, larger yields of NO would accompany only relatively rare grazing impacts. Oblique impact of a 10 km object with a velocity of 20 km s^{-1} , impacting at 10° to the horizontal, could ricochet many 0.1–1 km fragments at hypervelocity, producing a global swarm of Tunguska-scale events. Nitrate production from such a swarm could greatly exceed that of a single vertical impactor. Energy partitioned to the target apparently increases for impact angles between 45° and 15° , increasing the ability of the impact to vaporize potentially volatile targets.

Effects of global wildfires

The immediate creation of a large, heated mass of low-density air with peak temperatures of more than 20,000 K at the impact site and the intense heat emitted globally by impact ejecta re-entering the atmosphere are calculated to ignite combustible material and to create widespread wildfires (Melosh et al., 1990). Vegetation killed by the lack of sunlight and the abrupt cooling would have provided abundant fuel for the wildfires.

Large amounts of soot were discovered at the K/T boundary (estimated at $>5 \times 10^{16}$ g worldwide), which supports the burning of a significant fraction of the terrestrial biomass (Wolbach et al., 1988). This amount of soot in the atmosphere would have yielded a soot optical depth of about 10^3 , capable of causing climatic effects similar to those of the fine dust produced by the impact. The soot produced by the fires would have added to the opacity of the atmosphere, exacerbating the scenario of darkness and cooling following an impact.

Calculations suggest that such forest fires could have produced more than 10^{19} g of CO_2 , 10^{18} g of CO, 10^{17} g of CH_4 , and 10^{16} g of N_2O , in addition to reactive hydrocarbons and

oxides of nitrogen ($\text{NO} + \text{NO}_2$). This might have led to an intense photochemical smog, and a short-term increase in the greenhouse effect estimated to produce a global warming of roughly 10°C (Toon et al., 1997).

Effects of impacts on targets containing carbonates or sulfates

The target material of the impact can be important in terms of climatic impact. For example, impact of a 10 km diameter asteroid into thick carbonate deposits (like those at the Chicxulub Crater) might have released 10^3 – 10^4 Gigatons (10^{12} tons) of CO_2 that could have increased atmospheric carbon dioxide levels by factors of 2–10. This increase in CO_2 could have caused a rise in global temperatures of about 2 – 8°C , for 10^4 – 10^5 years after the impact.

The K/T impact site at Chicxulub was also underlain by thick Cretaceous evaporites including anhydrite (CaSO_4), and some K/T impact glasses are rich in calcium and contain up to 1 wt% SO_3 . Estimates of the increase in atmospheric SO_2 derived from degassing of deposits of anhydrite at the impact site range from about 10^{17} – 10^{19} g (independent of the sulfur released by the asteroid itself; Pierazzo et al., 1998). This can be compared with the 10^{13} g of SO_2 produced by the 1991 Pinatubo eruption or the 10^{15} g of SO_2 released by the Toba eruption (73,000 years ago), the largest volcanic eruption of the last few hundred thousand years. The formation of sulfuric acid aerosols from the large release of SO_2 by the Chicxulub impact would have sufficed to cause significant reduction of sunlight and global cooling after the dissipation of the short-lived dust/soot cloud. Estimates of cooling range from 5 to 31°C for as long as a decade, and even longer if ocean-temperature feedbacks come into play. The sulfuric acid fallout could have equaled or exceeded that proposed for the nitric acid produced by the impact.

Climatic changes from perturbations of biogeochemical cycles

The K/T boundary is marked by a major perturbation of the global carbon cycle, including severe reduction in pelagic carbonate deposition, decrease in biomass and oceanic productivity, and changes in organic carbon deposition (Kasting et al., 1986; Caldeira and Rampino, 1993). The primary source of alkalinity (excess positive charge) to the oceans is dissolved Ca and Mg derived from the chemical weathering of carbonate and silicate rocks. The two major sinks for alkalinity and carbon in the oceans are the deposition of shallow-water carbonate sediments, and the accumulation of deep-water carbonates derived from the calcareous tests of pelagic plankton.

A major disruption of the pelagic alkalinity and carbon sinks may have occurred in the aftermath of the mass extinction, with reduction in populations of calcareous plankton at the K/T boundary. The reduction of ocean primary productivity – the so-called “Strangelove Ocean” interval – lasted perhaps as long as 500,000 years (Caldeira and Rampino, 1993).

Kasting et al. (1986) performed model calculations with a two-box ocean model of the carbon-cycle perturbations that might accompany a large impact. They investigated the suggestion that an impact event would cause ocean surface waters to become under-saturated with respect to calcium carbonate, and hence lead to the extinction of calcareous organisms. This situation could also delay the recovery of calcareous plankton during the Strangelove Ocean period.

Global darkening could have killed off most of the existing phytoplankton within several weeks to months, while deposition of atmospheric NO_x created in the impact would have lowered the pH of ocean surface waters and released CO₂ into the atmosphere. However, model results indicated that mixing would have limited acidification of ocean surface waters to about 20 years or less. Kasting et al. (1986) also looked at the direct input of atmospheric CO₂ from a comet or from oxidation of terrestrial and marine organic matter. The net results might have been a greenhouse effect raising temperatures by several degrees, and perhaps a surface ocean uninhabitable by calcareous organisms for a couple of decades, but the model runs also suggested that the surface waters would not have remained corrosive for long, and thus could not have led to the Strangelove Ocean conditions of decreased carbonate productivity.

DMS reduction and climatic warming

Marine phytoplankton release dimethyl sulfide (DMS) gas, which oxidizes to form sulfuric acid aerosol that is the precursor for cloud condensation nuclei (CCN) over the oceans. The extinction of most marine calcareous phytoplankton at the K/T boundary would have drastically reduced output of DMS, and thus CCN and marine cloud coverage. Reduction of global cloud albedo would have led to a rapid warming of the global climate.

Rampino and Volk (1988) used model results that showed the effect of variations in CCN number density upon cloud albedo and climate. For a DMS reduction of ~80%, global temperature was predicted to rise by more than 6°C, and by nearly 10°C when the DMS was reduced by 90%. Even a 50% reduction in DMS should have produced a significant global warming of 3–4°C. The thermal mass and mixing structure of the ocean could have delayed the full surface warming by several 1,000 years.

Climate changes at the K/T boundary

Since many of the theoretical studies of impact processes predict significant climatic changes, it is worthwhile to ask if any clear evidence of such climate changes can be discerned in paleoclimatic data from the K/T boundary. For most paleoclimatic records, a brief “impact winter” would be impossible to resolve with present techniques. Paleobotanical evidence from western North America, however, has been interpreted by Wolfe (1991) as indicating a brief summer freeze (a temperature decrease of 25–30°C for less than 2 months). Leaf studies from the same area suggested a marked longer-term increase in temperature of 10°C that persisted for 500,000–1 million years after the impact (Wolfe, 1990).

Paleotemperatures based on oxygen-isotope studies suggest a very brief cooling at the K/T boundary, followed by a warming that lasted at least a few 1,000 years. Several analyses suggest a possible dramatic warming of ocean surface waters by as much as 10–12°C and bottom waters by 5°C. By contrast, some oxygen-isotope studies have reported “cold snaps” in the aftermath of the K/T impact event with 4–5°C regional coolings lasting from 5,000 to 10,000 years. These apparent climatic fluctuations following the K-T extinction event suggest that the paleotemperature data are unreliable, or that there was a basic instability in the post-impact climate regime (Rampino, 1995).

Galeotti et al. (2004) presented records of dinoflagellate cysts and benthic foraminifera across the K/T boundary at

El Kef, Tunisia. These records show a brief 20,000–40,000 year expansion of species from the Boreal Bio Province into the warmer western Tethys. This could have been caused by the formation of a large volume of cold surface waters during the K/T impact winter that later sank into the deeper ocean. Ocean-atmosphere modeling experiments provide support for such a prolonged cooling phase from the formation of a mass of cold sinking water.

Climate changes at times of other impacts

Little information exists as to climatic changes related to other known and well-dated Phanerozoic impacts (Rampino and Haggety, 1994), although these were all smaller in size than the Chicxulub event. The late Eocene Chesapeake Bay (90 km diameter) and Popigai (100 km diameter) impact craters (~35.7 million years ago) are probably related to a comet shower that lasted about 2.5 million years (Farley et al., 1998). This interval is marked by stepwise extinction of planktonic foraminifera (Hut et al., 1987), and a shift in species assemblage of calcareous nannoplankton (Monechi et al., 2000). In the well-studied Massignano Section in Italy, the iridium anomaly and shocked quartz most likely associated with the Popigai impact seem to be followed by a warming episode and a subsequent slight cooling episode that occurred about 60,000 years after the impact event (Coccioni et al., 2000). The relatively long duration of the environmental perturbation that followed the impact event(s) suggests feedback mechanisms that sustained the initial impact induced changes. The impacts may have accelerated global cooling (Vonhof et al., 2000). The major cooling and period of ice growth in the earliest Oligocene, however, followed the impacts/comet shower by about 2 million years.

Very little additional data exists as to the effects of impacts on climate. A possible impact shower in the Late Devonian that produced several layers of glassy microtektites (in Belgium and China) may be associated with a global climate cooling (see Rampino, 1995), but a cause-and-effect relationship is not clear.

Michael R. Rampino

Bibliography

- Alvarez, L.W., Alvarez, W., Asaro, F., and Michel, H.V., 1980. Extraterrestrial cause for the Cretaceous-Tertiary extinction. *Science*, **208**, 1095–1108.
- Caldeira, K., and Rampino, M.R., 1993. The aftermath of the end-Cretaceous mass extinction: Biogeochemical stabilization of the carbon cycle and climate? *Paleoceanography*, **8**, 515–525.
- Coccioni, R., Basso, D., Brinkhuis, H., Galeotti, S., Gardin, S., Monechi, S., and Spezzaferri, S., 2000. Marine biotic signals across a late Eocene impact layer at Massignano, Italy: Evidence for long-term environmental perturbations. *Terra Nova*, **12**, 258–263.
- Covey, C., Thompson, S.L., Weissman, P.R., and MacCracken, M.C., 1994. Global climatic effects of atmospheric dust from an asteroid or comet impact on Earth. *Glob. Planet. Change*, **9**, 263–273.
- Farley, K.A., Montanari, A., Shoemaker, E.M., and Shoemaker, C.S., 1998. Geochemical evidence for a comet shower in the late Eocene. *Science*, **280**, 1250–1253.
- Galeotti, S., Brinkhuis, H., and Huber, M., 2004. Records of post-Cretaceous-Tertiary boundary millennial-scale cooling from the western Tethys: A smoking gun for the impact winter hypothesis. *Geology*, **32**, 529–532.
- Hut, P., Alvarez, W., Elder, W.P., Hansen, T., Kauffman, E.G., Keller, G., Shoemaker, E.M., and Weissman, P.R., 1987. Comet showers as a cause of mass extinctions. *Nature*, **329**, 118–126.

- Kasting, J.F., Richardson, S.M., Pollack, J.B., and Toon, O.B., 1986. A hybrid model of the CO₂ geochemical cycle and its application to large impact events. *Am. J. Sci.*, **286**, 361–389.
- Kring, D.A., and Durda, D.D., 2002. Trajectories and distribution of material ejected from Chicxulub impact crater: Implications for postimpact wildfires. *J. Geophys. Res.*, **107**, 6-1–6-22.
- McKay, C.P., and Thomas, G.E., 1982. Formation of noctilucent clouds by an extraterrestrial impact. *Geol. Soc. Am. Spec. Pap.*, **190**, 211–214.
- Melosh, H.J., Schneider, N.M., Zahnle, K.J., and Latham, D., 1990. Ignition of global wildfires at the Cretaceous/Tertiary boundary. *Nature*, **343**, 251–254.
- Monechi, S., Bucciati, A., and Gardin, S., 2000. Biotic signals from nanoflora across the iridium anomaly in the upper Eocene of the Massignano section: Evidence from statistical analysis. *Mar. Micropaleontol.*, **39**, 219–237.
- Pierazzo, E., Kring, D.A., and Melosh, H.J., 1998. Hydrocode simulation of the Chicxulub impact event and the production of climatically active gases. *J. Geophys. Res.*, **103**, 28,607–28,625.
- Pope, K.O., 2002. Impact dust not the cause of the Cretaceous-Tertiary mass extinction. *Geology*, **30**, 99–102.
- Rampino, M.R., 1995. Catastrophe: impact of comets and asteroids. In Henderson-Sellers, A. (ed.), *Future Climates of the World: A Modeling Perspective, World Survey of Climatology*, vol. 16. Amsterdam: Elsevier, pp. 95–147.
- Rampino, M.R., and Haggerty, B.M., 1994. Extraterrestrial impacts and mass extinctions of life. In Gehrels, T. (ed.), *Hazards Due to Comets and Asteroids*. Tucson: University of Arizona Press, pp. 827–857.
- Rampino, M. R., and Volk, T., 1988. Mass extinctions, atmospheric sulphur and climatic warming at the K/T boundary. *Nature*, **332**.
- Toon, O.B., et al., 1997. Environmental perturbations caused by the impacts of asteroid and comets. *Rev. Geophys.*, **35**, 41–78.
- Vonhof, H.B., Smit, J., Brinkhuis, H., Montanari, A., and Nederbragt, A.J., 2000. Global cooling accelerated by early late Eocene impacts. *Geology*, **28**, 687–690.
- Wolbach, W.S., Gilmour, I., Anders, E., Orth, C.J., and Brooks, R.R., 1988. Global fire at the Cretaceous-Tertiary boundary. *Nature*, **334**, 670.
- Wolfe, J.A., 1990. Palaeobotanical evidence for a marked temperature increase following the Cretaceous/Tertiary boundary. *Nature*, **343**, 153–156.
- Wolfe, J.A., 1991. Palaeobotanical evidence for a June “impact winter” at the Cretaceous/Tertiary boundary. *Nature*, **352**, 420–423.

Cross-references

- Albedo Feedbacks
 Cretaceous/Tertiary (K/T) Boundary Impact, Climate Effects
 Paleoclimate Modeling, Pre-Quaternary
 Paleoclimate Modeling, Quaternary

BØLLING-ALLERØD INTERSTADIAL

Introduction

The Bølling-Allerød interstadial is the initial warm phase during the Weichselian late glacial that is followed by the cold Younger Dryas stadial.

The Weichselian late glacial, often referred to as *last glacial-interglacial transition* or *last termination* (ca. 13,000–10,000 ¹⁴C yr BP), was a period of rapid climate change. The late glacial is classically sub-divided into a series of stadials named after the occurrence of the characteristic arctic-alpine plant species *Dryas octopetala*, separated by interstadials named after the type localities Bølling and Allerød in Denmark. The biostratigraphic sub-division has been extensively used in north-west Europe, usually in a chronostratigraphic sense, and is still widely used globally.

History

Hartz and Milthers (1901) showed that, based on deposits in a clay-pit near Allerød (Denmark), a climatic warming had occurred during the late glacial. Between clay layers containing mountain avens (*Dryas octopetala*) and reindeer fossils, an organic layer containing birch (*Betula*) and elk fossils was present, indicating a change from tundra to a more forested environment followed by a return to tundra. Based on palynology, Jessen (1935) was able to define three subsequent pollen zones: Early Dryas (I), Allerød (II), and Late Dryas (III). This subdivision was further refined by Iversen (1942), who added another interstadial phase that supposedly occurred before the Allerød and was first described in Bølling Sø (Denmark).

The palynological sub-division of the Weichselian late glacial established by Jessen (1935) and Iversen (1942) was introduced into The Netherlands by van der Hammen, who recognized the Bølling and Allerød oscillations, separated by the Dryas stadials in a site named Hijkermeer. The interstadial deposits were characterized by a higher content of organics in comparison with the stadial deposits. Van der Hammen (1951) went on to demonstrate a similar vegetation development at different locations in The Netherlands. Since then, hundreds of pollen diagrams from late glacial deposits have been constructed using van der Hammen's scheme (Hoek, 1997).

Bio- and chronostratigraphy

Unfortunately, the boundaries of similar biostratigraphical zones defined in different regions are in most cases diachronous due to differences in vegetation response to changes in climate. This makes the use of the biostratigraphic zones defined in Scandinavia problematic outside this region. Furthermore, there are problems that can be regarded as inconsistencies in biostratigraphic definition. In northwestern Germany especially, an additional interstadial called Meiendorf is recognized, which correlates with the Bølling interstadial, while the term Bølling is used for the first part of the Allerød interstadial (Litt and Stebich, 1999). The discrepancy between the definition of Bølling and Allerød is mainly the result of a difference of opinion about the correlation with the section at Bølling Sø, first studied by Iversen (1942). In Britain, it is often difficult to recognize stadial conditions separating the individual interstadial phases (Lowe and Gray, 1980). Terms such as late glacial interstadial or Windermere interstadial have been used for the Bølling-Allerød interstadial complex. These examples all point towards the problems of transferring the biostratigraphic zonation scheme from one region to another. A detailed discussion regarding this issue is presented by de Klerk (2004).

With the introduction of the radiocarbon dating method, biostratigraphic correlation became less important and pollen diagrams were considered more frequently in a chronological context. Moreover, the terminology that was originally developed for biostratigraphical zones (Bølling, Allerød, etc.) has been used in a chronostratigraphic sense (Mangerud et al., 1974). Since then, the terms Bølling and Allerød have been connected worldwide to the time period between 13,000 and 11,000 yr BP, as defined by Mangerud et al. (1974). This chronological definition was, however, initially based on the radiocarbon-dated biostratigraphic zone boundaries from southern Scandinavia. Above this, the Mangerud et al. (1974) scheme has been constructed using bulk radiocarbon dates and was constructed when reservoir ages and radiocarbon-plateaux were not yet known (Wohlfarth, 1996). If the chronostratigraphic scheme is compared to the ¹⁴C-dated

biostratigraphy in The Netherlands, for instance, which is based on over 250 dates (Hoek, 1997), all zone boundaries appear to have different ages. The most striking differences can be seen in the ages for the start of the Bølling biozone or chronozone (Table B2).

Climate changes during the Bølling-Allerød interstadial

Although lithological and botanical evidence shows that strong environmental changes occurred during the late glacial period, it is ambiguous to translate these signals directly into climate. The AP (arboreal pollen) percentage was long considered as a temperature proxy. Based on the palynological records, in which the AP percentage increased during the course of the Bølling-Allerød interstadial, it was concluded that the warmest part of the late glacial fell towards the end of the Allerød interstadial, just before the Younger Dryas stadial.

It appears that this classical interpretation of late glacial vegetation and climate development leads to a different picture than

the records obtained from, for instance, the Greenland ice cores (Johnsen et al., 1992; Grootes et al., 1993) and Coleoptera studies (Atkinson et al., 1987; Coope et al., 1998). Both oxygen isotopes and fossil Coleoptera are considered to reflect changes in temperature almost instantaneously, while vegetation responds more slowly, due to migration lags in particular. Temperature reconstructions based on isotopes and Coleoptera reach their highest values early in the late glacial. This implies that the warmest phase must have occurred during the Bølling, followed by a step-wise cooling during the Allerød (Figure B10).

Recent developments

Stuiver et al. (1995) presented a comparison between European pollen zone boundaries and the GISP2 $\delta^{18}O$ climate transitions, but only at a low resolution. It is apparent from these and from other data that the use of different timescales has impeded more precise correlation between ice core and terrestrial records.

Table B2 Chronostratigraphy of the late glacial based on ^{14}C dated biozone-boundaries in The Netherlands (after Hoek, 1997) compared with the classical Stratigraphy of Norden by Mangerud et al. (1974)

The Netherlands		Stratigraphy of Norden	
^{14}C age BP	biozone	chronozone	^{14}C age BP
	HOLOCENE	FLANDRIAN	
10,150	Late Dryas	Younger Dryas	10,000
10,950	<i>Pinus</i>	Allerød	11,000
11,250	Allerød		
	<i>Betula</i>		
11,900	Earlier Dryas	Older Dryas	11,800
12,100	Bølling	Bølling	12,000
12,450	Earliest Dryas		
12,900	PLENIGLACIAL	MIDDLE WEICHSELIAN	13,000

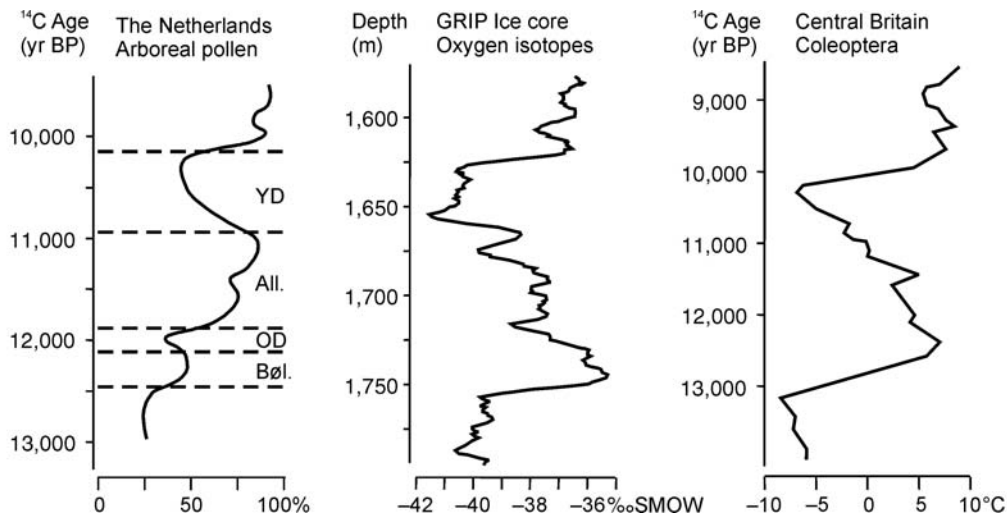


Figure B10 Comparison between the Bølling-Allerød interstadial, as recognized in the pollen record from the Netherlands (after Hoek, 1997), oxygen isotopes from the Greenland ice-core GRIP (Johnsen et al., 1992) and temperature reconstructions based on Coleoptera from Britain (Atkinson et al., 1987).

As described above, the application of biostratigraphic terminology to records from different regions and different sources may easily cause correlation problems. Therefore, the INTIMATE group of the INQUA Palaeoclimate Commission developed an event stratigraphy for the North Atlantic region, based on the stratotype of the GRIP ice-core record (Björck et al., 1998). This scheme defines a series of stadials and interstadials for the period 23.0–11.5 ice-core yrs BP, based on marked oxygen isotope variations in the GRIP ice core. Within Greenland interstadial 1, a subdivision is made into three warmer episodes GI-1a, 1c and 1e with intervening colder periods GI-1b and 1d (Figure B11). The INTIMATE event stratigraphy scheme has not been proposed as a replacement of the existing stratigraphic schemes, but as a *standard* against which to compare regional stratigraphic schemes including terms such as the Bølling-Allerød interstadial. Furthermore, the event stratigraphy is supposed to serve as a basis for establishing the synchronicity (or asynchronicity) of comparable events or sequences of events throughout the North Atlantic region (Lowe et al., 2001).

In the Swiss Alps, for instance, oxygen isotope analysis on calcareous lake deposits shows a strong correspondence to the Greenland ice-core records (Lotter et al., 1992). The same patterns have been recognized in lake deposits from

The Netherlands (Hoek and Bohncke, 2001), and central North America (Yu and Eicher, 1998), indicating a common temperature influence during the last glacial-interglacial transition in the Atlantic region.

The adoption of the Greenland ice-core record as the stratotype for the last glacial-interglacial transition, and thus as the standard chronology against which to compare the timing of regional events, has certain advantages over the use of the traditional scheme of Mangerud et al. (1974). The ice cores record the sequence of events at the highest available temporal resolution (potentially definable to sub-annual variations) and the chronologies derived from them, although not free of problems, are less problematic than radiocarbon dates, especially because several of the key transitions lie within radiocarbon plateaux (Stuiver et al., 1998).

It is to be expected that the term Bølling-Allerød interstadial will continue to be used, in particular for the warm phase during the Weichselian late glacial in northwest Europe. The ongoing effort in establishing the precise timing of climate changes during the last glacial-interglacial transition will hopefully provide the precise chronological framework with which to correlate other regional stratigraphies with each other and with the Greenland ice cores.

Wim Z. Hoek

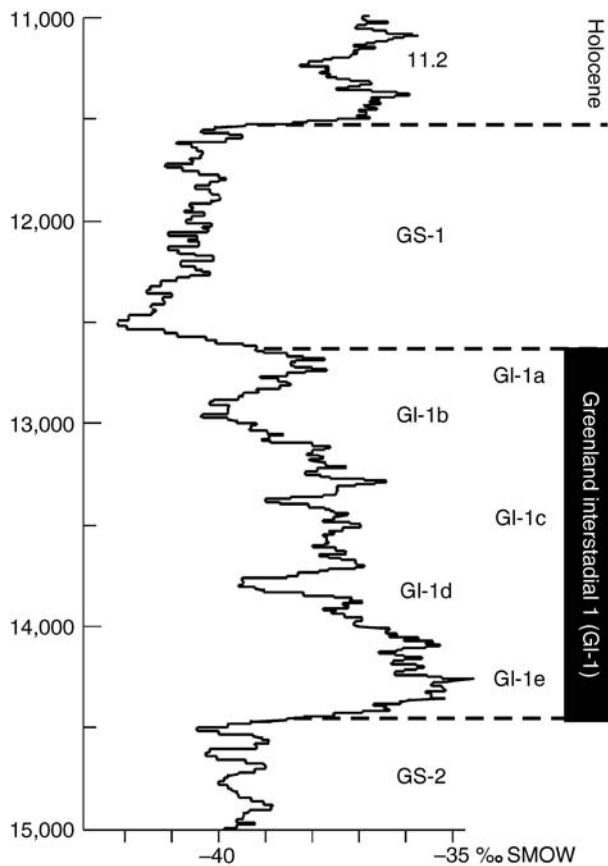


Figure B11 Stratigraphic position of Greenland interstadial 1 (GI-1) in the GRIP oxygen isotope record, corresponding to the Bølling-Allerød interstadial; age is in GRIP ice-core yrs BP. Within the Greenland interstadial, warm (GI-a,c,e) and cold (GI-b,d) events are given according to Björck et al. (1998).

Bibliography

- Atkinson, T.C., Briffa, K.R., and Coope, G.R., 1987. Seasonal temperatures in Britain during the past 22,000 years, reconstructed using beetle remains. *Nature*, **325**, 587–593.
- Björck, S., Walker, M.J.C., Cwynar, L.C., Johnsen, S., Knudsen, K.-L., Lowe, J.J., Wohlfarth, B., 1998. An event stratigraphy for the Last Termination in the North Atlantic region based on the Greenland ice-core record: A proposal by the INTIMATE group. *J. Quaternary Sci.*, **13**, 283–292.
- Coope, G.R., Lemdahl, G., Lowe, J.J., and Walkling, A., 1998. Temperature gradients in northern Europe during the Last Glacial-Holocene transition (14–9 kyr BP) interpreted from coleopteran assemblages. *J. Quaternary Sci.*, **13**, 419–433.
- De Klerk, P., 2004. Confusing concepts in Lateglacial stratigraphy and geochronology: Origin, consequences, conclusions (with special emphasis on the type locality Bøllingsø). *Rev. Palaeobot. and Palynol.*, **129**, 265–298.
- Groote, P.M., Stuiver, M., White, J.W.C., Johnsen, S., and Jouzel, J., 1993. Comparison of oxygen isotope records from the GISP2 and GRIP Greenland ice cores. *Nature*, **366**, 552–554.
- Hartz, N., and Milthers, V., 1901. Det senglaciale ler i Allerød Teglværksgrav. *Meddelelser fra Dansk Geologisk Forening*, **2**, 31–60.
- Hoek, W.Z., 1997. Late-Glacial and early Holocene climatic events and chronology of vegetation development in the Netherlands. *Vegetation Hist. Archaeobot.*, **6**, 197–213.
- Hoek, W.Z., and Bohncke, S.J.P., 2001. Oxygen-isotope wiggle-matching as a tool for synchronising ice-core and terrestrial records over Termination 1. *Quaternary Sci. Rev.*, **20**, 1251–1264.
- Iversen, J., 1942. En pollenanalytisk Tidsfaestelse af Ferskvandslagene ved Nørre Lyngby. *Meddelelser fra Dansk Geologisk Forening*, **10**, 130–151.
- Jessen, K., 1935. The composition of the forests in Northern Europe in epipalaeolithic time. *Biologiske Meddelelser*, **12**(1), 64pp.
- Johnsen, S.J., Clausen, H.B., Dansgaard, W., Fuhrer, K., Gundestrup, N., Hammer, C.U., Iversen, P., Jouzel, J., Stauffer, B., and Steffensen, J.-P., 1992. Irregular glacial interstadials recorded in a new Greenland ice core. *Nature*, **359**, 311–313.
- Litt, T., and Stebich, M., 1999. Bio- and chronostatigraphy of the lateglacial in the Eifel region, Germany. *Quaternary Int.*, **61**, 5–16.
- Lotter, A.F., Eicher, U., Birks, H.J.B., and Siegenthaler, U., 1992. Lateglacial climatic oscillations as recorded in Swiss lake sediments. *J. Quaternary Sci.*, **7**, 187–204.
- Lowe, J.J., and Gray, J.M., 1980. The stratigraphic subdivision of the Lateglacial of north-west Europe. In Lowe, J.J., Gray, J.M., and Robinson,

- J.E. (eds.), *Studies in the Lateglacial of North-west Europe*. Oxford: Pergamon, pp. 157–175.
- Lowe, J.J., Hoek, W.Z., and INTIMATE group, 2001. Inter-regional correlation of palaeoclimatic records for the Last Glacial-Interglacial Transition: A protocol for improved precision recommended by the INTIMATE project group. *Quaternary Sci. Rev.*, **20**, 1175–1187.
- Mangerud, J., Andersen, S.T., Berglund, B.E., and Donner, J.J., 1974. Quaternary stratigraphy of Norden, a proposal for terminology and classification. *Boreas*, **3**, 109–128.
- Stuiver, M., Grootes, P.M., and Braziunas, T.F., 1995. The GISP2 $\delta^{18}O$ Climate Record of the Past 16 500 Years and the Role of the Sun, Ocean, and Volcanoes. *Quaternary Res.*, **44**, 341–354.
- Stuiver, M., Reimer, P.J., Bard, E., Beck, W., Burr, G.S., Hughen, K.A., Kromer, B., McCormac, G., Van der Plicht, J., and Spurk, M., 1998. INTCAL98 radiocarbon age calibration 24,000–0 cal BP. *Radiocarbon*, **40**, 1041–1083.
- Van der Hammen, T., 1951. Late-Glacial flora and periglacial phenomena in The Netherlands. PhD Thesis, Leiden, Geologisch en Mineralogisch Instituut der Rijksuniversiteit te Leiden. *Leidse Geologische Mededelingen*, **17**, 71–183.
- Wohlfarth, B., 1996. The chronology of the Last Termination: A review of radiocarbon-dated, high-resolution terrestrial stratigraphies. *Quaternary Sci. Rev.*, **15**, 267–284.
- Yu, Z., and Eicher, U., 1998. Abrupt climate oscillations during the last deglaciation in Central North America. *Science*, **282**, 2235–2238.

Cross-references

Beetles as Quaternary and Late Tertiary Climate Indicators
 Dating, Biostratigraphic Methods
 Interstadials
 Last Glacial Termination
 Oxygen Isotopes
 Pollen Analysis
 Radiocarbon Dating
 Younger Dryas

BOREHOLE CLIMATOLOGY

Introduction

Past ground temperatures can be estimated by analyzing perturbations to the quasi-steady state equilibrium geothermal profile in the uppermost kilometer of the Earth's crust. In fact, it has been customary to eliminate the effects of known climatic events (mainly the last glacial termination) from the temperature profiles, in order to determine the internal heat output, an important quantity for the understanding of our planet's dynamics. Widespread concern about global warming and temperature changes during the last century prompted many in the geothermal community to reexamine the data for evidence of more recent temperature changes. Not surprisingly, we are finding coherent and systematic temperature perturbation patterns. What had previously been considered noise is now appearing to be a rich signal of local and regional climate change.

Consider the Earth's crust in thermal equilibrium. A temperature-depth profile starts at the surface at the mean-annual ground temperature and increases steadily with depth (Figure B12a). If the temperature at the upper boundary of the body is increased, additional heat propagates into the body causing an corresponding increase in temperature just below the surface (Figure B12b). The depth to which equilibrium temperatures are perturbed in a given time is governed by the thermal diffusivity of the body. For typical rocks, a thermal front (i.e., 5% change) propagates to about 16 m in one year, 50 m in 10 years, 160 m in 100 years,

and 500 m in 1,000 years. Thus the Earth's ground temperature history over the last millennium is captured in the uppermost kilometer of the crust. The depth of a temperature perturbation is related to the timing of surface changes. The shape of the perturbation reveals details of the surface temperature history. Positive and negative subsurface temperature anomalies are associated with ground surface warming and cooling respectively. The magnitude of surface temperature excursions that caused the subsurface anomalies is usually inferred directly by data inversion (Beltrami et al., 1997).

Although proxy indicators such as tree rings and oxygen isotope data are very useful as climatic indicators, they are not directly related to temperature at the Earth's surface. On the other hand, geothermal data are a direct reflection of the energy balance at the surface (Huang et al., 2000; Beltrami, 2002a,b). However, the heat conduction process acts as a low pass filter and smoothes the ground surface temperature perturbation as it propagates into the subsurface. As a result, geothermal data are useful to reconstruct the past climate through the last millennium, but with a resolution that decreases significantly in time.

Analyzes of geothermal data from the last century have revealed warming of between 2–4 °C in Alaska (Lachenbruch and Marshall, 1986), between 1–2 °C in eastern and central Canada (Beltrami and Mareschal, 1991; Beltrami and Mareschal, 1992; Shen and Beck, 1992; Beltrami et al., 2003), less than 1 °C in Utah (Chisholm and Chapman, 1992), etc. About half of this warming in Canada appears to be a recovery from a colder period that may be associated with the Little Ice Age, also documented from geothermal data in Europe (Grove, 1988).

Theory

One of the fundamental assumptions required for the reconstruction of ground temperature histories from geothermal data and eventually past climatic change is that the heat transfer regime within the ground be conductive (Beltrami, 2001a,b). In an ideal perfectly conductive soil, variations of surface temperature are propagated into the ground according to the heat conduction equation (Carslaw and Jaeger, 1959):

$$\frac{\partial T}{\partial z} = \kappa \frac{\partial^2 T}{\partial z^2}, \quad (1)$$

where κ is the thermal diffusivity of the rock controlling the rate of heat propagation into the solid as a response to temperature variations with time, T is temperature, and z is depth. The use of a one-dimensional equation is valid if long term surface temperature changes have a wavelength much larger than the depth to which they penetrate (usually less than 1 km).

In a source-free half space, the equilibrium heat-flow is constant and it is evaluated in the deeper part of the temperature profile least affected by the recent surface temperature changes. Following standard methods (Bullard, 1939), the equilibrium temperature is continued upward by assuming constant gradient over intervals of constant conductivity. The perturbation is determined as the difference between the measured temperature and the upward continuation of the deep temperature profile. The area between these curves represents the net heat absorbed by the ground, and the shape of the perturbation, if heat generation is ignored, is determined by the thermal history of the surface.

$$T(z) = T_0 + q_0 R(z) + T_i(z); \quad (2)$$

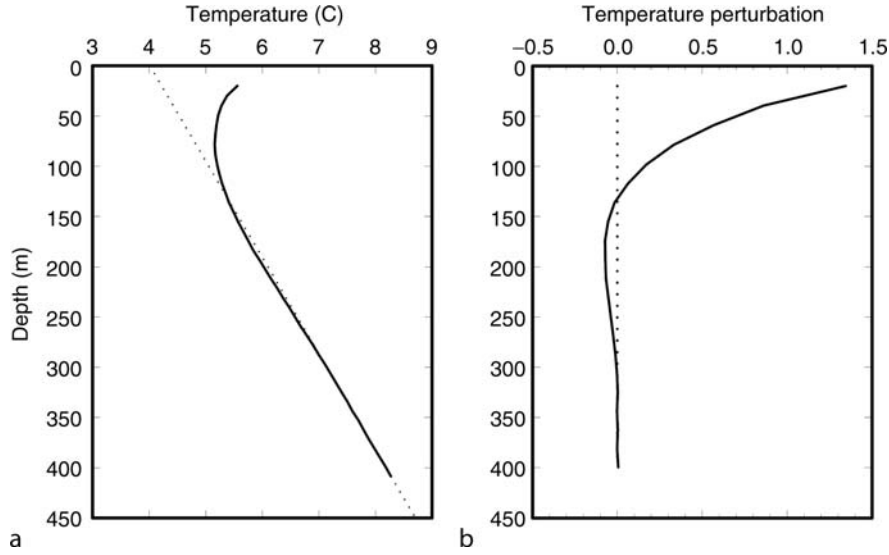


Figure B12 (a) Typical measured temperature-depth profile (solid line). The dashed line represents a background thermal profile least affected by recent climate change. (b) Temperature anomaly for the log shown at an expanded scale. Perturbation is calculated as the difference between measured temperature and background temperature for corresponding depths.

where $T(z)$ is the temperature at depth z , T_0 is the equilibrium ground surface temperature (in the deepest part of the borehole, the temperature is not affected by the changes of surface temperature: when $z \rightarrow \infty$, $T = T_0$, $t > 0$), q_0 is the equilibrium surface heat flow density, $R(z)$ is the thermal resistance, and $T_i(z)$ is the temperature perturbation arising from the time varying surface temperature.

For a one step change in ground surface temperature at time t before present ($\Delta T = T_s - T_0$), the temperature perturbation at depth z is given by (Carslaw and Jaeger, 1959):

$$T_i(z) = \Delta T \operatorname{erfc}\left(\frac{z}{2\sqrt{\kappa t}}\right), \quad (3)$$

where $\sqrt{\kappa t}$ is the characteristic thermal diffusion depth and erfc is the complementary error function.

Short period variations are attenuated rapidly with depth such that the ground surface temperature history can be approximated by the averaged surface temperature over a series of time intervals of equal duration.

For a model consisting of a series of step temperature changes, the temperature at depth z , Eqs. (2) and (3) yield:

$$T(z) = T_0 + q_0 R(z) + \sum_{k=1}^K T_k \left[\operatorname{erfc}\left(\frac{z}{2\sqrt{\kappa t_k}}\right) - \operatorname{erfc}\left(\frac{z}{2\sqrt{\kappa t_{k-1}}}\right) \right] \quad (4)$$

which is valid at each depth where data exist, becoming a system of linear equations that can be expressed as:

$$\Theta_j = A_{jl} X_l, \quad (5)$$

where Θ_j is a column vector containing the j -values of temperature measured at depth z_j , corrected for heat production between surface and depth z_j when necessary; X_l is a column vector containing the model parameters: $k+2$ unknowns (T_0 , q_0 , T_1 , ..., T_k); A_{jl} is a $(j \cdot l)$ matrix that contains 1 in the first

column, the thermal resistance to depth z_j , $R(z_j)$, in the second column and the difference between complementary error functions at times t_{k-1} and t_k for depth z_j in columns 3 to $k+2$.

$$\begin{pmatrix} T_1 \\ T_2 \\ \vdots \\ T_j \end{pmatrix} = \begin{pmatrix} 1 & R_1 & A_{1,3} & A_{1,4} & \dots & A_{1,k+2} \\ 1 & R_2 & A_{2,3} & A_{2,4} & \dots & A_{2,k+2} \\ \vdots & \vdots & \vdots & \vdots & \ddots & \vdots \\ 1 & R_j & A_{j,3} & A_{j,4} & \dots & A_{j,k+2} \end{pmatrix} \begin{pmatrix} T_0 \\ q_0 \\ T_1 \\ \vdots \\ T_k \end{pmatrix}, \quad (6)$$

$$A_{j,k+2} = \operatorname{erfc}\left(\frac{z_j}{2\sqrt{\kappa t_k}}\right) - \operatorname{erfc}\left(\frac{z_j}{2\sqrt{\kappa t_{k-1}}}\right) \quad (7)$$

This yields an under-determined system of linear equations that can be solved by singular value decomposition (SVD) (Lanczos, 1961; Jackson, 1972; Menke, 1989).

The model parameters can be written explicitly as:

$$X_l = \Theta_j \left(\frac{v_{lr} u_{rj}}{\lambda_{(r)}} \right) \quad (8)$$

with $r = 1, \dots, R$, $l = 1, \dots, M$, and $j = 1, \dots, N$. The summation is performed over repeated indices, and R is the rank of the matrix, M is the number of model parameters, and N is the number of data.

Equation (8) shows that any error in the data will be multiplied by $1/\lambda_{(r)}$ and will be amplified for the very small singular values. So, it is necessary to eliminate the singular values that are smaller than a cutoff value. The singular value decomposition selects the linear combination of model parameters that is best constrained by the data.

The model resolution matrix, \mathbf{R} , relates the parameters of an arbitrary model to the parameters that would be obtained by inversion of the corresponding data: $\mathbf{R} = \mathbf{V}\mathbf{V}^T$, $\mathbf{T}^{\text{est}} = \mathbf{R}\mathbf{T}^{\text{true}}$. The data resolution matrix, \mathbf{Q} , relates the observed data to those data that the inverted model parameters would produce: $\mathbf{Q} = \mathbf{U}\mathbf{U}^T$, $\Theta^{\text{pred}} = \mathbf{Q}\Theta^{\text{true}}$.

Energy balance at the earth's surface

There has been little work to infer variations of surface heat fluxes from geothermal data. Beltrami et al. (2000) estimated, using an analytical approximation, the average heat flux into the ground during the last 1,000 years, over a large region from eastern and central Canada. Results indicated average heat flux increases of 17.0 mWm^{-2} and 74.0 mWm^{-2} since 1,765 and in the last 100 years, respectively. They also identified a cold period between 1,500 and 1,800, indicated by a negative subsurface temperature anomaly.

More recently, singular value decomposition inversion was used to reconstruct surface heat flux histories from the heat flux anomalies detected in the subsurface (Beltrami, 2001a). In the Earth, the heat flux at any depth, ignoring the heat production, can be expressed as the sum of the quasi steady-state geothermal heat flux, q_{eq} , and the transient component, $\Delta q_0(z, t)$:

$$q(z, t) = q_{eq} + \Delta q_0(z, t) \quad (9)$$

If the surface heat flux history is modeled by a series of step heat flux changes at the surface, the heat flux at the depth z is given by:

$$q_t(z) = q_{eq} + \sum_{k=1}^K q_k \left[\text{erfc} \left(\frac{z}{2\sqrt{\kappa t_k}} \right) - \text{erfc} \left(\frac{z}{2\sqrt{\kappa t_{k-1}}} \right) \right] \quad (10)$$

$$q_0(t) = q_k; \quad t_{k-1} \leq t \leq t_k; \quad k = 1, \dots, K; \quad t_0 = 0 \quad (11)$$

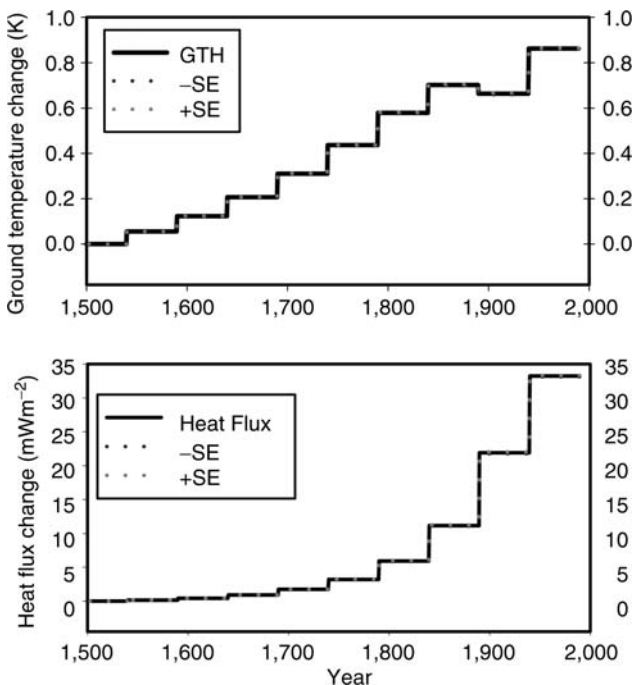


Figure B13 (a) Global mean ground surface temperature history (GSTH) from borehole temperature data. The dotted lines represent the stability of the GSTH for a data noise level of 0.02° K . (b) Global mean surface heat flux history (SHFH) for the same data set. The global SHFH describes the energy balance history at the Earth's surface for the last 500 years.

The system of linear equations can be resolved by singular value decomposition inversion in a similar fashion as for the ground surface temperature reconstruction.

An analytical estimate of the heat flux history from geothermal data (Beltrami et al., 2000), used an approximation based on fractional calculus (Wang and Brass, 1999). An equivalent expression for the heat flux history for a semi-infinite, homogeneous medium subjected to a series of sudden changes of surface temperature at any time between $[t_s, t]$, where t is the time at the moment of observation and t_s is time before present, is given by:

$$q_l = \frac{2\lambda}{\sqrt{\Delta t \kappa \pi}} \sum_{k=l+1}^N [(T_k - T_{k+1})(\sqrt{k-l} - \sqrt{k-l+1})] \quad (12)$$

Equation (12) is general and can be applicable to any time series at any time scale as long as the initial surface heat flux is zero, to avoid error accumulation in time (Beltrami, 2001b).

Observational results of Levitus et al. (2001) showed an increase in observed ocean heat content of $18.2 \times 10^{22} \text{ J}$ (over the past half-century) and an increase in atmospheric heat content $6.6 \times 10^{21} \text{ J}$, while the heat gained by the cryosphere is around $8.1 \times 10^{21} \text{ J}$. From the analysis of geothermal data Beltrami et al. (2002) estimated the heat gained by the lithosphere during the last half-century as $9.1 \times 10^{21} \text{ J}$. Recent inversion of the same data set yielded $7.1 \times 10^{21} \text{ J}$ for the heat absorbed during the same time period (Beltrami, 2002a) (Figure B13). These results are consistent with the idea that the observed warming of the Earth during the last fifty years has been global and affects all climate system components. Further information on the latest developments in borehole climatology can be found in Gonzalez-Rouco et al., 2008.

Hugo Beltrami and Daniela Nitoiu

Bibliography

- Beltrami, H., 2001a. Surface heat flux histories from geothermal data: Inference from inversion. *Geophys. Res. Lett.*, **28**, 655–658.
- Beltrami, H., 2001b. Surface heat flux histories from inversion of geothermal data: Energy balance at the Earth's surface. *J. Geophys. Res.*, **106**, 21,979–21,994.
- Beltrami, H., 2002a. Climate from borehole data: Energy fluxes and temperatures since 1500. *Geophys. Res. Lett.*, **29**(23), 2111, doi: 10.1029/2002GL015702.
- Beltrami, H., 2002b. Earth's long-term memory. *Science*, **297**, 206–207.
- Beltrami, H., and Mareschal, J.C., 1991. Recent warming in Eastern Canada inferred from geothermal measurements. *Geophys. Res. Lett.*, **18**, 605–60.
- Beltrami, H., and Mareschal, J.C., 1992. Ground temperature histories for central and eastern Canada from geothermal measurements: Little Ice Age signature. *Geophys. Res. Lett.*, **19**, 689–692.
- Beltrami, H., Cheng, L., and Mareschal, J.C., 1997. Simultaneous inversion of borehole temperature data for past climate determination. *Geophys. J. Int.*, **129**, 311–318.
- Beltrami, H., Wang, J.F., and Bras, R.L., 2000. Energy balance at the Earth's surface: Heat flux history in eastern Canada. *Geophys. Res. Lett.*, **27**, 3385–3388.
- Beltrami, H., Smerdon, J., Pollack, H.N., and Huang, S., 2002. Continental heat gain in the global climate system. *Geophys. Res. Lett.*, **29**, doi: 10.1029/2001GL014310.
- Beltrami, H., Gosselin C., and Mareschal, J.C., 2003. Ground surface temperatures in Canada: Spatial and temporal variability. *Geophys. Res. Lett.*, **30**(10), doi: 10.1029/2003GL017144.
- Bullard, E.C., 1939. Heat flow in South Africa. *Proc. R. Soc. London A.*, **173**, 474–502.
- Carslaw, H.S., and Jaeger, J.C., 1959. *Conduction of Heat in Solids*, 2nd ed. New York: Oxford University Press, 510pp.

- Chisholm, T.J., and Chapman, D.S., 1992. Climate change inferred from analysis of borehole temperatures: An example from western Utah. *J. Geophys. Res.*, **97**, 14155–14176.
- Grove, J.M., 1988. *The Little Ice Age*. London: Methuen, 498pp.
- Gonzalez-Rouco, J.F., Beltrami H., Zorita E., and Stevens M.B. (2008). Borehole climatology: A discussion based on contributions from climate modelling, *Climate of the Past Discussions*, **4**, 81–110.
- Huang, S., Pollack, H.N., and Shen, P.Y., 2000. Temperature trends over the last five centuries reconstructed from borehole temperatures. *Nature*, **403**, 756–758.
- Jackson, D.D., 1972. Interpretation of inaccurate, insufficient, and inconsistent data. *Geophys. J. R. Astron. So.*, **28**, 97–110.
- Lachenbruch, A.H., and Marshall, B.V., 1986. Changing climate: Geothermal evidence from permafrost in the Alaskan Arctic. *Science*, **234**, 689–696.
- Lanczos, C., 1961. *Linear Differential Operators*. Princeton, N.J: D. Van Nostrand, 564pp.
- Levitus, S., Antonov, J., Wang, J., Delworth, T.L., Dixon, K., and Broccoli, A., 2001. Anthropogenic warming of the Earth's climate system. *Science*, **292**, 267–270.
- Menke, W., 1989. *Geophysical Data Analysis: Discrete Inverse Theory, Int. Geophys. Ser.* vol. 45, San Diego, CA: Academic Press, 289pp.
- Shen, P.Y., and Beck, A.E., 1992. Paleoclimate change and heat flow density inferred from borehole temperature data in the Superior Province of the Canadian Shield. *Palaeogeogr. Palaeoclimatol. Palaeoecol. (Global and Planetary Change Section)*, **98**, 143–165.
- Wang, K., and Brass, R.L., 1999. Ground heat flux estimated from surface soil temperature. *J. Hydrol.* **216**, 214–226.

Cross-references

[Climate Variability and Change, Last 1,000 Years](#)
[Little Ice Age](#)

C

CARBON CYCLE

Historical background of the carbon cycle

The discovery that plants use carbon dioxide for growth in sunlight and return it to the atmosphere in darkness must have been the first scientific observation of part of the carbon cycle. The discovery of carbon dioxide as a gas that forms by fermentation and burning of charcoal, under the name of *spiritus silvestris*, is attributed to Jan Baptista (or Baptist) van Helmont, a man of medicine, alchemy, and early chemistry in the then Spanish Netherlands, in the first half of the 1600s (e.g., Graham, 1974). Presentation of the first general scheme of the carbon and nitrogen cycles was attributed to the French chemist, Jean Baptiste André Dumas, in 1841 (Rankama and Sahama, 1950, p. 535). Dumas (1842) described the cycle of CO₂ consumption and production by respiration, pointing to the sources of “carbonic acid” in the air and soil where it forms from decomposition of manure or organic fertilizers. He also pointed out that the Earth’s primordial atmosphere must have contained all the carbon dioxide and nitrogen that has been taken up by living organisms.

As to the geochemical cycles, in 1875, several chapters on the cycles of chemical elements appeared in a book on Earth history by Friedrich Mohr, a professor at the University of Bonn, with one short chapter on the carbon cycle among them (Mohr, 1875, pp. 397–398). The role of carbon dioxide as a gas warming the atmosphere, in addition to the similar role of water vapor that was known earlier, was demonstrated by Arrhenius (1896). The formation of organic matter from carbon dioxide and water under the action of light, the process known as photosynthesis, has been studied since the later part of the 1700s, when molecular oxygen was discovered to be part of the process and carbon dioxide was identified as a component of air. Short histories of successive discoveries in photosynthesis since the late 1,700s to the twentieth century have been published by several authors (Gaffron, 1964; Meyer, 1964, p. 21; Bassham, 1974; Whitmarsh and Govindjee, 1995). By the 1920s, the cycles of the chemical elements that are involved in biological processes – carbon, nitrogen, and phosphorus – and that are also transported between

soil, crustal rocks, atmosphere, land and ocean waters, and the Earth’s interior were sufficiently well recognized. Alfred Lotka’s book, *Elements of Physical Biology*, published in 1925, includes chapters on the cycles of carbon dioxide, nitrogen, and phosphorus that present a modern treatment of what are today called the biogeochemical cycles (Lotka, 1925). The term biogeochemical reflects the fact that biological, physical, and chemical processes play important roles and interact with each other in the carbon cycle. By 1950, the geochemical cycles of elements in the Earth’s interior and on its surface became textbook material, with the variable degree of detail in each cycle reflecting the knowledge of the reservoir contents and inter-reservoir fluxes at the time (Rankama and Sahama, 1950). Subsequent decades produced the knowledge we have today of the different chemical forms of carbon in the different compartments of the Earth, their abundances, and flows, all of which make the global biogeochemical cycle of carbon.

Structure of the carbon cycle

Geochemical or biogeochemical cycles of chemical elements are usually represented by environmental reservoirs and material flows or fluxes connecting them to each other. The structure of the global carbon cycle is shown in Figure C1 and the masses of carbon in the main environmental reservoirs are summarized in Table C1. The inventory of the reservoirs represents the geologic near-Recent, with atmospheric carbon given as the pre-industrial concentration of CO₂. Estimates of carbon masses in other reservoirs are subject to variable and greater uncertainties. The mass of carbon in land plants has been variably reported in the range of ±15–20% of the value given in Table C1, 700 Gt C (1 gigaton or 1 Gt = 10¹⁵ g). Large variations in the estimated global mass of peat and soil humus have also been reported in the literature. Thus, the numbers in Table C1 should be viewed as estimates for geologically recent time, and it should be kept in mind that the masses of carbon in the individual reservoirs have varied considerably throughout the Earth’s history. The carbon cycle is usually divided into a deeper part, called the *endogenic cycle*, and the *exogenic cycle* that includes the surface reservoirs of the sediments, oceanic and continental waters, land and aquatic biomass, soils, and the atmosphere.

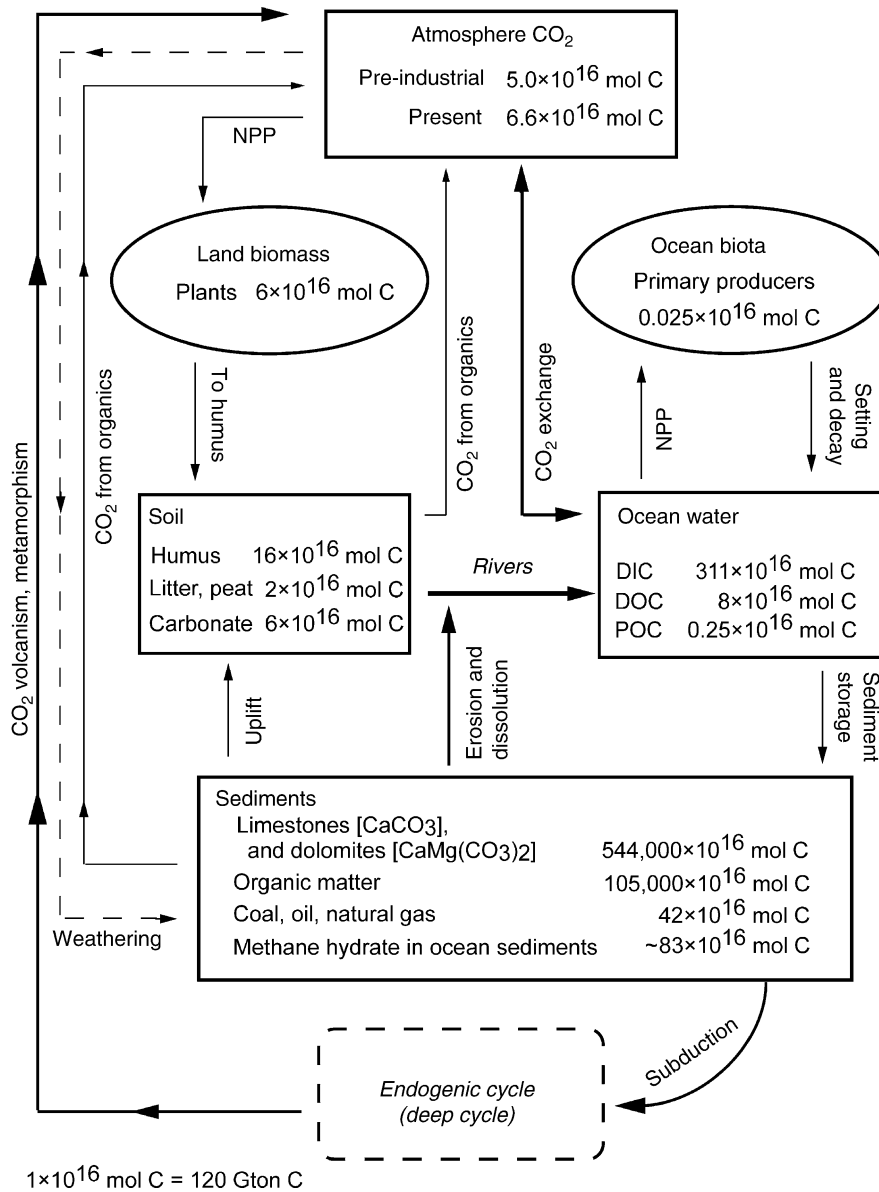


Figure C1 Global biogeochemical cycle of carbon. Reservoirs on the Earth surface represent the exogenic cycle. Masses of the major reservoirs given in Table C1. Mass units: 1 mol C = 12.011 g C or 1×10^{16} mol C = 120 Gt C. From Mackenzie and Lerman (2006).

The biggest reservoir of carbon near the Earth's surface lies in past and present oceanic sediments. These include carbonate rocks that comprise limestones, consisting mostly of the mineral calcite (CaCO₃), and dolomite rocks made predominantly of the mineral dolomite (CaMg(CO₃)₂); younger unconsolidated carbonate sediments on the ocean floor, composed to a large extent of skeletal remains of marine organisms; and organic matter in sediments that consists of many different organic compounds containing reduced carbon. Inorganic, oxidized carbon in carbonates accounts for about 84% of the sedimentary carbon mass, and the remaining 16% are in reduced organic matter. Both inorganic (oxidized) and organic (reduced) carbon, occurring in carbonate rocks and organic matter, make only 3.7 wt.-% of all the sediment preserved in the geologic record.

The planetary average abundance of carbon in the Earth as a whole is not well constrained because its abundance in the lower mantle and core is not well known, but its abundance in the Earth's mantle is much lower than in the sediments, 0.008–0.015 wt.-%.

Oxidized carbon is the most abundant form at the Earth's surface where it occurs as carbon dioxide gas, dissolved carbonate and bicarbonate ions, and carbonate ions in sedimentary minerals. In addition to carbonate minerals, pure elemental carbon occurs in nature in two minerals, diamond and graphite. Diamonds are a product of high temperature and pressure associated with explosive volcanic rocks called kimberlites and lamproites that formed in the mantle. Graphite deposits occur in different forms: hydrothermal veins in igneous rocks where

Table C1 Carbon masses in the major environmental reservoirs. From data in Li (2001), Mackenzie (2002), Ver et al. (1999), and Walker (1977). Units: 1 mol C = 12.011 g C

Reservoir	Mass of carbon	
	In grams C	In moles C
Atmosphere		
CO ₂ (at pre-industrial 280 ppmv)	5.94×10^{17}	4.95×10^{16}
CO (present)	1.24×10^{15}	4.42×10^{13}
CH ₄ (present)	4.82×10^{15}	3.01×10^{14}
Ocean		
Dissolved inorganic (DIC)	3.74×10^{19}	3.11×10^{18}
Dissolved organic (DOC)	1×10^{18}	8.33×10^{16}
Particulate organic (POC)	3×10^{16}	2.50×10^{15}
Ocean biota	3×10^{15}	2.50×10^{14}
Land biota		
Phytomass	7×10^{17}	5.83×10^{16}
Bacteria and fungi	3×10^{15}	2.50×10^{14}
Animals	$1 \text{ to } 2 \times 10^{15}$	1.25×10^{14}
Land		
Soil humus	1.5×10^{18}	1.25×10^{17}
Reactive fraction of humus		2×10^{16}
Dead organic matter, litter, peat	2.5×10^{17}	2.08×10^{16}
Inorganic soil (CaCO ₃)	7.2×10^{17}	6×10^{16}
Sediments		
Carbonates	6.53×10^{22}	5.44×10^{21}
Organic matter	1.25×10^{22}	1.05×10^{21}
Continental crust (layer 30 km thick)	2.58×10^{21}	2.14×10^{20}
Oceanic crust (layer 6.5 km thick)	9.20×10^{20}	7.66×10^{19}
Upper mantle (layer from 30 to 700 km)	$(8.9 \text{ to } 16.6) \times 10^{22}$	$\sim 1.1 \times 10^{21}$

crystalline graphite precipitated from hot fluids, thermally metamorphosed coal, and metamorphic rocks originally rich in organic matter. Another form of carbon occurring in igneous rocks is carbonatite, a rock made mostly of calcite, dolomite, and iron-containing dolomite (ankerite). Carbonatites are believed to form in the mantle, at high pressures of CO₂, and extrude as volcanic rocks or intrude into the upper lithosphere at the later stages of magmatic differentiation. The occurrence of carbonatites is limited to small areas at about 330 locations (Barker, 1997), and their total mass is very small in comparison to the sedimentary limestones and dolomites.

On Earth, the biological origin of organic matter is indicated by the abundance ratio of the two stable isotopes of carbon, ¹³C/¹²C: this ratio is lower in biologically-produced organic matter than in the source of CO₂ used in chemosynthesis or photosynthesis. However, organic compounds of non-biological origin occur in a class of meteorites known as chondrites, among which carbonaceous chondrites contain between 0.26 and 3.5 wt.-% carbon in organic compounds coexisting with aluminosilicate minerals. This abundance of organic carbon in extraterrestrial materials may be compared with its abundance of about 0.75 wt.-% in the entire preserved mass of sediments on Earth. Fossil fuels – coal, petroleum, and hydrocarbon gases – represent a very small part of the global reservoir of sedimentary organic matter (Figure C1). Known reserves of fossil fuels (coal, petroleum, and natural gas), recoverable with present-day technology, are estimated at about 800 Gt C or 7×10^{16} mol C. Estimates of total fossil fuel reserves are about 5,000 Gt C and, additionally, 10,000 Gt C in methane-hydrate deposits on the ocean floor and in the tundra, estimated within a range of a factor of 10 smaller or greater (Kvenvolden, 1988; Kvenvolden and Lorenson, 2001). These masses of fuel reserves and methane

hydrates make about 0.1 wt.-% of sedimentary organic carbon (Figure C1). The mass of atmospheric carbon dioxide would more than double if the known fossil fuels of 800 Gt C were burned to their commercial exhaustion and there were no removal of carbon dioxide from the atmosphere. A much greater potential increase in atmospheric carbon dioxide is indicated by the amounts of the estimated fuel reserves and methane hydrate.

The mass of carbon stored over the geologic history of the Earth in sedimentary limestones, dolomites, and undecomposed organic matter exceeds by a very large factor, about 100,000 the mass of carbon in atmospheric CO₂ at the present time.

Next in size is the carbon reservoir of the oceans or, more generally, of the oceanic and continental surface and ground waters that comprise most of the hydrosphere. The main form of carbon in the global water reservoir is dissolved carbon dioxide and its ionic species, and the generally less abundant dissolved organic carbon from incomplete decomposition of living and dead organic matter. These dissolved forms of carbon are usually denoted DIC, for dissolved inorganic carbon, and DOC, for dissolved organic carbon. Dissolved inorganic carbon (DIC) includes three aqueous species – CO₂, HCO₃⁻, CO₃²⁻ – and, to a lesser degree, their complexes with metal ions in solution. On the other hand, dissolved organic carbon includes a great variety of organic compounds ranging in molecular weight from light, simple organic acids to much heavier and structurally more complex species. Besides the dissolved forms of carbon, there are particles containing both inorganic and organic carbon in continental and ocean waters. Particulate inorganic carbon or PIC is mostly the grains of eroded carbonate rocks and skeletons of calcareous organisms formed in surface waters that sink to the ocean floor. Its organic counterpart, particulate organic carbon or POC, consists of undecomposed cells, products of metabolic excretion by zooplankton (fecal pellets), soft parts of dead organisms and organic matter adsorbed on mineral-particle surfaces such as clays.

The total mass of carbon in the global oceans, consisting mostly of DIC, is about 60 times greater than its atmospheric mass (Table C1). The greater mass of DIC in the ocean becomes either a source or sink of atmospheric carbon dioxide, depending on environmental conditions (Sect. *Running of the carbon cycle*).

In the atmosphere, carbon dioxide is the most abundant of the carbon-containing gases. At present, it forms a volume fraction 3.85×10^{-4} or 385 ppmv¹ of the atmosphere, increasing at a rate of approximately 1.5 ppmv per year. Other gases, such as methane (CH₄) from natural sources or agricultural activities, carbon monoxide (CO) and volatile organic compounds mainly from industrial activities, and the most recent emissions of the various chloro-fluoro-carbon compounds (CFCs) used as refrigerant and spray-propellant gases are believed to have a potentially much greater effect on atmospheric temperature, stratospheric and tropospheric ozone, and climate, despite their occurrences at concentrations much lower than those of atmospheric CO₂.

In the biosphere, land plants represent a major part of the carbon in living organic matter. This very large and diversified group includes predominantly photosynthetic plants ranging in

¹ppmv is parts per million by volume. In the atmosphere that is a mixture of ideal gases at the total pressure $P = 1$ atm, concentrations of individual gases in units of ppmv are also their partial pressures in units of 10^{-6} atm. CO₂ at a concentration of 370 ppmv has a partial pressure 3.70×10^{-4} atm.

size from short-lived unicellular organisms to trees whose lifetimes average several decades. Forests are the main reservoir of biotic carbon on land. In the ocean, most of the photosynthesizing organisms live in the upper layer of the oceans where sufficient light is available, called the euphotic zone, of an average thickness of 50 m, ranging up to about 200 m in very clear water. These free-floating organisms are the phytoplankton, and at least one group of the phytoplankton (coccolithophorids) are important producers of calcium carbonate shells that have made up a major part of the ocean-floor carbonate sediments since the middle of the Mesozoic Era. Additional aquatic photosynthesizers include the great variety of algae and bigger plants rooted to the bottom, known as macrophytes. The oceanic phytoplankton makes only a small fraction, about 0.5%, of carbon in the global biota. However, oceanic plants have a much shorter life cycle, about 20 days–1 month, than the land plants that turn carbon over approximately every 10 years. These differences account for the fact that flows of carbon through the land and oceanic phytomass are not too different (Table C4).

Carbon on the primordial earth

The Earth's history in its early stages went from the formation of the planet by accretion of a cloud of solid particles and gases to its partial melting after accretion, which resulted in the structural separation of its major units – the inner and outer core, the mantle and the lithosphere, and the crust. After the formation of the Earth nearly 4.55 billion years ago, a long period of some 650–800 million years preceded the appearance of life, the first fossil records of which are dated at 3.75–3.9 billion yr before present (Mojzsis et al., 1996; Rosing, 1999). This time of prebiotic Earth, known in the geologic time scale as the Hadean Eon, was a long period of environmental conditions very different from those of later time, when photosynthetic organisms emerged and modified greatly the Earth's surface environment. In this early, prebiotic stage of Earth history, when the temperatures near the Earth surface were considerably higher than at present, possibly near the 1,000 °C of silicate melts, the lighter chemical constituents of the Earth were separated or degassed from the solids and melt, forming the fluid layer of the primordial atmosphere. These volatile constituents became the major components of the outer shell of the Earth that comprises its atmosphere, hydrosphere, biosphere, and sediments.

The chemical elements and their compounds that escaped from the molten or solid Earth interior by degassing and made the primordial atmosphere are known as the *volatiles* (Rubey, 1951) or *hyperfusibles* (Poldervaart, 1955), mainly water

(H₂O), carbon (C), nitrogen (N), sulfur (S), and chlorine (Cl), as listed in Table C2. Rubey (1951, 1955) and later investigators who studied the balance of the volatiles at the Earth's surface demonstrated that their complete inventory includes some of the same constituents that had been added to the Earth's surface by the weathering of igneous rocks and, in general, by transfer of materials from the lithosphere to the oceans and sediments. These amounts are small fractions of the total masses of volatiles and the difference between the total and those derived from igneous rocks is known as *excess volatiles*. The masses of H₂O, C, N, S, and Cl in the present-day Earth's surface environment are approximately the masses of the volatiles on the primordial Earth that became incorporated in the differentiated outer shells of the cooler, later Earth. Water is the most abundant volatile and its mass exceeds the masses of other volatiles by a factor of 30–300. The individual estimates of H₂O and N, shown in Table C2, agree within 10–15%, but there is a much greater variation among the estimates of C, Cl, and S, attributable probably to the differences in the estimated masses of sedimentary rock salt, sulfates, sulfides, and the organic and inorganic carbon reservoirs. The view that most of the volatiles on the Earth's surface had been released from the mantle by degassing rather than remaining on the surface from an early stage of planetary accretion has been discussed by several authors (Rubey, 1951; Walker, 1977; Li, 2000). Degassing was probably not uniform and for such volatiles as carbon dioxide, water and perhaps sulfur, large fractions may still remain in Earth's upper mantle and possibly deeper in its interior.

The five primordial volatile gases were likely to have been H₂O (v), CO₂, N₂, HCl, and H₂S, although a number of authors have argued for different species of carbon, nitrogen, and sulfur as components of the primordial atmosphere: methane (CH₄) instead of carbon dioxide (CO₂), ammonia (NH₃) instead of molecular nitrogen (N₂), and sulfur dioxide (SO₂) instead of the reduced form of hydrogen sulfide (H₂S). Concerning the main chemical form of carbon in the early atmosphere, CO₂ rather than CH₄ is a thermodynamically stable species in the presence of even very low concentrations of oxygen gas (O₂), such as might have existed in contact with magmatic silicate melts. For the five volatiles to exist in a gaseous state, the temperature of the atmosphere should have been sufficiently high to prevent their condensation. Of the five, the highest critical temperature is that of H₂O, 374 °C, and this may be taken as a representative temperature of that stage of the early Earth before the volatiles began to condense to liquid water and form an aqueous solution of reactive and nonreactive gases. Although the time sequence and rate of Earth's cooling, the formation of the early oceans, and the reactions between minerals and water that led to the

Table C2 Volatiles in primordial Earth's surface environment (masses in grams of chemical species shown)

Major species	Rubey (1951)	Poldervaart (1955)	Walker (1977)		This entry ^a	
	Excess volatiles	Hyperfusibles	Total volatiles	From igneous rocks	Excess volatiles	Total volatiles on Earth surface
H ₂ O	1.66 × 10 ²⁴	1.66 × 10 ²⁴	1.590 × 10 ²⁴	0.031 × 10 ²⁴	1.559 × 10 ²⁴	1.430 × 10 ²⁴
C	2.48 × 10 ²²	6.22 × 10 ²²	7.609 × 10 ²²	0.804 × 10 ²²	6.805 × 10 ²²	7.784 × 10 ²²
N	4.20 × 10 ²¹	4.50 × 10 ²¹	4.892 × 10 ²¹	0.04 × 10 ²¹	4.852 × 10 ²¹	4.890 × 10 ²¹
Cl	3.00 × 10 ²²	3.40 × 10 ²²	3.120 × 10 ²²	0.1 × 10 ²²	3.020 × 10 ²²	4.311 × 10 ²²
S	2.20 × 10 ²¹	3.00 × 10 ²¹	5.220 × 10 ²¹	0.8 × 10 ²¹	4.420 × 10 ²¹	1.245 × 10 ²²
Volatiles total	1.721 × 10 ²⁴	1.768 × 10 ²⁴	1.707 × 10 ²⁴	0.041 × 10 ²⁴	1.667 × 10 ²⁴	1.568 × 10 ²⁴

^aFrom data in Li (2001) and other sources.

accumulation of dissolved solids in ocean water are known very incompletely, the prebiotic atmosphere and ocean likely evolved in three stages:

- (1) A hot atmosphere where the five volatiles could occur as gases.
- (2) A cooler atmosphere after the water has condensed and accumulated as a liquid on the Earth's surface, and hydrogen chloride and hydrogen sulfide were removed from the atmosphere by reactions with crustal rocks and transport of the reaction products to the primordial ocean.
- (3) An atmosphere where carbon dioxide and nitrogen remained the two main constituents, and CO₂ also dissolved in the primordial hydrosphere and reacted with crustal rocks.

After the Earth's surface had cooled, and HCl and H₂S were removed from the atmosphere by dissolution in the early hydrosphere and chemical reactions with crustal rocks, the two remaining main constituents of the atmosphere were CO₂ and N₂. Chemical neutralization of the chloride-ion from HCl and the sulfate-ion from the oxidized H₂S by reactions with silicate rocks would have added metal cations that doubled the salt content of the primordial ocean relative to the present-day value (70–80 g kg⁻¹ as compared to 35 g kg⁻¹ now). At a limiting, hypothetical case of no removal of CO₂ and N₂ from the atmosphere, the atmosphere would have been almost pure carbon dioxide at a concentration 97.4 vol.-% CO₂ with 2.6 vol.-% N₂ (the C and N masses of total volatiles given in the last column of Table C2 correspond to 6.481×10^{21} mol CO₂ and 0.175×10^{21} mol N₂). The combined mass of CO₂ and N₂ in this atmosphere, covering the Earth surface of 510×10^6 km², would have generated an atmospheric pressure of about 56 bar.

At a surface temperature of the Earth near 25–35 °C, about 25% of the CO₂ could dissolve in ocean water, with around 75% remaining in the atmosphere. Because N₂ gas at these temperatures is much less soluble in water than CO₂, the remaining atmosphere would have been 96.6 vol.-% CO₂ and 3.4 vol.-% N₂, with a total atmospheric pressure of about 40 bar. Dissolution of a large mass of CO₂ in the primordial hydrosphere would have resulted in very high concentrations of DIC in water, about 1 mol C kg⁻¹, in comparison to the present-day concentration in ocean water of about 2×10^{-3} mol C kg⁻¹. Because DIC reacts with Ca²⁺-ions in solution, making CaCO₃ as calcite and/or aragonite (Reaction (8) below), the solubility of CaCO₃ and the capacity of the solution to remain supersaturated with respect to these minerals place a limit on the mass of CO₂ and calcium that can remain in solution. For the removal of most CO₂ from the primordial atmosphere, a mass of CaCO₃ comparable to its present mass preserved in sediments might have formed during the first several hundred million years of Earth's prebiotic history. The higher concentrations of CO₂ in the primordial atmosphere, at the time when the solar luminosity was some 25–30% lower than at present, might have been responsible for the warming of the Earth's surface that kept it above freezing temperatures and enabled the emergence of life. (See *Archean environments; Atmospheric evolution, Earth; Faint young Sun Paradox*, this volume).

Running of the carbon cycle

The starting point of the carbon cycle is the Earth's mantle, from where it was degassed with other volatile elements in the early stage of the formation of the Earth. The processes of material exchange between the mantle and the Earth's surface belong in the endogenic cycle that operates on a much

longer time scale (10⁸–10⁹ years) and they are much slower than those among the surface reservoirs (Figure C1).

CO₂ in the atmosphere dissolves in rain, on land, and in ocean surface waters. It is also taken out of the atmosphere and surface waters by photosynthesizing organisms. Residues of living plants in part decompose to CO₂ and organic acids, and in part they become organic matter of soils and sediments. The solution of CO₂ in fresh water is mildly acidic and together with dissolved organic acids reacts with crystalline rocks of the continental crust, causing mineral dissolution and release of such major constituents of river waters as the metals sodium, magnesium, potassium, and calcium. Metal ions in rivers (Na⁺, K⁺, Mg²⁺, and Ca²⁺), balanced to a large degree by negatively-charged bicarbonate (HCO₃⁻) ions, are transported to the ocean. The calcium carbonate minerals, calcite and aragonite – both chemically the same (CaCO₃), but differing in their crystal structure – form in the ocean either as skeletons secreted by marine organisms that range in size from microscopic algae to large mollusks and corals, or by inorganic precipitation. Calcites containing up to about 15 mol-% Mg are formed by some groups of calcareous algae in shallow-water sections of the ocean. This calcium carbonate accumulates over large areas of the ocean floor in the form of settling shells of phytoplankton and zooplankton or in structures built of algae and corals, called reefs, in the shallower parts of the coastal zones. Aragonite and calcites rich in magnesium do not last long in the geologic record and they are transformed to calcite by recrystallization and/or dissolution and reprecipitation. Dolomite accounts for approximately 40% of the carbonate rock mass of the Phanerozoic Eon, the last 540 million years, but it is much less abundant, about 15%, in the carbonates of the younger Tertiary (Wilkinson and Algeo, 1989). At present, the formation of dolomite is much more restricted as, for example, in the highly saline coastal playas in the Persian Gulf.

In the present-day ocean, both the photosynthetically produced organic matter and calcium carbonate in surface waters have their own subcycles. As organic matter settles into the deeper ocean, it undergoes oxidation that returns CO₂ to ocean water (see *Carbon dioxide, dissolved (ocean)*). This process is also known as the biological pump. Some of the respired CO₂ is transported back to the surface layer by water mixing, but some of it is used in dissolution of CaCO₃ that rains down from the surface. An increase in concentration of dissolved CO₂ makes seawater more acidic and brings it to a level of undersaturation with respect to calcite and aragonite. Both of these minerals dissolve in the deep ocean, and their rates of dissolution are sufficiently fast to return most of the CaCO₃ to ocean water. Preservation of CaCO₃ in ocean-floor sediments is limited in the present-day ocean to depths smaller than approximately 3,500–4,000 m, which is a combined effect of a higher concentration of dissolved carbon dioxide that lowers the CO₃²⁻-ion concentration, an increase in the solubility of calcite with an increasing pressure, and a faster dissolution rate in a solution that is farther away from saturation with respect to the mineral. Over geologically long periods, much of the oceanic CaCO₃ was preserved in sediments that became the sedimentary cover of the present-day continents and some of it was transported into the mantle by the process of seafloor spreading and subduction of their margins in ocean trenches. This subduction process is part of the endogenic cycle (Figure C1) that breaks down CaCO₃ at high temperatures in the mantle and returns CO₂ to the surface, mostly in gases emitted by continental and oceanic volcanoes. The isotopic

composition of carbon in CO₂ in some of the volcanic emissions suggests that it is a mixture of carbon originally from the mantle and carbon from the Earth's surface.

The organic matter of terrestrial plants becomes incorporated in soils, where it is known as humus (a mixture of complex organic humic and fulvic acids), and the residues of fresh-water and oceanic plants are buried in sediments. Some of this organic matter decomposes more slowly, producing CO₂ and organic acids. The nutrient elements nitrogen and phosphorus return to soil water, where they become available once more for new plant growth. However, some fraction of this organic matter resists decomposition. This fraction becomes nearly permanently buried. Because land is at a higher elevation than the ocean surface, there is a continuous transport of running water carrying dissolved material and solid particles eroded from rocks, soils, and terrestrial organic matter to the ocean. Particles containing organic carbon (POC) are brought to the ocean where some of the POC decomposes. CO₂ thus produced by decomposition of terrestrial organic matter is added to CO₂ already present in ocean water.

In the ocean, atmospheric CO₂ dissolves in the surface water layer, a few hundred meters thick, which is well mixed by winds, and there it is used in photosynthetic production of organic matter, in addition to the production of calcium carbonate. The exchange of CO₂ between surface ocean water and the atmosphere depends on such factors as the mass of CO₂ in the atmosphere; temperature, salinity, and chemical composition of ocean water; the production and respiration of organic matter; and precipitation and dissolution of calcium carbonate minerals. For example, greater biological production of organic matter and its storage in sediments removes carbon dioxide from the atmosphere-ocean system; weathering of old organic matter in oceanic sediments exposed on land returns carbon dioxide to the atmosphere; and formation of calcium carbonate and its deposition in sediments removes carbon from the atmosphere-ocean system, yet it also changes the relative abundances of the three dissolved species of inorganic carbon in ocean water (CO₂, HCO₃⁻, and CO₃²⁻) and by this it affects the air-sea CO₂ exchange.

Net removal of carbon from ocean water by sedimentation of undecomposed organic matter and calcium carbonate must be balanced by inputs of carbon from other sources. One obvious but limited source is dissolution of atmospheric CO₂ in ocean water. Another important source is oxidation of carbon in organic matter that was eroded from older sediments on land and that was transported to the ocean. As atmospheric CO₂ is the source both of organic matter stored on land and in oceanic sediments, and the atmosphere and ocean water lose CO₂ by the formation of CaCO₃ and its storage in sediments, this CO₂ source would have been exhausted rapidly if it were not replenished. Replenishment comes from oxidation of old organic matter that is disseminated in sediments and more concentrated in black shales. Tectonic processes that cause uplift of continental masses and mountain building expose these older sediments to the atmosphere and to weathering and erosion on the Earth's surface, thereby providing input of CO₂ to the atmosphere. Volcanic emissions also add or, in part, return CO₂ to the atmosphere.

Main driving processes

Deep carbon cycle

Carbon dioxide is emitted from the Earth mantle through subaerial volcanism, in the spreading zones and ridges on the ocean floor, and from magmatic plumes and hot spots. The occurrence

of this chemically oxidized form of carbon in magmatic emissions indicates that CO₂ is not just a product of carbon oxidation at the Earth's surface but has a much longer geologic history on our planet. This view is consistent with the chemical thermodynamic properties of carbon and oxygen that tend to combine and form carbon dioxide, as in the reaction:



Over a wide range of temperatures, from those at the Earth's surface to those of molten silicate melts, chemical equilibrium in Reaction (1) is strongly shifted to the right, producing very high ratios of CO₂ to O₂. At the relatively low temperature of the Earth's surface, many processes represented by Reaction (1) do not go spontaneously from the left to the right, but carbon can exist metastably in contact with the oxidizing atmosphere for a very long time. Common examples of such occurrences are the pure forms of elemental carbon graphite and diamond; less pure forms, such as the coal varieties anthracite, and lignite; and fossilized organic compounds, such as amber.

A shorthand notation of the endogenic cycle of carbon is the chemical reaction between calcium carbonate carried into the mantle by tectonic plate subduction and silica, which produces calcium silicate minerals and carbon dioxide:

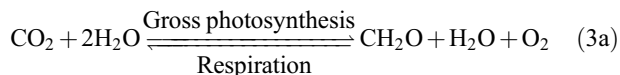


The reaction is generally known as the Urey reaction (Urey, 1952, pp. 148 and ff.), although J.J. Ebelmen was credited with introducing it much earlier, in 1845 (Berner and Maasch, 1996). In Reaction (2), CaSiO₃ represents various calcium silicate minerals that occur in igneous and metamorphic rocks. SiO₂ occurs either in the melt or in igneous rocks that can react with calcium carbonate. Reaction (2), going from left to right, describes the conversions of carbonates to calcium silicate and production of carbon dioxide during metamorphism. The reverse reaction, from right to left, represents chemical weathering of silicates in the continental crust by reactions with CO₂, and the final product CaCO₃. This omits intermediate reactions that involve Ca²⁺, HCO₃⁻, and CO₃²⁻ ions in aqueous solution.

Photosynthesis and respiration

Carbon is the main constituent of life on Earth. The main process that converts carbon dioxide into the organic molecules in cells of living plants is known as photosynthesis. Photosynthesis involves the chemical reduction of carbon, using the energy of sunlight to make organic matter in plants; the subsequent decomposition of organic matter is oxidation of carbon, also known as respiration or mineralization. These reactions are summarized in Reaction (3).

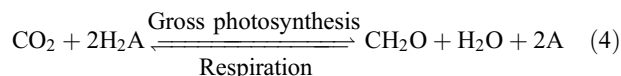
The respiration of organic matter is a process driven by bacteria that utilize the energy stored in CH₂O for their own metabolism. The common form of photosynthesis is the reaction between carbon dioxide and water that produces organic matter and free oxygen gas:



or, in a shorter form



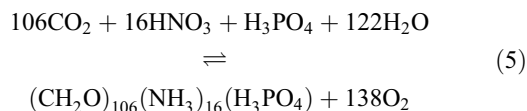
More generally, photosynthesis includes H_2A as a chemical compound where reduced A^{2-} transfers four electrons to oxidized carbon in CO_2 , to form organic matter of composition CH_2O and liberate $2A$ (Reaction (4)). Hydrogen sulfide, H_2S , is such an H_2A compound utilized by some photosynthetic sulfur-oxidizing bacteria:



The difference between gross photosynthetic production and respiration is net primary production, denoted NPP and usually given in units of carbon mass stored in living biomass in a unit of time (for example, mol C yr⁻¹). Reactions (3) and (4) are also often written with all the reactants and products multiplied by 6, giving the composition of organic matter as $C_6H_{12}O_6$, analogous to the sugar glucose. Organic matter produced by photosynthesis stores 470–490 kilojoules or 112–117 kilocalories of energy per 1 mole of carbon (1 mol C = 12.011 g C; 1 kcal = 4.184 kJ). When organic matter is oxidized, energy is released.

In photosynthesis, free molecular oxygen (O_2) is produced from water. Respiration generally oxidizes less reduced carbon than that produced by photosynthesis, which results in some surplus CH_2O and O_2 . This imbalance between photosynthesis and respiration has been of major importance to life on Earth because it enabled accumulation of molecular oxygen in the atmosphere and storage of organic matter in sediments over a period of perhaps the last 2 billion years or about one-half of the Earth's age of 4.6 billion years.

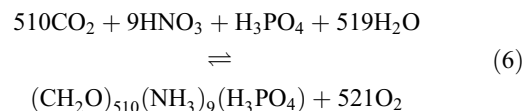
In addition to carbon, photosynthesizing organisms need nitrogen, phosphorus, sulfur, and trace elements. Mean atomic proportions of carbon, nitrogen, and phosphorus in photosynthesizing planktonic organisms are C:N:P = 106:16:1. The consistency and limited variability of this ratio, originally described by Redfield et al. (1963) and called the Redfield ratio since then, extend to oceanic zooplankton and to the plankton of continental waters. Oceanic phytoplankton uses nitrogen in the form of dissolved nitrate ions, NO_3^- , and phosphorus in the form of one of the dissolved phosphate ions, mostly HPO_4^{2-} . In solution, where the positively and negatively charged ions must balance, nitrogen and phosphorus used in the photosynthetic reaction can be written as neutral acid molecules, HNO_3 and H_3PO_4 , instead of the equivalent ($NO_3^- + H^+$) and ($HPO_4^{2-} + 2H^+$). The photosynthetic reaction of aquatic photosynthesis, similar to Reaction (4), is:



In Reaction (5), both carbon in CO_2 and nitrogen in NO_3^- are reduced, and the mass of oxygen produced is greater than the mass of carbon fixed in organic matter. In the absence of nitrate, ammonia (NH_3 or $NH_4^+ + OH^-$) may be utilized at least by some of the phytoplankton species, and organic matter of the same composition would be produced by a reaction with $16NH_3$ instead of $16NO_3^- + 16H^+$, then producing $106O_2$.

The Redfield ratio for land plants is less well constrained than for the aquatic phytoplankton, and C:N:P atomic ratios for land plants have been reported in a wide range from about 510:9:1 to 2057:17:1. Land plants are more efficient photosynthesizers

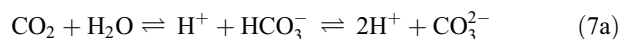
than marine organisms because they fix more carbon and produce more oxygen for each atom of phosphorus consumed. Higher land plants emerged in the Devonian Period that lasted from about 365 to 410 Ma ago. For a plant of C:N:P atomic ratio 510:9:1, the photosynthesis reaction based on carbon dioxide, nitrate, and phosphate, similar to Reaction (5), produces organic matter and oxygen in the following proportions:



In both Reactions (5) and (6), respiration or mineralization of organic matter is the reverse reaction (from right to left) that also consumes oxygen, but releases nitrogen and phosphorus to the environment, where they become available for new biological production. This recycling of nutrient nitrogen and, in particular, phosphorus is of major importance to biological productivity because the ultimate source of most phosphorus is in much slower leaching or dissolution from crustal rocks (see *Phosphorus cycle*).

Carbon in the atmosphere and hydrosphere

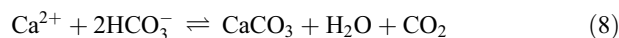
In an atmosphere containing oxygen, carbon dioxide is the only chemically stable form of carbon. More reduced carbon gases, such as carbon monoxide (CO), methane (CH_4), and volatile hydrocarbons are eventually oxidized to CO_2 . Carbon dioxide dissolved in water reacts to produce bicarbonate and carbonate ions:



An increase in concentration or partial pressure of CO_2 in the atmosphere results in its higher concentration in solution at equilibrium, and this further reduces the concentration of the carbonate ions and changes the relative proportions of the dissolved inorganic carbon species:



A higher CO_2 concentration can make the solution undersaturated with respect to $CaCO_3$ and cause dissolution, as shown in the following reaction going from the right to the left:



Reaction (8), proceeding from left to right, represents the formation of calcium carbonate minerals. As the bicarbonate ion, HCO_3^- , is the main species of DIC in ocean water and continental freshwaters, its reaction with Ca^{2+} removes 1 mole of carbon into sediments and produces 1 mole of CO_2 thereby restoring the balance of the carbonate species.

Dissolution of calcium carbonate by reaction with dissolved CO_2 represents the process of chemical weathering of limestones and silicate rocks on land, where they are exposed to atmospheric precipitation and groundwater containing elevated concentrations of CO_2 from respiration of organic matter in soils. The reaction of CO_2 with water that produces the bicarbonate and carbonate ions, the reactions of the latter with calcium, and the relatively low solubility of $CaCO_3$ minerals at the Earth's surface conditions are the factors behind the abundance of limestones and dolomites that once formed as oceanic sediments and became part of the continental crust and land surface.

Isotopic fractionation

In photosynthesis, plants use the lighter carbon isotope, ^{12}C , in preference to the heavier isotope, ^{13}C . This biological fractionation is a non-equilibrium process and results in marine and most terrestrial organic matter having a lower $^{13}\text{C}/^{12}\text{C}$ ratio than the atmospheric source. This difference, expressed as $\delta^{13}\text{C}$ (‰) (see *Carbon isotopes, stable*), amounts to organic matter being about 20–25‰ lighter than the value of $\delta^{13}\text{C} = -7\%$ of CO_2 in the present-day atmosphere. The land plants in the metabolic group C_3 that accounts for 85–95% of the present-day plant species, have an average $\delta^{13}\text{C} \approx -27\%$, with a range from -21 to -35% (O’Leary, 1988). A group of geologically younger land plants, the C_4 plants, is characterized by a smaller isotopic fractionation, -9 to -20% , with an average $\delta^{13}\text{C} \approx -13\%$. This metabolic pathway is only several million years old and it is believed to have evolved in response to lower atmospheric CO_2 concentrations. The third and smallest metabolic group, the CAM (crassulacean acid metabolism) plants, has carbon isotope fractionation values that extend from those of the C_3 to C_4 plants. In the ocean, the spread of $\delta^{13}\text{C}$ values for different groups of planktonic and benthic plants is considerable: -10 to -22% for algae and macrophytic plants, and -18 to -31% for plankton. Values of -20 to -21% are considered a representative average for marine plankton.

In the system of CO_2 gas, DIC, and CaCO_3 (calcite), isotopic fractionation at equilibrium between pairs of species is considerably smaller than in biological processes, as shown by the fractionation values in Table C3.

Equilibrium fractionation factor, α , is usually written in the δ notation of the two species exchanging their ^{13}C and ^{12}C . For the exchange between aqueous HCO_3^- and gaseous CO_2 the fractionation factor is, with the δ values taken as fractions:

$$\alpha_{\text{HCO}_3^-(\text{aq})-\text{CO}_2(\text{g})} = \frac{(^{13}\text{C}/^{12}\text{C})_{\text{aq}}}{(^{13}\text{C}/^{12}\text{C})_{\text{g}}} = \frac{1 + \delta^{13}\text{C}_{\text{aq}}}{1 + \delta^{13}\text{C}_{\text{g}}} \quad (9)$$

It should be noted that in the preceding notation the fractionation factor α is the quotient of the isotopic ratio in the aqueous phase to the ratio in the gaseous phase. As long as δ is much smaller than 1 and α is close to 1, the approximations $\ln(1 + \delta) \approx \delta$ and $\ln \alpha \approx \alpha - 1$ are used in Equation (9), giving logarithmic and linear forms of α :

$$\ln \alpha_{\text{HCO}_3^-(\text{aq})-\text{CO}_2(\text{g})} = \delta^{13}\text{C}_{\text{aq}} - \delta^{13}\text{C}_{\text{g}} \quad (10a)$$

or

$$\alpha_{\text{HCO}_3^-(\text{aq})-\text{CO}_2(\text{g})} - 1 = \delta^{13}\text{C}_{\text{aq}} - \delta^{13}\text{C}_{\text{g}} \\ = 9.6\text{‰}_{00} \text{ to } 7.9\text{‰}_{00} \quad (10b)$$

The preceding shows that the equilibrium fractionation is the difference between the $\delta^{13}\text{C}$ values of the two species. The bicarbonate ion in solution, as the main species of DIC, is isotopically heavier than CO_2 gas by 7.9‰ (at 25°C) to 9.6‰ (at 5°C) (Table C3). Isotopic fractionation of carbon between calcite and the bicarbonate ion in solution, as in Reaction (8), is small at Earth surface temperatures, where the $\delta^{13}\text{C}$ of calcite differs from HCO_3^- by -0.1 to $+0.9\%$ (Table C3). For this reason, changes in the isotopic composition of carbon in limestones through geologic time, such as those shown in Figure C2a, are considered as representative of the isotopic composition of DIC in ocean water, from which the rates of biological production and storage of organic carbon are estimated for different geologic periods.

Carbon fluxes

On the Earth’s surface with a climate and vegetation cover similar to those of pre-industrial times, the biggest carbon fluxes are those of net primary production (NPP) on land and in the ocean (Table C4). In Recent time, NPP on land recycles atmospheric CO_2 every 9 years:

$$\text{Recycling time} = \frac{\text{CO}_2 \text{ mass}}{\text{NPP}} \\ = \frac{4.95 \times 10^{16} \text{ mol C}}{5.25 \times 10^{15} \text{ mol C yr}^{-1}} = 9.4 \text{ yr}$$

Residence time of carbon in the individual reservoirs is a measure of the carbon cycle dynamics. Changes in reservoir sizes and fluxes in the geologic past produced great changes in the residence times of carbon in the different reservoirs. In particular, changes in atmospheric carbon dioxide and density of vegetation cover of land, discussed in the next section, were likely to result in changes in the residence times. The near-Recent mean residence time of carbon in land vegetation, from

Table C3 $^{13}\text{C}/^{12}\text{C}$ equilibrium fractionation between species shown as 1 and 2 in gaseous phase (g), aqueous solution (aq), and calcite (cal). Notation of the fractionation factor α_{12} is given in Equations (9)–(10). Temperature T is in Kelvin

No.	Species and phase		$\ln \alpha_{12}$ or $\alpha_{12} - 1$, as shown	T range (°C)	$(\alpha_{12} - 1) \times 10^3$ (‰)	
	1	2			5°C	25°C
1	$\text{CO}_2(\text{aq})$	$\text{CO}_2(\text{g})$	$\alpha_{12} - 1 = -0.373/T + 0.00019^a$	0–60	–1.1	–1.1
2	$\text{HCO}_3^-(\text{aq})$	$\text{CO}_2(\text{g})$	$\alpha_{12} - 1 = 9.552/T - 0.02410^b$	5–125	9.6	7.9
3	$\text{HCO}_3^-(\text{aq})$	$\text{CO}_2(\text{aq})$	$\alpha_{12} - 1 = 9.866/T - 0.02412^c$	5–125	10.7	9.0
4	$\text{CO}_3^{2-}(\text{aq})$	$\text{CO}_2(\text{g})$	$\ln \alpha_{12} = 8.886/T - 0.02225^d$	0–100	9.7	7.6
5	$\text{CaCO}_3(\text{cal})$	$\text{HCO}_3^-(\text{aq})$	$\ln \alpha_{12} = -4.232/T + 0.0151^e$	0–35	–0.1	0.9
6	$\text{CaCO}_3(\text{cal})$	$\text{HCO}_3^-(\text{aq})$		25		0.9 ± 0.2^f
7	$\text{CaCO}_3(\text{arag})$	$\text{HCO}_3^-(\text{aq})$		25		1.8 ± 0.2^f

^aEquation fitted by Mook et al. (1974) to data of Vogel et al. (1970).

^bMook et al. (1974), as recalculated by Friedman and O’Neil (1977, fig 27).

^cMook et al. (1974).

^dRegression fit to data of Thode et al. (1965, Table III).

^eEquation based on data of Salomons and Mook (1986, Table 6-2A) (Clark and Fritz, 1997).

^fRubinson and Clayton (1969).

Table C4 Carbon fluxes between major reservoirs in pre-industrial time (Figure C1). Data from Ver et al. (1999) unless indicated otherwise. (10^{15} g = 1 Gt)

Flux	Units	
	(10^{15} g C yr $^{-1}$)	(10^{12} mol C yr $^{-1}$)
Net primary production (NPP)	113.5	9,450
Land	63.1	5,250
Ocean	50.4	4,200
Volatilization from soil organic matter	62.5	5,200
Weathering consumption of CO $_2$	0.13	11
Net exchange atmosphere-ocean (dissolution 8×10^{15} , evasion 8.042×10^{15} mol yr $^{-1}$)	0.51	42
River input of dissolved C (DIC + DOC)	0.60	50
DIC	0.38	32
DOC	0.22	18
POC	0.19	16
PIC	0.18	15
Oceanic sediment long-term storage	0.28	23
Carbonates ^a	0.22 to 0.34	18 to 28
Organic matter ^a	0.06	5
Volcanism, metamorphism, hydrothermal ^b	0.22	18
Uplift ^b	0.40	33

^aPhanerozoic averages, from Figure C2b.

^bUplift assumed as balanced by subduction of ocean floor over geologically long periods (Mackenzie, 2002, p. 178).

the data in Tables C1 and C4, is about 11 years. Greater land coverage by either forests or grasses would lead to considerably longer or shorter, respectively, residence times of carbon in land phytomass. Recycling time by oceanic phytomass is about 0.06 yr or 20 days.

Volatilization of carbon from soil humus is due to respiration or mineralization of the reactive fraction of humus (15–20% of total). This implies a faster recycling of soil organic matter than may be suggested by the size of the whole reservoir.

The ratio of mean carbon fluxes of carbonate and organic carbon (carbonate/organic) in long-term storage or burial in sediments is 3.6–5.6, comparable to the mass ratio of 5.2 in sedimentary reservoirs (Tables C1 and C4). However, the rivers transport much more organic carbon relative to DIC, with the DIC to organic carbon ratio between about 1 and 1.8 (Table C4). This indicates that the rate of organic matter recycling in sediments is considerably faster than that of carbonates on a geologically long timescale.

Carbon trends through time

Sedimentary mass records

Preservation of sediments is subject to recycling, a process in which materials are eroded and dissolved, the products transported to the ocean where deposition or new mineral formation occurs, and ultimately the materials are reincorporated in the continental sediment cover or crystalline crust, through continental accretion and/or the endogenic cycle. As a result, the older the sediment, the less is preserved. Furthermore, most older sediments of the Early Proterozoic and Archean Eons, older than about 2 billion years (2 Ga), have been metamorphosed, and it is difficult to estimate the original proportions of the different sediment types in metamorphic rocks.

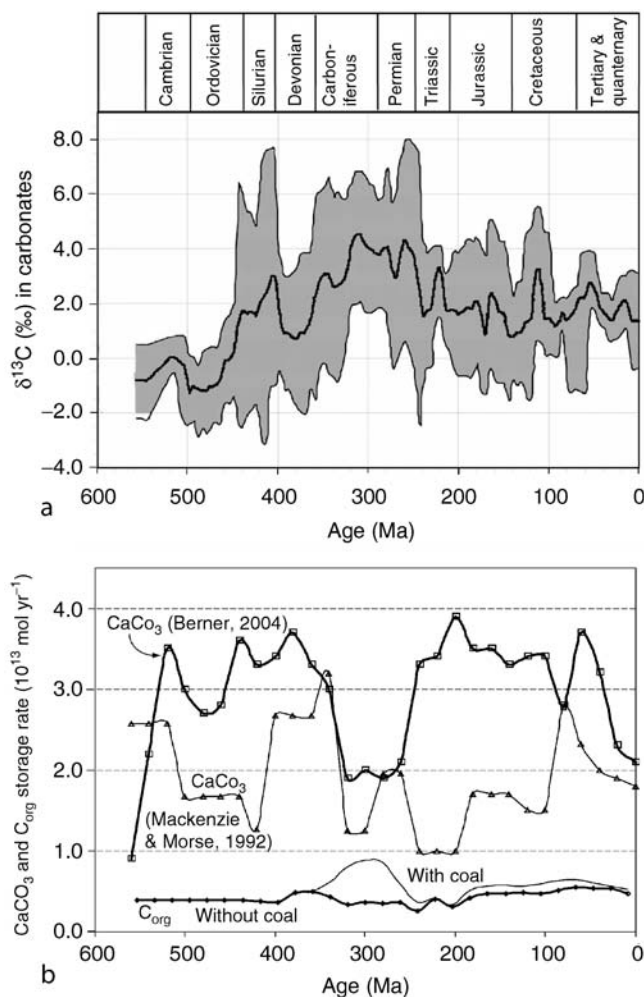


Figure C2 (a) Distribution of $\delta^{13}\text{C}$ in the shells of biogenic calcite during the Phanerozoic, based on approximately 4,500 samples. The black line is a running mean and the shaded area includes the 95% confidence limit about the mean (from Veizer et al., 1999). The base of the Phanerozoic Eon is the base of the Cambrian Period, 542 Ma BP, as given by the International Commission on Stratigraphy 2004. (b) Calculated CaCO_3 and organic carbon storage rates (accumulation rates) during the Phanerozoic (from data of Berner and Canfield, 1989; Mackenzie and Morse, 1992; Robert A. Berner, Yale University, personal communication, 2004).

The rates of carbonate storage during the last 550 Ma (Figure C2b) vary by about 50% from the mean, depending on the data source, but they show a decline from the higher values of the past to recent values. Organic carbon shows an increase in the storage rate around 300 Ma before present due to massive accumulation of coal in the Carboniferous Period. Variations in the rates of organic carbon storage result in variations of the rates of oxygen production, as shown in Reactions (3b), (5), and (6), with more oxygen generated when more photosynthetically produced organic carbon is sequestered.

A record of isotopic composition of organic carbon and carbonate carbon since the Late Proterozoic time, about 780 Ma ago, is shown in Figures C2a and C3. In general, an increase in the values of $\delta^{13}\text{C}_{\text{carb}}$ is accounted for by a greater rate of

storage of organic matter that incorporates ^{12}C in preference to ^{13}C . The fluctuating increase in $\delta^{13}\text{C}_{\text{carb}}$ during the earlier part of the Paleozoic Era, from 500 to 300 Ma ago, probably indicates long-term expansion of marine biological production and emergence of higher land plants in the Devonian Period, between about 400 and 360 Ma ago (see also *Carbon isotope variations over geologic time*). The magnitude of isotopic fractionation due to biological production and storage of organic carbon is the difference between the $\delta^{13}\text{C}$ values in carbonates (taken as representing the DIC isotopic composition in ocean water, Figure C2a) and organic carbon (Figure C3c; see preceding section on *Isotopic fractionation*).

The fractionation factor (ϵ , in ‰) varied within a range of 28–33‰ during the Paleozoic Era, from about 540 to 245 Ma. Departures outside this range, in geologically earlier and later periods may represent, at least to some extent, evolutionary changes in the oceanic and terrestrial biotas. In Late Proterozoic time, older than 540 Ma, large variations in the isotopic values of organic and carbonate carbon (Figure C3a, b) may correspond to the times of three major glaciations that occurred between 800 and 600 Ma ago, when rates of storage of organic carbon might have been relatively low (Hayes et al., 1999, p. 111). A decline in $\delta^{13}\text{C}_{\text{carb}}$ since the beginning of the Cenozoic Era about 65 Ma ago (Figures C2a and 3b) is usually attributed to the rise in the elevation of land and emergence of the major mountain terrains, such as the Alps and the Himalayas, which exposed more of the old organic carbon from shales to weathering, thereby adding more ^{13}C -depleted carbon to the oceans. However, the reasons behind a decrease in biological fractionation during the same period are not altogether clear.

As sedimentary carbonates and organic matter account for most carbon on the Earth's surface (Table C1), the isotopic

composition of these two reservoirs has been used to estimate their mass fractions in the sedimentary record. Because carbon on the Earth's surface ultimately originated in the mantle, $\delta^{13}\text{C}$ of the mantle should equal the mean $\delta^{13}\text{C}$ of the two major surface reservoirs (sedimentary carbonates and organic carbon). Thus, the isotopic composition balance requires that

$$\delta^{13}\text{C}_{\text{mean}} = f\delta^{13}\text{C}_{\text{carb}} + (1 - f)\delta^{13}\text{C}_{\text{org}} \quad (11)$$

where f is the mass fraction of carbonate carbon and $1 - f$ is the mass fraction of organic carbon in sediments. The mean $\delta^{13}\text{C}$ for mantle and surface carbon lies in the range of $-5 \pm 2\text{‰}$, the organic carbon reservoir in the Phanerozoic is about -28‰ , and the carbonate carbon is between $+1$ and $+2\text{‰}$ (Figure C3a, b). These values of $\delta^{13}\text{C}$, used in Equation (11), give the fraction of organic carbon in sediments, $1 - f = 0.15$ to 0.29 . The value given in Table C1 is 0.16.

Atmospheric CO_2

The latest major period of the Earth's history, the Phanerozoic Eon, covers approximately the last 550 Ma when such major evolutionary events occurred as the emergence of large vascular land plants and different groups of CaCO_3 -secreting organisms in the ocean. The biosphere and the global carbon cycle most likely affected one another interactively throughout the Earth's history, when atmospheric CO_2 undoubtedly played a major role in both because of the properties of the atmosphere. Apart from its interactions with the biosphere, atmospheric CO_2 is variably controlled by the major tectonic processes of the formation of the new ocean floor at the oceanic spreading zones, subduction of oceanic sediments, and emission of CO_2 from the deeper parts of the Earth by volcanism and

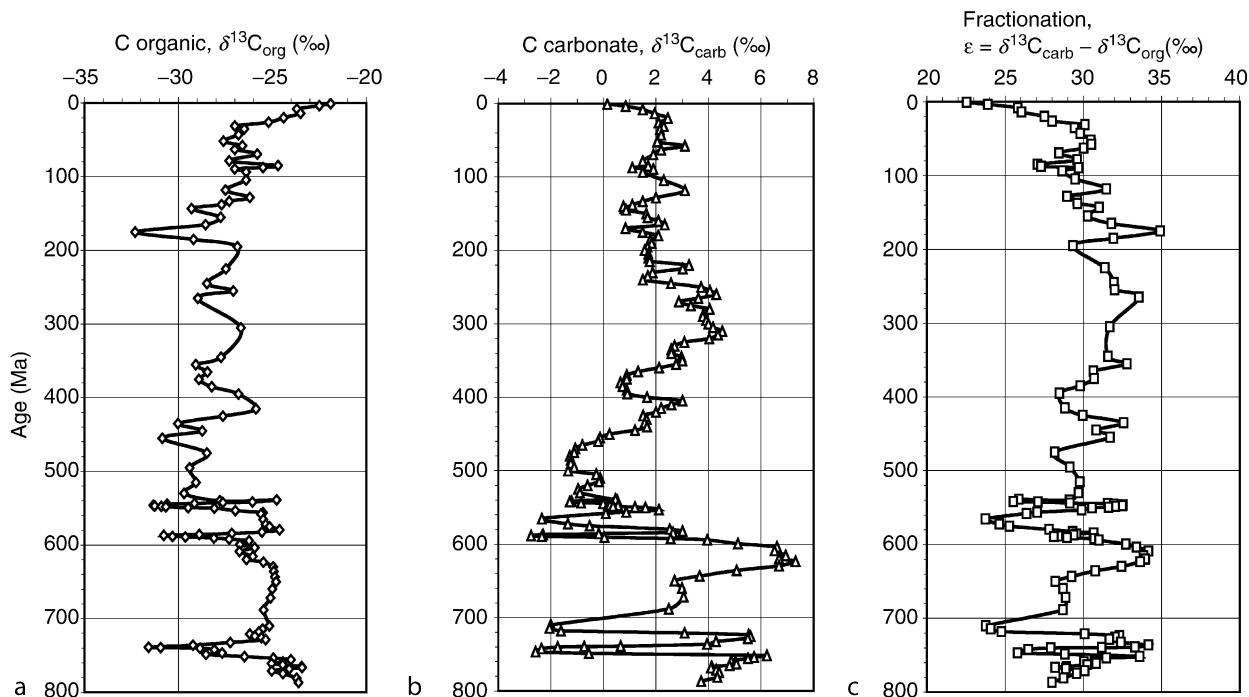


Figure C3 Carbon isotopic composition ($\delta^{13}\text{C}$, in ‰) in the Late Proterozoic (age > 570 Ma) and Phanerozoic time of (a) organic matter and (b) carbonates. (c) Fractionation between carbonate and organic carbon, ϵ in ‰ (from Hayes et al., 1999, and data provided by John M. Hayes, Woods Hole Oceanographic Institution, June 2003).

metamorphic processes. Furthermore, the rates of weathering on land, transport of weathered materials to the ocean, and sedimentary storage of organic matter and carbonates are all parts of the carbon cycle that involve the atmospheric CO₂ reservoir.

Atmospheric CO₂ underwent great changes in concentration during the Phanerozoic, as shown in Figure C4. Relative to its pre-industrial concentration of about 300 ppmv, CO₂ atmospheric levels might have been 15–25 times higher in the Early Paleozoic time, before a decline began about 380 Ma ago due to emergence of large vascular land plants. The high atmospheric CO₂ concentrations at that time might have been comparable to those of modern soils that contain about 30 times more CO₂ in their pore space than the atmosphere, due to the respiration or oxidation of organic matter. The calculated CO₂ curve, and its upper and lower limits of estimated error (e.g., Berner and Kothavala, 2001), is based on a geochemical model of the carbon cycle in a system of land-ocean-atmosphere reservoirs, and it includes numerous processes that affect weathering, biological production, and storage of reduced and oxidized carbon in sediments.

Among such processes are the increase in solar luminosity during the Phanerozoic, changes in the area and elevation of the global land mass, changes in the abundance of gymnosperm and angiosperm plants, water runoff from land, temperature, volcanic activity, and interactions among these processes. The low CO₂ values between about 380 and 280 Ma reflect the emergence of land plants in the Devonian and storage of coal in the Carboniferous Period. The higher values in the Mesozoic Era, from about 240 to 100 Ma, reflect a low relief of land and relatively low rate of utilization of atmospheric CO₂ in the weathering of continental rocks and old sediments. Thereafter, from the beginning of the Tertiary, the tectonically-driven rise of land resulted in higher weathering rates and a decline of atmospheric CO₂.

The variations in shallow ocean temperature and atmospheric CO₂ content during Phanerozoic time may be contrasted with those of the last 18,000 years, since the Last Glacial Maximum to the beginning of industrial time about 200 years ago and to the present. Since the Last Glacial Maximum, global mean temperature increased from about 9 °C to

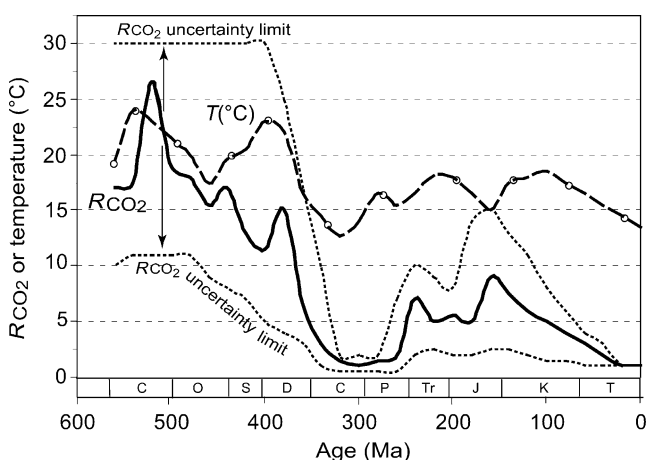


Figure C4 Calculated ratio of atmospheric CO₂ to the Holocene Epoch value taken as 300 ppmv (R_{CO_2}) and shallow ocean temperatures (from data of Berner and Kothavala, 2001, and Wallmann, 2004, as plotted in Locklair and Lerman, 2005).

15 °C and CO₂ from about 185 to 280 ppmv at the beginning of industrial time, indicating a change in R_{CO_2} from 0.66 to 1. Since 1861 to 2000, mean global temperature of the Earth's surface has increased further by about 0.7 °C and atmospheric CO₂ has risen by a factor of 1.33 since pre-industrial time. Concern is focused on the continued increase of atmospheric CO₂ due to burning of fossil fuels and human practices of land use, and the possible release of methane from the methane-hydrates due to warming (Figure C1). The rise in atmospheric carbon dioxide since the Last Glacial Maximum, and especially the last century, has not been countered by a greater biological production of organic carbon and, importantly, its sequestration in sediments that provide, together with mineral weathering, a powerful geological buffer of the carbon cycle.

Abraham Lerman

Bibliography

- Arrhenius, S., 1896. On the influence of carbonic acid in the air upon the temperature of the ground. *Phil. Mag.*, 5th ser., **41**, 237–276.
- Barker, D.S., 1997. Carbonatites. *McGraw-Hill Encycl. Sci. Technol.*, 8th ed., vol. 3, New York, NY: McGraw-Hill, pp. 239–240.
- Bassham, J.A., 1974. Photosynthesis. *Encycl. Brit., Macropaedia*, vol. 14, Chicago, IL: University of Chicago Press, pp. 365–373.
- Berner, R.A., and Canfield, D.L., 1989. A new model for atmospheric oxygen over Phanerozoic time. *Am. J. Sci.*, **289**, 333–361.
- Berner, R.A., and Kothavala, Z., 2001. Geocarb III: A revised model of atmospheric CO₂ over Phanerozoic time. *Am. J. Sci.*, **301**, 182–204.
- Berner, R.A., and Maasch, K.A., 1996. Chemical weathering and controls on atmospheric O₂ and CO₂: Fundamental principles were enunciated by J.J. Ebelmen, in 1845. *Geochim. Cosmochim. Acta*, **60**, 1633–1637.
- Clark, I.D., and Fritz, P., 1997. *Environmental Isotopes in Hydrology*. New York, NY: Lewis Publishers, 328pp.
- Dumas, J., 1842. *Essai de Statique Chimique des Êtres Organisés*. 2ème édit. Fortin, Masson, Paris, 4 + 88pp.
- Friedman, I., and O'Neil, J.R., 1977. Compilation of stable isotope fractionation factors of geochemical interest. In Fleischer, M. (ed.), *Data of Geochemistry*. 6th ed, U.S. Geol. Survey Prof. Pap. 440–KK.
- Gaffron, H., 1964. Photosynthesis. *Encycl. Brit.*, vol. 17, Chicago, IL: University of Chicago Press, pp. 855–856B.
- Graham, L., 1974. Heat. In *Encyclopedia Britannica, Macropaedia*, vol. 8, pp. 700–706; *Micropaedia*, vol. 4, p. 1007. Chicago, IL: University of Chicago Press.
- Hayes, J.M., Strauss, H., and Kaufman, A.J., 1999. The abundance of ¹³C in marine organic matter and isotopic fractionation in the global biogeochemical cycle of carbon during the past 800 Ma. *Chem. Geol.*, **161**, 103–125.
- Kvenvolden, K.A., 1988. Methane — a major reservoir of carbon on a shallow geosphere? *Chem. Geol.*, **71**, 41–51.
- Kvenvolden, K.A., and Lorenson, T.D., 2001. Global occurrences of natural gas hydrates. In Paull, C.E., and Dillon, W.P. (eds.), *Natural Gas Hydrates: Occurrence, Distribution, and Detection*. AGU Geophys. Monograph Series, vol. 124, pp. 3–18.
- Li, Y.-H., 2000. *A Compendium of Geochemistry: From Solar Nebula to the Human Brain*. Princeton, NJ: Princeton University Press, xiv + 475pp.
- Locklair, R.E., and Lerman, A., 2005. A model of Phanerozoic cycles of carbon and calcium in the global ocean: Evaluation and constraints on ocean chemistry and input fluxes. *Chem. Geol.*, **217**, 113–126.
- Lotka, A.J., 1925. *Elements of Physical Biology*. Baltimore, MD: Williams & Wilkins, xxx + 460pp. Also published as *Elements of Mathematical Biology*, 1956. New York, NY: Dover, pp. xxx + 465.
- Mackenzie, F.T., 2002. *Our Changing Planet*. Upper Saddle River, NJ: Prentice Hall, xii + 580pp.
- Mackenzie, F.T., and Lerman, A., 2006. Carbon in the Geobiosphere. Dordrecht, The Netherlands: Springer xxii + 402pp.
- Mackenzie, F.T., and Morse, J.W., 1992. Sedimentary carbonates through Phanerozoic time. *Geochim. Cosmochim. Acta*, **56**, 3281–3295.
- Meyer, B.S., 1964. Plant Physiology. *Encycl. Brit.*, vol. 18, Chicago, IL: University of Chicago Press, pp. 16–31.

- Mohr, F., 1875. *Geschichte der Erde*. 2. Aufl. Bonn, Germany: Verlag Max Cohen & Sohn, xx + 554pp.
- Mojzsis, S.J., Arrhenius G., McKeegan, K.D., Harrison, T.M., Nutman, A.P., and Friend, C.R.L., 1996. Evidence for life on Earth by 3800 Myr. *Nature*, **384**, 55–59.
- Mook, W.G., Bommerson, J.C., and Staverman, W.H., 1974. Carbon isotope fractionation between dissolved bicarbonate and gaseous carbon dioxide. *Earth Planet. Sci. Lett.*, **22**, 169–176.
- O'Leary, M.H., 1988. Carbon isotopes in photosynthesis. *Bioscience*, **38**, 328–335.
- Poldervaart, A., 1955. Chemistry of the Earth's surface. In Poldervaart, A. (ed.), *Crust of the Earth, Geol. Soc. Am. Spec. Pap.*, **62**, pp. 119–144.
- Rankama, K., and Sahama, Th.G., 1950. *Geochemistry*. Chicago, IL: Univ. Chicago Press, xvi + 912pp.
- Redfield, A.C., Ketchum, B.H., and Richards, F.A., 1963. The influence of organisms on the composition of seawater. In Hill, M.N. (ed.), *The Sea*, vol. 2, New York, NY: Wiley, pp. 26–77.
- Rosing, M.T., 1999. ¹³C-depleted carbon microparticles in >3700-Ma sea-floor sedimentary rocks from West Greenland. *Science*, **283**, 674–676.
- Rubey, W.W., 1951. Geologic history of seawater, an attempt to state the problem. *Geol. Soc. Am. Bull.*, **62**, 1111–1147.
- Rubey, W.W., 1955. Development of the hydrosphere and atmosphere, with special reference to probable composition of the early atmosphere. In Poldervaart, A. (ed.), *Crust of the Earth, Geological Society of America, Special Paper*, vol 62, pp. 631–650.
- Rubinson, M., and Clayton, R.N., 1969. Carbon-13 fractionation between aragonite and calcite. *Geochim. Cosmochim. Acta*, **33**, 997–1002.
- Salomons, W., and Mook, W.G., 1986. Isotope geochemistry of carbonates in the weathering zone. In Fritz, P., and Fontes, J. Ch. (eds.), *Handbook of Environmental Isotope Geochemistry*, vol. 2, The Terrestrial Environment, Amsterdam, The Netherlands: Elsevier, pp. 239–269.
- Thode, H.G., Shima, M., Rees, C.E., and Krishnamurty, K.V., 1965. Carbon-13 isotope effects in systems containing carbon dioxide, bicarbonate, carbonate, and metal ions. *Can. J. Chem.*, **43**, 582–595.
- Urey, H.C., 1952. *The Planets: Their Origin and Development*. New Haven, Conn.: Yale University Press, xvii + 245pp.
- Veizer, J., Ala, D., Azmy, K., Bruckschen, P., Buhl, D., Bruhn, F., Carden, G.A.F., Diener, A., Ebner, S., Godderis, Y., Jasper, T., Korte, C., Pawellek, F., Podlaha, O.G., and Strauss, H., 1999. ⁸⁷Sr/⁸⁶Sr, ^δ¹³C and ^δ¹⁸O evolution of Phanerozoic seawater. *Chem. Geol.*, **161**, 59–88.
- Ver, L.M.B., Mackenzie, F.T., and Lerman, A., 1999. Biogeochemical responses of the carbon cycle to natural and human perturbation: Past, present, and future. *Am. J. Sci.*, **299**, 762–801.
- Vogel, J.C., Grootes, P.M., and Mook, W.G., 1970. Isotopic fractionation between gaseous and dissolved carbon dioxide. *Zeitschr. Physik*, **230**, 225–238.
- Walker, J.C.G., 1977. *Evolution of the Atmosphere*. New York, NY: Macmillan Publishing, xiv + 318pp.
- Wallmann, K., 2004. Impact of atmospheric CO₂ and galactic cosmic radiation on Phanerozoic climate change and the marine ^δ¹⁸O record. *Geochim., Geophys. Geosyst.* doi: 10.1029/2003GC000683.
- Whitmarsh, J., and Govindjee, 1995. The photosynthetic process. In Singhal, G.S., Renger, G., Soppory, S.K., Irrgang, K.-D., and Govindjee (eds.), *Concepts in Photobiology: Photosynthesis and Photomorphogenesis*. Dordrecht, The Netherlands: Kluwer Academic, pp. 11–51.
- Wilkinson, B.H., and Algeo, T.J., 1989. Sedimentary carbonates record of calcium and magnesium cycling. *Am. J. Sci.*, **289**, 1158–1194.

Cross-references

[Archean Environments](#)
[Atmospheric Evolution, Earth](#)
[Carbon Dioxide, Dissolved \(Ocean\)](#)
[Carbon Isotope Variations Over Geologic Time](#)
[Carbon Isotopes, Stable](#)
[Faint Young Sun Paradox](#)
[Isotope Fractionation](#)
[Marine Biogenic Sediments](#)
[Marine Carbon Geochemistry](#)
[Methane Hydrates, Carbon Cycling, and Environmental Change](#)
[Ocean Paleoproductivity](#)
[Phosphorus Cycle](#)
[Weathering and Climate](#)

CARBON DIOXIDE AND METHANE, QUATERNARY VARIATIONS

Introduction

A straightforward method to reconstruct variations of atmospheric greenhouse gas concentrations during the past few hundred thousand years is the analysis of air enclosed in bubbles of suitable polar ice. For polar ice to be suitable, the possibility of any influence of melt water must be excluded, which is the case for very cold regions in the center of the Antarctic and the Greenland Ice Sheet, in part. Such ice is formed by the compaction of snow and firn by a dry sintering process. Atmospheric air is gradually enclosed in bubbles at the transition from firn to ice, typically 70–120 m below the surface. If the age of air in ice is defined as the time since its separation from the free atmosphere, it is clear that it is younger than the surrounding ice (defined as the time since deposition as snow). The age difference varies between a few decades for high accumulation rate sites and up to 5 millennia or more for low accumulation rate sites. For a given drilling site, the age difference generally varies with depth due to variations of temperature and accumulation rates in the past.

The gradual enclosure of air in bubbles also implies that air of an ice sample does not have a well-defined age but has a certain age distribution, depending on temperature and accumulation rate. This limits the possible time resolution of greenhouse gas records to a few years for high accumulation rate sites and more than a century for low accumulation rate sites. The air is well preserved in the bubbles. Diffusion of gases in cold ice is low. However, chemical reactions with impurities cannot be excluded, even in very cold ice.

The main foci of analyses of air samples extracted from air bubbles are the concentrations of the greenhouse gases CO₂ and CH₄, together with N₂O and the O₂/N₂ ratio. The isotopic composition of the gases is also of interest, especially in finding possible causes of observed variations. In the following description, only variations of the atmospheric concentration of the important greenhouse gases CO₂ and CH₄ will be discussed.

Records measured along the Antarctic Vostok (78° 28' S, 106° 48' E) core go back to 420,000 yrBP (Petit et al., 1999) and those from the recently drilled Dome C (75° 06' S, 123° 21' E) core date back to 740,000 yrBP (EPICA members, 2004). More detailed records are available for the last glacial epoch, the transition from the last glacial epoch to the Holocene, the Holocene and the last millennium. All these time intervals are discussed in separate sections.

Atmospheric CO₂ and CH₄ concentrations are relatively constant globally at any given time due to a short global mixing time. However, small CH₄ concentration differences between Greenland and Antarctica allow a rough estimate of the latitudinal distribution of CH₄ sources during different climatic epochs.

Analytical methods

To measure the CO₂ and CH₄ concentration of air enclosed in air bubbles of polar ice samples, the air has first to be extracted and then measured in a second step. For the extraction of air for CO₂ measurements, most laboratories use a dry extraction method to avoid any contamination with CO₂ that could be produced by the interaction of carbonates with water. Air

bubbles are opened mechanically by cracking, milling or grating ice samples at low temperature. For CH₄ measurements, air is removed by wet or dry extraction. In a typical wet extraction, ice is melted in an evacuated container and after all ice has melted, the sample is frozen very slowly from the bottom again to expel any air dissolved in the meltwater.

The CO₂ concentration in the air is measured by gas chromatography or by laser absorption spectroscopy. For the second method, a tunable infrared laser (wavelength about 4.23 μm) is tuned several times over the absorption line of a vibration-rotation transition of the CO₂ molecule. The CH₄ concentration is generally measured by gas chromatography. Measurement by laser absorption spectroscopy is possible but has not been used for routine measurements yet.

The minimal sample size for a single CO₂ measurement is 12 g ice; for a single CH₄ measurement, about 40 g ice is needed. Certain laboratories are using larger sample sizes but perform multiple analyses on the extracted air sample.

Reliability of CO₂ and CH₄ data from ice cores

The reproducibility of CO₂ measurements in air of polar ice samples is on the order of 1.5 ppmv. Results from direct atmospheric measurements of several ice cores that have an overlapping time period are in good agreement. However, this is no guarantee that the air in bubbles of older ice has exactly the composition of atmospheric air at the time of ice formation. CO₂ could be produced very slowly by carbonate-acid reactions or oxidation of organic material, or CO₂ dissolved or enclosed in micro bubbles in snowflakes could diffuse slowly into air bubbles. Only air from normal size bubbles and clathrates are extracted by dry extraction methods. The agreement of results for ice cores from various drill sites with different impurity concentrations show that the effect would be small, but cannot be excluded. For inland sites from Antarctica, it can be concluded that such artifacts are smaller than 5 ppmv.

The reproducibility of CH₄ measurements is about 10 ppbv. CH₄ is much less soluble in water than CO₂, but still twice as soluble as N₂. Therefore, it cannot be expected that analyses

of ice from locations with a mean temperature above -20°C will provide reliable results. Methane results are certainly less affected by chemical reaction between impurities in the ice, but a small production of CH₄ by chemical reactions or by biological activity cannot be excluded (Sowers, 2001).

Variations of atmospheric CO₂ and CH₄ concentrations during the past 650,000 years

Figure C5 shows variations of atmospheric CO₂ and CH₄ concentrations during the past 650,000 years compared with the Antarctic temperature derived from δD records. The CO₂ and CH₄ concentrations are based on analyses performed along the Vostok and the Dome C ice cores (Petit et al., 1999; Siegenthaler et al., 2005; Spahni et al., 2005). At Vostok, an ice core reached a depth of 3,623 m in 1998. The stratigraphy is undisturbed down to a depth of 3,310 m, and the ice at this depth is about 420,000 years old. More recently, an ice core was drilled at EPICA Dome C down to a depth of 3,270 m. The stratigraphy is probably undisturbed down to a depth of 3,200 m where the ice has an estimated age of about 800,000 years. Gas analyses have hitherto been published for ages up to 650,000 years. A very important result is that the atmospheric CO₂ and CH₄ concentrations never reached the present levels (about 370 ppm for CO₂ and 1,700 ppb for CH₄ in 2002) during this entire period.

The delta-deuterium (δD) record is a measure of regional temperature (see *Deuterium, deuterium excess*, this volume). A rather close correlation between variations of the two greenhouse gas concentrations and Antarctic temperature is obvious. CH₄ variations are more or less caused by climatic variations but there is also an important interplay between climatic and CO₂ variations, as will be discussed later.

Temperature during interglacial epochs before 430,000 yrBP was lower than in the subsequent interglacials but the duration of warm phases was longer. CO₂ concentrations were also lower in the interglacial epochs before 430,000 yrBP. At the end of glacial epochs, temperature started to increase between 600 and 2,800 years before the beginning of the increase in

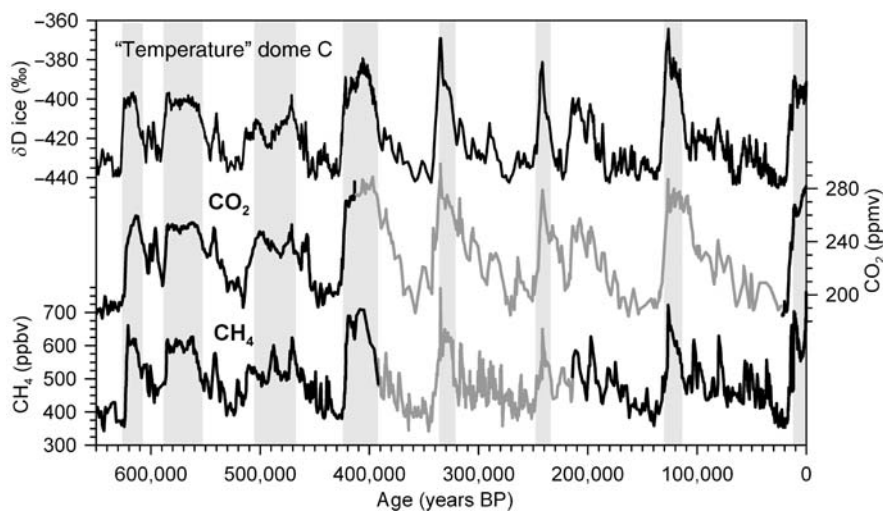


Figure C5 CO₂ and CH₄ records from Dome C and Vostok compared with the δD record from Dome C, which are characteristic for the local temperature (Petit et al., 1999; EPICA members, 2004; Siegenthaler et al., 2005; Spahni et al., 2005). Black lines are from Dome C, gray lines from Vostok. The shaded areas characterize interstadials.

the CO₂ concentration. This time lag does not call into question the interplay between temperature and CO₂ increase at the end of glacial epochs, which take place over several millennia.

The last glacial epoch

The last glacial epoch was characterized by large and fast temperature variations in Greenland, so called Dansgaard-Oeschger events, as documented by the $\delta^{18}\text{O}$ profile shown in Figure C6 (Dansgaard et al., 1993). The CH₄ concentration measured along the GRIP (Greenland Ice core Project) ice core shows variations parallel to the temperature variations, with higher concentrations during mild interstadials and lower concentrations in cold phases (Chappellaz et al., 1993). The variations are mainly caused by changes in CH₄ sources due to the productivity and the extension of wetlands in low and mid latitudes. The CH₄ variations are, therefore, a very convincing indication that Dansgaard-Oeschger events were not limited to Greenland but were climatic events of global significance.

The deuterium record from Antarctica and the $\delta^{18}\text{O}$ record from Greenland are scaled so that equal amplitudes correspond approximately to equal regional temperature variations. While these two records are quite different, the CH₄ records from Greenland and Antarctica are practically identical and show the same characteristics. Fast variations can, therefore, be used to synchronize age scales between Antarctic and Greenland ice core records (Blunier and Brook, 2001). This synchronization, however, shows an asynchrony in temperature variations between Greenland and Antarctica. As soon as a fast temperature increase in Greenland occurred, the temperature in Antarctica decreased.

The CO₂ concentrations measured along the Taylor Dome ice core (Indermühle et al., 2000) also show significant fluctuations but these are smoother and smaller than for CH₄. The variations are parallel to Antarctic temperature. Temperature variations in Antarctica were smaller than in Greenland, but

were accompanied by large variations in non-sea salt calcium deposition (nssCa) in Antarctica, indicating significant variations of terrestrial dust. A possible cause of the CO₂ variations with an amplitude of about 20 ppmv could, therefore, have been a variation of iron fertilization by eolian dust in the Southern Ocean (Röthlisberger et al., 2004).

The transition from the last glacial epoch to the Holocene

The transition from the last glacial epoch to the Holocene was the last large global temperature increase and was accompanied by a substantial increase in atmospheric CO₂ and CH₄. It is therefore a key period for investigating the interactions between global temperature and greenhouse gas concentrations. Figure C7 shows a section of Figure C6 with greater resolution (Monnin et al., 2001). The CO₂ concentration increased by 76 ppmv from 189 to 265 ppmv between about 17,000 and 11,100 yrBP in Antarctica. The increase occurred in four clearly distinguishable intervals. After a first, relatively fast (20 ppmv per thousand years) linear increase (I), a reduced linear increase followed in interval II, with a very fast increase of about 8 ppmv at its end. In interval III, characterized by a temperature decrease in Antarctica (Antarctic Cold Reversal), the CO₂ concentration also decreased slightly. In interval IV the CO₂ concentration increased at about the same rate as in interval I. This interval was concluded by another fast increase of about 6 ppmv, rising to 265 ppmv at the beginning of the Holocene.

The increase of the CO₂ concentration parallels the temperature increase in Antarctica, confirming that the Southern Ocean played a key role in causing the CO₂ increase. The rapid concentration increases at the end of interval II and IV occurred during rapid temperature increases in the Northern Hemisphere, indicating that it also had a significant global influence. Several

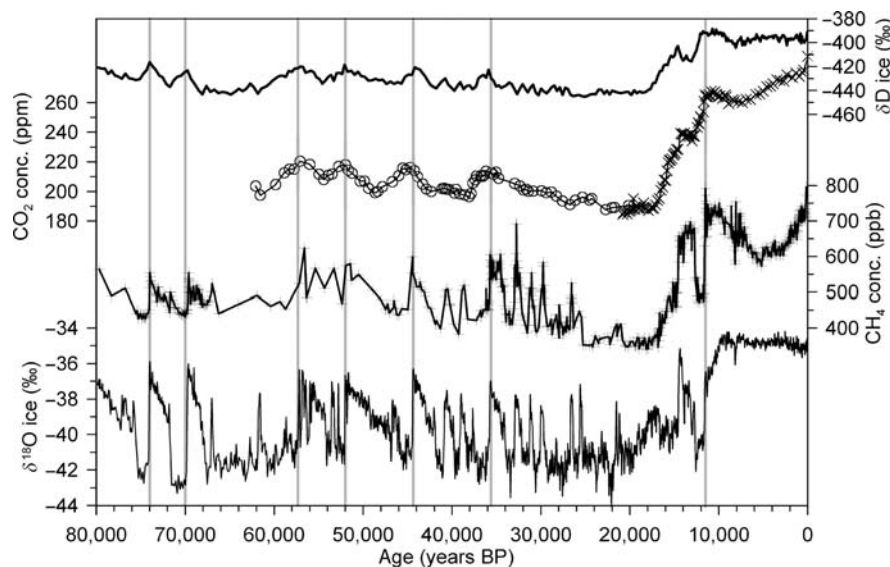


Figure C6 CO₂ and CH₄ records representing variations of the past 80,000 years compared with stable isotope records from Antarctica and Greenland, characterizing the corresponding local temperature (Chappellaz et al., 1993; Dansgaard et al., 1993; Indermühle et al., 2000; Blunier and Brook, 2001). Open circles of the CO₂ record are from Taylor Dome and diagonal crosses from Dome C ice cores (Antarctica). The δD record is also from Antarctica. The CH₄ record is from the Greenland GRIP ice core. Vertical lines highlight some important, fast temperature increases in Greenland ($\delta^{18}\text{O}$ curve).

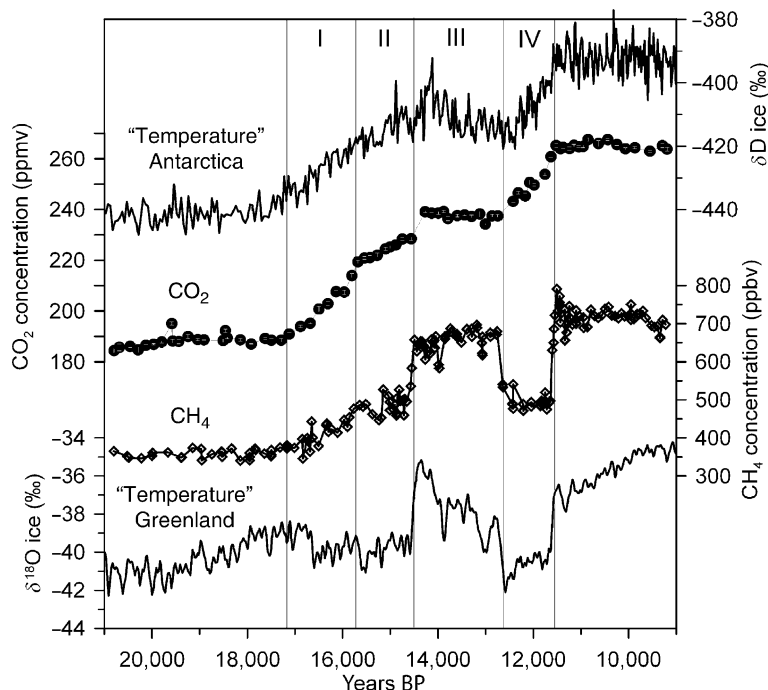


Figure C7 Evolution of the CO₂ and CH₄ concentration increases during the transition from the last glacial epoch to the Holocene, compared with records characterizing the temperature increases in Antarctica and Greenland (Monnin et al., 2001). Roman numerals mark the four time intervals mentioned in the text.

mechanisms have been suggested as causes for the atmospheric CO₂ increase: Reduced solubility of CO₂ in the Southern Ocean because of temperature increase, enhanced air-sea exchange due to reduced sea-ice extent, decreasing bioactivity due to reduced iron fertilization by eolian dust and changes in deepwater formation parallel to the fast temperature increases in the North Atlantic region.

The evolution of the atmospheric CH₄ concentration during the transitional periods is, as during Dansgaard-Oeschger events in the glacial epoch, approximately parallel to that of the Greenland δ¹⁸O record. However, the beginning of the CO₂ increase lags the beginning of the temperature increase by 800 ± 600 years (Monnin et al., 2001). This time lag is small compared with the duration of 6,000 years for the entire increase. It does not call into question the important amplification effect of the CO₂ increase with regards to the global temperature increase during the transition from the glacial epoch to the Holocene. The increase of atmospheric CO₂ concentration from 189 to 265 ppmv corresponds to a direct radiative forcing of about 2 W m^{-2} . The radiative forcing caused by CH₄ increase is about 10 times smaller (Joos, 2005). CH₄ increases parallel to fast temperature increases in Greenland are typically delayed by a few decades giving rise to the conclusion that CH₄ variations are mainly a response to abrupt northern climatic changes rather than a driver.

The Holocene

Ice cores from Taylor Dome and Dome C allow reconstruction of detailed records of the CO₂ and CH₄ concentration during the Holocene (Blunier et al., 1995; Flückiger et al., 2002; Indermühle et al., 1999; Monnin et al., 2004). Both records are shown in Figure C8. The CO₂ record clearly shows that the

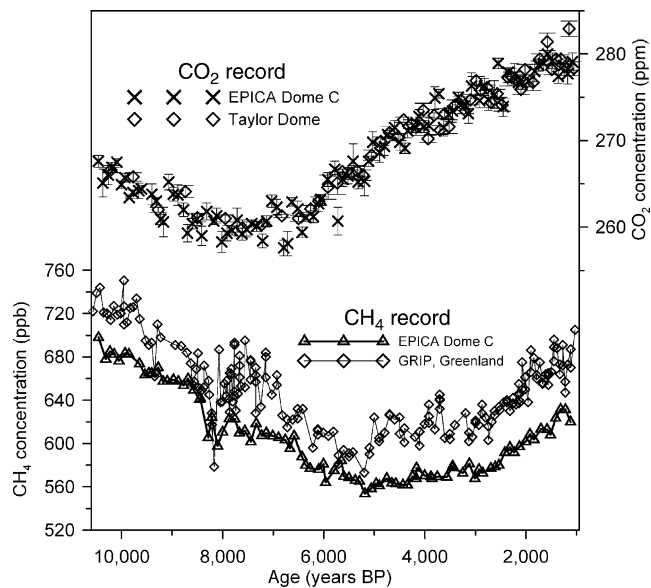


Figure C8 CO₂ and CH₄ records representing the pre-industrial Holocene (Blunier et al., 1995; Indermühle et al., 1998; Flückiger et al., 2002; Monnin et al., 2004). CH₄ concentrations in Greenland are on average about 40 ppbv higher than in Antarctica.

carbon cycle was not in a steady state during the Holocene. The CO₂ concentration decreased from 268 ppmv at 10,500 yBP to 260 ppmv at about 8,200 yBP and increased steadily in the following 7,000 years to about 280 ppmv at the beginning of

the last millennium. These variations are caused by the ocean and the terrestrial biosphere. An uptake of CO₂ by the terrestrial biosphere could be responsible for the decrease until 8,200 yrBP, with a release of CO₂ from the slightly relapsing biosphere and the ocean (due to an increase of the surface temperature) accounting for the increase afterwards. Because carbon in the terrestrial biosphere is significantly depleted in the carbon isotope ¹³C, it is quite clear that δ¹³C measured on CO₂ extracted from ice cores can help in estimating the relative contributions by the ocean and terrestrial biosphere. Based on presently available δ¹³C results, the CO₂ release by the ocean was responsible for about one third of the increase after 8,200 yrBP, and the release by the terrestrial biosphere responsible for about two thirds.

The atmospheric CH₄ concentration decreased in Antarctica from 720 ppbv at 10,500 yrBP to about 575 ppbv at about 5,000 yrBP. The results from the Greenland GRIP ice core show a larger scatter and are about 45 ppbv higher on average. The higher average in Greenland reflects the heterogeneous latitudinal distribution of CH₄ sources and the fact that the atmospheric residence time of CH₄ is only an order of magnitude longer than the inter-hemispheric exchange time. These differences between measured CH₄ concentrations in Greenland and Antarctica can be used to estimate a rough latitudinal distribution of CH₄ sources as will be outlined in a later section. The result of the estimate is that the CH₄ sources in the tropics were increasing from the Last Glacial Maximum until about 8,000 yrBP, then decreasing until about 5,000 yrBP and subsequently increasing again. Sources north of 30° N increased dramatically between the glacial maximum until about 10,000 yrBP, but surprisingly started to decrease again until 8,000 yrBP and increased again afterwards.

Remarkable is a significant CH₄ minimum that occurred for a short duration. It is synchronous with a temperature drop of about 7°C in Greenland and had a duration of 100–150 years. The CH₄ minimum is more pronounced in the Greenland record due to the higher accumulation rate. At Dome C in Antarctica, where the accumulation rate is more than six times lower, a signal of only about 100 year duration is attenuated by about 50% (Spahni et al., 2003).

The last millennium

The CO₂ and CH₄ concentrations were rather constant during the first eight centuries but increased dramatically during the last two centuries to values never experienced during the last 650,000 years, as shown in Figure C9. The CO₂ concentrations of different Antarctic ice cores are in good agreement, and also agree with the short overlapping interval and continuous direct atmospheric measurements, which started in 1958 (Blunier et al., 1995; Etheridge et al., 1996; MacFarling Meure et al., 2006). For the first eight centuries, they show a mean concentration of about 280 ppmv. Measurements from Greenland ice cores show significantly higher values, caused most probably by artifacts due to higher temperature and higher impurity concentrations. Greenland results are, therefore, not shown in Figure C9. The most detailed Antarctic record for the last millennium is available from the Law Dome ice core. The reproducibility of the measurements is 1.2 ppmv and individual results represent short time intervals due to a very high accumulation rate at the coastal Law Dome. The Law Dome record suggests an increase from about 279 ppmv at the beginning of the millennium to 282 ppmv at AD 1100, then a relatively

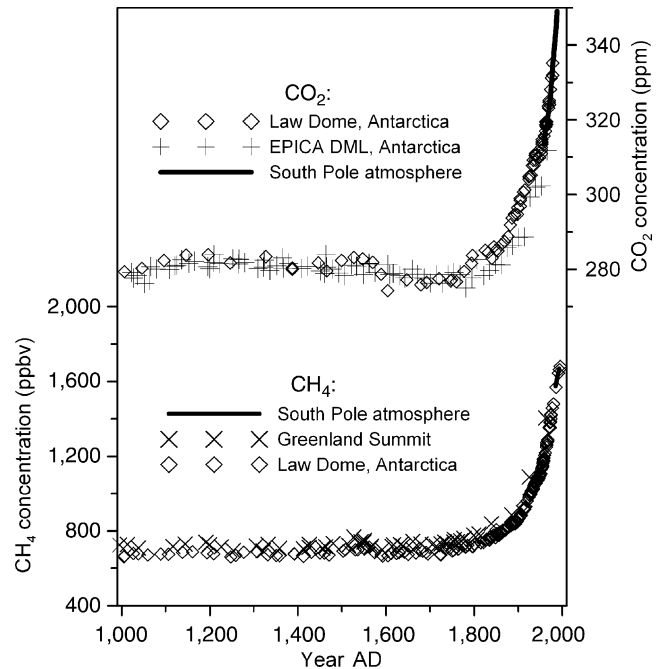


Figure C9 CO₂ records from Antarctica and CH₄ records from Greenland and Antarctica for the last millennium (Blunier et al., 1995; Etheridge et al., 1996; MacFarling Meure et al., 2006).

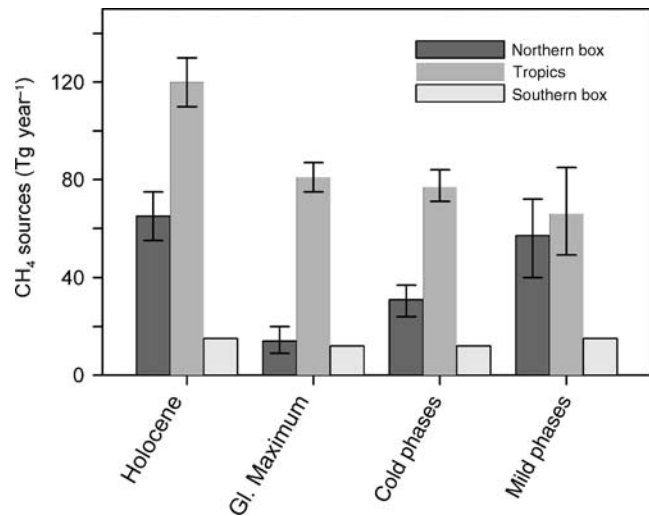


Figure C10 Estimated CH₄ sources for different climatic epochs from 90–30° N, 30° N–30° S and 30–90° S based on concentration differences between Greenland and Antarctica (Chappellaz et al., 1997; Dällenbach et al., 2000).

constant concentration until AD 1600, followed by a decrease to 277 ppmv, lasting until about AD 1750.

The CH₄ record shows relatively constant values of about 700 ppbv until AD 1750. Greenland values are slightly higher, but in this case it is assumed that this is not an artifact but is caused by the inter-hemispheric difference of the atmospheric concentration. Records from Law Dome again provide results that are more detailed. The concentration is about 640 ppbv at

the beginning of the millennium and shows smaller variations but also an increasing trend to a value of 700 ppbv at AD 1750. The increase could already be attributed to pre-industrial anthropogenic influences, such as expansion of rice cultivation and cattle.

Latitudinal distribution of pre-industrial CH₄ sources

Not only does the CH₄ concentration change with climatic variations but so does the inter-hemispheric concentration difference. This combination of results can be used to make a rough estimate of the latitudinal source distribution. In a simple model, sources in the three boxes 90–30° N (northern box), 30° N–30° S (tropical box) and 30–90° S (southern box) are taken into account (Chappellaz et al., 1997). It is assumed that the source in the southern box contributed 12 Tg yr⁻¹ during the cold periods of the last glacial period and 15 Tg yr⁻¹ during the mild periods of the last glacial epoch and the pre-industrial Holocene. The model results are shown in Figure C10 (Dällenbach et al., 2000). A remarkable, but still tentative, conclusion based on these estimates is that the CH₄ variations during the last glacial epoch were not mainly due to source changes in the tropics but in the northern box.

Bernhard Stauffer

Bibliography

- Blunier, T., and Brook, E.J., 2001. Timing of Millennial-Scale Climate change in Antarctica and Greenland during the Last Glacial Period. *Science*, **291**(5501), 109–112.
- Blunier, T., Chappellaz, J., Schwander, J., Stauffer, B., and Raynaud, D., 1995. Variations in atmospheric methane concentration during the Holocene epoch. *Nature*, **374**, 46–49.
- Chappellaz, J., Blunier, T., Raynaud, D., Barnola, J.M., Schwander, J., and Stauffer, B., 1993. Synchronous changes in atmospheric CH₄ and Greenland climate between 40 and 8 kyr BP. *Nature*, **366**, 443–445.
- Chappellaz, J., Blunier, T., Kints, S., Dällenbach, A., Barnola, J.-M., Schwander, J., Raynaud, D., and Stauffer, B., 1997. Changes in the atmospheric CH₄ gradient between Greenland and Antarctica during the Holocene. *J. Geophys. Res.*, **102**(D13), 15987–15999.
- Dällenbach, A., Blunier, B., Flückiger, J., Stauffer, B., Chappellaz, J., and Raynaud, D., 2000. Changes in the atmospheric CH₄ gradient between Greenland and Antarctica during the last glacial and the transition to the Holocene. *Geophys. Res. Lett.*, **27**(7), 1005–1008.
- Dansgaard, W., Johnsen, S.J., Clausen, H.B., Dahl-Jensen, D., Gundestrup, N.S., Hammer, C.U., Hvidberg, C.S., Steffensen, J.P., Sveinbjörnsdóttir, A.E., Jouzel, J., and Bond, G., 1993. Evidence for general instability of past climate from a 250 kyr ice-core record. *Nature*, **364**, 218–220.
- EPICA members, 2004. Eight glacial cycles from an Antractic ice core, *Nature*, **429**, 623–628.
- Etheridge, D.M., Steele, L.P., Langenfelds, R.L., Francey, R.J., Barnola, J.-M., and Morgan, V.I., 1996. Natural and anthropogenic changes in atmospheric CO₂ over the last 1000 years from air in Antarctic ice and firn. *J. Geophys. Res.*, **101**, 4115–4128.
- Flückiger, J., Monnin, E., Stauffer, B., Schwander, J., Stocker, T., Chappellaz, J., Raynaud, D., and Barnola, J.-M., 2002. High resolution Holocene N₂O ice core record and its relationship with CH₄ and CO₂. *Global Biogeochem. Cycles*, **16**(1), doi: 10.1029/2001GB001417.
- Indermühle, A., T.F. Stocker, F. Joos, H. Fischer, H.J. Smith, M. Wahlen, B. Deck, D. Mastroianni, J. Tschumi, T. Blunier, R. Meyer, B. Stauffer, 1999. Holocene carbon-cycle dynamics based on CO₂ trapped in ice at Taylor Dome, Antarctica. *Nature*, **398**, 121–126.
- Indermühle, A., Monnin, E., Stauffer, B., Stocker, T., and Wahlen, M., 2000. Atmospheric CO₂ concentration from 60 to 20 kyr BP from the Taylor Dome ice core, Antarctica. *Geophys. Res. Lett.*, **27**(5), 735–738.
- Joos, F., 2006. Radiative forcing and the ice core greenhouse gas record. *PAGES News*, **13**(3), 11–13.
- MacFarling Meure, C., Etheridge, D., Trudinger, C., Steele, P., Langenfelds, R., van Ommen, T., Smith, A., and Elkins, J., 2006. Law Dome CO₂, CH₄ and N₂O ice core records extended to 2000 years BP. *Geophys. Res. Lett.*, **33**, L14810, doi: 10.1029/2006GL026152.
- Monnin, E., Indermühle, A., Dällenbach, A., Flückiger, J., Stauffer, B., Stocker, T., Raynaud, D., and Barnola, J.-M., 2001. Atmospheric CO₂ Concentrations over the Last Glacial Termination. *Science*, **291**(5501), 112–114.
- Monnin, E., Steig, E.J., Siegenthaler, U., Kawamura, K., Schwander, J., Stauffer, B., Stocker, T.F., Morse, D.L., Barnola, J.-M., Bellier, B., Raynaud, D., and Fischer, H., 2004. Evidence for substantial accumulation rate variability in Antarctica during the Holocene, through synchronization of CO₂ in the Taylor Dome, Dome C and DML ice cores. *Earth Planet. Sci. Lett.*, **224**, doi: 10.1016/j.epsl.2004.05.007, 45–54.
- Petit, J.R., Jouzel, J., Raynaud, D., Barkov, N.I., Barnola, J.-M., Basile, I., Bender, M., Chappellaz, J., Davis, M., Delaygue, M., Delmotte, M., Kotlyakov, V.M., Legrand, M., Lipenkov, V.Y., Lorius, C., Pépin, L., Ritz, C., Saltzman, E., and Stievenard, M., 1999. Climate and atmospheric history of the past 420,000 years from the Vostok ice core, Antarctica. *Nature*, **399**, 429–436.
- Röthlisberger, R., Bigler, M., Wolff, E.W., Joos, F., Monnin, E., and Hutterli, M.A., 2004. Ice core evidence for the extent of past atmospheric CO₂ change due to iron fertilisation. *Geophys. Res. Lett.*, **31**, L16207, 1–4.
- Siegenthaler, U., Monnin, E., Kawamura, K., Spahni, R., Schwander, J., Stauffer, B., Stocker, T., Barnola, J.-M., and Fischer, H., 2005. Supporting evidence from the EPICA Dronning Maud Land ice core for atmospheric CO₂ changes during the past millennium. *Tellus*, **57B**, 51–57.
- Sowers, T., 2001. N₂O record spanning the penultimate deglaciation from the Vostok ice core. *J. Geophys. Res.*, **106**(D23), 31903–31914.
- Spahni, R., Schwander, J., Flückiger, J., Stauffer, B., Chappellaz, J., and Raynaud, D., 2003. The attenuation of fast atmospheric CH₄ variations recorded in polar ice cores. *Geophys. Res. Lett.*, **30**(11), 1571, doi: 10.1029/2003GL017093.
- Spahni, R., Chappellaz, J., Stocker, T.F., Loulergue, L., Hausammann, G., Kawamura, K., Flückiger, J., Schwander, J., Raynaud, D., Masson-Delmotte, V., and Jouzel, J., 2005. Atmospheric Methane and Nitrous Oxide of the Late Pleistocene from Antarctic Ice Cores. *Science*, **310**(5752), 1317–1321.

Cross-references

- [Antarctic Cold Reversal](#)
- [Carbon Isotopes, Stable](#)
- [Climate Variability and Change, Last 1,000 Years](#)
- [Dansgaard-Oeschger Cycles](#)
- [Deuterium, Deuterium Excess](#)
- [Holocene Climates](#)
- [Ice cores, Antarctica and Greenland](#)
- [Last Glacial Maximum](#)
- [Oxygen Isotopes](#)
- [Pleistocene Climates](#)
- [Quaternary Climate Transitions and Cycles](#)

CARBON DIOXIDE, DISSOLVED (OCEAN)

The ocean contains about 60 times more carbon in the form of dissolved inorganic carbon than in the pre-anthropogenic atmosphere (~600 Pg C). On time scales <10⁵ yr, the ocean is the largest inorganic carbon reservoir (~38,000 Pg C) in exchange with atmospheric carbon dioxide (CO₂) and as a result, the ocean exerts a dominant control on atmospheric CO₂ levels. The average concentration of inorganic carbon in the ocean is ~2.3 mmol kg⁻¹ and its residence time is ~200 ka.

Dissolved carbon dioxide in the ocean occurs mainly in three inorganic forms: free aqueous carbon dioxide (CO₂(aq)), bicarbonate (HCO₃⁻), and carbonate ion (CO₃²⁻). A minor form

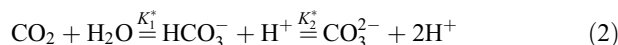
is true carbonic acid (H_2CO_3) whose concentration is less than 0.3% of $[\text{CO}_2(\text{aq})]$. The sum of $[\text{CO}_2(\text{aq})]$ and $[\text{H}_2\text{CO}_3]$ is denoted as $[\text{CO}_2]$. The majority of dissolved inorganic carbon in the modern ocean is in the form of HCO_3^- (>85%), as described below.

Carbonate chemistry

In thermodynamic equilibrium, gaseous carbon dioxide ($\text{CO}_2(\text{g})$), and $[\text{CO}_2]$ are related by Henry's law:

$$\text{CO}_2(\text{g}) \stackrel{K_0}{\rightleftharpoons} [\text{CO}_2] \quad (1)$$

where K_0 is the temperature and salinity dependent solubility coefficient of CO_2 in seawater (Weiss, 1974). The concentration of dissolved CO_2 and the fugacity of gaseous CO_2 , $f\text{CO}_2$, then obey the equation $[\text{CO}_2] = K_0 \times f\text{CO}_2$, where the fugacity is virtually equal to the partial pressure, $p\text{CO}_2$ (within ~1%). The dissolved carbonate species react with water, hydrogen and hydroxyl ions and are related by the equilibria:



The pK^* values ($= -\log(K^*)$) of the stoichiometric dissociation constants of carbonic acid in seawater are $pK_1^* = 5.94$ and $pK_2^* = 9.13$ at temperature $T = 15^\circ\text{C}$, salinity $S = 35$, and surface pressure $P = 1$ atm (Prieto and Millero, 2001). At typical surface seawater pH of 8.2, the speciation between $[\text{CO}_2]$, $[\text{HCO}_3^-]$, and $[\text{CO}_3^{2-}]$ is 0.5%, 89%, and 10.5%, respectively, showing that most of the dissolved CO_2 is in the form of HCO_3^- and not in the form of CO_2 (Figure C11). The sum of the dissolved carbonate species is denoted as total dissolved inorganic carbon (ΣCO_2):

$$\Sigma\text{CO}_2 = [\text{CO}_2] + [\text{HCO}_3^-] + [\text{CO}_3^{2-}] \quad (3)$$

This quantity is also represented as DIC, TIC, TCO_2 , and C_T . Another essential parameter to describe the carbonate system

is the total alkalinity (TA), a measure of the charge balance in seawater.

$$\text{TA} = [\text{HCO}_3^-] + 2[\text{CO}_3^{2-}] + [\text{B}(\text{OH})_4^-] + [\text{OH}^-] - [\text{H}^+] + \text{minor compounds} \quad (4)$$

ΣCO_2 and TA are conservative quantities, i.e., their concentrations measured in gravimetric units (mol kg^{-1}) are unaffected by changes in pressure or temperature, for instance, and they obey the linear mixing law. Therefore, they are the preferred tracer variables in numerical models of the ocean's carbon cycle. Of all the carbon species and carbonate system parameters described above, only $p\text{CO}_2$, pH, ΣCO_2 , and TA can be determined analytically. However, if any two parameters and total dissolved boron are known, all parameters ($p\text{CO}_2$, $[\text{CO}_2]$, $[\text{HCO}_3^-]$, $[\text{CO}_3^{2-}]$, pH, ΣCO_2 , and TA) can be calculated for a given T , S , and P (cf. Zeebe and Wolf-Gladrow, 2001).

Buffering

The dissolved carbonate species in seawater provide an efficient chemical buffer to various processes that change the properties of seawater. For instance, the addition of a strong acid such as hydrochloric acid (naturally added to the ocean by volcanism), is strongly buffered by the seawater carbonate system. In distilled water, the addition of HCl leads to an increase of $[\text{H}^+]$ and $[\text{Cl}^-]$ in solution in a ratio 1:1. This is not the case in seawater. For example, the addition of $1 \mu\text{mol kg}^{-1}$ HCl to distilled water at pH 7 reduces the pH to very close to 6. The same addition to seawater at pH 7 and $\Sigma\text{CO}_2 = 2,000 \mu\text{mol kg}^{-1}$ at $T = 15^\circ\text{C}$ and $S = 35$ only reduces the pH to 6.997. The seawater pH buffer is mainly a result of the capacity of CO_3^{2-} and HCO_3^- ions to accept protons.

One specific buffer factor, the so-called Revelle factor, is important in the context of the oceanic uptake of anthropogenic CO_2 . The Revelle factor, R , is given by the ratio of the relative

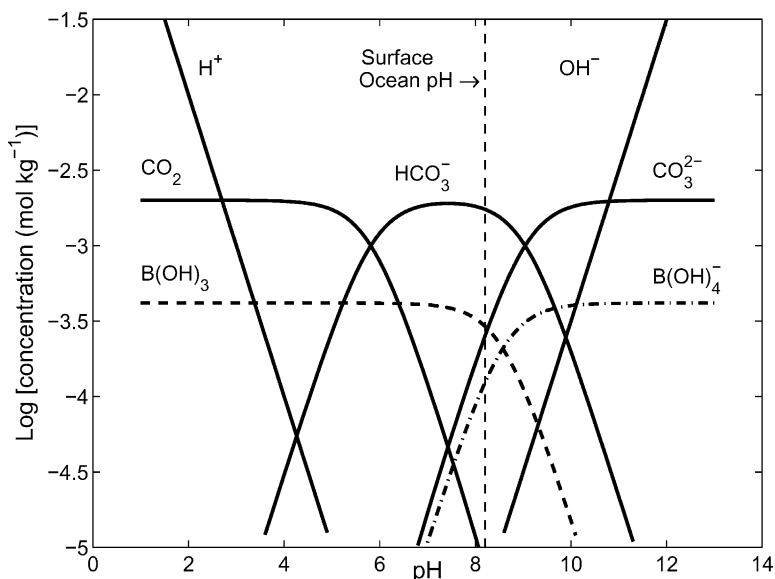


Figure C11 Concentrations of the dissolved forms of the carbonate system in seawater (so-called Bjerrum plot). $\Sigma\text{CO}_2 = 2,000 \mu\text{mol kg}^{-1}$, temperature $T = 15^\circ\text{C}$, salinity $S = 35$, and pressure $P = 1$ atm (after Zeebe and Wolf-Gladrow, 2001).

change of atmospheric $p\text{CO}_2$ (in equilibrium with dissolved CO_2) to the relative change of ΣCO_2 in seawater:

$$R = (d[p\text{CO}_2]/[p\text{CO}_2])_a / (d\Sigma\text{CO}_2/\Sigma\text{CO}_2)_{\text{sw}} \quad (5)$$

and varies roughly between 8 and 15, depending on temperature and $p\text{CO}_2$. As a consequence, the current increase of ΣCO_2 in surface seawater occurs not in a 1:1 ratio to the increase of atmospheric CO_2 (the latter being mainly caused by fossil fuel burning). Rather, a doubling of $p\text{CO}_2$ will only lead to an increase of ΣCO_2 of the order of 10%.

ΣCO_2 and TA of a water parcel

Important processes that can change the carbonate chemistry of a water parcel in the ocean can be described by considering changes in ΣCO_2 and TA (Figure C12). Invasion of CO_2 from (or release to) the atmosphere increases (or decreases) ΣCO_2 , respectively, while TA stays constant. This leads to a rise and drop of $[\text{CO}_2]$, respectively, with opposite change in pH (as CO_2 is a weak acid). Respiration and photosynthesis lead to the same trends, except that TA changes slightly due to nutrient release and uptake. CaCO_3 precipitation decreases ΣCO_2 and TA in a ratio 1:2, and, counterintuitively, increases $[\text{CO}_2]$ although inorganic carbon has been reduced. For a qualitative understanding, consider the chemical reaction



which indicates that during CaCO_3 precipitation CO_2 is liberated. Quantitatively, however, the conclusion that $[\text{CO}_2]$ in solution

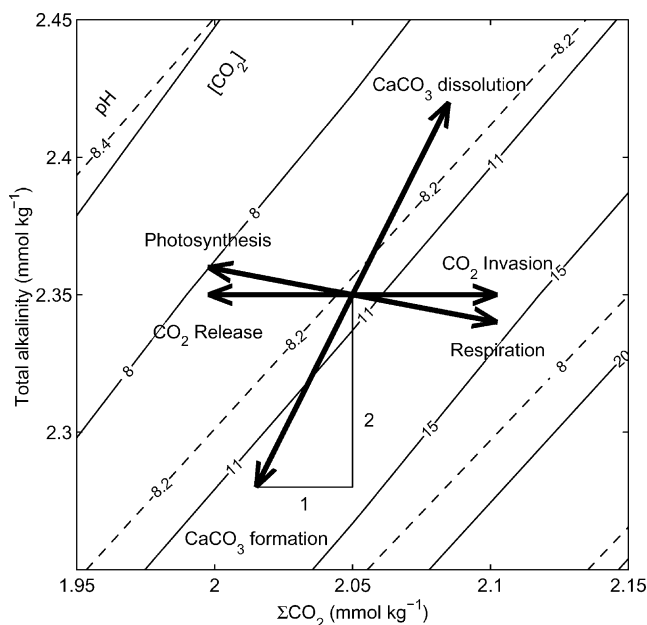


Figure C12 Important processes changing the carbonate chemistry of a water parcel in the ocean (values shown refer to $T = 15^\circ\text{C}$, $S = 35$, and $P = 1$ atm). Solid and dashed lines indicate contours of constant dissolved CO_2 and pH, respectively. Many processes are most easily described by considering changes in ΣCO_2 and TA. For example, the invasion of CO_2 increases ΣCO_2 while TA stays constant, which leads to an increase of dissolved CO_2 and a decrease of pH (as CO_2 is a weak acid).

is increasing by one mole per mole CaCO_3 precipitated is incorrect because of buffering. The correct analysis takes into account the decrease of ΣCO_2 and TA in a ratio 1:2 and the buffer capacity of seawater. That is, the medium gets more acidic because the decrease in alkalinity outweighs that of total carbon and hence $[\text{CO}_2]$ increases. For instance, at surface water conditions ($\Sigma\text{CO}_2 = 2,000 \mu\text{mol kg}^{-1}$, $\text{pH} = 8.2$, $T = 15^\circ\text{C}$, $S = 35$), $[\text{CO}_2]$ increases by only $\sim 0.03 \mu\text{mol}$ per $\mu\text{mol CaCO}_3$ precipitated.

Measurements and data

As stated above, the following parameters of the carbonate system can be determined experimentally: $p\text{CO}_2$, pH, ΣCO_2 , and TA. The $p\text{CO}_2$ of a seawater sample refers to the $p\text{CO}_2$ of a gas phase in equilibrium with that seawater sample. It is usually measured by equilibrating a small volume of gas with a large volume of seawater at given temperature. Then the mixing ratio of $\text{CO}_2(\text{g})$ in the gas phase is determined either using a gas chromatograph or an infrared analyzer. Finally, the $p\text{CO}_2$ is calculated from the mixing ratio. pH is routinely measured using a glass/reference electrode cell or spectrophotometrically using an indicator dye. ΣCO_2 is usually measured by an extraction/coulometric method or a closed cell titration. A potentiometric titration is used to determine TA. For summary, see DOE (1994) and Grasshoff et al. (1999).

A great volume of data on the carbonate chemistry of the oceans has been obtained over the last few decades through programs such as GEOSECS (Geochemical Ocean Sections Study), TTO (see Transient Tracers in the Oceans), and WOCE (World Ocean Circulation Experiment). Much of these data are available through CDIAC (Carbon Dioxide Information Analysis Center) at <http://cdiac.ornl.gov>.

Distribution of ΣCO_2 and TA

The vertical distribution of ΣCO_2 in the ocean is a result of the so-called biological and physical carbon pumps. Uptake of carbon into organic matter and production of CaCO_3 in the surface ocean, the transport to deeper layers, and the remineralization at depth (biological pump) reduces ΣCO_2 in surface waters while ΣCO_2 in deep water increases (Figure C13a). The increased solubility of CO_2 in high-latitudes at low temperatures where the ocean's deep water forms and descends to the abyss leads to the same vertical trend in ΣCO_2 (physical pump). Vertical profiles of TA in the ocean (Figure C13b) are mostly governed by production and dissolution of CaCO_3 . Generally, uptake of Ca^{2+} and CO_3^{2-} in the surface and release in the deep ocean reduces and increases TA, respectively. This is similar to the cycling of organic carbon and ΣCO_2 but the maximum in TA occurs at greater depth because CaCO_3 is mainly redissolved in deep water. The vertical distribution of ΣCO_2 and TA constitutes one major control on atmospheric CO_2 concentrations. For example, without the biological pump, the pre-anthropogenic atmospheric CO_2 concentration would have been >500 ppmv (parts per million by volume) rather than 280 ppmv (Maier-Reimer et al., 1996).

The horizontal distribution of CO_2 and ΣCO_2 in the surface ocean is mainly governed by the temperature-dependent solubility of CO_2 on interannual timescales. Warm low-latitude surface water generally holds less CO_2 ($\sim 10 \mu\text{mol kg}^{-1}$) and ΣCO_2 ($\sim 2,000 \mu\text{mol kg}^{-1}$) than cold high-latitude surface water ($\text{CO}_2 \sim 15 \mu\text{mol kg}^{-1}$ and $\Sigma\text{CO}_2 \sim 2,100 \mu\text{mol kg}^{-1}$), because of the enhanced solubility at low temperature. Locally,

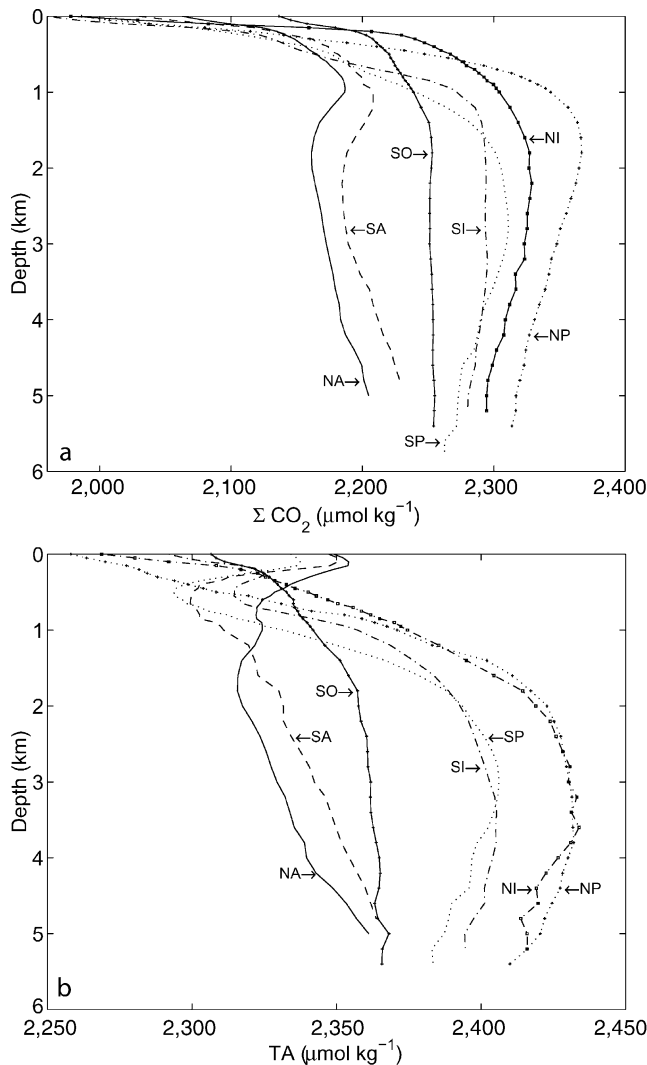


Figure C13 Average vertical distribution of ΣCO_2 (a) and TA (b) in the oceans. NA/SA: North/South Atlantic, SO: Southern Ocean, NI/SI: North/South Indian, NP/SP: North/South Pacific. The data (www.ewoce.org) were compiled using Ocean Data View (Schlitzer, R., www.awi-bremerhaven.de/GEO/ODV).

and on seasonal time scales, however, significant deviations from these general patterns may occur due to changes in salinity and processes such as biological activity, upwelling, temperature variations, river runoff, and other processes that affect ΣCO_2 and TA.

Deep ocean circulation, whose mass transport is predominantly from the North Atlantic through the Southern Ocean into the Indian and Pacific Ocean, produces horizontal deep-water gradients in ΣCO_2 and TA. While the details of deep ocean circulation are much more complex in general, the “youngest” water, which was most recently in contact with the atmosphere, resides in the Atlantic, whereas the “oldest” water resides in the Pacific. As a corollary, the water in the deep North Pacific has collected the most respired CO_2 on its way and thus has the highest ΣCO_2 (Figure C13a).

Inventories of ΣCO_2 and TA over time

Under most natural conditions, the global inventories of ΣCO_2 and TA constitute one major control on atmospheric CO_2 concentrations. Understanding changes of these inventories over time is therefore crucial to understanding climate. Thus, the characterization of the dominant carbon and alkalinity fluxes on different time scales is of fundamental importance. [Note that due to our limited knowledge on this subject, the following analysis is to be considered a simplification (Sundquist, 1986)].

Millennial ($<10^3$ yr) timescale

On timescales shorter than $\sim 10^3$ yr, the natural reservoirs that exchange carbon with the ocean are the atmosphere (pre-anthropogenic inventory ~ 600 Pg C), the biosphere (~ 550 Pg C), and soils ($\sim 1,500$ Pg C) and thus the oceanic inventory of ΣCO_2 ($\sim 38,000$ Pg C) can be considered essentially constant. Exceptions to this are potential rapid carbon inputs from otherwise long-term storage reservoirs. Examples are the current combustion of fossil fuel carbon by humans (which will eventually be mostly absorbed by the ocean), and catastrophic events such as possible impact events over carbonate platforms, or abrupt methane releases from gas hydrates (as postulated for the Paleocene-Eocene Thermal Maximum).

Glacial-interglacial (10^3 – 10^5 yr) timescale

On timescales of 10^3 – 10^5 yr, fluxes between reactive carbonate sediments ($\sim 5,000$ Pg C) and the ocean’s inventories of ΣCO_2 and TA have to be considered as well. Oceanic inventories may vary, for instance, during glacial cycles (see so-called calcite compensation below). The magnitude of these changes is, however, limited and so are associated changes in atmospheric CO_2 .

Tectonic ($>10^5$ yr) timescale

A large amount of carbon is locked up in the Earth’s crust as carbonate carbon ($\sim 70 \times 10^6$ Pg C) and as elemental carbon in shales and coals ($\sim 20 \times 10^6$ Pg C). On time scales $>10^5$ yr, this reservoir is active and imbalances in the fluxes to and from this pool can lead to drastic changes in ΣCO_2 and TA and atmospheric CO_2 . The balance between CO_2 consumption by subduction of marine sediments, weathering, subsequent carbonate burial, and volcanic degassing of CO_2 are the dominant processes controlling carbon fluxes on this time scale (Berner et al., 1983). This so-called rock cycle is driven by tectonic processes that lead to changes in seafloor spreading rates and continental uplift.

$[\text{CO}_3^{2-}]$ and CaCO_3 saturation

The accumulation and dissolution of reactive CaCO_3 sediments in the deep sea provide a powerful feedback to regulating the carbonate ion content ($[\text{CO}_3^{2-}]$) and thus the concentration of dissolved CO_2 in the ocean. The inventory of carbonate ion in the ocean cannot be viewed independently of carbonate sediments because of the control of CO_3^{2-} on the solubility of CaCO_3 . In today’s ocean, there is a close correspondence between $[\text{CO}_3^{2-}]$ of deep water and the observed distribution of CaCO_3 in deep sea sediments. Depending on the geographic location, there is a certain depth above which the ocean floor is mainly covered with calcite, while it is largely calcite-free

below this depth. The depth at which the sediments are virtually free of calcium carbonate is called the calcium carbonate compensation depth (CCD). The transition from calcite-rich to calcite-depleted sediments is not abrupt but gradual and the depth of rapid increase in the rate of dissolution as observed in sediments is called the calcite lysocline. Aragonite is more soluble than calcite and the aragonite lysocline occurs at shallower depth than the calcite lysocline. In the Pacific, the aragonite lysocline can be as shallow as 500 m and ~3 km in the Atlantic. The calcite lysocline lies at ~3–4 km in the Pacific and between 4 and 5 km in the Atlantic.

The reason for the disappearance of CaCO_3 at depth is the increase of solubility with pressure and thus with depth. The CaCO_3 saturation state of seawater is expressed by Ω :

$$\Omega = \frac{[\text{Ca}^{2+}]_{\text{sw}} \times [\text{CO}_3^{2-}]_{\text{sw}}}{K_{\text{sp}}^*} \quad (7)$$

where $[\text{Ca}^{2+}]_{\text{sw}}$ and $[\text{CO}_3^{2-}]_{\text{sw}}$ are the concentrations of Ca^{2+} and CO_3^{2-} in seawater and K_{sp}^* is the solubility product of calcite or aragonite at the in situ conditions of temperature, salinity, and pressure. Values of $\Omega > 1$ signify supersaturation and $\Omega < 1$ signify undersaturation. Because K_{sp}^* increases with pressure (the temperature effect is small) there is a transition of the saturation state from $\Omega > 1$ (calcite-rich) to $\Omega < 1$ (calcite-depleted) sediments at depth.

In the modern ocean, $[\text{Ca}^{2+}]_{\text{sw}}$ is large (compared to $[\text{CO}_3^{2-}]_{\text{sw}}$) and virtually constant (except for variations in salinity) and thus variations of the saturation state are controlled by variations in $[\text{CO}_3^{2-}]_{\text{sw}}$. The crossover of $[\text{CO}_3^{2-}]_{\text{sw}}$ and the carbonate ion concentration at calcite saturation is called calcite saturation horizon. The feedback that controls the average carbonate ion content of seawater and the distribution of CaCO_3 on a multi-millennial time scale via variations of the saturation horizon is called calcite compensation. This in turn exerts a major control on dissolved CO_2 and alkalinity in the ocean.

Calcite compensation

Calcite compensation maintains the balance between CaCO_3 weathering fluxes into the ocean and CaCO_3 burial fluxes in marine sediments on time scales of 10^3 – 10^5 yr (Broecker and Peng, 1987). In steady state, the riverine flux of Ca^{2+} and CO_3^{2-} ions from weathering must be balanced by burial of CaCO_3 in the sea, otherwise $[\text{Ca}^{2+}]$ and $[\text{CO}_3^{2-}]$ would rise or fall. The feedback that maintains this balance works as follows. Assume that there is an excess weathering influx of Ca^{2+} and CO_3^{2-} over burial of CaCO_3 . Then, the concentrations of Ca^{2+} and CO_3^{2-} in seawater increase, which leads to an increase of the CaCO_3 saturation state. This in turn leads to a deepening of the saturation horizon and to an increased burial of CaCO_3 just until the burial again balances the influx. The new balance is restored at higher $[\text{CO}_3^{2-}]$ than before.

ΣCO_2 and $\delta^{13}\text{C}$

In the ocean, there is an inverse relationship between the vertical distribution of ΣCO_2 and the stable carbon isotope ratio $^{13}\text{C}/^{12}\text{C}$ of ΣCO_2 ($\delta^{13}\text{C}_{\Sigma\text{CO}_2}$). In the surface ocean, phytoplankton takes up inorganic carbon to produce organic carbon via photosynthesis. This process discriminates against the heavy isotope ^{13}C such that the organic carbon is depleted in ^{13}C and, as a result, surface ΣCO_2 becomes enriched in ^{13}C . At

depth, the process is reversed. The organic carbon settling down to intermediate and deep waters is remineralized and the “isotopically light” carbon is set free, which causes deep ΣCO_2 to become enriched in ^{12}C (i.e., it has relatively less ^{13}C). In today’s ocean, the mean difference in $\delta^{13}\text{C}$ of ΣCO_2 between surface and deep ocean is $\Delta\delta^{13}\text{C} \cong 2\text{‰}$. In a very simple two-box view of the ocean, one can show that $\Delta\delta^{13}\text{C}$ depends on the strength of the carbon export to deep water (biological pump), the photosynthetic fractionation factor (Δ^{photo}), and mean ΣCO_2 of the ocean (Broecker, 1982):

$$\Delta\delta^{13}\text{C} = \Delta^{\text{photo}} \times \Delta\Sigma\text{CO}_2 / \Sigma\text{CO}_2 \quad (8)$$

where $\Delta\Sigma\text{CO}_2$ is the surface-to-deep difference in ΣCO_2 due to the biological pump. Given information on past $\Delta\delta^{13}\text{C}$ from differences in $\delta^{13}\text{C}$ of planktonic and benthic foraminifera, and assumptions regarding the strength of the biological pump, and Δ^{photo} , estimates of ΣCO_2 of past oceans have been derived (e.g., Shackleton, 1985).

Richard E. Zeebe and Dieter A. Wolf-Gladrow

Bibliography

- Berner, R.A., Lasaga, A.C., and Garrels, R.M., 1983. The carbonate-silicate geochemical cycle and its effect on atmospheric carbon dioxide over the past 100 million years. *Am. J. Sci.*, **283**, 641–683.
- Broecker, W.S., 1982. Ocean chemistry during glacial times. *Geochim. Cosmochim. Acta*, **46**, 1689–1705.
- Broecker, W.S., and Peng, T.-H., 1987. The role of CaCO_3 compensation in the glacial to interglacial atmospheric CO_2 change. *Global Biogeochem. Cycles*, **1**, 5–29.
- DOE 1994. *Handbook of methods for the analysis of the various parameters of the carbon dioxide system in sea water*, version 2, Dickson, A.G., and Goyet, C. (eds.), ORNL/CDIAC-74.
- Grasshoff, K., Kremling, K., and Ehrhardt, M. (eds.) 1999. *Methods of Seawater Analysis*, Weinheim: Wiley-VCH, 600pp.
- Maier-Reimer, E., Mikolajewicz, U., and Winguth, A., 1996. Future ocean uptake of CO_2 : Interaction between ocean circulation and biology. *Climate Dyn.*, **12**, 711–721.
- Prieto, F.J.M., and Millero F.J., 2001. The values of $\text{p}K_1$ and $\text{p}K_2$ for the dissociation of carbonic acid in seawater. *Geochim. Cosmochim. Acta*, **66**(14), 2529–2540.
- Shackleton, N.J., 1985. Oceanic carbon isotope constraints on oxygen and carbon dioxide in the Cenozoic atmosphere. In Sundquist, E.T., and Broecker, W.S. (eds.), *The Carbon Cycle and Atmospheric CO_2 : Natural Variations Archean to Present*. Geophys. Monogr. Ser., vol. 32, Washington DC: AGU, pp. 412–417.
- Sundquist, E.T., 1986. Geologic Analogs: Their value and limitations in carbon dioxide research. In Trabalka, J.R., and Reichle, D.E. (eds.), *The Changing Carbon cycle: A Global Analysis*. New York: Springer-Verlag, pp. 371–402.
- Weiss, R.F., 1974. Carbon dioxide in water and seawater: The solubility of a non-ideal gas. *Mar. Chem.*, **2**, 203–215.
- Zeebe, R.E., and Wolf-Gladrow, D.A., 2001. *CO_2 in Seawater: Equilibrium, Kinetics, Isotopes*. Amsterdam: Elsevier Oceanography Series, 346pp.

Cross-references

[Carbon Cycle](#)
[Carbon Dioxide and Methane, Quaternary Variations](#)
[Carbon Isotopes, Stable](#)
[Carbonate Compensation Depth](#)
[Marine Carbon Geochemistry](#)
[Methane Hydrates, Carbon Cycling, and Environmental Change](#)
[Paleo-Ocean pH](#)
[Quaternary Climate Transitions and Cycles](#)
[Thermohaline Circulation](#)

CARBON ISOTOPE VARIATIONS OVER GEOLOGIC TIME

In order to understand quantitatively the evolution of the Earth we have to deal with two types of records, direct and indirect (proxies). The isotopic composition of past seawater may be about the best proxy reflecting the evolution of our planet. This is because, due to its mixing rate of $\sim 1,000$ years, seawater is well mixed on million-year timescales and registers a globally averaged signal. The latter, however, is true only for chemical species with seawater residence times in excess of the mixing rate of the oceans. This contribution discusses the basic structures of the isotopic seawater curves for carbon on billion to million years of geologic history, a time scale well beyond the residence time of inorganic carbon in seawater that is about 2–4 thousand years (Ka).

The recording media

Apart from inclusions of possible modified seawater in Phanerozoic salts, no samples of ancient seawater are available for direct isotope studies. We have to rely therefore on biominerals and sediments precipitated from seawater, such as carbonate rocks and shells. Note that the evolution of seawater is a temporal continuum. In contrast, the recording media are generated by episodic events (sedimentation, biomineralization), that is they represent a point in time. It is estimated that for shallow marine sequences the sediments represent only $\sim 1/30$ of the elapsed time. The situation is somewhat better for deep-sea sediments, but in each case the erosional and non-depositional episodes represent more time than the actual sedimentary record. This imposes constraints on correlation of higher order patterns in the isotopic records of paleoseawater.

Carbonate components formed in seawater are orthorhombic aragonite (A) and rhombohedral calcite, the latter further subdivided into low-Mg calcite (LMC) with less than 4 mole% MgCO_3 and high-Mg calcite (HMC) with 4–28 mole-% MgCO_3 . The molar Mg/Ca ratio for present-day seawater is 5:1 and inorganically precipitated phases should be either A or HMC with about 7 mole-% MgCO_3 . LMC in marine environments is known mostly from the shells of some organisms, such as pelagic foraminifera, belemnites or brachiopods. Other organisms have shells composed of various combinations of A, HMC, and LMC. On average, shallow marine carbonate sediments, containing inorganically precipitated phases and skeletal debris, are composed of variable mixtures of HMC and A. Deep-sea oozes, on the other hand, consist almost exclusively of pelagic skeletal material and are predominantly LMC. The primary minerals that compose the sediment become exposed to the influence of meteoric waters and/or are subjected to higher pressures and temperatures during burial, rendering the original mineralogical assemblage unstable and converting them into a monomineralic limestone or dolostone.

Incorporation of carbon into carbonates

The incorporation of C isotopes into carbonate minerals (Hoefs, 1980) is governed by the so-called fractionation factor α :

$$R_S = \alpha_S - W R_W \quad (1)$$

where R is the ratio of relative abundances of isotopes, in this instance, $^{13}\text{C}/^{12}\text{C}$, the subscript S represents the solid carbonate

phase, and W stands for water (and its solutes, such as carbon species). Since α -values are close to unity and their variations are mostly in the third decimal place, the difference in α_{S-W} is better expressed in whole units as per mil ‰. Thus,

$$\Delta_{S-W} = \left[\left(\frac{R_S}{R_W} \right) - 1 \right] \times 10^3 = (\alpha_{S-W} - 1) \times 10^3 \quad (2)$$

For reasons connected with the design of mass spectrometers, it is easier to compare the measured isotope ratio (R_S) of an unknown sample to a standard with known R , and to express the measured difference as

$$\delta_S = \left[\left(\frac{R_S}{R_{\text{Standard}}} \right) - 1 \right] \times 10^3 \quad (3)$$

For carbon isotope studies in carbonate rocks, the standard usually utilized is the PDB (*Belemnitella americana* from the Cretaceous Peedee Formation of South Carolina).

The equilibrium isotopic fractionation factor α is inversely proportional to temperature and the relationship takes the form:

$$\ln \alpha = AT^{-2} + BT^{-1} + C \quad (4)$$

where A, B and C are constants determined experimentally and T is absolute temperature in degrees Kelvin. However, the temperature dependence of α for C isotopes is relatively small. Gaseous CO_2 that diffuses into seawater then dissociates and can finally precipitate as a CaCO_3 mineral, with fractionation involved at each step. The temperature dependencies of fractionation factors between $\text{CO}_2(\text{gas})$ and the $\text{CO}_2(\text{aq})$ (α_1), HCO_3^- (α_2), CO_3^{2-} (α_3) and calcite (α_4), respectively, are as follows:

$$1,000 \ln \alpha_1 = 0.0063 (10^6 T^{-2}) - 0.91 \quad (5)$$

$$1,000 \ln \alpha_2 = 1.099 (10^6 T^{-2}) - 4.54 \quad (6)$$

$$1,000 \ln \alpha_3 = 0.87 (10^6 T^{-2}) - 3.4 \quad (7)$$

$$1,000 \ln \alpha_4 = 1.194 (10^6 T^{-2}) - 3.63 \quad (8)$$

The overall variations in $\delta^{13}\text{C}$ of natural calcites induced by temperature are usually less than the scatter caused by other factors (about 0.04‰ per 1°C) and marine calcites have $\delta^{13}\text{C}$ mostly close to 0‰ PDB. Theoretically, the CaCO_3 should be enriched by about 1–3‰ in ^{13}C relative to the total dissolved C, because bicarbonate is the dominant C species in natural waters. In addition, aragonite should be somewhat enriched in ^{13}C relative to calcite. At 25°C , the theoretical calculations yield about a 0.9‰ enhancement, whereas the observed experimental enrichment has been about 1.8‰.

Disequilibrium phenomena

In nature, observed isotopic ratios deviate from the theoretical equilibrium values because of *kinetic factors*. Of these, perhaps the rate of precipitation of solid phases is the most important variable. Usually, the faster the rate, the closer α is to unity. The situation is still more complex if biomineralization is involved. Secretion of carbonate skeletons may proceed under equilibrium conditions or result in non-equilibrium fractionation of isotopes, known as *biogenic fractionations* or *vital effects* (Figure C14a). Such effects may be a consequence of biochemical processes that influence the kinetics of shell formation, result from incorporation of metabolic ^{13}C -depleted

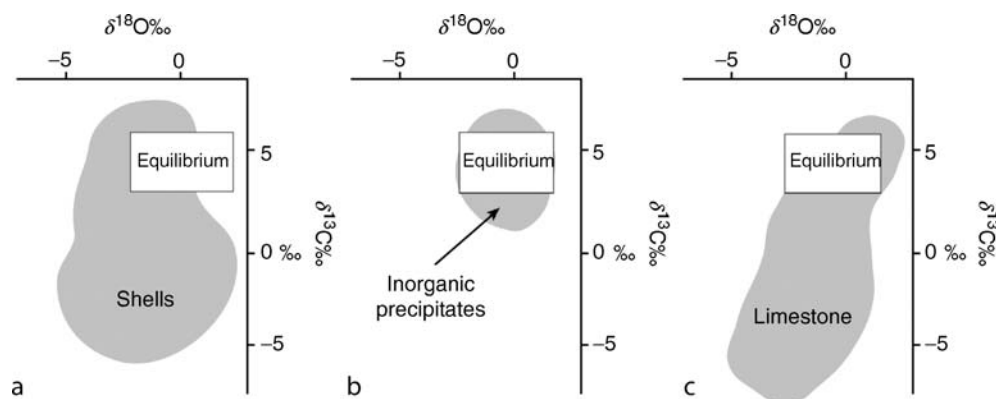


Figure C14 Oxygen and carbon isotopic composition of modern carbonate components. (a) The range observed in modern shells, (b) in “inorganic” precipitates, and (c) in diagenetically stabilized limestones. Box delineates the range of values in equilibrium with present day seawater. Modified from Veizer (1992).

CO₂ into CaCO₃ (McConnaughey, 1990a,b), or be due to a pH gradient between ambient water and intercellular fluid, the latter controlling the calcification process (Adkins et al., 2003). When this deviation is systematic, as for some foraminifera species, it can be corrected. In other cases, the degree, but not necessarily the sign of disequilibrium, is random. It is also possible, and by no means exceptional, to see different parts of the same skeleton having different isotopic compositions.

Recent marine carbonates

The components of recent marine carbonates include skeletal parts, chemical and/or biochemical precipitates, and early marine cements. Low-latitude shallow water assemblages are dominated by aragonitic corals and green algae, frequently accompanied by marine precipitates (whittings, ooids, peloids) and having ubiquitous early marine HMC and A cements. In contrast, carbonates of temperate zones, and of deeper slope settings in tropical regions, contain mostly skeletal remains with Mg-calcitic mineralogy. The dominant contributors are molluscs, foraminifera, and bryozoans. Early marine cements of Mg-calcitic composition in this assemblage are rare. Finally, the off-shore assemblage of pelagic organisms, such as calcitic foraminifera and coccoliths as well as aragonitic pteropods accumulate above their respective carbonate dissolution depths to produce *deep sea oozes* on the ocean floor.

The wide spread in O and C isotopic compositions (Figure C14) of recent marine carbonates reflects this complexity and the relative proportions of constituent components. Note that, for ecological reasons, even specific groups of organisms, such as shallow marine brachiopods that are of paleoclimatic interest, have a spread of oxygen and carbon isotopic values today of about 4‰, and this would also be expected to have been the case for their ancient counterparts. The inorganic (?) precipitates, such as ooids and early marine cements, tend to fall much closer to expected equilibrium values (Figure C14b). In detail, however, they may be characterized by slight ¹³C and/or ¹⁸O enrichment and, if so, biochemically-mediated processes may be involved in their precipitation.

Post-depositional diagenetic overprint

Diagenetic modification of freshly deposited sediments begins on the seafloor with mechanical and biological breakdown of the carbonate components and their binding by cements. This

process of rock generation from a loose sediment continues via two major pathways, designated here as meteoric (fresh water) and burial diagenesis (James and Choquette, 1990a, b; Choquette and James, 1990). These two pathways converge with time and some overlaps are possible even in the early stages of diagenesis.

Carbonate sediments deposited originally in *shallow marine environments* are exposed to the influence of continental, or meteoric, waters. Such waters are frequently charged with CO₂ and thus highly corrosive. The original marine mineralogical assemblage (A, HMC) transforms into a monomineralic (LMC) limestone via sequential dissolution-reprecipitation. This dissolution-reprecipitation process proceeds in a flow regime that is comprised of two components, regional flow and diffusion. The latter is relatively slow, on the order of a hundred meters in a million years, whereas the former can vary considerably. At high flow rates, the system is water-dominated. At slow flow-rates, local dissolution-reprecipitation gradients, maintained by diffusion and local physical parameters, are not entirely dissipated. This is a rock-dominated system, where the precursor phases play a considerable role in controlling the chemistry and isotopic composition of waters in the microenvironments and thus of the locally precipitated successor calcite. In most natural cases, there is a partially rock-dominated system, characterized by intermediate *water/rock ratios*. Nevertheless, C in the waters of these microenvironments originates mostly from the precursor carbonate phases (e.g., water/rock ratio ~10) and the δ¹³C therefore retains its near-original values.

The situation is complicated somewhat by the fact that oxidation of organic matter is an important diagenetic process. With burial, the sediment passes successively (Hesse, 1990) through the zones of (a) oxidation by dissolved O₂, (b) nitrate reduction, (c) sulfate reduction, (d) carbonate reduction, (e) fermentation, and (f) thermocatalytic decarbonation. The processes in the first five zones are mediated by assemblages of specific bacteria to temperatures of about 75°C. The mostly abiogenic zone (f) extends to about 150°C and at higher temperatures equilibria between graphite, CO₂, and CH₄ dominate. Processes (a) and (c) produce CO₂ and bicarbonate that are released to the pore space. The C in these species is thus derived from the oxidation of organic carbon, C_{org}, that is depleted in ¹³C, with δ¹³C usually around -25‰. The passage

of sediment into zone (d), particularly at the trailing edge of sulfate depletion, leads to production of methane. This CH_4 is isotopically very light ($-80 \pm 20\text{‰}$) and the residual C_{org} , which is subsequently oxidized to CO_2 , thus becomes exceptionally heavy ($\delta^{13}\text{C}$ in excess of $+10\text{‰}$). A return to ^{13}C -depleted values again characterizes zone (f).

In continually subsiding shallow water basins and in deep-sea environments, diagenetic stabilization is due to progressive *burial*. The entrapped pore waters are of marine origin and in equilibrium with the assemblage of carbonate minerals. The conversion of sediment into limestone in this case is achieved not by a chemical gradient but through loading of younger sediments. This results in a pressure and temperature rise that, in turn, increases the solubility of the solid phases. Their dissolution-reprecipitation proceeds sequentially in a manner similar to that described for the meteoric pathway, but at a slower rate. The recrystallization front, as it migrates upwards with continuous loading causes “smoothing” of the original isotope signals, but the overall shifts are similar to meteoric pathways, albeit of lesser magnitude.

The carbonate sediment, regardless whether following the meteoric or the burial pathway, eventually reaches the *deep burial* environment. The boundaries can be set at cessation of most bacterial processes at about 75°C (or ~ 2 km depth). The major process occurring at these depths is pressure-solution that results in dissolution of a portion of the already stabilized limestone and reprecipitation of this material as late, mostly iron-rich, blocky calcite cements that occlude the residual porosity. The deep meteoric waters that are involved in this process are mostly saline, but in terms of C isotopes, the system is mostly rock buffered. However, introduction of light $\delta^{13}\text{C}$ from thermocatalytic decarboxylation may be important locally.

It is essential to understand the fundamentals of these post-depositional processes if we are to interpret the origin of an isotopic signal preserved in the rock record (Figure C14c).

Sample selection

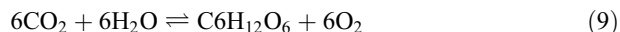
From the above discussion, it is clear that if we are to obtain a record of past seawater isotopic composition, it is essential that the samples be well preserved or at the minimum “least altered.” One alternative is to concentrate on phases that are relatively stable and resistant to diagenesis. Such a phase is the LMC of some fossil shells, such as foraminifera, belemnites, and brachiopods. Even with these samples, it is mandatory that they be screened by optical (microscope, cathodoluminescence, SEM) and chemical (trace element composition) techniques in order to ensure their good preservation. The details of these techniques are given, for example, in Veizer (1983), McArthur (1994), and Grossman et al. (1996). For whole rocks, or components composed originally of A and HMC, that were as a rule subjected to diagenetic stabilization, the effort has to concentrate on domains that were recrystallized at the lowest possible water/rock ratio, such as fine-grained limestones (micrites) or some types of cements. Note nevertheless that any given rock can contain, side by side, massively recrystallized and well-preserved domains.

Isotopic evolution of seawater

Based on the background understanding of isotope systematics in (bio)chemical sedimentary rocks, minerals, and fossils, we can now tackle the evolutionary history of this planet as

recorded by the isotopic composition of past seawater. In this outline, only the billion to million year time resolution will be considered. Discussion of the Quaternary record is beyond the scope of this contribution.

The two dominant exogenic reservoirs of carbon are carbonate rocks and organic matter in sediments. They are linked in the carbon cycle via atmospheric CO_2 and the C species dissolved in the hydrosphere. The $\delta^{13}\text{C}$ for the total dissolved carbon (TDC) in seawater is about $+1 \pm 0.5\text{‰}$, with surficial waters generally heavier and deep waters lighter than this average (Kroopnick, 1980). Atmospheric CO_2 in equilibrium with TDC of marine surface water has a $\delta^{13}\text{C}$ of about -7‰ . The CO_2 is utilized by photosynthetic plants for production of organic C causing depletion in ^{13}C .



Most land plants utilize the so-called C_3 , or Calvin, pathway that results in tissue with a $\delta^{13}\text{C}_{\text{org}}$ of about -25 to -30‰ . The situation for aquatic plants is somewhat different because they utilize dissolved and not gaseous CO_2 . Tropical grasses, on the other hand, utilize the C_4 (Hatch-Slack or Kranz) pathway and have a $\delta^{13}\text{C}$ of some -10 to -15‰ . A third group that combines these two pathways, the CAM plants (algae and lichens), has intermediate $\delta^{13}\text{C}$ values. In detail, the nature of the discussed variations is far more complex (Sackett, 1989) and depends on the types of organic compounds involved. For our purposes, however, it is only essential to realize that C_{org} is strongly depleted in ^{13}C . This organic matter, which is very labile, is easily oxidized into CO_2 that inherits the ^{13}C -depleted signal.

The $\delta^{13}\text{C}$ of mantle carbon is about -5‰ (Hayes et al., 1992) and in the absence of life and its photosynthetic capabilities, this would also be the isotopic composition of seawater (Figure C15). Yet, as far back as 3.5 billion years (Ga) ago, and possibly as far as ~ 4 Ga ago (Schidlowski et al., 1983),

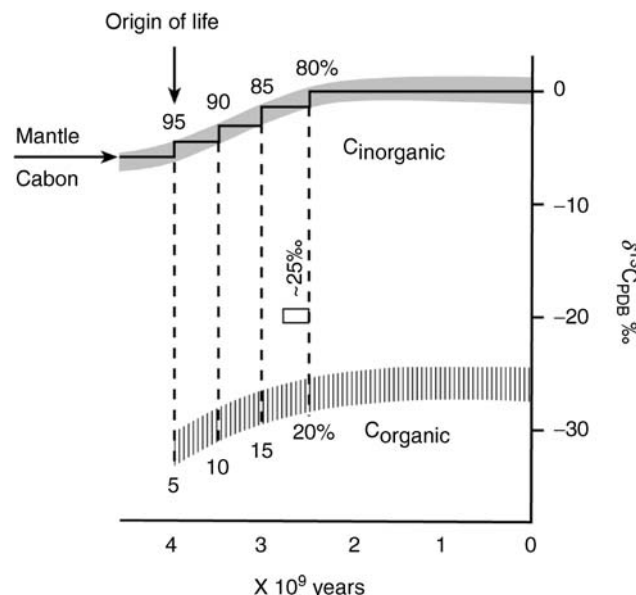


Figure C15 Theoretical evolution of $\delta^{13}\text{C}$ for inorganic (seawater) and organic matter, assuming that life originated ~ 4 Ga ago and the pool of organic carbon increased to its present day value (20% of all carbon) by ~ 2.5 Ga ago. Reproduced from Veizer (1988).

the carbonate rocks (\sim seawater) had $\delta^{13}\text{C}$ values of around 0‰ PDB (Figure C16). This suggests that a reservoir of reduced organic carbon that accounted for $\sim 1/5$ of the entire exogenic carbon existed already some 4 billion years ago, “pushing up” the residual 4/5 of carbon, present in the oxidized form in the ocean/atmosphere system, from -5 to 0‰. This is an oxidized/reduced partitioning similar to that of today. Stated in a simplified manner, life with its photosynthetic capabilities, and possibly of present day magnitude, can be traced almost as far back as we have a rock record. This photosynthesis may or may not have been generating oxygen as its by-product, but was essential in order to “lift” the seawater $\delta^{13}\text{C}$ to values similar to present day levels. In order to sustain seawater $\delta^{13}\text{C}$ at this level during the entire geologic history, it is necessary that inputs and outputs to the carbon cycle have the same $\delta^{13}\text{C}$. Since the input from the mantle, via volcanism and hydrothermal systems, has a $\delta^{13}\text{C}$ of -5 ‰ and the subducted carbonates are 0‰, the subduction process must also involve a complementary ^{13}C -depleted component of organic matter. This is possible to contemplate as long as oceanic waters were not fully oxygenated, such as may have been the case in the Archean (>2.5 Ga ago). This is either because oxygen generating photosynthesis was “invented” as late as the late Archean or early Proterozoic (Cloud, 1976), or because tectonic evolution led to a progressive oxygenation of the ocean/atmosphere system due to a switchover from a “mantle”-to a “river”-buffered ocean system (Goddéris and Veizer, 2000). For the latter alternative, it is possible to argue that the oxygen-generating photosynthesis (photosystem 2) may have been extant as far back as we have a geological record, without necessarily inducing oxygenation of the early ocean/atmosphere system (but see Lasaga and Ohmoto, 2002). Whatever the cause, the oxygenation of the system in the early Proterozoic (~ 2.5 – 1.8 Ga ago) would have resulted in oxidation of organic matter that was settling down through the water column. Today only $\sim 1\%$ of organic productivity reaches the ocean floor and $\sim 0.1\%$ survives into sedimentary rocks. As a result, the addition of mantle carbon, coupled with the subduction loss of the ^{13}C -enriched limestone carbon, would slowly force the $\delta^{13}\text{C}$ of seawater back to mantle values. In order to sustain the near 0‰ PDB of seawater during all of geologic history, it may be necessary to lower the input of mantle carbon into the ocean/atmosphere system by

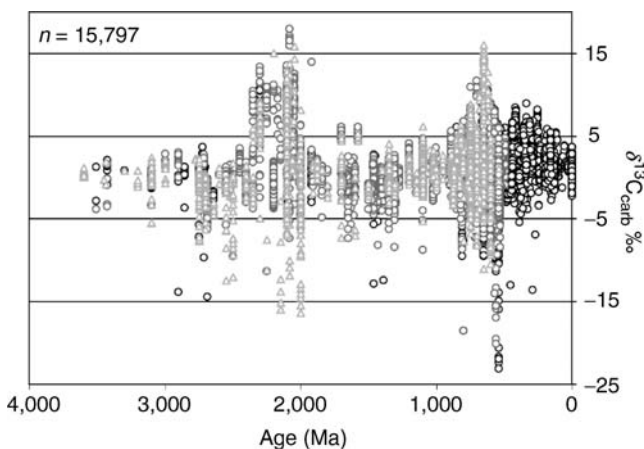


Figure C16 The record of $\delta^{13}\text{C}$ in limestones (circles) and dolostones (triangles) during geologic history. Reproduced from Shields and Veizer (2002), with permission from G³.

progressively diminishing the impact of hydrothermal and volcanic activity over geologic time.

Superimposed on this invariant Precambrian $\delta^{13}\text{C}$ seawater trend are two intervals with very heavy (and very light) values, at ~ 2.2 Ga ago and in the Neoproterozoic (Figure C16). The former has been interpreted as a result of the development of oxygen-generating photosynthesis that resulted in sequestration of huge quantities of organic matter (Karhu and Holland, 1996) into coeval sediments and the Neoproterozoic interval was the time of the proposed “snowball Earth” (Hoffman et al., 1998). At this stage, the reasons for the high frequency of the anomalous $\delta^{13}\text{C}$ values during these two intervals are not well known (see Rothman et al., 2003), but it is interesting that both were associated with large glaciations, as was the later discussed ^{13}C -enriched Permo/Carboniferous interval.

The sampling density and time resolution in the *Phanerozoic* enabled the delineation of a much better constrained secular trend (Figure C17), with a maximum in the late Permian, but even in this case we are dealing with a band of data. This reflects the fact that the $\delta^{13}\text{C}$ of total dissolved inorganic carbon ($\delta^{13}\text{C}_{\text{DIC}}$) of seawater is not uniform in time and space, that organisms can incorporate metabolic carbon into their shells (vital effect), and that some samples may also contain a diagenetic overprint. Superimposed on the overall trend are higher oscillations, on timescales of tens of millions of years and less, but their meaning is not yet understood.

It was proposed (Frakes et al., 1992) that the $\delta^{13}\text{C}_{\text{carbonate}}$ (seawater) becomes particularly heavy at times of glaciations, and that such times are also characterized by low CO_2 levels. The coincidences of the $\delta^{13}\text{C}$ peaks with the Late Ordovician and Permo-Carboniferous glacial episodes (Figure C17) appear to support this proposition, but the Mesozoic/Cenozoic record does not. Nevertheless, accepting the validity of the present $\delta^{13}\text{C}$ trend, it is possible to estimate the $\Delta^{13}\text{C}$ ($=\delta^{13}\text{C}_{\text{carb}}-\delta^{13}\text{C}_{\text{org}}$) that is proportional to $p\text{CO}_2$. Making a set of additional assumptions, one can then model $p\text{CO}_2$ levels of the ancient atmospheres. Three such *Phanerozoic* $p\text{CO}_2$ reconstructions do exist (Figure C18). However, they are internally inconsistent and not one of them shows any correlation

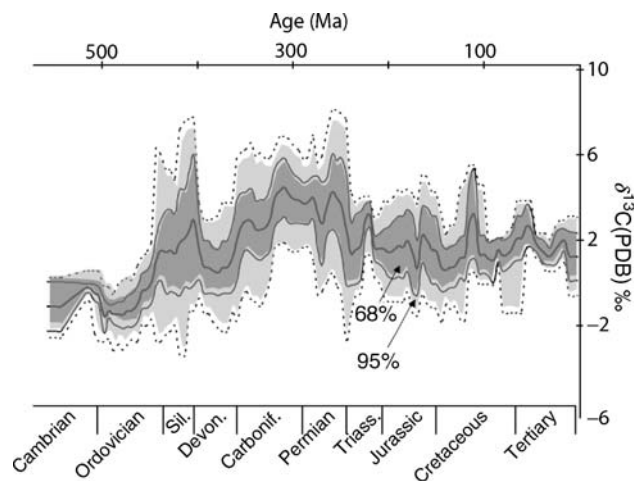


Figure C17 The *Phanerozoic* $\delta^{13}\text{C}$ trend for LMC shells. The running mean is based on a 20 Ma window and 5 Ma forward step. The shaded areas around the running mean include the 95% ($\pm 2\sigma$) of all data. Reproduced from Veizer et al. (1999), with permission from Elsevier Science.

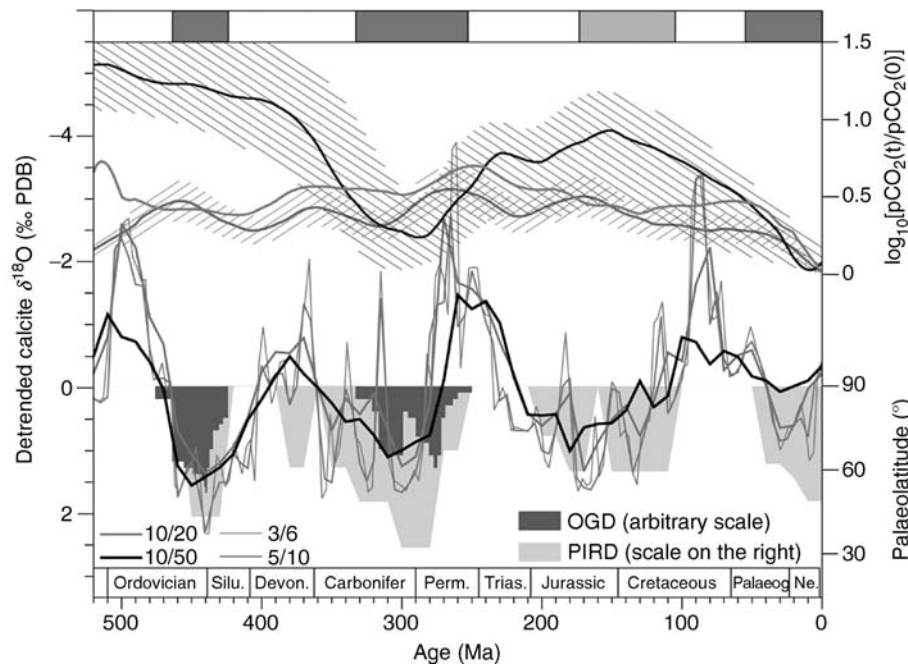


Figure C18 Phanerozoic climatic indicators and reconstructed $p\text{CO}_2$ levels. The bottom set of curves are the detrended running means of $\delta^{18}\text{O}$ values of calcitic shells over the Phanerozoic (3/6 means step 3 Myr, window 6 Myr). Histograms are paleolatitudes of ice-rafted debris (PIRD) and other glacial deposits (OGD) – such as tillites and glacial marine strata. The dark bars at the top represent cool climate modes (icehouses) and the white bars are the warm modes (greenhouses). The upper set of curves are reconstructed histories of the past $p\text{CO}_2$ variations. Modified from Shaviv and Veizer (2003).

with the paleoclimate deduced from sedimentological criteria. This led Veizer et al. (2000) to conclude that either the estimates of paleo- CO_2 were unreliable or there was no direct relationship between $p\text{CO}_2$ levels and climate for most of the Phanerozoic. In contrast, the “paleotemperature” trend for tropical Phanerozoic oceans, as deciphered from oxygen isotope record, correlates exceptionally well with the record of past variations in the flux of cosmic rays, suggesting that celestial phenomena were the primary driver of planetary climate (Shaviv and Veizer, 2003), at least on geological timescales.

Higher order peaks, at million-year resolution, have been observed in the geologic record, particularly in deep-sea borehole sections. An example of such an episode is the Cenomanian/Turonian boundary, some 91 million years ago, explained variously as due to a high organic carbon burial rate and draw-down of atmospheric CO_2 , increased thermohaline circulation, increased preservation of organic matter, or to diminished riverine input. However, the modeling of this excursion (Kump and Arthur, 1999) did not yield any unique solution.

Ján Veizer

Bibliography

- Adkins, J.F., Boyle, E.A., Curry, W.B., and Lutringer, A., 2003. Stable isotopes in deep-sea corals and a new mechanism for “vital effects.” *Geochim. Cosmochim. Acta*, **67**, 1129–1143.
- Choquette, P.W., and James, N.P., 1990. Limestones – the burial diagenetic environment. In McIlreath, I.A., and Morrow, D.W. (eds.), *Diagenesis. Geoscience Canada Reprint Series*. Geological Association of Canada, 4, pp. 75–112.
- Cloud, P., 1976. *Major features of crustal evolution*. Johannesburg, South Africa: Geological Society of South Africa Special Publications, 1–31.

- Frakes, L.A., Francis, J.E., and Syktus, J.I., 1992. *Climate Mode of the Phanerozoic: The History of the Earth's Climate over the Past 600 Million Years*. Cambridge, UK: Cambridge University Press, 286pp.
- Goddéris, Y., and Veizer, J., 2000. Tectonic control of chemical and isotopic composition of ancient oceans: the impact of continental growth. *Am. J. Sci.*, **300**, 434–461.
- Grossman, E.L., Mii, H.-S., Zhang, C., and Yancey, T.E., 1996. Chemical variation in Pennsylvanian brachiopod shells – effects of diagenesis, taxonomy, microstructure and paleoenvironment. *J. Sediment. Res.*, **66**, 1011–1022.
- Hayes, J.M., Des Marais, D.J., Lambert, I.B., Strauss, H., and Summons, R.E., 1992. Proterozoic biogeochemistry. In Schopf, J.W., and Klein, C. (eds.), *The Proterozoic Biosphere: A Multidisciplinary Study*. New York, NY: Cambridge University Press, pp. 81–134.
- Hesse, R., 1990. Early diagenetic pore water/sediment interaction: modern offshore basins. In McIlreath, I.A., and Morrow, D.W. (eds.), *Diagenesis. Geoscience Canada Reprint Series*, Geological Association of Canada, 4, pp. 277–316.
- Hoefs, J., 1980. *Stable Isotope Geochemistry*. Heidelberg: Springer Verlag, 208pp.
- Hoffman, P.F., Kaufman, A.J., Halverson, G.P., and Schrag, D.P., 1998. A Neoproterozoic snowball Earth. *Science*, **281**, 1342–1346.
- James, N.P., and Choquette, P.W., 1990a. Limestones – the seafloor diagenetic environment. In McIlreath, I.A., and Morrow, D.W. (eds.), *Diagenesis. Geoscience Canada Reprint Series*, Geological Association of Canada, 4, pp. 13–34.
- James, N.P., and Choquette, P.W., 1990b. Limestones – the meteoric diagenetic environment. In McIlreath, I.A., and Morrow, D.W. (eds.), *Diagenesis. Geoscience Canada Reprint Series*, Geological Association of Canada, 4, pp. 35–73.
- Karhu, J.A., and Holland, H.D., 1996. Carbon isotopes and the rise of atmospheric oxygen. *Geology*, **24**, 867–870.
- Kroopnick, P., 1980. The distribution of ^{13}C in the Atlantic Ocean. *Earth Planet. Sci. Lett.*, **49**, 469–484.
- Kump, L.R., and Arthur, M.A., 1999. Interpreting carbon-isotope excursions: Carbonates and organic matter. *Chem. Geol.*, **161**, 181–198.

- Lasaga, A.C., and Ohmoto, H., 2002. The oxygen geochemical cycle: Dynamics and Stability. *Geochim. Cosmochim. Acta*, **66**, 361–381.
- McArthur, J.M., 1994. Recent trends in strontium isotope stratigraphy. *Terra Nova*, **6**, 331–358.
- McConnaughey, T., 1990a. ^{13}C and ^{18}O isotopic disequilibrium in biological carbonates: 1. Patterns. *Geochimica et Cosmochimica Acta*, **53**, 151–162.
- McConnaughey, T., 1990b. ^{13}C and ^{18}O isotopic disequilibrium in biological carbonates: 2. In vitro simulation of kinetic isotope effects. *Geochimica et Cosmochimica Acta*, **53**, 163–171.
- Rothman, D.H., Hayes, J.M., and Summons, R., 2003. Dynamics of the Neoproterozoic carbon cycle. *Proceedings of the National Academy of Sciences*, **100**, 8124–8129.
- Sackett, W.M., 1989. Stable carbon isotope studies on organic matter in the marine environment. In Fritz, P., and Fontes, J.C. (eds.), *Handbook of Environmental Isotope Geochemistry*. Amsterdam: Elsevier, pp. 139–169.
- Schidlowski, M., Hayes, J.M., and Kaplan, I.R., 1983. Isotopic inferences of ancient biochemistries: Carbon, sulfur, hydrogen, and nitrogen. In Schopf, J.W. (ed.), *Earth's Earliest Biosphere: Its Origin and Evolution*. Princeton: Princeton University Press, pp. 149–187.
- Shaviv, N.J., and Veizer, J., 2003. Celestial driver of Phanerozoic climate? *GSA Today*, **13/7**, 4–10.
- Shields, G., and Veizer, J., 2002. Precambrian marine carbonate isotope database: Version 1.1. *Geochem. Geophys. Geosyst.*, **3/6**, 12pp.
- Veizer, J., 1983. Trace element and isotopes in sedimentary carbonates. *Rev. Mineral.*, **11**, 265–300.
- Veizer, J., 1988. The earth and its life: Systems perspective. *Origins of Life*, **18**, 13–39.
- Veizer, J., 1992. Depositional and diagenetic history of limestones: stable and radiogenic isotopes. In Clauer, N., and Chaudhuri, S. (eds.), *Isotopic signatures in Sedimentary Records*. Heidelberg: Springer, pp. 13–48.
- Veizer, J., Ala, D., Azmy, K., Bruckschen, P., Buhl, D., Bruhn, F., Carden, G. A. F., Diener, A., Ebner, S., Godd ris, Y., Jasper, T., Korte, C., Pawellek, F., Podlaha, O.G., and Strauss, H., 1999. $^{87}\text{Sr}/^{86}\text{Sr}$, $\delta^{13}\text{C}$ and $\delta^{18}\text{O}$ evolution of Phanerozoic seawater. *Chem. Geol.*, **161**, 59–88.
- Veizer, J., Godd ris, Y., and Fran ois, L.M., 2000. Evidence for decoupling of atmospheric CO_2 and global climate during the Phanerozoic eon. *Nature*, **408**, 698–701.

Cross-references

Atmospheric Evolution, Earth
Carbon Cycle
Carbon Dioxide, Dissolved (Ocean)
Carbon Isotopes, Stable
Isotope Fractionation
Marine Carbon Geochemistry

CARBON ISOTOPES, STABLE

General

Carbon has two stable (non-radioactive) isotopes. In nature, the ^{12}C isotope comprises 98.89% of all carbon and ^{13}C makes up the remaining 1.11%. A variety of physico-chemical processes whose rates are mass-dependent, such as kinetic reactions involving diffusion, and temperature-controlled equilibrium reactions serve to “fractionate” the isotopes into proportions slightly different from the bulk averages. These isotopes are therefore most useful when used in tandem as isotope ratios ($^{13}\text{C}/^{12}\text{C}$) in order to explore paleoclimates and paleoenvironments. Carbon isotopes are preserved and expressed in the bulk composition of a wide variety of materials such as shells, speleothems, bones, leaves, peat, soils, sediments, wood, and food, and more recently in the composition of specific compounds or

biomarkers contained therein. In some cases, the climate influence may be quite direct, but in many others the isotopic variations are less direct, linked to climate effects on the global carbon cycle and photosynthetic pathways of plants.

Notation

The $^{13}\text{C}/^{12}\text{C}$ in materials is measured with a stable-isotope ratio mass spectrometer (IRMS), taking advantage of the mass differences in ionized $^{13}\text{CO}_2$ molecules (or ^{13}CO molecules) relative to $^{12}\text{CO}_2$ (or ^{12}CO) that cause them to follow different trajectories in a magnetic field on the path to detectors. The isotopic ratio of an unknown sample is ultimately expressed in permil (‰) with the delta (δ) notation:

$$\delta^{13}\text{C} \text{ (in ‰)} = \left[\left(\frac{^{13}\text{C}}{^{12}\text{C}_{\text{sample}}} / \frac{^{13}\text{C}}{^{12}\text{C}_{\text{PDB}}} \right) - 1 \right] \times 1000 \quad (1)$$

where the conventional standard is PDB calcite from belemnite fossils of the Cretaceous PeeDee Formation of South Carolina. Although no original PDB standard remains from its initial adoption about five decades ago, there exist secondary standards such as NBS-21 graphite National Bureau of Standards-21) and V-PDB (Vienna PDB), whose isotopic composition is known with respect to PDB (Coplen, 1996). The $^{13}\text{C}/^{12}\text{C}$ ratio in PDB is 0.0112372, so positive $\delta^{13}\text{C}$ values have more ^{13}C (i.e., are “enriched”), and negative $\delta^{13}\text{C}$ values have less ^{13}C (i.e., are “depleted”). More generally when comparing $\delta^{13}\text{C}$ between samples, those with less negative (or more positive) $\delta^{13}\text{C}$ values are more enriched in ^{13}C relative to samples with more negative (less positive) $\delta^{13}\text{C}$. The range of $\delta^{13}\text{C}$ in many types of materials may be several permil but some, like ocean water dissolved inorganic carbon, are very homogeneous (Figure C19).

When examining carbon isotopic behavior of plants, discrimination (Δ) is often a useful parameter that eliminates the effect of any variability in atmospheric $\delta^{13}\text{C}$ ($\delta^{13}\text{C}_{\text{air}}$) in plant isotopic variation

$$\Delta = \frac{\delta^{13}\text{C}_{\text{air}} - \delta^{13}\text{C}_{\text{plant}}}{1 + \delta^{13}\text{C}_{\text{plant}}} \approx \delta^{13}\text{C}_{\text{air}} - \delta^{13}\text{C}_{\text{plant}} \quad (2)$$

Terrestrial environments

Most paleoclimate inferences from $\delta^{13}\text{C}$ in terrestrial settings are based on plant matter that acquires an isotopic composition related to the environment in which the plants grew. This signal may be subsequently passed on to other elements of the Earth system, to humans/animals from food consumption or to soils during plant respiration and decomposition of plant matter, for example. Temperature-dependent equilibrium reactions usually play a minor role, if any, in the source of the primary environmental signals in these materials.

Terrestrial vegetation is dominated by plants with the C_3 (Calvin-Benson) photosynthetic pathway for which carbon isotope composition is modeled by the equation of Farquhar et al. (1982):

$$\delta^{13}\text{C}_{\text{plant}} = \delta^{13}\text{C}_{\text{air}} - a - (b - a) \times \frac{C_i}{C_a} \quad (3)$$

where $\delta^{13}\text{C}_{\text{air}} = \delta^{13}\text{C}$ of the atmospheric CO_2 ; C_i/C_a = ratio of leaf intercellular CO_2 concentration to the atmospheric concentration; a = fractionation during CO_2 diffusion through stomata ($\sim 4.4\text{‰}$); and b = enzymatic fractionation by ribulose

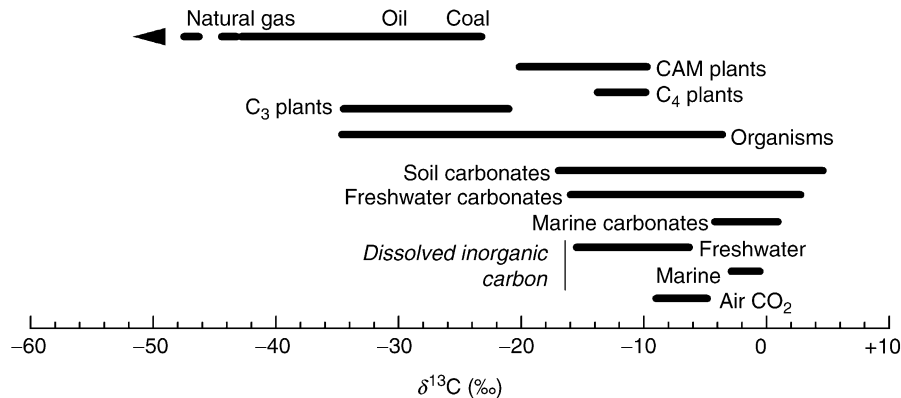


Figure C19 Typical stable-carbon isotope composition of natural materials.

bisphosphate carboxylase (Rubisco) ($\sim 27\%$). With regard to paleoclimate, C_i/C_a , and hence $\delta^{13}\text{C}_{\text{plant}}$, may be influenced by any and all environmental factors that affect rates of stomatal conductance and carbon fixation, such as light, temperature, relative humidity, and soil moisture (Farquhar et al., 1982). The $\delta^{13}\text{C}$ of C_3 plants generally falls into the range of -20 to -32% , with a mean of about -26 or -27% (Figure C19).

Equation 1 is a guide to interpreting possible climatic and environmental effects (relative humidity, temperature, soil moisture, etc.) on tree-ring $\delta^{13}\text{C}$ series in which the cellulose component is frequently isolated for higher fidelity of climate signal (Leavitt and Long, 1989; Robertson et al., 1997). There are also eco-physiological parameters such as water-use efficiency that may be reconstructed from the $\delta^{13}\text{C}$ of tree rings (Bert et al., 1997) and from plant macrofossils (Van de Water et al., 1994).

A second major group of plants uses the C_4 (Hatch-Slack) photosynthetic pathway, producing much more enriched $\delta^{13}\text{C}$ values (Figure C19), generally between -10 and -14% (mean -12%), largely because of reduced discrimination against ^{13}C by another enzyme, PEP-carboxylase, involved in the initial fixation of CO_2 (Farquhar, 1983). Trees, most shrubs and “cool-season” grasses tend to be C_3 plants (including crops such as wheat, alfalfa, and oats), whereas “warm-season” grasses (high summer precipitation in conjunction with high minimum temperatures, including crops such as maize, sorghum, and sugar cane) and some woody dicots adapted to arid conditions tend to be C_4 plants. It is suggested that the C_4 pathway may have evolved in response to periods of low atmospheric CO_2 concentrations whereby PEP-carboxylase serves to effectively pre-concentrate CO_2 at low atmospheric levels before the final carbon fixation by RuBP in bundle sheath cells (Ehleringer et al., 1997). C_3 plants are thought to be at a disadvantage at low CO_2 concentrations because oxygen will more readily react with Rubisco (a process called photorespiration). Theoretically, however, there are effects besides $p\text{CO}_2$, such as temperature, that can determine the success of C_3 versus C_4 (Figure C20), and there is direct evidence that climate may indeed be more important than CO_2 in determining C_4 plant distribution and expansion under some circumstances (Huang et al., 2001).

Because of the different climatic conditions favoring C_3 and C_4 plants, variations in their spatial and temporal proportions can be used as a paleoenvironmental indicator. The $\delta^{13}\text{C}$ of some materials can be used to estimate the proportion of

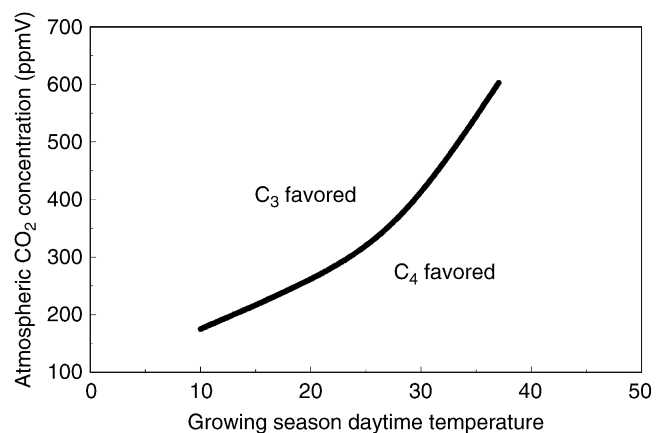


Figure C20 Approximate $p\text{CO}_2$ and temperature conditions that determine prevalence of C_3 versus C_4 plants based on their physiology. (After Ehleringer et al., 1997.)

C_3 and C_4 biomass present by means of a mixing model with -12% and -27% as approximate end members for pure (100%) C_3 and C_4 communities, respectively. For example, $\delta^{13}\text{C}$ of dated soil carbonates and soil organic carbon (and even teeth) has been used to estimate the global expansion of C_4 communities in the last 10 million years (Quade and Cerling, 1995; Cerling et al., 1998), and to infer regional vegetation shifts in the southern United States during the Quaternary (Monger et al., 1998). Even a shift in $\delta^{13}\text{C}$ of human bones in the U.S. Southwest (Figure C21) has been found to indicate a change in diet related to possible climate shifts (Coltrain and Leavitt, 2002).

Likewise, stalagmites and similar carbonate deposits deriving a substantial portion of their carbonate from respired soil CO_2 could record the $\delta^{13}\text{C}$ imprint of such C_3/C_4 changes. Even if C_3/C_4 has been constant, such as in the high-elevation C_3 landscape contributing carbonate to the hydrologic system producing vein calcite at Devil’s Hole, Nevada, the $\delta^{13}\text{C}$ variations have been used to infer density of past vegetation over tens of thousands of years (Coplen et al., 1994). Similarly, a strong correlation with El Niño/Southern Oscillation (ENSO) of a speleothem $\delta^{13}\text{C}$ record from Belize, Central America, might be related to teleconnected ENSO climate contributing to higher or lower ecosystem respiration (Frappier et al., 2002).

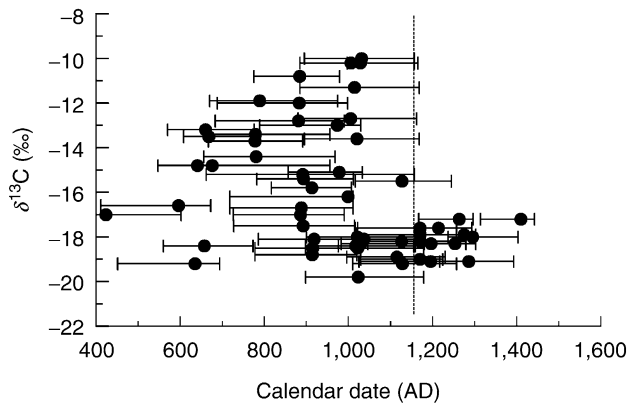


Figure C21 Shift in isotopic composition of bone collagen in the Fremont paleoculture of Utah from enriched values consistent with maize in the diet before AD 1100 and a C_3 -dominated diet afterward (after Coltrain and Leavitt, 2002). The period in which maize could be cultivated is attributed to farther northward penetration of the southwestern summer monsoon.

Marine environments

Initial isotopic analysis of foraminifera in Cenozoic marine sediment cores (Emiliani, 1972) was focused on the oxygen isotope composition as related to temperature or sea level (ice volume). Interpretation of $\delta^{13}C$ measurements on the same cores was delayed somewhat because of even more complicated environmental influences (Hoefs, 1987), but Shackleton and Kennett (1975) did find benthic forams consistently depleted relative to planktonic forams by about 1‰. In part, this is a consequence of planktonic forams incorporating dissolved carbonate species enriched by preferential removal of the isotopically light dissolved carbon during photosynthesis. There is now a 65 million-year record of $\delta^{13}C$ variation of carbonates in deep-sea sediment cores (Zachos et al., 2001) that shows overall variation of almost 4‰, with the lowest values occurring in the last 6 million years, and evidence of precipitous but brief $\delta^{13}C$ excursions (2–3‰), one of the largest occurring 55 million years ago.

The influences on this variability have been studied. Shackleton et al. (1983) used the $\delta^{13}C$ record of forams to infer greatly reduced CO_2 atmospheric concentrations (pCO_2) during the last full-glacial period, now known to be true in light of subsequent paleoatmosphere measurements in ice cores. Pagani et al. (1999) have since used compound-specific $\delta^{13}C$ analysis of alkenones derived from algae organic matter compared with $\delta^{13}C$ of planktonic forams to more precisely estimate pCO_2 (Figure C22). This is based on foram $\delta^{13}C$ representing the isotopic composition of aqueous CO_2 used in photosynthesis, and the fractionation between organic $\delta^{13}C$ and carbonate $\delta^{13}C$ being a function of aqueous CO_2 concentration (itself a function of pCO_2). The trend in calculated pCO_2 thus derived suggests CO_2 concentrations were very low 5–10 million years before a major continental C_4 plant expansion occurred around 8–4 million years ago, according to evidence from the $\delta^{13}C$ of teeth, soil carbonates, and terrestrial organic matter (Cerling et al., 1998). This implies that factors other than pCO_2 must have driven that C_4 boom.

Corals have provided a wealth of paleoenvironmental information from their chemical and isotopic composition. Coral

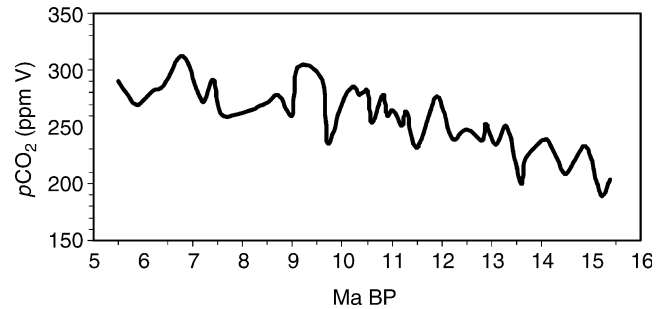


Figure C22 Atmospheric CO_2 concentrations between 16 and 5 million years ago, reconstructed from the difference between $\delta^{13}C$ of alkenones of organic matter and foram carbonates. (After Pagani et al., 1999.)

$\delta^{13}C$ variations have been attributed to a number of effects, such as variations in food source or dissolved carbonate isotopic composition (related to ecosystem productivity), but there is a growing body of evidence that at least in some cases light may be a dominating (and reconstructable) influence, whereby high levels promote more photosynthesis and less discrimination against ^{13}C (Swart et al., 1996).

Quay et al. (1992) demonstrated the merit in repeated measurement of $\delta^{13}C$ of dissolved inorganic carbon over two decades to help estimate ocean uptake of atmospheric CO_2 over time and space. Recent $\delta^{13}C$ investigations of calcareous sponges (Böhm et al., 2002), which deposit annual and subannual banding like corals, have further revealed their potential to reliably reconstruct $\delta^{13}C_{air}$ over hundreds of years or more.

A current area of great scientific interest is the possibility that methane (CH_4) in the form of hydrates or clathrates has periodically been released catastrophically from deep shelf sediments as a result of decreasing sea level, increasing temperature of the ocean water, or even submarine slope failure. Because methane is a powerful greenhouse gas, there is concern that any such future events might exacerbate global warming. Isotopic analysis of benthic foraminifera over the past 60,000 years from the Santa Barbara Basin reveals periodic large releases of methane (Kennett et al., 2000). Interstadials (warm intervals) are characterized by foram $\delta^{13}C$ values depleted by several permil. Detailed compound-specific $\delta^{13}C$ analysis of diplopterol, a product of methanotrophic bacteria, in sediments of the Santa Barbara Basin further confirms that the most negative values (interpreted as highest marine methane) occur during interstadials (Hinrichs et al., 2003).

Past and future

Stable carbon isotopes have been a highly valuable tool for the past 50 years in helping to build our current understanding of terrestrial and aquatic paleoenvironments, variously including past moisture conditions, temperature, light, plant productivity, the carbon cycle, and more. In some cases, $\delta^{13}C$ has provided a direct proxy of absolute conditions in past systems, and in others it has helped to constrain the range of likely paleoenvironmental conditions or provided independent support for conditions inferred from other evidence. With exciting improvements in mass-spectrometry, $\delta^{13}C$ measurements will unquestionably reveal even more about past changes in the Earth system. Advances such as compound-specific analysis are beginning to provide isotopic measurements of biomarkers exclusive to

land or aquatic organisms, to species or genera, and even to particular plant organs. Improvements in both the speed of analysis and ability to analyze extremely small quantities of compounds extracted from bulk samples enable even inherently microscopic materials such as pollen to be analyzed.

Steven W. Leavitt

Bibliography

- Bert, D., Leavitt, S.W., and Dupouey, J.-L., 1997. Variations of wood $\delta^{13}\text{C}$ and water-use efficiency of *Abies alba* during the last century. *Ecology*, **78**, 1588–1596.
- Böhm, F., Haase-Schramm, A., Eisenhauer, A., Dullo, W.-C., Joachimski, M.M., Lehnert, H., and Reitner, J., 2002. Evidence for preindustrial variations in the marine surface water carbonate system from coralline sponges. *Geochim. Geophys. Geosys.*, **3**(3), 10.1029/2001GC000264.
- Cerling, T.E., Ehleringer, J.R., and Harris, J.M., 1998. Carbon dioxide starvation, the development of C_4 ecosystems, and mammalian evolution. *Philos. Trans. R. Soc. Lond B*, **353**, 159–171.
- Coltrain, J., and Leavitt, S.W., 2002. Climate and diet in Fremont prehistory: Economic variability and abandonment of maize agriculture in the Great Salt Lake Basin. *Am. Antiquity*, **67**, 453–485.
- Coplen, T.B., 1996. New guidelines for reporting stable hydrogen, carbon and oxygen isotope-ratio data. *Geochimica et Cosmochimica Acta*, **60**, 3359–3360.
- Coplen, T.B., Winograd, I.J., Landwehr, J.M., and Riggs, A.C., 1994. 500,000-year stable carbon isotopic record from Devils Hole, Nevada. *Science*, **263**, 361–365.
- Ehleringer, J.R., Cerling, T.E., and Helliker, B.R., 1997. C_4 photosynthesis, atmospheric CO_2 , and climate. *Oecologia*, **112**, 285–299.
- Emiliani, C., 1972. Quaternary paleotemperatures and the duration of the high-temperature intervals. *Science*, **178**, 398–401.
- Farquhar, G.D., 1983. On the nature of carbon isotope discrimination in C_4 species. *Aust. J. Plant Physiol.*, **10**, 205–226.
- Farquhar, G.D., O'Leary, M.H., and Berry, J.A., 1982. On the relationship between carbon isotope discrimination and the intercellular carbon dioxide concentration in leaves. *Aust. J. Plant Physiol.*, **9**, 121–137.
- Frapplier, A., Sahagian, D., Gonzalez, L.A., and Carpenter, S.J., 2002. El Niño events recorded by stalagmite carbon isotopes. *Science*, **298**, 565.
- Hoeft, J., 1987. *Stable Isotope Geochemistry*. New York: Springer.
- Hinrichs, K.-U., Hmelo, L.R., and Sylva, S.P., 2003. Molecular fossil record of elevated methane levels in Late Pleistocene coastal waters. *Science*, **299**, 1214–1217.
- Huang, Y., Street-Perrott, F.A., Metcalfe, S.E., Brenner, M., Moreland, M., and Freeman, K.H., 2001. Dominant control on glacial-interglacial variations in C_3 and C_4 plant abundance. *Science*, **293**, 1647–1651.
- Kennett, J.P., Cannariato, K.G., Hendy, I.L., and Behl, R.J., 2000. Carbon isotopic evidence for methane hydrate instability during Quaternary interstadials. *Science*, **288**, 128–133.
- Leavitt, S.W., and Long, A., 1989. Drought indicated in carbon-13/carbon-12 ratios of southwestern tree rings. *Water Resour. Bull.*, **25**, 341–347.
- Monger, H.C., Cole, D.R., Gish, J.W., and Giordano, T.H., 1998. Stable carbon and oxygen isotopes in Quaternary soil carbonates as indicators of ecogeomorphic changes in the northern Chihuahuan Desert, USA. *Geoderma*, **82**, 137–172.
- Pagani, M., Freeman, K.H., and Arthur, M.A., 1999. Late Miocene atmospheric CO_2 concentrations and the expansion of C_4 grasses. *Nature*, **285**, 876–879.
- Quade, J., and Cerling, T.E., 1995. Expansion of C_4 grasses in the late Miocene of northern Pakistan: Evidence from stable isotopes in paleosols. *Palaeogeogr. Palaeoclimatol., Palaeoecol.*, **115**, 91–116.
- Quay, P.D., Tilbrook, B., and Wong, C.S., 1992. Oceanic uptake of fossil fuel CO_2 : Carbon-13 evidence. *Science*, **256**, 74–79.
- Robertson, I., Switsur, V.R., Carter, A.H.C., Barker, A.C., Waterhouse, J.S., Briffa, K.R., and Jones, P.D., 1997. Signal strength and climate relationships in $^{13}\text{C}/^{12}\text{C}$ ratios of tree ring cellulose from oak in east England. *J. Geophys. Res.*, **102**, 19507–19516.
- Shackleton, N.J., and Kennett, J.P., 1975. Paleotemperature history of the Cenozoic and initiation of Antarctic glaciation: Oxygen and carbon isotope analysis in the DSDP sites 277, 279 and 281. *Initial Rep. DSDP*, **29**, 743–755.

- Shackleton, N.J., Hall, M.A., Line, J., and Shuxi, X., 1983. Carbon isotope data in core V19-30 confirm reduced carbon dioxide concentrations in the ice age atmosphere. *Nature*, **306**, 319–322.
- Swart, P.K., Leder, J.J., Szmant, A., and Dodge, R.E., 1996. The origin of variations in the isotopic record of scleractinian corals: I Carbon. *Geochimica Cosmochimica Acta*, **60**, 2871–2886.
- Van de Water, P.K., Leavitt, S.W., and Betancourt, J.B., 1994. Trends in stomatal density and $^{13}\text{C}/^{12}\text{C}$ leaves during the last glacial-interglacial cycle. *Science*, **264**, 239–243.
- Zachos, J., Pagani, M., Sloan, L., Thomas, E., and Billups, K., 2001. Trends, rhythms, and aberrations in global climate 65 Ma to present. *Science*, **292**, 686–693.

Cross-references

[Alkenones](#)
[Carbon Cycle](#)
[Carbon Dioxide and Methane, Quaternary Variations](#)
[Carbon Isotope Variations over Geologic Time](#)
[Isotope Fractionation](#)
[Marine Biogenic Sediments](#)
[Marine Carbon Geochemistry](#)
[Methane Hydrates, Carbon Cycling, and Environmental Change](#)
[Radiocarbon Dating](#)
[Stable Isotope Analysis](#)

CARBONATE COMPENSATION DEPTH

Principles

The carbonate compensation depth (CCD) is the particular depth level in the oceans where the rate of supply of calcium carbonate to the sea floor is balanced by the rate of dissolution. In practice, the CCD is mapped as the level at which percent carbonate values in marine sediments drop towards zero, i.e., the depth transition from carbonate ooze to red clay or siliceous ooze. Because the supply and dissolution rates of carbonate differ from place to place, the depth of the CCD is variable. In the Indian Ocean and the Pacific, the CCD is typically found at depths between 3,500 and 4,500 m. In the North Atlantic and the eastern South Atlantic, the CCD occurs deeper than 5,000 m. Close to continental margins, the CCD tends to shoal due to higher biological productivity and hence respiration of organic matter in sediments, which releases metabolic CO_2 , in turn causing the dissolution of CaCO_3 . Beneath the equatorial upwelling zones, higher primary production of planktonic carbonate shells depresses the CCD by up to 500 m compared with the oligotrophic realms towards the north and south.

The depth of the CCD is determined by the kinetics of carbonate dissolution from sediments. If dissolution kinetics were infinitely fast, the CCD would coincide exactly with the saturation horizon of carbonate (the so-called chemical lysocline), which in turn is a function of pressure, temperature, salinity, and carbonate ion concentration of the overlying seawater (Figure C23), with generally increasing solubility in deeper waters. However, in real oceans the CCD is found at some degree of undersaturation, i.e., a few hundred meters below the lysocline (Archer, 1996). Because shells or skeletons made of aragonite (mainly corals and pteropods) dissolve more readily than those of calcite (coccoliths and foraminifers), the compensation depth for aragonite (ACD) is positioned some 1,000–2,000 m above the CCD. However, organic coatings of grains

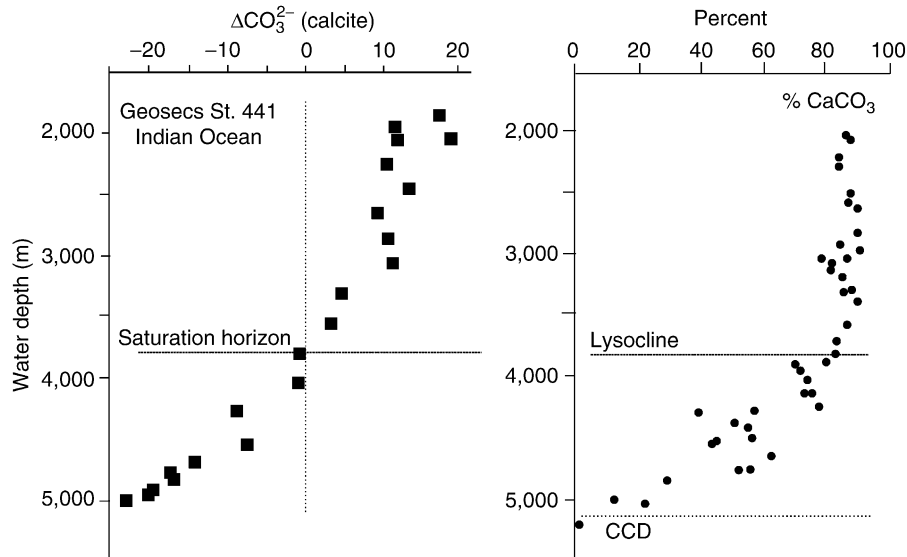


Figure C23 Calcite saturation data of GEOSECS station 441 ($5^{\circ}2'S$, $91^{\circ}47'E$) compared with carbonate contents (weight%) from surface sediment samples of the eastern equatorial Indian Ocean. (After Peterson and Prell, 1985.)

may inhibit the dissolution of sedimenting carbonate particles, thereby depressing the positions of lysocline and CCD below the predicted levels from carbonate chemistry. On the other hand, oxidation of organic matter in the sediments releases metabolic CO_2 and promotes CaCO_3 dissolution even above the chemical lysocline (Milliman et al., 1999).

Over longer timescales, the depth of CCD in the oceans is the expression of the mass balance of dissolved Ca^{2+} and HCO_3^- flowing into the oceans from weathering, and the removal of CaCO_3 from the ocean by burial. After an equilibration time of the order of 10,000 years, CaCO_3 compensation will have a profound impact on the buffering of the pH of the ocean. An imbalance between sources and sinks of CaCO_3 will drive the pH of the ocean toward restoring balance. For example, excess input of dissolved CaCO_3 will tend to drive the pH of the ocean toward higher, more basic values, deepening the CCD and increasing CaCO_3 accumulation on the seafloor until the rates return to balance.

Modern ocean distribution and Quaternary changes

The asymmetry of the modern ocean CCD pattern is largely a product of the thermohaline circulation. The greatest depth occurs in the eastern North Atlantic, where the production of supersaturated deep water increases the CCD to $>5,500$ m. The shallowest levels are in the northern North Pacific, where deep waters are old and enriched in CO_2 . This pronounced modern pattern has been termed basin-to-basin fractionation and is illustrated by the fact that roughly 65% of the present Atlantic seafloor is covered by carbonate ooze, while only 54% of the Indian Ocean sea floor and 36% of the Pacific sea floor share that distinction (Archer, 1996).

Regarding Quaternary times, observations from deep-sea sediment cores show that the CCD topography varied significantly over the glacial to interglacial cycles characteristic of the last 2.6 Myr of Earth history. The CCD fluctuations of the Pacific (first described by G. Arrhenius) are commonly described as dissolution cycles, with high dissolution

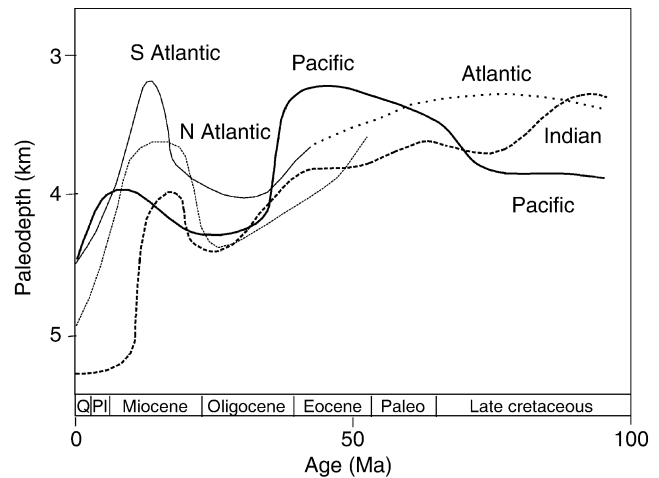


Figure C24 Carbonate compensation depth variation in different ocean basins through the late Cenozoic. (Redrawn from Van Andel, 1975.)

in interglacials and *vice versa*. Carbonate productivity plays a secondary role. On much of the Atlantic sea floor, the CCD fluctuations tend to change to counter those of the Pacific, with higher dissolution occurring during glacials. These changes in carbonate preservation are ascribed to changes in the formation of North Atlantic Deep Water, but also to changes in terrestrial carbon storage and in the fractionation between shallow and deep ocean carbonate deposition.

Pre-Quaternary history

Studies of longer cores from ocean floor drilling show that CCD fluctuations were similar in the various oceans and therefore driven by global mechanisms (Figure C24). The mean ocean CCD was about 1,000 m shallower than present during the Cretaceous and early Paleogene, followed by deepening levels going into

the Oligocene. Another shallowing occurred during the mid Miocene, before the CCD dropped to its present mean depth near 4,300 m. The drastic drop at the end of the Eocene is global in scale and reflects changes in the global carbon cycle, possibly linked to an increase in alkalinity due to higher silicate weathering caused by the Himalayan uplift (Francois and Walker, 1992). It might also be linked to the lowering of sea level at that time, reducing the area of shallow epicontinental seas available for the accumulation of coral reef carbonate. The late Neogene CCD drop is more pronounced in the North Atlantic as compared with that of all other ocean basins. It reflects mostly the increase in the production of North Atlantic Deep Water related to the opening and closing of ocean gateways at that time (Heinze and Crowley, 1997). However, there is still controversy about the cause of the CCD fluctuations in Earth history.

Torsten Bickert

Bibliography

- Archer, D.E., 1996. An atlas of the distribution of calcium carbonate in sediments of the deep sea. *Glob. Biochem. Cycles*, **10**, 159–174.
- Francois, L.M., and Walker, J.C.G., 1992. Modelling the Phanerozoic carbon cycle and climate: Constraints from the $^{87}/^{86}\text{Sr}$ isotopic ratio of seawater. *Am. J. Sci.*, **292**, 81–135.
- Heinze, C., and Crowley, T.J., 1997. Sedimentary response to ocean gateway circulation changes. *Paleoceanography*, **12**, 742–754.
- Milliman, J.D., Troy, P.J., Balch, W.M., Adams, A.K., Li, Y.H., and Mackenzie, F.T., 1999. Biologically mediated dissolution of calcium carbonate above the chemical lysocline? *Deep Sea Res. I*, **46**, 1653–1669.
- Peterson, L.C., and Prell, W.L., 1985. Carbonate dissolution in recent sediments of eastern equatorial Indian Ocean: Preservation patterns and carbonate loss above the lysocline. *Mar. Geol.*, **64**, 259–290.
- Van Andel, T.H., 1975. Mesozoic-Cenozoic calcite compensation depth and the global distribution of calcareous sediments. *Earth Planet. Sci. Lett.*, **26**, 187–194.

Cross-references

[Carbon Cycle](#)
[Carbonates, Cool Water](#)
[Carbonates, Warm Water](#)
[Marine Carbon Geochemistry](#)
[Paleo-Ocean pH](#)
[Pre-Quaternary Milankovitch Cycles and Climate Variability](#)
[Quaternary Climate Transitions and Cycles](#)

CARBONATES, COOL WATER

Introduction

The deposition of marine carbonate sediments in cool water environments has been long recognized (James, 1997). Despite this, the focus of study on carbonate sediments and their diagenesis has been carried out in warm, tropical waters in places such as the Caribbean, the Persian Gulf, the Great Barrier Reef, and Shark Bay. Not only do these places provide clear analogs for many ancient deposits, they are also often located in environments that are both pleasant to work in and easily accessible. Cool-water carbonates are, by way of contrast, deposited beneath some of the coldest and roughest waters of the world such as the Southern Ocean and North Atlantic. Furthermore, many of the best-exposed examples occur in Australia

([Figures C25 and C26](#)) and New Zealand, remote from European and North American centers of carbonate research.

Such disadvantages aside, understanding cool-water carbonates and their diagenesis is a vital component of carbonate sedimentology. They are currently being deposited across large areas of continental shelf, form extensive successions in Cenozoic basins, and are also known from many ancient high latitude environments. In addition, by virtue of their calcite-dominated mineralogy, cool-water carbonates provide excellent analogs for many Paleozoic limestones that were likewise dominated by calcite, in contrast to modern tropical carbonates, which are rich in aragonite.

History of investigations

Among the early studies, those of Chave (1967), Lees and Buller (1972) and Lees (1975) stand out as having established the conceptual framework for cool-water carbonate deposition. Meanwhile, Connolly and von der Borch (1967) and Wass et al. (1970) had discovered that cool-water carbonates were being deposited across the entire length and width of the southern Australian continental shelf. More recent compilations include the 1988 special issue of *Sedimentary Geology* (vol. 60), James and Clarke (1997), and Pedley and Carannante (2006). The last compilation paid particular attention to the cool-water carbonates of the Mediterranean Basin. Furthermore, ODP Leg 182 recovered a number of cores from the southern Australian margin in the Great Australian Bight (Feary et al., 2000).

Distinctive characteristics

James (1997) lists six characteristics for recognition of ancient cool-water carbonates. In decreasing order of reliability, these are:

1. Carbonates interbedded with glaciogene sediments
2. Carbonates situated in appropriate paleolatitudes
3. Glendonite-type minerals in carbonates
4. Carbonates composed wholly of the Heterozoan Association
5. Heterozoan Association outboard of mid to inner shelf/ramp Photozoan Association
6. Trace element and isotope geochemistry of skeletons

Of these, 1–3 are self explanatory but not always present, while 6 can be equivocal because of diagenesis. The following section therefore focuses on 4 and 5 as the characteristics that are most common and most readily determined by geological analysis.

Modern warm-water carbonates are dominated by photozoans, organisms that are either photosynthetic or are zooanthellate, with symbiotic photosynthetic organisms. These form the Photozoan Assemblage. In contrast, cool-water carbonates are predominantly dominated by Heterozoans, organisms that are non-photosynthetic and lack photosynthetic symbionts (James, 1997), and thus they are mostly dominated by bryozoans, with varying proportions of mollusks, foraminifers, echinoderms, brachiopods, barnacles, sponges, and coralline algae. As a result of this dichotomy, warm-water benthic carbonates are formed primarily in shallow water, especially in the first 30 meters where light is most intense. The biota that form cool-water carbonates are not limited to the photic zones, apart from coralline algae. Therefore, benthic carbonate production is not depth-limited but continues across the entire continental shelf and onto the upper continental slope. In addition to



Figure C25 The “Twelve Apostles,” sea stacks formed by erosion of the Oligo-Miocene Gambier Limestone, a cool-water carbonate on the south coast of Victoria, Australia (photo H. Apps).



Figure C26 Point Culver, Western Australia. Late Eocene cyclic cool-water chalky limestones rich in siliceous sponges, (photo by author).

the biota of the sediment surface, many of the organisms that contribute carbonate to these sediments grow prolifically on hard substrates, including rock reefs and sea floor hardgrounds. These rocky areas are in some ways analogous to the coral reefs of warm-water carbonates in that they provide a localized factory for carbonate production (Nelson et al., 1988a). Similarly, in shallow water, sea grass leaves provide a good substrate for epibionts, and the sheltered environment of sea grass banks (Figure C27) both encourages carbonate production and traps sediment (Gostin et al., 1984). In deeper water, bryozoan and sponge mounds are not uncommon (James et al., 2000), appearing in the geologic record both as discrete bioherms and biostromes.

In addition to their taxonomic distinctiveness, the Heterozan and Photozoan Assemblages differ in the dominant mineralogy produced. The Photozoan biotas produce skeletons that are predominantly aragonite and high magnesium calcite. Heterozan biotas are predominantly calcite, ranging from low to high magnesium contents. Aragonite is a comparatively minor component. This has major implications for the diagenesis of cool-water carbonates (see below).

Warm-water carbonates commonly contain ooids (formed in agitated shallow marine environments), abundant micrite (carbonate mud) formed either by disintegration of calcareous green algae or direct precipitation from seawater super-saturated with respect to carbonate, and intraclasts, formed by rapid sea floor



Figure C27 Seagrass beds and carbonate-rich sand, Esperance, Western Australia (photo by N. James).

cementation, again from super-saturated water. Ooids are absent in cool-water environments where saturation states are lower. True micrite is absent, and fine-grained carbonates are either carbonate silt formed by the erosion of other carbonates or coccoliths. Intraclasts are rare in cool-water successions, largely because the lower saturation state of carbonates in cooler marine waters reduces the rate of sea floor cementation.

Distribution

Modern marine carbonates occur wherever rates of biogenic carbonate production exceed terrigenous sediment supply. However, because biologic carbonate production is lower in cool as opposed to warm water, cool-water carbonates are generally found in areas of reduced terrigenous sedimentation (Chave, 1967). Gradations between warm and cool-water carbonates are known, such as on the west and southwest coasts of Australia (Cann and Clarke, 1993; Collins et al., 1997). However, a mean annual temperature of 22 °C or less serves as a useful dividing line between the warm and cool (or cold) water depositional realms (James, 1997). Cooler waters typically have a lower carbonate saturation than warmer waters, and this influences both the production of grains and the diagenesis of cool-water carbonates (see below).

Major settings for cool-water carbonate deposition include shelves and ramps, offshore banks, and large embayments. One of the largest and best-studied areas of cool-water carbonate shelf deposition is the continental shelf of southern Australia (James et al., 2001, and references therein). Rockhall (Scoffin et al., 1980) and Porcupine (Scoffin and Bowes, 1988) Banks in the North Atlantic are examples of modern offshore banks characterized by cool-water carbonate sediments. Large embayments floored by cool-water carbonates include Gulf St. Vincent (Shepherd and Sprigg, 1976) and Spencer Gulf of South Australia (Gostin et al., 1984).

In addition to temperature, several other processes can give rise to a cool-water aspect in otherwise warm water carbonate environments. One is turbidity, where high levels of suspended sediment reduce the competitive advantage of the photozoan biota so that, even in shallow water, the carbonate component

may be dominated by mollusks, bryozoan, and other heterozoan biota. The sediments in Bonaparte Gulf in northern Australia provide one such example (Clarke et al., 2001). Another is high nutrient loadings, which, in shallow water, will favor algal growth over that of zooanthellate organisms (James, 1997). In warmer waters, the algae will include calcareous green forms, but in areas where water temperatures are marginal for calcareous green algae, red algae and other components of the heterozoan biota will dominate. A third factor is water depth. Below the photic zone, biota is typically heterozoan in aspect. Deeper waters are cooler than shallow waters, especially where there is a well-developed thermocline. Deep shelf or upper slope carbonates of heterozoan aspect may therefore occur seaward either shallow cool-water shelf heterozoan carbonates or shallow warm-water shelf photozoan carbonates (James, 1997). Finally, cool or cold currents moving towards the equator along continental margins can result in conditions suitable for the Heterozoan Assemblage in low latitudes.

Diagenesis

Tropical carbonates often experience rapid seafloor cementation (Tucker and Wright, 1990). In contrast, cool-water carbonates for the most part experience limited seafloor cementation because of generally lower levels of carbonate saturation and the slower reaction times at lower temperatures. Rao (1981a) showed the presence of minor calcite seafloor cements in sediments on the Tasmania continental shelf. Ancient cool-water carbonates similarly show only limited seafloor cementation for the most part (e.g., Nicolaides, 1994 and Shubber et al., 1997). During exposure to meteoritic waters, limestones containing abundant aragonite have undergone extensive carbonate dissolution, which is reprecipitated as calcite. Dissolution and reprecipitation stabilizes the limestones and causes extensive lithification even in young carbonates that have undergone little burial, such as those of exposed Pleistocene reefs. Because aragonite is much less abundant in most cool-water carbonates, they do not undergo anywhere near as extensive dissolution and reprecipitation. In consequence, many cool-water carbonates that have undergone limited burial, such as



Figure C28 Oligo-Miocene Gambier Limestone exposed in cliffs near the Twelve Apostles, showing characteristic cyclic bedding (photo H. Apps).

the Oligocene carbonates of southern Australia, are only weakly lithified, despite their age (James and Bone, 1989). Most cementation in cool-water carbonates appears to be related to burial. This contrasts with aragonite-rich carbonates, where burial cements are more commonly associated with infill of remnant porosity after extensive seafloor and meteoric cementation. The Oligocene Te Kuiti Limestone of New Zealand has been buried to a depth of up to 1,100 m (Nelson et al., 1988b) and is, as a result, fully lithified and strongly stylolitized. It is likely that much of the carbonate needed to fully cement calcitic, cool-water limestones comes from pressure dissolution (Nicolaidis and Wallace, 1997). Pressure-dissolution appears to require at least ~200 m of burial to begin the process.

Examples of cool-water carbonates through geologic time

Cenozoic cool-water carbonates are best known from southern Australia, New Zealand, and southern Europe. The Australian examples range in age from Eocene to Pliocene and are very extensive, but have experienced little burial (rarely more than a few tens of meters), although some (Nicolaidis and Wallace, 1997) have had several hundred meters of burial (Figure C28). Most formed on Cenozoic shelves and slopes (e.g., Nicolaidis, 1994; Bernecker et al., 1997); however, some (Clarke et al., 1996; Shubber et al., 1997) formed in sheltered embayments similar to the modern gulfs of southern Australia. Because of their very limited burial diagenesis, they provide a useful link between the carbonates of modern cool-water environments and those that have experienced deep burial and subsequent uplift. Cool-water carbonates have also been documented from the margins of the Mediterranean, including examples from Spain (Franseen et al., 1997; Martin et al., 1996), Austria (Nebelsick, 1992), Italy (Bassi et al., 2006), and Greece (Spjeldnaes and Moissette, 1997). Cool-water carbonates of New Zealand, such as those of the Oligocene Te Kuiti Group

(Nelson et al., 1988b), have experienced deep burial and are fully lithified, unlike their Australian and Mediterranean counterparts. New Zealand carbonates were deposited on both shelf and platform environments (Nelson, 1978).

The well-known Cretaceous and Danian chalks of Europe (Scholle et al., 1983) are now regarded as cool-water carbonates. These were deposited in a range of environments directly analogous to those of modern southern Australia, from high-energy skeletal grainstones along the shores to offshore bryozoan mounds and deep shelf coccolith lime mudstones (Surlyk, 1997). Other documented examples of Mesozoic carbonates with cool-water affinities are the open shelf carbonates of Sardinia and the southern Appenines (Carannante et al., 1997).

The first Paleozoic carbonates recognized as being of cool-water origin were the Permian limestones of Tasmania. These were shown by Rao (1981b) to have formed on a polar shelf marginal to the Gondwana glaciation on the basis of their dropstones and close association with glaciomarine facies. In addition, they were deposited at a high paleolatitude and had a primary calcite-dominant mineralogy. Other cold-water carbonates of Tasmania include the Darlington Limestone (Brill, 1982), deposited in a near-shore facies. Equivalent sediments of the Northern Hemisphere are found in the Permian of the Sverdrup Basin (Beauchamp and Desrochers, 1997; Stemmerik, 1997).

Other known Paleozoic cool-water carbonates have been described from the Early Carboniferous of western Canada (Brandley and Krause, 1997; Martindale and Boren, 1997), to the Middle Ordovician of Canada by Brookfield (1988) and Kentucky by Pope and Read (1997). Lavoie (1995) provided a Late Ordovician example from Quebec. These three examples all occur at relatively low paleolatitudes. They are attributed to a combination of factors including upwelling, thermally stratified oceans, and cool or cold currents flowing towards the paleoequator.

Jonathan Clarke

Bibliography

- Bassi, D., Carannante, G., Murru, M., Simone, L., and Toscano, F., 2006. Rhodalgae/bryomol assemblages in temperate-type carbonate, channeled depositional systems: The Early Miocene of the Sarcidano area (Sardinia, Italy). In Pedley, H.M., and Carannante, G. (eds.), *Cool-water Carbonates: Depositional Systems and Palaeoenvironmental Controls*. London: Geological Society special publication **25**, pp. 23–52.
- Beauchamp, B., and Desrochers, A., 1997. Permian warm- to very cold-water carbonates and cherts in northwest Pangea. In James, N.P., and Clarke, J. (eds.), *Cool-water Carbonates*. Tulsa, OK: SEPM Special Publication **56**, pp. 327–348.
- Bernecker, T., Partridge, A.D., and Webb, J.A., 1997. Mid-late Tertiary deep-water temperate carbonate deposition, offshore Gippsland Basin, southeastern Australia. In James, N.P., and Clarke, J. (eds.), *Cool-water Carbonates*. Tulsa, OK: SEPM Special Publication **56**, pp. 221–236.
- Brandley, R.T., and Krause, F.F., 1997. Upwelling, thermoclines and wave-sweeping on an equatorial carbonate ramp: Lower Carboniferous strata of western Canada. In James, N.P., and Clarke, J. (eds.), *Cool-water Carbonates*. Tulsa, OK: SEPM Special Publication **56**, pp. 365–390.
- Brill, K.G., 1982. Palaeoenvironment of the Darlington Limestone (Early Permian), Tasmania. *Papers and Proceedings of the Royal Society of Tasmania* **116**, 67–84.
- Brookfield, M.E., 1988. A mid-Ordovician temperate carbonate shelf-the Black River and Trenton Limestone groups of southern Ontario, Canada. *Sediment. Geol.*, **60**, 137–153.
- Cann, J.H., and Clarke, J.D.A., 1993. The significance of Marginopora verbeulsi (Foraminifera) in surficial sediments at Esperance, Western Australia, and in last interglacial sediments in northern Spencer Gulf, South Australia. *Mar. Geol.*, **111**, 171–187.
- Carannante, G., Graziano, R., Ruberti, D., and Simone, L., 1997. Upper Cretaceous temperate-type open shelves from northern (Sardina) and southern (Appennines-Apulia) Mesozoic Tethyan margins. In James, N.P., and Clarke, J. (eds.), *Cool-water Carbonates*. Tulsa, OK: SEPM Special Publication **56**, 309–325.
- Chave, K.E., 1967. Recent carbonate sediments – an unconventional view. *J. Geol. Educ.*, **15**, 200–204.
- Clarke, J.D.A., Bone, Y., and James, N.P., 1996. Cool-water carbonates in an Eocene paleoestuary, Norseman Formation, Western Australia. *Sediment. Geol.*, **10**, 213–226.
- Clarke, J.D.A., Bone, Y., Cann, J.H., Davies, M., Macphail, M.K., and Wells, F., 2001. Post-glacial biota from the inner part of south-western Joseph Bonaparte Gulf. *Aust. J. Earth Sci.*, **48**, 63–79.
- Collins, L.B., France, R.F., Zhu, Z.-R., and Wyrwoll, K.-H., 1997. Warm-water platform and cool-water shelf carbonates of the Abrolhos Shelf, southwest Australia. In James, N.P., and Clarke, J. (eds.), *Cool-water Carbonates*. Tulsa, OK: SEPM Special Publication **56**, pp. 23–36.
- Connolly, J.R., and von der Borch, C.C., 1967. Sedimentation and physiography of the seafloor south of Australia. *Sedimentology*, **1**, 118–220.
- Feary, D.A., Hine, A.C., and Malone, M.J., et al., 2000. *Proceedings ODP, Initial Reports* 182 [Online]. Available from World Wide Web: http://www-odp.tamu.edu/publications/182_IR/182ir.htm. (Cited 2006-10-19).
- Franseen, E.K., Goldstein, R.H., and Farr, M.R., 1997. Substrate-slope and temperature controls on carbonate ramps: Revelations from upper Miocene outcrops, SE Spain. In James, N.P., and Clarke, J. (eds.), *Cool-water Carbonates*. Tulsa, OK: SEPM Special Publication **56**, pp. 271–190.
- Gostin, V.A., Hails, J.R., and Belperio, A.P., 1984. The sedimentary framework of northern Spencer Gulf, South Australia. *Mar. Geol.*, **61**, 111–138.
- James, N.P., 1997. The cool-water carbonate depositional realm. In James, N.P., and Clarke, J. (eds.), *Cool-water Carbonates*. SEPM Special Publication **56**, pp. 1–20.
- James, N.P., and Bone, Y., 1989. Petrogenesis of Cenozoic, temperate water calcarenites, south Australia: A model for meteoric/shallow burial diagenesis of shallow water calcite cements. *J. sediment. petrol.*, **59**, 191–203.
- James, N.P., and Clarke, J.D.A. (eds.), 1997. *Cool-water Carbonates*. Tulsa, OK: SEPM Special Publication **56**, pp. 1–20.
- James, N.P., Feary, D.A., Surlyk, F., Simo, J.A.T., Betzler, C., Holbourn, A.E., Li, Q., Matsuda, H., Machiyama, H., Brooks, G.R., Andres, M.S., Hine, A.C., and Malone, M., 2000. Quaternary bryozoan reef mounds in cool-water, upper slope environments; Great Australian Bight. *Geology*, **28**, 647–650.
- James, N.P., Bone, Y., Collins, L.B., and Kyser, T.K., 2001. Surficial sediments of the Great Australian Bight; facies dynamics and oceanography on a vast cool-water carbonate shelf. *J. Sediment. Res.*, **71**, 549–567.
- Lavoie, D., 1995. A late Ordovician high-energy, temperate-water carbonate ramp, southern Quebec, Canada: Implications for Late Ordovician oceanography. *Sedimentology*, **42**, 95–116.
- Lees, A., 1975. Possible influences of salinity and temperature on modern shelf carbonate sedimentation. *Mar. Geol.*, **19**, 159–198.
- Lees, A., and Buller, A.T., 1972. Modern temperate water and warm water shelf carbonate sediments contrasted. *Mar. Geol.*, **19**, 159–198.
- Martin, J.M., Braga, J.C., Betzler, C., and Bracher, T., 1996. Sedimentary model and high frequency cyclicity in a Mediterranean, shallow-shelf, temperate-carbonate environment (uppermost Miocene, Agua Amarga Basin, Southern Spain). *Sedimentology*, **43**, 263–277.
- Martindale, W., and Boreen, T.D., 1997. Temperature-stratified Mississippian carbonates as hydrocarbon reservoirs – examples from the foothills of the Canadian Rockies. In James, N.P., and Clarke, J. (eds.), *Cool-water Carbonates*. Tulsa, OK: SEPM Special Publication **56**, pp. 391–410.
- Nebelsick, J.H., 1992. Component analysis of sediment composition in Early Miocene temperate carbonates from the Austrian Paratethys. *Palaeogeogr. Palaeoclimatol. Palaeoecol.*, **91**, 59–69.
- Nelson, C.S., 1978. Temperate shelf carbonate sediments in the Cenozoic of New Zealand. *Sedimentology*, **25**, 737–771.
- Nelson, C.S., Keane, S.L., and Head, P.S., 1988a. Non-tropical carbonate deposits on the modern New Zealand shelf. *Sediment. Geol.*, **60**, 71–90.
- Nelson, C.S., Harris, G.J., and Young, H.R., 1988b. Burial-dominated cementation in non-tropical carbonate deposits of the Oligocene Te Kuiti group, New Zealand. *Sediment. Geol.*, **60**, 233–250.
- Nicolaides, S., 1994. Cementation in Oligo-Miocene non-tropical shelf carbonates, Otway basin, Australia. *Sediment. Geol.*, **95**, 91–121.
- Nicolaides, S., and Wallace, M.W., 1997. Pressure-dissolution and cementation in Oligo-Miocene non-tropical limestone (Clifton Formation) Otway Basin, Australia. In James, N.P., and Clarke, J. (eds.), *Cool-water Carbonates*. Tulsa, OK: SEPM Special Publication **56**, pp. 249–262.
- Pedley, H.M., and Carannante, G. (eds.), 2006. *Cool-Water Carbonates: Depositional Systems and Palaeoenvironmental Controls*. London: Geological Society special publication **25**, 373pp.
- Pope, M.C., and Read, F.J., 1997. High-resolution stratigraphy of the Lexington Limestone (Late Middle Ordovician), Kentucky, U.S.A.: A cool-water carbonate-clastic ramp in a tectonically active foreland basin. In James, N.P., and Clarke, J. (eds.), *Cool-water Carbonates*. Tulsa, OK: SEPM Special Publication **56**, pp. 411–430.
- Rao, C.P., 1981a. Cementation in cool-water bryozoan sand, Tasmania, Australia. *Mar. Geol.*, **40**, M23–M33.
- Rao, C.P., 1981b. Criteria for the recognition of cold-water carbonate sedimentation: Berridale Limestone (Lower Permian), Tasmania, Australia. *J. Sediment. Petrol.*, **51**, 491–506.
- Scholle, P.A., Arthur, M.A., and Ekdale, A.A., 1983. Pelagic environment. In Scholle, P.A., Bebout, D.G., and Moore, C.H. (eds.), *Carbonate depositional Environments*. Tulsa, OK: AAPG Memoir **33**, 619–691.
- Scoffin, T.P., and Bowes, G.E., 1988. The facies distribution of carbonate sediments on Porcupine Banks, northeast Atlantic. *Sediment. Geol.*, **60**, 125–134.
- Scoffin, T.P., Alexandersson, E.T., Bowes, G.E., Clokie, J.J., Farrow, G.E., and Milliman, J.D., 1980. Recent, temperate, sub-photic carbonate sedimentation: Rockall Bank, northeast Atlantic. *J. Sediment. Petrol.*, **50**, 331–356.
- Shepherd, S.A., and Sprigg, R.C., 1976. Substrate, sediments, and subtidal ecology of Gulf St. Vincent and Investigator Strait. In Twidale, C.R., Tyler, M.R., and Webb, B.P. (eds.), *Natural History of the Adelaide Region*. Adelaide: Royal Society of South Australia, pp. 161–174.
- Shubber, B., Bone, Y., James, N.P., and McGowran, B., 1997. Warming-upward subtidal cycles in mid-Tertiary cool-water carbonates, St. Vincent Basin. In James, N.P., and Clarke, J. (eds.), *Cool-water Carbonates*. Tulsa, OK: SEPM Special Publication **56**, pp. 237–248.
- Spjeldnaes, N., and Moissette, P., 1997. Cellaporid (bryozoan) thickets from the upper Pliocene of the island of Rhodes. In James, N.P., and Clarke, J. (eds.), *Cool-water Carbonates*. Tulsa, OK: SEPM Special Publication **56**, pp. 263–270.

- Stemmerik, L., 1997. Permian (Artinskian-Kazanian) cool-water carbonates in northern Greenland, Svalbard and the western Barents Sea. In James, N.P., and Clarke, J. (eds.), *Cool-water Carbonates*. Tulsa, OK: SEPM Special Publication 56, pp. 349–364.
- Surlyk, F., 1997. A cool-water carbonate ramp with bryozoan mounds: Late Cretaceous-Danian of the Danish Basin. In James, N.P., and Clarke, J. (eds.), *Cool-water Carbonates*. Tulsa, OK: SEPM Special Publication 56, pp. 293–308.
- Tucker, M.E., and Wright, V.P., 1990. *Carbonate Sedimentology*. Oxford: Blackwell Scientific Publications, 482pp.
- Wass, R.E., Connelly, J.R., and McIntyre, J., 1970. Bryozoan carbonate sand continuous along southern Australia. *Mar. Geol.*, 9, 63–73.

Cross-references

[Carbonates, Warm Water](#)
[Glacial Sediments](#)
[Glaciomarine Sediments](#)
[Glendonite/Ikaite](#)
[Marine Biogenic Sediments](#)

CARBONATES, WARM WATER

Sediments composed of calcium carbonate form a large, but not major, part of the world's continental shelf seas and deep ocean basins (Figure C29). The best-known examples of these sediments are coral reefs and white beaches made up of calcareous (CaCO_3) sand grains, typically seen in tropical environments.

What are warm-water carbonate sediments?

Most carbonate sediments are formed from the accumulation of skeletons and shells constructed by marine organisms through the precipitation of calcium carbonate (e.g., corals, mollusks and foraminifera). These are called skeletal, or bioclastic, carbonate sediments. Skeletal carbonates occur in both the warm and the cold waters of the shelf areas in the world (Figure C29). They are most common on continental shelves that are not diluted by large amounts of eroded and transported siliciclastic sediments, as is the case near major river mouths and adjacent to mountainous coastal regions. The composition of skeletal carbonates differs in warm and cool water areas because of the different skeletal organisms that live in these areas. Today's warm or tropical waters are characterized by sea-floor, or benthic, communities of the rapidly calcifying corals and calcareous green algae, together with mollusks, foraminifera, echinoids, bryozoans, etc. Coral reefs today are restricted to waters warmer than 18°C (Kleypas et al., 1999). Other carbonate sediments are formed by the chemical precipitation of crystals of calcium carbonate from seawater, with some authors arguing for a microbial mediation to this process (Riding and Awramik, 2000). Precipitation is favored in the warm, saline waters of some tropical seas and results in spherical, sand-sized grains known as ooids, aggregate grains, peloids and precipitated lime mud (for details, see below). These are labeled as non-skeletal carbonate sediments and are only found in warm-water areas. Lees and Buller (1972) found that modern ooids and grain aggregates form in waters with maximum annual temperatures $>20^\circ\text{C}$ and in waters with salinities greater than 37‰ (parts per thousand). This temperature together with the temperature

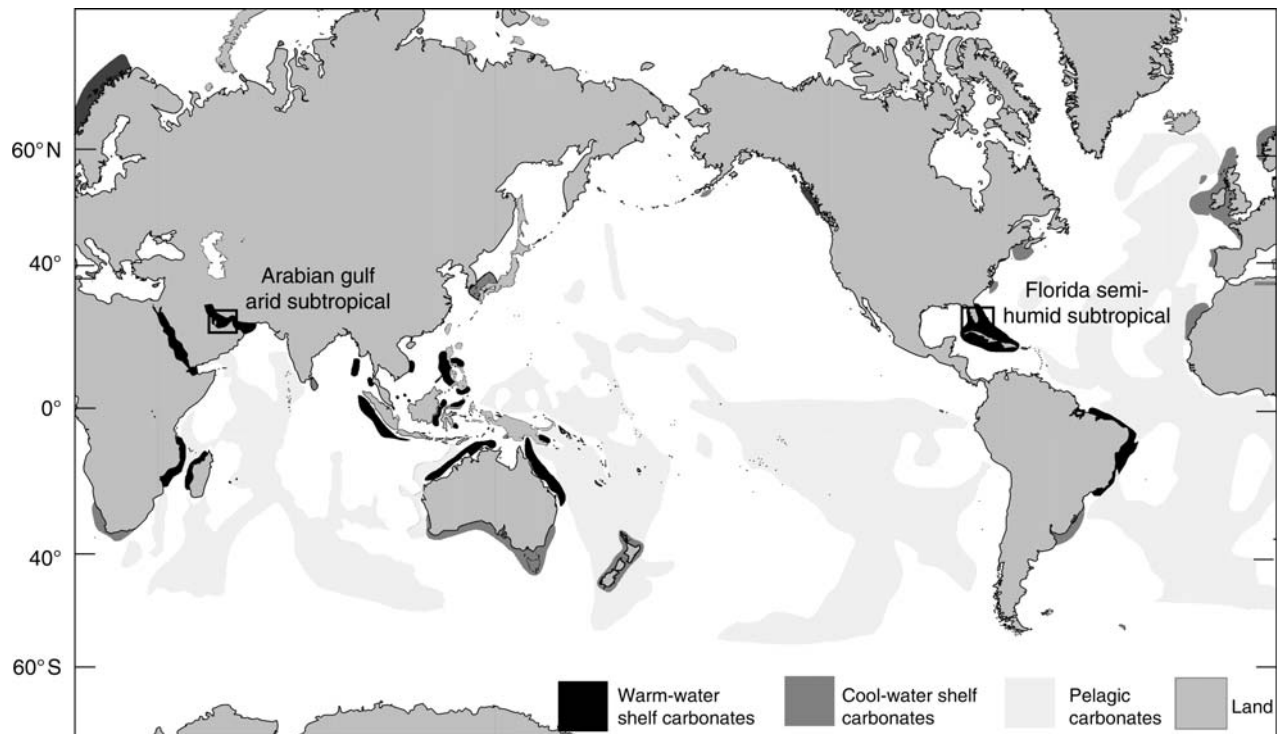


Figure C29 Global distribution of modern carbonate sediments. The two case studies discussed in the text are also located (after Bosence and Wilson, 2003).

restriction for coral reefs (i.e., 18–20°C) may therefore be taken as the boundary between what are regarded as warm (or tropical) and cool (or temperate) water carbonate sediments.

Warm-water carbonates through geological time

The abundance of carbonate rocks formed in marine shelf environments has varied considerably over geological time (Figure C30). Not surprisingly, they were most abundant when global sea levels were high and large areas of continents were flooded by shallow, warm-water, shelf seas. These conditions occurred several times in Earth history, during “greenhouse periods” when there were prolonged periods with no major ice caps covering the polar regions (Figure C30). The types of warm-water organisms that produced skeletal carbonates changed as life evolved, so that late Precambrian, early and late Paleozoic, Mesozoic and Cenozoic bioclastic limestones are quite different in their composition (Figure C30). An independent measure of paleotemperature may be made by analyzing the oxygen isotope ratios of original skeletal calcium carbonate of fossils within bioclastic limestones. Similarly, the mineralogy of ooids also changed through time in tune with greenhouse (low magnesium calcite ooids) and icehouse periods (aragonitic and high magnesium calcite ooids, Figure C30). The abundance of ooids has also changed with time, and possibly with sea-level changes, as peaks are found at times of major

long term sea-level change (Figure C30). Although the mineralogy of ooids has changed through time, and there is still debate as to what controls this (see discussion in Tucker and Wright, 1990), all indications are that ooids still represent ancient environments of increased temperature and increased salinity. The use of non-skeletal marine carbonate grains (such as ooids and grain aggregates) has proven to be more reliable than fossils as a warm-water indicator. This is because the formation of non-skeletal grains is predominantly controlled by the chemical conditions at or near the seafloor and, apart from the changes illustrated in Figure C30, these do not appear to have changed significantly through time. Studies on the nature of warm-water carbonate rocks over the last 650 Ma indicate that the present is not always the key to the past. A 400 Ma warm-water limestone will differ in its preserved biota and ooid mineralogy from its present day equivalent and care has to be taken in undertaking any paleoenvironmental analysis based on carbonate grain types.

Case studies of warm-water carbonate depositional environments; humid versus arid settings

Two case studies of present-day environments accumulating warm-water carbonate sediments are given below. These examples are used extensively in the interpretation of ancient environments as they illustrate the range of different sediment

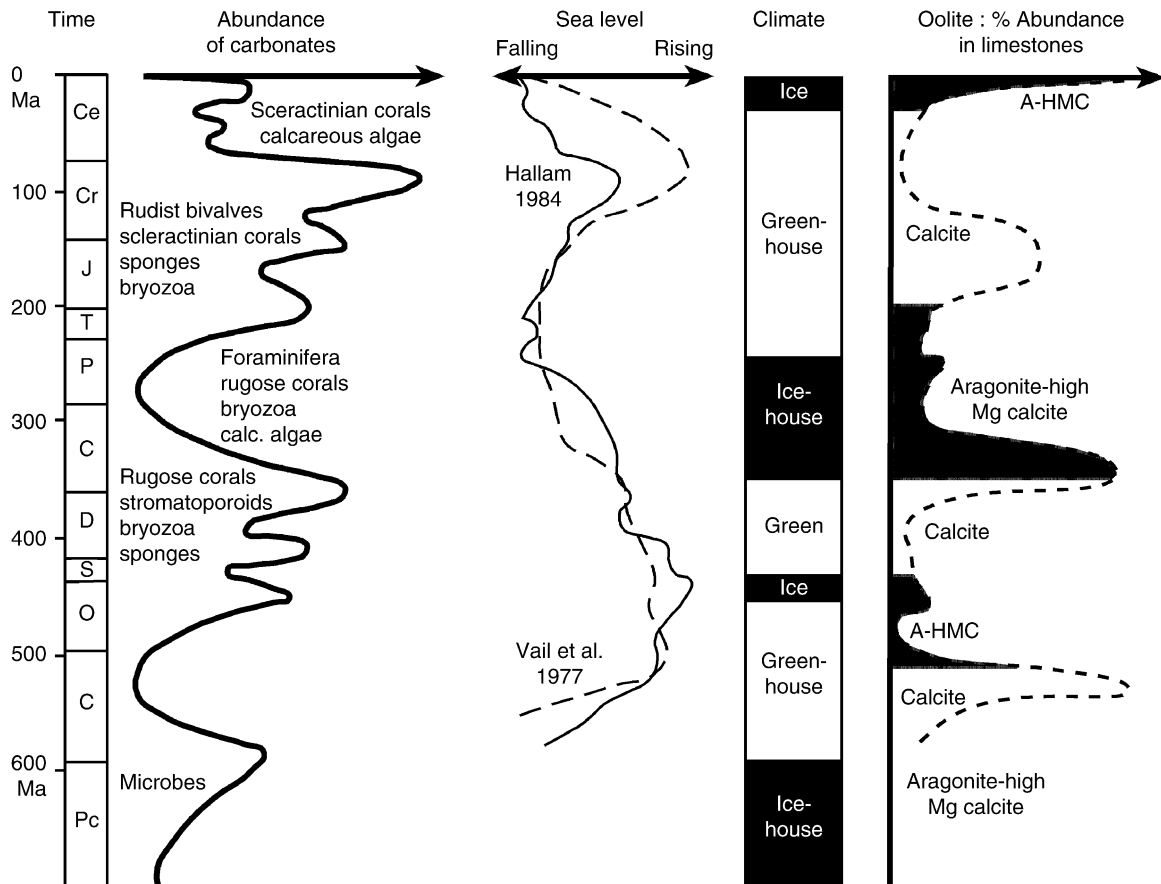


Figure C30 Secular changes in warm-water carbonate grains with respect to sea-level changes and icehouse–greenhouse periods. For details, see text (modified from many studies, for details see Tucker and Wright, 1990; Bosence and Wilson, 2003; Hallam, 1984; Vail et al., 1977).

grains and facies found in warm-water settings. They are both examples of carbonate shelves that are attached to continental areas, as opposed to isolated shelves, banks and atolls that form in offshore settings (for details see Tucker and Wright, 1990). They differ, however, in that South Florida is in a semi-humid subtropical setting and the Arabian Gulf is in an arid climate setting (Figure C29). The climatic setting is seen to have an overriding control on the nature of the sediments, particularly those accumulating in the shallow, nearshore areas.

South Florida

South Florida is a shelf with a large, low-lying hinterland (including the Everglades Swamps) set in a semi-humid, subtropical climate fringed by coastlines stabilized by mangroves (Figure C31a). Warm-water carbonate sediments accumulate throughout this shelf area and deep boreholes in the region show that this has been the case since Jurassic times. The platform comprises four main elements; a semi-enclosed lagoon (known as Florida Bay) that is partially isolated from open-marine waters by a chain of islands (the Florida Keys), a back reef area of normal marine waters that are protected from high

wave-energy by the rimmed margin, the reef and sand shoal margin to the platform, and the forereef slope that descends into the deep waters of the Strait of Florida (Figure C31f).

The semi-humid climate is seasonal, with a wet season from July to December (100–150 cm annual precipitation) when there is runoff of freshwater, reducing salinities in inner parts of Florida Bay to 6‰ (normal marine waters have on average 34–38‰). By contrast, in the warmer conditions of spring and summer, temperatures increase and salinities up to 60‰ are found in the restricted waters of Florida Bay. The reef areas experience normal marine salinities of 35–38‰ and water temperatures varying from 18–30 °C. The region has a very low tidal range, reaching 0.8 m in open-water settings and reducing to zero in the semi-enclosed lagoons of Florida Bay.

Organisms that are fully marine cannot survive in the semi-isolated shallow coastal waters of Florida Bay because of the variable salinities, dissolved oxygen levels and fine carbonate sediment suspended within the bay waters. Seagrass (e.g., *Thalassia*) beds (Figure C31b,e) and the calcareous organisms that encrust the grass blades (foraminifera, serpulid worms and bryozoa) are common, as are other skeletal organisms such

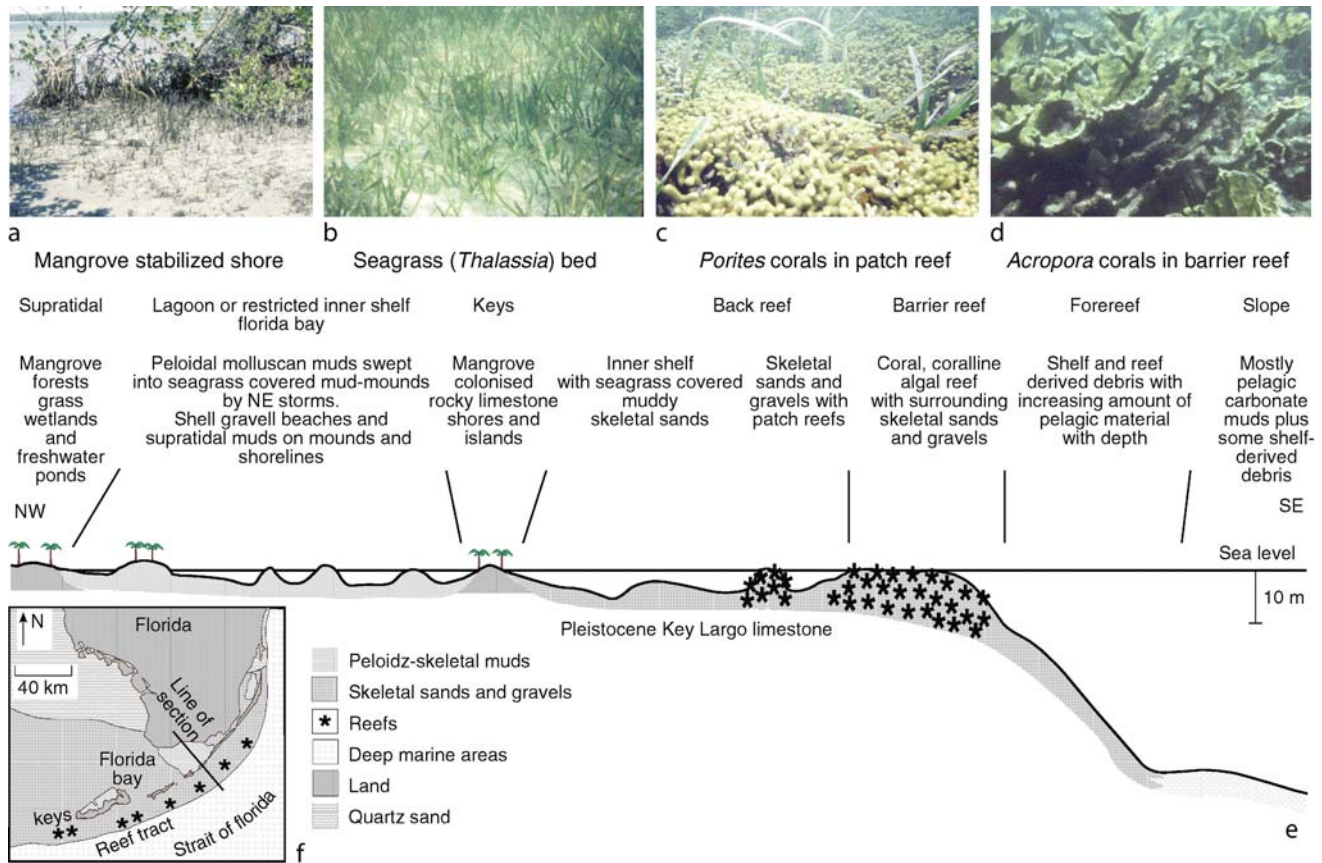


Figure C31 Nature and distribution of sediments in humid subtropical region of South Florida. Photographs (a)–(d) illustrate the control that organisms have on carbonate sediment production and accumulation. (a) Mangrove roots stabilizing the shoreline of Florida Bay (foreground 4 m across). (b) *Thalassia* seagrass bed. The grass leaves (20–30 cm high) act as a substrate for carbonate-secreting organisms whose skeletal debris is trapped and stabilized within the grass beds. (c) *Porites* coral (branches 1 cm across) are common reef builders in the back reef zone. Note also encrusted seagrass blades. (d) The shallow zone of the shelf margin barrier reef is mainly constructed by the elk horn coral, *Acropora palmata* (branches 15–20 cm across). Map and cross section ((e)–(f)) illustrate nature and distribution of sediments discussed in text (after Bosence and Wilson, 2003).

as mollusks, foraminifera and calcareous green algae (*Penicillus* and *Udotea*). When these organisms die, their skeletal debris accumulates as shelly muds that form bioclastic mudstones and wackestones in the geological record (for more details on these sediments, together with carbonate rock terminology, see Tucker and Wright (1990) and Flugel (2004)). Shells are concentrated on beaches and storm ridges as bioclastic gravels and sands. The carbonate mud has the same mineralogical (calcite and aragonite) and geochemical (Ca, Mg and Fe, etc.) composition as the skeletal organisms, which implies that most of the mud is produced from the breakdown of skeletons of algae and benthic invertebrates. Once formed, the mud is reworked by burrowing organisms (mainly shrimps and worms) that digest what they can from the mud and defecate the remainder as sedimentary faecal pellets or peloids.

Back reef areas are of normal marine salinity and more exposed to waves that generate well-oxygenated waters. These conditions favor a more diverse community of carbonate-secreting organisms such as corals, encrusting coralline algae, calcified plate-like green algae (*Halimeda*), mollusks, echinoderms and foraminifera. Corals are not abundant in this environment but they locally form small patch reefs constructed by corals and coralline algae overgrowing each other to form a rigid reef framework (Figure C31c,e). This framework forms an attractive habitat for many other organisms, including those that eat or bore into the coral such as sponges, worms, parrotfish, echinoids and mollusks. The coral debris they generate forms much of the skeletal carbonate sand and gravel that accumulates around the patch reefs. These, if lithified, will form skeletal or bioclastic packstones or grainstones in the geological record.

The rimmed margin of this platform comprises a barrier reef (because the reefs are detached from the shoreline and act as a barrier to the back reef and lagoonal areas inshore of them) with intervening high-energy, shallow-water shoals of coarse skeletal sand and gravel. These breaks in the arc of reefs are probably due to the fact that Florida is near the northernmost limit of both reef growth and warm-water carbonates (Figure C29). The shallowest zone of the reefs is formed by the branching coral *Acropora palmata* (Figure C31d,e), and by some round shaped (or head) corals and encrusting coralline algae. Deeper down the ocean-facing front of the reef, more massive and rounded coral growth forms are found that give way to deeper-water, flattened or plate-shaped corals. Lower areas of this fore reef slope are characterized by coarse-grained reef talus deposits formed of broken and bioeroded debris from the reef. Similar reef morphologies and coral zones are preserved in ancient reef limestones where they are called coral boundstones and are composed mainly of fossil corals. Reef corals are one of the most unequivocal biogenic indicators of warm, shallow-water conditions in the Cenozoic and Mesozoic.

Arabian Gulf

The southern coast of the Arabian (or Persian) Gulf offshore from the Gulf Coast States (Abu Dhabi, Dubai and Qatar) slopes gradually from the low relief desert of the coastal plain, through the coastal waters and down to a maximum depth of about 100 m over a distance of a couple of hundred kilometers (Figure C32). This gently sloping shelf morphology is the distinctive feature of what is known as a carbonate ramp. The shelf has no major reef systems or rimmed shelf margins as

are found in South Florida. The prevailing winds blow onshore from the northwest, which make this a storm-wave dominated coastline (Figure C32f). Due to the restricted opening to the Indian Ocean through the Strait of Hormuz and the arid climate setting, salinities in the Gulf are elevated to 40–45‰ and temperatures range annually from 20 to 34 °C. Details of the region and its sediments are given in Purser (1973).

Wave-base, the water depth at which wave-generated currents affect the sea floor, has an important control on sediment texture in gently sloping ramps and is used to subdivide ramps into zones (Figure C32e). In the Gulf, the outer ramp areas (below storm wave base) accumulate muds with a mixed composition (called marl); these are partly carbonate, of pelagic origin, and partly siliciclastic mud brought into the Gulf by rivers. These marls pass up-slope to the south into muddy and then clean skeletal and oolitic sands at the fair-weather wave base at around 10–20 m (Figure C32e, f). Moderate energy waters characterize this windward facing shore and hence areas of clean skeletal sand are found in inner ramp environments. These sands are commonly cemented at or just below the sea-floor to produce extensive hardgrounds, another feature of warm-water carbonates. Small patch reefs (Figure C32d) occur but with a low diversity coral fauna because of the elevated salinities and sometimes low winter temperatures.

The inner ramp in the Abu Dhabi area, prior to the extensive coastal developments of today, used to be dominated by ooid barrier beaches (with minor skeletal grains and peloids) (Figure C32c). Aragonitic ooids are precipitated in the relatively high salinity marine waters that have a moderate tidal and wave energy regime. Ooid barrier islands are situated up to 20 km away from the shoreline and broad, shallow lagoons have developed behind the barriers (Figure C32c). The lagoons have elevated salinities of 40–50‰ and so have a reduced diversity of marine faunas, comprising gastropods and ostracods that occur in lime muds and peloidal muddy sands. The lime muds are aragonitic and both the absence of calcified green algae (like those present in South Florida) and geochemical evidence from the lagoon waters and the deposited muds indicate that these muds were precipitated chemically within the lagoon (Kinsman and Holland, 1969) rather than having a skeletal origin such as those of Florida Bay.

The sabkhas are broad, saline, intertidal areas and coastal plains (Figures C32a, b, e, f) that may be flooded by lagoon waters during storms and high tides. The sabkhas have extensive microbial populations that alternate with sediment-rich layers to form stromatolites (Figure C32a, b). High aridity in the area leads to a net evaporation of floodwaters, and saline groundwaters in the sabkha, which results in the precipitation of evaporite minerals such as dolomite, gypsum and anhydrite.

Summary

From this review it can be seen that warm-water (>18–20 °C) continental shelf seas today have extensive areas of carbonate sediment accumulation. This, together with their relatively rapid accumulation rates, explains why limestones that deposited in warm-water shelf environments form the commonest types of limestone in the geological record. Warm-water carbonates have distinctive assemblages of component grains, both skeletal and non-skeletal in origin. However, these vary back through geological time so that the present is not always the key to the past and care must be taken with paleoclimatic and paleoenvironmental interpretations based on grain occurrences.

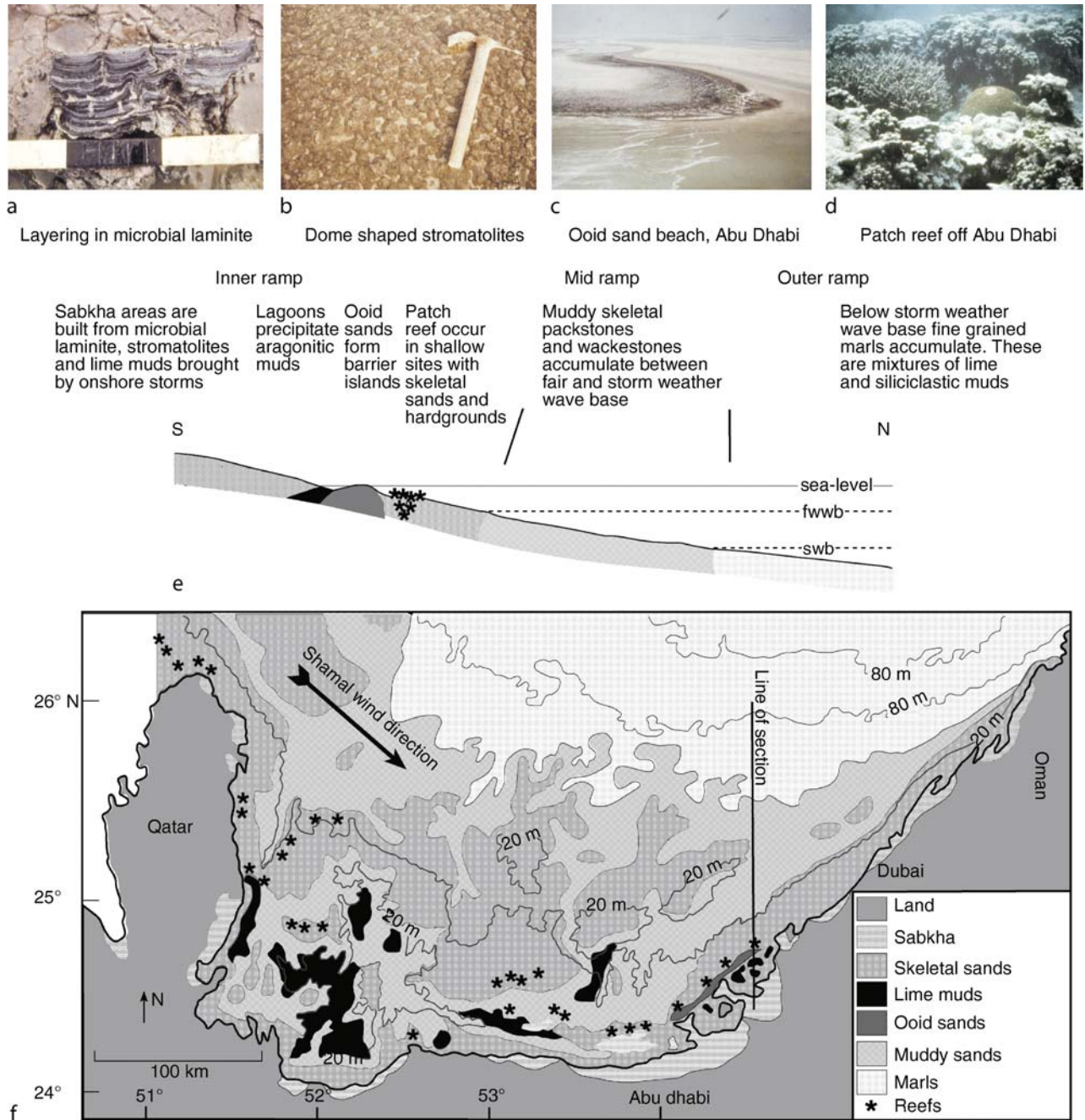


Figure C32 Nature and distribution of sediments in arid subtropical region of the Arabian Gulf. (a) Intertidal flats showing alternating microbial (dark) and sediment (light) layers: white patches within layering are precipitates of the calcium sulfate salt, anhydrite (scale in inches). (b) Dome-shaped stromatolites in intertidal sabkha. These result from upward growth of microbial mats and sediment with lighter colored sediment accumulating between domes. (c) Ooid sand beaches occur on barrier islands on the Abu Dhabi coast. Dark area by waters edge is microbial mat. (d) Patch reefs offshore from the barrier islands have a low diversity compared with reefs of the nearby Indian Ocean because of the high salinity of the Gulf waters. Map and cross-section ((e), (f)) of southeastern margin of the Arabian Gulf illustrate depth-related sediment types on carbonate ramp. Note change in sediment type with storm wave base (swb) and fairweather wave base (fwwb) (modified from Bosence and Wilson, 2003).

The two case studies of warm-water carbonate depositional systems illustrate the range of sedimentary grain types and sedimentary facies found in such environments today and explain how these are controlled by their climatic setting.

Studies such as these provide the raw data for interpretation of warm-water carbonates in the geological record.

Dan Bosence

Bibliography

- Bosence, D.W.J., and Wilson, R.C.L., 2003. Carbonate depositional systems. In Coe, A. (ed.), *The Sedimentary Record of Sea-level Change*. The Open University and Cambridge University presses, pp. 209–233.
- Flügel, E., 2004. *Microfacies of Carbonate Rocks*. Berlin, New York: Springer, 996pp.
- Hallam, A., 1984. Pre-Quaternary sea-level changes. *Annu. Rev. Earth Planet. Sci.*, **12**, 205–243.
- Kinsman, D.J.J., and Holland, H.D., 1969. The co-precipitation of cations with CaCO₃ IV. The co-precipitation of Sr²⁺ with aragonite between 16 °C and 96 °C. *Geochem. Cosmochim. Acta*, **33**, 1–17.
- Kleypas, J.A., McManus, J.W., and Meñez, L.A.B., 1999. Environmental limits to coral reef development: Where do we draw the line? *Am. Zool.*, **39**, 146–159.
- Lees, A., and Buller, A.T., 1972. Modern temperate water and warm water shelf carbonates contrasted. *Mar. Geol.*, **13**, 1767–1773.
- Purser, B.H. (ed.) 1973. *The Persian Gulf: Holocene Carbonate Sedimentation in a Shallow Epicontinental Sea*. Berlin: Springer, 471pp.
- Riding, R., and Awramik, S.M. (eds.) 2000. *Microbial Sediments*. Berlin: Springer, 332pp.
- Tucker, M.E., and Wright, V.P., 1990. *Carbonate Sedimentology*. Oxford, UK: Blackwell, 482pp.
- Vail, P.R., Mitchum, R.M. Jr., Todd, R.G., Widmier, J.M., Thompson, S. III, Sangree, J.B., Bub, J.N., and Hatlelid, W.G., 1977. Seismic stratigraphy and global changes of sea level. In Payton C.E. (ed.), *Seismic Stratigraphy – Applications to Hydrocarbon Exploration*. American Association of Petroleum Geologists Memoir, **26**, pp. 49–212.

Cross-references

Carbonates, Cool Water
 Coral and Coral Reefs
 Evaporites
 Greenhouse (warm) Climates
 Icehouse (cold) Climates
 Oxygen Isotopes

CENOZOIC CLIMATE CHANGE

The Cenozoic Era, or the last 65 million years, is a contrast of two worlds. Climates during the first 15 million years of the Cenozoic were generally warm and the Earth could be characterized as a greenhouse world. Fossil remains of early Eocene age (ca. 50 Ma) alligators found on Ellesmere Island (75°–80° N) contrast sharply with the polar climates that exist there today. This is not an isolated discovery or quirk of nature. An ever-growing body of faunal, floral, and geochemical evidence shows that the beginning of the Cenozoic Era was much warmer than the present time. What maintained such a warm climate and could it be an analog for future global warming? How did we go from the warm, greenhouse conditions to the cold poles that characterize today's world? To address these and other questions, it is necessary to consider more than a qualitative estimate of planetary temperatures. Quantitative temperature estimates (both magnitudes and rates of change) are required to depict how the Earth's climate has changed through time. One of the most powerful tools used to reconstruct past climates during the Cenozoic Era is the analysis of oxygen isotopes in the fossil shells of marine organisms. The calcium carbonate shells of the protist foraminifera are the most often analyzed organisms because the different species are distributed throughout surface (planktonic) and deep (benthic) marine environments.

Oxygen isotopes as a paleothermometer

The stable isotopes of oxygen used in paleoceanographic reconstructions are ¹⁶O and ¹⁸O. During the 1940s, Harold Urey at the University of Chicago predicted that the ¹⁸O/¹⁶O ratio in calcite (CaCO₃) should vary as a function of the temperature at which the mineral precipitated. His prediction spurred on experiments by himself and others at the University of Chicago, where they measured ¹⁸O/¹⁶O ratios in CaCO₃ precipitated in a wide range of temperatures, leading to the development of a paleotemperature equation based on oxygen isotopes.

The temperature during the precipitation of calcite can be estimated by measuring the δ¹⁸O value in calcite-secreting organisms (foraminifera, corals, and mollusks) and the δ¹⁸O value of the water in which the organisms live. The various paleotemperature equations all follow the original proposed by Sam Epstein and his colleagues (University of Chicago):

$$T = 16.5 - 4.3 \times (\delta^{18}O_{\text{calcite}} - \delta^{18}O_{\text{water}}) + 0.14 \times (\delta^{18}O_{\text{calcite}} - \delta^{18}O_{\text{water}})^2 \quad (1)$$

where T and $\delta^{18}O_{\text{water}}$ are the temperature (°C) and oxygen isotope value of the water in which the organism lived, and $\delta^{18}O_{\text{calcite}}$ is the oxygen isotope value of calcite measured in the mass spectrometer.

Equation 1 shows that the changes in $\delta^{18}O_{\text{calcite}}$ are a function of the water temperature and $\delta^{18}O_{\text{water}}$ value. A one-to-one relationship between $\delta^{18}O_{\text{calcite}}$ and $\delta^{18}O_{\text{water}}$ values dictates that a change in the $\delta^{18}O_{\text{water}}$ term will cause the exact change in the measured $\delta^{18}O_{\text{calcite}}$ value. However, an inverse relationship between $\delta^{18}O_{\text{calcite}}$ and T changes dictates that for every 1 °C increase in temperature, there is a 0.23‰ decrease in the measured $\delta^{18}O_{\text{calcite}}$ value. These relationships enable us to interpret $\delta^{18}O_{\text{calcite}}$ changes generated from foraminifera, corals, and mollusks. Most researchers follow a convention that plots $\delta^{18}O_{\text{calcite}}$ values with the axis reversed (higher values to the left or bottom) so that $\delta^{18}O$ records mimic temperature changes (e.g., colder to the left or bottom).

Temporal variations

Variations in the amount of water stored on land through time, usually in the form of ice, can have a significant effect on the mean ocean $\delta^{18}O_{\text{water}}$ value, and hence, the marine $\delta^{18}O_{\text{calcite}}$ record. At present, high-latitude precipitation returns to the oceans through summer ice/snow melting. During glacial periods, snow and ice accumulate into large ice sheets. Because the difference in ice sheet and mean ocean values is large ($\delta^{18}O_{\text{ice}} = -35$ to -40 ‰ vs. $\delta^{18}O_{\text{water}}$ mean ocean = ~ 0 ‰), ice sheet fluctuations are reflected in mean oceanic $\delta^{18}O_{\text{water}}$ values. This relationship can be illustrated by examining how the mean ocean $\delta^{18}O_{\text{water}}$ value increased during the Last Glacial Maximum (LGM) relative to the present (Figure C33). During the LGM, water stored in continental ice lowered global sea level by 120 m, removing $\sim 3\%$ of the ocean's volume. Thus, the mean ocean $\delta^{18}O_{\text{water}}$ value increased by 1.2‰ during the LGM relative to the present (Figure C33; the marine $\delta^{18}O_{\text{calcite}}$ record is also affected by mean ocean temperature).

Cenozoic δ¹⁸O records

The first Cenozoic $\delta^{18}O$ syntheses based on foraminiferal $\delta^{18}O$ records were produced during the mid-1970s. Nicholas Shackleton and James Kennett produced a composite benthic

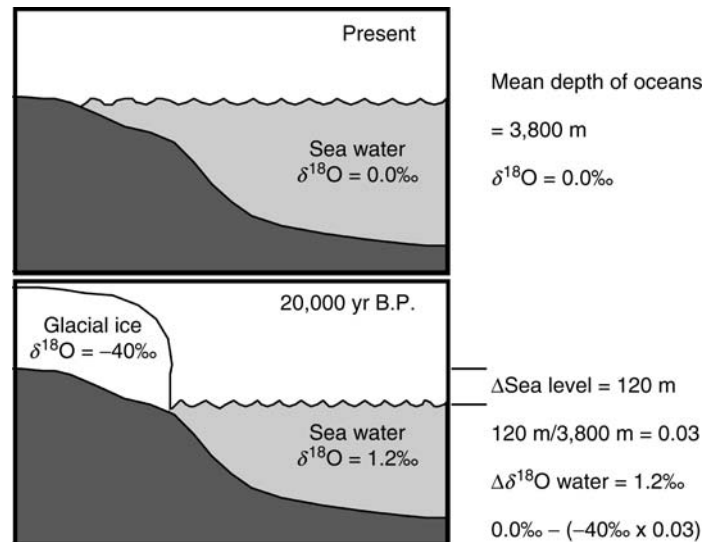


Figure C33 The growth and shrinkage of large ice sheets can have a significant effect on the $\delta^{18}\text{O}$ composition of the ocean. Removal of 3% of the ocean's water during the Last Glacial Maximum lowered sea level by 120 m. The $\delta^{18}\text{O}$ difference between the ocean and the ice is 40‰, causing a whole ocean $\delta^{18}\text{O}$ change of 1.2‰. The reverse process occurs during the melting of large ice sheets. If the Antarctic and Greenland ice were to melt, then sea level would rise ~ 70 m. The volume of water stored in these ice sheets is equivalent to $\sim 2\%$ of the water in the ocean. Therefore, the mean $\delta^{18}\text{O}$ value of the ocean would decrease by 0.7–0.8‰.

$\delta^{18}\text{O}$ record for the Cenozoic using cores from a region to the south of Australia. A second group led by Samuel Savin generated low-latitude planktonic and benthic foraminiferal $\delta^{18}\text{O}$ syntheses. Both records are important in understanding Cenozoic climate changes. Benthic foraminiferal records best reflect global temperature and ice volume changes. Additional advantages of the benthic foraminiferal composite include the following: (a) deep-ocean temperatures are more uniform than surface water with respect to horizontal and vertical gradients; (b) deep ocean $\delta^{18}\text{O}_{\text{water}}$ values are less variable than large surface water changes; (c) the deep ocean approximates high-latitude surface water conditions from which deep waters originated during the Cenozoic (i.e., Antarctica, northern North Atlantic); and (d) many benthic foraminiferal taxa are long-lived, therefore one species can be used to construct records spanning several millions of years, in contrast to planktonic taxa, which have shorter durations, such that records have to be spliced together from several species.

Low-latitude planktonic foraminiferal $\delta^{18}\text{O}$ records are good proxies for tropical sea-surface temperatures. Tropical temperatures are an important component of the climate system because they influence evaporation, and hence, total moisture in the atmosphere. A comparison of planktonic and benthic foraminiferal $\delta^{18}\text{O}$ values allows assessment of equator-to-pole as well as vertical temperature gradients during the Cenozoic, and thus, determination of planetary temperature changes. Much of the climatic change in the last 65 million years has been ascribed to poleward heat transport or greenhouse gas fluctuations. General circulation models indicate that each mechanism would produce different temperature patterns that can be validated using the planktonic and benthic $\delta^{18}\text{O}$ records.

The first benthic $\delta^{18}\text{O}$ syntheses generated, as well as more recent compilations, show the same long-term patterns. After the Cretaceous-Tertiary (K/T) boundary event, deep-water $\delta^{18}\text{O}$ values remained relatively constant for the first 7 million years of the Paleocene (Figure C34a). At 58 million years (Ma)

ago, benthic foraminiferal $\delta^{18}\text{O}$ values began a decrease over the next 6 Myr, which culminated during the early Eocene with the lowest recorded value (-0.5‰) of the Cenozoic. Following this minimum at 52 Ma, $\delta^{18}\text{O}$ values increased by 5.5‰, with maximum values ($\sim 5\text{‰}$) occurring during the glacial intervals of the Pleistocene. The first part of this long-term change was a gradual increase of 2‰ through the end of the Eocene (52–34 Ma). The remainder of the increase was accomplished through large steps at the Eocene/Oligocene boundary (~ 33.5 Ma), during the middle Miocene (ca. 15–13 Ma), and late Pliocene (ca. 3.2–2.6 Ma). After 2.6 Ma, the amplitude of the high-frequency signal increased to $>1\text{‰}$, reaching 1.8‰ over the past 800 thousand years.

Planktonic and benthic foraminiferal $\delta^{18}\text{O}$ values co-varied in general during the early Cenozoic (65–34 Ma). Planktonic values averaged about -1‰ between 65 and 58 Ma, before decreasing to -2.5‰ during the early Eocene, which were the lowest values of the Cenozoic (Figure C34a). From 52 to 33 Ma, planktonic foraminiferal values increased by 2‰. In spite of a break in the latest Eocene record, it appears that the tropical ocean differed from the deep ocean across the Eocene/Oligocene boundary. For much of the Oligocene (~ 33 –25 Ma), planktonic foraminiferal $\delta^{18}\text{O}$ values remained unusually high, averaging -0.5‰ . Beginning around the Oligocene/Miocene boundary (~ 25 Ma), planktonic foraminiferal $\delta^{18}\text{O}$ values began a long-term decrease, culminating in the Pleistocene, with average values of -1.5‰ . In contrast, the benthic $\delta^{18}\text{O}$ record permanently changed during the middle Miocene $\delta^{18}\text{O}$ shift and late Pliocene increase.

Apportioning the $\delta^{18}\text{O}$ changes recorded by the benthic and planktonic foraminifera between temperature and ice volume changes requires knowledge of or reasonable estimates for one of these parameters. One promising tool that may help discriminate between each effect is the Mg/Ca ratio measured in benthic foraminifera. Initial studies by a group at Cambridge University using Mg/Ca ratios confirmed the

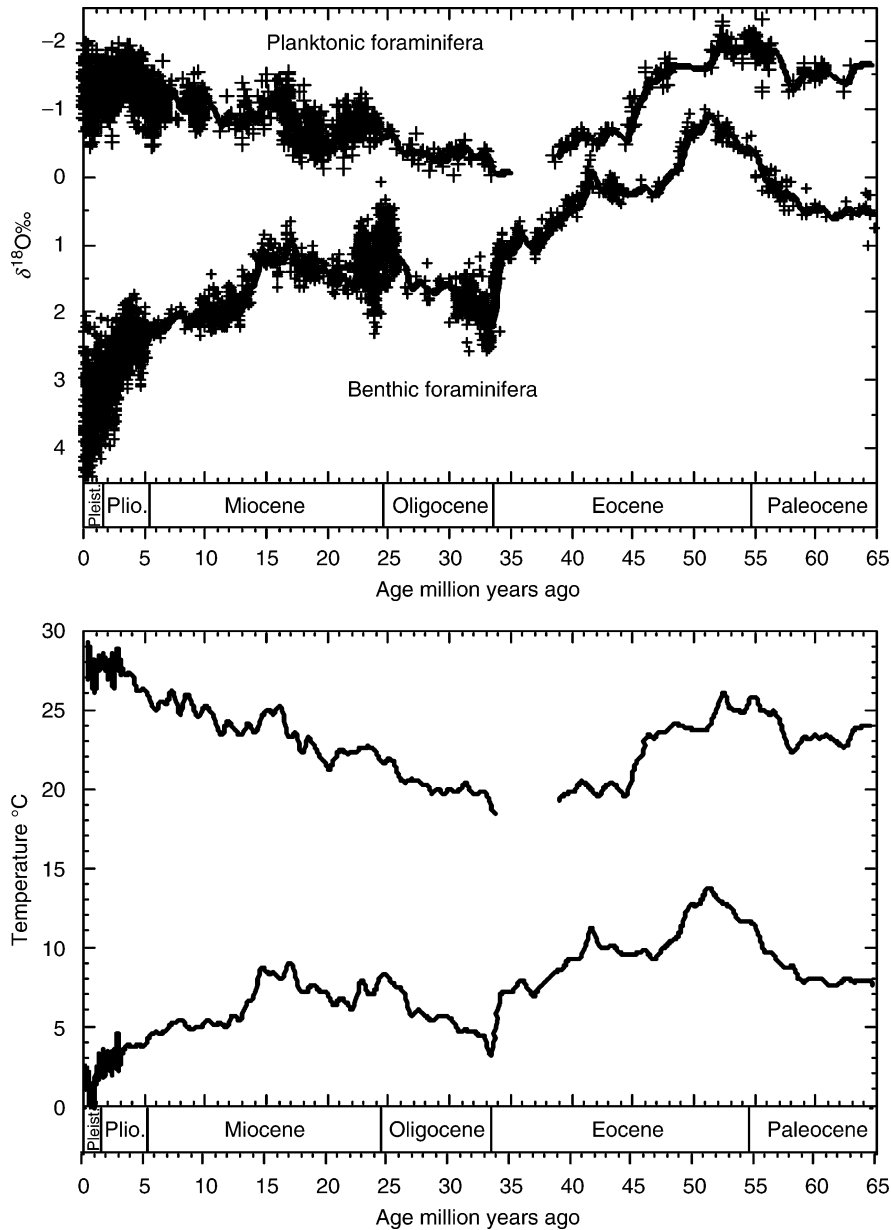


Figure C34 Planktonic and benthic foraminiferal $\delta^{18}\text{O}$ composite records, representing the tropical surface and deep ocean conditions. The *thick line* through both records was generated using a 1 million year Gaussian filter. Temperature estimates based on planktonic and benthic records and ice volume estimates discussed in the text are shown in (b).

long-term temperature changes during the Cenozoic that were calculated using the $\delta^{18}\text{O}$ record and other climate proxies. If verified, this record implies that small ice sheets grew during the middle and late Eocene and fluctuated in size throughout the Oligocene to Miocene. At present, the Mg/Ca record lacks the resolution for key intervals and still requires verification of interspecies offsets before it can be applied unequivocally to isolate the ice volume-induced $\delta^{18}\text{O}_{\text{water}}$ component in the foraminiferal $\delta^{18}\text{O}$ records. For the discussion that follows, glaciological evidence is used to estimate the ice volume/ $\delta^{18}\text{O}_{\text{water}}$ variations.

The greenhouse world

The oldest unequivocal evidence for ice sheets on Antarctica, ice-rafted detritus (IRD) deposited by icebergs in the ocean, places the first large ice sheet in the latest Eocene or earliest Oligocene. Thus, it is reasonable to assume that ice sheets were small to absent and that surface and deep-water temperature changes controlled much if not all of the $\delta^{18}\text{O}$ change prior to 34 Ma. The modern Antarctic and Greenland ice sheets lock up $\sim 2\%$ of the total water in the world's ocean. If melted, these ice sheets would raise global sea level by $\sim 70\text{--}75$ m and mean

ocean $\delta^{18}\text{O}_{\text{water}}$ value would decrease to -0.9‰ PDB. One can then apply Equation 1 to the benthic and planktonic foraminiferal $\delta^{18}\text{O}$ records to estimate deep- and surface-ocean temperatures for the first half of the Cenozoic (ca. 65–34 Ma).

During the early to middle Paleocene, deep-water temperatures remained close to 10°C (Figure C34b). The 1‰ decrease between 58 and 52 Ma translates into a deep-water warming of 4°C , reaching a high of 14°C . This is in sharp contrast to modern deep-water temperatures, which range between 0 and 3°C . Following the peak warmth at 52 Ma, the $\sim 2\text{‰}$ increase in benthic foraminiferal values indicates that the deep waters cooled by 7°C and were 7°C by the end of the Eocene. If small ice sheets existed during the Paleocene and Eocene, then temperature estimates would be on the order of 1°C warmer than those calculated for the ice-free assumption.¹

Tropical surface water temperatures warmed from 22 to 24°C , based on Equation 1, at the beginning of the Cenozoic to 28°C during the early Eocene (52 Ma; Figure C34b). The higher estimate is similar to temperatures in the equatorial regions of the modern oceans. Planktonic foraminiferal $\delta^{18}\text{O}$ values recorded a long-term increase of 2‰ (-2.5 to -0.5‰) through the remainder of the Eocene. Just prior to the Eocene/Oligocene boundary, tropical surface water temperatures were $\sim 21^\circ\text{C}$, ending the long-term tropical cooling of 7°C from 52 to 34 Ma.

The icehouse world of the last 33 million years

As mentioned above, southern ocean cores contain IRD at and above the Eocene/Oligocene boundary. Widely distributed IRD and glacial tills on parts of the Antarctic continental margin that represent the period from Oligocene to Recent mark the onset of large ice sheets. Whether these sediments represent persistent or periodic ice cover is uncertain. At least some ice was present on Antarctica during the Oligocene to early Miocene. Glaciological studies show that Antarctic ice sheet has been a fixture since the middle Miocene (~ 15 Ma). Our record of Northern Hemisphere ice sheets suggests that they were small or non-existent prior to the late Pliocene. For the purpose of estimating surface and deep temperatures, an ice volume estimate slightly lower than the modern ice volume will be applied for the interval that spans from the Oligocene into the middle Miocene (33–15 Ma). For the interval between 15 and 3 Ma, average ice volumes were probably similar to today's ice sheets. From 3 Ma, ice volumes varied between the modern and LGM. Using these broad estimates for ice volumes, mean ocean $\delta^{18}\text{O}_{\text{water}}$ values for those three intervals were -0.5 , -0.22 , and 0.4‰ PDB, respectively. The 0.4‰ estimate reflects the average between the maximum and minimum conditions during the Plio-Pleistocene. As discussed below, the largest portion of the high frequency signal is controlled by ice volume changes.

The benthic foraminiferal $\delta^{18}\text{O}$ increase at the Eocene/Oligocene boundary occurred rapidly (~ 100 kyr; Figure C35a). At the peak of the Eocene/Oligocene boundary event, benthic foraminifera recorded $\delta^{18}\text{O}$ values similar to modern values. Using the ice volume assumption from above, deep-water temperatures approached modern deep-ocean temperatures (3°C). This marks an important transition from the relatively warm

oceans of the Paleocene and Eocene to the cold deep waters of the Oligocene to present. This switch to a cold ocean where bottom waters formed at near-freezing temperatures heralded the development of the psychrosphere, where warm surface waters are found above the cold deep waters. Following the Eocene/Oligocene boundary, deepwater temperatures began a long-term warming over the next 18 million years (33–15 Ma). The coldest deep-water temperatures of 3°C were recorded at 33 Ma, while temperatures reached 9°C at ~ 25 and ~ 15 Ma (Figure C34b).

There is a gap in the planktonic foraminiferal $\delta^{18}\text{O}$ record for the latest Eocene that hampers our assessment of the tropical response during the Eocene/Oligocene climate event. However, it is clear from the data that do exist that the planktonic response across the Eocene/Oligocene boundary differed from the benthic response. The planktonic foraminiferal $\delta^{18}\text{O}$ values for the early Oligocene are similar to late Eocene values, whereas there was a 1.5‰ increase in benthic values. Planktonic foraminiferal records from other regions that span the Eocene/Oligocene boundary indicate that the surface water $\delta^{18}\text{O}$ increase was on the order of 0.5‰ . This change is approximately equal to the effect of the modern Antarctic ice sheet. Combined with the physical evidence, it seems probable that the planktonic foraminiferal $\delta^{18}\text{O}$ increase at the Eocene/Oligocene boundary recorded the ice volume influence with little temperature effect. Therefore, tropical surface temperatures remained around 22°C while the deep ocean cooled during this $\delta^{18}\text{O}$ shift. Following the boundary event, planktonic foraminifera $\delta^{18}\text{O}$ record during the Oligocene and early Miocene mirrored the benthic record in many respects. For much of the Oligocene and early Miocene, the absolute values were close to -0.5‰ , which translates into a temperature estimate of 21°C (Figure C34b). By 15 Ma, tropical surface waters had warmed to 26°C .

The middle Miocene $\delta^{18}\text{O}$ shift represents an increase of 1.5‰ in the benthic record between 15 and 13 Ma. This transition is composed of two sharp increases around 14 and 13 Ma (Figure C35b). These $\delta^{18}\text{O}$ steps occurred in less than 200 thousand years with each showing an increase of $\sim 1\text{‰}$ followed by a small decrease. During these two shifts, deepwaters cooled from 9 – 5°C . The planktonic foraminiferal $\delta^{18}\text{O}$ record from 15 to 13 Ma shows two increases as recorded in the benthic foraminiferal record (Figure C34). However, it does not show the large permanent shift recorded by the benthic foraminifera, indicating a small cooling from 26 to 24°C . From 13 to 3 Ma, the deep ocean cooled slightly from 5 to 3°C while the surface waters warmed from 24 to 26°C (Figure C34b).

The last of the large $\delta^{18}\text{O}$ steps in the Cenozoic was recorded during the late Pliocene from 3.2 to 2.6 Ma. This "step" is better characterized as a series of $\delta^{18}\text{O}$ cycles with increasing amplitudes and values over this interval (Figure C35c). The cycles have been subsequently determined to be 40 kyr obliquity cycles related to variations in the solar radiation received at high latitudes. This interval ushered in the growth of large-scale Northern Hemisphere ice sheets that have since dominated Earth's climate. At 2.6 Ma, the first ice-rafted detritus was deposited in the open North Atlantic and was coeval with the $\delta^{18}\text{O}$ maximum. Prior to 2.6 Ma, IRD was confined to the marginal basins to the north: Greenland and Iceland's continental margins. Subsequent $\delta^{18}\text{O}$ maxima were associated with ice-rafted detritus. Between 2.6 and 1 Ma, large Northern Hemisphere ice sheets waxed and waned on a 40 kyr beat.

¹Some data indicate that smaller ice sheets may have existed on the inland parts of Antarctica during the late Eocene. However, these were not large enough to deposit ice rafted detritus in the ocean. Therefore, their effect on the $\delta^{18}\text{O}$ values of the ocean was probably less than 0.3‰ .

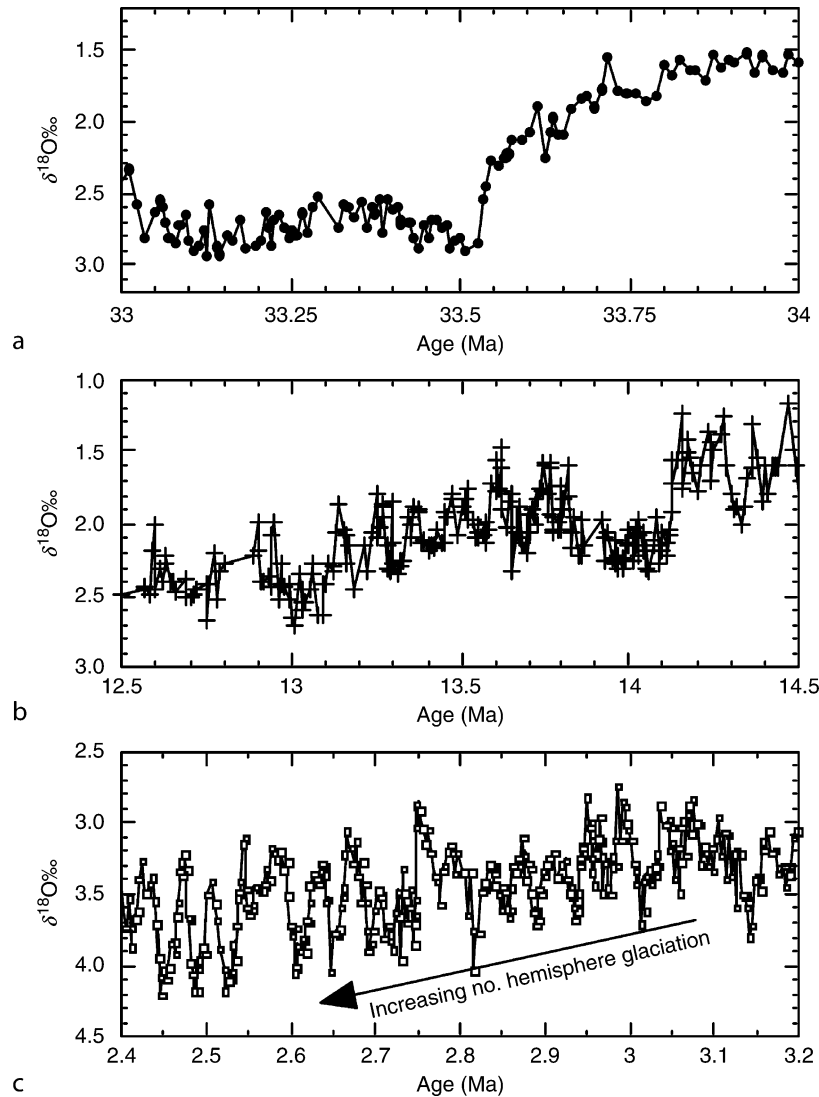


Figure C35 High-resolution $\delta^{18}\text{O}$ records representing the Eocene/Oligocene boundary (a), middle Miocene (b), and late Pliocene (c) $\delta^{18}\text{O}$ shifts.

Beginning around 1 Ma, the ice sheets increased in size and switched to a 100 kyr beat (Figure C36). During this interval, deep-water temperatures remained similar to those in the modern ocean (0–3 °C).

The planktonic foraminiferal $\delta^{18}\text{O}$ response during the late Pliocene event shows the cyclic behavior, but not the overall increase recorded by the benthic foraminifera. As with the middle Miocene $\delta^{18}\text{O}$ shift, the late Pliocene increase represents the cyclic build up of ice sheets accompanied by deep-water cooling. The tropical surface water temperatures, however, varied between 26 and 28 °C.

Pleistocene oxygen isotope variations

The first systematic downcore examination of the marine stable isotope record was made by Cesare Emiliani during the 1950s on $\delta^{18}\text{O}_{\text{calcite}}$ records generated from planktonic foraminifera in Caribbean deep-sea cores. Emiliani recognized the cyclic

pattern of low and high $\delta^{18}\text{O}_{\text{calcite}}$ values and concluded that these represented glacial-interglacial intervals. Emiliani identified the seven most recent climate cycles and estimated that they spanned the last 280,000 years.² To apply the paleotemperature equation to these records, Emiliani estimated that ice sheet induced ocean $\delta^{18}\text{O}_{\text{water}}$ variability was relatively small, 0.3‰.³ Therefore, most of the $\delta^{18}\text{O}_{\text{calcite}}$ variability between glacial and interglacial intervals represented temperature changes of 5–10 °C. Emiliani divided the $\delta^{18}\text{O}_{\text{calcite}}$ record into warm stages (designated with odd numbers counting down from the Holocene) and cold stages (even numbers). Hence, “Isotope Stage 1” refers to the present interglacial interval and “Isotope

²Current age estimates indicate that the duration of the cycles is approximately 525,000 years.

³As shown above, the maximum glacial – interglacial ice sheet signal was closer to 1.2‰.

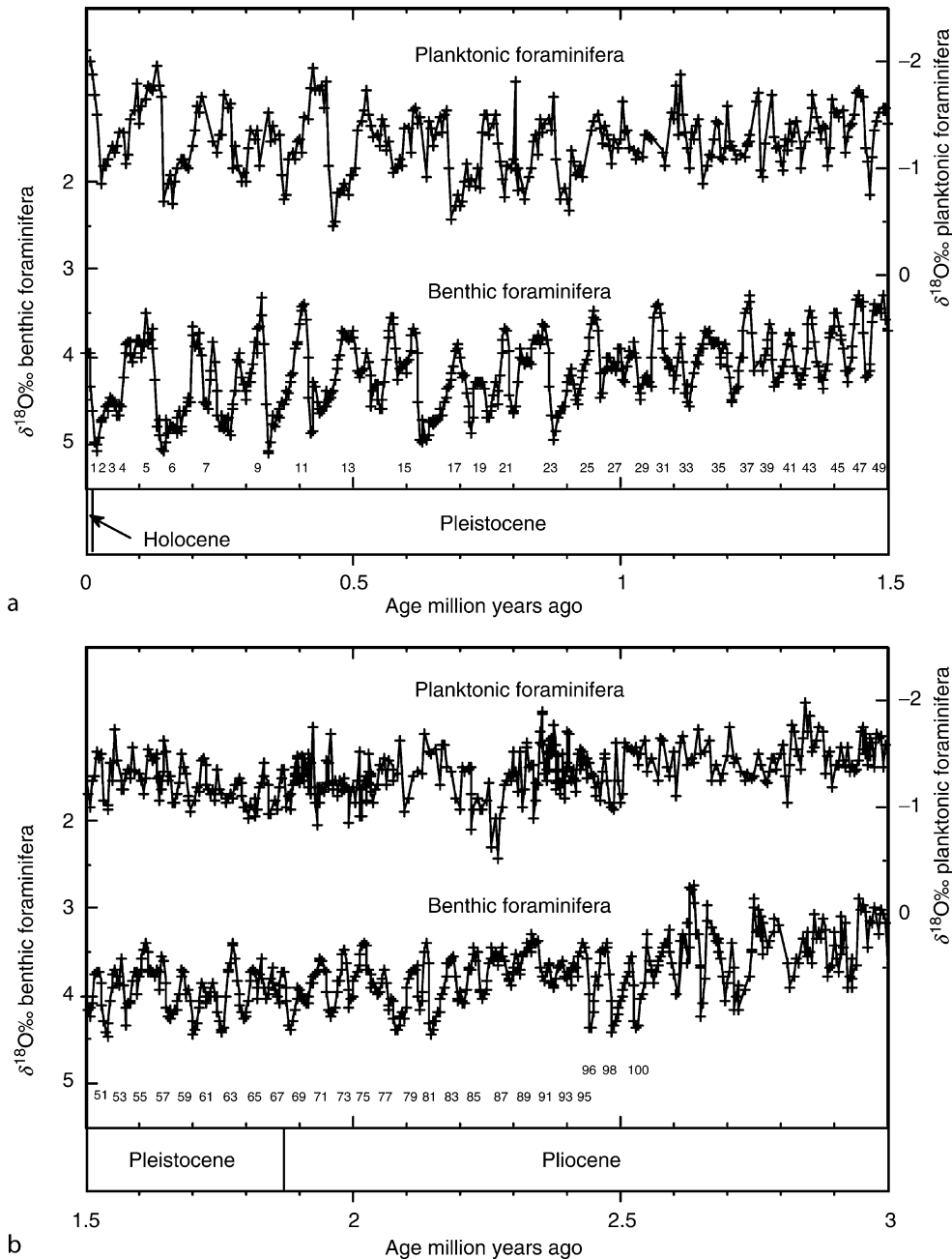


Figure C36 Planktonic and benthic foraminiferal $\delta^{18}\text{O}$ records for the last 3 million years. Note the high frequency signals in the records. For the interval between 3 and 1 Ma, a 40 kyr cycle dominates the records. After 1 Ma, the beat changes to a 100 kyr cycle and the amplitudes increase.

Stage 2" refers to the LGM (Figure C36). During the 1960s and 1970s, many argued that most of the glacial to interglacial difference in $\delta^{18}\text{O}_{\text{calcite}}$ values resulted from ice volume changes. Nicholas Shackleton of Cambridge University made the key observation that benthic foraminiferal $\delta^{18}\text{O}$ values show a glacial to interglacial difference of $\sim 1.8\text{‰}$ (which includes both ice volume and temperature effects). If the ice volume contribution were only 0.3‰ , as argued by Emiliani, then the deep

ocean temperatures would have been between 6 and 7°C colder than the present temperatures of 0 to 3°C . Seawater freezes at -1.8°C , precluding Emiliani's "low" ice volume estimate. By the early 1970s, numerous $\delta^{18}\text{O}$ records had been generated and showed a cyclic variation through the Pleistocene and into the late Pliocene. One hundred oxygen isotope stages, representing 50 glacial/interglacial cycles, have been identified for the interval since 2.6 Myr ago (Figure C36).

Mechanisms for climate change

Most climate change hypotheses for the Cenozoic focus on either oceanic heat transport and/or greenhouse gas concentrations. Each mechanism produces different responses in the equatorial-to-pole and surface-to-deep temperature gradients. An increase in the meridional heat transport generally cools the tropics and warms the poles. If poleward transport of heat decreases, then the tropics will warm and the poles will cool. Variations in greenhouse gas concentrations should produce similar changes in both the tropical and polar regions.

Tropical surface water and deep ocean records co-varied for the first part of the Cenozoic. The warming and subsequent cooling between 65 and 34 Ma are most often ascribed to changing greenhouse gas concentrations. The interval of warming that began around 58 Ma and peaked at 52 Ma coincided with the release of large amount of CO₂ into the atmosphere as a consequence of tectonic processes. The eruption of the Thulean basalts in the northeastern Atlantic Ocean began during the Paleocene and peaked around 54 Ma. It is also recognized that there was a large-scale reorganization of the mid-ocean ridge hydrothermal system beginning during the late Paleocene and extending into the Eocene. Both tectonic processes accelerate mantle degassing, which raises atmospheric levels of CO₂. Recently, evidence for another potentially large CO₂ reservoir was found along the eastern continental margin of North America. Methane hydrates frozen within the sediments appear to have been released catastrophically at least once and possibly multiple times during the latest Paleocene and early Eocene (~58–52 Ma). One or all of these sources could have contributed to the build-up of greenhouse gases in the atmosphere between 58 and 52 Ma.

Following the thermal maximum, the long-term cooling in both the surface and deep waters implies that greenhouse gas concentrations slowly decreased. Proxies for estimating pCO₂ concentrations ($\delta^{13}\text{C}$ fractionation within organic carbon and boron isotopes) are still being developed and refined. However, preliminary indications suggest that atmospheric pCO₂ levels were high (>1,000 ppm) during the early Eocene, dropped to ~400–500 ppm during the middle to late Eocene, and reached late Pleistocene concentrations (200–300 ppm) by the early Oligocene. It is generally thought that accelerated weathering of continents lowered atmospheric pCO₂ levels. The tectonic agent responsible was probably the uplift of the Himalayas and Tibetan Plateau.

The deepwater temperature cooling across the Eocene/Oligocene boundary (Figure C34b) was not accompanied by tropical cooling, and resulted from the first step in the thermal isolation of Antarctica. In the modern ocean, the Antarctic Circumpolar Current is a vigorous surface-to-bottom current that provides an effective barrier to southward-flowing warm surface waters. The development of this current during the Cenozoic hinged on the deepening of the Tasman Rise and the opening of the Drake Passage. Recent drilling indicates that marine connections developed across the Tasman Rise at or near the Eocene/Oligocene boundary (33.5 Ma). Tectonic constraints on the separation of the Drake Passage are less precise. Estimates range from 35 to 22 Ma for the opening of this gateway. The uncertainty lies in the tectonic complexity of the region, and the question of what constitutes an effective opening for water to flow through. The climatic consequence of creating a circum-polar flow was to thermally isolate Antarctica and promote the growth of the Antarctic ice sheet. As noted

above, the first large ice sheet developed beginning at the Eocene/Oligocene boundary.

The most notable divergence in the $\delta^{18}\text{O}$ records began during the middle Miocene (~15 Ma). For the first time during the Cenozoic, the tropical surface and deep waters recorded a clear divergence in $\delta^{18}\text{O}$ values, a trend that increased in magnitude and reached a maximum in the modern ocean. Any poleward transport of heat appears to have been effectively severed from Antarctica by 15 Ma, promoting further cooling. On the other hand, the tropics have been warming over the past 15 Ma. A combination of different factors fueled this warming. First, less heat was being transported out of the low- and mid-latitude regions to the high southern latitudes. Second, the opening of the Southern Hemisphere gateways that promoted the formation of the circumpolar circulation led to the destruction of the circum-equatorial circulation. The effects of the closure of the Tethys Ocean (predecessor to the Mediterranean) during the Miocene, shoaling of the Panamanian Isthmus (4.5–2.6 Ma), and constriction in the Indonesian Passage (~3 Ma to present) allowed the east-to-west flowing surface waters in the tropics to “pile” up and absorb more solar radiation. A consequence of the equatorial warming and high-latitude cooling was an increase in the equator-to-pole temperature gradient. As the gradient increased, winds increased, promoting the organization of the surface-ocean circulation patterns that persist today.

Some caveats

A concern in generating marine isotope records is that the isotopic analyses should be made on the same species. This is important because $\delta^{18}\text{O}_{\text{calcite}}$ values can vary between different species. Co-existing taxa of benthic foraminifera record $\delta^{18}\text{O}$ values that can differ by as much as 1‰. In planktonic foraminifera, variations between species can be as great as 1.5‰. For both the planktonic and benthic foraminifera, inter-specific differences are as large as the glacial-interglacial signal. These inter-specific $\delta^{18}\text{O}_{\text{calcite}}$ variations are often ascribed to a vital effect or kinetic fractionation of the oxygen isotopes within the organism. However, some of the difference in the planktonic taxa results from different seasonal or depth habitats and therefore provides important information about properties in the upper part of the water column. It is interesting to note that the first $\delta^{18}\text{O}$ syntheses were based on mixed species analyses and yet basic features captured in these curves still persist today. This attests to the robustness of these records and method for reconstructing climate changes in the ocean.

The high-frequency signal that dominates the late Pliocene to Pleistocene records is also present in the Miocene and Oligocene intervals. The cloud of points about the mean shown in Figure C34a reflects records that were sampled at a resolution sufficient to document the high frequency signal. For the interval between 35 and 1 Ma, the benthic foraminiferal $\delta^{18}\text{O}$ record has a 40 thousand year frequency superimposed on the long-term means that are represented by the smoothed line. The origin of the 40 thousand year cycles lies in variations in the tilt of the Earth’s axis (obliquity cycles) that influenced the amount of solar radiation received at high latitudes. This insolation signal was transmitted to the deep ocean because the high latitudes were the source regions for deep waters during much if not all of the Cenozoic. The record prior to 35 Ma is unclear with regard to the presence or absence of 40 thousand year cycles.

Finally, relatively high planktonic foraminiferal $\delta^{18}\text{O}$ values in the late Eocene to early Miocene indicate cooler than expected tropical temperatures. Recent work by Pearson and Palmer

(1999) indicates that post-burial diagenesis may have imprinted a cool signal on tropical planktonic foraminiferal calcite. Diagenesis occurs when calcium carbonate precipitates on the foraminiferal shells in the sediments in cold bottom water. Benthic foraminifera would not be adversely affected by this process since they grew in the cold bottom waters. If diagenesis did occur, one may conclude that the best estimate for tropical sea surface temperatures is that they have remained close to 28–30 °C for much of the Cenozoic. If verified, this would reconcile model results with observations. Climate models have a difficult time reconciling the cool tropics and warm poles paradox.

James D. Wright

Bibliography

- Craig, H., 1957. Isotopic standards for carbon and oxygen and correction factors for mass spectrometric analysis of carbon dioxide. *Geochemica et Cosmochemica Acta*, **12**, 133–149.
- Craig, H., 1965. The measurement of oxygen isotope paleotemperatures. In Tongiorgi, E. (ed.), *Stable Isotopes in Oceanographic Studies and Paleotemperatures*. Spoleto: Consiglio Nazionale delle Ricerche, Laboratorio di Geologica Nucleare, Pisa, pp. 161–182.
- Craig, H., and Gordon, L.I., 1965. Deuterium and oxygen-18 variations in the oceans and marine atmosphere. In Tongiorgi, E. (ed.), *Stable Isotopes in Oceanographic Studies and Paleotemperatures*. Spoleto: Consiglio Nazionale delle Ricerche, Laboratorio di Geologica Nucleare, Pisa, pp. 1–122.
- Emiliani, C., 1955. Pleistocene temperatures. *J. Geol.*, **63**, 539–578.
- Epstein, S., Buchsbaum, R., Lowenstam, H., and Urey, H.C., 1953. Revised Carbonate-water temperature scale. *Bull. Geol. Soc. Am.*, **64**, 1315–1326.
- Fairbanks, R.G., Charles C.D., and Wright, J.D., 1992. Origin of Melt Water Pulses. In Taylor, R.E., et al. (eds), *Radiocarbon After Four Decades*. New York: Springer, pp. 473–500.
- Imbrie, J., Hays, J.D., Martinson, D.G., McIntyre, A., Mix, A.C., et al., 1984. The orbital theory of Pleistocene climate: Support from a revised chronology of the marine $\delta^{18}\text{O}$ record. In Berger, A.L., Imbrie, J., Hays, J.D., Kukla, G., and Saltzman, B. (eds.), *Milankovitch and Climate* (Part I). Dordrecht: Reidel, pp. 269–305.
- Lear, C.H., Elderfield, H., and Wilson, P.A., 1999. Cenozoic Deep-Sea Temperatures and Global Ice Volumes from Mg/Ca in Benthic Foraminiferal Calcite. *Science*, **287**, 269–272.
- Miller, K.G., Fairbanks, R.G., and Mountain, G.S., 1987. Tertiary oxygen isotope synthesis, sea-level history, and continental margin erosion. *Paleoceanography*, **2**, 1–19.
- Miller, K.G., Wright, J.D., and Fairbanks, R.G., 1991. Unlocking the Ice House: Oligocene-Miocene oxygen isotopes, eustasy, and margin erosion. *J. Geophys. Res.*, **96**, 6829–6848.
- Pagani, M., Arthur, M.A., and Freeman, K.H., 1999. Miocene evolution of atmospheric carbon dioxide. *Paleoceanography*, **14**, 273–292.
- Palmer, M.R., Pearson, P.N., and Cobb, S.J., 1998. Reconstructing Past Ocean pH-Depth Profiles. *Science*, **282**, 1468–1471.
- Pearson, P.N., and Palmer, M.R., 1999. Middle Eocene Seawater pH and Atmospheric Carbon Dioxide Concentrations. *Science*, **284**, 1824–1826.
- Rozanski, K., Araguas-Araguas, L., and Gonfiantini, R., 1993. Isotopic Patterns in Modern Global Precipitation. In Swart, P.K., McKenzie, J., and Savin, S. (eds.), *Climate Change in Continental Isotopic Records* (Geophysical Monograph 78). Washington, DC: American Geophysical Union, pp. 1–35.
- Rye, D.M., and Sommer, M.A., 1980. Reconstructing paleotemperature and paleosalinity regimes with oxygen isotopes. In Rhoads, D.C., and Lutz, R.A. (eds.), *Skeletal Growth of Aquatic Organisms*. New York: Plenum Publishing, pp. 162–202.
- Savin, S.M., Douglas, R.G., and Stehli, F.G., 1975. Tertiary marine paleotemperatures. *Geol. Soc. Am. Bull.*, **86**, 1499–1510.
- Shackleton, N.J., 1967. Oxygen isotope analyses and Pleistocene temperatures re-assessed. *Nature*, **215**, 115–117.
- Shackleton, N.J., and Kennett, J.P., 1975. Paleotemperature history of the Cenozoic and initiation of Antarctic glaciation: Oxygen and carbon

- isotopic analysis in DSDP Sites 277, 279, and 281. *Initial Rep. Deep Sea Drill. Proj.*, **29**, 743–755.
- Shackleton, N.J., and Opdyke, N.D., 1973. Oxygen isotope and paleomagnetic stratigraphy of equatorial Pacific core V28–238: Oxygen isotope temperatures and ice volumes on a 10^5 year and 10^6 year scale. *Quaternary Res.*, **3**, 39–55.
- Shackleton, N.J., Berger, A., and Peltier, W.R., 1990. An alternative astronomical calibration of the Lower Pleistocene time scale based on ODP Site 677: Transactions of the Royal Society of Edinburgh. *Earth Sci.*, **81**, 251–261.
- Tiedemann, R.M., Sarnthein, M., and Shackleton, N.J., 1994. Astronomic calibration for the Pliocene Atlantic $\delta^{18}\text{O}$ and dust flux records of Ocean Drilling Program Site 659. *Paleoceanography*, **9**, 619–638.
- Urey, H.C., 1947. The thermodynamic properties of isotopic substances. *J. Chem. Soc.*, 562–581.

Cross-references

- [Greenhouse \(warm\) Climates](#)
- [Icehouse \(cold\) Climates](#)
- [Ice-Rafted Debris \(IRD\)](#)
- [Neogene Climates](#)
- [Obliquity](#)
- [Ocean Paleotemperatures](#)
- [Oxygen Isotopes](#)
- [Paleocene-Eocene Thermal Maximum](#)
- [Paleogene Climates](#)
- [Paleotemperatures and Proxy Reconstructions](#)
- [Plate Tectonics and Climate Change](#)
- [Quaternary Climate Transitions and Cycles](#)

CIRQUES

Cirques are glacially eroded features characteristic of mountain glaciation, and are also known as corries or cwms. They have been widely studied, and useful summaries of previous research are provided by Benn and Evans (1998) and Bennett and Glasser (1996).

Cirques are mountainside hollows, open on the downslope side but characteristically bounded on the upslope side by a steep slope or cliff (the headwall) that is arcuate in plan around the more gently sloping or over-deepened floor of the hollow. Glacial cirques are created by the erosional action of localized snow and ice patches, and during glaciation they contain “cirque glaciers” which may feed ice downstream into valley glaciers. Cirques evolve through time under continuing glacial activity by a combination of deepening of the base and headward erosion of the back wall. Early in the glaciation, nivation beneath snow accumulating in a mountainside hollow may be the chief process leading to the development of the cirque. As more snow and ice accumulates in the hollow, glacial erosion of the base and of the lower part of the headwall, combined with subaerial weathering and erosion of the upper parts of the headwall exposed above the ice, lead to the characteristic steep-walled basin of a mature cirque. Cirques tend to become more enclosed, and deeper, with longer glacial occupation. Long-term evolution of cirques can occur over several glacial cycles, and cirques may be altered by ice-sheet processes if glaciation increases beyond local cirque and valley glaciation. Cirque morphology is therefore often complex, and several small cirques may grow together to form one large, complex feature. Typically cirques are of the order of 10^2 – 10^3 m in diameter.

Cirque elevation and orientation can provide paleoclimatic information. The minimum elevation of cirques reflects the regional snowline at the time of their formation. The predominant orientation of cirques within a region can also indicate dominant wind direction, as snow may initially accumulate, and cirques form, on sheltered lee-side slopes, especially where these have a pole-ward aspect sheltered from insolation. Where precipitation shadows occur, on larger mountain masses, cirques are likely to develop with an aspect facing the dominant source of precipitation.

In postglacial environments cirques often contain lakes in their closed basins, and these lakes may drain by overflow across the lip or sill that marks the down-slope limit of the basin. In many locations the lip or sill is erosional in origin, marking the downstream limit of glacial over-deepening of the basin. However, the feature may be created or accentuated by the deposition of moraines marking the maximum extent of corrie glaciation.

Peter G. Knight

Bibliography

- Benn, D.I., and Evans, D.J.A., 1998. *Glaciers and Glaciation*. London, UK: Arnold, 734pp.
 Bennett, M.R., and Glasser, N.F., 1996. *Glacial Geology*. Chichester, UK: Wiley, 364pp.

Cross-reference

[Glacial Geomorphology](#)

CLAMP

Introduction

That a relationship exists between vegetation and climate is indisputable. The overall appearance of vegetation (i.e., its physiognomy), but not necessarily the species composition, tends to be characteristic of the particular climatic regime in which the vegetation grows (e.g., Holdridge, 1947). This is because many plant morphologies represent particular “engineering” solutions to particular environmental constraints. Only those plants with a genome that affords certain appropriate phenotypic expressions are able to survive in particular climatic regimes. Inappropriate phenotypes are eliminated, either by the physical environment taking its toll directly, or by competition from better-adapted plants.

Although all parts of a plant throughout all stages of the life cycle contribute to the overall success or failure of the individual, it is the leaf that plays the most critical role in environmental adaptation. Its photosynthetic function demands that a leaf be efficient at intercepting light and exchanging gases with the atmosphere, while affording the minimum water loss concomitant with maintaining water flow within the plant for solute transport and evaporative cooling. All this must be achieved with the minimum of structural tissue investment because building tissue costs energy and food resources. Thus, only a limited range of architectures satisfies the often conflicting constraints present in a given set of environmental conditions. Because the unchanging laws of gas diffusion, fluid flow, and mechanics impose these constraints, these forms are

convergent in time and space and independent of taxonomic affinity (Spicer, 2000).

So pervasive is the selective premium for leaf efficiency that physiognomic “tuning” to the environment exists across plant lineages and also within and between individual plants within lineages. For example, leaves at the top of a tree crown exposed to high light and wind energies tend to be small, thick “sun leaves.” In contrast, those in the darker, more sheltered, humid sub-canopy space tend to be larger and thinner (“shade leaves”). If the environment around a tree changes with time, through removal of surrounding trees, for example, then subsequent cohorts of leaves will display different appropriate morphologies.

Plants must produce leaves that are adaptive to the entire growing season and not just to the conditions that exist at the leaf development or expansion stage. This ability to seemingly “predict” future likely conditions must be genetically predetermined through ancestral selection. For example, plants in Mediterranean climates receive abundant rainfall during the spring when the new leaf crop expands, followed by summer drought. If plants responded only to the spring rains and produced large leaves, these leaves would be non-adaptive during the summertime. Clearly, selection favors genotypes that are tuned to the overall climatic conditions and not just those experienced at the time of leaf development.

Vegetation in recently glaciated and non-glaciated parts of the Northern Hemisphere is also correlated with climate, showing that genetic and phenotypic tuning of foliar physiognomy takes place over geologically short timescales (<1 million years) as a result of taxonomic elimination and migration, as well as selection for novel genotypes that arise as the result of chance mutation or hybridization.

The method

CLAMP (Climate Leaf Analysis Multivariate Program) (Wolfe, 1990, 1993; Kovach and Spicer, 1995; Wolfe and Spicer, 1999; Spicer, 2000) is a multivariate statistical technique that decodes the climatic signal inherent in the physiognomy of leaves of woody dicotyledonous plants. It is an evolutionarily robust, accurate, and precise quantitative proxy for direct atmospheric paleoclimate determinations over land, and as such complements marine-based climate proxies (e.g., oxygen isotopes). Moreover, where it is possible to compare temperatures derived from CLAMP with those from oxygen isotopes, both proxies are in close agreement (Kennedy et al., 2002).

CLAMP calibrates the foliar physiognomy of the woody dicots using reference datasets derived from modern vegetation growing under known conditions. Using these datasets, past climatic data are determinable from leaf fossil assemblages, provided that the characteristics of the living source vegetation are well represented in the sampling of the fossil assemblage. CLAMP calibration appears robust over time and has been applied effectively to fossil floras up to 96 Ma old (Herman and Spicer, 1996; Spicer et al., 2002), but is particularly powerful and reliable for late Tertiary (Wolfe, 1995; Spicer, 2000) and Quaternary assemblages.

The statistical engine used in CLAMP is Canonical Correspondence Analysis (CANOCO) (ter Braak, 1986), as this is robust for data that do not necessarily conform to normality in the statistical sense (i.e., the variables do not have a Gaussian distribution). Most importantly, the technique does not assume independence of variables. This is essential when leaf characters are the product of functional compromise,

constructional efficiency, and a finite genome. CANOCO is a direct ordination method, used widely in plant ecology, which orders samples, in this case vegetation sites, based on a set of attributes. In CLAMP, the attributes are numerical values assigned to each of 31 different leaf character states (size, shape, margin, apex, and base features) taken from more than 20 species of woody dicots in each vegetation site. The character states have been selected both for their ability to correlate with climate, and their survivability in even poorly-preserved fossil material. CLAMP calibration is not subject to diagenetic alteration.

The vegetation sites are positioned in 31 dimensional space, such that samples with the most similar physiognomic score plot closest together. Although climate data are not used to define the position of a vegetation site, it is clear from simple inspection that the vegetation sites are ordered in terms of climate variables, principally those relating to temperature and moisture (Figure C37). Instead of using subjective positioning of climate vectors (Wolfe, 1993), CANOCO defines the positions mathematically.

The largest publicly available calibration dataset now consists of foliar physiognomic measurements and climate observations from 173 modern vegetation sites mostly in the Northern Hemisphere (Physg3ar dataset). Earlier versions used fewer modern sites (e.g., 103 in Herman and Spicer, 1996) and different datasets can be used for different purposes. For example, if initial results indicate a warm climate, then a subset of the full dataset that excludes the sites that experience significant freezing conditions (the Physg3br dataset) offers greater precision (Table C5) (Wolfe, 1993; Wolfe and Spicer, 1999). Because climate variables for these sites are known (>30 year averages are used from climate

stations proximal to the sites), vectors for each of the measured climate variables can be calibrated.

Paleoclimate variables can be quantified by scoring a fossil assemblage in the same manner as for the modern vegetation. However, the fossil site is positioned in physiognomic space in a passive manner so it does not distort the calibration by its presence. By projecting the position of the fossil site on to the calibrated climate vector, the ancient paleoclimate can be derived (e.g., Figure C38).

Table C5 Standard CLAMP climate parameters for the Physg3ar and Physg3br datasets with the standard deviations of the residuals about the regressions, and the goodness of fit of the regressions

Parameter	Physg3br		Physg3ar	
	STDEV	r ²	STDEV	r ²
Mean annual temperature (°C)	1.17	0.95	1.72	0.92
Warm month mean temperature (°C)	1.58	0.83	1.80	0.83
Cold month mean temperature (°C)	1.88	0.93	2.54	0.91
Length of growing season (months)	0.70	0.93	0.85	0.91
Growing season precipitation (mm)	335.93	0.87	317.97	0.88
Mean monthly growing season precipitation (mm)	36.91	0.86	36.66	0.86
Precipitation in the three wettest months (mm)	140.29	0.86	138.05	0.86
Precipitation in the three driest months (mm)	92.99	0.86	89.85	0.85
Relative humidity (%)	7.36	0.73	8.17	0.66
Specific humidity (g kg ⁻¹)	0.90	0.87	0.98	0.86
Enthalpy (kJ kg ⁻¹)	3.18	0.92	3.54	0.92

Scoresheets, datasets and spreadsheets for determining paleoclimates can be downloaded from the CLAMP website: <http://www.open.ac.uk/earth-research/spicer/CLAMP/Clampset1.html>

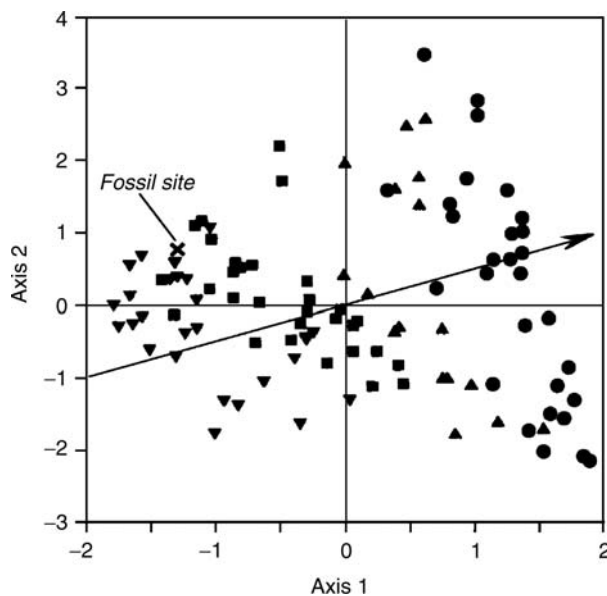


Figure C37 Plot of axes 1 and 2, the two axes of greatest variation, of the physiognomic space defined by the Physg3br CLAMP dataset. The positions of the samples are determined by the numerical description of the 31 different character states that summarize the leaf physiognomy. In this plot, the samples are coded to reflect the mean annual temperature (MAT) under which they grew: circles: 20.0–27.0°C; triangles: 15.0–19.9°C; squares: 10.0–14.9°C; inverted triangles: 4.8–9.9°C. The arrow shows the direction of the mean annual temperature vector as determined by CANOCO.

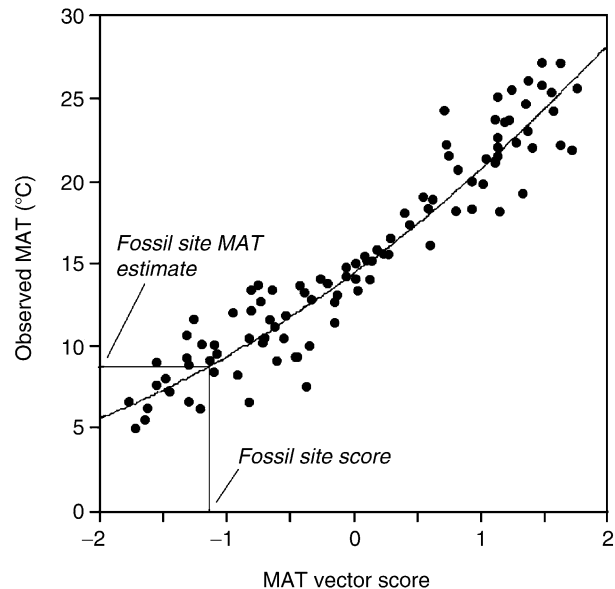


Figure C38 Mean annual temperature (MAT) vector score plotted against the observed MAT for the Physg3br dataset. The standard deviation of the residuals about the regression line is 1.17°C.

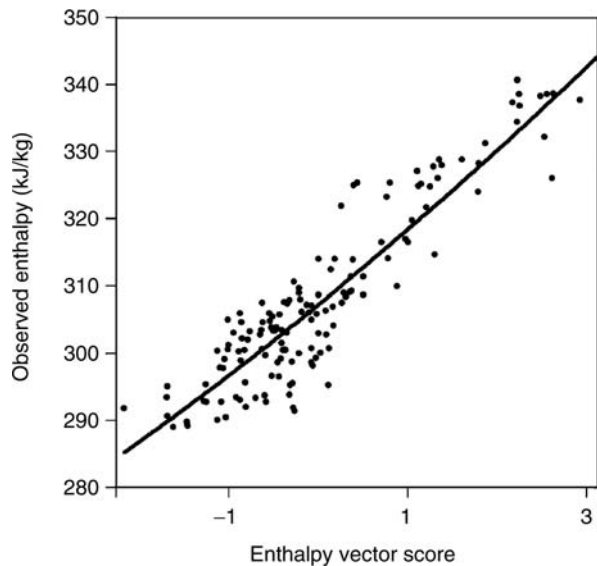


Figure C39 Enthalpy vector score plotted against the observed enthalpy using the CLAMP Physg3br dataset.

CLAMP is capable of determining not just mean annual temperature but a range of climate variables as shown in [Table C5](#).

Quantitative variables are critical for evaluating the performance of climate models but of particular importance is the ability of CLAMP to determine enthalpy. Enthalpy (H) is a function of both temperature and moisture:

$$H = c_p T + L_v q \quad (1)$$

where c_p is the specific heat capacity of moist air at constant pressure, T is temperature (in kelvin), L_v is the latent heat of vaporization, and q is the specific humidity. Leaves therefore exhibit a strong coding for enthalpy ([Figure C39](#)), with a high degree of precision.

The usefulness of enthalpy is that it can be used to determine paleoaltitude (Forest et al., 1995; Wolfe et al., 1998; Spicer et al., 2003) because the difference between two estimates of enthalpy for a given location yield an estimate of their difference in potential energy and hence height separation.

$$h = H + gZ \quad (2)$$

where h = moist static energy, g is gravitational acceleration, and Z is the altitude (see also *Energy budget climatology*, in *Encyclopedia of World Climatology*).

Limitations

Powerful as the technique is, there are some limitations. The current datasets include few vegetation/climate data for fully tropical wet regimes, continental interiors where there is a large mean annual range of temperatures, and sites in the southern hemisphere. The absence of such data currently constrains the types of paleoclimatic regimes that can be accurately retrodicted, but CLAMP development continues.

Robert A. Spicer

Bibliography

- Forest, C.E., Molnar, P., and Emanuel, K.A., 1995. Palaeoaltimetry from energy conservation principles. *Nature*, **374**, 347–350.
- Herman, A.B., and Spicer, R.A., 1996. Palaeobotanical evidence for a warm Cretaceous Arctic ocean. *Nature*, **380**, 330–333.
- Holdridge, L.R., 1947. Determination of world plant formations from simple climatic data. *Science*, **105**, 367–368.
- Kennedy, E.M., Spicer, R.A., and Rees, P.M., 2002. Quantitative paleoclimate estimates from Late Cretaceous and Paleocene leaf floras in the northwest of the South Island, New Zealand. *Palaeogeogr Palaeoclimatol Palaeoecol.*, **184**, 321–345.
- Kovach, W.L., and Spicer, R.A., 1995. Canonical correspondence analysis of leaf physiognomy: A contribution to the development of a new palaeoclimatological tool. *Palaeoclimates*, **1**, 125–138.
- Spicer, R.A., 2000. Leaf physiognomy and climate change. In Culver, S.J., and Rawson, P. (eds.), *Biotic Response to Global change: The Last 145 Million Years*. Cambridge, UK: University Press, Cambridge, pp. 244–264.
- Spicer, R.A., Herman, A.B., Ahlberg, A.T., Raikevich, M.I., and Rees, P.M.A., 2002. Mid-Cretaceous Grebenka flora of North-eastern Russia: Stratigraphy, palaeobotany, taphonomy and palaeoenvironment. *Palaeogeogr Palaeoclimatol Palaeoecol.*, **184**, 65–105.
- Spicer, R.A., Harris, N.B.W., Widdowson, M., Herman, A.B., Shuangxing, G., Valdes, P.J., Wolfe, J.A., and Kelley, S.P., 2003. Constant elevation of southern Tibet over the past 15 million years. *Nature*, **421**, 622–624.
- ter Braak, C.J.F., 1986. Canonical Correspondence Analysis: A new eigen-vector technique for multivariate direct gradient analysis. *Ecology*, **67**, 1167–1179.
- Wolfe, J.A., 1990. Palaeobotanical evidence for a marked temperature increase following the Cretaceous/Tertiary boundary. *Nature*, **343**, 153–156.
- Wolfe, J.A., 1993. A method for obtaining climate parameters from leaf assemblages. *U.S. Geol. Surv. Bull.*, **2040**, 71.
- Wolfe, J.A., 1995. Paleoclimatic estimates from Tertiary leaf assemblages. *Annu. Rev. Earth Planet Sci.*, **23**, 119–142.
- Wolfe, J.A., and Spicer, R.A., 1999. Fossil leaf character states: Multivariate analysis. In Jones, T.P., and Rowe, N.P. (eds.), *Fossil Plants and Spores: Modern Techniques*. London: Geological Society, pp. 233–239.
- Wolfe, J.A., Forest, C.E., and Molnar, P., 1998. Paleobotanical evidence of Eocene and Oligocene paleoaltitudes in midlatitude western North America. *Geol. Soc. Am. Bull.*, **110**, 664–678.

Cross-references

- [Cenozoic Climate Change](#)
- [Cretaceous Warm Climates](#)
- [Energy Budget Climatology, in Encyclopedia of World Climatology](#)
- [Glaciations, Quaternary](#)
- [Holocene Treeline Fluctuations](#)
- [Mountain Uplift and Climate Change](#)
- [Oxygen Isotopes](#)
- [Paleobotany](#)
- [Paleoclimate Proxies, an Introduction](#)
- [Paleo-Precipitation Indicators](#)
- [Paleotemperatures and Proxy Reconstructions](#)
- [Stable Isotope Analysis](#)

CLIMAP

Introduction

Ice ages, those times when great ice sheets spread across Northern Hemisphere continents, have been the subject of scientific and public interest for over 150 years. By the 1960s, the aerial extent of some ice ages had been established through the

mapping of the rocky debris left behind by the retreating ice and stratigraphic analyses of these deposits, which provided evidence of multiple ice advances and retreats. The accepted number of such advances was four, all occurring within the Pleistocene Epoch. Studies of deep-sea sediments, which have an advantage over the erosion-plagued record of glaciations on land because of their temporal continuity and spatial coverage, accelerated during this decade, providing further evidence of multiple major climate changes. This evidence was supplied through studies of the calcareous (limy) shells of microscopic plankton (foraminifera). When alive, these one-celled creatures are delicately adapted to the physical properties of the near-surface waters within which they live. Temperature exerts a strong influence on the geographical ranges of these species; therefore, some are restricted to the tropics while others live in the colder waters of high latitudes. Measuring warm-water species abundance variations down deep-sea cores generated qualitative estimates of ocean warming and cooling, which were interpreted as responses to ice sheet advances and retreats (Ericson and Wollin, 1968).

Laboratory studies in the 1950s had shown that the ratio of the isotopes ^{18}O to ^{16}O in the calcareous shells of some marine organisms decreases linearly with increasing temperature (Epstein et al., 1951). These changing ratios, when measured in the shells of planktonic foraminifera in deep-sea cores, were interpreted to allow measurement of changing ice age sea-surface-temperatures, with lower ratios (lighter) indicating warmer temperatures and higher ratios indicating colder temperatures (Emiliani, 1955). Doubt was cast on this interpretation, however, when it was shown that the Greenland and Antarctic Ice Sheets are isotopically light compared with seawater (Dansgaard, 1964). This is because water vapor, when moving from the tropics to high latitudes, preferentially precipitates water molecules with the heavier ^{18}O over those with the lighter ^{16}O , causing the ice sheets to be depleted in ^{18}O and enriched in ^{16}O relative to seawater. The building of ice sheets in the past could have further increased the $^{18}\text{O}/^{16}\text{O}$ ratio of seawater because the growing ice sheets preferentially leave ^{18}O behind as they move water from the ocean to the ice sheets. This in turn could increase the $^{18}\text{O}/^{16}\text{O}$ ratio in the shells of foraminifera. Thus, either cooling or ice sheet growth might have caused the increased $^{18}\text{O}/^{16}\text{O}$ ratios in the shells of foraminifera during ice ages. Regardless of which was responsible, there was no doubt that these isotopic and faunal variations recorded major climatic changes.

Hypotheses to explain these climatic changes abounded in the 1960s; Richard Foster Flint, the dean of Pleistocene geology at the time, put the number of hypotheses at 55. Some called on oscillators within the Earth's climate system (ocean, atmosphere, ice), such as the melting and refreezing of the Arctic Ocean to alternately increase and decrease the moisture supply to ice sheets bordering its rim (Ewing and Donn, 1956), or repeated surges of the Antarctic Ice Sheet, sending streams of ice into the ocean, which may have raised the Earth's albedo (reflectivity) and caused cooling (Wilson, 1964). Others called on changes outside the Earth's climate system, such as variations of solar output or variability in the concentration of interstellar dust through which the solar system traveled. The oldest idea, first proposed in the mid-nineteenth century, calls on variations in the geometry of the Earth's solar orbit, causing geographical and seasonal changes in the distribution of solar energy over the Earth's surface, and driving ice age climate change (Adhemar, 1842; Croll, 1864; Milankovitch, 1920). In the 1960s,

many thought these radiation changes were far too small to produce the great glacial advances and retreats; however, this hypothesis has advantages over others because its explicit prediction, that ice ages are periodic with periods of about 100, 40 and 23 thousand years, is testable. A period of nearly 100 thousand years should be present in the geological record if the Earth's climate system response to orbitally induced insolation changes is non-linear, as seemed likely. These specific predictions could be verified or rejected if the geological record of ice ages could be accurately dated; however, in the mid-1960s, dating of deep-sea cores was limited to the ^{14}C method, which extended back only some 25,000 ybp. Furthermore, there was no agreement on how to identify the base of the Pleistocene in deep-sea sediments, which was thought to mark the beginning of the ice ages.

The discovery that deep-sea sediments record reversals of the Earth's magnetic field (Harrison and Funnel, 1964) provided a new way to globally correlate and date deep-sea sediments. Magnetic minerals within the uppermost water-charged layer of seafloor sediment align themselves with the current direction of the field. As this layer is more deeply buried and compacted, the alignment of magnetic minerals becomes permanent. When the field reverses, the uppermost layer records the new field direction. If the field were to reverse today, an observer would see the needle of a magnetic compass swing from north to south, although it would take several thousand years to complete the swing. Geologically this is but an instant, therefore a record of a reversal in sediments is globally isochronous. Specific magnetic reversals, the last occurring some 700,000 years ago, were first dated in oceanic island lava flows (Cox et al., 1964). They can be uniquely identified in ocean sediments through their associated microfossil assemblages (Opdyke et al., 1966). Magnetic stratigraphy combined with biostratigraphy could consequently produce a global chronostratigraphy for deep-sea sediments over the last few million years (Hays et al., 1969; Opdyke and Foster, 1970; Hays and Berggren, 1971). These studies showed that there have been seven glaciations since the last magnetic field reversal and the Pleistocene's base is about 2 million years old.

Meanwhile, an ingenious technique to transform microfossil assemblage data into quantitative estimates of sea-surface temperature was being developed (Imbrie and Kipp, 1971). Factor analysis was used to identify microfossil assemblages in geographic arrays of sea-floor sediment samples and regression techniques were used to correlate the assemblage data with overlying sea-surface temperatures. In this way, equations were developed relating assemblage data to temperature. By using these equations and assemblage data from Pleistocene sediments, past sea-surface temperatures could be estimated. The technique assumes that the ecological tolerances of the selected species are little changed between Pleistocene and Recent time and the assemblage compositions are responses to physical gradients, dominated by temperature.

Finally, during the 1960s, the Lamont Geological Observatory, under the leadership of Maurice Ewing, more than tripled the size of its deep-sea core collection to more than 11,000 cores, making it a truly global collection.

The CLIMAP project

At the beginning of the 1970s, a group of young scientists trained in the study of deep-sea sediments and equipped with the new chronostratigraphic and paleoecological tools developed in the previous decade saw an opportunity to use the vast

Lamont core collection as a global climate monitoring system. Their objectives were to understand what causes ice ages and how the Earth as a whole responds to them. Through this better understanding, they hoped to predict future climate change. They called their project CLIMAP (Climate Long-range Investigation Mapping And Prediction). They were aided in this effort by a new program within the National Science Foundation, The International Decade of Ocean Exploration (IDOEO). It fostered ocean science research that included inter-institutional and international cooperation and had relevance to human needs.

CLIMAP initially proposed to study the spatial and temporal patterns of ice-age climate change in the North Atlantic, North Pacific and Antarctic. By generating seasonal maps of sea-surface temperatures at the last glacial maximum (LGM), they sought to measure the ocean's response to this most recent cooling extreme. Temporal changes were to be studied by generating time series of sea-surface temperature and other climatic indicators back to the last reversal of the Earth's magnetic field (700,000 yBP).

The project, consisting of scientists and students from Columbia University's Lamont Doherty Geological Observatory, Brown University and Oregon State University, faced challenges at its outset in 1971. The first was how to organize highly individualistic and competitive scientists, accustomed to working by themselves or with one or two others, into a cooperative productive team. This challenge was met, at least in part, by giving each investigator an individual as well as a group role. The individual roles, the study of an area of the ocean and regional time series, fed into the group task by providing regional information for the larger LGM mapping project and inter-regional comparisons of temporal climatic change. Task groups were formed to generate regional LGM sea-surface temperatures and regional time series, and others to address more general problems, e.g., the biotic index task group, under the leadership of John Imbrie, which served as a resource for regional task groups developing equations to estimate past sea-surface temperatures. CLIMAP quickly expanded to include European scientists: Drs. Shackleton (Cambridge, England), Seibold (Kiel, Germany), Dansgaard (Copenhagen, Denmark), Van der Hammen (Amsterdam, Netherlands) and Lamb (Norwich, England) were made corresponding members. These connections resulted in European conferences and a flow of students from Kiel to Lamont to work on specific CLIMAP objectives. At its peak, more than one hundred scientists and students were involved in this collaborative effort. The initial fears of internal conflict, whether because they were addressed or were ill-founded, did not materialize and the group worked together in remarkable harmony.

The second challenge stemmed from the group's commitment to generate maps of sea-surface temperature at the LGM as there was no easy way to identify this level in deep-sea cores short of ^{14}C dating at that time, and the group had budgeted insufficient funds for large numbers of ^{14}C dates. Furthermore, large areas of the ocean floor are carbonate-free, precluding ^{14}C dating. The solution to this problem happily came early in the project from a western equatorial Pacific core that just penetrated the last reversal of the Earth's magnetic field. Oxygen isotopic variations in the shells of both benthic and planktonic microfossils showed similar amplitudes throughout its length (Shackleton and Opdyke, 1973). Because ocean bottom temperatures are near zero today, they cannot get much colder during an ice age. Consequently, the large

changes in the oxygen isotopic ratios in benthic shells could not be caused by changing bottom water temperature, rather they must be caused by the changing isotopic composition of the ocean, driven by waxing and waning ice sheets. Hence, the changing isotopic composition of the ocean, due to changing ice sheet volume, must be responsible for most of the $^{18}\text{O}/^{16}\text{O}$ variations measured in foraminiferal shells. This isotopic signal mixes through the ocean within a thousand years; therefore, within this time, isotopic records from various parts of the world are synchronous. This meant that features of the oxygen isotopic record could be used to correlate deep-sea cores globally. The LGM could then be easily identified without multiple ^{14}C dates, as an isotopically heavy interval beneath the light values of the Holocene Epoch.

Criteria to identify the LGM in sediments containing biogenic silica but not calcium carbonate appeared in the form of a cosmopolitan radiolaria (*Cycladophora davisiana*) with high latitude temporal abundance changes strikingly similar to the $^{18}\text{O}/^{16}\text{O}$ record. In sub-Antarctic cores that contain both calcareous and siliceous microfossils, the abundance variations of *C. davisiana* were correlated with variations in the oxygen isotope record (Hays et al., 1976a), transferring the oxygen isotope chronostratigraphy to siliceous non-calcareous sediments in the high latitudes of both hemispheres (Robertson, 1975). Therefore, the CLIMAP team could accurately identify the LGM for their mapping task and globally correlate time series of estimated sea-surface temperature, the $^{18}\text{O}/^{16}\text{O}$ proxy for ice volume, and other climatically sensitive attributes of deep-sea cores.

Meanwhile, important advances were being made in another area that would soon intersect with CLIMAP's trajectory. The sophistication of numerical models of the atmosphere had been evolving since the early 1960s (Smagorinsky, 1963; Mintz, 1968; Sellers, 1969). These models are mathematical systems that simulate climatic states by solving equations representing physical processes. By the early 1970s, General Circulation Models (GCMs) could simulate the global distribution of such atmospheric properties as pressure, temperature, wind, and precipitation that are in equilibrium with a limited set of earth surface conditions (Gates, 1976). These surface conditions include sea-surface temperature, sea-ice extent, albedo, sea level and land elevation. CLIMAP was already reconstructing some of these for parts of the world ocean. If it expanded its LGM map to cover the world ocean, reconstructed the great continental ice sheets and estimated continental albedo, land elevation and sea level, it could model the LGM atmospheric circulation with the latest generation of GCMs.

The CLIMAP team quickly seized this opportunity and added a glacial geologist (George Denton) as well as an ice modeler (Terry Hughes) to the team, for if the perimeter of the great ice sheets could be determined and the assumption of ice sheet equilibrium (snow accumulation = ice ablation) accepted, ice sheet thickness could be modeled. The Denton-Hughes team recruited European scientists and together produced a book describing for the first time the area and thickness of all the great ice sheets at the LGM (Denton and Hughes, 1981). Dr. George Kukla, a student of the great dust deposits (loess) that accumulated on large areas of Eurasia during the last ice age, agreed to lead a group that would reconstruct continental albedo.

By 1975, under the leadership of Andrew McIntyre and Theodore Moore, the compilation of the first global LGM sea-surface temperature map for the month of August was complete and by the end of the decade, the group had doubled the

number of glacial maximum sea-surface temperature estimates and compiled maps for the months of February and August. These maps were merged, under the supervision of John Imbrie, with maps of continental albedo, land elevation, shorelines and the extent and thickness of the great ice sheets (Figure C40) (CLIMAP Project Members, 1976, 1981).

When compared with today, the LGM oceans showed large increases of winter sea-ice in both hemispheres and equator-ward expansion of polar water with pronounced steepening of temperature gradients across the polar fronts of both hemispheres. These changes were most dramatic in the North Atlantic, with this ocean's Polar Front shifting from its present position near the east coast of Greenland to a position running near Cape Hatteras to Spain. Temperatures were significantly colder in the tropical upwelling zones and along the western coasts of Africa, South America and Australia, probably in response to both increased upwelling and advection from higher latitudes. Temperatures within the great subtropical gyres, however, were little changed from today. On average, the ocean's surface temperature was 2.3 °C colder than today.

On the continents, immense ice sheets covered northern North America and Northern Europe. In North America, the

ice extended south to the present locations of New York City in the east, Seattle in the west and southern Illinois in the mid continent area. The northern European Ice Sheet extended into northwest Siberia; however, there was little or no ice on northern Alaska and northeast Siberia. The southern Andes generated expanding glaciers that spread to the lowlands of Patagonia. In general, there were huge differences in land ice extent in the Northern Hemisphere but very little difference in the Southern Hemisphere. This project produced the first reconstruction of Earth's surface conditions at a time that was climatically very different from today.

These surface conditions were then used as input to the two-level Mintz-Arakawa GCM. The model generated cooler and dryer continents, with the zone of westerly winds displaced southward near the great ice sheets. The mean temperature of the Earth's surface during the month of August was estimated to be on average nearly 5 °C lower than today's mean August temperature (Gates, 1976).

A modeling effort by the Geophysical Fluid Dynamics Laboratory of Princeton University focused on the simulation of tropical climate (Manabe and Hahn, 1977). CLIMAP's higher reconstructed LGM continental albedos produced greater negative departures of continental temperatures from

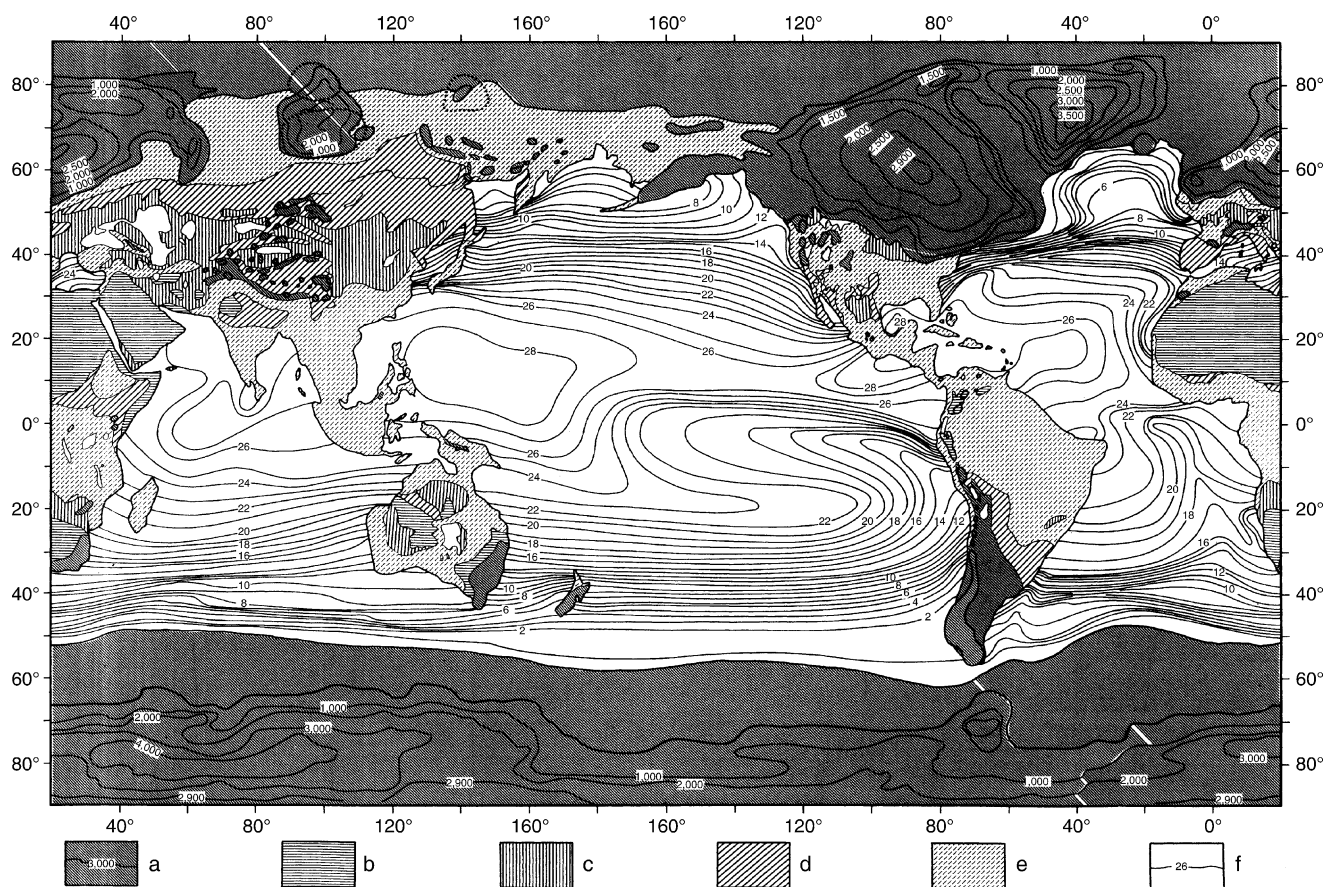


Figure C40 Surface of the ice age Earth in August 18,000 years ago. Contours are 1 °C for isotherms and 500 meters for ice elevation. Shorelines represent an 85 meter lowering of sea-level. Albedo values are given by the key; (a) snow and ice, albedo >40%, (b) sandy desert, patchy snow and snow-covered dense coniferous forests, albedo 30–90%, (c) loess, steppes and semi deserts, albedo 25–29%, (d) savannas and dry grasslands, albedo 20–24%, (e) forested and thickly vegetated land, albedo 15–18%, (f) ice-free ocean and lakes albedo <10% (modified from CLIMAP Project Members, 1984).

today's temperature than do air temperatures over the ocean. The model consequently predicts stronger surface outflows from the continents (or less surface inflow), resulting in increased tropical continental aridity. Evidence of such aridity was provided by mineralogical studies of tropical deep-sea cores (Damuth and Fairbridge, 1970). Manabe and Hahn (1977) also showed that an ice age increase in continental albedo over Tibet contributed to a weakening of the simulated Asian monsoon.

By the mid 1970s, CLIMAP had generated numerous time series in both hemispheres, some reaching back to the last reversal of the Earth's magnetic field (Cline and Hays, 1976). Because CLIMAP had demonstrated that oxygen isotopic variations (especially in benthic species) in deep-sea cores are primarily a response to changing Northern Hemisphere ice volume, Southern Hemisphere cores now offered a special opportunity to test the synchronicity of climate change between the two hemispheres. If local Southern Hemisphere temperatures could be estimated through faunal analysis in the same samples as oxygen isotopic ratios (reflecting Northern

Hemisphere ice sheet fluctuations) were measured, then the relative timing of climate change in the two hemispheres could be compared in the same core. Cores raised from the Indian Ocean sector of the sub-Antarctic region contained both siliceous and calcareous microfossils. Sea-surface temperature estimates, using siliceous microfossils, oxygen isotope measurements and measurements of the relative abundance of *C. davisiana*, showed that climatic change on ice age timescales is nearly in phase between the two hemispheres (Figure C41) (Hays et al., 1976b). This is not what the orbital theory of ice ages predicts; however, two cores from the sub-Antarctic sector of the Indian Ocean that together span more than 400,000 years (RC11-120 and E49-18) have sediment accumulation rates sufficient to resolve climate changes with periods of less than 20,000 years, which is adequate for a frequency test of the orbital theory. Spectral analysis of the three records yielded three spectral peaks in each record, centered at about 100,000, 41,000 and 23,000 years, very close to the orbital periods (Figure C42) (Hays et al., 1976b). The peak representing a period near 23,000 years is bimodal with power

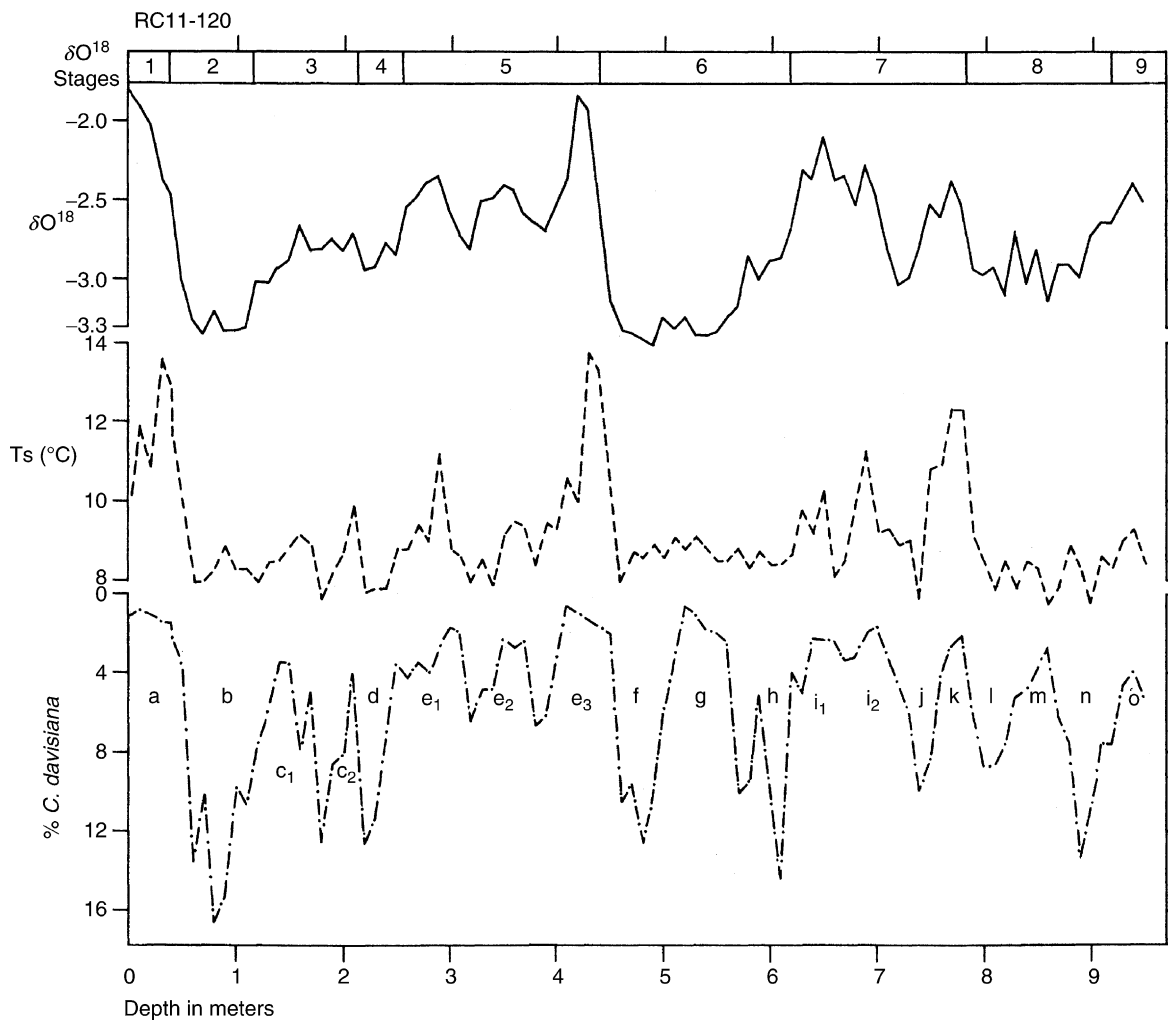


Figure C41 Depth plots of three records in sub Antarctic core RC11-120, from top to bottom: $\delta^{18}O$ a measure of the $^{18}O/^{16}O$ ratio, estimated sea-surface temperatures based on faunal analysis and % *C. davisiana* (after Hays et al., 1976b).

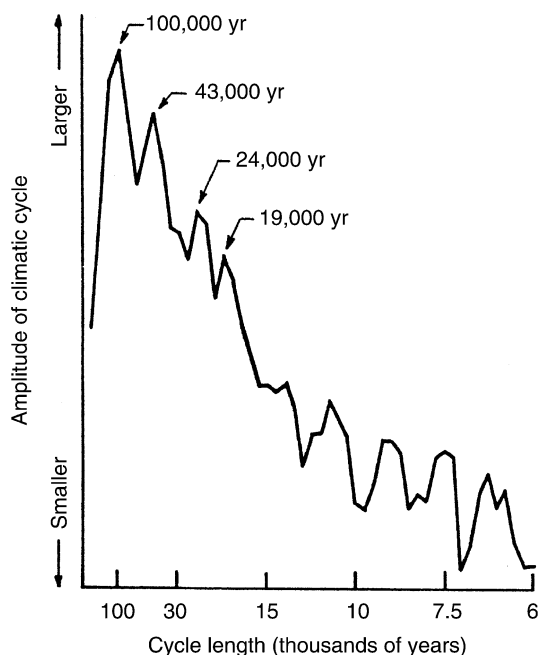


Figure C42 Periods in Northern Hemisphere ice volume variations during the last half million years (after Hays et al., 1976b).

centered near 23,000 and 19,000 years. Almost simultaneously with this study, André Berger, a Belgian scientist recalculated the orbital parameters and discovered that indeed there was also significant power in precession with a period near 19,000 years (Berger, 1977). The filtered 41,000 and 23,000-year signals show a constant phase relationship with tilt and precession over an interval of 300,000 years. These analyses provided convincing evidence that orbital variations are responsible for the timing of major glacial interglacial fluctuations, as had been suggested years before (Adhemar, 1842; Croll, 1864; Milankovitch, 1920). Why had CLIMAP succeeded in demonstrating the connection between orbital variations and climate change when many previous attempts had failed? – Emiliani, 1955, 1966; van den Heuvel, 1966; Kemp and Egger, 1967; Broecker and van Donk, 1970; Imbrie and Kipp, 1971. The clear reason is that by the time the CLIMAP team made their assessments, and very much due to their efforts, the knowledge of the age of geological features in deep-sea cores within the last half million years had improved to the point that it was sufficient to demonstrate the correlation between orbital variations and the geological record of climate change (Ninkovich and Shackleton, 1975; Hays and Shackleton, 1976; Shackleton and Opdyke, 1976; Thierstein et al., 1977).

CLIMAP workers then used the chronological information in the orbital calculations to more precisely date the geological record, first for the last 400,000 years (Hays et al., 1976b; Martinson et al., 1987) and then for the last 700,000 years (Kominz et al., 1979; Imbrie et al., 1984). The Kominz et al. (1979) work is noteworthy because, using orbital chronology mapped into an oxygen isotope record, they estimated the age of the last magnetic field reversal as 728,000 years and not 700,000 years, as had previously been thought. In the same year, additional K/Ar dates on lava flows confirmed this older age (Mankinen and Dalrymple, 1979). These nearly coincident

ages arrived at by independent methods were further confirmation of the orbital theory of ice ages as well as validation of the efficacy of mapping orbital chronological information into geological records.

The successful test of the orbital theory encouraged efforts to model the climatic consequences of radiation variations caused by precession and obliquity changes. Suarez and Held's (1976, 1979) energy balance model generates estimates of snow cover and temperature variations that, in a qualitative way, follow changes in temperature estimated from a North Atlantic core (Sanchetta et al., 1973). Imbrie and Imbrie (1980) using another model with orbital input generated variations in ice volume, which simulate the record of ^{18}O variations from deep-sea cores, and predicted future ice sheet variations.

CLIMAP's last major effort was the reconstruction of conditions at the last interglacial roughly 122,000 years ago, a time similar to the present day (CLIMAP Project Members, 1984). The group used the oxygen isotope record to identify the last interglacial and estimated temperatures through a time range of some 10,000 years. In this way, the temporal relationship between the melting of glacial ice before and re-growth after could be compared with the warming and cooling of sea-surface temperatures. In general, the sea-surface temperatures at the height of the last interglacial were not significantly different from those of the modern ocean. The project demonstrated that the oceanic sea-surface temperature change in much of the Southern Hemisphere precedes Northern Hemisphere ice volume change by several thousand years, while the reverse is true in the North Atlantic.

Conclusions

The CLIMAP project came to an end in 1981 but gave birth to project SPECMAP. Through the publication of more than 100 papers, CLIMAP contributed much to the nascent fields of paleoclimatology and paleoceanography. A few of its major contributions are listed below:

1. Presented the first detailed quantitative global reconstruction of the surface of the Earth at a time other than the present, i.e., the maximum of an ice age.
2. Through 1 (above), provided the boundary conditions for a global simulation of Earth's atmospheric circulation.
3. Provided the first quantitative measurement of how much the Earth cooled during an ice age.
4. Established a global chronostratigraphy for deep-sea sediments during the last 700,000 years with a resolution of less than a few thousand years.
5. Demonstrated that variations in the geometry of the Earth's orbit around the sun control the timing of ice age cycles.
6. By demonstrating that chronological information could be mapped from calculations of Earth's orbital variations to the climatic record in deep-sea sediments, it provided a new and accurate way to date deep-sea sediments.

James D. Hays

Bibliography

- Adhemar, J.A., 1842. *Revolutions de la mer*. Privately published, Paris.
- Berger, A., 1977. Support for the astronomical theory of climate change. *Nature*, **269**, 44–45.
- Broecker, W.L., and van Donk, J., 1970. Insolation changes, ice volumes and the $\delta^{18}\text{O}$ record in deep-sea cores. *Rev. Geophys. Space phys.*, **2**, 169–197.
- CLIMAP, 1976. The surface of the ice age Earth. *Science*, **191**, 1131–1137.

- CLIMAP Project Members, 1981. *Seasonal Reconstructions of the Earth's Surface at the Last Glacial Maximum*. Boulder, CO: Geological Society of America, Map and chart Series, **36**, 36pp.
- CLIMAP Project Members, 1984. The Last Interglacial Ocean. *Quaternary Res.*, **21**, 123–224.
- Cline, R.M., and Hays, J.D. (eds.), 1976. Investigation of Late Quaternary Paleocceanography and Paleoclimatology. 145. Boulder, CO: Geological Society of America, Geological Society of America Memoir 464pp.
- Cox, A., Doell, R.R., and Dalrymple, G.B., 1964. Reversals of the Earth's magnetic field. *Science*, **144**, 1537–1543.
- Croll, J., 1864. On the physical cause of the change of climate during geological epochs. *Philos. Mag.*, **28**, 121–137.
- Damuth, J.F., and Fairbridge, R.W., 1970. Equatorial Atlantic Deep-Sea arkosic sands and ice age aridity in tropical South America. *Geol. Soc. Am. Bull.*, **81**, 189–206.
- Dansgaard, W., 1964. Stable isotopes in precipitation. *Tellus*, **4**, 436–468.
- Denton, G.H., and Hughes, T.J. (eds.), 1981. The Last Great Ice Sheets. New York: Wiley-Interscience, 484p.
- Emiliani, C., 1955. Pleistocene temperatures. *J. Geol.*, **63**, 538–578.
- Epstein, S., Buchsbaum, R., Lowenstam, H., and Urey, H.C., 1951. Carbonate-water isotopic temperature scale. *Geol. Soc. Am. Bull.*, **62**, 417–425.
- Ericson, D.B., and Wollin, G., 1968. Pleistocene climates and chronology in deep-sea sediments. *Science*, **162**, 1227–1234.
- Ewing, W.M., and Donn, W.L., 1956. A theory of ice ages. *Science*, **123**, 1061–1066.
- Gates, W.L., 1976. The numerical simulation of ice-age climate with a general circulation model. *J. Atmos. Sci.*, **33**, 1844–1873.
- Harrison, C.G.A., and Funnel, B.M., 1964. Relationship between paleomagnetic reversals and micropaleontology in two late Cenozoic cores from the Pacific Ocean. *Nature (London)*, **204**, 566.
- Hays, J.D., and Berggren, W.A., 1971. Quaternary boundaries and correlations. In Funnel, B.M., and Riedel, W.R. (eds.), *Micropaleontology of the Oceans*. Cambridge, UK: Cambridge University Press, pp. 669–691.
- Hays, J.D., and Shackleton, N.J., 1976. Globally synchronous extinction of the radiolarian *Stylatractus universus*. *Geology*, **4**, 649–652.
- Hays, J.D., Saito, T., Opdyke, N.D., and Burckle, L.H., 1969. Pliocene-Pleistocene sediments of the Equatorial Pacific: Their paleomagnetic, biostratigraphic and climatic record. *Geol. Soc. Am. Bull.*, **80**, 1481–1514.
- Hays, J.D., Lazano, J., Shackleton, N., and Irving, G., 1976a. Reconstruction of the Atlantic and western Indian Ocean sectors of the 18,000 BP Antarctic Ocean. In Cline, R.M., and Hays, J.D. (ed.), *Investigations of Late Quaternary Paleocceanography and Paleoclimatology*. 145. Boulder, CO: Geological Society of America, Geological Society of America Memoir, 337–372.
- Hays, J.D., Imbrie, J., and Shackleton, N.J., 1976b. Variations of the Earth's orbit: Pacemaker of the Ice Ages. *Science*, **194**, 1121–1132.
- Imbrie, J., and Imbrie, J.Z., 1980. Modeling the climatic response to orbital variations. *Science*, **207**, 943–953.
- Imbrie, J., and Kipp, N.G., 1971. A new micropaleontological method for quantitative micropaleontology: Application to a late Pleistocene Caribbean core. In Turekian, K.K. (ed.), *Late Cenozoic Ice Ages*. New Haven, CT: Yale University Press, pp. 71–181.
- Imbrie, J., Hays, J.D., Martinson, D.G., McIntyre, A.C., Mix, A.C., Morley, J.J., Pisias, N.G., Prell, W.L., and Shackleton, N.J., 1984. The orbital theory of Pleistocene climate: Support from a revised chronology of the marine δO^{18} record. In Berger, et al., (ed.), *Milankovich and Climate*. Norwell, MA: D. Riedel, pp. 269–305.
- Kemp, W.C., and Egger, D.T., 1967. The relationship among sequences with application to geological data. *J. Geophys. Res.*, **72**, 739.
- Kominz, M.A., Heath, G.R., Ku, T.L., and Pisias, N.G., 1979. Brunhes time scales and the interpretation of climatic change. *Earth Planet. Sci. Lett.*, **45**, 394–410.
- Manabe, S., and Hahn, D.G., 1977. Simulation of the tropical climate of the ice age. *J. Geophys. Res.*, **82**, 3889–3911.
- Mankinen, E.A., and Dalrymple, G.B., 1979. Revised geomagnetic polarity time scale for the interval 0–5 m.y. BP. *J. Geophys. Res.*, **84**, 615.
- Martinson, D.G., Pisias, N.G., Hays, J.D., Imbrie, J., Moore, T.C., and Shackleton, N.J., 1987. Age dating and orbital theory of the ice ages: Development of a high-resolution, 0–300,000 year chronostratigraphy. *Quaternary Res.*, **27**, 1–27.
- McIntyre, A., Kipp, N.G., Be, A.W.H., Crowley, T., Kellogg, T., Gardner, J.V., Prell, W., and Ruddiman, W.F., 1976. Glacial North Atlantic 18,000 years ago: A CLIMAP reconstruction. In Cline, R.M., and Hays, J.D. (ed.), *Investigations of Late Quaternary Paleocceanography and Paleoclimatology*. 145. Boulder, CO: Geological Society of America, Geological Society of America Memoir 43–76.
- Milankovitch, M., 1920. *Theorie mathematique des phenomenes thermiques produits par la radiation solaire*. Paris: Gauthier-Villara.
- Mintz, Y., 1968. *Very Long-term Global Integration of the Primitive Equations of Atmospheric Motion: An Experiment in Climate Simulation*. 8, Boston, MA: American Meteorological Society. Meteorological Monographs, 20–36.
- Ninkovich, D., and Shackleton, N.J., 1975. Distribution and stratigraphic position and age of ash layer “L” in the Panama Basin region. *Earth Planet. Sci. Lett.*, **27**, 20–34.
- Opdyke, N.D., and Foster, J.H., 1970. Paleomagnetism of cores from the North Pacific. In Hays, J.D. (ed.), *Geological Investigations of the North Pacific*. 126. Boulder, CO: Geological Society of America. Geological Society of America Memoir, **126**, 83–119.
- Opdyke, N.D., Glass, B., Hays, J.D., and Foster, J., 1966. Paleomagnetic study of Antarctic deep-sea cores. *Science*, **154**, 349–357.
- Robertson, J.H., 1975. *Glacial to Interglacial Oceanographic Changes in the Northwest Pacific, including a Continuous Record of the Last 400,000 Years*. PhD Thesis, Columbia University, New York, 355pp.
- Sanchetta, C., Imbrie, J., and Kipp, N.G., 1973. Climatic record of the past 130,000 years in North Atlantic deep-sea core V23–82: Correlation with the terrestrial record. *Quaternary Res.*, **3**, 110–116.
- Sellers, W.D., 1969. A global climate model based on the energy balance of the Earth-atmosphere system. *J. Appl. Meteorol.*, **3**, 392–400.
- Shackleton, N.J., and Opdyke, N.D., 1973. Oxygen isotope and paleomagnetic stratigraphy of equatorial Pacific core V28–238: Oxygen isotope temperatures and ice volumes on a 10^5 and 10^6 timescales. *Quaternary Res.*, **3**, 39–55.
- Shackleton, N.J., and Opdyke, N.D., 1976. Oxygen-isotope and paleomagnetic stratigraphy of Pacific core V28–239 late Pliocene to latest Pleistocene. In Cline, R.M., and Hays, J.D. (eds.), *Investigations of Late Quaternary paleocceanography and paleoclimatology*. *Geol. Soc. Amer. Memoir*, **145**, 449–464.
- Smagorinsky, J., 1963. General circulation experiments with primitive equations: I the basic experiment. *Mon. weather rev.*, **91**, 99.
- Suarez, M.J., and Held, I.M., 1976. Modeling climatic response to orbital parameter variations. *Nature*, **263**, 46–47.
- Suarez, M.J., and Held, I.M., 1979. The sensitivity of an energy balance climate model to variations in the orbital parameters. *J. Geophys. Res.*, **84**, 4825–4836.
- Thierstein, H.R., Geitzenauer, K.R., Molfino, B., and Shackleton, N.J., 1977. Global synchronicity of late Quaternary coccolith datum levels: Validation by oxygen isotopes. *Geology*, **5**, 400–404.
- Van den Heuvel, E.P.J., 1966. On the precession as a cause of Pleistocene variations of the Atlantic Ocean water temperatures. *Geophys. J.R. Astron. Soc.*, **11**, 323–336.
- Wilson, A.T., 1964. Origin of ice ages: An ice shelf theory for Pleistocene glaciation. *Nature*, **201**, 147–149.

Cross-references

[Astronomical Theory of Climate Change](#)
[Dating, Magnetostratigraphy](#)
[Foraminifera](#)
[Ocean Paleotemperatures](#)
[Oxygen Isotopes](#)
[Radiolaria](#)
[SPECMAP](#)

CLIMATE CHANGE, CAUSES

To summarize evidence discussed elsewhere in this volume, past climate change can be detected on time scales of decades to hundreds of millions of years. Theories as to the causes for such changes extend back almost as far as the observations. James Croll (1867) was the first to seriously examine the role

of changes in the Earth's orbit, through their contribution to the waxing and waning of Pleistocene ice ages. In the early twentieth century, Alfred Wegener, in conjunction with the geographer Köppen (Köppen and Wegener, 1924), discussed how continental drift could explain the great Permo-Carboniferous ice age discovered in different parts of Gondwanaland. The tree ring laboratory at the University of Arizona was instituted in part to test hypotheses as to whether changes in the output of the sun may be responsible for decadal scale changes in drought in the western United States. In perhaps the first comprehensive assessment of the problem, Brooks (1926) estimated that there were already 56 different explanations for the ice ages.

Although many of the above ideas are still alive and well, one of the most significant advances in paleoclimatology in the last half century has been a considerable increase in quantifying past climate change, and in determining the chronology of past climate change. This last contribution is exceedingly important and sometimes either overlooked or taken for granted. As John Imbrie once remarked, "Stratigraphy is 90% of geology." By this, he meant that no sound testing of a cause is possible without a precise and accurate knowledge of the time relationships between different sources of forcing and the responses in the climate system.

The testing of hypotheses has also benefited greatly from the development of large-scale models of the atmosphere and ocean circulation and ice sheets, and the coupling of these models with both the biosphere and biogeochemical systems. One of the most significant advances by climate scientists in the last 30 years has been the recognition that not all climate change is related to some external type of forcing (e.g., volcanoes, solar and/or orbital insolation variations, motions of the continents, etc.). Rather, fluid systems can generate their own internal variability because of the different response times of different parts of the system, and this variability can account

for a very large part of the entire observed variability in the climate record.

The basic idea behind "internal variability" is that there are different time constants for different parts of the climate system – days to weeks for the atmosphere, months to years for the surface ocean (i.e., ocean mixed layer), centuries to a thousand years for the deep ocean circulation, thousands of years for ice sheets, and millions of years for continental drift. These time scales are not independent. Small, essentially random, variations in weather can sometimes store or remove heat temporarily from the ocean mixed layer. Because the ocean mixed layer has a heat capacity about 60 times that of the atmosphere, the time constant for integrating the atmospheric effects is longer in the surface ocean. Thus, there may be "decadal scale" climate variations driven simply by these random variations. In addition, planetary Rossby waves in the ocean can have time scales of years to a decade, so the propagation of these waves through the upper ocean can generate a more organized type of variability on decadal time scales. The great subtropical ocean gyres also have a time scale of a decade or two with respect to their transport of energy in the different ocean basins.

Given an infinite amount of time, the ocean would return any stored heat to the atmosphere, so that the long-term average exchange would be zero, but for finite periods, temperature can vary by 0.1–0.3 °C with respect to global mean temperature. In fact, all control runs of coupled models of the ocean-atmosphere circulation simulate such variability, which in one case has been extended to more than 10,000 model years. This variability is typically illustrated by variance versus frequency plots, which show increasing variance as the frequency of any forcing decreases (e.g., Figure C43). This pattern is known as a "red noise spectrum" and can be found in virtually all geophysical time series, including climate time series in the geologic record. The slope of the background spectrum is often in the range of -1 to -2 (the greater the slope, the greater the

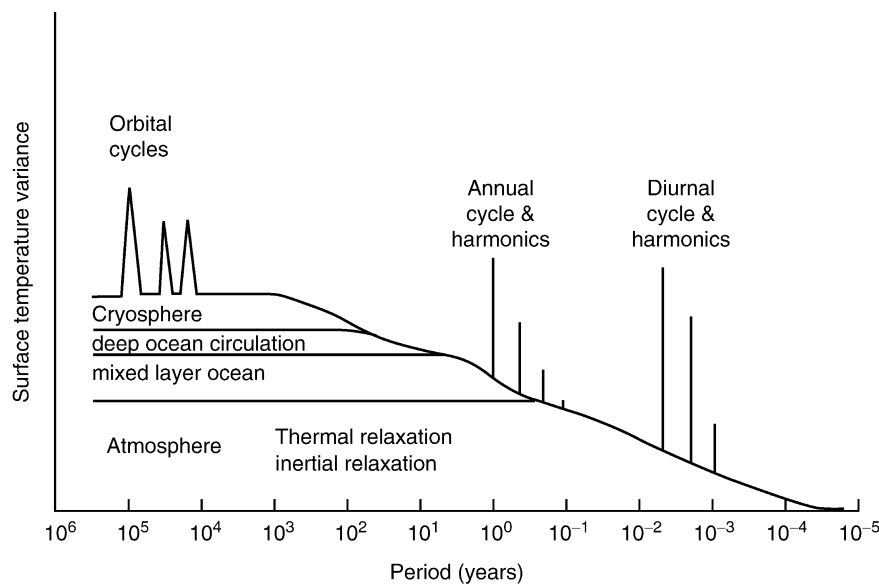


Figure C43 Schematic variance spectrum of the surface temperature versus frequency, f , (labeled in terms of period, which equals f^{-1} in years), illustrating the timescale for different components of the climate system and the relation between the background "red noise" variance and externally forced oscillations at distinct periods. (Modified from Crowley and North, 1991).

coupling between different time scales). This is the actual shape and range of slopes observed when high quality geologic observations have been used.

Only spectral peaks exceeding two standard deviations above the local background “red noise spectrum” require some type of additional explanation as to their origin, and even these must be checked with repeat analyses from other records as there is still a 5% chance that, in a fine length time series, a given peak can occur by chance alone above the 2-sigma level. These “stochastic” variations of climate should not be confused with chaos in the climate system. The latter can occur where random perturbations lead to some threshold “state change” in the system, after which there may be an abrupt change in system state. Such changes are inherently nonlinear, but the stochastic processes emphasized above are, to a large extent, linear processes.

The importance of the above discussion cannot be overemphasized, because there seems to be an inherent tendency to attribute any climate fluctuation, past or present, to some change in external forcing. However, the null hypothesis is to interpret the changes as being of internal origin unless there is some compelling evidence suggesting otherwise; for example, a strong correlation between an observed response and an external forcing term. Another, related test would be whether the observed response has a spectrum significantly different from the background climate spectrum. This is clearly the case for the annual cycle of temperatures and some of the climate changes on time scales of tens of thousands to hundreds of thousands of years that have been linked to periodic variations in the planet’s insolation.

Tectonic timescale

As indicated in Figure C44, the maximum variance in the paleoclimate system occurs on the tectonic time scale – millions to tens of millions of years. Here, the change is between times of little or no ice and times of major continental glaciation. Direct evidence of glaciations (striated rocks and pebbles, sedimentary deposits of likely glacial origin) indicates that there have been three main phases of major continental glaciation in the last 600 million years – in the late Precambrian (Neoproterozoic, ~600 Ma [million years ago]), the Permo-Carboniferous (~270–360 Ma), and the late Cenozoic (0–35 Ma). There are shorter glaciations (1–10 million years?) in the Late Ordovician (~440 Ma), in the mid-Devonian (~365 Ma) and perhaps in the middle Jurassic (~180 Ma). The magnitude and duration of the latter two is not well established, but it is likely they were less extensive in time and space than the late Cenozoic, Permo-Carboniferous, and Neoproterozoic glaciations. In total, direct evidence for glaciation occurs in about 25% of the record over the last 600 million years.

Changes in geography due to plate tectonic changes have long been explored as a mechanism of causing the “grand cycles” of Phanerozoic climate change (Donn and Shaw, 1977). However, in the early 1980s, paleoclimate-modeling exercises by Barron and Washington (1984, 1985) suggested that, although the climate effects of plate tectonic changes were significant, it was not possible to explain long-term changes in ice cover solely by this process (One exception is Greenland, where model results suggest that cooling could have been due to the northward migration of the landmass through the last 100 million years, plus deceased summer warming due to opening of the Greenland-Norwegian Seas (Crowley et al., 1986)). However, Barron and colleagues discovered that if

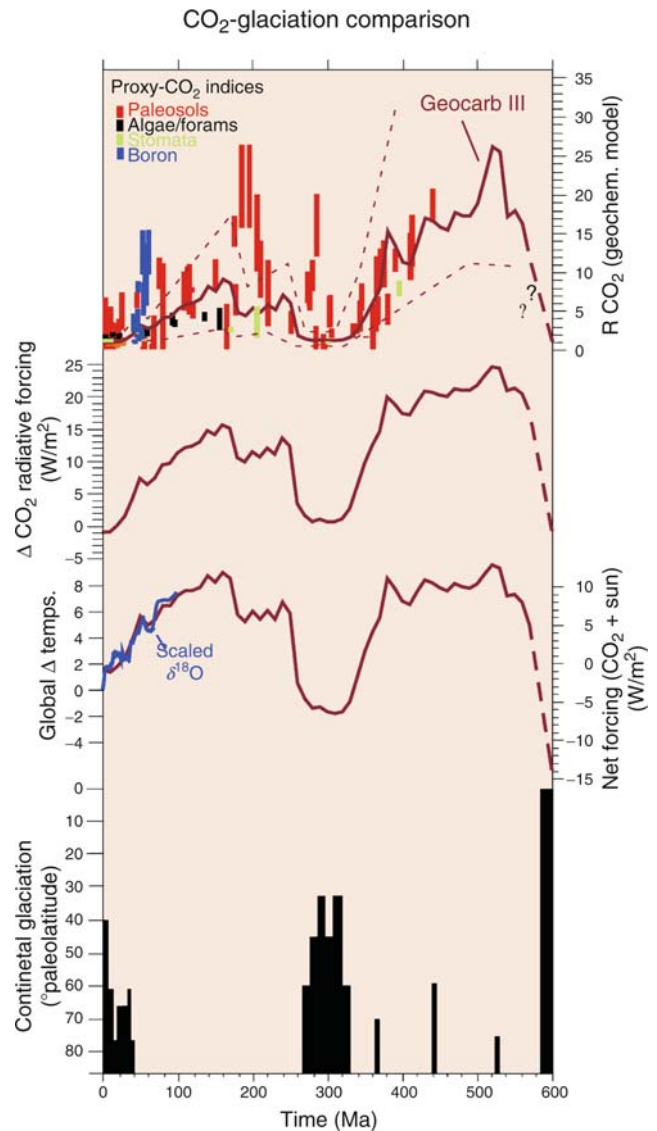


Figure C44 Comparisons of carbon dioxide changes from a geochemical model with various indices of climate change. From the top, comparison with various proxy CO₂ indices of the last 600 million years; next, adjusted radiative forcing after taking into account the logarithmic relation between CO₂ concentration and radiative forcing; second panel from bottom, radiative forcing after factoring in the evolution of solar output over the last 600 million years. On the left hand side of this panel is the oxygen isotope record of climate change for the last 100 million years, scaled to global temperatures. Bottom panel, comparison with best-documented evidence for continental glaciation. (Modified from Crowley and Berner, 2001).

carbon dioxide levels were changed, then a closer agreement between models and paleo-data could be obtained.

The results of Barron and colleagues meshed very well with independent studies of geochemistry. Berner et al. (1983) published a geochemical model suggesting that there could have been major changes in the natural CO₂ content of the atmosphere due to changes in the balance of sources and sinks of atmospheric CO₂ (e.g., outgassing from volcanoes, weathering,

and carbon burial). Changes in the latter two draw down CO_2 in the atmosphere. Changes in weathering can be related to uplift of landmasses, CO_2 -enhanced increases in weathering, and phases in the evolution of terrestrial life. For example, the present version of this model (Berner and Kothava, 2001; Figure C44) predicts a major period of high CO_2 levels in the early-mid Paleozoic (~ 300 – 540 Ma) followed by a significant decline in the later Paleozoic due to the evolution and expansion of land plants (which create an extra carbon sink of reduced carbon and also produce organic acids in the soil that accelerate the breakdown of silicate minerals). A later rise persists into the mid-Cretaceous period (~ 80 – 100 Ma) after which there is a slow decline to values at or near present by about 30 Ma.

Although considerable questions have been raised about this geochemical model, a separate line of testing, using geochemical analyses of various sedimentary constituents to derive “proxy” CO_2 estimates, agrees well with the model predictions to the first order. The calculated CO_2 levels also agree (to first order) with the amounts required by climate models to fit the paleo-data. On the 10-million year timescale (the resolution of the geochemical model), there is a good agreement (Figure C44) between the timing of CO_2 lows and major glaciation. On this timescale, it is necessary to factor in the evolution of solar irradiance due to the ever-increasing fusion-related conversion of hydrogen to helium in the sun’s core. The estimated increase amounts to about 1% per 100 million years. One also has to consider that radiative forcing from CO_2 changes is logarithmically related to CO_2 concentration because of the increased “saturation” of CO_2 absorption bands at high atmospheric CO_2 levels. Combining these two factors, and assuming for simplicity that the Earth’s planetary albedo of 30% remains constant with time, yields an estimate of net irradiance changes versus time that explains $\sim 50\%$ of the variance of continental glaciation on a time scale of 10 million years. There has been a separate but less conclusive line of discussion suggesting that CO_2 levels during the Neoproterozoic glaciation may also have been low. If so, about 60% of the major climatic variance over the last 600 million years can be explained by natural variations in the CO_2 content of the atmosphere.

There are still times when the simple CO_2 –ice relationship does not seem to hold – particularly in the Late Ordovician (~ 440 Ma) and the mid-Jurassic (~ 180 Ma). However, even these time intervals may not be totally at odds with the CO_2 model, for a number of climate modeling studies (Crowley and Baum, 1995) indicate that there is a small area of parameter space that allows high CO_2 and ice buildup. This parameter space is related to the configuration of the continents. When landmasses are close to the poles, the presence of open water suppresses the summer warming on these landmasses. Even small topographic highs can form permanent ice caps under such scenarios. Some preliminary work also suggests it may apply to the small ice advances in the Jurassic.

One peculiar feature of the above CO_2 –climate relationship is that the ocean appears to play a minor role in regulating the long-term global changes in climate. This is not to imply that the ocean did not change. The development of the Antarctic Circumpolar Circulation, after the opening of the Drake Passage (~ 20 – 30 Ma?), must have had a significant effect on the ocean circulation – at the minimum causing enhanced mixing between the deep and surface waters as the surface barriers disappeared. Modeling and observational studies (Maier-Reimer et al., 1990) suggest that final closure of the Central

American isthmus around ~ 3 Ma had a very significant effect on poleward heat transport in the Atlantic Basin (Figure C45). However, convincing links to the onset of late Cenozoic glaciation are surprisingly hard to establish. Enhanced poleward ocean heat transport in the North Atlantic since ~ 3.0 Ma coincides closely in time with the spread of Northern Hemisphere ice, but it is unclear why the ice would grow in the presence of greater warmth (summer temperatures seem more important than winter moisture as a limiting factor for ice initiation).

A more important role for the ocean response to higher CO_2 levels seems to involve the redistribution of heat on the planet. Geological data consistently indicate a very significant reduction in the equator-pole temperature gradient during times of extreme warmth. These reductions cannot be convincingly simulated with the present generation of climate models. This discrepancy represents perhaps the single largest uncertainty with respect to our understanding of how the Earth responded to past changes in forcings, and raises questions as to whether some unexpected changes may occur in the future due to society’s emissions of greenhouse gases into the atmosphere.

A related discrepancy between models and observations involves indications that winter warming in high latitudes appears to be greater than simulated by models with increased CO_2 and even a forced change in the polar temperature gradient. However, the disagreements may not be disastrous and could simply be explained by higher CO_2 levels in the atmosphere, or uncertainties in the paleo-latitude of the fossil sites.

In addition to modeling the steady-state nature of warm climates, some work has been done on the changes in climate through the Phanerozoic. In some cases, there are relatively abrupt transitions between states that imply either a rapid change in the forcing or instabilities in the climate system. In addition to the spectacular asteroid impact at the end of the Cretaceous (66 Ma), three noteworthy examples of shorter-term climatic

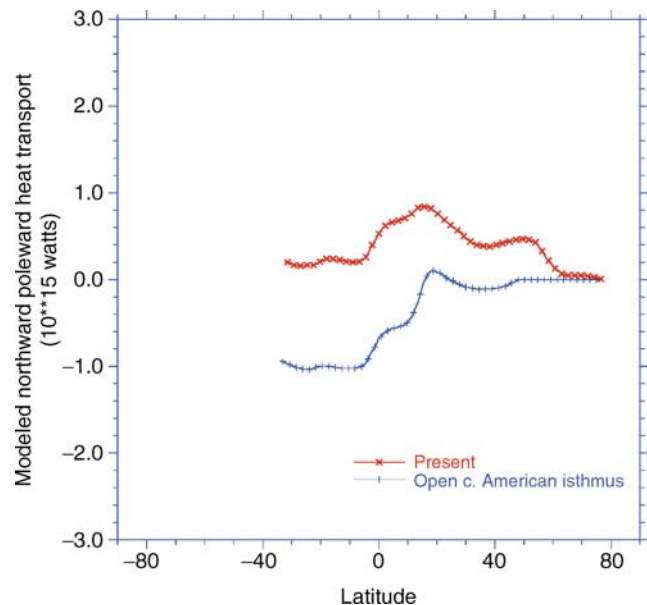


Figure C45 Comparison of polar heat transport in the Atlantic for an ocean model simulation with the present geography and with an open central American isthmus (based on results from Maier-Reimer et al., 1990).

events on long time scales (Zachos et al., 2001) involve an abrupt warming event that appears to have marked the warmest period of the Cenozoic around 55 Ma, the rapid expansion of ice on Antarctica around ~34 Ma, and another rapid climate change around 14 Ma. The first event (Paleocene-Eocene Thermal Maximum, or PETM) is associated (Zachos et al., 2003) with a rapid warming (order 10^3 – 10^4 year), a poleward expansion of subtropical biota, and abrupt warming of the deep-sea, which caused an extinction of some benthic organisms, an abrupt increase in global weathering rates, and a carbon isotope excursion that seems to be best explained by a sudden emission of methane clathrates buried on ancient continental margins (methane is a greenhouse gas that is rapidly converted to CO_2 in the atmosphere). This signal dissipated after about 200,000 years but may be the closest analog in the geologic record to how the climate system might respond to the current anthropogenic CO_2 perturbation.

The abrupt cooling around 34 Ma has long been known. It occurred over about 100,000 years and has been linked to an expansion of the Antarctic Ice Sheet and significant cooling of the deep oceans. Some recent modeling results (DeConto and Pollard, 2003) suggest that the rapid expansion of ice on Antarctica may reflect an unstable system response to slow decreases in atmospheric CO_2 . The third abrupt transition at about 14 Ma has been less examined. It has long been known from oxygen isotope records that an abrupt transition, perhaps as short as a few tens of thousands of years, occurred at this time and was associated with a further cooling of deep ocean waters. However, the precise nature of the triggering mechanism has been neither examined nor modeled.

As to reasons for the abrupt transitions, much effort over the last 20 years has been devoted to explaining and modeling abrupt climate shifts as a function of rapid reorganizations in the ocean-atmosphere system. However, for over 35 years, climate scientists have shown, first with simple energy balance models (Budyko, 1969) and later with more complex models, that it is also possible for models to rapidly evolve to a new climate state due to an instability related to the snow/ice albedo feedback. As temperatures cool due to, for example, CO_2 decreases, snow area either increases or (in the case of some regions) may be first preserved in summer. This new snow patch has much higher albedo (reflectivity) and further cools the system until it reaches a new equilibrium with significantly expanded ice area. General circulation model (GCM) experiments for the Permo-Carboniferous ice age (Crowley et al., 1994) provide some support for the idea that slow decreases in radiation (due to, for example, changes in CO_2 levels) result in a rapid increase in snow area at some critical point in the model (Figure C46). Further experiments linking GCMs to ice sheet models suggest that the abrupt change near the Eocene-Oligocene boundary (~34 Ma) may also be explained by this mechanism. Although still not widely accepted in the geological community, the snow-ice instability seems to be a very viable explanation for abrupt changes in ice extent in Earth history.

Glacial-interglacial timescale

For 50 years, it has been known from deep-sea records that there were numerous glacial-interglacial fluctuations in the late Pleistocene (Emiliani, 1955). With the advent of the Ocean Drilling Program, the record of glacial-interglacial fluctuations, as characterized by the oxygen isotope record of marine planktonic and benthic organisms, has been extended back millions of

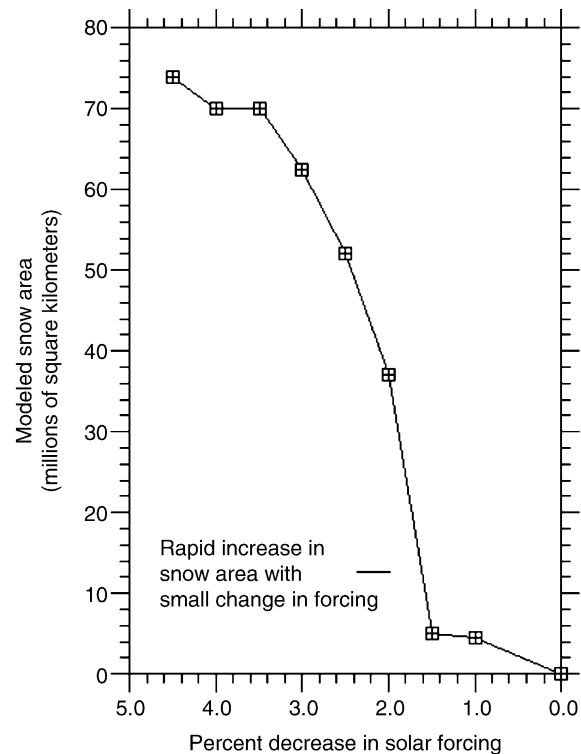


Figure C46 Model result illustrating the snowline instability. The figure shows the response of a snow cover in a general circulation model run for the Carboniferous ice age, versus changes in solar forcing (this is a conventional diagnostic tool for analyzing the response to any change in radiative forcing). Note that a decrease in solar radiation below a certain point results in rapid expansion of snow cover that would be associated with abrupt climate change, and glaciation, in the Earth record. (Modified from Crowley et al., 1994).

years. The records consistently show (Shackleton and Opdyke, 1976) that the expansion of Northern Hemisphere glaciation was a stepwise process, with Greenland glaciating first, then “small” ice sheets fluctuated at a ~41,000 year period, and in the last million years, very large ice sheets fluctuated primarily at the 100,000 year period.

It has now been established beyond a reasonable doubt that the primary factor responsible for the waxing and waning of the major ice sheets has been periodic seasonal variations of the Earth’s insolation due to orbital perturbations primarily from the gravitational fields of the Sun, moon, and Jupiter. This is the so-called Milankovitch Hypothesis or the Orbital Theory of Glaciation (Milankovitch, 1930) that was first convincingly demonstrated in an important paper by James Hays, John Imbrie, and Nicholas Shackleton (Hays et al., 1976). A key feature of this paper is that continental ice volume responds almost linearly to the orbital perturbations on shorter periods of ~41,000 years (obliquity or tilt of the Earth’s axis) and ~23,000 years (precession), while on the 100,000 year time scale the response to eccentricity variations is nonlinear. Another historic contribution comes from the Vostok (Antarctica) ice core (Figure C47), which indicates that CO_2 and Antarctic temperatures fluctuated almost in parallel for the last 400,000 years, with both strongly influenced by orbital variations (Petit et al., 1999). This result again implicates CO_2 variations as a major amplifying factor of past climate change.

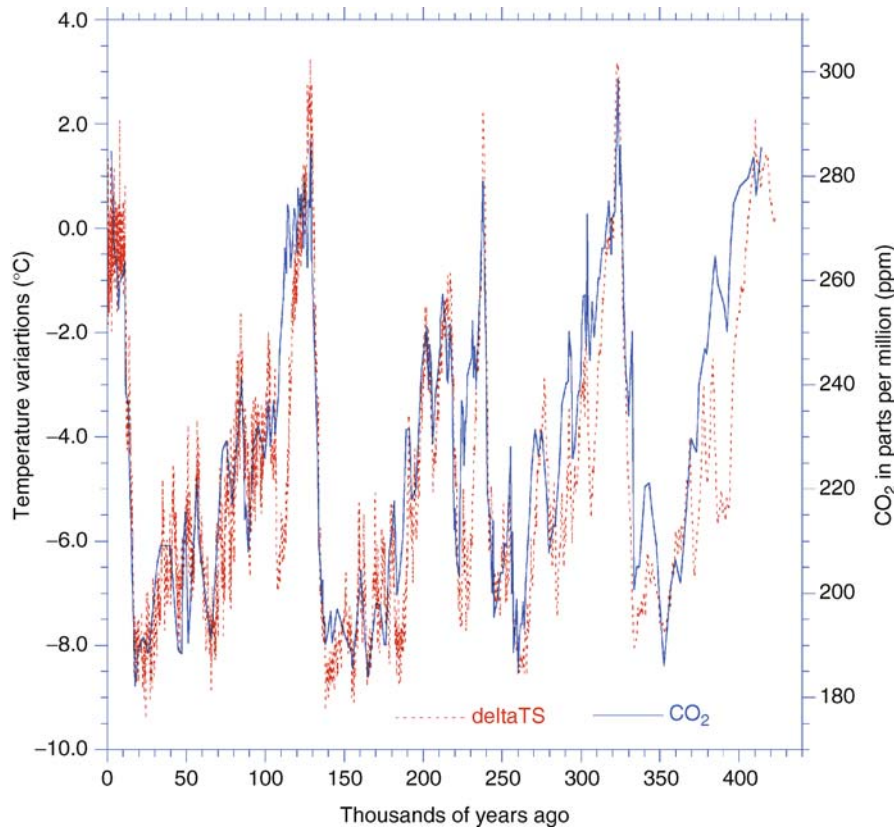


Figure C47 Comparison of carbon dioxide and deuterium temperature record from the Vostok ice core, illustrating a very tight coupling between the two records (the disjoint relationship in the oldest interglacial may reflect sampling problems at the bottom of the core). (Modified from data in Petit et al., 1999).

Since the Hays et al. (1976) paper, the principal modeling efforts have been associated with explaining how the ocean-atmosphere system translates orbital perturbations into ice volume fluctuations of the observed magnitude. A virtual mathematical zoo has been proposed as possible explanations for the 100,000 year cycle. Unfortunately, there has been little effort to cull among the different hypotheses, comparing predictions that can be falsified. Nevertheless, the dominant thinking at present is that the inherent nonlinearities associated with ice sheet dynamics are somehow responsible for the amplified response at the 100,000 period (e.g., Saltzman and Sutera, 1987). One example of how this process works is that, following an interglacial period, low summer insolation during a “cool summer orbit” leads to preservation of permanent snow fields, which over time build up into an ice sheet and flow into lower latitudes. At full glacial maximum conditions, the ice buildup depresses the Earth’s crust by as much as 1 km (Figure C48).

During a subsequent “warm summer orbit” configuration, melting of the ice sets in. Because the elastic rebound of the Earth’s crust is slower than the thinning of the ice sheet, the ice sheet is essentially “trapped” at low elevations, leading to catastrophic melting. The very rapid wastage in the time domain is translated into more power in the frequency domain at 100,000 year periods. CO₂ represents an important amplifier for the whole process. Application of a model of this type (Tarasov and Peltier, 1997) to the evolution of the last glacial cycle (Figure C49) suggests results in quite good agreement;

however, a fuller explanation for Pleistocene climate change requires understanding the origin of the CO₂ changes and further testing of the “ice trapping” model.

As with the tectonic timescale, there is also a great deal of interest in the role of abrupt climate instabilities facilitating the glacial-interglacial oscillations. For example, the first rapid melting of ice starting at about 19,000 calendar yBP seems to have occurred within a few centuries and caused about a 15 m increase in global sea level. A second phase of rapid melting began about 14,500 calendar yBP. This step was preceded by a slow but steady CO₂ increase, to about half of its Holocene value. There was also an abrupt increase in the overturning of the North Atlantic circulation that started at 14,500 yBP. Since the North Atlantic circulation provides substantial heat to the high latitudes in the strong overturning mode, this feedback presumably contributed to the rapid wasting of ice.

Some mechanism is needed to explain the rapid change in the state of the North Atlantic system. As Hays, Imbrie, and Shackleton demonstrated in 1976, some of the first signs of warming at the end of a glacial period occurred around Antarctica – perhaps because Antarctic sea ice has a far lower thermal inertia than the great northern hemisphere ice sheets. A number of recent studies now suggest that changes in the ocean circulation around Antarctica may have altered the production rate of Southern Ocean deep water, which, when it upwells in the North Atlantic, influences the production rate

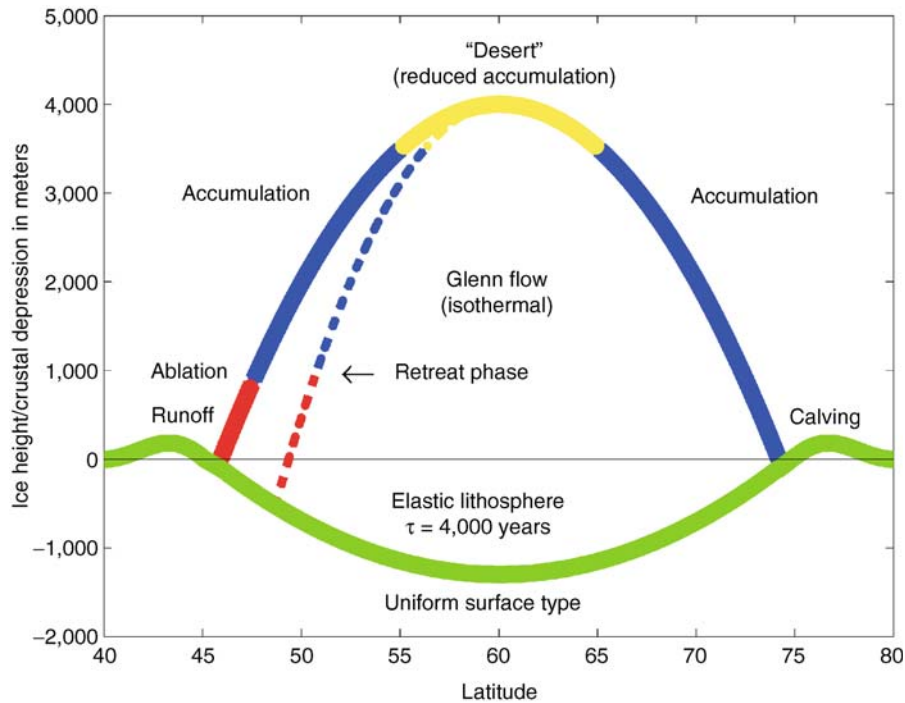


Figure C48 Schematic cross-section of Pleistocene ice sheets, illustrating zones of ablation and accumulation, and isostatic depression of the crust by the ice sheet. During times of rapid melting the ice will lay “trapped” in the depression due to the long response time of mantle rebound, resulting in rapid deglaciation (figure courtesy of William T. Hyde).

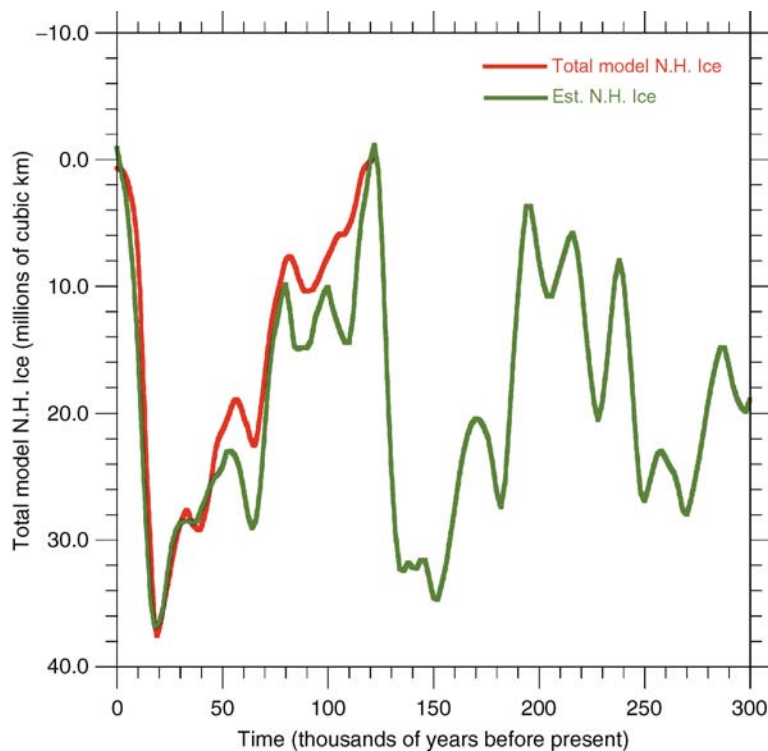


Figure C49 Comparison of modeled and observed Northern Hemisphere ice volume for the late Pleistocene. Observed variations based on marine oxygen isotope measurements converted to ice volume. Model result for the last glacial cycle based on the University of Toronto ice sheet model, which was driven by orbital forcing, CO_2 changes and variations in North Atlantic heat transport (model result courtesy of William Hyde).

of North Atlantic Deep Water. A sudden reduction of deep water formation around Antarctica might then have caused an abrupt “switch on” of the North Atlantic (Mikolajewicz, 1998). It is presently debated whether early CO₂ increases may have triggered the Antarctic changes around 19,000 BP, but the timing of the changes is sufficiently close to suggest such a possibility.

There has also been a great deal of interest in smaller but rapid changes in the ocean-atmosphere system during the “interstadial” period preceding the last glacial maximum. Records from Greenland ice cores, the North Atlantic, Eurasia, North America, and parts of the tropical regions of the South American-Indian Ocean sector indicate a fairly close correlation between the timing of abrupt changes in different regions that may reflect in part rapid and abrupt oscillations of the North Atlantic Deep Water circulation. The triggering link for the North Atlantic changes may involve some episodic outbursts of melted ice-rafted material from the continents that change the ocean salinity and short-circuit the overturning circulation.

The millennial and orbital scales cannot be viewed in isolation. It is clear that orbital forcing is virtually omnipresent in all paleoclimate records of at least the last million years. It is also clear that the system has undergone abrupt transitions. The relation between the two presumably involves the fact that, for glacial and interglacial transitions, slow changes in orbit forcing results in threshold responses in ice growth (e.g., snowline or thermohaline instabilities discussed above) and possibly CO₂. The system then goes through an abrupt transition on

its eventual trajectory to a state determined by the longer term forcing. The details of how these steps occur have yet to be elucidated.

Centennial-millennial timescale

Records primarily of the last 10,000 years provide information on shorter timescale climate that enable placement of the twentieth century warming in a longer-term perspective. Such data are also valuable in assessing different mechanisms for decadal-millennial climate change. Reconstructions (e.g., Figure C50) from the last 1,000 years of tree rings, ice cores, and corals provide a general picture of warm Middle Ages followed by a cold “Little Ice Age” that began in the late thirteenth century and persisted until the middle of the nineteenth century. Composites of such fluctuations generally agree with the lower resolution record derived from studies of the advance and retreat of alpine glaciers.

In addition to refining estimates of the magnitude and timing of past climate change, new paleotemperature reconstructions enable more precise estimates of the relative importance of different mechanisms for climate change. It has long been postulated that changes in the frequency of intense volcanic eruptions may have influenced climate on this time scale. Similarly, changes in the output of the Sun have also been postulated. Finally, there were small changes in the CO₂ content of the atmosphere during the Little Ice Age that have been recorded in ice cores, and also a long-term increase in trace gas concentrations for the last few thousand years.

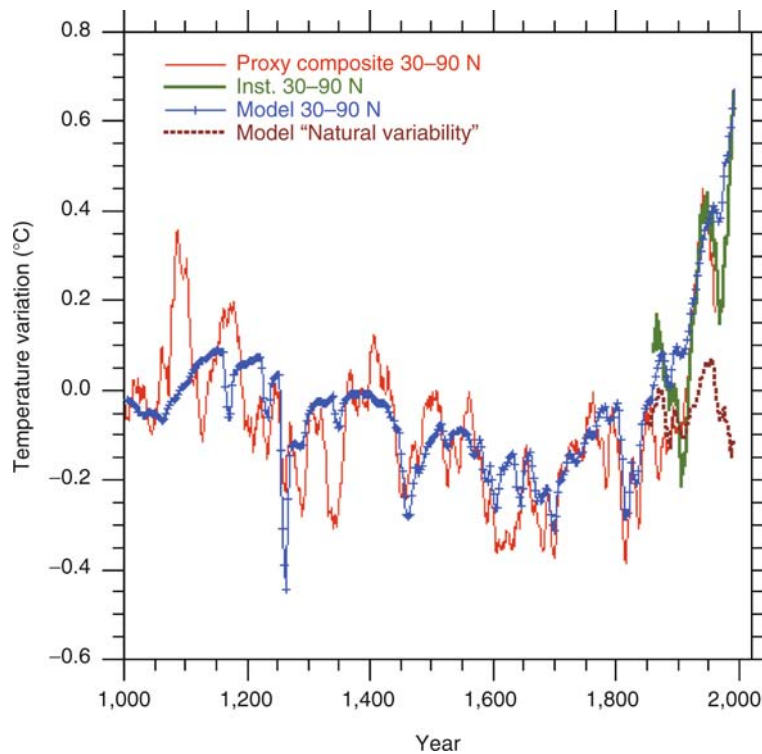


Figure C50 Sample comparison of model simulations of climate change over the last 1,000 years with observations from both the instrument and paleoclimate records. Reconstructed temperatures are for 30–90° N, where most of the long records are preserved. Model results driven by changes in greenhouse gases, volcanism, and output of the sun. Pulses of volcanism primarily account for climate change in the “Little Ice Age” (~1250–1850). Note that although the model does a good job of explaining about half of the decadal variance prior to about 1850, only the addition of greenhouse gases of anthropogenic origin can explain the late twentieth century temperature rise. (Modified from Crowley et al., 2003).

Reconstructions of volcanic, solar, and greenhouse gas forcing have enabled testing of the relative importance of different mechanisms for climate change. The volcanic reconstructions are based on sulfate deposited in Greenland and Antarctic ice cores. Solar variability can be inferred from variations of the cosmogenic isotopes ^{14}C and ^{10}Be . Trace gas concentrations are derived from ice cores. Experiments with both simple and complex climate models indicate that there is a surprisingly large forced response in the decadal-centennial band (Figure C50). More detailed analyses indicate that changes in volcanism can explain about 40% of the variance in the interval 1,000–1,850, i.e., prior to the enhanced disturbance of the system following the industrial revolution (Crowley et al., 2003). By contrast, solar variability and trace gas changes play only a secondary role on the largest scale (Hegerl et al., 2003); although there is some evidence that solar variability may occasionally be proportionately more important on smaller space scales.

The importance of solar variability seems to increase on the millennial timescale (Figure C51). There are a number of known millennial scale climate fluctuations that have long been identified as punctuating the generally warm time of the Holocene. In particular there are changes at about 5,500 BP (calendar years before present), 4,500 BP, and 2,700 BP. In the North Atlantic basin, these and other Holocene fluctuations bear a striking correspondence to solar forcing as inferred from variations of ^{14}C and ^{10}Be . These data suggest that the importance of solar forcing may be timescale-dependent – it is relatively weak on the decadal-centennial scale, but proportionately more important on the millennial scale. The general explanation for

such a frequency dependency may involve the fact that there is generally more variance at lower frequencies in geophysical systems. A weak solar signal at decadal-centennial scales may become sufficiently strong at the centennial-millennial scale to leave a clearer imprint on geologic records, especially since there is much less evidence in support of any millennial variability in volcanism.

The above analysis can explain the quasi-cyclical millennial scale oscillations of the Holocene that appear to be influenced by solar activity. However, volcanic activity in the last millennium has had a major effect on the system response during this time and has exerted a great influence on multi-decadal time scale fluctuations. This could explain why the Little Ice Age was the most extreme climate cooling of the last 1,000 years. This analysis therefore suggests that solar forcing may only reach significant levels for climate fluctuations greater than about a century in length.

The clarification of the relative importance of different types of natural forcing has enabled better understanding of the twentieth century trends in the instrumental record. Natural forcing alone, which can explain much of the pre-industrial interval, accounts for only a fraction of the twentieth century record. Viewed from the paleoclimate perspective (Figure C50), the recent temperature increase appears to be much more clearly driven by the anthropogenic greenhouse gas perturbation. Such a conclusion is consistent with an increasing body of analyses of instrumental records and points to the likelihood that the greenhouse perturbation has already manifested itself in the climate system.

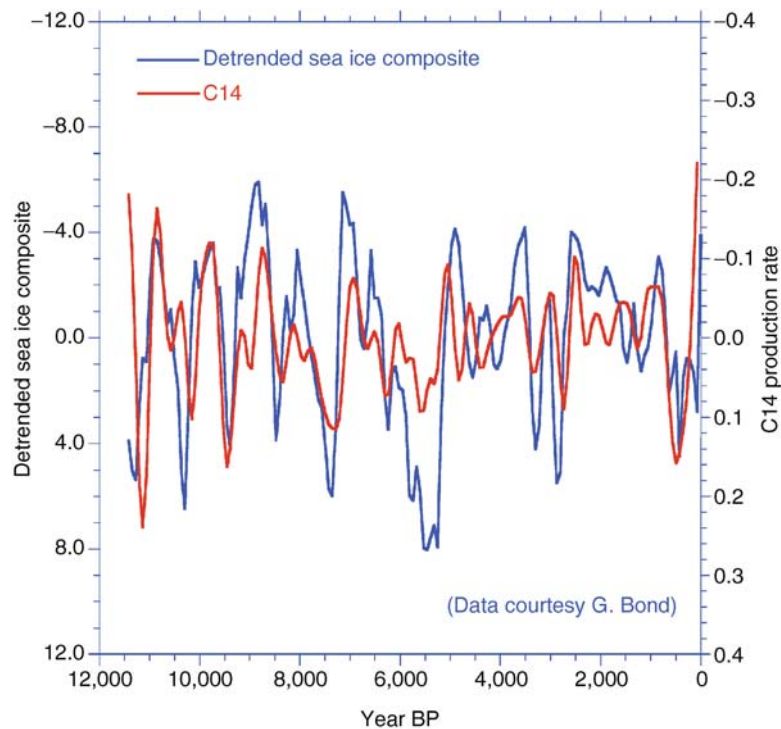


Figure C51 Comparison of atmospheric residual carbon-14 variations of the last 11,000 years with a record of sea ice variations in the subpolar North Atlantic. Positive values on the left axis indicate expansion of sea ice; positive values on the right axis indicates increase in C-14 production rate, which has been associated with a decreased output of solar irradiance. On century-millennial timescales, changes in solar variability may explain a proportionately larger amount of variance than volcanism in climate records (based on results from Bond et al., 2001).

Summary

A great deal has been learned about the causes of past climate change. CO₂ appears to play perhaps the dominant role as the first-order “driver” of climate change on tectonic timescales. However, CO₂ cannot explain everything. In particular, the altered planetary temperature gradient during warm time periods indicates a response of the ocean-atmosphere system that represents perhaps the most prominent difference between models and observations in the paleoclimate record. Understanding this response may enable more confident predictions of greenhouse model simulations of the future.

A second important consideration of climate change on tectonic timescales involves the rapid transitions to ice cover at various times in the Phanerozoic. Models suggest that this transition may be explicable by a snowline instability due to albedo discontinuities at the snow-ice edge. This instability has received much less attention than changes in the ocean circulation, but is fully deserving of equal prominence as a mechanism for rapid climate change.

On ice-age timescales, orbital forcing plays an important role in “pacing” the timing of glacial and interglacial advances. Instabilities appear to play a crucial role with respect to both ice advance and decay; the snowline instability may be more important for ice growth, but ocean changes coupled with ice sheet dynamics may be necessary to explain deglaciations. CO₂ is at the minimum an important amplifier of these responses and for deglaciation may play a fundamental and necessary role in driving the system to full interglacial conditions. Even after almost 25 years since its discovery, the cause of the ice age CO₂ changes continues to elude a satisfactory, consensus explanation.

Volcanism and solar variability appear to play the most important roles on decadal-millennial time scales. Solar variability appeared to have some influence on centennial-scale cooling events in the Holocene. However, the most severe cooling in the last 8,000 years – the Little Ice Age – may have resulted from a wave of volcanism superimposed on a modest cooling of solar origin. Projections of “natural forcing” into the twentieth century indicate that only a fraction of the observed warming can be explained by these processes; anthropogenic greenhouse warming appears to have established itself above the noise level of the geologic record. Future warming projections suggest that conditions comparable to the Pliocene-Miocene warm periods could occur by the end of the twenty-first century. Full utilization of the fossil fuel reservoir could drive temperatures up to levels not experienced since the Eocene warm period, 50 million years ago.

The greatest remaining issues involve:

1. Explanation for the altered equator-pole temperature gradient during past warm time periods.
2. Coupling between low-frequency orbital forcing and abrupt responses in the ocean-atmosphere system on ice age time scales.
3. The origin of ice age CO₂ changes.

Thomas J. Crowley

Bibliography

Barron, E.J., and Washington, W.M., 1984. The role of geographic variables in explaining paleoclimates: Results from Cretaceous climate model sensitivity experiments. *J. Geophys. Res.*, **89**, 1267–1279.

Barron, E.J., and Washington, W.M., 1985. Warm Cretaceous climates: High atmospheric CO₂ as a plausible mechanism. In Sundquist, E.T., and Broecker, W.S. (eds.), *The Carbon Cycle and Atmospheric CO₂*:

Natural Variations Archean to Present. 32. Washington, D.C.: AGU, pp. 546–553.

Berner, R.A., and Kothavala, Z., 2001. GEOCARB III: A revised model of atmospheric CO₂ over Phanerozoic time. *Am. J. Sci.*, **301**, 182–204.

Berner, R.A., Lasaga, A.C., and Garrels, R.M., 1983. The carbonate-silicate geochemical cycle and its effect on atmospheric carbon dioxide levels for the last 100 million years. *Am. J. Sci.*, **289**, 333–361.

Bond, G., Kromer, B., Beer, J., Muscheler, R., Evans, M.N., Showers, W., Hoffmann, S., Lotti-Bond, R., Hajdas, I., and Bonani, G., 2001. Persistent solar influence on North Atlantic climate during the Holocene. *Science*, **294**, 2130–2136.

Brooks, C.E.P., 1926. *Climate Through The Ages*. London: Dover Publications.

Budyko, M.I., 1969. The effect of solar radiation changes on the climate of the Earth. *Tellus*, **21**, 611–619.

Croll, J., 1867. On the eccentricity of the earth's orbit, and its physical relations to the glacial epoch. *Philos. Mag.*, **33**, 119–131.

Crowley, T.J., and Baum, S.K., 1995. Reconciling Late Ordovician (440 Ma) glaciation with very high CO₂ levels. *J. Geophys. Res.*, **100**, 1093–1101.

Crowley, T.J., and Berner, R.A., 2001. *Science*, **292**, 870–872.

Crowley, T.J., and North, G.R., 1991. *Paleoclimatology*. New York: Oxford University Press.

Crowley, T.J., Short, D.A., Mengel, J.G., and Short, D.A., 1986. Role of seasonality in the evolution of climate over the last 100 million years. *Science*, **231**, 579–584.

Crowley, T.J., Yip, K.-Y.J., and Baum, S.K., 1994. Snowline instability in a general circulation model: Application to Carboniferous glaciation. *Clim. Dyn.*, **10**, 363–374.

Crowley, T.J., Baum, S.K., Kim, K.-Y., Hegerl, G.C., and Hyde, W.T., 2003. Modeling ocean heat content changes during the last millennium. *Geophys. Res. Lett.*, **30** (18), 1932.

DeConto, R.M., and Pollard, D., 2003. Rapid Cenozoic glaciation of Antarctica induced by declining atmospheric CO₂. *Nature*, **421**, 245–249.

Donn, W.L., and Shaw, D.M., 1977. Model of climate evolution based on continental drift and polar wandering. *Geol. Soc. Am. Bull.*, **88**, 390–396.

Emiliani, C., 1955. Pleistocene temperatures. *J. Geol.*, **63**, 538–578.

Hays, J.D., Imbrie, J., and Shackleton, N.J., 1976. Variations in the Earth's orbit: Pacemaker of the ice ages. *Science*, **194**, 1121–1132.

Hegerl, G.C., Crowley, T.J., Baum, S.K., Kim, K.-Y., and Hyde, W.T., 2003. Detection of volcanic, solar and greenhouse gas signals in paleo-reconstructions of Northern Hemisphere temperature. *Geophys. Res. Lett.*, **30** (5), 1242.

Köppen, W., and Wegener, A., 1924. *Die Klimat der Geologischen Vorzeit*. Gebrüder Borntraeger: Berlin.

Maier-Reimer, E., Mikolajewicz, U., and Crowley, T.J., 1990. Ocean GCM sensitivity experiments with an open central American isthmus. *Paleoceanography*, **5**, 349–366.

Mikolajewicz, U., 1998. Effect of meltwater input from the Antarctic ice sheet on the thermohaline circulation. *Ann. Glaciol.*, **27**, 311–315.

Milankovitch, M., 1930. Mathematische Klimalehre und Astronomische Theorie der Klimaschwankungen. In Köppen, I.W., and Geiger, R. (eds.), *Handbuch der Klimatologie*. Berlin: Gebrüder Borntraeger.

Petit, J.R., Jouzel, J., Raynaud, D., et al., 1999. Climate and atmospheric history of the past 420,000 years from the Vostok ice core, Antarctica. *Nature*, **399**, 429–436.

Saltzman, B., and Sutera, A., 1987. The mid-Quaternary climatic transition as the free response of a three-variable dynamical model. *J. Atmos. Sci.*, **41**, 736–745.

Shackleton, N.J., and Opdyke, N.D., 1976. Oxygen isotope and paleomagnetic stratigraphy of Pacific core V28–239 late Pliocene to latest Pleistocene. In Cline, R.M., and Hays, J.D. (eds.), *Geol. Soc. Am. Mem.*, **145**, pp. 449–464.

Tarasov, L., and Peltier, W.R., 1997. Terminating the 100 ky ice age cycle. *J. Geophys. Res.*, **18**, 21665–21693.

Zachos, J., Pagani, M., Sloan, L., Thomas, E., and Billups, K., 2001. Trends, rhythms, and aberrations in climate, 65 Ma to present. *Science*, **292**, 686–693.

Zachos, J., Wara, M.W., Bohaty, S., Delaney, M.L., Petrizzo, M.R., Brill, A., Bralower, T.J., and Premoli-Silva, I., 2003. A transient rise in tropical sea surface temperature during the Paleocene-Eocene thermal maximum. *Science*, **302**, 1551–1554.

Cross-references

[Albedo Feedbacks](#)
[Astronomical Theory of Climate Change](#)
[Carbon Dioxide and Methane, Quaternary Variations](#)
[Cenozoic Climate Change](#)
[Climate Forcing](#)
[Climate Variability and Change, Last 1,000 Years](#)
[Cosmogenic Radionuclides](#)
[Glaciations, Pre-Quaternary](#)
[Glaciations, Quaternary](#)
[Heat Transport, Oceanic and Atmospheric](#)
[Little Ice Age](#)
[Medieval Warm Period](#)
[Paleocene-Eocene Thermal Maximum](#)
[Paleoclimate Modeling, Pre-Quaternary](#)
[Paleotemperatures and Proxy Reconstructions](#)
[Pre-Quaternary Milankovitch Cycles and Climate Variability](#)
[Sun-Climate Connections](#)
[Volcanic Eruptions and Climate Change](#)

CLIMATE FORCING

Climate forcings are usually thought of as being small, sustained changes that are externally imposed on either the solar or thermal component of the planet's radiation energy balance, thereby driving the climate system to a new thermal equilibrium. Climate change is frequently associated with changes in atmospheric circulation that alter the prevailing precipitation and temperature patterns. However, since the atmospheric circulation is ultimately driven by temperature contrasts, the climate forcings are ultimately radiative in nature.

Regarding climate forcings that are relevant to current climate, the gradual increase of greenhouse gases such as CO₂, CH₄, N₂O, CFC₃ and CF₂Cl₂ has the effect of strengthening the terrestrial greenhouse effect, and thus leading to enhanced global warming. Other contributors to current global climate change include changes in the amount and vertical distribution of ozone as well as the increase of both absorbing and non-absorbing aerosols whose differing radiative properties partially cancel each other's radiative forcing effects. Periodically, large volcanic eruptions inject large amounts of sulfur-bearing gases into the stratosphere. These gases become globally dispersed and are converted photochemically into sulfuric acid droplets, which block the incoming solar radiation and cool the ground surface until the aerosols fall out from the stratosphere. Changes in solar luminosity also contribute to climate forcing, although the observed variations in solar luminosity are small and coincide with sunspot activity during the course of the 11-year sunspot cycle. Larger changes in solar luminosity are believed to occur over longer time scales and are thought responsible for unusually cold periods such as the Little Ice Age during the Maunder Minimum in the seventeenth century, when sunspot activity had virtually ceased.

A change in radiative forcing does not necessarily have climatic consequences. Large changes in solar illumination occur as part of the diurnal cycle and large seasonal changes in solar heating take place in the polar regions. This produces largely repetitive short-term temperature fluctuations that are nevertheless part of what we regard as the prevailing equilibrium climate. The bona fide climate forcings are radiative forcings that are sufficiently large in magnitude, and/or are sustained enough to overcome the large heat capacity of the

ocean, land, and atmosphere, and thus produce a change in the annual mean radiative energy balance of the Earth sufficient to move the prevailing climate away from its reference norm.

Cataclysmic climate forcings

Astrophysical models of solar evolution indicate that the luminosity of the Sun was about 25% less than its present value in the early days of the solar system (see *Faint Young Sun Paradox*). This would have been a very large climate forcing, which, if applied to the present atmospheric composition, would quickly produce a solidly frozen planet from equator to pole. The fact that the Earth has maintained a viable biosphere for billions of years implies that a strong CO₂ greenhouse effect must have been operating at that time to have sustained temperatures that were sufficiently moderate for liquid water to exist in the environment. This also implies that, over the geological time frame, the biosphere of the Earth was able to successfully navigate the gradual reduction of atmospheric CO₂ to present-day levels as solar luminosity was increasing, thus avoiding the runaway greenhouse catastrophe that befell Venus and rendered it inhospitable to life.

The geological record is also punctuated by catastrophic climate forcings that are very likely the result of major comet or asteroid impacts, which in some cases have been linked to mass extinctions. Of these, perhaps the best documented is the end of Cretaceous mass extinction 65 million years ago, in which the dinosaurs and many other animal species of that time perished. This mass extinction has been associated with the multi-ringed, Chicxulub Crater, roughly 100 miles in diameter, which is located on the northern coast of the Yucatan Peninsula in Mexico, and which is believed to have been formed by the impact of a comet or asteroid perhaps ten miles in diameter. Another notable mass extinction occurred at the end of the Permian period 245 million years ago when 95% of the living species were wiped out. The geological record suggests that major extinctions have occurred roughly at intervals of 25–30 million years, a periodicity that according to one hypothesis has been associated with oscillations of the solar motion through the galactic plane. Encounters with the denser media of the galactic plane are thought to disturb the Oort Cloud of comets surrounding the Sun, causing an increased number of comets to drop down into the inner parts of the solar system, thereby "loading the dice" for catastrophic encounters. Such comet and asteroid impacts can release enormous amounts of energy; sufficient to vaporize hundreds of cubic kilometers of solid rock, which if dispersed globally would produce extensive clouds of light scattering particles high in the stratosphere. The initial firestorm of the impact would deposit a great deal of heat in the atmosphere, at least locally, and would be followed by prolonged global cooling that would last for several years until the dust settled out. This would have enormous climatic consequences; first by overheating the environment, then by blocking solar radiation from reaching the ground, stopping photosynthesis, and eliminating entire species unable to cope with the climatological consequences.

Geological scale climate forcings

Other climate forcings that have had a profound impact on climate are the changes in topography and continental layout that occur very gradually on a timescale of many millions of years. High mountain ranges such as the Andes and Himalayas strongly affect the local climate via altitude of the land. They also affect the atmospheric circulation and determine where

precipitation will fall and where arid conditions will prevail. Similarly, as the continental layout changes with continental drift, the ocean currents readjust and produce climate change. Absence of land in the polar regions to anchor potential ice sheets is believed to have been instrumental in maintaining the relatively mild temperatures during the Mesozoic period.

Another type of climate forcing and one that is responsible for the classical shifting of global climate between cold ice ages and warm interglacial periods over the past several million years is known as the astronomical or Milankovitch theory of climate change. This involves slow variations of the Earth's orbital parameters due to the gravitational influence of other planets. As a result, the tilt of the rotational axis of the Earth with respect to the orbital plane wobbles by more than a degree with a period of about 41,000 years. This affects the amplitude of the seasonal temperature change. Furthermore, because the orbit of the Earth is not fully circular, the Earth moves closer in and farther away from the Sun during the course of the year. At present, the closest point of approach, or perihelion, occurs in January, at which point the Earth receives about 7% more solar energy as compared with July when the Sun-Earth distance is at its maximum. The seasonal timing of perihelion occurrence is associated with the precession of the equinoxes, which takes about 22,000 years for a full cycle. In addition, the degree of oblateness of the Earth's orbit varies on a timescale of roughly 100,000 years. These perturbations have little effect on the annual mean solar energy that strikes the Earth, but they do alter the geographical and seasonal distribution of solar illumination by as much as 10–20%, being particularly effective in the polar regions.

Precisely how these slow variations in geographical and seasonal insolation act to produce an ice age climate is not yet fully understood. Ice core analysis of trapped air bubbles in the Antarctic and Greenland Ice Sheets indicates that atmospheric CO₂ levels 20,000 years ago were roughly half of present day concentrations. Climate model simulations of ice age climate show that the radiative forcing characteristic of ice age climate was about 6 W m⁻² less than for the current climate, due primarily to the effect of vast continental ice sheets that account for about 3.5 W m⁻², and to the decreased amount of greenhouse gases (CO₂, CH₄, and N₂O), which contribute about 2.5 W m⁻². This amount of radiative forcing was sufficient to maintain a global mean temperature 5 °C colder than the present global mean, consistent with the global mean temperature that has been inferred from polar ice core δ¹⁸O isotope ratios. This implies a climate sensitivity of nearly 1 °C global mean temperature change per 1 W m⁻² of radiative forcing for ice age climate, which is basically the same sensitivity that is obtained from climate model simulations conducted for current climate.

Nevertheless, a careful analysis of the ice core record shows that the observed temperature changes tend to precede the CO₂ and CH₄ changes by 500–1,000 years. This implies that the observed changes in CO₂ and CH₄ may be positive feedback responses by the ocean and the biosphere to the Milankovitch forcing. Just how this CO₂ and CH₄ feedback response might operate has not been fully demonstrated. The distinction between what constitutes a climate forcing and a climate feedback is not a clearly defined concept and depends on the timescales that are involved. On the one hand, there are fast feedback processes such as the evaporation and condensation of water vapor and the seasonal melting and freezing of snow and ice. These feedback processes respond quickly to changes

in radiative forcing and provide a positive feedback magnification of the original forcing. This is because water vapor is a strong greenhouse gas and the addition of more water vapor to the atmosphere produces more greenhouse warming. The melting of snow and sea ice lowers the albedo of the Earth and allows more solar radiation to be absorbed. Clouds also fall in the category of fast feedback processes, but are more complicated in that an increase in high-altitude cirrus would provide a positive feedback because of their strong greenhouse effect, while an increase in low-level clouds would increase the planetary albedo and thus provide a negative feedback. On the other hand, slow geophysical processes such as the growth and decay of continental ice sheets, changes in vegetation cover, and the gradual change in atmospheric CO₂ and CH₄ levels, may operate as feedback processes on geological timescales but act as radiative forcings on short (decadal) timescales.

The susceptibility of the Earth to ice age climate appears largest when alignment of the orbital parameters is most favorable for cold Northern Hemisphere summers. However, in climate model simulations, the Milankovitch forcing alone is not enough to initiate an ice age. It appears that a triggering mechanism, such as strong global cooling from a series of large volcanic eruptions, or a temporary decrease in solar luminosity, may be necessary to ensure that the winter snowfall accumulation does not melt during the following summer and becomes instead the foundation of a new continental ice sheet. However, once established, ice age climate is stable in the sense that the prevailing colder global temperature is in equilibrium with the combined radiative forcings due to the continental ice sheets and the depleted greenhouse gases.

A closer look at the geological temperature record based on isotope ratios found in Antarctic ice cores shows a complex time series of global mean temperature fluctuations. For most of the past 4 million years, the time series is characterized by a cold ice age climate. The warm interglacial periods appear to be relatively brief and tend to occur at intervals of roughly 100,000 years, and last perhaps 10,000–20,000 years. There are slow periodic fluctuations where the global temperature undergoes changes of more than several degrees on timescales of 10,000 years, on which are superimposed faster oscillations of less than 1,000 years in duration with amplitudes smaller than 1 °C. This only serves to illustrate the limitations of present day climate models, which appear capable of calculating the direct impact of radiative forcings with reasonable accuracy and in estimating the magnitude of feedback responses of the fast feedback processes but do not possess the necessary physics to model the full ice age cycle of climate change.

There may be additional uncertainties and non-linear effects involved in these slow-process climate forcings as suggested by the asymmetric nature of the more or less slow and steady growth of continental ice sheets followed by a more rapid ice sheet decay. The extent to which an ice sheet will grow or decay is determined by a complex balance between snow accumulation over the ice sheet relative to ice loss due to melting and ablation. A strong hydrological cycle is needed to supply ample moisture for ice sheet growth, and sufficiently cold summer temperatures are needed to sustain the accumulation of snow over the ice sheet. Ice sheet melting, however, is not simply the reverse process of ice accumulation. During ice sheet decay, ice dynamics aided by ice-melt lubrication injected via ice crevasses may undermine the ice sheets and lead to an accelerated breakup, processes that would not be operating during ice sheet buildup.

Radiative nature of climate forcings

The purely radiative aspects of climate forcing have been more thoroughly studied and can be described more quantitatively. As illustrated in Figure C52, the atmospheric temperature decreases steadily with height, due partly to radiative cooling by atmospheric gases but also due to the convective and dynamic transport of energy within the troposphere, which acts to maintain a global mean temperature gradient of about $5.5\text{ }^{\circ}\text{C km}^{-1}$. About half of the incident solar radiation is absorbed by the ground surface, from where the absorbed energy is transported upward in the form of latent and sensible heat and mixed throughout the troposphere by convective motions. For an atmosphere that is in radiative-convective equilibrium, convective heat transport along with longwave cooling by atmospheric water vapor, CO_2 , clouds, and other gases, work together to balance the atmospheric heating due to absorbed solar radiation. Convective heat transport also acts to bind the tropospheric temperature profile to the ground surface and to the very large heat capacity of the ocean. The stratosphere on the other hand is in a state of purely radiative equilibrium where the local heating due to the absorption of solar UV radiation by ozone is balanced by the longwave cooling due primarily to CO_2 . It is the local maximum concentration of ozone above the tropopause that produces the characteristic temperature profile in the stratosphere.

For the current climate, the global mean surface temperature is about 288K ($15\text{ }^{\circ}\text{C}$). The Earth has a planetary albedo of 0.3, because of which, the global mean solar energy absorbed is 239 W m^{-2} . For the Earth in radiative equilibrium, this dictates an effective Planck radiating temperature to space of 255K . The difference between the surface temperature and the effective radiating temperature ($33\text{ }^{\circ}\text{C}$) defines the total greenhouse strength of the Earth's atmosphere. This means that if the atmosphere of the Earth were totally transparent to all radiation (and if the Earth still had a global albedo of 0.3), the global mean surface temperature would be 255K ($-18\text{ }^{\circ}\text{C}$) instead of 288K . The point within the atmosphere where the physical temperature is equal to the effective radiating temperature is determined by the vertical distribution of the longwave

absorbing gases (H_2O , CO_2 , O_3 , CH_4 , N_2O) and clouds, and coincides with the point where the effective longwave opacity (as viewed from space) is unity. For the current climate, this point occurs at about a height of 6 km.

As illustrated in Figure C52a, the simplest measure of radiative climate forcing is the instantaneous forcing ΔF_i (W m^{-2}). When a radiative forcing such as doubled CO_2 is applied, the longwave fluxes change throughout the atmosphere. By evaluating the instantaneous radiative flux change at the tropopause, a reasonably good estimate of the eventual change in equilibrium surface temperature is obtained. This is because the tropospheric temperature profile is strongly bound to the surface temperature via convective heat transport, so that evaluating the flux imbalance at the tropopause gives a good estimate of the radiative forcing that is applied to the troposphere-ground system. A better estimate of the expected surface temperature change is obtained from the adjusted forcing, ΔF_a , whereby the stratosphere is allowed to adjust to its new radiative equilibrium before evaluating the radiative flux difference. This provides a more accurate measure of the radiative flux imbalance that actually drives the climate system. Because the heat capacity of the stratosphere is very small, the stratosphere will reach radiative equilibrium in a matter of months, long before the surface temperature has had a chance to respond appreciably.

Figure C53 shows the equilibrium surface temperature change, ΔT_o , which is obtained after the ocean, with its large heat capacity, has fully responded to the applied forcing, ΔF_a , in the artificial case that no feedback processes are allowed to operate. As might be anticipated, ΔT_o and ΔF_a , differ only by a relative scale factor where $\Delta T_o(^{\circ}\text{C}) \sim 0.3\Delta F_a$ (W m^{-2}), with the exact value of the constant depending somewhat on the latitudinal, spectral, and height distribution of the applied forcing. As indicated, instantaneous doubling of CO_2 increases the longwave opacity of the atmosphere. This forces the effective radiating level (the point where longwave opacity is unity) to a higher altitude where the temperature is colder; therefore, less thermal energy is radiated to space, thereby trapping the amount ΔF_a . Since the solar heat input remains fixed, the

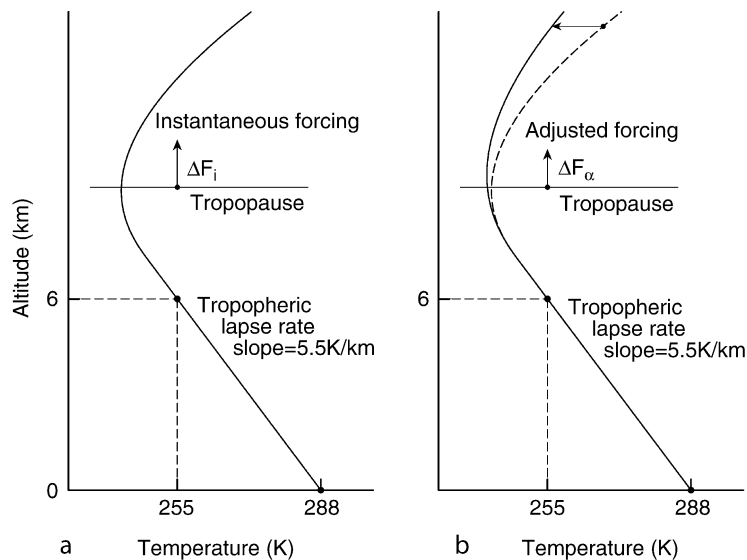


Figure C52 Schematic global mean temperature profile of the Earth. (a) Instantaneous forcing ΔF_i evaluated at the tropopause. (b) Adjusted forcing ΔF_a after allowing stratosphere to cool.

trapped thermal energy forces the atmospheric and surface temperatures to increase until radiative energy balance is restored.

When feedbacks are allowed to operate, there is a further increase in atmospheric temperature, as is shown in Figure C53b. This is because the initial warming of the atmosphere by the amount ΔT_o due to doubled CO_2 forcing induces more evaporation of water vapor, causes additional melting of snow and sea-ice, increases the amount of high-altitude cirrus, and decreases low-level clouds – all of which act to magnify the original temperature change of the initial radiative forcing perturbation.

The all-feedback response, ΔT_s , can be thought of as being the sum of the applied no-feedback forcing, ΔT_o , plus a contribution, ΔT_f , that arises entirely due to feedbacks, such that $\Delta T_s = \Delta T_o + \Delta T_f$. In typical doubled CO_2 climate experiments, $\Delta T_o = 1.2^\circ\text{C}$, with the global mean temperature change attaining $\Delta T_s = 4.0^\circ\text{C}$ at equilibrium. The ratio f , by which the no-feedback forcing is magnified, is called the climate feedback factor, such that $\Delta T_s = f\Delta T_o$, which for current climate yields $f = 3.3$.

The strength of the climate feedback response is given by the ratio $g = \Delta T_f / \Delta T_s$, which is also called the feedback gain

factor, and for current climate is about 0.7 (see *Albedo feedbacks*). From this we see that the feedback gain factor is related to the feedback factor by $f = (1 - g)^{-1}$. In this formulation, the relative strengths of individual feedback processes can be directly compared because the gain factors for water vapor, snow and ice, and cloud feedbacks combine linearly in the form $g = g_w + g_s + g_c$. Thus, the climate system of the Earth is seen to operate with a strongly positive overall feedback so that a relatively small change in the gain efficiency of any one of the feedback processes can have a disproportionately large effect in magnifying an applied radiative forcing.

The largest uncertainty in estimating the climate system response to an applied radiative climate forcing is associated with determining the strengths of the various feedback processes, which depend on complicated physical interactions that are difficult to model. Radiative forcings, on the other hand, can be calculated with good accuracy and can be expressed in terms of either the adjusted forcing, ΔF_a , or the no-feedback forcing response, ΔT_o . The radiative forcing due to changes in atmospheric CO_2 is shown in Figure C54a, and in Figure C54b for CH_4 and N_2O .

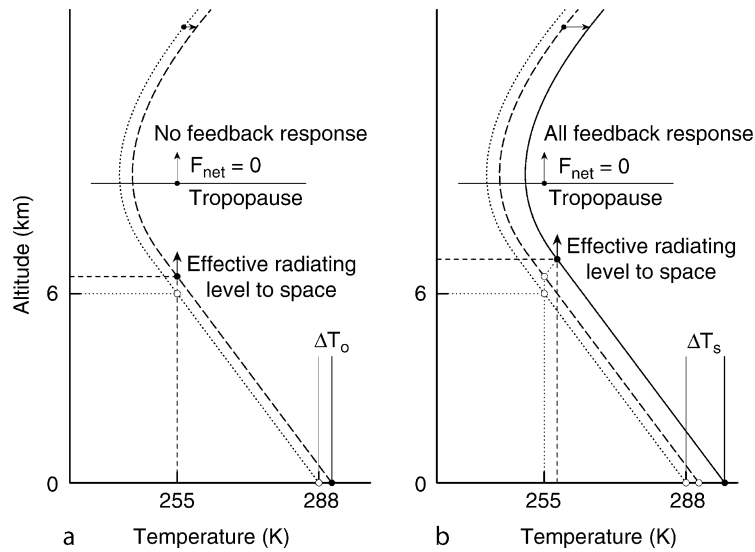


Figure C53 Schematic illustration of equilibrium response to doubled CO_2 . (a) No-feedback forcing response ΔT_o . (b) All-feedback response ΔT_s .

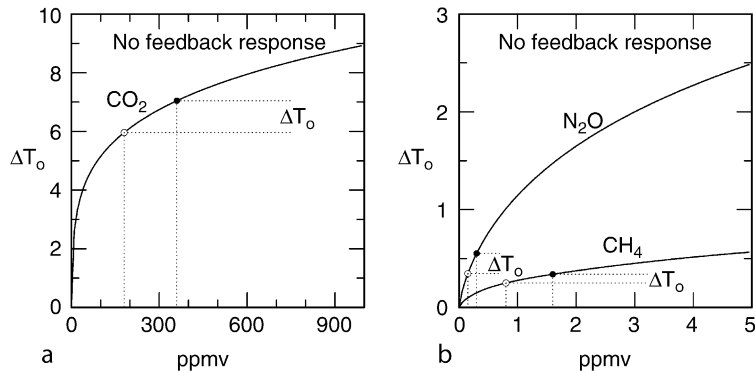


Figure C54 No-feedback forcing ΔT_o for (a) CO_2 , and (b) CH_4 and N_2O . Filled circles represent current atmospheric amounts. Open circles show ΔT_o for half of the current concentrations.

These no-feedback forcings show considerable saturation with increasing absorber concentration, particularly for CO₂. The curves are roughly logarithmic in nature; hence, the radiative forcing for a doubling of the gaseous concentration is not overly sensitive to the precise reference point. Also of note, if all CO₂ were removed from the atmosphere, the radiative forcing would be $\Delta T_0 \sim 7^\circ\text{C}$, and if we include also the radiative forcings for the current atmospheric amounts of CH₄, N₂O, the CFCs, and ozone, we obtain an additional $\Delta T_0 \sim 3^\circ\text{C}$. Together, the greenhouse forcing due to these non-volatile greenhouse gases (i.e., greenhouse gases that will not condense and precipitate from the atmosphere in response to temperature change) is approximately $\Delta T_0 \sim 10^\circ\text{C}$. The total greenhouse effect of the Earth's atmosphere (given by the difference between global mean surface temperature and the effective radiating temperature of the Earth) is $\Delta T_s \sim 33^\circ\text{C}$, which includes the contributions from all greenhouse gases, including water vapor, and also the greenhouse contribution due to clouds. From this, it follows that the ratio $f = \Delta T_s / \Delta T_0$, of the total terrestrial greenhouse effect to the total no-feedback forcing due to the non-volatile greenhouse gases, yields a climate sensitivity feedback factor of $f \sim 3.3$ for the entire atmosphere of the Earth, which is fully consistent with the feedback sensitivity that is obtained in climate change studies for relatively small climate forcings such as doubled CO₂.

Andrew A. Lacis

Bibliography

- Fleming, J.R., 1998. *Historical Perspectives on Climate Change*. NY: Oxford University Press, 194p.
- Hansen, J., Lacis, A., Rind, D., Russell, G., Stone, P., Fung, I., Ruedy, R., and Lerner, J., 1984. Climate sensitivity: Analysis of feedback mechanisms. In Hansen, J.E., and Takahashi, T. (eds.), *Climate Processes and Climate Sensitivity*, *Geophysical Monograph* 29, Washington, DC: American Geophysical Union, pp. 130–163.
- Hansen, J., Sato, M., and Ruedy, R., 1997. Radiative forcings and climate response. *J. Geophys. Res.*, **102**, 6831–6864.

Cross-references

- [Albedo Feedbacks](#)
- [Astronomical Theory of Climate Change](#)
- [Bolide Impacts and Climate](#)
- [Carbon Dioxide and Methane, Quaternary Variations](#)
- [Faint Young Sun Paradox](#)
- [Mass Extinctions: Role of Climate](#)
- [Maunder Minimum](#)
- [Paleoclimate Modeling, Quaternary](#)
- [Plate Tectonics and Climate Change](#)
- [Sun-Climate Connections](#)
- [Volcanic Eruptions and Climate Change](#)

CLIMATE VARIABILITY AND CHANGE, LAST 1,000 YEARS

Geologists and paleoclimatologists study the past on all time-scales as a basis for future predictions. The past is therefore highly relevant to modern climate change. It is essential to document past large-scale climate changes in order to place recent climate change in a longer-term context. The primary boundary conditions on the climate (e.g., Earth's orbital

geometry and global ice mass) have not changed appreciably over the past millennium. The variations in climate observed over this timeframe are hence likely to be representative of the natural climate variability that might be expected in the absence of any human influence. Placing modern climate change, including recent global warming, in a longer-term context can thus help establish the role of anthropogenic forcing (human greenhouse gas concentration increases and aerosol production) on past and future climate changes.

Approaches to estimating past changes

Instrumental meteorological records can only document large-scale climate changes over roughly the past 100–150 years. Relatively few instrumental records are available back into the eighteenth century. Several distinct approaches nonetheless exist for describing climate variations over a timeframe of roughly the past millennium. One such approach is the use of theoretical models of the climate system that are driven by estimated changes in external parameters or “forcings,” such as greenhouse gas concentrations and solar output, which tend to warm the climate, and the frequency and intensity of explosive volcanic eruptions, which tend to cool the climate through injecting reflective sulfate aerosol into the atmosphere (Free and Robock, 1999; Crowley, 2000; Gerber et al., 2003). This approach to reconstructing climate history is limited by the imperfectly known history of these changes in forcing, which are typically estimated indirectly from trapped gas, radioisotopes, and volcanic dust signals left behind in ice cores. Moreover, the reconstruction is limited by any uncertainties in the model's representation of actual climate processes and responses. Finally, the approach only indicates the forced component of climate change; it cannot estimate the possible role of internal dynamics (e.g., natural changes in ocean circulation) in the actual climate changes in past centuries, which are, in part, unpredictable from a model simulation.

Human documentary evidence provides another source for reconstructing climate in past centuries. Records of frost dates, droughts, famines, the freezing of water bodies, duration of snowcover, and phenological evidence (e.g., the dates of flowering of plants, and the ranges of various species of plants) can provide insight into past climate conditions (Wigley et al., 1981; Bradley, 1999). Furthermore, human accounts of mountain glacier retreats and advances during past centuries, widespread historical documentation of weather conditions, and even a handful of several centuries-long thermometer measurements are available in Europe for more than 1,000 years. Plentiful human documentary evidence is limited, however, to those regions (primarily Europe and Eastern Asia) where a written tradition existed. They are thus not useful for documenting truly global-scale climate variations. Human documentary records must furthermore be interpreted with caution, as they are not equivalent in their reliability to actual instrumental measurements of meteorological variables. Typically, these records provide indirect and potentially biased snapshots in time of potentially climate-related phenomena.

We must thus turn to more widespread, quantifiable measures of climate to document the large-scale climate variations of past centuries. Geological evidence from terminal glacial moraines indicating the advance of mountain glaciers in past centuries can also provide inferences into past climate changes. However, owing to the complex balance between local changes in melting and ice accumulation, and the effects of topography, all of which influence mountain glacier extents, it is difficult to

ascertain the true nature of temperature changes simply from evidence of retreat of mountain. Both increased winter precipitation and cooler summer temperatures can lead to the growth of a glacier, and large or even moderate glaciers respond slowly to any underlying climate changes (Folland et al., 2001). Estimates of long-term ground temperature trends from temperature profiles retrieved from terrestrial borehole data over the globe can also provide complementary large-scale information regarding ground-surface temperature trends in past centuries. However, impacts of changes in seasonal snow cover, land-surface changes, and other factors unrelated to surface air-temperature changes may complicate the interpretation of these data (Folland et al., 2001; Mann and Jones, 2003).

“Proxy” climate reconstruction

The most reliable estimates of climate changes in past centuries are provided by “proxy” indicators of climate change. These indicators are natural archives of information that, by their biological or physical nature, record climate-related phenomena. Certain proxy indicators, including most sediments cores, ice cores, and preserved pollen cannot record climate changes at high temporal resolution, and are thus generally not useful for reconstructing climate changes on centennial or shorter timescales. However, high-resolution, annually and/or seasonally resolved proxy climate records such as growth and density measurements from tree rings, laminated sediment cores, annually resolved ice cores, and isotopic information from corals can be used to describe year-to-year patterns of climate in past centuries (Jones et al., 2001; Mann, 2001). These indirect measurements of climate change vary considerably in their reliability as indicators of long-term climate. While tree-ring data are the most widespread source of annual proxy climate information, they are limited in a number of ways. They only provide information on sub-polar terrestrial regions, and generally, only extratropical species are useful for climate reconstruction. Thus, tree ring data are poorly representative of the full surface of the globe. The issue of how best to estimate climate variability on multi-centennial timescales from tree ring data, moreover, remains unresolved (Briffa and Osborn, 2002; Esper et al., 2002; Mann and Hughes, 2002), rendering long-term estimates based solely on tree ring data somewhat perilous. Coral information (e.g., oxygen isotopes and chemical species ratios that

respond to both temperature and salinity changes near the ocean surface), in contrast, offer information regarding tropical and subtropical climate changes, represent maritime regions, and continuously sample their environment over the full year. However, very long, multi-century records are rare, and the nature of the possible influence of “vital effects” (e.g., non-climatic influences on the coral’s biochemistry) has not yet been confidently established. Ice cores typically provide information from polar regions (and, in some cases, high-elevation tropical and extratropical environments), so that they are spatially complimentary to tree-rings and corals, but they sample a very small fraction of the global surface. An incontrovertible interpretation of ice-core oxygen isotopes in terms of e.g., atmospheric temperature variability, moreover, remains elusive, and precise annual dating is difficult. However, when taken together, and particularly when combined with historical documented information and the few long instrumental climate records available, these various proxy sources can provide a mutually complementary, global sampling (Figure C55) of climate changes in past centuries.

Such “multiproxy” assemblages of data can be used to reconstruct past large-scale patterns of surface temperature change, drought, and atmospheric circulation, by establishing a statistical relationship between the proxy data network and modern instrumental climate records (Mann, 2001). Indices of modes or patterns of climate variability, such as the El Niño/Southern Oscillation or ENSO and the North Atlantic Oscillation (NAO), which may play an important role in determining patterns of past climate variability, can also be reconstructed in a similar manner (see e.g., Jones et al., 2001 for a summary). This approach has also been used to reconstruct annual patterns of surface temperature change in past centuries (Mann et al., 1998; Briffa et al., 2001). Hemispheric or global mean surface temperature estimates can be derived by spatial averaging of such estimates of past large-scale patterns of surface temperature change. It is most meaningful to estimate the average surface temperature changes for the Northern Hemisphere, where considerably more widespread past data is available (e.g., Figure C55).

Climate history of the past 1,000 years

Climate reconstructions from proxy data networks have allowed for reconstructions of large-scale temperature patterns

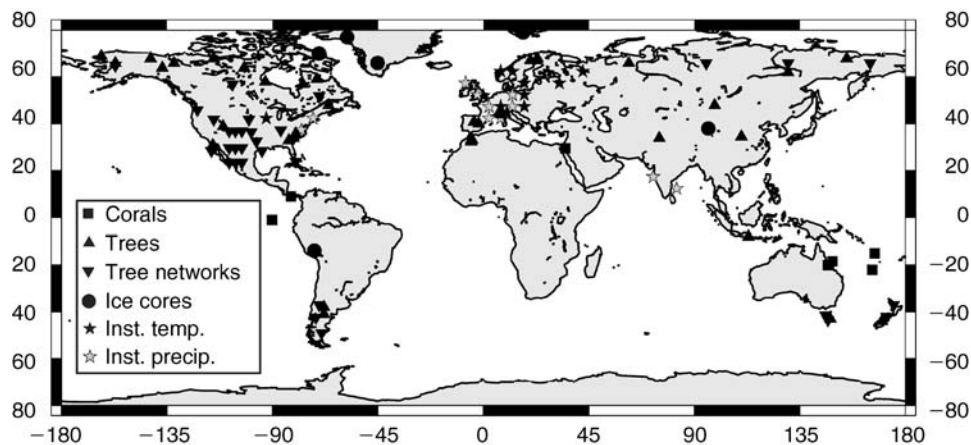


Figure C55 Geographic distribution of “proxy” and historical/instrumental indicators used in large-scale annual surface temperature reconstructions back to AD 1400 (adapted from Mann et al., 1998).

over roughly the past millennium. The detailed spatial patterns of these reconstructions provide insights into the underlying governing factors. For example, substantial patterns of warming and cooling over the extratropical Northern Hemisphere that vary from year-to-year appear to relate to the influence of the North Atlantic Oscillation (NAO) or Arctic Oscillation (AO) atmospheric circulation pattern. A related pattern of climate variability that appears to have an origin in internal, natural variations in the North Atlantic ocean-atmosphere system (Delworth and Mann, 2000) also appears to be important on multidecadal and century timescales. Other patterns of surface temperature variability appear to be associated with the global impacts of the El Niño/Southern Oscillation phenomenon. The complexity of the resulting regional variations in temperature trends underscores the premise that it is perilous to draw conclusions regarding hemispheric or global temperature trends from isolated regional information.

Different estimates of Northern Hemisphere mean temperature changes over the past millennium have been made, using different sources of proxy data, some of which are representative of the full Northern Hemisphere, and others which are more indicative of the extratropical regions of the Northern Hemisphere. These reconstructions can also be compared with model estimates of forced Northern Hemisphere mean temperatures changes over the past millennium (Figure C56). These various estimates indicate relatively modest variations in Northern Hemisphere mean temperature over the past 1,000 years, prior to the marked warming of the twentieth century. Hemispheric mean temperatures appear, for example, to have been slightly higher (by a couple of tenths of a degree Celsius) during the period AD 1000–1400 relative to the later, colder period AD 1400–1900 (associated, respectively, with the often-used labels of “Medieval Warm Period” and “Little Ice Age”). However, even the early interval of relative warmth does not approach the magnitude of the hemispheric warmth

of the latter twentieth century. The modest estimated changes in Northern Hemisphere average temperatures are consistent with evidence of the amplitude of natural (pre-anthropogenic) changes in the carbon cycle estimated from long-term carbon dioxide measurements (Gerber et al., 2003).

Some reconstructions of hemispheric temperature changes based on extratropical, continental tree-ring data suggest wider swings in temperature, including greater cooling during the seventeenth to nineteenth century than is evident in the instrumental, model, or other proxy-based estimates (Esper et al., 2002). The greater variability in this case probably arises from the emphasis on extratropical continental regions and the exclusive use of summer-temperature-sensitive tree ring chronologies (Mann, 2002). While European temperatures, for example, indicate a distinct cold phase from the seventeenth to nineteenth centuries, most hemispheric estimates (Figure C56) suggest a relatively steady, long-term cooling. It is probable that greater cooling in continental regions such as Eurasia and North America during the “Little Ice Age” resulted from changes in the NAO atmospheric circulation pattern. Recent evidence suggests that the NAO can be altered, for example, by changes in the output of the Sun (Shindell et al., 2001). Such changes may have led to enhanced winter cooling in Europe during the eighteenth century, when solar output was slightly weaker, and winter atmospheric circulation patterns in Europe appear to have been significantly altered, favoring exposure to cold, dry, Siberian air masses. Other complications arise from the use of summer temperature-sensitive tree-ring proxy information alone, which may exaggerate the cooling response to volcanic eruptions, which is greatest both over the continents and during summer (Mann, 2002).

Ground temperature changes estimated from boreholes in past studies (Huang et al., 2000) appeared to conflict with the hemispheric temperature trends evident in the instrumental and proxy-based estimates shown in Figure C56. Recent work has shown, however, that once these estimates are adjusted

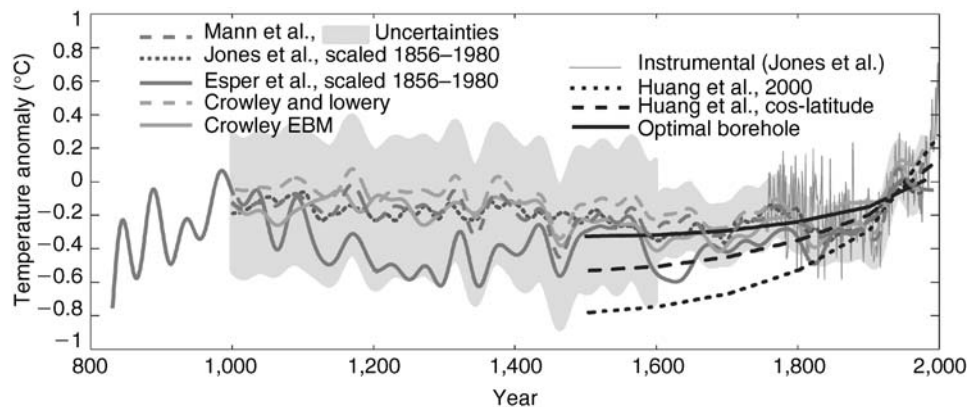


Figure C56 Comparison between various estimates of Northern Hemisphere temperature changes in past centuries. Annual mean Northern Hemisphere surface temperatures are reconstructed from proxy data (Crowley and Lowery, 2000; Mann et al., 1999) and theoretical energy balance models (Crowley, 2000), as well as *warm-season, extratropical Northern Hemisphere* temperature trends (Esper et al., 2002; Jones et al., 1998), scaled to match the *full Northern Hemisphere annual* temperature record for direct comparison (Jones et al., 1999). The smoothed reconstructions highlight variations on timescales greater than 40 years; uncertainties (95% confidence interval) in the smoothed Mann et al. (1999) reconstruction are also shown, as are the instrumental Northern Hemisphere temperature records through the mid eighteenth century (Mann and Jones, 2003). Estimates of ground surface temperature changes from terrestrial borehole data based are also shown, based on (a) a simple (unweighted) arithmetic average of available borehole data (Huang et al., 2000), (b) an areal-weighted average of the borehole data, and (c) statistically optimal hemispheric surface temperatures from available borehole data (Mann and Jones, 2003).

for spatial sampling biases (Briffa and Osborn, 2002; Mann and Jones, 2003) and the influence of factors unrelated to annual mean surface temperature changes, such as changes in the extent and duration of seasonal snowfall (Mann and Jones, 2003), the borehole estimates come into reasonable agreement with the other proxy and model-based estimates (Figure C56).

Implications

Recent research seeking to reconstruct and model climate changes of the past 1,000 years highlights the importance of taking into account regional variations in estimating climate changes in past centuries. While reconstructions of Northern Hemisphere temperature changes in past centuries, for example, confirm other (e.g., human documentary) evidence of the phenomenon of a 1–2 °C cooling in the winter during the “Little Ice Age” of the seventeenth to nineteenth centuries in Europe, they do not indicate a continuous period of similar magnitude cooling that is synchronous with cold conditions in Europe. The best current estimates suggest modest amplitude changes (considerably less than 1 °C) at the hemispheric scale, prior to the twentieth century warming trend. While internal climate factors are important in describing regional patterns of climate change, most of the observed variations in hemispheric mean temperature are consistent with the response of the climate to external forcing including volcanic and solar influences and, during the twentieth century in particular, anthropogenic influences. The comparisons between estimated and modeled changes imply a sizeable sensitivity of the climate system to anthropogenic influences of roughly 2 °C warming for a doubling of carbon dioxide concentrations from their pre-industrial levels.

Michael E. Mann

Bibliography

- Bradley, R.S., 1999. *Paleoclimatology: Reconstructing Climates of the Quaternary*. San Diego: Harcourt, Academic Press, 610pp.
- Briffa, K.R., and Osborn, T.J., 2002. Blowing hot and cold. *Science*, **295**, 2227–2228.
- Briffa, K.R., Osborn, T.J., Schweingruber, F.H., Harris, I.C., Jones, P.D., Shiyatov, S.G., and Vaganov, E.A., 2001. Low-frequency temperature variations from a northern tree ring density network. *J Geophys. Res.*, **106**, 2929–2941.
- Crowley, T.J., 2000. Causes of climate change over the past 1000 years. *Science*, **289**, 270–277.
- Crowley, T.J., and Lowery, T., 2000. How warm was the Medieval Warm Period? *Ambio*, **29**, 51–54.
- Delworth, T.L., and Mann, M.E., 2000. Observed and simulated multidecadal variability in the Northern Hemisphere. *Clim. Dyn.*, **16**, 661–676.
- Esper, J., Cook, E.R., and Schweingruber, F.H., 2002. Low frequency signals in long tree-ring chronologies for reconstructing past temperature variability. *Science*, **295**, 2250–2253.
- Folland, C.K., Karl, T.R., Christy, J.R., Clarke, R.A., Gruza, G.V., Jouzel, J., Mann, M.E., Oerlemans, J., Salinger, M.J., and Wang, S.-W., 2001. Observed climate variability and change. In Houghton, J.T. et al., (eds.) *Climate Change 2001: The Scientific Basis*. Cambridge, UK: Cambridge University Press, pp. 99–181.
- Free, M., and Robock, A., 1999. Global warming in the context of the Little Ice Age. *J. Geophys. Res.*, **104**, 19057–19070.
- Gerber, S., Joos, F., Bruegger, P.P., Stocker, T.F., Mann, M.E., Sitch, S., and Scholze, M., 2003. Constraining temperature variations over the last millennium by comparing simulated and observed atmospheric CO₂. *Clim. Dyn.*, **20**, 281–299.
- Huang, S., Pollack, H.N., and Shen, P.-Y., 2000. Temperature trends over the past five centuries reconstructed from borehole temperature. *Nature*, **403**, 756–758.
- Jones, P.D., Briffa, K.R., Barnett, T.P., and Tett, S.F.B., 1998. High-resolution paleoclimatic records for the last millennium: Interpretation,

- integration and comparison with circulation model control-run temperatures. *The Holocene*, **8**, 455–471.
- Jones, P.D., New, M., Parker, D.E., Martin, S., and Rigor, J.G., 1999. Surface air temperature and its changes over the past 150 years. *Rev. Geophys.*, **37**, 173–199.
- Jones, P.D., Osborn, T.J., and Briffa, K.R., 2001. The evolution of climate over the Last Millennium. *Science*, **292**, 662–667.
- Mann, M.E., 2001. Climate during the past millennium. *Weather*, **56**, 91–101.
- Mann, M.E., 2002. The value of multiple proxies. *Science*, **297**, 1481–1482.
- Mann, M.E., and Hughes, M.K., 2002. Tree-ring chronologies and climate variability. *Science*, **296**, 848.
- Mann, M.E., and Jones, P.D., 2003. Global surface temperatures over the past two millennia. *Geophys. Res. Lett.*, **30**(15), 1820.
- Mann, M.E., Bradley, R.S., and Hughes, M.K., 1998. Global scale temperature patterns and climate forcing over the past six centuries. *Nature*, **392**, 779–787.
- Mann, M.E., Bradley, R.S., and Hughes, M.K., 1999. Northern Hemisphere temperatures during the Past Millennium: Inferences, uncertainties, and limitations. *Geophys. Res. Lett.*, **26**, 759–762.
- Shindell, D.T., Schmidt, G.A., Mann, M.E., Rind, D., and Waple, A., 2001. Solar forcing of regional climate change during the Maunder Minimum. *Science*, **294**, 2149–2152.
- Wigley, T.M.L., Ingram, M.J., and Farmer, G., 1981. Past climates and their impact on man: A review. In Wigley, T.M.L., Ingram, M.J., and Farmer, G. (eds.), *Climate and History*. Cambridge, UK: Cambridge University Press, pp. 3–50.

Cross-references

- [Climate Forcing](#)
[Little Ice Age](#)
[Medieval Warm Period](#)
[North Atlantic Oscillation \(NAO\) Records](#)
[Paleoclimate Proxies, an Introduction](#)
[Sun-Climate Connections](#)
[Volcanic Eruptions and Climate Change](#)

COAL BEDS, ORIGIN AND CLIMATE*

Introduction

Coal is defined in the Glossary of Geology (1997, p. 122) as follows:

“A readily combustible (sedimentary) rock containing more than 50% by weight and more than 70% by volume of carbonaceous material, including inherent moisture, formed from compaction and induration of variously altered plant remains similar to those in peat. Differences in the kinds of plant materials (type), in degree of metamorphism (rank), and in the range of impurity (grade) are characteristic of coal.”

Although coal, by definition, may be composed of nearly 50% mineral matter, most commercial-grade coal in the United States is mined from coal beds that generally contain less than 20% mineral matter by weight (excluding mineral partings), and commonly less than 10% by weight. The U.S. Geological Survey excludes impure coal/coal material containing more than 33% ash by weight from resource/reserve estimates (Wood et al., 1983, p. 8). Coal with these grade characteristics can develop only under very limited conditions of peat formation. Grade characteristics indicate that resource-quality coal beds are derived from peat that formed in environments that were relatively free of dissolved solids and mineral content.

*All rights reserved

Furthermore, in order to form commercial grade coal beds, the concentration of mineral matter in the original peat must have been relatively low, because metamorphism following burial of peat tends to increase mineral content. The heat and pressure involved in the transformation (metamorphism or “coalification”) of peat to coal liberates significant amounts of the original organic matter in the form of carbon dioxide, methane, and water. The liberation and loss of organic matter during this transformation (metamorphism) of peat to coal may effectively double the mineral content. For example, 25% mineral matter in peat (dry basis) may be concentrated to 50% mineral matter when peat is transformed (coalified) to a medium volatile rank coal.

Climate and peat/coal formation

Although modern wetlands containing organic-rich sediment occur in a variety of climate settings around the world, only those deposits that contain less than approximately 25% (dry basis) mineral matter should be considered as precursors for coal. Other organic-rich deposits where mineral matter concentrations are greater than 25% will become carbonaceous shale or marl following burial and metamorphism. Cecil et al. (1985) pointed out a relation between climate and modern precursors of most commercial-grade coal. These modern coal precursors occur predominantly in two types of peat-forming environments, designated as type A and type B (Table C6 and Table C7), which can be differentiated, respectively, by selected parameters and conditions of peat-formation.

The primary variables that control the mineral matter content of peat (i.e., peat quality) are nutrient availability and pH of peat-forming environments. Thus, the highest quality peat/coal precursors have the lowest mineral matter content, and

they tend to have both a low pH and a low nutrient status (oligotrophic conditions). Oligotrophic peat deposits occur under humid to perhumid climates (see Cecil, 2003 for climate definitions), where relatively high precipitation causes intense chemical weathering (leaching) and removal of soluble mineral matter from peat. These climates also cause removal of nutrients and alkaline materials from mineral soils (pedogenesis) that are spatially and temporally associated with peat formation. Mesotrophic peat deposits tend to occur where the climate is marginally humid. The quality of mesotrophic peat is marginal as a precursor to coal because nutrients are available that promote microbial decay of organic matter. Furthermore, the nutrients tend to remain sequestered in peat as mineral matter through ion exchange processes. Eutrophic peat deposits, by definition, have a relatively high nutrient status and they generally contain relatively high concentrations of alkaline materials, which result in a near neutral pH that is conducive to high rates of microbial degradation of organic matter. These deposits tend to occur in climates that are moist subhumid or sometimes in drier climates, where soluble salts are enriched in surficial waters through evapotranspiration. As a result, eutrophic peat is invariably enriched in mineral matter to the extent that the peat would become very impure coal or carbonaceous shale upon burial and metamorphism.

In the modern world, the distribution of peat deposits (as precursors of coal beds) empirically illustrates climate controls on peat formation. Laterally extensive, high quality (low ash) peat deposits form predominantly in regions where monthly precipitation approximates or exceeds evapotranspiration (humid to perhumid climates). These regions include certain global climatic belts and regions that have maritime climates. The most widespread modern global climate belt of peat formation

Table C6 Parameters and conditions that control peat formation for the two predominant types of peat-forming environments (modified from Cecil et al. (1985) with climate terminology from Cecil, 2003)

Parameter	Type A condition	Type B condition
Climate	Perhumid	Humid
Water source	Ombrogenous (rain)	Topogenous (rain water, surface water, and ground water)
Nutrient availability	Oligotrophic (impoverished)	Oligotrophic to mesotrophic to eutrophic (impoverished to rich)
pH	<4	4 to ~7
Eh	?	?
Microbial activity	Low (cellulose preserved)	High (cellulose degraded)
Mechanism of degradation	Primarily chemical	Primarily microbial

Table C7 Descriptors and relative characteristics of peat-forming environments (modified from Cecil et al., 1985)

Descriptors of peat environments	Type A characteristics	Type B characteristics
Surface morphology	Domed	Planar
Flora communities	Low diversity; Zoned distribution; Xeromorphic physiognomy	High diversity; Random distribution; Luxuriant physiognomy
Ash content	Uniformly low	Low to high
Sulfur content	Uniformly low	Low to high
Nitrogen content	Uniformly low	Low to high
Cation exchange capacity	High	High
Specific conductivity	Low	High
Base saturation	Low	High
[Ca ²⁺]	Low	High
Fiber content	Fibric	Hemic to sapric
Bioorganic sulfide	Low	High
Bioorganic methane	Low	High

occurs in the vicinity of 60° North latitude along the edge of the atmospheric polar front. Polar fronts result from high atmospheric pressure and descending air at the poles that moves out from the polar region where it is then overridden by warmer and moister air in the vicinity of 60° latitude. The cooling of the warmer and moister air as it rises results in condensation and precipitation at the polar front. Even though precipitation is not particularly high in the region of polar fronts, the climate is humid to perhumid because cool summer temperatures and often freezing winter temperatures inhibit evaporation. At 60° South latitude, however, the absence of landmasses precludes widespread peat at this latitude in the Southern Hemisphere.

Areally extensive peat deposits also occur in certain equatorial regions. Thick (up to 13 meters) and extensive (over 50 km across) modern deposits of domed peat occur in equatorial Indonesia and Malaysia. Domed peat deposits, whose moisture source is exclusively precipitation, form in this region in response to a perhumid climate. The perhumid climate results from the presence of the nearly permanent low pressure, induced by the rising air of the intertropical convergence zone (ITCZ). In addition, a maritime effect occurs as moisture-laden weak winds cool as they move inland and rise over the island landmasses, thus causing precipitation that supplements rainfall associated with the low pressure of the ITCZ.

Further examples of peat formation controlled by maritime climate can be found in the British Isles where prevailing westerlies from the Atlantic Ocean cool as they rise upon reaching landmasses. The cooling of the westerly winds results in precipitation that contributes to the formation of peat deposits that blanket upland slopes. The climate in this cool temperate region is humid to perhumid because humidity and precipitation (in the form of fog, mist, and rain) are relatively high, whereas evapotranspiration is relatively low. Although it is highly unlikely that blanket peat deposits in upland areas can be preserved in the rock record, such deposits nevertheless serve to illustrate the relation between peat formation and wet climates.

Summary and conclusions

Modern peat deposits that could be precursors of resource-quality coal beds occur predominantly under humid to perhumid climatic conditions (Cecil, 2003; Cecil and Dulong, 2003). By analogy, coal beds containing less than approximately 30% ash must have been derived from peat that formed under humid to perhumid climatic conditions. Although some coalified terrestrial organic matter may have been deposited in sedimentary strata that were deposited under a wider range of climatic conditions, resource-quality coal beds that are discrete and areally extensive accumulated under humid to perhumid paleoclimate conditions.

C. Blaine Cecil and Sandra G. Neuzil

Bibliography

- Cecil, C.B., 2003. The concept of autocyclic and allocyclic controls on sedimentation and stratigraphy, emphasizing the climatic variable. In Cecil, C.B., and Edgar, N.T. (eds.), *Climate Controls on Stratigraphy: SEPM (Society for Sedimentary Geology)*. Special Publication, 77, pp. 13–20.
- Cecil, C.B., and Dulong, F.T., 2003. Precipitation models for sediment supply in warm climates. In Cecil, C.B., and Edgar, N.T. (eds.), *Climate Controls on Stratigraphy: SEPM (Society for Sedimentary Geology)*. Special Publication, 77, pp. 21–27.

- Cecil, C.B., Stanton, R.W., Neuzil, S.G., Dulong, F.T., Ruppert, L.F., and Pierce, B.S., 1985. Paleoclimate Controls on Late Paleozoic Sedimentation and Peat Formation in the Central Appalachian Basin (U.S.A.). *Int. J. Coal Geol.*, 5, pp. 195–230.
- Jackson, J.A., (ed.), 1997. *Glossary of Geology*, 4th edn. American Geol. Institute, Virginia, 469p.
- Wood, G.H., Kehn, T.M., Carter, M.D., and Culberston, W.C., 1983. *Coal Resource Classification of the U.S. Geological Survey: Geological Survey Circular 891*. Reston, VA: U.S. Geological Survey, 65p.

Cross-references

- [Continental Sediments](#)
[Sapropels](#)
[Sedimentary Indicators of Climate Change](#)

COASTAL ENVIRONMENTS

Introduction

The coastal zone, extending from ca. 10 m depth on the inner shelf to the landward limit of tidal action in rivers, occupies a small fraction of the Earth's surface. Despite this, coastal deposits are an important component of the stratigraphic record because they contain a large amount of information about the environmental conditions that prevailed during deposition. The geomorphology of the coastal zone (Figure C57) and the characteristics and stratigraphic architecture of the corresponding deposits (Figure C58) are influenced by many interdependent factors. The most notable of these are: (a) the history of sea (or lake) level, which, together with sediment input, determines whether the coastline is migrating landward (i.e., transgressing) or seaward (i.e., regressing or prograding); (b) the relative influence of waves, tidal currents, and river outflow, which determines the nature of the resulting facies; (c) the geologic setting, which controls the uplift or subsidence history and the resulting stratigraphic stacking pattern of coastal deposits; and (d) the climate, which determines the sea-level history, the intensity of wave action, the amount of fluvial runoff, the presence of ice, and the role of plants and animals. The interaction of these many factors produces enormous geomorphic variability and complexity in both modern coastal environments (Bird, 2000; Woodroffe, 2002) and their ancient counterparts (Pratt et al., 1992; Reading and Collinson, 1996).

Relative sea-level history

The direction of shoreline movement is the single most important control on the geomorphology and preserved stratigraphic expression of coastal environments (Boyd et al., 1992). Regressive situations are associated with the seaward growth of deltas (Figure C57a, b), the development of strandplains (also called beach-ridge plains) by prograding beaches and shorefaces, and the seaward build-out of open-coast tidal flats (Figure C57c). On the other hand, barrier islands, lagoons, and estuaries (Figure C57d) exist only where there is, or very recently has been, transgression. Thus, such environments are particularly common along modern coasts because of the post-glacial sea-level rise. Here, we follow the geological definition of "estuary" proposed by Dalrymple et al. (1992), in which an estuary is a transgressive coastal embayment (usually a drowned river valley) that receives sediment from both river and marine sources. This definition is preferred to the salinity-based formulation of Pritchard

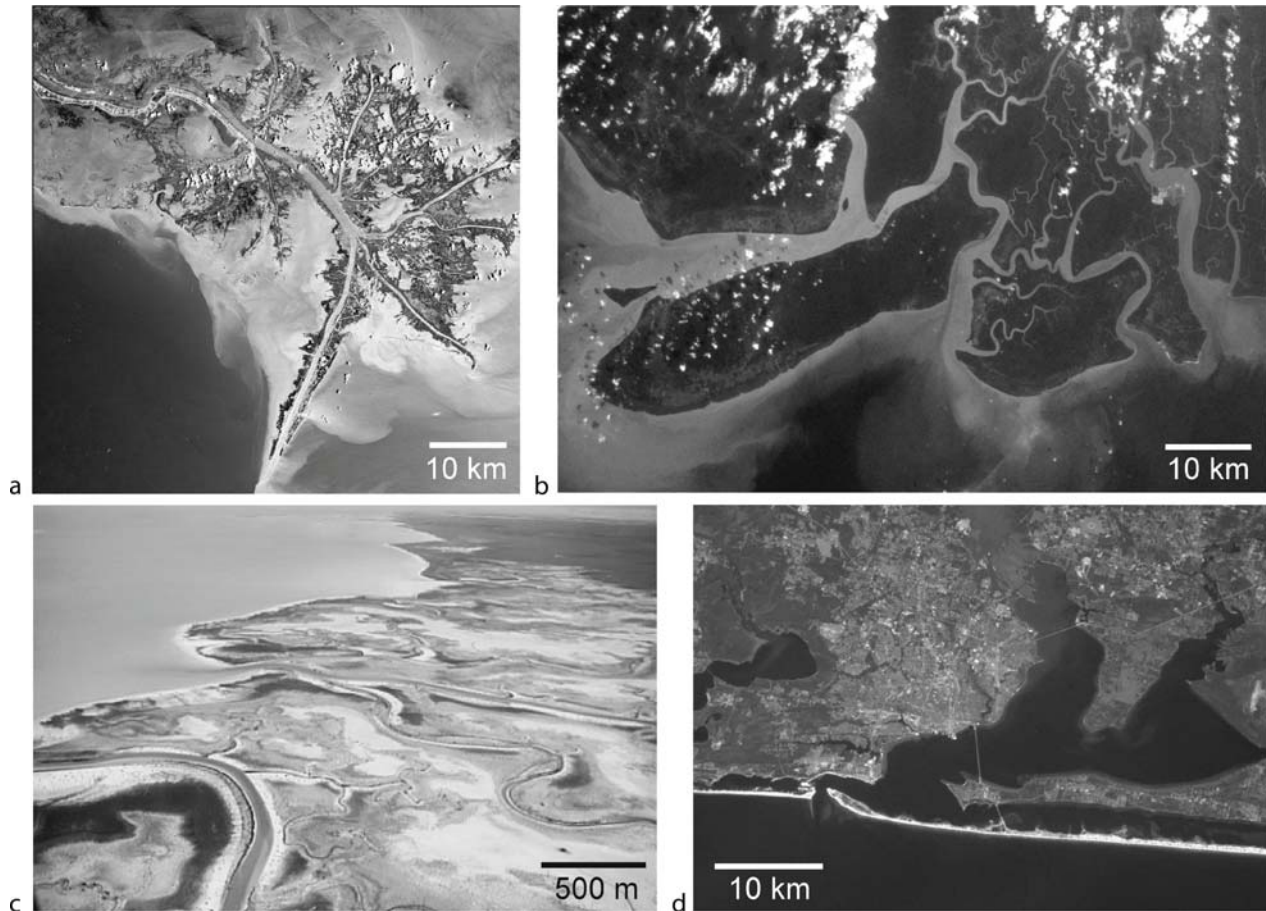


Figure C57 Typical examples of modern coastal environments. (a) The presently active birdsfoot delta of the Mississippi River, United States. Note the elongate distributary channels, flanked by levees and separated by shallow bays and marshes. (b) Subaerial plain of the tide-dominated Rajang River delta, Malaysia. Note the complex network of sinuous tidal channels. (c) Muddy, carbonate tidal flats, cut by meandering tidal channels, Andros Island, Bermuda. (d) Transgressive coast with barrier islands, tidal inlet, back-barrier lagoon, and drowned river-mouth estuaries (upper right), Pensacola, Florida, United States. The elongate area of land immediately behind the modern barrier is an older barrier island formed during a late Pleistocene highstand of sea level (all photos except c courtesy of NASA; c courtesy of N. P. James, Queen's University).

(1967), which considers any semi-enclosed coastal area with brackish water an estuary, regardless of whether it is regressive or transgressive.

The distinction between regressive and transgressive coasts is reflected in the vertical stacking pattern of coastal facies: shallower-water facies overlay deeper-water deposits in regressive settings, and the reverse in transgressive successions. Regressive successions are usually more or less complete and gradational (Figure C58a) because the shoreline is migrating into deeper water. Only in situations where regressions occur under conditions of falling sea level (i.e., a forced regression; Posamentier et al., 1992) is it common to generate a succession that may contain an erosion surface, with sandy, shallow-water facies lying abruptly on muddy, offshore deposits (Figure C58a). By contrast, transgressive successions are almost everywhere punctuated by one or more discontinuities (Figure C58b,c) at which the deposits of a more seaward environment lie abruptly on a more landward facies (e.g., brackish-water lagoonal mud overlying fluvial deposits). Such discontinuities are called flooding surfaces; if there is significant erosion, such as occurs where the shoreface migrates landward, they are also termed a ravinement surface (Figure C58a,c).

Physical processes

River currents, waves, and tidal currents are responsible for the geomorphology of coastal environments (Hayes, 1975; Wright, 1985; Boyd et al., 1992) and the nature of the associated deposits. Consequently, coastal environments and their ancient counterparts are commonly classified as river-, wave- or tide-dominated.

River-dominated coastal environments occur at the mouths of rivers, in settings where wave and tidal influence are not important, and generally consist of deltas with either a birds-foot or lobate morphology (Figure C57a; Wright, 1985). Distributary mouth bars occur directly seaward of the river mouth(s) and consist of a succession that passes upward from prodeltaic mud to the sand of the mouth bars. Interdistributary bays are developed between the distributary mouths (Figure C57a) and are sites where muddy and organic-rich sediments accumulate.

Wave-dominated coasts are generally straight or cusped, and are fronted by beaches that pass seaward into the shoreface and offshore shelf (Figure C57d). In progradational settings, progressive seaward migration of the coast produces a strandplain, on

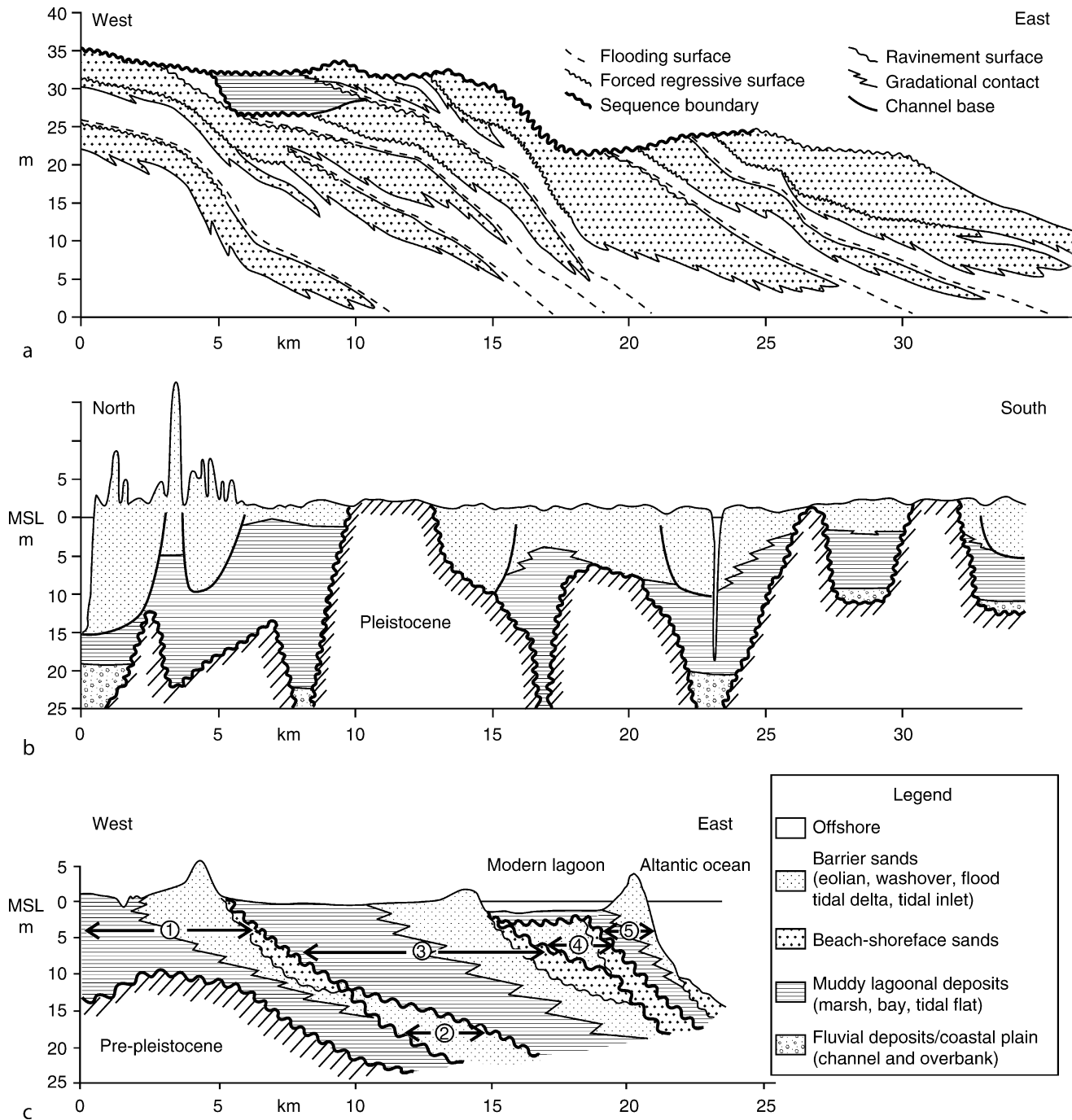


Figure C58 Vertical cross sections showing typical stratigraphic expressions of coastal deposits. (a) Prograding, wave-dominated shoreline, formed during a time of “greenhouse” climate. Note the episodic vertical offset of sandy beach-shoreface deposits, caused by small-scale sea-level changes. Iles Formation (Cretaceous), northwestern Colorado, United States (after Crabaugh, 2001, figure 2.8). (b) Coast-parallel section, Delaware, United States. The valleys cut during the last glacial maximum have been filled by a transgressive succession of fluvial, estuarine/lagoonal, and barrier-island deposits. All deposits above the -6 m level will be removed by landward migration of the shoreface, which will generate a ravinement surface (after Kraft et al., 1987, figure 3). (c) Coast-normal section perpendicular to **b**, showing the stacking and amalgamation of coastal deposits of five sea-level highstands during the Pleistocene. Each lowstand generated a through-going unconformity termed a sequence boundary. Each sequence (numbered oldest to youngest) contains a transgressive stacking of back-barrier mud and barrier-island sand. Note the erosional truncation of barrier sands in more down-dip areas. Most of this erosion is caused by transgressive shoreface ravinement. The greater degree of stratigraphic complexity relative to **a** is a result of the high-amplitude sea-level changes that characterized the “icehouse” conditions of the Pleistocene (after Demarest and Kraft, 1987, figure 4).

which eolian dunes may be important. The deposits generated by coastal progradation consist of a succession that coarsens upward from offshore mud into shoreface sand (Figure C58a). Such successions are abundant in the stratigraphic record and may be stacked on each other, reflecting repeated transgression and regression of the paleo-shoreline. Each upward-coarsening succession, termed a parasequence (Van Wagoner et al., 1988), is separated from the next one by a flooding surface, across which offshore shale rests abruptly on more nearshore deposits.

Transgressive, wave-dominated conditions are very common along modern coasts. Where the hinterland is low lying, as would be the case in most ancient sedimentary basins, the coastline is fronted by barrier islands that are separated by tidal inlets (Figure C57d). Drowned river-valley estuaries and lagoons lie behind these sandy islands. In such back-barrier areas, tidal action is commonly the dominant physical process. Tidal channels radiate from the tidal inlets, cutting through the flood-tidal deltas that lie immediately landward of inlets. Tidal flats rim the lagoons and estuaries; muddy deposits accumulate in the deeper-water areas. Bayhead deltas, which typically exhibit a river-dominated morphology, may be developed at river mouths. Such wave-dominated estuaries display a characteristic tripartite facies zonation, from sandy sediments at the barrier, through muddy lagoonal deposits, to more sandy sediments in the bayhead area, and are a common component of valley-fill successions (Figure C58b). The more seaward portions of the estuary, including the sandy barrier and related environments, are rarely preserved, however, because they are eroded by the landward passage of the shoreface, which generates a ravinement surface (Figure C58b).

Tide-dominated coastal environments most commonly occur in macrotidal areas (i.e., tidal ranges >4 m). At locations where there is a significant coast-normal tidal flux, a network of tidal channels is generally developed (Figure C57b,c). The migration of these channels produces an architecturally complex succession of lateral-accretion deposits. These deposits are commonly very heterolithic because of the high suspended-sediment concentrations. Tide-dominated sedimentation is favored in transgressive settings, because the flooding of an irregular topographic surface (i.e., a sequence boundary) generates many embayments that are sheltered from wave action and enhance the influence of tidal currents. However, large tidal ranges and tidal dominance can occur at any point in a relative sea-level cycle because tidal resonance is dependent on instantaneous, regional-scale basin morphology.

Geologic setting

The geologic setting creates the general context for the coastal zone. Coastal zones in tectonically active areas (e.g., coastlines on subducting or strike-slip continental margins, or in young rift basins) tend to be bordered by rugged hinterlands, especially if the location of the coastline is determined by an active fault. As a result, they are typically fed by small rivers that supply relatively coarse-grained sediment. The extent of estuarine environments is minimized because the steep fluvial gradient limits the intrusion of salt water and tidal action. Coastlines along passive continental margins or in foreland or intracratonic basins generally have lower gradients and may be fed by a smaller number of large rivers (Wright, 1985). The sediment reaching the river mouth is typically relatively fine-grained. Slow subsidence in tectonically stable areas causes transgressive coastal erosion to have a more profound influence than in areas of high subsidence rates. Thus, coastal deposits

will tend to be truncated to a greater degree, leading to a more fragmentary record of sea-level variations than in more rapidly subsiding areas (Figure C58c).

Influence of climate

Climate also influences the general context in which coastal environments exist. For example, the frequency and intensity of storms, which determine the intensity of wave action, is a function of the climatic belt. Mid-latitude coasts are subject to frequent storms, which favors the occurrence of high-energy, wave-dominated shorelines. By comparison, areas approximately 30° north and south of the equator tend to have low average wind speeds, with infrequent but intense hurricanes.

Humid climates have significant river flow, which delivers large amounts of sediment and fresh water to river mouths. This favors the development of deltas and prograding coastal environments, as well as the widespread occurrence of brackish-water conditions. Coastal vegetation is generally abundant and vegetated salt marshes are widespread in the upper intertidal zone (Luternauer et al., 1995). In tropical to sub-tropical settings, mangroves grow into the intertidal zone. Arid climates with high evaporation rates promote the development of hypersaline conditions in areas with limited tidal circulation (e.g., coastal lagoons and estuaries). Terrestrial vegetation is sparse and evaporite minerals such as gypsum and halite can grow in the surficial sediments of the intertidal zone. Caliche (also called calcrete) is commonly present in paleosols formed in areas with a semi-arid climate.

Organically produced carbonate sediment is abundant in areas with limited freshwater input and a consequent scarcity of terrigenous-clastic sediment. The nature of these carbonate sediments is strongly controlled by water temperature, as well as the availability of nutrients (James, 1997). In tropical and subtropical areas where water temperatures are higher than ca. 20°C, the fauna today is dominated by corals and calcareous algae that produce reefs. These reefs, together with the associated shallow carbonate platform, damp wave action and allow tidal flats to develop along many shorelines (Figure C57c). The repeated progradation and transgression of these flats produces stacked successions of upward-shallowing packages, typically 1–3 m thick, separated by flooding surfaces (Pratt et al., 1992). In temperate and polar areas, by contrast, reef-producing organisms do not thrive. Sediment-production rates are low and gently sloping offshore ramps occur instead of flat-topped platforms. Because of this, wave energy can reach the shoreline more readily, causing beaches to be more widespread than in tropical areas.

Polar areas experience seasonal or permanent growth of sea ice that limits the impact of wave energy. As a result, coastlines tend to be of lower energy and muddier than might be the case otherwise. Soft-sediment deformation caused by the grounding of ice pushed onshore by winds may be significant (Dionne, 1985). Permafrost is also an important constraint on coastal morphology.

Climate change at Milankovitch frequencies has had a profound influence on modern coastal areas because of the frequent, high-amplitude, sea-level cycles that have occurred throughout the “icehouse” conditions of the Quaternary. Each of the last few interglacial highstands has reached approximately the same elevation (Chappell et al., 1996), leading to the amalgamation and superposition of coastal deposits of significantly different ages but similar facies (Figure C58c). Significant time gaps (i.e., sequence boundaries) occur between these packages because of non-deposition and/or erosion

during the sea-level lowstands. For example, along much of the east and southern coasts of the United States, Holocene barrier-lagoon complexes lie only a short distance seaward of similar deposits of late Pleistocene age (Figure C57d; Demarest and Kraft, 1987). This leads to enormous stratigraphic complexity, especially in areas of low sediment supply. Sea-level oscillations with a similar period but much reduced amplitude probably occurred during “greenhouse” times such as the Cretaceous. Coastal deposits formed under these conditions may not show as much complexity because a smaller number of significant unconformities will be present (Figure C58a).

Summary

The coastal zone is arguably the most complex environment on earth because of the many independent factors that influence its characteristics. Pronounced spatial gradients in the intensity of the main physical processes (river currents, waves, and tidal currents) create complex assemblages of facies, which are then stacked in complex stratigraphic successions because of the migration of the shoreline in response to sea-level change and sediment addition or removal. The geologic setting and climate have less direct, but nevertheless important, influences on the nature of coastal environments. As a result of the interplay of these many factors, coastal deposits are a rich source of information about past environmental conditions.

Robert W. Dalrymple and Kyungsik Choi

Bibliography

- Bird, E., 2000. *Coastal Geomorphology: An Introduction*. New York: Wiley.
- Boyd, R., Dalrymple, R.W., and Zaitlin, B.A., 1992. Classification of coastal sedimentary environments. *Sediment. Geol.*, **80**, 139–150.
- Chappell, J., Omura, A., Esat, T., McCulloch, M., Pandolfi, J., Ota, Y., Pillans, B., 1996. Reconciliation of late Quaternary sea levels derived from coral terraces at Huon Peninsula with deep sea oxygen isotope records. *Earth Planet. Sci. Lett.*, **141**, 227–236.
- Crabough, J.P., 2001. *Nature and Growth of Nonmarine-to-Marine Clastic Wedges: Examples from the Upper Cretaceous Iles Formation, Western Interior Basin (Colorado) and the Lower Paleogene Wilcox Group of the Gulf of Mexico Basin (Texas)*. Ph.D. Thesis, Laramie, Wyoming: University of Wyoming.
- Dalrymple, R.W., Zaitlin, B.A., and Boyd, R., 1992. Estuarine facies models: Conceptual basis and stratigraphic implications. *J. Sediment. Petrol.*, **62**, 1130–1146.
- Demarest, J.M., II, and Kraft, J.C., 1987. Stratigraphic record of Quaternary sea levels: Implications for more ancient strata. In Nummedal, D., Pilkey, O.H., and Howard, J.D. (eds.), *Sea-Level Fluctuation and Coastal Evolution*. Tulsa, OK: SEPM, Society of Economic Paleontologists and Mineralogists, Special Publication 41, pp. 223–239.
- Dionne, J.-C., 1985. Formes, figures et faciès sédimentaires glaciels des estrans vaseux des régions froides. *Palaeogeogr. Palaeoclimatol. Palaeoecol.*, **51**, 415–451.
- Hayes, M.O., 1975. Morphology of sand accumulations in estuaries: An introduction to the symposium. In Cronin, L.E. (ed.), *Estuarine Research*, vol. II. New York: Academic Press, pp. 3–22.
- James, N.P., 1997. The cool-water carbonate realm. In James, N.P., and Clarke, A.D. (eds.), *Cool-Water Carbonates*. Tulsa, OK: SEPM, SEPM (Society for Sedimentary Geology), Special Publication 56, pp. 1–20.
- Kraft, J.C., Chrzastowski, M.J., Belknap, D.F., Toscano, M.A., and Fletcher, C.H., III, 1987. The transgressive barrier-lagoon coast of Delaware: Morphostratigraphy, sedimentary sequences and responses to relative rise in sea level. In Nummedal, D., Pilkey, O.H., and Howard, J.D. (eds.), *Sea-level Fluctuation and Coastal Evolution*. Tulsa, OK: SEPM, Society of Economic Paleontologists and Mineralogists, Special Publication 41, pp. 129–143.
- Luternauer, J.L., Atkins, R.J., Moody, A.I., Williams, H.F.L., and Gibson, J.W., 1995. Salt marshes. In Perillo, G.M.E. (ed.), *Geomorphology and Sedimentology of Estuaries. Developments in Sedimentology*, vol. 53. Amsterdam: Elsevier. pp. 307–332.
- Posamentier, H.W., Allen, G.P., James, D.P., and Tesson, M., 1992. Forced regressions in a sequence stratigraphic framework: concepts, examples, and exploration significance. *Am. Assoc. Pet. Geol. Bull.*, **76**, 1687–1709.
- Pratt, B.R., James, N.P., and Cowan, C.A., 1992. Peritidal carbonates. In Walker, R.G., and James, N.P. (eds.), *Facies Models—Response to Sea-level Change*. St. John's: Geological Society of Canada, pp. 303–322.
- Pritchard, D.W., 1967. What is an estuary? Physical viewpoint. In Lauff, G.H. (ed.), *Estuaries*. Washington, DC: American Association for the Advancement of Science. AAAS Publication 83, pp. 3–5.
- Reading, H.G., and Collinson, J.D., 1996. Clastic coasts. In Reading, H.G. (ed.), *Sedimentary Environments: Processes, Facies and Stratigraphy*. Oxford: Blackwell Science, pp. 154–231.
- Van Wagoner, J.C., Posamentier, H.W., Mitchum, H.W., Vail, P.R., Sarg, J.F., Loutit, T.S., and Hardenbol, J., 1988. An overview of sequence stratigraphy and key definitions. In Wilgus, C.K., Hastings, B.S., Kendall, C.G. St. C., Posamentier, H., Ross, C.A., and Van Wagoner, J. (eds.), *Sea-level Changes – an Integrated Approach*. Tulsa, OK: SEPM, Society of Economic Paleontologists and Mineralogists, Special Publication 42, pp. 39–45.
- Woodroffe, C.D., 2002. *Coasts: Form, Process and Evolution*. Cambridge, UK: Cambridge University Press.
- Wright, L.D., 1985. River deltas. In Davis, R.A., Jr. (ed.), *Coastal Sedimentary Environments*, 2nd edn. New York: Springer, pp. 1–76.

Cross-references

[Astronomical Theory of Climate Change](#)
[Carbonates, Cool Water](#)
[Carbonates, Warm Water](#)
[Cretaceous Warm Climates](#)
[Deltaic Sediments, Climate Records](#)
[Glacial Eustasy](#)
[Greenhouse \(warm\) Climates](#)
[Icehouse \(cold\) Climates](#)
[Sea Level Change, Last 250 Million Years](#)
[Sea Level Change, Post-Glacial](#)
[Sea Level Change, Quaternary](#)
[Sea Level Indicators](#)
[Sedimentary Indicators of Climate Change](#)

COCCOLITHS

Coccoliths are an important group of microfossils much used in paleoceanographic studies. They are minute (typically 1–10 μ) calcite platelets that are produced by unicellular planktonic algae, coccolithophores. In life, the individual coccolithophore cell is typically almost entirely covered by coccoliths, forming an exoskeleton or coccosphere. In the fossil record, coccoliths are often accompanied by nannoliths, i.e., similar sized calcite fossils of uncertain affinities (e.g., discoasters, nannoconids). Geologists study coccoliths and nannoliths together and refer to them as calcareous nannofossils.

Coccolithophores belong to the algal division (phylum) Haptophyta, which also includes many non-calcifying taxa (e.g., *Phaeocystis*, *Prymnesium* and *Pavlova*). Haptophytes are distinguished from other algae by their possession of two smooth flagella and a unique third flagellum-like organelle, the haptonema. Molecular genetic research has confirmed that the Haptophyta are a discrete clade that probably diverged from other protists in the Early Paleozoic and subsequently

acquired chloroplasts by endosymbiosis, possibly in the Early Mesozoic. Non-calcifying haptophytes, especially *Phaeocystis*, are important in shelf environments but coccolithophores are predominant in oceanic environments and the only group with a fossil record. The coccolithophore *Emiliana huxleyi* produces spectacular blooms with very high abundances of loose liths, which are readily identified by satellite (Figure C59).

Haptophytes typically have a life-cycle with discrete haploid and diploid phases, both of which are capable of indefinite asexual reproduction (Billard, 1994). In coccolithophores, the two phases produce different coccolith types. The haploid phase is usually motile and if it calcifies, it produces coccoliths formed of numerous euhedral crystallites; these “holococcoliths” are very small and rarely preserved. The diploid phase is often non-motile (i.e., flagella and haptonema are not developed) and produces more robust coccoliths formed of a few radial cycles of elaborate-shaped interlocking crystal units – “heterococcoliths” (Young et al., 1999). Both life-cycle stages are fully planktonic and there is no cyst-stage in the life cycle. The alternation between two life-cycle strategies may, however, aid adaptation to the open-marine environment – the haploid holococcolith-bearing phase typically occurs in shallower and more oligotrophic environments than the diploid heterococcolith-bearing phase. The haploid phase may also be mixotrophic. In any case, it is clear that coccolithophores are particularly well-adapted to oligotrophic open-ocean conditions and they often dominate the phytoplankton in such areas. In more eutrophic areas, coccolithophore numbers may increase but they become subordinate to the much more abundant diatoms. Similarly, coccolithophore blooms usually occur later in the seasonal succession than diatom blooms (Winter and Siesser, 1994).

In the fossil record, coccoliths are very important as open ocean sediment formers. They are usually the dominant calcareous component of pelagic deposits, including both Late Cretaceous chalks and modern deep sea oozes. They have proven invaluable as biostratigraphic marker fossils in such sediments and are the prime means of dating sediments recovered by the DSDP and ODP projects (Bown, 1998). Despite the minute size of coccoliths, such studies are usually carried out by light microscope, since the high birefringence of calcite means they are readily identified in cross-polarized light. Electron microscopy is only used for special studies. Numerous studies of nanofloral change have elucidated responses of coccoliths to oceanographic change and they can provide key constraints to hypotheses of change in the phytoplankton

based on indirect geochemical evidence – e.g., an inference of productivity change based on carbon isotopes can be tested by determining if concomitant change occurs in the phytoplankton. However, reliable quantitative nanofloral proxies and transfer functions are still at a relatively early state of development. The most important coccolithophore-derived geochemical proxy is the uk37 alkenone paleothermometer. There has also been much recent study of stable isotope and Sr/Ca records from coccoliths.

Jeremy R. Young

Bibliography

- Billard, C., 1994. Life cycles. In Green, J.C., and Leadbeater, B.S.C. (eds.), *The Haptophyta Algae*. Oxford: Clarendon Press, 51, pp. 167–186.
- Bown, P.R., 1998. *Calcareous Nannofossil Biostratigraphy*. British Micropalaeontological Society Publication Series, London: Chapman & Hall, pp. 315.
- Young, J.R., Davis, S.A., Bown, P.R., and Mann, S., 1999. Coccolith ultrastructure and biomineralisation. *J. Struct. Biol.*, 126, 195–215.
- Winter, A., and Siesser, W.G. (eds.), 1994. *Coccolithophores*. Cambridge, UK: Cambridge University Press, pp. 242.

Cross-references

[Alkenones](#)
[Dating, Biostratigraphic Methods](#)
[Deep Sea Drilling Project \(DSDP\)](#)
[Diatoms](#)
[Marine Biogenic Sediments](#)
[Ocean Drilling Program \(ODP\)](#)

COHMAP

Introduction

Climate change is global in scope, multivariate in character, and varies both temporally and spatially. Single investigator studies of sediment cores can provide individual data points for studying past climate, but as CLIMAP (Climate: Mapping and Prediction) demonstrated, it takes internationally and inter-institutionally organized groups of interdisciplinary investigators to compile the global data sets and models needed to construct a global view. Patterned after CLIMAP (1981), COHMAP (Cooperative Holocene Mapping Project) featured researchers who assembled continental-to-global data sets primarily of radiocarbon-dated pollen and lake-level data and analyzed these data to produce time series of maps of estimated climate variables that show the changing synoptic patterns of climate change during the late Quaternary. During its 18 years of existence from 1977 to 1995, COHMAP evolved from four principal investigators focusing on mapping late Quaternary climates in eastern North America to over 30 cooperating scientists who together were mapping and modeling the temporal changes in spatial patterns of climate from all continents but Antarctica, and from the Atlantic, Pacific, and Indian Oceans (Wright et al., 1993). Starting with the Last Glacial Maximum (LGM) at 21,000 calendar years ago (or 18,000 radiocarbon yBP), COHMAP members twice made a sequence of model runs that showed the simulated impact of the changing boundary conditions on late Quaternary climates (Kutzbach et al., 1993, 1998) and then thoroughly checked the model results against the data (COHMAP, 1988; Wright et al., 1993; Webb,

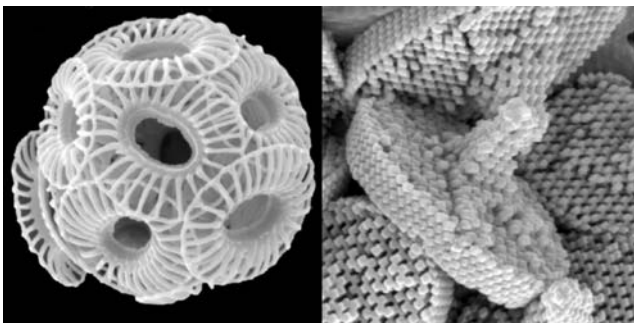


Figure C59 Left: Coccosphere of *Emiliana huxleyi* heterococcoliths. Right: Several *Helicosphaera carteri* holococcoliths.

1998). A key finding was the direct impact of orbitally forced changes in seasonal insolation on monsoon climates in Africa and southern Asia (Kutzbach, 1981; Kutzbach and Street-Perrott, 1985), which demonstrated how the climate forcing postulated by Adhemar, Croll, and Milankovitch (Imbrie and Imbrie, 1979) affected tropical climates without ice sheets being involved. By formulating a mechanism involving the enhancement and weakening of monsoons and then testing its plausibility with models and data, COHMAP investigators discovered one way for orbital forcing to affect global climates throughout Earth history. Geological evidence showing periodic frequencies on orbital time scales is abundant from the Permian, Triassic, Cretaceous, and other geological periods (DeBoer, 2004).

History, investigators, and meetings

COHMAP was a group of active researchers interacting and collaborating in productive ways (Wright and Bartlein, 1993). The group began as the brainchild of H. E. Wright and E. J. Cushing, established Quaternary geologists and paleoecologists, and J. E. Kutzbach and T. Webb III, meteorologically trained paleoclimatologists, who were both students of R. A. Bryson from whom they gained training in climate history and climate dynamics. In initial discussions at the 1974 AMQUA (American Quaternary Association) meetings in Madison, WI, these researchers identified a major opportunity to compile radiocarbon-dated pollen data into continental data sets for mapping and climatic reconstructions (Webb and Bryson, 1972). By 1977, when they were first funded by the National Science Foundation (NSF), the project had the potential to check the results of general circulation models (Peterson et al., 1979). Within a year, they began collaborating with F. A. Street-Perrott, who was developing a global lake level database and had good dated coverage in Africa and other tropical areas where pollen data were sparse (Street and Grove, 1979). Street-Perrott soon became a member of the executive committee along with paleoceanographers W. Ruddiman and W. Prell, who provided a CLIMAP perspective and SST estimates from the Atlantic, Pacific, and Indian Oceans, where sedimentation rates were high enough to allow resolution within the Holocene. In the early 1980s, P. J. Bartlein added his climatic, statistical, and cartographic expertise to the leadership group. By then, Kutzbach (1980, 1981) had developed methods for estimating precipitation from lakes levels and had begun using general circulation models (GCMs) to simulate the impact of orbital forcing of Holocene climates. The modeling studies evolved into a time series of runs in 3,000 year intervals from 18,000 radiocarbon years ago to present (Kutzbach et al., 1993). With a goal of global mapping of pollen and lake level data for data/model comparisons, the COHMAP executive committee recruited regional experts for acquisition, quality control, and interpretation of the pollen and lake-level data (COHMAP, 1988; Wright et al., 1993). A policy of subsidizing the radiocarbon dating of pollen data from critical areas encouraged many North American palynologists to contribute their data to the North American database.

Key to research planning and coordination was regular meetings involving either just the executive committee members or all cooperating scientists. At these meetings, investigators shared their expertise and educated each other across their diverse disciplines. They gained a common understanding of the global controls on the climate system and its spatio-temporal nature of variation. With a sophisticated view of the climate system, they used climate-modeling results to simulate possible changes in circulation patterns and teleconnections that helped explain

why the timing and magnitude of changes in the data differed among regions. They also used their continental-to-global data sets to test the accuracy of the model simulations. The meetings allowed both the modelers and the data compilers to learn from each other and to formulate productive plans for mutual research. Root and Schneider (1995) cited COHMAP as a model for “cooperative SCS (strategic cycle scaling)-like research” because of its integration of modeling and data analysis and its “interdisciplinary multi-institutional research” and education.

Key methods, findings and new concepts

In the beginning, COHMAP researchers aimed to compile and add to sets of modern and fossil pollen data for climate calibration and mapping in eastern North America. The goal was to map geographic patterns of vegetation and climate variables that show how and perhaps even why past climates had changed. Fieldwork was central to the project in order to fill gaps in the data networks, especially in critical regions. The Radiocarbon Laboratory directed by Margaret Bender at the Center for Climatic Research in Madison, Wisconsin, provided many dates to improve chronologies within sites with fossil pollen data. Two sets of pollen data were compiled. One was a calibration data set of over 900 sites with modern pollen data collected from surface sediments. When combined with the modern climate data for each site, these data were used to calculate transfer functions and later response surfaces that provided estimates of climate variables from the fossil pollen data (Bartlein et al., 1984, 1986). The fossil pollen data were in the second data set, which included site information, the pollen counts, and depth-date files for constructing chronologies. These data sets are now archived

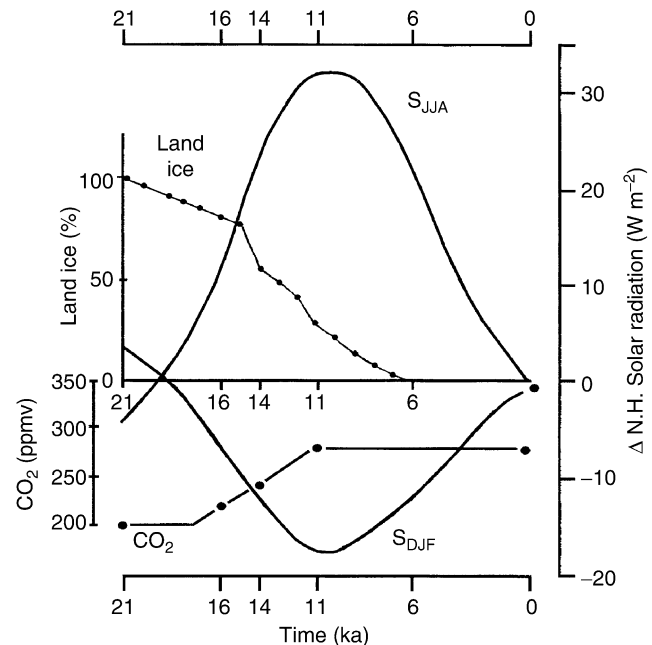


Figure C60 Changes in key climate controls during the last 21,000 years including (1) percentage coverage by terrestrial ice sheets, (2) concentration of atmospheric carbon dioxide, and (3) orbitally controlled insolation at the top of the atmosphere for the northern hemisphere for summer (June, July, and August) and winter (December, January, and February) (modified from Kutzbach et al., 1998).

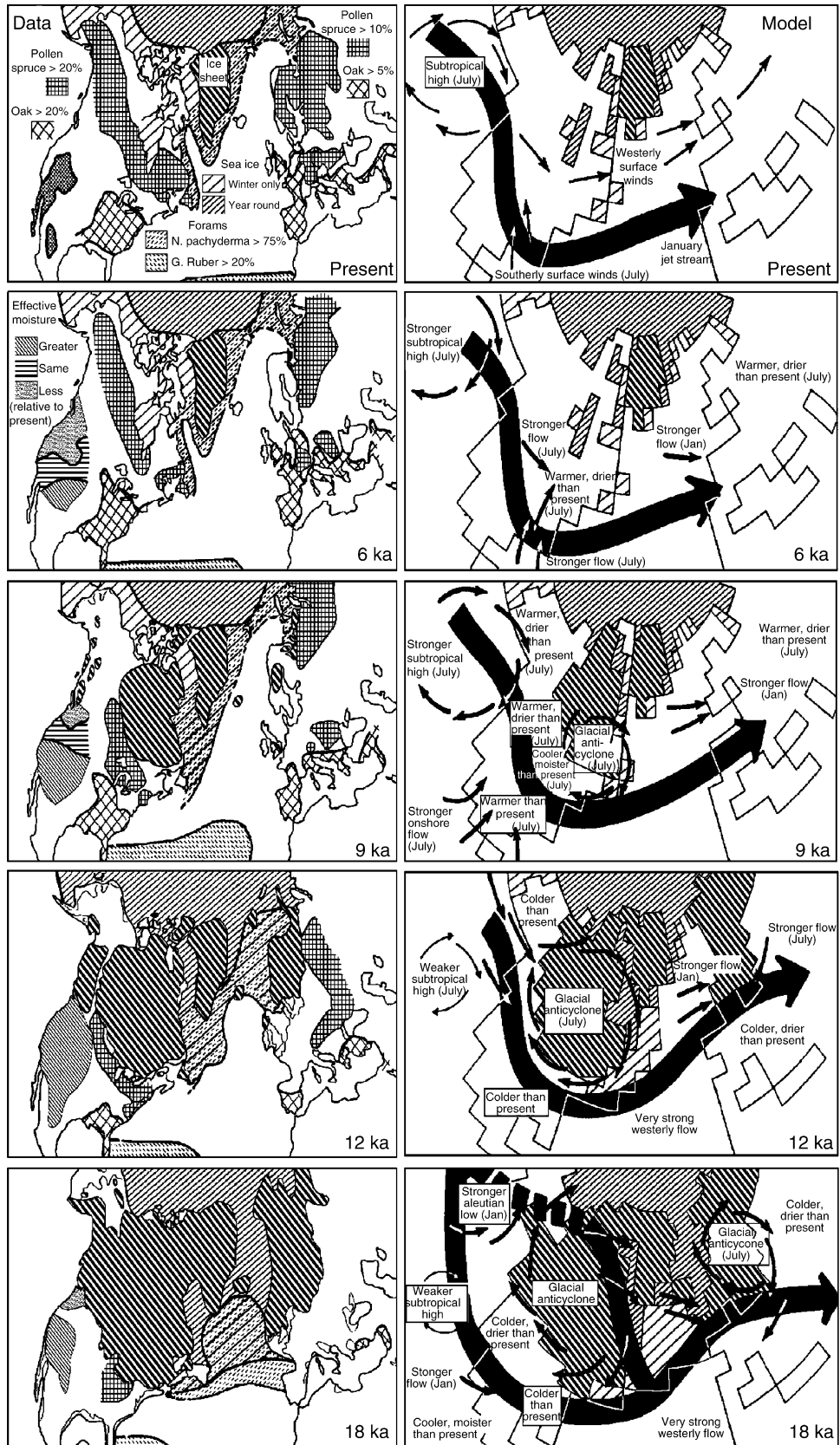


Figure C61 Continued.

and in active use at the NOAA World Data Base (<http://www.ngdc.noaa.gov/paleo/napd.html>).

With the addition of climate modeling, lake level data, and pollen data from other regions, the COHMAP effort expanded to a global program with a focus on comparing maps and time series of the model results with the data (Wright et al., 1993). CLIMAP's modeling of the LGM at 18,000 radiocarbon years ago or 21,000 calendar years ago was expanded by Kutzbach et al. (1993, 1998), who ran a global climate model to equilibrium with the boundary conditions at each 3,000-radiocarbon- or 5,000-calendar-year-interval between the LGM and present day (Figure C60). The climate model allowed COHMAP researchers to show the regional climatic impact of the broad-scale controls, such as ice sheet size, seasonal insolation, and greenhouse gas concentrations. The modeling results aided development of conceptual models for late Quaternary climate changes by illustrating mechanisms and circulation changes, and provided results that could be compared and thus tested by the data (Figure C61). Because the successful testing of the model results was key to their use in helping to explain late Quaternary climate changes, COHMAP researchers developed several methods for comparing the data to the model results. For each method, regional to continental-wide data sets were essential because of the 500-by-700-km gridding for the model results, which meant that only the broadest scale patterns could be compared.

In one approach, calibration data sets were used to calculate multiple regression equations and response surfaces that turned fossil pollen data into temperature and moisture estimates that, when mapped, could be compared to comparable maps of the model simulations. Hydrological models were also used to obtain moisture-balance estimates from lake-level data. In a second approach, response surfaces were used to turn model-simulated temperature and moisture values into maps of pollen or P-PE (precipitation minus potential evaporation) values that then could be compared to the pollen and lake-level data. In a final, more heuristic approach, cartoon-like maps illustrated the main features of the data and model simulations and allowed these visual representations to be compared (Figure C61). Such visualizations combined information from many diverse sets of data on the maps and brought focus to regions where the climate estimates from the data were robust.

COHMAP (1988) illustrated the first results of data-model comparisons in the context of time-series model simulations, as described in Wright et al. (1993). For the LGM over North America, these show that, in the model simulations, the high Laurentide Ice Sheet forced the winter jetstream southward over California, where winter storms brought moisture to fill the pluvial lakes (Figure C61). At the same time, the simulated glacial anticyclone produced anomalous easterly winds that created drier-than-present conditions in the Pacific Northwest just south of the ice sheet. As the ice sheet retreated, the jet and glacial anticyclone shifted in position, which altered the

pattern of moisture conditions across the west. In the east, much colder-than-present temperatures at the LGM favored spruce trees growing where oaks grow today. Then, the retreating ice sheet delayed the timing of peak warm temperatures during the Holocene in northeastern North America compared with the northwest and MacKenzie Delta areas. For the monsoonal regions of Africa and southern Asia, the climate model simulations showed an immediate (vs. delayed) response to orbital forcing and a much enhanced monsoonal circulation from 12,000 to 6,000 radiocarbon years ago when the contrast in seasonal insolation was greatest. Raised lake levels and steppe and savannah vegetation from western Africa into southern Asia fit well with the pattern of changes there.

These initial modeling results used version 0 of the NCAR Community Climate Model (CCM0), for which sea-surface temperatures needed to be prescribed. COHMAP researchers then updated the results using CCM1 with a mixed-layer ocean for a second set of time series runs (Kutzbach et al., 1998). They also used calendar-year calibrations for the radiocarbon dates and an ice sheet reconstruction that estimated a lower height for the Laurentide Ice Sheet at the LGM. The new simulations showed no split jet over North America in winter for the LGM, but showed most of the other main results (described above) to be robust and in good agreement with the data (Webb, 1998). A global biome model provided a new approach for data-model comparisons, and several papers illustrate its use to good effect. The simulated surface energy balance was also analyzed in detail and helped COHMAP researchers to separate dynamic from thermodynamic controls of regional climates (Bartlein et al., 1998). The data and model results showed clearly that climate changes vary spatially in magnitude as well as in timing and that phenomena like the "hypsithermal" were not globally uniform, either in magnitude or timing. With the patterns in moisture variations and seasonality varying along with temperature, no simple description of late Quaternary climates is possible.

Conclusions

Besides the key synthesis work (COHMAP, 1988; Wright et al., 1993; Webb, 1998), COHMAP results appear in over 200 journal articles and in edited books and journal issues by Wright (1983), Webb and Dubois (1985), Ruddiman and Wright (1987), and Huntley and Webb (1988). COHMAP research showed the broad impact of orbital forcing on late Quaternary climates and provided a background of forced changes onto which the many millennial-scale changes can be superimposed. Subsequent work has led to the mapping and modeling of Younger Dryas age climates; a study of possible feedbacks that affect the magnitude, pattern, and timing of late Quaternary climates; and an understanding of how climate patterns unlike any today have resulted in vegetation assemblages unlike any today.

Thompson Webb III

Figure C61 Changes in the atmosphere, geosphere, and biosphere that accompanied the transition from glacial to interglacial conditions during the past 18,000 years (18 ka), as illustrated by geological and paleoecological evidence (*left panels*) and features of the climate-model simulations (*right panels*). The maps of the data show the extent of ice sheets and of year-round and winter-only sea ice. For 18 ka, sea level lowering resulted in a broadened land area. The distributions of oak and spruce are inferred from pollen data, and the status of effective moisture (relative to present) in western North America is inferred from lake level records. The present region where annual precipitation is less than 300 mm is shown on the map for Present. The maps for the model simulations show the distribution of ice sheets and sea ice that served as boundary conditions for the simulations. *Thin black arrows* show the surface winds and *thick black arrows* show the jet stream position. The *broken line* for 18 ka over Alaska indicates a weakened jet (modified from color version in COHMAP, 1988).

Bibliography

- Bartlein, P.J., Webb, T. III., and Fleri, E.C., 1984. Holocene climatic change in the northern Midwest: Pollen-derived estimates. *Quaternary Res.*, **22**, 361–374.
- Bartlein, P.J., Prentice, I.C., and Webb, T. III., 1986. Climatic response surfaces based on pollen from some eastern North America taxa. *J. Biogeogr.*, **13**, 35–57.
- Bartlein, P.J., Anderson, P.M., Anderson, K.H., Edwards, M.E., Thompson, R.S., Webb, R.S., Webb, T. III., and Whitlock, C., 1998. Paleoclimate simulations for North America for the past 21,000 years: Features of the simulated climate and comparisons with paleoenvironmental data. *Quaternary Sci. Rev.*, **17**, 549–585.
- CLIMAP, 1981. *Seasonal Reconstruction of the Earth's Surface at the Last Glacial Maximum*. Boulder, CO: Geological Society of America. Geological Society of America Map Chart Series, MC-36.
- COHMAP Members, 1988. Climatic changes of the last 18,000 years: Observations and model simulations. *Science*, **241**, 1043–1052.
- DeBoer, P.L. (ed.), 2004. *Orbital Forcing and Cyclic Sequences*. Oxford, UK: Blackwell Science, 576pp.
- Huntley, B., and Webb, T. III. (eds.), 1988. *Vegetation History. Handbook of Vegetation Science*, vol. 7. Dordrecht, The Netherlands: Kluwer, 803pp.
- Imbrie, J., and Imbrie, K., 1979. *Ice Ages Solving the Mystery*. Hillside, NJ: Enslow Publishers.
- Kutzbach, J.E., 1980. Estimates of past climate at paleolake Chad, North Africa, based on a hydrological and energy budget model. *Quaternary Res.*, **14**, 210–223.
- Kutzbach, J.E., 1981. Monsoon climate of the early Holocene: Climatic experiment using the earth's orbital parameters for 9000 years ago. *Science*, **214**, 59–61.
- Kutzbach, J.E., and Street-Perrott, F.A., 1985. Milankovitch forcing of fluctuations in the level of tropical lakes from 18 to 0 kyr BP. *Nature*, **317**, 130–134.
- Kutzbach, J.E., Guetter, P.J., Behling, P., and Selin, R., 1993. Simulated climatic changes: Results of the COHMAP climate-model experiments. In Wright, H.E., Jr., Kutzbach, J.E., Webb, T. III., Ruddiman, W.F., Street-Perrott, F.A., and Bartlein, P.J. (eds.), *Global Climates Since the Last Glacial Maximum*. Minneapolis, MN: University of Minnesota Press, pp. 24–93.
- Kutzbach, J.E., Gallimore, R., Harrison, S.P., Behling, P., Selin, R., and Laarif, F., 1998. Climate and biome simulations for the past 21,000 years. *Quaternary Science Rev.*, **17**, 473–506.
- Peterson, G.M., Webb, T. III., Kutzbach, J.E., van der Hammen, T., Wijmstra, T.A. and Street, F.A., 1979. The continental record of environmental conditions at 18,000 B.P.: An initial evaluation. *Quaternary Res.*, **12**, 47–82.
- Root, T.L., and Schneider, S.H., 1995. Ecology and climate: Research strategies and implications. *Science*, **269**, 334–341.
- Ruddiman, W.F., and Wright, H.E., Jr. (eds.), 1987. *North America and Adjacent Oceans during the Last Deglaciation*, Decade of North American Geology. Boulder, CO: Geological Society of America.
- Street, F.A., and Grove, A.T., 1979. Global maps of lake-level fluctuations since 30,000 yr B.P. *Quaternary Res.*, **12**, 83–118.
- Webb, T. III. (ed.), 1998. *Late Quaternary Climates: Data Syntheses and Model Experiments*. *Quaternary Sci. Rev.*, **17**, 465–688.
- Webb, T. III., and Bryson, R.A., 1972. Late- and post-glacial climatic change in the northern Midwest, U.S.A.: Quantitative estimates derived from fossil pollen spectra by multivariate statistical analysis. *Quaternary Res.*, **2**, 70–115.
- Webb, T. III., and Dubois, J.M. (eds.), 1985. Tendances climatiques l'Holocène en Amérique du Nord. *Géographie physique et Quaternaire*, **39**, 113–226.
- Wright, H.E., Jr. (ed.), 1983. *Late-Quaternary Environments of the United States*, vol. 2: The Holocene, Minneapolis, MN: University of Minnesota Press.
- Wright, H.E., Jr., and Bartlein, P.J., 1993. Reflections on COHMAP. *The Holocene*, **3**, 89–92.
- Wright, H.E., Jr., Kutzbach, J.E., Webb, T. III., Ruddiman, W.F., Street-Perrott, F.A., and Bartlein, P.J. (eds.), 1993. *Global Climates Since the Last Glacial Maximum*. Minneapolis: University of Minnesota Press, 569pp.

Cross-references

[Astronomical Theory of Climate Change](#)
[Atmospheric Circulation During the Last Glacial Maximum](#)
[Carbon Dioxide and Methane, Quaternary Variations](#)
[CLIMAP](#)
[Climate Change, Causes](#)
[Dating, Radiometric Methods](#)
[Foraminifera](#)
[Heat Transports, Oceanic and Atmospheric](#)
[Holocene Climates](#)
[Hypsithermal](#)
[Ice Cores, Antarctica and Greenland](#)
[Interstadials](#)
[Lake Level Fluctuations](#)
[Last Glacial Maximum](#)
[Last Glacial Termination](#)
[Late Quaternary-Holocene Vegetation Modeling](#)
[Laurentide Ice Sheet](#)
[Monsoons, Quaternary](#)
[North Atlantic Deep Water and Climate Change](#)
[Obliquity](#)
[Ocean Paleotemperatures](#)
[Oxygen Isotopes](#)
[PAGES](#)
[Paleobotany](#)
[Paleoclimate Modeling, Quaternary](#)
[Paleoceanography](#)
[Paleolimnology](#)
[Paleo-Precipitation Indicators](#)
[Paleotemperatures, Proxy Reconstructions](#)
[Pollen Analysis](#)
[Precession, Climatic](#)
[Quaternary Vegetation Distribution](#)
[Radiocarbon Dating](#)
[Sea Level Change, Post-Glacial](#)
[SPECMAP](#)
[Transfer Functions](#)
[Wisconsinan \(Weichselian, Würm\) Glaciation](#)

CONTINENTAL SEDIMENTS

Introduction

Continental sediments can be very sensitive paleoclimate indicators because they are commonly deposited either in direct contact with the atmosphere or in close proximity to it. Relative to marine sediments, however, terrestrial sedimentary records of paleoclimate can be more difficult to interpret, due to incomplete preservation, fluctuating rates of sedimentation that commonly include significant periods of erosion, and post-depositional modification by bioturbation or diagenesis. This chapter first focuses on the broad association of various continental depositional systems (glacial, lacustrine, fluvial, and eolian) with specific climatologic settings. Following, several important paleoclimatologic indicators common to continental sediments are discussed.

Continental depositional systems and paleoclimate Glacial systems

The preservation of pre-Quaternary and Quaternary continental glacial deposits indicates that the Earth's climate has oscillated between an "icehouse" (i.e., glacial) and a "greenhouse" (i.e., interglacial) mode. Observations of modern glacial systems,

theoretical studies of glacial dynamics, and documentation of Quaternary glacial sediments form the basis for development of glacial system depositional models. However, because of the difficulty in examining modern subglacial processes and the fact that glacial environments are not at present extensive, the detailed environmental interpretation of ancient continental glacial sediments is not always straightforward. What is clear is that widespread deposition of glacial sediments on the continents, particularly in low latitude situations, indicates periods of significant global cooling.

Terrestrial glacial systems range in scale from local, alpine glaciers to continent-scale ice sheets. Glacial systems of all scales contain a variety of subenvironments that may be recognizable in the ancient sedimentary record. Among the most important are subglacial settings (under the glacier) and proglacial settings (in front of or adjacent to the glacier). Both environments may involve ice contact. Supraglacial settings (on top of the glacier) and englacial settings (within the glacier) have low preservation potential and will not be discussed here.

Subglacial ice contact deposits typically include some sort of glacial till – characterized by its very poor sorting and abundance of angular clasts, some of which may be glacially striated. Three till types are commonly recognized in ancient continental glacial deposits. Lodgement till typically forms by basal slip of the glacier against the sediment substrate. It is typically rather compacted and characterized by weak clast imbrication. More common is deformation till that forms through subglacial sediment shearing and is characterized by extremely poor sorting, random clast orientation, and evidence of soft-sediment deformation. Also common is melt-out till that usually contains evidence of subglacial water-reworking of sediment.

Although their sedimentology is not well documented, subglacial lakes of significant volume and longevity may be present beneath continental glaciers because of the insulation effects of the ice and internal heat of the underlying crust. For example, glacial Lake Vostok is estimated to be 70 km long and to have existed for up to 20 million years under the Antarctic Ice Sheet (Siegert et al., 2001). Although not a universally accepted idea, some workers have speculated that large subglacial lakes may have contributed significantly to glacial outwash flows, particularly during periods of deglaciation (Shaw et al., 1999).

Proglacial lakes can provide some of the best evidence for ancient glaciation because they commonly contain a variety of easily recognizable sedimentary structures. Perhaps most important are glacial-lacustrine rhythmites. Many (though not all) such rhythmites result from annual seasonal changes in sediment flux. Typically, glacial varves are characterized by a sharp base, corresponding to the onset of spring melt-out, overlain by relatively coarse-grained sediment deposited during spring and summer, followed by decreasing sediment sizes during the return to winter conditions. Sedimentation rates in proglacial lakes in which varves are being formed can be extremely high – commonly cm yr^{-1} (Ashley, 1975). In addition to rhythmites resulting from seasonal changes, proglacial lake environments are commonly characterized by widespread sediment gravity flow deposition, including overflows, interflows, and underflows (Gustavson, 1975). These result mainly through introduction of sediment by subglacial currents as well as through remobilization of sediments from lake margins. Ice-rafted debris (IRD), another common attribute of proglacial lake systems, consists of randomly-oriented coarse clasts (pebbles, cobbles, boulders) that are encased in

deeper-water glacial lake sediments (Levish, 1997). In the absence of association with other glacial sediments, IRD may be difficult to distinguish from poorly-sorted sediment associated with other sedimentary environments (e.g., some mud-rich debris flows).

In addition to lakes, proglacial settings can contain a spatially complicated suite of environments that may include bedload-dominated streams (glacial outwash) and eolian environments. Bedload-dominated streams associated with glacial outwash are difficult to distinguish from those not associated with glacial settings and thus are not by themselves good indicators of glaciation. Widespread eolian deposits in proglacial settings are commonly produced by adiabatic winds flowing off continental ice sheets. Proglacial eolian deposits can include both sand dunes and silt-sized loess, commonly occurring in paired dune-loess systems. Loess deposits typically consist of tabular beds of well-sorted silt that may contain included ventifacts and well-developed paleosols.

Lake systems

Lakes can contain some of the highest resolution sedimentary records of paleoclimate preserved in continental settings, because many of the physical, chemical, and biological processes that directly control sediment type and flux in lakes are driven by seasonal changes. Importantly, the preservation potential of lakes is generally high because lakes commonly form in areas where tectonic subsidence is significant.

Rates of lake basin infill by sediment and water are a function both of climate (e.g., effective precipitation rates) and tectonics (e.g., rate of subsidence of the lake basin bottom). This important relationship led Carroll and Bohacs (1999) to classify modern and ancient lakes as underfilled, balanced-filled, and overfilled. This is a useful classification because it can be readily applied to ancient lacustrine basins without the need for paleogeomorphic reconstructions. Underfilled lake basins typically reflect the inability of the delivery rate of sediment plus water to keep up with tectonic subsidence. Such lakes are typically closed and commonly retain some evidence of water column stratification, reduced bottom oxygen levels, and increased salinity levels. Overfilled lakes are usually open and reflect the inability of the subsidence rate to keep up with the delivery rate of sediment plus water. Such lakes are usually well-oxygenated and are characterized by progradation of deltas into the lake and a non-stratified water column. As the name implies, balanced-filled lakes occur in settings where subsidence and the rate of lake-basin infill by sediment and water are co-equal.

Climate records in lake sediments can be reflected by a multitude of sedimentologic, biologic, and geochemical characteristics that change over timescales ranging from 10^0 to 10^5 years. Annual seasonality may be faithfully recorded in lake sediments in the form of varve laminations that are controlled by seasonal environmental changes, such as variations in sedimentation flux, lake chemistry, or biology (Nuhfer et al., 1993). At longer time scales, oscillations in climate have been interpreted from a variety of sedimentologic characteristics in which some element of cyclicity is preserved. For example, Olsen (1990) described a series of upward-shoaling cycles within lake sediments from the Triassic rift basin of the eastern US. Applying spectral analysis to the temporal variations in relative lake depth, Olsen (1990) demonstrated that the frequency of water depth variation was consistent with that expected from astronomically-driven changes in the Earth's orbital parameters

(i.e., Milankovitch cyclicality). In a second example, Trauth et al. (2001) studied variations in sedimentology, diatom assemblages, and geochronology from East African lakes and concluded that the lakes alternated between deep freshwater conditions and shallow highly alkaline conditions on a 23-kyr-frequency band that is consistent with Milankovitch-driven cyclicality.

In addition to interpretation of orbitally-forced Milankovitch cyclicality in ancient lake deposits, lake sediments have proven useful in revealing the presence of other cyclic frequencies that may reflect atmospheric or coupled oceanic-atmospheric processes that are as yet poorly understood. For example, Munoz et al. (2002) studied laminated lake sediments from Spain and concluded that cyclic sedimentation reflected climate variations due to the El Niño Southern Oscillation (ENSO) and the North American Oscillation (NAO).

Three types of end-member lake types have been recognized as having particular paleoclimatologic significance. These are glacial lakes, playa lakes, and organic-rich lakes. Glacial lakes are discussed above. Playa lakes are shallow, closed lakes formed in areas of low effective precipitation and high rates of evaporation. Playa lakes usually have alkaline or saline water chemistries. Common characteristics include: (a) deposition of evaporites or alkaline minerals such as dolomite, various zeolites, and Mg-rich clays; (b) organic-rich laminated mudrock in the central part of the lake basin; and (c) abundant mudcracks – particularly in lake margin facies. The margins of saline or saline, alkaline lakes commonly interfinger with alluvial fan sediments, indicating the important role of tectonics not only in creating the lake basin, but also in the production of orographic climate effects (e.g., rain shadows) in some cases. Organic-rich lakes occur in a variety of tectonic and climatologic settings, so it is typically necessary to supplement climate interpretations based on sedimentary character with those from other data sets such as organic geochemistry or the composition of diatom assemblages. Organic-rich bottom sediments are commonly deposited in lakes with permanent thermal or salinity stratification, and anoxic bottom conditions develop in tropical climates with low seasonality and high humidity. For example, organic-rich lakes are common in equatorial Africa (Talbot, 1988) – an area characterized by little seasonality but abundant rainfall. In contrast, organic-rich lakes also are common in temperate North America (between 42° N and 55° N latitude) where seasonality is strong but annual productivity is high (Anderson et al., 1985).

River and alluvial fan systems

River system dynamics are controlled by a large number of variables that may be influenced by climate but may also reflect other external controls such as rates of subsidence and sedimentation. Unfortunately, the geomorphology of ancient fluvial systems is rarely preserved in the rock record. As a result, paleoclimatologic interpretations of ancient fluvial systems typically have focused on documenting the nature and geometry of sand bodies deposited by riverine processes and on determining whether ancient streams were ephemeral (i.e., not flowing continuously) or perennial (flowing continuously).

Use of fluvial sand body geometries to infer paleoclimate, though qualitative, usually focuses on distinguishing between mud-dominated streams that are inferred to be meandering, and bedload-dominated streams that are inferred to be more braided. Although both stream types can occur in a wide variety of climate settings and both are controlled by numerous factors other than climate – tectonics in particular – the implication is

that mud-dominated streams usually represent a more humid climate than bedload-dominated streams. Meandering stream channel sands tend to be isolated, with well-preserved channel forms and relatively few internal scours, a relatively fine overall grain size, and common preservation of lateral accretion surfaces within channel deposits. Paleocurrent indicator directions tend to be widely dispersed. Overbank regions are characterized by abundant evidence of plant colonization and, commonly, the occurrence of coal. Braided river deposits are usually characterized by sand bodies that are multistoried and multilateral, an abundance of cut and fill scour surfaces, relatively coarser and less well sorted sediment, and common planar and trough cross-bedding. Individual channels are rarely preserved, the ratio of sand to mud is higher than meandering streams, and evidence of plant colonization is less common. Overbank regions commonly contain well-developed calcsol (caliche) horizons (Miall, 1992, 1996).

Distinguishing between ancient ephemeral and perennial stream flow may be a somewhat more reliable means of interpreting paleoclimate than determining whether ancient streams were mud- or bedload-dominated, although both forms of interpretation are qualitative assessments of paleoclimate. Generally, ephemeral streams are more likely to represent dry climates than perennial streams. Common features of ancient ephemeral streams include: (a) relatively small sandstone bodies with upper flow regime structures produced by short but powerful flash floods; (b) abundant reworked sand and mud intraclasts, suggesting short duration flows; (c) common desiccated mud drapes and/or interbedded eolian deposits; (d) abundant root traces within the channel system, and (e) well-developed calcsols in overbank regions (Parrish, 1998). In contrast, perennial streams are typically characterized by larger sandstone bodies and low flow regime sedimentary structures, such as subaqueous dunes and current ripples, which are interpreted to reflect lower velocity and more sustained flows.

Alluvial fans are generally not regarded as good indicators of paleoclimate, although specific climatologic indicators (e.g., evaporites, coal) can be associated with alluvial fan systems. Alluvial fans are generally more useful as evidence of tectonic activity, because steep topographic gradients are required for alluvial fan formation. Nevertheless, climate can be an important influence on fan sedimentation. For example, Blair and McPherson (1994) described alluvial fans in terms of two end-members: debris-flow dominated fans, generally associated with more arid climate regimes; and sheet flood dominated fans, generally associated with more humid climate regimes. In many ancient cases, alluvial fans are indistinguishable from braided river deposits. Although this similarity might imply that alluvial fans are mostly associated with arid environments, fans are also common in well-watered environments as, for example, proglacial outwash fans, which commonly occur downstream from alpine glaciers.

Deserts and eolian systems

Deserts are generally defined as areas characterized by low rates of precipitation and high rates of evaporation. More specifically, the definition depends on the ratio of actual precipitation (P) to evaporation and evapo-transpiration (E_t). Deserts are usually characterized by P/E_t ratios of 0.2 (Parrish, 1998). Modern deserts generally occur in three different settings, each of which is characterized by air masses that retain moisture as they heat up, thereby inhibiting atmospheric condensation and resulting precipitation. The largest modern deserts (e.g., the Sahara) occur at lower middle latitudes (~30° N and 30° S) where dry,

descending upper-atmospheric flow heats up, inhibiting precipitation and enhancing evaporation. Deserts are also common in coastal areas where cool offshore air is brought onshore, where it heats up and retains excess moisture. The Namibian and Atacama Deserts are good examples. Lastly, deserts can be produced by orographic effects such as rain shadows (e.g., the Great Basin, western USA).

Modern and ancient deserts contain a variety of recognizable sedimentary facies that are good indicators of low effective moisture. Among the best of these are eolian sands. Eolian sands are readily recognizable in the ancient rock record because they are typically well sorted, commonly contain frosted grains produced by elastic grain-to-grain collisions in air, and usually include grain flow, grain fall, and wind ripple sedimentary structures (Kocurek and Dott, 1981). Grain flows result from avalanching of grains down the steep, lee side of sand dunes. Grain flow deposits are typically only a few cm thick, usually massive, and thin towards the bottom of the dune. Grain fall deposits, on the other hand, result from eolian transport of grains and deposition as a thin drape over pre-existing topography. Grain fall deposits are usually rather thin (1–2 mm thick) and are somewhat finer-grained than surrounding deposits. Wind ripple deposits are particularly diagnostic of eolian environments because wind ripples form by a fundamentally different process to subaqueous ripples and bear correspondingly different internal architectures. Wind ripples form by ballistic impacts of saltating grains on the bed surface. These ballistic impacts tend to organize the bed into ripples characterized by coarser grain populations (so-called “creeping population”) on ripple crests and in relatively protected ripple lee sides, and finer grain populations in ripple troughs and in less protected windward sides of ripples. As wind ripples migrate downwind and aggrade vertically, they leave behind mm-scale laminations of sand that typically coarsen upward as coarser-grained ripple crests migrate over finer-grained ripple troughs. Interfingering of wind ripple deposits with grain flow deposits at the base of dunes is generally regarded as unequivocal evidence of eolian sedimentation.

In addition to eolian sands, eolian systems commonly contain a variety of other environments that can yield important paleoclimatologic information. Most important of these are interdune depressions. Interdune depressions can be the sites of playa lakes, deflation flats, or ephemeral fluvial systems. The presence of interdune playa lakes is commonly controlled by the elevation of the water table relative to the dune surface. Although water table elevation can fluctuate out of phase with climate, it commonly provides some indication of moisture availability. For example, elevated water tables that tend to stabilize interdune areas commonly reflect greater availability of moisture (Havholm et al., 1993). In “wet” eolian systems, the area represented by interdune areas may be greater than that represented by eolian sandy bedforms. In dry eolian systems where the water table elevation is considerably below the bedform surface, interdune flats may be absent altogether (Herries, 1993).

In addition to their utility as indicators of low effective moisture, eolian sand deposits may be the best indicators of paleowind direction. Modern and ancient eolian sands typically accumulate in a variety of dune morphologies. Although not always straight-forward, the internal architectural elements of these dunes can provide direct evidence of paleowind direction. For example, unimodal wind directions commonly produce transverse dunes. As these dunes migrate, sand is eroded from the windward side of the dune and accumulates near the crest

of the dune. This accumulation eventually destabilizes and flows down the steep front side of the dune, producing a slip face that slopes downwind. As the dune migrates with time, these slip faces are commonly preserved as internal bounding surfaces. In ancient dune deposits, the orientation of such bounding surfaces can be measured and used to infer paleowind directions (Parrish and Peterson, 1988).

Despite the utility of dune slip facies for inferring paleowind directions, wind regimes are not typically unimodal but vary seasonally in their direction. The long axes of dunes deposited under such changing wind regimes are usually oriented obliquely to the average annual wind direction. Essentially, the dune is oriented in the position that is most transverse to each wind direction, weighted by wind energy. Thus, use of internal dune architecture to infer paleowind directions commonly requires three-dimensional modeling of dune morphology (e.g., Rubin, 1987) and resulting bounding surfaces. Given well-preserved three-dimensional exposures of ancient dunes and recognition of relationships among dune morphology, internal architecture, and prevalent wind direction(s), measurement of bounding surface orientations can provide paleowind information that is directly comparable with output from global atmospheric circulation models. For example, Parrish and Peterson (1988) measured the orientation of sedimentary structures produced by paleowinds as preserved in Lower Jurassic strata of the Colorado Plateau. These paleocurrent data contained convincing evidence both of summer monsoonal flow and summer subtropical high-pressure atmospheric gyres associated with the Pangean supercontinent and predicted by global circulation models.

Specific lithological indicators of climate found in continental sediments

Coal

Coal is a sedimentary rock that contains >70% organic carbon and is formed by lithification of peat, consisting of accumulations of vegetation that is adapted to saturated (waterlogged) conditions. Coal is generally described in terms of four lithotypes: vitrain, clairain, durain, and fusain (Teichmüller, 1989). Lithotypes, in turn, are composed of three types of coal macerals: vitrinite, liptinite (exinite), and inertinite. Each of these is further subdivided into a number of submacerals that typically can be recognized through petrographic analysis (Stach et al., 1982).

Peat accumulations form in raised mires or swamps under anaerobic, acidic conditions in which the local water table is at or above that of the surrounding area. This water table configuration generally inhibits the deposition of clastic sediment (clay, silt) and results in acidic conditions that inhibit bacterial decay of the peat itself. Peat accumulations also are characterized by relatively low nutrient (phosphorus and nitrogen) levels, because these elements are introduced mainly through precipitation rather than groundwater influx, particularly in the case of raised mires.

Peat, and by extension coal, is generally regarded as being associated with environments that are characterized by abundant precipitation. High precipitation not only can maintain a shallow water table, but also can promote plant growth and enhance the development of anoxic conditions within the peat accumulation. Although peat is generally associated with environments in which mean annual precipitation exceeds evaporation, Gyllenhaal (1991) demonstrated that many peats occur in environments where precipitation and evapotranspiration are roughly balanced. Ziegler

et al. (1987) and Gyllenhaal (1991) both suggested that peat accumulations are favored in environments characterized by a consistent, year-round minimum amount of monthly precipitation in the range of 20–40 mm/month. That is, peat formation is promoted more by a steady source of precipitation, rather than an annualized average net precipitation.

Despite the common association between peat formation and abundant precipitation, the interpretation of paleoclimate from coal occurrence is not straightforward. Firstly, though uncommon, a number of modern peat accumulations have been documented for areas in which the mean annual precipitation rate is less than the mean annual rate of evapotranspiration (Gyllenhaal, 1991). Second, preservation of coal in the rock records depends on a delicate balance between peat formation and subsidence of the sedimentary basin in which the peat occurs. Too rapid a rate of subsidence will drown the peat deposit. Too low a rate of subsidence will not allow sufficient peat to accumulate to produce very thick beds of coal. Thus, it is commonly difficult to formulate interpretations regarding paleoclimate based solely on the presence of coal, particularly for local basin-scale studies. On the other hand, global paleoclimate studies seeking to identify large-scale, regional trends have successfully demonstrated a link between coal occurrence and predicted distributions of high precipitation based on modeling (Parrish et al., 1982).

The petrography of coal can yield considerable information regarding the macerals that make up a coal, and many workers have attempted to link various maceral types with paleoclimatologic conditions in which the precursor peat accumulated. For example, Teichmüller (1989) proposed that abundant vitrinite in coal could be interpreted as reflecting a high rate of precipitation and a raised water table, whereas inertinite-rich coal forms under dry conditions with relatively low or seasonally fluctuating water tables. Other workers have attempted to tie the petrographic characteristics of coal to temperature (e.g., Diessel, 1992) or the taxonomic composition of the mire vegetation, which depends on both paleoclimate and geologic age (Cameron et al., 1989).

The ash and sulfur content of coal – two major considerations for determining the economic value of a coal deposit – also have been proposed as reflecting the paleoclimatologic conditions in which peat accumulates. Cecil et al. (1982) proposed three end-member conditions for the formation of peat that are related to paleoclimate and may be recognized through coal geochemistry. First, peats forming under permanently waterlogged conditions give rise to low ash, low sulfur, vitrinite-rich coals. Permanently saturated conditions inhibit the influx of detrital clays (resulting in low ash content), promote an acidic geochemical environment (pH <4.5) that inhibits the ability of sulfate-reducing bacteria to fix iron (resulting in low sulfur), and ultimately favor the preservation of abundant woody vegetation (vitrinite). Second, peats forming in planar mires under anaerobic conditions with pH >4.5 give rise to high ash, high sulfur, liptinite-rich coals, because of the introduction of significant detrital siliciclastic material, the ability of sulfate-reducing bacteria to fix iron as pyrite (FeS₂), and the accumulation of waxy cutaneous organic matter (liptinite). Third, peats forming in planar mires under conditions of lower annual rainfall or a seasonally fluctuating water table are characterized by a higher percentage of siliciclastic sediment (ash), development of aerobic conditions that inhibit sulfate reducing bacterial activity (low sulfur) and the accumulation of relatively abundant charcoal and carbonized woody debris (inertinite).

Evaporites

Most studies that use facies distributions to reconstruct global paleoclimate include evaporites. Although evaporites commonly involve the influx of marine waters as a source of dissolved ions, this is not always the case. Many modern evaporite deposits are forming in hypersaline lacustrine settings, such as the Dead Sea. The largest modern evaporite-forming environments are located in mid-latitudes (approximately 30° N and 30° S), where dry upper atmospheric air descends, heats up, and loses humidity. This humidity loss may lead to the formation of ergs (large sand seas) and associated evaporites.

As the name implies, the formation of evaporites involves concentration of dissolved ions to the point where salt precipitation occurs. Controls on evaporite mineralogy include the concentration and composition of dissolved ions. Progressive evaporation of normal marine seawater, for example, typically results first in the formation of carbonates, then sulfates, then halides. In continental environments not involving marine water as an ionic source, unusual evaporite minerals may be formed that differ from those formed at the marine-nonmarine interface. For example, economically valuable deposits of borate evaporites have formed in Death Valley, California, as a result of the weathering of surrounding hydrothermally-altered bedrock.

Environmental conditions needed for the formation of evaporite minerals typically involve low rates of precipitation, although many evaporite-forming environments involve monsoonal flow of moisture during the “wet” season. In such cases, the influx of monsoonal moisture is usually not high, and evaporation during the dry season typically exceeds precipitation during the wet season, resulting in net annual concentration of dissolved ions in surface and shallow groundwater. In many modern and ancient evaporite-forming environments, topography plays an important role in creating the aridity that leads to evaporite deposition. For example, Death Valley is located in the rain shadow of the Sierra Nevada.

Red beds

The term “red beds” is commonly applied to red-colored clastic sedimentary deposits associated with seasonally arid paleoclimate and warm temperatures. The red color is usually caused by hematite (Fe₂O₃) staining and is a function of grain size and the time elapsed since deposition, with finer grained and older deposits typically being redder. Hematite in terrestrial settings also can be formed from dehydration of hydrous iron oxides or precipitation in the presence of alkaline ground water. Terrestrial red beds associated with warm, seasonally arid climate include desert red beds (ephemeral stream, eolian, and some playa lake deposits), monsoonal “savannah” red beds in which annual wet and dry seasons are subequal in duration, and tropical red beds formed in conditions of intense chemical weathering. Tropical red beds usually contain an abundance of iron and aluminum sesquioxides (e.g., bauxite deposits) and typically form in strongly monsoonal climates. Although the term “red bed” is very common in the literature and many terrestrial clastic sedimentary deposits are likely formed in warm seasonally arid paleoclimatic conditions, red color is not diagnostic of these conditions and care should be exercised in making this interpretation.

Paleosols

Paleosols are ancient, buried weathering surfaces (soils) that are very common in the continental rock record and contain

considerable information about the nature of paleoclimatic conditions during the weathering process. Many classification schemes for paleosols have been developed (Retallack, 1988, 1990; Mack et al., 1993); in general, these classification systems are based on textural and compositional features that are quite different from the criteria that form the basis for classification of modern soils.

Physical and chemical characteristics of paleosols are determined from the duration of exposure to weathering and the composition of exposed bedrock, the availability of water, and diagenesis. Paleosols are commonly rich in carbonate, silica, organic matter, and sesquioxides such as Fe_2O_3 and Al_2O_3 and are generally more colorful than the surrounding rock. Paleosols commonly display a variety of distinctive textural features such as nodules, concretions, root traces, vertical or horizontal jointing, and hackly fracture.

Paleosols that are qualitatively associated with specific paleoclimate conditions include oxisols, vertisols, calcisols, gypsisols, histisols, and spodosols. Oxisols are characterized by low amounts of organic matter and abundant Fe or Al sesquioxides (laterites or bauxites) that typically are concentrated by poor drainage in areas of intense chemical weathering. These environments tend to be tropical with abundant rain for most of the year, followed by a several-month-long dry season. Vertisols are named so for the common presence of vertically-oriented fractures, called peds, that result from swelling and shrinkage (pedoturbation) of expandable clays (smectite or mixed layer smectite/illite). Climate regimes in which vertisols form are usually strongly seasonal with respect to rainfall (i.e., strongly monsoonal). Calcisols and gypsisols typically contain little organic matter and are named for the presence of pedogenic calcite and gypsum, respectively. Both paleosol types – gypsisols in particular – are associated with arid climates that are seasonal with respect to rainfall. Histisols are organic-rich soils that form in areas characterized by poor drainage, high rates of precipitation, and low rates of evaporation. Histosols can form in temperate or tropical areas. Spodosols can also be organic-rich and are characterized by a distinct horizon of concentrated organic matter and iron oxides formed by downward movement and accumulation (illuviation) of amorphous material during weathering. Spodosols are typically associated with cool climates in which precipitation exceeds evaporation. Lastly, argillisols, characterized by a distinct subsurface accumulation of clay, also reflect significant illuviation and commonly form in mid-latitude paleoclimates that are characterized by an excess of precipitation relative to evaporation.

Summary and conclusions

Continental sediments can provide an important basis for the interpretation of paleoclimate, including qualitative estimates of paleotemperature (hot vs. cold), annual precipitation (wet vs. dry), seasonality, and paleowind direction. However, care must be exercised in using the sedimentology or geochemistry of continental deposits to infer paleoclimate because of the wide range of influences that may control sediment composition and sedimentary architectures, the susceptibility of continental sediments to diagenetic overprinting, and the bias introduced through erosional deletion of significant portions of the sediment record.

Marc S. Hendrix

Bibliography

- Anderson, R.Y., Dean, W.E., Bradbury, J.P., and Love, D., 1985. *Meromictic Lakes and Varved Lake Sediments in North America*. U.S Geological Survey Bulletin 1607, 19pp.
- Ashley, G.M., 1975. Rhythmic sedimentation in glacial Lake Hitchcock, Massachusetts-Connecticut. In Jopling, A.V., and McDonald, B.C. (eds.), *Glaciofluvial and Glaciolacustrine Sedimentation*. Tulsa, OK: SEPM Special Publication 23, pp. 304–320.
- Blair, T.C., and McPherson, J.G., 1994. Alluvial fans and their natural distinction from rivers based on morphology, hydraulic processes, sedimentary processes, and facies assemblages. *J. Sediment. Res. A Sediment. Petrol. Process.*, 64, 450–489.
- Cameron, C.C., Esterle, J.S., and Palmer, C.A., 1989. The geology, botany and chemistry of selected peat-forming environments from temperate and tropical latitudes. *Int. J. Coal Geol.*, 12, 105–156.
- Carroll, A.R., and Bohacs, K.M., 1999. Stratigraphic classification of ancient lakes: Balancing tectonic and climatic controls. *Geology*, 27(2), 99–102.
- Cecil, C.B., Stanton, R.W., Dulong, F.T., and Renton, J.J., 1982. Geologic factors that control mineral matter in coal. In Filby, B.S., Carpenter, B.S., and Ragaini, R.C. (eds.), *Atomic and Nuclear Methods in Fossil Energy Research*. New York: Plenum Press, pp. 323–335.
- Diessel, C.F.K., 1992. *Coal-Bearing Depositional Systems*. Berlin: Springer-Verlag, 721pp.
- Gustavson, T.C., 1975. Sedimentation and physical limnology in proglacial Malaspina Lake, southeastern Alaska Connecticut. In Jopling, A.V., and McDonald, B.C. (eds.), *Glaciofluvial and Glaciolacustrine Sedimentation*. Tulsa, OK: SEPM Special Publication 23, pp. 249–263.
- Gyllenhaal, E.D., 1991. How accurately can paleoprecipitation and paleoclimatic change be interpreted from subaerial disconformities? Unpublished Ph.D. dissertation, University of Chicago, Chicago, IL.
- Havholm, K.G., Blakey, R.C., Capps, M., Jones, L.S., King, D.D., and Kocurek, G., 1993. Aeolian genetic stratigraphy: An example from the Middle Jurassic Page Sandstone, Colorado Plateau. In Pye, K., and Lancaster, N. (eds.), *Aeolian Sediments, Ancient and Modern*. Oxford: Blackwell Scientific. International Association of Sedimentologists Special Publication 16, pp. 87–107.
- Herries, R.D., 1993. Contrasting styles of fluvial-aeolian interaction at a downwind erg margin: Jurassic Kayenta – Navajo transition, north-eastern Arizona, USA. In North, C.P., and Prosser, D.J. (eds.), *Characterization of Fluvial and Eolian Reservoirs*. Geological Society of London Special Publication 73, pp. 199–218.
- Kocurek, G., and Dott, R.H.Jr., 1981. Distinctions and uses of stratification types in the interpretation of eolian sand. *J. Sediment. Petrol.*, 51, pp. 579–595.
- Levish, D.R., 1997. Late Pleistocene sedimentation in glacial Lake Missoula and revised glacial history of the Flathead lobe of the Cordilleran Ice Sheet, Mission Valley, Montana. Unpublished Ph.D. dissertation, University of Colorado, Boulder, CO, 191pp.
- Mack, G.H., James, W.C., and Monger, H.C., 1993. *Classification of paleosols*. Geological Society of America Bulletin 105, pp. 129–136.
- Miall, A.D., 1992. Alluvial models. In Walker, R.G., and James, N.P. (eds.), *Facies Models, Response to Sea Level Change*. Ontario: Geological Association of Canada, pp. 119–142.
- Miall, A.D., 1996. *The Geology of Fluvial Deposits: Sedimentary Facies, Basin Analysis, and Petroleum Geology*. New York: Springer, 582pp.
- Munoz, A., Ojeda, J., and Sanchez, V.B., 2002. Sunspot-like and ENSO-NAO-like periodicities in lacustrine laminated sediments of the Pliocene Vallarroya Basin (La Rioja, Spain). *J. Paleolimnol.*, 27, 453–463.
- Nuhfer, E.B., Anderson, R.Y., Bradbury, J.P., and Dean, W.E., 1993. Modern sedimentation in Elk Lake, Clearwater County, Minnesota. In Bradbury, J.P., and Dean, W.E. (eds.), *Elk Lake, Minnesota: Evidence for Rapid Climate Change in the North-Central United States*. Geological Society of America Special Paper 276, pp. 75–96.
- Olsen, P.E., 1990. Tectonic, climatic, and biotic modulation of lacustrine ecosystems – examples from Newark Supergroup of eastern North America. In Katz, B.J., (ed.), *Lacustrine Basin Exploration; Case Studies and Modern Analogs*. American Association of Petroleum Geologists Memoir 50, pp. 209–224.
- Parrish, J.T., 1998. *Interpreting Pre-Quaternary Climate from the Geologic Record*. New York: Columbia University Press, 338pp.
- Parrish, J.T., and Peterson, F., 1988. Wind directions predicted from global circulation models and wind directions determined from eolian sandstones of the western United States – A comparison. *Sediment. Geol.*, 56, pp. 261–282.

- Parrish, J.T., Ziegler, A.M., and Scotese, C.R., 1982. Rainfall patterns and the distribution of coals and evaporates in the Mesozoic and Cenozoic. *Paleogeogr. Palaeoclimatol. Palaeoecol.*, **40**, 67–101.
- Retallack, G.J., 1988. Field recognition of paleosols. In Reighardt, J., and Sigeo, W.R. (eds.), *Paleosols and Weathering through Geologic Time: Principles and Applications*. Geological Society of America Special Paper 216, pp. 1–20.
- Retallack, G.J., 1990. *Soils of the Past: An Introduction to Paleopedology*. Boston: Unwin Hyman, 520pp.
- Rubin, D.M., 1987. *Cross-Bedding, Bedforms, and Paleocurrent: Concepts in sedimentology and paleontology*, vol.1. Tulsa, OK: Society of Economic Paleontologists and Mineralogists, 187pp.
- Shaw, J., Munro-Stasiuk, M., Sawyer, B., Beaney, C., Lesemann, J.E., Musacchio, A., Rains, B., and Young, R.R., 1999. The Channeled Scabland: Back to Bretz?. *Geology*, **27**, 605–608.
- Siegert, M.J., Eyers, R.D., and Tabacco, I.E., 2001. Three-dimensional ice sheet structure at Dome C, central East Antarctica; implications for the interpretation of the EPICA ice core. *Antarct. Sci.*, **13**, 182–187.
- Stach, E., Mackowsky, M.T., Teichmüller, M., Taylor, G.H., Chandra, D., and Teichmüller, R., 1982. *Stach's Textbook of Coal Petrology* (3rd edn.). Berlin: Gebrüder Borntraeger, 535pp.
- Talbot, M.R., 1988. The origins of lacustrine oil source rocks: Evidence from the lakes of tropical Africa. In Fleet, A.J., Kelts, K., and Talbot, M.R. (eds.), *Lacustrine Petroleum Source Rocks*. Geological Society of London Special Paper 40, pp. 29–43.
- Teichmüller, M., 1989. The genesis of coal from the view point of coal petrology. *Int. J. Coal Geol.*, **12**, 1–87.
- Trauth, M.H., Deino, A., and Strecker, M.R., 2001. Response of the East African climate to orbital forcing during that last interglacial (130–117 ka) and the early last glacial (117–60 ka). *Geology*, **29**, 499–502.
- Ziegler, A.M., Raymond, A.L., Gierlowski, T.C., Horrell, M.A., Rowley, D.B., and Lottes, A.L., 1987. Coal, climate and terrestrial productivity: The present and Early Cretaceous compared. In Scott, A.C. (ed.), *Coal and Coal-Bearing Strata*. Geological Society of London Special Publication 32, pp. 25–49.

Cross-references

[Arid climates and indicators](#)
[Astronomical theory of climate change](#)
[Coal beds, origin and climate](#)
[Eolian sediments and processes](#)
[Evaporites](#)
[Glacial geomorphology](#)
[Glacial sediments](#)
[Ice-rafted debris \(IRD\)](#)
[Lacustrine sediments](#)
[Laterite](#)
[Loess deposits](#)
[Mineral indicators of past climates](#)
[Paleosols, pre-Quaternary](#)
[Proglacial lacustrine sediments](#)
[Red beds](#)
[Sedimentary indicators of climate change](#)
[Tills and tillites](#)
[Varved sediments](#)
[Weathering and climate](#)

CORALS AND CORAL REEFS

Nowhere do the sciences of biology and geology come closer together than in the study of coral reefs. Reefs can be considered as geological structures – massive ramparts of rock – that have been built by organisms in the distant past, or they can be considered as ecosystems that are as fragile as any other on Earth. Reefs, the geological structures, are the direct products of diverse living ecosystems and as such, their formation has

-
- Phylum Cnidaria
 Class Hydrozoa
 Order Hydroidea (hydroids)
Order Milleporina (including Genus *Millepora*)
Order Stylasterina (including Genera *Distichopora* and *Stylaster*)
 Class Scyphozoa (jellyfishes)
 Class Cubozoa (sea wasps)
 Class Anthozoa
 Subclass Octocorallia
Order Helioporacea (*Heliopora coerulea*)
Order Alcyonacea (soft corals, *Tubipora*, sea fans and relatives)
 Order Pennatulacea (sea pens)
 Subclass Hexacorallia
 Order Actiniaria (simple sea anemones)
 Order Zoanthidia (colonial anemones)
 Order Corallimorpharia (corallimorpharians)
Order Scleractinia (true stony corals)
Order Rugosa (Paleozoic corals)
Order Tabulata (Paleozoic corals)
 Subclass Ceriantipatharia
 Order Antipatharia (black corals)
 Order Ceriantharia (tube anemones)
-

Groups having some or all species with stony skeletons are indicated in bold.

always been controlled by the sorts of events that control other ecosystems, both marine and terrestrial.

The term “coral” is commonly used for both “soft” and “hard” corals and sometimes includes other colonial Cnidaria (also commonly called Coelenterata). The term “coral,” used without a qualifying term, most commonly refers to hard or skeletonized corals and it is used this way here. The taxonomic relationship between the taxa is indicated in the box below. This classification does not include many extinct orders of skeletonized Cnidaria with uncertain affinities.

Of the orders listed above, the three hexacoral orders (shown in **bold**) are, or were, dominant faunas of coral reefs as well as non-reef habitats. Scleractinia occur in the Mesozoic and Cenozoic; Rugosa and Tabulata occur in the Paleozoic. The four octocoral and hydrozoan orders (**bold**) are all primarily or entirely Cenozoic.

Of the four extant orders, all except the Stylasterina are partly or wholly zooxanthellatooxanthellatee (corals that have symbiotic blue-green algae called zooxanthellate in their tissues, see below) and are therefore restricted to sun-lit depths and warm water. Whether or not Rugosa and Tabulata were also zooxanthellate has long been debated without definite outcome.

Paleozoic corals

Many Cambrian fossils have at times been called “corals.” The most coral-like of these are small, cup-shaped, mostly solitary organisms with septa. Some have an operculum over the calice opening (Jell and Jell, 1976). In total, seven orders of Paleozoic corals may be recognized, of which the Tabulata and Rugosa are by far the most important. Unlike the Scleractinia, these two groups have left good fossil records, as their skeletons are calcitic and thus more stable than the aragonite skeletons of Scleractinia.

Order Tabulata (Early Ordovician–Permian)

Tabulata are much less variable than rugose or scleractinian corals. They are all colonial and consist of slender tube-like corallites

1–3 mm diameter, crossed internally by transverse partitions, the tabulae. Colonies are typically incrusting, flat or massive, but may be branching. Individual corallites may be in contact or widely separated. Each corallite has a theca (enveloping sheath) and groups of corallites are enclosed in a sheath-like epitheca. The corallites may be connected by fine tubules forming a three-dimensional structure. Where corallites are in close contact, internal horizontal partitions (tabulae) are usually found. Where corallites are separated, external horizontal plates (dissepiments) also occur. Radially arranged spine-like septa, sometimes forming vertical structures, may be present.

The morphology of the Tabulata does not indicate whether they were zooxanthellate or not. However, as they were colonial, had small corallites, and had growth rates comparable to those of zooxanthellate Scleractinia (up to 18 mm per year), it seems probable that they were.

The Tabulata are first seen as a distinct group in the Early Ordovician and thus pre-date the Rugosa (Figure C62). There is no evidence of common ancestry. By Middle Ordovician, there was a radiation in Tabulata diversity, with six families recognized. These are mostly associated with soft substrates rather than carbonate platforms of high-energy environments. Tabulata became significant frame builders during the Silurian but were relatively unimportant during intervals of maximum reef development in the Devonian. They appear to have not re-gained diversity during the Carboniferous or Permian, although they were periodically abundant.

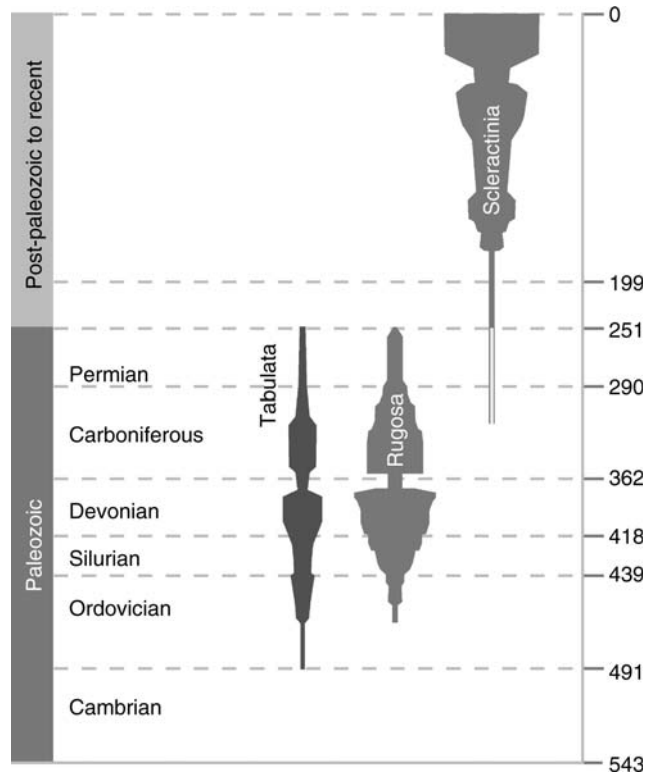


Figure C62 Approximate generic diversity of the three main orders of corals over time. Numbers to the right indicate millions of years ago. (After Stanley and Fautin, 2001.)

Order Rugosa (Mid Ordovician–Permian)

Rugosa have a much greater resemblance to Scleractinia than to Tabulata. Mature colonies have an array of growth forms comparable to Scleractinia (see below), although the majority of taxa are solitary or form colonies where individual corallites are large and dominant. Rugosa have basic structural components at least superficially similar to Scleractinia, the main difference being in the arrangement of the septa (Figure C63). Tabulae analogous to those of Tabulata are usually very abundant and so is a complex array of dissepiments that appear analogous to those of Scleractinia.

The earliest Rugosa were solitary and of simple construction. Complex colonies had evolved by Late Ordovician and thereafter the few evolutionary trends that are seen are mostly in skeletal detail and most have reversed one or more times. Differences in the pattern of insertion of septa make it unlikely that the Scleractinia arose from the Rugosa although this view is disputed.

Paleozoic coral reefs

Reef-like carbonate structures of one form or another have existed on Earth for at least 2.7 billion years (Wood, 1999). The first reef-like limestone accumulations (excluding microbial carbonates), found in Proterozoic rocks the world over, were simple structures formed by stromatolites, hemispherical mounds of what were probably blue-green algae that entrapped fine sediment much as stromatolites do today. The first reef-like structures of animal origin were built by archaeocyath sponges of the Lower Cambrian (530–520 MyBP). What reef-building there was after the extinction of the archaeocyaths was mostly due to cyanobacteria, stromatolites and some coral-like Anthozoa, all growing in shallow protected waters and containing abundant trilobites together with a wide diversity of mollusks.

Late Cambrian ecosystems persisted into the Middle Ordovician, when complex algae and invertebrate reef communities became widespread and reef biota greatly diversified. Stromatoporoïd sponges and tabulate corals radiated at this time. Rugose corals first appeared in the Middle Ordovician and rapidly increased in number and diversity (Figure C62). Thus, algal communities were largely replaced by communities of skeletonized metazoans. By Late Ordovician, colonial rugose and tabulate corals had greatly diversified in shallow water and formed coral patch reefs, along with stromatoporoids, other sponges and calcareous red algae. These reefs had little wave

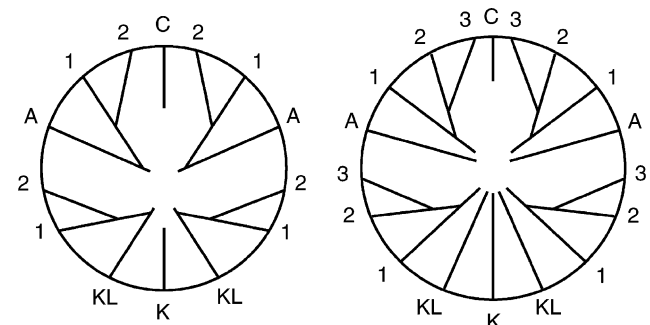


Figure C63 The basic septal pattern of Rugosa corallites. This pattern is usually unrecognizable in mature corallites. C = cardinal septum, K = counter septum, A = alar septa, KL = counter-lateral septa. (After Oliver, 1980.)

resistance and did not form solid platforms, although stromatoporoids and tabulate corals formed massive colonies several meters diameter. These are the oldest-known reef coral communities and were possibly the outcome of endo-symbiotic animal/algal associations. For at least 150 million years, different combinations of these algae, sponges, and corals built reefs around the tropical world (Wood, 1999). Silurian reefs became abundant and diverse and some reached massive proportions, the first truly wave-resistant carbonate platforms.

In the Devonian, especially the Middle to Late Devonian, reefs reached maximum development for the Paleozoic, if not the entire Phanerozoic. What remains today of these reefs are sometimes of awesome size and have the full range of zonation seen in modern reefs. They had a high diversity of frame builders including microbialites, calcifying cyanobacteria, stromatoporoid and other sponges as well as tabulate and rugose corals. They also contained a diversity of other fauna and flora perhaps comparable to modern reefs. However, before the close of the Devonian, reef building ceased abruptly and thus it remained until scleractinian-built reefs first emerged in the Late Triassic. This Late Devonian to Late Triassic interval is the longest hiatus in reef building in the geological record.

Latest Devonian reefs are relatively rare, and most reef-like constructions were relegated to relatively deep water throughout the entire Carboniferous. This was an interval of great climatic upheavals, sea-level fluctuation, and low ocean temperatures, all probably contributing to environments hostile to reef development. During the Late Carboniferous to Early Permian, phylloid (leaf-like) algae so completely dominated would-be reef substrates that most reef biota may have been displaced. Late Permian reef-like structures are characterized by frondose bryozoans, a wide range of sponges, algae, and encrusting tube-like *Tubiphytes* (of unknown taxonomic affinity), all with little cementation. Corals are uncommon everywhere.

The causes of the end-Permian extinctions are elusive, but as far as reef biota are concerned they were probably the result of a rapid drop in sea level succeeded by extensive volcanism and anoxic conditions, followed by an extensive sea-level rise. It has been estimated that 80–95% of all species became extinct. Apparently, among these were all corals.

Mesozoic and Cenozoic corals

Order Scleractinia (Middle Triassic to present)

Extant Scleractinia have similar numbers of zooxanthellate and azooxanthellate genera and species. These two groups are not taxonomically separate although they are almost all sharply eco-physiologically distinct. Zooxanthellate Scleractinia (sometimes called “reef-building corals”) are primarily colonial and are responsible for the construction of most Mesozoic to present coral reefs. Azooxanthellate Scleractinia are primarily solitary and most occupy deep water.

Structure. The simplest skeleton of an individual polyp, the corallite, is a tube-like structure, the corallite wall. Radially arranged vertical plates, the septa, are the dominant structures within the wall (Figure C64). Corallites may be solitary or joined by horizontal plates and other structures, collectively called the coenosteum. Some polyps or colonies have an epitheca, a thin film of skeleton surrounding the lower wall or colony perimeter. Complex colonies of many types are derived from this basic structure (Veron, 2000).

The sac-like body cavity of the coral polyp is the coelenteron, which serves many functions including digestion and

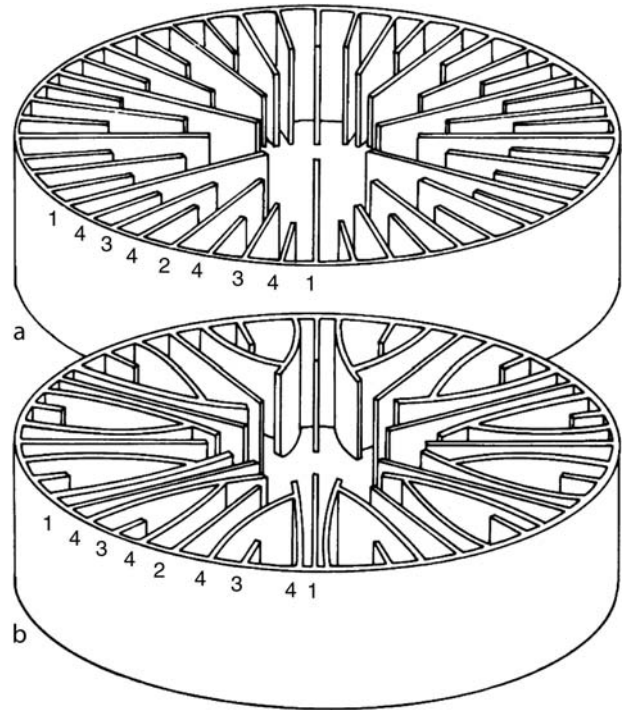


Figure C64 Septal patterns of Scleractinia showing simple radial symmetry (above) and poutales plan (below). The latter is found in several different families. *Porites* has a distinctive bi-radial symmetry of septa.

the circulation of fluids for respiration and nutrition. It is partitioned by vertical mesenteries that have coiled filaments along their inner margins.

Most Scleractinia have tentacles. These are smooth in corals that feed on detritus but most taxa have stinging cells (nematocysts) for defense and food capture. Nematocysts are commonly grouped into wart-like batteries.

Cnidaria are the simplest organisms to have discrete nervous, muscular and reproductive systems, and these are all well developed in Scleractinia. Some corals have separate male and female sexes but most are hermaphrodites.

Evolutionary history. The first organisms that might be called scleractinians are known from Paleozoic fossils from China and Scotland (Ezaki, 1998), but the earliest proliferation of organisms that were clearly ancestral Scleractinia are Middle Triassic and consisted of at least seven, but possibly nine, suborders. These corals did not build reefs; they were small solitary or phaceloid organisms of the shallow Tethys of southern Europe and Indo-China (Stanley and Fautin, 2001; Stanley, 2003).

There is current debate about whether the Scleractinia are a single lineage (monophyletic) or whether the order also includes non-skeletal taxa such as extant Corallimorpharia or other anemone-like taxa that are now extinct (Stolarski and Roniewicz, 2001; Stanley, 2003). Molecular studies (Veron et al., 1996; Romano and Cairns, 2000) are inconclusive so far, although they strongly indicate that any common ancestor would have been Paleozoic and thus were presumably Rugosa (see above) or, more likely, soft-bodied. Certainly, Scleractinia without skeletons may have existed both before and after the Middle Triassic (Oliver, 1980; Buddemeier and Fautin, 1997; see review in Stanley, 2003).

During the Middle and Late Triassic, corals became widespread throughout the Tethys region and their fossils are now found around much of the equatorial Panthalassa Ocean rim. There was an enormous time interval of 20–25 million years between the earliest Triassic corals and the earliest widespread coral reefs. Most noteworthy of Triassic corals is that they had a wide range of skeletal micro-structures, suggesting that any common ancestry would have been remote. Nevertheless, Triassic corals were not the ecological equivalents of modern corals; corallites were large and poorly integrated, such that phacelloid growth forms (where branches are composed of individual corallites) were dominant.

There was a 5–8 million year hiatus between the collapse of Triassic reef development and the onset of Jurassic reefs, a time of origin of many new scleractinian families (Beauvais, 1989). The Late Jurassic was probably the all-time global maximum of Mesozoic coral diversity with at least 150 genera recorded in the European Tethys and 51 in the Panthalassa. Paleobiogeographic provinces can be recognized that reflect continental plate movements, especially the increasing width of the Protoatlantic. By the Late Jurassic, the paleobiogeographic pattern that had developed was the precursor to the pattern that persisted into the Cenozoic. It was dominated by massive reef development throughout the Tethys, the Atlantic, and the far eastern Panthalassa. The vast expanse of the eastern Panthalassa was probably a barrier to east-west dispersion, just as the far eastern Pacific is today.

A high proportion of the families of extant Scleractinia have their origins in the Middle to Late Jurassic. For most, the fossil record is not clear and thus there are few links between the main branches of the Family Tree (Figure C65). The Jurassic was the time of proliferation if not the origin of two of the major groups of corals, the Fungiina and the Faviina. The Fungiina dominated much of the Jurassic and the Cretaceous. As a group, it was greatly diminished by the end-Cretaceous mass extinctions and the families attributed to it today have uncertain affinities. The Faviina, on the other hand, are a well-defined group and the Faviidae have remained a major family for 150 million years.

Early Cretaceous corals are broadly similar to those of the Late Jurassic (Beauvais, 1992). However, relatively little is known of the Middle Cretaceous corals. The continuity of families indicated in Figure C65 is largely due to extrapolations between Early and end-Cretaceous fauna, with poorly-known families omitted. This is because, by Middle Cretaceous, reefs worldwide had become dominated by rudist bivalves and environmental perturbations greatly affected reef development. It was not until the very late Cretaceous, following an unexplained total extinction of the rudists, that corals returned to a position of dominance. At this time reefs probably again occurred worldwide, but there are few remains of them today.

One-third of all families and over 70% of all genera became completely extinct at the end-Cretaceous boundary. The Faviidae and the Caryophylliidae are the only families that were major components of Mesozoic reefs and that also proliferated in the Cenozoic (Veron, 1995).

The evolutionary history of modern corals is divisible into three geological intervals: (a) the Paleogene, when the few survivors of the end-Cretaceous extinctions proliferated into a diverse cosmopolitan fauna; (b) the Miocene, when this fauna became subdivided into the broad biogeographic provinces we have today and pre-cursors of most extant species evolved; and (c) the Plio-Pleistocene to present, when the world went into full glacial mode and modern distribution patterns emerged.

For the 12 million years after the end-Cretaceous extinctions, only 13 new genera of corals have been recorded. It was thus a radiation of new zooxanthellate genera that populated the seas of the Eocene. By Late Oligocene, reef development became world-wide and diversity reached an all-time high in the Tethys and Caribbean (Frost, 1981).

The Miocene is the time of origin of non-Oligocene extant genera (primarily Indo-Pacific) and the immediate ancestors of extant species. It is also the time of obliteration of the Tethys, the extinction of non-zooxanthellate corals from the Mediterranean, and the start of the separate evolutionary histories of Atlantic and Indo-Pacific species.

Compared with most other major groups of animals, coral genera are long-lived in geological time and have low extinction rates: nearly half of all extant genera extend as far back as the Oligocene and nearly a quarter extend back to the Eocene.

The history of corals subsequent to the Miocene (Veron, 1995) becomes decreasingly visible in the fossil record and increasingly visible in the taxonomy and distribution of living corals. The Plio-Pleistocene fossil record of the Caribbean is better than that of the Indo-Pacific and it is in the Caribbean that the impacts of the Pleistocene glaciations were greatest. The progressive closure of the Central American Seaway was one of the most important events in the history of modern corals. Before the closure, there may have been no distinction between the corals of the far eastern Pacific and those of the Caribbean. After the closure (3.4 MyBP), the corals of the Pacific side of the Isthmus were extinguished, or nearly so.

There are no zooxanthellate scleractinian species common to the Indo-Pacific and the Caribbean today.

Order Milleporina

This order of hydrozoans is represented by several extinct genera and one common extant genus, *Millepora*, with approximately 50 species. All are zooxanthellate.

Millepora have growth forms ranging from branching to submassive and encrusting. Tiny polyps are mostly imbedded in the skeleton where they are linked by a network of minute canals (the cyclosystem). All that can be seen on the smooth surface are the pores of two types of polyps, gastropores and dactylopores. Reproductive ampullae, which produce medusae, can also be seen on the colony surface. Generations of sexual medusae alternate with generations of asexual polyps. Almost all records are Cenozoic, but as polyps are very small they are seldom distinct in fossils.

Order Stylasterina

The second group of hydrozoans is mostly found only in deep water. All are azooxanthellate. Two genera, *Distichopora* and *Stylaster*, are commonly found in caves and under overhangs in shallow reef environments.

Distichopora are ornate corals that branch in one plane. They have no cyclosystem; instead, gastropores are aligned along the edge of branches and these are flanked on each side by a row of dactylopores. Reproductive ampullae are clustered towards the ends of side branches.

Stylaster also branch in one plane but branches are fine, tapered and delicate. Gastropores are linked by individual cyclosystems and surrounded by dactylopores. These alternate on the sides of branches, giving the latter a zig-zag pattern. Wart-like reproductive ampullae occur on the sides of older branches. Almost all records are Cenozoic.

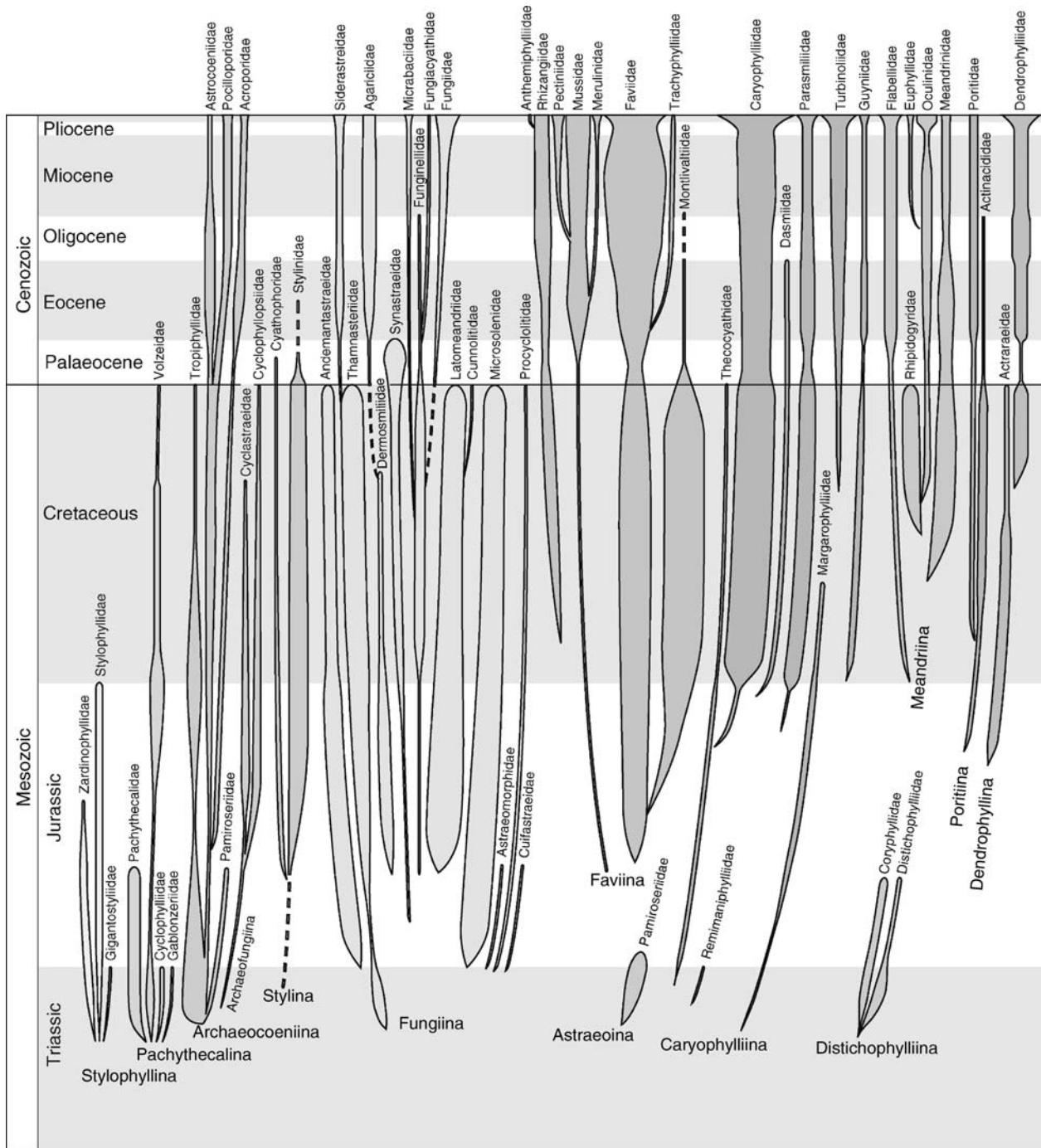


Figure C65 The “family tree” of Scleractinia. Reconstructing the evolutionary sequences of Scleractinia is a complicated process for it must encompass the fossil records over very great intervals of time, the taxonomic relationships of extant corals, and studies of coral systematics using molecular techniques. The top of the “tree” (the families of extant corals) is well established, as are the main branches through the Cenozoic, since most of these have extant representatives. However, little is known about the Mesozoic ancestors of Scleractinia, for the majority of families are extinct (simplified from Veron, 2000).

Order Helioporacea

Heliopora coerulea or “blue coral” is the sole member of Order Helioporacea. *Heliopora* is zooxanthellate and blue or greenish underwater. The skeleton, composed of fibrocrystalline

aragonite, is always permanently blue. Polyps are small and superficial and are interconnected by minute solenial tubes.

Heliopora is easily recognized in fossil outcrops by its color and therefore can be traced back to the Cretaceous. Throughout

this time, it appears to have remained a single species, in which case it would have by far the greatest geological longevity of any coral.

Order Alcyonacea

The second group of octocorals (corals which have eight tentacles) to form skeletons is part of the very large Order Alcyonacea. One genus, *Tubipora* the “organ-pipe” coral, has a skeleton. Only one species, *T. musica*, is currently named. It has an isolated taxonomic position.

Structure and evolutionary history. *Tubipora* are zooxanthellate. The skeleton is permanently colored dark red. Polyps are long and tubular and are interconnected by horizontal tabulae or stolons, which form transverse platforms. Corallites grow from the platforms, not from the branching of corallites. Living colonies have brown pinnate tentacles.

Heliopora is known only from the Plio-Pleistocene, but is widely distributed across the Indo-west Pacific.

Mesozoic and Cenozoic coral reefs

Intervals of change

Coral reef development is clearly correlated with extinction events and intervals of proliferation and diversification. The first major interval of reef development occurred after diversification of reef biota in the Middle Ordovician and lasted until the end-Devonian extinctions. The second occurred with the proliferation of Scleractinia in the Middle Triassic and ended with the end-Triassic extinctions. The third started with the proliferation of corals in the Middle to Late Jurassic and, punctuated by a 30 million year interval of rudist dominance, ended with the end-Cretaceous extinctions. The fourth started with the diversifications of the Early and Middle Eocene and, interrupted by a relatively minor end-Eocene extinction event and the Pleistocene glaciations, resulted in the reefs and the coral fauna we have today.

Although reef development is not closely linked to coral biodiversity *per se*, not surprisingly reef development clearly follows intervals of coral diversification and abundance, whilst cessation of reef development is absolutely linked to mass extinctions. The causes of mass extinctions, coral diversification, and abundance changes are not clear and may well be different in each case. However, all are underpinned by the gradual yet decisive control of the marine environment created by continental movements.

Perhaps surprisingly, the Earth’s great era-long cycles of temperature change show no dominating impact on coral or reef development, other than by controlling latitudinal spread. This is not true of shorter intervals of climate change, especially those that created sea-level changes. More rapid sea level changes have greater impact. It is very likely that these occurred at a much greater frequency, and were of greater importance, than suggested by the fossil record.

Mesozoic reefs

No reef building occurred for 12–14 million years after the end-Permian mass extinctions (Stanley, 2003). Only stromatolites remained common and it was not until the Middle Triassic that the first reef-like structures appeared; these had a fauna dominated by sponges, algae, bryozoa and *Tubiphytes*, much like those of the Late Permian. However, by Late Triassic, massive scleractinian reefs were abundant, especially in the Tethys, which remained a center of reef development throughout the Mesozoic.

The end of the Triassic was marked with a mass extinction. It was not the equal of the extinctions that marked the end of the Paleozoic 45 million years earlier, but it may have rivaled the extinctions at the end of the Mesozoic. The main impact on reefs was the collapse of the reefs of the Tethys, perhaps because of anoxic conditions correlated with sea-level and climatic changes. Whatever the cause, reef building did not recover for 6–8 million years. The inheritance of the Jurassic was a remnant of these extinctions, a depauperate although diverse suite of scleractinian genera. Early Jurassic reefs are rare everywhere in the world and all Triassic genera had become extinct by then.

The Jurassic recovery was slow, but by Middle Jurassic, reef development had again proliferated in the Tethys of Europe and in the Mediterranean. Complex ecosystems underwent a major radiation, enhanced by a warming climate and extensive flooding of shallow shelf areas. Elsewhere reefs remained poorly developed, especially in the Panthalassa and thus it may have remained throughout most of the Jurassic.

The beginning of the Cretaceous was not marked by any extinction event that had a major impact on reefs, and they continued to thrive throughout the Early Cretaceous. There was, however, an increasingly drastic change in coral communities over this time. Rudist bivalves, a previously obscure group of mollusks, progressively displaced corals as the dominant reef biota, and thus it remained for 30 million years. During this interval, zooxanthellate corals coexisted with rudists, but largely in separate, deeper habitats. The reefs of that time probably resembled the inshore fringing reefs of today, repeatedly destroyed by changing sea levels and consisting mostly of banks of entrapped sediment, with no algal cementation. Rudists were probably zooxanthellate and, as they had a lesser amount of aragonite in their shells than corals, probably survived acidic conditions better than the corals.

Repeated environmental upheavals probably had a greater influence on evolutionary change in the Cretaceous than did continental movements. The Late Cretaceous was a time of extreme sea level change, with periodic flooding of nearly 40% of the continents. Significantly for corals, this created a Super-Tethys Ocean, which covered much of present-day Europe. The consequences for reefs are unknown, but the continually decreasing sea levels of the Late Cretaceous would have had a great impact on coral communities (Kauffman and Fagerstrom, 1993).

Much of the Middle Cretaceous was characterized by release of carbon dioxide due to extensive volcanism around the continental plate margins and this, together with the accumulation of organic matter associated with sea level changes, may have increased the acidity of much of the ocean surface. Ocean and atmospheric temperatures over a range of latitude from the equator to the poles were much higher than they are now. This would have varied greatly over time, but subtropical conditions may have periodically extended to 45° N and possibly 70° S, and there were no polar ice caps. These conditions would have resulted in weaker ocean currents than we have today. Corals would have been far more widely dispersed and there would have been a much greater development of distinctive regional provinces.

Cenozoic reefs

By the close of the Mesozoic, the flooding of the continents had ceased and the warm climates that had dominated the Cretaceous had begun a long and irregular decline towards a

glacial mode (Perrin, 2002). Extensive reef development did not commence for some 12 million years after the end-Cretaceous extinctions. Eocene reefs are mostly poorly preserved, but were extensive in area. An end-Eocene extinction event, combined with progressive blockages of the Tethys Sea in the Early Oligocene created a hiatus in reef development, but did not greatly diminish coral diversity. Extensive reef development occurred throughout the Miocene. Plate tectonics remained an important aspect of reef development throughout the Cenozoic.

There were two post-Miocene events that greatly affected reef development. The first was the closure of the Central American Seaway, finally separating the coral faunas of the Indo-Pacific and Caribbean. The second was the Pleistocene glaciations, which, because of low sea temperatures, stopped reef development in the far eastern Pacific, much of the Caribbean, and high latitude locations of the western Pacific.

More importantly, low sea levels exposed all coral reefs world-wide. This clearly would have devastated all coral reefs, but the main impact was on the shallow reefs of central and western Indonesia, part of the global center of coral and coral reef biodiversity (see Figure C67).

During the Holocene, when both climate and sea levels became relatively stable, coral communities remained in constant flux as a result of changing surface currents. These create repeated changes to the distribution ranges of species and reticulate evolutionary changes resulting from repeated divergence and convergence of phylogenetic lineages.

Holocene environments are recorded in annual growth bands of massive corals like *Porites*. These bands provide proxy indicators of several environmental parameters notably temperature and rainfall, the latter where colonies grow near river mouths (Figure C66).

Types of reefs

Reefs are made of consolidated limestone and unconsolidated rubble. Consolidated reefs are usually constructed of solid limestone, made hard by the combined action of cementing (“coralline”) algae, the mechanical action of pounding waves, and the chemical action of rainwater.

There have been many attempts to classify different types of reefs. All lack general agreement because there is continual variation from one reef type to another, also because they can be classified according to their geological history, their shape, their position relative to land masses and by the material they are made of. In principle, these types of classification can be merged into three broad categories: “fringing reefs,” “barrier reefs” and “atolls” (Darwin’s original groups).

Fringing reefs are mostly close to coastlines, are usually unconsolidated wherever protected from wave action, and usually have a high component of non-carbonate sediment. Barrier reefs are off-shore and are composed of wave-resistant consolidated limestone. Atolls are usually (but not necessarily) a wall of reefs enclosing a central lagoon. As the shape of both barrier reefs and atolls is largely determined by the bathymetry of the substratum, there are all manner of intergrades between them. Likewise, “fringing reefs” gradually become “barrier reefs” with increasing distance from the shore. Reefs that do not conform to any of these descriptions are commonly called “platform” reefs.

The term “coral reef” is usually used in association with massive shallow-water limestone structures with a high coral

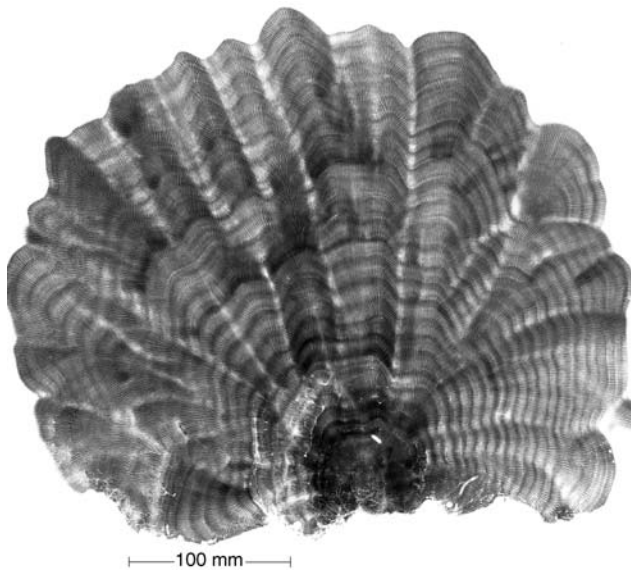


Figure C66 An X-rayed section through *Porites* showing annual growth bands. Study of these bands in fossil as well as in extant corals indicate annual growth rates and may also indicate environmental parameters, notably temperature and rainfall (image courtesy Janice Lough).

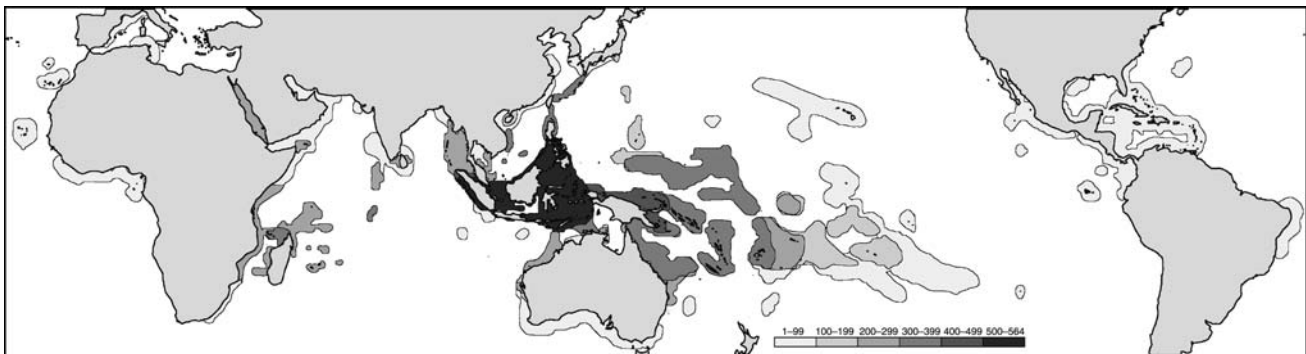


Figure C67 Species diversity contours of zooxanthellate corals. (After Veron, 1995, 2000.)

diversity, but other types of coral accumulations found in deep water are also of great size. These structures, sometimes called “bioherms,” are commonly formed of skeletal debris accumulated from one or a few species of azooxanthellate corals.

Zonation

Most accounts of coral reefs draw attention to the coral zones that they invariably display. These zones have been likened to zones of vegetation found on mountain slopes but on coral reefs they are mostly created by decreasing light and turbulence with increasing depth and, even in very clear water, this occurs within a depth range of less than 50 meters. Contrary to popular belief, species diversity is not at its highest on the scenically attractive reefs found in clear oceanic water. It reaches a peak for any given region on fringing reefs protected from strong wave action, where the water is slightly turbid. This is probably because *Acropora*, by far the most common Indo-Pacific coral, does not dominate these habitats, allowing for a higher diversity of other groups of coral.

Distribution patterns

The global distribution of reefs and the global pattern of coral diversity are linked, but not strongly (Figure C67). The Indonesian/Philippines archipelago has the world’s greatest concentration of reefs and the greatest coral diversity. Other areas of reef concentration are the Great Barrier Reef of Australia, the Red Sea and the Caribbean, the latter having a much lower diversity than all major Indo-Pacific regions. The reefs and coral faunas of each geological period are a combination of inheritance from the past and the outcome of more contemporary events. The distribution of modern reefs are an inheritance of the Tethys-dominated world of the Eocene (Figure C68), subsequently modified by the obliteration of both the Tethys Seaway (Miocene) and the Central American Seaway (Pliocene).

Reef environments

Calcareous algae thrive, but corals are uncommon on parts of reefs exposed to extreme wave action. Where there is some protection and where the water is clear, Indo-Pacific reef flats are usually dominated by *Acropora*. Unconsolidated rubble accumulations occur primarily where conditions for coralline

algae growth are poor: where wave action is weak, the water turbid, or the temperature frequently falls below 18 °C. Conditions for coral growth, however, may be good in such places.

Environmental factors. Substrate availability, sedimentary regimes, bathymetry, tidal regimes, turbulence, water quality, nutrients and biotic factors all affect reef development by controlling coral growth. These operate on local scales in shallow tropical seas primarily by affecting substrate conditions and light availability. On larger scales of space and time, sea levels and temperature are the most important limiting environmental parameters.

Sea level. Because coral reefs built by zooxanthellate corals can exist only in very shallow water, they are continually at the mercy of sea-level changes due to the land or sea rising or falling. Darwin recognized this long before the phenomenon of changing sea levels per se was actually discovered, yet even now it is not generally appreciated that coral reefs have not always looked like they do today. In times past, sea-level changes have been so rapid and so frequent that what are reefs today would have alternated between being exposed limestone islands and submerged limestone pinnacles. The reefs of today are artifacts of an unusually long period of relatively stable sea level.

Temperature. Reef-building corals and the reefs that they build have similar, tropical, distributions. This creates an interesting dilemma: which comes first, the coral or the reef? There have been many theories, all assuming some effect of ocean temperature. There is no correlation between coral diversity and reef formation: only a small number of coral species are needed to build the most massive reefs. There is, however, a clear correlation between ocean temperature and zooxanthellate coral distribution, and between the former and formation of highly consolidated reefs. The latter only occur where sea temperature does not fall below 18 °C for extended periods of time, a restriction that does not apply to those corals where approximately half of all species occur where temperatures regularly fall to 14 °C (Veron, 1995). The likely solution to the dilemma is that temperature controls the formation of reefs through ecological processes. Reef building requires carbonate production and that requires coral-dominated ecosystems. In the tropics, coral ecosystems exist because they are able to out-compete algae-dominated ecosystems, but this is not the case in higher

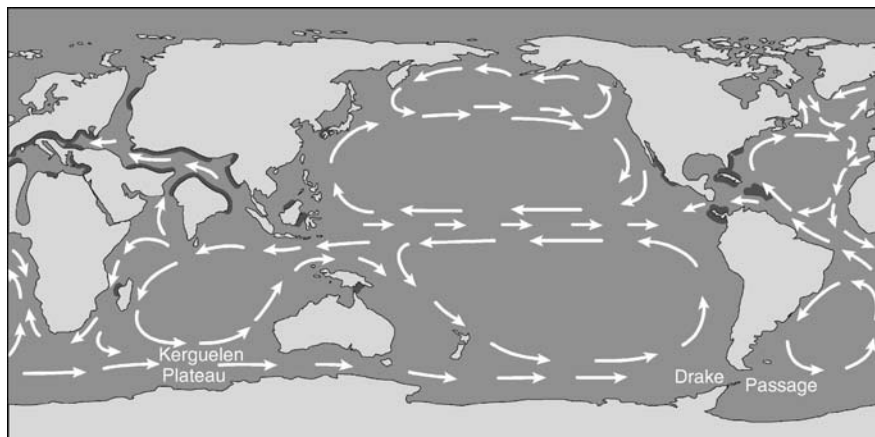


Figure C68 The distribution of coral reefs of the Eocene. (After Veron, 2000.)

latitudes. Thus, the highest latitude coral reefs in the world all have mixtures of coral and algal communities, which compete, and the corals struggle to get enough light and space to survive.

Symbiosis

Reefs of today are an ancient phenomenon without parallel in nature – a specific example of a symbiotic relationship between plants and animals. The sort of plants and animals is not critical, but the relationship between them is. Symbiosis allows the limitless resources of sunlight and carbon dioxide to be harnessed and used to construct a place to live. In effect, symbiosis allows reefs to be built by animals because it gives them the energy-generating capacity of plants. What the animal gives the plant is a medium in which to live that is stable yet exposed to sunlight. What the plant gives the animal is an enhanced capacity to remove metabolic waste, an enhanced capacity to calcify, a direct nutrient source and a capacity to concentrate and re-cycle limited nutrients, including nitrogen and phosphate. Symbiosis allows corals to exist in an almost nutrient-free environment, including the nutrient deserts of the emptiest oceans.

Clearly, the evolutionary advantage of symbiosis is very great, but the evolutionary cost is great also. Zooxanthellate corals are constrained to live near the ocean surface, the most hostile of marine environments both physically and biologically. Most importantly, symbiosis constrains corals to live in places where they must compete with macroalgae. Coral-algae symbiosis is therefore ultimately responsible for the geographic constraints of reefs as well as their construction.

When did symbiosis evolve? This question has been debated almost since coral/algal symbiosis was first discovered, and the debate continues. It is tempting to conclude that the building and maintenance of wave-resistant carbonate platforms requires sunlight as the primary energy source. If so, such platforms, found as reefs worldwide, especially in the Silurian, Devonian, Jurassic and Cenozoic, could only have been built by calcifying plants or by plant-animal symbioses. This is not true for the reefs of most other periods or those which were not wave resistant or which were not exposed to high-energy conditions. Nor can it be supposed that symbioses or capacity for skeletonization are irreversible conditions. Indeed, it is quite possible that corals are anemone-like organisms of many unrelated groups that can, over geological time intervals of environmental change, develop or lose the capacity for symbiosis concurrently or separately from the capacity for skeletonization.

John E. N. Veron

Bibliography

- Beauvais, L., 1989. Jurassic corals from the circum-Pacific area. *Mem. Assoc. Australasian Paleontol.* **8**, 291–302.
- Beauvais, L., 1992. Paleobiogeography of the Early Cretaceous corals. *Palaeogeogr. Palaeoclimatol. Palaeoecol.*, **92**, 233–247.
- Buddemeier, R.W., and Fautin, D.G., 1997. Saturation state and the evolution and biogeography of symbiotic calcification. In *International Symposium on Biomineralization*, Monaco, (Alleman, D., and Cuif, J.-P. eds.), pp. 23–32.
- Ezaki, Y., 1998. Paleozoic Scleractinia: Progenitors or extinct experiments? *Paleobiology*, **24**(2), 227–234.
- Frost, S.H., 1981. Oligocene reef coral biofaces of the Vicentin, northeast Italy. *Soc. Econ. Paleontol. Mineral. Spec. Publ.*, **30**, 483–539.
- Jell, P.A., and Jell, J.S., 1976. Early middle Cambrian corals from western New South Wales. *Alcheringa*, **1**, 181–195.

- Kauffman, E.G., and Fagerstrom, J.A., 1993. The Phanerozoic evolution of reef biodiversity. In Ricklefs, R.E., and Schluter, D. (eds.), *Species Diversity in Ecological Communities*. Chicago, IL: University of Chicago Press, pp. 314–329.
- Oliver, W.A., 1980. The relationship of the scleractinian corals to the rugose corals. *Paleobiology*, **6**(2), 146–160.
- Perrin, C., 2002. *Tertiary: The emergence of modern reef ecosystems*. Tulsa, OK: Society of Economic Paleontologists and Mineralogists. SEPM Special Publication 72, pp. 587–621.
- Romano, S.L., and Cairns, S.D., 2000. Molecular phylogenetic hypotheses for the evolution of scleractinian corals. *Bull. Mar. Sci.*, **67**(3), 1043–1068.
- Stanley, G.D., 2003. The evolution of modern corals and their evolutionary history. *Earth-Sci. Rev.*, **60**, 194–225.
- Stanley, G.D., and Fautin, D.G., 2001. The origins of modern corals. *Science*, **291**, 1913–1914.
- Stolarski, J., and Roniewicz, E., 2001. Towards a new synthesis of evolutionary relationships and classification of the Scleractinia. *J. Paleontol.*, **75**(6), 1090–1108.
- Veron, J.E.N., 1995. *Corals in Space and Time: The Biogeography and Evolution of the Scleractinia*. Sydney, Australia: University of New South Wales Press, 321pp.
- Veron, J.E.N., 2000. *Corals of the World* (3 vols.). Townsville, Australia: Australian Institute of Marine Science, 463, 429 and 489pp.
- Veron, J.E.N., Odorico, D.M., Chen, C.A., and Miller, D.J., 1996. Re-assessing evolutionary relationships of scleractinian corals. *Coral Reefs*, **15**, 1–9.
- Wood, R., 1999. *Reef Evolution*. Oxford: Oxford University Press, 414pp.

Cross-references

- [Cenozoic Climate Change](#)
[Cretaceous/Tertiary \(K-T\) Boundary Impact, Climate Effects](#)
[Early Paleozoic Climates \(Cambrian-Devonian\)](#)
[Late Paleozoic Paleoclimates \(Carboniferous-Permian\)](#)
[Mesozoic Climates](#)
[Neogene Climates](#)
[Ocean Anoxic Events](#)
[Plate Tectonics and Climate Change](#)

CORDILLERAN ICE SHEET

The Cordillera of western Canada was repeatedly enveloped by a continental ice sheet, known as the Cordilleran Ice Sheet, during the Pleistocene and latest Pliocene (Flint, 1971; Clague, 1989; Jackson and Clague, 1991). At its maximum extent, the Cordilleran Ice Sheet and its satellite glaciers covered almost all of British Columbia, southern Yukon Territory, and southern Alaska, and extended south into the northwestern conterminous United States (Figure C69 and C70). The ice sheet, to a considerable extent, was confined between the high mountain ranges bordering the Canadian Cordillera on the west and east, but large areas on the east flank of the Rocky Mountains and west of the Coast Mountains were also covered by ice. Glaciers in several mountain ranges, such as the Olympic, Cascade, and Mackenzie Mountains, were more or less independent of the ice sheet, even at times of maximum ice cover.

The Cordilleran Ice Sheet attained its maximum size in British Columbia where it was up to 900 km wide and reached to 2,000–3,000 m elevation over the plateaus of the interior (Wilson et al., 1958). When fully formed, the ice sheet probably had the shape of an elongate dish, with gentle slopes in the interior region and steeper slopes at the periphery. It closely resembled the present-day Greenland Ice Sheet at such times. More commonly, the interior of the ice sheet had an irregular,

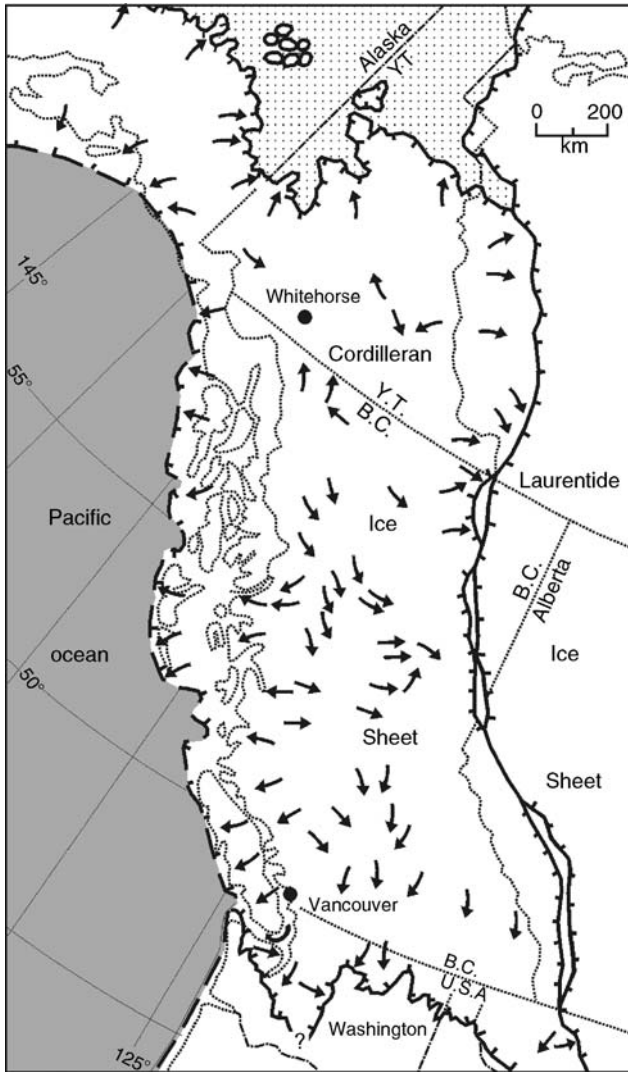


Figure C69 The Cordilleran Ice Sheet about 17,000 years ago at the maximum of the last glaciation. The upper surface of the ice sheet reached up to 2,000–3,000 m a.s.l. Arrows indicate directions of ice flow.

undulating surface, with several ice divides that shifted through time. These ice divides were subordinate to the main divide along the axis of the Coast Mountains.

In western British Columbia, ice streamed down fjords and valleys in the coastal mountains and covered large areas of the Pacific continental shelf. Some lobes extended to the shelf edge where they calved into deep water. Glaciers issuing from the southern Coast Mountains and Vancouver Island Ranges coalesced over the Strait of Georgia to produce a great outlet glacier that flowed far into Puget Lowland in Washington State (Waitt and Thorson, 1983). Glaciers streaming down valleys farther to the east likewise terminated as large lobes in eastern Washington, Idaho, and Montana (Waitt and Thorson, 1983).

Glaciers in southern Alaska were connected to the Cordilleran Ice Sheet and are considered by most researchers to be part of that ice sheet (Hamilton and Thorson, 1983). They flowed from



Figure C70 The Homathko Icefield in the southern Coast Mountains of British Columbia. Most of the Cordillera of western Canada looked something like this 16,000 years ago (photo by J. J. Clague).

mountain source areas across the continental shelf to the south and into the broad low country drained by the Yukon River to the north. Most of interior Alaska and northern Yukon Territory (Beringia) were extremely dry throughout the Pleistocene and consequently remained unglaciated. The Cordilleran Ice Sheet in southern Yukon was fed principally from the Selwyn and Cassiar Mountains, although some ice was supplied from the St. Elias Mountains (Jackson et al., 1991).

To the east, ice flowed out of the Rocky Mountains and locally coalesced with ice originating in the Keewatin sector of the Laurentide Ice Sheet (Clague, 1989). Some valley glaciers in the eastern Mackenzie Mountains also came into contact with Laurentide ice (Duk-Rodkin and Hughes, 1991). These ice masses coalesced only rarely, at times of maximum glaciation, most recently about 20,000 years ago. At other times, an ice-free zone (the “ice-free corridor”) existed between the Cordilleran and Laurentide Ice Sheets.

Growth and decay of Cordilleran Ice Sheet

The Cordilleran Ice Sheet nucleated in the high mountains of British Columbia, Yukon, and Alaska (Figure C71a and C72a). Small mountain ice fields grew and valley glaciers advanced when climate deteriorated early during each glaciation (Figure C71b; Kerr, 1934; Davis and Mathews, 1944). With continued cooling and an increase in precipitation, glaciers expanded and coalesced to form a more extensive cover of ice in mountains (Figure C72). The glaciers advanced out of the mountains and across plateaus and lowlands (Figure C72c), eventually coalescing to form an ice sheet that covered most of British Columbia and adjacent areas (Figure C71c and C72d). During this period, which spanned thousands of years, the major mountain ranges remained the principal sources of ice, and ice flow was controlled by topography. Ice thickened to such an extent during the final phase of glaciation that one or more domes became established over the interior of British Columbia, with surface flow radially away from their centers. This full continental ice sheet phase of glaciation was rarely achieved. The transition into this final phase was accompanied by a local reversal of ice flow in the

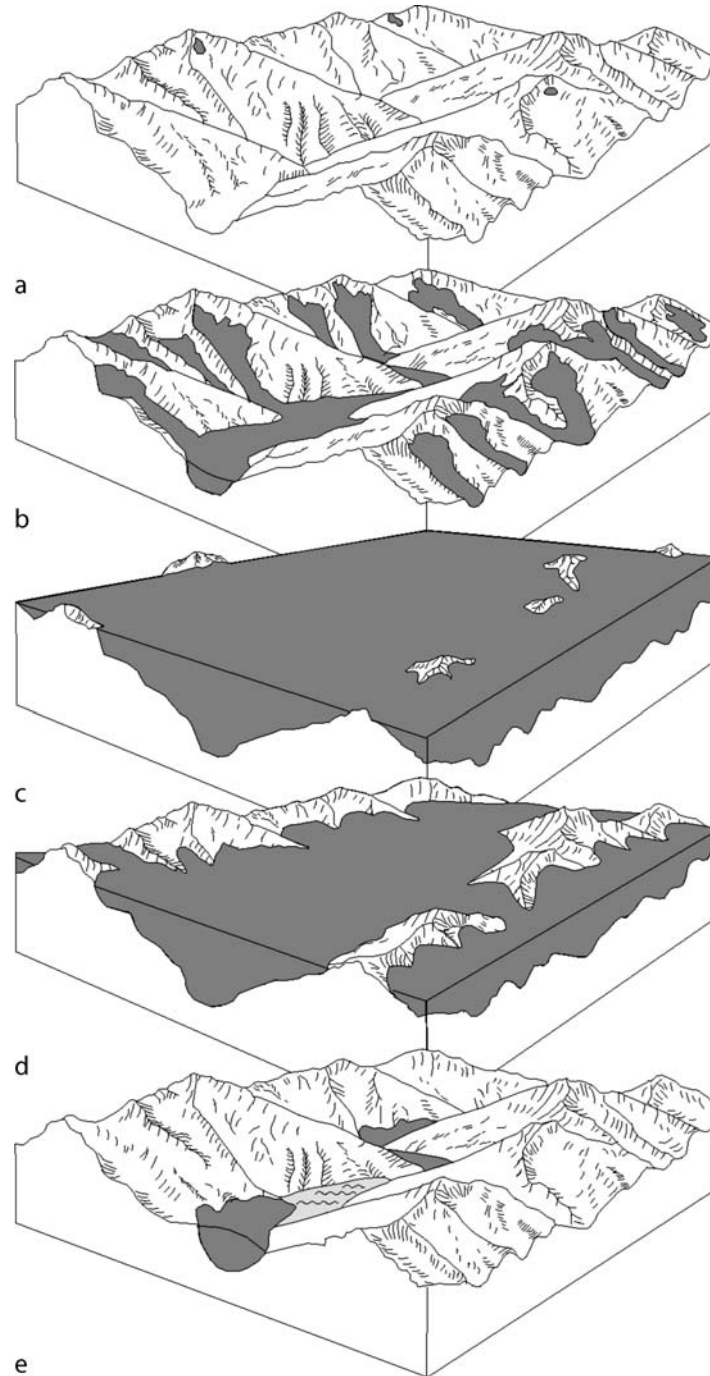


Figure C71 Schematic diagram showing growth and decay of the Cordilleran Ice Sheet. (a) Mountain area at the beginning of a glaciation. (b) Development of a network of valley glaciers. (c) Coalescence of valley and piedmont lobes to form an ice sheet. (d) Decay of ice sheet by downwasting; upland areas are deglaciated before adjacent valleys. (e) Residual dead ice masses confined to valleys. (Modified from Clague, 1989, figure 1.13).

Coast Mountains as the ice divide shifted eastward, from the mountain crest to a position over the British Columbia interior. A comparable westward shift and reversal of flow may also have occurred locally in the Rocky Mountains. The flow reversals resulted from the buildup of ice in the interior to

levels higher than the main accumulation areas in the flanking mountains.

The model outlined in the preceding paragraph provides a framework for conceptualizing the growth of the Cordilleran Ice Sheet, but the actual history of the ice sheet is more

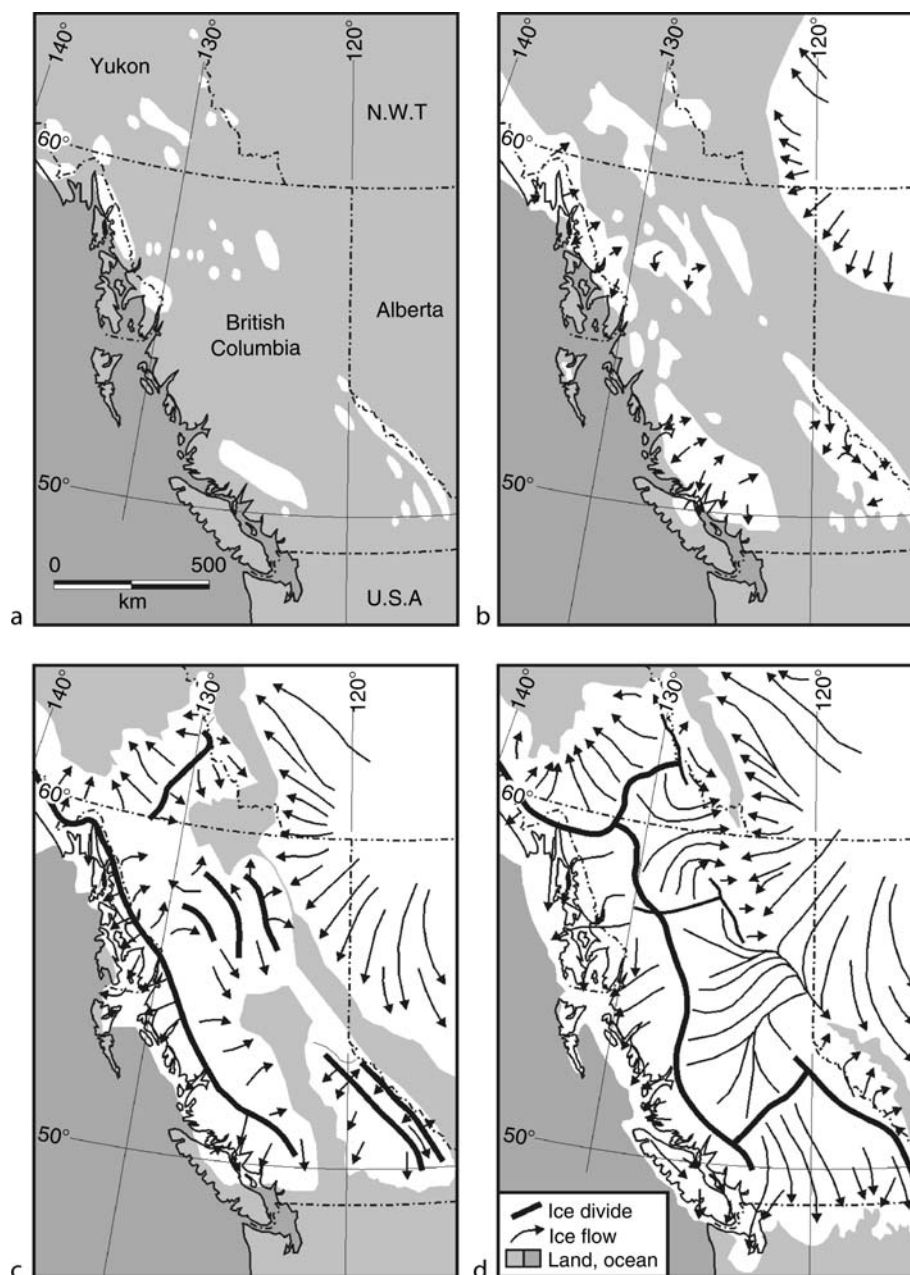


Figure C72 Schematic maps of ice cover in British Columbia during the growth phase of the last glaciation, about (a) 35,000, (b) 30,000, (c) 25,000, and (d) 18,000 years ago. Ice distributions are inferred from limited data and should only be considered approximations. (Modified from Clague et al., 2004, figure 4).

complicated (Clague, 1989). Ice did not build up in a uniform, monotonic fashion; rather, periods of growth were interrupted by intervals during which glaciers stabilized or receded.

Most glacial cycles terminated with rapid climate warming. Deglaciation was characterized by complex frontal retreat in peripheral glaciated areas and by downwasting accompanied by widespread stagnation throughout the Cordilleran interior. The western periphery of the ice sheet became unstable due,

in part, to the global rise in sea level that occurred at such times. The British Columbia continental shelf was rapidly freed of ice as glaciers calved back to fjord heads and valleys. Frontal retreat also occurred elsewhere along the periphery of the ice sheet, for example in northern Washington and southern Yukon.

A different style of deglaciation has been documented for areas of low and moderate relief nearer the center of the ice

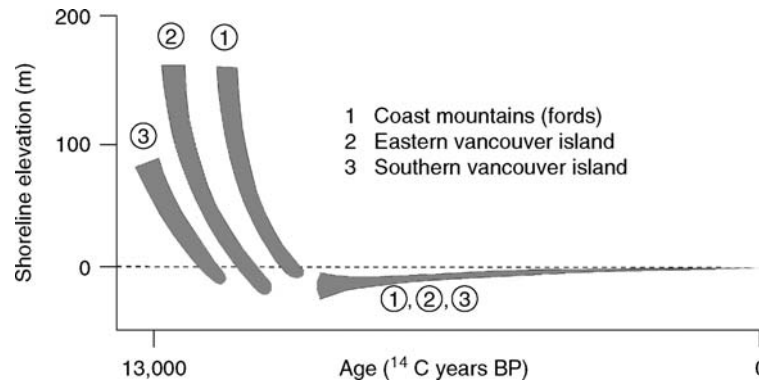


Figure C73 Generalized patterns of sea-level change on the British Columbia coast since the end of the last glaciation. Deglaciation and isostatic rebound occurred later in the Coast Mountains than on Vancouver Island. (Modified from Muhs et al., 1987, figure 10).

sheet. Deglaciation in these areas occurred mainly by downwasting and stagnation and proceeded through four stages (Fulton, 1967): (a) active ice phase – regional flow continued but diminished as ice thinned (Figure C71d); (b) transitional upland phase – the highest uplands became ice free, but regional flow continued in valleys; (c) stagnant ice phase – ice was confined to valleys but was still thick enough to flow; and (d) dead ice phase – ice tongues in valleys thinned to the point that they no longer flowed (Figure C71e).

The first areas to become ice-free were those near the periphery of the ice sheet, for example British Columbia's continental shelf and the plateaus of the northwestern United States (Clague, 1989). Active glaciers probably persisted longest in high mountain valleys, but they may have coexisted with large masses of dead ice on the plateaus of the Cordilleran interior. In general, retreat in the interior proceeded from both southern and northern peripheral areas towards the center of the ice sheet. In detail, however, the pattern of retreat was complex, with uplands in each region becoming ice-free before adjacent valleys.

Decay of the Cordilleran Ice Sheet at the close of each glaciation was interrupted repeatedly by glacier readvances (Clague, 1989). Most readvances affected relatively small areas and may not have been synchronous from one region to another.

Glacial erosion and deposition

The ice sheet and the alpine glaciers from which it formed modified the late Tertiary landscape of British Columbia and Yukon Territory. Mountain areas are dominated by erosional glacial landforms, whereas plateaus, coastal lowlands, and intermontane valleys record both the erosional and depositional effects of glaciers. In high mountains, classic alpine forms were created, including cirques and overdeepened valley heads, horns, and comb ridges. Most mountain valleys are typical glacial troughs. Some valleys in the westernmost Cordillera extend into fjords, which attain water depths of up to 750 m. Much of the sediment produced by glacial erosion was transported beyond the periphery of the ice sheet. Considerable sediment, however, was deposited in valleys, on coastal lowlands, and on the plateaus of the Cordilleran interior as proglacial and ice-contact sediments, mainly during the advance and recessional phases of the last glaciation. Deposits of older glaciations are less common, because they have been extensively eroded by the last Cordilleran Ice Sheet. Even in areas

where these older deposits are present, they are covered by younger sediments and, consequently, are poorly exposed.

Ice sheet glaciation and sea-level change

Growth and decay of the Cordilleran Ice Sheet triggered crustal movements that were dominantly isostatic in origin (Clague, 1983; Clague and James, 2002). The crust was displaced downward during periods of ice-sheet growth. Initially, the depression was localized beneath the mountain ranges that were loci of glacier growth. The area of crustal subsidence grew larger as glaciers advanced out of mountains and into lowlands. At times of maximum ice cover, the entire area of the ice sheet was displaced downward.

The amount of isostatic depression during times of maximum ice cover depended primarily on the thickness and extent of the ice sheet, the length of time over which it formed, and the structure and composition of the crust and mantle (James et al., 2000). Isostatic depression was greatest beneath the center of the ice sheet and decreased west of the Coast Mountains and Strait of Georgia toward the continental margin, and south into Washington State.

Elevated glaciomarine sediments and shoreline features along the British Columbia and northern Washington coasts provide evidence for isostatic depression at the end of the last glaciation (Clague et al., 1982a; Thorson, 1989). The elevation of the late-glacial marine limit differs in relation to distance from former centers of ice accumulation and time of deglaciation. In general, the marine limit is highest (ca. 200 m a.s.l.) on the British Columbia mainland coast and drops towards the west, southwest, and south. Many mainland fjords, however, were deglaciated after much of the local isostatic rebound had occurred; consequently, the marine limit in those areas is relatively low. Late-glacial shorelines on Haida Gwaii (Queen Charlotte Islands) were lower than at present, indicating that glacio-isostatic depression was less than the coeval global (eustatic) lowering of sea level (Clague et al., 1982b; Clague, 1983; Josenhans et al., 1997; Barrie and Conway, 2002).

Rapid deglaciation at the end of each glaciation triggered isostatic adjustments that were opposite in direction to those that occurred during ice-sheet growth (Figure C73; Clague, 1983; Clague and James, 2002). Material moved laterally in the mantle, from extraglacial regions towards the center of the decaying ice sheet. Areas at the periphery of the ice sheet, which

were deglaciated earliest, rebounded first. The total amount of uplift in these areas, however, was less than at the center of the ice sheet where ice thicknesses generally were greater. As deglaciation progressed, the zone of rapid isostatic uplift migrated in step with receding glacier margins (Figure C73; Clague, 1983). The rate of uplift in each region decreased exponentially with time, and rebound was largely complete within several thousand years of deglaciation (Clague et al., 1982a; James et al., 2000).

John J. Clague

Bibliography

- Barrie, J.V., and Conway, K.W., 2002. Rapid sea-level change and coastal evolution on the Pacific margin of Canada. *Sediment. Geol.*, **150**, 171–183.
- Clague, J.J., 1983. Glacio-isostatic effects of the Cordilleran Ice Sheet, British Columbia, Canada. In Smith, D.E., and Dawson, A.G. (eds.), *Shorelines and Isostasy*. London: Academic Press, pp. 321–343.
- Clague, J.J., 1989. Cordilleran Ice Sheet, chap. 1. In Fulton, R.J. (ed.), *Quaternary Geology of Canada and Greenland*. Ottawa, ON: Geological Survey of Canada, pp. 40–43.
- Clague, J.J., and James, T.S., 2002. History and isostatic effects of the last ice sheet in southern British Columbia. *Quaternary Sci. Rev.*, **21**, 71–87.
- Clague, J., Harper, J.R., Hebda, R.J., and Howes, D.E., 1982a. Late Quaternary sea levels and crustal movements, coastal British Columbia. *Can. J. Earth Sci.*, **19**, 597–618.
- Clague, J.J., Mathewes, R.W., and Warner, B.G., 1982b. Late Quaternary geology of eastern Graham Island, Queen Charlotte Islands, British Columbia. *Can. J. Earth Sci.*, **19**, 1786–1795.
- Clague, J.J., Mathewes, R.W., and Ager, T.A., 2004. Environments of northwestern North America before the last glacial maximum. In Madsen, D. (ed.), *Entering America: Northeast Asia and Beringia before the Last Glacial Maximum*. Salt Lake City, UT: University of Utah Press, pp. 63–94.
- Davis, N.F.G., and Mathewes, W.H., 1944. Four phases of glaciation with illustrations from southwestern British Columbia. *J. Geol.*, **52**, 403–413.
- Duk-Rodkin, A., and Hughes, O.L., 1991. Age relationships of Laurentide and montane glaciations, Mackenzie Mountains, Northwest Territories. *Géogr. physique Quaternaire*, **45**, 79–90.
- Flint, R.F., 1971. *Glacial and Quaternary Geology*. New York, NY: Wiley, 892pp.
- Fulton, R.J., 1967. *Deglaciation Studies in Kamloops Region, An Area of Moderate Relief, British Columbia*. Ottawa, ON: Geological Survey of Canada, 36pp.
- Hamilton, T.D., and Thorson, R.M., 1983. The Cordilleran Ice Sheet in Alaska. In Porter, S.C. (ed.), *Late-Quaternary Environments of the United States, Vol.1: The Late Pleistocene*. Minneapolis, MN: University of Minnesota Press, pp. 38–52.
- Jackson, L.E., Jr., and Clague, J.J. (eds.), 1991. The Cordilleran Ice Sheet. *Géogr. physique et Quaternaire*, **45**, 261–377.
- Jackson, L.E., Jr., Ward, B.C., Duk-Rodkin, A., and Hughes, O.L., 1991. The last Cordilleran Ice Sheet in southern Yukon Territory. *Géogr. physique et Quaternaire*, **45**, 341–354.
- James, T.S., Clague, J.J., Wang, K., and Hutchinson, I., 2000. Postglacial rebound at the northern Cascadia subduction zone. *Quaternary Sci. Rev.*, **19**, 1527–1541.
- Josenhans, H., Fedje, D., Pienitz, R., and Southon, J., 1997. Early humans and rapidly changing Holocene sea levels in the Queen Charlotte Islands-Hecate Strait, British Columbia, Canada. *Science*, **277**, 71–74.
- Kerr, F.A., 1934. Glaciation in northern British Columbia. *Roy. Soc. Can., Trans.*, **28**(4), ser. 3, 17–31.

Cross-references

Glacial geomorphology
 Glacial isostasy
 Glaciations, Quaternary
 Laurentide Ice Sheet
 Quaternary climate transitions and cycles
 Sea level change, Quaternary

COSMOGENIC RADIONUCLIDES

In contrast to stable isotopes, cosmogenic isotopes or radionuclides are continuously produced and destroyed by nuclear reactions. The fact that their sources and sinks (the radioactive decay) are well known makes them extremely useful tools in environmental sciences.

Sources and sinks

The main source of cosmogenic radionuclides is nuclear interactions caused by galactic cosmic rays. Solar cosmic rays are too low in energy to contribute significantly to the total production rate. Production induced by decay or fission of uranium or thorium, for instance, is only important under special circumstances (for example, underground).

The galactic cosmic rays are composed of protons (91%), helium nuclei (8%), and heavier nuclei (1%). Coming from space, cosmic rays first interact with the atmosphere. When they collide with nitrogen, oxygen or argon, a cascade of secondary particles is produced. Among them are mainly neutrons and protons, which interact with atmospheric nuclei producing a variety of cosmogenic nuclides with masses equal to or smaller than the target nucleus. The majority of these nuclides is unstable and they decay within a very short time into stable nuclides. Only few cosmogenic nuclides live long enough to be detected and useful for applications (Table C8).

Cosmogenic nuclides are detected using decay counting for short-lived nuclides or accelerator mass spectrometry (AMS) techniques for long-lived nuclides. The detection limits are on the order of a million atoms.

Before reaching the atmosphere, the cosmic rays have to cross the heliosphere, which expands to about 100 astronomical units (1.5×10^{10} km) and is filled with solar plasma of a very low density. This plasma streams out from the Sun (so-called solar wind) and carries solar magnetic fields, which deflect especially low-energy galactic cosmic ray particles and therefore reduce the production rate of cosmogenic nuclides depending on the solar activity. In addition, the geomagnetic dipole field prevents cosmic ray particles with too low a magnetic rigidity (momentum per charge) from penetrating into the atmosphere. This geomagnetic shielding effect is largest at low latitudes, where the field lines are parallel to the Earth's surface, and negligible at high latitudes, where the charged particles are guided into the atmosphere by the field lines. The dependence of the production rate on atmospheric depth (expressed in g cm^{-2}) and latitude is shown in Figure C74a using ^{10}Be as an example. As a result of these interactions, the intensity of the galactic cosmic rays is reduced within the atmosphere by almost three orders of magnitude. Therefore, the production of cosmogenic nuclides within the lithosphere is much smaller. However, due to a large number of heavier target nuclei, a variety of additional cosmogenic nuclides is produced in the lithosphere that cannot be produced in the atmosphere.

Some of the nuclides also have anthropogenic sources. During the nuclear bomb tests from the 1940s to 1970s, the atmospheric amount of several nuclides was considerably increased: ^{14}C by a factor of 2 and ^3H and ^{36}Cl by almost three orders of magnitude. Additional sources are nuclear power and reprocessing plants.

Table C8 List of some of the main cosmogenic nuclides with half-lives longer than 1 month that are produced by cosmic rays in the atmosphere (after Masarik and Beer, 1999)

Nuclide	Half-life	Target	Reaction	Production rate [$\text{cm}^{-2} \text{s}^{-1}$]	Decay (keV)	Detection
^3H	12.34 yr	N, O	Spallation	0.28	β^- (0.02)	Decay
^7Be	53.4 d	N, O	Spallation	0.035	ε (487)	Decay
^{10}Be	1.5 706 yr	N, O	Spallation	0.018	β^- (0.6)	AMS
^{14}C	5,730 yr	N	$^{14}\text{N}(n, p) ^{14}\text{C}$	2.0	β^- (0.2)	AMS/Decay
^{26}Al	740,000 yr	Ar	Spallation	7×10^{-5} *	β^- (5.1)	AMS
^{32}Si	150* yr	Ar	Spallation		β^- (0.2)	Decay/AMS
^{36}Cl	301,000 yr	Ar	Spallation	8.8×10^{-4} *	β^- (0.7)	AMS

*Indicate values with a large uncertainty.

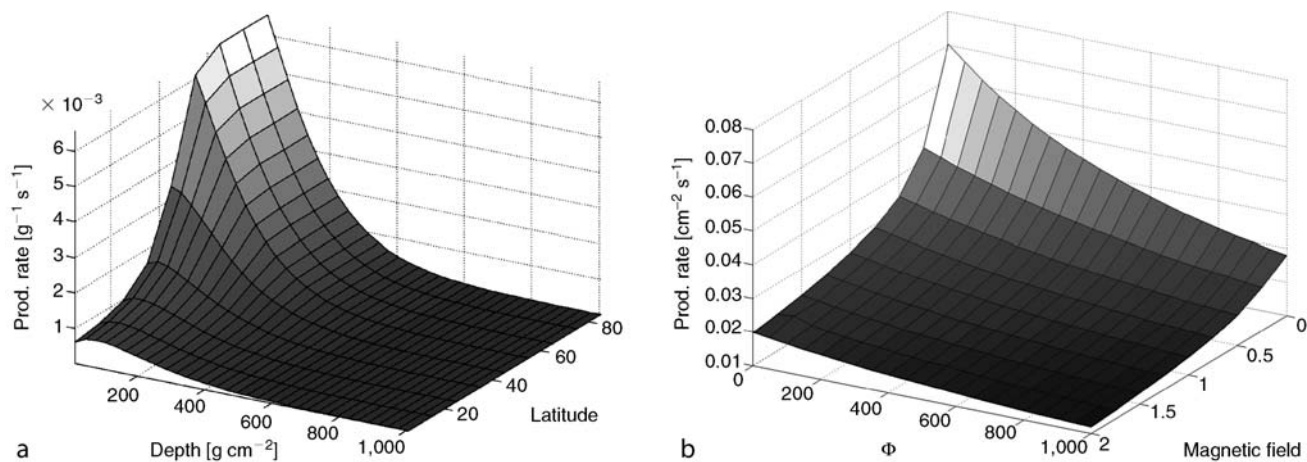


Figure C74 (a) Dependence of the ^{10}Be production rate on the atmospheric depth (0 g cm^{-2} : top of the atmosphere; $1,033 \text{ g cm}^{-2}$: sea level) and the latitude (Masarik and Beer, 1999). (b) Dependence of the mean global ^{10}Be production rate on the solar activity ($\phi = 0$, quiet sun; $\phi = 1000$, very active sun) and the geomagnetic field intensity (relative units, 1 = present field) (Masarik and Beer, 1999). The dynamic range between high solar activity/large magnetic field and quiet sun/no field is about an order of magnitude.

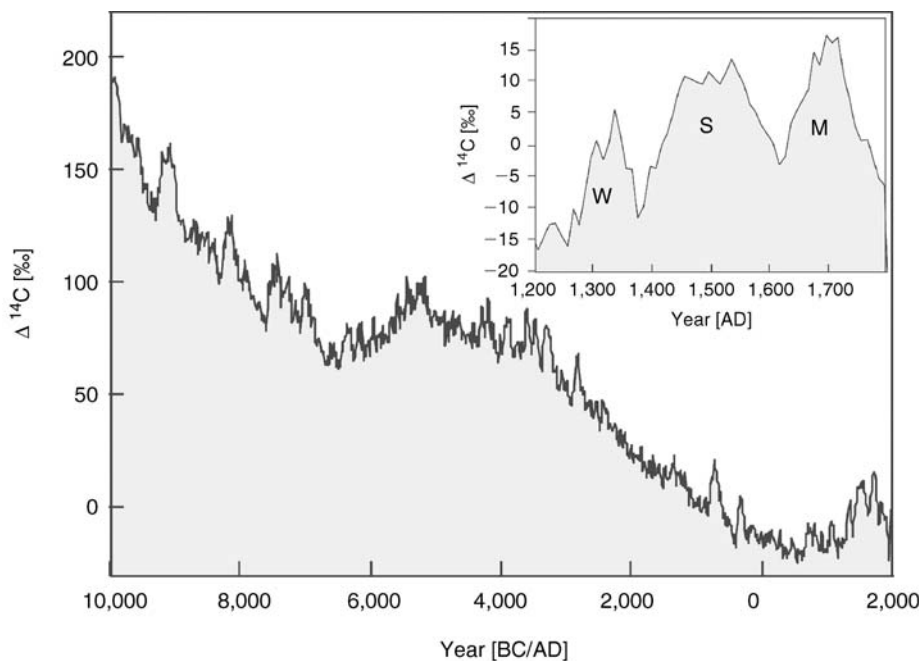


Figure C75 Deviations of the atmospheric $^{14}\text{C}/^{12}\text{C}$ ratio from the value of 1950 as a result of changes in the production rate caused by geomagnetic (long-term trend) and solar (short-term fluctuations) modulation of cosmic rays. (Modified from Stuiver et al., 1998; Stuiver and Braziunas, 1993.)

Applications

The two main fields of application of cosmogenic radionuclides are dating and tracing. In the case of dating, decay dating and exposure dating can be distinguished.

Dating

Decay dating makes use of the law of radioactive decay:

$$A(t) = A_0 \cdot \exp\left(-\frac{\ln 2}{T_{1/2}} \cdot t\right), \text{ with}$$

$A(t)$ = number of radioactive atoms, their concentration or their isotopic ratio at time t

$A_0 = A$ at the time zero

$T_{1/2}$ = half-life

If A_0 is constant or known and $A(t)$ is measured, the time t can be calculated. The crucial point is A_0 . By radiocarbon dating of tree-rings with known ages, the deviation of A_0 ($^{14}\text{C}/^{12}\text{C}$ ratio) from A_0 of 1950 could be determined for the past 12,000 years. These deviations in ‰, called $\Delta^{14}\text{C}$, are plotted in [Figure C75](#). The curve shows a long-term trend related to changes in geomagnetic field intensity and superimposed short-term fluctuations caused by changes in solar activity [Figure C74b](#), such as the well known Maunder, Spoerer and Wolf minima (see insert in [Figure C75](#)). The curve of [Figure C75](#) provides the basis to convert radiocarbon ages into calendar ages.

In contrast to decay dating, the exposure dating technique is based on the increasing number of cosmogenic nuclides that are produced in matter (e.g., rocks) previously shielded, for example, by a glacier. If the production rate is known, the exposure time can be calculated from the measured total number of produced atoms (Lal, 1988).

Tracing

In the case of tracer applications, cosmogenic nuclides can be used according to their specific properties to study a large variety of different physical, chemical and biological processes. They are particularly useful in investigating the behavior of their stable counterparts, such as, for example, the carbon cycle. Examples of ^{10}Be applications are given in the article on ^{10}Be .

Jürg Beer

Bibliography

- Lal, D., 1988. In situ-produced cosmogenic isotopes in terrestrial rocks. *Annu. Rev. Earth Planet Sci. Lett.*, **16**, 355–388.
- Masarik, J., and Beer, J., 1999. Simulation of particle fluxes and cosmogenic nuclide production in the Earth's atmosphere. *J. Geophys. Res.*, **104**(D10), 12099–12111.
- Stuiver, M., and Braziunas, T.F., 1993. Sun, Ocean, Climate and Atmospheric $^{14}\text{CO}_2$, an evaluation of causal and spectral relationships. *The Holocene*, **3**, 289–305.
- Stuiver, M., et al., 1998. INTCAL98 radiocarbon age calibration, 24,000–0 cal BP. *Radiocarbon*, **40**(3), 1041–1083.

Cross-references

[Beryllium-10](#)
[Dating, Radiometric Methods](#)
[Maunder Minimum](#)
[Radiocarbon Dating](#)
[Sun-Climate Connections](#)

CRETACEOUS WARM CLIMATES

Introduction

The Cretaceous period spans approximately 70 million years of Earth's history, from 135 to 65.4 million years ago. Warm intervals of the Cretaceous account for almost half the duration of the period. A cool temperate climate in the Early Cretaceous was followed by a warm to extremely warm Middle and Late Cretaceous, and the warmth persisted into the Paleogene. The Cretaceous and Paleogene greenhouse interval was longer in duration than the ensuing icehouse intervals of the Neogene. The termination of the Cretaceous is coincident with a major mass extinction event in Earth's history and a meteorite or bolide impact at the Cretaceous-Tertiary (K/T) boundary.

In describing the world during the Cretaceous period, geochemical model results indicate that atmospheric CO_2 levels were at least 2–10 times higher than present day values (Berner, 1994). The lack of permanent ice in the polar regions resulted in a low equator to pole thermal gradient. Processes that distributed the warmth from the low to high latitudes were the oceans and the atmosphere, but the amount of heat apportioned to each process is debated for these warm intervals (Barron et al., 1993). The driver of circulation lies in the tropical world, at least for atmospheric and surface ocean currents. Subsurface circulation of the Late Cretaceous Campanian oceans was probably initiated from high latitudes (DeConto et al., 2000a).

The warm intervals of the Cretaceous are known for the abundance of unique marine bivalve groups such as the ubiquitous inoceramids and the reef-building rudists. Major terrestrial floral groups such as the gymnosperms persisted during the warm climates, and angiosperms flourished during the Late Cretaceous. Dinosaurs of various groups, such as ceratopsians hadrosaurs, tyrannosaurs, and ornithomids, roamed the land.

The techniques used to infer Cretaceous climates have evolved over the decades. Traditional tools applied the distribution, abundance, and ecological associations of biota toward climatic interpretations. In particular, the geographic dispersion patterns of bivalves, gastropods, and foraminifera allowed for the original establishment of Cretaceous climate zones across the globe, as biotas were designated the most sensitive indicators of paleoclimatic conditions. Research directions then shifted to include stable isotopes to infer temperatures for the marine realm. Analyses focused on isotopes of carbon and oxygen, first for whole rock, later for ecological associations of foraminifers and inoceramid bivalves, and eventually for individuals from a specific species group. Single crystals of unaltered calcite, as preserved in the inoceramid bivalves, or original shell material containing calcite or aragonite provided the most reliable database from which thermal interpretations were developed. Currently, organic geochemical techniques such as TEX_{86} (see below) are applied toward the investigation of Cretaceous warmth in the marine realm (see also: *Geochemical proxies (non-isotopic)*; *Organic geochemical proxies*). Research on the terrestrial domain has not kept pace with that of the oceanic world, but land-ocean correlations and interpretations of interactions have accelerated in recent years.

Concurrent with the utilization of empirical and analytical data toward climate sensors was the development of the numerical climate model, three-dimensional General Circulation Models (GCMs) simulating atmospheric and/or oceanic conditions. Models contributed to understanding mechanisms of the atmosphere

and oceans by providing sensitivity experiments encompassing the entire globe. Advances in paleoclimate modeling, and limits to the models as applied to paleoclimate studies, are summarized in DeConto et al. (2000b). Valdes (2000) provides a comprehensive review of factors included in models for warm climates, and feedback mechanisms. One of the greatest challenges for modeling warm Cretaceous climates is in keeping the polar regions free of ice while not overheating the tropics. Ocean heat transport, high atmospheric CO₂ levels, and forest vegetation at high latitudes are the proposed mechanisms for modifying polar climates during Cretaceous warm intervals (Rind and Chandler, 1991; Barron et al., 1993; Otto-Bliesner and Upchurch, 1997).

Atmosphere

Extra-terrestrial and terrestrial sources influenced Cretaceous climate. Extra-terrestrial climatic forcing is expressed in Cretaceous rocks across the globe (Fischer, 1993; Park et al., 1993; Herbert et al., 1999). Cycles of precession, obliquity, and eccentricity, indicating a Milankovitch-style expression of climatic conditions, modulated the distribution of energy and the surface temperature of the Earth. Cool-wet and warm-dry climatic conditions controlled deposition of sediments during these cycles. Siliclastic input was higher than carbonate production during the cool-wet phase, resulting in deposition of calcareous shale and marlstone, and carbonate deposition dominated during the warm-dry phase of the cycle, resulting in the deposition of limestone and chalk.

Terrestrial forcing of climate occurred through sea floor spreading and volcanism that released CO₂ into the atmosphere. Although the warmth of the Cretaceous is attributed primarily to atmospheric CO₂ levels higher than those of today, the exact levels of CO₂ contributing to the warmth are under investigation. Model

experiments center on 2–4 times present-day values to match the distribution of temperatures inferred from macrofaunal and floral paleobiogeographic ranges. Continued production of CO₂ over millions of years, and retention of this greenhouse gas in the atmosphere, set up the conditions for warmth that extended from the middle through the Late Cretaceous stages.

Across the Cretaceous globe, the effects of global warmth resulted in the disappearance of the North and South Polar to Subpolar climatic zones, and their replacement by North and South Cold-Temperate zones (Figure C76). No permanent ice existed at the poles (Frakes, 1979), although slush caps and the periodic development of ice on the South Pole have been suggested. Cold Temperate, Mild Temperate, and Warm Temperate zones extended from the polar region through southern Canada. Episodically during highstands, subtropical conditions extended from approximately the Canadian-US border southward to the tropics. The tropical zone existed in the southern parts of the Gulf Coast states and north-central Mexico. A supertropical or Supertethyan zone, characterized by unusually high temperatures and salinities, emerged episodically within the tropics and included the islands of Puerto Rico, Cuba, and Hispaniola, as well as southern Mexico, northern Venezuela, and northern Columbia. These global climate zones were originally determined through the geographic mapping of bivalve genera and subgenera (Kauffman, 1973; Johnson and Kauffman, 1996).

In North America, atmospheric conditions were influenced by the presence of the Western Interior Basin, a fully marine seaway that extended from Arctic Canada and Alaska to the Gulf of Mexico during peak sea level highstand. This large seaway serves as a model for equivalent bodies of water across the globe. A relatively flat landmass bordered the eastern coastal plain, and a mountain belt developed to the west. A westerly

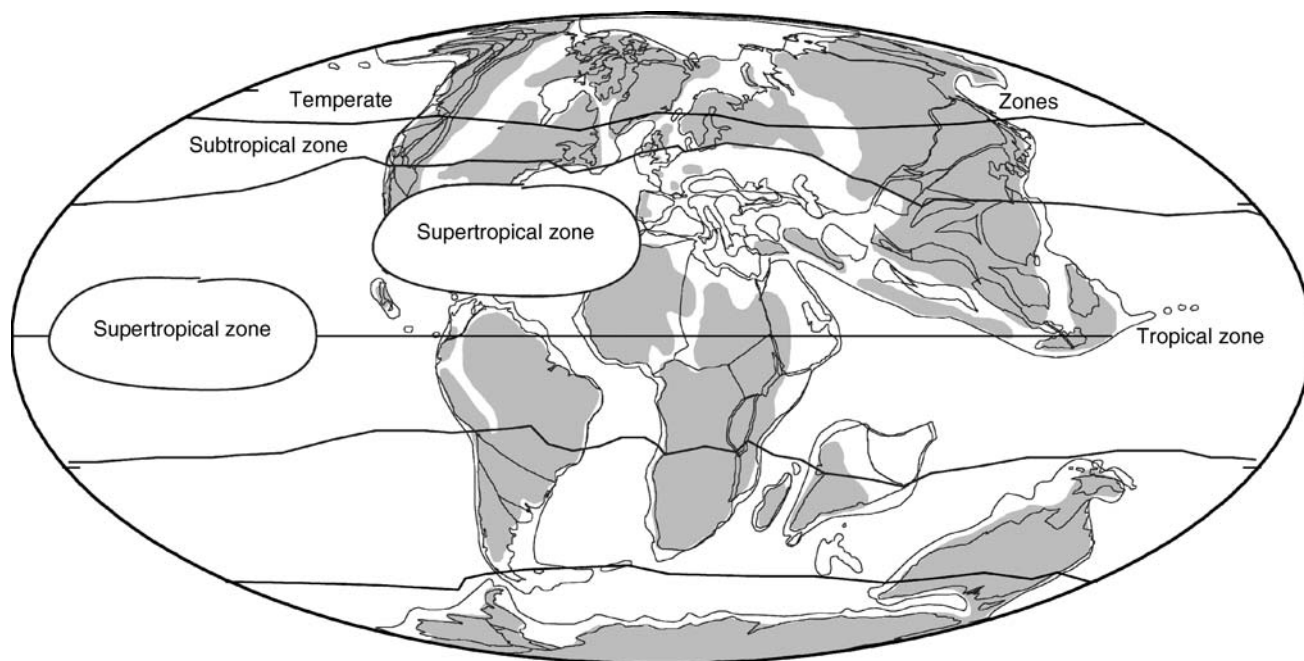


Figure C76 Cretaceous climate zones for paleolatitudes across the globe. Cold, Mild, and Warm Temperate Zones replaced the Polar Zones in the highest latitudes. Subtropical, Tropical, and Supertropical Zones expanded during the warmest stages of the Cretaceous, as indicated in text (base map for 80 Myr from C. R. Scotese).

wind system, as today, was prevalent. As the mountains rose progressively through the Late Cretaceous and especially the Paleogene, a more variable wind system developed. Updrafts carried moisture to heights where they produced rain. Progressive runoff into river systems formed a freshwater cap at the riverine mouths. On the western side of the Seaway, large deltas formed from Coniacian-Maastrichtian time and into the Paleogene, reflecting the rising Rocky Mountains. Paleoenvironments became marginal marine during deltaic deposition, and fully marine offshore. Along the eastern shoreline, deltaic deposition was restricted both spatially and temporally.

In essence, the presence of the Western Interior Seaway brought an abundance of tropical moisture from the Gulf of Mexico northward, and cool-temperate waters from Arctic Canada and Alaska southward across a large portion of North America. This conduit, 3,000 km long by 1,000 km wide, and 500 m to 1,000 m at its deepest during maximum transgression, provided a region for mixing of atmospheric and oceanic air masses and ocean currents, with potential for CO₂ exchange across the atmosphere-oceanic boundary.

During the past several decades, the Cretaceous world was viewed as one in which global atmospheric circulation was sluggish due to a low thermal gradient from the equator to the poles. In this scenario, meridional heat transport from the low to high paleolatitudes was apportioned more to the oceans than to the atmosphere (Barron et al., 1993). Newer interpretations from the oceanic realm, however, indicate that the tropics superheated, probably several times, between the middle and latest Cretaceous interval. In this revised scenario, a thermal gradient strong enough to induce atmospheric circulation may have been established between the superheated tropics and the cool polar regions (Norris et al., 2002).

Oceans

Sea level

Progressively through the Lower Cretaceous, sea level rose and advanced with each pulse, and the climate warmed across the globe. In North America, the Upper Albian marked the first north-south connection of the Western Interior Seaway. In South America and Africa, vast warm seas were connected in the Late Albian. In Europe, northern cold-temperate and subtropical seas linked up in at least two broad areas, one in western Europe during the Albian and later, and the other in western Russia, Poland, Czechoslovakia, Hungary, and Bulgaria.

Sea level reached a peak near the Cenomanian-Turonian boundary, fell in the Upper Turonian, and rose again at the Turonian-Coniacian boundary. Sea level remained high through the Coniacian and Santonian and until the Lower Campanian, as expressed in the Niobrara Formation and its equivalents where limestones and/or chalks, chalky shales, and calcareous shales were deposited continuously through the interval. Sea level fell in the Lower Campanian, rose moderately in the Middle Campanian, fell in the Upper Campanian, transgressed even more moderately in the Lower Maastrichtian, underwent a mild regression in the Middle Maastrichtian, and after a relative rise in the early Late Maastrichtian, fell at the end of the latest Maastrichtian. The extent of sea level fall in the Maastrichtian is much debated, although a small Antarctic ice sheet has been proposed (Miller et al., 1999; see also *Sea level change, last 250 million years*).

In the absence of ice during the Cretaceous, variations in sea level are attributed to variable rates of sea floor spreading

and volumetric changes in the ocean basins. The net effect of high sea level on climate in epicontinental seaways is in the production of maritime climatic conditions within and adjacent to the seaways, especially in the direction of the prevailing winds.

Pulses of elevated seas brought tropical surface waters from the Gulf Coast through the Western Interior Seaway to Canada. Most important in this migration of surface currents was the northward transport of tropical larvae, humidity, and relatively high temperatures. Likewise, in the western European region of the Northern Hemisphere, conduits for surface currents developed during high stands of the sea and carried heat northward. These simplified scenarios of heat export from the tropics by surface currents were complicated by regional and local tectonic episodes.

Elevated sea levels that flooded continents and tectonic subsidence that occurred in active basins combined to create silled basins with restricted circulation (Hay, 1988). Large portions of the temperate water columns became oxygen-restricted and had limited faunas. The higher the anoxic conditions, the more depauperate the fauna was in calcareous shales, limestones, and chalks. Ultimately, during the most anoxic of conditions, there was little or no macrofauna or burrowing, and organic carbon was preserved in the rock record as oceanic anoxic events.

The rise and fall of sea level affected climatic conditions in the atmosphere, which in turn affected hydrologic conditions on the land and deposition in the sea. The atmosphere contained latent moisture; rainy and dry seasons alternated. During the rainy season, the land was flooded and streams and rivers rose, with the runoff resulting in deltaic construction, downcutting, and an increase in sediment load and the rate of sedimentation for quite a distance offshore. Increased rainfall resulted in a reduction in the salinity of the sea and lack of clarity of the water. Marine chemistry, sediment types, and biotic compositions were affected. Likewise, during dry seasons, evaporative conditions prevailed and moisture returned to the atmosphere. The strength of the hydrologic cycle during the Cretaceous was reported as being more vigorous than that of today (White et al., 2001).

Marine temperatures

Cautions exist regarding our ability to predict pre-Pleistocene mean annual temperatures because of salinity uncertainties and potential problems with alkalinity/diagenesis (Crowley and Zachos, 2000). Yet, new fossil discoveries and excellent preservation of fossils, precision in analytical equipment, and further understanding of diagenetic effects allow for continued refinement of interpretations regarding temperatures from the marine realm. For example, based on oxygen isotopes derived from well-preserved planktic foraminifers, estimated sea surface temperatures (SSTs) for the Late Albian and Early Cenomanian were 30–31 °C (Norris and Wilson, 1998). From calculations, the authors determined that SSTs of 35–37 °C would be necessary to support hypersaline conditions. A few years later, isotopic determinations from planktic foraminifers yielded SST interpretations of 33–34 ± 2 °C (Norris et al., 2002), thus moving into the range of hypersaline conditions.

A SST proxy that is free from diagenetic effects and salinity corrections has emerged recently from organic chemical analyses (Schouten et al., 2003). TEX₈₆ (tetraether index of 86 carbon atoms) is based on membrane lipids of marine crenarchaeota. Crenarchaeota comprise 20–30% of the picoplankton component

in today's ocean; they adjust the composition of their tetraether membranes lipids in response to SST. This response, quantified as TEX₈₆, shows a strong linear relationship to today's SST and was used to evaluate middle Cretaceous sea surface temperatures. Results yielded high SSTs (e.g., Early Aptian equatorial Pacific 27–32°C, Late Albian 30° N Atlantic 35°C, Cenomanian/Turonian equatorial Pacific 34–36°C, Cenomanian/Turonian 30° N Atlantic 34–36°C), indicating extreme warmth from the low latitudes for the middle Cretaceous and giving support to the concept of a more vigorous atmospheric circulation than that envisioned 10 years ago.

Subsurface circulation from hypersaline waters in low latitudes was a prediction of Chamberlin (1906), with support from Brass et al. (1982). Newest model results from the Campanian indicate that deep water formation likely occurred at high southern latitudes (Deconto et al., 2000a), rather than in saline pools at low latitudes, and the process of subsurface circulation was more like today's thermohaline circulatory process during this stage.

The land

Investigations into the role of vegetation and its effect on the distribution of warmth across the Cretaceous globe are evolving rapidly, especially with numerical models. Otto-Bliesner and Upchurch (1997) examined the interrelationships between high- and middle-latitude forests and surface temperature regulation. Model results for the K/T indicated that forest vegetation warmed the global climate by 2.2°C. Forests caused warming in the high-latitude land areas, heat was transferred to the oceans, sea-ice formation was delayed, and winter temperatures over coastal land increased. DeConto et al. (2000a) used an OGCM that was forced by the Campanian climate simulated by the climate-vegetation model. The inclusion of plant community information into numerical models thus appears to assist with determinations of meridional thermal gradients and ocean heat-transport mechanisms, long-standing endeavors in the Cretaceous research community.

Correlation of events from terrestrial to marine sequences was difficult in the past due to the relatively poor temporal precision extracted from terrestrial rocks and fossils. Recently, however, analyses of co-equal events occurring between the two realms have been accomplished through correlation of the isotopic excursions of terrestrial and marine organic carbon, and marine carbonate carbon (Hasegawa, 2003). For example, based on a comparison of these species of carbon, it was proposed that the climatic optimum of warm and humid conditions occurred during the latest Cenomanian in northeastern Asia. This is significant in that data from the large continental landmass can now be integrated into the global database and used not only for climatic interpretations, but also for purposes of model-data comparisons.

Pulses of warming associated with Deccan volcanism and release of CO₂ are among the most current avenues of marine-terrestrial investigation, and these are achieved by analysis of the ¹⁸⁷Os/¹⁸⁸Os record. The seawater osmium ratio was declining during the Maastrichtian and prior to the K/T boundary. The drop in this ratio was identified from several Deep Sea Drilling Project (DSDP) sites and shows an abrupt decline more than 100,000 years before the boundary. The decline is coincident with Deccan volcanism from continental flood basalts (leading to release of CO₂), and the Late Maastrichtian warming of 3–5°C that is separate from that of the K/T

boundary extinction (Ravizza and Peucker-Ehrenbrink, 2003). In a similar manner, terrestrial evidence for a warming is also derived from carbon and oxygen isotopes from paleosol carbonates. Through this method, it was determined that atmospheric warming events occurred between 70 and 69 Myr, and also 65.5 and 65 Myr ago (Nordt et al., 2003), indicating that dramatic climatic fluctuations occurred several million years before as well as during the K/T boundary extinction interval. Although a wealth of empirical data has been accumulated from the K/T boundary extinction interval, definitive processes causal to the mass extinction continue to be debated vigorously.

Summary and conclusions

Empirical, analytical, and experimental techniques have been applied toward understanding the development and persistence of processes that produced Cretaceous warm climates. Used in combination, biotic distributions, isotopic and/or geochemical analyses, and numerical climate models yield the most comprehensive results and the most robust interpretations on Cretaceous climates.

The role of the atmosphere, and of the oceans, in distributing the warmth across the globe is as yet unresolved. The process of atmospheric circulation transporting heat across the latitudes may have been the same for icehouse and greenhouse intervals, but the actual temperatures for each steady state system were quite distinct. Cretaceous oceans distributed warmth across latitudes *via* surface currents, but subsurface circulation commenced in high latitudes, at least during the Campanian. Determination of sea surface temperatures and the interaction of the sea surface with atmospheric CO₂ exchange remain active research areas.

Thermal changes in the Cretaceous tropics dispute the theory of time-stable biotic evolution within equable tropical environments, and suggest an important role for large-scale disturbance in the evolution of tropical, and perhaps temperate, ecosystems (Johnson et al., 1996).

Erle G. Kauffman and Claudia C. Johnson

Bibliography

- Barron, E.J., Peterson, W.H., Pollard, D., and Thompson, S., 1993. Past climate and the role of ocean heat transport: Model simulations for the Cretaceous. *Paleoceanography*, **8**, 785–798.
- Berner, R.A., 1994. GEOCARB II: A revised model of atmospheric CO₂ over Phanerozoic time. *Am. J. Sci.*, **294**, 56–91.
- Brass, G.W., Southam, J.R., and Peterson, W.H., 1982. Warm saline bottom water in the ancient ocean. *Nature*, **296**, 620–623.
- Chamberlin, T.C., 1906. On a possible reversal of deep-sea circulation and its influence on geologic climates. *J. Geol.*, **14**, 363–373.
- Crowley, T.J., and Zachos, J.C., 2000. Comparison of zonal temperature profiles for past warm time periods. In Huber, B.T., MacLeod, K.G., and Wing, S.L. (eds.), *Warm Climates in Earth History*. Cambridge, UK: Cambridge University Press, pp. 50–76.
- DeConto, R.M., Brady, E.C., Bergengren, J., and Hay, W.W., 2000a. Late Cretaceous climate, vegetation and ocean interactions. In Huber, B.T., MacLeod, K.G., and Wing, S.L. (eds.), *Warm Climates in Earth History*. Cambridge, UK: Cambridge University Press, pp. 275–296.
- DeConto, R.M., Thompson, S.L., and Pollard, D., 2000b. Recent advances in paleoclimate modeling: Toward better simulations of warm paleoclimates. In Huber, B.T., MacLeod, K.G., and Wing, S.L. (eds.), *Warm Climates in Earth History*. Cambridge, UK: Cambridge University Press, pp. 21–49.

- Fischer, A.G., 1993. Cyclostratigraphy of Cretaceous chalk-marl sequences. In Caldwell, W.G.E., and Kauffman, E.G. (eds.), *Evolution of the Western Interior Basin*. St. Johns: Geological Association of Canada, pp. 283–295.
- Frakes, L.A., 1979. *Climates Throughout Geologic Time*. Amsterdam: Elsevier, 310pp.
- Hasegawa, T., 2003. Cretaceous terrestrial paleoenvironments of north-eastern Asia suggested from carbon isotope stratigraphy: Increased atmospheric pCO₂-induced climate. *J. Asian Earth Sci.*, **21**, 849–859.
- Hay, W.W., 1988. Paleooceanography: A review for the GSA Centennial. *Geol. Soc. Am. Bull.* **100**, 1934–1956.
- Herbert, T.D., Gee, J., and DiDonna, S., 1999. Precessional cycles in the Upper Cretaceous pelagic sediments of the South Atlantic: Long-term patterns from high-frequency climate variations. In Barrera, E., and Johnson, C.C. (eds.), *Evolution of the Cretaceous Ocean-Climate System*. Boulder, CO: Geological Society of America, pp. 105–120.
- Johnson, C.C., and Kauffman, E.G., 1996. Maastrichtian extinction patterns of Caribbean Province rudistids. In MacLeod, N., and Keller, G. (eds.), *The Cretaceous-Tertiary Mass Extinction: Biotic and Environmental Events*. New York: W.W. Norton & Co., pp. 231–273.
- Kauffman, E.G., 1973. Cretaceous bivalvia. In Hallam, A. (ed.), *Atlas of Paleobiogeography*. Amsterdam: Elsevier, pp. 353–383.
- Miller, K., Barrera, E., Olsson, R., Sugarman, P., and Savin, S., 1999. Does ice drive early Maastrichtian eustasy? *Geology*, **27**, 783–786.
- Nordt, L., Atchley, S., and Dworkin, S., 2003. Terrestrial evidence for two greenhouse events in the Latest Cretaceous. *GSA Today*, **13**, 4–9.
- Norris, R.D., and Wilson, P.A., 1998. Low-latitude sea-surface temperatures for the mid-Cretaceous and the evolution of planktic foraminifera. *Geology*, **26**, 823–826.
- Norris, R.D., Bice, K.L., Magno, E.A., and Wilson, P.A., 2002. Jiggling the tropical thermostat in the Cretaceous hothouse. *Geology*, **30**, 299–302.
- Otto-Bliesner, B.L., and Upchurch, G.R., 1997. Vegetation-induced warming of high-latitude regions during the Late Cretaceous period. *Nature*, **385**, 804–807.
- Park, J., D'Hondt, S.L., King, J.W., and Gibson, C., 1993. Late Cretaceous precessional cycles in double time: A warm-Earth Milankovitch response. *Science*, **261**, 1431–1434.
- Ravizza, G., and Peucker-Ehrenbrink, B., 2003. Chemostratigraphic evidence of Deccan volcanism from the marine osmium isotope record. *Science*, **302**, 1392–1395.
- Rind, D., and Chandler, M., 1991. Increased ocean heat transports and warmer climate. *J. Geophys. Res.*, **96**, 7437–7461.
- Schouten, S., Hopmans, E.C., Forster, A., van Breugel, Y., Kuypers, M.M.M., and Damste, J.S.S., 2003. Extremely high sea-surface temperatures at low latitudes during the middle Cretaceous as revealed by archaeal membrane lipids. *Geology*, **31**, 1069–1072.
- Valdes, P.J., 2000. Warm climate forcing mechanisms. In Huber, B.T., MacLeod, K.G., and Wing, S.L. (eds.), *Warm Climates in Earth History*. Cambridge, UK: Cambridge University Press, pp. 3–20.
- White, T., Gonzalez, L., Ludvigson, G., and Poulsen, C., 2001. Middle Cretaceous greenhouse hydrologic cycle of North America. *Geology*, **29**, 363–366.

Cross-references

[Animal Proxies, Invertebrates](#)
[Animal Proxies, Vertebrates](#)
[Cretaceous/Tertiary \(K-T\) Boundary Impact, Climate Effects](#)
[Flood Basalts: Climatic Implications](#)
[Geochemical Proxies \(Non-Isotopic\)](#)
[Greenhouse \(Warm\) Climates](#)
[Heat Transport, Oceanic and Atmospheric](#)
[Mesozoic Climates](#)
[Ocean Anoxic Events](#)
[Ocean Paleotemperatures](#)
[Organic Geochemical Proxies](#)
[Paleoclimate Modeling, Pre-Quaternary](#)
[Sea Level Change, Last 250 Million Years](#)
[Stable Isotope Analysis](#)

CRETACEOUS/TERTIARY (K-T) BOUNDARY IMPACT, CLIMATE EFFECTS

Introduction

Collisions of asteroids and comets with the Earth's surface are rare events that punctuate the geologic record. The collision of a large asteroid or comet with a planetary surface produces a tremendous explosion, equivalent to thousands of times the explosive energy of the world's combined nuclear arsenal. The end result is a crater tens to hundreds of kilometers in size. Although the existence of large impact structures on Earth is undisputed, the possible climatic effects of an impact were not seriously considered until 1980, when a team led by the famous physicist Luis Alvarez and his son, the geologist Walter Alvarez, suggested that the profound end-Cretaceous mass extinction might have been caused by the impact of a 10-km diameter asteroid or comet (Alvarez et al., 1980). Dated to 65 million years ago, this extinction is the last of the large, known mass extinctions on Earth and defines a major geologic boundary between the Cretaceous and Tertiary (or Paleogene, as it is often referred to in the recent literature) periods, the K/T boundary. The discovery by the Alvarez team of an anomalous enrichment of extraterrestrial iridium at the K/T boundary in the sections at Gubbio, Italy and Stevns Klint, Denmark opened a whole new era of reanalysis of the geologic record in search of more clues that could confirm the impact hypothesis. Since 1980, the list of "clues" has become long and overwhelming, culminating with the discovery of the K/T boundary crater, the Chicxulub structure, in the Yucatán Peninsula, Mexico (Figure C77). That region is a partially submerged continental platform consisting of a thick sedimentary sequence of carbonates and evaporites overlying continental crust. At the time of impact, a shallow sea a few tens to several hundreds of meters deep covered the impact region. The crater is roughly 180–200 km in diameter and currently buried under about 1 km of Tertiary sediments. Such a large impact event would affect the environment and climate worldwide. However, while several impact structures larger than 100 km in diameter have been identified on the Earth's surface, to this date Chicxulub is the only large, known crater that closely coincides in time with a mass extinction event.

Several short-term and long-term environmental effects result from a large impact event (e.g., see Toon et al., 1997). Short-term effects extend up to few weeks after the impact and are generally believed to have little influence on the long-term evolution of the climate. They include the localized direct effects of shock waves generated by the impact in the atmosphere, like blast waves (high pressure pulses traveling through the atmosphere at high velocity), and at the Earth's surface, such as earthquakes and tsunamis. Effects that are more widespread include the production of toxic gases like nitrogen oxides (NO, NO₂) and nitric acid (HNO₃) by shock heating of the atmosphere from the entering projectile as well as the atmospheric re-entry of material initially ejected well beyond the stratosphere by the impact. These gases also caused massive destruction of stratospheric ozone. The re-entering ejecta also produced intense friction heating of the atmosphere, leading to major wildfires that, in turn, filled the lower atmosphere with smoke, dust and pyrotoxins in a scenario reminiscent of a nuclear winter. Indication that much of the end-Cretaceous land biomass was consumed by fire is provided by widespread evidence of soot at the K/T boundary,

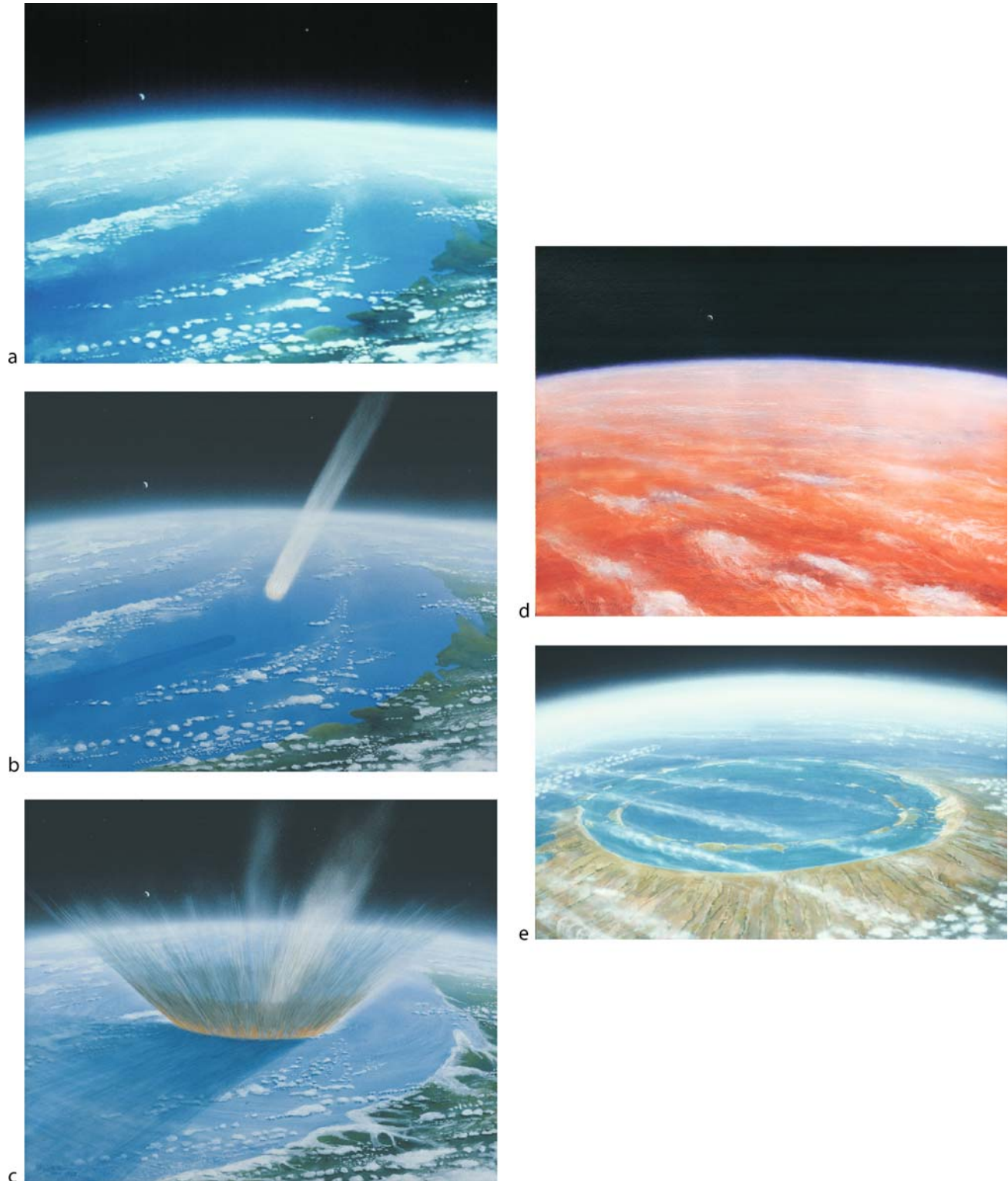


Figure C77 Artistic view of the Chicxulub impact event: (a) end-Cretaceous, 5 s before impact (Yucatan peninsula, Mexico); (b) end-Cretaceous, 1 s before impact (approaching asteroid or comet); (c) end-Cretaceous, the impact event; (d) beginning of Tertiary, about 1 month after impact (dust and sulfate clouds blocking sunlight); (e) Early Tertiary, 1,000 years after impact (final multiring Chicxulub structure) (paintings by William K. Hartmann).

consisting of up to 2% of the carbon content of the end-Cretaceous biosphere. Soot is a strong absorber of solar radiation, thus preventing it from reaching the surface.

Long-term effects extend over months to decades after the impact, and can have profound effects on the environment both directly and indirectly by perturbing the overall climate. They include the radiative effects due to the stratospheric loading of small size dust (e.g., Alvarez et al., 1980; Covey et al., 1994; Luder et al., 2003), and greenhouse gases such as carbon dioxide (CO₂) and water vapor (H₂O). Unique to the Chicxulub impact is the climatic effect of sulfur-bearing gases (Ivanov et al., 1996; Pierazzo et al., 1998), whose importance has been inferred from the climatic effects associated with major volcanic eruptions (see below).

The geologic record of the end-cretaceous climate and its perturbation

The end-Cretaceous geologic record can provide some constraints on the climatic effects of the Chicxulub impact event. The Cretaceous Period is characterized by one of the warmest climates documented in Earth's history (Barron et al., 1995). No evidence of extensive glaciation has yet been found for any time during this geologic period (although late-Cretaceous eustatic sea level fluctuations have been interpreted as being caused by the growth and shrinkage of minor ice sheets on Antarctica (see *Sea level change, last 250 million years*, ed.). The late-Cretaceous climate was slightly cooler than the mid-Cretaceous (up to 8–10°C), but its estimated mean global surface temperatures were still several degrees (°C) higher than present. Oceanic and continental data suggest equatorial paleotemperatures similar to the present-day, but a much lower latitudinal temperature gradient and thus warmer high-latitude temperatures.

Moving across the K/T boundary, the plant records of the Northern Hemisphere (mainly North America) indicate a major ecological disruption and quick recovery, which has been attributed to a brief low temperature excursion and change in the hydrologic cycle. This excursion, however, may not have affected the Southern Hemisphere as much, since only minor palynological changes have been found at the few investigated Southern Hemisphere locations. The marine isotopic record, on the other hand, shows little convincing evidence for either warming or cooling across the K/T boundary (see *Bolide impacts and climate*). This suggests that if any climate change occurred as a result of the impact event, it must have been of very short duration. The mean early Paleocene climate (~64 Ma) was very similar to that of the latest Maastrichtian (~67 Ma). It must be kept in mind, however, that the pre-Paleogene geologic record is characterized by rather low resolution, at best of the order of a few thousands years; time-averaging effects (like bioturbation) may further hide short-lasting shifts in the signal. Consequently, if evidence from a climate change spanning a few hundred years is averaged within a 10,000-year record, it may be very difficult to resolve in the geologic record.

Impact-related climatic effects

The most widely discussed climatic effect of a large impact is caused by dust loading of the upper atmosphere. Alvarez et al. (1980) suggested that dust raised by the impact would have spread worldwide in clouds thick enough to cause an endless night and block photosynthesis for periods longer than a year, with catastrophic consequences for the terrestrial biota. Today, the original Alvarez's scenario has been scaled down to a much

less catastrophic view where only the stratospheric portion of the fine (sub-micron) dust from the impact can affect the climate on a global scale (Toon et al., 1997). It is well known (and well-illustrated by the aftermath of the impact of comet Shoemaker-Levy 9 on Jupiter, in July 1994), both from observations and computer modeling, that large impacts can inject hot, melted or vaporized debris from the projectile and target well above the tropopause and beyond the stratosphere, and ballistically distribute it globally over the Earth.

The "darkness-at-noon" scenario (which incidentally led to the "nuclear winter" idea) was first explored using simple numeric models of the atmosphere's radiative balance. The results initially indicated that even a rapidly coagulating dust layer caused sub-freezing temperatures in continental interiors for at least 2 months after the impact and a global loss of photosynthesis for about half that time. Subsequently it was realized that most of the impact-generated dust (large particles) would have a very short residence time in the atmosphere. Furthermore, only the stratospheric portion of the fine (sub-micron) dust, which corresponds to a very small fraction of the impact-produced dust (Toon et al., 1997), would affect climate globally and over a significant period of time. Therefore, the initial "darkness-at-noon" hypothesis was scaled down to a less catastrophic view. There is still much uncertainty on the amount and size distribution of dust injected into the atmosphere by the impact, thus causing equal uncertainty on the extent of the climatic change. An early three-dimensional (3D) atmospheric general circulation model was used to investigate the effect of a uniform, thick stratospheric dust-layer that would decay in about a year (Covey et al., 1994). The results indicate a strong and "patchy" cooling on land, with temperature declining by up to ~12°C, and a mild cooling (few degrees) over the oceans, accompanied by a collapse of the hydrologic cycle. Although the climate model was extended to only one year after the impact, it suggested that the climate would probably recover in about a decade. Recently, the role of the oceans in the long-term response of the radiative perturbation following a Chicxulub-type dust loading of the atmosphere was explored using a two-dimensional (2D), zonally-averaged dynamic ocean circulation model (Luder et al., 2003). The model results indicate that in the first year after the impact the sea surface temperature dropped by several degrees, with the strongest effects in the equatorial regions, but this change remained confined to the upper 200 m of the oceans. Deep-sea temperatures started to change only after ~100 years, but never exceeded few tenths of °C. Overall, the dust-related climatic change did not affect the structure of the ocean circulation. These studies confirm the deep ocean's crucial role as moderator of the Earth's climate.

The presence of a thick sequence of carbonates and evaporites at the impact location brings into the discussion the atmospheric release of large amounts of carbon dioxide (CO₂), sulfur-bearing gases, and water vapor from the sedimentary layer (e.g., Ivanov et al., 1996; Pierazzo et al., 1998). Large amounts of greenhouse gases could be responsible for an abrupt and long lasting climate shift. Various computer simulations have been carried out to assess the influence of the sedimentary layer in the climatic effects of the Chicxulub impact. Early models suggested the release of CO₂ amounts large enough to affect the global climate significantly. However, more detailed modeling studies (Ivanov et al., 1996; Pierazzo et al., 1998) strongly revised the amount of CO₂ released in the impact, and consequently its climatic effects (even these lower estimates may have to be further downsized in light of new laboratory and field studies on the behavior of carbonates in impacts). Considering that the estimated atmospheric inventory

of CO₂ toward the end of the Cretaceous was about 2–10 times pre-industrial values, it is doubtful that the CO₂ directly released by the Chicxulub impact event would have increased the end-Cretaceous atmospheric inventory of CO₂ by more than ~50%. The radiative forcing associated with the impact-released CO₂ is in the range of 1.2–3.4 W m⁻², comparable to the estimated forcing from greenhouse gases due to industrialization (Pierazzo et al., 2003). This forcing is not considered to be large enough to cause a climate change capable of a major mass extinction. A bigger contribution to the atmospheric CO₂ inventory may come from the impact-related wildfires. Estimates from the identified soot layer at the K/T boundary suggest at most a doubling of the preimpact CO₂ inventory (Toon et al., 1997).

The release of sulfur-bearing gases and water vapor in the stratosphere results in the production of sulfate aerosols, as documented by volcanic eruptions. Sulfate aerosols are strong absorbers of long-wave (LW) radiation, while they mainly scatter short-wave (SW) radiation, resulting in a net cooling of the Earth's surface. The effect of injecting sulfur-bearing gases and water vapor into the stratosphere has been investigated with simple atmospheric models. Using a general planetary radiative transfer model, Pope et al. (1997) modeled the solar flux through a sulfate aerosol cloud. Sulfate formation from over 2×10^{17} g of sulfur dioxide (SO₂) and of water vapor (average K/T boundary impact scenario) was modeled with a simple coagulation model. Their results indicate that solar transmission would be significantly reduced (below 50% of normal) for about 8–13 years after the impact and cause a negative forcing (300 W m⁻²) about two orders of magnitude larger than the estimated forcing from CO₂. The presence of dust and soot grains could speed up the coagulation process, significantly decreasing the overall duration of the effect, but increasing its magnitude by further decreasing the solar transmission. Pope et al. (1997) estimated that forcing from the sulfates would cause the continental surface temperature to drop by several degrees, approaching freezing for several years. Using a similar approach but assuming that S would be released as a mixture of SO₂ and SO₃ Pierazzo et al. (2003) suggest a slightly shorter duration of the sulfate effect, with a 50% reduction in solar transmission for 4–5 years after the impact, but a stronger overall forcing (over 500 W m⁻²). They also found no significant change in the maximum forcing for sulfur loadings above about 3×10^{16} g of S (or 6×10^{16} g of SO₂; minimum K/T boundary impact scenario), suggesting a saturation of the sulfur-related forcing. In particular, in investigating the immediate (few days) post-impact climate responses using a single column version of an atmospheric general circulation model, Pierazzo and colleagues found strong temperature drops over the summer hemisphere continents, with milder effects over winter hemisphere continents and oceans. Adding impact-loads of CO₂ to the sulfate effects mitigates the overall cooling only slightly (0.5 °C at most). More comprehensive and detailed 3D climate system models of the impact-related climate change at the end-Cretaceous are still not available.

Study of the responses of terrestrial biota to impact-related climatic effects is still in its infancy. Lomax et al. (2000, 2001) used a dynamic global vegetation-biogeochimistry model to investigate the potential global-scale response of terrestrial ecosystems to an increase in atmospheric CO₂, and to a combined initial cooling plus greenhouse warming resulting from a Chicxulub-type impact. They found that a four to tenfold increase of the atmospheric end-Cretaceous CO₂ inventory produces spatially heterogeneous increases in the distribution of canopy structure, net primary

productivity, and soil carbon concentrations, possibly causing a biotic feedback mechanism that would ultimately help long-term climate stabilization (Lomax et al., 2000). They then investigated the overall combined effect of dust/sulfates and CO₂ loading on the terrestrial ecosystem by artificially reducing the mean annual temperature in the model by 6 °C and the solar irradiance by 30% for 100 years, and simulating the effects of wildfires by burning 25% of the vegetation carbon and setting the CO₂ concentration to ten times pre-impact levels (Lomax et al., 2001). The model results indicate a collapse of the terrestrial net primary productivity that recovered to pre-impact values within a decade. In particular, they found that the overall change in productivity and vegetation biomass is stronger at low latitudes than at high latitudes, and is consistent with ecological extinction gradients derived from terrestrial paleobotanical data.

Conclusions

The Chicxulub structure, 65 million years in age, is the youngest of the known terrestrial impact structures larger than 100 km in diameter. Structures of this size are associated with impact events that are capable of perturbing the environment and climate worldwide. Likely global scale effects include depletion of stratospheric ozone, ignition of global wildfires, release of climatically active gases, production of toxic oxides and acid rain, and atmospheric loading of dust and smoke. When looking at the geologic record, it appears that any climatic change introduced by the Chicxulub impact event did not destabilize the paleoclimate, which was able to recover to the pre-impact state over a geologically short timescale (<10,000 years). On the other hand, a sudden, large climate change lasting a few hundred years would still have enormous repercussions on the evolution of the biosphere.

Various investigations on the climatic effects associated with the K/T boundary impact indicate that an abrupt cooling episode occurred immediately after the impact and could have extended for a few years. The atmospheric loading of impact-produced CO₂ could then have caused a mild warming that may have helped climate recovery. The impact apparently did not affect the deep ocean. The slow response of the deep ocean and the quick reaction of the terrestrial ecosystem contribute to a fast recovery of the climate system.

To this day, the magnitude of the end-Cretaceous climate change is still an open question; answering it may shed new light on our understanding of the end-Cretaceous mass extinction.

Elisabetta Pierazzo

Bibliography

- Alvarez, L.W., Alvarez, W., Asaro, F., and Michel, H.V., 1980. Extraterrestrial cause for the Cretaceous-Tertiary extinction. *Science*, **208**, 1085–1108.
- Barron, E.J., Fawcett, P.J., Peterson, W.H., and Pollard, D., 1995. A "simulation" of mid-Cretaceous climate. *Paleoceanography*, **10**, 953–962.
- Covey, C., Thompson, S.L., Weissman, P.R., and MacCracken, M.C., 1994. Global climatic effects of atmospheric dust from an asteroid or comet impact on Earth. *Glob. Planet. Change*, **9**, 263–273.
- Ivanov, B.A., Badjukov, D.D., Yakovlev, O.I., Gerasimov, M.V., Dikov, Y.P., Pope, K.O., and Ocampo, A.C., 1996. Degassing of sedimentary rocks due to Chicxulub impact: Hydrocode and physical simulations. In Ryder, G., Fastovsky, D., and Gartner, S. (eds.), *The Cretaceous-Tertiary Event and Other Catastrophes in Earth History*. Boulder, CO: Geological Society of America. Geological Society Of America Special Paper 207, pp. 125–139.
- Lomax, B.H., Beerling, D.J., Upchurch, G.R. Jr., and Otto-Bliessner, B.L., 2000. Terrestrial ecosystem responses to global environmental change

- across the Cretaceous-Tertiary boundary. *Geophys. Res. Lett.*, **27**, 2149–2152.
- Lomax, B., Beerling, D., Upchurch, G. Jr., and Otto-Bliesner, B., 2001. Rapid (10-yr) recovery of terrestrial productivity in a simulation study of the terminal Cretaceous impact event. *Earth Planet. Sci. Lett.*, **192**, 137–144.
- Luder, T., Benz, W., and Stocker, T.F., 2003. A model for long-term climatic effects of impacts. *J. Geophys. Res.*, **108**, DOI: 10.1029/2002JE001894.
- Pierazzo, E., Kring, D.A., and Melosh, H.J., 1998. Hydrocode simulations of the Chicxulub impact event and the production of climatically active gases. *J. Geophys. Res.*, **103**, 28, 607–28, 626.
- Pierazzo, E., Hahmann, A.N., and Sloan, L.C., 2003. Chicxulub and Climate: Effects of stratospheric injections of impact-produced S-bearing gases. *Astrobiology*, **3**, 99–118.
- Pope, K.O., Baines, K.H., Ocampo, A.C., and Ivanov, B.A., 1997. Energy, volatile production, and climatic effects of the Chicxulub Cretaceous/Tertiary impact. *J. Geophys. Res.*, **102**(E9), 21, 645–21, 664.
- Toon, O.B., Zahnle, K., Morrison, D., Turco, R., and Covey, C., 1997. Environmental perturbations caused by the impacts of asteroids and comets. *Rev. Geophys.*, **35**, 41–78.

Cross-references

- [Bolide Impacts and Climate](#)
- [Cretaceous Warm Climates](#)
- [Sea Level Change, Last 250 Million Years](#)

CRYOSPHERE

Introduction

The cryosphere (derived from the Greek *kryos* for “cold”) comprises all of the frozen water and soil on the surface of the Earth. While this term is often used by climatologists, a more accurate name for the study of all aspects of ice and snow is *glaciology*. Ice in clouds is also an important element of climate but is not considered part of the cryosphere. Because the freezing point of water lies in the center of the range of terrestrially achieved temperatures, the cryosphere is a very changeable feature of the Earth’s surface. Its six main elements, in diminishing order of area for today’s climate, are: (a) seasonal snow cover, (b) sea ice, (c) permafrost, (d) ice sheets, (e) river and lake ice, and (f) mountain glaciers and small ice caps.

Seasonal snow cover is the most dynamic element of the cryosphere. It responds rapidly to atmospheric conditions on timescales of days to weeks and, in fact, exhibits the greatest seasonal variation of any geophysical element on the Earth’s surface. Although it has a small seasonal heat storage capacity, its main effect on climate comes from its high albedo (fraction of incident solar radiation reflected back to space). Fresh snow has an albedo of 0.9. *Sea ice* forms when sea water is cooled below its freezing point. This freezing is a complex process because the freezing point of water depends on the salt concentration of the ocean. A sea ice field usually consists of numerous individual floes, typically 0.5–4 m thick, with diameters between 1 meter and many kilometers. Sea ice has a high albedo and therefore the effect its seasonal cycle exerts on the surface heat balance of the Earth is similar to, though smaller than, that exerted by seasonal snow cover. Sea ice also acts as a barrier to the exchange of heat, moisture, and momentum between the atmosphere and the ocean, and furthermore plays a role in the formation of deep water masses in some oceanic areas. Sea ice is covered by snow for much of its lifetime. *River and lake ice* form in a similar manner to sea ice but without

the complications of high salt concentrations. Their climatic behavior resembles that of sea ice. *Ice sheets* are quasi-permanent features, responding to environmental changes on time scales of millennia. Today, only the two polar ice sheets on Antarctica and Greenland remain. Together, they contain by far the greatest proportion of mass of the cryosphere but are least sensitive to climate change on the shorter timescales. Ice sheets have a high elevation and high albedo, and so act as elevated cooling surfaces for atmospheric heat balance. They also play an important role in the freshwater balance of the oceans. Changes in their volume, though slow, are the main cause for sea-level changes on geological timescales. *Mountain glaciers* and small ice caps are a small component of the cryosphere. They are distinguished from the large ice sheets by their size and by the fact that they are topographically controlled. They are too small to have a direct influence on climate; however, their high rates of mass turnover allow rapid changes in response to climatic change (timescales of the order of decades to centuries). *Permafrost* is ground material that remains below freezing for at least two consecutive years, whether or not it contains ice. It may be continuous, underlying the whole of a region, or discontinuous, occurring in patches. In many regions the uppermost, so-called active layer, thaws annually to a depth of 1 to a few meters. Permafrost is a product of heat exchange between the land surface and the atmosphere, changing on timescales of centuries. It affects surface ecosystems and river discharge, and changes in its extent can control rates of trace gas emissions, especially of methane. Permafrost records temperature changes, hence its role as geo-indicator for monitoring and assessing environmental change.

Current distribution of ice in the cryosphere

Today, nearly 80% of the Earth’s freshwater is stored on the continents in the form of ice, almost all of it in the polar regions and in high mountain areas, cf. [Table C9](#) and [Figure C78](#). Perennial ice covers 10% of the Earth’s land surface and 4% of the oceans. The seasonal distribution of snow, lake and river ice, and to a lesser extent, sea ice, is closely linked with atmospheric conditions, in particular with temperature.

Seasonal snow

Seasonal snow reaches its maximum extent in late winter, when it covers almost 50% of the land surface of the Northern Hemisphere. It is almost absent in the Southern Hemisphere, where it is limited to the mountainous areas of New Zealand, southeastern Australia, and South Africa; it is more widespread only in Patagonia and ice-free regions of Antarctica and on sub-Antarctic islands.

Sea ice

The seasonal variation of sea ice is much smaller in the Arctic than in the Antarctic owing to the different geography of the two polar regions. The Arctic Ocean is a truly polar ocean surrounded by land, with only a limited range of longitudes within which sea ice can expand seasonally into lower latitudes. By contrast, in the Southern Hemisphere the central polar region is covered by the continent of Antarctica, preventing sea ice from extending to the highest latitudes in summer but at the same time allowing winter sea ice to extend in a roughly concentric zone around Antarctica at almost all longitudes. A second contrast between the two hemispheres is the larger upward oceanic heat flux in the Antarctic, as less fresh water enters the ocean to cause a low-salinity layer of polar surface water

Table C9 Size of the present-day cryosphere and average mass turnover times of its main components as given by the ice flux and average residence time (adapted from Fitzharris et al., 1996; Vaughan et al., 1999; Zhang et al., 1999; Huybrechts et al., 2000; Church et al., 2001; Lythe et al., 2001)

Cryospheric element	Area (10 ⁶ km ²)	Ice volume (10 ⁶ km ³)	Ice flux (km ³ yr ⁻¹)	Residence time ^a (yr)
Seasonal snow cover	47.2	~0.01	~25,000	~0.4
Northern Hemisphere (max)	46.3			
Southern Hemisphere (max)	0.9			
Sea ice				
Northern Hemisphere (max/min)	16.0/9.0	0.05/0.03	~40,000	~1
Southern Hemisphere (max/min)	22.0/4.0	0.03/ <0.01	~20,000	~1
Permafrost	25.4	~0.02	~40	~500
Ice sheets				
Antarctic Ice Sheet (grounded ice)	12.37	25.71	2,100	~12,500
Antarctic ice shelves	1.49	0.66	540	~1,200
East Antarctic Ice Sheet	10.09	22.59	1,350	~17,000
West Antarctic Ice Sheet	2.28	3.12	750	~4,000
Greenland Ice Sheet	1.71	2.85	570	~5,000
River and lake ice	<1.0			~0.3
Mountain glaciers and small ice caps	0.68	0.18	~750	~250

^aThe residence time is defined as the ice volume divided by the ice flux.

hampering vertical heat exchange from below. For these reasons, the Arctic features a thicker permanent sea ice cover of multiyear ice, augmented in winter by a seasonal ice cover of first-year ice extending into the surrounding subpolar seas. Around Antarctica, however, almost all of the winter ice melts in summer, leaving multiyear ice confined only to the western Weddell Sea, the Bellingshausen and Amundsen Seas, and coastal embayments. Arctic sea ice generally reaches its maximum extent in March and minimum extent in September. By contrast, Antarctic autumnal ice growth is slower and spring decay about one month faster.

Polar ice sheets

Present-day continental ice cover is entirely dominated by the Antarctic Ice Sheet, which is responsible for 90% of the volume and 85% of the area of all land ice. Most of this ice is in the East Antarctic Ice Sheet, which constitutes a vast, relatively flat dome with a maximum elevation of 4,030 m and a maximum known thickness of 4,776 m. The Transantarctic Mountains divide the East Antarctic Ice Sheet from the West Antarctic Ice Sheet and the Antarctic Peninsula. The West Antarctic Ice Sheet rests on bedrock below sea level and largely drains into two big ice shelves in the Ross and Weddell Seas. These ice shelves are up to 1,000 m thick and float in equilibrium with the ocean water. Smaller ice shelves fringe the Antarctic coastline elsewhere. Ice flow towards the margin results mainly from internal ice deformation under the action of gravity. At the margin, the flow is often channeled in outlet glaciers and in ice streams, in which the dominant flow mechanism is basal sliding, and that are responsible for the bulk of the ice discharge across the grounding line into the ice shelves.

Mass is lost from the ice shelves by bottom melting and by calving of icebergs from their ice fronts. Current Antarctic surface temperatures are so low that there is virtually no surface melting. These low temperatures also limit the amount of water vapor that can be advected inland. Accumulation rates over the vast interior of the continent are only a few cm per year and this makes the central Antarctic Plateau one of the driest places on Earth.

The only Arctic ice mass of significance is the Greenland Ice Sheet. It is a relict from the ice ages that overlies a bowl-shaped continent and has a maximum surface elevation of 3,230 m. In contrast to Antarctica, summer temperatures on Greenland are high enough to cause widespread summer melting, resulting in a negative mass balance below elevations of about 500 m in the north and 1,800 m in the south. Greenland has no major ice shelves apart from a few small ones along the north and northeast coast. Ice not lost by ablation is discharged into the ocean by iceberg calving from glaciers, in roughly the same amount as runoff. Complete melting of both polar ice sheets would raise global sea level by about 70 m.

Glaciers and ice caps

The water currently contained in glaciers and ice caps (excluding Antarctica and Greenland) is equivalent to about 0.5 m of global sea level. Half of it is in small ice caps, mostly in the Arctic, and the other half is stored in mountain glaciers elsewhere. Most mountain glacier ice is in Alaska, followed by Central Asia and Patagonia. Ice volume contained in the Alps is less than 1% of total glacier volume, but its glaciers have been studied the most. There are more than 160,000 glaciers worldwide. Glaciers enlarge when the accumulation of snow and ice exceed the loss by melting, and sometimes calving. Net accumulation occurs at higher altitude, net ablation at lower altitude. To compensate for net accumulation and ablation, the ice flows downhill by internal deformation and basal sliding. The primary controls on glacier mass balance are temperature, especially in summer, and accumulation, especially in winter. The nature of the response varies from glacier to glacier depending on mass-balance gradient, hypsometry, and glacier length.

Permafrost

About 24% of the exposed land area of the Northern Hemisphere is currently underlain by permafrost, most of it in the tundra of Canada, Alaska, and Russia (Zhang et al., 1999). It is also present under shallow polar sea beds, in ice-free areas in Antarctica, on some sub-Antarctic islands, and in many mountain areas and high plateaus of the world. Its distribution roughly follows the pattern of air temperature, though some of it is relict, having formed during colder glacial periods and having melted only very slowly since then. Sizeable areas below the polar ice sheets and small ice caps are also below freezing. This thermal condition of the ground extends to maximum depths of about 1,500 m in Siberia, 1,000 m in the Canadian Arctic, and 680 m in Alaska, but often it is also less than 20 m thick. Generally, permafrost with high ice content (>20% by volume) is found at high latitudes, and permafrost with low ice content (<10% by volume) mainly in mountainous regions and high plateaus. Almost half of the total permafrost area is continuous permafrost. The remaining part is made up of discontinuous and sporadic permafrost or occurs in isolated patches.

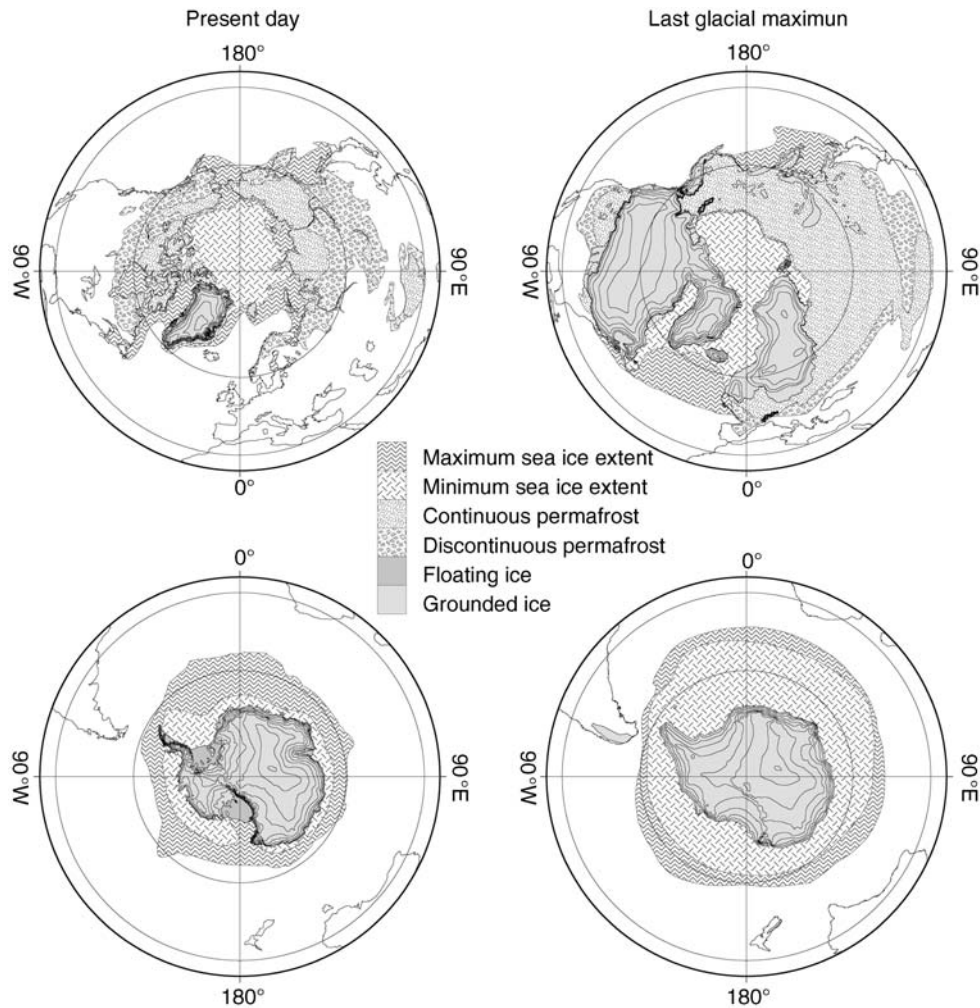


Figure C78 Geographic extent of main components of the cryosphere in both hemispheres. The *left panels* are for the present distribution, the *right panels* depict the situation during the Last Glacial Maximum between 23,000 and 19,000 years ago (adapted from maps presented in Cooke and Hays, 1982; Untersteiner, 1984; Frenzel et al., 1992; Fitzharris et al., 1996; Van Vliet-Lanoë and Lisitsyna, 2001, and the author's own ice sheet model results).

Current evolution of the cryosphere

The current evolution of many elements of the cryosphere, especially of those with the shorter response times, appears well correlated with the recent global warming trend of about 0.6°C since the late nineteenth century.

Snow covers in temperate regions are usually thin and often close to their melting point, hence they are sensitive indicators of climate change. Monitoring of seasonal snow is practical only with satellites, so there are no reliable records prior to 1971. Visible-band and passive microwave data since then show considerable variability from year to year, but also reveal a decline in the extent of snow cover in the Northern Hemisphere by about 10% since the mid-1980s, largely due to a decrease in spring extent (Robinson et al., 1993). This reduction in snow cover is highly correlated with increasing air temperature. Snow-cover observations at ground stations have been recorded for many decades and suggest that Northern Hemisphere spring extents are currently at their lowest values in the past 100 years. Numerous small perennial snow patches have

disappeared over the twentieth century, commensurate with the general warming trend.

Like seasonal snow, *sea ice* is also thought to be sensitive to climate change but the mechanisms are less well understood as additional processes such as ice transport, ocean circulation, and convection depths come into play. Warming is nevertheless thought to cause a reduction in both area and thickness of sea ice, which sets in motion a positive feedback, as more solar radiation is absorbed and more oceanic heat is transferred to the atmosphere. Satellite passive microwave data show a marked decrease of perennial Arctic sea ice extent for the period 1978–2000 of 9% per decade consistent with a summer warming of 1.2°C per decade over the same period (Comiso, 2002). Antarctic records of sea-ice extent, on the other hand, show large variability but a negligible, albeit slightly positive, overall trend. Knowledge of sea-ice thickness largely comes from upward sonar profiling from submarines in the Arctic and more recently, from buoys moored to the sea floor. Observations of sea ice thickness have also been derived from satellite altimetry of the freeboard height, but

geographical coverage and/or record length do not yet allow for strong conclusions. Summer Arctic sea ice cover and thickness have decreased in recent years (e.g., Lindsay and Zhang, 2005; Serreze et al., 2007).

Observations of *lake and river ice* exist primarily in the form of freeze-up and break-up dates. Records for the Northern Hemisphere since 1850 show significant evidence of later autumn freeze-up and earlier spring break-up of on average 5.8 days and 6.5 days per 100 years, respectively, consistent with the warming trend from the beginning of the twentieth century (Magnuson et al., 2000).

The present evolution of the *polar ice sheets* is still not known with confidence but a picture is starting to emerge from a combination of mass budget studies, satellite altimetry, and modeling (Rignot and Thomas, 2002). Current evidence indicates that the Antarctic Ice Sheet has probably lagged behind in the last glacial cycle of retreat. Most of the ongoing shrinking probably occurs in West Antarctica as a delayed response to post-glacial sea-level rise, whereas the East Antarctic Ice Sheet may be close to a stationary state, or growing slightly in response to increased accumulation rates. Superimposed on this long-term trend is a likely thickening effect of modern accumulation increases. Larger imbalances have recently been detected in West Antarctica, positive for the Siple Coast ice stream area and negative for the Pine Island/Thwaites catchment area. These probably represent local ice-dynamic effects that are unrelated to climate. The Greenland Ice Sheet is believed to be close to an overall neutral equilibrium. Current data show a consistent picture of a small thickening of the accumulation zone offset by larger thinning rates at lower altitudes. According to the Intergovernmental Panel on Climate Change (IPCC), both ice sheets together may have contributed between -2 cm and $+6$ cm to the observed twentieth century sea-level rise (Church et al., 2001).

A wealth of data exists on the geometry of valley *glaciers*. A large amount of information is available from sketches, etchings, paintings, and old photographs. In many cases, information from terminal moraines and trimlines is available to construct the history of a glacier over the last few centuries. An overwhelming characteristic of global glacier length records is the almost uniform recession of glaciers, which started about 1850 at the end of the Little Ice Age and is still continuing today. Rising global temperature is the most likely explanation and so the worldwide glacier retreat is probably one of the strongest measures of global warming. The only exceptions today are Norwegian and New Zealand glaciers, which are currently advancing, due to local increases in precipitation. However, this is an exceptional state that can probably not be sustained in the long term. Global glacier melt assessments indicate that since the late nineteenth century, glaciers and ice caps have lost between 5 and 10% of their volume and a little less than that in area. The IPCC reports a glacier contribution to global sea-level rise of between 2 and 4 cm over the last 100 years, less than the contribution from thermal expansion but similar to the combined contribution from the Antarctic and Greenland Ice Sheets. Findings of ancient remains in the European Alps (e.g., the 5,000-year old Oetztal “ice man”) indicate that current glacier recession is reaching levels not seen for probably several millennia. Recent studies suggest that the twentieth century rate of glacier wastage in Alaska and the Patagonian Andes doubled after the mid-1990s (Arendt et al., 2002; Rignot et al., 2003).

Deep *permafrost* temperatures change by conduction and therefore are a manifestation of past climatic conditions over long spans of time. Permafrost is also very sensitive to changes in its surface energy balance. Very small changes in surface climate can produce robust changes in permafrost temperatures. Long-term measurements in deep boreholes in Alaska, Canada, and elsewhere demonstrate a distinct but spatially heterogeneous warming trend in low-land permafrost (Romanovsky and Osterkamp, 2001). Temperature measurements in northern Alaska have demonstrated a warming of the permafrost of $2-4^{\circ}\text{C}$ over the last century. In North America, the southern extent of the discontinuous permafrost zone has migrated northward in response to warming after the Little Ice Age, and continues to do so today. In China, both an increase in the lower altitudinal limit of mountain permafrost and a decrease in areal extent have been observed. Increases of the thickness of the active layer in response to climate warming have also been reported.

The cryosphere during the last glacial cycle

During the last ice age, which was most severe from about 23,000 to 19,000 years ago, an extensive ice complex stretched across North America, Greenland, the polar seas, and parts of northern Eurasia. It consisted of huge land-based glaciers, marine-based ice sheets, and either permanent pack-ice or shelf ice. Ice increased synchronously over Antarctica and the Southern Ocean. Sea levels were 125 m lower than today because water was bound up in continental ice sheets that increased their total mass by about a factor of three (Clark and Mix, 2002; Figure C78 and Table C10).

The surface of the Earth during the Last Glacial Maximum (LGM) was comprehensively mapped by the CLIMAP (Climate: Long-range Investigation, Mapping, and Prediction) project in the 1970s from a combination of biological and lithological evidence from deep-sea cores and from the land (CLIMAP, 1976). Best documented is the chronology of Northern Hemisphere ice-sheet extent. The largest glacier complex was situated over North America. It is inferred to have consisted of several domes centered over the high plateaus of eastern Canada and the Rocky Mountains. An ice-free corridor separated the Cordilleran Ice Sheet from the Laurentide Ice Sheet until late in the glacial

Table C10 Size of main cryospheric elements during the Last Glacial Maximum (adapted from Denton and Hughes, 1981; Cooke and Hays, 1982; Van Vliet-Lanoë and Lisitsyna, 2001; Huybrechts, 2002; Clark and Mix, 2002)

Cryospheric element	Area (10^6 km ²)	Ice volume (10^6 km ³)	Excess ice-equivalent sea level (m)
All land ice	41.8	75–88	110–135
Laurentide Ice Sheet	14.6	31–38	75–88
Fennoscandian Ice Sheet	6.2	5.8–7.5	14–18
Greenland Ice Sheet	2.6	4.0–4.5	2–3
Antarctic Ice Sheet (grounded)	15.1	33–36	15–20
Other ice caps and glaciers	3.3	1.4–2.2	4–6
Northern Hemisphere sea ice (max/min)	18/11	–	–
Southern Hemisphere sea ice (max/min)	35/25	–	–
Exposed permafrost (continuous and discontinuous)	30	–	–

period. The glaciation of Eurasia had an ice sheet centered over the British Isles in the west and that extended beyond the present day shoreline onto the then emerged shelf of the North Sea. The Fennoscandian Ice Sheet spread into the same area from the east but did not coalesce into the British Isles at the LGM. To the east, the Fennoscandian Ice Sheet extended into the northern part of the Russian plain and the Barents Sea, which in the northwest was also covered by ice from Novaya Zemlya. The Kara Sea, except at its western margin, was not glaciated at the LGM, but likely at an earlier stage of the last glacial cycle. The thickness of the ice sheets cannot be reconstructed from glacial-geological observations but it has been inferred to have been up to 4 km from indirect evidence such as uplift rates of the land, and from modeling.

By comparison, the Antarctic and Greenland Ice Sheets underwent only small changes in volume and extent during the last glacial cycle. Volume changes of the Antarctic Ice Sheet were largely concentrated in West Antarctica and the Antarctic Peninsula. At the LGM, grounding lines advanced close to the continental shelf break almost everywhere as global sea level dropped. It is unclear whether extensive ice streams continued to exist in the Ross basin and elsewhere. Ice over interior East Antarctica was generally thinner than today because of lower accumulation rates. The Greenland Ice Sheet also extended beyond the present coastline to cover at least the inner continental shelf. Summer melting ceased and mass was lost by calving only. The Greenland Ice Sheet extended northwest to join the Laurentide Ice Sheet flowing out of Canada. Ice retreat of the Antarctic and Greenland Ice Sheets was in full progress between 13,000 and 8,000 years ago, several thousand years later than for the North American and European Ice Sheets (Huybrechts, 2002).

To date, no criteria have been developed to recognize paleo-ice shelves. It has been speculated that the Antarctic continent was entirely encircled by a vast ice shelf that merged imperceptibly with the permanent pack ice and possibly extended as far as 800 km beyond the continental shelf (Denton and Hughes, 1981). Russian scientists have hypothesized a 1 km thick Arctic ice shelf from glacial scouring of ridges at the sea floor, but its dating is uncertain (Polyak et al., 2001).

Small ice caps and glaciers merged to larger glacier complexes in Patagonia, the Alps, and many presently glaciated areas elsewhere (Pyrenees, Caucasus, eastern Siberia, New Zealand Alps, and other mountain areas). There is no convincing evidence for the occurrence of a Tibetan Ice Sheet, but glacier fronts in the Himalayas descended by about 1,000 m elevation.

In the Southern Hemisphere, the most striking difference was the winter extent of sea ice, which was significantly greater than it is today (Cooke and Hays, 1982). Summer extent was probably similar to today's winter extent. Permanent sea-ice cover also existed in the Norwegian, Greenland, and Labrador Seas coincident with a large shift in the path of the Gulf Stream, which flowed due east at 40°N during the glacial maximum. A striking and unexplained difference was the comparably small amount of cooling in the North Pacific and the associated southward extension of sea ice at LGM compared with equivalent latitudes in the North Atlantic.

There are no proxy data to infer the seasonal variation of snow cover and river and lake ice. Nevertheless, winter cover must have been greatly expanded, commensurate with Northern Hemisphere continental coolings of up to -20°C (CLIMAP Project members, 1981; Frenzel et al., 1992). There are also many fossil periglacial features at the surface that show that permafrost at the LGM was more extensive than today. In North America,

discontinuous permafrost extended up to 1,000 km south of the southern margin of the Laurentide Ice Sheet. Permafrost was also present on most of Europe, the Atlas Mountains, Turkey, Iran, the whole of Siberia, the Tibetan Plateau, northern China, and Hokkaido. In the Southern Hemisphere, widespread permafrost extended at mid altitude in southern America, as far north as 40°S, and was present in Patagonia, the southern island of New Zealand, and on all sub-Antarctic islands. It occurred isolated in mountainous areas of Tasmania and southeast Australia, and even in the highest mountains of East Africa and the high Andes. It never existed in South Africa, with the exception of a small spot of mountain permafrost in the Drakensberg (Van Vliet-Lanoë and Lisitsyna, 2001).

The last glacial cycle was enclosed by two periods when the cryosphere was smaller than today. During the Last Interglacial, which culminated 125,000 years ago, Northern Hemisphere temperatures at mid-latitudes were 2–3°C warmer than today, increasing towards the pole to more than 4°C. The Greenland Ice Sheet may have retracted to a small central ice dome, thus providing most of the melt to explain the inferred sea-level stand of approximately 6 m higher than today (Letréguilly et al., 1991; Cuffey and Marshall, 2000). The Holocene Climatic Optimum occurred around 6,000 years ago. The warming was of a similar magnitude as that of the Eemian warming, but it was shorter-lived. At that time, the Greenland Ice Sheet margin receded inland from its present position. The other components of the cryosphere, except the Antarctic Ice Sheet, were also smaller.

The cryosphere before the last glacial cycle

In geological terms, the last ice age ended a short time ago. It was the last episode of a period of climate oscillations between glacial and relatively ice-free environments that began about 2.3 million years ago. Over the last 800,000 years, such ice ages had a period of about 100,000 years; before that, 41,000-year cycles dominated. The penultimate glacial cycle, which ended 130,000 years ago, was probably the most severe. Periods of extensive glaciation also existed prior to those of the Pleistocene epoch. Though the record of early climates is dominated by evidence of global warmth and likely almost total absence of land and sea ice, there were intervals of widespread ice cover during Paleoproterozoic times, at around 2.3 billion years ago and perhaps also between 3.1 and 2.9 billion years ago.

The most extreme glacial climate in the Earth's history probably occurred during the Late Precambrian between 900 and 600 million years ago, and is known as the *Proterozoic ice house*. In its extreme version, ice sheets extended to the equator and the world's ocean was virtually entirely frozen over (Hoffman et al., 1998). At that time, the Earth experienced anomalously low atmospheric carbon dioxide concentrations, possibly as a result of mountain building and continental weathering, in addition to the Sun being 6% fainter than it is today. Recovery from such a *snowball Earth* could have resulted from volcanic outgassing of greenhouse gases. Glaciation of the Earth also occurred in the Late Ordovician at 450 million years ago, and during Carboniferous-Permian times between 320 and 250 million years ago. At this time, a single supercontinent, Gondwanaland, lay over the South Pole, which suggests that the presence of a large land mass at high latitude is a critical element for glaciation.

Glaciation on Earth started again during the Cenozoic Era, from 65 million years ago to the present. It started first in the

Southern Hemisphere and was punctuated by two periods of significant ice growth. The first ice increase occurred near the Eocene-Oligocene boundary 36 million years ago and saw frequent ice sheets growing and decaying on East Antarctica, reaching the margin of the continent in a few places (Barker et al., 1999). Global ice sheet volume increased again in the middle Miocene around 15 million years ago with the formation of a quasi-permanent East Antarctic Ice Sheet that may have reached its maximum extent. The first period of ice increase was probably driven by declining levels of atmospheric carbon dioxide, while the second period has been linked to the thermal isolation of Antarctica, as newly formed continents moved to the north and the Antarctic Circumpolar Current developed. The West Antarctic Ice Sheet likely formed later, during the Late Miocene. By 2 million years ago, the Antarctic glacial regime was much as at present and ice ages started to occur on the Northern Hemisphere, as did mountain glaciers in midlatitude highlands.

Philippe Huybrechts

Bibliography

- Arendt, A.A., Echelmeyer, K.A., Harrison, W.D., Lingle, C.S., and Valentine, V.B., 2002. Rapid wastage of Alaska glaciers and their contribution to rising sea levels. *Science*, **297**, 382–386.
- Barker, P.F., Barrett, P.J., Cooper, A.F.K., and Huybrechts, P., 1999. Antarctic glacial history from numerical models and continental margin sediments. *Palaeogeogr., Palaeoclimatol., Palaeoecol.*, **150**, 247–267.
- Church, J.A., Gregory, J.M., Huybrechts, P., Kuhn, M., Lambeck, K., Nhuon, M.T., Qin, D., and Woodworth, P.L., 2001. Changes in sea level. In Houghton, J.T., Ding, Y., Griggs, D.J., Noguer, M., Van der Linden, P.J., Dai, X., Maskell, K., and Johnson, C.A. (eds.), *Climate Change 2001: The Scientific Basis: Contribution of Working Group I to the Third Assessment Report of the Intergovernmental Panel on Climate Change*. Cambridge, UK/New York: Cambridge University Press, pp. 639–694.
- Clark, P.U., and Mix, A.C., 2002. Ice sheets and sea level of the Last Glacial Maximum. *Quaternary Sci. Rev.*, **21**(1–3), 1–7.
- CLIMAP, 1976. The surface of the ice-age earth. *Science*, **191**, 1131–1137.
- CLIMAP Project Members, 1981. Seasonal reconstructions of the Earth's surface at the Last Glacial Maximum (Geological Society of America Map and Chart Series, MC-36). Boulder, CO: Geological Society of America.
- Comiso, J.C., 2002. A rapidly declining perennial sea ice cover in the Arctic. *Geophys. Res. Lett.*, **29**(20), 1956, doi:10.1029/2002GL015650.
- Cooke, D.W., and Hays, J.D., 1982. Estimates of Antarctic ocean seasonal sea-ice cover during glacial intervals. In Craddock, C. (ed.), *Antarctic Geoscience* Madison: University of Wisconsin Press, pp. 1017–1025.
- Cuffey, K.M., and Marshall, S.J., 2000. Substantial contribution to sea-level rise during the last interglacial from the Greenland ice sheet. *Nature*, **404**, 591–594.
- Denton, G.H., and Hughes, T.J. (eds.), 1981. *The Last Great Ice Sheets*. New York: Wiley, 485pp.
- Fitzharris, B.B., 1996. The cryosphere: Changes and their impacts. In Watson, R.T., Zinyowera, M.C., and Moss, R.H. (eds.), *Climate Change 1995: Impacts, Adaptations and Mitigations of Climate Change: scientific-technical analysis*. Cambridge, UK: Cambridge University Press, pp. 241–266.
- Frenzel, B., Pecsí, M., and Velichko, A.A., 1992. Atlas of palaeoclimates and palaeoenvironments of the Northern Hemisphere, Late Pleistocene-Holocene. Stuttgart: Gustav Fisher Verlag, 153pp.
- Hoffman, P.F., Kaufman, A.J., Halverson, G.P., and Schrag, D.P., 1998. A Neoproterozoic Snowball Earth. *Science*, **281**, 1342–1346.
- Huybrechts, P., 2002. Sea-level changes at the LGM from ice-dynamic reconstructions of the Greenland and Antarctic Ice Sheets during the glacial cycles. *Quaternary Sci. Rev.*, **21**(1–3), 203–231.
- Huybrechts, P., Steinhage, D., Wilhelms, F., and Bamber, J.L., 2000. Balance velocities and measured properties of the Antarctic Ice Sheet from a new compilation of gridded datasets for modeling. *Ann. Glaciol.*, **30**, 52–60.
- Letréguilly, A., Reeh, N., and Huybrechts, P., 1991. The Greenland Ice Sheet through the last glacial-interglacial cycle. *Global and Planetary Change*, **4**(4), 385–394.
- Lindsay, R.W., and Zhang, J., 2005. The thinning of arctic sea ice, 1988–2003: Have we passed a tipping point? *J. Climate*, **18**, 4879–4894.
- Lythe, M., and Vaughan, D.G., 2001. BEDMAP: A new ice thickness and subglacial topographic model of Antarctica. *J. Geophys. Res.*, **106** (B6), 11335–11351.
- Magnuson, J.J., and 13 co-authors. 2000. Historical trends in lake and river ice cover in the Northern Hemisphere. *Science*, **289**, 1743–1746.
- Polyak, L., Edwards, M.H., Coakley, B.J., and Jakobsson, M., 2001. Ice shelves in the Pleistocene Arctic Ocean inferred from glaciogenic deep-sea bedforms. *Nature*, **410**, 453–457.
- Rignot, E.J., and Thomas, R.H., 2002. Mass balance of polar ice sheets. *Science*, **297**, 1502–1506.
- Rignot, E.J., Rivera, A., and Casassa, G., 2003. Contributions of the Patagonia Icefields of South America to sea level rise. *Science*, **302**, 434–437.
- Robinson, D.A., Dewey, K.F., and Heim, R.R., 1993. Global snow cover monitoring: An update. *Bull. Am. Meteorol. Soc.*, **81**, 1281–1299.
- Romanovsky, V.E., and Osterkamp, T.E., 2001. Permafrost: Changes and impacts. In Paepe, R., and Melnikov, V. (eds.), *Permafrost Response on Economic Development, Environmental Security and Natural Resources* Dordrecht: Kluwer, pp. 297–315.
- Serreze, M.C., Holland, M.M., and Stroeve, J., 2007. Perspectives on the Arctic's shrinking sea-ice cover. *Science*, **315**, 1533–1536.
- Untersteiner, N., 1984. The cryosphere. In Houghton, J.T. (ed.), *The Global Climate*. Cambridge, UK: Cambridge University Press, pp. 121–140.
- Van Vliet-Lanoë, B., and Lisitsyna, O., 2001. Permafrost extent at the Last Glacial Maximum and at the Holocene Optimum. The CLIMEX Map. In Paepe, R., and Melnikov, V. (eds.), *Permafrost Response on Economic Development, Environmental Security and Natural Resources* (NATO Science Series, 76). Dordrecht: Kluwer, pp. 215–225.
- Vaughan, D.G., Bamber, J.L., Giovinetto, M.B., Russell, J., and Cooper, A.P.R., 1999. Reassessment of net surface mass balance in Antarctica. *J. Climate*, **12**, 933–946.
- Zhang, T., Barry, R.G., Knowles, K., Heginbottom, J.A., and Brown, J., 1999. Statistics and characteristics of permafrost and ground-ice distribution in the Northern Hemisphere. *Polar Geogr.*, **23**(2), 132–154.

Cross-references

[Antarctic Glaciation History](#)
[Borehole Climatology: Climate Change from Geothermal Data](#)
[CLIMAP](#)
[Cordilleran Ice Sheet](#)
[Glaciations, Pre-Quaternary](#)
[Glaciations, Quaternary](#)
[Icehouse \(cold\) Climates](#)
[Last Glacial Maximum](#)
[Laurentide Ice Sheet](#)
[Mountain Glaciers](#)
[Periglacial Geomorphology](#)
[Pleistocene Climates](#)
[Proterozoic Climates](#)
[Scandinavian Ice Sheet](#)

CYCLIC SEDIMENTATION (CYCLOTHEM)

The term “cyclic sedimentation” is generic and can be applied to any type or scale of repetitive sedimentation (Einsele et al., 1991). Conversely, the term “cyclothem” has a much more specific application. The concept has mostly been applied to stratigraphic successions of middle to late Pennsylvanian (upper Carboniferous) rocks that were deposited in cratonic basins of the eastern and mid-continental USA. Well-developed

cyclic sedimentation was first noted in Illinois Basin (Eastern Interior Coal Basin), within late Paleozoic rocks in the state of Illinois. These lithological cycles exhibited vertical oscillations between coal bearing, siliciclastic-rich facies and carbonate-rich facies (Udden, 1912; Weller, 1930, 1931). The term “cyclothem” was subsequently applied to this style of cyclic sedimentation (Wanless and Weller, 1932).

The siliciclastic-rich facies were traditionally viewed as terrestrial or continental facies, however, tidal influences are now widely recognized (Archer and Kvale, 1993; Archer et al., 1994a,b). The carbonate-rich facies commonly contain marine fossils. Thus, cyclothem were commonly interpreted as resulting from changes in base level brought about by sea level fluctuations. These changes could be related to basinal tectonics, or most commonly, to global glacioeustatic changes that are related to Gondwanaland paleoglaciations. More recently, climatic oscillations and the resultant changes in rates of clastic flux into subsiding basins have been advocated as a potential driving mechanism (Cecil, 1990).

A recurring problem that haunts the application of cyclothem models is that there are a great number of different models at different scales. Reger (1931) employed an unusual and extreme application of the cyclothem paradigm for cycles in the Appalachian Basin. In sections that did not conform to his idealized model, he insisted that any missing units would be given stratigraphic names, but referred to as “phantoms” since they did not occur at that specific locality.

Commonly, a cyclothem model, which was derived from a specific basin and from a specific stratigraphic interval, has subsequently been applied far from its original areas of suitability. On the other hand, some general models, which do have a wide-ranging applicability, are named such that they imply occurrence only within a specific basin. For example, a common model is the “Illinois-Basin cyclothem,” which was applied originally by Wanless and Weller (1932) to coal-bearing sequences in middle Pennsylvanian rocks of southern Illinois (see also Wanless and Wright, 1978). Initially, the concept was thought to be a mapable entity and was applied as a formation-level stratigraphic entity. Another popular model is the “Kansas cyclothem,” which was described from non-coal bearing, more marine cycles in upper Pennsylvanian rocks of eastern Kansas (Moore, 1936, 1949, 1964). Similar to the application within the Illinois Basin, the cyclothem was used commonly as a mapable, lithostratigraphic entity.

The use of geographic descriptors for the names of these different types of cyclothem has continued to create confusion. For example, the “Illinois-Basin cyclothem” not only occurs in the middle Pennsylvanian of Illinois, but is also the typical sequence seen in age-equivalent rocks of Kansas. Similar, the “Kansas cyclothem” is the typical sequence observed in upper Pennsylvanian in eastern Kansas but also in age-equivalent strata of the Illinois Basin. Thus, there is a far greater similarity of the Pennsylvanian system in Illinois and Kansas than is commonly supposed. Largely, these misunderstandings have been perpetuated by the superficial application of the standard cyclothem models.

Although the cyclothem concept was originally conceived in the 1930s for sequences in Illinois, it was subsequently discarded as a meaningful stratigraphic entity in the land of its origin. However, the concept was developed in far greater detail for strata within the U.S. mid-continent (particularly within Kansas and adjacent states). Over a period of decades, ranging from the 1930s to the 1960s, increasingly more complex

models of cyclothem were discussed by Moore (1931, 1936, 1949, 1964). It is perhaps Moore’s near obsession and his dominating role in mid-continent geology that did much to entrench the concept of a “cyclothem” into the field of sedimentary geology. At its most complex, Moore’s models included cycles of cyclothem, which he termed a “megacyclothem.”

Later, Moore’s megacyclothem concept was modified and simplified by Heckel (1977, 1986). This adapted model was itself termed a “cyclothem”; thus, Moore’s earlier definition and Heckel’s subsequent modification of the term referred to different scales of stratigraphic sequences. This also increased the confusion over the historical use of the term. The reinterpretation of Moore’s cyclothem concepts included a reinterpretation of organic-rich facies as deep-water deposits and an inferred and hypothetical depth zonation based upon conodont distributions (Heckel and Baesemann, 1975). West et al. (1997) presented a summary of the various cyclothem models and discussions on their potential eustatic and climatic controls.

Attempts have made to quantify cyclothem and to develop a mathematical or statistical model. Such attempts have never been successful (see Pearn, 1964; West et al., 1997). Arguments have been proposed that a search for cyclicity in lithological successions is an inherent human bias (Zeller, 1964).

There are many drawbacks that exist with the traditional usage of the cyclothem concept. The biggest limitation is that most of the work has focused on the more regular and recurring parts of the cycle, which consist of the more-marine, carbonate-dominated portions of the sedimentary cycle. These units, which also include organic-rich laminated black shales, are the easiest to correlate, particularly when using subsurface, geophysical logs. The more clastic components, which have been referred to as clastic wedges (Wanless, 1964; Archer and Kvale, 1993) of the cycle, are far more variable and are much harder to adapt to simple cyclothem models. Subsequent work on the clastic wedges suggests that these facies were formed by deltaic and tidal-estuarine depositional systems (Archer et al., 1994a). From a sequence stratigraphic perspective, these clastic wedges include incised valley-fill (IVF) facies (Archer et al., 1994b).

Ongoing appreciation and application of sequence-stratigraphic models (see Van Wagoner et al., 1990), particularly to the clastic components of cyclothem, suggest that the cyclothem concept is largely obsolete. However, because of the extensive historical literature that has applied the various permutations of cyclothem models, the concept still creates considerable confusion in studies of cyclic sedimentation. Postdating the influence of Moore, the subsequent compendia of formal stratigraphic units of Kansas no longer attempted to apply the cyclothem concept (Zeller, 1968).

Allen W. Archer

Bibliography

- Archer, A.W., and Kvale, E.P., 1993. Origin of gray-shale lithofacies (“clastic wedges”) in U.S. midcontinental coal measures (Pennsylvanian). In Cobb, J.C., and Cecil, B. (eds.), *Modern and Ancient Coal-Forming Environments*. Boulder, CO: Geological Society of America. 286, pp. 181–192.
- Archer, A.W., Feldman, H.R., Kvale, E.P., and Lanier, W.P., 1994a. Pennsylvanian (Upper Carboniferous) fluvio- to tidal-estuarine coal-bearing systems: Delineation of facies transitions based upon physical and biogenic structures. In Calder, J.H., and Gibling, M.R. (eds.), *Palaeogeography, Palaeoclimatology, and Palaeoecology*, **106**, 171–185.

- Archer, A.W., Lanier, W.P., and Feldman, H.R., 1994b. Stratigraphy and depositional history within incised-paleovalley and related facies, Douglas Group (Missourian/Virgilian; Upper Carboniferous) of Kansas, USA. In Dalrymple, R.W., Boyd, R., and Zaitlin, B. (eds.), *Incised-Valley Systems: Origin and Sedimentary Sequences*. Tulsa, OK: Society of Economic Paleontologists and Mineralogists. 51, 176–190.
- Cecil, C.B., 1990. Paleoclimate controls on stratigraphic repetition of chemical and siliciclastic rocks. *Geology*, **18**, 533–536.
- Einsele, G., Ricken, W., and Seilacher, A., 1991. Cycles and events in stratigraphy—basic concepts and terms. In Einsele, G., Ricken, W., and Seilacher, A. (eds.), *Cycles and Events in Stratigraphy*. Berlin: Springer-Verlag, pp. 1–19.
- Heckel, P.H., 1977. Origin of phosphatic black shales in Pennsylvanian cyclothems of mid-continent North America. *Am. Assoc. Pet. Geol. Bull.*, **61**, 1045–1068.
- Heckel, P.H., 1986. Sea-level curve for Pennsylvanian eustatic marine transgressive-regressive depositional cycles along midcontinental outcrop belt, North America. *Geology*, **14**, 330–334.
- Heckel, P.H., and Baesemann, J.F., 1975. Environmental interpretations of conodont distribution in Upper Pennsylvanian (Missourian) megacyclothems in eastern Kansas. *Am. Assoc. Pet. Geol. Bull.*, **59**, 1058–1074.
- Moore, R.C., 1931. *Pennsylvanian Cycles in the Northern Mid-Continent Regions*. Illinois Geological Survey Bulletin **60**, pp. 247–257.
- Moore, R.C., 1936. *Stratigraphic Classification of the Pennsylvanian Rocks of Kansas*. Kansas Geological Survey Bulletin **22**, pp. 1–256.
- Moore, R.C., 1949. *Divisions of the Pennsylvanian System in Kansas*. Kansas Geological Survey Bulletin **83**, pp. 1–203.
- Moore, R.C., 1964. *Paleoecological Aspects of Kansas Pennsylvanian Rocks of Kansas*. Kansas Geological Survey Bulletin **169**, pp. 287–380.
- Pearn, W.C., 1964. Finding the ideal cyclothem. In Merriam, D.F. (ed.), *Symposium on Cyclic Sedimentation*. Kansas Geological Survey Bulletin **169**, pp. 399–413.
- Reger, D.B., 1931. *Pennsylvanian Cycles in West Virginia*. Illinois State Geological Survey Bulletin **60**, pp. 217–239.
- Udden, J.A., 1912. *Geology and Mineral Resources of the Peoria Quadrangle, Illinois*. U.S. Geological Survey Bulletin **506**, pp. 1–103.
- Van Wagoner, J.C., Mitchum, R.M., Campion, K.M., and Rahmanian, V.D., 1990. *Siliciclastic Sequence Stratigraphy in Well Logs, Cores, and Outcrops: Concepts for High-Resolution Correlation of Time and Facies*. Tulsa, OK: American Association of Petroleum Geologists. 7, 55pp.
- Wanless, H.R., 1964. Local regional factors in Pennsylvanian cyclic sedimentation. In Merriam, D.F. (ed.), *Symposium on Cyclic Sedimentation*. Kansas Geological Survey Bulletin **169**, pp. 593–606.
- Wanless, H.R., and Weller, J.M., 1932. Correlation and extent of Pennsylvanian cyclothems. *Geol. Soc. Am. Bull.*, **169**, 593–606.
- Wanless, H.R., and Wright, C.R., 1978. *Paleoenvironmental Maps of Pennsylvanian Rocks, Illinois Basin and Northern Mid-Continent Region*. Boulder, CO: Geological Society of America.
- Weller, J.M., 1930. Cyclical sedimentation of the Pennsylvanian Period and its significance. *J. Geol.*, **38**, 97–135.
- Weller, J.M., 1931. *The Conception of Cyclical Sedimentation during the Pennsylvanian Period*. Illinois State Geological Survey Bulletin **60**, pp. 163–177.
- West, R.R., Archer, A.W., and Miller, K.B., 1997. The role of climate in stratigraphic patterns exhibited by late Palaeozoic rocks exposed in Kansas. *Palaeogeogr. Palaeoclimatol., Palaeoecol.*, **128**, 1–16.
- Zeller, E.J., 1964. Cycles and psychology. In Merriam, D.F. (ed.), *Symposium on Cyclic Sedimentation*. Kansas Geological Survey Bulletin **169**, pp. 631–636.
- Zeller, D.E., 1968. *The Stratigraphic Succession in Kansas*. Kansas Geological Survey Bulletin **189**, pp. 1–81.

Cross-references

- [Coal Beds, Origin and Climate](#)
- [Continental Sediments](#)
- [Dating, Biostratigraphic Methods](#)
- [Deltaic Sediments, Climate Records](#)
- [Glacial Eustasy](#)
- [Late Paleozoic Paleoclimates \(Carboniferous-Permian\)](#)
- [Varved Sediments](#)

D

DANSGAARD-OESCHGER CYCLES

Dansgaard-Oeschger (D-O) cycles are oscillations of the climate system during the Wisconsinan glacial, where the climate switched between a cold glacial climate and a “warm” glacial climate. The glacial climate, which ended around 11,500 years ago, was colder than the present warm period (the Holocene) and variations were of much greater amplitude than those recorded during the Holocene.

D-O cycles are not regular sinusoidal cycles, but are characterized by rapid warming events. Such events occurred 24 times during the Wisconsinan glacial ($\sim 115\text{--}10\text{ kyBP}$) ($\text{ky} = 10^3$ years). The magnitude of the warming over Greenland is estimated to be approximately $10\text{--}15^\circ\text{C}$ based on data from Greenland ice cores. However, these temperatures did not reach the warm temperatures of the Holocene. A cycle is characterized by a rapid transition from the cold glacial climate to a warmer phase (which is also called a D-O event) within only 20–50 years. After this rapid warming, the warmer climate persists for hundreds to thousands of years. A slow decline in temperatures (recorded in the $\delta^{18}\text{O}$ values) occurs during D-O events, until the climate finally “jumps” back to the colder glacial climate (see [Figures D1](#) and [D2](#)). The cold phase does not show any characteristic behavior; it may be described as stable with a noisy signal. This cyclical behavior is what gives the D-O events their characteristic sawtooth shape.

Ocean sediment records show an oscillation of $\sim 1,500$ years (Bond and Lotti, 1995) during the Wisconsinan glacial period. These cycles are considered to originate from the D-O cycles (Bond and Lotti, 1995; Alley et al., 1999).

Occurrence and labeling of D-O cycles

The record of D-O cycles has been labeled by dividing each cycle into a warm and a cold phase, where the warm phases are named Greenland interstadials (GI) and the cold phases are named Greenland stadials (GS) (Björck et al., 1998; [Table D1](#) and [Figure D1](#)). Each GI/GS is associated with a number (1, 2, 3...) and each numbered GI/GS is then subdivided by

alphabetic letters (a, b, c...), which can be divided further by numbers associated with warm and cold phases. This numbering system allows the incorporation of data from new sites if additional variations or oscillations are found within a specific GI/GS. For example, GI-1 contains three warm periods, where the two oldest are the well-known Allerød and Bølling. GS-1 is also called Younger Dryas. Older Dryas (GI-1d), however, is the cold spell between the before-mentioned Allerød (GI-1c) and Bølling (GI-1e) in GI-1. This shows that the naming has been confusing in the past. The INTIMATE name convention (see Björck et al., 1998) has been used for the D-O cycles presented in [Table D1](#), which shows the dating of each GI and GS and its duration for the GRIP ice core.

History

D-O cycles are named after the two scientists who led the work on the phenomena, namely the Danish scientist Willy Dansgaard and the Swiss scientist Hans Oeschger. They were the first to relate the changes in the $\delta^{18}\text{O}$ record from the Greenland ice cores to a possible climate change over the North Atlantic region, and to changes in the thermohaline circulation (THC) (Dansgaard et al., 1983).

D-O cycles were first seen in the $\delta^{18}\text{O}$ record from the Camp Century ice core (Hansen and Langway, 1966) that was drilled in northwestern Greenland (see *Oxygen isotopes and Paleotemperatures, proxy reconstructions* to understand how $\delta^{18}\text{O}$ is used as a proxy for temperature). However, the climatic significance was not realized until the same behavior was seen in the $\delta^{18}\text{O}$ record of the Dye 3 ice core (from southern Greenland). Finally, the climatic relevance of the D-O cycles in Greenland ice cores was confirmed when the two Summit drillings, GRIP (Dansgaard et al., 1993) and GISP2 (Groote et al., 1993), were finished. At Summit, where horizontal movement is slow, the changes in the oxygen isotope record cannot originate from internal folding of the ice layers due to ice movement over rough bedrock. Therefore, they must be a signal of actual climate changes occurring over most of Greenland. At first, the signal was circumspectly attributed to climatic changes in the Greenland/North Atlantic region. Later, the area was enlarged to include Europe when evidence of D-O cycles was found in

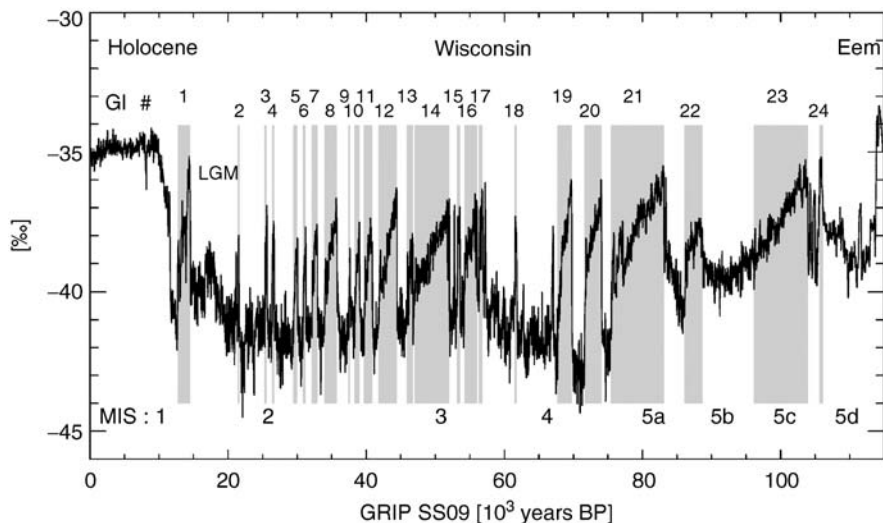


Figure D1 The GRIP $\delta^{18}\text{O}$ record is shown for the last 115,000 years. The Dansgaard-Oeschger events (GI/warm phase of the D-O cycle) are shaded and numbered accordingly (Björck et al., 1998). Note the sawtooth shape. During MIS 3, the two Bond cycles, consisting of GI:12-11-10-9 and GI:8-7-6-5, LGM denotes last glacial maximum. Only the last ~4,000 years of the last warm period (Eemian) is shown to the right. The time scale is the GRIP time scale SS09 (after Johnsen et al., 1995).

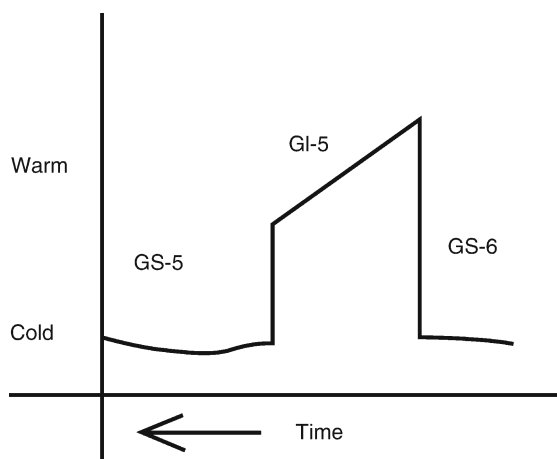


Figure D2 The figure shows schematically the name convention of the INTIMATE group for the Greenland stadials (GS) and Greenland interstadials (GI). It should be clear from the figure that each Dansgaard-Oeschger cycle consists of a GS and a GI. For the whole glacial record see Figure D1.

Europe (Thouveny et al., 1994; Allen and Huntley, 2000). The area influenced by the D-O cycles was once again enlarged to encompass most of the Northern Hemisphere and even across the Equator. Evidence of D-O cycles has been found in paleo-data from different regions of the world, for an up-to-date overview see Voelker et al. (2002) and Figure D3.

Dansgaard-Oeschger cycles in ocean sediment cores

Ocean sediment cores, particularly from the North Atlantic and Nordic seas, have also shown evidence of D-O cycles (Rasmussen et al., 1996; Elliot et al., 1998; Dokken and Jansen, 1999; van Kreveld et al., 2000). In ocean sediment cores, D-O cycles can be identified in many of the different climate proxy records, a few of which will be mentioned below.

Table D1 The transitions from stadials to interstadials and vice versa use the GRIP SS09 time scale; the names for the Dansgaard-Oeschger cycles are based on Björck et al. (1998). The ages correspond to the GIs and GSs shown in Figure D1. Stadial numbers that have a "H" and a number are stadials in which Heinrich events took place, and the number of the Heinrich event. This is not part of the INTIMATE naming convention, but is added for illustrative reasons

Events	GRIP age (years bp)	Duration	Events	GRIP age (years bp)	Duration
Holocene	11,551		GS-1	12,711	1,160
GI-1	14,491	1,780	GS-2 _{H1}	21,391	6,900
GI-2	21,631	240	GS-3 _{H2}	25,271	3,640
GI-3	25,571	300	GS-4	28,111	2,540
GI-4	28,311	300	GS-5 _{H3}	29,451	1,140
GI-5	30,011	560	GS-6	30,831	820
GI-6	31,191	360	GS-7	32,121	930
GI-7	32,911	790	GS-8	33,921	1,010
GI-8	35,731	1,810	GS-9 _{H4}	37,431	1,700
GI-9	37,671	240	GS-10	38,311	640
GI-10	38,991	680	GS-11	39,671	680
GI-11	40,851	1,180	GS-12	41,811	960
GI-12	44,371	2,560	GS-13 _{H5}	45,891	1,520
GI-13	46,751	860	GS-14	47,011	260
GI-14	51,991	4,980	GS-15	53,171	1,180
GI-15	53,571	400	GS-16	54,231	660
GI-16	56,011	1,780	GS-17	56,291	280
GI-17	56,851	560	GS-18 _{H6}	61,491	4,640
GI-18	61,771	280	GS-19	67,691	5,920
GI-19	69,751	2,060	GS-20	71,611	1,860
GI-20	74,041	2,430	GS-21	75,471	1,430
GI-21	83,091	7,620	GS-22	86,091	3,000
GI-22	88,700	2,609	GS-23	96,100	7,400
GI-23	103,946	7,846	GS-24	105,601	1,655
GI-24	106,180				

Layers of ice-rafted debris (IRD) are observed just before D-O events. Hence, it is thought that the warming is preceded by large amounts of icebergs carrying the IRD, which is then deposited in the North Atlantic region. The IRD signal is

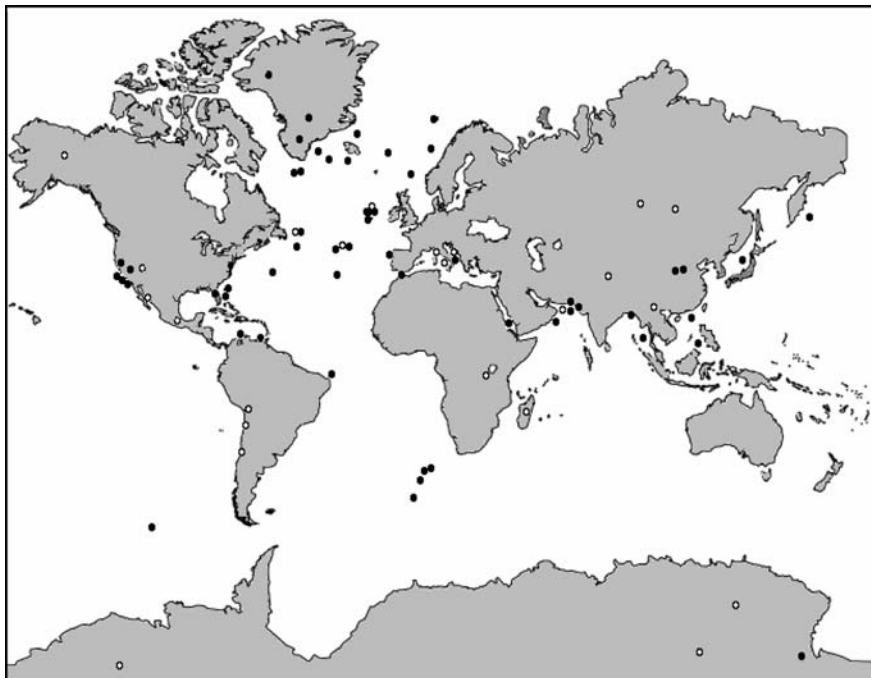


Figure D3 Global spatial distribution of sites where impacts of Dansgaard-Oeschger cycles have been recorded in paleorecords. *Black dots* indicate sites with a clear D-O type oscillation, *open circles* show sites where no or unclear D-O cycles have been found (after Voelker et al., 2002).

mostly of local character; the IRD has been shown to originate from the Fennoscandian (also known as the Scandinavian Ice Sheet), Greenland and Icelandic Ice Sheets. A few of these IRD events are also called Heinrich events; in these cases, the IRD mostly originates from the Laurentide Ice Sheet. Heinrich events are very large outbreaks of IRD/icebergs and only occurred six times during the Wisconsinan glacial (see Table D1). IRD events associated with outbreaks of icebergs are considered to imply a freshwater input into the North Atlantic, with a succeeding cooling of the region. After each cooling, the region warms very rapidly, this is seen for example in the abundance of the planktonic species (near surface) *Neogloboquadrina pachyderma* (sin). *N. pachyderma* is a cold water species and therefore it almost disappears during the warm phases. Another indicator of these climate changes is the $\delta^{18}\text{O}$ record in benthic (bottom) species, where the fluctuations in marine sediments mirror the $\delta^{18}\text{O}$ fluctuations in ice cores. For the benthic $\delta^{18}\text{O}$, low isotopic values indicate stadials (cold phases) and high values indicate interstadials (warm phases). A climate change that can be detected in the fauna at 1,000 meter depth indicates that the climate change must have affected not only the atmosphere, but also the ocean circulation (Rasmussen et al., 1996) and deep water convection in the North Atlantic in particular, which is important for the THC.

The changes in the ocean sediment cores indicate that the THC was weaker during stadials, and became enhanced to almost Holocene strength during interstadials. There are also indications of changes in the geographical occurrence of deep water convection. It can be seen that convection only occurred south of Iceland during the stadials, and both south and north of Iceland (in the Nordic seas) during the interstadials (Ganopolski and Rahmstorf, 2001).

Dansgaard-Oeschger cycles – a global phenomenon?

As mentioned above and shown in Figure D3, evidence of D-O cycles has been found over large parts of the globe. Therefore, it is particularly puzzling why there is no clear signal of D-O cycles in Antarctic ice cores (e.g., compare Figure D4, profiles A and E).

Antarctic ice cores show a different signal in the $\delta^{18}\text{O}$ record, looking completely different to the Greenland $\delta^{18}\text{O}$ record (see Figure D4). In Antarctica, the sawtooth shape is not present at all. The cycles look more like a triangle during the warm phase, with a slow warming, which, after peaking, immediately starts to slowly decline back to its cold period values. Due to uncertainty in the time scales of the Greenland and Antarctic ice cores, it was long discussed which came first – the Greenland or the Antarctic warming, or whether they were synchronous. This controversy was finally resolved when Blunier et al. (1998) measured atmospheric methane in microscopic air bubbles in the ice cores. The methane is well mixed globally within a year, and is therefore an inter-hemispheric marker that can be used to link the records from Greenland and Antarctica, respectively. It was shown that Antarctica was warming while Greenland was in the cold phase, and when the Greenland $\delta^{18}\text{O}$ record jumped into a warm phase of a D-O cycle, Antarctica started to cool. This asynchronous see-saw mechanism between the two hemispheres still lacks a full explanation. However, it is believed to arise from changes in the oceanic heat transport from the Southern Hemisphere to the Northern Hemisphere, which is believed to have differed during the different phases of the D-O cycles.

The trigger of Dansgaard-Oeschger events/cycles

D-O cycles have become a large research field within paleoclimatology. Evidence of D-O cycles in many different

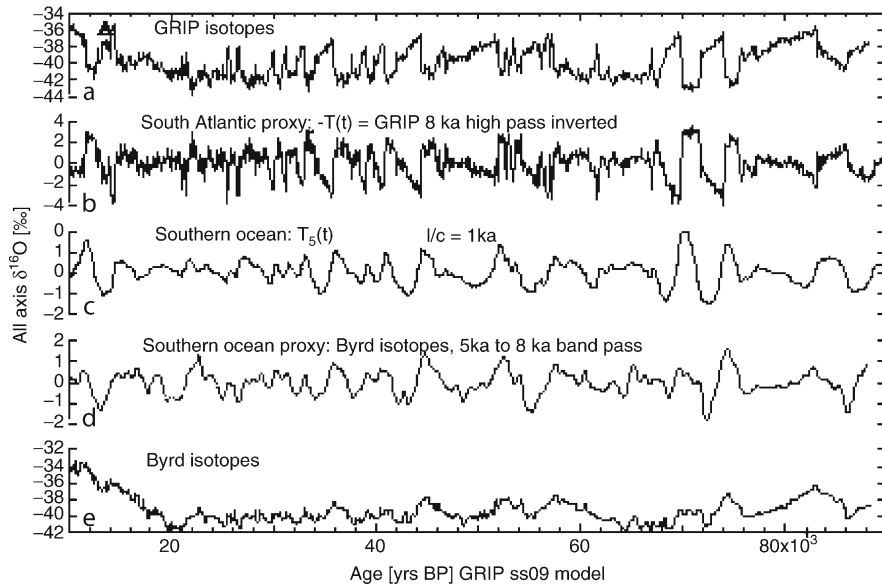


Figure D4 The GRIP isotope profile is shown in (a). (b) shows a 8 ky high pass filtering of *a* after inversion, which is considered the S-Atlantic temperature proxy. Folding *b* with $e^{-t/\tau}$, where $1/\tau = 1,000$ years, results in the profile shown in *c*; this profile depends on the time constant (τ) used. The 0.5 to 8 ky band pass filtering of the Byrd isotope profile (e) is shown in (d). The profiles in *c* and *d* are quite similar in shape and give a very high correlation coefficient of 0.87 for $\tau = 1$ ky in MIS 3 (22 to 58 kyrBP) (after Johnsen and Stocker, 2003).

paleorecords from around the world have made the understanding of these rapid and abrupt climate changes an intriguing challenge.

Retrieval of ocean sediment cores has shed some light on the magnitude of the impact of the D-O cycles. However, looking to the ocean for a possible mechanism for the triggering of D-O events is problematic, as the natural time scale of the THC is much longer than the 20–50 years it takes to switch into a D-O event. Furthermore, the ice sheets react on much longer time scales, and there is no astronomical forcing with a period of $\sim 1,500$ years. Sea ice has been mentioned as a possible trigger mechanism that would influence the deep water convection, and hence the THC. Another possibility that has been proposed is surging glaciers from the surrounding ice sheets, but simultaneously surging glaciers also lack an explanation or a trigger. Therefore, the triggering mechanism is still being debated.

Data analysis (Alley et al., 2001) and model studies (Ganopolski and Rahmstorf, 2002) have shown that a possible trigger of the D-O events could be stochastic resonance in the climate system under glacial conditions. A stochastic resonance implies that small changes, i.e., in the freshwater flux into the northern North Atlantic, could cause large rapid changes of the ocean circulation during the glacial period and hence large climate changes such as the D-O cycles (Ganopolski and Rahmstorf, 2002).

Irene A. Mogensen

Bibliography

- Allen, J.R.M., and Huntley, M.B., 2000. Weichselian palynological records from southern Europe; correlation and chronology. *Quaternary Int.*, **73/74**, 111–125.
- Alley, R.B., Clack, P.U., Keigwin, L.D., and Webb, R.S., 1999. Making sense of millennial-scale climate change. In Clark, R.B., Webb, P.U., Keigwin, L.D. (eds.), *Mechanisms of Global Climate Change at Millennial Time Scales*. Washington DC: American Geophysical Union, pp. 385–394.
- Alley, R.B., Anandakrishnan, S., and Jung, P., 2001. Stochastic resonance in the North Atlantic. *Paleoceanography*, **16**(2), 190–198.
- Björck, S., Walker, M.J.C., Cwynar, L.C., Johnsen, S., Knudsen, K.-L., Lowe, J.J., Wohlfarth, B., and intimate members, 1998. An event stratigraphy for the Last Termination in the North Atlantic region based on the Greenland ice-core record: A proposal by the INTIMATE group. *J. Quaternary Sci.*, **13**(4), 283–292.
- Blunier, T., Chappellaz, J., Schwander, J., Dällenbach, A., Stauffer, B., Stocker, T.F., Raynaud, D., Jouzel, J., Clausen, H.B., Hammer, C.U., and Johnsen, S.J., 1998. Asynchrony of Antarctic and Greenland climate change during the last glacial period. *Nature*, **394**, 739–743.
- Bond, G.C., and Lotti, R., 1995. Iceberg discharges into the North Atlantic on millennial time scales during the last glaciation. *Science*, **267**, 1005–1010.
- Dansgaard, W., Oeschger, H., Langway, C.C., Jr., 1983. Ice core indications of abrupt climate changes. In *Palaeoclimatic Research and Models. Proceedings of Workshop, Brussels, Dec. 1982*. Dordrecht/Boston/Lancaster: D. Reidel Publishing Company, pp. 72–73.
- Dansgaard, W., Johnsen, S.J., Clausen, H.B., Dahl-Jensen, D., Gundestrup, N.S., Hammer, C.U., Hvidberg, C.S., Steffensen, J.P., Sveinbjörnsdottir, A.E., Jouzel, J., and Bond, G., 1993. Evidence for general instability of past climate from a 250-kyr ice-core record. *Nature*, **364**, 218–220.
- Dokken, T.M., and Jansen, E., 1999. Rapid changes in the mechanism of ocean convection during the last glacial period. *Nature*, **490**, 458–461.
- Elliot, M., Labeyrie, L., Bond, G., Cortijo, E., Turon, J.-L., Tisnerat, N., and Duplessy, J.-C., 1998. Millennial-scale iceberg discharges in the Irminger Basin during the last glacial period: Relationship with the Heinrich events and environmental settings. *Paleoceanography*, **13**(5), 433–446.
- Ganopolski, A., and Rahmstorf, S., 2001. Rapid changes of glacial climate simulated in a coupled climate model. *Nature*, **409**, 153–158.
- Ganopolski, A., and Rahmstorf, S., 2002. Abrupt Glacial Climate change due to Stochastic Resonance. *Phys. Rev. Lett.*, **88**(3), 1–4.
- Groote, P.M., Stuiver, M., White, J.W.C., Johnsen, S.J., and Jouzel, J., 1993. Comparison of oxygen isotope records from the GISP2 and GRIP Greenland ice cores. *Nature*, **366**, 552–554.

- Hansen, B.L., and Langway, C.C., Jr., 1966. Deep core drilling and core analysis at Camp Century, Greenland 1961–1966. *U.S. Antarct. J.*, **1**, 207–208.
- Johnsen, S.J., and Stocker, T., 2003. Identifying the bipolar seesaw from polar Ice Core Data using a simple Model. *EGS-AGU-EUG Joint Assembly*, Nice, France, 6–11 April, 2003. *Geophys. Res. Abstr. V.5*, 13454, 2003.
- Johnsen, S., Dahl-Jensen, D., Dansgaard, W., and Gundestrup, N., 1995. Greenland palaeotemperatures derived from GRIP bore hole temperature and ice core isotope profiles. *Tellus*, **47B**, 624–629.
- Rasmussen, T.L., Thomsen, E., van Weering, T.C.E., and Labeyrie, L., 1996. Rapid changes in surface and deep water conditions at the Faeroe Margin during the last 58,000 years. *Paleoceanography*, **11**(6), 757–771.
- Thouveny, N., de Beaulieu, J.L., Bonifay, E., Creer, M.K., Guiot, J., Icole, M., Johnsen, S., Jouzel, J., Reille, M., Williams, T., and Williamson, D., 1994. Climate variations in Europe over the past 140 kyr deduced from rock magnetism. *Nature*, **371**, 503–506.
- van Kreveld, S., Sarnhein, M., Erlenkeuser, H., Grootes, P., Jung, S., Nadeau, M.J., Pfaumann, U., and Voelker, A., 2000. Northeast Atlantic sea surface circulation during the past 30–10 14C kyr. *BP. Paleoceanography*, **14**(5), 616–625.
- Voelker, A.H.L., and workshop participants, 2002. Global distribution of centennial-scale records for Marine Isotope Stage (MIS) 3: A database. *Quaternary Sci. Rev.*, **21**, 1185–1212.

Cross-references

Carbon Dioxide and Methane, Quaternary Variations
 Foraminifera
 Heinrich Events
 Ice Cores, Antarctica and Greenland
 Ice-Rafted Debris (IRD)
 Interstadials
 Isotopic Fractionation
 Last Glacial Maximum
 Laurentide Ice Sheet
 Millennial Climate Variability
 Oxygen Isotopes
 Paleotemperatures, Proxy Reconstructions
 Scandinavian Ice Sheet
 Thermohaline Circulation
 Wisconsinan (Weichselian, Würm) Glaciation
 Younger Dryas

DATING, AMINO ACID GEOCHRONOLOGY

Dating Earth history using the racemization of amino acids preserved in biominerals belongs to the chemical family of dating methods. Chemical methods differ from radioactive dating techniques in that their reaction rates depend on one or more environmental parameters, whereas radioactive decay remains constant regardless of most environmental conditions. Amino acids, derived from indigenous protein residues protected by the skeletal hardparts of organisms, survive in most environments for thousands to millions of years. The extent of racemization (defined below) of these amino acids is dependent primarily on the time elapsed since death of the organism and the integrated thermal history experienced by the biominerals, and to a lesser extent on vital effects unique to each taxon.

Amino acids are simple organic molecules that are the fundamental building blocks of proteins. They are exceptionally stable, with lifetimes for most of the more stable forms exceeding a million years at ambient temperatures. Although there are a large number of possible amino acids, only about 20 are common constituents of proteins. Amino acid geochronology (often

referred to as simply Amino Acid Racemization, or AAR) relies on the chiral nature of most amino acids. Chiral (derived from the Greek word for “hand”) molecules are asymmetric, or exhibit “handedness.” Chiral molecules are not superimposable on their mirror image. All but the simplest protein amino acid can exist in either a “left-” or “right-” handed configuration (enantiomers). The designation of the handedness for chemical compounds is determined by the direction they rotate plane-polarized light when in solution. Molecules that rotate polarized light are said to be optically active, whereas an equilibrium mixture of left- and right-handed amino acids (a racemic mixture) is “achiral,” or optically inactive, and will not rotate polarized light. The interaction of chiral molecules with other chiral molecules can be different to interactions with achiral molecules. A simple analog for a chiral compound is a glove, where the left and right hand gloves are mirror images of each other but they are not superimposable, whereas a ski pole is achiral. Bare hands (also chiral) inserted into a box containing only right-hand gloves, will only emerge with a gloved right hand, never with a gloved left hand, whereas bare hands inserted into a box of ski poles would always emerge with a ski pole, regardless of which hand was inserted. These principles are exploited by analytical procedures to separate chiral forms of amino acids.

It is a quirk of nature that the proteins of almost all living organisms utilize exclusively amino acids of the “left hand” configuration. Left-handed forms are given the abbreviation “L,” for levorotatory (they rotate polarized light in the left-hand direction), whereas right-hand forms are dextrorotatory, or D-amino acids. All amino acids have a three-letter abbreviation. Thus the common amino acid alanine, is abbreviated Ala, and its left- and right-handed forms are then D-Ala and L-Ala, respectively. The extent of amino acid racemization is expressed as the proportion of D- relative to L-amino acids, or D/L.

Amino acid geochronology capitalizes on the original uniquely left-handed character of amino acids preserved in skeletal hard parts or biominerals. Once the biological constraints that created optically active assemblages of amino acids are removed, usually at death of the organism, amino acids begin to spontaneously invert to their right-handed, or D-configuration. The process by which amino acids of one configuration convert into their opposite handedness is known as racemization. The rate at which this inversion occurs is strongly dependent on ambient temperature and, to a lesser extent, vital effects and environmental pH. At room temperature (22 °C), conversion from an optically pure amino acid (protein from a living organism has a D/L = 0) to a racemic mixture lacking optical activity (D/L = 1.0 for most amino acids) requires several thousands to several tens of thousands of years for most amino acids. The racemization reaction rate is exponentially related to temperature; at 160 °C, a racemic mixture is reached in 10–20 h, whereas in Arctic regions (–10 °C) equilibrium requires 1–2 million years. As a rule of thumb, at normal ambient temperatures (0–25 °C), the rate of racemization doubles for every 4 °C increase in temperature. [Figure D5](#) illustrates the useful time range for AAR dating under different mean annual temperatures for isoleucine; aspartic acid racemizes about an order of magnitude faster and is widely used for very young materials, or extremely cold sites (e.g., Goodfriend, 1992; Goodfriend et al., 1996; [Figure D6](#)). The effect of temperature on reaction rate is readily apparent in a plot of racemization levels for last interglacial “moderate” racemization-rate mollusks from the European Arctic to the Mediterranean ([Figure D7](#)).

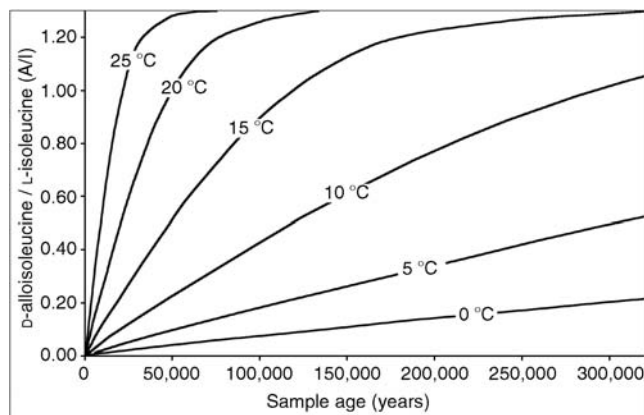


Figure D5 Relation between the extent of isoleucine epimerization (A/I) and sample age for effective diagenetic temperatures between 0 and +25 °C showing the strong dependence of epimerization rate on temperature. Lines derived from kinetics in eggshells of the Australian emu (*Dromaius*) shown in Miller et al. (2000).

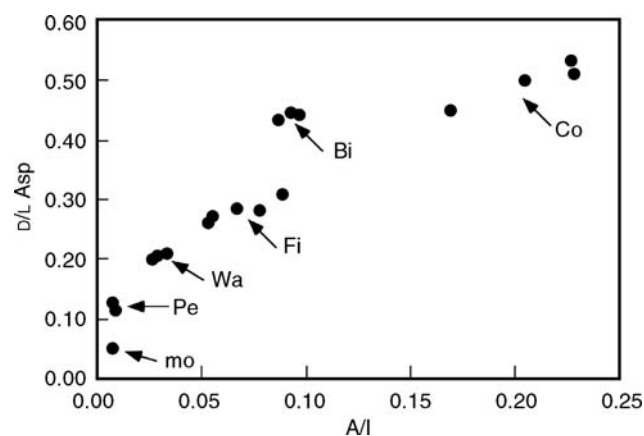


Figure D6 Fast-racemizing amino acids provide superior resolution for cold or very young samples. In this figure, D/L aspartic acid and D-alloisoleucine/L-isoleucine (A/I) were measured in the marine bivalve *Hiatella arctica*, collected from raised marine terraces along the north coast of Alaska (mean annual temperature ca. -12 °C). For the younger shorelines, D/L Asp provides a clearer separation of the sites, but this difference decreases for the older shorelines. (mo = modern; Pe = Pelukian shoreline (last interglacial); Wa = Wainwrightian shoreline; Fi = Fishcreekian shoreline; Bi = Bigbendian shoreline; Co = Colvillian shoreline (probably late Pliocene)). Modified from Goodfriend et al. (1996).

Racemization of amino acids in fossils

Fifty years ago, Abelson (1954) first showed that amino acids could be preserved in biominerals for hundreds of millions of years, and in a series of papers a few years later with P.E. Hare, outlined the potential of amino acid racemization as a geological dating method (Hare and Abelson, 1968). They showed that mollusks of known age exhibited increasing levels of racemization with increasing age, and the dating method of Amino Acid Geochronology was launched. Recent summaries of the methods are given by Miller and Brigham-Grette (1989), Wehmiller (1993), Wehmiller and Miller (2000).

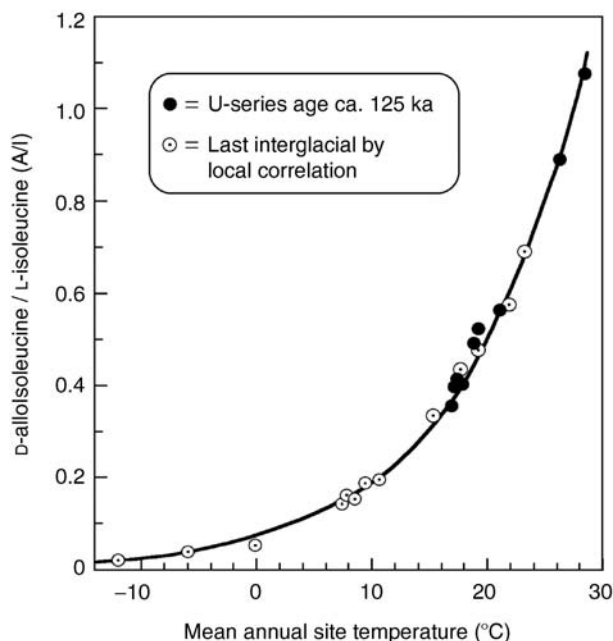


Figure D7 D-alloisoleucine/L-isoleucine (A/I) in moderate-racemization-rate mollusks from last interglacial (ca. 125 ka) sites across western Europe, ranging from Svalbard and Arctic Russia to the Mediterranean Basin, plotted against current mean annual site temperature. Last interglacial sites are dated by U/Th on corals or correlated to the last interglacial on the basis of diagnostic marine faunal elements. The data document the exponential dependency of racemization rate on site temperature. Unpublished data from G.H. Miller and P.J. Hearty.

Not all amino acids are suitable for geochronology. Glycine, the simplest and one of the most common amino acids, is not a chiral molecule. Other simple amino acids, such as alanine, are created in fossils by the decomposition of other more complex amino acids. Thermodynamically unstable amino acids, like serine and threonine, have half-lives too short for most geological applications. The most widely used slow-racemizing amino acids are isoleucine, leucine, valine and glutamic acid, whereas aspartic acid racemizes much more rapidly (Figure D6). All of these amino acids except isoleucine have a single chiral carbon atom, and can exist in either their D- or L-forms, which have identical physical and chemical properties except in their interaction with other chiral substances. Isoleucine, in contrast, has two chiral carbon atoms and can racemize about either carbon, or both. In nature, isoleucine racemizes almost exclusively about the alpha carbon, producing a new molecule, D-alloisoleucine, which has different chemical and physical characteristics, making it easier to separate in the laboratory. This reaction is known as epimerization, and the extent of isoleucine epimerization is abbreviated A/I or alle/Ile.

The separation, detection and quantification of the D- and L-amino acids are accomplished by either gas or liquid chromatography. L-isoleucine can be separated from its D-alloisoleucine pair by conventional ion-exchange high-pressure liquid chromatography (HPLC), whereas most other amino acids are separated by gas chromatography (GC) or reverse-phase liquid chromatography (RPLC) using a chiral stationary or mobile phase to separate the enantiomers.

Prerequisites of racemization dating

To utilize amino acid racemization as a dating tool requires a medium that not only preserves indigenous protein amino acids from bacterial attack, but that also excludes contamination by other amino acids. The more tightly the amino acids are integrated into the biominerals, the closer the medium will be to a closed system. The most common media that meet this prerequisite are carbonate biominerals, including the carbonate exoskeletons of bivalve and gastropod mollusks, foraminifera, and ostracods, bird eggshells and fish otoliths. Extensive studies on bone and wood have produced mixed results, largely due to the relatively porous nature of these media. Carbonate minerals also have the advantage that they provide a buffered system (pH = 8), eliminating pH as an environmental variable. Carbonate media in ideal preservation settings have been shown to preserve indigenous amino acids from mollusks more than 100 million years old.

Protein residues that occupy intracrystalline positions are less susceptible to diffusional loss than those that occur between mineral crystals. For example, almost all of the amino acids in bird eggshell are intracrystalline, and fossils show virtually no loss of amino acids over hundreds of thousands of years, whereas most of the amino acids in bivalve mollusks are situated between mineral layers, and exhibit slow diffusional loss over tens of thousands of years (Miller et al., 2000). A small amount of mollusk protein occupies intracrystalline positions, and targeting these residues may avoid uncertainties related to the slow diffusional loss of bulk analyses (Collins and Riles, 2000).

Each species that secretes a skeletal hard part containing amino acids incorporates different suites of proteins, so that the relative proportion of each amino acid in protein differs between taxa. A consequence of this variability is that the rates of racemization exhibit subtle but frequently significant differences between taxa (Figure D8); this vital effect is almost always significant at the genus level, occasionally at the species level. Racemization rates for isoleucine in different mollusk genera may be twice as fast for “fast” racemizers as for “slow” racemizers. Furthermore, some broad groups of mollusks, such

as the cockles, are less suitable for racemization studies. For these reasons, each species used must be rigorously evaluated. The activation energy for racemization appears to exhibit little variation across all carbonate biominerals, with most reported activation energies falling within $29 \pm 1 \text{ kcal mol}^{-1}$. But the entropy factor shows strong variability so that some amino acids racemize as much as 10 times more rapidly than others (Figure D6).

Once a suitable medium has been evaluated, certain site-selection criteria must be met. Because of the exponential sensitivity of reaction rate to temperature, near-surface samples that experience high seasonal temperature fluctuations will racemize more rapidly than deeply buried samples with the same arithmetic mean temperature but without seasonal fluctuations. Samples must have been buried deeply enough to avoid seasonal temperature oscillations with amplitudes more than 6°C . In most settings, this translates to a burial depth of at least 1 and preferably 2 meters. A short time in a near-surface setting has negligible influence,

Aminostratigraphy

Amino acid racemization can be applied as a geological dating tool in both a relative and absolute sense. As a relative dating tool, the technique is known as Aminostratigraphy. The premise is that over a limited geographic range and elevation, all sites can be expected to have experienced a similar thermal history ($\pm 1^\circ\text{C}$). Over this limited region, samples with similar D/L ratios are of the same age, those sites with higher D/L ratios are older, and those with lower ratios are younger. Samples with similar D/L ratios are typically grouped into aminozones (Figure D9). Aminostratigraphy does not require an assessment of racemization kinetics or estimates of past thermal histories. It is the least ambiguous application of Amino Acid Geochronology.

Aminostratigraphy has been commonly applied to mollusks excavated from raised marine terraces in coastal regions throughout the world. One example is a series of uplifted interglacial terraces along the Peruvian coast from which bivalve mollusks exhibit a regular increase in D/L leucine in higher (older) terraces, with corresponding absolute ages derived from electron-spin resonance (ESR) dating (Figure D9).

Absolute age and paleothermometry

Once the kinetics of racemization in a particular biomineral have been derived, the equation describing racemization contains only three unknowns: D/L (the extent of the reaction, which can be measured in the laboratory); t, the time since death; and T, the integrated thermal history. Theoretically, if either t or T is known, the other can be predicted. In an evaluation of uncertainties, McCoy (1987) showed that predicting paleotemperatures is inherently more precise than predicting ages. Unlike most biological proxies that record the temperature at which an organism lived, racemization-derived paleotemperatures reflect the integrated thermal history since the organism died. In the case of deeply buried samples, this equates to the mean annual temperature. If samples with independently derived ages are available from a limited region, then the evolution of temperature across the region can be calculated.

Comparing the extent of racemization in a series of radiocarbon-dated samples provides a powerful tool to derive quantitative estimates of the glacial-age temperature depression during the last glacial maximum. The glacial/Holocene temperature change in semi-arid Australia was quantified from A/I in emu

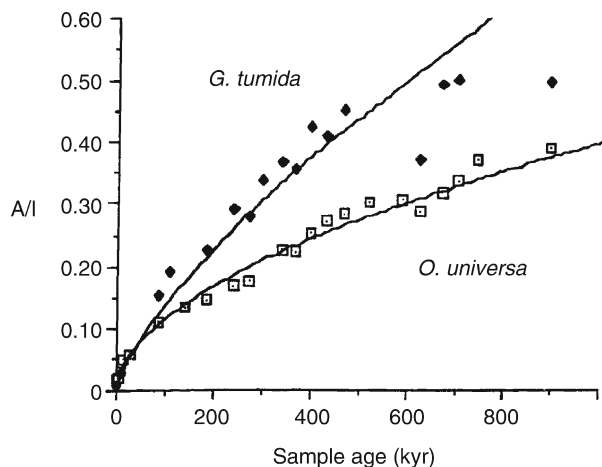


Figure D8 Comparison of the extent of isoleucine epimerization against sample age for two foraminifera taxa from deep-sea sediment cores. Both the vital effect (*Globobulimina tumida* epimerizes almost twice as fast as *Orbulina universa*), and non-linear kinetics are apparent. Modified from Müller (1984).

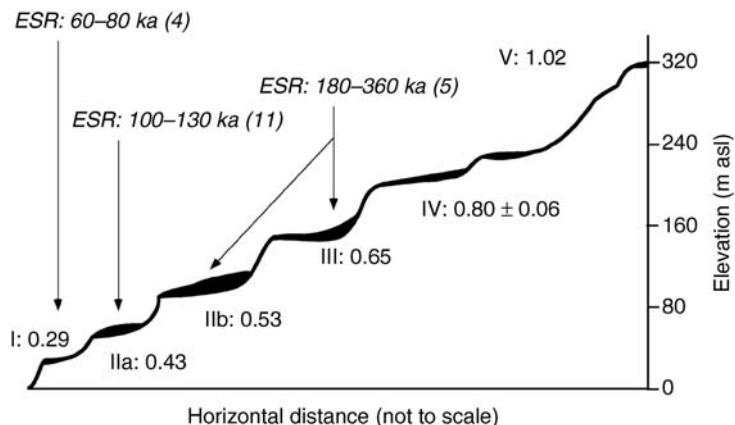


Figure D9 Schematic cross-section through a flight of raised marine terraces on the coast of Peru with aminozones (in roman numerals) defined by the extent of leucine racemization. ESR dates provide additional chronological control. The highest terraces are of early Quaternary age. Modified from Wehmiller (1993).

eggshells, each of which had also been dated by ^{14}C . The dataset spanned the last 40,000 years. Not all samples were deeply buried, hence some samples exhibited more advanced levels of racemization than expected. However, the change in slope between samples younger than about 16,000 years ago and those older than 16,000 years was unambiguous, and reflected at least 7°C warming from the cold last glacial maximum to the warmth of the present interglacial (Miller et al., 1997).

In theory, deriving absolute ages from the extent of amino acid racemization requires only a reasonable estimate ($\pm 1^\circ\text{C}$) of the average diagenetic temperature. For samples of Holocene age, this can be reasonably estimated from the instrumental record, but secure estimates for the time-dependent changes in mean annual temperatures across glacial/interglacial cycles are rarely possible. Age estimates are further complicated by kinetic uncertainties for many biominerals. An inherent assumption is that racemization follows simple, reversible first-order kinetics. While this assumption is met during the early stages of racemization, most mollusk and foraminifera shells deviate from predicted kinetics in the later stages of diagenesis (e.g., Figure D8). This has led several researchers to utilize an empirically derived parabolic kinetic model (Figure D10) that more closely approximates the observed change in D/L with time (Kaufman, 2000, 2003) instead. A common approach to absolute dating is to calibrate the reaction rate on a sample for which the age is independently determined, and then use the same rate constant for other samples in the same region. For Quaternary samples, a reasonable assumption is that a last interglacial calibration has an integrated thermal history that is a reasonable estimate for most of the Quaternary, and the calibrated rate constant can then be used to date other samples in the region to at least 1 Myr.

Conclusions

Amino Acid Geochronology offers a simple, but powerful relative dating tool (Aminostratigraphy) that provides temporal constraints beyond the range of radiocarbon dating. In all but the hottest regions, this includes all or most of the middle and late Quaternary. When independent dates are available, the extent of racemization can be used to reconstruct past thermal histories with a precision of $\pm 1^\circ\text{C}$. Moreover, with suitable

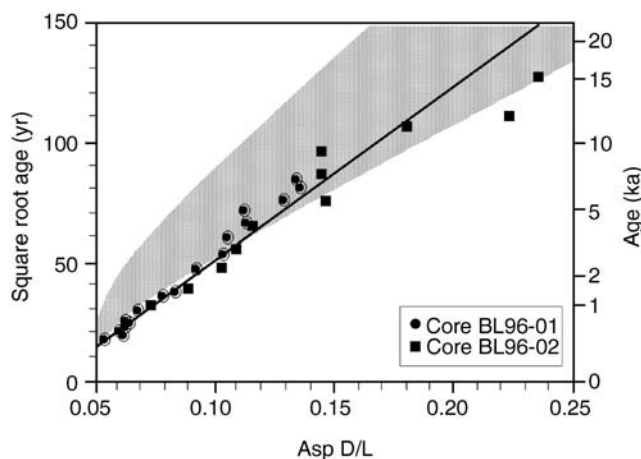


Figure D10 Plot of aspartic acid racemization (D/L Asp) against the square root of time for the ostracod genus *Candona* in two independently dated sediment cores from Bear Lake, Utah/Idaho, showing an essentially parabolic relation between D/L and time. Gray area shows the expected racemization ($\pm 1\sigma$) based on equations in Kaufman (2000), with temperature set to 4°C . Modified from Kaufman (2003).

calibration, racemization levels can be converted to reliable absolute ages. Although the measured extent of racemization depends heavily on temperature, the racemization reaction does not involve the loss of reactants. For the most stable amino acids, the concentration of the summed D - and L -forms at racemic equilibrium is about the same as the concentration of the original L -amino acid, providing there has been no diffusional loss from the biomineral matrix. Consequently, the precision of the method is almost as good at the end of the time range as at the beginning, unlike radiocarbon, where the loss of the primary isotope, ^{14}C , means that dates close to the limit of the method are susceptible to large analytical errors and trace levels of contamination.

Gifford H. Miller

Bibliography

Abelson, P.H., 1954. Organic constituents of fossils. *Carnegie Inst. Wash. Yearb.*, **53**, 97–101.

Collins, M.J., and Riles, M., 2000. Amino acid racemization in biominerals: The impact of protein degradation and loss. In Goodfriend, G., Collins, M., Fogel, M., Macko, S., and Wehmiller, J. (eds.), *Perspectives in Amino Acid and Protein Geochemistry*. New York: Oxford University Press, pp. 120–142.

Goodfriend, G.A., 1992. Rapid racemization of aspartic acid in mollusc shells and potential for dating over recent centuries. *Nature*, **357**, 399–401.

Goodfriend, G.A., Brigham-Grette, J., and Miller, G.H., 1996. Enhanced age resolution of the marine Quaternary record in the Arctic using aspartic acid racemization dating of bivalve shells. *Quaternary Res.*, **45**, 176–187.

Hare, P.E., and Abelson, P.H., 1968. Racemization of amino acids in fossil shells. *Carnegie Inst. Wash. Yearb.*, **66**, 526–528.

Kaufman, D.S., 2000. Amino acid racemization in ostracodes. In Goodfriend, G., Collins, M., Fogel, M., Macko, S., and Wehmiller, J. (eds.), *Perspectives in Amino Acid and Protein Geochemistry*. New York: Oxford University Press, pp. 145–160.

Kaufman, D.S., 2003. Dating deep-lake sediments by using amino acid racemization in fossil ostracodes. *Geology*, **31**, 1049–1052.

McCoy, W.D., 1987. The precision of amino acid geochronology and paleothermometry. *Quaternary Sci. Rev.*, **6**, 43–54.

Miller, G.H., and Brigham-Grette, J., 1989. Amino acid geochronology: Resolution and precision in carbonate fossils. *Quaternary Int.*, **1**, 111–128.

Miller, G.H., Magee, J.W., and Jull, A.J.T., 1997. Low-latitude glacial cooling in the Southern Hemisphere from amino acids in emu eggshells. *Nature*, **385**, 241–244.

Miller, G.H., Hart, C.P., Roark, E.B., and Johnson, B.J., 2000. Isoleucine Epimerization in Eggshells of the Flightless Australian Birds, *Genyornis and Dromaius*. In Goodfriend, G., Collins, M., Fogel, M., Macko, S., and Wehmiller, J. (eds.), *Perspectives in Amino Acid and Protein Geochemistry*. New York: Oxford University Press, pp. 161–181.

Müller, P.J., 1984. Isoleucine epimerization in Quaternary planktonic foraminifera: Effects of diagenetic hydrolysis and leaching, and Atlantic-Pacific intercore correlations. *Meteor. Forsch. Ergeb. C.*, **38**, 25–47.

Wehmiller, J.F., 1993. Applications of Organic Geochemistry for Quaternary Research: Aminostratigraphy and amino chronology. In Engel, M., and Macko, S. (eds.), *Organic Geochemistry*. New York: Plenum, pp. 755–783.

Wehmiller, J.F., and Miller, G.H., 2000. Aminostratigraphic dating methods in Quaternary Geology. In Noller, J., Sowers, J., and Lettis, W. (eds.), *Quaternary Geochronology: Methods and Applications*. Washington D.C.: American Geophysical Union, pp. 187–222.

Cross-references

- Dating, Biostratigraphic Methods
- Dating, Radiometric Methods
- Paleotemperatures, Proxy Reconstructions
- Radio Carbon Dating
- Uranium-Series Dating

DATING, BIOSTRATIGRAPHIC METHODS

Historic overview

Biostratigraphers study the distribution of fossils in sedimentary strata. They have two motives – reconstructing the history of life and developing a relative time scale for other geologic studies. More than two hundred years ago, before formulation of the theory of evolution, it became apparent that the same general succession of faunas could be recognized in different rocks at widely

separated locations. Trilobites appeared before ammonites, for example, and dinosaurs became abundant before mammals. Such observations led to the major divisions of the Phanerozoic time scale – the Paleozoic, Mesozoic, and Cenozoic eras – and to attempts to resolve much finer subdivisions using fossil species. These subdivisions enable time correlation – the identification of strata in different places that were deposited during the same time interval. The resolving power of correlation improved significantly when petroleum companies began to apply sequences of microfossil species to the task. The Deep Sea Drilling Project standardized high-resolution subdivisions based on microfossils extracted from cores of the ocean floors.

The basic practices of biostratigraphic correlation adapted to the availability of radioisotopic dates and personal computers. Initially biostratigraphy sought to divide the geologic time scale into biozones based on index species. Radioisotopic dates changed the focus to the age-calibration of species appearances and disappearances, which could then be used as biohorizons for indirect dating. Personal computers made determination of the likely sequence of large numbers of uncalibrated biohorizons practical.

The fundamental challenge in the use of biostratigraphy as a means of dating is the discrepancy between biostratigraphic horizons and time horizons (Figure D11). To step from biostratigraphic description to time correlation, it is necessary to compensate for the ecological and stochastic factors that inevitably cause the time of appearance and disappearance of fossil species to vary from place to place. In spite of some contention about the best way to handle this problem, it is evident that, in practice, there has been no more cost effective, more generally successful, or more readily available means than fossils to correlate rock strata (Ludvigsen et al., 1986).

Terms and basic data

A biozone is a body of rock characterized by the fossils it contains (Salvador, 1994). The bounding surfaces of such a unit are almost certainly diachronous; that is, the ages of the highest and lowest finds of the definitive species usually vary from place to place. The reasons are simple and unavoidable: new species evolve at unique places and times; their ranges expand to wider but patchier distributions that change over time; the geographic range dwindles more or less rapidly as the species is replaced by others; and incomplete preservation leaves a fossil record of the species that is patchier still. Furthermore, even

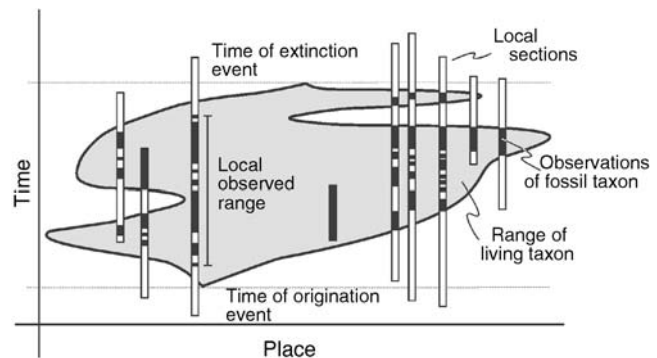


Figure D11 Range of a taxon in life (gray), the observed range of the fossil taxon (black) in stratigraphic sections (rectangles), and the time lines defined by the origination and extinction of the taxon.

deep marine sequences of sedimentary strata do not accumulate continuously (Aubry, 1995); they include gaps at all scales and some observed ranges end artificially at such gaps.

Portions of the bounding surface of a biozone are biohorizons – stratigraphic surfaces characterized by a faunal change, such as the lowest or highest local observations of a fossil taxon. The observed biozone is smaller than the range of the living species because of the vagaries of fossil preservation and collection. The corresponding time interval (chronozone) extends beyond the living range to encompass all the rocks deposited during the life span of the species, whether or not they contain the fossil. In spite of their essentially diachronous nature, biozones and biohorizons are routinely used to estimate the position of datum surfaces that correspond everywhere to the time of origination or extinction of a taxon.

The raw data of biostratigraphy are faunal lists – inventories of fossil taxa that coexist in the same stratum. Ideally, numerous faunas can be placed in sequence at individual stratigraphic sections, permitting local range charts to be constructed that show the span of strata from the lowest to the highest find of each taxon (Figure D12). The range ends, highest and lowest local finds of a taxon, are local estimates of the first and last appearance datums (FADs and LADs). The diachronous nature of biohorizons becomes evident when lines connecting the horizons of numerous highest and lowest finds are drawn between stratigraphic sections to form a fence diagram (Figure D13). Typically many of the correlation lines cross one another and it is clearly not possible to consider them all time-lines.

Biozones

Although many types of biozone have been proposed (Salvador, 1994), they result from only two significantly different practices. The choice is often dictated by the nature of the available data – faunal lists or range charts. One practice characterizes zones by their content, typically the co-occurrence of two or more taxa. Sequences of such “assemblage” zones (Figure D12) can be extracted from analysis of faunal lists alone (Guex, 1991; Alroy, 1994), but precise placement of the zone boundaries can be elusive. The other practice is more conducive to very fine subdivision (Murphy, 1994); it defines the limits of “interval” zones to coincide with highest- or lowest-find biohorizons. This practice requires good range charts. It seeks to avoid the inherent diachronism in biohorizons by selecting from all possible horizons only a subset that is always observed in the same sequence (Scott, 1985). Contradictory sequences of observed range ends can be observed only for taxa whose true ranges overlap in time. Consequently, the quest for robust sequences of range ends succeeds most readily if the range end events are widely spaced.

Resolving power is retained by selecting, as “index fossils,” short-lived species from rapidly evolving lineages. Ideally, these species are also abundant, distinctive, and widespread. Most are pelagic or wind-borne; e.g., conodonts (Ordovician-Triassic), graptolites (Ordovician-Silurian), ammonoids (Devonian-Cretaceous), foraminifera (Cambrian-Recent), calcareous nannofossils (Jurassic-Recent), diatoms (Cretaceous-Recent), radiolaria (Cambrian-Recent), spores (Silurian-Recent) and pollen (Pennsylvanian-Recent).

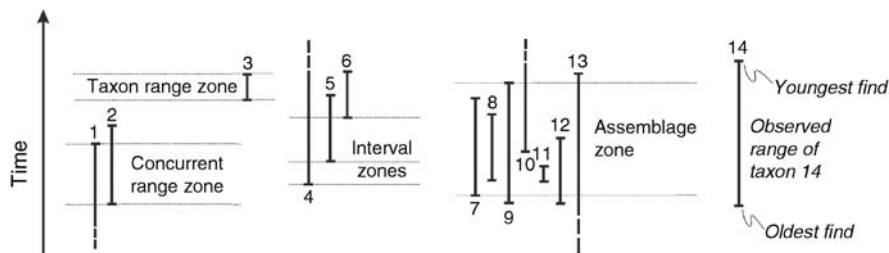


Figure D12 Biozones defined by subdivision of a range chart.

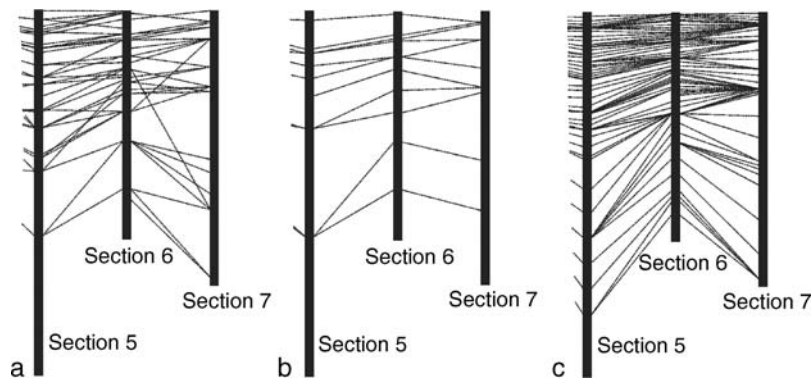


Figure D13 Biostratigraphic correlation as a fence diagram: part of a 7-section project. (a) Literal correlation of observed range ends.

(b) Range ends culled to those found in the same sequence in all 7 sections. (c) Adjustment of all range ends to the sequence that best fits all local observations.

FADs and LADs (biohorizons)

Rather than using a few biohorizons to define zones, modern biostratigraphy seeks to retain as many biohorizons as possible and determine the sequence of the corresponding datums. An essential difference is that this approach must evaluate and adjust the local biohorizons (Figure D13c). The elimination of cross-cutting biohorizons (Figure D13a, b) removes the most obvious appearance of diachronism but does not guarantee that the remaining correlation lines are isochronous. Three means of correction for diachronism are noteworthy. The first uses the gaps within the preserved ranges to add confidence intervals to the observed range ends (Marshall, 1990); it corrects only the stochastic component of the difference between biostratigraphy and time. The second method uses radioisotopic dates and calibrated paleomagnetic reversals to determine the age of range ends at different locations. It is best developed for Neogene FADs and LADs in cores from the ocean floor. The third strategy uses the observed sequences and/or coexistences in many locations and the principle of parsimony: it searches for a composite sequence of events to which all the local range charts can be fit with the minimum of adjustment. Assuming that most observed ranges are shorter than the true range, observed ranges are extended as necessary to fit them to a single global sequence. Initially, the method was implemented graphically as a form of regression (Shaw, 1964). Now, computer algorithms search for the best-fit sequence (Sadler, 2004). If available, horizons of known age, such as dated ash falls and calibrated paleomagnetic reversals, may be included to constrain the search for the best sequence.

Sometimes, especially over short distances, it is possible to exploit ecologic factors to achieve finer correlation. Short-lived changes in global temperature or the pattern of winds and ocean currents may become correlatable events when they cause changes in the relative abundances of pollen or foraminiferan taxa, for example. Distinctive fluctuations in stratigraphic trends of the relative abundances of taxa may then indicate correlative strata in different locations.

Resolving power

In favorable situations, zonation based upon pelagic marine organisms can resolve intervals that are on average less than one million years in duration. Usually such sets of zones are based upon a single biological clade. Conventional ammonite zones and subzones in the Mesozoic resolve 0.4–0.75 million year intervals, on average. Mesozoic zones based on foraminifera and calcareous nannofossils resolve 2–3 million years. Cenozoic zones and subzones for the same microfossils have average durations of 0.75–1.0 million years. Often, it is necessary to establish separate sets of zones for different climate belts. For Cenozoic radiolarians there are 32 low latitude zones and 11 mid latitude zones, for example. Ordovician conodonts support “North Atlantic” and “Mid continent” zones with resolving power of the order of 2–4 million years. For the Ordovician and Silurian, finer resolution (1–3 million years) is afforded by the more cosmopolitan graptolite zones.

Biohorizons offer the promise of better resolving power. For the Ordovician and Silurian, over 3,000 graptolite appearance and extinction events have been sequenced. For the Cenozoic there are of the order of 100 calibrated biohorizons each for foraminifera and calcareous nannofossils. Average resolving power of the order of 0.25 million years or better would appear to be possible by using biohorizons from more than one fossil

clade. Whether this is attempted by recourse to radioisotopic calibration or computer optimization of observed sequences, however, there are always clusters of range-end biohorizons whose relative age remains irresolvable. Nevertheless, the resolvable events and clusters of events are often sufficient to increase the resolving power 5- to 10-fold over traditional biozones (Harries, 2003). It appears that biostratigraphically based timescales might soon resolve intervals as short as 500,000 years, and even less, through most of the Phanerozoic. This approaches the size of analytical errors quoted for radioisotopic dates on Paleozoic ash falls. It is likely shorter than the time taken by many taxa to spread from their point of origin to their full geographic extent – an inevitable source of discrepancy between biohorizons and time lines. These figures concern the resolving power of timescales for global correlation. As the distance of correlation is reduced, more biohorizons and strata approximate time lines and potential resolution improves (Harries, 2003). The actual resolving power of any given correlation will be limited by the fossil content of the strata.

Peter M. Sadler

Bibliography

- Alroy, J., 1994. Appearance event ordination: A new biochronological method. *Paleobiology*, **20**, 191–207.
- Aubry, M.P., 1995. From chronology to stratigraphy: Interpreting the Lower and Middle Eocene stratigraphic record in the Atlantic Ocean. *SEPM Spec. Publ.*, **54**, 213–274.
- Guex J., 1991. *Biochronological Correlations*. Berlin: Springer, 252pp.
- Harries, P., 2003. *High Resolution Approaches in Paleontology*. Kluwer: Dordrecht.
- Ludvigsen, R., Westrop, S.R., Pratt, B.C., Tufnell, P.A., and Young, G.A., 1986. Dual Biostratigraphy: Zones and biofacies. *Geosci. Canada*, **13**, 139–154.
- Marshall, C.R., 1990. Confidence intervals on stratigraphic ranges. *Paleobiology*, **16**, 1–10.
- Murphy, M.A., 1994. Fossils as a basis for chronostratigraphic interpretation. *N. Jb. Geol. Palaeont. Abh.*, **192**, 255–271.
- Sadler, P.M., 2004. Quantitative Biostratigraphy – achieving finer resolution in global correlation. *Annu. Rev. Earth. Planet. Sci.*, **32**, 187–213.
- Salvador, A., 1994. *International Stratigraphic Guide*. Boulder, USA: Geological Society of America, 214pp.
- Scott, G.H., 1985. Homotaxy and biostratigraphical theory. *Palaeontology*, **28**, 777–782.
- Shaw, A.B., 1964. *Time in Stratigraphy*. New York, USA: McGraw Hill, 365pp.

Cross-references

- [Animal Proxies, Invertebrates](#)
[Animal Proxies, Vertebrates](#)
[Deep Sea Drilling Project \(DSDP\)](#)

DATING, DENDROCHRONOLOGY

Introduction

Dendrochronology is the science that deals with the absolute dating and study of annual growth layers in woody plants such as trees. The name derives from the Greek root words *dendron* for tree and *chronos* for time. The notion that variability in ring widths in trees relates to variability in climate dates back at least as far as Leonardo da Vinci, whose writing translates thus: *The rings from cut stems or branches of trees show their*

number of years, as well as those years that are more moist or dry, according to the size of their rings.

In addition to Leonardo, others also noted that ring width and climate were linked, and that patterns in trees could be matched across space and time. However, it was never pursued to the extent that chronologies were built and reconstructions of climate into the past were attempted. The development of dendrochronology as a scientific field came later, in the early twentieth century, under the guidance of Andrew Ellicott Douglass.

Douglass was an astronomer residing at the Lowell Observatory in Flagstaff Arizona (Webb, 1983). In 1904, he found that a distinct pattern of narrow and wide growth rings in conifer log sections, cut from the Flagstaff area, could be matched with trees from as far away as Prescott, some 150 kilometers distant. This led him to recognize the nature of a general control on tree-growth that was variable on an annual time scale and was most likely related to climate. Later, in 1911, Douglass recognized the real significance of his observation, and determined that the influence of climate was the major contributor to the common variability evident in the annual radial growth of trees. He recognized that, in the arid American Southwest, precipitation was the factor most limiting to tree growth. Therefore, tree growth could in turn be used as a proxy for rainfall before the time of the instrumental record.

Douglass had developed and utilized the principle of *cross-dating*, or pattern matching, as the basis for the science of dendrochronology. He realized that the simple counting of growth rings could result in errors of years or even decades over a span of hundreds of years of record. Douglass' procedure involved the rigorous detection of "locally absent" and "false" rings through sample replication and reproducibility of specific patterns. This procedure, facilitated by graphical *skeleton plotting* (Stokes and Smiley, 1968), allowed Douglass to accurately assign calendar dates to rings even when growth was highly stressed, as in the case of arid site conifers (Douglass, 1919). Through the development of *master chronologies* he was able to use this powerful new tool to compare and match growth patterns across a very broad region, allowing for the exact dating of annual rings from both living and dead trees. It was not long before this process led to the dating of aboriginal ruins from across the desert Southwest (Haury, 1962), making dendrochronology one of the most significant tools in the field of archaeology.

Dendrochronology makes use of distinct annual growth ring patterns as markers in time. Wood volume (ring width) and density are the two most common features used for the cross-dating procedure. By matching the patterns of growth from living trees of known age with similar patterns in the wood from progressively older trees, one can extend the time scale backward into the distant past. These distinct patterns can then be used for the accurate dating of events that somehow affected the growth or life of individual trees (Fritts, 1976). Any event that kills one or more trees, or otherwise leaves an impact at a particular year, can be fixed accurately in time through dendrochronology and crossdating. Examples of this can be seen throughout the literature, from the dating of buildings and other wooden artifacts (Haury, 1962; Baillie, 1982), to the determination of precise years of earthquake movements (Jacoby et al., 1989; Sheppard and Jacoby, 1989), and to the detection of epic droughts that caused mass mortality in the early North American settlements (Stahle et al., 1998). The application of dendrochronology can be used as an

important tool in many different fields, including ecology, archaeology, geomorphology, hydrology, and biogeography, to name a few. However, in no field has dendrochronology played a more significant role than in the field of climatology (see *Dendroclimatology*).

Dendrochronology is possible because climate influences tree growth across space and time to such an extent that there will be common variability expressed in the pattern of annual radial growth across broad regions (Douglass, 1919; Fritts, 1976; Hughes et al., 1982; Cook and Kairiukstis, 1990). The extent to which climate exerts its uniform influence determines how strong the agreement between trees will be. For that reason, the tree ring chronologies with the greatest fidelity are from regions where climate is at its most limiting to growth, and most regionally coherent. Extremes of temperature and moisture availability produce the greatest variability in annual radial growth, and are therefore the areas where crossdating is most readily achieved. Trees growing in regions with little climate variability and optimum conditions for growth are less likely to produce the high variability in growth pattern that allows for accurate crossdating. This simple tenet has become known as the *Principle of Limiting Factors* (Fritts, 1976), and along with crossdating forms the nucleus for the field.

The annual growth ring

The annual growth layer or "tree ring" is central to the science of dendrochronology. It can be described as a growth band in the xylem of a tree or shrub with anatomically definable boundaries, and is formed during a single annual period of cambial activity (Kozłowski, 1971; Fritts, 1976; Esau, 1977; Salisbury and Ross, 1992). Growth rings are actually sheaths of cells generated in the vascular cambium, between the prior year's growth and the bark, and they appear as concentric rings in a cross section of the stem. The annual growth cycle is described using the simplest case scenario of a temperate zone conifer. In the spring when moisture is plentiful, energy is devoted to the production of new growth cells. These first new growth cells are large, but as the summer progresses, cell size decreases until the short days and cool temperatures of autumn arrive and growth stops altogether. This process is called "hardening off," where the cell walls thicken in preparation for the freezing temperatures of winter. New growth begins anew the following spring with the arrival of longer days and warming temperatures. The contrast between the smaller, thicker-walled old cells of the end of the growth season (*latewood*) and the following year's larger, thinner-walled new cells (*earlywood*) forms the visible ring boundary typical of conifers (Figure D14). Initiation of cambial activity in the spring appears to be related to the resumption of bud growth, while its termination is likely correlated with the cessation of shoot extension (Digby and Wareing, 1966). While initial cambial activity has been linked to the downward movement of growth substances from the expanding buds, continued cambial growth is driven by a local source of auxin that is probably supplied by the differentiating xylem (Samish, 1954; Sheldrake, 1971).

During cambial activity, the newly formed cells differentiate into phloem and xylem. The phloem forms on the bark side of the cambium and serves as a conduit for transporting photosynthate downward from the leaves, while the xylem grows on the inner side of the cambium and transports water and nutrients upward (Nobel, 1974; Shigo, 1984). In some sense, each new ring can be viewed as a whole new functioning tree that completely envelops and replaces the previous year's

growth flush (Shigo, 1984). While there is some interaction between the latest, active growth rings and their predecessors, growth rings become effectively non-functional with time (Esau, 1977; Shigo, 1984).

Though conifers comprise the most widely used trees for dendrochronology, they are not the only trees used for chronology building. Many of the angiosperms, both deciduous and evergreen, have been successfully used. However, the growth rings in many of these species are often far less visible, and entirely different criteria must be used (Figure D15). Multiple, annual growth bands may occur under certain conditions but there are few documented cases of consistent, systematic multiple-banding in trees. Many tropical regions have few species that exhibit clearly defined annual banding that can be detected by conventional dendroclimatic methods, and it is this

fact that has hampered such studies in the tropical regions (Jacoby, 1989; Buckley et al., 1995; Worbes, 1995). Without being able to absolutely identify annual banding in a given species it is not possible to pursue dendrochronological studies.

Factors affecting tree growth

When annual growth rings are formed in trees, it is likely that those layers reflect the environmental conditions under which they were formed (Douglass, 1914; Fritts, 1966). Annual variability in ring width (or some other characteristic such as density or isotopic composition), when synchronous in many trees within a region, indicates a common set of external factors that are influencing tree growth within that region. Such external forcing factors, particularly where they are spatially-extensive, are most likely related to climate, as no other external factors are likely to act over a similar range in the space, time and frequency domains (Fritts, 1976; Hughes et al., 1982). It is therefore possible to extract the climatic “signal” from the annual record of tree growth in such instances, and it is this objective that forms the underlying basis for dendroclimatology research (see *Dendroclimatology*).

Tree growth, in an absolute sense, is an integration of all aspects of the operational environment. Climate is arguably the most important factor controlling overall growth. However, annual radial growth is also strongly influenced by stand dynamics effects that are related to the competition for light, water, and nutrients. Other factors that influence growth include the type, texture and mineral content of soils; the drainage, latitude, elevation, slope and aspect of the site; and the amount of solar radiation, available moisture and average temperature during the growing season, and perhaps previous seasons (Fritts, 1976). Natural disturbances, such as earthquakes and landslides, snow avalanches, fire, volcanic eruptions and ash fall, and herbivorous insect attack, can all influence tree growth for one or more seasons. Anthropogenic factors that can affect growth include groundwater pollution, fire, cutting, gouging and harvesting of shoots and leaves. Nearby disturbances that affect drainage or the availability of light may also play a significant role in ring width variability.

In addition to the effects of such external factors, there are several internal factors that can influence growth. These include the availability of nutrients, minerals, growth regulators, enzymes and water (Nobel, 1974; Fritts, 1976; Salisbury and Ross, 1992). Such internal factors are, however, influenced by external forcing from temperature and moisture availability, and typically play no role in the annual variability of growth. The genetics of a given species may be important in regulating these internal factors in a general sense. However, external variables (particularly those related to climate) may be more

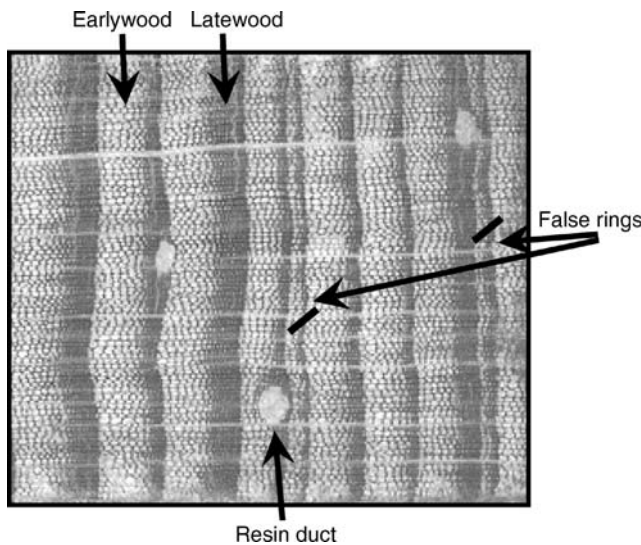


Figure D14 Typical conifer growth rings and associated features. This transverse view of *Pinus merkusii*, from north Thailand, reveals the cells that comprise the annual growth ring. Individual cells are divided into two general types: earlywood (light color) and latewood (dark color). The earlywood cells form at the beginning of the growth season and are usually larger, thinner-walled, and far less dense than latewood cells due to a lesser degree of lignification. The latewood cells form near the end of the growth season as part of the “hardening off” period before dormancy, in this case induced by annual drought. It is the delineation between these two cellular types that allows for the identification of annual growth rings in some trees, and hence crossdating of annual ring sequences. Two “false rings” are indicated that are the result of intra-annual periods of dormancy that result from intermittent drought.

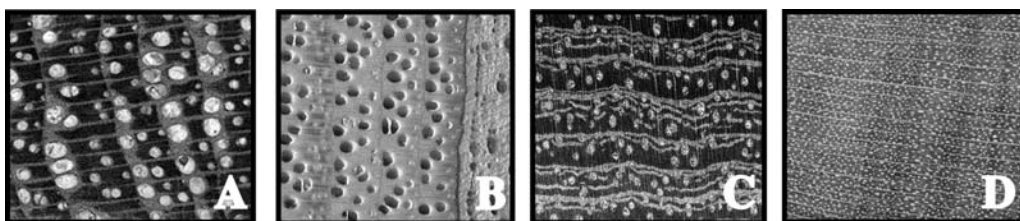


Figure D15 Different types of growth rings. (a) *Tectona grandis* (teak) from Indonesia classified as semi-ring porous to porous wood; (b) the ring porous wood of *Fraxinus americanus* (white ash) from New Hampshire; (c) the semi-porous rings of *Gluta usitata* of the family Anacardiaceae from Thailand; and (d) the diffuse porous wood of *Acer saccharum* (sugar maple) from New York State.

important on a year-to-year basis and are therefore reflected in the annual variability of ring width. It is this fact that makes absolute crossdating of ring sequences, and therefore dendrochronology, possible (Fritts, 1966).

Importance of site selection

Dendrochronology can only be successful if the trees selected are sensitive enough to climate to exhibit some annual variability (Fritts, 1976; Hughes et al., 1982). There are two basic principles of dendrochronology underlying climatic sensitivity in trees, which therefore relate directly to site selection: the *Principle of Limiting Factors*, and the *Principle of Ecological Amplitude* (Fritts, 1976).

The Principle of Limiting Factors states that a biological process such as growth cannot proceed faster than is allowed by its most limiting factor. Although the same factors may limit growth to some extent in all years, the degree and duration of their limiting influence may vary annually. When one factor is no longer limiting (e.g., when adequate moisture is available to drought-stressed trees), growth will systematically increase until another factor becomes limiting (Fritts, 1976). This becomes important in dendrochronology because tree rings can only be cross-dated when one or more environmental factor is *uniformly* limiting to growth across time and space.

The Principle of Ecological Amplitude refers to a species' range of potential habitats. Every species may grow and reproduce over a certain range of habitats, dependant upon certain hereditary factors that determine its phenotype (Fritts, 1976). Species that thrive on a wide range of habitats are said to have a large ecological amplitude, while those restricted to very specific habitat requirements have a small ecological amplitude. Near the center of its ecological amplitude, a species may be found on the widest range of sites, and climate may only rarely be limiting to growth. Near the margins, however, it may be restricted to very specific habitats, and it is in these marginal zones where climate is likely to be the most growth-limiting factor, and the most climatically sensitive trees should be found (Fritts, 1976; Hughes et al., 1982).

Site selection, therefore, becomes a matter of maximizing the desired climatic signal by sampling trees on sites where that parameter is likely to be growth limiting. In a dendroclimatic study of rainfall, such trees might be found in areas of steep slope, with well-drained, rocky soils, and an aspect facing the direct rays of the sun (Stokes and Smiley, 1968). It would also be advantageous to search for a species growing near the limits of its ecological amplitude, with regard to its need for moisture. If the aim of the study is to reconstruct temperature, trees should be sampled from the altitudinal or latitudinal limits of the species range where temperature should be the factor most limiting to growth. Dendrochronology can therefore only be successful if the following conditions are met:

1. There must be quantifiable variability in some aspect of the climate in the region of interest. For example, there must be a distinct wet and dry, or warm and cold, phase of the annual cycle. There must also be measurable annual variability within these seasons.
2. There must be at least one tree species available within the study region that exhibits distinct, annual growth rings with reasonably uniform ring widths. In some regions of the world, such as in the tropics, there are few species with distinct annual growth boundaries, and some may also exhibit intra-annual banding, where more than one growth ring is formed in some
3. Some definable aspect of annual growth (e.g., ring width or latewood density) must be uniformly variable in all trees at the site, so that sequences of wide and narrow, or dense and less dense, rings can be matched between trees. This "cross-dating" of annual ring sequences assures the temporal control that is central to dendrochronology.
4. The researcher must be able to link the common, synchronous variability in growth of all trees at a site to some recorded climatic parameter (e.g., rainfall, temperature, or mean sea-level pressure). If the climate/tree growth link is significantly strong, then a reconstruction of the selected climatic parameter can be considered.

A conceptual model for tree growth

A simple way of conceptualizing tree growth, in terms of dendrochronology, is the *linear aggregate model* developed by Cook (1990). The equation for this model is as follows:

$$R_t = A_t + C_t + dD1_t + dD2_t + E_t \quad (1)$$

where

R_t = the observed ring-width series;

A_t = the age-size-related trend in ring width;

C_t = the climatically-related environmental signal;

$D1_t$ = the disturbance pulse caused by a local endogenous disturbance;

$D2_t$ = the disturbance pulse caused by a stand wide exogenous disturbance;

E_t = the largely unexplained year-to-year variability not related to the other signals.

The model is expressed in linear form for purposes of simplification, in spite of known non-linear relationships associated with ring-width, such as that between the mean and standard deviation (Fritts, 1976). However, such relationships can be made linear by log transformation, indicating the intrinsically linear nature of the process (Cook, 1990). The d associated with $D1_t$ and $D2_t$ is a binary indicator of the presence or absence of either class of disturbance at some time t in the ring widths: when $d = 1$ the disturbance is present, when $d = 0$ it is absent. Therefore A_t , C_t , and E_t are all assumed to be continuously present in R_t , and depending on whether the intervention of some disturbance has occurred at some time t , $D1_t$ and $D2_t$ may not be present (Cook, 1990).

The age-size-trend (A_t) is a non-stationary process that partially reflects the geometrical constraint of adding a volume of wood to a stem of increasing radius (Fritts, 1969). If this constraint is the primary source of the trend then A_t will exhibit an exponential decay as a function of time, subsequent to the juvenile period of increasing radial growth (Fritts, 1976; Cook, 1990). This type of growth trend is typified by trees that grow in very open environments, where the effects of competition and disturbance are minimized (Stokes and Smiley, 1968; Fritts, 1976). In closed canopy stands where the effects of competition and endogenous disturbances are more frequent, the behavior of A_t may be strongly influenced in ways that may not be synchronous in all trees in the stand (Fritts, 1976; Cook, 1985, 1990). Figure D16 illustrates some typical growth trends found in ring width data. There is no predictable shape for A_t , in that it does not necessarily arise from any family of

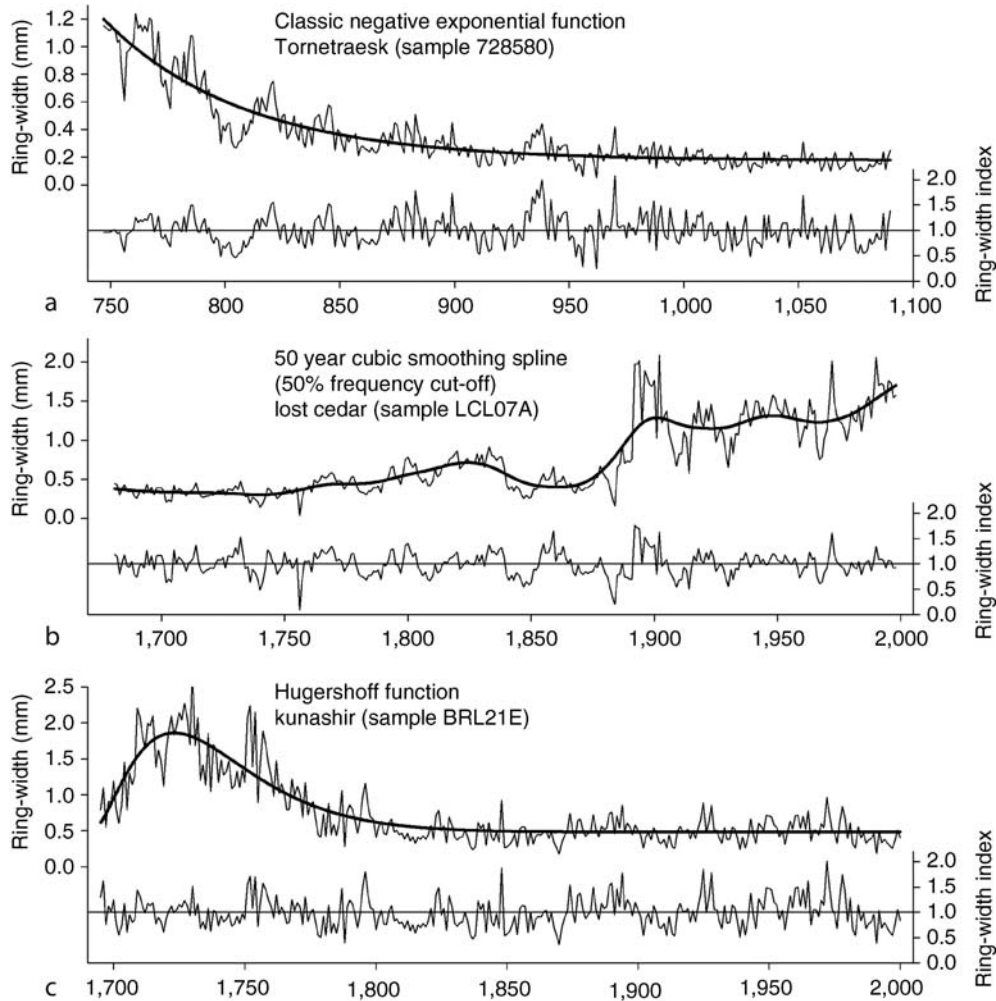


Figure D16 Three common growth trends associated with tree-ring time series and their standardized indices. (a) (top) represents a *Pinus siberica* tree growing in the Tornetraesk region of Fennoscandia. This tree shows a “classic” negative exponential growth trend that results from adding a given volume of wood to a cylinder of increasing diameter. The resulting indices generated from fitting this curve to the data are shown below the raw measurements. This type of growth trend occurs when effects of competition and disturbances are minimal, such as in open canopy forests. (b) (middle) is from a talus slope stand of *Thuja occidentalis* from the Bruce Peninsula of Ontario, Canada that has experienced the effects of rock fall and a large fire in the 1880s. This series illustrates the effects of disturbances (localized or regional) on the expected negative exponential growth curve, resulting in a disturbance pulse and an increasing trend that is removed here with a flexible smoothing spline. (The cubic smoothing spline was developed to remove disturbance effects from individual time series, while maximizing the common signal amongst all trees in the stand. If indiscriminately applied, this type of curve fitting can result in loss of signal). (c) (bottom) shows a Hugershoff curve fit on a *Quercus crispula* time series from Kunashir, in the Kurile Islands north of Japan. This type of growth curve is typical of a tree beginning as an understory tree, shaded from direct sunlight and in greater competition for resources, before emerging into the canopy and commencing an approximate negative exponential growth trend.

deterministic growth curve models such as the negative exponential curve. It should instead be thought of as a non-stationary, stochastic process that may, in special circumstances, be treated as a deterministic process (Cook, 1990; Cook et al., 1990a).

C_t is representative of the aggregate influence of all climate variables on tree growth. The typical variables that comprise C_t include precipitation, temperature and solar radiation. These variables combine to influence tree growth by controlling photosynthesis and the amount of available moisture for physiological activity within the constraints of the phenology of a given species (Fritts, 1976; Salisbury and Ross, 1992). It is the broad scale quality of these climate variables that is

typically of interest to the dendroclimatologist, as all trees in a stand will be affected in a similar manner, thereby maximizing the common signal (Fritts, 1976). These climate variables may usually be thought of as stationary, stochastic processes, though there may be some persistence in an autoregressive sense (Cook, 1985, 1990).

The endogenous disturbance pulses represented by $D1_t$ vary from tree to tree. They are typified by gap-phase stand development in which trees are removed from the canopy by localized processes affecting only those trees adjacent to the gap (White, 1979). They usually create patterns of suppression and release in the ring widths of affected trees. Truly endogenous disturbances are random events in space and time,

and the corresponding effect in a ring width series will be largely uncorrelated with similar pulses in other trees, even from the same stand (Cook, 1990). Exogenous disturbances, denoted by $D2_t$, are characterized by stand-wide disturbances attributed to such phenomena as fire, insect damage, disease, logging effects and pollution, though they may also result from episodic climate-related events like frost, wind or ice damage. The key factor, which may distinguish $D2_t$ from $D1_t$, is the synchrony in time of the former across the stand, unlike the latter, which will exhibit non-synchronous, random behavior in individual trees (Fritts, 1976).

The final term in the equation is E_t , which represents the variance in the ring widths that remains unexplained after accounting for A_t , C_t , $D1_t$, and $D2_t$ (Cook, 1990). Sources for this unexplained variance include micro-site characteristics such as variability in soil quality or type across the stand, hydrological gradients across the site or measurement error. It is assumed that E_t is serially uncorrelated within, and spatially uncorrelated between, trees in the stand.

Chronology building

The development of a master chronology series, or chronology *indices*, involves much more than just the averaging of individual tree ring measurements. The single most important, and undoubtedly controversial, aspect of chronology development is *standardization*. Standardization is the procedure by which tree ring time series, each having their own mean, standard deviation and overall growth characteristics, are converted to dimensionless indices that can be compared with one another. The first step is a curve-fitting procedure aimed at removal of a "biological growth trend" that is thought to be unrelated to climate. The idealized biological growth curve would be negative exponential in character, based on the geometry of adding a constant volume of wood to a cylinder of ever-increasing size. The "signal" that makes dendrochronology possible is the annual variability of climate forcing that is superimposed on the growth curve and commonly expressed in all trees. Thereby, traditionally, the measured ring width values would be divided by the "expected" values for each year, resulting in a set of standardized indices with a mean of 1.0 and the growth trend removed (Fritts, 1976). Often the growth trend takes on a form other than negative exponential, however, and in such cases other *a priori* detrending methods are routinely applied (Cook and Peters, 1981; Cook and Kairiukstis, 1990).

Standardization becomes increasingly complicated in more closed-canopy forests due to the effects of endogenous stand dynamics that may be the source of the principal low-frequency "signal" (Cook, 1985, 1987). Such disturbances can often introduce a low-frequency trend to the data that masks or negates the putative biological growth curve described above. In addition, variable rates of growth through time pose another problem for dendrochronologists, due to the *heteroskedastic* nature of tree ring series (i.e., changing variance through time due to direct relationship between mean and standard deviation). Comparing periods of growth between trees of different age and growth rate requires a normalization procedure to stabilize this changing variance, because this (like growth trend) is also unrelated to climate. Importantly, the annual variability superimposed on these growth rates will be proportional through time, resulting in the ability to crossdate the samples by their annual departures from the local mean. So, individualized local trends in data (i.e., not common among all trees at the stand) are typically removed through curve-fitting procedures such as the cubic smoothing

spline (Cook and Peters, 1981), a data-adaptive curve that can be altered to remove more or less of the trend in mean associated with such growth.

After the de-trending procedure has been applied individually to a suite of crossdated tree ring series, they can be averaged together into the master site chronology. It is this normalized chronology index that is used for further study. Thus, the purpose of the standardization procedure is to remove non-climatic trends, correct for heteroskedastic variance and equalize the resulting overall growth rate from tree to tree. It is important to note that Douglass (1919, 1928) had recognized these concepts, but it required the tremendous iterative power of high-speed computers to accomplish them for large numbers of trees.

The "traditional" method for generating indices (i.e., using division to produce ratios of the actual values divided by the expected values) has been shown to potentially introduce bias into the indexing procedure that may result in "over-fitting" the data, particularly in the outer end of the time series (Eriksson, 1989). This bias may have the effect of exaggerating recent trends in growth, and thereby any inferences of climate made from them. The source of the bias is related to the inherent asymmetry of radial growth in trees, where growth has a defined lower boundary of zero, and a poorly defined, highly variable maximum value. This asymmetry fosters dependence between the local mean and standard deviation by roughly defining the overall corridor within which a tree can respond to environmental inputs such as climate. Trees growing at faster rates have a wider corridor within which to respond to climate than do slower growing trees. Thus, the variance increases in proportion to the mean, and the effect of division on the resultant index can be highly non linear, especially where the estimated growth curve approaches zero.

A method described by Cook and Peters (1997) and first used by Cook et al. (1992) eliminates this potential bias by using residuals instead of ratios from the growth curve. The series are transformed prior to standardization by using a data adaptive power transformation based on the relationship between the local spread and level (standard deviation S , and mean M , respectively) for the best power transformation (Emerson and Strenio, 1983). The model is as follows:

$$\log S = k + b \log M \quad (2)$$

which is a simple linear regression in logarithmic space, where $S = cM^b$ and $k = \log c$, and b is the slope of the spread versus level relationship. This being the case, then $p = 1 - b$ is the appropriate value for the exponent used for the power transformation (Emerson and Strenio, 1983). Following this variance stabilization procedure, the residuals are taken rather than the ratios, resulting in unbiased estimates of tree growth (Cook and Peters, 1997).

Estimating the mean value function

Three general methods have been used for estimating the mean value function, subsequent to detrending of ring-width series: the arithmetic mean, a mean based on testing for a mixture of normal distributions in the sample and the biweight robust mean that discounts outliers (Cook et al., 1990a). The latter method automatically discounts the influence of outlier values in the computation of the mean, thereby reducing variance and bias likely to be caused by these outliers (Mosteller and Tukey, 1977; Cook, 1985). Outlier values may result from

endogenous disturbances that behave as random events in space and time, particularly in ring-width series from closed-canopy, mesic forests like those used for this study (Cook et al., 1990b). The biweight mean for a given year t is computed through iteration as:

$$\bar{I}_r = \sum_{j=1}^m w_j I_t \tag{3}$$

where

$$w_t = \left(1 - \left(\frac{I_t - \bar{I}_r}{cS_{I_r}} \right)^2 \right)^2 \tag{4}$$

when

$$\left(\frac{I_t - \bar{I}_r}{cS_{I_r}} \right)^2 < 1 \tag{5}$$

The weight function is denoted by w_t and is symmetric and therefore unbiased in its estimation of central tendency, provided that the data are symmetrically distributed (Cook, 1985). S_{I_r} is a robust measure of the standard deviation of the frequency distribution, which is defined here by the median absolute deviation, or MAD, calculated as follows:

$$S_{I_r}^* = \text{median} \{ |I_t - \bar{I}_r| \} \tag{6}$$

and c is a constant, often given as six or nine (Mosteller and Tukey, 1977). This constant, c , determines the point at which an outlying value is given a weight of zero, at which point the outlier is discounted and has no influence on the estimation of the mean index (Cook et al., 1990b). When c is set to nine, for example, any value exceeding ± 6 standard deviations from the mean is rejected (Mosteller and Tukey, 1977). A potential drawback of using the biweight robust mean is its lower statistical efficiency compared to the arithmetic mean when the sample population is devoid of outliers and approximates a Gaussian distribution (Cook, 1985). However, in most closed-canopy forests the biweight robust mean is justified as insurance against outliers in the estimation of the mean value function.

Autoregressive modeling, based on ARMA time-series modeling (Box and Jenkins, 1970), has also been shown to be an effective way of generating a more statistically efficient estimate of the mean value function (Cook, 1985; Guiot, 1987). This is particularly true where autocorrelation within individual time-series is high and out-of-phase between series. Tree ring indices can be expressed as an ARMA process of order p and q , in difference equation form as:

$$I_t = \phi_p I_{t-p} + \dots + \phi_1 I_{t-1} + e_t - q_1 e_{t-1} \dots - q_q e_{t-q} \tag{7}$$

where e_t values are serially random inputs or shocks driving tree growth as reflected in the ring widths, the ϕ_i values are the p autoregressive (AR) coefficients and the q_i values are the q moving average (MA) coefficients. These two coefficients combine to produce the characteristic persistence or “memory” exhibited in the I_t (Fritts, 1976; Cook, 1985). For each ring-width series, the values for e_t are assumed to be a combination of inputs related to the factors C_t , $D1_t$ and E_t as outlined in equation (1). The age-size trend, A_t , is considered to be either nonexistent in the raw ring width series (in other words $I_t = R_t$) or sufficiently removed by the detrending process (Guiot, 1987).

Tree-ring indices can be modeled and prewhitened as AR(p) or ARMA (p,q) processes in order to remove the effects of unwanted, disturbance-related transience on the common signal (Cook, 1985; Guiot, 1987). The Akaike Information Criterion, or AIC (Akaike, 1974) is a criterion for selecting the correct AR model and can be used to effectively determine the order of the process (Cook, 1985). Prewhitening is carried out following the estimation of the ARMA (p,q) coefficients, and converts the tree-ring series to *white noise* (Cook, 1985), calculated in difference equation form as:

$$e_t = I_t - \phi_1 I_{t-1} - \dots - \phi_p I_{t-p} + q_1 e_{t-1} + \dots + q_q e_{t-q} \tag{8}$$

The result is an e_t that represents the contributions of C_t , $D1_t$, and E_t , while $D2_t$ is assumed to be absent (Cook et al., 1990b). The transient effects of the endogenous disturbance pulses are also reduced, and thus foster an increase in fractional common variance in the mean-value function of e_t . Combined with the biweight robust mean for the computation of e_t , an improved estimate of C_t is derived. However, this estimate of C_t , in the form of e_t , is lacking the natural persistence that is related to climate and tree physiology (Fritts, 1976; Hughes et al., 1982; Cook and Kairiukstis, 1990), and during climatic reconstruction the persistence from the original climate calibration variable must be added back to the reconstructed series.

In order to completely model the common signal within an ensemble, it is necessary to estimate the common persistence structure among all detrended tree ring series. A pooled estimate of autoregression is computed directly from lag-product sum matrices of the ensemble, including information on persistence both within and among series (Cook, 1985). This pooling procedure is quite robust for dealing with high levels of out-of-phase fluctuations among series that are the result of endogenous disturbances, and is easy to apply for pure AR models. However, it is not easily applied to the ARMA modeling procedure due to the highly nonlinear MA coefficients (Cook, 1985; Cook et al., 1990b). A final tree-ring chronology (I_t) can be created, following the estimation of the common signal components as outlined above, by convolving the pooled AR coefficients with the e_t upon the selection of appropriate starting values (Cook, 1985).

Retaining low frequency variance

Perhaps the prime concern regarding tree-ring standardization procedures is the potential for a loss of low-frequency climate information due to “over-standardizing.” An important paper by Cook et al. (1995b) discussed the need for maximizing individual segment length of tree-ring series, due to a maximum retention of variance of about two-thirds the length of the segment. The segment length curve means that chronologies comprised of trees averaging 100 years in length, even if the overall chronology extends for 3,000 years, will only retain low frequency information on about a 66 year timescale. Aggressive detrending can remove even more of the low frequency variance, resulting in high-frequency “white noise” time series. This has become hugely important in recent debate about global warming, because of the need for placing recent trends in the context of natural variability (Cook et al., 1995a).

Two recent, very important and controversial papers, Mann et al. (1999) and Esper et al. (2002), used tree ring data for reconstructing Northern Hemisphere temperature for the past millennium. At the center of the controversy were the standardization of tree ring data and the retention

of low-frequency variance. The Mann reconstruction shows an extremely marked warming trend in the recent century that is virtually unmatched for the past 1,000 years. There is little evidence of a Medieval Warm Period (MWP) or a Little Ice Age (LIA) signature, such as has been indicated from prior tree ring studies (Jacoby and D'Arrigo, 1989). The Esper reconstruction uses entirely different standardization procedures designed to maximize low-frequency variability, and only long individual tree ring series from selected sites. This reconstruction shows a millennium of more prolonged changes with a clear MWP and LIA. The debate over these two reconstructions, their underlying methodologies and their implications for the global warming debate, has served a valuable purpose for the paleoclimate community. It is through such, often heated, exchanges that major advances are made in the field.

There is little doubt that tree rings have played an important role in the global warming debate, due to their ability to reproduce high resolution, absolutely dated records of climate over broad geographic areas and for the past millennium and beyond. This should continue to be the case for the foreseeable future, largely due to new techniques that will allow for use of previously unworkable species and environments. For example, recent improvements in isotopic research are allowing scientists to explore variability in the tropical regions that have not previously been allowed through traditional ring width analyses (White et al., 1994). These authors produced high-resolution oxygen 18 ($\delta^{18}\text{O}$) records from a *Podocarpus neriifolius* section from north Thailand, a tree with very faint growth rings that are difficult to crossdate visually. Since the species can attain ages that are estimated to be greater than three or four centuries (Buckley et al., 1995), it is a species worth pursuing. The $\delta^{18}\text{O}$ tracks the seasonal cycle in the growth for a period of 6 years following deliberate wounding in 1992, and re-sampling in 1999. The changes in $\delta^{18}\text{O}$ are related to changes in relative humidity and gives hope for pursuing dendroclimatic studies with species that have proven difficult with traditional methods (Poussart et al., 2004). This and other dendrochemistry techniques will ensure that tree rings will continue to provide new and important information to the paleoclimate community for many decades to come.

Examples of tree ring dating

The earliest examples of using tree rings for dating purposes, as noted at the beginning of this chapter, were in the American Southwest. Douglass' tree ring research on wood from pueblo ruins across the region firmly established the history of occupation and abandonment, and more importantly placed these human events in the context of past climate (Douglass, 1929; Haury, 1962). The dating of a charred beam from one such ruin, marked as HH-39, resulted in the extension of Douglass' Flagstaff living-tree chronology back to A.D. 1237. By continuing to date pueblos across the region, Douglass pieced together a regional chronology back to A.D. 700, and dated hundreds of pueblos against this regional master. This work was immensely important for archaeology as it established the occupation history across much of the American Southwest. Since that time, dendrochronology has been used as a dating tool for buildings and other wooden structures throughout the world.

Any event that kills or leaves its mark in the woody tissue of a tree, or groups of trees, can be dated to the precise year or season in which the event occurred. This principle has been used to date a wide range of geomorphic events. For

example, Yamaguchi (1985) dated volcanic eruptions on Mount St. Helens and determined that there was a 2-year interval between prehistoric events. Palmer et al. (1988) built a floating chronology from trees buried by the eruption of Mt. Taupo in New Zealand, and fixed a tentative date by radiocarbon dating the outer rings. McCord (1990) used flood scars in addition to ring width data to reconstruct past hydrology and maximum flow events. Jacoby et al. (1992) dated past landslides under Lake Washington in Seattle, using the rings of trees that had been submerged, still rooted, for the past thousand years. Wiles et al. (1995) used tree rings to date glacial fluctuations in Alaska, as trees "pushed" by glacial moraines are scarred in the season of the injury. Dendrochronology has proven to be a valuable dating tool for a wide range of events. Future application of dendrochronology as a dating tool is only limited by the imagination of those who would use it.

Brendan M. Buckley

Bibliography

- Akaike, H., 1974. A new look at the statistical model identification. *IEEE Trans. Autom. Control*, **AC-19**, 716–723.
- Baillie, M.G.L., 1982. *Tree-Ring Dating and Archaeology*. Chicago: The University of Chicago Press.
- Box, G.E.P., and Jenkins, G.M., 1970. *Time Series Analysis: Forecasting and Control*. San Francisco: Holden-Day.
- Buckley, B.M., Barbetti, M., Watanasak, M., D'Arrigo, R.D., Boonchirdchoo, S., and Sarutanon, S., 1995. Dendrochronological investigations in Thailand. *IAWA J.*, **16**(4), 393–409.
- Cook, E.R., 1985. *A time series analysis approach to tree-ring standardization*. PhD Thesis, University of Arizona.
- Cook, E.R., 1987. The decomposition of tree-ring series for environmental studies. *Tree-Ring Bull.*, **47**, 37–59.
- Cook, E.R., 1990. A conceptual linear aggregate model for tree rings. In Cook, E.R., and Kairiukstis, L.A. (eds.), *Methods of Dendrochronology: Applications in the Environmental Sciences*. Dordrecht: Kluwer, pp. 98–104.
- Cook, E.R., and Kairiukstis, L.A. (eds.), 1990. *Methods of Dendrochronology: Applications in the Environmental Sciences*, 1st edn. Dordrecht: Kluwer, 394pp.
- Cook, E.R., and Peters, K., 1981. The smoothing spline: A new approach to standardizing forest interior tree-ring width series for dendroclimatic studies. *Tree-Ring Bull.*, **41**, 45–53.
- Cook, E.R., and Peters, K., 1997. Calculating unbiased tree-ring indices for the study of climatic and environmental change. *The Holocene*, **7**(3), 359–368.
- Cook, E.R., Briffa, K., Shiyatov, S., and Mazepa, V., 1990a. Tree-ring standardization and growth-trend estimation. In Cook, E.R., and Kairiukstis, L.A. (eds.), *Methods of Dendrochronology: Applications in the Environmental Sciences*. Dordrecht: Kluwer, pp. 104–123.
- Cook, E.R., Shiyatov, S., and Mazepa, V., 1990b. Estimation of the mean chronology. In Cook, E.R., and Kairiukstis, L.A. (eds.), *Methods of Dendrochronology: Applications in the Environmental Sciences*. Dordrecht: Kluwer, pp. 123–133.
- Cook, E.R., Bird, T., Peterson, M., Barbetti, M., Buckley, B., D'Arrigo, R., and Francey, R., 1992. Climatic change over the last millennium in Tasmania reconstructed from tree rings. *The Holocene*, **2**, 205–217.
- Cook, E.R., Buckley, B.M., and D'Arrigo, R.D., 1995a. Decadal-scale oscillatory modes in a millennia-long temperature reconstruction from Tasmania. In Martinson, D.G., Bryan, K., Ghil, M., Hall, M.M., Karl, T.R., Sarachik, E.S., Sorooshian, S., and Talley, L.D. (eds.), *Natural Climate Variability on Decade-to-Century Time Scales*. Washington, D.C.: National Academy Press, pp. 523–532.
- Cook, E.R., Briffa, K.R., Meko, D.M., Graybill, D.A., and Funkhouser, G., 1995b. The 'segment length curse' in long tree-ring chronology development for palaeoclimatic studies. *The Holocene*, **5**(2), 229–237.
- Digby, J., and Wareing, P.F., 1966. The relationship between endogenous hormone levels in the plant and seasonal aspects of cambial activity. *Ann. Bot.*, **30**, 608–622.

- Douglass, A.E., 1914. A method of estimating rainfall by the growth of trees. In Huntington, E. (ed.), *The Climatic Factor*. Washington, D.C.: Carnegie Institute of Washington Publications, pp. 101–122.
- Douglass, A.E., 1919. *Climatic Cycles and Tree Growth*. Washington, D.C.: Carnegie Institution of Washington, Publication No. 289
- Douglass, A.E., 1928. *Climatic Cycles and Tree Growth, vol. II, A Study of the Annual Rings of Trees in relation to Climate and Solar Activity*. Washington, D.C.: Carnegie Institute of Washington, Publication No. 289.
- Douglass, A.E., 1929. The secret of the Southwest solved by talkative tree-rings. *Natl. Geogr. Mag.*, **56**(6), 736–770.
- Emerson, J.D., and Strenio, J., 1983. Boxplots and batch comparisons. In Hoaglin, D.C., Mosteller, F., and Tukey, J.W. (eds.), *Understanding Robust and Exploratory Data Analysis*. New York: Wiley, pp. 58–96.
- Eriksson, M., 1989. *Integrating Forest Growth and Dendrochronological Methodologies*. PhD Thesis, University of Minnesota.
- Esau, K., 1977. *Anatomy of Seed Plants*, 2nd ed. New York: Wiley, 550pp.
- Esper, J., Cook, E.R., and Schweingruber, F.H., 2002. Low-frequency signals in long tree ring chronologies for reconstructing past temperature variability. *Science*, **295**, 2250–2253.
- Fritts, H.C., 1966. Growth-rings of trees: Their correlation with climate. *Science*, **154**(3752), 973–979.
- Fritts, H.C., 1969. *Bristlecone pine in the White Mountains of California: Growth and Ring-width Characteristics (Papers of the Laboratory of Tree-Ring Research No. 4)*, Tucson, AZ, USA: University of Arizona Press.
- Fritts, H.C., 1976. *Tree Rings and Climate*. London: Academic Press. 567pp.
- Guiot, J., 1987. Standardization and selection of the chronologies by the ARMA analysis. In Kairiukstis, L., Bednarz, Z., and Feliksik, E. (eds.), *Methods of Dendrochronology - I*. Laxenburg, Warsaw: International Institute for Applied Systems Analysis, and the Polish Academy of Sciences-Systems Research Institute, pp. 97–105.
- Haury, E., 1962. HH-39: Recollections of a dramatic moment in southwestern archaeology. *Tree-Ring Bull.*, **24**, 11–14.
- Hughes, M.K., Kelly, P.M., Pilcher, J.R., and LaMarche, V.C. Jr. (eds.), 1982. *Climate From Tree Rings*. Cambridge, UK: Cambridge University Press. 223pp.
- Jacoby, G.C., 1989. Overview of tree-ring analysis in tropical regions. In Baas, P., and Vetter, R.E. (eds.), *Growth Rings in Tropical Woods*. IAWA Journal New Series, **10**, pp. 99–108.
- Jacoby, G.C., and D'Arrigo, R.D., 1989. Reconstructed Northern Hemisphere annual temperature since 1671 based on high-latitude tree-ring data from North America. *Clim. Change*, **14**, 39–59.
- Jacoby, G.C., Williams, P.L., and Buckley, B.M., 1992. Tree-ring correlation between prehistoric landslides and abrupt tectonic events in Seattle, Washington. *Science*, **258**, 1621–1623.
- Jacoby, G.C., Sheppard, P.R., and Sieh, K.E., 1998. Irregular recurrence of large earthquakes along the San Andreas fault: Evidence from trees. *Science*, **241**, 196–199.
- Kozłowski, T.T., 1971. *Growth and Development of Trees*, vol. 1. New York and London: Academic Press, 443pp.
- Mann, M.E., Bradley, R.S., and Hughes, M.K., 1999. Northern Hemisphere temperatures during the past millennium: Inferences, uncertainties, and limitations. *Geophys. Res. Lett.*, **26**, 759–762.
- Mariaux, A., 1981. Past efforts in measuring age and annual growth in tropical trees. In Bormann, F.H., and Berlyn, G. (eds.), *Age and Growth Rate of Tropical Trees: New Directions for Research*. New Haven, CT, USA: School of Forestry and Environmental Studies, Yale University.
- McCord, V.A.S., 1990. *Augmenting Flood Frequency Estimates Using Flood-Scarred Trees*, Tucson, AZ: PhD Dissertation, University of Arizona, 182pp.
- Mosteller, F., and Tukey, J.W., 1977. *Data Analysis and Regression*, Reading, MA, USA: Addison-Wesley.
- Nobel, P.S., 1974. *Introduction to Biophysical Plant Physiology*. San Francisco: W.H. Freeman and Company.
- Palmer, J.G., Ogdén, J., and Patel, R.N., 1988. A 426-year floating tree-ring chronology from *Phyllocladus trichomanoides* buried by the Taupo eruption at Pureora central North Island, New Zealand. *J. R. Soc. N.Z.*, **18**(4), 407–415.
- Poussart, P.F., Evans, M., and Schrag, D.P., 2004. Resolving seasonality in tropical trees: Multi-decade, high-resolution oxygen and carbon isotope records from Indonesia and Thailand. *Earth Planet. Sci. Lett.*, **218**, 301–316.
- Salisbury, F.B., and Ross, C.W., 1992. *Plant Physiology*, 4th edn. Belmont, California: Wadsworth Publishing Co. 682pp.
- Samish, R.M., 1954. Dormancy in woody plants. *Annu. Rev. Plant Physiol.*, **5**, 183–204.
- Sheldrake, A.R., (1971). Auxin in the cambium and its differentiating derivatives. *J. Exp. Bot.*, **22**, 735–740
- Sheppard, P.R., and Jacoby, G.C., 1989. Application of tree-ring analysis to paleoseismology: Two case studies. *Geology*, **17**, 226–229.
- Shigo, A.L., (1984). Compartmentalization: A conceptual framework for understanding how trees grow and defend themselves. *Annu. Rev. Phytopathol.*, **22**, 189–214.
- Stahle, D.W., Cleaveland, M.K., Blanton, D.B., Therrell, M.D., and Gay, D.A., 1998. The lost colony and Jamestown droughts. *Science*, **280**, 564–567.
- Stokes, M.A., and Smiley, T.L., 1968. *An Introduction to Tree-Ring Dating*. Chicago: University of Chicago Press.
- Webb, G.E., 1983. *Tree Rings and Telescopes: The Scientific Career of A.E. Douglass*. Tucson: The University of Arizona Press. 242pp.
- White, J.W.C., Lawrence, J.R., and Broecker, W.S., 1994. Modeling and interpreting D/H ratios in tree rings: A test case of white pine in the northeastern United States. *Geochimica et Cosmochimica Acta*, **58**(2), 851–862.
- White, P.S., (1979). Pattern, process and natural disturbance in vegetation. *Bot. Rev.*, **45**, 229–299.
- Wiles, G.C., Calkin, P.E., and Post, A., 1995. Glacier fluctuations in the Kenai Fjords, Alaska, U.S.A.: An evaluation of controls on iceberging glaciers. *Arct. Alp. Res.*, **27**(3), 234–245.
- Worbes, M., 1985. Structural and other adaptations to long-term flooding by trees in central Amazonia. *Amazonia*, **9**(3), 459–484.
- Worbes, M. 1995. How to measure growth dynamics in tropical trees - A review. *IAWA J.*, **16**(4), 337–352.
- Yamaguchi, D.K., 1985. Tree-ring evidence for a two-year interval between recent prehistoric explosive eruptions of Mount St. Helens. *Geology*, **13**(8), 554–557.

Cross-references

- [Climate Variability and Change, Last 1,000 years](#)
- [Dendroclimatology](#)
- [Little Ice Age](#)
- [Medieval Warm Period](#)
- [Time-Series Analysis of Paleoclimate Data](#)

DATING, FISSION-TRACKS

Fission-track (FT) dating is a powerful and relatively simple method of radiometric dating that has made a significant impact on understanding the thermal history of the upper crust, the timing of volcanic events, and the source and age of archaeological artifacts. Unlike most other dating techniques, FT dating is uniquely suited to dating low-temperature thermal events with common accessory minerals over a very wide geological range (as much as 0.004–4,000 Ma and typically 0.1–2,000 Ma). The method involves using the number of fission events produced from the spontaneous decay of ^{238}U in common accessory minerals to date the time of rock cooling below closure temperature. Most current research using FT dating focuses on: (a) thermochronological studies of orogenic belts, (b) provenance and thermal analysis of basin sediments, (c) age control of poorly dated strata including tephrochronology, and (d) archaeological applications.

FT dating relies on the formation of damage zones, or fission tracks, in a crystal from the spontaneous decay of uranium. Unlike other isotopic dating methods, the daughter

used in FT dating is an effect in the crystal rather than a daughter isotope. As such, the technique requires measurement of the parent isotope (^{238}U) and the daughter-like effect (fission tracks shown in Figure D17). Note that uranium and thorium also disintegrate through the process of α -decay through decay series that result in lead isotopes; this forms the basis of U-Pb dating. Both processes of nuclear disintegration (α -decay and fission) occur simultaneously, but the rate of fission decay ($\lambda_f = \sim 7 \times 10^{-17} \text{ yr}^{-1}$ for ^{238}U) is about 1 million times less frequent than that of α -decay ($\lambda_a = 1.5 \times 10^{-10} \text{ yr}^{-1}$ for ^{238}U). The vast majority of fission events in typical Phanerozoic rocks are from ^{238}U , due to its abundance and spontaneous fission decay rate.

Fission tracks are produced and retained in a number of minerals and solid materials (Fleischer et al., 1975), but currently the only routinely dated minerals are apatite, zircon, and to a lesser extent titanite (sphene). Fission-track dating is possible in garnet, pyroxene, and epidote among other common rock forming minerals, but these are rarely exploited. The nearly exclusive use of apatite and zircon in current studies stems from their very common occurrence as accessory minerals in sedimentary rocks and granites and their metamorphic equivalents. Fission tracks are also routinely measured in volcanic glass (Westgate, 1989).

Fission tracks form when two sub-equal fission fragments recoil and create end-to-end zones of disorder in the crystal lattice. This zone, long considered a result of the charged fission fragments stripping electrons from adjacent atoms (i.e., the “ion spike” mechanism of Fleischer et al., 1975), is a narrow zone, or trail, in the crystal. Once enlarged by chemical etching, typical tracks in apatite are ca. 14 μm and ca. 12 μm long in zircon, although they shorten when brought to elevated temperatures. While these zones of disorder were recognized in the late 1950s (Silk and Barnes, 1959), it was not until the early 1960s when researchers at General Electric in Schenectady, NY realized that these tracks were susceptible to

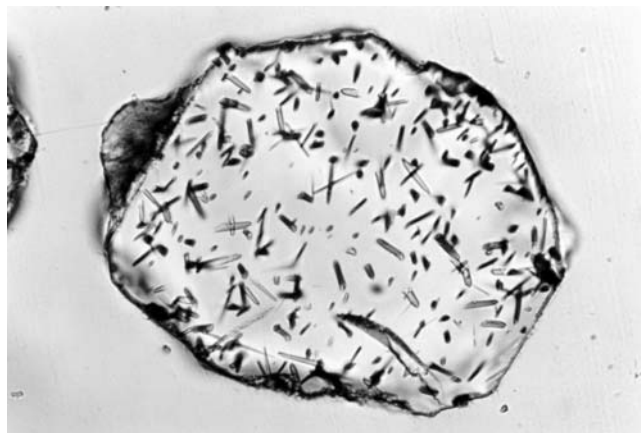


Figure D17 Photograph of fission tracks in a detrital apatite crystal from the mid-Cretaceous Jackass Mountain Formation, British Columbia. This apatite has a mid-Tertiary cooling age, so the strata were buried, heated, and then cooled in the Eocene. This apatite is about 150 μm across and horizontal tracks are about 12 μm long. This apatite crystal is mounted in epoxy, polished so an internal surface is exposed, and the chemically etched tracks are oriented in all directions, so some are short vertical track tips, while others are nearly horizontal and a full length can be seen. (Photo: J. I. Garver.)

chemical attack, and as such could be etched large enough to be visible with an ordinary optical microscope (i.e., 200x to 1,500x – Fleischer et al., 1975). Thus the technique of FT dating was born and the first reported fission track ages on ordinary minerals were reported soon thereafter (Fleischer et al., 1964).

The FT methodology is technically simple and requires little in the way of specialized equipment (Naeser, 1976). Fission-track ages are now routinely determined in many academic laboratories and several commercial labs throughout the world. The most common approach to FT dating is through the external detector method using a *zeta* calibration factor, which is based on repeated measurements of standards of known age (Fleischer and Hart, 1972; Hurford and Green, 1983). For an age to be calculated, the spontaneous track density (or fossil track density – ρ_s) and the uranium concentration in a single crystal need to be determined. Together these measurements are accomplished by mounting the crystals in a solid medium (epoxy or Teflon[®]), polishing to expose crystal interiors, and then enlarging the tracks with a chemical etchant. The measurement of uranium is typically accomplished by neutron irradiation, but other methods could in principle be used. In this step, the mount is covered with an external track detector (mica or plastic), and irradiated in a nuclear reactor with slow neutrons. This thermal neutron irradiation causes uranium to fission in the minerals of interest, and some fission fragments are ejected into the overlying external track detector. Because the thermal cross-section for fission of ^{235}U is large relative to that for ^{238}U , the track density on the external detector is a function of the thermal neutron flux (or fluence) and the concentration of ^{235}U . To determine total uranium, the ratio of $\text{U}^{235}/\text{U}^{238}$ is assumed to be constant. In practice, therefore, an age is determined by measuring the spontaneous track density (ρ_s), the induced track density (ρ_i), and the thermal fluence as determined from a dosimeter with known uranium concentration (ρ_d).

Fission tracks are constantly formed through the spontaneous fission of uranium, but only the ^{238}U isotope contributes significantly to the total accumulated fission tracks due to its abundance and relative decay rate (Roberts et al., in Fleischer et al., 1975). Tracks are only preserved in the crystal when temperatures fall below the annealing temperature (similar to the closure temperature of other isotopic systems), which varies from mineral to mineral and is the basis for determining low-temperature vs. time histories. While the details of closure temperatures are complicated, they are approximately 100–110 $^{\circ}\text{C}$ for typical apatite, ca. 230–250 $^{\circ}\text{C}$ for zircon, and ca. 300 $^{\circ}\text{C}$ for titanite. As with other isotopic systems, closure temperature is affected by the rate of cooling (Gallagher et al., 1998).

Tracks anneal by shortening or disappearing if they reside at elevated temperatures for an appreciable time. As such, it was discovered that the statistical distribution of track lengths could be used to understand the amount of time a sample spent at temperatures sufficient to anneal or partially anneal tracks. The partial annealing zone (PAZ) is generally regarded as the temperature range at which fission tracks are progressively shortened. Quantitatively this is regarded as the temperatures between 90% annealing and 10% annealing. At temperatures below the PAZ, fission tracks are more or less fully retained. At temperatures above the PAZ, fission tracks are formed, but then fully erased over geological times.

The relationship between track-length distributions and annealing rates is well established for apatite, but no other

minerals (Gallagher et al., 1998). For apatite, crystal composition controls annealing rates and the relative proportions of Cl, F, and OH appear to be most important. In laboratory and geological experiments, F-rich apatite is more resistant to annealing than Cl-rich apatite. For zircon, radiation damage appears to be the major influence on annealing rates and temperatures (Brandon et al., 1998).

The FT technique is widely used in understanding the thermal structure of the upper crust, especially in orogenic settings. Studies include understanding the offset of faults, the local exhumation of rock and regional denudation, the relationship between exhumation and orogenic relief, and the large-scale movement of rock in deforming orogenic wedges. These exhumation studies of the tectonic evolution of orogenic belts are perhaps the most widely used application of the FT technique. FT dating is also widely applied to understanding sedimentary basins and specific applications are aimed at deciphering the thermal history of sedimentary basins in the context of the thermal maturation of oil generation, and the provenance of sedimentary detritus (Naeser et al., 1989; Garver et al., 1999). Fission-track dating has also seen a variety of other uses including dating burnt coal seams, diatreme eruption, volcanic ash deposition, meteoritic impacts, tektite strewn fields, and the formation of precious metal deposits (Wagner and Van den Haute, 1992; Fleischer, 1998). In archeological applications, FT dating has been used to understand the age and source of obsidian artifacts, and fire-heated implements and hearthstones. The technique has also been used to date uranium-doped glasses and vases that are less than 200 year old (Fleischer et al., 1975; Wagner and Van den Haute, 1992).

John I. Garver

Bibliography

- Brandon, M.T., Roden-Tice, M.R., and Garver, J.I., 1998. Late Cenozoic exhumation of the Cascadia accretionary wedge in the Olympic Mountains, northwest Washington State. *Geol. Soc. Am. Bull.*, **100**, 985–1009.
- Fleischer, R.L., 1998. *Tracks to Innovation: Nuclear Tracks in Science and Technology*. New York: Springer-Verlag, 193pp.
- Fleischer, R.L. and Hart, H.R., Jr., 1972. Fission track dating: Techniques and problems. In Bishop, W.W., Miller, J.A., and Cole, S. (eds.), *Proc. of Burg Wartenstein Conf. on Calibration of Hominoid Evolution*. Edinburgh: Scottish Academic Press, pp. 135–170.
- Fleischer, R.L., Price, P.B., and Walker, R.M., 1964. Fission-track ages of zircon. *J. Geophys. Res.*, **69**(22), 4885–4888.
- Fleischer, R.L., Price, P.B., and Walker, R.M., 1975. *Nuclear Tracks in Solids*. Berkeley CA: University of California Press, 605pp.
- Gallagher, K., Brown, R., and Johnson, C., 1998. Fission track analysis and its application to geological problems. *Annu. Rev. Earth and Planetary Sci.*, **26**, 519–572.
- Garver, J.I., Brandon, M.T., Roden-Tice, M., and Kamp, P.J.J., 1999. Erosional denudation determined by fission-track ages of detrital apatite and zircon. In Ring, U., Brandon, M.T., Willett, S., and Lister, G. (eds.), *Exhumation Processes: Normal Faulting, Ductile Flow, and Erosion*. London: Geological Society of London Special Publication 154, pp. 283–304.
- Hurford, A.J., and Green, P.F., 1983. The zeta age calibration of fission-track dating. *Chem. Geol. (Isotope Geoscience Section)*, **1**, 285–317.
- Naeser, C.W., 1976. Fission-track dating. *U.S. Geological Survey, Open File Report* 76–190, 65pp.
- Naeser, N.D., Naeser, C.W., and McCulloh, T.H., 1989. The application of fission-track dating to the depositional and thermal history of rocks in sedimentary basins, in thermal history of sedimentary basins, methods and case histories. In Naeser, N.D., and McCulloh, T.H. (eds.), New York: Springer, pp. 157–180.
- Silk, E.C.H., and Barnes, R.S., 1959. Examination of fission fragment tracks with an electron microscope. *Phil. Mag.*, **4**, 970–972.
- Wagner, G.A., and Van den Haute, P., 1992. *Fission-Track Dating*. Dordrecht: Kluwer, 285pp.
- Westgate, J.A., 1989. Isothermal plateau fission-track ages of hydrated glass shards from silicic tephra beds. *Earth Planet. Sci. Lett.*, **95**, 226–234.

Cross-references

Dating, Radiometric Methods
Uranium-Series Dating

DATING, LUMINESCENCE TECHNIQUES

Introduction

Quartz, feldspar, zircon, and calcite are the most important minerals for luminescence geochronology, and they can produce several different types of luminescence. Thermally stimulated luminescence (or thermoluminescence, TL) is a cold light that is emitted upon heating minerals to a temperature (e.g., 450 °C) below that of incandescence (Aitken, 1985). Photon-stimulated luminescence (PSL) is emitted when minerals are exposed to visible or infrared wavelengths of light, and radioluminescence (RL) is emitted during mineral exposure to nuclear radiation (e.g., gamma rays). Other terms for PSL dating are optical dating or OSL dating. Through optical filters the PSL signal is observed at shorter wavelengths (higher photon energies) than the stimulating light (“anti-Stokes” emission). TL dates the last heating and last daylight exposure, while PSL and RL date only the last exposure to daylight, providing a family of related dating procedures for heated and unheated sediments (Aitken, 1998; Wagner, 1998; Krbetschek et al., 2000; Troja and Roberts, 2000).

Both quartz and potassium-(K)-rich feldspars are ubiquitous in natural sedimentary deposits, and both emit strong TL and PSL signals (and RL in the case of K-feldspars). The TL and PSL emissions from zircon crystals and from volcanic and archeological glass have also been used for dating, but these materials are more problematic and restricted in their application. The age range of luminescence sediment dating is from decades to 500 kyr (or 800 kyr in favorable circumstances, Berger, 1995), depending on the particular mineral and luminescence signal used. The significance of luminescence geochronometry lies not in the attainable precision (usually 5–15% at 1 σ), but in the ability to date directly, in calendar years, the burial or heating age of ubiquitous minerals, and to exceed the usual range (35–40 kyr) of ¹⁴C dating.

Concepts

Luminescence dating methods are based on the principles of radiation dosimetry. Buried sediments and artifacts are exposed to a continuous flux of low level, ambient ionizing radiation (α , β , and γ nuclear radiations, plus a smaller intensity of cosmic radiation). These generate a *dose rate* (D_R) (absorbed energy/unit time: Gray (Gy) kyr⁻¹, 1 Gy = 1 J kg⁻¹) that gives rise to the production of free charge carriers (electrons and holes) inside the mineral grains. Some electrons and holes are trapped at crystal lattice defects for several millions of years (having long *lifetimes* because they reside at energetically deep

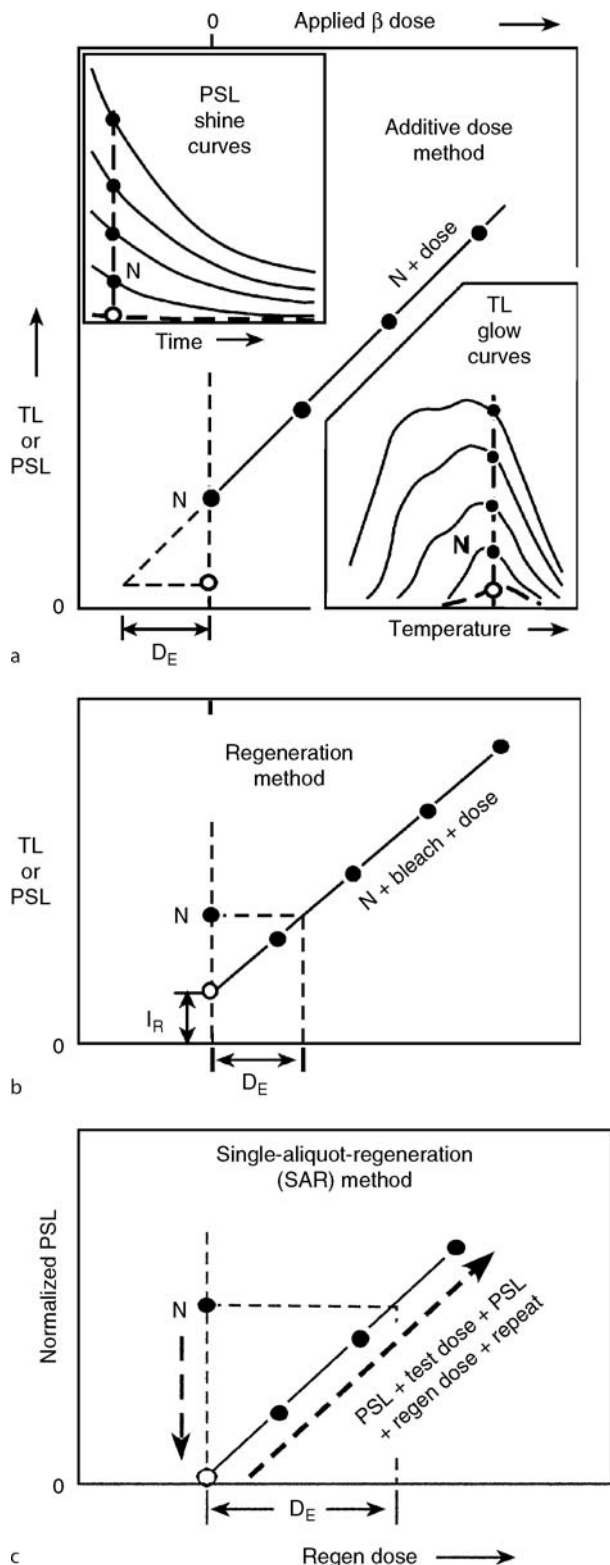


Figure D18 (a) Form of the luminescence readout curves for PSL and TL, and the construction of an “additive-dose” response curve to obtain a D_E value. N means unirradiated or “natural.” The open circle represents either a light-resistant signal (TL) or a combination of such with a

traps). However, in some zircons and some feldspars (e.g., of volcanic origin), significant leakage (by “quantum mechanical tunneling”) of electrons occurs from deep traps at ambient temperature, resulting in *anomalous fading* of the TL and PSL signals, causing under-estimation of age. The population of deeply-trapped electrons increases with further irradiation and hence with time, though filling of the traps leads to “saturation” and an upper age limit, dependent upon several variables. One may call this method “trapped electron” dating.

When the electron traps are emptied in the laboratory, TL, PSL or RL emissions arise from the recombination of ejected electrons with holes trapped at “luminescence centers” (ionized crystal defects, usually chemical impurities). The type of center determines the color of the luminescence. Typical impurities in quartz generate ultraviolet emissions, sometimes red; those in feldspars, violet, yellow-orange, and sometimes deep red. The intensity of the luminescence at a particular color (or wavelength) is proportional to the time since traps were last emptied. The clock-zeroing event is either daylight exposure (which empties light-sensitive traps) or heating (which empties all traps).

Historical development

The physics-concept foundations for luminescence dating were laid only in the late 1940s. TL dating of fired ceramics was first successfully developed at the University of Oxford (England) during the 1960s and 1970s (Aitken, 1985), following some pioneering work in North America during the 1950s and 1960s using TL from rock minerals for characterization. The potential for TL dating the last exposure of unheated sediments to sunlight was first recognized by Morozov and Shelkopyas (1968–1971) at the Ukrainian Academy of Sciences in Kiev. TL sediment dating was then developed into practical, accurate procedures at Simon Fraser University (Canada) in the late 1970s and early 1980s, with the use of laser-light (or photon) stimulated luminescence (PSL) also originating at Simon Fraser University, in 1985.

Since then there have been two major methodological developments in PSL dating: (a) the introduction and refinement of “single-aliquot” procedures, and (b) their extension to single grains. Previously, multiple aliquots were required for measurement of each D_E (equivalent dose – see below) value. The first attempt to obtain a PSL D_E value from only two aliquots was made at the University of Wales (UK) in 1991, and subsequently modified for true single-aliquot dating at the University of Edinburgh (UK) in 1996. The single-aliquot approach was first adapted for single grains (of feldspar) at the University of Quebec at Montreal (Canada) in 1994. The first successful use of single aliquots and single grains for dating employed sand-sized quartz grains from Australia in 1998. Methods were later refined to a universally adopted single-aliquot procedure (Murray and Wintle, 2000). The essentials of “single-grain” dating of quartz were clearly outlined by Olley et al. (1999). Single-grain dating of thousands of sand-sized grains per sample is now automated, using a micro-focused, scanning, high powered laser (Duller et al., 1999).

thermal-transfer signal (PSL). This “residual” is always proportionately much smaller for PSL than for TL. (b) An interpolation procedure for obtaining a D_E value. I_R is near zero for PSL. (c) A simplified illustration of the regeneration procedure used for single aliquots or single grains. The required heating steps are omitted for clarity.

Techniques

To derive an age in calendar years, two independent tasks are performed: (a) the measured natural luminescence signal is compared to that induced in subsamples (“aliquots”) by known radiation doses from calibrated laboratory sources (usually β or γ), thus scaling the natural signal and yielding an *equivalent dose* (D_E) or *paleodose* value (in Gy); and (b) the burial dose rate D_R is calculated from elemental measurements on portions of the sample grains and the surrounding sediments. This yields a luminescence age = D_E/D_R , independent of any other geochronometric technique.

Dose rate

Assuming secular equilibrium, one can use the concentrations of the ^{40}K , ^{238}U -series, and ^{232}Th -series radionuclides (Aitken, 1985) along with measured inter-grain water concentration, plus estimates of cosmic-ray flux (at the sample’s altitude, depth, and geomagnetic latitude) to calculate the dose rate. Inter-granular water absorbs ionizing radiation, so it must be estimated. Thick-source α -particle-counting can be used to provide the absorbed energy contributions from the several α -emitting nuclides in the U and Th decay series. This is more accurate than methods (e.g., neutron activation) that determine the concentration only of the parent nuclides, if there is or has been radon escape or other disequilibria, but is not generally as accurate as high-resolution γ spectrometry. If disequilibrium occurs (e.g., in sandy fluvial deposits), it is more likely to be in the ^{238}U series than in the ^{232}Th series.

If sand-sized grains are dated, then corrections (Aitken, 1985) must be made for the attenuation of β particles (2 mm range) across the dimensions of the grains. The effects of α particles (20 μm range) can be removed by HF-acid etching, or ignored for feldspars. The internal K concentration of feldspars needs to be determined in representative populations of grains. This is most accurately accomplished by the use of SEM-EDX (scanning-electron-microscopy-energy-dispersive-X-ray analysis) discrete-grain mapping for K (usually the highest-K grains are the brightest luminescence emitters).

Equivalent dose

Quartz and K-rich feldspar grains are selected most often for dating, using either sand-sized (e.g., 100–300 μm diameters) grains or the fine-silt (5–10 μm) fraction. The traditional multi-aliquot method for measuring D_E values is to extrapolate a dose-response curve to its intersection with some residual (light-insensitive) TL or PSL value (Figure D18a). This is done at each of successive intervals in the readout curves. In TL, a “plateau” in such D_E values can indicate a thermally stable signal. Alternatively, an interpolation procedure (Figure D18b) can be more precise, but most samples exhibit a change in slope (“sensitivity change”) of the regeneration curve compared to the additive-dose curve that is difficult or impossible to accommodate.

The single-aliquot-regeneration (SAR) technique (Murray and Wintle, 2000) overcomes the effect of such a sensitivity change by the use of a constant “test dose” (Figure D18c) and consequent normalization of signals. Relatively high precision in SAR D_E values can be attained. The greatest advantage of the single-aliquot and single-grain procedures is their potential ability to sort aliquots/grains that have not been exposed to much daylight from those that have (Figure D19). Age overestimates would be expected with the application of multi-aliquot methods to most fluvial (and similar) deposits.

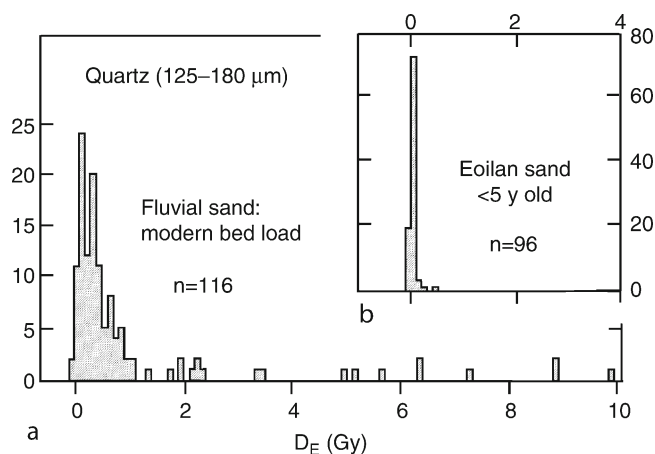


Figure D19 Histograms of D_E values for small (60–100 grains) single aliquots of quartz grains from (a) a modern fluvial bed-load sand, and (b) a modern (<5 year) eolian sand (modified from Olley et al., 1998).

Applications

Applications of multi-aliquot TL and PSL procedures have been reviewed by Aitken (1998) and Berger (1995). Applications of single-aliquot and single-grain PSL procedures have been reviewed by Lian and Roberts (2006), Murray and Olley (2002), Stokes and Walling (2003) and Wallinga (2002). Applications are being extended to types of deposits and regions of the globe (e.g., polar) previously considered impracticable. Quartz SAR can now date eolian deposits precisely at the century and decadal scale (e.g., special issue of *Quaternary Science Reviews*, 2003, 22(10–13)). However, unless the dose rates are unusually low (e.g., $<1 \text{ Gy kyr}^{-1}$), the upper age range of quartz remains ca. 150 kyr. Feldspars can be used further back in time, but more testing is required to understand how universal anomalous fading is, and what can be done about it.

Conclusions

There has been a rapid evolution in luminescence dating technique since the introduction of PSL methods in 1985, attaining a revolution in capability with the development of single-grain techniques. Remaining problems concern how to interpret histograms of SAR D_E values, and how to finesse internal age-consistency checks. Some approaches involve isolation and testing of properties of PSL signals having different lifetimes (so-called “fast,” “medium,” and “slow” components in quartz PSL). There is increasing interest in extracting the red emissions from feldspars to overcome the perennial problem of anomalous fading.

Glenn W. Berger

Bibliography

- Aitken, M.J., 1985. *Thermoluminescence Dating*. London, UK: Academic Press, 349pp.
 Aitken, M.J., 1998. *An Introduction to Optical Dating*. Oxford, UK: Oxford University Press, 262pp.
 Berger, G.W., 1995. Progress in luminescence dating methods for Quaternary sediments. In Rutter, N.W. and Catto, N.R. (eds.), *Dating Methods for Quaternary Deposits*. GEOtext2, St. John’s, NFLD: Geological Association of Canada, pp. 81–104.

- Duller, G., Boettler-Jensen, L., Murray, A., and Truscott, A., 1999. Single grain laser luminescence (SGLL) measurements using a novel automated reader. *Nucl. Instrum. Methods Phys. Res. B*, **155**, 506–514.
- Krbetschek, M.R., Trautmann, T., Dietrich, A., and Stolz, W., 2000. Radioluminescence dating of sediments: Methodological aspects. *Radiat. Meas.*, **32**, 493–498.
- Lian, O.B., and Roberts, R.G., 2006. Dating the Quaternary: progress in luminescence dating of sediments. *Quatern. Sci. Rev.*, **25**, 2449–2468.
- Murray, A.S., and Olley, J.M., 2002. Precision and accuracy in the optically stimulated luminescence dating of sedimentary quartz: A status review. *Geochronometria*, **21**, 1–15.
- Murray, A.S., and Wintle, A.G., 2000. Luminescence dating of quartz using an improved single-aliquot regenerative-dose protocol. *Radiat. Meas.*, **32**, 57–73.
- Olley, J.M., Caitcheon, G.C., and Murray, A.S., 1998. The distribution of apparent dose as determined by optically stimulated luminescence in small aliquots of fluvial quartz: Implications for dating young sediments. *Quat. Sci. Rev.*, **17**, 1033–1040.
- Olley, J.M., Caitcheon, G.C., and Roberts, R.G., 1999. The origin of dose distributions in fluvial sediments, and the prospect of dating single grains from fluvial deposits using optically stimulated luminescence. *Radiat. Meas.*, **30**, 207–217.
- Stokes, S., and Walling, D.E., 2003. Radiogenic and isotopic methods for the direct dating of fluvial sediments. In Piegay, H., and Kondolf, M. (eds.), *Tools in Fluvial Geomorphology: A Handbook for Geologists, Hydrologists, Engineers, Biologists, and Planners*. New York, NY: Wiley, pp. 233–267.
- Troja, S.O., and Roberts, R.G., 2000. Luminescence dating. In Cilberto, E., and Spoto, G. (eds.), *Modern Analytical Methods in Art and Archaeology*. New York, NY: Wiley, pp. 585–640.
- Wagner, G.A., 1998. *Age Determination of Young Rocks and Artifacts*. New York, NY: Springer, 453pp.
- Wallinga, J., 2002. Optically stimulated luminescence dating of fluvial deposits: A review. *Boreas*, **31**, 303–322.

Cross-references

Dating, Radiometric Methods
 Mineral Indicators of Past Climates
 Potassium-Argon/Argon-Argon Dating
 Quaternary Climate Transitions and Cycles
 Radiocarbon Dating
 Sedimentary Indicators of Climate Change
 Uranium-Series Dating

DATING, MAGNETOSTRATIGRAPHY

Introduction

Magnetostratigraphy refers to the application of the well-known principles of stratigraphy to the observed reversal pattern of the geomagnetic polarity recorded in rock sequences. This recording of the ancient geomagnetic field reveals successive intervals with alternating normal and reversed polarity in lava piles and sedimentary sequences. Normal means parallel to the present-day magnetic field (north-directed), while reversed refers to an antipodal south-directed field (Figure D20). As a rule, it appears that these successive intervals of different polarity show an irregular thickness pattern, caused by the irregular duration of the successive polarity zones. This produces a “bar code” in the rock record, which often is distinctive. Polarity intervals have a mean duration of some 250,000 years during the last 35 Myr, but large variations have occurred, ranging from 20,000 yr to several Myr. Once a calibrated “standard” or a so-called “geomagnetic polarity timescale” (GPTS) is constructed, dated by radiometric methods and/or by orbital tuning, one can match the observed pattern with this standard and hence derive the age of

the sediments. Magnetostratigraphy and correlation to the GPTS has become a standard tool in Earth sciences, especially because it can be applied to a wide variety of rock types (volcanic, sedimentary) and in different kinds of environment (continental, lacustrine, marine, etc.) (Butler, 1992; Opdyke and Channell, 1996; Tauxe, 1998; McElhinny and McFadden, 2000).

Historical background

In 1269, Petrus Peregrinus carried out a remarkable series of experiments with a spherical lodestone from which he deduced the dipolar nature of the magnet, and he reported his conclusions in his famous “*Epistola de Magnete*,” which is regarded as the first scientific treatise ever written. He also found that the magnetic force is both strongest and vertical at the poles, and became the first person to formulate the law that like poles repel and opposite poles attract. William Gilbert in 1600 published the results of his experimental studies in magnetism in “*De Magnete*.” He investigated the variation in inclination over the surface of a spherical lodestone and concluded for the first time that “*magnus magnes ipse est globus terrestris*” (the Earth itself is a great magnet). Apart from the spherical form of the Earth, magnetism was the first physical property to be attributed to the body of the Earth as a whole. The physical property of gravitation came 87 years later with the publication of Newton’s “*Principia*.”

Paleomagnetic studies of igneous rocks provided the first reliable information on reversals. In 1906, Brunhes observed lava flows magnetized in a direction approximately anti-parallel to the present geomagnetic field, and suggested that this was caused by a reversal of the field itself, rather than by some physicochemical property (“self-reversal” mechanism) of the rock. Matuyama (1929) demonstrated that young Quaternary lavas were magnetized in the same direction as the present field (normal polarity), whereas older lavas were consistently magnetized in the opposite direction. In the earliest 1950s, Jan Hospers and his supervisors were the first to realize that the polarity of lava flows could be a powerful stratigraphic correlation tool (Irving, 1988). Improved techniques and the undertaking of extensive investigations in many parts of the world have drastically increased the amount of paleomagnetic information and have now provided us with a very detailed GPTS (e.g., Berggren et al., 1995).

The geomagnetic polarity time scale

For the construction of the “bar code” pattern of magnetic polarity intervals, scientists rely on two fundamentally different records of geomagnetic polarity history: the marine magnetic anomaly record and the magnetostratigraphic record. Surveys over the ocean basins carried out from the 1950s onward found linear magnetic anomalies, parallel to mid-oceanic ridges, using magnetometers towed behind research vessels. During the early 1960s, it was suggested and soon confirmed that these anomalies resulted from the remanent magnetization of the oceanic crust. This remanence is acquired during the process of seafloor spreading, when uprising magma beneath the axis of the mid-oceanic ridges cools through its Curie temperature (The temperature at which thermal vibrations overcome the tendency toward magnetization. The Curie temperature of magnetite is 575°C) in the ambient geomagnetic field, thus acquiring its direction and polarity (Figure D21). The continuous process of rising and cooling magma at the ridge results in magnetized crust of alternating normal and reversed polarity, which

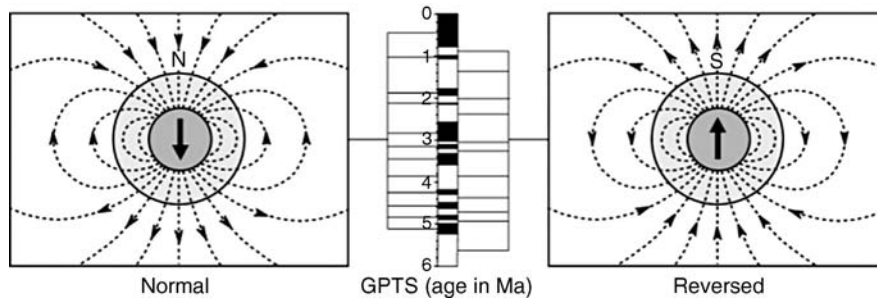


Figure D20 Schematic representation of the geomagnetic field of a geocentric axial dipole (“bar magnet”). During normal polarity of the field, the average magnetic north pole is at the geographic north pole, and a compass aligns along magnetic field lines, the inclination being positive (downward-directed) in the northern hemisphere and negative (upward-directed) in the southern hemisphere. Conversely, during reversed polarity, the compass needle points to the south, and the inclination is negative in the northern and positive in the southern hemisphere. In the GPTS, periods of normal and reversed polarity are represented by black and white colored intervals, respectively.

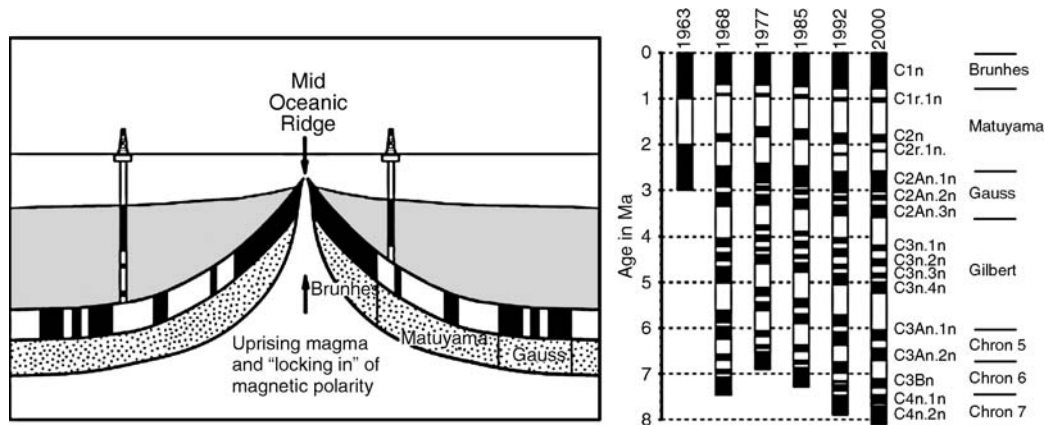


Figure D21 Formation of marine magnetic anomalies during seafloor spreading (*left*). The oceanic crust is formed at the ridge crest, and while spreading away from the ridge it is covered by an increasing thickness of oceanic sediments. The black (white) blocks of oceanic crust represent the original normal (reversed) polarity thermoremanent magnetization (TRM) acquired upon cooling at the ridge. The black and white blocks in the drill holes represent normal and reversed polarity depositional remanent magnetization (DRM) acquired during deposition of the marine sediments. Development of the geomagnetic polarity time scale (GPTS) through time (*right*) shows that the initial assumption of periodic behavior (in 1963) was soon abandoned as new data became available. The first modern GPTS based on marine magnetic anomaly patterns was established in 1968. Subsequent revisions show improved age control and increased resolution.

produces a slight increase or decrease of the measured field: the marine magnetic anomalies. It was also found that the magnetic anomaly pattern is generally symmetric on both sides of the ridge, and, most importantly, that it provides a wonderfully continuous tape recording of the geomagnetic reversal sequence.

The template of magnetic anomaly patterns from the ocean floor has remained central for constructing the GPTS from the late Cretaceous onward (110–0 Ma). In addition, combined magnetostratigraphic, biostratigraphic and radiometric results of deep-sea sediments (see *Deep Sea Drilling Project (DSDP)*) and land-based sections have confirmed and refined the general validity and accuracy of the GPTS.

The development of the GPTS continuously shows increasing detail and gradually improved age control through time (Figure D21). Periods of a predominant (normal or reversed) polarity are called chrons, and the four youngest ones are named after persons: Brunhes (normal) who suggested field reversal, Matuyama (reversed) who proved this, Gauss (normal) who mathematically described the field, and Gilbert (reversed) who discovered that the Earth itself is a big magnet. Chrons may contain short intervals of opposite polarity called

subchrons, which are named after the locality where they were discovered, e.g., the normal Olduvai subchron within the Matuyama reversed chron is named after Olduvai Gorge in Tanzania, and the Kaena reversed subchron within the Gauss normal chron after Kaena Point on Hawaii. Older periods of the GPTS have been subdivided into polarity chrons designated by the numbers correlated to oceanic magnetic anomalies (e.g., C3An). The polarity chron nomenclature has evolved progressively to accommodate additional polarity chrons (C3An.1n; C3An.2n) according to the chron nomenclature described in Cande and Kent (1992).

The oldest substantial parts of oceanic crust remaining in ocean basins are late Jurassic in age. The determination of the GPTS for older intervals must therefore be done by paleomagnetic studies of exposed stratigraphic sections on land. The best age control for Mesozoic sequences is in the late Triassic, where magnetostratigraphy in combination with cyclostratigraphy on long scientific drill cores in the continental sequences of the Newark basin (NE America) provided a high-resolution, astronomically calibrated GPTS (Kent and Olsen, 1999). For other Mesozoic and older periods, our knowledge of the polarity

time scale is much less refined and various intervals are still subject to lack of data and often to serious controversies.

The latest development in constructing a GPTS comes from orbital tuning of the sediment record (see *SPECMAP*). It differs essentially from the conventional GPTS where reversal ages are interpolated between a limited number of (radiometric) calibration points, essentially assuming constant sea-floor spreading between these calibration points. In the astronomically tuned time scale, each reversal boundary – or any other geological boundary for that matter, e.g., biostratigraphic datum levels or stage and epoch boundaries – is dated individually (Hilgen et al., 1997). This directly determines the age of each reversal and has important consequences for (changes in) spreading rates of plate pairs. Instead of having to assume constant spreading rates between calibration points, one can now accurately determine these rates and changes therein. The astronomical polarity time scale (APTS) has provided a breakthrough in dating of the geological record and has significantly increased our understanding of, for example, the (paleo)climate system, since astronomical tuning relies on deciphering and understanding environmental changes driven by climate change, which in turn is orbitally forced (see *Cyclic sedimentation (cyclothem)*).

The paleomagnetic signal in rocks

The ancient geomagnetic field can be reconstructed from its recording in rocks during the geological past (Figure D22). Almost every type of rock contains magnetic minerals, usually iron (hydr)oxides or iron sulfides. During the formation of rocks, these magnetic minerals (or more accurately: their magnetic domains) statistically align with the then ambient field, and will subsequently be “locked in,” preserving the direction of the field as a natural remanent magnetization (NRM): the paleomagnetic signal.

The type of NRM depends on the mechanism of recording the geomagnetic signal, and we distinguish three basic types: TRM, CRM and DRM. A thermoremanent magnetization

(TRM) is the magnetization acquired when a rock cools below the Curie temperature of its magnetic minerals, thereby “locking” the magnetic domains to be statistically aligned along the ambient field. A chemical remanent magnetization (CRM) is the magnetization acquired when a magnetic mineral grows through a critical “blocking diameter” or grain size. Below this critical grain size, the magnetic domains align along the ambient field, while above it the field will be locked and the acquired remanence may again be stable over billions of years. A depositional remanent magnetization (DRM) is the magnetization acquired when magnetic grains, either of detrital origin or formed in situ, and thus already carrying a TRM or CRM, are deposited. The grains statistically align with the ambient field as long as they are in the water column or in the soft water-saturated topmost layer of the sediment. Upon compaction and dewatering, the grains are mechanically locked – somewhere in a “lock-in depth zone” – and will preserve the direction of the ambient field.

As a rule, the total NRM is composed of different components. Ideally, the primary NRM, i.e., originating from the time of rock formation, has been conserved, but often this original signal is contaminated with or even completely overprinted by remanence components acquired later in its geological history, e.g., through weathering, metamorphism or tectonics. A parasitic component or partial overprint can be removed through “magnetic cleaning” or demagnetization procedure. This implies that rock samples must be subjected to various methods to remove stepwise any unwanted or non-original magnetization component, either by increased temperatures or alternating magnetic fields. Such experiments are routine paleomagnetic lab procedures, aimed at retrieving the original acquired magnetization that has recorded the ancient geomagnetic field.

Applications

Once the originally recorded geomagnetic field has been retrieved with sufficient accuracy and resolution, the successive intervals of normal and reversed polarity can be faithfully

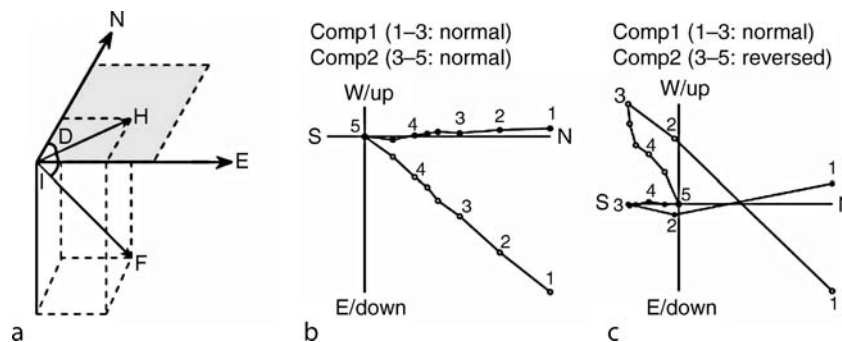


Figure D22 (a) The magnetic field on any point on the Earth's surface is a vector (F) that possesses a component in the horizontal plane called the horizontal component (H), which makes an angle (D) with the geographical meridian. The declination (D) is an angle from north measured eastward ranging from 0° to 360° . The inclination (I) is the angle made by the magnetic vector with the horizontal. By convention, it is positive if the north-seeking vector points downward and negative if it points upward. (b,c) To resolve the different magnetic components that can be acquired in a rock during its geological history, rock samples are subjected to a process of stepwise demagnetization. The standard method for presentation and analysis of the results of demagnetization are called Zijderveld diagrams (after Zijderveld, 1967). Changes in vector magnetization during demagnetization involve both its direction and its intensity. The orthogonal vector Zijderveld diagrams show both the changes in intensity and direction. The endpoint of the vector measured after each demagnetization step is then projected both onto the horizontal plane (*closed symbols*) and onto the vertical plane (*open symbols*). Difference vectors (*lines between end points*) then show the behavior of the total vector upon stepwise removal (see text for details).

determined. Still, there are several prerequisites for a successful application of magnetostratigraphy as a dating technique for sedimentary sequences. First, one needs to have some approximate (biostratigraphic or radiometric) age control. In addition, the studied sequences must represent a sufficiently long period to reveal a characteristic pattern of reversals (generally >1 Myr during the Cenozoic) to be unambiguously correlated with the standard (GPTS or APTS). Naturally, hiatuses and major changes in sedimentation rate may obscure this “fingerprint” pattern, requiring careful field observations, while sampling resolution must ideally be several times higher than the shortest duration of (sub)chrons (20–30 kyr).

Often, these prerequisites can be met, enabling magnetostratigraphy to be used as a high-resolution age control, which has several fundamental advantages over other dating techniques. Contrary to biostratigraphic datum levels, reversals of the geomagnetic field are fundamentally globally-synchronous events, within sampling resolution, allowing precise correlations between different parts of the world and between different environments (marine vs. continental), regardless of their fossil content or radiometric suitability. Hence, it can be used to study the paleogeographic evolution and paleoclimatic history of different regions over long periods. This enables, for example, detailed continental-marine correlations and hence the determination of synchrony or diachrony of regional or even global paleoclimatic or tectonic events. A successful correlation of the recorded polarity pattern to the GPTS provides accurate ages of every recognized reversal boundary, allowing establishment of rates and rates of change.

Finally, it is very compelling to combine magnetostratigraphy with astrochronology, because (a) it can be used to improve the age control of the standard GPTS (since individual reversals can be directly dated), and (b) it can help increase the resolution of the standard GPTS, since subchrons shorter than 30 kyr are generally not resolved from the ocean floor anomaly patterns. The reliability and completeness of the GPTS is not only crucial for geochronological purposes, but also for understanding the long-term statistical properties of the geomagnetic field.

Wout Krijgsman and C. G. Langereis

Bibliography

- Berggren, W.A., Kent, D.V., Aubry, M.-P., and Hardenbol, J., 1995. *Geochronology, Time Scales and Global Stratigraphic Correlations: A Unified Temporal Framework for an Historical Geology*. Tulsa, Oklahoma: SEPM, Special Volume, **54**, 386pp.
- Brunhes, B., 1906. Recherches sur la direction d'aimantation des roches volcaniques. *J. Phys.*, **5**, pp. 705–724.
- Butler, R.F., 1992. *Paleomagnetism, magnetic domains to geologic terranes*. Boston, USA: Blackwell Scientific Publications, 319pp.
- Cande, S.C., and Kent, D.V., 1992. A new geomagnetic polarity time-scale for the Late Cretaceous and Cenozoic. *J. Geophys. Res.*, **97**, 13917–13951.
- Hilgen, F.J., Krijgsman, W., Langereis, C.G., and Lourens, L.J., (1997). Breakthrough Made in Dating of the Geological Record. *EOS, Trans. AGU*, **78**, 285–288.
- Irving, E., (1988). The paleomagnetic confirmation of continental drift. *EOS*, **69**, 994–999.
- Kent, D.V., and Olsen, P.E., 1999. Astronomically tuned geomagnetic polarity time scale for the Late Triassic. *J. Geophys. Res.*, **104**, 12831–12842.
- Matuyama, M., 1929. On the direction of magnetization of basalt in Japan, Tyosen and Manchuria. *Japon. Acad. Proc.*, **5**, 203–205.
- McElhinny, M.W., and McFadden, Ph. L., 2000. *Paleomagnetism: Continents and oceans*. San Diego, USA: Academic Press, 386pp.
- Opdyke, N.D., and Channell, J.E.T., 1996. *Magnetic stratigraphy*. San Diego, USA: Academic Press, 346pp.
- Tauxe, L., 1998. *Paleomagnetic principles and practice*. Dordrecht, The Netherlands: Kluwer Academic, 299pp.
- Zijderveld, J.D.A., 1967. Demagnetisation of rocks: Analysis of results. In Collinson, D., Creer, K., and Runcorn S. (eds.), *Methods in Paleomagnetism*. New York, USA: Elsevier, pp. 254–286.

Cross-references

[Cyclic Sedimentation \(Cyclothem\)](#)
[Dating, Biostratigraphic Methods](#)
[Dating, Radiometric Methods](#)
[Deep Sea Drilling Project \(DSDP\)](#)
[Mineral Indicators of Past Climates](#)
[SPECMAP](#)

DATING, RADIOMETRIC METHODS

General principles

The discovery of radioactivity by Henri Becquerel in 1896 had a profound impact not only in the fields of physics and chemistry, but also in the earth sciences. Naturally occurring radioactivity immediately solved the problem of controversy over the Earth's internal heat. Lord Kelvin had used Earth's internal heat to estimate the age of the Earth as being about 20 Myr. This estimate, which assumed that the Earth's internal temperature structure was purely the result of passive heat diffusion since the formation of the planet, was highly unpopular with the geologists of the day, who argued that the processes that they witnessed on the Earth's surface required far more time. In one stroke, an otherwise unknown heat source could be invoked to extend the Earth's apparent age.

Radioactivity was also seen to provide a standard and reliable clock that had not yet existed in the earth sciences. As early as 1904, Rutherford proposed the use of U decay and its production of the newly discovered element, helium, as a method of dating rocks. This oldest of radiometric dating methods, though long abandoned, has made a recent come-back and is in the midst of a renaissance for dating near-surface processes. For an excellent overview of the history of radiometric dating methods and their basic principles, see York and Farquhar (1972) and also Faure (1986).

Radiometric dating methods rely on the presence of naturally occurring radioactive isotopes that decay into stable daughter products. Radioactivity is the process by which unstable atomic nuclei change into more stable and long-lived forms. The most important decay processes for earth scientists involve the expulsion of a ^4He nucleus (alpha particle, or α decay), an electron (β^- decay), or the capture of a free electron by the nucleus (electron capture or K-capture). A rare decay form that, for the purposes of radiometric dating, is equivalent to K-capture, involves the expulsion of a positron from the nucleus (β^+ decay).

These radioactive decay mechanisms involve not only the release of considerable amounts of energy (typically in the neighborhood of 1 million electron Volts or 1 MeV per decay) but they also transform the parent isotope into an isotope of another chemical element. The utility of radioactive decay to the field of geochronology derives from it providing the possibility of detecting either the buildup of decay products or the

decay of radioactive parent isotopes. From laboratory measurements over the past century, it has been possible to measure directly the rate at which radioactive isotopes decay. The energies involved in radioactivity are many orders of magnitude greater than the energies involved in normal chemical processes (typically about 1 eV). Furthermore, the physical scale of the nucleus is tiny compared with the cloud of electrons surrounding the nucleus that are involved in chemical reactions. This leads directly to the first assumption made in all radiometric dating techniques: radioactive decay processes are immune to the effects of chemical reactions or the presence or absence of other atoms.

This is almost certainly true for the α and β decay systems. However, there is a slight caveat with respect to the K-capture decay system, where high pressure can increase the electron density in the vicinity of the nucleus and therefore it can slightly raise the natural decay rate. This effect has been documented for the decay of ^7Be , but for the extremely important decay system involving the decay of ^{40}K into ^{40}Ar , it is not expected to be significant, even for pressures experienced in the upper mantle. In any event, the dating of material involved in the study of paleoclimates will always involve near surface processes, and the possible variability of K-capture decay is not likely to be a concern.

The second critical assumption in radiometric dating is that the process of decay is a random event and that the probability of the decay happening per unit time is a constant. This leads directly to the essential differential equation of radioactivity:

$$\frac{dP}{dt} = -\lambda P \quad (1)$$

where P is the concentration of the parent isotope and λ is called the decay constant. For geologically important isotopes, it is given in units of yr^{-1} . Equation (1) merely states that the rate of decay of a radioactive isotope is a simple linear function of the isotope's concentration. The solution of Equation (1) is given by:

$$P(t) = P_0 e^{-\lambda t} \quad (2)$$

where P_0 is the parent isotope concentration at formation or at zero time. One can also solve Equation (2) for the time that it will take for the parent isotope concentration to be one half of its original value, or its half life ($t_{1/2}$), and this time is given by $\ln(2)/\lambda$. The decay of the parent isotope as a function of half-lives is shown in Figure D23.

Short-lived systems

An important class of radiometric dating methods uses the decay of short-lived radioactive isotopes. In this case, $t_{1/2}$ is much lower than the age of the Earth, and the parent isotope is continually being produced in nature, usually by the action of energetic cosmic rays on the atmosphere or the Earth's surface. Typically, the daughter product is a common isotope and its buildup is not detectable. Instead, the concentration of the parent is measured, and the age equation for this class of methods can be solved from Equation (1) by:

$$t = \frac{1}{\lambda} \ln\left(\frac{P_0}{P}\right) \quad (3)$$

where P is the present day isotope concentration, and P_0 is the concentration at time zero.

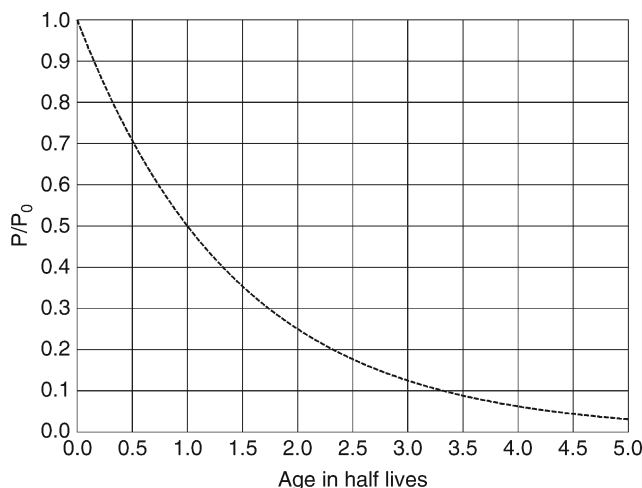


Figure D23 Decay of parent as given by Equation (2).

A critical assumption common to all of these dating methods is that one must know the value of P_0 . Frequently, this is based on the present day production rate of the isotope and it is assumed that this production rate has remained constant through time. Unfortunately, this assumption is often only approximately correct. The Earth's magnetic field strength, which varies significantly over both historical and geological time scales, can modulate the flux of cosmic rays and solar wind particles striking the Earth, and the assumption of constant production rate is not, strictly speaking, correct. However, there are often other methods that can be used to calibrate the parent isotope production rate, such as the use of dendrochronology to calibrate the ^{14}C technique.

From Equation (3), it can be determined that the highest parent isotope concentration is occurring now, and the parent isotope concentration will be lower for older and older samples. Eventually, for material older than about 10 half-lives, the measured concentration will only be less than 1/1,000 of the original value and will be very difficult to estimate accurately. This means that there is a basic time limit for short-lived decay methods, and they are most accurate for relatively young samples (Figure D23).

Ideally, one would like an independent test for, or a correction for, the assumption that the parent isotope's production rate is constant. Using two different parent isotopes as independent chronometers can sometimes achieve this. Specifically, by combining the decay of ^{10}Be and ^{36}Cl , and assuming that their production rates keep the same proportion, it is possible to eliminate uncertainties in the absolute production rate.

Long-lived systems

Typically, for samples that are more than a few half-lives old in short-lived systems, one must employ a different strategy, in which the daughter product of a long-lived radioactive isotope is measured. Such a parent isotope has to exist since the formation of the Earth, and therefore its half-life will be measured in billions of years. Examples of useful isotopes with this property are ^{40}K , ^{87}Rb , ^{147}Sm , ^{235}U , and ^{238}U . For such systems, the ratio of the daughter isotope to the parent isotope in the laboratory is

a monotonically increasing function of the geological age of the sample. The differential equation that governs the buildup of the daughter isotope D is given by:

$$\frac{dD}{dt} = \lambda P \tag{4}$$

As with Equation (1), the rate of daughter product production is a simple linear function of the concentration of radioactive parent (see Figure D24). When combined with the solution to Equation (1), the fundamental equation of long-lived radiometric dating systems results:

$$t = \frac{1}{\lambda} \ln \left(1 + \frac{D}{P} \right) \tag{5}$$

Here D is the present-day concentration of the daughter product that is present in the sample due to radioactive decay, and P is the present-day concentration of the radioactive parent. One of the simplest examples for the use of Equation (5) is for the Rb-Sr chronometer, where P is the concentration of ^{87}Rb and D is the concentration of “radiogenic” ^{87}Sr . “Radiogenic” means that the ^{87}Sr present in the rock is present due to the decay of ^{87}Rb .

Related to the long-lived clocks are a host of systems that, instead of measuring a radiogenic daughter product, measure some effect that slowly increases in the sample either due to in situ radioactive decay or some external source of radiation. Examples include fission track dating, where the “parent” is naturally fissionable ^{238}U and the effects are tracks of crystal damage due to collisions from the fission fragments; thermoluminescence (TL), where the effects are photons released from meta-stable electrons trapped in crystal defects; and cosmic ray exposure ages (e.g., Ne dating), where the effect is a build up of a nucleogenic product from the interaction of energetic cosmic rays. Many of these techniques require the estimation of a radiation dose rate, and some (e.g., TL) have an effective upper limit to the age they can measure. That is, the effect saturates and after a certain amount of crystal damage, no more time can be recorded.

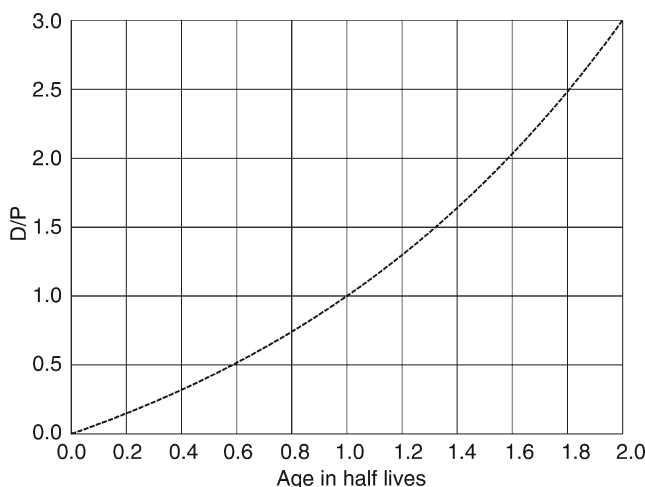


Figure D24 Graphical representation of the solution to Equation (4).

What makes a good clock?

A good geological clock, like a good wristwatch, must run at a known rate and it must record events faithfully. What does that mean in a geological setting? First, the rate of decay of the radioactive parent into the daughter product should be constant over time. This is essentially true for all radiometric systems. Second, the clock must record an event. This involves some chemical reaction that either isolates the parent isotope from the environment, in the case of short-lived systems, or it involves the chemical separation of the parent chemical from the daughter for long-lived systems. This event essentially “resets” the clock. Thereafter, the isotopic clock must record time faithfully, which means that the concentrations of both parent and daughter are only determined by time, and not by the geochemical environment. For example, in the Rb-Sr system, one wants a rock or mineral that has an enrichment of Rb and a removal of all radiogenic Sr from the sample at some zero time, such as at the mineral’s formation. Subsequently, there should be no addition or loss of either Rb or Sr until the sample can be analyzed in the laboratory. Under such conditions, Equation (5) will correctly give the age of the sample.

Unfortunately, perfection in a radiometric clock is hard to achieve. For example, some chronometers, such as Rb-Sr and Sm-Nd often only have small separations of parent isotopes from daughter isotopes during formation or alteration, so there is frequently a significant quantity of daughter isotope present at time zero. However, there are usually other non-radiogenic isotopes of the daughter element (e.g., ^{86}Sr) that can be used to correct for the presence of initial daughter isotope concentrations.

The most powerful short-lived clocks have a homogeneous concentration of the parent isotope until time zero, whereupon the parent is perfectly isolated from the environment and its decay faithfully records geological time. The most powerful long-lived radiometric clocks have extremely efficient separations of parent isotopes from daughter isotopes, thereby clearly resetting the clock at a distinct time. Subsequently, the rock must tenaciously retain both the parent and radiogenic isotopes. Currently, the most widely used short-lived system is based upon the decay of ^{14}C and the event measured is the time for an organic sample to become isolated from the environment’s homogeneous concentration of ^{14}C relative to the stable isotope of carbon, ^{12}C . The most powerful long-lived radiometric systems are based on the decay of ^{40}K to ^{40}Ar , or the decay of U isotopes into isotopes of Pb. In both of these cases, geologically important events can cause extremely large separations of parent from daughter and the retained radiogenic daughter isotopes are relatively easy to identify.

What does an “age” mean?

This is a central philosophical concept in the whole field of radiometric dating that is sometimes not considered by people trying to use this kind of data. Simply put, a radiometric date is a measure of the time needed to go from some known or presumed initial isotopic state to the state measured in the laboratory. For ^{14}C , this will be the time since the sample was isolated from the biosphere’s C reservoir; for Ar, it is the time since the sample started to retain Ar; for Sr, it is the time needed to increase the measured $^{87}\text{Sr}/^{86}\text{Sr}$ ratio above a known initial value. What starts the clock may be the formation of the rock or mineral, as is frequently the case for U-Pb ages of zircons

and Ar ages of young volcanic sanidine crystals, but it might be something more subtle.

Chemical alteration or other metamorphic processes can partially or completely reset the radiometric clock; the apparent age may therefore be the time of metamorphism or a value between formation and alteration. Some chronometers are especially sensitive to temperature, such as fission track, TL, K-Ar dating of feldspars, and the U-Th-He system. In such cases, the age that is measured is often the time since the sample has been cool enough to retain either the buildup of an effect (e.g., crystal damage as in TL and fission track) or the retention of a daughter isotope (e.g., ^4He , ^{40}Ar). Such ages are often referred to as “blocking temperature” ages, where the age represents the time since the sample cooled below the temperature at which the slow resetting of the clock is blocked. This is a particularly powerful concept for the U-Th-He system, where the effective blocking temperatures are extremely low and thus the clock is very useful for measuring the exposure ages of rapidly uplifted and cooled terranes.

Thus, it is important to take into account the context of the material that is being measured when assessing radiometric ages. The sample’s physical form and knowledge of the processes that can “reset the clock” are vital for understanding the numbers produced by the laboratory instruments.

Methodology

For the vast majority of radiometric dating methods, the basic instrument that is used is the mass spectrometer. Mass spectrometers take samples, separate them by mass into constituent isotopes, and measure the relative concentrations of these isotopes with electronic detectors. The instrument consists of three main parts: an ion source in which the sample’s atoms are ionized and accelerated by an electric potential; an analyzer region in which the ions are separated by mass, typically by bending the path of the ions with a magnetic field; and a detector section where the ions are collected and measured.

Ion sources

The first main distinction between different mass spectrometer types occurs at the ion source end. The choice of machine is largely determined by the element to be analyzed and how difficult that atom is to ionize. The elements with the highest ionization potential and that are the most difficult to convert to positive ions are the noble gases. For these elements, the ionization method of choice is the electron bombardment source. In this type of ion source, an electron beam with an energy of about 100 eV bombards the sample, knocking off an electron and converting the sample atom into a positive ion. The sample must be introduced under vacuum into the source in gas form and hence these machines are often called gas source mass spectrometers. This type of ion source is ideal for Ar dating, but it is inconvenient for other metallic radiogenic elements, such as Sr, Rb, or Pb, where it is difficult to convert the sample into a gas.

Fortunately, most metals have much lower ionization potentials than the noble gases. For them, the machines of choice are thermal ionization mass spectrometers (TIMS). In TIMS machines, the sample is chemically separated from other elements and it is dissolved in an aqueous solution. This solution is loaded onto a thin filament of a refractory metal such as tungsten or rhenium. After the filament is loaded into the ion

source and a high vacuum is achieved, an electric current is passed through the filament to heat it to a high temperature. In some cases, the metal is ionized by thermal energy directly on the original filament, but in other cases, the sample is expelled from the original filament as a neutral atom and contacts another hot filament where it is ionized. In any case, the method works using the relatively low energy ($\sim\text{eV}$) available from the white-hot filament material. For positive ion sources, it is also necessary for the sample element to have a significantly lower ionization potential than the filament material, otherwise the ions produced will mostly be from the filament itself. This means that hard to ionize elements like tungsten, hafnium, and the platinum group elements are difficult or impossible to measure using TIMS machines.

Sometimes, however, the tenacity with which sample atoms want to retain electrons can be used as an asset. For osmium, for example, thermal ionization produces a significant number of negative ions, where the sample atoms actually steal electrons from the filament metal. Negative thermal ionization mass spectrometers (NTIMS) are similar in form to TIMS machines, but all of the ion acceleration potentials and magnetic fields must be reversed.

Electron bombardment can ionize anything, but requires that the sample be in gas form. TIMS can be used for most, but not all metals. An ion source that can ionize almost any element and that has gained considerable favor in the past two decades is the inductively coupled plasma (ICP) source (Halliday et al., 1995). This source uses a high-powered radio-frequency induction coil to create plasma in a carrier gas, usually argon. Samples are dissolved in a liquid and introduced into the plasma using an aerosol device. The plasma itself is a gas of argon ions and free electrons that interacts with the sample atoms, ionizing them in the process. The energies available in an ICP source are typically about 5–10 eV, and are therefore intermediate between the ionization energies possible for electron bombardment and TIMS sources.

For in situ ionization of elements within a rock or mineral, the method of choice is frequently a focused ion beam that strikes a sample under vacuum, causing not only ablation of a variety of elements, but also causing ionization as well. This method is the front end of ion microprobes and with advances in analyzer sections and detection systems, these machines can collect precise isotope ratio data on elements in extremely small spots. There are a host of difficulties involved with this approach, not least of which is the fact that many different ion species are produced, thereby requiring an extremely high mass resolving power to separate ions that might only differ in mass by a few parts per thousand. However, the ion microprobe technique has been extremely valuable in geochronology, especially for U-Pb dating of zircons, which frequently have complex mixtures of domains of different ages. The high spatial resolution afforded by ion microprobes is essential, in such cases, for unraveling the detailed histories often recorded within a single grain.

Mass analyzers

Isotopes are separated for analysis by three main types: electrostatic analyzers (e.g., quadropoles), magnetic sector machines, and time of flight instruments. In electrostatic analyzers, the ion beam accelerated out of the source is put through a region of static and oscillating electric fields. It is possible to tune the frequency of the oscillating field such that nearly all isotopes

follow a path that is unstable and causes collision with the sides of the analyzer section. Only isotopes with masses within a narrow range of values follow an oscillating path narrow enough to survive the trip all the way through the analyzer and into the detector section. Electrostatic instruments have several advantages: they are relatively inexpensive; they tolerate a wide range of instrument pressures; and they can be small and light, making them attractive for space science applications. Traditionally, quadropole machines have been comparatively low precision machines because it has been difficult to establish conditions where the selected isotope has perfect transmission all the way from source to detector, making the measurement of extremely accurate isotope ratios harder to achieve than with magnetic sector machines. However, when isotope ratios do not need extremely high accuracy, and when mass resolution requirements are not too high, quadropoles can be very useful. In particular, they seem to be the instrument of choice for U-Th-He dating.

The vast majority of instruments used for precision radiometric dating utilize a magnetic sector analyzer. Simply put, the ion beam is fired into a zone where there is a strong magnetic field at right angles to the direction of flight of the ions. This causes a sideways acceleration, which in turn forces the ions into a circular path. The mass separation occurs because heavy isotopes "corner" this race-track in a wider arc than do light isotopes. This geometry has the additional advantage that there is a natural focusing effect so that ions leaving from a small spot in the ion source are refocused into a similarly small region at the detector. Thus, it is possible to have very high resolving power between similar masses and it is possible to assure that all of the ions of a given mass that leave the source can arrive at the detector. Determining which mass strikes the detector is done by varying the magnetic field, the accelerating voltage, or both.

Ion microprobes sometimes use a time-of-flight mass analyzer. In this type of analyzer, atoms are released from a spot on a sample using a short burst of ions, ionized, and accelerated down a flight tube by an accelerating voltage pulse that is precisely timed to coincide with the formation of the ions. To keep our race-track analogy, the time-of-flight machine is like a straight sprint. The lightest ions rush out in front of the heavier ions. In this type of machine, the mass separation occurs at the detector, which must be able to time resolve individual ions striking within microseconds of each other. This calls for both a sensitive and a fast detector.

Detectors

The simplest kind of ion detector, and the detector of choice when high precision is essential and where sample size is not a limitation, is the Faraday detector. This detector is simply a metal bucket placed at the end of the analyzer, which is in turn electrically connected to an electrometer. An electrometer is an exceptionally sensitive ammeter that converts the ion current entering the bucket into a measurable voltage using a high-sensitivity pre-amplifier and a high resistance feedback resistor. For Faraday detectors, the dominant form of noise is usually thermal or "Johnson" noise caused by thermal agitation within the feedback resistor. The importance of thermal noise can be minimized by having as high a value of resistance as possible, and this is typically 10^{11} Ohms. That means that an ion current of 10^{-11} A will create and output signal of 1 Volt. The performance of Faraday detectors is limited by thermal noise, slow

response due to capacitative effects, and non-ideal behavior in high value resistors. When the sample size is large enough, however, Faraday detectors can have extremely high precision.

The highest precision isotope ratios are measured using multiple collector (MC) Faraday detector systems. In MC-TIMS or MC-ICP machines, having multiple collectors allows for simultaneous collection of different mass isotopes. This eliminates any difficulties caused by instabilities in the source region (especially important for ICP sources), and it is often possible to quickly measure isotope ratios to within a few parts in 10^6 .

When speed or extremely high sensitivity is required, a "multiplier," or related device is almost always used. This might be an electron multiplier directly detecting individual ions, or it could be a so-called Daly detector, which fires off a few electrons from the ion impact site and those electrons in turn cause a flash of light at a scintillation window. The light is then amplified using a photo-multiplier. Multipliers operate as extremely high-gain, low-noise amplifiers by creating an ever-increasing cascade of electrons from a single ion/electron/ photon impact. Multipliers can operate in analog mode, where the incoming ion stream is merely amplified, usually by 10^4 to 10^6 or so. In this mode, the effectiveness at low levels is limited by so-called dark current, where a small current flows through the multiplier with no input signal.

The best performance is achieved when multipliers are operated in ion counting mode, where each incoming ion produces a discrete current pulse that is individually counted, thereby providing for single atom detection. There are limits to the effectiveness of multipliers, however, as they have a fundamental quantum noise limit (so-called "shot noise"). The counting of individual ions is similar to a public-opinion survey, and it is governed by the same Poisson statistics. This means that if, in a given time period, one counts n ions, that rate is representative of the true concentration only to within about the square root of n and the relative error estimate for the measurement will be the reciprocal of the square root of n . Therefore, to be able to measure to within one part in 10^5 , a precision quite achievable for Faraday detectors, about 10^{10} ions must be counted. The maximum count rate for multipliers is typically about 10^6 ions per second, which means a single channel would need to be counted for almost 3 h to match Faraday precision. For most cases, multipliers are used for low intensity ion beams where extremely high precision is not necessary.

Accelerator mass spectrometers

Accelerator mass spectrometers (AMS) are a class of machines that combine many of the techniques mentioned above with extremely high accelerating voltages in the analyzer sections, typically more than 1 million Volts. AMS has especially revolutionized the field of ^{14}C dating by allowing for the direct detection of miniscule quantities of ^{14}C in a vast ocean of other isotopic species or molecular fragments. This is accomplished by analyzing only negative ions (eliminating the ubiquitous ^{14}N) and using the high voltage to smash apart possible interfering molecules by passing the ions through a foil or gas barrier. The combination of methods allows for extremely high sensitivity, and AMS machines are vital for measurement of other rare short-lived species, such as ^{36}Cl .

Analysis and interpretation techniques

Mass spectrometers are excellent at measuring isotope ratios, but it is very difficult to directly measure absolute quantities

of material. For this reason, almost all interpretation involved in radiometric dating involves the use of isotope ratios. In fact, when an absolute concentration measurement is needed, it is usually performed with a technique called isotope dilution, where a known quantity of a rare isotope (a “spike”) is added to a sample and the sample’s concentration is deduced by the ratio of its main isotope to that of the spike. An example of this is in U-Th-He dating, where a known volume of the extremely rare ^3He isotope is added to the ^4He in the sample, and the sample concentration is calculated from the measured $^4\text{He}/^3\text{He}$ ratio.

In some cases, resetting the radiometric “clock” involves such an efficient separation of parent from daughter that at zero time there is essentially no daughter isotope present. In such cases, the daughter to parent ratio can be immediately measured and Equation (5) can be used to calculate an age. However, in most systems, there is a significant presence of daughter isotope in the sample inherited at time zero. A variety of methods that can be generally classified as “isochron” techniques have been developed to allow for the presence of initial daughter isotope and to calculate the amount of daughter present due to the in situ decay, i.e., the radiogenic component. As usual, one of the simplest systems to illustrate this is the Rb-Sr system, where the isotope method is almost always crucial for an accurate age determination.

Isochron analysis in the Rb-Sr system assumes that all of the mineral phases of a rock share the same initial $^{87}\text{Sr}/^{86}\text{Sr}$ ratio, where ^{87}Sr is a daughter product of the radioactive parent ^{87}Rb , and ^{86}Sr is non-radiogenic. Different minerals will tend to have varying Rb/Sr ratios, however. At the limit of zero Rb, the measured $^{87}\text{Sr}/^{86}\text{Sr}$ ratio should be the initial Sr isotopic composition inherited at time zero. For mineral phases with non-zero Rb, the measured $^{87}\text{Sr}/^{86}\text{Sr}$ ratio should be a linearly increasing function of Rb concentration whose slope is in turn a function of the age of the sample. This relationship is given by:

$$\frac{^{87}\text{Sr}}{^{86}\text{Sr}} = \left(\frac{^{87}\text{Sr}}{^{86}\text{Sr}}\right)_0 + (e^{\lambda t} - 1) \frac{^{87}\text{Rb}}{^{86}\text{Sr}} \quad (6)$$

In practice, different mineral separates or chemical leaches are analyzed for Rb and Sr, and the $^{87}\text{Sr}/^{86}\text{Sr}$ ratios are plotted

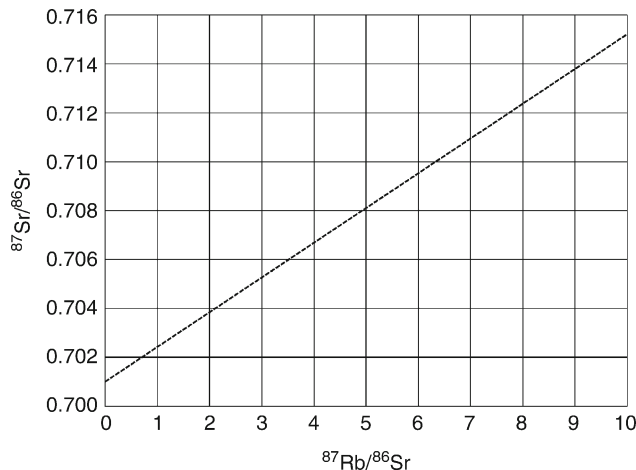


Figure D25 Synthetic isochron plot for a 100 million year old rock with an initial $^{87}\text{Sr}/^{86}\text{Sr}$ ratio of 0.701.

against $^{87}\text{Rb}/^{86}\text{Sr}$. If the isochron assumptions are valid, the data points will form a linear array where the intercept yields the initial Sr isotopic composition and the slope give a measure of the sample’s age (Figure D25).

All of the radiometric techniques have some analogous analysis system and some complexities (e.g., U-Th disequilibrium). Consult the individual topics listed under “Cross-references” for more details.

Chris M. Hall

Bibliography

- Faure, G., 1986. *Principles of Isotope Geology*. New York: Wiley, 608pp.
 Halliday, A.N., Lee, D.-C., Christensen, J.N., Walder, A.J., Freedman, P., Jones, C.E., Hall, C.M., Wen Yi., and Teagle, D., 1995. Recent developments in inductively coupled plasma magnetic sector multiple collector mass spectrometry. *Int. J. Mass Spectrom. Ion Proc.*, **146/147**, 21–33.
 York, D., and Farquhar, R.M., 1972. *The Earth’s Age and Geochronology*. Oxford, UK: Pergamon. 178pp.

Cross-references

- [Beryllium-10](#)
- [Cosmogenic Radionuclides](#)
- [Dating, Dendrochronology](#)
- [Dating, Fission-Tracks](#)
- [Dating, Luminescence Techniques](#)
- [Potassium-Argon/Argon-Argon Dating](#)
- [Radiocarbon Dating](#)
- [Strontium Isotopes](#)
- [Uranium-Series Dating](#)

DEEP SEA DRILLING PROJECT (DSDP)

The Deep Sea Drilling Project (1968–1983) was a 15 year program of exploration of the sediments on the ocean floor and the upper part of the underlying crust, recovering cores from 624 sites throughout the oceans (Figure D26). In 1981, Emiliani described it as “*unquestionably . . . the largest and most successful program of geological investigation ever undertaken by man.*”

Origin

The idea of drilling a hole in the ocean floor originated in 1957 from a group of American geoscientists led by Walter Munk and calling themselves the “American Miscellaneous Society” (Emiliani, 1981; Winterer, 2000). They believed that a major advance in knowledge would result from sampling the Earth’s mantle, and that this could be most effectively accomplished in the ocean where the thickness of the Earth’s crust is minimal. The idea was to drill through the Mohorovičić discontinuity (“the Moho”), the level where a sharp increase in velocity of seismic waves is taken as defining the boundary between the crust and the mantle. This became known as Project Mohole. It was thought that some incidental information on the history of the Earth might also be obtained. At that time most American geologists considered the ocean basins to be permanent ancient features, and the deep sea to be an unchanging environment. It was assumed that its sediments would contain a monotonous 4 billion year history.

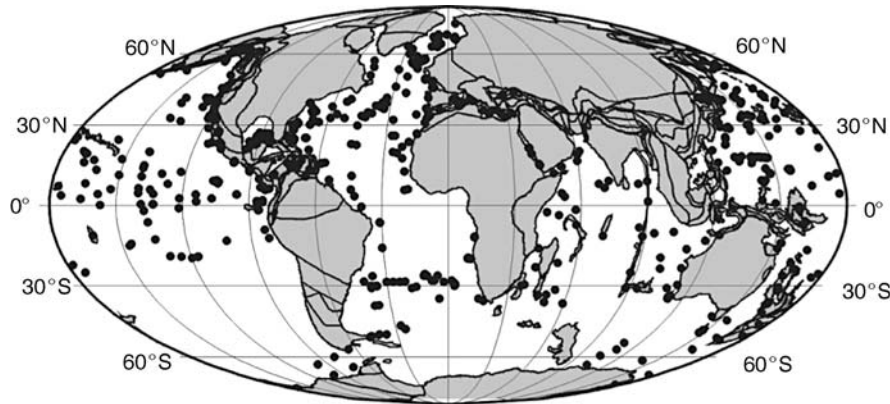


Figure D26 Sites cored by the Deep Sea Drilling Project (1968–1983). Map made using the ODSN plate tectonic mapping program (www.odsn.de).

To drill through the ocean floor in water 4–5 km deep would require that the drilling platform be nearly stationary for long periods of time. Anchors could not achieve this – the platform would need to be a vessel “dynamically positioned” by propellers. Further, it would be necessary to pull up the string of drill pipe, change the drill bit, lower the bit and pipe back down to the sea floor and re-enter the hole in the ocean floor. None of the necessary technology existed at that time.

Tests of the feasibility of drilling into the ocean floor were carried out as “Phase I” of Project Mohole, using a drilling barge, *CUSS I*, in the spring of 1961. For this work *CUSS I* was specially outfitted with outboard propellers and a system for positioning it relative to anchored buoys using radar. Its first test was in 948 m of water off La Jolla, California, penetrating 315 m of sediment. The barge was then moved to a site in 3,558 m of water 40 km east of Guadalupe Island off Baja, California, where it penetrated 170 m of sediment and 13 m of seafloor basalt. Encouraged by these results, Phase II of Project Mohole was to design the drilling vessel to reach the Moho. By 1966 the Phase II engineering had cost \$25,000,000 and the United States (U.S.) Congress cancelled the project.

Other geoscientists, notably Maurice Ewing and Cesare Emiliani, believed that much could be learned from the sedimentary record in the deep sea. At that time sediment cores were limited to the 20 m or so that could be recovered by piston coring devices. Ewing had approached several petroleum companies proposing a program of drilling and coring on a latitude-longitude grid. Emiliani argued that much more could be learned by drilling and recovering long sediment cores designed to investigate the history of the ocean (“Project LOCO”) rather than one single hole into the mantle. A LOCO advisory committee was established with scientists from several oceanographic institutions. Project LOCO was initiated using a small drilling vessel, *SUBAREX*, in November and December of 1963, coring late Tertiary and Quaternary sediments on the Nicaragua Rise.

Four oceanographic institutions, Lamont Geological Observatory (now Lamont Doherty Earth Observatory), Woods Hole Oceanographic Institution, Scripps Institution of Oceanography, and the University of Miami’s Rosenstiel School of Marine and Atmospheric Science then joined together as “JOIDES” (Joint Oceanographic Institutions for Deep Earth Sampling) in 1964. They proposed a program of coring a

transect of holes to depths of several hundred meters on the Blake Plateau east of Jacksonville, Florida. This was accomplished using the drill ship, *CALDRILL*, in 1965, with the Lamont Geological Observatory as the operating institution. A party of shipboard scientists from a variety of institutions was aboard and performed initial analysis of the samples. This was to become the model for future operations. The sediment cores were much more complete than those of the earlier feasibility tests, and it was evident that obtaining long sequences of sediment from the ocean floor was a practical endeavor.

Geology in the 1960s and the Deep Sea Drilling project proposal

In 1966 JOIDES proposed a program of ocean drilling as the “Deep Sea Drilling Project (DSDP)” to the U.S. National Science Foundation. The proposal was for 18 months of drilling on transects across the North Atlantic, South Atlantic, Caribbean Sea and Pacific Oceans. The project was proposed at a critical moment in the history of geology. When Project Mohole had been conceived it was widely accepted that the ocean basins were ancient features, but some geologists noted that there were odd features about the ocean floor: Why was there only an average of 0.5 km of sediment in the deep sea? Why was there no sediment on the ridge that extended down the middle of the Atlantic? Further, in 1954 Emiliani had discovered that oxygen isotope ratios in the shells of deep sea benthic foraminifera indicated the deep ocean to have been warm in the middle Cenozoic, not cold as it is today – challenging the idea of an unchanging environment. The mid-1960s saw the publication of geophysical data suggesting that the ocean basins were young dynamic features. Mapping of the Earth’s magnetic field over the ocean south of Iceland and west of British Columbia and Washington showed alternating bands of magnetization. These magnetic stripes were thought to be produced by rocks that had formed and acquired their magnetization when the Earth’s magnetic field was alternately “normal” (magnetic north near the North Pole) and “reversed” (magnetic north near the South Pole). The hypothesis was that ocean crust formed along the mid-ocean ridge system and then moved away as new crust was emplaced. Ocean crust is returned to the Earth’s mantle along zones of convergence, such as oceanic trenches. In effect, the ocean floor consists of several large rigid plates, with new crust being added on one side, and older crust being lost

on the other side. If these hypotheses of “seafloor spreading” and “plate tectonics” were true, then the scientific assumptions that had gone into the design of Project Mohole were wrong. A single hole into the Earth’s mantle would not have globally applicable results.

The engineering work that had been carried out for Project Mohole became important for the DSDP. The dynamic positioning system designed for the Mohole vessel became a reality, and the technology for re-entering the drill hole on the sea floor was further developed. In 1967, a ship already under construction for Global Marine Corporation was modified to have thruster propellers installed; these can move the ship sideways to help maintain position. The ship’s location on the sea surface, relative to the position of the hole on the seafloor, would be determined using sonic beacons dropped onto the sea floor before starting the drilling procedure. The computer program to carry out the necessary calculation was the first of its kind. The ship was also equipped with the first commercial satellite navigation instrument to assist in finding the site for drilling. A rapid method of recovering cores was developed for use in the project. “Wireline coring” involves dropping a core barrel down inside the drill pipe to latch into the drill bit. The core is taken through an opening in the center of the bit by drilling ahead. When the core barrel is thought to be full, a recovery tool is dropped down on a wireline. On impact with the core barrel, this tool unlatches the core barrel from the drill bit so that it can be hauled back up to the ship. The uniquely outfitted research drill ship was christened *GLOMAR Challenger* in honor of *HMS Challenger*, the British ship that collected samples from the ocean floor from 1872 to 1876 (Figure D27).

The initial phase of DSDP

Scripps Institution of Oceanography was selected by JOIDES to be the operating institution for the DSDP. The *GLOMAR Challenger* sailed from Orange, Texas on 20 June, 1968. The project consisted of nine two-month “Legs.” The first Leg, in the Gulf of Mexico and off the Bahamas, produced a series of surprises. Some of the first coring efforts recovered no sediment at all in the core barrel, but some smears of sediment were found on the drill bit and outside of the core barrel. It turned out that these small smears of sediment contained large numbers of calcareous nannofossils. The nannofossils, carbonate skeletal objects only a few microns across, suddenly became



Figure D27 The *GLOMAR Challenger* (DSDP archive photograph).

one of the most important tools for dating ocean sediments. The second site drilled was “Challenger Knoll” – one of the hills on the Sigsbee Abyssal Plain that floors the deep Gulf of Mexico. One of the cores recovered was oil-saturated sediment, and other cores showed that the Knoll was the top of a salt dome. This discovery showed that petroleum could be found in the deep sea, a revolutionary idea at the time. It also meant that a safety review procedure was needed to ensure that no sites that might cause pollution or endanger the ship would be drilled. Off the Bahamas, cores of early Cretaceous (120 million year old) sediment consisted of black shales rich in organic carbon, indicating that the deep sea had been anoxic at times in the past, a condition that geochemists at the time considered impossible. Leg 1 also drilled to “Horizon A,” a prominent seismic reflector that extends throughout much of the North Atlantic and that had been thought to represent the Cretaceous-Tertiary boundary. It turned out to be Eocene cherty turbidite.

Leg 2 was a transect across the North Atlantic from the U.S. to Africa, intended to be a test of the seafloor spreading hypothesis. Horizon A was drilled at several sites but drilling was stopped by hard layers of middle Eocene chert. Except at three sites, the chert layers prevented drilling into the basement. Evidence for seafloor spreading was favorable but not conclusive. However, the extent of chert accompanied by layers of abundant diatom and radiolarian remains in the central North Atlantic was a mystery. Today such deposits form only in upwelling regions in the polar oceans, along the equator, and along the western margins of the continents. How they came to be deposited in what was the middle of the North Atlantic at that time remains an unsolved puzzle even today. Leg 2 also made the discovery that carbonate ooze could be underlain by red clay. The boundary between carbonate ooze found in shallower depths today, and red clay, which is deposited in greater depths, had been discovered in modern sediments in the 1920s. It was interpreted as representing the level at which the rain of carbonate shells from planktonic organisms living in the upper ocean encounters carbonate-corrosive deep ocean waters, and was termed the “calcium carbonate compensation depth (CCCD).” In 1968 it was thought that the CCCD was either a pressure-induced phenomenon or the top of frigid bottom waters emanating from the Antarctic. The presence of red clay beneath carbonate ooze was contrary to the notion of subsidence of the sea floor away from the mid-ocean ridges and was interpreted as reflecting tectonic movement, a change in the depth of the CCCD, or a change in organic productivity. It was concluded that the latter was most likely.

Leg 3 was a transect across the South Atlantic from Africa to South America and yielded a most spectacular result. No chert was present and the holes were continuously cored to the basaltic basement. It became evident that the sediments immediately overlying the ocean crust were younger toward the Mid-Atlantic Ridge. A plot of the age of oldest sediment versus distance from the ridge crest produced a straight line indicating that the age of the ocean floor in the South Atlantic was a linear function of distance from the crest of the mid-ocean ridge. Although many geophysicists already believed in seafloor spreading and plate tectonics, it was the results of Leg 3 that convinced the geological community. The impact of Leg 3 on the history of geology was the serendipitous result of the concurrent development of a revolutionary hypothesis and the appropriate instrument – the *GLOMAR Challenger* – to test it. Leg 3 also confirmed that large fluctuations of the CCCD had taken place in the South Atlantic. The shipboard

party proposed that there had been vertical motions of the entire sea floor of 1 km or more.

In Leg 4, the DSDP investigated the Caribbean. The purpose was to recover complete reference sections rich in the fossils, particularly planktonic foraminifera, used for global stratigraphic correlation. Most of the information on the stratigraphic distribution of these fossils came from the margins of the Caribbean Basin, notably from Trinidad and Venezuela. The Caribbean was also interesting because its structure appears to be intermediate between continent and ocean basin. The expert stratigraphic micropaleontologists who were on board for this coring program were surprised that the stratigraphic sections in the Caribbean Basin were much less complete than along the margins. Much of the sediment had been deposited below the CCCD and contained no calcareous fossils at all. Synthesis of the CCCD records from this and earlier Legs suggested that it was related not to organic productivity or vertical motions of the seafloor but to changes in the water masses in the deep sea. The “floor” of the Caribbean was found to consist of basalt sills of late Cretaceous age, although older rocks were known from some of the Antilles islands. The origin of the Caribbean remained enigmatic.

The *GLOMAR Challenger* planned to explore the eastern Pacific by a multi-leg north-south transect. However, it was found that much of the stratigraphic record in the northern part of the transect had been destroyed by dissolution of the carbonate sediment. Plans were quickly changed to substitute an east-west transect in hopes of obtaining a more complete record. This showed that the location and strength of the equatorial upwelling system reflected not only the postulated northwestward movement of the Pacific Plate, but other less well-understood factors. Attempts to sample the oldest ocean crust in the western Pacific were unsuccessful, with the drilling often being stopped by layers of chert.

The results of Phase 1 of the DSDP are summarized in reports in Anonymous (1975).

The extensions of the DSDP

The DSDP continued with a series of proposals from JOIDES providing for extensions funded as amendments to the contract from NSF. From its beginning, DSDP had a unique structure for selecting scientific topics to be investigated. JOIDES selected drill sites using advisory panels composed of scientists from a number of institutions. In 1971 the DSDP was placed under the direction of a scientist, M. N. A. Peterson, as Project Director. From then on, the entire program was guided by scientists at the working level.

The first extension, Phase 2 of the DSDP, was for 30 months and almost immediately resulted in a major discovery. Seismic profiles off eastern North America showed a peculiar feature in some areas, reflectors that cut across strata but paralleled the sea floor. The suspicion was that these “bottom simulating reflectors” might represent the base of a layer containing gas hydrates. Gas hydrates are ices in which a cage of water molecules surrounds a gas molecule, usually methane. They are stable solids at temperatures above the freezing point of water and under the high pressures produced by several hundred meters or more of water. Leg 11 drilled a section on the Blake Outer Ridge, between the United States and Bermuda. The cores contained white ices, which rapidly decomposed. The discovery of gas clathrates in the deep sea had a number of implications. Originally it was thought that they might serve as seals for reservoirs of methane in the deep sea (as they do

in Siberia), and might be a major natural resource. Calculations of the volume of gas that might be trapped beneath and within hydrates indicated that these might be the largest deposits of methane on Earth although it was not clear how they might be exploited. They also serve to cement and stabilize sediment on the continental slopes. If gas clathrates were to suddenly decompose as a result of warming of the deep ocean, for example, slopes might become unstable, resulting in massive submarine landslides. These topics are actively being explored today.

It was always planned that after each extension, the program would return to the original problem of sampling the Earth’s mantle, but the difficulties of such a task became ever more apparent as experience was gained in drilling into the deep sea floor. An important problem was re-entry into the hole on the sea floor. The basic engineering design had been produced as a study for Project Mohole, and on Leg 15 in the winter of 1970–1971, the first successful re-entry was accomplished. The procedure involves setting a large steel cone on the sea floor, and drilling through a hole in its center until the drill bit must be changed. The drill string is then hauled back up to the ship and the bit changed. Sonar and a television camera are inserted into the drill bit and the drill string is lowered to the sea floor. The sonar seeks reflections from reflectors on the re-entry cone, and the ship is guided manually over it. The final location is determined by the television camera, and when the drill bit appears to be directly over the hole, it is dropped into the cone and, with luck, re-enters the hole in the sea floor. Over the years, this procedure has become routine, and by the end of the DSDP 124 holes had been outfitted with cones and re-entered.

Phase 2 included drilling in the North Atlantic, Mediterranean Sea, central Atlantic, North Pacific, southwestern Pacific, Indian Ocean, and Red Sea. Drilling and coring in the Mediterranean indicated that it had been cut off from the world ocean. The intense evaporation at this latitude had dried it out completely, so that it was a desert at the end of the Miocene. The “Mediterranean Salinity Crisis” was almost unimaginable to many geologists even though late Miocene gypsum and anhydrite deposits had been known from sections exposed on land around the Mediterranean. The basin was suddenly filled with ocean water again at the beginning of the Pliocene. It has remained flooded ever since.

Phase 3 of the DSDP allowed the ship to continue to explore the Indian Ocean and to go to high latitudes in both the Atlantic and Pacific Oceans, to initiate exploration of the history of the Arctic in the Norwegian-Greenland Sea, and of the Antarctic with drilling in the Southern Ocean and Ross Sea, and to return to the Mediterranean and explore the Black Sea.

The results of Phases 2 and 3 of the DSDP are summarized in reports (Anonymous, 1975, 1976).

The international program of ocean drilling (IPOD)

Expansion of JOIDES from the four original institutions began in 1968 with the addition of the University of Washington. However, in 1972, JOIDES member institutions began discussions with potential foreign partners. In 1975 the JOIDES membership was expanded to include institutions and funding from the USSR, the Federal Republic of Germany, Great Britain, France and Japan, and five other U.S. institutions, providing both additional expertise and funding. The new phase was designated the International Program of Ocean Drilling (IPOD). It continued for 76 months, ending on 19 November 1983. During this phase, the ship drilled extensively in the Atlantic and Pacific Oceans, focusing on a series of specific topics. During the IPOD, it became mandatory for the sites to

be cored continuously. This had the advantage that a large number of complete Neogene sections have been recovered, as shown in Figure D28, but the disadvantage that much less is known about the Paleogene (Figure D29) and the Cretaceous (Figure D30).

There were major technological advances achieved during the IPOD. The hydraulic piston corer was introduced in 1978.

This is similar in function to the piston corer used to take samples from oceanographic vessels, but it replaces the normal core barrel at the base of the drill string. A moving piston remains in place as the core barrel is pushed into the sediment, and the result is much less disturbance of the core in soft sediments. This device has made it possible to recover the upper part of the sedimentary sequence in exquisite detail, and

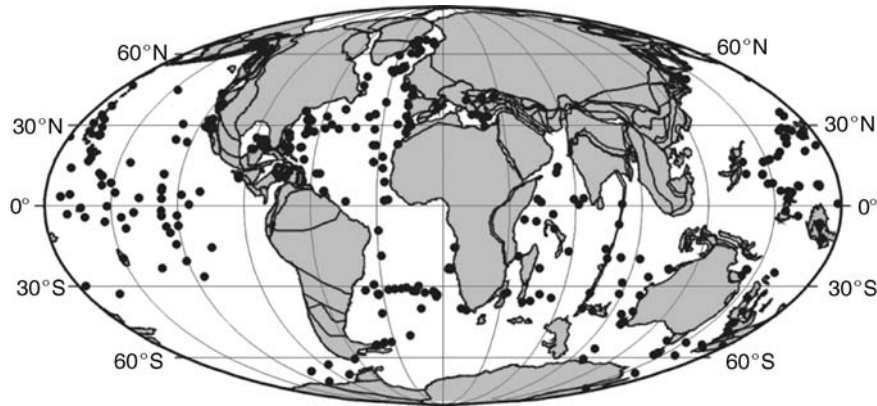


Figure D28 DSDP Sites penetrating the entire Neogene (ODSN plate tectonic mapping program).

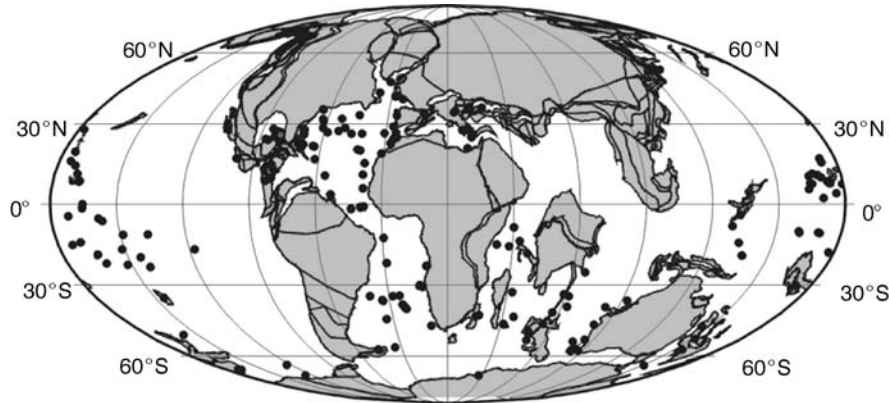


Figure D29 DSDP Sites penetrating the entire Cenozoic (ODSN plate tectonic mapping program).

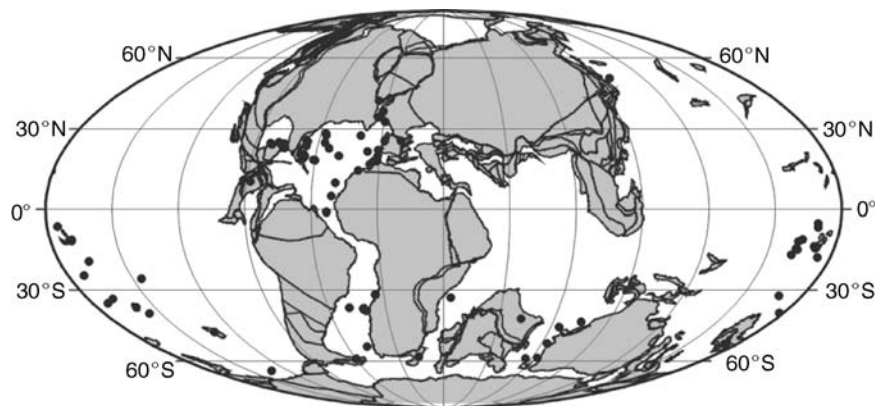


Figure D30 DSDP Sites penetrating the late Cretaceous. Recovery at Pacific sites is poor, and paleolocations in this sector are uncertain (ODSN plate tectonic mapping program).

permitted high-resolution analysis of the geologic record. Improved methods of measuring paleomagnetism in the cores, also introduced on board ship in 1978, made it possible to retrieve the magnetic signal from the cores much more reliably, with the result that determination of the magnetic stratigraphy could become a routine matter.

Coincidentally, refinement of methods of mass spectrometry made it possible to carry out measurements on stable isotopes on ever-smaller samples. It became feasible to measure isotopic ratios of oxygen and carbon on a massive scale and even to use these isotopic variations for stratigraphy. Again, this is an extraordinary example of serendipity in science, where the DSDP advances in core recovery technology and the advances in analytical technology combined to open new vistas.

The scientific results of the IPOD phase of the DSDP are summarized in reports in Anonymous (1979), Hay (1988), and Winterer (2000). Much of the work planned during IPOD carried over into the successor Ocean Drilling Program (ODP).

William W. Hay

Bibliography

- Anon., 1975. *Deep Sea Drilling Project, Legs 1–25*. AGI Reprint Series 1. Falls Church, VA: American Geological Institute, 93pp.
- Anon., 1976. *Deep Sea Drilling Project, Legs 26–44*. AGI Reprint Series 2. Falls Church, VA: American Geological Institute, 82pp.
- Anon., 1979. *Deep Sea Drilling Project, Legs 45–62*. AGI Reprint Series 3. Falls Church, VA: American Geological Institute, 77pp.
- Emiliani, C., 1954. Temperature of Pacific bottom waters and polar superficial waters during the Tertiary. *Science*, **119**, 853–855.
- Emiliani, C., 1981. A new global geology. In Emiliani, C. (ed.), *The Oceanic Lithosphere, The Sea, Vol. 7*. John Wiley and Sons, pp. 1685–1716.
- Hay, W.W., 1988. Paleooceanography: A review for the GSA Centennial. *Geol. Soc. Am. Bull.*, **100**, 1934–1956.
- Winterer, E.L., 2000. Scientific ocean drilling, from AMSOC to COMPOST. In *50 Years of Ocean Discovery*. Washington D.C.: National Academy Press, pp. 117–127.

Cross-references

[Carbonate Compensation Depth](#)
[Cenozoic Climate Change](#)
[Cretaceous Warm Climates](#)
[Cretaceous/Tertiary \(K-T\) Boundary Impact, Climate Effects](#)
[Dating, Magnetostratigraphy](#)
[Marine Biogenic Sediments](#)
[Methane Hydrates, Carbon Cycling, and Environmental Change](#)
[Messinian Salinity Crisis](#)
[Neogene Climates](#)
[Ocean Anoxic Events](#)
[Ocean Drilling Program \(ODP\)](#)
[Ocean Paleocirculation](#)
[Ocean Paleotemperatures](#)
[Paleoclimate Proxies, an Introduction](#)
[Paleogene Climates](#)
[Paleoceanography](#)

DELTAIC SEDIMENTS, CLIMATE RECORDS

Introduction

Deltas are low-lying alluvial plains formed near the mouth of a river, either along a lake or ocean shoreline, and commonly with a sizeable subaqueous deposit that extends offshore. The surface morphology of deltas typically consists of multiple

tributary channels that deliver sediment to different portions of the delta plain and nearshore. At the coast and onto the shelf, sediment deposition and morphological development in deltas are largely controlled by waves, tides, and riverine processes (Galloway, 1975). These factors dominate on shorter timescales of tens to hundreds of years. However, over millennial and longer periods it is generally agreed that delta evolution and sequence formation are controlled by: (a) climate, (b) tectonics, and (c) sea level. Unfortunately, these controls are not independent and so their relative roles in margin sequence development, particularly for deltas, remains a primary question in sedimentary geology.

Unraveling mixed signals of climate, tectonics, and sea level in deltas remains a difficult task, but the development of secular paleoclimate records in recent decades has, for the first time, allowed scientists to more faithfully (re)interpret stratigraphic and sedimentary records in the context of climate change. Previously, the impact of climate on delta systems had to be inferred through somewhat circular and indirect means (i.e., little independent confirmation of the presumed climatic forcing). Although this is also true of tectonics and sea level, the study of these controls had advanced decades before paleoclimate research and thus offered better-understood mechanisms and histories of change. However, it is now recognized that climate can vary at a much greater magnitude and more rapid rate than previously considered, and this dynamism prompts reconsideration of the role that climate plays in sedimentary processes and sequence development of deltas. Furthermore, significant advances in the numerical modeling of sedimentary and stratigraphic systems have for the first time allowed conceptual field-based models to be tested. In the case of climate records in deltas, this is particularly important because modeling can help deconvolve multiple forcing mechanisms and complex system responses.

Deltaic settings have not traditionally been targeted for paleoclimate reconstructions specifically because of their multiple environmental controls. Nevertheless, there remains intrinsic value in studying paleoclimate signatures in deltas because they serve both as: (a) primary receiving basins for land-derived erosional and weathering products, and as (b) point-sourced gateways for terrestrial fluxes to the ocean where many paleoclimatic records are deposited. Thus, the effects of climate change on entire watersheds are captured in deltaic deposits, which consequently filter climatic signals as they are transferred to marine repositories. Furthermore, deltaic settings and related marine deposits are generally important sites of carbon sequestration, closely tying carbon reservoirs with longer-term (>10⁴ yr) climate variations.

Influences of climate on deltas

Deltas can largely be considered a function of: (a) riverine water and sediment discharge to the continental margin, and (b) the interaction of these fluxes with coastal and marine processes. In this way, climate plays a major role in both the downstream forcing of the fluvial system and the modulation of sea level and coastal weather conditions. As such, there is strong overprinting of climate on deltaic systems, but precise signals are difficult to quantify because of complex feedbacks and secondary influences.

In the terrestrial realm of a delta system (i.e., the catchment basin), perhaps the most prevalent role that climate plays is via precipitation. With regard to sediment production, precipitation

is a primary control on glacial and fluvial incision, weathering, and slope failure. However, sediment is readily produced across a range of climates, from arid to humid and polar to tropical. What differs among such environments in terms of climate is hydrological runoff (=precipitation – evaporation) and thus the ability to transport sediment to the delta. In other words, sediment can be produced in many settings but is only transported to the delta with sufficient water discharge, which is primarily controlled by climate. Other important characteristics of precipitation include its phase (liquid vs. frozen), seasonality, and episodicity. First, the phase of precipitation controls the relative role of glacial and fluvial erosion in sediment production, as well as the timing and nature of water discharge (i.e., the river hydrograph). Each affects sediment-load grain size and weathering characteristics and, hence, the downstream development of delta stratigraphy. Second, the seasonality of river discharge affects the relative interaction of fluvial and marine processes, whereby strongly seasonal systems are subject to specific periods of river and marine-dominated conditions during the year. Similarly, the episodic discharge typified by storm-dominated or semi-arid river systems leaves a strong imprint on deltas, because sediments are delivered in large but infrequent pulses. Finally, precipitation exhibits strong secondary control on delta systems through the type and density of catchment vegetation, which affects runoff via overland flow and evapotranspiration rates as well as soil erosion rates. Quantitative modeling efforts have made progress in capturing the net effect of complex climate, hydrological, and sedimentary interplay, with Syvitski et al. (2003) recently showing that catchment-integrated temperature is a good predictor of fluvial sediment discharge. This strong relationship is linked directly with temperature's influence on precipitation, water phase, evaporation and consequently vegetation and discharge dynamics.

From the marine side of a delta, climate change plays primary roles in modulating both eustatic and relative sea level. Probably the strongest link between climate change and eustatic sea level has been the orbitally-tuned advance and retreat of continental ice sheets in the Plio-Pleistocene. The fate of deltaic systems under these 20–120 m sea level fluctuations has long been considered in the context of sequence stratigraphy (Vail et al., 1977), whereby the architecture and distribution of continental margin deposits has been used to reconstruct records of sea level change for much of the Phanerozoic. These general sequence models have been rigorously critiqued, though, with less than ideal results in reconstructing truly eustatic records of sea level change. However, among the major findings emerging from these studies are that sea level is not the overarching control previously thought and that influences of climate and tectonics on the terrestrial catchments are often of a similar magnitude to that for sea level (Shanley and McCabe, 1998). This further illustrates the frustratingly circular process of reconstructing climatic paleorecords based on stratigraphic sequences that are simultaneously being interpreted based on the same sequence-derived paleorecords. Hence, the secular derivation of climate history from lake, ice, and speleothem records bodes well for the unbiased interpretation of deltaic stratigraphic records.

Climatic signals in deltas

Because climate plays multiple roles in controlling deltaic systems, its signals and impacts may be looked for across a range of spatial and temporal scales. Typically, climate impacts on

larger fluviodeltaic systems are expected to be attenuated in the sizeable catchment, resulting in a weakened and delayed (10^4 – 10^5 yr) downstream signal (Castellort and Van Den Driessche, 2003). However, recent research has suggested that even large systems may respond rapidly to climate change when climate is a dominant control, such as in semi-arid and sub-tropical monsoon regions (Goodbred, 2003; Thomas, 2003). In smaller fluviodeltaic settings, high-frequency climate changes (10^{-1} – 10^2 yr) have a greater chance of influencing the entire sedimentary system and being preserved in the stratigraphic record, because the small catchment basin has limited storage capacity and signals are thus transferred more rapidly to the delta and shelf.

Climate impacts on deltaic systems may be manifested as geomorphic, stratigraphic, and sedimentological signals. Along the landward side of a delta, upstream of major subsidence (flexure) and accretion, geomorphic features are most likely to remain exposed and accessible for study. In such fluviually dominated reaches of a delta system, riverine terrace sequences and slackwater deposits have been used to reconstruct past hydrologic conditions. The terraces and slackwater deposits form at different elevations depending on the height of bankfull river stage, and hence water discharge. In several systems recently, the dating of bankfull features using cosmogenic radionuclides and optically stimulated luminescence have revealed that their timing and height correlates strongly with known Quaternary climatic variations (Repka et al., 1997; Yang et al., 2000). These records indicate that hydrologic conditions in fluviodeltaic systems vary significantly with millennial and orbital-scale climate change. A related manifestation of changing climate and hydrology is found in river planform morphology, which may vary in its degree of braiding and/or sinuosity (Bogaart and van Balen, 2000). Furthermore, river planforms reflect both sediment load and hydrology as they are largely controlled by ratios of total load/discharge and bedload/suspended load. However, as sediment load can also vary due to tectonic influences, river planforms are perhaps a more ambiguous link to climate than terraces and flood deposits.

Climate signals may also be preserved in delta stratigraphy, which similar to geomorphic signals, generally reflects changes in hydrology and sediment supply. Unlike upstream geomorphic records, though, delta sequences commonly preserve a relatively continuous stratigraphic record due to margin subsidence. Two signals of climate change recognized in delta stratigraphy include channelized-flood deposits, comprising coarse-grained sands to cobbles, and the architecture of deltaic strata and their stacking patterns, which reflect varying sediment inputs due to changing hydrological conditions. In hemipelagic deposits of the marine prodelta, climatically driven variation in river discharge are frequently recorded by alternations of bioturbated hemipelagic layers and organic-rich lithic sapropels reflecting dry and wet periods, respectively. The sapropels form due to high river discharge that: (a) supports high primary productivity and particulate carbon flux under elevated nutrient loading; and (b) enhances water-column stratification and the development of suboxic bottom waters, which limits organic matter degradation. For sedimentological records of climate change, such as microfossils, aeolian flux and grain size, these are also preserved in delta sequences but in many instances are overwhelmed by fluviually derived inputs. However, carbonate ooids that have formed locally off large sub-tropical river deltas likely reflect glacial period aridification and decreased fluvial discharge. Reduced discharge is implicated because modern ooids form

only in shallow waters of evaporative high-salinity settings. Furthermore, formation of carbonates at the rivermouths suggests limited sediment discharge, which would bury carbonate deposits and preclude their development.

Site cases

Until recently, few studies have specifically investigated climate signals and impacts in delta systems. The current knowledge base on this subject comes from several modeling groups, some field studies, and also by revisiting existing data with a better understanding of climate change from secular records. Although the list of site cases discussed below is not exhaustive, there are two relevant trends. First, the number of modeling studies equals or exceeds those based on field investigations, and second, the majority of delta systems in which climate has been investigated are located in the subtropics (the Rhine/Meuse a notable exception). Subtropical systems tend to be highly seasonal, receiving nearly all of their precipitation during the wet summer monsoon when the intertropical convergence zone (ITCZ) is most proximal. At orbital timescales, both the position and strength of the ITCZ varies in response to global boundary conditions (i.e., extent of continental ice sheets) and maximum summer insolation, respectively.

Nile delta (North Africa)

The Nile delta is located on the arid north coast of Africa, but the river's headwaters and main discharge source lie in East Africa where runoff is seasonally derived from the summer SW Asian monsoon. As such, water and sediment discharge to the delta have varied significantly with orbitally-tuned changes in monsoon precipitation. These variations are recorded in prodelta turbidites of the Nile system, which show alternating hemipelagic marls and organic-rich laminites that correlate with stable-isotope proxies for freshwater input. The individual marl/sapropel couplets track the 41-kyr precessional cycle, with packages at the 100-kyr and 400-kyr eccentricity cycles (Postma, 2001). These specific turbidite sequences are described from late Miocene to early Pliocene deposits. Younger records of climatic control have been recognized from fluvial terraces and channel planform along the Nile's middle reaches (Williams et al., 2000). Although these records are upstream of the delta, the changes in water and sediment discharge are almost certainly recorded at the margin but are yet to be described.

Ganges-Brahmaputra (South Asia)

The Ganges and Brahmaputra rivers drain the foreslope and backslope of the Himalayan front range, respectively. The two rivers coalesce near the Bengal margin to form the world's largest subaerial delta and deep-sea fan system. The rivers are also solely driven by the wet summer monsoon, when over 80% of water and 95% of sediment discharge occurs in only four months. Given global significance of the Himalayan/Tibetan uplift and its associated drainage systems, many portions of the Ganges fluvial delta system have been independently investigated in the past 15 years, revealing important variations in glacial activity, alluvial fan and floodplain development, delta evolution, and regional oceanography.

Taken together, the observed patterns show the immense Ganges dispersal system to respond to multi-millennial-scale ($<10^4$ yr) climate change in a system-wide and largely contemporaneous manner, and that major sedimentary signals are

transferred rapidly from source to sink with little apparent attenuation (Goodbred, 2003). Some of the major signals of climate change recorded in the delta stratigraphy include: (a) a thick (20–30 m) coastal mangrove facies that was deposited during rapid sea level rise in the early Holocene, and (b) a massive stored sediment volume stored during this period that reflects a sediment discharge at least 250% higher than the world's largest modern load of 1 billion tonnes (Goodbred and Kuehl, 2000). This high discharge period corresponds to the early Holocene hypsithermal, when peak regional insolation supported a stronger than present monsoon and associated precipitation. In contrast, signals recorded in the delta during the Last Glacial Maximum (18–20 ka) reflect aridification and very low river discharge. Carbonate ooids, typical of shallow, evaporative tropical waters, formed on the Bengal shelf at this time directly adjacent to the rivermouth (Wiedicke et al., 1999). Similarly, reconstructed planktonic foraminifera assemblages from the northern Bay of Bengal (Ganges discharge basin) indicate peak surface-water salinities corresponding to the LGM and apparently arid conditions (Cullen, 1981). These records from the delta and margin correlate well with findings from the catchment basin, and reflect the overall dominance of climate change in controlling this large fluviodeltaic system during the Quaternary.

Colorado, Brazos, and Trinity deltas (south-central North America)

These three rivers comprise a series of small catchments draining the semi-arid to moderately humid hills of central Texas, USA and discharging to the Gulf of Mexico. Presently, the rivers are driven by episodic floods and are forming small deltas at best. However, studies of the Texas shelf have revealed expansive fluviodeltaic sequences formed during a lower stand of sea level, and that they extend laterally and coalesce into an alongshelf composite delta system (Rodriguez et al., 1998). The shelf delta and its connection to upstream alluvial valleys are significantly larger than can be explained by modern hydrology and discharge, indicating an important change in climate or drainage basin character. The region is not tectonically active, but recent paleosol studies in the catchment reveal periods of significantly higher rainfall that are roughly correlative with the delta formation (Stiles et al., 2003). Although a definitive connection between the large Texas shelf deltas and a previously more humid climate has not been established, available data and examples from other similar systems imply a probable and significant linkage.

Rhine-Meuse delta (north-central Europe)

The Rhine-Meuse river drains central Europe and discharges to the southern North Sea coast. Much of the research on this system during the past decade has had a focus on understanding the signatures of climate and eustasy contained in the late Quaternary stratigraphy and geomorphology (Törnqvist, 1998; Veldkamp and Tebbens, 2001). Being a temperate river system, climatic forcings have probably not varied as dramatically as in the sub-tropical systems, but nonetheless the magnitude, timing, and nature of discharge appear to have played a role in shaping the fluviodeltaic system upstream of the hinge line. Terrace development in this river-dominated reach of the system is recognized as a primarily climate-controlled process through both modeling and field studies. However, the downstream impacts of such hydrological changes in the Rhine-Meuse

system appear to be insufficient to overcome the dominant influence of glacioeustasy during the Quaternary. There are likely climate impacts at the delta and margin but these are indistinguishable at the current resolutions of data and modeling.

Modeling studies

Climate has long been recognized as an important control on fluviodeltaic systems, but it has been difficult to confidently link observed stratigraphic and sedimentological signatures to climatic forcing. Such limits of field investigations are reflected in the relatively restricted results discussed above. However, exponential increases in computing power have allowed major advances to be made in the numerical modeling of fluvial and deltaic systems. Several current models offer the opportunity to compare results of system forcing by any combination of climate, eustasy, and tectonics, thereby helping to elucidate the specific character of climate impacts on stratigraphic sequences. In addition to modeling of the Rhine-Meuse mentioned above, the Niger delta sequence has also been investigated using an industry-based model (Van der Zwan, 2002). Investigation of the Niger was aimed at testing the impact of presumed Milankovitch-scale variations in sediment discharge over the Neogene. The orbitally linked forcing of regional climate and sediment occurred via global climate, insolation-control of monsoon strength, and vegetation. Results suggest that sediment supply does vary at both the large-scale (Ma) and Milankovitch-scale time frames under climatic forcings, and that there was a modest impact on stratigraphy. However, under icehouse conditions with rapid glacioeustatic sea level change, fluctuations in climate-forced sediment supply were greatly overshadowed. These findings echo those of other modeling studies in that climate is often found to be an important, but secondary, control on fluviodeltaic sequences. Furthermore, most modeling studies strongly suggest that climatic signals at the margin greatly lag the actual forcing in the catchment basin (Castelltort and Van Den Driessche, 2003). This notion conflicts with recent field evidence from several of the sub-tropical rivers discussed above. Much of these discrepancies likely arise from our limited knowledge of appropriate input values for pre-modern climate, riverine, and coastal conditions.

Conclusions

Deltas are heterogeneous systems controlled by a suite of processes, which altogether makes it challenging to isolate climate signals and their impacts. Nevertheless, climate is well recognized as a primary control of deltaic systems, and the ongoing reconstructions of secular climate records will allow better linkages to be made between climate and the stratigraphic record. If recent trends in both field and modeling efforts continue, then our understanding of climate's role in controlling river deltas and seaward basins is almost certain to advance quickly with the application of available paleoclimate records. Ultimately, our understanding of such systems will be sufficiently advanced that new information about climate change and its impacts can be determined by specifically targeting the complex, but high-resolution, archives contained in deltaic sequences.

Steven L. Goodbred, Jr.

Bibliography

- Bogaart, P.W., and van Balen, R.T., 2000. Numerical modeling of the response of alluvial rivers to Quaternary climate change. *Glob. Planet. Change*, **27**, 147–163.
- Castelltort, S., and Van Den Driessche, J., 2003. How plausible are high-frequency sediment supply-driven cycles in the stratigraphic record? *Sediment. Geol.*, **157**, 3–13.
- Cullen, J.L., 1981. Microfossil evidence for changing salinity patterns in the Bay of Bengal over the last 20 000 years. *Palaeogeogr., Palaeoclimatol., Palaeoecol.*, **35**, 315–356.
- Galloway, W.E., 1975. Process framework for describing the morphologic and stratigraphic evolution of deltaic depositional systems. In Broussard, M.L. (ed.), *Deltas, Models for Exploration*. Houston, Texas: Houston Geological Society, pp. 87–98.
- Goodbred, S.L., Jr., 2003. Response of the Ganges dispersal system to climate change: A source-to-sink view since the last interstade. *Sediment. Geol.*, **162**, 83–104.
- Goodbred, S.L., Jr., and Kuehl, S.A., 2000. Enormous Ganges-Brahmaputra sediment discharge during strengthened early Holocene monsoon. *Geology*, **28**, 1083–1086.
- Postma, G., 2001. Physical climate signatures in shallow- and deep-water deltas. *Glob. Planet. Change*, **28**, 93–106.
- Repka, J.L., Anderson, R.S., and Finkel, R.C., 1997. Cosmogenic dating of fluvial terraces, Fremont River, Utah. *Earth Planet. Sci. Lett.*, **152**, 59–73.
- Rodriguez, A.B., Anderson, J.B., and Bradford, J., 1998. Holocene tidal deltas of the Trinity incised valley; analogs for exploration and production. *Trans. Gulf Coast Assoc. Geol. Soc.*, **48**, 373–380.
- Shanley, K.W., and McCabe, P.J. (eds.), 1998. Relative role of Eustasy, Climate, and Tectonism in Continental Rocks, Special Publication 59. Tulsa OK, USA: SEPM (Society for Sedimentary Geology), 234pp.
- Stiles, C.A., Mora, C.I., Driese, S.G., and Robinson, A.C., 2003. Distinguishing climate and time in the soil record; mass-balance trends in Vertisols from the Texas coastal prairie. *Geology*, **31**, 331–334.
- Syvitski, J.P.M., Peckham, S.D., Hilberman, R., and Mulder, T., 2003. Predicting the terrestrial flux of sediment to the global ocean: A planetary perspective. *Sediment. Geol.*, **162**, 5–24.
- Thomas, M.F., 2003. Late Quaternary sediment fluxes from tropical watersheds. *Sediment. Geol.*, **162**, 63–81.
- Törnqvist, T.E., 1998. Longitudinal profile evolution of the Rhine-Meuse system during the last deglaciation; interplay of climate change and glacio-eustasy? *Terra Nova*, **10**, 11–15.
- Vail, P.R., Mitchum, R.M., Jr., Todd, R.G., Widmier, J.M., Thompson, S., III, Sangree, J.B., Bub, J.N., Hatlelid, W.G., 1977. Seismic stratigraphy and global changes of sea level. In Payton, C.E. (ed.), *Seismic Stratigraphy - Application to Hydrocarbon Exploration, Memoir 26*. Tulsa, OK: American Association of Petroleum Geologists, pp. 49–212.
- Van der Zwan, C.J., 2002. The impact of Milankovitch-scale climatic forcing on sediment supply. *Sediment. Geol.*, **147**, 271–294.
- Veldkamp, A., and Tebbens, L.A., 2001. Registration of abrupt climate changes within fluvial systems: Insights from numerical modelling experiments. *Glob. Planet. Change*, **28**, 129–144.
- Wiedicke, M., Kudrass, H.-R., and Hübscher, C., 1999. Oolitic beach barriers of the last glacial sea-level lowstand at the outer Bengal shelf. *Mar. Geol.*, **157**, 7–18.
- Williams, M.A.J., Adamson, D., Cock, B., and McEvedy, R., 2000. Late Quaternary environments in the White Nile region, Sudan. *Glob. Planet. Change*, **26**, 305–316.
- Yang, D., Yu, G., Xie, Y., Zhan, D., and Li, Z., 2000. Sedimentary records of large Holocene floods from the middle reaches of the Yellow River, China. *Geomorphology*, **33**, 73–88.

Cross-references

Continental Sediments
 Cyclic Sedimentation (Cyclothem)
 Glacial Eustasy
 Hypsithermal
 Last Glacial Maximum
 Monsoons, Quaternary
 Paleohydrology
 Sapropels
 Sea Level Change, Last 250 Million Years

DENDROCLIMATOLOGY

Introduction

Dendroclimatology is the branch of dendrochronology that utilizes absolutely dated and annually resolved growth layers in woody plants, such as trees, for the reconstruction and analysis of past climate variability. The same underlying principles of dendrochronology (described in *Dating, dendrochronology*) still apply. At the core of dendroclimatology lies the central tenet of all dendrochronological applications; the accurate *crossdating* of multiple tree ring samples that are all uniformly controlled by climate, such that the same signature of narrow and wide (or dense and less dense) rings can be identified in all of the sampled trees across time and space. The stronger the common “signal” between trees (i.e., the greater the degree to which narrow or wide rings are consistently narrow or wide), the stronger will be any reconstruction of climate that is derived from them. Methodologies have been developed for testing *signal strength* in chronology indices, and for *calibration* and *verification* of climate/tree-growth models, and these will be discussed in the ensuing sections.

As suggested above, climate may influence tree growth across space and time and can result in a high degree of common variability expressed in the pattern of annual growth rings in trees across broad regions (Douglass, 1919; Fritts, 1976; Hughes et al., 1982; Cook and Kairiukstis, 1990). The tree ring chronologies with the highest degree of strength in their common signal tend to be from regions where climate is at its most limiting to growth, and is most regionally coherent, and where other non-climatic factors such as competition and disturbance are at a minimum. Trees growing in regions with little climate variability and optimum conditions for growth are less likely to produce the high variability in annual growth necessary for robust reconstructions of climate. It is for this reason that *dendroclimatologists* seek out trees from those areas where trees are most likely to be limited by climatic factors such as temperature or drought, normally at the limits of their ecological range (see *Dating, dendrochronology*).

Describing tree-growth/climate relationships

The response of tree growth to climatic forcing involves the interaction of many complex factors. Due to this complexity there are no suitable theoretical models to allow for the extraction of a climatic signal from tree rings based on ecophysiological or mechanistic studies alone (Fritts, 1976; Hughes et al., 1982; Cook and Kairiukstis, 1990). Dendroclimatologists therefore rely upon semi-empirical relationships between tree growth and climate for calibrating the climate response of a given chronology (Fritts, 1976; Guiot et al., 1982). The multivariate statistical analyses used include principal component or eigenvector analysis, and canonical correlation and regression (Fritts et al., 1971; Fritts, 1976, 1991; Guiot et al., 1982).

The procedure that estimates the statistical growth-environment relationship is called *calibration*. The tree-growth/climate relationships revealed in this manner, called *response functions*,

may not necessarily reflect a directly coupled response. Rather, they may involve long chains of interacting cause and effect linkages that ultimately effect growth in the trees, resulting in enhanced or suppressed growth for a particular year. The climate response is evident because the elements of weather and climate affect the microclimates for individual trees, and thereby the physiological processes that in turn control growth (Gates, 1968a,b; Fritts et al., 1971; Fritts, 1976; Salisbury and Ross, 1992). When a sufficiently strong relationship has been established between tree growth and some parameter of climate (e.g., temperature or precipitation), the statistically-calibrated relationship can be used to generate a *transfer function* for the reconstruction of climate from tree growth for the period prior to the available climatic data set (Lofgren and Hunt, 1982).

For calibration, standardized tree ring indices (typically, ring width or maximum latewood density) are compared with the longest available instrumental records of climate, from meteorological stations that most closely represent conditions at the site. Long climatic time-series are required for a proper and robust statistical comparison (Fritts, 1976; Hughes et al., 1982; Cook and Kairiukstis, 1990). However, baseline weather data for a given tree site are usually lacking, and the nearest meteorological stations may be many kilometers from the location of the trees. This problem is compounded by the search for the oldest and least disturbed trees available, which are likely to be in areas remote from most weather stations, and at substantially higher elevations. Hughes et al. (1978) illustrated how the percentage of chronology variance explained by climate and prior growth, respectively, could change from 34% and 31% to 45% and 28%, respectively, when rainfall data from sites 60 km and 6 km distant were used. To some extent, this problem may be ameliorated by analyzing broad scale parameters such as sea level pressure (SLP) and sea surface temperature (SST) anomaly patterns, which may in turn influence local conditions at the site (e.g., Douglas, 1973; D'Arrigo et al., 2003). In most instances, temperature exhibits far less spatial variability than precipitation. It may therefore be more accurately represented by relatively distant instrumental records.

It is desirable to have monitored radial growth in conjunction with daily or even sub-daily environmental conditions over successive seasons at important dendroclimatic sites. This allows for a more mechanistically based climate/growth model. Such models are actively being pursued though at present they are limited to open-canopy, arid-site conifers with wide rings and uncomplicated growth structure (e.g., Fritts and Shaskin, 1994). Application of such mechanistic models to more mesic, closed-canopy forest environments is not yet viable.

In traditional dendroclimatological studies, tree growth for an entire season, as determined from the mean value function for each annual ring, is usually compared against monthly or seasonal climate parameters for the determination of the most significant factors affecting growth at the site (Fritts, 1982). In reality, climatic conditions on daily or even shorter time-scales may have a significant impact on the annual growth ring. Transient climate features such as severe frosts, very high temperatures, heavy snowfall, or windstorms may impact on growth for a given year, *t*. In most instances, however, such short-term factors can only be modeled when they leave obvious features in growth rings (e.g., traumatic resin ducts, frost-rings, false-rings), and monthly and seasonal data are more reliably modeled.

Some important assumptions and limitations exist for dendroclimatic reconstructions, which must be carefully considered:

1. It is assumed that the Uniformitarian Principle applies; i.e., the physical and biological processes that link the present environment with present variations in tree growth are the same processes that will have been in operation throughout any segment of the pre-calibration period (Fritts, 1976).
2. Similarly, the climatic conditions that produced past anomalies in tree growth are assumed to be analogous to the same processes enacting upon tree growth during the calibration period.
3. It is usually assumed that the systematic relationship between the limiting climatic parameter and the biological responder (tree growth) can be approximated by a linear mathematical expression. Lofgren and Hunt (1982) note, however, that in the case of transfer functions, the predictand set need not be a linear function of climate; e.g., the logarithm of a precipitation record could be used and therefore the linearity constraint is not so severe a restriction as it might first appear.
4. The data are assumed to be normally distributed when parametric statistics are tested for significance, as the effects of outliers and any other non-normal data may distort the testing of significance (Fritts, 1990). Non-normal data can be normalized prior to regression through several techniques outlined in Fritts (1976) and Cook and Kairiukstis (1990).
5. The observations must also be assumed to be independent of each other for most statistical testing procedures. A serial-dependence or autocorrelation among successive observations, or among observations in space, may seriously reduce the number of degrees of freedom used for statistical significance testing. The effects of autocorrelation may be removed by prewhitening the data through autoregressive modeling (e.g., Cook et al., 1992). Alternatively, prior growth can be included in the regression as a predictor variable, lagged up to m prior years.

It is clear that the assumptions listed above are not completely met by the climate/growth relationship used for calibration and climate reconstruction procedures. They may instead be regarded as comprising the limitations of the system (Fritts et al., 1971; Lofgren and Hunt, 1982) and, within these limitations, some percentage of the variability of climate will be explained by a dendroclimatic reconstruction. The quality and the length of both the tree ring and climatic data play a crucial role in the validity of the resulting models, and results derived from their calibrations and climate reconstructions should be verified, as discussed below.

Calibration of the climate response

The word *calibration* in dendroclimatology refers to the fitting of statistical models that can be applied to one or more *predictor* variables in order to estimate or reconstruct one or more *predictand* (Fritts, 1990). The term *response function* refers to the weights or coefficients of the statistical model that describes the manner in which trees respond to climate (Fritts et al., 1971; Fritts, 1976). The response function does not measure the climate-growth response directly but rather the effectiveness of a particular statistical model at predicting the element of tree ring variation forced by external factors (Hughes et al., 1982).

Climate parameters are often highly intercorrelated, making classical multiple regression analyses difficult to apply directly

for response function analysis. Instead, the principal components of climate are often used in order to provide orthogonalized data sets for use in regression (Fritts et al., 1971; Fritts, 1976; Guiot et al., 1982; Briffa and Cook, 1990). Additional complications may arise from the autoregressive properties of the tree ring series, where the growth in a particular year is not only dependent upon conditions in the season of growth but also in one or more previous seasons (Fritts et al., 1971; Fritts, 1976). Some form of prior growth parameter is often employed through lagging the tree ring series up to m prior years. Alternatively, both the tree ring time-series and the climate data can be prewhitened through autoregressive modeling to remove the effects of autocorrelation prior to response functions analysis (e.g., Cook et al., 1992).

There are several response function procedures in use at present. The primary differences relate to the manner in which relatively unimportant predictor PCs are removed from consideration during regression screening (Briffa and Cook, 1990). Blasing et al. (1984) noted that this is not always a straightforward procedure. Decisions regarding the number of climatic variables to include, confidence limits, and the number of eigenvectors to allow as candidate predictors in the regression, can affect the response function in unpredictable ways, leading to errors in interpretation. Blasing et al. (1984) recommended using the correlation function as an initial, interpretive guide prior to response function analysis, since the correlation functions are easier to understand, easier to replicate, and more difficult to alter subjectively. They also demonstrated how prior tree growth variables used in the regression can mask true climatic effects, and noted the usefulness of the correlation function for detecting such masking. The effect of prior growth variables can lead to mistakenly attributing real climatic effects to prior growth. They should therefore be considered separately from the response functions.

The simple correlation functions between the tree ring chronologies and the climate variables are used to interpret the climate response. Both the tree rings and the climate variables (where warranted) are first prewhitened as an order- p autoregressive (AR) process of the form:

$$X_t = \sum_{i=1}^p f_i X_{t-i} + e_t \quad (1)$$

where X_t is the time series being modeled, the f_i are the p autoregressive coefficients, and e_t is the series of random shocks or white noise residuals unexplained by the AR(p) model (Box and Jenkins, 1970). The e_t of the tree rings and climate variable are used to develop the regression model and subsequent climate reconstructions, with persistence due to climate added back (where warranted).

Reconstructing climate

Transfer functions are statistically derived equations that relate two sets of variables for which a causal relationship can be described, but for which the derivation of an analytical expression cannot be achieved (Fritts et al., 1971; Lofgren and Hunt, 1982). In the case of dendroclimatology, one set of variables consists of the tree ring indices, and the other the climatic parameter of interest (e.g., temperature or precipitation). The calibrated function of tree growth with the appropriate climate parameter can then be used to transfer the annual patterns of tree growth into yearly estimations of the climate variable, for

periods of time prior to the recording of that variable (Fritts, 1976; Lofgren and Hunt, 1982).

For many studies, PC regression analysis can be used to transform tree ring indices into estimates of a single climate variable (i.e., temperature). Prior to regression, the tree ring chronologies and climate variables are pre-whitened as order- p AR processes, as per Equation (1). The reconstruction of climate (Y) is therefore accomplished by estimating the regression equation over the calibration period as:

$$Y = Xb + E \quad (2)$$

where matrix X is the tree ring predictor set, b is the column vector of standardized regression coefficients used to estimate climate from tree rings, and E is the column vector of errors due to unexplained variance in the regression model. b can be estimated by ordinary least squares (OLS) as:

$$b = (XTX)^{-1} \cdot X^T Y^1 \quad (3)$$

where the superscript T denotes the transpose of matrix X and $(X^T X)^{-1}$ denotes the inverse of $X^T X$. In the form of normalized departures, estimates of climate from tree rings (\hat{Y}) can be obtained by multiplying X by b as follows:

$$\hat{Y} = Xb \quad (4)$$

When PCA is performed on the tree ring chronologies, values of X are multiplied by the eigenvector loadings (E), producing a new set of predictors:

$$U = XE \quad (5)$$

These are the PC amplitudes or *scores*. Prior to regression, each amplitude is normalized by the square root of its respective eigenvalue. The yearly variations in each amplitude reflect the relative importance of its eigenvector in describing the overall pattern of variance seen in the original data.

At this stage, a subset of amplitudes that explain most of the original variance in each data set is selected for regression analysis, after deleting the higher order eigenvectors. The eigenvalue-1 criterion (e.g., Guttman, 1954) is used here for screening predictors, deleting those eigenvectors with eigenvalues less than 1.0. This selection criterion is conservative in that it only retains around 20–40% of the eigenvectors, which may explain 60–70% of the total variance in the original data (Cook et al., 1994). In this way, the number of candidate predictors is reduced and, therefore, so is the potential for artificial predictability that might arise from the inclusion of too many predictors in the model (Davis, 1976; Lofgren and Hunt, 1982).

Once a subset of the predictor eigenvectors is selected, the predictand is regressed on selected predictor PCs, and the standardized regression coefficients are nothing more than the simple correlations between the two. The best-order regression model is selected by the minimum AIC criterion (Akaike, 1974), and the regression model is then:

$$Y = U' B' + E \quad (6)$$

where the prime denotes the reduced-order model of PC amplitudes and regression coefficients selected by the AIC. The matrix B' of regression coefficients can then be expressed in terms of the original predictors as

$$b = E' B' \quad (7)$$

This back-transformation to coefficients on the original predictors eliminates the interpretational disadvantage of working with regression weights of the PC amplitudes (Cook et al., 1994).

Verification of results

The statistical verification of climatic reconstructions is an integral part of dendroclimatology (Fritts, 1976; Hughes et al., 1982; Cook and Kairiukstis, 1990). Both response function and transfer function procedures can be verified through statistical analyses. The climate response equations are verified by comparing estimated values of tree growth with the actual values over an independent period (Briffa, 1984; Briffa and Cook, 1990). For this purpose, the climatic data are split into two equal segments (Figure D31). Identical predictor-selection criteria are used for both time periods to enable a more direct comparison of results, as recommended by Briffa and Cook (1990). Standardized periods of analysis, each of sufficient length to minimize sample-to-sample variability in the PC loading patterns (i.e., usually greater than 25–30 years) are also used. The problem of determining the confidence limits, both on R^2 and on the original climate predictors, is due to the fact that the selection of final PC predictors is an a posteriori decision, with an unclear definition of what the correct degrees of freedom are (Briffa and Cook, 1990).

The reliability of a particular model is assessed directly by calculating a number of verification statistics that measure the degree of similarity between independent estimates of climate from the model, and the corresponding instrumental data from independent time periods (Gordon, 1982; Fritts et al., 1990). Verification procedures may employ several statistics: parametric statistics that involve assumptions of the underlying probability distributions of the data, and are therefore sensitive to violations of these assumptions, and nonparametric statistics that are insensitive to such violations.

Following are several verification statistics that are commonly used: the Pearson product-moment correlation (R_p), the sign test (ST), the reduction of error test (RE), the product means test (PM), and the coefficient of efficiency (CE). Full descriptions of these tests can be found in the following: Fritts et al., 1990; Cook et al., 1992, 1994; Salinger et al., 1994.

The R_p statistic is one of the simplest and most commonly used verification statistics. It measures the relative variation (covariance) between two data sets, and is completely insensitive to differences in the mean and variance between the two (Fritts et al., 1990). Since it reflects the entire spectrum of variation (both high and low frequencies) its value can be affected by trends in the two data sets. This is resolved by calculating a new correlation coefficient from the first differences of the two data sets, thereby measuring only the high-frequency variance in common. The data sets are assumed to be normally distributed, and the variance is assumed to be linearly related (Fritts, 1976; Fritts et al., 1990).

The ST is a nonparametric measurement of reliability that counts the number of times the signs of the departures from the sample means agree or disagree, and offers the advantage of measuring the associations at all frequencies. Results are based on two possible outcomes: (+1) when the estimate and observations agree (i.e., are on the same side of the dependent data mean) and (−1) when they disagree (Fritts et al., 1990). A successful ST is indicated when the signs of the estimates are correct more often than would be expected from random numbers.

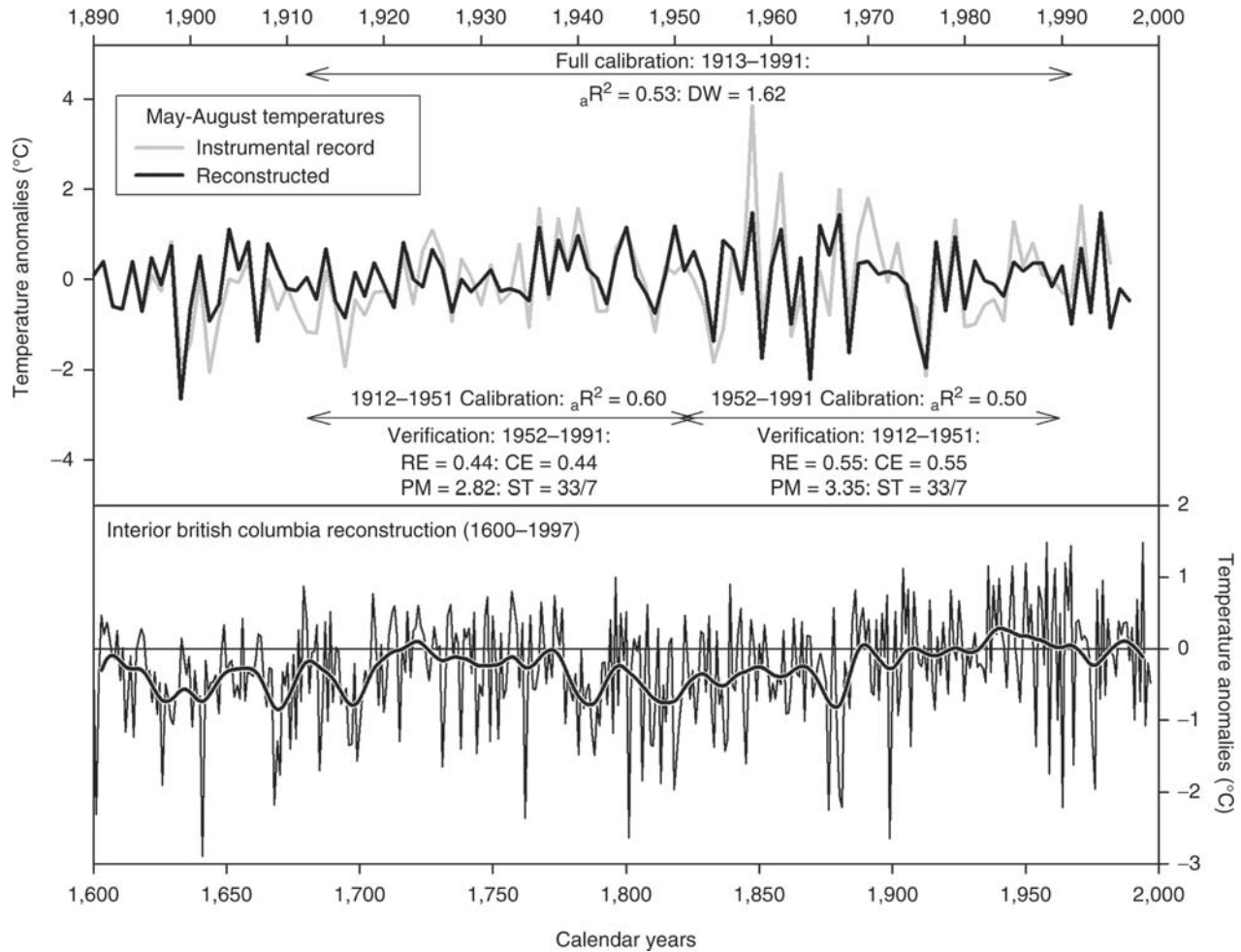


Figure D31 Tree ring reconstruction of temperature anomalies from Interior British Columbia (*bottom*), showing calibration and verification statistics and comparisons between actual and reconstructed temperatures (*top*). The full calibration period explains 53% of the variance in the original temperature series. Calibrating with the early (1912–1951) and late periods (1952–1991) independently, explains 60% and 50%, respectively, reflecting better fidelity in the early half of the record (data courtesy of R.J. Wilson).

The RE statistic offers a highly sensitive measure of reliability. It is similar to the explained variance statistic obtained with the calibration of the dependent data, and values range from negative infinity to a maximum of 1.0, which indicates a perfect estimation (Fritts et al., 1990). The RE is calculated by dividing the sum of the squared differences between actual and estimated values by the sum of the squared differences between actual values and the mean of the calibration period, then subtracting that value from 1.0. The significance of RE cannot be tested, though positive values indicate some degree of model skill. Errors are unbounded, so that even one extreme error in an otherwise nearly correct set of estimates may result in a negative RE and unfounded rejection of the model. While RE does estimate the explained variance with considerable accuracy (Gordon and LeDuc, 1981), the size of the sample being analyzed (n') may markedly affect its significance. For example, with $n' = 20$, an RE of zero was roughly equivalent to the 0.95 confidence limit, but for $n' = 10$ or 15 an RE statistic significantly different from zero would have to be greater than 0.25 and 0.12, respectively (Fritts et al., 1990).

The CE was introduced into dendroclimatology by Briffa et al. (1988) and is very similar to the RE, with values ranging from negative infinity to a maximum value of 1.0. The only difference is that the CE statistic uses the mean of the verification period in the denominator, instead of the mean of the calibration period. Consequently, if the verification and calibration means are identical, then $CE = RE$. However, when the means are not equal, RE will be greater than CE by a factor related to that difference (Cook et al., 1994). Since the value of the CE statistic will usually be less than for RE, it is an even more difficult test to pass. Although there is no significance test for CE, any value greater than zero indicates some degree of model skill (Cook et al., 1994).

The PM test takes into account both the sign and magnitude of the departure from the calibration average, and is computed from the product of the actual and estimated annual departures from the mean, with positive and negative means summed separately (Fritts, 1976). The product is positive when the departure sign is estimated correctly, and negative when incorrectly estimated. If randomly guessed, the means of the positive

and negative products are approximately the same (ignoring their signs); while for a correct reconstruction, the mean is larger for the positive products (Fritts, 1976). The difference between positive and negative products is tested with the t statistic, and is considered statistically significant when the value of t is higher than the expected value at the appropriate confidence level. A mean positive product that is significantly larger indicates a tendency for both actual and estimated departures from the average value to be large when the sign is correctly estimated, and small when the sign is incorrectly estimated. The latter case indicates that approximately average conditions both occurred and were estimated, thereby indicating the correctness of the reconstruction in spite of its incorrect sign (Fritts, 1976).

Reconstructions of climate from tree rings

Through his research on trees of the arid American southwest (see *Dating, dendrochronology*), A.E. Douglass came to understand the connection between climate and tree growth. In one of his earliest attempts to reconstruct climate, Douglass (1909), in his paper “*Weather cycles in the growth of big trees*,” described the connection between available moisture, food supply and annual incremental growth, and extrapolated long records of Ponderosa pine as proxy records of rainfall for northern Arizona. All of the methodological applications were done manually; curve fitting, standardization and chronology building, and all correlation analyses were done without the benefit of computers. This, of course, limited the numbers of trees used and the numbers of calculations made. For the next few decades, much work was done in this manner and climate reconstructions were laboriously produced.

Harold C. Fritts introduced a more biological, plant physiology-based research focus to the field of dendrochronology in the 1950s and 1960s (e.g., Fritts and Fritts, 1955; Fritts, 1956, 1960a). He employed the use of dendrographs that measured daily changes in stem growth to help in understanding the climate tree growth relationship in greater detail. He also introduced high-level statistical methods and the use of main-frame computing to process large sets of data (e.g., Fritts, 1960b, 1962, 1963). In addition, his work introduced the use of canonical regression and large regional networks of tree ring chronologies for the spatial reconstruction of climate (e.g., Fritts et al, 1971). These were highly innovative and important

works, made possible by the use of computers, which led to major advances in the methodology used for reconstructing climate from tree rings. The list of researchers who made significant contributions to the field of dendroclimatology, both before and after the work of Fritts, is impressive, but goes far beyond the scope of this chapter. Some important highlights are noted below.

One of the more important reconstructions of climate from tree rings was a reconstruction of streamflow from the Colorado River (Stockton, 1976; Stockton and Jacoby, 1976) shown in Figure D32. This work was important because it demonstrated that the estimates for overall streamflow of the Colorado River, upon which western states water rights were calculated, had substantially overestimated the average annual amount of water by more than 4 million acre feet (maf). The official measurements of 17.3 maf were dominated by data from the early 1900s, which Stockton’s work showed to encompass the wettest 30-year period of the past 500 years. The overall average based on the long tree ring reconstruction was 13.5 maf, and clearly illustrated the pitfalls of making decisions based on short-term data.

With the development of microcomputing in the 1970s and 1980s it became possible to generate large numbers of iterations of data, making it reasonable to reconstruct climate from multiple well-replicated tree ring chronologies. This has led to the present day scenario where synoptic scale reconstructions of climate can be made from hundreds of tree ring chronologies built from thousands of trees, using desktop computers. A recent example of such spatial reconstruction work is Cook et al. (1999) who reconstructed drought indices for the contiguous USA based on a gridded network of 425 moisture-sensitive tree ring chronologies that were calibrated and verified against 286 grid-points of PDSI (Palmer drought severity index). The reconstruction spanned the period from 1700–1978. This work has recently been expanded to include 835 tree ring series, and an increased overall length of reconstruction back to 1 AD for the western USA. The chronologies and PDSI grid points now extend into Canada and Mexico, giving far greater scope to the analyses of past drought. A drought area index (Figure D33) for the western USA shows evidence of a prolonged period of drought that lasted for much of the 10th–13th centuries, coinciding with the Medieval Warm Period (MWP). A current, prolonged drought in the western USA can now be better assessed within the

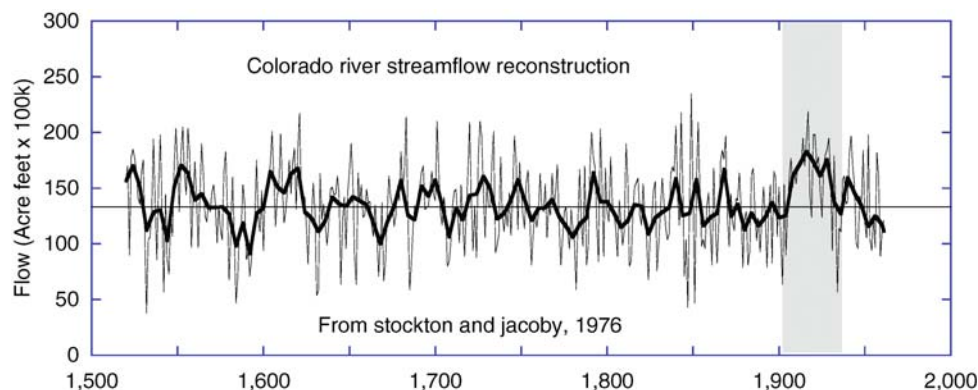


Figure D32 Colorado River streamflow reconstruction based on tree ring sites from the river’s catchment. The grey shaded area shows the period that the Colorado River Treaty was based on, which turned out to be the wettest period of the past 500 years. More water was divided between states than existed for the long-term mean.

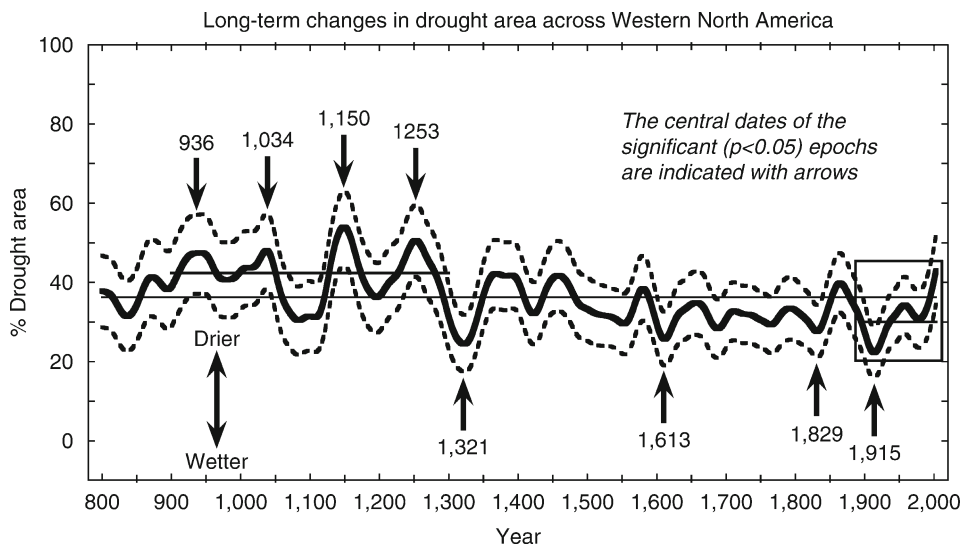


Figure D33 Tree ring based reconstruction of drought indices for the western USA depicted as drought area indices (DAI), expressed as percentage of area in drought with a PDSI of <-2 . This is a smoothed plot that accentuates decadal scale variability. Of particular interest is a "Medieval Dry Period" of extended drought from the mid 10th to late 13th centuries that is unmatched in intensity for the past 1,200 years (data courtesy of E.R. Cook).

context of the natural variability for the past 2,000 years. The current drought is shown to be orders of magnitude less than the MWP drought, suggesting dire consequences to a water-hungry society if MWP-like conditions returned. Much of these data and their reconstructions, as well as numerous other climate reconstructions from tree rings can be downloaded from the NOAA paleoclimatology website and the International Tree-Ring Data Bank (<http://www.ncdc.noaa.gov/paleo/>).

Tree rings and global warming

Tree rings have proven to be one of the most important proxies of climate in the global warming debate. This is due to their ability to reproduce high-resolution, absolutely dated records of climate over broad geographic areas for the past millennium and beyond. This work has been largely centered on tree ring sites from the boreal forests where temperature is the most limiting factor to growth. Early work in Alaska by Giddings (1938, 1943) showed the potential for working with northern treeline trees and explored their relationship to climate. Jacoby et al. (1985) followed up on this research, producing reconstructions of degree-days in Alaska. Meanwhile some of the first attempts to reconstruct large scale Arctic and Northern Hemisphere temperatures based on networks of temperate to sub-Arctic trees were being undertaken (e.g., Jacoby and D'Arrigo, 1989; D'Arrigo and Jacoby, 1993). Much recent attention has been focused on a multi-proxy reconstruction of Northern Hemisphere temperature by Mann et al (1998), which included tree ring series and showed the recent warming trend to be unmatched for the past 1,000 years. Esper et al. (2002) used networks of tree ring sites and novel standardization procedures (see *Dating, dendrochronology*) to produce a Northern Hemisphere temperature reconstruction that placed the recent warming within the scope of the natural variability of climate for the past 1,000 years, and suggested a MWP warming that rivaled the current temperature increase. D'Arrigo et al. (2006) provide a recent version of a Northern Hemisphere temperature reconstruction

that includes newly collected data and different methodologies from previous versions. While the scientific debate surrounding global warming goes on, tree rings remain among the most important proxies used for paleoclimate research.

Brendan M. Buckley

Bibliography

- Akaike, H., 1974. A new look at the statistical model identification. *IEEE Trans. Automat. Contr.*, **AC-19**, 716–723.
- Blasing, T.J., Solomon, A.M., and Duvick, D.N., 1984. Response functions revisited. *Tree-Ring Bull.*, **44**, 1–15.
- Box, G.E.P., and Jenkins, G.M., 1970. *Time Series Analysis: Forecasting and Control*. San Francisco, CA: Holden-Day.
- Briffa, K.R., 1984. *Tree-Climate Relationships and Dendroclimatological Reconstruction in the British Isles*. PhD thesis, University of East Anglia, Norwich, England.
- Briffa, K.R., and Cook, E.R., 1990. Methods of response function analysis. In Cook, E.R., and Kairiukstis, L.A. (eds.), *Methods of Dendrochronology: Applications in the Environmental Sciences*. Dordrecht: Kluwer Academic, pp. 240–247.
- Briffa, K.R., Jones, P.D., Pilcher, J.R., and Hughes, M.K., 1988. Reconstructing summer temperatures in northern Fennoscandia back to A.D. 1700 using tree-ring data from Scots pine. *Arct. Alp. Res.*, **20**, 385–394.
- Cook, E.R., and Kairiukstis, L.A. (eds.), 1990. *Methods of Dendrochronology: Applications in the Environmental Sciences*, (1st ed.). Dordrecht: Kluwer Academic, 394pp.
- Cook, E.R., Bird, T., Peterson, M., Barbetti, M., Buckley, B., D'Arrigo, R., and Francey, R., 1992. Climatic change over the last millennium in Tasmania reconstructed from tree rings. *The Holocene*, **2**, 205–217.
- Cook, E.R., Briffa, K.R., and Jones, P.D., 1994. Spatial regression methods in dendroclimatology: A review and comparison of two techniques. *Int. J. Climatol.*, **14**, 379–402.
- Cook, E.R., Meko, D.M., Stahle, D.W., and Cleaveland, M.K., 1999. Drought reconstructions for the continental United States. *J. Clim.*, **12** (4), 1145–1162.
- D'Arrigo, R., Wilson, R., and Jacoby, G., 2006. On the long-term context for late 20th century warming. *J. Geophys. Res.*, **111**, D031103, doi: 10.1029/2005JD006352.

- D'Arrigo, R.D., Buckley, B.M., Kaplan, S., and Woollett, J., 2003. Inter-annual to multidecadal modes of Labrador climate variability inferred from tree rings. *Clim. Dyn.*, **20**, 219–228.
- D'Arrigo, R.D., and Jacoby, G.C., 1993. Secular trends in high northern latitude temperature reconstructions based on tree rings. *Clim. Change*, **25**(2), 163–177.
- Davis, R.E., 1976. Predictability of sea surface temperature and sea level pressure anomalies over the North Pacific Ocean. *J. Phys. Oceanogr.*, **6**(3), 249–266.
- Douglas, A.V., 1973. *Past Air-Sea Interactions Off Southern California as Revealed by Coastal Tree-Ring Chronologies*. MS thesis, University of Arizona.
- Douglass, A.E., 1909. Weather cycles in the growth of big trees. *Mon. Weather Rev.*, **37**(5), 225–237.
- Douglass, A.E., 1919. *Climatic Cycles and Tree Growth (Publication 289)*. Washington, D.C.: Carnegie Institution of Washington.
- Esper, J., Cook, E.R., and Schweingruber, F.H., 2002. Low-frequency signals in long tree-ring chronologies for reconstructing past temperature variability. *Science*, **295**, 2250–2253.
- Fritts, H.C., 1956. Radial growth of beech and soil moisture in a central Ohio forest during the growing season of 1952. *Ohio J. Sci.*, **56**(1), 17–28.
- Fritts, H.C., 1960a. Daily radial growth in mature forest trees. *Yearbook of the American Philosophical Society*, Philadelphia, PA: 311–314.
- Fritts, H.C., 1960b. Multiple regression analysis of radial growth in individual trees. *Forest Science*, **6**(4), 334–49.
- Fritts, H.C., 1962. An approach to dendroclimatology: screening by means of multiple regression techniques. *J. Geophys. Res.*, **67**(4), 1413–20.
- Fritts, H.C., 1963. Computer programs for tree-ring research. *Tree-Ring Bull.*, **25**(3–4), 2–7.
- Fritts, H.C., 1976. *Tree Rings and Climate*. London: Academic Press, 567pp.
- Fritts, H.C., 1982. The climate-growth response. In Hughes, M.K., Kelly, P.M., Pilcher, J.R., and LaMarche V.C., Jr. (eds.), *Climate From Tree Rings*. Cambridge, UK: Cambridge University Press.
- Fritts, H.C., 1990. Methods of calibration, verification, and reconstruction: introduction. In Cook, E.R., and Kairiukstis, L.A. (eds.), *Methods of Dendrochronology: Applications in the Environmental Sciences*. Dordrecht: Kluwer Academic, pp. 163–165.
- Fritts, H.C., 1991. *Reconstructing Large-Scale Climatic Patterns from Tree-Ring Data: a Diagnostic Analysis*. Tucson, AZ, USA: University of Arizona Press.
- Fritts, H.C., Blasing, T.J., Hayden, B.P., and Kutzbach, J.E., 1971. Multivariate techniques for specifying tree growth and climate relationships and for reconstructing anomalies in paleoclimate. *J. Appl. Meteorol.*, **10**(5), 845–64.
- Fritts, H.C., and Shaskin, A.V., 1994. Modeling tree-ring structure as related to temperature, precipitation, and day length. In Lewis, T.E. (ed.), *Tree rings as Indicators of Ecosystem Health*. Boca Raton, FL: CRC Press, pp. 17–57.
- Fritts, H.C., Guiot, J., and Gordon, G.A., 1990. Verification. In Cook, E.R., and Kairiukstis, L.A. (eds.), *Methods of Dendrochronology: Applications in the Environmental Sciences*. Dordrecht: Kluwer Academic, pp. 178–185.
- Fritts, H.C., and Fritts, E.C., 1955. A new dendrograph for recording radial changes of a tree. *For. Sci.*, **1**(4), 271–6.
- Gates, D.M., 1968. Transpiration and leaf temperature. *Ann. Rev. Plant Physiol.*, **19**, 211–238.
- Giddings, J.L., Jr., 1938. Recent tree-ring work in Alaska. *Tree-Ring Bull.*, **5**(2), 16.
- Giddings, J.L., Jr., 1943. Some climatic aspects of tree growth in Alaska. *Tree-Ring Bull.*, **9**(4), 26–32.
- Gordon, G.A., 1982. Verification of dendroclimatic reconstructions. In Hughes, M.K., Kelly, P.M., Pilcher, J.R., and LaMarche, V.C., Jr. (eds.), *Climate From Tree Rings*. Cambridge, UK: Cambridge University Press, pp. 58–61.
- Gordon, G.A., and LeDuc, S.K., 1981. Verification statistics for regression models. In *Proceedings of the Seventh Conference on Probability and Statistics in Atmospheric Sciences*. Monterey, CA, USA.
- Guiot, J., Berger, A.L., and Munaut, A.V., 1982. Response functions. In Hughes, M.K., Kelly, P.M., Pilcher, J.R., and LaMarche, V.C., Jr. (eds.), *Climate From Tree Rings*. Cambridge, UK: Cambridge University Press, pp. 38–47.
- Guttman, L., 1954. Some necessary conditions for common-factor analysis. *Psychometrika*, **19**, 149–161.
- Hughes, M.K., Leggett, P., Milsom, S.J., and Hibbert, F.A., 1978. Dendrochronology of oak in North Wales, U.K., *Tree-Ring Bull.*, **38**, 15–24.
- Hughes, M.K., Kelly, P.M., Pilcher, J.R., and LaMarche, V.C., Jr. (eds.), 1982. *Climate From Tree Rings*. Cambridge, UK: Cambridge University Press, 223p.
- Jacoby, G.C., Cook, E.R., and Ulan, L.D., 1985. Reconstructed summer degree days in central Alaska and northwestern Canada since 1524. *Quaternary Res.*, **23**, 18–26.
- Jacoby, G.C., and D'Arrigo, R.D., 1989. Reconstructed northern hemisphere annual temperature since 1671 based on high-latitude tree-ring data from North America. *Clim. Change*, **14**, 39–59.
- Lofgren, G.R., and Hunt, J.H., 1982. Transfer Functions. In Hughes, M.K., Kelly, P.M., Pilcher, J.R., and LaMarche, V.C., Jr. (eds.), *Climate From Tree Rings*. Cambridge, UK: Cambridge University Press, pp. 50–56.
- Mann, M.E., Bradley, R.S., and Hughes, M.K., 1998. Northern hemisphere temperatures during the past millennium: Inferences, uncertainties, and limitations. *Geophys. Res. Lett.*, **26**(6), 759–762.
- Salisbury, F.B., and Ross, C.W., 1992. *Plant Physiology*, (4th ed.). Belmont, CA: Wadsworth Publishing Co., 682pp.
- Salinger, M.J., Palmer, J.G., Jones, P.D., and Briffa, K.R., 1994. Reconstructions of New Zealand climate indices back to AD 1731 using dendroclimatic techniques: some preliminary results. *Int. J. Climatol.*, **14**, 1135–1149.
- Stockton, C.W., 1976. Long-term streamflow reconstruction in the upper Colorado River basin using tree rings. In Clyde, C.B., Falkengberg, D.H., and Riley, J.P. (eds.), *Colorado River Basin Modeling Studies*. Logan, UT: Utah State University, pp. 401–441.
- Stockton, C.W., and Jacoby, G.C., 1976. Long-term surface-water supply and streamflow trends in the Upper Colorado River basin based on tree-ring analyses. *Lake Powell Res. Proj. Bull.*, **18**, 1–70.

Cross-references

[Dating, Dendrochronology](#)
[Medieval Warm Period](#)
[Paleoclimate Proxies, an Introduction](#)
[Transfer Functions](#)

DESERT VARNISH AS A PALEOCLIMATE PROXY

Desert varnish, a paper-thin accretion on rock surfaces (Figure D34), greatly alters the appearance of bare rock faces. Almost any lithology can host varnish, but the surface must remain stable for thousands of years in order to accumulate varnish in most desert environments. Rock varnish is the better term because this same rock coating forms on rocks in all environments, for example, alpine, Antarctic, Arctic, periglacial, stream, temperate, and tropical environments. The term desert varnish is most often used in arid regions (Dorn, 1998).

Environmental changes influence varnish. Lichens and many fungi, for example, secrete biological acids that destroy desert varnish by dissolving the manganese and iron oxides. Where rocks exist in a desert pavement or in other settings such as an opened rock crevice, local environmental conditions play the key role in varnish development. However, where rock surfaces are not greatly influenced by the local microenvironment, varnish layers, called visual microlaminations (VML), record changes in the aridity of an area. Varnishes seen in ultra thin sections (<5 μm) with a light microscope reveal orange-yellow and black layers.

In these boulder-top positions, wetter climates favor bacterial enhancement of manganese (Figure D35), producing the black layers. Drier climates with more alkaline dust foster development of orange-yellow (Mn-poor) layers that record arid periods (Dorn, 1990). In places where VMLs have been calibrated by radiometric dating methods, they can yield

correlated ages for rock surfaces (Liu, 2003, 2006), as revealed in a recent test: "... results of the blind test provide convincing evidence that varnish microstratigraphy is a valid dating tool to estimate surface exposure ages" (Marston, 2003, p. 197). Based on a decade of detailed analyses of over 10,000 microsedimentary basins, Liu (2003, 2006) found that black varnish layers correspond with Heinrich events, the Younger Dryas (Figure D36), and wet events during the Holocene.

The wet periods recorded in rock varnish, however, do vary in timing regionally. Cremaschi (1996), for example, found a mid-Holocene Mn-rich layer in Tunisian varnish correlating with a regional wet pulse in North Africa. When regionally calibrated, varnish microlaminations provide archaeologists and geomorphologists a powerful Quaternary tool (Liu and Broecker, 2008), because they reveal both climatic change and a time signal (Figure D37). The potential of VML extends beyond the Quaternary in circumstances where varnish is

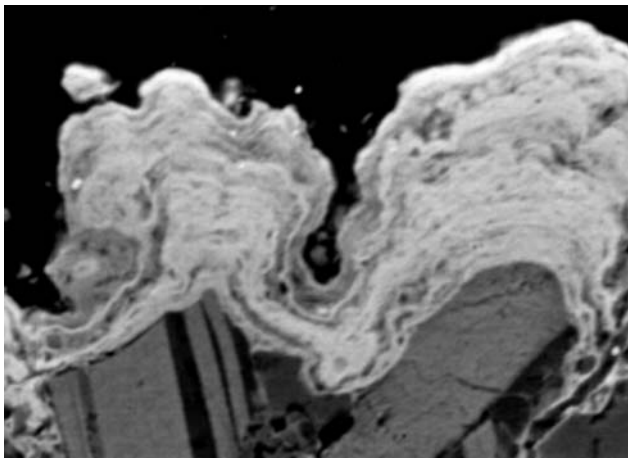
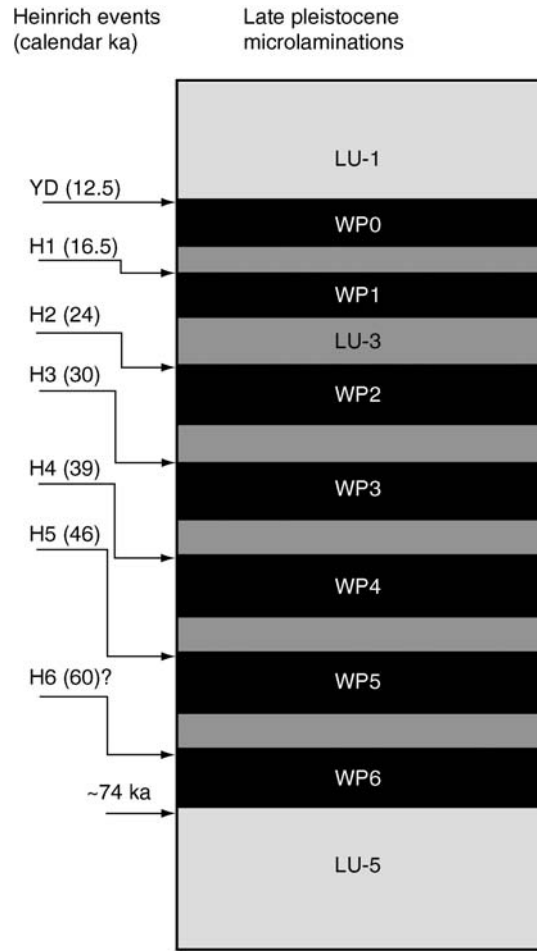


Figure D34 Backscattered electron microscope view of brighter rock varnish formed on granodiorite (feldspar and quartz minerals) at Kitt Peak, Arizona. The varnish is only about 0.05 mm thick. Note the distinct boundary between varnish and rock, indicating that varnish is an accretion.



Graph not drawn to scale

Figure D36 Calibration of varnish microlaminations from the basin and range of western North America (based on data in Liu, 2003), where ka is thousands of years.

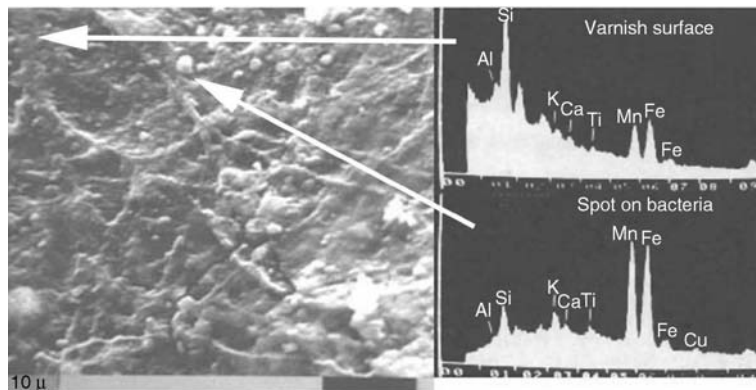


Figure D35 Budding bacteria concentrate manganese in rock varnish, as seen here through electron microscopy and energy dispersive chemical analyses of Negev Desert varnish.

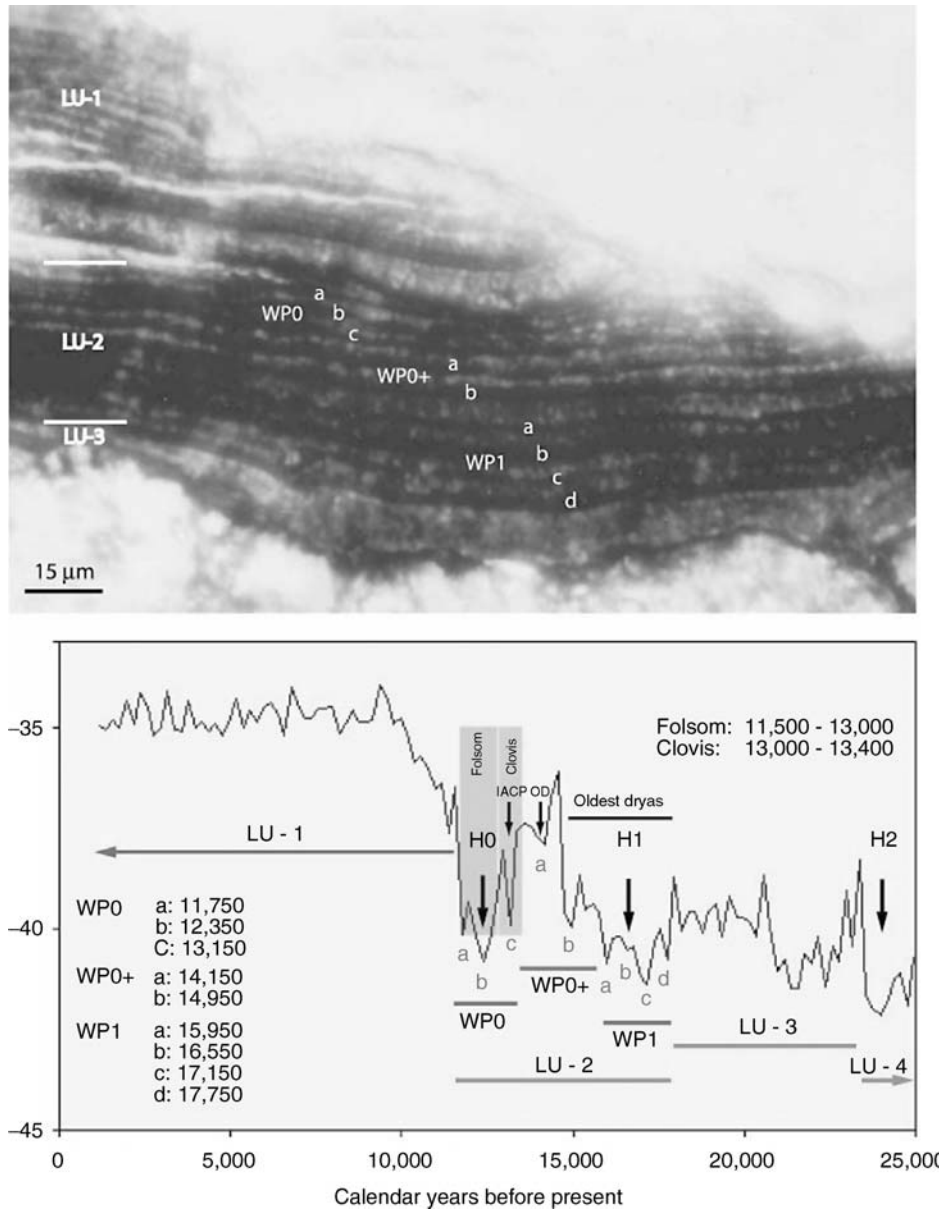


Figure D37 Rock varnish record of the latest Pleistocene wet events in Death Valley, California and its possible correlation with GISP2 $\delta^{18}\text{O}$ ice core record in Greenland (below), where the graphic is modified from Liu (2006). In fast accumulating varnishes, such as this sample from Death Valley, there are three wet phases in the Younger Dryas event (WPO), four wet phases in Heinrich event 1 (WP1), and two wet phases between them (WPO+) that can discriminate different events in the terminal Pleistocene.

preserved in sedimentary environments; investigators can infer from VML that the environment probably fluctuated between arid and less arid environments (Dorn and Dickinson, 1989).

There are other paleoclimatic indicators found in association with desert varnish. When other types of rock coatings (Dorn, 1998) alternate with desert varnish, the change in coating type often has implications for environmental change. Changes in the trace element geochemistry of varnish, for example, changes in carbon isotopes and lead (Dorn, 1998), also record environmental changes. Still other indicators include micromorphological changes in varnish layering that provide an indicator

of the dustiness of the depositional setting. Because desert varnish is a weathering feature, sensitive to climatic change, changes in its physical and chemical structure provides researchers opportunities to understand paleoclimatic changes in arid regions.

Ronald I. Dorn

Bibliography

Cremaschi, M., 1996. The desert varnish in the Messak Sattafet (Fezzan, Libyan Sahara), age, archaeological context and paleo-environmental implication. *Geoarchaeology*, **11**, 393–421.

- Dorn, R.I., 1990. Quaternary alkalinity fluctuations recorded in rock varnish microlaminations on western U.S.A. volcanics. *Palaeogeogr. Palaeoclimatol. Palaeoecol.*, **76**, 291–310.
- Dorn, R.I., 1998. *Rock Coatings*. Amsterdam: Elsevier, 429pp.
- Dorn, R.I., and Dickinson, W.R., 1989. First paleoenvironmental interpretation of a pre-Quaternary rock varnish site, Davidson Canyon, south Arizona. *Geology*, **17**, 1029–1031.
- Liu, T., 2003. Blind testing of rock varnish microstratigraphy as a chronometric indicator: Results on late Quaternary lava flows in the Mojave Desert, California. *Geomorphology*, **53**, 209–234.
- Liu, T., 2006. VML Dating Lab, <http://www.rmldatinglab.com/> (accessed June 24, 2006).
- Liu, T., and Broecker, W.S., 2008. Rock varnish microlamination dating of late quaternary geomorphic features in the drylands of western USA. *Geomorphology*, **93**, 501–523.
- Marston, R.A., 2003. Editorial note. *Geomorphology*, **53**, 197.

Cross-references

Dating, Radiometric Methods
 Heinrich Events
 Mineral Indicators of Past Climates
 Weathering and Climate
 Younger Dryas

DEUTERIUM, DEUTERIUM EXCESS

Measurements

Deuterium is the heavy stable isotope of hydrogen, ^2H or D, with a natural occurrence on Earth ($^2\text{H}/^1\text{H}$ isotopic ratio, hereafter D/H) of $\sim 153 \times 10^{-6}$ (Lécuyer et al., 1998). For the purpose of reconstructing paleoenvironments, it is commonly measured in paleowaters (e.g., groundwaters, ice, fluid inclusions), organic matter (e.g., tree cellulose), and hydroxylated minerals (e.g., clays, hydroxides), in which the D/H ratio ranges between approximately 160×10^{-6} and 80×10^{-6} (Mook, 2001; Jouzel, 2003).

The D/H ratio of a sample is measured by mass spectrometry on H_2 (hydrogen gas), after either a total reduction of the water, or a catalytic equilibration with H_2 . Both techniques allow some automation, but the latter requires larger sample volume (few ml, compared with few μl for the former). A new laser spectrometric technique is achieving promising results (Kerstel et al., 1999). The isotopic composition is usually expressed relative to a standard, currently the Vienna Standard Mean Ocean Water (V-SMOW), defined in 1966 by the International Atomic Energy Agency (IAEA), with a D/H ratio close to 155.75×10^{-6} . The relative composition is expressed with the δ notation:

$$\delta D = [(D/H)_{\text{sample}} / (D/H)_{\text{V-SMOW}} - 1] (\times 1,000, \text{ per mil})$$

It is recommended that isotopic measurements be expressed with respect to V-SMOW, and normalized on a two-standard scale, V-SMOW and SLAP (Standard Light Antarctic Precipitation), assuming a value $\delta D = -428\text{‰}$ for SLAP (Coplen, 1995). The different measurement techniques achieve a precision usually better than 1‰, but with a lower accuracy, as shown by interlaboratory comparisons (Meijer, 1999).

Reconstruction of paleoenvironments

The deuterium composition δD allows similar reconstructions of paleohydrological and paleoclimatic conditions as can be

achieved with the $\delta^{18}\text{O}$, both quantities being related by the ratio of their fractionation factors. Because condensation of water occurs mainly at equilibrium in the atmosphere, and because the ratio of their equilibrium fractionation factors is more or less constant with temperature, the δD and $\delta^{18}\text{O}$ values of precipitation (and of most surface waters) are linearly related with a slope close to 8, the so-called “Meteoric Water Line” (Craig, 1961). In contrast, kinetic conditions prevailing at evaporation modify both the slope and the intercept of this line (Merlivat and Jouzel, 1979). To infer these kinetic conditions, a second order isotopic parameter, the deuterium excess d , has been defined as $d = \delta D - 8 \times \delta^{18}\text{O}$ (Dansgaard, 1964).

Gilles Delaygue

Bibliography

- Coplen, T.B., 1995. Reporting of stable carbon, hydrogen, and oxygen isotopic abundances. In *Proc. Meet. Reference and Intercomparison Materials for Stable Isotopes of Light Elements*, Vienna, IAEA TecDoc 825, pp. 31–34 (available online at www.iaea.org).
- Craig, H., 1961. Isotopic variations in meteoric waters. *Science*, **133**, 1702–1703.
- Dansgaard, W., 1964. Stable isotopes in precipitation. *Tellus*, **16**, 436–468.
- Jouzel, J., 2003. Water stable isotopes: Atmospheric composition and applications in polar ice core studies. In Holland, H.D., and Turekian, K.K. (eds.), *Treatise on Geochemistry*. Amsterdam: Elsevier.
- Kerstel, E.R.T., van Trigt, R., Reuss, J., Meijer, H.A.J., and Dam, N., 1999. Simultaneous determination of the $^2\text{H}/^1\text{H}$, $^{17}\text{O}/^{16}\text{O}$, and $^{18}\text{O}/^{16}\text{O}$ isotope abundance ratios in water by means of laser spectrometry. *Anal. Chem.*, **71**, 5297–5303.
- Lécuyer, C., Gillet, P., and Robert, F., 1998. The hydrogen isotope composition of seawater and the global water cycle. *Chem. Geol.*, **145**, 249–261.
- Meijer, H.A.J., 1999. Isotope ratio analysis on water: A critical look at developments. In *Proc. Meet. New approaches for stable isotope ratio measurements*, Vienna, IAEA TecDoc 1247, pp. 105–112 (available online at www.iaea.org).
- Merlivat, L., and Jouzel, J., 1979. Global climatic interpretation of the deuterium–oxygen 18 relationship for precipitation. *J. Geophys. Res.*, **84**, 5029–5033.
- Mook, W.G. (ed.), 2001. *Environmental Isotopes in the Hydrological Cycle: Principles and Applications*. IHP Tech. Doc. 39, UNESCO/IAEA. (available online at: <http://www.iaea.org/programmes/ripc/ih/volumes/volumes.htm>).

Cross-references

Ice cores, Antarctica and Greenland
 Isotope Fractionation
 Oxygen Isotopes
 Paleoclimate Proxies, an Introduction
 Paleohydrology
 Paleotemperatures, Proxy Reconstruction
 Stable Isotope Analysis

DIAMICTON

Diamicton is a general term used to describe a non-sorted or poorly sorted, sometimes non-calcareous, terrigenous or marine sediment containing a wide range of particle sizes derived from a broad provenance (Harland et al., 1966). Diamictons may have sorted and stratified subfacies, usually contain “floating” clasts of a wide provenance, and may have a fine-grained matrix (Dreimanis and Lundqvist, 1984). The term diamictite

is used to describe a lithified diamicton. The term, today, also carries with it the connotation of a glacial origin but diamictons can be deposited within a variety of geological settings.

The term, diamictite, and, from it diamicton, was first proposed by Flint et al. (1960) to replace the term symmictite. (Diamicton comes from the Greek, *diamognymi* – to mangle thoroughly.) Often synonymous with diamicton is the term “till” but not all diamictons are tills. The term “diamict” has been used occasionally as a separate term but has become an alternative to diamicton (Hambrey and Harland, 1981, p. 23).

Tills are, in general, poorly sorted glaciogenic sediments, with occasional sorted subfacies, that subdivide into lodgment, flow, and meltout (Dreimanis, 1988). As till research expanded, it became clear that tills form within terrestrial and marine environments but such origins are not always easily ascertained.

Diamictons can be, in general, classified as conglomerates or various forms of cataclastics that contain varying proportions of fine-grained matrix within which “floating” clasts of a range of sizes and shapes occur (Pettijohn, 1975; Allen, 1982). Some classifications use different terms depending on the percentage of clasts or the degree of fine-grained matrix present (Folk, 1954; Schermerhorn, 1966; Pettijohn, 1975); however, essentially all of these types are diamictons as defined above. As such, diamictons can be derived from three dominant sources: glacial, mass movement, or endogenic. All three types can also be formed in terrestrial and subaqueous environments and in many instances appear remarkably similar in hand-specimen. One distinguishing characteristic of glacial diamictons may be the presence of striations on the surfaces of clasts, but caution must be exercised in using this diagnostic criterion (Gravenor et al., 1984; Iverson, 1991).

Glacial diamictons represent the largest group of diamictons both on land and on the ocean floor. Although the three classes of tills, as noted above, have become accepted, newer research suggests that all tills are formed under stress conditions such that it may be more appropriate to group lodgment and flow tills as part of a spectrum of glacial mélange (Ruszczynska-Szenajch, 1983; Menzies, 1990). Meltout tills are a special group of diamictons that deposit under relatively low stress conditions such that deformation is limited (Lawson, 1981); their global extent, however, is limited (Rappol, 1987; Paul and Eyles, 1990). In using micromorphology, it is apparent that the dominant three till (diamicton) types need to be revisited since most glacial diamictons are products of various ductile and brittle deformation processes of deposition or emplacement (Hiemstra and Meer, 1997; Meer van der, 1997). It has been proposed that these glacial diamictons be renamed “tectomicts,” indicative of the deformation history undergone in the processes of deposition (Meer et al., 2003).

John Menzies

Bibliography

- Allen, J.R.L., 1982. *Sedimentary Structures: Their Character and Physical asis* (2 vols.). Amsterdam: Elsevier Science Publishing, pp. 611–679.
- Dreimanis, A., 1988. Tills, their genetic terminology and classification. In Goldthwait, R.P., and Matsch, C.L. (eds.), *Genetic Classification of Glaciogenic Deposits*. Rotterdam: A.A. Balkema, pp. 17–83.
- Dreimanis, A., and Lundqvist, J., 1984. What should be called till? *Striae*, **20**, 5–10.
- Flint, R.F., Sanders, J.E., and Rodgers, J., 1960. Diamictite, a substitute term for symmictite. *Geol. Soc. Am. Bull.*, **71**, 1809–1810.
- Folk, R.L., 1954. The distinction between grain size and mineral composition in sedimentary rock nomenclature. *J. Geol.*, **62**, 344–359.

- Gravenor, G.P., von Brunn, V., and Dreimanis, A., 1984. Nature and classification of waterlain glaciogenic sediments, exemplified by Pleistocene, Late Paleozoic and Late Precambrian deposits. *Earth Sci. Rev.*, **20**, 105–166.
- Hambrey, M.J., and Harland, W.B. (eds.), 1981. *Earth's Pre-Pleistocene Glacial Record*. Cambridge, UK: Cambridge University Press, 1004pp.
- Harland, W.B., Herod, K.N., and Krinsley, D., 1966. The definition and identification of tills and tillites. *Earth Sci. Rev.*, **2**, 225–256.
- Hiemstra, J.F., and van der Meer, J.J.M., 1997. Pore-water controlled grain fracturing as indicator for subglacial shearing in tills. *J. Glaciol.*, **43**, 446–454.
- Iverson, N.R., 1991. Morphology of glacial striae: Implications for abrasion of glacier beds and fault surfaces. *Geol. Soc. Am. Bull.*, **103**, 1308–1316.
- Lawson, D.E., 1981. Distinguishing characteristics of diamictons at the margin of the Matanuska glacier, Alaska. *Ann. Glaciol.*, **2**, 78–84.
- Meer, van der J.J.M., 1997. Particle and aggregate mobility in till: Microscopic evidence of subglacial processes. *Quaternary Sci. Rev.*, **16**, 827–831.
- Meer, van der J.J.M., Menzies, J., and Rose, J., 2003. Subglacial till: The deforming glacier bed. *Quaternary Sci. Rev.*, **22**, 1659–1685.
- Menzies, J., 1990. Sand intraclasts within a diamicton mélange, southern Niagara Peninsula, Ontario, Canada. *J. Quaternary Sci.*, **5**, 189–206.
- Paul, M.A., and Eyles, N., 1990. Constraints on the preservation of diamict facies (Melt-out tills) at the margins of stagnant glaciers. *Quaternary Sci. Rev.*, **9**, 51–69.
- Pettijohn, F.J., 1975. *Sedimentary Rocks*. New York: Harper Row.
- Rappol, M., 1987. Saalian till in The Netherlands: A review. In van der Meer, J.J.M. (eds.), *Tills and Glaciotectonics*. Rotterdam: A.A. Balkema, pp. 3–21.
- Ruszczynska-Szenajch, H., 1983. Lodgement tills and syndepositional glaciogenic processes Related to subglacial thermal and hydrologic conditions. In Schlüchter, Ch., Rabassa, J., and Evenson, E.B. (eds.), *Tills and Related Deposits: Genesis, Petrology, Application, Stratigraphy*. Rotterdam: A.A. Balkema Publishers, pp. 113–117.
- Schermerhorn, L.J.G., 1966. Terminology of mixed coarse-fine sediments. *J. Sediment. Petrol.*, **36**, 831–835.

Cross-references

- [Glacial Geomorphology](#)
[Glaciomarine Sediments](#)
[Ice-Rafted Debris \(IRD\)](#)
[Sedimentary Indicators of Climate Change](#)
[Tills & Tillites](#)

DIATOMS

Diatoms, a type of unicellular algae, are one of the most abundant groups of phytoplankton and are an essential component of the oceanic food web. As autotrophs, their primary requirements for survival are adequate light and nutrients. Their primary photosynthetic pigments are chlorophyll a and c, xanthophylls and fucoxanthin. They are widely distributed in a variety of marine and freshwater environments, including open ocean and lake waters, shallow marine and lake sediments, sea ice, soils and even aerial habitats (such as wet rocks and bark). Diatoms can exist in a free-floating or planktonic form, or can be attached to a substrate, including rocks, other algae or sea ice. Species live both as solitary cells and colonially. One of their most important distinguishing characteristics is that their cell walls are impregnated with opaline silica. These paired silica valves fit together much like a box, with the larger epitheca fitting on top of the smaller hypotheca. They are held together with overlapping connecting bands, collectively termed the girdle and, together, these components comprise a frustule. These tests, which are intricately

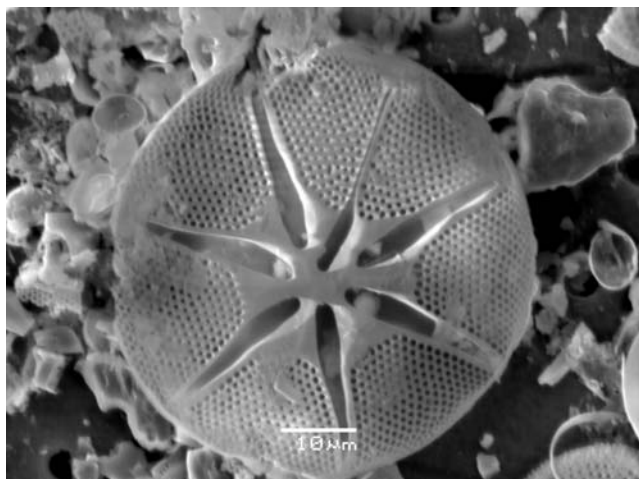


Figure D38 *Asteromphalus* sp., Southern Ocean, west of the Antarctic Peninsula, core NBP0107 KC8.

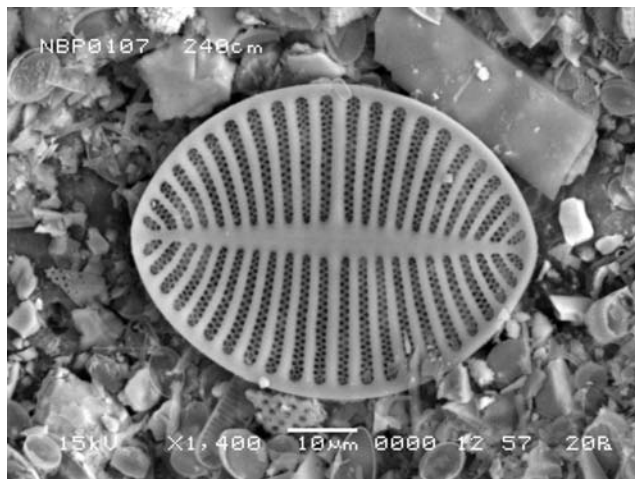


Figure D40 *Cocconeis* sp., Southern Ocean, west of the Antarctic Peninsula.

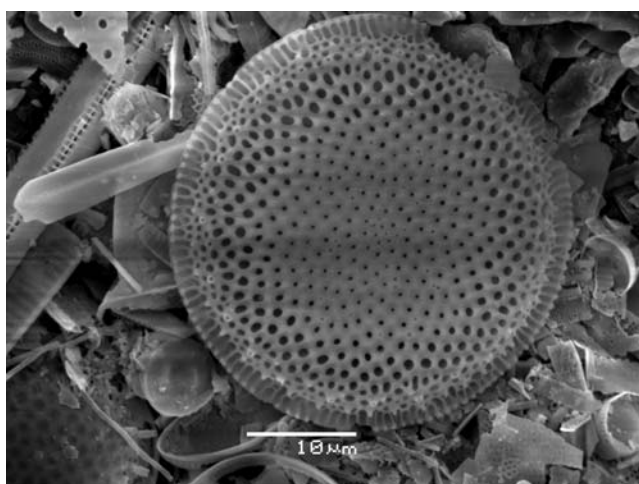


Figure D39 *Thalassiosira antarctica*, Southern Ocean, west of the Antarctic Peninsula, core NBP0107 KC8.

ornamented and taxonomically diagnostic, are often well-preserved in the fossil record, hence their use in paleoecologic and stratigraphic studies. They generally range in size from a few microns to a few hundred or even thousand microns, though most are around tens of microns in size (see [Figures D38–D40](#)).

Taxonomically, diatoms are placed in the class Bacillariophyceae, and are grouped with the Chrysophyceae (includes silicoflagellates and calcareous nannofossils) and Xanthophyceae in the phylum Chrysophyta. Two orders are distinguished, the Centrales, with radial symmetry, and the Pennales, which have bilateral symmetry. Over 100,000 different species (extinct and extant) have been described but perhaps only 15,000 of these are valid species, since many of the taxa described are now known to be variations of a single species. For example, through culturing work, workers have documented morphologic variability at different life cycle stages. A sparse fossil record of marine diatoms might date as far back as the Jurassic; however, these reports of Jurassic diatoms are not universally accepted. Certainly, a diverse flora of marine diatoms extends back to the

lower Cretaceous, suggesting their previous evolution. Lower Cretaceous diatoms are known from California, Russia, Antarctica and the southwest Pacific and Indian Oceans. Freshwater diatoms are known only as far back as the Paleocene.

Data on past and present abundance and distribution of diatom assemblages are used to reconstruct and document changes in environment, including those occurring today, for example, in the acidification and eutrophication of lakes, and pollution of freshwater and marine systems. Diatoms are particularly sensitive to a number of different environmental parameters, such as temperature, salinity, water chemistry (pH, alkalinity, nutrient concentration) and light levels, so analysis of assemblages over time is used as a proxy for these factors. The rapid regeneration rate of diatoms allows them to respond quickly to environmental change; their siliceous tests provide long-term documentation of these changes. Diatom data also provide important biostratigraphic information and have been used extensively as a correlation tool. Finally, diatoms have proven useful in a variety of other settings, such as archeological work, forensic studies and industrial use of diatomite (sedimentary rock formed by the accumulation and lithification of diatomaceous deposits), primarily for filtration.

Amy Leventer

Cross-references

[Lacustrine Sediments](#)
[Marine Biogenic Sediments](#)
[Paleoclimate Proxies, an Introduction](#)

DINOFLAGELLATES

The ecology of dinoflagellates

Dinoflagellates are microscopic unicellular organisms or protists belonging to the division of Dinoflagellata (Fensome et al., 1993). They inhabit most types of aquatic environments, from lakes to open ocean, and from equatorial to arctic settings.

When blooming, dinoflagellates can be responsible for “red tides”, so called because the very large number of cells in the surface water induces a color change. A few dinoflagellate species produce neurotoxins that may be bioconcentrated by filtering organisms, notably shellfishes, which then become poisonous and dangerous for the health of animals feeding on them.

Living dinoflagellates are characterized by two flagella, which permit swimming motion. Many dinoflagellates are phototrophic (i.e., undergoing photosynthesis) and form an important part of the planktonic primary production in lakes and oceans. Some dinoflagellates are heterotrophic (i.e., feeding on other organisms), and others are symbionts of marine invertebrates such as corals, in which they are known as zooxanthellae.

The life cycle of dinoflagellates and the cyst stage

Most dinoflagellates have a complex life cycle involving several stages, asexual and sexual, motile and non-motile (see Figure D41). During the course of sexual reproduction, some species form a diploid cell (i.e., with $2n$ chromosomes following the fusion of the gametes) that is protected within a cyst, permitting survival of the organism during a dormancy period of variable length (Fensome et al., 1993).

The motile and cyst stages are characterized by distinct morphologies. The cell wall or theca of many motile dinoflagellates is armored and consists of cellulose plates that form a distinctive geometry or tabulation, whereas the cysts only bear traces of the theca tabulation.

The organic-walled dinoflagellate cysts or dinocysts

Many species of dinoflagellates produce fossilizable cysts that are composed of highly resistant organic matter, similar in composition to the sporopollenin of pollen grains. The

organic-walled cysts, also known as “dinocysts” and previously called “hystrichospheres” by paleontologists, are usually well preserved in sediment. The dinocysts are typically 15–100 μm in diameter, and are observed in palynological slides prepared by standard laboratory procedures used for the study of pollen and spores, which involve treatments with hydrofluoric and hydrochloric acids. The study of dinocysts is thus considered a sub-discipline of palynology.

Dinocysts in paleoecology, paleoceanography and paleoclimatology

Fossil dinocysts are mainly known from marine sediments. They appear to be particularly abundant along continental margins (estuaries, continental shelves and slopes, epicontinental seas). Dinocysts were widely used in biostratigraphy and paleoecology of the Mesozoic and Cenozoic. In the field of Quaternary paleoceanography and paleoecology, the study of dinocysts is of growing interest. Because they are very resistant, dinocysts are generally well preserved in sediment despite dissolution that may affect calcareous or siliceous biological remains. Moreover, the development of reference databases from surface sediment samples (Dale, 1996; Rochon et al., 1999; Matthiessen and de Vernal, 2001; Zonneveld and Marret, 2003) has led to the documentation of strong relationships between the distribution of dinocyst assemblages and sea-surface parameters, including productivity and hydrographical conditions. Transfer functions derived from these databases have permitted the quantitative reconstruction of temperature, salinity, and sea-ice cover extent. For example, hydrographical maps of the northern North Atlantic during the Last Glacial Maximum (21 ka) were established using dinocyst data (de Vernal et al., 2000), and many regional reconstructions are currently being developed.

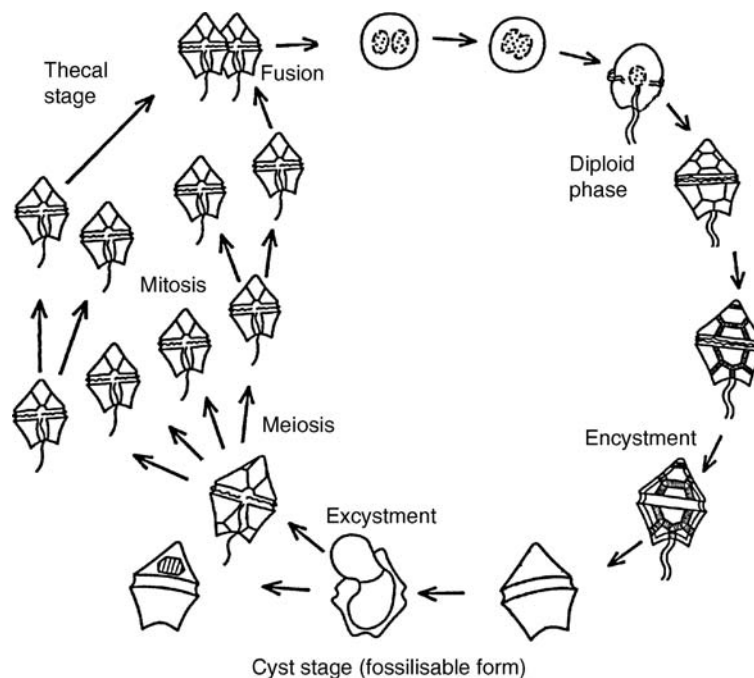


Figure D41 Schematic illustration of idealized dinoflagellate life-cycle (adapted from Fensome et al., 1993).

The calcareous dinoflagellates

In addition to organic-walled cysts or dinocysts, some dinoflagellate taxa yield calcareous microfossils generally associated with the cyst stage (Vink et al., 2000). Calcareous dinoflagellates appear to be abundant in oceanic sediments at middle to low latitudes, where they can be used as tracers of hydrographic conditions in the upper water column.

Anne de Vernal

Bibliography

- Dale, B., 1996. Dinoflagellate cyst ecology: Modelling and geological applications. In Jansonius, J., and McGregor, D.C. (eds.), *Palynology: Principles and Applications*. Texas: American Association of Stratigraphic Palynologists Foundation, College Station, 1249–1275.
- de Vernal, A., Hillaire-Marcel, C., Turon, J.L., and Matthiessen, J., 2000. Sea-surface conditions in middle to high latitudes of the North Atlantic during the last glacial maximum (LGM): The cold paradigm revisited. *Can. J. Earth Sci.*, **37**, 725–750.
- Fensome, R.A., Taylor, F.J.R., Norris, G., Sarjeant, W.A.S., Wharton, D.I., and Williams, G.L., 1993. A classification of living and fossil dinoflagellates. *Micropaleontology*, **7**, 1–351 (Special Publication).
- Matthiessen, J., and de Vernal, A. (eds.), 2001. Marine dinoflagellate cysts and high latitude Quaternary paleoenvironmental reconstructions. *J. Quaternary Sci.*, **16**(7), 595–751.
- Rochon, A., de Vernal, A., Turon, J.-L., Matthiessen, J., and Head, M.J., 1999. Distribution of dinoflagellate cyst assemblages in surface sediments from the North Atlantic Ocean and adjacent basins and quantitative reconstruction of sea-surface parameters. *Special Contribution Series of the American Association of Stratigraphic Palynologists*, **35**, Dallas, TX, pp. 1–152.
- Vink, A., Zonneveld, K.A.F., and Willems, H., 2000. Distributions of calcareous dinoflagellate cysts in surface sediments of the western equatorial Atlantic Ocean, and their potential use in paleoceanography. *Mar. Micropaleontol.*, **38**, 149–180.
- Zonneveld, K.A.F., and Marret, F., 2003. Atlas of the global geographic distribution of modern organic-walled dinoflagellate cysts. *Rev. Palaeobot. Palynol.* **125**, 1–200.

Cross-references

Coral and Coral Reefs
 Lacustrine Sediments
 Marine Biogenic Sediments
 Palynology

DOLE EFFECT

In 1935–1936, Dole (Dole, 1935) and Morita (Morita and Titani, 1936) discovered independently that the isotopic composition of atmospheric oxygen ($^{18}\text{O}/^{16}\text{O}$) is enriched relative to oceanic water. This isotopic enrichment of molecular oxygen in the heavier ^{18}O was named the Morita-Dole effect or just the Dole effect (DE in the following). The exact value of the enrichment was badly constrained for a long time after the discovery of the DE. It was not until 1972 that Kroopnick and Craig (Kroopnick, 1987) determined the DE with sufficient precision. Expressed relative to the Vienna Standard of Mean Ocean Water (V-SMOW) (Craig, 1961), they identified a value for the modern DE of

$$\begin{aligned}\delta^{18}\text{O}_{\text{Atm}} &= (^{18}\text{O}/^{16}\text{O})_{\text{Atm}} / (^{18}\text{O}/^{16}\text{O})_{\text{V-SMOW}} - 1 \\ &= 23.5 \pm 0.1\text{‰}.\end{aligned}$$

However, the reasons for this relatively strong enrichment of 23.5‰ were not clear for a long time and still are disputed to some extent. The first assumption was that photosynthesis produces an enriched O_2 flux; however, measurements did not confirm this hypothesis (Ruben et al., 1941; Dole and Jenks, 1944). Subsequently, various other hypotheses have been formulated: photochemical isotopic exchange between O_2 and H_2O (Roake and Dole, 1950) or between O_2 and CO_2 in the stratosphere (Dole et al., 1954), or, alternatively, preferred consumption of the light ^{16}O of dissolved oxygen by marine organisms (Rakestraw et al., 1951) or by soil bacteria during respiration processes (Dole et al., 1947). In each case, the measured enrichment due to the different processes could not confirm the corresponding hypothesis. Lane and Dole (1956) demonstrated convincingly that respiration processes in the ocean are indeed at least one important contribution to the DE. They measured a progressive isotopic enrichment of dissolved oxygen in oceanic water samples due to remineralization of organic material and demonstrated therewith that the biochemistry of plants must be studied to determine the origin of the DE.

Bender et al. (1994a) gave a detailed overview of current knowledge of processes contributing to the DE (see Figure D42 for a scheme of the global ^{18}O budget). Photosynthesis and respiration are the principal global O_2 fluxes. Photosynthetic production of O_2 tags the outgoing O_2 flux with the isotope signal of ambient water without any further fractionation (Guy et al., 1993). In the marine biosphere, the water of the euphotic surface layer has an isotopic composition of approximately 0‰ globally. In the terrestrial biosphere, the isotopic signature of water adjacent to photosynthetic production is characterized by large geographical and temporal variability. Following Farquhar et al. (1993), Bender et al. (1994a) opted for a global value of 4.4‰. This isotope signal of ambient water in leaves is significantly enriched as compared to oceanic surface waters and is mainly responsible for the different contribution to the DE by the terrestrial and the marine biosphere.

The most important contribution to the high value of the DE takes place during autotrophic and heterotrophic respiration. Various respirative O_2 fluxes (photorespiration, Mehler reaction, cyanide-sensitive and cyanide-insensitive pathways in dark respiration) fractionate ^{16}O against ^{18}O differently, but the mean fractionation is close to 20‰ in both the terrestrial and the marine environment. In the ocean, part of the respiration takes place in the deep ocean, isolated from the atmospheric oxygen reservoir. This slightly reduces the overall marine contribution to the DE due to a fraction of oxygen that fractionates against an already enriched oxygen pool.

Furthermore, there is a small temperature dependent fractionation during the dissolution of O_2 in water ($\sim 0.7\text{‰}$) (Benson and Krause, 1984). Equally, a small fractionation (0.4‰) takes place in the stratosphere during the photochemical exchange between CO_2 and O_2 . When adding up all these different fractionations, weighted with the corresponding fluxes, Bender et al. (1994a) computed a global equilibrium of $\delta^{18}\text{O}_{\text{Atm}} = 20.8\text{‰}$, underestimating by approximately 3‰ relative to the observed value. Besides a number of uncertainties in the considered processes, there might also be some processes neglected in this global budget such as fractionation during the diffusive mixing of O_2 in the upper soil column (Angert et al., 2001).

There are a number of applications of the DE (or of the $\delta^{18}\text{O}_{\text{Atm}}$ signal respectively) in paleoclimate studies. Past $\delta^{18}\text{O}_{\text{Atm}}$ can be reconstructed by analyzing the isotopic composition of air bubbles enclosed in the deep ice from Greenland

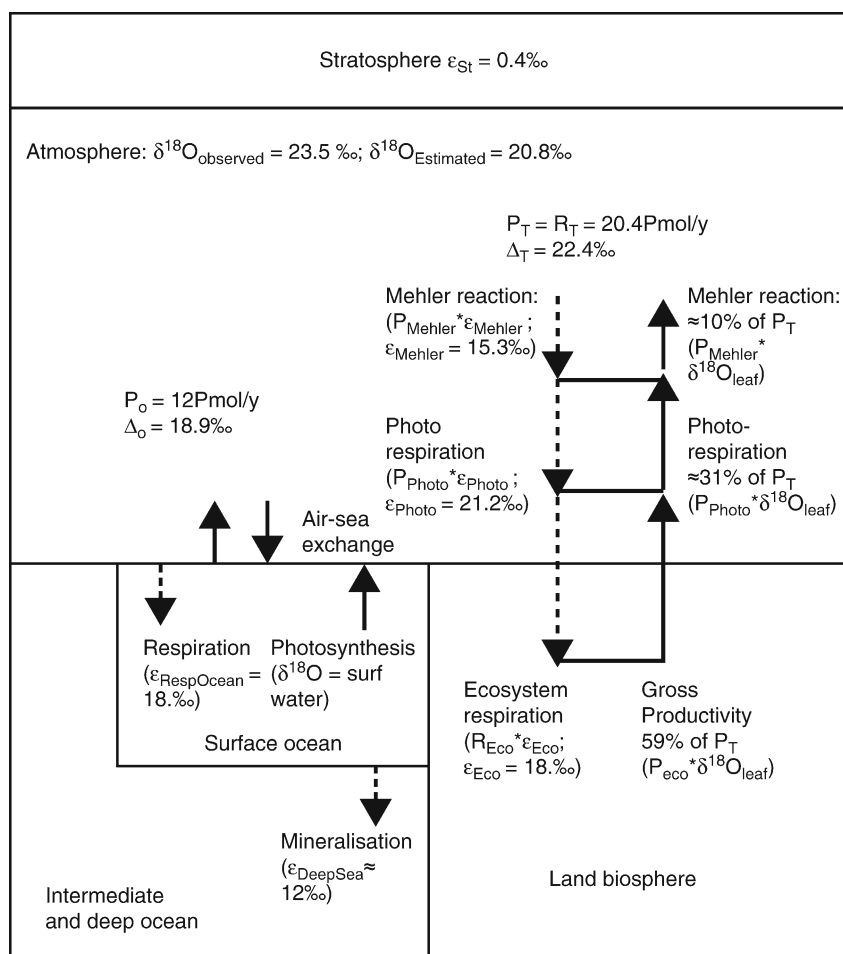


Figure D42 Scheme of the modern Dole effect according to Bender et al. (1994b). Three different oxygen consuming respirative fluxes (dark respiration, photorespiration, Mehler reaction) contribute to the total ecosystem respiration, R_{eco} , each with a different specific fractionation ϵ . This oxygen consuming process is exactly balanced by oxygen production during photosynthesis tagged isotopically with the isotopic composition of leaf water $\delta^{18}O_{leaf}$. The total terrestrial DE is 22.4‰ with a terrestrial O_2 flux of 20.4 Pmol yr^{-1} . Respirative fractionation in the ocean is slightly smaller than on land mainly due to respiration of already enriched oxygen in the deep and intermediate ocean. The photosynthetically produced O_2 flux has an isotopic signal of approximately 0‰ resulting in an oceanic contribution to the DE of 18.9‰ with an oceanic productivity of 12 Pmol yr^{-1} . The steady state solution of this best estimate is 20.8‰ compared to an observed DE of 23.5‰.

and Antarctica. The $\delta^{18}O_{Atm}$ signal is globally uniform within today's instrumental precision. Its variations in the past can therefore be used to synchronize ice cores from the Northern and Southern Hemisphere (Sowers et al., 1991; Bender et al., 1994b). Furthermore, the $\delta^{18}O_{Atm}$ signal was shown to be remarkably in phase with precessional insolation variations during the last four glacial/interglacial cycles (Petit et al., 1999). This observation was used to establish a more precise dating of polar ice cores (Parrenin et al., 2000; Shackleton, 2000). Modeling the DE also offers the potential of quantitatively constraining marine and terrestrial productivity in the past (Leuenberger, 1997; Hoffmann et al., 2003).

Georg Hoffmann

Bibliography

Angert, A., Luz, B., and Yakir, D., 2001. Fractionation of oxygen isotopes by respiration and diffusion and its implications for the isotopic composition of atmospheric O_2 . *Global Biogeochem. Cycles*, **15**(4), 871–880.

- Bender, M., Sowers, T., and Labeyrie, L., 1994a. The Dole effect and its variations during the last 130,000 years as measured in the Vostok ice core. *Global Biogeochem. Cycles*, **8**, 363–376.
- Bender, M., Sowers, T., Dickson, M.-L., Orchado, J., Grootes, P., Mayewski, P.A., and Meese, D.A., 1994b. Climate correlations between Greenland and Antarctica during the past 100,000 years. *Nature*, **372**, 663–666.
- Benson, B., and Krause, D., 1984. The concentration and isotopic fractionation of oxygen dissolved in fresh water and seawater in equilibrium with the atmosphere. *Limnol. Oceanogr.*, **318**, 349–352.
- Craig, H., 1961. Standard for reporting concentrations of deuterium and oxygen-18 in natural water. *Science*, **133**, 1833–1834.
- Dole, M., 1935. The relative atomic weight of oxygen in water and in air. *J. Am. Chem. Soc.*, **57**, 2731.
- Dole, M., and Jenks, G., 1944. Isotopic composition of photosynthetic oxygen. *Science*, **100**, 409.
- Dole, M., Hawkins, R.C., and Barker, H.A., 1947. Bacterial fractionation of oxygen isotopes. *J. Am. Chem. Soc.*, **69**, 226–228.
- Dole, M., Lane, G.A., Rudd, D.P., and Zankelies, D.A., 1954. Isotopic composition of atmospheric oxygen and nitrogen. *Geochim Cosmochim Acta*, **6**, 65–78.

- Farquhar, G.D., Lloyd, J., Taylor, J.A., Flanagan, L.B., Syvertsen, J.P., Hubick, K.T., Wong, S.C., and Ehleringer, J.R., 1993. Vegetation effects on the isotope composition of oxygen in atmospheric CO₂. *Nature*, **363**, 439–443.
- Guy, R.D., Fogel, M.L., and Berry, J.A., 1993. Photosynthetic fractionation of the stable isotopes of oxygen and carbon. *Plant Physiol.* **101**, 37–47.
- Hoffmann, G., Cuntz, M., Weber, C., Ciais, P., Friedlingstein, P., Heimann, M., Jouzel, J., Kaduk, J., Maier-Reimer, E., Six, K., and Seibt, U., 2003. A model of the Earth's Dole effect. *Global Biogeochem. Cycles*, **17**, 103–114.
- Kroopnick, P.M., 1987. Oxygen 18 in dissolved oxygen. In Oestlund, G., Craig, H., Broecker, W.S., and Spencer, D. (eds.), *GEOSECS Atlantic, Pacific and Indian Ocean Expeditions*. Washington D.C.: U.S. Government Printing Office, pp. 27–182.
- Lane, G.A., and Dole, M., 1956. Fractionation of oxygen isotopes during respiration. *Science*, **123**, 574–576.
- Leuenberger, M., 1997. Modeling the signal transfer of seawater $\delta^{18}\text{O}$ to the $\delta^{18}\text{O}$ of atmospheric oxygen using a diagnostic box model for the terrestrial and marine biosphere. *J. Geophys. Res.*, **102**, 26841–26850.
- Morita, N., and Titani, T., 1936. Über den Unterschied in der Isotopenzusammensetzung von Luft- und Wassersauerstoff. *Bull. Chem. Soc. Japan*, **11**, 36–38.
- Parrenin, F., Jouzel, J., Waelbroeck, C., Ritz, C., and Barnola, J.-M., 2000. Dating the Vostok ice core by an inverse method. *J. Geophys. Res.*
- Petit, J.R., Jouzel, J., Raynaud, D., Barkov, N.I., Barnola, J.M., Basile, I., Bender, M., Chappellaz, J., Davis, J., Delaygue, G., Delmotte, M., Kotlyakov, V.M., Legrand, M., Lipenkov, V., Lorius, C., Pépin, L., Ritz, C., Saltzman, E., and Stievenard, M., 1999. 420,000 years of climate and atmospheric history revealed by the Vostok deep antarctic ice core. *Nature*, **399**, 429–436.
- Rakestraw, N.W., Rudd, D.P., and Dole, M., 1951. Isotopic composition of oxygen in air dissolved in Pacific ocean water as a function of depth. *J. Am. Chem. Soc.*, **73**, 2976.
- Roake, W.E., and Dole, M., 1950. Oxygen isotope exchange in the electric discharge. *J. Am. Chem. Soc.*, **72**, 36–40.
- Ruben, S., Randall, M., Kamen, M., and Hyde, J.L., 1941. Heavy oxygen (¹⁸O) as a tracer in the study of photosynthesis. *J. Am. Chem. Soc.*, **63**, 877–879.
- Shackleton, N.J., 2000. The 100,000-Year Ice-Age Cycle Identified and Found to Lag Temperature, Carbon Dioxide, and Orbital Eccentricity. *Science*, **289**, 1897–1902.
- Sowers, T., Bender, M., Raynaud, D., Korotkevich, Y.S., and Orchado, J., 1991. The ¹⁸O of atmospheric O₂ from air inclusions in the Vostok ice core: Timing of CO₂ and ice volume changes during the penultimate deglaciation. *Paleoceanography*, **6**, 679–696.

Cross-references

[Ice cores, Antarctica and Greenland Isotope Fractionation](#)
[Oxygen Isotopes](#)

DRUMLINS

A drumlin is a subglacial landform that appears as a distinctive streamlined hill of sediment in the postglacial landscape. The term is derived from a Gaelic word meaning a mound or rounded hill. Drumlins vary significantly in size, shape and composition, and their origins remain controversial.

Drumlins are streamlined in the direction of ice movement, with a degree of elongation typically about 3:1 but sometimes as much as 60:1. At higher elongations drumlins grade into megaflutes. The up-glacier (stoss) end is typically the steeper and blunter while the downstream (lee) face is more gently sloping and more sharply pointed in plan form. Drumlins may occur singly or in “swarms” containing hundreds or thousands of hills. The largest drumlins reach 50 m in height and may be 20 km long, while the smallest examples are only 10 m long and grade

into other classes of smaller streamlined features such as flutes. Small drumlins can be superimposed on larger ones.

The composition of drumlins is variable but typically dominated by massive diamicton usually interpreted as till. Some drumlins contain a rock core and many include coarse stratified glaciofluvial deposits. The material is often highly deformed.

Several different origins for drumlins have been proposed and it is likely that different drumlins are formed in different ways. Some models suggest that drumlins are remnants of subglacial erosion of previously deposited sediments. It has been suggested that erosion was accomplished by huge subglacial “megafloods.” Other models suggest that drumlins are depositional features reflecting either subglacial lodgment or meltout. Many theories propose that the key processes are deformational. A widely accepted model is that drumlins are created by differential movement of material within a deforming subglacial sediment layer. The drumlins reflect areas of less mobile sediment while intervening areas reflect more rapidly moving material. Stratified sediments in some drumlins have been interpreted as lee side stratification sequences in water-filled cavities on the downstream end of drumlins. The flow of water through subglacial sediment under varying pressures, and the deformation of material in response to both glacial and water pressure are central to much current thinking about drumlins.

It has been suggested that drumlins form in a narrow belt only 20–30 km wide close to an ice-sheet margin. As the margin retreats, the zone migrates, and extensive fields of drumlins can be created in a time-transgressive sequence. It has also been suggested that drumlin fields mark the positions of former ice streams. Although drumlins are possibly the most intensively studied glacial landform, our understanding of them remains incomplete. However, it is clear that they have the potential to provide important information about former ice sheets both through their geographic distribution and through their sedimentology. Useful reviews are provided by Benn and Evans (1996), Bennett and Glasser (1996) and Hambrey (1994).

Peter G. Knight

Bibliography

- Benn, D.I., and Evans, D.J.A., 1998. *Glaciers and Glaciation*. London, UK: Arnold, 734pp.
- Bennett, M.R., and Glasser, N.F., 1996. *Glacial Geology*. Chichester, UK: John Wiley and sons, 364pp.
- Hambrey, M.J., 1994. *Glacial Environments*. London, UK: UCL Press Ltd., 296pp.

Cross-references

[Basal ice](#)
[Diamicton](#)
[Glacial geomorphology](#)
[Glaciofluvial sediments](#)
[Late Quaternary megafloods](#)
[Tills & tillites](#)

DURICRUSTS

Duricrusts are near-surface geochemical crusts formed as a result of low-temperature physicochemical processes operating within the zone of weathering that lead to the absolute or relative accumulation of minerals through the replacement



Figure D43 A 10 m thick exposure of silcrete and calcrete in the flanks of the Auob Valley at Kalkheuvall, Namibia (photograph: David J. Nash).

and/or cementation of pre-existing soil, sediment, bedrock, or weathered material. They can vary in hardness from powdery to highly indurated, and may reach thicknesses of >50 m although 1–10 m is more common (Goudie, 1973). Calcrete or caliche (cemented by calcium carbonate) is the most widespread form and is estimated to underlie >13% of the Earth's land surface (Wright and Tucker, 1991). Iron- and aluminum-rich ferricretes and alcretes are the next most common, and occur over large areas of west, central and east Africa, Australia, and India. Silica-rich silcrete is less widespread but is locally important in southern Africa, Australia, and Europe (Watson and Nash, 1997). Other accumulations such as calcium sulfate-cemented gypcrete are sometimes defined as duricrusts but are less likely to persist within the landscape. In contrast, durable duricrust varieties such as ferricrete and silcrete can act as important controls upon landscape evolution once exposed since they may form resistant caprocks (Figure D43).

There is no single model to explain the formation of all duricrusts. Ferricretes and alcretes commonly form by the relative accumulation of iron and aluminum oxides and hydroxides in seasonally-wet humid to sub-humid tropical environments as other more mobile elements are leached from weathering profiles. Absolute accumulation may also occur where iron and aluminum are transported downslope mechanically or in solution, or are mobilized within the weathering mantle. Silcretes and calcretes usually develop through the absolute accumulation of silica and calcium carbonate derived from rock weathering, dust, rainfall, surface- and groundwater, or biogenic sources. The translocation of solid or dissolved materials to sites of accumulation can be achieved via lateral movement of solutions through fluvial, lacustrine, or groundwater systems, and/or by vertical transfer mechanisms such as percolation and capillary rise (often in association with pedogenesis). Once at a site of accumulation, silica and calcium carbonate precipitation can be triggered by evaporation, pH changes, reactions with other cations, and organic activity.

Duricrusts may act as important paleoenvironmental indicators, particularly when found beyond their zone of contemporary formation or within the geological record. However, it is vital that the factors controlling formation are understood prior

to their use as such indicators. Low relative relief appears to be a requirement for the development of all varieties since the rate of formation must exceed that of removal of material by erosion. Topography may also influence the ability of a host material to retain moisture or permit leaching. The availability of a source material is critical in determining the degree and rate of formation. There is less agreement about the climatic requirements for duricrust formation. Calcretes are known to be forming today in dryland regions with rainfall in the range 200–600 mm (Goudie, 1973), and may, therefore, be a useful indicator of semi-arid climates. The environment of silcrete formation is more complex, with pedogenic varieties thought to develop under humid tropical climates and non-pedogenic silcretes under arid tropical conditions. However, as silcretes are only forming in one location today (through fixation by cyanobacteria in the highly alkaline Sua Pan, Botswana), it is difficult to identify representative modern analogs. The requirement of intensive leaching for ferricrete and alcrete development makes them a potentially useful indicator of humid tropical climates, with alcretes more prevalent where contemporary rainfall levels are particularly high.

David J. Nash

Bibliography

- Goudie, A.S., 1973. *Duricrusts in Tropical and Subtropical Landscapes*. Oxford, UK: Clarendon Press, 174pp.
- Watson, A., and Nash, D.J., 1997. Desert crusts and varnishes. In Thomas, D.S.G. (ed.), *Arid Zone Geomorphology*. Chichester, UK: Wiley, pp. 69–107.
- Wright, V.P., and Tucker, M.E. (eds.), 1991. *Calcretes*. Oxford, UK: Blackwell Scientific, 352pp.

Cross-references

[Arid Climates and Indicators](#)
[Laterite](#)
[Paleosols, Pre-Quaternary](#)
[Paleosols – Quaternary](#)
[Sedimentary Indicators of Climate Change](#)
[Weathering and Climate](#)

DUST TRANSPORT, QUATERNARY

The atmospheric cycle of soil-derived dust aerosol is expected to respond to changes in global climate conditions, such as the overall intensity of winds that entrain dust, and changes of the hydrological cycle that can affect the extent and dryness of source areas as well as the length of time that dust remains in the atmosphere. At the same time, dust can potentially impact global and regional climate conditions in several ways, by impacting the radiative balance of the atmosphere or by providing micronutrient fertilizers to marine and terrestrial plants, thereby modulating atmospheric CO₂ concentrations. Major dust source regions today are the Saharan desert, Arabia, the Asian deserts, Australia, and North America. The majority of atmospheric dust comes out of North Africa (50–70%) and Asia (10–25%).

Dust is particularly important within the context of the Quaternary because large fluctuations and overall increases in atmospheric dust concentrations coincided with the onset of Northern Hemisphere glacial cycles, approximately 2.8 Ma. The longest land records suggest that relatively continuous atmospheric dust deposition occurred on the Chinese Loess Plateau since about 7 Ma (Ding et al., 1999). These records, along with marine records from the North Pacific (Rea et al., 1998), suggest that dust deposition was enhanced following a geologically more recent phase of uplift of the Tibetan Plateau (approximately 3.6 Ma). This uplift blocked Indian moisture sources from reaching East Asia and created conditions favorable for the development of the East Asian monsoon, which modulates the southward flow of cold dry air masses across the East Asian continent in winter. As glacial cycles intensified, they enhanced conditions of stronger winds and higher aridity that favor dust emission during cold periods.

Marine sediment records of dust from around Africa also suggest a shift from a predominantly monsoon-driven climate before 2.8 Ma towards more arid conditions modulated by the periodicity of Northern Hemisphere glaciations after 2.8 Ma (deMenocal, 1995). The intensification of Northern Hemisphere glaciations resulted in cooler North Atlantic surface ocean temperatures that inhibited the expansion of the North African summer monsoon into the African continent, thereby increasing Saharan and Sahelian aridity.

Dust deposited over land, ocean or ice surfaces can be preserved in the geologic record and serve as archives of periods of past dustiness. Determining exact changes in deposition rates between different time periods is limited by the many different techniques used to measure dust, as well as the limited number of precise dates generated on these different sediment types. Nevertheless, significant efforts have been made to quantify changes in dust deposition through time, and the best-documented period of intensified dustiness in the Quaternary is the Last Glacial Maximum (approximately 17–23 ka). From these records, we know that dust was about 2–3 times increased globally during glacial periods compared with interglacial periods (Figure D44). During the last glacial period, North Africa remained the most important source of dust, but both data and models suggest an additional expansion of Asian, Australian, and South American dust sources during this time.

Loess deposits

During the last glacial period, loess deposition was greatly expanded, mostly in periglacial regions such as North America,

the Eurasian continent, and the South American Pampas region. The source of dust forming loess deposits is largely material that has been ground by glaciers and subsequently becomes available following fluvial transport to arid, non-vegetated source regions. Loess deposits are indicators of changes in both the extent and activity of dust sources, but also strongly depend on local conditions like terrain forms. For example, flat basins are relatively stable sites of continuous deposition. River terraces very near sources frequently show amplified deposition rates and are more likely to contain erosional discontinuities. Dust particles deposited in loess regions consist of relatively coarse particles (10–63 μm size) that have not been transported over large distances. As a result, deposition rates in loess deposits have been measured to be as high as 20,000 g m⁻² yr⁻¹ in the mid-continental USA (Roberts et al., 2003), while much of the loess deposited on the Chinese Loess Plateau falls in the range of 300–500 g m⁻² yr⁻¹.

Patterns of thickness and loess grain size can provide information about surface transport trajectories of loess. For example, in the mid-continental USA, thickness trends in the last glacial loess indicate that predominant surface winds came from the west and northwest (Figure D45). Loess thicknesses are greatest near dust sources along rivers, at the southern edge of the North American ice sheet, and directly downwind of the Rocky Mountains, and rapidly decrease to the east of these source regions.

Marine sediments

In order to examine dust records in marine sediments, one must first isolate the terrigenous material within marine sediments, and then avoid contamination by non-eolian terrigenous material such as turbidites, river plumes, ice bergs, and deep currents ice-rafted detritus. Once these complications are circumvented, marine sediment records can be good indicators for intermediate and long-distance transport of dust particles. Mean grain sizes in marine sediments are usually much less than 10 μm, although larger grains are found in sediments close to continental source areas. Accumulation rates in marine sediments can be as high as 100 g m⁻² yr⁻¹, but are usually in the order of 1–10 g m⁻² yr⁻¹.

Overall, marine sediments suggest about a 2-fold increase in glacial compared with interglacial dust deposition in the tropics and mid-latitudes, where the records are reliable. Different regions experienced different changes in dust deposition during glacial-interglacial cycles. Marine sediments in the North Pacific region suggest a 1–3-fold increase in dust deposition at the LGM compared to the late Holocene period, deposition off Africa increased by approximate 2–5 times, and deposition to the southeast of Australia shows 2–9-fold increases in dust deposition during glacial periods. In contrast, although the absolute magnitude of dust entering the Arabian Sea is high, increases in glacial dust deposition over the Arabian Sea are relatively small (60–80% increase at the LGM compared to today). In general, the spatial patterns of where dust was deposited did not undergo major changes, suggesting that the actual transport pathways of dust did not shift significantly between glacial and interglacial periods for most parts of the world.

Ice cores

Ice cores provide a record of long-distance transport of dust that reflects combined changes in source strengths, transport, and deposition through time. Grain sizes of dust found in ice cores are almost always smaller than 5 μm in diameter. Glacial increases in dust fluxes are highest in the Antarctic ice cores, with an approximately 10-fold increase in the Vostok Ice Core

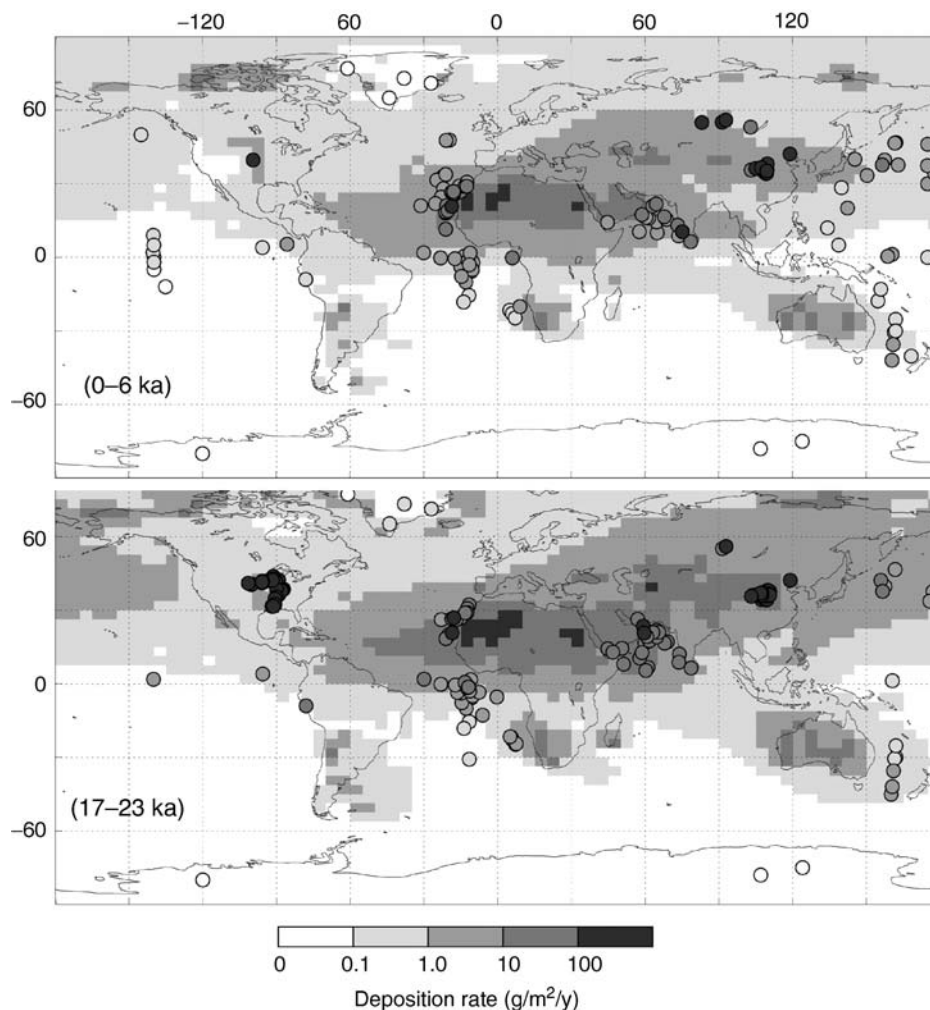


Figure D44 Simulated and observed glacial-interglacial changes in dust deposition between the late Holocene (0–6 ka) and the last glacial period (17–23 ka). Geological data are represented by circles taken from the Dust Indicators and Records of Terrestrial and Marine Paleoenvironments (DIRTMAP) database (Kohfeld and Harrison, 2001) superimposed on model results of Werner et al. (2003).

(Petit et al., 1999). While the changes in dust fluxes at these locations are very high, the actual fluxes are low (on the order of $0.0001\text{--}0.01\text{ g m}^{-2}\text{ yr}^{-1}$).

Mineralogical and isotope studies of the dust from ice cores in both Greenland and Antarctica have been used to constrain the polar transport and origins of dust. Current studies indicate that glacial dust arriving at Antarctica originates in southern South America (which is the dominant source), with lesser amounts possibly derived from northern New Zealand and the Antarctic dry valleys (Delmonte et al., 2002). Dust arriving in Greenland originates in the Asian deserts. Ice-core dust concentrations during interglacial periods are generally so low that their source regions cannot be pinpointed. However, studies on snow pits near the Greenland ice cores suggest that modern dust is still derived from Asian deserts (specifically the Takla Makan and Inner Mongolian deserts of northern China (Bory et al., 2002).

Ice core data from Vostok have also revealed the relative timing of changes in dust fluxes compared with other environmental parameters such as temperature and CO_2 (Figure D46).

In these records, dust increased well after the onset of glacial cooling and lowering of atmospheric CO_2 , with peak dust fluxes occurring only during peak glacial periods. This timing may provide insights into the causes of increased dustiness, as well as feedbacks of dust on climate parameters such as temperature, precipitation, and radiative balance.

Causes of increased glacial dustiness

Possible causes for increased dust emissions in glacial periods are stronger surface wind speeds that could lift higher amounts of dust aerosols from surfaces compared to modern conditions; increased aridity, which would expand the areas with drier soils and reduced vegetation where soil deflation by wind is possible; and increased availability of fine sediments that could easily be picked up by surface winds. Atmospheric loading of dust particles could also be increased under cold climate conditions as a consequence of the weakened hydrological cycle. (This can be deduced from the Clausius-Clapeyron relationship, which predicts lower atmospheric water content at lower temperatures.) The decrease in atmospheric water content leads

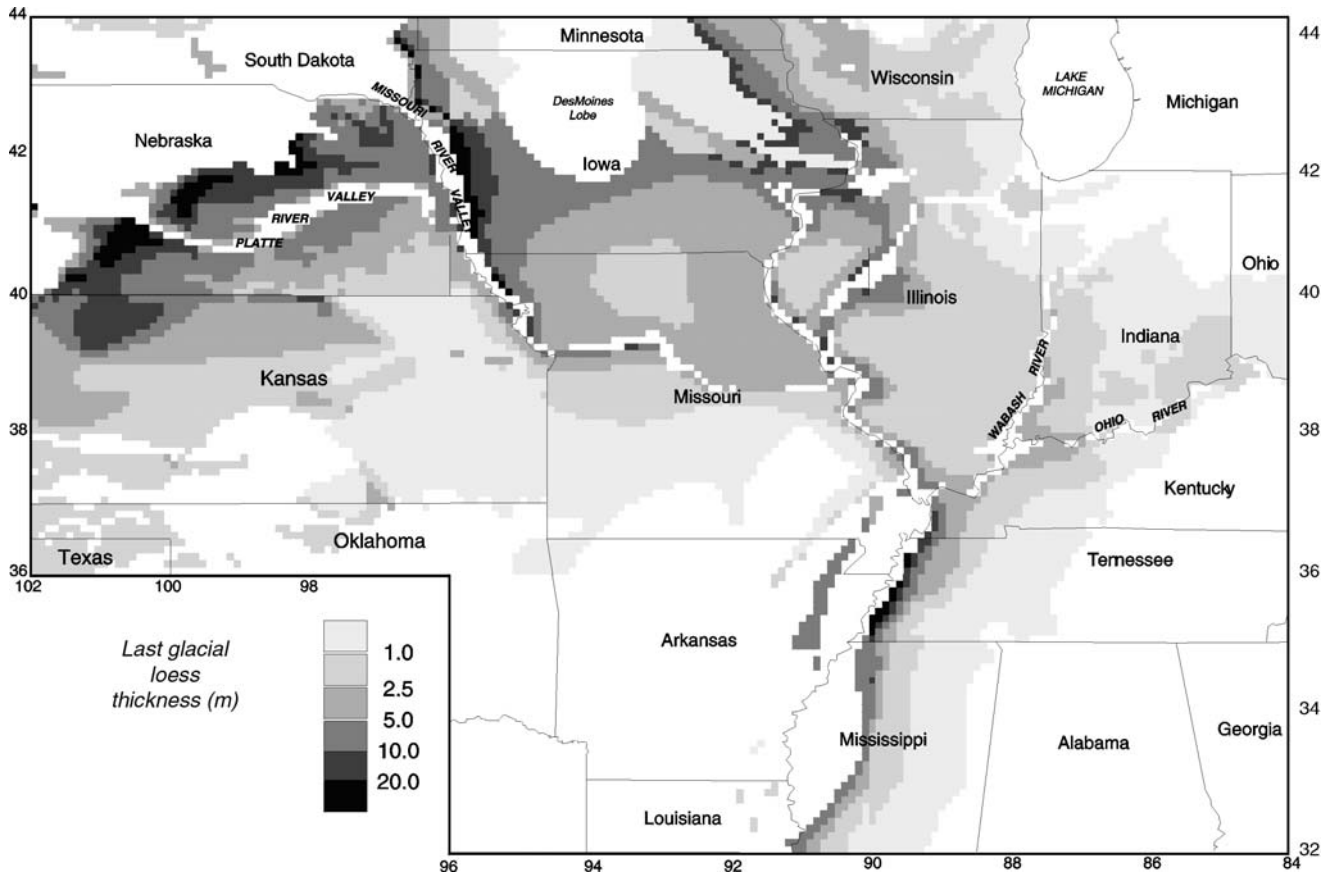


Figure D45 Thickness of last glacial loess from the midcontinental USA (Kohfeld and Harrison, 2001).

to decreased precipitation, reducing the washout of atmospheric dust particles and thus leading to longer atmospheric lifetimes.

The Last Glacial Maximum (LGM) has been a major focus of dust cycle modeling (e.g., Joussaume, 1993; Andersen et al., 1998; Mahowald et al., 1999; Reader et al., 1999; Lunt and Valdes, 2002; Werner et al., 2003), partly because dust deposition rates were high and well-documented for comparison (e.g., DIRTMAP, Kohfeld and Harrison, 2001), and partly because the changes in boundary conditions (e.g., ice sheet extent, atmospheric composition) are relatively well known.

Global dust models can only reproduce the increase in glacial dust deposition observed at high latitudes when the combined impact of increased wind speeds, reduced intensity of the hydrological cycle, and vegetation changes are included together. Neither increase in surface wind speeds and decrease in soil moisture alone (Joussaume, 1993; Andersen et al., 1998; Reader et al., 1999), nor additional increase in dust source areas caused by exposure of continental shelves can explain the observed increased high latitude dust (Andersen et al., 1998; Reader et al., 1999). Incorporating increases in dust source areas from changes in vegetation cover (Mahowald et al., 1999; Lunt and Valdes, 2002) produces a 20-fold increase in atmospheric dust loads at high latitudes, which is consistent with the high dust fluxes observed in polar ice cores. An LGM simulation using a full seasonal cycle of vegetation cover as a mask for dust emissions, as well as dried lake-beds as preferential dust emission regions, shows a more moderate increase in dust emissions, of a factor

of 2–3 during the LGM, in agreement with the available marine sediment and ice core data (Werner et al., 2003). The potentially large effect of dust supplied by glacial outwash, and increase in dry lake-beds at the LGM has not yet been evaluated by such global dust cycle models.

Effects of increased glacial dust

Dust may impact the climate by its direct radiative effect, i.e., it may either decrease or increase surface temperatures and modify atmospheric circulation depending on its optical properties and the albedo of the surface underlying the dust cloud. Overpeck et al. (1996) hypothesized that absorption of solar radiation over bright, ice covered surfaces in the Northern Hemisphere could cause warmer temperatures compared with those that would have occurred without increased dustiness at the LGM. In contrast, Claquin et al. (2003) showed that warming by dust would have a negligible effect at high latitudes when compared to the cooling impact of increased albedo due to the tremendous ice sheet expansion at the LGM. On the other hand, Claquin et al. (2003) estimated that the albedo feedback due to increased glacial atmospheric dust could reduce the incoming radiation in the tropics by as much as 2 W m^{-2} , which is the same order of magnitude as the decrease in greenhouse forcing due to reduced atmospheric CO_2 . This decrease in solar radiation at the surface might have caused additional cooling at low latitudes during the LGM. So far, no estimates regarding the impact of increased glacial dust on cloud

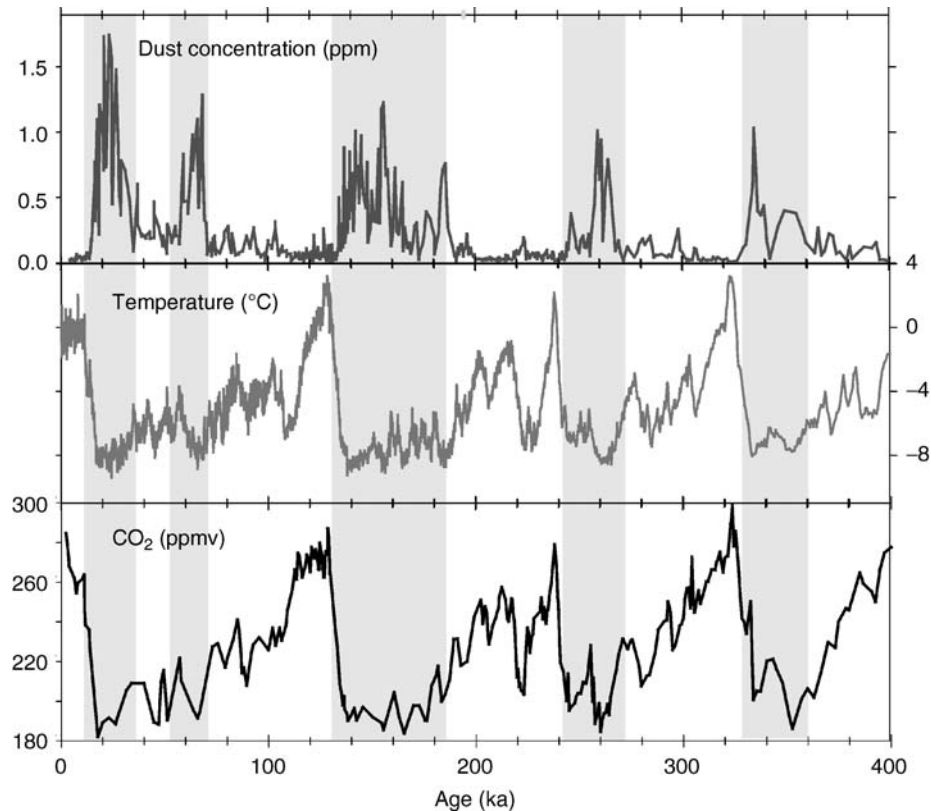


Figure D46 Records of temperature, carbon dioxide, and dust concentrations taken from the Vostok Ice Core, Vostok, Antarctica (Petit et al., 1999).

properties exist, but it is suspected that the presence of dust particles could have a significant impact on the brightness of clouds and precipitation formation (Rosenfeld et al., 2001).

In addition to the radiative effects of dust, the addition of iron from the increased dust deposited over the ocean could have fertilized the oceanic biosphere and subsequently enhanced the drawdown of atmospheric CO₂. This effect has been estimated to lie between 10 and 40 ppm of the observed glacial-interglacial atmospheric CO₂ change (Archer et al., 2000; Watson et al., 2000; Bopp et al., 2003). However, these estimates still incorporate large uncertainties, ranging from the estimation of Fe solubility to the exact role of Fe within marine ecosystems.

Karen E. Kohfeld and Ina Tegen

Bibliography

- Andersen, K.K., Armengaud, A., and Genthon, C., 1998. Atmospheric dust under glacial and interglacial conditions. *Geophys. Res. Lett.*, **25**, 2281–2284.
- Archer, D., Winguth, A., Lea, D., and Mahowald, N., 2000. What caused the glacial/interglacial atmospheric pCO₂ cycles? *Rev. Geophys.*, **38**, 159–189.
- Bopp, L., Kohfeld, K.E., Le Quéré, C., and Aumont, O., 2003. Dust impact on marine biota and atmospheric CO₂ during glacial periods. *Paleoceanography*, **18**, doi: 10.1029/2002PA000810.
- Bory, A.J.-M., Biscaye, P.E., Svensson, A., and Grousset, F.E., 2002. Seasonal variability in the origin of recent atmospheric mineral dust at NorthGRIP, Greenland. *Earth Planet. Sci. Lett.*, **196**, 123–134.
- Claquin, T., Roelandt, C., Kohfeld, K.E., Harrison, S.P., Tegen, I., Prentice, I.C., Balkanski, Y., Bergametti, G., Hansson, M., Mahowald, N., Rodhe, H., and Schulz, M., 2003. Radiative forcing of climate by ice-age atmospheric dust. *Climate Dyn.*, **20**, 193–202, doi: 10.1007/s00382-002-0269-1.
- Delmonte, B., Petit, J.R., and Maggi, V., 2002. Glacial to Holocene implications of the new 27000-year dust record from the EPICA Dome C (East Antarctica) ice core. *Climate Dyn.*, **18**, 647–660.
- deMenocal, P.B., 1995. Plio-Pleistocene African climate. *Science*, **270**, 53–59.
- Ding, Z.L., Xiong, S.F., Sun, J.M., Yang, S.L., Gu, Z.Y., and Liu, T.S., 1999. Pedostratigraphy and paleomagnetism of a similar to 7.0 Ma eolian loess-red clay sequence at Lingtai, Loess Plateau, north-central China and the implications for paleomonsoon evolution. *Palaeogeogr. Palaeoclimatol. Palaeoecol.*, **152**, 49–66.
- Joussaume, S., 1993. Paleoclimate Tracers: An investigation using an atmospheric general circulation model under ice age conditions 1. Desert dust. *J. Geophys. Res.*, **98**, 2767–2805.
- Kohfeld, K.E., and Harrison, S.P., 2001. DIRTMAP: The geologic record of dust. *Earth Sci. Rev.*, **54**, 81–114.
- Lunt, D.J., and Valdes, P.J., 2002. Dust deposition and provenance at the last glacial maximum and present day. *Geophys. Res. Lett.*, **29**, 2085, doi: 10.1029/2002GL015656.
- Mahowald, N., Kohfeld, K.E., Hansson, M., Balkanski, Y., Harrison, S.P., Prentice, I.C., Schulz, M., and Rodhe, H., 1999. Dust sources and deposition during the last glacial maximum and current climate: A comparison of model results with palaeodata from ice cores and marine sediments. *J. Geophys. Res.*, **104**, 15,895–15,916.
- Overpeck, J., Rind, D., Lacs, A., and Healy, R., 1996. Possible role of dust-induced regional warming in abrupt climate change during the last glacial period. *Nature*, **384**, 447–449.
- Petit, J.R., Jouzel, J., Raynaud, D., Barkov, N.I., Barnola, J.M., Basile, I., Bender, M., Chappellaz, J., Davis, M., Delaygue, G., Delmotte, M., Kotlyakov, V.M., Legrand, M., Lipenkov, V.Y., Lorius, C., Pepin, L., Ritz, C., Saltzman, E., and Stievenard, M., 1999. Climate and atmospheric history of the past 420,000 years from the Vostok ice core, Antarctica. *Nature*, **399**, 439–436.

- Rea, D.K., Snoeckx, H., and Joseph, L.H., 1998. Late Cenozoic eolian deposition in the North Pacific: Asian drying, Tibetan uplift, and cooling of the northern hemisphere. *Paleoceanography*, **13**, 215–224.
- Reader, M.C., Fung, I., and McFarlane, N., 1999. The mineral dust aerosol cycle during the Last Glacial Maximum. *J. Geophys. Res. Atmos.*, **104**, 9381–9398.
- Roberts, H.M., Muhs, D.R., Wintle, A.G., Duller, G.A.T., and Bettis, III, E.A., 2003. Unprecedented last-glacial mass accumulation rates determined by luminescence dating of loess from western Nebraska. *Quat. Res.*, **59**, 411–419.
- Rosenfeld, D., Rudich, Y., and Lahav, R., 2001. Desert dust suppressing precipitation: A possible desertification feedback loop. *Proceedings of the National Academy of Sciences U.S.A.*, **98**, 5975–5980.
- Watson, A.J., Bakker, D.C.E., Ridgwell, A.J., Boyd, P.W., and Law, C.S., 2000. Effect of iron supply on Southern Ocean CO₂ uptake and implications for glacial atmospheric CO₂. *Nature*, **407**, 730–734.
- Werner, M., Tegen, I., Harrison, S.P., Kohfeld, K.E., Prentice, I.C., Balkanski, Y., Rodhe, H., and Roelandt, C., 2003. Seasonal and interannual variability of the mineral dust cycle under present and glacial climate conditions. *J. Geophys. Res.*, **108**, doi: 10.1029/2002JD002365.

Cross-references

[Aerosol \(Mineral\)](#)
[Atmospheric Circulation During the Last Glacial Maximum](#)
[Eolian Dust, Marine Sediments](#)
[Eolian Sediments and Processes](#)
[Ice Cores, Antarctica and Greenland](#)
[Last Glacial Maximum](#)
[Loess Deposits](#)
[Monsoons, Quaternary](#)
[Mountain Uplift and Climate Change](#)
[Quaternary Climate Transitions and Cycles](#)

E

EARLY PALEOZOIC CLIMATES (CAMBRIAN-DEVONIAN)

Introduction

Early Paleozoic climates obviously cannot be studied directly. Proxies for climate must be employed as a substitute for direct observations. These proxies include lithological indicators, such as evaporites, calcretes, tillites, coals, kaolins, and bauxites. Evaporites, marine and nonmarine, are evidence of climatic conditions adequate to permit precipitation of salts from concentrated seawater or freshwater, i.e., arid climates. Marine evaporites are formed only in shoreline regions and not in the open ocean or in estuarine, lagoonal, or other situations where seawater is subject to enough evaporation to permit precipitation of its load of dissolved salts. This is also the case with nonmarine evaporites formed in permanent (lakes) or temporary (playa) environments. The evaporate minerals commonly preserved in the geological record are calcium carbonate (most commonly calcite), sodium chloride (halite), and calcium sulfate (anhydrite [anhydrous] or gypsum [hydrated]). Evaporites are overwhelmingly representative of arid, desert type environments. Calcretes are lumps (nodules) or layers (limestones) of calcium carbonate precipitated in the lower layers of ancient soil profiles under semiarid conditions. Tillites are lithified glacial deposits, and may also include glaciomarine deposits. Coals are chiefly lithified higher land plant materials, representing overall humid conditions, warm to cold, that first appeared in the Late Devonian when woody plants became widely preserved in what were peats in swamp or bog environments. Kaolins are clay deposits dominated by the hydrated aluminum silicate kaolin, or transported grains of the mineral derived from nonmarine clay deposits, formed under at least annually warm, humid weathering conditions. Bauxite is a lateritic product formed under tropical-subtropical, annually humid weathering conditions. Note that all of these materials are basically nonmarine in origin, although their salts are of marine origin. "Marine" evaporites occur in the shoreline region, although they commonly mix with nonmarine evaporitic materials in the landward direction. An extended discussion of these items is

provided by Boucot et al. (in press). Other potential climatic proxies, such as oolitic sedimentary iron ores and sedimentary phosphate deposits, are still too poorly understood in this context to be employed.

Additionally, there is an important suite of sedimentary rocks and associated cool/cold climate faunas in the Cambrian through the early half of the Middle Devonian that provide evidence about very high southern latitude conditions, the so-called Malvinokaffric and Atlantic realms (see Boucot and Blodgett, 2001, for an example).

Geographically, it is important to understand that the present distribution of these climatic proxy materials commonly does not correspond to their original geographic position owing to subsequent movements of varied crustal blocks following the Early Paleozoic, as well movements that occurred during the lengthy Cambrian-Devonian. With this in mind, the Cambrian-Devonian climatic proxy distributions may, in principle, be used to estimate the changing positions of Cambrian-Devonian climatic belts. However, owing to the somewhat limited known record of Cambrian-Devonian climatic proxy materials, there are limitations imposed on these climatic reconstruction possibilities. For example, there are no known Silurian bauxites, with very few in the Ordovician and none in the Cambrian, although a few that are present in the very late Precambrian permit estimation of where bauxite-forming environments might have been located in the Cambrian.

It has been concluded that there were several significant changes in the global climatic gradient during the Cambrian-Devonian (i.e., the Equator to polar temperature gradients, which are high during times of polar glaciation and low during times of polar warm temperate conditions), from moderately high in the Cambrian through earlier Middle Ordovician, very high during the later Middle to Late Ordovician, back to moderately high in the Silurian through earlier Middle Devonian, followed by a globally lower later Middle Devonian, a relatively low Late Devonian, and terminating in a relatively high gradient in the very latest Late Devonian.

Atmospheric and oceanic composition

There is no direct information about Cambrian-Devonian atmospheric or oceanic composition(s). Boucot and Gray (2001)

summarized current information about atmospheric carbon dioxide tenor that discounts earlier modeling attempts by others. [Figure E1](#) provides a summary of changing Cambrian-Devonian global climatic gradients. If atmospheric carbon dioxide concentrations are a direct function of global climatic gradient (i.e., global mean temperature with carbon dioxide assumed to be the major greenhouse gas), the Cambrian through earlier Middle Devonian concentrations were probably not much higher than today, but were significantly higher for the much lower global climatic gradients of the later Middle Devonian through much of the Late Devonian.

Oceanic composition, i.e., major and trace element ionic composition and concentration, cannot be directly measured. However, when one the physiological requirements of marine organisms, chiefly megascopic, are considered, it can be concluded that it is unlikely that oceanic composition has changed significantly from the Cambrian to the present unless there have been varied evolutionary changes affecting their physiologies, which is unsupported by available data.

Global climatic gradients

Boucot and Gray (2001) summarized Phanerozoic global climatic gradients ([Figure E1](#)). It is clear from the evidence that average global mean annual temperatures have changed back and forth over time. High global climatic gradients featuring continental glaciation are present only in the later Ordovician (part of the Caradocian plus the Ashgillian epochs) where a large Southern Hemisphere region, including at least Africa, the southern two-thirds of South America, and glaciomarine conditions extending into Central Europe, are involved. The later Devonian is characterized by a far lower global climatic gradient than at present.

Cambrian climatic evidence

The Cambrian features the beginning of high latitude Southern Hemisphere cool/cold regions that include Africa; South America, except for the Argentine Precordillera, where evaporites and calcrete are recognized; parts of easternmost North America; and most of Europe, except for Sardinia, where local evaporites are known. Arid conditions are indicated for a widespread, lower latitude Southern Hemisphere belt to the north of the cool/cold climate belt, which includes North America, the Near East and Arabia, northwestern peninsular India, North and South China, southern Siberia, and Australia. There is no evidence for a tropical-subtropical belt owing to the nonrecognition of bauxites, but such a belt is inferred by extrapolating from the prior late Precambrian and subsequent Ordovician situations.

Early Ordovician

The known Early Ordovician climatic distribution data are similar to that for the Cambrian. Cool/cold, high southern latitude rocks and faunas are known from parts of South America and North Africa as well as most of Southern and Central Europe. To the north of these, there is widespread evidence of arid conditions at lower latitudes, with widespread evaporites in North America, the Argentine Precordillera, North China, Australia, southern parts of the Siberian Platform, and southern Thailand (the Shan-Thai Terrane), together with an occurrence in Northern India. Again, there are no known bauxites but evidence extrapolated from the overlying Middle Ordovician suggests the presence of a warm, humid tropical-subtropical belt. Climatic evidence is lacking for Antarctica, Northern Europe, and Central Asia.

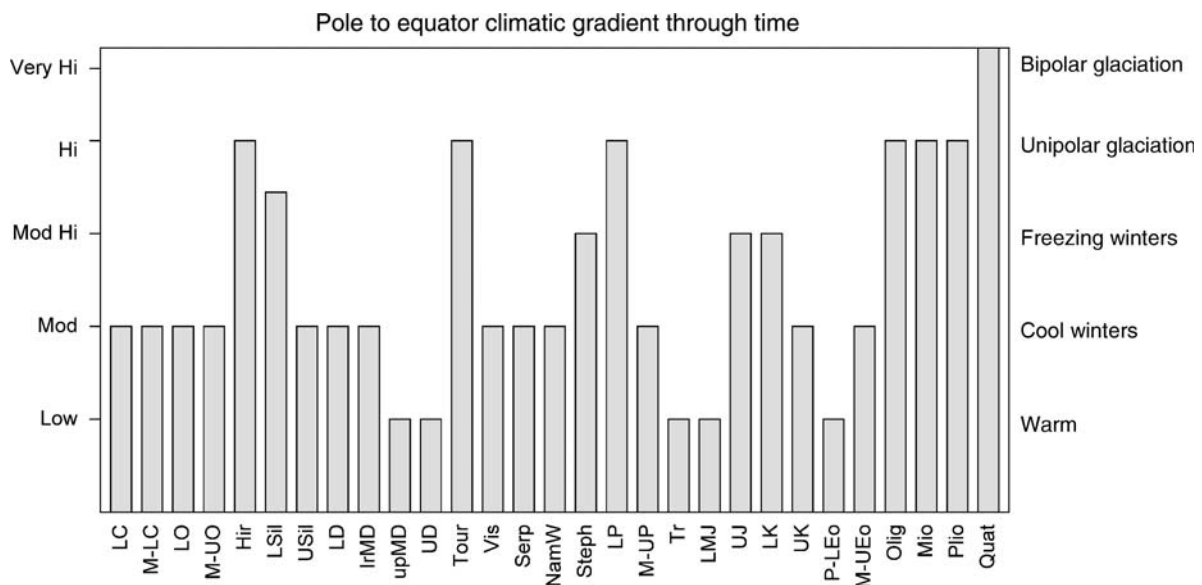


Figure E1 Periods when warm temperature indicators are present at high latitudes are taken as representative of intervals of low climatic gradient. Periods of temperate indicators at high latitudes display moderate climatic gradients, while times of cool to cold climate indicators near the poles suggest freezing winters, indicating “moderately high” climatic gradients. Continental glaciation at one pole represents an interval of high climatic gradient. Continental glaciation at both poles (i.e., the Quaternary), represents a period of “very high” climatic gradient (based on data from Boucot et al., in press).

Middle through end Ordovician

The middle to end Ordovician features later Ordovician evidence of global heightening of the climatic gradient, culminating in widespread latest Ordovician, Southern Hemisphere, high latitude, continental glaciation. Prior to this glaciation, there is evidence for cooler climates occurring earlier in the later-Ordovician, indicated by dropstones in North Africa and tillites in South Africa that are earlier in time than the latest Ordovician continental glaciation. Evidence of the latest Ordovician includes widespread sites in North Africa and Arabia, scattered localities in South America from southern Peru south, and widespread dropstones in central and Southern Europe, all of which probably reflect freezing winters at the very least, if not actual glaciation. Throughout this interval in the Southern Hemisphere, there is faunal and lithological evidence for cool/cold water conditions at higher latitudes. At lower southern latitudes, there is widespread evidence of an arid belt with widespread evaporites and calcretes in North America, and evaporites in Northern Europe (Baltic region and northern Russia), North and South China, Australia, and southern Siberia. Evidence for a humid tropical-subtropical belt is provided by Middle Ordovician bauxites in southeastern Kazakhstan and on part of the Siberian Platform. A Northern Hemisphere arid belt is indicated by the presence of evaporites in southern Siberia. The presence of kaolins in the same region as evaporites, in North America for example, is most easily explained by at least annually humid intervals at higher elevations with overall arid conditions widespread at lower elevations.

The presence of later Ordovician bauxites in northwestern Sudan is supportive of a brief incursion of warm climate conditions during the later Ordovician featuring warm water fauna and limestone in Central and Southern Europe and North Africa.

Silurian

There is widespread, high southern latitude lithological and faunal evidence for cool/cold climate conditions, with associated tillites, in the earlier Silurian at scattered Brazilian localities and dropstones at several North African localities. At lower southern latitudes, there is widespread evidence, including both calcretes and evaporites, from North America, Europe, Iran, northern India, and Australia that is indicative of a Southern Hemisphere arid belt. Evaporites in southern Siberia are consistent with the presence of a Northern Hemisphere arid belt. No bauxites are presently recognized in the Silurian, but a tropical-subtropical belt is extrapolated from later Ordovician and Devonian data.

Early Devonian

Climatically useful data for the Early Devonian indicates the presence of a high southern latitude cool/cold climate region, consistent with both faunal and lithological evidence. A lower latitude Southern Hemisphere arid belt is indicated by North American evaporates; calcretes and evaporites in Europe; evaporites in Iran, Libya, and northwestern Arabia; calcretes and evaporites in North and South China and Tarim; and evaporites in Australia. A Northern Hemisphere evaporate belt is suggested by widespread evaporites in Southern Siberia. Tropical-subtropical belt evidence is restricted to bauxite occurrences in the northern part of the eastern Urals and the Salair.

Middle Devonian

The Middle Devonian features the presence of the same cool/cold climate high southern latitude region indicated both faunally and lithologically for the earlier half of the Middle Devonian, followed by a lowering of the global climatic gradient consistent with the disappearance of this cool/cold climate region in the latter half of the interval. A warm temperate, mid southern latitude belt is consistent with North African coal at a single locality, more widespread kaolins in northern South America and North Africa, and coal in Libya. At still lower southern latitudes, there are widespread evaporites and calcretes in North America and Europe, evaporites in Australia, and calcrete in the later Middle Devonian of Antarctica. Evaporites in southern Siberia are consistent with a Northern Hemisphere arid belt. A tropical-subtropical belt is consistent with bauxites in southern Siberia, southeastern Kazakhstan, and northeastern Russia as well as coal from Central Asian and South China. In the later Middle Devonian, coals overlying earlier Middle Devonian evaporites in Arctic North America indicate movement into the tropical-subtropical belt.

Upper Devonian

The Upper Devonian features a latest Devonian restricted region of continental glaciation in the region from Bolivia through the Amazon and Parnaíba Basins, plus possible occurrences in Chad. A lower latitude Southern Hemisphere arid belt is represented by widespread North American calcretes and evaporites (except for northernmost coals), European and Australian evaporites and calcretes, plus evaporates and calcretes in localities in northern India, Asiatic Russia, Kazakhstan, Iran, and Turkey, and calcretes in Vietnam. Northern Hemisphere arid conditions are represented by Siberian Platform evaporites. The tropical-subtropical belt is represented by coals in South China, Bear Island and Svalbard; and bauxites in South China, the Salair and southern Siberia, the Urals, southeastern Kazakhstan, and the Russian Tien Shan and Timan.

Arthur J. Boucot

Bibliography

- Boucot, A.J., and Blodgett, R.B., 2001. Silurian-Devonian biogeography. In Brunton, C.H., Cocks, L.R.M., and Long, S.L. (eds.), *Brachiopods Past and Present*. The systematics Association Special Vol. series 63, London: Taylor & Francis, pp. 335–344.
- Boucot, A.J., and Gray, J., 2001. A critique of Phanerozoic climatic models involving changes in the CO₂ content of the atmosphere. *Earth-Sci. Rev.*, **56**, 1–159.
- Boucot, A.J., Chen, X., and Scotese, C.R., Preliminary compilation of Cambrian through Miocene climatically sensitive deposits (In press). Tulsa, OK: Society of Sedimentary Geology.

Cross-references

[Arid Climates and Indicators](#)
[Coal Beds, Origin and Climate](#)
[Duricrusts](#)
[Evaporites](#)
[Glacial Sediments](#)
[Glaciomarine Sediments](#)
[Laterite](#)
[Mineral Indicators of Past Climates](#)
[Paleosols, Pre-Quaternary](#)
[Sedimentary Indicators of Climate Change](#)
[Tills and Tillites](#)

EARTH LAWS AND PALEOCLIMATOLOGY

Introduction

Paleoclimatology, as one of the Earth Sciences, is subject to the laws of physics, chemistry and biology. Specifically, five “Earth laws” apply to this planet. Four of these, with limitations, also apply to other celestial bodies in the Solar System (Shirley and Fairbridge, 1997). Paleoclimatology falls within the scope of all five Earth laws.

The five laws, proposed here, are modified from earlier writings (Fairbridge, 1980). They are summarized as follows but discussed in some more detail (with selected references) later in this entry.

- *First Earth law: Stellar evolution and history of the Sun.* The Solar System has a finite existence that depends upon the evolution of the Sun, which behaves as a “main-sequence” star, burning hydrogen into helium, with nuclear fusion as its primary source of energy. The Sun’s energy is in part gravitational, relating to the inertial effects of its angular momentum developed by its rotation (axial spin), and to its orbital motions, which are accelerated by those of the planets (and cumulative). In addition, there are two types of solar emissions: electromagnetic radiation (dominated by optical wavelengths, e.g., 400–750 nm) and ionized, magnetic particles in the solar wind. Of importance to Earth history and climate is the long-term stability of the Solar System due to the Sun’s estimated 10 billion-year lifespan, thus enabling evolution to progress to more advanced forms of life.
- *Second Earth law: Galactic cycles.* As components of the Milky Way Galaxy, the Sun and Solar System are subject to its motions and history, following an inertial orbit from *perigalacticum* (closest approach to the center, a “black hole”) to *apogalacticum*, the farthest, with the cycle lasting about 240 Myr. On Earth, the ice ages, long-term geomagnetic reversals, and organic evolution may be modulated by it.
- *Third Earth law: Physical evolution of the Earth and Moon.* The physical evolution of the planet Earth, through 4.6 billion years, involves the gravitational ordering of its successive spheres – core, mantle, lithosphere, hydrosphere and atmosphere – a process known as differentiation, which occurred early in Earth history. This evolution has subsequently been modulated by the motions and tides of the Earth’s only natural satellite, the Moon, which has a revolution closely locked into its own 365.25 d period. Earth’s history and climate have also been influenced by secular changes in the obliquity of its spin axis.

Changes in the state of the Earth over time are recorded in the rock strata. Cutler (2003), in a recent biography of Nicolaus Steno (1638–1686), a Danish priest and early geologist, points out Steno’s fundamental observation that sedimentary rocks were laid down in water sequentially, establishing the geological “law of superposition.” It was based on exhaustive field work and proved conclusively the principle of physical evolution. It also provided evidence for the immensity of geological time. This latter inference remained to be demonstrated some two centuries later when applied to biological evolution.

- *Fourth Earth law: The organic or biological evolution of the Earth.* This has proceeded without interruption following

the first appearance of self-reproducing organisms at a very early stage in its history (“Hadean”). A certain degree of planetary stability is implied by the continual existence of life on Earth for over 3 billion years. During this time, the Earth has not undergone a runaway greenhouse effect, as on Venus (see *Atmospheric evolution, Venus*, this volume), nor has it frozen entirely (placing constraints on the concept of “Snowball Earth,” Hyde et al., 2000; Hoffman and Schrag, 2000; *Snowball Earth hypothesis* – this volume). Increases in species and speciation (as shown by stratigraphic paleontology) have accelerated through time, in spite of periodic mass extinctions that appear to be due to asteroid impacts, volcanism, ice ages and plate-tectonically forced isolation. Each mass extinction creates an ecologic “vacuum” that leads to an abruptly accelerated new speciation. Classical biological evolution *per se* through mutations (such as shown by embryology or DNA) or natural selection are of secondary significance compared with the dramatic speciation demonstrated by the paleontological/stratigraphic sequence following such extinction events. The “biosphere” (habitable region of the planet) interacts closely with the atmosphere, hydrosphere and superficial lithosphere (“pedosphere”), with mainly biogeochemical changes through time.

- *Fifth Earth law: Principle of Homeostasis.* The fifth law refers to dynamic equilibrium, a multi-feedback mechanism that tends to keep all natural systems in relative balance. On the planetary scale, that balance is represented by the “invariable plane” of the Solar System – the ecliptic. Passage through it affects the physics of every planet and their satellites. The 88-day highly elliptical orbit of Mercury (reflected in the Sun’s radiation spectrum) contrasts with the ecliptic-crossing orbits of Neptune and Pluto (with a revolution of 248 years). The Earth’s lunar orbit crosses this plane in an orbit of about 25,500 years ($1,370 \times 18.6134$ year, the Moon’s nodal cycle). During ice ages, Earth’s spin rate increases with near-axial ice loading, and the lunar orbit becomes shorter. During deglaciation the spin and orbit changes are opposite, but with distinct lags.

This law also applies to such terrestrial processes as *isostasy*, which determines how a crustal uplift or downwarp will be compensated in various ways (exhibited by gravitational “anomalies”). “Glacio-isostasy” applies to ice loading or melting on land and “hydro-isostasy” concerns the effect of adding glacial meltwater to the ocean, both processes affect global sea level. Another aspect of the equilibrium law is shown in orogeny, where mountain-building uplift leads to accelerated erosion, transport and sedimentation. This erosion in turn leads to renewed uplift due to isostatic rebound. The “penepplain” represents a long pause in crustal movements and is the theoretical end-phase of this equilibrium.

Earth laws: discussion and some climatological consequences

External influences on climate

The Sun

The Sun is a spinning body, tilted at about 5° from the mean plane of the planetary orbits. Its internal spin rate is about 25 days, while the photosphere’s rotation is slower, about 26–28 days, varying with solar latitude and time. The Sun also undergoes an inertial orbital revolution around the barycenter of the entire solar system. These patterns repeat sequentially but unevenly over about 178 years (Fairbridge and Sanders,

1987; Charvátová, 1995; Windelius and Carlborg, 1995). Long-term climate proxy data also disclose 178 year cycles (Windelius and Carlborg, 1995).

Inasmuch as planetary orbits are elliptical, their effects are variable, generally calculated by the beat frequencies of adjacent pairs. They are strongly cyclical. The “heartbeat” of the Solar System is approximately 19.859 years, the beat frequency of the two largest planets, Jupiter and Saturn.

The astronomic alignments of planets on one side of the Sun sets up an inertial momentum that develops a looping solar orbit around the solar system’s center of mass (the “barycenter”), as specified in the First Earth Law. Its 9.8 year cycle, generated by Jupiter, is amplified to a 19.859 year periodicity when Saturn is added, the resultant double loop being an epistrochoid with a heliocenter-barycenter distance that may sometimes exceed 1.5 million km (see Fairbridge and Sanders, 1987, fig. 26–6).

Solar energy is expressed in part gravitationally with respect to the planetary orbits, and in part by radiations that are intercepted by the surfaces of the planets. The gravitational relationship is not tidal but expressed by a torque applied both to the photosphere and to the orbiting and spinning planets, as shown by changes in their angular orbital momentum ($M \times D \times V$; mass, distance and velocity, with only mass being constant).

Solar radiations are of two types. One is essentially electromagnetic (over a wide spectrum, but dominantly in the optical range), and the other consists of ionized, magnetized particles (in the plasma of the solar wind). The first is felt primarily in the equatorial plane of the Earth (traveling at the speed of light), and fluctuates with the 11/22 year sunspot cycle. The second is highly variable in travel time, from hours to days, but the particles tend to be funneled into the Earth within the auroral oval of the magnetic poles; high-energy events often have a climatic impact. Although of low energy, the UV radiation is responsible for stratospheric ozone, which is important in climate modulation.

The Solar System is presently located about 3.6 million light-years above the mean plane of the galactic disk, a multi-arm spiral structure. Viewed from galactic “north,” this disk rotates clockwise at 160–220 km s⁻¹. However, relative to a given point on it, the Solar System moves counter-clockwise in a quasi-elliptical orbit around the galactic center, a “black hole” (Weissman, 1999). The closest approach of the Sun to the center of the galaxy, or “periglacticum,” is expected in a few thousand years, in contrast to its last “epogalacticum,” which would have been during the early Cretaceous. A complete cycle around the galaxy takes ~240 million years (see Second Earth Law). The trajectory also undulates in a vertical sense above and below the galactic plane with a period of 52–74 million years. Its last passage in an upward or “northerly” direction was about 2–3 million years ago (the beginning of the Pleistocene). Galaxies vary in structure but the Milky Way galaxy may be compared with the classical M-81, which has two very distinctive spiral arms. The passage of the Solar System through such an arm would subject the Earth to an accelerated infall of dust and comets. Such events tend to “punctuate” the planetary climate history!

“Icehouse” climates or major cooling intervals during the Earth’s history may be in part correlated with the galactic cycle, when passage of the Solar System through the galactic arms would increase the rain of cometary and possibly extra-galactic objects, which could affect terrestrial climates (e.g., cooling). Global cooling would coincide with a fall in atmospheric

CO₂, reflecting decreased land vegetation (extensive deserts), and colder seawater (reduced evaporation and lower pH). The cooling from impacts (nuclear winter scenario) would be counteracted to a small extent by warming due to CO₂ and CH₄ increase from burning wildfires, decaying organic matter, etc. (see *Bolide impacts and climate*, this volume). Alternatively, global cooling could be attributed to reduced levels of volcanism or to solar weakening.

A geologic “icehouse” may recur at intervals of about 120 Myr as the Solar System passes through the galactic arms, and may be amplified during the 240 Myr return of the perigalactic geometry, but nevertheless is always subject to a favorable paleogeography (“Susceptibility” or “Eiszeitvorbereitung” of Schwarzbach, 1963). The absence of glaciation at the Jurassic-Cretaceous boundary (expected in a 120 Myr cyclicity) has long been a point of discussion. In neritic (shallow, near-shore marine) regions it was certainly marked by a major eustatic withdrawal, but the principal factor was the global paleogeography dominated by Tethys, which maintained a warming effect on the world ocean.

While the passage of the Solar System through the galactic arms could possibly lead to cooling of the Earth, it is clear that not every such event result has resulted in an ice age. The explanation appears to lie in the unfavorable distribution of land masses and the related oceanographic circulation, as outlined below. Such periods constitute the inverse to Schwarzbach’s “susceptibility” or “preparation” rule. Thus, besides the ice ages, as climaxed in long-term “icehouse” climates, long-term (30–50 Myr) high susceptibility intervals have alternated with long-term low susceptibility “hothouse” or “greenhouse” conditions when, for example in the late Cretaceous, warm ocean temperatures extended to polar latitudes.

Milankovitch orbital cycles

Within a given ice age, there is an alternation between glacial and interglacial conditions, which are forced by Milankovitch orbital cycles of the Earth-Moon-Sun. The 90,000–100,000 year eccentricity cycle – dominant over the last 800,000 years – also has peaks at about 413,000 year. Secondary modulations are provided by the 40,036 obliquity period and two axial precessional cycles of around 19,000 or 23,000 years.

The sequence of glacial to interglacial states tends to follow a saw-tooth pattern, asymmetrically skewed toward the deglaciation phases. This is because of the latent heat of the ocean, which has a great heat-conserving potential and therefore cools slowly. When deglaciation starts, there is a tendency for run-away warming, aided by the feedback from eustatic rise of sea level, increasing global oceanicity and precipitation, spread of vegetation to semi-arid regions, and drop in albedo, due to shrinkage of ice sheets. The flood of freshwater from melting glaciers also affects ocean circulation, and produces important hydroisostatic effects. An interglacial is generally limited to about three warm pulses of only a few thousand years in an overall interval of about 20,000 years.

QBO and sunspot cycles

The most universal climate cycle over 12 months is the Quasi-biennial Oscillation (QBO) at 2.172 year, which Lamb (1977) recognized as a world-wide terrestrial phenomenon. With improved solar emission monitoring, it is now also recognized as extraterrestrial (Coughlin and Tung, 2004). Although the QBO is equatorial in its initial focus, it even reaches to the North Pole in the stratosphere (Kodera, 1993).

Spectrum analyses of all climatic and proxy time series discloses powerful spikes clustering about certain intervals. Comparison between different series at less than 22–23 years is sometimes confusing because of two factors (a) the 12-month seasonality, and (b) the ± 6 year variability of the sunspot cycle (Haigh, 2002). A great deal depends upon the source material and the length of the series. To overcome such barriers it is customary to select long series beginning at over the 22–23 years hurdle, for example the 2,600 year series of sunspots and auroras combined by Schove (1983) and analyzed by Jelbring (1995). Those peaks were identified by letters: A – 200 year, B – 133 year, C – 79 year, D – 50 year, E – 42 year, F – 33 year and G – 29 year. By selecting segments of the Schove series and analyzing them separately, Jelbring was able to (a) confirm the consistency of the Schove series, and (b) identify the major long-term peaks. Using the more precise data of the last century or so (since 1854) a 2.17 year QBO peak stood out clearly (Currie, 1995), with the same pattern occurring when the analysis was extended back to 1749.

Sea level-lunar modulation and meridional heat transport

Solar and lunar cycles appear to play a role in Earth's climate (e.g., Landscheidt, 1988; Charvátová, 1995; Hoyt and Schatten, 1997; Bond et al., 2001; Haigh, 2002; *Sun-climate connections*, this volume). A large number of regional climatic time series analyses (e.g., Currie, 1995) showed the universal presence of solar (11–22 year) and lunar (18.6134 year) forcing. The latter is further complicated by the principal oceanic tide at 18.03 year (“Saros” of the Babylonians), which in long-term records can be in or out of phase from time to time. Use of an 11-year average may be simple and straightforward, but is often wrong. Seasonality is often critical, as in the timing of El Niño before or after perihelion (around January 1–3 in the Northern Hemisphere, at present). In addition, the North Magnetic Polar oval and geographic latitude affect the concentration of the electromagnetic and particulate (solar wind) forcing. Nevertheless, it is apparent from Currie's pioneer labors that these two world-wide and astronomically predictable forcing functions (i.e., solar and lunar) should be included in all climatic studies.

The North Atlantic provides the sole significant oceanic connection with the Arctic Ocean and thus has a major effect on its circulation. The Bering Strait link plays only a minor role. The North Atlantic is modulated by the lunar tidal influence on its principal geostrophic current, the Gulf Stream. This is mediated by the zenith shift of the Moon (by over 1,100 km) every 9 years in its nodal cycle (18.6134 year). This acceleration and warming pulse is recognized not only by tide gauges and ocean temperatures but also by fishery statistics and sea-ice as far north as the Murmansk Current in the Barents Sea (Lamb, 1977, 1979). Increased evaporation in the westerly system occurs during the warming phase, raising winter snowfall in Scandinavia (small glacier advances) and increasing albedo all across central Asia (Kukla, 1981). Inasmuch as increased snowfall in the Himalayas and other Asiatic mountain systems leads to a retardation of the summer monsoon, sometimes there are droughts and famine in India, as was noted nearly a century ago by Sir Gilbert Walker. A giant feedback loop is thus created that further modulates the Indonesian wind reversal and the climate of northern Australia.

In the North Pacific, the Kuroshio is a geostrophic current analogous to the Gulf Stream, but it is mainly deflected south of the

Aleutian Islands to form the south-moving California Current off the west coast of North America. Although in its north-setting phase it has warming effects, it is cooled along the Aleutians and provides a cool pulse to North America in contrast to the warm pulse delivered by the Gulf Stream in Europe.

Tide gauge data disclose that when geostrophic currents accelerate worldwide, mean sea level responds, even in opposite hemispheres, because of the Coriolis effect. An accelerating current heading north off North America causes a fall in mean sea level near the coast, while the same trend in the Canaries Current heading south will also lower sea level off Africa. The twentieth century global rise of sea level (from about 1–2 mm yr⁻¹; Houghton et al., 2001), suggests, however, not only a sterically warmer ocean but also a more sluggish overall circulation. Climatologically, this is to be expected because the thermal gradient from the North Pole to the Equator is being reduced. Although Arctic and high latitude temperatures rise, equatorial sea-surface temperatures (SSTs) remain almost constant. The less the temperature contrast, the flatter the gradient, therefore mean sea level (MSL) rises on all continental coasts (Holgate and Woodworth, 2004). On the other hand, in mid-ocean situations (e.g., Turk Atoll in the mid-Pacific) there is remarkably little change.

Plate tectonics and paleogeography

A second very important factor in climate change and ice ages is the plate tectonic control of planetary paleogeography, specifically the relative patterns of land and sea (see *Plate tectonics and climate change*, this volume). A land-mass clustering (e.g., Pangaea) favors continentality and climatic extremes. An equatorial seaway, such as “Tethys,” on the other hand, would bring warm currents to all low- and mid-latitude land masses, incompatible with an ice age (Schwartzbach, 1963). Closure of seaways, for example at the Isthmus of Panama, the Strait of Gibraltar and the Sinai-Red Sea link, had the effect of isolating regional water bodies such as the North Atlantic and Mediterranean, and thus blocking the equalizing effect of marine circulation. The warm, open seaway of the Cretaceous Tethys therefore contrasts with the progressive blockages of Tethys that began in the early Tertiary and presaged the eventual Quaternary ice age (Fairbridge, 1961, 1967).

During the nineteenth century, it was recognized that the Earth's crust was subject to orogenic folding and faulting, but continents and oceans were taken to be permanent (“fixism”). Early in the twentieth century came “mobilism” and Wegener's theory of continental drift. With improved technology and marine geophysics in the late twentieth century, drift evolved into the plate-tectonic paradigm, which introduced crustal fracturing, sea-floor spreading, subduction and the systematic rearrangement of crustal blocks. Recently, global reconstructions became feasible.

Major break-ups of crustal plates, termed “*taphrogenesis*” (Fairbridge, 1982), once initiated, were followed by progressive dismemberment of former megacontinental blocks. Major changes in paleogeography and re-organization of continental plates can cause fundamental changes in the Earth's climate. Actualistic examples are the late Cenozoic opening of the Red Sea and the East African rifts with their major lakes. Climatologically, such taphrogenesis may introduce major moderating systems into an arid high-pressure region. In contrast, subduction and plate collisions can lead to major plateau uplift, as in Tibet, which can affect global climate (Ruddiman and Kutzbach, 1990,

1991; Raymo and Ruddiman, 1992). In a low-latitude maritime setting, numerous volcanic cones such as in the Caribbean or the Indonesian Archipelago favor micro-climates of highly varied nature. Paleogeographic reconstructions can therefore help to map out paleoclimates.

Thanks to its pre-existing physiographic irregularities, the present-day Earth is subject to a wide range of climatic variables (Oliver and Fairbridge, 1986; Hewitt and Jackson, 2003). Global average climate, however, can conceal opposing trends of temperature, pressure and precipitation, which in effect are often not only contradictory but often appear to generate spurious, random products. The search for regionally coherent patterns has proven to be much more rewarding, as was pioneered a century ago by Sir Gilbert Walker for the meteorological service of India. Notably, the most successful example has been the SOI, *Southern Oscillation Index*, which is based on regional data from the southeast Pacific (El Niño history), seawater temperatures and atmospheric pressure from the Pacific in general, and likewise from the northeast Indian Ocean. A more complex example is the *North Atlantic Oscillation* (NAO), based on the pressure difference between Iceland and the Azores, but it is susceptible to modulations of the Northern Hemisphere jet streams. These, in turn, are often subject to the influence of the North Magnetic Pole on incoming magnetized particles in the solar wind and on the locus of the Polar Vortex (see for example Boberg and Lundstedt, 2002; Thejll et al., 2003).

Global climatic asymmetry

The base of the atmosphere is the Earth's surface, two thirds of which is ocean and one third composed of rock, soil and vegetation. The land interface is subject to extreme seasonality and vegetation changes, instantly visible by satellite monitoring, and measurable most importantly in terms of *albedo*. In each hemisphere this value rises dramatically in winter over the high-latitude oceans, due to snow covered sea-ice, and over land with snow cover. However, this occurs mainly in the Northern Hemisphere because of the distribution of the continents, such that a gross *climatic asymmetry* is created in the annual heat budget. An additional albedo factor (also asymmetric) is created by the intertropical deserts (mainly Northern Hemisphere) and summer expansion of semi-arid Mediterranean lands. Global asymmetries produce non-linear responses and fluctuations in cyclic processes.

Climatologically, the Earth is not a perfect sphere but is subject to its physiography, which has a great influence on its annual heat budget. Its principal physiographic features are:

- The threefold equatorial inequality, consisting of two rainforest basins (Amazon and Congo, marked by endogenetic hydrologic systems) and the Indonesian Volcanic Archipelago (marked by about 10,000 micro-climates). Of the three, the latter constitutes the most important "center of action" on the globe. Satellite monitoring for more than a decade has shown its dominating role, with towering cumulus rising more than 15 km. The region is also unique oceanographically, straddling the two largest continental shelves in the world (the Sunda and Sahul Shelves, each more than 1.5 million km²), with the warmest ocean waters in the world. The surface water flow is always from east to west, partly tidal and partly the return phase of the "conveyor" thermohaline circulation. The resultant currents are quite powerful. They are subject to a strong lunar

cyclicality because the cold offshore water brought in over the shelf at high spring tides leads to thermal exchange with the atmosphere.

- The global continent/ocean asymmetry leads to a dominance of water in the Southern Hemisphere and land in the Northern Hemisphere. In contrast, the polar areas of the Southern Hemisphere are land, versus those of the North, which are water. The high elevation (ca. 3,000 m) of the former is distinctive. Both poles are largely covered by ice and snow, so that the albedo is always high but is variable perennially. North/south contrasts are most important at mid-latitudes. In the Southern Hemisphere, continents alternate with oceans, whereas in the Northern Hemisphere, the amalgamation of Eurasia and North Africa is not balanced by North America. Climatologically, this imbalance generates powerful fluctuations between zonal (westerly) and meridional (south-north) modes of circulation. "Oceanicity," or maritime air flow, alternates with "continentality," or turbulent and meridional air flow. In the Southern Hemisphere, the greater dominance of oceans means that strong continent/ocean contrasts are absent. Global climate systems are therefore dominated by the Northern Hemisphere, given the present continental configuration. Therefore, the Northern Hemisphere will dictate global periodicities during Ice Age fluctuations between glacial and interglacial states.

Geomagnetic reversals

The geomagnetic history of planet Earth demonstrates periodic polarity reversals of both brief and extended intervals (Lowrie, 1997). The explanation of the brief reversals could lie in reversals of flow within the molten iron core or possibly changes in mass loading, for example the growth of ice caps asymmetric to the Earth's spin axis, which would introduce a major wobble in the rotation that could be repeated during the melt phases. Another form of mass loading is by volcanic plateau eruptions, and yet another is the erosional unloading of mountains and the sediment filling of adjacent basins.

Long-term geomagnetic reversals may possibly coincide with perigalactic and apogalactic phases of Solar System history. Even more speculatively, the reversal process could influence rates of organic evolution as well as stratigraphic and climatologic history (McCrae, 1981). Links between reversals and galactic motions have been suggested by Negi and Tiwari (1983), as have links with mass extinctions (Raup and Sepkoski, 1984). The periodicity of the geomagnetic reversals has been analyzed by Stothers (1986), and locked into planetary and solar motions (Tsurutani et al., 1990).

Asymmetry of North Magnetic Pole – consequences

The North Magnetic Pole is not fixed but shifts from year to year. At present, it is west of Greenland, moving northwards. During the seventeenth century, when it was first measured, it lay east of Greenland, and the declination measured in London and Paris pointed east of Greenwich.

The charged particles of the solar wind are largely shielded from the Earth by the magnetosphere. The latter, however, is a toroid (doughnut shaped) and some of the particles are funneled into the Earth at the magnetic poles. Collisions with atmospheric atoms result in isotopic "spalling" and the creation of larger and denser atmospheric components. The periodic solar flares and magnetic storms set up strong atmospheric

turbulence (Bucha, 1976, 1984, 1988). From time to time, this could lead to a great outburst of cold anticyclonic polar air (Leroux, 1996); over North America such outbreaks can at times reach as far as the Canary Islands and the western Sahara. Short-term averages of the solar flares are about 0.417 year, but longer mean values of 13.4 years may correspond to the alignment frequencies of Jupiter and Uranus with the system bary-center (Landscheidt, 1988). Planetary triggering of dynamic events on the Sun is believed to operate through exchanges of spin and revolutionary torque. Sunspots tend to develop on the near side of the Sun and die out on the far side (with respect to the Earth).

Just as the Indonesian mega-center of action provides an equatorial climatic node in the Earth's dynamic systems, so the North Magnetic Pole provides a second, but much weaker node, asymmetrically located in the Northern Hemisphere, centered on about 70° west longitude. While the north geographic pole provides a normal center for the polar anticyclonic vortex, its locus shifts from time to time into the western hemisphere, thus modulating the pattern of the mean jet stream. This could influence the decadal to bi-decadal NAO (Lamb, 1977; see also Boberg and Lundstedt, 2002; Thejll et al., 2003).

Threshold effects

Following the Fifth Earth Law (Principle of Homeostasis), each phase of an ice age, glacial or interglacial, tends to maintain a *steady state* until a certain *threshold tolerance* is exceeded, whereupon a rapid (“runaway”) shift takes place in all parameters – including temperature, precipitation, current velocities, mean sea level, aerosols, trace gases, etc. This bimodal alternation within an ice age is mimicked by the icehouse/hot-house bimodality of long-term geologic history, but on much shorter timescales.

A critical threshold for the onset of glaciation is summer snow-melt. Once melting fails for several decades, a snow patch will increase in size and build its load to the point where old snow is converted to ice. Albedo increases and the snow patch expands. This condition tends to develop first in highland areas, leading to mountain (“valley”) glaciers, which eventually merge into an ice cap. The site of continental ice sheets is determined by the gross asymmetry of the two Northern Hemisphere landmasses, most importantly North America (fed by moisture from two sides) and secondly Northern Europe (fed only on one side). The Antarctic ice sheet, fed from all sides and symmetrical to the South Pole, is too large and too stable to melt in less than 100,000 yr. Consequently, it will remain more or less as a quasi-stable entity until the entire ice age ends.

Retardation, or delayed response to solar radiation forcing

A cooling cycle is signaled by the expansion of sea-ice. As its area increases, so does the albedo, leading to a positive feedback that accelerates the cooling. The season of snow-cover on land consequently increases. However, critical limits exist. During a warming cycle, the enormous heat capacity of the ocean retards its response to rising insolation. Therefore, both global cooling and post-glacial warming are out-of-phase with the actual glaciation and its related glacio-eustasy. There is evidence of ice-floes and ice-transport of large boulders in the English Channel (Fairbridge, 1971) near the beginning of the last (Weichselian) glaciation, up to 10,000 years before the general fall of sea level.

Likewise, during deglaciation there is a “retardation” effect of the same order, such as when, for example, the Virginia oyster (*Crassostrea virginica*) and other warming indicators appeared in the Canadian Maritime provinces up to 6,000 year before world sea level reached its peak (Fairbridge, 1961). Recent paleoclimate proxy records from both deep sea and polar ice cores confirm that during deglaciation, the retreat of ice sheets lags several thousand years behind insolation, temperature rises, and changes in atmospheric greenhouse gases (Petit et al., 1999; Raynaud et al., 2000).

Glacial environments

Periglacial environments develop on land areas during a glacial phase, in a broad marginal belt south of the ice sheets. In many regions, this belt is marked by extreme aridity, associated with high winds and dust storms that generate loess deposits. Dating from the numerous glacial cycles of the Pleistocene, these deposits have weathered, rich loamy soils and can now be traced all the way from the Atlantic coasts of Western Europe to the Pacific shores of China, as well as being found in North America, Australia and New Zealand.

In mountainous terrain the summer ice melt is likely to develop so-called “refugia,” in the form of humid oases and “pluvial” lakes (as in the Rocky Mountain region). A vast increase in desert areas, however, is the normal condition during a glacial period, such as is seen in Africa, India and Australia. Without adequate dating, when early explorers during the first half of the twentieth century found former lakes and riverbeds in desert regions, they tended to equate “glacial” with “pluvial” conditions, even in the total absence of evidence for former glaciers. Now, with radiogenic isotopic dating, Rocky Mountain pluvials have been correlated with displaced jet streams during glaciation and periodic glacier-melt conditions, whereas Saharan pluvials, in contrast, correlate with interglacial monsoon maxima. Based on climate modeling, the colder ocean surfaces of glacial phases and their reduced oceanic surface areas would logically lead to drier conditions on the continents (Fairbridge, 1967; Kutzbach et al., 1993). Even equatorial waters were as much as 5 °C cooler, and many subtropical seas in marginal belts became too cold to support coral-reef growth.

Glacial-phase desiccation led to wholesale conversion of vegetation cover toward more arid types, e.g., from rainforest to savanna, and even to total desertification. Radiocarbon-dated fluvial deposits on the Congo River (near the equator) are found interbedded with desert sands – deposits are derived from sources in the Kalahari to the south and the Sahara to the north (Fairbridge, 1976). In the upper Amazon rainforest of today, there are traces of sub-Andean dunes oriented northward. Biotic survival of tropical organisms, including primates, was only possible in “Refugia,” the oasis-like sanctuaries where rainforest could be maintained. In the northern Mediterranean, the cold adiabatic winds radiating from the Alpine ice caps led to frost action on a giant scale and sheets of cryoclastic debris (“grèzes litées” in French) and solifluction contributed to the periglacial colluvium (Lowe and Walker, 1997).

Probably the most dramatic evidence of glacial-phase aridity is found in the ice-cores of Antarctica and Greenland. Everywhere, precisely at the interglacial/glacial boundary, the amount of terrigenous, airborne debris (aerosols: dust and silt) rises by one to two orders of magnitude (Jouzel et al., 1993).

Glacial-stage winds of great intensity were dominated by convective turbulence in contrast to the zonal circulation of the interglacials (Lamb, 1977). Monsoonal winds virtually ceased as year-round snow cover helped create a quasi-permanent central Asian anticyclone. Even in northern Australia, the summer monsoon failed and sand dunes spread out across the continental shelf.

High-resolution proxy chronologies

The relatively short cycles can only be identified by a combination of astronomic analyses with the natural records as preserved in “proxy” sequences of uniform periodicities and quality. Such climatic proxies are provided by the annual layers in ice cores or in lake sediments and by similar seasonal banding in tree rings or stalactite growth (see *Paleoclimate proxies, introduction*; this volume). Geochemical studies of the various types of materials disclose seasonal and long-term fluctuations that help determine the various cycles. Most instructive are the ^{14}C flux rates analyzed in the wood of tree rings because these values reflect (inversely) the Sun’s particulate radiation. Thus, the radiation cause can be monitored and compared with the climatic effect (Stuiver and Braziunas, 1993).

Of the many proxies, tree ring densities have been checked and rechecked against hundreds of time series, extending now over more than 12,000 years. Their most consistent and stable periodicities determined by power-spectrum analysis (Thomson, 1990) fall into a harmonic series: 104.26, 208.52, 417.045, . . . Extending it one more step gives 834.09, which corresponds to 75×11.12 year, the mean sunspot cycle, thus providing a simple linkage of solar events and terrestrial climate.

Use of long proxy time series (ice cores, tree ring ^{14}C flux, sediment cores) is highly desirable for the bridging of certain solar disturbances, but can be susceptible to small errors and regional bias. Of these, the series with the strongest planetary-solar links is the 69.507–208.52–417.04–834 year sequence seen in the tree-ring ^{14}C flux (Stuiver and Braziunas, 1993). It conforms precisely to the 2.172 year QBO ($69.507 = 32$ QBO), thus linking the short-term solar flux with long-term planetary periods (69.507 year = Uranus-Jupiter-Venus Lap) (see also Fairbridge and Sanders, 1987).

Confusing to many analysts are the luni-solar forcings that were postulated by Ekholm and Arrhenius (1898) when they showed that both the 18.6 year nodal cycle and the 22–23 year solar cycle were present in the 800 year Scandinavian history of auroras. Also from Scandinavia came herring fisheries data of the same length (Pettersson, 1912, 1914), together with the longer cycle of 93 years. Wood (2001) studied oceanographic tide systems and found that the 93 year period represented “maximized declination and nutation, at alternating lunar syzygy phases.” Basically, he found only two tide cycles, “type A,” 1.1318 year (14 lunar months), and “type B,” 18.03 year, which is also recognized in astronomic observations as the “Saros” of the Babylonians.

Attention should be paid to the high latitudes, particularly the North Magnetic Pole and the auroral oval, because of the ^{14}C isotopes produced by high-energy extra-galactic (“cosmic”) particle collisions with atmospheric nitrogen. Measured in tree rings, this ^{14}C flux is modulated by sunspot and other cycles in the (magnetic) solar wind.

The existence of see-saw atmospheric pressure fluctuations at high latitudes was first drawn to attention by Sir Gilbert Walker

as the “North Atlantic Oscillation.” It was first associated with storminess cycles by Fairbridge and Hillaire-Marcel (1977), which were discovered in the periodicity of emerged beach ridges on the eastern Hudson Bay, dating back 8,300 years. Further work on the ridges in the southwestern part of the bay by Douglas Grant (pers. comm.) permitted the construction of a histogram showing that the storminess cycles occurred in three peaks, approximately 11–12, 22–24 and 45–47 years. Higher harmonics occur in the extreme fluctuations of the ^{14}C flux rates and the peaks in beach ridge heights.

Astronomic relationships between planetary motions, solar activity and terrestrial climate have long been controversial. First proposed two centuries ago for the sunspot cycle by Sir William Herschel, the variability of that cycle (11 ± 6 year) made it extremely difficult to handle as a statistical parameter. However, the 45 year mean periodicity of the 8,300 year Hudson Bay beach series is incontrovertible. After glacio-isostatic correction, the data plot on a practically straight line, dating back to the inundation of Hudson Bay (“Tyrrell Sea”) by the postglacial global eustatic rise.

The construction of a given beach ridge at this latitude requires a gradual transgression, i.e., a warm-summer climate cycle accompanied by mild-wet westerly airflow. Its building phase terminates with a rapid regression and cooling associated with easterly or northerly winds due to a high pressure system in the northeast. Hudson Bay is frozen over in winter, so the winter season’s climate is irrelevant. Diaries kept by the fur-trading officials indicate the length of ice-free conditions. The longest ice-free seasons were 1750–1800, a trend confirmed by tree-ring evidence for Kuujuarapik (Great Whale River) by Jacoby and D’Arrigo (1989) and other sources.

A related problem is the precise astronomic phase of the 45 year cycle. For example, the years AD 1761–1762 were marked by the triple conjunctions of Jupiter-Saturn-Uranus, together with secondary (but brief) alignments with the inner planets, Mars-Earth-Venus-Mercury (46.3383 year). The key sunspot maximum was 1761. Further discussion of solar and planetary cycles and their climatic consequences can be found in Fairbridge and Sanders (1987); also see Charvátová (1995) and Jelbring (1995).

Conclusions

The biogeophysical laws that govern this planet can be summarized in five general “Earth Laws” that have influenced the course of the Earth’s paleoclimatic history. The first law relates to the long-term evolution of the Sun, its sources of energy and to planetary dynamics. As a member of the Solar System, the Earth is also affected by the Sun’s electromagnetic radiation, mainly in the visible range, and by a stream of ionized, magnetized particles (the solar wind).

The Solar System is subject to cyclical phenomena on many timescales. Cyclical variations in the Earth’s orbital parameters (eccentricity, obliquity, precession) on the order of 2×10^4 to 10^5 years have led to the Quaternary ice ages (i.e., the astronomical theory of glaciations proposed by Milankovitch). Less well established are the possible climatic effects of variations in sunspot activity at around 11 years, the 18.6 lunar nodal cycle, or of planetary alignments, such as the beat frequency of the two largest planets, Jupiter and Saturn, at ~ 19.86 year, the “heartbeat” of the Solar System. Indications of these

cycles appear in a number of paleoclimate proxies, such as the ^{14}C flux recorded in tree rings. The longest cycle is the rotation of the Solar System about the galactic disk at ~ 240 Myr (second Earth Law). It has been suggested that passage of the Solar System through the spiral arms of the galaxy might subject the Earth to an increased rate of comet infall, possibly leading to cooling episodes.

The Earth is a dynamic planet. Although the gravitational differentiation of the Earth occurred early in its history, the surface and atmosphere have continuously changed over time, shaped by internal driving forces such as plate tectonics and volcanism (third Earth Law), as well as interactions with the Sun, the Moon, giant planets (first Earth Law) and the biosphere (fourth Earth Law). The history of the Earth is recorded in its rocks.

The long-term stability of the Sun on the main sequence has enabled the development of more advanced forms of life without interruption for over 3 billion years (fourth Earth Law). The significance of this for paleoclimatology is that the Earth has always had a sufficient reservoir of liquid water to maintain life. In other words, the Earth has never experienced a runaway greenhouse effect, as on Venus, nor a totally frozen state, as on Mars.

The fifth Earth Law relates to the principle of homeostasis – that of a dynamic equilibrium, involving complex feedback loops that tend to keep natural systems in relative balance. In spite of severe perturbations, such as produced by bolide impacts or volcanic mega-eruptions, a tendency exists for a return to previous conditions. Although relatively abrupt wide excursions or swings may occur, these always remain within limits.

In summary, the Earth's paleoclimate history is the consequence of a complex interplay of internal and external forcing through multiple feedback loops. Plate tectonics shapes paleogeography, which in turn determines land-sea differences in albedo and in the heat budget. These in turn affect its atmospheric and oceanic circulation patterns. Quasi-periodic changes in the Earth's orbital cycles lead to slight variations in incoming solar radiation, producing glacial-interglacial climate oscillations. More speculative is the role of solar activity, and lunar and planetary dynamics on climate. Implicit in such proposed correlations are several important inferences that are still rather controversial and will require more thorough investigation: for example, suggestions that (i) planetary dynamics control solar emission variability; and that (ii) solar emissions, both electromagnetic and particulate, control short-term terrestrial climate variables.

Rhodes W. Fairbridge and Vivien Gornitz

Bibliography

- Boberg, F., and Lundstedt, H., 2002. Solar wind variations related to fluctuations of the North Atlantic Oscillation. *Geophys. Res. Lett.*, **29**(15), 10.1029/2002GL014903.
- Bond, G., et al., 2001. Persistent solar influence on North Atlantic climate during the Holocene. *Science*, **294**, 2130–2136.
- Bucha, V., 1976. Changes in the geomagnetic field and solar wind—Causes of changes of climate and atmospheric circulation. *Studia Geophysica et Geodetica*, **20**, 346.
- Bucha, V., 1984. Mechanism for linking solar activity to weather-scale effects, climatic changes and glaciations in the Northern Hemisphere. In Mörner, N.-A., and Karlén, W. (eds.), *Climatic Changes on a Yearly to Millennial Basis*. Dordrecht, the Netherlands: D.Reidel, pp. 415–448.
- Bucha, V., 1988. Influence of solar activity on atmospheric circulation types. *Annales Geophysicae*, **6**, 513–524.
- Charvátová, I., 1995. Solar-terrestrial and climatic variability during the last several millennia in relation to solar intertial motion. *J. Coast. Res., Special Issue No. 17*, 343–354.
- Church, J.A., et al., 2001. Changes in Sea Level. In Houghton, J.T., Ding, Y., Griggs, D.J., Noguer, M., van der Linden, P.J., Dai, X., Maskell, K., and Johnson, C.A. (eds.), *Climatic Change 2001: The Scientific Basis*. Cambridge, UK: Cambridge University Press, Chapter 11, pp. 639–693.
- Currie, R.C., 1995. Variance contribution of M_n and S_n signals to Nile river data over a 30–8 year bandwidth. *J. Coast. Res., Special Issue No. 17*, 29–38.
- Coughlin, K., and Tung, K.K., 2004. Eleven-year solar signal throughout the lower atmosphere. *J. Geophys. Res.*, **109**, 7, D.21105.
- Cutler, A., 2003. *The Seashell on the Mountaintop: A Story of Science, Sainthood, and the Humble Genius who Discovered a New History of the Earth*. Dutton, Penguin Group: New York.
- Ekholm, N., and Arrhenius, S.A., 1898. Über den Einfluss des Mondes auf die Polarlichter und Gewitter. *Kongl. Svenska Ventenskaps Akademiens Handlingar. Stockholm*, **31**(2), 77–156.
- Fairbridge, R.W., 1961. Eustatic changes in sea level. In Ahrens, L.H., et al., (eds.), *Physics and Chemistry of the Earth*, vol.4. London: Pergamon, pp. 99–185.
- Fairbridge, R.W. (ed.), 1967. *The Encyclopedia of Atmospheric Sciences and Astrogeology*. New York: Reinhold, 1200pp.
- Fairbridge, R.W., 1971. Quaternary shoreline problems at INQUA 1969. *Quaternia*, **15**, 1–18.
- Fairbridge, R.W., 1976. Effects of Holocene climate change on some tropical geomorphic processes. *Quaternary Res.*, **6**, 529–556.
- Fairbridge, R.W., 1980. Prediction of long-term geologic and climatic changes that might affect the isolation of radioactive waste. *Underground Disposal of Radioactive Wastes*, **2**, 285–405. (Vienna, International Atomic Energy Agency, IAEA-SM-243/43, Appendix).
- Fairbridge, R.W., 1982. The fracturing of Gondwanaland. In Scrutten, R.A., and Talwani, M. (eds.), *The Ocean Floor*. Chichester, New York: Wiley, pp. 229–235.
- Fairbridge, R.W., and Hillaire-Marcel, C., 1977. An 8,000 year paleoclimatic record of the 45-yr “Double-Hale” solar cycle. *Nature*, **268**, 413–416.
- Fairbridge, R.W., and Sanders, J.E., 1987. The Sun's orbit, A.D. 750–2050: Basis for new perspectives on planetary dynamics and Earth-Moon linkage. In Rampino, M.R., Sanders, J.E., Newman, W.S., and Königsson (eds.), *Climate: History, Periodicity, and Predictability*. New York: Van Nostrand Reinhold, pp. 446–471.
- Haigh, J., 2002. The effects of solar variability on the Earth's climate. *Phil. Trans. R. Soc. Lond., sec.A*, **361**(1802), 95–111.
- Hewitt, C.N., and Jackson, A., 2003. *Handbook of Atmosphere Science*. Oxford: Blackwell Publishing, 684pp.
- Hoffman, P.F., and Schrag, D.P., 2000. Snowball Earth. *Sci. Am.*, Jan., 68–75.
- Holgate, S.J., and Woodworth, P.L., 2004. Evidence for enhanced coastal sea level rise during the 1990s. *Geophys. Res. Lett.*, **31**, LO7305, doi: 10.1029.
- Hoyt, D.V., and Schatten, K.H., 1997. *The Role of the Sun in Climate Change*. New York: Oxford University Press.
- Hyde, W.T., Crowley, T.J., Baum, S.K., and Peltier, W.R., 2000. Neoproterozoic ‘snowball earth’ simulations with a coupled climate/ice sheet model. *Nature*, **405**, 425–429.
- Jacoby, G.C., and D'Arrigo, R.D., 1989. Reconstructed Northern Hemisphere annual temperature since 1671 based on high-latitude tree-ring data from North America. *Clim. Change*, **14**, 39–59.
- Jelbring, H., 1995. Analysis of sunspot cycles phase variations: Based on D. Justin Schove's proxy data. *J. Coast. Res., Special Issue no. 17*, 363–369.
- Jouzel, J., et al., 1993. Extending the Vostok ice-core record of paleoclimate to the penultimate glacial period. *Nature*, **364**, 407–412.
- Kodera, K., 1993. The quasi-decadal modulation of the influence of the equatorial QBO on the north-polar stratospheric temperatures. *J. Geophys. Res.*, **98**, 7245–7250.

- Kukla, G.J., 1981. Surface albedo. In Berger, A. (ed.), *Climatic Variations and Variability: Facts and theories*. Dordrecht: Reidel, pp. 85–109.
- Kutzbach, J.E., et al., 1993. Simulated climatic changes. In Wright, H.E., et al., (eds.), *Global Climates since the Last Glacial Maximum*. Minneapolis, MN: University of Minnesota Press, pp. 24–93.
- Lamb, H.H., 1977. *Climate History and the Future*. London: Methuen (and Princeton University Press), 835pp.
- Lamb, H.H., 1979. Climatic variation and changes in the wind and ocean circulation: the Little Ice Age in the northeast Atlantic. *Quaternary Res.*, **11**, 1–20.
- Landscheidt, T., 1988. Solar rotation, impulses of the torque in the Sun's motion, and climatic variation. *Clim. Change*, **12**, 265–295.
- Leroux, M., 1996. *La Dynamique du Temps et du Climate*. Paris: Masson, 310pp.
- Lowe, J.J., and Walker, M.J.C., 1997. *Reconstructing Quaternary Environments* (2nd edn.) London: Prentice Hall, 446pp.
- Lowrie, W., 1997. Geomagnetic polarity reversals and the geological record. In Shirley, J.H., and Fairbridge, R.W. (eds.), *Encyclopedia of Planetary Science*. London: Chapman Hall (now Springer), pp. 269–272.
- McCrae, W.H., 1981. Long time-scale fluctuations in the evolution of the Earth. *Proc. R. Soc. Lond.*, **A375**, 1–41.
- Oliver, J.E., and Fairbridge, R.W. (eds.), 1986. *The Encyclopedia of Climatology*. New York: Van Nostrand Reinhold, 986pp.
- Negi, J.G., and Tiwari, R.K., 1983. Matching long-term periodicities of geomagnetic reversals and galactic motions. *Geophys. Res. Lett.*, **10**, 713–716.
- Pettersson, O., 1912. The connection between hydrographical and meteorological phenomena. *R. Meteor. Soc. Q. J.*, **38**, 173–191.
- Pettersson, O., 1914. Climatic variations in historic and prehistoric time. *Svenska Hydrogr. Biol. Komm., Skriften*, 26pp.
- Petit, J.R., et al., 1999. Climate and atmospheric history of the past 420,000 years from the Vostok ice core, Antarctica. *Nature*, **399**, 429–436.
- Raup, D.M., and Sepkoski, J.J. Jr., 1984. Periodicity of extinctions in the geologic past. *Proc. Natl. Acad. Sci.*, **81**(3), 801–805.
- Raymo, M.E., and Ruddiman, W.F., 1992. Tectonic forcing of late Cenozoic climate. *Nature*, **359**, 117–122.
- Raynaud, D., Barnola, J.M., Chappellaz, J., Blunier, T., Indermühle, and Stauffer, B., 2000. The ice core record of greenhouse gases: A view in the context of future changes. *Quaternary Sci. Rev.*, **19**, 9–17.
- Ruddiman, W.F., and Kutzbach, J.E., 1990. Late Cenozoic plateau uplift and climate change. *Trans. R. Soc. Edinb.: Earth Sci.*, **81**, 301–314.
- Ruddiman, W.F., and Kutzbach, J.E., 1991. Plateau uplift and climatic change. *Sci. Am.*, **264**(3), 66–75.
- Schove, D.J. (ed.), 1983. *Sunspot Cycles*, Benchmark Papers in Geology, vol. 68. Stroudsburg: Hutchinson Ross Publ. Co., 392pp.
- Schwartzbach, M., 1963. *Climates of the Past*. London: Van Nostrand Co., 328pp (transl. by R.O. Muir).
- Shirley, J.H., and Fairbridge, R.W. (eds.), 1997. *Encyclopedia of Planetary Sciences*. London: Chapman and Hall, 990pp.
- Stothers, R.B., 1986. Periodicity of earth's magnetic reversals. *Nature*, **322**, 444–446.
- Stuiver, M. and Braziunas, T.F., 1993. Sun, ocean, climate and atmospheric ^{14}C : An evaluation of causal and spectral relationships. *The Holocene*, **3**(4), 289–305.
- Thejll, P., Christiansen, B., and Gleisner, H., 2003. On correlations between the North Atlantic Oscillation, geopotential heights and geomagnetic activity. *Geophys. Res. Lett.*, **30**(6), 1347, doi:10.29/2002GL016598.
- Thomson, D.J., 1990. Time series analysis of Holocene climate data. *Philos. Trans. R. Soc. Lond.*, **A330**, 601–616.
- Tsurutani, Goldstein, B.E., and Smith, E.J., 1990. The interplanetary – solar causes of geomagnetic activity. *Planet. Space Sci.*, **38**, 109–126.
- Weissman, P.R., 1999. The Solar System and its place in the Galaxy. In Weissman, P.R., McFadden, L.A., and Johnson, T.V. (eds.), *Encyclopedia of the Solar System*. San Diego, CA: Academic Press, pp. 1–34.
- Windelius, G., and Carlborg, N., 1995. Solar orbital angular momentum and some cyclic effects on earth systems. *J. Coast. Res., Special Issue* **17**, 383–395.
- Wood, F.J., 2001. *Tidal Dynamics* (2 vol.) (3rd edn.). West Palm Beach, FL: Coastal Education and Research Foundation.

Cross-references

Astronomical Theory of Climate Change
 Atmospheric Evolution, Mars
 Atmospheric Evolution, Venus
 Bolide Impacts and Climate
 Carbon Cycle
 Dendroclimatology
 Eccentricity
 Glacial Eustasy
 Glacial Isostasy
 Glaciations, Quaternary
 Greenhouse (warm) Climates
 Icehouse (cold) Climates
 North Atlantic Oscillation (NAO) Records
 Obliquity
 Paleoclimate Proxies, an Introduction
 Paleo-EL Niño-Southern Oscillation (ENSO) Records
 Plate Tectonics and Climate Change
 Precession, Climatic
 Pre-Quaternary Milankovitch Cycles and Climate Variability
 Quasi-Biennial Oscillation (Encyclopedia of World Climatology)
 Snowball Earth Hypothesis
 Sun-Climate Connections

ECCENTRICITY

The orbit of the Earth around the Sun is an ellipse. The eccentricity of the orbit is a measure of its elliptical shape, i.e.,

$$e = \frac{\sqrt{a^2 - b^2}}{a}$$

a being the semi-major axis and b the semi-minor axis. Its present-day value is 0.0167, a small value corresponding to a nearly circular orbit. The eccentricity varies through time because of the mutual gravitational forces exerted on each other by the Earth, the Sun and the other planets of the solar system. The value of the eccentricity has remained less than 0.07 over the last 3 million years. (Berger and Loutre, 1991).

The amount of energy received by the Earth from the Sun is directly dependent on the eccentricity. Its global annual mean value per unit area is

$$\frac{S}{4\sqrt{1 - e^2}}$$

with S the total solar irradiance measured at a distance a from the Sun (Berger and Loutre, 1994). This annual mean irradiance is only slightly variable with eccentricity. The maximum change reached for the largest value of e is less than 0.2%. On the other hand, the eccentricity plays a role on insolation by modulating the amplitude of climatic precession.

Eccentricity varies with a quasi-period of $\sim 100,000$ years superimposed on a longer quasi-period of $\sim 400,000$ years (Berger, 1978). The eccentricity becomes very close to zero every 400,000 years (Figure E2).

Marie-France Loutre

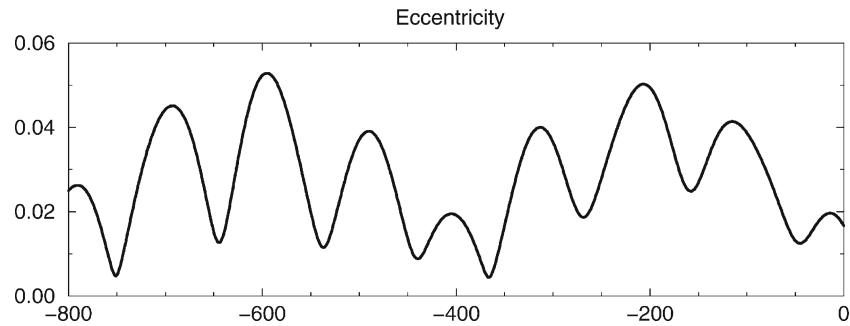


Figure E2 Long term variations of the eccentricity over the last 800,000 years.

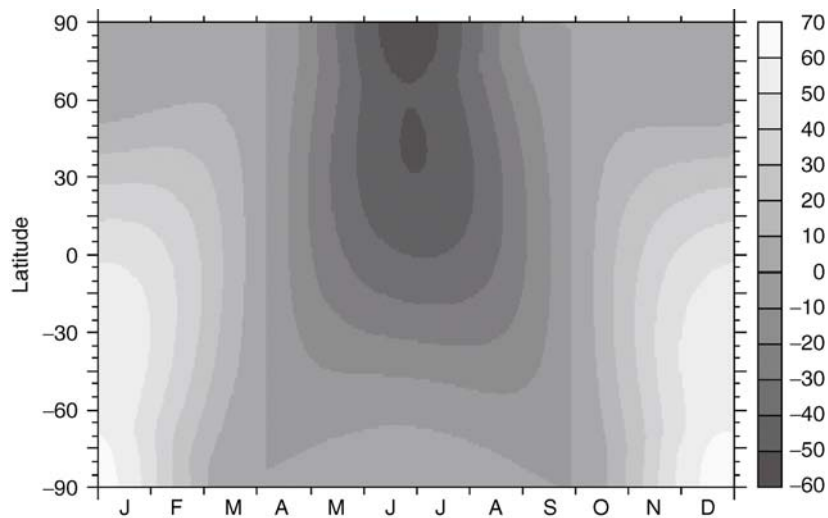


Figure E3 Variation of the mean irradiance (W m^{-2}) following an increase of the eccentricity from 0 to 0.055 (for the present-day value of obliquity, $\varepsilon = 23.446^\circ$ and longitude of perihelion, $\bar{\omega} = 102.04^\circ$). The mean irradiance is presently maximum at the South Pole at the December solstice (563 W m^{-2}), with a secondary maximum at the North Pole at the June solstice (527 W m^{-2}). At the equator, it is 439 W m^{-2} at the March equinox and 433 W m^{-2} at the September equinox. The difference between the polar values reflects the difference in the distance from the Earth to the Sun for these two solstices. The same holds for the equatorial values for the two equinoxes.

Bibliography

- Berger, A.L., 1978. Long-term variations of daily insolation and quaternary climatic changes. *J. Atmos. Sci.*, **35**(12), 2362–2367.
- Berger, A., and Loutre, M.F., 1991. Insolation values for the climate of the last 10 million years. *Quaternary Sci. Rev.*, **10**, 297–317.
- Berger, A., and Loutre, M.F., 1994. Precession, eccentricity, obliquity, insolation and paleoclimates. In Duplessy, J.C., and Spyridakis, M.-T. (eds.), *Long Term Climatic Variations, Data and Modelling*, vol. 22. Berlin: Springer. Nato ASI series, Serie I: Global Environmental Change, pp. 107–151.

Cross-references

[Astronomical Theory of Climate Change](#)
[Climate Forcing](#)
[Obliquity](#)
[Precession, Climatic](#)
[Pre-Quaternary Milankovitch Cycles and Climate Variability](#)
[Quaternary Climate Transitions and Cycles](#)
[SPECMAP](#)

EEMIAN (SANGAMONIAN) INTERGLACIAL

The Eemian has been defined as an interval dominated by forest elements that were preceded by an open vegetation cover of the previous glacial and succeeded by open vegetation of the last glacial complex (Turner and West, 1968). Thus, the Eemian is a terrestrial biostratigraphic unit associated with the last interglacial. Due to plant migration as well as climate and vegetation gradients, the lower and upper boundaries of the Eemian are time-transgressive. Eemian forests dominated NW Europe from ~ 126 to 115 kyBP, whereas Eemian forests in SW Europe may have persisted 5,000 year longer, from ~ 126 to 110 kyBP (Kukla et al., 2002). In practice, the term Eemian is widely applied to pedostratigraphic, biostratigraphic, and chronostratigraphic aspects of the last interglacial. The regional equivalents of the Eemian are known as Mikulinian in eastern

Europe, Kazantsevo in Siberia, Ipswichian in Great Britain, Ribains or Luhe in France, and Riss/Würm in the Alpine region.

In contrast to the Eemian, the last interglacial is a chronostratigraphic unit, i.e., boundaries are time-parallel. The last interglacial is the most recent interval when the global climate was as warm or even warmer than today (Kukla et al., 2002). The eustatic sea-level record is recommended as a master reference for the timing of the last interglacial (Muhs, 2002), because sea-level change represents a climate proxy that is globally in phase and its relicts such as coral reefs can be dated accurately. Furthermore, the boundaries of the interglacial can be defined reasonably well: when sea level was as high or higher than today, it can be assumed that the global climate was as warm or warmer than today. High-precision uranium-thorium dating of raised coral reefs indicates that the most recent interval when global sea level was as high or even higher than present occurred between 128 and 116 kyrBP (Muhs, 2002). Thus, the last interglacial lasted 12,000 years from 128 to 116 kyrBP. An alternative approach to delimit the last interglacial is to adopt arbitrarily the quasi-isochronous boundaries of marine isotope substage MIS 5e. When so defined, however, the last interglacial envelops the major cold event Heinrich 11 (H11).

The Sangamonian in North America is based on the Sangamon Geosol, a strongly weathered and traceable paleosol developed in the parent material of the penultimate glacial and buried by sediments of the last glacial. Thus, the Sangamon Geosol is a pedostratigraphic unit associated with the last interglacial. The lower and upper boundaries of the Sangamon Geosol are diachronous due to changes in parent material, drainage, and climate. The formation of the Sangamon Geosol lasted about 100 kyr, therefore much longer than the last interglacial (Hall and Anderson, 2000). Nevertheless, the Sangamonian Stage has been defined as a chronostratigraphic unit. Some authors correlate the Sangamonian Stage with the interval of MIS 5 (~130–75 kyrBP), whereas others restrict it to MIS 5e (~130–115 kyrBP).

Environmental conditions of the last interglacial world (128–116 kyrBP) were relatively similar to those of our current warm period, the Holocene. The major difference from the present is that early humans living at that time, such as the Neanderthals, did not influence the last interglacial environments. In general, the last interglacial world was slightly warmer and moister. The atmospheric composition was comparable to that of the pre-industrial Holocene. The continents were in their present position and the global sea level was at its maximum about 5 m higher than today. The principal features of atmospheric and oceanic circulation approached those of the current world. The coastlines were, aside from areas affected by isostatic depression, similar. The mountain ranges were the same as today, although their morphology has been further modulated in areas glaciated during the last ice age. The global landscape zones paralleled those of today: Polar ice caps existed in Greenland and Antarctica, although they were reduced in dimension. Frost-deserts and open tundra-type formations were present in the polar regions. Dense coniferous forests covered the higher latitudes of the Northern Hemisphere. Broad-leaved woodlands existed in large territories of the mid latitudes, being replaced by steppe communities in regions with lower precipitation. In the lower latitudes, desert-type areas were reduced in favor of savannahs. Species-rich rainforests covered vast areas of the inner tropics.

Because of the close similarity to Holocene environments, the last interglacial is considered to represent the most recent geological analog of our current warm period. Although the

human impact on the atmosphere makes the present climate different from any one in the past, study of the last interglacial and its transition to the next glacial can teach us a great deal about how the climate system operates (Kukla et al., 2002).

Insolation and climate response

Periodic long-term changes in the orbital configuration between the Sun and the Earth result in cyclic variations of the insolation, which are considered to be the main driving force of the glacial-interglacial cycles. The combination of orbital parameters such as precession, eccentricity, and obliquity leads to the occurrence of interglacial climates every ~100 kyr. The duration of interglacials is in general around half of a precession cycle. An exception from this rule might be applied to the present Holocene and the interglacial associated with MIS 11c around 400 kyr ago. Then and now, the influence of precession on insolation variations was damped down due to the almost circular orbit of the Earth. During the last interglacial period, in contrast, the eccentricity was higher and therefore the effects of precession on insolation were pronounced. Hence, warm conditions during the last interglacial lasted around 0.5 precession cycles, i.e., 11 kyr.

The mechanisms of climate response to insolation changes is not clear. It is assumed that the driver of climate is the summer insolation in the high northern latitudes and that due to the inertia of the global system there is a substantial delay in the climate response. Thus, the climatic optimum of the present interglacial was reached some millennia after the insolation maximum. A postponed climate response to insolation changes is also observed at the end of the last interglacial. Once the global system is in an interglacial mode of operation (oceanic and atmospheric circulation patterns approaching those of today), it stays in this mode even when the insolation is continuously reduced (Figure E4). At a certain critical threshold, however, the system shifts abruptly back into a glacial mode of operation. Most likely the concert of continuously reduced insolation, slowly extending ice shields at high latitudes with associated albedo feedbacks, and increasing freshwater input into the region of North Atlantic deep water production forced the system steadily to cross a critical threshold, triggering the abrupt reorganization of oceanic and atmospheric circulation. Such shifts into colder modes of operation occurred at around 115 and 110 kyr BP at the inception of the last glacial (Müller and Kukla, 2004). The Holocene insolation peaked 11 kyr ago. Today, the insolation intensity is as low as during most of the last glacial. Nevertheless, we are still in an interglacial mode due to the inertia of the global climate system.

The climate during the last interglacial has been reconstructed based on various climate proxies such as foraminiferal or pollen assemblages, the ratio of stable isotopes, and macrofossil remains. The reconstructions suggest mean annual temperatures up to 4 °C higher than today in northern Europe, in the northern latitudes of North America, and in northern Asia. More to the south, in Central Europe and in the mid latitudes of North America and Asia, the mean annual temperature rose up to 2 °C above the current values. In the lower latitudes of the Northern Hemisphere, in contrast, the mean annual temperature was similar to the present or even up to 1 °C lower. Thus, the meridional temperature gradient was lower during the climatic optimum of the last interglacial than today. The different meridional heat distribution might be explained by variations in the obliquity of the Earth's axis. During the early part of the last

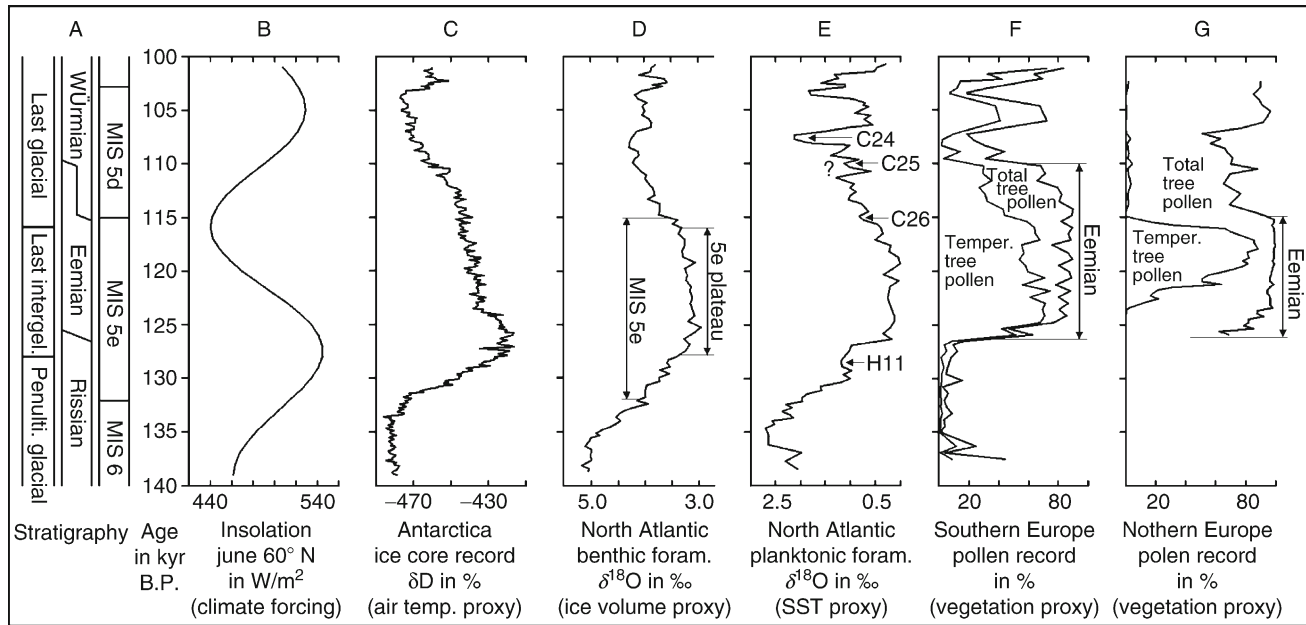


Figure E4 Tentative correlation of last interglacial records: (a) stratigraphy, (b) variations of June insolation at 60° N (Berger and Loutre, 1991), (c) δD record from the Vostok ice core (Petit et al., 1999), (d) benthic $\delta^{18}O$ record from core MD95–2042 off Portugal (Shackleton et al., 2003), (e) planktonic $\delta^{18}O$ record from core MD95–2042 off Portugal (Shackleton et al., 2003), (f) simplified pollen record from Tenaghi Philippon in Greece adopted from Wijmstra (1969), (g) simplified pollen record from Gröbern in Germany adopted from Litt (1994).

interglacial and during its climatic optimum at around 126 kyr BP (Figure E4c), the obliquity was higher than today, providing a stronger insolation to high latitudes, but weaker to the low ones. Furthermore, the perihelion occurred in boreal summer during the early part of the last interglacial, whereas perihelion is in boreal winter today.

Marine environments

A close representative of the last interglacial in deep sea sediments is MIS 5e. The marine oxygen isotope record, measured at benthic foraminifera, reflects mainly the total global ice volume. Consequently, oxygen isotope ratios are also an inverse proxy of global sea level. The changes in the benthic isotope records from various sites on the globe are generally considered to be synchronous. In fact, they might be quasi-synchronous as the mixing of oceanic water masses due to the large-scale overturning takes around 1,000–2,000 years. However, in contrast to the Eemian, the MIS 5e is customarily interpreted as a chronostratigraphic unit. The lower boundary of MIS 5e is defined at the midpoint of the transition between the heaviest $\delta^{18}O$ values during MIS 6 and the lightest $\delta^{18}O$ values during MIS 5e. The upper MIS 5e boundary is defined at the midpoint of the subsequent transition towards the heaviest $\delta^{18}O$ values during MIS 5d. Applying this concept to an oxygen isotope record on a timescale inferred from radiometric dating of coral reefs, MIS 5e lasted from 132 to 115 kyr BP (Figure E4a,d). The benthic isotope record from this site off Portugal shows an interval of quasi-constant light $\delta^{18}O$ values within MIS 5e. It has been assumed that this MIS 5e “plateau” correlates with the period when global sea level was as high or higher than at present, i.e., from 128 to 116 kyr BP (Shackleton et al., 2003). A comparison of the timing of this MIS 5e plateau with European pollen records (Figure E4f,g) suggests that

major global ice sheets, such as the Laurentide and the Scandinavian, had melted $\sim 2,000$ years before the spreading of Eemian woodlands in Europe.

Subsequent to the end of the MIS 5e $\delta^{18}O$ plateau, continental ice accumulated substantially, as reflected by the benthic oxygen isotope record of the interval 116–107 kyr BP (Figure E4d). Most likely, ice accumulation started in the area of the Laurentide and later the Scandinavian Ice Sheets. Eemian woodlands persisted in southern Europe for another $\sim 5,000$ years, well into MIS 5d. Thus, the onset of the last glacial was associated with the establishment of steep meridional climate gradients. Some authors question whether such steep gradients are feasible.

The sea-surface temperature (SST) change during the last interglacial has been reconstructed based on planktonic foraminiferal assemblages, the occurrence of ice-rafted detritus (IRD), $\delta^{18}O$ measurements from planktonic foraminifera, and alkenone. The occurrence of distinct IRD layers within otherwise mainly fine-grained deep sea sediments provides a correlation tool for the North Atlantic. It is assumed that the deposition of these IRD layers occurred within brief episodes (< 500 year) when icebergs moved far south and eastward accompanied by the expansion of cold surface water masses (McManus et al., 2002). The most prominent IRD layers during MIS 5e and 5d are the cold events H11 and C24 (Figure E4e). The H11 Heinrich event occurs at ~ 129 kyr BP, just before the onset of the last interglacial, and C24 at ~ 107 kyr BP, during the first stadial after the last interglacial. As H11 represents a major cold event, which occurred in the lower part of MIS 5e (Figure E4e), it is recommended not to adopt the boundaries of MIS 5e as the delimitation of the last interglacial. This approach would conflict the definition stating “... climate was as warm or even warmer than today” (Kukla et al., 2002).

Less-pronounced IRD layers have also been found at the transition from MIS 5e to 5d and during MIS 5d. The two ice rafting events C26 (at ~115 kyBP) and C25 (at ~110 kyBP) can be traced into the central part of the North Atlantic. A prominent cooling of 3 °C in SST at the transition from MIS 5e to 5d, derived from alkenone records from the Bermuda Rise, may correlate with the C26 event in the North Atlantic. The cold-water event C26 in the North Atlantic most likely relates to the opening of woodlands in NW Europe. If this is so, the event C26 marks the end of the classical Eemian in NW Europe (Figure E4e–g). Based on pollen analysis and varve counts at lake sediments from the famous Bispingen site in northern Germany, it has been determined that Eemian woodlands existed for around 11,000 years (Müller, 1974). Thus, the classical Eemian lasted from 126 to 115 kyr.

Recurring cold events, averaging one event every ~1,500 year, have been recognized in North Atlantic sediments of MIS 5e and Eemian lake sediments in Central Europe (Bond et al., 2001; Müller et al., 2005). By analogy with findings from the Holocene in the North Atlantic, the trigger for this last interglacial cyclic climate variability may have been changes in solar activity, possibly amplified by changes in North Atlantic ocean currents and/or the North Atlantic Oscillation. This sub-orbital cyclicality during the time of minimum global ice volume, however, was strongly subdued in comparison with the high-amplitude climate fluctuations of the last glacial.

Terrestrial environments

The term “Eem” was introduced by Harting (1874), based on the identification of a fauna of Lusitanian and even Mediterranean shells in marine clays buried by the last glacial deposits near the river Eem in the Netherlands. Today, it is customary to interpret the Eemian in a pollen record as an interval dominated by forest elements and associated with the climatic amelioration of the last interglacial. The terms “Eemian” and “last interglacial” should not be used synonymously. The Eemian, is strictly speaking, a biostratigraphic representative of the last interglacial in Europe. The onset of the Eemian is defined at the point in the pollen record when tree taxa exceed 50% of the total terrestrial pollen sum. The Eemian ends at the point when even the percentages of coniferous trees decline significantly. Obviously, this concept implies that, for reasons of climate gradients and plant migration, the onset and end of the Eemian did not occur at the same time in different areas of Europe. Therefore, the Eemian is time-transgressive and should not be used in a chronostratigraphic sense. In fact, it now appears that Eemian woodlands persisted considerably longer in southern Europe (126–110 kyBP) than in northwest Europe (126–115 kyBP) (Figure E4f,g). This implies the establishment of steep vegetation and climate gradients at the inception of the last glacial. The steepening of vegetation gradients might have been influenced by the steepening of meridional SST gradients in the North Atlantic, which in turn is suggested to be connected to a southward displacement of the North Atlantic Current at around 115 kyBP (Müller and Kukla, 2004).

The identification of the Eemian in a pollen record is based on a specific composition and succession of forest elements. In contrast to older interglacials, Eemian pollen records in Europe do not contain *Carya*, *Celtis*, *Eucommia*, *Pterocarya*, *Sequoia*, *Thuja*, and *Tsuga* as these taxa became extinct in this region earlier in the Quaternary. A peculiarity of the Eemian north of the Alps and Pyrenees is the absence of *Fagus* as

today this tree dominates quasi-natural forests in most of these areas. The typical composition and succession of the Eemian is known from master pollen records that reflect the biostratigraphy of several glacial-interglacial cycles (e.g., Reille et al., 2000). Absolute dating of interglacial sediments provides a tool to verify the biostratigraphic evaluation at other sites.

In Central Europe, the typical pollen zones of the Eemian have a remarkable consistency. This consistency is believed to be linked to an open seaway from the English Channel through the North and Baltic Seas to the White Sea, which supported the influence of mild oceanic climates over the entire region. The typical composition and succession of Eemian forest elements in Central Europe is shown in Figure E5. After a pioneer phase with *Juniperus*, *Betula*, and *Pinus*, the Eemian is characterized by the early spread of the deciduous taxa *Ulmus*, *Quercus*, and *Fraxinus* and the subsequent spread of *Corylus*. Within the *Corylus* phase there is a *Taxus* peak (sometimes featured as a double peak). Subsequently, an Eemian pollen record displays the spread of *Carpinus* and *Abies*. The maximum amount of *Carpinus* and *Abies* in the late-temperate phase varies in relation to altitude and proximity to mountain ranges (Müller, 2000). The major spread of *Picea*, occurs in the post-temperate phase of the Eemian. The final phase of the Eemian shows the spread and dominance of *Pinus* before coniferous forests decline.

In northern Europe, Eemian pollen records vary from those in Central Europe. In general, the composition of taxa stays the same. However, the further north a site is located, the more reduced is the percentage of the temperate taxa *Ulmus*, *Quercus*, *Fraxinus*, *Corylus*, and *Carpinus* to the benefit of *Betula*, *Pinus*, *Alnus*, and *Picea*. In northern Scandinavia, Eemian pollen diagrams do not show a temperate phase anymore, but a constant dominance of *Pinus* and *Betula*. Nevertheless, the long-distance wind transport of pollen resulted in grains from Central Europe found even far in the north of Scandinavia (Robertsson, 2000). There, the grains from temperate taxa sometimes reflect the typical Eemian succession of Central Europe.

In southern Europe, the boreal taxa *Betula* and *Picea* are absent south of the Alps and Pyrenees or do not play an important role in the record. The onset of the Eemian starts directly with the spread of deciduous *Quercus*, *Ulmus*, *Corylus*, and subsequently of *Carpinus* and *Quercus* evergreen. Mediterranean taxa such as *Pistacia*, *Olea*, and *Phillyrea* contributed pollen during the first half of the Eemian. Deciduous *Quercus* and *Carpinus* are the dominant taxa during the late-temperate phase of the Eemian. *Abies* was of minor importance. There was no post-temperate boreal forest phase such as in Central Europe, therefore late-deciduous woodlands persisted to the end of the Eemian at around 111 kyBP (Tzedakis et al., 2002). *Fagus* has been found south of the Alps in Italy and Austria during the Eemian.

In North America, pollen investigations in interglacial sediments have not hitherto had the same significance as in Europe. This might be due to the scarcity of interglacial lake sediments or a lack of exploration drilling.

Other representatives of the last interglacial in terrestrial environments are buried soils and geomorphologic features testifying to the absence of glaciers. This is how the classic Sangamonian interglacial has been described in North America. The term “Sangamon” was introduced by Leverett (1898), based on identification of a soil buried beneath till and loess of the last glacial that he observed in railroad cuts in Sangamon

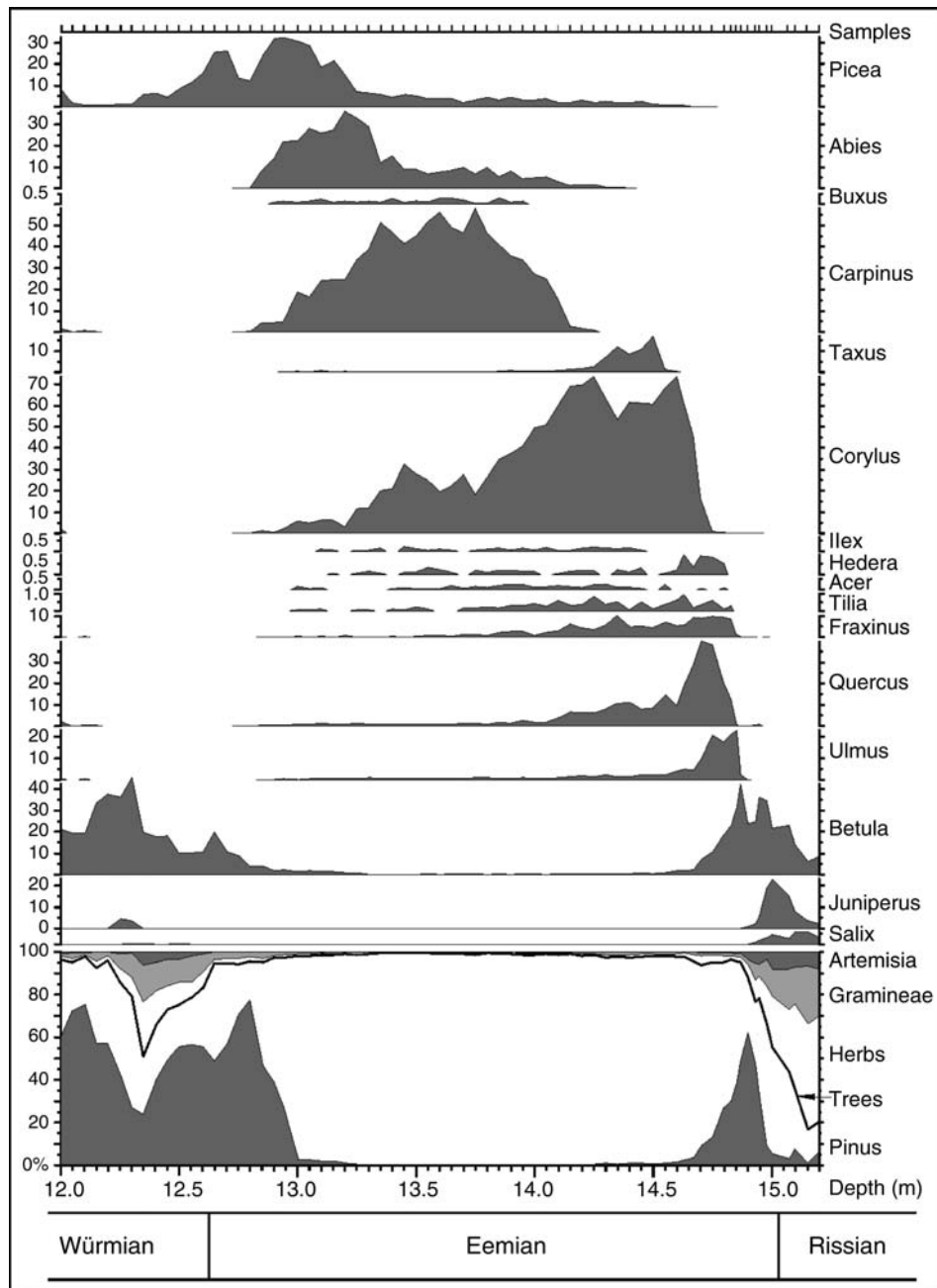


Figure E5 Characteristic taxa composition and succession of an Eemian pollen record in Central Europe (data from Jammertal in SW Germany, adopted from Müller et al., 2005).

County, Illinois. The Sangamon Geosol is a strongly developed paleosol in the parent material from the penultimate glacial (named Illinoian in the USA), and buried by the sediments of the last glacial (Wisconsinan). This paleosol has been described from many locations in the USA. It can be traced from the Great Lakes to Texas, and is frequently used as a marker horizon. The type of soil development varies with changes in parent material and regional climate conditions. In its type area at Athens Quarry, Illinois, the Sangamon Geosol is developed in loess colluvium and shows a remarkable thick Ab-horizon

on top of a Bt-horizon. Overall, soil proxies show that the Sangamon Geosol is more strongly developed than the Holocene soil. However, the differences in soil properties between the Sangamon Geosol and Holocene soil are interpreted primarily to reflect soil development duration, with climatic imprint being secondary. It is assumed that the Sangamon Geosol formed over a much longer time interval than the last interglacial, as is understood in Europe (Grimley et al., 2003). The weathering features of the Sangamon Geosol at its type region indicate that the formation persisted longer than the complete

MIS 5. The time represented in the Sangamon Geosol depends upon whether burial occurred and pedogenesis ceased during the early or late part of the Wisconsin glacial. In contrast to the Sangamon Geosol, the Sangamonian Stage has been defined as a chronostratigraphic unit by the Illinois State Geological Survey. The delimitation of the Sangamonian Stage is arbitrary. Some authors adopt the boundaries of MIS 5, whereas others restrict the Sangamonian Stage to MIS 5e.

The last interglacial paleosol in Europe, frequently found in loess sections, is in general preserved as a well-developed textural Bt-horizon. The last interglacial soil is known as Rocourt soil in NW Europe, as B1b of PK III in the Czech Republic, and as the Salyn soil of the Mezin Complex in Central Russia. The Bt-horizon is usually truncated and partly covered by humus soil sediments (Antoine et al., 2001). In high accumulation loess records, three humus zones have been found on top of the truncated last interglacial Bt-horizon (Bibus et al., 2002). The chernozem-like humus zones are separated from each other and from the Bt-horizon by loess colluvium that contains a mollusk fauna indicative of colder climate conditions. Therefore, it has been concluded that the humus zones developed during MIS 5a to 5c whereas the Bt-horizon is associated with MIS 5e.

Conclusions

- The last interglacial is the most recent interval prior to the Holocene when the global climate was as warm as or even warmer than today.
- Eustatic sea-level changes, a proxy of mean global climate, indicate that the last interglacial as a chronostratigraphic unit lasted from 128 to 116 kyrB.
- The Eemian is a biostratigraphic representative of the last interglacial in Europe.
- The Sangamon Geosol is a pedostratigraphic representative of ice-free conditions between the last and penultimate glaciation in North America.
- Both the Sangamon Geosol and Eemian have time-transgressive boundaries.
- MIS 5e, a close representative of the last interglacial in deep-sea sediments, records the time when total global volume of land-based ice was reduced.

Ulrich C. Müller

Bibliography

- Antoine, P., Rousseau, D.-D., Zöller, L., Lang, A., Munaut, A.-V., Hatté, C., and Fontugne, M., 2001. High-resolution record of the last interglacial-glacial cycle in the Nussloch loess-Palaeosol sequences, Upper Rhine area, Germany. *Quaternary Int.*, **76–77**, 211–229.
- Berger, A., and Loutre, M.F., 1991. Insolation values for the climate of the last 10 million years. *Quaternary Sci. Rev.*, **10**, 297–317.
- Bibus, E., Rähle, W., and Wedel, J., 2002. Profilaufbau, Molluskenführung und Parallelisierungsmöglichkeit des Altwürmabschnittes im Lössprofil Mainz-Weisenau. *Eiszeitalter und Gegenwart*, **51**, 1–14.
- Bond, G., Kromer, B., Beer, J., Muscheler, R., Evans, M.N., Showers, W., Hoffmann, S., Lotti-Bond, R., Hajdas, I., and Bonani, G., 2001. Persistent solar influence on North Atlantic climate during the Holocene. *Science*, **294**, 2130–2136.
- Grimley, D.A., Follmer, L.R., Hughes, R.E., and Solheid, P.A., 2003. Modern, Sangamon and Yarmouth soil development in loess of unglaciated southwestern Illinois. *Quaternary Sci. Rev.*, **22**, 225–244.
- Hall, R.D., and Anderson, A.K., 2000. Comparative soil development of Quaternary paleosols of the central United States. *Palaeogeogr. Palaeoclimatol. Palaeoecol.*, **158**, 109–145.

- Harting, P., 1874. De bodem van het Eemdal. Verlagen en Mededelingen van de Koninklijke Akademie van Wetenschappen, afdeling. *Natuurkunde II*, **8**, 289–290.
- Kukla, G.J., Bender, M.L., Beaulieu, J.-L., de, Bond, G., Broecker, W.S., Cleveringa, P., Gavin, J.E., Herbert, T.D., Imbrie, J., Joutel, J., Keigwin, L.D., Knudsen, K.-L., McManus, J.F., Merkt, J., Muhs, D.R., Mueller, H., Poore, R.Z., Porter, S.C., Seret, G., Shackleton, N.J., Turner, C., Tzedakis, P.C., and Winograd, I.J., 2002. Last Interglacial Climates. *Quaternary Res.*, **58**, 2–13.
- Leverett, F., 1898. The weathered zone (Sangamon) between the Iowan loess and Illinoian till sheet. *J. Geol.*, **6**, 171–181.
- Litt, T., 1994. Paläoökologie, Paläobotanik und Stratigraphie des Jungquartärs im nordmitteleuropäischen Tiefland unter besonderer Berücksichtigung des Elbe-Saale-Gebietes. *Dissertationes Botanicae*, **227**, 1–185.
- McManus, J.F., Oppo, D.W., Keigwin, L.D., Cullen, J.L., and Bond, G.C., 2002. Thermohaline circulation and prolonged interglacial warmth in the North Atlantic. *Quaternary Res.*, **58**, 17–21.
- Muhs, D.R., 2002. Evidence for the timing and duration of the last interglacial period from high-precision Uranium-Series Ages of corals on tectonically stable coastlines. *Quaternary Res.*, **58**, 36–40.
- Müller, H., 1974. Pollenanalytische Untersuchungen und Jahresschichtenzählungen an der eemzeitlichen Kieselgur von Bispingen/Luhe. *Geologisches Jahrbuch*, **A21**, 149–169.
- Müller, U.C., 2000. A late Pleistocene pollen sequence from the Jammertal, SW Germany with particular reference to location and altitude as factors determining Eemian forest composition. *Vegetation History and Archaeobotany*, **9**, 125–131.
- Müller, U.C., and Kukla, G.J., 2004. North Atlantic Current and European environments during the declining stage of the last interglacial. *Geology*, **32**, 1009–1012.
- Müller, U.C., Klotz, S., Geyh, M.A., Pross, J., and Bond, G.C., 2005. Cyclical climate changes during the Eemian interglacial in Central Europe. *Geology*, **33**, 449–452.
- Petit, J.R., Jouzel, J., Raynaud, D., Barkov, N.I., Barnola, J.M., Basile, I., Bender, M., Chappellaz, J., Davis, M., Delaygue, G., Delmotte, M., Kotlyakov, V.M., Legrand, M., Lipenkov, V.Y., Lorius, C., Pepin, L., Ritz, C., Saltzman, E., and Stievenard, M., 1999. Climate and atmospheric history of the past 420,000 years from the Vostok ice core, Antarctica. *Nature*, **399**, 429–436.
- Reille, M., Beaulieu, J.-L., Svobodova, H., Andrieu-Ponel, V., and Goegy, C., 2000. Pollen analytical biostratigraphy of the last five climatic cycles from a long continental sequence from the Velay region (Massif Central, France). *J. Quaternary Sci.*, **15**, 665–685.
- Robertsson, A.-M., 2000. The Eemian interglacial in Sweden, and comparison with Finland. *Geologie en Mijnbouw*, **79**, 325–333.
- Shackleton, N.J., Sanchez-Goni, M.F., Pailler, D., and Lancelot, Y., 2003. Marine Isotope Substage 5e and the Eemian Interglacial. *Glob. Planet. Change*, **36**, 151–155.
- Turner, C., and West, R.G., 1968. The subdivision and zonation of interglacial periods. *Eiszeitalter und Gegenwart*, **19**, 93–101.
- Tzedakis, P.C., Frogley, M.R., and Heaton, T.H.E., 2002. Duration of Last Interglacial conditions in Northwestern Greece. *Quaternary Res.*, **58**, 53–55.
- Wijmstra, T.A., 1969. Palynology of the first 30 meters of a 120 m deep section in northern Greece. *Acta Botanica Neerlandica*, **18**, 511–527.

Cross-references

- [Astronomical Theory of Climate Change](#)
[Dating, Biostratigraphic Methods](#)
[Eccentricity](#)
[Glacial Eustasy](#)
[Heinrich Events](#)
[Ice-Rafted Debris \(IRD\)](#)
[Laurentide Ice Sheet](#)
[Obliquity](#)
[Oxygen Isotopes](#)
[Paleosols, Quaternary](#)
[Precession, Climatic](#)
[Pollen Analysis](#)
[Scandinavian Ice Sheet](#)
[Sea Level Change, Quaternary](#)
[Uranium-Series Dating](#)

ELECTRICAL CONDUCTIVITY

Electrical measurements are frequently used to determine the chemical characteristics of ice cores in paleoclimate studies. Electrical measurements on ice cores can be made quickly, non-destructively, and with high spatial resolution, but they do not provide information on specific ions. Electrical measurements are used to identify the seasonal variations in chemistry that define the annual layers in an ice core that are used to determine the age of ice, and to determine if the layers in an ice core have been distorted by abnormal ice flow. For these tasks the high spatial resolution and efficiency of the electrical measurements is more important than information on specific ions. Electrical measurements can be classified into two general categories: direct current and alternating current methods.

Direct current methods are conventionally referred to as the Electrical Conductivity Method (i.e., ECM) (Hammer, 1983) and measure the current flow between two electrodes with a potential difference of about 1,000 V. The electrodes typically have a surface area of about 16 mm² and are separated by about 1 cm. Direct comparison of measurements made with different instruments is complicated because of differences in the electrode geometry and the potential difference. Measurements are typically made every 1 mm along a prepared flat surface of the core that is parallel to the axis of the core. The ice lattice prevents lateral movement of all ions except free protons, and hence only protons can carry the direct current. The ECM method is therefore sensitive only to the concentration of H⁺ ions associated with strong acids. The ECM record is typically presented as a continuous high spatial resolution record indicative of the acidity of the ice core. It is particularly well suited for indicating the presence of acids from volcanic activity and identifying annual layers.

Alternating current methods are referred to as Dielectric Property (DEP) measurements. They utilize a capacitor consisting of ice as the dielectric material between two conductive plates (Moore et al., 1989). A thin insulating layer prevents electrical connection between the conductive plates and the ice. The impedance of the ice-filled capacitor is typically measured over a range of frequencies every 1 cm along the core. The ice lattice prevents the lateral movement of all ions except free protons, but the other ions can conduct the electrical current by rotating around a stationary location. The DEP method is therefore sensitive to the concentration of a wide range of ions. The DEP record is typically presented as a continuous record indicative of the total ion content of the ice core. A variation on the DEP method is complex conductivity that uses an alternating current with an electrode geometry similar to the ECM method (Taylor et al., 2004). The complex conductivity method is also sensitive to the total ion content of the ice but has more spatial resolution than the DEP method.

The DEP and ECM methods are typically presented as a single profile along the length of an ice core. Multitrack measurements utilize multiple adjacent profiles that are measured on a flat surface parallel to the axis of the core (Taylor and Alley, 2004). This is presented as a two dimensional image of the conductivity in a vertical plane through the ice core. This enables the inclination and continuity of annual layers to be observed.

Kendrick Taylor

Bibliography

- Hammer, C.U., 1983. Initial direct current in the buildup of space charges and the acidity of ice cores. *J. Phys. Chem.*, **87**(21), 4099–4103.
- Moore, J.C., Mulvaney, R.L., and Paren, J.G., 1989. Dielectric stratigraphy of ice; a new technique for determining total ionic concentrations in polar ice cores. *Geophys. Res. Lett.*, **16**(10), 1177–1180.
- Taylor, K.C., and Alley, R.B., 2004. Two dimensional electrical stratigraphy of the Siple Dome, Antarctica ice core. *J. Glaciol.*, **50**, 231–235.
- Taylor, K.C., Alley, R.B., Meese, D.A., Spencer, M.K., Brook, E.J., Dunbar, N.W., Finkel, R., Gow, A.J., Kurbatov, A.V., Lamorey, G.W., Mayewski, P.A., Meyerson, E., Nishiizumi, K., and Zielinski, G.A., 2004. Dating the Siple Dome, Antarctica ice core by manual and computer interpretation of annual layering. *J. Glaciol.*, **50**, 453–461.

Cross-reference

Ice cores, Antarctica and Greenland

EOLIAN DUST, MARINE SEDIMENTS

Introduction

Charles Darwin was the first scientist to comment formally on the red dusts blowing from Africa out across the Atlantic, an event he observed while on the *Beagle* (Darwin, 1846). Marine geologists have known since the late 1950s that dust storms originating in the arid and semi-arid regions of continents carry dust long distances, and that sea-floor sediments in regions far from continents, out of the reach of river-borne sediment, are dominated by eolian dust.

Atmospheric scientists find that most of the dust is transported by a few spring storms. These storms raise the dust high up into the troposphere where it is transported for long distances and eventually removed by both dryfall and rainout (Prospero et al., 1983; Pye, 1987). Satellites now routinely track dust storms that move from the semiarid regions of central China all the way across the North Pacific to California, and from the Sahara across the Atlantic Ocean to the Caribbean and Florida. Since most of the world's continental surface area is in the Northern Hemisphere, the Northern Hemisphere is far dustier than the Southern.

Sources of atmospheric dust

Three main source regions provide dust to the atmosphere and ocean. The two largest are the deserts and basins of central China, north of the Tibetan Plateau, and the Sahara and Sahel regions of North Africa. The third important source of dust is the deserts of Arabia and the Horn of Africa, which provide dust to the northwestern Indian Ocean. The amount of material available for dust transport depends on the climate of the source region, with arid and semi-arid climates providing the most material, and more humid – vegetated – regions providing less. There are, however, hyperarid regions where rain falls very rarely. In these regions, there is not enough water to break down the feldspar minerals that are common in continental rocks into clays. Therefore, this weathering process does not create enough fine-grained material for long-range transport. What little material there was has been stripped away by the wind long ago, a condition known as deflation. The deserts

of Australia fit this description; they are hyperarid, deflated, and supply surprisingly little dust to the oceans. As a result of this physical and climatic geography, there is about an order of magnitude less dust deposited in the Southern Hemisphere. The total amount of dust delivered to the ocean is estimated to be about 0.1 to 0.2×10^{15} t yr⁻¹, which is roughly 1% of the total river load of 15 to 20×10^{15} t yr⁻¹ (Rea, 1994). Nonetheless, pelagic clays composed of eolian dust characterize the surface sediments of about one third of the ocean floor, an area similar to that of all land surfaces.

Size of dust grains

The large spring dust storms raise a broad mixture of grains from the desert floors, but after a transport distance of 1,000 or 2,000 km, the sand and coarse silt sized grains have fallen out and the remaining suspended minerals are fine silt and clay-sized. The size of these distal dust grains, now preserved in abyssal sediments, reflects the dynamic equilibrium between the supporting energy of the transporting winds and gravitational settling. Equilibrium grain size changes very little with increasing distance from the source region, and maps of the median grain size of dust in North Pacific sediments show little variation across this broad expanse of ocean (Rea and Hovan, 1995). Thus, at any one location, the size of these equilibrium dust grains preserved in deep sea sediments is a record of the energy of the transporting winds, with stronger winds resulting in coarser grains. Numerous grain size studies of dust show that it has a median diameter of 2–4 microns. The hypothesis that dust grain size provides a record of wind strength was tested by examining dust captured in sediment traps during an experiment conducted in the Arabian Sea. There, the dust grain size was coarsest when winds were strongest, but not necessarily when the most material was being transported (Clemens, 1998).

This observation indicates one more aspect of dust deposition that is important: that dust grain size is independent of the amount (and source) of dust deposited. Cross-plots of grain size and dust supply data from any one core show a random scatter. This independence means that scientists may discover the source area climate from the dust supply data and the wind intensity from the grain size data, both from the same set of samples.

Composition, mineralogy and geochemistry

The first modern reports on the subject of Saharan dust in the central Atlantic recognized the red-stained quartz grains accumulating in Atlantic sediments as being from the Sahara. Marine geologists studying the surface sediments of the North Pacific have understood for more than 40 years that the band of quartz-rich sediment extending east from the deserts of central and eastern Asia represented dust coming from China. Studies comparing the detailed mineralogy of the dust with that of the surface sediment show them to be indistinguishable. For the North Pacific region, the average composition of the <2 μm mineral component is dominated by illite, which is 30–40% of the total, with subequal amounts of quartz, chlorite, kaolinite, and plagioclase (10–15% each). Chlorite increases in abundance to the north, and smectite becomes a noticeable minor component nearer to North America (Leinen, 1989).

In the past decade, various technical advances with regard to geochemical analyses have made it possible to perform other studies that provide important information about dust transport and deposition. Trace element geochemistry and radiogenic

isotopic analysis of the dust have allowed scientists to resolve questions of source and how sources have changed over time. The first broadly-based study was of the geochemistry of the surficial sediment of the North Pacific. It showed that dust from China dominates the Pacific surficial sediment all the way south to the Intertropical Convergence Zone (ITCZ) and almost all the way east to North America. North America, on the other hand, supplies very little dust to the North Pacific Ocean. The neodymium, lead, and strontium isotope geochemistry of the dust isolated from sea-floor sediment samples is identical to that of Chinese loess, with a similar bulk geochemistry to that of Paleozoic shales (Jones et al., 1994, 2000). Over the years, scientists have used both the mineralogy, especially the clay mineralogy, and the geochemistry of the dust to determine its provenance, with excellent results. As a result of this kind of work, it is possible to understand the changing sources of dust to the oceans, and that the dust in the Greenland ice cores and Antarctic ice cores originates from Asia and southern Argentina, respectively (see Biscaye et al., 1997).

History of dust deposition

Long-term changes in dust deposition

Several studies of the long-timescale record of dust deposition have been carried out in both the Atlantic Ocean, downwind from the Sahara, and in the North Pacific, downwind from the deserts of central and eastern Asia. Most of this work has aimed to determine the mass accumulation rate of the dust, which is interpreted in terms of the aridity of the continental source regions. Some of these studies have also analyzed the grain size of the dust as an indication of wind strength, and aimed to determine the geochemistry of the dust in order to understand changes in the source region. Furthermore, all of this long-term work has been carried out in the Northern Hemisphere; the history of the Southern Hemisphere is assumed to be similar but that has yet to be shown conclusively. Deposits of nearly pure eolian sediment are known as pelagic clays or red clays after their brick-red to brown color. There are very few fossils in these cores, and because of their slow sedimentation rate, often 30–50 cm per 10⁶ yr, magnetic reversal stratigraphy generally does not work. Thus, age control is poor; often done on the basis of fossil fish teeth, or ichthyoliths. Improving the age control in red clays is an ongoing research topic (Gleason et al., 2002).

Two North Pacific cores have been studied in detail: a giant piston core LL44-GPC3 (this coding refers to the ship that raised the core, the AT&T cable-laying ship *Long Lines*, and that this core was the third Giant Piston Core recovered), and the cores from Ocean Drilling Program (ODP) Site 885/886. Core GPC3 came from the central North Pacific at about 30.3° N, 157.8° W, and ODP Site 885/886 is at 44.7° N, 168.3° W. Both sites now underlie the zonal winds of the prevailing westerlies. The record at GPC3 spans the entire Cenozoic, covering the last 70 million years. The iridium layer corresponding to the meteorite impact at the Cretaceous-Tertiary boundary that may have caused the ultimate extinction of the dinosaurs lies in the lower portion of the core. The materials recovered farther north at Site 885/886 provide a very good record of the last 12 million years. Together, these two records define the eolian depositional record for the latest Cretaceous and Cenozoic time.

Dust accumulation recorded in core GPC3 (Figure E6; Janecek and Rea, 1983; Rea et al., 1985) shows a very low

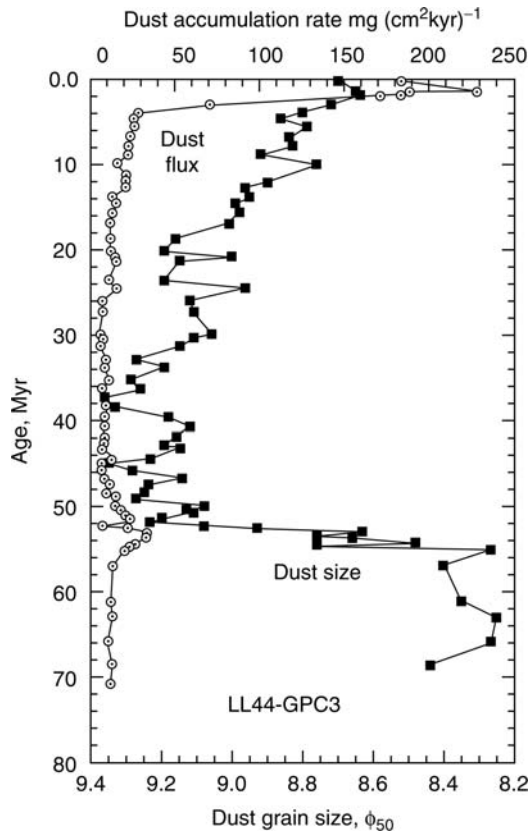


Figure E6 The Cenozoic record of dust deposition from core LL44-GPC3. Grain size values are median diameter in phi-units, where phi is the negative logarithm to the base 2 of the grain diameter in millimeters ($\phi = -\log_2 D_{mm}$). Thus $9\phi = 2 \mu\text{m}$, $8\phi = 4 \mu\text{m}$, etc.

input of dust through most of the Cenozoic. There is doubling of flux values at about 25 Ma, moving upcore from the Paleogene to the Neogene, and a further large increase in dust input at 3 or 4 Ma. This history can be interpreted in terms of changing climates, in this case increasing aridity, in the eolian source region. The size of the eolian grains is a measure of the wind intensity. In the younger part of the record, the size of the dust grains increases towards the present from low values in the Eocene, likely a result of increasing wind intensity accompanying the mid to late Cenozoic cooling of the higher latitudes. The big surprise in the GPC3 data was the very large change in dust grain size in the lower part of the core. We have found this same shift in grain size in other cores from the North Pacific. It represents, apparently, a sudden decline in wind intensity associated with several global changes that occurred in conjunction with the Paleocene/Eocene boundary (Rea et al., 1990) and the onset of unusually warm Eocene climates.

Sediments recovered from ODP Site 885/886 are characterized by a reliable magnetic reversal stratigraphy and so are much better constrained as to age and rate than those from GPC3. Nevertheless, the major late Cenozoic increase in dust flux seen in GPC3 is also the most significant change in this record (Figure E7). This order of magnitude increase in flux begins at 3.6 Ma and represents a significant drying in the eolian source regions in China. Other data indicate a rapid

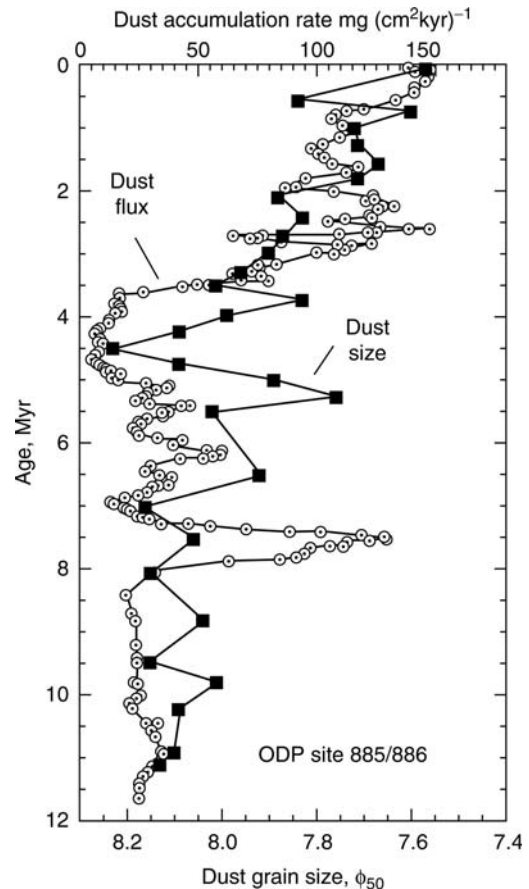


Figure E7 The record of dust deposition and grain size from core ODP Site 885/886 for the last 12 million years.

uplift of the northeastern portion of the Tibetan Plateau then, the deserts of central China being cut off from the moisture source to the south (Rea et al., 1998). The interpretation of the dust flux peak at about 8 Ma is less clear. The size of the eolian grains increases in younger materials. The increase is not regular, and the last shift towards coarser dust grains, hence stronger winds, begins about 4.5 Ma. Many studies of late Cenozoic climate change have shown that major Northern Hemisphere glaciation, the ice age we are in currently, began at 2.6 Ma. Other kinds of paleoclimate records suggest that this time of increasing continental ice cover was preceded by an increase in wind intensity two million years earlier, and an increase in the atmospheric dust loading one million years earlier. It can be concluded that different aspects of the world's climate system change sequentially, one after the other, rather than all at the same time.

Eolian records from the Atlantic and Indian Oceans indicate a late Cenozoic drying of Saharan and Sahelian Africa. The general sense of more dust coming into the oceans during the past three or four million years holds for these studies, but the timing of the aridity increases does not seem to be exactly the same for northern Africa and eastern Asia. A drying of the Northern Hemisphere continents in general concordance with Northern Hemisphere cooling and the ultimate beginning of the Plio-Pleistocene glacial ages has been clearly demonstrated by all studies of dust depositional history.

Orbital timescale changes in dust deposition

The classic terrestrial, Quaternary record of climate change is found in the loess horizons, interspersed with soils, that sweep across the Loess Plateau of China. Loess, a wind blown silt, forms during the relatively cold and dry glaciations, and the soils form during the warmer and wetter interglacial periods. In marine geology, the classic record of Quaternary climate change is found in the oxygen-18 ($\delta^{18}\text{O}$) values of seawater, which respond to the amount of glacial ice piled onto the continents. Linking these two paleoclimate records has been a long-standing goal of paleoclimatologists. The chance to achieve this objective was provided by a core raised from the Shatsky Rise, an oceanic plateau in the northwest Pacific. A study of dust deposition in this core captured the past 500,000 years (Figure E8) of the joint continental and marine history of climate change (Hovan et al., 1991). The flux of dust to the North Pacific varies by a factor of three to five on these glacial-interglacial timescales, with fluxes reaching a maxima during glaciations. As the dust flux maximal also correspond with the timing of loess formation, it is possible to determine the temporal relation between loess formation and the oxygen isotopic record generated from the same core. Spectral analysis of these and other eolian records of suitable resolution have shown the importance of the orbital variability that was first well quantified by Milankovitch in these

paleoclimatic records (Pisias and Rea, 1988; Clemens and Prell, 1990; Hovan et al., 1991).

Provenance studies

The geochemistry of the dust accumulated on the sea floor provides clues as to the source of the dust and the nature of any one source region. Knowing which continent, Asia or America, has provided the dust to the core location is a critical first step in the interpretation of source area climate. Here, again, the best-studied core is GPC3. Kyte and others (1993) analyzed samples from throughout GPC3 and were able to demonstrate that the dust in the upper portion of that core came from Asia, and dust in the lower part came from America. This observation regarding a change in the bulk geochemistry from a younger material of Asian affinity to an older sediment of American affinity was also noted by Pettke et al. (2002) who measured the Nd and Pb isotopic ratios of the dust. In the present climate regime, the change in dust geochemistry from Asian to American happens at the Intertropical Convergence Zone, and not, as might be expected, at the boundary between the zonal westerlies and the tradewinds. If this observation remains true during the Cenozoic, then the mid-Cenozoic geochemical transition observed in GPC3 marks the past location of the ITCZ, a location far north of the equator, perhaps 20° – 25° N (Rea, 1994; Rea et al., 2000; Pettke et al., 2002).

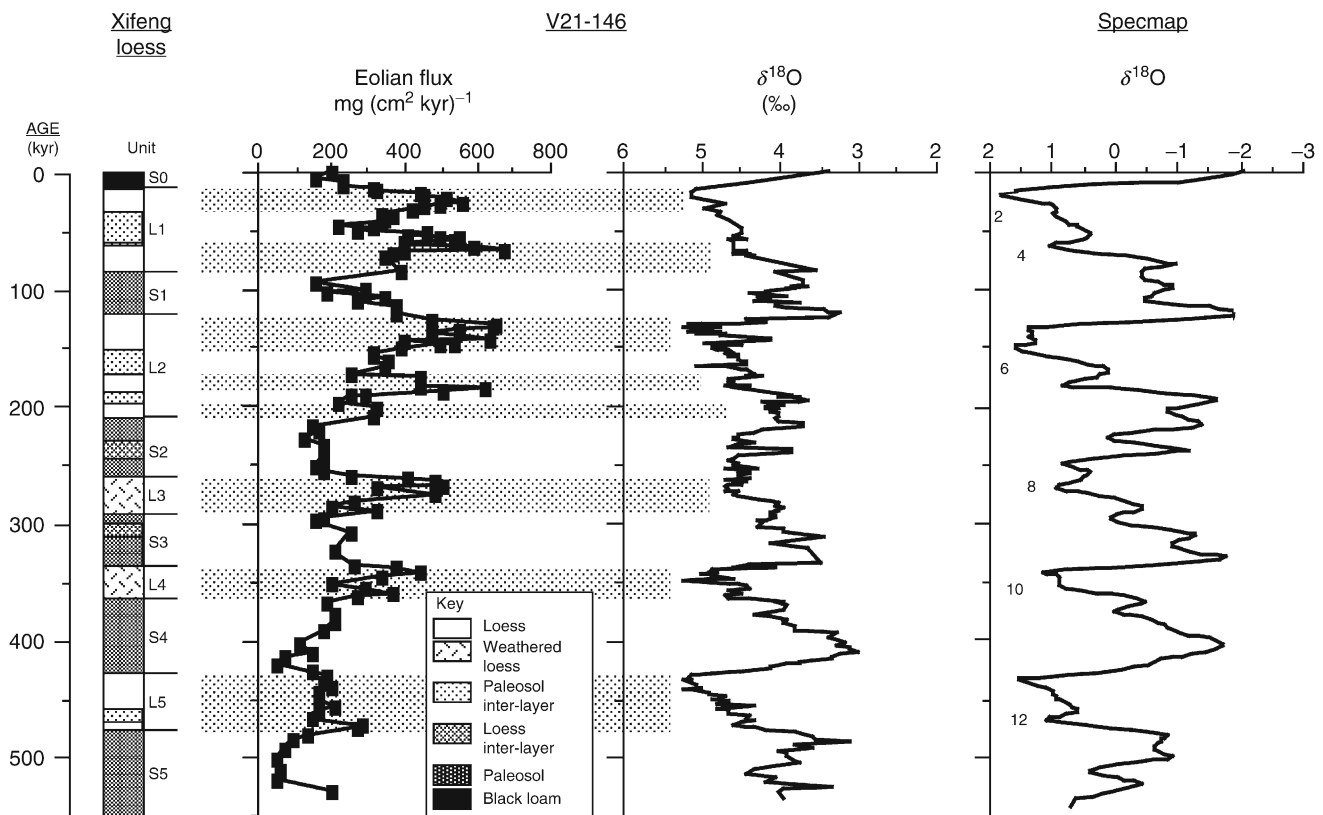


Figure E8 The record of dust deposition in the northwestern Pacific Ocean for the past 500,000 years. The column on the left shows the classic Chinese loess stratigraphy from the section at Xifeng. Data from core V21-146 raised from Shatsky Rise at 37.7° N, 163.0° E includes eolian flux and the $\delta^{18}\text{O}$ values measured by N. Shackleton on benthic foraminifera. The right column is the standardized $\delta^{18}\text{O}$ record of the marine geologists developed by the SPECMAP project. Even numbers denote glacial stages where isotopic values are more positive.

It is also possible to learn more about the eolian source areas than just where they are. For instance, Pettke et al. (2000) examined samples from ODP Site 885/886 and determined the $^{40}\text{Ar}/^{39}\text{Ar}$ ages of six dust samples whose stratigraphic ages ranged from 1.2 to 11.1 Ma. The mineral ages of those samples, dominated by illite, is about 200 million years. The 200 Myr age was interpreted to represent the formation age of the illites, and demonstrates that the processes of weathering, erosion, and late Cenozoic transport of those illites has not affected their argon-argon ages. This implies that other geochemical attributes of dust minerals may reflect the ultimate origin of those minerals and not the continental climate regime immediately prior to their transport to the sea.

Summary

Wind-blown dust forms a minor portion of deep sea sediment on a volumetric basis, but much of the world's ocean basins are characterized by a terrigenous sediment component that is dominated by eolian dust. These dust deposits provide paleoclimatic information not available from any other source. Studies of wind-blown dust fall into three categories: determination of its mass accumulation rate, an indicator of source area aridity; dust grain size, an indicator of transport energy; and dust composition, used for provenance studies. Dust records provide a useful and direct method to examine the evolution, usually climate related, of continental surfaces, and the only method to examine the geologic history of the Earth's wind systems (Rea, 1994). This last aspect is particularly important, as atmospheric circulation is an equal partner with ocean circulation as a global agent of climate change.

David K. Rea

Bibliography

- Biscaye, P.E., Grousset, F.E., Revel, M., Van der Gaast, S., Zielinsky, G.A., Vaars, A., and Kukla, G., 1997. Asian provenance of glacial dust (stage 2) in the Greenland Ice Sheet Project 2 ice core, Summit, Greenland. *J. Geophys. Res.*, **102**, 26765–26781.
- Clemens, S.C., 1998. Dust response to seasonal atmospheric forcing: Proxy evaluation and calibration. *Paleoceanography*, **13**, 471–490.
- Clemens, S.C., and Prell, W.L., 1990. Late Pleistocene variability of Arabian Sea summer monsoon winds and continental aridity: Eolian records from the lithogenic component of deep-sea sediments. *Paleoceanography*, **5**, 109–145.
- Darwin, C., 1846. An account of the fine dust which often falls on vessels in the Atlantic Ocean. *Q. J. Geol. Soc. Lond.*, **2**, 26–30.
- Gleason, J.D., Moore, T.C., Rea, D.K., Johnson, T.M., Owen, R.M., Blum, J.D., Hovan, S.A., and Jones, C.E., 2002. Ichthyolith strontium isotope stratigraphy of a Neogene red clay sequence: Calibrating eolian dust accumulation rates in the central North Pacific. *Earth Planet. Sci. Lett.*, **202**, 625–636.
- Hovan, S.A., Rea, D.K., and Piasias, N.G., 1991. Late Pleistocene continental climate and oceanic variability recorded in northwest Pacific sediments. *Paleoceanography*, **6**, 349–370.
- Janecek, T.R., and Rea, D.K., 1983. Eolian deposition in the northeast Pacific Ocean: Cenozoic history of atmospheric circulation. *Geol. Soc. Am. Bull.*, **94**, 730–738.
- Jones, C.E., Halliday, A.N., Rea, D.K., and Owen, R.M., 1994. Neodymium isotopic variations in North Pacific modern silicate sediment and the insignificance of detrital REE contributions to seawater. *Earth Planet. Sci. Lett.*, **127**, 55–66.
- Jones, C.E., Halliday, A.N., Rea, D.K., and Owen, R.M., 2000. Eolian inputs of lead to the North Pacific. *Geochimica et Cosmochimica Acta*, **64**, 1405–1416.
- Kyte, F.T., Leinen, M., Heath, G.R., and Zhou, L., 1993. Cenozoic sedimentation history of the central North Pacific: Inferences from the

- elemental geochemistry of core LL44-GPC3. *Geochimica et Cosmochimica Acta*, **57**, 1719–1740.
- Leinen, M., 1989. The pelagic clay province of the North Pacific Ocean. In Winterer, E.L., Hussong, D.M., and Decker, R.W. (eds.), *The Eastern Pacific Ocean and Hawaii*. Boulder, CO: Geological Society of America. The geology of North America, Volume N, pp. 323–335.
- Pettke, T., Halliday, A.N., Hall, C.M., and Rea, D.K., 2000. Dust production and deposition in Asia and the North Pacific Ocean over the past 12 Myr. *Earth Planet. Sci. Lett.*, **178**, 1–17.
- Pettke, T., Halliday, A.N., and Rea, D.K., 2002. Cenozoic evolution of Asian climate and sources of Pacific seawater Pb and Nd derived from eolian dust of sediment core LL44-GPC3. *Paleoceanography*, **17**, 3.1–3.13.
- Piasias, N.G., and Rea, D.K., 1988. Late Pleistocene paleoclimatology of the central Equatorial Pacific: Sea-surface response to the southeast trade-winds. *Paleoceanography*, **3**, 21–37.
- Prospero, J.M., Charlson, R.J., Mohnen, V., Jaenicke, R., Delany, A.C., Moyers, J., Zoller, W., and Rahn, K., 1983. The atmospheric aerosol system: An overview. *Rev. Geophys. Space Phys.*, **21**, 1607–1629.
- Pye, K., 1987. *Aeolian Dust and Dust Deposits*. New York: Academic Press, 334p.
- Rea, D.K., 1994. The paleoclimatic record provided by eolian deposition in the deep sea: The geologic history of wind. *Rev. Geophys.*, **32**, 159–195.
- Rea, D.K., and Hovan, S.A., 1995. Grain size distribution and depositional processes of the mineral component of abyssal sediments: Lessons from the North Pacific. *Paleoceanography*, **10**, 251–258.
- Rea, D.K., Leinen, M., and Janecek, T.R., 1985. Geologic approach to the long-term history of atmospheric circulation. *Science*, **227**, 721–725.
- Rea, D.K., Zachos, J.C., Owen, R.M., and Gingerich, P.D., 1990. Global change at the Paleocene-Eocene boundary: Climatic and evolutionary consequences of tectonic events. *Palaeogeogr. Palaeoclimatol. Palaeoecol.*, **79**, 117–128.
- Rea, D.K., Snoeckx, H., and Joseph, L.H., 1998. Late Cenozoic eolian deposition in the North Pacific: Asian drying, Tibetan uplift, and cooling of the Northern Hemisphere. *Paleoceanography*, **13**, 215–224.
- Rea, D.K., Moore, T.C., Jr., and Lyle, M., 2000. Atmospheric and oceanic circulation dynamics in the equatorial Pacific of the Paleogene world. *GFF*, **122**, 135–136.

Cross-references

[Astronomical Theory of Climate Change](#)
[Cenozoic Climate Change](#)
[Dust Transport, Quaternary](#)
[Eolian Sediments and Processes](#)
[Ocean Drilling Program \(ODP\)](#)
[SPECMAP](#)

EOLIAN SEDIMENTS AND PROCESSES

Introduction

The word “eolian” (or “aeolian”) comes from the Greek “Aeolus.” Aeolus, in Greek mythology, was the god of the winds. “Eolian” thus refers to any process of sediment entrainment, transport and deposition by wind. Study of eolian processes and sediments is a part of the disciplines of geomorphology, sedimentology and paleoclimatology. Extensive reviews of the use of eolian deposits in paleoclimatology can be found in Pye (1987), Pye and Tsoar (1990), Lancaster (1995), Livingstone and Warren (1996) and Kohfeld and Harrison (2001).

Eolian deposits of interest to paleoclimatologists include, in order of decreasing particle size, windblown sand, loess, and long-range-transported (“LRT” or “aerosolic”) dust. Syers et al.

(1969) presented a useful fivefold classification of eolian materials based on dominant particle size, transport pathway and range and persistence in the atmosphere. In their scheme, there are continua of (a) coarse-to-fine grained materials, (b) kilometer-to-10¹³ km ranges of transport, and (c) ground level-to-interplanetary space levels of transport (Figure E9). Thus, eolian sand is in a boundary-layer zone of transport (within 2 m of the ground surface) and loess occupies a range of relatively short-to-intermediate-distance transport within the lower troposphere. It is important to note, however, that some near-source loesses contain eolian sand. Similarly, most loess deposits contain some particles that are in the size range of aerosolic dust (10–1 μm) and these particles are capable of much longer-distance transport in the middle and upper troposphere. There is even a fraction of most loesses that contains particles in the stratospheric dust particle size range (<1 μm). These particles are capable of transport at very high altitudes in the stratosphere over thousands of kilometers of distance.

Eolian sand

Eolian sand consists of all deposits of sand-sized particles (2.00–0.05 mm diameter) that have been transported by the wind. Although most investigators think of dunes when considering eolian sand, there are also low-relief landforms composed of wind-blown sand called sand sheets. Most investigators, however, have directed attention to dunes in studies related to paleoclimatology. Hack (1941), in studying the origin of dunes in the Navajo Country of northeastern Arizona, proposed that the degree of activity of sand dunes (as well as the specific type of dune form) is a function of the balance between sand supply,

wind strength and duration, and amount of vegetation cover. Sixty years of study since that time have confirmed this basic model. Lancaster (1988) showed that the degree of activity of linear dunes in the Namib and Kalahari Deserts of southwestern Africa is a function of the amount of time that wind is above the threshold velocity for entrainment of sand grains and the balance between precipitation and potential evaporation, a proxy for amount of vegetation cover. Muhs and Holliday (1995) confirmed that the Lancaster “dune mobility index,” as it has come to be called, explains the varying degrees of dune activity in the Great Plains and desert southwest of the United States.

The importance of the Hack-Lancaster models of dune activity to paleoclimatology is that they provide a basis for interpreting past periods of eolian sand deposition or eolian sand stability. Assuming that there is an adequate supply of sand, the entrainment and transport of sand by wind will occur when a vegetation cover is lacking. Plant-covered dunes remain stable because much of the shear stress from wind is imparted to the vegetation rather than to the sediment grains. Lack of a protective vegetation cover usually occurs when potential evapotranspiration exceeds precipitation, a condition that characterizes arid, semiarid and subhumid regions. Thus, in a stratigraphic sequence of eolian sand and intercalated buried soils (paleosols), periods of relatively greater aridity are represented by eolian sand and periods of relatively greater humidity are represented by paleosols (Figure E10).

Because they are transported by the wind, stabilized eolian sands are also a direct reflection of past atmospheric circulation.

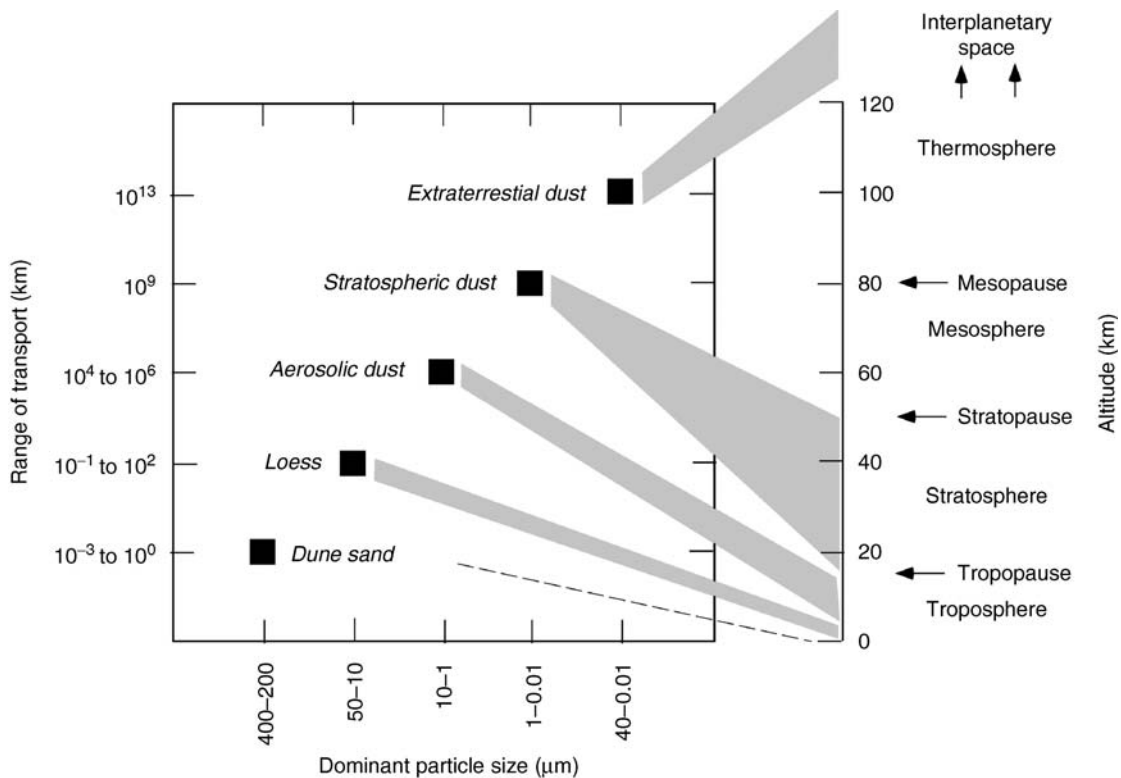


Figure E9 Diagram showing the continuum of eolian materials, with range of transport as a function of dominant particle size and generalized zone of transport in the atmosphere (based on Syers et al., 1969).

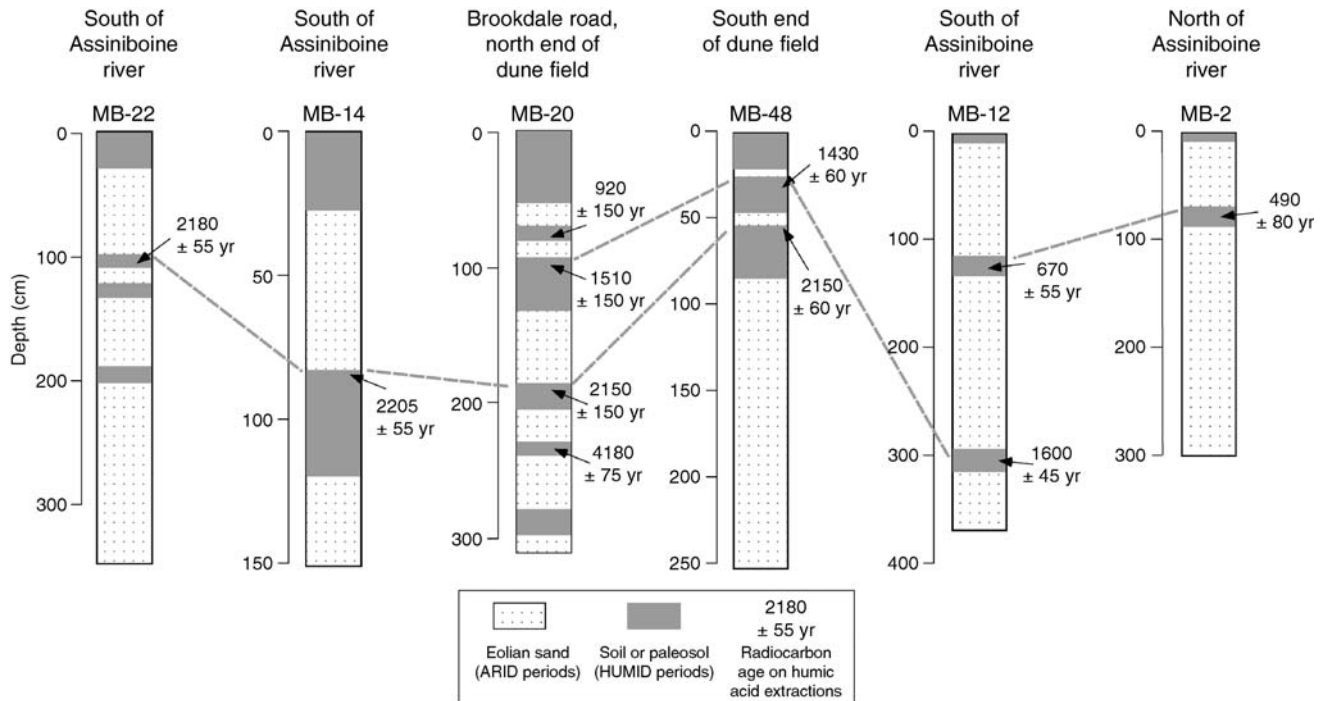


Figure E10 Stratigraphy and uncalibrated radiocarbon ages of late Holocene eolian sands from sections in the Brandon Dune Field, southern Manitoba, Canada. Episodes of eolian sand deposition represent relatively arid periods in the region, whereas paleosols represent less-arid periods when vegetation stabilized the dunes (redrawn from Wolfe et al., 2000).

Based on observations of actively moving sand dunes, eolian geomorphologists have developed an extensive classification of dune types that can be related to dominant wind directions (Pye and Tsoar, 1990; Lancaster, 1995; Livingstone and Warren, 1996). Linear dunes have long axes that parallel the dominant sand-moving winds and barchanoid ridges have long axes that are orthogonal to the predominant wind direction. Some dune types with superficially similar forms are actually formed by opposing directions of dominant winds. For example, barchan dunes have a crescentic shape with arms that point downwind, whereas parabolic dunes have a crescentic shape with arms that point upwind. Recognition of the differences between these two dune types requires field study. Nevertheless, stabilized dunes that have preserved their original forms provide valuable information about past wind regimes.

Field studies have shown that combined geomorphic, stratigraphic and geochronologic studies can document regional-scale changes in atmospheric circulation. For example, Lancaster et al. (2002) showed that linear dunes in western Mauritania are of three different ages, based on optically stimulated luminescence (OSL) ages, ~25–15 ka (last-glacial age), 13–10 ka (Younger Dryas), and <5 ka (late Holocene). These investigators found that last-glacial dunes are oriented northeast and Younger Dryas-age dunes are oriented north-northeast (Figure E11). In contrast, late Holocene dunes are oriented north-to-south, consistent with modern northerly winds that characterize the dominance of the Azores high over the region in summer. Thus, the greater proportion of easterly and northeasterly winds that built the last-glacial and Younger-Dryas-aged dunes reflect a different circulation regime at those times.

Other regions also show considerable change in the directions of dune-building winds over short timescales. In the central Great

Plains of the United States, late Holocene dunes are parabolic forms and have orientations that are very similar to modern dune-forming winds. For example, late Holocene parabolic dunes in the Great Bend area of central and western Kansas have arms that point to the southwest, consistent with modern southwesterly winds. However, prior to the late Holocene (perhaps during a mid-Holocene warm-dry period), winds apparently came from the northwest, based on geochemical trends (Arbogast and Muhs, 2000). Thus, dune-forming winds shifted at least 90° from their mid-Holocene direction to their present direction in the late Holocene. These data suggest a more zonal circulation pattern in the central Great Plains during the mid-Holocene than occurs today.

Loess

Loess, or windblown silt, is one of the most extensive surficial deposits on the Earth and may occupy as much as 10% of the land's surface, worldwide. Loess consists dominantly of particles between 50 and 2 microns, although some sand (>50 microns) and clay (<2 microns) are typically present. Unlike eolian sand, loess does not form distinctive landforms. Commonly, loess forms a blanket over a pre-existing landscape without much geomorphic expression. Loess ranges in thickness from a few decimeters to many tens of meters. It covers extensive areas of central North America, Alaska, Europe, Russia, Central Asia, China, Argentina and New Zealand and is the parent material for some of the world's most fertile soils. Extensive areas of loess occur near regions of active or past glaciation or in semiarid regions where there are abundant supplies of silt-rich sediments.

Loess has several distinctive characteristics that are important in paleoclimatology. Because much loess is glaciogenic,

a first-order significance of this sediment is that in many areas it marks glacial periods of the past. In some parts of North America and Europe, loess can be linked directly to its glacial sources, which supports the interpretation that it is primarily a record of past major ice sheet advances (see review in Bettis et al., 2003). The general model in such regions is that glacial grinding produces abundant silt-sized particles, which, after deposition in outwash deposits, are entrained by the wind. Thus, in a sequence of loess deposits with intercalated paleosols, unaltered loess marks periods of glaciation whereas paleosols mark interglacial or interstadial periods.

It is not always certain that loess is derived strictly from glaciers, however. For example, there has been a vigorous debate on the issue of whether Chinese loess has glacial or non-glacial (“desert”) sources and it is possible that it has both (Smalley, 1995; Derbyshire et al., 1998; Wright, 2001; Muhs

and Bettis, 2003). It is known, for instance, that loess in some regions, such as eastern Colorado in central North America, definitely contains a substantial nonglaciogenic component (Aleinikoff et al., 1999). Nevertheless, radiocarbon dating shows that the most recent period of thick loess deposition in Colorado was similar to that in areas proximal to the Laurentide Ice Sheet (see review in Muhs and Zarate, 2000). Thus, it appears that even where loess has its sources in non-glacial materials, the combination of dry, sparsely vegetated landscapes, a reduced intensity of the hydrological cycle and stronger winds may enhance the production and transport of windblown silt. These conditions are thought to be characteristic of glacial periods in many regions. Records of loess deposition in areas such as the Great Plains of North America and China have, therefore, records of glacial-interglacial cycles that compare favorably to the long-term record of such cycles in deep-sea cores (Figure E12). It is often possible to make what appears

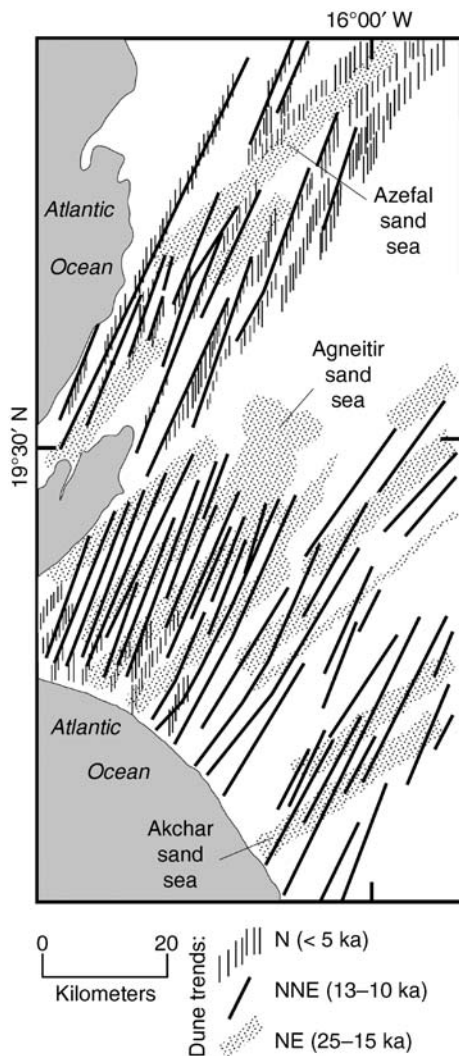


Figure E11 Map showing orientations of three ages of dunes in the western Sahara Desert of Mauritania, mapped from Landsat imagery (northerly dunes are shown schematically). The changes in orientation of the long axes of the different-aged dunes reflect shifts in wind direction (redrawn from Lancaster et al., 2002).

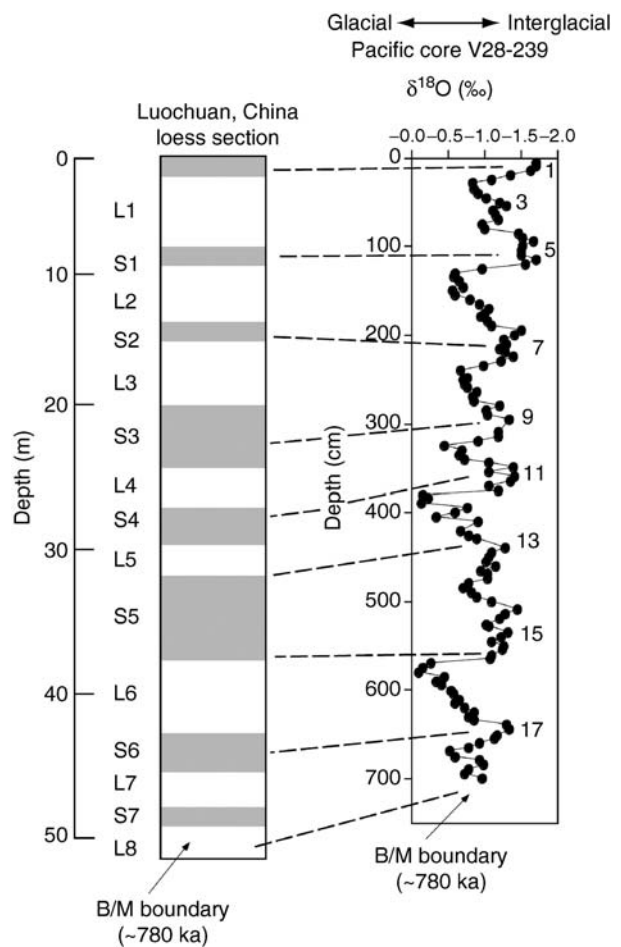


Figure E12 Stratigraphy of the Luochuan loess section, Chinese Loess Plateau, and proposed correlations to the deep-sea oxygen isotope record. Interglacial periods (odd numbers) are indicated by paleosols (shaded) in the loess record and by lighter (i.e., more negative) oxygen isotope values in the deep-sea record. Luochuan loess stratigraphy and location of the Brunhes-Matuyama (B/M) boundary (~780,000 year ago) are from Kukla and An (1989); oxygen isotope data and Brunhes-Matuyama (B/M) boundary) data for Pacific core V28-239 are from Shackleton and Opdyke (1976).

to be a one-to-one correlation between interglacial paleosols in a loess column and periods of isotopically light values (= interglacials) in a deep-sea core. However, it is important to note that the loess record is often incomplete. Erosion of either loess or paleosols can remove key periods that represent glacial or interglacials, respectively. On the other hand, if loess deposition rates are low during a particular glacial period, then a single paleosol may represent an interglacial period, a succeeding glacial period and the next-youngest interglacial period.

Beyond the identification of glacial-interglacial cycles, loess can provide valuable data for other paleoclimatic questions. Because it is transported by the wind, loess, as with eolian sand, can provide a direct record of past atmospheric circulation. Many studies have shown that loess has distinct decreases in thickness, grain size, carbonate content and geochemical properties away from a source (Ruhe, 1983; Muhs and Bettis, 2000; Porter, 2001). These distance-decay functions reflect the downwind processes of sediment-load reduction, coarse-load winnowing and syndepositional weathering. Identification of distance-decay functions in a number of loess bodies can yield paleowind directions, which in turn can be used to reconstruct regional circulation

patterns. Muhs and Bettis (2000) showed that in the North American midcontinent, loess-transporting winds were dominantly from the west or northwest during the last glacial period. Such a paleowind reconstruction has an apparent disagreement with atmospheric general circulation models (AGCMs) that simulate a northeasterly flow of air over central North America during the last glacial period, due to the presence of an anticyclone over the Laurentide Ice Sheet (COHMAP Members, 1988; Bartlein et al., 1998; Kutzbach et al., 1998). Modeling by Bromwich et al. (2005), however, shows that the zone of northeasterly winds may have been relatively narrow.

Because stronger winds can transport coarser-diameter grains, changes in mean particle size at a given locality indicate changes in the strength of particle-transporting winds. On the Chinese Loess Plateau, the median diameter of loess particles is a function of winds driven by the East Asian winter monsoon (Porter and An, 1995). Thus, at a single site, coarser particles indicate stronger winds and therefore a stronger East Asian winter monsoon. Porter and An (1995) showed that during the period since the last interglacial complex (i.e., since ~80,000 year ago), there have been 10 maxima in median particle diameter over the period of loess deposition (Figure E13).

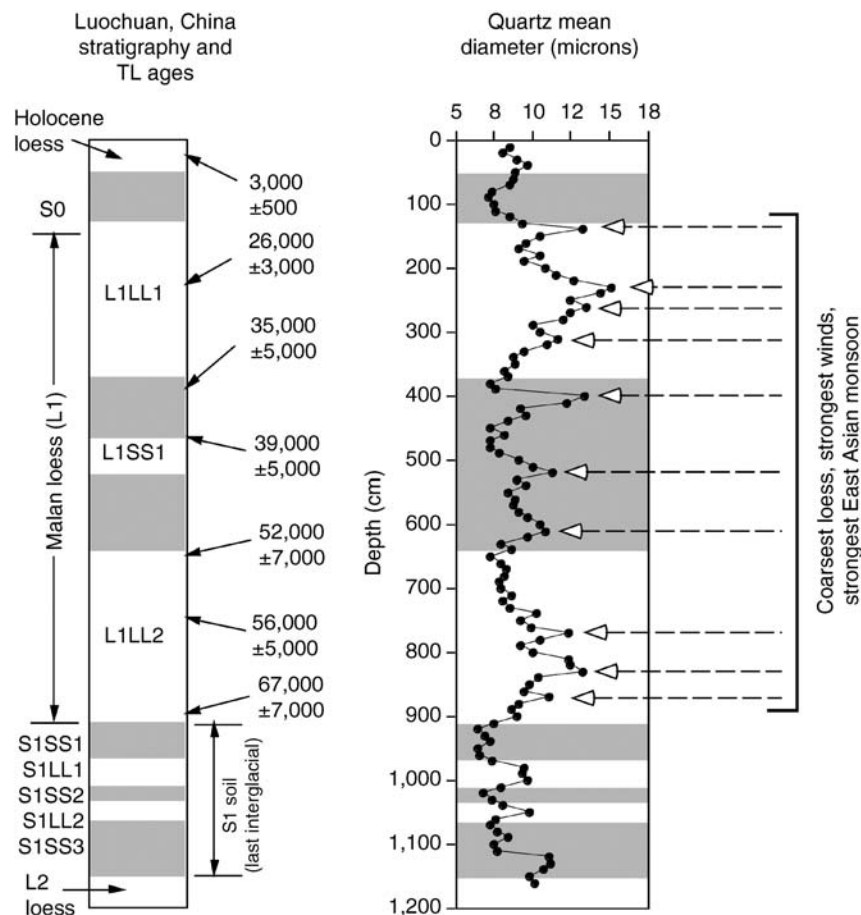


Figure E13 Stratigraphy, thermoluminescence ages, quartz mean diameter and inferred wind strengths over the last interglacial-glacial cycle at Luochuan, China. Loess units are white with an "L" prefix; paleosols are shaded with an "S" prefix. Stratigraphy and quartz mean diameter are based on Porter and An (1995) and Xiao et al. (1999); thermoluminescence ages are from Forman (1991).

Aerosolic (LRT) dust

Geologists, soil scientists and atmospheric scientists now recognize that fine-grained, aerosolic (<10 microns diameter) dust can travel distances of an intercontinental scale. Dust from the Sahara and Sahel regions of Africa travels yearly across the Atlantic Ocean on the easterly trade winds and what has been called the “Saharan Air Layer” to the Americas. Deposition occurs over a latitudinal span from northern South America at least to Florida (Prospero et al., 1970, 1981; Prospero and Lamb, 2003). The volume of this dust is large enough that it is easily visible on satellite imagery (e.g., Chiapello et al., 1999). Asian dust is transported east to the western Pacific Ocean basin and to islands at least as far as Hawaii (e.g., Olivarez et al., 1991). Dust from Australia tracks both to the northwest, towards the Indian Ocean, and southeast, towards New Zealand (McTainsh, 1989; Hesse and McTainsh, 1999).

There are excellent long-term records of LRT dust flux in diverse geologic settings (Figure E14 and E15). Dust can be recognized in (a) deep-ocean basin cores (e.g., Hovan et al., 1989; Ruddiman, 1997); (b) ice cores from Greenland and Antarctica, as well as smaller ice caps (e.g., Mayewski et al., 1994; Petit et al., 1999); and (c) lake basins (e.g., Xiao et al., 1999; Muhs et al., 2003). In addition, under favorable circumstances (a basaltic or carbonate bedrock that is compositionally distinct from dust) LRT dust can be identified as a contributor to soils on oceanic islands (see review in Birkeland, 1999).

In ocean cores and ice cores, where interglacial-glacial cycles are easily identified, it is apparent that global dust flux was high during glacial periods and low during interglacial

periods (Figure E14 and E15). Mahowald et al. (1999), Kohfeld and Harrison (2000) and Harrison et al. (2001) have reviewed the possible causes of higher dust flux during glacial periods, particularly the last glacial period. These factors include stronger or more persistent winds, greater aridity, decreased intensity of the hydrological cycle, decreased vegetation cover, increased sediment availability, or some combination of these factors. If sources of the dust in ocean, lake and ice cores can be identified, it is possible to reconstruct global-scale circulation during past periods of high dust flux.

Effects of dust on climate

There is an increasing recognition that dust, in addition to being a robust recorder of climate change, has possible effects on climate itself (Tegen, 2003). A traditional view has been that high dust flux cools the atmosphere, due to radiative backscatter to space. However, while this process has been well documented (e.g., Tegen et al., 1996), it is now known that the effect of dust on climate is actually quite complicated, and depends on the size, mineralogy and chemistry of the particles, plus the albedo of the surface over which particles are being transported (Arimoto, 2001). For example, Tegen et al. (1996) point out that over light surfaces (i.e., those with a high albedo, such as glaciers, snow-covered landscapes and sparsely vegetated landscapes) airborne dust absorbs radiation and reduces the solar flux that otherwise would be reflected back to space. Overpeck et al. (1996) generated an atmospheric model in which increases in airborne dust could produce a warming effect over such regions, downwind of dust sources. They point

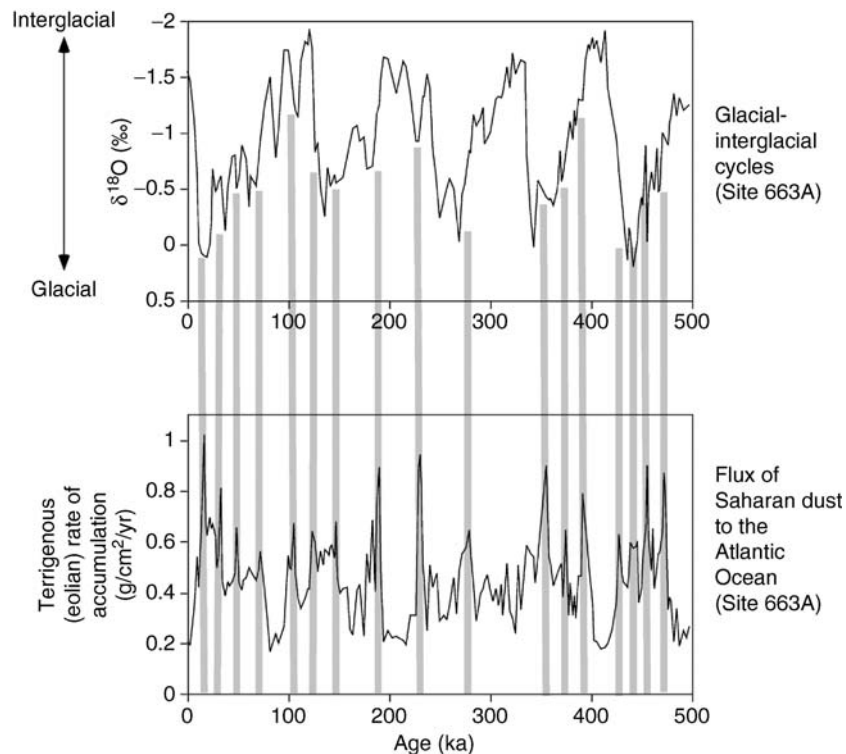


Figure E14 Records of dust flux from Saharan Africa to the Atlantic Ocean over glacial-interglacial cycles of the past 500,000 year. *Top:* Glacial-interglacial cycles in oxygen isotope record of foraminifera in deep-sea sediments at site 663A in the Atlantic Ocean. *Lower:* Accumulation rates of terrigenous sediments at site 663A – a measure of Saharan dust flux to the Atlantic Ocean. *Grey bands* show correspondence between generally cold (glacial or stadial) periods with periods of maximum dust flux. Site 663A data from deMenocal et al. (1993).

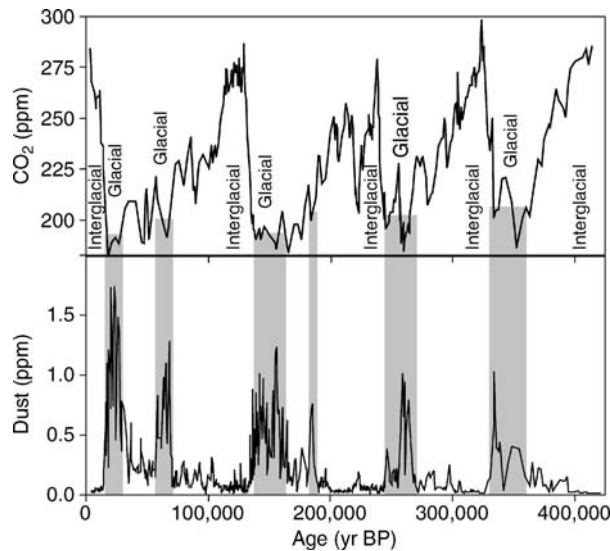


Figure E15 Top: Glacial-interglacial cycles in Vostok, Antarctica ice cores over the past ~400,000 year, as recorded by atmospheric carbon dioxide concentrations in gas bubbles. Bottom: Concentrations of dust in the same Vostok ice core record, showing correspondence between times of high dust flux and glacial periods (all data from Petit et al., 1999, 2001).

out that peaks in dust flux, as recorded in ocean cores and ice cores, occur just before glacial terminations, suggesting a causal relation.

In addition, dust can have indirect effects on climate. For example, phytoplankton growth in the oceans is limited in part by the degree of iron fertilization (e.g., Hutchins and Brunland, 1998). Fine-grained airborne dust has relatively high amounts of iron and iron content increases in a downwind direction in both China and North America (Eden et al., 1994; Muhs and Bettis, 2000). Thus, increased delivery of available iron to the oceans from the continents could, in principle, increase phytoplankton production, which in turn could draw down atmospheric carbon dioxide. Field studies show that in fact increased concentrations of dust-derived iron do enhance such primary production (Boyd et al., 2000). A decreased concentration of carbon dioxide in the atmosphere could result in cooling, due to a decreased greenhouse effect.

Summary

Eolian sediments consist of wind-blown sand, silt (loess) and fine-grained, long-range-transported (LRT or aerosolic) dust. For paleoclimatologists, eolian sand deposits may indicate periods of relative dryness in a region when vegetation cover is minimal. Buried soils in the same eolian sand sequences usually indicate periods of greater humidity and vegetation cover. Orientations of stabilized dunes can indicate past wind directions. Loess, or wind-blown silt, is often linked to glacial source sediments, although some loess may have a non-glaciogenic origin. Thus, loess deposits may mark glacial periods, but may also indicate dry, windy conditions in a sparsely vegetated source area. The geologic record indicates that major periods of loess deposition, whether glaciogenic or non-glaciogenic, occurred during glacial periods, when, in general, climates were drier than today. Although loess does not form distinctive landforms such as dunes, trends

in particle size, thickness and geochemistry can identify the dominant silt-transporting wind direction and yield valuable information to the paleoclimatologist about past circulation regimes. Aerosolic, or very fine-grained LRT dust, is best recorded in ocean sediments, ice caps and lake sediments. As with loess, the greatest flux of LRT dust during the Quaternary was during glacial periods. In addition to serving as a paleoclimate proxy, fine-grained dust may also affect climate itself, by warming or cooling the atmosphere through radiative scatter and by providing nutrients to the oceans and the continents.

Daniel R. Muhs

Bibliography

- Aleinikoff, J.N., Muhs, D.R., Sauer, R., and Fanning, C.M., 1999. Late Quaternary loess in northeastern Colorado, Part II—Pb isotopic evidence for the variability of loess sources. *Geol. Soc. Am. Bull.*, **111**, 1876–1883.
- Arbogast, A.F., and Muhs, D.R., 2000. Geochemical and mineralogical evidence from eolian sediments for northwesterly mid-Holocene paleowinds, central Kansas, U.S.A. *Quaternary Int.*, **67**, 107–118.
- Arimoto, R., 2001. Eolian dust and climate: Relationships to sources, tropospheric chemistry, transport and deposition. *Earth-Sci. Rev.*, **54**, 29–42.
- Bartlein, P.J., Anderson, K.H., Anderson, P.M., Edwards, M.E., Mock, C.J., Thompson, R.S., Webb, R.S., Webb, T., III, and Whitlock, C., 1998. Paleoclimate simulations for North America over the past 21,000 years: Features of the simulated climate and comparisons with paleoenvironmental data. *Quaternary Sci. Rev.*, **17**, 549–585.
- Bettis, E.A., III, Muhs, D.R., Roberts, H.M., and Wintle, A.G., 2003. Last glacial loess in the conterminous U.S.A. *Quaternary Sci. Rev.*, **22**, 1907–1946.
- Birkeland, P.W., 1999. *Soils and Geomorphology*. London: Oxford University Press, 430pp.
- Boyd, P.W., Watson, A.J., Law, C.S., Abraham, E.R., Trull, T., Murdoch, R., Bakker, D.C.E., Bowie, A.R., Buesseler, K.O., Chang, H., Charette, M., Croot, P., Downing, K., Frew, R., Gall, M., Hadfield, M., Hall, J., Harvey, M., Jameson, G., LaRoche, J., Liddicoat, M., Ling, R., Maldonado, M.T., McKay, R.M., Nodder, S., Pickmere, S., Pridmore, R., Rintoul, S., Safi, K., Sutton, P., Strzepek, R., Tanneberger, K., Turner, S., Waite, A., and Zeldis, J., 2000. A mesoscale phytoplankton bloom in the polar Southern Ocean stimulated by iron fertilization. *Nature*, **407**, 695–702.
- Bromwich, D.H., Toracinta, E.R., Oglesby, R.J., Fastook, J.L., and Hughes, T.J., 2005. LGM summer climate on the southern margin of the Laurentide Ice Sheet: Wet or dry? *J. climate*, **18**, 3317–3338.
- Chiapello, I., Prospero, J.M., Herman, J.R., and Hsu, N.C., 1999. Detection of mineral dust over the North Atlantic Ocean and Africa with the Nimbus 7 TOMS. *J. Geophys. Res.*, **104**, 9277–9291.
- COHMAP Members., 1988. Climatic changes of the last 18,000 years: Observations and model simulations. *Science*, **241**, 1043–1052.
- DeMenocal, P.B., Ruddiman, W.F., and Pokras, E.M., 1993. Influences of high- and low-latitude processes on African terrestrial climate: Pleistocene eolian records from equatorial Atlantic Ocean Drilling Program site 663. *Paleoceanography*, **8**, 209–242.
- Derbyshire, E., Meng, X., and Kemp, R.A., 1998. Provenance, transport and characteristics of modern aeolian dust in western Gansu Province, China, and interpretation of the Quaternary loess record. *J. Arid Environ.*, **39**, 497–516.
- Eden, D.N., Qizhong, W., Hunt, J.L., and Whitton, J.S., 1994. Mineralogical and geochemical trends across the Loess Plateau, North China. *Catena*, **21**, 73–90.
- Forman, S.L., 1991. Late Pleistocene chronology of loess deposition near Luochuan, China. *Quaternary Res.*, **36**, 19–28.
- Hack, J.T., 1941. Dunes of the western Navajo Country. *Geogr. Rev.*, **31**, 240–263.
- Harrison, S.P., Kohfeld, K.E., Roelandt, C., and Claquin, T., 2001. The role of dust in climate changes today, at the last glacial maximum and in the future. *Earth-Sci. Rev.*, **54**, 43–80.
- Hesse, P.P., and McTainsh, G.H., 1999. Last glacial maximum to early Holocene wind strength in the mid-latitudes of the Southern

- Hemisphere from aeolian dust in the Tasman Sea. *Quaternary Res.*, **52**, 343–349.
- Hovan, S.A., Rea, D.K., Piasis, N.G., and Shackleton, N.J., 1989. A direct link between the China loess and marine $\delta^{18}\text{O}$ records: Aeolian flux to the north Pacific. *Nature*, **340**, 296–298.
- Hutchins, D.A., and Brunland, K.W., 1998. Iron-limited diatom growth and Si:N uptake ratios in a coastal upwelling regime. *Nature*, **393**, 561–564.
- Kohfeld, K.E., and Harrison, S.P., 2000. How well can we simulate past climates? Evaluating the models using global paleoenvironmental datasets. *Quaternary Sci. Rev.*, **19**, 321–346.
- Kohfeld, K.E., and Harrison, S.P., 2001. DIRTMAP: The geological record of dust. *Earth-Sci. Rev.*, **54**, 81–114.
- Kukla, G., and An, Z., 1989. Loess stratigraphy in central China. *Palaeogeogr. Palaeoclimatol. Palaeoecol.*, **72**, 203–225.
- Kutzbach, J.E., Gallimore, R., Harrison, S.P., Behling, P., Selin, R., and Laarif, F., 1998. Climate simulations for the past 21,000 years. *Quaternary Sci. Rev.*, **17**, 473–506.
- Lancaster, N., 1988. Development of linear dunes in the southwestern Kalahari, southern Africa. *J. Arid Environ.*, **14**, 233–244.
- Lancaster, N., 1995. *Geomorphology of Desert Dunes*. London: Routledge, 290pp.
- Lancaster, N., Kocurek, G., Singhvi, A., Pandey, V., Deynoux, M., Ghienne, J.F., and Lo, K., 2002. Late Pleistocene and Holocene dune activity and wind regimes in the western Sahara Desert of Mauritania. *Geology*, **30**, 991–994.
- Livingstone, I., and Warren, A., 1996. *Aeolian geomorphology: An introduction*. Essex, England: Addison Wesley Longman Limited, 211pp.
- Mahowald, N., Kohfeld, K., Hansson, M., Balkanski, Y., Harrison, S.P., Prentice, I.C., Schulz, M., and Rodhe, H., 1999. Dust sources and deposition during the last glacial maximum and current climate: A comparison of model results with paleodata from ice cores and marine sediments. *J. Geophys. Res.*, **104**, 15895–15916.
- Mayewski, P.A., Meeker, L.D., Whitlow, S., Twickler, M.S., Morrison, M.C., Bloomfield, P., Bond, G.C., Alley, R.B., Gow, A.J., Grootes, P.M., Meese, D.A., Ram, M., Taylor, K.C., and Wumkes, W., 1994. Changes in atmospheric circulation and ocean ice cover over the North Atlantic during the last 41,000 years. *Science*, **263**, 1747–1751.
- McTainsh, G.H., 1989. Quaternary aeolian dust processes and sediments in the Australian region. *Quaternary Sci. Rev.*, **8**, 235–253.
- Muhs, D.R., and Bettis, E.A. III., 2000. Geochemical variations in Peoria Loess of western Iowa indicate paleowinds of midcontinental North America during last glaciation. *Quaternary Res.*, **53**, 49–61.
- Muhs, D.R., and Bettis, E.A. III., 2003. Quaternary loess-paleosol sequences as *Examples of Climate-Driven Sedimentary Extremes*. Boulder, CO: Geological Society of America. GSA Special Paper 370, pp. 53–74.
- Muhs, D.R., and Holliday, V.T., 1995. Evidence for active dune sand on the Great Plains in the 19th century from accounts of early explorers. *Quaternary Res.*, **43**, 198–208.
- Muhs, D.R., and Zarate, M., 2000. Eolian records of the Americas and their paleoclimatic significance. In Markgraf, V. (ed.), *Interhemispheric Climate Linkages*. San Diego, CA: Academic Press, pp. 183–216.
- Muhs, D.R., Ager, T.A., Been, J., Bradbury, J.P., and Dean, W.E., 2003. A late Quaternary record of eolian silt deposition in a maar lake, St. Michael Island, western Alaska. *Quaternary Res.*, **60**, 110–122.
- Olivarez, A.M., Owen, R.M., and Rea, D.K., 1991. Geochemistry of eolian dust in Pacific pelagic sediments: Implications for paleoclimatic interpretations. *Geochimica et Cosmochimica Acta*, **55**, 2147–2158.
- Overpeck, J., Rind, D., Laci, A., and Healy, R., 1996. Possible role of dust-induced regional warming in abrupt climate change during the last glacial period. *Nature*, **384**, 447–449.
- Petit, J.R., Jouzel, J., Raynaud, D., Barkov, N.I., Barnola, J.M., Basile, I., Bender, M., Chappellaz, J., Davis, J., Delaygue, G., Delmotte, M., Kotlyakov, V.M., Legrand, M., Lipenkov, V., Lorius, C., Pépin, L., Ritz, C., Saltzman, E., Stievenard, M., 1999. Climate and Atmospheric History of the Past 420,000 years from the Vostok Ice Core, Antarctica. *Nature*, **399**, 429–436.
- Petit, J.R., et al., 2001. Vostok Ice Core Data for 420,000 Years, IGBP PAGES/World Data Center for Paleoclimatology Data Contribution Series #2001–076. NOAA/NGDC Paleoclimatology Program, Boulder CO, USA.
- Porter, S.C., 2001. Chinese loess record of monsoon climate during the last glacial-interglacial cycle. *Earth-Sci. Rev.*, **54**, 115–128.
- Porter, S.C., and An, Z., 1995. Correlation between climate events in the North Atlantic and China during the last glaciation. *Nature*, **375**, 305–308.
- Prospero, J.M., and Lamb, P.J., 2003. African droughts and dust transport to the Caribbean: Climate change implications. *Science*, **302**, 1024–1027.
- Prospero, J.M., Bonatti, E., Schubert, C., and Carlson, T.N., 1970. Dust in the Caribbean atmosphere traced to an African dust storm. *Earth Planet. Sci. Lett.*, **9**, 287–293.
- Prospero, J.M., Glaccum, R.A., and Nees, R.T., 1981. Atmospheric transport of soil dust from Africa to South America. *Nature*, **289**, 570–572.
- Pye, K., 1987. *Aeolian Dust and Dust Deposits*. San Diego, CA: Academic Press, 334pp.
- Pye, K., and Tsoar, H., 1990. *Aeolian Sand and Sand Dunes*. London: Unwin Hyman, 396pp.
- Ruddiman, W.F., 1997. Tropical Atlantic terrigenous fluxes since 25,000 yrs BP. *Marine Geol.*, **136**, 189–207.
- Ruhe, R.V., 1983. Depositional environment of late Wisconsin loess in the midcontinental United States. In Wright, H.E. Jr., and Porter, S.C. (eds.), *Late-Quaternary environments of the United States*. vol. 1: The late Pleistocene. Minneapolis, MN: University of Minnesota Press, pp. 130–137.
- Shackleton, N.J., and Opdyke, N.D., 1976. Oxygen-isotope and paleomagnetic stratigraphy of Pacific core V28-239 late Pliocene to latest Pleistocene. *Geological Society of America Memoir* **145**, pp. 449–464.
- Smalley, I.J., 1995. Making the material: The formation of silt-sized primary mineral particles for loess deposits. *Quaternary Sci. Rev.*, **14**, 645–651.
- Syers, J.K., Jackson, M.L., Berkheiser, V.E., Clayton, R.N., and Rex, R.W., 1969. Eolian sediment influence on pedogenesis during the Quaternary. *Soil Sci.*, **107**, 421–427.
- Tegen, I., 2003. Modeling the mineral dust aerosol cycle in the climate system. *Quaternary Sci. Rev.*, **22**, 1821–1834.
- Tegen, I., Laci, A.A., and Fung, I., 1996. The influence on climate forcing of mineral aerosols from disturbed soils. *Nature*, **380**, 419–422.
- Wolfe, S.A., Muhs, D.R., David, P.P., and McGeehin, J.P., 2000. Chronology and geochemistry of late Holocene eolian deposits in the Brandon Sand Hills, Manitoba, Canada. *Quaternary Int.*, **67**, 61–74.
- Wright, J.S., 2001. “Desert” loess versus “glacial” loess: Quartz silt formation, source areas and sediment pathways in the formation of loess deposits. *Geomorphology*, **36**, 231–256.
- Xiao, J.L., An, Z.S., Liu, T.S., Inouchi, Y., Kumai, H., Yoshikawa, S., and Kondo, Y., 1999. East Asian monsoon variation during the last 130,000 years: Evidence from the Loess Plateau of central China and Lake Biwa of Japan. *Quaternary Sci. Rev.*, **18**, 147–157.

Cross-references

[Aerosol \(Mineral\)](#)
[Arid Climates and Indicators](#)
[Atmospheric Circulation During the Last Glacial Maximum](#)
[Dust Transport, Quaternary](#)
[Eolian Dust, Marine Sediments](#)
[Iron and Climate Change](#)
[Loess Deposits](#)
[Paleosols, Quaternary](#)

EOLIANITE

The abundance of sand and scarcity of land plants within deserts and along wave-dominated beaches allows the wind to build dunes. Along many mid-latitude coasts, much of the material available for transport is composed of calcium carbonate minerals – calcite and aragonite. Although the term *eolianite* is sometimes used by geologists for “all consolidated sedimentary rocks that were deposited by the wind” (Sayles, 1931), it has also been

used for carbonate-rich coastal dunes of Quaternary age. Here the term is used for eolian deposits of any age in which carbonate grains constitute greater than 50% of all detrital grains (carbonate eolianite of Abegg et al., 2001).

Most Quaternary carbonate eolianites appear to have been deposited during interglacial episodes within a high sea-level setting. Abundant calcareous skeletal material was generated in the warm, clear, shallow water that covered broad coastal platforms, and dune ridges were built by onshore winds. In some areas, however, it has been demonstrated that eolianites developed during glacial episodes when low sea level exposed the platforms to wind action. Low sea level, however, facilitates cementation of carbonate sediment by rainwater. Thus, even though glacial episodes may have been windier than interglacials, a greater quantity of uncemented carbonate sand was probably available for wind transport during interglacials.

Large-scale cross-stratification produced by deposition of sand on the steep leeward faces of migrating dunes is ubiquitous within most carbonate eolianites. Similar cross-strata can be produced in certain subaqueous settings, however. The best criterion for recognizing ancient eolian deposits is the inverse-graded lamination produced by migrating wind ripples (Hunter, 1977). The shells of land snails are relatively common within Quaternary eolianites; these typically are the only carbonate skeletons larger than sand-size. A diverse assemblage of trace fossils is also commonly present, and can include insect and crustacean burrows (Curran and White, 2001) as well as vertebrate tracks (Fornos et al., 2002). Rhizoliths – organo-sedimentary structures produced by the growth of plant roots – are abundant in many carbonate eolianites. Cementation of the dune sand can be quite rapid, and thick caliche (calcrete) develops in areas with a seasonal water deficit. This tendency toward early lithification enhances the geologic preservation of eolianite.

Numerous carbonate eolianites have been recognized among the late Paleozoic limestones of North America. Like Quaternary eolianites, these strata accumulated during a time when shorelines migrated rapidly due to the waxing and waning of large polar ice sheets (Rice and Loope, 1991). More recently, however, carbonate eolianites have also been found within Jurassic and Cretaceous sections, suggesting that these rocks are not necessarily indicative of “icehouse” conditions (Loope and Abegg, 2001).

The deposition of carbonate eolianites is ultimately dependent on the availability of sand-sized, unlithified carbonate sediment. This material is most voluminous in areas where the supply of terrigenous (siliciclastic) sediment is low. Areas with an arid climate, low relief, and high wave and wind energy are thus especially favorable; the southern and western coasts of Australia have generated huge deposits during the Quaternary (Brooke, 2001).

David B. Loope

Bibliography

- Abegg, F.E., Loope, D.B., and Harris, P.M., 2001. Deposition and diagenesis of carbonate eolianites. In Abegg, F.E., Harris, C.M., and Loope, D.B. (eds.), *Modern and Ancient Carbonate Eolianites*. Tulsa, OK: SEPM (Special Publication No. 71), pp. 17–30.
- Brooke, B., 2001. The distribution of carbonate eolianite. *Earth Sci. Rev.*, **55**, 135–164.
- Curran, H.A., and White, B., 2001. Ichnology of Holocene carbonate eolianites of the Bahamas. In Abegg, F.E., Harris, C.M., and Loope, D.B. (eds.), *Modern and Ancient Carbonate Eolianites*. Tulsa, OK: SEPM (Special Publication No. 71), pp. 47–56.
- Fornos, J.J., Bromley, R.G., Clemmensen, L.B., and Rodriguez-Perea, A., 2002. Tracks and trackways of *Myotrachus balearicus* Bate (Artiodactyla,

Caprinae) in Pleistocene aeolianites from Mallorca (Balearic Islands, Western Mediterranean). *Palaogeogr. Palaeoclimatol. Palaeoecol.*, **180**, 277–313.

- Hunter, R.E., 1977. Basic stratification types in small eolian dunes. *Sedimentology*, **24**, 361–387.
- Loope, D.B. and Abegg, F.E., 2001. Recognition and geologic preservation of ancient carbonate eolianites. In Abegg, F.E., Harris, C.M., and Loope, D.B. (eds.), *Modern and Ancient Carbonate Eolianites*. Tulsa, OK: SEPM (Special Publication No. 71), pp. 3–16.
- Rice, J.A., and Loope, D.B., 1991. Wind-reworked carbonates, Permian-Pennsylvanian of Arizona and Nevada. *Geol. Soc. Am. Bull.*, **103**, 254–267.
- Sayles, R.W., 1931. Bermuda during the Ice Age. In Proceedings of the American Academy of Arts and Sciences, vol. **66**, pp. 381–486.

Cross-references

Carbonates, Cool Water
 Carbonates, Warm Water
 Coastal Environments
 Paleosols, Pre-Quaternary
 Paleosols–Quaternary
 Sea Level Indicators
 Sedimentary Indicators of Climate Change

ESKERS

Eskers are ridges of glaciofluvial sediment deposited in ice-walled channels or subglacial tunnels. Those deposited supraglacially are closely related to kames. Eskers appear in the postglacial landscape as long sinuous ridges of sand and gravel, and can be used to reconstruct glacial drainage patterns. Because eskers form in a variety of different glacial settings and take a variety of specific forms they are valuable indicators of former glacial conditions.

Subglacial eskers most commonly form in channels running through the ice at the glacier bed and are sometimes referred to as tunnel-fill eskers. Where water flow in the tunnel is at high pressure the routing is controlled by ice surface gradient and the pattern of water pressure beneath the glacier, so eskers can flow uphill as well as down and do not follow the topography. Similarly, supraglacial eskers draped onto the ground when lowered by ice wastage will not necessarily follow the topography. However, water flowing through a subglacial tunnel at atmospheric pressure must follow the topography and eskers of this type will not flow uphill. Eskers can occur as single ridges or in braided patterns, and can also be discontinuous or “beaded.” The morphology of eskers has been related to the hydraulic conditions in which they form, but the origins of many specific eskers remain disputed. For example, some models propose that braided eskers occur subglacially in response to very high water pressures, while others suggest that braiding is a characteristic of supraglacial systems. Eskers are uncommon in areas characterized by widespread subglacial deformation. This is partly because deformation would destroy eskers even as they form and, more importantly, because deforming bed environments are not typically characterized by water drainage through tunnels cut into the ice. Eskers have therefore been cited as evidence against subglacial deformation in areas where they occur.

Eskers comprise a variety of facies ranging from silt and sand to gravel and boulders. Some sedimentary structures are similar to those in open-channel fluvial deposits, but some

characteristics of esker sediments are specific to tunnel hydraulics. Many eskers have a core of poorly sorted sands and gravels. It has been suggested that in pressurized tunnels all of the sediment may be in motion as a single mass and that deposition occurs rapidly when the tunnel is blocked or water supply decreases at the end of the melt season. Above the unsorted core many eskers display arched bedding of sorted sands and gravels. These may be deposited during low discharge periods following the deposition of the core.

The largest eskers are hundreds of kilometers in length, hundreds of meters wide and tens of meters high. In some areas they stand prominently above the surrounding landscape and provide convenient route ways for road building. Benn and Evans (1998), Bennett and Glasser (1996) and Hambrey (1994) provide useful reviews.

Peter G. Knight

Bibliography

- Benn, D. I., and Evans, D.J.A., 1998. *Glaciers and Glaciation*, London, UK: Arnold, 734pp.
 Bennett, M.R., and Glasser, N.F., 1996. *Glacial Geology*, Chichester, UK: Wiley, 364pp.
 Hambrey, M.J., 1994. *Glacial Environments*, London, UK: UCL Press, 296pp.

Cross-references

Basal Ice
 Glacial Geomorphology
 Glaciofluvial Sediments
 Kames

EVAPORITES

General features

Evaporites are rocks formed by minerals that precipitate from brines concentrated by solar evaporation. Evaporite minerals may precipitate in subaqueous environments from a standing body of water as surface and bottom nucleates (syndimentary or primary deposition) or in subaerial and shallow subsurface settings as intrasediment crystal growth, cement and replacement (diagenetic or secondary deposition).

Evaporites may form by evaporation of seawater, non-marine waters (such as meteoric, hydrothermal, volcanogenic and diagenetic reaction waters) or by mixing of various proportions of these waters. Non-marine evaporites may show a distinctively different mineralogy, but most saline minerals precipitate from the evaporation of any kind of water mixtures (Table E1; Hardie, 1984).

The main conditions for evaporite formation in a basin are:

1. evaporation rate exceeding rainfall, surface water and groundwater inflows (negative water balance),
2. closed or restricted hydrologic circulation, and
3. sufficient solute supply in the inflow waters.

Evaporite sedimentation may occur in a variety of depositional settings and may show complex associations of depositional features, including clastic structures.

The interpretation of ancient evaporite sequences is complicated by the common tendency of most evaporite minerals to undergo strong modifications during diagenesis and burial that partially or completely obliterate their original sedimentary features. For example primary gypsum is transformed into anhydrite during diagenesis and/or burial and is converted back to gypsum at surface exposure (Murray, 1964). Since evaporite rocks are composed of soluble minerals, their preservation in the rock record is critical. Evaporite deposits can be partially or completely dissolved just after deposition or later at burial and exposure conditions.

Evaporite minerals are highly sensitive to tectonics and may recrystallize, may be easily deformed and may flow to form salt pillows and diapirs. The presence of evaporite deposits in sedimentary successions may also influence mountain chain development by acting as detachment layers for thrusting (salt tectonics).

Evaporite sediments may be a source of hydrocarbons, but most importantly, salt tectonics may be responsible for the creation of complex hydrocarbon traps. Loading of evaporites by the overlying sediments and/or extensional tectonics lead to flowage of salts with the formation of salt domes that generate positive subsurface structures. These structures are potential hydrocarbon traps and evaporites, being relatively impermeable, may also act as seals for hydrocarbon reservoirs.

Table E1 Some of the most common saline minerals in marine and non-marine settings (data from Hardie, 1984)

Mineral	Composition	Marine	Non-Marine
Anhydrite	CaSO ₄	X	X
Aphthitalite (glaserite)	K ₂ SO ₄ · (Na, K)SO ₄		X
Antarcticite	CaCl ₂ · 6H ₂ O		X
Aragonite	CaCO ₃	X	X
Bischofite	MgCl ₂ · 6H ₂ O	X	X
Bloedite (astrakanite)	Na ₂ SO ₄ · Mg SO ₄ · 4H ₂ O	X	X
Burkeite	Na ₂ CO ₃ · 2Na ₂ SO ₄		X
Calcite	CaCO ₃	X	X
Carnallite	MgCl ₂ · KCl · 6H ₂ O	X	X
Dolomite	CaCO ₃ · MgCO ₃	X	X
Epsomite	MgSO ₄ · 7H ₂ O	X	X
Gaylussite	CaCO ₃ · Na ₂ CO ₃ · 5H ₂ O	X	X
Glauberite	CaSO ₄ · Na ₂ SO ₄	X	X
Gypsum	CaSO ₄ · 2H ₂ O	X	X
Halite	NaCl	X	X
Hanksite	9Na ₂ SO ₄ · 2Na ₂ CO ₃ · KCl		X
Hexahydrate	MgSO ₄ · 6H ₂ O	X	X
Kainite	MgSO ₄ · KCl · 11/4H ₂ O	X	X
Kieserite	MgSO ₄ · H ₂ O	X	X
Leonhardtite	MgSO ₄ · 4H ₂ O	X	
Leonite	MgSO ₄ · K ₂ SO ₄ · 4H ₂ O	X	X
Mirabilite	Na ₂ SO ₄ · 10H ₂ O	X	X
Nahcolite	NaHCO ₃		X
Natron	Na ₂ CO ₃ · 10H ₂ O		X
Pentahydrate	MgSO ₄ · 5H ₂ O	X	
Pirssonite	CaCO ₃ · Na ₂ CO ₃ · 2H ₂ O		X
Polyhalite	2CaSO ₄ · Mg SO ₄ · K ₂ SO ₄ · 2H ₂ O	X	X
Shortite	2CaCO ₃ · Na ₂ CO ₃		?
Sylvite	KCl	X	X
Tachyhydrite	CaCl ₂ · 2MgCl ₂ · 12H ₂ O		X
Thenardite	Na ₂ SO ₄		X
Thermonatrite	Na ₂ CO ₃ · H ₂ O		X
Trona	NaHCO ₃ · Na ₂ CO ₃ · 2H ₂ O		X

The interpretation of ancient evaporite sequences is challenged also by the observation that only a small proportion of the deposits in the rock record formed in settings like those of today, but most thick and extensive deposits of the past (saline giants) apparently have no modern equivalent. To study these deposits, non-actualistic models have been proposed.

Evaporites have an important economic value both intrinsic and indirect, because of their association with base metal ore deposits and hydrocarbon accumulations.

Seawater evaporation

The evaporation of seawater leads to the precipitation of an ordered sequence of minerals of increasing solubilities. The marine evaporite minerals are many (Table E1), but the most common are gypsum (anhydrite) and halite (Table E2). First to precipitate from evaporating seawater is CaCO_3 , but in very small amounts. Gypsum precipitation starts after carbonates, when 85% of seawater is lost by evaporation. Deposition of gypsum accounts for 3.6% of the total volume of precipitates. Halite precipitates when 90% of the water has evaporated and forms 78% of the volume of solids (Table E2). After halite precipitation the mineral succession (potassic salts) is complex because the residual brine tends to react with the precipitates (back reactions).

Allowing a column of 1,000 m of seawater to evaporate completely, only about 14 m of precipitates would form and among them halite is the predominant salt (Table E2). This indicates that the thickness of evaporite deposits is directly controlled by the rate and mode of replenishment of evaporated seawater. Thick marine evaporites may thus accumulate only in basins where hydrologically restricted circulation allows large seawater volumes to be introduced and evaporated without a significant dilution of the basinal brines.

Rates of evaporite deposition from marine waters are potentially higher than those of any other sediment. In optimum artificial environments, such as solar evaporation works, accumulation rates of up to 40 m and 100 m per 1,000 years have been reported for gypsum and halite, respectively (Schreiber and Hsü, 1980). These data suggest that an evaporite basin may be filled extremely rapidly, for example, the > 2 km of salts beneath the floor of the Mediterranean that accumulated during the Messinian in less than approximately 640 kyr (Krijgsman et al., 1999).

Modern evaporites

Climatic conditions and geologic context

Modern evaporite deposits accumulate in arid and semi-arid regions of the world in the global high pressure belts of the subtropical horse latitude and the poles, and in the midlatitude intracontinental desert and steppes that are isolated from oceanic

moisture (Figure E16). These desert areas are located in two belts approximately between 15° and 45° north and south of the equator. Other arid areas where evaporites can form are the rain shadows of high mountain chains, which may be present at any latitude. Examples are the Patagonian and Nevada-Utah orographic deserts, which are located in the Andes and the Sierra Nevada rain shadows, respectively.

The great part of present-day evaporite deposition occurs in closed continental basins (playa lakes), whereas coastal settings are volumetrically less significant. Marine evaporites are confined to coastal supratidal settings (sabkhas) and to low-lying areas where seawater seeps into pools and small basins (salinas). Even in Antarctica small amounts of evaporite minerals are forming in lakes by brine mixing, freezing, evaporation and sublimation (Carlson et al., 1990).

Closed basin conditions may have various origins: (a) tectonic basins, including fault-bounded intermontane basins and intracratonic structural sags, (b) interdunal depressions in sand seas, (c) wind deflation hollows, (d) abandoned fluvial channels, (e) volcanic or bolide impact craters and (f) depressions formed by combinations of the above (Smoot and Lowenstein, 1991). Solutes are supplied by rivers, springs, groundwater and rainwater and by wind-blown aerosols and dust.

Supratidal evaporites: sabkhas

Sabkhas are salt-encrusted surfaces commonly associated with brine bodies. They can be continental or marine, the latter being the most common and the most studied (see Kendall and Harwood, 1996 for review). Coastal sabkhas form prograding supratidal flats, commonly adjacent to protected lagoons. These supratidal flats consist of marine or continental carbonate and/or siliciclastic sand and mud sediments with binding microbial and algal mats. The sabkhas are subaerially exposed for most of the time and are strongly influenced by wind scour and storm-driven floods that truncate their top, maintaining flat deflation surfaces. The wind erodes the topmost dry and uncemented sediments lying above the capillary zone.

Evaporite minerals (gypsum, anhydrite and halite) are precipitated within the sediments by evaporation of capillary brines (evaporite pumping) and as surface crusts. Brines are supplied by marine seepage, marine flooding, inflowing continental groundwaters and ephemeral sheet floods (Yechieli and Wood, 2002). Gypsum forms as discoidal crystals, rosettes, clusters and cement. Anhydrite commonly replaces gypsum and forms single nodules, layers and contorted bands of coalesced nodules displacing or replacing the host sediments (entherolitic anhydrite). Halite is less common and is found as ephemeral surficial crusts and displacive cube crystals within the sediments (e.g., Gornitz and Schreiber, 1981).

Table E2 The theoretical precipitation sequence of salts from seawater as a function of evaporated seawater, salinity and density at the beginning of each salt precipitation (data from Sonnenfeld and Perthuisot, 1989). Also shown are the approximate thickness of the various salts precipitated by the evaporation of a column of seawater 1,000 m high and the percentage of precipitated salts (recalculated data from Handford, 1991)

Component	Evaporated seawater (wt-%)	Salinity (wt-‰)	Density (cm^{-3})	Salt thickness from 1,000 m of seawater (m)	Total precipitates (%)
Mg and K salts	99	variable	1.283–1.3235	2.9	17.7
Halite	90	350	1.212–1.2185	12.9	78
Gypsum	85	250	1.0897–1.115	0.6	3.6
Carbonates	75	140	1.10	0.1	0.4
Seawater		35	1.0245		

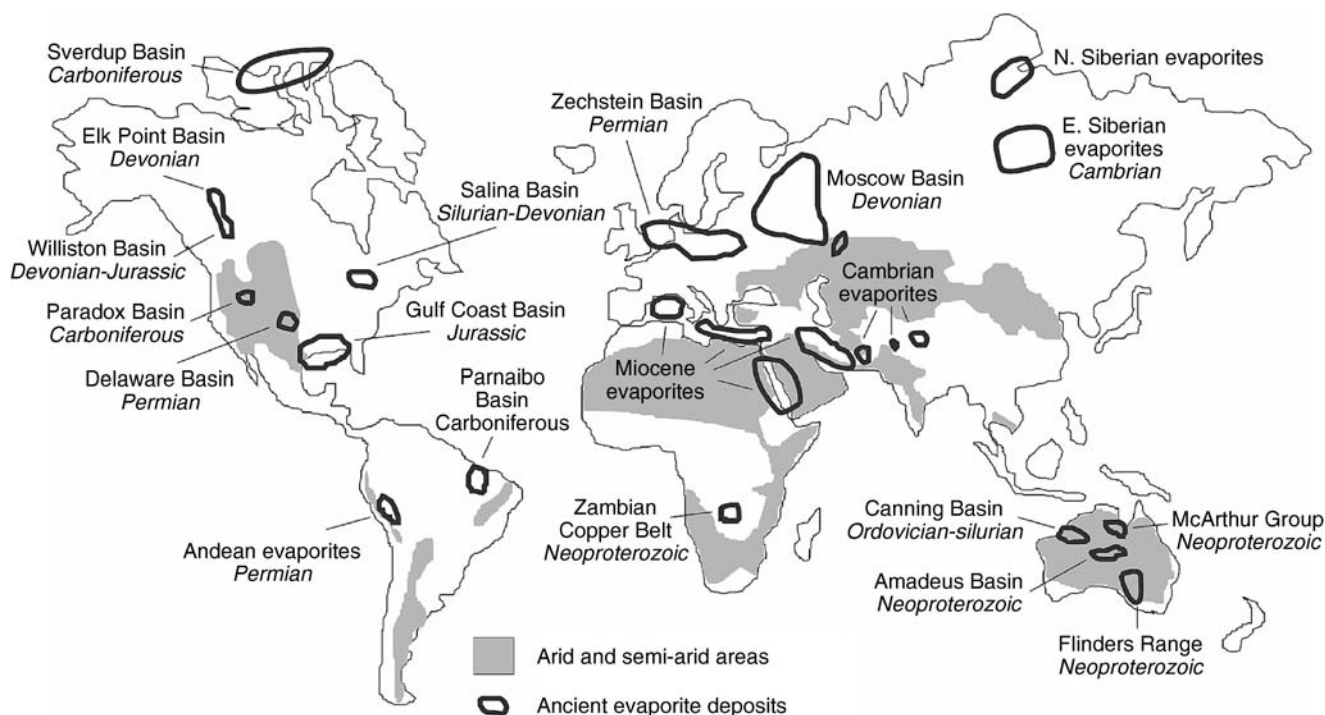


Figure E16 Map showing location, approximate size and age of the major ancient evaporite deposits of the world (simplified from Warren, 1999). Also shown are the arid and semi-arid climate areas where present-day evaporites are forming (simplified from Yechieli and Wood, 2002).

Coastal sabkhas are found: (a) as prograding supratidal flats above sea level along protected coastlines, (b) in depressions associated with salt pans between dunes or beach ridges, (c) at the margin of salinas associated with salt lakes fed by marine seepage through barriers, and (d) at the top of evaporite-filled salinas. Coastal sabkhas may pass landward into continental sabkhas as marine brines are replaced by continental waters during coastal plain progradation (Kendall and Harwood, 1996). Rates of deposition in modern sabkhas are high: thickness may reach 1 m in 1,000 years with 1 km progradation (Schreiber and Hsü, 1980). Sabkhas are present along the shores of the Persian Gulf, The Red Sea, west and southern Australia and North Africa.

Shallow-water evaporites: salinas

Modern shallow-water evaporites form in small salt lakes, commonly associated with sabkhas, fed by marine (salinas) or non-marine waters (playas). Salinas may be desiccated (salt pan), periodically dried out (ephemeral) or permanently covered by water (perennial). Desiccated and ephemeral salinas produce brine-pan sequences, whereas perennial salinas generate continuous subaqueous deposits.

Carbonates associated with shallow-water evaporites are characterized by biologically induced micrites and pelletal muds with microbial mats. The evaporite sedimentary features include tiny prismatic gypsum laminites (cumulates), beds consisting of large, commonly twinned, vertically-oriented bottom-grown gypsum crystals and clastic gypsum (Schreiber, 1988; Schreiber and El Tabakh, 2000). Precipitation of halite occurs at the bottom of the basin or more commonly at air-brine interface, with the formation of floating pyramidal hopper crystals

that may coalesce to form rafts. These halite rafts sink to the bottom of the basin and continue their growth as vertically-oriented crystal (chevrons). These crystals are milky-colored because they contain a large amount of fluid inclusions. Successive phases of halite deposition truncated by dilution episodes produce layered cuboid and chevron halite beds with microkarst pits (Shearman, 1970). Desiccation and dissolution features are common in shallow-water evaporite settings.

Modern salinas and playas are small and in many cases have been converted into sabkhas and brine pans by rapid evaporite filling. They are located in the coastal plain of the Gulf of Eilat (Red Sea), along the coast of south and western Australia and Baja California (Mexico). Useful modern examples for studying shallow-water evaporites are the artificial solar works, such as those of the Dead Sea.

Ancient evaporites

Evaporites through time and space

The oldest evaporite deposits that are still preserved in the rock record are present in Oman and Australia and date back to the Neoproterozoic. Pseudomorphs after evaporite minerals are common in the Proterozoic but have been reported in rocks as old as the Archean. The oldest pseudomorphs (3.45 Ga) have been described in South Africa and Australia and consist of barite, although their origin as actual evaporite replacements has been strongly argued (Nijman et al., 1998).

The frequency of evaporite deposition has oscillated significantly during the geological past. Peaks of large-scale evaporite deposition occurred in the Cambrian, Permian and Jurassic-Cretaceous, with less significant concentrations during the Triassic and the Tertiary (Figure E16).

Some of these deposits have huge dimensions: hundreds of kilometers in size and several kilometers thick (Figure E16). None of the evaporite giants of the past compare in extent and thickness to the scarce modern evaporite deposition and some of the facies observed in the rock record have no present-day analogs. Some of the reasons for these discrepancies are: (a) wider arid and semi-arid belts in the past because of warmer world climates; (b) larger shallow epeiric seas formed by long-term tectonic quiescence and low amplitude sea level fluctuations; (c) restricted seawater inflow to large oceanic margins and lake basins formed by rifting, continental collision and trans-tensional faulting combined with climate changes.

Another problem in studying ancient deposits is the difficulty in distinguishing between marine and non-marine evaporites (Hardie, 1984; Smoot and Lowenstein, 1991). A distinction can be possible when diagnostic saline mineral assemblages, associated fossils and regional depositional settings are recognized, but these criteria can be ambiguous or inapplicable. Any mineral combinations precipitated by seawater evaporation can be reproduced in non-marine settings, including gypsum and halite. The only mineral associations that cannot be produced by seawater without major modification by non-marine inflow are: (a) Na-carbonates, (b) Na-silicates and (c) Na- and Ca-borates.

Many deposits in the rock record have both marine and non-marine influences or alternations between them. These influences and alternations may be the result of mixing of marine and non-marine waters in isolated coastal lakes and intercalations of continental with coastal marine deposits.

Ancient sabkhas

Ancient sabkhas are identified by comparison with their modern analogs. Ancient sabkha evaporite beds are thin (less than 1 m), show evidence of exposure and erosion at the top and occur in basin margin settings. Gypsum in ancient sabkhas has been replaced by anhydrite during burial diagenesis.

Many evaporite deposits have been interpreted as sabkhas in the past based on the sole presence of anhydrite nodules (called "chicken wire") in thick evaporite cycles. We know today that the presence of anhydrite nodules by itself cannot be considered a criterion for sabkha identification because they can form in a variety of conditions, including early and late diagenesis (Schreiber and El Tabakh, 2000). Some thick sequences previously interpreted as sabkhas have been reinterpreted as subaqueous deposits (Warren and Kendall, 1985; Kendall and Harwood, 1996). The best known example of an ancient sabkha in the rock record is the Jurassic Purbeck of southern England (Shearman, 1966).

Ancient shallow-water evaporites

Shallow-water evaporites formed huge deposits in the geologic past on wide shelves and platforms that have no modern analog (basin-marginal platform evaporites). These deposits consist mostly of large vertically-oriented gypsum crystals associated with carbonate and bedded halite. Gypsum in ancient deposits has been commonly replaced by nodular anhydrite during burial diagenesis. Characteristic of shallow water deposits is the presence of dissolution surfaces and clastic evaporites. Clastic gypsum, commonly converted into anhydrite, shows all ranges of sedimentary features, indicating that gypsum can be eroded, transported, and deposited in the same fashion as other clastic sediments (Schreiber, 1988).

Ancient bedded halite rocks commonly recrystallize to form banded sequences composed of clear crystals, usually free of fluid inclusions, and do not retain their original sedimentary features, although a number of early Phanerozoic halites still maintain their depositional characteristics.

Typical ancient shallow water evaporites are described in the San Andres Formation of the Palo Duro Basin, Permian of Texas (USA) and in the marginal facies of the Messinian evaporites in the Mediterranean.

Ancient deep-water evaporites

Deep-water evaporites form saline giants precipitated from large-size brine bodies that lack any modern analog and can thus be identified solely by their vertical and lateral continuity (basin-central or basinwide evaporites). The modern Dead Sea, which is a closed perennial saline lake, may be considered a sort of deep-water analog just from the hydrodynamic point of view, because its water composition and mineral associations are peculiar (Hardie, 1984; Kendall and Harwood, 1996).

Ancient deep-water evaporites are composed mostly of finely laminated sulfate-carbonate couplets and laminar and bedded halite, commonly organic-rich, that can be correlated over wide areas (several hundreds of km in some cases; Dean and Anderson, 1982).

Most of these deposits are crystal cumulates that sank from the brine surface down to the bottom of the basin. The deepwater origin is inferred also by the absence of dissolution surfaces, a feature related to a vertical density stratification that is thought to be typical of deep evaporite basins. Mass-flow and turbidite deposits produced by the resedimentation of shallow-water evaporites are commonly associated with deep evaporite facies.

Deepwater evaporites are described in the Castile Formation of the Delaware Basin, Permian of Texas and New Mexico (USA), the central portion of the Salina Formation, Upper Silurian of the Michigan Basin (Canada and USA) and the central part of the Zechstein evaporates (Permian of northern Europe).

Evaporite geochemistry

Geochemistry is a significant tool that can help in documenting the origin and the post-depositional evolution of the evaporite deposits. Investigations may include analyses of fluid inclusions, trace elements (Br, Sr, Rb, Cs and Pb), Br/Cl ratios, $^{87}\text{Sr}/^{86}\text{Sr}$ ratios and S and O isotopes. Among these, the Br/Cl ratios in the chloride salts provide information on the evaporative concentrations and the hydrologic history record. The marine evaporite rocks may be dated by comparing their $^{87}\text{Sr}/^{86}\text{Sr}$ and $\delta^{34}\text{S}$ values with the secular variation curves of these isotopes in seawater.

Composition of fluid inclusions in marine halites has been used to constrain secular variations in the major ion chemistry of Phanerozoic seawater (Mg^{2+} , Ca^{2+} , Na^+ , K^+ , Cl^- and SO_4^{2-}) as a function of seafloor spreading rates, volcanism, global sea level, and mineralogy of marine limestones and evaporites (Lowenstein et al., 2001; Horita et al., 2002).

Microthermometric measurements on fluid inclusions in halite have been used to reconstruct the paleoclimate record of the past 200 kyr in Death Valley (Lowenstein et al., 1999) and the mid-Permian of western Kansas (Benison and Goldstein, 1999). This can be done because homogenization temperatures of fluid inclusions in subaqueously-formed halite record brine temperatures during salt crystallization that closely correlate with air temperatures.

Bibliography

- Benison, K.C., and Goldstein, R.H., 1999. Permian paleoclimate data from fluid inclusions in halite: *Chemical Geology*, **154**, 113–132.
- Carlson, C.A., Phillips, F.M., Elmore, D., and Bentley, H.W., 1990. Chlorine-36 tracing of salinity sources in the Dry Valley of Victoria Land, Antarctica. *Geochim. Cosmochim. Acta*, **54**, 311–318.
- Dean, W.E., and Anderson, R.Y., 1982. Continuous subaqueous deposition of the Permian Castile evaporites, Delaware Basin, Texas and New Mexico. In Handford, C.R., Loucks, R.G., and Davies, G.R. (eds.), *Depositional and Diagenetic Spectra of Evaporites – A Core Workshop* (SEPM Core Workshop No. 3), pp. 395.
- Gornitz, V.M., and Schreiber, B.C., 1981. Displacive halite hoppers from the Dead Sea: some implications for ancient evaporite deposits. *J. Sediment. Petrol.*, **51**, 787–794.
- Handford, R.C., 1991. Marginal marine halite: sabkhas and salinas. In Melvin, J.L. (ed.), *Evaporites, petroleum, and mineral resources*. New York: Elsevier. *Developments in Sedimentology*, **50**, pp. 1–66.
- Hardie, L.A., 1984. Evaporites: marine or non-marine. *Am. J. Sci.*, **284**, 193–240.
- Horita, J., Zimmermann, H., and Holland, H.D., 2002. Chemical evolution of seawater during the Phanerozoic: implications from the record of marine evaporites. *Geochim. Cosmochim. Acta*, **66**, 3733–3756.
- Kendall, A.C., and Harwood, G.M., 1996. Marine evaporites: arid shorelines and basins. In Reading, H.G. (ed.), *Sedimentary Environments: Processes, Facies and Stratigraphy*. Oxford: Blackwell, pp. 281–324.
- Krijgsman, W., Hilgen, F.J., Raffi, I., Sierro, F.J., and Wilson, D.S., 1999. Chronology, causes and progression of the Messinian salinity crisis. *Nature*, **400**, 652–655.
- Lowenstein, T.K., Li, J., Brown, C.B., Roberts, S.M., Ku, T.L., Luo, S., and Yang, W., 1999. 200 k.y. Paleoclimate record from death valley salt core. *Geology*, **27**, 3–6.
- Lowenstein, T.K., Timofeeff, M.N., Brennan, S.T., Hardie, L.A., and Demicco, R.V., 2001. Oscillations in Phanerozoic seawater chemistry: evidence from fluid inclusions. *Science*, **294**, 1086–1088.
- Murray, R.C., 1964. Origin and diagenesis of gypsum and anhydrite. *J. Sediment. Petrol.*, **34**, 515–523.
- Nijman, W., Debruijne, K.H., and Valkering, M.E., 1998. Growth fault control of Early Archean cherts, barite mounds and chert-barite veins, North Pole Dome, eastern Pilbara, Western Australia. *Precambrian Res.*, **88**, 25–52.
- Schreiber, B.C., 1988. Subaqueous evaporite deposition. *Evaporites and Hydrocarbons*. New York: Columbia University Press, pp. 182–255.
- Schreiber, B.C., and El Tabakh, M., 2000. Deposition and early alteration of evaporites. *Sedimentology*, **47**, 215–238.
- Schreiber, B.C., and Hsü, K.J., 1980. Evaporites. *Developments in Petroleum Geology*. vol. 2, Barking, England: Applied Science, pp. 87–138.
- Shearman, D.J., 1966. Origin of evaporites by diagenesis. *Trans. Inst. Mining Metall.*, **75**, 208–215.
- Shearman, D.J., 1970. Recent halite rock, Baja California, Mexico. *Trans. Inst. Min. Metall.*, **79B**, 155–162.
- Smoot, J.P., and Lowenstein, T.K., 1991. Depositional environments of non-marine evaporites. *Evaporites, petroleum, and mineral resources*. New York: Elsevier. *Developments in Sedimentology*, **50**, 189–347.
- Sonnenfeld, P., and Pertuisot, J.P., Brines and evaporites. 1989. *Short Course in Geology*, vol. 3, Washington, DC: American Geophysical Union, 126 pp.
- Warren, J.K., 1999. *Evaporites: Their Evolution and Economics*, Blackwell Science, 438 pp.
- Warren, J.K., and Kendall, C.G.St.C., 1985. Comparison of sequences formed in marine sabkha (subaerial) and salina (subaqueous) settings—modern and ancient. *Am. Ass. Petrol. Geol. Bull.*, **69**, 1013–1023.
- Yechieli, J., and Wood, W.W., 2002. Hydrogeologic processes in saline systems: playas, sabkhas, and saline lakes. *Earth Sci. Rev.*, **58**, 343–365.

Cross-references

[Arid Climates and Indicators](#)
[Coastal Environments](#)
[Continental Sediments](#)
[Marine Biogenic Sediments](#)
[Messinian Salinity Crisis](#)
[Mineral Indicators of Past Climates](#)
[Sedimentary Indicators of Climate Change](#)
[Stable Isotope Analysis](#)

EVOLUTION AND CLIMATE CHANGE

Introduction

Darwin's model (1859) for evolutionary change was based on a single branching tree of life, originating with one species at a point in deep time and concluding with the spectacular organic variety of modern ecosystems. Through time, the splitting of species developed both the biocomplexity and biodiversity of life present today, during some 4,000 million years of organic evolution. Nevertheless the process was not a gradual progression; life evolved at variable rates, commonly punctuated by a series of catastrophic events of varying magnitudes (Benton, 1995). Patterns, rates and trends in evolution were governed by a range of biological, chemical and physical factors; moreover their distributions and affects were rarely even or random. Climate is the manifestation of long-term, time-averaged atmospheric change, in simple terms, weather. The various patterns of climate change exerted a strong influence on a number of types of evolutionary process. Temperature was probably the most important climatic factor in marine environments, whereas in the more complex terrestrial milieu, temperature together with rainfall, solar luminosity and wind strength exerted their influence on the distribution and evolution of biotas. Climate, particularly temperature, is thus one of a number of factors including also sea-level change and volcanicity that may have been associated with both small and larger-scale evolutionary events (Figure E17). Climatic change has demonstrably driven the migration of biotas; less clear, however, is its control on microevolution processes at the species level. On a larger scale, extreme climate change has forced the restructuring of the planet's ecosystems and more rarely caused major extinction events.

Climatic fluctuations through time

Short-term trends

Many climatic events are short term, occurring within a time span of 100,000 years (Cronin, 1999). Many Earth surface processes respond rapidly to climate change, for example the atmosphere and ocean surface waters can change within days to a few years whereas the deep water of the ocean basins and terrestrial vegetation may take centuries to alter; the buildup of ice sheets and associated sea-level changes, however, occur over millennia. Changes in precipitation and temperature in the recent past may have influenced the course of human events and almost certainly impacted on the direction of hominid evolution during the late Pliocene and Pleistocene. Many short-term climatic fluctuations have been related to Milankovitch cycles associated with the eccentricity, obliquity and precession of the Earth's orbit, and generally lasted from 20,000 to 400,000 years. These short-term trends are associated with evolutionary changes at the speciation level and more local regional changes in the composition and structure of ecosystems.

Long-term trends

Data available for the late Proterozoic and Phanerozoic suggest that during the last 900 million years the Earth oscillated between greenhouse and icehouse conditions at least five times (Frakes, 1979; Frakes et al., 1992). These megacycles, first developed by Alfred Fischer, have been compared with patterns of change in extinctions, sea-level and volcanicity (Figure E18). Moreover, there may be a correlation between all three of these

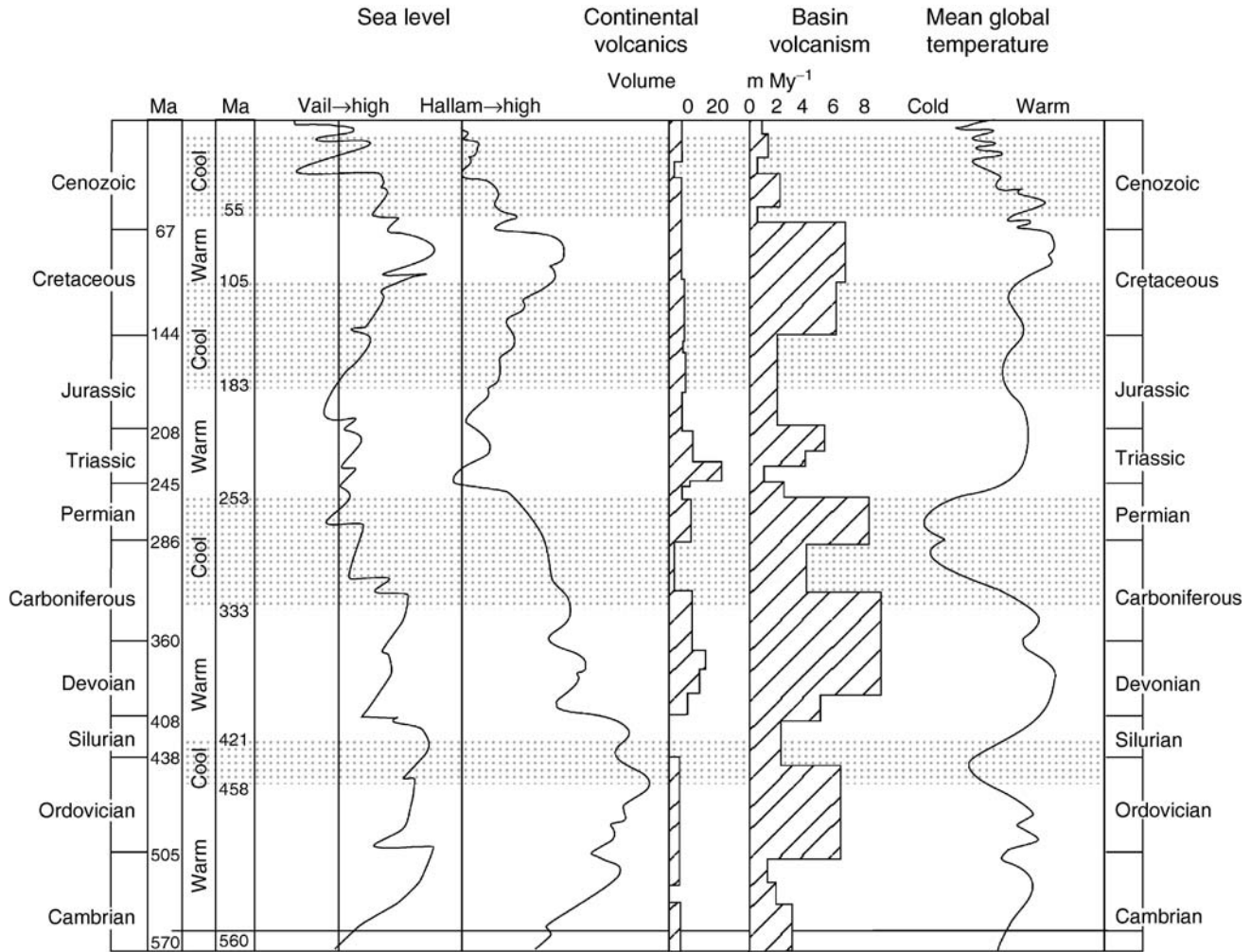


Figure E17 The relationships between temperature, volcanism and sea-level change during the last 570 million years (redrawn and replotted from Frakes et al., 1992).

variables and the assembly and breakup of the supercontinents. In marine environments, two extreme states occurred: The ice-house state involved stratified, stable oceans, cool surface waters between 2 and 25 °C and bottom waters ranging from 1 to 2 °C, together with rapidly moving bottom waters, rich in oxygen and with high productivity in areas of upwelling. On the other hand, greenhouse oceans were less stable and poorly stratified, with surface waters ranging in temperature from 12 to 25 °C and deep-water temperatures between 10 to 15 °C. Slow bottom currents carried little oxygen and productivity was generally low. Extinctions were associated with the transitions between these oceanic states. In addition to these major climatic fluctuations, a series of major extinction events, some associated with extra-terrestrial causes, clearly prompted major climate change over several million years. Such events caused major taxonomic extinctions together with major restructuring of the marine and terrestrial ecosystems. Generally, greenhouse biotas were most susceptible to extinction; their species were more specialized and thus exposed to environmental change.

Biocomplexity

Microevolution

Evolution at the species level is based on the natural selection of individuals from genetically and morphologically variable populations. Parts of populations with different samples of genetic material may become isolated from the parent population by physical or ecological barriers, leaving this subset free to evolve in a different direction, where selection pressures may also be different. Allopatric speciation based on the founder principle has been widely used to account for evolutionary change. A further mechanism is genetic drift, whereby small peripheral isolates of a population may break away from the parent population to establish new species eventually. Moreover, species evolution may have occurred in two quite different ways. Phyletic gradualism implies gradual morphological change whereas the punctuated equilibrium model involves rapid, sudden changes in morphology followed by intervals of no change, or stasis. Microevolution has been demonstrated

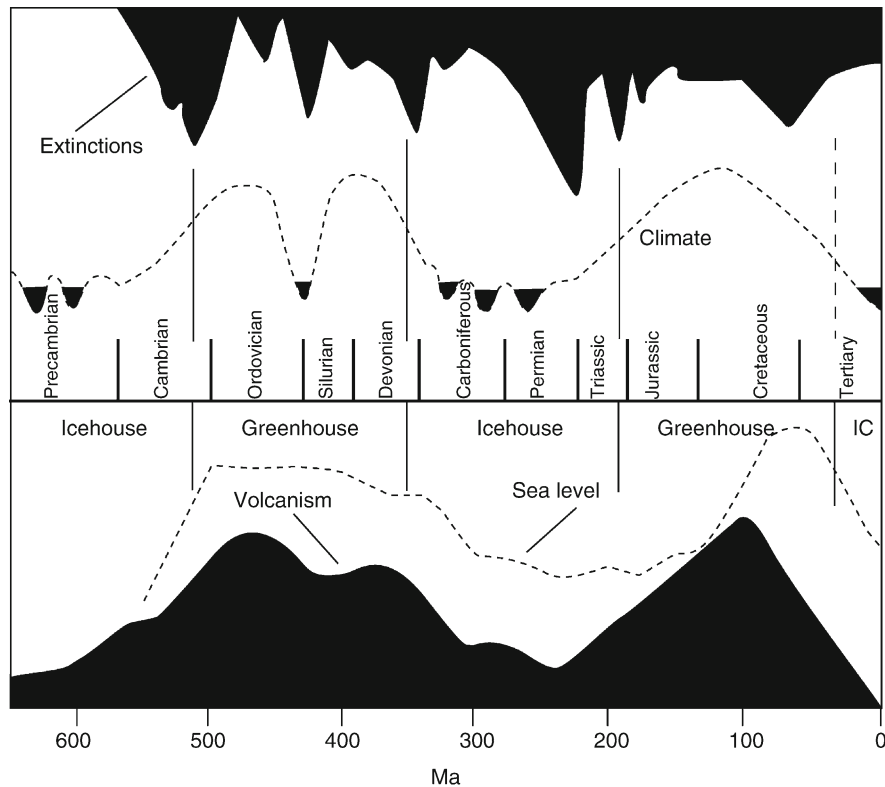


Figure E18 Alternations between icehouse and greenhouse states: the so-called “Fischer cycles.” The relationships between climate, extinctions, sea-level and volcanism are also indicated (adapted and redrawn from Fischer in Berggren and van Couvering, 1982).

in many fossil lineages (Benton and Pearson, 2001) although the link between speciation events and climatic change is more controversial. In general terms, marine plankton show gradual evolution whereas marine invertebrates and vertebrates display punctuated equilibria. Moreover, it is probable that narrowly fluctuating, changing environments hosted persistent gradualistic evolution whereas widely fluctuating environments were better characterized by morphological stasis (Sheldon, 1996). This resistance to morphological change has been demonstrated in a number of lineages such as Ordovician trilobites (Sheldon, 1987) and Pliocene mollusks (Williamson, 1981).

Short-term climatic fluctuations, for example those associated with Milankovitch cycles, can clearly disrupt and promote the reassembly of both marine and terrestrial communities (Bennett, 1997) and in some cases drive local extinctions and radiations, for example in the conodont and graptolite faunas of the Silurian (Jeppson, 1990). Regarding possible speciation, at least two outcomes are possible: Widespread evolutionary stasis or the development of isolated populations forming the focus of genetic and morphological divergence (Sepkoski, 1998). The Plio-Pleistocene deposits of East Africa have provided some of the best constrained studies of the relationship of climatic change to evolution. Datasets comprising a variety of mammals including hominoids have formed the focus for microevolutionary studies (Vrba, 1993). Cooler climates in the early Neogene prompted biotic turnovers in the evolution of animals with larger bodies and either relatively smaller or larger body parts (Vrba, 1996). The relative enlargement of the hominoid brain

exemplifies the latter. Some similar trends are apparent in Jurassic and Cretaceous marine environments. Deeper-water pelagic faunas are more diverse, such that communities that are more complex and have larger predators occur in oceans with raised temperatures.

Macroevolution

Macroevolution involves the study of larger scale evolutionary processes, usually involving major and rapid morphological change in a number of contemporary organisms. Generally, the appearance and disappearance of higher taxonomic groups during adaptive radiations or mass extinctions signal macroevolutionary change. Adaptive radiations are usually associated with the development of a successful morphological innovation and the exploitation of new ecospace. Such major evolutionary changes depend on many factors, both intrinsic and extrinsic, and are difficult to relate directly to climate. Many adaptive radiations, however, occur following major extinction events and take advantage of a range of vacant niches. Nevertheless, many, such as the diversification of skeletal organisms, reef-building organisms and the first predators, are clustered at the Precambrian-Cambrian boundary (Benton and Harper, 1997), associated with increasingly warm climates and higher sea levels. On land, the radiation of early terrestrial tetrapods in the early Carboniferous together with the diversification of large flying insects in the first extensive forests during the late Paleozoic, in cooler climates and more exposed land areas, have also been correlated with higher levels of atmospheric oxygen (Bernier et al., 2000).

Megaevolution

The appearance of entire new biotas and commonly grades of organization, for example the origin of life itself, the development of photosynthesis and the appearance of the metazoans rank, together with the origin and diversification of skeletal organisms, are megaevolutionary events (Benton and Harper, 1997). Data are as yet too imprecise to relate these events to climate change. However, there are a few indications. The first two events have been associated with a stable Archean crust and relatively cooler climates, favorable for carbon-based life to evolve. Metazoans appeared and diversified after the decay of the near global ice sheets of Snowball Earth whereas skeletal organisms radiated during the greenhouse climates of the early Cambrian.

Biodiversity

The fossil record holds a unique database of the diversification of life on land and in the sea (Harper and Benton, 2001). Range data of animals and plants through time form the basis of the study of biodiversity (Conway Morris, 1999). Qualitative and quantitative analyses have revealed that time trends are not random; biodiversity dynamics and the appearance of evolutionary innovations suggest that a nonrandom group of both intrinsic and extrinsic processes controlled changes in biodiversity (Jablonski, 1999). Climate is one of a number of important factors that mediates the planet's biodiversity through time.

Extinctions

During the Phanerozoic, animals and plants experienced a steady turnover in species. Clearly, climate change was one of a range of causes for background extinctions, particularly when habitats were destroyed and the tolerance range of individual species was exceeded. In addition, five major extinctions and a number of more minor events have been recognized in the fossil record, based primarily on paleontological data (Hallam and Wignall, 1997). All five, the end-Ordovician, late Devonian, end-Permian, end-Triassic and end-Cretaceous have been associated with major climatic changes linked to a range of terrestrial and extra-terrestrial causes (Brenchley and Harper, 1998). The end-Ordovician event was marked by a rapid transition from greenhouse to icehouse conditions associated with an increase in polar ice, a cooling of oceanic surface water and cycling of carbon within a changing oceanic system; most clades and ecological groups were affected and up to 85% of all species probably disappeared. The late Devonian event was less severe with the loss of about 80% of species during a phase of climatic cooling associated with sea-level change and anoxia. The end-Permian extinction was the most marked with about 95% of all species affected. All clades and ecological groups were devastated during a range of climatic changes, linked to a runaway greenhouse (Benton and Twitchett, 2003). The end-Triassic event witnessed the demise of about 75% of species, particularly the terrestrial vertebrates, during an event dominated by climate and sea-level changes together with anoxia. The end-Cretaceous event was near instantaneous with the disappearance of about 75% of species across a number of clades, including the ammonites and dinosaurs but particularly the plankton. Major climatic change has been linked to a bolide impact. Two more minor events, the Turonian-Cenomanian (loss of 50% of species) and the Eocene-Oligocene (loss of 35% of species) events have been linked to climatic changes associated with bolide impact or comet showers, respectively.

Radiations

Some intervals of apparent adaptive and rapid speciation can be related to climate change. Most profound was the emergence of the soft-bodied Ediacara fauna following the reversal of Snowball Earth. These remarkably diverse animals occupied a range of marine environments and ecological niches during the warmer climates of the late Proterozoic. The Cambrian explosion, marked by the rapid diversification of skeletal organisms with a spectrum of new body plans within the early part of the period, may have been associated with a continued rise in temperature, intense biological production and high rates of phosphate deposition coincident with changing patterns of oceanic circulation. The Ordovician radiation nevertheless marked the most significant diversification in numbers of marine organisms. The firm establishment of greenhouse conditions is correlated with widespread carbonate platforms and relatively high sea levels. This radiation set the agenda for Paleozoic marine life or perhaps marine biotas throughout the entire Phanerozoic (Alroy et al., 2001). The progressive diversification of marine life within the Modern evolutionary fauna following the end-Permian extinction event is again associated with persistent rises in temperature and sea level within a prolonged greenhouse phase.

On land some broad patterns are recognizable; for example the radiation of the pteridophyte plants together with the amphibians and mammal-like reptiles occurred during the cooler climates of the Carboniferous and Permian whereas the large reptiles, for example the dinosaurs, diversified during the warmer climates of the Jurassic and Cretaceous, together with the gymnosperm plants. Following the end-Cretaceous extinction event, angiosperm plants together with the mammals continued to diversify against a background of declining temperature.

Biotic change

In addition to the development of biocomplexity and biodiversity, a number of patterns of long-term change in the Earth's paleobiotic ecosystems can be detected (Figure E19a–c). Such large-scale ecologic changes are more closely related to major swings in climate associated with extinction events. Nevertheless, in many cases the severity of the ecologic crisis was decoupled from changes in biodiversity (Droser et al., 2000) suggesting that the environmental controls on both processes were different.

Precambrian

The Precambrian covers some 80% of geological time but organic remains are relatively few and many are controversial (Brasier et al., 2004). The era includes a series of major biological events, for example the origin of life and photosynthesis and the appearance of multicellular organisms together with the rise of the earliest metazoans and the evolution of the first skeletal animals. The origin of life (Rosing, 1999) and photosynthesis (Rosing and Frei, 2003) may have marked the establishment of more stable but warm climates on Earth following the development of continental crust together with marine basins and coincident with the cessation of meteorite showers. The role of climate during much of the later Archean and Proterozoic is unclear, while the development of an oxygenated atmosphere and hydrosphere favored the radiation of aerobic multicellular organisms (Knoll, 2003). Anaerobic environments and their organisms were marginalized. Moreover, the greater availability of atmospheric oxygen around 2.5–2.3 Ga may

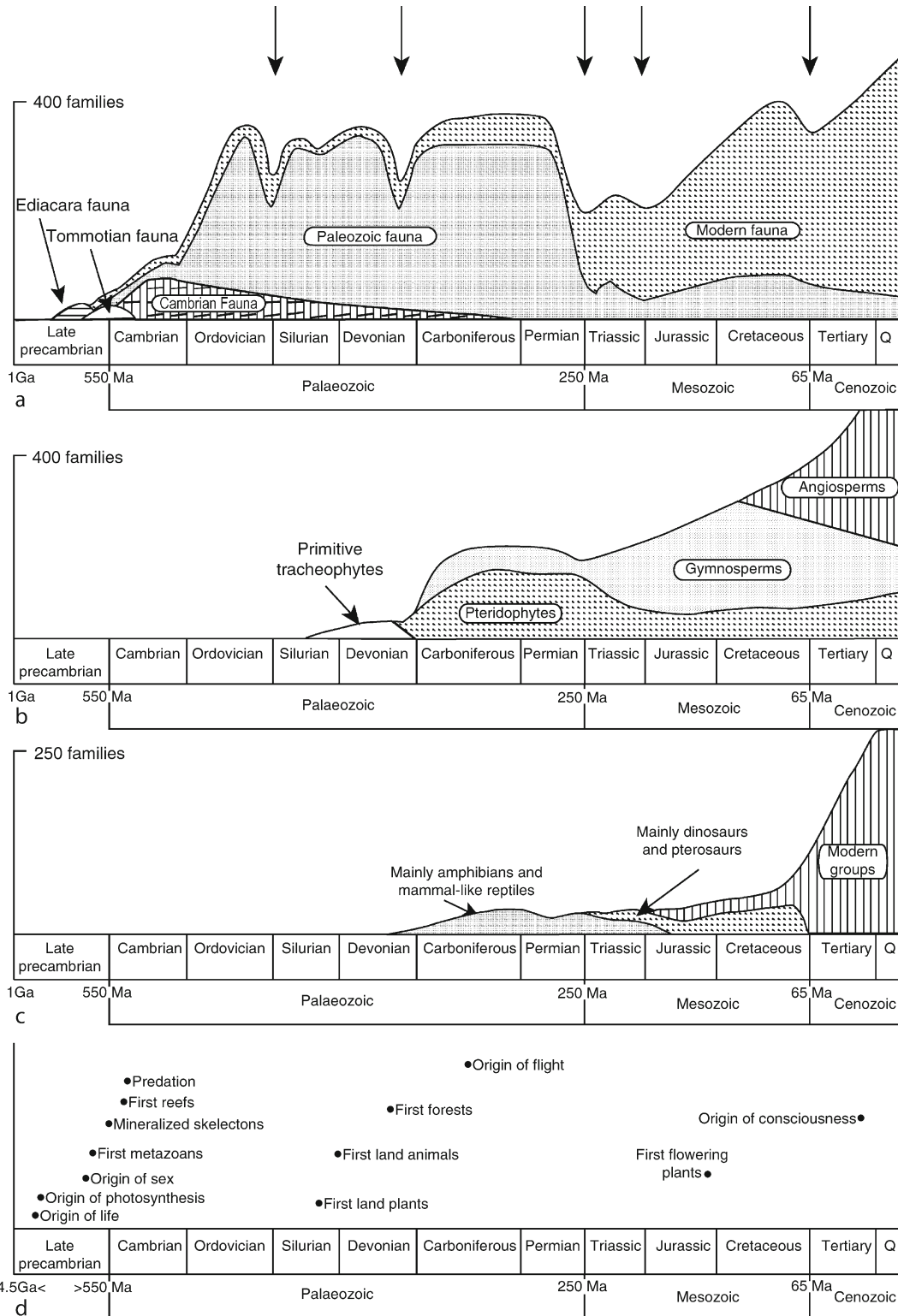


Figure E19 a. The marine evolutionary faunas together with the five big extinction events indicated by arrows, b. The nonmarine evolutionary floras, c. The nonmarine evolutionary tetrapod faunas and, d. Origins for some of the main mega and macroevolutionary events (replotted from various sources including Benton and Harper, 1997).

have reduced concentrations of methane, possibly driving the Huronian glaciation (Kasting et al., 2001). Nevertheless, major climate changes at the end of the Proterozoic virtually annihilated life on the planet; subsequent climatic amelioration may have strongly influenced the direction of metazoan life. The Snowball Earth hypothesis (Hoffman et al., 1998) envisages a runaway extreme icehouse state, with ice sheets extending from pole to pole and the oceans covered by sea ice. Marine organisms were thus restricted to refugia as the majority of marine habitats were destroyed. Earth emerged into a subsequent greenhouse state, populated initially by mutations generated during periods of extreme environmental stress. The first signs of relatively abundant metazoan life, the soft-bodied Ediacara biota, occurred globally above the late Proterozoic glacial deposits associated with Snowball Earth. They form the basis for the Ediacara Fauna (Figure E19a).

Phanerozoic

Phanerozoic life can be organized into a number of major evolutionary faunas and floras (Figure E19a). In the sea, the Cambrian evolutionary fauna was characterized by loosely-structured communities with morphologically varied species dominated by trilobites and primitive echinoderms and molluscs. It followed sequentially the appearance of the Tommotian (or Small Shelly) Fauna, dominated by small skeletal organisms. These first skeletal-dominated evolutionary faunas developed during the warmer climates of the early Cambrian. The Paleozoic evolutionary fauna (Ordovician-Permian) was dominated by abundant suspension feeders such as the brachiopods, bryozoans and corals, whereas the Modern evolutionary fauna (Triassic-Recent) consisted predominantly of detritus feeders with a substantial bioturbation of the seabed, together with efficient predators that participated in an arms race with their prey. The sharp transition between the Paleozoic and Modern evolutionary faunas is marked by the end-Permian extinction event (Benton and Twitchett, 2003), when over 95% of all species disappeared.

Similar models have been developed for terrestrial biotas (Figure E19b and E19c). The sequential appearance of evolutionary faunas dominated by the amphibians and mammal-like reptiles, the dinosaurs and pterosaurs and finally the modern groups is partly determined by extinction events: the end-Triassic event marked the transition between the first two groups and the end-Cretaceous event witnessed the demise of the dinosaurs and the rise of the mammals. The floral history of the planet was most affected by the end-Permian event (subsequent rise of the gymnosperms) and the end-Cretaceous event (subsequent dominance of the angiosperms).

Biological feedbacks

The relationship between climate and life suggests the existence of a feedback between the two over time. Today and during the recent past much discussion has been focused on the anthropogenic influences on our climate as we move again into a greenhouse phase. The industrial revolution set the agenda for the sustained use of fossil fuels and the persistent generation of greenhouse gases. Climatic warming will have a greater impact on the biotas of the cold-temperate and polar regions, with a pole-ward shift in climate on the order of 100 km per century (Wilson, 1992). Nevertheless, a number of models for long-term climatic change have also involved the role of feedbacks from biological organisms (Figure E20). Most marked

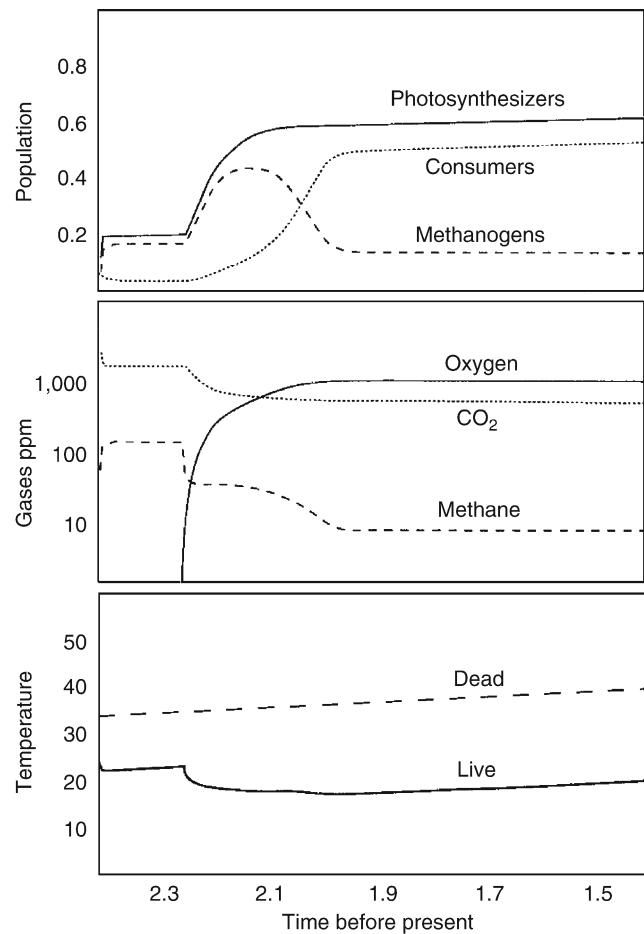


Figure E20 Populations of photosynthesizers, consumers and methanogens (top), the relative ppm of atmospheric gases (middle) and the influence of life on planet Earth during mid Precambrian (replotted from Lovelock, 1998).

are changes during the Precambrian, predicted by the Gaia hypothesis (Lovelock, 2000). The diversification of photosynthesizers, together with consumers from the early Proterozoic onwards, hiked oxygen levels concomitant with declines in greenhouse gases. Such models promote the vital effects of life as a stabilizing influence on the planet's climate, reducing the otherwise steady rise in the Earth's surface temperatures. In the same way, the extensive coal swamps and forests of the later Paleozoic may also have contributed to an interval of cooler climate, as diversifying land plants mediated atmospheric oxygen levels, anticipating the importance of modern rainforests as a climatic buffer.

David A. T. Harper

Bibliography

Alroy, J., Marshall, C.R., Bambach, R.K., Bezusko, K., Foote, M., Fürsich, F.T., Hansen, T.A., Holland, S.M., Ivany, L.C., Jablonski, D., Jacobs, D. K., Jones, D.C., Kosnik, M.A., Lidgard, S., Low, S., Miller, A.I., Novack-Gottshall, P.M., Olszewski, T.D., Patzkowsky, M.E., Raup, D.M., Roy, K., Sepkoski, J.J., Jr. Sommers, M.G., Wagner, P.J., and Webber, A., 2001. Effects of sampling standardization on estimates of Phanerozoic marine diversification. *Proc. Natl. Acad. Sci.*, **98**, 6261–6266.

- Bennett, K.D., 1997. *Evolution and Ecology: The pace of Life*. Cambridge, UK: Cambridge University Press, 241pp.
- Benton, M.J., 1995. Diversification and extinction in the history of life. *Science*, **268**, 52–58.
- Benton, M.J., and Harper, D.A.T., 1997. *Basic Palaeontology*. Harlow: Addison Wesley Longman, 342pp.
- Benton, M.J., and Pearson, P.N., 2001. Speciation in the fossil record. *Trends Ecol. Evol.*, **16**, 405–411.
- Benton, M.J., and Twitchett, R.J., 2003. How to kill (almost) all life: The end-Permian extinction event. *Trends Ecol. Evol.*, **18**, 358–365.
- Berner, R.A., Petsch, S.T., Lake, J.A., Beerling, D.J., Popp, B.N., Lane, R.S., Laws, E.A., Westley, M.B., Cassar, N., Woodward, F.I., and Quick, W.P., 2000. Isotope fractionation and atmospheric oxygen: Implications for Phanerozoic O₂ evolution. *Science*, **287**, 1630–1633.
- Brasier, M., Green, O., Lindsay, J., and Steele, A., 2004. Earth's oldest (~3.5 Ga) fossils and the “early Eden Hypothesis”: Questioning the evidence. *Orig. Life Evol. Biosph.*, **34**, 257–269.
- Brenchley, P.J., and Harper, D.A.T., 1998. *Palaeoecology: Ecosystems, Environments and Evolution*. Cheltenham: Nelson Thornes, 402pp.
- Conway Morris, S., 1999. The evolution of diversity in ancient ecosystems: A review. *Philos. Trans. R. Soc. Lond.*, **B 353**, 327–345.
- Cronin, T.M., 1999. *Principles of Paleoclimatology: Perspectives in Paleobiology and Earth History*. New York: Columbia University Press, 560pp.
- Darwin, C., 1859. *On the Origin of Species by means of Natural Selection, or Preservation of Favoured Races in the Struggle for Life*. New York: Mentor Edition, 479pp.
- Droser, M.L., Bottjer, D.J., Sheehan, P.M., and McGhee, G.R. Jr., 2000. Decoupling of taxonomic and ecologic severity of Phanerozoic marine mass extinctions. *Geology*, **28**, 675–678.
- Fischer, A.G., 1982. The two Phanerozoic supercycles, 129–150. In Berggren, W.A., and van Couvering, J.A. (eds.), *Catastrophes in Earth History*. Princeton: Princeton University Press.
- Frakes, L.A., 1979. *Climates Throughout Geologic Time*. Amsterdam: Elsevier, 310pp.
- Frakes, L.A., Francis, J.E., and Syktus, J.I., 1992. *Climate Modes of the Phanerozoic*. Cambridge, UK: Cambridge University Press, 274pp.
- Hallam, A., and Wignall, P.B., 1997. *Mass Extinctions and their Aftermath*. Oxford: Oxford University Press, 320pp.
- Harper, D.A.T., and Benton, M.J., 2001. History of Biodiversity. *Geol. J.*, **36**, 185–362.
- Hoffman, P.F., Kaufman, A.J., Halverson, G.P., and Schrag, D.P., 1998. A Neoproterozoic snowball Earth. *Science*, **281**, 1342–1346.
- Jablonski, D., 1999. The future of the fossil record. *Science*, **284**, 2114–2115.
- Jeppson, L., 1990. An oceanic model for lithological and faunal changes tested on the Silurian record. *J. Geol. Soc. Lond.*, **147**, 663–674.
- Kasting, J.F., Pavlov, A.A., and Siefert, J.L., 2001. A coupled ecosystem-climate model for predicting the methane concentration in the archaean atmosphere. *Orig. Life Evol. Biosph.*, **31**, 271–285.
- Knoll, A.H., 2003. *Life on a Young Planet*. Princeton and Oxford: Princeton University Press, 277pp.
- Lovelock, J., 1998. *The ages of Gaia*. New York: Bantam Books, 252pp.
- Lovelock, J., 2000. *Gaia: A new look at life on Earth*. Oxford: Oxford University Press, 176pp.
- Rosing, M.T., 1999. C-13-depleted carbon microparticles in > 3700-Ma sea-floor sedimentary rocks from west Greenland. *Science*, **283**, 674–676.
- Rosing, M.T., and Frei, R., 2003. U-rich Archaean sea-floor sediments from Greenland – indications of > 3700 Ma oxygenic photosynthesis. *Earth Planet. Sci. Lett.*, **6907**, 1–8.
- Sheldon, P.R., 1987. Parallel gradualistic evolution of Ordovician trilobites. *Nature*, **330**, 561–653.
- Sheldon, P.R., 1996. Plus ça change – a model for stasis and evolution in different environments. *Palaeogeogr. Palaeoclimatol. Palaeoecol.*, **127**, 209–227.
- Sepkoski, J.J. Jr., 1998. Rates of speciation in the fossil record. *Philos. Trans. R. Soc. Lond.*, **B 353**, 315–326.
- Vrba, E.S., 1993. Turn-over pulses, the Red Queen, and related topics. *Am. J. Sci.*, **293-A**, 418–452.
- Vrba, E.S., 1996. Climate, heterochrony, and human evolution. *J. Anthropological Res.*, **52**, 1–28.
- Williamson, P.G., 1981. Palaeontological documentation of speciation in Cenozoic molluscs from the Turkana Basin. *Nature*, **293**, 437–443.
- Wilson, E.O., 1992. *The Diversity of Life*. Cambridge, MA: Belknap Press, 424pp.

Cross-references

- [Astronomical Theory of Climate Change](#)
- [Bolide Impacts and Climate](#)
- [Greenhouse \(warm\) Climates](#)
- [Human Evolution and Climate Change](#)
- [Icehouse \(cold\) Climates](#)
- [Snowball Earth Hypothesis](#)
- [Volcanic Eruptions and Climate Change](#)

F

FAINT YOUNG SUN PARADOX

Standard models of solar evolution indicate that the intensity of solar radiation should have increased by about 25–30% over the 4.6 billion year duration of geologic time (Gilliland, 1989). The phrase “faint young Sun” was coined by Sagan and Mullen (1972) to describe the implications of these standard models for Earth’s climate, because early in the Sun’s lifetime, the radiation reaching a planet like Earth today (with both similar orbit and amount of greenhouse forcing) would not have been sufficient to prevent the planet’s average temperature from dropping below the freezing point of water. Sagan and Mullen evaluated the implications of the faint young Sun paradox in the context of geologic evidence from early in Earth’s history that rules out a long-lived frozen state. They argued that a greater amount of greenhouse gas forcing was required to offset the lower solar luminosity of the young Sun. The faint young Sun hypothesis is still being evaluated today and many hypotheses reconcile the reduced solar luminosity with geologic evidence, using refinements of the greenhouse gas arguments of Sagan and Mullen (1972), but some other hypotheses raise the possibility of variations of Earth’s orbital properties and even call into question the standard models of solar evolution.

A significant part of the Sun’s evolution is thought to occur along the main sequence, a field defined by observations of many stars and represented on a Hertzsprung-Russell diagram of luminosity versus temperature. Like other stars, the Sun derives its energy from nuclear fusion in its core and radiates most of this energy from its surface, the solar disc, as continuous blackbody radiation with a maximum in the visible region and tails that extend to the infrared and microwave and also into the ultraviolet and X-ray regions of the spectrum. The amount and spectral characteristics of this blackbody radiation can be described by one principal equation, the Planck function, and two derivative laws, the Stephan Boltzman Law and Wien’s Law. The Planck function describes the spectral characteristics of blackbody radiation (B_λ), and takes the form:

$$B_\lambda = \frac{2hc^2}{\lambda^5 \pi (e^{hc/\lambda kT} - 1)}$$

where c is the speed of light, λ is the wavelength, k is Boltzman constant, T is temperature, and h is Planck’s constant. The Stephan Boltzman Law describes the total energy emitted by a blackbody and is given by:

$$E = 4\pi R^2 \sigma T^4$$

where σ is the Stephan-Boltzman constant ($5.67 \times 10^{-8} \text{ W m}^{-2} \text{ K}^{-4}$) and $4\pi R^2$ is the surface area. At its present size and average surface temperature of 5,785 K, the Sun emits a total blackbody energy of approximately $3.8 \times 10^{26} \text{ W}$. The standard solar model indicates that the size of the Sun has increased with time, resulting in an increase in solar radiation (brightening of the Sun) over the course of its 4.6 billion year existence (Gilliland, 1989).

Wien’s Law describes the wavelength of the maximum of Planck’s function as

$$\lambda_{\text{max}} \approx \frac{2898 \mu\text{m K}}{T}$$

where λ is given in μm . Wien’s Law places the peak of radiation in the visible region and this is essential for the Earth’s greenhouse effect.

The underlying principle of the greenhouse effect requires a planetary energy balance (e.g., $E_{\text{incident}} = E_{\text{radiated to space}}$), and an atmosphere that transmits incoming radiation, but absorbs energy radiated from the planet’s surface. Greenhouse gases in the Earth’s atmosphere are transparent to visible radiation, transmitting a high dose of incident solar radiation through the atmosphere to warm the Earth’s surface, but these same gases absorb and reradiate the infrared radiation emitted from the surface. The energy recycled (absorbed and reradiated) by greenhouse gases in the atmosphere contributes a finite amount of surface warming beyond that provided by incoming solar radiation. In today’s atmosphere, the greenhouse effect contributes approximately 33 K of warming, raising the average surface temperature to 298 K.

The warming provided by the present-day greenhouse effect is essential for keeping the average surface temperature of Earth above the freezing point of water, but as recognized by Sagan and Mullen (1972), this amount of warming would not have been sufficient to have kept the surface temperatures above freezing if solar radiation had been lower by more than ~10%. Furthermore, the standard solar model points to as much as 25–30% lower solar luminosity 4.6 billion years ago than today. Moreover, for the vast majority of geologic time, this standard solar model predicts that incident solar radiation would have been less than 90% of present-day values. It was also recognized that if the mean surface temperature of Earth fell below the freezing point of water, the oceans would have frozen, leading to a negative feedback involving planetary albedo and planetary ice. The amount of radiation available to warm the climate would thus have decreased as ice cover expanded, because more radiation would have been reflected back to space rather than absorbed by the surface and transformed into heat.

Geologic evidence, however, does not point to a long-lived frozen state for early Earth. Rather, the presence of sedimentary rocks suggests the existence of liquid water throughout much of geologic history (Cloud, 1972). In addition, chemical and isotopic characteristics of 4.3–4.4 billion year old zircon grains from the Jack Hills of Australia point to the presence of liquid water within a few million years of the formation of Earth (Mojzsis et al., 2001; Wilde et al., 2001). Sagan and Mullen (1972) argued that the faint young Sun paradox could be reconciled with the geological observations if the Earth's early greenhouse effect provided enough additional warming of the planet (beyond that of the present greenhouse effect) to offset the lower luminosity of a faint young Sun.

Central to the hypothesis of a more efficient greenhouse is the identification of the gas that is responsible for the enhanced greenhouse forcing. Three gases (NH₃, CO₂, and CH₄) have been suggested as the principal cause of the enhanced greenhouse effect during the early parts of Earth's history. Sagan and Mullen (1972) and Sagan and Chyba (1997) argued that NH₃ was the gas responsible for the enhanced greenhouse. Debate about the suitability of NH₃ as an early Earth greenhouse gas has focused on its lifetime in the atmosphere. While Owen et al. (1979) argued that high UV fluxes in a low O₂/O₃ atmosphere would destabilize NH₃, making CO₂ or even CH₄ which are stable in high-UV environments more likely candidates, Sagan and Chyba (1997) argued that a high altitude organic haze, similar to that observed on Saturn's moon Titan, could provide a sufficient UV shield to stabilize NH₃. Most workers agree that CO₂ played a significant role as a greenhouse gas throughout Earth's history, and the debate revolves around its sources and sinks and whether it was the principal greenhouse gas, or whether a second or third greenhouse gas would have been required to sustain the greenhouse forcing necessary to offset the effects of a faint young Sun (Walker et al., 1981; Kasting, 1993; Kasting and Catling, 2003). Using arguments structured around mineral equilibrium and stability of siderite (an iron carbonate) and greenalite (an iron-bearing phyllosilicate mineral) in the 2.7 billion year old Mount Roe paleosol, Rye et al. (1995) placed limits on the amount of carbon dioxide in the atmosphere that would have been too low to have kept Earth's surface above freezing, and called instead for a second greenhouse gas in the early atmosphere, such as CH₄. Pavlov et al. (2000) used an energy balance model to demonstrate that a combination of CO₂ and CH₄ would have sufficed

to offset the effects of the faint young Sun. It is also thought that such a greenhouse gas mixture might carry other consequences for the Earth's early atmosphere and this has been demonstrated for methane by Catling et al. (2001) who explored its sources and its implications for the oxidation state of the early Earth's atmosphere.

Other hypotheses have been proposed to reconcile the geological evidence with the faint young Sun paradox. These include the hypothesis that the standard solar model and its implications about main sequence evolution are not relevant for the Sun. This alternate hypothesis centers around a more massive and more luminous young Sun than that predicted by the standard model and argues that a more massive (larger) Sun would radiate more rather than less energy (Graedel et al., 1991). A second hypothesis calls on changes in Earth's obliquity (tilt of the rotational axis), which if it remained at high values throughout much of Earth's history could have sustained liquid water by keeping parts of the Earth facing the Sun over longer periods of time, which would have led to hotter summers (Jenkins, 2000). This hypothesis is similar to that envisioned by Milankovich for the orbital forcing of glacial and interglacial cycles. These two hypotheses remain to be tested, leaving the most widely held hypothesis – that of enhanced greenhouse gas forcing early in Earth's history – as the preferred one. Among the fundamental issues in identifying the implications of greenhouse gas forcing and climate through deep time is the characterization of the sources, sinks, and stability (feedbacks) of greenhouse gases in models of early Earth atmospheres, such that climate was stabilized over the first 3 billion years of geologic history.

James Farquhar

Bibliography

- Catling, D.C., Zahnle, K.J., and McKay, C.P., 2001. Biogenic methane, hydrogen escape, and the irreversible oxidation of early Earth. *Science*, **293**, 839–843.
- Cloud, P., 1972. Working model of primitive Earth. *Am. J. Sci.*, **272**(6), 537–548.
- Graedel, T.E., Sackmann, I.J., Boothroyd, A.I., 1991. Early solar mass-loss- a potential solution to the weak Sun paradox *Geophys. Res. Lett.* **18**(10), 1881–1884.
- Gilliland, R.L., 1989. Solar evolution. Global and planetary change, Vol. 75, 1-2, Elsevier. pp. 35–55.
- Jenkins, G.S., 2000. Global climate model high-obliquity solutions to theancient climate puzzles of the Faint-Young Sun Paradox and low-altitude Proterozoic Glaciation. *J. Geophys. Res. Atmos.*, **105**, 7357–7370.
- Kasting, J.F., 1993. Earths Early Atmosphere. *Science*, **259**(5097), 920–926.
- Kasting, J.F., and Catling, D., 2003. Evolution of habitable planet. *Annu. Rev. Astron. Astrophys.*, **41**, 429–463.
- Mojzsis, S.J., Harrison, T.M., and Pidgeon, R.T., 2001. Oxygen-isotope evidence from ancient zircons for liquid water at the Earth's surface 4,300 Myr ago. *Nature*, **409**, 178–181.
- Owen, T., Cess, R.D., Ramanathan, V., 1979. Enhanced CO₂ greenhouse to compensate for reduced solar luminosity on early Earth. *Nature*, **277**, 640–642.
- Pavlov, A.A., Kasting, J.F., Brown, L.L., Rages, K.A., and Freedman, R., 2000. Greenhouse warming by CH₄ in the atmosphere of early Earth. *J. Geophys. Res. Planets*, **105**, 11981–11990.
- Rye, R., Kuo, P.H., and Holland, H.D., 1995. Atmospheric carbon dioxide concentrations before 2.2 billion years ago. *Nature*, **378**, 603–605.
- Sagan, C., Chyba, C., 1997. The early faint Sun paradox: Organic shielding of ultraviolet-labile greenhouse gases. *Science*, **276**, 1217–1221.
- Sagan, C., and Mullen, G., 1972. Earth and Mars: Evolution of atmospheres and surface temperatures. *Science*, **177**(4043), 52–56.

- Walker, J.C.G., Hays, P.B., and Kasting, J.F., 1981. A negative feedback mechanism for the long-term stabilization of Earth's surface temperature. *J. Geophys. Res. Oceans Atmos.*, **86**, 9776–9782.
- Wilde, S.A., Valley, J.W., Peck, W.H., and Graham C.M., 2001. Evidence from detrital zircons for the existence of continental crust and oceans on the Earth 4.4 Gyr ago. *Nature*, **409**(6817), 175–178.

Cross-references

Albedo Feedbacks
 Archean Environments
 Atmospheric Evolution, Earth
 Climate Forcing
 Greenhouse Effect and Greenhouse Gases (*Encyclopedia of World Climatology*)
 Mineral Indicators of Past Climates
 Obliquity

FLOOD BASALTS: CLIMATIC IMPLICATIONS

Introduction

Flood basalts represent large-volume, predominantly effusive, eruptions of magma onto the Earth's surface. The volume of the largest flows exceeds 1,000 km³, some two orders of magnitude greater than the historic basalt flows found on Iceland and Hawaii. Magma contains dissolved volatiles that exsolve as the magma depressurizes and may be released into the atmosphere during and after the eruption. It is these aerosols, a cocktail including dust, H₂O, CO₂, SO₂, HF, and HCl, that have been implicated in climatic change. This has led some authors to propose causative links between flood basalt volcanism, climate change, and mass extinctions (McLean, 1985; Courtillot, 1999; Wignall, 2001). They suggest that dust and volatiles injected into the atmosphere lead to successive, short-term changes in atmospheric composition and temperature, leading ultimately to collapse of global ecosystems. The causative links between large-scale flood basalt volcanism and mass extinctions are, however, poorly defined.

Flood basalts may be erupted onto the Earth's continental crust, in which case they are called *continental flood basalts* (CFB). Most continental flood basalts are erupted subaerially, and any gases that are released enter directly into the atmosphere. Alternatively, flood basalts may erupt in the ocean basins (where they build large *oceanic plateaus*). In this environment, the eruption may be submarine, in which case the volatiles initially dissolve in the ocean. Both continental flood basalt provinces and ocean plateaus comprise the so-called *large igneous provinces* (LIPs) (Coffin and Eldholm, 1994). Most large igneous provinces – and hence flood basalts – originate from mantle plumes, regions of hot mantle ascending from the deep Earth interior.

Volcanism and climate forcing

It is widely recognized that explosive volcanic eruptions can perturb the Earth's climate. The eruption of Pinatubo in 1991 resulted in a small but significant cooling at the Earth's surface, and the much larger eruption of Tambora in 1815 caused even greater cooling (Oppenheimer, 2002). Climate-forcing agents include gases and aerosols, and volcanic eruptions (especially basaltic ones) often produce considerable masses of CO₂ and SO₂. The residence times of sulfate and dust aerosols in the lower atmosphere (troposphere) are short, usually of the order of a few days or weeks. The greatest effects on climate are caused by injection above the tropopause and into the stratosphere,

where the residence times are greater (on the order of 2 years, the turn-over time of the stratosphere). Injection of material above the tropopause adds to the Junge Layer (or Stratospheric Aerosol Layer), a sulfate-bearing layer in the lower stratosphere. This in turn leads to heating (through absorption of incident radiation) of the stratosphere, and concomitant cooling of parts of the troposphere. For example, the radiative forcing 1 year after the Pinatubo eruption (when ~20 Mt of SO₂ was injected in to the stratosphere), was about -4 W m^{-2} (IPCC, 2001).

Lakagigar, Iceland, 1783

While explosive volcanic eruptions are usually considered as transitory events for the purposes of climate modeling, effusive flood basalt events are different, because the source may be active for several months, years or even decades. The Lakagigar (“Laki”) eruption in SE Iceland in 1783 is the best documented and most recent basalt eruption, and offers an analog of much larger eruptions in the geological past. Approximately 15 km³ of basalt was erupted over a period of about 8 months (the bulk being erupted in a series of short explosive pulses during the first few months), causing local environmental devastation (most notably the Haze Famine), and cooling of the Northern Hemisphere climate (Thordarson and Self, 2004). Three aspects of the Laki eruption are important here: firstly, compared with explosive eruptions such as Pinatubo and Tambora, the eruption was prolonged, facilitating aerosol formation over several months. Secondly, some episodes of the eruption were sufficiently vigorous to enable injection of material into the lower stratosphere, thus producing hemispheric, as well as local, effects. And thirdly, the aerosols were sulfur-rich, a characteristic of iron-rich basaltic magmas.

Most basaltic eruptions are effusive in nature, producing lava fountains and flows. They contrast with eruption of more silicic magmas, which tend to be explosively ejected, forming tall eruption columns and widely dispersed pyroclastic fallout. The Laki eruption was, however, moderately violent during its early, peak stages, with Strombolian or even sub-Plinian episodes, and eruption columns that may have reached altitudes in excess of 13 km (Thordarson and Self, 2004). Most of the time, however, venting was effusive. Volatile dispersal was therefore both local, with low-level emissions from the vent and lava flow, and more widespread, with injection into the tropopause and lowermost stratosphere.

The volatile budget of the Laki eruption has been extensively investigated (Thordarson et al., 1996). Pre-eruption concentrations of volatile species were determined from glass inclusions and these were used to estimate the total volatile release from the erupted magma. During the eruption period, ~122 Mt of SO₂ (approximately the current global annual anthropogenic output) was released into the atmosphere, together with a mixture of F (7 Mt), Cl (~15 Mt) and H₂O (~235 Mt) (Thordarson et al., 1996). Most of these volatiles were released during the first three months of the eruption. It is estimated that approximately 80% of the SO₂ mass (~100 Mt) was injected into the lower stratosphere, the bulk of which was probably rapidly converted to sulfuric acid aerosols (equivalent to ~190 Mt) (Thordarson and Self, 2004). The remainder (~20 Mt SO₂, equivalent to ~40 Mt of H₂SO₄), was emitted from the cooling lava flow and formed a local, low-altitude, toxic haze.

The injection of sulfuric acid into the lower stratosphere and polar jet stream is thought to have been responsible for the atmospheric haze observed over large parts of Europe

throughout 1783. This haze is estimated to have extended to an altitude of at least 16 km, resulting in substantial dimming of the Sun.

during several of the summer months of the year 1783, when the effect of the Sun's rays to heat the Earth in these northern regions should have been greatest, there existed a constant fog over all Europe

this fog was of a permanent nature; it was dry, and the rays of the sun seemed to have little effect towards dissipating it. (Benjamin Franklin, 1784)

The eruption and the accompanying haze have been implicated in the subsequent high temperatures recorded in July, 1783, and the successive Northern Hemisphere cold winters of 1783/1784 to 1785/1786 (for a more complete description, see Grattan, 2005). It is likely that the high July temperatures resulted from the development of anticyclones over central or northern Europe, allowing warm air to flow from southern Europe (Thordarson and Self, 2004). Whether or not these changes in large-scale weather systems were influenced by the Laki eruption is not known. The winters of 1783/1784 to 1785/1786 were unusually cold, with an average temperature drop of 1.5 C over Europe and North America (Thordarson and Self, 2004). This temperature drop is consistent with the radiative forcing predicted by the injection of SO₂ into the stratospheric aerosol layer.

A full understanding of the Laki flood basalt eruption is important for two reasons. Firstly, such eruptions are not uncommon. On Iceland, for example, there have been four such eruptions in the last 1,200 years, Laki merely being the latest. Similar (but often larger) lava flows have built the Icelandic crust, dating back more than 12 million years, and similar eruptions may occur in other basaltic provinces associated with mantle plumes (e.g., Afar, Ethiopia; Hawaii). Secondly, the eruption provides important information about much larger events that have occurred in the geological past, and which have been implicated in mass extinction events.

Columbia river flood basalt province

The Miocene flood basalts of the Columbia River Province in northwest USA are among the best studied on Earth. The total volume of the province is of the order of 175,000 km³, and many of the individual flows have eruptive volumes in excess of 1,000 km³. Most the province was erupted between about 16.5 and 14.5 Ma. It is estimated that the eruption of the Roza flow (ca. 1,300 km³ of basalt; ~14.7 Ma) produced a phenomenal mass of aerosols: approximately 12,000 Mt of SO₂ (equivalent to 23,000 Mt of H₂SO₄), 680 Mt of Cl and 1690 Mt of F (Thordarson and Self, 1996). The effect of this aerosol loading on the global climate is likely to have been substantial, but with our current understanding of the duration and eruption intensity of large flood basalts, it is difficult to quantify. Estimates of the duration of large flood basalt eruptions vary from a few weeks (Shaw and Swanson, 1970) to a few years (Self et al., 1996). Given the eruption profile of Laki, where 80% of the magma was released during the first 3 months of the eruption, it is possible that the bulk of the Roza magma was also extruded within a relatively short time (months?), even if the eruption subsequently continued to be active for several years. If this is the case, then a substantial proportion of the SO₂ could have been injected into the stratosphere atop vigorous fire fountains and Plinian-style eruption columns (Stothers et al., 1986). Repeated SO₂ and dust injection, over a period of

several years, may also have occurred. Substantial cooling of at least the Northern Hemisphere troposphere would have ensued, but given that the response of the global climate to such (cumulative) mass loading is likely to be strongly non-linear, the precise outcome is difficult to predict. Immediate and dramatic cooling (for at least the duration of the eruption) would have been likely; transient "volcanic winters" could have ensued, and acid rain would have caused local environmental devastation.

Even more difficult to predict is the global response to successive flood basalt eruptions. The Columbia River Province comprises some 300 flow units, mostly erupted over a period of about 2 Ma. This gives an average interval between each flood basalt eruption of 7,000 years. The repose time between individual eruptions is clearly sufficient for the climate to recover, at least from the cooling effects of sulfate injection, although Thordarson and Self (1996) have suggested that the eruption of the Columbia River flood basalts was a contributory factor in the Miocene global cooling event that began at about 15–14.5 Ma.

Not only did the flows release large quantities of SO₂, however, but they also vented prodigious masses of CO₂, which, being a greenhouse gas, could have caused global warming. Are these masses significant? Estimates of the CO₂ content of basaltic magma vary dramatically, because the gas has a low solubility in the melt at near-surface conditions, and is rapidly exsolved. However, based on pre-eruptive values of 7,000 ppm CO₂ in basalts from ocean island volcanoes (Bureau et al., 1999), and assuming that 99% of the CO₂ is lost to air, then 1 m³ of basalt will release a little over 18 kg of CO₂. Using these figures, the total amount of CO₂ released from the Laki eruption was of the order of 270 Mt (or 73 Mt carbon), and from the Roza flow, a little over 23,000 Mt (6,300 Mt C). As the residence time of CO₂ in the atmosphere is much greater than that of SO₂, knowledge of the eruption profile is less important than it is for SO₂.

The current anthropogenic output is approximately 7,000 Mt C yr⁻¹. The mass erupted from Laki was insignificant, on a global scale. The flux from the Roza flow was likely to have been enhanced by burning vegetation, etc., but even assuming that the bulk of the CO₂ was degassed in the early stages of the eruption, the flux rates were not substantially greater than today's anthropogenic output. Note that total C release from the whole of the eruptive portion of the Columbia River basalt province was on the order of 800,000 Mt, a seemingly vast amount, but given that the eruption occurred over a period about 2 million years, the average flux was only 0.4 Mt C yr⁻¹, a fraction of the current anthropogenic output.

Flood basalts and mass extinctions

The "big three" mass extinctions of the last 300 Ma all coincide (within the precision of current dating techniques) with major flood basalt events. These are the Siberian Traps with the end-Permian extinction at 250 Ma; the Central Atlantic Magmatic Province with the end-Triassic extinction (200 Ma); and the Deccan Traps with the end-Cretaceous (K-T) extinction (65 Ma; Figure F1). The likelihood of these associations being pure chance is remote: about 1 in 2,000 (White and Saunders, 2005), and several other volcanic provinces – either continental or oceanic – are contemporaneous with other mass extinction events and other evidence of significant changes in ocean chemistry (for example, formation of black shales during periods of oceanic anoxia at 90 Ma; Kerr, 1998). Both the Siberian and

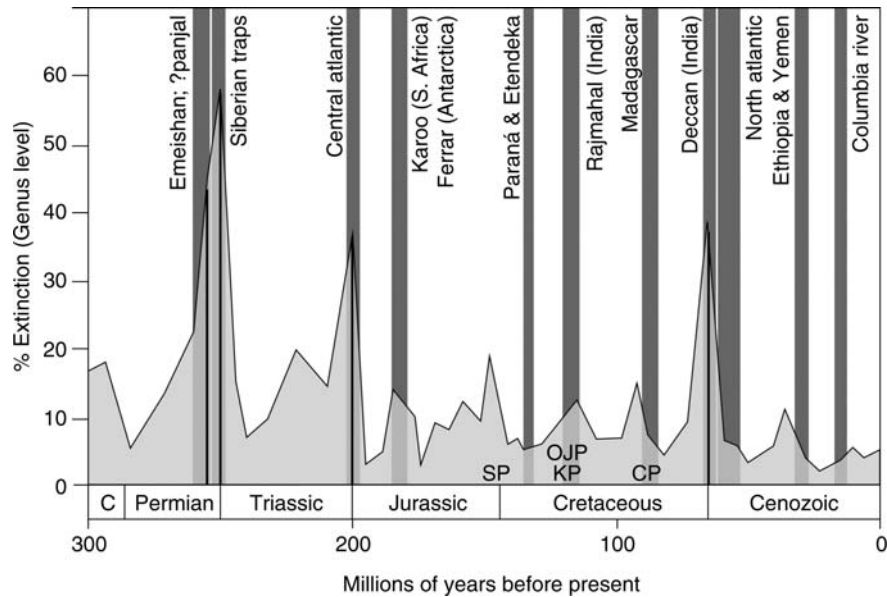


Figure F1 Extinction rate versus time (multiple-interval marine genera: modified from Sepkoski, 1996) compared with eruption ages of continental flood basalt provinces. Three of the most severe extinctions, the P-Tr, the Tr-J, and the K-T, correspond with eruption of the Siberian Traps, Central Atlantic Magmatic Province, and Deccan Traps, respectively. Oceanic plateaus may also have had profound environmental consequences (Kerr, 1998) (S: Sorachi Plateau, Japan; K: Kerguelen Plateau; OJ: Ontong Java Plateau; C: Caribbean-Colombian) (modified from White (2002) and White and Saunders (2005)).

Deccan Traps are substantially larger than the Columbia River Province, with eruptive volumes of the order of 3.5 million km³ (Reichow et al., 2002) in the case of the former, and around 0.75 million km³ in the case of the Deccan Traps. The total eruption duration may have been as short as 0.5 Ma, but is likely to have been longer than this; there is considerable uncertainty about the duration of volcanic activity in both provinces. Assuming this “worst case” scenario (0.5 Ma), and using the same volatile concentrations as in the Roza flow, produces average fluxes of 20 and 34 Mt C yr⁻¹ for the Deccan and Siberian Traps, respectively, and 38 and 66 Mt SO₂ yr⁻¹ for the two provinces. At face value it is difficult to see how these fluxes could lead directly to global ecosystem collapse; they are too low. Magmatic fluxes are far from regular, however, and successive flows may occur sufficiently frequently that SO₂ could accumulate in the atmosphere over several years or decades. This would lead to substantial climate forcing and, initially, tropospheric cooling. Meanwhile, simultaneous release of CO₂ could, on a longer time-scale, lead to an *increase* in global temperatures. This in turn could trigger the catastrophic release of carbon from terrestrial and marine methane hydrates, as indicated by the isotopically light carbon signature found in several horizons associated with mass extinction and flood basalt events (Wignall, 2001).

Conclusions

From the historical observations of the 1783 Laki event, it is evident that even a relatively small basalt eruption is capable of causing climate change on a hemispheric scale. This is in addition to the local devastation caused by acid rain and release of a range of toxic gases. The height of the convection column associated with basaltic eruptions is less than with major explosive events, but injection of gas and dust into the stratosphere is likely given the high magmatic flux rates. Unlike explosive

eruptions, flood basalts can erupt for several months if not years, leading to prolonged discharge of volatiles. The largest documented flood basalts indicate release of prodigious volumes of gas, especially SO₂, into the atmosphere, leading to the likelihood of substantial, short-term cooling of the lower atmosphere. Simultaneous release of carbon dioxide may cause longer-term global warming if the excess volcanic CO₂ cannot be removed (e.g., by biological activity) sufficiently quickly, and if flood basalt eruptions occur in rapid succession. This may trigger release of methane hydrates and initiate collapse of global ecosystems. Detailed modeling of the effects of flood basalt eruptions on global climate is required to ascertain the full significance of volcanic forcing.

Andrew D. Saunders

Bibliography

- Bureau, H., Métrich, N., Semet, M.P., and Staudacher, T., 1999. Fluid-Magma decoupling in a hot-spot volcano. *Geophys. Res. Lett.*, **26**, 3501–3504.
- Coffin, M.F., and Eldholm, O., 1994. Large igneous provinces: Crustal structure, dimensions, and external consequences. *Rev. Geophys.*, **32**, 1–36.
- Courtillot, V., 1999. *Evolutionary Catastrophes: The Science of Mass Extinction*. Cambridge: Cambridge University Press, 173pp.
- Grattan, J., 2005. Pollution and Paradigms: Lessons from Icelandic volcanism for continental flood basalt studies. *Lithos*, **79**, 343–353.
- IPCC, 2001. *Climate Change 2001: The Scientific Basis*. Houghton, J.T., Ding, Y., Griggs, D.J., Noguer, M., van der Linden, P.J., Dai, X., Maskell K., and Johnson C.A. (eds.), *Intergovernmental Panel on Climate Change*. Cambridge, UK: Cambridge University Press.
- Kerr, A.C., 1998. Oceanic plateau formation: A cause of mass extinction and black shale deposition around the Cenomanian-Turonian boundary? *J. Geol. Soc. London*, **155**, 619–626.
- McLean, D.M., 1985. Deccan traps mantle degassing in the terminal Cretaceous marine extinctions. *Cret. Res.*, **6**, 235–259.

- Oppenheimer, C., 2002. Limited global change due to the largest known Quaternary eruption, Toba, ~74 kyr BP. *Quaternary Sci. Rev.*, **21**, 1593–1609.
- Reichow, M.K., Saunders, A.D., White, R.V., Pringle, M.S., Al'Mukhamedov, A.I., Medvedev, A., and Korda, N., 2002. New $^{40}\text{Ar}/^{39}\text{Ar}$ data on basalts from the West Siberian Basin: Extent of the Siberian flood basalt province doubled. *Science*, **296**, 1846–1849.
- Self, S., Thordarson, T., Keszthelyi, L., Walker, G.P.L., Murphy, M.T., Long, P.E., and Finnemore, S., 1996. A new model for the emplacement of Columbia River basalt as large, inflated, pahoehoe lava sheets. *Geophys. Res. Letts.*, **23**, 2689–2692.
- Sepkoski, J.J., 1996. Patterns of Phanerozoic extinction: A perspective from global data bases. In Walliser, O.H. (ed.), *Global Events and Event Stratigraphy*. Berlin: Springer, pp. 35–51.
- Shaw, H.R., and Swanson, D.A., 1970. Eruption and flow rates of flood basalt. In Gilmore, E.H., and Stradling, D.F. (eds.), *Proceedings of the Second Columbia River Basalt Symposium*. Cheney: East Washington State College Press, 271–299.
- Stothers, R.B., Woolf, J.A., Self, S., and Rampino, M.R., 1986. Basaltic fissure eruptions, plume heights, and atmospheric aerosols. *Geophys. Res. Letts.*, **13**, 725–728.
- Thordarson, Th., and Self, S., 1996. Sulfur, chlorine, and fluorine degassing and atmospheric loading by the Roza eruption, Columbia River Basalt Group, Washington, USA. *J. Volcanol. Geotherm. Res.*, **74**, 49–73.
- Thordarson, Th., and Self, S., 2004. Atmospheric and environmental effects of the 1783–1784 Laki eruption: A review and reassessment. *J. Geophys. Res.*, **108**, 1 (20030116), 29pp.
- Thordarson, Th., Self, S., Óskarsson, N., and Hulsebosch, T., 1996. Sulfur, chlorine, and fluorine degassing and atmospheric loading by the 1783–1784 AD Laki (Skaftár Fires) eruption in Iceland. *Bull. Volcanol.*, **58**, 205–222.
- White, R.V., 2002. Earth's biggest 'whodunnit': unravelling the clues in the case of the end-Permian mass extinction. *Philos. Trans. R. Soc. Lond.*, **360**, 2963–2985.
- White, R.V., and Saunders, A.D., 2005. Volcanism, impact and mass extinctions: Incredible or credible coincidences? *Lithos*, **79**, 299–316.
- Wignall, P.B., 2001. Large igneous provinces and mass extinctions. *Earth Sci. Rev.*, **53**, 1–33.

Cross-references

Aerosol (Mineral)
 Atmospheric Evolution, Earth
 Carbon Isotopes, Stable
 Climate Forcing
 Cretaceous/Tertiary (K-T) Boundary Impact, Climate Effects
 Evolution and Climate Change
 Methane Hydrates, Carbon Cycling, and Environmental Change
 Volcanic Eruptions and Climate Change

FORAMINIFERA

Foraminifera are single-celled eukaryotic organisms that live in both the marine and fresh water environment. They range in size from 100 μm –15 cm in length. Foraminifera (often referred to as forams) are classified primarily by the composition and morphology of their tests (shells). Tests can be made of organic compounds, sand grains, and other particles cemented together (agglutinated), or secreted calcium carbonate (CaCO_3). Many groups are commonly made of a number of chambers, added during growth (Figure F2). The arrangement of these chambers and the position and shape of apertures are important for taxonomic classification.

Foraminifera exhibit both benthic (live on (*epifaunal*) or in (*infaunal*) the substrate) and planktonic (passive floating)

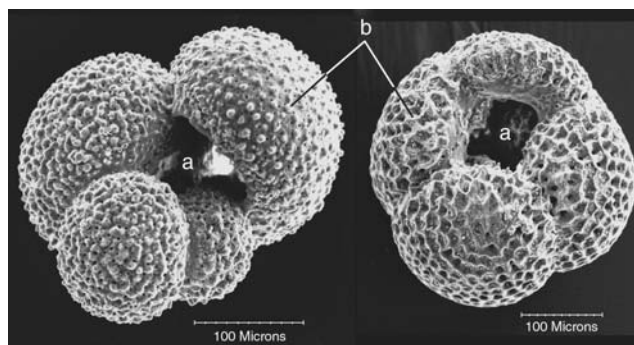


Figure F2 SEM image of the planktonic foraminifera *Globigerina bulloides* d'Orbigny (left) and *Dentoglobigerina altispira* Cushman and Jarvis (right) showing apertures (a) and chambers (b).

lifestyles. There are approximately 40 species of planktonic foraminifera in the ocean today. This comprises about 1% of the extant species of foraminifera. In the open marine environment, benthic foraminifera are usually much more diverse yet occur in lower abundances than planktonic foraminifera.

The geologic history of fossil foraminifera begins in the earliest Cambrian. Foraminifera probably existed as cells without fossilizable coverings long before that. In the Jurassic, foraminifera adapted to a planktonic mode of life.

Foraminifera were probably first recorded by the Greek historian Herodotus in the fifth century BC in his observations of large disc-shaped fossils (now known as the benthic foraminifer *Nummulites gizehensis*) found in the building stones of the Egyptian pyramids (Haynes, 1981). Prior to the advent of the microscope, seventeenth century naturalists observed foraminifera with hand lenses and often classified them as gastropods or cephalopods because many possess a coiled chamber arrangement. As microscopy advanced, more detail in the structure of foraminiferal tests was observed and they were recognized as single-celled organisms.

Foraminiferal studies advanced with the advent of the *Challenger* expedition of 1872–1876. Brady (1884) illustrated a number of foraminifera from this first oceanographic cruise and our understanding of foraminiferal biogeography began to take shape. During the early to mid twentieth century, the petroleum industry's need for age control and environmental interpretation led to great advances in micropaleontology, more in general, and much more data on foraminifera. The next major advance was the development of scanning electron microscopy, which enabled detailed analysis of test wall ultrastructure for the first time. The Deep Sea Drilling Project and its successor, the Ocean Drilling Program, have provided a wealth of quantitative data on both temporal and geographic distribution of benthic and planktonic foraminifera.

Applications in paleoclimatology

Foraminifera have been widely used in several areas of paleoclimatology. Calcium carbonate tests are thought to be secreted in equilibrium with sea water at the time of formation. For this reason, foraminifera have been the most widely used organisms for shell chemistry (Mg:Ca) and stable isotope geochemistry ($\delta^{18}\text{O}$, $\delta^{13}\text{C}$). Their small size, abundance, and distribution make them ideal environmental indicators. With the knowledge

that different species of planktonic foraminifers live at different depths and reach maximum abundance at different times of the year, geochemical analyses of foram tests can provide a wealth of information on the composition and structure of the water column. With benthic foraminifers providing information on bottom waters, elaborate paleoenvironmental and paleoclimatic information can be obtained from samples containing foraminifers.

Quantitative analysis of assemblages of planktonic foraminifers has been widely used to reconstruct past sea-surface temperatures using a transfer function or nearest analog approach. Transfer functions range from simple (Ericson and Wollin, 1956) to complex factor analytic approaches pioneered by Imbrie and Kipp (1971). This later technique formed the basis of the CLIMAP Last Glacial Maximum reconstruction (CLIMAP, 1981) and has been modified and used to reconstruct paleoclimate conditions during other time periods back to the mid-Pliocene warm period (Dowsett et al., 1999). With the recognition that planktonic foraminiferal distribution on the sea floor closely matches overlying oceanic conditions, total faunal analysis has become a mainstay of paleoenvironmental and paleoclimatic reconstruction.

The temporal framework upon which paleoclimate reconstructions are based is of fundamental importance. The same characteristics that make planktonic foraminifers so useful for geochemical analysis—high abundance, small size, facies independence, ease of identification and high preservation potential—make foraminifers ideal for biochronological (including biostratigraphy and correlation of marine sediments) analyses. For any pre-Pleistocene study, foraminiferal biochronology is usually still one of the leading tools in terms of accuracy and utility. Planktonic foraminifer zonations have been developed by a number of workers and individual biotic events (first and last appearances in a temporal sense) have been dated by calibration to magnetostratigraphy (Berggren et al., 1985, 1995; Dowsett, 1989).

In summary, foraminifers are the original multi-tool for paleoclimatology. The quantitative distribution of foraminifers in both temporal and spatial dimensions provides information on age of sample and any number of aspects of the paleoceanographic environment. When combined with geochemical and isotopic

analysis of foraminifer tests, no other fossil group has provided so much to the field of paleoclimatology.

Harry J. Dowsett

Bibliography

- Berggren, W.A., Kent, D.V., and Van Couvering, J.A., 1985. Neogene geochronology and chronostratigraphy. In Snelling, N.J. (ed.), *The Chronology of the Geological Record*. London: Geological Society of London, Memoir 10, pp.211–260.
- Berggren, W.A., Kent, D.V., Swisher, C.C., and Aubry, M.-P., 1995. A revised Cenozoic geochronology and chronostratigraphy. In Berggren, W.A., Kent, D.V., Aubry, M.-P., and Hardenbol, J. (eds.), *Geochronology, Time Scales and Global Stratigraphic Correlation*. Tulsa: Society for Sedimentary Geology, Special Publication 54, pp.129–212.
- Brady, H.B., 1884. Report on the foraminifera dredged by H.M.S. Challenger, during the years 1873–1876. *Report of the scientific results of the voyage of H.M.S. Challenger, 1873–1876, Zoology*, 9, 1–814.
- CLIMAP, 1981. Seasonal reconstruction of the Earth's surface at the last glacial maximum. *Geological Society of America Map and Chart Series MC-36*, 1–18.
- Dowsett, H.J., 1989. Application of the graphic correlation method to Pliocene marine sequences. *Mar. Micropaleontol.*, 35, 279–292.
- Dowsett, H.J., Barron, J.A., Poore, R.Z., Thompson, R.S., Cronin, T.M., Ishman, S.E., and Willard, D.A., 1999. Middle Pliocene paleoenvironmental reconstruction: PRISM2. *U.S. Geological Survey Open File Report 99–535*.
- Ericson, D.B., and Wollin, G., 1956. Correlation of six cores from the equatorial Atlantic and the Caribbean. *Deep Sea Res.*, 3, 104–125.
- Haynes, J.R. 1981. *Foraminifera*. New York: Wiley, 433pp.
- Imbrie, J., and Kipp, N.G., 1971. A new micropaleontological method for quantitative paleoclimatology: Applications to a late Pleistocene Caribbean core. In Turekian, K.K. (ed.), *The Late Cenozoic Glacial Ages*. New Haven: Yale Univ. Press, pp.71–181.

Cross-references

Carbon Isotopes, Stable
 CLIMAP
 Dating, Biostratigraphic Methods
 Dating, Magnetostratigraphy
 Deep Sea Drilling Project (DSDP)
 Ocean Drilling Program (ODP)
 Oxygen Isotopes
 Transfer Functions

G

GEOCHEMICAL PROXIES (NON-ISOTOPIC)

Introduction

The utility of geochemical proxies requires chemical analysis of geological samples. Since there is no means of directly measuring past climates and environments, proxy indicators are employed as indirect measures of the main processes. Information for environmental reconstruction comes from both organic and inorganic sources, even though organic matter (OM) typically constitutes a minor fraction of sediments. These proxies may reveal details about paleotemperature, phytoplankton community structure, vegetation history, dust provenance, nutrient cycles and availability, ocean circulation and paleoredox conditions (Figure G1).

Technical terms and concepts

Since sedimentary organic matter is the residue of past biota, its type and quantity reflects environmental conditions affecting past ecosystems. Analysis of organic matter involves identifying both its general source from bulk elemental compositions, stable isotopes and Rock-Eval pyrolysis data, and its detailed origins from analyses of biomarker molecular compositions (see below). Changes in organic *composition* can be interpreted as proxies for varying sea-level, ocean currents, temperature and continental climates, while changes in *abundance* may signify variable paleoproduction or preservation conditions.

Inorganic proxies are typically measured from constituents of the hard parts of previously living biota such as calcitic plankton and coral. The rate of incorporation of metal ions as compared with the principal component calcium varies according to environmental conditions. Therefore, proxies for past temperature and nutrients are derived from metal ratios such as Mg/Ca, Sr/Ca and Cd/Ca. Complementary information from multiple proxies can be obtained during a single suite of analyses for major and minor metal abundances.

The longevity of a particular record has a profound effect upon its constituent components. Geochemically, these components can be classified as either *labile* (readily undergoing

change or breakdown), or *refractory* (resistant to change, especially to heat). As a deposit ages, more refractory components become relatively enriched, while labile components are scarcely preserved. *Diagenesis* causes both the concentration and composition of sedimentary organic matter to diverge from the original biologically synthesized material. The lability of geochemical components renders them more susceptible to diagenesis. Ultimately, the geochemical composition of a paleoenvironmental record may look a lot different from the time of its creation or original deposition. Comparison of multiple geochemical proxies helps to compensate for the effects of diagenetic alteration and improves their interpretation for a more complete paleoenvironmental reconstruction.

Significance of geochemical proxies

The faithful reconstruction of paleoclimates and paleoenvironments requires the availability of reliable records. For placement in a temporal framework, the age of a particular record must be known, or assumptions regarding its continuity must be made. While “geochemical fossils” exist and are readily exploited for their paleoenvironmental data, fossil records are typically incomplete. Furthermore, the preservation of these records is rarely uniform. For this reason, continental (terrestrial) records of paleoenvironmental change (e.g., coal, evaporites, loess) have generally been regarded as discontinuous or a palimpsest, written and rewritten throughout the history of geologic time. Sedimentary records from lakes and other terrestrial depositional environments are typically Holocene (post-glacial) in age, although some low-latitude lakes (e.g., Lake Tanganyika) and cave deposits (e.g., speleothems) have yielded longer records. Conversely, vast sediment deposits underlying the world’s oceans may have been accumulating quasi-periodically for millions of years. For this reason, the majority of geochemical proxies are derived from aquatic-environment sediments, though many techniques may be universally applicable. Deep-sea sedimentation rates are typically a few centimeters per 1,000 years and with few exceptions reveal only decadal to millennial-scale changes in paleoclimate. Conversely, lacustrine records may offer short and regional records of paleoenvironmental change at a seasonal or annual scale.

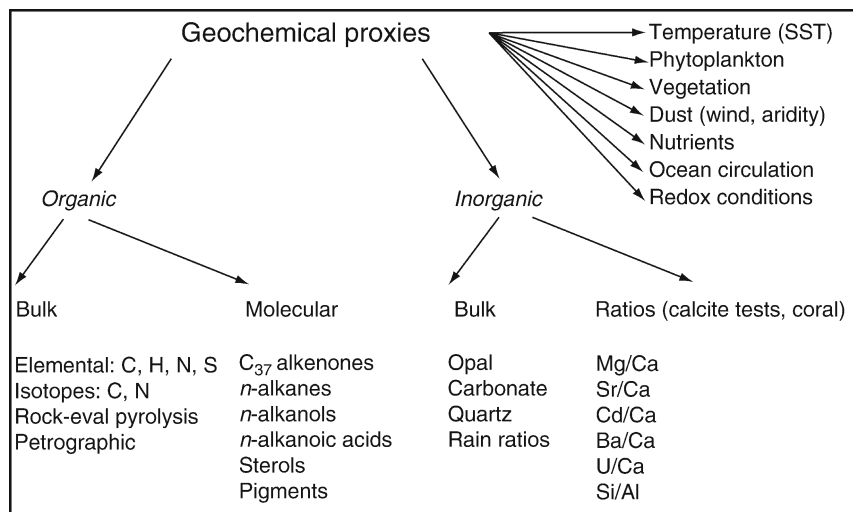


Figure G1 Summary of principal geochemical proxies and derived information used for environmental reconstruction.

Bulk organic geochemistry

Organic molecules are created in the biosphere by biological processes. The geosphere (lithosphere, hydrosphere and atmosphere) provides the substrate for these biological processes and is the ultimate sink for residual organic molecules. Organic geochemistry reveals the origin and fate of organic molecules and their utility as geochemical and paleoenvironmental proxies as they are preserved in the geosphere. Since both production and preservation of organic matter are affected by environmental change, bulk sedimentary organic matter and a large number of biomarker compounds, together with patterns of compound classes and their isotopic compositions, have enabled organic geochemists to deduce much about the environmental conditions that impacted ecosystems at different times and places in the geological past.

The primary source of organic matter in aquatic systems is planktonic photosynthetic production. Large variations in the rate of production are effected by nutrient availability in surface waters. Availability is controlled by nutrient (nitrate, phosphate) transport from land to lakes and oceans, and the efficiency of nutrient recycling within these systems. Animals and microbes may use such primary organic matter as a source of carbon and nutrients for significant secondary production of reworked, degraded organic matter with its own distinctive geochemical signature. Detritus from land plants and a small amount of organic matter from animals may make additional contributions to sedimentary organic content. Therefore, determinations of the relative importance of algal productivity, land-plant productivity and transport processes are a critical part of paleoenvironmental reconstruction.

The information obtained from organic geochemical proxies is diverse. Mass accumulation rates of organic carbon reveal the biological paleoproductivity and the environmental conditions that influenced the preservation of this organic matter. The composition of organic matter can be informative about aquatic and continental vegetation, which in turn depends on climatic factors such as temperature, moisture availability and wind strength. Quantities and isotopic contents of sedimentary organic matter (carbon, nitrogen) provide detailed histories of elemental cycling at both local and global scales. Environmental

(e.g., sea surface) temperatures can be deduced from the sedimentary molecular residues of organisms that lived at such times in the past. The typically small eolian (wind-derived) fraction of an organic mixture may contain distinctive components that record atmospheric transport processes. Comparison of multiple indicators (the “multi-proxy” approach) typically leads to better, more confident interpretations.

Preservation of the organic signal

Of the proxy indicators that depend on fluxes, bulk organic carbon accumulation measurements are perhaps the most widely used and common. Organic matter is intrinsically unstable in oxidizing environments and degrades in the photic zone, during particulate sinking and subsequent sediment bioturbation. Many attempts to relate total sedimentary organic input to surface net export have been made since the ground-breaking work of Suess (1980) and Berger et al. (1987). It has been shown that after remineralization, rarely more than a few percent remains to form the organic geochemical sedimentary record. The fraction of carbon buried is primarily a function of water depth, deep water oxygenation and linear sedimentation rate (Müller and Suess, 1979). Away from potential allochthonous (e.g., downslope) sources and under oxygenated states, environmental conditions cause the organic matter flux (amount per unit time) surviving degradation to decrease with increasing water column (depth) due to microbial oxidation (Figure G2). Degradation rates are greatest for fresh organic matter, but decline with depth as the residual detritus contains progressively more resistant organic matter. If a significant proportion of the accumulating sediment constitutes lithogenic particles, then this additional flux (ballast) may improve preservation of the organic flux to the seafloor. An important bias in the source of sedimentary carbon can affect the record of low (export) productivity zones, such as the inner ocean, where lateral advection from the continental shelf is often significant.

Former rates of primary production can be estimated from the organic carbon content of marine sediments according to the productivity-depth relationship and knowledge of the mass accumulation rate. For example, Stein (1986) proposed

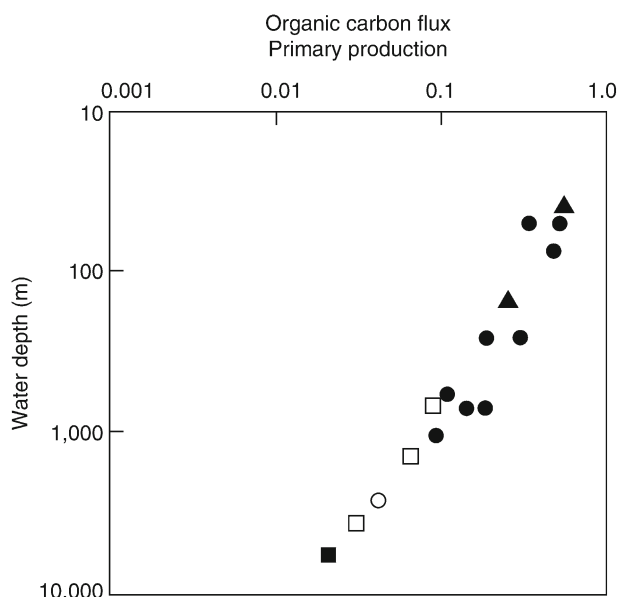


Figure G2 Concentrations of organic carbon on sinking particles collected by sediment traps at various depths in the ocean (figure compiled from Meyers, 1997; reprinted from *Organic Geochemistry*, 27, Meyers P.A., *Organic geochemical proxies of paleoceanographic, paleolimnologic, and paleoclimatic processes*, pp. 213–250, Copyright (1997), with permission from Elsevier).

Paleoproductivity, $\text{gC m}^{-2} \text{yr}^{-1}$

$$= 5.31 [C_{\text{org}}(\text{DBD})]^{0.71} \times \text{SR}^{0.07} \times \text{WD}^{0.45} \quad (1)$$

where C_{org} is weight percentage of marine organic carbon, DBD is dry bulk density in g cm^{-3} , SR is sedimentation rate in cm kyr^{-1} , and WD is water depth in meters at time of deposition.

The oxidation of organic matter and animal respiration removes dissolved oxygen in aquatic environments. Where this rate of removal exceeds the rate of replenishment (from the atmosphere), water column anoxia may develop. Under conditions of high primary production or strong water-column stratification, organic matter fluxes do not appear to decrease with depth (Karl and Knauer, 1991) and sedimentary preservation may be improved (Figure G3).

The rate of delivery of organic matter to the surface layer of sediments effectively determines the amount of benthic alteration in the bioturbated layer. Benthic oxidation will initially utilize interstitial oxygen, but as conditions become progressively more anoxic, nitrate, oxides of manganese, iron and eventually sulfate reduction will occur. These reduced species may be later interpreted as geochemical proxies of anoxia.

Physical sorting during transport and sinking of organic matter can create compositional artifacts since different components are commonly associated with different particle sizes. This complicates the interpretation of co-occurring sedimentary proxies, which may not share the same temporal or spatial origins. For example, C/N ratios of OM can be affected by hydrodynamic sorting: they are generally lower in fine-grained than in coarse-grained sediments, which typically contain more intact land-plant debris. Fine sediments may contain more clay with greater potential for ammonium adsorption. This highlights the problems

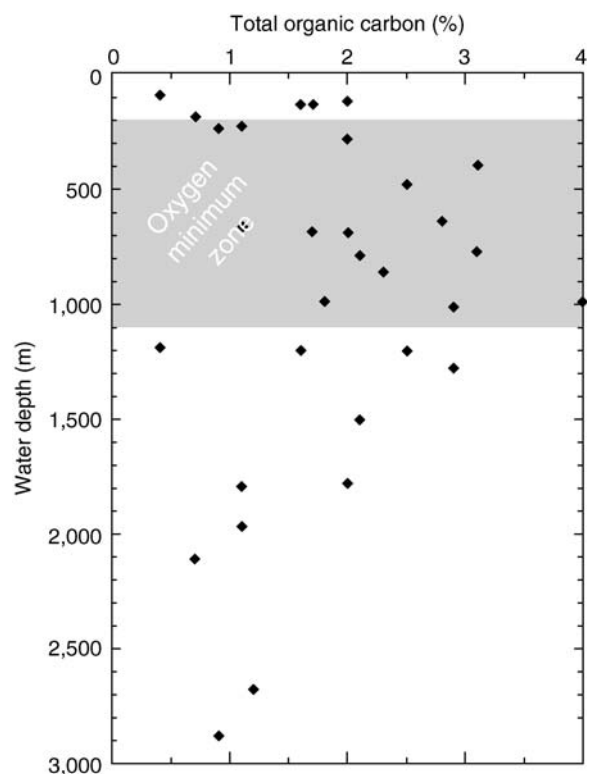


Figure G3 Distribution of total organic carbon in surface sediments of the Arabian Sea as a function of water depth. The shaded area denotes the approximate depth range of the present oxygen minimum zone (OMZ) (reprinted from *Organic Geochemistry*, 31, Schulte S., Mangelsdorf K., and J. Rullkötter, *Organic matter preservation on the Pakistan continental margin as revealed by biomarker geochemistry*, pp. 1005–1022, Copyright (2000), with permission from Elsevier).

of bulk analysis, especially where low organic content results in samples with a significant inorganic nitrogen fraction. Molecular-level analyses are not immune to such biasing of the source information they yield; organic molecules with radiocarbon ages several thousand years older than co-occurring calcitic plankton remains have been found in drift-deposit sediments from the Bermuda Rise (Ohkouchi et al., 2002). Furthermore, geo-lipids typically constitute a small fraction of the residual (sedimentary) organic matter, making insidious abundance variations more common. Although *biomarkers* are relatively resistant to microbial degradation, they may still be subject to diagenetic overprinting.

Analysis of bulk organic matter

Petrographic analysis of sedimentary records can reveal the origin of organic matter, its mode of transport and degree of degradation through microscopic study. Unstructured, amorphous organic flakes and intact debris of algae such as cell walls constitute *autochthonous* organic matter. *Allochthonous* material includes variably-preserved lignin and cellulose debris and soil-derived organic material. Spores, pollen and the residue of forest fires transported by wind form the *eolian* organic fraction. By determining the petrographic composition of sedimentary organic matter, it is possible to supplement information provided by other techniques concerning changes in origins of organic matter over time and sedimentary intervals where diagenesis may have altered or biased the bulk geochemical indicators.

Algal and terrestrial plant origins of sedimentary organic matter can be distinguished on the basis of its elemental C/N ratio. Reliable source information can be derived in moderately preserved organic matter since algae typically have atomic C/N ratios of 4–10, while vascular plants (that is, those composed in part of vascular tissue, including all flowering plants and the higher cryptogamous plants) have C/N ratios of ≥ 20 (Meyers, 1994). This difference relates to the proteinaceous nature of algal matter compared with the abundance of cellulose in (vascular) plants. Diagenesis has the potential to alter the C/N ratio, causing it to increase during preferential degradation of proteinaceous components of algal OM, but decrease during carbon remineralization due to preferential absorption of ammonium(-nitrogen) by clay minerals (Müller, 1977).

Rock-Eval pyrolysis

Quantification of hydrocarbons generated by progressive heating of sediment samples from 200 °C to 600 °C, related to the origin of OM, generates three distinct signals related to the quantity of hydrocarbons, which are gaseous (S_0), volatile (S_1) and released by thermal cracking of kerogen (S_2). Total organic carbon is the sum of the residual and pyrolyzed organic carbon (S_3) content. From these results are derived: (a) the Hydrogen Index (HI), the hydrocarbon potential of the total OM (mg HC/g C_{org}), a proxy for the H/C of OM; and (b) the Oxygen Index (OI), the amount of oxygen (mg CO_2 /g C_{org}), a proxy for the O/C ratio (Espitalié et al., 1977). Values are typically plotted against each other on a van Krevelen plot and grouped according to three main types of organic matter: (a) rich in HC content, derived from microbial biomass or waxy coatings of plants; (b) moderately rich in HC, originating from algae; (c) poor in hydrocarbons, rich in carbohydrates, typical of woody plant material (Figure G4). Values may be affected by organic matter oxidation, particularly after deposition. Oxidation causes a reduction in total organic carbon (TOC)

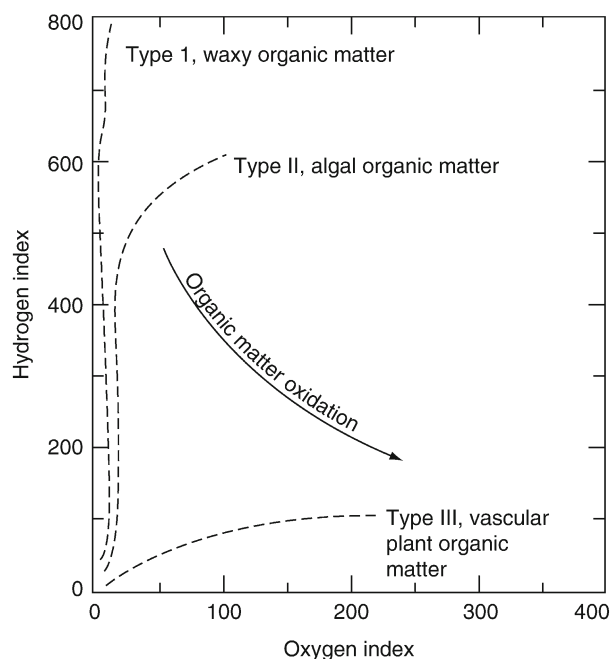


Figure G4 Rock-Eval van Krevelen plot for differentiating sources of sedimentary organic matter.

concentration, C/N ratio and HI values while oxygen content increases, thereby reducing HI/OI and causing Type I or II organic matter to resemble Type III.

Bulk inorganic geochemistry

Bulk geochemical proxies such as opal, carbonate and quartz dust have been traditionally employed to attempt to reconstruct paleoclimate. However, more recent advances in understanding the constraints on delivery and preservation of these sedimentary components limit the usefulness of the data obtained. An alternative technique that overcomes many of the problems of bulk organic matter analysis involves the application of rain ratios between the organic and inorganic components of the sediment record. Berger and Keir (1984) proposed that ratios of organic carbon:carbonate and organic carbon:opal may increase with export production. The ratio of detrital to biogenic content may also be employed to estimate paleoproductivity. The concentrations of certain inorganic proxies, such as aluminum and potassium, have been measured to represent the major part of the detrital sediment content. Found mostly in clays, their sediment depth profile is considered typical for the bulk detrital elements. Thus, the content of elements sensitive to productivity changes or inherently involved in biological and authigenic processes, such as cadmium, barium and silicon, can be successfully normalized with respect to the detrital signal. One limitation of this technique is that it is restricted to areas of predominantly clay deposition, and cannot thus be applied on the continental margins where silt is commonly the dominant matrix size fraction. Nevertheless, several such rain ratios are commonly used. For example, cadmium has been found to be depleted in the surface ocean relative to deeper waters (Boyle et al., 1976), indicating uptake by organisms at the surface and regeneration from deeper sinking biomass. Profiles of cadmium generally resemble those of phosphate (especially enriched in upwelling regions), rather than silicate, confirming shallow cycling in association with labile nutrients.

Inorganic nutrient indicators

More detailed information for the reconstruction of upper ocean nutrient concentrations and water mass formation and circulation has been retrieved from trace metal/calcium ratios in the calcitic tests of planktonic organisms such as foraminifera and coccolithophorids. The ratio of Cd:Ca in carbonate plankton tests has been used to reconstruct the cadmium content of the water in which the organisms grew and to detect changes in the position of the nutricline relative to the thermocline and water column stratification. The ratio of Si:Al content of biogenic opal has been similarly used (Martinez et al., 1996). Cd resembles phosphate in terms of its behavior in seawater (Figure G5). Therefore, measurement of Cd/Ca ratios in the tests of shallow water column foraminiferal species has been employed as a paleonutrient (PO_4^{3-}) proxy in thermocline waters (Boyle, 1988).

The response of benthic foraminiferal cadmium to deep-water Cd concentrations has also been established (Boyle, 1992). Benthic shell Cd/Ca and Ba/Ca have been used to interpret changes in deep-water circulation since the long residence time of Cd limits the impact of changes in mean ocean Cd on glacial/inter-glacial timescales (<5%, Rosenthal et al., 1995), relative to the short residence time of Ba (~10 kyr). Coupled Cd/Ca and Ba/Ca records have proven useful because Cd/Ca is a labile nutrient tracer and Ba/Ca is a refractory nutrient tracer,

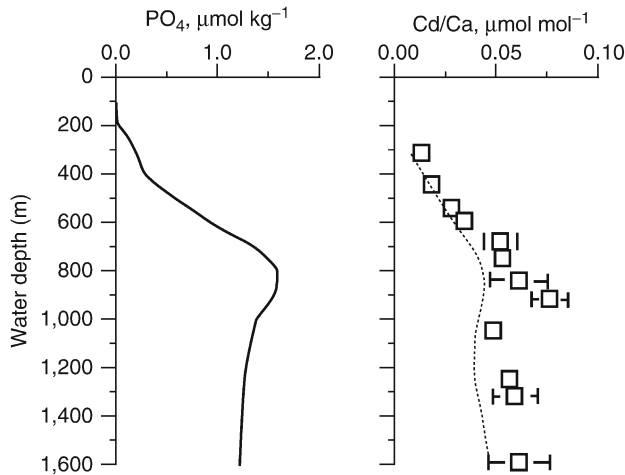


Figure G5 Dissolved PO_4^{3-} water-column profile from the sub-tropical western North Atlantic compared with Cd/Ca concentrations in calcitic foraminifera at similar depths (reprinted from *Geochimica et Cosmochimica Acta*, 61, Rosenthal Y., Boyle E.A., and N. Slowey, Temperature control on the incorporation of magnesium, strontium, fluorine, and cadmium into benthic foraminiferal shells from Little Bahama Bank: Prospects for thermocline paleoceanography, pp. 3633–3643, Copyright (1997), with permission from Elsevier).

each involved differently in biogeochemical cycling. However, there is an apparent depth-related change in the partition coefficient of Cd in calcitic foraminifera. The effects of algal symbionts (Mashiotta et al., 1997) and temperature (Rickaby and Elderfield, 1999) may also influence such estimates.

Trace metal ratios in foraminifera are subject to elevation in instances of (sedimentary) secondary overgrowth or carbonate precipitation on shell surfaces, which can trap contaminants between the shell and the overgrowth layer. Such overgrowths form where Mn^{2+} is mobilized (under oxic conditions), and can therefore be detected in shells with relatively elevated Mn/Ca values (Boyle et al., 1995).

Inorganic temperature indicators

Strontium and magnesium occur in seawater in approximately constant proportions to calcium, and all three elements have long oceanic residence times. Based on this constant source ratio, variations in Sr/Ca and Mg/Ca in foraminifera shells are due to the influence of environmental conditions that control their incorporation or preservation during the process of calcification. Experimental evidence indicates that temperature exerts the dominant control on shell Mg/Ca. Cultured planktonic foraminifera *Globigerina bulloides* and *Orbulina universa* exhibit an increase in shell Mg/Ca of 8–10‰/°C (Nürnberg et al., 1996; Lea et al., 1999). This temperature regulation of co-precipitation of shell Mg probably involves both a thermodynamic response of the inorganic distribution coefficient, and a temperature effect on physiological processes regulating cellular Mg uptake. Secondary influences are attributable to seawater pH and salinity. A smaller but similar kinetic influence of calcification has been recorded in Sr/Ca of coccoliths. However, global foraminiferal Sr/Ca data exhibit a linear decrease with increasing water depth, suggesting that the Sr partition coefficient is most likely a pressure related phenomenon (Rosenthal et al., 1997). Interpretations based on Sr/Ca are also complicated by the much

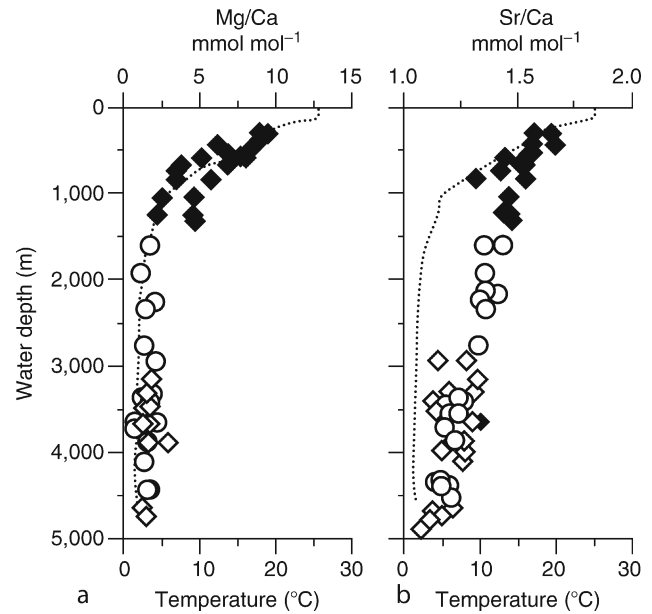


Figure G6 Ocean-wide *Cibicidoides* (a) Mg/Ca, and (b) Sr/Ca data from Little Bahama Bank (\square), Sierra Leone Rise and Ceara Rise (\square), and Ontong Java Plateau (\circ) (reprinted from *Geochimica et Cosmochimica Acta*, 61, Rosenthal Y., Boyle E.A., and N. Slowey, Temperature control on the incorporation of magnesium, strontium, fluorine, and cadmium into benthic foraminiferal shells from Little Bahama Bank: Prospects for thermocline paleoceanography, pp. 3633–3643, Copyright (1997), with permission from Elsevier).

smaller range of Sr/Ca values than Mg values in shells (Figure G6).

Records of Mg/Ca ratios in benthic foraminifera also have been interpreted as an independent proxy for reconstructing the history of Quaternary bottom water temperatures (e.g., Martin et al., 2002). Mg-paleothermometry offers an advantage over other proxies of sea-surface temperatures (SST) because Mg/Ca is measured on the same phase as $\delta^{18}\text{O}$ (a function of both the oxygen isotopic composition of sea water and temperature of calcification) and therefore should record the same calcification temperature. Consequently, paired measurements of $^{18}\text{O}/^{16}\text{O}$ and Mg/Ca can permit an accurate reconstruction of $\delta^{18}\text{O}_{\text{water}}$ and, by inference, paleosalinity. Paired measurements on the same sample may also resolve leads and lags between changes in SST and sea level (Lea et al., 2000, 2002; Figure G7). Unfortunately, there remain some uncertainties about Mg enrichment in species that have undergone gametogenesis, suggesting a significant alteration of Mg/Ca during gametogenic calcite precipitation. This effect has the potential to confound Mg paleothermometry in sedimentary shells containing a varying mixture of gametogenic and ontogenetic calcite. However, recent studies indicate a strong covariance between shell Mg/Ca and ambient temperatures and suggest that, with careful calibration (of single species), it may be a reliable proxy for seawater paleotemperature reconstruction.

Element/Ca ratio analyses of coral skeletal material have also been used to reconstruct SSTs of the tropical oceans. Scleractinian corals secrete skeletons composed of aragonite (CaCO_3), which incorporates both Sr and Ca into its structure. Similar to foraminifera, the incorporation ratio of Sr/Ca is determined by both the Sr/Ca of ocean water and the Sr/Ca distribution coefficient between aragonite and seawater. The former has remained

essentially constant over 10^5 yr timescales because of its long elemental residence times, while the latter is determined principally by the temperature of seawater in which the coral grew (Beck et al., 1992). Not surprisingly, measurements of skeletal Sr/Ca on samples of coral typically show a very strong coherence with SST over seasonal and interannual timescales (e.g., Linsley et al.,

2000; Figure G8). Such SST proxy variations have also been used to reconstruct El Niño Southern Oscillation (ENSO) changes (e.g., Tudhope et al., 2001). By making paired measurements of $\delta^{18}\text{O}$, derived tropical sea-surface salinity (SSS) reconstructions agree with SSS observations at the interannual timescale (Quinn and Sampson, 2002). There also appears to be a relationship between

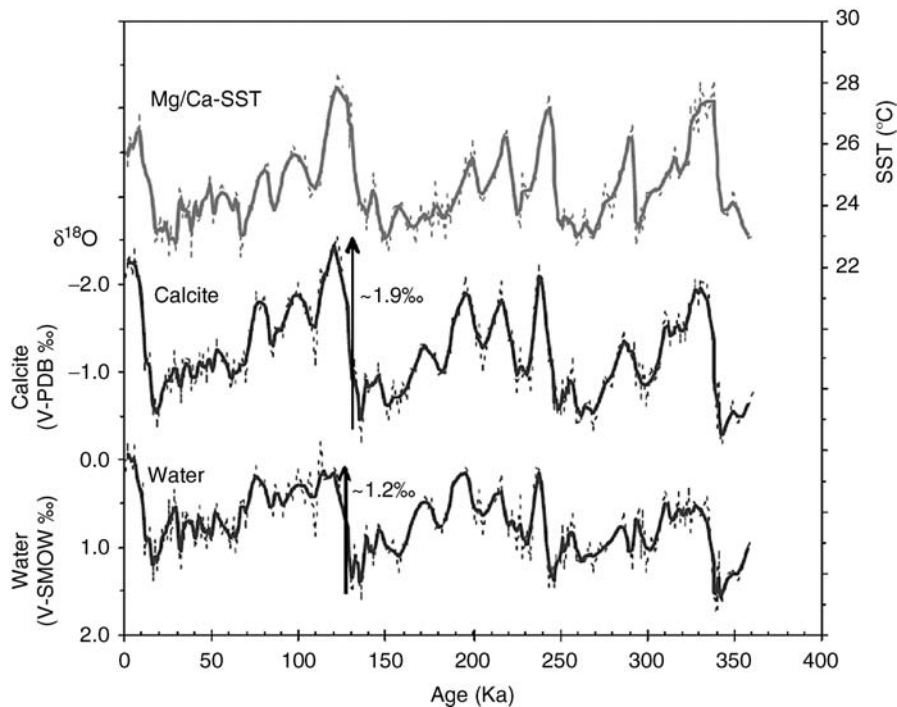


Figure G7 Sea surface temperature (SST) (based on Mg/Ca), $\delta^{18}\text{O}_{\text{calcite}}$ (V-PDB scale), and $\delta^{18}\text{O}_{\text{water}}$ (V-SMOW scale) records from Cocos Ridge core TR163-19, using *G. ruber*-white variety (Lea et al., 2000). The $\delta^{18}\text{O}_{\text{water}}$ record is calculated from the SST and $\delta^{18}\text{O}_{\text{calcite}}$ values. Dashed lines are the measured and calculated data. Heavy lines indicate filtered data (reprinted from Quaternary Science Reviews, 21, Lea D.W., Martin P.A., Pak D.K., and H.J. Spero, Reconstructing a 350 ky history of sea level using planktonic Mg/Ca and oxygen isotope records from a Cocos Ridge core, pp. 283–293, Copyright (2002), with permission from Elsevier).

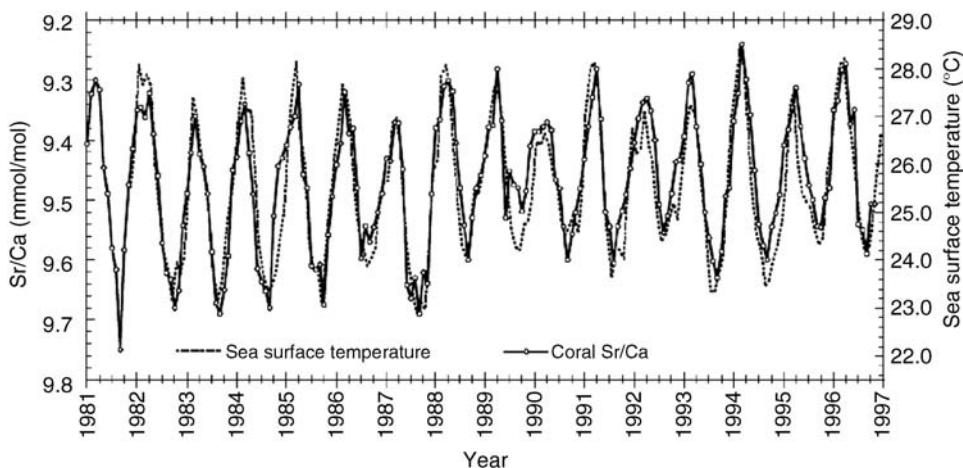


Figure G8 Comparison of instrumental monthly SST for Rarotonga and near-monthly Rarotonga coral Sr/Ca, spanning the interval from 1981 to 1997 (reprinted with permissions from Linsley B.K., G.M. Wellington, and D.P. Schrag, 2000, Decadal sea surface temperature variability in the sub-tropical South Pacific from 1726 to 1997 A.D., Science, 290, pp. 1145–1148, Copyright (2000) AAAS. Permission from AAAS is required for all other uses).

SST and Mg/Ca (Mitsuguchi et al., 1996), and also SST and U/Ca (Min et al., 1995), although such correlations are rarely constant within an individual coral or different corals from the same location and have not received widespread utility in paleoenvironmental reconstruction. Similar measurements have also been made on bivalve shells and fish otoliths. All may be subject to *vital effects* (less predictable physiological variations associated with the life cycle of an organism) and micro-environmental (habitat) variations.

Measurement techniques

While early work on temperature reconstruction from scleractinian coral Sr/Ca ratios had a precision of just $\pm 3^\circ\text{C}$, close to the seasonal SST range of their tropical habitat, the use of thermal ionization mass spectrometry (TIMS) and subsequently (sector field) inductively coupled plasma atomic emission spectrophotometry (ICP-ES) has led to an order of magnitude improvement in precision. Similarly, advances in combining laser ablation technology with inductively coupled plasma-mass spectrometry (ICP-MS) offer the opportunity to measure multiple elemental ratios simultaneously and rapidly on individual foraminifera or calcitic coccolith platelets.

Molecular source indicators

Organisms can regulate the production of constituent lipids, dependent on variable prevailing environmental conditions such as temperature, light, salinity and nutrient availability. The preservation of such compounds in the molecular sedimentary record provides a sink for potentially reconstructing environmental and climatic variations. Therefore, the molecular composition of sedimentary organic matter can reveal detailed information about its production, transport and preservation. Research since the 1970s has sought to identify and characterize a complex suite of sedimentary organic compounds diagnostic of their biological origins, and to relate these compounds to likely sources of OM (e.g., Brassell et al., 1986; Repeta et al., 1992). *Biological marker compounds*, or simply *biomarkers*, are extractable sedimentary lipids with relatively specific biological origins that can provide equally specific organic matter source information (Eglinton and Calvin, 1967). They are typically less sensitive to degradation than the average for bulk organic matter, and may follow an established pattern of alteration during diagenesis, resulting in predictable lipid end-products (“geolipids”). Several hundred biomarkers have been identified in marine sediments, of which only those most commonly investigated in sedimentary records with potential to reconstruct paleoclimate are discussed here; the long-chain C_{37} alkenones, *n*-alkanes, *n*-alkanols, *n*-alkanoic acids, sterols and pigments.

Several factors are prerequisites for the utility of any specific biomarker. The survival of the biomarker signal during sedimentation is crucial to its use. Unfortunately, some of the most diagnostic biomarkers, such as carotenoids, are frequently the most labile. Alternatively, a biomarker may be ubiquitous or too widespread in the sedimentary record, such as long chain *n*-alkanes, to provide detailed diagnostic information about a specific organism, but may still be informative about a particular environment. Thus, it is important for the utility of a biomarker that it should originate from a specific organism or type of organism, from a restricted environment, with modern analogous organisms. It is preferable that a biomarker occurs widely, thus providing information about a variety of sedimentary regimes, and over an extended period of geological time. Finally, it is also

preferable that the biomarker be generated and buried during a short time period, preserving a time-dependent signal useful in high-resolution environmental reconstructions.

Variable lipid contributions from vascular land plants or algae can be distinguished according to consistent differences in molecular chain-length. For example, there is significant variation in the distribution of *n*-alkanes between organisms: aquatic algae are dominated by the presence of lower (shorter chain) *n*-alkanes, such as C_{15} and C_{17} (e.g., Blumer et al., 1971; Simoneit, 1977; Cranwell et al., 1987), whereas the leaf waxes of higher plants are typically dominated by longer chain C_{27} , C_{29} and C_{31} *n*-alkanes in the sedimentary record (e.g., Eglinton and Hamilton, 1967; Rieley et al., 1991). The distributions of long-chain *n*-alkanols and *n*-alkanoic acids can be similarly related to long-term variations in organic matter supply. The waxy coatings of land-plant leaves, flowers and pollen contain C_{24} , C_{26} and C_{28} long-chain *n*-alkanoic acids, whereas C_{12} , C_{14} and C_{16} *n*-acids are dominant in algae. A ratio of these source indicators has been used to identify changes in the terrigenous versus aquatic organic matter contribution (e.g., Bourbonniere and Meyers, 1996). Those properties of vascular plants that protect them against environmental change, such as desiccation, similarly favor the survival of longer chain *n*-alkanes during microbial degradation, eolian transportation over long distances (e.g., Gagosian and Peltzer, 1986) and sinking in aquatic environments. Conversely, lake and marine sediment trap studies of settling particles indicate that the contribution of short-chain biomarkers from algal material is selectively depleted during sinking, presumably because such material is fresher and more labile (Meyers and Eadie, 1993). Combined with palynological information, the lipid data can provide important paleoclimatic evidence regarding wind strength and direction and changing environmental conditions in source areas such as the Chinese Loess Plateau or Sahara. Studies have shown a correspondence between the flux of higher plant *n*-alkanes and *n*-alkanols in sediments and climatic severity, especially during cold glacial intervals (e.g., Poynter et al., 1989; Pelejero et al., 1999; Figure G9).

Sterol biomarkers

A number of sterols (tetracyclic alcohols) have been exploited as paleoenvironmental proxies, differentiated by the presence/absence of double bonds, positions of methyl groups and length of the C_{17} branched sidechain (Volkman, 1986; de Leeuw and Baas, 1986). Individual sterols have been assigned specific organisms of origin, such as dinosterol (dinoflagellates), brassicasterol (diatoms) and cholesterol (Figure G10a). In addition, algal and vascular plant contributions have been differentiated by the presence or absence of particular sterols, for example on the basis that leaf waxes contain C_{28} and C_{29} , but not C_{27} sterols (Rieley et al., 1991; Figure G10b). However, sedimentary sterols are practically ubiquitous, and many sources in marine and terrestrial environments remain uncharacterized (Volkman, 1986). The distribution of sterol biomarkers appears most informative when there are successive variations in abundance and precursor/product relationship within a single sedimentary sequence (e.g., Higginson and Altabet, 2004).

Alkenones

The most widely applied biomarkers for paleoceanographic reconstruction are temperature-sensitive lipids comprising the series of C_{37} – C_{39} di-, tri- and tetra-unsaturated methyl and

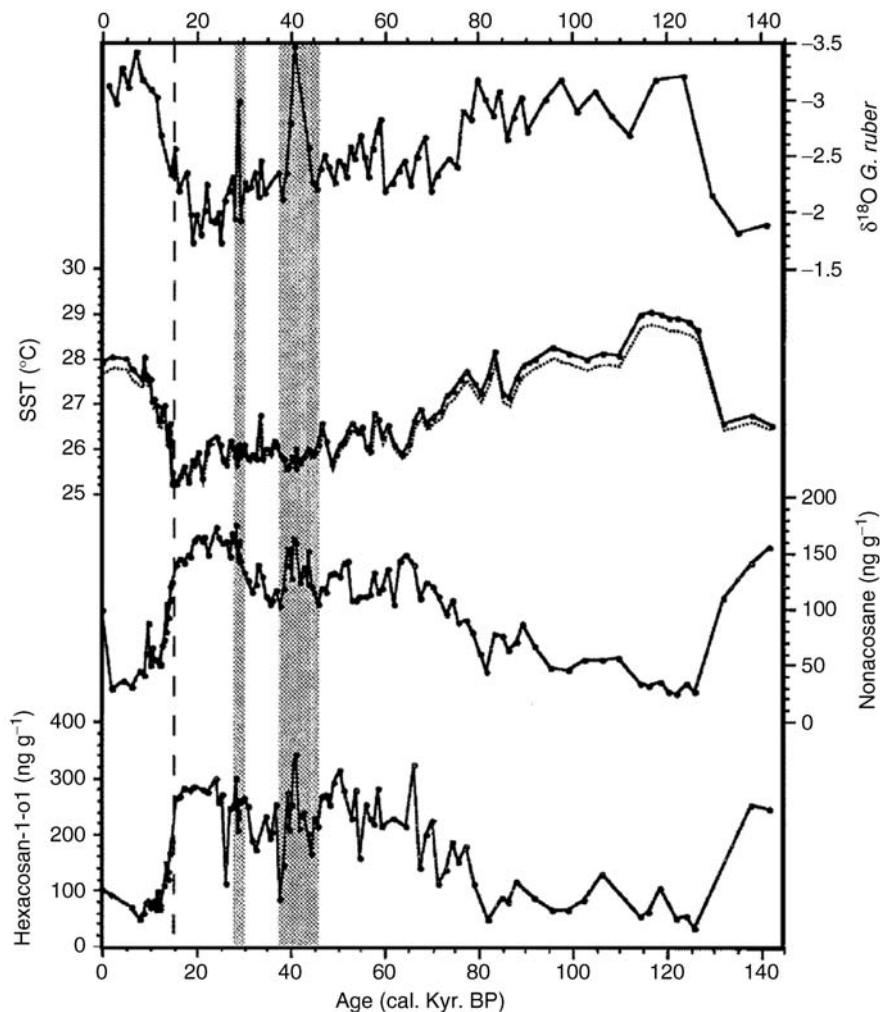


Figure G9 $\delta^{18}\text{O}$ isotopic composition of *G. ruber*, U_{37}^K , sea surface temperature (SST), *n*-nonacosane, and *n*-hexacosan-1-ol abundances in a core from the South China Sea covering the last 140 kyr (after Pelejero et al., 1999; reprinted from Marine Geology, 156, Pelejero C., Grimalt J.O., Sarnthein M., Wang L., and J.-A. Flores, Molecular biomarker record of sea surface temperature and climatic change in the South China Sea during the last 140,000 years, pp. 109–121, Copyright (1999), with permission from Elsevier).

ethyl ketones (“alkenones”; Figure G11a,b). First identified in sediments from Walvis Ridge off southwest Africa during DSDP Leg 40 (Boon et al., 1978), they are now known to occur in marine sediments from all oceans (e.g., Brassell, 1980; Marlowe et al., 1984). Their detection in sediments of Cretaceous age confirmed their production over an extended period of geological time (Farrimond et al., 1986). The compounds were initially traced to the abundant marine unicellular coccolithophorid, *Emiliania huxleyi* (Volkman et al., 1980). However, they have subsequently been identified in other members of the Gephyrocapsaceae algal family (e.g., *Gephyrocapsa oceanica*; Marlowe et al., 1984; Conte et al., 1998). Because alkenones are specific biomarkers of coccolithophorids, quantification of the abundance of the long-chain alkenones in deep-sea sediments is used as a proxy for changing paleoproductivity (e.g., Prahl et al., 1988; Madureira et al., 1997). More significantly, the distribution of marine sedimentary alkenones appears to be related to growth temperature of their source algae, and thus climate (Brassell and Eglinton, 1984). Subsequent

testing of this hypothesis in laboratory cultures grown at different temperatures (e.g., Brassell et al., 1986 and references therein; Conte et al., 1998) has verified the temperature dependence in the biosynthetic production of alkenone unsaturation. This may be related to the ability of such aquatic organisms to change the molecular composition of their lipid bilayer to maintain a constant cell membrane fluidity under a range of thermal conditions, although this remains to be proven.

Values of U_{37}^K , defined as the alkenone unsaturation index, are calculated from the relative concentrations of the $C_{37:2}$, $C_{37:3}$ and $C_{37:4}$ alkenones according to the formula (Brassell et al., 1986; Prahl and Wakeham, 1987):

$$U_{37}^K = [C_{37:2}] - [C_{37:4}] / ([C_{37:2}] + [C_{37:3}] + [C_{37:4}]) \quad (2)$$

These values appear to increase linearly with growth temperature, and may be converted to ambient water temperatures through a calibration equation according to the prevailing oceanic setting (e.g., Prahl and Wakeham, 1987; Prahl et al.,

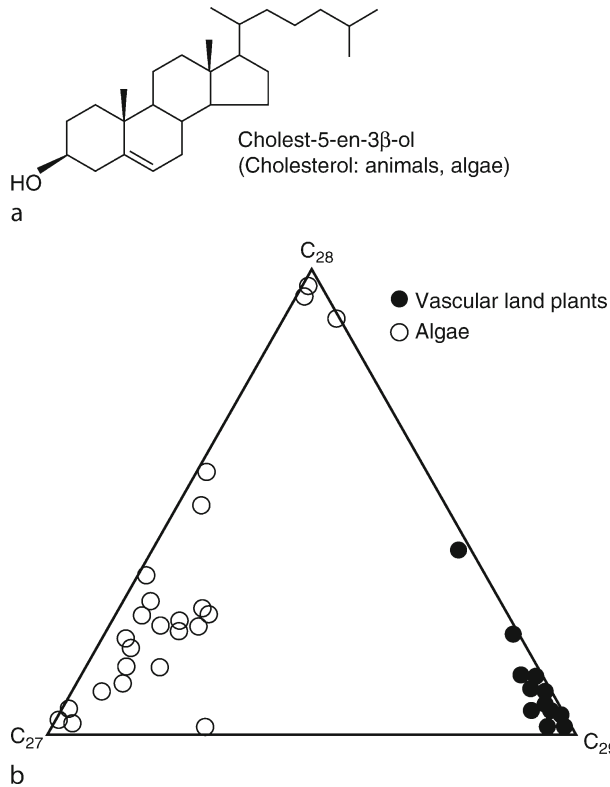


Figure G10 (a) Chemical structure of cholesterol. (b) C₂₇, C₂₈, and C₂₉ sterol source characteristics (compiled from Meyers, 1997; reprinted from *Organic Geochemistry*, 27, Meyers P.A., *Organic geochemical proxies of paleoceanographic, paleolimnologic, and paleoclimatic processes*, pp. 213–250, Copyright (1997), with permission from Elsevier).

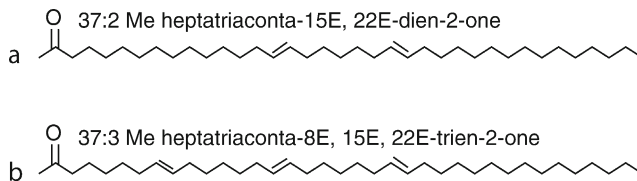


Figure G11 Molecular structures of (a) C_{37:2} alkenone; (b) C_{37:3} alkenone.

1988; Figure G12). Where the C_{37:4} alkenone is absent, such as in warm tropical waters, the U₃₇^{K'} index, which excludes this component, is more commonly used (Müller et al., 1998; cf. Figure G13a–c). The index relates to the general chemical property that the number of carbon-carbon double bonds in related organic molecules varies inversely with their melting points. As a consequence, values of relative abundance of the di- and tri-unsaturated alkenones for bottom sediments in equatorial regions are close to unity. Conversely, the C_{37:3} alkenone dominates in sediments from beneath the much cooler Southern Ocean (Sikes and Volkman, 1993). Since the algae generating the alkenones synthesize their lipid constituents within the photic zone, their rapid response to changes in water temperatures produces relative abundances in bottom sediments that

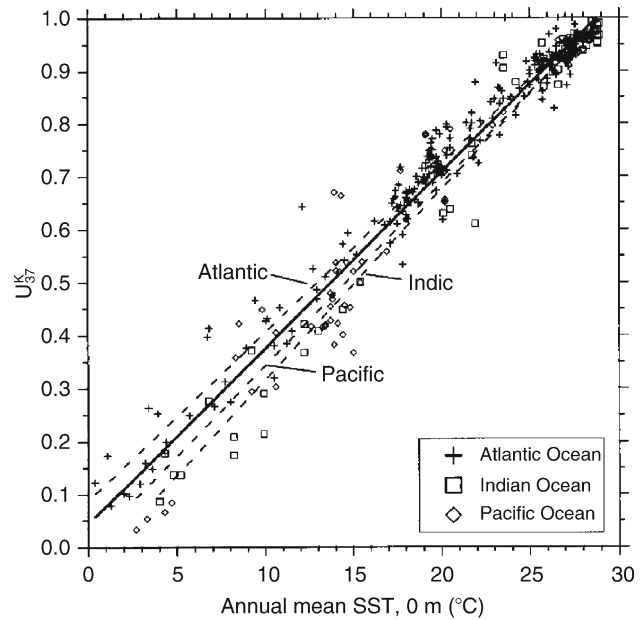


Figure G12 Relationships between U₃₇^{K'} index and annual mean SST (0 m) for surface sediments from the global ocean, 60° S–60° N. The global core-top calibration (U₃₇^{K'} = 0.033SST + 0.044) is equivalent to that obtained from cultures of *E. huxleyi* by Prah and Wakeham (1987) (reprinted from *Geochimica et Cosmochimica Acta*, 62, Müller P.J., Kirst G., Ruhland G., Von Storch I., and A. Rosell-Melé, Calibration of the alkenone paleotemperature index U₃₇^{K'} based on core-tops from the eastern South Atlantic and the global ocean (60° N–60° S), pp. 1757–1772, Copyright (1998) with permission from Elsevier).

approximate near-surface temperatures at the time of maximum biosynthesis during spring blooming (e.g., Herbert et al., 1998). The algal source of alkenones discovered in lacustrine sediments has not been similarly resolved, thereby precluding any specific paleoenvironmental reconstruction from such records.

Reconstruction of sea surface temperature is informative about changing ocean circulation, upwelling intensity (wind strength) and near-surface stratification. The alkenone method conveniently avoids biases inherent to temperature calibrations based upon variable biological groups since production has been shown to be specific to haptophytes (Marlowe et al., 1984), and the production ratio/temperature relationships of the two most common individuals (*Emiliania huxleyi* and *Gephyrocapsa oceanica*) are statistically inseparable (Conte et al., 1998). Although alkenones experience degradation, especially under oxic conditions (Prah et al., 1989), this seems to affect all alkenones roughly comparably, and has little significant effect on U₃₇^{K'} values (Marlowe et al., 1984; Rontani et al., 1997; Hoefs et al., 1998). Site-specific biases in temperature reconstruction have been associated with alkenone incorporation, differential preservation of the chemical species, and region-specific inconsistencies of growth seasonality. Furthermore, alkenones can be produced at various depths (and temperatures) by populations of a single species (Conte et al., 1998) and there may be temperature-independent differences in alkenone unsaturation rates due to regional nutrient variations affecting coccolithophorid growth depth. Nevertheless, in areas and times in which *E. huxleyi* has been dominant (since first occurrence at 268 ka), such as in the North Atlantic, paleotemperature and paleoclimatic reconstructions have

proven valuable (e.g., Weaver et al., 1999) since they are otherwise independent of past changes in sea water salinity and ice volume.

Pigments

Changes in past higher plant and algal populations can be recorded in pigment compositions preserved in sediments since such molecules are essential for photosynthesis. Some organic compounds exhibit specificity to certain types of plants and

have therefore been used as paleoenvironmental biomarkers. The role of pigments is to absorb (light) energy at certain wavelengths, converting it into chemical energy. They are found on the chloroplast membranes and are physically arranged to maximize light absorption. Since each pigment may only be active within a narrow wavelength range, several kinds of pigments are often found together. Photosynthetic pigments can be grouped into three classes: chlorophyll, carotenoid and xanthophyll. Each contains a chemical group capable of selective light absorption (resulting in characteristic coloration) known as a chromophore, which typically involves conjugated C=C double bonds (each separated from the other by a single bond). Combined with oxygen-containing functional groups that are common to many, these sites render pigments susceptible to diagenetic alteration to more stable sedimentary end-products.

Chlorophylls are the principal photosynthetic pigments common to all plants. They contain a central tetrapyrrole ring, and differ according to the nature of the attached alkyl sidechain. The most common, chlorophyll *a*, has an ester-linked diterpenoid alcohol sidechain, phytol. Diagenesis affects the amount and types of pigments preserved in sediments. Specifically, chlorophyll is rare in marine sediments, especially where there is a deep water column and similar pigments are degraded if they are not rapidly incorporated into sediments. Even after incorporation, pigments continue to undergo diagenesis. Sedimentary studies have led to the establishment of predictable conversion routes for chlorophyll pigments, including de-metallization to form pheophytins, ester hydrolysis to form pheophorbides and transesterification to form the more resistant steryl chlorin esters (Keely and Brereton, 1986). These products have been given the collective name "chlorins" (Higginson, 2000).

Chlorophylls absorb solar energy most efficiently at longer wavelengths of the visible spectrum, wavelengths that are also readily absorbed by water. Therefore, aquatic plants have evolved *carotenoid* accessory pigments to expand energy capture to a wider range of wavelengths useful for photosynthesis. Carotenoid pigments such as β -carotene (Figure G14a) are composed of two six-carbon rings separated by a conjugated carbon chain. The *xanthophylls* such as fucoxanthin (Figure G14b) are also classified as secondary pigments, since they do not transfer energy directly from sunlight to the photosynthetic pathway, but involve chlorophyll as an intermediary. These secondary pigments are present in different amounts in different plants/algae and therefore act as discrete source identifiers for sedimentary organic matter.

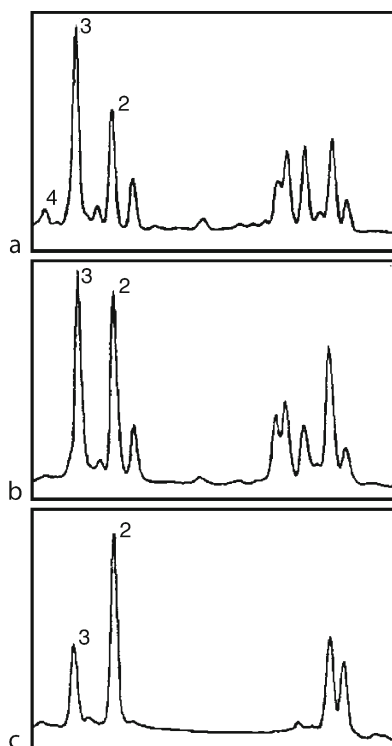


Figure G13 Representative partial gas chromatograms of the relative abundance of $C_{37:2}$ (2), $C_{37:3}$ (3), and $C_{37:4}$ (4) long-chain alkenones in surface sediments from (a) Norwegian Sea (72° N), (b) North Atlantic Ocean (54° N), and (c) tropical Atlantic Ocean (4° N) (after Rosell-Melé, 1994).

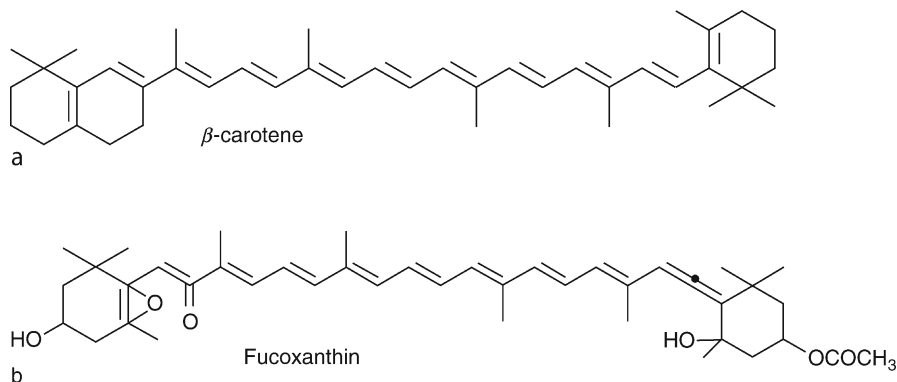


Figure G14 (a) Chemical structure of β -carotene. (b) Chemical structure of fucoxanthin.

Combined sedimentary lipid/pigment studies can yield important information regarding the history of regional phytoplankton community structure. For example, pigment and lipid analyses of a core of marine sediments recovered from the northeast Arabian Sea revealed that four biomarker compounds, dinosterol, alkenones, brassicasterol and chlorins, attributed to dinoflagellate, prymnesiophyte, diatom, and chlorophyll production, respectively, exhibited concordant concentration maxima coincidental with total organic carbon peaks over the past 200 kyr (Schubert et al., 1998; Figure G15). The similarity of the individual biomarker distributions and good correlations with total chlorins indicated a stable phytoplankton community structure driven by nutrient upwelling. A lack of correlation with records of long-chain *n*-alkanes and *n*-alcohols illustrates the independence of the terrestrial organic contribution.

Techniques

The analysis of organic geochemical proxies is heavily reliant upon liquid and gas chromatographic techniques. The term chromatography arises from the Greek words for color and writing and accordingly involves the separation of components of a mixture (such as colored pigments) by the differential distribution of those components between a mobile and a stationary phase. Mobile phases can be gas, liquid or supercritical fluids; stationary phases can be solids or liquids adsorbed to a solid. Separation depends on the differential affinities of solutes for a mobile and stationary phase.

Gas chromatography (GC) developed rapidly in the 1960s after the epic pioneering work of James and Martin (1952). For the modern analysis of lipids, sufficient quantities of lipids to quantify terrestrial or aquatic inputs, or to determine $U_{37}^{K'}$ values, are typically extracted from <1 g of freeze-dried, well-homogenized bulk

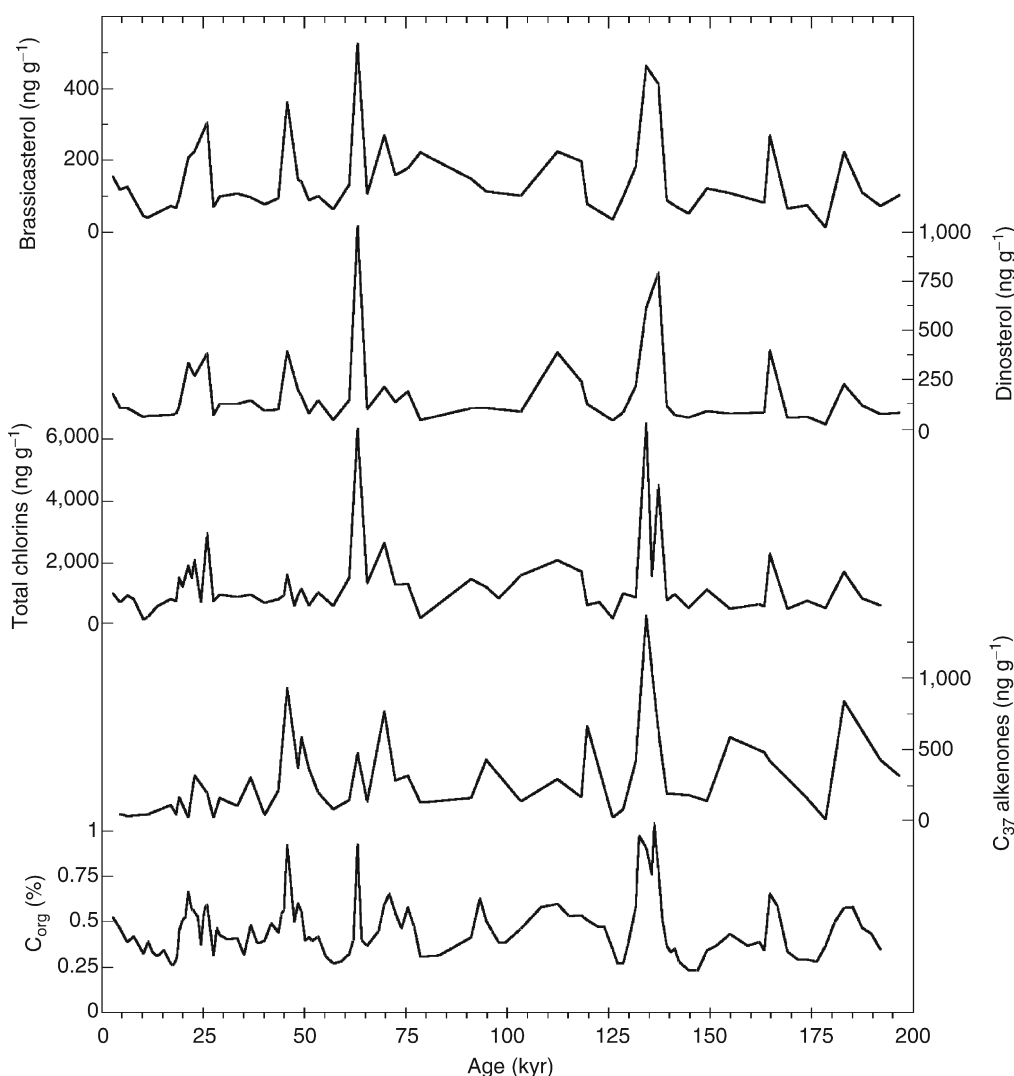


Figure G15 Abundance data for paleoproductivity biomarkers (organic carbon, C₃₇ alkenones, chlorins, dinosterol and brassicasterol) plotted against age for Arabian Sea sediment core 94KL (reprinted with permission from Nature, 394, Schubert C.J., Villanueva J., Calvert S.E., Cowie G.L., von Rad U., Schulz H., Berner U., and H. Erlenkeuser, Stable phytoplankton community structure in the Arabian Sea over the past 200,000 years, pp. 563–566, Copyright (1998)).

sediment by (Soxhlet) solvent extraction. This process can be expedited using an accelerated solvent extractor (ASE) at high temperature and pressure using small solvent volumes for a short duration (e.g., >100 °C, >1,000 psi, 20 min per sample). Organic extracts are typically evaporated under a N₂ stream and then rediluted (e.g., with toluene) and spiked with recovery standards. Each sample is vaporized and injected onto the head of the chromatographic column, which contains a stationary phase adsorbed onto the surface of an inert solid, for example chemically bonded to the inside of a fused silica tube. The sample is transported through the column in its vapor phase by the flow of an inert, gaseous mobile phase such as helium, separated into its components according to volatility under a temperature gradient program. The response of each component is precisely quantified in a detector such as an FID (flame ionization detector). For alkenones, the analytical procedure typically has a reproducibility of better than $\pm 0.005 U_{37}^{K'}$ units, corresponding to a temperature uncertainty of ± 0.2 °C.

High Pressure Liquid Chromatography (HPLC) was developed in the mid-1970s following a variety of older techniques for chemical separations, including open-column chromatography, paper chromatography and thin-layer chromatography, begun by Tswett (1905). HPLC quickly improved with the development of column packing materials and the additional convenience of on-line detectors. It is now routinely employed for the separation, identification and quantification of pigments and sterols. It utilizes a liquid mobile phase to separate the components of a mixture (dissolved in a solvent), which are forced to flow through a chromatographic column under high pressure. The mixture is resolved into its components in the column according to their interaction with the stationary phase (column packing material). As each component emerges from the column, it is carried in the mobile phase to a flow cell in which detection occurs. Typical detectors include fixed/variable wavelength and diode array UV/Visible, and fluorescence detectors. Each component is identified according to its characteristic emission spectrum response.

Summary

Geochemical proxy indicators for environmental reconstruction rely on both organic and inorganic sources. They may reveal the history of temperature, vegetation, wind, aridity, nutrients, ocean circulation, and plankton trophic structure. Analysis of organic matter involves both identification and quantification of its bulk and molecular composition. Complementary information is derived from inorganic proxies reliant upon biogenic/lithogenic and metal/Ca ratios in sediment and skeletal material. Geochemical proxy interpretations may be confounded by post-depositional diagenesis, especially in environments exposed to non-stable temperature, oxidation or biological activity. The lability of geochemical components typically renders them more susceptible to diagenesis. Abundance records are susceptible to systematic bias from preservation effects such as dissolution or water column depth. Ratio proxies may overcome such difficulties, but their link with the primary signal (such as paleoproduction, nutrients or temperature) is typically more tenuous and usually wholly empirical. Although ideally the interpretation of a proxy record relies upon the laws of thermodynamics, most paleoceanographic data are at least partly governed by poorly understood biological processes. Because further biological processes following the production of geochemical markers by organisms can create

additional biases in the sedimentary record, multiple proxy studies are favored to identify the primary signals of interest. A multi-proxy approach, such as combining analysis of alkenones and planktonic Mg/Ca for SST reconstruction, may compensate for post-depositional effects and improve the interpretation of paleoclimates and ancient environments.

Matthew J. Higginson

Bibliography

- Beck, J.W., Edwards, R.L., Ito, E., Taylor, F.W., Recy, J., Rougerie, F., Joannot, P., and Henin, C., 1992. Sea-surface temperature from coral skeletal Sr/Ca ratios. *Science*, **257**, 644–647.
- Berger, W.H., and Keir, R., 1984. Glacial-Holocene changes in atmospheric CO₂ and the deep-sea record. In Hansen, J.E., and Takahashi, T. (eds.), *Climate Processes and Climate Sensitivity*, *Geophysical Monograph* 29, 337–351. Washington, DC: American Geophysical Union.
- Berger, W.H., Fischer, K., Lai, C., and Wu, G., 1987. Ocean productivity and organic carbon flux. I. Overview and maps of primary production and export production. San Diego: University of California, SIO Reference 87–30.
- Blumer, M., Guillard, R.R.L., and Chase, T., 1971. Hydrocarbons of marine plankton. *Mar. Biol.*, **8**, 183–189.
- Boon, J.J., van der Meer, F.W., Schuyf, P.J.W., de Leeuw, J.W., Schenck, P.A., and Burlingame, A.L., 1978. 1. Organic geochemical analysis of core samples from site 362 Walvis Ridge, DSDP Leg 40. In Bolli, H.M., and Ryan, W.B.F. (Hrsg.) Initial Reports of the Deep Sea Drilling Project, vols. 38, 39, 40, and 41, Supplement, Walvis Ridge DSDP Leg 40. Washington, DC: U.S. Government Printing Office, pp. 627–637.
- Bourbonniere, R.A., and Meyers, P.A., 1996. Sedimentary geolipid records of historical changes in the watersheds and productivities of Lakes Ontario and Erie. *Limnol. Oceanogr.*, **41**, 352–359.
- Boyle E.A., 1988. Cadmium: Chemical tracer of deep-water paleoceanography. *Paleoceanography*, **3**, 471–489.
- Boyle, E.A., 1992. Cadmium and $\delta^{13}C$ paleochemical ocean distributions during the stage 2 glacial maximum. *Ann. Rev. Earth Planet. Sci.*, **20**, 245–287.
- Boyle, E.A., Sclater, F.R., and Edmond, J.M., 1976. On the marine geochemistry of cadmium. *Nature*, **263**, 42–44.
- Boyle, E.A., Labeyrie, L., and J.C. Duplessy, 1995. Calcitic foraminiferal data confirmed by cadmium in aragonitic *Hoeglundina*: Application to the last glacial maximum in the northern Indian Ocean. *Paleoceanography*, **10**, 881–900.
- Brassell, S.C., 1980. The lipids of deep sea sediments: Their origin and fate in the Japan Trench. Ph.D. Thesis, University of Bristol.
- Brassell, S.C., and Eglinton, G., 1984. Lipid indicators of microbial activity in marine sediments. In Hobbie, J.E., and Williams, P.J.leB. (eds.), *Heterotrophic Activity in the Sea*. New York: Plenum Press, pp. 481–503.
- Brassell, S.C., Eglinton, G., Marlowe, I.T., Pflaumann, U., and Sarnthein, M., 1986. Molecular stratigraphy: A new tool for climatic assessment. *Nature*, **320**, 129–133.
- Conte, M.H., Thompson, A., Lesley, D., and Harris, R.P., 1998. Genetic and physiological influences on the alkenone/alkenoate versus growth temperature relationship in *Emiliania huxleyi* and *Gephyrocapsa oceanica*. *Geochim. Cosmochim. Acta*, **62**, 51–68.
- Cranwell, P.A., Eglinton, G., and Robinson, N., 1987. Lipids of aquatic organisms as potential contributors to lacustrine sediments – II. *Org. Geochem.*, **11**, 513–527.
- De Leeuw, J., and Baas, M., 1986. Early-stage diagenesis of sterols. In Johns, R.B. (ed.), *Biological Markers in the Sedimentary Record*. Amsterdam: Elsevier, pp. 101–123.
- Eglinton, G., and Calvin, M., 1967. Chemical Fossils. *Sci. Am.*, **216**, 32–43.
- Eglinton, G., and Hamilton, R.J., 1967. Leaf epicuticular waxes. *Science*, **156**, 1322–1335.
- Espitalié, J., Laporte, J.L., Madec, M., Marquis, F., Leplat, P., Paulet, J., and Boutefeu, A., 1977. Méthode rapide de caractérisation des roches mères de leur potentiel pétrolier et de leur degré d'évolution. *Revue de l'Institut Français du Pétrole*, **32**, 23–42.
- Farrimond, P., Eglinton, G., and Brassell, S.C., 1986. Alkenones in Cretaceous black shales, Blake-Bahama Basin, western North Atlantic. In Leythaeuser, D., and Rullkötter, J. (eds.), *Advances in Organic Geochemistry, 1985*. *Org. Geochem.*, **10**, 897–903.

- Gagosian, R.B., and Peltzer, E.T., 1986. The importance of atmospheric input of terrestrial organic material to deep sea sediments. *Org. Geochem.*, **10**, 661–669.
- Herbert, T.D., Schuffert, J.D., Thomas, D., Lange, C., Weinheimer, A., Peleo-Alampay, A., and Herguera, J.C., 1998. Depth and seasonality of alkenone production along the California margin inferred from a core top transect. *Paleoceanography*, **13**, 263–271.
- Higginson, M.J., 2000. Chlorin pigment stratigraphy as a new and rapid palaeoceanographic proxy in the Quaternary. Ph. D. Thesis, University of Bristol.
- Higginson, M.J., and Altabet, M.A., 2004. Initial test of the silicic acid leakage hypothesis using sedimentary biomarkers. *Geophys. Res. Lett.*, **31**, L18303, doi:10.1029/2004GL020511.
- Hoefs, M.J.L., Versteegh, G.J.M., Rijpstra, W.I.C., de Leeuw, J.W., and Sinninghe Damsté, J.S., 1998. Post-depositional oxic degradation of alkenones: Implications for the measurement of palaeo sea surface temperatures. *Paleoceanography*, **13**, 42–49.
- James, A.T., and Martin, A.J.P., 1952. Gas-liquid partition chromatography: The separation and micro-estimation of volatile fatty acids from formic acid to dodecanoic acid. *Biochem. J.*, **50**, 679–690.
- Karl, D., and Knauer, G., 1991. Microbial production and particle flux in the upper 350 m of the Black Sea. *Deep Sea Res.*, **38**, 921–942.
- Keely, B.J., and Brereton, R.G., 1986. Early chlorin diagenesis in a Recent aquatic sediment. *Org. Geochem.*, **10**, 975–980.
- Lea, D.W., Mashiotta, T.A., and Spero, H.J., 1999. Controls on magnesium and strontium uptake in planktonic foraminifera determined by live culturing. *Geochim. Cosmochim. Acta*, **63**, 2369–2379.
- Lea, D.W., Pak, D.T., and Spero, H.J., 2000. Climate impact of Late Quaternary equatorial Pacific sea surface temperature variations. *Science*, **289**, 1719–1724.
- Lea, D.W., Martin, P.A., Pak, D.K., and Spero, H.J., 2002. Reconstructing a 350 ky history of sea level using planktonic Mg/Ca and oxygen isotope records from a Cocos Ridge core. *Quaternary Sci. Rev.*, **21**, 283–293.
- Linsley, B.K., Wellington, G.M., and Schrag, D.P., 2000. Decadal sea surface temperature variability in the sub-tropical South Pacific from 1726 to 1997 AD. *Science*, **290**, 1145–1148.
- Madureira, L.A.S., van Kreveld, S.A., Eglinton, G., Conte, M., Ganssen, G., van Hinte, J.E., and Ottens, J.J., 1997. Late Quaternary high-resolution biomarker and other sedimentary climate proxies in a northeast Atlantic core. *Paleoceanography*, **12**, 255–269.
- Marlowe, I.T., Brassell, S.C., Eglinton, G., and Green, J.C., 1984. Long chain unsaturated ketones and esters in living algae and marine sediments. *Org. Geochem.*, **6**, 135–141.
- Martin, P.A., Lea, D.W., Rosenthal, Y., Shackleton, N.J., Sarnthein, M., and Papenfuss, T., 2002. Quaternary deep sea temperature histories derived from benthic foraminiferal Mg/Ca. *Earth Planet. Sci. Lett.*, **198**, 193–209.
- Martinez, P.H., Bertrand, P.H., Bouloubassi, I., Bareille, G., Shimmield, G., Vautravers, B., Grousset, F., Guichard, S., Ternois, Y., and Sicre, M.A., 1996. An integrated view of inorganic and organic biogeochemical indicators of palaeoproductivity changes in a coastal upwelling area. *Org. Geochem.*, **24**, 411–420.
- Mashiotta, T.A., Lea, D.W., and Spero, H.J., 1997. Experimental determination of cadmium uptake in the shells of the planktonic foraminifera *Orbulina universa* and *Globigerina bulloides*: Implications for surface water palaeoceanography. *Geochim. Cosmochim. Acta*, **61**, 4053–4065.
- Meyers, P.A., 1994. Preservation of elemental and isotopic source identification of sedimentary organic matter. *Chem. Geol.*, **144**, 289–302.
- Meyers, P.A., 1997. Organic geochemical proxies of paleoceanographic, paleolimnologic, and paleoclimatic processes. *Org. Geochem.*, **27**, 213–250.
- Meyers, P.A., and Eadie, B.J., 1993. Sources, degradation, and resynthesis of the organic matter on sinking particles in Lake Michigan. *Org. Geochem.*, **20**, 47–56.
- Min, G.R., Edwards, R.L., Taylor, F.W., Recy, J., Gallup, C.D., and Beck, J.W., 1995. Annual cycles of U/Ca in coral skeletons and U/Ca thermometry. *Geochim. Cosmochim. Acta*, **59**, 2025–2042.
- Mitsuguchi, T., Matsumoto, E., Abe, O., Uchida, T., and Isdale, P.J., 1996. Mg/Ca thermometry in coral skeletons. *Science*, **274**, 961–963.
- Müller, P.J., 1977. C/N ratios in Pacific deep-sea sediments: effect of inorganic ammonium and organic nitrogen compounds sorbed by clays. *Geochim. Cosmochim. Acta*, **41**: 765–776.
- Müller, P.J., and Suess, E., 1979. Productivity, sedimentation rate, and sedimentary organic matter in the oceans – I. Organic carbon preservation. *Deep Sea Res. I*, **26**, 1347–1362.
- Müller, P.J., Kirst, G., Ruhland, G., Von Storch, I., and Rosell-Melé, A., 1998. Calibration of the alkenone paleotemperature index $U^{K_{37}}$ based on core-tops from the eastern South Atlantic and the global ocean (60° N–60° S). *Geochim. Cosmochim. Acta*, **62**, 1757–1772.
- Nürnberg, D., Bijma, J., and Hemleben, C., 1996. Assessing the reliability of magnesium in foraminiferal calcite as a proxy for water mass temperatures. *Geochim. Cosmochim. Acta*, **60**, 803–814.
- Ohkouchi, N., Eglinton, T.I., Keigwin, L.D., and Hayes, J.M., 2002. Spatial and temporal offsets between proxy records in a sediment drift. *Science*, **298**, 1224–1227.
- Pelejero, C., Grimalt, J.O., Sarnthein, M., Wang, L., and Flores, J.A., 1999. Molecular biomarker record of sea surface temperature and climatic change in the South China Sea during the last 140,000 years. *Mar. Geol.*, **156**, 109–121.
- Poynter, J.G., Farrimond, P., Robinson, N., and Eglinton, G., 1989. Aeolian-derived higher plant lipids in the marine sedimentary record: Links with palaeoclimate. In Leinen, M., and Sarnthein, M. (eds.), *Paleoclimatology and Paleometeorology: Modern and Past Patterns of Global Atmospheric Transport*. Dordrecht: Kluwer, pp. 435–462.
- Prahl, F.G., and Wakeham, S.G., 1987. Calibration of unsaturation patterns in long-chain ketone compositions for paleotemperature assessment. *Nature*, **330**, 367–369.
- Prahl, F.G., Muelhausen, L.A., and Zahnle, D.L., 1988. Further evaluation of long-chain alkenones as indicators of paleoceanographic conditions. *Geochim. Cosmochim. Acta*, **52**, 2303–2310.
- Prahl, F.G., de Lange, G.J., Lyle, M., and Sparrow, M.A., 1989. Post-depositional stability of long-chain alkenones under contrasting redox conditions. *Nature*, **341**, 434–437.
- Quinn, T.M., and Sampson, D.E., 2002. A multiproxy approach to reconstructing sea surface conditions using coral skeleton geochemistry. *Paleoceanography*, **17**(4), 1062, doi: 10.1029/2000PA000528.
- Repeta, D.J., McCaffrey, M.A., and Farrington, J.W., 1992. Organic geochemistry as a tool to study upwelling systems: Recent results from the Peru and Namibian shelves. In Summerhayes, C.P., Prell, W.L., and Emeis, K.C. (eds.), *Upwelling Systems: Evolution Since the Early Miocene*. Geological Society Special Publication No. 64, pp. 257–272.
- Rickaby, R., and Elderfield, H., 1999. Planktonic Cd/Ca: Paleonutrients or paleotemperature? *Paleoceanography*, **14**, 293–303.
- Rieley, G., Collier, R.J., Jones, D.M., and Eglinton, G., 1991. The biogeochemistry of Ellesmere Lake, U.K. – I. source correlation of leaf wax inputs to the sedimentary lipid record. *Org. Geochem.*, **17**, 901–912.
- Rontani, J.F., Cuny, P., Grossi, V., Beker, B., 1997. Stability of long-chain alkenones in senescing cells of *Emiliania huxleyi*: effect of photochemical and aerobic microbial degradation on the alkenone unsaturation ratio ($U^{K_{37}}$). *Org. Geochem.*, **26**, 503–509.
- Rosell-Melé, A., 1994. Long-chain alkenone and alkyl alkenoate, and total pigment abundances as climatic proxy-indicators in the northeastern Atlantic: Analytical methods, calibration and stratigraphy. Ph.D. Thesis, University of Bristol.
- Rosenthal, Y., Boyle, E.A., Labeyrie, L., and Oppo, D., 1995. Glacial enrichments of authigenic Cd and U in glacial sub-Antarctic sediments: A climatic control on the elements' oceanic budget? *Paleoceanography*, **10**, 395–413.
- Rosenthal, Y., Boyle, E.A., and Slowey, N., 1997. Temperature control on the incorporation of magnesium, strontium, fluorine, and cadmium into benthic foraminiferal shells from Little Bahama Bank: Prospects for thermocline paleoceanography. *Geochim. Cosmochim. Acta*, **61**, 3633–3643.
- Schubert, C.J., Villanueva, J., Calvert, S.E., Cowie, G.L., von Rad, U., Schulz, H., Berner, U., and Erlenkeuser, H., 1998. Stable phytoplankton community structure in the Arabian Sea over the past 200,000 years. *Nature*, **394**, 563–566.
- Schulte, S., Mangelsdorf, K., and Rullkötter, J., 2000. Organic matter preservation on the Pakistan continental margin as revealed by biomarker geochemistry. *Org. Geochem.*, **31**, 1005–1022.
- Sikes, E.L., and Volkman, J.K., 1993. Calibration of alkenone unsaturation ratios $U^{K_{37}}$ for paleotemperature estimation in cold polar waters. *Geochim. Cosmochim. Acta*, **57**, 1883–1889.
- Simoneit, B.R.T., 1977. Organic matter in eolian dusts over the Atlantic Ocean. *Mar. Chem.*, **5**, 443–464.
- Stein, R., 1986. Surface-water paleoproductivity as inferred from sediments deposited in oxic and anoxic deepwater. In Degens, E.T., Meyers, P.A., and Brassell, S.C. (eds.), *Biogeochemistry of Black Shales*. Hamburg: Selbstverlag Universität Hamburg, pp. 55–70.

- Suess, E., 1980. Particulate organic carbon flux in the oceans: Surface productivity and oxygen utilisation. *Nature*, **288**, 260–263.
- Tswett, M.S., 1905. Trudy Varshavskogo Obshchestva Estestvoispytatelei. *Otdelenie Biologii*, **14**, 20–39.
- Tudhope, A.W., Chilcott, C.P., McCulloch, M.T., Cook, E.R., Chappell, J., Ellam, R.M., Lea, D.W., Lough, J.M., and Shimmield, G.B., 2001. Variability in the El Niño–Southern Oscillation through a glacial–interglacial cycle. *Science*, **291**, 1511–1517.
- Volkman, J.K., 1986. A review of sterol markers for marine and terrigenous organic matter. *Org. Geochem.*, **9**, 83–99.
- Volkman, J.K., Eglinton, G., Corner, E.D.S., and Sargent, J.R., 1980. Novel unsaturated straight-chain C₃₇–C₃₉ methyl and ethyl ketones in marine sediments and a coccolithophore *Emiliania huxleyi*. In Douglas, A.G., and Maxwell, J.R. (eds.), *Advances in Organic Geochemistry*. Oxford: Pergamon Press, pp. 219–227.
- Weaver, P.P.E., Chapman, M.R., Eglinton, G., Zhao, M., Rutledge, D., and Read, G., 1999. Combined coccolith, foraminiferal, and biomarker reconstruction of paleoceanographic conditions over the past 120 kyr in the northern North Atlantic (59° N, 23° W). *Paleoceanography*, **14**, 336–349.

Cross-references

Alkenones
 Carbon Cycle
 Coccoliths
 Coral and Coral Reefs
 Foraminifera
 Ocean Paleotemperatures
 Organic Geochemical Proxies
 Oxygen Isotopes
 Paleoclimate Proxies, an Introduction
 Phosphorus Cycle

GLACIAL ERRATICS

A glacial erratic is a glacially transported clast of non-local provenance. Some erratics are noteworthy because of their large size or exotic bedrock type. Erratics were pivotal to the development of the Ice Age theory, popularized by Louis Agassiz. They continue to be used to determine the limits and flow paths of past glaciers. Erratics have also been useful in mapping ore minerals.

Saussure was the first to use the term erratic (in 1779) for granite boulders overlying limestone in the western Alps (Flint, 1971). Like others, he believed they were transported by water. In 1787, Benard Friederich Kuhn was the first to interpret that they were carried by more extensive glaciers (Imbrie and Imbrie, 1979). James Hutton reached the same conclusion in 1795. Inhabitants of the Alps recognized that they were carried by past glaciers (e.g., Jean-Pierre Perraudin in 1815). Both Ignaz Venetz (from 1816–1829) and Jean de Charpentier (from 1829–1833) further developed this hypothesis after conversations with Perraudin. Jens Esmark in Norway (in 1824) and Reinhard Bernhardt (in 1832) in Germany both noted erratics and argued that they indicated glaciation of northern Europe. Jean de Charpentier introduced Louis Agassiz to erratics in 1836. In 1837, Agassiz presented an expanded version of Charpentier's ideas. Agassiz proposed that a great Ice Age had once gripped Europe. During the next 30 years, Agassiz championed the Ice Age. Upon landing in North America in 1848, Agassiz found erratics there also. Louis Agassiz is buried in Boston's Mount Auburn Cemetery and his grave is marked by an erratic of gray granite.

Glacial erratics are commonly found in till and on end moraines. They may also be found overlying bare bedrock. In alpine glaciers, large erratics can be carried on the surface of the ice onto which they fall during landslides. In ice sheets such as those that covered North America and Europe 20,000 years ago, erratics must have been eroded near their beds and then transported in the ice or on the ice surface. The exact processes by which the very largest erratics become incorporated and transported great distances is not completely understood, but erratic paths indicate that transport may occur in stages during more than one glaciation.

Erratics range in size from pebbles to megaliths of well over 100 tons. Many erratics have clearly traveled more than 500 km, but none appears to have traveled farther than 1,200 km (Flint, 1971). Erratics form boulder fans or erratic trains, which are fan-shaped distributions of boulders downstream from the outcrop of origin. Some of the most famous indicator erratics in northern Europe include the Rapakivi granites and copper of Finland, and the porphyries of Sweden. In North America, some of the most famous include the Alberta erratic trains, the Sioux Quartzite of South Dakota and Minnesota, and native copper from the Lake Superior region. Diamonds are found as erratics in glacial till of the western Great Lakes. A diamond-bearing kimberlite pipe in the Canadian Northwest Territory was discovered by tracking indicator minerals in erratics (Kjarsgaard and Levinson, 2002). In Finland, numerous studies have located ores by mapping and tracing erratic trains.

Patrick M. Colgan

Bibliography

- Flint, R.F., 1971. *Glacial and Quaternary Geology*. New York: Wiley, 892pp.
- Imbrie, J., and Imbrie, K.P., 1979. *Ice Ages: Solving the Mystery*. Cambridge, MA: Harvard University Press, 224pp.
- Kjarsgaard, B.A., and Levinson, A.A., 2002. Diamonds in Canada. *Gems & Gemology*, **38**, 208–238.

Cross-references

Glacial Geomorphology
 Glacial Sediments
 History of Paleoclimatology
 Moraines
 Mountain Glaciers
 Tills and Tillites

GLACIAL EUSTASY

Introduction

Glacioeustasy is defined as global sea-level changes resulting from terrestrial ice-volume changes. Sea level is defined as the distance of the sea surface relative to the center of the Earth, which closely coincides with the geoid – a surface of equal potential gravitational energy. A more accurate definition would take into consideration undulations due to continents or mountain ranges, or ocean currents. Two factors control sea level. The first is the volume of water in the ocean, which is largely dependent on glacial eustasy and to a lesser extent on the volume of water in terrestrial aquifers, as well as thermal

expansion and contraction of seawater. The second are changes in the shape and volume of the ocean basin, which is controlled by continental collision, spreading rates of mid-ocean ridges, and the formation of large oceanic igneous provinces. Of these mechanisms, only glacial-eustatic changes are both large (>10 m) and rapid (<<1 Myr).

As sea level either rises or falls eustatically, flooded portions of the crust experience water loading or unloading, so that observed fluctuations in water depth relative to the ocean floor (termed apparent sea-level (ASL) changes; Pekar et al., 2002a) exceed the original eustatic changes by a factor of ~ 1.48 (Kominz and Pekar, 2001). Changes in ASL are solely of eustatic origin, but they differ in amplitude because their reference frame is different. The concept of ASL change also differs from that of water-depth change at passive continental margins and other sedimentary basins, because water depth at such locations is influenced by sediment accumulation and by subsidence unrelated to changes in water loading (Pekar et al., 2003). The concept of relative sea-level change, as widely used in the stratigraphic literature, implicitly includes the effects of sediment loading (e.g., Posamentier et al., 1988). In the literature today, many of the sea-level estimates are not strictly eustatic, in that these estimates include water loading. For example, the sea-level changes observed at small islands in the ocean (e.g., Barbados; Fairbanks, 1989) are ASL changes because the crust that underlies such islands is regionally loaded by water. The ice-volume-related changes in sea level obtained from such locations for calibration against oxygen isotope records need to be multiplied by 0.68 to obtain eustatic changes (Pekar et al., 2003).

Today most of the Earth's ice is stored in the East Antarctica Ice Sheet (26 km³) with lesser volumes in the ice sheets of Greenland (2.7 km³) and West Antarctica (3 km³). Portions of the ice sheet that are below sea level do not contribute to sea-level rise given that they already displace ocean water, as in the example of the West Antarctic Ice Sheet, which mainly resides below sea level. The portion of the East and West Antarctic Ice Sheets above sea level contains the water equivalent of a ~ 66 m sea-level rise. The Greenland Ice Sheet lacks large floating ice shelves and contains the water equivalent of a ~ 7 m sea-level rise. Ice stored by mountain or alpine glaciers (0.2 km³) is minor in comparison and would be equivalent to less than a meter of eustatic change. If the total stored ice volume today were to melt, this would result in a eustatic rise equivalent to ~ 73 m. In contrast, as recent as 20 ka B.P., sea level was ~ 120 m lower than today because of large continental ice sheets in the Northern Hemisphere (e.g., Fairbanks, 1989).

Methods for estimating glacial eustasy

Within historical time scales (10^0 – 10^2 yr), tide gauges have provided estimates of local sea-level changes. Although these sea-level changes at any particular site contain a glacial-eustatic signal, they are also controlled by expansion of sea-surface waters due to global warming and by local crustal movement of the area. The latter is controlled by uplift or subsidence on tectonically active margins (e.g., California), subsidence due to sediment loading, thermal cooling of the crust, and uplift from isostatic adjustments after the retreat of an ice sheet. By examining tide gauges globally and removing local effects, the global mean sea-level rise is estimated to be 1 to 2 mm yr⁻¹ (e.g., Houghton et al., 2001). However, it is uncertain how much of this signal is due to the expansion of water as the oceans warm.

Measuring sea-level changes from Holocene and late Pleistocene records have been accomplished mainly by examining records from shoreline emergent reefs (e.g., Fairbanks and Matthews, 1978; Fairbanks, 1989; Chappell et al., 1996) and salt-water marshes (e.g., Scott and Medillio, 1978; Goodbred et al., 1998). In the case of emergent reefs, the species *Acropora palmata* was used as a sea-level indicator as this coral typically lives on reef crests in 5 m of water or less. Glacial-eustatic changes were estimated by making assumptions of uplift rates of the reef. Sea-level estimates based on salt marsh studies have used benthic foraminiferal and plant zonation to provide sea-level estimates for the Holocene with accuracy to ± 10 cm. Furthermore, modeling of the quantity of ice volume that existed during the Last Glacial Maximum (Peltier, 1998) has provided an additional means to constrain glacial-eustatic change.

For pre-Pliocene times, methods for constraining glacioeustasy have relied on stratigraphic records from passive margins and $\delta^{18}\text{O}$ records from both planktonic and benthic foraminiferal shells (called tests) obtained from deep-sea cores. Although stratigraphic records have been especially useful in constraining pre-Pliocene eustatic changes (e.g., Vail et al., 1977; Haq et al., 1987; Miller et al., 1998; Kominz and Pekar, 2001), a triad of processes controls these records: eustasy, sediment supply, and local tectonics. Evaluation of eustatic changes from stratigraphic records requires estimates of the effects of sediment compaction as well as subsidence due to flexural sediment loading of the margin and thermal contraction of the crust (e.g., Steckler and Watts, 1978; Steckler et al., 1999; Kominz and Pekar, 2001). Various methods have been used to estimate eustatic changes from continental margins. In 1977, the Exxon Production Research Company (EPR) demonstrated the relationship of the stratigraphic record to sea-level change by estimating sea level from calculations of sediment aggradation on passive margins using seismic reflection profiles and core material (Vail et al., 1977; Haq et al., 1987). Nevertheless, controversies have arisen over the specific methodologies used and the proprietary nature of the data (Christie-Blick, 1991; Christie-Blick and Driscoll, 1995). However, non-proprietary studies have verified both the number and timing of many of the sea-level changes identified in the EPR records (e.g., Eberli, 2000; Miller et al., 1996; Pekar and Miller, 1996; Miller et al., 1998), although the amplitudes appear to be overestimated by up to a factor of two for many of them (e.g., Miocene: Miller et al., 1997; Oligocene: Miller et al., 1985; Pekar et al., 2002a; Eocene: Browning et al., 1996; Pekar et al., 2005; Cretaceous: Miller et al., 1999).

Recent studies have modeled the effects of compaction, sediment loading, and crustal cooling in order to isolate a eustatic signal from stratigraphic records (i.e., backstripping). Kominz et al. (1996) provided constraints on Eocene through Miocene times using one-dimensional backstripping. These methods provided quantitative constraints on the subsidence due to compaction, but not on the rates of subsidence due to flexure loading and thermal contraction. More recently, Kominz and Pekar (2001), using two-dimensional flexural backstripping, have provided perhaps the best-constrained estimates of pre-Pliocene sea-level changes (between 34 and 23 Ma), which they attribute mainly to ice-volume changes in Antarctica.

In cases when flexural backstripping is not used, stratigraphers have relied on correlating sequence boundaries (e.g., water depth lowering) to other sites globally as well as to oxygen isotope increases (inferred glacioeustatic lowerings) in order to indicate a eustatic control (e.g., Browning et al., 1996; Pekar and Miller, 1996; Oleg et al., 1999). Oxygen isotopes obtained from

marine carbonates vary as a function of ice-volume changes, as well as the temperature and precipitation/evaporation history (i.e., salinity effect) of the seawater in which the carbonate formed. Thus, glacial-eustatic estimates derived from $\delta^{18}\text{O}$ records (e.g., Miller et al., 1985, 1991, 1998; Abreu and Anderson, 1998) require an evaluation of the temperature signal and the “salinity effect”. Studies using coupled Mg/Ca ratios and $\delta^{18}\text{O}$ measurements have begun to provide estimates of bottom-water temperature for the Quaternary (Martin et al., 2002), which have permitted evaluation of the $\delta^{18}\text{O}$ of the seawater and thus placed constraints on ice volume. This technique has been extended through most of the Cenozoic, with limited application in older records due to diagenesis affecting the original seawater value of the calcite (e.g., Lear et al., 2000; Martin et al., 2002; Billups et al., 2002). Although questions have been raised about possible oceanic Mg/Ca ratio changes through time (Billups and Schrag, 2003) and isotopic species offset, bottom-water temperature estimates have begun to allow the isotopic proxy for continental ice volume to be evaluated for these older times. Finally, direct evidence of ice sheet extent, such as ice rafted debris (IRD), has demonstrated the presence of continental ice sheets beginning no later than the base of the Oligocene (Breza and Wise, 1992). However, IRD provide evidence for existence of an ice sheet only when glaciers reach the coastline.

History of glacial eustasy

Holocene and Pleistocene glacial-eustatic changes

During the past 18,000 years, the collapse of large ice sheets in the Northern Hemisphere as well as ice volume reductions in Antarctica have resulted in a sea-level rise of about 120 m (e.g., Fairbanks, 1989). The decay of the ice sheets occurred in several steps, with two meltwater pulses occurring at ~ 12 ka and ~ 9.5 ka, and rates of sea-level rise ranging from 24 to 28 meters per 1,000 years (Fairbanks, 1989). With the final demise of the Northern Hemisphere ice sheet around 8 ka B.P., the rate of sea-level rise has slowed continuously since about 8 ka (Peltier, 1999), with the current eustatic rise due to ice melting estimated at ~ 1 mm yr^{-1} .

The late Pleistocene contains the largest glacial-eustatic changes of the past 200 Ma with a number of amplitudes >100 m. In $\delta^{18}\text{O}$ records, these glacial cycles have followed a sawtooth shape for the past 800 ka with a periodicity in phase with the eccentricity cycle (the “100-kyr cycle”) of Milankovitch (Shackleton and Opdyke, 1973). Beyond ~ 800 ka, $\delta^{18}\text{O}$ records indicate that the obliquity cycle (41-kyr cycle) dominated the record through the Pliocene, coupled with smaller glacial-eustatic amplitudes. Large scale Northern Hemisphere glaciation was initiated at approximately 2.4 Ma (Raymo et al., 1989), as evidenced by $\delta^{18}\text{O}$ excursions concomitant with the occurrence of IRD in the North Atlantic, providing unequivocal evidence for proximal continental ice sheets (Shackleton et al., 1984). Between 2.4 and 2.7 Ma, evidence for glacial-eustatic changes less than half those of the late Pleistocene are implied by $\delta^{18}\text{O}$ values (Raymo et al., 1989; Jansen et al., 1990; Raymo, 1994), which are thought to have originated from Antarctic and limited Northern Hemisphere ice growth. An early Pliocene warming has been suggested to have resulted in at least a partial collapse of the Antarctic Ice Sheet (Raymo et al., 1989; Hearty et al., 1999). Eustatic estimates also indicate that sea level was up to 40 m higher, supporting the notion of a significant deglaciation (Haq et al., 1987; Dowsett and Cronin, 1990). However, this is still controversial, with further studies required (Denton et al., 1984).

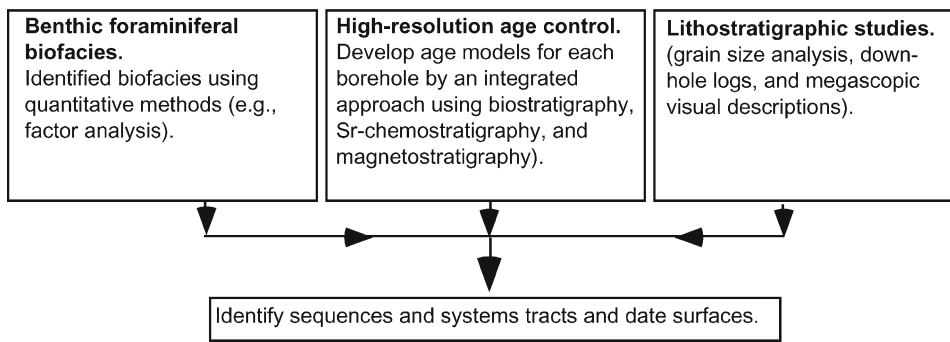
Pre-Pliocene glacial-eustatic changes

Unlike Pleistocene glacial-eustatic changes that were the result of both Northern and Southern Hemisphere ice sheets, pre-Pliocene glacial eustasy is mainly the result of ice-volume changes in Antarctica. Most of our understanding of glacial-eustatic changes for the Tertiary comes from the Ocean Drilling Program drilling of shallow marine strata (Bahamas, Eberli, 2000; Miller et al., 1996; Miller et al., 1998) and deep-sea $\delta^{18}\text{O}$ records (e.g., Miller et al., 1987; Miller et al., 1991; Zachos et al., 2001). Miller et al. (1991) noted that covariance between subtropical planktonic and benthic foraminiferal $\delta^{18}\text{O}$ records plus large $\delta^{18}\text{O}$ amplitudes ($<0.5\%$) with high $\delta^{18}\text{O}$ values ($<2\%$) in benthic $\delta^{18}\text{O}$ records from the Miocene and Oligocene implied the growth of ice sheets. Subsequent stratigraphic studies showed that sequence boundary development and $\delta^{18}\text{O}$ events correlate well, indicating a global mechanism (e.g., Eberli et al., 2000; Miller et al., 1996; Pekar and Miller, 1996; Miller et al., 1998). Furthermore, estimates of eustatic amplitudes used paired Mg/Ca ratios and $\delta^{18}\text{O}$ ratios to place constraints on ice-volume changes and thus glacial-eustatic changes for the past 50 Ma (Lear et al., 2000; Billups et al., 2002; Pekar et al., 2002b). Results from stratigraphic records (Miller et al., 1998) indicate that glacial-eustatic changes ranged up to perhaps 40 m ASL during the early Miocene (21–16 Ma). In contrast, using calibrated $\delta^{18}\text{O}$ records, estimates of ice volume ranged from 125% to $\sim 25\%$ of the present-day Antarctic Ice Sheet during glacial maxima and glacial minima, respectively (Pekar and DeConto, 2006).

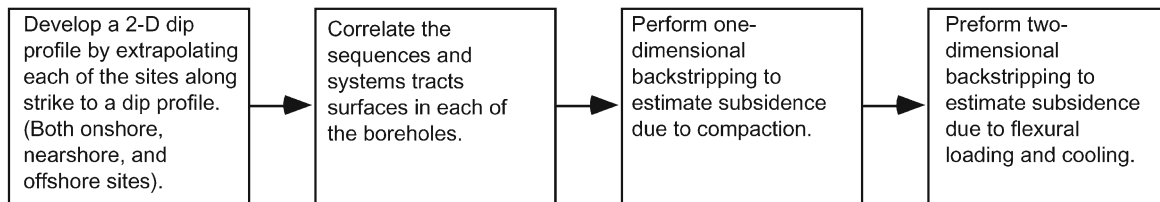
The Oligocene is considered the start of the Icehouse World of the Cenozoic (Miller et al., 1991) and contains perhaps the best estimates of sea level for a pre-Pliocene time. Kominz and Pekar (2001) and Pekar and Kominz (2001) estimated glacial-eustatic changes for the period between 23 and 34 Ma by combining two-dimensional flexural backstripping with two-dimensional paleoslope modeling of foraminiferal biofacies and lithofacies of the New Jersey Coastal Plain (Figure G16). Results indicate ASL amplitudes ranging from 20 ± 10 to 80 ± 20 m, with the largest sea-level change occurring during the earliest Oligocene (33.5 Ma). The size of this change implies that the Antarctic Ice Sheet was small or absent at the end of the Eocene, but grew rapidly (<100 kyr; Zachos et al., 1996) to nearly the present size of the East Antarctic Ice Sheet, or perhaps up to 30% larger (Kominz and Pekar, 2001; Lear et al., 2004; Coxall et al., 2005; Pekar and Christie-Blick, 2007) (Figure G17).

The late Oligocene Epoch has presented a climatic conundrum because of low $\delta^{18}\text{O}$ values from deep-sea records, which suggest bottom water warming, coupled with at least partial collapse of the Antarctic Ice Sheet. However, Antarctic drilling results (e.g., Cape Roberts Project), indicate that East Antarctica was heavily glaciated during the late Oligocene (Naish et al., 2001; Roberts et al., 2003). Additionally, high $\delta^{18}\text{O}$ values from Weddell Sea Sites 689 and 690 (2.9 and 3.3‰) are consistent with a fully-glaciated East Antarctic Continent (EAC) and cold bottom water temperatures (2.0–2.5 °C) (Pekar et al., 2005a). This paradox can be explained by spatial restriction of deep waters produced near the Antarctic Continent (proto-AABW), coupled with the presence of a large ice sheet covering most of East Antarctica. Bottom waters elsewhere may have been influenced by a combination of proto-AABW and warmer, more saline deep waters (Pekar et al., 2006). Glacial-eustatic estimates at higher frequency timescales during the Oligocene have been developed by calibrating amplitudes

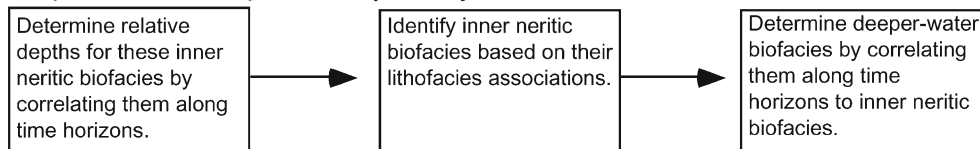
Step 1. Develop a sequence and chronostratigraphic framework by integrating:



Step 2. Reconstruct the original depositional stratal geometry of the margin.



Step 3. Determine paleobathymetry for each of the benthic foraminiferal biofacies.



Step 4. Determine the apparent sea-level and eustatic change.

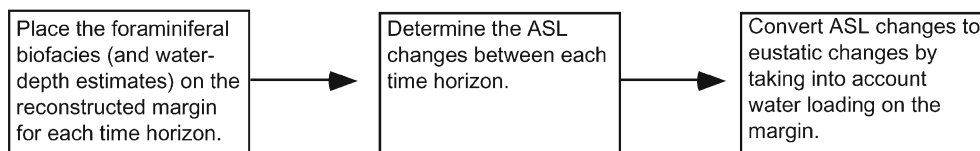


Figure G16 Flow chart showing method for determining paleobathymetric estimates for benthic foraminiferal biofacies, apparent sea-level, and eustatic changes using two-dimensional paleoslope modeling and two-dimensional flexural backstripping.

of $\delta^{18}\text{O}$ events (Oi-events, Miller et al., 1991; Pekar and Miller, 1996) to sea-level estimates (Pekar et al., 2002a) and then applying them to high-resolution $\delta^{18}\text{O}$ records (Pekar et al., 2006). At 100- to 400-kyr timescales (corresponding to orbital eccentricity cycles) glacial-eustatic changes ranged between 20 and 35 m, and at the 40-kyr timescales (obliquity cycle), 20–30 m eustatic changes were inferred.

Recent studies indicate that during the late middle to late Eocene (42–34 Ma) there were at least episodically significant ice sheets in Antarctica (Browning et al., 1996; Miller et al., 1998). Sequence boundaries, interpreted to represent sea-level changes and dated between 42–34 Ma, were correlated with $\delta^{18}\text{O}$ increases identified in deep-sea records, indicating a global causal mechanism, such as glacial eustasy (Browning et al., 1996; Miller et al., 1998).

The early to middle Eocene (55–42 Ma) has been dubbed the “doubt house” world. Although Browning et al. (1996)

determined that late Middle to late Eocene (<42 Ma) sequence boundaries in New Jersey were controlled by glacioeustasy, they concluded that it was unlikely that early to early-middle Eocene sequence boundaries were the result of ice-volume changes. Subsequently, Miller et al. (1998) concluded that there were hints of glacioeustasy operating during the early to early-middle Eocene. Pekar et al. (2005) identified seven sequence boundaries of late early to Middle Eocene age (51–42 Ma) in core material from ODP Leg 189 Site 1171 (South Tasman Rise). These sequence boundaries correlate well with deep-sea $\delta^{18}\text{O}$ increases and sequence boundaries identified from other margins. The synchronous nature of sequence boundary development from globally distal sites together with $\delta^{18}\text{O}$ increases suggests a global control. The only mechanism that can explain these significant and rapid changes is glacial eustasy, indicating that large ice sheets existed in this supposedly ice-free world. Modeling studies and atmospheric $p\text{CO}_2$

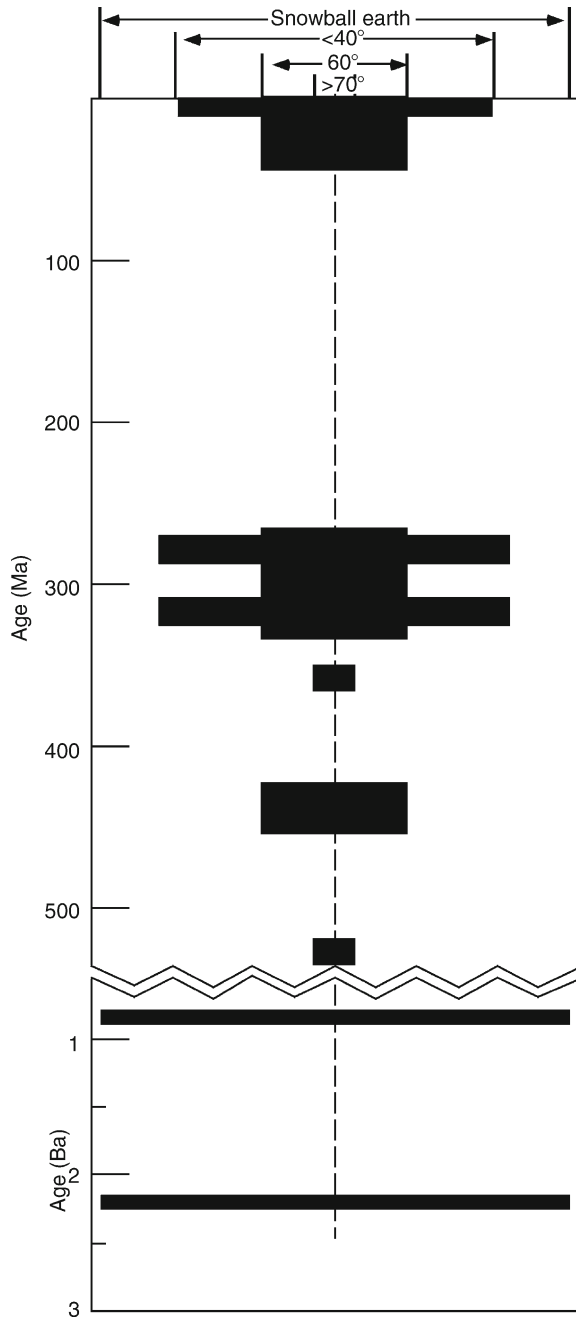


Figure G17 The paleolatitudinal distribution of glacial evidence during geological time (adapted from Crowley and Burke, 1998).

estimates show that the first time $p\text{CO}_2$ levels decreased below a threshold that could support the development of an Antarctic Ice Sheet occurred at ~ 51 Ma (Pearson and Palmer, 2000; DeConto and Pollard, 2003). Sea-level amplitudes estimated from $\delta^{18}\text{O}$ records ranged from ~ 20 m for the early Eocene (51–49 Ma) and ~ 25 m to ~ 45 m for the middle Eocene (48–42 Ma) (Pekar et al., 2005).

The glacial-eustatic record for the Paleocene remains cryptic. Oxygen isotope values during this time were relatively

low ($\sim 1.0\%$), although these values are similar to those of the middle Eocene. Additionally, stratigraphic studies have identified sequence boundaries that may be due to ice volume changes (Haq et al., 1987; Liu et al., 1997). Thus, it is reasonable to infer that small (< 25 m), ephemeral ice sheets may have existed during this time.

The Mesozoic era

The Mesozoic was a time of generally warm equable climates that extended to high latitudes, thus the existence of significant ice sheets was unlikely. Yet, rapid and large sea-level changes, recognized in stratigraphic records, present a conundrum in this supposedly ice-free world (Haq et al., 1987; Hallam, 1992). These greenhouse sequences can be explained as follows: (a) they are locally controlled (e.g., delta lobe switching, local tectonics); (b) they formed from low amplitude sea-level changes (sea-level changes of up to 10 m on a million-year timescale can be caused by a number of mechanisms such as thermal expansion or contraction of ocean water); (c) in as much as the mechanisms of large rapid sea-level changes are poorly understood, there could have been significant ice sheets during so-called greenhouse worlds (Miller et al., 2004).

Recent stratigraphic studies from a number of sites around the world (New Jersey: Miller et al., 2004; NW European sections: Hancock, 1993; and Russian sections: Sahagian et al., 1996) have lent credence to the idea that significant ice sheets existed at least intermittently during the Cretaceous, by identifying and dating large and rapid sea-level changes. The good correlation between the timing of these sea-level changes and increases observed in oxygen isotope records supports this hypothesis (Miller et al., 2004). The paradox of high-latitude warmth during the Cretaceous together with significant ice volume can be resolved if one assumes ephemeral, areally limited ice sheet development in Antarctica. The estimated size of ice sheets would have been restricted to the interior of the Antarctic Continent. Thus coastal waters around Antarctica could have remained relatively warm, while at the same time, ice sheets equivalent to ~ 10 – 40 m of sea-level change could have grown and decayed (Miller et al., 2004).

Evidence for extensive glacial-eustatic changes for the remainder of the Mesozoic era remains largely uncertain. This period of rising sea level during the fragmentation of the super-continent Pangaea was associated with generally warm and equable climates and was largely ice free. A number of studies suggest numerous rapid sea-level changes during the lower Cretaceous down through the base of the Triassic (Haq et al., 1987; Hallam, 1992). Nevertheless, it is uncertain whether these were due to tectono-eustasy or local changes in sedimentation or tectonics.

The Paleozoic era

Large-scale waxing and waning of ice sheets in the southern super-continent Gondwanaland occurred episodically throughout the Paleozoic (Figure G17). Glacial-eustatic changes during the late Paleozoic have been ascribed to at least three glacial periods in Gondwanaland (e.g., Isbell et al., 2003). The late Carboniferous and early Permian contain perhaps the best evidence for large (> 30 m) glacial-eustatic events. This includes glaciogenic sediments in Gondwanaland and transgressive/regressive cycles observed mainly in North America and Europe. Stratigraphic evidence indicates large eustatic amplitudes ranging from ~ 60 – 70 m (Moore, 1964; Adlis et al., 1988; Crowley and Baum,

1991) to ~100 m (Smith and Read, 2000; Heckel, 1994) and as high as 200 m (Soreghan and Giles, 1999; Ross and Ross, 1987). Cyclothem deposits (transgressive/regressive sedimentary packages) characterize Carboniferous to lower Permian strata in both North America and Europe and have been ascribed to glacial-eustatic changes. The deposits display a cyclicity between 44 and 412 kyr, which falls within the range of Milankovitch orbital cycles (Isbell et al., 2003; Imbrie, 1985). In contrast, smaller eustatic amplitudes have been suggested based on the aerial extent of Gondwanaland glaciogenic sediments of no more than 50 m (Isbell et al., 2003). Two other glacial events (late Devonian and late Mississippian to early Pennsylvanian) were probably smaller in extent and consequently resulted in smaller glacial-eustatic changes. Cyclothem and longer timescale sea-level changes have been correlated between stratigraphic sections in North America and Europe, indicating a global mechanism. The lower Paleozoic records contain evidence for glacial events in Gondwanaland and glacial-eustatic sea-level changes in the stratigraphic record. One of the largest Paleozoic glaciations occurred during a two million year span (437–435 Ma) in the late Ordovician, as northern Africa drifted over the South Pole (e.g., Berry et al., 1995). Glaciogenic sediments typical of large continental ice sheets have been identified in Saharan Africa and Saudi Arabia (e.g., Vaslet, 1990). Geological data suggest that southern ice sheets may have reached paleolatitudes near 50° S (Brenchley and Newell, 1984).

Snowball earth episodes in the proterozoic

The largest glacial events in Earth's history occurred during the early Proterozoic (~2.3 Ga) and Neo-Proterozoic (~0.7 Ga) when cold glacial conditions extended into the tropics. Ice-volume extent and subsequent glacial-eustatic amplitudes are uncertain during the Neo-Proterozoic, with estimates ranging from 160 m, inferred from stratigraphic records of an incised valley, to perhaps several times that of the Pleistocene glaciation (Hyde et al., 2000). A debate continues over the extent of the sea ice and whether the Earth did indeed become a true "snowball" or whether it remained a "slush ball", with the tropics remaining mainly ice-free (Hoffman et al., 1998; Christie-Blick et al., 1999). In both glacial periods, decreases in greenhouse gases are thought to have been a primary mechanism for the initiation of these colder periods. It has also been speculated that the Earth's tilt may have been higher (>54°) during these periods, which could have resulted in low latitude glaciation without the entire Earth experiencing glacial conditions (Jenkins, 2003).

Stephen F. Pekar

Bibliography

- Abreu, V.S., and Anderson, J.B., 1998. Glacial eustasy during the Cenozoic: Sequence stratigraphic implications. *Am. Assoc. of Pet. Geol. Bull.*, **82**, 1385–1400.
- Adlis, D.S., Grossma, E.L., Yancey, T.E., and McLerran, R.D., 1988. Isotope stratigraphy and paleodepth changes of Pennsylvanian cyclical sedimentary deposits. *Palios*, **3**, 487–506.
- Berry, W.B.N., Quinby-Hunt, M.S., and Wilde, P., 1995. Impact of late ordovician glaciation-deglaciation on marine life. In Stanley, S.M., Knoll, A.H., Kennett, J.P. (eds.), *Effects of Past Global Change on Life*. Washington, DC: The National Academy Press, pp. 34–46.
- Billups, K., and Schrag, D.P., 2003. Application of benthic foraminiferal Mg/Ca ratios to questions of Cenozoic climate change. *Earth Planet. Sci. Lett.*, **209**, 181–195.
- Billups, K., Channell, J.E.T., and Zachos, J., 2002. Late Oligocene to early Miocene geochronology and paleoceanography from the subantarctic South Atlantic. *Paleoceanography*, **17**, 1, doi: 10.1029/2000PA000568.
- Brenchley, P.J., and Newell, G., 1984. Late Ordovician environmental changes and their effect on faunas. In Bruton, D.L. (ed.), *Aspects of the Ordovician System*. Paleontological Contributions for the University of Oslo No **295**, pp. 65–79.
- Breza, J., and Wise, S.W., 1992. Lower Oligocene ice rafted debris on the Kerguelen Plateau: evidence for east Antarctic continental glaciation. In Schlich, R., Wise, S.W. Jr., et al. (eds.), *Proceedings of the Ocean Drilling Program Scientific Results*, vol. 120. College Station, TX: Ocean Drilling Program, pp. 161–178.
- Browning, J.V., Miller, K.G., and Pak, D.K., 1996. Global implications of lower to middle Eocene sequence boundaries on the New Jersey coastal plain: The icehouse cometh. *Geology*, **24**, 639–642.
- Chappell, J., Omura, A., Esat, T., McMulloch, M., Pandolfi, J., Ota, Y., and Pillans, B., 1996. Reconciliation of Late Quaternary sea levels derived from coral terraces at Huon Peninsula with deep-sea oxygen isotope records. *Earth Planet. Sci. Lett.*, **141**, 227–236.
- Christie-Blick, N., 1991. Onlap, offlap, and the origin of unconformity-bounded depositional sequences. *Mar. Geol.*, **97**, 35–56.
- Christie-Blick, N., and Driscoll, N.W., 1995. Sequence stratigraphy. *Annu. Rev. Earth Planet. Sci.*, **23**, 451–478.
- Christie-Blick, N., Sohl, L.E., and Kennedy, M.J., 1999. Considering a Neoproterozoic snowball Earth (Technical Comment). *Science*, **284**, 1087.
- Coxall, H.K., Wilson, P.A., Palike, H., Lear, C.H., and Backman, J., 2005. Rapid stepwise onset of Antarctic glaciation and deeper calcite compensation in the Pacific Ocean. *Nature*, **433**, 53–57.
- Crowley, T.J., and Baum, S.K., 1991. Estimating Carboniferous sea-level fluctuations from Gondwana ice extent. *Geology*, **19**, 975–977.
- Crowley, T.J., and Burke, K.C. (eds.), 1998. *Tectonic Boundary Conditions for Climate Reconstructions*. New York: Oxford University Press, pp. 3–17.
- DeConto, R.M., and Pollard, D., 2003. Rapid Cenozoic glaciation of Antarctica induced by declining atmospheric CO₂. *Nature*, **421**, 245–249.
- Denton, G.H., Prentice, M.L., Kellogg, D.E., and Kellogg, T.B., 1984. Late Tertiary history of the Antarctic Ice Sheet: evidence from the Dry Valleys. *Geology*, **12**, 263–267.
- Dowsett, H.J., and Cronin, T.M., 1990. High eustatic sea level during the middle Pliocene: Evidence from the southeastern U.S. Atlantic Coastal Plain. *Geology*, **18**, 435–438.
- Eberli, G.P., 2000. The record of Neogene sea-level changes in the prograding carbonates along the Bahamas Transect – Leg 166 synthesis. In Swart, P.K., et al. (eds.), *Proceedings of the Ocean Drilling Program, Scientific Results*, vol 166. College Station, TX: Ocean Drilling Program, pp. 167–177.
- Fairbanks, R.G., 1989. Glacio-eustatic record 0–16,000 years before present: Influence of glacial rates on Younger Dryas event and deep ocean circulation. *Nature*, **342**, 637–642.
- Fairbanks, R.G., and Matthews, R.K., 1978. The marine oxygen isotopic record in Pleistocene coral, Barbados, West Indies. *Quaternary Res.*, **10**, 181–196.
- Goodbred, S.L., Wright, E.W., and Hine, A.C., 1998. Sea-level change and storm-surge deposition in a late Holocene Florida salt marsh. *J. Sediment. Res.*, **68**, 240–252.
- Hallam, A., 1992. *Phanerozoic Sea-Level Changes*. New York: Columbia University Press, 266pp.
- Hancock, J.M., 1993. Transatlantic correlations in the Campanian-Maastrichtian stages by eustatic changes of sea-level. In Hailwood, E.A., and Kidd, R.B. (eds.), *High Resolution Stratigraphy*. Geological Society Special Publication, vol. 70. London: The Geological Society, pp. 241–256.
- Haq, B.U., Hardenbol, J., and Vail, P.R., 1987. Chronology of fluctuating sea levels since the Triassic. *Science*, **235**, 1156–1167.
- Hearty, P.J., Kindler, P., Cheng, H., and Edwards, R.L., 1999. A+20 m middle Pleistocene sea-level highstand (Bermuda and the Bahamas) due to partial collapse of Antarctic ice. *Geology*, **27**, 375–378.
- Heckel, P.H., 1994. Evaluation of evidence for glacio-eustatic control over marine Pennsylvanian cyclothem in North America and consideration of possible tectonic effects. In Dennison, J.M., and Eddensohn, F.R. (eds.), *Tectonic and Eustatic Controls on Sedimentary Cycles*. SEPM Concepts in Sedimentology and Paleontology, vol. 4. Tulsa OK: Society for Sedimentary Geology, pp. 65–87.
- Hoffman, P.F., Kaufman, A.J., Halverson, G.P., and Schrag, D.P., 1998. A Neoproterozoic snowball Earth. *Science*, **281**, 1342–1346.
- Houghton, J.T., Ding, Y., Griggs, D.J., Noguier, M., van der Linden, P.J., Dai, X., Maskell, K., and Johnson, C.A., 2001. *Climate Change 2001: The Scientific Basis*, Cambridge: Cambridge University Press, 881pp.

- Hyde, W.T., Crowley, T.J., Baum, S.K., and Peltier, W., 2000. Neo Proterozoic 'snowball Earth' simulations with a coupled climate ice-sheet model. *Nature*, **405**, 425–429.
- Imbrie, J., 1985. A theoretical framework for the Pleistocene ice ages. *J. Geol. Soc.*, **142**, 417–432.
- Isbell, J.L., Miller, M.F., Wolfe, K.L., and Lenaker, P.A., 2003. Timing of late Paleozoic glaciation in Gondwana: Was glaciation responsible for the development of Northern Hemisphere cyclothem? In Chan, M.A., and Archer, A.W. (eds.), *Extreme Depositional Environments: Mega End Members in Geologic Time*. Geological Society of America Special Paper, 370. Boulder, CO: Geological Society of America, pp. 5–24.
- Jansen, E., Sjolholm, J., Bleil, U., and Erichsen, J.A., 1990. Neogene and Pleistocene glaciations in the Northern Hemisphere and the late Miocene-Pliocene glacial ice volume fluctuations: Evidence from the Norwegian Sea. In Bleil, U., and Thiede, J. (eds.), *Geological History of the Polar Oceans: Arctic versus Antarctic*. Amsterdam: Kluwer, pp. 677–705.
- Jenkins, G.S., 2003. GCM greenhouse and high-obliquity solutions for early Proterozoic glaciation and middle Proterozoic warmth. *J. Geophys. Res.*, **108**, NO. D3, 4118, doi:10.1029/2001JD001582.
- Kominz, M.A., Miller, K.G., and Browning, J.V., 1996. Long-term and short-term global Cenozoic sea-level estimates. *Geology*, **26**, 311–314.
- Kominz, M.A., and Pekar, S.F., 2001. Oligocene eustasy from two-dimensional sequence stratigraphic backstripping. *Geol. Soc. Am. Bull.*, **113**, 291–304.
- Lear, C.H., Elderfield, H., and Wilson, P.A., 2000. Cenozoic deep-sea temperature and global ice volumes from Mg/Ca in benthic foraminiferal calcite. *Science*, **287**, 269–272.
- Lear, C.H., Rosenthal, Y., Coxall, H.K., and Wilson, P.A., 2004. Late Eocene to early Miocene ice sheet dynamics and the global carbon cycle. *Paleoceanography*, **19**, PA4015, doi: 10.1029/2004PA001039.
- Liu, C., Browning, J.V., Miller, K.G., and Olsson, R.K., 1997. Paleocene benthic foraminiferal biofacies and sequence stratigraphy. In Miller, K.G., and Snyder, S.W. (eds.), *Proc. ODP Sci. Results*, vol 150X. College Station, TX: Ocean Drilling Program, pp. 267–276.
- Martin, P.A., Lea, D.W., Rosenthal, Y., Shackleton, N.J., Sarntheim, M., and Papenfuss, T., 2002. Quaternary deep-sea temperature histories derived from benthic foraminiferal Mg/Ca. *Earth Planet. Sci. Lett.*, **198**, 193–209.
- Miller, K.G., Mountain, G.S., and Tucholke, B.E., 1985. Oligocene glacioeustasy and erosion on the margins of the North Atlantic. *Geology*, **14**, 257–261.
- Miller, K.G., Fairbanks, R.G., and Mountain, G.S., 1987. Tertiary oxygen isotope synthesis, sea-level history, and continental margin erosion. *Paleoceanography*, **2**, 1–19.
- Miller, K.G., Wright, J.D., and Fairbanks, R.G., 1991. Unlocking the icehouse: Oligocene-Miocene oxygen isotopes, eustasy, and margin erosion. *J. Geophys. Res.*, **96**, 6829–6848.
- Miller, K.G., Mountain, G.S., Blum, P., Gartner, S., Alm, P.G., Aubry, M. P., Burckle, L.H., Guerin, G., Katz, M.E., Christensen, B.A., Compton, J., Damuth, J.E., Deconinck, J.F., de Verteuil, L., Fulthorpe, C.S., Hesselbo, S.P., Hoppie, B.W., Kotake, N., Lorenzo, J.M., McCracken, S., McHugh, C.M., Quayle, W.C., Saito, Yoshiki, S., S.W., ten Kate, W.G., Urrutia, M., Van Fossen, M.C., Vecsei, A., Sugarman, P.J., Mullikins, L., Pekar, S., Browning, J.V., Liu, C., Feigenson, M.D., Goss, M., Gwynn, D., Queen, D.G., Powars, D.S., Heibel, T.D., and Bukry, D., 1996. Drilling and dating New Jersey Oligocene-Miocene sequences; ice volume, global sea level, and Exxon records. *Science*, **271**, 1092–1095.
- Miller, K.G., Rufolo, S., Gwynn, D., and Pekar, S.F., 1997. Miocene benthic foraminiferal biofacies and sequences. In Miller, K.G., and Snyder, S.W., (eds.), *Proceedings of the Ocean Drilling Program, Scientific Results*, vol. 150X. College Station, TX: Ocean Drilling Program, pp. 169–186.
- Miller, K.G., Mountain, G.S., Browning, J.V., Kominz, M., Sugarman, P.J., Christie-Blick, N., Katz, M.E., and Wright, J.D., 1998. Cenozoic global sea level, sequences, and the New Jersey Transect: Results from coastal plain and continental slope drilling. *Rev. Geophys.*, **36**, 569–601.
- Miller, K.G., Barrera, E., Olsson, R.K., Sugarman, P.J., and Savin, S.M., 1999. Does ice drive Maastrichtian eustasy? *Geology*, **27**, 783–786.
- Miller, K.G., Sugarman, P.J., Browning, J.V., Kominz, M.A., Olsson, R.K., Feigenson, M.D., and Hernandez, J.C., 2004. Upper Cretaceous sequences and sea-level history, New Jersey Coastal Plain. *Geol. Soc. Am. Bull.*, **116**, 368–393.
- Moore, R.C., 1964. Paleocological aspects of Kansas Pennsylvanian and Permian cyclothem. In Merriam, D.F. (ed.), *Symposium on Cyclic Sedimentation*. Kansas Geological Survey Bulletin, 169, pp. 287–380.
- Naish, T.R., Woolfe, K.J., Barrett, P.J., Wilson, G.S., Cliff, A., Bohaty, S.M., Buckler, C.J., Claps, M., Davey, F.J., Dunbar, G.B., Dunn, A.G., Fielding, C.R., Florindo, F., Hannah, M.J., Harwood, D.M., Henrys, S.A., Krissek, L.A., Lavelle, M., Van der Meer, J., McIntosh, W.C., Niessen, F., Passchier, S., Powell, R.D., Roberts, A.P., Sagnotti, L., Scherer, R.P., Strong, P.C., Talarico, F., Verosub, K.L., Villa, G., Watkins, D.K., Webb, P.N., and Wonik, T., 2001. Orbitally induced oscillations in the East Antarctic Ice Sheet at the Oligocene/Miocene boundary. *Nature*, **413**, 719–723.
- Oleg, P.V., Akhmetiev, M.A., and Sahagian, D.L., 1999. Sequence stratigraphy and sea-level history of Oligocene strata of the northern Aral Sea region (Kazakhstan): Implications for glacioeustatic reconstructions. *Geol. Soc. Am. Bull.*, **111**, 1–10.
- Pearson, P.N., and Palmer, M.R., 2000. Atmospheric carbon dioxide concentrations over the past 60 million years. *Nature*, **406**, 695–699.
- Pekar, S.F., and Christie-Blick, N., 2007. Resolving apparent conflicts between oceanographic and Antarctic climate records and evidence for a decrease in pCO₂ during the Oligocene through early Miocene (34–16 Ma). *Paleoceanography, Palaeoclimatology, Palaeoecology*, **26**(1–2) p. 41–49.
- Pekar, S.F., and DeConto, R., 2006. High-resolution ice-volume estimates for the early Miocene: Evidence for a dynamic ice sheet in Antarctica. *Paleoceanogr. Palaeoclimatol. Palaeoecol.*, **231**, 101–109.
- Pekar, S.F., and Kominz, M.A., 2001. Two-dimensional paleoslope modeling: A new method for estimating water depths for benthic foraminiferal biofacies and paleo shelf margins. *J. Sediment. Res.*, **71**, 608–620.
- Pekar, S., and Miller, K.G., 1996. New Jersey Oligocene "Icehouse" sequences (ODP Leg 150X) correlated with global $\delta^{18}\text{O}$ and Exxon eustatic records. *Geology*, **24**, 567–570.
- Pekar, S.F., Christie-Blick, N., Kominz, M.A., and Miller, K.G., 2002a. Calibrating eustasy to oxygen isotopes for the early icehouse world of the Oligocene. *Geology*, **30**, 903–906.
- Pekar, S.F., Marchitto, T., Lynch-Steiglitz, J., White, T., and Ennyu, A., 2002b. Evidence for a tropical source for climate change during the early Miocene (19–16 Ma): Stable isotopic and Mg/Ca records from ODP Leg 189 Site 1168. *EOS, Transactions, American Geophysical Union*, F927.
- Pekar, S.F., Christie-Blick, N., Miller, K.G., and Kominz, M.A., 2003. Evaluating factors controlling stratigraphic architecture at passive continental margins: Oligocene sedimentation in New Jersey. *J. Sediment. Res.*, **73**, 227–245.
- Pekar, S.F., Hucks, A., Fuller, M., and Li, S., 2005. Glacioeustatic changes during the early and middle Eocene (51–42 Ma) greenhouse worlds based on shallow-water stratigraphy from ODP Leg 189 Site 1171 and oxygen isotope records. *Geol. Soc. Am. Bull.*, **117**, 1081–1093.
- Pekar, S.F., Harwood, D., and DeConto, R., 2006. Resolving a late Oligocene conundrum: Deep-sea warming versus Antarctic glaciation. *Paleoceanogr. Palaeoclimatol. Palaeoecol.*, **231**, 29–40.
- Peltier, W.R., 1998. Postglacial variations in the level of the sea: Implications for climate dynamics and solid-earth geophysics. *Rev. Geophys.*, **36**, 603–689.
- Peltier, W.R., 1999. Global sea-level rise and glacial isostatic adjustment. *Global Planet. Change*, **20**, 93–123.
- Posamentier, H.W., Jervey, M.T., and Vail, P.R., 1988. Eustatic controls on clastic deposition I – Conceptual framework. In Wilgus, C.K., et al. (eds.), *Sea-Level Changes: An Integrated Approach*. Society of Economic Paleontologists and Mineralogists Special Publication No. **42**, pp. 109–124.
- Raymo, W.E., 1994. The initiation of Northern Hemisphere glaciation. *Annu. Rev. Earth Planet. Sci.*, **22**, 353–383.
- Raymo, M.E., Ruddiman, W.F., Backman, J., Clement, B.M., and Martinson, D.G., 1989. Late Pliocene variation in Northern Hemisphere ice sheets and North Atlantic deep circulation. *Paleoceanography*, **4**, 413–446.
- Roberts, A.P., Wilson, G.S., Harwood, D.M., and Verosub, K.L., 2003. Glaciation across the Oligocene-Miocene boundary in southern McMurdo Sound, Antarctica: New chronology from the CIROS-1 drill hole. *Paleoceanogr. Palaeoclimatol. Palaeoecol.*, **198**, 113–130.
- Ross, C.A., and Ross, J.R.P., 1987. Late Paleozoic sea levels and depositional sequences. *Cushman Foundation for Foraminiferal Research Special Publication*, **24**, 137–149.
- Sahagian, D., Pinous, O., Olfieriev, A., Zakharov, V., and Beisel, A., 1996. Eustatic curve for the Middle Jurassic-Cretaceous based on Russian

- platform and Siberian stratigraphy: Zonal resolution. *Am. Assoc. Petrol. Geol. Bull.*, **80**, 1433–1458.
- Shackleton, N.J., and Opdyke, N.D., 1973. Oxygen isotope and paleomagnetic evidence for early Northern Hemisphere glaciation. *Nature*, **270**, 216–219.
- Shackleton, N.J., Backman, J., Zimmerman, H., Kent, D.V., Hall, M.A., and Roberts, D.G. et al. 1984. Oxygen isotope calibration of the onset of ice-raftering and history of glaciation in the North Atlantic region. *Nature*, **307**, 620–623.
- Scott, D.B., and Medioli, F.S., 1978. Vertical zonations of marsh foraminifera as accurate indicators of former sea levels. *Nature*, **272**, 528–531.
- Smith, L.B., and Read, J.F., 2000. Rapid onset of late Paleozoic glaciation on Gondwana: Evidence from Upper Mississippian strata of the Mid-continent, United States. *Geology*, **28**, 279–282.
- Soreghan, G.S., and Giles, K.A., 1999. Amplitudes of late Pennsylvanian glacioeustasy. *Geology*, **27**, 255–258.
- Steckler, M.S., and Watts, A.B., 1978. Subsidence of the Atlantic-type continental margin off New York. *Earth Planet. Sci. Lett.*, **41**, 1–13.
- Steckler, M.S., Mountain, G.S., Miller, K.G., and Christie-Blick, N., 1999. Reconstruction of Tertiary progradation and clinoform development on the New Jersey passive margin by 2-D backstripping. *Mar. Geol.*, **154**, 399–420.
- Vail, P.R., Mitchum, R.M. Jr., and Thompson, S. III., 1977. Seismic stratigraphy and global changes of sea level. III. Relative changes of sea level from coastal onlap. In Payton, C.E. (ed.), *Seismic Stratigraphy – Applications to Hydrocarbon Exploration*; American Association of Petroleum Geologists, Memoir **26**, 63–81.
- Vaslet, D., 1990. Upper Ordovician glacial deposits in Saudi Arabia. *Episodes*, **13**, 147–161.
- Zachos, J.C., Quinn, T.M., and Salamy, S., 1996. High-resolution (10^4 yr) deep-sea foraminiferal stable isotope records of the earliest Oligocene climate transition. *Paleoceanography*, **9**, 353–387.
- Zachos, J.C., Pagani, M., Sloan, L., Thomas, E., and Billups, K., 2001. Trends, rhythms, and aberrations in global climate 65 Ma to present. *Science*, **292**, 686–693.

Cross-references

Antarctic Glaciation History
 Cenozoic Climate Change
 Cyclic Sedimentation (cyclothem)
 Glacial Isostasy
 Greenhouse (warm) Climates
 Icehouse (cold) Climates
 Neogene Climates
 Oxygen Isotopes
 Paleogene Climates
 Sea-Level Change, Last 250 Million Years
 Sea-Level Change, Post-Glacial
 Sea-Level Change, Quaternary
 Sea-Level Indicators
 Snowball Earth Hypothesis

GLACIAL GEOMORPHOLOGY

Glacial geomorphology is the scientific study of the processes, landscapes, and landforms produced by ice sheets, valley glaciers, and other ice masses on the surface of the Earth. These processes include understanding how ice masses move, and how glacial ice erodes, transports, and deposits sediment. Landscapes and landforms that developed as a result of glaciation are the dominant focus of this field since they carry distinctive features and forms related specifically to glacial processes. Likewise, glacial geomorphology encompasses the impacts of glaciation upon floral and faunal evolution, modification, and distribution; and includes study of those areas peripheral to glaciated terrains, where drainage pattern alteration, climate, vegetation, and soil conditions are all severely affected by glaciation. This field

includes studies of the causes of glaciation, the chronology of glaciation through geologic time (the retreat and advance of ice masses), glacial sediment stratigraphy, and the global impact of glaciations on oceans, climate, flora, fauna, and human society (Mickelson & Attig, 1999; Bennett & Glasser, 1996; Benn & Evans, 1998; Menzies, 2002). Closely allied to glacial geomorphology are studies into the physics of ice masses (glaciology), global climatology (paleoclimatology), and paleoenvironmental reconstructions (paleoecology). It is generally accepted that glacial geomorphology has become synonymous with glacial geology.

In every geological period, other than the Jurassic, there appears to have been at least one, if not several, global glaciations. Earth is a “glacial planet” where ice masses have covered at least 30–60% of the Earth’s surface (continents and ocean basins) approximately every 100,000–150,000 years over the past 800,000 years. Glacial sediments, both lithified and unlithified, are found on every continent, and the present oceanic basins of the Earth are covered by great thicknesses of glaciomarine sediments. At the maximum of the last Pleistocene glaciation, sea levels were at least 120 m below the present sea level, permitting temporary land bridges in the immediate postglacial period to appear between Siberia and Alaska, South Asia and the Indonesian Archipelago, and between continental Europe and the British Isles. Such land bridges acted as corridors through which flora, fauna, and humans colonized North America, northwestern Europe, and parts of Australasia.

The impact of glacial geomorphology upon human society is immense especially in the mid-latitudes and poleward in both North and South Hemispheres. Soils and construction engineering are, for example, affected by glacial sediments and glaciated terrains. Cities such as Boston, Massachusetts and Glasgow, Scotland have been built on drumlin fields such that urban planning and transportation systems must adapt to this “peculiar” hummocky topography. The siting of dams, the intricacies of groundwater pathways, and the location and discovery of minerals are tied to glaciations and problems in glaciated terrains. The impact of glaciation is enormous in the continental USA where at least 60% of the population live and work in areas once covered by the last glaciation (the Wisconsinan). Likewise, in Canada, a comparative figure would be closer to 99% of the Canadian population, and in Western Europe at least 50–60% of the population inhabit formerly glaciated terrain.

Extent of glaciation at present and in the past

Today approximately 10% of the Earth’s surface is covered by ice masses. The two largest ice masses are the Greenland, and the West and East Antarctic Ice Sheets. The remaining ice masses are various mountain valley, cirque, hanging, and piedmont glaciers, small ice caps and fields, and ice shelves attached to the fringes of the Antarctic and the Canadian Arctic Archipelago (Figure G18a). Present ice sheet thickness varies from around 2,500 m in central Greenland to over 4,600 m in Antarctica. Valley glaciers and smaller ice masses are considerably thinner. During the maximum extent of the last glaciation in North America, the thickness of the Laurentide Ice Sheet over Hudson Bay would have been similar to that of Antarctic today (Mickelson & Attig, 1999).

The extent of glaciation during the Pleistocene may have covered at least 30% of the continents. If the oceanic basins in the Arctic, north Pacific, north Atlantic, and Southern Oceans are included, then over 60% of the Earth’s surface would have been ice-bound (Figure G18b). Similar percentages of ice cover may have occurred in earlier geological times.

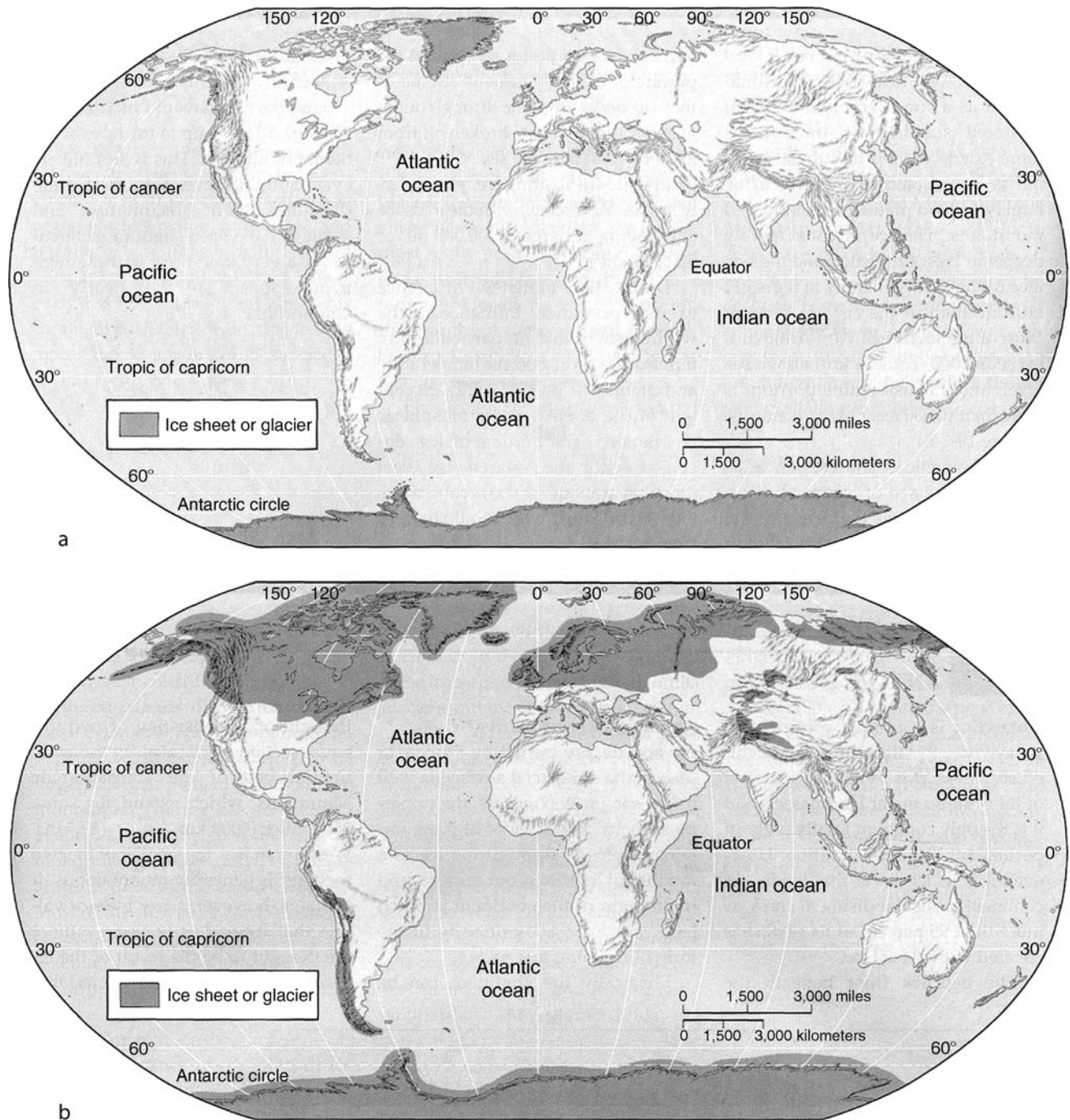


Figure G18 (a) Present worldwide distribution of glacial ice (modified from McKight and Hess, 2000). (b) Extent of worldwide glaciation approximately 18,000 years ago, at the maximum of the Late Wisconsinan (modified from McKight and Hess, 2000).

The Earth as a “Glacial Planet”

The Earth has alternated between interglacial and glacial conditions on an approximate 100,000–150,000 year cycle during most of the Quaternary. Recognition of the recurrence of glaciation in the geologic past is a relatively new concept. In

the nineteenth Century, glacial lithified sediment (the Talchir Boulder Beds) had been recognized in India, and the Permian glacial sediments of Shropshire in England had been identified, but a full recognition of repeated global glaciations only became established in the mid-twentieth Century.

In Europe and North America, during the late nineteenth and early twentieth Centuries, only one single glacial period, the Pleistocene (“The Ice Age,”) was initially recognized. The “Ice Age” was perceived as an unusual aberration of nature, not a repetitive cyclic event. During the Pleistocene, which began around 1.8 million years ago (Ma), much of today’s flora and fauna developed and evolved, and likewise the emergence of our human ancestors stemmed from this period. The Pleistocene was also a time of considerable upheaval in terms of plant speciation and the demise of several larger animals, such as the woolly Rhinoceros, the giant Elk and the Mammoth, towards the end of this period.

As ice ages began to be recognized in Europe, a subdivision of 4 major glaciations was established (Table G1). This four-fold division was further used in North America. Only with oceanic deep drilling programs (ODP) in the North Atlantic and Pacific Oceans that began in 1968 did it become apparent that instead

of 4, at least 17, if not 20, major glaciations had occurred during what was a much longer and colder Pleistocene Period. In the past, it was thought that glaciations worldwide were synchronous in their advances and retreats, but it has become apparent that fluctuations in ice mass margins vary considerably between continents and along different margins of the same ice sheet. For example, along the margins of the Laurentide Ice Sheet in North America, retreat and advance of margins differed considerably between the east coast of New England and the Canadian Maritimes as compared with the margin in the Dakotas and the Canadian Prairies. This lack of synchronicity, certainly over periods of time less than 2,000 years, suggested a much more complex glacial history than previously considered. With modern dating methods and the use of oxygen isotope ratios (establishing the basis for marine Oxygen Isotope Stages), warm (interglacial) and cold (glacial) periods can be determined where the sediment record permits (Figure G19). We now appear to live an interglacial period that may be further prolonged in time or heightened in temperature due to global “greenhouse” warming.

Table G1 Major glaciations of North America and western Europe

European Alps	Northwest Europe	Britain	North America
Würm <i>R/W</i>	Weichsel <i>Eem</i> Warthe	Devensian <i>Ipswichian</i>	Wisconsinan <i>Sangamon</i>
Riss	Saale Drenthe	Wolstonian	Illinoian
<i>M/R</i>	<i>Holstein</i>	<i>Hoxnian</i>	<i>Yarmouth</i>
Mindel	Elster	Anglian	Kansan
<i>G/M</i>	<i>Cromerian</i>	<i>Cromerian</i>	<i>Aftonian</i>
Günz			Nebraskan

Interglacials in *italics*; glaciations in **bold**.

Glacial landscapes – today

In the Pleistocene, vast ice sheets covered the Earth’s surface beginning with a relatively slow build up to repeated maximum extensions into the mid-latitudes (Figure G18b). These ice sheets had an enormous impact in moving across terrain and eroding, transporting, and depositing vast quantities of sediments both on land and in the ocean basins. The surface topography of the continents today, for example in the northern states of USA and throughout Canada and northern Europe, was totally modified, with distinctive landscapes and landforms repeatedly overprinted until the terrain was finally exposed from beneath the ice some 10,000 years ago. Although ice

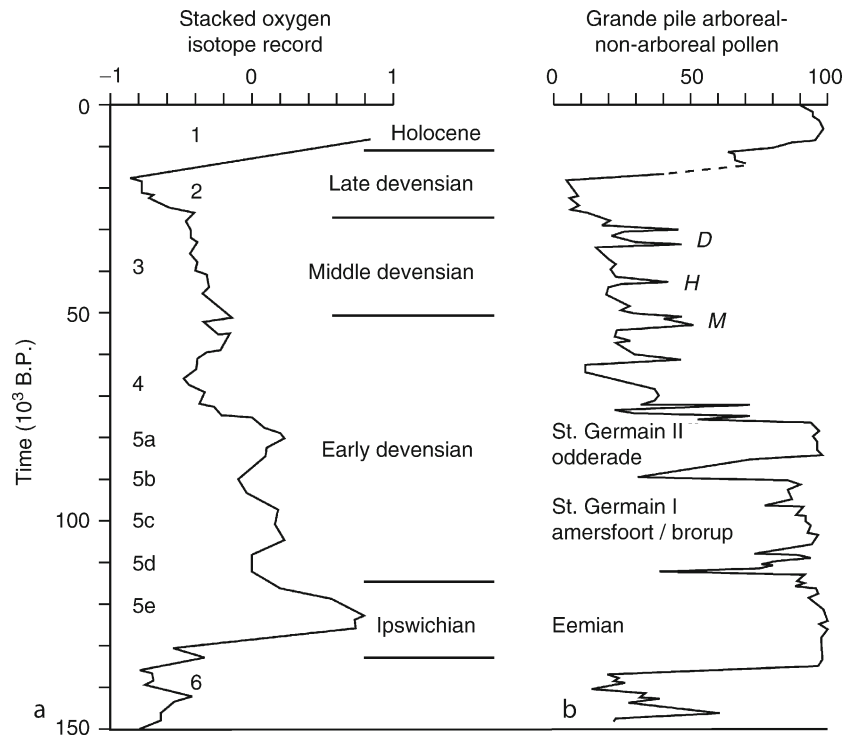


Figure G19 Oxygen isotope record of glaciations for the past 130,000 years (modified after Bowen, 1994).

sheet build-up was relatively slow, the downwasting and melting of the ice sheets was remarkably fast. With the rapid demise of the ice sheets, sea level very quickly rose and, since the ice sheets had isostatically depressed the continental land masses, in many instances sea level rose above present levels, drowning large coastal areas. Much later, continental land masses readjusted to the loss of the ice sheet load and slowly rose. Raised shorelines and cliffs began to re-appear above sea levels. These raised beaches and strandlines, for example in Europe, became the colonization pathways for early humans as they moved northward.

Glacial erosion can be seen on bedrock surfaces in the form of glacial striae and chattermarks, and the effects of high



Figure G20 Striated boulder within a clast-rich till, Steingletscher, Switzerland (boulder is approximately 11 cm across).

pressure meltwater scour (Figure G20). Evidence of glacial transport can be observed in the form of boulder trains and isolated erratic boulders left strewn across glaciated landscapes (Figure G21). Finally, the effects of glacial deposition can be seen as thick glacial sediments, and landforms such as moraines, drumlins and eskers, glacial lake sediments, and immense thicknesses of glacial sediments within marine environments (Menzies, 2002).

Glacial erosion – processes, landforms, and landscape systems

The processes of glacial erosion produce sediments for transport and later glacial deposition. Processes of erosion occur in all glacial environments. Although rather limited, supraglacial erosion in the form of abrasion and meltwater action occurs on the surfaces of ice masses, especially during the summer months when melted ice and snow move across glacier surfaces. In mountainous areas, considerable windblown detritus and debris deposited by avalanches and mass movement often ends up in the supraglacial environment where it may undergo abrasion and meltwater action. Even more limited is the amount of erosion that occurs within ice masses in englacial tunnels where glacial sediment is transported spasmodically depending on meltwater activity within an ice mass. Proglacial erosion is considerable since significant volumes of debris are released from ice masses either along lateral and frontal margins in valley glaciers, along the front margins of large ice sheets, or into oceanic basins where ice margins are floating or have attached ice shelves and thus debris is removed via a grounding-line. In all these locations, sediment entering the proglacial environment is subject to substantial erosion largely due to meltwater transport and mass movement. Most glacial erosion, however, occurs in the subglacial environment where high stress levels, meltwater under hydrostatic pressures, and a vast source of erodable material are available (Figure G22).



Figure G21 Erratic boulder sitting on outwash plain in front of the Mont Miné Glacier, Valais, Switzerland (boulder approximately 2 m high).



Figure G22 Subglacial deposits directly beneath a glacier in Switzerland.

Processes

Glacial erosional processes can be subdivided under five main headings: abrasion, plucking/quarrying, meltwater action, chemical action, and freeze-thaw processes. In general, all of these processes may operate on the same rock surfaces such that examples of glacial erosion typically possess all the characteristic “marks” of all these processes Benn & Evans, 1998; Menzies, 2002.

Abrasion is the wearing down of bedrock and rock fragment surfaces by the scouring of debris-laden ice and meltwater. In both instances, as the debris at the base of the ice or moving within high pressure meltwater passes over the surface of bedrock or other rock surfaces, scratching and wearing down of the surface occurs. The evidence takes the form of minute scratches or striae (Figure G20) on rock surfaces, or extremely polished rock faces with smoothly sculpted geometries that illustrate rapid wear. These latter forms of erosion are termed P-forms (Figure G23). To be effective, such abrasion processes demand high basal ice debris concentrations and/or elevated debris content in high pressure meltwater streams – debris that is sharp, angular, and harder than the rock surfaces being cut; sufficiently strong basal ice pressures; and finally an effective means of evacuation of the abraded debris. This latter requirement is essential if the abrasion process is to continue and not become “clogged.” The production of immense volumes of abraded debris is apparent in the down-stream “milky” nature of glacial streams that exhibit a blue or greenish-blue color due to the high fine debris content referred to as “glacial milk” or “rock flour.”

Plucking or quarrying is a set of processes that removes fractured, jointed, or disaggregated rock fragments from bedrock or the rock surface. Typically, rocks fracture under tensile or compressive stresses produced by the overall stress levels created by the overlying moving ice mass, or by percussive processes where rock fragments crash against rock surfaces and produce flakes and shards of rock materials. Rock plucking can produce enormous boulders and minuscule rock flakes.



Figure G23 P-forms from Espanola, Ontario (scale card 8.5 cm long).

Where large bedrock knobs have been overridden, roche moutonnée may be produced as distinctive erosional landforms with smooth up-ice (stoss) sides and steep craggy down-ice (lee) sides (Figure G24). Where percussive plucking occurs on rock surfaces, tiny chattermarks and lunate fractures develop (Figure G23).

Meltwater, in association with high debris content and high pressure discharge, creates other forms of abrasive wear on rock surfaces. A little-understood process is the effects of chemical weathering beneath ice masses where hydrostatically pressured meltwater, high stress levels, and fluctuating temperatures lead to carbonate, silicate, and iron solution and re-precipitation down-ice. Characteristically, such chemical processes can usually be observed as distinctive stains or “trails” on rock

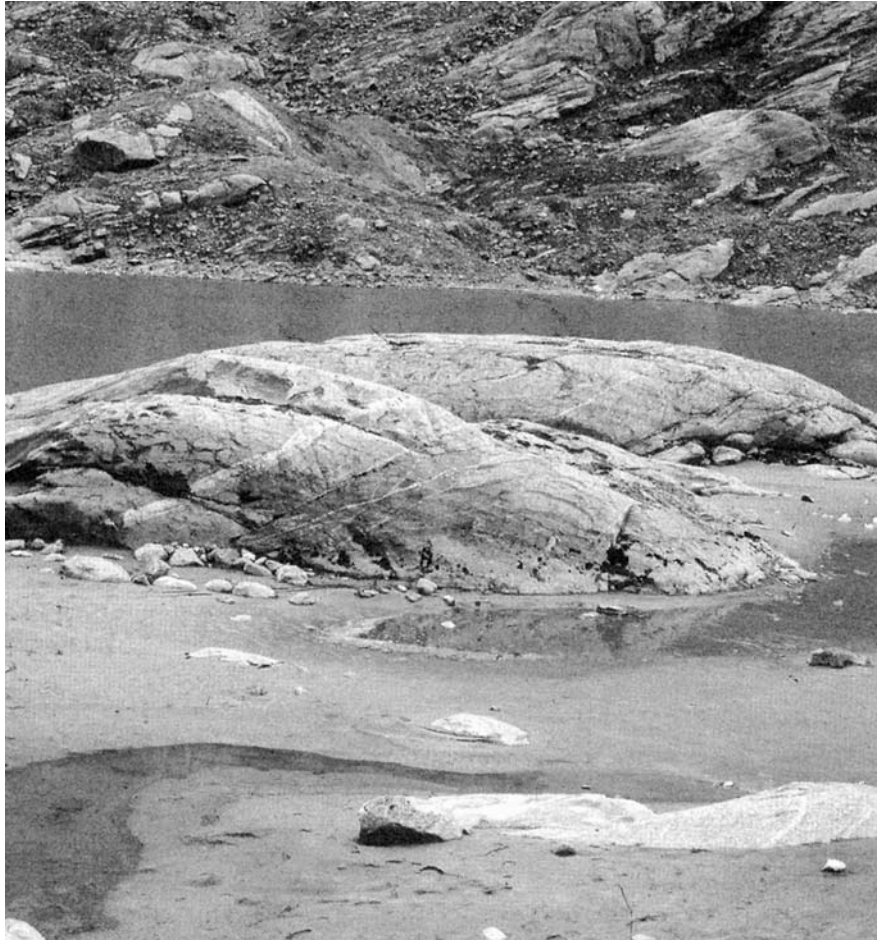


Figure G24 Roche moutonnée (approx. 25 m in length) in front of Nigardsbreen, Norway; ice moving from right to left.

surfaces, often on the lee-side of bedrock protrusions. Finally, in glacial environments, freeze-thaw processes are active, seasonally and diurnally, producing large volumes of frost shattered rock materials.

Landforms

Glacial erosional landforms can be subdivided into areal and linear forms. The range of scale of these landforms can be immense, from centimeter sized “rats-tails” and flutes on rock surfaces (Figure G25) to roche moutonnée, tens of meters in height (Figure G24). Vast areas of the Canadian and Fennoscandian Shields best portray widespread areal glacial erosion (Figure G26). Linear forms such as fjords, troughs (U-shaped valleys) (Figure G27), finger lakes, tunnel valleys, and, at a much smaller scale, fluted bedrock knobs (P-forms) and roche moutonnée, occur in all glaciated regions. All of these landforms reflect the erosive power of glaciers and ice sheets, and their associated meltwater action.

Landscape systems

Perhaps the best known example of a glaciated landscape system is that of high mountain glaciation where pyramidal peaks



Figure G25 Various fluted and streamlined bedrock forms – small-scale flutes, Wilton, Ontario.

(horns), arêtes, cirques, tarn lakes, rock steps (riegels), and hanging valleys are found in close association (Figure G28). No similar landscape system exists for ice sheet erosive landscapes except for the areal scour, bedrock trough, fluted

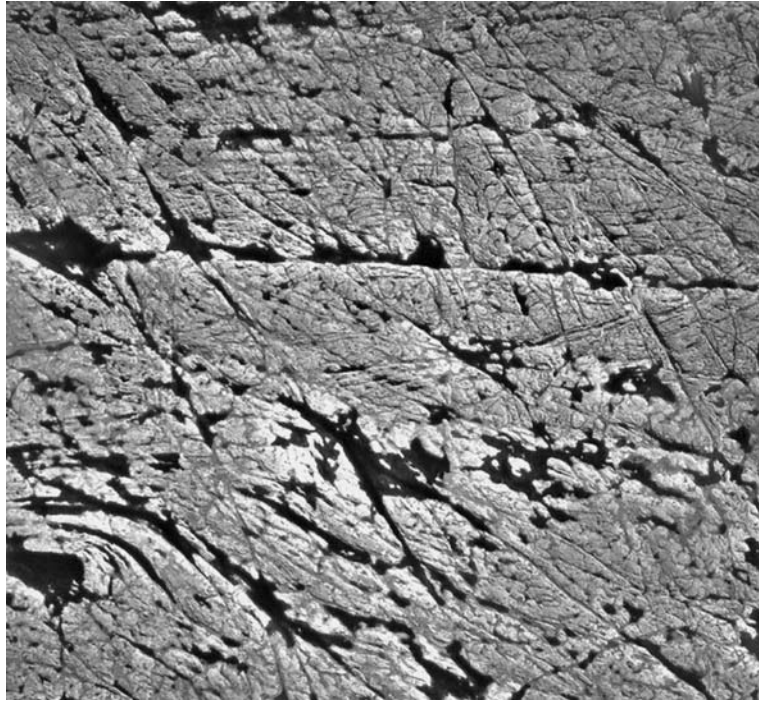


Figure G26 Aerially scoured glacialiated terrain near Lac Troie, Quebec, Canada.



Figure G27 Princess Louise Inlet, British Columbia, Canada.

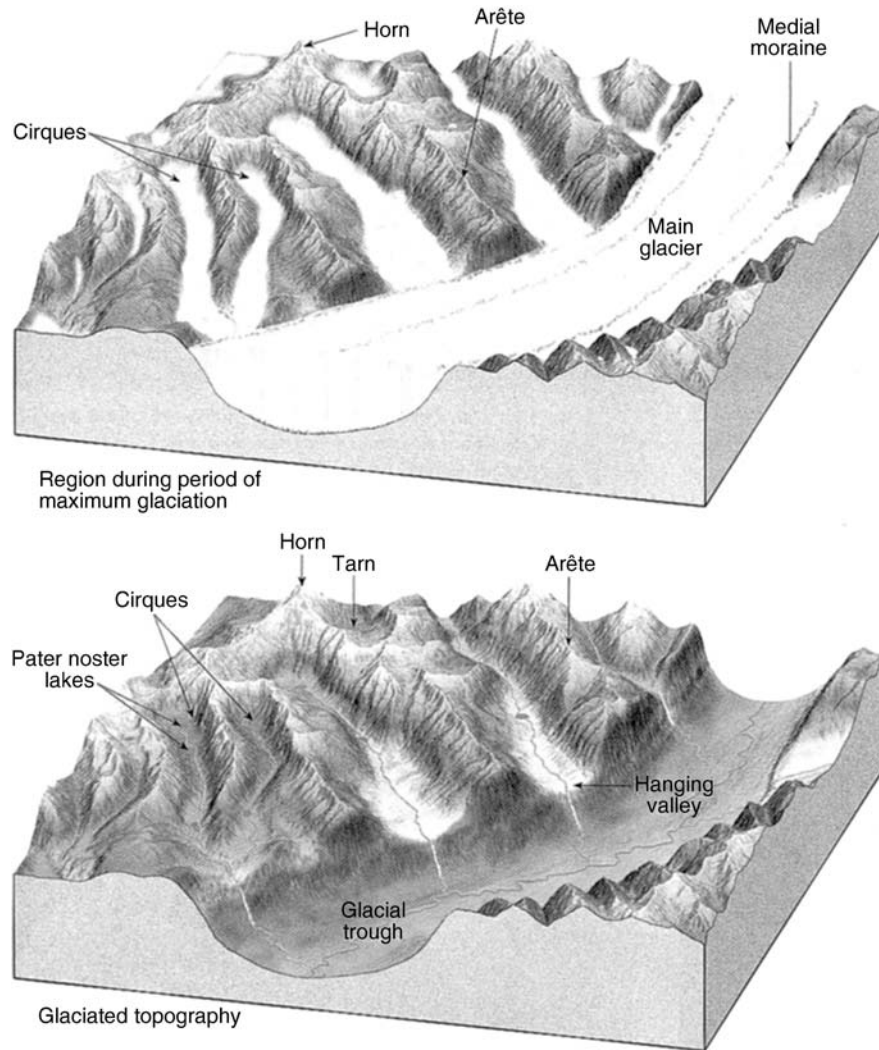


Figure G28 Erosional landscape system for alpine glaciation (modified from Tarbuck and Lutgens, 2003).

bedrock knob landscapes, such as the Canadian and Fennoscandian Shields, for example Bennett & Glasser, 1996; Benn & Evans, 1998.

Glacial transport

Glaciers and ice sheets transport vast quantities of sediment from fine-grained clays and silts to huge boulders. Sediment is transported on the surface of the ice as supraglacial debris, within the ice as englacial debris, beneath the ice as subglacial debris, and beyond the ice margins as proglacial sediment. Each environment affixes the transported sediment with a potentially distinctive signature that, although complex due to overprinting and re-transportation, can be used, at times, to differentiate glacial sediment types Bennett & Glasser, 1996; Benn & Evans, 1998; Menzies, 2002. Sediment is transported encased within the basal layers of the ice, on the surface of the ice, and beneath the ice within deforming soft sediment beds.

Glacial deposition: processes, landforms, and landscape systems

The deposition of glacial sediment is largely a function of the means of sediment transportation. Since ice masses scavenge sediments from their glaciated basins, and in the case of ice sheets this may be continental landmasses, the provenance of glacial sediment is typically immense, containing far-traveled sediment and boulders as well as local rock materials. In fact, most glacial sediments reflect a provenance only a few 10s of kilometers up-ice from any point of deposition. However, repeated glaciation may greatly increase the original distance from the origin to the final deposition site.

Glacial deposits occur as unsorted sediments with a wide range of particle sizes and as sorted sediments deposited by meltwater. Unsorted sediments are typically referred to as till or glacial diamicton. These sediments are exceedingly complex sedimentologically and stratigraphically. They occur in all sub-environments of the glacier system and range from subglacial clay-rich,

consolidated lodgement tills to coarse supraglacial flow tills, and subglacial and submarginal areas of basal ice melting leading to melt-out tills. However, this classification with reference to subglacial tills is probably inaccurate. It would be more rigorous to term these tills “tectomicts,” products of the complex subglacial environment.

The sorted or fluvio-glacial sediments range from fine-grained clays deposited in glacial lakes (glaciolacustrine) to coarser sands and gravels deposited in front of ice masses as outwash fans or sandur, and rain-out sediments deposited in marine settings (glaciomarine).

Processes

The processes of glacial deposition range from direct smearing of subglacial debris as lodgement tills to mass movement of sediments from the frontal and lateral margins of glaciers as flow tills, and to direct ablation of ice forming melt-out tills in front of ice masses in proglacial areas and within subglacial cavities.

Landforms

Glacial landforms include those formed (a) transverse to ice motion, (b) parallel to ice motion, (c) unoriented, non-linear, (d) ice marginal, and (e) fluvio-glacial. Although a complex myriad of glacial depositional forms occur in most glaciated areas, the dominant landforms discussed below include (a) Rogen moraines, (b) drumlins and fluted moraines, (c) hummocky moraines, (d) end moraines, and (e) eskers and kames.

Rogen moraines or ribbed moraines are a series of conspicuous ridges formed transverse to ice movement. These ridges typically rise 10–20 m in height, 50–100 m in width, and are spaced 100–300 m apart. They tend to occur in large numbers as fields, for example, in the Mistassini area of Quebec. They are composed of a range of subglacial sediments and are

thought to be formed by the basal deformation of underlying sediment, possibly in association with a floating ice margin at times (Figure G29) Menzies, 2002.

Drumlins are perhaps one of the most well known glacial landforms. Considerable literature exists on their formation and debate continues on their mechanic(s) of formation. Drumlins are streamlined, roughly elliptical or ovoid-shaped hills with a steep stoss side facing up-ice and a gentler lee-side facing down-ice (Figure G30a). Drumlins range in height from a few meters to over 250 m, and may be from 100 m to several kilometers in length (Figure G30b). They tend to be found in vast swarms or fields of many thousands (Figure G30b). In central New York State, for example, over 70,000 occur, and vast fields likewise exist in Finland, Poland, Scotland, and Canada. Drumlins are composed of a wide range of subglacial sediments and may contain boulder cores, bedrock cores, sand dikes, and “rafted” non-glacial sediments. It seems likely that these landforms develop below relatively fast moving ice beneath which a deforming layer of sediment develops inequalities and preferentially stiffer units become nuclei around which sediment accumulates and the characteristic shape evolves. Other hypotheses of formation range from the streamlining of pre-existing glacial sediments by erosion, to changes in the dilatancy of glacial sediments leading to stiffer nuclei at the ice-bed interface, fluctuations in porewater content and pressure within subglacial sediments again at the ice-bed interface, and the infilling of subglacial cavities by massive subglacial floods.

Fluted moraines are regarded as subglacial streamlined bedforms akin to drumlins (Figure G31). These landforms are typically linked in formation with drumlins and Rogen moraines. They tend to be much smaller in height and width than drumlins but may stretch for tens of kilometers in length. They are typically composed of subglacial sediments. Fluted moraines have been found to develop in the lee of large boulders



Figure G29 Rogen moraine near Uthusslön, Sweden (photo from Jan Lunqvist).

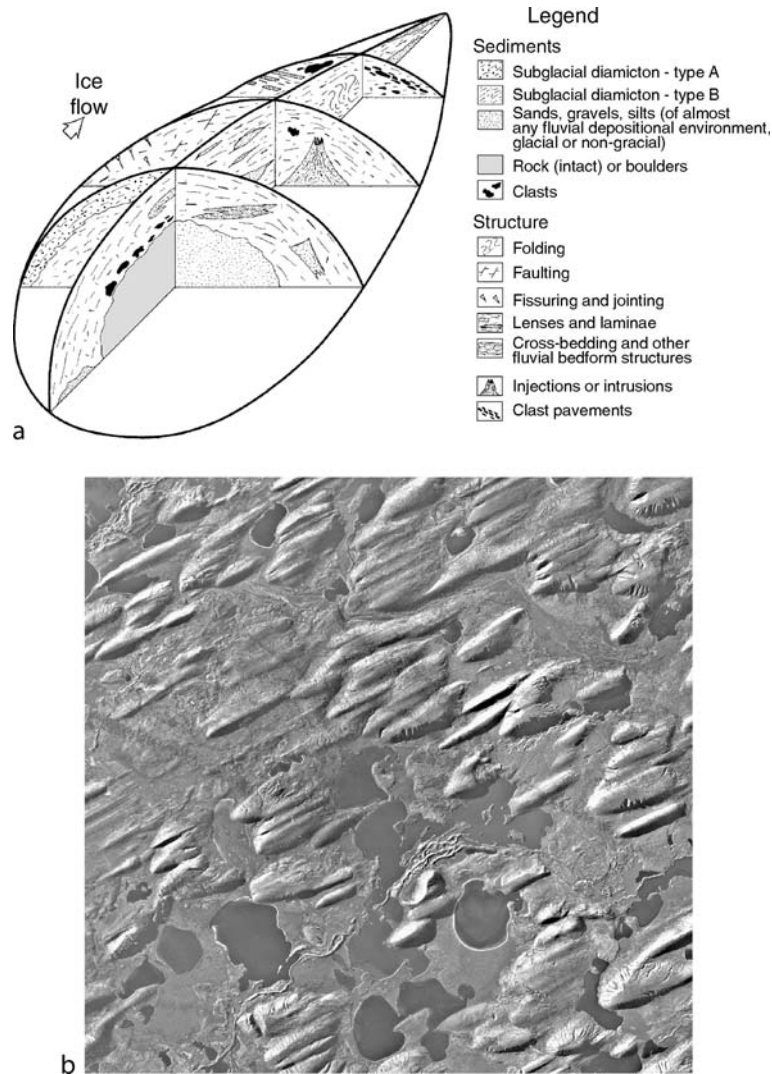


Figure G30 (a) General model of drumlin plan and variability of internal composition, (b) drumlin field in Saskatchewan (ice direction from upper right to lower left).

but may also be attenuated drumlin forms, the result of high basal ice shear stress and high ice velocities. In central New York State, fluted moraines occur beside and amongst the large drumlin fields.

Hummocky moraine is a term used to denote an area of terrain in which a somewhat chaotic deposition pattern occurs, similar to a series of small sediment dumps (Figure G32). These moraines rarely rise above a few meters but may extend over considerable areas. Hummocky moraines often mark locations where massive down-wasting of an ice mass may have occurred.

End or terminal moraines and retreat or frontal moraines occur at the front margins of ice masses. Typically, these landforms, transverse to ice motion, are a few meters to tens of meters in height and, if built-up over several years, may be even higher and of some considerable width (1–5 km). Moraines contain subglacial and supraglacial debris, and often have an accurate shape closely mirroring the shape of an ice front. Since these moraines mark the edge of an ice mass at any given

time, the longer ice remains at that location, the higher and larger the moraines become. However, as an ice mass retreats, with periodic stationary periods (stillstands), a series or sequence of moraines (i.e., recessional moraines) develop that mark the retreat stages of the ice (Figure G33). Sequences of end moraines can be observed in the mid-west states of Illinois, Ohio, and Michigan Mickelson & Attig, 1999.

Eskers are products of subglacial meltwater streams in which the meltwater channel has become blocked by fluvio-glacial sediments. Eskers are long ridges of sands and gravels that form anatomizing patterns across the landscape (Figure G34). They range in height from a few meters to > 50 m and may run for tens of kilometers. In Canada, some eskers cross the Canadian Shield for hundreds of kilometers. These landforms often have branching ridges and a dendritic morphology. Eskers are dominantly composed of fluvio-glacial sands and gravels with distinctive faulted strata along the edges where the ice tunnel wall melted and collapsed. In many instances



Figure G31 Fluted moraine, Storbreen Glacier, Norway (boulder at the head of the flute; ice direction bottom right to middle left).



Figure G32 Hummocky moraine, Glen Turret, Scotland.

eskers are observed “running” uphill or obliquely crossing over drumlins, a testament to their formation within high pressure subglacial meltwater tunnels Benn & Evans, 1998.

In many glaciated areas during ice retreat, large, roughly circular dumps of fluvio-glacial sands and gravels occur. These forms, termed kames, appear to form when infilled crevasses

or buried ice melt, leaving the sediment behind in a complex but chaotic series of mounds. The term kame or kame-delta has been applied to fluvio-glacial sediments that have formed temporary deltas into long-gone glacial lakes. In Finland, a long line of such kame-deltas formed into a moraine-like series of linear ridges transverse to ice front retreat (Salpuasselkä).



Figure G33 Late Wisconsinan end moraines (black) of the Green Bay Lobe (Wisconsin), Lake Michigan Lobe, and Huron-Erie Lobe (Indiana) (modified after Frye and Willman, 1973).

Glacial depositional landscape systems

Distinctive suites of glacial depositional landforms can be found in valley glacier, and ice sheet settings (Figure G35). Typically, these sequences of landforms are often overprinted due to subsequent glaciations but in the mid-west of the USA, such suites of depositional landforms from the last glaciation to affect the area (Late Wisconsinan) can be clearly discerned (Figure G33). Distinctive landscape systems attributable to the marginal areas of ice sheets also carry a unique supraglacial suite of landforms, as can be observed in parts of the mid-western USA (Figure G36).

The impact of glaciation beyond ice limits

Areas beyond the ice limits are greatly influenced by glaciation due to deteriorating climatic conditions, the deposition of wind-blown dust (loess), the divergence of river systems where headwaters or partial drainage basins may be intersected by advancing ice, the impact of outburst floods from ice fronts (jökulhlaups), and major faunal and floral changes due to encroaching ice. In terms of the impact of ice masses on human life and society, the only evidence is somewhat anecdotal. At the close of the Late Wisconsinan, ice masses may have acted to spur human migration, for example through the short-lived ice-free corridor between the Cordilleran and Laurentian Ice Sheets in central Alberta, Canada into the prairies to the south.

Within a few hundreds of kilometers of the vast ice sheets that covered North America and Europe, significant climatic conditions must have been severe with strong katabatic cold winds descending from the ice. Associated with these severe climates, periglacial conditions must have prevailed, in which the ground became permanently frozen to a considerable depth. The effects of periglacial activity produced frozen ground phenomena such as solifluction sediments down slopes, ice and sand wedges, and localized ice lenses and pingo formation. Dramatic changes in vegetation types and animal life occurred, with the southern migration of many species in the Northern Hemisphere. For example, unlike today, central southern Texas



Figure G34 Esker Ridge, Bylot Island, Canada (photograph courtesy of C. Zdanowicz).

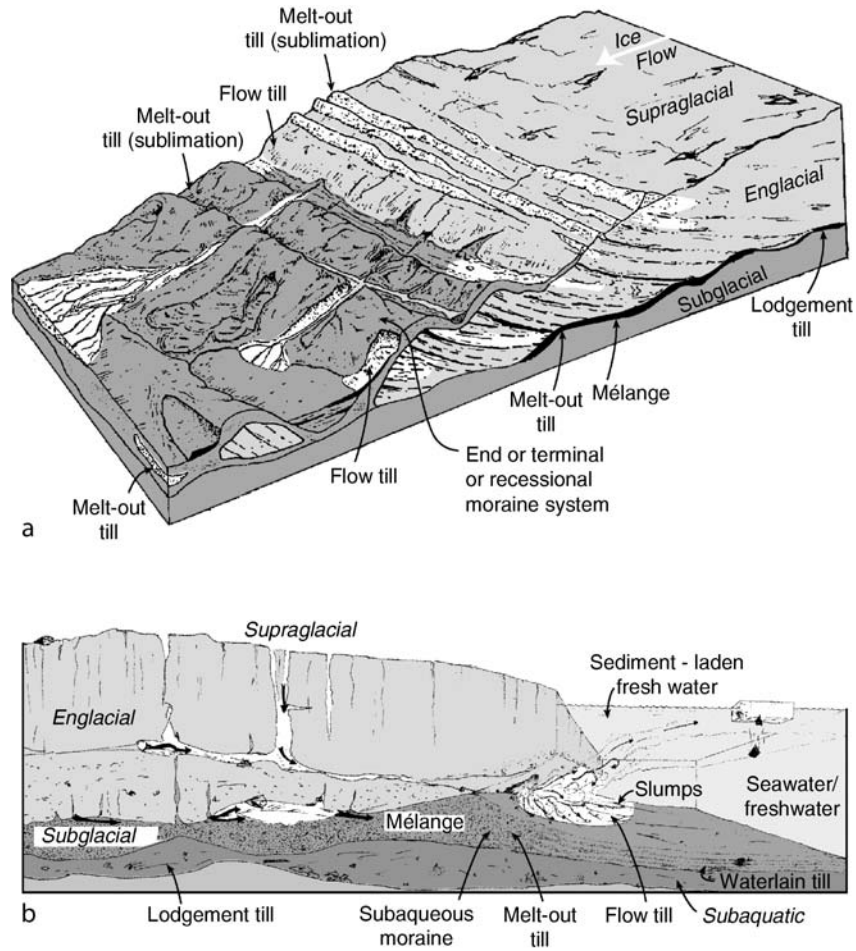


Figure G35 (a) Model of land-based glacial depositional system. (b) Model of depositional system of an ice mass with a marine margin.

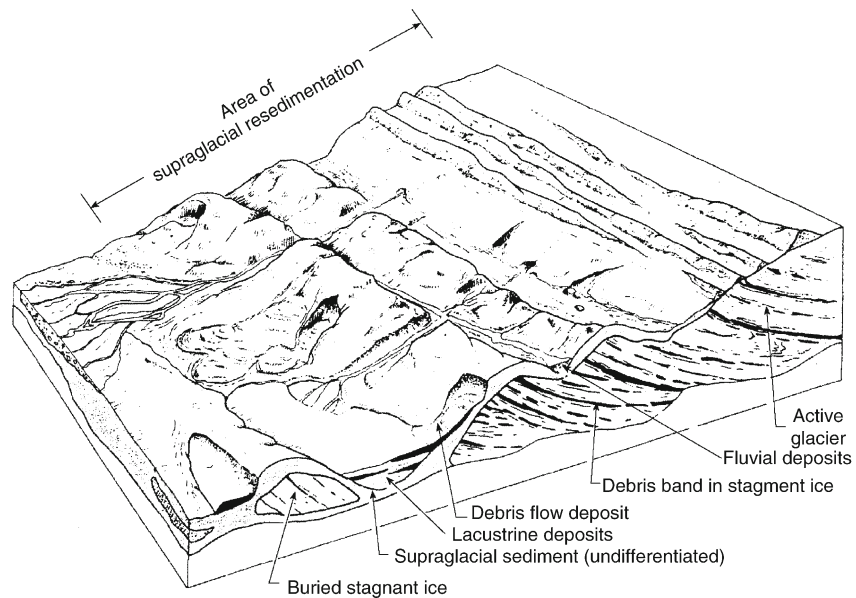


Figure G36 (a) Model of supraglacial and ice-marginal landscape systems (modified from Edwards, 1986). (b) Supraglacial and ice-marginal landscapes, Findeln Glacier, Switzerland.

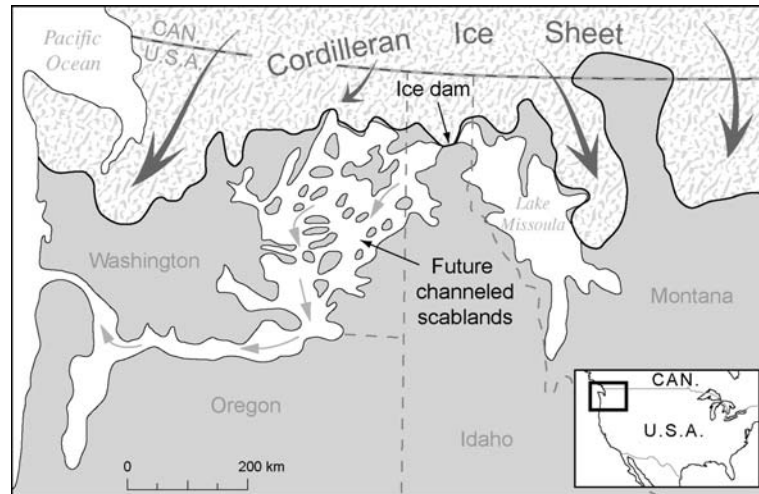


Figure G37 Jökulhlaup resulting from catastrophic drainage of glacial Lake Missoula has led to the formation of the Channeled Scablands of Washington and Oregon.

would have supported hardwood forests of the type now found in Ohio and Pennsylvania.

Due to the katabatic winds, fine sediments were picked up from the proglacial areas along the margins of the ice sheets and the dust was transported away from the ice and deposited as thick, massive loess sediments (glacioaeolian sediments). Considerable thicknesses of these sediments occur in the mid-western states of the USA, especially in Iowa and Kansas, and also in central Europe, Hungary, Central Asia, and China.

In some instances, vast outpourings of meltwater (jökulhlaups) flooded from the ice fronts, leading to distinctive, heavily dissected terrains being formed (badlands). Such an occurrence is recorded in the Columbia River Badlands of Washington and Oregon States where a huge lake formed and then dramatically drained (Lake Missoula floods) (Figure G37).

John Menzies

Bibliography

- Benn, D.I., and Evans, D.J.A., 1998. *Glaciers and Glaciation*. London: Arnold Publishers, 734pp.
- Bennett, M.R., and Glasser, N.F., 1996. *Glacial Geology*. Chichester: Wiley publishers.
- Menzies, J. (ed.), 2002. *Modern and Past Glacial Environments* (Student Edition). Oxford: Butterworth-Heinemann, 543pp.
- Mickelson, D., and Attig, J. (eds.), 1999. *Glacial Processes Past and Present*. Special paper 337, Boulder, CO: Geological Society of America.

Cross-references

[Cirques](#)
[Cryosphere](#)
[Diamicton](#)
[Drumlins](#)
[Eskers](#)
[Glacial Erratics](#)
[Glacial Megalakes](#)
[Glaciations, Quaternary](#)
[Glaciations, Pre-Quaternary](#)
[Glaciofluvial Sediments](#)
[Icehouse \(cold\) Climates](#)
[Kames](#)
[Kettles](#)

[Late Quaternary Megafloods](#)
[Loess Deposits](#)
[Moraines](#)
[Mountain Glaciers](#)
[Periglacial Geomorphology](#)
[Pingos](#)
[Roche Moutonnées](#)

GLACIAL ISOSTASY

Glacial isostasy refers to the response of the solid Earth to any changes in the planet's ice sheets. The Earth is not a rigid body and it will deform when subjected to forces or to changes in surface loads. The nature of this deformation depends largely on the time scale, magnitude, and wavelength of the deforming force or load. Examples include the very rapid crustal fracturing at the time of earthquakes, the semi-diurnal and diurnal tidal deformations of the solid planet due to the changing gravitational attraction by the Sun and Moon, and the seasonal changes in the mass distribution within the atmosphere. Examples on longer, geological timescales include the redistribution of surface loads during erosion and sediment deposition or by the formation of large volcanic complexes. At the high frequency part of the spectrum, the response is primarily elastic but with decreasing frequency the response becomes increasingly viscous.

To a first approximation, the Earth is a layered body whose outer shell, the lithosphere, acts essentially as an elastic layer. The mantle below is more viscous and flows when subject to non-hydrostatic stress and for very long term loads, of the order of a million years or more, this region behaves largely as a fluid. The outer core acts as a fluid even at high frequencies. The lithosphere comprises the crust, which is relatively cold and brittle, and the uppermost part of the mantle that is relatively cool, strong, and elastic.

Isostasy is a concept that describes the response of the planet to a change in surface load. It was originally developed to describe the mechanism by which mountains and plateaus were supported by the crust for long periods of time. In its simplest

form, the surface load is assumed to be underlain by lower-than-normal densities such that below the crust or lithosphere the pressures are hydrostatic everywhere. The manner in which this “compensating” mass is distributed gives rise to different models of isostasy: Airy, Pratt, or regional. The first two models are local compensation models in which the compensating mass is located immediately below the load but in the third model, a local load is supported regionally. The underlying assumption in these models is that the surface loads are supported by stresses within the crust-lithosphere and that the sub-lithospheric mantle is fluid, an assumption that is operationally effective on long timescales of many tectonic processes.

Glacial isostasy is concerned with the planet’s response to the changing surface loads of ice and water during the waxing and waning of large ice sheets. To a first approximation of local isostasy, the crust beneath the ice sheet is depressed by the product of the ratio of ice and mantle densities and the thickness of the ice, such that somewhere below the ice-loaded lithosphere the vertical pressures are constant at constant depth. For a 3 km thick ice cap, this would mean a crustal depression of about 800 m. On timescales of glacial cycles (10^4 – 10^5 years), the mantle does not behave as a fluid and the load will be partly supported by viscous stresses in the sub-lithospheric region. Thus, the initial response to a large ice load will be by elastic deformation of the entire lithosphere-mantle followed by a viscous creep as the mantle stresses relax and the load is increasingly supported by the lithosphere. The local isostatic depression will be attained as a limit. Likewise, when the ice sheet is removed, the initial response is elastic followed by a viscous rebound. The rate at which this occurs will be a function of the mantle viscosity and observations of this rebound, in fact, provide the primary evidence for this viscosity.

Large ice sheets have periodically formed on the Earth’s surface in response to changes in planetary configurations and the resulting changes in solar insolation (e.g., the Milankovitch theory). Thus, water mass is withdrawn from the oceans and localized at high latitudes when large ice sheets form, and more than 50×10^6 km³ of water is periodically moved between the ice sheets and the oceans, resulting in a global lowering of sea level by 130–150 m. This is the most direct consequence of glacial isostasy: global fluctuations in sea level that mirror the growth and decay of ice sheets during the glacial cycles of the past two million years. The spatial pattern of this sea-level change is, however, complex. What is observed is that the position of past shorelines relative to the present shoreline position and the crust – which forms the reference surface for the measurement – is itself displaced during the surface-loading cycles. Moreover, as the Earth deforms and mass is redistributed around the globe, the gravity field of the planet changes and surfaces of constant gravitational potential, e.g., the geoid or sea level in the absence of oceanographic and meteorological forcing, are modified as well. Thus, the relative sea-level observation at a locality is a measure of the change in ocean volume, of the radial deformation of the Earth’s surface under the changing surface load, and of the change in gravitational potential. The globally averaged sea-level change resulting from a change in ice volume is referred to as the ice-volume-equivalent sea-level change and, in the absence of other processes that change ocean volume, this corresponds to eustatic sea-level change.

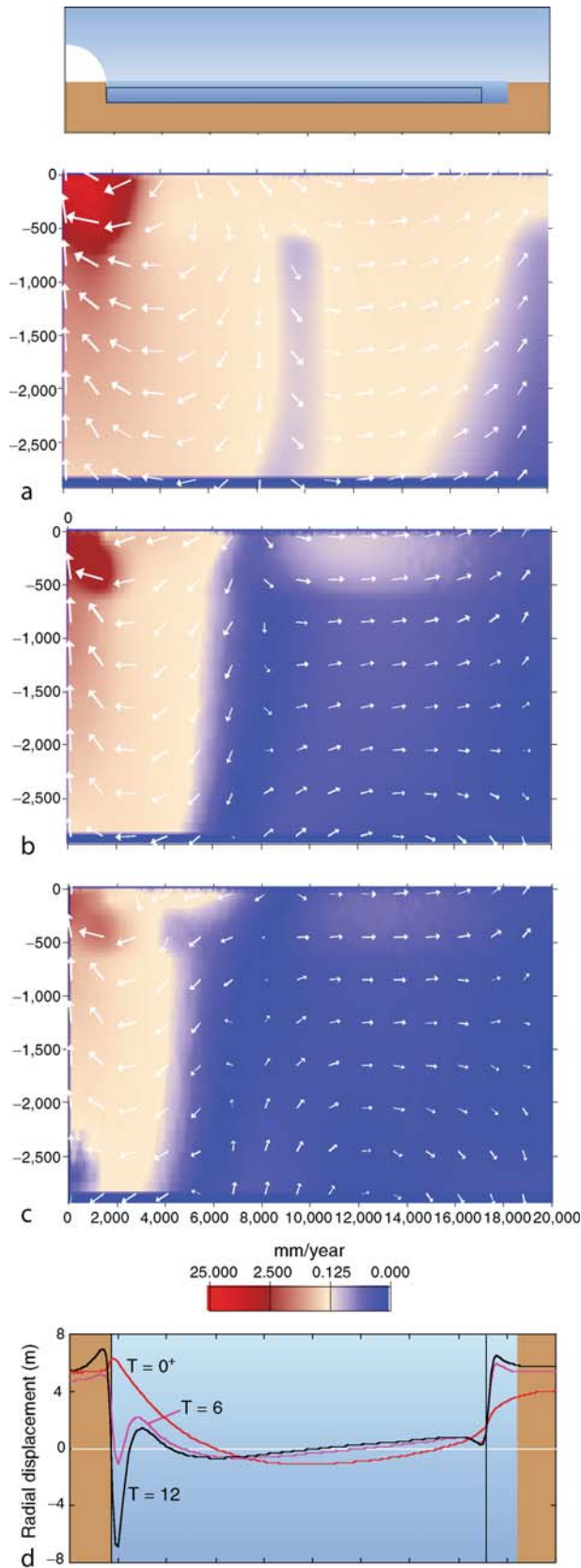
The Earth is presently in an interglacial period and the last of the large ice sheets over North America and Europe disappeared before ~7,000 years ago. The remaining ice sheets of Greenland and Antarctica also, in a first approximation,

stabilized by about this time. However, while ocean volumes remained nearly constant during the interglacial period, sea levels have continued to change as a result of the viscous or delayed response of the Earth to the removal of the ice load and the redistribution of the melt water into the oceans. The amount of this post-glacial change at any location depends on the relative importance of the different components contributing to the sea-level change: the crustal deformation under the changing ice and water load, the changes in gravitational potential, and the changes in ocean volume. The relative sea level changes with location and with time and gives rise to the complex spatial and temporal pattern of sea-level change that has been observed.

The most obvious deformational effect of the glacial cycles occurs in the areas of glaciation where, as illustrated above, the crust may be depressed by hundreds of meters beneath large ice sheets. However, the removal of water from the ocean basins also adds to the deformation. The removal of 150 m of water from an ocean basin would result in a rebound of the ocean floor, and of islands within the basin, of up to 30–40 m according to the local isostatic formulation. Thus, in any rigorous formulation of glacial isostasy the total load of the ice and oceans needs to be considered.

Sea level is not the only process perturbed by the glacial cycles. Gravity is time dependent and this can be measured instrumentally in areas of ongoing rebound. The radial and horizontal changes in position of the crust can also be measured by space-geodesy methods (the glacial rebound contains a horizontal surface velocity signal as well as the radial signal). The planetary rotation is modified as the inertia tensor evolves through time, and the motions of satellites around the planet are perturbed. All of these signals provide evidence for the Earth’s viscous response function, but the sea-level signal remains the most important because it has been preserved in the geological record, primarily for the period since the last deglaciation and, in a more fragmentary form, for earlier periods.

If the Earth’s viscosity and elastic structure as well as the history of the ice sheets are known, then physically consistent models can be developed that rigorously predict the observed phenomenon: models that describe the deformation of the entire planet, that distribute the meltwater in a self-consistent way into time-dependent and realistic ocean basins, and that include the effects of the changing water load as well as ice load. The theory has to be a global one because all parts of the mantle are affected by the deglaciation of one ice sheet. This is illustrated in Figure G38 for a simplified model in which the ice sheet, land mass, and ocean basin are longitude independent. In this case, a continent-based ice sheet at the north pole, with dimensions approximating the North American Ice Sheet, has been rapidly removed and only the rates of mantle displacement caused by the changing ice loads are shown for three epochs, 100 years after the unloading, and 6,000 and 12,000 years later. The deformation extends throughout the mantle, down to the core-mantle boundary at ~2,900 km depth, and to the antipodes of the ice cap. The contribution to this deformation field from the water loading is much smaller in amplitude and this is shown here only as the radial displacement of the sea surface for three epochs, immediately after unloading and showing the elastic deformation, and at 6,000 and 12,000 years later. These signals, while relatively small, are observationally significant and important for estimating the mantle rheology, particularly at margins far from the former ice sheets, such as across the antipodal margin illustrated.



If the parameters defining the Earth's response function (its rheology) are only partly known, then the comparison of predictions with observations provides a means of estimating this function. If the ice history, the location and thickness of ice through time, is not fully known then such a comparison may contribute to the description of the past ice sheets. In fact, neither the rheology nor ice history are perfectly known and the primary motivation for the study of glacial isostasy is to better understand the solid planet's response to stress in support of dynamical planetary studies, and to improve the description of the past ice sheets in support of palaeoclimate studies.

As sea level rises and falls, it leaves behind signals of its past position. Submerged terrestrial materials, such as in-situ tree stumps, indicate that sea levels were lower at the time of tree growth than today. Coral reefs above present sea levels are indicative of sea levels having been higher in the past. Thus, if the age of the tree stump or of the coral can be measured, limiting values to past sea levels can be established. In some instances, high resolution observations are possible. The submerged sediments may contain faunal or floral fossils of species that lived only in a narrow tidal range or the morphology of the reef may indicate that it formed at the upper growth limit of corals. In either case, the paleoshoreline can be precisely identified. Some examples of results from different parts of the world are illustrated in Figure G39 and these, for the period since the Last Glacial Maximum (LGM) at $\sim 30,000$ – $20,000$ years ago, reveal some of the principal spatial variabilities of the sea-level signal.

The results for Ångermanland, northern Sweden, and Richmond Gulf, Canada, are characteristic for locations that are near the former centers of glaciation, where the dominant contribution to the relative sea-level change is from the crustal rebound upon removal of the ice. Note that in the Swedish example, the last ice disappeared about 9,000 years ago but since then more than 200 m of rebound has occurred, testimony to the viscous relaxation of the mantle. The example from the Norwegian coast at Andøya is characteristic of the sea-level signal from near ice margins. A similar result is observed at Vestfold Hills in Antarctica, although the early part of the record here does not appear to have been preserved in the sediments, or deglaciation occurred late. The result from the Bristol Channel is representative of areas beyond but not far from the ice margins and here sea levels have not been higher than present at any time since the LGM. Similar signals are seen along the North American Atlantic coast south of around New York. The observations from

Figure G38 Mantle deformation as the result of glacial loading at one pole. The model is axisymmetric about the pole of the ice sheet, which rests on a continent of the same dimension (*left hand side, top panel*). A second, unloaded continent occurs at the antipodes (*right hand side*). The ice sheet is assumed to melt instantaneously and the water is added into the ocean basin between the two continents. The panels (a–c) illustrate the rates of displacement of mantle material at three epochs: (a) soon after the unloading and upon completion of the elastic response, (b) 6,000 years after unloading, and (c) 12,000 years after unloading. The *arrows* indicate the direction of flow and their lengths are proportional to the magnitude of the flow rate on a logarithmic scale. The *color coding* indicates the magnitudes of the rates. Panel (d) gives the radial displacement of the ocean surface immediately after melting (at time $T = 0^+$) and at 6,000 and 12,000 years ago ($T = 6, 12$ ka) due to the addition of the water load into the ocean basin.

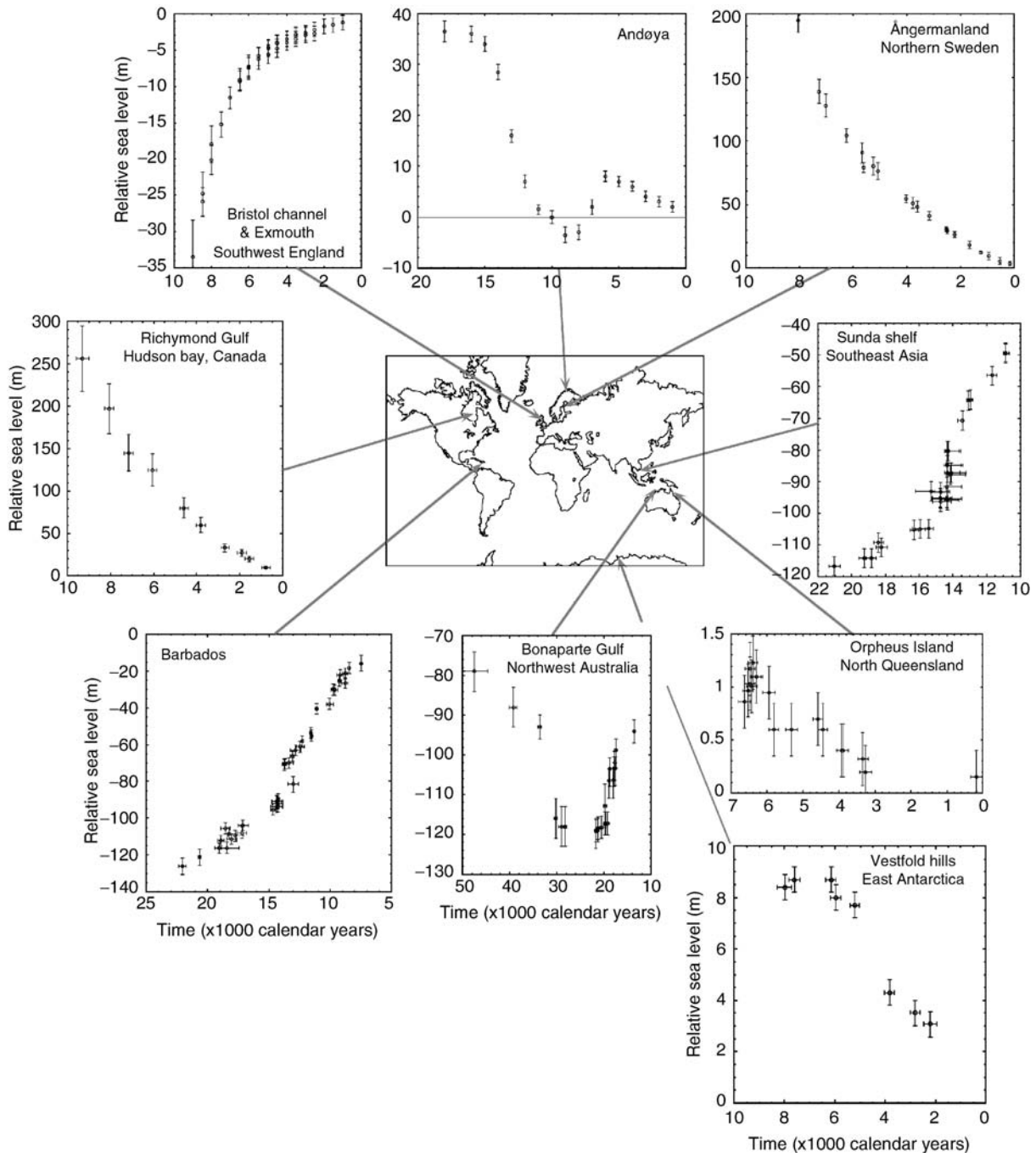


Figure G39 Observations of relative sea-level change from different locations and for different time intervals. All observation sites are believed to have been tectonically stable except for Barbados where a small correction for such motion has been applied. Note the different scales used for the various time-height plots. All observed depths and elevations have been reduced to mean sea level and all timescales correspond to calendar years (adapted from Lambeck and Chappell, 2002).

Barbados, the Sunda Shelf, and the Bonaparte Gulf are representative of sites far from former ice margins, where sea levels experienced a sustained rise until about 7,000 years ago. The onset of this rise appears to occur shortly after 20,000 years ago and its rate appears to have been variable. The record from the Bonaparte Gulf indicates that the low sea levels persisted for

an interval of about 10,000 years, starting at ~30,000 years ago. Detailed observations for the past 7,000 years from such localities distant from the former ice sheets, e.g., Orpheus Island, Australia, also indicate that sea levels at continental margins have actually been falling slowly as a result of the oceanic mantle response to the changing water load.

This spatial variability can be understood in terms of the several components contributing to the signal and, in particular, from the interplay between local rebound and global ocean volume change. For sites far from the ice sheets, the isostatic contributions are relatively small, about 10–15% of the eustatic change, and insensitive to the details of the melting history. Observations from “far-field” sites such as Barbados or the Bonaparte Gulf therefore constrain the change in total ice volume once the small isostatic corrections are applied. For the sites near the centers of former glaciation, the observed signal is predominantly from the crustal rebound that dominates the ocean volume signal. If the eustatic change is known from the analysis of far-field data, the rebound term can be determined and this is primarily a function of rheology parameters and ice thickness. When melting ceases abruptly, a small cusp may occur in the sea-level data and this becomes more pronounced when the rebound contribution is reduced relative to the eustatic change. This occurs, for example, at Andøya and establishes the time of the end of major glaciation. At these sites the signal is initially dominated by the rebound but at a certain time this is reduced and equal in magnitude but opposite in sign to the global eustatic term so that sea level is constant for a period. Later the eustatic term dominates and sea level again rises until melting ceases and it is the residual relaxation of the unloading that dominates the signal. This latter part of the signal provides a useful constraint on mantle rheology while the earlier part of the signal provides constraints on the ice distribution at its margins. The Andøya signal, for example, indicates that the outer Vesterålen of Norway were ice free at about 19,000 years ago, but that the ice must have extended offshore before that time in order to produce the elevated sea levels once the area became ice free.

Beyond the ice margin, the rebound signal during deglaciation becomes one of subsidence. During the loading phase, mantle material is displaced beneath the area of loading and because mass is conserved, a broad but shallow bulge forms around the periphery of the ice sheet (c.f. Figure G38). Then, as the ice melts, this bulge subsides and results, in the absence of other contributions, in an apparent rise in sea level. Thus, here the sea-level change is initially rapid as the ice decays and, when melting has ceased, the rise is slow and reflects the isostatic change. The early part of the record represents mainly the eustatic contribution and the latter part reflects mainly the rheology. Much further from the ice sheets, the deformation resulting from the changing ice load is reduced and the major isostatic term comes from the change in water load (Figure G38). This effect is most pronounced at continental margins where the extra water during deglaciation depresses the ocean floor, pulling sea level down with it, and resulting in a fall in sea level at the coast. This signal becomes most visible when melting has ceased and results in small-amplitude highstands at about 6,000–7,000 years ago, as observed in many places along the Australian coast (the Orpheus Island result).

What these examples illustrate is that the isostatic signals, by taking advantage of their spatial and temporal variability, provide a means of estimating both the mantle rheology and aspects of the ice history. This is important because generally the distribution of the ice during the recent glaciation is not well known. Most of the observational evidence is from the last 20,000 years, older information being scarce because it has been largely destroyed by an earlier ice advance or phase of sea-level rise and also because the commonly used radiocarbon dating method becomes unreliable or imprecise.

The limits of the ice sheets over North America and Europe for the LGM and for the subsequent ice retreat have been mostly well mapped but major differences of opinion remain for some locations, most notably for Arctic Russia. Sea-level observations may help here. For example, if a large ice sheet existed over the Kara Sea and western Siberia during the LGM, then a raised shoreline pattern similar to that observed for adjacent Fennoscandia resulting from glacial rebound would be expected, but the absence of such a pattern indicates that any LGM ice over the region must have been unimportant. For regions such as this, the glacial isostasy analysis provides more insight into the ice history than into the Earth rheology. Debate also occurs over the extent to which the large ice sheets extended onto the continental shelves. Did the Scandinavian Ice Sheet extend across the North Sea and overrun the northern British Isles or did the two ice sheets form separately? Again, the glacial isostatic analyses for the two areas provide useful constraints. If thick ice did extend across the North Sea during the LGM then the rebound in southwestern Norway would have been greater than that actually observed and the center of rebound over the British Isles would lie in eastern Scotland rather than where it is observed in western Scotland. Where were the LGM North American ice margins in northeastern Canada? Was the ice restricted to the upper fiords of Baffin Island or did it extend far onto the continental shelf? The presence of well-elevated shorelines at outer coastal sites, with early Holocene ages, points to substantial rebound having occurred here and to early ice over the region and onto the shelf. Another area of uncertainty concerns the ice thickness at the LGM and during the subsequent deglaciation phase. Only in special cases where mountains protruded through the ice are there observational constraints on the thickness and this is not the case for the large former ice sheets other than near their margins. Instead, the ice thickness is based on glaciological and climate assumptions, for example about the conditions at the base of the ice sheet, the coupling of the ice to the underlying rock and sediments, and the supply of moisture. Alternative, but yet plausible, assumptions can lead to distinctly different results for the ice thickness, and the glacial isostatic inversions must include a strategy for estimating ice thickness. Because of the good distribution in time and space of the observational evidence across northern Europe, the Fennoscandian rebound problem is particularly well posed and inversion schemes can be developed that solve the problem for both rheology and ice sheet parameters.

Figure G40 illustrates the isostatic rebound of Scandinavia based on model calculations constrained by a variety of geological, geodetic, and geomorphological data. The results are shown for three epochs: (a) an early stage of the LGM when ice margins were at their maximum extent, (b) about 12,000 years ago when the southern ice margins had retreated across the Baltic Sea and when the retreat was momentarily halted during the climatic cold interval of the Younger Dryas, and (c) at present, some 9,000 years after all the Scandinavian ice had vanished. At the time of the second epoch, the Baltic was closed to the Atlantic both by the ice barrier in southern Sweden and by the land barrier through the Danish Bælts. This formed the Baltic Ice Lake at an elevation of about 25–30 m higher than coeval sea level. It left well-defined shorelines across the region, which today are strongly inclined relative to present sea level, and this information has been used to constrain the model parameters. Tide-gauge observations of sea-level change for the past century as well as Global Positioning

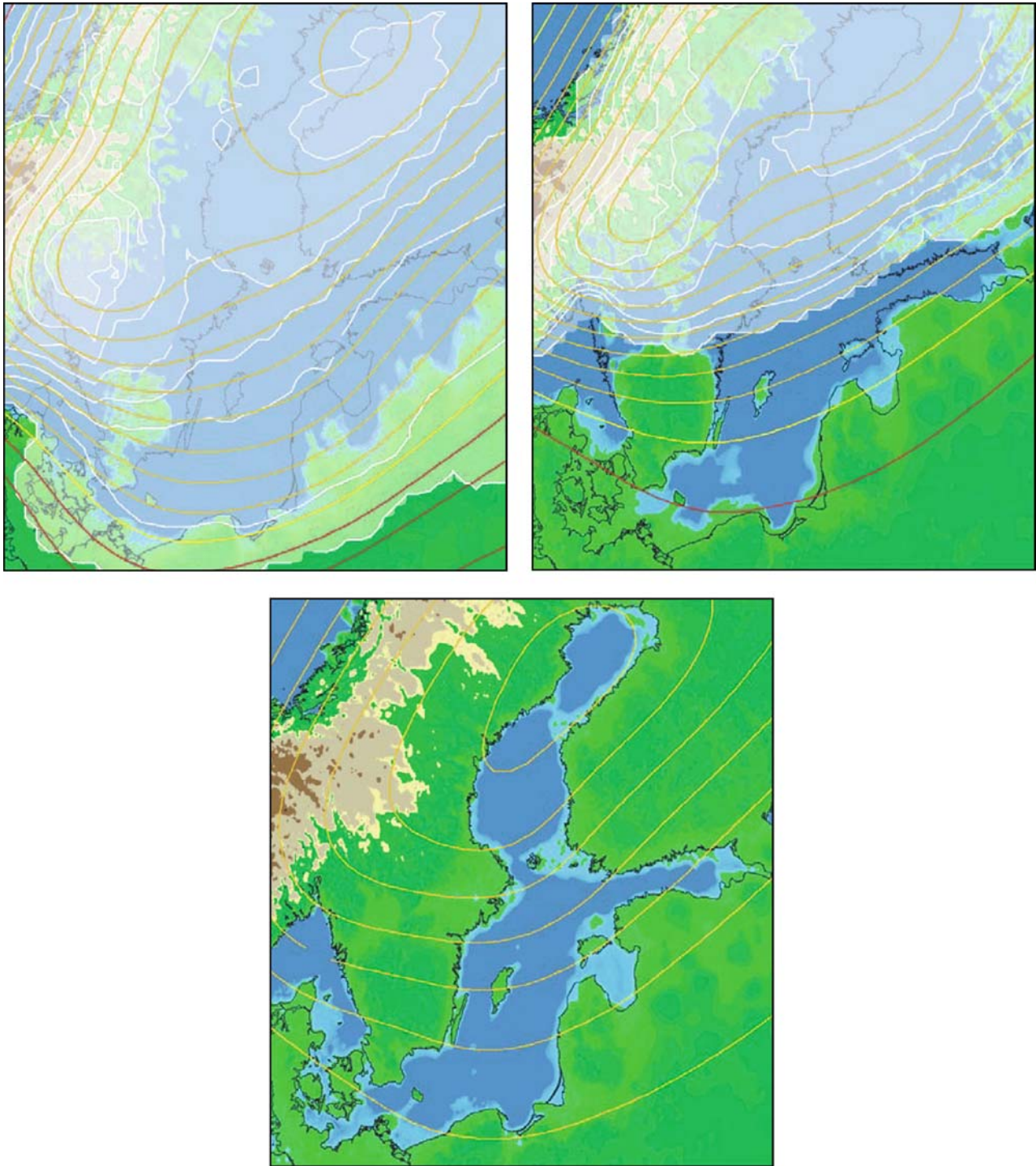


Figure G40 Paleogeographic reconstructions for Fennoscandia at three epochs: ~20,000 years ago corresponding to the end of the Last Glacial Maximum (LGM), ~12,000 years ago, corresponding to the Younger Dryas (YD), and for the present. The ice sheets are shown by the translucent regions with the ice thickness contours, in *white*, corresponding to 400 m intervals. Areas with underlying blue correspond to regions below sea level for the epoch given. The paleoshorelines are defined by the *green-blue* boundary for each epoch. During the Younger Dryas, the Baltic Ice Lake was about 25–30 m higher than the Atlantic Ocean and formed a frozen freshwater lake. For the LGM and YD the *yellow* and *red* contours correspond to the change in local sea level that occurred since the present. The *yellow* contours are positive and in this area the paleoshorelines, if preserved, will occur above present sea level. The zero value is identified as the first *yellow* contour. The *red* contours are negative. The contour values are 100 m for the LGM, and 50 m for the YD. The third panel illustrates the present-day rate of change in sea level rise (contour interval is 1 cm yr^{-1}) with the maximum rate in the northern Gulf of Bothnia approaching 8 cm yr^{-1} .

System (GPS) observations of crustal rebound for the past decade provide additional constraints on the rebound models.

The essential rheological result from this and inversions of data sets from other localities is that the viscosity can be adequately described by a linear relation between stress and rate of strain over the range of stress magnitudes and duration of stress cycles encountered. The resulting “effective” viscosity is depth-dependent, with the lower mantle below about 670 km depth being of distinctly higher viscosity than the upper mantle. Some viscosity stratification occurs within the upper mantle, with the depth dependence broadly following the depth of seismic parameters of shear velocity and attenuation. Lateral variation in the upper mantle also occurs, again broadly following the seismic parameters. Beneath the continental margins of Australia, for example, the upper mantle viscosity is less than beneath Scandinavia, where in the former case the estimates of viscosity come from analysis of the water loading effects. Such variation is not unexpected since both mantle viscosity on time scales of thousands of years and the propagation of seismic waves at periods of seconds and minutes are likely to be temperature controlled.

Mantle viscosity is a fundamental parameter for describing the Earth’s dynamical behavior because it controls the rates of convection and thermal evolution of the mantle. The challenges for future work in glacial isostasy are to refine this viscosity structure, not only its depth and lateral variability but also its behavior over time. Is the evidence for linear behavior supported when some of the longer cycles in glacial loading are examined? This will require new information for the earlier periods of the glacial cycles of both the ice sheets and the Earth’s response. Improved observational evidence for the present rates of post-glacial deformation will also contribute to an improved understanding of the viscosity structure. These measurements will include high-precision measurements of the displacements of points on the Earth’s surface and changes in gravity. The challenge here will be to separate these changes from tectonic signals.

Kurt Lambeck

Bibliography

- Lambeck, K., 2002. Sea-level change from mid-Holocene to recent time: An Australian example with global implications. In Mitrovica, J.X., and Vermeersen, B. (eds.), *Ice Sheets, Sea Level and the Dynamic Earth*. Washington, DC: American Geophysical Union, pp. 33–50.
- Lambeck, K., 2004. Sea-level change through the last glacial cycle. *Compt. Rendus Geosci.*, **336**, 677–689.
- Lambeck, K., and Chappell, J., 2001. Sea-level change through the last glacial cycle. *Science*, **292**, 679–686.
- Watts, A.B., 2001. *Isostasy and Flexure of the Lithosphere*. Cambridge: Cambridge University Press.

Cross-references

Glacial Eustasy
 Sea-level Change, Post-Glacial
 Sea-Level Change, Quaternary
 Sea-Level Indicators

GLACIAL MEGALAKES

Continental ice sheets that form during epochs of glaciation exert immense influences on water drainage across the land. Their huge loads depress the underlying land surface, and lakes

form in the moats that surround the ice sheets. They can block the lower courses of major rivers, impounding flow, and even diverting it into adjacent drainage basins. Meltwater from glacial margins may introduce huge discharges into land-surface depressions that hold much smaller lakes during nonglacial periods. The lakes may climatically alter water balances, promoting further glaciation by a kind of positive feedback.

Glacial megalakes are exceptional for their extent and/or their volume. They may form in direct contact with glacial ice, or they may form in nearby depressions under the pronounced influence of glaciers in the regional drainage basin. There are modern examples for all these situations, but the relatively small size and different thermal regimes of modern versus ice-age glaciers pose problems of extrapolation to the past conditions of major continental glaciation that favored the development of glacial megalakes.

Types of glacial megalakes

Ice-marginal lowland megalakes

The classic example of an ice-marginal lowland megalake is the Baltic Ice Lake, which formed about 14,500 calendar years ago, in the ice-marginal moat to south and east of the retreating Fennoscandian Ice Sheet. Prominent, well-dated glacial moraines mark the recession of this ice sheet from northern Germany and Poland to positions in Denmark and southern Norway and Sweden, which blocked the outlet of glacial meltwater from the Baltic to the North Sea until about 11,200 years ago. The lake then drained through a spillover across the Mt. Billingen Area, southern Sweden (Björck, 1995). There followed a period of alternation between marine and saline conditions, as land rebounded from the load of the disappearing ice sheet and global sea level rose from the melting of ice on all the continents. At its maximum extent, the Baltic Ice Lake covered nearly 400,000 km² in a relatively shallow inundation with a volume of about 9,000 km³. Its modern successor, the Baltic Sea, is the world’s largest brackish water body.

Structural/tectonic basin megalakes

Basins formed by tectonic processes may hold lakes that are strongly influenced by glaciers in their drainage basins. Classic examples occur in the Basin and Range tectonic province of the western United States, where Lake Bonneville, the mega-lake predecessor of the Great Salt Lake, formed during the last ice age. This paleolake achieved a maximum area of 52,000 km² and a volume of 7,500 km³ between about 22,000 and 17,500 calendar years ago. The lake filled to the level of a spill point in south-central Idaho, and then dropped 100 m as it eroded into the outlet, releasing the catastrophic Bonneville Flood down the Snake River (O’Connor, 1993).

Another megalake formed at the elevation of 3,800 m in the Altiplano of southern Bolivia and northern Peru. The modern Altiplano depression contains Lake Titicaca (8,800 km² in area), Lake Poopo, and the great salt pans of Ciopasa and Uyuni. Paleolake Tauca covered the whole depression (about 50,000 km²) to a depth of around 100 m. It achieved its maximum stage after the Last Glacial Maximum in the nearby mountains (about 22,000–20,000 calendar years ago).

Intermontane, ice-dammed megalakes

Very deep lakes can form when a glacier advances down a mountain valley to block a river. Perhaps the most famous example is Glacial Lake Missoula, which formed between about

17,500 and 14,500 calendar years ago (Atwater, 1986). At maximum extent this lake covered 7,500 km², and it held a volume of about 2,500 km³. Cataclysmic failure of the ice dam impounding this lake resulted in the release of water over 600 m deep, thereby generating some of the largest known glacial megafloods (Baker and Bunker, 1985).

Subglacial megalakes

Ice-penetrating radar mapping of the sub-ice floors of portions of the Antarctic Ice Sheet has identified over 70 subglacial lakes. Largest of these is Lake Vostock, which occupies an interior subglacial trench of tectonic origin. The lake measures 240 by 50 km and holds between 2,000 and 5,000 km³ of water (subject to interpretive uncertainty as to the lake depth). Because the water in this lake is isolated from the surface environment by 4 km of overlying ice, it likely contains very interesting biota, surviving in an extreme environment similar to those inferred to be present on Mars and on Jupiter's icy moon, Europa. A project is currently underway to sample the water in this remarkable lake.

Glacial Lake Agassiz and the Laurentide Ice Sheet

Perhaps the largest well-documented glacial megalake formed in north-central North America in association with the largest glacier of the last ice age, the Laurentide Ice Sheet. This ice sheet is known to have been highly unstable throughout much of its history. Not only did freshwater discharges from the glacier result in ice-marginal lakes; outbursts of meltwater into the Atlantic Ocean may have generated climate changes by influencing the thermohaline circulation of the North Atlantic Ocean (Teller et al., 2002).

During the Last Glacial Maximum, the Laurentide Ice Sheet achieved its maximum extent about 20,000 years ago. The initial glacial retreat generated relatively small lakes because of the regional river drainage to the south, away from the ice front. The ice sheet surged and readvanced at times, leading to a very complex history in the basins that now contain the Great Lakes. However, when the ice sheet advanced north of this area into the Canadian Shield, Lake Agassiz formed in the trough between the ice and drainage divides to the south and west, in parts of present-day North Dakota, Manitoba, and western Ontario. The megalake seems to have been initiated close to the time of the Younger Dryas cooling event, which began about 12,700 years ago. One explanation for this cooling is diversion to the St. Lawrence River of the Laurentide meltwater that previously flowed to the Gulf of Mexico via the Mississippi. The outflow of great quantities of freshwater into the North Atlantic disrupted the salinity gradient that drives the thermohaline circulation of the oceans by the formation of deepwater in the North Atlantic (Broecker and Denton, 1989).

As the southern margin of the Laurentide Ice Sheet retreated northward into the present Hudson Bay region, Lake Agassiz adjusted to a succession of overflow or spill points, approximately as follows: (a) It drained southward via the Minnesota River to the Mississippi and Gulf of Mexico (about 12–13,000 years ago). (b) It then entered Lake Superior via a route near Thunder Bay. (c) It shifted to the northwest via the Clearwater spillway to the Mackenzie River and the Arctic Ocean (about 11,000 years ago). (d) It then flowed eastward again to Lake Superior through a succession of spillways (about 10,000 years ago). (e) It shifted to the Ottawa River and the St. Lawrence. (f) Finally, it flowed to the Hudson Bay area (about 8,400 years

ago). This 5,000-year history resulted in inundation at one time or other of 1.5 million km², but its maximum one-time extent was not achieved until a union occurred with glacial Lake Ojibway in northern Ontario about 8,400 years ago. At this maximum, terminal stage, the resulting megalake covered about 840,000 km², and held about 160,000 km³ of water (Leverington et al., 2002). This is double the volume of the largest modern lake, the Caspian Sea, but the paleolake was highly unstable. It was dammed by remnants of the Laurentide Ice Sheet, which was severely weakened by the influx of marine water into Hudson Bay. The stage was set for a massive sub-glacial outburst of the Lake Agassiz water through Hudson Strait into the Labrador Sea, a probable trigger for the 8,200 yr B.P. cold event – the most abrupt and widespread global climatic cooling event to have occurred within the last 10,000 years (Clarke et al., 2003).

Central Asian paleolakes

In the mountain areas of central northern Asia, there were probable ice-dammed expansions of modern Lakes Baikal (31,500 km² area; 23,000 km³ volume) and Issyk-Kul (6,000 km² area; 4,000 km³ volume). In the Altai Mountains, great megafloods emanated from the late Pleistocene ice-dammed Chuya-Kuray paleolake, covering 12,000 km² and holding 1,000 km³ of water, perhaps 900 m deep at the ice dam (Baker et al., 1993).

The lowland glacial lakes of Siberia involved the expansion of huge ice sheets that covered the shallow seas north of Eurasia and blocked north-flowing rivers, notably the Ob, Irtysh and the Yenesei. Grosswald (1980) interpreted this blockage to be Late Weichselian in age (about 15–20,000 years ago), but more recent work considers the events to be Early Weichselian (about 90,000 years ago) (Arkhipov et al., 1995). The largest lake, formed on the west Siberian plain, was estimated by Mangerud et al. (2001) to cover 600,000 km² at a surface elevation of 60 m. However, both Arkhipov et al. (1995) and Grosswald (1980) postulate a much larger paleolake, about 1,200,000 km² in area, with a volume of about 75,000 km³ at a surface elevation of 128 m. This west Siberian megalake was the Asian equivalent of Agassiz. It drained southward, through the Turgai divide of north-central Kazakhstan, to the basin of the modern Aral Sea. The latter rose from its 1960 elevation of 53 m to 70 or 80 m, enlarging from 60,000 km² (1960 area) to about 100,000 km² in the Pleistocene. This paleolake then drained southwestward through the Uzboi Channel into the basin of the modern Caspian Sea. Also fed by glacial meltwater from northern Europe via the Volga, the Caspian expanded during its late glacial Khvalyn phase to an area of 950,000 km², holding a volume of 135,000 km³ at an elevation of 50 m (the modern Caspian level is –28 m). The Khvalyn paleolake drained via the Manych paleochannel and the Don River to the basin of the modern Black Sea. The Black Sea was then disconnected from the Aegean and filled by freshwater (the New Euxine phase); the glacial meltwater filled the basin to an elevation of –60 m. This basin functioned in two modes during the Quaternary. Its cold-climate mode was a freshwater lake (that may have filled and drained through the northwestern Turkey to the Aegean). Its warm-climate phase involved rising global sea level, inducing salt-water invasions through the Turkish straits to form the saline Black Sea, the last of which occurred about 8,000 years ago, an inundation that may have inspired the story of Noah (Ryan et al., 2003).

Victor R. Baker

Bibliography

- Arkipov, S.A., Ehlers, J., Johnson, R.G. and Wright, H.E. Jr., 1995. Glacial drainage towards the Mediterranean during the Middle and Late Pleistocene. *Boreas*, **24**, 196–206.
- Atwater, B.F., 1986. Pleistocene Glacial-lake Deposits of the Sanpoil River Valley Northeastern Washington. U.S. Geological Survey Bulletin 1661, 39pp.
- Baker, V.R., and Bunker, R.C., 1985. Cataclysmic late Pleistocene flooding from glacial Lake Missoula: A review. *Quaternary Sci. Rev.*, **4**, 1–41.
- Baker, V.R., Benito, G., and Rudoy, A.N., 1993. Paleohydrology of late Pleistocene superflooding, Altai Mountains, Siberia. *Science*, **259**, 348–350.
- Björck, S., 1995. A review of the history of the Baltic Sea, 13.0–8.0 ka BP. *Quaternary Int.*, **27**, 19–40.
- Broecker, W.S. and Denton, G.H., 1989. The role of ocean-atmosphere reorganizations in glacial cycles. *Geochim. Cosmochim. Acta*, **53**, 2465–2501.
- Clarke, G., Leverington, D., Teller, J., and Dyke, A., 2003. Superlakes, megafloods, and abrupt climate change. *Science*, **301**, 922–923.
- Grosswald, M.G., 1980. Late Weichselian Ice Sheet of northern Eurasia. *Quaternary Res.*, **13**, 1–32.
- Leverington, D., Mann, J.D., and Teller, J.T., 2002. Changes in the bathymetry and volume of glacial Lake Agassiz between 9,200 and 7,700 ¹⁴C yr B.P. *Quaternary Res.*, **57**, 244–252.
- Mangerud, J., Astakhov, V., Jakobsson, M., and Svendsen, J.I., 2001. *J. Quaternary Res.*, **16**, 773–777.
- O'Connor, J.E., 1993. Hydrology, hydraulics and sediment transport of Pleistocene lake Bonneville flooding on the Snake River, Idaho. Geological Society of America Special Paper 274, 83pp.
- Ryan, W.B.F., Major, C.O., Lericolais, G., and Goldstein, S.L., 2003. Catastrophic flooding of the Black Sea. *Annu. Rev. Earth Planet. Sci.*, **31**, 525–554.
- Teller, J.T., Leverington, D.W., and Mann, J.D., 2002. Freshwater outbursts to the oceans from glacial Lake Agassiz and their role in climate change during the last deglaciation. *Quaternary Sci. Rev.*, **21**, 879–887.

Cross-references

Cordilleran Ice Sheet
 Last Glacial Termination
 Late Quaternary Megafloods
 Laurentide Ice Sheet
 Proglacial Lacustrine Sediments
 Quaternary Climate Transitions and Cycles
 Scandinavian Ice Sheet
 The 8,200-year BP Event
 Thermohaline Circulation
 Younger Dryas

GLACIAL SEDIMENTS

Glacial sediments are formed in association with glacier ice in subglacial, ice marginal, lacustrine and marine environments. In such diverse environments, sediment can be reworked and deposited by a very wide range of processes, including subglacial lodgement, deformation and melt-out, subaerial and subaqueous mass-movements, fluvial processes, and settling through a water column. Numerous attempts have been made to classify the resulting range of sediments in schemes of greater or lesser complexity (Dreimanis, 1989), incorporating many varieties of “till” (e.g., flow till, lowered till, waterlain till, iceberg till). Many of these proposed sediment types are difficult to distinguish in the field, however, and a simple classification scheme is now favored by most workers. A fundamental distinction can be made between *primary glaciogenic deposits*, formed by exclusively glacial processes (such as subglacial lodgement, melt-out and deformation),

and *secondary deposits*, formed by the reworking of glaciogenic debris by processes not unique to glacial environments (Lawson, 1989). In terms of their internal characteristics, secondary glaciogenic deposits can be indistinguishable from sediments formed by similar processes in non-glacial environments and so, seen in isolation, they do not provide unequivocal evidence for the former presence of glacier ice. A glacial origin, however, can be determined from the *context* of such sediment facies, particularly the range of associated facies and structures, and the form and distribution of overlying landforms. It is therefore helpful to take a hierarchical approach to the analysis and interpretation of glacial sediments, in which individual facies are interpreted in terms of their *process* of deposition, and sediment-landform associations (comprising suites of genetically-related facies) are used to reconstruct former depositional *environments* (cf. Walker, 1992; Benn and Evans, 1998).

The characteristics of glacial sediments reflect the processes of entrainment, transport, and deposition experienced by debris as it travels through a glaciated basin. One of the most distinctive characteristics of glacial sediments is the presence of *erratics*, or exotic, far-traveled material. For Quaternary deposits, the provenance of erratics can often be pinpointed, allowing patterns of glacier flow to be reconstructed with some accuracy. For older successions, however, this may not be possible, especially if sediment exposure or preservation is poor. Erratics do not occur in all glacial deposits, however, and some are dominated by local material, eroded and redeposited close to its source. Transport processes can also impart a distinctive glacial signature on sediments. Debris transported at glacier beds is commonly subjected to high inter-particle contact forces, and the resulting abrasion and crushing of particles produces distinctive clast morphologies and particle size distributions. Clasts are commonly striated (particularly finer lithologies) with smooth, polished facets on their upper and lower surfaces, and may have asymmetrical *stoss-lee* or bullet-shaped forms. The presence of such clasts in a deposit does not necessarily mean, however, that it was deposited in a subglacial environment, because glacial debris can be carried far beyond glacier margins by various processes prior to final deposition. Some of these processes (such as fluvial transport) will result in rapid clast rounding and obliteration of striae and other glacial signatures, whereas others (such as iceberg rafting) may carry debris for hundreds of kilometers with little or no modification. Particle size distributions of subglacially-transported debris commonly exhibit a very broad range of grain sizes, from clay or silt up to pebbles or larger, and are typically bimodal or polymodal. The finer particles (<63 μm) are formed during subglacial abrasion, and are sometimes known as *rock flour*. Other particle size modes may reflect fracturing or crushing of larger clasts along joints, grain boundaries and other weaknesses. Whereas subglacial transport produces distinct debris characteristics, debris transported in englacial and supraglacial positions generally undergoes little or no modification and commonly retains the character of the parent debris. For this reason, supraglacial and englacial debris transport is known as *passive transport*, in distinction to *active* subglacial transport (Boulton, 1978; Benn and Evans, 1998), although some limited clast modification can occur during passive transport. Passive transport is particularly important in mountain environments, where large quantities of debris are delivered to glacier surfaces by rockfall and other mass movement processes. Fluvial processes can also transport significant quantities of sediment through some glaciers, resulting in significant clast rounding and size sorting. Thus, although striated, faceted clasts and rock flour are typical of subglacially transported debris, they are not essential

characteristics of glacial sediments, nor do they provide unequivocal evidence of ice-contact deposition.

Debris can be released from glacial transport at the glacier bed, or at subaerial or subaqueous glacier margins. In the former case, *tills* can be formed by the frictional lodgement of particles against the bed, the deformation of weak subglacial materials, or the melt-out of debris-rich ice. Subglacial deformation is now thought to be a very important till-forming process, especially where ice-sheets override soft sedimentary rocks or unlithified sediments. High cumulative strains may result in the complete mixing of the parent materials, creating diamicts which may be hard to distinguish from other till types. Paradoxically, subglacially deformed sediments are often easier to identify where cumulative strains are lower, because structures and textures inherited from the parent material are more likely to survive, and patterns of deformation easier to recognize. Such *glaciotectonites* are typically heterogeneous, incorporating laminae, boudins or rafts of pre-existing materials, often complexly folded and faulted. Glaciotectonites and deformation tills often occur in close association. Lodgement is an important process beneath wet-based ice; large boulders are especially likely to lodge against the bed, and are then molded by overpassing ice into asymmetrical stoss-lee forms resembling roches moutonnées. Although the term *lodgement till* is widely used (especially in the older literature) it is unlikely that lodgement, acting alone, can result in thick till units, and it is likely that most subglacial tills have undergone some degree of deformation. Melt-out tills are susceptible to reworking by slope processes or during dewatering, and thick, undeformed melt-out till sequences generally have low preservation potential. Sediments deposited below active ice are commonly streamlined. Long, narrow ridges of till (fluted moraines, or flutes) may extend downglacier from boulders or other obstructions on the bed, reflecting till deformation into cavities at the glacier sole. Drumlins are larger streamlined bedforms, commonly with complex internal stratigraphies. They may have rock or sediment cores (which may be deformed or undeformed), with an outer carapace of till or glaciotectonite. The most widely accepted origin for drumlins involves selective deformation, erosion and deposition of a soft glacier bed, although other ideas have been proposed.

Debris released by melting at a glacier surface or along terrestrial ice margins is commonly reworked by a wide variety of processes, including debris flow, other mass movements such as falls, slides and slumps, and the action of flowing water and wind. All of these processes will modify sediment characteristics to some degree. In particular, grain-size distributions are strongly influenced by fluvial action, fall sorting, winnowing by wind, and other processes, and many secondary glacial deposits exhibit a narrower range of grain sizes than subglacial tills. The simplest ice-marginal deposits consist of aprons of diamicts (debris flow and other mass movement deposits), and gravels and sands (glaciofluvial deposits) built up around the ice margin. Such *dump moraines* have a fan-like internal geometry, with beds dipping out from the ice margin at angles up to $\sim 35^\circ$. Dump moraines are particularly common around debris-covered glaciers in high mountain environments, and may form steep-sided ramps >100 m high. In many ice-marginal environments, however, sediments may be deposited and reworked several times as the local topography is altered by ice melting and oscillations of the glacier margin. Consequently, many ice-marginal sediment sequences have complex stratigraphies consisting of complexly interbedded diamicts, gravels, sands and silts, affected by faults and folds. Advances of the ice margin can

bulldoze ice-marginal and proglacial sediments into push moraines, or larger-scale glaciotectonic thrust-block moraines, with complex internal deformation structures (Benn and Evans, 1998).

Many glaciers terminate in lakes or the sea, and a large part of the glacial geologic record consists of glaciolacustrine and glaciomarine sediments. The character of subaqueous glacial sediments depends on the activity of the ice margin, sediment supply, meltwater discharges, and whether the ice is grounded or floating. At temperate glacier margins, where meltwater discharges are high, sedimentation may be dominated by subaqueous outwash, forming fans of crudely-sorted gravels and sands interbedded with fine-grained drapes deposited from meltwater plumes. If glacier margins are sufficiently stable, subaqueous fans can accumulate to the waterline, whereupon they evolve into ice-contact deltas. These have a three-fold internal stratigraphy, consisting of (a) low-angle topsets of gravel or sand, formed at the delta top; (b) dipping foresets formed on the delta foreslope; and (c) low gradient bottomsets, formed by the settling of fine sediments from turbidity currents beyond the delta front. Progradation of a delta can result in these sediments forming a vertical succession. Some subaqueous ice margins are dominated by mass movements, including debris flows, slumps and slides. Such mass movements tend to become more dilute and finer-grained down-flow, forming turbidity currents. These are particularly common in glaciolacustrine environments, where they form distinctly laminated successions consisting of basal graded sands, rippled sands and silts, laminated silts, and an upper drape of fine-grained sediment. Glaciolacustrine turbidites should not be confused with varves, which are annually deposited couplets consisting of a clay layer deposited during the winter (when the lake surface is frozen and sediment input is small) and a coarser layer deposited in summer. In contrast, turbidites are deposited rapidly (over a few minutes to hours in glacial settings), and lack a winter clay layer. Where glacier ice is in direct contact with lake- or seawater, calved icebergs can transport debris far beyond ice margins, then release it as they progressively melt or overturn. Dropstones can occur as isolated particles within fine-grained sediments, or in iceberg dump mounds. Sediments with high concentrations of dropstones are termed dropstone muds or dropstone diamicts.

During the last three decades, glacial geologists have amassed a large amount of data on modern glacial sedimentary environments in different climatic and topographic settings. This information has been used to define a range of glacial land system models, which can guide the interpretation of the glacial geologic record of the Pleistocene and older glacial epochs (Evans, 2003). Caution must be employed when appealing to modern analogs in glacial geology, because some former events or environments may not have modern equivalents, either in kind or in magnitude. With due care, however, modern analogs provide a powerful means of extracting maximum information about former depositional processes, environments, ice-margin activity, and climatic setting from Earth's rich glacial geologic record.

Douglas I. Benn

Bibliography

- Benn, D.I., and Evans, D.J.A., 1998. *Glaciers and Glaciation*. London: Arnold.
- Boulton, G.S., 1978. Boulder shapes and grain-size distributions of debris as indicators of transport paths through a glacier and till genesis. *Sedimentology*, **25**, 773–799.

- Dreimanis, A., 1989. Tills: Their genetic terminology and classification. In Goldthwait, R.P., and Matsch, C.L. (ed.), *Genetic Classification of Glacigenic Deposits*. Rotterdam: Balkema, pp. 17–84.
- Evans, D.J.A. (ed.), 2003. *Glacial Landscapes*. London: Arnold.
- Lawson, D.E., 1989. Glacigenic resedimentation: Classification concepts and application to mass-movement processes and deposits. In Goldthwait, R.P., and Matsch, C.L. (eds.), *Genetic Classification of Glacigenic Deposits*. Rotterdam: Balkema, pp. 147–169.
- Walker, R.G., 1992. Facies, facies models and modern stratigraphic concepts. In Walker, R.G., and James, N.P. (eds.), *Facies Models: Response to Sea-level Change*, 1–14. Toronto: Geological Association of Canada.

Cross-references

Drumlins
 Glacial Erratics
 Glaciofluvial Sediments
 Glaciomarine Sediments
 Ice-Rafted Debris (IRD)
 Moraines
 Roche Moutonnées
 Tills and Tillites

GLACIATIONS, PRE-QUATERNARY

Introduction

Earth has experienced recurring periods of glaciation (icehouse climatic conditions) alternating with periods of warm climate (greenhouse climatic conditions) (Figure G41; Hambrey and Harland, 1981; Eyles, 1993; Crowell, 1999). Glaciations have occurred on one continent or another, except for the Mesoproterozoic (ca. 2–1 Ga) in Precambrian times and the Mesozoic (250–65 Ma) in Phanerozoic times (Figure G42).

Changes in insolation, agglomeration, splitting and drifting of continents and associated orogenies are the first-order controls for changing climatic conditions on Earth. Some glacial periods correlate reasonably well with major orogenic phases (Figure G41); that is, with the agglomeration of continents and the change in distribution and volume of oceanic basins. The relative position and elevations of continents affected oceanic and atmospheric circulation, along with redistribution of heat, as well as degree of weathering of exposed rock and associated sequestration of atmospheric CO₂. These factors all contributed to the development of greenhouse and icehouse conditions and glaciations. Other factors such as orbital parameters further modulated the behavior of glaciers during ice-house periods.

Recognition of ancient glaciations is based on type and distribution of sedimentary deposits, fossil assemblages and their isotopic composition, and, in some cases, on erosional features. However, the older the glaciation, the less reliable and abundant the information is. Ancient glacial deposits may have been deeply buried, modified by metamorphism or selectively preserved in basins not subsequently affected by erosion. In addition, it is more difficult both to interpret the paleoenvironment of older deposits as different processes may have formed similar features, and also to date them because fossils or other suitable dateable material may be absent, and chemical (isotopic) composition of waters and atmosphere may have been different or altered.

The following are the most common, effective lines of evidence used to establish the occurrence of an ancient glaciation. No single indicator, however, provides unequivocal proof of

glaciation; it is the assemblage of several criteria, abundantly present in an area, which can be used to infer cold climate and presence of glaciers.

Depositional features

The presence of widespread *diamictite* (thick when marine), associated with cold-climate indicators is the most frequently used criterion to establish glacial conditions. Diamictite is a rock derived from diamicton – a poorly sorted mixture of mud, sand and gravel (Figure G43). Diamicton may be deposited directly by glaciers (till; tillite when cemented), or formed by other sedimentary processes, such as rainout of fine-grained suspended sediment and ice rafted debris, and debris flow in terrestrial or subaqueous conditions. The presence of extensive diamictite that contains faceted clasts is a strong initial clue of glaciation, when tectonic influences (such as non-glacial debris flow caused by tectonic activity) can be confidently discarded. However, it is difficult to determine whether diamictite is of glacial or non-glacial origin. It is therefore critical to look at the characteristics and distribution of associated deposits in order to establish the paleoclimatic significance of diamictite. When abundant, *shape and surface texture of clasts*, from bullet-shaped, faceted, and striated pebbles and boulders, to imprints and chattermarks on sand grains, are powerful indicators of glacial action. However, these may not always demonstrate direct deposition by ice, as clasts may be reworked under other depositional conditions. Although *boulder pavements* are commonly used as glacial indicators in the Quaternary, they are rarely identified in more ancient examples. *Dropstones* (lonestones) and deposits with textural inversions (such as randomly distributed lenses or pockets of sand and/or coarser-grained material in fine-grained deposits) are interpreted to indicate ice rafting and dumping from iceberg and seasonal ice floes, although they need to be distinguished from material rafted by floating organic debris (algae, trees) in the Phanerozoic. Presence of sand, silt, and clay *rhythmites* in lacustrine and marine deposits may contribute to a glacial interpretation, although they may also be formed by turbidity currents not necessarily derived from glaciers. True *varves*, the typical clay-silt or silt-sand couplets formed annually in ice-covered lakes, are rarely identified in pre-Quaternary successions because it is usually impossible to confirm that each couplet represents a year of deposition. Of interest is the fact that loess, so common in Pleistocene periglacial settings, is rarely reported from pre-Quaternary glacial deposits. This may be a matter of poor preservation of exposed terrestrial material; its ancient equivalent would likely be subaqueous silty deposits. Depositional landforms such as drumlin and eskers have rarely been used to establish glaciation, one of the debatable exceptions being for the Carboniferous in Brazil.

Biological and geochemical features

Cold climate *flora* (mainly terrestrial) and *fauna* (terrestrial and marine) and their related deposits, such as coal and ooze, are strong indicators of cold settings during Phanerozoic times. *Isotope* (such as O, C) analyses of skeletal marine microfossils can also provide indication on the presence and amount of glacial ice.

Erosional/deformation features

Abraded pavements on bedrock are often found with striations, and some chatter marks, crescent gouges, and lunate fractures.

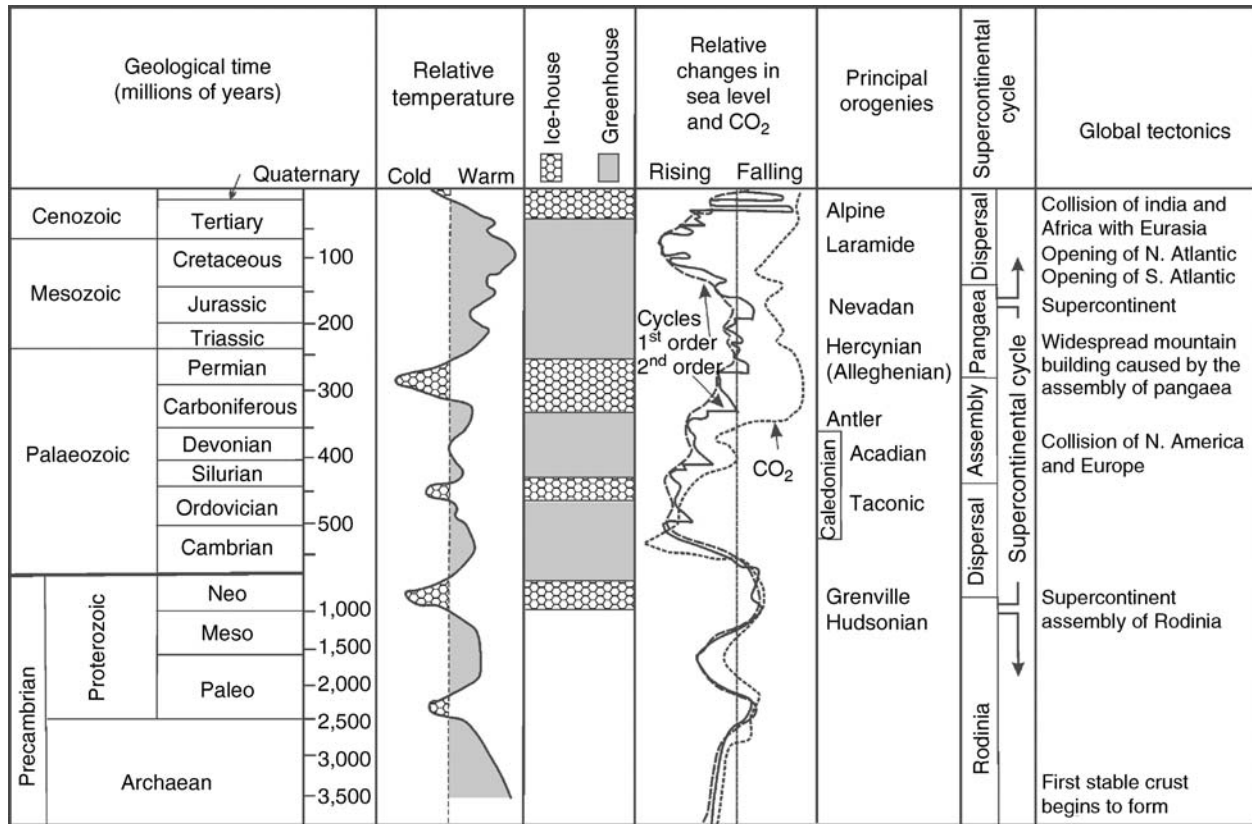


Figure G41 Major tectonic, environmental and climatic change on Earth (after Doyle et al., 1995; with data from Berner, 1990; Young, 1999).

Striated pavements are common throughout the ages (Laajoki, 2002). They can be formed by glaciers, but also by other unrelated tectonic (slickensides) and depositional (debris flows) processes. *Large-scale erosional features* such as *roche moutonnées*, crag and tails, and rock channels have rarely been used to establish glaciation, except in exhumed Ordovician surfaces in northwest Africa. When extensive, *furrows* in marine and lacustrine deposits are occasionally taken to indicate scouring by icebergs or seasonal ice floes (such as for the Ordovician in Brazil). Associated with other cold climate evidence, *sandstone wedges* have also been used to infer frozen ground conditions.

Precambrian glaciations

Archean

Archean-age glacial deposits (2,990–2,870 Ma) have been reported from South Africa. Diamictites are observed with occasional striated and faceted clasts at three different stratigraphic levels within the Witwatersrand Basin, both in outcrops and subsurface mining walls. Diamictite up to 80 m thick containing glacially striated and faceted clasts has also been found in the Pongola Basin. Other diamictites have been observed in northern Europe and North America but their glacial origin is debated.

Paleoproterozoic

Glacigenic deposits of Paleoproterozoic age have been documented in North America (Huronian), South Africa (Makganyene),

Finland-Russia (Karelian) and western Australia (Hammersley). Good exposures of Paleoproterozoic glacial deposits occur within the Huronian Supergroup in Ontario, Canada. The Gowganda Formation consists of diamictites with some faceted clasts overlying striated pavements, and thinly laminated argillites with abundant dropstones. These diamictites have accumulated in a predominantly glaciomarine setting. The laminated argillites were thought to be varves formed in a glacially influenced, subaqueous setting, but this cannot be confirmed in the absence of high resolution (annual) dating of these deposits.

The age of the Gowganda Formation has been bracketed between 2,670 and 2,220 Ma by underlying volcanic rock and a cross-cutting diabase. The ages of other Paleoproterozoic glacigenic successions are equally poorly constrained and range between 2,050 and 2,700 Ma, whereas the deposits in South Africa, Finland-Russia and western Australia are thought to be broadly correlative with the North American Huronian glacial deposits, their synchronous deposition is speculative.

Neoproterozoic

The striated pavement and overlying diamictite exposed on the shores of Varangerfjorden, Norway (Figure G43) were first described in 1891 and used to infer a Precambrian-age glaciation. This was one of the first Neoproterozoic glacial deposits to be described; others have since been documented from every continent (Crowell, 1999). Evidence for glacial conditions includes striated pavements, striated and faceted clasts, marine diamictite and laminated mudstone with dropstones.

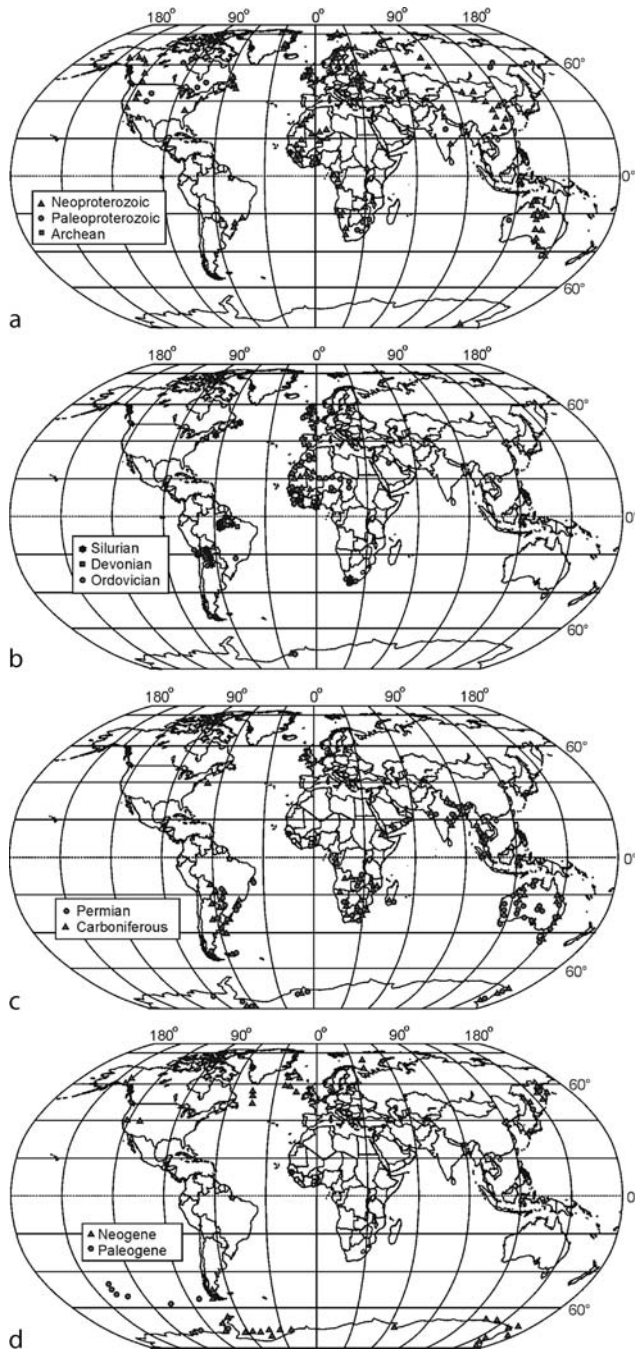


Figure G42 Maps of locations showing the recorded glacial features on Earth: (a) Precambrian; (b) Early Paleozoic; (c) Late Paleozoic; (d) Cenozoic (after Hambrey and Harland, 1981; Martini et al., 2001; and some data from Evans, 2000).

Two major glacial periods have been established in the Neoproterozoic, with growing evidence for a third. Glacial deposits are commonly ascribed to either of the two glacial periods based on lithological characteristics, biostratigraphy (acritarchs and Ediacaran fauna), chemostratigraphy ($\delta^{13}\text{C}$) of associated carbonates and radiometric dates (Hambrey and Harland,



Figure G43 Neoproterozoic diamictite of the Smallfjord Formation overlying a striated pavement, Bigganjargga, northern Norway.

1985; Knoll, 2000). The oldest glaciation (ca. 750–670 Ma) is commonly referred to as Sturtian, whereas the youngest (ca. 635 Ma) has been referred to as Marinoan (Australia, Canada) or Varangian (North Atlantic). However, there is still much debate about the age and stratigraphic correlation of these glacial deposits and the number and extent of Neoproterozoic glaciations (Knoll, 2000; Kendall et al., 2006).

Various aspects of the Neoproterozoic geologic record suggest that glaciations of this time may have been more severe than those of the Phanerozoic. The widespread distribution of diamictites, including some at low paleolatitude, has been used to infer that ice possibly covered the entire world (Harland, 1964). Inferred glacial deposits are commonly associated with carbonates that exhibit strong fluctuations in $\delta^{13}\text{C}$. The close juxtaposition of glacial deposits and presumably warm water carbonates has been used to suggest relatively rapid climate change between glacial and warm conditions, whereas the $\delta^{13}\text{C}$ fluctuations imply significant perturbations in seawater geochemistry (Harland, 1964; Hoffman et al., 1998). The low latitude (equatorial) deposition of some glacial deposits has been suggested by paleomagnetic analyses, although it has only been confidently demonstrated for the Elatina Formation in Australia (Evans, 2000). Nevertheless,

several scenarios have been proposed to explain low latitude glaciations, including a “snowball” Earth encased in ice as a result of increased reflectivity or “runaway albedo,” glaciations during a significant change in tilting of the Earth’s rotating axis, and high-mountain glaciers associated with tectonic uplift. Further research on Neoproterozoic successions and a more robust geochronological framework are needed to fully evaluate the plausibility of these scenarios.

Phanerozoic glaciations

Extensive glaciations occurred during the Phanerozoic. The Ordovician and Permo-Carboniferous ones were widely distributed across mid-to high-latitudes (Evans, 2003). No glaciations have been recorded during the Mesozoic, although the presence of ice at the poles has been suggested by local occurrence of rafted debris.

Paleozoic glaciations

The Paleozoic is characterized by three periods of icehouse conditions centered over North Africa and South America (Ordovician), South America (Devonian), and Australia, Africa, South America, India and the Arabian Peninsula (Carboniferous) (Figure G42). This reflects, for the most part, polar wandering and drifting of the continents into and away from mid-high latitudes where glaciers could develop (Caputo and Crowell, 1985).

The *Ordovician* glaciation (ca. 440 Ma) was the first major Phanerozoic glaciation; it was centered in northwestern Africa (Ghienne, 2003). The evidence consists of a widespread exhumed surface with striated pavements, polished surfaces and other erosional features, and well-developed diamictites (presumably tillites). Glaciomarine deposits of equivalent age are reported from farther south, in Sierra Leone. One apparent anomaly is that the Ordovician glaciation occurred when the tropical water temperature was just 3 °C cooler and the CO₂ partial pressure was about 15 times higher than the present (Figure G41). This suggests that cooler conditions are not always related to low concentrations of CO₂ in the atmosphere. Perhaps the location of continents near the poles offset these apparently adverse conditions in order for glaciation to occur.

The Ordovician glaciation had a worldwide effect on relative sea-level change. It contributed to the interruption of the major, early Phanerozoic transgression, forcing a regression from the Ordovician to the Silurian. The postglacial transgression led to the re-establishment of normal fauna, and extensive development of reefs and of several, early Silurian euxinic basins. This cycle is recognized in various places, such as South Africa, Turkey, South America, Europe and North America, where either thin diamictites and/or significant unconformities mark or occur stratigraphically close to the Ordovician-Silurian boundary.

Though not yet well studied, early *Silurian* deposits of possible glacial origin have been reported from southwestern South America (Argentina, Brazil, Bolivia).

The *Devonian* glaciation was mostly limited to South America (Caputo and Crowell, 1985). The evidence consists mainly of widespread, thick (up to 600 m) marine diamictite whose origin has been indirectly related to regional glaciations.

During the *Late Carboniferous–Early Permian* (~350–250 Ma), Earth experienced some of the most widespread and longest glaciations recorded during the Phanerozoic. These glaciations affected the southernmost part of Pangea with terrestrial (tillites?) and widespread marine diamictites occurring

primarily in Australia, South Africa, South America and southern Asia. The growing and waning glaciers also had significant impact on distant northern lands, where thick, coal-bearing deposits show cyclicity (cyclothems) that ultimately records relative sea-level changes. For the first time in Earth’s history, cold climate conditions are also indicated by terrestrial plants and coal deposits (Figure G44). Although these ancient plant assemblages were very different from the present ones, they occupied analogous environments and produced similar products (peat; coal upon diagenesis). In most cases, the Permian-Carboniferous diamictites are overlain by marine deposits, and these in turn by continental deposits, some bearing coal derived from warm-climate peat. In other instances though, glacial deposits are interlayered with and overlain by coal-bearing units, where the cold climate origin of the coal can be established through pollen and plant macrofauna analysis. A good record of climatic changes from Upper Carboniferous-lowermost Permian glacial cold conditions to middle-upper Permian-Triassic warm settings has been established in South Africa (Figure G44; Falcon, 1989).

Cenozoic glaciations

The Tertiary (65–2 Ma) and Quaternary (2 Ma to Present) periods constitute the Cenozoic Era. Here we deal with the deteriorating Tertiary climate and possible glaciations that developed at high latitudes. The warm climate conditions persisted throughout the globe during the early Tertiary with its warmest time about 50 Ma (Eocene); this is indicated by vertebrate fossils such as alligators in Arctic islands and tropical marine microfossils (foraminifera and coccoliths) in North Atlantic deposits. Climatic deterioration occurred from 40 to 25 Ma (late Eocene and Oligocene), leading to the colder conditions of the late Cenozoic Era. Ice rafted material and $\delta^{18}\text{O}$ of marine microfossils indicate that Antarctic polar sea ice and continental glaciations may have developed by about 36–34 Ma (early Oligocene). The Antarctic glaciations expanded considerably between 15–10 Ma (Miocene). Associated large sea-level changes dramatically influenced distant areas. For example, the connection between the Mediterranean Sea and the Atlantic Ocean was cut off at this time, leading to widespread deposition of evaporites and what is commonly referred to as the Mediterranean (or Messinian) salinity crisis. The onset of glaciations in the Northern Hemisphere dates from about 6 Ma and the mid-latitude continental ice sheets started developing approximately 3 Ma ago (Pliocene). This is indicated by variations in marine microfossil fauna and abundance of ice-rafted material in northern seas.

Conclusion

Glaciations have existed on various continents throughout Earth history, although some local records are still debated. Many hypotheses have been put forward to explain the distribution of glacial periods in time and space, none of which is all encompassing. Every major glaciation has its own peculiarities, but all appear to require a cool atmosphere, the presence of continents at or near the poles, and some region-wide obstruction that impedes the redistribution of heat across latitudes. An intriguing correlation that has long been noted is the development of icehouse conditions with major orogenies that change the physiography of a significant part of the Earth’s surface and may indirectly affect the composition of the atmosphere. In addition, the two longest cold periods (Neoproterozoic and Permian-Carboniferous) coincide with periods of time where global

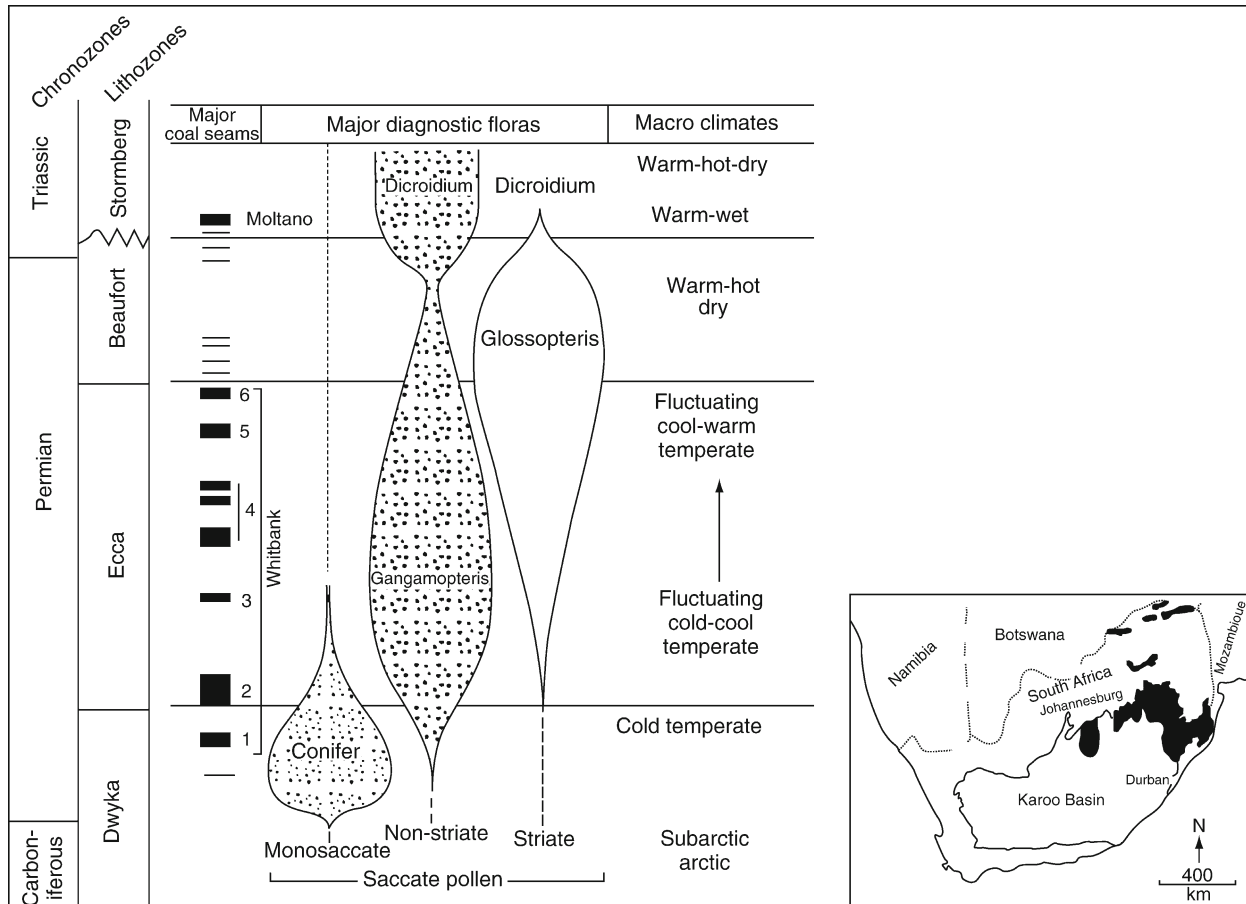


Figure G44 Schematic diagram showing the stratigraphy, major coal seams, diagnostic floras and inferred macroclimates for the Upper Carboniferous to Triassic succession in South Africa. The succession records the following changes in depositional environment: glacially-influenced marine conditions (Dwyka Group), deep to shallow marine environments (Ecca Group) and fluvial environments (Beaufort and Stormberg Groups). Note the change in diagnostic flora from the glacial conditions of the Late Carboniferous-early Permian to the temperate-cold middle Permian, and to the warm late Permian-Triassic (from Martini et al., 2001; after Falcon, 1989). Inset: distribution of coal.

paleogeography was characterized by supercontinents. Recent developments in various fields of geology (such as isotope geochemistry and geochronology) provide promising avenues of research in pre-Quaternary glacial geology.

Emmanuelle Arnaud and I. Peter Martini

Bibliography

- Berner, R.A., 1990. Atmospheric carbon dioxide over Phanerozoic time. *Science*, **249**, 1382–1386.
- Caputo, M.V., and Crowell, J.C., 1985. Migration of glacial center across Gondwana during the Paleozoic Era. *Geol. Soc. Am. Bull.*, **96**, 1020–1036.
- Crowell, J.C., 1999. Pre-Mesozoic ice ages: Their bearing on understanding the climate system. *Geol. Soc. Am., Memoir*, **192**, 106pp.
- Doyle, P., Matthew, R.B., and Baxter, A.N., 1995. *The Key to Earth History: An Introduction to Stratigraphy*. New York: Wiley, 231pp.
- Evans, D.A.D., 2000. Stratigraphic, geochronological, and paleomagnetic constraints upon the Neoproterozoic climatic paradox. *Am. J. Sci.*, **300**, 347–433.
- Evans, D.A.D., 2003. A fundamental Precambrian-Phanerozoic shift in Earth's glacial style? *Techonophysics*, **375**, 353–385.
- Eyles, N., 1993. Earth's glacial record and its tectonic setting. *Earth Sci. Rev.*, **35**, 1–248.
- Falcon, R.M.S., 1989. Macro- and micro-factors affecting coal seam quality and distribution in southern Africa with particular reference to the No. 2 Seam, Witbank coalfield, South Africa. *Int. J. Coal Geol.*, **12**, 681–731.
- Ghienne, J.F., 2003. Late Ordovician sedimentary environments, glacial cycles and post glacial transgression in the Taoudeni Basin, West Africa. *Palaeogeogr. Palaeoclimatol. Palaeoecol.*, **189**, 117–145.
- Hambrey, M.J., and Harland, W.B. (eds.), 1981. *Earth's pre-Pleistocene glacial record*. Cambridge Earth Science series. Cambridge: Cambridge University Press, 1004pp.
- Hambrey, M.J., and Harland, W.B., 1985. The late Proterozoic glacial era. *Palaeogeogr. Palaeoclimatol. Palaeoecol.*, **51**, 255–272.
- Harland, W.B., 1964. Critical evidence for a great infra-cambrian glaciation. *Geol. Rundsch.*, **54**, 45–61.
- Hoffman, P.F., Kaufman, A.J., Halverson, G.P., and Schrag, D.P., 1998. A Neoproterozoic snowball earth. *Science*, **281**, 1342–1346.
- Kendall, B., Creaser, R.A., and Selby, O., 2006. Re-Os geochronology of postglacial black shales in Australia. Constraints on the timing of "Sturtian" glaciation. *Geology*, **34**, 729–732.
- Knoll, A.H., 2000. Learning to tell Neoproterozoic time. *Precambrian Res.*, **100**, 3–20.
- Laajoki, K., 2002. New evidence of glacial abrasion of the Late Proterozoic unconformity around Varangerfjorden, northern Norway. In Altermann, W., and Corcoran, P. (eds.), *Precambrian Sedimentary Environments: A Modern Approach To Ancient Depositional Systems*. Oxford: Blackwell Science, pp. 450.

- Martini, I.P., Brookfield, M.E. and Sadura, S., 2001. *Principles of Glacial Geomorphology and Geology*. Upper Saddle River: Prentice Hall, 381pp.
- Young, G.M., 1999. The Precambrian atmosphere. In Marshall, C.P. and Fairbridge, R.W. (eds.), *Encyclopedia of Geochemistry*. Dordrecht: Kluwer, pp. 526–532.

Cross-references

Cenozoic Climate Change
 Climate Change, Causes
 Coal beds, Origin and Climate
 Diamicton
 Early Paleozoic Climates (Cambrian-Devonian)
 Glacial Sediments
 Glaciations, Quaternary
 Icehouse (cold) Climates
 Ice-Rafted Debris (IRD)
 Late Paleozoic paleoclimates (Carboniferous-Permian)
 Messinian Salinity Crisis
 Proterozoic Climates
 Snowball Earth Hypothesis
 Tills and Tillites
 Varved Sediments

GLACIATIONS, QUATERNARY

Overview

The Quaternary Period spans the last 2 million years (Myr) and includes the Pleistocene Epoch of Earth history, which prevailed for most of the Quaternary, and the Holocene Epoch beginning around 11,000 years ago. The Quaternary Period has been a time of profligate environmental and climatic change, characterized by a sequence of roughly 30 glacial-interglacial cycles in the Northern Hemisphere (Figure G45). This period of Earth history is colloquially known as the “Ice Age,” the time when ice sheets rolled up and down “like great white window blinds” over the landscape (Annie Dillard, *Pilgrim at Tinker Creek*).

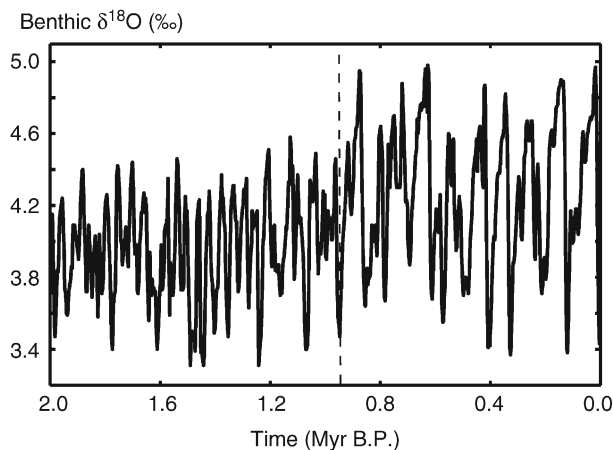


Figure G45 Marine benthic $\delta^{18}\text{O}$ variability over the last 2 Myr, from ODP core 677 (0.4–2 Myr B.P.) and SPECMAP stacked data (0.4 Myr B.P. to present) (based on Imbrie et al., 1993, SPECMAP Archive #4; IGBP PAGES/World Data Center-A for Paleoclimatology, data contribution series 93-031, NOAA/NGDC Paleoclimatology Program, Boulder CO).

This article summarizes the geological and paleoceanographic evidence of the Quaternary ice sheets, with emphasis on the chronology of glacial-interglacial cycles and the geographic distribution of the ice sheets. This is followed by an expanded discussion of ice sheet-climate interactions and the potential causes of Quaternary ice sheet growth and decay. Although the exact forcing mechanisms and internal climate-system interactions that cause glacial-interglacial cycles are not fully understood, many of the principal ingredients in Quaternary climate dynamics have been identified. Outstanding questions and puzzles about the Quaternary glaciations are highlighted throughout the discussion.

Observations

The glacial-interglacial cycles that distinguish the Quaternary are recorded in a number of geological and paleoceanographic archives, including deep-sea and lake sediments, ice cores, glacial landforms, coral reefs, ancient groundwater, cave records, over-consolidated sediments, loess deposits, fossil pollen, and relative sea-level reconstructions. This rich array of geological data cannot be fully summarized here, but interested readers are referred to Bradley (1999) for an expanded discussion of methods of paleoclimate reconstruction.

Marine sediments

The most detailed record of glaciation during the Quaternary comes from the marine deep-sea sediment record (e.g., Figure G45). Foraminifera in both the surface- and deep-sea (benthic) water column make use of ambient seawater to build calcium carbonate shells. Individual planktonic shells are labeled with oxygen isotope ratios, $\delta^{18}\text{O}$, that are representative of the local water. Upon their demise, foraminifera sink to the bottom and are entombed in sediments. Rainout of marine sediments and carbonate shells is slow in deep-water environments, typically on the order of cm per 1,000 years. Deep-sea sediment cores therefore permit continuous stratigraphies that extend millions of years into the past, with numerous chemical and isotopic signatures of paleoenvironmental conditions.

Oxygen-18 in the CaCO_3 of marine foraminifera varies as a function of both ocean temperature and overall ocean chemistry (see *Oxygen isotopes*). During evaporation of surface water, it is energetically favorable to vaporize the lighter isotope ^{16}O in H_2O . This causes a net depletion of ^{16}O in surface waters and a concomitant enrichment of ^{18}O . In an equilibrium state of the hydrological cycle, water vapor precipitates over the ocean and continents, and continental precipitation returns to the oceans as river runoff, giving a net isotopic balance on time scales of months to years. During glacial times, however, continental ice sheets build up on the land and there is a net accumulation of light water isotopes on the continents. Sea level falls and the oceans become isotopically heavier. In Figure G45, benthic $\delta^{18}\text{O}$ therefore indicates the history of continental ice volume through the Quaternary. Heavy $\delta^{18}\text{O}$ values correspond to glacial times and light values represent interglacial conditions, such as the contemporary Holocene epoch. Modern benthic values in this reconstruction are 3.43‰, while the mean Quaternary value is 4.10‰. Up to 30 glacial-interglacial cycles are apparent in Figure G45, increasing in both amplitude and duration during the last 900 kyr.

Ice cores

While the marine sediment record provides the best available chronology of Quaternary ice volume, more direct proxies of Quaternary temperature are available from ice cores (see *Ice cores*,

Antarctica and Greenland). Ice from the summit region of the Greenland Ice Sheet provides high-resolution records of the last glacial cycle, ca. 120 kyr B.P. to present, with $\delta^{18}\text{O}$ and δD in the ice providing a proxy for glacial-period atmospheric temperatures in central Greenland (Figure G46; Dansgaard et al., 1993). The Greenland ice cores also illustrate a complex array of millennial-scale climate variability during glacial periods. In Vostok, East Antarctica, a 3,623-m ice core provides a detailed record of the last 420 kyr, a period that spans three glacial-interglacial cycles (Figure G47a; Petit et al., 1999). Accumulation rates are lower on the Antarctic Plateau than in Greenland, so climate reconstructions for the last glacial cycle

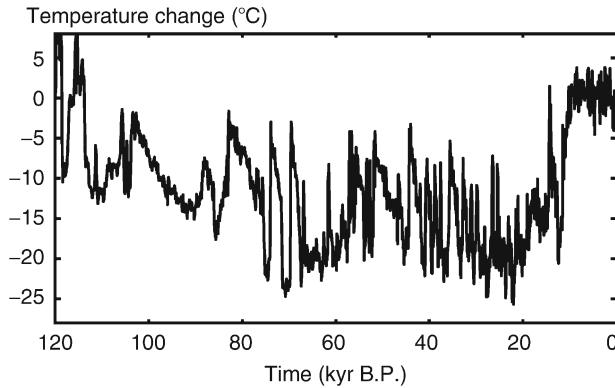


Figure G46 Temperature reconstructions for the last 120 kyr from the GRIP ice core, Summit Greenland (Dansgaard et al., 1993). Temperature reconstructions are based on $\delta^{18}\text{O}$ in the ice core and are expressed as perturbations from the modern surface temperature, using the isotope-temperature transfer function derived by Cuffey and Clow (1997).

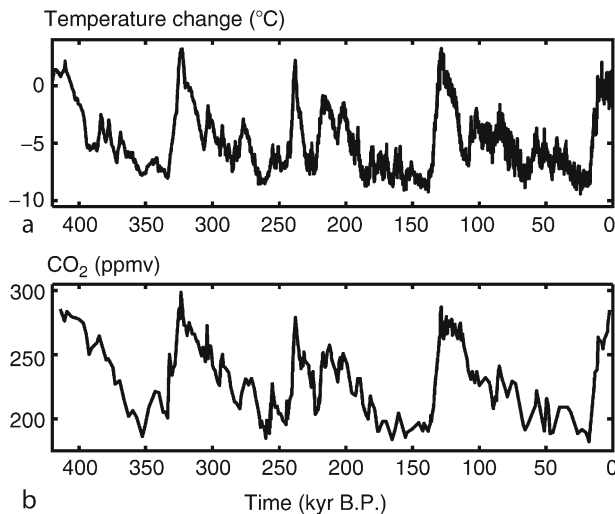


Figure G47 Temperature and carbon dioxide reconstructions for the last 420 kyr from the Vostok, Antarctica ice core. Temperature reconstructions are based on δD in the ice core and are expressed as perturbations from the modern surface temperature at Vostok (data from Petit et al., 2001, IGBP PAGES/World Data Center for Paleoclimatology, data contribution series 2001-076, NOAA/NGDC Paleoclimatology Program, Boulder CO).

have lower temporal resolution. Taking this into account, the record from Antarctica closely mirrors what is seen in Greenland.

Many other paleoenvironmental records are available from ice cores of Antarctica, Greenland, tropical glaciers, and Arctic icefields (see *Ice cores, Antarctica and Greenland*, this volume). These include samples of atmospheric gases in air bubbles that are trapped in the ice cores (Figure G47b), atmospheric aerosols and dissolved ions, and both direct and indirect climate proxies (for temperature and snow accumulation rates). While ice core stratigraphies offer superb detail, they broadly reflect what is seen in less-resolved stratigraphies from lake, loess, marine, and cave records in many regions of the world.

The last glacial cycle

The glacial geologic record on land does not afford the continuous chronology available from marine or ice cores, but it offers insights into the geographic distribution of ice sheets during glacial episodes. Evidence of multiple glaciations is clear in most regions of the Northern Hemisphere, but the terrestrial record has been largely obliterated by the most recent (Wisconsinan) advance and retreat of ice, beginning about 120 kyr B.P. Ice sheet nucleation appears to have occurred at this time in the Scandinavian mountains, Russian Arctic islands, and northeastern North America, with ice dispersal centers in the Queen Elizabeth Islands and highlands of Labrador and Quebec. There is no evidence of major ice advance in western North America at this time.

Multiple sequences of advance and retreat are apparent in the geologic record as ice sheets in North America and Eurasia grew fitfully to their Last Glacial Maximum (LGM) configuration at roughly 21 kyr B.P. (Dyke and Prest, 1987). The timing of maximum ice sheet extent differed in different regions, with 21 kyr B.P. marking the minimum sea level of the last glacial cycle (120–130 m below present). Ice sheets then melted back over the period 21–8 kyr B.P., with ice retreat punctuated by periods of rapid sea-level rise.

Table G2 presents estimates of present-day and LGM global ice sheet volume. Modern ice sheets harbor an amount of ice equivalent to almost 69 m of global sea level. At the peak of the last glaciation, terrestrial ice volume increased by roughly 270%, to 179–198 m sea-level equivalent. All of the world's ice masses grew during the last glaciation, including the Antarctic Ice Sheet and icefields in New Zealand, Patagonia, and tropical mountains. However, the bulk of additional ice at the height of the last glaciation built up in the Northern Hemisphere, when the confluent Laurentide, Cordilleran, and Innuitian ice complexes in North

Table G2 Ice sheet volume reconstructions for modern day and at the Last Glacial Maximum, 21 kyr B.P., expressed as sea-level equivalent

Region	Ice volume (msl)	
	LGM	Modern
North America ^a	78–88	0.2
Eurasia ^b	10–14	0.2
Antarctica ^c	75–79	61.1
Greenland ^c	9–10	7.2
Other ^d	6	0.1
Total	178–197	68.8

^aMarshall et al. (2002).

^bSiegert et al. (1999).

^cHuybrechts (2002).

^dClark and Mix (2002).

America were greater in size than modern-day Antarctica. A recent special volume of *Quaternary Science Reviews* (vol. 21, 2002) presents details on ice sheet, ocean, and climate conditions at the LGM.

Ice sheet area and volume at the Last Glacial Maximum is believed to be close to the maximum Quaternary extent of ice sheets in many regions. However, earlier glaciations reached further south in parts of the northern interior USA, and Quaternary ice sheet maxima in most of the high Arctic also predates the LGM. This is consistent with glacial-interglacial chronologies in marine and ice cores (Figures G45, G47a), which indicate a remarkably similar structure and amplitude of glacial-interglacial cycles over the last 900 kyr. The seemingly sudden switch in demeanor of glacial-interglacial cycles at 900 kyr, known as the mid-Pleistocene transition, is discussed in the next section on Quaternary climate dynamics.

Quaternary climate processes

Orbital variations

The underlying causes of Quaternary ice sheet advance and retreat are not fully understood, although there are convincing links with variations in the Earth's axis of rotation and its orbit around the Sun. Most important among these astronomical variations are changes in the eccentricity of Earth's orbit, the tilt of the rotational axis relative to the plane of the ecliptic, and the orientation of Earth's tilt axis (see *Astronomical theory of climate change*; Imbrie et al., 1993). Tilt axis orientation varies as Earth precesses like a top, with the effect of changing the latitude (hemisphere) that receives the most direct solar radiation at perihelion. This effect, known as the precession of the equinoxes, combines with orbital eccentricity to produce seasonal variations in insolation on long time scales; there would be no effect if Earth's orbit were circular.

These "Milankovitch" variations are regular cycles with periodicities of 100 kyr (eccentricity), 41 kyr (tilt), and 19 and 23 kyr (precession). Of these influences, only the first changes global annual insolation. Variations in tilt and precession change the geographic distribution and seasonality of insolation, and this appears to be key for triggering Northern Hemisphere (NH) glaciation and deglaciation. Cool NH summer configurations occur when there is high eccentricity and low axial tilt, and when NH summer coincides with aphelion, the moment in Earth's orbit when it is furthest from the sun.

Following up on the theoretical suggestions of Adhemar and Croll, Milankovitch surmised that cool summers at high northern latitudes were the key to ice sheet nucleation. His calculations of the orbital parameters and the associated variations in NH insolation bear a remarkable correlation with the marine record of continental ice volume (Figure G45). While the orbital variations are more purely periodic, orbital periodicities of 19, 23, 41 and 100 kyr are clearly evident in the marine sediment and ice core records. Therefore, astronomical variations have been called the "pacemaker of the Ice Ages" (Imbrie and Imbrie, 1979).

The orbital theory of the Ice Ages cannot explain many aspects of glacial-interglacial cycles, however. The direct radiative forcing associated with Milankovitch variations is too small to have acted as the sole control of glaciations. Orbital variations also produce insolation perturbations that are out-of-phase in the Northern and Southern Hemispheres, whereas both hemispheres experienced essentially simultaneous episodes of ice sheet advance and temperature depression during the Quaternary glaciations.

Additional difficulties are introduced by the time scales of variability. As detailed in Imbrie and Imbrie (1979) and Imbrie et al. (1993), the dominant period of late Pleistocene glacial cycles is close to 100 kyr, while orbital forcing is strongest at 19, 23 and 41 kyr. The mid-Pleistocene transition that is vividly evident in Figure G45 represents a switch from an early Pleistocene "Milankovitch world," where glacial-interglacial cycles occurred at 40-kyr time scales, to the late Pleistocene 100-kyr cycles noted above. This switch must have been caused by changes in internal climate and ice sheet dynamics, as the periodicity and amplitude of orbital variations have not changed during the Quaternary. Millennial-scale climate variability during glacial periods (Figure G46) also requires a non-orbital explanation, as the dramatic temperature changes witnessed in the Greenland ice cores occur at sub-Milankovitch frequencies (Clark et al., 1999a).

In summary, orbital influences are clearly evident in the timing and duration of glacial-interglacial cycles, but orbitally-driven insolation changes cannot explain many important aspects of ice sheet growth and Quaternary climate. Internal climate system amplifiers and feedbacks must have acted in concert with orbital variations to produce glacial-interglacial cycles. Subsections below introduce a number of these internal dynamical processes. Interested readers are referred to Clark et al. (1999a) for expanded discussion.

Internal dynamics: greenhouse gases

The Vostok ice core provides a remarkable record of carbon dioxide and methane variations over the last 420 kyr (Figure G47b; Petit et al., 1999). These gases are trapped in air bubbles in the ice, providing samples of the ancient atmosphere. Because CO₂ and CH₄ are well mixed in the troposphere, with a mixing time of less than a decade, these gas concentrations represent global levels of CO₂ and CH₄ through the last three glacial cycles. Concentrations closely track the change in atmospheric temperature that is recorded in the Vostok ice core (Figure G47a), which is calculated from deuterium and oxygen isotope ratios in the ice crystals.

CO₂ and CH₄ are radiatively active greenhouse gases and the reduced glacial concentrations of CO₂ and CH₄ would cause a direct global cooling effect, reinforcing cold conditions in glacial times. Similarly, elevated interglacial CO₂ and CH₄ concentrations are certain to have augmented interglacial warmth. Temporal variability in these gases therefore represents a significant internal climate feedback/forcing that is essentially phase-locked with global temperature and ice volume, within dating uncertainty. Because greenhouse gas impacts are global (that is, hemispherically-mixed), the reductions in glacial CO₂ and CH₄ concentrations help to transform the Northern Hemisphere orbital forcing into a global temperature perturbation.

The causes of glacial-interglacial CO₂ and CH₄ variations are a matter of debate. Variability in CO₂ concentrations arises from transfers between carbon reservoirs in the atmosphere, terrestrial biosphere, ocean mixed layer, and deep ocean. Because the deep ocean has a long residence time and is capable of holding huge carbon reserves, most theories of glacial CO₂ sequestration involve increased biological and physical uptake in the oceans. Glacial-interglacial variations in CH₄ are expected to have different causes and are more likely related to low-latitude terrestrial biological activity. Ruddiman (2001) offers a thorough introduction to Quaternary fluctuations in CO₂ and CH₄ and potential causes of CO₂ and CH₄ variability on glacial-interglacial time scales. Improved understanding of the glacial carbon cycle poses a high-priority challenge in current studies of Quaternary climate dynamics.

Internal dynamics: ice sheets

Glaciers and ice sheets exert a cooling influence on the climate by increasing the average topographic elevation of the landscape and by reflecting a large fraction of incoming solar radiation back to space. Both of these influences act as positive feedbacks to promote ice expansion once ice sheets are nucleated and to accelerate ice sheet retreat during deglaciation. These influences, particularly the ice-albedo (reflectivity) feedback, are believed to be critical to amplifying the modest changes in insolation associated with orbital perturbations. In modeling studies, cooling feedbacks from these processes make it difficult to melt away an ice sheet once it has established itself; model studies that permit free simulations of the ice-climate system have yet to simulate glacial terminations – transitions from glacial to interglacial conditions – in a satisfactory manner.

Additional ice sheet feedbacks arise due to internal, long-timescale processes associated with ice dynamics and glacial isostasy. Ice sheets flow by two principal mechanisms: (a) internal visco-plastic deformation (“creep” flow), and (b) basal flow, via either decoupled sliding over the bed or subglacial sediment deformation. The first mechanism, internal deformation, produces relatively low ice fluxes in most situations, giving rise to steep, thick ice sheets such as those of present-day Greenland and East Antarctica. In West Antarctica, where basal flow dominates ice-sheet flux, ice sheets are low-sloping and significantly thinner. Ice streams that drain the West Antarctic Ice Sheet appear to flow over a thin layer of deforming sediment, lubricated by high subglacial water pressures. Melting conditions and free water at the bed enable this fast-flow mechanism, and it creates a situation where the West Antarctic Ice Sheet has a high rate of ice transport to the continental margins and a relatively short response time to climate perturbations.

A growing body of geologic evidence suggests that fast-flowing ice lobes and marine ice sheet instabilities were prevalent in the Eurasian and Laurentide Ice Sheets during the glacial period (Clark, 1994; Heinrich, 1988). Modeling studies indicate that the largest former ice sheet, the Laurentide, could have been substantially thinner and more responsive to climate change in a flow regime dominated by basal flow (Fisher et al., 1985), similar to modern-day West Antarctica. This would sensitize the ice sheet to warming trends and make it easier to achieve ice sheet deglaciation during warm orbital periods.

The geological record is inconclusive with respect to the reconstructions of the thickness and dynamics of the former ice sheets, but ice sheet modeling studies indicate a potential connection between intrinsic time scales of ice sheet thermodynamic evolution and the 100-kyr glacial cycle (Marshall and Clark, 2002). Basal flow cannot become widespread until the ice sheet reaches the pressure-melting point at the base. This takes on the order of tens of thousands of years, such that a switch to West Antarctic-style ice dynamics is not possible until late in the glacial cycle. Once a large fraction of the ice sheet bed is at the melting point, subglacial water builds up at the bed and basal flow takes over from internal deformation as the dominant flow mechanism. This transfers large quantities of ice to the southern and marine margins, where there is surplus energy available for ablation, greatly facilitating ice sheet retreat during glacial terminations.

This internal ice sheet instability offers one means by which orbital forcing on 19, 23, and 41 kyr cycles is filtered to produce a 100-kyr response time in the Earth system. Glacial isostasy offers another long-timescale mechanism. The weight of

the ice sheets and the changing ocean-water load causes elastic deflection of the Earth’s crust and viscous flow of deep mantle material, giving rise to topographic deflections of more than 1,000 m in central regions of the former ice sheets. This isostatic response has a timescale of several kyr, introducing a lag between ice volume and isostatically-driven surface draw-down. This effect is believed to be critical to ice sheet deglaciation and the 100-kyr glacial cycle because the thick, mature (e.g., LGM) ice sheets will depress their bed enough to lower a large portion of the ice sheet to altitudes where melting dominates snow accumulation.

Internal dynamics: ocean circulation

Ice sheets also interacted in complex ways with the oceans during glacial episodes. There is strong evidence that changes in the freshwater budget of the North Atlantic during the glaciation were sufficient to weaken or shut down deepwater formation, reducing North Atlantic thermohaline circulation. This diminished the poleward transfer of heat and increased the intensity of cold conditions in the mid-latitude and subpolar North Atlantic.

Reduced deepwater formation was probably a consequence of decreased evaporation and increased freshwater runoff from the continents during the glacial period, through both meltwater runoff and circum-Atlantic iceberg fluxes. It is also believed that the location of meltwater injections to the North Atlantic is critical for destabilizing the thermohaline circulation. Retreating ice sheets during the last deglaciation caused a runoff diversion from the Mississippi River Basin (Gulf of Mexico) to the eastern North American seaboard, via the Hudson and St. Lawrence Rivers, which appears to have perturbed the North Atlantic and sent the Northern Hemisphere climate into a temporary return to glacial conditions, known as the Younger Dryas cold episode (see Clark et al., 1999b).

North Atlantic deepwater communicates with the global ocean on times scales of the order of 1 kyr, while ocean-atmosphere interactions via energy, moisture, and momentum exchange are essentially instantaneous. These exchanges appear to have been important during glaciations, as North Atlantic thermohaline changes are rapidly communicated throughout the Northern Hemisphere, and possibly the globe. Cold/warm cycles associated with North Atlantic variability are accentuated in the North Atlantic region, however, and are widely considered to be the cause of the dramatic millennial-scale climate variability seen in Greenland ice cores (Figure G46; Dansgaard et al., 1993; Clark et al., 1999b). This high-frequency temperature flicker is a significant fraction of the glacial-interglacial temperature shift in Greenland, so the dynamics of the paleohydrological cycle and the ocean-atmosphere-ice sheet system are likely to prove integral to Quaternary climate dynamics.

Other climate system influences

Clark et al. (1999a) list a number of additional ways in which ice sheets influence climate, including topographic perturbations to atmospheric circulation. This alters storm tracks and probably contributes to the specific geographic pattern of glaciation. Other factors that contribute to global cooling during glacial episodes include an order-of-magnitude increase in windblown atmospheric dust and an expected reduction in water vapor, the most powerful tropospheric greenhouse gas. Enhanced dust content of the ice age atmosphere is evident in ice cores and may contribute to cooling during glacial periods

through the role of dust in scattering (hence, diminishing) incoming solar radiation. Airborne dust levels increase during the glaciation as a result of several influences, including: (a) more arid conditions in many regions of the world, (b) exposed continental shelves due to sea-level drawdown (creating a larger terrestrial source area), and (c) higher surface winds, due to increased baroclinic instability as a result of greater meridional temperature gradients.

While there is no clear geological proxy for water vapor content in the ice age troposphere, globally depressed temperatures would cause reduced evaporation rates and lower saturation specific humidity values. These effects would have the greatest impact in tropical regions, where more than two-thirds of the total present-day evaporation occurs. The tropics cooled by as much as 5°C at the LGM. The resulting effects on the atmosphere are more difficult to predict. Reductions in greenhouse gas effects would cause a cooling, but changes in cloud cover could provide either warming or cooling influences. With less water vapor in the atmosphere, less cloud cover might be expected, causing a warming effect due to increased global albedo. However, the cooler glacial atmosphere would have a lower saturation threshold, meaning that cloud cover during the glacial period may have increased or been similar to present in some regions.

Summary

The discussion above identifies the roles of orbital forcing and internal climate feedbacks in generating glacial-interglacial cycles in the Quaternary. While the exact processes that give rise to ice sheet nucleation and decay have yet to be elucidated, the feedbacks and internal mechanisms introduced in this article are all expected to play a role in amplifying the insolation changes caused by orbital variations. These internal amplifiers include ice-albedo feedbacks, orographic changes, shifts in ocean and atmospheric circulation, and major regime changes in the carbon cycle and global hydrological cycle during glaciations. In addition, isostatic adjustments and internal dynamical processes in ice sheets probably play a role in the 100-kyr glacial cycle of the last 900 kyr, through the introduction of long-timescale lags in the ice sheet system. This essentially acts to precondition the ice sheets for collapse over tens of thousands of years, delaying the glacial termination until a warm orbital period when the ice sheet is prone to instability and is capable of rapid response to climate warming.

Many outstanding questions remain, including the cause(s) of millennial-scale climate variability during the Quaternary and the puzzle of the mid-Pleistocene transition from 40-kyr to 100-kyr glacial cycles. It is possible that early Pleistocene ice sheets were small enough to remain climatically sensitive, making it easier to precipitate a deglaciation. The shift to higher-amplitude glaciations at ca. 900 kyr B.P. still needs to be explained, but it may reflect a non-linear threshold response to a gradual Quaternary cooling trend, similar to what must have occurred at the Pliocene-Pleistocene transition that ushered in the Quaternary ice ages.

Shawn J. Marshall

Bibliography

Bradley, R.S., 1999 *Paleoclimatology: Reconstructing Climates of the Past*, 2nd ed., International Geophysica series. San Diego: Harcourt Academic Press, 613pp.

- Clark, P.U., 1994. Unstable behaviour of the Laurentide Ice Sheet over deforming sediment and its implications for climate change. *Quat. Res.*, **41**, 19–25.
- Clark, P.U., and Mix, A.C., 2002. Ice sheets and sea level of the last glacial maximum. *Quat. Sci. Rev.*, **21**, 1–7.
- Clark, P.U., Alley, R.B., and Pollard, D., 1999a. Northern hemisphere ice-sheet influences on global climate change. *Science*, **286**, 1104–1111.
- Clark, P.U., Webb, R.S., and Keigwin, L.D. (eds.), 1999b. Mechanisms of Global Climate Change at Millennial Timescales. Geophysical Monograph 112. Washington, D.C: American Geophysical Union.
- Cuffey, K.M., and Clow, G.D., 1997. Temperature, accumulation, and ice sheet elevation in central Greenland through the last deglacial transition. *J. Geophys. Res.*, **102**, 26, 383–326, 396.
- Dansgaard, W., Johnsen, S.J., Clausen, H.B., Dahl-Jensen, D., Gundestrup, N.S., Hammer, C.U., Hvidberg, C.S., Steffensen, J.P., Sveinbjörnsdóttir, A.E., Jouzel, J., and Bond, G.C., 1993. Evidence for general instability of past climate from a 250-kyr ice-core record. *Nature*, **364**, 218–220.
- Dyke, A.S., and Prest, V.K., 1987. Late Wisconsinan and holocene history of the Laurentide ice sheet. *Géog. phys. Quat.*, **41**, 237–264.
- Fisher, D.A., Reeh, N., and Langley, K., 1985. Objective reconstructions of the late Wisconsinan Laurentide Ice Sheet and the significance of deformable beds. *Géog. Phys. et Quat.*, **39**, 229–238.
- Heinrich, H., 1988. Origin and consequences of cyclic ice-rafting in the northeast Atlantic Ocean during the past 130,000 years. *Quat. Res.*, **29**, 141–152.
- Huybrechts, P., 2002. Sea-level changes at the LGM from ice-dynamic reconstructions of the Greenland and Antarctic Ice Sheets during the last glacial cycles. *Quat. Sci. Rev.*, **21**, 203–231.
- Imbrie, J., and Imbrie, K.P., 1979. *Ice Ages: Solving the Mystery*. Cambridge MA: Harvard University Press, 224pp.
- Imbrie, J., Boyle, E.A., Clemens, S.C., Duffy, A., Howard, W.R., Kukla, G., Kutzbach, J., Martinson, D.C., McIntyre, A., Mix, A.C., Molfino, B., Morley, J.J., Peterson, L.C., Pisias, N.G., Prell, W.L., Raymo, M.E., Shackleton, N.J., and Toggweiler, J.R., 1993. On the structure and origin of major glaciation cycles. II. The 100,000-year cycle. *Paleoceanography*, **8**, 699–735.
- Marshall, S.J., and Clark, P.U., 2002. Basal temperature evolution of the North American Ice Sheets and implications for the 100-kyr glacial cycle. *Geophys. Res. Lett.*, **29**(18), doi: 10.1029/2002GL015192.
- Marshall, S.J., James, T.S., and Clarke, G.K.C., 2002. North American Ice Sheet reconstructions at the last glacial maximum. *Quat. Sci. Rev.*, **21**, 175–192.
- Petit, J.R., Jouzel, J., Raynaud, D., Barkov, N.I., Barnola, J.M., Basile, I., Bender, M., Chappellaz, J., Davis, J., Delaygue, G., Delmotte, M., Kotlyakov, V.M., Legrand, M., Lipenkov, V., Lorius, C., Pépin, L., Ritz, C., Saltzman, E., and Stievenard, M., 1999. Climate and atmospheric history of the past 420,000 years from the Vostok Ice Core, Antarctica. *Nature*, **399**, 429–436.
- Ruddiman, W.H., 2001. *Earth's Climate: Past and Future*. New York, NY: W.F. Freeman and Company.
- Siegert, M.J., Dowdeswell, J.A., and Melles, M., 1999. Late Weichselian glaciation of the Eurasian high Arctic. *Quat. Res.*, **52**, 273–285.

Cross-references

[Albedo Feedbacks](#)
[Astronomical Theory of Climate Change](#)
[Binge-purge Cycles of Ice Sheet Dynamics](#)
[Carbon Dioxide and Methane, Quaternary Variations](#)
[Dust Transport, Quaternary](#)
[Glacial Isostasy](#)
[Ice Cores, Antarctica and Greenland](#)
[Last Glacial Maximum](#)
[Laurentide Ice Sheet](#)
[Millennial Climate Variability](#)
[Ocean Drilling Program](#)
[Oxygen Isotopes](#)
[Pleistocene Climates](#)
[Quaternary Climate Transitions and Cycles](#)
[Scandinavian Ice Sheet](#)
[Sea-level Change, Quaternary](#)
[SPECMAP](#)

GLACIOFLUVIAL SEDIMENTS

Glaciofluvial (also known as glacifluvial or fluvio-glacial) sediments are deposited by glacier melt-streams, in either ice-contact or proglacial settings (Benn and Evans, 1998). Glacier-fed rivers exhibit large diurnal and annual fluctuations in discharge, and commonly have an abundant supply of coarse, cohesionless sediment. Sediment motion is strongly episodic, with entrainment and transport occurring during rising discharge, and deposition during falling stages. Typically, large amounts of sediment are transported as bedload (rolling or sliding close to the stream bed) especially during high stages, when even large boulders can be set in motion. Suspended sediment concentrations can also be high, particularly during early summer when they can reach a few tens of grams per liter. (Glacier meltstreams often also have high dissolved loads, but this is not considered here.)

Proglacial river networks tend to consist of braided channel networks with intervening gravelly barforms. Active channels periodically switch position or are abandoned as the evolving sediment surface interacts with patterns of water flow. The dynamic nature of proglacial streams is reflected in the characteristics of glaciofluvial sediments. The two most important effects of glaciofluvial transport on sediments are *size sorting* and *particle rounding*. Glaciofluvial gravels, sands and silts are typically well sorted, with approximately Gaussian particle-size distributions, although bimodal distributions can result from the infilling of openwork gravels with finer particles during falling stages. Some facies, however, can be poorly sorted, especially those deposited from *hyperconcentrated flows* with high suspended load. Pebbles are rapidly rounded by abrasive wear (corrasion), and may evolve from sub-angular or sub-rounded forms close to glaciogenic sediment sources to well-rounded forms within a few kilometers of the source. The internal structure of glaciofluvial sediment facies reflects the local geometry of the river bed and the characteristics of the depositing flow. Horizontally bedded or laminated facies reflect *vertical accretion* (or aggradation) of sediment and cross-bedded and cross-laminated facies form during *lateral accretion* during the migration of bedforms such as ripples, dunes and bars. Glaciofluvial sediments tend to exhibit recurrent large-scale structures mirroring the three-dimensional form of elements such as channels and bars, and their evolution through time. Miall (1985) recognized eight such architectural elements in fluvial sediments: (a) channel fills (CH); (b) downstream accretion macroforms (DA), recording the downstream migration of ripples, dunes and bars; (c) lateral accretion macroforms (LA) recording lateral migration of bank-attached or mid-channel bars; (d) gravel bars and bedforms (GB) consisting of extensive tabular gravel sheets; (e) sediment-gravity flows (SG); (f) sandy bedforms (SB), deposited in chutes and minor channels and on bar tops; (g) laminated sand sheets (LS) laid down in ephemeral sheet floods; and (h) overbank fines (OF), deposited by the settling of suspended load following flood events. These architectural elements occur in different combinations in different settings, and can be used to reconstruct aspects of the hydrology of former fluvial systems, yielding important paleoenvironmental information.

Accumulation of glaciofluvial sediments forms outwash plains, also known by the Icelandic word *sandar* (singular = *sandur*). These typically exhibit down-stream reduction of channel gradient and sediment grain size. Sandar commonly have multiple levels, which may be terraces that are formed by sediment incision due to changes in hydrology, sediment availability, or a drop in local

base level that leaves abandoned terraces above the active part of the sandur. Terraces may be paired (at the same height on both sides of the sandur) or unpaired, depending on the relative rates of incision and lateral channel migration. The retreat of ice can cause the abandonment of outwash surfaces, leaving a steep reverse slope at the up-valley limit of glacio-fluvial deposits. Such slopes are known as *outwash heads*, and are particularly common in humid climatic settings with high water and sediment discharges. Where glaciofluvial sediments are deposited in contact with buried ice, subsequent melt of the ice causes subsidence and collapse of the overlying sediment forming *kettle holes*. In the case of isolated ice blocks, ice melt creates *pitted outwash*, but where buried ice bodies are more extensive, the resulting landforms consist of irregular mounds and ridges of sediment known as *kame* and *kettle topography*. Eskers are a distinctive type of glacio-fluvial deposit, formed in ice-walled channels or tunnels in supraglacial, englacial or subglacial positions. On ice melting, eskers are left as upstanding, often meandering ridges of sand and gravel. These may exhibit widespread internal collapse structures resulting from the disappearance of supporting ice.

The highest discharges in glacierized catchments occur in association with *glacier lake outburst floods* (GLOFs), triggered by the failure of moraine- or ice dams, or subglacial volcanic activity. GLOFs, also widely known by the Icelandic term *jökulhlaups*, can have discharges several orders of magnitude greater than normal peak flows, and are capable of transporting and depositing large volumes of material, including very large boulders and ice blocks. GLOF deposits are very variable, depending on discharges, sediment availability and topographic setting (see Maizels, 1993, 1995; Lord and Kehew, 1987). Massive facies deposited by hyper-concentrated flows and debris flows are common, although they may be extensively reworked during the falling stage of the flood. The largest GLOF known was the drainage of Glacial Lake Missoula across Idaho, Washington and part of Oregon at the end of the last glaciation. Giant fluvial forms, including networks of channels, and huge ripples and bars in the channeled scablands record glaciofluvial erosion and deposition on a truly massive scale (Baker, 1981).

Douglas I. Benn

Bibliography

- Baker, V.R., 1981. *Catastrophic Flooding: The Origin of the Channeled Scabland*. Stroudsburg, PA: Dowden, Hutchinson and Ross, 360pp.
- Benn, D.I., and Evans, D.J.A., 1998. *Glaciers and Glaciation*. London: Arnold.
- Lord, M.L., and Kehew, A.E., 1987. Sedimentology and palaeohydrology of glacial-lake outbursts in southeastern Saskatchewan and northwestern North Dakota. *Geol. Soc. Am. Bull.*, **99**, 663–673.
- Maizels, J.K., 1993. Lithofacies variations within sandur deposits: The role of runoff regime, flow dynamics and sediment supply characteristics. *Sediment. Geol.*, **85**, 299–325.
- Maizels, J.K., 1995. Sediments and landforms of modern proglacial terrestrial environments. In Menzies, J. (ed.), *Modern Glacial Environments*. Oxford: Butterworth-Heinemann, pp. 365–416.
- Miall, A.D., 1985. Architectural-element analysis: A new method of facies analysis applied to fluvial deposits. *Earth Sci. Rev.*, **22**, 261–308.

Cross-references

Eskers
 Glacial Sediments
 Kames
 Kettles
 Late Quaternary Megafloods
 Moraines
 Outwash Plains

GLACIOMARINE SEDIMENTS

Glaciomarine sediment is a general term to describe inorganic and organic material deposited in a marine setting by a combination of glacier- and marine-related processes. (This term is equivalent to glaciomarine and glacial marine). These sediments provide valuable records of ice sheet fluctuations because they occur beyond the limit of glacial erosion or cover older glacial erosional surfaces. The appearance and physical characteristics of glaciomarine sediments can be highly varied depending on the relative influence of marine and glacial depositional processes. Primary factors controlling the sediment characteristics include: volume of meltwater input, residence time and melt rate of icebergs, and biogenic production (Figure G48). Debris concentrations in glacier ice, extent of sea ice, and the strength of ocean currents are also important. Sediment redeposition by mass movements is common in glacio-marine environments; debris flow and turbidite deposits may be interbedded with primary glaciomarine sediments. Glaciomarine sediments exhibit gradational changes in particle size, depositional rates and organic content with distance from the glacier front. Generally, the particle size and depositional rate of inorganic material decreases with distance from the glacier front whereas the organic fraction increases (Figure G49).

The processes controlling the characteristics of glaciomarine sediments are related to climate conditions (e.g., Powell and Domack, 2002). In polar regions where summer temperatures are $<0^{\circ}\text{C}$, ablation is the result of sublimation and calving; little meltwater is produced. Most marine-terminating Antarctic glaciers are in this group and they deliver glacial sediment via icebergs with a minor contribution from subglacial meltwater (Anderson, 1999). In temperate regions, such as southeast Alaska, where summer temperatures are $>10^{\circ}\text{C}$, ice is at the pressure melting point and ablation is dominated by melting. Sediment is primarily delivered by debris-laden meltwater plumes and sedimentation from icebergs is minor. In these regions sediment accumulation is strongly seasonal. Between these two end members, where summer temperatures are $<10^{\circ}\text{C}$, the dominant mechanism of sediment delivery varies spatially and temporally and spans the continuum between iceberg- and meltwater-dominated systems.

Rates of deposition decrease in a non-linear fashion away from the grounding line (Figure G49) (Boulton, 1990). In the ice-proximal zone, sediment accumulation rates vary widely depending on the flux of debris-laden meltwater. For instance, glaciomarine sediments deposited within 2 km of the ice front on the Antarctic margin typically have accumulation rates $<2\text{ cm yr}^{-1}$ whereas accumulation rates within 2 km of the ice front in southeast Alaska are $200\text{--}2,000\text{ cm yr}^{-1}$ (Cowan and Powell, 1991). Since Earth's climate changes over time, glaciomarine sediment accumulation rates change with time as well.

Diamictos

Glaciomarine diamictos are poorly-sorted sediments that may be stratified or structureless with particle sizes ranging from clay to boulders. Glaciomarine diamictos are typically associated with ice-proximal environments. In polar regions, these diamictos originate as debris meltout from the base of glacier ice within a few kilometers of the grounding line where the glacier terminates as an ice shelf or ice tongue (Anderson, 1999). In sub-polar fjords, glaciomarine diamictos may be deposited beyond the limit of meltwater influence within a zone dominated by iceberg rafted debris (O'Cofaigh et al., 2001). The abundance of fine particles is a function of current strength. Strong currents may advect fines prior to deposition or may winnow fine-grained sediment deposited near the grounding line. Late Quaternary ice-proximal glaciomarine diamictos from the Antarctic (Ross Sea) continental shelf are extremely similar in appearance to glacial till, suggesting little meltwater and weak ocean currents at the time of deposition (Licht et al., 1999).

At the front of meltwater-dominated glaciers, diamictos may be deposited locally at the site of meltwater discharge from the ice front as fan-shaped or delta-like deposits (Powell, 1990). These ice-proximal diamictos are dominated by sand and gravel and may be stratified; the grain size distribution changes toward a higher proportion of fine-grained material with distance from the meltwater source. In addition to point-source deposits, glaciomarine diamictos may be deposited relatively continuously along the ice front from debris melting out of the ice front or falling off a debris-rich ice surface.

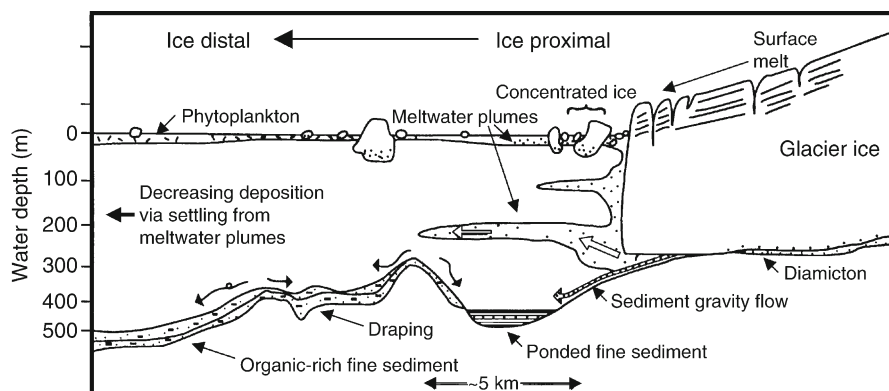


Figure G48 This conceptual model shows the depositional processes and glaciomarine sediment types for a subpolar glacier. Density of meltwater plumes controls their position in the water column and iceberg concentrations partially control the nature of ice-distal sediments. Sea-ice cover may affect iceberg drift and primary productivity. The geometry of sedimentary deposits is controlled by the position of the glacier front, seafloor bathymetry and ocean currents (Syvitski et al., 1987; Anderson, 1999) (modified from Powell and Domack, 2002).

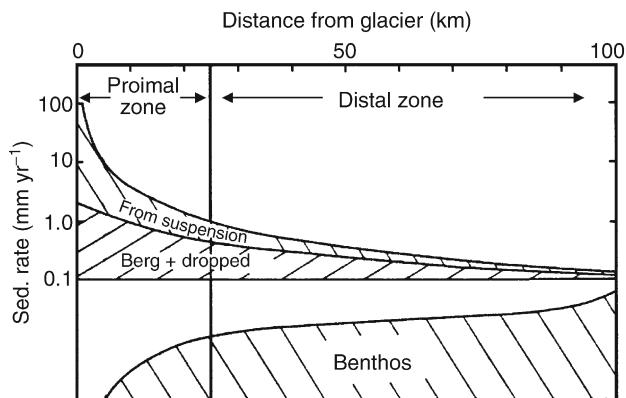


Figure G49 Generalized relationship between glaciomarine depositional processes and distance from glacier front. Sediment accumulation rates decrease in non-linear fashion away from the ice front (modified from Boulton, 1990).

Fine sediment

Fine sediment refers to that which is dominated by silt and clay with minor amounts of sand and pebbles; these sediments may be massive or stratified. The appearance of these fine sediments can be highly variable over small spatial scales in the glaciomarine environment because the depositional processes may be localized. Fine sediment is usually associated with ice-distal deposits on continental margins and in fjords. These glaciomarine sediments settle through the water column after being released by meltwater plumes or icebergs. Stratification may be caused by annual variations in meltwater production, iceberg rafting events or turbidites. Accumulation rates are highly variable and are related to climate conditions. Fine sediments from East Greenland fjords look nearly identical to those deposited in southeast Alaska, however the rates of deposition differ by several orders of magnitude (Smith and Andrews, 2000). Organic carbon content is typically higher in fine sediment than in diamictos because there is less dilution by inorganic (terrestrial) material. Biologically-produced siliceous muds and ooze are extensive in the modern glaciomarine environment on Antarctica's continental shelves and the total organic carbon content of the sediments is commonly 1–3% (Domack et al., 1999).

Kathy Licht

Bibliography

- Anderson, J.B., 1999. *Antarctic Marine Geology*. Cambridge, UK: Cambridge University Press, 289pp.
- Boulton, G.S., 1990. Sedimentary and sea-level changes during glacial cycles and their control on glaciomarine facies architecture. In Dowdeswell, J.A., and Scourse, J.D. (eds.), *Glaciomarine Environments: Processes and Sediments*. London, UK: Geological Society of London, Special Publication 53, pp. 15–52.
- Cowan, E.A., and Powell, R.D., 1991. Ice-proximal sediment accumulation rates in a temperate glacial fjord, southeastern Alaska. In Anderson, J.B., and Ashley, G.M. (eds.), *Glacial Marine Sedimentation: Paleoclimatic Significance*. Geological Society of America, Special Paper 261, pp. 61–73.
- Domack, E.W., Jacobsen, E.A., Shipp, S.S., and Anderson, J.B., 1999. Late Pleistocene-Holocene retreat of the West Antarctic Ice-Sheet system in the Ross Sea: A new perspective: Part 2, Sedimentologic and stratigraphic signature. *Geol. Soc. Am. Bull.*, **111**, 1517–1536.
- Licht, K.J., Dunbar, N., Jennings, A.E., and Andrews, J.T., 1999. Sedimentological evidence for the maximum extent of grounded ice in the western Ross Sea during the last glacial maximum. *Geol. Soc. Am. Bull.*, **111**, 91–103.

- O'Cofaigh, C., Dowdeswell, J.A., and Grobe, H., 2001. Holocene glaciomarine sedimentation, inner Scoresby Sund, East Greenland: The influence of fast-flowing ice-sheet outlet glaciers. *Mar. Geol.*, **175**, 103–129.
- Powell, R.D., 1990. Glaciomarine processes at grounding-line fans and their growth to ice-contact deltas. In Dowdeswell, J.A., and Scourse, J.D. (eds.), *Glaciomarine Environments: Processes and Sediments*. London, UK: Geological Society of London, Special Publication 53, pp. 53–73.
- Powell, R., and Domack, E., 2002. Modern glaciomarine environments. In Menzies, M. (ed.), *Modern and Past Glacial Environments*. Oxford, UK: Butterworth-Heinemann, pp. 361–389.
- Smith, L.M., and Andrews, J.T., 2000. Sediment characteristics in iceberg dominated fjords, Kangerlussuaq region, East Greenland. *Sed. Geol.*, **130**, 11–25.
- Syvitski, J.P.M., Burrell, D.C., and Skei, J.M., 1987. *Fjords: Processes and Products*. New York, NY: Springer-Verlag, 379pp.

Cross-references

- Diamicton
 Glacial Geomorphology
 Glacial Sediments
 Glaciations, Quaternary
 Ice-rafted Debris (IRD)
 Sedimentary Indicators of Climate Change
 Till and Tillites

GLENDONITE/IKAITE*

The term “glendonite” does not refer to a mineral, but to a class of pseudomorphs. A pseudomorph is a mineral that has taken the characteristic crystal shape of another mineral by processes such as replacement or recrystallization. Glendonites are pseudomorphs after the mineral ikaite, a monoclinic mineral with composition $\text{CaCO}_3 \cdot 6\text{H}_2\text{O}$.

Ikaite forms in near-freezing waters. It requires pressures exceeding those of the deepest ocean to be thermodynamically stable (Marland, 1975). Therefore when present in recent sediments it is always metastable. Ikaite may be “stabilized” by the presence of orthophosphate, an inhibitor of the precipitation of anhydrous CaCO_3 .

There have been few observations of ikaite in nature, probably reflecting its rapid decomposition into water and CaCO_3 when removed from cold waters. It may well be a rather common mineral. It appears to occur in two forms: as crystals (Stuess et al., 1982), often in muddy sediment, and as massive tufa towers; e.g., Ikka Fjord, southwest Greenland (Buchardt et al., 1997).

Dana (1884) examined the pseudomorphs and observed “a square prism,” and in cross-section “two sets of distinct diagonal lines intersecting at right angles,” characteristic of tetragonal symmetry. This led to several false attributions as to the precursor mineral. Monoclinic ikaite strongly approximates such orthogonal forms (to within ca. $\pm 0.5^\circ$) due to an accidental near-equivalence in the crystallography (Swainson and Hammond, 2001). Canted pyramidal faces usually terminate the prism. More common than well-formed isolated crystals are multi-crystal rosettes, consisting mostly of pyramidal faces, or their molds (Figure G50).

The use of pseudomorphs as proxies for ancient climates is unusual, yet it seems that the case for the use of glendonites is strong. The unusual morphology of glendonites provides a strong link to the crystallography of ikaite, which has highly specific conditions of formation.

*All rights reserved

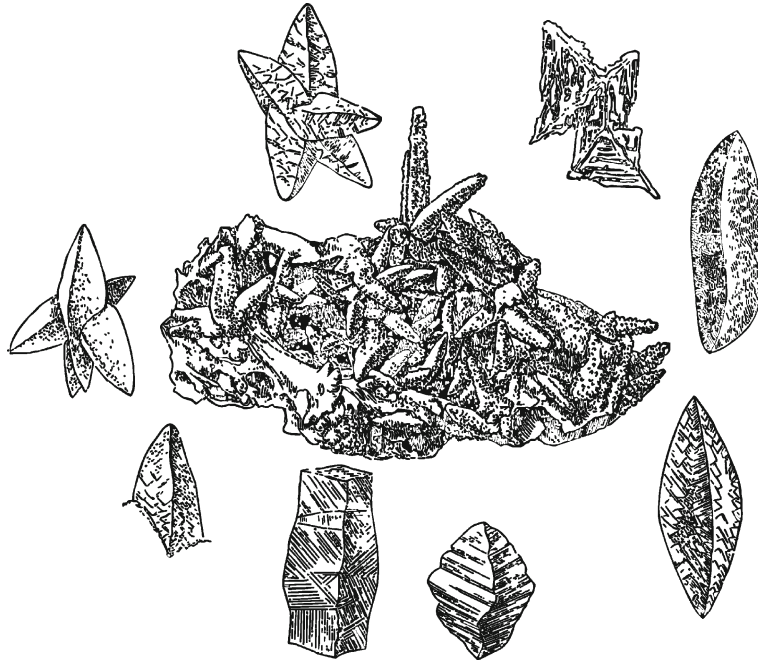


Figure G50 Images of some pseudomorphs after ikaite (Dana, 1884, U.S. Geological Survey).

While many glendonites are found in high latitudes associated with cold climates, they should not be used in isolation as paleolatitude indicators: e.g., ikaite has been reported in deep sea fan sediments off Congo, and in the Nankai Trough off Japan. Ikaite is not exclusively marine. Pseudomorphs have been reported in estuarine deposits. The famous 'thinolite' pseudomorphs of western Nevada and eastern California, USA, formed in a Pleistocene lake and may represent pseudomorphs of the tower-like tufa form.

Ian P. Swainson

Bibliography

- Buchardt, B., Seaman, P., Stockmann, G., Vous, M., Wilken, U., Düwel, L., Kristiansen, A., Jenner, C., Whittar, M.J., Kristensen, R.M., Petersen, G.H., and Thorbjørn, L., 1997. Submarine columns of ikaite tufa. *Nature*, **390**, 129–130.
- Dana, E.S., 1884. *A Crystallographic Study of the Thinolite of Lake Lahontan*. Washington DC: U.S. Government Printing Office. U.S. Geological Survey Bulletin No. 12, pp. 429–450.
- Marland, G., 1975. The stability of $\text{CaCO}_3 \cdot 6\text{H}_2\text{O}$. *Geochim. Cosmochim. Acta*, **39**, 83–91.
- Suess, E., Balzer, W., Hesse, K-F., Müller, P.J., Ungerer, C.A., and Wefer, G., 1982. Calcium carbonate hexahydrate from organic-rich sediments of the Antarctic shelf: Precursors of glendonites. *Science*, **216**, 1128–1131.
- Swainson, I.P., and Hammond, R.P., 2001. Ikaite, $\text{CaCO}_3 \cdot 6\text{H}_2\text{O}$: Cold comfort for glendonites as paleothermometers. *Am. Mineral.*, **86**, 1530–1533.

Cross-references

Carbonates, Cool Water
 Geochemical Proxies (non-isotopic)
 Marine Carbon Geochemistry
 Mineral Indicators of Past Climates
 Paleotemperatures and Proxy Reconstructions

"GREENHOUSE" (WARM) CLIMATES

Definition and origins of the term "greenhouse"

The term "greenhouse" is defined, as follows, from a climatological standpoint in the online 'Oxford English Dictionary' (OED), based on the textbook by Trewartha (1937, p. 25):

"The phenomenon whereby the surface and the lower atmosphere of a planet are maintained at a relatively high temperature owing to the greater transparency of the atmosphere to visible radiation from the sun than to infra-red radiation from the planet."

It is now becoming clear that although Trewartha (1937) may have been the first person to use the term "greenhouse effect," the concept and discussion of ancient cold/warm climates began in the previous century. Although many sources cite Jean Baptiste Joseph Fourier as the originator of the greenhouse effect (Fourier, 1827), this has been called into question. The most significant attack on the abuse of Fourier's work has been published by Fleming (1999), who states that most of the citations regarding Fourier are "unreliable, misdirected and anachronistic," and possibly stem from one of the most cited pieces of work on global warming (Arrhenius, 1896) that originally misquoted Fourier (1827). Although Fourier (1824, 1827) made analogies to the greenhouse effect, his work was focused more on terrestrial temperatures and ultimately the theory of heat (Fleming, 1999).

Charles Babbage in 1847 may have been the first person to propose the greenhouse effect (Steel, 1992) in the following text taken from 'The Works of Charles Babbage' (Campbell-Kelly, 1989),

"It is on this principle that greenhouses act as traps for catching and imprisoning the sun's rays: probably some very slight difference in the composition of the glass of which they consist may considerably alter this power. . . If the solids of the fluids on the surface,

or if the atmospheres of distant plane[t]s possess the properties of reflection, radiation and absorption in certain degrees, it is by no means impossible that some of the most remote of them may be hotter than those which are much nearer to the central body. . . . When however the heat communicated from the sun is confined and prevented from escape, and so forced to accumulate, very high temperatures are attained. . . . Under the varied circumstances of climate, which might arise from differences in the reflecting, the radiating, the absorbing, and the conducting power of the moon's surface, as well as from different degrees of central heat, the presence of water upon its surface might produce very different effects."

A major advance in understanding climates and climate change was published by John Tyndall (1861) who conducted physical experiments demonstrating that vapors and gases are able to absorb and subsequently emit radiative heat. Some thirty-five years later, Arrhenius (1896) took the findings of Tyndall and others and showed that the Earth's heat budget could be dramatically affected by the abundance of carbonic acid (a reaction product of water and CO₂) in the atmosphere. Arrhenius (1896) went on to conclude, with the assistance of geologist Arvid Gustaf Högbom, that changes in the total abundance of carbonic acid in the atmosphere could have been effective enough to cause glacial/interglacial cycles. Based on his model, Arrhenius made calculations as to the effect of increased (and decreased) carbon dioxide on temperature, and his results are very similar to modern sophisticated models.

Chamberlain (1897) used the findings of Arrhenius and Högbom in order to understand the development of glaciations in the geological record through a drawdown in carbon dioxide and hence mountain uplift and, consequently, increased weathering. Although many researchers highlight Chamberlain as one of the fathers of the global carbon cycle model, Berner (1995) demonstrated that a great deal of Chamberlain's work was actually based on Högbom's work. However, it was Chamberlain who further developed the CO₂ theory of climate change, which forms the basis of many paleoclimatic investigations of the geological record (see Berner, 1995; Fleming, 2000).

Arrhenius subsequently published a general audience book entitled *'Worlds in the Making'*, wherein he discusses the

effects of greenhouse gases in the atmosphere and their contributions towards climate change (Arrhenius, 1908). In this book, he gave an account of the "hot-house" theory, hence the birth of the concept of "greenhouse" (warm) climates.

The greenhouse effect and the climate system

The Earth is a unique dynamic system, with close links and feedbacks between the hydrosphere, atmosphere, biosphere, lithosphere, convecting mantle and outer space. Changes in these links and feedback mechanisms can dramatically affect the magnitude of exchange between the components of this dynamic system that ultimately drive climate and determine whether the environment remains in a warm or cool mode (Figure G51). Although the importance of the atmosphere as a geological agent was recognized long ago, it has been somewhat neglected in studies of past climate change until fairly recently. It is now widely accepted that greenhouse gases significantly affect the Earth's climate both on short- and long-term cycles, especially the global carbon cycle (Berner, 1999). Many greenhouse gases can cause both warming and cooling, due to the absorptive and radiative properties of those gases (Khalil, 1999). The most common greenhouse gases that are considered when discussing climate change on glacial/interglacial cycles and short- and long-term geological cycles are provided in Table G3.

One of the key components in Figure G51 is the amount of incoming radiation versus that which is being emitted back to space. In principle, if the budget of incoming *versus* outgoing radiation were equal and all components within the climate system were static then the climate would also remain static. However, if radiation input is less than output, the Earth climate system would become cooler, whereas if radiation input is greater than output, the Earth would become warmer: this is essentially the "greenhouse effect." Due to the absorptive and radiative properties of the greenhouse gases listed in Table G3, their relative abundance in the atmosphere can significantly affect the global temperature of the Earth. High abundances of CO₂ and H₂O_{vap} in the atmosphere will increase re-radiation and thus prevent heat from escaping. Of great interest to society at present is CO₂, mainly because of the effects of

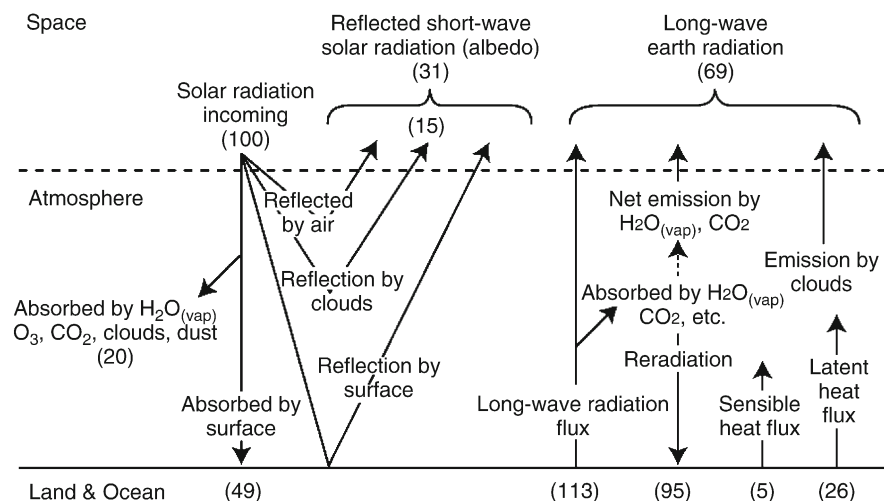


Figure G51 The mean annual radiation and heat balance (modified from Berner and Berner, 1996). Numbers in brackets represent percentages that are either absorbed or re-radiated.

Table G3 Common greenhouse gases

Greenhouse gas	Formula
Carbon dioxide	CO ₂
Methane	CH ₄
Water vapor	H ₂ O
Nitrous oxide	N ₂ O
Sulfur dioxide	SO ₂
Ozone	O ₃

the rise of industrialization and burning of fossil fuels and thus an increased abundance of atmospheric greenhouse gases. However, in recent years carbon-isotope ratios in the deep geologic record have been applied to infer methane dissociation events and subsequent global warming (Hesselbo et al., 2000; Dickins, 2001; Beerling et al., 2002).

The abundance of greenhouse gases in the atmosphere is not the only factor influencing the global climate on geological timescales. The schematic diagram in Figure G52 includes the long-term and short-term carbon cycle (Jenkyns, 2003), primarily identified through our ability to obtain high-resolution records in the deep geologic record. This figure illustrates the majority of pathways in the short- and long-term carbon cycle, and in particular considers the most relevant processes that imprint on and affect the geoclimatic record. Long-term events can be referred to as "greenhouse (warm) episodes", while short-term events are termed a "transient climate events". More detailed analyses of biotic feedbacks in paleoclimatology are given in Woodwell and Mackenzie (1995), Hay et al. (1997), Berner (1999) and Huber et al. (2001).

Paleoclimates in the geologic record

Understanding the causes and consequences of global climate change is one of the most important issues of modern science, and includes the investigation of climatic variations in the geologic record (paleoclimatology). Fueled by concerns about the impact of human activities on the physical and biological environment of the Earth, an increasing amount of research has been devoted to untangling records and mechanisms of past and present climate variation. The Intergovernmental Panel on Climate Change (IPCC, 2007) constitutes a large international assemblage of scientists and data that attempts to investigate the effects of modern climate change (in part induced by anthropogenic activities) through modeling projections of future climatic scenarios (see <http://www.ipcc.ch/>). Although largely focused on recent and future climate change until recently, the latest assessment of the IPCC includes many research areas that attempt to uncover the causes of ancient climatic variability, including its magnitude, variability, frequency, and impacts on the Earth system. Our understanding of ancient climates, let alone rapid climate change in the geologic record, is still in its infancy even 100 years since the work of Arrhenius and others. This is reiterated by Huber et al. (2001), who write in the preface of *Warm Climates in Earth History*:

"In spite of the prevalence of warm climates in Earth history and the potential practical significance of understanding them, the fundamental causes, nature, and mechanics of warm climates are still poorly understood. . . Perhaps most importantly, though, integrated studies have revealed consistent areas of disagreement between empirical and theoretical analyses. Increasing temporal and geographic resolution in models and proxy data will only improve the ability to use deep time as a testing ground for our understanding of the causes, nature, and mechanics of globally warm climates."

Many methods can be used to determine whether a time period in the geological record experienced a warm or cool climate, for example, the presence or absence of climate-sensitive sediments (e.g., evaporites, coals, corals, bauxites), geochemical data (e.g., negative and positive excursions in oxygen- and carbon-isotope ratios of foraminifera), faunal distributions (e.g., the presence of crocodiles at high latitudes), floral physiology (e.g., stomatal indexes, leaf margin analysis), and many other techniques. It is beyond the scope of this entry to discuss all the periods in the geologic record; however, a summary of warm climate modes will be provided with appropriate references for further study (Figure G53). More specific discussion of certain key intervals that illustrate rapid climatic warming will also be provided. However, we refer the reader to the many other entries in this encyclopedia.

Figure G53 depicts the climate modes of the Phanerozoic as determined through paleoclimatic analysis (Frakes et al., 1992) and oxygen isotopic evolution of the ocean (Veizer et al., 1999; Shaviv and Veizer, 2003; Royer et al., 2004). The warm (greenhouse) climate mode, as defined by Frakes et al. (1992), is a climate that is

"globally warm, as indicated by the abundance of evaporites, geochemical data, faunal distributions, etc., and with little or no polar ice."

On the other hand, Fischer (1986) defines a greenhouse mode as a period that has low latitudinal temperature gradients, high mean ocean temperatures, a sluggish ocean, and marine anoxia. Notwithstanding variations in the definition of a greenhouse mode, there are four major warm modes in the Phanerozoic that will be discussed in detail below (note, that this discussion considers the broader nature of greenhouse modes with only minor discussion on transient climate events). What is apparent in Figure G53 is a lack of co-variation between reconstructed and modeled atmospheric CO₂ levels with warm and cool climate modes; such a finding was reported by Shaviv and Veizer (2003), and vehemently debated by Royer et al. (2004). Although this apparent disparity may invoke the conclusion that CO₂ is *not* a controlling factor on temperature in geologic time (Boucot and Gray, 2001; Shaviv and Veizer, 2003; Wallmann, 2004), it should be noted that the effect of CO₂ and many other environmental factors (e.g., carbon burial, seawater pH, sea level, volcanism, weathering, cosmic rays) coalesce to generate paleoclimatic cycles. It is apparent, however, that during periods of major glaciations (e.g., Early Carboniferous–Late Permian and Early Eocene–Present), atmospheric CO₂ levels are low, and that other cool climate modes are only 'less warm' periods (Royer et al., 2004). In general, there has been less scientific effort on the cause and effects of "greenhouse" (warm) climates in the geological record compared with "icehouse" (cool) climates.

Early Earth

Our interpretation of the early Earth climate is at best poor, and as Lyons (2004) eloquently states:

"a universal theme in studies of the early Earth is that big stories are told with little data and lots of speculation."

This applies particularly to our understanding of the faint young Sun paradox (Longdoz and Francois, 1997), which states that the power of the sun was only 70% of what it is today, and thus other mechanisms for global warmth were required to prevent the Earth from remaining frozen. The major factor causing warmer early Earth temperatures is attributed to

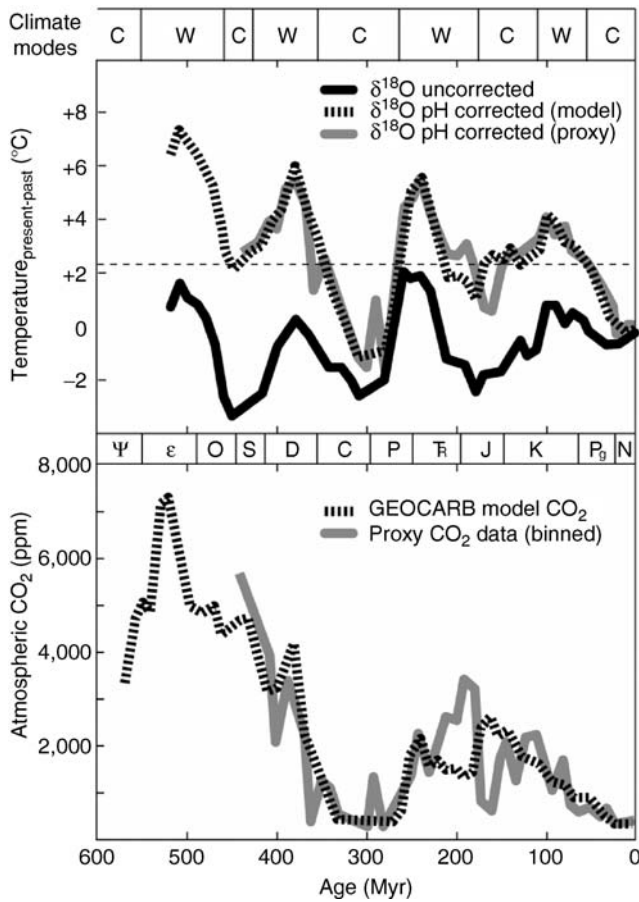


Figure G53 Climate modes through the Phanerozoic based on paleoclimatic analysis (Frakes et al., 1992) and oxygen isotopic evolution of the ocean (Shaviv and Veizer, 2003; Royer et al., 2004). Climate modes: C = cool; W = warm (see definitions in Frakes et al., 1992). *Top panel:* Temperature curves represent present global average minus the reconstructed temperatures: the modern global average temperature in the geologic record would have a value of zero (see Royer et al., 2004 for details). The three temperature curves are: (1) an uncorrected curve (Veizer et al., 1999) [solid line], (2) a pH-adjusted curve based on modeled CO₂, and (3) pH-adjusted proxy CO₂ data (Royer et al., 2004) [dashed and gray line respectively]. The horizontal dashed line is based on the Paleogene glaciation in the Cenozoic (Zachos et al., 2001), which would give a temperature of ca. +2.2°C above the present global average. If this horizontal dashed line is used as an estimate for warm (above) and cool (below) climates, then correspondence with the climate modes of Frakes et al. (1992) is much better. Ψ = Ediacaran; ε = Cambrian; O = Ordovician; S = Silurian; D = Devonian; C = Carboniferous; P = Permian; Tr = Triassic; J = Jurassic; K = Cretaceous; Pg = Paleogene; N = Neogene. *Bottom panel:* Phanerozoic atmospheric CO₂ concentrations based on the GEOCARB III model (dashed line) and proxy CO₂ data (solid grey line) after Royer et al., 2004.

exceptionally high levels of greenhouse gases, such as CH₄ (Pavlov et al., 2003) and CO₂ (Hessler et al., 2004; Ohmoto et al., 2004; Pierrehumbert, 2004; Fowler et al., 2003).

Early Cambrian to Late Ordovician periods

Our understanding of this warm episode is somewhat skewed, as continental reconstructions suggest that landmasses occupied

low latitudes (Golonka, 2002). The use of paleontology in the Cambrian as an indicator of warmth is difficult due to the great number of unoccupied ecological niches and limited biological diversification (Frakes et al., 1992). Therefore, other proxies of climatic warmth must be utilized. The earliest part of the Cambrian is poorly understood, primarily because of a lack of pristine marine carbonate available for paleotemperature reconstructions. An isotope curve indicates that by the Middle–Late Cambrian, paleotemperatures far exceeded present temperatures (Figure G53), which coincided with extremely high atmospheric CO₂ levels at that time (Royer et al., 2004), possibly as a result of intense volcanism over the Precambrian–Cambrian transition (Doblas et al., 2002). Karhu and Epstein (1986) suggest Cambrian paleotemperatures as high as 50°C, although it is not yet fully understood whether changes in the oxygen-isotope composition of seawater (δ_w) may have exacerbated the reconstructed paleotemperatures, which far exceeded normal marine faunal tolerances. However, paleotemperatures during the Ordovician became more reasonable at ~30–38°C (Veizer et al., 1999; Brand, 2004), although a suggested Ordovician δ_w value of –3‰ would have lowered the temperatures further to ~27°C (Wallmann, 2001; Shields et al., 2003). Other evidence for a greenhouse climate during this interval includes the presence of massive evaporites at low latitudes (Alvaro et al., 2000; Baikov, 2004), carbonate expansion to high latitudes (Frakes et al., 1992), lateritic and bauxitic profiles (Sturesson, 2003), and increased phosphorite accumulation (Meng et al., 1997). The presence of oolitic ironstones has also been suggested as an indicator of warmth during a marine transgressive phase (Frakes et al., 1992; Yapp, 2004). During the Ordovician, abundant black-shale deposition supports a transgressive sea-level phase, accompanied by high oceanic productivity (Easto and Gustin, 1996).

Late Silurian to Early Carboniferous periods

After the Late Ordovician glaciation, the Late Silurian still experienced relatively cool temperatures, although by the beginning of the Devonian, temperatures begin to rise sharply, reaching a peak in the Middle Devonian before decreasing again (Figure G53). By comparison to the Cambrian–Ordovician greenhouse episode, this time interval was relatively cooler and coincided with decreasing atmospheric CO₂ levels (Wallmann, 2001), increasing volcanism, and tectonic activity during the Caledonian and Arcadian Orogenies (Torsvik and Cocks, 2004). Peak paleotemperature in the Middle Devonian also coincided with large evaporite deposits in west Canada, Siberia, and North Africa (Frakes et al., 1992). Carbonate deposition increased during the Devonian, bioherms were dominant and reef systems extended latitudinally up to ~60° (Frakes et al., 1992; Dubalatorov and Krasnov, 2000; Edinger et al., 2002). A humid environment is believed to have been initiated in the Late Silurian, when the Coal Age began (Calder and Gibling, 1994), and is concurrent with the first record of fossil charcoal, suggesting wildfires (Glasspool et al., 2004). During the Devonian, marine faunas became more cosmopolitan (Babin, 2000), soils were well-developed latitudinally in the terrestrial environment, and plant communities diversified, with the occurrence of the first trees (Retallack, 1997). The most prominent feature depicting an arid climate was the widespread deposition of red beds, such as the Old Red Sandstone and Catskill Formation. As with the previous greenhouse mode, phosphorite accumulation increased (Martin, 1995), as did upwelling and oceanic productivity (Caplan and Bustin, 2001), culminating in major marine anoxia during the Frasnian–Famnenian interval

of the Devonian sea-level rise (see Rackian and House, 2002). However, the Late Devonian–Early Carboniferous climate switched dramatically from a greenhouse to icehouse world, which is believed to be caused by intensified silicate weathering and organic carbon burial (Averbuch et al., 2005).

Late Permian to Middle Jurassic periods

One of the most intensely studied greenhouse intervals occurred during the Permian–Triassic boundary (Kidder and Worsley, 2004). This boundary interval is believed to have coincided with the onset of a greenhouse climate with widespread marine anoxia (Grice et al., 2005), a global coal gap (Retallack et al., 1996), the disappearance of *Glossopteris* (Spalletti et al., 2003), and a massive increase in phosphate accumulation, classically described by the Phosphoria Formation, USA (Knudsen and Gunter, 2002). The Carboniferous–Permian record had atmospheric CO₂ levels that were comparable to present-day concentrations, although by the Middle Permian they began to rise to levels of ~2,000 ppmV, peaking at the Permian–Triassic boundary. Paleotemperatures rose sharply during this interval, from cool to warm, but peaked during the Early Triassic (Figure G53). Extensive evaporite deposits occurred in the Triassic and Early Jurassic, although the Late Triassic has scarce bauxite and laterite deposits (Frakes et al., 1992). A number of paleoproxies for the Triassic suggest that it was a period with climates alternating between arid and humid: (a) paleosols from the Middle Triassic of Argentina (Tabor et al., 2004), (b) foliar physiognomy and tree-rings from Antarctica (Cúneo et al., 2003), (c) sediment analysis from the Late Permian–Early Triassic indicating fluctuating precipitation regimes with a peak in the Early Triassic (Wopfner, 2002), and (d) clay mineral analysis from Europe (Ruffell et al., 2003). On the basis of tree-ring widths, Pires et al. (2005) suggested that the climate became more uniform by the Late Triassic, which is also indicated by clay-mineral analysis (Ruffell et al., 2003). However, the Late Triassic was heavily influenced by monsoonal conditions, as implied by the strong orbital cyclicity recorded in the Newark Basin (LeTourneau and Olsen, 2003). By the Late Triassic, a number of bolide impacts and extensive volcanism altered the Earth system, possibly resulting in a climate with less fluctuations but growing warmth (see Tanner et al., 2004). One of the major episodes that occurred at the Triassic–Jurassic boundary, which has been attributed to climate change, is the emplacement of the Central Atlantic Magmatic Province (Hames et al., 2003), which contributed to a transient climate event and possibly the turnover or extinction of many floral and faunal groups (Pálfy et al., 2000; Hesselbo et al., 2002). The Early Jurassic also witnessed the diversification and latitudinal spread of floras (Krassilov, 2003) and the global distribution of black shales, which occurred most prominently during the early Toarcian (Hesselbo et al., 2000). The early Toarcian oceanic anoxic and transient climate event has been attributed to the massive dissociation of methane gas hydrates (clathrates), as recorded by a rapid negative $\delta^{13}\text{C}$ excursion in both the marine and terrestrial carbon reservoirs (Hesselbo et al., 2000; Kemp et al., 2005). A similar explanation has also been proposed for the Permian–Triassic boundary (Krull et al., 2004). Paleotemperatures rose significantly over the Toarcian, as recorded by belemnite oxygen-isotope ratios (Jenkyns et al., 2002; van de Schootbrugge et al., 2005). However, this is not apparent in Figure G53. Both the early Toarcian oceanic anoxic event and Permian–Triassic boundary event are related to periods of major volcanism, such as the Karoo–Ferrar continental flood basalts (Duncan et al., 1997) and Siberian Traps (Renne et al., 1995), respectively. These

volcanic outpourings are potentially the original source of greenhouse gases and consequent global warming episodes (Huyn and Poulsen, 2005).

Mid-Cretaceous period to Early Cenozoic era

The initiation of this greenhouse (warm) mode has been revised from that given in Frakes et al. (1992) and is now placed at the Barremian–Aptian boundary 125 Myr ago, where it records a major shift in climate, oceanic structure, and environment (Gröcke, 2002; Jenkyns, 2003; Erba, 2004). Based on obtaining pristine marine microfossil records from Ocean Drilling Program cores, our understanding of the Cretaceous and Cenozoic climate is vastly improved (e.g., Jenkyns, 2003). Significant Pacific Ocean large igneous province formations began at the Barremian–Aptian boundary with the formation of the Ontong Java Plateau (Larson and Erba, 1999) and consequent increasing atmospheric CO₂ levels and warming (Huber et al., 2002; Leckie et al., 2002). Major sea-level transgression and regressions occurred during the Cretaceous periods, although the ocean remained sluggish, with high productivity resulting in significant deposition of black shales (Poulsen et al., 2001; Wilson and Norris, 2001; Leckie et al., 2002). The Cretaceous oceanic anoxic events record a significant temperature increase with the maximum occurring during the Cenomanian–Turonian event (Norris et al., 2002; Poulsen, 2004). However, this event also records a decrease in atmospheric CO₂ levels (Kuypers et al., 1999). Extreme Cretaceous warmth is also shown by Antarctic and Arctic floral and faunal compositions and the prevalence of opportunism (Herman and Spicer, 1996; Tarduno et al., 1998; Huber, 2000; Francis and Poole, 2002). Whether volcanism and/or methane dissociation were prevalent during the Cretaceous (e.g., the Aptian oceanic anoxic event) and Cenozoic (e.g., Paleocene-Eocene Thermal Maximum) is still a matter of debate (Bains et al., 1999; Gröcke et al., 1999; Dickens, 2001; Beerling et al., 2002). However, a number of paleoclimatic indicators (e.g., oxygen isotopes, black shales, rapid carbon-isotope excursions) suggest sustained warmth with several transient climate events (e.g., Aptian, Cenomanian–Turonian oceanic anoxic events, the Paleocene-Eocene Thermal Maximum ELMO and X-event layer). Recent evidence also indicates that the Cretaceous warmth was interrupted by rapid short-lived cooling (icehouse) episodes and potentially glaciation (Stoll and Schrag, 2000; Gale et al., 2002; Pirrie et al., 2004; Gröcke et al., 2006; Bornemann et al., 2008).

Summary

Our understanding of greenhouse (warm) climates in geologic time has been limited since a primary focus of deep time research to date has been on icehouse (cool) climates, which are more easily recognized in the sedimentological record. A concerted effort is required to integrate multi-proxy approaches to estimate ancient temperatures and atmospheric CO₂ levels more accurately. In addition, based on the modern focus on rapid climate change in today's society, there is a greater need to identify and research transient climate events in deep time. Studies of the Paleocene-Eocene Thermal Maximum, Toarcian, Aptian, and Cenomanian/Turonian oceanic anoxic events, the Permian–Triassic boundary and Frasnian–Famennian boundaries are needed. Our knowledge of early Earth climates (bar Snowball Earth episodes) is limited due to a lack of reliable proxies indicative of greenhouse modes. Four major greenhouse (warm) modes have been

identified in the Phanerozoic (Figure G53), and within these intervals, several (or many) transient climate events conducive with rapid, extreme warming can be identified. Equally important is that within these greenhouse (warm) modes, rapid icehouse (cool) climates are also becoming recognized, suggesting that the Earth's climate could flip rapidly between warm and cool modes in deep geologic time.

Darren R. Gröcke

Bibliography

- Álvaro, J.J., Rouchy, J.M., et al. 2000. Evaporitic constraints on the southward drifting of the western Gondwana margin during Early Cambrian times. *Palaeogeogr. Palaeoclim. Palaeoecol.*, **160**, 105–122.
- Arrhenius, S., 1896. On the influence of carbonic acid in the air and upon the temperature of the ground. *Phil. Mag. J. Sci. Series 5*, **41**, 237–276. [For more information on Svante Arrhenius see the special issue in *AMBIO*, **26** (1) in 1997.]
- Arrhenius, S., 1908. *Worlds in the Making*. New York, USA: Harper & Brothers.
- Averbuch, O., Tribouillard, N., Devleeschouwer, X., Riquier, L., Mistiaen, B., and van Vliet-Lanoe, B., 2005. Mountain building-enhanced continental weathering and organic carbon burial as major causes for climatic cooling at the Frasnian–Famennian boundary (ca. 376 Ma)? *Terra Nova*, **17**, 25–34.
- Babin, C., 2000. Ordovician to Devonian diversification of the Bivalvia. *Am. Malacol. Bull.*, **15**, 167–178.
- Baikov, A.A., 2004. Duration of the lateral paragenetic reef–evaporite system formation. *Lith. Min. Res.*, **39**, 135–144.
- Beerling, D.J., Lomas, M.R., and Gröcke, D.R., 2002. On the nature of methane gas-hydrate dissociation during the Toarcian and Aptian oceanic anoxic events. *Am. J. Sci.*, **302**, 28–49.
- Berner, R.A., 1995. A. G. Högbom and the development of the concept of the geochemical carbon cycle. *Am. J. Sci.*, **295**, 491–495.
- Berner, R.A., 1999. A new look at the long-term carbon cycle. *GSA Today*, **9**, 1–6.
- Berner, E.K., and Berner, R.A., 1996. *Global Environment: Water, Air, and Geochemical Cycles*. New Jersey, USA: Prentice Hall, 376pp.
- Bornemann, A., Norris, R.D., Fridrich, O., Beckmann, B., Schocten, S., Sinninghe Damsté, J.S., Vogel, J., Hofmann, P., and Wagner, T., 2008. Isotopic evidence for glaciation during the Cretaceous super greenhouse. *Science*, **319**, 189–192.
- Boucot, A.J., and Gray, J., 2001. A critique of Phanerozoic climatic models involving changes in the CO₂ content of the atmosphere. *Earth Sci. Rev.*, **56**, 1–159.
- Brand, U., 2004. Carbon, oxygen and strontium isotopes in Paleozoic carbonate components: an evaluation of original seawater-chemistry proxies. *Chem. Geol.*, **204**, 23–44.
- Calder, J.H., and Gibling, M.R., 1994. The Euramerican Coal Province – controls on Late Paleozoic peat accumulation. *Palaeogeogr. Palaeoclim. Palaeoecol.*, **106**, 1–21.
- Campbell-Kelly, M. (ed.), 1989. *The Works of Charles Babbage, Volume 4, Scientific and Miscellaneous Papers I*. London, UK: William Pickering, 217pp.
- Caplan, M.L., and Bustin, R.M., 2001. Palaeoenvironmental and palaeoceanographic controls on black, laminated mudrock deposition: example from Devonian–Carboniferous strata, Alberta, Canada. *Sed. Geol.*, **145**, 45–72.
- Chamberlain, T.C., 1897. The method of multiple working hypotheses. *J. Geol.*, **6**, 837–848.
- Cúneo, N.R., Taylor, E.L., Taylor, T.N., and Krings, M., 2003. In situ fossil forest from the upper Fremouw Formation (Triassic) of Antarctica: paleoenvironmental setting and paleoclimate analysis. *Palaeogeogr. Palaeoclim. Palaeoecol.*, **197**, 239–261.
- Dickins, G.R., 2001. Carbon addition and removal during the Late Palaeocene Thermal Maximum: Basic theory with a preliminary treatment of the isotopic record at Ocean Drilling Program Site 1051, Blake Nose. *Geol. Soc. Lon. Spec. Publ.*, **183**, 293–305.
- Doblas, M., López-Ruiz, J., Cebriá, J.-M., Youbi, N., and Degroote, E., 2002. Mantle insulation beneath the West African craton during the Precambrian–Cambrian transition. *Geology*, **30**, 839–842.
- Dubalato, V.N., and Krasnov, V.I., 2000. Middle Devonian and Frasnian seas of Siberia. *Strat. Geol. Corr.*, **8**, 557–578.
- Duncan, R.A., Hooper, P.R., Rehacek, J., Marsh, J.S. and Duncan, A.R., 1997. The timing and duration of the Karoo igneous event, southern Gondwana. *J. Geophys. Res.*, **102**, 18,127–18,138.
- Easto, C.J., and Gustin, M.M., 1996. Volcanogenic massive sulfide deposits and anoxia in the Phanerozoic oceans. *Ore Geol. Rev.*, **10**, 179–197.
- Edinger, E.N., Copper, P., Risk, M.J., and Atmojo, W., 2002. Oceanography and reefs of recent and Paleozoic tropical epeiric seas. *Facies*, **47**, 122–149.
- Erba, E., 2004. Calcareous nannofossils and Mesozoic oceanic anoxic events. *Mar. Micropaleon.*, **52**, 85–106.
- Fischer, A.G., 1986. Climatic rhythms recorded in strata. *Ann. Rev. Earth Planet. Sci.*, **14**, 351–376.
- Fleming, J.S., 1999. Joseph Fourier, the ‘greenhouse effect’, and the quest for a universal theory of terrestrial temperatures. *Endeavour*, **23**, 72–75.
- Fleming, J.R., 2000. T. C. Chamberlain, climate change, and cosmogony. *Stud. Hist. Phil. Mod. Phys.*, **31**, 293–308.
- Fourier, S.B.J., 1824. Remarques générales sur les températures du globe terrestre et des espaces planétaires. *Ann. Chim. Phys. Series 2*, **27**, 136–167. [An English translation of Fourier's 1824 paper by Ebeneser Burgess can be found in the *Am. J. Sci.*, **32**, 1–20 (1837).]
- Fourier, S.B.J., 1827. Mémoire sur les températures du globe terrestre et des espaces planétaires. *Mém. Acad. Sci. Series 2*, **7**, 569–604.
- Fowler, C.M.R., Ebinger, C., and Hawksworth, C.J., 2003. The Early Earth: Physical, Chemical and Biological Development. *Geological Society of London Special Publication* **199**, pp. 1–352.
- Frakes, L.A., Francis, J.E., and Syktus, J.I., 1992. *Climate modes of the Phanerozoic: The history of the Earth's climate over the past 600 million years*. Cambridge: Cambridge University Press, 286pp.
- Francis, J.E., and Poole, I., 2002. Cretaceous and early Tertiary climates of Antarctica: evidence from fossil wood. *Palaeogeogr. Palaeoclim. Palaeoecol.*, **217**, 223–242.
- Gale, A.S., Hardenbol, J., Hathway, B., Kennedy, W.J., Young, J.R., and Phansalkar, Y., 2002. Global correlation of Cenomanian (Upper Cretaceous) sequences: Evidence for Milankovitch control on sea level. *Geology*, **30**, 291–294.
- Glasspool, J.J., Edwards, D., and Axe, L., 2004. Charcoal in the Silurian as evidence for the earliest wildfire. *Geology*, **32**, 381–383.
- Golonka, J., 2002. Plate-tectonic maps of the Phanerozoic. In: Kiessling, W., Flügel, E., and Golonka, J. (eds.), *Phanerozoic Reef Patterns*. Tulsa, OK: SEPM Society for Sedimentary Geology Special Publication, **72**, 21–75.
- Grice, K., Cao, C.Q., et al. 2005. Photic zone euxinia during the Permian–Triassic superanoxic event. *Science*, **307**, 706–709.
- Gröcke, D.R., 2002. The carbon isotope composition of ancient CO₂ based on higher-plant organic matter. *Phil. Trans. R. Soc. Lond. A*, **360**, 633–658.
- Gröcke, D.R., Hesselbo, S.P., and Jenkyns, H.C., 1999. Carbon-isotope composition of lower Cretaceous fossil wood: ocean-atmosphere chemistry and relation to sea-level change. *Geology*, **27**, 155–158.
- Gröcke, D.R., Ludvigson, G.A., Witzke, B.L., Robinson, S.A., Joeckel, R.M., Ufnar, D.F., and Ravn, R.L., 2006. Recognizing the Albian–Cenomanian (OAE1d) sequence boundary using plant carbon isotopes: Dakota Formation, Western Interior Basin, USA.
- Hames, W.E., McHone, J.G., Renne, P.R., and Ruppel, C. (eds.), 2003. *The Central Atlantic Magmatic Province: insights from fragments of Pangaea*. American Geophysical Union Monograph, **136**, 267pp.
- Hay, W.W., DeConto, R.M., and Wold, C.H.N., 1997. Climate: Is the past the key to the future? *Geol. Rundsch.*, **86**, 471–491.
- Herman, A., and Spicer, R.A., 1996. Palaeobotanical evidence for a warm Cretaceous Arctic ocean. *Nature*, **380**, 330–333.
- Hesselbo, S.P., Gröcke, D.R., et al. 2000. Massive dissociation of gas hydrate during a Jurassic oceanic anoxic event. *Nature*, **406**, 392–395.
- Hesselbo, S.P., Robinson, S.A., Surlyk, F., and Piasecki, S., 2002. Terrestrial and marine extinction at the Triassic–Jurassic boundary synchronized with major carbon-cycle perturbation: a link to initiation of massive volcanism? *Geology*, **30**, 251–254.
- Hessler, A.M., Lowe, D.R., Jones, R.L. and Bird, D.K., 2004. A lower limit for atmospheric carbon dioxide levels 3.2 billion years ago. *Nature*, **428**, 736–738.
- Huber, B.T., 2000. Tropical Paradise at the Cretaceous poles? *Science*, **282**, 2199–2200.

- Huber, B.T., MacLeod, K.G., and Wing, S.L., 2001. *Warm Climates in Earth History*. Cambridge: Cambridge University Press, 462pp.
- Huber, B.T., Norris, R.D., and MacLeod, K.G., 2002. Deep-sea paleo-temperature record of extreme warmth during the Cretaceous. *Geology*, **30**, 123–126.
- Huyn, T.T., and Poulsen, C.J., 2005. Rising atmospheric CO₂ as a possible trigger for the end-Triassic mass extinction. *Palaeogeogr. Palaeoclim. Palaeoecol.*, **217**, 223–242.
- IPCC. 2007. Climate Change 2007: The Physical Science Basis. Contribution of Working Group I to the Fourth Assessment Report of the Intergovernmental Panel on Climate Change. In Solomon, S., Qin, D., Manning, M., Chen, Z., Marquis, M., Averget, K.B., Tignor, M., and Miller, H.L., Cambridge, Cambridge University Press, 996pp.
- Jenkyns, H.C., 2003. Evidence for rapid climate change in the Mesozoic–Palaeogene greenhouse world. *Phil. Trans. R. Soc. Lond. A*, **361**, 1885–1916.
- Jenkyns, H.C., Jones, C.E., Gröcke, D.R., Hesselbo, S.P., and Parkinson, D.N., 2002. Chemostratigraphy of the Jurassic System: Applications, limitations and implications for palaeoceanography. *J. Geol. Soc. Lond.*, **159**, 351–378.
- Karhu, J. and Epstein, S., 1986. The implication of the oxygen isotope records in co-existing cherts and phosphates. *Geochim. Cosmochim. Acta*, **50**, 1745–1756.
- Kemp, D.B., Coe, A.L., Cohen, A.S., and Schwark, L., 2005. Astronomical pacing of methane release in the Early Jurassic period. *Nature*, **437**, 396–399.
- Khalil, M.A.K., 1999. Non-CO₂ greenhouse gases in the atmosphere. *Ann. Rev. Energy Environ.*, **24**, 645–661.
- Kidder, D.L., and Worsley, T.R., 2004. Causes and consequences of extreme Permo-Triassic warming to globally equable climate and retention to the Permo-Triassic extinction and recovery. *Palaeogeogr. Palaeoclim. Palaeoecol.*, **203**, 207–237.
- Knudsen, A.C., and Gunter, M.E., 2002. Sedimentary Phosphates – An example: Phosphoria Formation, southeastern Idaho, U.S.A. In Kohn, M.J., Rakovan, J., and Hughes, J. (eds.), *Reviews in Mineralogy and Geochemistry, Phosphates: Geochemical, Geobiological, and Materials Importance*. vol. 48, pp. 363–389.
- Krassilov, V.A., 2003. *Terrestrial Paleocology and Global Change*. Bulgaria: Pensoft Publishers, Russian Academic Monographs No. 1 464pp.
- Krull, E.S., Lehmann, D.J., Druke, D., Kessel, B., Yu, Y.Y., and Li, R., 2004. Stable carbon isotope stratigraphy across the Permian–Triassic boundary in shallow marine carbonate platforms, Nanpanjiang Basin, south China. *Palaeogeogr. Palaeoclim. Palaeoecol.*, **204**, 297–315.
- Kuypers, M.M.M., Pancost, R.D., and Sinninghe-Damsté, J.S., 1999. A large and abrupt fall in atmospheric CO₂ concentration during Cretaceous times. *Nature*, **399**, 342–345.
- Larson, R.L. and Erba, E., 1999. Onset of the mid-Cretaceous greenhouse in the Barremian–Aptian: igneous events and the biological, sedimentary, and geochemical responses. *Paleoceanography*, **14**, 663–678.
- Leckie, R.M., Bralower, T.J., and Cashman, R., 2002. Oceanic anoxic events and plankton evolution: biotic response to tectonic forcing during the mid-Cretaceous. *Paleoceanography*, **17** (3), 1041 (doi:10.1029/2001PA000623).
- LeTourneau, P.M., and Olsen, P.E., 2003. *The Great Rift Valleys of Pangea in Eastern North America* vol. 2, New York: Columbia University Press, 384pp.
- Longdoz, B., and Francois, L.M., 1997. The faint young sun climatic paradox: Influence of the continental configuration and of the seasonal cycle on the climatic stability. *Glob. Planet. Change*, **14**, 97–112.
- Lyons, T.W., 2004. Warm debate on early climate. *Nature*, **428**, 359–360.
- Martin, R.E., 1995. Cyclic and secular variation in microfossil biomineralization: clues to the biogeochemical evolution of Phanerozoic oceans. *Glob. Planet. Change*, **11**, 1–23.
- Meng, X., Ge, M., and Tucker, M.E., 1997. Sequence stratigraphy, sea-level changes and depositional systems in the Cambro–Ordovician of the North China carbonate platform. *Sed. Geol.*, **114**, 189–222.
- Norris, R.D., Bice, K.L., Magno, E.A., and Wilson, P.A., 2002. Jiggling the tropical thermostat in the Cretaceous hothouse. *Geology*, **30**, 299–302.
- Ohmoto, H., Watanabe, Y., and Kumazawa, K., 2004. Evidence from massive siderite beds for a CO₂-rich atmosphere before ~1.8 billion years ago. *Nature*, **429**, 395–399.
- Pálffy, J., Mortensen, J.K., Carter, E.S., Smith, P.L., Friedman, R.M., and Tipper, H.W., 2000. Timing the end-Triassic mass extinction: first on land, then in the sea? *Geology*, **281**, 39–42.
- Pavlov, A.A., Hurtgen, M.T., Kasting, J.F., and Arthur, M.A., 2003. Methane-rich Proterozoic atmosphere? *Geology*, **31**, 87–90.
- Pires, E.F., Sommer, M.G., and Scherer, C.M.D.S., 2005. Late Triassic climate in southernmost Parana Basin (Brazil): Evidence from dendro-chronological data. *J. South Am. Earth Sci.*, **18**, 213–221.
- Pierrehumbert, R.T., 2004. High levels of atmospheric carbon dioxide necessary for the termination of global glaciation. *Nature*, **429**, 646–649.
- Pirrie, D., Marshall, J.D., Doyle, P., and Riccardi, A.C., 2004. Cool early Albian climates; new data from Argentina. *Cret. Res.*, **25**, 27–33.
- Poulsen, C.J., 2004. A balmy Arctic. *Nature*, **432**, 814–815.
- Poulsen, C.J., Barron, E.J., Arthur, M.A., and Peterson, W.H., 2001. Response of the mid-Cretaceous global oceanic circulation to tectonic and CO₂ forcings. *Paleoceanography*, **16**, 576–592.
- Rackay, G., and House, M.R. (eds.), 2002. Late Devonian biotic crisis: ecological, depositional and geochemical records. *Palaeogeogr. Palaeoclim. Palaeoecol.*, **181**, 1–386.
- Renne, P.R., Zichao, Z., Richards, M.A., Black, M.T., and Bassu, A.R., 1995. Synchrony and causal relations between Permian–Triassic boundary crises and Siberian flood volcanism. *Science*, **269**, 1413–1416.
- Retallack, G.J., 1997. Early forest soils and their role in Devonian global change. *Science*, **276**, 583–585.
- Retallack, G.J., Veevers, J.J., and Morante, R., 1996. Global coal gap between Permian–Triassic extinction and Middle Triassic recovery of peat-forming plants. *Geol. Soc. Am. Bull.*, **108**, 195–207.
- Royer, D.L., Berner, R.A., Montañez, I.P., Tabor, N.J., and Beerling, D.J., 2004. CO₂ as a primary driver of Phanerozoic climate. *GSA Today*, **14**, 4–10.
- Ruffell, A., McKinley, J.M., and Worden, R.H., 2003. Comparison of clay mineral stratigraphy to other proxy palaeoclimate indicators in the Mesozoic of NW Europe. *Phil. Trans. R. Soc. Lond. A*, **360**, 675–693.
- Shaviv, N.J., and Veizer, J., 2003. Celestial driver of Phanerozoic climate? *GSA Today*, **13**, 4–10.
- Shields, G.A., Carden, G.A.F., Veizer, J., Meidla, T., Rong, J.-Y. and Li, R.-Y., 2003. Sr, C, and O isotope geochemistry of Ordovician brachiopods: a major isotopic event around the Middle–Late Ordovician transition. *Geochim. Cosmochim. Acta*, **67**, 2005–2025.
- Spalletti, L.A., Artabe, A.E., and Morel, E.M., 2003. Geological factors and evolution of southwestern Gondwana Triassic plants. *Gondwana Res.*, **6**, 119–134.
- Steel, D., 1992. Charles Babbage, the craters of the Moon, and the greenhouse effect. *J. Br. Astron. Assoc.*, **102**, 246–247.
- Stoll, H.M., and Schrag, D.P., 2000. High-resolution stable isotope records from the Upper Cretaceous rocks of Italy and Spain: glacial episodes in a greenhouse planet? *Geol. Soc. Am. Bull.*, **112**, 308–319.
- Sturesson, U., 2003. Lower Palaeozoic iron oolites and volcanism from a Baltoscandian perspective. *Sed. Geol.*, **159**, 241–256.
- Tabor, N.J., Montañez, I.P., Zierenberg, R., and Currie, B.S., 2004. Mineralogical and geochemical evolution of a basalt-hosted fossil soil (Late Triassic, Ischigualasto Formation, northwest Argentina): Potential for paleoenvironmental reconstruction. *Geol. Soc. Am. Bull.*, **116**, 1280–1293.
- Tanner, L.H., Lucas, S.G., and Chapman, M.G., 2004. Assessing the record and causes of Late Triassic extinctions. *Earth Sci. Rev.*, **65**, 103–139.
- Tardunno, J.A., Brinkman, D.B., Renne, P.R., Cottrell, R.D., Scher, H., and Castillo, P., 1998. Evidence for extreme climatic warmth from Late Cretaceous Arctic vertebrates. *Science*, **282**, 2241–2244.
- Torsvik, T.H., and Cocks, L.R.M., 2004. Earth geography from 400 to 250 Ma: a palaeomagnetic, faunal and facies review. *J. Geol. Soc. Lond.*, **161**, 555–572.
- Trewartha, G.T., 1937. *An Introduction to Weather and Climate*. New York, USA: McGraw-Hill, 373pp.
- Tyndall, J., 1861. On the absorption and radiation of heat by gases and vapours, and on the physical connection of radiation, absorption, and conduction. *Phil. Mag. Ser. 4*, **22**, 169–194, 273–285.
- van de Schootbrugge, B., et al. 2005. Early Jurassic climate change and the radiation of organic walled phytoplankton in the Tethys Ocean. *Paleobiology*, **31**, 73–97.

- Veizer, J., et al. 1999. $^{87}\text{Sr}/^{86}\text{Sr}$, $\delta^{13}\text{C}$ and $\delta^{18}\text{O}$ evolution of Phanerozoic seawater. *Chem. Geol.*, **161**, 59–88.
- Wallmann, K., 2001. The geological water cycle and the evolution of marine $\delta^{18}\text{O}$ values. *Geochim. Cosmochim. Acta*, **65**, 2469–2485.
- Wallmann, K., 2004. Impact of atmospheric CO₂ and galactic cosmic radiation on Phanerozoic climate change and the marine $\delta^{18}\text{O}$ record. *Geochem. Geophys. Geosys.*, **5**, (doi:10.1029/2003GC000683).
- Wilson, P.A., and Norris, R.D., 2001. Warm tropical ocean surface and global anoxia during the mid-Cretaceous period. *Nature*, **412**, 425–429.
- Woodwell, G.M., and Mackenzie, F.T. (eds.), 1995. Biotic Feedbacks in the Global Climatic System. Will the Warming Feed the Warming? New York, USA: Oxford University Press, 416pp.
- Wopfner, H., 2002. Tectonic and climatic events controlling deposition in Tanzanian Karoo basins. *J. Afr. Earth Sci.*, **34**, 167–177.
- Yapp, C., 2004. Rusty relics of Earth history: Iron(III) oxides, isotopes, and surficial environments. *Ann. Rev. Earth Planet. Sci.*, **29**, 165–199.

Cross-references

[Carbon Cycle](#)
[Carbon Isotope Variations Over Geologic Time](#)
[Cretaceous Warm Climates](#)
[Early Paleozoic Climates \(Cambrian-Devonian\)](#)
[Faint Young Sun Paradox](#)
[Greenhouse Effect in Encyclopedia of World Climatology](#)
[History of Paleoclimatology](#)
[Late Paleozoic Paleoclimates \(Carboniferous-Permian\)](#)
[Mesozoic Climates](#)
[Methane Hydrates, Carbon Cycling, and Environmental Change](#)
[Ocean Anoxic Events](#)
[Oxygen Isotopes](#)
[Paleocene-Eocene Thermal Maximum](#)

H

HEAT TRANSPORT, OCEANIC AND ATMOSPHERIC

Ocean-atmosphere interactions control Earth's climate in many ways. The most important of these controls is the heat transport of energy by atmosphere and ocean.

The only source of heat on Earth is solar radiation. As any physical body with a temperature above absolute zero, Earth loses heat in the form of infrared radiation proportional to the fourth power of its absolute temperature. The Earth as a planet is in almost perfect thermal steady state and therefore the top of the atmosphere must be in a complete globally-averaged radiative balance.

However, because of Earth's sphericity, solar radiation in high latitudes spreads over larger areas than in low latitudes, and the net radiative balance at the top of the atmosphere is positive in low latitudes and negative in high latitudes (Figure H1). The atmosphere and oceans must transport heat from low to high latitudes to balance these heat surpluses and deficits. In the absence of the meridional heat transport (for example, on a planet without oceans or atmospheres), the surface temperature at the tropics would be much higher than the observed temperature and would be much lower at the poles.

Meridional poleward heat transport in the atmosphere and oceans provides an effective feedback for constraining the equator-to-pole thermal contrasts to certain limits. These limits determine the Earth's climate extremes, which have varied throughout geological time. As the air and water motions depend on thermal gradients, heat transport is a highly nonlinear and sensitive feedback, and so is the climate system.

The sum of the meridional heat transport expedited jointly by the ocean and atmosphere can be determined from the divergence of the zonally averaged heat budget at the top of the atmosphere. About 5–6 PW (1 PW is equal to 10^{15} W) of energy is carried poleward by the ocean-atmosphere system in both hemispheres (Peixoto and Oort, 1992). Atmosphere carries heat directly, by transporting warmer air poleward, and indirectly, by carrying latent heat in water vapor.

Until recently, it was thought that roughly half of the poleward heat transport is expedited by the atmosphere, and half by the ocean. Based on a re-analysis of data gathered between February 1985 and April 1989, Trenberth and Caron (2001) have found that the atmospheric heat transport is at least twice larger than the oceanic in the Northern Hemisphere, with this ratio even higher in the Southern Hemisphere. However, because the heat capacity and density of sea water are much larger than those of air, changes in the oceanic budget, as reflected in oceanic heat transport, have profound and much longer-lasting effects on climate.

The atmosphere and the ocean transfer heat differently. The atmosphere transports heat meridionally mainly by large transient eddies in the middle and high latitudes. The ocean carries heat mainly by the large-scale horizontal gyres, and by the meridional overturning cells driven by the sinking and spreading of cold water. These gyres and overturning cells comprise the global ocean circulation system, also known as the global ocean conveyor (Broecker, 1991).

The meridional oceanic heat transport by ocean currents, Q_{adv} across a zonal coast-to-coast and top-to-bottom section can be computed as follows:

$$Q_{adv} = \rho_0 c \int_{-H}^0 \int_{\lambda_W}^{\lambda_E} v \theta a dz d\lambda$$

where ρ_0 is constant sea water density ($1,028 \text{ kg m}^{-3}$), c is the specific heat of water at constant pressure, v is the meridional component of velocity, H is the depth of the ocean, θ is potential temperature (i.e., in situ temperature corrected for heating by compression), a is the Earth's radius, and λ_W and λ_E are the longitudes of the west and east coasts of the ocean basin at the chosen latitude, respectively. Total water transport across such a coast-to-coast and top-to-bottom section must be zero. However, the total heat transport across this section is modulated by spatially-inhomogeneous temperature and is not zero, and the total meridional oceanic heat transport depends on both the intensity of meridional flows and steepness of temperature gradients.

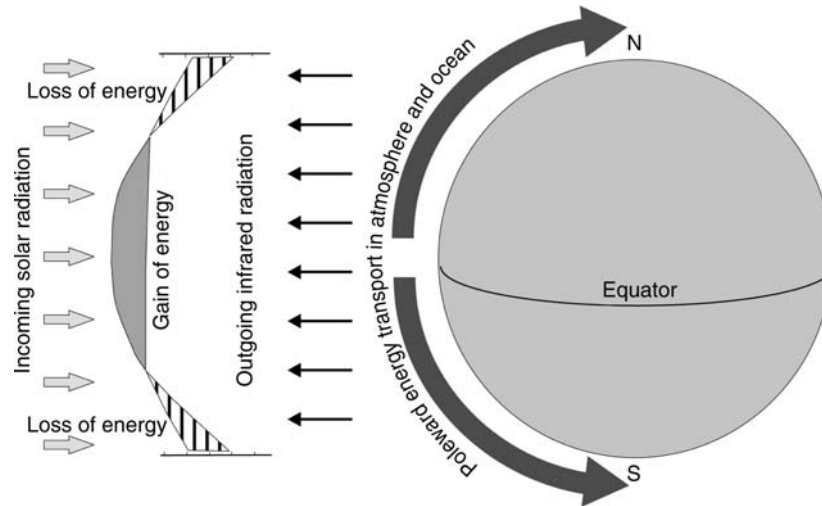


Figure H1 Simplified scheme of radiative balance and compensating heat transport in the ocean and atmosphere.

The present-day global thermohaline conveyor is driven by deep convection associated with the formation of the North Atlantic Deep Water (NADW). The North Atlantic Current carries warm and salty surface water to the northern North Atlantic and Norwegian Seas where it cools and sinks to the deep sea. Continuity of the ocean currents requires that the southward cross-equatorial deep-ocean outflow of NADW (about $16 \times 10^6 \text{ m}^3 \text{ s}^{-1}$) must be compensated by an equal amount of northward flowing water in the upper layers. The combined effect of these two opposite flows leads to large (up to 1 PW) northward cross-equatorial heat transport in the Atlantic Ocean.

Since sea water density depends on both temperature and salinity, freshwater balance at the sea surface may have a strong effect on ocean circulation and its associated heat transport (Bryan, 1986). Modeling studies have revealed that the ocean meridional overturning has strong sensitivity to relatively small inputs of freshwater, which are capable of capping the convection at key sites. Paleoclimatographic data support these simulations and indicate that changes in ocean overturning intensity and pattern might have happened many times through geologic history, especially during glacial-interglacial cycles of the Pleistocene.

The NADW dominance is challenged by a powerful southern deepwater source. In the Southern Ocean, chilled surface water descends to the bottom and forms the ocean's densest water mass – the Antarctic Bottom Water (AABW). The competition between NADW and AABW leads to unstable meridional overturning characterized by rebounds on centennial to millennial time scales. The idea of a bipolar seesaw has been invoked to explain the oscillations of meridional overturning by NADW-AABW wrestling (Broecker, 1998).

Numerical simulations offer an ocean seesaw scenario explained in Figure H2. Present-day overturning is driven by a relatively strong NADW formation instigating a strong northward overturning pattern in the Atlantic Ocean, as shown in Figure H2a. A glacial overturning pattern, e.g., during the Last Glacial Maximum, is a reduced and shallowed version of the present-day pattern, with NADW reduced yet still functioning (not shown in Figure H2). After a glacial termination,

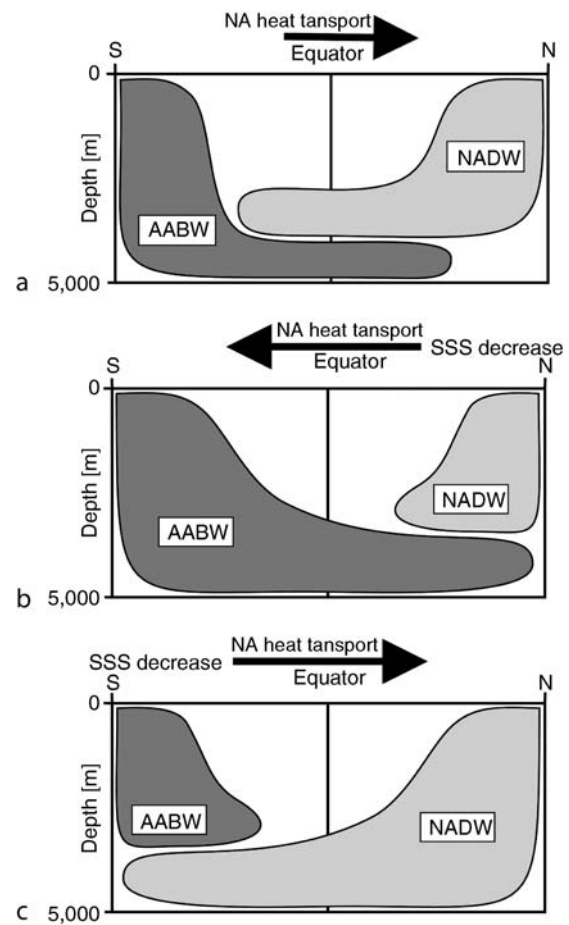


Figure H2 Schemes of water mass layering and overturning structure; (a) present-day mode of overturning; (b) northern meltwater event; (c) southern meltwater event. Direction of cross-equatorial oceanic heat transport is shown by arrows above each scheme (from Seidov et al., 2001).

a post-glacial iceberg armada from a collapsing ice sheet surged into the northern North Atlantic. Melting of the icebergs created a freshwater layer that may have capped NADW formation in key convection areas, shown as the northern low surface salinity impact in [Figure H2b](#). Paleoclimate proxies, including ice-rafted debris, suggest that such freshwater impacts, some known as Heinrich events, have indeed happened and might have caused great reductions in NADW formation. As NADW subsided, stronger AABW allowed the southward cross-equatorial heat transport in the Atlantic Ocean ([Figure H2b](#)). The heat surplus in the Southern Ocean warmed surface water in the Southern Ocean and sea ice there began to melt. Freshwater from melting ice (shown as a southern low salinity impact in [Figure H2c](#)) then slowed AABW formation, with the North Atlantic Ocean's surface water concurrently becoming colder because of southward rather than northward cross-equatorial heat transport.

The northern surface waters became colder and at some point dense enough to restore or even overshoot NADW formation ([Figure H2c](#)), followed by a seesaw-cycle repeat.

Oceanic heat transport is also thought to be a crucial element for climate change on geological time scales of millions of years and longer. Because of continental drift, the sea-land distribution has been changing throughout geologic history. The ocean circulation is sensitive to continental geometry and position, especially to opening and closing of major oceanic gateways, such as the Drake Passage, Indonesian Throughflow, Bering Strait, etc. One of the explanations of past warm climates, e.g., during the Cretaceous, is that both polar areas were open oceans.

Our knowledge of the ocean-atmosphere interactions is not yet complete. Improving this knowledge is essential for understanding past, present, and anticipated future climate change. For that reason, more research effort is still needed to observe and model heat transport in the ocean and atmosphere.

Dan Seidov

Bibliography

- Broecker, W., 1991. "The great ocean conveyor." *Oceanography*, **1**, 79–89.
- Broecker, W.S., 1998. "Paleocean circulation during the last deglaciation: A bipolar seesaw?" *Paleoceanography*, **13**, 119–121.
- Bryan, F., 1986. "High-latitude salinity effects and interhemispheric thermohaline circulations." *Science*, **323**, 301–304.
- Peixoto, J.P., and Oort, A.H., 1992. *Physics of Climate*. New York: American Institute of Physics.
- Seidov, D., Haupt, B.J., Barron, E.J., and Maslin, M., 2001. "Ocean bi-polar seesaw and climate: Southern versus northern meltwater impacts". In Seidov, D., Haupt, B.J., and Maslin, M. (eds.), *The oceans and rapid climate change: Past, present, and future*. Washington, D.C.: AGU, pp. 147–167.
- Trenberth, K.E., and Caron, J.M., 2001. "Estimates of meridional atmosphere and ocean heat transports." *J. Climate*, **14**, 3433–3443.

Cross-references

[Antarctic Bottom Water and Climate Change](#)
[Climate Change, Causes](#)
[Heinrich Events](#)
[Ice-rafted Debris \(IRD\)](#)
[Last Glacial Termination](#)
[North Atlantic Deep Water and Climate Change](#)
[Paleocean Modeling](#)
[Paleoceanography](#)
[Sun-climate Connections](#)
[Thermohaline Circulation](#)

HEINRICH EVENTS

Introduction

Heinrich (1988) first reported on the occurrence of six layers with high ice-rafted detritus (IRD) concentrations within the last glacial cycle, and they have been dubbed Heinrich layers since correlative layers were discovered in marine core DSDP609 and in the Labrador Sea in the North Atlantic Ocean (Bond et al., 1992; Broecker et al., 1992; Andrews et al., 1994). The six IRD layers can be correlated across the North Atlantic ([Figures H3](#) and [H4](#)). The high percentage of IRD in Heinrich layers is due to a high IRD flux in four of the six Heinrich layers over the last 60 kyr, namely H1, H2, H4 and H5 ([Figure H5](#)). These detrital carbonate-bearing Heinrich layers (Bond et al., 1992; Andrews et al., 1994) appear to require a series of repeated, anomalous, glaciological processes in or near the Hudson Strait. They have razor-sharp bases, and thus must have had extremely sharp onsets. Broecker et al. (1993) made a detailed assessment of H1 and H2 from DSDP core 609. Their results emphasize the decline in numbers of foraminifera during the Heinrich events within the IRD belt and the change in the slope of the ^{14}C age versus depth across these intervals. Although overall foraminifera abundance is low, shells that are found are in good condition, so that it is not a question of preservation. As well as can be recorded in marine sediments, Heinrich layers occur within the coldest parts of this record. These Heinrich layers are rapidly followed by dramatic warm intervals.

Heinrich layers H3 and H6 are different from the other Heinrich layers ([Figure H5](#)). For example, they show only a modest increase in flux (McManus et al., 1998) and in the number of lithic grains per gram (Bond et al., 1992, 1993) despite their high %IRD. Gwiazda et al. (1996) concluded that H3 and H6 were not really ice-rafting events, but instead were low foraminifera intervals, which would account for the high %IRD.

Provenance

The provenance of Heinrich layers H1, H2, H4 and H5 within the IRD belt is very distinctive and hence can be mapped by any number of geochemical measurements, as well as magnetic susceptibility (Grousset et al., 1993; see [Figure H5](#)) and detrital carbonate content (Bond et al., 1992). The data that have been collected reveal a remarkably complete story of the provenance of the Heinrich layers (Hemming, 2004). Nd isotope compositions of bulk terrigenous detritus and Pb isotope compositions of individual feldspar grains reveal an Archean source area for the Heinrich layers. Furthermore, the Pb isotope compositions of individual feldspar grains and $^{40}\text{Ar}/^{39}\text{Ar}$ ages of individual hornblende grains indicate a profound Paleoproterozoic metamorphic overprint on the Archean terrain. The presence of detrital carbonate grains, organic geochemistry, clay mineralogy, and K/Ar and Rb/Sr ages of the fine fractions also reveal a substantial sedimentary contribution to the layers. The entire spectrum of provenance observations for the H1, H2, H4 and H5 layers is consistent with a derivation from near the Hudson Strait.

In the eastern North Atlantic, events H3 and H6 have compositions that are distinct from those of H1, H2, H4, and H5. Using Pb isotope compositions of composite feldspar samples, Gwiazda et al. (1996) found that H3 and H6 resemble ambient sediment in V28–82, suggesting a large European source

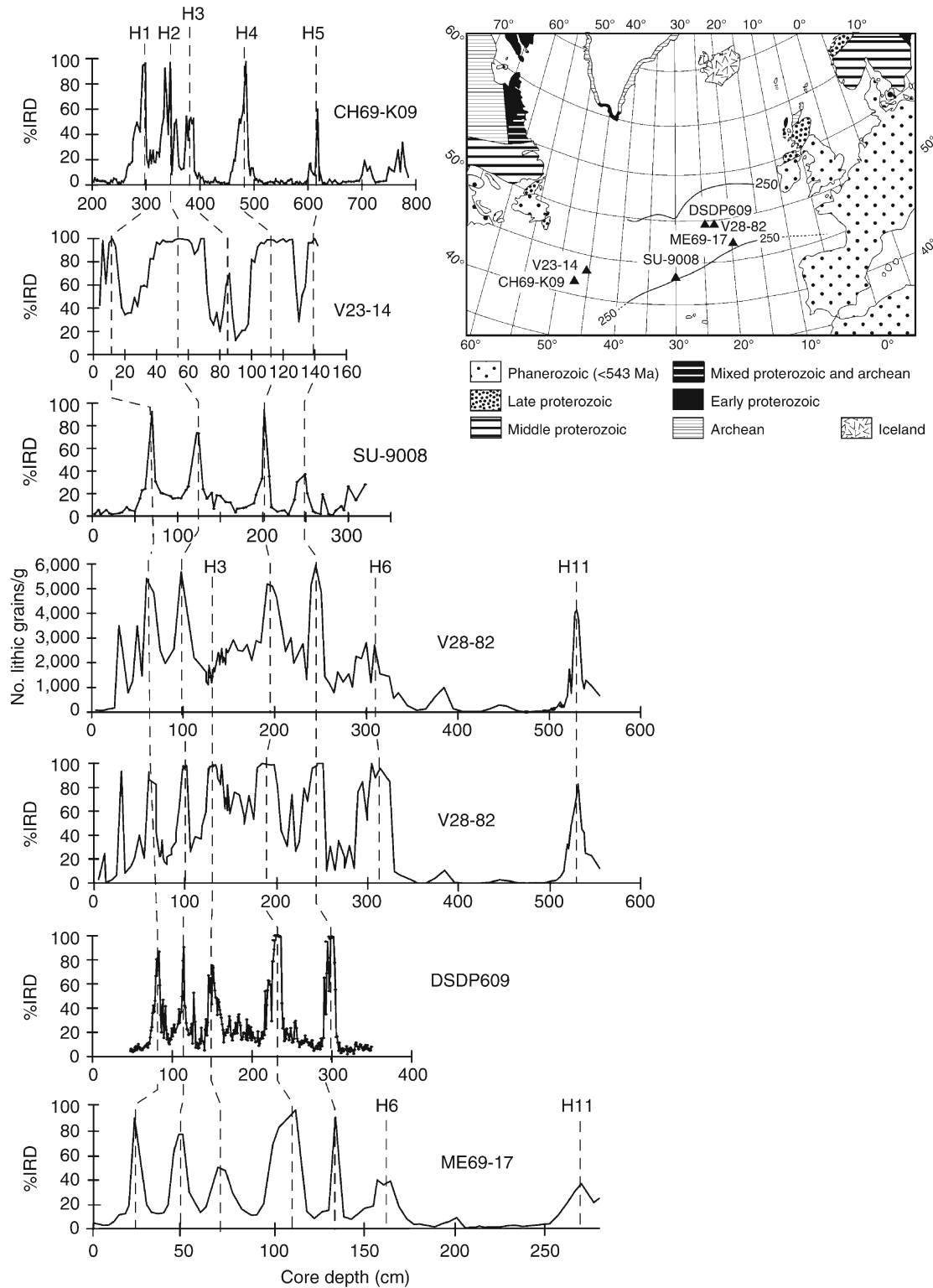


Figure H3 Ice rafted detritus data for North Atlantic sediment cores with Heinrich layers. Most of the data are % of lithic grains in the >150 μm fraction; however the data from ME69-17 (Heinrich, 1988) is % of lithic grains in the 180–3,000 μm fraction. Also shown is the record of number of lithic grains >150 μm per gram of dry sediment from core V28-82. Map shows the location of the cores. Data sources are: for CH69-K09 (Labeyrie et al., 1999), V23-14 (Hemming and Hajdas, 2003), SU-9008 (Grousset et al., 1993), V28-82 (Gwiazda et al., 1996; Hemming et al., 1998; McManus et al., 1998), DSDP609 (Bond et al., 1992; Broecker et al., 1992), ME69-17 (Heinrich, 1988).

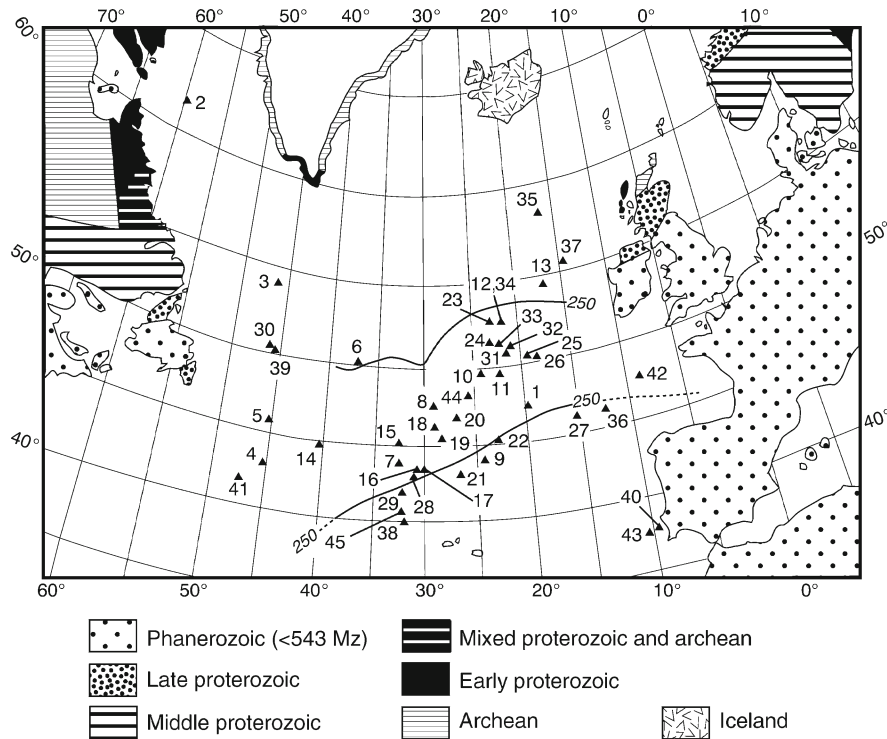


Figure H4 Map showing locations of cores with identified Heinrich layers. Simplified geological provinces are shown for reference. Map template and the $250 \text{ mg cm}^{-2} \text{ kyr}^{-1}$ flux lines from 25–13 kyr are from Ruddiman (1977); Ruddiman's "IRD belt" is shown for reference.

contribution, which agrees with the conclusion of Grousset et al. (1993). As mentioned above, H3 and H6 seem to be low foraminifera intervals rather than major ice-rafting events. These conclusions are consistent with other observations around the North Atlantic. Although Heinrich layer H3 appears to be a Hudson Strait event (Grousset et al., 1993; Bond and Lotti, 1995; Rashid et al., 2003), it does not spread Hudson Strait-derived IRD as far to the east as the other Heinrich events (Grousset et al., 1993). The map pattern of Sr isotope data from H3 shows a striking pattern of decrease in $^{87}\text{Sr}/^{86}\text{Sr}$ nearly perpendicular to the IRD belt (Hemming, 2004), consistent with a mixture of sediments from the Labrador Sea icebergs with those derived from icebergs from eastern Greenland, Iceland and Europe.

Chronology and duration of the Heinrich layers

Constraining the chronology and duration of the Heinrich layers is critical to understanding their origin as well as their role in global abrupt climate change. The duration of Heinrich layers has been estimated by the difference in ^{14}C ages across Heinrich layers, particularly H1 and H2 (Bond et al., 1992, 1993), as well as by measurements of sediment flux by the $^{230}\text{Th}_{\text{xs}}$ method (Francois and Bacon, 1994; Thomson et al., 1995; McManus et al., 1998).

The ages of Heinrich layers H1 and H2 are reasonably certain based on radiocarbon measurements, but estimations of their duration are compromised by the events themselves because they represent a large sediment flux increase (Manighetti et al., 1995). Within the IRD belt, the estimated age at the base of the layers is a maximum due to capping of the bioturbated layer by the Heinrich layer. The estimated age at the

top is a minimum due to bioturbation after the events. Additionally, the likelihood that Heinrich events are associated with major deep-ocean circulation changes (Vidal et al., 1997; Kissel et al., 1999; Elliot et al., 2001, 2002) and thus changes in the atmospheric radiocarbon content (Yokoyama et al., 2000; Waelbroeck et al., 2001) means that it is uncertain how to interpret the value of the radiocarbon measurements near these events. Data published by Bond et al. (1992, 1993) for core V23–81 give the best greatest density of data, but reveal age plateaus above both H2 and H1. Published estimates of Heinrich layer duration range from 208 to 2,280 years. Taking the best estimates, the average duration is 495 years and the standard deviation in this duration is 255 years (Hemming, 2004).

Precursor events

Understanding the origin of Heinrich layers relies on constraining the provenance of the layers themselves, and also in reconstructing the events leading up to their occurrence, the so-called precursor intervals (Bond and Lotti, 1995). Percentages of fresh basaltic glass and hematite-stained grains, counted at high resolution in several North Atlantic cores, vary on a 1- to 2-kyr interval, and the pacing of petrological changes in IRD appears to be similar to that of $\delta^{18}\text{O}$ in Greenland ice (inferred to be a proxy of air temperature changes) (Bond and Lotti, 1995; Bond et al., 1997, 1999). Bond and Lotti (1995) showed that peaks in Icelandic glass and hematite-stained grain abundances fall within the broad lithic peaks that encompass Heinrich layers, and that they precede detrital carbonate peaks for Heinrich layers H1, H2, H3, and H4 in cores DSDP609 and V23–81 (see also Bond et al., 1999). Grousset et al. (2001) showed a series of provenance changes that are consistent with

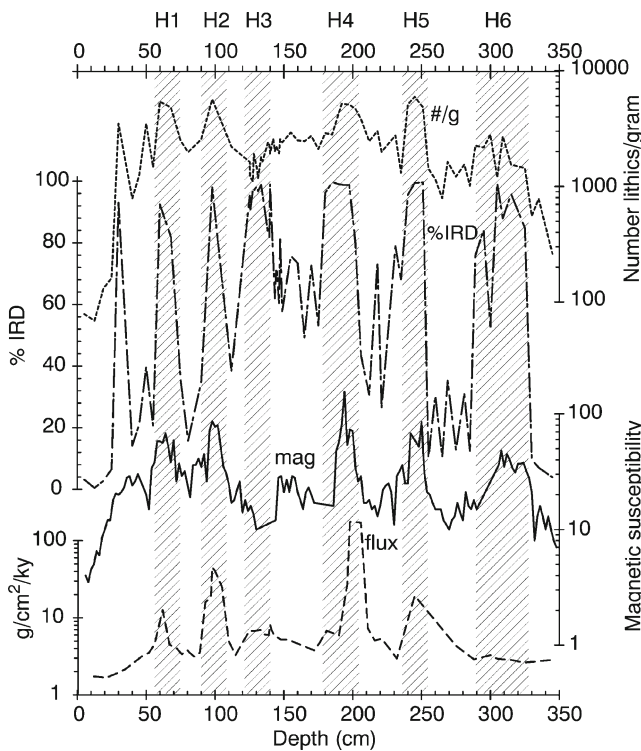


Figure H5 Different measures of IRD in core V28-82. Note that the Heinrich intervals defined by number of grains per gram do not appear to be precisely correlated with those defined by %IRD. Additionally, the intervals of high flux measured by ^{230}Th excess are smaller than those defined by counts. The intervals of high magnetic susceptibility are also smaller and appear to be offset from the flux peaks. These records reflect at least four independent samplings of the core, so partly the apparent offsets could be related to that. However, they are too large to be entirely explained in this way. Data sources are: %IRD and number of lithic grains per gram (Gwiazda et al., 1996; McManus et al., 1998; Hemming et al., 1998), flux (McManus et al., 1998), magnetic susceptibility (Greg Downing, unpublished data).

these observations. They found that during Heinrich layers H1 and H2 there appear to be sequential increases in volcanic grains, quartz grains, and carbonate grains at core SU9009 in the south-central part of the IRD belt. This observation of a precursor with greater lithic grains of non-Hudson Strait source suggested that the Laurentide Ice Sheet was not always responding to the same climate forcing as the Dansgaard-Oeschger (D-O) cycles, or was doing so later than other ice sheets. Furthermore, Vance and Archer (2002) have found that the provenance of precursory intervals to H4 and H2 are not similar based on radiogenic isotope studies of DSDP609 sediments.

One view of these precursors is that they simply represent the IRD signals of D-O cool phases in the North Atlantic (Bond et al., 1999; G. Bond, personal communication in 2002), and their appearance before the Hudson Strait-derived detritus means that the sea surface cooled prior to the input of Heinrich layers. Icelandic glass is an important component in Iceland Sea (Voelker et al., 1998) and Irminger Basin sediments (Elliot et al., 1998; van Kreveld et al., 2000), and East Greenland may be a significant source of hematite-stained grains (Bond et al., 1999; van Kreveld et al., 2000).

Although there is contention about whether Heinrich layers have correlatives in the Nordic seas (Fronval et al., 1995 and Elliot et al., 2002 vs. Dowdeswell et al., 1999), it is clear that the pattern is different. In the IRD belt, Heinrich layers are outstanding IRD events while events in between are modest although apparently correlative with Greenland cooling events (Bond et al., 1993, 1999; Bond and Lotti, 1995). In contrast, there is apparently an IRD event of equal magnitude for each of the Greenland cooling events, although there is a larger flux in general during the Last Glacial Maximum.

The key precursory events to Heinrich events may be preserved in Labrador Sea sediments. The recognition that the carbonate-rich intervals in the Labrador Sea marine sediment cores are approximately synchronous with Heinrich events (Bond et al., 1992; Andrews et al., 1994) helped to explain the source of the Heinrich ice armadas. However, in contrast to the case in the open ocean, where icebergs are the major sediment contributors, a large fraction of the sediment deposited near the Hudson Strait is brought by meltwater. Hesse and Khodabakhsh (1998) showed that the carbonate-rich layers near the mouth of Hudson Strait differ in sedimentological character from the Heinrich layers in the open ocean, and in particular are much finer-grained. They described a series of facies: nepheloid-layer deposits (or type I Heinrich layers), mud-turbidites (or type II Heinrich layers), laminae of IRD (or type III Heinrich layers), and fine suspended sediment and dropstones supplied by ice rafting (type IV Heinrich layers). These facies are generally arranged proximal to distal from the Hudson Strait, with type IV being the character of Heinrich layers in the IRD belt. Clarke et al. (1999) suggest that at Orphan Knoll site HU91-045-094 Heinrich events are separable into two distinct depositional processes. Turbidite sedimentation with high fine-grained carbonate concentrations is followed by a brief interval of increased IRD. The observations from the Labrador Sea suggest an interval where sediments were derived from subglacial meltwater prior to the launching of iceberg armadas to the North Atlantic.

Processes that may produce Heinrich layers

The timing of Heinrich events is in striking coincidence with the pattern of climate fluctuations documented from ice cores (Bond et al., 1993; Broecker, 1994). There is also good evidence for a global, or at least Northern Hemisphere wide, footprint (Broecker and Hemming, 2001; Hemming, 2004). Although the mechanism that drives the events remains a matter of debate, there is no doubt that they are spectacular examples of interactions among Earth's atmosphere, oceans and cryosphere. Most of the individual studies of sites outside the North Atlantic ice-rafting zone conclude that the Heinrich-correlated events are caused by changes in winds; stronger trade winds in the tropics, stronger winter monsoon winds in China (Porter and An, 1995; Wang et al., 2001) and the Arabian Sea, stronger northerly winds in the western Mediterranean. When compared to the ambient glacial conditions, there appears to be a general pattern of tendency for wetter (milder?) conditions along the western North Atlantic margin during Heinrich events, and perhaps along the eastern South Atlantic margin. In contrast, more extreme cold/dry glacial conditions prevailed during Heinrich intervals on the eastern North Atlantic margin and western Mediterranean. The pattern of differences between Heinrich events and ambient glacials, as well as the geographic distribution of sites that are sensitive to Heinrich events versus D-O events, may provide important clues as to the driving forces of these abrupt climate

changes. The coincidence in timing with the D-O pattern and the broad pattern of Northern Hemisphere correlations imply an important climate connection to Heinrich events. The layers themselves, however, reflect anomalous glaciological processes, and proposed mechanisms for their origin are discussed below.

Three broad categories of proposed mechanisms for Heinrich layers are reviewed by Hemming (2004): (a) catastrophic purging of the Laurentide Ice Sheet (MacAyeal, 1993) or episodic activity of an ice stream in the Hudson Strait (Marshall and Clarke, 1997), (b) jökulhlaups (Johnson and Lauritzen, 1995), and (c) ice shelf breakup (Hulbe, 1997; Hulbe et al., 2004). All appear to be capable of producing the first order features of the Heinrich layers, including the large injection of fresh water into the North Atlantic Current (with volume depending on duration) and the large volume of sediment deposited rapidly in these events.

Hemming (2004) concluded that glaciological instability (episodic purging) is the most likely explanation for the Heinrich layers unless it can be demonstrated that these events are much shorter than the estimated 500 year duration (essentially instantaneous). Although it is conceivable that the Heinrich layers represent instantaneous deposition as required by the ice shelf and jökulhlaup scenarios, the data appear to be more consistent with at least hundreds of year duration for the layers. Further examination of hydrographic changes in the North Atlantic may provide additional constraints on the ice-derived water volume by documenting the mixed layer thickness. Additionally, further examination of detailed sedimentology and hydrography proxies in the Labrador Sea provides constructive ways to decide among the proposed possibilities.

Summary

Heinrich layers are spectacular IRD deposits in the North Atlantic that resulted from massive discharges of icebergs from the Laurentide Ice Sheet through the Hudson Strait. They are clearly linked to dramatic climate shifts in the Northern Hemisphere. Detailed studies of the interval containing H1 through H4 in the IRD belt have demonstrated a strong connection between the timing of Heinrich layers and the pace of climate variability in the North Atlantic. More work is needed in the Southern Hemisphere in order to evaluate whether or not an inter-hemispheric correlation truly exists at the times of Heinrich events.

Much effort has gone into characterizing the Heinrich events in the North Atlantic and in identifying potentially correlative climate events globally, and from this effort a picture is emerging about the causes and effects related to them. They occurred during extreme cold periods in the North Atlantic, followed abruptly by dramatic warming trends. A large influx of ice-derived water into the North Atlantic accompanied these events, and it appears that a major reorganization of deep ocean circulation was produced. What remains to be better understood is whether the correlations were global or only Northern Hemisphere-wide, and what was the ultimate driver of these dramatic events.

Sidney Hemming

Bibliography

Andrews, J.T., Tedesco, K., Briggs, W.M., and Evans, L.W., 1994. Sediments, sedimentation rates, and environments, southeast Baffin Shelf and northwest Labrador Sea, 8-26 ka. *Can. J. Earth Sci.*, **31**, 90-103.

- Bond, G., Heinrich, H., Broecker, W., Labeyrie, L., McManus, J., Andrews, J., Huon, S., Jantschik, R., Clasen, S., Simet, C., Tedesco, K., Klas, M., Bonani, G., and Ivy, S., 1992. Evidence for massive discharges of icebergs into the North Atlantic ocean during the last glacial period. *Nature*, **360**, 245-249.
- Bond, G., Showers, W., Cheseby, M., Lotti, R., Almasi, P., deMenocal, P., Priore, P., Cullen, H., Hajdas, I., and Bonani, G., 1997. A pervasive millennial-scale cycle in North Atlantic Holocene and glacial climates. *Science*, **278**, 1257-1266.
- Bond, G.C., and Lotti, R., 1995. Iceberg discharges into the North Atlantic on millennial time scales during the last glaciation. *Science*, **267**, 1005-1010.
- Bond, G.C., Broecker, W.S., Johnsen, S., McManus, J.F., Labeyrie, L., Jouzel, J., and Bonani, G., 1993. Correlation between climate records from North Atlantic sediments and Greenland ice. *Nature*, **365**, 143-147.
- Bond, G.C., Showers, W., Elliot, M., Evans, M., Lotti, R., Hajdas, I., Bonani, G., and Johnsen, S., 1999. The North Atlantic's 1-2 kyr climate rhythm: Relation to Heinrich Events, Dansgaard/Oeschger cycles and the little ice age. In Clark, P.U., Webb, R.S., and Keigwin, L.D. (eds.), vol. 112. *Mechanisms of Global Climate Change at Millennial Time Scales*, Washington D.C.: American Geophysical Union, pp. 35-68.
- Broecker, W., Bond, G., and McManus, J., 1993. Heinrich events: Triggers of ocean circulation change? In Peltier, W.R. (ed.), vol. I 12. *Ice in the Climate System*, Berlin, Heidelberg: Springer, pp. 161-166.
- Broecker, W.S., 1994. Massive iceberg discharges as triggers for global climate change. *Nature*, **372**, 421-424.
- Broecker, W.S., and Hemming, S., 2001. Paleoclimate- climate swings come into focus. *Science*, **294**, 2308-2309.
- Broecker, W.S., Bond, G.C., Clark, K.M.E., and McManus, J.F., 1992. Origin of the northern Atlantic's Heinrich events. *Climate Dyn.*, **6**, 265-273.
- Clarke, G.K.C., Marshall, S.J., Hillaire-Marcel, C., Bilodeau, G., and Veiga-Pires, C., 1999. A glaciological perspective on Heinrich Events. In Clark, P.U., Webb, R.S., and Keigwin, L.D. (eds.), vol. 112. *Mechanisms of Global Climate Change at Millennial Time Scales*, Washington D.C.: American Geophysical Union, pp. 243-262.
- Dowdeswell, J.A., Elverhøi, A., Andrews, J.T., and Hebbeln, D., 1999. Asynchronous deposition of ice-rafted layers in the Nordic seas and North Atlantic Ocean. *Nature*, **400**, 348-351.
- Elliot, M., Labeyrie, L., Bond, G., Cortijo, E., Turon, J.-L., Tisnerat, N., and Duplessy, J.-C., 1998. Millennial-scale iceberg discharges in the Irminger Basin during the last glacial period: Relationship with the Heinrich events and environmental settings. *Paleoceanography*, **13**(5), 433-446.
- Elliot, M., Labeyrie, L., Dokken, T., and Manthe, S., 2001. Coherent patterns of ice-rafted debris deposits in the Nordic regions during the last glacial (10-60 ka). *Earth Planet Sci. Lett.*, **194**(1-2), 151-163.
- Elliot, M., Labeyrie, L., and Duplessy, J.C., 2002. Changes in North Atlantic deep-water formation associated with the Dansgaard-Oeschger temperature oscillations (60-10 ka). *Quaternary Sci. Rev.*, **21**(10), 1153-1165.
- Francois, R., and Bacon, M., 1994. Heinrich events in the North Atlantic: Radiochemical evidence. *Deep-Sea Res.*, **41**(2), 315-334.
- Fronval, T., Jansen, E., Bloemendal, J., and Johnsen, S., 1995. Oceanic evidence for coherent fluctuations in Fennoscandian and Laurentide ice sheets on millennium timescales. *Nature*, **374**, 443-446.
- Grousset, F.E., Cortijo, E., Huon, S., Hervé, L., Richter, T., Burdloff, D., Duprat, J., and Weber, O., 2001. Zooming in on Heinrich layers. *Paleoceanography*, **16**(3), 240-259.
- Grousset, F.R., Labeyrie, L., Sinka, J.A., Cremer, M., Bond, G., Duprat, J., Cortijo, E., and Huon, S., 1993. Patterns of ice-rafted detritus in the glacial North Atlantic (40-55°N). *Paleoceanography*, **8**(2), 175-192.
- Gwiazda, R.H., Hemming, S.R., and Broecker, W.S., 1996. Provenance of icebergs during Heinrich event 3 and the contrast to their sources during other Heinrich episodes. *Paleoceanography*, **11**, 371-378.
- Heinrich, H., 1988. Origin and consequences of cyclic ice rafting in the northeast Atlantic Ocean during the past 130,000 years. *Quaternary Res.*, **29**, 142-152.
- Hemming, S.R., 2004. Heinrich Events: Massive Late Pleistocene detritus layers of the North Atlantic and their global climate imprint. *Rev. Geophys.*, **42**, 1-43. RG1005, doi: 10.1029/2003RG000128.

- Hemming, S.R., and Hajdas, I., 2003. Ice rafted detritus evidence from $^{40}\text{Ar}/^{39}\text{Ar}$ ages of individual hornblende grains for evolution of the southeastern Laurentide ice sheet since 43 ^{14}C kyr. *Quaternary Int.*, **99–100**, 29–43.
- Hemming, S.R., Broecker, W.S., Sharp, W.D., Bond, G.C., Gwiazda, R.H., McManus, J.F., Klas, M. and Hajdas, I., 1998. Provenance of the Heinrich layers in core V28–82, northeastern Atlantic: $^{40}\text{Ar}/^{39}\text{Ar}$ ages of ice-rafted hornblende, Pb isotopes in feldspar grains, and Nd-Sr-Pb isotopes in the fine sediment fraction. *Earth Planet Sci. Lett.*, **164**, 317–333.
- Hesse, R., and Khodabakhsh, S., 1998. Depositional facies of late Pleistocene Heinrich events in the Labrador Sea. *Geology*, **26**(2), 103–106.
- Hulbe, C.L., 1997. An ice shelf mechanism for Heinrich layer production. *Paleoceanography*, **12**, 711–717.
- Hulbe, C.L., MacAyeal, D.R., Denton, G.H., Kleman, J., and Lowell, T.V., 2004. Catastrophic ice-shelf breakup as the source of Heinrich event icebergs. *Paleoceanography*, **19**, PA1004, doi: 10.1029/2003PA00089.
- Johnson, R.G., and Lauritzen, S.-E., 1995. Hudson Bay–Hudson Strait jökulhlaups and Heinrich events: A hypothesis. *Palaeogeogr., Palaeoclimatol., Palaeoecol.*, **117**, 123–137.
- Kissel, C., Laj, C., Labeyrie, L., Dokken, T., Voelker, A., and Blamart, D., 1999. Rapid climatic variations during marine isotopic stage 3: Magnetic analysis of sediments from Nordic Seas and North Atlantic. *Earth Planet Sci. Lett.*, **171**, 489–502.
- Labeyrie, L., Leclaire, H., Waelbroeck, C., Cortijo, E., Duplessy, J.-C., Vidal, L., Elliot, M., and Le Coat, B., 1999. Temporal variability of the surface and deep waters of the North West Atlantic Ocean at orbital and millennial scales. In Clark, P.U., Webb, R.S., and Keigwin, L.D. (eds.), *Mechanisms of Global Climate Change at Millennial Time Scales*, vol. 112. Washington D.C.: American Geophysical Union, pp. 77–98.
- MacAyeal, D.R., 1993. Binge/purge oscillations of the Laurentide ice sheet as a cause of the North Atlantic's Heinrich Events. *Paleoceanography*, **8**(6), 775–784.
- Manighetti, B., McCave, I.N., Maslin, M., and Shackleton, N.J., 1995. Chronology for climate change: Developing age models for the Biogeochemical Ocean Flux Study cores. *Paleoceanography*, **10**(3), 513–525.
- Marshall, S.J., and Clarke, G.K.C., 1997. A continuum model of ice stream thermomechanics in the Laurentide ice sheet 2. Application to the Hudson Strait ice stream. *J. Geophys. Res.-Solid Earth*, **102**(B9), 20615–20637.
- McManus, J.F., Anderson, R.F., Broecker, W.S., Fleisher, M.Q., and Higgins, S.M., 1998. Radiometrically determined sedimentary fluxes in the sub-polar North Atlantic during the last 140,000 years. *Earth Planet Sci. Lett.*, **155**, 29–43.
- Porter, S.C., and An, Z.S., 1995. Correlation between climate events in the North Atlantic and China during the last glaciation. *Nature*, **375**, 305–308.
- Rashid, H., Hesse, R., and Piper, D.J.W., 2003. Distribution, thickness and origin of Heinrich Layer 3 in the Labrador Sea. *Earth and Planetary Sci. Lett.*, **205**(3–4), 281–293.
- Ruddiman, W.F., 1977. Late Quaternary deposition of ice-rafted sand in the subpolar North Atlantic (lat 40 to 65°N). *Geological Soc. Am. Bull.*, **88**, 1813–1827.
- Thomson, J., Higgs, N.C., and Clayton, T., 1995. A geochemical criterion for the recognition of Heinrich events and estimation of their depositional fluxes by the $^{230}\text{Th}_{\text{excess}}$ profiling method. *Earth Planet Sci. Lett.*, **135**, 41–56.
- van Krevelend, S., Sarnthein, M., Erlenkeuser, H., Grootes, P., Jung, S., Nadeau, M.J., Pflaumann, U., and Voelker, A., 2000. Potential links between surging ice sheets, circulation changes, and the Dansgaard-Oeschger cycles in the Irminger Sea, 60–18 kyr. *Paleoceanography*, **15**(4), 425–442.
- Vance, D., and Archer, C., 2002. Isotopic constraints on the origin of Heinrich event precursors. *Geochimica et Cosmochimica Acta*, **66** (15A Suppl. 1), A798.
- Vidal, L., Labeyrie, L., Cortijo, E., Arnold, M., Duplessy, J.C., Michel, E., Beccuqué, S., and van Weering, T.C.E., 1997. Evidence for changes in the North Atlantic Deep Water linked to meltwater surges during the Heinrich events. *Earth Planet Sci. Lett.*, **146**, 13–27.
- Voelker, A.H.L., Sarnthein, M., Grootes, P.M., Erlenkeuser, H., Laj, C., Mazaud, A., Nadeau, M.-J., and Schleicher, M., 1998. Correlation of marine ^{14}C ages from the Nordic seas with the GISP2 isotope record: Implications for ^{14}C calibration beyond 25 ka BP. *Radiocarbon*, **40**, 517–534.
- Waelbroeck, C., Duplessy, J.C., Michel, E., Labeyrie, L., Paillard, D., and Duprat, J., 2001. The timing of the last deglaciation in North Atlantic climate records. *Nature*, **412**, 724–727.
- Wang, Y.J., Cheng, H., Edwards, R.L., An, Z.S., Wu, J.Y., Shen, C.-C., and Dorale, J.A., 2001. A high-resolution absolute-dated late Pleistocene monsoon record from Hulu Cave, China. *Science*, **294**, 2345–2348.
- Yokoyama, Y., Esat, T.M., Lambeck, K., and Fifield, L.K., 2000. Last ice age millennial scale climate changes recorded in Huon Peninsula corals. *Radiocarbon*, **42**(3), 383–401.

Cross-references

Dansgaard-Oeschger Cycles
 Deep Sea Drilling Project (DSDP)
 Ice-Rafted Debris (IRD)
 Millennial Climate Variability
 Quaternary Climate Transitions and Cycles

HISTORY OF PALEOCLIMATOLOGY

The roots of paleoclimatology

This narrative will treat sequentially (i) the discovery phase of the evidence (which still continues to this day) and (ii) the causative and experimental phase. Short biographies of major paleoclimatologists are presented in a companion piece.

Earliest observations

The elemental concept of climate change probably evolved in documentary form in ancient Egypt (Nile Valley), Mesopotamia, the Indus Valley and in China, where exceptional river floods or extended droughts were experienced. Decadal to century-long variations in the amplitudes of the Nile floods were more or less paralleled by the fortunes of successive dynasties. Times of drought and famine were socially more serious than episodic experiences of excessive (summer) floods. Early chapters of the Judeo-Christian Bible, notably *Genesis*, recounted the tale of the forty-day rain, resulting in the “flood of Noah,” and the subsequent recovery. Other oriental cultures contained comparable traditional sagas. It can therefore be a reasonable speculation that the concept or idea of periodic climate change was not only firmly established in human folklore, but also justified by periodic reinforcement provided by anomalous climatic events (as discussed below); see especially Ryan and Pitman (1999).

During the last 10,000 years or so, climatic events have affected human history on various scales, evidence for which is now being uncovered with increasing frequency. The role of external events, large or small, as causative factors in human history, thus became a central feature in Aristotelian thinking, and this approach tended to dominate “natural history” for the next two millennia (Schramm, 1963). For example, the development of huge pro-glacial lakes across North America during the retreat of the Laurentian Ice Sheet was accompanied by iso-static crustal rebound that eventually tilted the lakes seawards, resulting in great floods of freshwater that spread out and eventually diluted adjacent ocean surfaces, causing paleoclimatic crises with global repercussions. This may have contributed to universal flood mythology.

Another single-event phenomenon was the drowning of the Euxinic freshwater lakes in the Black Sea region when the postglacial sea-level rise surpassed the threshold sill of the Bosphorus (Zenkovitch in Fairbridge, 1966, p.146). Recent

oceanographic exploration here has disclosed abundant evidence of the former littoral, its fauna and human inhabitants (Ryan and Pitman, 1999).

From a historical point of view, the rejection of catastrophic hypotheses illustrates the innate conservatism of geologists raised on a philosophy of Lyellian uniformitarianism (see discussion, below). The eventual acceptance of such “outrageous” hypotheses has gradually led to a modified philosophy of neocatastrophism.

Dawn of reason

Even prior to the time of Lyell (1797–1875), gradual build-up of an anti-catastrophic and anti-miracle camp had begun. By the eighteenth century, observations could often be supplemented by chemistry and geological fieldwork, and the latter presented the endless paradoxes of paleoclimatology (although this term did not emerge until the twentieth century). At first, the observers were like the hunter-gatherers of anthropology. They simply explored. They started recording their observations on maps. Specialized concepts like petrology, stratigraphy, structure, mineralogy and paleontology emerged only in the early nineteenth century. The observers of the eighteenth to early nineteenth centuries were in two categories: (i) the gentlemen-traveler, i.e., personages with “private funds” who explored the world out of curiosity; and (ii) the commercially funded people who were “mission-oriented,” searching specifically for resources such as coal or metallic minerals such as gold, silver, iron, copper, zinc and lead; or engineer-trained, who were planning canals or water-supplies. Those observers who asked questions about the climatic conditions indicated by this or that proxy at the time of its formation had both leisure and literacy. An early discussion of scientific questions was by Emanuel Swedenborg (1688–1772), the Swedish scientist and theologian, who attributed elevated shorelines to progressive desiccation of the world ocean following the Biblical flood (see further, below).

Oddly enough, the people asking questions were frequently members of the clergy, who were not only literate but whose duties called for considerable traveling. Thus, Nicolaus Steno (Stensius; 1638–1686), the “father of stratigraphy,” although trained in the flat terrain of Denmark, spent most of his (theological) career in northern Italy, where he found time to accurately observe and record the stratification and structures of rock formations.

The scientific approach

The earth-science historian Schwarzbach (1963, 1974) recognized Robert Hooke (1635–1703), the English physicist, as the first scientist in paleoclimatology. He observed giant turtles and oversized ammonites in the Portlandian (uppermost Jurassic) of Dorset in England and concluded that they indicated a once warmer climate. This he believed could only be explained by a shift in the Earth’s axis.

Another imaginative pioneer was George L. Leclerc, Conte de Buffon (1707–1788), a celebrated French natural scientist. In his book “*Epoques de la Nature*” (1778), Buffon described the gradual cooling of a once-molten Earth, a cooling that began at the poles. Formerly warm temperatures at high latitudes were demonstrated by discoveries of large mammal remains, such as elephants and rhinoceroses, in these regions; such creatures are only found in warm climates today.

Then came Thomas Jefferson (1743–1826), third president of the United States, who had also served as ambassador to France and had become acquainted with Buffon. In his book “*Notes on the State of Virginia*” (1785), Jefferson discussed the discovery of fossil mammoth bones in what he regarded as anomalistically high latitudes. He believed this could possibly be explained by a change in the angle of the Earth’s ecliptic, and thus the tilt of the spin axis that controls the annual distribution of the seasons. At present, the Southern Hemisphere summer coincides with the Earth’s closest approach to the Sun and the Northern Hemisphere summer comes when they are farthest apart. About 9,000 years ago, the northern summer came when the Earth’s orbit was closest to the sun, so that mid-latitude mean summer temperatures were 2–3 °C warmer than today. The question of the mammoths in North America could alternatively be explained by a change in the creatures’ preferred habitat, a choice also considered (and favored) by Jefferson.

The classic “gentleman-scientist-traveler” was Alexander von Humboldt (1769–1859), who became the most famous German earth scientist of the nineteenth century, notably for his work in South America. He also lived for nearly 20 years in Paris and thus had the good fortune to gain access to its scientific libraries and to contemporary naturalists and thinkers like Buffon. To begin with, in 1799, however, he succumbed to A. G. Werner’s “Neptunian” concept of water-laid granites and basalts, a false idea, albeit contributing to a once warmer Earth. Later, after observing active volcanoes, he was probably the first to recognize the potential influence of ash and dust clouds on cooling of the climate (1823).

Idea of climate cycles

The classic concept of climatic cycles is probably that attributed to Joseph who was a member of the Israelite community in the Egypt of the New Kingdom, perhaps around the fourteenth century BC. Joseph (in the scriptures) warned of 7 years of bounty followed by 7 years of lean conditions. The message was clear: climates fluctuate, so, take care and plan ahead! Egyptological data include evidence of high-water marks (carbonate crusts) on temple columns, alternating with signs of erosional dissection in Nile terraces, which point to times when the flow was sluggish. Papyrus descriptions can now be confirmed by geological surveys (Fairbridge, 1962).

Systematic measurement of Nile flood cycles was initiated during the Moslem era (AD. 610), with many centuries of accurate data. Both short and long cycles have been identified (Hassan, 1981), which reflect monsoonal rainfall, mainly in the Ethiopian headwaters of the Blue Nile. Spectrum analysis (Currie, 1995) discloses both solar (11 years) and lunar (18.6 years) periodicities.

The first discussion of elevated shorelines (around the Baltic) appears to have been by Emanuel Swedenborg (1688–1772), mentioned above, who attributed them to traces of former levels accumulated or eroded during the progressive desiccation of the world ocean after the Biblical flood. An experimental approach was that of Carl Linneus (1707–1778), a Swedish professor from Uppsala, jointly with Anders Celsius, the professor of physics. Linneus was best known for his systematic biologic classification (having introduced the structured nomenclature of biology with species, genus, and so on). Together they made a remarkable contribution to climatic history when they disproved the “Desiccation Theory,” which had been widespread in the eighteenth century. The theory was formulated by the Bishop of Åbo (now Turku, in Finland) and based on the gradual emergence of the

coasts of Scandinavia, which he and fellow-theologians interpreted as conclusive evidence for the Bible story of the Noachian Flood and its subsequent recession. Linneus and Celsius devised a practical experiment to test the Biblical Desiccation Theory. Having heard that southern Sweden was emerging more slowly than the northern part of the country, they decided on a summer vacation on horseback and chiseled a series of water-level marks along the coast. Each site was revisited annually for 10 years, after which they announced their results. In the north around the Gulf of Bothnia, the coast appeared to be rising at 6–8 mm a year, while in the south, the Baltic shore was progressively sinking; in places it was even negative (the water marks were submerged). A desiccation of the world ocean would be uniform, but relative motion must reflect motion of the Earth's crust. This was probably the first practical experiment in both crustal change and paleoclimatology. (However, they did not perceive the connection to isostatic rebound due to removal of the former ice load [Ed]).

Anders Celsius (1701–1744), the Swedish physicist and astronomer at Uppsala at the same time as Linneus, was distinguished for his early observations of the aurora borealis (1716–1732). Besides helping to measure the arc of the meridian in Lapland (with colleagues from the French Academy of Science, in 1736), he became known for developing the centigrade scale, later known as the “Celsius scale” for thermometers. Accurately calibrated instruments were distributed to the physics departments of all major universities. For the first time, temperatures could be measured quantitatively.

In connection with the Linneus-Celsius experiments should be mentioned the experience of Baron Christian Leopold von Buch (1774–1853), a famous German geologist who had been a fellow student with von Humboldt at the Freiberg Mining Academy in Saxony. He made extensive trips by boat around northern Norway, as well as in the Baltic. Von Buch confirmed that the coast was indeed rising at Åbo, as was most of Scandinavia. Northern Norway, exposed to severe storm waves of the North Atlantic, is subject to spectacular coast erosion. The crustal uplift in northern Norway, however, created a succession of emerged benches in the form of a staircase. These dramatic landforms are repeated along the coast for more than 1,000 km. In 1810, Von Buch attributed the uplifting not to cyclical climate factors but to pulsatory magmatic causes, such as he had seen operating in the Canary Islands and other volcanic regions. (The glacioisostatic explanation for the uplift had to wait for over one hundred years: see below.)

Reusch, in 1894, coined the term “strandflat,” for the wide shore platforms. However, storm waves were not responsible because shore erosion is also found on the inner sides of fjords. To explain them, Nansen (1922) proposed a two-stage process: (i) frost action at or above sea level, followed by (ii) freezing and transport of the debris by floating ice. First observations in Quebec by Lyell helped his drift theory (see below). Traces of “fossil” strandflats and ice-transported boulders are seen on the Channel coasts of England and France, and as far south as northwest Spain (Fairbridge, 1977).

Could cyclical processes be triggered extraterrestrially? The idea that the Sun might have something to do with climatic events was to tread on delicate ground. When Galileo Galilei (1564–1642) first observed sunspots, it implied to some theologians an imperfection in the face of God's creation, the Sun, and that was anathema. Astronomy led nevertheless to the idea of predictable cycles. When Sir Edmond Halley (1656–1742) successfully anticipated the return of his eponymous comet in

1758 (from earlier orbits in 1531, 1607, and 1682), the case was established. The comet returned again in 1835, 1910 and 1986. He also laid the foundations for the new science of geomagnetism, which eventually helped to link endogenetic forces with paleo-climatology. Later, Sir William Herschel (1738–1822), when astronomer-royal of England, hinted that not only did the sunspots fluctuate in a cyclical manner, but that they might also relate to some climatic fluctuations that could affect the price of wheat.

Systematic observations of sunspots were begun in 1826 by an amateur astronomer, S. H. Schwabe, of Dessau, Germany, who announced a roughly 10-year cycle in 1843. At that time, Sir Edward Sabine had been monitoring geomagnetic fluctuations in Canada and found a similar variation, even hinting at “a common cause.” This was also suggested independently in 1852, by R. Wolf and A. Gautier, in Switzerland and France, respectively, and by R. C. Carrington in 1860, in England.

A century of controversy about Sun-climate relations has followed. An abundant literature accumulated over the decades, summarized in “*Sunspot Cycles*” (Schove, 1983). Today, the concept of a solar forcing cycle is beginning to be recognized, but the “how” and “why” are still elusive (e.g., Bond et al., 2001; Shindell et al., 2001; Rind, 2002). Systematic measurement of temperature opened the door (very gradually) to the idea of climatic cycles. This practical step was made possible by Celsius in the early eighteenth century, and two centuries later came the first analysis of an instrumental temperature time series (which had been assembled by the Dutch meteorologist Labrijn during World War II) that clearly displayed climate cycles (Fairbridge, 1968, p.210).

Labrijn's time series disclosed temperature cycles corresponding to the 22-year solar magnetic reversals and radiation fluctuations. These observations applied only to the North Atlantic-European area covered by the temperature recordings initiated by Celsius, but they opened the way to some twentieth century thinking.

The existence of that 22-year cycle was later confirmed by Schuurmans (in Flohn and Fantechi, 1984). The cycle was further strengthened when small errors caused by the urban heating effect were skillfully removed in a 250-year study of Stockholm temperatures by Anders Moberg (1995). The statistical procedure that made Labrijn's study so impressive used the mean summer months (June, July, August) minus the mean winter months (December, January, February) (3-month values) to create an oceanicity/continentality record.

One clue to solar-climatic relationships lies in the Moon. The role of the Moon in weather cycles has long been established in folklore, for better or worse. In science, George Schübler a professor of physics at the University of Tübingen, Germany, presented a paper in 1836 containing statistical analysis of his 60 years of systematic measurements of rainfall, which disclosed the 18.6 years lunar nodal cycle (see: “Earth-Moon system – dynamics” in Shirley and Fairbridge, 1997). Also worth mentioning is a fifteenth century agronomy text published in Italy that pointed out the advantage in seeding time because of the rainfall indications of the 18.6 years cycle. Sir Arthur Schuster of Manchester (U.K.), known for his invention of the time-series periodogram, published on the lunar and solar periodicities in earthquakes (1897) and on the influence of planets on sunspot formation (1911). In the late twentieth century, R. G. Currie disclosed lunar cycles in practically all geophysical and climatic time series, not least the nearly 1,400 years' record of the Nile floods (Currie, 1995).

William Gilbert's (1544–1603) pioneering discoveries in geomagnetism eventually led to an understanding of the aurora borealis and later the aurora australis as expressions of the Earth's magnetic field in the face of an initially mysterious solar force. A comprehensive review of the history of this subject was done by Siscoe (1980), establishing their correlations with sunspot cycles, but he set aside specific linkage with the solar wind and the geomagnetic field.

Scientific observations of the aurora and the geomagnetic field were begun in Scandinavia in the nineteenth century. Because of the high latitude, the common folk of Norway and Sweden had been observing these phenomena for many centuries. Country pastors recorded many sightings and these were analyzed by two distinguished scientists Nils Ekholm and Svante Arrhenius (a meteorologist and a geochemist) in a publication of the Royal Swedish Academy of Science. They identified both the 11-year solar cycle and the 18.6-year lunar cycle, as well as their climatic associations (Ekholm and Arrhenius, 1898). Today, a century later, this seminal paper is never cited and these relationships are still very little understood.

Popularization of paleoclimatology

Popularization of scientific thought became the fashion in early nineteenth century Europe and North America. Hugh Miller (1802–1856) made fossil discoveries that became a basis for paleogeographic and paleoclimatic reconstructions in his writings. They proved to be immensely exciting for his non-technical audiences.

A Swiss naturalist and professor of botany in Zürich, Oswald Heer (1809–1883) was the first to discover evidence (fossil leaves and fruit) of a warm climate during an interglacial interval in the Alps. Heer's epoch-making book "*The Primeval World of Switzerland*" (2 vols., 1865, transl. 1876) was very widely read and helped establish him as one of the founders of paleoclimatology and of paleogeography. By assuming that fossilized plants could be used as analogues for modern ones, the present-day habitats (in terms of temperature and precipitation) could be used for calculating proxy temperatures and rainfall. Bearing in mind that during the early Cenozoic the Tethys seaway was open to the Indian Ocean and Pacific, Heer's calculation of a mean warming of 7° F (3.5 °C) at that time was "probably the best approximation" (Brooks, 1949). Intervals of the warm paleoclimates in the Cenozoic would appear to have been achieved by three synergetic global paleogeographic factors: (i) open Tethyan seaway worldwide; (ii) limited orographic blocking; (iii) restricted Antarctic mountain glaciers (Fairbridge, 1961).

Uniformitarianism and actualism

The Scottish "gentleman-farmer" James Hutton (1726–1797) was the first to examine climate as a global phenomenon, although this work was largely eclipsed by his revolutionary role in geology as a whole. His original "*Theory of the Earth*" (a paper to the Royal Society of Edinburgh, 1785) endeavored to set out the natural laws by which the dynamics of Earth history could be explained. To explain erosion of the Earth's surface, he introduced the idea of climate and the atmosphere, and the year before (1784) he outlined his "*Theory of Rain*." This included a global review of climate, recognizing that atmospheric humidity was the key to rainfall, and that precipitation must occur when a warm air mass encounters a cooler one. An invaluable summary of his ideas was published by John

Playfair in 1803 (see also below). Hutton contributed fundamentally to the eighteenth century concept that eventually came to be called "uniformitarianism." Lyell (1830) reasoned that the "laws of nature" were immutable and permanent, which permits one "to reason by analogy." The standard aphorism is: "the Present is the Key to the Past." Whereas Nicolaus Steno (1631–1687) discovered the idea of sequence, or time-ordering, it was Hutton, after his famous discovery of a stratigraphic unconformity, who realized that geological processes should not be seen as a continuum but as subject to periodic upsets or revolutions. Thus, the concept of a *cycle* of events or processes emerged, to be further consolidated by Lyell in his stratigraphic sequences. It was not, however, until the late twentieth and early twenty first centuries that those sequences became locked into a paleoclimatologic framework, when Milutin Milankovitch (1879–1958) and Frederick Zeuner (1905–1963) developed, respectively, astronomic forcing potentials, with their stratigraphic representation.

A slightly different concept of uniformitarianism and terminology had already emerged in Russia and eastern Europe, the word "actualism" being coined by M. V. Lomonosov (1711–1765), Russia's "Father of Science." As generally conceived, actualism was practical methodology. It was therefore an investigative tool based on laws derived from quantitative models and would justify predictions as well as past events. In contrast, uniformitarianism was more a philosophy of "geohistory," subject to many potential dangers of interpretation (Albritton, 1975). Today, the actualistic approach is preferred.

In northern Germany the late eighteenth century was marked by frequent observations of exotic boulders (mainly granite or ancient limestones), called "Findlinge" (foundlings). Both country people and geologists recognized they did not belong in the local suite of outcrops. In folklore, they were generally attributed to relics of the Biblical Flood. In 1802, John Playfair (1748–1819), the Scottish geologist and follower of James Hutton, appreciated that these blocks or boulders were similar to others in the peripheral valleys of the Alps, where local scientists attributed them to glaciers that were formerly more extensive.

The glacial theory

The "glacial theory" was to become one of the scientific world's preoccupations during the first half of the nineteenth century. Good summaries are to be found in Flint (1971), Schwarzbach (1963, 1974) and Imbrie and Imbrie (1979, 1986).

The glacial theory received a significant spurt when, in 1817, the Swiss Natural Science Society announced a competition for members to demonstrate the former extension of the Alpine glaciers. This was rewarded in 1822 by a key lecture delivered by the Swiss engineer, Ignatz Venetz (although it was not published until 1833). The theme was taken up enthusiastically by geologist Louis Agassiz (1805–1873) who eventually came to teach at Harvard University.

Scandinavia was also a potential source of erratic blocks, but the glaciers there were smaller and less known than those of Switzerland. Nevertheless, in 1824 Jens Esmark of Denmark (1762–1829) proposed a former glacial source for northern Europe's widespread erratics.

At this point in history, the "establishment" struck back, through the powerful and colorful pen of the Reverend Dean William Buckland (1784–1856), first professor of geology at Oxford, and president of the Geological Society of London in

1824 and in 1840. Bearing in mind that his income depended in large measure on his religious observances, it should be no surprise that the Noachian Flood should feature in his public utterances. Thus, his first major work in 1823 was entitled "*Reliquiae Diluvianae, or Observations on the Organic Remains, contained in Caves, Fissures and Diluvial Gravel, attesting the Action of a Universal Deluge.*" Buckland coined the term "diluvium" (i.e., flood formation) for deposits of the Pleistocene ice age and this label came into widespread use in Europe, retained even into the twentieth century, long after the Biblical Flood story was quietly abandoned. Buckland's enthusiasm and extrovert nature brought him some criticism; nevertheless, he firmly established the concept of stratigraphic paleontology, the contrasting sequences of which constitute the very core of paleoclimatology.

From drift ice to glaciation

The glacial theory was the first of those remarkable revolutions in thought that directly concerns paleoclimatology. From the question of erratic boulders to continental glaciation calls for a great leap in scale, but it was scarcely more than a decade before this intellectual leap was achieved. The key was field demonstration. On Alpine excursions in 1836, Ignatz Venetz and then Jean de Charpentier persuaded Louis Agassiz of the former expansion of the mountain glaciers over the surrounding lowland terrain, and in 1837 Agassiz presented his general theory of a "Great Ice Age" to the Swiss Society of Natural Sciences in Neuchâtel. His regular correspondence with geologists in Britain led to Alpine excursions by Buckland (in 1838) and exchange trips by Agassiz (first, in 1840) to England, Scotland and Wales. Charles Lyell was shown the evidence, and eventually there was consensus. Almost the whole of the British Isles must have been glaciated according to T. F. Jamieson (1829–1913). The first general survey of the subject in Britain was in 1874 by James Geikie (1839–1915), who had been professor of geology at the University of Edinburgh. North America also provided important clues (Flint, 1971).

Lyell, curiously enough, was not an instant convert. He made two trips to North America, including one to the St. Lawrence valley and Bay of Fundy in Canada. Here he observed glacial boulders embedded in floating ice, and in the first edition of his "*Principles of Geology*" (1830) he attributed all erratics to drifting ice. Indeed, for a long time (over a century) all superficial deposits of evidently glacial origin were classified in both Britain and the United States as "drift." This was more a habit than belief. It was only in the later editions of Lyell that "drift" became divorced from floating ice. In the United States, it served as a synonym for glacial deposits in general and a "driftless area" is still recognized in the upper Midwest (Flint, 1971, p. 478).

In Germany, the reception of the glacial theory was also not instantaneous (Schwarzbach, 1974). Nevertheless, the German word "Eiszeit" (ice age) was the first such expression used by Karl Schimper in 1837, though it was quickly adopted worldwide. Von Buch, professor of geology in Berlin, had an enormous influence but considered the erratics to be transported by mudflows. In a letter of 1850 (Schwarzbach, 1974, p.5), he refers to the glacial theory as "a strange aberration of the human mind." Eventually, in Germany, the concept became universally accepted after a visit to Berlin in 1875 by the Swedish geologist Otto Torell (1828–1900).

In Scotland, Charles MacLaren, in 1842, reasoned that if this huge amount of ice had been derived by evaporation from the ocean, then sea level at the glacial maximum must have

been much lower than today. Unfortunately he overestimated the former ice volume and calculated the fall of sea level at 800 feet, which later proved to be somewhat exaggerated (by a factor of about 2). The principle, however, was important, and a globally significant phenomenon was now established, although it was more than 100 years before it was incorporated in general geological reasoning. Not only were vast climatic changes possible, but they also affected sea level and the relative size of continents and oceans from which climatic feedback processes were inevitable (Valentine and Moores, 1970).

Pre-Quaternary ice ages

Before the end of the nineteenth century, other, even more extensive glaciations were discovered to have occurred prior to the Quaternary "Great Ice Age." First to be found was the Permo-Carboniferous Ice Age (in multiple phases). Evidence for these glaciations was widely greeted with incredulity, partly because their situations were often close to the equator and, as more and more sites were added, it was seen that they were (improbably) spanning the width of an entire hemisphere (Du Toit, 1937).

Possibly one of the most courageous acts that can be imagined was when a very youthful new arrival to the Geological Survey of India, W. T. Blanford, in 1856, announced that he had just discovered indisputable evidence of a former ice age in the Permo-Carboniferous sediments of the Deccan (between 17° and 24° N), at a distance of only a little over 2,000 km from the equator. At that time, fixed continents, fixed planetary orbits and fixed ideas were rather rigidly established. Nevertheless, cynics may be astonished to learn that Blanford later became Director of the Survey, his extraordinary discovery being later confirmed elsewhere in India, as well as in all parts of the Southern Hemisphere. In fact, this glacial formation, to be known as the Talchir Tillite, over 100 m thick in places, became a key factor in the concept of a former giant continent, called (in 1883) "Gondwanaland" by Suess (1831–1914), parts of which today straddle the equator.

Permo-Carboniferous glacial deposits and striated pavements were then discovered all across Gondwanaland (Frakes, 1979). They were reported in Australia (eventually in all seven states); in Africa, from the extreme south to north of the Congo; and Arabia (Crowell, 1999). They were also discovered in South America (from Brazil to Patagonia and the Falkland Islands), and finally in Antarctica. Historically, these discoveries generated many interesting and some altogether exotic hypotheses. The most significant of these was the "Theory of Continental Drift" of Alfred Wegener (1926; translated 1966) which proved to be the forerunner of the modern plate-tectonic paradigm (summarized by Emiliani, 1992, p. 234–253). In this way, with the aid of marine geology and geophysics, a solution was found for what at first sight was an insoluble problem in paleoclimatology.

Further great ice age intervals were subsequently discovered in earlier geologic periods. One of the largest of these was that of the late Ordovician, which eventually was found to have extended from Brazil through West Africa and completely across the Sahara to Ethiopia and Saudi Arabia. Interestingly it was only discovered in the 1970s, initially by French oil geologists. Its presence was anticipated through paleontological indicators and based on paleomagnetic data (Fairbridge, 1971, 1973).

Discovered earlier was a late Proterozoic ice age, known as the Varangian due to the site of its first discovery on the

Varanger Fjord in the Finnmark district of northernmost Norway. Its present latitude, about 100 km north of the Arctic Circle, presents no problem in climatology (Schwarzbach, 1974; Frakes, 1979). Eventually an “Eocambrian” glaciation was also discovered in South America, West Africa, in South Australia and elsewhere, leading to the concept of a “Snowball Earth” at one stage. Plate-tectonic reconstructions were needed, however, in order to apply “actualistic” models.

Still earlier Precambrian tillites, which are more difficult to date, have been traced back in time (For example, the Gowganda Tillite in Canada at about 2.8 billion years BP). The problem of correct identification rises as one goes back in time and, when in doubt, the terms “pebbly mudstone” and “diamictite” have been used.

Causality: climatic changes

Visher (1986) wrote: “Geology as a predictive science may find its roots in the naturalism of the eighteenth century. The need for a naturalistic philosophy was developed due to the discovery of the predictability of the motion of bodies useful in discovering the array of order throughout the solar system.” Progress called for inductive reasoning, and, in addition, “bold hypotheses” were needed. In 1830, Lyell had already written: “Geology is the science which investigates the successive changes that have taken place in the organic and inorganic kingdoms of nature; it inquires into the causes of these changes, and the influence which they have exerted in modifying the surface and external structure of our planet.”

These generalized principles can now be applied to paleoclimatology, provided that its highly interdisciplinary nature is clearly understood: Astronomy, meteorology, geophysics, biology, geochemistry, sedimentology and stratigraphy are all involved.

One of the lengthy treatments of paleoclimates in general was by Eugène Dubois (1858–1940), who discovered the “Java (Trinil) Man” (while working in the Dutch East Indies). Dubois (1893) believed that an evolving Sun was a factor in paleoclimatology, but the time-scale was a difficulty. Evidence of remarkable climatic fluctuations that completely changed the physical geography of central Asia and its human environments on scales of 10^4 years or less was found in central Asia (Huntington and Visher, 1922).

Early works on paleoclimatology include “*Climate Through the Ages*” (Brooks, 1949, 1970). Brooks (1949, p. 382–386) conveniently tabulated a series of potential forcing agencies, with numerous references. Schwarzbach (1974) and Frakes (1979) have greatly expanded this database. The actual term “*Palaeoklimatologie*” (in German) was used in a book-length text by a paleobotanist, F. Kerner-Marilaun (1930).

Cosmic variables

In the late twentieth century, increasing knowledge of outer space afforded, for example, by the Hubble Telescope, has greatly expanded our concepts of the galaxies, and particularly of our own, the Milky Way galaxy. A major climate-modulating agent that has been proposed is intergalactic dust, as well as gas clouds. The earliest suggestion of the latter appears to be by Calverwell in 1895. Cosmic dust in outer space was also favored by Noelke (1908). Two Cambridge astronomers, Hoyle and Lyttleton (1919), speculating on the potential for interstellar “matter” to modify climate, have both been severely criticized for their unconventional (but often stimulating) ideas.

Particles in the galactic arms

Twentieth century studies of the Milky Way galaxy have shown that there is a high concentration of particulate matter embedded in the two spiral arms. Further, their distal parts display a regular undulation through which the Solar system must pass in its revolution around the galaxy. This periodicity is around $30 (\pm 3)$ Myr, which provides a potential forcing function for extinction/evolution spurts (Eldredge and Gould’s “punctuated” evolutionary model, 1972), for which Rampino and Haggerty (1996) proposed the term “Shiva Hypothesis”.

Solar radiation

Two categories of radiation (or energy emission) from the Sun are especially relevant for climate and paleoclimate studies. More than 99% of that energy is in electromagnetic form, the spectrum ranging from gamma and X-rays through UV to visible and IR to radio waves. Only the UV to near IR spectrum is relevant for climate (Peixoto and Oort, 1992). It travels in a rectilinear sense at the speed of light ($2.9973 \times 10^8 \text{ m s}^{-1}$, or approximately 186,000 miles s^{-1}), and accordingly has its terrestrial impact maximized at the Earth’s equator and as far north and south as the two tropics, Cancer and Capricorn, decreasing polewards. Heat flow from inside the Earth, generated by nuclear reactions, is about 3.5 orders of magnitude less than the exogenetic source.

The second solar source is particulate emission traveling through the solar wind; a plasma flux, which travels at variable speeds but generally requires several days to reach this planet. The solar wind carries magnetized particles and consequently is deflected by the Earth’s magnetosphere and funneled into the lower atmosphere at the two magnetic poles. Passage through the atmosphere results in collisions with molecules of nitrogen, oxygen, and CO_2 , resulting in isotopic spalling (e.g., ^{14}C , etc.). The discovery of sunspots by Galileo Galilei (1564–1642) in 1610 opened the door to the concept of a small-scale variable in solar radiation. It just so happened that the weak sunspots of the “Maunder Minimum” during the Little Ice Age (approximately 1650–1730) immediately followed Galileo’s discovery, but stronger sunspots became visible at that time in China and Korea so that some continuity was maintained. From archaeological magnetic studies, it is now known that, at that time, the magnetic pole lay in the Eastern Hemisphere, north of Siberia, and thus much closer to China and Korea (Schove, 1983).

Orbital variations

Although precise calculations of orbital characteristics of Earth-Moon-Sun motions have only become possible in the computer age, useful hand calculations have been available for more than 300 years. Linkage with terrestrial climate was proposed by Adhémar (1842) and developed by James Croll (1875) and Sir Robert Ball in 1891. An excellent account of the nineteenth century debates can be found in Imbrie and Imbrie (1979).

With the twentieth century came the Yugoslav engineer-mathematician Milutin Milankovitch (1941, 1969). Earliest discussions with geological applications had been offered by Frederick Zeuner (1945, 1959), and these had a worldwide impact. The “Establishment” reaction was almost unanimously negative. Science historians will probably argue this question for a long time to come, but the present writer (R. W. F.), having been a close friend of Zeuner (and other major “players”), believes that this opposition was driven by multiple

factors: xenophobia, religious conservatism and professional narrowness, to name a few. The early history of the controversy is well treated by Imbrie and Imbrie (1979). Subsequent developments were noted at several international conferences (e.g., Berger et al., 1984, 1991, 1992).

The final face-to-face conference was held in 1984 at the Lamont-Doherty Geological Observatory of Columbia University in New York when all the leading experts gathered in one room, together with the surviving relatives of the Milankovitch family who were present as visitors (Berger et al., 1984). The evidence of (i) astronomy was precise; (ii) the chronology of deep-sea deposits with ^{18}O isotopic paleoclimatic proxies was incontrovertible; (iii) the deep-sea record was identical with the continental time-series developed from glacio-eolian loess deposits alternating with interglacial soil deposits with type sections in Moravia (Kukla, 1972) and China (see discussion, below), and (iv) dating the marine coastal deposits had disclosed a eustatic synchrony between them and the Milankovitch-predicted glacial/interglacial cycles as anticipated already by Maclaren (1842) and brought into the orbital perspective by Zeuner (1945/1959) and Fairbridge (1961).

Inasmuch as the three principal variables of the Milankovitch "canon" (effective terrestrial insolation results from changes in precession (18–23 kyr), obliquity (41 kyr), and eccentricity (100 kyr)), long-term extrapolation is difficult, but is assisted by power-spectrum analysis. Methods for the latter have been greatly refined (Berger, 1995). (See also *Astronomical theory of climate change*, and *SPECMAP*.) Insolation values have been calculated for the last 10 million years (Berger and Loutre, 1991, 1992; Berger et al., 1992).

Thanks to work mainly by petroleum geologists, the apparent recurrences of Milankovitch-type cycles are now known for further back than 500 million years (see *Pre-Quaternary Milankovitch cycles and climate variability*). As might be expected with a three-fold forcing mechanism, there have been periods when one or another of the cycles was dominant, and other intervals when antiphase blocking and paleogeographic smoothing weakened them practically to extinction.

Asteroid impact events

Small asteroid or bolide impacts are traceable from the evidence of craters in semi-arid terrain back in time for about 5–10 Myr, but are very difficult to trace in older sedimentary basins and in submarine settings, thus including much more than two-thirds of the Earth's surface (Shirley and Fairbridge, 1997).

Major asteroid events, on the other hand, are mainly deduced from secondary evidence, such as geophysical anomalies, debris rings and organic extinctions (Rampino and Haggerty, 1996; Rampino, 1998). The instantaneous result is a catastrophic heat surge, as evidenced by widespread charcoal fragments (Lewis and Anders, 1985). This, however, is brief but followed by acid rain and protracted global cooling. The 1906 Tunguska event in eastern Siberia was not really a major one but the destruction of forests was dramatic. Paleontological data suggest an impact event is followed by a climatic deterioration of 10^5 – 10^6 years, initiated by a relatively short-term particle loading of the stratosphere, but triggering positive feedback of some variety, from plate excitation, tectonic uplifts and rain-shadow desiccation to lowered tree-lines.

The massive extinction at the K/T boundary event was documented by Gramletter in 1965, two decades *before* the discoveries by Alvarez (1986). If the asteroid fell in the sea, some

1,250 billion tons of water (following Alvarez) would have loaded the atmosphere, and would not only have effectively quenched the initial forest fires, but its toxicity (sulphuric, nitric and hydrochloric acids) must have been inimical to most forms of life. The survivors were mostly sheltered by burrows on land, deep lakes or oceanic depths. Stenothermal (ecologically limited) forms of life perished. Eurythermal ones had much better chances of survival. The initial tsunami waves reached more than 1,000 km to central Texas from Chicxulub in Yucatan (Bourgeois, et al., 1985), so that marine littoral biotas would not have time to adapt or migrate.

Following any major impact event, there is now a general consensus that a "nuclear winter" would ensue. Besides the climatic effect, the impact area (larger than the Gulf of Mexico) would be a biological wasteland, a biotic vacuum into which new populations would be slow to penetrate. Thus, the climatic relations associated with soil development would be significantly delayed.

The impact model for the K/T event has not been universally accepted and a well-reasoned volcanic alternative (Officer and Page, 1996) has its adherents. In contrast, the Eocene-Oligocene boundary event (~34 Myr) also saw major extinctions and good evidence for an asteroid collision (~35 Myr ago, at the mouth of Chesapeake Bay, USA; Poag, 1997), but in this case an orogenic and tectono-eustatic model may also offer a reasonable explanation (Mörner, 1984). All these factors are possibly interconnected.

Endogenic terrestrial heating

Heat flow from the Earth's interior was evident since the early days of coal mining in the eighteenth century. Confirmed by deep mining for gold and other metals in the nineteenth century, it became a topic of geophysical interest in the twentieth century. Sir Edward Bullard of Cambridge (U.K.) devised "heat probes" for use at sea. A source of internal heating of the planet Earth would be provided by radioactive decay. During initial planetesimal infall, short-term (brief half-life) radioactive elements would generate considerable heat, but it is only the long-lived isotopes that would generate heat sources surpassing the age of the planet. Systematic heat-flow measurements around the globe disclose energy sources adequate to mobilize convective circulation and thereby drive plate tectonics (see below).

Plate tectonics and redistribution of continents and oceans

In the nineteenth century, there was a general assumption that continents and oceans occupied more or less permanent positions in the Earth's crust, although marine transgressions and regressions were universally recognized and orogeny was generally an accepted concept, albeit in an episodic sense. A brief historical review is provided by Gohau (1990).

With the early twentieth century came Alfred Wegener (1880–1930) and the theory of continental drift (Wegener, 1926, 1966). It was received rather favorably in Australia, South Africa, South America and India (e.g., Du Toit, 1937), but much less so in the Northern Hemisphere, where the evidence was not as striking.

Coastal matching had already been noted for Africa and South America by Francis Bacon (1561–1626) in spite of the rather poor maps of Elizabethan times. Critical factors were the paleoclimatic indicators, discovered in the nineteenth century. Pea-sized seeds of the Permian *Glossopteris* flora could not be

carried throughout Gondwanaland by wind. Richly fossiliferous (plant) remains in coal seams were interstratified with indubitably glacial deposits on each of the Gondwana continents. Wegener's drift theory, critics claimed, however, was (i) impossible in terms of geophysics, but (ii) more importantly, it was contrary to religious concepts and conservative philosophy.

After World War II, new geophysical instruments together with worldwide marine geological surveys and the Deep-Sea Drilling Program led to total rethinking. Ocean paleomagnetic anomalies were the key to understanding the dynamic history of the oceans. Sea-floor spreading opened oceanic seaways (Dietz, 1961, 1977; Pitman and Heirtzler, 1966), and subduction-driven orogenic structures closed them (Isacks et al., 1968). Permanence (or "fixism") was OUT and mobilism was IN. This "Theory of Plate Tectonics" then became the geological paradigm of the late twentieth century. A historical review is provided by Marvin (1973).

While plate boundaries are determined by seismic belts today and by structural or petrological indicators in the past, they do not determine paleogeographic boundaries, nor do they relate to climatic systems. Specifically it is the former shorelines that are of particular interest in terms of paleoclimatology. Nevertheless, the plates are essential for continental reconstruction, and thence for paleoceanographic reconstruction, but the latter requires a eustatic treatment, as, for example, in the Mesozoic trans-America and trans-Africa seaways (unrelated to plate boundaries).

For the Mesozoic-Cenozoic eras, there were two critical water bodies that profoundly affected and controlled global paleoclimatology: (i) the gigantic proto-Pacific "Panthalassa" of Wegener (1929) and (ii) "Tethys," which was formally established by Edvard Suess (1885–1909; translated 1904–1924) long before plate tectonic reconstructions. Over about 250 million years, the Panthalassa progressively shrank in size as the two Americas shifted westward while the eastern Pacific was subducted. At the same time, the west-central and southwest Pacific became segmented into back-arc basins and island arcs. "Tethys" was linked equatorially to Panthalassa. The Tethyan link was always equatorial, with oceanic circulation going east to west. The climatic consequence was a global warming system of extraordinary effectiveness and continuity. As long as it remained in place, no terrestrial ice age could develop. This global oceanic circulation acted like a clean radiator for an automobile in maintaining a constant global temperature for the "climate machine."

As Africa, India and Australia drifted northward, they helped to create the continuous Southern Ocean, creating a second global circulation that dominates Southern Hemisphere climate systems today (Fairbridge, 1982). This feature has developed in stages over the last 200 million years or so. In contrast to Tethys, the Southern Ocean has always been in the higher (southern) latitudes, with its circulation west to east, i.e., in the Prevailing Westerlies.

Plate migrations in the Cenozoic gradually constricted the formerly open Tethys. The present Mediterranean is all that remains of the once mighty Tethys (Emiliani, 1992). Eventually South America closed in on the Caribbean and North America plates. A volcanic belt sealed the Panama Isthmus (Kennett, 1982). Tethys ceased to exist (apart from the Mediterranean) as a world-encircling "radiator," and the global climate machine went into a cooling mode, part of the "paleogeographic preparation" (Schwarzbach, 1974) that was inevitably the forerunner of the Quaternary ice age (see also *Cenozoic climate change*).

Plate tectonic controls for this ice-age preparation were three in number (and in importance): (i) partial blockage of warm E-W equatorial ocean currents (Fairbridge, 1973); (ii) presence of a pole-oriented land mass (Antarctica; Schwarzbach, 1963); and (iii) orographic growth (in central Asia, Europe and North America; Raymo and Ruddiman, 1992; Raymo, 1994).

Two further climatic systems relate to the plate-tectonic dictates: (i) relative to crustal rifting of continents and sea-floor spreading and (ii) relative to subduction zones, orogeny and volcanism (see below).

Orographic response to plate tectonics, and eustasy

Examples of Quaternary and present-day continental rifts are seen in East Africa, with a transition to oceanic setting in the Red Sea and Gulf of Aden. Climatically, the Red-Sea type linear basins that were periodically closed generated either euxinic or evaporating troughs, as well as sites for future hydrocarbon concentration. In Brazil (see Bigarella, in Fairbridge, 1975), the uplifted rift shoulders generate a rainforest belt as far south as Santa Catarina, but on the opposite side of the Atlantic, in Namibia, the SE trade wind creates a desert; and in Angola, a savanna.

Rifting of continents and its effects on the vertical state of the Earth's crust can be measured to some degree by dating the trace of ancient shorelines. This introduces the complex problem of "eustasy" or universal shift of mean sea level, which approximates the geoid (Fairbridge, 1961). This is only an approximation because the actual mean sea level can vary considerably in both space and time. Mentioned already is the effect of glaciation on global sea level (e.g., *glacial eustasy*). However, the field evidence for a former shoreline, as represented by an ancient beach deposit, an erosion bench, the surface of a now-dead coral reef or other geomorphic features, can reflect a range of distinctive causative processes. Actual sea level represents the homogeneous sum of all those processes, but the role of each varies from place to place and time to time.

Edvard Suess, professor of geology at the University of Vienna, invented the expression "eustatic fluctuations" of sea level (1885–1909; 1904–1924). He saw that there were repeated, large-scale fluctuations of world sea level throughout geological time. Oddly enough, however, he did not associate these with glaciation, magmatism or tectonism, but with sedimentation. Thus, he reasoned, the gradual filling of ocean basins would be achieved by erosion and sediment-transport from the uplifted land masses. *Ergo*, sea level would rise. Although the expression he created was excellent, his version proved to be the least important of varied causes. These fall into three categories:

1. *Tectono-eustasy* (operating by structural deformation of ocean basins, as during pulsations of plate tectonics, with an "Archimedean effect"; Pitman, 1978);
2. *Glacio-eustasy* (operating by change in the hydrologic state, water being transported from ocean to land and being converted to glacier ice, and vice versa);
3. *Sedimento-eustasy* (operating by sediment-infilling of ocean basins; the corollary of land erosion; mainly unidirectional, the sedimental cycles alternating with tectonic uplift followed by erosion cycles).

Mountain uplift and terrestrial cooling

Paleogeographic evidence shows that during the last 65 million years (since the end of the Cretaceous) there has been a

progressive (but fluctuating) fall in mean global surface temperatures. Subduction at active convergent plate margins has led to intermittent surges of orogenic uplift, including high plateau formation, e.g., Tibet, Iran, Anatolia, Bolivia and Colorado. High elevations have led to increased snowfall on the mountains, but drier conditions in rain-shadow plateaus. Both continentality and global albedo have risen, leading also to progressive global cooling. Brooks (1949, p.385) lists numerous references to such processes, and the uplift of Tibet has produced a flood of publications (Raymo and Ruddiman, 1992). (See also *Mountain uplift and climate change*.)

Oceanic circulation

At present, there is a general global circulation in the ocean, first recognized by Stommel (1958), following his studies of the Gulf Stream. It was seen as operating in the manner of a conveyor belt, now referred to as the "Conveyor" (Broecker, 1991). The essential conception recognizes a cold-water sink that becomes a cold, dense deepwater flow that heads south from near Greenland to the Southern Ocean where it turns eastward and is strengthened by cold, high density waters from below the Antarctic peripheral sea-ice. Tongues of this deep-water stream reach northwards into the Indian Ocean and western Pacific. At the surface, equatorial easterlies lead to upwelling. A counter flow of warm water leads back through the East Indies to the Indian Ocean, around the Cape of Good Hope, and joins the Benguela Current up the coast of southwest Africa, thence across the equator westwards to join the Gulf Stream. Paleomonsoons mark Holocene fluctuations in the tropics (Maley, 1997), but the cold cycles of the Pleistocene saw almost complete cessation of monsoonal systems (see also *Monsoons, Quaternary*).

A critical submarine ridge extends from the Faroe Islands to Iceland and operates as a modulator of the conveyor due to periodic eustatic shallowing. On a large scale, this may operate as a major on-off switch for amplifying glacial/interglacial climatic cycles.

Geological activity along other submarine ridges has probably played analogous roles from time to time in the remote past. For example, Brooks (1949, p.386) cites E. Hull who in 1897 suggested an "Antillean continent" that could once have caused a major deflection of the Gulf Stream. This entire region has undergone fundamental reorganizations since the Cretaceous, eventually leading to the blocking of Tethys and the repeated opening and closing of the Panama Strait. The final closure in the late Pliocene permitted two-way migrations by land animals and blocked the marine connections (Stewart, in Fairbridge, 1975, p. 418,).

With reference to the global warming of Cretaceous times, T. C. Chamberlin (1897) suggested that at a critical point, increased evaporation in the low latitudes could reverse the present circulation. The global salinity sink would then be equatorial. Upwelling in polar regions would keep them permanently warm. Studies of $\delta^{18}\text{O}$ records in high latitude Cretaceous and Cenozoic fossils and recent drilling show that this was indeed true.

Sea-ice and glacier fluctuation

The presence of sea-ice in winter is said to be the origin of the naming of Iceland, which was settled by Scandinavian (Viking) migrants after the eighth century, about the time of Charlemagne and the Holy Roman Empire. Climatically, it was a

period of remarkable warmth: the "Little Climatic Optimum" or "Medieval Warm Period" (Lamb, 1977). A rich flora at that time flourished in Spitsbergen (now largely ice-bound). It lasted until about AD. 1300 which marked the beginning of a fluctuating series of cold intervals, the "Little Ice Age," which persisted until about AD. 1725, or even 1850 according to some opinions. The Vikings could not have been more fortunate in their colonization voyages, because there is evidence that at that time the westerly storm tracks in summer tended to head over Greenland and Spitzbergen. Accordingly, there were frequently light easterlies to fill their sails. For a short time, ca. AD. 1000, they had an outpost at Anse-les-Meadows in Newfoundland, the first European settlement in the New World. Its fireplaces have been radiocarbon-dated. With the Little Ice Age, conditions turned against them. Despite warm cycles, the general trend was from bad to worse. The South Greenland colony gradually perished, and the last Viking died around AD. 1400 (McGovern, 2000).

Sea ice on the north coast of Iceland develops occasionally today in winters when a tongue of the Gulf Stream weakens. Major and protracted incursions were recorded during the Little Ice Age (Schell, in Fairbridge, 1967; Grove, 1988). Greatest severity, however, was seen during the seventeenth, eighteenth and nineteenth centuries. Lamb (1977) regarded sea ice, through its albedo, as a major factor in high-latitude cooling.

Today, Iceland's biggest (ice-cap) glacier, Vatnajökull, covers about 8,300 km², and there are six smaller ones. The first systematic study of the mass balance on Vatnajökull was on the joint Swedish-Icelandic expedition, led by Hans Ahlmann, a Stockholm professor, and Jon Eythorsson. There had been some confusion earlier about the response of glaciers to climatic forcing (temperature vs. precipitation), but Ahlmann (1938) was able to show that, in this case at least, climatic cooling was the dominant control. The Ewing-Donn theory of ice ages (Ewing and Donn, 1956, 1958), on the other hand, claimed that precipitation was the key. They proposed instead that during interglacial warmings of the world ocean, the Arctic Ocean was largely ice-free, with more moisture evaporating and returning as snow; thus, all glaciers would expand and advance. However, the Arctic Ocean does not appear to have been totally ice-free for several million years (see *Arctic sea ice*). In the second half of the twentieth century, there has been a retreat of both sea ice and mountain glaciers (Kerr, 2006).

Changes in atmospheric composition

Since earliest Precambrian times, geological evidence reveals episodic and secular changes in the Earth's atmosphere (see also separate entries). These changes have been forced by various agencies, which have been subject to progressive modification. Not all of these factors are well understood, but one quite indisputable fact emerges from the geologic record: the continuous existence of water (H₂O) in a fluid state. From this it follows that Earth-Moon-Sun interactions and planetary orbits must have been maintained in a dynamic balance on multi-billion year time scales (Shirley and Fairbridge, 1997); further, it follows that secular or cyclical variations in solar radiation must be balanced by powerful feedback mechanisms that have maintained a quasi-stable climate ($18 \pm 5^\circ\text{C}$) and prevented the Earth's mean temperature from ever suffering either a runaway heating (e.g., to a Venusian state) or a runaway icehouse condition (e.g., a Martian state), although arguments for a "snowball" state have been presented (see *Snowball Earth hypothesis*).

Secular changes over geologic time are demonstrated by the sedimentological-stratigraphic-paleontologic record and its successive biogeochemical revolutions. These are summarized (Fairbridge, in Oliver and Fairbridge, 1987, p. 301):

1. First Life, in CH₄ or CO₂ environment (ca. 4.0 billion years)
2. Mid-Precambrian oxygen threshold (ca. 2.5 billion years)
3. Eocambrian/Cambrian CaCO₃-exoskeletal life (ca. 540 million years)
4. Late Paleozoic “Great Coal Age” carbon storage (ca. 350–290 million years)
5. Cretaceous-Paleocene pelagic carbonate storage (ca. 150–50 million years)

Secondary, largely cyclical changes have amplified or decelerated the great secular trends. Periodicities of the cyclical changes range from fluctuations in the galactic arms at about 30 ± 2 million years (Rampino and Haggerty, 1996) to the Milankovitch orbital parameters, as noted earlier.

Besides biogeochemical processes that mainly depend on climatically controlled environments, there are also asteroid impacts, and volcanological and tectonic processes that are largely non-cyclical, or only marginally so. Volcanoes, depending on their magmatic characteristics, emit H₂O vapor, CO₂, SO₂ and CH₄. Climatically important is the fact that H₂O, CO₂ and CH₄ are “greenhouse” gases; that is, they tend to be environmentally warming, in contrast with the volcanic aerosol SO₂, which is a cooling agent.

Methane (CH₄) is the most effective greenhouse gas. In nature, it is produced by a wide range of organisms, from termites and ungulate cattle to swamp bacteria. These sources in general lean towards a tropical climatic bias, but subarctic tundra swamps are also significant.

Greenhouse gases not only affect climate but also global hydrology (see Herschy and Fairbridge, 1998) and eustatic fluctuations of sea level (Fairbridge, 1961). The two are linked, for example, during a major cold cycle when sea level is low and biotic (metabolic) activity is globally reduced. During glaciations, low temperatures generally reduce metabolic rates, water is scarce and deserts are widespread; atmospheric H₂O, CO₂ and CH₄ levels are all reduced. Also related to the hydrology-eustasy link are the soil biotas. World soils are commonly ignored by both geologists and climatologists but their atmospheric role is of major importance. As mentioned above, Erhart’s “biostatic” condition is a long-term, warm, stable, high-eustatic state, with stable CO₂ (Fairbridge and Finkl, 1980; Erhart, 1956). This is contrasted by Erhart’s “rhexistatic” conditions that are marked by sharp cooling events, with eustatic fall (often by 100 m or more) leading to extensive erosion, resulting in transfers of iron oxides to sedimentary storage. Natural deforestation due to glacial advance and desertification shifts CO₂ to the atmosphere, so the pendulum swings abruptly into a warming mode once more.

In the twenty first century, considerable attention is being paid to the question of “greenhouse warming.” This condition has been brought about by anthropogenic activity, principally expressed by increasing levels of CO₂, SO₂, and CH₄, mainly consequent upon deforestation and the burning of fossil hydrocarbons (coal, oil and natural gas). This activity began with transition of *Homo sapiens* from the Stone Age to the era of metals, starting about 4000 BC. with charcoal-based smelting (Ruddiman, 2005). Deforestation also expanded with the need for increased pasturage and cereal crop planting (Lamb, 1977). The last naturally warm climatic cycle, or *Medieval*

Warm Period (q.v.) was roughly AD. 800–1300, from the time of Charlemagne to the beginning of the *Little Ice Age* (q.v.). Evidence for late twentieth century warming is accumulating. However, but is difficult to distinguish natural climate variability from evidence of anthropogenic modification of atmospheric gases. How much is natural fluctuation? Recent evidence, however, supports an anthropogenic role (e.g., see *Encyclopedia of World Climatology*).

The Moon, luni-solar tides and related solar, planetary and terrestrial cycles

The Earth’s only satellite, the Moon has a uniquely large mass ratio (1:81) and the two behave almost as twin planets, revolving about a common center of mass located approximately 4,800 km from the geo-center. The Moon’s orbital plane is inclined at an angle of $5^{\circ}10'$ to the Earth’s orbital plane (ecliptic), and the point where they cross is called the *Node*. The Moon’s elliptical orbit at *perigee* radius is about 365,000 km and at *apogee* about 409,000 km, on average (Shirley and Fairbridge, 1997). This leads to cyclical changes in both tides and climate-related periodicities (Currie, 1995). The principal climate effect in the 18.6-year nodal cycle, observed in both rainfall and temperature time series.

The tide-raising force of the Moon, on average, is 2.17 times that of the Sun, and the resultant is a luni-solar tide, which generates an oceanic “tidal wave” (not related to tsunamis) that circles the globe every day, though modified by land barriers. Over the period of nearly a fortnight (27 days, 7 h, 43 min), the range varies from “spring” to “neap” tide (at 90°), depending on the relative alignment of Sun and Moon. Amplification of the range occurs at *perihelion* (early January around the year AD. 2000) when the Earth in the Northern Hemisphere is closest to the Sun. In the Southern Hemisphere, it is in July (the axial precession effect). Tide is also higher at *perigee* (close lunar approach) and more so at *syzygy* (approximate alignment of all three bodies). Very close line-ups occur at 558.4-year intervals (30×18.6 years) and at 93.067-year intervals (5×18.6 years). These multiples of the 18.6-year nodal cycle are seen in long climatic proxies (Currie, 1995) as well as its short-term harmonics, which link with El Niños (Fairbridge, 1990).

Otto Pettersson (1912, 1930), the Swedish oceanographer, found that the 18.6-year nodal cycle generated an internal wave in the North Sea at the boundary of the rising offshore saline waters and the partly fresh outflow from the Baltic Sea. As it approached the coast across the progressively shallowing North Sea, the wave also becomes larger and steeper. At a tidal station on the Gulmar Fjord it can approach 25 m and set up dangerous currents. Extremes are reached at 93.067 years, a five-cycle repeat at the same season, and likewise 15 317.75 h (which has a ratio of 17:28 for the principal lunar and solar cycles). Pettersson discovered that rising super-tides brought a flood of young herrings that flourished and brought considerable profits to the fishermen of the Hanseatic League. He was able to trace their fish trade back to the twentieth century, with this proxy, peaking always at ca. 93 years and longer intervals.

The year 1912 brought the highest predicted astronomical tide of the twentieth century. In Greenland, super-tides cause floating glacier-snout calving and so in 1912 an exceptional stream of icebergs came directly in the course of the ill-fated *Titanic* (Wood, 2001). Warming waters plus the buoyancy effect triggers major iceberg launching and NOT cooling cycles as sometimes assumed. Long-term lunar cycles may

also be involved in “Heinrich events” that mark the last 80,000 years or so in the North Atlantic. A “staircase” of 185 isostatically emerged beachridges on the Hudson Bay at about 45-year periodicity suggest storm cycles (warm phases create open-water, ice-free conditions) of synergetic luni-solar forcing (Fairbridge and Hillaire-Marcel, 1977), with peaks at 317 years. Comparable but less-complete sequences occur elsewhere in the Arctic and in northern Norway (Fletcher et al., 1993).

The lunar nodal (or nodical) cycle of 18.6 year marks variations of the Moon’s declination (Wood, 2001). This results in the Moon’s zenith position shifting over $28^{\circ}45'$ or 1,568 km N or S in a 9.3 year interval, returning at about the same season in the 317-year luni-solar period. As the zenith position shifts north or south it has the effect of amplifying or decreasing normal meridional tidal current velocities and their heat transport. The effect is most apparent in the great meridional currents like the Gulf Stream, which disclose a $>1^{\circ}\text{C}$ rise or fall in related long-term surface temperatures. The Russian oceanographer Maksimov (Lamb, 1977) found that it also affected the length of the sea-ice in the Barents Sea and Russian Arctic. It could therefore affect global albedo.

It seems probable that the Moon may also play a climatic role in the equatorial belt. Particularly significant is the bottleneck created by the East Indies with their narrow straits and shallow seas, partially blocking the return flow of the “Conveyor” system as well as the east to west tidal “wave” as it moves from the Pacific to the Indian Ocean. This archipelago occupies a unique place on the planet; the many volcanic cones concentrate the rising warm-humid air, feeding it in diurnal pulses to the stratosphere. The latter is subject to modulation by incoming solar radiation, the mean pulse being the QBO (“quasibiennial oscillation”) of solar emissions at 2.172 year, which is also a distinctive terrestrial climate cycle (Schove, 1983). Five QBO cycles ($5 \times \text{QBO} = 10.86$ year) is close to the sunspot period. A 13.03-year period ($6 \times \text{QBO}$) coincides very closely with the lunar perihelion return and thus with the Earth’s tides. Solar emissions are thus linked chronologically both to terrestrial climate and tidal system. According to Lamb (1977), the QBO (2.172 year) is the most universal climate cycle above the annual one. It is also the most omnipresent solar emission period.

As suspected by Pettersson (op.cit.), the Moon is so large and close to the Earth that it greatly modulates the Earth’s orbit, which in turn shows linkages to the periodicities of other planetary orbits (Fairbridge and Sanders, 1987) and to the Sun’s 19.8593-year motion around the systemic barycenter. This cycle is locked into the beat frequency of the two largest planets, Jupiter and Saturn. Multiples of all the planetary beats are whole integer fractions of the longer cycles and multiples of the Sun’s inner spin rate (n : 0.0678785 year). They are linked by a simple formula, $BF = n + 2n^2$, where BF is the particular beat frequency. The beat frequency of the U-J-V planets (Uranus-Jupiter-Venus) is interesting because it seems to correspond to clustering of El Niño periods, thus $69.5076 (0.0678785)^{-1} = 1,024$ [$\sqrt{1,024} = 32$]. This U-J-V period ($\times 590.00$) is almost an exact fraction of the Milankovitch 41,009.5 ecliptic cycle. It is also exactly one third of 208.52 years, the ^{14}C tree-ring flux (Stuiver and Brazunas, 1989). The inner planets (mean beat frequency 46.3388 years) can be included with Saturn-Jupiter (19.8593 years) thus: $278.03 (0.0678785)^{-1} = 4,096$ [$\sqrt{4,096} = 64$]. This value corresponds to 25×11.1212 years, the mean sunspot cycle.

Consequences

Volcanic and desert dusts

Major volcanic eruptions of the historical era, such as Tambora (1815) and Krakatoa (1883), have been associated with several years of global cooling (Lamb, 1977; see also: *Volcanic eruptions and climate change*).

The atmospheric effects of the Krakatoa eruption and its dust clouds were explored by the Sarasin brothers in 1901, and a general theory presented by Humphreys in 1913. The database was greatly strengthened by a worldwide catalog of more than 1,000 years of geological and historical records (Sigurdsson et al., 2000, p. 249–269). Bryson (1997) suggested that large temperature and precipitation fluctuations, especially in the mid-Holocene, reflected planetary-scale volcanic-dust triggering. From Indian environmental indicators (mainly lake pollen), he concluded that cooling trends were marked by strengthening of the circum-polar vortex and southward shift of the jet stream. This shift is particularly clear in the Mediterranean and northern India, which are then visited by plentiful winter rains. In contrast, when the warm phases shift the winter jet north of the Himalayas, there are (often catastrophic) droughts. In the monsoon belt, however, the summer rains are strengthened. A NATO-sponsored conference in Turkey (Dalfes et al., 1997) considered these questions, notably in connection with the classical collapse of the advanced civilizations there in the third millennium BC.

Lee-desert dusts were first documented by Charles Darwin on the voyage of H.M.S. *Beagle* in 1832 off the coast of West Africa. Distinctive traces of microfossils from Lake Chad have now been tracked westwards as far as the Caribbean, Florida and even New York City. Caribbean deep-sea cores (Emiliani, 1966) and Antarctic ice cores (Petit et al., 1999; EPICA, 2004) showed that, during the last seven glacial cycles, the dust-load rose as water temperatures fell.

During the last glacial stage of the Quaternary ice age, which reached its maximum about 18,000–25,000 years ago, the lower sea levels led to increased continentality, and colder ocean temperatures to decreased evaporation. There was widespread aridity that extended from present-day Mediterranean belts and in places reached to the equator (Fairbridge, 1964). In Africa, dune belts crossed the Congo, both from the Sahara and the Kalahari. Long-distance dust transport from these vast deserts was universal (Jelbring, 1998), as shown by deep-sea sediment cores worldwide, but even more dramatically in the ice cores of Greenland and Antarctica. Stronger meridional atmospheric circulation was calculated by Lamb and Woodroffe (1970) for glacial-stage paleogeography, with weakened westerly systems.

Loess and paleosols

Loess is a German agricultural term, with the same root as the English word “loose,” for a friable soil (see also *Loess deposits*). Loess is a climatically-specific wind-blown silt, actualistically seen today in the lower Yukon delta area, where strong winds affect a tree-less area of braided stream channels and dry alluvial tracts. Although extremely restricted in extent today, during the maximum and waning stages of the glacial stages, loess distribution was almost worldwide. Classical loess is a slightly calcareous, siliclastic silt that extends across western and eastern Europe into southern Russia, Mongolia and northern China. In the Southern Hemisphere, limited areas occur in Patagonia and New Zealand (South Island). It was

first positively attributed to eolian activity by Baron von Richthofen (1877–1885), but it has long remained controversial. During warm cycles, loess weathering produces a distinctive red paleosol.

The loess/paleosol cycles in Moravia (eastern part of Czech Republic) are exposed in a spectacular sequence tens of meters thick in a brick-clay quarry at Cerveny Vlchy (appropriately: the “red hills”) near Brno. George Kukla collected carefully oriented samples for paleomagnetic measurement, which provided the chronologic key (see *Dating, magnetostratigraphy*). The upper part of the sequence was “normal,” oriented to the current North magnetic pole; the lower part was “reversed,” thus oriented to the south. (The last paleomagnetic reversal occurred 780 kyr ago). Later, Kukla compared his terrestrial climatic sequence with the $\delta^{18}\text{O}$ paleotemperature oscillations in the deep-sea sediment cores at Lamont Doherty Earth Observatory, Columbia University. An identical number of climate cycles down to the Bruhnes-Matuyama boundary was found in both sequences (Kukla, 1972). This was one of the greater paleoclimatic discoveries of the century. It demonstrated conclusively that climate oscillations in the mid-ocean are synchronous with those in the mid-continent; furthermore, in the latter, the temperature oscillations can be quantified with proxy data. Using the Kukla-devised model, the vast loess deposits of northern China have been systematically surveyed, disclosing not only a perfect correlation with the deep-sea and central European sequence, but still earlier stages, including the early Pleistocene and even Pliocene (Gauss magnetic epoch).

Eolization and eolianite

The expression “eolization” (see also *Eolianite*) was invented by the French sedimentologist André Cailleux. Many sands and sandstones of the Paris Basin were eolian or primarily marine, but during negative eustatic oscillations and exposure to wind action during long periods of desiccation they became redistributed, thus, “eolization.” In warm coastal belts where comminuted molluscan shells, fragmented corals and carbonate foraminifera commonly constitute the predominant beach sands, even short phases of lowered sea level favor the build-up of carbonate shore dunes. Climatic oscillations during the Holocene repeatedly led to eustatic withdrawal by up to 1 m or so, which led to massive coast-parallel dunes, in places exceeding 20 m in height. Winds with sustained high wind velocities could create sporadic “blowouts” at gaps in the shore-parallel dune belt, thus feeding linear dunes that extend inland, up to 1 km or more. Such high velocities were favored from time to time in particular regions where the normal westerly airflow would be amplified by the sea-breeze effect characteristic of the margins of the subtropical anticyclones. Rainfall during the cool interval led to partial solution of the carbonate dune sand to consolidate it into a dune rock or *eolianite*. Ice-age winds were undoubtedly stronger than the prevailing winds in the same localities today (Jelbring, 1998).

The essential synergy between carbonate sand supply, sustained westerlies and subtropical sea breeze was provided during the Quaternary period at times corresponding to the frequent negative sea-level oscillations with amplified wind velocities (especially winter seasons in cold intervals of 1–3 centuries) but also where abundant supplies of carbonate sand were available, implying relatively warm ocean waters. Ideal sites for such highly specific paleoclimatic indicators were

oceanic islands and continental shores between 25 and 35° N and S, for example in the Bahamas, Bermuda, Morocco and North Africa to Egypt, Palestine, Israel and Lebanon, South Africa (Cape Province), Madagascar, India (Gujarat), western Australia, South Australia, Victoria, and Hawaii.

At the time of the Napoleonic wars, a certain British naval officer, Lt. Nelson (not the admiral), noticed the curious dune features converted to a hard rock (eolianite) in Bermuda, which provides an excellent, easily sawn building stone (Sayles, 1931). In SW Australia, in 1791, another British naval officer, Capt. George Vancouver, had also commented on them (Fairbridge and Teichert, 1948), as did Charles Darwin on the voyage of H.M.S. *Beagle*, who remarked on how the dune rock can be seen disappearing below modern sea level. Later, Charles Darwin also noticed eolianite on the islands of Ascension and St. Helena. He reasoned that because there were essentially no beaches on those islands today, the dune sands must have been blown up on the higher slopes during periods when sea level was lower, and winds were stronger. That reasoning was, of course, prior to the glacial theory and the mechanism of glacioeustasy (Fairbridge, 1961).

Eolization and eolianites are thus two of the most incontrovertible paleoclimate indicators. Eolization calls for extreme aridity and sustained high winds where there is a plentiful supply of sand, pebbles or rock fragments (as in some modern deserts, e.g., Sahara, Gobi, Atacama, Namibia and the “dry-valley” areas of Antarctica). Eolianites are even more specific, being restricted to “Mediterranean” latitudes 25–35° N and S, that is, to littoral belts where warm offshore waters favor a rich carbonate-shelly fauna.

Lake levels and fluvial indicators

Lakes and lake-levels constitute a persuasive basis for past-climate appraisal. They may act as a measurable rain-gauge but this must be interpreted with caution because of the evaporation-precipitation balance and other factors. A systematic treatment of lake level chronology has been presented by Street and Grove (1976, 1979), with Africa and Australia as the most coherent grouping (Rognon and Williams, 1977). North American “pluvial” conditions were essentially independent (Bradley, 1985; Nicholson and Flohn, 1980; see also *Lake level fluctuations*).

Input and overflow of lakes may be quite significant. The role of fluvial input may be quite simple in a small area but in the case of a major river like the Amazon, the Nile or the Mississippi, a complex analysis is essential.

Historically, the Nile is by far the best documented, starting with Herodotus about 450 BC., who as librarian in Alexandria was undoubtedly familiar with the delta and the pyramids. The upper course was poorly known but Eratosthenes had drawn a reasonable map of the Blue Nile, though the White Nile’s course was still uncertain. The principal annual flood (mid-summer) was recognized as coming from the Blue Nile, while the weaker, winter-season flood was from the White Nile. The former is fed by the monsoonal rains in Ethiopia, which decrease when the atmospheric pressure in Cairo is high and vice versa, according to measurements by Sir Henry Lyons published in 1905 (cited by Brooks, 1926/1949). Brooks observed that the same relationship exists throughout most of the Asian monsoon belt as far east as Hong Kong. The White Nile floods, however, appear to reflect the general equatorial circulation. The dynastic history and “prehistory” of the Nile

is unique among rivers in that it has provided investigators with a rather secure system of dates based on both archaeology (Wendorf and Schild, 1976) and radiocarbon-dated sedimentology and geomorphology (Fairbridge, 1962; Williams and Faure, 1980).

Precise measurements of the Nile floods were apparently made since the time of the Ptolemy pharaohs, for the good reason that Egypt's wealth depended on the agriculture maintained by the Nile flood, but they were only systematically recorded until the Islamic era. We now have complete records from AD. 641 to 1480 but they were only sporadic from then until 1830. Brooks (op.cit., p. 331) cites a general monograph on the subject by Prince Omar Tousoun, which describes pre-Islamic Nile floods simply as "weak," "good" or "strong" for various periods since the fifth century BC. Modern power spectrum analyses have disclosed the 11–22-year sunspot cycle and the 18.6-year lunar cycle in the accurately recorded data (Currie, 1995; El Fandy et al., 1994) but long-term changes are also apparent. The same periodicities were obtained from historical flood records from China (Currie and Fairbridge, 1985). Sporadic material provides dates for the floods of the Yangtzi and Hwang-Ho (Yellow River).

No long-term precise records of other major rivers are available, but many written accounts exist for the great European rivers (Rhine, Danube, etc.). Within the last century or so the hydrometrics of all major rivers have been measured but this interval has coincided with the worldwide explosion of dam construction for hydro-electric, flood-control, irrigation and urban uses; thus, the data have been strongly influenced by anthropogenic effects. For a general treatment, *The Encyclopedia of Hydrology and Water Resources* (Herschy and Fairbridge, 1998) may be helpful.

Rhodes W. Fairbridge

Bibliography

- Ahlmann, H.W., 1938. *Land of Ice and Fire*. London: Kegan Paul, 271p.
- Albritton, C.C. Jr., 1975. *Philosophy of Geohistory*. (Benchmark Papers in Geology, vol. 13). Stroudsburg: Dowden, Hutchinson & Ross, 386pp.
- Adhémar, J., 1842. "Les Révolutions de la mer. Déluges périodiques." Paris.
- Alvarez, W., 1986. Toward a theory of impact crises. *EOS*, **67**, 649, 658.
- Berger, A., 1995. Modelling the astronomical theory of paleoclimates. In Finkl, C.W. (ed.), *Cycles*, *J. Coast. Res.*, **17**, pp. 355–362 (special issue).
- Berger, A., Imbrie, J., Hays, J., Kukla, G., and Saltzman, B. (eds.), 1984. *Milankovitch and Climate: Understanding the Response to Astronomical Forcing*. Dordrecht: Reidel, 895pp.
- Berger, A., and Loutre, M.F., 1991. Insolation values for the climate of the last 10 million years. *Quaternary Sci. Rev.*, **10**, 297–317.
- Berger, A., and Loutre, M.F., 1992. Astronomical solutions for paleoclimate studies over the last 3 million years. *Earth Planet. Sci. Lett.*, **111**, 369–382.
- Berger, A., Loutre, M.F., and Laskar, J., 1992. Stability of the astronomical frequencies over the Earth's history for paleoclimatic studies. *Science*, **255**, 560–566.
- Bond, G., Kromer, B., Beer, J., Muscheler, R., Evans, M.N., Showers, W., Hoffmann, S., Lotti-Bond, R., Hadjas, I., and Bonani, G., 2001. Persistent solar influence on North Atlantic climate during the Holocene. *Science*, **294**, 2130–2136.
- Bourgeois, J. et al., 1985. A tsunami deposit at the Cretaceous-Tertiary boundary in Texas. *Science*, **241**, 567–570.
- Bradley, R.S., 1985. *Quaternary paleoclimatology: Methods of Paleoclimatic Reconstruction*. London: Allen and Unwin.
- Broecker, W.S., 1991. The great ocean conveyor. *Oceanography*, **4**, 79–89.
- Brooks, E.P., 1926/1949. *Climate Through the Ages* London: Ernest Bonn. 395pp.
- Bryson, R.R., 1997. Proxy indications of Holocene winter rains in southwest Asia compared with simulated rainfall. In Dalfes, H.N., Kukla, G., and Weiss, H. (eds.), *Third Millennium BC Climate Change and Old World Collapse*. NATO ASI Series, vol. 149, Berlin and Heidelberg: Springer, p. 465.
- Chamberlin, T.C., 1897. A group of hypotheses bearing on climate change. *J. Geol.*, **5**, 653–683.
- Croll, J., 1875/1885. *Climate and Time, in their Geological Relations; a theory of secular changes of the Earth's Climate*. (2nd ed.) London and New York: Appleton, 577pp.
- Crowell, J.C., 1999. Re-Mesozoic ice ages. *Geol. Soc. Am. Mem.*, **192**, 106pp.
- Currie, R.G., 1995. Variance contribution of M_n and S_c signals to Nile River data over a 30–8 year bandwidth. *J. Coast. Res.*, **17**, 29–38.
- Currie, R.G., and Fairbridge, R.W., 1985. Periodic 18.6-year and cyclic 11-year induced drought and flood in Northeastern China and some global implications. *Quaternary Sci. Rev.*, **4**, 109–134.
- Dalfes, H.N., Kukla, G., and Weiss, H. (eds.), 1997. *Third Millennium BC Climate Change and Old World Collapse*, NATO ASI Series., vol. 149, Berlin and Heidelberg: Springer
- Dietz, R.S., 1961. Continent and ocean basin evolution by spreading of the sea-floor. *Nature*, **190**, 854–857.
- Dietz, R.S., 1977. Plate tectonics: a revolution in geology and geophysics. *Tectonophysics*, **38**, 1–6.
- Dubois, E., 1893. *Die Klimate der geologischen Vergangenheit und ihre Beziehungen zur Entwicklungsgeschichte der Sonne*. Leipzig.
- Du Toit, A.L. 1937. *Our Wandering Continents*. Edinburgh: Oliver and Boyd, 366pp.
- Ekelund, N., and Arrhenius, S.A., 1898. Über den Einfluß des Mondes auf die Polarlichter und Gewitter. *Kongl. Svenska Vetenskaps Akademiens Handlingar*, **31**(2), 77–156.
- Eldredge, N., and Gould, S.J., 1972. Punctuated equilibria: An alternative to phyletic gradualism. In Schopf, T.J.M. (eds.), *Models of Paleogeology*. San Francisco: Freeman Cooper, pp. 82–115.
- El Fandy, M.G., et al., 1994. Time series models adaptable for forecasting Nile floods and Ethiopian rainfalls. *Bull. Am. Met. Soc.*, **75**(1), 83–94.
- Emiliani, C., 1966. Isotope paleotemperatures. *Science*, **154**, 851–857.
- Emiliani, C., 1992. *Planet Earth*. Cambridge, UK: University Press, 718pp.
- EPICA, 2004. Eight glacial cycles from an Antarctic ice core (Benchmark Papers in Geology, vol.13). *Nature*, **429**, 623–628.
- Erhart, H. (1956). *La Genèse des Sols—Esquisse d'une Théorie Géologique: Biostasie et Rhexistasie*, Paris: Masson. 90pp.
- Ewing, M., and Donn, W.L., 1956. A theory of ice ages. *Science*, **123**, 1061–1066.
- Ewing, M., and Donn, W.L., 1958. A theory of ice ages, II. The theory that certain local conditions caused Pleistocene glaciations discussed further. *Science*, **127**, 1159–1162.
- Fairbridge, R.W., 1961. Eustatic changes in sea level. In Ahrens, L.H. et al., (eds), *Physics and Chemistry of the Earth*. London: Pergamon Press, vol. 4, pp. 99–185.
- Fairbridge, R.W., 1962. New radiocarbon dates of Nile sediments. *Nature*, **196**, 108–110.
- Fairbridge, R.W. 1964. The importance of limestone and its Ca/Mg content to paleoclimatology. In Nairn, A.E.M. (ed.), *Problems in Paleoclimatology*. New York: Wiley, pp. 431–530.
- Fairbridge, R.W. (ed.), 1966. *The Encyclopedia of Oceanography*. New York: Reinhold, 1021pp.
- Fairbridge, R.W. (ed.), 1967. *The Encyclopedia of Atmospheric Sciences and Astrogeology*. New York: Reinhold, 1200pp.
- Fairbridge, R.W. (ed.), 1968. *The Encyclopedia of Geomorphology*. New York: Van Nostrand Reinhold, 1295pp.
- Fairbridge, R.W., 1971. Upper Ordovician glaciation in Northwest Africa? *Geol. Soc. Am. bull.*, **82**, 269–274.
- Fairbridge, R.W., 1973. Glaciation and plate migration. In Tarling, D.H., and Runcorn, K. (eds.), *Implications of Continental Drift to the Earth Sciences*. London: Academic Press, vol. 1, pp. 503–515.
- Fairbridge, R.W., (ed.), 1975. *The Encyclopedia of World Regional Geology, part 1: Western Hemisphere*. Stroudsburg, Dowden: Hutchinson & Ross, 704pp.
- Fairbridge, R.W., 1977. Rates of sea ice erosion of Quaternary littoral platforms. *Studia Geol. Polonica*, **52**, 135–141.
- Fairbridge, R.W., 1982. The fracturing of Gondwanaland. In Scrutton, R.A., and Talwani, M. (eds.), *The Ocean Floor*. Chichester, NY: Wiley, pp. 229–235.

- Fairbridge, R.W., 1990. Solar and lunar cycles embedded in the El Niño periodicities. *Cycles*, **41**, 66–72.
- Fairbridge, R.W., and Finkl, C.W., Jr., 1980. Cratonic erosional unconformities and peneplains. *J. Geol.*, **88**, 69–86.
- Fairbridge, R.W., and Hillaire-Marcel, C., 1977. An 8,000 year paleoclimatic record of the 45-yr “Double-Hale” solar cycle. *Nature*, **268**, 413–416.
- Fairbridge, R.W., and Sanders, J.E., 1987. The Sun’s orbit, A.D. 750–2050: Basis for new perspectives on planetary dynamics and Earth-Moon linkage. In Rampino, M.R., Sanders, J.E., Newman, W.S., and Königsson, L.K. (eds.), *Climate: History, Periodicity, and Predictability*. New York: van Nostrand Reinhold, pp. 446–471.
- Fairbridge, R.W., and Teichert, C., 1948. The Low Isles of the Great Barrier Reef: A new analysis. *Geogr. J.*, **111**, 67–88.
- Fletcher, C.H. III, et al., 1993. Emergence of the Varanger Peninsula, Arctic Norway, and climate changes since deglaciation. *The Holocene*, **3**(2), 116–127.
- Flint, R.F., 1971. *Glacial and Quaternary Geology*. New York: Wiley, 892pp.
- Flohn, H., and Fantechi, R. (eds.), 1984. The climate of Europe: Past, present, and future. Dordrecht, The Netherlands: Reidel Publishing Co.
- Frakes, L.A., 1979. *Climates Throughout Geologic Time*. Amsterdam: Elsevier, 379pp.
- Gohau, G., 1990. *A History of Geology*. New Brunswick, NJ: Rutgers University Press, 259pp.
- Grove, J.M., 1988. *The Little Ice Age*. London: Methuen, 498pp.
- Hassan, F.A., 1981. Historical Nile floods and their implications for climate change. *Science*, **212**, 1142–1144.
- Heer, O., 1865, transl. 1876. *The Primeval World of Switzerland*, 2 vol., London.
- Hersch, R.W. and Fairbridge, R.W., (eds.), 1998. *Encyclopedia of Hydrology and Water Resources*. Dordrecht: Kluwer Academic Publishers, 803pp.
- Hoyle, F., and Littleton, R.A., 1919. The effect of interstellar matter on climatic variation. *Proceedings of the Cambridge Philosophical Society*, **35**, 405–418.
- Huntington, E., and Visher, S.S., 1922. *Climatic Changes, Their Nature and Causes*. New Haven, CT: Yale University Press, 329pp.
- Imbrie, J., and Imbrie, K.P. (1979/1986). *Ice Ages: Solving the Mystery*. Cambridge, MA: Harvard University Press, 224pp.
- Isacks, B.L., Oliver, J., and Sykes, L.R., 1968. Seismology and the new global tectonics. *J. Geophys. Res.*, **73**, 5855–5899.
- Jelbring, H., 1998. *Wind controlled climate*. Ph.D. Thesis, Akademityrk AB, Sweden: Stockholm University, 111pp.
- Kennett, J.P., 1982. *Marine Geology*. Englewood Cliffs, NJ: Prentice-Hall.
- Kerner-Marilaun, F., 1930. “Paläoklimatologie.” Berlin: Gebr. Borntraeger.
- Kerr, R.A., 2006. A worrying trend of less ice, higher seas. *Science*, **311**, 1698–1701.
- Kukla, G.J., 1972. Insolation and glacials. *Boreas*, **1**, 63–96.
- Lamb, H.H., 1977. *Climate History and the Future*. London: Methuen (and Princeton University Press), 835pp.
- Lamb, H.H., and Woodroffe, A., 1970. Atmospheric circulation during the last Ice Age. *Quaternary Res.*, **1**, 29–58.
- Lewis, R.S., and Anders, E., 1985. Cretaceous extinctions: Evidence for wildfires and search for meteoritic material. *Science*, **230**, 167–170.
- Lyell, C. (1830–1833). *Principles of Geology*. London: John Murray, 3 vols. [facsimile reprint, New York: Johnson Reprint Corp., 1969, introduction by M.J.S. Rudwick].
- Maclaren, C., 1842. The glacial theory of Professor Agassiz of Neuchatel. *Am. J. Sci.*, **42**, 346–365.
- Maley, J., 1997. Middle to late Holocene changes in tropical Africa and other continents: Paleomonsoon and sea surface temperature variations. In Dalfes, H.N., Kukla, G., and Weiss, H. (eds.), *Third Millennium BC Climate Change and Old World Collapses*. Berlin: Springer-Verlag, pp. 611–640.
- Marvin, U.B., 1973. *Continental Drift, the Evolution of a Concept*. Washington, D.C.: Smithsonian Institution press, 205pp.
- McGovern, T.H., 2000. The Demise of Norse Greenland. In Fitzhugh, W.W., and Ward, E.I. (eds.), *Vikings: The North Atlantic Saga*. Washington and London: Smithsonian Institution Press and National Museum of Natural History, pp. 327–393.
- Milankovitch, M., 1941. Kanon der erdbestrahlung und seine Anwendung auf das Eiszeitenproblem. *Roy. Serb. Acad.*, Special Publication 133, 633pp. (Engl. transl. 1969 as “Canon of Insolation and the Ice-Age Problem”, by Israel Progr. Sci. Transl., U.S. Dept. Commerce, Washington, 484pp.)
- Moberg, A., 1995. Multi-taper spectral analysis of the Stockholm air temperature record: A significant 22.8yr cyclic pulse observed. *J. Coast. Res.*, **17**, 39–44
- Mörner, N.A., 1984. Low sea levels, droughts, and mammalian extinctions. In Berggren, W.A., and Van Couvering, J.A. (eds.), *Catastrophes and Earth History*. Princeton, NJ: Princeton University Press, pp. 387–394.
- Nansen, F., 1922. The strandflat and isostasy. *Vitenskapsselskapets skrifter, I matematisk-Naturevitenskapelig Klasse 1921*, No. 11, Kristiana I, Kommission hos Jacob Dybwad.
- Nicholson, S., and Flohn, H., 1980. African environmental and climatic changes and the general circulation in late Pleistocene and Holocene. *Climatic change*, **27**, 20–34.
- Noelke, F., 1908. “Das Problem der Entwicklungsgeschichte unseres Planetensystems.” Berlin.
- Officer, C., and Page, J., 1996. *The Great Dinosaur Extinction Controversy*. Reading, MA: Addison & Wesley, 209pp.
- Oliver, J.E., and Fairbridge, R.W., 1987. *The Encyclopedia of Climatology*. New York: Van Nostrand Reinhold, 986pp.
- Petit, J.R. et al., 1999. Climate and atmospheric history of the past 420,000 years from the Vostok ice core, Antarctica. *Nature*, **399**, 429–436.
- Peixoto, J.P., and Oort, A.H. (1992). *Physics of Climate*. New York: American Institute of Physics, 512pp.
- Pettersson, O., 1912. The connection between hydrographical and meteorological phenomena. *Quarterly J. Roy. Meteor. Soc.*, **38**, 173–191.
- Pettersson, O., 1930. The tidal force. *Geogr. Annaler*, **12**, 261–322.
- Pitman, W.C., 1978. Relationship between eustasy and stratigraphic sequences of passive margins. *Geol. Soc. Am. Bull.* **89**, 1389–1403.
- Pitman, W.C. III, and Heirtzler, J.R., 1966. Magnetic anomalies over the Pacific-Antarctic Ridge. *Science*, **154**, 1164–71.
- Poag, C.W., 1997. The Chesapeake Bay bolide impact: A convulsive event in Atlantic Coastal Plain Evolution. *Sediment. Geol.*, **108**, 45–90.
- Rampino, M.R. 1998. The galactic theory of mass extinctions: An update. *Celestial Mech. Dyn. Astron.* **69**, 49–58.
- Rampino, M.R., and Haggerty, B.M., 1996. “The ‘Shiva Hypothesis’: Impacts, Mass Extinctions and the Galaxy.” *Earth, Moon, and Planets*, **72**, 441–460.
- Raymo, M.E., 1994. The initiation of Northern Hemisphere glaciation. *Annu. Rev. Earth Planet. Sci.*, **22**, 353–383.
- Raymo, M.E., and Ruddiman, W.F., 1992. Tectonic forcing of late Cenozoic climate. *Nature*, **359**, 117–122.
- Rind, D., 2002. The sun’s role in climate variations. *Science*, **296**, 673–677.
- Rognon, P., and Williams, M.A.J., 1977. Late Quaternary climatic changes in Australia and North Africa: a preliminary interpretation. *Palaeo-geogr. Palaeo-climatol. Palaeo-ecol.*, **21**, 285–327.
- Ruddiman, W.F., 2005. *Plows, Plagues and Petroleum: How Humans Took Control of Climate*. Princeton, NJ: Princeton University Press, 272pp.
- Ryan, W.B.F., and Pitman, W.C., 1999. *Noah’s Flood: The New Scientific Discoveries About the Event That Changed History*. New York, NY: Simon & Schuster, 320pp.
- Sayles, R.W., 1931. Bermuda during the Ice Age. *Proceedings of the American Academy of Arts & Sciences*, **66**, 382–467.
- Schöve, D.J., 1983. *Sunspot Cycles* (Benchmark Papers in Geology, vol. 68). Stroudsburg: Hutchinson Ross Publ. Co., 392pp.
- Schramm, M., 1963. Aristotelianism: Basis and Obstacle to Scientific Progress in the Middle Ages. *History of Science*, **2**, 91–113.
- Schwarzbach, M., 1974. *Das Klimate der Vorzeit*, 3rd ed. Stuttgart: F. Enke Verlag, (English edition, 1963). New York: Van Nostrand.
- Shindell, D.T., Schmidt, G.A., Mann, M.E., Rind, D., and Waple, A., 2001. Solar forcing of regional climate change during the Maunder Minimum. *Science* **294**, 2149–2152.
- Shirley, J.H., and Fairbridge, R.W. (eds.), 1997. *Encyclopedia of Planetary Sciences*, London: Chapman & Hall, 990pp.
- Siscoe, G.L., 1980. Evidence in the auroral record for secular solar variability. *Rev. Geophys. Space Phys.*, **18**, 647–658.
- Sigurdsson, H., Houghton, B.F., McNutt, S.R., Rymer, H., and Stix, J. (eds.), 2000. *Encyclopedia of Volcanoes*. San Diego, CA: Academic Press, 1417pp.
- Stommel, H., 1958. *The Gulf Stream*. Berkeley, CA: University of California Press, 202pp.

- Street, F.A., and Grove, A.T., 1976. Environmental and climatic implications of late Quaternary lake-level fluctuations in Africa. *Nature*, **281**, 380–385.
- Street, F.A., and Grove, A.T., 1979. Global maps of lake-level fluctuations since 30,000 years BP. *Quaternary Res.*, **12**, 83–118.
- Stuiver, M., and Braziunas, T.F., 1989. Atmospheric ¹⁴C and century-scale solar oscillations. *Nature*, **388**, 405–408.
- Suess, E., 1885–1909. *Das Antlitz der Erde*, Vienna: F. Tempsky. (Engl. Transl. “The Face of the Earth”. Oxford: Clarendon Press, 1904–1924). 5 vols.
- Valentine, J.W., and Moores, E.M., 1970. Plate-tectonic regulation of faunal diversity and sea level: A model. *Nature*, **228**, 659–669. (reprinted in Shea, 1985, 281–283).
- Visher, G.S., 1986. A history of geological thought. *Earth Sciences History*, **5/2**, 137–143.
- Von Richthofen, F., (1877–1885). *China: Ergebnisse eigener Reisen und darauf gegründeter Studien*. Berlin, 4 vols.
- Wegener, A., 1929. *Die Entstehung der Continente und Ozeane*. F. Vieweg & Son, Braunschweig, 4th ed. (trans. by J. Binram as “The Origin of Continents and Oceans”, 1966). New York: Dover Publications, 346pp.
- Wendorf, F., and Schild, R., 1976. *Prehistory of the Nile Valley*. New York: Academic Press, 404pp.
- Williams, M.A.J., and Faure, H. (ed.), 1980. *The Sahara and the Nile*. Rotterdam: A.A. Balkema, 607pp.
- Wood, F.J., 2001. *Tidal dynamics*, 3rd ed. West Palm Beach: Coastal Education and Research Foundation, 2 vols.
- Zenkovitch, A., 1966. Fairbridge, R.W., (ed.), *The Encyclopedia of Oceanography*. New York: Reinhold, p. 146.
- Zeuner, F.E., 1945/1959. *The Pleistocene Period* (2nd ed. 1959, Hutchinson & Co., 447pp). London: Royal Society.

Cross-references

Arctic Sea Ice
 Astronomical Theory of Climate Change
 Atmospheric Evolution, Earth
 Climate Change, Causes
 Cretaceous/Tertiary (K-T) Boundary Impact, Climate Effects
 Dating, Magnetostratigraphy
 Eolian Sediments and Processes
 Eolianite
 Glacial Eustasy
 Glacial Geomorphology
 Glacial Isostasy
 Glaciations, Pre-Quaternary
 Glaciations, Quaternary
 History of Paleoclimatology – Biographies
 Lake Level Fluctuations
 Little Ice Age
 Loess Deposits
 Maunder Minimum
 Medieval Warm Period
 Monsoons, Quaternary
 Mountain Uplift and Climate Change
 Paleoclimate Proxies, an Introduction
 Plate Tectonics and Climate Change
 Pre-Quaternary Milankovitch Cycles and Climate Variability
 Snowball Earth Hypothesis
 Sun-Climate Connections
 Thermohaline Circulation
 Volcanic Eruptions and Climate Change

HISTORY OF PALEOCLIMATOLOGY – BIOGRAPHIES

Abbot, Charles Greeley (1872–1973)

Abbot was an American astrophysicist who was active for many years in studies relating solar emissions to terrestrial climates. Born in Wilton, N. H., he was long involved with the Smithsonian Institution in Washington, D.C., first as director of the astrophysical

observatory (1907), and later as secretary of the institution (1928–1944). Abbot completed the infrared spectrum and organized studies of the so-called “solar constant.” Following one cycle of the 11 year sunspot period after another, he demonstrated remarkable solar variability together with difficult-to-explain climatic fluctuations. He obtained patents for his instruments for measuring solar activity and energy.

Adhémar, Joseph (1797–1862)

The French mathematician, J. Adhémar, is believed to have been the first to recognize the fundamental role of the *Precession of the Equinoxes* in ice ages and paleoclimatology, in a book published in 1842. Only 5 years after the announcement of the former ice age by Agassiz, Adhémar came up with his new concept: precession must have a climatic effect. He argued that because of the inclination of the Earth’s spin axis, there would be a reverse of the seasons receiving maximum solar radiation every hemicycle of the precession. At the present time, the Southern Hemisphere receives maximum radiation in the southern summer. Due to the eccentricity of the Earth’s orbit around the Sun, winters in the Southern Hemisphere are longer than those in the Northern Hemisphere. The precession is about 26,000 years but inasmuch as the eccentricity major axis is likewise moving counter-clockwise, the effective period is about 21,000 years. An important forcing paleoclimatic mechanism was thus provided, although additional orbital forcings were needed to generate the glacial/interglacial oscillations of ice ages (see Croll, 1875; Milankovitch, 1941).

Agassiz, Louis Jean Rodolphe (1807–1873)

Agassiz was a Swiss paleontologist and Quaternary glaciologist who was the first prominent geologist to adopt the “Glacial Theory,” pioneered in 1824 by Jens Esmark in Denmark, and by I. Venetz and Jean de Charpentier in Switzerland (1830s). The theory evolved in steps from being an explanation for the transport of erratic blocks down-valley from Alpine-type glaciers, to the concept of a formerly much greater ice-cap, and eventually to the recognition of ice sheets of near-continental dimensions in northern Europe and North America (Carozzi, 1966). His most famous work was *Études sur les Glaciers* (1840). He even suggested that the interior of Greenland was covered by ice, a very daring hypothesis in the mid-nineteenth century. Eventually, Fridtjof Nansen, the Norwegian explorer-scientist-humanitarian, crossed (and proved the existence of) the Greenland ice cap in 1888. Agassiz was so carried away by the ice sheet idea that in 1837 he proposed a giant glacial cover for most of the Northern Hemisphere.

In 1846, Agassiz emigrated to the United States and became professor of zoology and geology at Harvard University (1847). He traveled extensively in the southern states, Canada and Brazil. At an early stage in his career, he spent a year in Paris, studying under Cuvier. Therefore, it is not surprising that he adopted the Cuvier model of organic evolution: repeated extinctions and re-creations, being strongly opposed to the Darwinian model (Carozzi, 1973; Lurie, 1966).

Arrhenius, Svante August (1859–1927)

A Nobel prize-winner in chemistry (1903), Arrhenius is important in the field of paleoclimatology for his research into CO₂, which led to modern work on the greenhouse/icehouse concepts (1959), supporting the theory of J. Tyndall (1863) that enhanced infrared reflection from the Earth’s surface warms

the lower atmosphere in proportion to the CO₂ and H₂O vapor trapped there (1896).

Arrhenius, who served as Rector of the University of Stockholm (1887–1902) and later as the Director of the Nobel Institute for Physical Chemistry, was also interested in cosmology and was aware of the role of magnetized solar emissions in the fluctuations of the Earth's geomagnetic field (pioneer observations were being made in Norway at that time). Jointly with the meteorologist, Nils Ekholm, he analyzed the periodicities of aurora observations (which were often recorded by country pastors, and traced back for up to 800 years) and their geomagnetic correlations, discovering both the 22 year solar cycle and the 18.6 year lunar cycle.

Blanford, William Thomas (1832–1905)

Blanford's major contribution to paleoclimatology was that he discovered, mapped and announced the presence of Permian-Carboniferous glacial striations and deposits in the Deccan of India. This was the first discovery of "exotic" paleoclimatic evidence from the subtropics and was destined to become the nucleus of the Suess concept of Gondwanaland, the continental drift theory of Wegener, and finally the plate tectonics theory of the late twentieth century.

Blanford graduated from the Royal School of Mines in London and served on the Geological Survey of India (1855–1882), being the author of a major work on the Gondwana (Permian-Mesozoic) formations. He also made surveys in Burma, Sikkim and Iran. Vertebrate paleontology being among his many interests, he became vice president of the Zoological Society, F.R.S. and Fellow of the Geological Society (Anon, 1905; Bonney, 1907; Holland, 1905).

Bond, Gerard Clark (1940–2005)

Bond was one of the first researchers who identified that the "Heinrich events" documented in sediment cores in the northwest Atlantic Ocean indicated abrupt climatic fluctuations, using the deep-sea cores of the Lamont-Doherty Earth Observatory of Columbia University. Those sediment cores are marked by whitish layers that reflect limestone debris carried by glaciers melting in eastern Canada and swept out to sea by icebergs. For this work, he received the Maurice Ewing Medal from the American Geophysical Society in 2003. Later, he recognized that climate changes over the last 10,000 years were driven by variations in solar radiation, which fluctuates inversely with cosmic rays and whose flux is clearly recorded in the ¹⁴C measurements obtained from tree rings and thus chronologically fixed in time.

Chamberlin, Thomas Chrowder (1843–1928)

One of America's greatest earth scientists, educators and Quaternary glaciation specialists, Chamberlin initially taught at Beloit College, Wisconsin (1872–1882), serving also as director of the state geological survey and later with the U.S. Geological Survey. President of the University of Wisconsin (1887–1892), he moved on to the University of Chicago (1892–1919) when he founded the prestigious *Journal of Geology* (Willis, 1929).

In paleoclimatology, his leading role was in helping to identify and name the primary four-fold division of Laurentian glaciations and their interglacial paleosols (Alden, 1929). An expedition to Greenland in 1894 gave Chamberlin the idea of an ice-sheet anticyclone, which had only limited validity. With his astronomical colleague, F. R. Moulton, he developed the "Planetesimal Hypothesis" for the evolution of the Solar System.

Chambers, Robert (1802–1871)

Chambers was a self-taught Scottish geologist who developed early ideas about isostasy and made a comprehensive study of sea level and its climatic message, writing the first book on the subject (1844), which contains a general review that spans the British Isles, Scandinavia and North America. Field work in Scotland and Norway prompted several papers on the glacial striations and deposits (in 1851) that provided "an important service" towards the acceptance of Agassiz's glacial theory (Geikie, 1905) (Milhauser, 1959).

Charpentier, Jean de (1786–1855)

Born in Germany, Charpentier spent most of his life in Silesia, but worked professionally in Switzerland, France and Spain, becoming the first to postulate that the entire Alpine chain was once covered by a thick ice cap, from which radiated many ice streams as valley glaciers. He wrote earlier on the geology and tectonics of the Pyrenees, but from the paleoclimatic point of view his major work was *Sur les glaciers et sur les terrains erratiques du bassin du Rhône* (1841), which described the field work and outlined his general theory.

Charpentier contested the early catastrophist view of Agassiz, which visualized a giant Northern Hemisphere ice sheet, and argued persuasively for the more modern mountain chain ice cap. He also wrote on non-marine mollusca (Lugeon, 1920; Teller, 1983).

Croll, James (1821–1890)

Croll was a Scottish geologist who served with the H. M. Geological Survey (1867–1881) and made a fundamental contribution to the orbital theory of paleoclimatology and ice ages (Imbrie and Imbrie, 1979) that incorporated the Earth's axial precession (but not the other orbital elements; those had to await the twentieth century work of Milankovitch, 1941). He published several full-length books on the nature of ancient climates and ice ages. Furthermore, he examined the oceanic circulation of the past and the physics of glacier flow (Irons, 1897). In climate studies, he established a "retardation" principle, whereby the melting of the glacial ice would be retarded with respect to climatic warming by the latent heat of the melting. (Eustatic "retardation" or lag was later shown diagrammatically in Fairbridge, 1961, and subsequently by stable isotope and trace gas analysis of polar ice cores – see Shackleton (2000)).

Daly, Reginald Aldworth (1871–1957)

A remarkably versatile Canadian geologist and geomorphologist, Daly originally worked with the Canadian Geological Survey (1901–1907) (Birch, 1960). He then moved to M.I.T. (until 1912) and finally transferred to Harvard (until 1942). As a petrologist, he went to American Samoa in the South Pacific but, observing emerged coral reefs and shore platforms there, he focused on the question of ice ages and eustasy. He proposed a "Glacial Control Theory" for coral reef growth. His book on the ice ages is certainly the best in the early to mid-twentieth century; it was still in reprint three decades later. His "marginal bulge hypothesis," which postulated a positive peripheral crustal response to the ice loading in the interior, has stimulated innumerable calculations concerning the strength of the Earth's crust and rates of adjustment, and in relation to hydroisostasy. It also introduced the idea of a "zero isobase" that shifts progressively inland during the glacial retreat (Fairbridge, 1968, p. 885).

DeGeer (Baron) Gerhard Jacob (1858–1943)

The leader in Swedish Quaternary science, deGeer formed his first ideas about deglaciation on several expeditions to Spitzbergen between 1882 and 1910. He also elaborated on the theory of eskers that cross Sweden from north to south, and demonstrated how end moraines were built up during pauses in the glacial retreat. This was the first clear demonstration of cyclical dynamics in the paleoclimatic record.

DeGeer served as professor of geology at the University of Stockholm (1897–1924). His major contribution was a year-by-year chronology of the entire Holocene epoch based on the painstaking counting of annual varves measured in an overlapping sequence from one postglacial lake to another, as exposed in brick-clay pits from the south of Sweden to the north. The lake chronologies permitted the exact dating of the pauses in the glacial retreat, i.e., the cold climatic fluctuations in the otherwise warming secular trend. DeGeer's work was extended to North America and South America by his students Antevs (1944) and Caldenius (1948), respectively. His chronology was widely welcomed by archaeologists, but was less enthusiastically received by geologists, because of questions about interpretation and continuity. His surveys were repeated by the Swedish Geological Survey in 1970–1980, and found to be substantially correct. Radiocarbon dating (after isotopic corrections) confirmed the chronology.

Douglass, Andrew Ellicott (1867–1962)

Born in Vermont and educated at Trinity College, Hartford, Connecticut, Douglass was hired by Percival Lowell to select the best locality for a major telescope, choosing Flagstaff, with the objective of mapping the alleged Martian canals suspected by Lowell to reflect the activity of intelligent life on that planet. Inevitably, they disagreed, but Douglass remained in Arizona and became interested in tree rings, which he used to identify past solar cycles and predict future solar cycles. Appointed to the University of Arizona in Tucson in 1906, he initiated the science of dendrochronology, creating an unbroken record in Ponderosa pine tree rings extending back many thousand years. With this, he could date (to the year) the archeological record of early human activity in the American Southwest.

Douglass' main achievement was the technique of "cross-dating" whereby matching portions of tree ring patterns from different ruins could be overlapped, thus extending the chronological record. By overlapping tree ring records from many different sites in the region, a complete dendrochronology could be constructed. Douglass also realized that differing patterns of narrow versus wide growth rings reflected variations in climatic factors, thus laying the foundation of dendroclimatology (Webb, 1983). The Laboratory of Tree-Ring Research, which he instituted, is now a division of the College of Arts and Sciences at the University of Arizona.

Dubois, Eugène (1858–1940)

Sometimes confused with French and Swiss scientists with the same name, Eugène Dubois was in fact a Dutchman, who was working in the East Indies when (in 1891–1892) he discovered the "Java (Trinil or Solo) Man," an early primate that was identified as *Homo erectus* (More specimens were found in 1938 by Von Koenigswald).

Dubois has the distinction of writing the first book-length work on paleoclimatology. He recognized that the Sun as a heat-generating star would be expected to evolve through time,

and thus would influence terrestrial climates. However, he intuitively assumed it was cooling, whereas modern astronomy suggests it to be experiencing a slowing in warming. A critical question concerns Precambrian temperatures: were they warmer or colder than today? Current opinions favor the latter (Schwarzbach, 1974, p. 295).

Dunn, Edward John (1844–1937)

A stratigrapher and economic geologist, Dunn was preparing the first geological map of the Cape Colony in South Africa (publ. 1873), when he recognized a tillite, later named the "Dwyka Conglomerate," the first formally named Permo-Carboniferous glacial formation in South Africa (Molengraaff, 1898). Although some unquestionable tillites, varves, and erratics (up to 2 m across) had been found earlier in Natal (Zululand) by P. C. Sutherland (in 1868), they were not dated until Dunn's work suggested their contemporaneity.

Dunn was born in England, migrated to Australia, worked in South Africa and then returned to Australia to become director of the Geological Survey of Victoria (1904–1912). He published very little, except for government reports and a semi-popular book entitled *Pebbles* (1911) (DuToit, 1938).

Emiliani, Cesare (1922–1995)

Born in Bologna, Italy, Emiliani went to the United States in 1948 and obtained his Ph.D. from the University of Chicago in 1950. Moving to the University of Miami in 1957, he became one of the founders of the new science of paleoceanography. He was an early pioneer in the use of oxygen isotopes in marine fossils as a paleoclimate proxy, attributing variations in $^{18}\text{O}/^{16}\text{O}$ ratios to both changes in ocean temperature (60%) and glacial ice volume (40%). Based on sawtoothed patterns in oxygen isotope records from long ocean cores, he recognized many more than the traditionally-accepted four major Pleistocene glaciations. His dating of an ocean core spanning multiple climate cycles in calcareous ooze fundamentally contributed to the ultimate acceptance of the Milankovitch theory of climate change, as forced by changes in planetary orbits.

Emiliani was a natural born educator and produced many volumes on the earth sciences. In his last years, he was intrigued by the anomalous lack of a zero year in the classical calendar and explored the possibilities of selecting a new astronomically chosen zero year close to 10,000 yBP, such as would eliminate the AD/BC division of recent millennia (Hay and Zakevich, 1999).

Esmark, Jens (1762–1829)

The name Esmark (also spelled Esmarch) must always be associated with the Glacial Theory, although his paper of 1826 did not receive the recognition that came to Agassiz a decade or more later (Charlesworth, 1957).

Esmark was born and raised in Denmark, trained as a geologist and traveled widely. He became professor of mineralogy in Oslo. Esmark recognized that steep fjord-valley walls (U-shaped) were drowned relics of former glacial erosion. He had also seen the so-called "Findlinge" (foundlings) or glacial erratics all across northern Europe, and traced their lithological identities with specific source areas in Scandinavia. For example, the very distinctive Rapakivi granite came uniquely from only one area in Finland. A particular fossiliferous Ordovician limestone came only from the island of Gotland in the Baltic. Norwegian granites reached England and Scotland. Only a

continental-sized ice sheet could have been the mode of transport. Esmark believed the ice sheet responsible was at least 1,000 m thick.

Ewing, William Maurice (1906–1974)

Ewing was one of the founders of marine geophysics and first director of the Lamont Geological Observatory (now Lamont-Doherty Earth Observatory), Columbia University. Ewing's major contribution to the earth sciences was his leadership in worldwide oceanographic expeditions to map the sea floor, and his involvement with students and international associates that paved the way to the chronology of sea-floor spreading and the seismic location of tectonic plate boundaries (Wertembaker, 1974). Through his participation in the Deep-Sea Drilling Project (DSDP), the stratigraphic history of the last 150 million years was enriched with an absolute chronology including isotopically identified climatic fluctuations that were further characterized geomagnetically. The Ewing-Donn theory of ice ages was flawed, being based on a model of ice-sheet growth that depended mainly upon warming oceans (which increased the evaporation rate and hence Arctic snowfall (Bullard, 1975)).

Fairbridge, Rhodes W. (1914–2006)

Rhodes Fairbridge was ahead of his time in his early acceptance of Wegener's theory of continental drift, the role of orbital cycles in climate change (e.g., the Milankovitch theory), solar influence on climate, and recognition of general aridity during glacial periods. He was among the first to detect the twentieth century rise in global sea level in the 1960s. Fairbridge was active in many international scientific organizations, including INQUA and NATO-sponsored paleoclimate symposia. His numerous publications cover a broad range of subjects in paleoclimatology, Holocene sea level change and geomorphology, among others (Finkl, 1987; 2005).

Fairbridge was born in 1914 in Fairbridge Village, Western Australia, which established by his parents for disadvantaged and troubled youths. He studied at Queen's University (Kingston, Ontario) and Oxford University (England), and later received his Ph.D. from the University of Western Australia in 1944. During World War II, Fairbridge served in the Royal Australian Air Force in intelligence, and after the war he taught at the University of Western Australia between 1946 and 1953. In the early 1950s, his discovery of Permian tillites and Mesozoic plant fossils near the Irwin River, Western Australia that were Gondwanan age provided important evidence for Wegener's theory. In 1951, on the *Capricorn* expedition to the South Pacific with Roger Revelle, he investigated biogeochemical erosion of calcareous eolianites and coral reefs (Revelle and Fairbridge, 1957). Subsequent observations of emergent islands and shorelines in the Pacific and Indian Oceans pointed to the role of hydro-isostatic uplift. Correlation of data from many of the world's shorelines convinced Fairbridge that global sea level had fluctuated during the Holocene, in contrast to Francis Shepard's smooth sea level curve. (For a current view, see *Sea level change, post-glacial*).

Following a one-year teaching appointment (1953–1954) at the University of Illinois (Urbana), Fairbridge went to Columbia University in 1954, where he remained until his retirement in 1982. A keen interest in cyclical terrestrial phenomena is one of the recurrent themes in Fairbridge's long career. A 1961 symposium that he organized explored the effects of solar variability and other cyclic phenomena on

climate. Later, Fairbridge and Claude Hillaire-Marcel found a 45-year periodicity in raised beachridges at Hudson Bay, which they attributed to climate-related changes in sea level. With John Sanders, he investigated the role of planetary alignments on solar activity and Earth's climate. While the proposed linkages remain controversial, studies by G. Bond and others, for example, point to some solar influence (see *Sun-climate connections*). Furthermore, variations in the Earth's orbital parameters leading to changes in insolation are now accepted as an underlying cause of the Pleistocene ice ages (see *Astronomical theory of climate change*). After retirement, he continued working as Series Editor for the Earth Science Series Encyclopedias (of which this volume is one) at the nearby Goddard Institute for Space Studies until shortly before his death.

Flint, Richard Foster (1902–1976)

A long-time professor of geology at Yale University (New Haven, Connecticut), "Rocky" Flint played a leading role in the twentieth century development of a Quaternary stratigraphy in North America that was based upon meticulous field work, calling for close attention to the paleoclimatic forcing of the sequences of glacial deposits (tills of various sorts, "lodgment," etc.). Interglacial weathering profiles were recognized as warm climate products (Porter, 1978).

Through his key textbooks, Flint made an important contribution to the education of American geologists of the mid-twentieth century, for most of whom serious geological time ceased at the end of the Pliocene, although an "overburden" of Pleistocene was sometimes noted. Flint's first full-length textbook was *Glacial and Pleistocene Geology* (1957). The concept of the Holocene as a distinct geologic epoch was slow to penetrate and although first proposed at the International Geological Congress in 1885, it was long called "Recent."

Forbes, James David (1809–1868)

Best known for his work on the physics of glacier flow, Forbes was a professor at the University of Edinburgh (1833–1855) with many interests. He devised the first seismograph. In experiments on the physics of heat, he described the polarization of radiant infrared heat. He pioneered the field of geothermal heat flow with field measurements in mines at various depths and studied volcanology in the Auvergne. He traveled (and climbed) extensively in the Alps and Norway, examining the effects of glaciation on the geomorphology of the area and he applied these findings to the geomorphology of Scotland (Cunningham, 1990; Anon, 1869; 1871).

Forbes helped pioneer the mathematical modeling of paleoclimates, recognizing that they (a) are latitude dependent, and (b) vary according to local distribution of land and sea (Forbes, 1861). He saw that continentality lowers mean temperatures towards the poles, but raises them towards the equator (Brooks, 1949, p. 133).

Galileo Galilei (1564–1642)

The first use of the telescope in observing sunspots places Galileo in a special position concerning paleoclimatology and the dynamic universe, because this initiated studies of solar activity and established the concept that the Sun was subject to some "imperfections." This particular observation brought him into some disfavor with the theological Establishment. Galileo's epoch-making discoveries in celestial mechanics are

generally regarded among historians of science as marking the beginnings of the “Age of Enlightenment.” His adoption of the Copernican view of the Solar System brought him into trouble with the authorities, but also heralded the intellectual revolution of the age (Berry, 1898; Drake, 1972; Winkler and Van Helden, 1992).

Gauss, Carl Friedrich (1777–1855)

Born in Brunswick, Germany, in humble circumstances, Gauss was to become a celebrated astronomer and geophysicist and was director of the Göttingen Observatory for 47 years. He independently worked out the interplanetary ratios of the Titius-Bode Law. Largely concerned with geodesy, he became interested in sea level and its fluctuations, which played an important role in the history of the North German coast because of catastrophic dike-breaks and flooding during the amplified lunar forcing of the Little Ice Age (cf. Pettersson, O.). He met Alexander von Humboldt who interested him in geomagnetism, and by 1834 no less than 23 magnetic observing stations were set up. Jointly with Weber, their *Atlas des Erdmagnetismus* was published in 1840. The link between magnetic fluctuations and the solar cycle was to be discovered somewhat later by Sabine. One of the paleomagnetic epochs is named after him (Dunnington, 1955; May 1972).

Gilbert, William (1540–1603)

Thanks to his seminal work *De Magnete*, Gilbert established the basic attributes of geomagnetism, a study that has led to paleomagnetism, and in turn to the chronology of rock magnetism. Magnetostratigraphy has become a useful dating tool in paleoclimatology.

During the reign of Queen Elizabeth I, Gilbert was undoubtedly England’s most distinguished man of science. Widely traveled, he was a friend of Kepler and Galileo. Studying the regional nature of magnetism, Gilbert came to view the Earth as a giant bar magnet, a “lodestone” (a concept pioneered by Peregrinus in 1269). Increasing ship-use of the magnetic compass disclosed regional anomalies. Furthermore, but without using the word “gravity,” he anticipated Newton in postulating “*a mutual bodily affection between allied bodies, tending towards that union or junction.*”

Grabau Amadeus William (1870–1946)

Grabau was a professor of geology at Columbia University, but went to China in 1920 to become professor at the National University in Peking, chief paleontologist at the Geological Survey, and founder of the Geological Society of China (Sun, 1947).

His early work on the paleontology and stratigraphy of the American midwest and Appalachian belt convinced Grabau of the rhythmic nature of the geologic record, and he presented his “Pulsation Theory” at the International Geological Congress in Washington in 1933 (Grabau, 1936a, b). This was the most systematic approach at that time to the idea of long-term (>20 Myr) global cycles in paleoclimatology and paleogeography.

Grabau’s ideas of a general ordering of geologic processes are probably his lasting contribution. One concept of particular interest to paleoclimatology is quasi-actualist, that is to say based on historical records in part: the process of “marining” as displayed over the Yellow River (Huang-Ho) delta in northern China. This involves the simultaneous result of overwhelming discharge by a major river and an upward swing of mean sea level (eustatic), resulting in the general inundation of a delta and coastal plain on the order of >100,000 km².

These represent major paleoclimatic events that have occurred repeatedly in China (and also in the Mississippi, Nile and other major deltas).

An early adherent of Wegener’s theory of continental drift, Grabau prepared paleogeographic maps that reflected continental reconstructions based on paleontological reasoning. Grabau had observed that modern-day organisms, notably molluscan faunas, tend to suffer depauperization, reduction in size (within a species) and in population as one goes polewards. Vectors could thus be drawn for any period converging on the polar area. Particularly striking is his map (1940) of the Upper Ordovician, which illustrates a South Pole in the middle of the Sahara Desert. It was more than 30 years later that field evidence for glaciation was to be discovered there (Beuf et al., 1971; Fairbridge, 1973).

Granlund, Erik (1892–1938)

Swedish Quaternary geologist of the Svenska Geologiska Undersökning in Uppsala, Granlund made valuable discoveries in peat formation and pollen analysis (Lundquist, 1938). In an intensive study of Swedish peat bogs, he established that evidence existed for five dry intervals in the postglacial period, marked by oxidation and reddish colors. Using the varve-based chronology of deGeer (see above), their dates were approximately: 2,300, 1,200 and 600 BC and AD 400 and 1,200. The best developed is the 600 BC layer, which is the so-called “Grenzhorizont,” marking the boundary between the warm-wet climates of the subboreal stage and the cool-wet characteristics of the subatlantic stage. Rainfall comparisons are shown in Brooks (1949, p. 299).

Heer, Oswald (1809–1883)

One of the founders of paleogeography and paleoclimatology, Heer was a Swiss professor at the University of Zürich. He was particularly interested in the message of paleobotany in permitting the scientific reconstruction of past landscapes. His major work *Die Urwelt der Schweiz* (1865), later translated into English as *The Primeval World of Switzerland* (2 vols., translated 1876), played an important role in bringing the Earth’s ancient past into the forefront of literature (Grey, 1884).

Howchin, Reverend Walter (1845–1937)

A minister of the Church of England, Howchin emigrated to South Australia and took up church duties. Among his geological discoveries were striated pavements, erratics and glacial sediments associated with fossiliferous Permo-Carboniferous sediments, traces of which had been reported earlier (Alderman, 1967). These paleoclimatic discoveries were sensational in view of their distance from the Talchir glacials in India and the Dwyka of South Africa. They helped to consolidate the Suess concept of Gondwanaland, and thus became an integral link in the continental drift theory of Wegener, which later became incorporated into the current theory of plate tectonics.

Huntington, Ellsworth (1876–1947)

American geographer Ellsworth Huntington took part in expeditions to Turkistan (1903–1904) and western China (1905–1906). In 1907, he joined the faculty at Yale and in 1909 led their expedition to Palestine and Asia Minor. With the Carnegie Institution of Washington, he studied climate in the U.S., Mexico and Central America. In paleoclimatology, his name is associated with the history of the semi-arid lands of central

Asia. In geomorphology, he established an important concept, now known as the “Huntington Principle” (Fairbridge, 1970), that fluvial terraces tend to accumulate during semiarid regimes, whereas they become dissected during wetter cycles. A comprehensive rearrangement of ancient river systems was observed in central Asia, implying major changes in climatic regimes. He later became interested in solar activity and other paleoclimate changes.

Jamieson, Thomas Francis (1829–1913)

A Scottish geologist and agriculturalist at the University of Aberdeen (appointed 1862), Jamieson played a key role in the Quaternary geology and geomorphology of Scotland (Woodward, 1913). His great distinction was to have developed the concept of glacio-isostatic rebound (though he did not use that expression). He observed uplifted shorelines and coastal deposits and reasoned their origin as an isostatic crustal response to unloading of glacial ice, a critical concept in the study of ancient glaciations. Jamieson’s “classic” field evidence definitively negated the early idea of a marine ice-flow agency for glacial deposits. He was also convinced that the lowered evaporation rates during glacial times led to pluviation in closed basins like the Dead Sea, and the Caspian and Aral Seas. He coined the term “Pluvial Period” (More recent evidence points to generally more arid conditions and lower lake levels during glaciations, except where lakes are fed by glacial melt-water [Ed.]).

Kerner-Marilaun, Fritz (von) (1866–1944)

An Austrian paleobotanist, Fritz Kerner was the author of the first major textbook with the title: *Paläoklimatologie* (Borntraeger, 1930), although earlier studies of climate history had been made. Kerner went to some pains to stress the uncertainties of many would-be paleoclimatic proxies. Quoting his own words (translated, R. W. Fairbridge): “*There can be no shadow of doubt that an examining magistrate would declare such a family of evidence or testimony completely inadequate for the explanation of what is a very complicated case.*”

Kerner developed mathematical formulas for modeling paleotemperatures appropriate for specific latitudes and continentality in relation to geostrophic currents (Brooks, 1949, p. 41). He recognized the low equator-pole thermal gradient for non-glacial world climates (with an ice-free Arctic). These he called “acryogenic” (*akryogenen*), in contrast to glacial phases: “cryogenic” (*kryogenen*) (Brooks, 1949; Fairbridge, 1964; Schwarzbach, 1974, p. 269–267). Kerner recognized causal relationships between paleogeographic changes and oceanic circulation. He also suggested various proxy-sediments (e.g., bauxite and brown coal) for past climates.

King, Lester C. (1907–1989)

A New Zealander who spent most of his professional life in Africa, King was well-traveled and worked in seven continents. Primarily a geomorphologist, he viewed earth history globally, and accepted Wegener’s crustal mobilism well before plate tectonics became established. King’s great contribution to paleoclimatology was his identification of world-wide phases of terrestrial (non-marine) sedimentation, paleosol building, landforms, etc., that reflect synchronous global events, clearly relating to planetary climate change but with details unspecified. He noted that Phanerozoic time is marked by long intervals of warm humid climates leading to deeply weathered paleosols,

which alternate with short, sharp interruptions associated with tectonism (uplift or depression).

Milankovitch, Milutin (1879–1958)

Of Serbian origin, born in Dalj, Slavonia (in what is now Croatia), Milankovitch was destined to become one of the world’s central figures of late twentieth century paleoclimatology, although considered highly controversial in his own lifetime. His belief in the long-term climatic significance of the Earth-Moon orbital variables followed in the footsteps of Adhèmar, Croll, Ball and others, but he added the essential refinements of meticulous astronomic calculations, long before electronic calculators were invented. In a curious way, he was helped by two world wars (Imbrie and Imbrie, 1979, 1986). During long periods of captivity he was able to complete the mathematical foundations for his *Kanon der Erdbestrahlung* (1941; English translation, 1969), which disclosed the effective radiation or “insolation” at various latitudinal belts and at various time epochs.

Supported on climatic grounds by Köppen and Wegener (1924) and on geological grounds by Zeuner (1959), the Milankovitch theory was violently opposed or ignored by the scientific establishment until marine geologists were able to prove the same orbital chronology and paleotemperatures in deep-sea deposits (Broecker, 1968; Berger et al., 1984), which were confirmed in the chronology of loess and in paleosols on land (Kukla, 1970). Acceptance of the Milankovitch Theory opened the way to serious studies of cyclical processes and the role of external forcing in climate change.

Oeschger, Hans (1927–1998)

Oeschger founded the Division of Climate and Environmental Physics at the Physics Institute, University of Bern, and remained as Director until his retirement in 1992. Oeschger was an innovator and leader in the use of polar ice cores as important paleoclimate archives. He and his colleagues were the first to discover and measure large glacial to interglacial variations in atmospheric CO₂ concentrations in the air bubbles trapped in ice. Together with his colleagues, he detected a series of abrupt climate changes in the Greenland ice cores, now called “Dansgaard-Oeschger events.”

Pettersson, Otto (Sven Otto) (1848–1941)

Swedish professor of oceanography at Stockholm University, Otto Pettersson was one of a family of marine scientists with strong international ties. While associated with the Swedish Fisheries Commission, he observed that the rising tide at their laboratory and tide station on the Gulmarfjord, on Sweden’s west coast, would form an internal wave up to 25 m high at the boundary of the (cold, dense) offshore water and the out-flowing (somewhat fresher and less dense) Baltic water. At the peak of the 18.6 year nodal cycle, the tide produced a dramatic effect near the head of the fjord. Sweeping into the Baltic, it carried young herrings, providing a bounty for the fishermen. Herring statistics, reaching back to about the twelfth century in Hanseatic League archives, showed this luni-solar orbital cycle to increase harmonically at the same season: 18.6/93.067/186.134 year, with effects on regional climate as well. Pettersson’s tidal force theories were summarized in the *Geografiska Annaler* (1930, v. 18).

The oceanographic and climatic effects of the 18.6 year lunar nodal cycle are well known (Lamb, 1977), and the coexistence

of the sunspot cycle and the nodal cycle was recognized in auroral and geomagnetic records by Ekholm and Arrhenius (1898), and in the Nile floods and climate data by Currie (1995).

Ramsay, Wilhelm (1865–1928)

A Finnish mineralogist and Quaternary geologist, Ramsay was the proponent of the “Relief Theory” in paleoclimatology (Spencer, 1936). The role of uplift was neglected as a climate-forcing process until the late twentieth century when plate-tectonic studies drew attention to the progressive underthrusting of the Himalayas and general uplift of the Tibetan plateau, especially during the Quaternary. Simultaneous uplifts occurred in the Rocky Mountains, Andes and Alps.

Ramsay was also very interested in eustasy. However, his estimate of lowest Pleistocene sea level (1930) was 275 m, approximately double the present estimates. He investigated the meltwater filling of the Russian closed basins, at one stage forming a giant Aralo-Caspian lake. Ramsay also visualized a post-glacial downcutting of the Dardanelles and Bosphorus to drown the Black Sea, a concept recently embraced by Ryan and Pitman. In terms of the glacio-isostatic uplift of Fennoscandia (he appears to have invented the concept), he allows a considerable lag time by reducing the theoretical crustal response (see discussion by Daly, 1934, p. 71).

Reusch, Hans Henrik (1852–1922)

A Norwegian geologist, Reusch (1890) discovered the first unquestionably glacial deposits stratigraphically related to the lowest Cambrian, on the north shore of the Varanger Fjord in the Finnmark district of Norway (Kaiser, 1923). The tillite is diagenetically lithified, but not structurally deformed, and rests on beautifully striated and grooved bedrock of Proterozoic age. Its discovery triggered the recognition of comparable tillites elsewhere in the Caledonian belt, in Scotland, Spitsbergen, and elsewhere in the Arctic. Analogous formations were then found on every continent, which has led to the concept of “Snowball Earth.” Harland (1964) called it “the great Infra-Cambrian glaciation” (Schwarzbach, 1974), also known as the “Eocambrian glaciation,” or “Vendian” or “Upper Riphean” in Russia. Today, several Neoproterozoic glaciations between 750 and 542 Myr are recognized: the Sturtian (~750 to ~720 Myr) and the Marindan (~620 to 600 Myr).

Revelle, Roger Randall Dougan (1909–1991)

Roger Revelle, standing six feet and four inches tall, has been described as a “scientific giant,” both literally and figuratively. He was one of the first scientists to study marine geology and the role of ocean carbonates in global warming. He was also involved in many international scientific programs, showing concern over issues of population growth, adequate food and energy resources.

Born in Seattle in 1909, Revelle obtained his B.A. in geology from Pomona College in 1929 and Ph.D. in oceanography from the University of California, Berkeley in 1936. Shortly thereafter, he was appointed an instructor at the Scripps Institution of Oceanography in San Diego. By 1951, he had become director of Scripps. During his years as director, he attracted many prominent scientists and expanded the laboratory facilities and fleet, stimulating Pacific basin geophysical studies, which played a key role in the discoveries leading to plate tectonics.

One of his major contributions to climatology was the finding that excess atmospheric carbon dioxide, produced by

anthropogenic greenhouse gas emissions, was being absorbed by the ocean at a much slower rate than previously thought, thereby contributing to recent global warming (Revelle and Suess, 1957). He hired David Keeling to monitor atmospheric carbon dioxide levels, initially at Mauna Loa in Hawaii, and elsewhere. The “Keeling Curve,” showing rising carbon dioxide levels since 1957, has become a key piece of evidence in the ongoing debate over global warming.

Schimper, Karl Friedrich (1803–1867)

The first person to use the term “Ice Age” (“Eiszeit” in German, 1837), Schimper certainly deserves a place in paleoclimatology’s history (Volger, 1889). He was a naturalist and paleontologist, and was also interested in glacial geomorphology. After discussions in the field with Agassiz, he coined the term “Eiszeit,” which may have owed something to the German poet J. W. Goethe, who referred to an “epoch of great cold” in a romantic novel of 1829.

Selwyn, Alfred Richard Cecil (1824–1902)

Selwyn, an English geologist, was director of the Geological Survey of Victoria (1852–1869). Later, he held a similar position in Canada (1869–1894), contributing to the stratigraphy of Quebec and vertebrate footprints. He was the first to discover (in 1859) the Permo-Carboniferous glacial formations and elegant grooved and striated pavements in the Inman valley of South Australia, which were the first to be identified on the Australian continent (Whitaker, 1904).

Shackleton, Nicholas J. (1937–2006)

Nicholas Shackleton received his B.A. in 1961 and Ph.D. in 1967 at Cambridge University, where he remained during his professional career. Over many productive years, Shackleton made numerous contributions to paleoclimatology, primarily through his pioneering work using marine oxygen isotopes to unravel the climate record contained in ocean cores. Working closely with Neil Opdyke, who dated the sequence of paleomagnetic reversals, he developed a chronology of oxygen isotope variations, which led to the recognition of numerous Quaternary glacial to interglacial cycles on roughly 100,000-year timescales. Once a reasonably accurate timescale had been established, the observed climate cycles, including cycles at 23,000 years (precession) and 41,000 years (obliquity), could be linked to Earth’s orbital parameters, thus confirming the Milankovitch theory of the ice ages (Hays et al., 1976). The CLIMAP project (see *CLIMAP*) grew out of these early studies. The marine oxygen isotope curves derived from benthic foraminifera form the basis of the widely-used SPECMAP chronology (see *SPECMAP*). Shackleton was also one of the first researchers to apply carbon isotopes to paleoclimate studies, in particular using ¹³C values in benthic foraminifera as a marker for major changes in deepwater ocean circulation (Ruddiman, 2006).

In collaboration with John Chappell in 1986, Shackleton compared marine oxygen isotope oscillations with eustatic sea level variations recorded in emergent reef terraces on the Huon Peninsula, New Guinea, and assessed the role of variable deep-sea temperatures. A more recent comparison with Antarctic ice cores, however, also indicated that a substantial fraction of the foraminiferal oxygen signal stemmed from variations in deep-ocean temperature rather than ice volume (Shackleton, 2000). Furthermore, ice volume was found to lag behind fluctuations in orbital eccentricity and carbon dioxide, thus pointing to the role of feedbacks involving CO₂ (Shackleton, 2000).

Shackleton was the Director of the Godwin Institute of Quaternary Research at Cambridge University for many years, officially retiring in 2004, yet remaining active until shortly before his death. In recognition of his many scientific contributions, he received numerous honors and awards, including a knighthood in 1998 for his services to earth science, appointment as Fellow of the Royal Society (1985) and Foreign Member of the U.S. Academy of Sciences, the Crafoord Prize (1995), the Milankovitch Medal (1999), the Vetlesen Prize (2004), and Japan's Blue Planet Prize (2005).

Suess, Eduard (1831–1914)

Suess, professor of geology at the University of Vienna (1857–1908), saw the Earth's crust as undergoing long-term cycles of extension with subsidence, alternating with horizontal compression and uplift, a revolutionary idea at that time (Gohau, 1990). His *Antlitz der Erde* (in 5 parts, 1885–1909) was immediately translated into French and then into English (as *The Face of the Earth*, 1904–1924).

From his worldwide reviews of stratigraphy and paleontology, Suess became convinced about the worldwide rise and fall of the ocean level, and coined the expression “eustatic movements” (1888). Particularly in the rocks of the region between the Alpine belt and the Mediterranean, he perceived a regular and universal ebb and flow like a giant tide. He understood that the basins opened tectonically and closed by sedimentary infilling, but climatic forcing was not considered (Tietze; 1916).

His grandson was the celebrated geochemist Hans Suess at the Scripps Institution of Oceanography, La Jolla, a branch of the University of California. Hans was the first to demonstrate the cyclical fluctuations of ^{14}C in the wood of tree rings (a proxy for solar-wind energy flux) and found that the thickness of these tree rings coincided with climatic variables (Suess, 1981).

Swedenborg, Emanuel (1688–1772)

A Swedish scientist, philosopher and religious mystic, Swedenborg traveled widely and wrote extensively about all branches of science, but also noted the elevated beachlines that mark the boundaries of Scandinavia. However, following the beliefs of the day, he attributed them to pauses in the gradual desiccation of the world ocean after the Biblical flood of Noah. Nevertheless, he was credited with the earliest work on paleontology in Sweden, and attempted a systematic approach to mineralogy. In 1734, he outlined his nebular hypothesis for the universe, long before Kant. Swedenborg was one of the first to attempt some reconciliation between scientific developments and the literal interpretation of the Bible (Tufel, 1875–1877).

Urey, Harold C. (1893–1981)

Harold Urey was one of the most prominent and influential scientists of the twentieth century. His research contributed to nuclear physics, chemistry, and the earth sciences. His work on elemental isotopes led to the development of entirely new disciplines such as cosmochemistry, geochronology, stable isotope geochemistry and paleoclimatology. He also took a keen interest in the origins of the Solar System and of life on Earth.

Born in Walkerton, Indiana in 1893, Harold Urey received his B.A. in 1917 from the University of Montana and his Ph.D. in chemistry in 1923, from the University of California, Berkeley. He worked on atomic structure with Niels Bohr at the Institute

for Theoretical Physics in Copenhagen for several years. Upon his return to the United States, Urey became associate professor in chemistry at John Hopkins University, and later taught chemistry at Columbia University between 1929 and 1936. His research in nuclear systems and isotopic variations resulted in the discovery of deuterium – “heavy” hydrogen, with mass 2. This discovery earned Urey the Nobel Prize in 1934.

Contributing to the Manhattan Project during World War II, Urey designed methods for separating and enriching ^{235}U , the fissionable isotope of uranium needed for making an atomic bomb. After the war, he became professor at the Institute for Nuclear Studies, Chicago University. During the course of his work with oxygen isotopes, Urey noticed a temperature dependence in the fractionation factor of $^{18}\text{O}/^{16}\text{O}$ between carbonates and water and realized that this could be used to measure paleotemperatures. Several papers published between 1948 and 1951 became the basis for stable isotope paleothermometry, which is so widely used in paleoclimatology today (Epstein et al., 1951; Urey et al., 1948, 1951).

After retirement in 1958, Urey became professor of chemistry-at-large at the newly-formed University of California in San Diego. He became interested in the origin of the Solar System and of life on Earth. In 1959, he and his then-graduate student Stanley Miller simulated early Earth conditions by passing an electric discharge into a flask containing a mixture of methane, ammonia, and water, and obtained a variety of amino acids, precursors of the proteins that are essential to living systems (Miller and Urey, 1959).

In addition to the Nobel Prize, Urey received numerous awards and honors, among which are the Medal of Merit from President Harry S. Truman, the National Medal of Science, and the 400th Anniversary of John Kepler Medal and Citation from the American Academy of Arts and Sciences.

Von Richthofen, Baron Ferdinand (1833–1905)

Often considered as one of the founders of the science of geomorphology, Baron (Freiherr) von Richthofen was born in what was German Silesia (now Poland); he studied in Breslau (now Wroclaw) and later Berlin. Von Richthofen's many interests eventually earned him a university chair in Leipzig (1883) and then in Berlin (1886) (Ravenstein, 1905; Beckinsdale, 1975).

He joined the Austrian geological survey, his work taking him to China, Southeast Asia and California. In the 200 m high cliffs of the Chinese loess plateau, he first recognized non-actualistic phenomena, i.e., sediments that could not possibly be explained by modern-day processes (Tiessen, 1907). Von Richthofen correctly interpreted the loess as an eolian deposit of silt to dust-sized particles that had accumulated during glacial cycles. He viewed the upper part as a paleosol, modified by weathering and soil-forming processes that suggested mild interglacial climates. The loess sections of the world are now known to constitute unique records of continental climatic oscillations that have been dated to show contemporaneity with (a) glacier oscillations in ice sheets such as Greenland and Antarctica; and (b) deep-sea sediments with similar oscillations characterized by micropaleontology and $\delta^{18}\text{O}$ temperature data. Von Richthofen's eolian loess thus forms the third leg of our ice age chronology (Hettner, 1906).

Some confusion arose during the twentieth century when water-laid loess was discovered in central and eastern Europe. At one stage, this was the “official” Soviet interpretation. Von Richthofen in fact had remarked on loess dust that in places

had fallen into lakes or had been reworked to become a fluvial deposit. While cliffs along the Danube clearly display lenses of water-lain loess, the uniquely periglacial hyperaridity of loess episodes has been abundantly confirmed.

Another of his important paleoclimatic discoveries was in the Dolomite Alps (then part of Austrian Tyrol). He viewed each mountain block as an original coral reef of Triassic age, evidently a subtropical facies in cool latitudes today. The original limestone had been altered to dolomite (named for Deodet de Dolomieu, 1750–1801).

Zeuner, Frederick Everard (1905–1963)

Paleoclimatologist, prehistorian, geologist and all-round naturalist, Zeuner was one of the “greats” of the early twentieth century. Trained at the universities in Berlin, Tübingen and Breslau, he became a lecturer at Freiburg im Breisgau in 1931, where he worked with Walter Soergel on the fluvial evidence for the Milankovitch orbital hypothesis. At that time, the very idea of extraterrestrial forcing was very tentative, and violently opposed by many authorities. Although the astronomic basis was fairly sound, the geological record was pitifully bereft of a quantitative chronology. Nevertheless, Zeuner took the astronomic record as a basis for that chronology.

Fleeing persecution in Germany in 1934, Zeuner found sanctuary in London, at the British Museum of Natural History, where he worked on fossil insects, the paleoclimatic value of which was already recognized. Zeuner then became honorary lecturer, later professor, and finally director of the London Institute of Archaeology. He elaborated on the orbital theory and found it to be compatible with the geological record of glaciations, paleosols, eustatic sea levels, and other paleoclimatic indicators and proxies. Two of his books, *The Pleistocene Period* (1945, 1959) and *Dating the Past* (1946) had a worldwide impact.

The chronology problem had been partially solved by the Swedish varve-dating system of Baron deGeer, which had been integrated with Holocene sea-level fluctuations. The last 10,000 years were seen to span a precession hemicycle (Fairbridge, 1961, 1981). Radiocarbon dating subsequently expanded the chronology to over 40,000 year, taking the record back two precession cycles.

Rhodes W. Fairbridge and Vivien Gornitz

Bibliography

- Abbot, G.G., 1918. On periodicity in solar variation. *Smithsonian Miscellaneous Collections*, **69**(6), 8pp.
- Abbot, G.G., 1936. Cycles in tree-ring widths. *Smithsonian Miscellaneous Collections*, **95**(19), 5pp.
- Abbott, C.G., 1948. Magnetic storms, solar radiation, and Washington temperature departures. *Smithsonian Miscellaneous Collections*, **110**(6).
- Abbot, C.G., 1963. Solar variation and weather. *Smithsonian Miscellaneous Collections*, **146**, no.3, 61pp.
- Adhémar, J., 1842. *Révolutions de la Mer: Déluges Périodiques*. Paris: Carilian-Goeury et V. Dalmont, (2nd edn. 1860).
- Alden, W.C., 1929. Contributions to glacial geology. *J. Geol.*, **37**, 293–319.
- Alderman, A.R., 1967. The development of geology in South Australia: A personal view. *Rec Aust. Acad. Sci.*, **1**(2), 30–52.
- Anon., 1869. Forbes–Obituary. *Geol. Mag.*, **6**, 95–96.
- Anon., 1871. Forbes–Obituary. *Proc. R. Soc. London*, **19**, i–ix.
- Anon., 1905. Blandford–Biography. *Geol. Mag.*, **42**, 1–15.
- Antevs, E., 1944. DeGeer–Memorial, *Geological Society American, Proceedings*, Report for 1943, 117–133.
- Arrhenius, G.O.F., 1959. Svante Arrhenius’ contributions to earth sciences and cosmology. *Kungl. Vetensk. Akad., Åsbok*, Bil., 101–115.

- Arrhenius, S.A., (1896). On the influence of carbonic acid in the air on the temperature of the ground. *Phil. Mag.*, **41**, 237–276.
- Beckinsale, R.P., 1975. Richthofen, Ferdinand von. *Dict. Sci. Biogr.*, **11**, 438–441.
- Berger, A., Imbrie, J., Hays, J., Kukla, G., and Saltzman, B. (eds.), 1984. *Milankovitch and Climate*. Dordrecht: Reidel, 895pp.
- Berry, A., 1898. *A Short History of Astronomy*. London: J. Murray (Dover Publ., Inc., 1961).
- Beuf, S., Biju-Duval, B., De Charpal, O., Rognon, P., Gariel, O., and Benacef, A., 1971. *Les Grès du Paléozoïque inférieur au Sahara*. Paris: Editions Technip, 464pp.
- Birch, F., 1960. Daly–Obit. *Biogr. Mem. Natl. Acad. Sci.*, **34**, 31–64.
- Bonney, T.G., 1907. Blandford–Obit. *Proc. R. Soc. Lond.*, **79**, xxvii–xxxii.
- Broecker, W.S., 1968. Milankovitch hypothesis supported by precise dating of coral reefs and deep sea sediments. *Science*, **159**, 297–300.
- Brooks, C.E.P., 1926/1949. *Climate Through the Ages*. London: Ernest Bonn. (2nd ed. 1949). New York: McGraw-Hill, 395pp. (Dover reprint, 1970).
- Bullard, E.C., 1975. *Biogr. Mem. Fell. R.S.* (London), **21**, 269–311.
- Caldenius, C., 1948. *Orbit. Geol. För. Stockholm, Förh.*, vol. 70, pp. 513–527.
- Carozzi, A.V., 1966. William Maurice Ewing, 12 May 1906 – 4 May 1974. Agassiz’s amazing geological speculation: The Ice Age. *Studies in Romanticism*, **5**, 57–83.
- Carozzi, A.V., 1973. Agassiz’s influence on geological thinking in the Americas. *Arch. Sci. Genève*, **27**, 5–38.
- Chambers, R., 1844. *Vestiges of the Natural History of Creation*, Edinburgh.
- Chambers, R., 1848. *Ancient Sea-Margins, as Memorials of Changes in the Relative Level of Sea and Land*. Edinburgh and London: Chambers, Orr and Co., 388pp.
- Chappell, J., and Shackleton, N.J., 1986. Oxygen isotopes and sea level. *Nature*, **324**, 137–140.
- Charlesworth, J.K., 1957. *The Quaternary Era*. (2 vols.) London: E. Arnold, 1700pp.
- Cornwall, I.W., 1964. Zeuner–Obituary. *Zeitschr. F. Geomorph.*, **8**, 382–383.
- Croll, J., 1875. *Climate and Time, in their Geological Relations: A Theory of Secular Changes of the Earth’s Climate*. Appleton: London and New York, 577p. (2nd ed., 1885).
- Cunningham, F.F., 1990. *James David Forbes: Pioneer Scottish Glaciologist*. Edinburgh: Scottish Academic Press, 32pp.
- Currie, R.G., 1995. Variance contribution of M_0 and S_c signals to Nile River data over a 30–8 year bandwidth. *J. Coastal Res.*, **17**, 29–38.
- Daly, R.A., 1934. *The Changing World of the Ice Age*. New Haven: Yale University Press, 271pp.
- Drake, S., 1972. Galilei, Galileo. *Dict. Sci. Biogr.*, **5**, 237–250.
- Dubois, E., 1893. *Die Klimate der geologischen Vergangenheit und ihre Beziehungen zur Entwicklungsgeschichte der Sonne*. Leipzig.
- Dunnington, G.W., 1955. *Carl Friedrich Gauss: Titan of Science*. New York.
- Du Toit, A., 1938. Dunn–Obit. *Trans. Geol. Surv. S. Africa*, 45–46.
- Eckholm, N., and Arrhenius, S.A., 1898. Ueber den Einfluss des Mondes auf die Polarlichter und Gewitter. *Kongl. Svenska Vetenskaps Akademiens Handlingar* **31**(2), 77–156.
- Epstein, S., Buchsbaum, R., Lowenstam, H.A., and Urey, H.C., 1951. Carbonate-water isotopic temperature scale. *Bull. Geol. Soc. Am.*, **62**, 417–426.
- Esmark, J., 1826. Remarks tending to explain the geological history of the Earth. Kristiania (reprinted in *Edinburgh New Philosophical Journal*, 1827, **2**, 107–121).
- Fairbridge, R.W., 1961. Eustatic changes in sea level. In Ahrens, L.H. et al., (eds), *Physics and Chemistry of the Earth*. London: Pergamon, 4, pp. 99–185.
- Fairbridge, R.W., 1964. The importance of limestone and its Ca/Mg content to paleoclimatology. In Nairn, A.E.M. (ed.), *Problems in Paleoclimatology*. New York: Wiley, pp. 431–530.
- Fairbridge, R.W. (ed.), 1968. *The Encyclopedia of Geomorphology*. New York: Van Nostrand Reinhold, 1295pp.
- Fairbridge, R.W., 1970. World paleoclimatology of the Quaternary. *Revue Géographique Phys. Géologie Dynamique*, vol. 12 (2), 97–104.
- Fairbridge, R.W., 1973. Glaciation and plate migration. In Tarling, D.H., and Runcorn, K. (eds.), *Implications of Continental Drift to the Earth Sciences*. London: Academic Press, vol. 1, pp. 503–515.
- Fairbridge, R.W., 1981. Holocene sea-level oscillations. In Königsson, L.K. and Paabo, K. (eds.), *Striae, Florilegium Florinis Dedicatum*. vol. 14, pp. 131–141, Uppasala, Sweden.

- Fairbridge, R.W., 1995. Foreword: Some personal Reminiscences of the idea of cycles, especially in the Holocene. In Finkl, C.W. Jr., *Holocene Cycles: Climate, Sea Levels, and Sedimentation*. J. Coastal Res., No. 17, pp. 5–10 (special issue).
- Fairbridge, R.W., and Sanders, J.E., 1987. The Sun's orbit, A.D. 750–2050: Basis for new perspectives on planetary dynamics and Earth-Moon linkage. In Rampino, M.R., Sanders, J.E., Newman, W. S., and Königsson (eds.), *Climate: History, Periodicity, and Predictability*. New York: van Nostrand Reinhold, pp. 446–471.
- Fenton, C.L., and Fenton, M.A. 1952. *Giants of Geology*. Garden City, N.Y.: Doubleday Doran, 301pp.
- Finkl, C.W., Jr., 1987. Rhodes W. Fairbridge: An Appreciation. In Rampino, M.R., Sanders, J.E., Newman, W.S., and Königsson (eds.), *Climate: History, Periodicity, and Predictability*. New York: van Nostrand Reinhold, pp. 1–34.
- Finkl, C.W., Jr., (ed.), 2005. The Sun, Earth, and Moon: In Honor of Rhodes W. Fairbridge. *J. Coastal Res.*, Special Issue, No. 42.
- Flint, R.F., 1957. *Glacial and Pleistocene Geology*. New York: Wiley, 553pp.
- Flint, R.F., 1971. *Glacial and Quaternary Geology*. New York: Wiley, 892pp.
- Forbes, J.D., 1861. Inquiries about terrestrial temperature. *Trans. R. Soc. Edinb.*, **22**, 75.
- Geikie, A., 1905. *The Founders of Geology*. (2nd. edn.) London: Macmillan, 486pp.
- Gilbert, W., 1600. De Magnete, Magneticisque Corporibus, et de Magno Magnete Tellure. London.
- Gilbert, W., 1651. De Mundo Mostro Sublunari Philosophia Nova. Amsterdam (posthumously).
- Gohau, G., 1990. *A History of Geology*. New Brunswick, N.J.: Rutgers University Press, 259pp.
- Grabau, A.W., 1936a. The great Huangho plain of China. *Assoc. Am. & Chinese Engineers J.*, **17**, 247–266.
- Grabau, A.W., 1936b. Oscillation or Pulsation. *International Geological Congress Report*, Washington, **1**, 539–553.
- Grabau, A.W., 1940. *The Rhythm of the Ages*. Peking: Henri Vetch, 561p.
- Grey, A., 1884. Heer–Memorial. *Am. J. Sci.*, **28**, 67–69.
- Harland, B., 1964. Critical evidence for the great Infra-Cambrian glaciation. *Geolog. Rundschau*, **54**, 45–61.
- Hay, W.W., Zakevich, E., 1999. Cesare Emiliani (1922–1995): The founder of paleoceanography. *Int. Microbiol.*, **2**, 52–54.
- Hays, J.D., Imbrie, J., and Shackleton, N.J., 1976. Variations in the earth's orbit: Pacemaker of the ice ages. *Science*, **194**, 1121–1132.
- Heer, O., 1865, (transl. 1876). *The Primeval World of Switzerland*, 2 vols. Ed. J. Heywood, Trans W.S. Dallas, 2 vol., 716pp. London: Longmans, Greene & Co.
- Hettner, A., 1906. Ferdinand von Richthofen's Bedeutung für die Geographie. *Geographische Zeitschr.*, **12**, 1–11.
- Holland, T.R., 1905. Blanford–Obit. *Records, Geological Survey of India*, vol. 32.
- Howchin, W., 1912. Australian glaciations. *J. Geol.*, **20**, 193–227.
- Howchin, W., 1918/1929. *Geology of South Australia*. Adelaide: Gillingham
- Huntington, E., and Visher, S.S., 1922. *Climatic Changes. Their Nature and Causes*. New Haven: Yale University Press, 329pp.
- Imbrie, J., and Imbrie, K.P., 1979/1986. *Ice Ages: Solving the Mystery*. Cambridge, MA: Harvard University Press, 224pp.
- Irons, J., 1897. Croll–Obit. *Geol. Mag.*, **34**, 71–77.
- Kaiser, E., 1923. Reusch–Obit. *Zentralbl. Min.*, 156–160.
- Kerner-Marilaun, F., 1921, 1930. *Paläoklimatologie*. Berlin, Gebr. Borntraeger.
- King, L.C., 1962/1967. *The Morphology of the Earth*. Edinburgh: Oliver & Boyd (2nd edn., 1967).
- King, L.C., 1983. *Wandering Continents and Spreading Sea Floors on an Expanding Earth*. Chichester: Wiley, 232pp.
- Köppen, W., and Wegener, A., 1924. *Die Klimate der Geologischen Vergangenheit*. Berlin (revised edition 1940).
- Kukla, G.J., 1970. Correlation between loesses and deep-sea sediments. *Geol. Fören. Förh. Stockholm*, **92**, 148.
- Lamb, H.H., 1977. *Climate History and the Future*. London: Methuen, (and Princeton University Press) 835p.
- Lugeon, M., 1920. Jean de Charpentier. *Bull. Soc. Vaud. Sci. Nat.*, **53**, 465–481.
- Lundquist, G., 1938. Granlund–Obit. *Geol. För. Stockholm, Förh.*, **60**, 525–542.
- Lurie, E., 1960. *Louis Agassiz: A Life in Science*. Chicago and London: Chicago University Press, 448pp.
- May, K.O., 1972. Gauss, Carl Friedrich. *Dict. Sci. Biogr.*, **5**, 298–315.
- Milankovitch, M., 1941. Kanon der erdbestrahlung und seine Anwendung auf das Eiszeitenproblem. *Roy. Serb. Acad., Sp. Publ.*, **133**, 633p. (Engl. Transl. 1969 as “Canon of Insolation and the Ice-Age Problem”, by Israel Progr. Sci. Transl., U.S. Dept. Commerce, Washington, 484pp).
- Milhauser, M., 1959. *Just Before Darwin: Robert Chambers and “Vestiges.”* Middletown, CT: Wesleyan University Press, 246pp.
- Miller, S.L., and Urey, H.C., 1959. Organic compound synthesis on the primitive earth. *Science*, **130**, 245–251.
- Molengraaff, G.A.F., 1898. Glacial origin of the Dwyka conglomerate. *Trans. Geol. Soc. South Africa*, **4**, 103–115.
- Oeschger, H., Langway, C.C., Jr. (eds.), 1989. *The Environmental Record in Glaciers and Ice Sheets*. Chichester, UK: Wiley.
- Pettersson, O., 1914a. Climatic variations in historic and prehistoric time. *Svenska Hydrogr. Biol. Komm. Skrifter.*, **5**, 26pp.
- Pettersson, O., 1914b. On the occurrence of lunar periods in solar activity and the climate of the Earth: A study in geophysics and cosmic physics. *Svenska Hydrogr. Biol. Komm.*, **5**:26.
- Pettersson, O., 1930. The tidal force. *Geogr. Annaler*, **12**, 261–322.
- Porter, S.C., 1978. Flint–Memorial. *Geol. Soc. Am. Memorials*, **8**, 7pp.
- Ramsay, W., 1910. Orogenesis und Klima. *Overs. Finska Vet. Soc. Föhr.*, vol.52(a) [see also *Geol. Mag.* V.21, 1924].
- Ravenstein, E.G., 1905. Ferdinand Freiherr von Richthofen. *Geogr. J.* (London), **26**, 679–682. (Benchmark Papers in Geology, v.13).
- Revelle, R., and Fairbridge, R.W., 1957. Carbonates and carbon dioxide. *Geol. Soc. Am. Memoir* **67**(1), 239–295.
- Revelle, R., and Suess, H.H., 1957. Carbon dioxide exchange between atmosphere and ocean and the question of an increase of atmospheric CO₂ during the past decades. *Tellus*, **9**, 18–27.
- Ruddiman, W.R., 2006. Nicholas J. Shackleton (1937–2006). *Science*, **312**, 711.
- Sarjeant, W.A.S., 1980. *Geologists and the History of Geology*. (5 vols.) New York: Arno Press.
- Schwarzbach, M., 1963. *Climates of the Past*. London: Van Nostrand Co., 328
- Schwarzbach, M., 1974. *Das Klimate der Vorzeit*, 3rd edn. Stuttgart: F. Enke Verlag, (English translation, 1963). New York: Van Nostrand.
- Shackleton, N.J., 2000. The 100,000-year ice-age cycle identified and found to lag temperature, carbon dioxide and orbital eccentricity. *Science*, **289**, 1897–1902.
- Singer, C., 1959. *A Short History of Scientific Ideas to 1900*. Oxford: Clarendon Press, 525pp.
- Spencer, L.J., 1936. Ramsey–Obit. *Min. Mag.*, **22**, 403–404.
- Suess, E., 1885–1909. *Das Antlitz der Erde*, Vienna: F. Tempsky.
- Suess, E., 1916. Eduard Suess, Erinnerungen. 451pp., Leipzig (Hirzel).
- Suess, H.E., 1981. Solar activity, cosmic-ray produced carbon-14, and the terrestrial climate, p.307–310 In: *Sun and climate.*: Proceedings of the Conference on Sun and climate. Toulouse, 1980: Centre national d'Etudes spatiale, 471pp.
- Sun, Y.C., 1947. Grabau–Obit. *Bull. Geol. Soc. China*, **27**, 1–26.
- Teller, J.T., 1983. Jean de Charpentier 1786–1855. *Geographers Biobibliographical Studies*, **7**, 17–22.
- Tiessen, E., 1907. Ferdinand von Richthofen's Tagbücher aus China, 2 vols. Berlin: Dietrich Reimer, V.I., 588pp., V.II, 375pp.
- Tietze, E., 1916. Einige Seiten über Eduard Suess. *J.b.k.k. Geol. Reichsanstalt*, **66**, 33–556 (reprint: 1917).
- Tufel, R.L. (ed.), 1875–1877. Documents Concerning the Life and Character of Swedenborg, collected, translated and annotated. (3 vols.). London: Swedenborg Society.
- Urey, H.C., Epstein, S., McKinney, C., and McCrea, J., 1948. Method for measurement of paleotemperatures. *Bull. Geol. Soc. Am.*, **59**, 1359–1360.
- Urey, H.C., Lowenstam, H.A., Epstein, S., McKinney, C.R., 1951. Measurements of paleotemperatures of the upper Cretaceous of England, Denmark, and the southeastern United States. *Bull. Geol. Soc. Am.*, **62**, 399–416.
- Volger, G.H.O., 1889. *Leben und Leistungen des Naturforschers Karl Schimper*. Frankfurt-am-Main, 56pp.
- Von Richthofen, F., 1886. “Führer für Forschungsreisende,” Hannover, Jänecke, 734pp.
- Walter, J., 1928. Arrhenius memorial lecture. *J. Chem. Soc.*, 1380–1401 (London).
- Webb, G.E., 1983. *Tree Rings and Telescopes: The Scientific Career of A. E. Douglass*. Tucson: University of Arizona Press, 242pp.
- Wertembaker, W., 1974. *The Floor of the Sea*. Boston: Little, Brown, 275pp.
- Whitaker, W., 1904. Selwyn–Obit. *Proc. R. Soc. Lond.*, **75**, 325–328.
- Willis, B., 1929. Chamberlin–Memorial. *Geol. Soc. Am. Bull.*, **40**, 23–45.

- Winkler, M.G., and Van Helden, A., 1992. Representing the heavens: Galileo and visual astronomy. *ISIS*, **83**, 195–217.
- Woodward, H.B., 1913. Jamieson–Obit. *Geol. Mag.*, **50**, p.332–333.
- Zeuner, F.E., 1945/1959. *The Pleistocene Period*. London: Royal Society, 2447p.
- Zeuner, F.E., 1946. *Dating the Past*. London: Methuen, 444pp.

Cross-references

Astronomical Theory of Climate Change
 CLIMAP
 Dendroclimatology
 Glacial Geomorphology
 Glaciations, Quaternary
 History of Paleoclimatology
 Oxygen Isotopes
 Plate Tectonics and Climate Change
 Sea Level Change, Post-Glacial
 SPECMAP
 Stable Isotope Analysis
 Sun-Climate Connections
 Tills & Tillites

HOLOCENE CLIMATES

Introduction and definition

The Holocene – or “wholly recent” – epoch is the youngest phase of Earth history, which began when the last glaciation ended, and for this reason it is sometimes also known as the post-glacial period. In reality, the Holocene is one of many interglacials that have punctuated the late Cenozoic ice age. The term was introduced by Gervais in 1869 and was accepted as part of valid geological nomenclature by the International Geological Congress in 1885. A summary account of Holocene environmental history is provided by Roberts (1998). A commission of the International Union for Quaternary Research (INQUA) has been devoted to the study of the Holocene, and it is also a major focus of the PAGES (Past Global Changes) program. Since 1991, the journal *The Holocene* has been dedicated exclusively to Holocene research.

There are three principal schools of thought about how the Holocene should be formally defined. Because the Holocene still “lives,” debate has focused on defining its onset, namely the Pleistocene-Holocene boundary. The first school of thought (Watson and Wright, 1980) believes that the beginning of Holocene is easily recognized in individual records of deglaciation or biotic change (e.g., in pollen diagrams), but that because these changes are not exactly the same age everywhere, the Pleistocene-Holocene boundary should therefore be time-transgressive. A second school prefers the “type-section” approach commonly used in geology to define stratigraphic boundaries. Mörner (1976), for example, proposed that a sequence in southern Sweden might be the standard reference point for the Pleistocene-Holocene boundary. The third view, and one which is supported by INQUA, is that the Holocene is simply defined as beginning 10,000 radiocarbon (^{14}C) years ago.

^{14}C chronologies count AD 1950 as being the “present-day” and also underestimate true – or calendar – ages by several centuries for most of the Holocene. Cross-dating of pines from

the western United States and northwest Europe has revealed a systematic divergence between ^{14}C and tree-ring ages in samples more than 2,500 years old, with a discrepancy amounting to 600 years (or 12%) at 5,000 yBP. Moreover, the calibration curve is not a smooth line but contains a number of deviations that represent short-term variations in atmospheric ^{14}C production. This is significant in that some ^{14}C dates have more than one calendar age. Current estimates for the beginning of the Holocene put it at around 11,500 yBP in calendar years, based on counts of tree rings and annual ice layers (Alley et al., 1993; Gulliksen et al., 1998). It is now possible to calibrate ^{14}C dates for the whole of the Holocene (Stuiver and Reimer, 1993), and because it is better to use calendar rather than radiocarbon years as a time frame for past global changes, the former (i.e., cal. yBP) will be used in this entry.

Various attempts have been made to subdivide the Holocene, usually on the basis of inferred climatic changes. Blytt and Sernander, for instance, proposed a scheme of alternating cool-wet and warm-dry phases based on shifts in peat stratigraphy in northern Europe. However, with the systematic application of ^{14}C dating it has become clear that Holocene vegetation and climatic changes were more often than not time-transgressive, and as a result most researchers prefer to use age (e.g., 8,000 cal. yBP) rather than stage (e.g., Boreal-Atlantic transition) for defining past events.

Data sources

For the last few centuries of the Holocene, instrumental data are available and can be used to build up high-quality time-series for individual climate variables. However, because the climate system varies over timescales longer than can be observed directly, it is also necessary to turn to longer-lived human and natural archives. For intermediate time-scales, documentary sources can be used (Bradley and Jones, 1992), although these data were not always collected in a form ideal for the analysis to which we wish to subject them. The length of the “historical” time period also varies greatly in different parts of the world, extending back around 5,000 years in regions such as Egypt, but little more than a few decades in places like Papua-New Guinea. A third group of techniques operates over longer Holocene timescales. These are proxy-climate methods such as dendroclimatology and pollen analysis, which can sometimes be combined within a single sequence to create a multi-proxy approach.

In environments with little human disturbance, it is widely believed that organisms – terrestrial, aquatic or marine – will eventually achieve a state of equilibrium with the prevailing climate. Modern data on climate-species relationships can therefore be applied to paleoecological data from sediment cores to produce quantitative estimates of past temperatures or rainfall levels, using transfer functions or other multivariate statistical methods. Climatic calibration of modern and fossil pollen data has allowed maps to be produced showing temperature, precipitation or air mass distribution for different times during the Holocene over eastern North America (Webb et al., 1993). An alternative, complementary approach involves calibrating proxy-climate indicators, such as the stable isotope signature in cave speleothems, against local meteorological records for the last 50–100 years. If a statistically significant correlation can be found, the proxy-climate records can then be used to extend the time series back to before the beginning of recorded weather observations.

The last deglacial climatic transition

The Last Glacial Maximum occurred around 25,000–18,000 years ago, according to calibrated radiocarbon dating. At this time, temperatures on land were lowered by as much as 20 °C although ocean temperatures changed much less. Under the full glacial climate, ice sheets more than 4 km thick lay across northern Europe and North America, and smaller ice caps existed in the Alps, the southern Andes, and parts of East Asia. Climatic warming, and the consequent deglaciation of these continental regions, took place in a series of steps that appear to have been broadly synchronous over large parts of the globe, although there may have been some asynchrony between the Northern and Southern Hemispheres.

Deglaciation, which took about 9,000 years to complete in Europe and North America, was an unsteady process, and at various times towards the tail end of the Pleistocene ice sheets temporarily re-advanced. In at least some cases, this was the result of a temporary but sharp oscillation in climate, which represented a false start to the present interglacial. In the circum-North Atlantic region, this late Pleistocene thermal oscillation comprised a warming event often known as the Bølling-Allerød interstadial (~15,000–12,700 cal. yBP) followed by a cooling event called the Younger Dryas stadial (12,700–11,500 cal. yBP). Evidence from coleopteran (beetle) and chironomid (midge) fossils shows that summer temperatures warmed rapidly to reach – or even exceed – those of today soon after 15,000 cal. yBP.

Ice cores provide some of our most important paleoclimatic data for ice age climate, with Greenland possessing the most important record in the Northern Hemisphere. Ice has accumulated faster here than in Antarctica and it therefore offers a more detailed sequence of past climatic change, with an annual time resolution for the part covering the late Pleistocene and Holocene. The GRIP and GISP2 cores drilled at the summit of the Greenland ice sheet between 1988 and 1993 provide especially important climate records. They show the same late-glacial climatic oscillation as revealed in biotic records, and confirm that the warming steps were extremely rapid. The last of these, marking the transition from the Younger Dryas stadial to the Holocene interglacial proper, involved a temperature rise of 7 °C over no more than 50 years (Alley et al., 1993). These sudden jumps in climate may be linked to periodic on and off switching of the thermohaline “conveyor belt” circulation in the Atlantic Ocean (Bard and Broecker, 1992). The Younger Dryas climatic reversal, for example, was most probably the result of a partial shut-down of the Atlantic conveyor caused by large pulses of meltwater from adjacent Northern Hemisphere ice sheets.

The early Holocene climatic optimum

Because climatic change was especially rapid during the millennia either side of the Pleistocene-Holocene boundary, many Earth surface systems experienced lagged responses. Global (eustatic) sea levels, for example, lay at about –40 m at 11,000 cal. yBP and only reached modern elevations around 6,000–5,000 years ago (Edwards et al., 1993). Similarly, because soil formation and vegetation cover often lagged behind the climate, many landscapes experienced a phase of temporary geomorphic instability during the Pleistocene-Holocene transition, with high rates of erosion and sediment flux.

In many mid-latitude Northern Hemisphere regions, a thermal optimum can be identified between ~10,000 and ~6,000 cal. yBP from the extension of species such as the water chestnut and the pond tortoise north of their present European climatic limits.

The cause of these long-term climatic changes lies in astronomically-controlled variations in the Earth’s receipt of solar radiation (Figure H6). At the start of the Holocene, one of the three *Croll-Milankovitch* cycles – the precession of the equinoxes – lay at the opposite point on the cycle from where it lies today. Therefore, the Northern Hemisphere received nearly 8% more solar radiation during summer months than at present, and northern summers were considerably warmer in consequence.

Because climatic conditions exert a powerful influence over geomorphic processes, relict landforms can furnish indications about past climates. In the tropics and sub-tropics, two of the most climatically-sensitive geomorphic regimes are desert dunes and lakes. As a result of the close relationship between eolian processes and climatic aridity, fossil dunes have helped to provide an indication of the changing extent and location of the World’s arid zones (Goudie, 1983). Eolian landforms not only indicate times of climatic aridity but also reveal former wind strengths and directions. While dunes indicate periods of climatic aridity, high-level lakes reflect periods of positive water balance, and in the Holocene at least, these are associated with phases of wetter climate. Direct geomorphic evidence of former high levels derives from shoreline terraces and related landforms left above present-day lakes.

It was recognized in the early twentieth century that deserts were not always as arid as they are today. In addition to the evidence of high-level lakes, ancient rock paintings from the Sahara depict herds of savanna mammals, while pollen diagrams and rodent nests indicate much richer, often wooded, vegetation cover. Within the tropics, ¹⁴C dating has shown that the last “pluvial” (or wet) period started during the terminal Pleistocene and continued through the first half of the Holocene (14,000–5,500 cal. yBP). Water-balance calculations for these enlarged early Holocene lakes indicate that rainfall in East Africa, the Sahara, and northwest India increased by between 150 and 400 mm per year (Street-Perrott et al., 1991). This increase was caused by an enhanced monsoon circulation that brought summer rains further north than they occur today. The

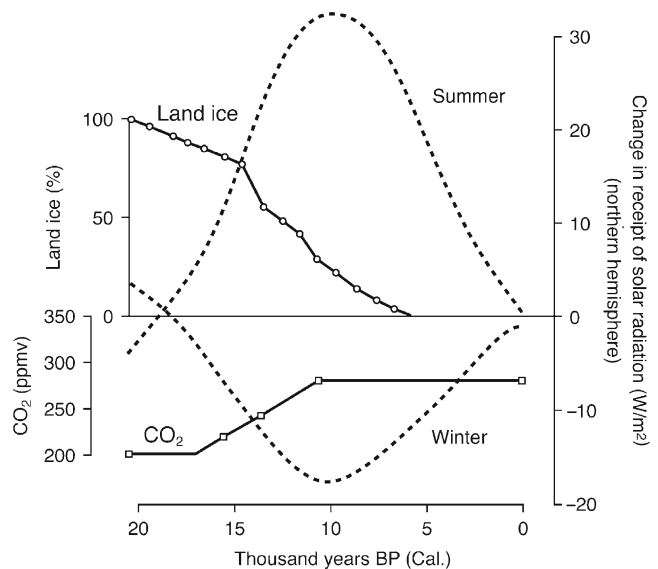


Figure H6 Changing receipt of solar radiation and other climatic controls in the Northern Hemisphere since the Last Glacial Maximum (modified after Kutzbach and Street-Perrott, 1985)

stronger monsoon was itself generated by the “thermal optimum,” which led to greater heating over the land – especially over south Asia – and caused low pressure, which sucked in the humid, monsoonal air masses from the south.

In mid-latitude regions such as the North American prairie, a different pattern of climate change occurred around this time. Pollen data show that the mid-western prairie-forest boundary moved eastwards until 8,000 cal. yBP, but subsequently shifted back in the opposite direction. As this boundary is today controlled by moisture availability, it is reasonable to use it as a proxy climatic indicator, recording climatic conditions between 8,000 and 4,500 cal. yBP that were drier than at present. Sediment cores from some of the many small lakes of the North American Great Plains also record this climatic phase. Diatom and geochemical analyses, for example, show high salinities during the first half of the Holocene, while before and after this phase the lake water was relatively fresh (Haskell et al., 1996).

This orbital forcing of the early Holocene climatic optimum appears to have been amplified by the biosphere itself. Modeling experiments have shown that vegetation had a significant effect on climatic conditions in key boundary areas, such as the edges of forest and desert biomes, by changing the surface albedo and moisture conditions. Along the boreal-tundra ecotone, for example, calculations suggest that the expanded forest caused an additional warming of about 4 °C in spring temperatures 6,000–7,000 years ago, over and above that caused directly by solar heating (Foley et al., 1994).

These longer-term climatic trends were interrupted on several occasions during the Holocene by abrupt events of shorter, centennial duration. In the tropics, they are recorded in abrupt lake-level falls, dated in Africa to ~12,000, 8,200 and 5,200 cal. yBP (Gasse, 2000). As with the rapid rises in temperature at the Pleistocene-Holocene transition, these hydrological changes occurred so rapidly that their true rate cannot be determined by ¹⁴C dating. The abrupt arid events are also recorded by the Greenland ice core record as sharp troughs in atmospheric methane, implying a reduction in tropical wetlands, which are a major source of this greenhouse gas (Figure H7).

Late Holocene climatic variability

Although less marked than during the early Holocene, the later Holocene nonetheless experienced some significant shifts in climate. Among these were the progressive cooling following the Holocene thermal optimum and the climatic desiccation of the northern sub-tropics after 6,000 cal. yBP that created the modern Saharan, Arabian and Thar deserts. The water levels of some low-latitude lakes fell abruptly at this time (Figure H7), suggesting rapid suppression of the monsoonal circulation system, which controls tropical rainfall (Street-Perrott et al., 1991; Gasse, 2000).

Superimposed on longer-term climatic trends linked to orbital insolation forcing were shorter-term secular variations from wet to dry, or cold to warm, recorded in the stratigraphy of peat bogs (Charman et al., 1999) or the advance and retreat of mountain glaciers. Whether these oscillations represent true, regular cycles is uncertain, as is the question of the causes of these climatic changes. Among the most likely controlling mechanisms for sub-Milankovitch climatic variations are changes in the radiation output of the Sun, linked to sunspot cycles, and the heat-shielding effect of volcanic eruptions with large dust emissions.

Volcanic aerosols can play an important role in disturbing the Earth’s climate, for example by creating a dust veil that reduces the transparency of the atmosphere. After major

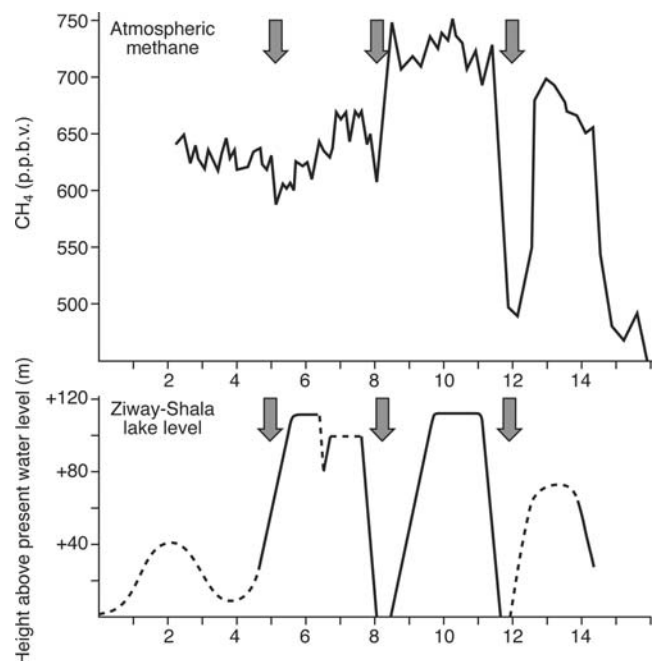


Figure H7 Tropical African lake-level record compared with atmospheric methane concentration recorded in a Greenland ice core (modified after Roberts, 1998; data from Gillespie et al., 1983; Blunier et al., 1995). Arrows show abrupt arid events interrupting longer-term climatic trends. Ages are in 1000 yBP (cal).

historically-recorded eruptions like that at Laki in Iceland in AD 1783, contemporary writers such as Benjamin Franklin recorded severe late frosts and peculiar hazes in regions far removed from the volcanoes themselves (Grattan and Brayshay, 1995). Some earlier Holocene eruptions were substantially larger than the Laki fissure eruption, and it has been suggested that they may have had a proportionately bigger climatic impact (Zielinski et al., 1994). For example, in about 1628 BC (3,578 cal. yBP), the Aegean island of Santorini (Thera) exploded catastrophically, forcing its Bronze Age population to flee or perish. Dendroclimatology studies have shown that the tree rings of Irish bog oaks were unusually narrow at this time, while bristlecone pine growth rings of the same age in California show signs of frost damage. These have been interpreted as the result of a cooler and/or wetter climate. However, in Turkey, which is warm and dry in summer, the same climatic change appears to have given rise to more, not less, favorable growing conditions and to broader tree rings (Kuniholm et al., 1996). While the evidence linking tree-rings, climate and volcanic eruptions is impressive, it also suggests that in most cases the climate perturbation was short-lived, typically a decade or less.

Increasing evidence is also being found to support a role for variations in solar radiation upon Holocene climates, typically based on the observation that cyclic fluctuations in climate proxies have periodicities close to those found in the record of solar activity (Bond et al., 2001). In some cases, well-dated climatic anomalies have been to correlate with a known forcing function, such as European temperature minima coinciding with the Maunder minimum in solar activity of AD 1650–1715 (Mauquoy et al., 2002).

In addition to these external mechanisms, variations in Holocene climate will also have been forced by cyclic

processes originating within the Earth system, such as the quasi-periodic ~1500-year long Bond cycles during which ice-berg “armadas” drifted southward into the North Atlantic, slowing down the oceanic thermohaline conveyor belt. A comparable but much higher-frequency auto-cyclic phenomenon is the well-known El Niño-Southern Oscillation (ENSO). Although ENSO-type events appear to have operated throughout the Holocene, there is evidence, especially from high-resolution stable isotope analysis of corals, that the current ENSO frequency spectrum was not established until mid-Holocene times (Gagan et al., 2000).

The period during the Holocene with the best-resolved and most reliably calibrated climate data is the last millennium, including both the Mediaeval Climate Anomaly (~AD 1000–1250) and Little Ice Age (~AD 1250–1850, particularly AD 1590–1850) during which major rivers like the Thames and the Tiber regularly froze over. Data come from proxy-climate records, notably tree rings, from historical observations and – for the last two centuries – from instrumental records. Following the initial work of Mann et al. (1999) a number of synthetic curves have been generated from available data sets for Northern Hemisphere temperature changes. Source of these have a “hockey-stick” shape, in which temperatures fell progressively to reach a minimum in the seventeenth century, before rising sharply during the last 150 years. It remains an unresolved question how much of the observed rise of ~1 °C since the mid-nineteenth century is due to anthropogenic increases in atmospheric greenhouse gases, and how much is due to natural variability. However, global temperatures are probably now higher than at any time during the last 1,000 years, and it is likely that most of the post-1980 warming is of human origin.

To judge by recent experience, drought-prone regions can be expected to have been at least as severely affected by any climatic fluctuations as mid- and high-latitude areas, not only because of temperature change, but also due to rainfall variability. During the last millennium, greater aridity appears to have marked the North American Great Plains at the time of the Little Ice Age to judge from lake salinity variations, while increased dust flux onto the ice caps of the Andes suggests a similar tendency towards drought during this time interval. By contrast, East African lakes were at low levels at the time of the Mediaeval Climate Anomaly and were often higher during the Little Ice Age (Verschuren et al., 2004).

Conclusion

It is clear that since the end of the last glacial stage, climatic stability over decadal to millennial timescales has been far from the norm. A Holocene perspective can help to disentangle the different factors that determined these variations in global climate. Secular climatic cycles are recorded by many paleoclimatic indicators, including peat bog profiles, salinity fluctuations in non-outlet lakes, and in cores from ice caps. Some of these archives, such as variations in tree ring widths, can be resolved to individual years, and this permits investigation of the potential causes of short-term changes to the climate.

A Holocene timescale is also valuable if we want to establish how typical current rates of climatic change are, compared to those of the recent geological past. During the last major global warming around 11,500 years ago, a gradual orbital forcing of climate was amplified by a series of positive feedback mechanisms to cause an abrupt switch from glacial to interglacial conditions within the span of a human lifetime. The current temperature rise is therefore not unprecedented, although the climate is heading

towards conditions warmer than at any time during the Holocene. Past climatic changes offer further warnings about the potential instability of climate and the consequent hazards of climate prediction. On at least three occasions within the last 10,000 years, the climate deteriorated abruptly, only to return to its previous state within a few centuries.

If it is climatically calibrated and homogenized, proxy data for the Holocene can also be compared against numerical (global circulation models) GCM experiments run with different boundary conditions (COHMAP, 1988). Such data versus model comparisons allow the sensitivity and reliability of GCMs to be tested, hence improving their ability to predict future climates. The climate during the early Holocene “thermal optimum,” in particular, has been used to test and calibrate numerical models of the atmosphere. On the other hand, the Holocene does not offer a direct analogue for a future greenhouse gas-warmed climate, because it was dominated by seasonal, rather than mean annual, changes in the Earth’s net receipt of solar radiation.

Neil Roberts

Bibliography

- Alley, R.B., Meese, D.A., Shuman, C.A., Gow, A.J., Taylor, K.C., Grootes, P.M., White, J.W.C., Ram, M., Waddington, E.D., Mayewski, P.A., and Zielinski, G.A., 1993. Abrupt increase in Greenland snow accumulation at the end of the Younger Dryas event. *Nature*, **362**, 527–529.
- Bard, E., and Broecker, W.S. (eds.), 1992. *The Last Deglaciation: Absolute and Radiocarbon Chronologies*. NATO ASI Series. Berlin: Springer.
- Blunier, T., Chappellaz, J., Schwander, J., Stauffer, B., and Raynaud, D., 1995. Variations in atmospheric methane concentration during the Holocene epoch. *Nature*, **374**, 46–49.
- Bond, G., Kromer, B., Beer, J., Muscheler, R., Evans, M.N., Showers, W., Hoffmann, S., Lotti-Bond, R., Hajdas, I., and Bonani, G., 2001. Persistent Solar Influence on North Atlantic climate during the Holocene. *Science*, **294**, 2130–2136.
- Bradley, R.S. and Jones, P.D. (eds.), 1992. *Climate since A.D. 1500*. London: Routledge.
- Charman, D.J., Hendon, D., and Packman, S., 1999. Multi-proxy surface wetness records from replicate cores on an ombrotrophic mire: Implications for Holocene palaeoclimate records. *J. Quaternary Sci.*, **14**, 451–463.
- COHMAP members, 1988. Climatic changes of the last 18,000 years: Observations and model simulations. *Science*, **241**, 1043–1052.
- Edwards, R.L., Beck, J.W., Burr, G.S., Donahue, D.J., Chappell, J.M.A., Bloom, A.L., Druffel, E.R.M., and Taylor, F.W., 1993. A large drop in atmospheric $^{14}\text{C}/^{12}\text{C}$ and reduced melting in the Younger Dryas, documented with ^{238}Th ages of corals. *Science*, **260**, 962–968.
- Foley, J.A., Kutzbach, J.E., Coe, M.T., and Levis, S., 1994. Feedbacks between climate and boreal forests during the Holocene epoch. *Nature*, **371**, 52–54.
- Gagan, M.K., Ayliffe, L.K., Beck, J.W., Cole, J.E., Druffel, E.R.M., Dunbar, R.B., and Schrag, D.P., 2000. New views of tropical paleoclimates from corals. *Quaternary Sci. Rev.*, **19**, 45–64.
- Gasse, F., 2000. Hydrological change in the African tropics since the Last Glacial Maximum. *Quaternary Sci. Rev.*, **19**, 189–212.
- Gillespie, R., Street-Perrot, F.A., and Switsur, R., 1983. Post-glacial arid episodes in Ethiopia have implications for climate prediction. *Nature*, **306**, 681–683.
- Goudie, A.S., 1983. The arid Earth. In Gardner, R., and Scoging, H. (eds.), *Megageomorphology*. Oxford: Clarendon Press, pp. 152–171.
- Grattan, J., and Brayshay, M., 1995. An amazing and portentous summer: Environmental and social responses in Britain to the 1783 eruption of an Iceland volcano. *Geogr. J.*, **161**, 125–134.
- Gulliksen, S., Birks, H.H., Possnert, G., and Mangerud, J., 1998. The calendar age of the Younger Dryas – Holocene transition at Kråkenes, western Norway. *The Holocene*, **8**, 249–260.
- Haskell, B.J., Engstrom, D.R., and Fritz, S.C., 1996. Late Quaternary paleohydrology in the North American Great Plains inferred from the

- geochemistry of endogenic carbonate and fossil ostracods from Devils Lake, North Dakota, USA. *Palaeogeogr. Palaeoclimatol. Palaeoecol.*, **124**, 179–193.
- Kuniholm, P.I., Kromer, B., Manning, S.W., Newton, M., Latini, C.E., and Bruce, M.J., 1996. Anatolian tree rings and the absolute chronology of the eastern Mediterranean, 2220–718 BC. *Nature*, **381**, 780–783.
- Kutzbach, J., and Street-Perrott, F.A., 1985. Milankovitch forcing of fluctuations in the level of tropical lakes from 18 to 0 kyr BP. *Nature*, **317**, 130–134.
- Mann, M.E., Bradley, R.S., and Hughes, M.K., 1999. Northern Hemisphere temperatures during the past millennium: Inferences, uncertainties and limitations. *Geophys. Res. Lett.*, **26**, 759–762.
- Mauquoy, D., van Geel, B., Blaauw, M., and Plicht, van der J., 2002. Evidence from northwest European bogs shows “Little Ice Age” climatic changes driven by variations in solar activity. *The Holocene*, **12**, 1–6.
- Mörner, N.-A., (ed.), 1976. The Pleistocene/Holocene boundary: A proposed boundary-stratotype in Gothenberg, Sweden. *Boreas*, **5**, 193–275.
- Roberts, N., 1998. *The Holocene. An environmental history*. Oxford/Boston: Blackwell.
- Street-Perrott, F.A., Mitchell, J.F.B., Marchand, D.S., and Brunner, J.S., 1991. Milankovitch and albedo forcing of the tropical monsoons: A comparison of geological evidence and numerical simulations for 9,000 yr BP. *Trans. R. Soc. Edinb., Earth Sci.*, **81**, 407–427.
- Stuiver, M., and Reimer, P.J., 1993. Extended ¹⁴C database and revised CALIB radiocarbon calibration program. *Radiocarbon*, **35**, 215–230.
- Verschuren, D., Briffa, K., Hoelzmann, P., Barker, P., Scott, L., Barber, K., Snowball, I., and Roberts, N., 2004. Holocene climate variability in Europe and Africa: A PAGES PEP III time-stream 1 synthesis. In Battarbee R.W., Gasse F., and Stickley C.E., (eds.), *Past Climate Variability through Europe and Africa*. Dordrecht: Kluwer, pp. 567–582.
- Watson, R.A., and Wright, H.E. Jr., 1980. The end of the Pleistocene: A general critique of chronostratigraphic classification. *Boreas*, **9**, 153–163.
- Webb, T., Bartlein, P.J., Harrison, S.P., and Anderson, K.H., 1993. Vegetation, lake levels and climate in eastern North America for the past 13,000 years. In Wright, H.E. Jr., Kutzbach, J.E., Webb, T., Ruddiman, W.F., Street-Perrott, F.A., and Bartlein, P.J. (eds.), *Global Climates since the Last Glacial Maximum*. Minneapolis: University of Minnesota Press, pp. 415–467.
- Zielinski, G.A., Mayewski, P.A., Meeker, L.D., Whitlow, S., Twickler, M.S., Morrison, M., Meese, D.A., Gow, A.J., and Alley, R.B., 1994. Record of volcanism since 7000 B.C. from the GISP2 Greenland ice core and implications for the volcano-climate systems. *Science*, **262**, 948–952.

Cross-references

Arid Climates and Indicators
 Astronomical Theory of Climate Change
 Bölling-Allerød Interstadial
 Climate Variability and Change, Last 1000 Years
 COHMAP
 Dating, Dendrochronology
 Dendroclimatology
 Eolian Sediments and Processes
 Hypsithermal
 Ice Cores, Antarctica and Greenland
 Lake Level Fluctuations
 Last Glacial Termination
 Late Quaternary-Holocene Vegetation Modeling
 Little Ice Age
 Medieval Warm Period
 Millennial Climate Variability
 PAGES
 Paleoclimate Modeling, Quaternary
 Paleo-El Niño-Southern Oscillation (ENSO) Records
 Pollen Analysis
 Sea Level Change, Post-Glacial
 Sun-Climate Connections
 Thermohaline Circulation
 Volcanic Eruptions and Climate Change
 Younger Dryas

HOLOCENE TREELINE FLUCTUATIONS

Timberline and treeline

Treelines are climatically sensitive transitional zones between closed forests and alpine, polar, or dry grassland communities. In most cases, temperature and precipitation thresholds determine whether a site is treeless or not (Arno and Hammerly, 1993; Körner, 1999). However, many other factors, such as vegetation type, soil type, snow cover, topography, and wind can locally co-determine the boundary of tree growth. Independently from the biotic and abiotic causes that form this conspicuous vegetation limit, the spatial position of treeline depends on the definition of “tree.” The most commonly used criterion to define “tree” at treeline is a minimum height between 8 and 2 m (Arno and Hammerly, 1993; Körner, 1999). Some studies prefer to distinguish between timberline and treeline (e.g., using the height of trees as a diagnostic criterion: 8 m for timberline and 2 m for treeline). The width of the transitional zone separating closed forests from treeless plant communities is not uniform: polar treelines and drought-caused treelines can form very broad transition zones such as parklands with widely spaced trees (Arno and Hammerly, 1993). Conversely, mountain treelines have rather narrow transitional zones (i.e., 100–200 m of vertical extent). It has been suggested that this range overlaps with the altitudinal span between timberline and treeline as defined above (8 vs. 2 m of tree height, Tinner and Theurillat, 2003).

The climatic sensitivity of treelines has led to much effort on the reconstruction of past treeline positions in order to quantify Holocene climatic changes. The significance of the method for paleoclimatology lies mainly in two factors: (a) Treeline studies have local to regional spatial resolutions and therefore provide valuable information about climatic changes of mountainous or polar sites, and (b) If combined with independent environmental proxies (e.g., oxygen isotopes as climatic proxy), treeline studies can give insights into biosphere responses to rapid environmental changes.

Reconstructing treeline fluctuations

The reconstruction of treeline fluctuations can be performed using different approaches. Analysis of pollen, stomata, macrofossils, and megafossils (including tree rings) are the most important methods. In addition, charcoal, soil, and phytolith analysis may be applied to determine maximum treeline positions. The methods have different spatial resolutions. Since pollen is easily lifted, transported, and deposited by winds over long distances, pollen records have rather low spatial resolutions. Thus, it is difficult to reconstruct treeline fluctuations by using the pollen approach alone. Macrofossil and megafossil analyses are considered to be more reliable tools for reconstruction of timberline fluctuations (Birks, 2001; Tinner and Theurillat, 2003) since they have higher taxonomic and spatial resolutions (meters to decameters) than pollen studies (decimeter to kilometers). A disadvantage of macrofossil and megafossils is that, in contrast to pollen, they are not ubiquitous in Holocene deposits. Producing treeline reconstructions requires records from today’s treelines that reach back to the late glacial. Two preconditions are essential: (a) the chronology of the treeline records must be fixed to an absolute scale with sufficient ¹⁴C-dates of terrestrial fossils, and (b) the study sites should be situated near to the present-day treeline position.

To assess the magnitude of past climate changes, reconstructions of Holocene treeline fluctuations must be related to modern treeline positions. For estimations of past temperature changes it is assumed that today's occurrence of trees is in equilibrium with the climate of the past few decades. In regions affected by strong human impact (e.g., the Alps), single trees in remote areas may still indicate the potential altitudinal limit of forest and tree growth. Using today's lapse rates (under the assumption of Holocene stability), it is possible to convert past treeline fluctuations (m) into (summer) temperature changes ($^{\circ}\text{C}$) (Haas et al., 1998), although it must be considered that higher treelines in the past reflected warmer periods that were stable enough to allow subalpine forest to migrate up-slope (100–200 years of potential response lags). In an attempt to synthesize common patterns across two continents, we focus on a few well-documented but representative case studies from temperature-controlled mountain treelines in Europe and Northern America.

Holocene treeline dynamics

Since reconstructions of Holocene treeline fluctuations reflect past local dynamics, comparisons among the sites are needed

to assess larger-scale patterns that could be related to climatic changes. Comparisons among pollen and macrofossil stratigraphies in the Swiss and Italian Alps allowed the detection of phases of warm (dry) and cool (wet) phases (Wick and Tinner, 1997) that are in agreement with lake-level fluctuations in the alpine forelands (CE-1 to CE-8, Haas et al., 1998) and glacier oscillations (Figure H8). The analysis of pollen and macrofossils from lake and mire deposits along altitudinal transects permits the reconstruction of treeline fluctuations during the Holocene (Tinner and Theurillat, 2003). These reconstructions show that the positions of timberline and treeline fluctuated within a band of 100–180 m during the Holocene and that treeline was at its uppermost limit (ca. 180 m higher than today) during the period 10,000–6,000 cal. yBP (Figure H9). Severe diebacks of treeline vegetation occurred during cold (humid) periods (CE-1 to CE-8 as well as during the Little Ice Age; Figures H8 and H9). A severe treeline decline lasted from 8,200 to 7,500 cal. yBP (CE-3), with two minima at 8,000 and 7,600 cal. yr B.P. (Figure H8, sites Gouillé Rion and Lengi Egga). After 6,000–5,000 cal. yBP, timberline and treeline progressively declined by about 180 m and 300–400 m, respectively (Figure H9). The regression of densely forested areas

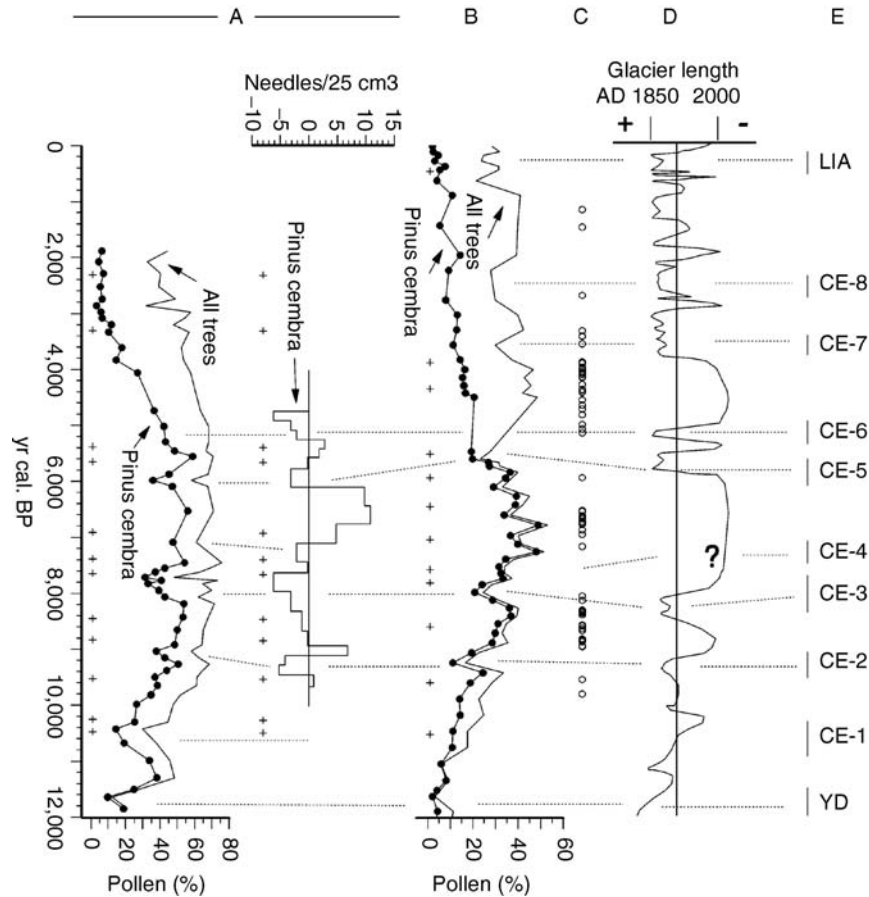


Figure H8 Comparison between pollen and macrofossil records of high-elevation sites and glacier fluctuations during the past 12,000 years; (a) pollen percentages and macrofossil concentrations at Gouillé Rion (Swiss Alps); (b) pollen percentages at Lengi Egga (Swiss Alps); (c) radiocarbon dates of wood and organic debris collected in front of Alpine glaciers (Hormes et al., 2001); (d) estimated length variation of Swiss glaciers (Maisch et al., 1999); (e) central European cold-humid phases (Haas et al., 1998). +in a and b show the chronological position of radiocarbon dates used for depth-age models.

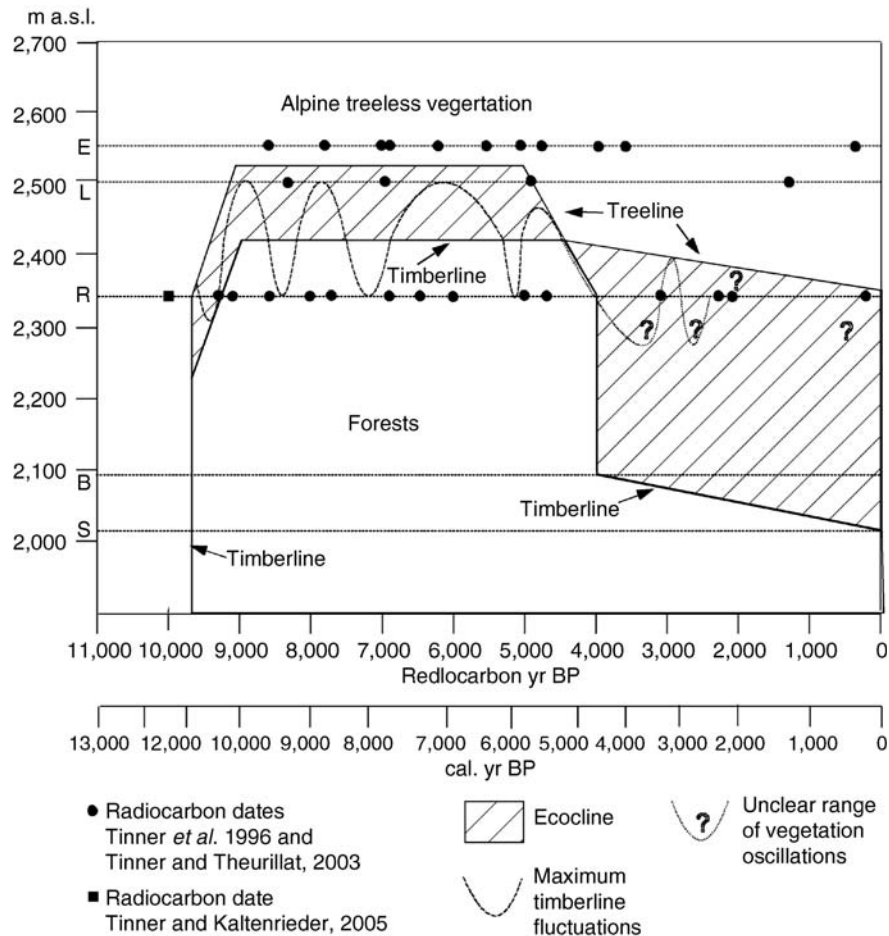


Figure H9 The approximate Holocene timberline and treeline elevation (m) in the Swiss central Alps based on radiocarbon-dated macrofossil and pollen sequences (modified from Tinner and Theurillat, 2003).

(timberline) in the Alps during the past 5,000 years was primarily caused by human impact, whereas the course of treeline gives a more realistic estimation of the climatic influence (Figure H9). Assuming constant lapse rates of $0.7^{\circ}\text{C}/100\text{ m}$, it is possible to estimate the range of Holocene temperature oscillations in the Alps to $0.8\text{--}1.2^{\circ}\text{C}$ between 10,500 and 4,000 cal. yBP, when average (summer) temperatures were about $0.8\text{--}1.2^{\circ}\text{C}$ higher than today. After 4,000 cal. yBP, summer temperatures successively declined to values comparable to those of the twentieth century (Figure H9).

The general course of Holocene treeline fluctuations in the Alps is similar to that reconstructed for Scandinavian sites. Megafossil, macrofossil, and pollen studies suggest that treeline was at its uppermost limit between 9,500(–9,000) and 6,500 (–6,000) cal. yBP in Norway and Sweden, about 200–400 m above today's treeline position (Kullman, 1995; Dahl and Nesje, 1996; Barnekow, 1999; Barnett et al., 2001). At some study sites, treelines declined temporarily between 8,300 and 8,000 cal. yBP (Dahl and Nesje, 1996; Barnekow, 1999; Barnett et al., 2001). Using today's lapse rates, it has been estimated that temperatures were $1.3\text{--}2.0^{\circ}\text{C}$ higher than today during the period of highest treeline positions.

A number of pollen profiles from western North America provide multi-millennial year records of alpine timberline fluctuations. These records were derived primarily from sediments deposited in high-elevation lakes and bogs, and, in most cases, limited dating control of the sedimentary records restricts their application to the reconstruction of only the general trends in treeline position throughout the Holocene. A more detailed picture of timberline fluctuations during the last 1,000 years has emerged from the study of tree rings taken from living trees or dead snags situated near the alpine timberline in the North American Cordillera. Most pollen records indicate that the alpine timberline was higher than present during the early to mid-Holocene and a general and widespread decline was underway by ca. 6,000–5,000 cal. yBP (Hebda, 1995). Pollen-based estimates of Holocene timberline position have been corroborated by several complementary proxies for estimating past environmental and climatic conditions. Taken together, these data suggest that mean growing season temperature in western North America was on the order of $1\text{--}4^{\circ}\text{C}$ warmer than present during the early-mid Holocene.

Perhaps the most direct and unequivocal evidence for past high stands of alpine timberline in western North America is

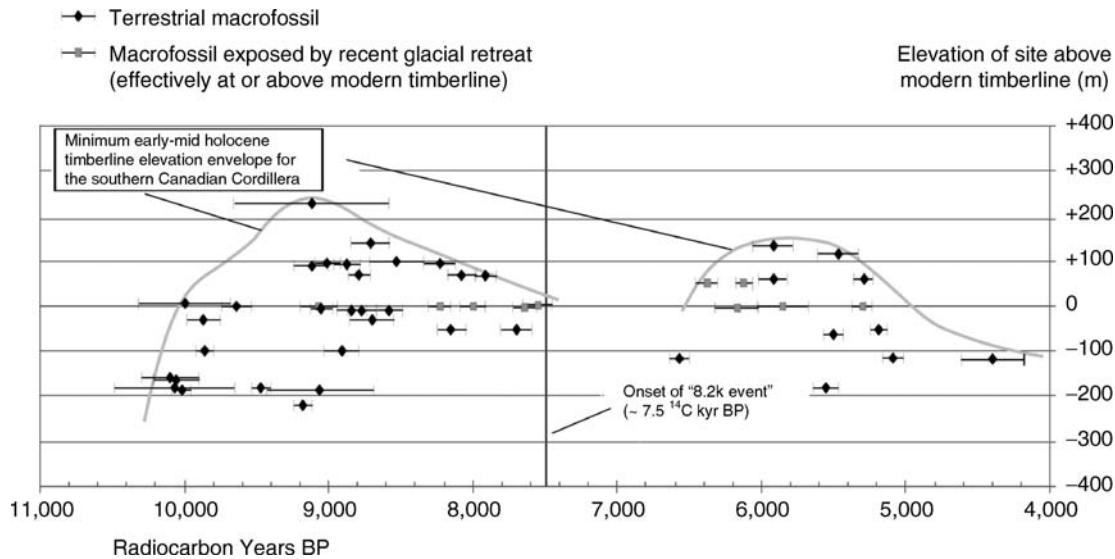


Figure H10 The approximate minimum early-mid Holocene treeline elevation in the southern Canadian Cordillera, based on radiocarbon-dated wood macrofossils recovered from high-elevation sites (modified from Reasoner et al., 2001).

radiocarbon-dated macrofossils that have been preserved in alpine environments. In some cases these data are derived from abundant conifer needles preserved in lacustrine sediments at sites that are currently above natural treeline (Reasoner and Hickman, 1989) and in others they are obtained from logs (megafossils) preserved in alpine bogs or soil profiles (Kearney and Luckman, 1983; Carrara, et al., 1991). Similarly, fossil wood dating to the early Holocene has been recovered from retreating termini of a number of glaciers in western Canada (Luckman, 1988), which indicates that early Holocene forests occupied areas now covered by ice. The recovery of wood ranging in age from ca. 10,000–5,000 cal. yBP from sites situated 100–200 m above the present timberline clearly indicates that subalpine forests reached at least this elevation during the early Holocene. Reasoner et al. (2001) compiled early-mid Holocene macrofossil information from across southwestern Canada and plotted this information relative to modern timberline. The results indicate two clear periods of higher-than-present timberline during the early Holocene: an early phase from the onset of the Holocene to approximately 8,200 cal. yBP (7,500 ^{14}C yBP) and a later phase between 7,300 and 5,700 cal. yBP (6,400 and 5,000 ^{14}C yBP, Figure H10). These data are in general agreement with European records (e.g., Figure H9) that indicate the timberline was higher than present during the early-mid Holocene and suggest the 8.2 event may have also impacted alpine treelines in western North America. Additional high-resolution records for the North American Cordillera are necessary to resolve this issue.

Several small-scale fluctuations of the alpine timberline have been documented during the last millennium, primarily from dendrochronological analyses of living trees near alpine timberline and in situ dead snags. For example, the abrupt synchronous termination of 92 tree-ring records related to the 1690's "cold snap" (Luckman, 1994) clearly indicates that significant changes to the position of the alpine timberline have occurred on decadal timescales and that these changes have been driven by natural variability of the regional climate (Figure H11).

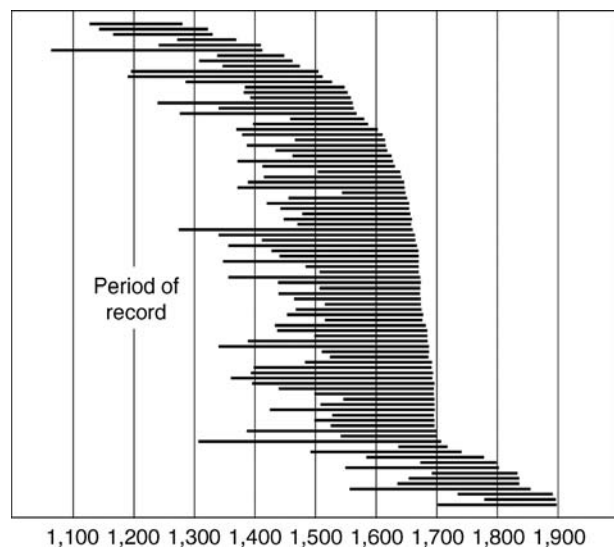


Figure H11 Length of record preserved in calendar-dated snags recovered from the Athabasca Glacier Site, Central Canadian Rockies. The standing and fallen snags occur at and above the present treeline or where these snags are considerably larger than trees presently growing at the site. One of the main Little Ice Age advances of the Athabasca Glacier has been dated at 1714 (modified from Luckman, 1994).

Linking the past to the future

It is clear that the position and composition of the timberline ecotone has been sensitive to Holocene climate change. The millennial-scale trends generally reflect gradual decline in Northern Hemisphere insolation from approximately 11% higher-than-present in the early Holocene. Superimposed on this long-term trend are higher-frequency fluctuations related to changes in oceanic circulation, volcanic activity, and solar

irradiance or a combination of these factors. It is also clear that anthropogenic climate forcing over the next 100 years is likely to rival or exceed the warmest conditions of the Holocene. Concerns about global warming involve adjustments, collapses, migrations, or extinctions of boreal and alpine life. Surprisingly, relatively few studies have addressed past responses of ecosystems such as treeline communities to climatic change. One of the reasons for avoiding this topic is that accurate studies require independent climatic proxies and very high temporal resolution (<10–20 years/sample). To assess how tree-lines could respond to global change, high resolution studies including macrofossil analysis are urgently needed.

Mel A. Reasoner and Willy Tinner

Bibliography

- Arno, S.F., and Hammerly, R.P., 1993. *Timberline - Mountain and Arctic Forest Frontiers*. Seattle: The Mountaineers, 304pp.
- Barnekow, L., 1999. Holocene tree-line dynamics and inferred climatic changes in the Abisko area, northern Sweden, based on macrofossil and pollen records. *Holocene*, **9**, 253–265.
- Barnett, C., Dumayne-Peaty, L., and Matthews, J.A., 2001. Holocene climatic change and tree-line response in Leirdalen, central Jotunheimen, south central Norway. *Rev. Palaeobot. Palynol.*, **117**, 119–137.
- Birks, H.H., 2001. Plant macrofossils. In Smol, J.P., Birks, H.J.B., and Last, W.M. (eds.), *Tracking Environmental Change Using Lake Sediments*. Dordrecht: Kluwer, 49–74.
- Carrara, P.E., Trimble, D.A., and Rubin, M., 1991. Holocene treeline fluctuations in the Northern San-Juan Mountains, Colorado, USA, as indicated by radiocarbon-dated conifer wood. *Arct. Alp. Res.*, **23**, 233–246.
- Dahl, S.O., and Nesje, A., 1996. A new approach to calculating Holocene winter precipitation by combining glacier equilibrium-line altitudes and pine-tree limits: A case study from Hardangerjokulen, central southern Norway. *Holocene*, **6**, 381–398.
- Haas, J.N., Richoz, I., Tinner, W., and Wick, L., 1998. Synchronous Holocene climatic oscillations recorded on the Swiss Plateau and at timberline in the Alps. *Holocene*, **8**, 301–309.
- Hebda, R.J., 1995. British Columbia vegetation and climate history with a focus on 6 ka BP. *Géographie physique et Quaternaire*, **49**, 55–79.
- Hormes, A., Müller, B.U., and Schlüchter, C., 2001. The Alps with little ice: Evidence for eight Holocene phases of reduced glacier extent in the Central Swiss Alps. *Holocene*, **11**, 255–265.
- Kearney, M.S., and Luckman, B.H. 1983. Holocene timberline fluctuations in Jasper National Park, Alberta. *Science*, **221**, 261–263.
- Körner, C., 1999. *Alpine Plant Life*. Berlin: Springer, 338pp.
- Kullman, L., 1995. Holocene Tree-Limit and Climate History from the Scandes-Mountains, Sweden. *Ecology*, **76**, 2490–2502.
- Luckman, B.H., 1988. 8000 year old wood from the Athabasca Glacier, Alberta. *Can. J. Earth Sci.*, **25**, 148–151.
- Luckman, B.H., 1994. Evidence for climatic conditions between ca. 900–1300 A.D. in the Southern Canadian Rockies. *Clim. Change*, **26**, 171–182.
- Maisch, M., Wipf, A., Denneler, B., Battaglia, J., and Benz, C., 1999. Die Gletscher der Schweizer Alpen. Gletscherhochstand 1850, Aktuelle Vergletscherung, Gletscherschwund-Szenarien. Zürich: vdf, 373pp.
- Reasoner, M.A., and Hickman, M., 1989. Late Quaternary Environmental-Change in the Lake Ohara Region, Yoho-National-Park, British-Columbia. *Palaeogeogr. Palaeoclimatol. Palaeoecol.*, **72**, 291–316.
- Reasoner, M.A., Davis, P.T., and Osborn, G., 2001. Evaluation of proposed early-Holocene advances of alpine glaciers in the North Cascade Range, Washington State, USA: Constraints provided by palaeoenvironmental reconstructions. *Holocene*, **11**, 607–611.
- Tinner, W., and Kaltenrieder, P., 2005. Rapid responses of high-mountain vegetation to early Holocene environmental changes in the Swiss Alps. *Journal of Ecology*, **93**(5): 936–947.
- Tinner, W., and Theurillat, J.-P., 2003. Uppermost limit, extent, and fluctuations of the timberline and treeline ecocline in the Swiss Central Alps during the past 11,500 years. *Arct., Antarct., Alp. Res.*, **35**, 158–169.
- Wick, L., and Tinner, W., 1997. Vegetation changes and timberline fluctuations in the Central Alps as indicator of Holocene climatic oscillations. *Arct. Alp. Res.*, **29**, 445–458.

Cross-references

[Dendroclimatology](#)
[Holocene Climates](#)
[Hypsithermal](#)
[Macrofossils](#)
[Palynology](#)
[Pollen Analysis](#)
[The 8,200-Year b.p. Event](#)

HUMAN EVOLUTION AND CLIMATE CHANGE

Introduction

How, where, and why humans evolved are fundamental questions that capture our attention and spark curiosity. A number of recent hominin fossil discoveries as old as 6 Ma and advances in DNA research have now documented that humans evolved in Africa and then migrated to other parts of the world starting as early as 2.0 Ma. Hominins are living or fossil members of the family Hominidae. Evidence of their early exodus from Africa has raised other questions. Why did humans leave the safety of trees? What were the drivers that may have nudged hominins toward bipedalism and developed species that failed, while only one ultimately succeeded? Were the development of tools, the exodus from Africa, and the brain development that led to language, art and imagination a passive or direct response to some paleoenvironmental stresses?

During the last few decades, the need to understand the Earth's climate system and evaluate the potential threat of global warming has yielded a wealth of knowledge on climate and paleoclimate. This research has led to the exciting potential of GCMs (global climate models) – computer models that facilitate the analysis of present, past, and future climates. However, understanding the paleoenvironmental and paleoclimatic context of human evolution can only be accomplished using an interdisciplinary approach integrating geologic, biologic, and anthropologic data and the knowledge of global climate change.

The hominin fossil record reaches back in time to ~6 million years ago and stone tools to ~2.5 million years ago. The general framework of global climate during the Plio-Pleistocene is well documented from the oxygen isotope record from deep sea cores, but the details of paleoclimate on the continents is just now starting to emerge. There have been a few attempts to synthesize within regions and to place key sites within a broader temporal and spatial context, e.g., Turkana, northern Kenya (Brown and Feibel, 1991; Feibel et al., 1991), Ologesalie, southern Kenya (Behrensmeier et al., 2002) and Olduvai Gorge, northern Tanzania (Hay, 1976; Ashley and Hay, 2002). However, most geological studies of hominin-bearing deposits have typically focused on correlation and chronology of sites, with usually only local site-based descriptions accompanying each find. With the growing realization of the importance of tectonism, volcanism, and astronomic climate forcing during the Plio-Pleistocene, there is now an opportunity to integrate what is known about the paleoenvironment and paleocli-

mate from the geologic record and the evolutionary history from archaeological and paleo-anthropological records. A number of scientists have attempted to relate climate to hominin evolution, with some success (Brain, 1981; Behrensmeier, 1982; Boaz and Burckle, 1983; Foley, 1994; deMenocal, 1995; Potts, 1996b; Feibel, 1997), and a series of international workshops and conferences have been held to address the problem (Vrba et al., 1995; Bromage and Schrenk, 1999).

In order to examine the relationship between climate and human evolution, the following will:

1. Review the phylogeny (family evolutionary record) of the hominins
2. Describe the evolution of aspects of hominins that are distinctively “human”
3. Summarize briefly what is known about global climate during the period of hominin evolution

4. Examine possible links between climate change and human evolution

Hominin family tree

Despite the meager fossil record of hominins prior to appearance of modern humans (probably less than a few thousand individuals total) the main pattern of the hominin family tree is evident (Figure H12). Prior to about 4 million years ago, the record is so poor and the connections between fossils so uncertain that each hominin fossil has been given its own genus name: *Sahelanthropus tchadensis*, ~6–7 million years from Chad (Brunet et al., 2002); *Orrorin tugenensis*, ~6 million years from Kenya (Pickford and Senut, 2001; Senut et al., 2001); *Ardipithecus kadabba*, 5.77–5.54 million years from Ethiopia (Haile-Selassie et al., 2004); and *Ardipithecus ramidus*, 4.4 million years from Ethiopia (White et al., 1994). The fact

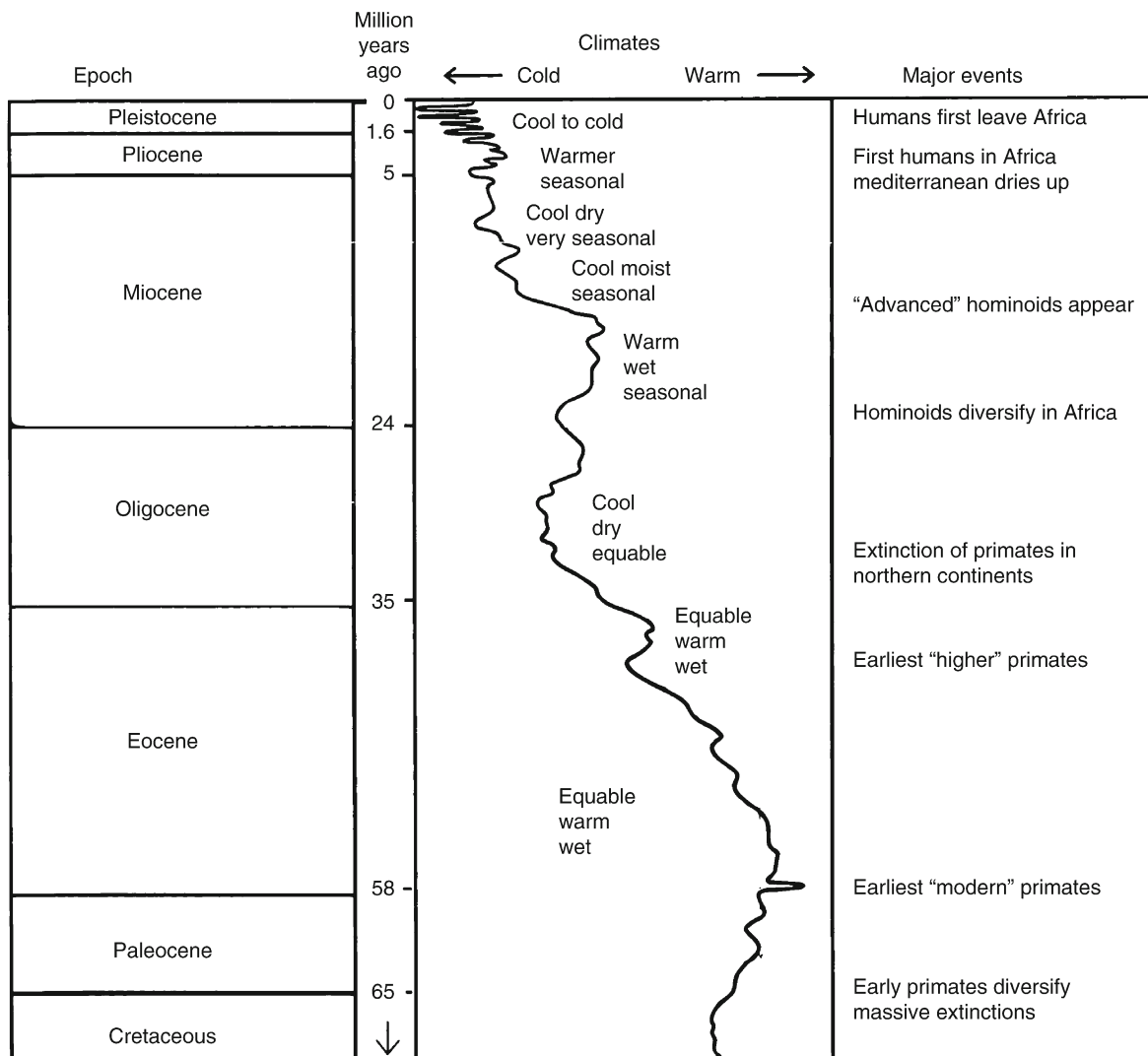


Figure H12 The graph traces the trend of climate during the Cenozoic era, showing a general cooling and culminating with the ice ages of the Pleistocene epoch. The relative temperatures are interpreted from the oxygen isotope record of foraminifers found in marine sediment records. Major events in primate evolution are indicated on the right (Tattersall, 1993) (modified from Partridge et al., 1995).

that hominins existed at least 6 Ma suggests that the divergence between apes and humans took place earlier, during the late Miocene, perhaps between 7 and 9 Ma.

The gracile australopithecines were the dominant hominin group from about 4–2.5 Ma and it is likely that several species existed at the same time; *A. africanus* and *A. afarensis* were important species. One of the earliest australopithecines, *Australopithecus anamensis*, dated at 4.2 Ma, was found in northern Kenya (Leakey et al., 1995) and the group lived in a large region stretching from South Africa to Ethiopia. Two hominin lineages diverged at about 2.5 Ma from the early more gracile australopithecines, leading to the robust australopithecines (e.g., *Paranthropus boisei*), who eventually went extinct, and the earliest members of the genus *Homo* that led to modern humans (Figure H12). There is some uncertainty, however, concerning the age of the earliest *Homo*. The genus may be as old as 2.4 Ma, but it was definitely present by 1.9 Ma, when the lineage had radiated to produce three species: *H. habilis*, *H. rudolfensis* and *H. erectus* (Wood, 1992). The genus *Homo* overlapped in both space and in time with the robust australopithecines, but eventually became the single survivor. Anatomically modern humans, *Homo sapiens*, are recognized from about 200,000 years ago.

Evolution of hominin traits

There are two key physical traits that can be tracked in the hominin fossil record: (a) bipedal locomotion (which appeared early on and characterizes all hominins), and (b) an increase in brain capacity relative to body size (associated with genus *Homo*). Average cranial capacity ranges from ~400 cm³ in australopithecines, ~650 cm³ in early *Homo* to ~1,400 cm³ in modern humans (*Homo sapiens*). The two characteristics were assumed to be linked somehow and early models of human evolution envisioned that hominins would leave the safety of trees, develop bipedalism, and then the increase in brain size would follow. However, the fossil evidence suggests that bipedalism and an increase in brain size were independent. The fossil evidence of one of the oldest hominins, *Orrorin tugenensis* (6 Ma), reveals it was a good tree climber, but it had already adapted to bipedalism when on the ground (Senut et al., 2001). A study of *A. africanus* fossils from South Africa dated between 2 and 3 Ma showed a bipedal creature that had a “primitive” body with a more “advanced” cranial capacity (ranging from 435 to 530 cm³) (McHenry and Berger, 1998). The primitive body consisted of a large chest and long upper limbs with a small pelvic girdle and short lower limbs. These

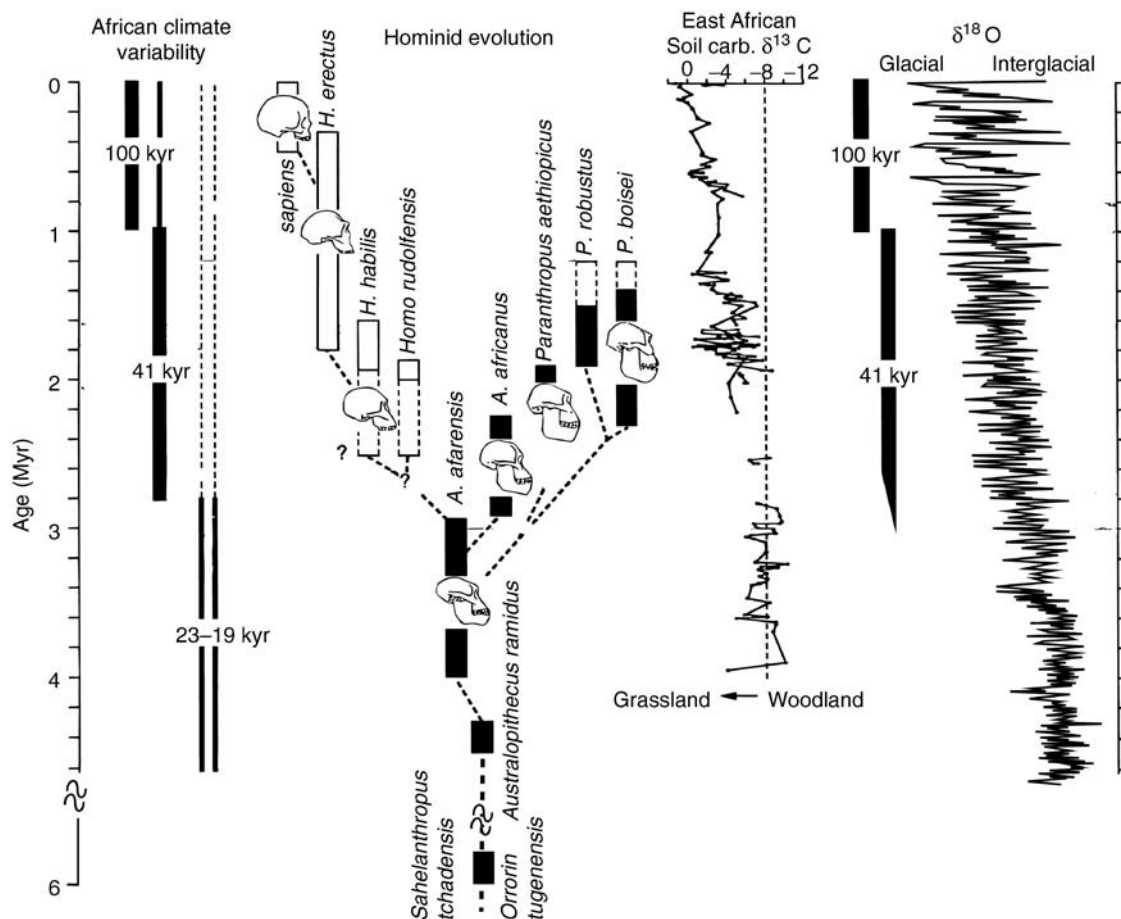


Figure H13 A comparison of the African climate variability represented by the dominance of Milankovitch cycles (*far right*); a graph of human phylogeny (Wood, 1992); vegetation record interpreted from the carbon isotopes in soils (Cerling and Hay, 1988; Cerling, 1992); global temperatures interpreted from oxygen isotopes from the marine record (Shackleton et al., 1990) (modified from deMenocal and Bloemendal, 1995).

characteristics suggest tree climbing was still important to some hominins despite the ability to walk on two legs and the possession of a larger brain.

The development of technology, abstract thought, language, and culture are thought to develop when the brain attains significant cranial capacity. As body size and sex affects cranial capacity, a direct correlation is not appropriate. Primitive stone tool making, the first evidence of technology, dates to 2.5 Ma (Semaw et al., 1997). These tools are assumed to be a product of *Homo*, but there is no direct evidence of this. The human abilities of language and complex cognitive thought leave no record, but it appears that these had evolved in hominins 200,000–300,000 years ago, based on dated archaeological sites containing grindstones, pigments, and stone blades (McBrearty and Brooks, 2000). By 100,000 years ago, there are records of long distance exchange, fish hooks, and mining, and by 50,000 years ago, beads and other art forms are found (McBrearty and Brooks, 2000).

Global climate change

The Earth's climate has varied significantly over its 4.6 billion year history. The climate system, a complex interaction of five components (oceans, land surface, ice, atmosphere, and vegetation) is forced by the tectonics, variations in strength of the Sun, and astronomic forcing, i.e., changes in the Earth's orbit (Ruddiman, 2001). The most continuous and complete record of climate change since the evolution of primates (<65 million years ago) occurs in marine sediments. Microfossils and minerals collected in long sediment cores from ocean basins around the world are analyzed for variations. Oxygen isotopes in foraminifers and diatoms (tiny marine organisms) and dust blown from continental deserts are used as proxies for climate change over time. The isotope variability reflects global temperature (ice volume) changes, whereas the dust signifies moisture changes (Hays et al., 1976; deMenocal, 1995). More fragmentary continental records that occur in lakes or in soils are used to provide additional climate information. For example, carbon isotopes in soil carbonates serve as a proxy for vegetation change and have been used to determine the proportion of forests, open woodland and savannah (Cerling, 1984; Cerling et al., 1993).

Both the marine and terrestrial records during the Cenozoic era (last 65 million years) point to general cooling and drying that ultimately led to the ice ages of the Pleistocene epoch (Figure H12). There were times of particularly abrupt cooling (14 and 2.8 Ma) that brought on increases in global ice volumes. At 14 Ma, the Antarctic glaciers increased in size and became permanent; 2.8 Ma marks the onset of Northern Hemisphere continental-scale glaciation. The general cooling of the Earth has been linked to plate tectonics that led to massive uplifts (i.e., mountain building in the Tibetan Plateau and western North America) and later (10–4 million years) the closing of the Isthmus of Panama, which changed oceanic circulation (Stanley, 1995; Ruddiman, 2001).

Although the long-term trend has been toward a cooler and drier climate, the record clearly shows oscillations on a variety of time scales and more importantly an increase in the magnitude of these climate swings, particularly in recent times (Figure H12). Many have been related to long-term variations in solar radiation caused by the relative position of the Earth with respect to the Sun (Milankovitch cycles), as well as short-term variations (solar radiance). Milankovitch cycles

include 100 ka cycles, which are due to eccentricity of the Earth's orbit; ~41 ka cycles, reflecting the tilt of the Earth (obliquity); and ~21 ka cycles, related to the precession of the equinoxes. The ice ages that dominated the Northern Hemisphere in the Pleistocene are related to both the 100 and 41 kyr Milankovitch cycles (Ruddiman, 2001).

Climate during the last 6 million years, when hominins evolved into modern humans, has been characterized by high variability. 6 million years ago, it was cooler and drier, but with more seasonal continental conditions and the periodic enhancement of the Indian monsoon system (Ruddiman, 2001). Monsoon strength is directly related to the 21 ka precession cycle that changes amount of solar radiation reaching the Earth. Lake levels rose and fell to the rhythm of this shortest Milankovitch cycle and wet-dry cycles dominated the tropics where human evolution took place. This climate variability would have had a significant impact on hominins and is likely to have been a key factor in human evolutionary response.

Evolution and climate

It is tempting to begin to make correlations between the dramatic evolutionary changes of hominins from tree dweller to modern humans capable of space travel and the climatically turbulent environment of Africa in which much of this evolution took place. Speciation events are commonly attributed to climate change, because without the catalyst of environmental change, most species and ecosystems would remain in equilibrium and unchanged (Vrba et al., 1995; Poirier and McKee, 1999). Linking a specific climate circumstance to a specific evolutionary change is problematic. Some question whether global climate signatures are felt at the environmental level important to human survival (Behresmeyer, 1982). Despite the fact that the hominin fossil record is meager and widely dispersed and the paleoclimate record, particularly on land, is scanty, there are some generalizations that can be made.

During the last 5–7 million years, general cooling and drying in Africa caused a decrease in forest and an increase in open woodland and savannah grasslands. Coincidentally, this is the time that hominins began to develop bipedal locomotion, although early fossil evidence indicates they retained their tree climbing skills for a considerable time. Approximately 2.5 million years ago, the World's climate system experienced increasing variability, continental glaciers developed in the Northern Hemisphere, and the tropics became drier (Figure H12). Coincidentally, the first appearance of the genus *Homo* occurred at about this time along with the first appearance of hominin "technology," i.e., stone tools. The discovery of primitive tools and hominins (*Homo*) in the Republic of Georgia at 1.75 Ma may record the migration out of Africa to seek a more stable environment (Gabunia et al., 2000). There are now indications that other animals in Africa showed an evolutionary response to the changing environment. In a study of grazing and browsing fauna in northern Kenya and Ethiopia, Behresmeyer et al. (1997) found that the cooling and drying climate gradually nudged the population toward more grassland-adapted species.

How does climate change trigger evolution? Climate may act more like a filter. Potts (1996a, b) proposed an ecological model termed "variability selection" to explain patterns of hominin evolution. He suggests that dramatic climate shifts favor animals that can readily adapt to new environments. He points out the

trend toward survival of the generalist, rather than the specialist. Those lineages capable of living in varied environments and adapting to change succeed. Whereas, those more specialized go extinct when they fail to adapt to new conditions. Humans have survived droughts and ice ages and live in every possible ecological niche from high altitudes (~4,500 m) to sea level and from arctic sea ice to tropical jungles.

Conclusions

Specific climatic events cannot be linked directly to a specific evolutionary response in the family Hominidae. However, there is a broad coincidence between aridification of Africa (and the associated expansion of open woodlands and grasslands) over the last 7 Ma and the development of bipedalism. Increasing climate variability at about 2.5 Ma is associated with the first record of genus *Homo*, the first appearance of stone tools (evidence of technological capabilities), the increase in cranial capacity, and eventually the migration of hominins out of Africa. The development of complex cognitive processes, language, art, etc. cannot be tied directly to climate, but may fall into the “variability selection” theory where dramatic climatic shifts favor animals that are truly generalists and can adapt to a wide range of environmental conditions (Potts, 1996a).

Gail M. Ashley

Bibliography

- Ashley, G.M., and Hay, R.L., 2002. Sedimentation patterns in a Plio-Pleistocene volcanoclastic rift-margin basin, Olduvai Gorge, Tanzania. In Renaut, R.W., and Ashley, G.M. (eds.), *Sedimentation in Continental Rifts*. (SEPM Special Publication 73) Tulsa, OK: SEPM (Society for Sedimentary Geology), pp. 107–122.
- Behresmeier, A.K., 1982. The geological context of human evolution. *Annu. Rev. Earth Planet. Sci.*, **10**, 39–60.
- Behresmeier, A.K., Todd, N.E., Potts, R., and McBrinn, G.E., 1997. Late Pliocene faunal turnover in the Turkana Basin, Kenya and Ethiopia. *Science*, **278**, 1589–1594.
- Behresmeier, A.K., Potts, R., Deino, A., and Ditchfield, P., 2002. Olorgesailie, Kenya: A million years in the life of a rift basin. In Renaut, R.W., and Ashley, G.M. (eds.), *Sedimentation in Continental Rifts*. (SEPM Special Publication 73) Tulsa, OK: SEPM (Society for Sedimentary Geology), pp. 97–106.
- Boaz, N.T., and Burckle, L.H., 1983. Paleoclimatic framework for African hominid evolution. In: *SASQUA International Symposium Proceedings*, pp. 483–490. Location: Transvaal Museum, Swaziland, Africa; Time: 29 August to 2 September, 1983.
- Brain, C., 1981. Hominid evolution and climate change. *S. Afr. J. Sci.*, **77**, 104–105.
- Bromage, T., and Schrenk, F. (eds.), 1999. African Biogeography, Climate Change, and Human Evolution. New York: Oxford University Press, 485pp.
- Brown, F.H., and Feibel, C.S., 1991. Stratigraphy, depositional environments and paleogeography of the Koobi Fora Formation. In Harris, J.M. (ed.), *Koobi Fora Research Project, Volume 3. Stratigraphy, artiodactyls and Paleoenvironments*. Oxford, UK: Clarendon Press, pp. 1–30.
- Brunet, M., Guy, F., Pilbeam, D. et al., 2002. A new hominid from the Upper Miocene of Chad, Central Africa. *Nature*, **418**, 145–151.
- Cerling, T.E., 1984. The stable isotopic composition of modern soil carbonate and its relation to climate. *Earth Planet. Sci. Lett.*, **71**, 229–240.
- Cerling, T.E., 1992. Development of grasslands and savannas in East Africa during the Neogene. *Palaeogeogr. Palaeoclimatol. Palaeoecol.*, **97**, 241–247.
- Cerling, T.E., and Hay, R.L., 1988. An isotopic study of paleosol carbonates from Olduvai Gorge. *Quaternary Res.*, **25**, 63–78.
- Cerling, T.E., Wang, Y., and Quade, J., 1993. Global ecological change in the late Miocene: Expansion of C₄ ecosystems. *Nature*, **361**, 344–345.
- deMenocal, P.B., 1995. Plio-Pleistocene African climate. *Science*, **270**, 53–59.
- deMenocal, P.B., and Bloemendal, J., 1995. Plio-Pleistocene climatic variability in subtropical Africa and the paleoenvironment of hominid evolution: A combined data-model approach. In Vrba, E.S., Denton, G.H., Partridge, T.C., and Burckle, L.H. (eds.), *Paleoclimate and Evolution with Emphasis on Human Origins*. New Haven, CT: Yale University Press, pp. 262–288.
- Feibel, C.S., 1997. Debating the environmental factors in hominid evolution. *GSA Today*, **7**, 1–7.
- Feibel, C.S., Harris, J.M., and Brown, F.H. 1991. Neogene paleoenvironments of the Turkana Basin. In Harris, J.M. (ed.), *Koobi Fora Research Project, Volume 3. Stratigraphy, artiodactyls and Paleoenvironments*. Oxford: Clarendon Press, pp. 321–370.
- Foley, R.A., 1994. Speciation, extinction and climatic change in hominid evolution. *J. Hum. Evol.*, **26**, 275–289.
- Gabunia, L., Vekua, A., Lordkipanidze, D., Swisher, C.C. III, Ferring, R., Justus, A., Nioradze, M., Tvsatchretidze, M., Anton, S.C., Bosinski, G., Jöris, O., de Lumley, M.A., Majsuradze, G., and Mouskhelishvili, A., 2000. Earliest Pleistocene hominid cranial remains from Dmanisi, Republic of Georgia: Taxonomy, geological setting, and age. *Science*, **288**, 1019–1025.
- Haile-Selassie, Y., Suwa, G., White, T.D., 2004. Late Miocene teeth from Middle Awash, Ethiopia, and early hominid dental evolution. *Science*, **303**, 1503–1505.
- Hay, R.L., 1976. *Geology of the Olduvai Gorge, a Study of Sedimentation in a Semi-arid Basin*. Berkeley, CA: University of California Press, 203pp.
- Hays, J.D., Imbrie, J., and Shackleton, N.J., 1976. Variations in the earth's orbit: Pacemaker of the ice ages. *Science*, **194**, 1121–1131.
- Leakey, M.G., Feibel, C.S., McDougall, I., and Walker, A., 1995. New four-million-year-old hominid species from Kanapoi and Allia Bay, Kenya. *Nature*, **376**, 565–571.
- McBrearty, S., and Brooks, A.S., 2000. The revolution that wasn't: A new interpretation of the origin of modern human behavior. *J. Hum. Evol.*, **39**, 453–563.
- McHenry, H.M., and Berger, L.R., 1998. Limb proportions in *Australopithecus africanus* and the origins of the genus *Homo*. *J. Hum. Evol.*, **35**, 1–22.
- Partridge, T.C., Bond, G.C., Hartnady, C.J.H., deMenocal, P.B., Ruddiman, W.F., 1995. Climatic effects of Late Neogene tectonism and volcanism. In Vrba, E.S., Denton, G.H., Partridge, T.C., and Burckle, L.H. (eds.), *Paleoclimate and Evolution with Emphasis on Human Origins*. New Haven, CT: Yale University Press, pp. 8–23.
- Pickford, M., and Senut, B., 2001. The geological and faunal context of Late Miocene hominid remains from Lukeino, Kenya. C.R. Academy Science Paris, Sciences de la Terre et des planètes, *Earth Planet. Sci.*, **332**, 145–152.
- Poirier, F.E., and McKee, J.K., 1999. *Understanding Human Evolution*, 4th edn. Upper Saddle River, NJ: Prentice Hall, 386pp.
- Potts, R., 1996a. Evolution and climate variability. *Science*, **273**, 922–923.
- Potts, R., 1996b. *Humanity's Descent: The consequences of ecological instability*. New York: W. Morrow, 325pp.
- Ruddiman W.F., 2001. *Earth's Climate, Past and Future*. New York: W.H. Freeman, 465pp.
- Shackleton, N.J., Berger, A., and Peltier, W.R., 1990. An alternative astronomical calibration of the Lower Pleistocene timescale based on ODP Site 677. *Trans. R. Soc. Edinb. Earth Sci.*, **81**, 251–261.
- Semaw, S., Harris, J.W.K., Feibel, C.S., Renne, P., Bernor, R.L., Fessaha, N., and Mowbray, K., 1997. The oldest archaeological sites with an early Oldowan Industry from the Gona River deposits of Ethiopia. *Nature*, **385**, 333–336.
- Senut, B., Pickford, M., Gommery, D., Mein, P., Cheboi, K., and Coppens, Y. 2001. First hominid from the Miocene (Lukeino Formation) Kenya. C.R. Academy Science Paris, Sciences de la Terre et des planètes. *Earth Planet. Sci.*, **332**, 137–144.
- Stanley, S.M., 1995. Climatic forcing and the origin of the human genus. In *Effects of past global change in life*. “National Research Council (U.S.)” Washington, DC: National Academy Press, pp. 233–243.
- Tattersall, I., 1993. *The Human Odyssey: Four Million Years of Human Evolution*. New York: Prentice Hall, 191pp.
- Vrba, E.S., Denton, G.H., Partridge, T.C., and Burckle, L.H., 1995. *Paleoclimate and Evolution, with Special Emphasis on Human Origins*. New Haven, CT: Yale University Press, 547pp.

- White, T.D., Suwa, G., and Asfaw, B., 1994. *Australopithecus ramidus*, a new species of early hominid from Aramis, Ethiopia. *Nature*, **371**, 306–312.
- Wood, B., 1992. Origin and evolution of the genus *Homo*. *Nature*, **355**, 783–790.

Cross-references

Carbon Isotopes, Stable
 Cenozoic Climate Change
 Climate Change, Causes
 Evolution and Climate Change
 Neogene Climates
 Oxygen Isotopes
 Pleistocene Climates

HYPsITHERMAL

Hypsithermal is derived from the Greek root *hypsos*, meaning “high.” In geology, the A.G.I. *Glossary* states that hypsithermal is “a term proposed by Deevey and Flint (1957) as a substitute for *climate optimum* and *thermal maximum*” (see also Charlesworth, 1957; Schwarzbach, 1963; Nilsson, 1983), in reference to a warm period during the early to middle Holocene.

The original concept of a postglacial “climatic optimum” first emerged in the nineteenth century among paleobotanists in northern Europe from evidence of hazel nuts and leaves discovered at anomalously high latitudes and later from pollen analyses (mostly in core samples). Three pollen zones were recognized as discrete subdivisions of this climatic optimum, following the original nineteenth century pollen-based plan of Blytt and Sernander (see Sernander, 1908): boreal (V, VI), Atlantic (VII) and subboreal (VIII) (now classified internationally as “biozones”).

The proof of an exceptionally warm phase in the early to middle Holocene is attributable to L. von Post, the Swedish “father” of modern pollen analysis. In 1946, he recognized three post-glacial climatic phases, stage II being warmer than present. Antevs (1953) named them *anathermal* (“warming”), *althethermal* (“high thermal”), and *medithermal* (“moderating”). However, the last two are linguistic hybrids and should be replaced respectively by *hypsithermal* and *katathermal* (Nilsson, 1983). Synonymous terms are *althethermal* (now obsolete), *megathermal* (likewise, see Judson, 1953, p. 59) and *xerothermal* (specifically hot, dry climates of the postglacial interval). None of the above is mentioned in the newest edition of *The Holocene* (Roberts, 1998). These terms have mostly been limited to North American authors and have now largely fallen into disuse.

A distinct climatic negative swing in the mid-hypsithermal at about 3850 BC (5,000 ¹⁴C yBP) was first recognized by Tage Nilsson in 1935 and attributed by many writers to the recent immigration of human settlers with associated forest clearing. However, the same negative swing has subsequently been established worldwide (e.g., the Rotmoos Neoglacial in the Alps), even in uninhabited areas, as well as in a negative swing of eustatic sea level (the “Bahama Low”). Thus, its natural (non-anthropogenic) forcing is now accepted (Nilsson, 1983). It marks the AT-2/SB-1 biozone boundary. This negative swing was marked by a dramatic fall in the elm pollen, the so-called “*ulmus decline*,” although after a few centuries it recovered somewhat and the Greenland ice cores show some warming

trends. Significantly, the negative “spike” is seen also in the solar modulated (¹⁴C flux record of tree rings Stuiver’s “S” type), and must therefore be forced by a major fluctuation in the Sun’s radiation (Stuiver and Braziunas, 1989).

The chronology of these intervals is confused by the difference between “absolute” ages (now based on varves, tree rings and ice cores) and the radiocarbon ages (which require calibration). The hypsithermal interval is traditionally given as 9,000–2,500 BP (by radiocarbon, from AD 1950), i.e., boreal to subboreal biozones. However, the oxygen-isotopic temperature records of the Greenland ice cores suggest a much younger limit. In Dansgaard et al. (1971), the “climatic optimum” lasts from only about 8,300–4,800 BP, thus a span of 3,500 sidereal years. It is therefore practically limited to the Atlantic biozone (AT-1 and AT-2).

Besides the pollen evidence, there are also clear traces of the “tree line” (the northern limit of tree growth at the edge of the treeless tundra, or in mountains at a critical elevation; Markgraf, 1974). A very stylized approximation of this boundary was presented by Firbas (1949), who also showed that it did not coincide with the effective radiation curve for these latitudes of Milankovitch. This roughly 10,000 yr lag or “retardation” factor is also observed in worldwide eustatic sea-level curves (Fairbridge, 1961, 1983; Lowe and Walker, 1997). Unfortunately, all regional sea-level curves are different because of isostatic and tectonic variables. Probably the nearest approach to a “standard” curve is that of Ters (1987) or Fairbanks (1989). The explanation of retardation lies both in the onset of ice-age glaciation and in its general retreat. Atmospheric cooling precedes the glacial advance (and sea-level fall), just as warming precedes post-glacial melting, although both are associated with secondary climatic fluctuations (notably the Allerød-Younger Dryas oscillation).

Climatic fluctuations within the hypsithermal interval became recognized rather widely in all parts of the world after the 1950s, following the development of radiocarbon dating. The incidents of neoglacial advance were seen first in the Alps (e.g., by Patzelt, 1974), and then extended progressively worldwide (Denton and Porter, 1970; Denton and Karlén, 1973; Röthlisberger, 1986). In her comprehensive volume on the Little Ice Age, Jean Grove (1988) drew attention to preceding Holocene cycles of climatic cooling during the alleged hypsithermal, marked in the Alps by the Venediger, Frossnitz (or Larstig), Rotmoos, Löbber and Goschener advances. In the more recent Scandinavian papers, even more frequent oscillations are documented (Karlén et al., 1995).

In North America, the Alaskan glaciers have also been found to fluctuate more or less synchronously with the European ones. In the semiarid Southwest, there were major lake-level fluctuations, but their interpretation has been complicated by seasonality contrasts, notably the incidence of winter rains during cold cycles, as opposed to summer, monsoonal rains during warm cycles.

Globally, the fluctuations of the hypsithermal are registered most dramatically by proxies other than neoglacial and their associated melt-water lakes. The best dated and most homogeneous of these are the ¹⁴C flux measurements from tree rings (Stuiver and Braziunas, 1989). When standardized and reduced to 10–20 years means, the results disclose an alternation of major intervals of more than 100 years duration. Each positive departure is matched by a negative one of equal dimensions. These are interpreted as being due to fluctuations in solar radiation, and thus affect terrestrial climates (Fairbridge and Sanders, 1987; Charvátová and Štěpánek, 1991; Windelius and

Carlborg, 1995). During the 10,500 year history of the Holocene, there have been approximately 20 of these major perturbations.

The amplitudes and lengths of these solar perturbations display a variance that decreases over the second half of the hypsithermal interval. This decrease is apparent in the glacier fluctuations, as well as in sea level, in fluvial discharge (reflecting flood/drought alternations), and in other proxies. This systematic behavior is mainly registered in the Northern Hemisphere proxies and may therefore reflect the gradual decrease in ecliptic angle that accompanies the Earth/Moon precession cycle, a major climatic forcing of the Milankovitch parameters. It is now approaching a minimum contrast between Northern and Southern Hemispheres.

To summarize, the “hypsithermal” is a semi-formal interval, defined climatically, in Holocene history, originally taken as between roughly 9,000–2,500 yBP (radiocarbon years), but now restricted to about 8,300–5,000 sidereal yBP. It corresponds to the “Atlantic” biozone, and appears to be related to the Northern Hemisphere phase of the Milankovitch precession when high continentality led to warmer summers and colder winters.

Rhodes W. Fairbridge

Bibliography

- Antevs, E., 1953. Geochronology of the deglacial and neothermal ages. *J. Geol.*, **61**, 195–230.
- Charlesworth, J.K., 1957. *The Quaternary Era* (2 vols.). London: E. Arnold, 1700pp.
- Charvátová, I., and Štřešník, J., 1991. Solar variability as a manifestation of the Sun's motion. *Jour. Atm. Terr. Phys.*, **53**, 1019–1025.
- Dansgaard, W., Johnsen, S.J., Clausen, H.G., and Langway, C.C. Jr., 1971. Climatic record revealed by the Camp Century ice core. In Turekian, K.K. (ed.), *The Late Cenozoic Glacial Ages*. New Haven, CT: Yale University Press, pp. 37–56.
- Deevey, E.S., and Flint, R.F., 1957. Postglacial Hypsithermal interval. *Science*, **125**, 182–185.
- Denton, G.H., and Karlén, W., 1973. Holocene climatic variations: Their pattern and possible cause. *Quaternary Res.*, **3**, 155–205.
- Denton, G.H., and Porter, S.C., 1970. Neoglaciation. *Sci. Am.*, **222**, 101–110.
- Fairbanks, R.G., 1989. A 17,000-year glacio-eustatic sea level record: Influence of glacial melting on the Younger Dryas event and deep-ocean circulation. *Nature*, **342**, 637–642.
- Fairbridge, R.W., 1961. Eustatic changes in sea level. In Ahrens, L.H. et al., (eds), vol. 4, *Physics and Chemistry of the Earth*. London: Pergamon, pp. 99–185.
- Fairbridge, R.W., 1983. Isostasy and eustasy. In Smith, D., and Dawson, A. (eds.), *Shorelines and Isostasy*. London: Academic Press, pp. 3–25.
- Fairbridge, R.W., and Sanders, J.E., 1987. The Sun's orbit, A.D. 750–2050: Basis for new perspectives on planetary dynamics and Earth-Moon linkage. In Rampino, M.R. et al., (eds.), *Climate-History, Periodicity, and Predictability*. New York, NY: Van Nostrand Reinhold, pp. 446–471 (bibliography, 475–541).
- Firbas, F., 1949. Spät- und nacheiszeitliche Waldgeschichte Mitteleuropas nördlich der Alpen. Jena: Fischer, 480pp.
- Grove, J.M., 1988. *The Little Ice Age*. London: Methuen, 498pp.
- Judson, S.S., jr., 1953. *Geology of the San Juan site, eastern New Mexico*. Smithsonian Miscellaneous Collections, v. **121**, no.1, 70pp.
- Karlén, W., et al., 1995. Climate of northern Sweden during the Holocene. *J. Coastal Res.*, Special Issue, **17**, 49–54.
- Lowe, J.J., and Walker, M.J.C., 1997. *Reconstructing Quaternary Environments*, 2nd (edn.). London: Longman.
- Markgraf, V., 1974. Palaeoclimatic evidence derived from timberline fluctuations, 67–83. In Labeyrie, J. (ed.), *Les Méthodes quantitatives d'étude des variations du climat au cours du Pléistocène*. Colloques internat. 219. Paris: C.N.R.S., 317pp.
- Nilsson, T., 1983. *The Pleistocene*. Stuttgart: F. Enke Verlag, 651pp.
- Patzelt, G., 1974. Holocene variations of glaciers in the Alps, Paris: Colloques Internationaux du Centre National de la Recherche Scientifique no. 210. *Les Méthodes quantitative d'étude des variations du climat au cours du Pléistocene*, 51–59.
- Roberts, N., 1998. *The Holocene: An Environmental History*, 2nd (edn.). Oxford: Blackwell, 316pp.
- Röthlisberger, F., 1986. *10,000 Jahre Gletchergeschichte der Erde*. Aarau, Verlag Sauerländer, 416pp.
- Schwarzbach, M., 1963. *Climates of the Past*. London: Van Nostrand, 328
- Sernander, R., 1908. On the evidence of postglacial changes of climate furnished by the peat mosses of northern Europe. *Geol. Foren., Förh. Stockholm*, **30**, 465–473.
- Stuiver, M., and Braziunas, T.F., 1989. Atmospheric ¹⁴C and century-scale solar oscillations. *Nature*, **338**, 405–408.
- Ters, M., 1987. Variations in Holocene sea level on the French Atlantic coast and their climatic significance. In Rampino, M.R., Newman, W.S., and Sanders, J.E. (eds.), *Climate: History, Periodicity and Predictability*. New York: Van Nostrand-Reinhold, pp. 204–237.
- Windelius, G., and Carlborg, N., 1995. Solar orbital angular momentum and some cyclic effects on Earth systems. *J. Coastal Res.*, **17**, 383–395 (special issue).

Cross-references

- [Astronomical Theory of Climate Change](#)
- [Holocene Climates](#)
- [Holocene Treeline Fluctuations](#)
- [Ice cores, Antarctica and Greenland](#)
- [Palynology](#)
- [Pollen Analysis](#)
- [Quaternary Vegetation Distribution](#)
- [Radiocarbon Dating](#)
- [Sun-climate Connections](#)

ICE CORES, ANTARCTICA AND GREENLAND

Introduction

Polar ice results from the progressive densification of snow deposited at the surface of the ice sheet. The transformation of snow into ice generally occurs within the first 100 meters and takes from decades to millennia, depending on temperature and accumulation rate, to be completed. During the first stage of densification, recrystallization of the snow grains occurs until the closest dense packing stage is reached at relative densities of about 0.55–0.6, corresponding to the snow-firn transition. Then plastic deformation becomes the dominant process and the pores progressively become isolated from the surface atmosphere. The end product of this huge natural sintering experiment is ice, an airtight material. Because of the extreme climatic conditions, the polar ice is generally kept at negative temperatures well below the freezing point, a marked difference to the ice of temperate mountain glaciers.

Ice cores are cylinders of ice with a diameter of ~10 cm. They are obtained by drilling through glaciers or ice sheets. This entry deals with ice cores recovered in the two ice sheets existing today at the surface of the Earth: in Antarctica and Greenland. Ice cores from mountain glaciers are handled in another section (see *Ice cores, mountain glaciers*). Ice cores range from shallow (from the surface to 100 m), to intermediate (down to about 1,000 m) and deep (>1,000 m), and are recovered using specific technologies, including thermal and electro-mechanical drilling systems. The main purposes of recovering ice cores in Antarctica or Greenland are to describe the past changes in atmospheric composition and climate of our planet, understand the past behavior of the ice sheets and the mechanisms controlling ice flow, and ultimately contribute to an improved understanding of the Earth system.

The main Antarctic and Greenland ice cores

Apart from several shallow drilling sites in the most coastal area and a few drillings through the ice shelves, a total of 14 drill cores have reached bedrock or a depth close to bedrock

in Antarctica and Greenland. Therefore, the current number of drill sites is still fairly limited in relation to the large dimensions of these ice sheets. [Table II](#) provides information on the ten deepest drilling operations; [Figures I1](#) and [I2](#) show their location in Antarctica and Greenland.

Two pioneering long ice cores, the Camp Century (Greenland) (Hansen and Langway Jr., 1966; Dansgaard et al., 1971) and the Byrd (West Antarctica) (Gow et al., 1968; Epstein et al., 1970) cores, drilled in the 1960s, provided the first continuous and already detailed record back to the last deglaciation and the last ice age.

Three deep Antarctic ice cores record several glacial-interglacial cycles: Vostok (4 cycles, back to 420 kyBP; Petit et al., 1999), Dome Fuji (DF) (3 cycles, 330 kyBP; Watanabe et al., 2003) and EPICA Dome C (EDC) (8 cycles, 740 kyBP; EPICA Community Members, 2004, [Figure I3](#)).

The Vostok drill site holds the world's record in terms of depth, as of 2007. The EDC core, although shorter by a few hundred meters, provides the longest record, approximately twice as old as the Vostok record. New measurements are performed to extend the EDC record back to 800,000 yBP. Furthermore, a new deep drilling at DF, completed in 2006, lies close to bedrock. It should provide the second longest record, covering ~700,000 years.

Three long Greenland ice cores, GRIP, GISP2 and NGRIP cover the last 100,000 years; i.e., most of the last glacial-interglacial cycle, but only the NGRIP core provides an undisturbed record back to the latest part of the penultimate interglacial (also called Eemian) (North Greenland Ice Core Project Members, 2004). A new drilling operation (called NEEM) is planned in Greenland to recover an ice core able to provide a complete record of the Eemian. In addition, a number of intermediate-type cores recovered from both ice sheets sample the Holocene (our current interglacial) and part of the last glacial period with good resolution.

Establishing an ice core chronology

Establishing the chronology of Antarctic and Greenland ice cores is essential for interpreting ice core records. The age of the ice corresponds to the time the snow is deposited at

Table 11 Major ice cores: sites, depth, length of record. Please, note that in most cases, we use the first publication that provides the basic information, rather than the most recent or most relevant ones

Site	Ice sheet	Year of recovery	Depth (m)	Temporal length of the record
Camp Century (Dansgaard et al., 1971)	Greenland	1966	1,387.4	Back to the last ice age
Byrd (Epstein et al., 1970; Gow et al., 1968)	West Antarctica	1968	2,164	Back to the last ice age
Dye 3 (Dansgaard et al., 1985)	Greenland	1981	2,037	Back to the last ice age
GRIP (GREENLAND-SUMMIT-ICE-CORES, 1997)	Greenland	1992	3,029	~105 ka
GISP 2 (GREENLAND-SUMMIT-ICE-CORES, 1997)	Greenland	1993	3,053	~105 ka
Vostok (Petit et al., 1999)	East Antarctica	1998	3,623	~420 ka
North GRIP (NORTH-GREENLAND-ICE-CORE-PROJECT-MEMBERS, 2004)	Greenland	2003	3,085	~120 ka
EPICA DC (EPICA-COMMUNITY-MEMBERS, 2004)	East Antarctica	2004	3,270	~800 ka
EPICA DML (EPICA-COMMUNITY-MEMBERS, 2006)	East Antarctica	2006	2,774	More than one glacial-interglacial cycle
Dome Fuji	East Antarctica	2006	3,029	The age at the bottom is estimated to be ~700 ka

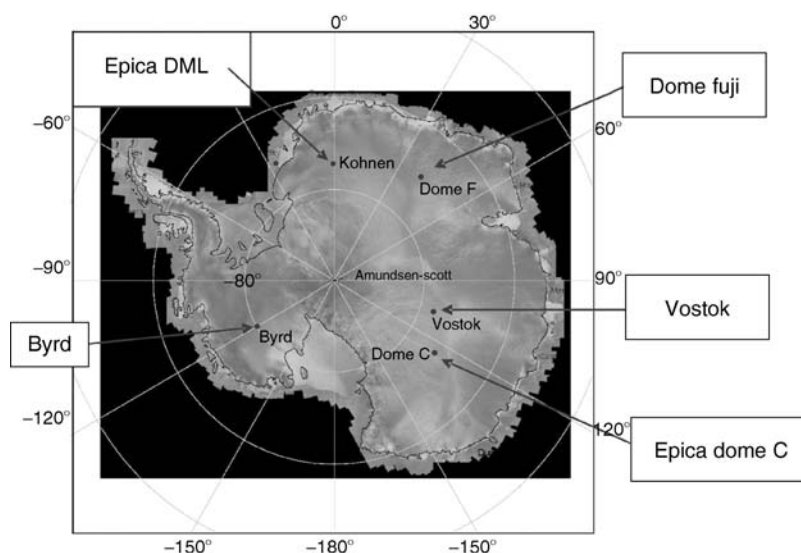


Figure 11 Index map showing the locations of ice cores from Antarctica that are listed in Table 11.

the surface of the ice sheet and its chronology can be established using different tools including layer counting, synchronization to the Earth orbital variations (orbital tuning approach), synchronization to other well dated archives, and glaciological modeling. On the other hand, during snow densification, interstitial air can exchange with the atmosphere at the surface through the firm porosity until it is trapped in the form of bubbles. Therefore, in any ice core, contemporaneous gas and ice signals are not recorded at the same depth and air occluded in air bubbles is younger than its surrounding ice.

Note that methods based on radioactive decay are not of use to date polar ice directly. In particular, ^{14}C dating of the CO_2 trapped in air bubbles is possible but limited in accuracy because of in situ production in the firm.

Counting preserved annual layers through the seasonal variations of different properties, like ice isotopic composition, aerosol chemical composition or dust content, works in sites with high accumulation rates and is especially appropriate for Greenland ice cores. For instance, the method has been used on the DYE-3, GRIP, GISP2 and NGRIP cores, and can be

especially accurate for Holocene ice (maximum counting error estimated to be up to 2%; Rasmussen et al., 2006). This layer counting method is, however, not applicable for low accumulation sites such as those of the East Antarctic Plateau. Orbital variations of the Earth impact the solar radiation received at the top of the atmosphere (generally called insolation), and in turn the Earth's climate. The orbital tuning approach consists of tuning ice core climatic records to those changes in insolation that can be accurately calculated for the past millions of years (Berger, 1978; Laskar et al., 2004). This approach has been used in the case of the long, 420-kyr Vostok record. Unfortunately, the phasing between insolation and the climatic response is generally poorly constrained and not likely to be constant due to the non-linearity of the climatic system, which is a major limitation of the orbital tuning approach. As a consequence, the chronological uncertainty of the orbital tuning approaches is about 5 kyr. Nevertheless, it has been recently suggested that ice core properties recording local insolation directly may overcome this limitation (Bender, 2002; Raynaud et al., 2007).

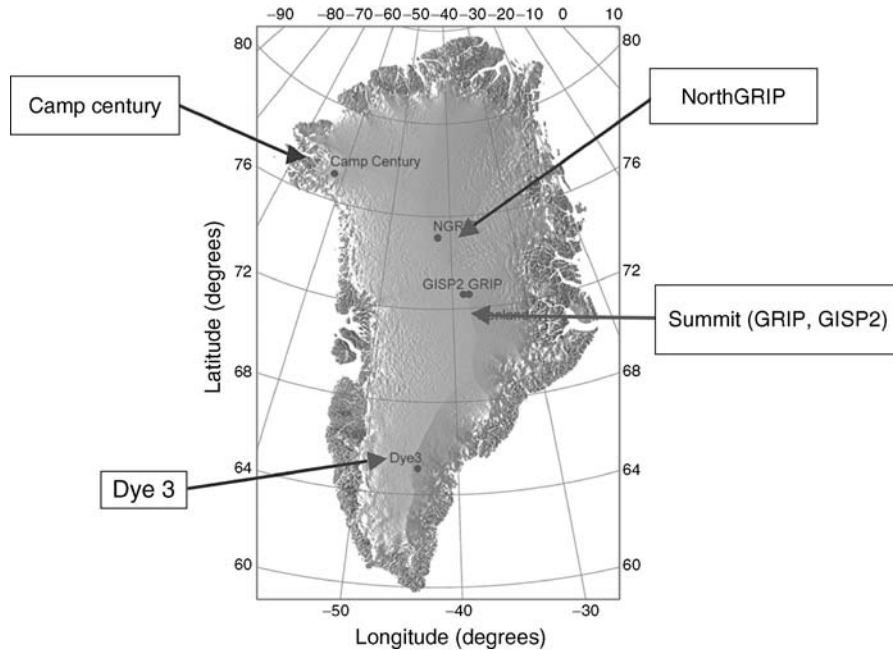


Figure 12 Index map showing the locations of ice cores from Greenland that are listed in Table 11.



Figure 13 Ice core protruding from the drill head from EPICA Dome C, Antarctica (photo courtesy of Eric Lefèvre, LGGE, Grenoble).

Ice cores can also be dated by synchronization with other well-dated archives. For example, back to the last glacial period, ice cores from Antarctica can be synchronized with the Greenland ice cores using the CH_4 records or the Be-10 records (Yiou et al., 1997; Blunier and Brook, 2001). A second example is the identification of well-dated volcanic eruptions in the ice cores.

In order to provide a method independent of the orbital tuning approach, glaciologists have proposed to date ice cores continuously using snow accumulation and ice flow models for calculating the annual layer thickness at each depth. In this case the main limitations include the uncertainties in our

knowledge of past accumulation changes, basal conditions (melting, sliding) and rheological conditions.

Finally, it has been recently proposed to use an inverse method, which associates the information of the different dating methods available on one core to obtain an optimal chronology. This inverse method has been applied on the Vostok (Parrenin et al., 2001; Parrenin et al., 2004), Dome Fuji (Watanabe et al., 2003) and EPICA Dome C (EPICA Community Members, 2004) cores. In the future, such an inverse method could be applied to several drilling sites simultaneously, obtaining a common and optimal chronology for those drilling sites.

The difference between the ages of gas bubbles and the surrounding ice can be computed with a firm model (see Goujon et al., 2003 and references therein). Under present-day conditions, this difference is on the order of a few centuries for high accumulation/high temperature sites and of several thousands of years in sites of the high Antarctic Plateau with low accumulation and temperature conditions (e.g., $\sim 3,000$ years at Vostok). Under glacial conditions it increases significantly due to colder climate, which is paralleled by lower accumulation rates, but the accuracy of the calculation under past conditions is limited due to uncertainty in past accumulation rates and temperatures.

Antarctic and Greenland ice core: an archive of the atmospheric composition and climate

The Antarctic and Greenland ice cores contain a wide spectrum of information on past changes in the environmental conditions of the Earth. Examples are given in Table 12.

Polar ice cores record both variations in climate and in atmospheric composition. They essentially provide a pure record of solid precipitation, atmospheric gases, dust and aerosols and are, in fact, a unique archive of past changes of our atmosphere. For their part, deep oceanic and continental sediments are recording oceanic, vegetation or soil changes.

Table 12 Climatic or environmental parameters and corresponding properties measured in ice. Note the diversity of the information contained in ice cores, which deals with the atmosphere, the cryosphere, the oceans and the continents

Climatic and environmental parameter	Ice properties
Temperature change at the surface of the ice sheet	Isotopic composition of the ice ($^{18}\text{O}/^{16}\text{O}$, D/H); Isotopic composition of the air trapped in ice (^{15}N , ^{40}Ar)
Variations of atmospheric greenhouse trace gases	Greenhouse trace gas concentrations in the air trapped in ice (CO_2 , CH_4 , N_2O)
Origin of the precipitation	Deuterium excess of ice
Atmospheric transport and circulation; Source (marine, continental, volcanic, anthropogenic) of dust and aerosols	Dust and aerosols in ice
Changes in continental ice volume and sea level; Changes in hydrological cycle and biological activity	Isotopic composition ($^{18}\text{O}/^{16}\text{O}$) of the atmospheric oxygen trapped in ice
Local insolation changes due to orbital cycles	O_2/N_2 of air trapped in ice; Air content of ice
Changes in surface elevation of the ice sheet	Air content of ice; Isotopic composition of ice
Changes in ice flow	Physical properties of ice
Solar activity and Earth's magnetic field intensity	Beryllium-10 (^{10}Be)

Continuous changes in temperature at the surface of the ice sheet are revealed by measuring the isotopic composition of the ice (deuterium or oxygen-18), and more sporadic abrupt temperature changes are accurately recorded by the isotopic composition of N_2 and Ar found in the air trapped in ice.

Polar ice cores also provide the most reliable paleo-archive of air composition, by directly recording atmospheric composition in the form of air bubbles when the firm becomes ice. They allow the reconstruction of the past evolution of important greenhouse gases (see section on carbon dioxide and methane, Quaternary variations). Thus, the Vostok and the new EPICA DC record produce clear evidence of the strong correlation between greenhouse gases (CO_2 and CH_4) and climate over glacial-interglacial cycles (EPICA Community Members, 2006; see also *Carbon dioxide and methane, Quaternary variations*).

Dust and aerosols found in Antarctic or Greenland ice cores have been collected at the surface of the ice sheets by dry or wet deposition. The ice record of their concentration and size distribution provides information about past extent of marine and continental sources as well as variations in atmospheric transport. Since marine sources can be influenced by the extent of sea ice, it may also be able to reconstruct past changes in sea ice. Ice cores also provide a precious volcanic record in the same way.

Apart from these natural variations in gases, dust and aerosols, ice cores record the impact of human activities, especially on greenhouse trace gases and sulfate compounds. They also document paleometallurgy activities from as early as Greek and Roman times and, during the last few decades, radioactive fallout and added lead in gasoline.

The ice core record also contains information about past changes of the ice sheets. The air content of polar ice depends on the atmospheric pressure when bubbles close-off, and thus gives information about past surface elevation. Physical properties of ice such as grain size and orientation are indicators of past ice flow in the vicinity of the drilling site.

Conclusion

Polar ice cores provide a wide range of information on the Earth system, some of which have a real impact on societal and educational issues. Because they play a central role in global change research, the international ice coring community is planning new projects in both Antarctica and Greenland under the International

Partnerships in Ice Core Sciences (IPICS) initiative (Brook and Wolff, 2006). IPICS aims to extend the ice core record in time and enhance spatial resolution. Concerning deep ice coring, one of the projects is to search for a 1.5 million year record of climate and greenhouse gases in Antarctica, during a time period when Earth's climate shifted from $\sim 40,000$ year to $\sim 100,000$ year cycles. In northwest Greenland, a deep ice core is planned to recover a complete record of the Eemian for the first time.

Dominique Raynaud and Frédéric Parrenin

Bibliography

- Bender, M., 2002. Orbital tuning chronology for the Vostok climate record supported by trapped gas composition. *Earth Planetary Sci. Lett.*, **204**, 275–289.
- Berger, A.L., 1978. Long-term variations of daily insolation and Quaternary climatic changes. *J. Atmos. Sci.*, **35**, 2362–2367.
- Blunier, T., and Brook, E.J., 2001. Timing of millennial-scale climate change in Antarctica and Greenland during the last glacial period. *Science*, **291**, 109–112.
- Brook, E., and Wolff, E.W., 2006. The future of ice core science. *Eos Trans. AGU*, **87**(4), 39.
- Dansgaard, W., Johnsen, S.J., Clausen, H.B., and Langway Jr., C.C. 1971. Climatic record revealed by the camp century ice core. In Turekian, K.K. (ed.), *The Late Cenozoic Glacial Ages*. New Haven, London: Yale University Press, pp. 37–56.
- Dansgaard, W., Clausen, H.B., Gundestrup, N., Johnsen, S.J., and Rygner, C., 1985. Dating and climatic interpretation of two deep Greenland ice cores. In Langway Jr., C.C., Oeschger, H., and Dansgaard, W. (eds.), *Greenland Ice Core: Geophysics, Geochemistry and the Environment*. Washington, DC: Geophysical Monograph. American Geophysical Union.
- EPICA Community Members, 2004. Eight glacial cycles from an Antarctic ice core. *Nature*, **429**(6992), 623–628.
- EPICA Community Members, 2006. One-to-one coupling of glacial climate variability in Greenland and Antarctica. *Nature* **444**(7116), 195–198.
- Epstein, S., Sharp, R.P., and Gow, A.J., 1970. Antarctic ice sheet: stable isotope analyses of Byrd station cores and interhemispheric climatic implications. *Science* **168**, 1570–1572.
- Goujon, C., Barnola, J.-M., and Ritz, C., 2003. Modeling the densification of polar firm including heat diffusion: Application to close-off characteristics and gas isotopic fractionation for Antarctica and Greenland sites. *J. Geophys. Res.*, **108**. doi:10.1029/2002JD003319.
- Gow, A.J., Ueda, H.T., and Garfield, D.E., 1968. Antarctic ice sheet: Preliminary results of first core hole to bedrock. *Science* **161**, 1011–1013.
- Greenland Summit Ice Cores, 1997. *J. Geophys. Res.*, **102**(C12), 26315–26886.
- Hansen, B.L., and Langway Jr., C.C., 1966. Deep core drilling in ice and core analysis at camp century, Greenland, 1961–1966. *Antarctic J. US*, **1**, 207–208.

- Laskar, J., Robutel, P., Joutel, F., Gastineau, M., Correira, A.C.M., and Levrard, B., 2004. A long-term numerical solution for the insolation quantities of the Earth. *Astron Astrophys* **428**, 261–285.
- North Greenland Ice Core Project Members, 2004. High-resolution record of Northern hemisphere climate extending into the last interglacial period. *Nature*, **431**, 147–151.
- Parrenin, F., Jouzel, J., Waelbroeck, C., Ritz, C., and Barnola, J.-M., 2001. Dating the Vostok ice core by an inverse method. *J. Geophys. Res.*, **106** (D23), 31837–31851.
- Parrenin, F., Rémy, F., Ritz, C., Siebert, M.J., and Jouzel, J., 2004. New modeling of the Vostok ice flow line and implication for the glaciological chronology of the Vostok ice core. *J. Geophys. Res.*, **109**. doi:10.1029/2004JD004561.
- Petit, J.R., Jouzel, J., Raynaud, D., Barkov, N.I., Barnola, J.-M., Basile, I., Bender, M., Chappellaz, J., Davis, M., Delaygue, G., Delmotte, M., Kotlyakov, V.M., Legrand, M., Lipenkov, V.Y., Lorius, C., Pépin, L., Ritz, C., Saltzman, E., and Stievenard, M., 1999. Climate and atmospheric history of the past 420,000 years from the Vostok ice core, Antarctica. *Nature*, **399**, 429–436.
- Rasmussen, S.O., Andersen, K.K., Svensson, A.M., Steffensen, J.P., Vinther, B.M., Clausen, H.B., Siggaard-Andersen, M.-L., Johnsen, S. J., Larsen, L.B., Dahl-Jensen, D., Bigler, M., Rothlisberger, R., Fischer, H., Goto-Azuma, K., Hansson, M.E., and Ruth, U., 2006. A new Greenland ice core chronology for the last glacial termination. *J. Geophys. Res.*, **111**, D06102. doi:10.1029/2005JD006079.
- Raynaud, D., Lipenkov, V., Lemieux-Dudon, B., Loutre, M.-F., Lhomme, N., 2007. The local insolation signature of air content in Antarctic ice: A new step toward an absolute dating of ice records. *Earth and Planetary Science Letters*, **261**, 337–349.
- Watanabe, O., Jouzel, J., Johnsen, S., Parrenin, F., Shoji, H., and Yoshida, N., 2003. Homogeneous climate variability across East Antarctica over the past three glacial cycles. *Nature*, **422**, 509–512.
- Yiou, F., Raisbeck, G.M., Baumgartner, S., Beer, J., Hammer, C., Johnsen, J., Jouzel, J., Kubik, P.W., Lestringuez, J., Stievenard, M., Suter, M., and Yiou, P., 1997. Beryllium 10 in the Greenland ice core project ice core at summit, Greenland. *J. Geophys. Res.*, **102**, 26783–26794.

Cross-references

Beryllium-10
 Carbon Dioxide and Methane, Quaternary Variations
 Deuterium, Deuterium Excess
 Dust Transport, Quaternary
 Ice Cores, Mountain Glaciers
 Oxygen Isotopes
 Quaternary Climate Transitions and Cycles
 SPECMAP

ICE CORES, MOUNTAIN GLACIERS

Introduction

With the help of recent innovations in light-weight drilling technology, ice core paleoclimatic research has been expanded from the polar regions to ice fields in many of the world's mountain ranges and on some of the world's highest mountains. Over the last few decades, much effort has been focused on the retrieval of cores from sub-polar regions such as western Canada and eastern Alaska, the mid-latitudes such as the Rocky Mountains and the Alps, and tropical mountains in Africa, South America, and China. Unlike polar ice cores, climate records from lower-latitude alpine glaciers and ice caps present information necessary to study processes where human activities are concentrated, especially in the tropics and subtropics where 70% of the world's population lives. During the last 100 years, there has been an unprecedented acceleration

in global and regional-scale climatic and environmental changes affecting humanity. The following is an overview of alpine glacier archives of past changes on millennial to decadal time scales. Also included is a review of the recent, global-scale retreat of these alpine glaciers under present climate conditions, and a discussion of the significance of this retreat with respect to the longer-term perspective, which can only be provided by the ice core paleoclimate records.

Locations of mountain ice core retrieval

The sites from which many of the high-altitude ice cores have been retrieved are shown in [Table I3](#). Among the earliest efforts to retrieve climate records from mountain glaciers were programs involving surface sampling on the Quelccaya Ice Cap (13°56' S, 70°50' W; 5,670 m a.s.l.) in southern Peru (1974–1979). The results from this preliminary research, conducted by the Institute of Polar Studies (now the Byrd Polar Research Center) at The Ohio State University, paved the way for the first high-altitude tropical deep-drilling program on Quelccaya in 1983, which yielded a 1,500-year climate record. Meanwhile, in western Canada, a 103-m ice core was drilled on Mt. Logan (60°35' N, 140°35' W; 5,340 m a.s.l.) by Canada's National Hydrology Research Laboratory. The record from this core extends back to 1736 AD. Recently, the ice caps on both these mountains have been redrilled, Mt. Logan in 2002 and Quelccaya in 2003. During the intervening decades, mountain ice core research has expanded significantly throughout the world, with programs successfully completed on the Tibetan Plateau and the Himalayas, the Cordillera Blanca of Northern Peru, Bolivia, East Africa, the Swiss and Italian Alps, Alaska, and the Northwest United States ([Table I3](#)).

Climatic and environmental information from mountain ice cores

The records contained within the Earth's alpine ice caps and glaciers provide a wealth of data that contribute to a spectrum of critical scientific questions. These range from the reconstruction of high-resolution climate histories to help explore the oscillatory nature of the climate system, to the timing, duration, and severity of abrupt climate events, and the relative magnitude of twentieth century global climate change and its impact on the cryosphere. Much of the variety of measurements made on polar ice cores, and the resulting information, is also relevant to cores from mountain glaciers. Researchers can utilize an ever-expanding ice core database of multiple proxy information (i.e., stable isotopes, insoluble dust, major and minor ion chemistry, precipitation reconstruction) that spans the globe in spatial coverage and is of the highest possible temporal resolution. The parameters that can be measured in an ice core are numerous and can yield information on regional histories of variations in temperature, precipitation, moisture source, aridity, vegetation changes, volcanic activity and anthropogenic input ([Figure I4](#)). Many of these physical and chemical constituents produce wet and dry/cold and warm seasonal signals in the ice, which allow the years to be counted back similar to the counting of tree rings.

Isotopic ratios of oxygen and hydrogen ($\delta^{18}\text{O}$ and δD , respectively) are among the most widespread and important of the measurements made on ice cores. Early work on polar ice cores on these "stable" (i.e., as opposed to unstable, or radioactive) isotopes indicated that they provide information on the precipitation temperature (Dansgaard, 1961), based on

Table 13 A sampling of mountain glaciers sites from which ice cores have been retrieved since 1980. This is by no means a complete inventory of all alpine ice cores ever collected

Mountain	Location	Elevation (m a.s.l.)	Year drilled	Leading organization	Length of core (m)	Length of record (yr)
Bona Churchill	61°24' N, 141°42' W	4,420	2002	BPRC	460	1700
Mt. Logan	60°35' N, 140°35' W	5,340	1980 2002	NHRI NGP, AINA NIPR IQCS, UNH	103 190 220 345	225 NA NA NA
Eclipse Dome	60°51' N, 139°47' W	3,017	1996	UNH	160	NA
Fremont Glacier	49°07' N, 109°37' W	4,100	1991 1998	USGS	160 50, 160	275, NA
Belukha	49°48' N, 86°34' E	4,062	2001	PSI, UNIBE	140	200+
Fiescherhorn	46°32' N, 8°02' E	3,880	1988 2002	PSI, UNIBE	30 150	42
Coropuna	15°32' S, 72°39' W	6,450	2003	BPRC	146.3, 34.3, 34.3	16,000+
Col du Dôme	45°50' N, 6°50' E	4,250	1994	LGGE, IFU	139	75
Mont Blanc	45°45' N, 6°50' E	4,807	1994	LGGE	140	200+
Djantugan	43°12' N, 42°46' E	3,600	1983	IGRAS	93	57
Gregoriev	41°58' N, 77°55' E	4,660	1991 2001 2003	IGRAS, BPRC IGRAS IGRAS	20, 16 21.5 22	53 NA NA
Dunde	38°06' N, 96°24' E	5,325	1987	BPRC, LIICRE	138	10,000+
Malan	35°50' N, 90°40' E	6,056	1999	LIICRE	102	112+
Guliya	35°17' N, 81°29' E	6,200	1992	BPRC, LIICRE	302	110,000+
Puruogangri	33°55' N, 89°05' E	6,000	2000	BPRC, LIICRE	208	7000
Dasuopu	28°23' N, 85°43' E	7,200	1996	BPRC, LIICRE	162	1,000+
Qomolangma	27°59' N, 86°55' E	6,500	1998	UNH, LIICRE	80	154
Kilimanjaro	3°04' S, 37°21' E	5,895	2000	BPRC	52	11,700
Huascarán	9°06' S, 77°36' W	6,050	1993	BPRC	166	19,000
Quelccaya	13°56' S, 70°50' W	5,670	1983 2003	BPRC	155, 164 168, 129	1,500 1780
Illimani	16°37' S, 67°47' W	6,350	1999	IRD, PSI	137, 139	18,000
Sajama	18°06' S, 68°53' W	6,540	1996	BPRC	132	20,000

NA: Data not available.

Abbreviations: *BPRC*, Byrd Polar Research Center, The Ohio State University (USA); *NHRI*, National Hydrology Research Institute (Canada); *NGP*, National Glaciology Program (Canada); *AINA*, Arctic Institute of North America, University of Calgary (Canada); *NIPR*, National Institute of Polar Research (Japan); *IQCS*, Institute for Quaternary and Climate Studies, University of Maine (USA); *USGS*, United States Geological Survey (USA); *PSI*, Paul Scherrer Institute (Switzerland); *IRD*, Institute of Research and Development (France); *LGGE*, Laboratoire de Glaciologie et Geophysique de l'Environnement (France); *IGRAS*, Institute of Geography, Russian Academy of Science (Russia); *IFU*, Institut für Umweltphysik (Germany); *UNIBE*, University of Bern (Switzerland); *LIICRE*, Key Laboratory of Ice Core and Cold Regions Environment (China); *UNH*, Institute for the Study of Earth, Oceans and Space, University of New Hampshire (USA).

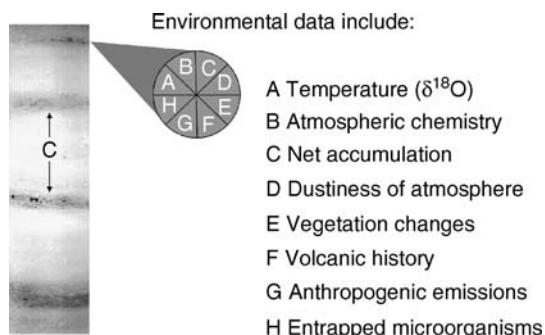


Figure 14 A large variety of environmental information can be obtained from high-altitude ice cores. On the left is an image of a core from a typical mountain glacier in Tibet. The dust bands were deposited during the dry seasons, and the space between them is cleaner ice from snow deposited during the wet seasons.

the fractionation of the oxygen and hydrogen atoms into their light and heavy isotopes (^{16}O and ^{18}O , ^1H and ^2H or deuterium (D)), and on the higher vapor pressure of H_2^{16}O over HD^{16}O and H_2^{18}O . The resulting ratios of the light and heavy isotopes

of these elements act as recorders of temperature both at the moisture source and at the deposition site.

The use of $\delta^{18}\text{O}$ and δD as temperature proxies for polar ice is now widely accepted; however, it is still a source of controversy for lower-latitude cores. Some who have studied the problem suggest that $\delta^{18}\text{O}$, rather than being a temperature recorder at lower latitudes, is a function of precipitation amount (Rozanski et al., 1993; Dahe et al., 2000; Shichang et al., 2000; Baker et al., 2001; Tian et al., 2001). However, real-time comparisons of air temperature and $\delta^{18}\text{O}$ measured on precipitation on the Northern Tibetan Plateau reveal a very close relationship between the two (Yao et al., 1996). Correlations between ice core records from the Himalayas and the Northern Hemisphere temperature records show that on longer time scales (longer than annual) the dominant factor controlling mean $\delta^{18}\text{O}$ values in snowfall must be temperature rather than precipitation (Thompson et al., 2000; Davis and Thompson, 2003). On seasonal to annual time scales, both temperature and precipitation influence the local $\delta^{18}\text{O}$ signal (Vuille et al., 2003).

The annual precipitation rate on an ice cap, or net balance, can be reconstructed by measuring the length of ice between seasonal variations in one or more parameters (e.g., $\delta^{18}\text{O}$ indicating warm or cold seasons or high aerosol concentrations characterizing dry seasons, Figure 14) Since ice is viscous, it

tends to flow not only horizontally but also vertically, resulting in annual layer thinning with depth. In order to correct for this deformation and reconstruct the original thickness of an annual layer at the time of its deposition in the past, vertical strain models are used that take into account the changing densities with depth, the thickness of the glacier, and the rate of thinning (Bolzan, 1985; Reeh, 1988; Meese et al., 1994).

Aerosols in the atmosphere are either deposited on mountain ice fields and glaciers as nuclei of snow (wet deposition) or carried by turbulent air currents to high altitudes (dry deposition). Either way, these insoluble mineral dust particles and soluble salts, such as chlorides, record variations in environmental conditions such as regional aridity. The concentration and size distribution of insoluble dust particles are also helpful for qualitative reconstructions of wind strength. Evidence of volcanic eruptions in the ice is provided by sulfate concentrations and/or the presence of microscopic tephra particles. If these volcanic layers are identifiable (e.g., the 1815 eruption of Tambora or the 1883 eruption of Krakatoa), they can serve as valuable reference horizons to calibrate the time scale. Biological aerosols, such as pollen grains (Liu et al., 1998) and nitrates that may have been injected into the atmosphere by vegetation upwind of a glacier (Thompson et al., 1995; Thompson, 2000), have been useful for reconstructing past climate and environmental changes that have had impacts on regional flora.

The record of human activity is also available from ice cores, although this type of research on high-altitude glaciers lags behind polar ice sheets. Research on heavy metal types and concentrations in high-altitude glaciers is relatively new, but what is available from Mont Blanc in the French-Italian Alps provides information about increasing industrial production and other activities associated with expanding populations and urbanization (Van DeVelde et al., 1999). Measurements of carbon dioxide and methane, as well as lesser gases, trapped in ice bubbles are not as extensive on ice from mountain glaciers as they are from polar cores; however, the research that has been done shows correlations of so-called "greenhouse" gas concentrations with the temperature proxy $\delta^{18}\text{O}$ (Yao et al., 2002a, b). The information from these ice core studies complements other proxy records that compose the Earth's climate history, which is the ultimate yardstick by which the significance of present and projected anthropogenic effects will be assessed.

The significance of climate records from mountain glaciers

Ice core records from high-altitude glaciers, when combined with high-resolution proxy histories such as those from tree rings, lacustrine and marine cores, corals, etc., provide an unprecedented view of the Earth's climatic history that can extend over several centuries or millennia. The longest of them have revealed the nature of climate variability since the Last Glacial Maximum (LGM), 18–20 thousand years ago, and even beyond. The more recent parts of the climate records, which are of annual and even seasonal resolution, can yield high-resolution temporal variations in the occurrence and intensity of coupled ocean-atmosphere phenomena such as El Niño and monsoons, which are most strongly expressed in the tropics and subtropics, and are of world-wide significance. This is particularly valuable information since meteorological observations in these regions are scarce and of short duration.

Four records from the Andes (Huascarán in Northern Peru, Coropuna in Southern Peru and Sajama and Illimani in Bolivia) and one from the Western Tibetan Plateau (Guliya) extend to or

past the end of the last glacial stage and confirm, along with other climate proxy records (e.g., Guilderson et al., 1994; Stute et al., 1995), that the LGM was much colder in the tropics and subtropics than previously believed. Although this period was consistently colder, it was not consistently drier through the lower latitudes as it was in the polar regions. For example, the effective moisture along the axis of the Andes Mountains during the end of the last glacial stage was variable, being much drier in the north than in the Altiplano region in the central part of the range (Thompson et al., 1995, 1998; Ramirez et al., 2003). In another example in Western China, the Guliya Ice Cap is partly affected by the variability of the southwest Indian monsoon system, which was much weaker during the last glacial stage than during the Holocene. However, this region of the Tibetan Plateau also receives (and received) moisture generated from the cyclonic activity carried over Eurasia by the prevailing wintertime westerlies. Not only were lake levels in the Western Kunlun Shan higher than tropical lakes during the LGM (Li and Shi, 1992), but the dust concentrations in the Guliya ice core record were consistent with those of the Early Holocene when the summer Asian monsoons became stronger, suggesting that local sources of aerosols were inhibited during this cold period by higher precipitation and soil moisture levels (Davis, 2002).

Ice cores from the Andes can also contribute to what is known about past environmental and climatic conditions of the Amazon Basin. The extent of biological activity in the Amazon rainforest during the LGM is controversial, and the nitrate concentration record from the Huascarán ice core has been included in the argument (Colinvaux et al., 2000). Pollen studies from the Amazon Basin suggest that the extent of the rainforest has not changed much between the glacial maximum and the Holocene. However, proponents of the "refugia" theory (i.e., Clapperton, 1993) assert that the cold, dry climate in the tropics caused a major retreat of the rainforest flora into a small, geographically isolated area, leaving most of the Basin covered by grasslands. In the Huascarán core, the nitrate concentration profile is similar to the $\delta^{18}\text{O}$ levels throughout most of the record, and the very low concentrations of nitrate, which are concurrent with very depleted $\delta^{18}\text{O}$, suggest that biological activity upwind of the Cordillera Blanca was impeded by the cold and dry climate ~19,000 years ago.

Most of the deep cores from the low latitudes extend through at least the Holocene, and show spatial variations in climate, even between records from the same region. For example, the Holocene $\delta^{18}\text{O}$ profiles from Huascarán and Illimani, while similar to each other in that they show Early Holocene isotopic enrichment, are different from that on Sajama, which has a relatively stable isotopic record through the last 10,000 years. Although Sajama and Illimani, both in Bolivia, are geographically close to each other, they are on opposite sides of the Andean Mountains, with Illimani located in the eastern range. Like Huascarán far to the north, it received most of its precipitation from the northeast after it had been recycled through the Amazon Basin. Sajama, which is located on the high, dry Altiplano, is more subject to Pacific influences and local hydrological effects.

Holocene ice core records from mountain glaciers around the world show evidence of major climatic disruptions, such as droughts and abrupt cold events during this period, which previously was believed to have been stable. Major dust events, beginning between 4.2 and 4.5 ka and lasting several hundred years, are observed in the Huascarán and Kilimanjaro ice cores

(Thompson, 2000; Thompson et al., 2002, respectively), and the timing and character of the dust spikes are similar to one seen in a marine core record from the Gulf of Oman (Cullen et al., 2000) and a speleothem $\delta^{13}\text{C}$ record from a cave in Israel (Bar-Matthews et al., 1999). This dry period is also documented in several other proxy climate records throughout Asia and Northern Africa (see contributions in Dalfes et al., 1994). Two other periods of abrupt, intense climate change in east Africa are observed in the Kilimanjaro ice core at ~ 8.3 ka and 5.2 ka (Thompson et al., 2002). The latter event is associated with a sharp decrease in $\delta^{18}\text{O}$, indicative of a dramatic but short-term cooling.

More recently, a historically documented drought in India in the 1790s, which was associated with monsoon failures and a succession of severe El Niños, was recorded in the insoluble and soluble aerosol concentration records in the Dasuopu ice core (Thompson et al., 2000). Another recorded Asian Monsoon failure in the late 1870s (Lamb, 1982) is noticeable in the Dasuopu dust flux record, which is a calculation that incorporates both the dust concentration and the annual net balance. The dust concentration on Dasuopu is also linked to the magnitude of the Southern Oscillation and the phase of the Pacific Decadal Oscillation (Davis, 2002), thus indicating a linkage between these tropical processes. However, recent research on Tibetan Plateau ice cores drilled north of 32°N shows that their climate records are not only influenced by the South Asian Monsoon and other tropical coupled atmospheric-oceanic processes such as the El Niño-Southern Oscillation (ENSO), but also by atmospheric pressure variations such as those seen in the North Atlantic Oscillation (Davis and Thompson, 2003; Wang et al., 2004). Thus, the high resolution isotope, chemistry, dust, and accumulation records from

ice cores retrieved from across the Plateau help us to reconstruct the spatial and temporal variability of the climate in this region.

There is little purpose in trying to reconstruct the history of global climate change from one ice core, especially at high resolution on short time scales. However, as discussed above, it is clear that certain parameters such as $\delta^{18}\text{O}$ do record large-scale regional variability in sea surface temperatures, while others such as aerosols may be more sensitive to local as well as regional conditions. Although the mountain ice core records that extend back through the last millennium show regional differences with each other and with the polar records, many of them also document common climatic variations on hemispheric, and even global, scales. This is illustrated in Figure 15, where composites of the decadal-averaged $\delta^{18}\text{O}$ profiles of three South American cores (Huascarán, Quelccaya, and Sajama) and three Tibetan Plateau cores (Dunde, Guliya and Dasuopu) show different interhemispheric trends (Thompson et al., 2003) (Figures 15a and 15b, respectively). For example, the “Little Ice Age,” a cold event between the fifteenth and nineteenth centuries that is recorded in many Northern European climate records, is more evident in the South American ice core composite than in the Tibetan Plateau. The “Medieval Warming,” a period before the “Little Ice Age,” which appears in the Greenland ice core records, is also obvious in the Andean ice cores. However, both the composites show isotopic enrichment (indicating warming) beginning in the late nineteenth century and accelerating through the twentieth century. When all six of the profiles from these mountain glaciers are combined, the resulting composite (Figure 15c) is similar to the Northern Hemisphere temperature records of Mann et al. (1998) and Jones et al. (1998) covering the last 1,000 years (Figure 15d).

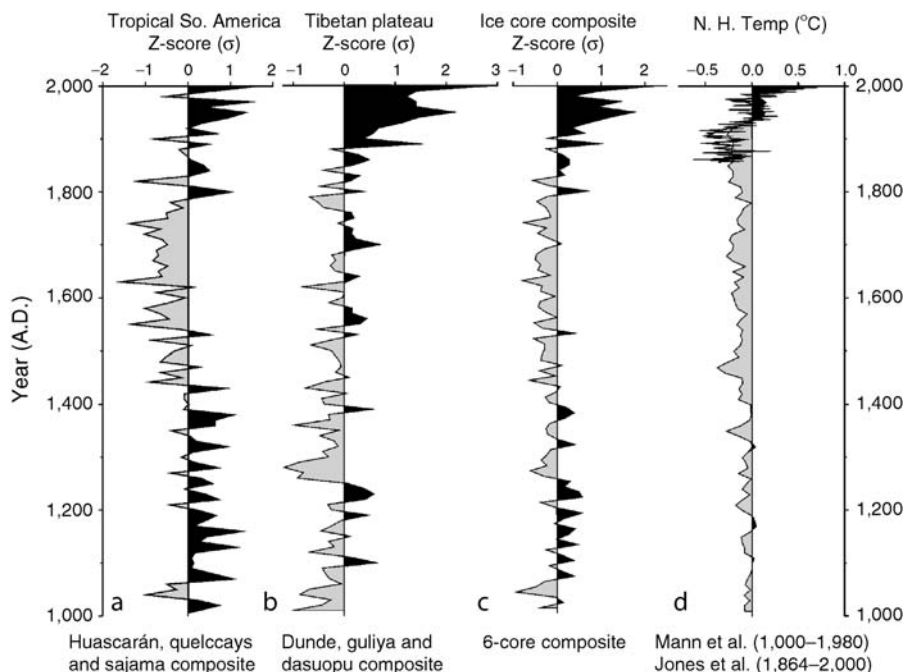


Figure 15 Composite records of decadal averages of $\delta^{18}\text{O}$ from ice cores from (a) the South American Andes (Huascarán, Quelccaya, Sajama) and (b) the Tibetan Plateau (Dunde, Guliya and Dasuopu) from 1000 AD to the present. All six ice-core records are combined (c) to give a total view of variations in $\delta^{18}\text{O}$ over the last millennium in the tropics, which is compared with the Northern Hemisphere reconstructed temperature record (d) (from Thompson et al., 2003).

Not only do these comparisons argue for the important role of temperature in the composition of oxygen isotopic ratios in glacier ice, but they also demonstrate that the abrupt warming from the late nineteenth century through the twentieth century (and continuing into this century) transcends regional variations, unlike earlier climatic variations. Indeed, on a global basis, the twentieth century was the warmest period in the last 1,000 years, which also encompasses the time of the “Medieval Warming.”

The modern climate warming and its effects on mountain glaciers

Meteorological data from around the world suggest that the Earth’s globally averaged temperature has increased 0.6°C since 1950. The El Niño year of 1998 saw the highest globally averaged temperatures on record, while 2002 (a non-El Niño year) was the second warmest, followed by 2003 and 2001 (a la Niña year). The recent warming of the past century, which has been accelerating in the last two decades, is recorded in alpine glaciers in other ways, both within the ice core records and by the rapid retreat of many of the ice fields. This glacier retreat is observed in almost all regions, from the Caucasus and other Eurasian mountain ranges in the mid-latitudes (Mikhaleenko, 1997), to central Europe and western North America (Huggel et al., 2002; Meier et al., 2003), and to the Tibetan Plateau and the tropics (Thompson et al., 1993; Dahe et al., 2000; Thompson et al., 2000). In the Andes, on the Tibetan Plateau and in the East Africa Rift Valley region, this climate change has left its mark. The many ice fields on Kilimanjaro covered an area of 12.1 km^2 in 1912, but today only 2.6 km^2 remains (Figure 16). If the current rate of retreat continues, the perennial ice on this mountain will likely disappear within the next 20 years (Thompson et al., 2002).

Future priorities

Ice cores from mountain glaciers, especially those from the tropical and subtropical latitudes where most of the world’s

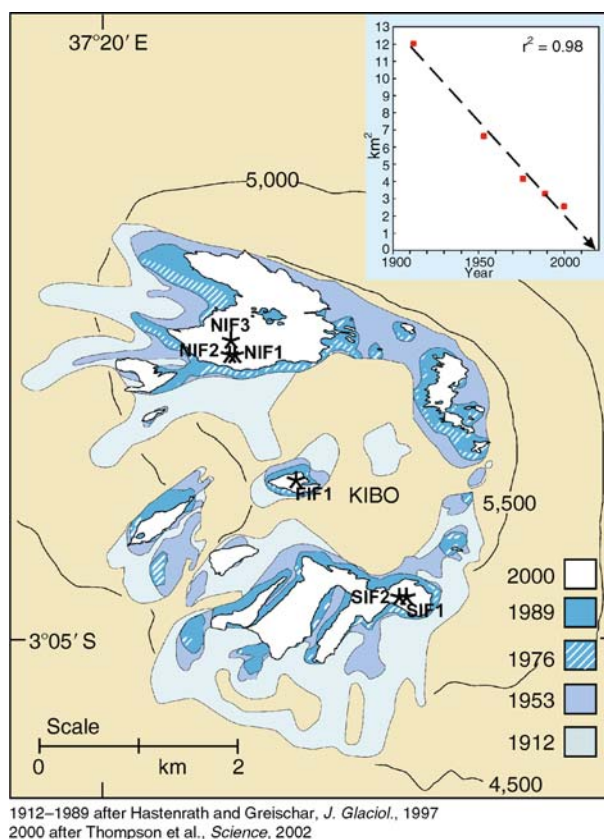


Figure 16 Retreat of ice fields in the Kibo Crater of Kilimanjaro, Tanzania. Shaded areas show “snapshots” of areas of ice cover at five times over the twentieth Century. At the rate of retreat shown here, all the ice on this mountain will disappear within the first half of the twenty first century (insert) (from Thompson et al., 2002).

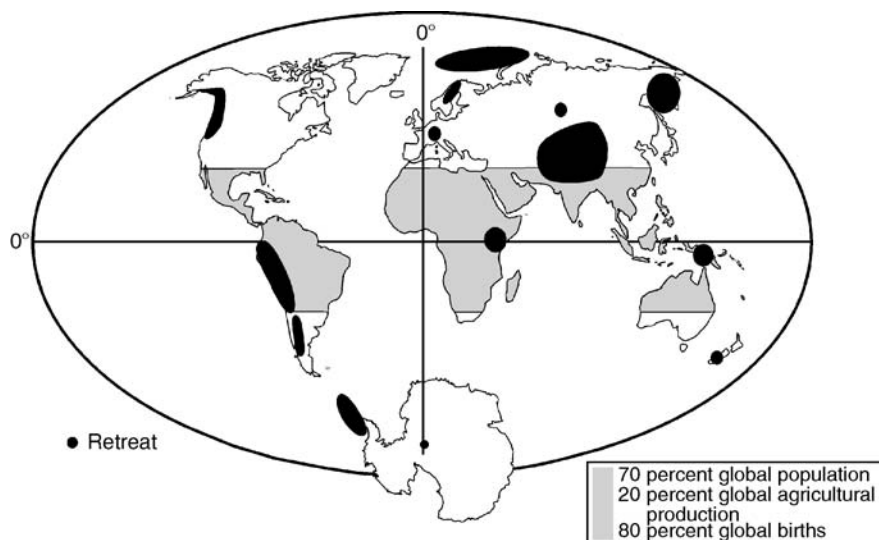


Figure 17 Map demonstrating the current condition of the Earth’s cryosphere. Dark shading depicts regions where glacier retreat is underway. The light shading represents over land between 30°N and 30°S .

population is concentrated, provide unique and valuable archives of climate information because they are able to record variations in atmospheric chemistry and conditions. Since 1982, the El Niño-Southern Oscillation phenomenon has gained worldwide attention as populations and governments have come to realize the extent of its widespread and often devastating effects on weather. As we begin to understand how this coupled atmospheric-oceanic process works, we also see its linkages with other important systems such as the Asian/African Monsoons. Because both of these tropical systems influence precipitation and temperature over large regions, their effects are also recorded by the chemistry and the amount of snow that falls on alpine glaciers. Seasonal and annual resolution of chemical and physical parameters in ice core records from the Andes Mountains has allowed reconstruction of the variability of the ENSO phenomenon over several hundred years (Thompson et al., 1984, 1992; Henderson, 1996; Henderson et al., 1999). Because the effects of El Niño and La Niña events are spatially variable, ice core records from the northernmost (Colombia) and southernmost (Patagonia) reaches of the Andes Mountains will help further resolve the frequency and intensity of ENSO, along with temperature variations, from long before human documentation. This will aid in placing the modern climate changes and the modern ENSO into a more comprehensive perspective. Variability of the South Asian Monsoon is also of vital importance for a large percentage of the world's population that lives in the affected areas. Cores from the Tibetan Plateau have yielded millennial-scale histories of monsoon variability across this large region and information on the interaction between the monsoon system and the prevailing westerlies that are traced back to the Atlantic Ocean.

The clearest evidence for major climate warming underway today comes from the mountain glaciers, recorded in both the ice core records and in the drastic reductions in both total area and total volume. The rapid retreat causes concern for two reasons. First, these glaciers are the world's "water towers," and their loss threatens water resources necessary for hydroelectric production, crop irrigation and municipal water supplies for many nations. The ice fields constitute a "bank account" that is drawn upon during dry periods to supply populations downstream. The current melting is cashing in on that account, which was built over thousands of years but is not currently being replenished. As Figure 17 illustrates, almost all the Earth's mountain glaciers are currently retreating. The land between 30° N and 30° S, which constitutes 50% of the global surface area, is home to 70% of the world's population and 80% of the world's births. However, only 20% of the global agricultural production takes place in these climatically sensitive regions. The second concern arising from the disappearance of these ice fields is that they contain paleoclimatic histories that are unattainable elsewhere and, as they melt, the records preserved therein are forever lost. These records are needed to discern how climate has changed in the past in these regions and to assist in predicting future changes.

Lonnie G. Thompson

Bibliography

- Baker, P.A., Seltzer, G.O., Fritz, S.C., Dunbar, R.B., Grove, M.J., Tapia, P.M., Cross, S.L., Rowe, H.D., and Broda, J.P., 2001. The history of South American tropical precipitation for the past 25,000 years. *Science*, **291**, 640–643.
- Bar-Matthews, M., Ayalon, A., Kaufman, A., and Wasserburg, G.J., 1999. The Eastern Mediterranean paleoclimate as a reflection of regional events: Soreq Cave, Israel. *Earth Planet. Sci. Lett.*, **166**, 85–95.
- Bolzan, J.F., 1985. Ice flow at the Dome C ice divide based on a deep temperature profile. *J. Geophys. Res.*, **90**(D5), 8111–8124.
- Clapperton, C., 1993. *Quaternary Geology and Geomorphology of South America*, Amsterdam, The Netherlands: Elsevier, 779pp.
- Colinvaux, P.A., DeOliveira, P.E., and Bush, M.B., 2000. Amazonian and neotropical plant communities on glacial time-scales: The failure of the aridity and refuge hypotheses. *Quaternary Sci. Rev.*, **19**, 141–170.
- Cullen, H.M., deMenocal, P.B., Hemming, S., Hemming, G., Brown, F.H., Guilderson, T., and Sirocko, F., 2000. Climate change and the collapse of the Akkadian empire: Evidence from the deep sea. *Geology*, **28**, 379–382.
- Dahe, Q., Mayewski, P.A., Wake, C.P., Shichang, K., Jiawen, R., Shugui, H., Tandong, Y., Qinzhaoh, Y., Zhefan, J., and Desheng, M., 2000. Evidence for recent climate change from ice cores in the central Himalaya. *Ann. Glaciol.*, **31**, 153–158.
- Dalfes, H.N., Kukla, G., and Weiss, H. (eds.), 1994. *Third Millennium BC Climate Change and Old World Collapse*. Berlin: Springer, 723pp.
- Dansgaard, W., 1961. The isotopic composition of natural waters with special reference to the Greenland Ice Cap. *Meddelelser om Grønland*, **165**, 1–120.
- Davis, M.E., 2002. *Climatic Interpretations of Eolian Dust Records from Low-Latitude, High-Altitude Ice Cores*, The Ohio State University: PhD Thesis.
- Davis, M.E., and Thompson, L.G., 2004. Four centuries of climatic variation across the Tibetan Plateau from ice-core accumulation and $\delta^{18}\text{O}$ records. In Cecil, L.D., Thompson, L.G., Steig, E.J., and Green, J.R. (eds.), *Earth Paleoenvironments: Records Preserved in Mid and Low Latitude Glaciers*. New York: Kluwer, pp 145–162.
- Guilderson, T.P., Fairbanks, R.G., and Rubenstone, J.L., 1994. Tropical temperature variations since 20,000 years ago: Modulating inter-hemispheric climate change. *Science*, **263**, 663–665.
- Hastenrath, S., and Greischar, L., 1994. Glacier recession on Kilimanjaro, East Africa, 1912–89. *J. Glaciol.*, **43**, 455–459.
- Henderson, K.A., 1996. *The El Niño-Southern Oscillation and other modes of Interannual Tropical Climate Variability as Recorded in Ice Cores from the Nevado Huascarán col, Peru*, The Ohio State University: M.S. Thesis.
- Henderson, K.A., Thompson, L.G., and Lin, P.-N., 1999. Recording of El Niño in ice core $\delta^{18}\text{O}$ records from Nevado Huascarán, Peru. *J. Geophys. Res.*, **104**(D24), 31053–31065.
- Huggel, C., Kaab, A., Haeberli, W., Teyssere, P., and Paul, F., 2002. Remote sensing based assessment of hazards from glacier lake outbursts: A case study in the Swiss Alps. *Can. Geotech. J.*, **39**(2), 316–330.
- Jones, P.D., Briffa, K.R., Barnett, T.P., and Tett, S.F.B., 1998. High-resolution palaeoclimatic records for the last millennium: Interpretation, integration and comparison with general circulation model control-run temperatures. *Holocene*, **8**, 455–471.
- Lamb, H.H., 1982. *Climate History and the Modern World*, London, UK: Methuen, 387pp.
- Li, S., and Shi, Y., 1992. Glacial and lake fluctuations in the area of the west Kunlun Mountains during the last 45,000 years. *Ann. Glaciol.*, **16**, 79–84.
- Liu, K.B., Yao, Z., and Thompson, L.G., 1998. A pollen record of Holocene climate changes from the Dunde ice cap, Qinghai-Tibetan Plateau. *Geology*, **26**(2), 135–138.
- Mann, M.E., Bradley, R.S., and Hughes, M.K., 1998. Global-scale temperature patterns and climate forcing over the past six centuries. *Nature*, **392**, 779–787.
- Meese, D.A., Gow, A.J., Grootes, P., Mayewski, P.A., Ram, M., Stuiver, M., Taylor, K.C., Waddington, E.D., and Zielinski, G.A., 1994. The accumulation record from the GISP2 core as an indicator of climate change throughout the Holocene. *Science*, **266**, 1680–1682.
- Meier, M.F., Dyurgerov, M.B., and McCabe, G.J., 2003. The health of glaciers: Recent changes in glacier regime. *Clim. Change*, **59**(1–2), 123–135.
- Mikhaleiko, V.N., 1997. Changes in Eurasian glaciation during the past century: Glacier mass balance and ice-core evidence. *Ann. Glaciol.*, **24**, 283–287.

- Ramirez, E., Hoffmann, G., Taupin, J.D., Francou, B., Ribstein, P., Caillon, N., Ferron, F.A., Landais, A., Petit, J.R., Pouyaud, B., Schotterer, U., Simoes, J.C., and Stievenard, M.A., 2003. A new Andean deep ice core from Nevado Illimani (6,350 m), Bolivia. *Earth Planet. Sci. Lett.*, **212** (3–4), 337–350.
- Reeh, N., 1988. A flow-line model for calculating the surface profile and the velocity, strain-rate, and stress fields in an ice sheet. *J. Glaciol.*, **34**(116), 46–54.
- Rozanski, K., Araguás-Araguás, L., and Gonfiantini, R., 1993. Isotopic patterns in modern global precipitation. In Swart, P.K., Lohmann, K.C., McKenzie, J., and Savin, S. (eds.), *Climate Change in Continental Isotopic Records*. Washington, D.C.: American Geophysical Union, pp. 1–36.
- Shichang, K., Wake, C.P., Dahe, Q., Mayewski, P.A., and Tandong, Y., 2000. Monsoon and dust signals recorded in Dasuopu glacier, Tibetan Plateau. *J. Glaciol.*, **46**(153), 222–226.
- Stute, M., Forster, M., Frischkorn, H., Serejo, A., Clark, J.F., Schlosser, P., Broecker, W.S., and Bonani, G., 1995. Cooling of tropical Brazil (5° C) during the last glacial maximum. *Science*, **269**, 379–383.
- Thompson, L.G., 2000. Ice-core evidence for climate change in the Tropics: Implications for our future. *Quaternary Sci. Rev.*, **19**, 19–36.
- Thompson, L.G., Mosley-Thompson, E., and Armao, B.M., 1984. El Niño–Southern Oscillation events recorded in the stratigraphy of the tropical Quelccaya ice cap, Peru. *Science*, **226**, 50–52.
- Thompson, L.G., Mosley-Thompson, E., and Thompson, P.A., 1992. Reconstructing interannual climate variability from tropical and subtropical ice-core records. In Diaz, H.F., and Markgraf, V. (eds.), *El Niño: Historical and Paleoclimatic Aspects of the Southern Oscillation*. Cambridge, UK: Cambridge University Press, pp. 295–322.
- Thompson, L.G., Mosley-Thompson, E., Davis, M., Lin, P.-N., Yao, T., Dyurgerov, M., and Dai, J., 1993. "Recent warming": Ice core evidence from tropical ice cores with emphasis upon Central Asia. *Global Planet. Change*, **7**, 145–146.
- Thompson, L.G., Mosley-Thompson, E., Davis, M.E., Lin, P.-N., Henderson, K.A., Cole-Dai, J., Bolzan, J.F., and Liu, K.-b., 1995. Late Glacial Stage and Holocene tropical ice core records from Huascarán, Peru. *Science*, **269**, 47–50.
- Thompson, L.G., Davis, M.E., Mosley-Thompson, E., Sowers, T.A., Henderson, K.A., Zagorodnov, V.S., Lin, P.-N., Mikhailenko, V.N., Campen, R.K., Bolzan, J.F., Cole-Dai, J., and Francou, B., 1998. A 25,000 year tropical climate history from Bolivian ice cores. *Science*, **282**, 1858–1864.
- Thompson, L.G., Yao, T., Mosley-Thompson, E., Davis, M.E., Henderson, K.A., and Lin, P.-N., 2000. A high-resolution millennial record of the South Asian Monsoon from Himalayan ice cores. *Science*, **289**, 1916–1919.
- Thompson, L.G., Mosley-Thompson, E., Davis, M.E., Henderson, K.A., Brecher, H.H., Zagorodnov, V.S., Mashiotta, T.A., Lin, P.-N., Mikhailenko, V.N., Hardy, D.R., and Beer, J., 2002. Kilimanjaro ice core records: Evidence of Holocene climate change in tropical Africa. *Science*, **298**, 589–593.
- Thompson, L.G., Mosley-Thompson, E., Davis, M.E., Lin, P.-N., Henderson, K., and Mashiotta, T.A., 2003. Tropical glacier and ice core evidence of climate change on annual to millennial time scales. *Clim. Change*, **59**(1–2), 137–155.
- Tian, L., Masson-Delmotte, V., Stievenard, M., Yao, T., and Jouzel, J., 2001. Tibetan Plateau summer monsoon northward extent revealed by measurements of water stable isotopes. *J. Geophys. Res.*, **106**(D22), 28081–28088.
- van De Velde, K., Ferrari, C., Barbante, C., Moret, I., Bellomi, T., Hong, S., and Boutron, C., 1999. A 200 year record of atmospheric cobalt, chromium, molybdenum, and antimony in high altitude alpine firn and ice. *Environ. Sci. Tech.*, **33**(20), 3495–3501.
- Vuille, M., Bradley, R.S., Healy, R., Werner, M., Hardy, D.R., Thompson, L.G., and Keimig, F., 2003. Modeling $\delta^{18}\text{O}$ in precipitation over the tropical Americas, Part II: Simulation of the stable isotope signal in Andean ice cores. *J. Geophys. Res.*, **108**(D6), 4175–4192.
- Wang, N., Thompson, L.G., Davis, M.E., Mosley-Thompson, E., Tao, T., and Pu, J., 2003. Influence of variations in NAO and SO on air temperature over the northern Tibetan Plateau as recorded by $\delta^{18}\text{O}$ in the Malan ice core. *Geophys. Res. Lett.*, **30**(22), 2167–2170.
- Yao, T., Thompson, L.G., Mosley-Thompson, E., Yang, Z., Zhang, X., and Lin, P.N., 1996. Climatological significance of $\delta^{18}\text{O}$ in north Tibetan ice cores. *J. Geophys. Res.*, **101**(D23), 29531–29537.
- Yao, T., Duan, K., Xu, B., Wang, N., Pu, J., Kang, S., Qin, X., and Thompson, L.G., 2002a. Temperature and methane changes over the past 1,000 years recorded in Dasuopu glacier (central Himalaya) ice core. *Ann. Glaciol.*, **35**, 379–383.
- Yao, T., Thompson, L.G., Duan, K., Xu, B., Wang, N., Pu, J., Tian, L., Sun, W., Kang, S., and Qin, X., 2002b. Temperature and methane records over the last 2 ka in Dasuopu ice core. *Sci. China Ser. D: Earth Sci.*, **45**(12), 1068–1074.

Cross-references

Aerosol (Mineral)
 Deuterium, Deuterium Excess
 Ice Cores, Antarctica and Greenland
 Little Ice Age
 Medieval Warm Period
 Monsoons, Quaternary
 Mountain Glaciers
 North Atlantic Oscillation (NAO) Records
 Oxygen Isotopes
 Paleo-El Niño–Southern Oscillation (ENSO) Records
 Paleo-precipitation Indicators

"ICEHOUSE" (COLD) CLIMATES

Earth's climate has changed, within life-sustaining bounds, from warm to cool intervals, on scales from thousands to hundreds of millions of years. In the Phanerozoic Eon there have been three intervals of glaciation (Ordovician, Carboniferous and Cenozoic) lasting tens of millions of years, with ice down to sea level at mid-latitudes (Frakes et al., 1992; Crowell, 1999). These cool "icehouse" intervals were generally times of lower sea level, lower CO₂ percentage in the atmosphere, less net photosynthesis and carbon burial, and less oceanic volcanism than during alternating "greenhouse" intervals (Fischer, 1986). The transitions from Phanerozoic icehouse to greenhouse intervals were synchronous with some biotic crises or mass extinction events, reflecting complex feedbacks between the biosphere and the hydrosphere.

Figure 18 summarizes Earth's entire paleoclimate history, and Figure 19 shows the better-known Phanerozoic Eon, with carbon, strontium and sulfur isotopic ratios that are linked to major climate changes. Figure 110 shows an anti-correlation between atmospheric CO₂ levels and $\delta^{18}\text{O}$ values (proxy for oceanic temperature), which tracks the latitude of ice-rafted glacial debris.

The Cryogenian Period of Neoproterozoic time (about 750–580 Ma) contains rocks deposited in two or more severe Icehouse intervals (Harland, 1964; Knoll, 2000). Laminated cap carbonates with depleted $\delta^{13}\text{C}$ ratios are found on top of glacial marine diamictites in many successions (Kauffman et al., 1997). The sharp juxtaposition of icehouse versus greenhouse deposits has led some to suggest that rapid and extreme climate changes took place in Neoproterozoic time. The Snowball Earth hypothesis proposes that during these Neoproterozoic glaciations, the world ocean froze over. The cap carbonates are thought to have been deposited during a subsequent alkalinity event, caused by rapid warming and supersaturation of sea water on shallow continental shelves (Hoffman et al., 1998; Kennedy et al., 2001; Hoffman and Schrag, 2002).

The Earth's temperature has remained relatively constant for 3.8 by, within a range where life could exist (Figure 111), even though solar luminosity has increased and atmospheric

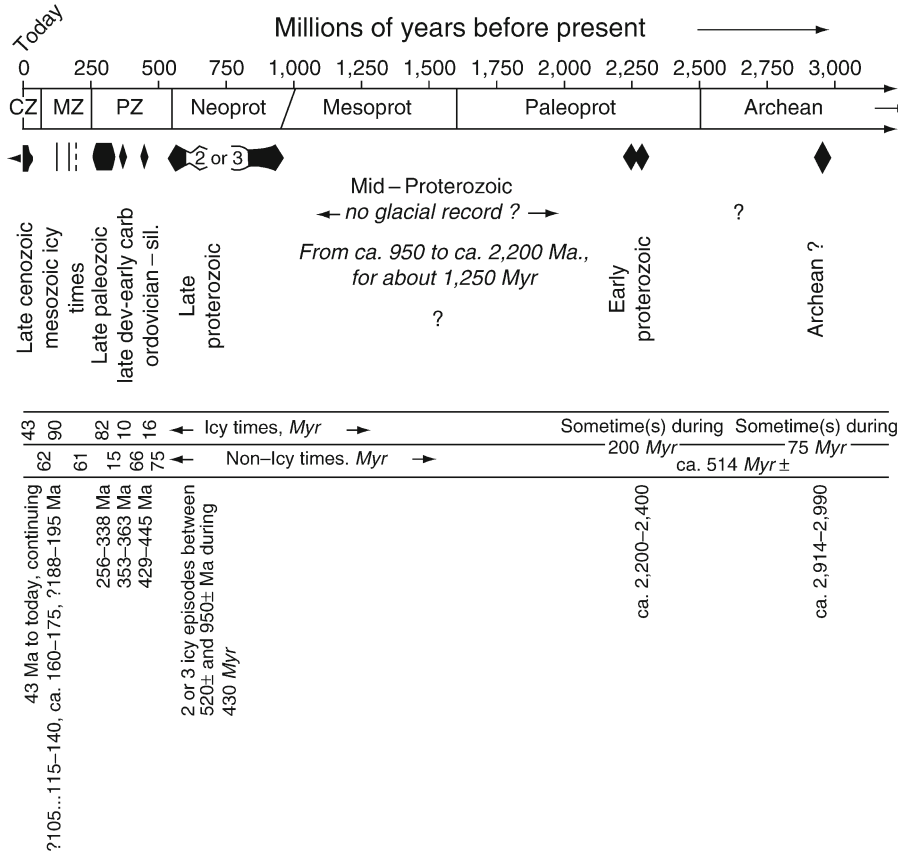


Figure 18 Major ice ages on Earth when the extent of continental glaciers was so great that tongues of ice reached the sea. Duration of icy and non-icy times is shown in the middle of the figure. CZ = Cenozoic; MZ = Mesozoic; PZ = Paleozoic; NEOPROT = Neoproterozoic; MESOPROT = Mesoproterozoic; PALEOPROT = Paleoproterozoic (from Crowell, 1999, Figure 1, used by permission of Geological Society of America).

CO₂ levels have steadily decreased, since Archean time. In the Phanerozoic, the atmospheric CO₂ concentration has varied drastically between icehouse and greenhouse times (Figure I10) (Berner, 1990, 1991; Veizer, 2000; Crowley and Berner, 2001). These concentrations are buffered by feedback loops involving water vapor within the hydrosphere and complex relations in the biosphere (Kump, 2002).

Icehouse characteristics

In general, icehouse conditions occur at times of lower sea level, less cumulative volcanic activity, more vigorous oceanic circulation and bottom water oxidation, less diversity in marine organisms, and deeper levels of the carbonate compensation depth. Relatively warmer, greenhouse intervals are characterized by marine transgression, extensive carbonate bank systems, organic-rich shale basins, marine chert and phosphorite deposition, and nutrient upwelling (Fischer and Arthur, 1977). During icehouse intervals, several or all of the tectonic, geochemical, and astronomical events discussed below coincide. However, determination of the relative cause and effect of each factor, each with its own feedback system, is complex. Both terrestrial and celestial components are involved.

Glaciation to sea level at mid latitudes

The empirical definition of an icehouse state as seen in the geological record is the presence of floating sea-ice at mid-latitudes (30°),

and therefore the presence of ice-rafted debris (dropstones) in marine sediments (Frakes et al., 1992). Glacial ice has likely been present in high mountains throughout the Phanerozoic but the preservation potential of such alpine glacial deposits is low (Crowell, 1999) (see *Ice-rafted debris (IRD)*; *Glacial geomorphology*).

Well-mixed and colder oceans

During an icehouse, the deep ocean floor is oxygenated, and oceans are well-mixed. Icehouse conditions are favored when continental positioning allows north-south ocean circulation to bring warm equatorial water into polar latitudes where it evaporates and generates snowfall. This was the case during the Quaternary. Pleistocene oceanic bottom water temperatures were 15 °C lower than during the Mesozoic greenhouse (Crowley and Berner, 2001).

Carbon dioxide in atmosphere is lower

The percent of CO₂ in the atmosphere is lower in icehouse times, and generally tracks, and partly causes, the net change in temperature (Berner, 1990). Today's CO₂ percentage is in the icehouse range, at 300–370 ppm (Crowley and Berner, 2001). Models show this to be 17% of the Late Cretaceous greenhouse value, and perhaps only 5% of Cambrian Greenhouse CO₂ levels (Figure I10) (Chen and Drake, 1986; Berner, 1990). CO₂ percentage dropped with the Devonian advent of land plants and resulting accelerated silicate weathering.

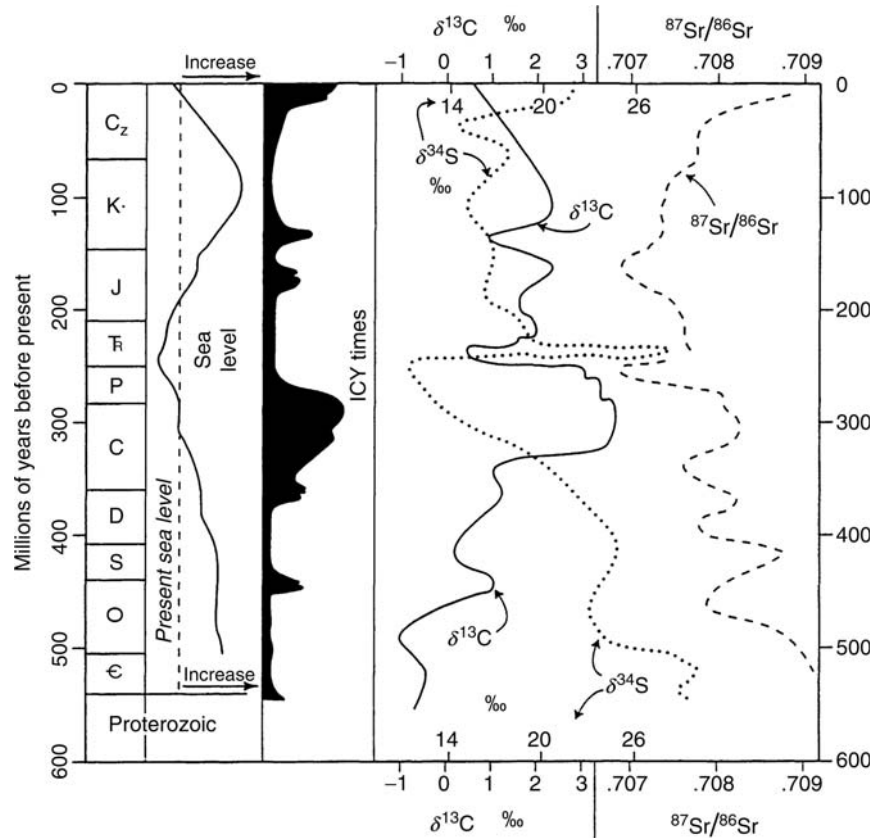


Figure 19 Carbon ($\delta^{13}\text{C}$), strontium ($^{87}\text{Sr}/^{86}\text{Sr}$), and sulfur ($\delta^{34}\text{S}$) isotopic ratios through Phanerozoic time compared with sea level and icy times. Cz = Cenozoic; K = Cretaceous; J = Jurassic; Tr = Triassic; P = Permian; C = Carboniferous; D = Devonian; S = Silurian; O = Ordovician; = Cambrian (from Crowell, 1999, Figure 25; originally modified from Veevers, 1994, Figure 1, used by permission of Geological Society of America).

Carbon isotope values are complex

Carbon is fractionated between organic matter (which is relatively concentrated in ^{12}C) and carbonate (inorganic carbon (which is heavier in $\delta^{13}\text{C}$). Mantle carbon and methane (organic carbon) are both depleted in ^{13}C . The more sedimentary carbon that is buried as organic matter, the heavier will be the remaining carbonate carbon (Knoll, 1991). Further, increased weathering of sediments that contain isotopically light organic carbon, in orogenic belts, or from exposed continental shelves during times of low sea level, will shift the $\delta^{13}\text{C}$ ratio in carbonate sediments to more negative values.

In the Pleistocene, more negative $\delta^{13}\text{C}$ values correspond with times of greater glaciation. In the Neoproterozoic, major negative $\delta^{13}\text{C}$ spikes are found in carbonate rocks deposited on top of glacial marine sediments.

However, for the Late Paleozoic Ice Age and the Ordovician glaciation, $\delta^{13}\text{C}$ values are heavier than during the intervening greenhouse intervals (Figure 19). This apparent ambiguity has caused much controversy.

Global sea level is lower

Sea level is relatively lower during icehouse modes (Figure 19). At such times, water is stored in glacial ice, causing significant drops in global sea level on timescales of 10^5 yr (100 kyr). The extent of sea ice has an important positive feedback on the

albedo or reflectivity of the Earth, which increases as sea level drops and ice expands. As the albedo increases, the Earth absorbs less solar radiation, and the climate becomes cooler. Conversely, during warmer, more humid times, sea level is high and polar ice is minimal, lowering the Earth's albedo. The ultimate long-term (10^8 years – first order) controls on sea level are tectonic, expressed as the average elevation of water-displacing, thermally inflated ocean floor, which is itself a function of the average rate of sea-floor spreading.

Bioherms and evaporites restricted to low latitude: aragonite seas

During icehouse intervals, bioherms and evaporites are restricted to less than 20° latitude. There is lower invertebrate diversity in high latitudes. Like today, aragonite and high-Mg calcite ooids precipitate in shallow marine environments (as opposed to low-Mg calcite ooids during greenhouse times) (Stanley and Hardie, 1998).

Reduced pelagic diversity

Diversity of the pelagic marine realm was reduced (oligotaxy) during icehouse intervals. Such oligotaxic times fostered intense blooms of opportunistic pelagic organisms at times of cumulative lowest diversity (Fischer and Arthur, 1977; Fischer, 1982, 1986).

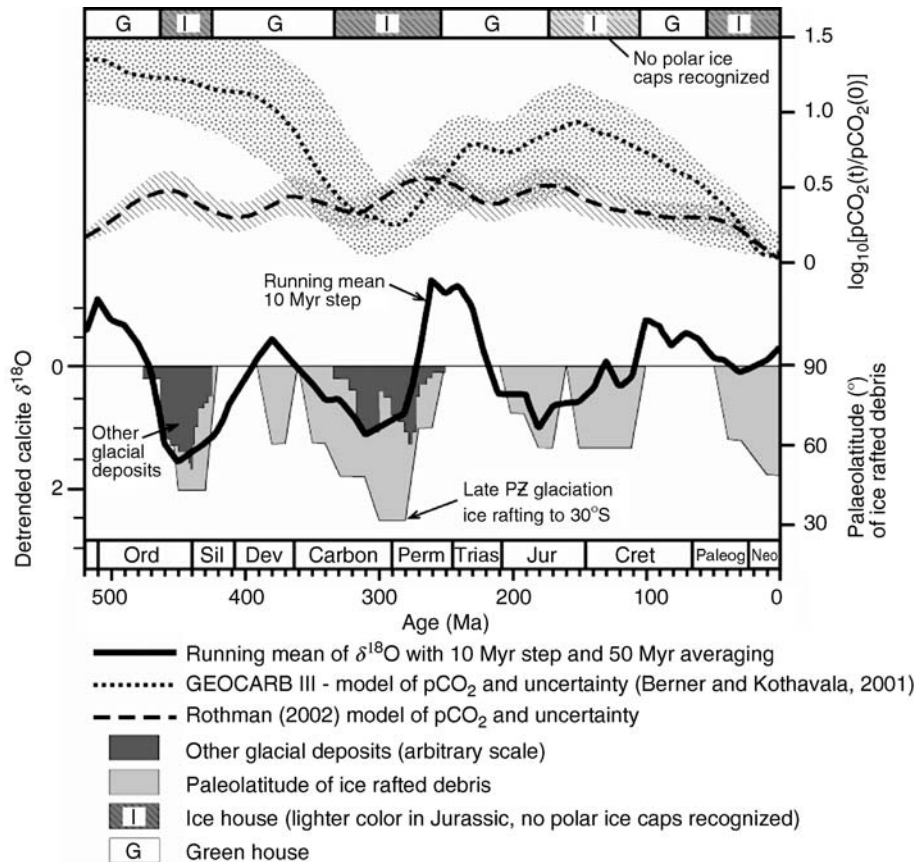


Figure 110 Phanerozoic climatic indicators and reconstructed $p\text{CO}_2$ levels (adapted from Shaviv and Veizer, 2003, Figure 1). Icehouse and greenhouse intervals are shown at the top of the diagram. Upper two curves represent estimated $p\text{CO}_2$ from the GEOCARB III CO_2 model (Berner and Kothavala, 2001) and the model of Rothman (2002). Oxygen isotope values from shells are shown with 10-Myr steps and 50-Myr averages. This smooths the curve and eliminates the highest readings. Paleolatitude of ice rafted debris and qualitative estimate of other glacial deposits are shown in the lower part of the diagram.

Carbonate compensation depth is deeper

During icehouse intervals, the CCD (carbonate compensation depth) is relatively deep within the world ocean, caused by the cooler oceanic temperatures and the resulting greater solubility of carbonate. Such conditions may not, however, apply to the Neoproterozoic, before the advent of pelagic carbonate-secreting organisms (Ridgwell et al., 2003).

Rates of carbon burial are reduced

In general, rates of carbon burial, or sequestration of organic carbon, are reduced in icehouse times, because the oceans are better aerated and the area of dysoxic restricted basins is smaller. The locations of such basins and associated carbon sinks are determined by plate configuration, global and local sea level, and by local organic productivity (controlled by upwelling). Low rates of accumulation of marine organic matter in Late Paleozoic time suggest well-ventilated Icehouse oceans.

Volcanic production of CO_2 is lower

In Phanerozoic cool periods, net production of CO_2 by volcanic activity is lower than during greenhouse events. Plate tectonic and mantle events cause these changes in net volcanic eruption

rates, with decreased rates reflecting periods of supercontinents and slow sea-floor spreading.

Plate tectonic causation

Icehouse climates are favored during times of relatively slow sea-floor spreading, which, in the Phanerozoic, have been times of supercontinent persistence. In general, large continents favor formation of ice sheets (Frakes et al., 1992). For the Late Paleozoic and Late Cenozoic ice ages, a north-south arrangement of continents, fostering longitudinal ocean circulation, was a first-order cause of climate cooling.

A decrease in worldwide volcanic activity, with reduction in CO_2 emission, is controlled by the rate of sea-floor spreading. Such a decrease is favorable for a long-term icehouse event. Slower sea-floor spreading leads to lower global sea level, another icehouse characteristic.

Veevers (1990) suggests that supercontinent cycles are the ultimate cause of icehouse climates, which occur at times of maximum continentality and slower sea-floor spreading. Apparent long-term periodicities in global tectonic phenomena and impact cratering have been linked to motions of the solar system through the galaxy (e.g., Rampino and Stothers, 1986).

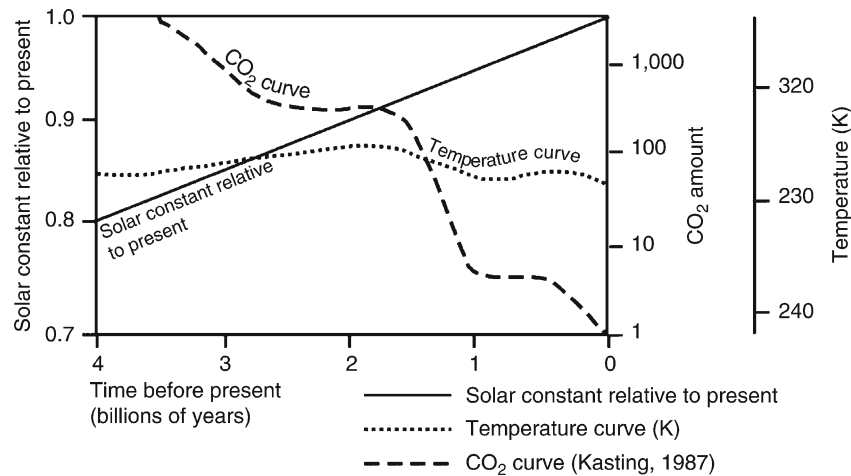


Figure I11 Variation of surface temperature, solar constant and atmospheric CO₂ over geologic time. Temperature curve refers to average surface temperature at 35° latitude. Note that CO₂ percentage has been falling steadily since the Archean, while solar output has been increasing. The net temperature has remained quite constant. Small-scale CO₂ changes, related to icehouse cycles, are superposed on this decreasing secular trend (simplified from Frakes et al., 1992, Figure 1.1).

However, Crowell (1999) does not recognize these tectonic supercycles. The presence or absence of deterministic chrono-tectonic supercontinent cycles is a recurring point of discussion in the study of Earth history.

Records of ancient glaciations

Glaciers are manifested differently at different latitudes, and include ice sheets, valley glacier and piedmont glacier complexes and mountain glaciers. Geological evidence for glaciation and glacial sedimentation are important to paleoclimatologists and sedimentologists, because they can indicate former cold climates (Harland, 1964; Deynoux et al., 1994; Crowell, 1999). Definitive ancient glacial deposits include poorly sorted diamictites, which may contain striated clasts and be associated with dropstone facies in proglacial lakes or seas (Link and Gostin, 1981).

A brief summary of the main icehouse intervals since 1,000 Ma follows. More detail is given in Crowell (1999).

Neoproterozoic (Cryogenian) glacial interval

Late Proterozoic glacial strata are found on all continents. The first evidence for ice sheets at low latitudes was marshaled by Harland (1964) who proposed the Great Infra-Cambrian ice age. Neoproterozoic paleocontinental positions suggest that most landmasses were at low latitudes, in areas of intense silicate weathering (Evans, 2000). This intense weathering traps carbonate and lowers global atmospheric CO₂ percentage (Kirschvink, 1992). Repeated studies have demonstrated low paleolatitudes for Neoproterozoic glacial marine strata (Sohl et al., 1999).

The Cryogenian Period of the Neoproterozoic is named for these icehouse intervals and has been investigated by the International Union of Geological Sciences (Knoll and Walter, 1992; Knoll, 2000; Narbonne, 2003).

Only recently have sufficiently accurate geochronologic data been obtained to place constraints on the Neoproterozoic glacial intervals, so that issues of synchronicity and extent of specific glacial advances remain controversial. Figure I12 shows the time and isotopic constraints, grouped into two broad icehouse

intervals, Sturtian (730–670 Ma) and Marinoan (640–580 Ma), each tens of millions of years long in duration and each with several glaciations. The Marinoan glacial interval is used here in the inclusive sense (Knoll, 2000) to encompass the Varanger, Ghaub, and Gaskiers glaciations and is succeeded by the Ediacaran (Vendian) Period. New radiometric ages from glacial strata reveal multiple ages for ice advance, rather than two synchronous global ice ages (Bowring et al., 2003; Lund et al., 2003; Calver et al., 2004; Fanning and Link, 2004; Hoffmann et al., 2004; Zhou et al., 2004). Purely lithostratigraphic correlations have been a first start, but, to be credible, must be verified by geochronology.

Cap carbonates

Neoproterozoic glacial marine diamictites are often overlain by laminated cap carbonates that have strongly negative $\delta^{13}\text{C}$ values (e.g., Kauffman et al., 1997; Hoffman et al., 1998; Kennedy et al., 2001). Some cap carbonates contain spectacular aragonite crystal fans that grew rapidly on the sea floor. The juxtaposition of glacial (icehouse) deposits with carbonate (greenhouse) deposits is striking. In the Snowball Earth scenario, which proposes that the world oceans froze entirely over (Hoffman et al., 1998; Hoffman and Schrag, 2002), cap carbonates play an integral role and are thought to have been deposited rapidly during a post-glacial marine alkalinity event that was fed by a deeply weathered carbonate-rich regolith formed during the glaciation.

The severity of Cryogenian climate cycles is represented by the wide range of $\delta^{13}\text{C}$ values from Neoproterozoic carbonates (Figure I12) (Kaufman et al., 1997; Lorentz et al., 2004). Documented negative $\delta^{13}\text{C}$ isotopic excursions for carbonates immediately above the glacial rocks are as great as 16‰, going from +10 to –6‰, which exceeds the magnitude of Phanerozoic excursions (Hoffman and Schrag, 2002). Levels of –6‰ suggest near-shutdown of the fractionation of ¹²C in organic matter, as would happen with rapid deposition of shallow-marine carbonate during post-glacial transgression.

Crowell (1999) points out that these carbonates may not represent immediately warmed ocean water, but rather, slowly

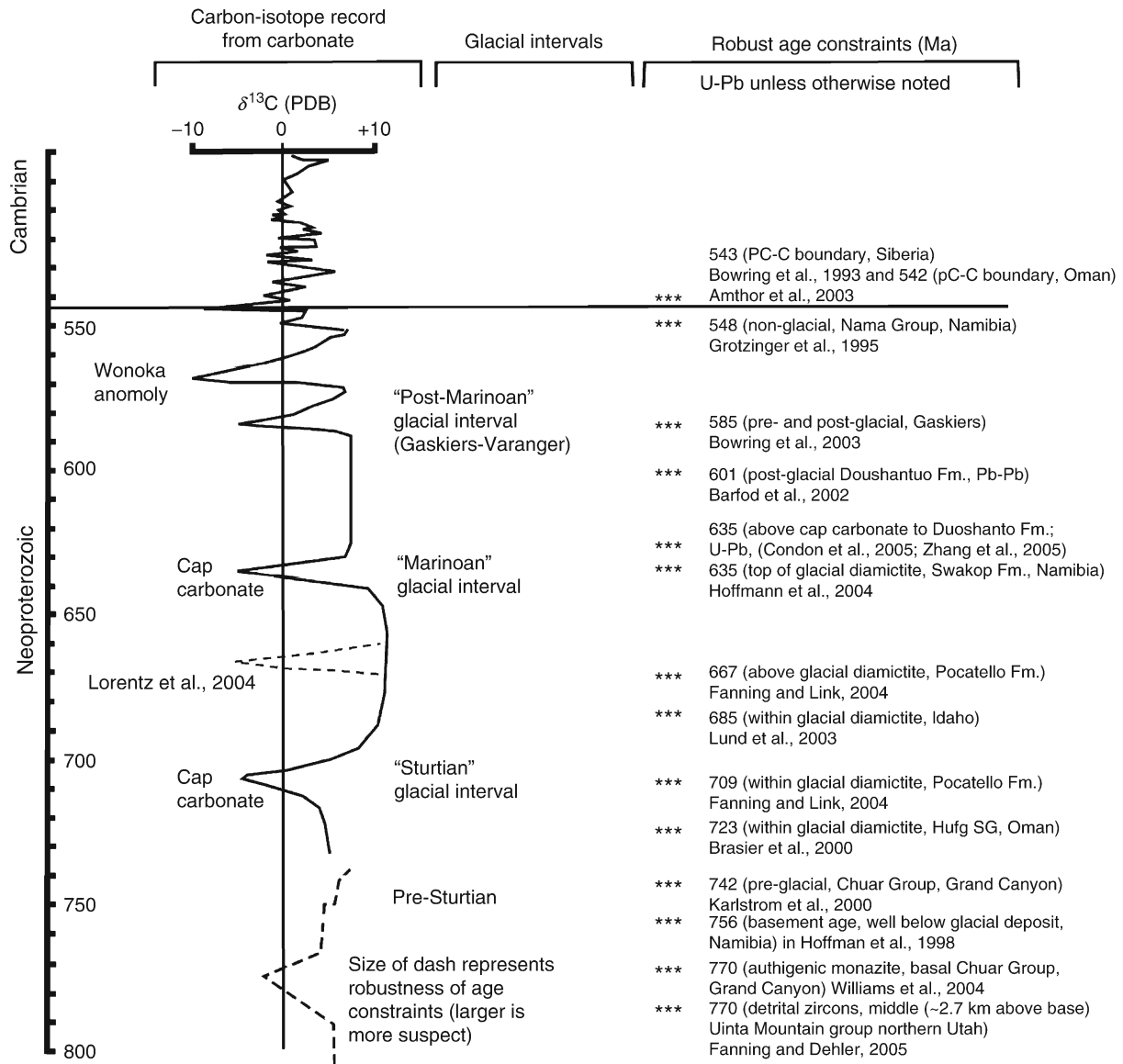


Figure 112 Late Neoproterozoic glacial intervals, carbon isotope values (Kaufman et al., 1997; Kennedy et al., 2001), and geochronologic constraints. Figure prepared by F. A. Corsetti, University of Southern California.

warming transgressive shelves above marine tillites. At least one post-glacial cap carbonate in south China has extremely low $\delta^{13}\text{C}$ values of -45% , suggesting local methane release caused by post-glacial sea level rise and flooding of continental shelves (Jiang et al., 2003).

Proposed explanations of low-latitude Cryogenian glaciation

Low latitude glaciation has been explained by several hypotheses:

1. A climate system similar to that of today with unusual paleogeographic and tectonic factors combining to allow low-latitude glaciation;
2. A Snowball Earth with an ice shelf covering the ocean. (Note that a modification into a "Slushball Earth" may be

necessary to account for evidence of meltwater during Neoproterozoic glaciations).

3. A greater inclination of Earth's spin axis such that polar regions have more equable climates than low-latitude positions (Williams, 1975);
4. True polar wander, where the lithosphere decouples from the asthenosphere and moves with respect to the magnetic field. This would cause inconsistent paleomagnetic pole positions on different continents;
5. Extraterrestrial influences, which may trigger climate cooling by the presence of abundant air-borne ejecta.

Late Ordovician and Early Silurian glaciations

During the Late Ordovician to early Silurian (~ 458 – 421 Ma), short but severe glaciations affected areas of South Africa,

the Saharan region of North Africa, and South America as the continents drifted over the South Pole. These glaciations were primarily due to continental positioning, and did not represent a global icehouse event. Atmospheric CO₂ percentage was high (Figure I10), but its effects were overridden by favorable continental positioning of Gondwanaland near the South Pole (Crowley and Berner, 2001).

Late Devonian and Early Carboniferous glaciations

Late Devonian and Early Carboniferous ice ages are recognized in isolated places in Brazil, in what were then high southern polar latitudes. Crowell (1999) includes these in his major episodes of glaciation, though Frakes et al. (1992) do not do so.

Late Paleozoic ice age

The Late Paleozoic ice age, from early Carboniferous to late Permian time (Figure I13) (~350–253 Ma) is the period of the

well-known Gondwanan glaciations. It produced striated surfaces and tillites on all Gondwanan continents (Australia, India, Asia, Antarctica, South America and Africa). Glaciers extended away from the South Pole as far as 40° S latitude. In most places, several advance and retreat cycles can be recognized, and they are diachronous on different continents, tracking movement through high southern latitudes. In the Northern Hemisphere, glacio-eustatic cyclothem are recognized in the North American mid-continent. Gondwanan glacial deposits were part of the evidence used by Wegener for continental drift. Stones derived from southern and western Africa are found in glacial deposits in Brazil and Argentina.

The Late Paleozoic ice ages ended at least 5 Myr before the mass extinction at the end of the Permian. The warming process may have been facilitated by the outpouring of the Siberian trap lavas and associated CO₂ emission (see *Glaciations, pre-Quaternary; Late Paleozoic climates*).

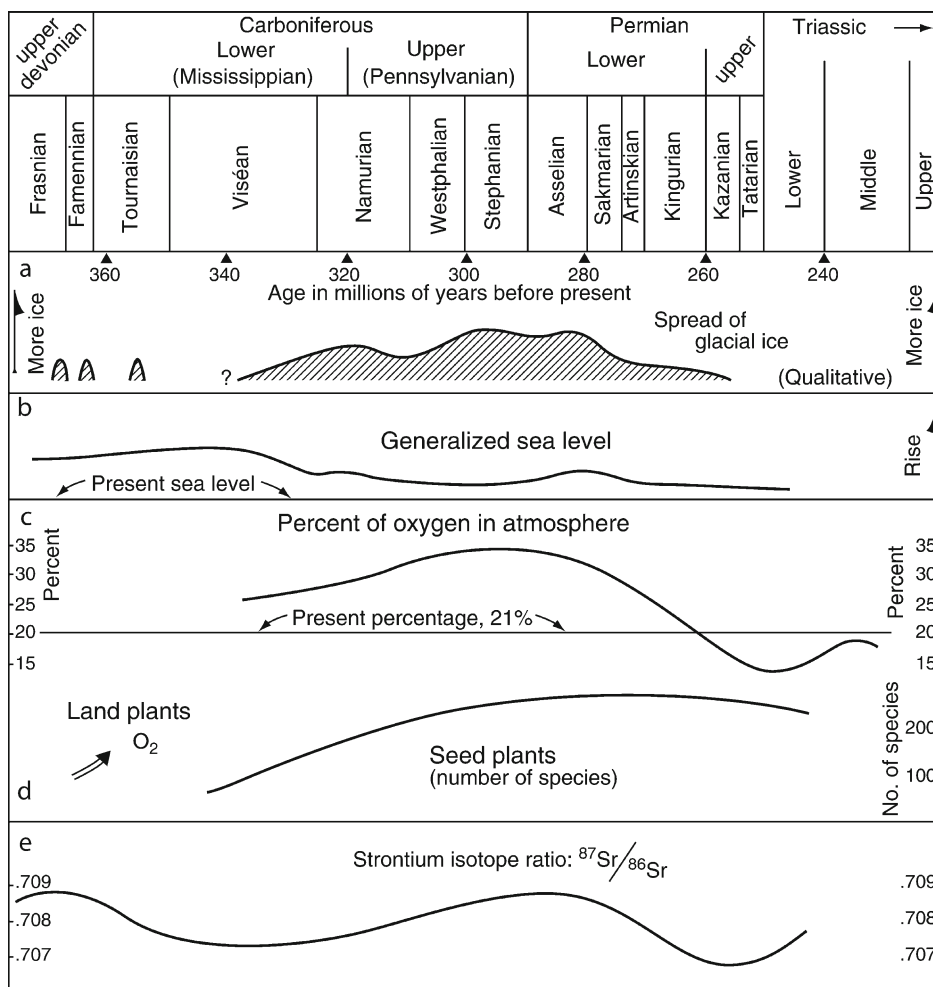


Figure I13 Time plot of glacial expansions during the Late Paleozoic ice age from Devonian through Triassic time. Figure shows several possible cause and effect factors related to glacial advances. Geologic time scale calibrations from Harland et al. (1990), generalized sea-level curve from Vail et al. (1977), percent of oxygen in atmosphere from Berner (1990), number of species of land plants from Niklas et al. (1985), strontium isotopic ratios simplified from Burke et al. (1982) and Holser et al. (1988) (from Crowell, 1999, Figure 39; used with permission of the Geological Society of America).

Late Cenozoic ice age

The Late Cenozoic, Eocene to Recent glaciation (~55–0 Ma) (Frakes et al., 1992) began slowly and locally in the Antarctic. Ice-rafterd sediment is present in 35 Ma Antarctic sediments. Worldwide cooling ensued by early Miocene time (22 Ma). Northern Hemisphere climates got progressively colder, as reflected by paleobotanical records of the southward migration of the extent of broad-leafed evergreen vegetation. The Cenozoic rise of the Himalayas intensified the Indian monsoon, and affected climate in numerous ways, including favoring Arctic cooling. The collision of India and Asia also created a CO₂ sink, due to enhanced chemical weathering of the uplifted Himalayan orogenic belt, which removed CO₂ from the atmosphere (see *Mountain uplift and climate change*). The greatest extent of glaciation was reached in the Pleistocene. Pleistocene climate cyclicity is recorded in δ¹⁸O curves as measured from CaCO₃ shells of foraminifera, with the δ¹⁸O values inversely related to ocean-water temperature (i.e., positive values indicate cold ocean temperatures and vice-versa; see *Oxygen isotopes*). Pleistocene glacial cyclicity generally follows Milankovich astronomical controls (see *Astronomical theory of climate change; Pleistocene climates; Glaciations, Quaternary*).

Summary

Earth has undergone several Icehouse periods, with the Pleistocene being the most recent. The controlling factors are both cyclic (external or astronomical) and secular (internal to the Earth), largely the product of plate tectonics (see *Climate change, causes*). In his synthesis of pre-Mesozoic ice ages, Crowell (1999) sees an irregular pattern of major glaciations, caused by changes in paleogeography and driven by plate tectonics, with secondary atmospheric and astronomical influence.

Earth's orbital variations are surely cyclic: "Alloccyclic sedimentary rhythms – driven by orbital reaction of the Earth with this moon, its sibling planets, and the Sun, and transmitted through climate – are real" (Fischer, 1986). Luckily for us, Earth's history of extraterrestrial interactions has not fundamentally disrupted the life-sustaining Earth-Ocean-Lithosphere system. As shown in Figure I11, Earth's surface temperature has remained relatively constant within limits since the Archean, even though the luminosity of the Sun has increased and the amount of CO₂ in the atmosphere has decreased. Water vapor has acted as a buffer and climate moderator (Kump, 2002; Shaviv and Veizer, 2003).

CO₂ cycling through the biosphere is internal to the climate system, and thus cannot drive a secular change through time, but does affect feedbacks (see *Carbon cycle*). Net volcanism, related to sea-floor spreading rate, is an external forcing factor to the climate system, and had a major effect on the levels of CO₂ during the Mesozoic Greenhouse period (Kump, 2002). Even though the burning of fossil fuels has caused atmospheric CO₂ concentration to rise steadily since observations on Mauna Kea began in 1958 (Chen and Drake, 1986), changes in climate owing to human activity are geologically ephemeral. In taking a long-time view of the Earth's history, they represent but a quick excursion.

Paul K. Link

Bibliography

Amthor, J.E., Grotzinger, J.P., Schroeder, S., Bowring, S.A., Ramezani, J., Martin, M.W., and Matter, A., 2003. Extinction of *Cloudina* and *Namacalathus* at the Precambrian-Cambrian boundary in Oman. *Geology*, **31**, 431–434.

- Barfod, G.H., Albarede, F., Knoll, A.H., Xiao, S., Telouk, P., Frei, R., and Baker, J., 2002. New Lu-Hf and Pb-Pb age constraints on the earliest animal fossils. *Earth Planet. Sci. Lett.*, **201**, 203–212.
- Berger, W.H., 1982. Climate steps in ocean history—Lessons from the Pleistocene. In Berger, W.H., Crowell, J.C., et al. (eds), *Climate in Earth History, Studies in Geophysics*. Washington, DC: National Academy Press, pp. 43–54.
- Berner, R.A., 1990. Atmospheric carbon dioxide levels over Phanerozoic time. *Science*, **249**, 1382–1386.
- Berner, R.A., 1991. A model of atmospheric CO₂ over Phanerozoic time. *Am. J. Sci.*, **291**, 339–376.
- Berner, R.A., and Kothavala, Z., 2001. GEOCARB III: A revised model of atmospheric CO₂ over Phanerozoic time. *Am. J. Sci.*, **301**, 182–204.
- Bowring, S., Myrow, P., Landing, E., Ramezani, J., and Grotzinger, J., 2003. Geochronological constraints on terminal Neoproterozoic events and the rise of Metazoans. *Geophys. Res. Abstr.*, **5**, 13,219.
- Brasier, M., McCarron, G., Tucker, R., Leather, J., Allen, P., and Shields, G., 2000. New U-Pb zircon dates for the Neoproterozoic Ghubrah glaciation and for the top of the Huqf Supergroup, Oman. *Geology*, **28**, 175–178.
- Burke, W.H., Denison, R.E., Hetherington, E.A., Koepnick, R.B., Nelson, H.F., and Otto, J.B., 1982. Variations of seawater ⁸⁷Sr/⁸⁶Sr throughout Phanerozoic time. *Geology*, **10**, 516–519.
- Calver, C.R., Black, L.P., Everard, J.L., and Seymour, D.B., 2004. U-Pb zircon age constraints on late Neoproterozoic glaciation in Tasmania. *Geology*, **32**, 893–896.
- Chen, C.-T.A., and Drake, E.T., 1986. Carbon dioxide increase in the atmosphere and oceans and possible effects on climate. *Annu. Rev. Earth Planet. Sci.*, **14**, 201–236.
- Condon, D., Zhu, M., Bowring, S., Wang, W., Yang, A., and Jin, Y., 2005. U-Pb ages from the Neoproterozoic Doushantuo Formation, China. *Science*, **308**, 95–98.
- Crowell, J.C., 1999. *Pre-Mesozoic Ice Ages: Their Bearing on Understanding the Climate System*. 192, Boulder, CO: Geological Society of America Memoir 106pp.
- Crowley, T.J., and Berner, R.A., 2001. CO₂ and climate change. *Science*, **292**, 870–872.
- Deynoux, M., Miller, J.M.G., Domack, E.W., Eyles, N., Fairchild, I.J., and Young, G.M. (eds.), 1994. *Earth's Glacial Record*. Cambridge, UK: Cambridge University Press, 266pp.
- Evans, D.A.D., 2000. Stratigraphic, geochronological, and paleomagnetic constraints upon the Neoproterozoic climatic paradox. *Am. J. Sci.*, **300**, 347–433.
- Fanning, C.M., and Dehler, C.M., 2005. Constraining depositional ages for Neoproterozoic siliciclastic sequences through detrital zircon ages: A ca. 770 maximum age for the lower Uinta Mountain Group. *Geological Society of America Abstracts with Programs*, **37**.
- Fanning, C.M., and Link, P.K., 2004. 700 Ma U-Pb SHRIMP ages for Neoproterozoic (Sturtian) glaciogenic Pocatello Formation, southeastern Idaho. *Geology*, **32**, 881–884.
- Fischer, A.G., 1982. Long-term climatic oscillations recorded in stratigraphy. In Berger, W. (ed.), *Climate in Earth History*. National Research Council, Studies in Geophysics, Washington, DC: National Academy Press, pp. 97–104.
- Fischer, A.G., 1986. Climatic rhythms recorded in strata. *Annu. Rev. Earth Planet. Sci.*, **14**, 351–376.
- Fischer, A.G., and Arthur, M.A., 1977. Secular variations in the pelagic realm. In Cook, H.C., and Enos, P. (eds.), *Deep Water Carbonate Environments*. SEPM Special Publication 25, pp. 18–50.
- Frakes, L.A., Francis, J.E., and Syktus, J.I., 1992. *Climate modes of the Phanerozoic*. New York: Cambridge University Press, 274pp.
- Grotzinger, J.P., Bowring, S.A., Saylor, B.Z., and Kaufman, A.J., 1995. Biostratigraphic and geochronologic constraints on early animal evolution. *Science*, **270**, 598–604.
- Harland, W.B., 1964. Critical evidence for a great infra-Cambrian glaciation. *Geologische Rundschau*, **54**, 45–91.
- Harland, W.B., Armstrong, R.L., Cox, A.V., Craig, L.E., Smith, A.G., and Smith, D.G. (eds.), 1990. *A Geologic Time Scale 1989*. Cambridge, UK: Cambridge University Press, 263pp.
- Hoffman, P.F., and Schrag, D.P., 2002. The snowball Earth hypothesis: testing the limits of global change. *Terra Nova*, **14**, 129–155.
- Hoffman, P.F., Kaufman, A.J., Halverson, G.P., and Schrag, D.P., 1998. A Neoproterozoic snowball Earth. *Science*, **281**, 1342–1346.

- Hoffmann, K.-H., Condon, D.J., Bowring, S.A., and Crowley, J.L., 2004. U-Pb zircon date from the Neoproterozoic Ghaub Formation, Namibia: Constraints on Marinoan glaciation. *Geology*, **32**, 817–820.
- Holser, W.T., Schidlowski, M., Mackenzie, F.T., and Maynard, J.B., 1988. Biogeochemical cycles of carbon and sulfur. In Gregor, C.B., Garrels, R.M., Mackenzie, F.T., and Maynard, J.B. (eds.), *Chemical Cycles in the Evolution of the Earth*. New York: Wiley, pp. 105–173.
- Jiang, G., Kennedy, M.J., and Christie-Blick, N., 2003. Stable isotopic evidence for methane seeps in Neoproterozoic postglacial cap carbonates. *Nature*, **426**, 822–826.
- Karlstrom, K.E., Bowring, S.A., Dehler, C.M., Knoll, A.H., Porter, S.M., DesMarais, D.J., Weil, A.B., Sharp, Z.D., Geissman, J.W., Elrick, M.B., Timmons, J.M., Crossey, L.J., and Davidek, K.L., 2000. Chuar Group of the Grand Canyon: Record of breakup of Rodinia, associated change in the global carbon cycle, and ecosystem expansion by 740 Ma. *Geology*, **28**, 619–622.
- Kasting, J.F., 1987. Theoretical constraints on oxygen and carbon dioxide concentrations in the Precambrian atmosphere. *Precambrian Res.*, **34**, 205–229.
- Kaufman, A.J., Knoll, A.H., and Narbonne, G.M., 1997. Isotopes, ice ages, and terminal Proterozoic Earth history. *Proc. Natl. Acad. Sci.*, **94**, 6600–6605.
- Kennedy, M.J., Christie-Blick, N., and Sohl, L.E., 2001. Are Proterozoic cap carbonates and isotopic excursions a record of gas hydrate destabilization following Earth's coldest intervals? *Geology*, **29**, 443–446.
- Kirschvink, J.L., 1992. Late Proterozoic low-latitude global glaciation: The snowball Earth. In Schopf, J.W., and Klein, C. (eds.), *The Proterozoic Biosphere*. New York: Cambridge University Press, pp. 51–52.
- Knoll, A.K., 1991. End of the Proterozoic Eon. *Sci. Am.*, **265**, 64–73.
- Knoll, A.K., 2000. Learning to tell Neoproterozoic time. *Precambrian Res.*, **100**, 3–20.
- Knoll, A.H., and Walter, M.R., 1992. Latest Proterozoic stratigraphy and Earth history. *Nature*, **356**, 673–677.
- Kump, L.R., 2002. Reducing uncertainty about carbon dioxide as a climate driver. *Nature*, **419**, 188–190.
- Link, P.K., and Gostin, V.A., 1981. Facies and paleogeography of Sturtian glacial strata (Late Precambrian), South Australia. *Am. J. Sci.*, **281**, 353–374.
- Lorentz, N.J., Corsetti, F.A., and Link, P.K., 2004. Seafloor precipitates and C-isotope stratigraphy from the Neoproterozoic Scout Mountain Member of the Pocatello Formation, southeast Idaho: implications for Earth System behavior. *Precambrian Res.*, **130**, 57–70.
- Lund, K., Aleinikoff, J.N., Evans, K.V., and Fanning, C.M., 2003. SHRIMP U-Pb geochronology of Neoproterozoic Windermere Supergroup, central Idaho: Implications for rifting of western Laurentia and synchronicity of Sturtian glacial deposits. *Geol. Soc. Am. Bull.*, **115**, 349–372.
- Narbonne, G.M., 2003. I.U.G.S. Subcommittee on the Terminal Proterozoic System, 18th circular (September 2003). <http://geol.queensu.ca/people/narbonne/trm-prot/> (June 2004).
- Niklas, K.J., Tiffney, B.H., and Knoll, A.H., 1985. Patterns in vascular land plant diversification: an analysis at the species level. In Valentine, J.W. (ed.), *Phanerozoic Diversity Patterns: Profiles in macroevolution*. Princeton, NJ: Princeton University Press, pp. 97–128.
- Parrish, J.T., 1982. Upwelling and petroleum source beds, with reference to the Paleozoic. *AAPG Bull.*, **66**, 750–774.
- Rampino, R., and Stothers, R.B., 1986. Geological periodicities and the galaxy. In Smoluchowski, R., Bahcall, J.N., and Matthews, M.S. (eds.), *The Galaxy and the Solar System*. Tucson, AZ: University of Arizona Press, pp. 241–259.
- Ridgwell, A.J., Kennedy, M.J., and Calderia, K., 2003. Carbonate deposition, climate stability, and Neoproterozoic ice ages. *Science*, **302**, 859–862.
- Rothman, D.H., 2002. Atmospheric carbon dioxide levels for the last 500 million years. *Proc. Natl. Acad. Sci.*, **99**, 4167–4171.
- Shaviv, N.R., and Veizer, J., 2003. Celestial driver of Phanerozoic climate? *GSA Today*, **13**, 4–10.
- Sohl, L.E., Christie-Blick, N.M., and Kent, D.V., 1999. Paleomagnetic polarity reversals in Marinoan (ca. 600 Ma) glacial deposits of Australia: implications for the duration of low-latitude glaciations in Neoproterozoic time. *Geol. Soc. Am. Bull.*, **111**, 1120–1139.
- Stanley, S.M., and Hardie, L.A., 1998. Secular oscillations in the carbonate mineralogy of reef-building and sediment-producing organisms driven by tectonically forced shifts in seawater chemistry. *Palaeogeogr. Palaeoclimatol. Palaeoecol.*, **144**, 3–19.
- Vail, P.R., Mitchum, R.M. Jr., Todd, R.G., Widmier, J.M., Thompson, S., III, Sangree, J.B., Bubb, J.N., and Hatlelid, W.G., 1977. Seismic stratigraphy and global changes of sea level. In Payton, C.E. (ed.), *26, Seismic stratigraphy—Application to Hydrocarbon Exploration*. Tulsa, OK: American Association of Petroleum Geologists Memoir pp. 29–212.
- Veevers, J.J., 1990. Tectonic-climatic supercycle in the billion-year plate-tectonic eon: Permian Pangean icehouse alternates with Cretaceous dispersed continent Greenhouse. *Sediment. Geol.*, **68**, 1–16.
- Veevers, J.J., 1994. Pangea: Evolution of a supercontinent and its consequences for Earth's paleoclimate and sedimentary environments. In Klein, G.D. (ed.), *Geological Society of America Special Paper 288, Pangea: Paleoclimate, Tectonics, and Sedimentation During Accretion, Zenith, and Breakup of a Supercontinent*. Boulder, CO: Geological Society of America, pp. 13–23.
- Veizer, J., Godderis, Y., and Francois, L.M., 2000. Evidence for decoupling of atmospheric CO₂ and global climate during the Phanerozoic eon. *Nature*, **408**, 698–701.
- Williams, G.E., 1975. Late Precambrian glacial climate and the Earth's obliquity. *Geol. Mag.*, **112**, 441–444.
- Williams, M. and 2004. Dating sedimentary sequences: in situ U/Th-Pb microprobe dating of early diagenetic monazite and Ar-Ar dating of marcasite nodules: Case studies from Neoproterozoic black shales in the southwestern U.S. *Geological Society of America Abstracts with Programs*, **35**, 595.
- Worsley, T.R., Nance, R.D., and Moody, J.B., 1986. Tectonic cycles and the history of the Earth's biogeochemical and paleoceanic record. *Paleoceanography*, **1**, 233–263.
- Zhang, S., Jiang, G., Zhang, J., Song, B., Kennedy, M.J., and Christie-Blick, N., 2005. U-Pb sensitive high-resolution ion microprobe ages from the Doushantuo Formation in south China: Constraints on late Neoproterozoic glaciations. *Geology*, **33**, 473–476.
- Zhou, C., Tucker, R.D., Xiao, S., Peng, Z., Yuan, X., and Chen, Z., 2004. New constraints on the ages of Neoproterozoic glaciations in south China. *Geology*, **32**, 437–440.

Cross-references

Albedo Feedbacks
 Astronomical Theory of Climate Change
 Carbon Cycle
 Carbon Isotope Variations over Geologic Time
 Carbon Isotopes, Stable
 Cenozoic Climate Change
 Climate Change, Causes
 Glacial Geomorphology
 Glaciations, Pre-Quaternary
 Glaciations, Quaternary
 Greenhouse (warm) Climates
 Ice-rafted Debris (IRD)
 Late Paleozoic Paleoclimates (Carboniferous-Permian)
 Mountain Uplift and Climate Change
 Oxygen Isotopes
 Plate Tectonics and Climate Change
 Sea Level Change, Last 250 Million Years
 Snowball Earth Hypothesis

ICE-RAFTED DEBRIS (IRD)

Introduction

Ice-rafted debris (IRD) is sediment of any grain size that has been transported by floating ice and released subsequently into an aqueous environment; the ice acts as a raft, providing buoyancy to any debris included within it or on its surface. Although IRD is often assumed to be transported by icebergs, the ice raft can be in the form of either icebergs, derived from

glaciers and ice sheets, or from sea ice formed by the freezing of sea water. IRD is usually deposited by icebergs and sea ice floating in marine waters, but icebergs, lake and river ice can also transport debris and release it subsequently into lakes.

Sources and distribution of debris

The best-known source of IRD is from glaciers and ice sheets. This form of IRD is heterogeneous in grain size, ranging from fine clays and silts to large boulders. This is because glacier ice can erode and transport material of all grain sizes. Sediments produced in the zone of shearing and crushing at the base of an ice sheet often show microscopic and larger edge rounding, together with striations and faceting of their surfaces. The modal shape class of this debris is sub-rounded in terms of Powers' visual roundness index. Such basally-derived glacial debris is usually found in the lowermost few centimeters to meters of glacier ice, at concentrations ranging from a few percent to a few tens of percent (Anderson et al., 1980). It can be present at higher levels in a glacier, usually in discrete bands of debris-rich ice, as a result of glaciotectonic processes such as folding and thrusting.

By contrast, debris incorporated at the glacier surface is usually derived from either rockfall or dirty-snow avalanching onto the ice, although finer-grained material can be deposited by the action of wind. Rockfall and avalanche debris is produced predominantly from weathering of exposed rock on valley walls, and is often relatively coarse-grained and angular in shape, with a sub-angular or angular modal Powers' roundness. Wind-blown debris is of silt and clay size, and is well sorted. Except locally, where significant rockfalls and avalanches have taken place, most of the debris load of glaciers is of basally-derived debris that is eroded or reworked at the glacier bed (Dowdeswell, 1986).

Sea ice also provides a vehicle for the long-distance ocean transport of sediments, although its load is typically of fine-grained material with rather few large clasts (Nürnberg et al., 1994). Fine sediments, entrained in shallow waters during storms, are incorporated when the sea-surface freezes during winter (Barnes et al., 1982). In addition, sediments can be entrained from the sea floor where the ice contacts it in shallow water, or where supercooled water freezes at the sea bed and entrains debris – such anchor ice can incorporate sand and coarser debris. Finally, debris can be introduced to the sea-ice surface through delivery by wind action or from the sediment load of rivers which can flow across shorefast sea ice during spring melting.

Debris release by melting and dumping

Icebergs are formed when ice breaks off, or calves, from the marine or lake margins of glaciers and ice sheets. The icebergs, and any included debris, then drift under the action of ocean currents and, to a lesser extent, wind. The icebergs melt and fragment during their drift. As they melt, at a rate dependent on the temperature of the water, and their size and velocity, any included sediment is released. Coarser material rains out to the sea floor directly, whereas silts and clays have a residence time in the water column linked to particle size, surface roughness and water viscosity. Those parts of an iceberg exposed above water also melt, and debris released there can build up on the surface to be deposited as a single event when the iceberg fragments or overturns. Icebergs vary in diameter from meters to tens and even over 100 km on initial calving,

and can be hundreds of meters in thickness. They may travel up to several thousand kilometers from their glacier source before complete melting, providing a mechanism of long-distance transport for included debris.

Sea ice forms during winter as the sea-surface freezes. Its drift is controlled mainly by wind because, at only a few meters in thickness but covering millions of square kilometers of the ocean, wind shear on its surface is particularly important. Sea ice melts from its base as it drifts into warmer waters, and at its surface due to increased radiative energy in summer. Predominantly fine-grained sediments are released in this way, in contrast to the delivery of material of heterogeneous grain size from icebergs.

Sedimentology of IRD

Deep-ocean sediments are usually fine-grained muds or ooze that are deposited in an environment of low energy. Floating ice, mainly in the form of icebergs, is the only mechanism by which significant quantities of very coarse-grained debris can be delivered into such environments. Individual pebbles, sometimes referred to as dropstones or lonestones, within fine-grained massive muds are a clear indicator of IRD deposition. Often dropstones exhibit striated and faceted surfaces, confirming their glacial origin. In higher energy marine environments, closer to the glacier source of icebergs and meltwater, isolated pebbles can be found within laminated silts and clays. Sometimes the laminations beneath the pebble have been deformed downward by the clast, and overlying sediments are, in turn, draped over it. Where large numbers of icebergs have traversed an area, releasing debris on melt or overturn, layers of sandy material have been observed, known as ice-rafted debris layers (Bond et al., 1992).

Paleoenvironmental significance

At timescales of hundreds of millions of years, the occurrence of isolated dropstones has been used to provide evidence of past ice ages, during which sufficient ice built up on land to reach the sea and produce sediment-laden icebergs. The occurrence of six ice ages over the past thousand million years of Earth history has been inferred using this and other evidence (Eyles, 1993). The first occurrence of IRD in long cores from the Late Cenozoic geological record has also been used to identify the initial growth of ice sheets on Antarctica and Northern Hemisphere landmasses.

The record of IRD deposition is usually constructed by counting the numbers of grains larger than a given size, often between 0.5 and 2 mm, per increment of core depth. Cores spanning the last glacial-interglacial cycle of about 115,000 years have also been examined at high resolution. The most easily distinguished ice-rafted layers yet found are the six so-called "Heinrich Layers," deposited as six events in North Atlantic cores over the past 60,000 years or so (Heinrich, 1988; Bond et al., 1992). Each IRD layer represents a collapse of the Hudson Bay-Hudson Strait drainage basin of the North American Ice Sheet, with the discharge of huge numbers of icebergs into the North Atlantic. The thickness of these Heinrich Layers decreases from about 0.5 m offshore of eastern Canada, to just a few centimeters some 3,000 km away off western Europe (Dowdeswell et al., 1995). Other IRD layers, less thick and continuous over space, probably indicate instabilities within smaller ice-sheet drainage basins, and have also been used to infer regional climatic and sea-level changes. However, IRD

layers are sometimes difficult to correlate over large distances because the very nature of iceberg drift and fragmentation is statistical, and long-distance correlations of IRD layers may be restricted to the products of major ice-sheet collapse events (Dowdeswell et al., 1999).

Finally, the sources and drift tracks of icebergs can be reconstructed from the mineralogical analysis of IRD grains. Debris derived from characteristic source rocks can be identified several thousands of kilometers distant, allowing patterns of past ocean currents to be reconstructed. The work of Bischof (2001) on the sources and drift tracks of icebergs in the Arctic Ocean provides an example of the use of mineralogical tracers.

Julian A. Dowdeswell

Bibliography

- Anderson, J.B., Domack, E.W., and Kurtz, D.D., 1980. Observations of sediment-laden icebergs in Antarctic waters: Implications to glacial erosion and transport. *J. Glaciol.*, **25**, 387–396.
- Barnes, P.W., Reimnitz, E., and Fox, D., 1982. Ice rafting of fine-grained sediment, a sorting and transport mechanism, Beaufort Sea, Alaska. *J. Sediment. Petrol.*, **52**, 493–502.
- Bischof, J., 2001. *Ice Drift, Ocean Circulation and Climate Change*. Heidelberg: Springer.
- Bond, G., Heinrich, H., Broecker, W., Labeyrie, L., McManus, J., Andrews, J., Huon, S., Jantschik, R., Clasen, S., Simiet, C., Tedesco, K., Klas, M., Bonani, G., and Ivy, S., 1992. Evidence for massive discharges of icebergs into the North Atlantic during the last glacial period. *Nature*, **360**, 245–249.
- Dowdeswell, J.A., 1986. The distribution and character of sediments in a tidewater glacier, southern Baffin Island, N.W.T., Canada. *Arctic Alpine Res.*, **18**, 45–56.
- Dowdeswell, J.A., Maslin, M.A., Andrews, J.T., and McCave, I.N., 1995. Iceberg production, debris rafting, and the extent and thickness of Heinrich layers (H-1, H-2) in North Atlantic sediments. *Geology*, **23**, 301–304.
- Dowdeswell, J.A., Elverhøi, A., Andrews, J.T., and Hebbeln, D., 1999. Asynchronous deposition of ice-rafted layers in the Nordic seas and North Atlantic Ocean. *Nature*, **400**, 348–351.
- Eyles, N., 1993. Earth's glacial record and its tectonic setting. *Earth Sci. Rev.*, **35**, 1–248.
- Heinrich, H., 1988. Origin and consequences of cyclic ice rafting in the north-east Atlantic during the past 130,000 years. *Quaternary Res.*, **29**, 143–152.
- Nürnberg, D., Wollenburg, I., Dethleff, D., Eicken, H., Kassens, H., Letzig, T., Reimnitz, E., and Thiede, J., 1994. Sediments in Arctic sea ice: Implications for entrainment, transport and release. *Mar. Geol.*, **119**, 185–214.

Cross-references

[Binge-Purge Cycles of Ice Sheet Dynamics](#)
[Diamicton](#)
[Glaciomarine Sediments](#)
[Heinrich Events](#)

INTEGRATED OCEAN DRILLING PROGRAM (IODP)

Introduction

Studies of the ocean floor have greatly improved our understanding of processes responsible for the evolution of oceans and continents. Because the geology of oceans is simpler than that of continents and because the oceans are relatively young, reconstruction of their geologic history is simpler. However, the

oceans hide crustal rocks under sediment cover that can be several kilometers thick. We can study the underlying rocks by remote-sensing geophysical means and geochemical analyses of rocks recovered by coring and dredging. Definitive knowledge about the composition of underlying rocks and the processes responsible for their formation can only be obtained by acquiring samples, and that can only be accomplished by drilling and coring operations. It is not surprising, therefore, that scientific deep-ocean drilling, which started in 1968, has greatly increased our knowledge about the Earth. The Integrated Ocean Drilling Program is a complex international scientific drilling program that currently operates throughout the world.

Legacy programs

Scientific deep-ocean drilling started in 1968 with the Deep Sea Drilling Project (DSDP). The project's drillship was the *GLOMAR CHALLENGER*, whose operations were managed by the Scripps Institution of Oceanography. The drillship succeeded in overcoming several technical challenges, including dynamic positioning (how to keep the drillship positioned over the borehole in the presence of currents) and heave compensation (how to compensate for the ship's heave, so that the cores represent proper vertical positioning of the rock layers). DSDP's spectacular achievements became evident through the wealth of scientific results that emerged after drilling and coring at more than 600 sites throughout the world's oceans – all oceans except the Arctic. The DSDP verified seafloor spreading in the South Atlantic – ages were determined from examination of marine magnetic anomalies and were confirmed radiometrically, by comparing age from basement core samples. By obtaining core samples in all the oceans and by correlating the layering in the samples to environmental conditions, the field of paleoceanography was launched. Before DSDP started, a large number of seismic reflection profiles had been obtained in the world's oceans. Drilling, however, established the identity of layering in the seismic reflection profiles.

DSDP was succeeded by the Ocean Drilling Project (ODP) in 1985. The *JOIDES RESOLUTION* was the drillship used and the project was run by Texas A&M University. This program continued until 2003 and involved drilling at more than 650 sites. As more and more complex targets were attempted, technical innovations became necessary and a number of scientific discoveries were made. Among these were the presence of extensive microbial populations and the recovery of frozen methane reservoirs beneath the deep seafloor. It became possible to investigate fluid flow in the crust in several environments. The presence of vast sand deposits in deep water was discovered. Much was learned about the evolution of continental margins and new investigations probed the enigmatic large igneous provinces in the oceans.

Some of the major paleoclimate discoveries made under DSDP and ODP include:

- *Development of the field of paleoceanography.* The near-global network of continuous stratigraphic sections obtained by ocean drilling is the foundation of the field of paleoceanography.
- *Orbital variability during the Cenozoic.* By linking the record of climatic variation preserved in deep-sea sediments to calculated variations in Earth's orbital parameters, scientists have demonstrated the role of orbital variability in driving climate change.

- *Development of high-resolution chronology.* Complete recovery of fossiliferous marine sedimentary sections has greatly facilitated linking Earth's geomagnetic polarity reversal history to evolutionary biotic changes and to the isotopic composition of the global ocean.
- *Ocean circulation changes on decadal to millennial time-scales.* The record preserved in marine sediments and recovered by ocean drilling has clearly demonstrated that deep- and surface-ocean circulation is variable on decadal to millennial timescales, confirming results from polar ice cores.
- *Global oceanic anoxic events.* Deep-sea sediments exhibit specific times when the surface water productivity of large areas of the ocean was unusually high.
- *Timing of ice-sheet development in Antarctica and the Arctic.* Drilling has revealed that Earth's entry into its current Ice Age extended over 50 Myr.
- *Sea-level change and global ice volume.* Marine sediments recovered from shallow water areas have shown that important global sea-level changes have occurred synchronously through at least the past 25 Myr, and that these changes can be matched to oxygen isotope records of climate produced from the deep sea.
- *Uplift of the Himalayas and the Tibetan Plateau.* Drilling results have shown that the onset and development of both the Indian and Asian monsoons are the result of climate change associated with this uplift.

The Initial Science Plan for IODP

The success of DSDP and ODP encouraged scientists interested in scientific drilling to inquire whether a new program could be launched aimed at previously unreachable drilling targets. Some of these targets were located beneath the ice-covered Arctic Ocean. Others involved drilling to great depths, where the stability of the borehole could not be assured with existing techniques, or where the release of hydrocarbon fluids under pressure could lead to blow-outs. A number of international conferences were held based on the premise that the drilling program needed enhancements – new drilling platforms were needed that could deal with problems associated with stability of drill hotels, with blow-out prevention, and with difficult locations such as ice-covered seas and shallow water depths (where the *JOIDES RESOLUTION* could not be used). These conferences included the Conference on Cooperative Ocean Riser Drilling (CONCORD) in Tokyo (1997), the Conference on Multiple Platform Exploration of the Ocean (COMPLEX) in Vancouver (1999), and a workshop on Alternate Drilling Platforms (APLACON) in Brussels (2001), as well as several other workshops and conferences. The conclusions from these meetings formed the basis of deliberations by an Integrated Ocean Drilling Program (IODP) Planning Subcommittee (IPSC), which provided a report entitled “Earth, Oceans, and Life.” The report outlines the IODP Initial Science Plan for 2003–2013 and constitutes the program's scientific basis. It outlines three principal scientific themes and eight new initiatives derived from these themes, as well as principles of implementation.

The principal themes include *the deep biosphere and the sub-seafloor ocean; environmental change, processes, and effects; and solid Earth cycle and geodynamics.*

Within the science plan themes, the following initiatives are detailed:

- *Deep biosphere*

“Define bounding temperatures, pH and redox potential of the subseafloor biosphere ecosystem.”

“Evaluate the biogeochemical impacts of the subseafloor microbiota.”

“Provide uncontaminated samples necessary for high priority studies of deep-biospheric trophic strategies.”

- *Gas hydrates*

“Explore the nature of gas hydrates and the range of depositional settings; study the origin of the gas and the processes of its migration and entrapment.”

- *Extreme climates*

“Understand the mechanisms by which climate extremes develop and are maintained.”

Understanding the mechanisms by which climactic extremes develop, are maintained and end is fundamental to a quantitative description of global change. Earth is now in one of those extremes, the geologically unusual situation of bipolar glaciation. Our knowledge of how Earth's system operates to maintain the current climate is relatively good, but we are still debating how the climate has reached this state.

A question of fundamental importance is how, once established, Earth's climate system operated to maintain the low thermal gradients indicated by warm, high-latitude climates. The paradox in this case is the apparent requirement to transport the great amount of heat needed to warm the poles, versus the sluggish oceanic and atmospheric circulation suggested by low pole-to-equator thermal gradients.

- *Rapid climate change*

“Recover detailed marine sedimentary records to examine the presence of rapid climate changes in the past.”

One of the most striking results of recent paleoclimate research has been the determination that climate can change abruptly across the globe. For example, during the last glacial cycles, jumps between warmer and colder states occurred within decades, and these jumps were often associated with alternations in ocean circulation patterns.

Records of “natural” rapid climate change provide an indispensable context for evaluating contemporary anthropogenic inputs to the environment. The timing and distribution of the present warming trend may match those of previous times, or they may differ in some way explainable only by anthropogenic forcing. Such comparisons are greatly facilitated by recovery and use of detailed marine sedimentary records with resolutions approaching those of instrumental records.

The Arctic Ocean is essentially unknown, yet has the potential to advance our knowledge of rapid climate change processes enormously.

- *Continental break-up and sedimentary basin formation*

“Investigate difference in continental break-up and sediment basin formation at volcanic and non-volcanic margins.”

- *Large igneous provinces*

“Understand mantle behavior during the massive episodic magmatic events that are responsible for the formation of large igneous provinces and determine potential causal relationships and feedback mechanisms between their formation and environmental change.”

- *Twenty-First Century Mohole*

“Recover a complete section of oceanic crust and uppermost mantle and advance significantly our understanding

of the processes governing the formation and evolution of oceanic crust.”

- *Seismogenic zone*

“Understand the nature of the seismogenic zone and mechanics of the earthquake cycle through a comprehensive, multidisciplinary project focused on the behavior of rocks, sediments and fluids in the fault zone region.”

The above initiatives give a flavor of IODP plans. IODP is to be dynamic in nature and further initiatives will result as drilling proceeds.

Certain principles have been agreed on during IODP’s implementation. Foremost is the coordinated use of multiple drilling platforms. (The individual drilling platforms will be discussed in the next section.) A comprehensive engineering development program will be developed to provide a number of special measurement and sampling tools. Existing logging programs will be reviewed and enhanced as necessary. Boreholes drilled as part of IODP will be instrumented to serve as sub ocean-bottom observatories. These initiatives will require coordination with other scientific programs that demonstrate interest in such observatories. For example, coordination and cooperation with programs involved in climate change may be desirable, as well as with industry, which shares similar goals with IODP.

Drilling ships and platforms

Scientists participating in the IODP will be able to make use of three drilling platforms:

- The riser-equipped drilling vessel, the *CHIKYU*, built by JAMSTEC (acronym for the Japan Agency for Marine-Earth Science and Technology);
- A riserless platform provided by the United States, the *JOIDES RESOLUTION*, a 143-m long drillship used in IODP and for the first phase of IODP operations has recently undergone major renovations.
- Mission-specific platforms contributed by European countries that can operate in ice-covered oceans, shallow water zones, and areas inaccessible to the drilling vessels *CHIKYU* and *JOIDES RESOLUTION*.

The centerpiece of IODP is the drilling vessel *CHIKYU*. Built at a cost of more than \$500 million, the ship is 210 m long, and has a gross tonnage of 57,500 tons. The top of her 70-m derrick rises 116 m above the waterline. A dynamic positioning system can keep her within a 15-m radius above a drill hole. The *CHIKYU* contains a number of laboratories for intensive, non-destructive core analysis. These include a microbiology laboratory, a paleomagnetism laboratory, and a laboratory that includes an X-Ray CT scanner. It can drill 7 km beneath the ocean floor and can thus penetrate oceanic crust and reach the mantle. Drilling at a water depth of 2.5 km, the *CHIKYU* can wield a total drill pipe length of 9.5 km. Other distinguishing features of the *CHIKYU* include the availability of a riser and a blow-out preventer. The riser consists of a large diameter pipe which connects the drillship to the wellhead on the ocean floor and contains the drill pipe. Drilling fluid, which consists of “drilling mud,” is pumped down through the drill pipe together with the cuttings (ground up bits of rock), and returns through the space between the drill pipe and the riser pipe to the drillship. The cuttings are separated by filtering, and the drilling fluid is recycled. Circulating the drilling mud through the riser pipe provides several advantages.

Drilling mud is superior to seawater (which has to be used if there is no return circulation) in flushing the cuttings out, which otherwise could clog the drill hole. Appropriately dense mud can be used to line the drill hole and prevent it from caving in. In the absence of coring, the cuttings provide information about the formation that is being drilled through. When a riser is being used, a blow-out preventer sits over the drill hole. It acts as an automated shut-off device which provides protection against unintentional release of high pressure fluids and gases. The *CHIKYU* uses a massive 380-ton blow-out preventer, which contains a pressure-control system that maintains pressure at 15,000 pounds per square inch.

Mission-specific platforms are chosen for each mission-specific expedition. The Arctic Coring Expedition (ACEX) included a fleet of three icebreaker-class ships: a drilling vessel, the *VIDAR VIKING*, which remained at a fixed location and suspended more than 1,600 m of drill pipe through the water column and into the underlying sediments; a Russian nuclear icebreaker, the *SOVETSKIY SOYUZ*; and a diesel-electric icebreaker, the *ODEN*. The *SOVETSKIY SOYUZ* and *ODEN* protected the *VIDAR VIKING* by breaking “upstream” floes into smallish iceberg bits that allowed the *VIDAR VIKING* to stay positioned and recover sediment cores.

IODP structure

The IODP organization is complex. It includes Funding Agencies; Implementing Organizations, which run the drillships; the Science Advisory Structure, which provides scientific advice; and a Central Management Organization. The two Lead Funding Agencies are the U.S. National Science Foundation (NSF) and the Japanese Ministry of Education, Culture, Sports, Science and Technology (MEXT). They provide equal funds for the program. Funds also are contributed by the European Consortium for Ocean Research Drilling (ECORD), which consists of 17-member countries. China’s Ministry of Science and Technology (MOST) is an associate funding agency. The Implementing Organizations (IOs) include: the USIO comprising the Consortium for Ocean Leadership, Texas A&M University, and Lamont-Doherty Earth Observatory – the USIO operates the *JOIDES RESOLUTION*; CDEX, the Center for Deep Earth Exploration, part of JAMSTEC, operates the *CHIKYU*; and ESO, the European Consortium for Research Drilling (ECORD) Science Operator, which operates mission-specific platforms. The Science Advisory Structure (SAS) includes a number of committees and panels that provide scientific advice. Several hundred scientists serve on these committees and panels. IODP Management International (IODP-MI), a nonprofit corporation, serves as the Central Management Organization.

The structure of IODP can be perceived as a matrix with international funding agencies as program sponsors along one axis, and the Science Advisory Structure and Implementing Organizations along another axis, with the Central Management Office providing program focus.

Expeditions

IODP’s first two expeditions (in 2004) were the Juan de Fuca Hydrogeology Expedition and ACEX. IODP’s inaugural voyage was conducted at the Juan de Fuca Ridge in the summer of 2004, 200 km off the coast of British Columbia. Its objective was to conduct a series of studies to evaluate how fluid flows within oceanic crust. To succeed, the science party had to establish three “borehole observatories.” Two new observatories were

installed nearly 600 m below the seafloor, and another was established to replace an existing observatory. When completed within the next few years, the observatory network will enable scientists to discern the flow pattern in the oceanic crust. Expedition 301, the Juan de Fuca, also sampled sediments, basalt, fluids and microbial samples, and collected wireline logs in the deepest borehole.

The Arctic Coring Expedition, the first scientific drilling expedition to the central Arctic Ocean followed, in late summer 2004. Expedition 302 recovered sediment cores deeper than 400 m below seafloor in water depths of ~1,300 m at a location only 250 km from the North Pole.

ACEX's destination was the Lomonosov Ridge, hypothesized to be a sliver of continental crust that broke away from the Eurasian Plate at ~56 Ma. As the ridge moved north and then subsided, marine sedimentation occurred and continued to the present, resulting in what was anticipated (from seismic data) to be a continuous paleoceanographic record. The elevation of the ridge above the surrounding abyssal plains (~3 km) ensures that sediments atop the ridge are free of turbidites. ACEX's primary scientific objective was to continuously recover this sediment record and sample the underlying sedimentary bedrock by drilling and coring from a stationary drillship.

ACEX's biggest challenge was maintaining the drillship's location while drilling and coring 2–4-m thick sea ice that moved at speeds approaching half a knot. Sea-ice cover over the Lomonosov Ridge moves with the Transpolar Drift and responds locally to wind, tides, and currents. Never before had the high Arctic Ocean Basin (known as "mare incognitum" within the scientific community) been deeply cored, primarily because of these challenging sea-ice conditions.

Initial offshore results, based on analysis of core catcher sediments, demonstrated that biogenic carbonate only occurs in the Holocene-Pleistocene interval. The upper ~170 m represent a record of the past ~15 Myr composed of sediment with ice-rafted sediment and occasional small pebbles, suggesting that ice-covered conditions extended at least this far back in time. Earlier in the record, spanning a major portion of the Oligocene to late Eocene, an interruption in continuous sedimentation occurred. This may represent a hiatus encompassing a time interval of non-deposition or an erosional episode that removed sediment of this age from the ridge. The sediment record during the middle Eocene is of dark, organic-rich siliceous composition. Isolated pebbles, interpreted as ice-rafted dropstones, are present well into the middle Eocene section. An interval recovered around the lower/middle Eocene boundary contains an abundance of *Azolla* spp., suggesting that a fresh/low-salinity surface-water setting dominated the region during this time period. Drilling revealed that, during the latest Paleocene to the earliest Eocene boundary interval known as the Early Eocene Thermal Maximum (EETM) or the Paleocene-Eocene Thermal Maximum (PETM), the Arctic Ocean was subtropical with warm surface-ocean temperatures. ACEX penetrated into the underlying sedimentary bedrock, revealing a shallow-water depositional environment of Late Cretaceous age.

IODP expeditions aboard the *JOIDES RESOLUTION* continued through 2005 into 2006. As of July 2005, six riserless expeditions were completed. Of the six, five occurred in the North Atlantic; the sixth was conducted in the deep Gulf of Mexico. The *JOIDES RESOLUTION* proceeded to the Pacific for the remainder of 2005 and a portion of 2006.

Two mission-specific operations, the Tahiti Sea Level and the New Jersey Sea Level Expeditions, were planned for implementation by ESO.

Brief descriptions of 2004–2005 IODP expeditions follow.

North Atlantic Climate

The objective of these two back-to-back expeditions was to establish the intercalibration of geomagnetic paleointensity, isotope stratigraphy, and regional environmental stratigraphies for the Late Neogene to Quaternary period, and to develop a millennial-scale stratigraphic template for the North Atlantic. Other objectives were: (a) to better understand the relative phasing of atmospheric, cryospheric, and oceanic changes central to the mechanisms of global climate change on orbital or millennial timescales; and (b) to improve our knowledge of the temporal and spatial behavior of the geomagnetic field through high-resolution records of directional secular variation and geomagnetic paleointensity. A total of 36 holes was drilled at 11 sites, and 6,998 m of core were retrieved from beneath the seafloor.

Complete sedimentary sections were drilled by multiple advanced piston coring directly south of the Central Atlantic "ice-rafted debris belt" and on the southern Gardar Drift. In addition to the North Atlantic paleoceanography study, a borehole observatory was successfully installed in a new 170 m deep hole close to an earlier Ocean Drilling Program site.

Core Complex

This two-expedition program was aimed at documenting the conditions under which oceanic core complexes (OCCs) develop. These large shallow seafloor features appear to be related to rifting and accretion at slow-spreading mid-ocean ridges. However, currently available data are inadequate to characterize the magmatic/tectonic/metamorphic history, which is needed to better understand the mechanisms of OCC uplift and emplacement. Two sites were drilled: a deep-penetration site on the central dome of Atlantis Massif to sample the detachment fault zone and the alternation front and to drill into unaltered mantle (core and logging analyses were planned); and a shallower-penetration site through the hanging wall to sample rock just above the detachment, the shallowest part of the unexposed fault, and through the fault zone (core and logging analyses were planned). Twenty-two holes were drilled at four sites, with a total of 1,113 m of core retrieved. Unfortunately, the unaltered mantle was not reached.

Porcupine Basin Carbonate Mounds

The Porcupine Basin Carbonate Mounds Expedition included drilling a downslope suite of three sites on the eastern slope of Porcupine Sea Bight, west of Ireland. The sites are centered on "Challenger mound," a 170-m high, partly buried carbonate mound in the "Belgica mound province," topped by dead, cold-water coral rubble. The Belgica mound province belongs to one of the world's most well-documented carbonate mound provinces. The on-mound site was expected to unveil the environmental record locked in a carbonate mound and to shed light on the processes which may have controlled the genesis of the mound – in particular to test the hypothesis of the possible role of fluid venting as a trigger for mound growth and to assess the importance of environmental forcing factors. Particular attention was paid to microbiological and biogeochemical processes in mound genesis and development.

Deepwater Gulf of Mexico

This expedition was named "Overpressure and Fluid Flow Processes in the Deepwater Gulf of Mexico: Slope Stability, Seeps,

and Shallow Water Flow.” It was designed to explore the relationships that exist among and between overpressure, flow, and deformation in passive margin settings, and to test a multi-dimensional flow model by examining how physical properties, pressure, temperature, and pore fluid composition vary within low-permeability mudstones that overlie a permeable and over-pressured aquifer.

Superfast Spreading Crust

Two expeditions to examine the superfast spreading crust returned to an earlier ODP borehole to recover a complete section through $>200 \text{ m yr}^{-1}$ oceanic crust. Multiple trips to the drill sites resulted in retrieval of gabbros from intact ocean crust. In addition, for the first time, Scientists were able to drill through the entire sequence of volcanic rocks that cap the ocean crust to reach a fossil magma chamber 1.4 km beneath the seafloor. A complete section of the upper oceanic crust, drilled 1005 meters into the basement, was recovered.

Tahiti Sea Level

This expedition drilled a series of boreholes along a number of transects to: (a) reconstruct the deglaciation curve for the period 20,000–10,000 yBP in order to establish the minimum sea-level during the Last Glacial Maximum (LGM), and to assess the validity, timing and amplitude of meltwater pulses (so-called MWP-1A and MWP-1B events; ca. 13,800 and 11,300 cal. yBP), which are thought to have disturbed the general thermohaline oceanic circulation and, hence, global climate; (b) establish the sea surface temperature (SST) variation accompanying the transgression at each transect. These data will allow the examination of the impact of sea-level changes on reef growth, geometry and biological makeup, especially during reef drowning events, and will help improve the modeling of reef development; and (c) identify and establish patterns of short-term paleoclimatic changes that are thought to have punctuated the transitional period between present-day climatic conditions following the LGM. It is proposed to quantify the variations of sea surface temperatures based on high-resolution isotopic and trace element analyses on massive coral colonies. A attempt was made to identify specific climatic phenomena such as El Niño-Southern Oscillation (ENSO) in the time frame prior to 10,000 yBP.

Cascadia Margin Gas Hydrates

The Cascadia Margin Gas Hydrates proposal, designed in an accretionary prism environment, aimed to better constrain the models concerning the formulation of gas hydrates. Expedition 311 drilled a series of sites across the northern Cascadia accretionary prism to improve understanding of the deep origin of methane, its upward transport, its incorporation in gas hydrate, and its subsequent loss to the seafloor.

New Jersey Sea Level

This IODP expedition is to obtain continuous cores and down-hole logging measurements of siliciclastic sequences from this modern continental margin within crucial paleo-inner-shelf facies at three sites that represent the most sensitive and accessible locations for deciphering amplitudes and testing facies models.

Conclusion

While surface samples in the ocean bottom can be recovered by coring and dredging, samples of deep rocks can only be

recovered by deep drilling and coring. The deep drilling programs DSDP, ODP, and now IODP are programs that obtain rocks at great depths by coring and are therefore, by examination of these rocks, able to tell us much of climate conditions and ocean conditions at the time that the sediments that constitute the rocks were laid down. The science of paleoceanography can thus be said to have developed largely as a result of these drilling programs. Climate changes with frequencies ranging from several hundreds of thousands of years to the millennial scale have thus been elaborated through an examination of the cored rocks. The goals of IODP with respect to paleoceanography are focused on a number of specific problems; these include the studies of rapid climate change, as well as extreme climates and the variables that relate oceans to climate. During the next five years we expect major discoveries with respect to climates and oceans of the past, which in turn may give us clues as to what we can expect of climate and oceans in the future.

Manik Talwani

Bibliography

- Farrell, J.W., and Prell, W.L., 1989. Climatic change and CaCO_3 preservation: An 800,000-year bathymetric reconstruction from the central equatorial Pacific. *Paleoceanography*, **4**, 447–466.
- Hays, J.D., Imbrie, J., and Shackleton, N.J., 1976. Variations in Earth's orbit: Pacemaker of ice ages. *Science*, **194**, 1121–1132.
- Kennett, J.P., 1977. Cenozoic evolution of Antarctic glaciation, the circum-Antarctic Ocean, and their impact on global paleoceanography. *J. Geophys. Res.*, **82**, 3843–3860.
- Raymo, M.E., and Ruddiman, W.F., 1992. Tectonic forcing of late Cenozoic climate. *Nature*, **359**, 117–122.
- Schrag, D.P., Hampt, G., Murray, D.W., 1996. The temperature and oxygen isotopic composition of the glacial ocean. *Science*, **272**, 1930–1932.
- Zachos, J.C., Pagani, M., Sloan, L., Thomas, E., and Billups, K., 2001. Trends, rhythms, and aberrations in global climate 65 Ma to Present. *Science*, **292**, 686.

Cross-references

Deep Sea Drilling Project (DSDP)
Methane Hydrates, Carbon Cycling, and Environmental Change
Ocean Drilling Program (ODP)
Paleocene-Eocene Thermal Maximum
Paleoceanography

INTERSTADIALS

Definitions

Interstadials are regarded as the relatively short-lived periods of thermal improvement during a glacial phase, when temperatures did not reach those of the present day and, in lowland mid-latitude regions, the climax vegetation was boreal woodland (Lowe and Walker, 1997). Jessen and Milthers (1928) defined interstadials as periods that are either too short or too cold to allow the development of temperate deciduous forest of interglacial type in the same region. Interstadials are, however, not only defined on biostratigraphical grounds. In the USA, for instance, an interstadial is formally regarded as a climatic episode within a glaciation during which a secondary recession or standstill of glaciers took place (Gibbard and West, 2000).

Table 14 Interstadials during the Weichselian in Europe: Denmark (DK), The Netherlands (NL), Germany (D) France (F), Great Britain (UK), compared to GRIP Summit glacial interstadials IS as defined by Dansgaard et al. (1993)

Terrestrial sequences Europe	IS
Bølling-Allerød (DK), Windermere (UK)	1
Denekamp (NL)	8
Hengelo (NL)	12
Moershoofd (NL)	13
Glinde (D)	14
Oerel (D)	16
Odderade (D) St. Germain II (F)	21
Brørup (DK), St. Germain I (F), Chelford (UK)	23
Amersfoort (NL)	

Interstadials during the Weichselian

Many different interstadials are defined in Europe based on palynology. The interstadials that occurred during, for instance, the Weichselian Glacial have been named after the place where the interstadial was described for the first time. Many of these Weichselian interstadial stratotypes have been defined in NW Europe and are described by Behre (1989), Zagwijn (1989), and de Beaulieu and Reille (1992) (Table 14). Dansgaard et al. (1993) described 24 interstadial phases in the GRIP oxygen isotope record from the Greenland ice, characterized by a sudden increase and gradually decrease of oxygen isotope values. Recent evidence points to a total of 25 interstadial phases that are resolved in the Greenland ice core (NGRIP Members, 2004). These so-called Dansgaard-Oeschger interstadial events can be correlated with low percentages of the planktonic cold water foraminifera *Neogloboquadrina pachyderma* in high-resolution records from the North Atlantic (Bond et al., 1993).

Wim Z. Hoek

Bibliography

- Behre, K.E., 1989. Biostratigraphy of the last glacial period in Europe. *Quaternary Sci. Rev.*, **8**, 25–44.
- Bond, G., Broecker, W., Johnsen, S., McManus, J., Labeyrie, L., Jouzel, J., and Bonani, G., 1993. Correlations between climate records from North Atlantic sediments and Greenland ice. *Nature*, **365**, 143–147.
- Dansgaard, W., Johnsen, S.J., Clausen, H.B., Dahl-Jensen, D., Gundestrup, N.S., Hammer, C.U., Hvidberg, C.S., Steffensen, J.P., Sveinbjörnsdóttir, A.E., Jouzel, J., and Bond, G., 1993. Evidence for general instability of past climate from a 250-kyr ice-core record. *Nature*, **364**, 218–220.
- de Beaulieu, J.L., and Reille, M., 1992. The last climatic cycle at La Grande Pile (Vosges, France): A new pollen profile. *Quaternary Science Reviews*, **11**, 431–438.
- Jessen, K., and Milthers, V., 1928. Stratigraphical and palaeontological studies of interglacial freshwater deposits in Jutland and north-west Germany. *Danmarks Geologiske Undersøgelse II*, **48**, 380pp.
- Gibbard, P.L., and West, R.G., 2000. Quaternary chronostratigraphy: The nomenclature of terrestrial sequences. *Boreas*, **29**, 329–336.
- Lowe, J.J., and Walker, M.J.C., 1997. *Reconstructing Quaternary Environments*. London, UK: Longman, 446pp.
- North Greenland Ice Core Project (NGRIP) Members, 2004. High-resolution record of Northern Hemisphere climate extending into the last interglacial period. *Nature*, **431**, 147–151.
- Zagwijn, W.H., 1989. Vegetation and climate during warmer intervals in the Late Pleistocene of western and central Europe. *Quaternary Int.*, **3–4**, 57–67.

Cross-references

Bølling-Allerød Interstadial
 Millennial Climate Variability
 Dansgaard-Oeschger Cycles
 Ice Cores, Antarctica and Greenland
 Oxygen Isotopes
 Palynology
 Pollen Analysis

IRON AND CLIMATE CHANGE

Iron availability limits the ability of phytoplankton in some parts of the surface ocean to photosynthesize biomass from dissolved CO₂ in seawater. An important source of iron to phytoplankton is the deposition of dust from continents. The sensitivity of dust deposition to climatic factors such as aridity and windiness makes iron a possible link between climate and the CO₂ concentration in the atmosphere. Iron climate linkages and their biogeochemical ramifications are explored further in a recent article by Jickels et al. (2005).

The element iron is abundant in the core and crust of the Earth. In the early Earth, the oceans contained high concentrations of dissolved iron in the form of Fe²⁺. However, as the oceans became oxidized by increasing O₂ concentrations in the atmosphere, iron oxidized to the relatively insoluble state Fe³⁺, and deposited into sedimentary structures known as Banded Iron Formations. Except for anoxic regions such as in sediments or isolated basins such as the Black Sea, dissolved iron concentrations have remained low in the oceans ever since.

However, iron is not absent in the oxic ocean. Fe³⁺ is stabilized in the dissolved form by complexing organic compounds called chelators or siderophores (Rue and Bruland, 1995). These compounds appear to be biogenic, but little is known of their structure, lifetime, or origins. Similar compounds are secreted in soil and freshwater systems to enable plants, fungi, and bacteria to acquire iron. A vast majority of the iron in seawater is found to be complexed to siderophores. In addition, the precipitation of Fe³⁺ into solid form does not result in its immediate removal by sinking when the particles generated are very small. More than half of the Fe³⁺ in seawater is found in colloidal form, too small to sink but potentially too large to be biologically useful. In particular, the diffusion coefficient of colloidal complexed iron will be slower than that for truly dissolved iron, and its availability for biological uptake will be correspondingly less (Wu et al., 2001).

In spite of its scarcity, iron is an essential co-factor in enzymatic systems such as the light-harvesting photosynthesis systems, and in nitrogenase, the enzyme which fixes NH₄⁺ from molecular N₂ (Falkowski et al., 1998). Because of its low solubility in oxic seawater, iron has been shown to limit the production of biomass in several regions of the surface ocean. These regions, historically called High Nutrient Low Chlorophyll (HNLC) regions, include the equatorial Pacific, the North Pacific, and the Southern Ocean. When the iron concentration in the surface ocean is artificially increased in these areas, the iron stimulates increases in chlorophyll concentration, photosynthetic efficiency, and phytoplankton growth rates (Coale et al., 1996). These iron fertilization experiments constitute one of the most dramatic breakthroughs in biological oceanography in several decades.

The link between phytoplankton and the CO₂ concentration of the atmosphere occurs via the biological pump in the ocean. Photosynthesis produces particles that can leave their source waters by sinking. The downward net flux of biological material leaves the surface ocean depleted in nutrients such as NO₃⁻ and PO₄⁻, as well as dissolved CO₂. CO₂ gas dissolves into surface seawater, or evaporates into the atmosphere, according to its concentration in seawater or air, and its solubility (mostly controlled by temperature). Depletion of CO₂ from surface waters by biological activity therefore draws down the CO₂ concentration of the atmosphere. In the present-day ocean, Southern Ocean surface waters contain the majority of the potentially biologically usable nutrients NO₃⁻ and PO₄⁻. In addition, because the Southern Ocean is a conduit to the largest oceanic carbon reservoir – the deep ocean, atmospheric pCO₂ in models is more sensitive to surface chemistry changes in the Southern Ocean than other oceanographic regions. Therefore, the search for an explanation for lower glacial pCO₂ values has centered on deposition of iron onto the Southern Ocean.

There are arguments for and against the Southern Ocean fertilization hypothesis. On the positive side, the deposition of dust and Fe in Antarctic ice cores was indeed higher during glacial times, by more than an order of magnitude. Most of this dust appears to originate from a specific region in Patagonia, but dust deposition increased globally by a factor of two or more. The decline in Antarctic dust deposition is also one of the earliest indicators of the coming deglaciation (suggesting that dust decrease could be an ultimate cause for the other aspects of the deglaciation) (Broecker and Henderson, 1998).

On the other hand are arguments against the Southern Ocean fertilization hypothesis. Several models of iron geochemistry in the ocean conclude that the dominant iron source to the Southern Ocean surface is from below, in the upwelling water, and that increasing the negligible deposition flux will have little effect (Archer and Johnson, 2000). Fertilization experiments in the Southern Ocean have not resulted in increased sinking of organic matter into deep waters, but rather an increased standing biomass stock in surface waters as the added iron is efficiently recycled (Boyd et al., 2000). Trace element tracers for sea surface nutrient concentration in the Southern Ocean have not shown a substantial drawdown during glacial time (Boyle, 1992). Furthermore, the pCO₂ sensitivity to the Southern Ocean decreases with increasing model complexity and realism, such that even a complete drawdown of Southern Ocean nutrients would not be enough to generate glacial pCO₂ values (Archer et al., 2000). Finally, an increase in the biological pump would result in a decrease in the O₂ concentration of the deep ocean, which is not apparent in the sedimentary record.

With these counter-arguments in mind, the community is also investigating the possibility that an increased glacial iron supply might stimulate an increase in nitrogen fixation, resulting in an increase in the nitrate inventory of the ocean (Broecker and Henderson, 1998). A release from nitrogen limitation might result in a stronger biological pump, although phosphorus availability could limit this effect. In addition, iron fertilization is being explored as a potential fix for rising CO₂ concentrations resulting from fossil fuel consumption.

David Archer

Bibliography

Archer, D.E., and Johnson, K., 2000. A model of the iron cycle in the ocean. *Global Biogeochem. Cycles*, **14**, 269–279.

- Archer, D., Eshel, G., Winguth, A., Broecker, W.S., Pierrehumbert, R.T., Tobis, M., and Jacob, R., 2000. Atmospheric pCO₂ sensitivity to the biological pump in the ocean. *Global Biogeochem. Cycles*, **14**, 1219–1230.
- Boyd, P.W., Watson, A.J., Law, C.S., Abraham, E.R., Trull, T., Murdoch, R., Bakker, D.C.E., Bowie, A.R., Buesseler, K.O., Chang, H., Charette, M., Croot, P., Downing, K., Frew, R., Gall, M., Hadfield, M., Hall, J., Harvey, M., Jameson, G., LaRoche, J., Liddicoat, M., Ling, R., Maldonado, M.T., McKay, R.M., Nodder, S., Pickmere, S., Pridmore, R., Rintous, S., Safi, K., Sutton, P., Strzepek, R., Tannaberger, K., Turner, S., Waite, A., and Zeldis, J., 2000. A mesoscale phytoplankton bloom in the polar Southern Ocean stimulated by iron fertilization. *Nature*, **407**, 695–702.
- Boyle, E.A., 1992. Cadmium and δ¹³C paleochemical ocean distributions during the Stage 2 glacial maximum. *Annu. Rev. Earth Planet. Sci.*, **20**, 245–287.
- Broecker, W.S., and Henderson, G., 1998. The sequence of event surrounding termination II and their implications for the cause of glacial-interglacial CO₂ changes. *Paleoceanography*, **13**, 352–364.
- Coale, K.H., Johnson, K.S., Fitzwater, S.E., Gordon, R.M., Tanner, S., Chavez, F.P., Ferioli, L., Sakamoto, C., Rogers, P., Millero, F., Steinberg, P., Nightingale, P., Cooper, D., Cochlan, W.P., Landry, M. R., Constantinou, J., Rollwagen, G., Trasvina, A., and Kudela, R., 1996. A massive phytoplankton bloom induced by an ecosystem-scale iron fertilization experiment in the equatorial Pacific Ocean. *Nature*, **383**, 495–501.
- Falkowski, P.G., Barber, R.T., and Smetacek, V., 1998. Biogeochemical controls and feedbacks on ocean primary production. *Science*, **281**, 200–206.
- Jickels, T.D., 2005. Global iron connections between desert dust, ocean biogeochemistry, and climate. *Science*, **308**, 67–71.
- Rue, E.L., and Bruland, K.W., 1995. Complexation of iron(III) by natural organic ligands in the Central North Pacific as determined by a new competitive ligand equilibration/absorptive cathodic stripping voltammetric method. *Mar. Chem.*, **50**, 117–138.
- Wu, J., Boyle, E., Sunda, W., and Wen, L.-S., 2001. Soluble and colloidal iron in the oligotrophic North Atlantic and North Pacific. *Science*, **293**, 847–849.

Cross-references

Banded Iron Formations and the Early Atmosphere
Marine Carbon Geochemistry

ISOTOPE FRACTIONATION

Isotopes are atoms whose nuclei contain the same number of protons but a different number of neutrons. The term ‘isotope’ is derived from a Greek word meaning equal place: the various isotopes of an element occupy the same position in the periodic table. Isotopes of an element can be either stable or unstable (radioactive). Differences in chemical and physical properties arising from variations in atomic mass of an element are called ‘*isotope effects*’. The partitioning of isotopes between two substances or two phases of the same substance with different proportions of isotopes is called ‘*isotope fractionation*’ (Hoefs, 1997; Criss, 1999).

The isotopic composition of materials contains information that can be used, for example, to reconstruct the palaeo-environment and to understand the hydrological cycle and biochemical pathways.

History

In 1913, isotopes were discovered by J. J. Thomson who found that the element neon has two different kinds of atoms with atomic weights 20 and 22. A few years later, 212 of the 287

naturally occurring isotopes were known. The reason for the existence of isotopes was, however, unclear until the discovery of the neutron by Chadwick in 1932. The seminal papers by Urey (1947) and Bigeleisen and Mayer (1947) on the thermodynamic properties of isotopic substances provided the basis for the utilization of stable isotopes in geology, geochemistry, biogeochemistry, paleoceanography and elsewhere.

Notation, definitions

Isotopic ratios, R , are measures of the relative abundances of isotopes of an element, E ; they are usually arranged so that the lightest stable isotope (index a), which is often also the most abundant isotope, appears in the denominator: ${}^bR = {}^bE/{}^aE$ (stable boron isotopes are an exception: ${}^{11}\text{B}$ is about four times more abundant than ${}^{10}\text{B}$). The three stable oxygen isotopes ${}^{16}\text{O}$, ${}^{17}\text{O}$, and ${}^{18}\text{O}$ will be used to explain the notation and basic definitions.

The oxygen isotope with mass number 16 contains 8 protons and 8 neutrons and is denoted by ${}^{16}\text{O}$. It is by far the most abundant (99.76%) of the three stable oxygen isotopes. For example, the ratio of ${}^{17}\text{O}$ to ${}^{16}\text{O}$ in water, or the ratio of ${}^{18}\text{O}$ to ${}^{16}\text{O}$ in carbon dioxide can be written as:

$${}^{17}R_{\text{H}_2\text{O}} = \frac{[\text{H}_2^{17}\text{O}]}{[\text{H}_2^{16}\text{O}]}, \quad {}^{18}R_{\text{CO}_2} = \frac{2[\text{C}^{18}\text{O}^{18}\text{O}] + [\text{C}^{18}\text{O}^{16}\text{O}]}{2[\text{C}^{16}\text{O}^{16}\text{O}] + [\text{C}^{18}\text{O}^{16}\text{O}]}$$

The *isotopic composition*, δ , of a sample, determined by mass spectrometric methods, is measured with respect to a standard (std):

$$\delta^b E_{\text{sample}} = \left(\frac{{}^bR_{\text{sample}}}{{}^bR_{\text{std}}} - 1 \right) \cdot 1,000$$

where b is the atomic mass of the isotope and the factor 1,000 converts the δ value to per mil. The standards (cf. Hoefs, 1997) used for stable oxygen isotopes are V-SMOW (Vienna-Standard Mean Ocean Water; ${}^{18}R_{\text{V-SMOW}} \cdot 10^6 = 2,005.20 \pm 0.43$) and V-PDB (Vienna-Pee-Dee Belemnite, ${}^{18}R_{\text{V-PDB}} \cdot 10^6 = 2,067.1 \pm 2.1$).

The *fractionation factor*, α , is defined as the ratio between the isotopic ratio in compound X and that in compound Y:

$${}^b\alpha_{(X-Y)} = \frac{{}^bR_X}{{}^bR_Y} = \frac{\delta^b E_X + 1,000}{\delta^b E_Y + 1,000}$$

It is a measure of the partitioning of isotopes between two or more phases in response to an isotope effect.

Whereas the δ value is the result of the whole history of the sample, the α value is characteristic for, say, an equilibrium between X and Y or for a process that leads from X to Y. Since α values are usually very close to 1.0, the ϵ notation is commonly used to express isotope fractionations in per mil ($\pm\%$):

$${}^b\epsilon_{(X-Y)} = ({}^b\alpha_{(X-Y)} - 1) \cdot 1,000$$

Isotope effects

The most important isotope effects arise from differences in: (a) random mean velocities and (b) vibrational frequencies of molecules.

a) Random mean velocity effects. In (local) thermodynamic equilibrium, the mean kinetic energy is equal for all molecules and determined by temperature alone:

$$\langle E_{\text{kin},j} \rangle = \frac{1}{2} m_j \langle v_j^2 \rangle = \frac{3}{2} k_B T = E_{\text{thermal}}$$

$$\text{where } m_j \text{ and } v_{\text{rms},j} = \sqrt{\langle v_j^2 \rangle}$$

are mass and random mean square (rms) velocity of molecule j , k_B is Boltzmann's constant, and T is absolute temperature. At a given temperature, the rms velocity varies with the mass of the molecule: light molecules are faster than heavy molecules (Graham's law of diffusion):

$$v_{\text{rms},1}/v_{\text{rms},2} = \sqrt{m_2/m_1}$$

As a consequence, molecules containing the light isotope diffuse faster. The ratio of the diffusion coefficients D_v for the light (mass m_a) and the heavy molecule (mass m_b) of a gas that diffuses through air (mass $m_c = 29$) is given by

$$\alpha_{(a-b)} = \frac{D_b}{D_a} = \sqrt{\frac{m_b + m_c}{m_b \cdot m_c} \frac{m_a \cdot m_c}{m_a + m_c}}$$

For ${}^{13}\text{CO}_2$ and ${}^{12}\text{CO}_2$, one obtains

$${}^{13}\alpha_{\text{diff. CO}_2 \text{ in air}} = \sqrt{\frac{45 + 29}{45 \cdot 29} \frac{44 \cdot 29}{44 + 29}} \approx 0.9956$$

The relation does not apply, however, for diffusion of gases through liquids where the ratio of the diffusion coefficients is closer to one (${}^{13}\alpha_{\text{diff. CO}_2 \text{ in water}} \approx 0.9993$). The variation of the rms velocity with mass also leads to differences in evaporation.

b) Effects due to molecular vibrations. The zero-point energy of vibrations in molecules, E_0 , is mass dependent. For diatomic molecules $E_0 = hv/2$, where h is Planck's constant and ν is the (vibration) frequency. The ratio of frequencies ν and ν' for two diatomic molecules of different isotopic composition is approximately given by $\nu'/\nu = (\mu/\mu')^{1/2}$ where $\mu = m_1 \cdot m_2/(m_1 + m_2)$ is the reduced mass and m_1 and m_2 are the masses of the two atoms involved.

Example: compare the frequencies for ${}^{16}\text{O}^{16}\text{O}$ ($\nu, \mu = 16 \cdot 16/(16 + 16) = 8$), ${}^{17}\text{O}^{16}\text{O}$ ($\nu', \mu' = 17 \cdot 16/(17 + 16) \approx 8.2424$), and ${}^{18}\text{O}^{16}\text{O}$ ($\nu'', \mu'' = 18 \cdot 16/(18 + 16) \approx 8.4706$): $\nu'/\nu \approx 0.9852$, $\nu''/\nu \approx 0.9718$, i.e., the strength of the isotope effect increases with the mass difference and thus it is not surprising that the resulting isotope fractionation is also 'mass-dependent', as a rule.

Isotope fractionation

The difference in isotopic composition between various compounds or between various phases of a single compound is called isotope fractionation. It is noted that even the largest isotope effect may not cause fractionation if the reaction goes to completion, i.e., a quantitative reaction in which the reactant is completely transformed into the product. However, an isotopic fractionation will always be observed when a reaction has an isotope effect and the formation of the product is not quantitative (Hayes, 1982).

Equilibrium isotope fractionation

Isotope fractionation can occur in equilibrium, for example, between the various isotopic forms of carbon dioxide, bicarbonate, and carbonate ions (Zeebe and Wolf-Gladrow, 2001). As a rule: "The heavy isotope goes preferentially to the chemical compound in which the element is bound most strongly." (Bigeleisen, 1965). For example, in the temperature range between 0 and 25°C, the

$\delta^{13}\text{C}_{\text{CO}_2}$ in seawater is 8–10‰ lower (“isotopically lighter”) than $\delta^{13}\text{C}_{\text{HCO}_3^-}$.

The fractionation factors for equilibrium fractionation involving three isotopes with masses $m_1 < m_2 < m_3$ usually scale such that $\alpha_{2/1} = \alpha_{3/1}^\beta$, where $\beta = (1/m_1 - 1/m_2)/(1/m_1 - 1/m_3)$ (Young et al., 2002). For the three stable oxygen isotopes: $^{17}\alpha = (^{18}\alpha)^{0.529}$.

Nonequilibrium (“kinetic”) isotope fractionation

Nonequilibrium effects are associated with incomplete or unidirectional processes such as evaporation, kinetic isotope effects in chemical reactions, diffusion, or metabolic effects. Kinetic isotope effects in chemical reactions occur when reaction rates for compounds containing light or heavy isotopes are different, which is almost always the case and thus isotope fractionation can be expected. If the reservoir of reactants is finite, the isotope effect associated with the reaction will not only yield a product of different isotopic composition but will lead to a change in the isotopic composition of the reservoir as well (*Rayleigh distillation*; Bigeleisen and Wolfsberg, 1958). Kinetic isotope effects can quantitatively be understood on the basis of the ‘transition state theory’ (Bigeleisen and Wolfsberg, 1958). The fractionation factors for kinetic fractionation involving three isotopes with masses $m_1 < m_2 < m_3$ often scale such that $\alpha_{2/1} = \alpha_{3/1}^\beta$, where $\beta = I_n(m_1/m_2)/I_n(m_1/m_3)$ (Young et al., 2002). For the three stable oxygen isotopes: $^{17}\alpha = (^{18}\alpha)^{0.515}$.

“Mass-independent” fractionation

A mass-independent fractionation of stable oxygen isotopes was reported (for the first time) in 1973 in meteorites and in 1983 in laboratory studies (Thiemens and Heidenreich, 1983). These studies show differences in the isotopic compositions for certain compounds that contain ^{16}O only (Substance X) and Compounds X and compound Y with fractionation factors $^{17}\alpha$ and $^{18}\alpha$ (between X and Y) that are almost equal, i.e., $^{17}\alpha \approx ^{18}\alpha$. These fractionation processes are called ‘mass-independent’. They may occur at low pressures and, for example, play an essential role for stratospheric ozone. The resulting unusual composition of atmospheric oxygen has been used in the so-called ‘triple-isotope method’ to derive estimates of the biosphere productivity (Luz et al., 1999). A theoretical

explanation based on an extension of the Rice, Ramsperger, Kassel, Marcus (RRKM) theory has been developed only recently (Gao and Marcus, 2001). A mass-independent isotope effect has also been observed during thermal decomposition of carbonates in vacuo (Miller et al., 2002).

Dieter A. Wolf-Gladrow and Richard E. Zeebe

Bibliography

- Bigeleisen, J., 1965. Chemistry of isotopes. *Science*, **147**, 463–471.
- Bigeleisen, J. and M.G. Mayer. Calculation of equilibrium constants for isotopic exchange reactions. *J. Chem. Phys.*, **15**: 261–267, 1947.
- Bigeleisen, J., and Wolfsberg, M., 1958. Theoretical and experimental aspects of isotope effects in chemical kinetics. *Adv. Chem. Phys.*, **1**, 15–76.
- Criss, R.E., 1999. *Principles of Stable Isotope Distribution*. New York: Oxford University Press, 264pp.
- Gao, Y.Q., and Marcus, R.A., 2001. Strange and unconventional isotope effects in ozone formation. *Science*, **293**, 259–263.
- Hayes, J.M., 1982. Fractionation et al.: An introduction to isotopic measurement and terminology. *Spectra*, **8**(4), 3–8.
- Hoefs, J., 1997. *Stable Isotope Geochemistry*, (4th edn.). Heidelberg: Springer.
- Luz, B., et al., 1999. Triple-isotope composition of atmospheric oxygen as a tracer of biosphere productivity. *Nature*, **400**, 547–550.
- Miller, et al., 2002. Mass-independent fractionation of oxygen isotopes during thermal decomposition of carbonates. *Proc. Natl. Acad. Sci.*, **99**(17), 10988–10993.
- Thiemens, M.H., and Heidenreich, J.E. III., 1983. The mass-independent fractionation of oxygen: A novel isotope effect and its possible cosmochemical implications. *Science*, **219**, 1073–1075.
- Urey, H.C., 1947. The thermodynamic properties of isotopic substances. *J. Chem. Soc.*, 562–581.
- Young, et al., 2002. Kinetic and equilibrium mass-dependent isotope fractionation laws in nature and their geochemical and cosmochemical significance. *Geochim. Cosmochim. Acta*, **66**(6), 1095–1104.
- Zeebe, R.E., and Wolf-Gladrow, D., 2001. *CO₂ in Seawater: Equilibrium, Kinetics, Isotopes*. Amsterdam: Elsevier.

Cross-references

[Carbon Isotopes, Stable](#)
[Oxygen Isotopes](#)
[Paleotemperatures and Proxy Reconstructions](#)
[Stable Isotope Analysis](#)
[Strontium Isotopes](#)
[Sulfur Isotopes](#)

K

KAMES

A kame is an ice contact glaciofluvial landform. It is composed of sediment deposited by water in contact with glacier ice either at the side of, or on the surface of a glacier. The sediment fills of supraglacial streams and lakes, ice marginal channels and ice-dammed lakes often form flat-topped hills or terraces after the ice has disappeared. The term kame is a Scottish word to describe such flat-topped hills. Kames are closely related to eskers, and transitional forms between the two occur. Generally kames are less continuous and are associated with supraglacial or ice-marginal water, whereas eskers are more continuous and are associated with subglacial water. The presence of flat or gently sloping surfaces, representing fluvial surfaces, is sometimes said to be a diagnostic characteristic of kames. However, postglacial collapse following the loss of ice support can seriously disturb kame morphology.

Kames generally consist of well-sorted, stratified sediments. If deposited by glacial streams they are dominated by sands and gravels. If deposited in lakes they are characterized by clay, silt and fine sand. Kames can occur as individual hills, as plateau areas or as terraces. At the smallest end of the spectrum of kame forms are supraglacial crevasse fillings. Where many kames occur together within an area the term kame field is sometimes used. Kames are often associated with kettle holes to produce “kame and kettle” topography. Kame landscapes tend to reflect environments where ice retreat was accompanied by abundant meltwater and sediment supply.

The term “kame” is often applied to mean “ice contact” in compound terms such as kame terrace, kame delta or kame plateau. Terraces generally form where streams flow along margins of glaciers, and therefore they lie parallel to the ice margin where the margin lies on a reverse slope. So-called “flights” of terraces at different levels may be created as a glacier surface reduces in elevation during ice retreat. Kame deltas, also known as delta moraines or simply ice-contact deltas, form where glacial streams emerge from the glacier into water.

As they are created in ice-contact situations kames are prone to collapse as ice retreats. Their sedimentary architecture

therefore reflects not only the processes of deposition but also the processes of structural collapse. Supraglacially-derived sediments are likely to be more disturbed than ice marginal deposits. Survival of extensive kames indicates that an area was dominated by down-wasting and meltout of ice after any phase of extensive proglacial fluvial erosion, which would have removed the kames. Benn and Evans (1998), Bennett and Glasser (1996) and Hambrey (1994) provide useful reviews of this topic.

Peter G. Knight

Bibliography

- Benn, D.I., and Evans, D.J.A., 1998. *Glaciers and Glaciation*, London, UK: Arnold, 734pp.
Bennett, M.R., and Glasser, N.F., 1996. *Glacial Geology*. Chichester, UK: Wiley, 364pp.
Hambrey, M.J., 1994. *Glacial Environments*, London, UK: UCL Press, 296pp.

Cross-references

[Eskers](#)
[Glacial Geomorphology](#)
[Glacial Sediments](#)
[Glaciofluvial Sediments](#)
[Kettles](#)

KETTLES

A kettle, or kettle hole, is an enclosed depression within glacial sediments, caused by the melting of ice that was buried within the sediments. The ice may be a remnant of the glacier margin detached by ablation, or an ice block deposited from a glacial stream. Kettles are characteristic of proglacial outwash plains and areas of stagnant ice. They very often fill with water to form kettle lakes. Kettles vary in size and may be just a few meters or several hundred meters in diameter.

Some kettles form from the melting of completely buried ice blocks, others from the melting of partially covered ice blocks,

and the morphology of the holes created reflects their origin. Where ice is completely buried, as may be the case when stagnant glacier ice is blanketed by supraglacial meltout sediment or where ice blocks in a proglacial flood are deeply buried in glacialfluvial deposits, kettles form by subsidence and may initially be very steep sided. Where ice blocks are partially exposed, as may be the case where ice blocks are deposited on a sandur plane during a short proglacial flood, the debris content of the ice block and the depth of burial have a significant impact on the form of the kettle. Debris released from the melting ice block may create a ridge around the edge of the kettle or may completely fill the kettle with debris, creating a mound rather than a hollow (Maizels, 1992). Different forms that have been described include “rimmed,” “crater,” and “till-fill” kettles. Where an outwash plain is marked by a large number of kettles the term “pitted plain” is sometimes used. Many ice blocks are deposited on outwash plains during glacial floods, and the distribution of kettles on an outwash plain can be used to reconstruct the routing and magnitude of flow during flood events.

Kettles may be completely filled with sediment if deposition occurs after the ice has completely melted, but will still be recognizable in the sedimentary record. The kettle will be represented

by a downfaulted block, and the amount of downfaulting at different levels in the profile will indicate the depth above which sediment was deposited after the ice completely melted. Benn and Evans (1998) and Bennett and Glasser (1996) provide useful reviews of this topic.

Peter G. Knight

Bibliography

- Benn, D.I., and Evans, D.J.A., 1998. *Glaciers and Glaciation*, London, UK: Arnold, 734pp.
- Bennett, M.R., and Glasser, N.F., 1996. *Glacial Geology*, Chichester, UK: Wiley, 364pp.
- Maizels, J., 1992. Boulder ring structures produced during Jökulhlaup flows. *Geogr. Ann.*, **74A**, 21–33.

Cross-references

[Glacial Geomorphology](#)
[Glacial Sediments](#)
[Kames](#)
[Outwash Plains](#)

L

LACUSTRINE SEDIMENTS

Introduction

Concerns about global change and its potential effects on human activities, including economic, social, and political affairs, are exerting great pressure on science to produce models and predictions for future climatic variability. In this regard, the key to the future is a proper understanding of the past. In principle, data sources for past climatic variations are instrumental meteorological and historical data. However, meteorological time series are rather short and thus limited for interpretation (Bradley, 1999). Historical data are available for the last couple of centuries, prior to the instrumental record, and these enable a more or less accurate determination of natural climatic and anthropogenic changes. These data, however, become scarce and unreliable for longer timescales and thus need to be complemented by information from indirect archives for a better interpretation of the past. On the continents, lacustrine sediments provide an excellent archive for the extension of instrumental and historical data of environmental and climatic changes on a high-resolution decadal or even annual timescale.

Lacustrine sediments contain a wide variety of information indirectly reflecting environmental conditions. They can be analyzed by sedimentological, geochemical, geophysical, and biological methods combined within the field of paleolimnology (Berglund, 1986; Last and Smol, 2001; Cohen, 2003). The obtained data are generally called “paleoclimate proxy data” or “proxies” and are used to evaluate the variability of past climatic conditions as well as human influences on the lake system and on the catchment basin. This is possible because lacustrine sediments record many environmental processes that occur in the water column and in the drainage area of the lake.

Due to this availability of multi-proxy data sets in combination with high resolution and accurate dating, lacustrine sediments often provide a more comprehensive environmental interpretation than other continuous continental records like

tree rings, peat bogs, and speleothems. Discontinuous records like fluvial, colluvial, and loess deposits or soils are prone to hiatuses and therefore are only suitable for environmental reconstructions under special circumstances, for short time intervals, or for certain scientific questions.

The formation of lacustrine sediments is controlled by atmospheric processes (climate) but also by the geology of the catchment basin, which is connected to the lake system through (climatically-controlled) hydrology (Figure L1). Climate and geology also control the formation of soils and plant cover in the catchment as well as water chemistry and plankton communities in the lake (Wetzel, 2001). As geology does not change significantly through the life span of most lakes, variations recorded in the sedimentary record are almost certainly related to climate variability, which itself is controlled by solar forcing. However, in the most recent past anthropogenic influences have become increasingly important.

Occurrence

Lakes are standing bodies of water that accumulate sediments from the surrounding environment and from their water column. Lakes are relatively young features ($\leq 10^4$ years) that have predominantly been formed during the last cold period of the Pleistocene by glacial activities (Hutchinson, 1957; Gierlowski-Kordesch and Kelts, 1994). Sediments deposited in these lakes generally provide excellent archives for a large variety of Late Glacial and Holocene paleoenvironmental investigations. Lakes can also be found in volcanic regions (crater lakes). In some rare occurrences, lakes of tectonic origin (e.g., along the Great African Rift System) or impact crater lakes exist, all of which may contain much longer sediment records than glacial lakes, covering several glacial/interglacial cycles or even the entire Quaternary (up to 10^6 years).

Formation of lacustrine sediments

The formation of lacustrine sediments depends on climatic factors and therefore, under natural conditions, the dominating regional climate controls the type of lacustrine sedimentation (clastic, biogenic, or evaporitic). Lacustrine sediments are the

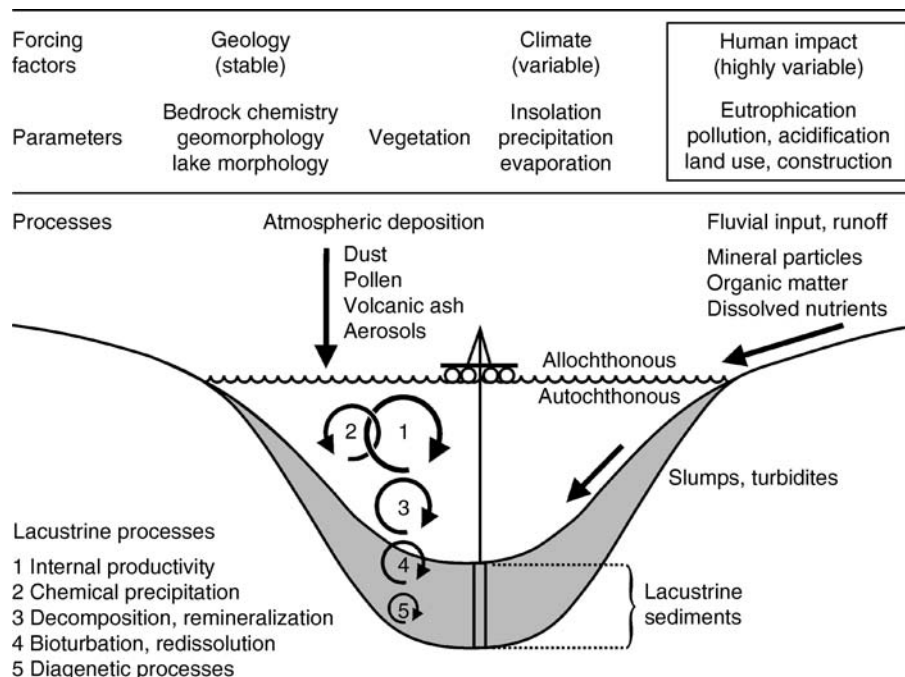


Figure L1 Simplified illustration of forcing factors and parameters as well as processes that lead to the formation of lacustrine sediments.

result of three different mechanisms (Håkanson and Jansson, 1983):

- The flux of mineral particles through fluvial input from the catchment area or by atmospheric deposition forms clastic sediments, which to a certain extent may contain organic particles, e.g., leaves or pieces of wood carried into the lake by runoff.
- Biological productivity in the lake generates organic or biogenic sediments as the dead organic matter sinks and accumulates at the lake bottom.
- Chemical precipitation of minerals from the water column forms evaporitic sediments.

In general, sediment components can be classified into two groups: those produced in the lake (autochthonous components) and those formed in the catchment basin (allochthonous components), which are transported to the lake by overland flow, rivers and streams, or by eolian activities. Although there are clear constraints for the environmental conditions necessary for the formation of clastic, organic, or evaporitic sediments, lacustrine sediments usually are the result of a combination of these processes.

Clastic lacustrine sediments

Clastic (detrital) sediments predominate under cold climatic conditions, e.g., at high latitudes or in alpine regions. Such clastic or minerogenic sediments are typical of proglacial lakes. Intensive physical weathering and the lack of a dense vegetation cover provide high amounts of minerogenic detritus, which can easily be eroded and transported to the lake. In general, the sediment transfer from the catchment area into the lake is correlated with the amount of runoff. In regions with a continental climate, runoff is governed by the melting of snow and ice through solar insolation during the summer. Under oceanic

climatic conditions, runoff is controlled either by the melting of snow and ice through advective heat transport associated with increased rainfall or solely by precipitation. Lakes with clastic deposits are generally poor in nutrients (oligotrophic) inhibiting high organic productivity.

Organic lacustrine sediments

Under temperate or warm, humid climatic conditions, the catchment area is vegetated, reducing the availability and the transport capability of clastic material into the lake. Chemical weathering prevails and releases nutrients from the bedrock that are incorporated into plant organic matter, buffered in soils, or washed out and transported as dissolved ions into the lake. This results in higher nutrient levels in the lake (mesotrophic to eutrophic conditions) and the related increase of organic productivity leads to the formation of organic or biogenic sediments. Algal blooms start with diatoms in spring, are followed by green and blue-green algae during summer, and are sometimes terminated by a second diatom bloom in fall. While green and blue-green algae are easily decomposed during deposition, siliceous diatom frustules are much more resistant to dissolution and are generally well preserved in the sedimentary record. In addition to this autochthonous sedimentary component, an allochthonous component may occur during winter: as the plant cover is reduced and thus soils become more susceptible to erosion, runoff increases and transports minerogenic as well as organic debris of littoral and terrestrial origin to the lake. The latter two components are washed into the central part of the lake basin during runoff events related to fall or winter rains.

If carbonates are present in the catchment area, autochthonous calcite precipitation adds an additional component to the organic sediment fraction. Carbonaceous rocks are dissolved and the solutes are transferred into the lake. In these hard water

lakes, calcite crystals are produced by autochthonous biochemical precipitation: Ca^{2+} and HCO_3^- in the lake water stay in solution only until the saturation point is reached. This is partly achieved by the seasonal temperature increase in the surface water layer during the summer insolation maximum. As CaCO_3 is less soluble with increasing temperature, calcite may precipitate due to this effect alone. However, even more important is the temperature-related increase of photosynthetic activities in the water column through phytoplankton blooms. As a result of enhanced photosynthesis, CO_2 is withdrawn from the lake water and thus the pH rises up to pH 9 with a consequent reduction in CaCO_3 solubility. This combination of temperature increase and phytoplankton activity contributes to additional precipitation of calcite crystals. Under such conditions, the shells of calcifying organisms (e.g., ostracods, mollusks) may also be a significant sediment constituent.

Evaporitic lacustrine sediments

Under arid or semiarid climatic conditions, evaporitic sediments are formed as the salinity and the pH of a lake increase through enhanced evaporation of the lake water. This results in the saturation of specific mineral compounds (salts), which then precipitate out of the lake's water column. In addition to calcite, which can precipitate either biogeochemically in mid-latitudes or physicochemically under semi-arid climatic conditions, evaporitic sediments are also composed of calcium sulfate (gypsum) and sodium chloride (halite), both precipitating only under arid climates.

Modification of lacustrine sedimentation

Several processes may alter lacustrine sedimentary records:

- Especially in deep lakes with steep sidewalls, turbidity currents may transport large amounts of sediment from the lake-shores into the central basin. Turbidites may be associated with erosion at their base, which causes a hiatus in the sedimentary record.
- In shallow parts of lake basins or if strong winds induce deep-reaching water movements, currents can cause resuspension of fine-grained sediments and redeposition somewhere else.
- Bioturbation caused by the burrowing activities of benthic fauna mixes the uppermost sediment layers. The effects of bioturbation are reduced if anoxic conditions prevent the presence of higher organisms at the lake floor. For example, organic rich muds (sapropels) cause anoxic conditions near the sediment/water interface due to oxygen consumption during the decomposition of organic matter.
- In the course of early diagenesis the growth of iron- and manganese-minerals like vivianite, siderite, pyrite, or rhodochrosite may also disturb the original layering of the soft sediments.

If one or more of these processes are or have been present in a lake, they can introduce hiatuses and mixing into the record and make high-resolution investigations difficult or impossible.

Sedimentation rates

The rapid reaction of the local hydrological regime to environmental change is coupled with changes in sedimentation rates (mm yr^{-1}) and accumulation rates ($\text{g cm}^{-2} \text{yr}^{-1}$). Lacustrine sedimentation rates are in the range of 0.3 mm to several mm per year, which is up to three magnitudes higher than in marine

sediment records. As a consequence, this high sedimentation rate reduces the length of the time window that might be studied to ca. 10^4 years, whereas marine records reach up to 10^8 years.

Therefore, lacustrine sediments facilitate stratigraphic studies with centennial to decadal resolution. If annually laminated (varved) sediments are preserved, annual to even seasonal time resolution is possible (Zolitschka, 2003). Thus, different kinds of abrupt changes can be detected by the wide variety of applicable sedimentological, geochemical, geophysical, and biological analytical methods (Last and Smol, 2001). Lately, multi-proxy investigations of lake sediments became more and more important because they provide several independent lines of evidence for a common observation – environmental change as the response to climate change and human impact – and therefore improve the reliability of the interpretation.

Dating

Time control is one of the most important issues in the study of lacustrine sediments. Without an accurate timescale a comparison of the sample proxy data with historical and archaeological data and with other lacustrine archives as well as with other proxy records on a local, regional, or global scale is impossible. Among all sedimentary records, lake sediments provide the best time control, as different dating methods can be applied to the same cores. Usually, radiometric dating methods are carried out depending on the decay rates of radiogenic isotopes, e.g., ^{14}C dating for the last ca. 50,000 years and ^{137}Cs and ^{210}Pb for the last 50 and 200 years, respectively. Radiometric measurements are related to time by the half-life of the isotope and through models of production and deposition of radiogenic isotopes. The time is provided in isotopic years and needs to be calibrated into calendar years by comparison with monitoring data of radioactive fallout (^{137}Cs), by using depositional models (^{210}Pb), or with the help of dendrochronology (^{14}C).

In many regions, the annual climatic cycle represents the strongest observed cyclicity. Under permanent or seasonal anoxic conditions near the lake bottom, this cyclicity can be preserved as annually laminated or varved sediments. However, varved sediments are not the rule because processes like bioturbation in well-oxygenated lakes disturb this cyclical layering. Incremental dating can be applied (Zolitschka, 2003) to well-preserved annually laminated sediments. This method is based on cyclical accumulation of biological or lithological material with time, leading to the formation of organic (biogenic) or clastic varves. The major control mechanisms of this cyclicity are the seasonal climatic variations that produce an “internal clock.” Such a varve chronology provides either an absolute chronology in calendar years, if the varves continue to the present, or a floating chronology, if the record is not annually laminated to the top of the sequence.

In addition to these “absolute” dating methods, stratigraphic methods are often applied to provide further time control and to facilitate correlation between neighboring sites of investigation. Most common is the biostratigraphic method of pollen analysis (palynology) where distinct changes in the regional pattern of vegetation are used. For a larger regional scale, paleomagnetic studies are also sensible and might even reveal global variations of inclination and declination changes of the Earth's magnetic field. For very long records, reversals or event-like excursions of the polarity of the Earth's magnetic field can be used as a stratigraphic tool (magnetostratigraphy). If a lake is situated in a volcanic region, tephra layers are another possibility to elaborate an independent time-frame through tephrochronology. Lacustrine

sediments have the advantage that one record provides several different dating methods, which allows significant improvement of the overall dating accuracy.

Proxy data recorded in lacustrine sediments

Since meteorological parameters are not directly recorded in lacustrine sediments, indirect information has to be used for climatic reconstruction. These so-called proxy data are either quantitative or descriptive information about sedimentological, geophysical, geochemical, or biological processes that are dominantly controlled by climatic conditions and thus provide a good approximation of climatic variability. Three major groups of proxy data are used with lake sediments to reconstruct past climatic and related environmental changes:

- Biological proxies (e.g., pollen, diatoms, chironomids) are calibrated using regional training sets, which are statistically transformed into quantitatively reconstructed values of temperature, pH, salinity, or total phosphorus concentration.
- Physicochemical proxies (e.g., isotopes) can be analyzed relatively fast and easily compared with biological proxies. Carbon isotopes of bulk organic matter provide information about changes in the trophic condition of a lake while oxygen isotopes of authigenic carbonates or calcareous skeletons of microfossils like ostracods provide quantitative information that can be linked to temperature and precipitation on a global scale. Furthermore, as water residence times in lakes are rather short, isotope records provide data about climatic changes almost without any time lags whereas lag effects of decades or more are typical for biological systems.
- Sedimentary proxies (e.g., flux rates, grain sizes, elemental composition, magnetic properties, clay minerals) provide qualitative information about major environmental changes in the lake and the catchment basin. These data are usually more complex than biological proxies and therefore much more difficult to interpret.

If several different proxy data are used for a combined interpretation (multi-proxy approach), the overall significance of the results is improved considerably.

Modern calibration

The key to an improved interpretation of lacustrine sediment records is a proper understanding of present-day processes leading to the formation of such deposits. The primary climatic signal can be modified and transformed in several ways. For this reason it is necessary to establish correlations between run-off events, sediment sources, and sediment deposition as well as between climatic parameters and biological sedimentary proxies, e.g., vegetation (pollen), diatoms, or chironomids. Correlations need also to be established between climatic parameters and stable isotopes or between sediment texture, structure, and composition. The period of monitoring should ideally exceed several years to obtain site-specific calibration data sets and transfer functions valid for larger regions. These can then be used to reconstruct quantitative variations of climatic variables like temperature or precipitation, which are crucial for the evaluation and refining of global to regional climate models.

Conclusions

Evidence of past and present climate variability as well as more recent anthropogenic influences on lakes and their catchment basins are recorded in lacustrine sediments. The major difficulties

in employing these natural archives for paleoenvironmental and paleoclimatic reconstructions are in establishing a precise and reliable timescale and interpreting the record properly. Ideally, both obstacles can be circumvented if lake sediments are studied, obtaining multi-proxy data on multiple-dated timescales. Successfully applied, lacustrine sedimentary archives provide a unique opportunity to study the past dynamics of environmental systems on local, regional, and even global scales. This geological perspective is necessary in order to generate realistic projections of future environmental changes that might, at least in part, result from human activities.

Bernd Zolitschka and Dirk Enters

Bibliography

- Berglund, B.E. (ed.), 1986. *Handbook of Holocene Palaeoecology and Palaeohydrology*. Chichester & New York: Wiley, 869pp.
- Bradley, R.S., 1999. *Paleoclimatology – Reconstructing Climates of the Quaternary*. San Diego, CA: Harcourt Academic Press. International Geophysics Series, 64, 613pp.
- Cohen, A.S., 2003. *Paleolimnology: The History and Evolution of Lake Systems*. Oxford: Oxford University Press, 528pp.
- Gierlowski-Kordesch, E., and Kelts, K. (eds.), 1994. *Global Geological Record of Lake Basins*. Cambridge, UK: Cambridge University Press, 427pp.
- Håkanson, L., and Jansson, M., 1983. *Principles of Lake Sedimentology*. Berlin, Heidelberg: Springer-Verlag, 316pp.
- Hutchinson, G.E., 1957. *A Treatise on Limnology. I. Geography, Physics and Chemistry*. New York: Wiley.
- Last, W.M., and Smol, J.P. (eds.), 2001. *Tracking Environmental Change Using Lake Sediments*. Developments in Paleoenvironmental Research, vol. 1–4. Dordrecht: Kluwer.
- Wetzel, R.G., 2001. *Limnology: Lake and River Ecosystems*. San Diego, CA: Academic Press, 1006pp.
- Zolitschka, B., 2003. Dating based on freshwater and marine laminated sediments. In Mackay, A., Battarbee, R., Birks, J., and Oldfield, F. (eds.), *Global Change in the Holocene: Approaches to Reconstructing Fine-resolution Climate Change*. London: Edward Arnold, 92–106.

Cross-references

[Carbon Isotopes, Stable](#)
[Climate Forcing](#)
[Climate Variability and Change, Last 1,000 Years](#)
[Continental Sediments](#)
[Cyclic Sedimentation \(Cyclothem\)](#)
[Dating, Biostratigraphic Methods](#)
[Dating, Magnetostratigraphy](#)
[Dating, Radiometric Methods](#)
[Diatoms](#)
[Evaporites](#)
[Geochemical Proxies \(Non-Isotopic\)](#)
[Holocene Climates](#)
[Lake Level Fluctuations](#)
[Mineral Indicators of Past Climates](#)
[Ostracods](#)
[Oxygen Isotopes](#)
[Paleoclimate Proxies, an Introduction](#)
[Paleohydrology](#)
[Paleolimnology](#)
[Palynology](#)
[Pleistocene Climates](#)
[Pollen Analysis](#)
[Proglacial Lacustrine Sediments](#)
[Quaternary Climate Transitions and Cycles](#)
[Radiocarbon Dating](#)
[Sapropels](#)
[Sedimentary Indicators of Climate Change](#)
[Stable Isotope Analysis](#)
[Tephrochronology](#)
[Transfer Functions](#)
[Varved Sediments](#)

LAKE-LEVEL FLUCTUATIONS

Introduction

Lake-level changes can occur as a consequence of climatic change, tectonic activity, erosion at the outlet, or human activity. Water-level fluctuations associated with climate changes are a response to variations in precipitation-evaporation (P-E) over the watershed. A particular lake's sensitivity to P-E variations is primarily related to basin hydrology, or whether inflow exits the lake basin via a surface outflow (overflowing, open) or is confined to the lake basin (non-overflowing, closed). The water level of a closed lake system, in the absence of tectonic activity, erosion at the outlet, or human influence, represents an equilibrium state between: (a) input (catchment runoff and groundwater inflow), and (b) output (evaporation and sub-surface seepage). In a closed-basin system, changes in effective moisture will cause the volume of the lake to either increase or decrease until a new equilibrium is achieved. In overflowing lakes, climatically driven lake-level changes are limited to P-E decreases, because further increases are compensated by greater outflow (Harrison and Digerfeldt, 1993). The magnitude of lake-level response to climate change can be calculated from known or estimated hydrological budgets if the geomorphic characteristics of the lake and its watershed are known, including bathymetry, catchment and shoreline topography, soil type, and vegetation (Hostetler, 1995). Various combinations of precipitation and evaporation can produce the same effective moisture, but if other climate proxy data can be used to constrain one of the variables, then the range of the other can be determined (e.g., Barber and Finney, 2000).

A lake's water-level history is the result of its response to climate over a range of timescales ($1-10^5$ years). Large water-level fluctuations at 10^3 to 10^5 -year timescales correspond to global climate changes associated with glacial-interglacial periods and global ice volume (e.g., Benson et al., 1989; Finney et al., 1996). Lake-level data can provide important Pleistocene and Holocene P-E information at $<10^3$ -year timescales or better when chronological control for water-level variations can be established (Abbott et al., 1997). Historical gauge and climate observational records are available that document lake-level variations and climate fluctuations at 10^2 -year timescales for the last 50–100 years (Street-Perrott and Harrison, 1985).

Lakes are distributed globally, providing regional paleoclimatic information for low latitudes (Kutzbach and Street-Perrott, 1985; Street-Perrott and Perrott, 1990; Abbott et al., 1997; Seltzer et al., 1998) and semi-arid regions at middle to high-latitudes (Benson, 1981; Benson et al., 1989; Harrison and Digerfeldt, 1993; Thompson et al., 1993; Yu et al., 1997; Abbott et al., 2000; Anderson et al., 2005). In many tropical and sub-tropical locations, lake-level variations are of particular paleoclimatic significance. Region-wide changes in drought patterns have been identified as coincident with significant cultural change or collapse (e.g., Binford et al., 1997; Bookman et al., 2004). Well-dated lake-level data have also been used to identify feedbacks between tropical rainfall and global heat transport by thermohaline circulation (e.g., Street-Perrott and Perrott, 1990). In the middle latitudes, lake levels have been used to determine quantitative estimates of paleoprecipitation (e.g., Benson, 1981; Hastenrath and Kutzbach, 1983, 1985), and to verify paleoclimate model simulations (e.g., Webb et al., 1993).

Lake-level reconstructions

Past lake-level variations may be indicated by geomorphic evidence within a lake basin. Raised shoreline features and wave-cut platforms indicate higher lake levels (e.g., Gilbert, 1890; Oviatt et al., 1994). Evidence for past lake-level variations is also found within the stratigraphy of lacustrine deposits. It is difficult to identify basin-wide sedimentary changes from observations of a single core with a small cross section of 2–10 cm. Multiple cores collected on a shallow to deep water transect provide more reliable lake-level information for quantification of lake-level changes (e.g., Digerfeldt, 1986). Sediment stratigraphy and facies changes may record water-level shifts in several ways because lake-level fluctuations affect numerous limnological and sedimentological processes. Consequently, evidence from core studies may be subject to more than one interpretation. However, consensus developed from multiple lines of evidence can be used to build a compelling lake-level reconstruction. Sedimentary changes can be identified by visual stratigraphy, changes in color, pollen, grain size distribution, and organic matter concentration. Multiple lines of evidence commonly include physical, chemical, paleolimnological, and paleoecological analyses and studies of these are known as “multi-proxy” studies, with age control determined by high precision geochronological techniques, such as accelerator mass spectrometer (AMS) radiocarbon dating in combination with ^{210}Pb and ^{137}Cs assays for the youngest sediments. Correlation of multiple cores recovered from different water depths can be used to detect unconformities that form hiatuses in the sediment record and determine the timing of these events.

Stratigraphically-based multi-proxy lake-level reconstructions increase the ability to identify links between lake-level reconstructions and climate fluctuations (Digerfeldt, 1986; Dearing, 1997). Although the most useful combination of multi-proxy studies varies from lake to lake, the three major categories of sedimentary evidence are: (a) the distribution and pattern of littoral vegetation, (b) sediment compositional variations with varying depths, and (c) the shallowest depth where fine-grained, organic-rich sediment accumulates (i.e., the sediment limit). Lundqvist (1925, 1927) pioneered the use of core transects from shallow to deep water to investigate how macrofossil content, pollen concentration, and sediment composition varied with changing depth. Digerfeldt (1986) and Dearing (1997) further modified these methods. The use of core transects to investigate lake-level change is most commonly applied to lakes with small catchment to lake surface-area ratios that have relatively shallow underwater slopes.

The distribution of shoreline (littoral zone) macrophyte vegetation is largely determined by lake-water depth for many closed-basin lakes. Characteristic zonation of emergent, floating-leaved, and submerged vegetation extends outwards from the shoreline. A decrease in water depth (lower lake level) will commonly result in macrophyte vegetation migrating toward the lake. However, such a vegetation response may also occur over time because of progressive sedimentary infilling. In contrast, an increase in water depth (higher lake level) will result in landward macrophyte vegetation migration away from the lake. It is more difficult to find alternative explanations for landward expansion of shoreline vegetation than higher lake level.

Depending on the character of shoreline deposits, littoral zone sediments may contain higher proportions of reworked

mineral particles than offshore zones. This is caused by wave action or wind-induced currents that winnow fine-grained sediments from shoreline deposits and transport them into deeper water, toward the center of the lake. Generally, grain size decreases gradually away from shore, forming a fining outward facies. Lowstands lead to displacement of the shore towards the center of the lake and may be recognized by an increase in grain size and mineral quantity. Lake highstands, in turn, are recognized by a decrease in grain size. Similarly, the level below which fine organic or fine-grained mineral sediments accumulate is usually determined by location with respect to the shoreline. This level represents the limit between dominantly erosional and depositional sedimentary processes. Lake highstands will often be recorded as an increase in the sediment limit and lowstands as a lowering of the sediment limit. However, lower lake levels are accompanied by erosion and redeposition of older sediments away from shore, these would previously have accumulated in near-shore sedimentary environments.

The most appropriate location and group of lake-level proxies to investigate must be determined from the limnological and sedimentological properties of each individual watershed and lake basin. Additionally, geomorphic processes and basin bathymetry are important factors to consider when investigating lake-level changes using core transect studies. Variations of shore character and lake basin bathymetry will dictate whether sediment accumulation is continuous or interrupted by periods of erosion or non-deposition with considerable variability in sediment thickness and composition in shallow-water environments. For example, vegetation changes can be easily recognized in eutrophic lakes with high macrophyte production and diversity, but in oligotrophic lakes, coarse minerogenic material is often a more dominant signal. Lake-level variations will most likely be recorded by changes in the fine-grained sediment limit in lakes with sandy shorelines. In stratified marl lakes, changes in the location of marl sediment accumulation are often the dominant water-level indicator. Yu et al. (1997) used sediment hiatuses, detritus layers, and terrestrial moss layers from five cores with calcium-carbonate oxygen isotopes to identify lake-level changes. Anderson et al. (2005) used palynology, calcium carbonate proportions, and bulk organic carbon and nitrogen isotopes on four cores from Marcella Lake, Yukon Territory. Numerous studies have also investigated relationships between changes in lake level and variation in diatoms, ostracods and chironomids (Hoffman, 1998; Alin and Cohen, 2003; Yang et al., 2003).

Another approach is to use seismic surveys to identify lake-level changes and determine where to collect sediment cores. The seismic profiles allow for the identification of erosion surfaces and on-lap and off-lap sedimentary structures, and provide information regarding changes in sediment thickness across the lake basin. Abbott et al. (2000) used seismic profiling and multi-proxy sedimentary analyses including bulk sedimentology and palynology on Birch Lake, Alaska to determine the sediment limit. Keely et al. (2005) used seismic profiling on Lake Bosumtwi, Ghana. These seismic investigations improved the determination of coring locations that yielded optimal information on water-level changes.

Resolving the timing and rate of lake-level variations requires an accurate and precise chronology. Early lake-level reconstructions, prior to the advent of AMS radiocarbon dating, were commonly based on beta-counting analytical techniques using bulk sediment samples. Bulk sedimentary material is typically composed of organic matter derived from aquatic

organisms and can be older than the true age of the deposit because of a reservoir or hardwater effect. This reservoir effect is the result of either a long lake-water residence time or the presence of limestone in the drainage basin, which is a source of ancient carbon. AMS radiocarbon dating requires samples containing around 1 milligram of organic material for accurate and precise ages. Furthermore, the technique eliminates uncertainty regarding the source of the organic material because terrestrial macrofossils (as little as 0.5 mg) can be identified and dated. However, it is still possible that terrestrial macrofossils can be reworked from older sediments during water-level changes. High resolution lake-level studies based on AMS radiocarbon measurements of identified macrofossils have been conducted on Lake Titicaca, Bolivia (see case study below); Birch Lake, Alaska (Abbott et al., 1997, 2000); Marcella Lake, Yukon, Canada (Anderson et al., 2005); and the Dead Sea (Bookman et al., 2004).

Lake level variations are important for studying the mechanisms of climate change if both the spatial and temporal resolution of the data is sufficiently extensive and detailed to describe patterns on the scale of the climate process. For example, Brenner et al., (2001) used a synthesis of finely resolved lake-level reconstructions from the circum-Caribbean and Andean altiplano to evaluate paleoclimatic variations during the period when the Mayan and Tiwanaku cultures arose. Additionally, Kutzbach and Street-Perrott (1985) and Street-Perrott and Harrison (1985) verified paleoclimatic model simulations since 15,000 yBP at 3,000 year intervals by comparing the model-based closed-lake area estimates in the Northern Hemisphere tropics with the geologically-based lake-level evidence. Holocene lake-level variations in Europe and Central and North America are explained in other studies by the direct effects of sea-level, solar insolation, and atmospheric circulation changes (Hodell et al., 1991; Harrison and Digerfeldt, 1993; Wright et al., 1993; Yu et al., 1997; Abbott et al., 2000; Anderson et al., 2005). The sensitivity of lake systems to climate is evident by the distribution, size, and thermal structure of lakes throughout the world (Hostetler, 1995). Lake-level variations, by providing effective moisture balance information unavailable from temperature-sensitive paleoclimatic sources, are indispensable archives of paleoclimatic information with which to study climate change.

Case study: Lake Titicaca, Bolivia/Peru

A multi-proxy high-resolution lake-level study of Lake Titicaca documented periods of severe drought during the last 4,000 years in the central Andean altiplano in order to investigate relationships between climatic and cultural change during the late Holocene (Abbott et al., 1997). Fifteen sediment cores were collected on a transect from shallow (1.9 m) to deep (20.2 m) water from Lago Wiñaymarka, an isolated section of the larger Lake Titicaca basin, connected by a 21 m-deep channel through the Tiquina Strait (Binford et al., 1997). Lake Titicaca is a large (8,300 km²), deep (280 m) water body located on the border of Bolivia and Peru. During the late Pleistocene and Holocene, the lake alternated between an open and closed hydrological system. It is in the upper reaches of a much larger endorheic system that includes Lago Poopo and the salares of central and southern Bolivia. Today, water drains out of Lake Titicaca over a bathymetric sill at 3,804 m a.s.l. down the Río Desaguadero from the southwest corner of Lago Wiñaymarka (Wirmann, 1992). The lake has undergone

measurable water-level changes during the historic period (AD 1914 to present), ranging from 3,806.2 m a.s.l. in 1943 to 3,812.6 m a.s.l. in 1986, with an average annual fluctuation of 0.8 m (Roche et al., 1992). The Lake Titicaca basin is particularly sensitive to drought because even with the overflowing conditions that prevail today, only 1 to 3% of the lake water is lost by surficial overflow. The majority of the balance is lost to evaporation in the high altitude semi-arid environment.

The water-level history of Lake Titicaca was reconstructed from the lithostratigraphy and 60 radiocarbon measurements. First, the dated cores were used to identify stratigraphic levels where erosion surfaces occurred, indicating that the lake level was below that point (Figure L2). Second, for the periods with erosional surfaces, the transect of cores was used to identify the highest stratigraphic level where lacustrine sediments were preserved, indicating that water level was above that point. Using this twofold stratigraphic approach, five periods of significant lake-level depression forming five erosion surfaces were defined by the following criteria: (a) scour marks, (b) mud cracks, (c) abrupt transitions (<1 cm) characterized by coarser-grained (fine-sand) sediments with high bulk density (>1 g cm⁻³) overlying fine-grained organic-rich mud (>20% organic matter), (d) an abrupt increase in both iron and potassium concentration associated with the reducing conditions

in water-saturated soils, and (e) highly fragmented shell material in the overlying mud. The presence of one or more of these characteristics combined with an abrupt change in the radiocarbon age of adjacent strata indicates erosion or non-deposition. Detailed core descriptions, smear-slide mineralogy, and radiocarbon stratigraphy were used to delimit water-saturated soils and erosion surfaces formed during low water stands and sub-aerial exposure. Shallow-water subfacies (<2 m water depth) were identified by: (a) the presence of high concentrations of achenes (seeds) of the littoral sedge *Schoenoplectus tatora* in a coarse-grained matrix (silt to sand), (b) large amounts of aquatic plant macrofossils (*Myriophyllum*, *Chara*, and *Potamogeton*), and (c) sediments containing >90% CaCO₃ composed of calcified macrophyte coatings and fragmented mollusk shells.

This study demonstrated the presence of middle to late Holocene hydrological fluctuations on the South American altiplano as shown by five periods of low water stands in Lake Titicaca. The water level of Lake Titicaca fluctuated >22 m during the past 3,500 years. Four of the lowstands were profound (indicated water lowering depth) and occurred abruptly over a period of 100–200 years. The earliest occurred during a prolonged middle Holocene dry phase that ended after 3,500 BP. All of the cores collected in Lago Wiñaymarka

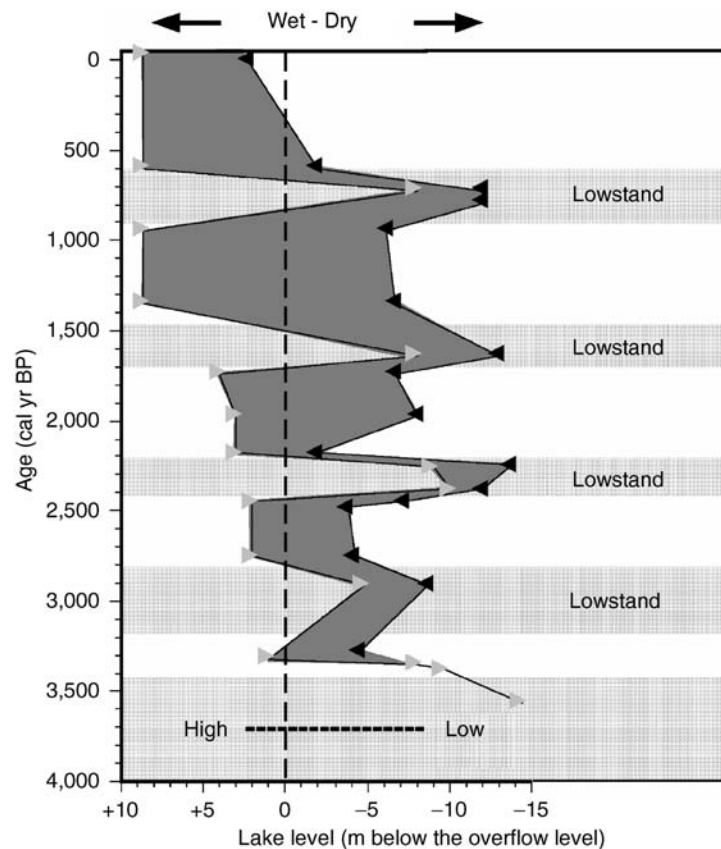


Figure L2 Lake-level reconstruction from Lake Titicaca based on lithostratigraphy from four cores and 60 AMS ¹⁴C measurements. The Gray Triangle symbol signifies the lowest stratigraphic level in cores A-D where an erosion surface occurs, indicating that lake level was below this point at the time indicated. Likewise, the Black Triangle symbol indicates the highest stratigraphic level where lacustrine sediments are preserved, implying water level was above this level.

for this study penetrate into previously sub-aerially exposed sediments, indicating that Lake Titicaca was >15 m below overflow level (BOL) prior to 3,500 BP. A second lowstand of 5–8 m BOL occurred between 3,200 and 2,800 BP. Shallow-water sub-facies between 3,500 and 2,800 BP suggest the lake remained below the overflow stage during this period. The third lowstand of 10–12 m BOL ended after 2,200 BP. The duration of this dry phase is estimated at 200 years. The fourth lowstand of 10–12 m BOL ended after 1,450 BP. The duration of this phase remains unknown, but is likely to have been near 250 years based on sediment accumulation rates. The final low lake level of 7–12 m BOL began prior to 900 BP and ended after 600 BP. Shallow-water subfacies suggests that water level probably remained low until 500 BP. The final lowstand is coincident with the decline of raised-field agriculture and collapse of Tiwanaku culture.

Mark B. Abbott and Lesleigh Anderson

Bibliography

- Abbott, M.B., Binford, M.W., Brenner, M., and Kelts, K., 1997. A 3500 ¹⁴C yr high-resolution record of water level changes in Lake Titicaca, Bolivia/Peru. *Quaternary Res.*, **47**, 169–180.
- Abbott, M.B., Finney, B.P., Edwards, M.E., and Kelts, K.R., 2000. Lake-Level reconstructions and paleohydrology of Birch Lake, Central Alaska, based on seismic reflection profiles and core transects. *Quaternary Res.*, **53**, 154–166.
- Alin, S.R., and Cohen, A.S., 2003. Lake-level history of Lake Tanganyika, East Africa, for the past 2500 years based on ostracod-inferred water-depth reconstruction. *Palaeogeogr. Palaeoclimatol. Palaeoecol.*, **199**, 31–49.
- Anderson, L., Abbott, M.B., Finney, B.P., and Edwards, M.E., 2005. Paleohydrology of the southwest Yukon Territory, Canada, based on multi-proxy analyses of lake sediment cores from a depth transect. *The Holocene*, **15**(8), 1172–1183.
- Barber, V.A., and Finney, B.P., 2000. Late Quaternary paleoclimatic reconstructions for interior Alaska based on paleolake-level data and hydrologic models. *J. Paleolimnol.*, **24**, 29–41.
- Benson, L.V., 1981. Paleoclimatic significance of lake level fluctuations in the Lahontan Basin. *Quaternary Res.*, **16**, 390–403.
- Benson, L.V., Curry, D.R., Dorn, R.I., Lajoie, K.R., Oviatt, C.G., Robinson, S.W., Smith, G.I., Stine, S., and Thompson, R.S., 1989. Variations in sizes of four Great Basin lake systems during the past 35,000 years. *Palaeogeogr. Palaeoclimatol. Palaeoecol.*, **78**, 241–268.
- Binford, M.W., Kolata, A.L., Brenner, M., Janusek, J., Abbott, M.B., and Curtis, J., 1997. Climate variation and the rise and fall of an Andean civilization. *Quaternary Res.*, **47**, 171–186.
- Bookman, R., Yehouda, E., Agnon, A., Stein, M., 2004. Late Holocene lake levels of the Dead Sea. *Geol. Soc. Am. Bull.*, **116**, 555–571.
- Brenner, M., Hodell, D.A., Curtis, J.H., Rosenmeier, M.F., Binford, M.W., and Abbott, M.B., 2001. Abrupt climate change and Pre-Columbian cultural collapse. In Markgraf, V. (ed.), *Interhemispheric Climate Linkages*. San Diego, CA: Academic Press, pp. 87–103.
- Dearing, J.A., 1997. Sedimentary indicators of lake-level changes in the humid temperate zone: A critical review. *J. Paleolimnol.*, **18**, 1–14.
- Digerfeldt, G., 1986. Studies on past lake-level fluctuations. In Berglund, B.E. (ed.), *Handbook of Holocene Palaeoecology and Palaeohydrology*. Chichester: Wiley, pp. 127–143.
- Finney, B.P., Scholz, C.A., Johnson, R.C., Trumbore, S., 1996. Late Quaternary lake-level changes of Lake Malawi. In Johnson, T.C., Odada E.O. (eds.), *Limnology, Climatology and Paleoclimatology of the East African Lakes*. Australia: Gordon and Breach Publishers, 495–508.
- Gilbert, G.K., 1890. Lake Bonneville. United States Geological Survey Monograph, **volume 1**, pp. 213.
- Harrison, S.P., and Digerfeldt, G., 1993. European lakes as palaeohydrological and palaeoclimatic indicators. *Quaternary Sci. Rev.*, **12**, 223–248.
- Hastenrath, S., and Kutzbach, J.E., 1983. Paleoclimatic estimates from water and energy budgets of East African lakes. *Quaternary Res.*, **19**, 141–153.
- Hastenrath, S., and Kutzbach, J.E., 1985. Late Pleistocene climate and water budget of the South American Altiplano. *Quaternary Res.*, **24**, 249–256.
- Hodell, D.A., Curtis, J.H., Jones, G.A., Higuera-Gundy, A., Brenner, M., Binford, M.W., and Dorsey, K.T., 1991. Reconstruction of Caribbean climate change over the past 10,500 years. *Nature*, **352**, 790–793.
- Hoffman, W., 1998. Cladocerans and chironomids as indicators of lake level changes in north temperature lakes. *J. Paleolimnol.*, **19**, 55–62.
- Hostetler, S.W., 1995. Hydrologic and thermal response of lakes to climate: Description and modeling. In Lerman, A., Imboden, D.M., Gat, J.R. (eds.), *Physics and Chemistry of Lakes* (2nd edn.). New York/Amsterdam: Springer, pp. 63–82.
- Keely, B., Scholz, C.A., King, J.W., Peck, J., Overpeck, J.T., Russell, J.M., and Amoako, P.V.O., 2005. Late Quaternary low stands of Lake Bosumtwi, Ghana: Evidence from high resolution seismic reflection and sediment core data. *Palaeogeogr. Palaeoclimatol. Palaeoecol.*, **216**, 235–249.
- Kutzbach, J.E., and Street-Perrott, F.A., 1985. Milankovitch forcing of fluctuations in the level of tropical lakes from 18 to 0 kyr BP. *Nature*, **317**, 130–134.
- Lundqvist, G., 1925. Utvecklingshistoriska insjostudier I Sydsvrige. *Sveriges Geologiska Undersokning*, **C 330**, 1–129.
- Lundqvist, G., 1927. Bodenablagerungen und Entwicklungstypen der Seen. *Die Binnengewasser*, **2**, 1–122.
- Oviatt, C.G., Sack, D., and Curry, D.R., 1994. The Bonneville basin, Quaternary, western U.S. In Gierlowski-Kordesch, E., and Kelts, K. (eds.), *Global Geologic Record of Lake Basins* (vol. 1). Cambridge, UK: Cambridge University Press, pp. 371–375.
- Roche, M.A., Bourges, J.C., and Mattos, R., 1992. Climatology and hydrology of the Lake Titicaca basin. In Dejoux, C., and Iltis, A. (eds.), *Lake Titicaca: A Synthesis of Limnological Knowledge*. Boston: Kluwer, pp. 63–83.
- Seltzer, G.O., Baker, P.B., Cross, S., Fritz, S.C., and Dunbar, R., 1998. High-resolution seismic reflection profiles from Lake Titicaca, Peru/Bolivia. *Geology*, **26**, 167–170.
- Street-Perrott, F.A., and Harrison, S.P., 1985. Lake levels and climate reconstruction. In Hecht, A.D. (ed.), *Lake Levels and Climate Reconstruction*. New York, NY: Wiley, pp. 291–340.
- Street-Perrott, F.A., and Perrott, R.A., 1990. Abrupt climate fluctuations in the tropics: The influence of Atlantic ocean circulation. *Nature*, **343**, 607–612.
- Webb, T. III., Ruddiman, W.F., Street-Perrott, F.A., Markgraf, V., Kutzbach, J.E., Bartlein, P.J., Wright, H.E., and Prell, W.L., 1993. In Vegetation, lake levels, and climate in eastern North America for the past 18,000 years. Wright, H.E., Kutzbach, J.E., Webb, T. III., Ruddiman, W.F., Street-Perrott, F.A., and Bartlein, P.J. (eds.), *Global climate since the Last Glacial Maximum*. Minneapolis, MN: University of Minnesota Press, pp. 514–535.
- Wirmann, J.P., 1992. Morphology and bathymetry. In Dejoux, C., and Iltis, A. (eds.), *Lake Titicaca: A Synthesis of Limnological Knowledge*. Boston: Kluwer, pp. 16–23.
- Wright, H.E., Kutzbach, J.E., Webb, T. III., Ruddiman, W.R., Street-Perrott, F.A., and Bartlein, P.J., 1993 (eds.). *Global Climate Since the Last Glacial Maximum*. Minneapolis, MN: University of Minnesota Press, pp. 569.
- Yang, X., Kamenick, C., Schmidt, R., and Sumin, W., 2003. Diatom based conductivity and water level inference models from eastern Tibetan (Qinghai-Xizang) Plateau lakes. *J. Paleolimnol.*, **30**, 1–19.
- Yu, Z., McAndrews, J.H., and Eicher, U., 1997. Middle Holocene dry climate caused by change in atmospheric circulation patterns: Evidence from lake levels and stable isotopes. *Geology*, **25**, 251–254.

Cross-references

Lacustrine Sediments
 Paleoclimate Proxies, an Introduction
 Paleolimnology
 Paleo-Precipitation Indicators
 Radiocarbon Dating

LAST GLACIAL MAXIMUM

Introduction

The Last Glacial Maximum (LGM) occurred when ice sheets and glaciers throughout the world were at their maximum extent during the last ice age. Once dated as 18,000 radiocarbon (21,500 calibrated/sidereal/“calendar”) years ago, the LGM is now believed to have occurred between 23,000 and 19,000 (cal) years ago (Clark and Mix, 2002). However, debate continues regarding its extent, timing and the nature of its ice sheets (below). The LGM is believed to have resulted from climate change caused by changes in the orbital configuration of the Earth. However, the LGM was synchronous in both hemispheres, suggesting that poorly understood feedback factors probably operated. Somehow, they provided sources of precipitation for ice growth and maximum expansion at the LGM.

The LGM is an important “time-slice” for paleogeographic reconstruction and computer simulation because the configuration of the Earth differed so greatly from that of the present. Extensive mid-latitude ice sheets existed in North America, northwest Europe and, controversially, in northern Russia and Siberia. The shape of ocean basins and coastlines was different because water abstracted from the ocean and locked in the ice sheets lowered sea level by between 120 and 130 m. This altered the chemistry of the ocean, which became more saline and isotopically ($\delta^{18}\text{O}$) heavier. Atmospheric circulation was modified by the large ice sheets: for example, the LGM Laurentide Ice Sheet (LIS) split the jet stream into two arms. Thick ice sheets caused the Earth’s crust to subside glacio-isostatically, the extent of which is partly revealed by raised shorelines fashioned as the crust recovered and sea level rose during and after deglaciation. Modeling these effects has provided constraints on the rheology of the Earth’s mantle and crust. The concentration of greenhouse gases in the atmosphere (CO_2 and CH_4) was lower than at present, at a time of reduced ocean and continental temperatures throughout the world. Vegetational zones were compressed by latitude and altitude. General aridity prevailed as deserts expanded and extensive dust storms deposited sand and silt (loess) deposits. However, in some regions that are arid today, extensive lakes occurred, such as Lake Bonneville and Lake Lahontan in America (Benson, 2004).

History

The term “Last Glacial Maximum” is relatively recent and refers to the time of maximum global ice volume inferred from the oxygen isotope stratigraphy ($\delta^{18}\text{O}$) of ocean sediments (CLIMAP, 1976, 1981). While the $\delta^{18}\text{O}$ signal is a global one, it conceals a wide variety of temporal responses by different ice masses caused by regional climate variation as well as the glaciological and environmental characteristics of individual ice sheets and glaciers. This was recognized when the LGM was re-defined as having occurred between 23,000 and 19,000 (cal) years ago (Clark and Mix, 2002).

The LGM concept has older antecedents that identified the maximum extent of continental ice sheets during the “latest” or “last” glaciation (Flint, 1971; Sibrava et al., 1986). This was based on field mapping of “fresh” and relatively unmodified glacial and glaciofluvial landforms, such as moraines, drumlins and eskers. First developed in the midwestern USA,

where the ice maximum became known as the “Classical Wisconsin” (Flint, 1971), this method was also applied to Great Britain and Ireland where a “newer drift” (LGM) was distinguished from an older one. However, this criterion is not always reliable: the “fresh” moraines of the Warthe glaciation in Germany were once thought to be LGM, but are older than the Eemian (“last interglacial”). Only the late Weichselian glaciation is of LGM age.

Techniques

Glacial geology in the field provides evidence regarding ice source regions, ice movement and the extent of LGM ice. Estimating the precise age of the glaciation is essential for determining its timing and regional variability. Since 1950, radiocarbon dating has been used to accomplish this essential task, with ^{14}C accelerator mass spectrometry (AMS) providing greater precision and accuracy. Where ^{14}C dating of organic samples is impossible, cosmogenic rock exposure ages can now date glacial boulders and glaciated rock surfaces (Gosse and Phillips, 2001). Uranium series dating of corals provides information on the LGM sea level – a means of estimating continental ice volume. Within this dating framework, a whole range of environmental disciplines use data from continents and oceans to complete the picture beyond the LGM ice sheets. These data form the basis of computer simulations of the LGM climate and, reciprocally, provide validation or question such simulations (Ruddiman, 2000). LGM ice sheets have also been simulated as three-dimensional thermodynamic ice-sheet models.

Extent of glaciation

Two versions of the possible extent of ice in the Northern Hemisphere at the LGM were assembled by Denton and Hughes (1981) and CLIMAP (1981): a minimum and a maximum reconstruction (Figure L3). The main differences involve the extent of glaciation in northern Russia and Siberia and Arctic Canada (below). In the Southern Hemisphere, the Antarctic ice sheet extended across the continental shelf to its edge and large ice caps expanded in the Himalayas, South America and New Zealand. High altitude small ice caps and glaciers at lower latitudes expanded in East Africa, the Andes, New Guinea and Hawaii. However, the greatest expansion occurred in the mid- to higher-latitudes of North America and Europe, for which there is no present-day analogue.

The extent of ice at the LGM is well established on the southern margins of Northern Hemisphere mid-latitude ice sheets. The LIS, which was coextensive with the Cordilleran Ice Sheet of the Rocky Mountains, advanced to Long Island, Ohio, Illinois, Iowa and South Dakota. In Europe, the Fennoscandian Ice Sheet advanced to Berlin and Warsaw. However, the northern margins of LGM ice continue to be the subject of debate (Andrews, 1987). Ongoing controversy continues regarding northwestern Russia and eastern Siberia, where a major expansion of the Barents Sea and Kara Sea ice sheets may predate the LGM. Much of the evidence is submarine and insufficient reliable age estimates are available on land.

Ice sheet reconstructions

The LGM reconstructions of CLIMAP were based to a large extent on a “marine-based” ice sheet model from Antarctica (Denton and Hughes, 1981). For example, in North America, the LIS reconstruction was a high-elevation, over 4 km thick, single ice dome centered over Hudson’s Bay. Similarly, the

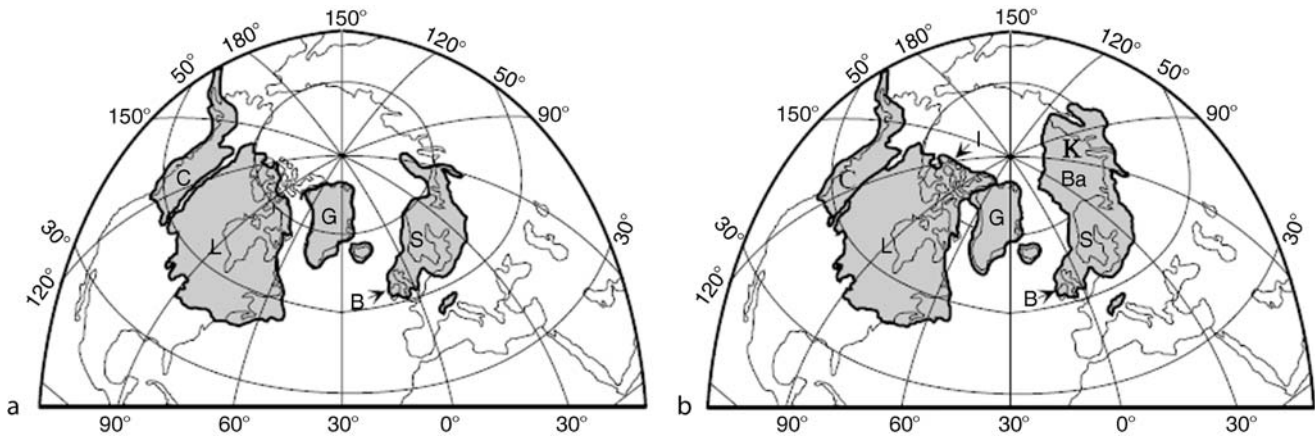


Figure L3 (a) The CLIMAP minimum reconstruction of Northern Hemisphere LGM ice sheets; (b) The CLIMAP maximum reconstruction of Northern Hemisphere ice sheets. L: Laurentide Ice Sheet; C: Cordilleran Ice Sheet; I: Innuitian Ice Sheet; G: Greenland Ice Sheet; B: Great Britain and Ireland Ice Sheet; S: Scandinavian (Fenno-Scandian) Ice Sheet; Ba: Barents Sea Ice Sheet; K: Kara Sea Ice Sheet. This does not show smaller ice caps: for example, in the western USA or the Pyrenees. See text for the location of the smaller Southern Hemisphere ice sheets and ice caps.

Fenno-Scandian ice sheet was centered over the Gulf of Bothnia, where it exceeded 3 km in thickness. These became standard ice-sheet boundary conditions for computer simulations of the LGM climate. More recent ice sheet modeling suggests an ice thickness of over 3.8 km for the LIS, with mean volumetric estimates of 10^{15} m^3 (Marshall et al., 2002).

Glacial geology in the field, however, especially indicators of ice movement from glacial erratics, is not consistent with the CLIMAP reconstruction. Instead the field evidence points to a multi-domed and thinner LIS. The LIS was less extensive in the Canadian Arctic and, as such, supports the minimum view of LGM glaciation (Andrews, 1987; Dyke et al., 2002). A thinner, multi-domed ice sheet is believed to have responded more rapidly to changes in climate: for example, Heinrich events, massive ice discharges into the ocean once thought to have lasted about 2,000 years, are now believed to have lasted only 250 years. Such rapid changes are consistent with climate events inferred from ice core records in Greenland.

Timing of the LGM

Table L1 shows estimates of ice volume and the amount of sea lowering at the LGM. Recent estimates based on hundreds of AMS ^{14}C and uranium series ages from corals in Barbados suggest that the lowest sea level occurred 26,000 years ago (Fairbanks and Peltier, 2004).

Radiocarbon dating indicates that the LIS may have advanced rapidly to its maximum extent as early as 27–29 cal ka BP, well before the LGM, and remained near that limit until 17 ka (cal). However, the Cordilleran Ice Sheet in the Puget Sound region did not reach its maximum extent until 4,000 years later. Similarly, the Antarctic Ice Sheet reached its maximum extent at different times in different sectors. The Scandinavian and British ice sheets were not joined at the LGM (compare with Figure L3), but may have been joined somewhat earlier. They reached their maximum extent about >26 (cal) ka along western margins, but about 23–22 (cal) ka on their southern margins.

The age of the LGM on the northern margin of the LIS is unknown and may be much younger than on its southern margin. All that is known is that deglaciation commenced about 15,000 years ago, an age probably close to maximum expansion

Table L1 Estimates of ice equivalent sea level (m) for LGM ice sheets (adapted from Clark and Mix, 2002)

Ice sheet	CLIMAP min.	CLIMAP max.	Model min.	Model max.
Antarctica	24.5	24.5	14	21
North America	77	92	82.4	82.4
Greenland	1	6.5	2	3
Eurasia	20	34	13.8	18
All Others	5	6	6	6
TOTAL	127.5	163	118.2	130.4

(Andrews, 1987; Dyke et al., 2002). Uncertainty in establishing the age of the LGM in some regions arises because suitable samples are unavailable for radiocarbon dating, a deficiency now being addressed by cosmogenic rock exposure ages.

David Q. Bowen

Bibliography

- Andrews, J.T., 1987. The Late Wisconsin glaciation and deglaciation of the Laurentide Ice Sheet. In Ruddiman, W.F., and Wright, H.E. Jr. (eds.), *North America and Adjacent Oceans during the Last Deglaciation*. Boulder, CO: Geological Society of America. *Geology of North America*; K-3, pp. 13–38.
- Benson, L., 2004. Western Lakes. In Gillespie, A.R., Porter, S.C., and Atwater, B.F. (eds.), *The Quaternary Period in the United States*. Amsterdam/New York: Elsevier, pp. 185–204.
- Clark, P.U., and Mix, A.C., 2002. Ice Sheets and sea level of the Last Glacial Maximum. *Quaternary Sci. Rev.*, **21**, 1–7.
- CLIMAP (*Climate Long Range investigation, Mapping and Prediction*), 1976. The surface of the ice age Earth. *Science*, **191**, 1131–1144.
- CLIMAP, 1981. *Seasonal Reconstructions of the Earth's Surface at the Last Glacial Maximum*. Geological Society of America Map Series, MC-36. Boulder, CO: Geological Society of America.
- Denton, G.H., and Hughes, T.J., 1981. *The Last Great Ice Sheets*. New York: Wiley, pp. 1–484.
- Dyke, A.S., Andrews, J.T., Clark, P.U., England, J.H., Miller, G.H., Shaw, J., and Veillette, J.J., 2002. The Laurentide and Innuitian ice sheets during the Last Glacial Maximum. *Quaternary Sci. Rev.*, **21**, 9–31.
- Fairbanks, R.G., and Peltier, W.R., 2004. Reanalysis and Extension of the Barbados Sea Level Record. *Eos Transactions American Geophysical Union*, 85 (47).

- Flint, R.F., 1971. *Glacial and Quaternary Geology*. New York: Wiley.
- Gosse, J.C., and Phillips, F.M., 2001. Terrestrial in situ cosmogenic nuclides: Theory and application. *Quaternary Sci. Rev.*, **20**, 1475–1560.
- Marshall, S.J., James, T.S., and Clarke, G.K.C., 2002. North American Ice Sheet reconstruction at the Last Glacial Maximum. *Quaternary Sci. Rev.*, **21**, 175–192.
- Ruddiman, W.F., 2000. *Earth's Climate*. New York: W.H. Freeman.
- Sibrava, V., Bowen, D.Q., and Richmond, G.M., 1986. (eds.). Glaciations in the Northern Hemisphere. (Project 24 International Geological Correlation Programme). *Quaternary Sci. Rev.*, **5**, 1–511.

Cross-references

Atmospheric Circulation during the Last Glacial Maximum
 CLIMAP
 Cordilleran Ice Sheet
 Cosmogenic Radionuclides
 Cryosphere
 Eemian (Sangamonian) Interglacial
 Glacial Geomorphology
 Glacial Megalakes
 Glacial Sediments
 Heinrich Events
 Ice cores, Antarctica and Greenland
 Ice-Rafted Debris (IRD)
 Laurentide Ice Sheet
 Oxygen Isotopes
 Paleoclimate Modeling, Quaternary
 Paleotemperatures and Proxy Reconstructions
 Pollen Analysis
 Radiocarbon Dating
 Scandinavian Ice Sheet
 Sea Level Change, Quaternary
 Thermohaline Circulation
 Uranium-Series Dating
 Wisconsinan (Weichselian, Würm) Glaciation

LAST GLACIAL TERMINATION

Late Quaternary climates are characterized by successive glacial and interglacial periods. While glacial inceptions are usually progressive, the transitions from full glacial conditions to full interglacial ones occur within about 10 kyr or less. During these remarkable time periods, named terminations, the climate system experiences considerable reorganizations. The Last Glacial Termination, between approximately 20 and 8 kyBP, is of particular interest since it can be studied in detail and can be dated with good accuracy using radiocarbon methods. If, by definition, the major event is the disappearance of the large Northern Hemisphere ice sheets (Laurentide and Fennoscandian) with a resulting sea-level rise of about 120 m, this is associated with many other important changes. First, the warming recorded in Greenland ice cores or in marine cores at high northern latitudes does not smoothly follow the decreasing size of continental ice areas. On the contrary, abrupt warmings and coolings, associated with changes in ocean circulation punctuate the transition. Second, many well-dated climatic proxies suggest that some generalized warming that was recorded in tropical or southern marine cores occurred before any major reduction of northern ice sheets. Third, the rise in atmospheric carbon dioxide concentration from glacial levels around 180–200 ppm towards interglacial levels around 260–280 ppm also occurred several thousands of years before the continental ice volume decrease. All these facts are not

easily explained in the context of the Milankovitch theory, which claims that astronomical changes affect the mass balance of ice sheets, and consequently lead to global climatic changes. Understanding the dynamics of the Last Glacial Termination is therefore a critical step both for the theory of glacial-interglacial cycles as well as for understanding millennial scale climatic variability.

Astronomical forcing and ice volume changes

Terminations attracted the attention of paleoclimatologists when they examined the first continuous marine isotopic records. The characteristic sawtooth character of climatic changes was first outlined by Emiliani (1966). The notion of terminations was introduced by Broecker and van Donk (1970) and it was already clear at this time that the astronomical theory would not easily explain this structure (Broecker and van Donk, 1970): “... the cause of the primary sawtoothed cycle is still an open question.”

Though this early definition of terminations was descriptive, it is interesting to note that terminations do systematically correspond to deviations that would be predicted by a linear astronomical theory of Quaternary climate, as illustrated in Figure L4. If the origin of these sawtoothed 100 kyr glacial-interglacial cycles is linked to astronomical parameters, it remains to be explained what amplifying feedbacks are involved during terminations. When examining the last five or ten terminations, there is no direct correspondence between the timing or intensity of terminations and the insolation forcing. On the contrary, termination V, between isotopic stages 12 and 11, was one of the largest transitions, although it occurred about 425 kyBP when insolation changes were quite small. Conversely, termination III, between stages 8 and 9, was not a large transition although seasonal insolation changes were considerable about 243 kyBP.

Probably the simplest way to explain terminations is to envision the sawtooth-like 100 kyr cycles as relaxation oscillations. In this concept, the ultimate cause of terminations would be found in the preceding glacial maximum, and the insolation forcing only acts as a favorable external influencing factor. This can quite successfully explain the timing of events (Paillard, 1998) as well as the amplitude and phase of terminations (Parrenin and Paillard, 2003). However, a mechanistic understanding of terminations needs a closer inspection of the evolution of different climatic parameters like temperatures at different Earth locations, deep oceanographic properties, sea level, or greenhouse gas concentrations. A detailed sequential chronology of these changes is available for the last termination.

The sequence of events during the Last Glacial Termination

The summer insolation forcing at high northern latitudes (taken at the summer solstice) steadily increased from the Last Glacial Maximum (LGM) about 21 kyBP up to 11 kyBP, in the middle of the termination, at the peak insolation time. However, the mid-transition actually occurred around 12 kyBP, while the maximum insolation forcing happened later, around 11 kyBP for June insolation, around 8 kyBP for August insolation, and around 9 kyBP for the averaged summer forcing. This highlights the fact that the phase relationship between astronomical forcing and global ice sheet volume is poorly understood on a millennial time scale. However, as shown in Figure L5, the temperature variations have a much more complex history.

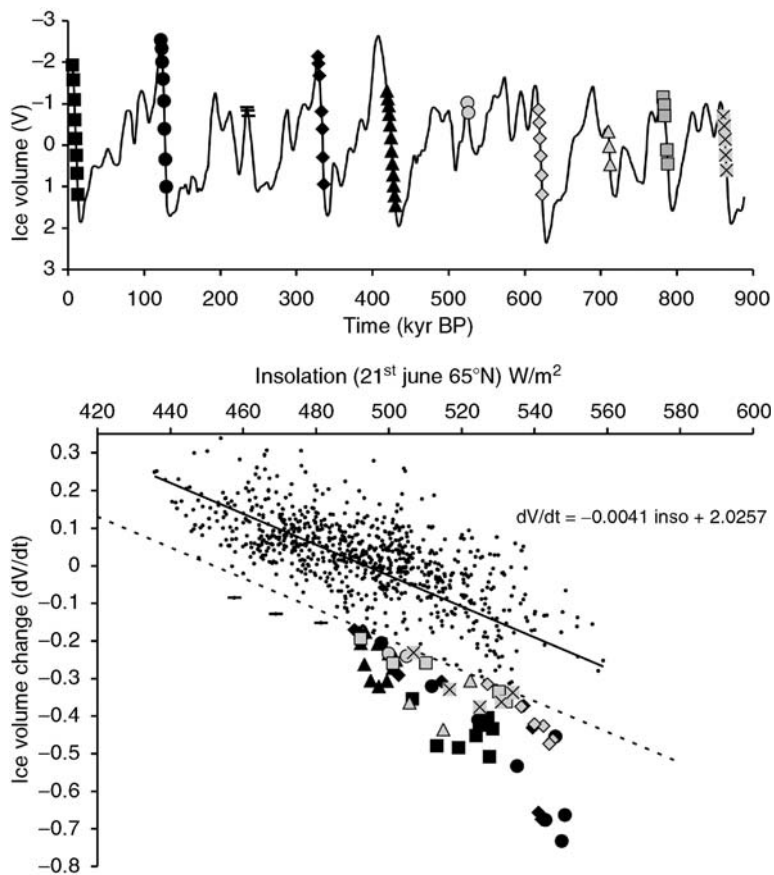


Figure L4 The *top curve* is a classical reconstruction of glacial-interglacial cycles, based on the $\delta^{18}\text{O}$ of foraminifera, and interpreted here as normalized ice volume V (Bassinot et al., 1994). On the *diagram below*, the derivative (dV/dt) is plotted as a function of the insolation forcing. A clear linear relationship is obtained, in large part due to the tuning methodology used to build a timescale for the ice volume data. However, marked points are significantly below the regression line (*heavy line*). It is then possible to define terminations as time periods during which ice volume decreases much faster than a linear astronomical theory could predict (*below the dotted line*). They occur about every 100 kyr, as can be seen on the *top panel* where the same marked points are represented.

At high northern latitudes, an abrupt warming was observed in Greenland around 14 kyrBP, as well as in many other locations in Europe and in the North Atlantic. The following warm interval (Bølling-Allerød) only lasted about two thousand years and ended with an abrupt cooling event into the Younger Dryas time interval. This cold period was shorter than a thousand years and also ended abruptly with a warm period that progressively led into the Holocene and the present-day climate. The same pattern is also visible in the atmospheric methane (CH_4) concentration recorded in Greenland ice cores. However, records from Antarctica or from the Southern Ocean have almost the opposite pattern, with a cooling occurring in the middle of the transition, the Antarctic Cold Reversal, during the northern warm Bølling-Allerød interval. The explanation for such rapid climatic changes, as shown for example by $^{231}\text{Pa}/^{230}\text{Th}$ records, involves major changes in the Atlantic deep circulation, which transports heat from one hemisphere to the other. This opposition has been named the “bipolar-seesaw” (Stocker, 1998). These abrupt changes recorded during the last termination are a clear indication that the internal variability of our climate is of primary importance in accounting for the dynamics of glacial-interglacial transitions.

The atmospheric CO_2 concentration closely follows the evolution of Antarctic temperatures, although some secondary features are probably linked to the northern climate (Monnin et al., 2001). Interestingly, this southern temperature rise started around 18 kyrBP, when the northern ice sheets were still close to their maximum volume. Explaining this southern warming with an astronomical forcing appears quite problematic, although the annual mean insolation and the obliquity forcing may have some importance (Loutre et al., 2004). More than half of the glacial-interglacial pCO_2 increase, from 180 to 240 ppm, occurred during this early phase, between 18 kyrBP and 14 kyrBP, while sea level rose by about only 20 m above glacial levels. Furthermore, an early warming has also been found in many other locations, like the tropics (Lea et al., 2000). It is therefore reasonable to assume that this early atmospheric CO_2 rise and the associated warming had a critical role in the triggering of the deglaciation. In this context, the key to understanding the terminations probably lies in the carbon cycle (Paillard, 2001), and the fundamental question is not in understanding why pCO_2 was low during LGM, but why it rose rapidly just afterwards. If maximum global ice volume was a trigger for some Southern Ocean warming and pCO_2

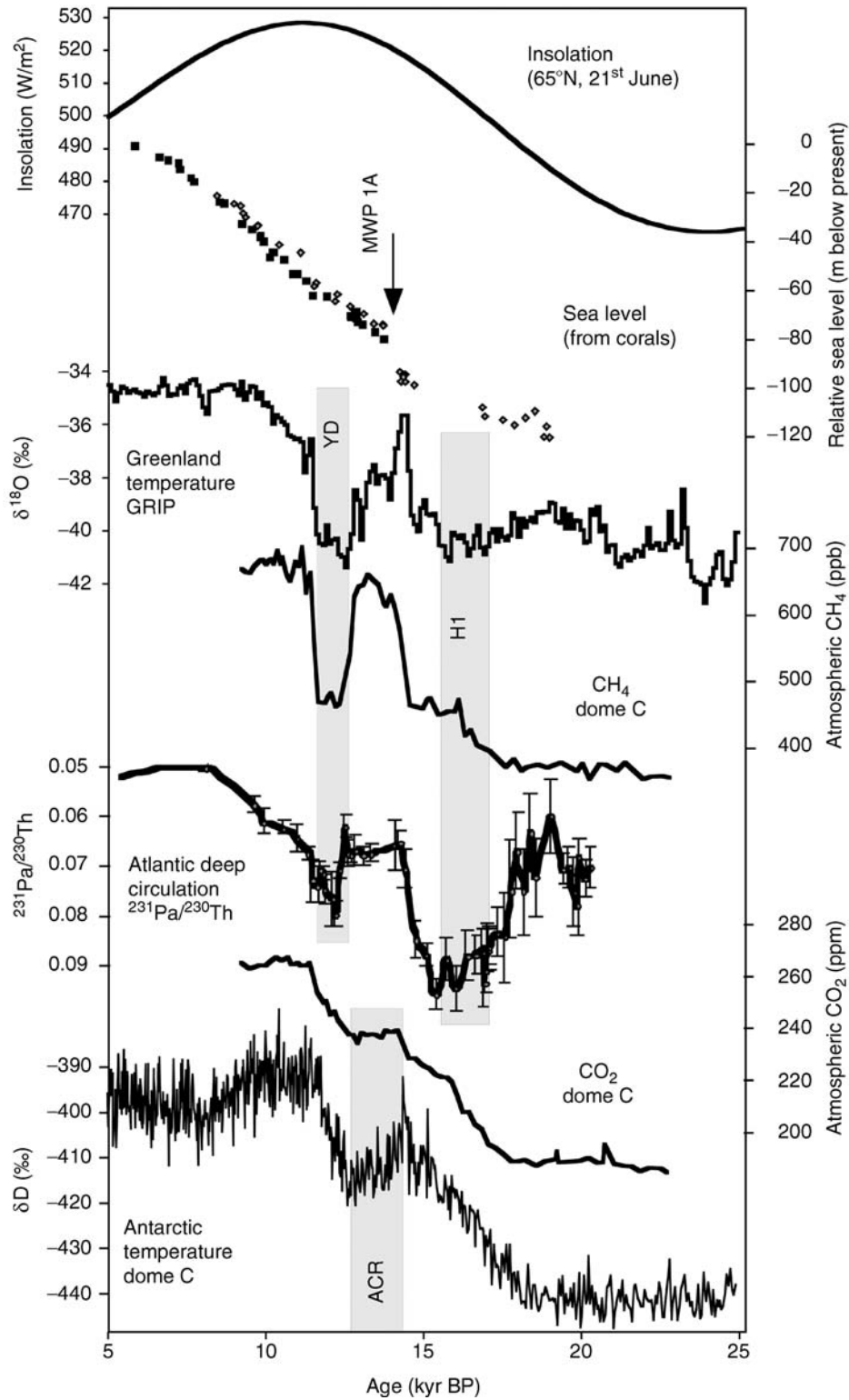


Figure L5 From top to bottom, daily insolation forcing at the summer solstice at $65^\circ N$ (Berger, 1978); sea level reconstructed from corals (Fairbanks, 1989; Bard et al., 1996); Greenland temperature based on oxygen isotopes (Dansgaard et al., 1993); atmospheric CH_4 concentration recorded at Dome C (Monnin et al., 2001); intensity of the deep oceanic circulation based on $^{231}Pa/^{230}Th$ ratio (McManus et al., 2004); atmospheric CO_2 concentration (Monnin et al., 2001); Antarctic temperature based on deuterium measured at Dome C (Stenni et al., 2001). Cold events are highlighted: Heinrich event 1 (H1), Younger Dryas (YD), Antarctic Cold Reversal (ACR).

increase, as required by the relaxation oscillation paradigm, it is natural to look at the evolution of the Antarctic Ice Sheet at this time. Since it is largely driven by sea-level changes, the Antarctic continental ice reached its maximum by entirely covering the continental shelves several thousands of years after the LGM (Denton and Hughes, 2002). A possible scenario is to assume that this could affect sea ice formation and bottom water formation around Antarctica. If we furthermore hypothesize that low CO₂ levels during glacial times are linked to Southern Ocean bottom water characteristics, then expansion of the Antarctic Ice Sheet could lead to the atmospheric pCO₂ increase. This would account both for the triggering of terminations and for the observed sequence of events (Paillard and Parrenin, 2004).

Millennial scale variability and terminations

The role of the millennial-scale climatic variability on the dynamics of the last termination remains an open question. As shown in Figure L5, the southern warming and pCO₂ increase are associated with a major decrease in the deep Atlantic Ocean circulation. This oceanic slowdown is traditionally explained by the massive iceberg discharge from the Laurentide Ice Sheet, known as Heinrich event 1, which occurred around 17 kyBP. A reasonable hypothesis would be to put these millennial scale changes at the center of the dynamics of terminations, but many questions still need to be resolved: What triggers Heinrich events? Are deep circulation slowdowns caused solely by iceberg discharges? What is the role and dynamics of the Younger Dryas and, more generally, of Dansgaard-Oeschger events? How can a Southern Ocean warming explain a rapid pCO₂ increase by 40–60 ppm in only 3 or 4 thousand years? All these questions are currently being closely examined by paleoclimatologists, and their answers should lead to a new understanding of the Last Glacial Termination. They also highlight how far we have come from the traditional Milankovitch theory in which Quaternary ice volume changes were tentatively explained only by insolation and ice sheet mass balance. If Dansgaard-Oeschger events, the Younger Dryas, Heinrich events, associated Antarctic warmings, and finally glacial-interglacial cycles appear today to be rather different topics, the detailed history of the Last Glacial Termination suggests that understanding the links between these different aspects of climatic variability could provide the clue to a revised and a more integrated theory of Quaternary climates.

Didier Paillard

Bibliography

- Bard, E., Hamelin, B., Arnold, M., Montaggioni, L., Cabioch, G., Faure, G., and Rougerie, F., 1996. Deglacial sea-level record from Tahiti corals and the timing of global meltwater discharge. *Nature*, **382**, 241–244.
- Bassinot, F.C., Labeyrie, L.D., Vincent, E., Quidelleur, X., Shackleton, N.J., and Lancelot, Y., 1994. The astronomical theory of climate and the age of the Brunhes-Matuyama magnetic reversal. *Earth Planet. Sci. Lett.*, **126**, 91–108.
- Berger, A.L., 1978. Long-term variations of daily insolation and Quaternary climatic change. *J. Atmos. Sci.*, **35**, 2362–2367.
- Broecker, W.S., and van Donk, J., 1970. Insolation changes, ice volumes and the O¹⁸ record in deep-sea cores. *Rev. Geophys. Space Phys.*, **8**, 169–197.
- Dansgaard, W., Johnsen, S.J., Clausen, H.B., Dahl-Jensen, D., Gundestrup, N.S., Hammer, C.U., Hvidberg, C.S., Steffensen, J.P., Sveinbjörnsdóttir, A.E., Jouzel, J., and Bond, G., 1993. Evidence for general instability of past climate from a 250-kyr ice-core record. *Nature*, **364**, 218–220.
- Denton, G.H., and Hughes, T.J., 2002. Reconstructing the Antarctic ice sheet at the Last Glacial Maximum. *Quaternary Sci. Rev.*, **21**, 193–202.

- Emiliani, C., 1966. Paleotemperature analysis of Caribbean cores P6304–8 and P6304–9 and a generalized temperature curve for the past 425,000 years. *J. Geol.*, **74**, 109.
- Fairbanks, R.G., 1989. A 17,000 year glacio-eustatic sea level record: Influence of glacial melting rates on the Younger Dryas event and deep ocean circulation. *Nature*, **342**, 637–642.
- Lea, D.W., Pak, D.K., and Spero, H.J., 2000. Climate Impact of late Quaternary Equatorial Pacific sea surface temperature variations. *Science*, **289**, 1719–1724.
- Loutre, M.F., Paillard, D., Vimeux, F., and Cortijo, E., 2004. Does mean annual insolation have the potential to change the climate? *Earth Planet. Sci. Lett.*, **221**, 1–14.
- McManus, J.F., Francois, R., Gherardi, J.-M., Keigwin, L.D., and Brown-Leger, S., 2004. Collapse and rapid resumption of Atlantic meridional circulation linked to deglacial climate changes. *Nature*, **428**, 834–837.
- Monnin, E., Indermühle, A., Dällenbach, A., Flückiger, J., Stauffer, B., Stocker, T.F., Raynaud, D., and Barnola, J.-M., 2001. Atmospheric CO₂ concentrations over the Last Glacial Termination. *Science*, **291**, 112–114.
- Paillard, D., 1998. The timing of Pleistocene glaciations from a simple multiple-state climate model. *Nature*, **391**, 378–381.
- Paillard, D., 2001. Glacial cycles: Toward a new paradigm. *Rev. Geophys.*, **39**, 325–346.
- Paillard, D., and Parrenin, F., 2004. The Antarctic ice-sheet and the triggering of deglaciations. *Earth Planet. Sci. Lett.*, **227**, 263–271.
- Parrenin, F., and Paillard, D., 2003. Amplitude and phase of glacial cycles from a conceptual model. *Earth Planet. Sci. Lett.*, **214**, 243–250.
- Stenni, B., Masson-Delmotte, V., Johnsen, S., Jouzel, J., Longinelli, A., Monnin, E., Röthlisberger, R., and Selmo, E., 2001. An oceanic cold reversal during the last deglaciation. *Science*, **293**, 2074–2077.
- Stocker, T.F., 1998. The seesaw effect. *Science*, **282**, 61–62.

Cross-references

- [Antarctic Cold Reversal](#)
[Astronomical Theory of Climate Change](#)
[Bølling-Allerød Interstadial](#)
[Dansgaard-Oeschger Cycles](#)
[Heinrich Events](#)
[Last Glacial Maximum](#)
[Millennial Climate Variability](#)
[North Atlantic Deep Water and Climate Change](#)
[Quaternary Climate Transitions and Cycles](#)
[Sea Level Change, Quaternary](#)
[Thermohaline Circulation](#)
[Younger Dryas](#)

LATE PALEOZOIC PALEOCLIMATES

Introduction

The climate of the late Paleozoic, particularly the Pennsylvanian and Early Permian, was very similar to the present-day climate. During both intervals, the South Pole experienced significant glaciation and the North Pole experienced intermittent glaciation (Hambrey and Harland, 1981; Zachos et al., 2001). Because of this, the term “ice house” has been used to describe the climate of both intervals. Paradoxically, although the poles were frigid, warm, wet climates prevailed at the equator during both intervals. In both intervals, glaciation occurred in the context of a major continental collision: between Laurussia and Gondwana to form Pangaea in the late Paleozoic; and between India and Asia to form Eurasia in the Cenozoic. Finally, in both intervals, an extended period of “hot-house” climate, with warm poles and shallow pole-to-equator temperature gradients, preceded glaciation (Ziegler et al., 1981; Zachos et al., 2001; Raymond and Metz, 2004).

Late Devonian glaciation (Glacial I) and paleoclimate

The onset of Southern Hemisphere glaciation in the Late Devonian is a logical place to begin our consideration of late Paleozoic paleoclimates. Although this glaciation was relatively short, perhaps less than 0.5 million years (McGhee, 1996; Streele et al., 2000), it signals the beginning of the transition between the early Paleozoic “hot-house” and the late Paleozoic “ice-house” or glacial climates. Isbell et al. (2003) referred to this glaciation as Glacial I (Figure L6). Late Famennian (Glacial I) sediments appear in a number of South American basins (Bolivia, Madre de Dios, Solimoes, Amazonas, Paranaiba) and possibly in Libya (Isaacson et al., 1999; Streele et al., 2000). This glaciation coincided with the deposition of the Hangenberg Shale, a black, organic-rich shale deposited on top of ramp and platform carbonates in low and mid-latitudes (Caplan and Bustin, 1999). The

Hangenberg is one of a series of organic-rich shales and limestones deposited on Devonian and early Mississippian continental shelves, termed “Kellwasser event beds” after the extensive Kellwasser Horizon that marks the Frasnian-Famennian boundary (House, 1985). During Kellwasser events, anoxic or dysoxic water flooded continental shelves and the burial rate of organic carbon increased (Buggisch, 1991).

The terrestrial floras and marine faunas of the Late Devonian and Mississippian were extremely cosmopolitan (Ziegler et al., 1981; McGhee, 1996; Streele et al., 2000; Raymond and Metz, 2004), suggesting a shallow pole-to-equator temperature gradient. In the Mesozoic and early Cenozoic, shallow latitudinal temperature gradients reflect extremely warm poles (Valdes, 2000). In the Late Devonian, however, cosmopolitan floral and faunal assemblages may reflect equatorial cooling. Evidence for cool equatorial temperatures associated with Late Devonian glaciation includes contraction of the ranges of calcareous foraminifera toward the equator (Kalvoda, 1986) and the increasing diversity of deep-water siliceous sponges in the latest Devonian (McGhee, 1996).

Late Devonian glaciation was preceded by mass extinction at the Frasnian/Famennian boundary: 13–38% of marine families, 29–60% of marine genera and 82% of marine species became extinct (Sepkoski, 1986; McGhee, 1996). This mass extinction appears to have been related to equatorial cooling and flooding of continental shelves with anoxic or dysoxic water, although other mechanisms have been proposed (see Raymond and Metz, 2004 and references therein). In the Late Devonian mass extinction, equatorial taxa suffered higher percentages of extinction than southern cold-temperate and polar taxa; and, shallow water, presumably warm-adapted corals suffered greater percentages of extinction than deep water, presumably cold-adapted, corals (Scrutton, 1988; McGhee, 1996).

Late Devonian glaciation coincided with a second interval of increased extinction at the Devonian-Carboniferous boundary: approximately 16% of marine families and 21% of marine genera became extinct (Sepkoski, 1986). However, these extinctions show no clear latitudinal pattern.

Witzke (1990) reviewed the use of sedimentological indicators (coals, bauxite, kaolinite, evaporites and calcretes) to define climate zones. Based on sedimentological indicators, we can identify the following Late Devonian climate zones: (a) a wet, equatorial zone, coincident or slightly to the north of the paleoequator; (b) two arid, subtropical zones to the north and south of the equatorial zone and a southern wet, warm temperate zone; and (c) a southern cool temperate zone associated with South Polar glaciation (Figure L7).

Mississippian paleoclimate

Late Devonian glaciation may have persisted into the earliest Mississippian (Isaacson et al., 1999; Isbell et al., 2003), although earliest Mississippian glacial sediments are poorly dated (Streele et al., 2000). Aside from these putative earliest Mississippian glacial deposits, the first two stages of the Mississippian, the Tournaisian and Viséan, were apparently free of significant glacial ice.

Based on sedimentary indicators, the following climate zones can be identified: (a) a zone of wet “equatorial” climate, which lay to the north of the paleoequator on the northwest side of Pangaea and coincided with the paleoequator on the east side of the continent; (b) a zone of arid climate to the south; (c) a southern warm temperate zone to the south of the arid zone; (d) a southern cool temperate zone to the

Paleozoic	Carboniferous	Permian	Late	Lopingian	?	Glacial III	
			Middle	Guadalupian	Zechstein		?
			Early	Cisuralian	Rotliegendes		?
		Pennsylvanian	Gzhelian	Stephanian	***		
			Kasimovian		***		
			Moscovian	Westphalian	*****		
	Mississippian	Bashkirian	Namurian B & C	***	Glacial II		
		Late		Serpukhovian		***	
		Middle	Viséan	*			
	Devonian	Early	Tournaisian	***	Glacial I		
		Late	Famennian Frasnian	***			
		Middle	Givetian Eifellian	***			
		Early	Emsian Pragian Lochkovian	***			

Figure L6 The timing and duration of late Paleozoic glaciation. *: Glacial I, II, and III of Isbell et al. (2003); **: mid-to-late Westphalian glaciation of Veevers and Powell (1987), Frakes et al. (1992), and Crowell (1999). While glaciation may have persisted until the end of the Permian (Frakes et al., 1992; Crowell, 1999; Isbell et al., 2003); others have suggested that glaciation ended in the mid-Permian (Veevers and Powell, 1987; Gibbs et al., 2002; Rees et al., 2002).

south of the arid zone; and (e) a northern warm temperate zone to the north of the equatorial wet zone (Figure L8).

Rowley et al. (1985) reviewed the phytogeography of Tournaisian and Visean floras. In both intervals, northern warm temperate floras from Siberia are distinct. In both, wet tropical assemblages from Europe and South China appear distinct from arid tropical assemblages found in the Canadian Maritimes. Few Tournaisian Gondwanan assemblages were included in their study; however, Visean Gondwanan assemblages from the warm temperate zone have a distinct floral assemblage (Iannuzzi and Pfefferkom, 2002).

The migration patterns of marine invertebrates allow us to trace the relative climate of the Mississippian. In the mid-to-late Visean, a statistically significant percentage of articulate brachiopod genera expanded their range toward the poles,

suggesting that both poles became warmer in the late Visean. Although the biostratigraphic resolution of land plant migrations is not as precise as that of brachiopods, Northern Hemisphere land plants show a similar range expansion toward the pole in the Visean (Raymond, 1985; Raymond et al., 1990; Kelley and Raymond, 1991).

Late Mississippian-Permian glaciation (Glacial II and III) and paleoclimate

Marine invertebrate migration patterns suggest that the North Pole remained warm into the Sepukhovian (Raymond et al., 1990). In the Southern Hemisphere, however, a significant percentage of genera migrated away from the South Pole in the late Visean to Sepukhovian, suggesting South Polar cooling during the Serpukovian (Kelley and Raymond, 1991). A growing

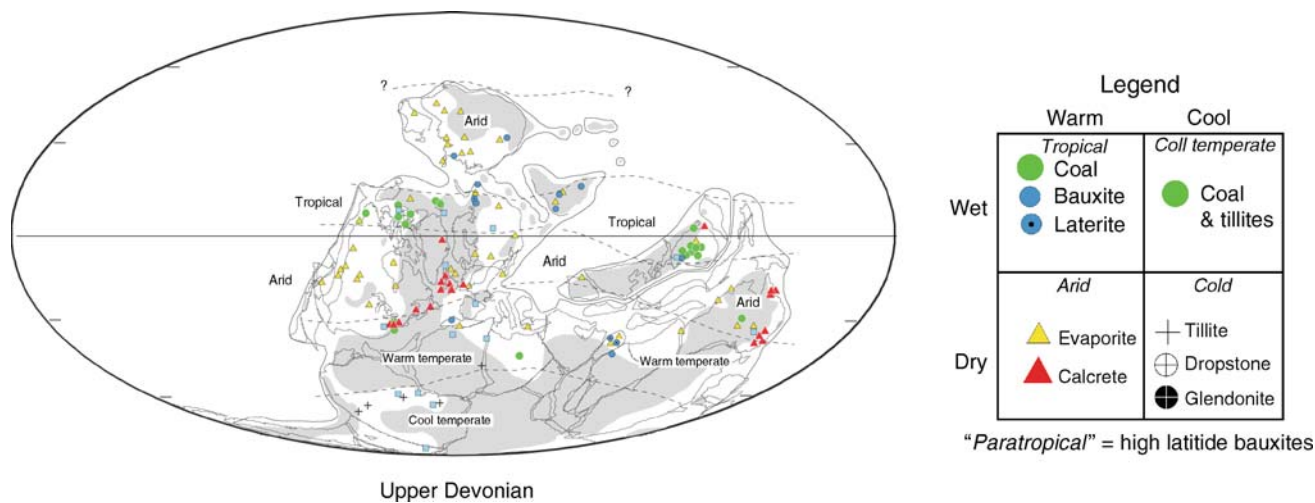


Figure L7 Late Devonian paleogeographic reconstruction showing climate zones and the distribution of sedimentary indicators of Late Devonian climate (based on unpublished data of A. J. Boucot, C. Xu, and C.R. Scotese).

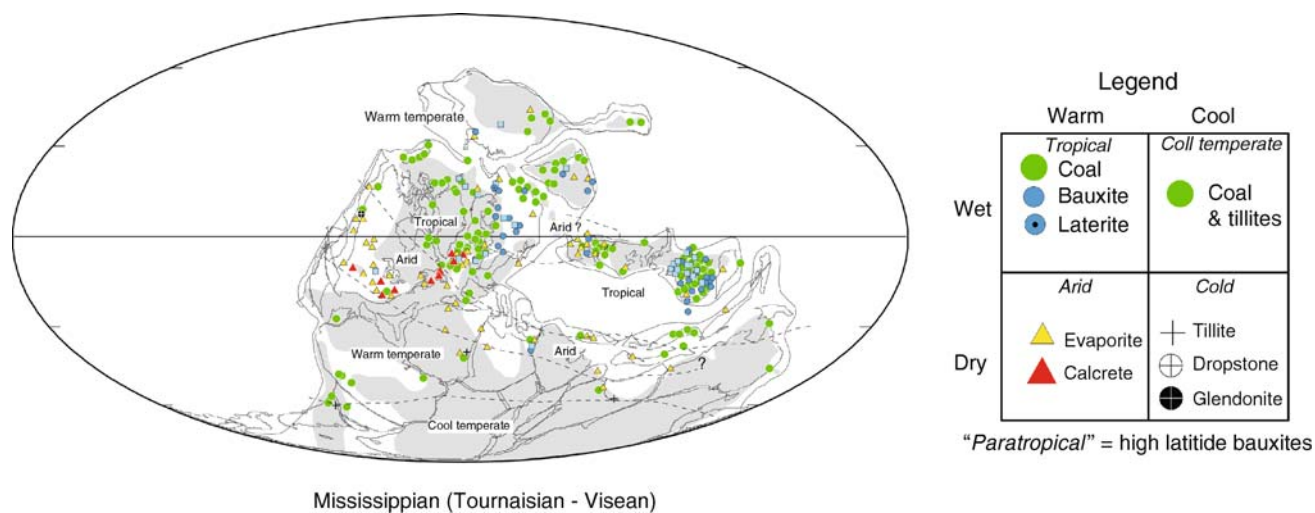


Figure L8 Lower Carboniferous (Mississippian) paleogeographic reconstruction showing climate zones and the distribution of sedimentary indicators of early-middle Mississippian (Tournaisian and Visean) climate (unpublished data, A. J. Boucot, C. Xu, and C. R. Scotese).

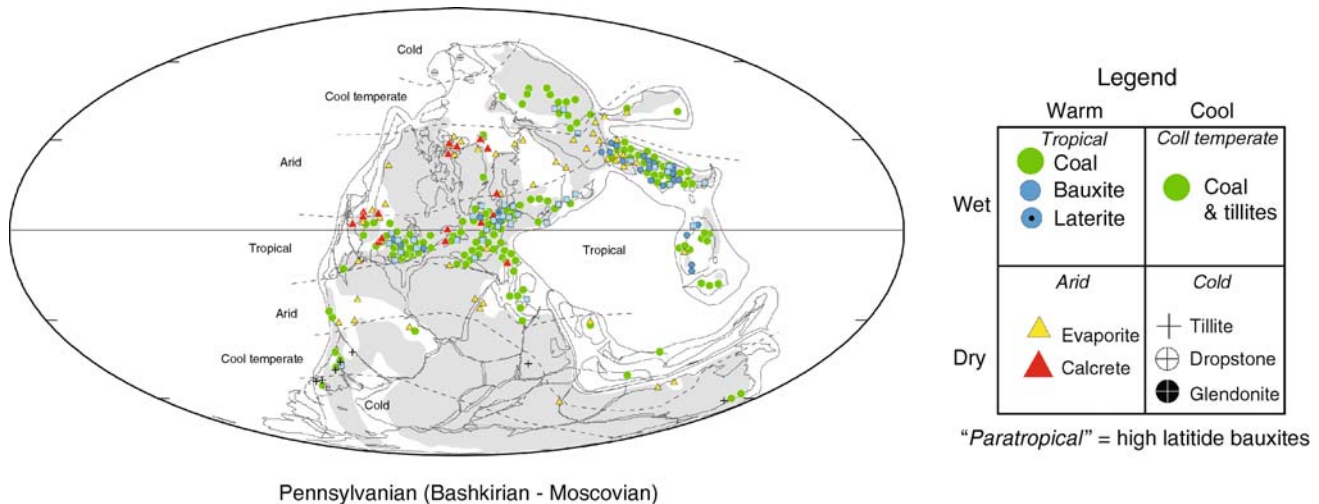


Figure L9 Upper Carboniferous (Pennsylvanian) paleogeographic reconstruction showing climate zones and the distribution of sedimentary indicators of Pennsylvanian climate (unpublished data, A. J. Boucot, C. Xu and C. R. Scotese).

body of evidence suggests that this migration away from the South Pole was related to the onset of significant glaciation in the Southern Hemisphere (Isbell et al., 2003). Global regression in the late Serpukhovian has been linked to the onset of Southern Hemisphere glaciation (Bourotz et al., 1978; Ross and Ross, 1988). Glacial sedimentary deposits of Namurian through earliest Westphalian age occur in South America and Australia (Isbell et al., 2003). In addition, shifts in the isotopic composition ($\delta^{18}\text{O}$ and $\delta^{13}\text{C}$) of marine carbonates from North America, Europe, and the Russian Platform in the Serpukhovian may signal the onset of significant glaciation (Bruckschen et al., 1999; Mii et al., 2001).

Although many lines of evidence suggest that glaciation began in the Serpukhovian, the nature of this glaciation remains uncertain. Isbell et al. (2003) argued that Glacial II sediments resulted from alpine rather than continental glaciation. Others (Veevers and Powell, 1987; Crowell, 1999) argued for continental glaciation during this interval. Resolution of this controversy will require additional data; nonetheless, the biogeographic patterns discussed below indicate that the onset of glaciation in the Serpukhovian had a profound effect on Carboniferous biotas. The biotic response to Serpukhovian glaciation was similar to the biotic response to continental glaciation in the late Tertiary-Recent and very different from the biotic response to Late Devonian glaciation.

The biogeographic differentiation of land plants and marine invertebrates increased dramatically in the early Pennsylvanian (Ziegler et al., 1981). This increase in biogeographic differentiation reflected the biotic response to the establishment of a steep pole-to-equator temperature gradient as a result of glaciation. Crame and Rosen (2002) noted a similar biogeographic response to late Cenozoic glaciation. Late Devonian glaciation occurred during an interval of low biogeographic differentiation, which persisted into the early Mississippian (Raymond and Metz, 2004).

As the poles became frigid, the equatorial climates of the Pennsylvanian became wetter and perhaps warmer as well. Late Visean "equatorial" coal deposits have a broad latitudinal distribution, ranging from 20° S paleolatitude to 30° N paleolatitude on a variety of paleogeographic reconstructions (Raymond, 1996).

A pronounced paleoequatorial coal belt, centered on the paleo-equator, became established in the Serpukhovian and continued throughout the Pennsylvanian and into the Permian (Figures L8–L10). As the equatorial coal belt became established, the diversity of equatorial land plants rose relative to the diversity of mid-latitude and high-latitude land plants (Raymond, 1996). The presence of a pronounced paleoequatorial coal belt and the increased diversity of paleoequatorial land plants during this interval suggest that equatorial climates became wetter during glacial onset. Bande and Prakash (1986) noted a similar increase in the diversity of equatorial land plants between the early and late Cenozoic, which may be tied to late Cenozoic glaciation.

Coal distribution data suggest that the paleo-equator became wetter during glacial onset. Marine invertebrate migration patterns suggest that it may have become warmer as well. A small, but statistically significant percentage of Northern Hemisphere brachiopod genera vacated the equatorial zone in the Serpukhovian by moving their southern boundary away from the equator (Raymond et al., 1989; Raymond et al., 1990). Valentine (1984) noted similar migration patterns for marine invertebrates associated with late Cenozoic glaciation, which he interpreted as evidence for equatorial warming. During Late Devonian glaciation, calcareous foraminifera contracted their ranges toward the pole (Kalvoda, 1986). This migrational pattern is exactly opposite from that of Carboniferous brachiopods and late Tertiary marine invertebrates, and suggests that the low-latitudes became cooler during Late Devonian glaciation.

Ziegler et al. (1987) linked the presence of equatorial coal to cold or glaciated poles. Otto-Bliesner (1993) attributed Pennsylvanian paleoequatorial coal to the orientation and latitudinal placement of the Ouachita and Alleghany Mountains, along an east to west trend, close to the paleo-equator. Paleoclimate models suggested that east-west trending equatorial mountain belts might constrain the position of the inter-tropical convergence zone (the zone of ever-wet, ever-warm climate) to a narrow latitudinal belt, centered on the equator. In the latest Mississippian and early Pennsylvanian, glacial onset and continental collision were so closely spaced in time that it is impossible to distinguish the contribution of mountain building and glaciation from the formation of the paleoequatorial coal belt.

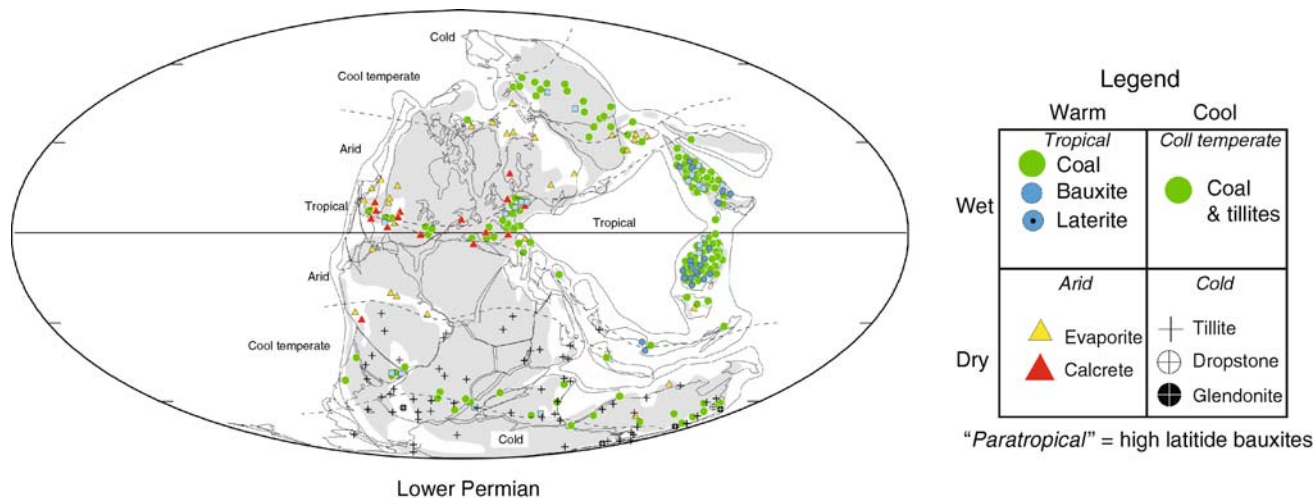


Figure L10 Lower Permian paleogeographic reconstruction showing climate zones and the distribution of sedimentary indicators of early Permian climate (unpublished data, A. J. Boucot, C. Xu, and C.R. Scotese).

The continuity of glaciation during the rest of the Pennsylvanian and into the Permian remains controversial. Isbell et al. (2003) argued for substantially ice-free poles during most of the Westphalian, followed by renewed glaciation in the late Pennsylvanian (Stephanian). Other workers suggested that Gondwana remained glaciated from the Namurian into the Permian and argued for peak glaciation in the Westphalian (Veevers and Powell, 1987; Frakes et al., 1992; Crowell, 1999). Isotopic studies, which suggest warming rather than cooling at the Westphalian/Stephanian boundary (Bruckschen et al., 1999; Mii et al., 2001), appear to contradict Isbell et al. (2003).

The abundance of 4th and 5th order transgressive-regressive cycles, known as cyclothem, in Carboniferous and Permian strata from the Paleo-Northern Hemisphere has been interpreted as evidence for continental glaciation (Ross and Ross, 1988; Heckel, 1994). According to Heckel and others (see Heckel, 1994 and references therein), Milankovitch orbital cycles caused late Paleozoic continental glaciers to advance and retreat, which resulted in the deposition of repeated transgressive-regressive sedimentary cycles in equatorial and low latitudes. Cyclothem are usually linked to continental glaciation because only continental glaciers contain enough water to affect global sea level (Isbell et al., 2003). If cyclothem reflect glacial-eustasy, the presence of Westphalian cyclothem in North America, Europe, the Russian Platform, the Moscow Basin, and the Urals argues for significant Westphalian glaciation. Conversely, Isbell et al. (2003), who felt that the middle and late Westphalian were ice-free, suggested that Carboniferous and Permian cyclothem could have other causes aside from glaciation.

A full understanding of the significance of 4th and 5th order transgressive-regressive cycles known as cyclothem requires more research. The earliest reported cyclothem occur in the early Visean of Great Britain (Wright and Vanstone, 2001), before other signs of significant glaciation, such as increased biogeographic differentiation, the development of the paleoequatorial coal belt, and isotopic shifts indicating global cooling and the growth of glaciers (Bruckschen et al., 1999; Mii et al., 2001; Raymond and Metz, 2004). Some Carboniferous 4th and 5th order transgressive-regressive cycles attributed to glacial-eustasy

may have a different cause. However, glacial-eustasy appears to be a reasonable explanation for repeated 4th and 5th order transgressive-regressive cycles that can be correlated across North America (Heckel, 1994).

Widespread glaciation may have ended in the Middle Permian (Veevers and Powell, 1987; Gibbs et al., 2002; Rees et al., 2002) (Figures L10 and L11). Others (Frakes et al., 1992; Crowell, 1999; Isbell et al., 2003) suggest that Gondwanan glaciers may have persisted to the end of the Permian. Pennsylvanian and Permian marine and terrestrial biotas retained a high amount of biogeographic differentiation, suggesting a relatively steep pole to equator temperature gradient throughout the Pennsylvanian and Permian (Ziegler et al., 1981; Rees et al., 2002). Nonetheless, the presence of fossil forests, reconstructed as cool-temperate deciduous vegetation, in Late Permian sediments from Antarctica, suggests that the Late Permian South Pole was warmer than it was during the Pennsylvanian and Early Permian (Rees et al., 2002). Compared to Pennsylvanian and Early Permian climate, the climate of the Middle and Late Permian was more influenced by monsoonal circulation patterns (Parrish, 1993). As a result, the equatorial zone of the supercontinent Pangea was relatively arid in the Middle and Late Permian and the paleotropical coal belt was confined to island continents, such as South China, which straddled the paleoequator to the east of Pangea at that time.

Summary

In summary, the late Paleozoic was a time of dramatic climatic shifts, punctuated by glaciation events. Clues to these climate changes can be found in sediments, the stable isotopic composition of marine carbonates, and the biogeographic distribution of land plants and marine animals. Late Devonian glaciation (Glacial I of Isbell et al., 2003), which started the interval, appears more similar to Late Ordovician "hot-house" glaciation than subsequent ice-house glaciations in the mid-Carboniferous-to-Permian and late Cenozoic (Raymond and Metz, 2004). The glaciation event that began in the late Serpukhovian or at the Mississippian-Pennsylvanian boundary (Glacial II of Isbell et al., 2003) appears very similar to late Cenozoic glaciation. During both intervals, the poles were cold,

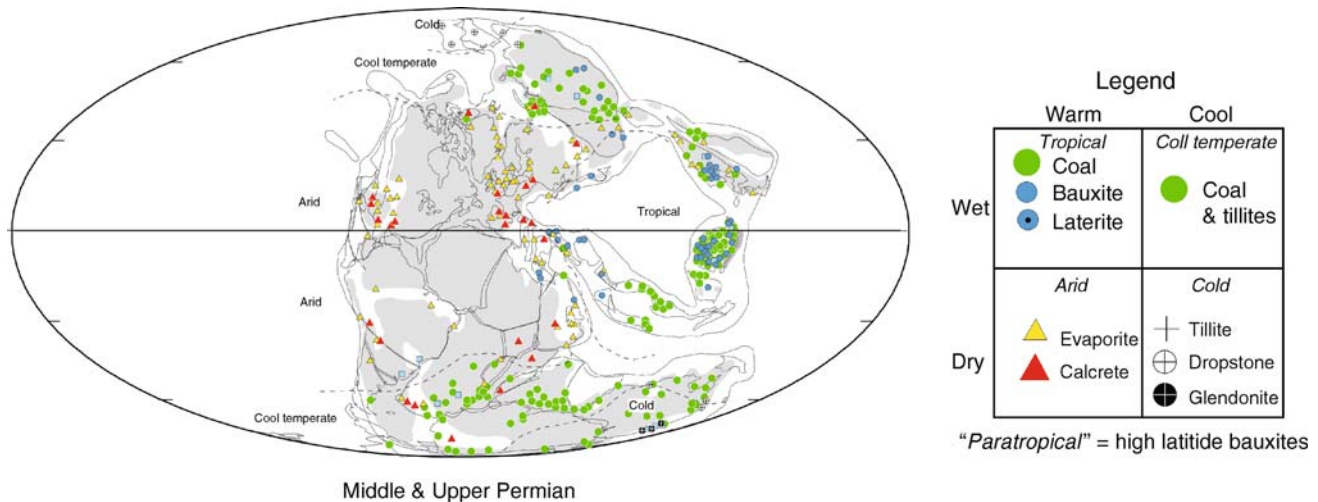


Figure L11 Middle and Upper Permian paleogeographic reconstruction showing climate zones and the distribution of sedimentary indicators of middle and late Permian climate (unpublished data, A. J. Boucot, C. Xu, and C.R. Scotese).

the equator was warm, and there was abundant biogeographic differentiation. Unlike the hot-house glaciations of the Late Ordovician and Late Devonian, Pennsylvanian-Permian glaciation was not marked by mass extinction. Sources differ on the continuity of glaciation in the mid-to-late Pennsylvanian (mid Westphalian through Stephanian) and after the Middle Permian (Veevers and Powell, 1987; Frakes et al., 1992; Bruckschen et al., 1999; Crowell, 1999; Isbell et al., 2003). However, the persistence of biogeographic differentiation throughout the Pennsylvanian to the end of the Permian argues for steep latitudinal temperature gradients, cold poles, and warm, wet equatorial climates until the end of the Paleozoic (Ziegler et al., 1981; Rees et al., 2002).

Anne Raymond and Christopher R. Scotese

Bibliography

- Bande, M.B., and Prakash, U., 1986. The Tertiary flora of Southeast Asia with remarks on its palaeoenvironment and phytogeography of the Indo-Malayan region. *Rev. Palaeobot. Palynol.*, **49**, 203–234.
- Bourot, A., Einor, O.L., Gordon, M., Meyen, S.V., and Wagner, R.H., 1978. Proposals for an international chronostratigraphic classification of the Carboniferous. Huitieme Congres International de Stratigraphie et de Geologie Carbonifere, Compte Rendu, 1, 36–52.
- Bruckschen, P., Oesmann, S., and Veizer, J., 1999. Isotope stratigraphy of the European Carboniferous: Proxy signals for ocean chemistry, climate and tectonics. *Chem. Geol.*, **161**, 127–163.
- Buggisch, W., 1991. The global Frasnian-Famennian 'Kellwasser' Event. *Geologische Rundschau*, **80**, 49–72.
- Caplan, M.L., and Bustin, R.M., 1999. Devonian-Carboniferous Hangenberg mass extinction event, widespread organic-rich mudrock and anoxia: Causes and consequences. *Palaeogeogr. Palaeoclimatol. Palaeoecol.*, **148**, 187–207.
- Crame, J.A., and Rosen, B.R., 2002. Cenozoic palaeogeography and the rise of modern diversity patterns. In Crame, J.A., and Owen, A.W. (eds.), *Palaeobiogeography and Biodiversity Change: The Ordovician and Mesozoic-Cenozoic Radiations*. London: Geological Society of London, pp. 153–168.
- Crowell, J.C., 1999. *Pre-Mesozoic Ice Ages: Their Bearing on Understanding the Climate System*. Boulder, CO: Geological Society of America, pp. 1–106.
- Frakes, L.A., Francis, J.E., and Syktus, J.I., 1992. *Climate Modes of the Phanerozoic*. Cambridge, UK: Cambridge University Press, 274pp.
- Gibbs, M.T., Rees, P.M., Kutzbach, J.E., Ziegler, A.M., Behling, P.J., and Rowley, D.B., 2002. Simulations of Permian climate and comparisons with climate-sensitive sediments. *J. Geol.*, **110**, 33–55.
- Hambrey, M.J., and Harland, W.W., 1981. *Earth's Pre-Pleistocene Glacial Record*. Cambridge, UK: Cambridge University Press, 1004pp.
- Heckel, P.H., 1994. Evaluation of evidence for glacio-eustatic control over marine Pennsylvanian cyclothem in North America and consideration of possible tectonic events. In Dennison, J.M., and Etensohn, F.R. (eds.), *Tectonic and Eustatic Controls on Sedimentary Cycles*. Tulsa, OK: SEPM, pp. 65–88.
- House, M.R., 1985. Correlation of mid-Paleozoic ammonoid evolutionary events with global sedimentary perturbations. *Nature*, **313**, 17–22.
- Iannuzzi, R., and Pfefferkorn, H.W., 2002. A pre-glacial, warm-temperate floral belt in Gondwana (Late Viséan, Early Carboniferous). *Palaios*, **17**, 571–590.
- Isaacson, P.E., Hladil, J., Shen, J.-W., Kalvoda, J., and Grader, G., 1999. Glaciation in South America and marine offlap on other continents. In Feist, R., Talent, J.A., and Daurer, A. (eds.), *Noth Gondwana: Mid-Paleozoic Terranes, Stratigraphy, and Biota*. pp. 239–257.
- Isbell, J.L., Miller, M.E., Wolfe, K.L., and Lenaker, P.A., 2003. Timing of late Paleozoic glaciation in Gondwana: Was glaciation responsible for the development of northern hemisphere cyclothem? In Chan, M.A., and Archer, A.W. (eds.), *Extreme Depositional Environments: Mega end Members in Geologic Time*. Boulder, CO: Geological Society of America, pp. 5–24.
- Kalvoda, J., 1986. Upper Frasnian and lower Tournaisian events and evolution of calcareous foraminifera - close links to climatic changes. In Walliser, O. (ed.), *Global Bio-Events*. Berlin: Springer, pp. 225–236.
- Kelley, P.H., and Raymond, A., 1991. Migration, origination, and extinction of Southern Hemisphere brachiopods during the Middle Carboniferous. *Palaeogeogr. Palaeoclimatol., Palaeoecol.*, **86**, 23–39.
- McGhee, G.R. Jr., 1996. *The Late Devonian Mass Extinction*. New York: Columbia University Press, 303pp.
- Mii, H.-S., Grossman, E.L., Yancey, T.E., Chuvashov, B., and Egorov, A., 2001. Isotopic records of brachiopod shells from the Russian Platform - evidence for the onset of mid-Carboniferous glaciation. *Chem. Geol.*, **175**, 133–147.
- Otto-Bliessner, B., 1993. Tropical mountains and coal formation: A climate model study of the Westphalian (306 MA). *Geophys. Res. Lett.*, **20**, 1947–1950.
- Parrish, J.T., 1993. Climate of the Supercontinent Pangea. *J. Geol.*, **101**, 215–233.
- Raymond, A., 1985. Floral diversity, phytogeography, and climatic amelioration during the Early Carboniferous (Dinantian). *Paleobiology*, **11**, 293–309.
- Raymond, A., 1996. Latitudinal patterns in the diversification of mid-Carboniferous land plants: Climate and the floral break. In Leary,

- R.L. (eds.), *Patterns in Paleobotany: Proceedings of a Czech-U.S. Carboniferous Paleobotany Workshop*. Springfield, IL: Illinois State Museum, pp. 1–18.
- Raymond, A., and Metz, C., 2004. Ice and its consequences: Late Ordovician, Late Devonian, Pennsylvanian-Permian, and Cenozoic glaciation compared. *J. Geol.*, **112**, 655–670.
- Raymond, A., Kelley, P.H., and Lutken, C.B., 1989. Polar glaciers and life at the equator: The history of Dinantian and Namurian (Carboniferous) climate. *Geology*, **17**, 408–411.
- Raymond, A., Kelley, P.H., and Lutken, C.B., 1990. Dead by degrees: Articulate brachiopods, paleoclimate, and the mid-Carboniferous extinction event. *Palaios*, **5**, 111–123.
- Rees, P.M., Ziegler, A.M., Gibbs, M.T., Kutzbach, J.E., Behling, P.J., and Rowley, D.B., 2002. Permian phytogeographic patterns and climates: New data and model comparisons. *J. Geol.*, **110**, 1–31.
- Ross, C.A., and Ross, J.A., 1988. Late Paleozoic transgressive and regressive deposition. In Wilgus, C.K., Hastings, B.S., Kendall, C.G.S.C., Posamentier, H.W., Ross, C.A., and Wagoner, Van J.C. (eds.), *Sea-Level Changes: An Integrated Approach*. Tulsa, OK: Society of Economic Paleontologists and Mineralogists, pp. 227–247.
- Rowley, D.B., Raymond, A., Parrish, J.T., Lottes, A.L., Scotese, C.R., and Ziegler, A.M., 1985. Carboniferous paleogeographic, phytogeographic, and paleoclimatic reconstructions. *Int. J. Coal Geol.*, **5**, 7–42.
- Scrutton, C.T., 1988. Patterns of extinction and survival in Paleozoic corals. In Larwood, G.P. (eds.), *Extinction and Survival in the Fossil Record*. Systematics Association, pp. 65–88.
- Sepkoski, J.J. Jr., 1986. Phanerozoic overview of mass extinctions. In Raup, D.M., and Jablonski, D. (eds.), *Patterns and Processes in the History of Life*. Berlin: Springer, pp. 277–295.
- Streel, M., Caputo, M.V., Loboziak, S., and Melo, J.H.G., 2000. Late-Frasnian-Famennian climates based on palynomorph analysis and the question of Late Devonian glaciations. *Earth Sci. Rev.*, **52**, 121–173.
- Valdes, P.J., 2000. Warm climate forcing mechanisms. In Huber, B.T., Macleod, K.G., and Wing, S.L. (eds.), *Warm Climates in Earth History*. Cambridge, UK: Cambridge University Press, pp. 3–20.
- Valentine, J.W., 1984. Neogene marine climate trends: Implications for biogeography and evolution of shallow-sea biota. *Geology*, **12**, 647–650.
- Veevers, J.J., and Powell, C.M., 1987. Late Paleozoic glacial episodes in Gondwanaland reflected in transgressive-regressive depositional sequences in Euramerica. *GSA Bull.*, **98**, 475–487.
- Witzke, B.J., 1990. Paleoclimates in Laurentia and Euramerica. In McKerrow, W.S., and Scotese, C.R. (eds.), *Paleozoic Palaeogeography and Biogeography*. Bath, UK: Geological Society of London, pp. 57–73.
- Wright, V.P., and Vanstone, S.D., 2001. Onset of Late Paleozoic glacio-eustasy and the evolving climates of low latitude areas: A synthesis of current understanding. *J. Geol. Soc. (Lond.)*, **158**, 579–582.
- Zachos, J., Pagani, M., Sloan, L., Thomas, E., and Billups, K., 2001. Trends, rhythms, and aberrations in global climate 65 Ma to present. *Science*, **292**, 686–693.
- Ziegler, A.M., Bambach, R.K., Parrish, J.T., Barrett, S.F., Gierlowski, E.H., Parker, W.C., Raymond, A., and Sepkoski, J.J.J., 1981. Paleozoic biogeography and climatology. In Niklas, K.J. (eds.), *Paleobotany, Paleocology, and Evolution*. New York: Praeger, pp. 231–266.
- Ziegler, A.M., Raymond, A.L., Gierlowski, T.C., Horrell, M.A., Rowley, D.B., and Lottes, A.L., 1987. Coal, climate and terrestrial productivity: The present and early Cretaceous compared. In Scott, A.C. (eds.), *Coal and Coal-Bearing Strata: Recent Advances*. London: Geological Society, pp. 25–49.

Cross-references

Animal Proxies, Invertebrates
 Coal Beds, Origin and Climate
 Cyclic Sedimentation (Cyclothem)
 Early Paleozoic Climates (Cambrian-Devonian)
 Glacial Eustasy
 Glaciations, Pre-Quaternary
 “Greenhouse” (warm) Climates
 “Icehouse” (cold) Climates
 Mass Extinctions: Role of Climate

Paleobotany
 Plate Tectonics and Climate Change
 Sedimentary Indicators of Climate Change
 Stable Isotope Analysis

LATE QUATERNARY MEGAFLOODS

The last major deglaciation of planet Earth (the last portion of Marine Isotope Stage 2, from about 20,000 to 11,000 calendar years ago) involved huge fluxes of water from the wasting continental ice sheets. It has become increasingly apparent that much of this water was delivered as floods of immense magnitude and relatively short duration. These late Quaternary megafloods had short-term peak flows, comparable in discharge to the more prolonged fluxes of ocean currents (The unit of discharge for both ocean currents and megafloods is the Sverdrup, equivalent to 1 million cubic meters per second). Some outburst floods likely induced very rapid, short-term effects on Quaternary climates. The late Quaternary superfloods also greatly altered drainage evolution and the planetary patterns of water and sediment movement to the oceans.

Historical context

During the eighteenth and early nineteenth centuries there were many studies of landscape phenomena that posited the action of phenomenally large floods. Some of these studies invoked a kind of biblical catastrophism, but other studies merely employed hypotheses of immense floods because these phenomena seemed to provide the best explanations for such features as scoured bedrock and accumulations of huge, water-transported boulders. Unfortunately, a logically flawed doctrine of uniformitarianism was promoted in the later eighteenth century (Baker, 1998), effectively retarding progress on understanding the role of cataclysmic flooding in Quaternary processes. The renaissance in catastrophic flood studies of the later twentieth century was made possible because of a long-lasting controversy over the origin of the Channeled Scabland in the northwestern United States. Extending from the 1920s to the 1960s, the great “scablands debate” eventually led to general acceptance of the cataclysmic flood origin that was championed by J Harlan Bretz, a professor at the University of Chicago.

Based on Bretz’s studies of the Channeled Scabland, the distinctive erosional and depositional features of cataclysmic flooding are well known. These include scabland bedrock erosion (Figure L12), streamlining of residual uplands, large-scale scour around obstacles, depositional bars, giant current ripples (fluvial gravel dunes), and huge sediment fans. These features can be identified by orbital remote sensing imagery and by field reconnaissance. These features could be used to discover and document cataclysmic flood effects on more river basins globally.

Megaflood landscapes

Cordilleran

The Channeled Scabland landscape developed south of the Cordilleran Ice Sheet, in the northwestern United States. The Purcell Lobe of the ice sheet extended south from British Columbia to the basin of modern Pend Oreille Lake in northern Idaho. It thereby impounded the Clark Fork River drainage to



Figure L12 Aerial view of giant potholes and butte-and-basin scabland eroded into the basalt bedrock of eastern Washington by the cataclysmic Missoula megafloods, approximately 15,000 years ago. These potholes measure about 15 m in depth and 40 in width. They are in Lenore Canyon, a part of the lower Grand Coulee. Lake Lenore is visible at the upper right.

the east, forming glacial Lake Missoula in western Montana. At maximum extent, this ice-dammed lake held a water volume of about 2,500 km³ with a depth of 600 m at the dam. Repeated failures through subglacial tunnels are inferred to have occurred between about 18,000 and 15,000 years ago (Waitt, 1985). However, these multiple outburst events were of greatly differing magnitudes. About 15 events exceeded 3 Sverdrups, and at least one of these reached about 10 Sverdrups in discharge (Benito and O'Connor, 2003). The largest failure or failures probably involved a different source mechanism than that envisioned by Waitt (1985).

Upon reaching the Pacific Ocean, the Missoula floodwaters continued flowing down the continental slope as hyperpycnally-generated turbidity currents (Normark and Reid, 2003). The sediment-charged floodwaters followed the Cascadia submarine channel into and through the Blanco Fracture Zone and out onto the abyssal plain of the Pacific. As much as 5,000 km³ of sediment may have been carried and distributed as turbidites over a distance of 2,000 km west of the Columbia River mouth.

Laurentide

As the Laurentide Ice Sheet of central and eastern Canada retreated from its late Quaternary maximum extent, it was bounded to the south and west by immense meltwater lakes, which developed in the troughs that surrounded the ice. As the lake levels rose, water was released as great megafloods, which carved numerous spillways into the drainages of the Mississippi, St. Lawrence, and Mackenzie Rivers (Kehew and Teller, 1994). The greatest megafloods developed from the last of the ice-marginal lakes, a union between Lake Agassiz in south-central Canada and Lake Ojibway in northern Ontario. The resulting megalake held about 160,000 km³ of water, which was released subglacially about 8,400 years ago, under the ice sheet and into the Labrador Sea via the Hudson Strait (Clarke et al., 2003).

Eurasian spillways

In the 1970s, Mikhail G. Grosswald recognized that the late Quaternary ice-sheet margins of northern Eurasia, like those

of northern North America, held huge proglacial lakes, and great spillways that developed for the diversion of drainage. Not only was meltwater diverted to the south-flowing Dnieper and Volga Rivers, but the great north-flowing Siberian rivers, the Irtysh, Ob, and Yenesei were impounded by ice sheets that covered the modern Barents and Kara Seas. Though Grosswald's reconstructions created considerable controversy, recent work shows that these impoundments did indeed occur. However, the largest diversions are now dated to about 90,000 years ago, when ice-sheet growth was enhanced by the climatic influence of the ice-dammed lakes (Krinner et al., 2004). The largest megalake, Lake Mansi, drained southward through the Turgai divide of north-central Kazakhstan to the basin of the modern Aral Sea. The Aral, in turn, drained through a spillway at its southwestern end into the Caspian, which expanded to a late Quaternary size over twice its modern extent, known as the Khvalyn paleolake. The Khvalyn paleolake spilled westward through the Manych spillway into the Don valley, then to the Sea of Azov, and through the Kerch Strait to the Euxine Abyssal Plain (the floor of the modern Black Sea). The huge size of the Manych spillway, up to 35 km wide, implies that flows may have reached a peak of 10 Sverdrups (Baker, 1996). During the last glaciation, the Black Sea was isolated from the Mediterranean Ocean, and it filled with fresh water derived from the great system of glacially augmented rivers entering it from the north. The freshwater faunal facies of the Black Sea show that the Caspian was spilling through the Manych spillway around 18,000 years ago and the Black Sea was spilling into the Sea of Marmara, which, in turn, spilled via the Hellespont into the Aegean Sea.

Central Asian uplands

A number of cataclysmic flood landscapes are now recognized in the mountain areas of central Asia. The best studied of these regions is the Altai Mountains of south-central Siberia (Carling et al., 2002). The Altai flooding derived from the Chuja-Kuray ice-dammed lake, which may have held as much as 1,000 km³ of water at a maximum depth of up to 900 m (Baker et al., 1993). Downstream of this ice dam, the Chuja and Katun River valleys are characterized by immense gravel bars, emplaced into various valley-side embayments by the flooding. The bars are up to 5 km long and 120 m in height. The bar surfaces and associated run-up layers of flood-transported gravel indicate maximum flow depths of about 320 m. Flow modeling of the associated paleoflood discharges retrodicts a peak flow of about 11 Sverdrups and mean flow velocities of about 30 m s⁻¹ (Herget and Agatz, 2003).

Another region with extensive evidence of late Quaternary megafloods is Tuva. The Tuvan paleofloods derived from an ice-dammed lake in the Darkhat depression of north-central Mongolia (Grosswald and Rudoy, 1996). The paleolake held about 250 km³ of water with a depth of 200 m at its ice dam. The paleoflooding entered the upper Yenesei River, and it was remarkable for the emplacement of spectacular trains of giant current ripples (gravel dunes) near the Tuva capital city of Kyzyl (Figure L13).

In Kirgizstan, Lake Issyk-Kul, the world's second largest modern mountain lake, was transformed into an even larger ice-dammed lake during the last glaciation. Iceberg-emplaced landforms rise to 300 m above the present lake level (Grosswald et al., 1994). Spectacular erosion at the full-glacial lake outlet, Boam Canyon, indicates that the paleolake failed by cataclysmic outburst flooding. This flood emplaced an enormous outwash fan, extending 85 km from the mouth of Boam

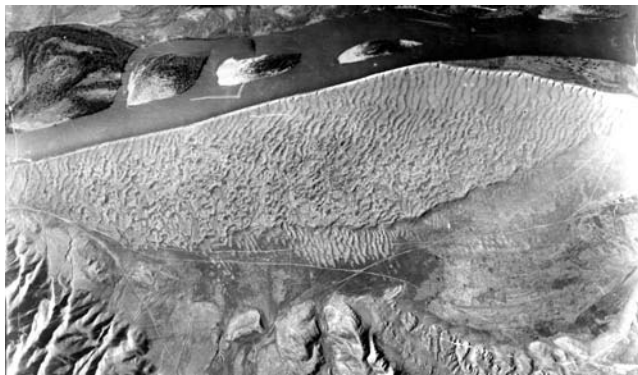


Figure L13 Aerial photograph of giant current ripples (gravel dunes) located near Kyzyl, Tuva. The ripples occur on a gravel bar just north of the Yenesei River (bottom of photograph) about 25 km southwest of Kyzyl. There are nearly 100 ripples on a bar 6 km in length. Ripple heights vary from 2 to 3 m. The photograph shows an area 6 by 4 kilometers. The paleoflood flow was moving from right (east) to left (west).

Canyon. A similar but smaller fan occurs on the upper Yenesei River, where the Tuvan floods emerged from canyons of the West Sayan Mountains and entered the Abakan Basin. Another area of probable glacial cataclysmic flooding is Lake Baikal, which may have expanded during full-glacial periods by ice blockage of its outlet, thereby raising its level of spill points.

Current controversies

Black Sea flooding

Although late Quaternary freshwater inundation of the Black Sea is well recognized, it is usually correlated with enhanced proglacial meltwater flow via the many rivers draining southward from the northern Eurasian ice sheets, as noted above. A recent controversy has arisen, however, over the marine influx to the Black Sea that occurred during rising Holocene sea level. This influx caused Mediterranean water to spill through the Hellespont and Bosphorus, reaching the Black Sea about 9,500 years ago. One view (Ryan et al., 2003) holds that the global ocean rose to the level of a relatively shallow sill of the Bosphorus outlet and catastrophically spilled into the Black Sea basin, which then was partly filled with freshwater to a level about 85 m below that of today. The resulting cataclysmic inundation presumably displaced a large human population in a calamity that is equated to the Noachian flood myth. An alternative view is that much of the Bosphorus is underlain by freshwater facies of late Pleistocene age, derived from the Black Sea. The minimal erosion of these sediments is not consistent with the idea that cataclysmic flooding led to the overlying Holocene marine facies of Mediterranean origin.

Subglacial megafloods

A variety of enigmatic landforms, involving water erosion and deposition, develop beneath very large continental ice sheets. These landforms include drumlins, Rogen moraines, large-scale bedrock erosional marks, and tunnel channels (valleys). Though commonly explained by subglacial ice deformational processes, the genesis of these features cannot be observed in modern glaciers that are much smaller than their late Quaternary counterparts. The assemblage of landforms as part of an erosional/depositional

sequence beneath continental ice sheets that precedes regional ice stagnation and esker formation was explained by Shaw (1996) as resulting from a phase of immense subglacial sheet floods, which, in turn, follow ice-sheet advances that terminate with surging, stagnation and melt-out. Shaw (1996) proposed that peak discharges of tens of Sverdrups are implied by the late Quaternary subglacial landscapes of the southern Laurentide Ice Sheet. Shoemaker (1995) provided some theoretical support for Shaw's model, though at smaller flow magnitude levels.

Global consequences

Ocean currents are integral to Earth's climate engine, distributing heat between the equator and the poles. For example, the Gulf Stream flows at discharges of up to 100 Sverdrups, involving relatively slow moving water 1 km in depth and 50–75 km wide. As this seawater evaporates and becomes more saline, it increases in density, eventually sinking in the northern Atlantic. This process forms a portion of the great thermohaline circulation, which acts as a conveyor belt for heat in the oceans. Cataclysmic megafloods can introduce relatively low-density, freshwater lids over large areas of ocean surface. Freshwater can enter the oceans very rapidly, at flow rates of up to 10 Sverdrups and volumes of thousands of km³. The resulting disruption of sea-surface temperatures and density structure can drastically alter climates, at least on time scales of decades to centuries.

The connections between Pleistocene ice sheets and the oceans are still very poorly understood. An important link is inferred from relatively brief (100- and 500-year) intervals in which thick marine layers of ice-rafted material were widely distributed across the North Atlantic. Called "Heinrich events," these layers are thought to record episodes of massive iceberg discharge from unstable ice sheets. The youngest Heinrich events date to 17,000 (H1), 24,000 (H2) and 31,000 (H3) years ago. Closely related is the Younger Dryas (YD) event, a global cooling at 12,000 years ago, which is also associated with North Atlantic ice-rafted rock fragments. There is evidence from corals in Barbados that sea level rose spectacularly, about 20 m during H1 and about 15 m just after YD. Such rises would require short-term freshwater fluxes to the oceans of about 14,000 and 9,000 km³ yr⁻¹, respectively. (Fairbanks, 1989). These events are thought to relate to ice-sheet collapse, reorganization of ocean-atmosphere circulation, and release of subglacial and proglacial meltwater, most likely during episodes of cataclysmic megaflooding.

Victor R. Baker

Bibliography

- Baker, V.R., 1996. Megafloods and glaciation. In Martini, I.P. (eds.), *Late Glacial and Postglacial Environmental Changes*. New York: Oxford University Press, pp. 98–108.
- Baker, V.R., 1998. Catastrophism and uniformitarianism: Logical roots and current relevance. In Blundell, D.J., and Scott, A.C. (eds.), No. 143, *Lyell: The Past is the Key to the Present*. London: Geological Society Special Publications, pp. 171–182.
- Baker, V.R., Benito, G., and Rudoy, A.N., 1993. Paleohydrology of late Pleistocene superflooding, Altai Mountains, Siberia. *Science*, **259**, 348–350.
- Benito, B., and O'Connor, J.E., 2003. Number and size of last-glacial Missoula floods in the Columbia River valley between Pasco Basin, Washington and Portland, Oregon. *Geol. Soc. Am. Bull.*, **115**, 624–638.

- Carling, P.A., Kirkbride, A.D., Parnachov, S., Borodavko, P.S., and Berger, G.W., 2002. Late Quaternary catastrophic flooding in the Altai Mountains of south-central Siberia: A synoptic overview and introduction to flood deposit sedimentology. In Martini, I.P., Baker, V.R., and Garzon, G. (eds.), *Flood and Megaflood Processes and Deposits: Recent and Ancient Examples*. International Association of Sedimentologists, Special Publication No. 32, pp. 17–35.
- Clarke, G., Leverington, D., Teller, J., and Dyke, A., 2003. Superlakes, megafloods, and abrupt climate change. *Science*, **301**, 922–923.
- Fairbanks, R.G., 1989. A 17,000-year glacio-eustatic sea level record: Influence of glacial melting rates on the Younger Dryas event and deep ocean circulation. *Nature*, **342**, 631–642.
- Grosswald, M.G., and Rudoy, A.N., 1996. Quaternary glacier-dammed lakes in the mountains of Siberia. *Polar Geogr.*, **20**, 180–198.
- Grosswald, M.G., Kuhle, M., and Fastook, J.L., 1994. Wurm glaciation of Lake Issyk-Kul area, Tian Shan Mts: A case study in glacial history of central Asia. *Geojournal*, **33**, 273–310.
- Herget, J., and Agatz, H., 2003. Modelling ice-dammed lake outburst floods in the Altai Mountains (Siberia) with HEC-RAS. In Thorndycraft, V.R., Benito, G., Barriendos, M. and Llasat, M.S. (eds.), *Palaeofloods, Historical Data and Climatic Variability: Applications in Flood Risk Assessment*. Madrid, Proceedings of the PHEFRA Workshop, Centro de Ciencias Medioambientales, pp. 177–181.
- Kehew, A.E., and Teller, J.T., 1994. History of the late glacial runoff along the southwestern margin of the Laurentide Ice Sheet. *Quaternary Sci. Rev.*, **13**, 859–877.
- Krinner, G., Mangerud, J., Jakobsson, M., Crucifix, M., Ritz, C., and Svendsen, J.I., 2004. Enhanced ice sheet growth in Eurasia owing to adjacent ice-dammed lakes. *Nature*, **427**, 429–432.
- Normark, W.R., and Reid, J.A., 2003. Extensive deposits on the Pacific Plate from Late Pleistocene North-American glacial lake bursts. *J. Geol.*, **111**, 617–637.
- Ryan, W.B.F., Major, C.O., Lericolais, G., and Goldstein, S.L., 2003. Catastrophic flooding of the Black Sea. *Annu. Rev. Earth Planet. Sci.*, **31**, 525–554.
- Shaw, J., 1996. A meltwater model for Laurentide subglacial landscapes. In McCann, S.B., and Ford, D.C. (eds.), *Geomorphology sans Frontières*. New York: Wiley, pp. 182–226.
- Shoemaker, E.M., 1995. On the meltwater genesis of drumlins. *Boreas*, **24**, 3–10.
- Watt, R.B. Jr., 1985. Case for periodic, colossal jokulhlaups from Pleistocene glacial Lake Missoula. *Geol. Soc. Am. Bull.*, **96**, 1271–1286.

Cross-references

[Cordilleran Ice Sheet](#)
[Drumlins](#)
[Glacial Geomorphology](#)
[Glacial Megalakes](#)
[Heinrich Events](#)
[Last Glacial Termination](#)
[Laurentide Ice Sheet](#)
[Proglacial Lacustrine Sediments](#)
[Thermohaline Circulation](#)
[Younger Dryas](#)

LATE QUATERNARY-HOLOCENE VEGETATION MODELING

Introduction

Vegetation modeling is central to understanding the role that plants have played in shaping the Earth's atmospheric composition and climate in the past, and the potential responses and feedbacks of vegetation to future climate changes. Over the past decade, a series of global vegetation models have been applied to the subject of late Quaternary and Holocene climate change. Because a vegetation model provides a complete

picture of the Earth's land surface, and because it produces a diagnostic that can be directly compared to paleo-observations (e.g., plant assemblages), vegetation models have been particularly useful for evaluating the output of general circulation models (GCMs). Progress in vegetation modeling has enabled the researcher to simulate vegetation patterns with more detail, and to evaluate other variables with paleoproxies, such as dust fluxes, methane emissions, and carbon storage. Current directions in late Quaternary and Holocene vegetation modeling include the incorporation of a vegetation model directly into the land surface scheme of GCMs so that vegetation may interact in real time with the climate system through the atmosphere and oceans.

Over the past decade, a variety of process-based, global vegetation models have been developed to study a variety of problems in biogeography, biogeochemistry, and atmospheric composition. These models have been primarily applied to the present-day, but are increasingly being used to study the recent geological past. For paleo-applications, global vegetation models play an important role, because other methods of inferring past vegetation patterns and processes leave the investigator with information gaps, either spatially, temporally, or both. Paleoproxy data from a variety of sources (e.g., pollen, packrat middens) can be used to infer vegetation history and biogeography at a point, but extrapolation is difficult given the sensitivity of vegetation to climatic and edaphic factors beyond the catchment area of the pollen source. The composition of trace gases measured in gas bubbles from ice cores contains some signal of the biogeochemical processes active in the terrestrial biosphere, such as vegetation productivity, methane emissions from wetlands, and compounds produced during biomass burning. However, these ice core records integrate the climatic or environmental signals over entire hemispheres, and thus provide little information about their spatial distribution, which is important in understanding the influence of the biosphere on the climate system and interactions between vegetation and the animal world. Furthermore, the land surface signal in ice cores must often be separated from oceanic activity. For some radiatively important trace gases, including CO₂, this is a difficult task. Thus, to study late Quaternary and Holocene vegetation history, a global vegetation model is an essential tool: as an integrator over both space and time and as a method to estimate the contribution of the land surface to the budgets of greenhouse gases, an important quantity not only at present but also in the past.

Vegetation model structure and processes

The past decade has seen great progress in the development and application of global vegetation models. The latest vegetation models incorporate both biogeographical and biogeochemical processes to simulate vegetation distribution and the fluxes of carbon, water, nutrients, and other trace gases through the terrestrial biosphere. This capability makes current vegetation models a powerful tool for investigating the Earth's surface during the late Quaternary and Holocene, as a variety of problems may be addressed.

Methods

The Plant Functional Type (PFT) is the basic unit of calculation in most global-scale vegetation models. Each PFT is defined to be a generic representation of all plant taxa that share specific characteristics such as growth form (e.g., tree or grass), phenological habit (e.g., deciduous or evergreen; summergreen or raingreen), leaf morphology (e.g., broadleaf or needleleaf),

and other parameters such as root depth distribution and maximum photosynthetic rate. At the computational core of a vegetation model is a scheme that determines the combination of PFTs that make up the vegetation at a certain location. PFT combinations are often combined into assemblages, termed “biomes”; these biomes represent the major vegetation types found on earth (Table L2).

The simplest form of vegetation model (e.g., BIOME1; Prentice et al., 1992) uses a set of rules based on absolute bioclimatic limits to determine the presence or absence of PFTs and then assigns a biome based on a simple hierarchy of these PFTs. More advanced vegetation models, e.g., BIOME4 (Kaplan, 2001), use a coupled carbon and water flux scheme to determine the leaf area index (LAI) that maximizes net primary productivity (NPP) for any given PFT. The PFT hierarchy, and thus the resulting biome, is determined by the list of PFTs ranked by LAI and NPP. Additional rules or climate-based indices may also be used to further refine the biome classification. An advantage of this type of coupled biogeography-biogeochemistry model is that both vegetation structure and the impact of vegetation on global biogeochemistry may be simultaneously investigated. Finally, dynamic vegetation models, e.g., LPJ or IBIS, explicitly simulate the competition among PFTs as they evolve through time.

In the most recent global vegetation models (e.g., BIOME4, LPJ), model operation is based on 12 or 13 PFTs representing physiologically distinct classes from arctic/alpine cushion forbs to tropical evergreen trees. Each PFT is assigned bioclimatic limits that determine whether its net primary productivity (NPP) is calculated for a given grid cell.

Table L2 Biomes simulated by BIOME4

Tropical forests

Tropical evergreen broadleaf forest
Tropical semi-evergreen forest
Tropical deciduous broadleaf forest and woodland

Temperate forests

Temperate deciduous broadleaf forest
Temperate evergreen needleleaf forest
Warm-temperate evergreen broadleaf and mixed forest
Cool mixed forest
Cool evergreen needleleaf forest
Cool-temperate evergreen needleleaf and mixed forest

Cold forests

Cold evergreen forest
Cold deciduous forest

Forest, Shrub and Grassland combinations

Tropical savanna
Tropical xerophytic shrubland
Temperate xerophytic shrubland
Temperate sclerophyll woodland and shrubland
Temperate deciduous broadleaf savanna
Temperate evergreen needleleaf open woodland
Cold parkland

Grassland

Tropical grassland
Temperate grassland

Tundra

Graminoid and forb tundra
Low- and high-shrub tundra
Erect dwarf-shrub tundra
Prostrate dwarf-shrub tundra
Cushion-forb, lichen, and moss tundra

Sparse or no vegetation

Desert

Equilibrium versus dynamic global vegetation models

Despite the recent focus on developing dynamic global vegetation models (DGVMs) for carbon cycle research (Cox et al., 2000; Sitch et al., 2003), equilibrium vegetation models that provide a “snapshot” view of the Earth’s surface at a given time remain important for late Quaternary and Holocene vegetation modeling. Equilibrium vegetation models are currently far more detailed and precise than DGVMs in their ability to simulate biogeographic patterns. Additionally, operation of a DGVM requires 10 to 100 times more overhead than an equilibrium vegetation model in terms of the size of input and output datasets and computing power. As such, a DGVM is neither necessary nor appropriate for addressing every research problem. Equilibrium vegetation models provide an efficient method to investigate global ecosystem theory and a required test-bed for developing methods for simulating the behavior of vegetation that may later be applied in a DGVM context. A DGVM is required to study periods of rapidly changing climate where ecosystem “memory” is important, e.g., biogeochemical feedbacks in the anthropogenically-modified environment of the present and the near future. Equilibrium models are more suited to “time slice” analyses where an equilibrium approximation is adequate and interest focuses on regional phenomena that are not as well simulated with current DGVMs.

On time scales greater than ca. 10^2 years, vegetation dynamics are controlled by two main factors: shifts in absolute limits of tolerance for certain plant types and competition among coexisting plant taxa due to shifts in disturbance regime or optimum climate. Thus, most modeling to date for late Quaternary and Holocene studies focuses on simulating the potential, natural equilibrium vegetation at an instant in time (i.e., a time slice). A major reason for choosing time slices for vegetation reconstructions is that paleodata have been assembled for particular time slices, which may be used to evaluate the performance of the model. Furthermore, the computational requirements of producing a time slice simulation of vegetation are much simpler than for a dynamic scenario.

Paleovegetation simulation

For simulation of vegetation of the past, a vegetation model requires paleoclimatology data, which are usually generated from one or an ensemble of paleoclimate simulations from a GCM. Vegetation models can be coupled to the GCM climatology in a variety of ways (Figure L14). In the simplest case, the vegetation model is run “offline” through one-way forward coupling to the GCM climatology. This method has the advantage of being computationally efficient and enables a great deal of flexibility in the choice of GCM output and particular vegetation model used.

To investigate certain phenomena where particular feedbacks between the terrestrial biosphere and the climate system are thought to be important, forms of coupling that are more complicated have been applied. Asynchronous coupling uses a GCM simulation to drive an offline vegetation model, which then provides the land surface conditions (primarily the distribution of the major biomes) to make a subsequent run of the GCM. After three or four iterations, the GCM climatology is usually in equilibrium with the vegetation model. Asynchronous coupling is particularly useful for simulating long-timescale climate changes, such as those that occur on millennial scales, and has been successfully applied to the problem of glacial inception and late Pleistocene deglaciation. Finally, a vegetation model

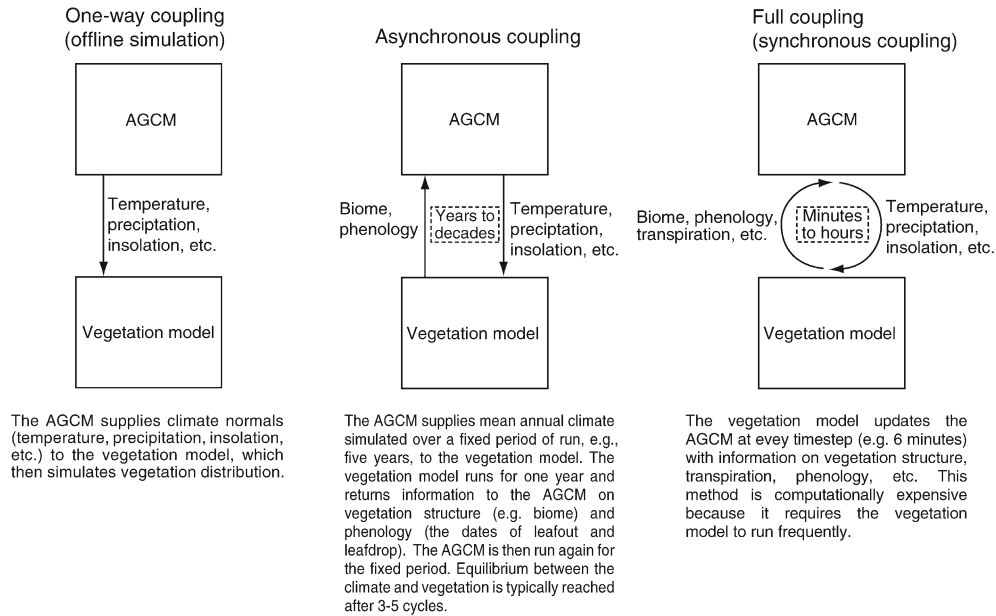


Figure L14 Types of atmosphere model (AGCM)-vegetation model coupling.

with prognostic biogeography may be fully incorporated within the land surface scheme of a GCM. This is the most computationally expensive method of making paleovegetation simulations and has been applied much less often than the other methods. The vegetation model is coded directly into the land surface scheme of the GCM, and vegetation dynamics are typically updated on an annual time-step. This configuration is particularly useful for studying rapid climate changes where changes in land surface conditions are suspected to have had a strong physical or biogeochemical feedback to the climate system. Such situations are frequent in the paleorecord, but uncertainties about the external forcing that drives the rapid climate change event have limited the application of such coupled models. Moreover, the biogeography component of a coupled atmosphere-vegetation GCM is usually a very small part of the total computational demand of the model; coupled atmosphere-vegetation models could be applied more widely.

Except in the case of fully coupled vegetation atmosphere models, paleovegetation simulation typically involves the preparation of an anomaly climatology, where the GCM paleoclimate simulation is subtracted from a control run simulation for the GCM. These anomalies are then applied to a gridded dataset of present-day observed climatology. The anomaly technique is used to avoid biases inherent in the GCM's control climatology, which is often in disagreement with observed climatology over large regions. The anomaly technique also offers a degree of standardization among GCM climatologies when it is desired to analyze the differences in the major features of the climate simulated by different GCMs.

Vegetation history

Most late Quaternary and Holocene vegetation modeling has focused on two key times in the past: the Last Glacial Maximum (LGM, ca, 21 ka) and the mid-Holocene (ca 6 ka; Figure L15). These two periods have been a major focus for paleoclimate simulations (e.g., Jousaume and Taylor, 1995;

Jousaume and Taylor, 2000; Kohfeld and Harrison, 2000) because they represent two extremes in climate forcing. At the LGM, the Earth's orbital configuration was fairly similar to today but greenhouse gas concentrations were low (Raynaud et al., 1993), Northern Hemisphere ice sheets were expanded (Denton and Hughes, 1981), and sea level was therefore lower (Fairbanks, 1989). In addition to the large changes in terrestrial geography, the ocean surface was significantly colder and the distribution of sea ice was expanded (CLIMAP, 1981). The configuration of the Earth's orbit around the Sun was, however, substantially different to that of today (and the LGM) during the early to mid-Holocene. The phasing of the precession (23 kyr) and obliquity (41 kyr) cycles of the orbit were such that the high latitudes of the Northern Hemisphere received a maximum in insolation (incoming solar radiation), both during boreal summer and annually, at ca. 11,000 calendar yBP. This anomaly decayed gradually towards the present. As a direct result of the changes in orbital forcing, many regions of the Arctic experienced summer temperatures considerably higher than at present during the early Holocene (see e.g., Ritchie et al., 1983; Bradley, 2000; MacDonald et al., 2000; Elias, 2001). Increased heating of the northern continents also influenced tropical climates; paleodata indicate that much wetter conditions existed in the Sahara and in south Asia in the early to mid-Holocene as compared to the present. However, at the time of the Northern Hemisphere insolation maximum, the Laurentide Ice Sheet, although substantially reduced from the LGM, was still sufficiently large to have a major downwind cooling effect (Mitchell et al., 1988; Harrison et al., 1992). Northern Europe and eastern North America therefore experienced a thermal maximum several thousand years after the insolation maximum (Wright et al., 1993). For this reason, investigations of the impact of insolation changes on climate have conventionally focused on 6,000 yBP, when the difference in orbital configuration was still large but the impact of the residual Laurentide Ice Sheet was small and essentially local.

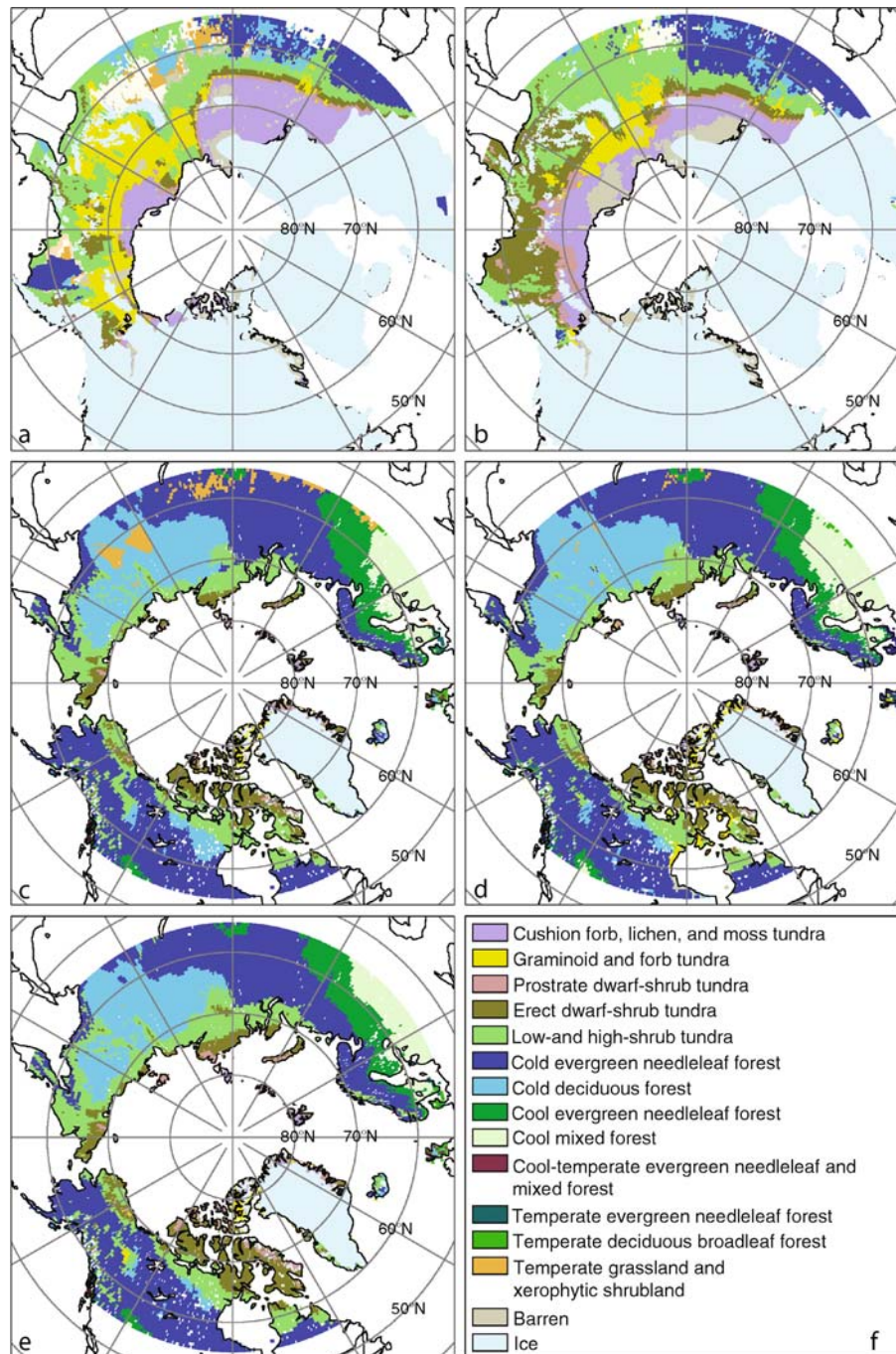


Figure L15 Paleovegetation simulations for the late Quaternary and Holocene. Offline simulation of the biomes of the Northern Hemisphere north of 55° N simulated by BIOME4: for the LGM using AGCM output from the (a) MRI2 and (b) LMDH models; for 6 ka using AOGCM output from (c) IPSL-CM1 and (d) HADCM2 models; and (e) for the present-day potential natural state using observed, gridded climatology; (f) legend for all panels. For a further explanation of these experiments see Kaplan et al. (2003).

The Last Glacial Maximum

A wide range of vegetation modeling has been performed for the LGM. This research has been motivated by the desire to understand the effect of the radically different climate on the Earth's surface at present. Major climate-driven changes in

the Earth's vegetation have implications for climate feedbacks, the distribution of animals and humans, and for the behavior of the biogeochemical Earth system. Studies in LGM vegetation modeling qualitatively describe changes in biogeography, the physiological effects of climate and low CO₂ levels on

vegetation structure and composition, implications of carbon storage on the global carbon cycle, and sources of radiatively active aerosols and trace gases. While most studies used simple one-way vegetation simulations based on a GCM climatology, a few studies have used asynchronous or fully interactive coupling between vegetation and atmosphere to investigate the role of vegetation in shaping the glacial climate. Finally, one study uses a vegetation model in “inverse” mode to estimate changes in climate variables using observed paleovegetation. This method allows accounting for the effect of CO₂ concentration on the observed vegetation.

Biogeography. LGM vegetation was dominated by grasses and shrubland in the tropics, tundra, and deserts in higher latitudes. The area of forest biomes was reduced as compared to present levels on all continents. Low CO₂ concentrations contributed to the expansion of C₄ grasses. The vegetation models simulate large, continuous areas of rainforest in the Amazon lowlands and on the exposed Sunda shelf, but do not display a high degree of fragmentation in rainforest biomes as has been suggested by some interpretations of the paleodata. Despite using an anomaly-based technique for developing the paleoclimate, the models are still somewhat sensitive to the GCM-simulated paleoclimate. No analog biomes – notably graminoid and forb tundra in the Arctic – are widespread, and the potential for more to appear is possible especially if they were defined in the models (Prentice et al., 1993; Kaplan et al., 2003).

Biogeography/plant physiology. Model simulations of LGM vegetation have been used to illustrate the effect of low CO₂ concentrations on vegetation structure and plant physiology. Jolly and Haxeltine (1997) showed that LAI and vegetation productivity in the mountains of tropical Africa result in the simulation of shrub and grassland and biomes in areas that might otherwise climatically support forests. These results indicate that attempts to use observed paleovegetation assemblages to reconstruct climate may be wrong if the direct effect of changes in atmospheric CO₂ concentrations on the vegetation was not taken into account. Furthermore, the low CO₂ concentrations may be responsible for thinner forests, such as the observed forest-parklands of North America that were abundant at the LGM but have no modern analog (Cowling, 1999).

Carbon storage/carbon cycle. A great deal of vegetation modeling has been done to estimate the role of the terrestrial biosphere in long-term oscillations in the global carbon cycle (Friedlingstein et al., 1992; Friedlingstein et al., 1995; François et al., 1999; François et al., 2000; Kaplan et al., 2002; Otto et al., 2002). All modeling studies indicate that the land biosphere stored considerably less carbon at the LGM as compared to the present; models predict a reduction in carbon storage from 200 to 1,000 Pg C. The general reduction in forest area, expansion of tundra and desert, and the effect of low atmospheric CO₂ concentrations on ecosystems were the main reasons for the reduction in carbon storage. In any reconciliation of the global glacial carbon budget, the low LGM terrestrial carbon storage must be accounted for with increases in carbon stored in the oceans.

Dust sources. Ice core measurements indicate that atmospheric dust concentrations at the LGM were up to 20 times greater than at present. These dramatic increases may be due to changes in climate and land surface conditions. A modeling study (Harrison et al., 2001) found that dust sources are highly sensitive to land surface conditions, where potential as a dust source increases exponentially as vegetation cover becomes sparser. Under LGM conditions, the vegetation model indicates

that large areas of the land surface were covered by very sparse vegetation or were completely barren, conditions ideal for dust deflation. The effect of the cold climate and low CO₂ concentrations on terrestrial vegetation may have increased global atmospheric dust loading significantly, with further feedbacks to the climate system through direct radiative effects and the export of nutrients to the ocean.

Methane. In contrast to the pattern shown in the dust record, atmospheric methane concentrations were less than half of those measured in the late Holocene, before strong anthropogenic influence. Earlier studies hypothesized that the reduction in atmospheric methane concentrations could be due to a reduction in global wetland area and productivity (Chappellaz et al., 1993). However, a detailed vegetation model study (Kaplan, 2002) demonstrated that wetland area did not change significantly between the LGM and the pre-industrial period, and therefore the reduction in methane source from wetlands was probably not responsible for the majority of the observed reduction in atmospheric methane concentrations. Lower vegetation productivity was responsible for a ca. 20% reduction in the wetland methane source. This conclusion remains robust even when the vegetation/wetland-methane model is driven by a number of different GCMs, each of which exhibited a wide range of change in global and regional climates in the LGM paleoclimate simulation (Pinot et al., 1999).

Asynchronous coupled modeling. Initial evaluation of vegetation model output from one-way coupling experiments regarding a GCM paleoclimate simulation indicated that in some areas, simulated vegetation could not be corroborated by paleovegetation observations. This was particularly true for the mid-latitude zone of unglaciated Eurasia, where vegetation models overpredicted the amount of forest. Asynchronous coupling of a vegetation model to an atmosphere model (Kubatzki and Claussen, 1998) improved on the result of the vegetation simulation, particularly in Siberia where the inclusion of vegetation-snow-albedo interaction proved to be the key in reducing forest area in the model results. The study also showed that vegetation-atmosphere interactions through albedo effects were important in other areas: a “bright” parameterization for the initial albedo of deserts resulted in the simulation of extensive subtropical deserts worldwide, whereas a “darker” model for desert albedo led to extensive colonization of the glacial western Sahara by plants and an intensification of the monsoon over India.

Interactive coupled modeling. A fully coupled atmosphere-vegetation model study of the LGM resulted in similar conclusions, most notably that the biophysical effect of changing vegetation cover resulted in grasslands and tundra largely replacing forests in Eurasia (Levis et al., 1999). This coupled model study had the benefit of being able to investigate the effect of the change in CO₂ concentrations on leaf stomatal conductance. Physiological studies have shown that plants at low ambient CO₂ concentrations and under well-watered conditions will lose more water for a given unit carbon gain; over large scales this could have an effect on atmospheric humidity and regional hydrology. Further sensitivity studies established that the effect of low CO₂ concentrations manifest themselves in the climate system much more strongly through direct changes in vegetation cover and density rather than through this potential enhancement in vegetation transpiration.

Inverse modeling. Guiot et al. (1999) used the novel technique of applying a vegetation model in inverse mode to investigate the changes in two climate variables (temperature of the

coldest month and total annual precipitation) given an observed vegetation distribution. By using a process-based vegetation model instead of the traditional response surface or regression methods for determining climate variables from observed vegetation, the authors were able to account for the changes in vegetation structure due to low CO₂ concentrations that have no modern analog. Applied to the Mediterranean basin and Eurasia, the technique showed that many GCMs might underestimate the extent of cooling and drying in the LGM climate.

The mid-Holocene

While climate change between the mid-Holocene and present was considerably smaller than the LGM-present difference, a decade of paleoclimate simulation work indicates that capturing these subtle changes in a climate model probably requires interactive simulation of the atmosphere with the land surface. Vegetation modeling efforts for the mid-Holocene have focused on land surface changes in the Sahara and the circumpolar north, where the expansion of vegetation as indicated by paleodata was greatest. Both of these regions have been shown to have important biophysical feedbacks to the climate system and the observed extent of vegetation change cannot usually be reproduced without some form of interactive coupling between the land surface and the atmosphere. In the case of the Sahara, even the most sophisticated coupled models still fail to reproduce the observed extent of vegetation change. Global vegetation response to mid-Holocene climate also has implications for the carbon cycle and the global budgets of radiatively active trace gases.

Biogeography. Initial simulations of mid-Holocene vegetation were performed in an offline experiment with paleoclimate simulation from the CCM1 GCM using prescribed present-day sea surface temperatures and preindustrial CO₂ concentrations (Prentice et al., 1998). These vegetation simulations were evaluated for Europe, where a dense network of paleodata allowed detailed model-data intercomparisons. Results indicated that the model could capture only few of the major vegetation changes observed in the data. The simulation did agree with data in that forest cover extended further north and to higher elevations as compared to the present, and excluded boreal conifers from central and eastern Europe. But the model simulation generally disagreed with observations, importantly in not simulating the observed extent of vegetation change in southern Europe and the extent of temperate forest types in the Fennoscandia, and by simulating a greatly expanded area of steppe in southeastern Europe that is not observed in the paleoecological record. In a series of similar offline experiments, Harrison et al. (1998) further demonstrated an ensemble of vegetation model simulations for the mid-Holocene driven by ten different GCMs showed quantitatively similar vegetation changes in the intertropical zone and the northern and southern extratropics, with drier equatorial forests and an increase in vegetation cover in the subtropical desert regions, and an expansion of forests to the north. An underestimate, relative to paleodata observations, of the magnitude of subtropical vegetation change was also a feature common to all models. The small differences among models were related to the simulation of features in the regional climate. Another recent study used a coupled atmosphere-ocean GCM with an offline vegetation model that focused specifically on vegetation change in northern latitudes of the Northern Hemisphere (Kaplan et al., 2003). This study found that both simulated and observed changes at the northern forest limit were small, but that significant changes probably occurred in the type

of tundra covering the area north of the forest boundary. While most vegetation models treat tundra as a single vegetation class with uniform physical properties, this study emphasized that the height, density, and phenology of tundra vegetation may be as important as the forest-tundra boundary itself as a biophysical feedback to the atmosphere. All of these uncoupled offline experiments emphasized the need for interactive coupling, both between the atmosphere and oceans and the atmosphere and land surface, to reproduce realistically the climate and vegetation of the mid-Holocene.

Biogeography / carbon storage. Another offline vegetation modeling study (Foley, 1994) attempted to estimate the change in global terrestrial carbon storage at the mid-Holocene compared with the present, taking into account the changes in vegetation distribution under a simulated mid-Holocene climate. Though significant changes in global biogeography were simulated in this experiment, including the northward expansion of the northern limit of forests and the expansion of grasslands area in the Sahara desert, the patterns were not in particularly good agreement with the paleobotanical record. Regionally, NPP and vegetation carbon storage increased significantly (up to 15%), but global carbon storage did not change significantly between the simulated present and mid-Holocene conditions.

Asynchronous coupling. In an effort to better capture the climate and biogeography of the mid-Holocene, a series of experiments used the asynchronous coupling technique (Kutzbach et al., 1996a; Kutzbach et al., 1996b; Texier et al., 1997; de Noblet-Ducoudré et al., 2000). All of these studies focused on the areas of greatest climate and vegetation change since the mid-Holocene, i.e., the Sahara region and the northern forest-tundra boundary. Texier et al. (1997) found that after the fourth iteration of an asynchronous coupling, global tundra area was reduced by 25% and the savanna-desert boundary in west Africa shifted 2.5 degrees north, as compared to the present. Finally, de Noblet-Ducoudré et al. (2000) concluded that vegetation conditions in the Sahara were dependent on both sea surface temperature and the simulation of atmospheric circulation, and that the observed changes in vegetation distribution could not be explained by including vegetation feedback alone. While no asynchronous coupling experiment was fully successful in reproducing the observed conditions of vegetation at the mid-Holocene, these experiments did show that interaction between the land surface and the atmosphere had an important influence on mid-Holocene climate.

Interactive coupling. Two recent studies used fully coupled atmosphere-vegetation models to study the mid-Holocene climate and biogeography (Ganopolski et al., 1998; Doherty et al., 2000). Doherty et al. (2000) showed that vegetation-atmosphere feedbacks had the effect of not only modifying the climate over the Sahara in general, but also the seasonal pattern of rainfall in North Africa, particularly by extending the length of the rainy season. This had the effect of producing an increase in vegetation over the Sahara region, but was still not consistent with the vegetation change observed in the data. A limitation of this study was that it used a GCM with fixed, present-day sea surface temperatures. Ganopolski et al. (1998) used an Earth system model of intermediate complexity (EMIC) to perform a study of mid-Holocene climate and vegetation that included fully coupled atmosphere, ocean, sea ice, and vegetation components at coarse spatial resolution. While analysis was possible only over large regions, the results indicated that ocean circulation, sea ice, and vegetation feedbacks were important controls on high latitude vegetation at the mid-Holocene. Alternatively, the response of North African climate was dominated by the land

surface feedback alone. Both studies showed importantly that only with the complex interaction of atmosphere and land surface can we begin to approach a realistic simulation of mid-Holocene climate and vegetation.

Conclusions

Late Quaternary and Holocene vegetation modeling experiments have, for the first time, allowed a complete picture of the Earth's land surface in the past to be presented in a systematic way. These experiments have also provided an important evaluation of climate model output, through the ability to make quantitative comparison of simulated to observed vegetation from proxy data. These model-data intercomparisons have highlighted deficiencies in both climate and vegetation models and led to improvements in modeling technique and a general trend towards full integration of vegetation models within GCMs. As both GCMs and vegetation models improve, we may expect to see more realistic paleoclimate simulations, and a clearer picture of the face of the Earth. These vegetation simulations will also see a wide range of new application to problems in archaeology and anthropology, biogeochemistry, and climate change research, all of which will present a clearer picture of the behavior of the earth system and help researchers reach a better understanding of the potential for future climate change.

Jed O. Kaplan

Bibliography

- Bradley, R.S., 2000. Past global changes and their significance for the future. *Quaternary Sci. Rev.*, **19**, 391–402.
- Chappellaz, J.A., Fung, I.Y., and Thompson, A.M., 1993. The atmospheric CH₄ increase since the Last Glacial Maximum (1). Source estimates. *Tellus*, **B 45**, 228–241.
- CLIMAP, 1981. *Seasonal Reconstructions of the Earth's Surface at the Glacial Maximum*. Boulder, CO: Geological Society of America.
- Cowling, S.A., 1999. Simulated effects of low atmospheric CO₂ on structure and composition of North American vegetation at the Last Glacial Maximum. *Glob. Ecol. Biogeogr.*, **8**, 81–93.
- Cox, P.M., Betts, R.A., Jones, C.D., Spall, S.A., and Totterdell, I.J., 2000. Acceleration of global warming due to carbon-cycle feedbacks in a coupled climate model. *Nature*, **408**, 184–187.
- de Noblet-Ducoudré, N., Claussen, R., and Prentice, C., 2000. Mid-Holocene greening of the Sahara: First results of the GAIM 6000 year BP Experiment with two asynchronously coupled atmosphere/biome models. *Clim. Dyn.*, **16**, 643–659.
- Denton, G.H., and Hughes, T.J., 1981. *The Last Great Ice Sheets*. New York: Wiley.
- Doherty, R., Kutzbach, J., Foley, J., and Pollard, D., 2000. Fully coupled climate/dynamical vegetation model simulations over northern Africa during the mid-Holocene. *Clim. Dyn.*, **16**, 561–573.
- Elias, S.A., 2001. Mutual climatic range reconstructions of seasonal temperatures based on Late Pleistocene fossil beetle assemblages in Eastern Beringia. *Quaternary Sci. Rev.*, **20**, 77–91.
- Fairbanks, R.G., 1989. A 17,000-year glacio-eustatic sea level record: Influence of glacial melting rates on the younger dryas event and deep-ocean circulation. *Nature*, **342**, 637–642.
- Foley, J.A., 1994. The sensitivity of the terrestrial biosphere to climatic change: A simulation of the middle Holocene. *Global Biogeochem. Cycles*, **8**, 505–525.
- François, L., Kaplan, J., Otto, D., Roelandt, C., Harrison, S.P., Prentice, I.C., Wamant, P., and Ramstein, G., 2000. Comparison of vegetation distributions and terrestrial carbon budgets reconstructed for the Last Glacial Maximum with several biosphere models. In Braconnot, P. (ed.), *Paleoclimate Modeling Intercomparison Project (PMIP)*. Canada: La Huardière, WMO/WCRP, WCRP-111, pp. 141–145.
- François, L.M., Goddérès, Y., Wamant, P., Ramstein, G., de Noblet, N., and Lorenz, S., 1999. Carbon stocks and isotopic budgets of the terrestrial biosphere at mid-Holocene and Last Glacial Maximum times. *Chem. Geol.*, **159**, 163–189.
- Friedlingstein, P., Delire, C., Muller, J.F. and Gerard, J.C., 1992. The climate induced variation of the continental biosphere - a model simulation of the Last Glacial Maximum. *Geophys. Res. Lett.*, **19**, 897–900.
- Friedlingstein, P., Prentice, K.C., Fung, I.Y., John, J.G., and Brasseur, G.P., 1995. Carbon-biosphere-climate interactions in the last glacial maximum climate. *J. Geophys. Res.-Atmos.*, **100**, 7203–7221.
- Ganopolski, A., Kubatzki, C., Claussen, M., Brovkin, V., and Petoukhov, V., 1998. The influence of vegetation-atmosphere-ocean interaction on climate during the mid-Holocene. *Science*, **280**, 1916–1919.
- Guiot, J., Torre, F., Cheddadi, R., Peyron, O., Tarasov, P., Jolly, D., and Kaplan, J.O., 1999. The climate of the Mediterranean basin and of Eurasia of the Last Glacial Maximum as reconstructed by inverse vegetation modelling and pollen data. *Ecologia mediterranea*, **25**, 193–204.
- Harrison, S.P., Kutzbach, J.E., and Behling, P., 1992. General circulation models, paleoclimatic data and last interglacial climates. *Quaternary Int.*, **10–12**, 231–242.
- Harrison, S.P., Jolly, D., Laarif, F., Abe-Ouchi, A., Dong, B., Herterich, K., Hewitt, C., Joussaume, S., Kutzbach, J.E., Mitchell, J., de Noblet, N., and Valdes, P., 1998. Intercomparison of simulated global vegetation distributions in response to 6 kyr BP orbital forcing. *J. Clim.*, **11**, 2721–2742.
- Harrison, S.P., Kohfeld, K.E., Roelandt, C., and Claquin, T., 2001. The role of dust in climate changes today, at the Last Glacial Maximum and in the future. *Earth-Sci. Rev.*, **54**, 43–80.
- Jolly, D. and Haxeltine, A., 1997. Effect of low glacial atmospheric CO₂ on tropical African montane vegetation. *Science*, **276**, 786–788.
- Joussaume, S., and Taylor, K.E., 1995. Status of the Paleoclimate Modeling Intercomparison Project (PMIP). In Gates, W.L. (ed.), *Proceedings of the First International AMIP Scientific Conference, May 15–19, 1995*. Monterey, CA: WMO/WCRP, WCRP 92, WMO/TD-No. 732, pp. 425–430.
- Joussaume, S., and Taylor, K.E., 2000. The paleoclimate modeling intercomparison project. In Braconnot, P. (ed.), *Paleoclimate Modeling Intercomparison Project (PMIP)*. La Huardière, Canada: WMO/WCRP, WCRP-111, WMO/TD-No. 1007, pp. 9–24.
- Kaplan, J.O., 2001. *Geophysical Applications of Vegetation Modeling*. Ph.D. Thesis. Lund: Lund University, 132pp.
- Kaplan, J.O., 2002. Wetlands at the Last Glacial Maximum: Distribution and methane emissions. *Geophys. Res. Lett.*, **29**, 3.1–3.4.
- Kaplan, J.O., Prentice, I.C., Knorr, W., and Valdes, P.J., 2002. Modeling the dynamics of terrestrial carbon storage since the Last Glacial Maximum. *Geophys. Res. Lett.*, **29**, 31.1–31.4.
- Kaplan, J.O., Bigelow, N.H., Bartlein, P.J., Christensen, T.R., Cramer, W., Harrison, S.P., Matveyeva, N.V., McGuire, A.D., Murray, D.F., Prentice, I.C., Razzhivin, V.Y., Smith, B., Walker, D.A., Anderson, P.M., Andreev, A.A., Brubaker, L.B., Edwards, M.E., and Lozhkin, A.V., 2003. Climate change and Arctic ecosystems: 2. Modeling, paleodata-model comparisons, and future projections. *J. Geophys. Res.-Atmos.*, **108**, (D19), 8171, doi:10.1029/2002JD002559.
- Kohfeld, K.E., and Harrison, S.P., 2000. How well can we simulate past climates? Evaluating the models using global palaeoenvironmental datasets. *Quaternary Sci. Rev.*, **19**, 321–346.
- Kubatzki, C., and Claussen, M., 1998. Simulation of the global biogeophysical interactions during the last glacial maximum. *Clim. Dyn.*, **14**, 461–471.
- Kutzbach, J., Bonan, G., Foley, J., and Harrison, S.P., 1996a. Vegetation and soil feedbacks on the response of the African monsoon to orbital forcing in the early to middle Holocene. *Nature*, **384**, 623–626.
- Kutzbach, J.E., Bartlein, P.J., Foley, J.A., Harrison, S.P., Hostetler, S.W., Liu, Z., Prentice, I.C., and Webb III, T., 1996b. Potential role of vegetation feedback in the climate sensitivity of high-latitude regions: A case study at 6000 years BP. *Global Biogeochem. Cycles*, **10**, 727–736.
- Levis, S., Foley, J.A., and Pollard, D., 1999. Potential high-latitude vegetation feedbacks on CO₂-induced climate change. *Geophys. Res. Lett.*, **26**, 747–750.
- MacDonald, G.M., Velichko, A.A., Kremenetski, C.V., Borisova, O.K., Goleva, A.A., Andreev, A.A., Cwynar, L.C., Riding, R.T., Forman, S.L., Edwards, T.W.D., Aravena, R., Hammarlund, D., Szeicz, J.M., and Gattaulin, V.N., 2000. Holocene treeline history and climate change across northern Eurasia. *Quaternary Res.*, **53**, 302–311.
- Mitchell, J.F.B., Grahame, N.S., and Needham, K.J., 1988. Climate simulations for 9000 years before present: seasonal variations and effect of the Laurentide ice sheet. *J. Geophys. Res.-Atmos.*, **93**, 8283–8303.

- Otto, D., Rasse, D., Kaplan, J., Warnant, P., and Francois, L., 2002. Biospheric carbon stocks reconstructed at the Last Glacial Maximum: comparison between general circulation models using prescribed and computed sea surface temperatures. *Glob. Planet. Change*, **33**, 117–138.
- Pinot, S., Ramstein, G., Harrison, S.P., Prentice, I.C., Guiot, J., Stute, M., Jousaume, S., and PMIP participating groups, 1999. Tropical paleoclimates at the Last Glacial Maximum: comparison of Paleoclimate Modeling Intercomparison Project (PMIP) simulations and paleodata. *Clim. Dyn.*, **15**, 857–874.
- Prentice, I.C., Cramer, W., Harrison, S.P., Leemans, R., Monserud, R.A., and Solomon, A.M., 1992. A global biome model based on plant physiology and dominance, soil properties and climate. *J. Biogeogr.*, **19**, 117–134.
- Prentice, I.C., Sykes, M.T., Lautenschlager, M., Harrison, S.P., Denissenko, O., and Bartlein, P.J., 1993. Modelling global vegetation patterns and terrestrial carbon storage at the last glacial maximum. *Glob. Ecol. Biogeogr.*, **3**, 67–76.
- Prentice, I.C., Harrison, S.P., Jolly, D., and Guiot, J., 1998. The climate and biomes of Europe at 6000 yr BP: Comparison of model simulations and pollen-based reconstructions. *Quaternary Sci. Rev.*, **17**, 659–668.
- Raynaud, D., Jouzel, J., Barnola, J.M., Chappellaz, J., Delmas, R.J., and Lorius, C., 1993. The ice record of greenhouse gases. *Science*, **259**, 926–934.
- Ritchie, J.C., Cwynar, L.C., and Spear, R.W., 1983. Evidence from northwest Canada for an early Holocene Milankovitch thermal maximum. *Nature*, **305**, 126–128.
- Sitch, S., Smith, B., Prentice, I.C., Arneth, A., Bondeau, A., Cramer, W., Kaplan, J.O., Levis, S., Lucht, W., Sykes, M.T., Thonicke, K., and Venevsky, S., 2003. Evaluation of ecosystem dynamics, plant geography and terrestrial carbon cycling in the LPJ dynamic global vegetation model. *Glob. Change Biol.*, **9**, 161–185.
- Texier, D., de Noblet, N., Harrison, S.P., Haxeltine, A., Jolly, D., Jousaume, S., Laarif, F., Prentice, I.C., and Tarasov, P., 1997. Quantifying the role of biosphere-atmosphere feedbacks in climate change: coupled model simulations for 6000 years BP and comparison with palaeodata for northern Eurasia and northern Africa. *Clim. Dyn.*, **13**, 865–882.
- Wright, H.E. Jr., Kutzbach, J.E., Webb, T., III, Ruddiman, W.F., Street-Perrott, F.A., and Bartlein, P.J., 1993. *Global Climates since the Last Glacial Maximum*. Minneapolis, MN: University of Minnesota Press, 569pp.

Cross-references

[Holocene Climates](#)
[Hypsithermal](#)
[Last Glacial Maximum](#)
[Paleoclimate Modeling, Quaternary](#)
[Pleistocene Climates](#)
[Quaternary Vegetation Distribution](#)

LATERITE

Laterite is an iron-rich, sub-aerial, weathering product, commonly believed to evolve as a result of intense, in situ substrate alteration under tropical or sub-tropical climatic conditions. It comprises an important subset of a wider range of ferruginous and related aluminous (i.e., bauxitic) weathering products, which include ferricretes and various iron-rich paleosols. Laterite weathering profiles often develop an indurated surface layer of resistant duricrust, forming laterally extensive sheets ca. 1–20 m in thickness (Figure L16). These lateritized surfaces are both chemically and physically resistant and may extend over areas of a few, to hundreds, or even thousands, of square kilometers.

Historical background and definitions

The term laterite (literally “brick rock”) was first used by Buchanan (1807) to describe a naturally occurring material from



Figure L16 Laterite profile (ca. 40 m) exposed at the edge of a mesa (i.e., table-land) at Panchgani (17°55'N, 73°48'E), Maharashtra, India. Mechanically resistant upper layers of the laterite profile typically form a protective capping overlying less altered materials below, producing a characteristic cliff-like morphology.

Angadipuram (10°58'N, 76°13'E), Kerala state, south-western India. Once cut and allowed to harden, laterite was used as building material (Figure L17). Since this first description, the term has had a long history of geological and geomorphological usage. However, the unfortunate early adoption of Buchanan's casual field description as a type definition has since caused considerable confusion. A more comprehensive and geologically rigorous description was provided by Newbold (1844) from studies of laterite-capped plateaux near Bidar, India (17°54'N, 77°32'E). He was the first to suggest that laterite developed in situ (in this instance upon Deccan flood basalt lavas), by segregation and subsequent rearrangement of minerals and elements that originally comprised the parent rock (Newbold, 1846). Despite this attempt to better define laterite and the lateritization process, the term “laterite” (sensu lato) was used throughout the nineteenth and twentieth centuries to describe a wide range of iron-rich, terrigenous weathering products and duricrusts. Unfortunately, many of these materials were often products of fundamentally different element enrichment and depletion processes (Schellmann, 1986; Ollier and Galloway, 1990; Bourman and Ollier, 2002; Schellmann, 2003).

Modern field studies make evident that the majority of examples of iron-rich duricrust typically occur as two genetically

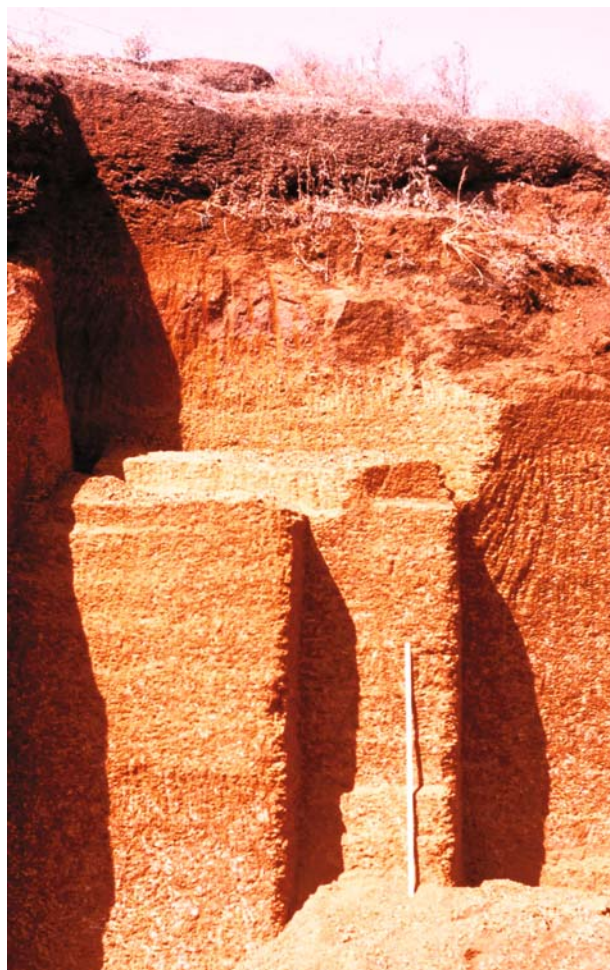


Figure L17 Laterite quarrying at Bidar, India, showing recently cut sections (with 1 meter scale rule) where material from the upper parts of the profile (Zone IV) has been extracted for laterite bricks. Bidar localities were used by Newbold (1846) to argue for laterite as an “in situ” (i.e., autochthonous) weathering product.

distinct types. Aleva (1994) distinguishes between *laterites*, which attain elevated iron contents entirely through autochthonous residual enrichment within the weathering profile (i.e., no net input of iron), and *ferricretes*, in which an absolute iron enrichment occurs (i.e., alteration profiles that receive an allochthonous net input of iron). This division represents a useful process-based distinction, but the practicality of determining allochthony or autochthony of the iron component is often problematic (e.g., Thomas, 1994). In practice, many lateritic weathering profiles are modified by the introduction of allochthonous materials. For instance, many elements (e.g., Fe, Al and some trace metals) can be introduced either in solution or as chelates by groundwaters passing through the evolving weathering profile. These elements can then be re-deposited at specific levels within the profile by redox reactions associated with variations in groundwater chemistry and water table fluctuation. Alternatively, allochthonous material (e.g., eolian dust) may also be introduced by mechanical accumulation through the exposed surface of the profile (e.g., Chadwick et al.,

Table L3 Geochemical analysis of the Bidar weathering profile illustrated in Figure L18

Sample	BB1	BB3	BB5	BB8	BB9
<i>Major elements (wt%)</i>					
SiO ₂	48.90	38.59	30.61	31.35	9.59
TiO ₂	2.16	5.11	5.76	2.33	2.03
Al ₂ O ₃	13.72	31.54	25.83	27.22	9.85
Fe ₂ O ₃	13.40	24.10	36.95	38.37	77.53
MnO	0.19	0.11	0.06	0.07	0.23
MgO	6.93	0.40	0.23	0.10	0.16
CaO	10.99	0.19	0.07	0.00	0.04
Na ₂ O	2.46	0.00	0.00	0.00	0.00
K ₂ O	0.16	0.02	0.02	0.07	0.03
P ₂ O ₅	0.16	0.18	0.08	0.08	0.12
<i>Total</i>	<i>99.07</i>	<i>100.25</i>	<i>99.61</i>	<i>99.59</i>	<i>99.58</i>
(LOI)	0.60	11.74	11.11	11.13	7.31
<i>Trace elements (ppm)</i>					
Ba	52.9	54.9	13.3	17.3	161.8
Ce	21.9	20.8	6.5	21.8	53.1
Cr	148.3	201.3	249.6	736.5	691.8
Cs	0.0	0.1	0.0	0.4	0.1
Cu	177.4	394.1	451.5	182.5	581.1
La	8.9	26.1	2.7	9.7	6.5
Nb	10.0	19.5	23.4	17.2	14.8
Nd	15.8	62.8	6.2	6.6	5.8
Ni	97.9	287.3	72.4	106.1	40.3
Pb	1.0	2.4	9.7	19.7	36.7
Rb	1.1	1.0	0.1	3.6	1.3
Sc	37.7	70.0	14.9	24.4	190.1
Sr	210.4	13.4	3.5	7.1	9.7
Th	1.0	1.9	1.4	6.0	6.9
U	0.2	1.0	2.1	1.8	1.6
V	371.3	687.0	1,846.0	967.3	2,985.7
Y	30.6	692.8	2.6	4.4	4.2
Zn	106.4	119.9	62.1	70.3	35.2
Zr	128.1	245.5	281.6	211.2	283.3

Chemical variations show an up-profile increase in the degree of alteration from basaltic bedrock (BB1) to indurated laterite cap (BB9). Note the enrichment of Fe and Al oxides, also metals like Cr, Cu, and V toward the surface, with concomitant depletion of silica, alkalis and alkali earths. (Establishment of a water table or fluvial and eolian inputs may modify these patterns).

1990; Brimhall et al., 1991). Nevertheless, the distinction between dominantly autochthonous or allochthonous weathering profiles remains important because it places constraints upon processes operating during duricrust evolution, and upon contemporaneous paleoclimatic and geomorphological conditions.

Characteristic properties

Laterites (*sensu stricto*) are, primarily, residual materials formed directly by in situ rock breakdown, and should not contain any significant allochthonous component. They owe their chief compositional characteristics to the relative enrichment of iron (and often aluminum), and the other less mobile parent rock (i.e., protolith) constituents. This enrichment occurs under aggressive weathering conditions as a consequence of the greater mobility, and hence loss, of constituent silica, alkalis, and alkaline earths from the protolith (Table L3). Since protolith materials nearer the surface are more subject to weathering, the degree of alteration will diminish with depth, thereby producing a weathering profile (Figure L18). Where such profiles are exposed, they typically consist of an uninterrupted progression from unaltered bedrock, through increasingly

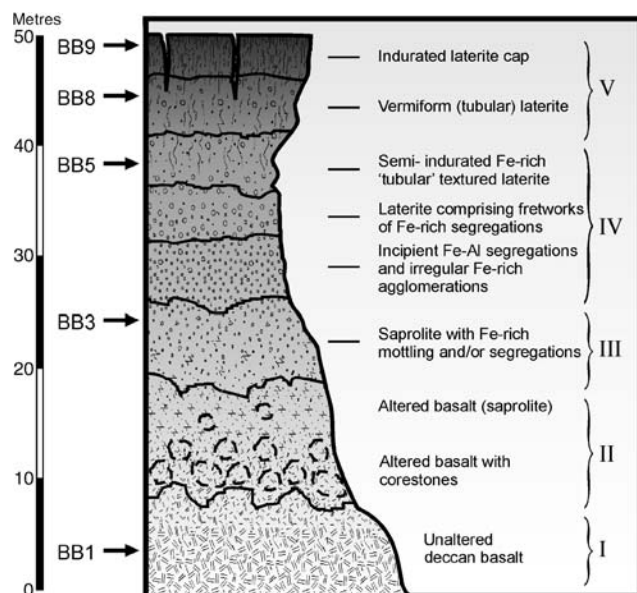


Figure L18 Generalized vertical section through the autochthonous Bidar laterite weathering profile (17°55'N, 77°32'E), illustrating the compositional (Table L3) and textural progression from unaltered basalt protolith to indurated laterite (after Borger and Widdowson, 2001). (I) unaltered basalt progressing up-profile to material displaying limited alteration of primary minerals; (II) altered basalt containing “unaltered” corestones within a soft saprolitic matrix, progressing upward into (III), a saprolitic to weakly-lateritized zone with residual lithological characteristics, increasingly obscured up-profile with increasing Fe-mottling and segregations; (IV) moderately lateritized zone comprising iron segregations and vermiform textures, and becoming increasingly indurated up-profile; (V) strongly lateritized, indurated laterite with vermiform textures, becoming highly ferruginous in the uppermost levels of the profile. (N.B. A similar alteration progression is commonly observed on other protolith substrates).

altered and iron enriched zones, to culminate in laterite at the top. Lateritic duricrusts typically form the uppermost layers of in situ weathering profiles, and crop out at the surface as a massive, interlocking fretwork of iron (and aluminum) oxides and hydroxides (i.e., sesquioxides, Figure L19).

Conditions of formation

The conditions under which lateritic profiles form include:

- (i) Favorable geomorphological environments characterized by limited runoff and lack of aggressive erosion. Ingress of rainfall and/or establishment of a water table serve to promote evacuation of the more mobile constituents.
- (ii) Favorable climatic conditions typified by seasonal, high annual rainfall (e.g., a monsoon-type climate). High humidity and high mean annual temperatures further promote alteration.
- (iii) Regions of relative tectonic stability, characterized by minimal uplift, crustal deformation, or erosion.

The chemical and mechanical durability of laterite confers a prominent role in tropical and sub-tropical landscape evolution. Studies of occurrences in India, Africa, and Australia have proved crucial in advancing tropical geomorphology (e.g., McFarlane, 1976; Summerfield, 1991; Thomas, 1994; Widdowson, 1997a, b). However, disturbance, by uplift, climate change,



Figure L19 Close-up of the uppermost, indurated layer (Zone V) of a lateritic duricrust revealing the massive, interlocking fretwork of iron and aluminum oxides and hydroxides (i.e., sesquioxides), and their associated ‘vermiform’ texture.

or both, is likely to terminate the lateritization process and lead to rapid erosion and stripping of the lateritic weathering profile (Borger and Widdowson, 2001). Consequently, laterite formation and preservation has been episodic throughout the geological record (Bardossy, 1981; McFarlane, 1983) with, for instance, acmes occurring within cratonic regions during the late Cretaceous “greenhouse climate,” and during the Tertiary thermal maxima.

Wider importance

Recently, ferricrete and laterite duricrusts, together with Fe-rich paleosols, have acquired renewed importance as paleoclimatic indicators because preservation of these materials records the occurrence of wet, tropical conditions during the geological past (e.g., Tsekhovskii et al., 1995; Tardy and Roquin, 1998). Such information is crucial in documenting changing regional and global climates (e.g., Bardossy, 1981; Thomas, 1994) and, together with other key climate proxies, aids in identifying periods of climatic perturbation arising either rapidly through volcanic and impact events or due to longer-term climate controls (i.e., Mikankovich-Croll cycles). Importantly, the presence of lateritic profiles in the geological record also confers wider

paleoenvironmental information, such as that concerning paleogeographic setting and the nature of paleolandscapes. For instance, laterite formation is likely to have always been restricted to humid tropical regions (or their climatic equivalents), and to those areas characterized by low runoff, ingress of precipitation, and the long-term establishment of a stable water table. Reconstruction of ancient lateritized paleosurfaces can also provide a useful tool for quantifying the degree of neotectonic deformation, since post-lateritization uplift can lead to the distortion of originally low-lying peneplains, and measurable increases in surface elevation (Widdowson and Cox, 1996).

Furthermore, appropriate mineralogical, geochemical, and isotopic studies on laterites are also beginning to reveal detailed information regarding past climatic and atmospheric conditions. Carbon, oxygen, uranium-thorium, and, most recently, lithium isotope systematics of weathering products offer the opportunity to investigate paleoatmospheric, paleoclimatic, and paleo-weathering conditions throughout the geological record (e.g., Bird and Chivas, 1989, 1993; DeQuincey et al., 2002; Pistiner and Henderson, 2003; Kisakurek et al., 2004). For instance, geochemical and isotopic analyses of Proterozoic laterites from South Africa (Gutzmer and Beukes, 1998), suggest not only an ancient oxidizing atmosphere, but also a hot and humid climate at ca. 2 Ga. Moreover, carbon isotope signatures preserved within these laterites may actually indicate the presence of early, terrestrially-based, photosynthesizing organisms. Finally, other isotopic systems, such as samarium–neodymium (Sm–Nd), have been successfully employed to identify and quantify allochthonous dust input into ancient weathering profiles, and as a proxy for monitoring the long-term chemical and isotopic balance between the evolving weathering profile and its associated hydrological characteristics (Viers and Wasserburg, 2004).

Mike Widdowson

Bibliography

- Aleva, G.J.J., (compiler) 1994. *Laterites. Concepts, Geology, Morphology and Chemistry*. Wageningen: ISRIC.
- Bardossy, G., 1981. Palaeoenvironments of laterites and lateritic bauxites - effect of global tectonism on bauxite formation. In Proceedings of the International Seminar on Lateritisation Processes, Trivandrum, India 11–14 December, 1979. Rotterdam: Balkema, pp. 287–294.
- Bird, M.I., and Chivas, A.R., 1989. Stable isotope geochronology of the Australian regolith. *Geochim. Cosmochim. Acta*, **53**, 3239–3256.
- Bird, M.I., and Chivas, A.R., 1993. Geomorphic and palaeoclimatic implications of an oxygen-isotope chronology for Australian deeply weathered profiles, regolith. *Aust. J. Earth Sci.*, **40**, 345–348.
- Borger, H., and Widdowson, M., 2001. Indian laterites, and lateritic residues of southern Germany: A petrographic, mineralogical, and geochemical comparison. *Z. Geomorph. N.F.*, **45**, 177–200.
- Bourman, R.P., and Ollier, C.D., 2002. A critique of the Schellmann definition and classification of “laterite.” *Catena*, **47**, 117–131.
- Brimhall, G.H., Lewis, C.J., Ague, J.J., Dietrich, W.E., Hampel, J., Teague, T., and Rix, P., 1991. Metal enrichment by deposition of chemically-mature aeolin dust. *Nature*, **333**, 819–824.
- Buchanan, F., 1807. *A journey from Madras through the Countries of Mysore, Kanara, and Malabar*, vol. 2. pp. 436–461; vol. 3. pp. 66, 89, 251, 258, 378. London: East India Co.
- Chadwick, O.A., Brimhall, G.H., and Hendricks, D.M., 1990. From a black to a gray box – mass balance interpretation during pedogenesis. *Geomorphology*, **3**, 369–390.
- DeQuincey, O., Chabaux, F., Clauer, N., Sigmarsson, O., Liewig, N., and Lepun, J.-C., 2002. Chemical mobilizations in laterites: Evidence from trace elements and ^{238}U - ^{234}U - ^{230}Th disequilibria. *Geochim. Cosmochim. Acta*, **66**, 1197–1210.
- Gutzmer, J., and Beukes N.J., 1998. Earliest laterites and possible evidence for terrestrial vegetation in the Early Proterozoic. *Geology*, **26**, 263–266.
- Kisakurek, B., Widdowson, M., and James, R.H., 2004. Behaviour of Li isotopes during continental weathering: The Bidar laterite profile, India. *Chem. Geol.*, **212**, 27–44.
- McFarlane, M.J., 1976. *Laterite and Landscape*. London: Academic Press, 151pp.
- McFarlane, M.J., 1983. The temporal distribution of bauxitisation and its genetic implications. In Melfi, A.J., and Carvalho, A. (eds.), Proceedings of the II International Seminar on Lateritisation Processes, Brazil, 4–12 July, 1982. Balkema, Rotterdam: Sao Paulo, pp. 287–294.
- Newbold, T.J., 1844. Notes chiefly geological, across the Peninsula from Masulipatam to Goa, comprising remarks on the origin of regur and laterite: Occurrence of manganese veins in the latter and on certain traces of aqueous denudation on the surface of southern India. *J. Asiat. Soc. Beng.*, **15**, 204–213, 224–231, 380–396.
- Newbold, T.J., 1846. Summary of the geology of Southern India, Part VI: Laterite. *R. Asiat. Soc.*, 227–240.
- Ollier, C.D., and Galloway, R.W., 1990. The laterite profile, ferricrete and unconformity. *Catena*, **17**, 97–109.
- Pistiner, J.S., and Henderson, G.M., 2003. Lithium-isotope fractionation during continental weathering processes. *Earth Planet. Sci. Lett.*, **214**, 327–339.
- Schellmann, W., 1986. A new definition of laterite. *Geol. Surv. India, Mem.* **120**, 1–7.
- Schellmann, W., 2003. Discussion of “A critique of the Schellmann definition and classification of laterite.” *Catena*, **52**, 77–79.
- Summerfield, M.A., 1991. *Global Geomorphology*. Harlow: Longman, 537pp.
- Tardy, Y., and Roquin C., 1998. *Dérive des continents, Paléoclimats et Altérations Tropicales*, Editions BRGM Orléans France, 473pp.
- Thomas, M.F., 1994. *Geomorphology in the Tropics*. Chichester, UK: Wiley, 460pp.
- Tsekhovskii, Yu. G., Shchipakina, I.G., and Khramtsov, I.N., 1995. Lateritic eluvium and its redeposition products as indicators of Aptian-Turonian climate. *Stratigr. Geol. Correl.*, **3**(3), 285–294.
- Viers, J., and Wasserburg, G.J., 2004. Behavior of Sm and Nd in a lateritic profile. *Geochimica and Cosmochimica Acta*, **68**(9), 2043–2054.
- Widdowson, M. (ed.), 1997a. *Palaeosurfaces: Recognition, reconstruction, and paleoenvironmental interpretation*. Geological Society of London Special Publication, **120**, 330pp.
- Widdowson, M., 1997b. Tertiary palaeosurfaces of the SW Deccan, Western India: Implications for passive margin uplift. In Widdowson, M. (ed) *Palaeosurfaces: Recognition, Reconstruction and Palaeoenvironmental Interpretation*. Geological Society of London Special Publication, **120**, pp. 221–248.
- Widdowson, M., and Cox, K.G., 1996. Uplift and erosional history of the Deccan traps, India: Evidence from laterites and drainage patterns of the Western Ghats and Konkan Coast. *Earth Planet. Sci. Lett.*, **137**, 57–69.

Cross-references

Duricrusts
 Paleosols, Pre-Quaternary
 Paleosols–Quaternary
 Sedimentary Indicators of Climate Change
 Weathering and Climate

LAURENTIDE ICE SHEET

The Laurentide Ice Sheet is that part of the North American ice sheet complex that was centered on the Canadian (Laurentian) Shield during Quaternary glaciations. Its configuration and history are fairly well known only for the Wisconsinan (last) Glaciation, and are known in outline only for preceding glaciations.

The late Wisconsinan (25–10 ka BP [ka = thousands of radiocarbon years]) North American ice sheet complex consisted of

three major ice sheets: the Laurentide Ice Sheet, which was centered on the Canadian Shield but also expanded across the Interior Plains to the west and south; the Cordilleran Ice Sheet, which inundated the western mountain belt between the northernmost coterminous United States and Beringia (unglaciated Yukon Territory and Alaska); and the Innuitian Ice Sheet, which covered most of the Canadian Arctic Archipelago north of about 75° N latitude (Figure L20). The ice cover over Newfoundland and the Maritime Provinces of Canada during this interval is usually referred to as the Appalachian Ice Complex, because ice flowed out from local centers within the region rather than from the Canadian Shield. All of the peripheral ice sheets were broadly confluent with the Laurentide Ice Sheet at the Last Glacial Maximum (LGM), and the Greenland Ice Sheet was confluent with the Innuitian Ice Sheet. The term Laurentide Ice Sheet is sometimes applied to this contiguous North American ice mass, though rarely in glacial geology. The North American ice sheet complex was by far the largest of former late Pleistocene ice sheets, with an area of about 15 million square kilometers (17.4 million, including Greenland ice). Its growth and decay thus accounts for more than half, possibly as much as three quarters, of global sea-level change during the last glacial cycle. Its presence profoundly affected the global climate system and the isostatic deformation of the planet.

The nucleus of this complex, the Laurentide, comprised three major sectors, the Labrador Sector, the Keewatin Sector, and the Baffin Sector. These sectors are named for areas of ice sheet inception and probable areas of outflow at the LGM. They were located respectively east, west, and north of Hudson Bay. Continental scale syntheses of ice recession following the LGM are given by Prest (1969), Bryson et al. (1969), Denton and Hughes (1981), Dyke and Prest (1987), and Dyke et al. (2003).

Wisconsinan history

Because the Laurentide Ice Sheet accounts for such a large proportion of global sea-level change, the oceanic record of global ice volume is a good proxy of its history for the period beyond the range of reliable radiocarbon dating (>30,000 yBP). On this basis, the ice sheet started to nucleate about 120,000 years ago, following marine isotopic stage 5e, and attained sequentially greater maxima at about 115,000, 70,000, and 20,000 years ago. It is generally agreed, though poorly demonstrated, that ice sheet nucleation resulted from snowline lowering to the point where snow persisted through the summers on the large plateau areas of the Canadian Arctic Archipelago, Quebec-Labrador, and the Arctic mainland west of Hudson Bay, formerly known as Keewatin. In the far north and possibly in Hudson Bay, formation and thickening of perennial sea ice may have assisted the process of englacialiation by eliminating iceberg calving when the ice caps advanced to shorelines. The outlines of early Wisconsinan ice sheets are poorly known because no moraines are now securely assigned to the maxima at 115 ka and 70 ka (Dyke et al., 2002). If interpretations of putative glaciolacustrine sediments (Scarborough Formation) and till in Sunnybrook Drift at Toronto and the ages of tills below and above the St. Pierre nonglacial sediments in the St. Lawrence River are accepted, ice sheets reached southernmost central Canada at these times but may not have extended into the United States. Similarly, the extent of ice at the middle Wisconsinan minimum (stage 3) is poorly known and has been variously portrayed. During the ice volume minimum at about 30 ka BP, ice cover approximately coincided with the Canadian Shield, leaving ice cover similar to present in the Cordillera and in the Canadian Arctic Archipelago (Dyke et al., 2002).

Late Wisconsinan glacial history is better known because it is based on well-mapped surface glacial features, such as end

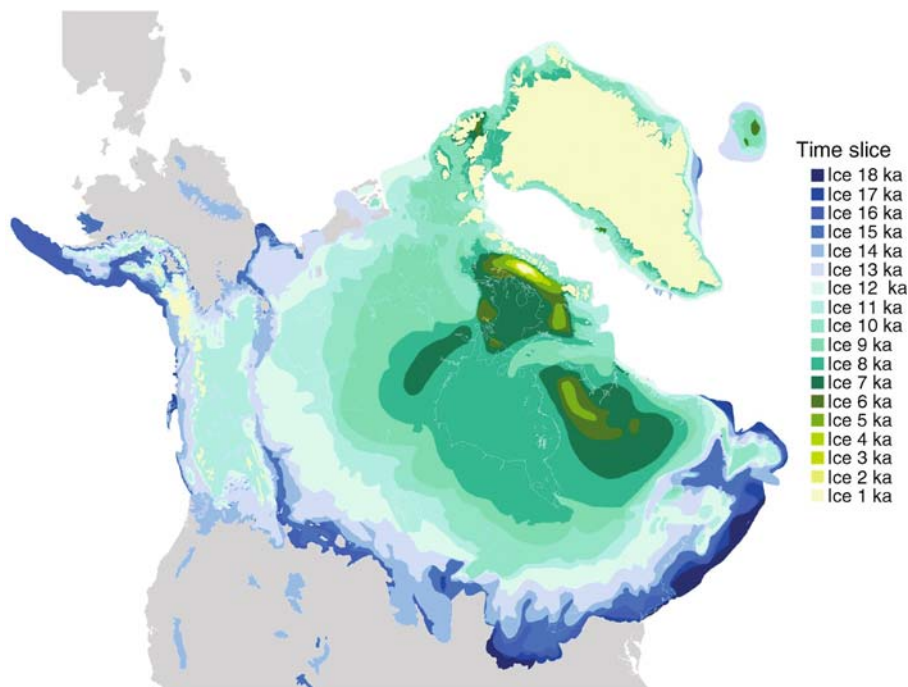


Figure L20 Isochrone map of deglaciation of North America, derived from Dyke et al. (2003).

moraines and ice-flow features (e.g., drumlins), and it is more abundantly constrained by radiocarbon dates. From its 30 ka BP position, Laurentide ice expanded to its late Wisconsinan maximum position in the northwest, south, and northeast about 23–24 ka BP and in the southwest and far north about 20–21 ka BP (Dyke et al., 2002). Hence, the general limit of glaciation expanded by 500–1,000 km in 7,000–10,000 years, including the inception and growth of the Innuitian and Cordilleran Ice Sheets. Relatively little recession occurred prior to 14 ka BP except in deep water on the continental shelf off New England and Atlantic Canada (Figure L20). Indeed, the southwestern margin of the Cordilleran Ice Sheet continued to advance through the Puget Lowland of Washington State until 14.5 ka BP. Thus, the period of generally maximum ice cover in North America spanned from about 22 to 14 ka BP, which is broader than the interval of the global sea-level minimum by several millennia on either side. This fact suggests that North America is more susceptible to glaciation than are the other large, periodically glaciated regions.

The recession of ice from the LGM is portrayed in Figure L20 at 1,000-year intervals in radiocarbon years, assembled from Dyke et al. (2003). The glacial geomorphology of the continent is the fundamental constraint on any interpretation of North American deglaciation. Two specific patterns, those of end moraines and other ice marginal features and those of ice flow features, are of primary importance. These broad patterns have been known for decades from large-scale compilations such as the Glacial Map of Canada (Prest et al., 1968; Dyke and Prest, 1987) and the Glacial Map of the United States east of the Rockies (Flint et al., 1959). The fundamental assumption in interpreting these patterns, in common with present and previous efforts, is that where moraines or other ice marginal features do not record specific ice margins, the margins tended to follow normal ice flow directions. This common assumption accounts for the fundamentally similar patterns seen in most reconstructions of Laurentide deglaciation over the decades, namely recession back to the three major centers of Keewatin, Quebec-Labrador, and Baffin Island.

The second major constraint in interpreting the history of deglaciation is the set of relevant numerical age determinations. New “exposure dating” studies have provided important tests of models of terrain age in the “weathering zones” along the mountainous eastern seaboard (e.g., Steig et al., 1998) and have reaffirmed the late Wisconsinan age of final coalescence of the Laurentide and Cordilleran Ice Sheets in Alberta (Jackson et al., 1997). However, only radiocarbon age determinations are sufficiently precise at this time to allow mapping of the deglaciation sequence at centennial resolution. The radiocarbon database of Dyke et al. (2003) provides direct and minimum-limiting dates on ice recession as well as maximum-limiting dates on readvances, including the advance to the late Wisconsinan glacial limit.

Most direct dates on ice marginal positions are from sites where moraines or meltwater features have been followed into shell-bearing marine deposits, such as commonly occur in ice-contact deltas. Opportunities to date ice marginal features landward of the limit of postglacial marine incursion directly are exceedingly rare, being limited to those few localities where ice readvanced across living or recently dead vegetation or where the varve chronologies of proglacial lakes can be tied into the radiocarbon time scale. The remaining age control is entirely in the form of minimum-limiting dates on lake sediments, peat, wood, plant macrofossils, foraminifera, and mammal bones. Reservoir corrections are applied to radiocarbon dates on foraminifera as they are to marine mollusks.

In summary, ages of deglaciation are reasonably well established in most coastal areas. Varve chronologies and dated readvances provide control at key inland sites. Elsewhere, minimum-limiting dates are valuable constraints. Recent improvements in age control and more detailed mapping of deglacial patterns have brought the North American deglaciation sequence more evidently into correlation with the major climatic events recognized in the North Atlantic region and in the Greenland ice cores. Thus, the acceleration of retreat at 14 ka BP corresponds to the sudden warming evident in the Summit, Greenland ice core record. More significantly, the Younger Dryas cooling now emerges as an important control of ice marginal behavior of the North American ice sheets, similar to that shown by the Scandinavian Ice Sheet, a result commensurate with growing recognition of this event in North American pollen records. Similarly, the prominent 8.2 cal ka BP cold event (7.5 ^{14}C ka BP) is now firmly correlated with the deglaciation of Hudson Bay and drainage of glacial lakes Agassiz and Ojibway (Barber et al., 1999).

The world’s largest ice sheet complex lost < 10% of its area prior to 14 ka BP. It then retreated nearly linearly until 7 ka BP, by which time only 10% of the area remained more glaciated than it is today. This linear reduction of area, as currently understood, was interrupted by two events: a reduced rate of recession during the later half of the Younger Dryas, and an increased rate as ice cleared from Hudson Bay (Figure L21). These events are clearer when plotted on the calendar time

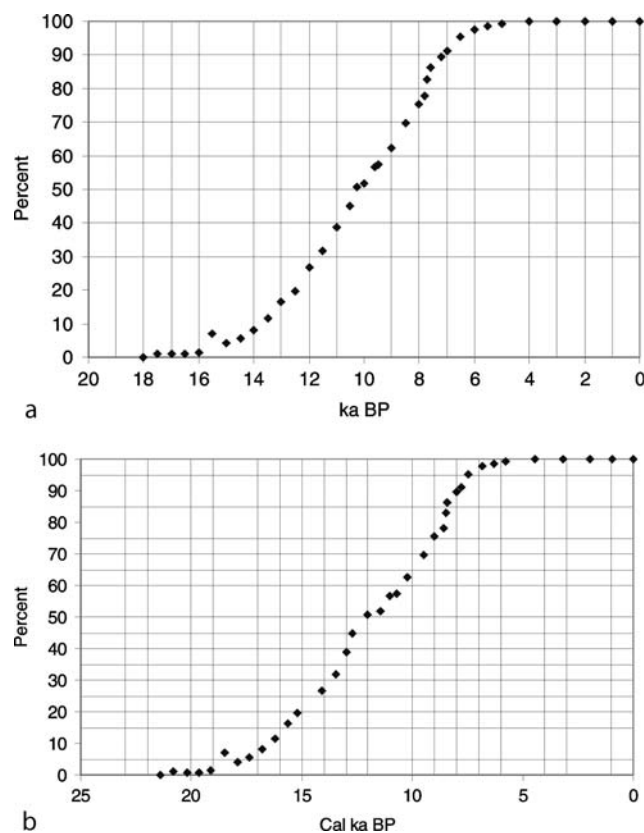


Figure L21 Percent area deglaciated in North America and Greenland, plotted on radiocarbon (a) and calendar (b) time scales.

scale, because the radiocarbon time scale abbreviates the duration of the Younger Dryas (Figure L21b).

The deglacial chronology accords reasonably well with the record of global sea-level rise (Fairbanks, 1989), which features two meltwater pulses separated by reduced melting during the Younger Dryas interval. During meltwater pulse IA (13–11 ka BP), the North American ice sheet complex decreased from about $14.9 \times 10^6 \text{ km}^2$ to $11.5 \times 10^6 \text{ km}^2$. During meltwater pulse IB (10.5–8.5 ka BP), ice area decreased from $10.5 \times 10^6 \text{ km}^2$ to $4.2 \times 10^6 \text{ km}^2$. These area reductions correspond approximately to volume losses of $10.8 \times 10^6 \text{ km}^3$ ($5,400 \text{ km}^3 \text{ a}^{-1}$) and $11.7 \times 10^6 \text{ km}^3$ ($5,600 \text{ km}^3 \text{ a}^{-1}$). These rates account for 40% of meltwater pulse IA and 60% of meltwater pulse IB. The relatively early demise of the Eurasian ice sheets accounts for their greater contribution to meltwater pulse IA.

Arthur S. Dyke

Bibliography

- Barber, D.C., Dyke, A.S., Hillaire-Marcel, C., Jennings, A.E., Andrews, J.T., Kerwin, M.W., Bilodeau, G., McNeely, R., Southon, J., Morehead, M.D., and Gagnon, J.-M., 1999. Forcing of the cold event of 8,200 years ago by catastrophic drainage of Laurentian lakes. *Nature*, **400**, 344–348.
- Bryson, R.A., Wendland, W.M., Ives, J.D., and Andrews, J.T., 1969. Radiocarbon isochrones on the disintegration of the Laurentide Ice Sheet. *Arct. Alp. Res.*, **1**, 1–14.
- Denton, G.H., and Hughes, T.J., 1981. *The Last Great Ice Sheets*. New York: Wiley, 484pp.
- Dyke, A.S., and Prest, V.K., 1987. The Late Wisconsinan and Holocene history of the Laurentide Ice Sheet. *Géographie physique et Quaternaire*, **41**, 237–263.
- Dyke, A.S., Andrews, J.T., Clark, P.U., England, J.H., Miller, G.H., Shaw, J., and Veillette, J.J., 2002. The Laurentide and Innuitian ice sheets during the Last Glacial Maximum. *Quaternary Sci. Rev.*, **21**, 9–31.
- Dyke, A.S., Moore, A., and Robertson, L., 2003. Deglaciation of North America. Geological Survey of Canada Open File, **1574**: Thirty-two digital maps at 1:7 000 000 scale with accompanying digital chronological database and one poster (two sheets) with full map series.
- Fairbanks, R.G., 1989. A 17,000-year glacio-eustatic sea level record: Influence of glacial melting rates on the Younger Dryas event and deep ocean circulation. *Nature*, **342**, 637–642.
- Flint, R.F., Colton, R.B., Goldthwait, R.P., and Wilman, H.B., 1959. Glacial Map of the United States east of the Rocky Mountains. Geological Society of America, 1:1,750,000.
- Jackson, L.E. Jr., Phillips, F.M., Shimamura, K., and Little, E.C., 1997. Cosmogenic ^{36}Cl dating of the Foothills erratics train, Alberta, Canada. *Geology*, **25**, 195–198.
- Prest, V.K., 1969. Retreat of Wisconsin and Recent ice in North America. Geological Survey of Canada Map, **1257A**, scale 1:5 000 000.
- Prest, V.K., Grant, D.R., and Rampton, V., 1968. Glacial Map of Canada. Geological Survey of Canada Map, **1253A**, scale 1:5 000 000.
- Steig, E.J., Wolfe, A.P., and Miller, G.H., 1998. Wisconsinan refugia and the glacial history of eastern Baffin Island, Arctic Canada: Coupled evidence from cosmogenic isotopes and lake sediments. *Geology*, **26**, 835–838.

Cross-references

Cordilleran Ice Sheet
 Glacial Geomorphology
 Glaciations, Quaternary
 Last Glacial Maximum
 Moraines
 Radiocarbon Dating
 Sea Level Change, Quaternary
 The 8200-Year BP Event
 Tills & Tillites
 Wisconsinan (Weichselian, Würm) Glaciation
 Younger Dryas

LITTLE ICE AGE

General description

The period known as the “Little Ice Age” spans roughly the sixteenth through the mid-nineteenth centuries. During this time, temperatures over much of Europe were frequently unusually cold, Alpine glaciers advanced, and European rivers froze much more often than during medieval times or during the past century and a half. Cold climates also prevailed over several other areas, especially those adjacent to the North Atlantic. The combination of cold conditions over both Europe and eastern North America, the two areas with the greatest amount of western record-keeping, led many to consider the period as one of global cooling, resulting in the label “Little Ice Age.”

Modern science has shown, however, that there is considerable regional variation in the extent of the cooling, with some areas even warming during this period. It now appears that the Northern Hemisphere as a whole cooled only moderately (Briffa et al., 1998; Jones et al., 1998; Mann et al., 1999; Crowley, 2000), by several tenths of a degree. However, not enough data exists to establish a reliable estimate for the Southern Hemisphere as a whole. Furthermore, even in the areas that cooled, there is a great deal of variability in the timing of the cooling. This latter fact has led to a proliferation of time-periods that are called the Little Ice Age, with some extending it to the fourteenth century (Fagan, 2000).

Despite the inhomogeneous cooling during the Little Ice Age, it remains important as it is the most reliably documented, relatively large climate anomaly during the last millennium (prior to the industrial revolution). Understanding the Little Ice Age is therefore an important test of our comprehension of natural climate variability.

Evidence

Based on early thermometer measurements, documentary evidence, and proxies for past temperatures (such as tree rings and glacier extents), it is believed that annually averaged European temperatures were roughly 1–1.5 °C colder during the Little Ice Age relative to preceding or subsequent periods (Pfister, 1995; Shindell et al., 2001). However, many winters appear to have been much colder (e.g., see Fagan, 2000). Dutch masterpieces from that time by Brueghel, van der Neer and others show people skating on canals and rivers that almost never freeze today. Ice was so prevalent in northern seas that Inuit fisherman were seen as far south as Scotland. Glaciers advanced in the Alps, Scandinavia and Iceland, destroying outlying farms and threatening to crush whole villages. Snow lay on the ground in Britain and the Netherlands an average of 20–30 days during the winter between 1680 and 1730, as opposed to an average of 2–10 days every winter during the twentieth century (Fagan, 2000). In North America, native tribes banded together to form the League of the Iroquois in the face of declining food supplies and other natural hardships during those cold years. During the American Revolutionary War, British soldiers were able to drag massive cannons across a frozen New York Harbor.

It is often claimed that the Viking settlements in Greenland and the New World were wiped out by the severe drop in

temperatures. Local climate conditions likely changed in these locations, but not necessarily in concert with those elsewhere. Additionally, it seems that the cutting off of trade routes back to Europe played a primary role in the settlements' demise. An increase in North Atlantic sea ice due to climatic changes may therefore have been more important than altered local conditions. Weather in Iceland illustrates the complexity of relating climate change to habitability. Iceland was locked in by sea ice for several months during most years of the Little Ice Age, but seldom after 1880. Barley was grown effectively in Iceland from the ninth century through the twelfth, after which this crop failed until the warming of the late 1900s. While conditions were certainly harsher in Iceland during the Little Ice Age, the cold weather there may have actually begun much earlier.

Causes of cooling

It has long been speculated that the drop in temperatures was due to a dimmer Sun. Galileo's development of the telescope for astronomy in the early 1600s allowed early observers to chart the behavior of the Sun. They regularly noticed dark spots, which cycled over a period of about 11 years, as they do today. After 1645, the spots largely vanished. They reappeared around 1715, and the sunspot cycle has been present ever since. The intervening years are now known as the Maunder Minimum, the most prolonged and dramatic of several decadal timescale reductions in solar irradiance during the last millennium. This period coincides with the coldest European temperatures. Modern satellite measurements have confirmed the early assumption that the number of sunspots is related to the total brightness of the Sun, though the exact relationship is not yet well quantified. The Maunder Minimum period, with almost no sunspots recorded by European astronomers, represents the extreme low of a multi-century period that appears to have been marked by generally lower solar output. Evidence from cosmogenic isotopes (atomic isotopes produced only by cosmic rays whose ability to reach the Earth depends on the sun) obtained from ice cores matches the general pattern of sunspot variability during past centuries, including the Little Ice Age (Stuiver and Braziunas, 1989). The reduction in solar output during the Maunder Minimum is estimated at about one-quarter of one percent (Lean et al., 1995). Though this is a very small change, the output of the Sun is so large that this can still have a sizeable impact. However, it is not enough to plunge the whole Earth into much colder conditions, and even to account for the modern view of the Little Ice Age as a regional phenomenon requires some amplification.

The other major factor in the cooling during this period was an increase in volcanic eruption frequency and size (Free and Robock, 1999; Crowley, 2000). Limited historical information is supplemented by the signature volcanic ash layers preserved in ice cores. Eruptions injected a larger number of aerosol particles into the atmosphere during the seventeenth century than during the period immediately following the Little Ice Age or during the Medieval Warm Period, which preceded it. These particles reflect solar radiation, and it is estimated that the additional eruptions of the seventeenth century would have reduced the radiation reaching the Earth by an amount comparable to the reduced solar output at that time (Crowley, 2000). The global average surface temperature response is proportional to this energy change; therefore,

volcanism could have played a role in the global or hemispheric mean response although the global effects lasted only 1–3 years. A combination of solar and volcanic influences seems the most likely explanation for the hemispheric-scale cooling of the Little Ice Age.

Regional climate change

Studies have shown that changes in stratospheric ozone in response to solar variations amplify the climate impact of those irradiance variations (Haigh, 1996; Shindell et al., 1999; Shindell et al., 2001). Incorporating those ozone changes, the most recent climate model simulations have found that the reduced brightness of the Sun during the Maunder Minimum causes global annual average surface temperature changes of only a few tenths of a degree, in line with the small hemispheric average cooling seen in the proxy data. However, regional wintertime cooling over Europe and North America is 5–10 times larger due to a shift in atmospheric winds (Shindell et al., 2001). Both the climate model and proxy data show that surface temperature changes associated with solar output variations exhibit alternating warm oceans and cold continents at mid-latitudes of the Northern Hemisphere (Figure L22). These seem to occur primarily through a slowdown in the speed of westerly winds at the Earth's surface associated with the North Atlantic Oscillation (NAO). Greater heating by the Sun in the tropics relative to high latitudes causes an equator-to-pole flow of air, which is turned towards the east by the Earth's rotation. A reduction in the amount of sunlight reaching the planet leads to a weaker equator-to-pole heating difference, and therefore slower winds. Ozone changes in the stratosphere amplify this effect.

Impacts on surface temperatures are particularly large in winter. Because the oceans are relatively warm during the winter due to their large heat storage, the diminished flow creates a cold-land/warm-ocean pattern (as shown in Figure L22) by reducing the transport of warm oceanic air to the continents, and vice versa. Changes in this wind flow have only a small impact on global temperatures as the warm and cold regions average out. However, they have a large regional effect and increase the frequency of extreme events, such that a reduction in winds would lead to many more extremely cold days over Europe and eastern North America (which may stand out in the historical record). The shift in circulation thus appears to be the solution to the apparent paradox of extreme cold with only a marginally dimmer sun. Ocean circulation may have also responded to solar irradiance fluctuations. Volcanic eruptions are known to induce a positive bias in the NAO during the winter following the eruption, but this is opposite to the pattern seen during the Little Ice Age. Their long-term impact is likely to be relatively minor, as the particles injected into the upper atmosphere typically remain there in sufficient numbers to affect climate for only a year or two.

Though early records of wind flow are extremely limited, historical data associates the European seventeenth century winter cooling with enhanced northeasterly advection of continental air, consistent with an anomalous negative phase of the NAO (Slonosky et al., 2001). Reconstructions of the strength of the NAO from instrumental and proxy data suggest that there may have been a long-term weakening during the Little Ice Age (Luterbacher et al., 1999). Ocean sediments show a decreased sea surface temperature of 1–2°C in the Sargasso Sea during the sixteenth to nineteenth centuries, and warmer

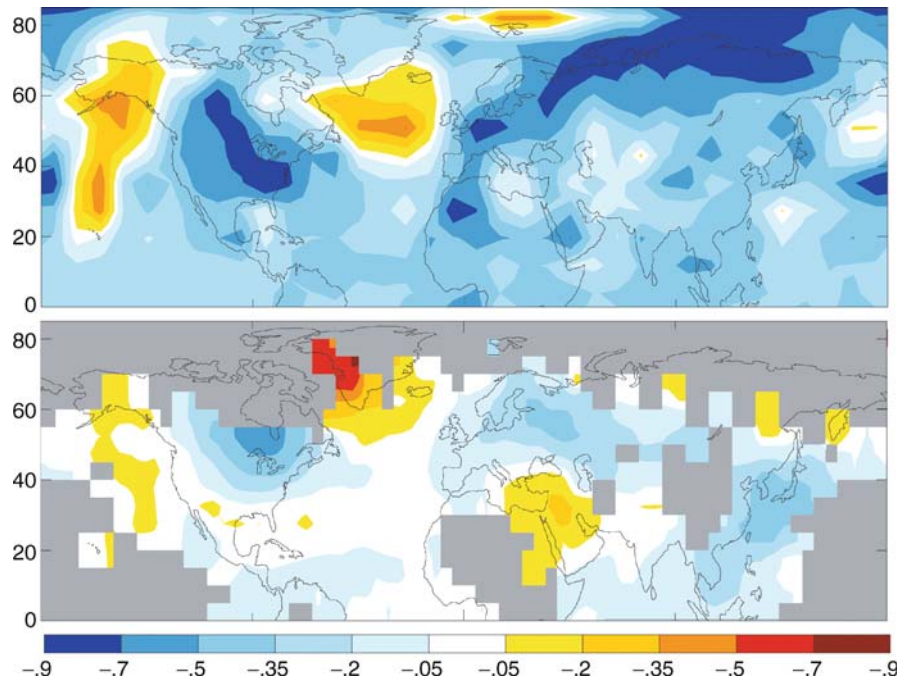


Figure L22 Annual average surface temperature change (C) due to solar irradiance change between the Maunder Minimum (late seventeenth century) and a century later, when solar output had returned to relatively large values, in the NASA Goddard Institute for Space Studies climate model (*top*) and in the historical temperature reconstructions (*bottom*).

Atlantic temperatures north of 44°N latitude, extending to the area off Newfoundland (Kiegwin and Pickart, 1999), consistent with a reduced NAO, but not with uniform basin-wide cooling.

Drew T. Shindell

Bibliography

- Briffa, K.R., Jones, P.D., Schweingruber, F.H., and Osborn, T.J., 1998. Influence of volcanic eruptions on Northern Hemisphere summer temperature over the past 600 years. *Nature*, **393**, 350–354.
- Crowley, T.J., 2000. Causes of climate change over the past 1000 years. *Science*, **289**, 270–277.
- Fagan, B., 2000. *The Little Ice Age*, New York: Basic Books, 272 pp.
- Free, M., and Robock, A., 1999. Global warming in the context of the Little Ice Age. *J. Geophys. Res.*, **104**, 19057–19070.
- Haigh, J.D., 1996. The impact of solar variability on climate. *Science*, **272**, 981–984.
- Jones, P., et al., 1998. High-resolution palaeoclimatic records for the last millennium: interpretation, integration and comparison with General Circulation Model control-run temperatures. *Holocene*, **8**, 455–471.
- Kiegwin, L.D., and Pickart, R.S., 1999. Slope water current over the Laurentian Fan on Interannual to Millennial Time Scales. *Science*, **286**, 520–523.
- Lean, J., Beer, J., and Bradley, R., 1995. Reconstruction of solar irradiance since 1610: Implications for climate change. *Geophys. Res. Lett.*, **22**, 3195–3198.
- Luterbacher, J., Schmutz, C., Gyalistras, D., Xoplaki, E. and Wanner, H., 1999. Reconstruction of monthly NAO and EU indices back to AD 1675. *Geophys. Res. Lett.*, **26**, 2745–2748.
- Mann, M.E., Bradley, R.S., and Hughes, M.K., 1999. Northern hemisphere temperatures during the past millennium: Inferences, uncertainties, and limitations. *Geophys. Res. Lett.*, **26**, 759–762.
- Pfister, C., 1995. Monthly temperature and precipitation in central Europe 1525–1979: Quantifying documentary evidence on weather and its effects. In Bradley, R.S., and Jones, P.D. (eds.), *Climate Since A.D. 1500*. London: Routledge, pp. 118–142.

- Shindell, D.T., Rind, D., Balachandran, N.K., Lean, J., and Lonergan, P., 1999. Solar cycle variability, ozone, and climate. *Science*, **284**, 305–308.
- Shindell, D.T., Schmidt, G.A., Mann, M.E., Rind, D., and Waple, A., 2001. Solar forcing of regional climate change during the Maunder Minimum. *Science*, **294**, 2149–2152.
- Slonosky, V.C., Jones, P.D., and Davies, T.D., 2001. Instrumental pressure observations and atmospheric circulation from the 17th and 18th centuries: London and Paris. *Int. J. Climatol.*, **21**, 285–298.
- Stuiver, M., and Braziunas, T.F., 1989. Atmospheric C-14 and century-scale solar oscillations. *Nature*, **338**, 405–408.

Cross-references

- [Climate Variability and Change, last 1,000 years](#)
- [Cosmogenic Radionuclides](#)
- [Maunder Minimum](#)
- [Medieval Warm Period](#)
- [North Atlantic Oscillation \(NAO\) Records](#)
- [Sun-Climate Connections](#)
- [Volcanic Eruptions and Climate Change](#)

LOESS DEPOSITS

Definition

Loess can be defined simply as a terrestrial clastic sediment, composed predominantly of silt-sized particles, which is formed essentially by the accumulation of wind-blown dust. Initially, von Leonhard (1823–1824) used the word “*Loeß*” for friable silty deposits near Heidelberg, based on the word “*Loesch*” for loose soil, which was the term used by the local people of the Rhine Valley. Lyell (1834–1845) brought the

term into widespread usage and was responsible for stimulating interest in similar deposits. However, the eolian origin of loess did not become widely accepted until the publications of von Richthofen (1870–1885). Several genetic and descriptive definitions of loess have been discussed since that time. Although the sub-aerial wind-fall origin, as well as silt-sized quartz particles domination, are the leading criteria of loess sediments, other additional definitive features (e.g., loose, unstratified, porous, calcareous, pale yellow, occurring in mantle form, etc.) are advocated by many scientists. In a historical perspective, the definition's use was controlled by its application.

Composition and features

Loess is relatively well-sorted clastic sediment that is homogeneous, porous and slightly altered. *Typical loess* (so called “*primary loess*”) usually has a yellow or pale yellow color. Coarse silt particles (10–50 μm in diameter) make 40–70% of typical loess by weight. This size fraction of particles is characteristic of eolian dust deposits and commonly is called the “*basic*,” “*loess*” or “*loessic*” fraction. The percentage of clay and sand content in loess is subordinate in importance (5–20%). Beside the prevailing quartz grains (40–80%), it may contain feldspar, calcite and dolomite. Quartz in loess occurs as irregular, subangular and angular grains with characteristic surfaces resulting from mechanical fragmentation. Among clay minerals, either illite or montmorillonite dominates are present, although kaolinite, vermiculite and chlorite may also be present in smaller amounts. Carbonate content is variable (ranging from 1 to 20%), depending on environmental conditions. Mineral grains are slightly cemented and partly aggregated mostly by carbonate. Primary carbonates usually are dolomite particles but secondary carbonates consist of calcite coatings on silt grains, fillings in interstices and vertical tubes left from the decay of grass roots. The void ratio is usually extremely high (45–55%) in loess, and the average diameter of aggregates is 10–15 μm . Loess is permeable to water and easily collapses when saturated with water. The compression strength of loess is about 1.5 kg dm^{-2} . The collapsibility leads to eventual problems for engineering activities in loess areas. Moreover, loess is easily eroded by surface water and liable to underground piping, though under dry conditions even steep loess walls are stable (Figure L23). Remnants of terrestrial materials, mostly of cryophile fauna and flora, are typical in the loess horizons. Individual loess



Figure L23 Peoria and Roxana loess horizons of the Wisconsinian time at Crowley's Ridge, Arkansas.

horizons are usually unstratified, but loess sequences often contain intercalated loam or sand beds (Liu et al., 1985; Pécsi, 1990).

Although the above features are characteristic of typical loess, non-typical loess or “*loess-like sediments*” of similar properties and genesis is widespread. In many loess sequences there is a continuum of modified loess, which ranges from weakly developed leached layers to intensely weathered paleosols and pedocomplexes. When altered by active soil formation, loess becomes more clay-like, hardens and can be either leached of primary carbonates or enriched by secondary carbonates. When redeposited by rainwater runoff, snowmelt and other processes, loess becomes slightly stratified. The terms “*secondary loess*,” “*altered loess*,” “*degraded loess*,” “*redeposited loess*,” “*loess derivatives*” and “*reworked loess*” have been used to describe such varieties of loess.

Origin

The origin of loess has a long history of controversy. Since von Richthofen suggested the “*subaerial*” theory of loess formation in 1870, the eolian origin of loess has been the most popular and best-documented. Succeeding investigations refined the process of eolian dust sedimentation and loess feature formation. The contributions of Tutkovskii, Obruchev and Kriger (Russia), von Richthofen and Grahmann (Germany), Liu (China), Fink (Austria), Kukla (Czechoslovakia) and Pécsi (Hungary), as well as Pye and Péwé (USA), are well known (Smalley, 1975; Liu et al., 1985; Pécsi, 1990; Pye, 1995).

Three conditions are required for loess deposition: (a) a large supply of suitable dust-sized particles that is sustained, at least episodically, over a period of tens to hundreds of thousands of years; (b) adequate wind energy to transport the dust, and (c) the existence of suitable dust traps downwind of the dust source area.

Although in situ weathering products may be directly deflated, in most instances at least one intermediate stage of alluvial or glaciofluvial transport and deposition is involved before it is picked up by wind and deposited as loess. Extensive loess deposits appear to be a Quaternary phenomenon and show a clear spatial relationship with areas of Pleistocene continental glaciation. Such deposits have been referred to as “*glacial*” or “*periglacial*” loess. The constituent silt particles were formed largely by sub-glacial grinding and subsequently deflated from glaciofluvial outwash deposits. Loess cover is particularly thick (almost up to 30 m) near valleys that served as meltwater drainageways, but thins and becomes finer away from valleys. Deposits of loess also occur on the semi-arid margins of some deserts (“*peridesert loess*”). In this case, significant amounts of quartz silt are probably produced by eolian abrasion and weathering processes in deserts or in adjacent mountain ranges before being deflated and deposited as loess. As opposed to the “*cold loesses*” of periglacial zones, the peridesert loesses are called “*warm loesses*” (Smalley, 1975, Liu, 1985, Pye, 1995).

The magnitude of the dust flux and pattern of dispersion from a potential source are strongly influenced by the nature of the prevailing regional winds. Local wind systems, such as valley winds, can be important in forming proximal dust deposits, but longer-range transport and formation of distal deposits requires the involvement of regional-scale wind systems. Dry deposition is enhanced wherever there is a reduction in wind speed or an increase in surface roughness. However, if dust passes over a water body, moist ground or a vegetated surface, the particles may be trapped. Subsequently, on impact of rainwater runoff, snowmelt or other processes on the slope, grains may be moved further away

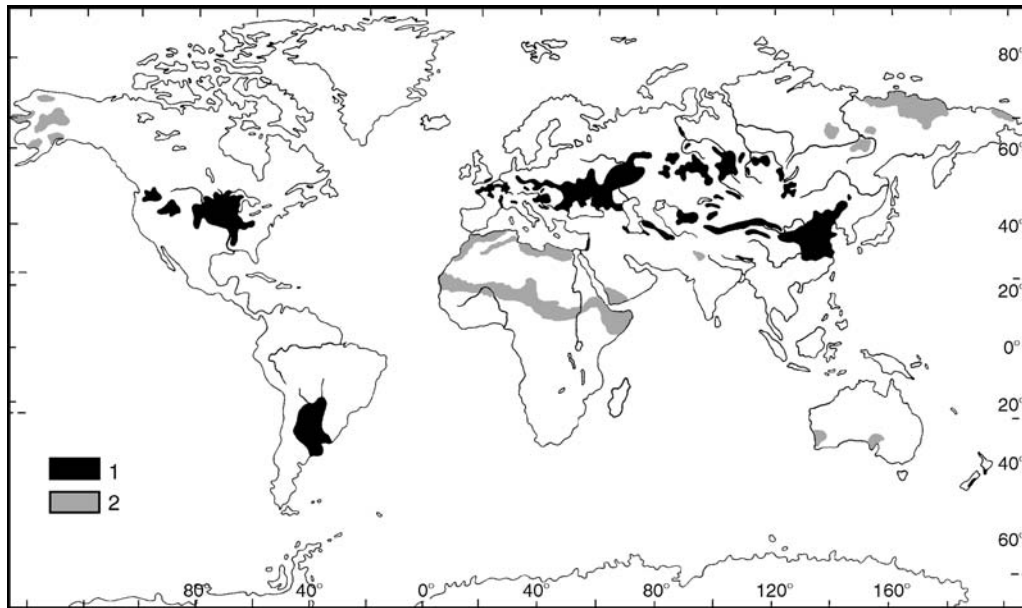


Figure L24 Distribution of loess and loess-like sediments. 1: Loess and loess-like sediments; 2: Loess derivatives and loess-like sediments (after Pécsi, 1990).

until they are stabilized by vegetation. Soil and related weathering processes are a syn- or post-depositional alteration of the primary deposit, and to some geologists are early stage diagenesis.

An alternative hypothesis (“soil-eluvial,” “in situ” or “back-swamp-loessification”) of loess formation was suggested by Berg in Russia in 1916, and then advocated by Russel and Fisk in the USA in 1944 (Smalley, 1975; Follmer, 1996). This hypothesis excludes the eolian factor and assumes most of loess sediments have a fluvial origin. According to this idea, any fine-grained deposits may be converted into typical loess as a result of weathering and soil forming processes. The in situ theory has not been well-documented or widely accepted since that time. The fundamental defect of the theory is that it creates a cascade of increasingly complex relationships that require unrealistic explanations, such as great tectonic uplift, excessive amounts of alluviation, and greater depths of valley cutting during erosion cycles. Also the characteristic angular grains of quartz are not explained by this theory.

Distribution

Loess is one of the widest-spread formations of the ice age, but it also forms on semi-arid desert margins and on foothills of mountain ranges. Loess sediments cover almost 10% of the world’s land surfaces. Extensive loess and loess-like sediments occur on plains, plateaus, pediments and major river basins (Figure L24). Loess reaches its maximum thickness (> 100 m) on the Loess Plateau of China, but usually loess series are not more than 30 m thick. In Eurasia, typical loess is also common in southern Siberia, central Asia, on the Russian Plain, in central Europe, and in isolated areas in Western Europe. Loess is widespread on the Columbia Plateau and Mississippi basin in North America and on La Plata basin in South America.

Outside the present-day temperate belt, non-typical loess varieties have developed. They vary in clay and sand content, mineral composition and color. Some loess, such as that in New Zealand and Argentina has a high content of volcanic glass and feldspars,

while loess in parts of Central Asia, the Rhine Valley and the Mississippi Valley has a high content of carbonate minerals (up to 30%). Some deposits, such as those of Nebraska, contain up to 40% sand (*sandy loess*). At the other end of the spectrum, fine-grained loesses on the southeastern and eastern margins of the Chinese Loess Plateau and Tadjikistan have more than 20% clay (*clayey loess*). Brownish-pink loess varieties are common in the Mediterranean climatic zone (Kashmir, Pakistan, Iran, Israel, North Africa and New Zealand) and non-calcareous loesses were formed under relatively humid environmental conditions in some regions. A special loess variety, the “*yedomas*” loess-ice complex, occurs in large patches in northeastern Siberia, in the permafrost tundra zone. Along Yukon River in Alaska and on the Loess Plateau of China, high rates of loess deposition continue today.

Konstantin G. Dlussky

Bibliography

- Follmer, L.R., 1996. Loess studies in central United States: Evolution of concepts. *Engin. Geol.*, **45**, 287–304.
 Liu, T., et al., 1985. *Loess and the environment*, Beijing, China: China Ocean Press, 251pp.
 Pécsi, M., 1990. Loess is not just the accumulation of dust. *Quat. Int.*, **7/8**, 1–21.
 Pye, K., 1995. The nature, origin and accumulation of loess. *Quat. Sci. Rev.*, **14**, 653–667.
 Smalley, I.J. (ed.), 1975. *Loess: lithology and Genesis. Benchmark Papers in Geology*, vol. 26. Stroudsburg, PA: Dowden, Hutchinson & Ross, 429pp.

Cross-references

- [Dust Transport, Quaternary](#)
[Eolian Sediments and Processes](#)
[Glaciations, Quaternary](#)
[Mineral Indicators of Past Climates](#)
[Paleosols – Quaternary](#)
[Sedimentary Indicators of Climate Change](#)
[Wisconsinan \(Weichselian, Würm\) Glaciation](#)

M

MARINE BIOGENIC SEDIMENTS

General features

Biogenic (or biogenous) sediments are ubiquitous in marine environments; the main divisions are readily classified with reference to the amount of carbonate present and the depth of water at which they are found (shallow or deep). The dominant types are (in the order of abundance): deep-sea carbonates (calcareous ooze, foraminifer ooze, nannofossil ooze); deep-sea siliceous deposits (siliceous ooze, diatom ooze, radiolarian ooze); hemipelagic silica-rich deposits (at continental margins below upwelling regions); shelf carbonate deposits (reef and platform carbonates, dominated by coral and algal debris or by foraminifer and mollusk materials, depending on circumstances; reefal debris, lagoonal carbonate muds, etc.); and various types of anaerobic deposits (rich in organic matter and with or without opal or carbonate). Because deep sea covers most of the surface of the planet, the dominant biogenic deposits are deep-sea sediments, and their dominant ingredient is pelagic plankton, reflecting the fact that production is tied to sunlight (Figure M1).

The key ingredients of biogenic sediments are therefore calcium carbonate, opaline silica, and organic matter; the first two of these ingredients are largely in the shape of microfossils on the deep-sea floor (Funnell and Riedel, 1971; H. C. Jenkyns, in Reading, 1986). Opaline fossils and organic matter tend to occur together (but not invariably so) and are generally found in high productivity regions. While carbonate is precipitated in such regions, it tends to be dissolved because a high supply of organic matter will increase carbon dioxide levels at the water-sediment interface, which produces carbonic acid. This circumstance was well understood by John Murray of the *Challenger* Expedition in the nineteenth century. Murray also provided the main subdivisions of deep-sea sediments and noted that deep-sea carbonates tend to occur in the shallower half of the deep-sea floor. The boundary is referred to as the “carbonate compensation depth” or CCD. It is the largest of the biogenic sedimentary features on Earth and reflects a balance

between rate of supply (almost all from calcareous plankton) and rates of dissolution (which increase with depth). The level of the CCD responds to the carbon chemistry of deep waters, and is quite different in the North Atlantic (deepest, below 5 km) and North Pacific (shallowest, above 4 km north of the equator). Roughly, this level runs parallel to the “apparent oxygen utilization”; that is, the amount of oxygen in deep water that has been converted to carbon dioxide. Because of this relationship, fluctuations of the CCD through time are useful in the reconstruction of the marine carbon cycle, and provide (some) clues to changes in the sharing of carbon dioxide between ocean and atmosphere. Quite generally, the deposition of biogenic sediments and the record contained therein are crucial ingredients in defining the machinery of global biogeochemical processes (e.g., Butcher et al., 1992).

Shallow-water carbonate deposits

Biogenic sediments in the sea consist of fossils or fragments of fossils. Initially, it was the study of fossils (paleontology) that dealt with their origin and applied this knowledge in biostratigraphy (the dating of sedimentary sequences and the tracing of evolution) and the reconstruction of environments of the past (paleoecology, paleoclimatology, paleoceanography). Geologists interested in these subjects studied modern shallow-water environments, beginning in the nineteenth century, with emphasis on corals, mollusks, foraminifers and other organisms producing hard parts of carbonate. Reefs provided an early focus and attractor because fossil diversity tends to be high in reefs (“bioherms”) preserved in the geologic record (for an overview, see B. W. Sellwood, in Reading, 1986). From the 1950s, developments in scuba diving opened entirely new avenues for direct observation and for experiments (Figure M2). Sampling submerged coral now routinely provides information about past conditions of growth, based on the measurement of growth bands, supplemented by chemical analysis. The study of modern environments and of the record preserved in skeletal structures has provided tools to study ancient environments as well, using fossils from the appropriate time. The information sought includes depth of water, temperature, productivity, dynamic interactions between organisms and environment and between

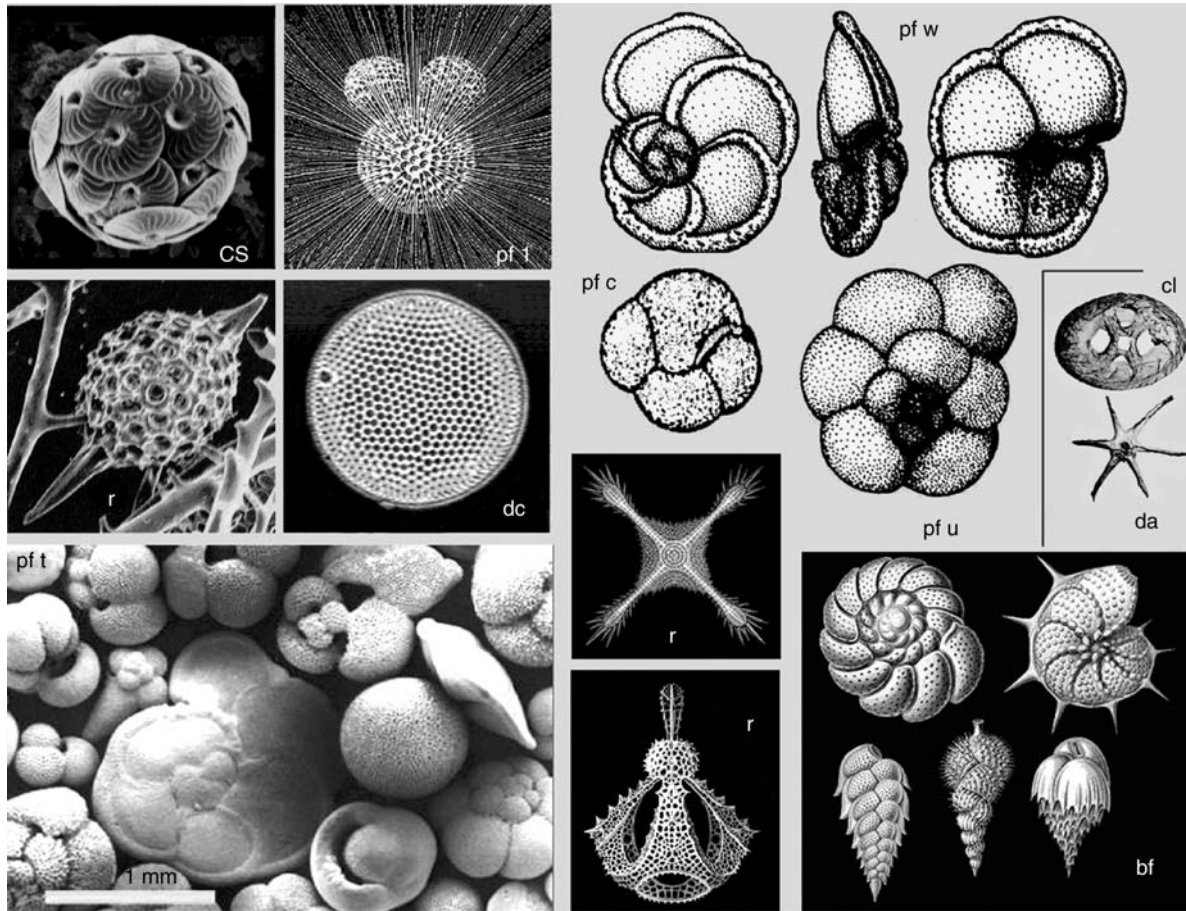


Figure M1 Key ingredients of the dominant biogenic sediments on Earth; that is, deep-sea calcareous and siliceous ooze. *cs*: Coccolithophorid (ca. 20 μm ; B. Donner, Bremen); *pf l*: living planktonic foraminifer within its halo of spines (E. Haeckel); *r*: (leftmost) radiolarian (C. Samtleben, Kiel); *dc*: centric diatom (O. Romero, Bremen); *pf t*: tropical assemblage of planktonic foraminifers (M. Yasuda, SIO); *pf w*: warm-water planktonic foraminifer (F. L. Parker, 1962); *pf c*: cold-water species; *pf u*: upwelling species; *cl*: coccolith; *da*: discoaster (both D. Bukry and M. N. Bramlette, 1969); *r*: radiolarians (E. Haeckel); *bf*: benthic foraminifers (E. Haeckel).

the organisms themselves, the role of disturbance, and seasonal variation. Above all, fossils – whether large or small (macro- or micro- or nanno-fossils) – record their environment of growth. If they do not like the extant conditions, they may shut down and record nothing (“biased reporting”). To gather information about past climate conditions, therefore, one has to employ several lines of evidence, using paleontology, sedimentology, geochemistry, and physical principles in a best-guess approach to reconstruction.

The largest biogenic structure on the planet is the Great Barrier Reef (GBR) off the northeastern coast of Australia. Drilling (by the drilling vessel *JOIDES Resolution*, in the context of the international Ocean Drilling Program (ODP, 1985–2003)) has demonstrated that the bulk of the structure is geologically young, less than one million years old. Presumably, the origin of the great reef is tied to the large sea level fluctuations that occurred after 800,000 years ago. Reefs are rubble factories, and sea level fluctuations stimulate rubble production. In particular, the periods of rapid rise during the melting of large ice sheets would have favored survival and expansion of rapidly growing species, such as those belonging to the genus *Acropora*. In addition, sometime after

the Mid-Pleistocene Climate Shift (see below), the Western Equatorial Warm Pool expanded southward to the region of the GBR, presumably aided by the clogging of the warm-water exit into the Indian Ocean and by the reef rubble produced around Indonesian islands. The GBR is a highly irregular structure (Figure M3). Its features and those of other reefs in the South Pacific erode during low stands of sea level (especially chemical erosion; Purdy, 1974), and build up during high stands favoring shallow ground. Without sea level fluctuation and attendant erosion, the product of reef growth is a carbonate platform.

Deep-sea carbonate deposits

Calcareous ooze rich in foraminifers was first discovered as a widespread deposit on the deep-sea floor in the middle of the nineteenth century. It was not clear, initially, whether the biogenic remains evident within the ooze originated on the sea floor or in the water. John Murray showed, by comparing plankton samples with sediment samples, that the bulk of the sand-sized material consists of planktonic foraminifers (“*Globigerina* ooze”). He also realized that the preservation of these fossils deteriorates with depth in the water, such that all carbonate would be dissolved below some depth (now known as the

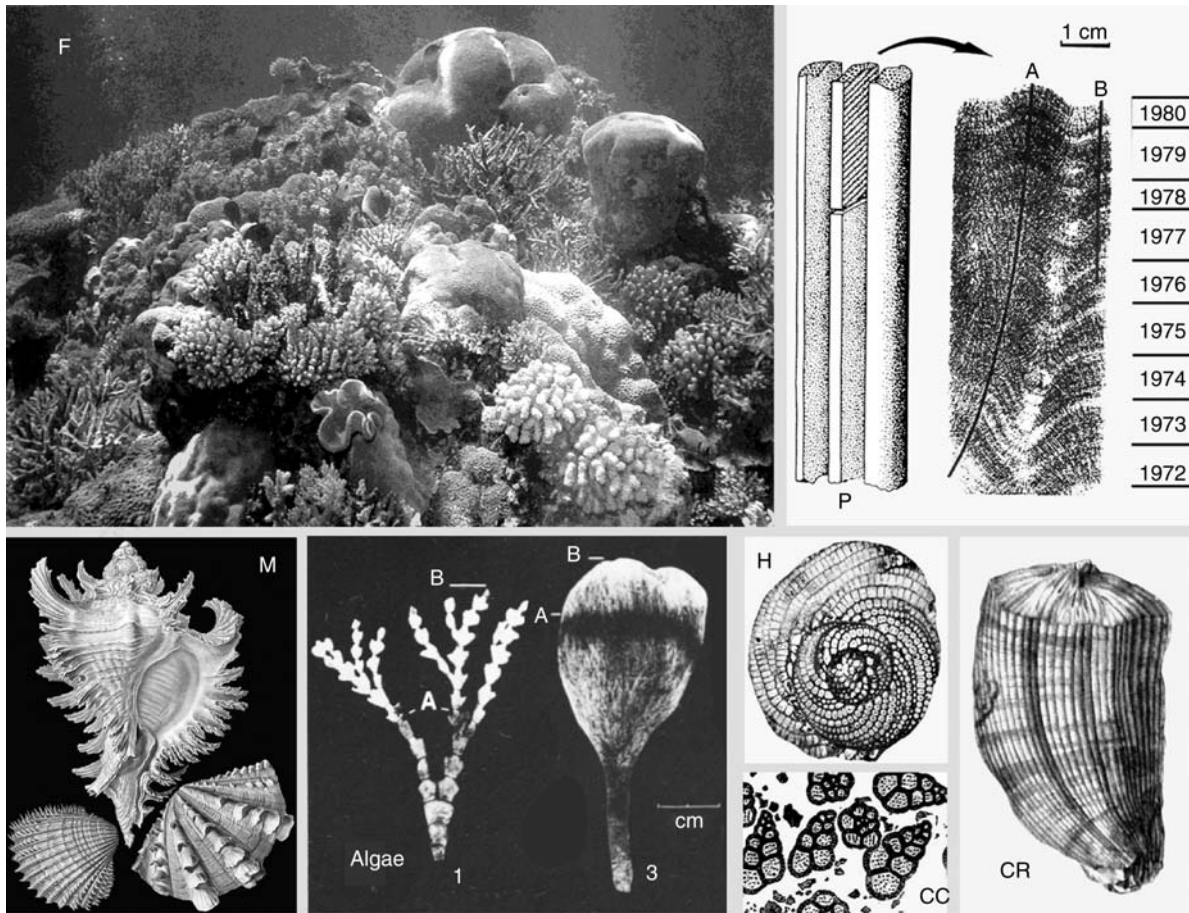


Figure M2 Shallow-water calcareous biogenic sediments originate from carbonate-secreting organisms such as corals, mollusks, algae, and foraminifers. *F*: Tropical coral reef at Fanning Island (SIO photo); *P*: core sample from a specimen of *Porites* from the western tropical Pacific (J. Pätzold, Bremen); *M*: armored mollusks (E. Haeckel); *A*: algae, in situ staining of calcareous algae in Bermuda (*Halimeda*, *Penicillus*) to determine rate of growth (G. Wefer); *H*: *Heterostegina*, a large benthic foraminifer bearing photosynthesizing symbionts (A. Loeblich and H. Tappan); *CC*: foraminifers in Cretaceous chalk (M. Neumayr); *CR*: Cretaceous mollusk, reef-forming in places (rudist pelecypod, M. Neumayr).

CCD), leaving only “Red Clay.” The CCD describes the narrow depth-dependent zone where carbonate-rich sediments give way to red clay and other carbonate-poor deposits bathed by undersaturated waters. A more subtle assessment of conditions on the sea floor at the time of deposition is possible by noting the state of preservation of calcareous fossils (Figure M4). A narrow zone separating well-preserved from poorly preserved fossils within the calcareous ooze defines the level of the “lysocline.” The lysocline fluctuates through time as a result of changes in deep circulation, which affects oxygen and carbon dioxide content of deep waters. Quite generally, patterns of preservation (taphonomy) hold a large amount of information regarding the environmental conditions during deposition of biogenic sediments.

The fact that rates of carbonate accumulation change considerably in a given region of the deep-sea floor was discovered during the Swedish Deep-Sea Expedition (1947–1948). It was especially obvious in the eastern equatorial Pacific, where sediments show regular cycles of light and dark colors, associated with high and low carbonate content. Both fluctuations in carbonate production and fluctuations in the intensity of carbonate dissolution can produce such cycles. The sediment cycles were

linked to productivity fluctuations that were in turn ascribed to changing trade wind intensities and equatorial upwelling, with ice ages having the stronger winds and increased upwelling (Arrhenius, 1952). In general, these concepts were supported by later studies, although the light-dark cycles are largely a result of variations in the intensity of carbonate dissolution.

Overall, calcareous nannofossils are the dominant component of calcareous ooze, especially in the large regions of low productivity below the central gyres. Thus, the typical biogenic deposit on the planet is coccolith ooze. Study of the minute coccoliths (platelets shed from coccolithophorids, Figure M1, upper left) requires the use of powerful microscopes. The invention and spread of scanning electron microscopes greatly aided in producing inventories and detailed descriptions of these fossils (Winter and Siesser, 1994). The pioneer work was done using petrologic microscopes, and these instruments still are the preferred tools for routine shipboard analysis, i.e., for the biostratigraphic dating of sediments during drilling expeditions. The presence of easily recognized nannofossils known as “discoasters” (Figure M1, far right) indicates an age greater than Quaternary, for example. Discoasters died out at the end of the Pliocene.

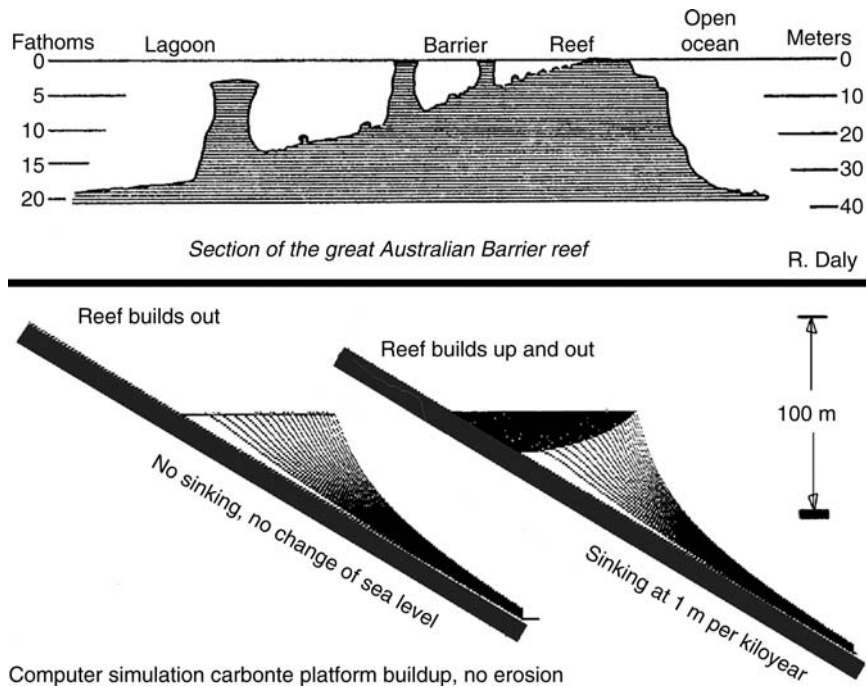


Figure M3 Nature of the Great Barrier Reef, as a product of differential buildup (during high sealevel stand) and erosion (during low stands). *Upper:* Profile through Great Barrier Reef, drawn by R. Daly (1934). *Lower:* basic structure of a carbonate platform as expected for constant sea level and slow sinking of the foundation (W.H.B., unpublished).

In places, especially on relatively shallow regions of the Atlantic, calcareous ooze contains the shells of pelagic gastropods, in varying proportions. Such shells are made of aragonite, a polymorph of calcium carbonate that is much more soluble than calcite. The shells are typically 1 cm long; where dominant (made so by bottom currents washing the sediment) they constitute "pteropod ooze."

The process of seafloor spreading slowly moves calcareous sediments to greater depth, on a million-year time scale. Thus, as a general rule, deep-sea sediments overlying basaltic basement (generated at the spreading center) should be rich in carbonate, while sediments overlying these older deposits should have less carbonate. That is, by the principles of "plate stratigraphy," sediments at the bottom of the stack were originally deposited at shallower depths above the CCD near the spreading center. As the plates moved apart and the ocean floor subsided, older sediments fell below the CCD. Reality is more complicated because of large fluctuations of the CCD through geologic time. The largest such excursion was the enormous drop of the CCD to deeper levels around 40 million years ago (Figure M5). This drop (toward the end of the Eocene) represents a large shift in carbonate accumulation patterns, from shelf to deep sea. It heralds the beginning of the great cooling that dominated the Cenozoic and illustrates the importance of mountain building (uplift on land removes shelf seas) in the course of this cooling. The marked drop of the CCD in the Atlantic since about 10 Ma marks the turning on of deepwater production there; that is, a filling of the basin with more saturated waters (said to be "young"). At the same time, opaline fossils on the sea floor dissolved more easily from that time onwards (young water bears less silicate than old) and there was an overall shift of silica deposition from the Atlantic to the Pacific.

The Auversian Facies Shift at 40 million years ago, when carbonate deposits become widespread on the deep-sea floor, is well expressed in the acoustic stratigraphy of deep-sea deposits. The shift is recognized in the western tropical Pacific as a marked change from highly reflective layers (interbedded limestones and chert) to more or less transparent (echo-lacking) chalk sequences. The fundamental reason for this development is twofold: the switch of carbonate deposition from shelves to the deep-sea floor, and the removal of opal into upwelling regions by diatom deposition, including in the belt around Antarctica. Upwelling is a function of winds, and winds are driven by temperature gradients, hence zonal winds that drive year-round upwelling increase with polar cooling.

Ocean and climate history

The study of biogenic sediments, especially those recovered from the deep-sea floor, provides the basis for reconstruction of ocean and climate history for the last 100 million years or so (paleoceanography). Information for periods before this time is difficult to obtain because seafloor subduction removes the evidence. The main tool in reconstruction is a detailed biostratigraphy (Berggren et al., 1985; Bolli and Saunders, 1985), greatly aided by coordination with the history of magnetic reversals. The main clues for reconstruction are derived from a combination of biogeography and stable isotopes, notable oxygen and carbon isotopes (Vincent and Berger, 1981; Kennett, 1985; Wefer and Berger, 1991), complemented by a large number of additional proxies for environmental conditions (Hay, 1988; Fischer and Wefer, 1999). The most detailed reconstructions have centered on the last glacial maximum (following the CLIMAP studies, 1976) and on the sequence

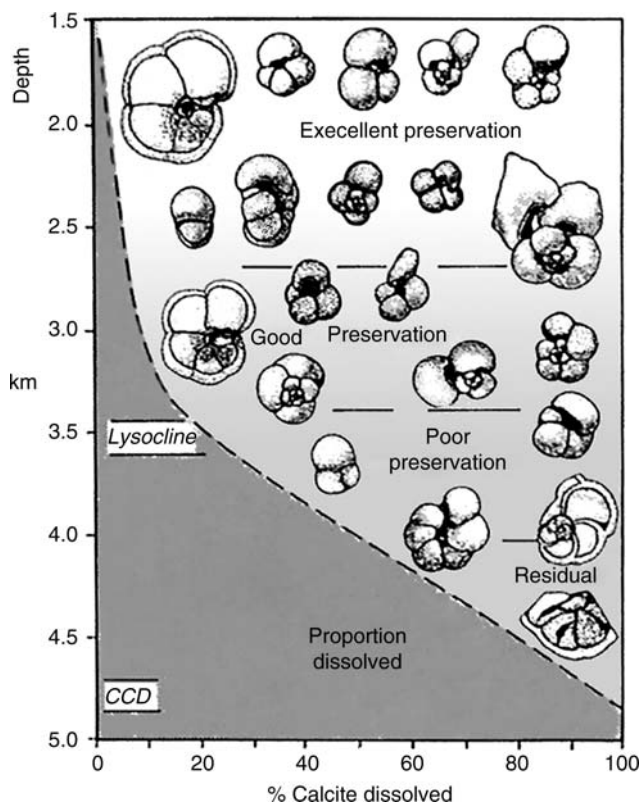


Figure M4 Deterioration of preservation of calcareous fossils (here: planktonic foraminifers) as a function of water depth, and definition of lysocline and CCD. The color of the calcareous ooze becomes darker with depth, as the proportion of carbonate decreases.

of events since that time, with some emphasis on the Younger Dryas cold spell during the period of ice melting (Fairbanks, 1989). As noted by Olausson (1965) and many since, the addition of large amounts of meltwater to the northern North Atlantic interferes with the formation of deep water and thus has many ramifications for the global thermohaline circulation (Broecker and Denton, 1989).

The pioneer work in the reconstruction of the history of the last million years was done on the cores obtained by the *Albatross* during the Swedish Deep-Sea Expedition (1947–1948, led by Hans Pettersson), by Gustaf Arrhenius, Cesare Emiliani, Eric Olausson, Frances Parker, and Fred Phleger. For the history of the last 100 million years, the pioneer studies were done by a rapidly growing community of biostratigraphers and paleoceanographers on material recovered by the drilling vessel *Glomar Challenger*, in the Deep Sea Drilling Project (1968–1983). Among the contributors to the first of the “Initial Reports on the Deep Sea Drilling Project” were M. N. Bramlette, W. R. Riedel, W. A. Berggren, E. A. Pessagno, J. D. Bukry, W. W. Hay, W. H. Blow, J. D. Hays, and A. G. Fischer. Project Chief Scientist was M. N. A. Peterson. Just as the *H.M.S. Challenger* symbolizes the beginning of modern oceanography, the *Albatross* and the *Glomar Challenger* are iconic for the beginnings of paleoceanography. A third vessel, the *JOIDES Resolution*, took over from 1985 and became the dominant tool for ocean history exploration at that time.

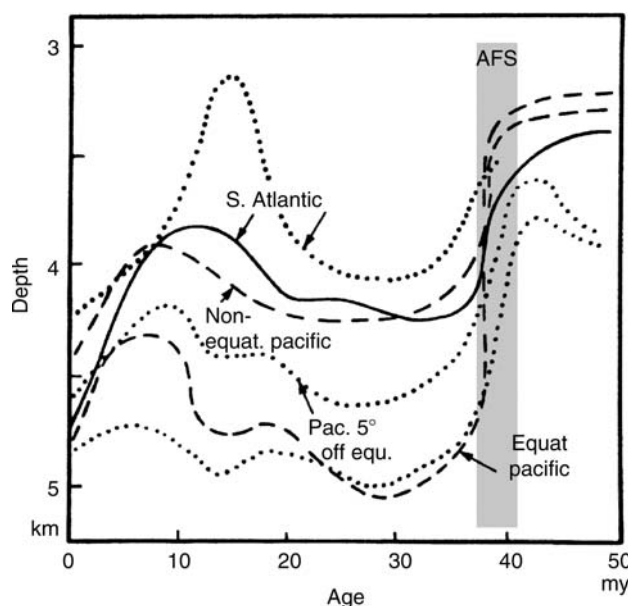


Figure M5 Reconstruction of CCD variations for various regions of the ocean. *Dotted lines*: According to Berger and Roth (1975). *Solid and dashed lines*: according to van Andel et al. (1977), as drawn in Seibold and Berger (1993). *AFS*: Auversian Facies Shift (Berger and Wefer, 1996). The AFS denotes an overall change in sedimentation patterns, whereby calcareous ooze becomes dominant in deep-sea deposits (carbonate deposition being shifted from shelf to deep sea) and opaline sediments are no longer widespread, but become concentrated below upwelling regions, including the sea around Antarctica.

The main result from the *Albatross* investigations was that biogenic deep-sea deposits show cyclic sedimentation, a finding that was linked to orbitally driven climate change and corresponding ice-age fluctuations. Much evidence has been found since to support this notion, especially from the analysis of oxygen isotopes of planktonic and benthic foraminifers, and from time series analysis using Fourier methods (Hays et al., 1976). The ice-age cycles are driven by changes in seasonal contrast, much as initially suggested by the Serbian mathematician Milutin Milankovitch (1930). The dominant cycles reflect the influence on seasonal contrast from changes in the obliquity of Earth’s axis (41,000 years) and in the eccentricity of the orbit (near 100,000 years) (Figure M6). Precession (the fact that summer solstice migrates between positions close to and far from the sun along the orbit) translates the eccentricity signal into 23,000-year amplitude variations in climate, which express themselves especially strongly in the productivity cycles of upwelling regions. A striking change in response of the climate system to the forcing occurs near 920,000 years ago: a strong long-term cycle sets in as the amplitude of the signal increases, first expressed as a doubling of the obliquity cycle, and then (near 700,000 year) moving into a 100,000-year cycle.

The main result from *Glomar Challenger* drilling concerned the evolution of a cold ocean from a warm one, with all its ramifications (Kennett, 1982). This general *leitmotif* governs the evolution of marine organisms during the Cenozoic, from nannoplankton to whales (which evolved blubber and baleen to gather krill in cold upwelling regions).

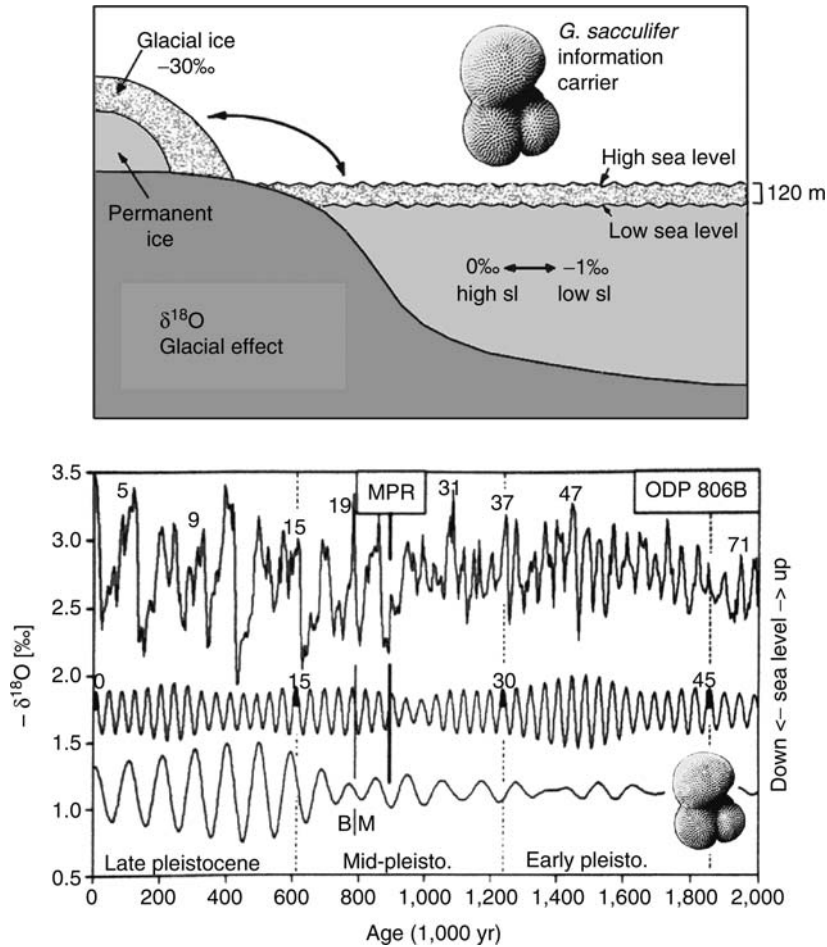


Figure M6 Oxygen isotope stratigraphy of Quaternary biogenic sediments from the western equatorial Pacific. *Upper:* Diagram showing how ice-mass changes are translated into variations of oxygen isotope composition of planktonic foraminifers (concept introduced by C. Emiliani, 1955). *Lower:* Stratigraphy of a sequence of cores from Ontong Java Plateau (modified after Berger and Wefer, 1992). *Numbers:* Emiliani isotope stages. *MPR:* Mid-Pleistocene Revolution (climate shift to long cycles with large amplitudes). *Top:* Original isotope sequence. *Below:* 41-kyr cycle contained in the series, and 100-kyr cycle, based on Fourier decomposition of the original record.

The chief drawback of early drilling was the mixing of sediment during drilling. This was largely eliminated during the Ocean Drilling Program (1985–2003), by sending a piston coring advice ahead of the drill bit. The cores allow for high-resolution studies, on a thousand-year scale, and this opened the door for “tuning” of the sedimentary record to Milankovitch forcing, which can be reconstructed rather precisely (Shackleton and Crowhurst, 1994). As a result, detailed records of climate change emerged, including the details and differences of ice-age cycles in various regions of the ocean. Other topics that have been studied in detail are Antarctic ice buildup and the response of the ocean in terms of changing productivity and deep-sea circulation, the nature of the climate change at the Eocene-Oligocene boundary (Prothero and Berggren, 1992), and the sequence of a strange carbon isotope excursion at the end of the Paleocene (thought to involve large-scale release of methane from submarine clathrates; Dickens et al., 1995). The series of events surrounding the grand extinction event 65 million years ago attracted much interest, as did many other examples of natural experiments that allow an assessment of

how the climate machine works and how the ocean responds to disturbance.

The great sustained stepwise cooling that characterizes global climate history since the late Eocene (Auversian Facies Shift, AFS, 40 million years ago) is well reflected in the oxygen isotopes of benthic foraminifers from the deep-sea floor of the Atlantic (Figure M7). The isotope index traces both ice and temperature; thus, it illustrates both the cooling of deep waters and the buildup of polar ice sheets, but at different proportions depending on the time span considered. Ice on Antarctica is thought to enter the picture around the time of the AFS, followed by major changes in circulation and associated sedimentation patterns. However, great ice sheets have presumably only covered the Antarctic continent since the middle Miocene. At the Pacific equator, the first indications for a narrowing of the zone of upwelling appear after the AFS, in the shape of a band of opaline sediments (that is, sediments rich in radiolarians and diatoms). These sediments are significant as a clue to the rise of zonal winds. An asymmetry of zonal wind activity about the equator would have been

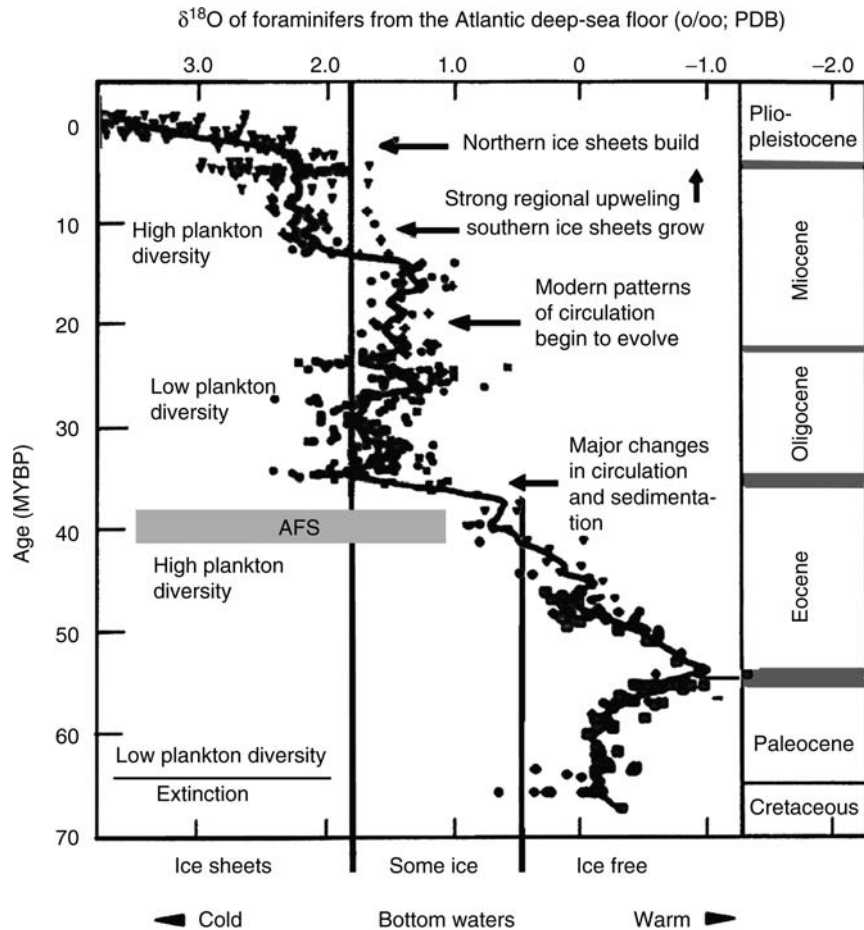


Figure M7 Stepwise cooling in the Cenozoic, since 40 million years ago (AFS, Auversian Facies Shift). The first step implies production of cold deep water (seen in the extinction of benthic foraminifers); the second, buildup of Antarctic ice caps; the third, buildup of ice in the northern polar regions (modified after a diagram in Miller et al., 1987).

present, similar to that found today but more pronounced. The southern trades helped to drive equatorial upwelling. A strong asymmetry presumably persisted until well into the late Neogene, when ice buildup in the Northern Hemisphere provided a counterweight to southern polar ice fields (Flohn, 1985).

The low plankton diversity during the Oligocene is puzzling. The rapid increase of diversity in the early Miocene, with the evolution of deep-living and shallow-living plankton, has been linked to the development of a thermocline. Certainly, the existence of a thermocline within the sunlit zone is a defining feature of the modern ocean. Photosynthesizing organisms must stay in the sunlit zone sufficiently long, on average, to produce more substance than they use up in respiration. Whenever the mixed layer is substantially thicker than the sunlit layer, this basic condition (Sverdrup's criterion of net photosynthesis) is not likely to be met. A deep and/or ill-defined thermocline will allow a thick mixed layer. This makes the pelagic realm an unfavorable habitat for production. In addition, the lack of opportunity for migrating up and down through the different environments defined by a thermocline precludes diversification. We may conclude, therefore, that in the Oligocene the thermocline was largely ineffective as an element

in structuring the pelagic environment; that is, the habitat of plankton.

Strong coastal upwelling, based on silica and organic matter content of hemipelagic sediments, is well documented for the last 10 million years or so, especially in the Southern Hemisphere (Summerhayes et al., 1992; Christensen and Giraudeau, 2002). Presumably, the resulting high abundance of plankton and associated herring-like fish favored the rapid evolution of warm-blooded predators, including sea birds, both with and without flight, and marine mammals.

A direct comparison of warm oceans (pre-AFS) and cool or cold oceans (post-AFS) is complicated by the fact that the former are associated with large shelf seas and the latter are not. Furthermore, the configuration of continents was quite different, with a broad seaway once connecting the Pacific, Indian and Atlantic Oceans in tropical latitudes – the Tethys (Barron and Peterson, 1989; Barrera and Johnson, 1999). Any efforts to relate differences or similarities in life habitat conditions and biodiversity to the warm-cold contrast may well be compromised by the presence or absence of large shelf seas and the Tethys seaway (The Tethys persisted well into the Cenozoic; Haq, 1981). There are some features of the warm ocean,

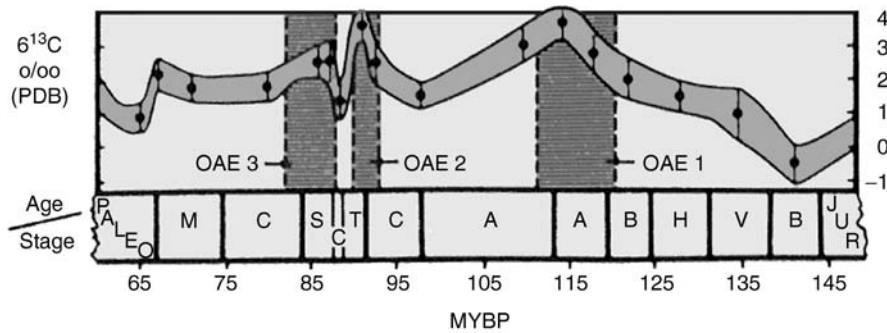


Figure M8 General trends of carbon isotope stratigraphy (pelagic marine limestones) in the Cretaceous, suggesting the removal of organic carbon during times of low oxygen availability (that is, during deposition of black mud) (modified from Arthur et al. 1985). OAE: Oceanic anoxic event.

however, that are quite different from those of a cold one on a fundamental level. Foremost among these is a dearth of oxygen in deep waters, which largely derives from the fact that oxygen is less soluble in warm water than in cold. This, presumably, greatly contributed to the fact that anaerobic conditions, reflected in the accumulation of black mud (now shale), were widespread during Cretaceous periods, and especially so during certain privileged intervals spanning the Albian-Aptian, Cenomanian-Turonian and Santonian-Campanian boundaries. The cause for extended anaerobic conditions, it is thought, is a greatly increased effusion of volcanic magma to the surface of the planet, bringing with it a corresponding increase of carbon dioxide in the atmosphere (Arthur et al., 1985). The system responds by burying organic carbon, which counteracts the geochemical imbalance. The burial of organic carbon preferentially removes C-12 from the carbon cycle, driving up the ratio between C-13 and C-12, which is then reflected in the stable isotope composition of calcareous fossils deposited at the time (Figure M8). The origin of much of the retrievable petroleum on the planet is linked to anaerobic conditions in the middle Cretaceous seas. The paleoceanographic implications of oxygen stress are vast, including widespread denitrification, which would have greatly impacted the level of productivity (For background on productivity in the sea, and reading the record of productivity in biogenic sediments, see Falkowski and Woodhead, 1992).

The great concepts of orbitally driven climate cycles during the Quaternary, of general cooling during the Cenozoic, and of warm oxygen-stressed seas in the Cretaceous, along with the revolutionary insights from plate tectonics, have fundamentally changed the way geologists look at the environmental history of the planet in the second half of the twentieth century. However, perhaps the single most important clue to the nature of Phanerozoic history, and especially regarding evolution, has been the recognition of the importance of the end-of-Cretaceous ("K-T") impact of a celestial body with Earth, producing widespread extinction (for discussions, see Berggren and van Couvering, 1984). It was within biogenic deposits that the extinction event was first clearly documented, in particular in calcareous shallow-water and pelagic deposits (e.g., Berggren, 1962; Bramlette, 1965). The evidence for impact was found in a famous pelagic carbonate section near Gubbio in Italy (Alvarez et al., 1980), where the exact horizon of extinction of planktonic foraminifers had been previously established (Luterbacher and Premoli-Silva, 1964).

Studies of the K/T boundary have greatly contributed to the reconstruction of the exact sequence of events, and especially to elucidating the early response of the system to stress (involving strange plankton blooms: Thierstein and Okada, 1979) and the course of recovery from the event in terms of biodiversity (in a time-span counted in millions of years).

Wolfgang H. Berger and Gerold Wefer

Bibliography

- Alvarez, L.W., Alvarez, W., Asaro, F., and Michel, H.V., 1980. Extraterrestrial cause for the Cretaceous-Tertiary extinction. *Science*, **208**, 1095–1108.
- Arrhenius, G.O.S., 1952. Sediment cores from the east Pacific. *Rep. Swed. Deep-Sea Exped. 1947–1948*, **5**(1), 1–227.
- Arthur, M.A., Dean, W.E., and Schlanger, S.O., 1985. Variations in the global carbon cycle during the Cretaceous related to climate, volcanism, and changes in atmospheric CO₂. In Sundquist, E.T., and Broecker, W.S. (eds.), *The Carbon Cycle and Atmospheric CO₂: Natural Variations Archean to Present*. Washington, DC: American geophysical union. AGU Geophysical Monograph, vol. 32, pp. 504–529.
- Barrera, E., and Johnson, C.C. (eds.) 1999. *Evolution of the Cretaceous Ocean-Climate System*. Boulder, CO: Geological Society of America. GSA Special Paper 332, 445pp.
- Barron, E.J., and Peterson, W.H., 1989. Model simulation of the Cretaceous ocean circulation. *Science*, **244**, 684–686.
- Berger, W.H., and Roth, P.H., 1975. Oceanic micropaleontology: Progress and prospects. *Rev. Geophys. Space Phys.*, **13**(3), 561–585 and 624–635.
- Berger, W.H., and Wefer, G., 1992. Klimageschichte aus Tiefseesedimenten – Neues vom Ontong-Java-Plateau (Westpazifik). *Naturwissenschaften*, **79**, 541–550.
- Berger, W.H., and Wefer, G., 1996. Expeditions into the past: Paleoceanographic studies in the South Atlantic. In Wefer, G. et al., (eds), *The South Atlantic: Present and Past Circulation*. Berlin: Springer, pp. 363–410.
- Berggren, W.A., 1962. Some planktonic foraminifera from the Maestrichtian and the Danian stages of southern Scandinavia. *Stockholm Univ. Contrib. Geol.*, **9**, 1–106.
- Berggren, W.A., and van Couvering, J.A. (eds.) 1984. *Catastrophes and Earth History*. Princeton, NJ: Princeton University Press, 464pp.
- Berggren, W.A., Kent, D.V., Flynn, J.J., and Van Couvering, J.A., 1985. Cenozoic Geochronology. *Geol. Soc. Amer. Bull.*, **96**, 1407–1418.
- Bolli, H.M., Saunders, J.B., and Perch-Nielsen, K. (eds.) 1985. *Plankton Stratigraphy*. Cambridge, UK: Cambridge University Press, 1032pp.
- Bramlette, M.N., 1965. Massive extinctions of biota at the end of Mesozoic time. *Science*, **148**, 1696–1699.
- Broecker, W.S., and Denton, G.H., 1989. The role of ocean-atmosphere reorganizations in glacial cycles. *Geochim. Cosmochim. Acta*, **53**, 2465–2501.
- Bukry, D., and Bramlette, M.N., 1969. Coccolith age determinations – Leg 1, Deep Sea Drilling Project. *Initial Rep. Deep Sea Drilling Project*, **1**, 369–387.

- Butcher, S.S., Charlson, R.J., Orians, G.H., and Wolfe, G.V. (eds.) 1992. *Global Biogeochemical Cycles*. London/San Diego, CA: Academic Press, 379pp.
- Christensen, B.A., and Giraudeau J. (eds.) 2002. Neogene and quaternary evolution of the Benguela coastal upwelling system. *Mar. Geol.*, **180** (Special Issue), 1–276.
- CLIMAP Project Members, 1976. The surface of the ice-age Earth. *Science*, **191**, 1131–1137.
- Daly, R.A., 1934. *The Changing World of the Ice Age*. New Haven: Yale University Press, 271pp.
- Dickens, G.R., O'Neil, R.R., Rea, D.K., and Owen, R.M., 1995. Dissociation of oceanic methane hydrate as a cause of the carbon isotope excursion at the end of the Paleocene. *Paleoceanography*, **10**, 965–971.
- Emiliani, C., 1955. Pleistocene temperatures. *J. Geol.*, **63**, 538–578.
- Fairbanks, R.G., 1989. A 17,000-year glacio-eustatic sea level record: Influence of glacial melting rates on the Younger Dryas event and deep-ocean circulation. *Nature*, **342**, 637–642.
- Falkowski, P.G., and Woodhead, A.D. (eds.) 1992. *Primary Productivity and Biogeochemical Cycles in the Sea*. New York: Plenum Press, 550pp.
- Fischer, G., and Wefer, G. (eds.) 1999. *Use of Proxies in Paleoceanography*. Berlin: Springer, 735pp.
- Flohn, H., 1985. *Das Problem der Klimaänderungen in Vergangenheit und Zukunft*. Darmstadt: Wissenschaftliche Buchgesellschaft, 228pp.
- Funnell, B.M., and Riedel, W.R. (eds.) 1971. *The Micropaleontology of Oceans*. Cambridge, UK: Cambridge University Press, 828pp.
- Haq, B.U., 1981. Paleogene paleoceanography: Early Cenozoic oceans revisited. *Oceanologica Acta*, **4** (Supplement), 71–82.
- Hay, W.W., 1988. Paleoceanography: A review for the GSA centennial. *Geol. Soc. Am. Bull.*, **100**, 1934–1956.
- Hays, J.D., Imbrie, J., and Shackleton, N.J., 1976. Variations in the Earth's orbit: Pacemaker of the ice ages. *Science*, **194**, 1121–1132.
- Kennett, J.P., 1982. *Marine Geology*. Englewood Cliffs, NJ: Prentice-Hall, 813pp.
- Kennett, J.P. (ed.) 1985. The Miocene Ocean: Paleoceanography and biogeography. *Geol. Soc. Am. Memoir*, **163**, 1–337.
- Luterbacher, H.P., and Premoli-Silva, I., 1964. Biostratigrafia del limite Cretaceo-Terziario. *Riv. Ital. Paleontol.*, **70**, 67–128.
- Milankovitch, M., 1930. *Mathematische Klimalehre und astronomische Theorie der Klimaschwankungen. Handbuch der Klimatologie, Bd 1, Teil A*, Berlin, Bornträger, 176pp.
- Miller, K.G., Fairbanks, R.G., and Mountain, G.S., 1987. Tertiary oxygen isotope synthesis, sealevel history, and continental margin erosion. *Paleoceanography*, **2**, 1–19.
- Olausson, E., 1965. Evidence of climatic changes in North Atlantic deep-sea cores, with remarks on isotopic paleotemperature analysis. *Prog. Oceanogr.*, **3**, 221–252.
- Parker, F.L., 1962. Planktonic foraminiferal species in Pacific sediments. *Micropaleontology*, **8**(2), 219–254.
- Prothero, D.R., and Berggren, W.A. (eds.) 1992. *Eocene-Oligocene Climatic and Biotic Evolution*. Princeton, NJ: Princeton University Press, 566pp.
- Purdy, E.G., 1974. Reef configurations: Cause and effect. In Laporte, L.F. (ed.), *Reefs in Time and Space*. Tulsa, OK: Society of Economic Paleontologists and Mineralogists. SEPM Special Publication 18, pp. 9–76.
- Reading, H.G. (ed.) 1986. *Sedimentary Environments and Facies*, 2nd edn. Oxford: Blackwell Scientific, 615pp.
- Seibold, E., and Berger, W.H., 1993. *The Sea Floor*. 3rd edn. Berlin: Springer, 356pp.
- Shackleton, N., and Crowhurst, S., 1994. Details that make the difference. *Oceanus*, **36**(4), 45–48.
- Summerhayes, C.P., Prell, W.L., and Emeis, K.C. (eds.) 1992. *Upwelling Systems: Evolution since the Early Miocene*. Piccadilly: Geological Society of London. Geological Society of London Special Publication 64, 519pp.
- Thierstein, H.R., and Okada, H., 1979. The Cretaceous/Tertiary boundary event in the North Atlantic. *Initial Rep. Deep Sea Drill. Proj.*, **43**, 601–616.
- van Andel, T.J.H., Thiede, J., Sclater, J.G., and Hay, W.W., 1977. Depositional history of the South Atlantic Ocean during the last 125 million years. *J. Geol.*, **85**, 651–698.
- Vincent, E., and Berger, W.H., 1981. Planktonic foraminifera and their use in paleoceanography. In Emiliani, C. (ed.), "The Sea, vol. 7, *The Oceanic Lithosphere*." New York: Wiley-Interscience, pp. 1025–1119.
- Wefer, G., and Berger, W.H., 1991. Isotope paleontology: Growth and composition of extant calcareous species. *Mar. Geol.*, **100**, 207–248.
- Winter, A., and Siesser, W.G., 1994. *Coccolithophores*. Cambridge, UK: Cambridge University Press, 242pp.

Cross-references

[Astronomical Theory of Climate Change](#)
[Carbonate Compensation Depth](#)
[CLIMAP](#)
[Coccoliths](#)
[Coral and Coral Reefs](#)
[Cretaceous/Tertiary \(K-T\) Boundary Impact, Climate Effects](#)
[Deep Sea Drilling Project \(DSDP\)](#)
[Diatoms](#)
[Foraminifera](#)
[Ocean Anoxic Events](#)
[Ocean Drilling Program \(ODP\)](#)
[Paleocene-Eocene Thermal Maximum](#)
[Quaternary Climate Transitions and Cycles](#)
[Radiolaria](#)

MARINE CARBON GEOCHEMISTRY

Introduction

The ocean contains approximately 50 times as much dissolved CO₂ as is contained in the atmosphere, and the carbon cycle in the ocean controls the pCO₂ of the atmosphere on time scales of thousands of years. The atmospheric CO₂ concentration today is rising because of human activities, such as fossil fuel combustion and deforestation. The CO₂ rise is faster than the century-scale ocean/atmosphere equilibration time, but the ocean will ultimately absorb most of the CO₂ that is released. In the past, changes in the carbon cycle of the ocean drove changes in atmospheric pCO₂ synchronously with the glacial/interglacial climate cycles. The orbital forcing which paces the glaciations (called Milankovitch cycles, see *Astronomical Theory of Climate Change*) is asynchronous across the equator; extra warmth in the north is balanced by decreased heating in the south. However, because of the rapid mixing of the atmosphere, the glacial CO₂ cycles tend to warm or cool the entire planet synchronously, and are largely responsible for the global synchrony of the glaciations. The carbon cycle of the ocean is therefore a primary determiner of the climate of the Earth, in the past and in the future.

The carbon cycle in the ocean begins with gas fluxes across the sea surface into the atmosphere. These depend on wind speed, temperature, and the chemistry of the water at the sea surface. Seawater chemistry of CO₂ is complicated by the presence of the carbonate pH buffer system pH. Only a tiny fraction of the dissolved carbon is present as the uncharged dissolved gas that can interact with the atmosphere. Because of this chemistry, a slight change in the pH of seawater can result in an enormous change in the concentration of dissolved CO₂, and in the equilibrium pressure of CO₂ in the atmosphere. The solubility of dissolved CO₂ depends on temperature and to a lesser extent salinity, so that a warming parcel of seawater will tend to push more CO₂ into the atmosphere. The CO₂ concentration of surface ocean waters is also affected by the growth and sinking of phytoplankton in the surface ocean. The carbon cycle of the ocean is therefore determined by a

combination of chemical, physical, and biological mechanisms (see also *Carbon cycle*).

The physical chemistry of carbon in seawater

Carbon is a unique element in the biosphere, in part because of its extremely varied chemistry. The oxidized form, CO_2 , is the dominant form in the atmosphere. In seawater, oxidized carbon undergoes hydration and pH reactions leading to generation of bicarbonate (HCO_3^-) and carbonate (CO_3^{2-}) ions. These species are collectively called “dissolved inorganic carbon” or DIC. The most reduced form of carbon is methane, CH_4 , while most biological carbon exists at intermediate oxidation states analogous to carbohydrates, which follow the approximate stoichiometry CH_2O . Reduced forms of carbon are collectively called “organic carbon.” Production of organic carbon from inorganic requires an input of energy, such as the light energy used in photosynthesis, or chemical energy used in chemosynthesis.

In the air, the CO_2 abundance can be defined as a concentration (molecules per volume), a proportion or “mixing ratio” (molecules of CO_2 per molecule total), or as the proportion of the total pressure that can be attributed to CO_2 . This last quantity is called the “partial pressure,” and at sufficiently low total pressures, the ideal gas law tells us that the partial pressure of a gas like CO_2 is very close to the total pressure of the mixture multiplied by the fraction of the molecules that are CO_2 . The atmospheric CO_2 abundance is commonly expressed either as a mixing ratio in units of parts per million (ppm), or as a partial pressure in units of microatmospheres ($10^{-6} \text{ atm} = \mu\text{atm}$). The numerical value of either of these measures in the atmosphere is close to 370 in both cases (and is presently rising by approximately 1.5 ppm or μatm per year). The abbreviation “ $p\text{CO}_2$ ” stands for partial pressure (and is unfortunately easy to confuse with the meaning of pH, defined as the negative logarithm of the concentration of H^+). For a detailed discussion of the physical chemistry of inorganic carbon in seawater, see Stumm and Morgan (1981).

A convenient way to think about CO_2 equilibrium between air and water is to take the chemistry of a water sample, and calculate how much CO_2 would exist in the air above it in equilibrium. In this way, we can define the $p\text{CO}_2$ of a water sample. This tells us nothing about the real physical pressure that a diver, for example, would feel in the water, but tells us what the composition of a bubble would be after it has had a chance to equilibrate. In nature, water and gas phases are not always in equilibrium; in fact, for CO_2 at the surface of the ocean, disequilibrium is the rule. If the $p\text{CO}_2$ of a water sample is higher than the $p\text{CO}_2$ of the air it is in contact with, then CO_2 will tend to evaporate from the water into the air, lowering the $p\text{CO}_2$ of the water and raising the $p\text{CO}_2$ of the air as the system approaches equilibrium (see *Carbon dioxide, dissolved (ocean)*).

The solubility of any gas in water depends on temperature, with increasing solubility as the water cools down. CO_2 gas is no exception. At a given concentration of dissolved CO_2 , the equilibrium partial pressure in the gas phase therefore decreases as the temperature drops (increasing solubility means less remains in the gas phase). The surface ocean is warm in the tropics and cold at the poles. Therefore, one component of the carbon cycle in the ocean is a tendency for CO_2 to escape to the atmosphere in the warm tropics, where it is less soluble, and to invade the ocean in the colder high latitudes.

Partitioning of carbonate species in seawater

CO_2 gas proper is but a minor participant in a larger chemical system called the carbonate buffer system. CO_2 gas combines with water (is “hydrated”) to form carbonic acid (H_2CO_3). Carbonic acid undergoes two proton dissociation reactions (loss of H^+) to form the charged (ionic) species bicarbonate (HCO_3^-) and carbonate ion (CO_3^{2-}). The hydration reaction is



In practice, it is analytically difficult to distinguish hydrated from unhydrated CO_2 , so these two species are lumped together into a single category that for simplicity we will just call dissolved CO_2 in the discussion that follows. The equilibration time of this reaction is roughly a minute, although it can be accelerated in biological systems by the enzyme carbonic acid anhydrase.

The dissociation reactions are governed by equilibrium expressions, denoted K_1 for the loss of the first proton and K_2 for the second. The dissociation constant K_1 can be written to determine the ratio of the products to the reactants of the reaction



while the second, K_2 , applies to



The ratios are taken between the activities of each of the solutes, which can be approximated by the concentrations in moles per liter, denoted by square brackets:

$$K_1 = [\text{HCO}_3^-][\text{H}^+]/[\text{CO}_2]$$

and

$$K_2 = [\text{CO}_3^{2-}][\text{H}^+]/[\text{HCO}_3^-]$$

Values of the dissociation constants are given by Dickson and Millero (1987).

Built upon these seemingly simple relations is a chemical system of rather counter-intuitive behavior. One example is the response of $[\text{CO}_3^{2-}]$ to changes in the CO_2 concentration of the solution (Equation 1). Carbonate ions determine whether CaCO_3 from coral reefs or planktonic shells dissolves (see *Carbonate compensation depth*). The response of an equilibrium reaction to an addition of a species on one side of the equilibrium is a tendency to shift the equilibrium toward the opposite direction, to “mop up” the added species. The response of the first dissociation (Equation 2) in isolation would be an increase in HCO_3^- and H^+ (an increase in H^+ is equivalent to a decrease in pH). The response of the second dissociation reaction might seem to be another shift to the right, increasing the concentration of CO_3^{2-} (and increasing the stability of CaCO_3). We could call this the “rising tide floats all boats” response.

However, this simple expectation is wrong. The flaw in our reasoning was to ignore the protons, which exist in much lower concentration than any of the carbon species. The rightward shift in Reaction 2 above generates a much more profound change in H^+ , relative to its concentration, than the change in HCO_3^- . H^+ therefore dominates the response of Reaction 3, which shifts to the left rather than to the right as we would assume. The behavior of the system can be seen more intuitively by combining both reactions, eliminating the troublesome

protons (and thereby conceptually forbidding them from changing their concentrations at all – a better approximation). This new reaction is:



When the reaction is written in this way, an addition of carbonic acid (or, equivalently, CO_2) can be seen to consume CO_3^{2-} , provoking the dissolution of coral reefs, rather than their growth. In spite of the fact that CaCO_3 contains carbon, it cannot act as a sink for CO_2 unless a source of base is added.

The buffer chemistry of seawater has an immediate implication for the interaction of seawater with rising atmospheric $p\text{CO}_2$, even in the absence of solid CaCO_3 . For a simple unbuffered gas like oxygen, for example, the solubility of the gas is expressed by Henry's law

$$K_{\text{h},\text{O}_2} = p\text{O}_2/[\text{O}_2]$$

which tells us that the concentration of the gas in solution goes up proportionately to a rising partial pressure in the gas phase. The relation also holds for CO_2 , as

$$K_{\text{h},\text{CO}_2} = p\text{CO}_2/[\text{CO}_2]$$

but the total amount of CO_2 that the seawater can absorb is affected by the buffer chemistry as expressed in Reaction 4 above. Dissolved carbonate ion (CO_3^{2-}) reacts with added CO_2 , effectively hiding it from the atmosphere and from Henry's law. The buffer works by reacting most of the invading CO_2 with CO_3^{2-} to form HCO_3^- , so the strength of the buffer is determined by the ratio of the CO_2 and CO_3^{2-} concentrations. Globally, the average ratio of CO_3^{2-} to CO_2 in surface waters is about 10, so seawater can hold 10 times as much CO_2 as it would without the buffer system. As atmospheric CO_2 rises, however, sea surface CO_3^{2-} concentrations will drop, and the buffer capacity of seawater will decline.

When the gas concentration in the surface ocean is out of equilibrium with the atmosphere, it relaxes toward equilibrium by a process known as gas exchange. The rate of gas exchange depends on the wind speed, surface roughness, bubbles and foam, the presence or absence of a surface microlayer, or skin of oils, and the diffusivity of the gas. A typical gas exchange rate is $3\text{--}5 \text{ m d}^{-1}$, meaning that a typical mixed layer of 100 m thick at the ocean surface will approach equilibrium with an e-folding time scale of $100 \text{ m}/5 \text{ m d}^{-1} = 20$ days (see Wanninkhof, 1992). For CO_2 , the factor of 10 buffering would increase the time scale to about 200 days. For the ocean as a whole, the rate at which gases invade the deep ocean is limited by the circulation time scale of the ocean, which is about a thousand years. For CO_2 , because the ocean is the larger reservoir, the atmosphere largely responds to ocean forcing, rather than the other way around, on the time scale of ocean overturning circulation.

The balancing of the various dissolved carbon species across the equilibrium reaction makes it somewhat more complicated to think about the carbon cycle in the ocean. For example, when seawater with one set of concentrations is mixed with a different seawater sample with a different set of concentrations, the mixed carbonate buffer system adjusts to re-establish pH balance. That is to say, if we combine one solution with $10 \mu\text{M}$ CO_2 with equal parts of another that starts with $20 \mu\text{M}$ CO_2 , we do not necessarily obtain a solution that contains $15 \mu\text{M}$ CO_2 , because some of the CO_2 reacts with CO_3^{2-} in

the resulting mixture. This makes life complicated for oceanographers, who would prefer that their chemical quantities be "conservative to mixing." The solution is a pair of derived quantities for seawater that do have the required conservation properties. One is the total concentration of all of the CO_2 species; this is called the "total CO_2 ," or ΣCO_2 . If we mix a solution that contains $1,800 \mu\text{M}$ ΣCO_2 with equal parts of another that contains $2,200 \mu\text{M}$ ΣCO_2 , we will obtain a solution that contains $2,000 \mu\text{M}$ ΣCO_2 , with no tricky business.

The other derived quantity is called the alkalinity, which is defined as the sum of all charges of the salts of weak acids in solution. One way to think about alkalinity is that if we were to add H^+ in an amount equal to the alkalinity, then all of the carbon in solution would be in the form of CO_2 , free to exchange with the atmosphere. Ignoring contributions from borate and other minor species, the "carbonate alkalinity" of seawater can be written as

$$\text{alk} = \text{HCO}_3^- + 2\text{CO}_3^{2-} \quad (5)$$

where the factor of two in front of CO_3^{2-} reflects the two protons it would take to produce carbonic acid from carbonate. The crucial point is that Reaction 4, above, has the same alkalinity on both sides of the reaction. As pH equilibrium redistributes carbon species toward one side or the other of Reaction 3, the alkalinity is unchanged. Therefore, if we combine two water parcels with different alkalinites, the alkalinity of the resulting mixture is a simple combination of the two. We say that both alkalinity and total CO_2 are conservative to mixing, and this simplifies our thinking about all kinds of processes that occur in the ocean carbon cycle.

How can we relate the alkalinity and total CO_2 to the equilibrium $p\text{CO}_2$ of surface waters, and exchange of CO_2 with the atmosphere? As we have already seen, dissolved CO_2 gas itself is only a minor part of the total carbon inventory of seawater, and the fraction of carbon in the form of CO_2 depends on the pH of the solution. Together, the alkalinity and the total CO_2 concentration can tell us everything there is to know about the carbon chemistry of the seawater. At a constant alkalinity, if we increase the total CO_2 concentration, the concentration of dissolved CO_2 and the equilibrium $p\text{CO}_2$ of the water sample will go up. This is easy to imagine, as an increase in the number of carbons without any change in the number of charges must lead to an increase in the number of uncharged carbons, that is CO_2 . In a similar way, if we maintain a constant total CO_2 and increase the alkalinity, then the number of charges per carbon atom goes up, and the proportion of uncharged CO_2 molecules goes down.

A useful property of the alkalinity is that it does not care about fluxes of CO_2 gas. An invasion of CO_2 from the atmosphere will increase the total CO_2 of the seawater, and alter the proportions of the various carbon species according to Reaction 3, but since shifts along Reaction 3 have no effect on the alkalinity, the alkalinity will be unchanged in response to gas exchange. In an analogous way, if we were to add strong acid to seawater somehow, this would change alkalinity while leaving the total CO_2 unchanged. This latter is a hypothetical example; natural fluxes of strong acid such as acid rain are generally negligible in the carbon chemistry of the surface ocean.

The biological pump

The other major mechanism governing the fluxes of CO_2 across the sea surface, nearly equal in magnitude to the effect of

temperature discussed above, is the growth and sinking of phytoplankton in the surface ocean. Geochemically, the effect of phytoplankton growth is to convert dissolved carbon into particulate carbon. Particles can sink, generating a net flux of carbon downwards in the ocean. Some of the phytoplankton (plants of the sea) sink on their own, while another fraction of the sinking carbon arises from the fecal pellets excreted by zooplankton grazers. This process has been called the “biological pump” (see Broecker and Peng, 1982). The atmosphere only sees the surface ocean, so the effect of the biological pump is to change the ocean chemistry so that the atmosphere sees, and therefore changes, the chemistry of the atmosphere itself.

It is helpful to divide the biological pump into two components, because these components have opposite effects on the CO_2 concentration and $p\text{CO}_2$ of the surface ocean. The first, and dominant, component is the organic carbon pump, comprised of the proteins, lipids, and other structural biochemical machinery of the cell. This is called the “soft tissue” pump. Only a small fraction of the plankton production is exported to depth; in very productive regions, the export fraction may reach half, while in the open ocean only 5–10% of the production is exported. The rest of the biomass produced is respired in the surface ocean, returning to dissolved carbon. Organic carbon production depletes the total CO_2 concentration of the seawater, but has only a small effect on the alkalinity. Therefore, the effect of the soft tissue pump is to decrease the $p\text{CO}_2$ of surface waters.

The second component of the biological pump is the production and sinking of the calcium carbonate (CaCO_3) shells of some plankton species. This process is called the “hard tissue” pump. The formation of CaCO_3 takes place by the reaction



Because one mole of CO_3^{2-} accounts for one mole of total CO_2 but two equivalents of alkalinity (see Equation 5), the effect of the CaCO_3 pump is a 2:1 change in alkalinity versus total CO_2 . A decrease in alkalinity leaves a greater proportion of uncharged carbon (CO_2), so the net effect of the CaCO_3 pump on the $p\text{CO}_2$ of surface waters is an increase in $p\text{CO}_2$.

When these two components of the biological pump are combined in the surface ocean, the rate of the soft tissue pump exceeds that of the hard tissues, so the overall effect of biological activity in the ocean is to decrease the $p\text{CO}_2$ of the atmosphere. CaCO_3 secreting plankton are favored in tropical surface waters, but even here the rate of organic carbon sinking from the surface ocean exceeds that of CaCO_3 by a factor of up to 10. In polar waters colder than 10°C , CaCO_3 production becomes even less important. If the biota of the ocean were killed and the contents of the ocean allowed to redistribute themselves in response to this, the $p\text{CO}_2$ of the atmosphere would perhaps double.

Photosynthesis in the ocean is limited by a number of factors that determine the extent to which biology affects ocean chemistry and atmospheric $p\text{CO}_2$ (Longhurst, 1998). The first factor is light; production of biomass requires energy, which is derived by sunlight via the photosynthetic apparatus. Although open ocean waters are clearer than any freshwater lakes on Earth, the incident sunlight is absorbed and scattered by phytoplankton, other particulate and dissolved material, and by the water itself. Although the absorption of light depends on wavelength (red is absorbed most quickly, which is why undersea scapes appear blue), in general the absorption of intensity of “photosynthetically available radiation” (PAR)

decreases over a depth scale of about 100 m. Below this depth, the metabolic costs of respiration exceed the available energy from photosynthesis, and phytoplankton are unable to thrive. The surface sunlit zone, capable of supporting phytoplankton, is called the “euphotic zone.” The production of CaCO_3 does not require energy in the same way as photosynthesis does, and there is some secretion of CaCO_3 by zooplankton such as foraminifera below the euphotic zone, but most CaCO_3 production is associated with phytoplankton called coccolithophorids in the euphotic zone.

A second factor influencing the availability of light to the phytoplankton is mixing. Winds tend to mix the surface waters of the ocean into a distinct mixed layer ranging from a few to a thousand meters thick. The thickness of the mixed layer depends on the contrast between the temperature (and to a lesser extent the salinity) of the surface ocean compared with the deep ocean. In the tropics, warm surface waters are more buoyant than the colder waters below. This density difference inhibits mixing of waters across the stratification boundary, and the mixed layer tends to be thin. Phytoplankton suspended in the surface euphotic zone tends to remain in the euphotic zone. However, at high latitudes, or in subpolar winter, the cooler surface waters mix more readily with subsurface waters, allowing the wind to create a deep mixed layer. The phytoplankton spend at least some of their time at depths deeper than the euphotic zone, limiting their growth. The “spring bloom” in the North Atlantic is a clear demonstration of the effect of mixing. As soon as spring warming stabilizes a shallow mixed layer, the phytoplankton concentrations and photosynthesis rates increase dramatically.

The end of the spring bloom in the North Atlantic (and in other regions) is caused by another factor that limits phytoplankton growth: nutrient ions such as NO_3^- and PO_4^{3-} , which are essential to the manufacture of the biochemical machinery of the cell. Nitrogen is used in the amino acid building blocks of proteins, and phosphorus is used in DNA and in an energy storage molecule called ATP. The elemental ratio of C:N:P in phytoplankton is relatively constant, and has been named the “Redfield ratio.” An astonishing fact about ocean chemistry is that the ratio of N:P in seawater is close to that of phytoplankton, so that to a first approximation, both elements get used up at the same time. Carbon, in contrast, exists in much greater abundance in seawater, so that the nutrients are always depleted first. The mean concentration of PO_4^{3-} in the ocean is $2.2 \mu\text{M}$; when this value is multiplied by a revised C:P Redfield ratio of 135 we estimate that approximately $200 \mu\text{M}$ of the roughly $2,000 \mu\text{M}$ ΣCO_2 concentration in the ocean (N10%) travels with PO_4^{3-} as “metabolic” CO_2 . The metabolic CO_2 represents the maximum impact of biology on the chemistry of the surface ocean.

The effect of the soft-tissue biological pump in the ocean is to deplete NO_3^- and PO_4^{3-} in surface waters by exporting them to the deep ocean. Primary production in the ocean is therefore tied intimately to upwelling or mixing of nutrient-rich subsurface waters into the surface euphotic zone. One place where this occurs is in near-shore waters, where winds drive offshore currents, pulling subsurface waters up from below. Another such place is along the equator, where the change of direction of the Coriolis force pulls surface waters away from the equator, leaving a void that must be filled by upwelling subsurface waters. A third mechanism for bringing nutrients to the surface takes us back to the spring bloom example above; deep wintertime mixing entrains nutrient-rich deep water into the euphotic

zone, recharging it with nutrients for the next spring bloom. After the nutrients are used up by the spring bloom, phytoplankton concentrations and photosynthesis rates decrease for the rest of the summer.

In contrast to the North Atlantic, some regions of the surface oceans, such as the Equatorial Pacific, the North Atlantic, and the Southern Ocean, maintain high concentrations of nutrients in the surface euphotic zone all year round, with no spring bloom. One of the more exciting discoveries of the past decade is that the phytoplankton may be limited by the availability of another nutrient, iron (Fe) (see *Iron and climate change*). Phytoplankton require iron in the minute ratio of approximately $1:10^5$ Fe:C. The oxic form of iron, Fe^{3+} , is relatively insoluble in water, and so seawater tends to become depleted in iron relative to their stocks of NO_3^- and PO_4^{3-} . When this water upwells, it must await the delivery of iron by deposition as dust from the atmosphere. The North Atlantic, according to this theory, is rich in dust deposition, so supports a spring bloom, while the equatorial Pacific is more remote, and is dust and iron limited.

There is a general correspondence between the temperature of the surface ocean and its nutrient content, although this relationship is not absolute. In part, this is because colder surface waters mix more readily with nutrient-rich subsurface. Deeper mixing also creates a situation of light limitation for phytoplankton, as explained above. At any event, the net effect of this correspondence is to set temperature and sea surface nutrients in opposition to each other in their effects on atmospheric $p\text{CO}_2$. The cold temperatures in the Southern Ocean, for example, tend to lower the $p\text{CO}_2$ of surface water, pulling CO_2 into the ocean. However, the high concentration of nutrients in Southern Ocean surface waters indicate that the ΣCO_2 concentration is higher there than it would be if nutrients were depleted, tending to increase atmospheric $p\text{CO}_2$ in the opposite direction from the thermal forcing. On the other hand, the region of the highest CO_2 flux from the ocean to the atmosphere is the equatorial Pacific, where nutrient-rich waters are warmed by the tropical sun, in other words where both temperature and nutrient forcing are working in the same direction.

Most of the organic matter that sinks out of the euphotic zone in the surface ocean never reaches the sea floor, typically 4 km below. It is subject to microbial degradation and to grazing by zooplankton in the mid-water column. The sinking flux of particles can be measured using a device called a sediment trap, which consists of a large funnel or cylinder with a carousel of sealable sample chambers that can sequentially store the falling debris (Honjo, 1996). Several traps are typically tied to a mooring, allowing an assessment of the sinking flux of carbon as a function of depth. These fluxes are generally found to decrease drastically over the top 500 m of the water column.

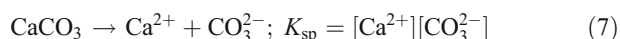
Different chemical components of the debris are removed selectively as they sink. The flux of organic carbon decreases more quickly with depth than does the flux of CaCO_3 or SiO_2 (another type of shelly hard part, the mineral opal is secreted by the phytoplankton diatoms) (see *Diatoms*). Nitrogen and phosphorus are removed more quickly than carbon, as indicated by increasing C:N and C:P ratios in sediment traps. The flux of CaCO_3 appears rather uniform with depth in sediment traps, but budgets for CaCO_3 production and deposition on the sea floor, and for alkalinity in the water column, seem to indicate a substantial dissolution of CaCO_3 in the mid-water column. The discrepancy with sediment trap results may be caused by biases in trap efficiency in shallow waters (Yu et al., 2001) or by CaCO_3 dissolution (Betzer et al., 1984) within the traps.

Organic carbon by itself is not sufficiently dense to sink very quickly through seawater, if at all, and so attention has focused on the role of CaCO_3 , SiO_2 , and wind-blown continental material as “ballast” (Armstrong et al., 2002; Klaas and Archer, 2002). This theory is consistent with the sediment trap data in that while the fluxes of the various constituents vary widely in space and time, the ratio of organic carbon to ballast in the deep traps, and in particular to CaCO_3 , seems much more stable. Only a small fraction of the organic matter produced in the surface ocean makes it to the deep sea, so the ballast model predicts that the absolute flux of organic carbon to depth might be determined by the fluxes of ballast. However, the ballast model does not explain the trap data in the top kilometer of the water column, where the organic carbon to ballast ratio is higher and more variable than in the deep sea.

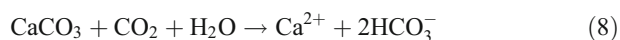
CaCO_3 compensation and the pH of the ocean

We have seen how the biological pump affects the $p\text{CO}_2$ of the atmosphere, by pumping carbon and nutrients from the surface ocean to the deep. In addition to this direct effect, the biological pump has an indirect effect on $p\text{CO}_2$, called carbonate compensation (Broecker and Peng, 1987). CaCO_3 is produced biologically, mostly in the surface ocean. Some fraction of this CaCO_3 reaches the sea floor, and its chemical constituents (Ca^{2+} , one ΣCO_2 , and two alkalinities) are permanently removed from the ocean as it is buried. This output is balanced by input from the dissolution of rocks, mostly sedimentary CaCO_3 , a process called weathering on land. The idea is that the pH of the ocean adjusts; acting as a stable negative feedback to insure that the output of CaCO_3 by burial balances the input from weathering. As we have seen, a change in seawater pH will have a large impact on the speciation of carbon, and therefore on $p\text{CO}_2$ (see *Paleo-ocean pH*).

The input of dissolved CaCO_3 to the ocean derives from the chemical weathering of rocks on land (see *Weathering and climate*). The saturation state for CaCO_3 dissolution is given by the reaction

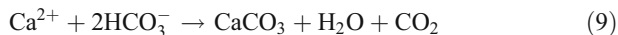


If the product of the reactants, Ca^{2+} and CO_3^{2-} , is less than the value of K_{sp} then the solution is undersaturated and CaCO_3 will tend to dissolve. In practice, the CO_3^{2-} combines with CO_2 and water to yield the overall reaction



where the Ca^{2+} and HCO_3^- reflect the dominant ion pair in most river water. The reactant CO_2 is derived ultimately from the atmosphere, but CO_2 partial pressures in soil gas are elevated to an order of magnitude higher than atmospheric values by the action of plants and the microbial respiration of soil carbon. River water, reflecting its origin as soil water, is typically strongly supersaturated in CO_2 , and close to saturation with respect to CaCO_3 at that $p\text{CO}_2$. In areas where the rate of freshwater runoff is extremely high, the dissolution reaction may not have time to keep up with the flux of distilled rainwater, and the solution concentrations will drop. The lithology, or rock type, of a region also has an impact on the chemistry of rivers. To a first approximation, however, we expect that the total flux of dissolved CaCO_3 to the ocean depends primarily on the total rate of fresh water runoff to the oceans, and secondarily on temperature, soil biological activity ($p\text{CO}_2$), terrain type,

and other variables. Once the Ca^{2+} and alkalinity are delivered to the ocean, they are used to produce CaCO_3 according to the reaction



returning the atmospheric CO_2 that weathering borrowed back to the atmosphere.

CaCO_3 production occurs in shallow ocean waters and in surface waters overlying the deep sea (Milliman, 1993). In many cases, in coral reefs for example, the production rate of CaCO_3 seems to mirror the rate of organic carbon production, as though the organisms calcified in order to shift the pH balance back toward the acidic, ensuring a readily available supply of dissolved CO_2 . Some fraction, roughly half, of the CaCO_3 produced in surface waters dissolves in the water column, and the rest reaches the sea floor to be redissolved or buried.

The fate of CaCO_3 landing on the sea floor depends strongly on depth in the ocean, because the solubility of CaCO_3 increases with pressure (Archer, 1996). This is because the dissolution reaction entails a small decrease in volume as CaCO_3 dissolves; an increase in pressure encourages the system to find the volumetrically smaller, dissolved, form. In addition, there is a surface/deep contrast in the concentration of CO_3^{2-} , resulting from the biological pump. We have already seen that the effect of the biological pump, dominated by the soft-tissue pump, on the carbon chemistry of the water column is to deplete the surface waters in ΣCO_2 . As a result of the pH equilibrium reaction 3, dissolved CO_3^{2-} is increased over the mean ocean value. The concentration of CO_3^{2-} goes down with depth, but the amount of CO_3^{2-} required in equilibrium goes up with depth. These factors combine to create a "saturation horizon" in the water column, above which CaCO_3 is supersaturated, and below which it is undersaturated. Some fraction of the CaCO_3 raining to the sea floor lands on topographic highs, in sediments overlain by supersaturated water, and tends to be buried. CaCO_3 landing in abyssal sediments tends to dissolve. The distribution of CaCO_3 on the sea floor resembles snow-capped mountains, with preservation on the mountaintops and none in the valleys. The depth of the "snow line," where CaCO_3 is no longer preserved in sediments, has been called the carbonate compensation depth, or CCD. In practice, sedimentary CaCO_3 dissolution is complicated by the rate of diffusive contact of the pore water with overlying water, and by other sediment reactions such as organic carbon respiration. Not all of the CaCO_3 deposited above the saturation horizon is buried, and some of the CaCO_3 flux to undersaturated sediments may be preserved. The CCD (a property of the solid sediment) is not the same as the saturation horizon (a property of the water column). In most parts of the ocean, the CCD is 0.5–1.5 km deeper than the saturation horizon (see *Carbonate compensation depth; Carbon dioxide, dissolved (ocean)*).

The pH-determining mechanism of the ocean, called carbonate compensation (beware of the unfortunate overlap with the separate concept of the carbonate compensation depth or CCD), arises from the need for the ocean to balance the input and burial rates of CaCO_3 . The way the ocean regulates burial to balance weathering is through the pH of the ocean. The input of CaCO_3 from weathering tends to drive the ocean towards the basic, as a source of excess alkalinity. The neutralization of the primary CO_3^{2-} dissolution product by atmospheric CO_2 to produce HCO_3^- in Reaction 8 is a consumption of the acid from the atmosphere and ocean by CaCO_3 , a base. If this source of base were unbalanced by CaCO_3 burial

in sediments, the ocean would get progressively more basic over time. This would increase the proportion of the dissolved carbon that is CO_3^{2-} , increasing the depth range over which CaCO_3 is stable and increasing the burial rate of CaCO_3 , until ultimately the burial rate would balance the weathering rate. The time scale over which this relaxation takes place is 5–10 kyr (Archer et al., 1997).

Numerous factors can drive CaCO_3 compensation. An increase in chemical weathering would drive the CCD deeper, lowering atmospheric $p\text{CO}_2$. Today, a significant fraction of CaCO_3 deposition occurs on continental shelves and carbonate platforms, which may have been exposed during times of lowered sea level such as the Last Glacial Maximum (LGM). A decrease in shallow-water burial would have required an increase in deep sea burial to compensate, also lowering $p\text{CO}_2$. A decrease in the production rate of CaCO_3 , driven perhaps by ocean chemistry or climate change, would require that a greater proportion of the CaCO_3 produced be buried, requiring a deeper saturation horizon and CCD, resulting in lower $p\text{CO}_2$. Finally, a CaCO_3 compensation response in the future will ultimately neutralize much of the fossil fuel CO_2 that humankind is releasing to the atmosphere. The CO_2 invasion will acidify the ocean, lowering $[\text{CO}_3^{2-}]$ and decreasing CaCO_3 burial. Excess CaCO_3 source to the ocean will drive the ocean toward the basic, neutralizing the excess CO_2 into the form of dissolved HCO_3^- in the ocean water column.

David Archer

Bibliography

- Archer, D.E., 1996. An atlas of the distribution of calcium carbonate in sediments of the deep sea. *Glob. Biogeochem. Cycles*, **10**, 159–174.
- Archer, D., Khesghi, H., and Maier-Riemer, E., 1997. Multiple timescales for neutralization of fossil fuel CO_2 . *Geophys. Res. Lett.*, **24**, 405–408.
- Armstrong, R.A., Lee, C., Hedges, J.I., Honjo, S., and Wakeham, S.G., 2002. A new, mechanistic model for organic carbon fluxes in the ocean based on the quantitative association of POC with ballast minerals. *Deep Sea Res. II*, **49**, 219–236.
- Betzer, P.R., Byrne, R.H., Acker, J.G., Lewis, C.S., and Jolley, R.R., 1984. The oceanic carbonate system: A reassessment of biogenic controls. *Science*, **226**, 1074–1077.
- Broecker, W.S., and Peng, T.H., 1982. *Tracers in the Sea*. Palisades, NY: Eldigio Press.
- Broecker, W.S., and Peng, T.H., 1987. The role of CaCO_3 compensation in the glacial to interglacial atmospheric CO_2 change. *Glob. Biogeochem. Cycles*, **1**, 15–29.
- Dickson, A.G., and Millero, F.J., 1987. A comparison of the equilibrium constants for the dissociation of carbonic acid in seawater media. *Deep Sea Res.*, **34**, 1733–1743.
- Honjo, S., 1996. Fluxes of particles to the interior of the open oceans. In Ittekkot, V., Aschauer, P., Honjo, S., and Depetris, P. (eds.), *Particle Flux in the Ocean*. New York: Wiley.
- Klaas, C., and Archer, D.E., 2002. Association of sinking organic matter with various types of mineral ballast in the deep sea: Implications for the rain ratio. *Glob. Biogeochem. Cycles*, **16**, 10.1029/2001GB001765.
- Longhurst, A., 1998. *Ecological Geography of the Sea*. San Diego, CA: Academic Press, 398pp.
- Milliman, J.D., 1993. Production and accumulation of calcium carbonate in the ocean: Budget of a non-steady state. *Glob. Biogeochem. Cycles*, **7**, 927–957.
- Stumm, W., and Morgan, J.J., 1981. *Aquatic Chemistry*. New York: Wiley, 780pp.
- Wanninkhof, R., 1992. Relationship between wind speed and gas exchange over the ocean. *J. Geophys. Res.*, **97**(C5), 7373–7382.
- Yu, E.-F., Francois, R., Bacon, M.P., Honjo, S., Fleer, A.P., Manganini, S.J., Loeff, M.M.R.v.d., and Ittekkot, V., 2001. Trapping efficiency of bottom-tethered sediment traps estimated from the intercepted fluxes of ^{230}Th and ^{231}Pa . *Deep Sea Res. I*, **48**, 865–889.

Cross-references

[Astronomical Theory of Climate Change](#)
[Carbon Cycle](#)
[Carbon Dioxide, Dissolved \(Ocean\)](#)
[Carbonate Compensation Depth](#)
[Coccoliths](#)
[Diatoms](#)
[Foraminifera](#)
[Iron and Climate Change](#)
[Paleo-Ocean pH](#)
[Phosphorus Cycle](#)
[Weathering and Climate](#)

MARINE CLAY MINERALS

Clay minerals found in the marine environment may be arbitrarily divided into two genetic groups: those forming in and those being transported into marine waters and sediments. Clay minerals forming in seawater and sediments link directly to diagenetic processes and are not examined in detail here. Detrital clay minerals can be compared to source terrain or provenance and hinterland climate, so are described here.

Clay minerals forming in the marine environment commonly display neoformal features, as they are often secondary to some precursor. Although this neoformalization can occur in the water column or within surficial sediments, this is patently a diagenetic process with links to adjacent sea and land surface conditions (such as paleoclimate) that are too tenuous for discussion here. Such links do exist; an example is given by Worden et al. (2000). Early (near-surface) diagenetic clay minerals include the group of clay minerals termed glauconite, which may replace shells (e.g. foraminifera) or clastic grains (e.g. feldspars). Deep burial diagenetic marine clay minerals are beyond the scope of this description.

Clay minerals being transported into the marine environment are detrital in origin, being transported by water, ice, air, or volcanic eruption. The types of clay minerals are thus variable, depending on the source terrain lithology, weathering characteristics during erosion and transport, transport time and method, and final depositional environment. Thus, a granitic source terrain will contain abundant feldspars; these may be weathered in humid conditions to form kaolinite which will be deposited close to shore as it flocculates and forms large clay crystals. However, at any point in this story, our assumptions may be incorrect! In an arid environment, kaolinite production will be diminished, even with the correct source lithology (granite). Clays may be deposited as floodplain soils where they become neoformal as successor clays during temporary storage prior to a second phase of erosion and marine deposition that will not reflect the hinterland lithology. The moral of this story is that caution is required during interpretation of both Recent and modern marine clay mineral assemblages, as well as the more problematic ancient materials.

The mineral structure of clays is problematic (Parker and Rae, 1998). Since clays are layer silicates, often around 2 μm in size, we are dependent on the Scanning Electron Microscope, Transmission Electron Microscope, and X-ray diffractometer in performing mineralogical analysis. This article follows the United States Geological Survey convention (<http://pubs.usgs.gov/of/of01-041/htmldocs/clay.htm>) of listing "groups" of minerals

where appropriate, roughly by overall abundance, examining the interpretation possibilities and problems in each case.

The abundant clay minerals of recent and ancient marine sediments (in no particular order)

Chlorite group

The chlorites are Mg, Al, Fe aluminosilicates of the brittle mica suite. They originate as hydrothermal minerals, but are most abundant in chlorite schists and greenschist metamorphic terrains (their most common provenance). Their occurrence in marine sediments as detrital components reflects this primary source terrain as the ultimate point of their origin and a clear association with physical weathering (as opposed to chemical weathering and thus mineral degradation). Rapid erosion by glaciers and rivers of mountain terrains are the most common "first pass" interpretation proxy for the chlorite group. The problems with chlorites stem from their widespread occurrence and robust nature. Thus, they may survive more than one cycle or erosion, being eroded out of their primary source terrain, and subsequently deposited and stored in a secondary sedimentary rock, before being re-eroded and deposited out of context from their original source. Chlorites may also form during burial diagenesis, thus potentially confusing any studies of paleoweathering or paleoclimates.

Illite. Illite comprises a K, Al aluminosilicate of the mica group. They originate as the weathering product of feldspars and other clay minerals, especially the degradation of muscovite. Illites may form hydrothermally in alkaline conditions rich in K, often as an inter-layered mineral structure with smectites ('mixed layer illite-smectites'). Thus, they have a similar, if lower, metamorphic grade origin to chlorites. A very common component of detrital marine sediments, illite is notable usually only by its absence or abundance. A common interpretation strategy is to consider illite as the ever-present "clay mineral rain" of the seas, to be used as a ratio against smectite or kaolinite in paleoweathering studies. The same interpretation problems pertain as with the chlorite group: illite is robust and may survive many sediment cycles; thus, its original provenance is rarely clear. The crystallinity of illite is often maintained during erosion, reflecting the metamorphic grade of the original hinterland.

Kaolinite group

The kaolinites comprise hydrous aluminosilicates of the serpentine-kaolin group. Their primary origin is associated with the hydrothermal alteration of feldspars and other silicates. Humid weathering also promotes similar degradation and the kaolinitization of feldspars is common under such climatic conditions and is accelerated by warm, humid conditions. Volcanic ashes often contain kaolinite. The kaolinites form one of the most abundant and useful paleoclimate proxy materials as their detrital presence always suggests humid conditions at some point in their origin. Interpretation problems are also abundant of course! A non-feldspar-bearing hinterland terrain may be humid and warm, yet produce no kaolinite. As mentioned above, kaolinite is also abundant and thus its presence is not always enough to determine changing paleoclimatic conditions. Ratios of kaolinite with other minerals have commonly been employed in determining horizons of paleoclimate change. Changing ratios, when compared favorably to other paleoclimate proxies (stable isotopes, palynomorphs) form a useful method of identifying episodes of past climate change (Chamley, 1989). The tendency of kaolinite to flocculate and settle close to shore thus means that changing ratios may also reflect variable

sea-levels, not changes in paleoweathering of the hinterland. Finally, kaolinite is a common shallow burial diagenetic mineral.

Smectite group

The smectites are variable composition Ca, Na, Al, Mg Fe aluminosilicates for which montmorillonite is a practical synonym. Smectites originate from the weathering of basic and intermediate igneous and meta-igneous rocks, as well as being a common constituent in volcanic ashes (bentonites, fuller's earths). As a result of weathering, soils forming in temperate and humid climates, especially where seasonally wet, commonly contain smectite. Thus, their proxy interpretation is similar to that of the kaolinites, if not quite as clear. Problems in interpreting the presence and changing abundance of smectites in rock successions include the inverse problem to kaolinite: commonly being a small crystal, smectite tends to stay buoyant for longer than other clays and thus is deposited offshore. For this reason, it has been associated with deep marine and transgressive conditions – the paleoclimate “signal” in its abundance may be masked by relative sea-level changes. An even greater hazard to smectite interpretation is its volcanic origin, as ash-falls can appear randomly in the sedimentary record, masking any paleoclimatic control. Detailed petrographic investigation of the presence of volcanic glass shards or ash-fall textures may resolve this interpretation hazard.

Mixed-layer clays. Many of the clay mineral crystal groups listed above and below can become interstratified. Most common are the illite-smectites and chlorite-smectites. Such clays often have a hydrothermal origin. In soils, they form when conditions are episodic, such as wetting and drying cycles. Thus, the presence of mixed-layer illite-smectites has been related to seasonal climates. Interpretation is hazardous, however, as these minerals are difficult to characterize.

The less abundant clay minerals of recent and ancient marine sediments (in no order)

For the sake of brevity, I have selected two of the many tens of rarer clay minerals to demonstrate their use in paleoclimatic interpretations.

Sepiolite and palygorskite

Sepiolite is part of the palygorskite group and possesses a Mg-bearing, hydroxide chain-like silicate structure. Palygorskite is chemically and structurally more complex. Both are of use to paleoclimatologists, especially palygorskite as it forms in near-surface arid conditions. If proven to be detrital and found in marine sediments, an arid hinterland can be assumed. The problem is its rarity and actual provenance as wind-blown dust may be transported in the stratosphere from arid zones to those of a humid nature, confusing the interpretation.

Alastair Ruffell

Bibliography

- Chamley, H., 1989. *Clay Sedimentology*. Berlin: Springer, 349pp.
 Parker, A., Rae, J.E. (eds.), 1998. *Environmental Interactions of Clays: Clays and the Environment*. Berlin: Springer/GmbH & Co. KG; 210pp.
 Worden, R.H., Ruffell, A.H., and Cornford, C., 2000. Surface temperature, sequence stratigraphy and deep burial diagenesis. *Clay Miner.*, **35**, 13–23.

Cross-reference

[Mineral Indicators of Past Climates](#)

MARS: WATER AND PAST CLIMATES

Mars has long been the focus of a great deal of attention, largely due to the presence of water and the potential for harboring life, either now or in the past. Until recently the question of life on Mars has focused on whether Mars was once “warm and wet” and Earthlike or “cold and dry” and barren like the Moon. The recent orbiter and rover missions have revealed that Mars is a remarkably diverse place and these simple labels no longer fit. Mars has experienced a striking diversity of environments from extremely arid deserts, to standing water in lakes, to a planet blanketed by snow and ice. The key questions in the search for life have therefore become how warm, how wet, and most importantly, for how long?

The evidence for these past environments is contained in the rocks, minerals, and landforms of Mars. Minerals in particular contain the record of geologic processes and ancient environments in which they formed; certain minerals only form in water, whereas others are rapidly destroyed in wet environments.

Mars is a volcanic planet

The first close-up images of Mars revealed a surface dotted with massive volcanoes and provided the first hints of a planet dominated by volcanic processes (Figure M9). However, the definitive information on the composition of Martian rocks has come from the visible, infrared, neutron, and gamma ray spectrometers that have been used to map mineral and elemental compositions. Spectral data from Earth-based telescopes and early spacecraft missions provided hints of compositional differences and the presence of iron-bearing minerals (e.g., Soderblom, 1992). The first global maps of the minerals, rocks, and ice on the surface, as well as the dust and condensates in the atmosphere of Mars were made using data from the Thermal Emission Spectrometer (TES) infrared spectrometer aboard the Mars Global Surveyor (MGS) spacecraft (e.g., Christensen et al., 2001). These observations have been followed up by near-IR spectra from the Mars Express OMEGA experiment (Mustard et al., 2005).

TES infrared spectra have shown that the rocks and sands are composed almost entirely of volcanic minerals characteristic of basaltic rocks (e.g., Christensen et al., 2001). These common minerals – feldspar, pyroxene, and olivine – are found in the basaltic lavas that also cover much of the Earth, from the ocean floor to the volcanic islands of Hawaii and Iceland. OMEGA has confirmed the widespread occurrence of olivine and pyroxene over much of the surface (Mustard et al., 2005). The rocks in the ancient cratered terrains are basaltic in composition, whereas the younger rocks of northern lowlands have more glass, more silica-rich minerals, and fewer iron-bearing pyroxene and olivine minerals (Christensen, 2001; Mustard, 2005). Volcanic rocks high in silica typically form by complex processes that include remelting of existing basalts, fractional crystallization, or melting of a water-rich source region. The possible existence of higher-silica rocks on Mars may imply more water in the mantle than on Earth, or differing temperatures or pressures at which melting occurred. Alternatively, the high-silica components may have been produced by minor aqueous weathering of basalt (e.g., Wyatt et al., 2004). In either case, the vast majority of the Martian rocks is volcanic in origin.



Figure M9 Apollinaris Patera, a 200 km wide ancient volcano, is seen in this mosaic of THEMIS infrared images. Apollinaris erupted huge volumes of ash that have been carved into channels by water.

Early fluvial activity

Many of the ancient, heavily-cratered terrains of Mars contain channels that were eroded by water. Analysis of the global distribution of these channels has shown that extensive fluvial activity occurred over portions of the ancient highlands (Figure M10). These data indicate a period of erosion early in Mars history that produced extensive infilling of craters, the development of local and regionally integrated drainage networks, and the formation of deltas and alluvial fan deposits (e.g., Gulick and Baker, 1989; Malin and Edgett, 2003; Howard et al., 2005). The development of these drainage networks and depositional fans is suggestive of runoff from precipitation or rapid melting of snow, possibly aided by groundwater sapping. It has also been suggested that Mars had extensive oceans on the basis of images and topographic data that suggest shorelines, smooth ocean floors, and glacial features (Baker et al., 1991).

The prevailing environment during the early period of fluvial erosion may have been one of a cold, thin atmosphere with very limited mechanical erosion, punctuated by short periods of thicker atmosphere and greater erosion. These thicker atmospheres may have been produced by periodic climate changes (e.g., Pollack and Toon, 1982), or generated in the impact cratering process and lasting hundreds to thousands of years (Segura et al., 2002). Fluvial erosion appears to have reached

a climax in the late Noachian period ($\sim 3\text{--}3.5$ Gyr) (Howard et al., 2005), with only limited activity since that time that is primarily associated with large catastrophic flood events, isolated channel formation, and minor incision of small gullies (Malin and Edgett, 2000).

A cold, dry Mars

Although there is strong evidence for early fluvial activity in isolated locations, the global mineral mapping shows an ancient, cratered surface whose original volcanic minerals are still largely preserved, implying very little alteration by water. Olivine and pyroxene form at very high temperatures ($>800^\circ\text{C}$), but are unstable in the presence of water at the surface as on Earth today. However, ancient pyroxene- and olivine-rich basalts are common; they are exposed more than 4.5 km below the surface in the walls of Valles Marineris and throughout the equatorial plains (Hoefen et al., 2003; Hamilton and Christensen, 2005; Mustard et al., 2005). Near the summit of Syrtis Major are a series of old, volcanic cones and flows composed of glassy lavas (Christensen et al., 2005) that are also highly susceptible to chemical erosion. The occurrence of these unstable minerals suggests that neither sub-surface hydrothermal activity nor surface aqueous weathering has significantly affected these very old rocks since they were emplaced.

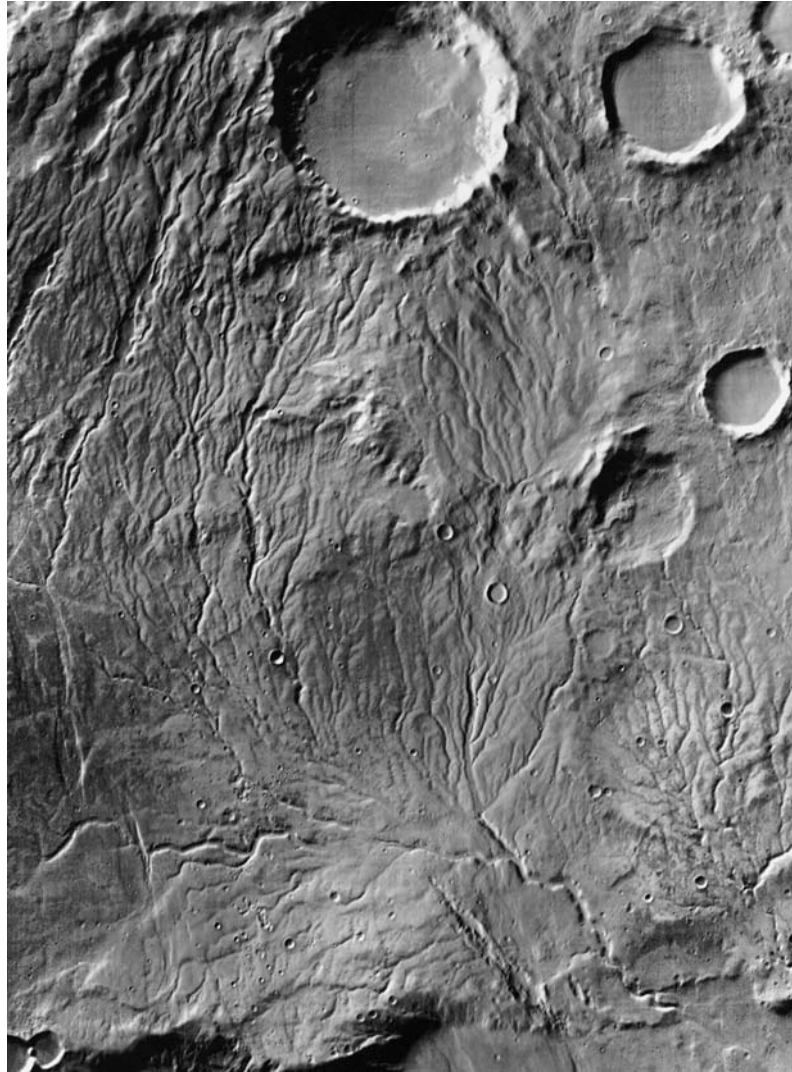


Figure M10 Evidence of fluvial processes early in Martian history is illustrated in the drainage network of Warrego Valles. This image is a mosaic of THEMIS daytime infrared images covering an area ~ 200 km wide centered near 42° S, 266° E.

The Spirit rover at Gusev Crater has provided additional mineralogical evidence for limited aqueous weathering. The rocks on the crater floor are volcanic and extremely old, perhaps as much as 3 billion years, yet the Mini-TES, Mössbauer, and Alpha Particle X-ray spectrometer (APXS) spectrometers and cameras on the rover clearly show the presence of olivine and pyroxene that have been very little altered since these lavas first cooled (McSween et al., 2004). These pristine volcanic rocks provide evidence that these plains have not been exposed to any significant amount of water since these lavas were erupted. They may have been “wetted,” as evidenced by thin coatings on some rocks, but they have not been “soaked.”

What is not found

In assessing the climate history of Mars, it is important to consider what rock types are not present. On Earth, vast deposits of carbonate rocks, composed of CO_3^{2-} with calcium, magnesium,

or iron, have precipitated from warm oceans through interactions between CO_2 gas, water, and mineral grains. If Mars ever had a warm ocean, it has been suggested that thick deposits of carbonates would have also formed through interactions with its CO_2 atmosphere. Spectra from TES and the Mini-TES on the Mars Exploration Rovers have shown that small amounts of carbonate are present in the ubiquitous Martian dust (Bandfield et al., 2003). These minerals most likely formed by direct interaction with water vapor in the atmosphere. However, no evidence of extensive carbonate rock layers has been found by the TES, THEMIS, or OMEGA instruments (Christensen et al., 2001; Bibring et al., 2005), suggesting that if Mars ever had oceans, they were either too cold, too short-lived, were covered by ice that limited interactions with the atmosphere, or had unique chemical conditions that prevented carbonates from forming. Clay minerals, which form primarily by aqueous weathering and are common on Earth, have also been shown by OMEGA and TES to be rare on Mars (Christensen et al.,

2001; Bibring et al., 2005), again suggesting that Mars has experienced little aqueous alteration.

While lakes and drainage networks clearly point to fluvial processes, the lack of extensive carbonates and clays, together with the presence of original olivine, pyroxene, and glass, argue that these processes must have been relatively short-lived. Thus, on a global scale, aqueous chemical weathering appears to have been a relatively minor process throughout much of Martian history.

Meridiani – a locally wet Mars

The Meridiani Planum site explored by the Opportunity rover was chosen based on spectral evidence from the TES for high abundances of crystalline hematite, an iron oxide that forms by several processes, most of which involve water (e.g., Christensen and Ruff, 2004) (Figure M11). Hematite can form by precipitation from fluids circulating through saturated sediments or by deposition of precursor water-bearing iron minerals that are dehydrated over time. The mineralogic evidence for water at Meridiani is corroborated by the unique appearance of the hematite-rich surface in Meridiani indicative of water deposition: the Meridiani rocks are finely layered and easily eroded, suggesting a sedimentary deposit; they sit atop an older, heavily cratered surface, implying a different process

of formation; and they embay pre-existing channels, suggesting that these rocks were deposited in water rather than covering the entire landscape as volcanic ash or windblown dust (Christensen and Ruff, 2004).

Upon landing, Opportunity's spectrometers and cameras confirmed the importance of water at Meridiani (Squyres et al., 2004). Outcrops of layered sedimentary rocks were observed by Opportunity's cameras, and the Mössbauer, APXS, and Mini-TES spectrometers found that these rocks contained high (30–40%) abundances of sulfates most likely formed by evaporation of sulfur-rich water. The hematite occurs as 1–5 mm diameter spheres that are embedded within the rock layers, and were likely formed by iron-rich fluids circulating through the lake sediments (e.g., Squyres et al., 2004). The margins of this body of water may not have extended much beyond the current deposits of hematite seen from orbit, making this a large lake (Christensen and Ruff, 2004), rather than part of a global ocean. Several nearby craters also have hematite-rich layered rocks, suggesting they may have held separate lakes (Christensen and Ruff, 2004).

The coarsely-layered rocks exposed at the base of Burns Cliff in Endurance Crater appear to have been formed by migrating dunes, whereas the layers at the top of the cliff are made of sulfate-rich sediments deposited in water (Grotzinger



Figure M11 The distribution of crystalline hematite discovered by TES in Meridiani Planum. The TES hematite abundances are shown superimposed over a mosaic of THEMIS daytime infrared images illustrating the complex morphology of the Meridiani region.

et al., 2005) (Figure M12). These layers may record variations in climate from arid eolian dunes, to wet evaporating playas where the sulfate salts were formed, to a groundwater system that formed the hematite spheres (Grotzinger et al., 2005). This system may have persisted for thousands of years.

Evidence for standing water is also seen at Aram Chaos, a 300-km diameter crater basin that is filled with layered rocks that contain both hematite and sulfate and show evidence for a lake created by the release of massive amounts of sub-surface water (Glotch and Christensen, 2005; Gendrin et al., 2005). Finely-layered erodable rocks that contain hematite and sulfate are also found in the troughs of Valles Marineris, suggesting that they also were deposited in standing water.

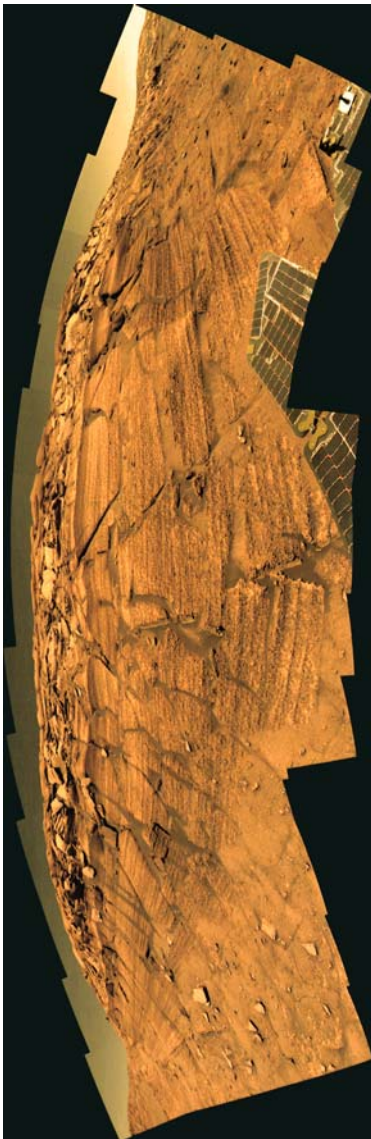


Figure M12 Burns Cliff, Endurance Crater. After descending into Endurance Crater, the Spirit rover drove to Burns Cliff, a spectacular rock outcrop ~7 m high made of finely-layered rock. These layers are composed of basaltic sands and evaporite minerals that were deposited in a varying environment of wind and water.

These discoveries provide strong evidence that water was stable in isolated regions for brief periods of time. The factors that caused water to accumulate and allowed it to remain at these sites (perhaps a combination of heat from sub-surface volcanic activity, high salt concentrations that lowered the freezing temperature, or a protective covering of ice over water released by catastrophic floods) are currently unknown.

Modern snow and ice

There is growing evidence that Mars has a large inventory of water, currently in the form of ice at mid- to high-latitudes. Both poles have deposits of ice or ice-rich sediments that are up to three km thick and cover more than 500,000 km². Temperature measurements have demonstrated that the perennial north polar cap was water ice, whereas a layer of CO₂ ice remains over much of the south polar cap even through the summer (Kieffer, 1979). Recent measurements by the MOC, THEMIS, and OMEGA instruments have shown that windows of water ice are exposed within the south polar cap, indicating that water ice is present there beneath a thin layer of overlying CO₂ ice (Byrne and Ingersoll, 2003; Titus et al., 2003; Langevin et al., 2004).

A substantial inventory of water ice was discovered using data from the Gamma Ray Spectrometer (GRS) and the High Energy Neutron Detector (HEND) instruments on Mars Odyssey (Feldman et al., 2002). The regions poleward of ~60° in both hemispheres are made up of more than 80% water ice (Figure M13). Such high ice abundances could not have formed by diffusion of water vapor from the atmosphere into the pores of the soil. Ice must have been deposited as a layer of snow or frost.

These ice deposits are reservoirs of water that can migrate as the climate changes. The Martian climate is predicted to change dramatically as the tilt of the Martian spin axis oscillates by as much as 20° on timescales of 10⁵–10⁶ years (Ward, 1974). These changes likely produce a significant mobilization of polar water, redistributing it to lower latitudes as snow and ice (e.g., Jakosky and Carr, 1985). When the axis is oriented more perpendicular to the Sun (low obliquity), the poles are the coldest places on the planet and water migrates to them. As the axis tilts toward the Sun (high obliquity) the poles warm, the mid-latitudes cool, and water, in the form of snow and ice, migrates to the mid-latitudes. Remnants of these ice deposits can be found in unusual landforms throughout the mid-latitudes. One type is a “basketball” textured terrain that only occurs between 30° and 50° latitude in both hemispheres and was suggested to have formed as soils cemented by ice deposited during the last “ice age” lost their ice and eroded as the climate warmed (Mustard et al., 2001).

A second type of deposit occurs preferentially on cold, pole-facing slopes (Carr, 2001). These “pasted on” slope mantles are up to 10 m thick, often occur in hollows, and can have features suggestive of flow (Figure M14). These characteristics suggest an ice-rich layer that was once more extensive but has been removed from all but the coldest, pole-facing slopes.

One of the more remarkable discoveries made by the MGS MOC camera is the small young gullies that also occur between ~30° and ~50° latitude in both hemispheres (Malin and Edgett, 2000) (Figure M14). These gullies have been proposed to form from discharge of liquid water from sub-surface aquifers, the rapid release of liquid CO₂, dry landslides, the melting of ground ice that percolates to an impermeable layer, the melting of pore ice that diffused inward from the atmosphere during periods of colder temperatures, or through

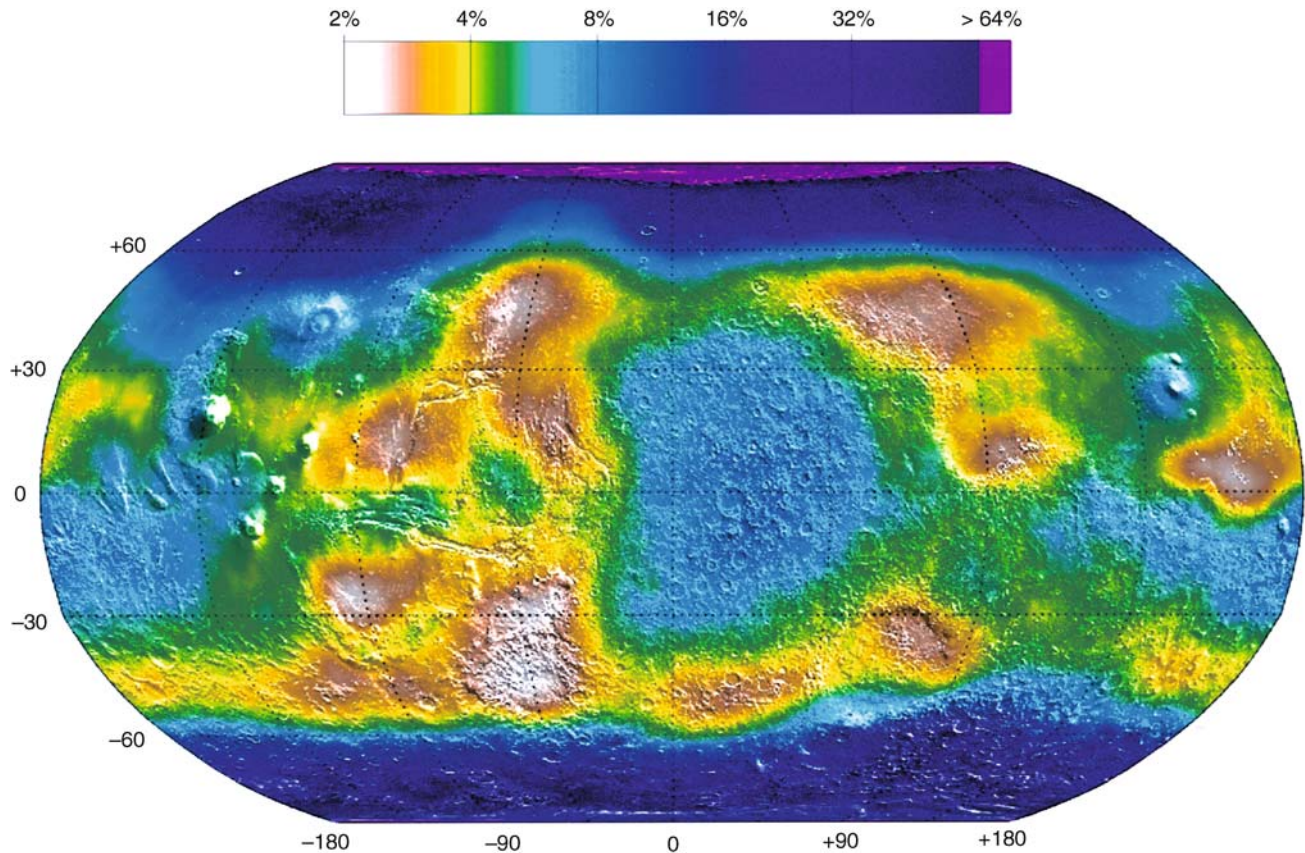


Figure M13 The distribution of sub-surface water ice. This global map was made using data from the Neutron Spectrometer that is part of the Odyssey Gamma Ray Spectrometer suite. Hydrogen in the form of water ice occurs in abundances $>80\%$ poleward of $\sim 60^\circ$ in both hemispheres (data are adapted from Feldman et al., 2002).

melting of a snow layer deposited during periods of higher obliquity when surface ice was stable at these latitudes (see recent review by Heldmann and Mellon, 2004).

The proposed melting of pore ice does not account for the fact that as the surface and sub-surface temperatures warm, the upper soil layer will become desiccated before significant liquid water can be produced (Mellon and Phillips, 2001). Water release from sub-aquifers can explain gully morphology, latitudinal distribution, and slope position (Heldmann and Mellon, 2004). The primary arguments against this model are the presence of gullies on isolated knobs and dunes with no obvious aquifer source. An aquifer source is a survival and recharge mechanism that would allow these aquifers to persist to the present, their formation only at latitudes poleward of 30° , and the ability of water to remain liquid long enough to carve gullies up to 2 km long under current atmospheric conditions.

In the snowmelt model (Lee et al., 2001; Christensen, 2003), the snow acts as a greenhouse, absorbing sunlight beneath the surface, but preventing the heat from being re-radiated (Clow, 1987). This layer of snow also acts as an insulating layer that limits evaporation of the melted water. As a result, snow can melt 10–20 cm beneath the surface and remain liquid, even when the surface temperatures are far below freezing (Clow, 1987). In this model (Christensen, 2003), a layer of snow is deposited at mid-latitudes during periods of high obliquity. As the obliquity decreases and the mid-latitude climate warms, the snow melts

and erodes gullies in the snow and underlying surface. Eventually most of the snow completely melts, revealing gullies carved in the hillsides. Patches of snow remain today as “pasted on” deposits where they are protected against sublimation by a layer of desiccated dust/sediment. Melting could be occurring at the present time in favorable locations in these snowpacks, and these patches may provide fascinating locales in which to search for life, if it exists (Christensen, 2003).

Summary – and where to look next

The new tools that have permitted a more detailed view of Mars from orbit and the surface have shown that Mars is remarkably diverse. The role of water has varied tremendously at different times and in different places on Mars. There is no doubt that Mars experienced periods of channel formation early in its history, yet those ancient rocks contain minerals that quickly break down in a wet environment, and also lack extensive clays and carbonates. The current climate is very dry and cold, yet the Opportunity rover landed on the floor of an ancient body of water. Finally, liquid water is not stable at the surface today, yet recent gullies emerge from modern aquifers or beneath modern snowpacks.

How can these apparently conflicting views be reconciled? One possibility is that the erosional periods were too brief for extensive chemical weathering to have occurred – mechanical erosion of channels can proceed much more rapidly than

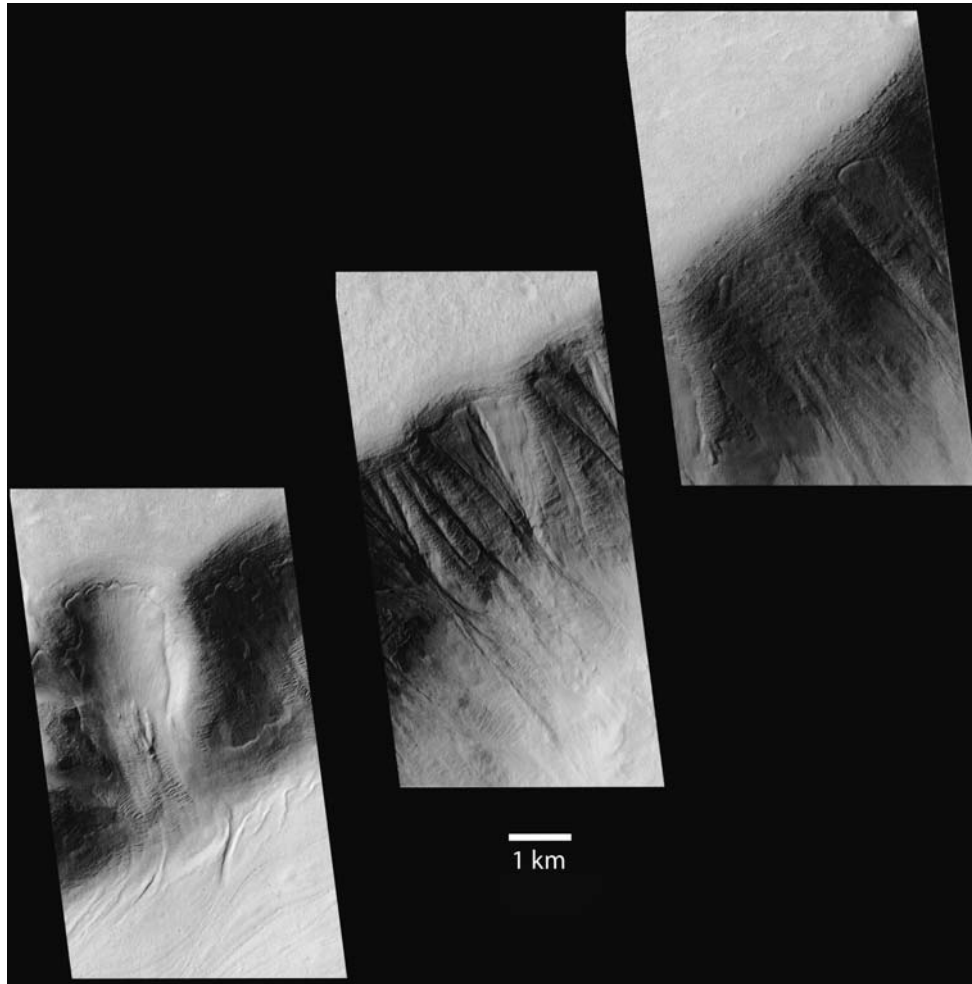


Figure M14 Ice-rich mantles and associated gullies on poleward facing slopes in the Southern Hemisphere. This collage shows MOC images from the northwest wall of Dao Valles, between 33° and 35° S. These images show well developed flow features with compressive ridges that are strongly suggestive of ice (*left panel*), mantles of ice-rich material with gullies that are only present where the mantles are lacking (*center panel*), and depressions with associated gullies, some of which still have mantles, whereas others are free of mantling material (*right panel*). These landforms could be explained by the melting of a snow mantle to form gullies, which are only visible in those locations where the snow has completely disappeared. MOC images left to right: M03-04950, M09-02885, and M0-3-6266.

chemical weathering. The erosional periods may have been caused by large impacts that produced very short-lived, thick atmospheres that allowed liquid water to persist (Segura et al., 2002). Thus, while Mars possesses a large inventory of water, it is likely that this water has remained frozen throughout much of its history, resulting in very little chemical weathering. Sporadically this water is released to form channels and lakes.

While neither typical nor common, the locations where liquid water may have been present for long periods of time – ancient lakes and modern snows – nonetheless hold the greatest promise for future exploration. In the modern gully systems, liquid water likely occurs very near the surface, is stable for extended periods of time, and is regenerated on the relatively short time-scales associated with climate oscillations. Repeated access to near-surface liquid water could provide a means for life to have survived over extended periods of Martian history, and could provide favorable sites for past or present life. Finally, the great diversity of surface environments from place to place and through

time on Mars is a sign of a complex climate history. It is also one of the most hopeful indicators for the possibility of Martian life, providing a rich suite of environments where life may have taken hold.

Phillip R. Christensen

Bibliography

- Baker, V.R., Strom, R.G., Gulick, V.C., Kargel, J.S., Komatsu, G., and Kale, V.S., 1991. Ancient oceans, ice sheets, and the hydrological cycle on Mars. *Nature*, **352**, 589–862.
- Bandfield, J.L., Glotch, T.D., and Christensen, P.R., 2003. Spectroscopic identification of carbonates in the Martian dust. *Science*, **301**, 1084–1087.
- Bibring, J.-P., Langevin, Y., Gendrin, A., Gondet, B., Poulet, F., Berthé, M., Soufflot, A., Arvidson, R., Mangold, N., Mustard, J., Drossart, P., and Omega-Team, 2005. Mars surface diversity as revealed by the OMEGA/Mars Express Observations. *Science*, **307**, 1576–1581, doi:10.1126/science.1108806.

- Byrne, S., and Ingersoll, A.P., 2003. A sublimation model for Martian south polar ice features. *Science*, **299**, 1051–1053.
- Carr, M.H., 2001. Mars global surveyor observations of fretted terrain. *J. Geophys. Res.*, **106**, 23571–23595.
- Christensen, P.R., 2003. Formation of recent Martian gullies through melting of extensive water-rich snow deposits. *Nature*, **422**, 45–48, doi:10.1038/nature01436.
- Christensen, P.R., and Ruff, S.W., 2004. The formation of the hematite-bearing unit in Meridiani Planum: Evidence for deposition in standing water. *J. Geophys. Res.*, **109**, E08003, doi:10.1029/2003JE002233.
- Christensen, P.R., Bandfield, J.L., Hamilton, V.E., Ruff, S.W., Kieffer, H. H., Titus, T., Malin, M.C., Morris, R.V., Lane, M.D., Clark, R.N., Jakosky, B.M., Mellon, M.T., Pearl, J.C., Conrath, B.J., Smith, M.D., Clancy, R.T., Kuzmin, R.O., Roush, T., Mehall, G.L., Gorelick, N., Bender, K., Murray, K., Dason, S., Greene, E., Silverman, S.H., and Greenfield, M., 2001. The Mars Global Surveyor Thermal Emission Spectrometer experiment: Investigation description and surface science results. *J. Geophys. Res.*, **106**, 23823–23871.
- Christensen, P.R., McSween, H.Y. Jr., Bandfield, J.L., Ruff, S.W., Rogers, A.D., Hamilton, V.E., Gorelick, N., Wyatt, M.B., Jakosky, B.M., Kieffer, H.H., Malin, M.C., and Moersch, J.E., 2005. Evidence for igneous diversity and magmatic evolution on Mars from infrared spectral observations. *Nature*, **436**, doi:10.1038/nature03639.
- Clow, G.D., 1987. Generation of liquid water on Mars through the melting of a dusty snowpack. *Icarus*, **72**, 95–127.
- Feldman, W.C., Boynton, W.V., Tokar, R.L., Prettyman, T.H., Gasnault, O., Squyres, S.W., Elphic, R.C., Lawrence, D.J., Lawson, S.L., Maurice, S., McKinney, G.W., Moore, K.R., and Reedy, R.C., 2002. Global distribution of neutrons from Mars: Results from Mars Odyssey. *Science*, **297**, 75–78.
- Gendrin, A., Mangold, N., Bibring, J.-P., Langevin, Y., Gondet, B., Poulet, F., Bonello, G., Quantin, C., Mustard, J., Arvidson, R., and LeMouelic, S., 2005. Sulfates in Martian layered terrains: The OMEGA/Mars Express view. *Science*, **307**, 1587–1590.
- Glotch, T.D., and Christensen, P.R., 2005. Geologic and mineralogic mapping of Aram Chaos: Evidence for a water-rich history. *J. Geophys. Res.*, **110**, E09006, doi:10.1029/2004JE2389.
- Grotzinger, J., Bell, J.F. III, Calvin, W., Clark, B.C., Fike, D., Golombek, M., Greeley, R., Herkenhoff, K.E., Jolliff, B., Knoll, A.H., Malin, M., McLennan, S.M., Parker, T., Soderblom, L., Sohl-Dickstein, J.N., Squyres, S.W., Tosca, N.J., and Watters, W., 2005. Stratigraphy, sedimentology and depositional environment of the Burns Formation, Meridiani Planum, Mars. *Earth Planet. Sci. Lett.*, **240**, 14–75.
- Gulick, V.C., and Baker, V.R., 1989. Fluvial valleys and Martian palaeoclimates. *Nature*, **341**, 514–516.
- Hamilton, V.E., and Christensen, P.R., 2005. Evidence for extensive olivine-rich bedrock in Nili Fossae, Mars. *Geology*, **33**, 433–436.
- Heldmann, J.L., and Mellon, M.T., 2004. Observations of Martian gullies and constraints on potential formation mechanisms. *Icarus*, **168**, 285–304.
- Hoefen, T., Clark, R.N., Bandfield, J.L., Smith, M.D., Pearl, J.C., and Christensen, P.R., 2003. Discovery of olivine in the Nili Fossae region of Mars. *Science*, **302**, 627–630.
- Howard, A.D., Moore, J.M., and Irwin, R.P. III., 2005. An intense terminal epoch of widespread fluvial activity on early Mars: I. Valley network incision and associated deposits. *J. Geophys. Res.*, **110**, E12S14, doi:10.1029/2005JE002459.
- Jakosky, B.M., and Carr, M.A., 1985. Possible precipitation of ice at low latitudes of Mars during periods of high obliquity. *Nature*, **315**, 559–561.
- Kieffer, H.H., 1979. Mars south polar spring and summer temperatures: A residual CO₂ frost. *J. Geophys. Res.*, **84**, 8263–8289.
- Langevin, Y., Poulet, F., Gendrin, A., Gondet, B., Berthé, M., Soufflot, A., Drossart, P., Combes, M., Bellucci, G., Moroz, V., Mangold, N., Schmitt, B., and Omega-Team, 2004. Perennial water ice identified in the south polar cap of Mars. *Nature*, **428**, 627–630.
- Lee, P., Cockell, C.S., Marinova, M.M., McKay, C.P., and Rice, J.W., 2001. Snow and ice melt flow features in Devon Island, Nunavut, Arctic Canada as possible analogs for recent slope flow features on Mars, in *Proceedings of the 32nd Lunar and Planetary Science Conference*, abstract 1809, March 12–16, Houston, Texas [CD-ROM].
- Malin, M.C., and Edgett, K.S., 2000. Evidence for recent ground water seepage and surface runoff on Mars. *Science*, **288**, 2330–2335.
- Malin, M.C., and Edgett, K.S., 2003. Evidence for persistent flow and aqueous sedimentation on early Mars. *Science*, **302**, 1931–1934.
- McSween, H.Y. Jr., et al., 2004. Basaltic rocks analyzed by the Spirit rover in Gusev Crater. *Science*, **305**, 842–845.
- Mellon, M.T., and Phillips, R.J., 2001. Recent gullies on Mars and the source of liquid water. *J. Geophys. Res.*, **106**, 23165–23180.
- Mustard, J.F., Cooper, C.D., and Rifkin, M.K., 2001. Evidence for recent climate change on Mars from the identification of youthful near-surface ground ice. *Nature*, **412**, 411–414.
- Mustard, J.F., Poulet, F., Gendrin, A., Bibring, J.-P., Langevin, Y., Gondet, B., Mangold, N., Bellucci, G., and Altieri, F., 2005. Olivine and pyroxene diversity in the crust of Mars. *Science*, **307**, 1594–1597.
- Pollack, J.B., and Toon, O.B., 1982. Quasi-periodic climate changes on Mars: A review. *Icarus*, **50**, 259–287.
- Segura, T.L., Toon, O.B., Colaprete, A., and Zahnle, K., 2002. Environmental effects of large impacts on Mars. *Science*, **298**, 1977–1980.
- Soderblom, L.A., 1992. The composition and mineralogy of the Martian surface from spectroscopic observations: 0.3 μm to 50 μm. In Kieffer, H.H., Jakosky, B.M., Snyder, C.W., and Matthews, M.S. (eds.), *Mars*. Tucson, AZ: University of Arizona Press, pp. 557–593.
- Squyres, S.W., Grotzinger, J.P., Bell, J.F., Christensen, P.R., Clark, B.C., Crisp, J.A., Farrand, W.H., Herkenhoff, K.E., Klingelhöfer, G., Knoll, A.H., McLennan, S.M., McSween, H.Y., Morris, R.V., Rieder, R., and Soderblom, L.A., 2004. In-situ evidence for an ancient aqueous environment on Mars. *Science*, **306**, 1709–1714.
- Titus, T.N., Kieffer, H.H., and Christensen, P.R., 2003. Exposed water ice discovered near the south pole of Mars. *Science*, **299**, 1048–1051.
- Ward, W.R., 1974. Climatic variations on Mars. I. Astronomical theory of insolation. *J. Geophys. Res.*, **79**, 3375–3386.
- Wyatt, M.B., McSween, H.Y. Jr., Tanaka, K.L., and Head, J.W. III., 2004. Global geologic context for rock types and surface alteration on Mars. *Geology*, **32**, 645–648, doi:10.1130/G20527.1.

Cross-references

[Astronomical Theory of Climate Change](#)
[Atmospheric Evolution, Mars](#)
[Mineral Indicators of Past Climates](#)
[Obliquity](#)
[Sedimentary Indicators of Climate Change](#)

MASS EXTINCTION: ROLE OF CLIMATE

Introduction

Mass extinction is a defining feature of life's history. Over short periods of geologic time, geographically widespread and ecologically diverse groups of organisms disappear from the fossil record. The five largest extinctions of the Phanerozoic occurred during the Late Ordovician, Late Devonian, and at the Permian-Triassic, Triassic-Jurassic, and Cretaceous-Tertiary boundaries, when over 40% of genera and 60% of species became extinct. Some mass extinctions completely restructured many components of the world's marine ecosystems, while others caused major loss of species but little ecological restructuring.

Major changes in the Earth's climate system have been proposed to explain mass extinctions and their associated geochemical anomalies. Current debate focuses on the nature of climatic change during mass extinction and whether it results from extra-terrestrial perturbations of the Earth system or from internal processes. Additional debate centers on whether changes in the physical climate system or chemistry of the atmosphere and oceans are most important. The search for the environmental cause(s) of mass extinction is a dynamic field with a voluminous literature. Outlined below are climatic mechanisms proposed for the five largest Phanerozoic extinctions and a few important references.

Gradual climatic cooling

Gradual climatic deterioration has long been cited as an agent of mass extinction (Stanley, 1984). Extinction is caused through the gradual contraction of ranges for tropical and subtropical species, which causes loss of diversity through loss of habitat. Gradual climatic cooling is commonly associated with major regression of the world's oceans, which shrinks habitat area for organisms of the continental shelf. Temperature decline and regression are causally linked through an inverse relationship between global sea level and the volume of glacial ice, and through a direct relationship between global sea level, plate spreading rates, and atmospheric $p\text{CO}_2$.

Gradual climatic cooling was initially proposed as the dominant agent of extinction for the end-Cretaceous, based on oxygen isotopic evidence for a gradual decline in temperature during the Late Cretaceous and evidence for long-term cooling at the Cretaceous-Tertiary boundary (Clemens, 1982). However, gradual cooling is contradicted by evidence for significant temperature fluctuations during the last few million years of the Cretaceous, warming at the Cretaceous-Tertiary boundary, rapid extinction of organisms coincident with a bolide impact, and mass mortality of the terrestrial biota (see below).

Stronger evidence exists for mass extinction by gradual climatic cooling during the Late Ordovician (Hirnantian). The Late Ordovician extinction occurred in two major pulses. The first pulse occurred at the onset of global cooling and lowering of sea level associated with the growth of continental glaciers on Gondwana, while the second occurred during the rise of global sea level associated with melting of glacial ice (Sheehan, 2001). Glaciation occurred under significantly increased levels of atmospheric $p\text{CO}_2$, perhaps 10-fold pre-industrial levels or greater. Glacial ice was able to develop during a short-term (<1 Myr) fluctuation in atmospheric $p\text{CO}_2$ because of reduced solar luminosity, low seasonality on Gondwana, and the absence of trees and shrubs (Crowley, 2000; Gibbs et al., 2000).

Catastrophic climatic cooling

Catastrophic cooling consists of a sharp drop in temperature that is caused by the rapid production of an optically dense and globally widespread aerosol cloud. The lowest temperatures occur in continental interiors, which are removed from the thermal buffering of the ocean, and at high latitudes in the summer hemisphere. The severity and duration of the low-temperature excursion depends on the type and quantity of materials present in the cloud, the optical properties of these materials, and the rapidity with which dust, soot, and aerosols are removed from the atmosphere by settling and precipitation (Covey et al., 1994; Toon et al., 1997).

"Volcanic winter" results from the production of a global aerosol cloud by massive volcanic eruption, in particular stratospheric sulfate aerosols, which cause cooling that can last for up to a decade (Rampino et al., 1988; Wignall, 2001). Volcanic ash enhances the radiative effects of sulfate aerosols. However, it is removed from the atmosphere within a few months. Historic volcanic eruptions have had minor effects on global temperature (<1 °C) but greater effects on regional temperature at high latitudes. Large explosive volcanic eruptions of the geologic past produced aerosol loading of the stratosphere at least one order of magnitude greater than that of recent eruptions. The potential short-term cooling effects of fissure eruptions, which produce flood basalts and large igneous provinces, are not well understood (Wignall, 2001).

"Impact winter" results from the vaporization and fragmentation of the bolide and its target rock (Alvarez et al., 1980). Dust is produced in large quantities but remains in the atmosphere for only a few months because coagulation of dust particles promotes rapid sedimentation from the atmosphere. Ignition of vegetation and formation of a smoke cloud is caused by the impact fireball and a broiler effect resulting from the reentry of rock fragments into the atmosphere. If the bolide strikes gypsum and anhydrite rocks, then the resulting impact vaporization will create stratospheric sulfate aerosols that persist for a decade or more and cause a period of "global twilight" following the attenuation of the dust cloud (Toon et al., 1997). (see *Bolide impacts and climate; Cretaceous/Tertiary (K-T) boundary impact, climate effects*; this volume).

Blockage of sunlight can produce freezing temperatures, which kill cold-sensitive organisms. Photosynthesis ceases in the absence of light, which causes starvation of animals and animal-like protists. Survivorship would be highest for organisms with well-developed dormancy mechanisms (e.g., seeds, resting spores) and lowest for organisms with no dormancy mechanisms. Tropical ecosystems would be highly vulnerable to the effects of cold temperatures and the cessation of photosynthesis, while temperate and boreal ecosystems would be less vulnerable. Surface waters of the open ocean would be highly vulnerable to the cessation of photosynthesis because photosynthesis is the major source of energy for consumer organisms. Nearshore marine and deep ocean ecosystems would be less vulnerable because of their dependence on detritus as a major source of energy. Freshwater ecosystems would be least vulnerable because of the high influx of detritus and widespread dormancy mechanisms in freshwater algae and invertebrates (Sheehan and Hansen, 1986; Upchurch, 1989).

Catastrophic climatic cooling caused by a bolide impact is best supported for the Cretaceous-Tertiary boundary, where extinction of many organisms occurred at the base of a boundary clay that contains elevated levels of iridium, shock-metamorphosed minerals, glassy spherules, and other evidence of impact. Terrestrial plants indicate mass mortality at the Cretaceous-Tertiary boundary through an anomalous abundance of fern spores. The Chicxulub impact structure dates to the Cretaceous-Tertiary boundary, and remnants of the impacting body have been found at the Cretaceous-Tertiary boundary in the Pacific, North America, and Europe. Some authors propose that three impacts occurred across the Cretaceous-Tertiary boundary based on the stratigraphic distribution of spherule-containing beds (Keller et al., 2003).

Catastrophic climatic cooling from multiple bolide impacts probably occurred during the Late Devonian mass extinction, but the relationship between impact and extinction is not fully resolved. Evidence for Late Devonian impacts includes iridium anomalies, impact spherules, and at least two impact craters (McGhee, 1996).

Catastrophic cooling probably occurred at or near the Triassic-Jurassic boundary, based on evidence for a bolide impact (Olsen et al., 2002). Evidence includes a small iridium anomaly associated with an anomalous abundance of fern spores. Disagreement exists over whether the impact was linked to major turnover in vertebrates and plants. Massive flood volcanism started near the Triassic-Jurassic boundary (Wignall, 2001) and might have produced significant sulfate aerosols and short-term cooling events.

Catastrophic cooling also may have taken place at the Permo-Triassic boundary. Evidence for impact includes high

concentrations of microspherules and noble gas ratios in fullerenes suggestive of an extra-terrestrial source, but the case for a bolide impact is not as strong as at the Cretaceous-Tertiary boundary. Terrestrial plants provide evidence for mass mortality at the Permo-Triassic boundary, in particular anomalous abundances of fungal spores indicative of increased rates of decomposition.

Storms

Catastrophic climatic cooling by a global aerosol cloud would create a strong temperature inversion and generally stable atmosphere. However, oceanic impact of a large bolide could create a hypercane, an intense cyclonic storm that forms over the impact site when water temperature exceeds 50 °C. Pressures in a hypercane can be as low as 500–600 mbar, wind speed can exceed Mach 1, and the storm top can extend into the middle stratosphere. A hypercane injects large quantities of water into the stratosphere. This would destroy significant amounts of ozone, increase the flux of UV radiation, and cause the death of terrestrial and shallow-water organisms (Emanuel, 2003).

Acid rain

Acid rain changes the pH of water and soils. The most widely proposed mechanism for the formation of acid rain is a bolide impact. Nitric acid forms after the passage of a bolide at high speed through the atmosphere, which creates nitrogen oxides through intense heat and pressure. Sulfuric acid forms after the impact vaporization of gypsum and anhydrite. The amount of acid created by impact depends on the size and velocity of the bolide, the mass of vaporized sulfate, and the extent to which basic minerals such as larnite form during impact (Maruoka and Koerber, 2003; Toon et al., 1997).

Volcanism is a second proposed mechanism for the formation of acid rain. Rapid extrusion of large masses of lava, such as those found in many flood basalts, would inject large quantities of sulfur dioxide into the atmosphere, which forms sulfuric acid (Wignall, 2001). This could lead to the formation of acid rain with a sufficiently high rate of influx.

Empirical evidence for the formation of acid rain at mass extinction boundaries is limited. Disproportionate extinction of calcareous organisms at the Cretaceous-Tertiary boundary is consistent with ocean acidification, but high survival of freshwater aquatic organisms is inconsistent with acid rain (Hallam and Wignall, 1997).

Long-term global warming

Long-term global warming results from changes in the levels of greenhouse gases, most notably carbon dioxide (CO₂) and methane (CH₄). Carbon dioxide enters the atmosphere by mantle outgassing at spreading ridges and volcanoes. It is removed from the atmosphere by silicate weathering and incorporation into organic matter and carbonate rock. Methane is produced by bacterial reduction of CO₂ under anaerobic aquatic conditions. It is oxidized in the atmosphere to form CO₂. Organic carbon is strongly depleted in ¹³C relative to atmospheric and carbonate because of enzymatic fractionation: carbon fixed by C₃ photosynthesis has ^δ¹³C ranging from –22 to –32 per mil, while biogenic methane has ^δ¹³C ranging from –55 to –85 per mil. Changes in the rate of transfer of carbon between different reservoirs can be detected by changes in the ^δ¹³C of the atmosphere, which is recorded in the ^δ¹³C of organic matter and carbonate.

Major perturbations to the global carbon cycle are indicated by excursions in the stable isotopic record. Simultaneous negative excursions in ^δ¹³C for organic matter and carbonate

indicate an increased rate of oxidation of organic carbon and/or a decrease in its rate of burial (Kump and Arthur, 1999), which indicates possible global warming through an increase in atmospheric *p*CO₂ and/or methane. Simultaneous positive excursions in ^δ¹³C for organic matter and carbonate indicate increases in the rate of burial for organic carbon and possible global cooling through a decrease in atmospheric *p*CO₂. Flood basalts from large igneous provinces can inject significant quantities of CO₂ into the atmosphere if they are extruded at a rapid rate (Wignall, 2001), but changes in the ^δ¹³C of the atmosphere are probably small. Proxies such as stomatal index in plants corroborate trends based on isotopes and provide independent estimates of *p*CO₂ (Royer et al., 2001).

Negative excursions in carbon isotopes and large igneous provinces occur at the Cretaceous-Tertiary, Triassic-Jurassic, and Permo-Triassic boundaries. Isotopic evidence for long-term warming at the Cretaceous-Tertiary boundary is corroborated by direct temperature proxies such as leaf physiognomy and oxygen isotopes, direct estimators of atmospheric *p*CO₂ such as stomatal index, and carbon cycle models (Beerling et al., 2002; Kaiho et al., 1999; Wolfe, 1990). Post-impact levels of *p*CO₂ may have exceeded 2,300 ppm. Simulation studies indicate that rapid extrusion of Deccan Intertrappan flood basalts is insufficient to explain the increase in *p*CO₂ and that impact vaporization of carbonate is needed (Beerling et al., 2002). The carbon isotopic excursion starts at the Cretaceous-Tertiary boundary and continues well into vegetation recovery, indicating that it is controlled by marine processes rather than biomass burning (Beerling et al., 2001).

A negative carbon isotope excursion occurs at the Triassic-Jurassic boundary and lasts for approximately 600,000 years (Hesselbo et al., 2002). Increases in *p*CO₂ are indicated by changes in stomatal index, and warming is indicated by major increases in *Classopollis*, a thermophilic plant. The first extrusions of the Central Atlantic Magmatic Province began ~20 kyr after the Triassic-Jurassic boundary and continued for 2 Myr.

The Permo-Triassic extinction is known as the “mother of mass extinctions” because of its extremely high mortality (Erwin, 1993). Not surprisingly, the carbon isotopic anomaly at the Permo-Triassic boundary is the largest negative excursion associated with a mass extinction event. Hypotheses to account for this excursion include massive release of CO₂ from an anoxic ocean, sudden release of CH₄ from ocean sediments, mass mortality of the biota, volcanic release of CO₂ from the Siberian traps, and reduced oxygen levels. Evaluation of these hypotheses with a global carbon cycle model (Berner, 2002) shows that methane release was probably the most important contributor to the isotopic excursion. This is interesting in light of Ryskin’s suggestion that mass mortality at the Permo-Triassic boundary was caused by the combustion of a methane-rich atmosphere (Ryskin, 2003). Carbon cycle modeling indicates a rise in *p*CO₂ > 1,000 ppm, while combined C-S cycle modeling and sulfur isotope analysis indicate a sudden drop in atmospheric O₂ from 30 to 15% at the Permo-Triassic boundary. These results corroborate suggestions that anoxia was an important contributor to the Permo-Triassic extinction (Berner, 2002; Berner et al., 2003).

Summary and conclusions

The cause(s) of mass extinction is still open to debate. Environmental change during mass extinctions appears to be more pronounced than environmental change at other times, but whether

all mass extinctions have a single underlying cause is unclear. Temperature change appears to be one common theme to the five major mass extinctions of the Phanerozoic, but the driving mechanism(s) can differ between extinctions. The Late Ordovician extinction, for example, is clearly related to a gradual decline in global temperatures, while the Cretaceous-Tertiary boundary extinctions are related (at least in part) to catastrophic temperature decline resulting from bolide impact. Each mass extinction event probably has its own unique set of environmental changes.

Further understanding of mass extinction will require an interdisciplinary effort involving geologists, paleontologists, geochemists, and geophysicists.

Garland R. Upchurch, Jr.

Bibliography

- Alvarez, L.W., Alvarez, W., Asaro, F., and Michel, H., 1980. Extraterrestrial cause for the Cretaceous-Tertiary extinction. Experimental results and theoretical interpretation. *Science*, **208**, 1095–1108.
- Beerling, D.J. et al., 2001. Evidence for the recovery of terrestrial ecosystems ahead of marine primary production following a biotic crisis at the Cretaceous-Tertiary boundary. *J. Geol. Soc. Lond.*, **158**, 737–740.
- Beerling, D.J., Lomax, B.H., Royer, D.L., Upchurch, G.R., and Kump, L.R., 2002. An atmospheric $p\text{CO}_2$ reconstruction across the Cretaceous-Tertiary boundary from leaf megafossils. *Proc. Natl. Acad. Sci. USA*, **99**, 7836–7840.
- Berner, R.A., 2002. Examination of hypotheses for the Permo-Triassic boundary extinction by carbon cycle modeling. *Proc. Natl. Acad. Sci. USA*, **99**, 4172–4177.
- Berner, R.A., Beerling, D.J., Dudley, R., Robinson, J.M., and Wildman, W.A., 2003. Phanerozoic atmospheric oxygen. *Annu. Rev. Earth Planet. Sci.*, **31**, 105–134.
- Clemens, W.A., 1982. Patterns of extinction and survival of the terrestrial biota during the Cretaceous/Tertiary transition. *Geol. Soc. Am. Spec. Pap.*, **190**, 407–414.
- Covey, C., Thompson, S.L., Weissman, P.R., and MacCracken, M.C., 1994. Global climatic effects of atmospheric dust from an asteroid or comet impact on Earth. *Glob. planet. Change*, **9**, 263–273.
- Crowley, T.J., 2000. Carbon dioxide and Phanerozoic climate. In Huber, B.T., MacLeod, K.G., and Wing, S.L. (eds.), *Warm Climates in Earth History*. Cambridge, UK: Cambridge University Press, pp. 425–444.
- Emanuel, K.A., 2003. Tropical cyclones. *Annu. Rev. Earth Planet. Sci.*, **31**, 75–104.
- Erwin, D.H., 1993. *The Great Paleozoic Crisis: Life and Death in the Permian*. New York, NY: Columbia University Press, 327pp.
- Gibbs, M.T., Bice, K.L., Barron, E.J., and Kump, L.R., 2000. Glaciation in the early Paleozoic ‘greenhouse’: the roles of paleogeography and atmospheric CO_2 . In Huber, B.T., MacLeod, K.G., and Wing, S.L. (eds.), *Warm Climates in Earth History*. Cambridge, UK: Cambridge University Press, pp. 386–422.
- Hallam, A., and Wignall, P.B., 1997. *Mass Extinctions and Their Aftermath*. Oxford, UK: Oxford University Press, 320pp.
- Hesselbo, S.P., Robinson, S.A., Surlyk, F., and Piasecki, S., 2002. Terrestrial and marine extinction at the Triassic-Jurassic boundary synchronized with major carbon-cycle perturbation: A link to the initiation of massive volcanism? *Geology*, **30**, 251–254.
- Kaiho, K., Kajiwara, Y., Tazaki, K., Ueshima, M., Takeda, N., Kawahata, H., Arinobu, T., Ishiwatari, R., Hirai, A., and Lamolda, M.A., 1999. Oceanic primary productivity and dissolved oxygen levels at the Cretaceous/Tertiary boundary; their decrease, subsequent warming, and recovery. *Paleoceanography*, **14**, 511–524.
- Keller, G., Stinnesbeck, W., Adatte, T., and Stuben, D., 2003. Multiple impacts across the Cretaceous-Tertiary boundary. *Earth Sci. Rev.*, **62**, 327–363.
- Kump, L.R., and Arthur, M.A., 1999. Interpreting carbon-isotope excursions: carbonates and organic matter. *Chem. Geol.*, **161**, 181–198.
- Maruoka, T., and Koeberl, C., 2003. Acid-neutralizing scenario after the Cretaceous-Tertiary boundary impact event. *Geology*, **31**, 489–492.
- McGhee, G.R., 1996. *The Late Devonian Mass Extinction: The Frasnian/Famennian Crisis*. New York, NY: Columbia University Press, 303pp.
- Olsen, P.E., Kent, K.V., Sues, H.-D., Koeberl, C., Huber, H., Montanari, A., Rainforth, E.C., Fowell, S.J., Szajna, M.J., and Hartline, B.W., 2002. Ascent of dinosaurs linked to an iridium anomaly at the Triassic-Jurassic boundary. *Science*, **296**, 1305–1307.
- Rampino, M.R., Self, S., and Stothers, R.B., 1988. Volcanic winters. *Annu. Rev. Earth Planet. Sci.*, **16**, 73–99.
- Royer, D.L., Berner, R.A., and Beerling, D.J., 2001. Phanerozoic CO_2 change: Evaluating geochemical and paleobiological approaches. *Earth Sci. Rev.*, **54**, 349–392.
- Ryskin, G., 2003. Methane-driven oceanic eruptions and mass extinctions. *Geology*, **31**, 741–744.
- Sheehan, P.M., 2001. The late Ordovician mass extinction. *Annu. Rev. Earth Planet. Sci.*, **29**, 331–364.
- Sheehan, P.M., and Hansen, T.A., 1986. Detritus feeding as a buffer to extinction at the end of the Cretaceous. *Geology*, **14**, 868–870.
- Stanley, S.M., 1984. Temperature and biotic crises in the marine realm. *Geology*, **12**, 205–208.
- Toon, O.B., Zahnle, K., Morrison, D., Turco, R.P., and Covey, C., 1997. Environmental perturbations caused by the impacts of asteroids and comets. *Rev. Geophys.*, **35**, 41–78.
- Upchurch, G.R., 1989. Terrestrial environmental changes and extinction patterns at the Cretaceous-Tertiary boundary, North America. In Donovan, S.K. (ed.), *Mass Extinctions: Processes and Evidence*. London, UK: Belhaven Press, pp. 195–216.
- Wignall, P.B., 2001. Large igneous provinces and mass extinctions. *Earth Sci. Rev.*, **53**, 1–33.
- Wolfe, J.A., 1990. Palaeobotanical evidence for a marked temperature increase following the Cretaceous/Tertiary boundary. *Nature*, **343**, 153–156.

Cross-references

- [Bolide Impacts and Climate](#)
- [Carbon Cycle](#)
- [Carbon Isotope Variations Over Geologic Time](#)
- [Cretaceous/Tertiary \(K-T\) Boundary Impact, Climate Effects](#)
- [Flood Basalts: Climatic Implications](#)
- [Late Paleozoic Paleoclimates \(Carboniferous-Permian\)](#)
- [Methane Hydrates, Carbon Cycling, and Environmental Change](#)
- [Paleobotany](#)
- [Volcanic Eruptions and Climate Change](#)

MAUNDER MINIMUM

The Maunder Minimum refers to the period from about 1645 to 1715 during which very few sunspots were observed. Following Galileo’s refinement of the telescope around 1610, observations of sunspots showed that they appeared to be a fairly regular phenomenon. One of the main features was that their abundances waxed and waned approximately every 11 years, which became known as the solar cycle or sunspot cycle. During the Maunder Minimum, however, relatively very few sunspots were seen for roughly seventy years, and the 11-year cycle was dramatically reduced (Eddy, J.A., 1976). After 1715, the cycle built up again, and such a dramatic decrease in sunspots has not been seen since. When the sun is more active there are a greater number of sunspots. Though these are dark patches that emit less radiation than normal, their abundance is correlated with overall greater solar output since bright spots (faculae) are more abundant at the same times. The Maunder Minimum, with an extremely quiescent sun, is therefore thought to have been a low point for solar output. This may have contributed to colder climate conditions over many regions of the Earth during this

period (see *Little Ice Age*). The name for the minimum honors the work of E. W. Maunder.

Other evidence agrees with that of the early astronomers. Records of two independent cosmogenic isotopes (^{10}Be , ^{14}C), chemical variants formed only from cosmic rays, have been obtained from ice cores and tree rings. Since the intensity of cosmic rays reaching the Earth is modulated by the Sun, these isotopes serve as a proxy for solar output. The abundance of these isotopes varies in concert with the sunspot record over the past several centuries during which they overlap. The isotopic records corroborate the astronomical evidence for reduced solar output during the Maunder Minimum. Based on both the sunspot and isotope records, several other periods of reduced solar activity have also been identified. The exact size of the change in solar output that took place during the Maunder Minimum (or during other historical times) is still uncertain. Most estimates place it in the range of 0.2–0.5 watts per meter squared less irradiance reaching the Earth’s surface.

Drew T. Shindell

Bibliography

Eddy, J.A., 1976. The Maunder Minimum. *Science*, 1182–1202.

Cross-references

- Beryllium-10
- Climate Variability and Change, Last 1000 Years
- Cosmogenic Radionuclides
- Little Ice Age
- Sun-Climate Connections

MEDIEVAL WARM PERIOD

Histories in western Europe have long recognized a “post-Carolingian” climatic amelioration, approximately since the death of Charlemagne (AD 814), the first of the “Holy Roman Emperors” of the early Middle Ages. The Medieval Warm Period (MWP) was also called the “Early Medieval Warm Epoch” (Lamb, 1977, 1982) and the “Neo-Atlantic” by some palynologists. The expression “Little Climatic Optimum” (LCO) has sometimes been employed to contrast it with the dramatic warming of the “Atlantic” phase of the late Mesolithic to Neolithic ages (about 6700–4200 BC, (sidereal year)). The Atlantic phase was long known in Scandinavia as the mid-Holocene “Climatic Optimum” (also termed the “Hypsithermal”), when local temperatures were 2–3 °C above present (Roberts, 1998).

Lamb (op cit. p. 35) identified a broad long-term “summer wetness index” (rising) and compared it with a “winter severity index” (falling), based on 50-year means. Both display a systematic lengthening of the wavelength of upper westerlies across northern Europe, reaching its peak around AD 1100. A comparable warming swing also marked the twentieth century. However, analysis of this period is complicated by anthropogenic greenhouse warming. The two most recent warm periods were separated by the “Little Ice Age” (LIA) from approximately AD 1300 to 1750. The warmest interval of the MWP in Europe was AD 1150–1300. A study of Canadian borehole temperatures (mentioned by Lamb, op .cit., p. 104–105) suggested that the mean MWP was up to 1.6 °C warmer than the average for the last millennium. In the Sargasso Sea area of the North Atlantic

(see [Figure M15](#)), studies of planktonicbenthic foraminifera suggest that the SST was about 1 °C warmer than today 1,000 years ago and above average for the last 3 millennia, about 2 °C higher than during the LIA (Keigwin, 1996).

Human responses to the MWP have been outlined by many writers (see LeRoy Ladurie, 1971; Bryson and Murray, 1977; Bryson and Swain, 1981). The dramatic start of the LIA has been eloquently described by Lamb (op. cit.), but less attention has been paid to the MWP as a whole. Biological proxies are very interesting. In central Europe history reports, incidents of locust (*Locusta migratoria*) plagues in the drought summers occurred as follows: nineteenth century, 8 seasons; tenth, eleventh, twelfth century, none or next to none; fourteenth century, 15 seasons; fifteenth century, none; sixteenth century, 6; seventeenth century, one only; eighteenth century, 6; nineteenth century, 4 summers. From recent data in North Africa, Landscheidt (1987) suggested there was a correlation between locust plagues and solar radiation.

Sea-surface temperatures in the North Atlantic were higher during the MWP, (by 5 °C or more), and sea-ice coverage was appreciably reduced (Mayewski et al., 1994). Wind and wave action were likewise reduced. In the Greenland ice cores, a marked lowering of sodium (from sea-salt) has been observed. These climatic factors played an important role in the occupation of Iceland by Viking (Norse) colonists in the nineteenth century (AD 860). In the North Atlantic, there were

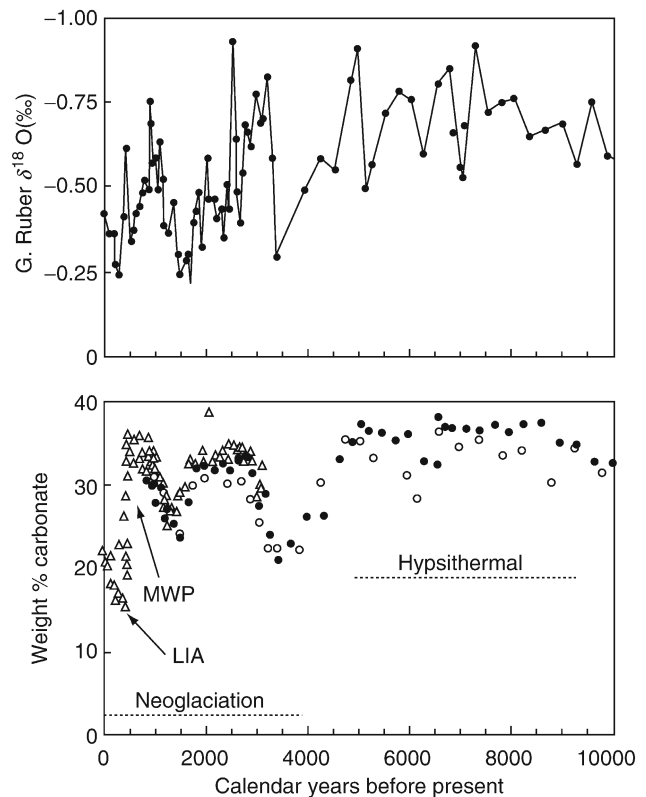


Figure M15 Variability in two proxies of sea-surface temperatures in the Sargasso Sea over the last three millennia, showing a marked contrast between the MWP and LIA (modified from Keigwin, 1996). (a) (top) $\delta^{18}\text{O}$ (‰) in the surface-dwelling foraminifera *Globigerinoides ruber* (white variety), Bermuda Rise, northern Sargasso Sea; (b) (bottom) weight % CaCO_3 .

frequent summers with calm seas and easterly winds that greatly favored their particular type of ships (shallow draft and square sails). Eventually, explorations were carried out by Eric the Red and Leif Ericsson, southern Greenland was colonized by the Norsemen (Dansgaard et al., 1975), and they settled briefly (AD 986) at Anse aux Meadows in Newfoundland ("Vinland"), the first European foothold in North America.

During the same MWP Arctic warming came a widespread development of Eskimo cultures, reaching as far north as Ellesmere Land (AD 900). From the Bering Sea, they spread out to northern Alaska, and in Siberia, they reached as far north as the New Siberian Islands. In the eleventh century a new wave of migrants brought the "Thule Culture" that spread from Alaska to northern Greenland.

In North America, native peoples spread northwards up the valleys of the Mississippi and Missouri, bringing an agricultural economy into Wisconsin and Minnesota, where pollen studies have shown there were reliable summer rains (Griffin, 1961). Eventually they reached the northern Rockies and even Utah. The Hohokam people were meanwhile developing agriculturally oriented communities in New Mexico and Arizona.

In Asia, the behavior of the Caspian Sea provides hydrographic evidence of the MWP climate. From the ninth to fourteenth Centuries, the rise of the Caspian Sea by 18 m flooded vast areas, notably in the Volga Delta. This reflected a general increase in precipitation over much of northern Russia. Clearly, this also reflects increased evaporation over the warming Gulf Stream and North Atlantic in general. The populations of central Asia showed a general expansion, but this only reached a crescendo in the early thirteenth century, which launched the celebrated conquests of Genghis Khan and his "Mongol Hordes" (AD 1205–1225).

It was the exploration of central Asia in the first decades of the twentieth century that provided the data base for Ellsworth Huntington's concept of climatic determinism (Huntington, 1924), which caused a great deal of controversy at a time when climate was assumed (by the conservative "Establishment") to be a changeless aspect of the environment. A long sediment core obtained from Lake Saki (Crimea) illustrates the higher precipitation levels of the MWP that also occurred in southern Russia. The thickness of clay varves suggests a heavier rainfall at this time (Lamb, 1977, p. 408; Xanthakis et al., 1995).

The MWP warm cycle was also seen in Scandinavia and the Alps, by glacier retreats (Röthlisberger, 1986; Karlén et al., 1995). Particularly in Sweden such glacier melts have been dated precisely by sedimentation measurements in the corresponding glacial lakes. Worldwide response was also marked by eustatic sea-level indicators including higher-than-normal beach ridges in many different regions, ranging from the Arctic coast of Alaska to the coasts of the Gulf of California and southwestern Florida (Fairbridge, 1992). The first radiocarbon dates of this higher sea-level stage were obtained in Western Australia, on Rottneest Island, and this therefore became known as the "ROTTNEEST STAGE" (Fairbridge, 1961). In Scandinavia, it is often referred to as the "Viking Stage" due to the abundant relics produced from the isostatic emergence around Stockholm and Uppsala. In northern Germany, the Netherlands and Belgium (Bennema, 1954), evidence for the higher sea level is partly drowned by tectonic subsidence but, after correction, its level was about 0.5 m above present MSL.

Inundation of low-lying coastal areas completely changed the geography in some areas. As sea level rose, there was frantic dike building in northern Germany, the Netherlands,

Belgium, northern France and in parts of eastern England. The critical moment when man-made dikes were overtopped in particular storms is recorded by historic disasters when tens of thousands of people and livestock were drowned and farms and whole villages were totally destroyed (Bakker, 1957). In the lower Rhine Valley, river floods amplified the oceanic factors (Berendsen, 1995). Outstanding events included the flooding of the lower IJssel valley in the Netherlands, with the creation of the Zuider Zee (1250–1251, 1287), and in Britain, with the creation of the Norfolk Broads (Lamb, 1977, p. 433). Other areas were affected including western France, the Rhone and Po Deltas.

The MWP ("Rottneest") rise of sea level had an important demographic effect inasmuch as it drove coastal dwellers inland, creating endless conflict with the people (mostly farmers and pastoralists) already occupying those areas. In the southern Baltic (modern Poland and northeast Germany), southern Denmark and the Frisian Belt in northwest Germany, post-glacial tectonic subsidence amplified the eustatic rise of the MWP.

An economic side effect of the MWP sea-level rise occurred in the salt industry (see a recent book, "Salt" by Mark Kurlansky). During periods of low sea level, as during much of the Roman Era, there were coastal salt pans with sea-water ponds that were organized in series to permit progressive evaporation. This was a major industry because common salt (NaCl) is an essential dietary condiment, as well as being in widespread demand for food preservation, leather tanning, etc. With the MWP rise, the salt pans were repeatedly inundated and in many cases could not be expanded inland because of low bluffs, dunes or cliffs. Industrial disaster was alleviated by a wholesale shift inland to "fossil" salt deposits, mostly of Triassic or Permian age, which had been long exploited since the Bronze Age or earlier. These deposits are known to occur in Britain, Spain, France, Germany, Austria, Poland and Russia (Moores and Fairbridge, 1997) (Many geographic names in central Europe incorporate the roots *Salz*, *Sal*, *Sel*, etc., e.g., Salzburg, Salzkammergut, Salzach).

Metallic ores were extensively mined (mainly by Saxon miners) in mountainous areas of Europe, where the Bronze Age had developed after the glaciers had receded and exposed dry outcrop areas. These expanded during the glacial recessions of the MWP. With the ensuing Little Ice Age (after 1300), there were neo-glacial advances and flooding of mines, leading to closures of the high passes in the Alps (Lamb, 1977, p. 273–274).

Lamb (1967, 1977, p. 276 ff) was fascinated by the history of grape vines and viticulture in Medieval Britain, a country not particularly celebrated today for its home-grown wines. South of lat. 53° N, this study disclosed widespread vineyards there in Medieval times, some 500 km north of present-day limits in France and Germany. To quote from William of Malmesbury writing in 1150 (tr. from *Latin*) of the vale of Gloucester "here you may behold highways and public roads full of fruit-trees, not planted, but growing naturally. . . No county in England has so many or so good vineyards as this, either for fertility or for sweetness of the grape. . ." The export of British wines to France and Germany was a major factor in international trade, and even led to diplomatic friction (when the British undersold the French). It should be recalled that in 1066 William of Normandy had led an invasion of Saxon Britain, at that time considered a remarkable prize. However, the Little Ice Age began and soon after 1300, the entire wine industry collapsed within 10 years, the vines surviving only in rare cases under the protection of walled gardens.

The abruptness of the LIA onset was a major aspect of the termination of the MWP, because it gave little leeway for organic adaptation. In human terms, this cultural shock is well dramatized by Tuchman (1978). Less well known is the effect on coral reefs that had grown vigorously to a low-tide limit about 60 cm higher than present. The fall by about 1 m created a small cliff on reef shores, with no gradual transition.

The eastern parts of North America and Greenland seem to have shared the European experience of the MWP equally (though detailed histories are lacking), as did New Zealand and some other parts of the Southern Hemisphere. However, in the North Pacific region, China, Japan and the western part of North America experienced the exact climatic opposite. In Japan, the mean blooming date of the cherry trees of the imperial gardens in Kyoto has long been monitored as the harbinger of spring and the occasion of joyful festivals. For the MWP, however, the mean blossoming date was a full 10 days later than the millennial average, or 11 days when comparing the mean for the twelfth century with that for the fifteenth century. To Lamb (1977, p. 400) "this suggests an eccentric position of the circumpolar vortex over the Northern Hemisphere in Europe's High Middle Ages, with the climatic zones persistently displaced north over the Atlantic sector and south over the whole Pacific sector and the Far East."

Archaeomagnetic studies employing the paleomagnetic orientation of baked bricks or fireplace clays indicate that the North Magnetic Pole at the time of the MWP lay in the eastern hemisphere, i.e., north of Siberia. A similar antiphase relationship is observed during Europe's cold phases (Bucha, 1984, 1988), but is not always consistent.

As noted earlier, at Mediterranean latitudes, there were commonly heavy summer rains during the MWP. In central America, these had an important role in bringing about the downfall of the Mayan civilization in Yucatan and elsewhere, as the maize (sweet corn) economy requires less humid seasons for ripening (Brooks, 1949); the maize culture required rainy and dry seasons. Repeated multiyear droughts between ca. AD 800 and AD 900 may have contributed to the collapse of the Classic Mayan civilization (Hodell et al., 2001; Haug et al., 2003).

The same delicate adjustment of agriculture to seasonal cycles may also help to explain the wonderful surge in culture and religious buildings at Angkor in Cambodia, which reached a maximum around AD 1000. During the Little Ice Age, these structures were seasonally inundated by the rise of the Mekong and back-filling of Tonle-Sap that eventually buried the entire complex in 10 m or more of sediment.

Northern Hemisphere synthesis

Basing his estimates mainly on botanical proxies (palynology), Lamb (1977, p. 404) presented a comparison between the major climatic intervals for Britain of the last 10,000 years. The MWP discloses the warmest annual mean temperatures since the Atlantic stage 6,000 years ago, 0.8 °C warmer than the warmest decades of the twentieth century. The MWP was also wetter, except for the two summer months July and August, which were characteristically dry.

A series of Northern Hemisphere oriented maps is presented by Lamb (1977, p. 444–5) for selected centuries, depicting troughs of the upper westerlies across Europe and the typical frontal depressions. For summer months during the MWP (AD 1000–1099), the mean polar jet swung from southern Greenland across northern Scandinavia to the Arctic shore of Siberia.

Meanwhile the major frontal depressions radiated from northern Greenland to east coast North America, from near Spitsbergen to Sicily, from near Lake Baikal to western China, and from Alaska to around Wake Island. For the same areas and season during the LIA (1550–1599), the polar jet ran across Scotland and southern Sweden, while the principal European frontal depressions ran from western Spain across the British Isles and the west of Norway.

For the winter seasons, the MWP polar jet crossed Quebec and swung north of Iceland to the Barents Sea while its southern branch crossed Spain and the Mediterranean to Syria. The latter brought plentiful winter rains and prosperity to the kingdom of Palmyra (Syria) and the peoples of Palestine and Mesopotamia. Five centuries later in the LIA, the winter jet unified and crossed Iceland to head for southern Russia, and to bring desertification to parts of Syria, Mesopotamia, and the Indian Peninsula (Bryson and Murray, 1977).

These mean jet trajectories help explain the antiphase relationships between climate proxies in Western Europe and the Far East. The inferred positions of the polar vortex swing to and fro, to eastern or western hemisphere; this appears to be analogous, on a greatly amplified (century) scale, with the "North Atlantic Oscillation" (NAO), which operates on a roughly decadal basis.

[Editor's note: More recent paleoclimate reconstructions over the last millennium provide additional support for the existence of a warmer period roughly 1,000 years ago, at least over the Northern Hemisphere. Less can be said about the Southern Hemisphere, inasmuch as reliable data are still fairly scarce. Based on long tree-ring records from 14 sites in North America and Eurasia, the warming of the MWP peaked between 950 and 1045, with temperatures comparable to those of the twentieth century prior to 1990 (Esper et al., 2002). A composite curve derived from multi-proxy data, including tree rings, boreholes, marine and lake sediments, and speleothems, also shows a period of higher temperatures around AD 1000 to AD 1100, followed by below average temperatures, with a minimum around AD 1600 (Moberg et al., 2005).]

Summary

1. The MWP (or Little Climatic Optimum) is a roughly 450-year climatic interval, at around AD 850–1300. Based on historical documentation, this was a warming cycle in Europe and eastern North America, but cooling in the north Pacific.
2. Based on (a) CO₂ and temperature indicators in the Greenland ice cores, and (b) C-14 flux (inverse) levels in the dendrochronology, this interval is confirmed as a warming cycle in the Atlantic realm, with temperatures at least 1 °C above millennial means, on average.
3. Based on astrochronology (using the 45.4-year resonance interval of the three major planets, Jupiter, Saturn and Uranus) there were three warm peaks: "Post-Carolingian" (AD 852), "Dunkerque-3" (944), and "Viking/Rottmest" (1125). Two cool peaks (marked by extended interruptions caused by low sunspots and reduced solar emissions) occurred at the "Normanian" (peak: AD 1034) and the "Ottoman" (AD 1307).
4. In general, precipitation rose in step with the mean temperature oscillations, but most glaciers tended to retreat. In exceptional areas, glaciers showed temporary advances.
5. Mean sea level rose and fell eustatically and caused coastal retreat matching eustatic rise in more or less stable crustal

- areas, and vice versa. However, in areas of crustal subsidence or rapid compaction, coasted retreat increased.
6. During much of the MWP, the general atmospheric circulation (prevailing westerlies, trade winds, etc.) slackened, but in the subarctic latitudes, the 45-year summer storminess cycle persisted. With weakening trade winds, El Niño cycles became more important (but detailed monitoring is not available). However, the associated warm coastal currents are known to have reached farther south in Peru, and farther north in California.
 7. The influence of the Gulf Stream and Kuroshio Currents were shifted northwards, together with their characteristic ameliorating effects in maritime areas (increased oceanicity), contrasted by reduced continentality.
 8. Sea ice coverage in the North Atlantic and Barents Sea decreased. Due to the longer ice-free seasons in areas of abundant sediment supply, the beach ridge buildup was anomalously high in places.
 9. In subarctic lakes and swamp deposits, the level of pine (or conifer) pollen rose in contrast to that of tundra species. Farther south, the mixed forest boundaries moved northwards.
 10. Equatorial lakes displayed localized change in level, as did rainfall, while savanna (monsoon) boundaries tended to shift poleward by some hundreds of km. The Southern Hemisphere was broadly in phase with the Northern Hemisphere, but out-of-phase for short cycles.

Rhodes W. Fairbridge

Bibliography

- Bakker, J.P., 1957. Relative sea-level changes in northwest floods in the Netherlands in recorded time. *Deutsch. Geogr. Verhandl.* (Tr. In Leatherman, S.P. (ed.), *Overwash Processes: Benchmark*, vol. 58. Stroudsburg, PA: DHR, pp. 51–56), vol. 31, pp. 233–237.
- Bennema, J., 1954. Holocene Movements of Land and Sea-Level in the Coastal Areas of the Netherlands. *Geologie en Mijnbouw*, **63**, 343–350.
- Berendsen, H.J.A., 1995. Holocene fluvial cycles in the Rhine delta? *J. Coast. Res.*, Special Issue **17**, 103–108.
- Brooks, C.E.P., 1926/1949. *Climate Through the Ages*, 2nd edn. (Dover reprint, 1970). New York: McGraw-Hill, 395pp.
- Bryson, R.A., and Murray, T.J., 1977. *Climates of Hunger*. Madison, WI: University of Wisconsin Press, 171pp.
- Bryson, R.A., and Swain, A.A., 1981. Holocene variations of monsoon rainfall in Rajasthan. *Quaternary Research*, **16**, 135–145.
- Bucha, V., 1984. Mechanism for linking solar activity to weather-scale effects, climatic changes and glaciations in the Northern Hemisphere, p. 415–448. In Mörner, N.-A., and Karlen, W. (eds.), *Climatic Changes on a Yearly to Millennial Basis*. Dordrecht, Netherlands: D. Reidel Publ. Co., 667pp.
- Bucha, V., 1988. Influence of solar activity on atmospheric circulation types. *Ann. Geophys.*, **6**(5), 513–524.
- Dansgaard, W., et al., 1995. Climatic changes, Norsemen and modern man. *Nature*, **255**, 24–28.
- Esper, J., Cook, E.R., and Schweingruber, F.H., 2002. Low-frequency signals in long tree-ring chronologies for reconstructing temperature variability. *Science*, **295**, 2250–2253.
- Fairbridge, R.W. (ed.) 1961. Solar variations, climatic change, and related geophysical problems. *Ann. N. Y. Acad. Sci.*, **95**, 1–740.
- Fairbridge, R.W., 1992. *Holocene Marine Coastal Evolution of the United States*. Tulsa, OK: Society of Economic Paleontologists and Mineralogists. SEPM Special Publication 48, pp. 9–20.
- Griffin, J.B., 1961. Some correlations of climate and cultural change in eastern American prehistory. *Ann. N. Y. Acad. Sci.*, **95**(1), 710–717.
- Haug, G.H., Günther, D., Peterson, L.C., Sigman, D.M., Hughern, K.A., and Aschlimann, B., 2003. Climate and the collapse of the Maya civilization. *Science*, **299**, 1731–1735.
- Hodell, D.A., Brenner, M., Curtis, J.H., and Guilderson, T., 2001. Solar forcing of drought frequency in the Maya lowlands. *Science*, **292**, 1367–1370.
- Huntington, E., 1924. *Civilization and Climate*, 3rd edn. New Haven, CT: Yale University Press, 453pp (reprinted 1977; Hamden, CT: Archon Books).
- Karlén, W., et al., 1995. Climate of northern Sweden during the Holocene. *J. Coast. Res.*, Special Issue **17**, 49–54.
- Keigwin, L.D., 1996. The Little Ice Age and Medieval Warm Period in the Sargasso Sea. *Science*, **274**, 1504–1508.
- Lamb, H.H., 1967. Britain's changing climate. *Geogr. Jour.*, **133**(4), 445–468.
- Lamb, H.H., 1977. *Climate History and the Future*. London: Methuen (and Princeton University Press), 835pp.
- Lamb, H.H., 1982. *Climate, History, and the Modern World*. London/New York: Methuen.
- Landscheidt, T., 1987. Long-range forecasts of solar cycles and climate change. In Rampino, M.R. et al., (eds), *Climate: History, Periodicity, and Predictability*. New York: Van Nostrand, pp. 421–445.
- LeRoy Ladurie, E., 1971. *Time of Feast: Times of Famine*. New York: Doubleday (transl. from French).
- Mayewski, P.A., et al., 1994. Changes in atmospheric circulation and ocean ice cover over the North Atlantic during the last 41,000 years. *Science*, **263**, 1747–1751.
- Moberg, A., Sonckhkin, D.M., Holmgren, K., Datsenko, N.M., and Karlen, W., 2005. Highly variable Northern Hemisphere temperatures reconstructed from low- and high-resolution proxy data. *Nature*, **433**, 613–617.
- Moore, E., and Fairbridge, R.W. (eds.), 1997. *Encyclopedia of European and Asian Regional Geology*. London: Chapman Hall.
- Roberts, N., 1998. *The Holocene: An Environmental History*, 2nd edn. Oxford: Blackwell Ltd., 316pp.
- Röthlisberger, F., 1986. 10,000 Jahre Gletchergeschichte der Erde: Aarau, Verlag Sauerländer, 416pp.
- Tuchman, B.W., 1978. *A Distant Mirror: The Calamitous 14th Century*. New York: Ballantine Books, 677pp.
- Xanthakis, J., Liritzis, I., and Poulakos, C., 1995. Solar-climatic cycles in the 4,190-year Lake Saki mud layer thickness record. *J. Coast. Res.*, Special Issue **17**, 79–86.

Cross-references

Climate Variability and Change, Last 1,000 Years
 Dendroclimatology
 Hypsithermal
 Little Ice Age
 Maritime Climate
 North Atlantic Oscillation (NAO) Records
 Paleoclimate Proxies, an Introduction

MESOZOIC CLIMATES

Introduction

The Mesozoic Era (250–65.5 million years ago) consists of the Triassic, Jurassic and Cretaceous Periods. Each of these periods is divided into many epochs and stages. The name Mesozoic comes from the Greek words “meso” meaning middle and “zoe” meaning life. The first to use the term Mesozoic was John Phillips in 1840. It has been considered to represent a time of greenhouse climates (e.g., Hallam, 1985), with elevated atmospheric CO₂ levels and higher mean global surface temperatures and is therefore considered as a possible analog for future climates.

Only sparse and often equivocal evidence for Mesozoic glacial sediments is seen, whereas abundant evidence for Precambrian, Paleozoic and late Cenozoic glaciations are recognized (Figure M16). Changes in continental configuration throughout the Mesozoic Era had important consequences for global climate.

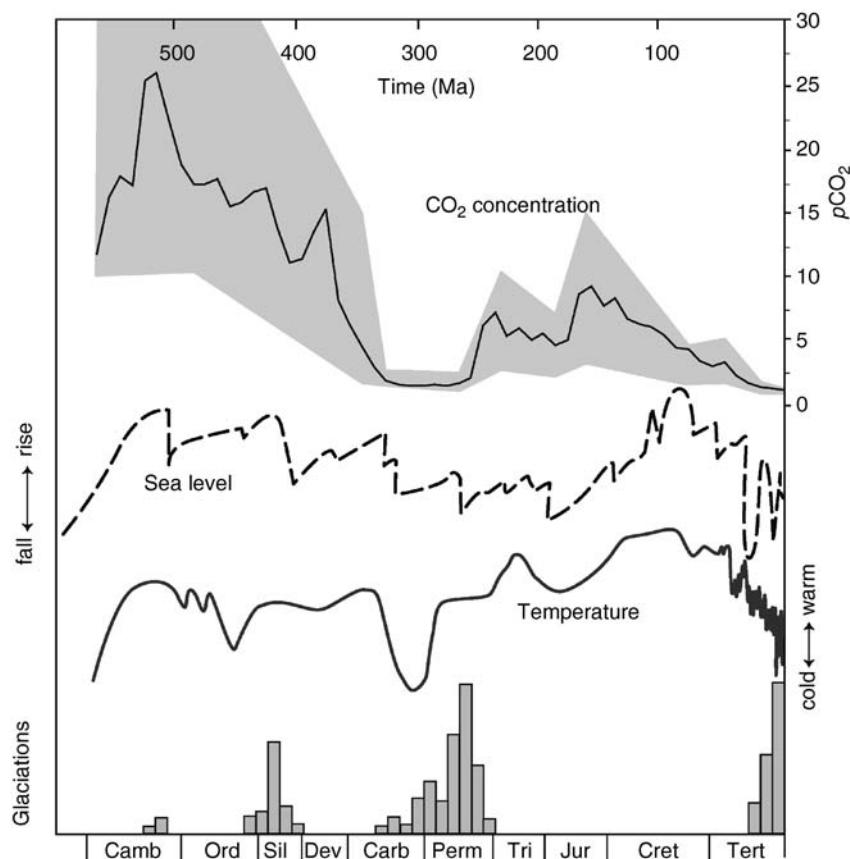


Figure M16 Phanerozoic climatic indicators and reconstructed $p\text{CO}_2$ levels. The upper set of curves describes the reconstructed histories of the past $p\text{CO}_2$ variations (GEOCARB III) by Berner and Kothavala (2001). The shaded region depicts the uncertainties quoted within the GEOCARB III reconstructions. Sea level data is from Vail et al. (1977) and temperature data from Merritts et al. (1998). The Phanerozoic distribution of glaciations is modified from Hambrey (1994). A semi-quantitative measure of the extent of the Earth's surface affected is indicated by the heights of the peaks.

At the end of the Paleozoic, as a result of the final Variscan suturing of all of the continent components, the supercontinent Pangea (meaning "all-earth") was formed. Very few continental fragments escaped incorporation into Pangea and because of its sheer size it was relatively unstable from its beginning. Hence, parts of the supercontinent began to break away, whilst collision was occurring in other areas. The break-up of the continent continued throughout the Mesozoic and into the Cenozoic.

The proportion of greenhouse gases, and in particular CO_2 , in the atmosphere of the Mesozoic has had a major control on global climate. CO_2 transmits incoming short-wave solar radiation, but greenhouse gases absorb outgoing long-wave radiation and the trapped radiation warms the lower part of the Earth's atmosphere. The atmospheric CO_2 curve shows low values during the Carboniferous, which then rise in the Permian, throughout the Triassic and Jurassic, followed by a gradual decline through both the late Mesozoic and Cenozoic (Berner and Kothavala, 2001). The long-term carbon cycle reflects atmospheric CO_2 exchange between the atmosphere and carbon stored in rocks. Loss of CO_2 from the atmosphere is accomplished by photosynthesis and burial of organic matter in sediments and by the reaction of atmospheric CO_2 with Ca and Mg silicates during continental weathering. The release of CO_2 to the atmosphere takes place by means of oxidative weathering of old organic matter and by the thermal

breakdown of buried carbonates and organic matter (via diagenesis, metamorphism and volcanism) resulting in degassing to the Earth's surface (Berner and Kothavala, 2001). The long-term global (eustatic) sea-level trend shows a gradual fall, from the end of the Paleozoic to the early Mesozoic, changing in the latest Triassic to a rising trend that continued into the middle Cretaceous. Sea levels only begin to fall again in the latest Cretaceous and into the Cenozoic (Figure M16). Although atmospheric levels of CO_2 are commonly assumed to be a main driver of global climate, clearly longer-term changes in sea level are also strongly influenced by other (tectonic) processes, the most important of which is sea-floor spreading, which changes the volume and elevation of ocean ridges. A first order correlation is seen between atmospheric CO_2 and global temperature estimates.

Early Mesozoic Pangean climates

The dawn of the Triassic saw the geography of the world looking quite similar to how it did during the Permian. Data suggest that sea level rose a little from its Permian low. The combination of a huge land mass and lower global sea level (related to the reduced rates of tectonic activity) should have resulted in extremely arid continental climatic conditions. Sedimentary deposits in Brazil and South Africa give us a window into the Triassic world. Many of the sedimentary rocks deposited in

Triassic terrestrial environments are dune-deposited sandstones or oxidized fluvial sandstones and mudstones (red beds). Additionally, evaporite deposits are more extensive in the Triassic than at any other time during the Phanerozoic. These deposits attest to the hot and dry conditions within the interior of Pangea. Modeling results suggest that the global average temperatures were up to 7°C warmer than today. Extreme temperature ranges >45°C are predicted for the lowland interior of Pangea. Precipitation in large areas of the interior was less than 0–2 mm d⁻¹, comparable with modern arid and semi arid deserts.

Temperatures of the equatorial oceans may have been 5–10°C warmer than those seen today, but data are scarce and are not derived from the most reliable sources. Nevertheless, warm conditions are thought to have extended to the poles. For example, a combination of roots, logs, and leaves of woody plants has been taken to be indicative of temperate climatic conditions in Antarctica during the middle Triassic. The wood samples of Antarctica exhibit distinct growth rings, which have also been analyzed for climate signals. Such analyses reveal that the climate was strongly seasonal and that light may have been a limiting factor in the growth of these forest trees. The distributions of fossil reefs and carbonate build-ups has also been interpreted as reflecting the presence of ancient warm water seaways analogous in terms of their distributions to those of the present day. However, the communities of organisms that constructed many ancient build-ups were often dissimilar to the coral-rich ecosystems represented by modern reefs. During the Late Triassic, carbonate build-ups became both large and widespread throughout the Tethyan margins, particularly along the western and northern borders. These were formed by corals, calcisponges, hydrozoans and algae.

The assumption that the climatic history of the Triassic was characterized by uninterrupted hot and arid conditions has, however, been questioned. Humid zones occurred close to the coast and at high latitudes, as shown by coals and bauxite deposits in these areas. A number of General Circulation Model simulations of the Triassic (e.g., Kutzbach, 1994; Wilson et al., 1994) predict that the geography of the supercontinent Pangea was conducive to the establishment of a “megamonsoonal” circulation (Parrish, 1993). Particularly in the late Triassic, the climate of the Colorado Plateau region became relatively wet, though still seasonal. Furthermore, Parrish (1993) suggests that evidence for monsoonal conditions is apparent at higher latitude locations such as Australia (beyond the normal influence of a monsoonal circulation), during the Late Triassic. The strength of the monsoon must therefore have been at its greatest at this time.

A few studies have also provided possible evidence of glacial conditions during the late Triassic. Breccia-like conglomerates of Triassic age containing large angular rock fragments from Japan and alleged tills from southern South America have also been recorded (see Price, 1999 for a summary). A glacial origin for these deposits has, however, been strongly questioned. The possible existence of sizeable ice cover during the middle and late Triassic, based upon evidence for high frequency Milankovitch-influenced sea level oscillations, has been recorded in platform carbonates from Europe. In as much as tectonic movements cannot operate on a sufficiently rapid timescale to account for the observed high frequency sea level changes, only glacio-eustatic mechanisms likely controlled such sea level change. If these sea level changes were glacio-eustatically controlled, this implies the occurrence of a significant number of sufficiently large glaciations affected global sea level during the Triassic. However, if ice caps were either absent or negligible during the Mesozoic,

alternative mechanisms to account for the observed changes in sea level are required, such as possibly regional tectonic events. However, tectonic movements have generally been considered to operate neither at a sufficiently rapid timescale, nor on a global scale. An alternative mechanism is that changes in plate density associated with tectonic-induced stresses could account for many of the transgressions and regressions traceable over areas larger than individual sedimentary basins. Other possibilities to account for short-term global changes in sea level include the thermal expansion and contraction of ocean water and desiccation of isolated ocean basins. The General Circulation Model simulations for the Triassic (e.g., Kutzbach, 1994; Wilson et al., 1994) using elevated CO₂ concentrations (ranging from 1,000 to 1,650 ppm) and relief reaching a maximum of 2 km also provide results consistent with extreme temperature variability at polar latitudes. For example, the model of Kutzbach (1994) simulated a mean annual temperature of -5°C, with winter temperatures of -30°C and summer temperatures of 25°C over parts of Antarctica. The simulation of Wilson et al. (1994) produced summer temperatures of 20°C and winter temperatures dropping to a minimum of -50°C over Antarctica and solid permafrost zone. Although a tract of sea-ice was simulated all year round, Wilson et al. (1994) considered the results to be inconsistent with polar ice sheet development.

The climate of disintegrating Pangea

Latest Triassic to Jurassic times saw the progressive break-up of Pangea. Ocean floor was present in the central Atlantic region by middle Jurassic times, heralding the separation of Gondwana and Laurasia. This rifting removed the major forcing factor of the monsoon, the distinctive Pangean geography (Parrish, 1993). The postulated warmth that characterized the Triassic appears to have continued into the Jurassic (Figure M16). Global sea level began to rise, possibly associated with the increased sea-floor spreading as Pangea began to break up. Based on the global distributions of lithological climate indicators such as coals, as well as evaporites and eolian sands, a general symmetry of climate zones about the paleoequator appeared throughout the Jurassic. Using lithological and floral data, Rees et al. (2000) suggested that the Jurassic world was one in which low latitudes were seasonally dry, succeeded polewards in both hemispheres by desert, seasonally dry, warm temperate and cool temperate biomes. Modeling studies (e.g., Moore et al., 1992) have implied that the tropical regions reached temperatures as high as 40°C during parts of the summer months. Precipitation in these regions during the summer months locally exceeded 16 mm per day. Siberian floras were assigned to a cool temperate biome, characterized by cold winters and warm summers, implying polar conditions considerably warmer than today. Rees et al. (2000) did not, however, identify any geological evidence for tropical year-round wet or, at the other extreme, tundra or glacial biomes. The occurrence of a theropod dinosaur of Jurassic age from Antarctica has likewise been used as evidence for a warm climate in polar regions.

One of the most common methods of establishing quantitative values for past ocean temperatures has been the use of oxygen isotopes derived from well-preserved biogenic carbonate material. Studies assessing Jurassic ocean temperature variation at high southern latitudes, using isotopic ratios from belemnites, certainly support the notion that high latitudes were significantly warmer than today and ice-free. Paleotemperature estimates for the European area range from 12 to 30°C, again considerably warmer than today. The Lower and Upper parts

of the Jurassic appear to have been the hottest periods. Such a trend possibly mirrors the CO₂ curve (Figure M16). A cooler middle Jurassic is not inconsistent with the findings of Frakes et al. (1992). A great deal of information regarding the temperature of Earth during the Jurassic has been gained from faunal data and in particular the analysis of the patterns and degree of provinciality. It has been widely considered that, in particular, the early Jurassic period was characterized by low faunal provinciality, possibly due to equable climates and the lack of polar ice caps. Faunal provinciality became more marked from Middle Jurassic times onwards and two major faunal provinces existed in the Northern Hemisphere, the northern Boreal realm and the lower latitude Tethyan realm. A Southern Hemisphere Austral realm corresponding to the northern Boreal realm has also been recognized. The possible existence of Boreal and Austral realms, delineated by temperature, during parts of the Mesozoic certainly does lend support to the existence of cold conditions at the poles for certain times.

In a similar fashion to the Triassic, General Circulation Model simulations of the Jurassic climate (e.g., Moore et al., 1992) reveal also that high latitude regions may have developed cold temperatures providing adequate leeway to argue for the presence or absence of high latitude ice. Siberian Jurassic tillites stretching from the Yenisey River eastwards to the Oloy Ridge have also been described (see Price, 1999, for a review). The principal characteristics of these deposits are non-bedded, silty and pebbly claystones that have been considered to be glacio-marine in origin or formed by seasonal ice of mountain rivers. A recent study by Chumakov and Frakes (1997) re-investigating some of these Jurassic deposits suggested, however, that sediments previously attributed to ice rafting display instead characteristics of mass movement, including contorted bedding and evidence of turbidity currents.

The late Jurassic–early Cretaceous was characterized in many areas of the world by a sea-level lowstand (Figure M16) possibly initiated by low spreading rates, resulting in large semi-restricted epicontinental seas and widespread deposition of non-marine sediments. The progressive weakening of the monsoonal circulation is also evident resulting from the increasing dispersion of continental components and increasing asymmetrical continental configuration. The latest Jurassic Purbeck group of the UK, which contains evidence of evaporite deposition, may be the local expression of the spread of an equatorial arid zone across Europe during these times. Clay mineral assemblages also reflect the expansion of the arid zone northwards during the middle to late Jurassic within the East European Platform.

The Cretaceous Period was a time of considerable tectonic activity. The supercontinent Gondwanaland began to break up in the early Cretaceous: India began to move northwards and the North Atlantic began to open. Early Cretaceous freshwater sediments and plants of Europe point to a change to warm and humid conditions. A warm and wet climate may be a result of the continents becoming significantly more dispersed and rising sea levels. By mid-Cretaceous times, the Tethys Ocean began closing. Evidence points towards an unusually high rate of volcanic activity, especially at mid-oceanic ridges. Magma erupted at oceanic ridges and created new oceanic crust, thereby forcing the continental landmasses apart. Rates of continental drift (i.e., sea-floor spreading rate) were then about three times as great as they are now. During the mid-Cretaceous (~90 million years ago), sea levels rose dramatically, possibly up to 200 m higher than present levels, flooding up to 40% of the continents and resulting in the widespread deposition

of chalk-dominated facies. The Western Interior Seaway of the USA was at this time at its maximum. Much of central and western Europe was under water. Hence, mid-Cretaceous indicators of aridity, such as evaporites, are generally restricted to low latitudes and occur within northern Africa, South America, the Gulf of Mexico and also in the middle East. By late Cretaceous times, the evaporate-producing arid zones had contracted to a Mesozoic minimum (Hallam, 1985). These areas generally correlate with areas of climate model-predicted warmth, coupled with low soil moisture. Year-round moist-wet conditions prevailed at higher latitudes. Extensive coal deposits of mid-Cretaceous age are found in Northern Eurasia and Eastern Europe. Abundant coals occur also in the USA, particularly adjacent to the Western Interior Seaway.

In addition, during the mid-Cretaceous, vast outpourings of lava created a succession of immense undersea plateaus beneath the Pacific Ocean between 135 and 115 million years ago. One of these – the Ontong Java Plateau in the southwest Pacific – may be the largest flood basalt province in the world (roughly the size of Alaska) and certainly led to an huge increase in hydrothermal activity and an increase in CO₂ outgassing, which was ultimately released to the atmosphere. Extensive outgassing of CO₂ would have led to climatic warming, due to the greenhouse effect. In addition to this increase in outgassing of CO₂, the reduced continental area (due to the sea level maximum) would presumably also have resulted in a decrease in continental weathering and a reduction in the drawdown of CO₂. Therefore, the global climate at this time should have been one of the warmest in Earth's history. Abundant isotopically-derived foraminiferal paleotemperature data, gathered particularly from equatorial latitudes, suggest that globally averaged ocean surface temperatures in the Cretaceous were as much as 6–12 °C higher than at present. Although changes in equatorial regions may not have been so marked, these data support the hypothesized “Cretaceous greenhouse” and a thermal maximum occurring at ~90 Ma. However, Figure M16 shows a mismatch between peak Cretaceous warmth (and sea level) and peak CO₂ production. A pulse of volcanic activity and crustal production and hence CO₂ outgassing appears absent or has yet to be identified at this time (Wilson et al., 2002).

The prospect of generally warmer tropics poses important implications for hurricane genesis. Frequency of hurricanes greatly increases during times when an extensive ocean area has surface temperatures in excess of 27 °C. As broad areas of the Cretaceous oceans were probably above this threshold temperature, in all likelihood hurricanes should have been substantially more frequent in the mid-Cretaceous than at present. Particularly compelling evidence for polar warmth is also provided by the analysis of fossil wood and by the physiognomic analysis of middle and late Cretaceous floras from Alaska and northeastern Asia (e.g., Herman and Spicer, 1997). Data from this latter study suggests that an Arctic Ocean with a winter surface temperature of ~6 °C maintained Northern Alaska coastal temperatures above freezing. Rich fern, gymnosperm and angiosperm floras are also known from the Cretaceous of Greenland, Siberia and Antarctica. Such warmer polar conditions would have been maintained by increased atmospheric and oceanic poleward heat transport. Significantly warmer tropical oceans also provided appropriate environmental conditions for enhanced evaporation and hence the production of warm saline bottom waters. Today, oceanic deep waters form in higher latitudes, where sea-ice formation increases the salinity and therefore the density of surface water.

It is possible that the extensive outgassing of CO₂ would have had other effects upon the oceans. Oxidation of reduced material in hydrothermal effluents and the stimulation of primary productivity owing to the injection of hydrothermal Fe into surface waters are both potential O₂ reducing mechanisms. Major episodes of organic carbon rich black shale deposition within the Cretaceous corresponded to Oceanic Anoxic Events. These have been interpreted in terms of increased burial of organic carbon, attributed to enhanced preservation under reduced O₂ conditions, or driven by changes in surface water productivity (that delivered more organic carbon to the sea floor). A loss of CO₂ from the atmosphere may well have resulted from enhanced organic-matter production and burial in the oceans, sequestering CO₂ and eventually leading to a reduction in paleotemperatures. Such trends may not necessarily be resolvable on the atmospheric CO₂ curves of Berner and Kothavala (2001).

Paleoclimate data for the early Cretaceous are derived largely from mid-low latitudes and may not necessarily reflect ambient climatic conditions at the poles. At least seasonally cold ocean temperatures and more controversially limited polar ice caps have been postulated to have existed during the early Cretaceous. Studies have revealed distinct faunal belts throughout parts of the early Cretaceous resulting from considerable temperature gradients from north to south. These paleobiogeographic patterns support the idea of a cooler phase for parts of the early Cretaceous and hence disagree with the suggestion of a globally warm equable climate throughout the Cretaceous. Many studies have recorded large and globally synchronous Milankovitch-influenced oscillations of Cretaceous sea level and fluctuating polar ice volumes have sometimes been invoked as a primary mechanism to account for such changes. Furthermore, Frakes et al. (1992) described tillites and dropstones, providing at least equivocal evidence for the presence of ice sheets. However, such data are poorly distributed in the Cretaceous. Short-term climatic cycles, related to variations in the geometry and mechanics of the Earth-Sun system (i.e., Milankovitch cycles), have been recognized throughout the Mesozoic. (The Milankovitch cyclic variations include eccentricity of the Earth's orbit with a periodicity of ~100 kyr, precession with a periodicity of ~21 kyr, and obliquity of the axis of rotation with a periodicity of ~41 kyr). Small-scale rhythms, often marl-limestone couplets within some Mesozoic sedimentary successions, have also been attributed to orbitally-modulated (Milankovitch) climatic change. Changes in productivity and temperature, for example, provide mechanisms for the translation of orbital variations into cyclic sedimentation during non-glacial times.

Towards the end of the late Cretaceous there was a decrease of temperature and a fall in global sea level (Figure M16), reducing the area of shallow marine environments. The close of the Cretaceous witnessed a major extinction event that saw the disappearance of at least 75% of the species on Earth, both in the oceans and on the continents. The most famous of these were the dinosaurs, although they represent only a small fraction of the plants and animals that disappeared. Although most agree that the Cretaceous-Tertiary extinction event was caused by a catastrophic bolide impact, climate change, continental reconfigurations and sea level change have also been considered as complementary mechanisms to account for the extinction events.

Summary

The Mesozoic Era has been considered to represent a time of greenhouse climates, with elevated atmospheric CO₂ levels and higher mean global surface temperatures. However,

empirical observations and modeling studies do not conclusively suggest high latitude ice-free environments during the whole of the Mesozoic. The combination of the massive size of the Pangean landmass and lower global sea level resulted in extremely arid continental climates, especially during the Triassic period. More humid zones did occur close to the coast and at high latitudes, as shown by coals and bauxite deposits in these areas. Associated with the progressive break-up of Pangea, global sea level began to rise. Aridity was slowly replaced by climates that were more humid during the late Mesozoic, although they were still punctuated by periods of extreme aridity. This increase in continental humidity certainly appears to have been related to an increasing maritime influence. Global temperatures and sea levels rose, reaching a maximum at ~90 Ma. The atmospheric CO₂ curve shows increasing values throughout the Triassic, with a maximum in the early Cretaceous, whereas temperatures and sea levels were at their highest somewhat later. Thus, mismatch between peak Cretaceous warmth (and sea level) and peak CO₂ production is observed.

Gregory D. Price

Bibliography

- Berner, R.A., and Kothavala, Z., 2001. GEOCARB III: A revised model of atmospheric CO₂ over Phanerozoic time. *Am. J. Sci.*, **301**, 182–204.
- Chumakov, N.M., and Frakes, L.A., 1997. Mode of origin of dispersed clasts in Jurassic shales: southern part of the Yana-Kolyma fold belt, North East Asia. *Palaeogeogr. Palaeoclimatol. Palaeoecol.*, **128**, 77–85.
- Frakes, L.A., Francis, J.E., and Syktus, J.I., 1992. *Climate Modes of the Phanerozoic*. Cambridge, UK: Cambridge University Press, 274pp.
- Hallam, A., 1985. A review of Mesozoic climates. *J. Geol. Soc. Lond.*, **142**, 433–445.
- Hambrey, M.J., 1994. *Glacial Environments*. London, UK: UCL Press, 296pp.
- Herman, A.B., and Spicer, R.A., 1997. New quantitative palaeoclimate data for the Late Cretaceous Arctic: Evidence for a warm polar ocean. *Palaeogeogr. Palaeoclimatol. Palaeoecol.*, **128**, 227–251.
- Kutzbach, J.E., 1994. Idealized Pangean climates: Sensitivity to orbital change. In: Klein, G.D. (ed.), *Pangea: Paleoclimate, Tectonics and Sedimentation during Accretion, Zenith and Breakup of a supercontinent*. Geological Society of American Special Paper, 288, pp. 41–55.
- Merritts, D., DeWet, A., and Menking, K., 1998. *Environmental Geology, an Earth System Science approach*. New York: Freeman.
- Moore, G.T., Hayashida, D.N., Ross, C.A., and Jacobson, S.R., 1992. Paleoclimate of the Kimmeridgian/Thonian (Late Jurassic) world: I. Results using a general circulation model. *Palaeogeogr. Palaeoclimatol. Palaeoecol.*, **93**, 113–150.
- Parrish, J.T., 1993. Climate of the supercontinent Pangea. *J. Geol.*, **101**, 215–233.
- Price, G.D., 1999. The evidence and implications of polar-ice during the Mesozoic. *Earth Sci. Rev.*, **48**, 183–210.
- Rees, P.M., Ziegler, A.M., and Valdes, P.J., 2000. Jurassic phytogeography and climates: New data and model comparisons. In Huber, B.T., Macleod, K.G., and Wing, S.L. (eds.), *Warm Climates in Earth History*. Cambridge: Cambridge University Press, pp. 297–318.
- Vail, P.R., Mitchum, R.M., Todd, R.G., Widmier, J.M., Thompson, S., Songree, J.B., Bubb, J.N., and Hatleid, W.G., 1977. Seismic stratigraphy and global changes of sea level. *Am. Assoc. Pet. Geol. Memoir*, **26**, 63–81.
- Wilson, K.M., Pollard, D., Hay, W.W., Thompson, S.L., and Wold, C.N., 1994. General circulation model simulations of Triassic climates: Preliminary results. In Klein, G.D. (ed.), *Pangea: Paleoclimate, Tectonics and Sedimentation during Accretion, Zenith and Breakup of a supercontinent*. Geological Society of American Special Paper, 288, pp. 91–116.
- Wilson, P.A., Norris, R.D., and Cooper, M.J., 2002. Testing the Cretaceous greenhouse hypothesis using glassy foraminiferal calcite from the core of Turonian tropics on Demerara Rise. *Geology*, **30**, 607–610.

Cross-references

Astronomical Theory of Climate Change
 Continental Sediments
 Cretaceous/Tertiary (K-T) Boundary Impact, Climate Effects
 Cretaceous Warm Climates
 Cyclic Sedimentation (cyclothem)s
 Greenhouse (warm) Climates
 Monsoons, Pre-Quaternary
 Ocean Anoxic Events
 Pre-Quaternary Milankovitch Cycles and Climate Variability

MESSINIAN SALINITY CRISIS

During the Messinian (uppermost Miocene), the Mediterranean area was involved in a rapid and dramatic salinity crisis, as indicated by the discovery of 1–2 km thick evaporite deposits beneath its sea floor (Hsü et al., 1973). The problems in envisioning viable depositional models for these evaporites generated a number of contrasting hypotheses regarding the timing (synchronous versus diachronous), the origin (glacioeustatic versus tectonic), the environmental conditions (deep versus shallow water) and the impact (global versus regional) of the salinity crisis. An international controversy arose mostly because different sub-basins could have experienced different evaporite deposition at the same time and direct data on the evaporite rocks in the deep Mediterranean depressions are limited to only a few meters of boreholes. Other significant problems were the absence of an accurate and reliable time frame for the Messinian, the difficult application of biostratigraphy in unfavorable hypersaline sediments, and lithologies that are not well suited to magnetostratigraphy (diatomites and evaporites).

Originally, three main models were proposed to explain the origin of the Mediterranean evaporite giant: (a) a shallow, rapidly subsiding basin able to create accommodation space for shallow-water to supratidal evaporite accumulation (Nesteroff, 1973); (b) a preexisting deep basin that became partially cut off from world sea level, resulting in drawdown and deposition of shallow-water to desiccated hypersaline facies (Hsü et al., 1973); and (c) a preexisting deep basin in which deposition occurred in deep hypersaline water (Busson, 1980). Other hypotheses integrate different environments of deposition to explain the complex array of evaporite facies throughout the Mediterranean Basin.

On a broad scale, the evaporite deposits beneath the deep Mediterranean depressions indicate progressive restriction of the Mediterranean-Atlantic connection. As suggested by seismic data, the evaporites can be divided into two main sulfate-bearing units, the Lower Evaporites (or First Cycle), containing thick halite deposits, and the Upper Evaporites (Second Cycle), separated by an interregional unconformity. The Second Cycle does not have a marine signature like that of First Cycle and is not evaporitic across all of the Mediterranean. In most land sections it consists of detrital sediments with a brackish fauna, the so-called “Lago Mare” (Lake Sea) facies, which represents a dominantly freshwater body of Paratethyan origin, marking the complete isolation of the Mediterranean from the ocean. Normal marine conditions were suddenly re-established at the beginning of the Pliocene as a consequence of flooding from the Atlantic.

Recently, astrochronology and integrated stratigraphy have demonstrated that the onset of evaporite formation was a

synchronous event over the entire Mediterranean basin, dated at 5.96 Ma (Krijgsman et al., 1999). Cyclic evaporite deposition is related to circum-Mediterranean climate changes driven by changes in the Earth’s precession with an average periodicity of 21.7 kyr. Isolation from the Atlantic Ocean was established between 5.59 and 5.33 Ma, causing a large fall in Mediterranean water level followed by erosion (5.59–5.50 Ma) and deposition of the non-marine “Lago Mare” sediments (5.50–5.33 Ma). According to these data, the total duration of the Messinian salinity crisis is approximately 640 kyr. This view is not shared by all authors (Butler et al., 1995; Clauzon et al., 1996; Riding et al., 1998), but the general consensus is toward a marked drawdown of the Mediterranean water level. Estimations of the water level drop range from a few hundred meters up to 3,000 m (Tay et al., 2002), but some parts of the Mediterranean appear to have remained under relatively deep-water conditions throughout the entire salinity crisis (Roveri et al., 2001).

Another common view is that the deeply incised subaerial erosional surface that produced the incised canyons of the Rhone, Ebro, Po and Nile Rivers represents the time interval during which evaporites accumulated in the deep basins. More controversial is the stratigraphic position of the marginal evaporites, which are placed by different authors either above or below the main unconformity (Riding et al., 1998; Clauzon et al., 1996), thus postdating or predating the desiccation phase in the deep basins.

The compilation of a detailed chronology challenged the original view that the Mediterranean isolation could have been triggered by glacioeustatic sea level lowering (Kastens, 1992). The latest Miocene glaciation occurred from 6.26 to 5.5 Ma. It was marked by 18 glacial-to-interglacial oscillations controlled by the 41-kyr cycle of obliquity (Hodell et al., 2001). Although the glaciation may have contributed to the isolation of the Mediterranean, it preceded the base of the Lower Evaporites by 300 kyr, supporting tectonic or local climatic forcing for the crisis inception (Krijgsman et al., 1999; Hodell et al., 2001). This hypothesis is supported by the discovery of large and rapid climate variations during the salinity crisis, as documented by biomarkers, stable hydrogen, and carbon isotope compositions (Andersen et al., 2001). Moreover, the end of the salinity crisis preceded the most prominent interglacial conditions by 170 kyr, suggesting that sea level outside the Mediterranean began to rise prior to the base of the Pliocene. This implies that tectonics were responsible for the end of the crisis or there was a significant lag between sea level rise and the resumption of normal marine conditions in the Mediterranean (Hodell et al., 2001).

Stefano Lugli

Bibliography

- Andersen, N., Paul, H.A., Bernasconi, S.M., McKenzie, J.A., Behrens, A., Schaeffer, P., and Albrecht, P., 2001. Large and rapid climate variability during the Messinian salinity crisis: Evidence from deuterium concentrations of individual biomarkers. *Geology*, **29**(9), 799–802.
- Busson, G., 1980. Les grandes cuvettes évaporitiques en milieu detritique: Comment elles se creusent, comment elles se remplissent. *Bulletin Centres de Recherches Exploration-Production Elf Aquitaine*, **4**, 557–588.
- Butler, R.W., Lickorish, H., Grasso, M., Pedley, H.M., and Ramberti, L., 1995. Tectonics and sequence stratigraphy in Messinian basins, Sicily: Constraints on the initiation and termination of the Mediterranean salinity crisis. *Geol. Soc. Am. Bull.*, **107**, 425–439.

- Clauzon, G., Sue, J.-P., Gautier, F., Berger, A., and Loutre, M.-F., 1996. Alternative interpretation of the Messinian salinity crisis: Controversy resolved? *Geology*, **24**, 363–366.
- Hodell, D.A., Curtis, J.H., Sierra, F.J., and Raymo, M.E., 2001. Correlation of late Miocene to early Pliocene sequences between the Mediterranean and North Atlantic. *Paleoceanography*, **16**, 164–178.
- Hsu, K.J., Ryan, W.B.F., and Cita, M.B., 1973. Late Miocene desiccation of the Mediterranean. *Nature*, **242**, 240–244.
- Kastens, K.A., 1992. Did glacio-eustatic sea level drop trigger the Messinian salinity crisis? New evidence from Ocean Drilling Program site 654 in the Tyrrhenian Sea. *Paleoceanography*, **7**, 333–356.
- Krijgsman, W., Hilgen, F.J., Raffi, I., Sierra, F.J., and Wilson, D.S., 1999. Chronology, causes and progression of the Messinian salinity crisis. *Nature*, **400**, 652–655.
- Nesteroff, W.O., 1973. Un modele pour les evaporites messiniennes en Mediterranee: des bassin peu pro fonds avec depots d'evaporites iagunaires, 1973. In Drooger, C.W. (ed.), *Messinian Events in the Mediterranean*. Amsterdam: Koninklijke Nederlandse Akademie Van Wetenschappen, North-Holland Publishing Company, pp. 68–81.
- Riding, R., Braga, J.C., Martin, J.M., and Sanchez-Almazo, I.M., 1998. Mediterranean Messinian salinity crisis: Constraints from a coeval marginal basin, Sorbas, southeastern Spain. *Mar. Geol.*, **146**, 1–20.
- Roveri, M., Bassetti, M.A., and Ricci Lucchi, F., 2001. The Mediterranean Messinian salinity crisis: An Apennine foredeep perspective. *Sediment. Geol.*, **140**, 201–214.
- Tay, P.L., Lonergan, L., Warner, M., Jones, K.A., and the IMERSE Working Group, 2002. Seismic investigation of thick evaporite deposits on the central and inner unit of the Mediterranean Ridge accretionary complex. *Mar. Geol.*, **186**, 167–194.

Cross-references

- [Astronomical Theory of Climate Change](#)
[Continental Sediments](#)
[Cyclic Sedimentation \(cyclothems\)](#)
[Evaporites](#)
[Neogene Climates](#)
[Plate Tectonics and Climate Change](#)
[Pre-Quaternary Milankovitch Cycles and Climate Variability](#)

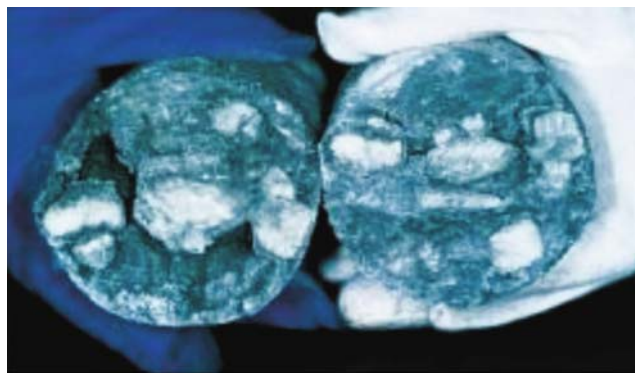
METHANE HYDRATES, CARBON CYCLING, AND ENVIRONMENTAL CHANGE

Overview

Enormous amounts of methane reside as solid gas hydrate and free gas bubbles in the pore space of marine sediment along continental margins. Most of this methane has formed through the microbial breakdown of organic matter originally deposited on the seafloor. At present, a small fraction escapes to ocean waters through seafloor venting. Reaction with dissolved sulfate consumes additional methane in pore waters of shallow sediment. These potentially important carbon fluxes, which remain absent from most global carbon cycle models, could change dramatically through time because the stability and distribution of gas hydrate and free gas depend on external conditions, particularly ocean temperature. Chemical anomalies in sediment or sedimentary rocks may document such variations in methane release and hint at an under-appreciated mechanism for past climate change.

Chemistry and theoretical occurrence

At relatively low temperatures, high pressures and high gas concentration, certain low-molecular-weight gases such as methane, ethane, propane, carbon dioxide and xenon can combine with water to precipitate crystalline substances



200--1244C-10H-2 (83.70-84.30 mbsf)

Figure M17 Example of natural gas hydrate recovered from Hydrate Ridge off the coast of Oregon (Shipboard Scientific Party, 2002).

resembling ice (Figure M17). These solid compounds are called clathrate hydrates of gas, or more conveniently “gas hydrates,” because the gas molecules exist within cages of water molecules. Three types of clathrate structures have been identified: Structure I, Structure II and Structure H. Each of these structures contains small and large cavities that can host guest gas molecules; their general formulae are $8C \cdot 46H_2O$ (S1), $24C \cdot 136H_2O$ (S2), and $4C \cdot 34H_2O$ (SH), where C is the total number of available cavities. The type of clathrate structure formed depends on the size and composition of the guest gases. Moreover, the chemical composition may differ from the ideal formulae because gas molecules need not occupy all cavities (Sloan, 1998). Indeed, natural clathrate hydrates of methane seem to be S1 with a composition of approximately $CH_4 \cdot 6H_2O$. For all three structures, the solid gas hydrate can dissociate to constituent water and gas phases with a decrease in pressure or increase in temperature, although gas chemistry and crystal structure determine the precise conditions (Sloan, 1998).

Gas hydrates naturally precipitate in the pore space of water-bearing sediments when gas concentrations exceed saturation conditions at appropriately high pressure, low temperature and low salinity (e.g., Dickens and Quinby-Hunt, 1997). These criteria are met in two general environments: Arctic regions beneath several hundreds of meters of permafrost, and along continental margins beneath several hundreds of meters of seawater (Kvenvolden, 1999). This article focuses on the latter because the marine realm hosts the vast majority of natural gas hydrate (>99%) (Kvenvolden and Lorenson, 2001).

Within deep-sea sediments, gas hydrates can potentially exist between the seafloor and a relatively shallow, sub-bottom depth where temperatures become excessively warm because of the geothermal gradient (Figure M18). This depth interval is commonly called the gas hydrate stability zone (GHSZ) and its lower bound generally increases with water depth because of greater pressure and invariant salinity. Thus, across a continental margin, the GHSZ forms a lens within sediment that starts at some shallow water depth and thickens beneath deeper water (Figure M18). This lens begins nominally at 250–500 m water depth at present, depending on local bottom water temperature and gas composition (Dickens, 2001). Below the GHSZ, where temperatures are too warm, free gas bubbles will exsolve from solution when gas concentrations exceed saturation (Holbrook et al., 1996;

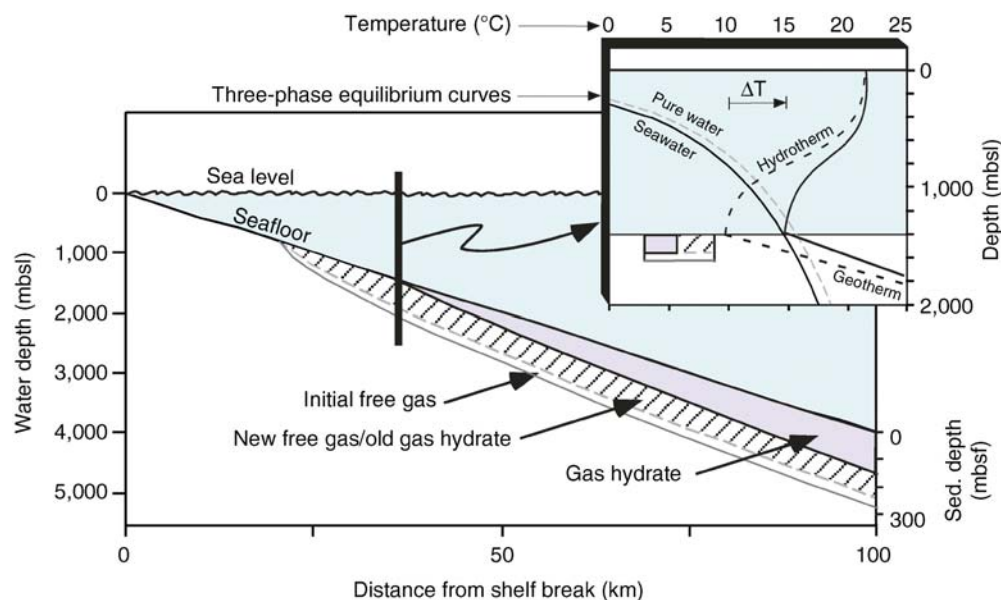


Figure M18 Theoretical location of crystalline gas hydrate and free gas bubbles below the seafloor before and after a 5 °C rise in bottom water temperature (after Dickens, 2001). The phase boundaries pertain to the pure methane system in pure water and seawater. Note that the diagram pertains to an initial bottom water temperature of 10 °C, as inferred for the Paleocene prior to the PETM.

Dickens et al., 1997). Significant amounts of gas hydrate cannot accumulate above the seafloor because, like ice, it has a density less than liquid water and floats.

Natural distribution and composition

Although appropriate pressure and temperature conditions exist throughout the deep ocean, insufficient concentrations of requisite gases preclude gas hydrate formation in many deep-sea sediment sequences. Along continental margins, however, the decomposition of organic matter through microbial activity or thermal cracking generates enough low molecular weight hydrocarbon gases to saturate pore waters within portions of the GHSZ.

Gas hydrates can be recovered from at or near the seafloor in a few places where hydrocarbon gases escape from sediment along fluid conduits such as faults. Locations documented to date include numerous sites in the Gulf of Mexico and on Hydrate Ridge off the coast of Oregon (Figure M17 and M19). Interestingly, these hydrates lie in contact with water containing very low concentrations of hydrocarbon gases. Evidently, a rapid supply of hydrocarbon gases can prevent the dissolution of gas hydrates on the seafloor.

Good evidence for gas hydrates has been documented in marine sediment well beneath the seafloor at over 60 locations in all oceans (Kvenvolden, 1999). Most of this evidence is indirect, coming from geophysical methods and an understanding of how sound waves propagate through sediment (Kvenvolden, 1999; Kvenvolden and Lorenson, 2001). Relative to sediment with pore space filled by water, the presence of solid gas hydrate and free gas bubbles increases and decreases the velocity of sound, respectively. A drop in sound velocity therefore occurs where gas hydrate directly overlies free gas bubbles at the base of the GHSZ. Seismic profiles generated on ships can image this acoustic interface (Figure M19), commonly named a bottom-simulating reflector (BSR) because it represents a solid/gas phase boundary,

parallels the seafloor and cross-cuts sedimentary strata (Holbrook et al., 1996; Kvenvolden, 1999). However, significant amounts of gas hydrate can exist at locations without a BSR, when insufficient gas concentrations to saturate pore waters occur at the bottom of the GHSZ (Dickens, 2001). Remote sensing of gas hydrate using current methods offers only a partial view of their distribution.

Considered unsafe for scientific drilling until the last decade, only a few areas of the seafloor with gas hydrate have been drilled so far in order to evaluate its vertical distribution and characteristics. These places include the Blake Ridge offshore of South Carolina, the Peruvian Margin, and Hydrate Ridge. In drill holes at each of these locations, some gas hydrate samples were recovered within the GHSZ. However, most gas hydrate eluded recovery and dissociated to constituent methane and water as pressure decreased and temperature increased during sediment core retrieval (Paull and Matsumoto, 2000; Shipboard Scientific Party, 2002). This inference comes from the results of various proxy techniques for measuring gas hydrate abundance. For example, a special tool was used at each drilled location to collect sediment cores at *in situ* pressure. The amounts of hydrocarbon gases released from these pressure cores (Figure M19) exceed gas hydrate saturation at many depths (Dickens et al., 1997; Milkov et al., 2003). In addition, the dissociation of gas hydrate is an endothermic reaction that decreases the temperature of sediment and releases fresh water to surrounding, relatively saline pore water. Anomalous low temperatures and fresh pore waters measured after core recovery can thus record the presence of gas hydrate in sediment at *in situ* conditions (Paull and Matsumoto, 2000; Shipboard Scientific Party, 2002). A major find resulting from this recent drilling is that gas hydrate in these locations is widely dispersed in sediment at low concentrations (<5% of pore space) except along local fluid conduits where, in some cases, the amount of gas hydrate exceeds the mass of sediment over m-scale intervals.

In most regions with gas hydrate, microbial production of gas dominates, and the gas within recovered samples of

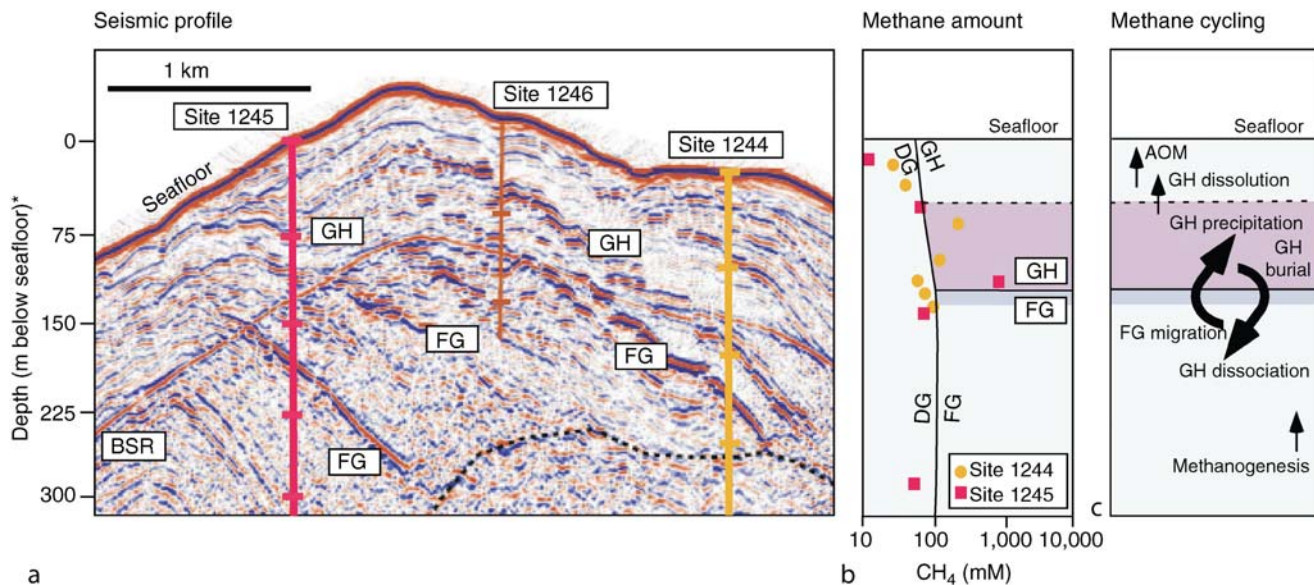


Figure M19 Seismic reflection profile across southern Hydrate Ridge on the Oregon Margin showing the bottom simulating reflector (BSR) and the location of three sites drilled during Leg 204 (Shipboard Scientific Party, 2002). Also shown are methane concentrations determined using pressure cores (Milkov et al., 2003), and the inferred dynamic cycling of methane in this region (modified from Dickens, 2003). The BSR is an acoustic interface separating gas hydrate from underlying free gas bubbles.

hydrate comprises mostly methane, often in excess of 99% (Kvenvolden and Lorenson, 2001). The microbial origin also leads to an exceptional depletion in the isotope ^{13}C (Kvenvolden and Lorenson, 2001). These microbial gas hydrates are Structure I clathrates. In some regions such as the Gulf of Mexico, however, thermogenic gas dominates, and gas hydrate samples may contain significant amounts of ethane and propane (Kvenvolden and Lorenson, 2001). These mixed hydrocarbon gas hydrates are often Structure II clathrates.

Global amount and significance

Estimates of the worldwide amount of gas hydrate in marine sediment remain poorly constrained and vary greatly. This reflects the intrinsic difficulty in quantifying the abundance of a phase that defies straightforward detection by remote methods and simple recovery by conventional drilling methods.

In theory, the global amount of gas hydrate in the oceanic realm can be calculated from two parameters: the volume of pore space within the GHSZ along all continental margins (Figure M18), and the average amount of pore space occupied by gas hydrate within this volume (Dickens, 2001). Estimates for the first parameter range from 1 to $6 \times 10^6 \text{ km}^3$ at present. On average, pore space within this volume probably contains between 1% and 10% gas hydrate. This implies that present-day oceanic gas hydrates hold somewhere between 1,000 and 22,000 Gt of carbon ($\text{Gt} = 10^{15} \text{ g}$) as methane (Dickens, 2001), with most but not all current literature typically suggesting about 10,000 Gt of carbon (cf. Kvenvolden, 1999; Milkov et al., 2003). Not included in these estimates are amounts of carbon stored in dissolved gas or in free gas bubbles beneath gas hydrate, which have not been assessed rigorously. Whatever the total, these amounts are enormous considering that the atmosphere contains about 700 Gt C, and the entire standing-stock of the terrestrial biosphere only accounts for about 500–1,000 Gt C.

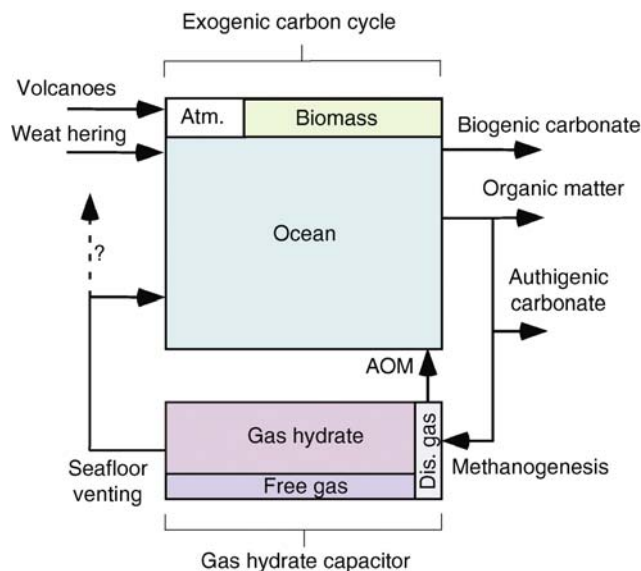


Figure M20 A basic, steady-state view of the exogenic global carbon cycle (ocean, atmosphere and biomass) with postulated connections to gas hydrates and free gas (after Dickens, 2003).

A dynamic view and a large capacitor

Oceanic gas hydrates and associated free gas constitute a major pool of ^{13}C -depleted methane intimately connected to the global carbon cycle (Figure M20). This view can be understood by considering individual deposits of gas hydrate and free gas in marine sediment as dynamic systems where carbon cycles between the ocean, sediments, dissolved gas, gas hydrate and free gas over time (Figure M19).

Photosynthetic organisms in surface waters produce complex organic molecules, which eventually sink through the water column to the seafloor. Within the sediment, bacteria utilize dissolved oxygen, nitrate, and sulfate to convert this organic matter to a series of products including carbon dioxide and acetate. Other microbes, probably archaea, use these simple carbon-based compounds to generate methane (e.g., Marchesi et al., 2001). This dissolved gas migrates both laterally and vertically via diffusion and fluid flow. Eventually, at sufficiently high gas concentrations and appropriate pressure and temperature conditions, gas hydrate can precipitate in pore space. Sediment burial over time slowly brings these solid methane-bearing molecules to higher temperatures. At some relatively shallow depth in the sediment column, gas hydrate is no longer stable and dissociates to gas-saturated water and free CH_4 gas bubbles.

Although much of the methane released from gas hydrate at depth migrates upward to recycle through the above processes, some quantity escapes these systems through one of two pathways. In many places, upward moving methane encounters sulfate diffusing down from the seafloor. This leads to anaerobic oxidation of methane (AOM), a biochemical reaction whereby consortia of archaea and bacteria convert methane to bicarbonate ion across a sulfate/methane transition (SMT) (e.g., Boetius et al., 2000). The SMT often occurs in the first 40 m below the seafloor (D'Hondt et al., 2002). However, in a few places with gas hydrate, notably where faults extend from the seafloor to depths below the GHSZ, high rates of fluid flow along conduits discharge methane into deep waters of the ocean. Aerobic oxidation of methane by bacteria probably consumes most of this methane in the water column (Valentine et al., 2001).

Pressure and temperature affect the location and fluxes of methane cycling within these dynamic carbon pools. As such, gas hydrate systems may serve as a large “capacitor” in the global carbon cycle, with relatively steady carbon inputs but highly variable carbon outputs (Dickens, 2003). The burial and degradation of organic carbon slowly contributes methane carbon to gas hydrate systems over time. At steady-state conditions, AOM and seafloor methane venting also slowly return methane carbon to the ocean. However, the rates of venting could change, perhaps dramatically, when deep ocean temperatures or sea level vary. Consider, for example, a modest rise in seafloor temperatures along continental margins from 0°C to 5°C (Figure M18). Once propagated into sediment, this perturbation would significantly shrink the global GHSZ, dissociating large amounts of gas hydrate to free gas bubbles. The build-up of free gas within sediment would lead to local pressures that exceed those from overlying water and, in some cases, overlying sediment. Such overpressure might cause sediment failure and rapid release of methane from the seafloor to the ocean or atmosphere through slumping or venting (Figure M21).

The capacitor concept is crucial for understanding gas hydrates throughout time in three regards (Dickens, 2003). First, widely accepted models for the global carbon cycle do not contain gas hydrates and methane fluxes to and from the seafloor. Nonetheless, these models may reasonably portray the fundamental operation of the carbon cycle when methane carbon inputs and outputs are small and roughly balanced, which is probably the case at present. Second, a capacitor allows for the production, storage and release of methane. Since sedimentary rocks show that organic carbon has accumulated in relatively cold deep waters ($<15^\circ\text{C}$) over significant intervals

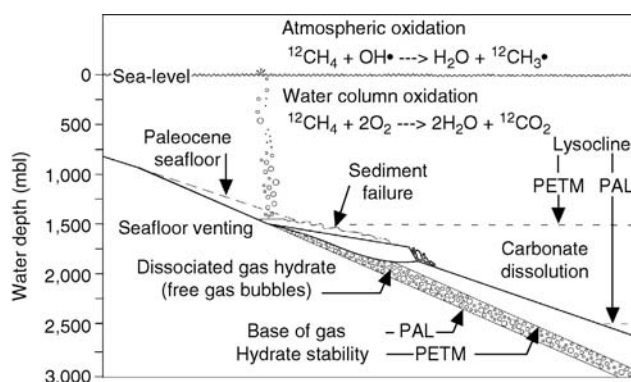


Figure M21 Schematic diagram highlighting the gas hydrate dissociation hypothesis for the Paleocene/Eocene boundary (modified from Katz et al., 1999). Large quantities of gas hydrate convert to free gas bubbles, which escape through sediment slumping (shown here) or venting to produce ^{13}C -depleted carbon dioxide in either the ocean or atmosphere.

of the geological record, presumably gas hydrates and free gas bubbles have always been a common phenomenon. Third, a capacitor allows for major injections of ^{13}C -depleted carbon to the ocean or atmosphere when external conditions change.

Potential climatic effects of seafloor methane release

Massive release of methane from marine gas hydrate systems to the atmosphere could significantly impact climate and the environment (Paull et al., 1991; Kvenvolden, 1999). Methane is a greenhouse gas with a much higher warming potential than carbon dioxide. Although methane molecules have a fairly short lifetime in the present-day atmosphere (about 10 years on average), this residence time depends strongly on atmospheric concentrations of methane and other species. Additionally, methane removal in the atmosphere eventually produces carbon dioxide. Consequently, a large transfer of methane from gas hydrate systems to the atmosphere could have a profound and lasting effect on earth surface temperatures (Schmidt and Shindell, 2003).

Microbes in the water column rapidly oxidize most methane venting above modern gas hydrate systems (Valentine et al., 2001). Therefore, direct injection of methane from gas hydrates to the atmosphere presents a conceptual problem (Kvenvolden, 1999). Conceivably, methane could escape oxidation if it was released sufficiently fast or if bubbles were coated with hydrate (Heeschen et al., 2003). Dislodged gas hydrate could also float toward the surface (Paull et al., 2002).

Substantial release of methane to the ocean could also affect the marine environment, primarily by changing the chemistry of deep ocean water (Dickens, 2000). Microbial oxidation of methane removes dissolved oxygen and produces carbon dioxide (Valentine et al., 2001), which decreases pH upon reaction with water, to form carbonic acid. In turn, increased acidity dissolves calcium carbonate, a common constituent of marine shells and seafloor sediment.

Irrespective of whether methane oxidation occurred in the atmosphere or ocean, its ultimate fate would be production of carbon dioxide, which could propagate throughout the ocean, atmosphere and terrestrial biomass. Consequently, a massive release of ^{13}C -depleted methane would decrease the $^{13}\text{C}/^{12}\text{C}$ ratio of all carbon upon the Earth's surface (Dickens, 2000).

Ancient methane release

Events of extreme environmental change punctuate Earth's history. Across some of these aberrations, the $^{13}\text{C}/^{12}\text{C}$ ratio of calcium carbonate and organic matter decreased at multiple locations, suggesting a major and rapid input of ^{13}C -depleted carbon to the atmosphere or ocean. Over the last 500 million years, such intervals include the Permian/Triassic boundary ca. 252 million years ago (Ma), several episodes in the Jurassic through middle Cretaceous ca. 183–120 Ma, and the Paleocene/Eocene boundary ca. 55 Ma. Increasingly, Earth scientists have argued that these abrupt geochemical anomalies signify massive release of methane from marine gas hydrate systems (e.g., Katz et al., 1999; Hesselbo et al., 2000; Beerling et al., 2002; Berner, 2002).

Of these events, the Paleocene/Eocene boundary (see *Paleocene-Eocene thermal maximum*, this volume) warrants special attention because evidence for massive methane release is compelling. First, unlike older intervals, stratigraphic relationships unequivocally demonstrate that the carbon isotope perturbation was global and rapid. At least 40 different stable isotope records, constructed using deep and shallow marine carbonate, and terrestrial carbonate and organic matter, now show a prominent drop in the $^{13}\text{C}/^{12}\text{C}$ ratio across the Paleocene/Eocene boundary (e.g., Katz et al., 1999; Bowen et al., 2002; Zachos et al., 2001). In records from open-ocean locations (Figure M22), the initial decrease occurs over 10–40 cm while the return to near initial values occurs over 100–400 cm, depending on sedimentation rate. The exact shape and timing of the carbon isotope excursion remain open issues, even at the same location. Nevertheless, on the basis of different dating methods (see Dickens, 2003), its decrease and return spanned <20 kyr and <220 kyr, respectively. Given the abruptness of this change, only methane release from the seafloor provides a satisfactory explanation for the very large drop in carbon isotope ratios (Dickens, 2003). Arguments for a comet impact (Kent et al.,

2003), while interesting, have little merit (Dickens and Francis, 2004; Schmitz et al., 2004).

Ancillary information from sediment cores across the Paleocene/Eocene boundary further supports a massive release of methane from gas hydrate systems. The $^{18}\text{O}/^{16}\text{O}$ ratio of carbonate shells precipitated by benthic foraminifera living on the seafloor also decreased significantly at this time (e.g., Katz et al., 1999; Zachos et al., 2001). This change suggests a major rise in deep ocean temperatures, perhaps upwards of 6°C , which would affect the distribution of gas hydrate dramatically (Figure M18 and M21). Deep marine sediment sequences furthermore display clear evidence for a substantial drop in dissolved oxygen and pronounced dissolution of calcium carbonate (e.g., Katz et al., 1999). In addition, these observations appear to coincide with unusual slumping along continental margins (Katz et al., 1999).

The cause and effects of presumed methane release during the Paleocene/Eocene boundary remain open issues, in large part because of intrinsic difficulties distinguishing the relative timing of rapid environmental changes in 55 million year old strata. However, all of the above observations closely correlate with a prominent benthic foraminifera extinction (e.g., Katz et al., 1999), extreme global warming (e.g., Zachos et al., 2001), and an extraordinary diversification of terrestrial mammals (e.g., Bowen et al., 2002).

Methane venting in the Quaternary

Major fluctuations in polar ice volume caused sea level to fall by greater than 100 m several times during the last few hundred thousand years. Several papers have speculated that these sea level drops may have released substantial quantities of methane from oceanic gas hydrate systems because of a decrease in the pressure within seafloor sediment (e.g., Kayen and Lee, 1991; Paull et al., 1991). If this idea is correct, methane must have come from sediment in shallow water depths or through other geological processes (e.g., sediment slumping) because the GHSZ would remain relatively unchanged at deeper water depths (Figure M18 and M21). A general correlation seems to exist between known locations of gas hydrate and sediment slumps formed during sea level low stands (e.g., Kennett et al., 2002). However, there is little if any ancillary data (e.g., carbon isotope deviations) to suggest that changes in sea level induce significant variations in global methane outgassing from deep marine sediment.

Climate records for the late Quaternary also indicate numerous brief atmospheric warming events that occurred during glacial times and that probably reflect some combination of changing ocean circulation patterns and elevated greenhouse gas concentrations. Notably, these “interstadial” events corresponded to prominent highs in atmospheric methane. Most literature has attributed the methane peaks to increased emissions from terrestrial wetlands (e.g., Severinghaus and Brook, 1999), although there is limited evidence in the geological record for their contemporaneous and requisite existence (Kennett et al., 2002). On the other hand, several lines of evidence suggest that water at intermediate depths in the ocean rose by several degrees centigrade prior to the atmospheric warming events. Recent papers have thus argued that these increases in bottom water temperature would propagate heat into sediment, dissociate gas hydrate to free gas, and release methane to the ocean and atmosphere through sediment failure (e.g., Kennett et al., 2002). Sediment records from the California margin provide some support for this interpretation. Immediately after episodes

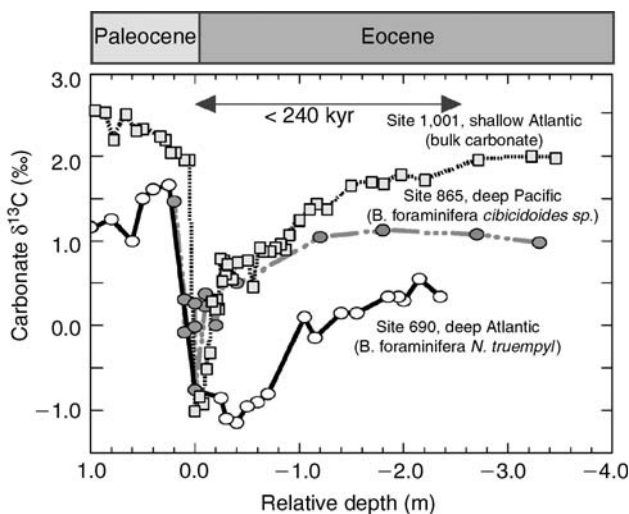


Figure M22 Carbon isotope records across the Paleocene/Eocene boundary in different phases at three deep-sea locations (see Dickens, 2003). Original records have been placed on a common depth scale with the carbon isotope minimum at 0.0 m. Note that the sedimentation rates vary between sites, giving different shapes to the excursion. Carbon isotopes are expressed in conventional delta notation ($\delta^{13}\text{C}$) so that negative values signify a drop in the $^{13}\text{C}/^{12}\text{C}$ ratio.

of intermediate water warming in the Santa Barbara Basin, the $^{13}\text{C}/^{12}\text{C}$ ratio of benthic foraminifera decreased (Kennett et al., 2000), and the abundance of organic compounds produced by methane-consuming bacteria increased (Hinrichs et al., 2003). To date, however, no compelling evidence has been provided to suggest that methane released from the seafloor during interstadial events escaped microbial consumption in the water column, or that atmospheric methane in fact initiated climate change.

Conclusions

A large although unconstrained mass of ^{13}C -depleted hydrocarbons, mostly methane, exists as crystalline gas hydrates and free gas bubbles along modern continental margins. Although specimens of massive gas hydrate can be recovered from the seafloor, the bulk of methane in these phases lies dispersed within the upper few hundreds of meter of sediment. Most methane in gas hydrates and free gas escapes collection during conventional sediment recovery, but can be detected through various proxy techniques. All information indicates that the overall distribution of methane depends on carbon fluxes to and from the ocean, and external conditions such as pressure and temperature. In all likelihood, gas hydrates have occurred throughout most of geological time. An open issue is whether gas hydrate systems can suddenly discharge large amounts of methane. If this is the case, rapid methane release could impact the environment by contributing to atmospheric warming or by changing ocean chemistry. A burgeoning body of literature suggests that methane released from gas hydrate systems explains unusual observations during certain intervals of extreme environmental change in the ancient geological record, such as the Paleocene/Eocene boundary. The idea that methane contributes significantly to changes in Quaternary climate is more controversial but has some support.

Gerald R. Dickens and Clayton Forswall

Bibliography

- Bowen, G.J., Clyde, W.C., Koch, P.L., Ting, S.Y., Alroy, J., Tsubamoto, T., Wang, Y.Q., and Wang, Y., 2002. Mammalian dispersal at the Paleocene/Eocene boundary. *Science*, **295**, 2062–2065.
- Beerling D.J., Lomas M.R., and Grocke D.R., 2002. On the nature of methane gas-hydrate dissociation during the Toarcian and Aptian oceanic anoxic events. *Am. J. Sci.*, **302**, 28–49.
- Berner, R.A., 2002. Examination of hypotheses for the Permo-Triassic boundary extinction by carbon cycle modeling. *Proc. Natl. Acad. Sci. USA*, **99**, 4172–4177.
- Boetius, A., Ravensschlag, K., Schubert, C.J., Rickert, D., Widdel, F., Gieseke, A., Amann, R., Jørgensen, B.B., Witte, U., and Pfannkuche, O., 2000. A marine microbial consortium apparently mediating anaerobic oxidation of methane. *Nature*, **407**, 623–626.
- D'Hondt, S., Rutherford, S., and Spivack, A.J., 2002. Metabolic activity of subsurface life in deep-sea sediments. *Science*, **295**, 2067–2070.
- Dickens, G.R., 2000. Methane oxidation during the late Palaeocene thermal maximum. *Bull. Soc. Géol. France*, **171**, 37–49.
- Dickens, G.R., 2001. The potential volume of oceanic methane hydrates with variable external conditions. *Org. Geochem.*, **32**, 1132–1193.
- Dickens, G.R., 2003. Rethinking the global carbon cycle with a large, dynamic and microbially mediated gas hydrate capacitor. *Earth Planet. Sci. Lett.*, **213**, 169–182.
- Dickens, G.R., and Francis, J.M., 2004. Comment: A case for a comet impact trigger for the Paleocene/Eocene thermal maximum and carbon isotope excursion. *Earth Planet. Sci. Lett.*, **217**, 197–200.
- Dickens, G.R., and Quinby-Hunt, M.S., 1997. Methane hydrate stability in pore water: A simple theoretical approach for geophysical applications. *J. Geophys. Res.*, **102**, 773–783.
- Dickens, G.R., Paull, C.K., Wallace, P., and ODP Leg 164 Scientific Party, 1997. Direct measurement of in situ gas volumes in a large gas hydrate reservoir. *Nature*, **385**, 426–428.
- Heeschen, K.U., Trehu, A.M., Collier, R.W., Suess, E., and Rehder, G., 2003. Distribution and height of methane bubble plumes on the Cascadia Margin characterized by acoustic imaging. *Geophys. Res. Lett.*, **30**, Art. No. 1643.
- Hesselbo, S.P., Gröcke, D.R., Jenkyns, H.C., Bjerrum, C.J., Farrimond, P., Bell, H.S.M., and Green, O.R., 2000. Massive dissociation of gas hydrate during a Jurassic oceanic anoxic event. *Nature*, **406**, 392–395.
- Hinrichs K.-U., Hmelo L.R., and Sylva, S.P., 2003. Molecular fossil record of elevated methane levels in late Pleistocene coastal waters. *Science*, **299**, 1214–1217.
- Holbrook, W.S., Hoskins, H., Wood, W.T., Stephen, R.A., Lizarralde, D., and Leg 164 Science Party, 1996. Methane hydrate and free gas on the Blake Ridge from vertical seismic profiling. *Science*, **273**, 1840–1843.
- Katz, M.E., Pak, D.K., Dickens, G.R., and Miller, K.G., 1999. The source and fate of massive carbon input during the Latest Paleocene Thermal Maximum. *Science*, **286**, 1531–1533.
- Kayen, R.E., and Lee, H., 1991. Pleistocene slope instability of gas hydrate-laden sediment on the Beaufort Sea Margin. *Mar. Geotech.*, **10**, 125–141.
- Kennett, J.P., Cannariato, K.G., Hendy, I.L., and Behl, R.J., 2000. Carbon isotopic evidence for methane hydrate instability during Quaternary interstadials. *Science*, **288**, 128–133.
- Kennett, J.P., Cannariato, K.G., Hendy, I.L., and Behl, R.J., 2002. *Methane Hydrates in Quaternary Climate Change*. Washington, DC: American Geophysical Union, 216pp.
- Kent, D.V., Cramer, B.S., Lanci, L., Wang, D., Wright, J.D., and Van der Voo, R., 2003. A case for a comet impact trigger for the Paleocene/Eocene thermal maximum and carbon isotope excursion. *Earth Planet. Sci. Lett.*, **211**, 13–26.
- Kvenvolden, K.A., 1999. Potential effects of gas hydrate on human welfare. *Proc. Natl. Acad. Sci. USA*, **96**, 3420–3426.
- Kvenvolden, K.A., and Lorenson, T.D., 2001. The global occurrence of natural gas hydrate. In Paull, C.K., and Dillon, W.P. (eds.), *Natural Gas Hydrates: Occurrence, Distribution and Detection*. Washington, DC: American Geophysical Union. Geophysical Monograph Series 124, pp. 3–18.
- Marchesi, J.R., Weightman, A.J., Cragg, B.A., Parkes, R.J., and Fry, J.C., 2001. Methanogen and bacterial diversity and distribution in deep gas hydrate sediments from the Cascadia Margin as revealed by 16S rRNA molecular analysis. *FEMS Microbiol. Ecol.*, **34**, 221–228.
- Milkov, A.V., Claypool, G.E., Lee, Y.-J., Xu, W., Dickens, G.R., Borowski, W.S., and ODP Leg 204 Scientific Party, 2003. In situ methane concentrations at Hydrate Ridge offshore Oregon: New constraints on the global gas hydrate inventory from an active margin. *Geology*, **31**, 833–836.
- Paull, C.K., and Matsumoto, R., 2000. Leg 164 overview, in *Proceedings of the Ocean Drilling Program, Scientific Results*, vol. 164, pp. 3–10. College Station, TX: Ocean Drilling Program.
- Paull, C.K., Ussler W., and III, Dillon, W.P., 1991. Is the extent of glaciation limited by marine gas-hydrates? *Geophys. Res. Lett.*, **18**, 432–434.
- Paull, C., Brewer, P., Ussler, W., Peltzer, E., Rehder, G., and Clague, D., 2002. An experiment demonstrating that marine slumping is a mechanism to transfer methane from seafloor gas-hydrate deposits into the upper ocean and atmosphere. *Geo-Mar. Lett.*, **22**, 198–203.
- Schmidt, G.A., and Shindell, D.T., 2003. Atmospheric composition, radiative forcing, and climate change as a consequence of a massive methane release from gas hydrates. *Paleoceanography*, **18**, article 10.1029/2002PA000757.
- Schmitz, B., Peucker-Ehrenbrink, B., Heilmann-Clausen, C., Aberg, G., Asaro, F., and Lee, C.T.A., 2004. Basaltic explosive volcanism, but no comet impact, at the Paleocene-Eocene boundary: High-resolution chemical and isotopic records from Egypt, Spain and Denmark. *Earth Planet. Sci. Lett.*, **225**, 1–17.
- Severinghaus, J.P., and Brook, E.J., 1999. Abrupt climate change at the end of the last glacial period inferred from air trapped in polar ice. *Science*, **286**, 930–933.
- Shipboard Scientific Party, (2002). Leg 204 Preliminary Report. *ODP Prelim. Rpt.*, 104 [Online]. Available from World Wide Web: http://www.odp.tamu.edu/publications/prelim/204_prel/204PREL.PDF.
- Sloan, E.D. Jr., 1998. *Clathrate Hydrates of Natural Gases*. New York: Marcel Dekker, 705pp.
- Valentine, D.L., Blanton, D.C., Reeburgh, W.S., and Kastner, M., 2001. Water column methane oxidation adjacent to an area of active hydrate

dissociation, Eel River Basin. *Geochim. Cosmochim. Acta*, **65**, 2633–2640.

Zachos, J., Pagani, M., Sloan, L., Thomas, E., and Billups K., 2001. Trends, rhythms, and aberrations in global climate 65 Ma to present. *Science*, **292**, 686–693.

Cross-references

[Carbon Cycle](#)

[Carbon Dioxide, Dissolved \(Ocean\)](#)

[Carbon Isotopes, Stable](#)

[Paleocene-Eocene Thermal Maximum](#)

[Paleogene Climates](#)

[Pleistocene Climates](#)

MID-PLIOCENE WARMING

The middle Pliocene is the most recent period in Earth history with temperatures as warm as those we expect the Earth to experience by the latter part of the 21st Century. Estimates of middle Pliocene warming are from 2.0 °C to 3.2 °C (Figure M23), placing them in the range of the Intergovernmental Panel on Climate Change (IPCC) projections of global temperature rise by the year 2100. Yet, in many respects, the mid-Pliocene is very much like the

modern world. Terrestrial geography and ocean basin configuration are largely unchanged, many floral and faunal species are still extant, and altered internal and external forcings (e.g., mid-ocean ridge spreading rates, solar luminosity) are not factors as they would have been for much more ancient periods. While most scientists are confident that we have identified the primary forcings triggering the present warming trend, no one is certain of the ultimate climate impact of those forcings, or their associated feedback processes. The middle Pliocene presents us with somewhat the reverse situation: extensive global data reveal the mature state of a warmer world, essentially the resulting climate impact of a prior global warming. The forcings that led to Pliocene warming may be only partially identified, but in both the mid-Pliocene and the present day, the myriad of feedbacks that exist between the forcing triggers and their eventual impacts remain the topic of extensive research.

Data collection, process studies, and numerical simulations, all of which provide both validation and predictive capacity, are targeted at narrowing estimates of climate change. The middle Pliocene world provides an excellent paleo-laboratory for testing the sensitivity of the physical models that we rely upon for estimating future warming impacts. It challenges our understanding of the sensitivity of key components of the climate system and how we simulate that system: polar vs. tropical sensitivity, the role of ocean circulation in a warming climate, the hydrological impact of altered storm tracks, and the regional

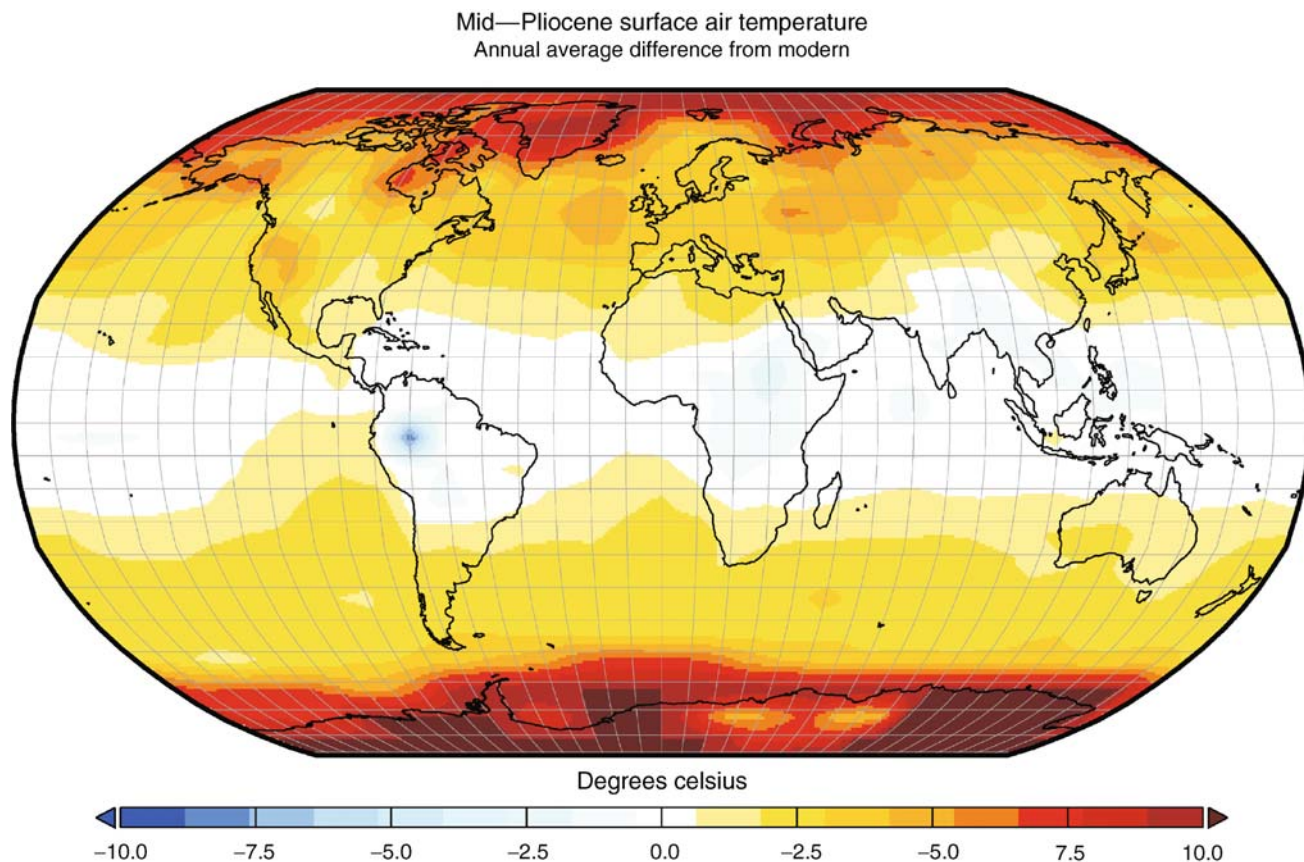


Figure M23 Simulations of mid-Pliocene surface air temperatures show that the Earth was more than 2 °C warmer than during the mid 20th century. Warming was greatest in high latitudes, particularly in regions where land and sea ice extent were lower. Slight cooling in some regions results from increased elevation, or increased standing water in the case of the Amazon River basin.

climate impacts of modified atmospheric and oceanic energy transport systems.

Issues in middle Pliocene warming

The interpretation of a mid-Pliocene global warming, where temperatures were significantly higher than modern, is supported by both terrestrial and marine paleoclimate proxies (e.g., Dowsett et al., 1996; Dowsett et al., 1999; Haywood et al., 2005; Thompson, 1991; Thompson, 1992; Thompson and Fleming, 1996; Wara et al., 2005). Marine microfaunal evidence suggests that warming was greatest at high latitudes (Dowsett et al., 1996), resulting in a reduced equator-to-pole temperature gradient and tropical oceans that were, in the end, far less sensitive to change. Estimates of paleo-CO₂ levels including analyses of the stomatal density of fossil leaves (Kürschner et al., 1996; vanderBurgh et al., 1993), analyses of $\delta^{13}\text{C}$ ratios of marine organic carbon (Raymo and Rau, 1992), and measurements of differences between the carbon isotope composition of surface and deep waters (Shackleton et al., 1992) all suggest an elevation of atmospheric CO₂ of roughly 60–100 ppmv above pre-industrial concentrations. Present-day atmospheric CO₂ levels are close to 384 ppmv (in 2008) and are, therefore, within the envelope predicted to have existed during the middle Pliocene (360–400 ppmv). Increases in additional greenhouse gases, such as methane, may have accompanied the CO₂ increase during the Pliocene. However, an open question is whether the middle Pliocene climate represents the lag effect of modest greenhouse warming, revealing how the oceans and ice-sheets integrate, redistribute, and even amplify climate impacts through longer-term feedback mechanisms (i.e., ocean circulation, sea level rise, permafrost melting, etc.).

Paleoclimate modeling studies have suggested that the middle Pliocene pattern of warmer sea surface temperatures and surface air temperatures is more consistent with enhanced ocean heat transports than with a simple increase in the atmospheric CO₂ level (Figure M24) because low latitude regions

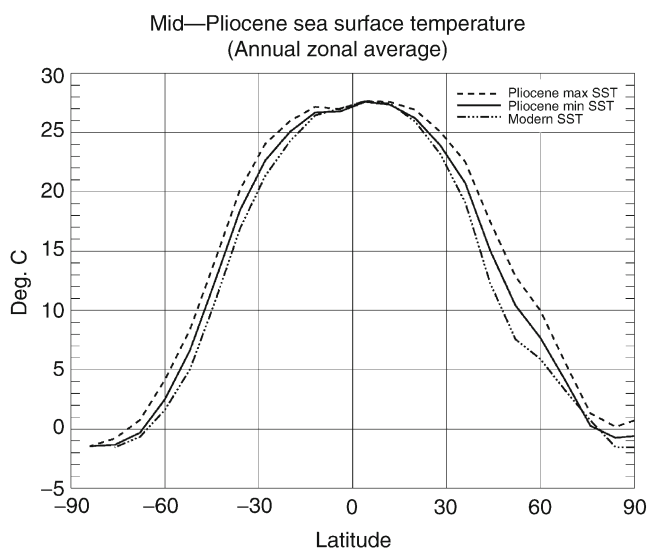


Figure M24 Modern and middle Pliocene sea surface temperatures show no significant difference in the tropics, in contrast to mid and high latitude regions, suggesting a role for altered ocean heat transports in surface warming.

show such limited warming compared to high latitudes. However, there is some disagreement between proxy records of tropical temperatures, particularly in the Pacific Ocean. Several recent studies using Mg/Ca ratios and alkenones find that the eastern equatorial Pacific may have been warmer than previously thought. These findings are somewhat more consistent with moderately increased greenhouse gas levels, and have been used to suggest that the middle Pliocene warming may have been characterized by a tropical sea-surface temperature pattern that is akin to a permanent El Niño. Although no study has yet determined a specific set of forcings and feedbacks that were responsible for triggering changes in ocean circulation during the Pliocene, data suggest that a combination of increased greenhouse gases and altered ocean heat transports, and perhaps additional factors, acted concurrently (linked by feedback relationships) to generate the middle Pliocene warming (e.g., Dowsett et al., 1996; Raymo et al., 1996).

Enhanced ocean heat transports may have been the result of strengthened thermohaline circulation (THC) and/or increased flow of surface ocean currents. The latter process has not been widely accepted, since generating enhanced wind stress under a regime of reduced latitudinal temperature gradients and a decreased dynamic circulation of the atmosphere is difficult (Crowley, 1996). Recently, however, Haywood et al. (2000) showed that regionally enhanced wind stress fields over the North Atlantic, North Pacific and Southern Ocean occur in middle Pliocene experiments using the Hadley Centre's General Circulation Model (GCM). Such regional increases may be sufficient to strengthen the gyre circulations in these ocean basins and cause an increase in meridional heat transport. Moreover, greater wind stress curl and consequent gyre strengthening in the North Pacific is supported by paleoceanographic evidence along the California margin (Ravelo et al., 1997).

Other factors must also be considered. Surface conditions in the middle Pliocene were somewhat different from present-day: vegetation distributions were altered (Thompson and Fleming, 1996) and sea level was probably around 15–25 meters higher than modern (e.g., Dowsett and Cronin, 1990). In addition, both the Greenland and Antarctic Ice Sheets were probably smaller (though the size of the Antarctic Ice Sheet remains a key Pliocene controversy), and topographic relief may not have reached modern proportions in the Western Cordillera, the East African Rift region and on the Tibetan Plateau (Raymo et al., 1988; Ruddiman and Kutzbach, 1989; Raymo and Ruddiman, 1992).

Middle Pliocene warming and estimates of future climate change

Despite these differences, the middle Pliocene displays more similarities with our anticipated future climate than almost any other period in Earth history. Foremost among these is the magnitude of warming in the middle Pliocene, which is similar to future global climate change simulations at high latitudes and over mid-latitude continental interiors. If forcings and associated feedbacks are proportional to the ultimate climate impacts, then the middle Pliocene is probably closer to what we can expect from future global warming than are the warm climates of the Holocene or Pleistocene interglacials. The potential to use the middle Pliocene as an analogue for future climate change is also reinforced by the fact that many key boundary conditions, such as the position of the continents, vegetation types and the intact state of the isthmus of Panama, were the same as or similar to those of the present day (Crowley, 1991; Crowley, 1996; Maier-Reimer et al.,

1990). The opportunity to conduct detailed data-model comparisons is also excellent as there is:

1. Abundant paleoclimatic information from both the marine and terrestrial realm (relative to older time periods);
2. A large number of extant species, making micropaleontologically-based climate interpretations feasible;
3. A reduced chance that diagenesis will hamper geochemical analyses and more precise dating of proxy data, and thus more precise validation of equilibrium GCM simulations (Chandler et al., 1994).

The ability to use numerical climate model simulations to study this past global warming is also greatly enhanced by the development of the PRISM (Pliocene Research, Interpretation and Synoptic Mapping) series of quantitative digital data sets produced by the United States Geological Survey since 1992. The ocean surface maps were updated using data from more than 170 sites worldwide, and are available as the PRISM2 data set of middle Pliocene conditions (Dowsett et al., 1999). Efforts are now underway to extend the PRISM data to include 3-dimensional temperature data for the mid-Pliocene oceans. These data are designed specifically for use in paleoclimate modeling studies utilizing GCMs. As such, the PRISM2 reconstruction represents the most detailed global paleoclimate reconstruction for any time other than the Last Glacial Maximum (21 ky BP), and the *only* major reconstruction of a globally warmer time period.

Mark A. Chandler

Bibliography

- Chandler, M.A., Rind, D., and Thompson, R.S., 1994. Joint investigations of the middle Pliocene climate II: GISS GCM Northern Hemisphere results. *Palaeogeogr. Palaeoclimatol. Palaeoecol.*, **9**, 197–219.
- Crowley, T.J., 1991. Modeling Pliocene warmth. *Quaternary Sci. Rev.*, **10**, 275–282.
- Crowley, T.J., 1996. Pliocene climates: The nature of the problem. *Mar. Micropaleontol.*, **27**, 3–12.
- Dowsett, H., Barron, J., and Poore, R.Z., 1996. Middle Pliocene sea surface temperatures: A global reconstruction. *Mar. Micropaleontol.*, **27**, 13–26.
- Dowsett, H.J., and Cronin, T.M., 1990. High eustatic sea level during the middle Pliocene: Evidence from southeastern U.S. Atlantic coastal plain. *Geology*, **18**, 435–438.
- Dowsett, H.J., Barron, J.A., Poore, R.Z., Thompson, R.S., Cronin, T.M., Ishman, S.E., and Willard, D.A., 1999. Middle Pliocene paleoenvironmental reconstruction: PRISM2. *US Geol. Surv. Open File Rep.*, 99–535.
- Haywood, A.M., Valdes, P.J., and Sellwood, B.W., 2000. Global scale paleoclimate reconstruction of the middle Pliocene climate using the UKMO GCM: Initial results. *Global Planet. Change*, **25**, 239–256.
- Haywood, A.M., Dekens, P., Ravelo, A.C., and Williams, M., 2005. Warmer tropics during the mid-Pliocene? Evidence from alkenone paleothermometry and a fully coupled ocean-atmosphere GCM. *Geochim. Geophys. Geosyst.*, **6**, Q03010 (doi:10.1029/2004GC000799).
- Kürschner, W.M., van der Burgh, J., Visscher, H., and Dilcher, D.L., 1996. Oak leaves as biosensors of late Neogene and early Pleistocene paleoatmospheric CO₂ concentrations. *Mar. Micropaleontol.*, **27**, 299–312.
- Maier-Reimer, E., Mikolajewicz, U., and Crowley, T., 1990. Ocean general circulation model sensitivity experiment with an open Central American isthmus. *Paleoceanography*, **5**, 349–366.
- Ravelo, A.C., et al., and ODP Leg 167 Shipboard Scientific Party, 1997. Pliocene carbonate accumulation along the Californian margin. *Paleoceanography*, **12**, 729–741.
- Raymo, M.E., and Rau, G., 1992. Plio-Pleistocene atmospheric CO₂ levels inferred from POM delta ¹³C at DSDP Site 607. *Eos Trans. AGU*, **73** (43), 95–96.
- Raymo, M.E., and Ruddiman, W.F., 1992. Tectonic forcing of Late Cenozoic climate. *Nature*, **359**, 117–122.
- Raymo, M., Grant, M., Horowitz, M., and Rau, G.H., 1996. Mid-Pliocene warmth: Stronger greenhouse and stronger conveyor. *Mar. Micropaleontol.*, **27**, 313–326.
- Raymo, M.E., Ruddiman, W.F., and Froelich, P.N., 1988. Influence of Late Cenozoic mountain building on ocean geochemical cycles. *Geology*, **16**, 649–653.
- Ruddiman, W.F., and Kutzbach, J.E., 1989. Forcing of Late Cenozoic Northern Hemisphere climate by plateau uplift in southern Asia and the American West. *JGR Atmos.*, **94**(D15), 18,409–18,427.
- Shackleton, N.J., Le, J., Mix, A., and Hall, M.A., 1992. Carbon isotope records from Pacific surface waters and atmospheric carbon dioxide. *Quaternary Sci. Rev.*, **11**, 387–400.
- Thompson, R.S., 1991. Pliocene environments and climates in the Western United States. *Quaternary Sci. Rev.*, **10**, 115–132.
- Thompson, R.S., 1992. Palynological data from a 989-ft (301-m) core of Pliocene and Pleistocene sediments from Bruneau, Idaho. *US Geol. Surv. Open File Rep.*, 92–713.
- Thompson, R.S., and Fleming, R.F., 1996. Middle Pliocene vegetation: Reconstructions, paleoclimate inferences, and boundary conditions for climate modeling. *Mar. Micropaleontol.*, **27**, 27–49.
- vanderBurgh, J., Visscher, H., Dilcher, D.L., and Kürschner, W.M., 1993. Paleoatmospheric signatures in Neogene fossil leaves. *Science*, **260**, 1,788–1,790.
- Wara, M.W., Ravelo, A.C., and Delaney, M.L., 2005. Permanent El Niño-like conditions during the Pliocene warm period. *Science*, **309**: 758–761 (doi:10.1126/science.1112596).

Cross-references

[Greenhouse \(Warm\) Climates](#)
[Paleoclimate Modeling, Pre-Quaternary](#)
[Pleistocene Climates](#)

MILLENNIAL CLIMATE VARIABILITY

Introduction

One of the most puzzling features of Earth's past climate is a series of strikingly abrupt and robust variations that occur roughly every 1,000–7,000 years. First recognized in temperature records from Greenland ice cores and North Atlantic deep-sea sediments, these millennial climate cycles are now known to have a global or nearly global footprint, and they have been found in records spanning at least the last half million years. Paleoclimate records reveal at least four modes of millennial climate change: Heinrich events, Bond cycles, and Dansgaard/Oeschger cycles that occur exclusively within glacials, and unnamed persistent cycles that punctuate both glacials and interglacials. (*Note that the term cycle, as used here, refers to a repeating process that is not necessarily periodic.*)

Records of millennial climate variations have drawn widespread attention because they produced the first convincing evidence that Earth's climate system is much less stable than once thought and can shift suddenly on human time scales. The millennial cycles typically exhibit threshold behavior; i.e., abrupt transitions from one mode of operation to another during which temperature changes of several degrees Celsius occur within decades if not years. Although these striking temperature jumps appear to have taken place predominantly during glaciations, results of some modeling experiments imply that they might be induced in the near future by continued global warming. Even though the likelihood of that happening might be low, the impact on society is potentially so severe that understanding why the climate system is prone

to such behavior has become a high priority. Yet after more than two decades of research, the underlying mechanisms remain elusive.

Millennial climate cycles: history and description

Heinrich events

Heinrich (1988) was the first to recognize that glacial sediments in a deep-sea core from the Dreizack Seamount (Figure M25) were punctuated by six distinct layers demarking brief ($\leq 1,000$ years) episodes of extreme ocean surface cooling, dramatic reductions in abundances of planktic foraminifera, depletions in planktic $\delta^{18}\text{O}$, and exceptionally large increases in IRD (ice-rafted debris) produced by melting of armadas of debris-laden icebergs discharged into the subpolar North Atlantic. Later, these six episodes were named Heinrich events by Broecker et al., (1992).

Building on Heinrich's discoveries, Bond et al. (1992, 1993) demonstrated that IRD maxima and the strong depletions in $\delta^{18}\text{O}$ in the six Heinrich events (H1–H6) occurred suddenly at the end of cooling ramps containing bundles of progressively colder Dansgaard/Oeschger (D/O) cycles (Figure M26a–e). The cooling ramps were followed abruptly by an unusually large warming that raised sea surface temperatures by several degrees Celsius to nearly Holocene values. Cores containing these features extend from the Labrador Sea eastward across the entire North Atlantic between latitudes of about 40°N and 55°N , the so called IRD belt (Figure M25). Petrologic and geochemical tracers in the IRD point to sources of the massive Heinrich iceberg discharges in eastern Canada, probably in the Hudson Strait region.

Heinrich events are sometimes defined as corresponding to the full range of the increases in IRD. Detailed analyses of the anatomy of Heinrich layers, however, demonstrate that the initial increase in IRD does not contain tracers linked to Hudson Strait sources. To avoid confusion over the age of Heinrich events the term should apply only to layers rich in IRD derived mainly from eastern Canada. For an excellent summary of Heinrich events see Hemming (2004) and this volume (*Heinrich events*).

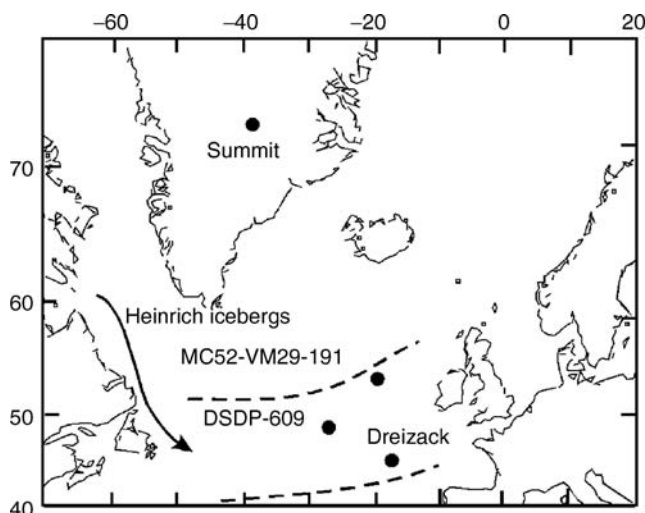


Figure M25 Locations of cores mentioned in text and location of the Ruddimann IRD belt (dashed lines).

Bond cycles

Named by Broecker (1994), a Bond cycle, first identified in Greenland ice cores and North Atlantic temperature records, begins with the post-Heinrich event warming, followed by a gradual cooling ramp that contains a bundling of progressively colder D/O cycles, and then ends abruptly at the peak cooling of the next Heinrich event (Figure M26a,b). The atmosphere and ocean surface temperature drop over the course of a Bond cycle is a few to several degrees Celsius. IRD concentrations in North Atlantic sediments follow this pattern, with short cycles of progressively larger amplitude, probably correlative with D/O cycles, developing as temperatures decrease (Figure M26c).

The shapes of Bond cycles were the basis for correlating temperature records from Greenland ice cores and North Atlantic deep-sea sediments over the entire last glacial cycle (Figure M26a,b). The correlation documented for the first time the relation between D/O cycles in the ice cores and Heinrich events in the ocean.

D/O cycles

The typical evolution of these abrupt events, also named by Broecker (1994), begins with a rapid ocean surface and atmospheric warming, completed usually within a few decades, followed by gradual cooling over a few hundred years, and a distinct cold phase afterwards for a few centuries to a millennium (Figure M26a). Approximately 23 D/O oscillations occurred during the last glacial cycle. The well-known Younger Dryas (YD) event is the last of these and was followed abruptly by the onset of the present interglacial or Holocene (Figure M26a). A recent revision of ice core temperature calibration suggests that the YD ended with a remarkable atmospheric warming of 10°C in decades or less (Grachev and Severinghaus, 2005).

Within the D/O stadials that terminate Bond cycles, the large IRD peaks of Heinrich events are confined to the last few hundred years, suggesting that the massive discharges of Heinrich icebergs came after several hundred years of cold temperatures (Bond et al., 1993). Cold phases of the other D/O cycles also contain peaks in the concentrations of IRD, although they are not as large as those during Heinrich events (Figure M26c). The sources of IRD in D/O cycles are diverse, including Europe, east Greenland, and Iceland (Hemming, 2004). Percentages of detrital carbonate remain low during the cold phases of D/O cycles (Figure M26d), suggesting that, in contrast to Heinrich events, sources in eastern Canada were not important.

Persistent multi-century to millennial cycles

High-resolution measurements of two IRD grain types, hematite-stained grains derived from red bed deposits and fresh volcanic glass derived from Iceland and or Juan Mayen have revealed robust oscillations that do not follow the D/O cycle pattern, but instead punctuate both cold and warm phases of those cycles (Figure M26f). Surprisingly, these persist across the glacial-interglacial transition and continue through the entire Holocene (Bond et al., 2001). The pacing of the cycles is highly irregular, varying from about 900 years to about 2,000 years. The petrologic changes are thought to reflect repeated southward advections of cooler waters carrying ice with debris rich in the two grain types from the polar seas north of Iceland. These shorter cycles are sometimes incorrectly called Bond cycles.

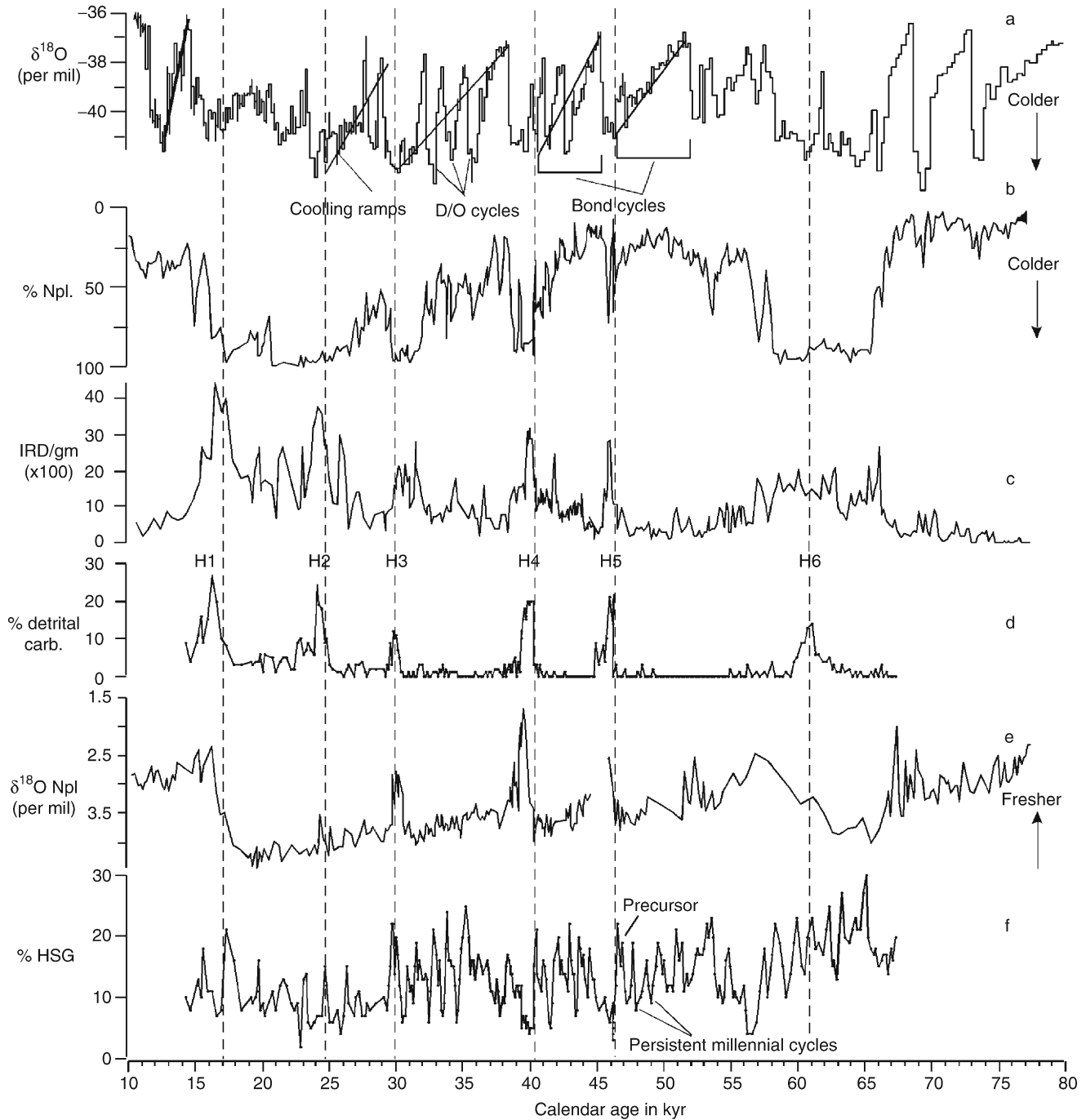


Figure M26 (a) Records from GISP2 ice core, and (b–f) DSDP 609. *Npl.*, *N. pachyderma* (s.); *HSG*, hematite-stained grains; *H*, Heinrich event. Dashed lines mark boundaries between increases in detrital carbonate (Heinrich events) and precursory events as defined by *HSG* record. See text for discussion (modified from Bond et al., 1999).

At least some of these persistent oscillations also occur in the Greenland ice core records where subtle variations in $\delta^{18}\text{O}$ and in estimates of temperature punctuate many of the stadial and interstadial intervals of D/O cycles (North Greenland Ice Core Project members, 2004; Landais et al., 2004). Prominent depletions in $\delta^{18}\text{O}$ also are present in early Holocene ice at about 11,300, 10,900, 10,300, 9,300, 8,200 years.

Global distribution of millennial variations

Heinrich events, Bond cycles and D/O cycles have now been found in climate records far from the North Atlantic where they were first identified. Voelker (2002) compiled evidence that revealed their presence in both hemispheres extending from high polar latitudes to the tropics. The best records, however,

are from stalagmite deposits, which can be dated accurately with uranium-thorium methods, and from ice cores whose chronology is constrained in part by layer counting. A map of the stalagmite and ice core sites (Figure M27) documents the global footprint of these three types of millennial variations. Outside of the North Atlantic the imprint of the persistent millennial cycles has been found in late Holocene sediments from the Cariaco Basin off Venezuela, in Holocene lake records from Ecuador, in glacial-Holocene loess deposits from the Mississippi Valley, China and Tibet, in tree ring records from Finland, and in a stalagmite record from Yemen.

Mechanisms

Oscillatory ice sheet dynamics

Although no consensus has been reached on the cause of millennial climate variability, one widely held view maintains that the fundamental mechanism arises from oscillatory internal dynamics of glaciers flowing into the northern North Atlantic. Recurring surges or collapses of those glaciers are thought to have caused

repeated and rapid increases in the flux of icebergs (i.e., freshwater) into the ocean. Upon reaching the convecting regions north and south of Iceland, the freshwater injections are presumed to have lowered ocean surface salinities enough to force ocean circulation across a threshold, induce a hysteresis behavior, and abruptly reduce or shut down North Atlantic Deep Water (NADW) formation (Ganopolski and Rahmstorf, 2001). Models of this process have shown that a shutdown of NADW production triggers a precipitous drop in ocean surface temperature that is broadly consistent with paleotemperature data.

To explain the oscillatory dynamics, MacAyeal (1993) proposed a free oscillation mechanism that has come to be known as the binge-purge model. A large glacier or ice sheet frozen to bedrock will slowly build up during the binge phase. The purge phase (i.e., the Heinrich event) occurs when geothermal heat melts the basal sediment and produces a lubricated discharge pathway. The model produced massive collapses of the ice every 7,000 years, agreeing reasonably well with the observed timing of Heinrich events. In a more elaborate development of the model, Greve and MacAyeal (1996) found that free oscillations from 1,000 to 10,000 years could occur within a large ice sheet, thereby potentially providing an explanation for both Heinrich events and the faster-paced D/O cycles.

Climate-centered mechanisms

The elegant glacier-centered hypothesis was called into question, however, by the results of efforts to test two of its corollaries. If the hypothesis were correct, the IRD increases in both Heinrich events and D/O cycles should occur at the same time as, or slightly lead, the ocean-climate response, and synchronicity of discharges from different glaciers would be unlikely owing to the vagaries of internal glacier dynamics. Instead, it was found in high-resolution North Atlantic records that the onset of ocean surface coolings actually preceded, by at least several hundred years, the IRD increases, and that the IRD in D/O cycles discharged from different glaciers at the same time (Bond et al., 1999; Hemming, 2004). Moreover, each Heinrich event appeared to have been immediately preceded by an increase in IRD (precursory events) whose composition recorded the same simultaneous discharges of icebergs from different sources that were found in D/O cycles (e.g., Figure M26c,f).

Those findings raised the specter of the chicken or egg problem. The lead of ocean surface coolings and the synchronous IRD discharges from different glaciers during D/O events seemed best explained by the effects of a climate-ocean mechanism that operated upon glaciers flowing into the North Atlantic. The observation of D/O-like IRD discharges immediately preceding each Heinrich event implied that even Heinrich events were triggered by the same climate mechanism. Attempts to identify the climate triggering mechanism have invoked changes in salinities in the Gulf Stream (Broecker et al., 1990), stochastic resonance (Alley et al., 2001), collapse of an ice shelf in the Labrador Sea (Hulbe et al., 2004), and super El Niños driven by ocean surface salinity changes in the tropical Pacific (Stott et al., 2002). None of these mechanisms, however, has been generally accepted.

The enigmatic 1,470-year cycle

Mayewski et al. (1997) were the first to recognize the presence of a spectral peak in $\delta^{18}\text{O}$ records from Greenland ice cores centered on about 1,470 years. The peak is narrow and statistically significant, suggesting to them that the cycle is truly periodic. Bond

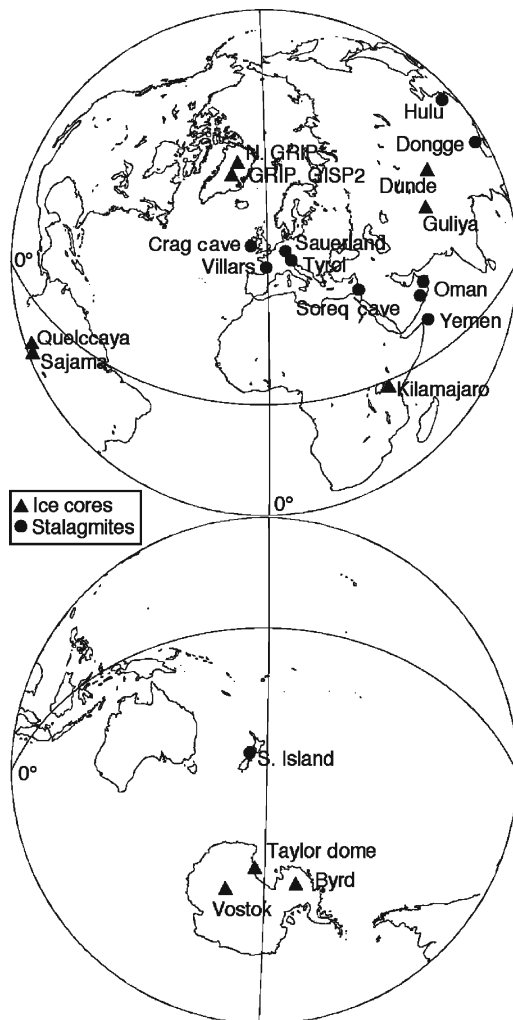


Figure M27 Locations of ice cores and stalagmite records with evidence of Heinrich events, Bond cycles, and D/O cycles.

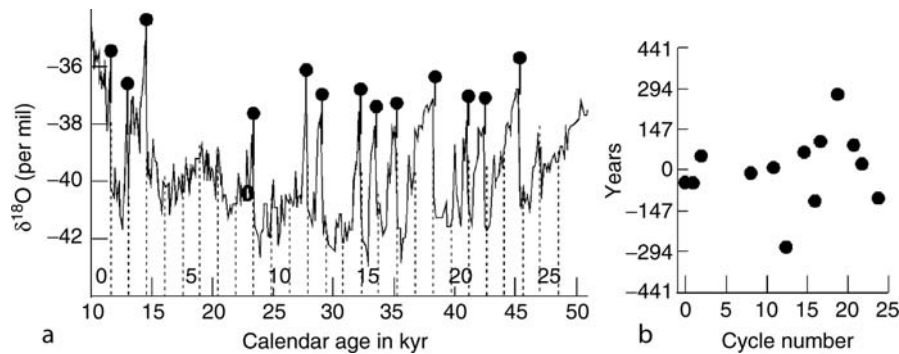


Figure M28 (a) The 1,470-year timing of D/O events from Rahmsdorf (2003). Dashed lines mark out exact 1,470-year intervals. Markers with solid dots denote onset of D/O cycles as defined by warming above a threshold defined by amplitude and range. (b) Deviation in years of onset of D/O cycles from an exact 1,470-year pacing (modified from Rahmsdorf, 2003).

et al., (1997, 1999) found that the pacing of the two petrologic tracers, hematite-stained grains and Icelandic glass, through the last glacial cycle had a mean value of $1,470 \pm 500$ years (1 sigma). Whether the cycle is truly periodic is unclear due to error in the radiocarbon-dated time series. Recently, Rahmstorf (2003), using non-spectral methods, demonstrated that the spacing of D/O cycles in the GISP2 ice core was exactly 1,470 years or even multiples of 1,470 years, thereby clearly tying the D/O oscillations to the 1,470-year cycle (Figure M28). From that finding, Rahmstorf argued that D/O events are discrete events paced by the 1,470-year cycle rather than being discrete cycles themselves.

The cause of the 1,470-year cycle remains a mystery. Rahmstorf (2003) argued that no internal processes in a complex non-linear system such as the Earth's climate system could produce such a regular oscillation, a conclusion supported by results of modeling experiments. He suggested that the cycle might have been produced by orbital variations within the Milankovitch band or by solar forcing.

The Holocene dilemma

Once regarded as a long period of climate stability, it is now clear from ice core, marine, and terrestrial records that the entire 12,000 years of the Holocene is punctuated by a series of robust cycles of millennial duration. The Holocene dilemma arises from evidence that, in many records, these cycles have about the same $\sim 1,500$ -year pacing found in records from the last glacial. In particular, after extending their analyses of the two petrologic tracers, hematite-stained grains and Icelandic glass, to the present, Bond et al. (1999, 2001) found that the Holocene cycle pacing fell within the same range as documented for the glacial record, $1,470 \pm 500$ -years. In addition, the amplitude of the cycles is about the same in both the glacial and Holocene intervals. One interpretation of those findings is that the Holocene and glacial $\sim 1,470$ -year cyclicity was produced by the same mechanism. Given the absence of large glaciers and ice sheets during most of the Holocene, the mechanism could not have been linked to oscillatory ice sheet dynamics. Moreover, the mechanism underlying the cyclicity must have operated independently of the glacial-interglacial climate state. Those arguments have been criticized, however, because the Holocene cycles do not have the precise 1,470-year periodicity of the D/O oscillations (e.g., Schulz and Paul, 2002).

Braun et al. (2005) have proposed an intriguing solution to this problem. Building on evidence in Bond et al. (2001) that the

Holocene cycles may have been forced by variations in solar irradiance, Braun and his colleagues made the remarkable discovery that their climate system model, CLIMBER-2, when forced by the DeVries solar cycle (210 years) and the Gleissberg solar cycle (88 years), can produce robust D/O events with a precise period of 1,470 years under glacial boundary conditions, but not under Holocene boundary conditions. Their surprising results have far-reaching implications for the fundamental mechanisms that underlie abrupt climate change, and they clearly deserve much further investigation and rigorous testing.

Summary

Views on what causes millennial climate variability fall into two camps. One is glacier-centered and assumes that free oscillations in glaciers and ice sheets cause repeated discharges of icebergs into the ocean. The iceberg freshwater injections force recurring changes in the North Atlantic's deep-water circulation that in turn produce a series of robust abrupt climate changes with a global or nearly global footprint. The other is climate-centered and assumes that a climate mechanism of unknown origin forces increases in iceberg discharge either through direct effects on glacier mass balance or through changes in the North Atlantic deep circulation. In this case the glacier activity and its effects on NADW production operates as a non-linear positive feed back that amplifies the climate signal and transmits a series of abrupt climate shifts well beyond the North Atlantic region. Both views have been criticized and neither can fully account for the 1,470-year pacing of the D/O cycles and the presence of similar cycles in the Holocene when the large glaciers and ice sheets were absent.

Gerard Bond

Bibliography

- Alley, R.B., Anandakrishnan, S., and Jung, P., 2001. Stochastic resonance in the North Atlantic. *Paleoceanography*, **16**(2), 190–198.
- Bond, G.C., Heinrich, H., Broecker, W., Labeyrie, L., McManus, J., Andrews, J., Huon, S., Jantschik, R., Clasen, S., Simet, C., Tedesco, K., Klas, M., Bonani, G., and Ivy, S., 1992. Evidence for massive discharges of icebergs into the North Atlantic ocean during the last glacial. *Nature*, **360**, 245–249.
- Bond, G., Broecker, W., Johnsen, S., McManus, J., Labeyrie, L., Jouzel, J., and Bonani, G., 1993. Correlations between climate records from North Atlantic sediments and Greenland ice. *Nature*, **365**, 143–147.

- Bond, G.C., Showers, W., Cheseby, M., Lotti, R., Almasi, P., deMenocal, P., Priore, P., Cullen, H., Hajdas, I., and Bonani, G., 1997. A pervasive millennial-scale cycle in North Atlantic Holocene and Glacial climates. *Science*, **278**, 1257–1266.
- Bond, G.C., Showers, W., Elliot, M., Evans, M., Lotti, R., Hajdas, I., Bonani, G., and Johnson, S., 1999. The North Atlantic's 1–2 Kyr climate rhythm: Relation to Heinrich events, Dansgaard/Oeschger cycles and the Little Ice Age. In Clark, P.U., Webb, R.S., and Keigwin, L.D. (eds.), *Mechanisms of global climate change at millennial time scales*. Washington, DC: AGU, Geophysical Monograph Series 112, pp. 35–58.
- Bond, G.C., Kromer, B., Beer, J., Muscheler, R., Evans, M., Showers, W., Hoffmann, S., Lotti-Bond, R., Hajdas, I., and Bonani, G., 2001. Persistent solar influence on North Atlantic climate during the Holocene. *Science*, **294**, 2130–2136.
- Braun, H., Christl, M., Rahmstorf, S., Ganopolski, A., Mangini, A., Kubatzki, C., Roth, K., and Kromer, B., 2005. Possible solar origin of the 1,470-year glacial climate cycle demonstrated in a coupled model. *Nature*, **438**, 208–211.
- Broecker, W.S., 1994. Massive iceberg discharges as triggers for global climate change. *Nature*, **372**, 421–424.
- Broecker, W.S., Bond, G., Klas, M., Bonani, G., and Wolff, W., 1990. A salt oscillator in the glacial North Atlantic? 1. The concept. *Paleoceanography*, **5**, 469–477.
- Broecker, W.S., Bond, G.C., Klas, M., Clark, E., and McManus, J.F., 1992. Origin of the northern Atlantic's Heinrich events. *Clim. Dynam.*, **6**, 265–273.
- Ganopolski, A., and Rahmstorf, S., 2001. Rapid changes of glacial climate simulated in a coupled climate model. *Nature*, **409**, 153–158.
- Grachev, A., and Severinghaus, J., 2005. A revised $+10 \pm 4$ °C magnitude of the abrupt change in Greenland temperature at the Younger Dryas termination using published GISP2 gas isotope data and air thermal diffusion constants. *Quaternary Sci. Rev.*, **24**, 513–519.
- Greve, R., and MacAyeal, D.R., 1996. Dynamic/thermodynamic simulations of Laurentide ice-sheet instability. *Ann. Glaciol.*, **23**, 328–335.
- Heinrich, H., 1988. Origin and consequences of cyclic ice rafting in the northeast Atlantic Ocean during the past 130,000 years. *Quaternary Res.*, **29**, 142–152.
- Hemming, S.R., 2004. Heinrich events: Massive late Pleistocene detritus layers of the North Atlantic and their global climate imprint. *Rev. Geophys.*, **42**, 1–43.
- Hulbe, C.L., MacAyeal, D.R., Denton, G.H., Kleman, J., Lowell, T.V., 2004. Catastrophic ice shelf breakup as the source of Heinrich event icebergs. *Paleoceanography*, **19**(1). doi: PA1004 10.1029/2003PA000890.
- Landais, A., Barnola, J.M., Masson-Delmotte, V., Jouzel, J., Chappellaz, J., Caillon, N., Huber, C., Leuenberger, M., and Johnsen, S.J., 2004. A continuous record of temperature evolution over a sequence of Dansgaard-Oeschger events during marine stage 4 (76–62 kyrBP). *Geophys. Res. Lett.*, **31**, 1–4, L22211. doi: 10.1029/2004GL021193.
- MacAyeal, D.R., 1993. Binge/purge oscillations of the Laurentide ice sheet as a cause of the North Atlantic's Heinrich events. *Paleoceanography*, **8**(6), 775–784.
- Mayewski, P.A., Meeker, L.D., Twickler, M.S., Whitlow, S., Yang, Q., Lyons, W.B., and Prentice, M., 1997. Major features and forcing of high-latitude Northern Hemisphere atmospheric circulation using a 110,000 year-long glaciochemical series. *J. Geophys. Res.*, **102**, 26345–26366.
- North Greenland Ice Core Project Members, 2004. High-resolution record of northern hemisphere climate extending into the last interglacial period. *Nature*, **431**, 147–157.
- Rahmstorf, S., 2003. Timing of abrupt climate change: A precise clock. *Geophys. Res. Lett.*, **30**(10), 1510. doi: 10.1029/2003GL017115.
- Schulz, M., and Paul, A., 2002. Holocene climate variability on centennial-to-millennial time scales 1. Climate records from the North-Atlantic realm. In Wefer, G., Berger, W.H., Behre, K.-E. and Jansen, E. (eds.), *Climate Development and History of the North Atlantic Realm*. Berlin: Springer, pp. 41–54.
- Stott, L., Poulsen, C., Lund, S., and Thunell, R., 2002. Super ENSO and global climate oscillations at millennial time scales. *Science*, **297**, 222–226.
- Voelker, A.H.L., 2002. Global distribution of centennial-scale records for marine isotope stage (MIS) 3: A database. *Quaternary Sci. Rev.*, **21**(10), 1185–1212.

Cross-references

Binge-Purge Cycles of Ice Sheet Dynamics
 Dansgaard-Oeschger Cycles
 Heinrich Events
 Ice-Rafted Debris (IRD)
 Quaternary Climate Transitions and Cycles
 Sun-Climate Connections
 Younger Dryas

MINERAL INDICATORS OF PAST CLIMATES

Introduction

A mineral is a naturally occurring crystalline solid created by geological or biogenic processes (e.g., calcite/aragonite in mollusk shells or coral). Minerals that form at or near the Earth's surface are products of chemical weathering, evaporation, authigenic crystallization, and bio-mineralization. They reflect ambient conditions at the Earth-atmosphere interface. Therefore they can furnish important clues about former climates. Minerals are utilized as paleoclimate indicators or proxies in several different ways:

1. To infer past climates and changes over time.
2. To deduce changes in atmospheric composition.
3. As mineralogical “markers” in provenance studies.
4. As “hosts” for climate-sensitive stable isotopes and trace elements.

The most direct mineral indicators or proxies are those that are generated under relatively narrow climatic ranges or within restricted environmental settings. Examples include chemical precipitates such as evaporites, low temperature minerals such as ikaite and hydrohalite, residual soils (iron and aluminum oxyhydroxides, kaolinite), and authigenic minerals (forming *in situ*, e.g., glauconite, berthierine, phillipsite, barite). Evaporite minerals (e.g., gypsum, anhydrite, halite, sylvite) are generally indicative of arid to hyperarid climates. They form in restricted marine basins, narrow rift valleys, coastal lagoons, sabkhas (salt flats), and internally-drained continental interiors, where rates of evaporation exceed rates of water supplied by rivers or rainfall (McLane, 1995; Parrish, 1998; *Evaporites*). The distribution of modern evaporites closely corresponds to the distribution of deserts. In addition, diagnostic of aridity are chemically-resistant minerals like quartz that are concentrated into eolian sand deposits (and ultimately sandstones) by wind transport and deposition. Sedimentary rocks of biogenic origin (e.g., chalks, cherts, phosphorites) provide information on paleotemperatures, productivity, and ocean circulation. Clay minerals derived from chemical weathering of rocks are relevant climate indicators, since they denote prevailing conditions at the time of formation. Kaolinite, for example, although widespread in many soils, is characteristic of tropical weathering, whereas chlorite is usually more abundant in colder regimes, where physical weathering predominates. Changes in composition of marine or lacustrine clays often parallel climate fluctuations (e.g., Mallinson et al., 2003; Robert and Kennett, 1997; Yuretich et al., 1999, see below).

Minerals that are sensitive to oxidation may provide information about past atmospheres. Pyrite and uraninite oxidize and alter rapidly under current atmospheric conditions. Their preservation in detrital grains from 3 billion year old sediments implies much lower atmospheric oxygen than at present (Fleet,

1998; Kirk et al., 2003). The abundance of *banded iron formations* (BIFs) older than 2 billion years also suggests reduced oxygen levels at that time. The accumulation of large BIF deposits required transport of dissolved ferrous iron over long distances, followed by precipitation in locally, more oxygenated environments (see *Banded iron formations and the early atmosphere; Atmospheric evolution, Earth*; McLane, 1995).

Minerals act as markers of provenance in paleoclimate studies. For example, changing pyroxene to amphibole ratios in late Quaternary Nile delta sediments point not only to variations in the relative contributions from the Blue and White Nile tributaries, but also to oscillations in rainfall in the two source areas that are linked to larger-scale climatic changes (Foucault and Stanley, 1989). An important clay mineral tracer is the latitudinally-sensitive kaolinite/chlorite ratio, one of several parameters used to establish an eastern Asian desert source for ice-age dust in the GISP2 (Greenland) ice cores (e.g., Biscaye et al., 1997).

Stable isotopes and trace elements housed in minerals furnish quantitative paleoclimate data. Oxygen isotope ratios in foraminiferal calcite are related to seawater temperatures and global ice volume (see *Stable isotope analysis*). Oxygen and carbon isotope ratio fluctuations in speleothem calcite reflect variability in atmospheric circulation, precipitation patterns, and vegetation cover (Genty et al., 2003; *Speleothems*). Oxygen isotope ratios in marine barite have been attributed to altered redox conditions, changes in continental shelf area, and sea level during the Plio-Pleistocene (Turchyn and Schrag, 2004). Magnesium/calcium and strontium/calcium ratios in foraminiferal calcite are also important paleo-ocean temperature indicators.

Mineral paleoclimate indicators are briefly described below and summarized in Table M1.

Ice

Ice (H₂O), the solid form of water at or below 0 °C and under normal atmospheric pressure, occurs in massive accumulations in polar ice sheets, and also in mountain glaciers, ice shelves, and sea ice (see *Cryosphere*). The lower density of ice (0.92 g cm⁻³) relative to water results from a relatively open crystal lattice, due to H-bonding of H₂O molecules. Ice, although solid, deforms readily under the force of gravity, which sets glaciers into motion.

Because the temperature of the water-ice phase transition lies within the diurnal or seasonal range of many regions, ice is sensitive to climate change on many time scales. The extent of the cryosphere has varied markedly during Quaternary glacial-interglacial cycles. The growth and decay of polar ice sheets can be reconstructed from the distribution of geomorphological features and marine oxygen isotope ratios that record paleosea-level variations (see *Glacial geomorphology, Stable isotope analysis*). Ice cores from Greenland, Antarctica, and mountain glaciers contain important archives of past temperatures and atmospheric trace gases (see *Ice cores, Antarctica and Greenland; Ice cores, mountain glaciers*).

Iron oxides and oxyhydroxides

Hematite

Hematite (α -Fe₂O₃) is a common constituent of sedimentary rocks formed under oxidizing conditions. Hematite occurs in Phanerozoic *ironstones*, iron-rich rocks that also contain goethite, berthierine, and siderite. Ironstones may be deposited in lakes, bogs or coal swamps, or on shallow marine shelves or under semi-arid

Table M1 Mineral indicators

Mineral	Paleoclimatic and/or paleo-environmental significance
<i>Oxides, hydroxyoxides</i>	
Ice	Cryosphere volume, glacial-interglacial cycles
Hematite	Oxic conditions; tropical/semi-tropical/temperate weathering
Goethite	Oxic conditions; tropical/semi-tropical/temperate weathering
Lepidocrocite	Oxic conditions; tropical/semi-tropical/temperate weathering
Maghemite	Magnetostratigraphic dating
Magnetite	Magnetostratigraphic dating
Gibbsite	Component of bauxite; humid, tropical chemical weathering
Boehmite	Component of bauxite; humid, tropical chemical weathering
Birnessite	Component of desert varnish; aridity
<i>Sulfides</i>	
Pyrite	Reducing (anoxic) conditions; low atmospheric O ₂ (as detrital grains)
<i>Halides</i>	
Halite	Evaporite; aridity
Sylvite	Evaporite; aridity
Hydrohalite	Evaporite; low temperature, hypersalinity
Antarcticite (rare)	Evaporite; low temperature, hypersalinity
<i>Carbonates</i>	
Calcite	Paleotemperatures (oxygen isotope, trace element ratios), "calcite seas – greenhouse climates"
Aragonite	Like calcite; "Aragonite seas – Icehouse climates"
Dolomite	Arid, hot-saline lakes, sabkhas
Siderite	Reducing (suboxic-anoxic) conditions
Ikaite (glendonite)	Low temperature, near-freezing
<i>Sulfates, phosphates</i>	
Gypsum	Evaporite; aridity
Anhydrite	Evaporite; aridity
Mirabilite	Evaporite; aridity, hypersalinity, low temperature
Barite	Ocean paleoproductivity
Franconite	Ocean paleoproductivity
<i>Silica minerals</i>	
Quartz	Eolian sand, sandstones – aridity; eolian dust (marine sediments, ice cores) – wind strengths, direction.
Opal, chert	Ocean paleoproductivity
<i>Clay minerals</i>	
Kaolinite	Tropical/semi-tropical chemical weathering
Chlorite	High latitude physical weathering
Sepiolite	Warm, semi-arid to arid climates
Palygorskite	Warm, semi-arid to arid climates
Glauconite	Weakly reducing (suboxic) conditions, low sedimentation rates
Berthierine	Reducing environments
<i>Zeolites</i>	
Analcime	Desert soils, alkaline lakes–aridity
Chabazite	Alkaline lakes; aridity
Phillipsite	Alkaline lakes; aridity
Clinoptilolite	Alkaline lakes; aridity

or seasonally-alternating wet/dry climates (Parrish, 1998). Hematite coats quartz and clay grains, and cements detrital particles in continental *red beds* (iron-stained sandstones, siltstones, and shales). These rocks occur in a variety of geologic settings, including desert sandstones, evaporitic tidal flats, lagoons, and savanna soils. Ferric iron, initially deposited as goethite, gradually transforms into hematite, intensifying the reddish color. The chemical reaction is enhanced by increasing temperature, alkalinity, and dehydration. Although once believed to be an indicator of arid climates, red beds are now thought to develop also in warm

climates with seasonal precipitation (Parrish, 1998; see also *Red beds*, this volume).

Hematite also concentrates within nodular horizons in *ferricrete* – an iron-rich lateritic duricrust (also termed “cuirasse”) that is a product of intense chemical weathering in semi-tropical to tropical climates, with seasonally varying rainfall ($T = 25\text{--}30^\circ\text{C}$, $P = 1,500\text{ mm yr}^{-1}$, $\text{RH} = 65\%$ (Tardy, 1992). Most silicates and even resistant minerals such as quartz are leached out, enriching the soil in residual iron oxides (hematite, goethite), and minor kaolinite.

Hematite-stained quartz and feldspar grains derived from sedimentary red beds have been used as lithologic tracers for late Quaternary to Holocene North Atlantic *ice-rafted debris* (IRD) (Bond et al., 1997). The hematite-stained grains were probably derived from eastern Greenland and Spitsbergen, in contrast to volcanic glass – another lithic tracer – from Iceland or Jan Mayen. Peaks in the record of hematite-coated grains provide a reliable and consistent proxy for estimating the pacing of IRD events.

Hematite, magnetite (Fe_3O_4) and siderite (FeCO_3) alternate with bands of chert (SiO_2) in early Proterozoic *banded iron formations* (BIFs). The accumulation of large BIF deposits implies the transport of soluble iron (as Fe^{2+}), likely derived from submarine volcanic sources, over long distances. Upwelling subsequently brought dissolved iron onto locally more oxygenated, shallow marine shelves, where oxidation of iron and precipitation occurred (McLane, 1995). Since most BIFs are older than 2 billion years, the availability of ferrous iron implies lower atmospheric oxygen levels than at present.

Maghemite

Maghemite ($\gamma\text{-Fe}_2\text{O}_3$) is a magnetic polymorph of hematite (with the same chemical composition, but a different crystal structure). It is a widespread, although minor component of paleosols and loess. Along with magnetite, it carries the magnetic signal employed in magnetostratigraphic dating.

Goethite

Goethite ($\alpha\text{-FeOOH}$) is an *oxyhydroxide*, widely distributed in sedimentary rocks, including ironstones, red beds, and also found in lateritic soils. Upon burial, it dehydrates and inverts to hematite. Lepidocrocite ($\gamma\text{-FeOOH}$), a polymorph of goethite, is also common in soils. Ferrihydrite ($\text{Fe}_2\text{O}_3 \cdot 2\text{FeOOH} \cdot 2.6\text{H}_2\text{O}$) is a poorly crystallized iron oxyhydroxide found in recent soils, sediments, and iron concretions. Since it is metastable, it slowly dehydrates and recrystallizes to goethite or hematite (Evans, 1992).

Magnetite

Magnetite (Fe_3O_4), a di- and tri-valent iron oxide, forms under somewhat more reducing conditions than hematite, in the absence of carbonate or sulfide (McLane, 1995). Magnetite, along with maghemite is the dominant source of magnetic signal in soils or sediments (Maher, 1998). Magnetic susceptibility (the ratio of induced magnetization to the inducing magnetic field) is a measure of the ability of a substance to be magnetized. It is directly proportional to the quantity of strongly magnetic minerals (i.e., magnetite and maghemite) present in loess, paleosols, and marine sediments.

Magnetite formation and soil magnetization increase in well-drained soils overlying Fe-rich source rocks that are exposed to seasonally-varying wet and dry cycles. On the other hand, excessively arid, wet, or acid soils show little magnetic enhancement.

Furthermore, magnetically-enhanced soils show some correlation between maximum soil susceptibility and annual precipitation (Maher, 1998). Thus, paleo-susceptibility values in carefully-selected soil or loess samples, as in the Loess Plateau, China, provide a useful proxy of annual rainfall, and potentially of changes in monsoonal patterns and atmospheric circulation.

The Earth’s magnetic field has reversed episodically over time, the last major reversal (Matuyama-Brunhes) occurring 780,000 yrBP. The timing of changes in direction of magnetization of rocks over time has therefore been used as a dating tool in paleoclimatology (see *Dating, magnetostratigraphy*). The time-varying magnetic properties of eolian loess deposits in a stratigraphic sequence also record a high-resolution history of climate change, including precipitation patterns. Paleoclimate studies show that paleosols formed under relatively warm, humid, interglacial conditions are characterized by relatively high magnetic susceptibilities that correlate with high illite/chlorite ratios in the southern Loess Plateau, China, signifying more intense chemical weathering (Zhao et al., 2005) and with more negative oxygen isotope ratios in deep sea sediments (Reynolds and King, 1995). The reverse is found during cold, dry glacial periods.

Aluminum oxides and oxyhydroxides

Gibbsite ($\text{Al}(\text{OH})_3$) and boehmite (AlOOH) are major constituents of *bauxite*. Bauxite (Figure M29) is a residual, lateritic soil that is formed by intense chemical weathering of rocks under wet, tropical climates with annual mean precipitation above $1,700\text{ mm yr}^{-1}$, whereas ferricretes (see above) develop under hot, but seasonally-variable precipitation ranging between $1,300\text{--}1,700\text{ mm yr}^{-1}$ (Tardy and Roquin, 1992). However, others have suggested that both bauxites and laterites were generated under similar tropical climates, with one or more dry

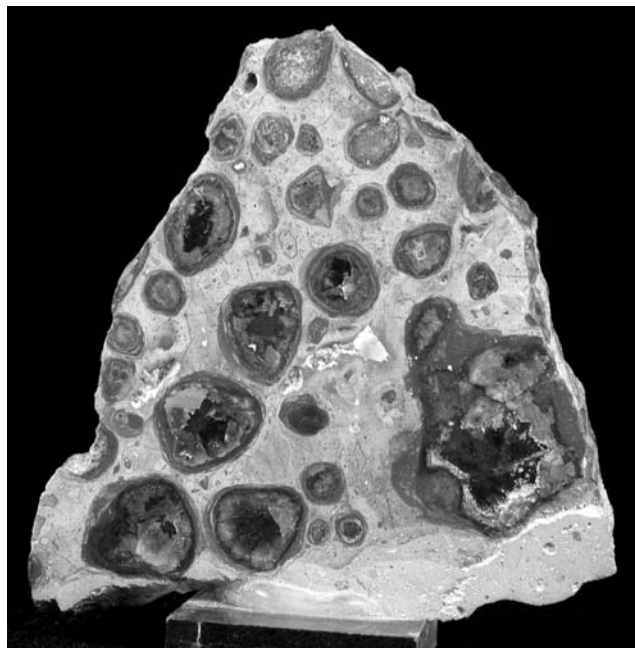


Figure M29 Bauxite with pisolitic texture, Arkansas ($6.4\text{ cm} \times 6.4\text{ cm}$). Bauxite is composed of a mixture of aluminum oxides and oxyhydroxides, resulting from intense chemical weathering under wet, tropical climates (specimen, V. Gornitz; photograph, John Betts).

months (Parrish, 1998). Under these climate regimes, most silicates and even resistant minerals such as quartz are destroyed, leaving insoluble aluminum minerals, such as gibbsite and boehmite, with lesser quantities of diaspore (AlOOH), kaolinite, hematite, and goethite.

The geographic distribution of bauxites has changed over time, reflecting not only changing climates, but also the northerly motion of the African and American plates since the opening of the Atlantic Ocean in the Jurassic period. Quaternary to Recent bauxites in Africa and South America are nearly equatorial, whereas pre-Quaternary bauxites on both continents tend to lie to the northeast (and also south) of their present positions (Tardy and Roquin, 1992).

Manganese oxides and oxyhydroxides

Manganese minerals occur in diverse environments, including terrigenous soils, rock varnish, and oceanic nodules. Among the more common phases in soils and sediments are pyrolusite (MnO_2), manganite ($\text{MnO}\cdot\text{OH}$), vernadite ($\delta\text{-MnO}_2$) or $((\text{Mn,Fe,Ca,Na})(\text{O,OH})_2\cdot n\text{H}_2\text{O})$, birnessite $((\text{Na,Ca})_{0.5}(\text{Mn}^{4+}, \text{Mn}^{3+})_2\text{O}_4\cdot 1.5\text{H}_2\text{O})$, hollandite $(\text{Ba}_2(\text{Mn}^{4+}, \text{Mn}^{2+})_8\text{O}_{16})$, and todorokite $(\text{Mn}^{2+}, \text{Ca, Mg})\text{Mn}_3^+\text{O}_7\cdot \text{H}_2\text{O}$. Manganese (and iron) oxides are concentrated in lateritic soils, ferricretes, and duricrusts (Tardy and Roquin, 1992). Iron-manganese nodules are also widespread in clay-rich soils of temperate to warm climates (Stiles et al., 2001). Initially depositing as hydrous phases, such as birnessite, these eventually dehydrate and invert to anhydrous phases such as hollandite during diagenesis. Total Fe content of Fe-Mn nodules in both modern and paleo-Vertisols has been used as a proxy for mean annual precipitation, showing a positive correlation (whereas total Mn varies inversely) with this climate parameter (Stiles et al., 2001).

Exposed rock surfaces in desert environments are frequently coated by thin laminations of manganese and iron oxides. Desert (or rock) varnish consists of around 70% clays and 30% Fe and Mn oxides, mainly hematite, birnessite, and lesser todorokite (McKeown and Post, 2001). Rock varnish is produced by oxidizing bacteria that extract iron, manganese, and other metals from airborne dust, and precipitation. The manganese content of varnish increases with mean annual precipitation, in contrast to that of soil Fe-Mn nodules. Accurate radiometric dating and chemical analyses of varnish laminations show promise as a paleoclimate proxy (Broecker and Liu, 2001; see also *Desert varnish as a climate proxy*).

Oceanic manganese nodules are rounded concretions that develop in areas of low sediment accumulation rates on the deep seafloor. The nodules are a complex intergrowth of poorly crystalline hydrous manganese and iron phases, including birnessite, todorokite, and vernadite (Li and Schoonmaker, 2003). Most nodules have accreted on nuclei of sharks' teeth, fish bone, shell or rock fragments.

Iron sulfides

Pyrite

Since iron can exist in two different oxidation states, iron minerals are potentially sensitive indicators of soil or sediment redox conditions, which are linked to biogeochemical cycles, and thus indirectly to climate. Pyrite (FeS_2), in particular, has been used an indicator of soil/sediment redox state. Decomposition of organic matter in sediments creates a locally anaerobic environment, in which bacterial reduction of sulfates

to hydrogen sulfide (H_2S) takes place. The H_2S reacts in turn with dissolved iron to precipitate pyrite or marcasite. Marcasite (FeS_2) is less stable in acidic solutions than pyrite, and is therefore less abundant in the geologic record. Deposition of pyrite is favored by euxinic lacustrine or marine environments (restricted water circulation), presence of organic-rich sediments, locally elevated CH_4 levels, and (on land), poorly-drained or water-logged soils. The degree of pyritization (DOP)¹ has frequently been taken as a marker for soil/sediment redox state. DOP values <0.46 represent aerobic conditions, with $0.46\text{--}0.75$ intermediate, and $\text{DOP} > 0.75$ euxinic conditions (Raiswell et al., 1988). However, DOP may also depend on iron availability. Furthermore, in certain shallow water environments, such as tidal salt marshes, DOP values may reflect pore water redox state and sediment chemistry rather than bottom water oxygen levels (Roychoudhury et al., 2003).

Pyrite is rapidly oxidized in today's atmosphere and thus generally does not occur as a detrital mineral. Therefore, well-rounded "detrital" grains of pyrite, also uraninite (UO_2), and siderite (FeCO_3), from the Witwatersrand basin in South Africa have been widely regarded as evidence for much lower than present atmospheric oxygen levels during the Archean eon ($>2,500$ million yBP). The significance of these grains as paleo-atmosphere indicators has been controversial, since a hydrothermal origin was proposed for "placer" gold nuggets associated with these minerals in conglomerates. However, several recent studies strengthen the case for the placer theory. Precise $^{187}\text{Re}/^{187}\text{Os}$ radiometric dating shows that the rounded gold nuggets (and associated pyrite and uraninite grains) are ~ 3 billion years old as compared to significantly younger ages of 2.76–2.89 billion years for the enclosing host conglomerates, and that therefore the heavy minerals must be detrital (Kirk et al., 2003). Textural and isotopic evidence also favors the placer theory. Rounded, As-bearing pyrite grains with truncated compositional growth bands clearly demonstrate that the grains were mechanically abraded (Fleet, 1998). The rounded pyrite exhibits a broader range in δS^{34} values, suggestive of a placer origin, in contrast to crystalline pyrite overgrowths, which probably were produced by later hydrothermal alteration or metamorphism (England et al., 2002).

Halides

Halite

Halite (NaCl) crystallizes from a supersaturated brine at the air-water interface as thin square plates, which grow faster at their edges. These expand into pyramidal crystals with hollowed centers (hoppers), and eventually coalesce into floating rafts and sink. The hopped crystals continue to grow on the basin floor, ultimately creating a distinctive layered, chevron-like pattern in sedimentary salt deposits (Figure M30). In addition to precipitating directly from brine, halite can also grow within soft mud or silt into large displacive cube crystals, often with hollow faces (Figure M31; Gornitz and Schreiber, 1981). Displacive halite is well-known from the geologic record. The presence of such crystals in sedimentary rocks suggests an origin within shallow marine sediments or from the intertidal to supratidal zone, in fairly hot, arid climates (Gornitz and Schreiber, 1981).

¹DOP = $\% \text{Fe}_{\text{pyrite}} / (\% \text{Fe}_{\text{pyrite}} + \text{reactive Fe})$, where $\text{Fe}_{\text{pyrite}}$ is the fraction of iron associated with pyrite, while reactive Fe is the fraction of iron that reacts with dissolved sulfur.

Halite crystals often trap droplets of the brine from which they precipitate. Such fluid inclusions, if primary (i.e., trapped at the time of growth), can supply useful information about the temperature and composition of the brine. For example, primary fluid inclusions in “chevron”-type halite from shallow ephemeral saline lakes or salt pans from the Permian Nippewalla Group, western Kansas yield homogenization temperatures in the range 21–50 °C. (Benison and Goldstein, 1999). Since these

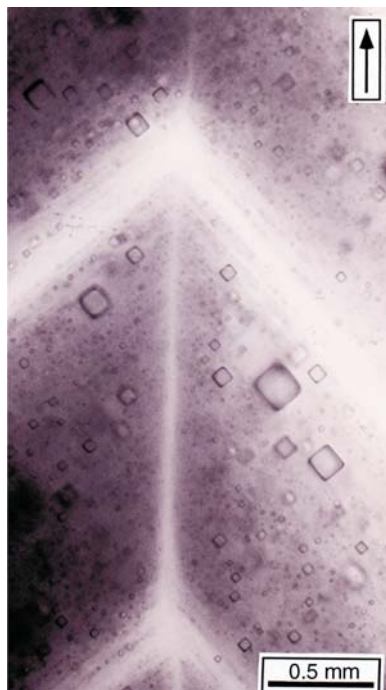


Figure M30 Chevron texture in bedded halite from the mid-Permian Nippewalla Group, western Kansas formed by precipitation of rafts of hopped halite in supersaturated brines (photograph, Kathy Benison, Central Michigan University; reproduced with permission).

shallow saline pools were exposed to the surface, these values closely reflect atmospheric temperatures and support other paleogeographic evidence pointing to a hot, arid climate of the mid-North American continent during the mid-late Permian. Primary inclusions in marine chevron halite have also been used to track major oscillations in Phanerozoic paleosea water chemistry (Lowenstein et al., 2001). Mg^{2+}/Ca^{2+} ratios of Phanerozoic seawater derived from the fluid inclusions show systematic variations over time, with peak Mg^{2+}/Ca^{2+} ratios occurring during the late Precambrian, Permian, and Neogene. These periods of high Mg^{2+}/Ca^{2+} values were associated with periods of enhanced aragonite ($CaCO_3$) and $MgSO_4$ deposition, as well as slower seafloor spreading rates.

Other halides

Sylvite (KCl) is an evaporitic salt, often associated with halite, which forms under similar conditions of high aridity. Hydrohalite ($NaCl \cdot 2H_2O$) is a form of salt that precipitates from highly saturated brines at low temperatures (Roberts et al., 1997). Because of its solubility, it is rarely preserved in the geologic record, but its former presence may be inferred from pseudomorphs of halite or other minerals. Antarcticite ($CaCl_2 \cdot 6H_2O$), is a rare soluble chloride, discovered in saline lakes from the dry valleys of Antarctica (Torii and Ossaka, 1965). It precipitates from saturated brines at below-freezing temperatures (see also *Evaporites*).

Carbonates

Calcite, aragonite, and dolomite

Calcite and aragonite are the common polymorphs of $CaCO_3$. (Vaterite is a much rarer form of $CaCO_3$). Aragonite is less stable than calcite, but is stabilized by magnesium in seawater (McLane, 1995). High Mg-calcite, a variety of calcite, may contain up to 10–18 mol-% $MgCO_3$. In dolomite ($CaMg(CO_3)_2$), the molar proportion of magnesium to calcium is 1:1. Calcite, aragonite, and dolomite occur over a broad range of geologic settings, including karst terrains, arid soils, lacustrine, coastal, and shallow to deep-water marine environments. These minerals can form as inorganic chemical precipitates and through biogenic processes.

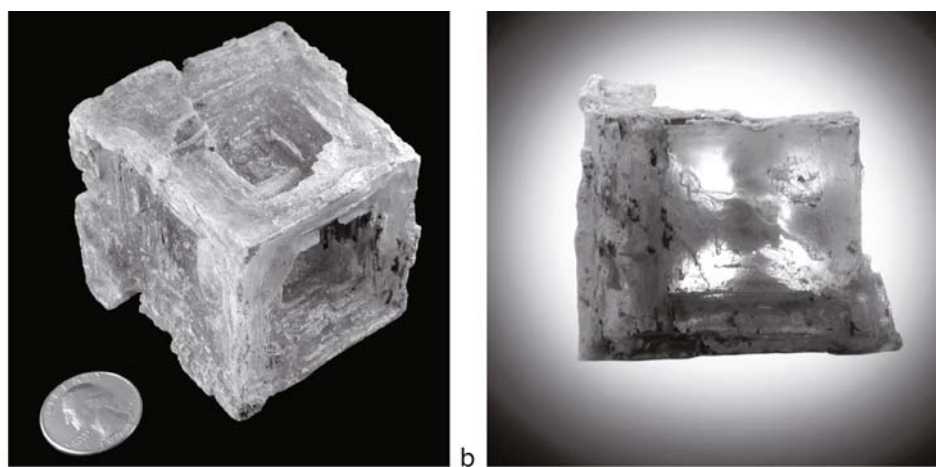


Figure M31 (a) Displacive halite, hopper (hollow) cube with mud inclusions, Dead Sea, Israel (6.3 cm × 6.3 cm). (b) Displacive halite, Dead Sea, Israel (2.5 cm × 3.2 cm). Mud inclusions have been incorporated into the halite along crystallographic directions during growth, forming a Maltese cross pattern (specimens, V. Gornitz; photographs, John Betts).

Calcite and, to a lesser extent, aragonite are the most common minerals in cave *speleothems* (i.e., stalactites and stalagmites). The concentric, layered rings in speleothems record annual climatic or environmental variations, much like tree rings. Thus, trace elements or oxygen and carbon isotope ratios in speleothems have been used as paleoclimate proxies (e.g., Genty et al., 2003; *Speleothems*). In arid to semi-arid climates, calcite and dolomite concentrate within hardpan soil layers, forming *calcrete* (or “caliche”), a type of *duricrust* (Milnes, 1992; *Duricrusts*). Calcite and aragonite constitute the bulk of carbonate-rich *eolianites*, which accumulate as wind-blown dunes adjacent to mid-latitude beaches (see *Eolianite*). Eolianites develop along dry, low relief coasts, with high wave and wind energy. Mg-calcite and aragonite are characteristic cements of *beachrock*, a clastic rock that is lithified within the intertidal zone of tropical to subtropical coasts (McLane, 1995; see *Beachrock*). Beachrock has been used as a paleo-sea-level indicator.

Calcite is the dominant bio-mineral of deep-sea calcareous oozes or chalk, which consists mainly of skeletal coccolithophores and foraminifera. Aragonite is derived from pelagic pteropods. Modern shallow-water carbonates, largely confined to subtropical and tropical climates, are dominated by aragonite and high Mg-calcite (Morse, 2003). Aragonite is produced by scleractinian coral, calcareous green algae, and some mollusks, whereas high Mg-calcite is created by benthic foraminifera and sea urchins. Oolitic carbonates (composed of aragonite or high Mg-calcite) are generally non-biogenic (Morse, 2003).

A number of trace elements, such as magnesium, strontium, or barium are incorporated into marine carbonates. Mg/Ca and Sr/Ca ratios in foraminiferal calcite serve as paleotemperature proxies, and Cd/Ca and Ba/Ca ratios as proxies of ocean paleoproductivity and circulation (Kastner, 1999; Parrish, 1998). Oxygen and carbon isotopes in foraminifer calcite yield information on ocean paleotemperatures, polar ice volume, and the carbon budget (Parrish, 1998). Coccoliths have been used for biostratigraphic dating of marine sediments.

The abundance of biogenic carbonates has varied considerably during the Phanerozoic eon. Periods of calcite dominance (“calcite seas”) from the Ordovician through Devonian periods and Jurassic-Cretaceous have alternated with periods of aragonite dominance (“aragonite seas”) during the Carboniferous-Triassic and more recently, the Neogene (Montañez, 2002). Calcitic corals and stromatoporoids dominated the reefs of calcite seas, in contrast to the aragonitic sponges, corals, algae, and Mg-calcite red algae that occupied the reefs of aragonite seas. Modern reefs are populated by aragonitic scleractinian corals and Mg-calcite coralline algae. The calcite-dominant periods are closely associated with “greenhouse” climates, whereas the aragonite-rich periods are linked to “icehouse” conditions. These temporal variations in marine bio-mineralogy have been attributed to changes in seawater Mg/Ca ratios, shifts in long-term rates of sea-floor spreading, eustatic fluctuations, and climate cycles. Periods when the seawater Mg/Ca mole ratio exceeds two favor the production of high Mg-calcite and aragonite, and vice-versa (Lowenstein et al., 2001).

Although dolomite occurs massive in sedimentary rocks, it forms at present in restricted environments such as highly saline lakes or sabkhas. These are coastal salt flats, or shallow, tidal pools in hot, arid regions (e.g., the Persian Gulf, also around the Caribbean, Southern California) that are periodically flooded by seawater and concentrated by evaporation. Gypsum (sometimes anhydrite) precipitates first, leaving the residual brine enriched in magnesium, which then reacts with

calcium carbonate sediments, resulting in the deposition of dolomite (McLane, 1995).

Ikaite (glendonite)

Ikaite ($\text{CaCO}_3 \cdot 6\text{H}_2\text{O}$) is a rare mineral that is stable only at very low temperatures and several kilobars pressure. It occurs in nature at temperatures up to 7°C in alkaline, phosphatic marine and continental waters (De Lurio and Frakes, 1999). Although ikaite has generally been replaced by calcite (“glendonite”), its original crystal habit of individual bipyramids or radiating clusters has been preserved in the sediments (Figure M32; Swainson and Hammond, 2001). Because of the rather restricted conditions under which ikaite/glendonite forms, it has been used as a proxy for near-freezing water temperatures (De Lurio and Frakes, 1999).

Siderite

Siderite (FeCO_3) occurs in minor amounts in reducing, low sulfide, lacustrine, deltaic environments (McLane, 1995), and on marine continental margins, where it forms during late diagenesis in suboxic to anoxic pore fluid waters near a source of detrital Fe (Kastner, 1999). *Sphaerosiderite* is a distinctive millimeter-sized, spherulitic variety of siderite found in silty mudstones from reducing soils in continental wetlands (Ludvigson et al., 1998). The $\delta^{18}\text{O}$ ratios of sphaerosiderite and co-existing calcite have been used to estimate paleotemperature and ground-water $\delta^{18}\text{O}$ values (Ludvigson et al., 1998). Careful selection of unaltered samples is necessary to avoid errors in the paleothermometry introduced by diagenetic alteration (Ludvigson et al., 2000).

Siderite figures prominently in the debate surrounding the composition of the Earth’s early atmosphere. The existence of ancient oceans presumes that the reduced luminosity of the



Figure M32 Glendonite (calcite pseudomorph after ikaite), Olenitsa River, Kola Peninsula, Russia, (2.5 cm) (specimen, V. Gornitz; photograph, John Betts). Ikaite, or glendonite, is an indicator of near-freezing water temperatures.

Sun prior to 3 billion years was offset by higher levels of greenhouse gases such as carbon dioxide or methane (see *Faint Young Sun Paradox*). The lack of siderite in paleosols older than ~2 billion years has been interpreted to indicate an insufficient amount of atmospheric CO₂ to compensate for the faint young Sun, and that therefore the major greenhouse gas was CH₄. However, Ohmoto et al. (2004) use thermodynamic arguments to conclude that massive Archean siderite deposits were laid down under a CO₂-rich atmosphere. The formation of iron (II)-rich carbonate (Fe_{0.53}Mg_{0.44}CO₃) weathering rinds on conglomerate pebbles from the 3.2 billion year old Barberton Greenstone Belt, South Africa also hints at higher paleo-atmospheric CO₂ levels than present (Hessler et al., 2004).

Sulfates

Gypsum and anhydrite

Gypsum (CaSO₄·2H₂O) and anhydrite (CaSO₄) are among the most abundant evaporite minerals. Gypsum also crystallizes within muds in desert playas or coastal sabkhas (Figure M33a–c). Gypsum nodules grow directly by displacing the enclosing mud sediment, coalescing into nodular layers. Gypsum dehydrates to anhydrite at the higher temperatures and pressures caused by burial to depths of several hundred meters (McLane, 1995). Anhydrite precipitates directly from highly saturated brines at temperatures above 22 °C (McLane, 1995).

Mirabilite

Mirabilite (Na₂SO₄·10H₂O) is a soluble evaporite mineral that precipitates under conditions of high salinity and at low temperatures.

Barite

Barite (BaSO₄) forms in hydrothermal and in sedimentary environments. It also precipitates from seawater, accumulating on the ocean floor, often in association with plankton and organic matter (Derry and Murray, 2004; Kastner, 1999). Furthermore, its insolubility and resistance to diagenetic alteration under oxic conditions help preserve it in marine sediments. These features make barite accumulation rates a useful marker for ocean paleoproductivity (Parrish, 1998; Paytan et al., 1996) (see *Ocean paleoproductivity*). Oxygen isotope ratios in marine barite record changes in exposure to sulfur oxidation on continental shelves during glacial-interglacial cycles and thus indirectly record fluctuations in sea level (Turchyn and Schrag, 2004).

Phosphates

Francolite, or carbonate-fluorapatite (Ca₅(PO₄,CO₃)₃(F,OH)), is the chief mineral in phosphorite, a sedimentary rock rich in phosphates (see *Phosphorite*). The chemical composition of francolite is variable, with differing amounts of Na, Sr, or Mg replacing Ca, and SO₄ substituting for PO₄. Francolite occurs as pellets, nodules, crusts, or laminations. Collophane is an amorphous or cryptocrystalline form of sedimentary phosphate.

Phosphorites accumulate on continental margins, epeiric seas, and to a lesser extent on seamounts or ocean islands. They are generally formed in zones of marine upwelling and high biologic productivity (Parrish, 1998). The main source of phosphorus comes from vertebrate skeletal remains, or breakdown of organic matter. Fish scales or bones frequently act as nuclei for the buildup of francolite pellets or nodules.

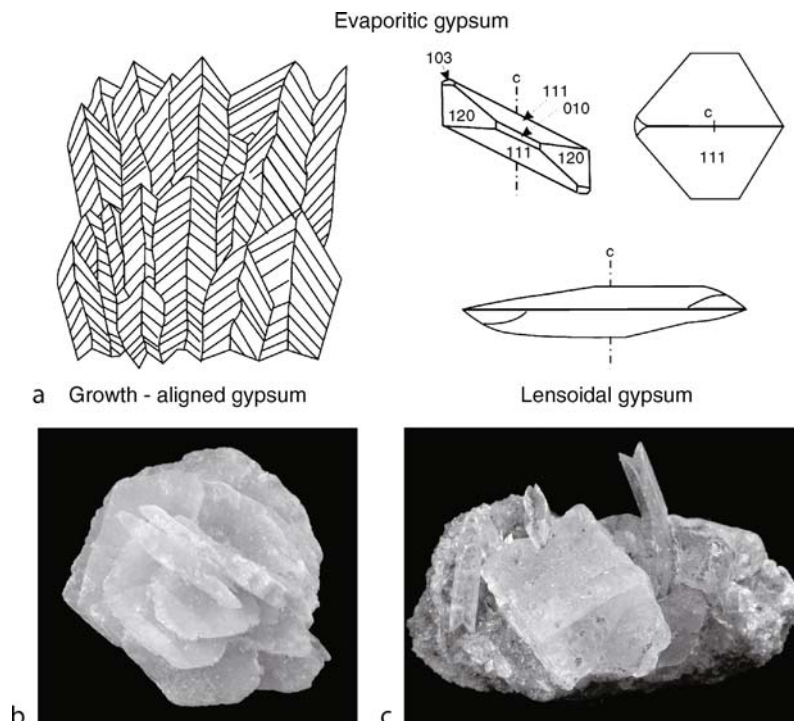


Figure M33 (a) Gypsum textures typical of evaporitic environments – growth aligned gypsum (left), lensoidal gypsum (right) (after Warren, 1999). (b) Gypsum rose, Chihuahua, Mexico (4.4 cm × 3.2 cm, specimen, V. Gornitz; photograph, John Betts). (c) Gypsum (prismatic, twinned crystals) and halite (cube) on fine-grained halite, salinas de otomo, Pisco Province, Ica Pagion, Peru (6.4 cm × 2.5 cm; specimen, V. Gornitz; photograph, John Betts).

Silica minerals

The most common varieties of silica found near the earth's surface include quartz, chalcedony, chert, and opal.

Quartz

Low-quartz (α -SiO₂) is the stable form of crystalline silica at the earth's surface and one of the most abundant minerals in crustal rocks. Quartz is a hard ($H = 7$ Mohs scale), chemically resistant mineral that survives the rock weathering cycle in nearly all climates, except for hot and humid tropical climates (e.g., see *Bauxite*, above). It is a major constituent of eolian desert deposits, sandstones, and many littoral beach sands. In deserts, winds concentrate quartz grains into dunes and huge sand seas (ergs). Fossil sand dunes show characteristic cross-bedding and wind-ripple forms. The orientation of cross-bedding and other sedimentological features enable the reconstruction of paleowind directions (Parrish, 1998). Examples of quartz-rich eolian sandstones include the Jurassic Navajo and Kayenta Sandstones of Utah and Colorado, the Permian Coconino Sandstone of the Grand Canyon region, New Red Sandstone (Permo-Triassic, England) and the Yellow Sands – Permian, England (Parrish, 1998). Quartz is also a significant component of eolian dust in marine sediments and in ice cores. Variations in concentrations and grain sizes of eolian dust grains provide information on changes in glacial to interglacial wind directions and intensities (*Eolian dust, marine sediments*).

Opal-A, opal-CT, chert, chalcedony

Opal-A is an amorphous, structurally disordered form of silica which contains several percent of water. Widespread in deep sea sediments (e.g., in siliceous oozes), it is largely derived from the remains of marine micro-organisms, such as diatoms, radiolarians, silicoflagellates, and siliceous sponge spicules (Parrish, 1998). (However, some marine opal may be of volcanic origin). Over time, opal-A gradually transforms to opal-CT, which shows domains of short-range order similar to the atomic arrangement in cristobalite and tridymite. Further diagenesis leads to opal-C and chert.

Chert is a sedimentary rock consisting of opal, crypto- to microcrystalline quartz, and chalcedony (a fibrous variety of quartz). Extensive bedded chert deposits are mostly products of former marine biogenic sedimentation. Bedded chert is often associated with phosphorites and black shales (see *Phosphorite*; McLane, 1995). Such cherts, or siliceous oozes, have deposited in zones of marine upwelling that are diagnostic of high organic primary productivity (Kastner, 1999; Parrish, 1998). Tracking shifts in the distribution of upwelling zones over time may also reveal information about changes in paleo-ocean circulation.

Clay minerals

Clay minerals are phyllosilicates, or sheet silicates, consisting of layers of silica tetrahedra attached to layers of aluminum or magnesium atoms, each of which is surrounded by six oxygen atoms or hydroxyl ions in octahedral layers. Other cations, such as iron, potassium, sodium, or calcium, can also be present. The clays differ in the nature of the cations within and between sheets and in their stacking arrangements. Important clay minerals and their ideal chemical formulas are listed in Table M2.

Clay minerals are produced by the chemical weathering of rocks near the earth's surface (Figure M34). The clay

Table M2 Common clay minerals

Kaolinite	Al ₂ Si ₂ O ₅ ·(OH) ₄
<i>Smectite group (expanding clays)</i>	
Montmorillonite	(Na,Ca) _{0.3} (Al,Mg) ₂ Si ₄ O ₁₀ (OH) ₂ ·nH ₂ O
Beidellite	(Na,Ca) _{0.3} Al ₂ (Si,Al) ₄ O ₁₀ (OH) ₂ ·nH ₂ O
Nontronite	Na _{0.3} Fe ₂ (Si,Al) ₄ O ₁₀ (OH) ₂ ·nH ₂ O
Saponite	(Ca,Na) _{0.3} (Mg,Fe) ₃ (Si,Al) ₄ O ₁₀ (OH) ₂ ·nH ₂ O
Illite	KAl ₂ (Si ₃ Al)O ₁₀ (OH) ₂
Glaucanite	(K,Na,Ca)(Fe ³⁺ ,Al,Fe ²⁺ ,Mg)(Si,Al) ₄ O ₁₀ (OH) ₂
Vermiculite	(Mg _{2.7} Fe _{0.3})(Si ₃ Al)O ₁₀ (OH) ₂ ·nH ₂ O
Chlorite group	(Mg _{2.6} Fe _{0.4})Si _{2.5} (Al,Fe) _{1.5} O ₁₀ (OH) ₈
Berthierine	(Fe ₅ ,Al) ₃ (Si,Al) ₂ O ₅ (OH) ₄
Sepiolite	Mg ₄ Si ₆ O ₁₅ (OH) ₂ ·6H ₂ O
Palygorskite	(Mg,Al) ₂ Si ₄ O ₁₀ (OH) ₂ ·4H ₂ O

detritus is removed by water erosion and accumulates in lacustrine, estuarine, and marine sediments. Clays are also major constituents of terrestrial soils and of airborne dust. The relative abundance of clays is closely related to climate or to environmental setting, although source rock mineralogy also influences their development. Kaolinite (Figure M34a), for example, is created by intense chemical weathering of warm, humid climates, in which silica is leached out, leaving soils enriched in alumina (Chamley, 1989). Chlorite (Figure M34b) and illite (Figure M34c) tend to form in soils dominated by physical weathering – both in colder, often formerly glaciated regions, and hot, dry climates (Chamley, 1989). Consequently, these clays generally reflect the composition of their parent rocks. Smectite (Figure M34d), illite, chlorite, and mixed-layer clays are more prevalent in temperate-cool, moist climates (Chamley, 1989). Well-crystallized iron-rich smectites (e.g., nontronite) occur in sub-arid climates (Chamley, 1989). Montmorillonite – a smectite – also forms by weathering of volcanic ash. Sepiolite, palygorskite, and attapulgite are three rather rare clay minerals found in calcrete soils, and in warm, semi-arid to arid climates (Chamley, 1989; Parrish, 1998; Watson, 1992).

Glaucanite, (K,Na,Ca)(Fe³⁺,Fe²⁺,Mg)(Si,Al)₄O₁₀(OH)₂, is a dark-green to black mineral, related to mica and mixed-layer clays, usually found as tiny rounded grains that most likely formed as fecal pellets. It occurs in weakly reducing environments, near upwelling zones on continental shelves and margins between depths of 100–250 m (Chamley, 1989), characterized by relatively slow sedimentation rates (Kastner, 1999; Parrish, 1998; Velde, 2003), and is often associated with phosphorites (McLane, 1995; Velde, 2003). The presence of potassium in glaucanite allows dating of sea level cycles in marine sediments, via the potassium-argon or rubidium-strontium methods (Velde, 2003).

Berthierine, (Fe₅,Al)₃(Si,Al)₂O₅(OH)₄, a dark-greenish phyllosilicate closely related to kaolinite and serpentine, occurs in near-shore or deltaic sediments (Velde, 2003) from chemically reducing environments, but more rarely in terrigenous soils. Its presence in early Triassic continental paleosols may indicate low atmospheric oxygen levels, possibly resulting from catastrophic methane release, mass mortality, and rise in CO₂ at the Permian-Triassic boundary (Sheldon and Retallack, 2002).

Inasmuch as non-biogenic marine sediments are largely derived from continental sources, the distribution of clay minerals in the oceans closely corresponds to that of adjacent landmasses. Thus, marine clays display a latitudinal zonation broadly paralleling the major climate zones (Chamley, 1989; Evans, 1992; Parrish, 1998). Kaolinite is abundant in equatorial waters, whereas chlorite

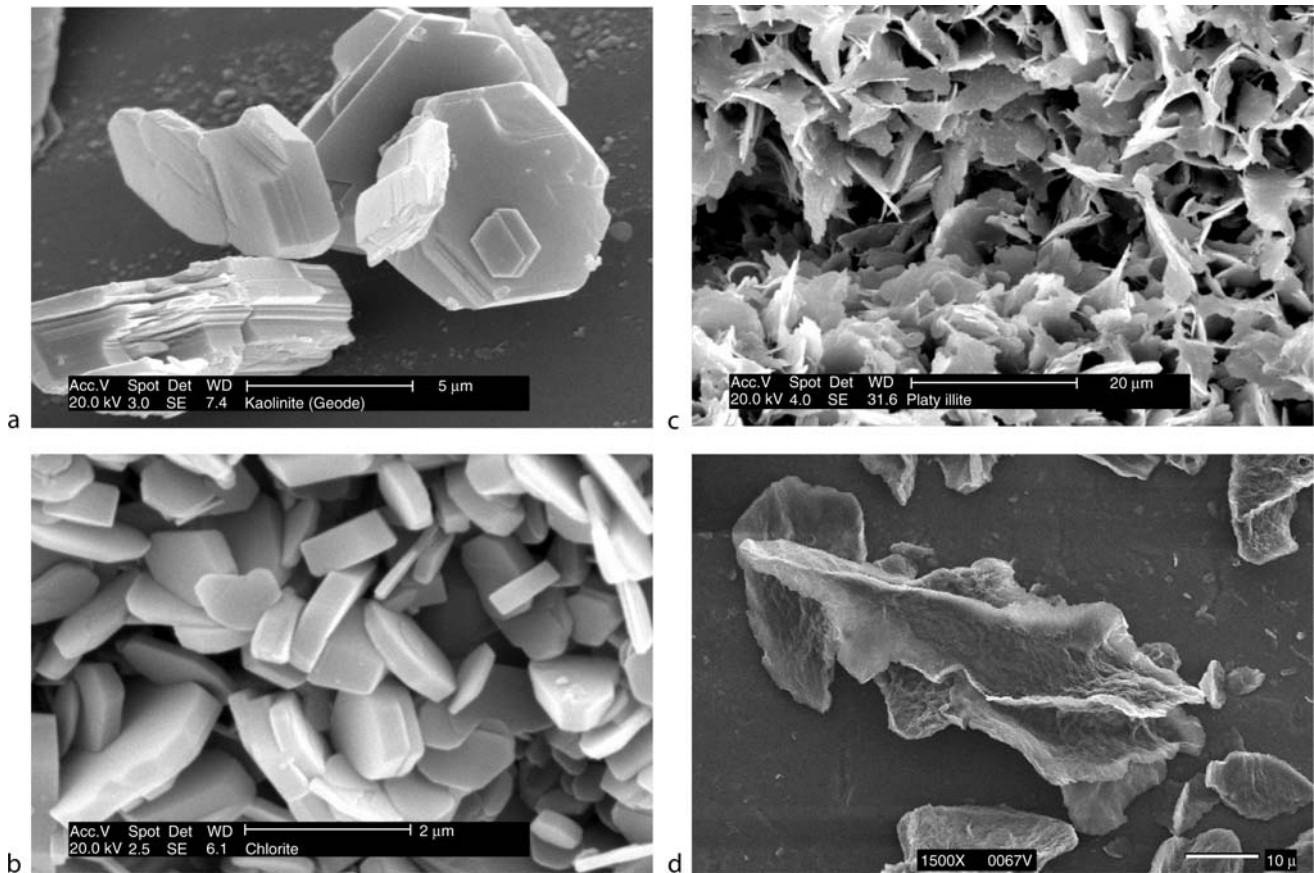


Figure M34 (a) Kaolinite, Keokuk geode, USA. (b) Iron-rich chlorite, Spiro Sandstone, Arkoma Basin, Oklahoma, USA. (c) Illite, Rotliegend Formation, Northern Germany. (d) Smectite, Ap horizon, Webster soil, University of Minnesota Southern Agricultural Station, Waseca, Minnesota. Reproduced with permission from the "Images of Clay" gallery published by the Clay Minerals Group of the Mineralogical Society and the Clay Minerals Society (www.minersoc.org/pages/gallery/claypix).

and illite concentrations increase toward higher latitudes. The distribution of smectites, on the other hand, is not quite as strongly zoned, indicating the influence of other, non-climate factors.

Temporal changes in clay mineralogy record important paleoclimate events. For example, Kennedy et al., (2006) associated a significant increase in clay minerals relative to quartz during the late Neoproterozoic (800–550 million years ago) with a growing degree of terrigenous chemical weathering, clay-organic matter burial, and increasing oxygen levels. Kaolinite and expandable clays (i.e., smectites) became more abundant at the expense of illite, chlorite, and mica during this period, consistent with development of soils, possibly promoted by biotic activity. Variations in relative abundances of kaolinite, smectite and mixed-layer illite/smectite have been used as a paleoclimate proxy for wet versus dry climates during the Mesozoic of northwestern Europe (Ruffell et al., 2002), with high kaolinite indicating humid periods. Elsewhere, increases in smectite and kaolinite relative to illite in marine sediments off Antarctica at around 33.5 Ma have been correlated with a marked positive δO^{18} shift and onset of significant Antarctic glaciation (Robert and Kennett, 1997). Decreasing kaolinite/illite, smectite/illite ratios after 33.4 Ma signal enhanced physical weathering under cooler, drier climates. A similar pattern of higher kaolinite/illite and smectite/illite ratios at ~33.5 and 33.4 Ma, succeeded by increased illite content is observed in cores

from the Great Australian Bight (Mallinson et al., 2003). These cores also show 22-Kyr cyclicality in kaolinite/smectite ratios, linked to precessional changes in precipitation, wind patterns and runoff that affected the mineralogy and transport of clays to the Bight.

Enhanced chemical weathering during warmer interglacials generated higher concentrations of interlayered illite-smectite in Lake Baikal sediments, Russia, whereas greater physical weathering during colder, glacial periods resulted in chlorite and illite enrichment (Yuretich et al., 1999). Changes in illite/chlorite ratios in Chinese loess sections have been used to reconstruct monsoonal activity during the late Pleistocene (Zhao et al., 2005). In the southern Loess Plateau, the illite/chlorite ratio and magnetic susceptibility are higher in interglacial paleosols and lower in glacial loess. More intense weathering of chlorite, leading to higher illite/chlorite ratios, indicates a stronger monsoonal regime operating during interglacial periods.

The distinctive mineral assemblage of high illite, low smectite, and low kaolinite/chlorite ratio in the dust from the GISP2 (Greenland) ice core pinpoints a likely source of the clays in deserts of eastern Asia. Although dust composition (and sources) remained fairly constant during the last glaciation, changes in total concentrations and grain sizes reveal

Table M3 Common zeolite minerals

Analcime	$\text{NaAlSi}_2\text{O}_6 \cdot \text{H}_2\text{O}$
Chabazite	$\text{Ca}_2(\text{Al}_4\text{Si}_8\text{O}_{24}) \cdot 12\text{H}_2\text{O}$
Clinoptilolite	$(\text{Na}, \text{K}, \text{Ca}_{0.5})_6(\text{Al}_6\text{Si}_{30}\text{O}_{72}) \cdot 24\text{H}_2\text{O}$
Erionite	$(\text{Na}, \text{K}_2, \text{Mg}, \text{Ca}_{1.5})(\text{Al}_8\text{Si}_{28}\text{O}_{72}) \cdot 28\text{H}_2\text{O}$
Mordenite	$\text{Na}_3\text{KCa}_2(\text{Al}_8\text{Si}_{40}\text{O}_{96}) \cdot 28\text{H}_2\text{O}$
Phillipsite	$(\text{K}, \text{Ca}_{0.5}, \text{Na})_4(\text{Al}_6\text{Si}_{10}\text{O}_{32}) \cdot 12\text{H}_2\text{O}$

significant variations in wind speed and strength during stadials and interstadials (Biscaye et al., 1997).

Zeolites

Zeolites (Table M3) are a group of hydrated aluminosilicate minerals with an open framework structure, into which various large ions and water molecules can fit and which possess a certain degree of mobility. They are widespread in cavities in basaltic lavas, as authigenic or diagenetic minerals in marine sediments, and in low-grade metamorphic rocks. Phillipsite is an authigenic zeolite that forms on the seafloor or at shallow depths (Kastner, 1999). Clinoptilolite forms in silica-rich marine sediments, derived from opal-A. Zeolites also form from the alteration of volcanic glass, tuff, or lavas in high pH, alkali-rich, semi-arid to arid environments. Analcime is common in sodium-rich alkaline desert soils (Watson, 1992). Zeolites from saline, alkaline lakes include analcime, chabazite, clinoptilolite, erionite, mordenite, and phillipsite. These zeolites are often associated with evaporites (Parrish, 1998). Zeolites in lacustrine deposits have been used as markers for dry, alkaline environments, as for example at Lake Naivasha, Kenya, where low lake levels are represented by the presence of chabazite and phillipsite, with even greater aridity indicated by clinoptilolite and analcime (Trauth et al., 2001). The East African lake level fluctuations have been linked to precessional cycles in springtime insolation and monsoonal precipitation.

Summary

Minerals that form at or near the earth's surface in contact with the atmosphere and hydrosphere can provide important information about former climates. They have been used to reconstruct past climates and changes over time, deduce changes in atmospheric composition, trace eolian and precipitation patterns, and serve as "hosts" for climate-sensitive stable isotopes and trace elements.

The most useful mineral indicators or proxies are those that are generated under relatively narrow climatic ranges or within restricted environmental settings. Examples include evaporites, low temperature minerals (e.g., ikaite and hydrohalite), residual soils (e.g., iron and aluminum oxyhydroxides, kaolinite), and certain authigenic minerals (that form *in situ*, e.g., glauconite, berthierine, phillipsite, barite). Minerals that are sensitive to oxidation (e.g., pyrite and uraninite) reflect past atmospheric oxygen levels. Distinctive detrital minerals in eolian deposits act as markers of wind direction and intensity. Similarly, minerals in deltaic sediments point not only to variations in the relative contributions from source tributaries, but can also indicate precipitation variability in source areas. Trace elements and stable isotope ratios contained within minerals such as calcite (both biogenic and non-biogenic) have provided a wealth of paleoclimatological information.

Vivien Gornitz

Bibliography

- Benison, K.C., and Goldstein, R.H., 1999. Permian paleoclimate data from fluid inclusions in halite. *Chem. Geol.*, **154**, 113–132.
- Biscaye, P.E., Grousset, F.E., Revel, M., Van der Gaast, Zielinski, G.A., Vaars, A., and Kukla, G., 1997. Asian provenance of glacial dust (stage 2) in the Greenland Ice Sheet Project 2 ice core, Summit, Greenland. *J. Geophys. Res.*, **10226**, 765–26, 781.
- Bond, G., Showers, W., Cheseby, M., Lotti, R., Almasi, P., deMenocal, P., Priore, P., Cullen, H., Hajdas, I., and Bonani, G., 1997. Massive millennial-scale cycle in North Atlantic Holocene and Glacial climates. *Science*, **278**, 1257–1266.
- Broecker, W.S., and Liu, T., 2001. Rock varnish: recorder of desert wetness? *GSA Today*, **11**(8), 10.
- Chamley, H., 1989. *Clay Sedimentology*. Berlin: Springer, 623p.
- De Lurio, J.I., and Frakes, L.A., 1999. Glendonites as a paleoenvironmental tool: implications for early Cretaceous high latitude climates in Australia. *Geochim. et Cosmochim. Acta*, **63**, 1039–1048.
- Derry, L.A., and Murray, R.W., 2004. Continental margins and the sulfur cycle. *Science*, **303**, 1981–1982.
- England, G.L., Rasmussen, B., Krapez, B., and Groves, D.I., 2002. Palaeoenvironmental significance of rounded pyrite in siliciclastic sequences of the Late Archean Witwatersrand Basin: Oxygen-deficient atmosphere or hydrothermal alteration? *Sedimentology*, **49** (6), 1133–1156.
- Evans, L.J., 1992. Alteration products at the Earth's surface—the clay minerals. In Martini, I.P., and Chesworth, W. (eds.), *Weathering, Soils, and Paleosols*, Amsterdam: Elsevier, Chap. 5, pp. 107–125.
- Fleet, M.E., 1998. Detrital pyrite in Witwatersrand gold reefs: X-ray diffraction evidence and implications for atmospheric evolution. *Terra Nova*, **10**(6), 302–306.
- Foucault, A., and Stanley, D.J., 1989. Late Quaternary palaeoclimatic oscillations in East Africa recorded by heavy minerals in the Nile delta. *Nature*, **339**, 44–46.
- Genty, D., Blamart, D., Ouahdi, R., Gilmour, M., Baker, A., Jouzel, J., and Van-Exter, S., 2003. Precise dating of Dansgaard-Oeschger climate oscillations in western Europe from stalagmite data. *Nature*, **421**, 833–837.
- Gornitz, V.M., and Schreiber, B.C., 1981. Displacive halite hoppers from the Dead Sea: implications for ancient evaporite deposits. *J. Sed. Petrol.*, **51**, 787–794.
- Hessler, A.M., Lowe, D.R., Jones, R.L., and Bird, D.K., 2004. A lower limit for atmospheric carbon dioxide levels 3.2 billion years ago. *Nature*, **428**, 736–738.
- Kastner, M., 1999. Oceanic minerals; their origin, nature of their environment, and significance. *Proc. Natl. Acad. Sci.*, **96**, 3380–3387.
- Kennedy, M., Droser, M., Mayer, L.M., Pevear, D., and Mrofka, D., 2006. Late Precambrian oxygenation; inception of the clay mineral factory. *Science*, **311**, 1446–1449.
- Kirk, J., Ruiz, J., Chesley, J., and Titley, S., 2003. The origin of gold in South Africa. *Am. Scientist*, **91**, 536–541.
- Li, Y.H., and Schoonmaker, J.E., 2003. Chemical composition and mineralogy of marine sediments. In: Mackenzie F.T. (ed.), *Sediments, Diagenesis, and Sedimentary Rocks* (vol. 7), *Treatise of Geochemistry*, Holland, H.D., and Turekian, K.K. (eds.). Amsterdam: Elsevier, pp. 1–35.
- Lowenstein, T.K., Timofeeff, M.N., Brennan, S.T., Hardie, L.A., and Demicco, R.V., 2001. Oscillations in Phanerozoic seawater chemistry: Evidence from fluid inclusions. *Science*, **294**, 1086–1088.
- Ludvigson, G.A., Gonzalez, L.A., Metzger, R.A., Witzke, B.J., Brenner, R.L., Murillo, A.P., and White, T.S., 1998. Meteoric sphaerosiderite lines and their use for paleohydrology and paleoclimatology. *Geology*, **26**, 1039–1042.
- Ludvigson, G.A., Ufnar, D.F., Gonzalez, L.A., White, T.S., Phillips, P.L., Witzke, B.J., and Brenner, R.L., 2000. When good sphaerosiderites go bad: Caveats in the application of a paleoclimate proxy. *Geol. Soc. Am. Abstr. Prog.*, **32**(7), pp. A–524.
- Maher, B.A., 1998. Magnetic properties of modern soils and Quaternary loessic paleosols: paleoclimatic implications. *Palaeogeog. Palaeoclim. Palaeoecol.*, **137**, 25–54.
- Mallinson, D.J., Flower, B., Hine, A., Brooks, G., and Garza, R.M., 2003. Paleoclimate implications of high latitude precession-scale mineralogical fluctuations during early Oligocene Antarctic glaciation: The Great Australian Bight record. *Glob. Planet. Change*, **39**, 257–269.

- McKeown, D.A.M., and Post, J.E., 2001. Characterization of manganese oxide mineralogy in rock varnish and dendrites using X-ray absorption spectroscopy. *Am. Min.*, **86**, 701–713.
- McLane, M., 1995. *Sedimentology*, New York: Oxford University Press, 432p.
- Milnes, A.E., 1992. Calcrete. In Martini, I.P., and Chesworth, W. (eds.), *Weathering Soils Paleosols*. Amsterdam: Elsevier, Chap. 13, pp. 309–347.
- Montañez, I.P., 2002. Biological skeletal carbonate records changes in major-ion chemistry of paleo-oceans. *Proc. Natl. Acad. Sci.*, **99** (25), 15852–15854.
- Morse, J.W., 2003. Formation and diagenesis of carbonate sediments. In Mackenzie, F.T. (ed.), *Sediments, Diagenesis, and Sedimentary Rocks* (vol. 7), *Treatise of Geochemistry*, Holland, H.D. and Turekian, K.K. (eds.). Amsterdam: Elsevier, pp. 67–85.
- Ohmoto, H., Watanabe, Y., and Kumazawa, K., 2004. Evidence from massive siderite beds for a CO₂-rich atmosphere before ~1.8 billion years ago. *Nature*, **429**, 395–399.
- Parrish, J.T., 1998. *Interpreting pre-Quaternary Climate from the Geologic Record*, New York: Columbia University Press, 338p.
- Paytan, A., Kastner, M., and Chavez, F.P., 1996. Glacial to interglacial fluctuations in productivity in the equatorial Pacific as indicated by marine barite. *Science*, **274**, 1355–1357.
- Raiswell, R., Buckley, F., Berner, R.A., and Anderson, T.F., 1988. Degree of pyritization of iron as a paleoenvironmental indicator of bottom-water oxygenation. *J. Sed. Petrol.*, **58**(5), 812–819.
- Reynolds, R.L., and King, J.W., 1995. Magnetic records of climate change. US National Report to IUGG, 1991–1994, *Rev. Geophys.*, **33** (Suppl. 95), RG00354.
- Robert, C., and Kennett, J.P., 1997. Antarctic continental weathering changes during Eocene-Oligocene cryosphere expansion: clay mineral and oxygen isotope evidence. *Geology*, **25**, 587–590.
- Roberts, S., Spencer, M., Yang, R.J., and Krouse, H.R., 1997. Deciphering some unique paleotemperature indicators in halite-bearing saline lake deposits from Death Valley, California, USA. *J. Paleolimnol.*, **17**, 101–130.
- Roychoudhury, A.N., Kostka, J.E., and Van Cappellen, 2003. Pyritization: A palaeoenvironmental and redox proxy reevaluated. *Estuar. Coast. Shelf Sci.*, **57**, 1–11.
- Ruffell, A., McKinley, J.M., and Worden, R.H., 2002. Comparison of clay mineral stratigraphy to other proxy palaeoclimate indicators in the Mesozoic of NW Europe. *Phil. Trans. Royal Soc. Lond. A*, **360**, 675–693.
- Sheldon, N.D., and Retallack, G.J., 2002. Low oxygen levels in earliest Triassic soils. *Geology*, **30**, 919–922.
- Stiles, C.A., Mora, C.I., and Driese, S.G., 2001. Pedogenic iron-manganese nodules in Vertisols: A new proxy for paleoprecipitation? *Geology*, **29**, 943–946.
- Swainson I.P., and Hammond, R.P., 2001. Ikaite, CaCO₃.6H₂O: cold comfort for glendonites as paleothermometers. *Am. Mineral.*, **86**, 1530–1533.
- Tardy, Y., 1992. Diversity and terminology of lateritic profiles. In Martini, I.P., and Chesworth, W. (eds.), *Weathering, Soils & Paleosols*. Amsterdam: Elsevier, Chap. 15, pp. 379–405.
- Tardy, Y., and Roquin, C., 1992. Geochemistry and evolution of lateritic landscapes. In Martini, I.P., and Chesworth, W. (eds.), *Weathering, Soils & Paleosols*, Amsterdam: Elsevier, Chap. 16, pp. 407–443.
- Torii, T., and Ossaka, J., 1965. Antarcticite: a new mineral, calcium chloride hexahydrate, discovered in Antarctica. *Science*, **149**, 975–977.
- Trauth, M.H., Deino, A., and Strecker, M.R., 2001. Response of the East African climate to orbital forcing during the last interglacial (130–117 ka) and the early last glacial (117–60 ka). *Geology*, **29**, 499–502.
- Turchyn, A.V., and Schrag, D.P., 2004. Oxygen isotope constraints on the sulfur cycle over the past 10 million years. *Science*, **303**, 2004–2007.
- Velde, B., 2003. Green clay minerals. In Mackenzie, F.T. (ed.), *Sediments, Diagenesis, and Sedimentary Rocks* (vol. 7), *Treatise of Geochemistry*, Holland, H.D. and Turekian, K.K. (eds.). Amsterdam: Elsevier, pp. 309–324.
- Warren, J., 1999. *Evaporites: Their Evolution and Economics*. Oxford, UK: Blackwell Science, Chap. 1, 19. p. 13, 19.
- Watson, A., 1992. Desert soils. In Martini, I.P., and Chesworth, W. (eds.), *Weathering, Soils & Paleosols*. Amsterdam: Elsevier, Chap.10, pp. 225–260.
- Yuretich, R., Melles, M., Sarata, B., and Grobe, H., 1999. Clay minerals in the sediments of Lake Baikal: A useful climate proxy. *J. Sed. Res.*, **69**, 588–596.
- Zhao, L., Ji, J., Chen, J., Liu, L., Chen, Y., and Balsam, W., 2005. Variations of illite/chlorite ratio in Chinese loess sections during the last glacial and interglacial cycle: Implications for monsoon reconstruction. *Geophys. Res. Lett.*, **32**, L20718. doi:10.1029/2005GL024145.

Cross-references

[Atmospheric Evolution, Earth](#)
[Banded Iron Formations and the Early Atmosphere](#)
[Beachrock](#)
[Carbonates, Cool Water](#)
[Carbonates, Warm Water](#)
[Cryosphere](#)
[Dating, Magnetostratigraphy](#)
[Desert Varnish as Climate Proxy](#)
[Duricrusts](#)
[Eolian Dust, Marine Sediments](#)
[Eolian Sediments and Processes](#)
[Eolianite](#)
[Evaporites](#)
[Faint Young Sun Paradox](#)
[Glacial Geomorphology](#)
[Glendonite/Ikaite](#)
[Ice Cores, Antarctica and Greenland](#)
[Ice Cores, Mountain Glaciers](#)
[Ice-Rafted Debris \(IRD\)](#)
[Laterite](#)
[Marine Biogenic Sediments](#)
[Marine Clay Minerals](#)
[Ocean Paleoproductivity](#)
[Paleosols, Pre-Quaternary](#)
[Paleosols-Quaternary](#)
[Phosphorite](#)
[Red Beds](#)
[Sedimentary Indicators of Climate Change](#)
[Speleothems](#)
[Stable Isotope Analysis](#)

MONSOONS: PRE-QUATERNARY

Monsoon circulation has existed throughout geological history whenever the tropics were occupied by both land and sea. Pre-Quaternary monsoons, however, are poorly understood because paleo-monsoon studies have been heavily biased toward variations of the Quaternary monsoon on the orbital and suborbital time scales. Pre-Quaternary monsoon systems are often considered over a much longer time span, so they show more significant variations in responding to tectonically-induced geographic and topographic changes. Pre-Quaternary monsoons have so far only sporadically been mentioned in the literature for most of the geological periods, except for two better studied intervals: the Permian and Triassic where a “megamonsoon” developed on the megacontinent Pangaea, and the late Cenozoic, which led to the establishment of the modern monsoon system.

Megamonsoon of the megacontinent

As monsoons are caused by land-sea contrast in the heating rate, the ideal conditions for a monsoon system to develop exist when only one major continent and one complementary ocean exist on Earth. This was the real case around 250–200 Myr ago, during the late Permian and Triassic, when all continents

assembled into two major landmasses, Laurasia and Gondwanaland, that joined near the equator to form the supercontinent Pangaea and the super-ocean Panthalassa (Figure M35a). The extensive distribution of evaporites and many biogeographic features indicate a maximum of continentality, leading to speculation about the association of monsoon-type seasonal rains with large landmasses at that time (Robinson, 1973). Parrish et al. (1982) used the basic principles of atmospheric and oceanic circulation to reconstruct global paleo-precipitation maps for seven time intervals of the Mesozoic and Cenozoic, and found patterns of a strong summer monsoon low over Laurasia

and a winter monsoon high over Gondwanaland in the Triassic and reversed monsoon features for opposite seasons. According to these authors, the Triassic was distinguished by maximal aridity with precipitation on the supercontinent provided only by monsoons (Figure M35b). Kutzbach and Gallimore (1989) were the first to use numerical modeling to explore the “megamonsoon of the megacontinent.” Applying a low-resolution general circulation model to the idealized Pangaea (Figure M35a), they found extreme continentality with a hot summer and cold winter, and large-scale summer and winter monsoon circulations (Figure M35c,d). At the same time, Crowley et al. (1989) used

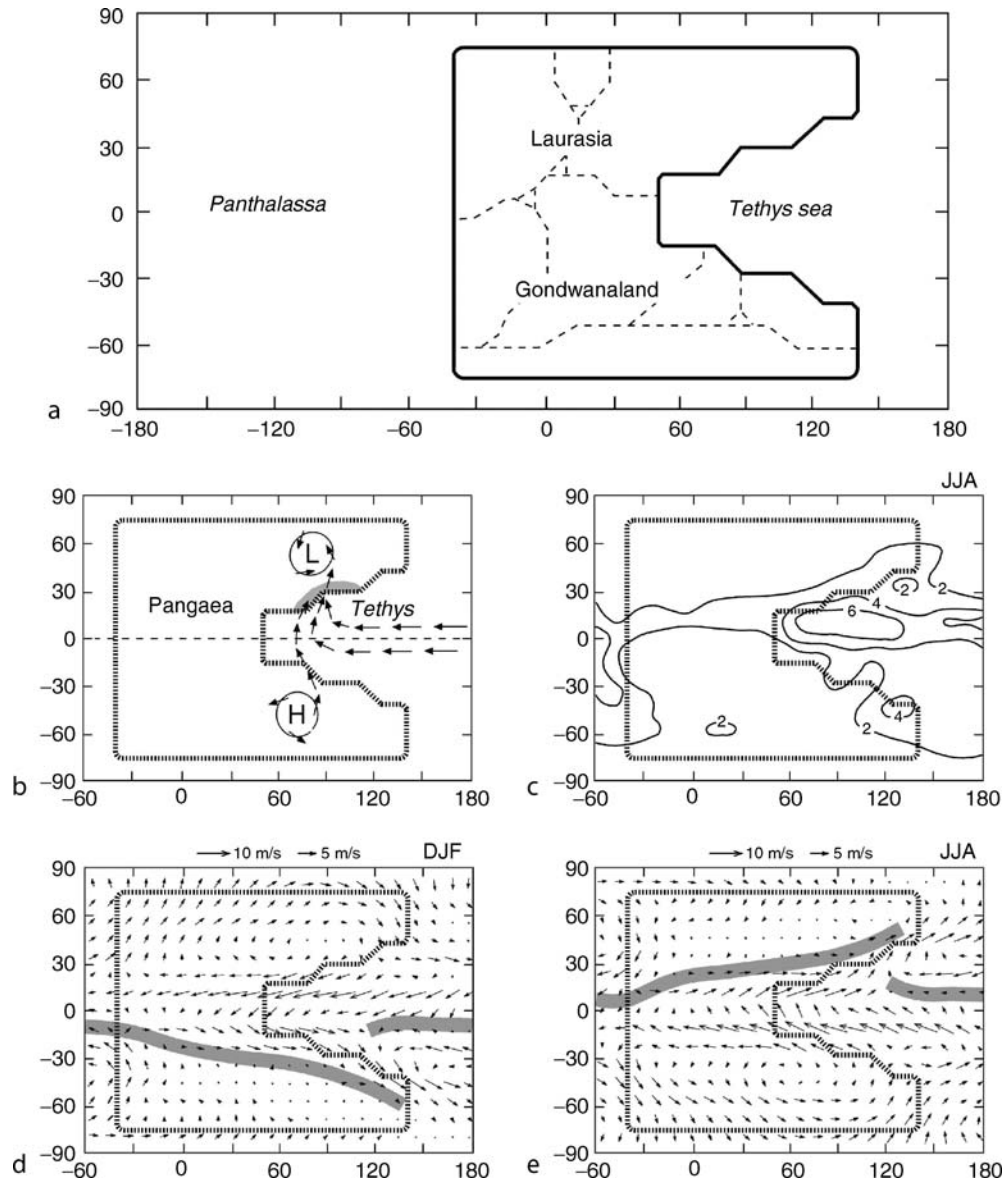


Figure M35 Megamonsoon of the Pangaea. (a) The idealized Pangaea continent. *Fine dashed lines* indicate the approximate outlines of modern landmasses (after Kutzbach and Gallimore, 1989). (b) Schematic diagram illustrating monsoonal circulation in northern summer. *Arrows* show surface winds, stippling indicates heavy seasonal rains (modified from Parrish and Peterson, 1988). (c) Modeled precipitation rate (mm d⁻¹) on Pangaea for summer. (d), (e) Modeled surface winds on Pangaea for winter (d) and summer (e), note the seasonal reversal of the wind direction. The *gray bar* shows the poleward limit of summer monsoon over land and the Intertropical Convergence Zone over ocean (modified from Kutzbach and Gallimore, 1989).

energy balance modeling (EBM) to study the late Permian climate. Both modeling results show an extremely wide annual range of temperature (50°C) for hinterland and strong monsoon circulation over Pangaea.

The geological record of the “megamonsoon” was found from the upper Triassic of North America: the Newark and related basins in the east and the Colorado Plateau in the west

(Figure M36a). Late Triassic lacustrine deposits from the Newark Basin, New Jersey, which were about 10°N in the monsoon-prevalent tropics at that time, display clear evidence of monsoon-driven seasonality and lake level fluctuations (Olsen, 1986). Part of the sequence consists of micro-laminated mudstones (varves) with 0.2–0.3 mm thin couplets of alternating light and dark layers, implying significant seasonal contrast

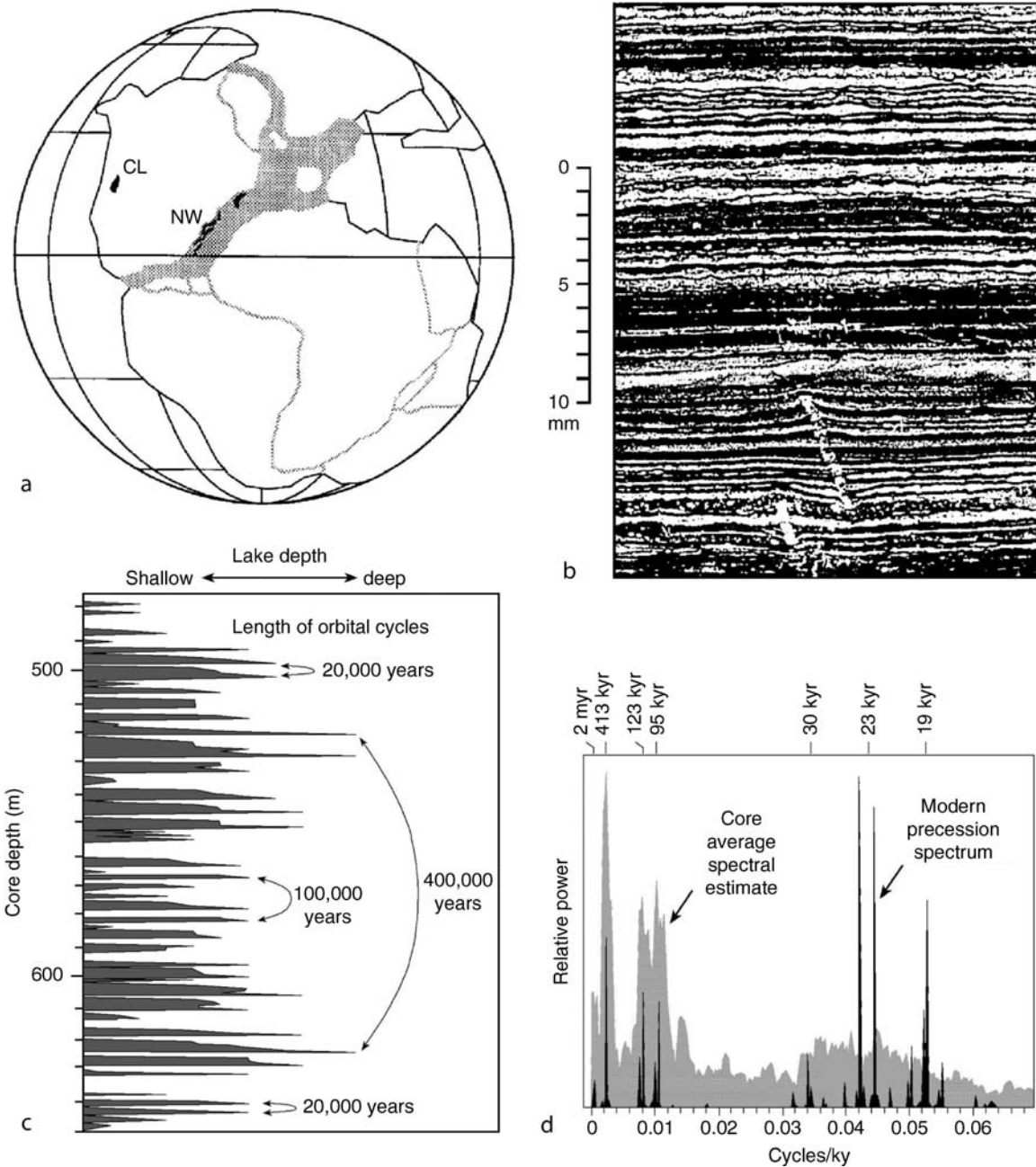


Figure M36 Late Triassic monsoon records from North America. (a) Locations of the Colorado Plateau with the Chinle Formation (CL) and, to the east, a chain of rifted basins containing the Newark Supergroup (NW). (b) Photograph of microlaminated mudstone showing organic-rich/carbonate-rich couplets as annual varves. (c) Lake-level fluctuations revealed in a section of the Newark lake sediments, showing 20-kyr, 100-kyr, and 400-kyr cycles. (d) Average spectral estimates of sediment cycles in the Newark Basin against the modern precession spectrum. (Modified from Olsen and Kent, 1996 and Ruddiman, 2001).

(Figure M36b). Detailed studies including spectral analyses on the nearly 7,000 m long section reveal a full range of precession-related periods of lake level change: the 20-kyr precession cycles, and 100-kyr and 400-kyr eccentricity cycles which modulate the amplitude of precessional cyclicity (Figure M36c,d). All these cycles are characteristic of the tropical response to orbital forcing and support a monsoon-climate origin of lake level change, whereas the absence of obliquity cycles preclude the possibility of direct linkages to high-latitude climate systems (Olsen and Kent, 1996). Similar records of the Pangaean “megamonsoon” were also found in the Chinle Formation, Colorado Plateau, on the tropical western margin of the supercontinent (Figure M36a; Dubial et al., 1991). During the Pangaean interval, eolian, playa deposits and evaporates were widespread on the Colorado Plateau, but the Chinle formation represents an unusually wet episode with well-developed fluvial and lacustrine deposits and paleosol sequences, indicating abundant moisture brought about by enhanced monsoon circulation and strong seasonality.

Establishment of the modern monsoon system

The modern Asian-Australian and African monsoons cover most of the Eastern Hemisphere, and fundamental questions in Cenozoic paleoclimatology ask when the modern monsoon system was established and how it has evolved since then. Three tectonic factors have been proposed to exert a control over the evolution of Asian monsoon circulation: plateau uplift, sea-land distribution, and closing of oceanic gateways. Continuous records of the monsoon history provided by Deep Sea

Drilling Project/Ocean Drilling Program (DSDP/ODP) cruises to the Arabian, Mediterranean and South China Seas, as well as from the Loess plateau in central China, have been used to verify the various tectonic hypotheses (Sun and Wang, 2005).

Tectonic forcing and numerical modeling

1. **Plateau uplift.** GCM experiments on the modern land-sea distribution indicate that strong monsoons can be induced by solar forcing only when the elevation of Tibet-Himalaya has reached at least half that of today (Prell and Kutzbach, 1992). A number of studies in the late 1980s investigated the climatic consequences of uplift (e.g., Ruddiman et al., 1989) and found that uplift may have been responsible for both the global cooling and significant strengthening of the Asian monsoon system in the late Cenozoic. According to the prevalent hypothesis, uplift of the Tibetan Plateau intensified around 8 Ma and caused enhanced aridity over the Asian interior and the onset of the Indian and east Asian monsoons (Figure M37a, Prell and Kutzbach, 1997; An et al., 2001). However, this cognition is challenged by the new discovery of Miocene loess (Guo et al., 2002) and other evidence that indicates an older age (see below).
2. **Sea-land distribution.** The results of Atmospheric General Circulation Model (AGCM) simulation by Ramstein et al. (1997) indicate that the Paratethys, an epicontinental sea stretching over Eurasia 30 Ma ago, had progressively receded during the Miocene, resulting in major continentalization of the Asian interior and enhancement of monsoon circulation. They consider the retreat of the Paratethys Sea as important as the uplift of the Himalayan/Tibetan Plateau

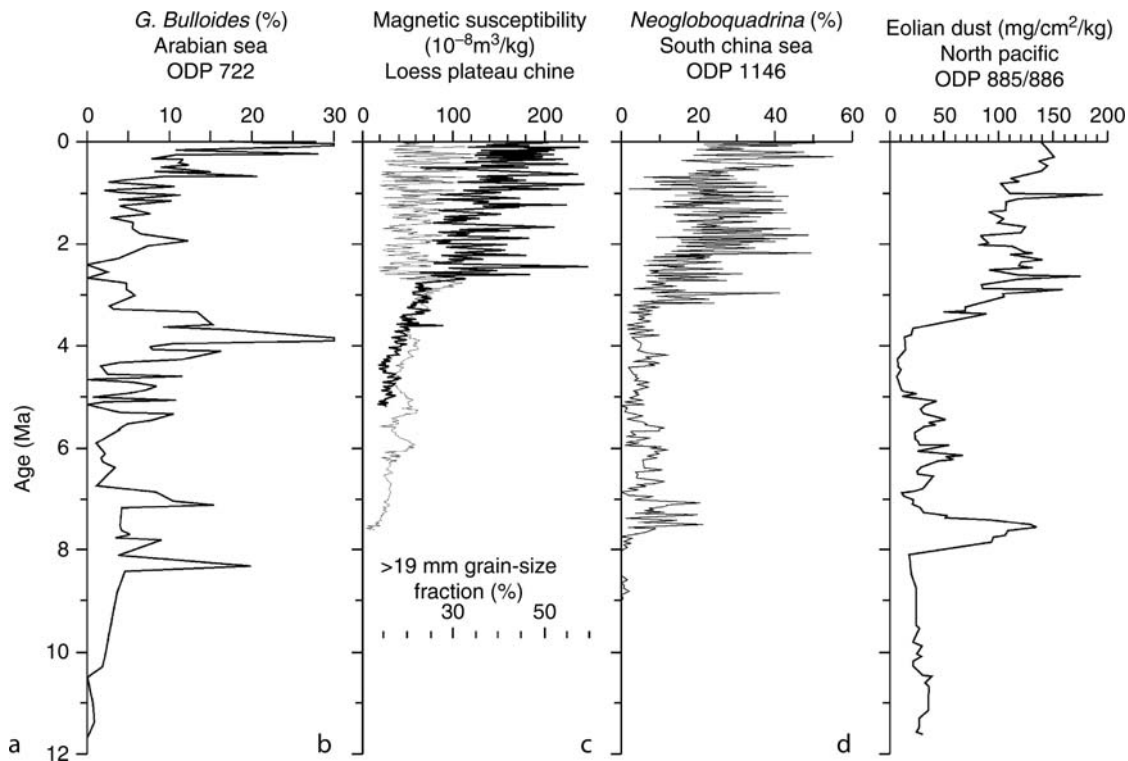


Figure M37 Records of Asian monsoon and aridity evolution over the past 12 Myr. (a) *Globigerina bulloides* % (>150 μm), ODP Site 722, Arabian Sea; (b) Magnetic susceptibility (thin line) and grain size fraction (thick line) from the Loess Plateau (An et al., 2001); (c) *Neogloboquadrina dutertrei* %, ODP Site 1146, South China Sea (Wang et al., 2003); (d) Dust flux ($\text{mg cm}^{-2} \text{ kyr}^{-1}$), ODP sites 885/886, north Pacific (Rea et al., 1998).

for development of the Asian monsoon. As the shrinkage of the Paratethys Sea occurred during the Oligocene-late Miocene, its effects on the monsoon may have lasted from 30 to 10 Ma, significantly earlier than the 8-Ma date implied by the uplift hypothesis.

3. **Oceanic gateways.** An oceanic circulation model reveals that the “closure” of the Indonesian seaway 3–4 Ma ago could be responsible for east African aridification (Cane and Molnar, 2001). The northward drift of the Australian Plate may have switched the source of the Indonesian Throughflow current from the warm South Pacific to the relatively cold North Pacific waters. This would have decreased Sea Surface Temperatures (SSTs) in the Indian Ocean and would have subsequently reduced precipitation over east Africa, as well as the overall strength of the Indian summer monsoon as recorded in marine deposits.

All of these three factors are believed to be significant in the development of the modern monsoon, but their relative roles remain unclear. To single out the role played by each of the factors, many more long-term sequences and better constraints on the timing of the tectonic and climate events are needed.

Geological records

Studies on the long-term evolution of the Asian monsoon started with ODP Leg 117 to the Arabian Sea in 1987. A sudden increase in the cool-water planktonic foraminifer *Globigerina bulloides* in sediment cores of Leg 117 around 8.5 Ma ago was considered by Kroon et al. (1991) as indicating the onset of monsoon-related upwelling (Figure M37a). This date is very close to the rapid ecological transition from C3-dominated to C4-dominated vegetation around 7.4–7.0 Ma, as revealed by the $\delta^{13}\text{C}$ data of pedogenic carbonates from northern Pakistan in the Himalayan foreland. These were interpreted as evidence for the origin or intensification of the Asian monsoon system (Quade et al., 1989). In addition, the dating of the extensive faults on the Tibetan Plateau suggests a significant uplift/extension period at about 8 Ma. On the basis of these findings and GCM simulations, Prell and Kutzbach (1992) hypothesized that uplift of the Tibetan Plateau to at least

half of its present height at ~8 Ma caused the intensification of the Asian monsoon.

In the Chinese Loess Plateau, the base of the loess-paleosol sequences dated to about 2.6 Ma was previously taken as indicating the initiation of the East Asian monsoon (Liu and Ding, 1993). Later, Chinese scientists found that the Red Clay underlying the loess sequence was also of wind-blown origin and indicative of monsoon transport (Table M4), so the history of eolian deposits of the Loess Plateau should be extended to 7–8 Ma (Figure M37b; An et al., 2001). Since the uplift of the Tibetan Plateau can lead to enhanced aridity in the Asian interior and to intensification of the Asian monsoon system (Kutzbach et al., 1993), a nearly concurrent beginning of both the Indian Ocean upwelling and dust accumulation in central China about 8 Ma ago has been interpreted as marking the onset of the Indian and East Asian monsoons, which in turn implies a significant increase in the altitude of the Plateau (An et al., 2001). However, the recent discovery by Guo et al. (2002) of a Miocene loess sequence from Qinan, western Loess Plateau, has further extended the Chinese dust history. Like the Pleistocene loess, the Miocene loess evinces enhanced aridity in the dust source areas and energetic winter monsoon winds required for dust transport, whereas paleosols point to increased moisture supply by summer monsoon winds. A total of 231 interbedded loess-paleosol layers, representing a nearly continuous history of eolian dust accumulation from 22 to 6.2 Ma, indicates that large source areas of eolian dust and energetic winter monsoon winds existed since early Miocene, at least 14 Ma earlier than previously thought (Table M4).

Noticeable climate change from arid to humid climatic conditions in East China occurred as early as around the Oligocene/Miocene boundary. The synthesized data from oil exploration and stratigraphic studies indicate that a broad aridity belt stretched across China from west to east during the Paleogene, particularly in the Paleocene, before it contracted to Northwest China in the Neogene (Figure M37), suggesting a transition from a planetary to monsoonal system in atmospheric circulation over the region. This climate transition, now confirmed by abundant paleobotanical/palynological and lithostratigraphic data, may further imply that monsoonal moisture brought westward from the ocean to East

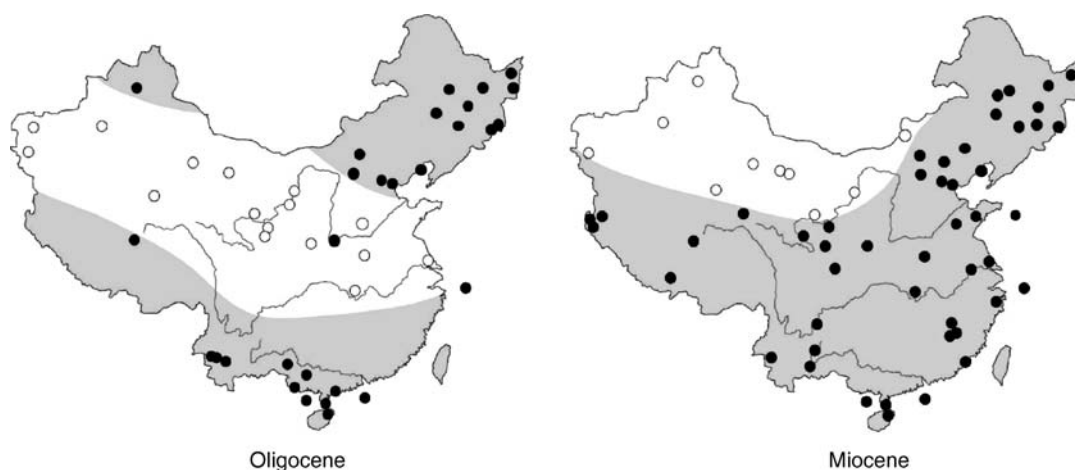


Figure M38 Distribution of arid climate zones in China based on paleobotanical and palynological data: (a) Oligocene; (b) Miocene. *Open dots* denote humid vegetation, *filled dots* denote arid vegetation. The Paleocene and Eocene patterns are similar to those of the Oligocene, while Pliocene and Pleistocene patterns are close to those of the Miocene. The drastic change between the Oligocene and Miocene implies the beginning of the modern East Asian monsoon system (Sun and Wang, 2005).

Table M4 Development of the dust history in the Loess Plateau, China

Deposits	Age	Reference
Loess-paleosol sequence	0–2.6 Ma	Liu and Ding, 1993
Red clay	2.6–8 Ma	An et al., 2001
Qinan loess sequence	6.2–22 Ma	Guo et al., 2002

China as a response to the reorganization of the climate system about 24 Ma ago was probably caused by an enhancement, if not the first establishment, of the East Asian summer monsoon (Sun and Wang, 2005). The loess-paleosol sequence at Qinan supports the Oligocene/Miocene climate transition. The existence of the Asian monsoon at about 16–14 Ma has been reported from northern Thailand, where middle Miocene mammalian faunas were found to have adapted to a monsoon-styled wet climate.

Sedimentological data from ODP Leg 116, Bay of Bengal also imply the intensification of uplift-induced monsoon in the early Miocene. Although the dramatic $\delta^{13}\text{C}$ increase of total organic carbon in Bengal Fan sediments at ca. 7 Ma supports the development of the monsoon in the Himalayan foreland at this time, the sediment accumulation records are in conflict with the 8 Ma uplift model. Accumulation rates at several DSDP/ODP Sites were high for the 17–7 Ma old Bengal Fan, but decreased from 7 to 1 Ma with the clay mineral assemblages indicating reduced physical erosion and strengthened chemical weathering (Derry and France-Lanord, 1997). No significant change in sediment accumulation around 8 Ma has been found at any ODP Leg 184 sites in the South China Sea (Wang et al., 2000). On the other hand, if using the planktonic foraminifer *Neogloboquadrina dutertrei* as an indicator of the East Asian monsoon and enhanced productivity in the South China Sea, its abundance peaks at 7.6 Ma and 3.2 Ma at Site 1146 on the northern slope correspond well to the Indian monsoon records (Figure M37c; Wang et al., 2003).

The dust record also indicates that the Asian monsoon system has a longer history and greater variability both in space and in time than previously thought. In the Miocene sequence of Qinan, two intervals are distinguished by higher dust accumulation: 15–13 Ma and 8–7 Ma (Guo et al., 2002). These might represent periods of enhanced aridity in the source areas, an interpretation supported by pollen data from Yumen, north-east of Tibet. Increased aridity over Asia around 8–7 Ma also explains a peak in dust accumulation rate in the North Pacific (Figure M37d; Rea et al., 1998).

Monsoon evolution in geological history

The number and geographic coverage of the monsoon records decrease with increasing age, resulting in relatively deficient knowledge of the pre-Quaternary monsoon history. Although it may be premature to discuss the evolution of the monsoon system through the entire geological history, the examples of the Pangaeian and late Cenozoic times provide convincing evidence that tectonically-induced changes in sea-land distribution and in topography have played the primary role in controlling the monsoon system over the 10^6 – 10^7 year and longer timescales. Tracing back the entire Phanerozoic history, the monsoon system strengthened with increased size of continents and increased altitude of mountains. With the collapse of the megacontinent, for example, the “megamonsoon” circulation over Pangaea was subsequently replaced by a basically zonal circulation (Parrish et al., 1982). The late paleozoic American

Appalachians (estimated average altitude of 4,500 m) and the European Variscan (2,000–3,000 m) in Pangaea might have played a role similar to the late Cenozoic Himalaya-Tibet in the intensification of the concomitant monsoon circulation (Fluteau et al., 2001).

The development of polar ice-sheets is another major control of the monsoon system. Clemens et al. (1996) found a non-stationarity in the phase of the summer monsoon system relative to a growing Northern Hemisphere ice volume over the past 3.5 Myr. During the initiation and the growth of the Northern Hemisphere ice sheets, the phase of strong monsoons moved away from the phase of maximum ice volume and systematically drifted in a similar pattern over the past 2.6 Myr. An intensified winter monsoon resulting from the growth of the boreal ice sheet was also reported from the Chinese loess records (Liu and Ding, 1993). Accordingly, the nature of the monsoon system in the ice-house vs. hot-house Earth must have been different, and the transition between hot- and ice-house regimes can be of paramount importance for reconstructing the monsoon history.

A trustworthy reconstruction of the monsoon history depends on the proxies adopted. Care is necessary to evaluate how the monsoon proxies that were developed for the Quaternary period can be applied to the earlier geological past. It is equally crucial to distinguish monsoon proxies from those driven by other factors. An example is the late Miocene development of C4 vegetation, exhibited by a $\delta^{13}\text{C}$ shift in pedogenic carbonates, which was considered by Quade et al., (1989) as a signal of the onset of the Indian monsoon when first found in Pakistan. Since many subsequent findings have occurred in various continents, this $\delta^{13}\text{C}$ shift has been re-interpreted as representing a large-scale vegetation change caused by decreased CO_2 concentration on the globe (Cerling et al., 1997).

Regardless of all the complexity, paleo-monsoons are increasingly important in pre-Quaternary studies. Climate variations throughout geological history have been driven not only by higher latitudes where ice-sheets develop but also by lower latitude factors, especially by the monsoons.

Pinxian Wang and Qianyu Li

Bibliography

- An, Z., Kutzbach, J.E., Prell, W.L., and Porter, S.C., 2001. Evolution of Asian monsoons and phased uplift of the Himalaya-Tibetan plateau since Late Miocene times. *Nature*, **411**, 62–66.
- Cane, M.A., and Molnar, P., 2001. Closing of the Indonesian seaway as a precursor to east African aridification around 304 million years ago. *Nature*, **411**, 157–162.
- Cerling, T.E., Harris, J.M., MacFadden, B.J., Leakey, M.G., Quade, J., Eisenmann, V., and Ehleringer, J.R., 1997. Global vegetation change through the Miocene/Pliocene boundary. *Nature*, **389**, 153–158.
- Clemens, S., Murray, D., and Prell, W., 1996. Nonstationary phase of the Plio-Pleistocene Asian monsoon. *Science*, **274**, 943–948.
- Crowley, T.J., Hyde, W.T., and Short, D.A., 1989. Seasonal cycle variations on the supercontinent of Pangaea. *Geology*, **17**, 457–460.
- Derry, L.A., and France-Lanord, C., 1997. Himalayan weathering and erosion fluxes: Climate and tectonic controls. In Ruddiman, W.F. (ed.), *Tectonic Uplift and Climate Change*. New York: Plenum Press, pp. 290–312.
- Dubial, R.F., Parrish, J.T., Parrish, J.M., and Good, S.C., 1991. The Pangaeian megamonsoon – Evidence from the Upper Triassic Chinle Formation, Colorado Plateau. *Palaios*, **6**, 347–370.
- Fluteau, F., Besse, J., Broutin, J., and Ramstein, G., 2001. The Late Permian climate. What can be inferred from climate modeling concerning Pangea scenarios and Hercynian range altitude? *Palaeogeogr. Palaeoclimatol. Palaeoecol.*, **167**, 39–71.

- Guo, Z.T., Ruddiman, W.F., Hao, Q.Z., Wu, H.B., Qiao, Y.S., Zhu, R.X., Peng, S.Z., Wei, J.J., Yuan, B.Y., and Liu, T.S., 2002. Onset of Asian desertification by 22 Myr ago inferred from loess deposits in China. *Nature*, **416**, 159–163.
- Kroon, D., Steens, T.N.F., and Troelstra, S.R., 1991. Onset of monsoonal related upwelling in the western Arabian Sea. In Prell, W.L., Niitsuma, N., et al., (eds), *Proceedings of ODP, Scientific Results*, Vol. 117. College Station, TX: Ocean Drilling Program, pp. 257–264.
- Kutzbach, J.E., and Gallimore, R.G., 1989. Pangean climates: Megamonsoons of the megacontinent. *J. Geophys. Res.*, **94**, 3341–3357.
- Kutzbach, J.E., Prell, W.L., and Ruddiman, W.F., 1993. Sensitivity of Eurasian climate to surface uplift of the Tibetan Plateau. *J. Geol.*, **101**, 177–190.
- Liu, T.S., and Ding, Z.L., 1993. Stepwise coupling of monsoon circulations to global ice volume variations during the late Cenozoic. *Global Planet. Change*, **7**, 119–130.
- Olsen, P.E., 1986. A 40-million-year lake record of Early Mesozoic orbital climatic forcing. *Science*, **234**, 842–848.
- Olsen, P.E., and Kent, D.V., 1996. Milankovitch climate forcing in the tropics of Pangaea during the Late Triassic. *Palaeogeogr. Palaeoclimatol. Palaeoecol.*, **122**, 1–26.
- Parrish, J.T., and Peterson, F., 1988. Wind directions predicted from global circulation models and wind directions determined from eolian sandstones of the western United States – a comparison. *Sediment. Geol.*, **56**, 261–282.
- Parrish, J.T., Ziegler, A.W., and Scotese, C.R., 1982. Rainfall patterns and the distribution of coals and evaporates in the Mesozoic and Cenozoic. *Palaeogeogr. Palaeoclim. Palaeoecol.*, **40**, 67–101.
- Prell, W.L., and Kutzbach, J.E., 1992. Sensitivity of the Indian monsoon to forcing parameters and implications for its evolution. *Nature*, **360**, 647–653.
- Prell, W.L., and Kutzbach, J.E., 1997. The impact of Tibetan-Himalayan elevation on the sensitivity of the monsoon climate system to changes in solar radiation. In Ruddiman, W.F. (ed.), *Tectonic Uplift and Climate Change*. New York: Plenum Press, pp. 171–201.
- Quade, J., Cerling, T.E., and Bowman, J.E., 1989. Development of Asian monsoon revealed by marked ecological shift during the latest Miocene in northern Pakistan. *Nature*, **342**, 163–166.
- Ramstein, G., Fluteau, F., Besse, J., and Joussaume, S., 1997. Effect of orogeny, plate motion and land-sea distribution on Eurasian climate change over the past 30 million years. *Nature*, **386**, 788–795.
- Rea, D.K., Snoeckx, H., and Joseph, L.H., 1998. Late Cenozoic eolian deposition in the North Pacific: Asian drying, Tibetan uplift, and cooling of the Northern Hemisphere. *Paleoceanography*, **13**, 215–224.
- Robinson, P.L., 1973. Palaeoclimatology and continental drift. In Tarlin, D.H., and Runcorn, S.K. (eds.), *Implications of Continental Drift to Earth Sciences*, Vol.1. London: Academic Press, pp. 451–476.
- Ruddiman, W.F., 2001. *Earth's Climate: Past and Future*. New York: Freeman, 465pp.
- Ruddiman, W.F., Prell, W.L., and Raymo, M.E., 1989. Late Cenozoic uplift in southern Asia and the American West: Rationale for General Circulation Modeling experiments. *J. Geophys. Res.*, **94**, 18,379–18,391.
- Sun, X., and Wang, P., 2005. How old is the Asian monsoon system? Paleobotanical records from China. *Palaeogeogr. Palaeoclimatol. Palaeoecol.*, **222**, 181–222.
- Wang P., Prell W., Blum P., et al., 2000. *Proceedings of the Ocean Drilling Program, Initial Reports*, Vol. 184. College Station TX: Ocean Drilling Program.
- Wang P., Jian Z., Zhao Q., Li Q., Wang R., Liu Z., et al., 2003. Evolution of the South China Sea and monsoon history revealed in deep-sea records. *Chinese Sci. Bull.*, **48**, 2,549–2,561.
- Wang, P., Clemens, S., Beaufort, L., Braconnt, P., Ganssen, G., Jian, Z., Kershaw, P., and Sarnthein, M., 2005. Evolution and variability of the Asian monsoon system: state of the art and outstanding issues. *Quaternary Sci. Rev.* **24**, 595–629.

Cross-references

Atmospheric Evolution, Earth
 Deep Sea Drilling Project (DSDP)
 Loess Deposits
 Monsoons, Quaternary
 Mountain Uplift and Climate Change

Ocean Drilling Program (ODP)
 Plate Tectonics and Climate Change
 Precession, Climatic
 Pre-Quaternary Milankovitch Cycles and Climate Variability
 Varved Sediments

MONSOONS, QUATERNARY

Definition

The word “monsoon” is from the Arabic word “mausim,” meaning *season of winds*, which is often applied to the seasonal reversals of the wind direction along the shores of the Indian Ocean and surrounding regions, especially in the Arabian Sea. The prevailing winds blow from the southwest during half of the year and from the northeast during the other (Figure M39).

Monsoons are driven by the land-sea thermal contrast as the continent heats up and cools down faster than the ocean. Thus, in summer, land reaches a higher temperature than the ocean and the hot air over the land tends to rise, creating an area of persistent low pressure. This produces an extremely constant wind blowing toward the land. Associated rainfall is generated as the moist ocean air is diverted upward by mountains, which causes cooling, and in turn, condensation. In winter, the land cools off quickly, but the ocean retains heat longer. The warmer air over the ocean rises, creating a low pressure area and a breeze from land to ocean. Because the temperature difference between the ocean and land is less than in summer, the winter monsoon winds are weak and variable. Monsoons are similar to sea breezes, but they are much larger in extent, stronger, and are more constant.

Monsoon systems

As monsoons have become better understood, the definition has broadened, indicating climatic systems in which the precipitation is largely confined to the warm season. Monsoons

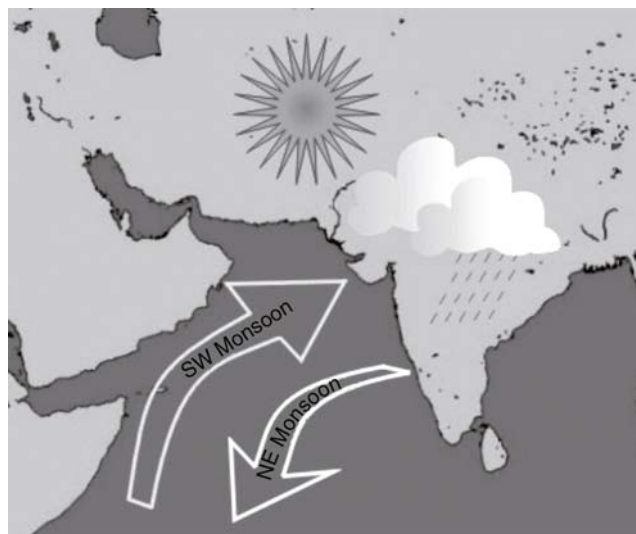


Figure M39 Asian monsoon circulation marked by the southwest or summer and northeast or winter monsoon winds. The Indian landmass receives maximum solar insolation during the summer monsoon months (June–September).

now include almost all of the phenomena associated with the annual weather cycle within the tropical and subtropical parts of Asia, Africa, Australia, North America and the adjacent seas and oceans.

The southwest or summer monsoon occurs from June to September, marked by wet and strong winds, providing maximum rainfall to the Asian landmass. The northeast or winter monsoon season ranges from December to early March, during which time the winds are dry and weak, and precipitation is reduced over the land. However, Australia and Southeast Asia receive enough rainfall during the winter monsoon. The North American monsoon occurs from mid-July to September, affecting mainly southwestern parts of the United States. The Indian or Asian monsoon, which affects South and Southeast Asia as well as northern Africa, is the best known and most regular of the world's monsoons, and one of the most spectacular features of the tropical climate system, affecting ~60% of world population between 30° N and S latitudes.

The Indian monsoon system

The Indian monsoon system is believed to have evolved in the late Oligocene or early Miocene, and appears to have had a major shift in its intensity and seasonal duration ~8.5 Ma BP. (e.g., Gupta et al., 2004). Rapid changes in the monsoon in the late Quaternary and the Holocene are documented in numerous papers based on proxies from marine records of the summer monsoon winds (Schulz et al., 1998; Gupta et al., 2003), cave deposits that record precipitation in Oman (Neff et al., 2001; Fleitmann et al., 2003), peat deposits that indicate humidity and temperature (Hong et al., 2003), runoff in the Bay of Bengal (Kudrass et al., 2001), and fluvial sediments indicating the intensity of rainfall (Sharma et al., 2004; also Figure M40). Strong monsoon events had a potentially dramatic effect on the fluvial systems (Goodbred and Kuehl, 2000), the terrestrial and marine fauna and flora, and human populations in Asia during the Holocene (past 10,000 years) (Gupta et al., 2003; Gupta, 2004).

Across the Asian region, the effects of the monsoon are preserved in numerous proxies that include tree rings, soils, ice, lake deposits, peat deposits, cave deposits and marine sediments. Paleoproxies provide evidence of slow changes in the monsoon related to solar insolation, and evidence of abrupt, multi-decadal to millennial scale events throughout the Quaternary and the Holocene.

Quaternary changes

As the climate entered the glacial-interglacial mode during the Quaternary, the Indian monsoon system also underwent parallel changes (e.g., Schulz et al., 1998; Leuschner and Sirocko, 2003). For instance, the intervals of cold spells in the North Atlantic have been found to be aligned with intervals of weak summer monsoon (e.g., Schulz et al., 1998), during which time the winter monsoon strengthened (Fontugne and Duplessy, 1986). The summer monsoon oscillated with millennial-scale variability (the Dansgaard-Oeschger (D-O) and Heinrich events), concentrated at periodicities of ~1,100, 1,450, 1,750 and 2,300 yr during the last glacial (Naidu and Malmgren, 1995; Sirocko et al., 1996). This pattern is almost similar to that of changes in the Greenland ice cores (Schulz et al., 1998; Leuschner and Sirocko, 2003) (also Figure M40).

Despite numerous assertions, the origins of millennial-scale (sub-Milankovich or sub-orbital scale) abrupt changes in the

monsoon remain elusive. Conceptual and numerical models indicate that these climate changes could originate in the tropics (e.g., Hoerling et al., 2001) or in the North Atlantic (Bond et al., 2001). Changes in tropical sea surface temperatures over the Indian and Pacific Oceans are capable of producing changes in the North Atlantic Oscillation in coupled climate model simulations, resulting in warmer temperatures associated with the positive phase of the North Atlantic Oscillation (Hoerling et al., 2001). Other changes linked to the hydrological cycle, such as changes in the quantity of water vapor in the atmosphere, or vegetation-driven greenhouse gases (Stott et al., 2002), could produce a cooling effect that is amplified at high latitudes. Alternately, the North Atlantic could drive the observed changes in the tropics (Bond et al., 2001).

Holocene variability

Repeated occurrences of millennial-scale weak and strong phases of the Indian summer monsoon characterize the Holocene record (Figure M41). The summer monsoon was stronger in the early Holocene, which is evident in the enormous Ganges-Brahmaputra sediment discharge (Goodbred and Kuehl, 2000), rapid speleothem growth reported in Oman (Burns et al., 2001) and the dominance of conifers and broad-leaved trees in the Central Higher Himalayas (Phadtare, 2000). During the period between ~10,400 and 5,500 cal yr BP, Northern Hemisphere temperatures peaked and the Indian, Southeast Asian and African monsoons reached their maximum – the so-called “Holocene Climatic Optimum.”

The early Holocene monsoon maximum was interrupted by an abrupt cooling peak ~8,200 cal yr BP. (Alley et al., 1997), during which time the summer monsoon over the Indian subcontinent and tropical Africa weakened (Gasse, 2000). Successive shifts towards drier conditions in northern Africa and Asia intensified after ~5,500 cal yr BP. (Overpeck et al., 1996; Gasse, 2000), which contributed to the termination of ancient civilizations in the region. Sustained drought due to aridification led to societal collapse of the Egyptian and Mesopotamian civilizations at around 4,200 cal yr BP. (Weiss et al., 1993; Cullen et al., 2000). The evaporation dropped during the arid phase in India (Sharma et al., 2004), and the Indus Valley civilization transformed from an organized urban phase to a post-urban phase of smaller settlements with southward migration of the population (Allchin and Allchin, 1997; Staubwasser et al., 2003; Gupta, 2004).

The summer monsoon was weakest from ~2,500 to 1,500 cal yr BP. in the late Holocene (Anderson et al., 2002; Gupta et al., 2003). During the Medieval Warm Period (AD. 900–1400), the summer monsoon strengthened (Gupta et al., 2003) whereas during the most recent climatic event, the Little Ice Age (AD. 1450–1850), there was a drastic reduction in the intensity of the summer monsoon (Gupta et al., 2003).

Centennial to millennial-scale changes and forcing mechanisms

Previous studies have demonstrated that the interannual variability of the Indian summer monsoon is controlled by the Eurasian snow cover (Bamzai and Shukla, 1999) and the amplitude and period of El Niño Southern Oscillation (ENSO) (Krishna Kumar et al., 1999). Long term variability in the Indian summer monsoon on millennial scales may be attributed to solar forcing (Neff et al., 2001; Fleitmann et al., 2003) and

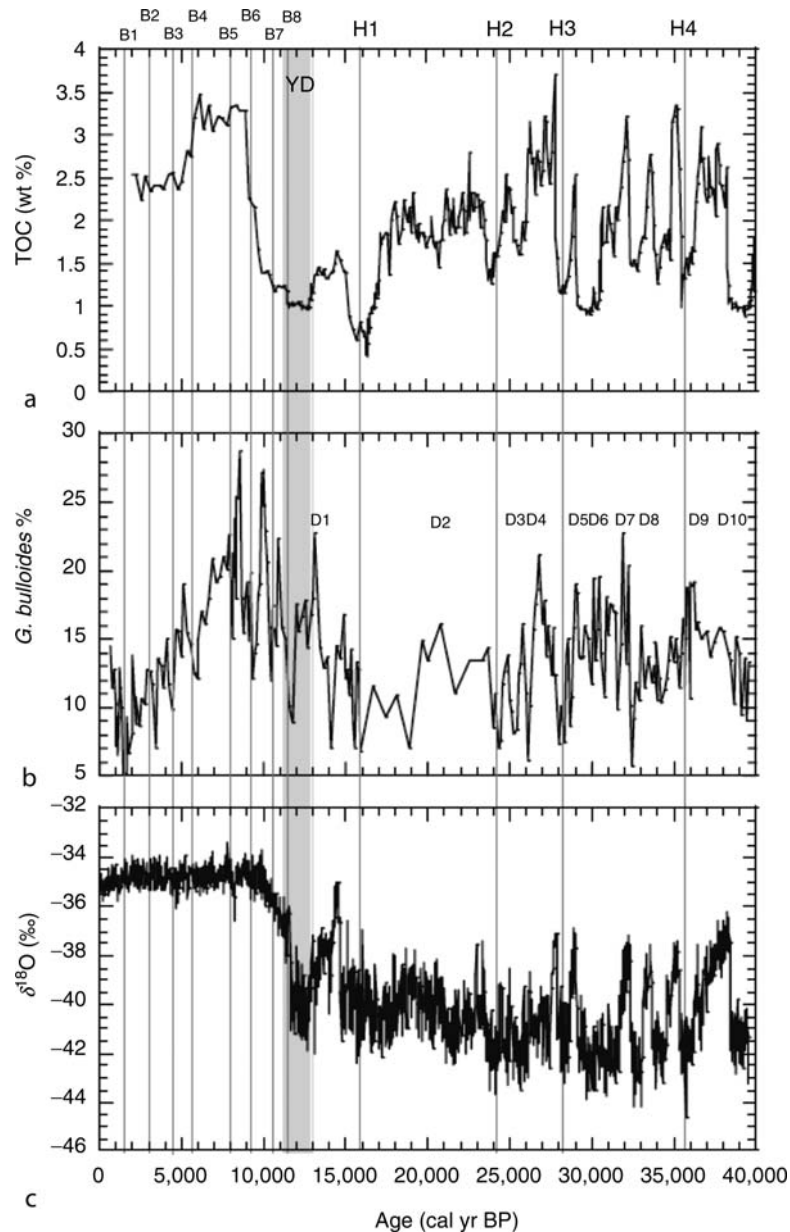


Figure M40 Summer monsoon proxy record for the late quaternary from the Arabian Sea. (a) Marine total organic carbon (TOC) record of SO90-111KL off Pakistan, northeastern Arabian Sea (Schulz et al., 1998); (b) *G. bulloides* percentages in ODP Hole 723A; (c) GISP2 $\delta^{18}\text{O}$ record (Grootes et al., 1993). B1-12: Bond events; H1-14: Heinrich events; D1-10: D-O events.

glacial interglacial boundary conditions (Burns et al., 2001). Major monsoon fluctuations on decadal to centennial scales during the Holocene have been attributed to changes in surface boundary conditions (Overpeck et al., 1996) and the North Atlantic climate due to changes in the North Atlantic Deep Water production (Gupta et al., 2003), and solar activity (Neff et al., 2001; Gupta et al., 2005).

The extent/duration of the snow and ice cover has been suggested as a cause of monsoon variability due to the albedo feedback of snow and ice-fields (Shukla, 1987). Increased albedo of

snow delays the seasonal heating cycle over Asia and thus delays and weakens the summer monsoon. Previous workers have also suggested that fluctuations in the monsoon intensity may be forced by variations in the tropical land-surface boundary conditions (Gasse and van Campo, 1994). Increased summer monsoon strength may lead to denser vegetation cover in Central Asia that reduces surface albedo of the region, increasing the land-sea thermal contrast and thus the summer monsoon strength.

Stuiver and Braziunas (1993) suggested that solar variability could be an important factor affecting climate variation during

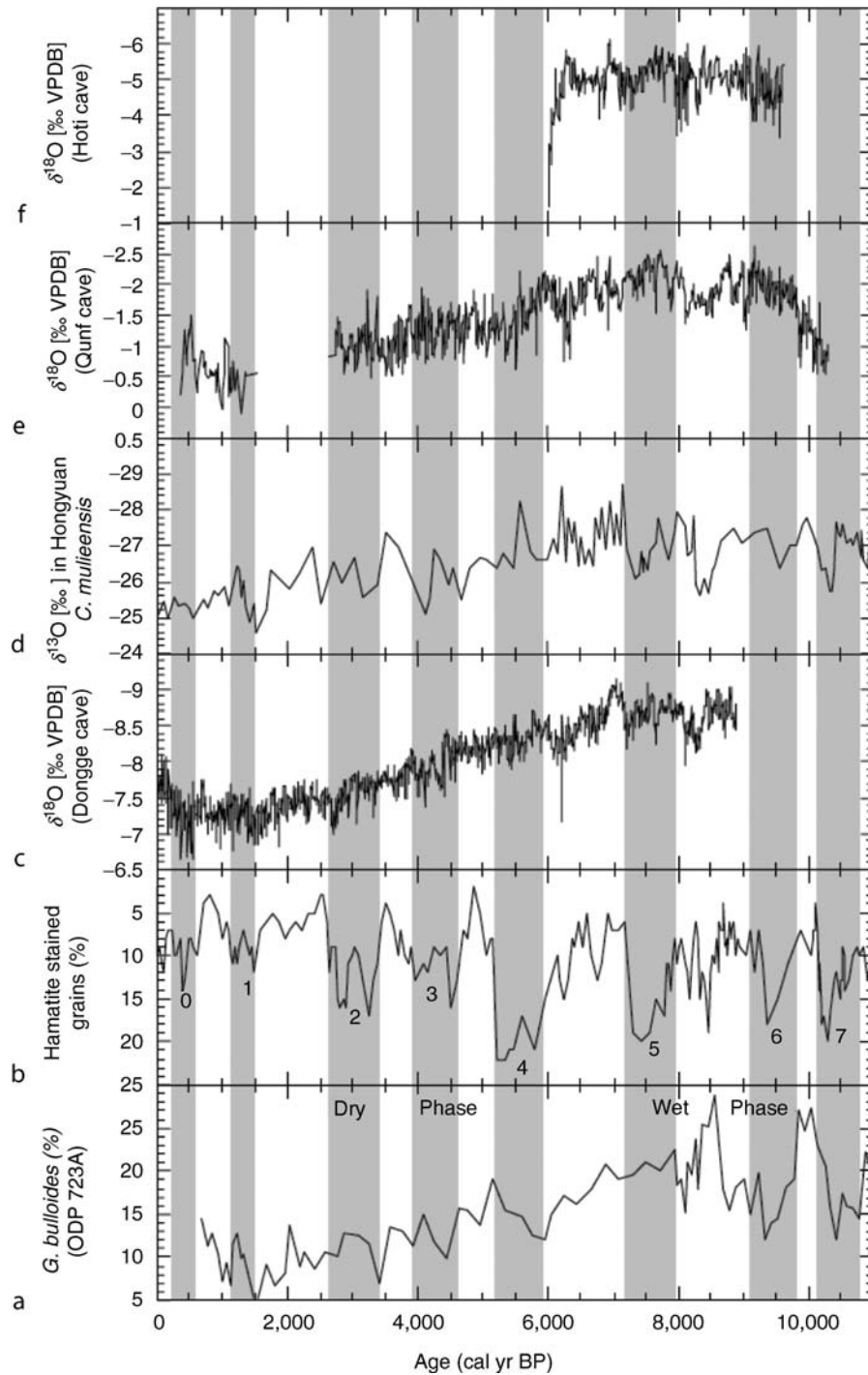


Figure M41 Visual correlation between proxy records. (a) *G. bulloides* percent from ODP Hole 723A, Arabian Sea (Gupta et al., 2003); (b) hematite % in core MC52 in the North Atlantic (Bond, et al., 2001); (c) oxygen isotope record from Dongge Cave, southern China (Wang et al., 2005); (d) Hongyuan peat deposit (Hong et al., 2003), (e) Qunf Cave $\delta^{18}\text{O}$ (Fleitmann et al., 2003), and (f) Hoti Cave $\delta^{18}\text{O}$ (Neff et al., 2001). Grey bars highlight the Bond events 0–7 (Bond, et al., 2001).

the Holocene on the basis of analysis of ^{14}C records from tree rings. The production rates of cosmogenic nuclides (^{14}C and ^{10}Be) that reflect changes in solar activity appear to be closely correlated to Bond Cycles (Bond et al., 2001). Although the

exact process by which global climate and solar forcing may be linked is not clearly understood, variations in ultraviolet radiation and cosmic ray flux may trigger abrupt climate changes by altering the heat budget of the stratosphere

(van Geel et al., 1999) and changing the atmosphere's optical parameters and radiation balance (Kodera, 2004). The summer monsoon intensity has been positively related to changes in solar insolation not only at the Milankovitch scale (Clemens et al., 1991; Leuschner and Sirocko, 2003), but also at decadal and centennial scales, as documented by various recent studies (Wang et al., 1999; Neff et al., 2001; Gupta et al., 2005). For example, Gupta et al. (2005) observed a relation between intervals of low sunspot activity and low intensity of the summer monsoon during the Holocene.

Solar variability may lead to changes in the circulation pattern of the atmosphere and may amplify the variability of the oceanic circulation. Model results have explained the mechanism of the dynamic response of atmospheres to solar forcing (Shindell et al., 2001). A recent study from the Arabian Sea suggests that even small changes in solar output can cause pronounced changes in the tropical climate, emphasizing the importance of a sun-monsoon link (Gupta et al., 2005).

Conclusions

Summer monsoon variability has important implications on the human population of the Asian-African region as the summer monsoon winds bring rainfall to most parts of the region, thus enhancing agricultural productivity. During the early Holocene, when the summer monsoon intensity was high, several Asian rivers were in their full vigor, and plants and animals were domesticated in the Indian subcontinent along the banks of the River Indus and its tributaries. However, prolonged droughts after the beginning of the arid phase (~5,000 cal yr BP) in the Indian subcontinent led to population dislocation, widespread migration, and state collapse of the Harappan Civilization. Some people resorted to modifying their dwelling environments by developing new strategies to optimize the utility of available water rather than migrating to safer places. It appears that the hydrological changes in South Asia had the greatest effect on human settlements, as opposed to the theory that temperature changes controlled the migration of the population. Intervals of weak summer monsoon and cold spells in the North Atlantic coincided with low sunspot activity during the Holocene, indicating that the response of both the tropics and high latitudes to solar variability was direct. The monsoon could be sensitive to relatively small changes in solar forcing. The sun-monsoon link can be explained by a direct solar influence on the Intertropical Convergence Zone that controls monsoonal precipitation. It can thus be concluded that solar variability plays an important role in driving multidecadal to millennial-scale changes in monsoon climate.

Anil K. Gupta

Bibliography

- Allchin, B., and Allchin, R., 1997. *Origins of a Civilization. The Prehistoric and Early Archaeology of South Asia*. New Delhi: Penguin Books India, 287pp.
- Alley, R.B., Mayewski, P.A., Sowers, T., Stuiver, M., Taylor, K.C., and Clark, P.U., 1997. Holocene climatic instability: A prominent, widespread event 8,200 years ago. *Geology*, **25**, 483–486.
- Anderson, D.M., Overpeck J.T., and Gupta, A.K., 2002. Increase in the Asian Southwest monsoon during the past four centuries. *Science*, **297**, 596–599.
- Bamzai, A.S., and Shukla, J., 1999. Relation between Eurasian snow cover, snow depth, and the Indian summer monsoon: An observational study. *J. Climatol.*, **12**, 3117–3132.

- Bond, G., Kromer, B., Beer, J., Muscheler, R., Evans, M.N., Showers, W., Hoffman, S., Lotti-Bond, R., Hajdas, I., and Bonani, G., 2001. Persistent solar influence on North Atlantic climate during the Holocene. *Science*, **294**, 2130–2136.
- Burns, S.J., Fleitmann, D., Matter, A., Neff, U., and Mangini, A., 2001. Speleothem evidence from Oman for continental pluvial events during interglacial periods. *Geology*, **29**, 623–626.
- Clemens, S., Prell, W., Murray, D., Schimmield, G., and Weedon, G., 1991. Forcing mechanisms of the Indian Ocean monsoon. *Nature*, **353**, 720–725.
- Cullen, H.M., deMenocal, P.B., Hemming, S., Hemming, G., Brown, F.H., Guilderson, T., and Sirocko, F., 2000. Climate change and the collapse of the Akkadian empire: Evidence from the deep sea. *Geology*, **28**, 379–382.
- Fleitmann, D., Burns, S.J., Mudelsee, M., Neff, U., Kramers, J., Mangini, A., and Matter, A., 2003. Holocene forcing of the Indian monsoon recorded in a stalagmite from Southern Oman. *Science*, **300**, 1737–1739.
- Fontugne, M., and Duplessy, J.C., 1986. Variations of the monsoon regime during the Upper Quaternary: Evidence from carbon isotopic record of organic matter in North Indian Ocean sediment cores. *Palaeoogeogr. Palaeoecol.*, **56**, 69–88.
- Gasse, F., 2000. Hydrological changes in the African tropics since the Last Glacial Maximum. *Quaternary Sci. Rev.*, **19**, 189–211.
- Gasse, F., and Van Campo, E., 1994. Abrupt post-glacial climate events in West Asia and North Africa monsoon domains. *Earth Planet. Sci. Lett.*, **126**, 435–456.
- Goodbred, S.L., and Kuehl, S.A., 2000. Enormous Ganges-Brahmaputra sediment discharge during strengthened early Holocene monsoon. *Geology*, **28**, 1083–1086.
- Grootes, P.M., Stuiver, M., White, J.M.C., Johnsen, S., Jouzel, J., 1993. Comparison of oxygen isotope records from the GISP2 and GRIP Greenland ice cores. *Nature*, **366**, 552–554.
- Gupta, A.K., 2004. Origin of agriculture and domestication of plants and animals linked to early Holocene climate amelioration. *Curr. Sci.*, **87**, 54–59.
- Gupta, A.K., Anderson, D.M., and Overpeck J.T., 2003. Abrupt changes in the Asian southwest monsoon during the Holocene and their links to the North Atlantic Ocean. *Nature*, **421**, 354–356.
- Gupta, A.K., Singh, R.K., Joseph, S., and Thomas, E., 2004. Indian Ocean high-productivity event (10–8 Ma): Linked to global cooling or to the initiation of the Indian monsoons? *Geology*, **32**, 753–756.
- Gupta, A.K., Das, M., and Anderson, D.M., 2005. Solar influence on the Indian summer monsoon during the Holocene. *Geophys. Res. Lett.*, **32**, L17703 (doi: 10.1029/2005GL022685).
- Hoerling, M.P., Hurrell, J.W., and Xu, T., 2001. Tropical origins for Recent North Atlantic climate change. *Science*, **292**, 90–92.
- Hong, Y.T., Hong, B., Lin, Q.H., Zhu, Y.X., Shibata, Y., Hirota, M., Uchida, M., Leng, X.T., Jiang, H.B., Xu, H., Wang, H., and Yi, L., 2003. Correlation between Indian Ocean summer monsoon and North Atlantic climate during the Holocene. *Earth Planet. Sci. Lett.*, **211**, 371–380.
- Kodera, K., 2004. Solar influence on the Indian Ocean monsoon through dynamical processes. *Geophys. Res. Lett.*, **31**, L24209, 1–4.
- Krishna Kumar, K., Kleeman, R., Cane, M.A., and Rajagopalan, B., 1999. Epochal changes in Indian Monsoon – ENSO Precursors. *Geophys. Res. Lett.*, **26**, 75–78.
- Kudrass, H.R., Hofmann, A., Doose, H., Emeis, K., and Erlenkeuser, H., 2001. Modulation and amplification of climatic changes in the Northern Hemisphere by the Indian summer monsoon during the past 80 k.y. *Geology*, **29**, 63–66.
- Leuschner, D.C., and Sirocko, F., 2003. Orbital insolation forcing of the Indian monsoon – A motor for global climate change. *Paleogeogr. Paleoclimatol. Paleoecol.*, **197**, 83–95.
- Naidu, P.D., and Malmgren, B.A., 1995. Do benthic foraminifer records represent a productivity index in oxygen minimum zone areas? An evaluation from the Oman Margin, Arabian Sea. *Mar. Micropaleontol.*, **26**, 49–55.
- Neff, U., Burns, S.J., Mangini, A., Mudelsee, M., Fleitmann, D., and Matter, A., 2001. Strong coherence between solar variability and the monsoon in Oman between 9 and 6 kyr ago. *Nature*, **411**, 290–293.
- Overpeck, J., Anderson, D., Trumbore, S., and Prell, W., 1996. The southwest Indian Monsoon over the last 18,000 years. *Clim. Dynam.*, **12**, 213–225.

- Phadtare, N.R., 2000. Sharp decrease in summer monsoon strength 4,000–3,500 cal yr B.P. in the Central Higher Himalaya of India based on pollen evidence from Alpine peat. *Quaternary Res.*, **53**, 122–129.
- Schulz, H., von Rad, U., and Erlenkuser, H., 1998. Correlations between Arabian Sea and Greenland climate oscillations of the past 110,000 years. *Nature*, **393**, 54–57.
- Sharma, S., Joachimski, M., Sharma, M., Tobschall, H.J., Singh, I.B., Sharma, C., Chauhan, M.S., and Morgenroth, G., 2004. Late glacial and Holocene environmental changes in Ganga plain, Northern India. *Quaternary Sci. Rev.*, **23**, 145–159.
- Shindell, D.T., Schmidt, G.A., Mann, M.E., Rind, D., and Waple, A., 2001. Solar forcing of regional climate change during the Maunder Minimum. *Science*, **294**, 2149–2152.
- Shukla, J., 1987. Interannual variability of monsoons. In Fein, J.S., and Stephens, P.L. (eds.), *Monsoons*. New York: Wiley, pp. 399–463.
- Sirocko, F., Garbe-Schönberg, D., McIntyre, A., and Molino, B., 1996. Teleconnections between the subtropical monsoons and high-latitude climates during the last deglaciation. *Science*, **272**, 526–529.
- Staubwasser, M., Sirocko, F., Grootes, P.M., and Segl, M., 2003. Climate change at the 4.2 ka B.P. termination of the Indus Valley civilization and Holocene south Asian monsoon variability. *Geophys. Res. Lett.*, **30**, 1425 (doi:10.1029/2002GL016822).
- Stott, L.W., Poulson, C., Lund, S., and Thunell, R., 2002. Super ENSO and global climate oscillations at millennial timescales. *Science*, **297**, 222–226.
- Stuiver, M., and Braziunas, T.F., 1993. Sun, ocean climate and atmospheric ¹⁴CO₂: An evaluation of casual and spectral relationships. *Holocene*, **3**, 289–305.
- van Geel, B., Raspopov, O.M., Renssen, H., van der Plicht, J., Dergachev, V.A., and Meijer, H.A.J., 1999. The role of solar forcing upon climate. *Quaternary Sci. Rev.*, **18**, 331–338.
- Wang, L., Sarnthein, M., Erlenkuser, H., Grimalt, J., Grootes, P., Heilig, S., Ivanova, E., Kienast, M., Pelejero, C., and Pflaumann, U., 1999. East Asian monsoon climate during the Late Pleistocene: High resolution sediment records from the South China Sea. *Mar. Geol.*, **156**, 245–284.
- Wang, Y., Cheng, H., Edwards, R.L., He, Y., Kong, X., An, Z., Wu, J., Kelly, M.J., Dykoski, C.A., and Li, X., 2005. The Holocene Asian monsoon: Links to solar changes and North Atlantic climate. *Science*, **308**, 854–857.
- Weiss, H., Courty, M.-A., Wetterstrom, W., Guichard, F., Senior, L., Meadow, R., and Curnow, A., 1993. The genesis and collapse of third millennium north Mesopotamian civilization. *Science*, **261**, 995–1004.

Cross-references

[Ancient Cultures and Climate Change](#)
[Dansgaard-Oeschger Cycles](#)
[Deltaic Sediments, Climate Records](#)
[Heinrich Events](#)
[Hypsithermal](#)
[Millennial Climate Variability](#)
[Monsoons and Monsoons Climate in *Encyclopedia of World Climatology*](#)
[Monsoons, Pre-Quaternary](#)
[North Atlantic Oscillation \(NAO\) Records](#)
[Paleo-El Niño-Southern Oscillation \(ENSO\) Records](#)
[Sun-Climate Connections](#)

MORAINES

A moraine is a glacial landform created by the deposition or deformation of sediment by glacier ice. Many different types of moraine exist, reflecting the many different processes by which glaciers deposit and deform sediment and the many locations and environments within the glacier system where

deposition can occur. Moraines are composed of till, which is also highly variable, as its characteristics depend on the characteristics of the debris supplied by the glacier as well as on the processes and environment of glacial deposition.

The morphology and sedimentology of moraines can be used to reconstruct the characteristics of former glaciers. Their distribution reflects the geography of former glaciers and glacial process environments. Sediment characteristics reflect the source location of the debris: supraglacial debris is characteristically angular, while basally derived debris is typically faceted, subrounded and striated. Structures within moraines can reveal seasonal and long term variations in processes of sedimentation.

Moraines are classified both genetically according to the process by which they are created and geographically according to their position within the glacier system. The principal processes by which moraines are created are the release of debris from ice by meltout and the deformation of proglacial or subglacial sediments by ice motion. Supraglacial moraines include lateral moraines, medial moraines and inner moraines. Subglacial moraines occur parallel or perpendicular to ice flow or in irregular patterns. Ice marginal moraines occur around the edges of glaciers and are defined by their position as either lateral or frontal moraines. Moraines marking the maximum extent of a glacial advance are referred to as terminal moraines. Moraines deposited at successive positions of the margin during a period of progressive retreat are recessional moraines. Marginal moraines at existing glaciers are typically ridges of sediment resting partially on the edge of the glacier. Upon deglaciation, ice-cored moraines lose their ice support and therefore tend to shrink in size and may become structurally unstable. Marginal moraines may be several tens of meters in height, tens or hundreds of meters across, and may stretch for hundreds of kilometers around the margins of large ice sheets.

Moraines provide long-term storage within the glacier sediment transfer system, and a supply of debris to the proglacial zone. Sediment flux within glaciated basins is very sensitive to the position of glaciers relative to their moraines. When glaciers lie behind marginal moraines the bulk of sediment produced at the margin can go into storage in the moraine belt and not reach the proglacial region. When glaciers have no marginal moraines, sediment passes directly into the proglacial system. Moraines can also focus meltwater discharge, localizing fluvial processes and causing moraine-dammed lakes. These lakes are potentially unstable and pose a serious threat of catastrophic flooding. Bennett and Glasser (1996) and Benn and Evans (1998) provide a useful review of this topic.

Peter G. Knight

Bibliography

- Benn, D.I., and Evans, D.J.A., 1998. *Glaciers and Glaciation*. London, UK: Arnold, 734pp.
- Bennett, M.R., and Glasser, N.F., 1996. *Glacial Geology*. Chichester, UK: Wiley, 364pp.

Cross-references

[Glacial Geomorphology](#)
[Glacial Sediments](#)
[Tills & Tillites](#)

MOUNTAIN GLACIERS

Mountain glaciers are constrained by the topography of the underlying bedrock. They can assume a wide variety of forms such as cirque glaciers and valley glaciers, which generally have unidirectional flow, and ice caps, which usually sit atop peaks and flow radially from central summit locations. Often, ice caps contain outlet glaciers at their bases. Mountain glaciers occupy the upper altitudes of many ranges on all the continents except Australia (although they also occur in New Zealand and New Guinea), and are most extensive on the Tibetan Plateau, in Southern Alaska, and in the South American Andes. In fact, 70% of all the world's tropical mountain glaciers are located in the Peruvian Andes. Mountain glaciers around the Gulf of Alaska cover an area of 32,400 square miles, about 13% of the world's ice coverage, and include some of the largest glaciers outside the polar regions. In general, the closer to the equator a glacier is located, the higher the elevation, since the 0°C isotherm (temperature at which ice ablates) increases in altitude with decreasing latitude. Thus, Alaskan and high Canadian mountain glaciers currently exist at altitudes as low as 3,000 meters above sea level (m a.s.l.), while some mountain glaciers near the equator, such as those on Huascarán in Peru (9° S) and Kilimanjaro in Tanzania (3° S), can only survive at altitudes greater than 5,500 m a.s.l. In the tropics, these glaciers are vital for the local populations since they are often important sources of drinking water and hydroelectric power.

Tropical mountain glaciers often occur in regions that are affected by strong seasonal variations in precipitation (for example, monsoon environments), thus wet and dry seasons are recorded as easily discernable layers. Because these glaciers are relatively small (compared with the polar ice sheets) and lie close to the 0°C isotherm, they can respond quickly to variations in temperature and effective moisture, and thus serve as reliable "barometers" of climate change. For these reasons, in the last 20 years mountain glaciers, particularly ice caps, have become valuable sources of information about past climate change and thus have placed the current global climate change in perspective. The length of the climate record contained in a mountain glacier is constrained primarily by two things: the net accumulation of snow each year, and the temperature of the

glacier at its base. A glacier that contains a climate record that covers several millennia often (but not always) occurs in regions where the annual snowfall is relatively low (less than a meter per year), but more importantly the temperatures are cold enough that the base of the ice is frozen to the bedrock. This prevents the removal of annual layers from the bottom, which is very important since ice is compressed during burial, and more annual layers are contained in smaller increments with depth. Mountain glaciers in such environments can be found in the highest altitudes of the Andes Mountains, the Tibetan Plateau, the Alaskan and Canadian Arctic region, and of course in the mountain ranges in Antarctica and Greenland. Temperate glaciers, in which some of the ice (usually at the base) is above the pressure melting point, usually contain shorter records of climatic and environmental variation, and these occur at lower altitudes and latitudes.

The clearest evidence for the current major climate warming comes from the tropical glaciers, recorded in both the ice core records and in the drastic and accelerating retreats of both total area and total ice volume. The recent warming trend has contributed greatly to the accelerating rates of mountain glacier retreat, especially in the climatically stable tropics where the average intraseasonal temperature change is usually no greater than 1–2°C. For example, the Qori Kalis Glacier in Peru now retreats on average over the last 15 years more than 60 meters per year, more than 10 times faster than during the first 15 years of measurement starting in 1963. Similarly, the ice on Mount Kilimanjaro, Africa, which covered ~4.3 square miles in 1912, only covers 0.94 square mile today. If the current rate of retreat continues, the perennial ice on Kilimanjaro will disappear within the next 15–20 years, the first time in the past 11,000 years that Kilimanjaro will be devoid of ice (Thompson et al., 2002). The documentation of this can be seen in the two photos in Figure M42 taken in 1912 and in 2000.

Dramatic mountain glacier retreat is also observed at high latitudes. The glaciers in southern Alaska are experiencing very high rates of precipitation and runoff, up to 400 cm yr⁻¹. Recent work suggests that melting and calving of Alaskan glaciers make up about one-half of the total global glacial contribution to sea level rise (Arendt et al., 2002). However, while the glaciers of Alaska are retreating due to marked warming in this region, some glaciers in Norway and Sweden which had been advancing because of the



Figure M42 The ice cap on Kilimanjaro in Tanzania (3° S) in 1912 (left) and in 2000 (right).

more northerly trajectory of storms that bring higher snowfall have since 1999 have also begun to retreat as the temperature rise has started to over shadow the increase in winter snowfall.

The rapid retreat of the world's mountains glaciers causes grave concern for three reasons. First, they are the world's "water towers," and their loss threatens water resources necessary for hydroelectric production, crop irrigation, and municipal water supplies for many nations of the world. The ice fields constitute a "bank account" that was built up over thousands of years, and is drawn upon during dry times to feed and energize populations downstream. The current melting is cashing in on that rapidly dwindling bank account. Second, these ice fields contain paleoclimate histories that are unattainable elsewhere and, as the ice fields melt, the records preserved therein are lost forever. The records are needed to discern how climate has changed in the past in these sensitive regions and to assist in predicting future change. Finally, one of the important aspects of glacier retreat on a global scale is the potential contribution that it makes to sea-level rise.

Lonnie G. Thompson

Bibliography

- Arendt, A.A., Echelmeyer, K.A., Harrison, W.D., Lingle, C.S., and Valentine, V.B., 2002. Rapid wastage of Alaska glaciers and their contribution to rising sea level. *Science*, **297**, 382–386.
- Thompson, L.G., Mosley-Thompson, E., Davis, M.E., Henderson, K.A., Brecher, H.H., Zagorodnov, V.S., Mashiotta, T.A., Lin, P.N., Mikhalenko, V.N., Hardy, D.R., and Beer, J., 2002. Kilimanjaro ice core records: Evidence of Holocene climate change in tropical Africa. *Science*, **298**, 589–593.

Cross-references

Cirques
 Cryosphere
 Greenhouse (Warm) Climates
 Ice cores, Mountain Glaciers
 Sea Level Change, Post-Glacial

MOUNTAIN UPLIFT AND CLIMATE CHANGE

Fossil shells in 400 million year old limestone near the arid, 8.8 km high summit of Mount Everest provide clear evidence for large-scale uplift of the Himalaya. South of the range crest, the southern flank of the Himalaya descends to near sea level and receives several meters of rain from the southeastern monsoon each summer. To the north, the Tibetan Plateau rises to an average elevation of 5 km and experiences a semi-arid climate.

The spatial juxtaposition of these contrasting physiographic regions and their strikingly different climates raise two fundamental questions: how does mountain uplift affect climate and climate change; and to what extent does climate change affect the uplift of mountain belts? Everyday experience indicates that mountains affect weather and climate. Clouds gather around mountain summits, rainfall is commonly greater at higher elevations, and precipitation is typically reduced downwind of mountain ranges. The provocative contention that climate could affect the growth of mountain ranges (Molnar and England, 1990) has motivated recent research efforts to explore the potential interactions between

climate, erosion, and tectonics. Numerical models that link geodynamic deformation with climate and erosion predict that gradients in climate can drive analogous spatial gradients in erosion, which, in turn, can modulate where deformation occurs within an orogen (Willett, 1999; Beaumont et al., 2001). Such reasoning suggests that the direction from which prevailing winds bring moisture into a mountain belt could ultimately determine the patterns and rates of strain and rock uplift within the orogen. Testing of these predictions has only recently begun, but synthesis of geodetic, geophysical, geological, climatic, and geomorphic data are beginning to provide insights on the nature, magnitude, and rates of the interactions that affect the Earth's surface and its deformation.

Initially, the impact of mountain uplift on climate and climate change is described. Subsequently the potential effects of climate on mountain uplift and evidence for such interactions are discussed.

Mountain uplift and climate

Orographic precipitation

Orographic precipitation refers to the impact that topography exerts on the distribution of precipitation. In the simplest form, mountain ranges cause enhanced rainfall on the upwind side of a range and generate decreased rainfall on the downwind flank. As air masses move across a landscape, mountains present topographic barriers that force diversion of the air mass through some combination of flow over the crest of the mountains and flow around its flanks. Two competing characteristics of air masses determine precipitation where moisture-laden air encounters mountainous topography (Roe et al., 2002). First, if relative humidity is constant in a static column of air then the moisture content decreases as temperature decreases with height (at a rate of $\sim 6.5^\circ\text{C km}^{-1}$). This lowered moisture content promotes decreasing precipitation at higher elevations (Figure M43). Second, as wind pushes moist air masses toward the flanks of mountains, the air is forced upslope, causing a convergence of moisture in the air column. The cooling that occurs as the air is lifted upslope increases the relative humidity. When combined with moisture convergence, the cooling leads to saturation and to rainfall of the moisture in excess of saturation (Roe et al., 2002). Hence, as air masses rise up the flanks of a mountain range, rainfall commonly increases (Figure M43). On the downwind side, as descending air masses warm adiabatically, their relative humidity drops and rainfall abruptly decreases, thereby creating a rain shadow.

Both the amount of moisture in an approaching air mass and the height of a given mountain range have finite limits. Two competing effects serve to determine the rainfall distribution. As more and more water is wrung out of the air due to orographic rainfall on upwind flanks of ranges, the reduced amount of remaining atmospheric moisture reduces the rainfall potential at higher elevations. In contrast, the steepening of slopes that characterizes the upper reaches of mountains (Brozovic et al., 1997) causes more rapid moisture convergence and tends to increase rainfall potential. The net result is that, for ranges of modest relief ($\sim 1\text{--}2$ km), rainfall tends to increase near the range crest, whereas for ranges with high relief (>3 km) rainfall can decrease on the upper parts of the windward flanks. The latter effect is well illustrated in the Himalaya, where the peak monsoonal precipitation of $4\text{--}5\text{ m yr}^{-1}$ occurs several kilometers below and >10 km to the south of the range crest (Figure M44). By 10 km north of the Himalayan crest, monsoonal rainfall has dropped to $<1\text{ m yr}^{-1}$, and at altitudes exceeding ~ 6.5 km, precipitation is negligible (Harper and Humphrey, 2003).

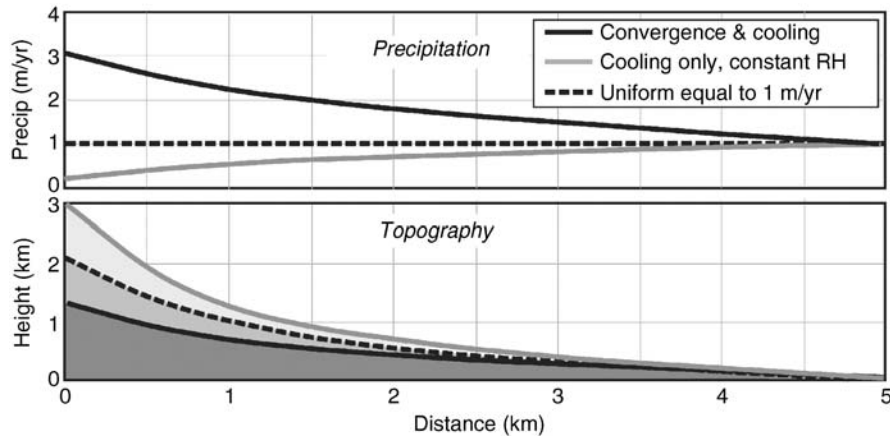


Figure M43 Orographic precipitation for a range experiencing rock-uplift rates of 2 mm yr^{-1} . (a) *Top*: Theoretical predictions of orographic precipitation with the range crest on the left of each panel. With increasing altitude (moving from right to left), air masses cool as they expand. If relative humidity (RH) is held constant, the air holds less moisture and produces less rainfall (“cooling only” curve *light gray line*). Wind blowing toward a mountain range causes vertical convergence of air masses and increases water content. Convergence and cooling increase RH, driving condensation and enhancing rainfall (the orographic effect *heavy, black line*). *Bottom*: Trends in rainfall with distance from the range crest affect equilibrium river profiles, such that river incision balances rock-uplift rates. With less rain toward the divide (cooling-only curve), the river channels are steeper and the height of the range crest is 50% greater than in the absence of orographic feedbacks, which tend to lower the range crest and channel gradients (*heavy black line*). Note the nearly 3-fold difference in ridge height between the “cooling-only” case and the “convergence and cooling” case. (Modified after Roe et al., 2002.)

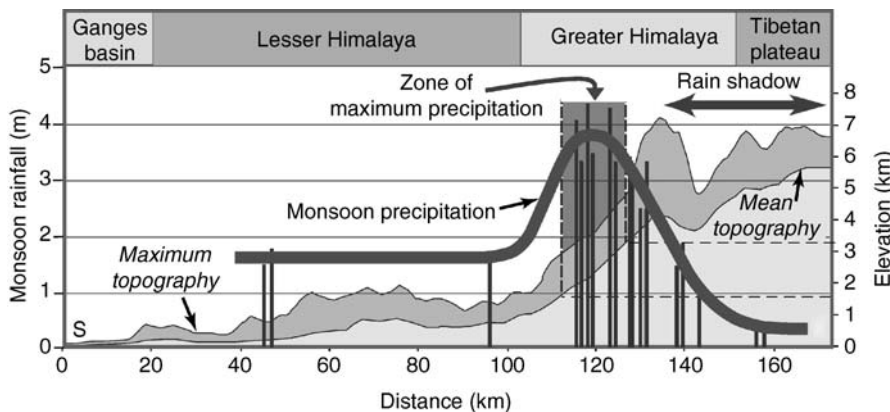


Figure M44 Example of orographic precipitation in the central Nepalese Himalaya. Orographic lifting caused by monsoonal storms from the Indian Ocean that impinge on the Himalaya enhances rainfall. The greatest rainfall occurs at $\sim 2,500 \text{ m}$ elevation, where the summertime maximum precipitation reaches $\sim 4 \text{ m yr}^{-1}$. Loss of moisture as the air masses cross the Himalaya creates a striking rain shadow to the north with only $\sim 10\%$ as much rain. (Modified from Burbank et al., 2003.)

As climate changes, the presence of mountains induces non-linear changes on orographic precipitation. For example, the typical average atmospheric cooling of $5\text{--}6^\circ\text{C}$ during glacial maxima dictates that air masses will, on average, hold less moisture. Such a reduction means that the total precipitation will be reduced overall and the zone of maximum rainfall may be moved farther from the range crest in ranges with high relief. As even less moisture creeps over the range crest, rain shadows can deepen. Although few reliable proxies exist for rainfall during glacial times, an observed steepening of regional glacial snowline gradients across high ranges like the Himalaya (Williams, 1983; Pratt et al., 2002; Burbank et al., 2003) implies an enhanced orographic effect on precipitation during glacial times.

Air mass trajectories

Mountain ranges represent physical barriers to air masses blown toward them. Two behaviors are commonly observed as air masses encounter topography: some air flows up and over the crest of the range, whereas some is diverted around the range margins. The balance between these two effects is determined by the height and lateral continuity of the range and by wind strength. Even when flowing over the mountains, much air flow is funneled through the lowest topography. Ranges with isolated high summits present less effective barriers than do more plateau-like ranges. Hence, volcanic arcs will cause less diversion than block uplifts. For example, both the Cascades of Washington and the Sierra Nevada of California are oriented nearly perpendicular to the prevailing storm tracks off the Pacific Ocean. Whereas isolated

volcanic peaks in the Cascades rise to elevations $>3\text{--}4$ km, many mountain passes lie below 2 km and much moisture funnels through these passes. The regional patterns of past glacial snowlines (a function primarily of precipitation and temperature) show that, similar to today, moisture was funneled up the major drainages during glacial climates (Figure M45). Although the Sierra Nevada also has summits rising to ~ 4 km, the passes along its crest are commonly >3 km in elevation, thereby creating a formidable barrier across the path of approaching storms and leading to diversion around the range's southern and northern ends. Similar to other ranges forming block-like barriers, the moisture that does penetrate the Sierra Nevada tends to be funneled along major river valleys (Burbank, 1991).

The impact of an individual range on regional climates can alter during climatic changes. As ice sheets accumulate at high latitudes during glacial times, the average position of the jet stream and the intertropical convergence zone migrates latitudinally. At the same time, storm trajectories also change with respect to ranges that could potentially block or divert them. As a consequence, the impact of mountainous topography on precipitation patterns will change coevally with major climatic variability, as storm tracks, total atmospheric moisture, and wind strength are altered.

Continentality and fringing ranges

As an air mass flows over ocean to land, it leaves its major source of evaporative moisture behind. Once over land, the normal extraction of moisture via rainfall commonly causes a progressive drying of the air mass, such that downwind regions will become increasingly dry, unless new moisture sources are added. Thus, farther inland on large land masses, continentality increases as the distance from major moisture sources grows.

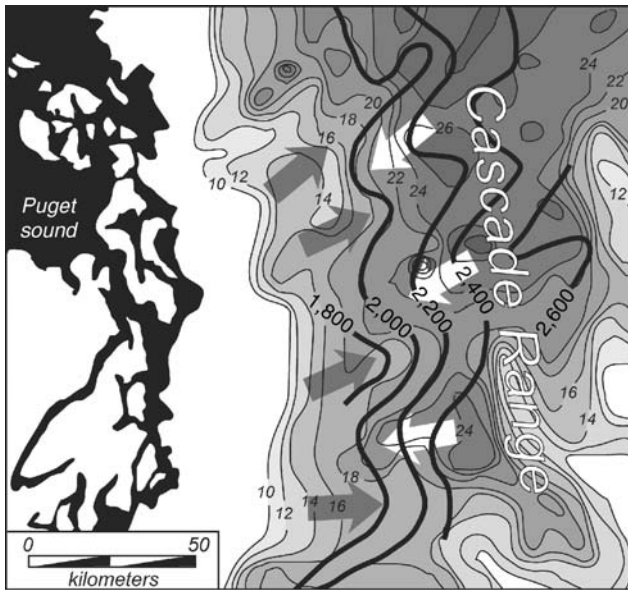


Figure M45 Pattern of glacier snow lines during the past glaciation as reconstructed from the height of cirques in the northern Cascade Range, Washington. The re-entrants (dark arrows) in the snowline elevations (heavy contours) correspond primarily with low topography along river drainages, whereas the salients (white arrows) correspond primarily with higher topography. River valleys funnel more moisture to the interior of the range, thereby lowering snowlines. (Modified after Porter, 1977.)

For example, central Asia's isolation from major moisture sources creates continental deserts in mid-latitude regions that normally experience temperate climates. Aridification of this region occurred at least 20 Ma ago (Guo et al., 2002) and was undoubtedly enhanced by the growth of the Himalaya that blocked northward moisture transport from the Indian Ocean.

The existence of fringing mountain ranges along the margins of continents can augment the magnitude of continentality. If the mountains are oriented across major storm trajectories, orography can efficiently extract moisture in the near-coastal region and create residual air masses that are even more depleted in moisture than they would be in the absence of coastal topography. Thus, north-south-oriented ranges like the Andes, Cascades, and Sierra Nevada have a larger impact on downwind continentality than do east-west-trending ranges like the Utiyas, European Alps, or Pyrenees that are oriented more parallel to prevalent storm trajectories. Even these storm-track-parallel ranges enhance continentality, however, because air masses diverted around their flanks travel a longer path and lose more moisture than they would in the absence of the range.

Plateau growth and monsoons

Summer monsoons, which can drop several meters of rainfall over 2–4 months, are one of the world's most dramatic climatic phenomena. The contrast in the heat capacity of water versus soils results in differential responses to seasonal changes in insolation. During summer months, terrestrial areas warm more rapidly than the oceans, causing lowered atmospheric pressure over the land as air masses warm, expand, and vertically ascend. The consequent lateral atmospheric flow from surrounding higher pressure zones over the oceans draws water vapor toward the continental interiors. Once over land, release of latent heat during precipitative condensation warms the surrounding air even more and creates a positive feedback by lowering atmospheric pressure over the land still further and enhancing the regional pressure gradient and resultant landward flow. Thus, differential heating and release of latent heat during rain storms can create a monsoon, an intensified summer precipitation cycle over continents.

Summer monsoons exist over northern Australia, the Amazon, and western Africa, but the Asian monsoon is the best known and typically the strongest. Much of the strength of the Asian monsoon derives from the presence of the Tibetan Plateau. The largest plateau on Earth, the Tibetan Plateau encompasses ~ 2.5 million km^2 , an area about one-third the size of the continental United States, and averages 5 km in elevation (Fielding et al., 1994). Although summertime temperatures in Tibet are cool by most human standards, Tibet is the warmest place on Earth at 5 km elevation. Because soils absorb, retain, and re-radiate heat much more effectively than does air, the Tibetan Plateau represents a hot island surrounded by an otherwise cool atmosphere at 5 km above sea level. This warmth drives the summertime low-pressure system over southern Asia and is the pump that primes and modulates the strength of the Asian monsoon.

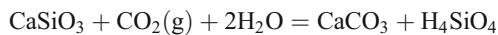
Numerical simulations reinforce this contention (Kutzbach et al., 1993), although definition of a specific altitudinal threshold or areal extent required to trigger a strong monsoon remains uncertain. Nonetheless, the causative linkage of a high and wide plateau to development of a strong Asian monsoon underpins interpretations that use geologic indicators of the onset of a strengthened monsoon as predictors of the timing of major

uplift of the Tibetan Plateau (Quade et al., 1989; Harrison et al., 1992; Molnar et al., 1993).

The growth of the Tibetan Plateau represents a clear case in which tectonically-driven surface uplift (i.e., an increase in mean elevation) has caused fundamental changes in regional climates. Moreover, the 5 km high topography of Tibet presents a physical barrier that impacts global patterns of atmospheric circulation and affects regional climates throughout the Northern Hemisphere (Kutzbach et al., 1993).

Active mountain building and climate change

The CO₂-weathering hypothesis suggests that weathering of silicate rocks can extract CO₂ from the atmosphere, thereby reducing the amount of greenhouse gases and causing global cooling (Raymo and Ruddiman, 1992). Such a reaction can be chemically expressed as:



in which calcium silicate combines with atmospheric CO₂ and creates calcium carbonate which is then precipitated and sequestered in oceans. Although drawdown of atmospheric carbon dioxide should happen all the time due to such a weathering process, the uplift of mountains is proposed to accelerate chemical weathering rates because rapid mechanical denudation in mountains will provide abundant fresh mineral surfaces for chemical attack. This theory, therefore, links orogenesis with changes in mineral weathering rates, greenhouse gases, and ultimately global temperature.

The growth of the Himalaya and secondarily of the Andes during the late Cenozoic (Raymo et al., 1988) has been cited as a potential trigger for enhanced rates of CO₂ drawdown and global cooling. These ranges are characterized by mechanical erosion rates averaging >1 mm yr⁻¹; rates far exceeding those at which rocks are converted to soils through chemical and mechanical weathering. The primary way in which these ranges sustain long-term erosion rates of this magnitude is via landslides involving bedrock, because soil-related processes are too slow (Burbank et al., 1996). Such landsliding persistently exposes fresh rock surfaces that are ideal sites for chemical weathering. Chemical weathering is enhanced by two additional features of the Himalaya and Andes. First, the tropical temperatures promote more rapid rates of chemical weathering than do cooler conditions at northern latitudes. Second, these ranges are sufficiently high to be glaciated. The “rock flour” that is produced by glacial grinding is perfect grist for chemical weathering because it commonly comprises tiny, unweathered rock particles with large surface area/mass ratios.

The drawdown of atmospheric CO₂ is counterbalanced by three feedbacks. First, more than 95% of the Earth’s surface is not experiencing mountain building. Erosion rates are low (commonly <0.01 mm yr⁻¹) in such areas, and chemical weathering also proceeds slowly even in the tropics, except in areas of higher relief. These areally extensive, low rates of atmospheric drawdown may balance the high rates of drawdown predicted for areas of rapid mountain building and erosion. Second, because erosion isostatically drives rock uplift, formerly buried carbon reservoirs can be exposed to erosion and returned to the atmosphere. Third, mountain building associated with subduction can lead to metamorphic degassing of carbon-rich rocks. These mechanisms serve to increase atmospheric CO₂ concentrations.

Impacts of climate and climate change on mountain uplift

Defining uplift

The term “uplift” should be defined in an appropriate context (e.g., Figure M46). The change of elevation at any point in a landscape (surface uplift at a point) is a function of the magnitude of erosion, deposition, and vertical movement of the underlying rock. Some coupling exists among these factors: erosion or deposition should induce a compensating isostatic response, such that ~5/6 (the ratio of crustal to mantle densities) of an instantaneous change in altitude due to erosion or deposition will be recovered over time. The vertical movement of rocks, whether in response to isostasy or tectonism, can be defined as “rock uplift” and should be measured in absolute terms with respect to a reference surface, such as the geoid or sea level. Whereas such measurements may be feasible at the coast, this formal reference frame is commonly lost inland. Nonetheless, relative amounts of rock uplift can be defined by comparing offset points that were once contiguous at the same altitude. The average change of all points on a surface serves to define “surface uplift” or the change in the mean elevation of an area (Figure M46). Although some geophysicists argue that the term surface uplift should be restricted to areas of a size (~10⁴ km²) capable of inducing a response to crustal loading (England and Molnar, 1990), changes of mean surface elevation of smaller areas can provide useful geomorphic and geologic insights (Medwedeff, 1992; Talling and Sowter, 1999).

Absolute field measurement of any form of uplift at geologic time scales (>10³ yr) is commonly difficult. The widespread availability of digital elevation models allows ready determination of modern surface elevations; a comparable reconstruction of ancient elevations could require many hundreds of points. Although the science of paleoaltimetry is improving (Sahagian and Maus, 1994; Forest et al., 1999), there are few reliable or precise measures of the previous altitude of the surface or rock beneath it. Even when the amount of erosion or deposition can be specified, the vertical movement of rocks in response to isostasy or to tectonic loading is hard to measure. Whereas coastal terraces provide a means to define rock-uplift (Lajoie, 1986), for most inland sites, relative displacements of surfaces or rocks are commonly studied with respect to a reference frame defined by an assumed earlier form, such as a river gradient (Thompson et al., 2002) or the surface of a former sedimentary basin (Burbank et al., 1999; Bullen et al., 2003).

What drives surface uplift of mountain ranges?

Four phenomena can commonly cause positive changes in mean elevation. Tectonic thickening of the crust will induce a change in the mean height equal to ~1/6 of the magnitude of thickening after the crust is compensated isostatically. The commonly observed low-density root beneath contractional ranges is at least partly responsible for elevated topography above it. Replacement of high-density mantle with lower density asthenosphere will drive a similar isostatic response, but in proportion to the density contrasts between them and the thickness of the replaced mantle. Dynamic support of topography can occur when the strength of the flexed crust induces surface uplift over a flexure. For example, underthrusting of old, thick, rigid crust can generate dynamic topography. In contrast to the previous two mechanisms, which cause surface uplift, dynamic support will create a range out of isostatic equilibrium. Finally, volcanism can cause surface uplift by two mechanisms. Heating of the crust lowers its density and makes it more buoyant, whereas addition of new volcanic material to the

surface or intrusion of plutons adds to the crustal mass and causes an isostatic response. Because crustal additions occur from point sources (vents) in volcanic systems, they generate more irregular, punctuated surface uplift than non-volcanic systems, because they create isolated high peaks or volcanic cones that may be widely separated.

Surface uplift of mountain peaks (positive elevation changes) will typically result from all of the processes described above. Because volcanoes add material to the Earth's surface, rock beneath will subside in response to new volcanic loads, such that only $\sim 1/6$ of any crustal thickening will be expressed as a long-term elevation change.

Erosion can also induce peak uplift. Consider the situation in which erosion is focused in only part of the landscape, such as the valley bottoms. The removal of mass by erosion will

cause a net thinning of the crust, and although the mean elevation will decrease, the crustal thinning induces isostatic uplift (rock uplift). If uneroded, the intervening peaks will rise by an amount equal to $\sim 5/6$ of the average amount of erosion (Molnar and England, 1990). Consequently, 1 km of erosion averaged across a region could cause the mean elevation to decrease by ~ 150 m, whereas uneroded peaks could uplift isostatically >800 m (Figure M47).

The erosional system

The primary means by which climate can affect tectonics is through the influence of climate on erosion. Isostasy requires that wherever erosion removes significantly more mass from an active orogen than elsewhere, differential rock uplift will occur preferentially beneath the more highly eroded area.

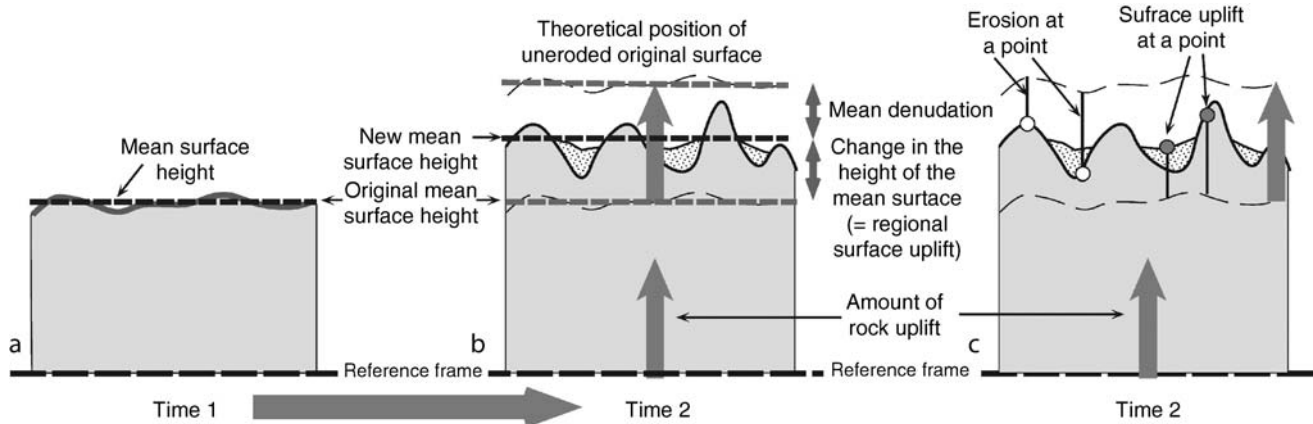


Figure M46 Definitions for aspects of "uplift." (a) Initial configuration depicting mean surface height. (b) Rock uplift (vertical arrows) represents the vertical motion of rock with respect to sea level or the geoid. "Regional surface uplift" is defined by changes in mean surface height (difference from "time 1" to "time 2"). The difference between the magnitude of rock uplift and the change in the mean surface height is the mean denudation. (c) "Surface uplift at a point" can depart from the mean surface uplift due to variations in erosion or deposition at specific sites in a landscape. (Modified after Burbank and Anderson, 2001.)

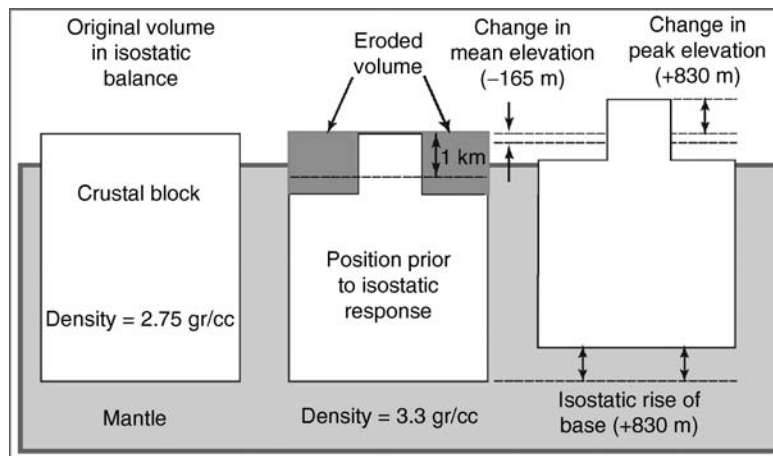


Figure M47 Isostatic responses to erosion. *Left:* An uneroded "crustal" block in isostatic balance with surrounding denser mantle; its upper surface floats above the surface of the denser material. *Center:* Square "valleys" 1.5 km deep remove mass across $2/3$ of the top of the crustal block (average erosion equals 1 km). Rebound is artificially restrained. *Right:* Following isostatic rebound, the mean elevation decreases by ~ 165 m, whereas the base of the block and the remaining part of its uneroded upper surface rebound ~ 830 m. The amount of rebound or "rock uplift" equals the average amount of erosion (1 km) times the ratio of the density of the crustal block ($\rho = 2.75 \text{ g cm}^{-3}$) to that of the mantle ($\rho = 3.3 \text{ g cm}^{-3}$).

Because differential rock uplift usually requires faulting, differential erosion can focus tectonic activity in regions where erosion is most rapid.

A linked climate-geomorphic system underlies this feedback. From a geomorphic framework, most mountain belts consist of networks of rivers and adjoining hillslopes (Figure M48). The rivers control the rate of lowering of base level within the mountains, whereas the hillslopes respond to base-level lowering and provide a flux of sediment to the rivers. Two classes of hillslope processes can be defined based on whether they involve primarily soil or bedrock. Soil erosion processes on hillslopes include rain splash, creep, bioturbation, and shallow (soil) landsliding. Because these occur primarily within soils, they cannot proceed at rates faster than soils are produced by weathering of bedrock. The best documented studies at present indicate that the conversion of rock to regolith or soil occurs at rates of $<0.5 \text{ mm yr}^{-1}$ (Heimsath et al., 1997). Thus, if hillslopes are eroding at rates slower than this, processes that move soils downslope may be sufficient to account for all hillslope sediment fluxes. As soon as rates climb above 1 mm yr^{-1} , bedrock landslides must begin to play an important role. For bedrock landslides to occur, a hillslope must be sufficiently steep to overcome the stabilizing forces resulting from cohesion (rock strength) and gravitational normal stresses on a potential failure plane. At equilibrium, slope angles should hover around that angle required for failure: the threshold slope angle. In many rapidly eroding terrains, hillsides are long and straight, with slope angles that are commonly clustered around $30^\circ\text{--}34^\circ$, independently of variations in erosion rates $>1 \text{ mm yr}^{-1}$. These characteristics are indicative of threshold slopes poised for failure (Figure M48). Any processes that decrease cohesion or normal stresses, and increase pore pressures or shear stresses, will tend to lead to bedrock landsliding. Thus, rock weathering, heavy rainfall, or seismic shaking will all tend to trigger landslides.

For ranges whose peaks rise above the regional snowline, glacial erosion becomes an important component of the geomorphic system (Figure M49). Glaciers that slide on their beds are very effective erosive agents, capable of eroding at rates exceeding 10 mm yr^{-1} (Hallet et al., 1996). Glacial erosion is commonly defined as a function of ice velocity (Humphrey and Raymond, 1994). Because velocity typically peaks near the glacial snowline, vertical erosion is considered to be maximized in the vicinity of the snowline (MacGregor et al., 2000). When coupled with enhanced vertical erosion, rapid headward erosion by glaciers causes a flattening of the slope of the long profile of glaciers (Brocklehurst and Whipple, 2002). Although glaciers are capable of overdeepening (scouring below the level of their toes), the rate of lowering of the entire glacial profile is ultimately regulated by the rate at which the rivers erode at the glacial terminus.

Mountains of sufficient height may have their upper reaches in a frozen zone that almost never rises above freezing. Here, glaciers are cold-based and frozen to their beds, freeze-thaw activity is minimal, and the primary means of erosion is through bedrock landslides (Figure M49). In such a setting, warm-based glaciers commonly occur at lower altitudes and cause both downward and headward erosion. Meanwhile, peaks within the frozen zone become higher and narrower. These steep-like summit regions episodically collapse via large-scale bedrock landslides.

Climatic impacts on the geomorphic system and mountain topography

During the repeated, large-scale Quaternary oscillations (Shackleton and Opdyke, 1976), changing temperature and precipitation regimes caused ice sheets and mountain glaciers to wax and wane. Snowlines generally were lowered 800–1,000 m in most temperate regions during maximum glacial times (Porter, 1989). This snowline shift displaced the predicted zone of maximum glacial erosion farther down the

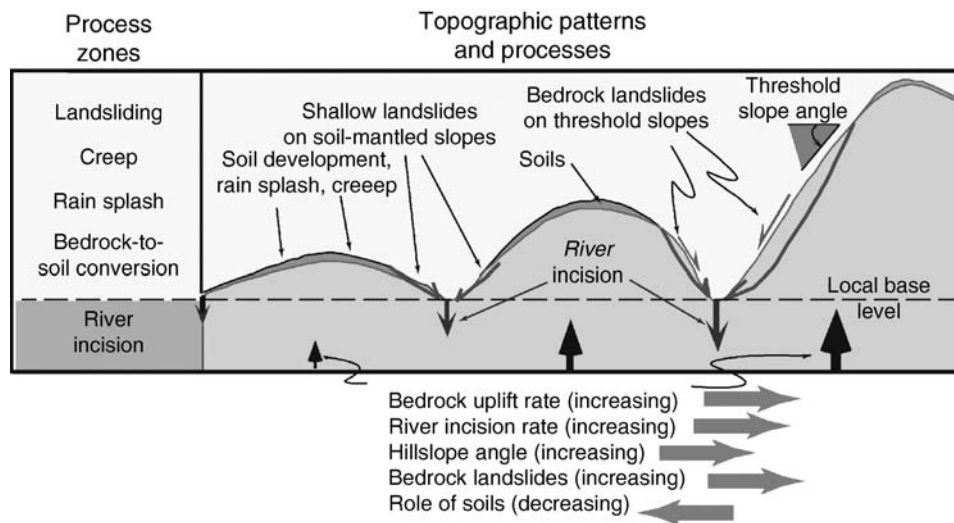


Figure M48 Hillslope and erosion processes in a steady-state, non-glaciated landscape. *Left panel:* Geomorphic process zones. River incision determines changes in local base level. Rates of rock-to-soil conversion limit the rate at which the landscape can erode (rain splash, creep, shallow landslides) in the absence of removal of unweathered bedrock. *Right panel:* Rates of relative rock-uplift increase from left to right. Assuming topographic steady-state, hillslope erosion and river incision match rock uplift rates. For slow uplift, soil processes (creep, rain splash) balance uplift rate. At higher uplift rates, shallow landslides rapidly strip soil from hillslopes. When relative rock-uplift rates exceed the rock-to-soil conversion rate, soil erosion balances uplift only if bedrock erosion, usually via landslides, also occurs. In most such landscapes, many hillslopes hover near the threshold angle for failure by landsliding. (Modified after Burbank, 2002.)

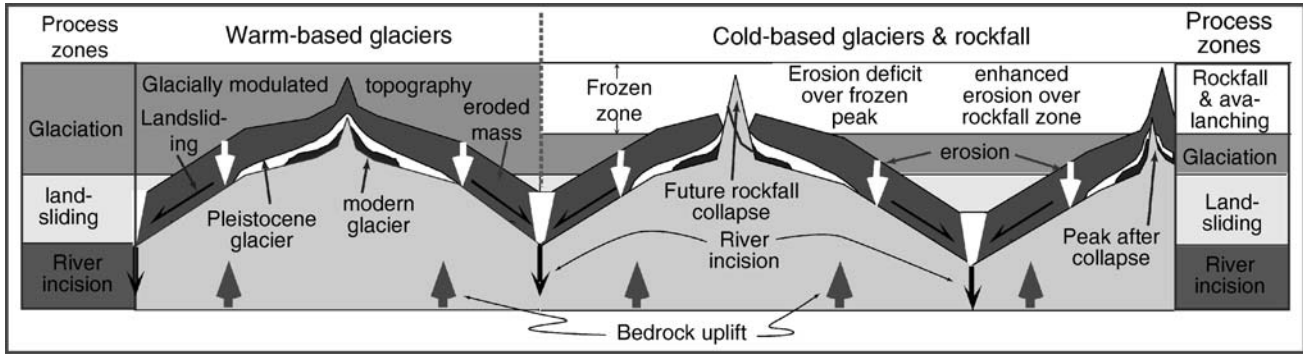


Figure M49 Erosion processes in steady-state, glaciated landscapes experiencing rapid relative rock uplift and erosion. Below the glacial limit, erosion (white downward arrows and dark gray region) via bedrock landsliding and river incision balance rock uplift (dark arrows along base). *Left panel:* Warm-based glaciers slide on their beds and erode bedrock, leading to a concentration of higher altitude topography near the glacial snowline. *Right panel:* Cold-based glaciers are frozen to their beds and, the absence of freeze-thaw cycles prevents erosion in the frozen zone. As warm-based glaciers continue to erode at lower altitudes, rock uplift steepens the summit regions, making them more unstable, and causing massive landslides. (Modified after Burbank, 2002.)

mountain flanks and was responsible for the low-gradient glacial troughs that exist downstream of modern glaciers. The vertical and lateral excavation of these troughs lowers base level and steepens adjacent valley walls, thereby promoting accelerated lowering of the ridges between glacial valleys. During glacial times, therefore, the average height of the glaciated parts of mountains should be lowered due to enhanced erosion of both valleys and ridges.

Changes in hydrology and sediment loads also affect fluvial erosion during climate changes. For any given climatic state, a river tends toward a graded condition, whereby its channel slope and width are adjusted to transport the sediment supplied to it from hillslopes. For a given discharge, steeper and narrower channels allow more sediment to be transported downstream. The longitudinal profiles of rivers typically show systematic downstream decreases in channel slope with increasing drainage area. The concavity (θ) of many river systems is defined by the relationship of channel slope (S) to drainage area (A): $S = kA^{-\theta}$, where k is a constant (Whipple et al., 1999). For most rivers, channel concavity hovers around 0.4–0.5. The constant k can be conceptualized as a ratio between rock uplift and climate or hydrology. If rock uplift rates increase, channel steepness should also increase, whereas if climatic conditions enhance erosiveness, channel steepness decreases (Whipple et al., 1999). In general, climatic conditions that lead to higher discharges will promote erosion and cause the entire stream profile to become less steep (Figure M50).

Sediments transported by rivers abrade the channel bed through repeated impacts. In the absence of sediment, rivers cannot erode efficiently, whereas too much sediment will cover the bed of the river and protect it from further erosion (Sklar and Dietrich, 2001). For underloaded rivers, i.e., where the sediment supply is much less than the transport capacity, a climatically-induced increase in the sediment supply may promote more rapid channel erosion. Irrespective of the cause (changing sediment or water discharge) of a lower channel slope, unless there is a compensating change in drainage spacing or rock strength, hillslopes and ridge crests will be lowered as well, and the mean elevation of a range should decrease (Figure M50). Because climate oscillates between glacial and interglacial conditions, the erosivity of fluvial systems should oscillate as well, such that the mean elevation, mean relief, and height of the ridge crests should vary with climate.

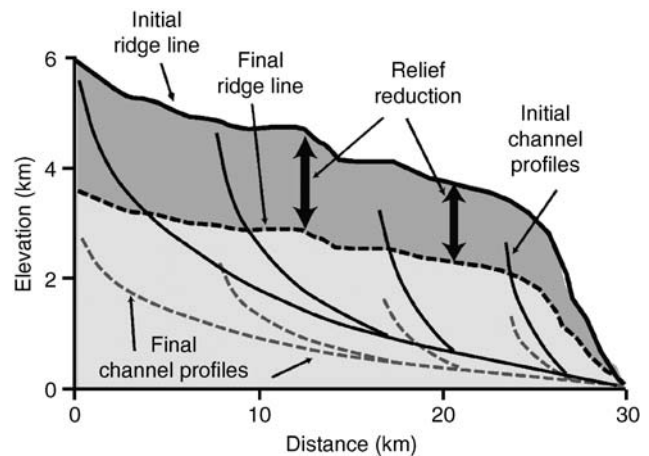


Figure M50 Predicted changes in river-channel and ridge-crest profiles that result from a sustained change from a less to more erosive climate state or from a regime of more rapid to slower rock uplift. More erosive climates increase discharge to each channel, thereby enhancing their ability to erode and lower river profiles. Because only a small fraction of a landscape typically lies between the channel head and ridge crest, a decrease in the channel gradient causes ridge lines to lower as well. (Modified after Whipple et al., 1999.)

The rapidity of climate change, however, often outpaces the response time of river systems (Whipple, 2001), such that the hillslopes and rivers will always tend to be somewhat out of equilibrium.

Because glaciers are very effective erosional agents, their presence will create a different mountain topography than would occur on the same range in the absence of glaciers. Two attributes influence glacial effects on topography. First, the focusing of bedrock erosion by glaciers at the altitude of the glacial snow line causes a lowering of mean elevation at that level. Second, as climate changes, the glacial snowline shifts altitudinally up or down, causing a synchronous shift in the zone of maximum glacial erosion. The well known elongate glacial troughs of alpine terrains are excavated by this mechanism. In comparison to the topographic profiles of rivers, glaciers produce high-altitude low-gradient profiles that extend

upward to the base of the cirque headwalls. Because the headwalls occupy only a small fraction of the landscape, the glacial troughs cause a concentration of landscape area in the altitude range defined by climatically-driven variations in snowline (Figure M51) (Brozovic et al., 1997). The net results of climatically-driven snowline variations are a lowering of the mean elevation, a focusing of land area near the snowline, and development of isolated horns or summits formed by coalescence of cirques. These summits may act as topographic “lightning rods” where storms gather along their flanks (Brozovic et al., 1997). The additional snow fed into the nearby glaciers would be expected to cause them to erode even more effectively.

Although reconstruction of the paleoaltitude of past mountain belts is difficult and typically contains large uncertainties (100s of m), changes in the flux of sediments from a mountain belt can be assessed through examination of the sedimentary record in basins adjacent to ranges. An enhanced sediment flux can occur either because erosion is occurring with greater efficiency compared to the past or because the rates of tectonic fluxes into an eroding mountain belt have increased. Compilation of sedimentation-accumulation rates from basins around the world indicate that both the volume and grain size of sediments has significantly increased since ~2–4 Ma (Zhang et al., 2001). The global synchrony of this change indicates that tectonics cannot be the cause: only climate change could cause such a pervasive and synchronous response. Whereas one might expect expanded glaciations to drive increases in erosion rates (Hallet

et al., 1996), many of the studied basins are not bounded by glaciated ranges. Instead, it is proposed that strongly oscillating Late Cenozoic climates have imposed such abrupt and frequent changes in precipitation, vegetation, and temperature that the landscape was always out of equilibrium and susceptible to rapid erosion (Zhang et al., 2001).

Steady-state orogens, topography, and climate

Conceptually, in a convergent mountain range, the flux of rock into an orogen could be balanced by the efflux through erosion, such that a steady-state mass would be maintained (Willett and Brandon, 2002). In a topographic steady state, the mean height and relief of the range would also remain steady through time. In such a condition, erosion by rivers, hillslopes, and glaciers must be adjusted so that they collectively erode at the same rate as rock moves into the orogen through tectonism. Steady-state topography requires a tectonic influx, because by itself the isostatic response to erosion will always result in a reduction in the mean height of a range. Given the rate of climatic change and the response time of geomorphic systems to approach equilibrium, orogenic topography should oscillate between higher and lower mean elevation and relief. Thus, at short time scales ($<10^5$ yr), steady state would never be strictly attained. However, if the average topography remained steady at time scales exceeding the primary glacial cycles (10^5 yr), the topography could be considered to be in a steady state.

Recent numerical models suggest that climate can play a major role in shaping orogens and determining where strain is focused within an orogenic belt (Beaumont et al., 1992; Willett, 1999). The models suggest that, in the absence of erosion, a convergent orogen will simply widen and thicken over time. If moisture is advected into the orogen from one side, the resultant asymmetric erosion causes profound changes in the shape of the orogen, precipitation patterns, and distribution of thickening and strain. Both the topographic divide and the zone of maximum crustal thickening shift away from the moisture source, whereas the region of maximum strain shifts toward the moisture (Figure M52). These changes all result from the preferential focusing of erosion on only one side of the orogen.

At a large scale, the predicted impacts of climate on orogenic growth may be well displayed by the Himalayan-Tibetan Orogen. Strong climatic contrasts exist on the northern and southern margins of the Tibetan Plateau. In the south, the Asian monsoon delivers 3–5 m of rain over the summer months to the southern flank of the Himalaya (Barros et al., 2000). In the north, generally arid to semi-arid conditions prevail along the margins of the Tarim Basin and the Hexi Corridor. After ~50 Myr of the ongoing Indo-Asian collision, 1,000s of km of convergence have been absorbed within the orogen. Accommodation of the converging crust can occur by thickening and widening, removal of mass through erosion, or lateral escape of mass out of the pathway of collision. The monsoon’s highly effective removal of mass from the Himalayan side of the Tibetan Plateau suggests that a near steady state may prevail there (Beaumont et al., 2001). Many of the major Himalayan structures that were active 10 million years ago are still active today, and the zone of active deformation has not significantly widened. In contrast, on the arid northern side of the Tibetan Plateau, extensive northward expansion of the Plateau has occurred during this same interval. Both northward propagation of active thrusting and the incorporation, shortening, and thickening of the former northern foreland has enabled large scale

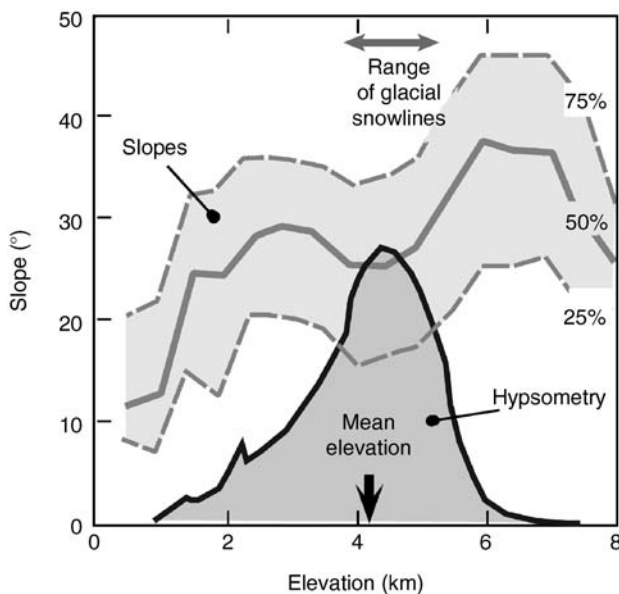


Figure M51 Hypsometry (altitude versus frequency) and mean hillslope angles of a glaciated Himalayan region. In glaciated regions above 3 km, much of the topography is concentrated between 4 and 5 km – a range coinciding with the altitudinal range of glacier snow lines between interglacial and glacial times. Glacial erosion is most efficient near the snow line, where ice flows fastest. Such altitudinally-dependent erosion focuses more topography near that altitude. Hillslope angles are steep in the zone just below the glaciers (<3.5 km) where bedrock landsliding occurs, but become more gentle in the altitude range where most glaciers occur, before steepening again in the headwalls and higher altitudes where cold-based glaciers prevail. (Modified after Brozovic et al., 1997.)

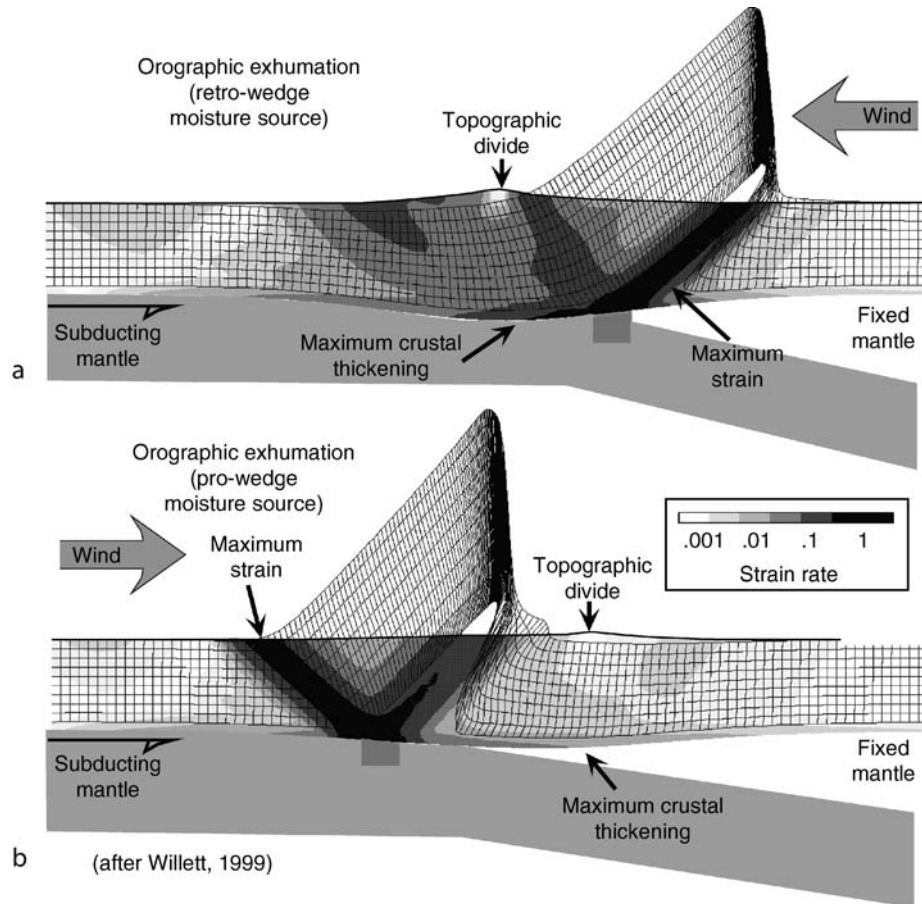


Figure M52 Contrasting magnitudes of geometries of erosion, strain, and crustal thickening resulting from the direction in which storms approach an orogen. In both cases, the tectonic framework is identical, with two blocks of continental lithosphere colliding and with the mantle lithosphere detaching on one side of the orogen. In each case, erosion and crustal strain are concentrated on the side from which moisture approaches the orogen, whereas the topographic divide and zone of maximum crustal thickening move away from the moisture source. The erosion resulting from greater rainfall on one side of the orogen creates fundamental contrasts in deformation patterns, despite the identical tectonic framework. (a) Moisture enters the orogen from above the retro-wedge side (the non-subducting side). (b) Moisture approaches from the pro-wedge side. (Modified after Willett, 1999.)

accretion of new mass into the northern edge of the Tibetan Plateau. The apparent steady state on one flank of the Himalayan-Tibetan Orogen and its obvious absence on the other flank support the prediction that large scale climatic contrasts exert a controlling influence on patterns of orogenic deformation (Willett, 1999).

Summary

Mountain ranges impact climate and climate change through multiple mechanisms, including the control of the pathways moisture follows across the landscape, patterns of orographic precipitation as storms impinge on the flanks of mountains, the enhancement of summer monsoons, and the magnitude of continentality. The chemical composition of the atmosphere and, in particular, the concentrations of CO_2 may be affected by rates of mountain building, whereby rapid mountain growth causes high rates of mechanical weathering and enhances the extent of glaciation – both of which serve to provide fresh rock surfaces for chemical weathering.

Climate can also exert some surprising controls on mountain topography and orogenic growth. In nonglaciated mountains, a

coupling exists between river erosion, bounding hillslopes, and climate. Rates of river downcutting control both local base-level lowering and incipient changes in the angle of hillslopes. Increased discharge during wetter climates will promote more rapid fluvial erosion and lower stream gradients. The flux of sediment off slopes represents the primary means of denudation in most orogens. As climate changes, precipitation variations alter hillslope pore pressures, change stable hillslope angles, and ultimately cause variability in hillslope sediment fluxes. When climates are wetter or more erosive, the mean altitude and relief of ranges should be lowered.

In glaciated ranges, glacial erosion commonly limits the mean height of mountain ranges by removing much of the topography above the snow line. Climatically-induced variations in the glacial snow line cause changes in the elevation of maximum glacial erosion and tend to define an altitudinal range within which most topography is concentrated. Overall, glaciated ranges will have lower mean elevations than would nonglaciated ranges under the same tectonic conditions.

In convergent orogens, gradients in erosion can cause gradients in crustal strain. Increased moisture on one flank of a

range will tend to increase erosion on that side and induce more rapid deformation in the underlying rock. Whereas a simple isostatic response can restore ~80% of the eroded mass, if rock is entering a convergent orogen from the side, then a steady state topography can be maintained at time scales ($>10^5$ yr) exceeding those of major climatic cycles.

Douglas W. Burbank

Bibliography

- Barros, A.P., Joshi, M., Putkonen, J., and Burbank, D.W., 2000. A study of the 1999 monsoon rainfall in a mountainous region in central Nepal using TRMM products and rain gauge observations. *Geophys. Res. Lett.*, **27**, 3683–3686.
- Beaumont, C., Fullsack, P., and Hamilton, J., 1992. Erosional control of active compressional orogens. In McClay, K.R. (ed.), *Thrust Tectonics*. London: Chapman and Hall, pp. 1–18.
- Beaumont, C., Jamieson, R.A., Nguyen, M.H., and Lee, B., 2001. Himalayan tectonics explained by extrusion of a low-viscosity crustal channel coupled to focused surface denudation. *Nature*, **414**, 738–742.
- Brocklehurst, S.H., and Whipple, K.X., 2002. Glacial erosion and relief production in the eastern Sierra Nevada, California. *Geomorphology*, **42**, 1–24.
- Brozovic, N., Burbank, D.W., and Meigs, A.J., 1997. Climatic limits on landscape development in the northwestern Himalaya. *Science*, **276**, 571–574.
- Bullen, M.E., Burbank, D.W., and Garver, J.I., 2003. Building the northern Tien Shan: Integrated thermal, structural, and topographic constraints. *J. Geol.*, **111**, 149–165.
- Burbank, D.W., 1991. Late Quaternary snowline reconstructions for the southern and central Sierra Nevada, California: Re-assessment of the Recess Peak Glaciation. *Quaternary Res.*, **36**, 294–307.
- Burbank, D.W., 2002. Rates of erosion and their implications for exhumation. *Mineral. Mag.*, **66**, 25–52.
- Burbank, D.W., and Anderson, R.S., 2001. *Tectonic Geomorphology*, 1st edn. Malden, MA: Blackwell Science, 273pp.
- Burbank, D.W., Leland, J., Fielding, E., Anderson, R.S., Brozovic, N., Reid, M.R., and Duncan, C., 1996. Bedrock incision, rock uplift and threshold hillslopes in the northwestern Himalayas. *Nature*, **379**, 505–510.
- Burbank, D.W., McLean, J.K., Bullen, M., Abdrakhmatov, K.Y., and Miller, M.G., 1999. Partitioning of intermontane basins by thrust-related folding, Tien Shan, Kyrgyzstan. *Basin Res.*, **11**, 75–92.
- Burbank, D.W., Blythe, A.E., Putkonen, J., Pratt-Sitaula, B., Gabet, E., Oskin, M., Barros, A., and Ojha, T.P., 2003. Decoupling of erosion and precipitation in the Himalayas. *Nature*, **426**, 652–655.
- England, P., and Molnar, P., 1990. Surface uplift, uplift of rocks, and exhumation of rocks. *Geology*, **18**, 1173–1177.
- Fielding, E.J., Isacks, B.L., Barazangi, M., and Duncan, C., 1994. How flat is Tibet? *Geology*, **22**, 163–167.
- Forest, C.E., Wolfe, J.A., Molnar, P., and Emanuel, K.A., 1999. Paleoaltimetry incorporating atmospheric physics and botanical estimates of paleoclimate. *Geol. Soc. Am. Bull.*, **111**, 497–511.
- Guo, Z.T., Ruddiman, W.F., Hao, Q.Z., Wu, H.B., Qiao, Y.S., Zhu, R.X., Peng, S.Z., Wei, J.J., Yuan, B.Y., and Liu, T.S., 2002. Onset of Asian desertification by 22 Myr ago inferred from loess deposits in China. *Nature*, **416**, 159–163.
- Hallet, B., Hunter, L., and Bogen, J., 1996. Rates of erosion and sediment evacuation by glaciers: A review of field data and their implications. *Glob. Planet. Change*, **12**, 213–235.
- Harper, J., and Humphrey, N.F., 2003. High altitude Himalayan climate inferred from glacial ice flux. *Geophys. Res. Lett.*, **30**, 10.1029/2003GL017329 (1764).
- Harrison, T.M., Copeland, P., Kidd, W.S.F., and Yin, A., 1992. Raising Tibet. *Science*, **255**, 1663–1670.
- Heimsath, A.M., Dietrich, W.E., Nishiizumi, K., and Finkel, R.C., 1997. The soil production function and landscape equilibrium. *Nature*, **388**, 358–361.
- Humphrey, N.F., and Raymond, C.F., 1994. Hydrology, erosion, and sediment production in a surging glacier: The Variegated Glacier surge, 1982–1983. *J. Glaciol.*, **40**, 539–552.
- Kutzbach, J.E., Prell, W.L., and Ruddiman, W.F., 1993. Sensitivity of Eurasian climate to surface uplift of the Tibetan Plateau. *J. Geol.*, **100**, 177–190.
- Lajoie, K.R., 1986. Coastal Tectonics. In *Active Tectonics*. Washington, DC: National Academy Press, pp. 95–124.
- MacGregor, K.R., Anderson, R.S., Anderson, S.P., and Waddington, E.D., 2000. Numerical simulations of glacial-valley longitudinal profile evolution. *Geology*, **28**, 1031–1034.
- Medwedeff, D.A., 1992. Geometry and kinematics of an active, laterally propagating wedge thrust, Wheeler Ridge, California. In Mitra, S., and Fisher, G.W. (eds.), *Structural Geology of Fold and Thrust Belts*. Baltimore, MD: Johns Hopkins University Press, pp. 3–28.
- Molnar, P., and England, P., 1990. Late Cenozoic uplift of mountain ranges and global climatic change: Chicken or egg? *Nature*, **346**, 29–34.
- Molnar, P., England, P., and Martinod, J., 1993. Mantle dynamics, uplift of the Tibetan Plateau, and the Indian monsoon. *Rev. Geophys.*, **31**, 357–396.
- Porter, S.C., 1977. Present and past glaciation threshold in the Cascade Range, Washington, U.S.A.: Topographic and climatic controls, and paleoclimatic implications. *J. Glaciol.*, **18**, 101–116.
- Porter, S.C., 1989. Some geological implications of average Quaternary glacial conditions. *Quaternary Res.*, **32**, 245–261.
- Pratt, B., Burbank, D.W., Putkonen, J., and Ojha, T., 2002. Climatic implications of modern and paleo ELAs in the central Nepal Himalaya. *EOS (Transactions of the American Geophysical Union)*, **83**, F319.
- Quade, J., Cerling, T.E., and Bowman, J.R., 1989. Development of Asian monsoon revealed by marked ecological shift during latest Miocene in northern Pakistan. *Nature*, **342**, 163–166.
- Raymo, M.E., and Ruddiman, W.F., 1992. Tectonic forcing of late Cenozoic climate change. *Nature*, **359**, 117–122.
- Raymo, M.E., Ruddiman, W.F., and Froelich, P.N., 1988. Influence of late Cenozoic mountain building on ocean geochemical cycles. *Geology*, **16**, 649–653.
- Roe, G.H., Montgomery, D.R., and Hallet, B., 2002. Effects of orographic precipitation variations on the concavity of steady-state river profiles. *Geology*, **30**, 143–146.
- Sahagian, D.L., and Maus, J.E., 1994. Basalt vesicularity as a measure of atmospheric pressure and palaeoelevation. *Nature (London)*, **372**, 449–451.
- Shackleton, N.J., and Opdyke, N.D., 1976. Oxygen-isotope and paleomagnetic stratigraphy of Pacific core V28–239 Late Pliocene to Latest Pleistocene. *Geol. Soc. Am. Mem.*, **145**, 449–464.
- Sklar, L., and Dietrich, W.E., 2001. Sediment supply, grain size and rock strength controls on rates of river incision into bedrock. *Geology*, **29**, 1087–1090.
- Talling, P.J., and Sowter, M.J., 1999. Drainage density on progressively tilted surfaces with different gradients, Wheeler Ridge, California. *Earth Surf. Processes and Landforms*, **24** (9), 809–824.
- Thompson, S.C., Weldon, R., III, Rubin, C.M., Abdrakhmatov, K.E., Molnar, P., and Berger, G.W., 2002. Late Quaternary slip rates across the central Tien Shan, Kyrgyzstan, central Asia. *J. Geophys. Res.*, **107**, 10.1029/2001JB000596.
- Whipple, K.X., 2001. Fluvial landscape response time; how plausible is steady-state denudation? The steady-state orogen; concepts, field observations, and models. *Am. J. Sci.*, **301**, 313–325.
- Whipple, K.E., Kirby, E., and Brocklehurst, S.H., 1999. Geomorphic limits to climate-induced increases in topographic relief. *Nature*, **401**, 39–43.
- Willett, S.D., 1999. Orogeny and orography: The effects of erosion on the structure of mountain belts. *J. Geophys. Res.*, **104**, 28957–28982.
- Willett, S.D., and Brandon, M.T., 2002. On steady states in mountain belts. *Geology*, **30**, 175–178.
- Williams, V.S., 1983. Present and former equilibrium-line altitudes near Mount Everest, Nepal and Tibet. *Arct. Alp. Res.*, **15**, 201–211.
- Zhang, P., Molnar, P., and Downs, W.R., 2001. Increased sedimentation rates and grain sizes 2–4 Myr ago due to the influence of climate change on erosion rates. *Nature*, **410**, 891–897.

Cross-references

[Glacial Geomorphology](#)
[Monsoons, Pre-Quaternary](#)
[Monsoons, Quaternary](#)
[Paleo-Precipitation Indicators](#)
[Plate Tectonics and Climate Change](#)
[Weathering and Climate](#)

N

NEAREST-LIVING-RELATIVE METHOD

The nearest-living-relative (NLR) method represents a standard and powerful tool in paleoclimatology and paleoecology. It uses the climatic or ecologic characteristics of the NLRs of fossil taxa or assemblages to estimate the paleoclimatic or paleoecologic conditions under which the fossil taxa or assemblages lived. Since the NLR method is based on the assumption that the climatic or ecologic characteristics of a fossil taxon or assemblage are similar to those of its nearest living relative, it is largely restricted to the Cenozoic. The paleobotanist Oswald Heer (1809–1883), who is also considered to be one of the founders of paleoclimatology, was probably the first to use this technique in order to estimate climate parameters for the Tertiary based on fossil floras (see *History of Paleoclimatology*). Since that time, numerous qualitative and quantitative variations of the NLR method have been developed, some of them based on fossil taxa, others based on fossil assemblages, all of them, however, have their specific advantages and limitations.

Qualitative techniques

The qualitative indicator taxon approach may be viewed as the classic variation of the NLR method: individual indicator taxa are used to derive information about the paleoenvironment or about paleoenvironmental trends. For instance, the modern bivalve species *Mytilus edulis* tolerates hyposaline conditions; hence, mass occurrence of *Mytilus* in a Cenozoic shell-bed may indicate brackish or varying salinities. Similarly, an increase in abundance of Lauraceae (laurel family) or Arecaceae (palm family) leaves in a sequence of fossil floras is typically interpreted as reflecting a warming trend since today both families show a predominantly tropical to subtropical distribution.

Although very simple and rapid to apply – at least if the ecology and climatology of the NLRs of the fossil taxa are known – this qualitative indicator taxon approach has serious limitations. First, it provides only qualitative and not quantitative data. Second, the accuracy and reliability of the paleoenvironmental information depends on the taxonomic level to

which the NLR of a fossil taxon can be determined and on the stratigraphic or evolutionary age of the fossil taxon. Typically, more detailed information can be extracted from fossil taxa if their NLRs can be identified not only on the family but also on the genus or even species level. The accuracy, however, to which the NLR of a given fossil can be determined, is a function of the evolutionary and stratigraphic age of the fossil. Angiosperms have their major radiations in the Cretaceous and Paleogene. Correspondingly, the NLR of Neogene angiosperms can mostly be identified on the genus level, Pleistocene angiosperms on the species level. The situation is completely different for mammals, which show important radiations in the Neogene and Pleistocene. Hence, the NLRs of many early Pleistocene mammals can only be identified on the family or genus level. A third shortcoming of the qualitative indicator taxon approach is its sensitivity to taphonomic effects since the presence or absence of certain indicator taxa may not only be controlled by paleoclimatic or paleoenvironmental change but also by taphonomy. For instance, Lauraceae are quite common in European Paleogene leaf floras but are rare in pollen floras due to differential degradation processes. For the same reason, angiosperms are rare in Cenozoic wood floras since their trunks and branches decay more rapidly than those of conifers. Finally, it should be emphasized that the qualitative indicator taxon approach is not a well-defined, objective and reproducible technique. The same fossil flora or fauna may hence lead to different interpretations if analyzed by different scientists.

Instead of indicator taxa, it is possible to use fossil indicator assemblages to obtain qualitative paleoenvironmental information. This qualitative indicator assemblage approach is particularly common in Quaternary research: pollen diagrams of sedimentary sequences are interpreted as a succession of characteristic vegetation types; from the vegetation succession, a qualitative or semi-quantitative climate trend or climate curve may then be derived. The technique can be applied to all kinds of fossil assemblages but it makes more rigorous assumptions than the qualitative indicator taxon approach. In the qualitative indicator assemblage approach, it is required that the NLRs of fossil taxa and of fossil assemblages are identified correctly and that both the fossil taxa and the fossil assemblages have

climatic or environmental requirements similar to those of their modern analogues. Hence, the qualitative indicator assemblage technique is more restricted in its applicability than the qualitative indicator taxon approach. In general, it works quite well in the Quaternary but becomes increasingly less reliable in the Neogene. In addition, it is even more sensitive to taphonomy than the indicator taxon approach because transportation and fossilization processes may heavily influence the composition of a fossil assemblage.

Quantitative techniques

Both the indicator taxon and indicator assemblage techniques may also be used in a more systematic and objective way in order to obtain quantitative paleoclimate or paleoenvironmental data. Grichuk (1969) was the first to develop Heer's indicator taxon approach into a well-defined methodology that allows determination of absolute climate estimates from fossil floras; his technique was later modified into the so-called "coexistence approach" and adapted to modern computer technology (Mosbrugger and Utescher, 1997). A similar methodology was developed by Atkinson et al. (1987) for beetles and applied to Quaternary beetle faunas. All these techniques are quite similar (Figure N1). Given a fossil fauna or flora with taxa A to Z for which the NLRs A' to Z' are known, if the climatic (or ecologic) tolerances of the modern taxa A' to Z' (e.g., concerning the various climatic parameters such as mean annual temperature, mean temperature of the warmest month, etc.) are known, then by overlapping all these tolerances the "coexistence interval" can be determined for any environmental or climatic parameter. This coexistence interval is interpreted to bracket the real climatic or environmental parameter value under which the fossil fauna or flora lived. The climatic resolution of the methodology can be improved if the various climatic parameters such as mean annual temperature, mean annual precipitation, etc. are not considered independently but if the multidimensional climatic spheres, which describe the climatic tolerances of the modern taxa A' to Z', are calculated and overlapped (e.g., Kühl et al., 2002).

All these quantitative techniques have found wide application in paleoclimatology and proved very useful and reliable in Cenozoic paleoclimate reconstructions (e.g., Utescher et al., 2000; Mosbrugger et al., 2005). Unfortunately, they suffer from similar shortcomings as the qualitative indicator taxon approach. However, the method becomes virtually independent from taphonomy if many taxa are included in the analysis. For instance, if some taxa are missing in the fossil fauna or flora

for taphonomic reasons, this will only influence the width of the resulting coexistence interval (cf. Figure N1) but the new interval will still bracket the real value. Similarly, the simultaneous consideration of many taxa will allow statistical tests to determine if some modern taxa have changed their climatic tolerances as compared to their fossil relatives. For instance, in Figure N1, the NLR taxon C' forms a climatic outlier with respect to parameter I, i.e., the climatic tolerance of C' does not overlap with the climatic tolerances of the other NLRs of the fossil flora/fauna. This clearly indicates that the climatic tolerance of modern taxon C' does not reflect the climatic tolerance of fossil taxon C. From many such analyses it turns out that all modern relict taxa, such as the conifer genus *Sequoia*, that today have a very restricted distribution, as compared to the distribution area of the fossil taxon, are not very useful in paleoclimate reconstructions.

A variety of assemblage-based methods that allow quantitative estimates of paleoclimate or paleoenvironment parameters also exists. The modern analogue technique may serve as an example. In a first step, a calibration dataset has to be established. For this purpose, many modern assemblages covering a wide range of climatic (or ecologic) conditions are characterized with respect to their climatic (or ecologic) requirements. Then for a given fossil assemblage, a certain number (e.g., 1–5) of the best "modern analogues" are picked from the calibration dataset; the climatic characteristics of these modern analogues are averaged and the mean value is used as a paleoclimate estimate for the fossil assemblage. The classic transfer functions may be viewed as just another variety of the quantitative assemblage-based methods.

The limitations of these techniques are similar to those described for the qualitative indicator assemblage approaches: the NLRs of the fossil taxa and of the fossil assemblages have to be identified and it is assumed that both fossil assemblage and its modern analogue have similar climatic or environmental requirements. Hence, quantitative assemblage-based paleoclimate reconstructions are again largely restricted to the Quaternary, with rapidly increasing uncertainties further back in time. Calibration of the modern data set and taphonomy play a crucial role in these techniques. It has to be kept in mind that there are fossil assemblages, such as the Pleistocene mammoth steppe, which have no close modern analogues. In addition, taphonomic filter processes may strongly influence the relative abundance of taxa in a fossil assemblage and thus hamper the identification of the nearest living relative assemblage.

Summary

The nearest-living-relative method exists in numerous taxon- and assemblage-based variations and is still one of the most powerful approaches to obtain qualitative and quantitative paleoclimate (or paleoenvironment) information. Taxon-based approaches relying only on the presence-absence of taxa are less sensitive to taphonomy than assemblage-based approaches, which typically also rely on the relative abundance of taxa. Stratigraphically, taxon-based methods are limited to periods after the time when the major evolutionary radiation of the respective taxon group occurred; typically, they cannot be applied to pre-Cenozoic times. In contrast, assemblage-based techniques are mostly restricted in their application to Quaternary sequences.

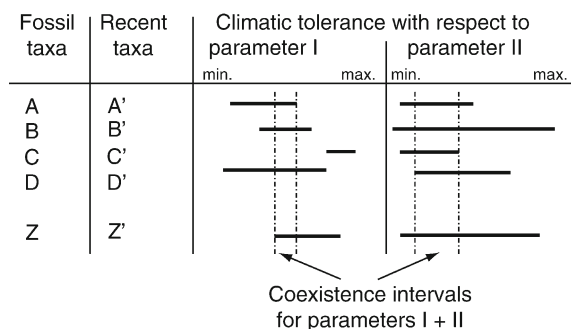


Figure N1 General concept of quantitative indicator taxon approaches. Taxon C' forms a climatic outlier (further explanation in the text).

Bibliography

- Atkinson, T.C., Briffa, K.R., and Coope, G.R., 1987. Seasonal temperatures in Britain during the past 22,000 years, reconstructed using beetle remains. *Nature*, **325**, 587–592.
- Grichuk, V.P., 1969. An attempt to reconstruct certain elements of the climate of the northern hemisphere in the Atlantic period of the Holocene. In Neishtadt, M.I. (ed.), *Golotsen*. Moscow: Izd-vo Nauka, pp. 41–57.
- Kühl, N., Gebhardt, G., Litt, T., and Hense, A., 2002. Probability density functions as botanical-climatological transfer functions for climate reconstruction. *Quaternary Res.*, **58**, 381–392.
- Mosbrugger, V., and Utescher, T., 1997. The coexistence approach - a method for quantitative reconstructions of Tertiary terrestrial palaeoclimate data using plant fossils. *Palaeogeogr. Palaeoclimatol. Palaeoecol.*, **134**, 61–86.
- Mosbrugger, V., Utescher, T., and Dilcher, D., 2005. Cenozoic continental climatic evolution of Central Europe. *Proc. Natl. Acad. Sci.*, **102**, 14964–14969.
- Utescher, T., Mosbrugger, V., and Ashraf, R.A., 2000. Terrestrial climate evolution in Northwest Germany over the last 25 million years. *PALAIOS*, **15**, 430–449.

Cross-references

- [Animal Proxies, Invertebrates](#)
- [Animal Proxies, Vertebrates](#)
- [History of Paleoclimatology](#)
- [Paleobotany](#)
- [Paleoclimate Proxies, an Introduction](#)
- [Pollen Analysis](#)
- [Transfer Functions](#)

NEOGENE CLIMATES

Introduction

The Neogene includes the Miocene and Pliocene epochs, which span 23.03–5.33 and 5.33–1.81 million years ago, respectively Loureus et al., 2004. The Neogene witnessed several major paleoclimatological changes. In general terms, the Neogene went from a warm climatic optimum in the late early Miocene through rapid cooling during the middle Miocene, to the onset of Northern Hemisphere Glaciation (NHG) in the Pliocene.

The Miocene

During the Miocene, especially the middle Miocene, the Earth went through several major changes – both climatic and tectonic. The climatic transition involved gradual cooling, starting about 15 million years ago, and establishment of major ice sheets on Antarctica by 10 million years ago (Zachos et al., 2001), as well as significant changes in global carbon cycling and deep ocean circulation. Initially, researchers argued for minimal continental ice from sometime in the Cretaceous to the Miocene, with a transition to so-called “icehouse” conditions in the middle Miocene. However, evidence now exists in support of the development of glacial conditions in the early Oligocene, with waxing and waning of global ice volume occurring through the Oligocene and early Miocene. Trends in microfossil stable oxygen isotope composition provide evidence for several glacial intervals during the Miocene (e.g., Miller et al., 1991). However, a period of global warmth followed a major glacial episode at the Oligocene/Miocene boundary, resulting in a reduced latitudinal temperature gradient and higher average surface water and deep-water temperatures (Zachos et al., 1997, 2001). At the height of the climatic optimum

(17–15 million years ago) deep-water and high-latitude surface water temperatures were as much as 6 °C warmer than today (Shackleton and Kennett, 1975; Savin et al., 1975). The most dramatic climatic change that occurred during the Miocene took place around 15 million years ago, during the middle Miocene, at which time there was evidence for rapid deep-water cooling and east Antarctic ice-sheet expansion (Figure N2). Evidence from ice-rafted debris indicates that glaciation in the Nordic seas and Arctic regions began in the late Miocene. During the late Miocene, glaciers reached sea level in both the North Atlantic and North Pacific, resulting in the deposition of ice-rafted debris across both these oceans.

There are several different hypotheses concerning the cause of the Miocene climatic optimum and the following cooling. One of these hypotheses involves changes in atmospheric CO₂ content, with an elevated *p*CO₂ possibly responsible for the global warmth in the late early Miocene optimum. Evidence for Neogene *p*CO₂ variability comes from different sources. Evidence regarding a possible organic carbon control on *p*CO₂ can be found in the stable carbon isotope composition of microfossils that live on the ocean floor. In the middle Miocene, there is a positive shift in the stable carbon isotope composition of marine carbonates, which is associated with organic carbon-rich deposits around the Pacific, such as the Monterey Formation (Vincent and Berger, 1985). Increased upwelling is thought to be the major cause for this increased organic carbon burial and subsequent CO₂ removal. The increase is followed by a positive shift in the stable oxygen isotope composition of marine carbonates, indicating a cooling associated with decreased levels of *p*CO₂. However, Raymo (1994) suggested that the primary cause of decreasing *p*CO₂ during the Miocene was due to changes in rates of continental chemical weathering. Based on a strontium isotope record, Raymo (1994) argued for increasing silicate chemical weathering rates as the primary mechanism of CO₂ removal. The enhanced weathering rate has been attributed to a major phase of deformation of the Himalayan orogen that occurred about 21–17 million years ago. On the other hand, reconstructions of the evolution of atmospheric *p*CO₂ during the Miocene that are based on the carbon analyses of diunsaturated alkenones and planktonic foraminifers from deep-sea sediment cores show no link between atmospheric *p*CO₂ and climate change during the late early and middle Miocene (Pagani et al., 1999). Another cause of the late early Miocene climate optimum and East Antarctic ice expansion in the middle Miocene could be the opening of the Drake Passage between South America and the Antarctic Peninsula. The opening of the Drake Passage had a great effect on Southern Ocean circulation.

Several different hypotheses tie Miocene climate change to deep-water circulation patterns (Wright et al., 1992 and references therein). Based on stable carbon and oxygen isotope records from the Atlantic, Pacific, Indian and Southern oceans, middle Miocene growth of the East Antarctic Ice Sheet was controlled by the interplay between Northern Component Water, Southern Component Water and a water mass originating in the eastern Tethys (Wright et al., 1992; Flower and Kennett, 1995). According to Wright et al. (1992) a combination of the relatively warm Northern Component Water and Tethyan water masses about 20–16 million years ago produced a significant meridional heat transport that warmed the deep ocean by several degrees. At around 16 million years ago, deep-water temperatures cooled after the fluxes of Northern Component Water and Tethyan outflow water were reduced, allowing the deep oceans to be ventilated by only Southern Component

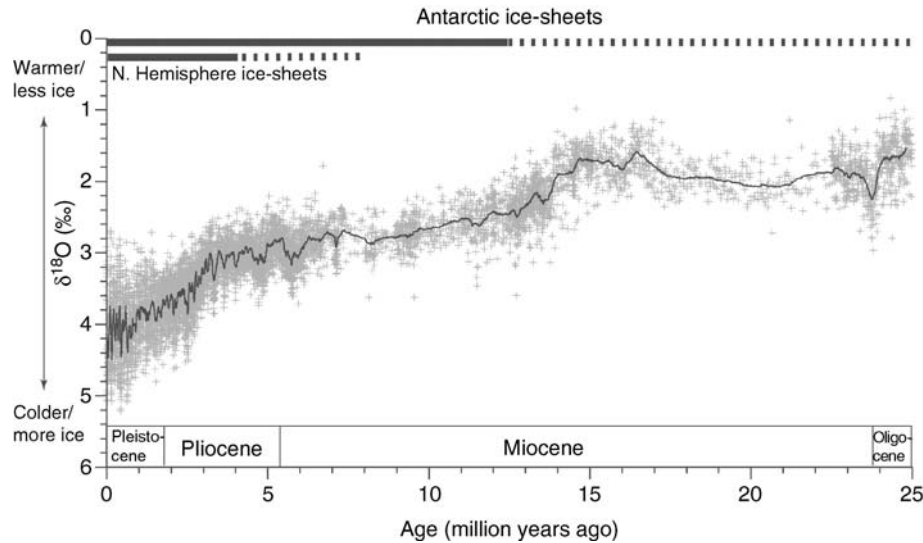


Figure N2 Trends in global climate change during the Neogene. The data shown are based on deep-sea stable oxygen isotope records ($\delta^{18}\text{O}$) from more than 40 Deep Sea Drilling Project and Ocean Drilling Program sites (Zachos et al., 2001). The stable oxygen isotope composition of bottom-dwelling foraminifers reflects changes in global ice-volume and/or changes in deep-water temperature. Solid black line corresponds to heavily smoothed values of raw data (grey crosses). Increases in $\delta^{18}\text{O}$ values correspond to climatic deterioration, i.e., larger global ice-volume and/or cooler deep-waters (after Zachos et al., 2001).

Water. Flower and Kennett (1995) suggested that with the cessation of Tethyan outflow around 14 million years ago, Southern Component Water production increased, thereby reducing the meridional heat transport and making an expansion of the East Antarctic Ice Sheet possible. Hence, reconstructions of the production rates of warm and cold deep-water masses suggest that the middle Miocene cooling and growth of the East Antarctic Ice Sheet were controlled by changes in ocean circulation.

The latest Miocene, during the Messinian stage (7.12–5.32 million years ago, Berggren et al., 1995) was a time of major climatic and paleoceanographic change. Large anhydrite/gypsum deposits from the Messinian are found around the Mediterranean region, suggesting that the Mediterranean Sea was desiccated during this time period. During the late Miocene, the connections between the Atlantic Ocean and Tethyan Ocean (a precursor to the Mediterranean) were through the Rifian Corridor in Morocco and the Iberian Portal in Spain. These passages allowed the inflow of Atlantic waters in to the Paleo-Mediterranean to replenish evaporative loss in this basin. With the progressive closure of the two straits that connected the Paleo-Mediterranean with the Atlantic, the Paleo-Mediterranean became isolated and desiccated (e.g., Benson et al., 1991; Hodell et al., 1994). This led to what is called the Messinian salinity crisis. The desiccation of the Paleo-Mediterranean affected oceanic salinity by removing an estimated 6% of dissolved salts from seawater. The cause of the Mediterranean salinity crisis was probably the interplay between tectonic changes, glacio-eustatic changes and climate changes within the Paleo-Mediterranean.

The Pliocene

The early Pliocene (~5–3 Ma) seems to be the most recent time period of sustained global warmth. During the mid-Pliocene (~3 Ma), prior to the onset of Northern Hemisphere glaciation, global mean temperatures may have been as much as 3.5 °C warmer than at present (Raymo et al., 1996). Much evidence comes

from the mid-Pliocene, when high-latitude sea surface temperature increases suggest strong thermohaline circulation.

The reasons for mid-Pliocene warmth are not yet clear. Crowley (1996) summarized several possible reasons: changing CO_2 levels, orographic effects related to late Cenozoic uplift and/or changes in meridional heat transport due to, for example, closure of the Central American Isthmus. Recent studies call on a combination of two main factors to explain Pliocene warmth: increased atmospheric CO_2 levels and enhanced thermohaline circulation. Because CO_2 is a “greenhouse” gas, changes in Pliocene atmospheric CO_2 levels could be the cause of the mid-Pliocene warmth. Raymo et al. (1996), for example, suggested that atmospheric CO_2 levels during the mid-Pliocene were on average about 35% higher than the pre-industrial value. CO_2 estimates for the mid-Pliocene come from different sources. Among these are studies of the carbon isotopic composition of marine organic matter (Raymo et al., 1996), stomatal densities in leaves (Van der Burgh et al., 1993) and the carbon isotope difference between surface and deep waters (Shackleton et al., 1992). However, the results from these different techniques show little increase in $p\text{CO}_2$ for the Pliocene.

In addition to changes in atmospheric CO_2 levels, change in ocean heat transport, i.e., thermohaline circulation is one of the major mechanisms used to explain past time intervals of greater warmth, like that of the mid-Pliocene. The thermohaline circulation plays a significant role in regulating global climate by redistributing heat and moisture and influencing the rate of CO_2 exchange between the ocean surface and deep-ocean. At present, the thermohaline circulation is composed of two major water masses: North Atlantic Deep Water (NADW) and Antarctic Bottom Water (AABW). NADW is produced in the northern North Atlantic and spreads towards the south, influencing other ocean basins. AABW, which is mainly produced in the Weddell Sea and Ross Sea, spreads towards the low latitudes in all ocean basins. The overturning cells of NADW and AABW are interrelated, which means that the relative

abundance of these water masses in ocean basins can be modified by a change in production rate of only one of them. However, there are problems associated with holding changes in ocean heat transport responsible for greater warmth (Crowley, 1996). One of them is the need to identify the factors responsible for changes in ocean circulation. Another is that increased heat transport would decrease low-latitude sea-surface temperatures (SST). Cooler tropical SSTs during past warm periods are matters of controversy. Raymo et al. (1996) presented evidence suggesting that the mid-Pliocene (~3 Ma) warmth was related to increased NADW production, in addition to slightly increased CO₂ levels. Although increased NADW production might be responsible for increased warmth in the North Atlantic, it is not clear how this would result in global warmth. Changes in thermohaline circulation primarily redistribute heat over the planet.

The initiation of NADW production occurred during the Neogene. Data from deep-sea cores suggests that NADW was being formed during parts of the middle Miocene (~17–11 million years ago) and that the flux of NADW increased in the late Miocene (~11–5 million years ago), approaching modern values in the early Pliocene (~5–3 million years ago). There are two major hypotheses for the cause of the initiation of NADW. One is that the shoaling and subsequent closure of the Central American Seaway allowed the North Atlantic to become saline enough for the formation of NADW (Maier-Reimer et al., 1990). The other is that changes in the sill depth of the Greenland-Scotland Ridge (Wright and Miller, 1996). Based on modeling studies, Mikolajewicz and Crowley (1997) suggested that the initiation of NADW might have been related to the closing of the Central American Seaway, but that the depth of the Greenland-Scotland Ridge controlled its outflow.

Paleoceanographic studies in the western equatorial Atlantic, the eastern equatorial Pacific and in the Caribbean indicate that the closure of the seaway between North and South America resulted in a distinct reorganization of ocean circulation starting at about 4.6 million years ago (Haug and Tiedemann, 1998). The emergence of the Panamanian Isthmus intensified the Gulf Stream and introduced warm, saline water masses to the high northern latitudes. Evaporative cooling of this warm, saline water mass would result in the formation of NADW. However, Kim and Crowley (2000) suggested, based on an ocean general circulation model, that the increased NADW production could be a consequence of Pliocene warming rather than a primary cause. Their results indicate that a warming over the Southern Ocean produces lower rates of sea ice formation and southern ocean deep-water outflow. This in turn, leads to an increase in NADW outflow in the Southern Ocean and an increase in poleward heat transport in the North Atlantic. Kim and Crowley further postulated that due to the greater sea ice area in the Southern Ocean, this region would be more sensitive to the inferred slightly higher CO₂ levels during the mid-Pliocene.

Onset of Northern Hemisphere Glaciation

The initiation of major NHG seems to have been the culmination of a longer-term high-latitude Cenozoic cooling that began in the early Eocene and is marked by the first indications of ice sheets in Antarctica about 36 million years ago. The long-term cooling brought the climate system of Earth to a critical state for ice-sheet buildup in the Northern Hemisphere. The glaciation of Greenland and the Arctic is believed to have begun in the late Miocene. Small amounts of ice-rafted debris (IRD)

are detected in Nordic Sea sediment cores back to about 11 million years ago (Jansen et al., 2000 and references therein). The timing of the onset of NHG varies to some extent between different regions. Although the initiation of major glacial intervals probably occurred close to the middle/late Miocene boundary, major glacial events are not apparent in the Nordic seas until just before 3 million years ago. An intensification of glacial conditions is recorded at about 3.3 million years ago. The onset of large-scale NHG is dated at approximately 2.75 million years ago on the Vøring Plateau and 3.3 million years ago on the Iceland Plateau (Fronval and Jansen, 1996; Jansen et al., 2000). The different timing probably reflects different responses of the Greenland Ice Sheet versus ice-sheets in northern Europe. IRD with an origin from the Laurentide Ice Sheet seem to appear around 2.74 million years ago. In general, enrichment of the stable oxygen isotope composition of benthic foraminifers suggests that there was significant deep-water cooling and an increase in global ice volume after 3.2 Ma (Tiedeman et al., 1994; Shackleton et al., 1995) (Figure N2).

Several different causes for the onset of NHG have been suggested. One theory attributes the onset of NHG to a decline in the concentration of atmospheric CO₂. This would reduce the amount of heat trapped in the atmosphere and lead to cooling. Changes in atmospheric CO₂ could arise from increased productivity or from a longer-term decline in CO₂ due to the burial of organic carbon and chemical weathering. It has also been hypothesized that the final closing of the South American Seaway was linked to the onset of NHG. The strengthened northward flow of warm, salty water would suppress sea-ice formation. With a reduced sea-ice cover, more moisture from the ocean would be available to the surrounding landmasses and trigger the growth of large ice sheets there. Haug and Tiedemann (1998), for example, proposed that increased atmospheric moisture supply was a necessary precondition for ice-sheet growth, which was then triggered by changes in the Earth's orbital obliquity. A contrasting argument is that increased deep-water formation could have worked against the initiation of NHG as greater heat transport to high latitudes would have tended to prevent ice-sheet formation.

The geological record shows strong evidence that the thermohaline circulation in the early Pliocene weakened as a response to the onset of Northern Hemisphere Glaciation (e.g., Raymo et al., 1992, 1996). Based on the stable carbon isotope composition in benthic foraminifera from the Atlantic and Pacific oceans, Raymo et al. (1992) associated the gradual cooling between 3 and 2 Ma with an increased suppression of the formation of NADW. Data from the eastern Pacific (Shackleton et al., 1995) shows an in-phase relationship between colder periods and those having decreased NADW formation during the Pliocene. It has been argued that tectonic changes such as the closing of the Central American Seaway, uplift of the Himalayan and Tibetan Plateaus, and deepening of the Bering Strait are too gradual to account entirely for the rapid onset of NHG. Although tectonic changes may have brought the global climate to a critical threshold, the rapid variations in Earth's orbital parameters and thus insolation are more likely to have triggered the intensification of NHG (e.g., see Lourens and Hilgen, 1997). Long-term periodic variations in the Earth's orbital parameters seem at least partially to have controlled the onset of NHG (see *Astronomical theory of climate change*).

Bibliography

- Benson, R.H., Rakic-El Bied, K., and Bonaduce, G., 1991. An important current reversal (influx) in the Rifian corridor (Morocco) at the Tortonian-Messinian boundary: The end of the Tethys Ocean. *Paleoceanography*, **6**(1), 164–192.
- Berggren, W.A., Kent, D.V., Swisher, C.C., and Aubry, M.-P., 1995. A revised Cenozoic geochronology and chronostratigraphy. In Berggren, W.A., Kent, D.V., Aubry, M.-P., and Hardenbol, J. (eds.), *Geochronology, time scales and global stratigraphic correlation*, Special Publication No. 54. Tulsa, OK: SEMP, pp. 129–212.
- Crowley, T.J., 1996. Pliocene climates: The nature of the problem. *Mar. Micropal.*, **27**, 3–12.
- Flower, B.P., and Kennett, J.P., 1995. Middle Miocene deepwater paleoceanography in the southwest Pacific: Relations with East Antarctic ice sheet development. *Paleoceanography*, **10**(6), 1095–1112.
- Fronval, T., and Jansen, E., 1996. Late Neogene paleoclimates and paleoceanography in the Iceland-Norwegian Sea: Evidence from the Iceland and Voring Plateaus. In Thiede, J., Myhre, A.M., Firth, J.V., Johnson, G.L., and Ruddimand, W.F. (eds.), *Proceedings of the ODP Science Results*, **151**, pp. 455–468.
- Haug, G.H., and Tiedemann, R., 1998. Effect of the formation of the Isthmus of Panama on Atlantic Ocean thermohaline circulation. *Nature*, **393**(6686), 673–676.
- Hodell, D.A., Benson, R.H., Kent, D.V., Boersma, A., and Rakic-El Bied, K., 1994. Magnetostratigraphic, biostratigraphic, and stable isotope stratigraphy of an Upper Miocene drill core from the Salé Briquerie (northwestern Morocco): A high-resolution chronology for the Messinian stage. *Paleoceanography*, **9**(6), 835–855.
- Jansen, E., Fronval, T., Rack, F., and Channell, J.E.T., 2000. Pliocene-Pleistocene ice rafting history and cyclicity in the Nordic Seas during the last 3.5 Myr. *Paleoceanography*, **15**, 709–721.
- Kim, S.-J., and Crowley, T.J., 2000. Increased Pliocene North Atlantic Deep Water: Cause or consequence of Pliocene warming? *Paleoceanography*, **15**(4), 451–455.
- Lourens, L.J., and Hilgen, F.J., 1997. Long-period variation in the Earth's obliquity and their relation to third-order eustatic cycles and the Late Neogene glaciations. *Quaternary Int.*, **40**, 43–52.
- Lourens, L., Hilgen, F., Shackleton, N.J., Laskar, J., Wilson, D., (2004) "The Neogene Period". In: Gradstein, F., Ogg, J., Smith, A.G. (eds.), *Geologic Time Scale*, Cambridge University Press, Cambridge.
- Maier-Reimer, E., Mikolajewicz, U., and Crowley, T., 1990. Ocean general circulation model sensitivity experiments with an open Central America Isthmus. *Paleoceanography*, **5**(3), 349–366.
- Mikolajewicz, U., and Crowley, T.J., 1997. Response of a coupled ocean/energy balance model to restricted flow through the central American isthmus. *Paleoceanography*, **12**(3), 429–441.
- Miller, K.G., Wright, J.D., and Fairbanks, R.G., 1991. Unlocking the ice house: Oligocene-Miocene oxygen isotopes, eustasy, and margin erosion. *J. Geophys. Res.*, **96**(B4), 6829–6848.
- Pagani, M., Arthur, M.A., and Freeman, K.H., 1999. Miocene evolution of atmospheric carbon dioxide. *Paleoceanography*, **14**(3), 273–292.
- Raymo, M.E., 1994. The Himalayas, organic carbon burial, and climate in the Miocene. *Paleoceanography*, **9**(3), 399–404.
- Raymo, M.E., Hodell, D.A., and Jansen, E., 1992. Response of deep ocean circulation to initiation of Northern Hemisphere glaciation (3–2 Ma). *Paleoceanography*, **7**(5), 645–672.
- Raymo, M.E., Grant, B., Horowitz, M., and Rau, G.H., 1996. Mid-Pliocene Warmth: Stronger greenhouse and stronger conveyor. *Mar. Micropal.*, **21**, 313–326.
- Savin, S.M., Douglas, R.G., and Stehli, F.G., 1975. Tertiary marine paleotemperatures. *Geol. Soc. Am. Bull.*, **86**, 1499–1510.
- Shackleton, N.J., and Kennett, J.P., 1975. Paleotemperature history of the Cenozoic and the initiation of Antarctic glaciation: Oxygen and carbon isotope analyses in DSDP sites 277, 279, and 281. *Init. Rep. DSDP Proj.*, **29**, 743–755.
- Shackleton, N.J., Le, J., Mix, A., and Hall, M.A., 1992. Carbon isotope records from Pacific surface waters and atmospheric carbon dioxide. *Quaternary Sci. Rev.* **11**, 387–400.
- Shackleton, N.J., Hall, M.A., and Pate, D., 1995. Pliocene stable isotope stratigraphy of Site 846. In Pisiias, N.G., Mayer, L.A., Janecek, T.R.,

- Palmer-Julson, A., and van Andel, T.H. (eds.), *Proceedings Of the ODP, Science Results*, **138**, pp. 337–355.
- Van der Burgh, J., Visscher, H., Dilcher, D.L., and Kürschner, W.M., 1993. Paleoatmospheric signatures in Neogene fossil leaves. *Science*, **260**, 1788–1790.
- Vincent, E., and Berger, W.H., 1985. Carbon dioxide and polar cooling in the Miocene: The Monterey hypothesis. In Sundquist, E.T., and Broecker, W.S. (eds.), *The Carbon Cycle and Atmospheric CO₂: Natural Variations From Archean to Present*. Geophysical Monograph Series, vol. **32**, pp. 455–468.
- Wright, J.D., Miller, K.G., and Fairbanks, R.G., 1992. Early and middle Miocene stable isotopes: Implications for deepwater circulation and climate. *Paleoceanography*, **7**(3), 357–389.
- Wright, J.D., and Miller, K.G., 1996. Control of North Atlantic Deep Water circulation by the Greenland-Scotland Ridge. *Paleoceanography*, **11**(2), 157–170.
- Zachos, J.C., Flower, B.P. and Paul, H., 1997. Orbitally paced climate oscillations across the Oligocene/Miocene boundary. *Nature*, **388** (6642), 567–570.
- Zachos, J., Pagani, M., Sloan, L., Thomas, E., and Billups, K., 2001. Trends, rhythms, and aberrations in global climate 65 Ma to present. *Science*, **292**, 686–693.

Cross-references

- [Antarctic Bottom Water and Climate Change](#)
- [Antarctic Glaciation History](#)
- [Astronomical Theory of Climate Change](#)
- [Carbon Isotopes, Stable](#)
- [Cenozoic Climate Change](#)
- [Ice-Rafted Debris \(IRD\)](#)
- [Marine Biogenic Sediments](#)
- [Messinian Salinity Crisis](#)
- [Mid-Pliocene Warming](#)
- [North Atlantic Deep Water and Climate Change](#)
- [Ocean Paleocirculation](#)
- [Oxygen Isotopes](#)
- [Plate Tectonics and Climate Change](#)
- [Pre-Quaternary Milankovitch Cycles and Climate Variability](#)
- [Thermohaline Circulation](#)
- [Weathering and Climate](#)

NITROGEN ISOTOPES

Introduction

Nitrogen, element number five in the Periodic Table, is a limiting nutrient to primary production (i.e., plant growth) on the continents and in the ocean (Dugdale and Goering, 1967). Phytoplankton productivity is generally high where fixed (i.e., soluble) nitrogen concentrations are elevated and low where they are diminished. Because primary productivity influences climate, via the uptake of atmospheric carbon dioxide, and is the precursor to petroleum deposits, it is important to understand nitrogen cycling in the environment. The stable isotopes of nitrogen, ¹⁴N and ¹⁵N, representing, respectively, 99.63% and 0.37% of nitrogen atoms in the solar system, provide a powerful tool for elucidating the processes that transfer nitrogen between reservoirs because many of them cause large isotopic fractionations that can be measured with a mass spectrometer.

The global nitrogen cycle

The largest reservoir of nitrogen on the planet is rocks, which contain 1.9×10^{11} Tg (10^{12} g) of nitrogen (Wada and Hattori, 1990). Nitrogen in rocks is not very reactive and therefore has a very long residence time. The largest available pool of nitrogen is atmospheric dinitrogen gas (N_2), consisting of 3.9×10^9 Tg N (Wada and Hattori, 1990). For comparison, the total amount of nitrogen contained in all plants and animals on the continents is 1.5×10^4 Tg N and in the ocean is 4.7×10^2 Tg N, both very much smaller than the reservoir of nitrogen in the atmosphere. While some specialized microbes are able to convert N_2 gas into ammonia (NH_3) – the biologically useful form of nitrogen – by a process called nitrogen fixation, most primary producers require fixed nitrogen in the form of nitrate (NO_3^-) or ammonium ion (NO_4^+). The pool of nitrate in the ocean is 5.7×10^5 Tg N and that of ammonium ion is 7×10^3 Tg N (Wada and Hattori, 1990).

The marine nitrogen cycle is complex and not well understood (Codispoti, 1995). Current estimates indicate that the total of all oceanic sinks for nitrogen are larger than combined sources by 75% (Codispoti and Christensen, 1985) but uncertainties of a factor of two to four exist regarding the magnitude of each. Sources of fixed nitrogen to the ocean are (a) nitrogen fixation ($30\text{--}130$ Tg N yr^{-1}), (b) atmospheric deposition ($30\text{--}83$ Tg N yr^{-1}), and (c) river runoff ($13\text{--}24$ Tg N yr^{-1}) (Wada and Hattori, 1990). Sinks of nitrogen in the ocean are (a) microbial denitrification, the conversion of nitrate to N_2 gas with its subsequent loss to the atmosphere ($25\text{--}180$ Tg N yr^{-1}), (b) burial in marine sediments (20 Tg N yr^{-1}), and (c) exports of organic nitrogen to the continents via fish catches, guano deposition, and atmospheric transport ($10\text{--}20$ Tg N yr^{-1}) (Codispoti and Christensen, 1985).

While the combined exports of nitrogen substantially exceed combined imports in the above tally, recent studies indicate that nitrogen fixation rates may have been drastically underestimated by a factor of two or more (Gruber and Sarmiento, 1997; Karl et al., 1997; Zehr et al., 2001). So the marine nitrogen cycle may be approximately in balance. Nevertheless future studies are needed to better constrain the sources and sinks of nitrogen in the ocean.

Nitrogen isotope ratios

Nitrogen isotopic ratios are typically measured on gaseous nitrogen (N_2 or N_2O) in a dual-inlet mass spectrometer. Very high precision, on the order of 0.01% or better, is obtainable using this technique. The isotope ratio of a sample is reported relative to that of a reference standard and reported in delta notation in units of per mil (‰), where one per mil is one-tenth of one percent, or one part per thousand, according to Equation (1):

$$\delta^{15}N = \left(\frac{^{15}N/^{14}N_{\text{sample}}}{^{15}N/^{14}N_{\text{standard}}} \right) - 1 \times 1,000/‰ \quad (1)$$

Atmospheric nitrogen (N_2) is the reference standard for nitrogen isotopic analyses and has a $\delta^{15}N$ value defined as 0‰.

The biologically-mediated reduction reactions that convert nitrogen from nitrate (NO_3^- , +5 oxidation state) to nitrite (NO_2^- , +3) to nitrous oxide (N_2O , +1), to nitrogen gas (N_2 , 0), and to ammonia (NH_3 , -3) are faster for ^{14}N than for ^{15}N as a result of higher vibrational frequency of bonding to ^{14}N than to ^{15}N (Owens, 1987). This results in products that are

^{15}N -depleted (i.e., have a lower $^{15}N/^{14}N$ ratio and lower $\delta^{15}N$) relative to the substrate. If the substrate reservoir is either closed or has inputs and outputs that are slow relative to one of the reduction processes then the reservoir will become enriched in ^{15}N . An example is the oxygen-depleted sub-surface water of the eastern tropical Pacific Ocean where high rates of denitrification cause large ^{15}N enrichments of the nitrate pool on the order of 1% (or 10‰) (Cline and Kaplan, 1975). Denitrification in low-oxygen regions of the ocean, such as the eastern tropical Pacific and the Arabian Sea cause the $\delta^{15}N$ value of the ocean nitrate reservoir to be high ($\sim 5\%$) relative to the atmosphere and to terrestrial nitrogen (Wada et al., 1975; Sigman et al., 1999).

During the reduction of N_2 to NH_3 by nitrogen fixing bacteria in the ocean, atmospheric nitrogen ($\delta^{15}N = 0\%$), which is already isotopically-depleted relative to ocean fixed nitrogen, is further depleted, resulting in organic nitrogen with a $\delta^{15}N$ value of -2.7% (c.f., Sachs and Repeta, 1999 and references therein). In regions of the ocean where nitrogen fixation is extensive, such as in the subtropical north Pacific (Liu et al., 1996; Karl et al., 1997) and in the Mediterranean Sea (Sachs and Repeta, 1999), $\delta^{15}N$ values are low in both phytoplankton and fixed nitrogen relative to global ocean average values.

Oxidation reactions that convert ammonia to N_2O , NO_2^- and NO_3^- during nitrification also result in isotopic fractionation (Mariotti et al., 1981; Yoshida et al., 1989).

Diagenetic alteration of nitrogen isotope ratios

Early diagenetic (i.e., decomposition) reactions in marine sediments can severely alter the isotopic composition of sedimentary organic nitrogen. This is critical to consider when attempting the interpretation of nitrogen isotopic ratios in whole sediment because the effect of diagenesis can be as large as the primary signal that is sought. For example, the diagenetic overprint of sedimentary nitrogen isotopic values typically ranges from 3–8‰ in sediments overlain by well-oxygenated water (Altabet and Francois, 1994; Sachs and Repeta, 1999), while the total range of isotopic variation is typically less than 5‰. The problem of diagenetic alteration of sedimentary $\delta^{15}N$ values is less of a concern in sediments overlain by oxygen-depleted water (Altabet et al., 1999; Sachs and Repeta, 1999).

One means of circumventing the issue of diagenesis is to measure nitrogen isotopic ratios on molecular fossils, or “biomarkers.” These molecules have a known source and, if found intact, are unlikely to have been altered isotopically. Chlorophyll and its decomposition products, chlorins, are ideal for this purpose because they are produced by all primary producers and persist in sediments for millions of years (Sachs and Repeta, 1999). Algal culture studies indicate that chlorophyll $\delta^{15}N$ values reflect those of the host alga with a constant isotopic depletion of 5.1‰ (Sachs et al., 1999). Methods for purifying chlorins for nitrogen (and carbon) isotopic analysis are described in Sachs and Repeta (2000).

Conclusion

Nitrogen isotopic ratios provide a powerful tool for evaluating processes within the nitrogen cycle and for reconstructing changes in the cycling of nitrogen through time. Because multiple nitrogen transformation reactions occur simultaneously in any environment, with some leading to nitrogen isotopic enrichment and some to isotopic depletion of the reservoir

of interest, it can be difficult to discern the most important processes. Nitrogen isotopes are therefore most useful in environments where one or more transformation processes can be ruled out.

Julian P. Sachs

Bibliography

- Altabet, M.A., and Francois, R., 1994. Sedimentary nitrogen isotopic ratio as a recorder for surface ocean nitrate utilization. *Global Biogeochem. Cycles*, **8**(1), 103–116.
- Altabet, M.A., Pilskaln, C., Thunnel, R., Pride, C., Sigman, D., Chavez, F., and Francois, R., 1999. The nitrogen isotope biogeochemistry of sinking particles from the margin of the eastern North Pacific. *Deep-Sea Res. I*, **46**, 655–679.
- Cline, J.D., and Kaplan, I.R., 1975. Isotopic fractionation of dissolved nitrate during denitrification in the eastern tropical North Pacific Ocean. *Mar. Chem.*, **3**, 271–299.
- Codispoti, L.A., 1995. Is the Ocean Losing Nitrate? *Nature*, **376**, 724.
- Codispoti, L.A., and Christensen, J.P., 1985. Nitrification, denitrification and nitrous oxide cycling in the eastern tropical South Pacific Ocean. *Mar. Chem.*, **16**, 277–300.
- Dugdale, R.C., and Goering, J.J., 1967. Uptake of new and regenerated forms of nitrogen in primary productivity. *Limnol. Oceanogr.*, **12**, 196–206.
- Gruber, N., and Sarmiento, J.L., 1997. Global patterns of marine nitrogen fixation and denitrification. *Global Biogeochem. Cycles*, **11**(2), 235–266.
- Karl, D., Letelier, R., Tupas, L., Dore, J., Christian, J., and Hebel, D., 1997. The role of nitrogen fixation in biogeochemical cycling in the subtropical North Pacific Ocean. *Nature*, **388**, 533–538.
- Liu, K.-K., Su, M.-J., Hsueh, C.-R., and Gong, G.-C., 1996. The nitrogen isotopic composition of nitrate in the Kuroshio Water northeast of Taiwan: Evidence for nitrogen fixation as a source of isotopically light nitrate. *Mar. Chem.*, **54**, 279–292.
- Mariotti, A., Germon, J.C., Hubert, P., Kaiser, P., Letolle, R., Tardieux, A., and Tardieux, P., 1981. Experimental determination of nitrogen kinetic isotope fractionation: Some principles; illustration for the denitrification and nitrification processes. *Plant and Soil*, **62**, 413–430.
- Owens, N.J.P., 1987. Marine variation in ^{15}N . *Adv. Mar. Biol.*, **24**, 390–451.
- Sachs, J.P., and Repeta, D.J., 1999. Oligotrophy and nitrogen fixation during eastern Mediterranean sapropels events. *Science*, **286**, 2485–2488.
- Sachs, J.P., and Repeta, D.J., 2000. The purification of chlorins from marine particles and sediments for nitrogen and carbon isotopic analysis. *Org. Geochem.*, **31**(4), 317–329.
- Sachs, J.P., Repeta, D.J., and Goericke, R., 1999. Nitrogen and carbon isotopic ratios of chlorophyll from marine phytoplankton. *Geochimica et Cosmochimica Acta*, **63**(9), 1431–1441.
- Sigman, D.M., Altabet, M.A., McCorkle, D.C., Francois, R., and Fischer, G., 1999. The $\delta^{15}\text{N}$ of nitrate in the Southern Ocean: Consumption of nitrate in surface waters. *Global Biogeochem. Cycles*, **13**(4), 1149–1166.
- Wada, E., and Hattori, A., 1990. *Nitrogen in the Sea: Forms, Abundances, and Rate Processes*. Boca Raton, FL: CRC Press.
- Wada, E., Kadonaga, T., and Matsuo, S., 1975. ^{15}N Abundance in Nitrogen of Naturally Occurring Substances and Global Assessment of Denitrification From an Isotopic Viewpoint. *Geochem. J.*, **9**, 139–148.
- Yoshida, N., Morimoto, H., Hirano, M., Koike, I., Matsuo, S., Wada, E., Saino, T., and Hattori, A., 1989. Nitrification Rates and ^{15}N Abundances of N_2O and NO_3^- in the Western North Pacific. *Nature*, **342**, 895–897.
- Zehr, J.P., Waterbury, J.B., Turner, P.T., Montoya, J.P., Omoregie, E., Steward, G.F., Hansen, A., and Karl, D.M., 2001. Unicellular cyanobacteria fix N_2 in the subtropical North Pacific Ocean. *Nature*, **412**, 635–638.

Cross-references

Isotope Fractionation
 Nitrogen Cycle, in *Encyclopedia of Geochemistry*
 Organic Geochemical Proxies
 Stable Isotope Analysis

NORTH ATLANTIC DEEP WATER AND CLIMATE CHANGE

Modern North Atlantic deep water

Together, the atmosphere and oceans transport $\sim 5\text{--}6$ PW (PW = 10^{15} W) of heat away from the tropics toward each pole in response to the latitudinal imbalance between incoming solar and outgoing long-wave radiation. In the Atlantic Ocean, net ocean heat transport is northward in both hemispheres, with a maximum of ~ 1.3 PW across northern middle latitudes (Ganachaud and Wunsch, 2000). This transport is dominated by the meridional overturning circulation, which transforms warm surface currents (moving predominately northward) into cold deep waters (moving predominately southward). The main product of this transformation is North Atlantic Deep Water (NADW), which forms poleward of 50°N and fills much of the Atlantic between ~ 1 and 4 km depth below sea surface. NADW formation is thus associated with the release of a great deal of heat to the high northern latitude atmosphere.

Modern NADW is ventilated in two main regions of wintertime deep convection: the Greenland Sea (producing Greenland Sea Deep Water) and the Labrador Sea (producing Labrador Sea Water) (Figure N3). In general, three factors may contribute to convective instability: cooling, increased salinity (lack of freshwater input, or active salinification due to sea ice formation), and winds/storminess. Sea ice also leads to the formation of dense Arctic shelf waters that entrain warm Atlantic waters. The resulting Arctic Intermediate/Deep Water mixes with Greenland Sea Deep Water to form the dense overflows that pass southward on each side of Iceland (Denmark Strait Overflow Water to the west, and Iceland-Scotland Overflow Water to the east). Each overflow

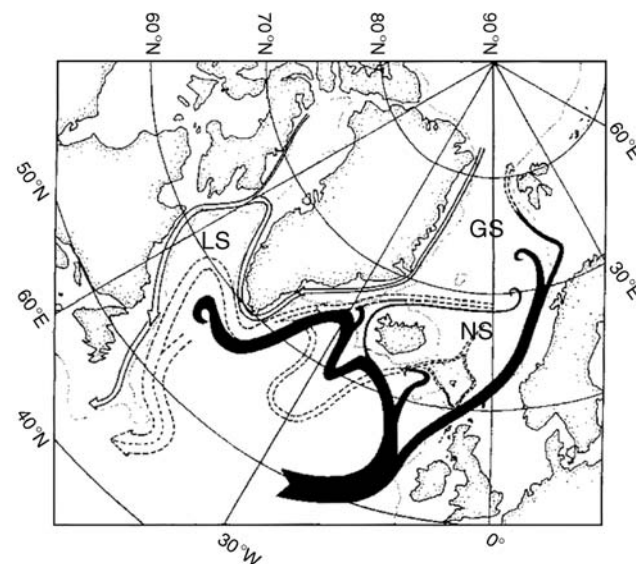


Figure N3 Schematic diagram of modern NADW formation, after McCartney and Talley (1984). Warm ($>4^\circ\text{C}$) surface currents are shown in black, and dense deep waters are dashed. The curled ends of the warm currents indicate sinking. Also shown are cold surface currents (open arrows). Labels denote the Labrador Sea (LS), Greenland Sea (GS), and Norwegian Sea (NS).

amounts to roughly 3 Sverdrups ($Sv = 10^6 \text{ m}^3 \text{ s}^{-1}$), and several additional Sv are entrained south of the sills as geostrophy concentrates the net flow into a western boundary current (Hansen and Østerhus, 2000). Labrador Sea Water adds perhaps another 5 Sv, yielding a total of 15 ± 2 Sv of NADW exiting the North Atlantic (Ganachaud and Wunsch, 2000). The overflows mainly contribute to NADW properties below 2 km depth while the less-dense Labrador Sea Water mainly affects the 1–2 km range.

Hydrographic time series indicate that fluxes of the various NADW components have varied slightly over recent decades (Dickson et al., 1996; Hansen et al., 2001). Changing patterns of surface salinity and winds may suppress deep convection in one region while enhancing it in another. Analogous but larger scale changes are believed to have occurred in the distant past, with dramatic impacts on climate.

Last Glacial Maximum

The importance of the North Atlantic's wind-driven circulation in explaining the climate of the last ice age was hypothesized by James Croll well over a century ago, but the abyssal circulation did not receive attention until much later. Weyl (1968) proposed that Pleistocene glaciations were initiated by reduced NADW formation and expanded sea ice coverage, with both being caused by lower sea surface salinities in the North Atlantic. Early reconstructions of Last Glacial Maximum (LGM, ~ 21 ka) North Atlantic surface temperatures based on assemblages of planktonic organisms suggested that polar waters and sea ice expanded southward, as expected if the warm, upper branch of the meridional overturning circulation was restricted. Reduced NADW has since come to be regarded as a response to (and amplifier of) glaciation, rather than its ultimate cause (Rahmstorf, 2002).

Most of what is known about the past distribution of NADW is based on paleonutrient proxies. Modern NADW is low in dissolved nutrients like phosphate and nitrate because it is formed from surface waters that have been stripped of these constituents by photosynthetic activity. In contrast, Atlantic deep waters of southern origin (Antarctic Bottom Water (AABW) and Circumpolar Deep Water (CDW)) are

formed from waters that contain abundant nutrients. Deep Atlantic nutrient distributions therefore reflect the spatial extent of these water masses and give some indication of "aging" (via the collection of nutrients remineralized from decomposing organic matter that rains from above) and mixing processes.

Since there is no way to directly measure past phosphate or nitrate distributions, nutrient proxies are relied upon for paleoceanographic reconstructions. One such proxy is $\delta^{13}\text{C}$, a measure of the ratio between ^{13}C and ^{12}C in the dissolved inorganic carbon (DIC) pool. The preferential uptake of ^{12}C during marine photosynthesis leaves low-nutrient surface waters, such as those that form NADW, enriched in $\delta^{13}\text{C}$ (Kroopnick, 1985) (Figure N4). The $\delta^{13}\text{C}$ of DIC is recorded by the $\delta^{13}\text{C}$ of benthic foraminiferal calcite (Duplessy et al., 1984), offering a way to reconstruct the distribution of NADW through time. Another important nutrient proxy is dissolved Cd, which is highly correlated with phosphate in the modern ocean. Some phytoplankton use Cd as a micronutrient and others may incorporate it incidentally during the uptake of other nutrients. The Cd concentration of seawater is reflected in the Cd/Ca ratio of benthic foraminiferal calcite (Boyle, 1992), again offering a method for tracing paleo-NADW. Discrepancies sometimes exist between $\delta^{13}\text{C}$ and Cd/Ca, however, pointing to complicating factors such as air-sea carbon exchange, benthic foraminiferal microhabitat effects, and calcite undersaturation or dissolution. Care must therefore be exercised when interpreting changes recorded by just one proxy.

Benthic foraminiferal $\delta^{13}\text{C}$ and Cd/Ca provide a relatively detailed picture of deep Atlantic water mass geometries during the LGM. Below ~ 2 km, both proxies indicate higher nutrient concentrations during glacial times, consistent with reduced NADW production (Boyle, 1992; Oppo and Lehman, 1993; Samthein et al., 1994; Curry and Oppo, 2005; Marchitto and Broecker, 2006). High $\delta^{13}\text{C}$ and low Cd/Ca values at intermediate depths (above ~ 2 km) suggest that NADW was partially replaced by a shallower water mass dubbed Glacial North Atlantic Intermediate Water (GNAIW). This apparent shoaling of northern source deep waters allowed high-nutrient

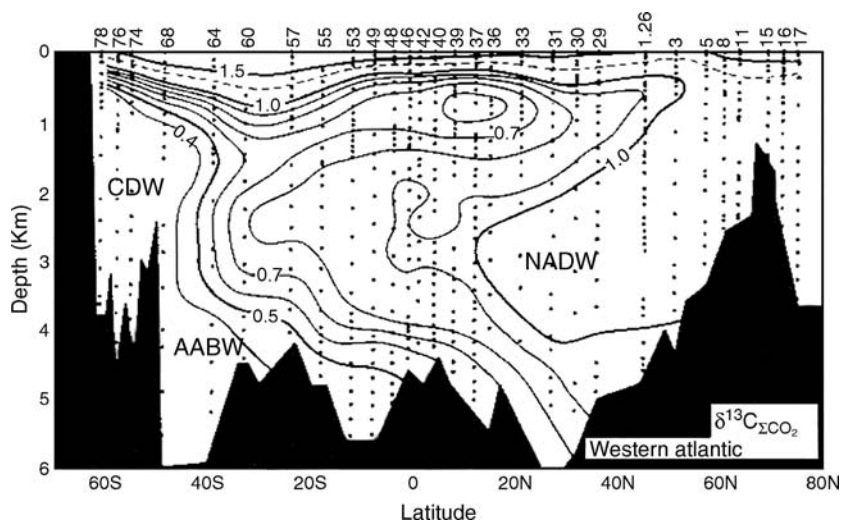


Figure N4 Section of modern seawater $\delta^{13}\text{C}$ in the western Atlantic Ocean, after Kroopnick (1985) (reprinted with permission from Elsevier). High values trace the southward flow of NADW, which mixes with low- $\delta^{13}\text{C}$ AABW and CDW. Dots indicate locations of samples, and numbers along the top axis indicate GEOSECS station numbers.

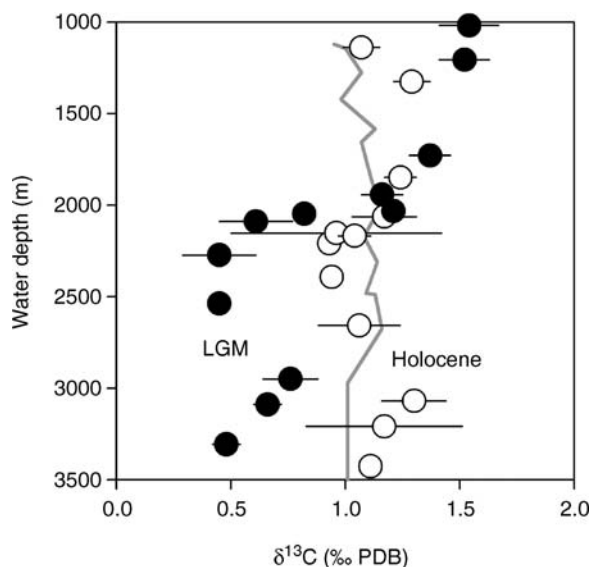


Figure N5 Vertical profiles of North Atlantic (>40° N) benthic foraminiferal $\delta^{13}\text{C}$ for the Holocene (open circles) and LGM (filled circles) (Oppo and Lehman, 1993; Marchitto et al., 2002). LGM data have been shifted upward by 120 m to account for the glacial lowering of sea level. Also shown are nearby modern seawater measurements (gray line) (Kroopnick, 1985). The LGM nutricline at ~2,000 m separates high- $\delta^{13}\text{C}$ GNAIW from low- $\delta^{13}\text{C}$ AABW/CDW.

southern source deep waters (AABW and/or CDW) to penetrate farther into the North Atlantic (Figure N5). Two additional paleonutrient tracers, Ba/Ca and Zn/Ca, support this view (Lea and Boyle, 1990; Marchitto et al., 2002).

Ocean circulation models suggest that reduced sea surface salinities and greater sea ice cover in the glacial North Atlantic could cause not only a shallower mode of deep water production (GNAIW), but also a shift in its production site to south of Iceland (Ganopolski et al., 1998). This change in deep convection sites would reduce ocean heat transport to higher latitudes even if the rate of deep water production was unchanged. The question of rate cannot be addressed with paleonutrient data alone, since their distributions depend on additional factors such as initial sea surface (“preformed”) values, biogeochemical cycling, and water mass mixing. One method that can potentially be used to assess actual flow rates is the ^{14}C age difference between coexisting benthic and planktonic foraminifera, which is an estimate of the time elapsed since the deep water mass was last in contact with the atmosphere (“ventilation age”). Mixing with old (poorly ventilated) AABW/CDW must be accounted for, however, to isolate any true aging of northern source waters. Limited LGM measurements are consistent with older waters in the deep (~3–4 km) Atlantic (Robinson et al., 2005), but the impact of mixing has not been well constrained. An additional complication for benthic-planktonic ages arises from temporal variations in the ^{14}C content of the atmosphere, a problem that can be avoided by obtaining paired ^{14}C and U-series dates on deep sea corals (Robinson et al., 2005). $^{231}\text{Pa}/^{230}\text{Th}$ patterns in marine sediments have been used to argue that LGM GNAIW must have been exported to the Southern Ocean at a rate similar to today, otherwise more Pa (which is less particle reactive than Th) would have been scavenged out of the water column within the Atlantic (Yu et al., 1996). The differential behavior of Pa and Th is dependent on

particle flux and composition, however, adding uncertainty to rate estimations.

A promising method for reconstructing the rate of the meridional overturning circulation is paleo-geostrophy. The northward flowing limb of the North Atlantic overturning is geostrophic, i.e., the flow is balanced by a horizontal pressure gradient and the Coriolis force. The strength of the flow can therefore be calculated from the magnitude of the pressure gradient. Above some “level of no motion” (where isobars are horizontal) the pressure gradient must be accompanied by lateral changes in density. Because benthic foraminiferal $\delta^{18}\text{O}$ is influenced by both temperature and salinity, it is a good recorder of density in waters warmer than ~5°C, allowing paleo-geostrophic calculations to be made. Lynch-Stieglitz et al. (1999) showed that Gulf Stream transport through the Florida Straits was only ~15–18 Sv during the LGM. Today the flow is ~30–32 Sv, with the wind-driven subtropical gyre accounting for ~17 Sv and the rest being due to meridional overturning. Since it is unlikely that the gyre circulation was slower during the LGM (models do not support weaker winds), this suggests that the overturning was either very weak, or was accomplished in a way that did not draw surface waters northward through the Florida Straits.

Although benthic foraminiferal $\delta^{18}\text{O}$ has also been used to infer deep ocean paleotemperatures, the influence of seawater $\delta^{18}\text{O}$ (which is related to both salinity and global ice volume) has been difficult to quantify. Fortunately, independent methods for separating temperature and salinity have recently become available. Initial indications from benthic foraminiferal Mg/Ca (a temperature proxy) are that the deep equatorial Atlantic was ~3–4°C colder during the LGM than during the Holocene, consistent with a greater influence of AABW (Martin et al., 2002). Semi-direct estimates of salinity and seawater $\delta^{18}\text{O}$ can also be made by analyzing glacial-age waters that have been partially preserved as sediment pore waters. When combined with benthic foraminiferal $\delta^{18}\text{O}$, these measurements suggest that the LGM deep Southern Ocean was much saltier and denser, but not discernibly colder, than the deep North Atlantic (Adkins et al., 2002). This is very different from the modern relationship (AABW colder and fresher than NADW), indicating a major change in the thermohaline properties of the deep circulation. All deep waters appear to have been formed close to the freezing point, with salinity dominating the deep stratification.

Dansgaard-Oeschger cycles and Heinrich events

During the last ice age, temperatures over Greenland and in the North Atlantic repeatedly and abruptly switched between cold stadials and warm interstadials, with a periodicity of approximately 1,500 years (Dansgaard et al., 1993). Broecker et al. (1985) suggested that these Dansgaard-Oeschger (D-O) cycles could have been caused by switches between “weak NADW” and “strong NADW” states, driven by oscillations in North Atlantic salinity. The first convincing evidence for a millennial-scale change in NADW flow was during the Younger Dryas (~13–11.6 ka), a brief return to glacial-like conditions in the middle of the last deglaciation. Benthic foraminiferal Cd/Ca and $\delta^{13}\text{C}$ imply a sharply reduced presence of NADW in the deep western North Atlantic at this time (Boyle and Keigwin, 1987). NADW suppression during the Younger Dryas may have been caused by an input of Laurentide Ice Sheet meltwater into the North Atlantic via the St. Lawrence River. Paleonutrient records (Keigwin

and Boyle, 1999; Boyle, 2000) and benthic foraminiferal faunas (Rasmussen et al., 1997) now suggest that NADW production was also reduced during D-O stadials and enhanced during interstadials (Figure N6). There is evidence for an opposite response (reduced during interstadials) for GNAIW (Zahn and Stüber, 2002), suggesting that stadials resembled the LGM state while interstadials approached the Holocene state. Some deep waters may have continued to form in the Norwegian-Greenland Seas during stadials because of brines resulting from sea ice formation (Dokken and Jansen, 1999).

Various ocean circulation models support the hypothesis that even small freshwater forcing can abruptly switch NADW between different equilibrium states (Rahmstorf, 2002). These models exhibit hysteresis behavior, whereby the system flips rapidly from strong to weak/no overturning, or vice versa, after crossing some surface salinity threshold. Furthermore, the overturning can be bistable, meaning that it can exist in either state for a given range of freshwater forcing. Glacial boundary conditions may narrow the hysteresis loop, such that a smaller range of salinity forcing is required to cause abrupt switches. Periodic or quasi-periodic salinity “triggers” may result from internal ice sheet dynamics (iceberg calving) (Schmittner et al., 2002) or possibly solar variations. When combined with white-noise salinity variability, the required magnitude of salinity forcing is further reduced, a phenomenon known as stochastic resonance (Alley et al., 2001).

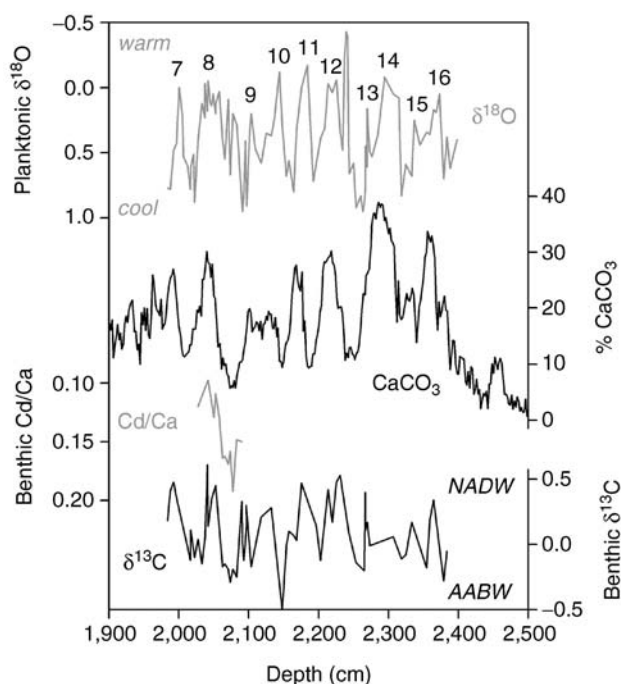


Figure N6 Last ice age climatic and deep water indicators from Bermuda Rise (~4,600 m) in the western North Atlantic (Keigwin and Boyle, 1999). Planktonic foraminiferal $\delta^{18}\text{O}$ shows warmings coincident with Dansgaard-Oeschger interstadials (numbered). Benthic foraminiferal $\delta^{13}\text{C}$ increased during interstadials, suggesting stronger production of NADW. Cd/Ca measurements across one stadial-interstadial transition are consistent with this (note reversed scale). Low bulk percent CaCO_3 during stadials may have been due, in part, to dissolution by corrosive AABW.

Some models' glacial responses may be grouped into three states: “warm” or strong NADW (interstadials), “cold” or weak GNAIW (stadials), and “off” (Heinrich events) (Rahmstorf, 2002). Heinrich events, which occurred during stadials every 6–10 Kyr, are marked by widespread ice-rafted debris layers believed to have resulted from ice sheet surging. The modeled Heinrich state thus results from a much larger freshwater (iceberg) forcing than in the normal stadial state. There is good paleonutrient evidence for reduced NADW during Heinrich events (Boyle, 2000; Elliot et al., 2002), and at least some GNAIW sites show strong nutrient enrichments (Zahn and Stüber, 2002). $^{231}\text{Pa}/^{230}\text{Th}$ measurements from Bermuda Rise suggest that the meridional overturning circulation was nearly or completely shut down during Heinrich event 1 (McManus et al., 2004).

Northern Hemisphere glaciations (past 3 Myr)

Composite records of deep ocean $\delta^{18}\text{O}$ indicate that significant Northern Hemisphere glaciations commenced during the late Pliocene, at ~3 Ma. Deep ocean $\delta^{13}\text{C}$ gradients suggest that a gradual weakening of NADW began around this time (Ravelo and Andreasen, 2000), probably as a response to (and amplifier of) surface cooling and freshening. The divergence of Nd isotopic values between the North Atlantic and Southern Ocean since ~3–4 Ma is consistent with this weakening (Frank et al., 2002). On the 41 Kyr scale of late Pliocene glacial-interglacial cycles, NADW was generally weakest during glaci- als and progressively deteriorated toward the Pleistocene. Glacial suppression of NADW intensified after ~1.5 Ma and was most severe during the 100 Kyr cycles of the mid-late Pleistocene (since ~0.9 Ma) (Raymo et al., 1997). GNAIW has appeared during glaciations (intermittently) since at least the early Pleistocene (McIntyre et al., 1999).

On a finer temporal scale, there appear to be lags between Pleistocene glacial cycles and NADW production changes (Wright and Flower, 2002). During glacial initiations, NADW initially strengthened as ice sheets began to grow, likely in response to increased salinities. The resulting continued sea surface warmth may have supplied excess moisture for the expanding ice. At least several millennia passed before reduced salinities caused NADW suppression and North Atlantic cooling. A similar (but opposite) progression seems to have occurred during deglaciations: GNAIW initially weakened due to meltwater addition, with NADW resumption and surface warming occurring several millennia later. Hence, NADW production changes have played an important role in modifying the character of glacial-interglacial transitions.

With still higher temporal resolution, it is apparent that the millennial scale variability characteristic of the last glaciation was also present during prior glaciations. Ice rafting events have been associated with NADW reorganizations since at least the early Pleistocene (Raymo et al., 1998). During the late Pleistocene (past 0.5 Myr), millennial-scale sea surface variability was strongest when ice sheets exceeded a certain threshold size (McManus et al., 1999). Benthic $\delta^{13}\text{C}$, however, suggests that NADW reductions occurred during intervals of cooling and ice rafting regardless of their magnitude, implying that rapid deep circulation changes may occur without large Northern Hemisphere ice sheets.

Earlier Cenozoic history

On longer timescales, tectonics played an important role in the broad evolution of NADW. Prior to the global cooling of

the Plio-Pleistocene, a relatively cold NADW mass (loosely defined) could only form at very high latitudes, such as in the Norwegian-Greenland Seas. During the early Cenozoic, a shallow Greenland-Scotland Ridge prevented any such waters from filling the open Atlantic. Attempts to date the onset of NADW formation, presumed to coincide with an opening in this barrier, have relied on two main methods: reconstructing deep ocean $\delta^{13}\text{C}$ gradients and identifying sedimentation patterns created by deep flow. It has been proposed that an early Oligocene initiation coincided with the formation of the Southeast Faroes Drift (Davies et al., 2001). Accumulation on Feni Drift also began around this time, though its link to NADW production is not straightforward. The opening of Drake Passage (probably during the Oligocene) may have also established the ocean dynamics necessary to sustain a meridional overturning circulation, thereby amplifying the cooling and glaciation of Antarctica (Toggweiler and Bjornsson, 2000). The transition of deep Southern Ocean $\delta^{13}\text{C}$ from low Pacific-like values toward high North Atlantic values during the early-middle Miocene (~ 20 – 15 Ma) has been interpreted as the first appearance of substantial NADW (Wright and Miller, 1996). The formation of other major North Atlantic drifts around this time may or may not be related to increased NADW flow.

Another tectonic change that affected NADW formation was the closing of the Isthmus of Panama. Although the closure began ~ 13 Ma, the gateway was not shallow enough to strongly impact NADW until ~ 4.6 Ma (Haug and Tiedemann, 1998). By this time, the flow of relatively fresh Pacific waters into the Atlantic was minimized, allowing the North Atlantic to become saltier. This excess salt intensified the production of NADW, which may have contributed to early Pliocene warmth. The stronger northward flow of warm waters may have also preconditioned the Northern Hemisphere for glaciation at ~ 3 Ma by supplying the requisite moisture for ice growth.

Thomas M. Marchitto, Jr.

Bibliography

- Adkins, J.F., McIntyre, K., and Schrag, D.P., 2002. The salinity, temperature, and $\delta^{18}\text{O}$ of the glacial deep ocean. *Science*, **298**, 1769–1773.
- Alley, R.B., Anandakrishnan, S., and Jung, P., 2001. Stochastic resonance in the North Atlantic. *Paleoceanography*, **16**, 190–198.
- Boyle, E.A., 1992. Cadmium and $\delta^{13}\text{C}$ paleochemical ocean distributions during the Stage 2 glacial maximum. *Annu. Rev. Earth Planet. Sci.*, **20**, 245–287.
- Boyle, E.A., 2000. Is ocean thermohaline circulation linked to abrupt stadial/interstadial transitions? *Quaternary Sci. Rev.*, **19**, 255–272.
- Boyle, E.A., and Keigwin, L.D., 1987. North Atlantic thermohaline circulation during the last 20,000 years linked to high latitude surface temperature. *Nature*, **330**, 35–40.
- Broecker, W.S., Peteet, D.M., and Rind, D., 1985. Does the ocean-atmosphere system have more than one stable mode of operation? *Nature*, **315**, 21–25.
- Curry, W.B., and Oppo, D.W., 2005. Glacial water mass geometry and the distribution of $\delta^{13}\text{C}$ of ΣCO_2 in the Western Atlantic Ocean. *Paleoceanography*, **20**(1), PA1017 (doi:10.1029/2004PA001021).
- Dansgaard, W., Johnsen, S.J., Clausen, H.B., Dahl-Jensen, D., Gundestrup, N.S., Hammer, C.U., Hvidberg, C.S., Steffensen, J.P., Sveinbjornsdottir, A.E., Jouzel, J., and Bond, G., 1993. Evidence for general instability of past climate from a 250-kyr ice-core record. *Nature*, **364**, 218–220.
- Davies, R., Cartwright, J., Pike, J., and Line, C., 2001. Early Oligocene initiation of North Atlantic Deep water formation. *Nature*, **410**, 917–920.
- Dickson, R., Lazier, J., Meincke, J., Rhines, P., and Swift, J., 1996. Long-term coordinated changes in the convective activity of the North Atlantic. *Prog. Oceanogr.*, **38**, 241–296.
- Dokken, T.M., and Jansen, E., 1999. Rapid changes in the mechanism of ocean convection during the last glacial period. *Nature*, **401**, 458–461.
- Duplessy, J.-C., Shackleton, N.J., Matthews, R.K., Prell, W., Ruddiman, W.F., Caralp, M., and Hendy, C.H., 1984. ^{13}C record of benthic foraminifera in the last interglacial ocean: Implications for the carbon cycle and the global deep water circulation. *Quaternary Res.*, **21**, 225–243.
- Elliot, M., Labeyrie, L., and Duplessy, J.-C., 2002. Changes in North Atlantic deep-water formation associated with the Dansgaard-Oeschger temperature oscillations (60–10 ka). *Quaternary Sci. Rev.*, **21**, 1153–1165.
- Frank, M., Whiteley, N., Kasten, S., Hein, J.R., and O’Nions, K., 2002. North Atlantic Deep Water export to the Southern Ocean over the past 14 Myr: Evidence from Nd and Pb isotopes in ferromanganese crusts. *Paleoceanography*, **17**(2), 1022 (doi:10.1029/2000PA000606).
- Ganachaud, A., and Wunsch, C., 2000. Improved estimates of global ocean circulation, heat transport and mixing from hydrographic data. *Nature*, **408**, 453–457.
- Ganopolski, A., Rahmstorf, S., Petoukhov, V., and Claussen, M., 1998. Simulation of modern and glacial climates with a coupled global model of intermediate complexity. *Nature*, **391**, 351–356.
- Hansen, B., and Østerhus, S., 2000. North Atlantic-Nordic Seas exchanges. *Prog. Oceanogr.*, **45**, 109–208.
- Hansen, B., Turrell, W.R., and Østerhus, S., 2001. Decreasing overflow from the Nordic seas into the Atlantic Ocean through the Faroe Bank channel since 1950. *Nature*, **411**, 927–930.
- Haug, G.H., and Tiedemann, R., 1998. Effect of the formation of the Isthmus of Panama on Atlantic Ocean thermohaline circulation. *Nature*, **393**, 673–676.
- Keigwin, L.D., and Boyle, E.A., 1999. Surface and deep ocean variability in the northern Sargasso Sea during marine isotope stage 3. *Paleoceanography*, **14**, 164–170.
- Kroopnick, P.M., 1985. The distribution of ^{13}C of ΣCO_2 in the world oceans. *Deep Sea Res.*, **32**, 57–84.
- Lea, D.W., and Boyle, E.A., 1990. Foraminiferal reconstruction of barium distributions in water masses of the glacial oceans. *Paleoceanography*, **5**, 719–742.
- Lynch-Stieglitz, J., Curry, W.B., and Slowey, N., 1999. Weaker Gulf Stream in the Florida Straits during the Last Glacial Maximum. *Nature*, **402**, 644–648.
- Marchitto, T.M., and Broecker, W.S., 2006. Deep water mass geometry in the glacial Atlantic Ocean: A review of constraints from the paleo-nutrient proxy Cd/Ca. *Geochem. Geophys. Geosys.*, **7**(12), Q12003 (doi: 10.1029/2006 GC001323).
- Marchitto, T.M., Oppo, D.W., and Curry, W.B., 2002. Paired benthic foraminiferal Cd/Ca and Zn/Ca evidence for a greatly increased presence of Southern Ocean Water in the glacial North Atlantic. *Paleoceanography*, **17**(3), 1038, (doi:10.1029/2000PA000598).
- Martin, P.A., Lea, D.W., Rosenthal, Y., Shackleton, N.J., Sarnthein, M. and Papenfuss, T., 2002. Quaternary deep sea temperature histories derived from benthic foraminiferal Mg/Ca. *Earth Planet. Sci. Lett.*, **198**, 193–209.
- McCartney, M.S., and Talley, L.D., 1984. Warm-to-cold water conversion in the northern North Atlantic Ocean. *J. Phys. Oceanogr.*, **14**, 922–935.
- McIntyre, K., Ravelo, A.C., and Delaney, M.L., 1999. North Atlantic Intermediate Waters in the late Pliocene to early Pleistocene. *Paleoceanography*, **14**, 324–335.
- McManus, J.F., Oppo, D.W., and Cullen, J.L., 1999. A 0.5-million-year record of millennial-scale climate variability in the North Atlantic. *Science*, **283**, 971–975.
- McManus, J.F., Francois, R., Gherardi, J.-M., Keigwin, L.D., and Brown-Leger, S., 2004. Collapse and rapid resumption of Atlantic meridional circulation linked to deglacial climate changes. *Nature*, **428**, 834–837.
- Oppo, D.W., and Lehman, S.J., 1993. Mid-depth circulation of the subtropical North Atlantic during the Last Glacial Maximum. *Science*, **259**, 1148–1152.
- Rahmstorf, S., 2002. Ocean circulation and climate during the past 120,000 years. *Nature*, **419**, 207–214.
- Rasmussen, T.L., van Weering, T.C.E., and Labeyrie, L., 1997. Climatic instability, ice sheets and ocean dynamics at high northern latitudes

- during the last glacial period (58–10 ka BP). *Quaternary Sci. Rev.*, **16**, 71–80.
- Ravelo, A.C., and Andreasen, D.H., 2000. Enhanced circulation during a warm period. *Geophys. Res. Lett.*, **27**, 1001–1004.
- Raymo, M.E., Oppo, D.W., and Curry, W., 1997. The mid-Pleistocene climate transition: A deep sea carbon isotopic perspective. *Paleoceanography*, **12**, 546–559.
- Raymo, M.E., Ganley, K., Carter, S., Oppo, D.W., and McManus, J.F., 1998. Millennial-scale climate instability during the early Pleistocene epoch. *Nature*, **392**, 699–702.
- Robinson, L.F., Adkins, J.F., Keigwin, L.D., Southon J., Fernandez D.P., Wang, S.L., and Scheicer, D.S., 2005. Radiocarbon variability in the western North Atlantic during the last deglaciation. *Science*, **310**, 1469–1473.
- Sarnthein, M., Winn, K., Jung, S.J.A., Duplessy, J.-C., Labeyrie, L., Erlenkeuser, H., and Ganssen, G., 1994. Changes in east Atlantic deep-water circulation over the last 30,000 years: Eight time slice reconstructions. *Paleoceanography*, **9**, 209–267.
- Schmittner, A., Yoshimori, M., and Weaver, A.J., 2002. Instability of glacial climate in a model of the ocean-atmosphere-cryosphere system. *Science*, **295**, 1489–1493.
- Toggweiler, J.R., and Bjornsson, H., 2000. Drake Passage and palaeoclimate. *J. Quaternary Sci.*, **15**, 319–328.
- Weyl, P.K., 1968. The role of the oceans in climatic change: A theory of the ice ages. *Meteorol. Mono.*, **8**, 37–62.
- Wright, A.K., and Flower, B.P., 2002. Surface and deep ocean circulation in the subpolar North Atlantic during the mid-Pleistocene revolution. *Paleoceanography*, **17**(4), 1068, (doi:10.1029/2002PA000782).
- Wright, J.D., and Miller, K.G., 1996. Control of North Atlantic Deep Water circulation by the Greenland-Scotland Ridge. *Paleoceanography*, **11**, 157–170.
- Yu, E.-F., Francois, R., and Bacon, M.P., 1996. Similar rates of modern and last-glacial ocean thermohaline circulation inferred from radiochemical data. *Nature*, **379**, 689–694.
- Zahn, R., and Stüber, A., 2002. Suborbital intermediate water variability inferred from paired benthic foraminiferal Cd/Ca and $\delta^{13}\text{C}$ in the tropical West Atlantic and linking with North Atlantic climates. *Earth Planet. Sci. Lett.*, **200**, 191–205.

Cross-references

[Antarctic Bottom Water and Climate Change](#)
[Carbon Isotopes, Stable](#)
[Cenozoic Climate Change](#)
[Dansgaard-Oeschger Cycles](#)
[Heinrich Events](#)
[Last Glacial Maximum](#)
[Ocean Paleocirculation](#)
[Ocean Paleoproductivity](#)
[Oxygen Isotopes](#)
[Quaternary Climate Transitions and Cycles](#)
[Thermohaline Circulation](#)

NORTH ATLANTIC OSCILLATION (NAO) RECORDS

Introduction

Natural climate variability in the Atlantic sector results from processes at work in the atmosphere and in the ocean, and interactions between the two. In general, Atlantic climate variability has been described as a function of three related components: (a) an *atmospheric* mode of variability known as the North Atlantic Oscillation (NAO), (b) an *oceanic* mode of variability known as Atlantic Meridional Overturning Circulation, and possibly (c) an *atmosphere-ocean* mode of dynamics in the tropical Atlantic (see review by Marshall et al., 2001).

The first component, the NAO, is the leading mode of atmospheric variability in the Atlantic sector and has been dubbed the regional manifestation of the Arctic Oscillation (AO) – the leading mode of large-scale atmospheric variability in the Northern Hemisphere (NH). The NAO/AO is second only to the El Niño-Southern Oscillation (ENSO) in terms of the range of its climate impacts.

Impacts

The NAO has a profound impact on both marine and terrestrial ecosystems (Stenseth et al., 2002) in the Atlantic sector and surrounding continents, stretching from the Caribbean to the Arctic and from the eastern seaboard of the United States to Siberia. In addition to temperature and precipitation, impacts of the NAO are seen in agricultural production (Souriau, 2001), yields from fisheries (Otterson and Stenseth, 2001), fertility and demographic trends of land animals (Post and Stenseth, 1998), snow depth (Beniston, 1997), water resource management (Cullen et al., 2002), hydropower generation (Visbeck et al., 2002), hurricanes (Landsea et al., 1999), and wave heights (Kushnir and Wallace, 1989; Kushnir et al., 1997). The NAO is also the major factor controlling air-sea interactions over the Atlantic Ocean; modulating the intensity and location of upwelling/downwelling centers of the Atlantic's Meridional Overturning Circulation (MOC). Furthermore, there exists the possibility that the NAO has been influenced by anthropogenically forced climate change. This has led to the suggestion that a significant NAO-related weakening of the MOC in global warming scenarios is – while contentious – a possibility (Marshall et al., 2001).

Definitions

The NAO refers to a meridional redistribution of atmospheric mass between the center of subtropical high surface pressure located near the Azores, known as the Azores High (AH), and the center of subpolar low surface pressure near Iceland, known as the Icelandic Low (IL). There is no single way to define the NAO. Techniques include one-point correlation maps that rely on identifying regions of maximum negative correlation (Wallace and Gutzler, 1981), principle component analysis using eigenvectors of the covariance matrix (Barnston and Livezey, 1987), and clustering algorithms that identify climate regimes corresponding to the peak in the probability density function (Cassou and Terray, 2001).

In general, the NAO is described as being in either a positive or a negative phase. Synchronous strengthening (positive NAO state) and weakening (negative NAO state) of the NAO centers-of-action have been shown to result in distinct, dipole-like climate change patterns between western Greenland/the Mediterranean and northern Europe/northeast US/Scandinavia (Walker, 1924; Walker and Bliss, 1932; van Loon and Rogers, 1978; Rogers and van Loon, 1979). A lower-than-normal (higher-than-normal) IL and higher-than-normal (lower-than-normal) AH result in an enhanced (reduced) pressure gradient and a positive (negative) NAO. During this +NAO (–NAO) phase, surface winds and wintertime storms moving from west to east across the North Atlantic are stronger (weaker) than usual. As a result, wetter and warmer (drier and cooler) winter conditions occur in northern Europe, Scandinavia and the east coast of the US, while cooler and drier (warmer and wetter) winters occur in eastern Canada and Greenland.

In addition to a sea-level pressure (SLP) signature, the NAO has a coherent signal in sea-surface temperature (SST) involving a tripole pattern of almost zonally-oriented anomalies with subtropical and high-latitude SSTs varying in-phase and mid-latitude SSTs varying out-of-phase (Seager et al., 2000). Figure N7 presents the classic SLP and SST pattern associated with the NAO. While the NAO reflects changes in the strength and orientation of mid-Atlantic westerlies that dictate heat and moisture flux trajectories, it is also expressed in terms of distinct North Atlantic SST, sub-surface temperature (Molinari et al., 1997; Reverdin et al., 1997) and sea-ice extent anomalies (Deser and Blackmon, 1993). During the positive phase of the NAO, SSTs in the eastern Labrador Sea, eastern Mediterranean, and subtropical Atlantic are anomalously cold by 0.5–1 °C, whereas SSTs in the North Sea and Sargasso Sea are anomalously warm by approximately the same amount (Cullen et al., 2002).

Given that there is no unequivocal method for defining the NAO, it follows that there is no universally accepted index of the temporal variability of the NAO. However, as the signature of the NAO is strongly regional, a simple NAO index has been defined as the difference between the normalized mean winter (December through March; DJFM) SLP anomalies at locations representative of the relative strengths of the AH and IL. A positive NAO index implies more meridional storm tracks while a negative NAO index implies more zonal storm tracks. It must be remembered, however, that indices of the NAO merely provide a temporal signature for the behavior of a phenomenon whose dynamics are not clearly understood.

Historical development

The NAO was first documented by the Danish missionary Hans Egede Saabye (Egede, 1745) who described it as a saw-saw in temperature between Greenland and Denmark. Sir Gilbert Walker eventually defined the NAO as a meridional alternation of atmospheric mass in the 1920s (Walker, 1924). In addition to the NAO, Walker was also the first to describe the Southern Oscillation and the North Pacific Oscillation in his attempt to forecast Indian monsoon rainfall (Brown and Katz, 1991).

Beginning with the work of Bjerknes (1964), considerable effort has been made to understand the extent to which preferred timescales apparent in observations of the North Atlantic Ocean are associated with interactions between the ocean and atmosphere. These processes can be either coupled, whereby the two systems generate important positive and negative feedbacks, or uncoupled, where communication does not lead to feedbacks. Coupled, or two-way, interactions between the ocean and atmosphere suggest the potential for a degree of predictability. Predictability resides primarily within the long-term memory of the ocean and provides the opportunity for long-range forecasting. One example, in fact the only unquestioned example, of a coupled ocean-atmosphere interaction is the El Niño-Southern Oscillation (ENSO). Like the ENSO, the NAO has been shown to have significant climate impacts. However, there is still considerable doubt as to whether the NAO is a coupled ocean-atmosphere process. The NAO is a fundamental mode of the atmosphere, that is, it appears in atmospheric general circulation models (AGCMs) with fixed surface boundary conditions, whereas the Southern Oscillation's existence is entirely dependent upon active ocean-atmosphere coupling.

Significance

Given its importance as a modulator of climate in the Atlantic sector, an increased understanding of how the NAO has varied in past centuries is of considerable interest to the climate community. However, unlike the tropics, where abundant maritime proxy climate data (e.g., coral records) are preserved for high-resolution reconstructions of ENSO variability over past centuries, extra-tropical regions such as the North Atlantic lack these primary archives for reconstruction. The best proxy archives of NAO variability come from terrestrial regions and include tree ring records from North America, Eurasia, Scandinavia, and the Middle East, documentary evidence from Europe, and ice cores from the Arctic.

The NAO has exhibited a significant trend towards more positive values over the past 30 years, steadily rising from a negative phase in the 1960s to a persistent positive phase in the early 1990s. This trend accounts for a significant portion of the wintertime (DJFM) temperature increase over Eurasia

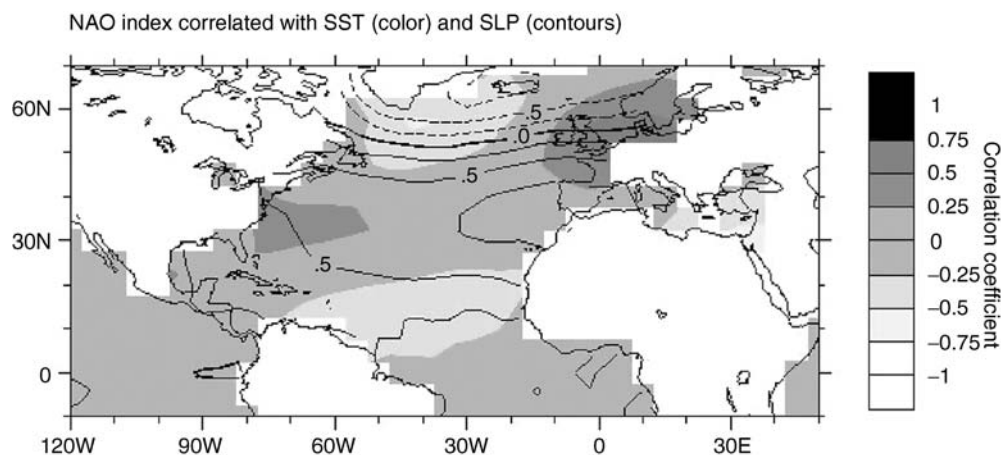


Figure N7 Correlation over the period 1865–2001 between the NAO index (Hurrell, 1995) and North Atlantic sector sea-level pressure (SLP; Kaplan, 2000) anomalies and sea-surface temperature (SST; Kaplan et al., 1998) anomalies. SLP correlation is shown as *contoured* r values (correlation coefficient) from -1.0 to 1.0 and SST correlation is shown as *shaded* r values (correlation coefficient) from -1.0 to 1.0 .

(Hurrell and van Loon, 1997). Consequently, the NAO has been introduced into the global warming debate with a search for mechanisms that could resolve whether this trend is due to anthropogenic perturbation or natural variability (Rodwell et al., 1999; Shindell et al., 1999). Coherent, large-scale changes in the NAO since 1981 were linked to recent dry conditions over western Greenland and the Mediterranean, and wetter and warmer than normal conditions in northern Europe, the northeast US, and parts of Scandinavia (Hurrell, 1995; Hurrell and van Loon, 1997). Using multivariate linear regression to quantify temperature variability associated with the NAO, it was shown that the NAO accounts for 31% of NH interannual variance (Hurrell, 1996). Moreover, the NAO accounts linearly for 0.15°C of the 0.29°C NH extratropical temperature increase for the period 1981–1994, with respect to the 1935–1994 mean. It should be noted, however, that the winters since 1995 have shown negative or neutral values – thereby interrupting the trend. In addition to being linked to widespread warming over the past three decades (Hurrell, 1996), it has been suggested that the NAO may have also played a role in maintaining climate anomalies during the Little Ice Age (Luterbacher et al., 1999, 2000; Shindell et al., 2001).

Proxy NAO records lengthen the relatively short observational record and provide the opportunity to assess both the low-frequency behavior of the NAO and the recent positive trend. Since the NAO is a natural mode of atmospheric variability, one could argue that much of the recent warming is natural and not related to the build-up of greenhouse gases in the atmosphere since the industrial revolution. This viewpoint, however, ignores the possibility that anthropogenic climate change might influence modes of natural variability, perhaps making it more likely that one phase or another of the NAO might be preferred.

Observational records

Table N1 details the most commonly used NAO indices. Most of the more commonly used NAO indices are derived from different representative SLP stations of the IL and AH. The principal component (PC) time series of the leading empirical orthogonal function (EOF) of Atlantic SLP is also commonly used. Walker and Bliss (1932) constructed the first index of the NAO using a linear combination of surface pressure and temperature measurements. Rogers (1984) constructed an NAO index beginning in 1895 using SLP anomalies from Ponta Delgados, the Azores, and Akuyreyri, Iceland. 1995) demonstrated that data from Lisbon, Portugal better captured the southern node variability of the NAO and used it along with data from Stykkisholmur, Iceland to develop an index that extends back to 1864. Figure N7 presents the correlation of the Hurrell (1996) NAO index with winter (DJFM) SLP (Kaplan et al., 2000) and SST (Kaplan et al., 1998) data. Jones et al.

(1997) further extended the NAO index back to 1821, using pressure data from Gibraltar and a composite southwest Iceland series. Jones et al. (2003) show that all of these indices are significantly correlated at interannual and decadal timescales but that choice of the southern node does make a difference.

Cullen et al. (2002) developed an SST anomaly index of the NAO, extending back to 1857, to extract the NAO-related component of Atlantic SST variability – similar in principle to the NINO3 SST-based index, which tracks ENSO in the tropical Pacific Ocean. Luterbacher et al. (1999) have developed the longest observational NAO record to date, going back to 1675, using instrumental station pressure, temperature and precipitation measurements, and proxy data. Each method has advantages and disadvantages. Indices based on station data are fixed in space and are therefore affected by small-scale transient non NAO-related weather events (Trenberth, 1984). Given the shifting of the NAO centers-of-action through the annual cycle, these indices cannot sufficiently capture the NAO over all months of the year (Hurrell and van Loon, 1997). One advantage of the PC time series approach is that it includes a larger spatial domain and hence provides a more optimal representation of the NAO pattern.

In addition to these commonly used NAO indices, several other methods for capturing temporal variability exist. During the 1950s, Namias, (1950) and Lorenz, (1951) were among the first to develop indices known as the “zonal index cycle.” These indices characterize NAO variability by looking at zonally averaged mid-latitude surface westerly wind fields. Stephenson et al. (2003) describe several less well-known NAO indices that have been developed by European scientists.

An investigation of the power spectrum of these NAO indices suggests little evidence that the NAO varies on any preferred timescale. Spectral analysis, used to quantify periodicities within time series, shows a slightly “red” spectrum (power increasing with period). There is somewhat enhanced variance on interannual (2–3 years) and decadal (8–10 years) bands as well as a trend over the last 30 years – but there are no significant peaks. Using a station-based index, Hurrell and van Loon (1997) demonstrated that the NAO index showed a greater degree of interannual variability during late nineteenth and early twentieth centuries, whereas decadal variability increased during the late twentieth century. Furthermore, Feldstein (2000) concluded that a role for forcings external to the atmosphere (i.e., the ocean) could not be ruled out despite the fact that interannual variability of the NAO arises primarily from noise. Czaja et al. (2003) caution that spectral analyses of dynamical NAO indices are not optimal for detecting the impact of the ocean.

Paleorecords

Instrumental records of the NAO, while useful in assessing seasonal and interannual variability, are not long enough to answer fundamental questions about low-frequency variability. In addition, recent observational records are not pure reflections of natural climate variability – they carry an imprint of anthropogenic forcing. As a result, a clear need exists to extend climate records back beyond the industrial era in order to understand: (a) the range of natural climate variability, (b) how quickly climate regimes can switch, and (c) how human activity might be influencing natural climate variability.

At present, paleoreconstructions are unable to accurately fingerprint the climate response to increasing greenhouse gas

Table N1 Instrumental records

Index	Season	Field	Begin
Cullen et al. (2002)	DJFM	SST	1856
Hurrell (1995)	DJFM	SLP	1864
Jones et al. (1997, 1999)	Monthly	SLP	1780
Luterbacher et al. (1999)	Monthly	SLP, SAT, P	1675
Rogers (1984)	DJFM	SLP	1874
Thompson and Wallace (2000)	Monthly	SLP	1899
Thompson and Wallace (1998)	JFM	SAT	1851

emissions as they cannot achieve the spatial (regional level) and temporal (season-specific) resolution required (Jones et al., 2001). Nevertheless, several attempts have been made to extend the NAO record back based on the rationale that large-scale climate variability can be represented successfully by integrating across a number of high-resolution “proxies” of past variability. Proxies can either be natural (physical or biological) or from a documentary source and generally act as an indicator of either temperature or precipitation or some combination of the two. The most widely used proxy for NAO reconstructions are trees, where ring density, ring width, and wood isotopic composition are generally measured. Ice cores are the second most widely used proxy, where isotope ratios, accumulation rates, and melt layers serve as proxies. Corals and stalagmites (Proctor et al., 2000) can also be used by measuring isotopic concentration, cation ratios, and growth thickness to provide an annual reconstruction; however, these records are generally restricted to the tropics and have not been widely employed as a tool for reconstructing the NAO. Whereas instrumental measurements have unique space and time coordinates, climate proxies often represent the combined influences of climatic and non-climatic factors, recorded at different times of the year depending on the type and location of the proxy. Calibration against instrumental records is critical for all proxies, and statistical regression is generally used to establish a relationship between observations of the climate in a given region and the variability of the proxy over the same time period.

Table N2 details the most commonly used NAO paleoproxy reconstructions. The longest record is that of Cook et al. (2002), extending back to AD 1400. The reconstructions of Luterbacher et al. (1999, 2002a,b) are the only reconstructions providing monthly resolution. Despite the inconsistencies between different records, this rich archive of tree rings, ice cores, and documentary data indicate that prolonged positive and negative NAO phases have occurred in the past (Appenzeller, 1998; Cook et al., 1998; Luterbacher et al., 1999; Schmutz et al., 2000; Cullen et al., 2001). This suggests that the extreme positive values of the index evident since the late 1980s are not unprecedented over the past five centuries (Luterbacher et al., 2002a,b). Proxy records also indicate that there is a degree of “intermittency” present in the NAO. This suggests the NAO does not contain a single, persistent frequency – but rather oscillates between low-frequency variability and periods more akin to white noise (Appenzeller et al., 1998). However, it should also be noted that the NAO index might simply be one particular realization of a white noise atmosphere initiating a red noise ocean response (Wunsch, 1999).

Due to the different methods, different time intervals, and different observational time series used for calibration, a direct comparison of the different indices shows little agreement before the 1820s (Schmutz et al., 2000; Cullen et al., 2001).

Schmutz et al. (2000) suggest that proxy-based NAO indices are unable to capture NAO variability in a consistent manner in the eighteenth and nineteenth centuries and speculate that the NAO includes several different circulation patterns with specific impacts on a given proxy, resulting in degrees of covariability. Prior to the twentieth century most NAO index reconstructions show an inconsistent picture and in the period before the 1820s these inconsistencies are greater.

Of the NAO records listed in Table N2, the reconstructions by Cook et al. (2002) and Luterbacher et al. (2002a,b) appear to have somewhat more consistent covariability – at least on interannual timescales. The winter (DJFM) multiproxy reconstruction by Cook et al. (2002) was constructed using tree ring and ice core data from the North Atlantic sector whereas the monthly (1659–1995) and seasonal (1500–1658) reconstructions by Luterbacher et al. (2002a,b) used both instrumental and documentary data from Eurasia. When the seasonal indices are compared, explained variances are higher in Luterbacher et al. (2002a,b) than in the Cook et al. (2002) reconstruction during and before the eighteenth century. Furthermore, Luterbacher et al. (2002a,b) suggests predominantly negative-phase NAO values before 1800, whereas Cook et al. (2002) indicate more positive-phase NAO values.

Predictability

In addition to the importance of assessing the role of increasing greenhouse gases, an improved dynamical understanding of the NAO may help provide a better understanding of NAO ocean-atmosphere dynamics as well as the potential predictability of large-scale climate fluctuations in the Atlantic sector. Current research efforts suggest a small degree of seasonal predictability of North Atlantic climate via two potential pathways. The ocean, with its significant thermal inertia, may provide one pathway for limited predictability (Rodwell, 2003). Statistical analyses have revealed that knowledge of North Atlantic (Kushnir et al., 2002) and tropical Pacific (Hoerling et al., 2001) SSTs may provide information about the NAO with a lead time of several months.

A second pathway that offers hope for improved predictability of the NAO involves links through which changes in stratospheric wind patterns might exert some downward control on surface climate (Thompson et al., 2003). The NAO is most active in the winter, a time when stratospheric circulation favors communication between the stratosphere and troposphere, which is consistent with the stratosphere as a potential mechanism. Traditionally, it was thought that the more massive troposphere was forcing the stratosphere, however, now it appears things may work the other way around. Changes in stratospheric circulation can be forced by several different mechanisms including ozone depletion, volcanic dust, and CO₂. Rising CO₂ concentrations cool the stratosphere and strengthen the stratospheric winter vortex, which

Table N2 Paleoproxy records

Reconstruction	Source	Location	Period
Appenzeller et al. (1998)	Ice core	Greenland	1648–1990
Cook et al. (2002)	Multiproxy	Northern Hemisphere	1400–1979
Cook et al. (1998)	Tree rings	North Atlantic sector	1701–1980
Cullen et al. (2001)	Multiproxy	North Atlantic sector	1750–1979
Glueck and Stockton (2001)	Multiproxy	Northern Hemisphere	1429–1983
Luterbacher et al. (2002a,b)	Instruments/documentary	Eurasia	1500–1995
Rodrigo et al. (2001)	Documentary	Spain	1501–1997

generates stronger surface winds through a complex dynamical interaction. These enhanced westerly surface winds are consistent with a positive NAO index. A statistical connection between the month-to-month variability of the NH stratospheric polar vortex and the tropospheric NAO was established several years ago (Perlwitz and Graf, 1995) and more recently it has been documented that large amplitude anomalies in the wintertime stratospheric winds precede anomalous behavior of the NAO by 1–2 weeks. (Baldwin and Dunkerton, 2001), perhaps providing some extended range predictability. Similarly, processes that affect the stratospheric circulation on longer timescales, such as reductions in stratospheric ozone, volcanic forcing, and increases in greenhouse gases, could factor into the trend in Atlantic surface climate observed over the past several decades (Gillett, 2003).

This leaves the interesting possibility that, while interannual to decadal variations in the NAO/AO exist simply because they represent a fundamental mode of climate variability, the trend may be anthropogenically forced. Using an AGCM, Shindell et al. (1999) tested the possibility that these observed trends could be simulated by realistic increases in greenhouse gas concentrations. Ultimately, Shindell et al. (1999) showed that rising greenhouse gases in an AGCM could create a trend in the NAO/AO. Greenhouse gases, therefore, may induce climate change through dynamical effects in addition to direct radiative forcing.

Conclusions

Records, both instrumental and paleoproxy reconstructions of the NAO, provide a temporal snapshot of the behavior of a large-scale climate phenomenon whose dynamics are not yet fully understood. Despite the fact that the NAO is indeed a mode of variability internal to the atmosphere, these records of the NAO exhibit low-frequency variability – both decadal variability and trends – that would not be expected from a fast acting atmospheric process. That not all of the variability associated with the NAO can be attributed to intraseasonal stochastic atmospheric processes suggests a possible role for external forcings. Furthermore, it suggests a small but perhaps useful amount of predictability.

Heidi M. Cullen

Bibliography

- Appenzeller, C., Stocker, T.F., and Anklin, M., 1998. North Atlantic oscillation dynamics recorded in Greenland ice cores. *Science*, **282**, 446–449.
- Baldwin, M.P., and Dunkerton, T.T., 2001. Stratospheric harbingers of anomalous weather regimes. *Science*, **294**, 581–584.
- Barnston, A.G., and Livezey, R.E., 1987. Classification, seasonality, and persistence of low-frequency atmospheric circulation patterns. *Mon. Weather Rev.*, **115**, 1083–1126.
- Beniston, M., 1997. Variations of snow depth and duration in the Swiss Alps over the last 50 years: Links to changes in large-scale climate forcings. *Clim. Change*, **36**, 281–300.
- Bjerknes, J., 1964. Atmospheric teleconnections from the tropical Pacific. *Mon. Weather Rev.*, **97**, 103–172.
- Brown, B.G., and Katz, R.W., 1991. Use of statistical methods in the search for teleconnections: Past, present, and future. In Glantz, M.H., Katz, R.W., and Nicholls, N. (eds.), *Teleconnections linking Worldwide Climate Anomalies*. Cambridge, UK: Cambridge University Press, pp. 371–400.
- Cassou, C., and Terray L., 2001. Oceanic forcing of the wintertime low frequency atmospheric variability in the North Atlantic European sector: A study with the ARPEGE model. *J. Clim.*, **14**, 4266–4291.
- Cook, E.R., Briffa, K.R., and Jones, P.D., 1994. A reconstruction of the North Atlantic Oscillation using tree chronologies from North America and Europe. *The Holocene*, **8**, 9–17.
- Cook, E.R., D'Arrigo, R.D., and Briffa, K.R., 1998. The North Atlantic Oscillation and its expression in circum-Atlantic tree ring chronologies from North America and Europe. *Holocene*, **9**, 9–17.
- Cook, E.R., D'Arrigo, and Mann, M.E., 2002. A well-verified, multiproxy reconstruction of the winter North Atlantic Oscillation index since AD 1400. *J. Clim.*, **15**, 1754–1764.
- Cullen, H.M., D'Arrigo, R.D., Cook, E.R., and Mann, M.E., 2001. Multiproxy reconstructions of the North Atlantic Oscillation. *Paleoceanography*, **16**, 27–39.
- Cullen, H.M., Kaplan, A., Arkin, P.A., and deMenocal, P.B., 2002. Impact of the North Atlantic Oscillation on Middle Eastern climate and streamflow. *Clim. Change*, **55**, 315–338.
- Czaja, A., Robertson, W., and Huck, T., 2003. The role of the Atlantic Ocean-atmosphere coupling in affecting North Atlantic Oscillation variability. In Hurrell, J.W., Kushnir, Y., Ottersen, G., and Visbeck, M. (eds.), *The North Atlantic Oscillation: Climate Significance and Environmental Impact*. Washington, DC: American Geophysical Union, 134, pp. 173–192.
- Deser, C., and Blackmon, M.L., 1993. Surface climate variations over the North Atlantic Ocean during winter: 1900–1989. *J. Clim.*, **6**, 1743–1753.
- Egede, H., 1745. *History of Greenland* (translated from the Danish). Picadilly, London: Pickering Bookseller, 220pp.
- Feldstein, 2000. Teleconnections and ENSO: The timescale, power spectra, and climate noise properties. *J. Clim.*, **13**, 4430–4440.
- Gillett, N.P., Graf, H.F., and Osborn, T.J., 2003. Climate change and the North Atlantic Oscillation. In Hurrell, J.W., Kushnir, Y., Ottersen, G., and Visbeck, M. (eds.), *The North Atlantic Oscillation: Climate Significance and Environmental Impact*. Washington, DC: American Geophysical Union, 134, pp. 173–192.
- Glueck, M.F., and Stockton, C.W., 2001. Reconstruction of the North Atlantic Oscillation 1429–1983. *Int. J. Clim.*, **21**, 1453–1465.
- Hoerling, M.P., Hurrell, J.W., and Xu, T., 2001. Tropical origins for recent North Atlantic climate change. *Science*, **292**, 90–92.
- Hurrell, J.W., 1995. Decadal trends in the North Atlantic Oscillation: Regional temperatures and precipitation. *Science*, **269**, 676–679.
- Hurrell, J.W., 1996. Influence of variations in extratropical wintertime teleconnections on Northern Hemisphere temperature. *Geophys. Res. Lett.*, **23**, 665–668.
- Hurrell, J.W., and van Loon, H., 1997. Decadal variations in climate associated with the North Atlantic Oscillation. *Clim. Change*, **36**, 301–326.
- Jones, P.D., Davies, Jónsson, T., Barring, and Wheeler, D., 1997. Extension of the North Atlantic Oscillation using early instrumental pressure observations from Gibraltar and south-west Iceland. *Int. J. Clim.*, **17**, 1433–1450.
- Jones, P.D., Davies, T.D., Lister, D.H., Slonosky, V., Jónsson, T., Barring, L., Jónsson, P., Maheras, P., Kolya-Machera, F., Barriendos, M., Martin-Vide, J., Rodriguez, R., Alcoforado, M.J., Wanner, H., Pfister, C., Luterbacher, J., Rickli, R., Schuepbach, E., Kaas, E., Schmith, T., Jacobeit, J., and Beck, C., 1999. Monthly mean pressure reconstructions for Europe for Europe for the 1780–1995 period. *Int. J. Clim.*, **19**, 347–364.
- Jones, P.D., Osborn, T.J., and Briffa, K.R., 2001. The evolution of climate over the last millennium. *Science*, **292**, 662–666.
- Jones, P.D., Osborn, T.J., and Briffa, K.R., 2003. Pressure-based measures of the North Atlantic Oscillation (NAO): A Comparison and an assessment of changes in the strength of the NAO and in its influence on surface climate parameters. In Hurrell, J.W., Kushnir, Y., Ottersen, G., and Visbeck, M. (eds.), *The North Atlantic Oscillation: Climate Significance and Environmental Impact*. Washington, DC: American Geophysical Union, 134, pp. 173–192.
- Kaplan, A., Cane, M.A., Kushnir, Y., Clement, A.C., Blumenthal, M.B., and Rajagopalan, B., 1998. Analyses of global sea surface temperature 1856–1991. *J. Geophys. Res.*, **103**, 18567–18589.
- Kaplan, A., Kushnir, Y., and Cane, M.A., 2000. Reduced space optimal interpolation of historical marine sea level pressure. *J. Clim.*, **13**, 2987–3002.
- Kushnir, Y., 2002. Pacific North America pattern. In *Encyclopedia of Global Environmental Change*. Chichester, UK: Wiley.
- Kushnir, Y., and Wallace, G.M., 1989. Low-frequency variability in the northern hemisphere winter: Geographical distribution, structure, and time scale dependence. *J. Atmos. Sci.*, **46**, 3122–3142.
- Kushnir, Y., Cardone, V.J., Greenwood, J.G., and Cane, M., 1997. On the recent increase in North Atlantic wave heights. *J. Clim.*, **10**, 2107–2113.

- Landsea, C.W., Pielke, R.A., Mestas-Nunes, A., and Knaff, J.A., 1999. Atlantic basin hurricanes: Indices of climatic changes. *Clim. Change*, **42**, 89–129.
- Lorenz, E.N., 1951. Seasonal and irregular variations of the Northern Hemisphere sea-level pressure profile. *J. Meteorol.*, **8**, 52–59.
- Luterbacher, J., Schmutz, C., Gyalistras, D., Xoplaki, E., and Wanner, H., 1999. Reconstruction of monthly NAO and EU indices back to AD 1675. *Geophys. Res. Lett.*, **26**, 2745–2748.
- Luterbacher, J., Rickli, R., Tinguely, C., Xoplaki, E., Schüpbach, E., Dietrich, D., Hüsler, J., Ambühl, M., Pfister, C., Beeli, P., Dietrich, U., Dannecker, A., Davies, T.D., Jones, P.D., Slonosky, V., Ogilvie, A.E.J., Maheras, P., Kolyva-Machera, F., Martin-Vide, J., Barriendos, M., Alcoforado, M.J., Nunes, M.F., Jónsson, T., Glaser, R., Jacobeit, J., Beck, C., Phillip, A., Beyer, U., Kaas, E., Schmith, T., Barring, L., Jónsson, P., Rácz, L., and Wanner, H., 2000. Monthly mean pressure reconstructions for the late Maunder Minimum period (AD 1675–1715). *Int. J. Clim.*, **20**, 1049–1066.
- Luterbacher, J., Xoplaki, E., Dietrich, D., Rickli, R., Jacobeit, J., Beck, C., Gyalistras, D., Schmutz, C., and Wanner, H., 2002a. Reconstruction of the sea level pressure fields over the Eastern North Atlantic and Europe back to 1500. *Clim. Dyn.*, **18**, 545–561.
- Luterbacher, J., Xoplaki, E., Dietrich, D., Jones, P.D., Davies, T.D., Portis, D., Gonzalez-Rouco, J.F., von Storch, H., Gyalistras, D., Casty, C., and Wanner, H., 2002b. Extending North Atlantic Oscillation reconstructions back to 1500. *Atmos. Sci. Lett.*, **2**, 114–124.
- Marshall, J., Kushnir, Y., Battisti, D., Chang, P., Czaja, A., Dickson, R., Hurrell, J., McCartney, M., Saravanan, R., and Visbeck, M., 2001. North Atlantic climate variability: Phenomena, impacts, and mechanisms. *Int. J. Climatol.*, **21**, 1863–1898.
- Molinari, R.L., Meyer, D.A., Festa, J.F., Bezdek, H.F., 1997. Multiyear variability in the near-surface temperature structure of the midlatitude western North Atlantic Ocean. *J. Geophys. Res.*, **102**, 3267–3278.
- Namias, J., 1950. The index cycle and its role in the general circulation. *J. Meteorol.*, **7**, 130–139.
- Ottersen, G., and Stenseth N.C., 2001. Atlantic climate governs oceanographic and ecological variability in the Barents Sea. *Limnol. Oceanogr.*, **46**, 1774–1780.
- Perlwitz, J., and Graf, H.F., 1995. The statistical connection between tropospheric and stratospheric circulation of the Northern-Hemisphere in winter. *J. Clim.*, **8**, 2281–2295.
- Post, E., and Stenseth, N.C., 1998. Large-scale climate fluctuation and population dynamics of moose and white-tailed deer. *J. Animal Ecol.*, **67**, 537–543.
- Proctor, C.J., Baker, A., Barnes, W.L., and Gilmour, M.A., 2000. A thousand year speleothem proxy record of North Atlantic climate from Scotland. *Clim. Dyn.*, **16**, 815–820.
- Reverdin, G., Cayan, D., Kushnir, Y., 1997. Decadal variability of the hydrography in the upper northern North Atlantic in 1948–1990. *J. Geophys. Res.*, **102**, 8505–8531.
- Rodrigo, F.S., Pozo-Vázquez, D., Esteban-Parra, M.J., and Castro-Diez, Y., 2001. A reconstruction of the winter North Atlantic Oscillation index back to AD 1501 using documentary data in Southern Spain. *J. Geophys. Res.*, **106**, 14804–14818.
- Rodwell, M.J., 2003. On the predictability of North Atlantic Climate. In Hurrell, J.W., Kushnir, Y., Ottersen, G., and Visbeck, M. (eds.), *The North Atlantic Oscillation: Climate Significance and Environmental Impact*. Washington, DC: American Geophysical Union, 134, pp. 173–192.
- Rodwell, M.J., Rowell, D.P., and Folland, C.K., 1999. Oceanic forcing of the wintertime North Atlantic Oscillation and European climate. *Nature*, **398**, 320–323.
- Rogers, J.C., 1984. The association between the North Atlantic Oscillation and the Southern Oscillation in the Northern Hemisphere. *Mon. Weather Rev.*, **112**, 1999–2015.
- Rogers, J.C., and van Loon, H., 1979. The seesaw in winter temperatures between Greenland and northern Europe. Part II: Some oceanic and atmospheric effects in middle and high latitudes. *Mon. Weather Rev.*, **107**, 509–519.
- Schmutz, C., Luterbacher, J., Gyalistras, D., Xoplaki, and Wanner, H., 2000. Can we trust proxy-based NAO index reconstructions? *Geophys. Res. Lett.*, **27**, 1135–1138.
- Seager, R., Kushnir, Y., Visbeck, M., Naik, N., Miller, J., Krahnemann, G., and Cullen, H., 2000. Causes of Atlantic Ocean climate variability between 1958 and 1998. *J. Clim.*, **13**, 2845–2862.
- Shindell, D.T., Miller, R.L., Schmidt, G.A., and Pandolfo, L., 1999. Simulation of recent northern winter climate trends by greenhouse-gas forcing. *Nature*, **399**, 452–455.
- Shindell, D.T., Schmidt, G.A., Miller, R.L., and Rind, D., 2001. Northern hemisphere winter climate response to greenhouse gas, ozone, solar, and volcanic forcing. *J. Geophys. Res.*, **106**, 7193–7210.
- Slonosky, V.C., Jones, P.D., and Davies, T.D., 2000. Variability of the surface atmosphere circulation over Europe 1774–1995. *Int. J. Clim.*, **20**, 1875–1897.
- Souriau, A., and Yiou, P., 2001. Grape harvest dates for checking NAO paleoreconstructions. *Geophys. Res. Lett.*, **28**, 3895–3898.
- Stenseth, N.C., Mysterud, A., Ottersen, G., Hurrell, J.W., Chan, K., and Lima, M., 2002. Ecological effects of climate fluctuations. *Science*, **297**, 1292–1296.
- Stephenson, D.B., Wanner, H., Brönnimann, S., and Luterbacher, J., 2003. The history of scientific research on the North Atlantic Oscillation. In Hurrell, J.W., Kushnir, Y., Ottersen, G., and Visbeck, M. (eds.), *The North Atlantic Oscillation: Climate Significance and Environmental Impact*. Washington, DC: American Geophysical Union, 134, pp. 173–192.
- Thompson, D.W., and Wallace, J.M., 1998. The Arctic Oscillation signature in the wintertime geopotential height and temperature fields. *Geophys. Res. Lett.*, **25**, 1297–1300.
- Thompson, D.W., and Wallace, J.M., 2000. Annular modes in the extratropical circulation. Part I: Month-to-month variability. *J. Clim.*, **13**, 1000–1016.
- Thompson, D.W., Lee, S., and Baldwin, M.P., 2003. Atmospheric processes governing the Northern Hemisphere Annular Mode/North Atlantic Oscillation. In Hurrell, J.W., Kushnir, Y., Ottersen, G., and Visbeck, M. (eds.), *The North Atlantic Oscillation: Climate Significance and Environmental Impact*. Washington, DC: American Geophysical Union, 134, pp. 81–112.
- Trenberth, K.E., 1984. Signal versus noise in the Southern Oscillation. *Mon. Weather Rev.*, **112**, 326–332.
- van Loon, H., and Rogers, J.C., 1978. Seasaw in winter temperatures between Greenland and northern Europe. Part I: General description. *Mon. Weather Rev.*, **106**, 296–310.
- Visbeck, M., Cherry, J., and Cullen, H., 2002. The North Atlantic Oscillation and energy markets in Scandinavia. *The Clim. Rep.*, **3**, 9–11.
- Walker, G.T., 1924. Correlation in seasonal variations of weather IX. A further study of world weather. *Memoirs of the India Meteorological Department*, **24**, 275–332.
- Walker, G.T., and Bliss, E.W., 1932. World Weather V. *Memoirs of the India Meteorological Department*, **IV**, 119–139.
- Wallace, J.M., and Gutzler, D.S., 1981. Teleconnections in the geopotential height field during the Northern Hemisphere winter. *Mon. Weather Rev.*, **109**, 784–812.
- Wunsch, C., 1999. The interpretation of short climate records, with comments on the North Atlantic Oscillation. *Bull. Am. Met. Soc.*, **80**, 245–255.

Cross-references

- [Climate Forcing](#)
- [Climate Variability and Change, Last 1000 Years](#)
- [Coral and Coral Reefs](#)
- [Dating, Dendrochronology](#)
- [Dendroclimatology](#)
- [Ice Cores, Antarctica and Greenland](#)
- [Little Ice Age](#)
- [Medieval Warm Period](#)
- [North Atlantic Deep Water and Climate Change](#)
- [Paleo-El Niño-Southern Oscillation \(ENSO\) Records](#)
- [Paleotemperatures and Proxy Reconstructions](#)
- [Speleothems](#)

O

OBLIQUITY

The Earth's axis of rotation is not perpendicular to the orbital plane (ecliptic). At present, there is an angle of 23.446° between the axis of rotation and the perpendicular to the ecliptic. This angle, called obliquity, governs the march of the seasons. The North Pole receives sun light during the entire boreal summer while the South Pole remains in the dark. It is the reverse for the boreal winter.

Obliquity results from the torque that the Sun and the Moon exert on the equatorial bulge of the Earth. Its value has varied from 22 to 25° over the last three million years, with a quasi-period of 41,000 years (Figure O1; Berger, 1978; Berger and Loutre, 1991). Obliquity plays a similar role in both hemispheres. Indeed, larger obliquity increases the energy received in each hemisphere during the local warm season. The highest latitudes are more sensitive to obliquity changes because the energy flux at the surface depends on the inclination of the solar beam (Berger and Loutre, 1994). Around the poles, a 1° obliquity change induces a change in the solar radiation at the top of the atmosphere by $\sim 4\%$ during summer time. Moreover, a larger obliquity reinforces the seasonal contrast in insolation because it increases the irradiance in summer and reduces it in winter. It also reduces the latitudinal contrast in annual irradiance because it increases the irradiance at mid-and high-latitudes and decreases it at low latitudes (Figure O2).

Marie-France Loutre

Bibliography

- Berger, A.L., 1978. Long-term variations of daily insolation and Quaternary climatic changes. *J. Atmos. Sci.*, **35**(12), 2362–2367.
- Berger, A., and Loutre, M.F., 1991. Insolation values for the climate of the last 10 million years. *Quaternary Sci. Rev.*, **10**, 297–317.
- Berger, A., and Loutre, M.F., 1994. Precession, eccentricity, obliquity, insolation and paleoclimates. In Duplessy, J.C., and Spyridakis, M.-T. (eds.), *Long Term Climatic Variations, Data and Modelling*. Nato ASI series, Series I: Global Environmental Change, Vol. 22. Berlin: Springer, pp. 107–151.

Cross-references

- [Astronomical Theory of Climate Change](#)
- [Climate Forcing](#)
- [Eccentricity](#)
- [Millennial Climate Variability](#)
- [Precession, Climatic](#)
- [Pre-Quaternary Milankovitch Cycles and Climate Variability](#)
- [Quaternary Climate Transitions and Cycles](#)
- [SPECMAP](#)

OCEAN ANOXIC EVENTS

Although black shales and carbon isotope anomalies are known from the Paleozoic, ocean crust older than approximately 150 Myr has been subducted and therefore oceanic anoxic events prior to the Mesozoic cannot be confirmed. Therefore, this discussion will focus mainly on Mesozoic events.

Mesozoic ocean anoxic events are defined based on the widespread occurrence of fine-grained sedimentary rocks that are highly enriched in organic carbon (e.g., black shales). Deposits of organic-carbon enriched strata (generally known as “black

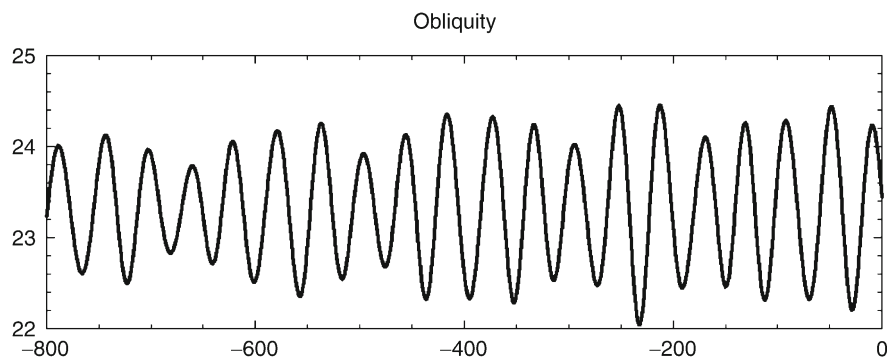


Figure O1 Long term variations of the obliquity over the last 800,000 years.

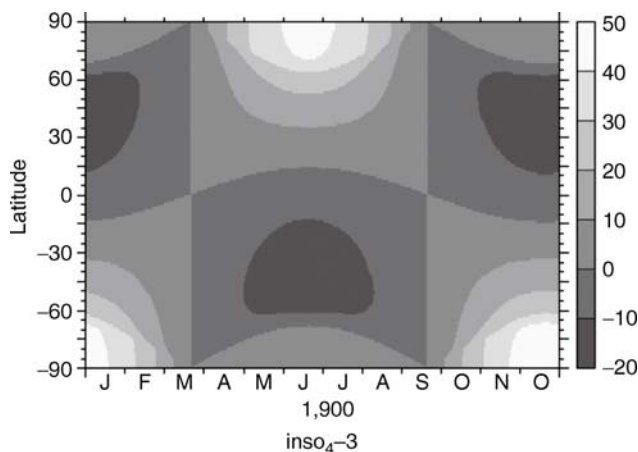


Figure O2 Variation of the mean irradiance (W m^{-2}) following an increase of the obliquity from 22 to 24° (at present-day eccentricity, $e = 0.0167$ and longitude of perihelion, $= 102.04^\circ$).

shales") were recognized as special features of the rock record early in the development of the geologic sciences because they require specific environmental conditions for formation that are not common or widespread in modern oceans. Nonetheless, these deposits store quantities of carbon sufficient to source all of the petroleum and natural gas that humans have thus far consumed, or will ever produce. In fact, it has been estimated that the highest proportion of petroleum source rocks were formed during the times in Earth history that were characterized by ocean anoxic events (Schlanger and Cita, 1982).

Based on observations of organic carbon burial rates in modern marine environments that are oxygen deficient, early black shale researchers concluded that the key factor leading to enhanced organic carbon preservation was decreased oxygen content in bottom waters (e.g., less than 1.0 ml O_2 per $\text{L H}_2\text{O}$). Oxygen deficiency was known to occur as a consequence of either (i) water column stratification, a process that prevents downward mixing of surface waters enriched in oxygen by photosynthesizing algae and/or gas exchange with the atmosphere, (ii) increases in primary production, which result in accumulation of excess decomposing organic matter and exhaustion of oxygen supply by aerobic bacteria. As the petroleum industry expanded in the twentieth century, the impetus to better understand the formation of organic carbon-enriched petroleum source rocks led to even more detailed studies of modern and ancient black shales. Following World War II, the development of research-related exploratory drilling in the ocean basins (the Deep Sea Drilling Project) resulted in a major discovery: many of the black shales known from shallower epicontinental basins could be traced to time equivalent strata in the deep sea record, suggesting that the conditions responsible for organic carbon burial and preservation had been extremely widespread, if not global, during certain intervals of Earth's history. This discovery led Schlanger and Jenkyns (1976) to propose the concept of Mesozoic oceanic anoxic events or OAEs.

The key features that first distinguished ocean anoxic events were the rapid onset, short duration ($\pm 0.5 \text{ Myr}$), and widespread distribution of highly organic-carbon enriched deposits, which suggested a profound and sudden change in the Earth's ocean-atmosphere system (Schlanger and Jenkyns, 1976; Schlanger et al., 1987). It was later shown that many of the OAEs were also

characterized by significant positive shifts in the stable isotopic composition of both organic and inorganic (carbonate) carbon contained within them (Arthur et al., 1985, 1987, 1988). This evidence indicated that the Earth's entire surface carbon reservoir had been depleted in the lighter stable isotope of carbon (^{12}C), likely due to a global increase in the burial of organic matter (which preferentially concentrates the lighter stable isotope). Had the entire global ocean turned rapidly anoxic (as suggested by the OAE term), leading to a worldwide increase in preservation of organic carbon? Alternatively, had rates of phytoplankton production dramatically risen so that the supply of organic matter sinking through the water column was so large that the respiratory demands of decomposers overwhelmed oxygen supplies, secondarily causing widespread anoxia? Was carbon burial in ocean sediments so massive that it turned the oceans into a net CO_2 sink, causing drawdown of atmospheric CO_2 and cooling of the warm greenhouse climate of the Mesozoic? Were these putative changes in marine and terrestrial environments responsible for the major changes in biodiversity revealed in fossil records spanning some of the OAEs? Lastly, what process(es) had initiated each OAE and what caused them to terminate? Such questions have been vigorously debated during almost thirty years of intensive research on these events, and although much has been learned, the largest questions remain unanswered. For this reason, Mesozoic OAEs remain one of the most actively studied examples of deep time perturbations in the Earth's ocean-climate system.

Organic carbon burial processes

The fundamental process underlying the formation of OAEs is the burial of organic carbon. Organic carbon is produced in sufficient quantities to form geologically significant accumulations mainly by primary photosynthesizers, including algae and bacteria in oceans and lakes and vascular plants on land. In most depositional environments, where oxygen is abundant, accumulating organic matter is efficiently decomposed and the CO_2 that was fixed by plants ("photosynthate") is returned to the surface reservoir with no net change in the global carbon cycle. Under certain conditions, however, where oxygen becomes limited due to a decrease in supply or an increase in demand (relative to supply), accumulating organic matter may be protected from aerobic decomposition long enough to be buried, thus preventing its remineralization to CO_2 (examples include bogs in which so much plant matter accumulates that available oxygen is consumed by respiration, or well-stratified tropical lakes and shallow seas in which a lack of seasonal overturn leads to oxygen-depleted bottom waters and improved conditions for preservation of algal organic matter). In these settings, carbon is removed from the surface short-term carbon cycle and it enters the long-term (lithospheric) carbon cycle, where it remains for timescales of millions to many millions of years. Ocean anoxic events represent extremely narrow time intervals in which large areas of the world's oceans shifted from carbon respiring to carbon preserving systems.

The exposure of organic matter to dissolved oxygen certainly exerts an important primary control on organic carbon burial rate (Hartnett et al., 1998), but it is not the only control. The main factors that regulate the rate of burial and long term preservation of organic matter in marine sediments include the rate of export production (fraction of primary photosynthate reaching the sediment), the rate of bulk sedimentation (which controls how fast organic matter is transferred into the anoxic zone within the sediment column), and the rate of organic decomposition (which is accomplished by aerobic and anaerobic microbial communities) (e.g., Arthur and Sageman, 1994;

Sageman and Lyons, 2003; Sageman et al., 2003). Although there has been much debate about the importance of production vs. preservation over the years, the current consensus views each of the aforementioned factors to be important, if not interdependent elements of organic matter burial. Their relative importance may vary from one depositional system to another.

Types of OAEs

Mesozoic OAEs occur in two major time intervals that are generally characterized by widespread development of black shales (Figure O3). Based on areal extent of organic carbon deposition and perturbation of the global carbon cycle, as reflected in carbon isotope excursions, the Toarcian event in the Jurassic (Jenkyns, 1988) and OAE Ia through III in the Cretaceous (Leckie et al., 2002) are the major designated OAEs. However, other stratigraphic intervals such as the Late Jurassic Kimmeridge Clay and Oxford Clay, or the Middle to Late Cenomanian Graneros and Greenhorn Formations (and time equivalent stratigraphic units), are also characterized by significant organic carbon enrichments, as well as some minor perturbations in the isotope record.

Although the difference between OAE and non-OAE black shales appears to be a matter of degree, the key question is degree of what? Both OAE and non-OAE black shales may exhibit spatial and temporal differences in the principal types of organic matter buried; the dominance of production, preservation, or sedimentation mechanisms; or the nature of the associated carbon isotope excursion. For example, the Toarcian event, OAE Ia, OAE Ib, OAE II and OAE III [all] contain mostly marine organic matter, but OAE Ic and OAE Id appear to be dominated by terrestrial organic material (Erbacher et al., 1996). Increase in primary production is currently viewed as the dominant mechanism driving carbon burial during OAEs in most settings. However, evidence for dominance of hydrogen-sulfide rich conditions in the deep ocean basins (e.g., Kuypers et al., 2002) combined with the recent demonstration of enhanced organic matter preservation due to sulfide-mediated hydrogenation reactions (Hebting et al., 2006) suggests that preservation may indeed also play an important role. Lastly, although the archetypal isotope excursion during an OAE is the positive shift believed to reflect greater burial of ^{12}C -enriched organic matter (e.g., OAE Ia, OAE II), some events are characterized by distinct negative shifts in $\delta^{13}\text{C}$ followed by a swing to positive values. This pattern is particularly well developed in the Toarcian event (Hesselbo et al., 2000, 2003).

Causal mechanisms for OAEs

If enhanced primary production initiates OAEs, then these events likely reflect major changes in nutrient availability. Several processes have been implicated as causal factors affecting nutrient budgets in Cretaceous seas, but none of them individually provides a satisfactory explanation for the observed features of OAEs. For example, changes in vertical circulation associated with the opening of ocean gateways has been suggested as a mechanism that might have upwelled phosphate-rich deep waters (Kuypers et al., 2002; Poulsen et al., 2003). Some investigators have suggested that micronutrients, such as reactive Fe, derived from hydrothermal activity associated with rapidly spreading ridges or emplacement of large igneous provinces may have played a role in driving OAEs (Sinton and Duncan, 1997; Kerr, 1998; Kerr et al., 2004; Leckie et al., 2002; Snow et al., 2005). This idea is quite intriguing, especially since the strontium isotope record (Figure O3) shows shifts toward less radiogenic values consistent

with global increases in oceanic volcanism and sea floor spreading during several OAEs (McArthur et al., 2001), and the ages of some large igneous provinces broadly overlap with OAEs (Wignall, 2001; Leckie et al., 2002). A terrestrial source of increased phosphorus is also a possibility given that many studies have shown changes in paleotemperature proxies consistent with significant warming during the time intervals containing OAEs (e.g., Huber et al., 2002; Norris et al., 2002; Wilson et al., 2002). Such temperature increases, initially caused by enhanced volcanic outgassing of CO_2 and global warming, could have driven up chemical weathering rates leading to greater terrigenous phosphorous input to the oceans (Föllmi, 1995). Lastly, it is clear from a comparison of the global relative sea level record and OAEs (Figure O3) that they occurred during rising sea level or highstand episodes when the area of shallow shelf seas was greatly expanded. As originally recognized by Schlanger and Jenkyns (1976), shelf sea area may have been a critical prerequisite for OAE development.

Although none of these proposed mechanisms alone explains the short-term character of all OAEs, some combination likely provides a plausible means to initiate and terminate these events. In addition, the role of phosphorus regeneration during anoxic organic matter decomposition has received increasing attention in recent years as a potential feedback mechanism for eutrophication and black shale deposition (Ingall et al., 1993; Van Cappellen and Ingall, 1994; Ingall and Jahnke, 1997; Murphy et al., 2000; Nederbragt et al., 2004). This process may have played a role in maintaining elevated organic carbon burial rates during OAEs.

Summary

Interest in OAEs was originally motivated, in part, by a desire to better understand the processes leading to formation of petroleum source rocks. As we look forward to the end of the Petroleum Era, due to occur in the next century, renewed interest in OAEs has been driven by a very different motivator: the need to better understand the processes and feedbacks involved in rapid perturbations of the Earth's biogeochemical cycles. OAEs include some of the most geologically rapid and pervasive changes of the oceans and atmosphere driven by changes in the carbon cycle, and they are associated with warm climates, rising sea levels, and possibly increased nutrient fluxes to the oceans. The development of sound environmental policy for the twenty first Century and beyond will depend on our ability to predict the response of the Earth System to anthropogenic CO_2 output, the climate warming predicted to result from this output, the increases in sea levels as continental ice sheets continue to melt, and the increase in agricultural runoff of nutrients associated with population-driven expansion of food production. Studies of Mesozoic OAEs provide a critical source of information to our ongoing effort to build accurate and predictive Earth System models.

Brad Sageman

Bibliography

- Arthur, M.A., and Sageman, B.B., 1994. Marine Black Shales: depositional mechanisms and environments of ancient deposits. *Annu. Rev. Earth Planet. Sci.*, **22**, 499–551.
- Arthur, M.A., and Schlanger, S.O., 1979. Cretaceous "oceanic anoxic events" as causal factors in development of reef-reservoired giant oil fields. *Am. Assoc. Pet. Geol. Bull.*, **63**(6), 870–885.
- Arthur, M.A., Dean, W.E., and Schlanger, S.O., 1985. Variations in the global carbon cycle during the Cretaceous related to climate, volcanism,

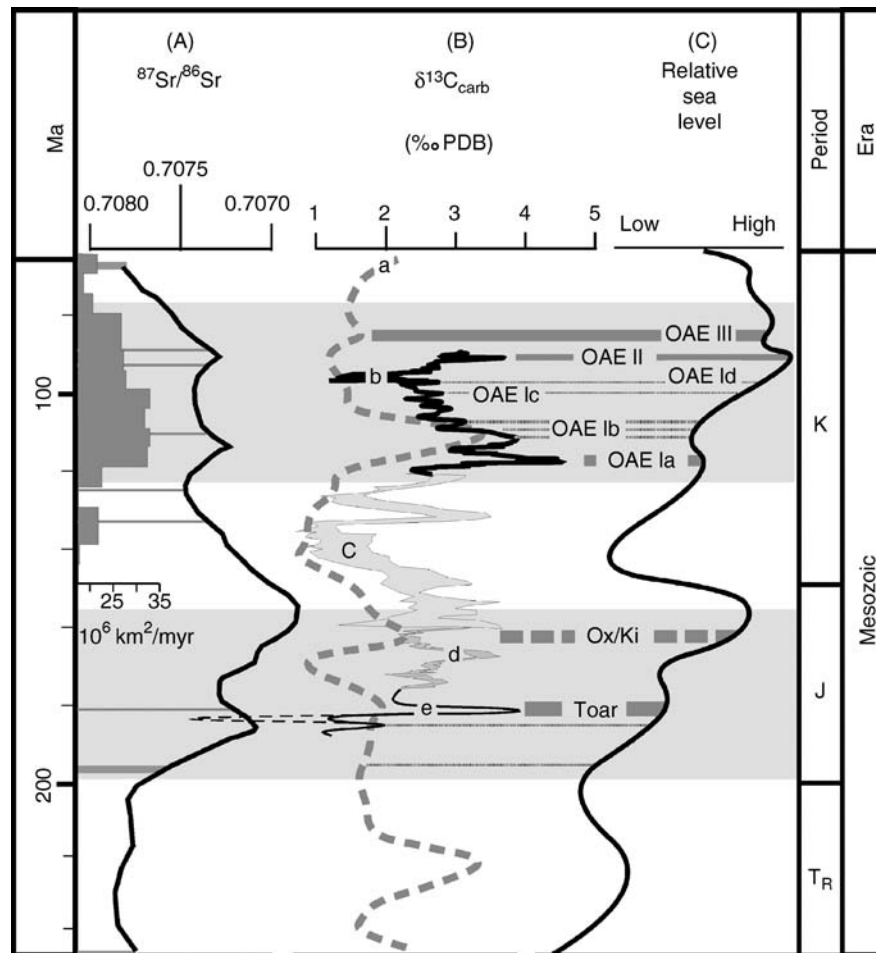


Figure O3 Mesozoic Ocean Anoxic Events occur in two broadly defined intervals shown by gray bands. A compilation of relevant data includes: (A) Marine Sr isotope curve from McArthur et al., 2001; horizontal lines within the curve represent times of continental and submarine volcanic eruptions; thick lines show the three most extensive continental flood basalts; dark gray histogram shows Larson's (1991) reconstruction of ocean crust production rates for the last 150 Myr (in 10^6 km^2 of crust per million years); (B) carbon isotope curves for bulk carbonate from (a) Veizer et al. (1999), (b) Leckie et al. (2002), (c) Weissert and Erba (2004), (d) Hesselbo et al. (2003), (e) Rey and Delgado (2002) and (thin dashed line) Hesselbo et al. (2000) – the wide curves represent envelopes of data, the single lines represent running averages or smaller data sets; (C) sea level history from Hallam (1981) and Haq et al. (1987, 1988) – the curve shows only relative changes (lower, higher) due to difficulties involved in determination of absolute global sea levels in deep time records. Ocean Anoxic Event designations are based on Arthur and Schlanger (1979) and Leckie et al. (2002) for the Cretaceous and include major events Ia and II, as well as OAE Ib–d (dashed lines) and OAE III. Jurassic events are based on Jenkyns (1988), Wignall and Hallam (1991), Tribovillard et al. (2005), and Röhl and Schmid-Röhl (2005) and include the Toarcian OAE (Toar), as well as the Oxford Clay and Kimmeridge Clay (Ox/Ki) and two regional black shale events in the Pliensbachian and Sinemurian (dashed lines).

- and changes in atmospheric CO_2 ; natural variations Archean to present. *Geophys. Monogr.*, **32**, 504–529.
- Arthur, M.A., Schlanger, S.O., and Jenkyns, H.C., 1987. The Cenomanian-Turonian Oceanic Anoxic Event II. Paleooceanographic controls on organic matter production and preservation. In Brooks, J., and Fleet, A. (eds.), *Marine Petroleum Source Rocks*. Geological Society London Special Publication, pp. 401–420.
- Arthur, M.A., Dean, W.E., and Pratt, L.M., 1988. Geochemical and climatic effects of increased marine organic carbon burial at the Cenomanian/Turonian boundary. *Nature*, **335**, 714–717.
- Erbacher, J., Thurow, J., and Littke, R., 1996. Evolution patterns of radiolaria and organic matter variations: A new approach to identify sea-level changes in mid-Cretaceous pelagic environments. *Geology*, **24**, 499–502.
- Follmi, K.B., 1995. 160 My record of marine sedimentary phosphorus burial – coupling of climate and continental weathering under Greenhouse and Icehouse conditions. *Geology*, **23**(9), 859–862.
- Hallam, A., 1981. A revised sea-level curve for the early Jurassic. *J. Geol. Soc.*, **138**, 735–743.
- Haq, B., Hardenbol, J., and Vail, P.R., 1987. The chronology of fluctuating sea level since the Triassic. *Science*, **235**, 1156–1167.
- Haq, B.U., Hardenbol, J., and Vail, P.R., 1988. Mesozoic and Cenozoic chronostratigraphy and eustatic cycles. In Wilgus, C.K. (eds.), *Sea-level changes: An integrated approach*. Tulsa, OK: SEPM, Special Publication – Society for Sedimentary Geology 42, pp. 71–108.
- Hartnett, H.E., Keil, R.G., Hedges, J.I., and Devol, A.H., 1998. Influence of oxygen exposure time on organic carbon preservation in continental margin sediments. *Nature*, **391**, 572–574.
- Hebting, Y., Schaeffer, P., Behrens, A., Adam, P., Schmitt, G., Schneckenburger, P., Bernasconi, S.M., and Albrecht, P., 2006. Biomarker evi-

- dence for a major preservation pathway of sedimentary organic carbon. *Science*, **312**, 1,627–1,631.
- Hesselbo, S.P., Grocke, D.R., Jenkyns, H.C., Bjerrum, C.J., Farrimond, P., Morgans Bell, H.S., and Green, O.R., 2000. Massive dissociation of gas hydrate during a Jurassic oceanic anoxic event. *Nature*, **406**, 392–395.
- Hesselbo, S.P., Morgans-Bell, H.S., McElwain, J.C., Rees, P.M., Robinson, S.A., and Ross, C.E., 2003. Carbon-cycle perturbation in the Middle Jurassic and accompanying changes in the terrestrial paleoenvironment. *J. Geol.*, **111**, 259–276.
- Huber, B.T., Norris, R.D., and MacLeod, K.G., 2002. Deep-sea paleotemperature record of extreme warmth during the Cretaceous. *Geology*, **30**(2), 123–126.
- Ingall, E., and Jahnke, R., 1997. Influence of water-column anoxia on the elemental fractionation of carbon and phosphorus during sediment diagenesis. *Mar. Geol.*, **139**(1–4), 219–229.
- Ingall, E.D., Bustin, R.M., and Van Cappellen, P., 1993. Influence of Water Column Anoxia on the Burial and Preservation of Carbon and Phosphorus in Marine Shales. *Geochim. Cosmochim. Acta*, **57**(2), 303–316.
- Jenkyns, H.C., 1988. The early Toarcian (Jurassic) anoxic event; stratigraphic, sedimentary and geochemical evidence. *Am. J. Sci.*, **288**, 101–151.
- Kerr, A.C., 1998. Oceanic plateau formation: A cause of mass extinction and black shale deposition around the Cenomanian-Turonian boundary. *J. Geol. Soc.*, **155**, 619–626.
- Kerr, A.C., Tarney, J., Kempton, P.D., Pringle, M., and Nivia, A., 2004. Mafic pegmatites intruding oceanic plateau gabbros and ultramafic cumulates from Bolivar, Colombia: Evidence for a “wet” mantle plume? *J. Petrol.*, **45**(9), 1877–1906.
- Kuypers, M.M.M., Pancost, R.D., Nijenhuis, I.A., and Sinninghe Damste, J.S., 2002. Enhanced productivity led to increased organic carbon burial in the euxinic North Atlantic basin during the late Cenomanian oceanic anoxic event. *Paleoceanography*, **17**(4), 13pp.
- Larson, R.L., 1991. Latest pulse of Earth; evidence for a Mid-Cretaceous super plume. *Geology*, **19**, 547–550.
- Leckie, R.M., Bralower, T.J., and Cashman, R., 2002. Oceanic anoxic events and plankton evolution; biotic response to tectonic forcing during the Mid-Cretaceous. *Paleoceanography*, **17**, 29pp.
- McArthur, J.M., Howarth, R.J., and Bailey, T.R., 2001. Strontium isotope stratigraphy; LOWESS Version 3; best fit to the marine Sr-isotope curve for 0–509 Ma and accompanying look-up table for deriving numerical age. *J. Geol.*, **109**, 155–170.
- Murphy, A.E., Sageman, B.B., Hollander, D.J., Lyons, T.W., and Brett, C.E., 2000. Black shale deposition in the Devonian Appalachian Basin: Siliciclastic starvation, episodic water-column mixing, and efficient recycling of biolimiting nutrients. *Paleoceanography*, **15**, 280–291.
- Nederbragt, A.J., Thurow, J., Vonhof, H., and Brumsack, H.J., 2004. Modelling oceanic carbon and phosphorus fluxes: implications for the cause of the late Cenomanian Oceanic Anoxic Event (OAE2). *J. Geol. Soc.*, **161**, 721–728.
- Norris, R.D., Bice, K.L., Magno, E.A., and Wilson, P.A., 2002. Jiggling the tropical thermostat in the Cretaceous hothouse. *Geology*, **30**(4), 299–302.
- Poulsen, C.J., Gendaszek, A.S., and Jacob, R.L. 2003. Did the rifting of the Atlantic Ocean cause the Cretaceous thermal maximum? *Geology*, **31**(2), 115–118.
- Rey, J., and Delgado, A., 2002. Carbon and oxygen isotopes; A tool for Jurassic and Early Cretaceous pelagic correlation (southern Spain). *Geol. J.*, **37**, 337–345.
- Röhl, H.J., and Schmid-Röhl, A., 2005. Lower Toarcian (upper Liassic) black shales of the Central European epicontinental basin; a sequence stratigraphic case study from the SW German Posidonia Shale. In Harris, N.B. (ed.), *The Deposition of Organic Carbon-Rich Sediments: Models, Mechanisms and Consequences*. Special Publication – Society for Sedimentary Geology 82, Tulsa, OK: SEPM, pp. 165–189.
- Sageman, B.B., and Lyons, T.W., 2003. Geochemistry of fine-grained sediments and sedimentary rocks. In MacKenzie, F. (ed.), *Treatise on Geochemistry*. vol. 7, New York: Elsevier, pp. 115–158.
- Sageman, B.B., Murphy, A.E., Werne, J.P., Ver Straeten, C.A., Hollander, D.J., and Lyons, T.W., 2003. A tale of shales: The relative roles of production, decomposition, and dilution in the accumulation of organic-rich strata, Middle-Upper Devonian, Appalachian basin. *Chem. Geol.*, **195**, 229–273.
- Schlanger, S.O., and Cita, M.B., 1982. Introduction to the Symposium: On the nature and origin of Cretaceous organic carbon-rich facies. In Schlanger, S.O., and Cita, M.B. (eds.), *On the Nature and Origin of Cretaceous Organic Carbon-Rich Facies*. New York, NY: Academic Press, pp. 1–6.
- Schlanger, S.O., and Jenkyns, H.C., 1976. Cretaceous oceanic anoxic events: Causes and consequences. *Geol. Mijnbouw*, **55**, 179–184.
- Schlanger, S.O., Arthur, M.A., Jenkyns, H.C., and Scholle, P.A., 1987. The Cenomanian-Turonian oceanic anoxic event; I, Stratigraphy and distribution of organic carbon-rich beds and the marine delta (super 138C excursion in Marine petroleum source rocks. In Brooks, J., and Fleet, A.J. (eds.), *Geological Society of London Special Publications* 26, pp. 371–399.
- Sinton, C.W., and Duncan, R.A., 1997. Potential links between ocean plateau volcanism and global ocean anoxia at the Cenomanian-Turonian boundary. *Econ. Geol. Bull. Soc. Econ. Geol.*, **92**(7–8), 836–842.
- Snow, L.J., Duncan, R.A., and Bralower, T., 2005. Trace element abundances in the Rock Canyon Anticline, Pueblo, Colorado, marine sedimentary section and their relationship to Caribbean plateau construction and oxygen anoxic event 2. *Paleoceanography*, **20**(4), 1–14.
- Tribovillard, N., Ramdani, A., and Trentesaux, A., 2005. Controls on organic accumulation in Upper Jurassic shales of northwestern Europe as inferred from trace-metal geochemistry. *Special Publication – Society for Sedimentary Geology* 82, Tulsa, OK: SEPM, pp. 145–164.
- Van Cappellen, P., and Ingall, E.D., 1994. Benthic phosphorus regeneration, net primary production, and ocean Anoxia – a model of the coupled marine biogeochemical cycles of carbon and phosphorus. *Paleoceanography*, **9**(5), 677–692.
- Veizer, J., Alab, D., Azmyb, K., Bruckschena, P., Buhla, D., Bruhna, F., Cardena, G.A.F., Dienera, A., Ebnetha, S., Godderisb, Y., Jaspersa, T., Kortea, C., Pawelleka, F., Podlahaa, O.G., and Straussa, H., 1999. ⁸⁷Sr/⁸⁶Sr, d¹³C and d¹⁸O evolution of Phanerozoic seawater. *Chem. Geol.*, **161**, 59–88.
- Weissert, H., and Erba, E., 2004. Volcanism, CO₂ and palaeoclimate; a Late Jurassic-Early Cretaceous carbon and oxygen isotope record. *J. Geol. Soc. Lond.*, **161**, 695–702.
- Wignall, P. B., 2001. Large igneous provinces and mass extinctions. *Earth Sci. Rev.*, **53**(1–2), 1–33.
- Wignall, P.B., and Hallam, A., 1991. Biofacies, stratigraphic distribution and depositional models of British onshore Jurassic black shales. *Geological Society of London Special Publications* **58**, 291–309.
- Wilson, P.A., Norris, R.D., and Cooper, M.J., 2002. Testing the Cretaceous greenhouse hypothesis using glassy foraminiferal calcite from the core of the Turonian tropics on Demerara Rise. *Geology*, **30**(7), 607–610.

Cross-references

Atmospheric Evolution, Earth
Carbon Cycle
Carbon Isotopes, Stable
Mesozoic Climates
Sapropels

OCEAN DRILLING PROGRAM (ODP)

History

For more than 30 years, the Ocean Drilling Program (ODP) has sent hundreds of scientists out from their universities and laboratories to the far corners of the world's oceans in search of sediments and rocks that tell the story of Earth's restless past. The ancient ocean depths, long thought to be a barren and unchanging primordial environment, have yielded their secrets of how our planet's powerful yet delicate ecosystem functions.

The Ocean Drilling Program constitutes one part of a systematic geologic investigation of the Earth that has been ongoing since the eighteenth century. It is only in the past thirty years that scientific ocean drilling conducted by ODP and its predecessor, the Deep Sea Drilling Project (DSDP) has taken

center stage as one of the main contributors to our understanding of the system that drives Earth's evolution. ODP focuses its inquiry into the physics, chemistry, and biology of the Earth's processes using two basic data collection strategies: (a) drilling holes in oceanic crust and extracting core samples and (b) inserting instruments into the holes to measure conditions such as pressure, temperature, and chemistry of the pore waters. Scientists from every major scientific specialty use all the tools available to them both in ship and shore-based laboratories to analyze samples and measurements in an effort to compile the data needed for a thorough, multidisciplinary understanding of the processes taking place in and on the seafloor.

Deep sampling of the sedimentary layer of oceanic crust actually began in 1947 with the invention of the Kullenberg piston corer which was able to penetrate to the Pleistocene and late Pliocene sedimentary layers. Through the 1950s and early 1960s, scientists were able to gather samples as old as the upper-Cretaceous (Kennett, 1982; Hay, 1988). Long piston cores provided the first evidence that sedimentary accumulations in deep sea basins are highly variable and subject to constantly changing environmental processes.

In the early 1960s, improvements in deep sea drilling technology warranted a proposal to launch a national program to drill through the Mohorovičić Discontinuity, the boundary between the crust and the mantle. The ambitious plan was to penetrate 6 km of crustal rock below the sea floor in the Pacific Ocean basin. Known as the Experimental Mohole Project, the plan was scrapped after a few test holes due to unanticipated technology problems resulting in substantial cost overruns. Even though the Project was thought to be a dismal failure, samples obtained while drilling from a floating vessel demonstrated to scientists the enormous potential value of geological explorations in oceanic crust, which covers over 70% of the Earth's surface, rather than restricting research to the continental crust.

By 1964, four U.S. oceanographic institutions (Miami University, Columbia University, Woods Hole, and Scripps) had joined together in a consortium known as the Joint Oceanographic Institutions for Deep Earth Sampling (JOIDES) and proposed to the National Science Foundation a program of continuous coring to depths of more than 1 km off the coasts of Florida and Trinidad. Deep sea sediments recovered from six drillholes contained long sequences of well-preserved microfossil assemblages useful for global stratigraphic correlations.

The Mohole Project and the JOIDES holes, as they were called, thus laid the foundation for a campaign of scientific ocean drilling that, over the past four decades, has yielded a treasure trove of core samples and downhole measurements available to scientists all over the world.

On July 20, 1968, the *Glomar Challenger*, an existing vessel modified specifically for scientific ocean drilling, set sail as the flagship of the Deep Sea Drilling Project (DSDP), initially designed as an 18-month project to drill in the Atlantic and Pacific oceans. DSDP was so successful that in the early 1970s other U.S. and foreign institutions joined JOIDES in support of the program, thus providing more stable funding for ongoing operations. DSDP continued operations for more than a decade, gradually increasing its international participation and its range of deep-sea explorations. In 1985, a new, larger, and more sophisticated scientific research vessel began operations, launching the Ocean Drilling Program, a brand new program of scientific ocean drilling. Operated by Texas A&M University, the drillship *JOIDES Resolution* is a "floating university," fitted with modern drilling

equipment as well as numerous fully-equipped laboratories for sample measurement and analysis.

ODP has explored all of the world's oceans, from the Arctic to the Weddell Sea near Antarctica, collecting sediment and rock samples, recording downhole geophysical and geochemical data, and establishing long-term borehole observatories. Since the *JOIDES Resolution* first sailed in January 1985, she has put to sea six times a year, every year with a contingent of scientists, students, drilling specialists and crew, who leave politics and national identity behind in favor of getting the job done. As of mid-2002, ODP has collected almost 700,000 feet (215 km) of cores from over 1,700 holes. Participants in the Ocean Drilling Program include 18 U.S. institutions and 22 international partners. An estimated 2,700 scientists from more than 40 nations have participated in ODP expeditions and countless more have used ODP samples and data in their research. All ODP core samples and related measurements are carefully preserved in depositories and archives and are made available for study to scientists from all countries, institutions, and disciplines.

ODP research objectives

The impetus for deep sea drilling has been to collect sediment and rock samples from oceanic crust in an effort to define and understand the evolution of the planet. One of the most fortuitous aspects of ODP is that evolving technology for scientific ocean drilling coincided with recently developed theories of continental drift, sea-floor spreading, and shifts in the planet's magnetic field. Theories of slowly drifting landmasses, known as plate tectonics, were first proposed in the early twentieth Century by Alfred Wegener, but scientists lacked the tools and technology to test his intriguing hypotheses. The advent of scientific ocean drilling has allowed the collection of data to test and confirm plate tectonics as well as many other hypotheses concerning the geodynamics of natural events like earthquakes and volcanoes, and theories of crustal age and its relationship to the magnetic properties of rocks.

From the outset, ODP researchers have sought to understand the dynamics of Earth's geophysical and geochemical processes, focusing on:

1. climate and sea level variability
2. the nature and movements of sediments and fluids in and on the oceanic crust
3. the deep structure of continental margins and mantle-crust interactions
4. the nature and functions of life forms within the oceanic crust

ODP contributions to Earth science

The Ocean Drilling Program's approach to scientific investigation derives from the recognition that Earth is a complex, multidimensional, dynamic system that is constantly changing. Some changes may be considered rapid in geologic time – for example, ice sheets can fluctuate dramatically over a few thousand years. Other changes occur so gradually that their effects are not at all apparent, even over hundreds of millennia. Geologists have learned to analyze data within theoretical models that can collapse millions of years into time scales in which changes can be described and interpreted. Although any division of the components of Earth's system is arbitrary, oceanographers must subdivide their theoretical approaches and hypotheses in order to tackle manageable scientific questions. Over the years, ODP has concentrated its

efforts within a number of broad scientific themes: climate and sea level variability; sediments, fluids, and bacteria as agents of system change; heat and mass transfer within the Earth's crust and mantle; and deformation mechanisms within the lithosphere which contribute to natural catastrophic events such as earthquakes, volcanoes, and massive landslides under the ocean.

Climate change

The Earth's climate exhibits cycles of warming and cooling as well as episodes of rapid climate change. Geologists from a wide variety of disciplines have employed an extraordinary number of investigative approaches to identify and quantify climate variability, and the various agents of change within Earth's dynamic climate system. This area of research is critical to understanding natural climate cycles, as well as impacts on local and global climate of natural and man-made perturbations in the system.

Climate is affected by atmospheric composition, planetary orbital oscillations, ocean circulation patterns and carbon flux, biological productivity and evolution, land surface alterations, sea-level fluctuations, and the global distribution and volume of ice. Climate change in turn impacts many of these factors such that a feedback system exists between physical, chemical, and other ecosystem elements (Figure O4). Identifying cause and effect relationships requires data from widely diverse geographic locations and from as many time periods as possible.

One method for measuring climate change comes from examining stable isotopes of oxygen, carbon, and nitrogen, and the presence of particular elements within microfossils in sediment deposits. The ratio of oxygen isotopes and the concentration of certain elements in the fossils vary predictably with the temperature at which the animals lived. These measurements allow scientists to extrapolate their findings to make predictions about

other parts of the climate system, such as the waxing and waning of ice volume over time (Lear et al., 2000).

Variations in carbon deposition is another indicator of climate change, since biologic productivity and turnover varies with climate, and rates of biological activity can be measured in depositions of biogenic sediments of the deep sea. The degree of preservation of organic carbon in sediments is controlled both by rates of productivity and degree of oxygenation of the bottom waters.

Plate tectonics, popularly known as continental drift, has also been implicated in major climatic variation due to alterations in the distribution of freshwater and heat transport in the global ocean. Through cores obtained from ocean drilling, scientists have identified shifts in ocean currents, seawater salinity, and rates and pathways of heat transport due to the reconfiguration of oceans and continents, particularly the opening and closing of oceanic gateways. One example is the closure of the Central American Seaway, near Panama, which initially resulted in climate warming but ultimately led to major ice sheet development in the Northern Hemisphere (Haug et al., 2001).

Fluctuations in sea-level are also seen as indicators of shifts in the global climate. While local sea-level changes can be the result of sediment shifting and plate movement, global sea-level fluctuation is usually the result of changes in the global volume of ice, and is directly associated with variations in atmospheric and ocean temperatures. ODP has drilled a number of sites, particularly in the New Jersey continental shelf and Bahama Islands, in an effort to identify those sea level variations that are the result of local effects versus those that result from global climate change.

Large shifts in climate can also occur as a result of catastrophic natural events. An event such as a volcanic eruption or a meteor striking the Earth can produce sufficient change in the composition of the atmosphere to cause an overall warm-

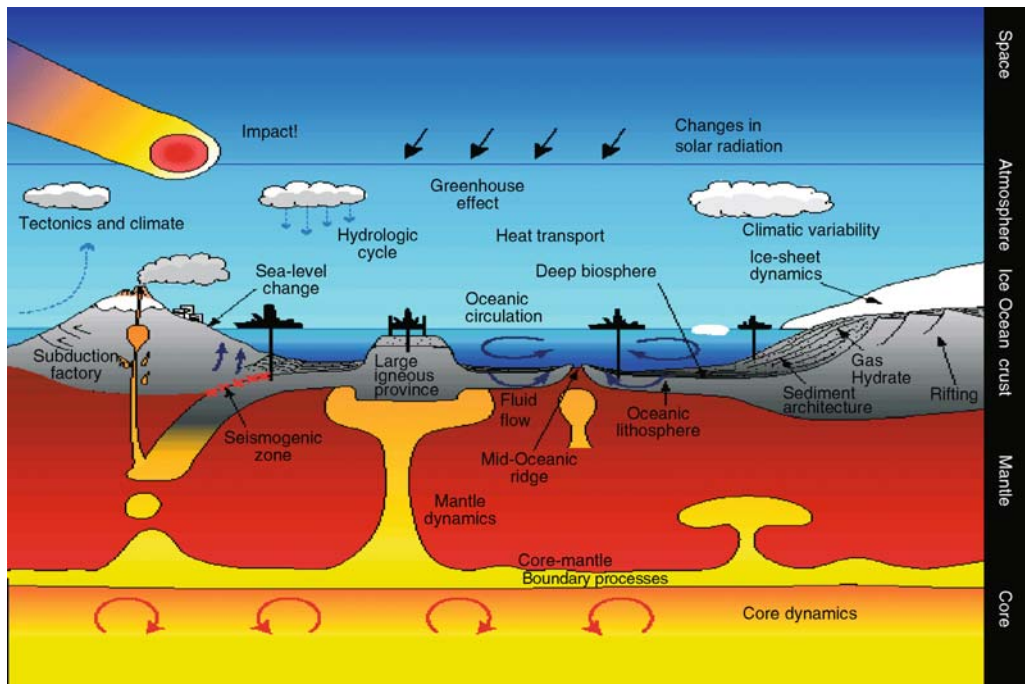


Figure O4 Earth system components, processes, and phenomena (courtesy of Asahiko Taira, Japan Marine Science and Technology Center).

ing of the global climate and even widespread extinctions of biological species. Such an event is thought to have occurred about 65 million years ago. A large extraterrestrial object, probably a meteor, apparently slammed into Earth at what is now Mexico's Yucatan Peninsula. In 1997, ODP drilled into sites 300 miles off northeastern Florida, extracting cores containing sedimentary layers that reveal in beautiful detail a cataclysmic story of destruction and biotic upheaval. The cores exhibit sedimentary layers of debris from the impact consisting of a layer of green, glassy globules and mineral grains, a succeeding layer showing remains of the meteorite but devoid of almost all life, and succeeding layers showing the return of microorganisms. The cores that document what is now known at the Cretaceous-Tertiary (K/T) boundary enable scientists to conduct geochemical and paleontological studies of the post-apocalyptic repopulation of the ocean (Norris, 1997).

Architecture of planet Earth

By convention, our planet is described as being made up of three major sections, an inner molten core, the mantle, which is composed mostly of solid igneous rock, and the crust, consisting of regions of consolidated rock, layers of sediment, and pockets of gases and fluids inhabited by microorganisms. In fact, these components of the planet are in motion and interacting with each other all the time. We see the effects of crustal and upper mantle motion in the form of volcanoes, earthquakes, faults, geysers, and other natural phenomena. The Ocean Drilling Program has focused a great deal of attention on describing the movement of rock, sediments, gases, and fluids in the oceanic crust and mantle. Core samples from the far reaches of the global ocean have confirmed the theory of plate tectonics by comparing sedimentary deposits, magnetic signatures, and crustal rocks from geographically disparate sites. Over the past two decades, ODP research has improved our understanding of Earth's deep mantle using numerical simulations, images derived from global seismic tomography, and experimental studies of materials at simulated mantle conditions. These studies suggest mantle architecture and dynamics that are considerably more complex than simple layering.

A dramatic example of plate tectonics, or continental drift, is apparent in the Atlantic Ocean. Until about 140 millions years ago, a narrow, shallow seaway lay between Europe and North America. The European and North American plates began to shift, resulting in a spreading of the seafloor and the formation of the Atlantic Ocean. A combination of geophysical measurements and studies of drill cores obtained by ODP off the coast of Portugal documents this gradual phenomenon by measuring the thickness of the crust and determining that the continental crust became shallower as it spread. It broke up when it had thinned to about 7 km, resulting in a crust-free zone of exposed mantle at the seafloor. Many of the rock cores have now been dated using radioactive isotopes to demonstrate that the focus of stretching of the crust and mantle migrated from the continent towards the ocean (Whitmarsh et al., 2001).

Another major focus of ODP technological and research effort has been the placement of long-term observatories in the ocean floor. Dubbed CORKs, these observatories are designed to document the flow of heat and chemicals within the interior of the crust by measuring temperatures, pressures, and compositions of fluids (Figure O5). CORKs have been placed on the axis and flank of the Juan de Fuca Ridge in the northern Pacific, and the flank of the Costa Rica Rift and the Nankai and Mariana subduction zones. Data from CORKs show that changes in mechanical and fluid-flow properties of rock formations result from plate strain,

notably at sites where earthquakes occur. Thus, research from CORKs is helping to explain the relationship between episodic plate motion, deformation, and earthquake energy release (Davis and Becker, 1998).

Observatories can also be used to measure seismic activity in crustal deformations offshore, too far for land-based measuring instruments to reach. ODP emplaced such an observatory offshore of northeast Japan, more than 1,000 m below the sea floor in water depths of 2,000 m. This observatory is designed to sense movement at plate boundaries, called subduction zones. Interpretations of measurements allow geophysicists to determine whether plate movement is creating plate boundary strain that could eventually erupt in a violent earthquake. Earth-

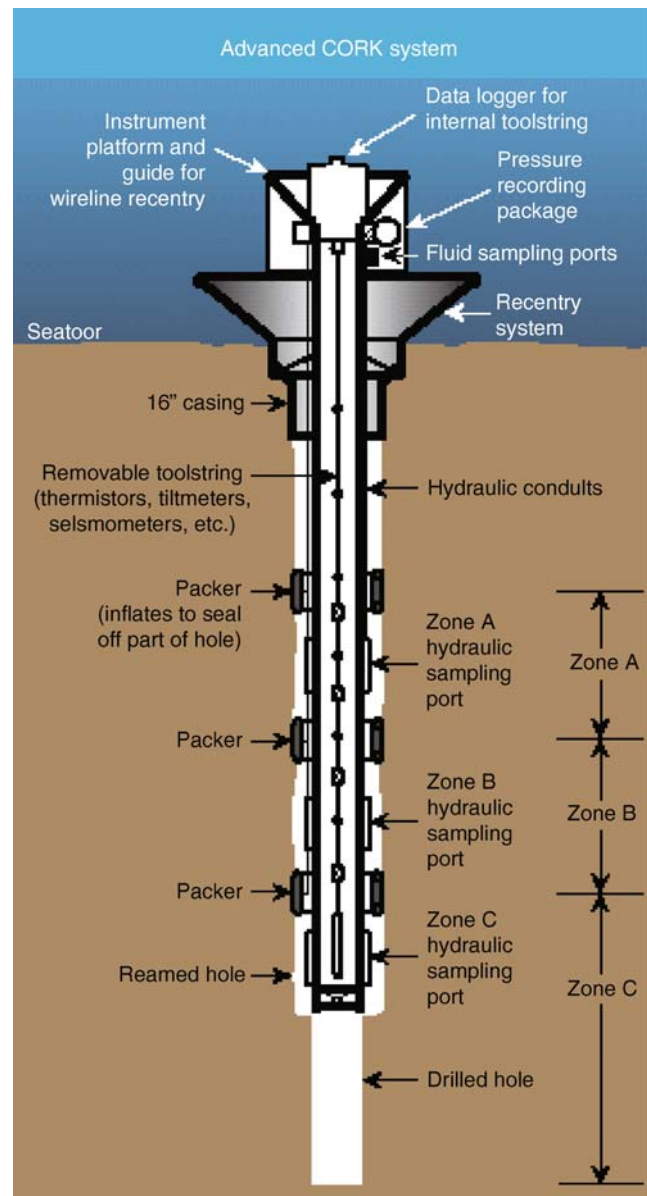


Figure O5 Advanced Cork System (courtesy of Earl Davis, Geological Survey of Canada and Keir Becker, University of Miami).

quakes are devastating manifestations of plate movement, but only represent a portion of the total energy storage and release being created at subduction zones. ODP observatories help us see the whole picture, allowing better prediction of natural hazards (Suyehiro, 2002).

Drilling through the entire thickness of Earth's crust has been a challenge since the very beginning of scientific ocean drilling. Scientists define the architecture of oceanic crust by comparing the seismic signature of the crust in the oceans to the various pieces of oceanic crust found on continents. ODP recently drilled one hole in the Pacific to a depth of 2,111 m below the sea floor – the deepest scientific hole drilled in the ocean. Another expedition extracted 1.5 km of rock core from below the seafloor at the Mid Atlantic Ridge. Core samples from the deep crust provide valuable information on deformation structures and rock composition from which interpretations of tectonic activity can be derived (Dick et al., 2000).

Deep biosphere

Living microorganisms have found a comfortable home in the various ecological niches of Earth's crust, from shallow sedimentary layers to deep regions of basalt rock. Until recently, it was assumed that the deep crust was a sterile, lifeless place, undisturbed by the messiness of organic metabolic processes. In the past two decades, ODP research has discovered a wide variety of microbial life forms deep within oceanic crust. Drilling has unearthed bacteria living as deep as 800 m below the seafloor, much deeper than was previously thought possible given the extreme temperatures and pressures in the deep crustal environment. Estimating the size and ecological impact of this so-called deep biosphere is a major scientific goal of ODP. While the concentration of living organisms in Earth's crust is small, the global volume of crust is enormous, indicating that crustal organisms may represent a significant fraction of the Earth's biomass (Parkes et al., 1994).

Recent research indicates that the ability of bacteria to cycle between active and dormant states in response to nutrient levels may answer one of the mysteries of how they survive in such inhospitable environments. Indeed, microbial activity has even been found in reservoirs of volcanic glass, suggesting that the microbes are metabolizing minerals as an energy source. Microbes in volcanic crust may be important catalysts of chemical change, and may help to regulate the cycling of elements between seawater and oceanic crust. The existence of such life forms that derive their energy from inorganic chemical reactions suggests that life may thrive in previously unsuspected places, such as on Mars and Europa (Fisk, 1997).

Bacteria isolated from continental hydrothermal environments have already made a major impact on biotechnology in areas like bioremediation, waste treatment, microbial enhanced oil recovery, and biominerals. Some bacterial populations appear to have survived for millions of years, suggesting they have some remarkable enzymes and metabolic processes. The seafloor may turn out to be an especially suitable setting for sampling the deep biosphere and measuring microbiological processes and fluid flow in support of biological communities. Subseafloor environments are often more stable and structurally less complicated than terrestrial environments. Drilling and core collection strategies are being developed to assure samples relatively uncontaminated by human activity.

Microbiology has become an integral part of ODP explorations. The drillship has a well-equipped microbiology laboratory that allows seagoing scientists to collect samples from

cores for experiments and analysis both immediately onboard and preserved for shore-based study. The results of these studies will contribute to our understanding of how the Earth and its inhabitants have co-evolved (Smith, 2002).

ODP technology

The ODP collects samples from the Earth's crust in locations that are not only great distances from shore-based laboratories but incredibly difficult to reach. ODP drilling sites may be thousands of miles from shore and more than 8 km below the ocean surface. ODP adapts technology developed by oil exploration companies, as well as engineering specialized drilling tools as required by scientists' research goals. The centerpiece of the ODP is the 143 m long drillship *JOIDES Resolution* (Figure O6). For more than two decades, this ship has made at least six expeditions a year to drill cores and take measurements inside the boreholes in all but very shallow, very deep, or ice-covered oceans. The ship is equipped with over a thousand square feet of state-of-the-art geophysical, geochemical, and microbiological laboratories, and accommodates 50 scientists and technicians and an equivalent complement of crew members.

ODP cores and downhole measurements are the priceless data that are used by both seagoing and shore-based scientists to conduct analyses, test hypotheses, and develop theories of how all the elements of the Earth system function. Cores are obtained by lowering a string of drill pipe through an opening in the ship's hull, called the moon pool, down to the seafloor. Core barrels, containers for the core, are lowered within the pipe. They collect core samples as the drill bit chews through the seafloor. Once the core arrives on deck, all scientists and technicians are busy taking measurements of its geophysical and geochemical properties, such as density, porosity, and magnetism. The core is then halved, with the working half being prepared for sampling and the archive half kept in pristine condition and saved for future research. Scientists spend much of their time on board measuring and analyzing core samples for composition, grain size, age, and color. At the end of the cruise, all cores are sent to one of four onshore repositories where they are stored in a temperature-controlled environment for future research.

The borehole left behind is also a source of valuable data that is collected and stored with care equal to the cores them-

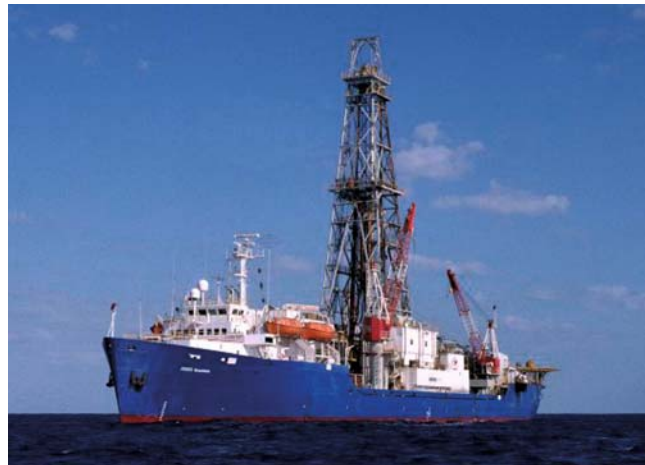


Figure O6 ODP drillship *JOIDES Resolution*.

selves. Downhole measuring tools are placed in the hole on wirelines both during and after extracting the core. Instruments attached to the wireline continuously measure geophysical conditions such as temperature, pressure, fluid flow, and magnetism, all of which are critical to understanding the dynamic processes in the environment from which the cores were extracted. These logging tools also include imaging tools that create a detailed “picture” of the inside of the borehole. These data help scientists to develop models and theories of sediment and rock structure, conditions and movements at plate boundaries, and shifts in crustal composition such as magma flows and intrusions (Goldberg, 1997).

ODP organization and funding

The ODP is an international partnership of scientists and research institutions organized to explore the evolution and structure of the Earth. Its composition and membership has grown throughout its thirty-year history to include the United States, Germany, Japan, the United Kingdom, the Australia/Canada/Chinese Taipei/Korea Consortium for Ocean Drilling, the European Science Foundation Consortium for Ocean Drilling (Belgium, Denmark, Finland, Iceland, Ireland, Italy, The Netherlands, Norway, Portugal, Spain, Sweden, and Switzerland), the People’s Republic of China, and France.

Member countries pool financial resources to fund ODP research. Program resources are managed by a non-profit corporation that subcontracts with various institutions to provide ship and logging operations, shore-based laboratories and core curation, and dissemination of samples, data, and research results.

ODPs research agenda has always been proposed and evaluated by participating ODP scientists. Individual scientists or groups of scientists propose research projects to ODP. Proposals are reviewed and evaluated by multidisciplinary panels representing scientists from all ODP member countries and institutions. The consortium of Joint Oceanographic Institutions for Deep Earth Sampling (JOIDES) constitutes a series of science advice panels and committees, which are charged with evaluating not only the scientific merit of proposals, but also considerations such as safety, likelihood of success, pollution prevention, and technological requirements.

This unique format brings together researchers and students from universities, industry, and government laboratories in member nations to work in modern, fully equipped shipboard laboratories on focused scientific projects. The results of research based on ODP cores, samples, and data are published openly in leading scientific journals and in ODP publications.

Joanne C. Reuss

Bibliography

- Davis, E., and Becker, K., 1998. Borehole observations record driving forces for hydrothermal circulation in young oceanic crust. *Eos, Trans. Am. Geophys. Union*, **79**(31), 377–378.
- Dick, H.J.B., et al., 2000. A long in-situ section of the lower ocean crust: results of ODP Leg 176 drilling at the Southwest Indian Ridge. *Earth Planet. Sci. Lett.*, **179**, 31–51.
- Fisk, M.R., 1997. Evidence for Microbes in Oceanic Balasts: Glass-Eating Bacteria? *ODP’s Greatest Hits; Contributions from the U.S. Scientific Community*. Washington, DC: Joint Oceanographic Institutions, 15.
- Goldberg, D., 1997. The role of downhole measurements in marine geology and geophysics. *Rev. Geophys.*, **35**–3, 315–342.
- Haug, G.H., Tiedemann, R., Zahn, R., and Ravelo, A.C., 2001. Role of Panama uplift on oceanic freshwater balance. *Geology*, **29**, 207–210.

- Hay, W.W., 1988. Paleooceanography: A Review for the GSA Centennial. *Geol. Soc. Am. Bull.*, **100**, 1,934–1,956.
- Kennett, J., 1982. *Marine Geology*. Englewood Cliffs, NJ: Prentice-Hall, 811pp.
- Lear, C.H., Elderfield, H., and Wilson, P.A., 2000. Cenozoic deep-sea temperatures and global ice volumes from Mg/Ca in benthic foraminiferal calcite. *Science*, **287**, 269–272.
- Norris, R.D., 1997. Records of the Apocalypse: ODP Drills the K/T Boundary. *ODP’s Greatest Hits; Contributions from the U.S. Scientific Community*. Washington, DC: Joint Oceanographic Institutions, 9.
- Parkes, R.J., Cragg, B.A., Bale, S.J., Getcliff, K., Goodman, P.A., Rochelle, J.J.F., Weightman, A.J., and Harvey, S.M., 1994. Deep bacterial biosphere in Pacific Ocean sediments. *Nature*, **371**, 410–413.
- Smith, D.C., 2002. Microbes: Life Deep Beneath the Seafloor. *ODP Highlights; International Scientific Contributions from the Ocean Drilling Program*. Washington, DC: Joint Oceanographic Institutions, 6.
- Suyehiro, K., 2002. The Earth’s Next Move. *ODP Highlights; International Scientific Contributions from the Ocean Drilling Program*. Washington, DC: Joint Oceanographic Institutions, 25.
- Whitmarsh, R.B., Manatschal, G., and Minshull, T.A., 2001. Evolution of magma-poor continental margins from final rifting to seafloor spreading. *Nature*, **413**, 150–154.

Cross-references

- [Carbon Isotopes, Stable](#)
[Climate Change, Causes](#)
[Cretaceous/Tertiary \(K-T\) Boundary Impact, Climate Effects](#)
[Deep Sea Drilling Project \(DSDP\)](#)
[Oxygen Isotopes](#)
[Plate Tectonics and Climate Change](#)
[Sea Level Change, Last 250 Million Years](#)
[Stable Isotope Analysis](#)

OCEAN PALEOCIRCULATION

Introduction

Because of its impact on global climate, one of the most important aspects of ocean circulation is the rate of meridional overturning (also called “Conveyor Belt” or thermohaline circulation) (Figure O7; see *Thermohaline circulation*). In the Atlantic Ocean, the meridional overturning circulation (MOC) brings heat from the tropics to high northern latitudes, which ameliorates the climate of the northern continents (Broecker, 1997). Changes in the rate of the Atlantic MOC and in the associated production of the North Atlantic Deep Water (NADW) may thus have been directly implicated in the large climatic cycles and abrupt climate changes that characterize the Quaternary period and may have contributed to the waxing and waning of the large continental ice sheets that covered North America and Northern Europe during glacial times (see *Quaternary climate transitions and cycles*). Changes in the global ocean circulation could have also played an indirect role in altering the Earth’s climate by influencing atmospheric CO₂ and greenhouse warming (see *Ice cores, Antarctica and Greenland*). Lower rates of deep-water ventilation would engender greater sequestration of carbon in the deep sea, resulting in lower atmospheric CO₂ and cooler temperatures (Toggweiler, 1999). Reconstructing past changes in ocean circulation (i.e., ocean paleocirculation) is thus an integral part of understanding the evolution of climate and has been subject to intensive scientific scrutiny for several decades.

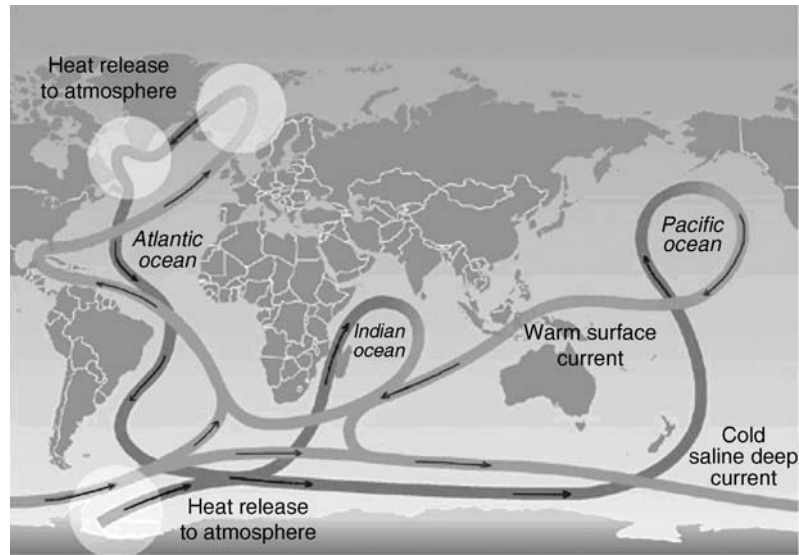


Figure O7 The thermohaline circulation of the ocean. Warm, shallow water is transported from the tropics to the high North Atlantic, where it comes in contact with cold air, cools down and eventually becomes dense enough to sink to the bottom. The newly-formed deep water flows to the south, goes around Antarctica and fills up the two other major ocean basins where it gradually mixes upward to return as a warmer shallower water mass to the North Atlantic (Intergovernmental Panel on Climate Change, 2001).

Reconstructing paleocirculation

The chemical and isotopic composition of marine sediments and skeletal remains of organisms that grow on the seafloor is one of our main sources of information for evaluating past changes in ocean circulation in relation to climatic variability. Changes in ocean circulation impart distinct chemical and isotopic signatures to seawater that are recorded in the carbonate shells of benthic foraminifera (i.e., protozoans living on the seafloor), in the carbonate skeletons of deep-sea corals and in the sediment accumulating on the seafloor. Results obtained from these geochemical tracers (or proxies) clearly reveal that significant changes both in the distribution of water masses and in the rate of deep-water circulation took place in the past, in concert with important climatic events. Reconciling the detailed interpretation of these different and sometimes conflicting proxies is yielding an increasingly clear depiction of how deepwater circulation contributed to or responded to past global climate changes.

Geochemical tracers of deep-water circulation can be broadly divided into two categories: (a) water mass tracers and (b) kinematic tracers of ocean circulation. Both types of tracers are complementary and necessary to fully document past changes in deep water circulation. The water mass tracers are better suited for reconstructing past expansions or contractions of the different water masses that fill the deep ocean basins, while kinematic tracers are necessary to constrain past changes in the rate at which volumes of deep water were produced (expressed in Sverdrups = $10^6 \text{ m}^3 \text{ s}^{-1}$).

Underlying principles

Proxies for water mass identification

In the deep Atlantic Ocean, two antagonistic water masses, the North Atlantic Deep Water (NADW) and the Antarctic Bottom Water (AABW), vie for spatial dominance. The NADW, which

initiates the global conveyor belt circulation (Figure O7), originates from the North Atlantic and flows southward towards the Southern Ocean, while the AABW originates from the Southern Ocean and flows northward. The latter water mass is denser, and wedges underneath the NADW.

In the modern ocean, these two deepwater masses can be clearly distinguished by their chemical and isotopic composition. Deep waters of southern origin have significantly higher dissolved nutrient concentrations (Figure O8). Nutrients consist of dissolved salts (nitrate, phosphate, silicate) that are taken up in surface waters to sustain the growth of phytoplankton and regenerated at depth from the decay of sinking organic matter. This biological cycling results in lower nutrient concentrations in surface waters and higher concentrations in deeper waters. Nutrient concentrations in deep waters have two components. When surface waters sink to produce deep waters, they already contain nutrients due to incomplete biological utilization and entrainment of nutrient-enriched water from intermediate depths. As newly formed deep waters age in deep ocean basins, they accumulate an increasing load of dissolved nutrients from the decay of organic matter exported from the surface. The former contribution to the total nutrient load of deep waters is the “preformed nutrient” concentration and the latter contribution is the “regenerated nutrient” concentration. Deep waters of southern origin have higher preformed nutrient concentrations because nutrient utilization in the surface waters around Antarctica is limited by the harsh environmental conditions that prevail in this region. This is the main reason why AABW has noticeably higher nutrient concentrations than NADW, which clearly identify its presence and its northward propagation above the seafloor (Figure O8). Assuming no changes in the preformed nutrient concentration of the two deep-water masses, further northward penetration of AABW would result in higher nutrient concentrations in the deep water of the Atlantic. Therefore, if we were able to estimate past

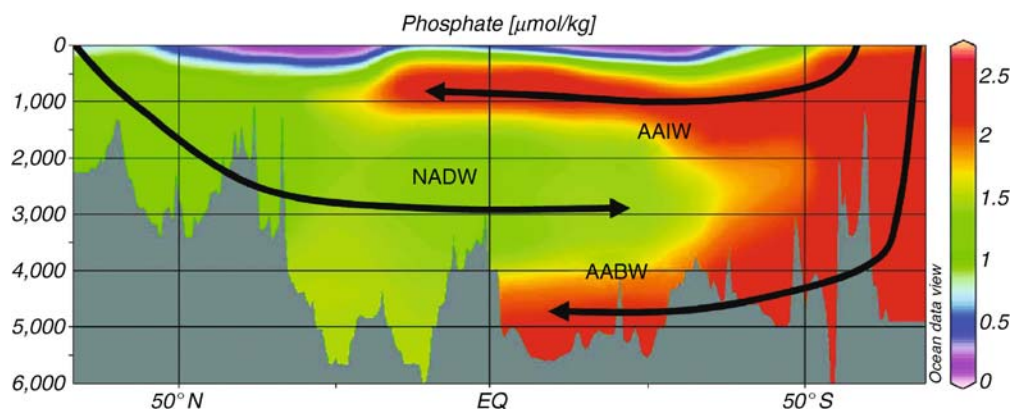


Figure O8 Latitudinal cross section of phosphate concentration in the Atlantic Ocean. The high phosphate concentrations in the two water masses of southern origin, the Antarctic Intermediate Water (AAIW) and the Antarctic Bottom Water (AABW), stand out in sharp contrast to the lower phosphate concentrations in the North Atlantic Deep Water (NADW).

changes in deep water nutrient concentrations, we could deduce the relative importance of these two water masses in the past. However, past changes in deepwater nutrient concentrations are not directly recorded in marine sediments. Instead, one has to find chemical and isotopic signatures (i.e., nutrient concentration proxies) that correlate closely with dissolved nutrient concentrations and become incorporated in marine archives (i.e., benthic foraminifera, deep-sea corals, or sediments). The most often used water mass proxies are the carbon isotopic composition ($\delta^{13}\text{C}$) of dissolved inorganic carbon and the dissolved concentration of several biologically recycled trace metals (Cd, Zn, Ba), which are recorded in the isotopic and chemical composition of benthic foraminifera and deep-sea corals that grow in contact with bottom water. Neodymium isotope ratio (ϵ_{Nd}) has also been used. Unlike the previous tracers, ϵ_{Nd} is recorded in the oxide coatings of settling particles that accumulate on the seafloor and is not directly affected by biological cycling.

$\delta^{13}\text{C}$ in benthic foraminifera

Carbon has two stable isotopes: ^{13}C ($\sim 1.1\%$) and ^{12}C ($\sim 98.9\%$). Isotopic compositions are reported in the “delta” notation, i.e., $^{13}\text{C}/^{12}\text{C}$ ratio expressed in permil deviation from a standard taken as reference:

$$\delta^{13}\text{C}_{\text{Sample}} = \left[\frac{\left(\frac{^{13}\text{C}}{^{12}\text{C}} \right)_{\text{Sample}}}{\left(\frac{^{13}\text{C}}{^{12}\text{C}} \right)_{\text{Standard}}} - 1 \right] 1,000$$

During photosynthesis, dissolved inorganic carbon, nitrate and phosphate are taken up by phytoplankton to produce organic matter in surface waters. Because ^{12}C is taken up preferentially to ^{13}C , the organic matter produced has a $\delta^{13}\text{C}$ value lower than the $\delta^{13}\text{C}$ of inorganic carbon dissolved in surface waters. Upon degradation and oxidation of organic matter in deep waters, the dissolved inorganic carbon produced has a similarly “light” isotopic composition (i.e., low $\delta^{13}\text{C}$). This isotopically light inorganic carbon is regenerated concurrently with nitrate and phosphate, resulting in a negative linear correlation between the nitrate or phosphate concentration and the $\delta^{13}\text{C}$ of dissolved

inorganic carbon in deep waters (Kroopnick, 1985; Figure O9a). The $\delta^{13}\text{C}$ of inorganic carbon dissolved in bottom waters is recorded by the carbon isotopic composition of the calcium carbonate produced by benthic foraminifera living on the seafloor, which thus indirectly record nutrient concentrations in bottom waters. By measuring the $\delta^{13}\text{C}$ of benthic foraminifera that lived in the past at different water depths, it is thus possible to reconstruct past changes in the $\delta^{13}\text{C}$ of seawater and deduce past changes in the concentration and vertical distribution of nutrients in deep waters (Samthein et al., 2001).

Cd/Ca, Ba/Ca and Zn/Ca ratios in benthic foraminifera or deep-sea corals

A similar principle can be applied to certain trace metals. Cadmium (Cd) is biologically recycled with phosphorus, resulting in a tight positive correlation between phosphate and dissolved Cd concentration in seawater (Figure O9b). As Cd becomes incorporated in biogenic carbonate minerals in proportion to its concentration in ambient seawater, the Cd/Ca ratio in fossil benthic foraminifera (Boyle, 1988) and deep-sea corals (Adkins et al., 1998) provides an independent means of reconstructing past changes in bottom water nutrient concentration. As for $\delta^{13}\text{C}$, this information can be used to contrast the relative contribution of NADW and AABW in the deep Atlantic Ocean, if we assume (i) no changes in the preformed nutrient concentrations in the water masses involved, and (ii) no changes in the rate of organic matter remineralization in deep waters.

Barium (Ba) and zinc (Zn) are also biologically recycled, but their regeneration from settling particles occurs at greater depth than for Cd. Instead of tightly correlating with phosphate, their seawater profiles mimic those of alkalinity or dissolved silicate (Figures O9c and O9d), which are controlled by the dissolution of carbonate and biogenic silica occurring in deeper water. As for Cd, the concentration of dissolved Ba and Zn in bottom water is recorded in the Ba/Ca and Zn/Ca ratios in the shells of benthic foraminifera (Lea and Boyle, 1989; Marchitto et al., 2000). Because of its deeper regeneration, the contrast in Zn concentration between NADW and AABW is more pronounced than for Cd. As a result, paired Zn and Cd measurement in the same foraminifera shells provides

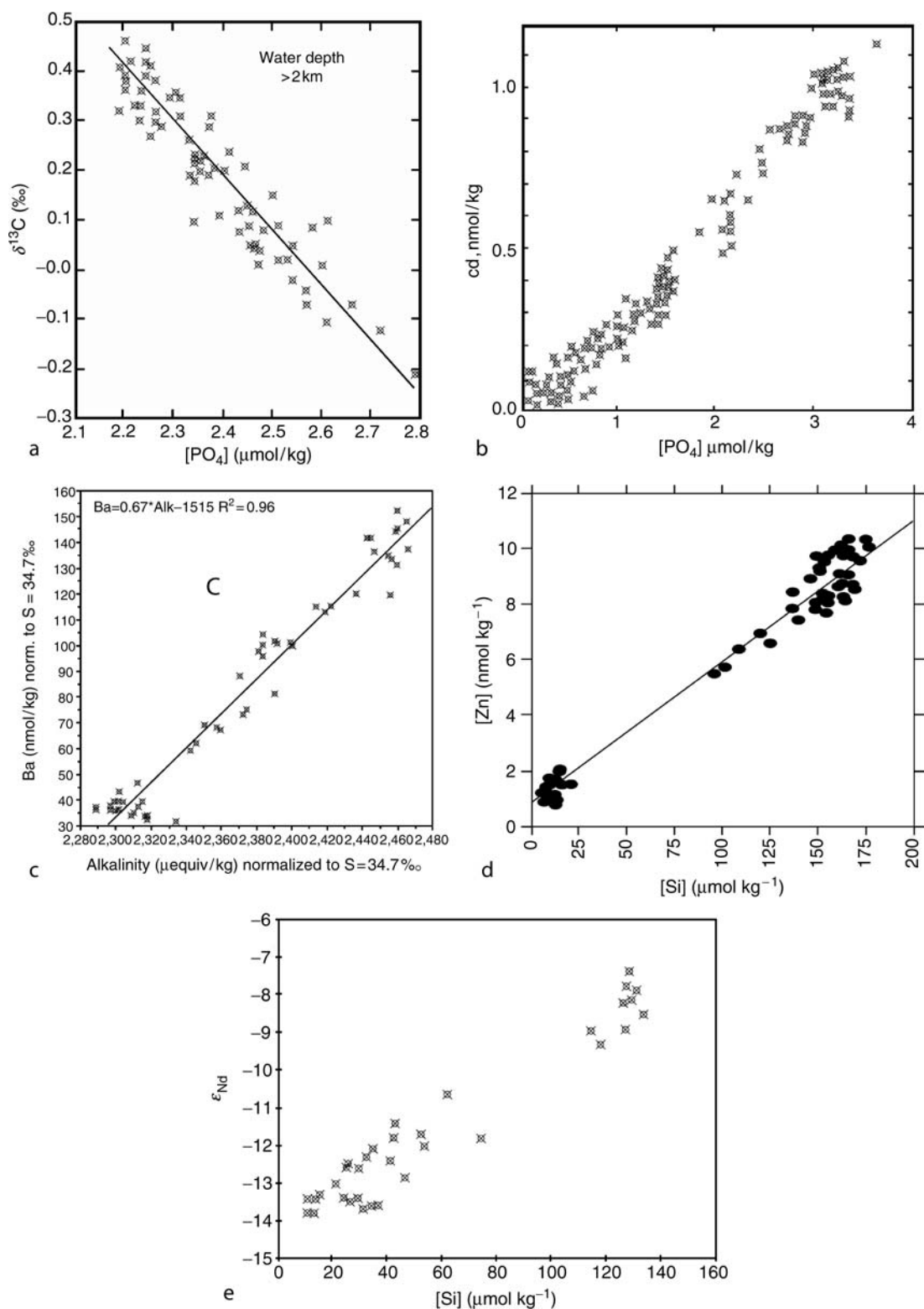


Figure O9 Correlations between seawater properties (nutrient concentration and alkalinity) and proxies used for their paleoceanographic reconstruction. (a) $\delta^{13}\text{C}$ of dissolved inorganic carbon vs phosphate concentration in deep water (adapted from Broecker and Maier-Reimer, 1992). (b) Dissolved cadmium vs. phosphate concentration in subsurface waters (adapted from Boyle, 1986). (c) Dissolved barium vs. alkalinity in surface and deep waters (adapted from Lea, 1993). (d) Dissolved zinc vs. dissolved silicate concentration in seawater deeper than 1,000 m (adapted from Marchitto et al., 2000). (e) ϵ_{Nd} vs. dissolved silicate concentration in the deep Atlantic Ocean (adapted from Rutberg et al., 2000).

a means of distinguishing between changes in AABW penetration and changes in preformed nutrient concentration (Marchitto et al., 2002).

Neodymium isotopic ratio (ϵ_{Nd}) in sedimentary oxides

Neodymium isotopic composition is reported as:

$$(\epsilon_{\text{Nd}})_{\text{Sample}} = \left[\frac{(^{143}\text{Nd}/^{144}\text{Nd})_{\text{Sample}}}{(^{143}\text{Nd}/^{144}\text{Nd})_{\text{Standard}}} - 1 \right] 10^4$$

Seawater ϵ_{Nd} reflects Nd input from nearby continental masses (von Blanckenburg, 1999). Deep waters formed in the North Atlantic acquire a Nd isotopic composition ($\epsilon_{\text{Nd}} = -13.5$) clearly distinct from that of the deep waters originating from the Southern Ocean ($\epsilon_{\text{Nd}} = -7$). There is a positive linear correlation between ϵ_{Nd} and silicate concentration (Figure O9e) in the deep Atlantic, reflecting a two end-member mixing between NADW (low silicate concentration and low ϵ_{Nd}) and AABW (high silicate, high ϵ_{Nd}). Dissolved Nd is removed from seawater by adsorption on iron and manganese oxides that precipitate in seawater and coat settling particles. The Nd isotopic composition associated with oxides, which can be chemically leached from sediment, thus provides a complementary means of estimating the northward penetration of deep waters of southern origin, which is independent of the biological recycling of nutrients (Rutberg et al., 2000). This is important, because changes in the concentration of the nutrient-related tracers described above could be affected by biological recycling, independently of circulation.

Kinematic proxies for estimating rates of circulation

Several proxies that provide information on changes in circulation rates have also been developed. They include (a) reconstruction of the $^{14}\text{C}/^{12}\text{C}$ ratio in the atmosphere, (b) paired planktonic-benthic ^{14}C age differences, (c) ^{14}C ages of ^{230}Th -dated deep-sea corals, (d) geostrophic flow reconstructions from benthic foraminifera $\delta^{18}\text{O}$, and (e) $^{231}\text{Pa}/^{230}\text{Th}$ in Atlantic sediments.

$^{14}\text{C}/^{12}\text{C}$ ratio in the atmosphere

^{14}C is a radioactive isotope of carbon that is continuously produced in the atmosphere by cosmic rays (cosmic rays are protons that shatter nuclei of atoms in the atmosphere, producing neutrons that become incorporated into the nuclei of nitrogen atoms while ejecting a proton; as a result ^{14}N becomes ^{14}C). After formation, ^{14}C enters the global carbon cycle and decays with a half-life of 5,730 years, thereby providing a clock to date carbon-containing samples during the last $\sim 50,000$ years. However, accurate dating must take into account past variations in the $^{14}\text{C}/^{12}\text{C}$ ratio of the atmosphere (expressed as $\Delta^{14}\text{C}_{\text{atm}}$; see *Radiocarbon dating*). To that end, $\Delta^{14}\text{C}_{\text{atm}}$ has been reconstructed for the past 50,000 years (Hughen et al., 2004) by measuring the $^{14}\text{C}/^{12}\text{C}$ ratio of samples that could be independently dated (tree rings, ^{230}Th -dated corals, annually-layered sediments, marine sediments correlated to the precise timescale of Greenland ice cores). An important fraction of $\Delta^{14}\text{C}_{\text{atm}}$ variability results from variations in the intensity of the Earth's magnetic field; these affect the influx of cosmic rays and hence the production rate of cosmogenic nuclides like ^{14}C . This variability can be estimated from paleomagnetic data (e.g., Laj et al., 2002). Additional $\Delta^{14}\text{C}_{\text{atm}}$ variability can also result from changes in the rate of deepwater formation, which

affect the residence time of ^{14}C in the atmosphere. Thus, the residual between the reconstructed history of $\Delta^{14}\text{C}_{\text{atm}}$ and the $\Delta^{14}\text{C}_{\text{atm}}$ predicted from the changes in the intensity of the geomagnetic field can be attributed to changes in the rate at which ^{14}C is transferred from the atmosphere to the deep sea as a result of deep water formation (Hughen et al., 2004). $\Delta^{14}\text{C}_{\text{atm}}$ higher than predicted from paleomagnetic data indicates slower rates of transfer of ^{14}C from the atmosphere to the deep sea, reflecting lower rates of deep-water formation. However, changes in the air-sea exchange rate of ^{14}C , in the solar component of ^{14}C production modulation, and in the terrestrial carbon reservoir, together with the effect of the biological export of ^{14}C to the deep sea, must also be considered.

Paired planktonic-benthic ^{14}C age differences

^{14}C age differences between the fossil shells of planktonic (i.e., living in surface waters) and benthic (i.e., living on the seafloor) foraminifera recovered from the same sediment horizon and presumed to be contemporaneous can potentially provide quantitative information on past changes in deepwater renewal rates. Larger differences in age have been taken to indicate older deep waters and slower renewal rates (Keigwin and Schlegel, 2002).

There are two potential complications, however, with that approach. One stems from the variability in $\Delta^{14}\text{C}_{\text{atm}}$ with time. Although the planktonic and benthic foraminifera are contemporaneous, the benthic species are growing in water that was in contact with the atmosphere at an earlier time when $\Delta^{14}\text{C}_{\text{atm}}$ may have been different. The $^{14}\text{C}/^{12}\text{C}$ ratio of the benthic and planktonic foraminifera cannot thus be compared directly but one must take into account this difference in initial conditions (Adkins and Boyle, 1997). The second complication may be even more problematic to resolve. It arises from the fact that foraminifera do not acquire their carbon directly from the atmosphere. Instead, their carbon source is inorganic carbon dissolved in ambient seawater. The $^{14}\text{C}/^{12}\text{C}$ ratio of surface waters, where planktonic foraminifera grow, is controlled by exchange of CO_2 with the atmosphere and mixing with older dissolved inorganic carbon from below. As a result, the $^{14}\text{C}/^{12}\text{C}$ ratio of oceanic surface waters and planktonic foraminifera is lower than that of the contemporaneous atmosphere. In the modern ocean, at low to mid latitudes, surface waters have a $^{14}\text{C}/^{12}\text{C}$ ratio that corresponds to an age of ~ 400 years. This so-called "reservoir age," however, can be significantly larger at high latitudes (up to 1,300 years), particularly in the Southern Ocean, where upwelling rates of older deeper waters are higher and CO_2 exchange with the atmosphere is limited by extensive sea ice cover (Bard, 1988). Because deep water is formed at high latitudes, benthic foraminifera growing on the seafloor at low to mid latitude record a $^{14}\text{C}/^{12}\text{C}$ ratio that has been affected by a significantly older "reservoir age" than their contemporaneous planktonic counterparts living in surface water. This difference must also be considered when calculating the ventilation age of deep water.

^{14}C ages of ^{230}Th -dated deep-sea corals

Some species of corals live at great depths, sometimes as deep as 4,000 m. They can be dated by measuring the growth of ^{230}Th from the decay of ^{234}U included in the coral's carbonate lattice. Decay-correcting $^{14}\text{C}/^{12}\text{C}$ measured in the same coral samples and comparing it to the corresponding $^{14}\text{C}/^{12}\text{C}$ ratio of the atmosphere thus provides a means of estimating the

age of deep water (Adkins et al., 1998). These estimates must also take into account possible changes in “reservoir age” and the variability in $\Delta^{14}\text{C}_{\text{atm}}$. However, unlike the sedimentary archives, which provide continuous but relatively low resolution records (millennial to centennial timescales, depending on the sedimentation rates), deep-sea corals provide narrow (~ 150 years dictated by the life span of coral specimens) but high-resolution (decadal-centennial timescales) windows on past changes in deep water ages.

Geostrophic flow reconstructions from benthic foraminifera $\delta^{18}\text{O}$

Most of the warm water flowing to the far North Atlantic for NADW formation is supplied by the Gulf Stream (Figure O10a). The Gulf Stream enters the North Atlantic through the Florida Strait at a flow rate of about 30 Sverdrups. As it moves to the north, it is continually accrued by entrainment of water coming from the North Atlantic Subtropical gyre, and its flow rate increases gradually, reaching 150 Sverdrups as it turns eastward. In the Florida Straits, the Gulf Stream is nearly in geostrophic balance, i.e., the Coriolis acceleration associated with the flow of water (C) is balanced by the lateral pressure gradient across the Strait (P; Figure O10b). This pressure gradient is associated with a lateral seawater density gradient and results in sloping surfaces of constant seawater density, called “isopycnals.” If the flow rate of the Gulf Stream were to accelerate, the Coriolis force would intensify. To maintain geostrophic balance, the lateral pressure gradient would have to increase, which would be reflected by steeper isopycnals. The slope of the isopycnals across the Florida Straits can be estimated from the oxygen isotopic composition ($\delta^{18}\text{O}$) of benthic foraminifera living on the seafloor on each side of the Straits, thereby providing a means of estimating the flow rate of water through the Strait in the geological past. To the extent that the contribution from the subtropical recirculation gyre (Figure O10a) remained con-

stant, changes in flow rate in the Florida Strait could be used to infer changes in the rate of NADW formation (Lynch-Stieglitz et al., 1999). The main difficulties with this approach are (a) ascertaining the contribution from the subtropical gyre, and (b) the requirement that current velocity must be known at one level taken as reference, which is very difficult to constrain for past circulation (Wunsch, 2003).

$^{231}\text{Pa}/^{230}\text{Th}$ in Atlantic sediments

^{231}Pa and ^{230}Th are two natural radionuclides produced at constant rates in seawater from the decay of dissolved uranium. Both are rapidly adsorbed on settling particles and removed to the underlying sediment (Figure O11). As ^{231}Pa has a lower affinity for most marine particles than ^{230}Th , it has a residence time in deep water approximately five times longer and equivalent to the mean residence time of deep water in the modern Atlantic (ca. 200 years). As a result, nearly 50% of the ^{231}Pa produced in the NADW as it transits through the Atlantic is exported to the Southern Ocean, while most of the ^{230}Th is removed in the Atlantic sediment (Yu et al., 1996). Reflecting this differential export, the mean $^{231}\text{Pa}/^{230}\text{Th}$ of Atlantic sediments (activity ratio ~ 0.05) is only slightly above half the ratio of the rate of production of the two nuclides in the water column (0.093). $^{231}\text{Pa}/^{230}\text{Th}$ in Atlantic sediments can thus record the rate at which NADW is produced and exported to the Southern Ocean. As the rate of NADW formation and export decreases, the extent of ^{231}Pa export to the Southern Ocean also diminishes, resulting in higher $^{231}\text{Pa}/^{230}\text{Th}$ in Atlantic sediments (Marchal et al., 2000). The interpretation of this proxy is complicated, however, by the fact that the removal rate of ^{231}Pa from seawater depends on particle flux and composition. Lower $^{231}\text{Pa}/^{230}\text{Th}$ in Atlantic sediments could also be due to higher particle flux or higher concentration of opal, a biogenic mineral produced by some plankton species. Past changes in particle flux and composition in the Atlantic Ocean must therefore be taken into account when

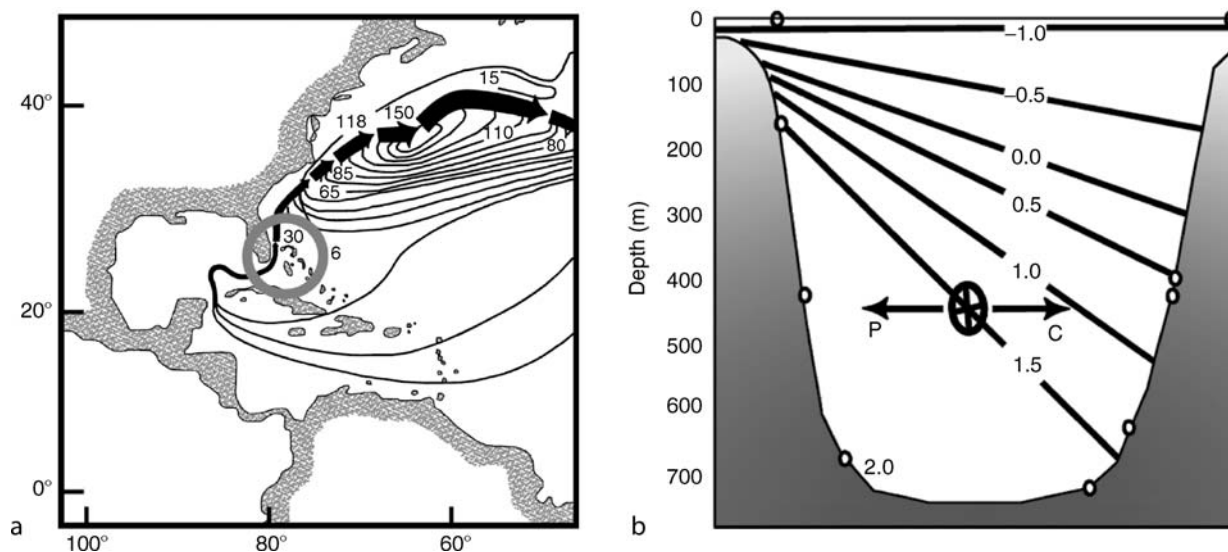


Figure O10 (a) Gulf Stream and recirculation in the North Atlantic subtropical gyre with total transport streamlines in Sverdrups, adapted from Worthington (1976). Red circle highlights the Florida Straits. (b) Cross-section in the Florida Straits showing sloping horizons of constant seawater density obtained from the $\delta^{18}\text{O}$ of modern benthic foraminifera (sampling depths are marked by open circles). The geostrophic flow that prevails in this region results from the balance between the Coriolis force due to the Earth's rotation (C) and the lateral pressure gradient created by the lateral density gradient (P). The cross indicates that the water flows away from the reader (adapted from Lynch-Stieglitz et al, 1999).

interpreting sediment $^{231}\text{Pa}/^{230}\text{Th}$ as a kinematic indicator of deepwater formation.

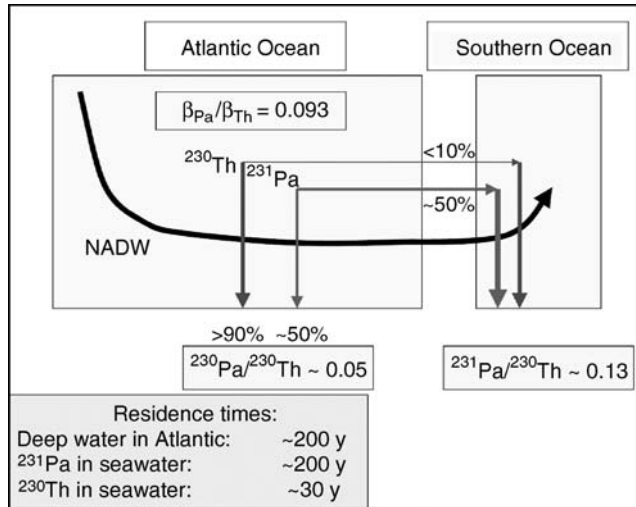


Figure O11 Schematic representation of the principle for estimating the rate of NADW formation from $^{231}\text{Pa}/^{230}\text{Th}$ in marine sediments. ^{231}Pa and ^{230}Th are produced uniformly in seawater from the decay of dissolved uranium ($\beta_{\text{Pa}}/\beta_{\text{Th}}$ = production rate ratio). Because of its shorter residence time in the water column, nearly all the ^{230}Th produced in the NADW during transit through the Atlantic is removed in the underlying sediment. On the other hand, since the residence time of ^{231}Pa in seawater is similar to the residence time of deep water in the Atlantic, approximately half of the ^{231}Pa produced in the Atlantic is exported into the Southern Ocean with NADW. The resulting deficit of ^{231}Pa in Atlantic sediment increases with the rate of NADW formation and export to the Southern Ocean.

Reconstruction of past changes in ocean circulation during the last glacial-interglacial cycle

Because of its half-life, information from ^{14}C can only be considered for the last 50,000 years and we can best constrain past changes in deep water circulation during that time span. This is a climatically important and interesting period, as it nearly encompasses the full range of Quaternary climatic variability. High-resolution climatic fluctuations over that time period are documented by the oxygen isotopic composition of the ice that has accumulated on Greenland (Figure O12), reflecting air temperature (see *Ice cores, Antarctica and Greenland*). The last ~10,000 years (i.e., the Holocene period) were characterized by relatively warm (i.e., higher $\delta^{18}\text{O}$ in ice) and stable conditions. In contrast, the preceding glacial period, when large ice sheets covered the North American and European continents, was characterized by large climatic fluctuations. These fluctuations are called Dansgaard-Oeschger cycles and consist of abrupt warmings followed by more gradual coolings. The transition to the Holocene, which coincided with the melting of most of the large northern continental ice sheets, was also punctuated by an abrupt warming ~15,000 years ago (Bølling), followed by a brief cold reversal (Younger Dryas) at ~12,800 yrBP, and a rapid final warming at 11,600 yrBP.

Changes in the distribution of deep-water masses

One of the most robust deductions derived from the water mass proxies is that climatic variability was associated with vertical redistribution of nutrient concentrations in the water column of the Atlantic. Nutrient concentrations at intermediate depths (above ~2,500 m) were lower during the last glacial period compared to today, while they were higher in deeper waters (below ~2,500 m). This has been corroborated by the $\delta^{13}\text{C}$, Cd/Ca and Zn/Ca ratios of benthic foraminifera (Figure O13). Lower nutrient concentrations in glacial intermediate waters have been taken as reflecting the formation of a shallower water mass in the North Atlantic (the Glacial North Atlantic Intermediate Water, GNAIW) in lieu of today's NADW, while higher nutrient concentrations in deep water have been taken

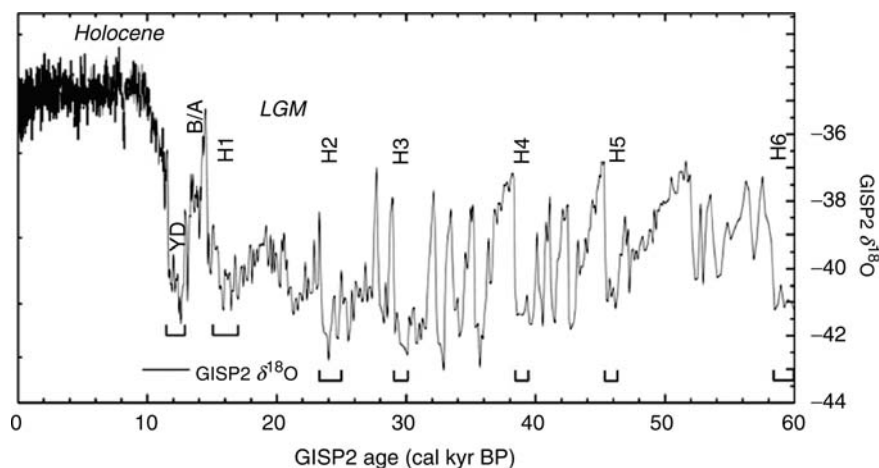


Figure O12 Oxygen isotopic composition ($\delta^{18}\text{O}$) of the ice that accumulated on Greenland during the last 60,000 years (Grootes et al., 1993). Higher $\delta^{18}\text{O}$ indicates higher temperature. LGM: Last Glacial Maximum (the time of maximum continental ice buildup). YD: Younger Dryas cold period. B/A: Bølling-Allerød warm period. H1 to H6 mark the timing of 6 massive iceberg discharge events recorded as high accumulation of ice-rafted debris in the North Atlantic, coinciding with the coldest periods (lowest $\delta^{18}\text{O}$) recorded in the ice core.

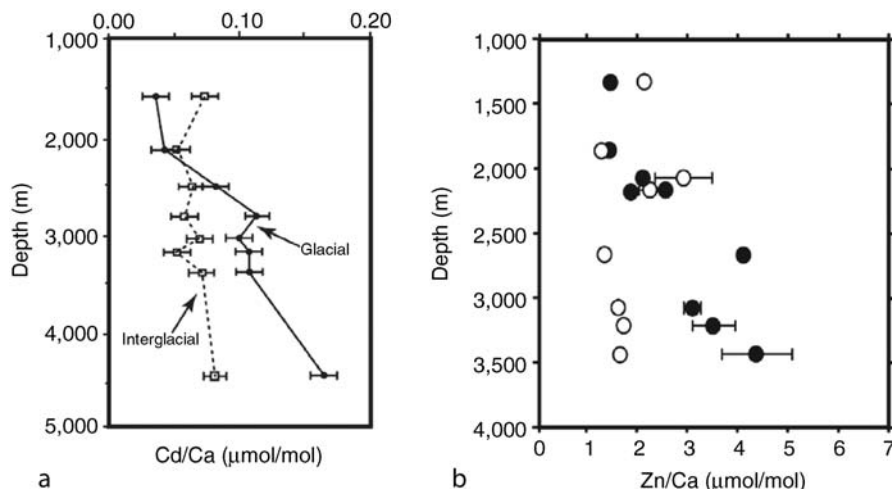


Figure O13 Vertical redistribution of nutrients in the Atlantic Ocean during the last glacial period recorded by (a) Cd/Ca (adapted from Boyle, 1988), (b) Zn/Ca (adapted from Marchitto et al., 2002) in benthic foraminifera. *Open symbols*: Holocene profile; *closed symbols*: glacial profile.

as indicating increased penetration of deep water of southern origin into the North Atlantic. Higher nutrient concentrations in the deep Atlantic could also reflect higher preformed nutrient concentration in North Atlantic surface waters or higher remineralization of organic matter in deep waters. However, the similarity between the benthic foraminifera record of Zn/Ca and Cd/Ca in the North Atlantic argues against dramatic changes in preformed nutrient concentrations (Marchitto et al., 2002). Increased penetration of southern water during the last glacial period has also been confirmed by ϵ_{Nd} , which is independent of nutrient recycling (Rutberg et al., 2000). The more extensive $\delta^{13}C$ database (Sarnthein et al., 2001) clearly shows increased northward penetration of southern water and replacement of the modern NADW by the shallower GNAIW during the last glacial maximum (Figure O14a,b). Combining $\delta^{13}C$ and Cd/Ca, Lynch-Stieglitz et al. (1996) provided evidence that the shallower GNAIW propagated to the Pacific Ocean, in a similar manner as today's NADW (Figure O7).

A third mode of deepwater mass distribution has also been identified from the distribution of benthic foraminifera $\delta^{13}C$, in which deepwater formation from the north was essentially eliminated and the entire water column of the Atlantic Ocean below the main thermocline was filled with water of southern origin (Figure O14c). This situation seems to arise during the coldest intervals of the glacial periods, which are associated with catastrophic iceberg discharges, called Heinrich Events (Figure O12). These events are recorded in the sediments of the North Atlantic as discrete layers of coarse-grained ice-rafted debris that are deposited as the icebergs melt. The shutdown of deep-water formation in the North Atlantic during these events has been attributed to melting of icebergs and lowering of the density of surface waters in areas of deepwater formation.

Changes in the rate of formation of deepwater masses

As pointed out by Legrand and Wunsch (1995), water mass tracers alone cannot uniquely constrain rates of deep-water formation. Doing so requires kinematic tracers. The initial study using $^{231}Pa/^{230}Th$ in Atlantic sediments (Yu et al., 1996) reached the surprising conclusion that the rate of deep water

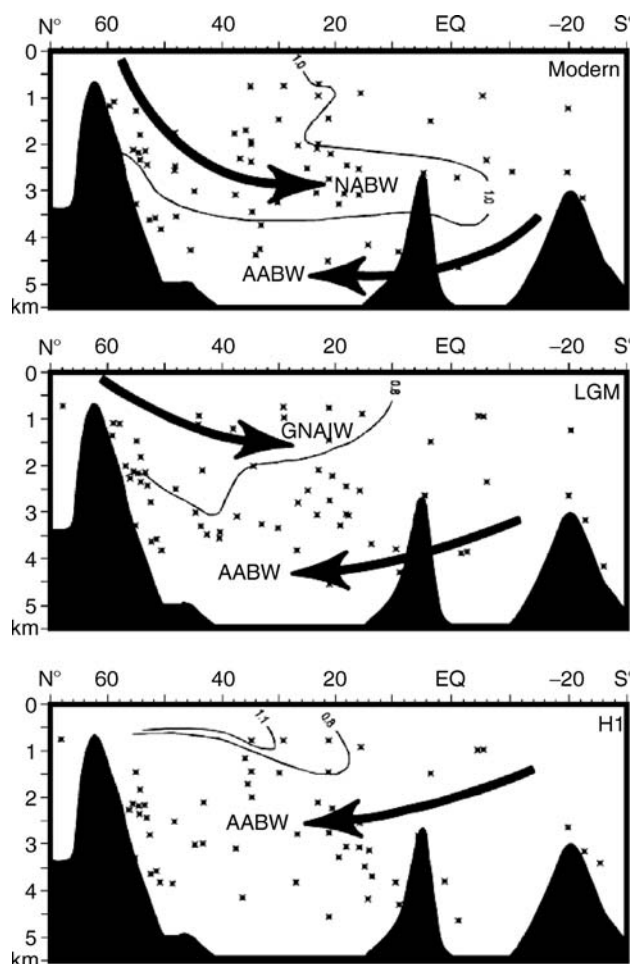


Figure O14 Vertical transects of benthic foraminifera $\delta^{13}C$ in the Atlantic Ocean (a) Modern (b) Last glacial maximum (c) Heinrich event H1 (adapted from Sarnthein et al., 2001).

formation in the North Atlantic during the last glacial maximum (GNAIW) and its export to the southern ocean was little different from today's rate of formation and export of NADW. The uncertainties on this estimate were quite large however, and the subsequent use of a zonally integrated general circulation model indicated that the existing data were not inconsistent with a possible 30% glacial reduction (Marchal et al., 2000). Reconstruction of the slope of the isopycnals in Florida Straits also suggested a 30% reduction in the rate of GNAIW formation (Lynch-Stieglitz et al., 1999), although this estimate also has very large uncertainties (Wunsch, 2003).

A high-resolution $^{231}\text{Pa}/^{230}\text{Th}$ profile obtained by analyzing a core retrieved from a drift deposit in the central North Atlantic provides important additional insights into the relationship between the rate of northern source deepwater formation and climatic variability (Figure O15). This record confirms the steady formation of NADW over the entire Holocene period at a rate similar to present (i.e., $^{231}\text{Pa}/^{230}\text{Th} \sim 0.055$). It also suggests a slight reduction of the rate of GNAIW formation during the last glacial maximum (i.e., $^{231}\text{Pa}/^{230}\text{Th} \sim 0.068$ between 17,500 and 20,000 yrBP), although this higher $^{231}\text{Pa}/^{230}\text{Th}$ may be partly due to the higher particle fluxes at that time. The most prominent feature of this new record, however, is the rapid increase in $^{231}\text{Pa}/^{230}\text{Th}$ to values similar to the rate of production (0.093) between 17,500 and 15,000 yrBP. This indicates that the formation of northern source deep water had totally ceased for a period of $\sim 2,500$ years (particle fluxes decreased during that time interval and cannot account for the observation), and coincided with the more recent Heinrich Event (H1; Figure O12). Deepwater formation in the North Atlantic re-started abruptly at 15,000 yrBP, coinciding with a rapid climate warming (Bølling) and a rapid rise in sea level. The latter must have been the result of accelerated melting of continental ice. A significant but lesser decrease in the rate of deepwater formation also occurred during the cold Younger Dryas period, followed by a gradual acceleration into the Holocene.

There is a good general agreement between this interpretation of $^{231}\text{Pa}/^{230}\text{Th}$ in North Atlantic sediment (McManus et al., 2004) and the reconstruction of atmospheric $\Delta^{14}\text{C}$ (Hughen et al., 1998, 2004). Comparing the latter with $\Delta^{14}\text{C}_{\text{atm}}$ predicted from the changes in the intensity of the geomagnetic field reveals deviations that are consistent with slower rates of transfer of ^{14}C from the atmosphere to the deep sea (i.e., lower rates

of deepwater formation) during the Younger Dryas cold period and Heinrich Event H1.

^{14}C ages of ^{230}Th -dated deep-sea corals suggest that changes in the rates of deepwater circulation may have been very abrupt. Adkins et al. (1998) have shown that within a period of 130 years, the ^{14}C age of bottom water at 40°N in the Western Atlantic at 1,800 m depth decreased by 670 years, suggesting an abrupt slowdown of deepwater formation rate at a time (15,400 yrBP) that preceded the Bølling warming. This observation indicates that deepwater formation rates could have fluctuated on centennial timescales, i.e., a "flickering" rate too rapid to be recorded in the $^{231}\text{Pa}/^{230}\text{Th}$ record. However, a detailed reconstruction of deep water circulation on this timescale, using the narrow windows of information both in time and space provided by deep-sea corals, requires the further analysis of a large number of widely-distributed coral specimens.

Conclusion

Much remains to be done to obtain a detailed and accurate reconstruction of past changes in deep water circulation, even during the relatively recent past of the late Quaternary. It is evident that none of the proxies used for water mass identification and circulation rates provides a simple, straightforward answer. Each proxy is affected by factors other than deepwater circulation and the circulation signal must be retrieved from a tangle of other influences. It is therefore important not to rely on a single tracer, but to use the full range of circulation proxies that is at our disposal. Apparent disagreements point to problems with the interpretation of at least some of the proxies and through an iterative process of proxy validations in the modern ocean, paleoceanographic reconstructions, and cross examinations, we gradually converge towards a better understanding of past ocean circulation. This endeavor is crucial not only to understand past climatic variations but also to improve our ability at predicting future climate changes that could potentially be triggered by human activity.

The picture that is slowly emerging suggests that during the last glacial period, GNAIW was generally produced at a rate that was not dramatically different from the modern rate of NADW formation. It also seems that, as is the case for the modern NADW (Figure O7), the GNAIW was part of a global "conveyor belt" circulation. However, this only ventilated the

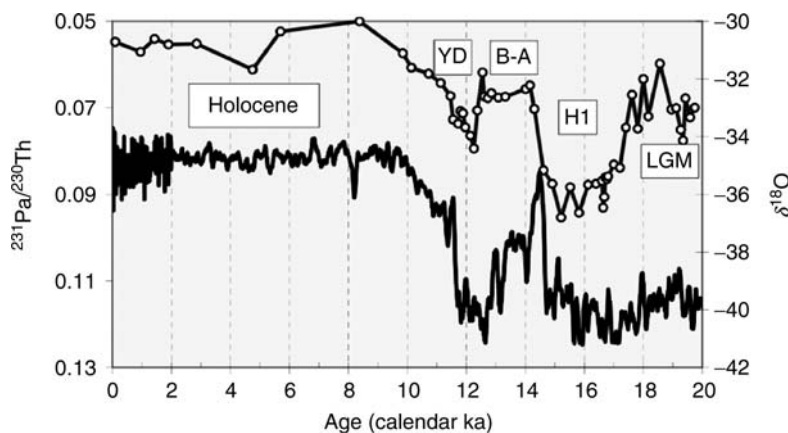


Figure O15 $^{231}\text{Pa}/^{230}\text{Th}$ in a high sedimentation rate core from the North Atlantic (adapted from McManus et al., 2004) compared to the $\delta^{18}\text{O}$ in Greenland ice. Low $^{231}\text{Pa}/^{230}\text{Th}$ = high NADW formation rate (note the reverse scale); higher $\delta^{18}\text{O}$ = warmer temperature.

upper 2,500 m of the ocean. Below that depth, deep waters presumably originating from the southern ocean were present. In contrast to this apparent lack of correlation between rates of deepwater formation and climate on these longer time scales, there seems to be a much closer relationship on shorter time-scales. During short periods of massive iceberg discharge (Heinrich Events) that punctuated the glacial period, deepwater formation in the North Atlantic may have totally ceased. The rapid warmings that followed these events seem to be the results of a rapid reinvigoration of the Atlantic MOC. Such a sequence of events has now been well documented for the last of the Heinrich Events (H1), which occurred during the early stages of the deglacial transition into the Holocene. Water mass proxies suggest similar sequences during the other Heinrich events, but confirmation with kinematic tracers is still required. The possibility that some of the abrupt climate changes in the past were associated with rapid changes in the rate of thermohaline circulation raises concerns that such events could happen in the near future.

Roger Francois

Bibliography

- Adkins, J.F., and Boyle, E.A., 1997. Changing atmospheric $\Delta^{14}\text{C}$ and the record of deep water paleoventilation age. *Paleoceanography*, **12**, 337–344.
- Adkins, J.F., Cheng, H., Boyle, E.A., Druffel, E.R.M., and Edwards, R.L., 1998. Deep-Sea coral evidence for rapid change in ventilation of the deep North Atlantic 15,400 years ago. *Science*, **280**, 725–728.
- Bard, E., 1988. Correction of accelerator mass spectrometry C-14 ages measured in planktonic foraminifera: Paleoceanographic implications. *Paleoceanography*, **3**, 635–645.
- Boyle, E.A., 1986. Paired carbon isotope and cadmium data from benthic foraminifera: Implications for changes in oceanic phosphorus, oceanic circulation, and atmospheric carbon dioxide. *Geochim. Cosmochim. Acta*, **50**, 265–276.
- Boyle, E.A., 1988. Cadmium: Chemical tracer of deepwater paleoceanography. *Paleoceanography*, **3**, 471–489.
- Broecker, W.S., 1997. Thermohaline circulation, the Achilles heel of our climate system: Will man-made CO_2 upset the current balance? *Science*, **278**, 1582–1588.
- Broecker, W.S., and Maier-Reimer, E., 1992. The influence of air and sea exchange on the carbon isotope distribution in the sea. *Global Biogeochem. Cycles*, **6**, 315–320.
- Hughen, K.A., Overpeck, J.T., Lehman, S.J., Kashgarian, M., Southon, J., Peterson, L.C., Alley, R.B., and Sigman, D., 1998. Deglacial changes in ocean circulation from an extended radiocarbon calibration. *Nature*, **391**, 65–68.
- Hughen, K.A., Lehman, S.J., Southon, J.N., Overpeck, J.T., Marchal, O., Herring, C., and Turnbull, J., 2004. ^{14}C activity and global carbon cycle changes over the past 50,000 years. *Science*, **302**, 202–207.
- Intergovernmental Panel on Climate Change 2001. *Climate Change 2001: Synthesis Report. Contribution of Working Group I, II and III to the Third Assessment Report of the Intergovernmental Panel on Climate Change*. Cambridge, UK: Cambridge University Press.
- Keigwin, L.D., and Schlegel, M.A., 2002. Ocean ventilation and sedimentation since the glacial maximum at 3 km in the western North Atlantic. *Geochem. Geophys. Geosyst.*, **3**(6), 1034 (doi: 10.1029/2001GC000283).
- Kroopnick, P.M., 1985. The distribution of C-13 of TCO_2 in the world oceans. *Deep Sea Res.*, **32**, 57–84.
- Laj, C., Kissel, C., Mazaud, A., Michel, E., Muscheler, R., and Beer, J., 2002. Geomagnetic field intensity, North Atlantic Deep Water circulation and atmospheric $\Delta^{14}\text{C}$ during the last 50 kyr. *Earth Planet. Sci. Lett.*, **200**, 177–190.
- Lea, D.W., 1993. Constraints on the alkalinity and Circumpolar deep water from benthic foraminiferal barium. *Global Biogeochem. Cycles*, **7**, 695–710.
- Lea, D., and Boyle, E.A., 1989. Barium content of benthic foraminifera controlled by bottom-water composition. *Nature*, **338**, 751–753.
- LeGrand, P., and Wunsch, C., 1995. Constraints from paleo-tracer data on the North Atlantic circulation during the last glacial maximum. *Paleoceanography*, **10**, 1011–1045.
- Lynch-Stieglitz, J., van Geen, A., and Fairbanks, R.G., 1996. Inter-ocean exchange of glacial North Atlantic Intermediate Water: Evidence from subantarctic Cd/Ca and carbon isotope measurements. *Paleoceanography*, **11**, 191–201.
- Lynch-Stieglitz, J., Curry, W.B., and Slowey, N.C., 1999. Weaker Gulf Stream in the Florida Straits during the last glacial maximum. *Nature*, **402**, 644–648.
- Marchal, O., Francois, R., Stocker, T.F., and Joos, F., 2000. Ocean thermohaline circulation and sedimentary $^{231}\text{Pa}/^{230}\text{Th}$ ratio. *Paleoceanography*, **15**, 625–641.
- Marchitto, T.M., Curry, W.B., and Oppo, D.W., 2000. Zinc concentrations in benthic foraminifera reflect seawater chemistry. *Paleoceanography*, **15**, 299–306.
- Marchitto, T.M., Oppo, D.W., and Curry, W.B., 2002. Paired benthic foraminifera Cd/Ca and Zn/Ca evidence for a greatly increased presence of southern ocean water in the glacial North Atlantic. *Paleoceanography*, **17**(3), 1038 (doi: 10.1029/2000PA00059).
- McManus, J.F., Francois, R., Gherardi, J., Keigwin, L.D., and Brown-Leger, S., 2004. Rapid deglacial changes in Atlantic meridional circulation recorded in sedimentary $^{231}\text{Pa}/^{230}\text{Th}$. *Nature*, **428**, 834–837.
- Rutberg, R.L., Hemming, S.R., Goldstein, S.L., 2000. Reduced North Atlantic Deep Water flux to the glacial southern ocean inferred from neodymium isotope ratios. *Nature*, **405**, 935–938.
- Sarnthein, M., and 18 others, 2001. Fundamental modes and abrupt changes in North Atlantic circulation and climate over the last 60 ky – Concepts, reconstruction and numerical modeling. In Schäfer, P., Ritzau, W., Schlüter, M., Thiede, J. (eds.), *The Northern North Atlantic: A Changing Environment*. Berlin: Springer Verlag, pp. 45–66.
- Toggweiler, J.R., 1999. Variation of atmospheric CO_2 by ventilation of the ocean's deepest water. *Paleoceanography*, **14**, 571–588.
- von Blanckenburg, F., 1999. Tracing past ocean circulation? *Science*, **286**, 1,862–1,863.
- Worthington, L.V., 1976. *On the North Atlantic circulation, The Johns Hopkins Oceanographic Studies*, Vol. 6. Baltimore, MD: Johns Hopkins University Press, 110pp.
- Wunsch, C., 2003. Determining paleoceanographic circulations, with emphasis on the last glacial maximum. *Quaternary Sci. Rev.*, **22**, 371–385.
- Yu, E.-F., Francois, R., and Bacon, M.P., 1996. Similar rates of modern and last-glacial ocean thermohaline circulation inferred from radiochemical data. *Nature*, **379**, 689–694.

Cross-references

[Antarctic Bottom Water and Climate Change](#)
[Carbon isotopes, Stable](#)
[Coral and Coral Reefs](#)
[Dansgaard-Oeschger Cycles](#)
[Dating, Radiometric Methods](#)
[Foraminifera](#)
[Heinrich Events](#)
[Ice Cores, Antarctica and Greenland](#)
[Last Glacial Termination](#)
[North Atlantic Deep Water and Climate Change](#)
[Ocean Paleoproductivity](#)
[Quaternary Climate Transitions and Cycles](#)
[Radiocarbon Dating](#)
[Thermohaline Circulation](#)
[Uranium-Series Dating](#)

Introduction

Ocean productivity – the uptake of dissolved inorganic carbon and its sequestration into organic compounds by marine primary producers – plays a major role in controlling the partitioning of carbon between the ocean and atmosphere. Productivity fluctuations can therefore influence climate by altering the atmospheric concentrations of the greenhouse gas carbon dioxide (Berger et al., 1989). In addition, changes in marine productivity have some bearing on the biogeochemistry of many trace elements (P, N, Si, Ba) and gases (dimethyl sulfide). The record of significant fluctuations in atmospheric carbon dioxide in air trapped within polar ice along with the increasing concern of potential climate warming induced by industrial carbon dioxide emissions has emphasized the need to understand the interrelationship between productivity, ocean chemistry, atmospheric carbon dioxide, and climate. Ocean paleoproductivity studies document past changes in the biological production of organic matter and skeletal material. These studies provide insight into the causes of such fluctuations, the consequences for biogeochemical cycles within the ocean, and their correspondence to Earth's climate.

There are two components of oceanic productivity that are of interest: (a) net primary production in the surface ocean; and (b) export production, which is the fraction of net primary production that leaves the surface ocean and sinks to the deep ocean. While the former is of interest for learning about oceanic ecosystems, and carbon and nutrient cycling within the ocean, the latter is more relevant for carbon sequestration and climate change. The unit for measuring productivity is flux of carbon ($\text{grams C m}^{-2} \text{ yr}^{-1}$) and typical values for open ocean net primary productivity today are 25–250 $\text{g C m}^{-2} \text{ yr}^{-1}$. Export production typically ranges from less than 10% and up to 50% of the net primary production.

The concept of changing oceanic productivity and the relation of such changes to climate stand at the beginning of paleoceanographic research. Arrhenius (1952) suggested such changes to explain the sedimentary record and in particular calcite accumulation and size distribution of a diatom (*Coscinodiscus nodulifer*) over time in the eastern Equatorial Pacific. Since direct measurements of carbon uptake or flux to the deep ocean cannot be done for past times, paleoproductivity reconstruction has been based on records obtained from marine sediments. Over the past 50 years, a large variety of methods has been applied to reconstruct productivity, attesting to the importance of this field. Some of these methods result only in qualitative estimates while others are more quantitative. Each of these methods (or proxy variables for productivity) has associated assumptions and limitations and therefore should be used with caution. Ideally, several proxies should be applied simultaneously at any given site or time interval to evaluate changes in marine productivity.

Reconstruction of productivity from organic matter or phosphorus in sediments

As a dominant biological component, measurements of organic carbon (C) content of sediments seem a logical choice for reconstructing biological C production. In areas removed from downslope transport of fine-grained material, it has been assumed that the flux of organic C reaching the sediment is proportional to its net export from the surface ocean (Figure O16). Indeed, sediment trap studies indicate that a general relation between the flux of organic matter to the deep sea and productivity exists. However, there is a strong depth dependence of the relation because of

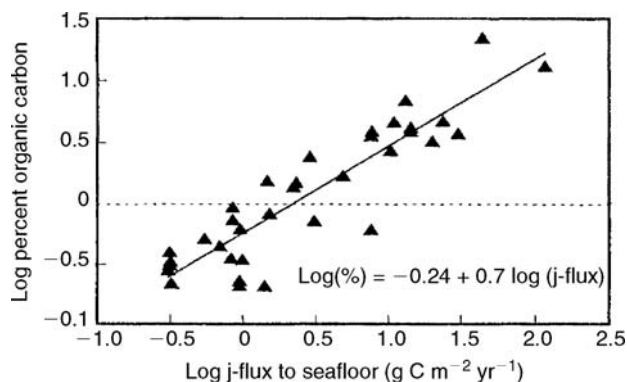


Figure O16 Correlation of organic carbon content in marine sediments with organic matter flux to the seafloor (after Berger and Herguera, 1992).

organic C degradation in the water column. Only a small fraction of the organic matter that arrives to the sediment is ultimately buried. However, at least at some oceanic locations, a relation between the abundance of organic matter in sediments and primary production has been observed. Empirical equations that quantitatively relate the accumulation rate of organic carbon in sediments to overlying productivity (Muller and Suess, 1979) or to the carbon flux to the seafloor (Sarnthein et al., 1988) have been suggested using data from the present ocean. The relation between organic matter content and productivity has been applied to reconstruct past oceanic productivity in various oceanic basins and for various time scales (Muller and Suess, 1979; Pedersen, 1983; Finney et al., 1988).

The interpretations of the fluctuations of organic carbon content in terms of paleoproductivity are complicated by processes affecting organic matter preservation such as sediment accumulation rates, deep water oxygen content, exposure time, and mineral surface area (Emerson, 1985; Keil et al., 1994). In addition, supply of organic C from terrestrial origin may result in overestimation of the oceanic productivity in coastal environments (Goni et al., 1998).

One of the elements directly related to organic matter is phosphorus (P). Phosphorus is an important nutrient to all living organisms. In general, marine phytoplankton incorporate P at a relatively constant ratio to their C content (the Redfield molar ratio of 106 C to 1 P). Accordingly, mapping past P accumulation may provide an indirect estimate of C flux and thus productivity (Delaney, 1998). Indeed, this proxy has been used to reconstruct past ocean productivity, typically over long geological time frames where organic C data is more likely to be compromised (Filippelli, 2002).

It must be kept in mind, however, that only a small fraction of P is preserved in the sediment (like C) and that, within the sediment after burial, P is transformed from the organic forms to authigenic minerals (Ruttenberg and Berner, 1993). To account for this complication, the “reactive P” fraction, which is the P that presumably was associated with organic matter, is used for paleoproductivity reconstruction (Delaney, 1998). In addition, post burial redox diagenesis may alter the P association and preservation in the sediment and therefore care must be taken to avoid samples that have been compromised by such processes (Delaney, 1998).

Reconstruction of productivity from carbonate or opal

Geologists have long recognized that variations in sediment composition parallel surface primary production. Indeed calcium carbonate and biogenic opal in marine sediments are predominantly composed of the hard parts of marine organisms (coccolithophores and diatoms). Sediment traps show a good correlation between the organic C flux and carbonate flux under certain conditions in the open ocean above the lysocline (Deuser et al., 1981; Ruhlemann et al., 1996) (Figure O17a). Similarly biogenic opal flux in sediment traps and on the seafloor generally correlates with the organic C flux (Calvert, 1966) (Figure O17b). These empirical relations based on traps and core top sediments can be used as a basis for reconstructing changes in location and intensity of export production. Indeed, Lyle et al. (1988) demonstrate linkage between mass accumulation rates of organic C, calcite, and biogenic opal and tie these to biological productivity.

Both these proxies, however, represent only changes in the export production of the specific organisms precipitating these minerals. One must therefore assume a predictable relation between total export production and the production of specific groups of organisms that are responsible for the precipitation of these minerals. Moreover, opal fluxes to the sediment may be dominated by event production such as during diatom blooms. In addition, both proxies are affected by a variety of physical and chemical oceanographic processes and not only by productivity. In particular, because the ocean is undersaturated everywhere with respect to opal, there is a major problem in quantitatively relating the amount of opal preserved in sediments to its production in the water column. Opal preservation rates depend on several factors including the global silica budget, pore water dissolved silica concentration, the thermal history of the sediment column, and the degree of silicification of the frustules (DeMaster, 1981; Treuger et al., 1995; Hutchins and Bruland, 1998). As a result, areas with high opal accumulation do not always correspond with areas of high productivity such as in the present-day Southern Ocean. Nevertheless, there do appear to be major trends in the history of opaline sedimentation over time and this proxy has been used to suggest qualitative changes in export production. Similarly, calcium carbonate accumulation in marine sediments may also suffer severe diagenetic modification of the original productivity-driven signal due to dissolution. This process, however, will occur predominantly in the deeper parts of the ocean where

seawater is undersaturated with respect to calcite. With proper site selection, or after accounting for dissolution (Mekik et al., 2002), it is possible to obtain representative patterns of carbonate production in most areas of the world's ocean.

Reconstruction of productivity from barite and Ba accumulation

Marine barite (BaSO_4), the major carrier of particulate Ba in the water column, is related to the marine carbon export flux (Bishop, 1988; Dymond et al., 1992). Barite precipitation in the water column is associated with decaying organic matter (Ganeshram et al., 2003). This results in a positive correlation between barite and excess-Ba (the Ba fraction not carried by terrigenous material – $\text{Ba}_{\text{excess}}$) and organic carbon fluxes in sediment traps and filtered particulate matter (Dehairs et al., 1980; Dymond et al., 1992). Based on this relationship in sediment traps, Dymond et al. (1992) predicted a positive correlation between the accumulation of $\text{Ba}_{\text{excess}}$ in marine sediments and carbon export (Figure O18a).

$\text{Ba}_{\text{excess}}$ has been used in many studies, to infer paleoproductivity (Nürnberg et al., 1997; Bonn et al., 1998; Bains et al., 2000). $\text{Ba}_{\text{excess}}$ is determined from the total Ba concentration in the sediment after subtracting the Ba associated with terrigenous material, which is calculated from total Al or Ti, and normalization to a constant detrital Ba/Al or Ba/Ti ratio. This calculation assumes that (a) all sedimentary particulate Ba besides the fraction associated with terrigenous aluminosilicates is predictably related to carbon export, (b) all of the Al (or Ti) is associated with terrigenous material, and (c) the Ba/Al (Ba/Ti) ratio used for normalization is in fact representative of each sample's terrigenous component and is constant in space and time. If the above assumptions are correct then $\text{Ba}_{\text{excess}}$ accumulation in sediments could be used to estimate carbon export.

Paytan et al. (1996) and Eagle et al. (2003) proposed an algorithm for paleoproductivity reconstruction based directly on barite accumulation in core top sediments (Figure O18b). In these studies, as in Dymond et al. (1992), the applicability of the proxy relies on the observation that barite forms and accumulates in proportion to biological productivity and the organic matter flux in the water column. In addition, barite shows promise as a paleoproductivity proxy because it is a highly refractory mineral with preservation as high as 30% in oxic sediments (Dymond et al., 1992). The barite accumulation

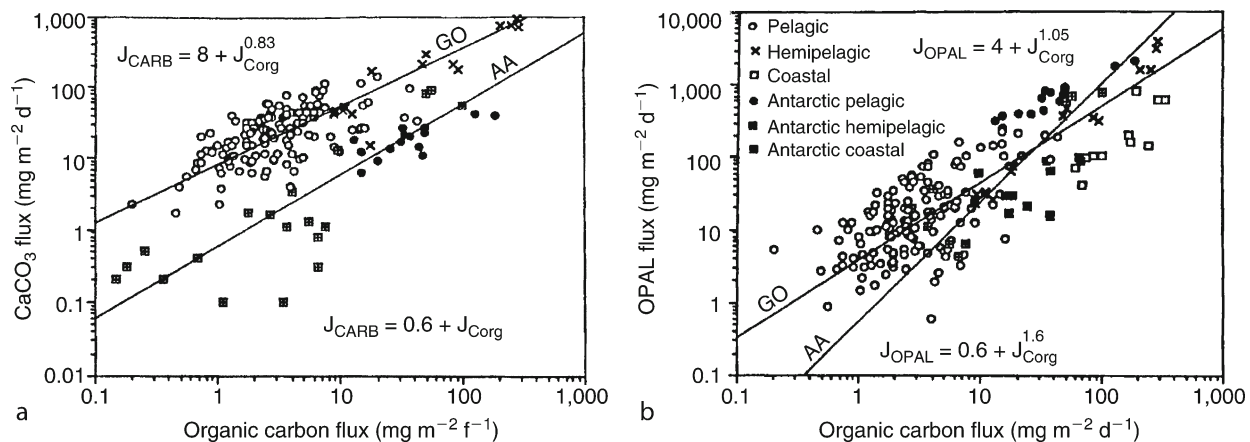


Figure O17 Relationship between (a) carbonate and (b) opal flux and organic carbon flux in sediment traps from various regions in the ocean. GO: global ocean; AA: Southern Ocean (after Berger and Herguera, 1992).

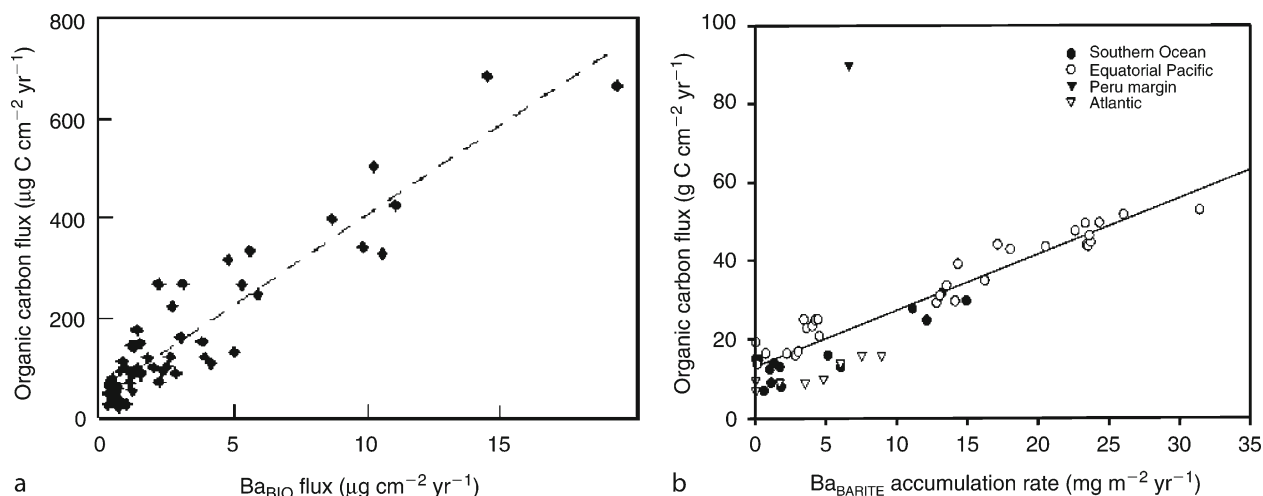


Figure O18 (a) Relation between excess Ba and organic C export in sediment traps (modified from Dymond et al., 1992). (b) Relation between barite accumulation rate in core top sediments and carbon export in the overlying water column (modified from Eagle et al., 2003).

rate in oxic sediments could therefore serve as a proxy for estimating paleocarbon export if the processes controlling barite formation and preservation are known and operate globally in the ocean.

Barium, however, is contained in other phases, some of which are biogenically-related (e.g., organic matter, biogenic silica, and biogenic carbonate), and others that are not directly related to carbon export (e.g., terrigenous silicates, Fe-Mn oxides, and hydroxides). The non-barite phases that are included in Ba_{excess} would not necessarily yield a predictable global $C_{\text{org}}/Ba_{\text{excess}}$ relationship as found by Dymond et al. (1992). This is because the ratio of organic carbon to these other biologically-related Ba phases varies spatially in the ocean, and because factors controlling Ba incorporation into Fe-Mn oxides and hydroxides are not directly biologically mediated. Although barite accumulation is not affected by the above factors, its preservation is affected by the dissolved Ba concentration in seawater; thus, some estimate of past oceanic Ba concentrations is needed for quantitative use of this proxy. In addition, barite in marine sediments is remobilized under sulfate-reducing conditions, so this proxy can only be applied when pore waters have remained saturated with respect to barite throughout the sedimentary record.

Reconstruction of productivity from microfossil assemblages

The use of species distribution has been widely applied for reconstructing productivity. Plankton assemblages in the surface ocean respond to nutrient concentrations, thus productivity. A number of foraminifera species have been identified as indicative of high productivity (*Globigerina bulloides*, *Neogloboquadrina dutertrei* and *Globorotalia tumida* at low latitudes, *Globigerina quinqueloba* in temperate latitudes and *Neogloboquadrina pachyderma* in cold upwelling waters). Single species abundances, however, may be more indicative of upwelling or other hydrographic physical processes rather than biological productivity. Multi-species based indexes using all of the foraminifera species in sediment cores to construct a quantitative estimate of productivity using standard transfer function

techniques are more robust (Imbrie and Kipp, 1971). The transfer functions (modern analogs) are constructed using modern primary production rates and a global coverage of core top foraminifera abundance data (Mix, 1989). The high abundance and diversity of foraminifera allows statistical analyses of small sediment samples (Figure O19a).

Similarly, the benthos biomass and the structure of the benthic community (species composition and size) reflect the supply of organic matter to the seabed, thus export production (Rowe, 1983). In particular, benthic foraminifera, which constitute a major portion of the benthic biomass, respond to changes in supply of organic carbon to the seafloor. Accordingly, changes in benthos abundance (population size) and benthic population composition (assemblage) have been used to qualitatively indicate changes in export production (Figure O19b). The biomass of total benthic foraminifera is positively correlated with the estimated local annual flux of organic C into the deep sea (Herguera, 2000). Specific species such as *Uvigerina peregrina* and *Globobulimina* sp. are characteristic of high nutrient fluxes, whereas *Cibicides wuellerstorfi* and *Cibicides kullenbergi* biofacies dominate areas of low productivity (Altenbach and Sarnthein, 1989). Transfer functions based on benthic communities and diatom assemblages have also been developed and applied to reconstruct past oceanic productivity (Loubere, 1999).

Many uncertainties remain, however, because our knowledge of the biology of the common fossil groups is limited. It is not clear to what extent the plankton assemblage reflects primary production, export production, or food availability. In addition, assemblages respond to a complex suite of environmental parameters that are not easily separated, thus are affected by other environmental variables (temperature, salinity, oxygen, etc.). Problems may arise from non-analog situations where the calibration using present-day core top samples does not represent past conditions. In addition, for all the species indices, there may be preservation effects and post-deposition changes in assemblages due to preferential dissolution, which will limit our ability to see true biological relationships. For longer time frames, evolution of species will also limit the utility of this type of index.

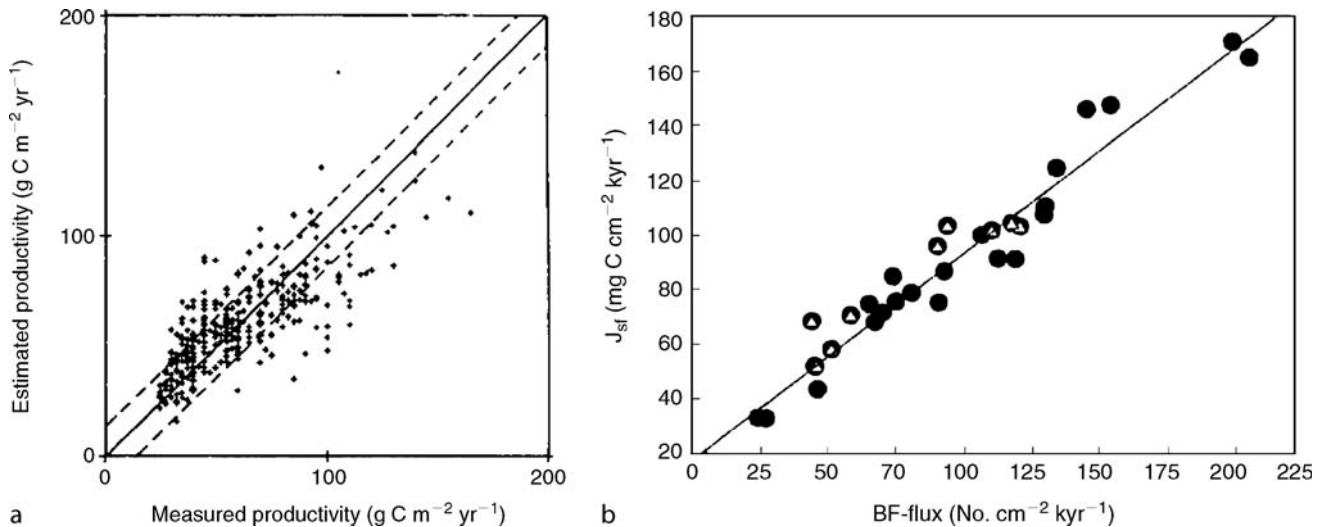


Figure O19 (a) Estimated versus measured values for productivity as generated from foraminiferal transfer functions. (b) Accumulation rate of benthic foraminifera (*BF-flux*) as a function of calculated flux of organic matter to the seafloor (*J_{sf}*) (after Berger and Herguera, 1992).

Reconstruction of productivity from carbon isotope records

A link between ocean productivity and carbon isotopes was first postulated by Tappan (1968), who suggested that change in $\delta^{13}\text{C}$ of carbonates towards heavier values is indicative of increased deposition of organic carbon, thus export production. The principle underlying this relation is carbon mass balance. During photosynthesis, since isotopically light carbon (^{12}C) is preferentially incorporated into the produced organic matter, the residual inorganic pool will become enriched in ^{13}C . This signature will be recorded in carbonate shells and therefore higher $\delta^{13}\text{C}$ of carbonates indicates increased burial of organic matter (with low $\delta^{13}\text{C}$ values) and hence higher productivity.

The difference between planktonic and benthic $\delta^{13}\text{C}$ compositions is a refinement of the above proxy (Figure O20). This difference is controlled by both the photosynthesis of organic matter in the surface ocean, which depletes the inorganic pool of ^{12}C , and the regeneration of this organic matter at depth, returning the ^{12}C to the deep-water inorganic pool. Thus, the larger the difference between the benthic and planktonic $\delta^{13}\text{C}$ (typically referred to as $\Delta^{13}\text{C}$), the higher the productivity (Shackleton et al., 1983; Curry and Crowley, 1987; Schneider et al., 1994).

It must be kept in mind that changes in oceanic circulation may modify the deepwater $\delta^{13}\text{C}$ independently of productivity. Moreover, when benthic foraminifera species are used for $\delta^{13}\text{C}$ analyses, it is important to choose species that indeed record the isotope ratio of dissolved inorganic carbon in seawater and not that of water within the sediment; thus only epifaunal species (organisms living on top and not within the sediments) should be used. In addition, because the isotopic fractionation during photosynthesis and shell production may vary between species and within each species depending on environmental parameters ($p\text{CO}_2$, carbonate ion concentrations, nutrient availability, etc.) a record obtained from a single species is preferable (Duplessy et al., 1984). Reconstruction of paleoproductivity via carbon isotopes becomes less reliable the farther back in time we go in the geological record. With now-extinct

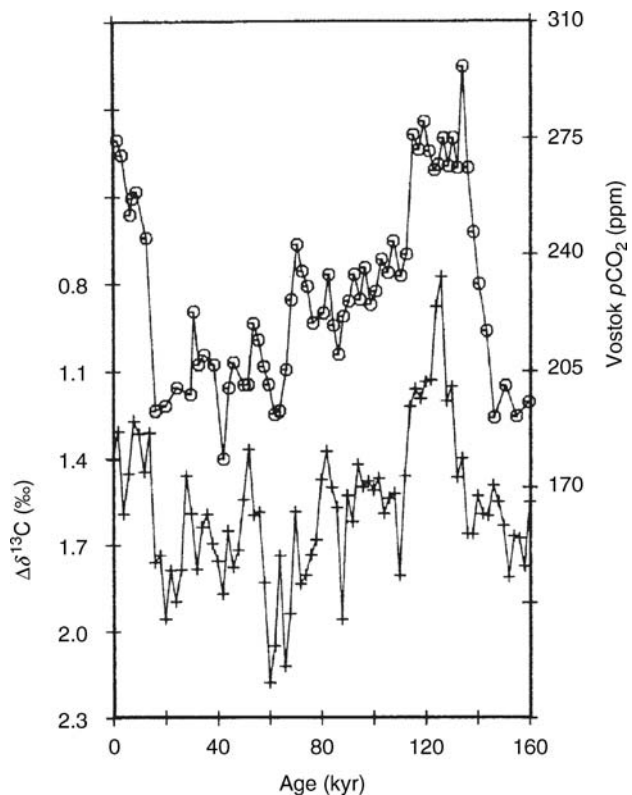


Figure O20 $\delta^{13}\text{C}$ difference ($\Delta\delta^{13}\text{C}$) between the benthic foraminifera *Uvigerina* sp. and the planktonic foraminifera *Neogloboquadrina dutertrei* in core V19-30 in the eastern Equatorial Pacific (+ symbols) (data from Shackleton and Pisias, 1985). Also plotted is the VOSTOCK ice core $p\text{CO}_2$ data from Barnola et al., (1987) (o symbols). The similarity between the records confirms the importance of export productivity variations (the biological pump) to atmospheric CO_2 (figure modified from Mix, 1985).

species, we can only indirectly verify the faithfulness of the C signal in their skeletons to the ambient water $\delta^{13}\text{C}$. In addition, the extent of diagenetic modification of carbonate $\delta^{13}\text{C}$ increases with time after burial and may be significant in areas where pore fluids contain “light” methanogenically-derived C.

Reconstruction of productivity from geochemical indicators

Several geochemical indicators that record particle flux in the water column have also been used as proxies for productivity (Al/Ti, Ba/Ti, $^{231}\text{Pa}/^{230}\text{Th}$, $^{10}\text{Be}/^{230}\text{Th}$). In vast areas of the open ocean, most of the particulate matter sinking in the water is of biogenic origin and thus is related to productivity.

Application of bulk Al/Ti and Ba/Ti ratios assumes that changes in the delivery of Al and Ba in non-lithogenic material are proportional to particle flux, which may then be related/converted to productivity. These proxy applications assume that in specific open-ocean locations (with low terrigenous input), total particle flux is proportional to C_{export} (Murray et al., 2000). Since Al is particle reactive, the adsorbed fraction of Al should increase with increasing particle flux; therefore, the excess Al content of deep-sea sediments (i.e., the fraction of Al not associated with aluminosilicate material) will increase with increasing particle flux (Murray and Leinen, 1996). Similarly, Ba/Ti should co-vary with bulk particle flux, and thus C_{export} (Figure O21; Murray et al., 2000). Bulk ratio proxies apply so long as Ti is exclusively of terrigenous origin, the fraction of Al or Ba associated with lithogenic Ti does not change significantly through time, and the excess Al or Ba is related to C_{export} in a predictable and consistent manner. The benefit of a normalizing ratio is that it does not require conversion of concentrations to accumulation rates, thus avoiding errors associated with such conversions.

In open ocean areas, a relationship exists between the mass flux of particulate matter and the unsupported $^{231}\text{Pa}/^{230}\text{Th}$ and $^{10}\text{Be}/^{230}\text{Th}$ activity ratios of recent sediments (Anderson et al., 1983; Rutsch et al., 1995). These ratios have been used as tracers to assess changes in productivity. The production rate of ^{231}Pa and ^{230}Th from dissolved U in seawater and the input of ^{10}Be to the ocean are known; however, the removal of these elements is not homogenous because they have variable residence times in

the ocean. Because ^{230}Th is more effectively scavenged, its flux to the seafloor is nearly equal to its rate of production; in contrast ^{231}Pa and ^{10}Be have longer residence times, which allows transport and preferential removal in high particle flux regions (Anderson et al., 1983). Therefore, high $^{231}\text{Pa}/^{230}\text{Th}$ and $^{10}\text{Be}/^{230}\text{Th}$ ratios indicate regions of extensive particle flux. The major advantage of the radionuclide ratios is that they are less sensitive to post-depositional diagenetic alteration. However, changes in ocean ventilation rate and dependence of scavenging efficiency in particle composition may influence the reliability of these proxies (Walter et al., 1999).

Accumulation of redox-sensitive metals in marine sediments is indirectly related to productivity, or more accurately, to the flux of C to the sediment. The higher the export production and organic C accumulation the more oxygen is consumed in the water column and sediment. As pore waters become sufficiently reducing, some metals precipitate and accumulate in the sediments. An example of an element that has been linked to organic C flux is uranium, which forms authigenic minerals in the sediment under reducing conditions (Kumar et al., 1995). Laminated sediments have also been linked to very high organic C fluxes. When the organic matter flux to the bottom waters is high, all of the dissolved oxygen is consumed, resulting in anoxic waters and low abundance of benthic organisms. This in turn reduces the degree of bioturbation and preserves the lamination in sediments. The above proxies, however, will also respond to changes in bottom water oxygen over time that are related to circulation and ventilation of the ocean and not to productivity, thus they are hard to interpret directly as reflecting changes in biological productivity.

It has recently been suggested that another geochemical proxy, the Sr/Ca ratio in coccolithophores, changes in proportion to calcification rates, which are higher when coccolith productivity is high (Stoll and Schrag, 2000). This proxy has been used for qualitative reconstruction of paleoproductivity; however, such reconstruction will only represent changes in coccolith productivity, which may be decoupled from total production. In addition, species-dependent Sr uptake rates and diagenetic alteration of original Sr/Ca ratios have not been completely ruled out and may complicate interpretation.

Reconstruction of productivity from nutrient content

Nutrient (N, P, Fe, Si) availability in many places controls the productivity in the surface ocean. Therefore, it has been suggested that knowledge of nutrient concentrations or their degree of utilization can be examined in the sedimentary record and may provide indirect information about past productivity. Such proxies include the nitrogen isotopic composition of organic matter (Altabet and Francois, 1994; Farrell et al., 1995), silicon isotopic composition of diatom frustules (De La Rocha et al., 1998), and the Cd/Ca ratio of planktonic foraminifera (Cd serves as an analog for P; Elderfield and Rickaby, 2000). The basic concept behind these proxies is that in areas where the nutrient pool (N, Si, P) in the surface ocean is not fully utilized, progressive assimilation of nutrients from surface seawater, accompanied by fractionation, produces strong gradients in the isotopic or elemental composition within the euphotic nutrient pool, which is then recorded by the plankton. This in turn leads to corresponding changes in the composition of particles that sink in the water column and accumulate in the sediment. For example, at high nutrient content relative to uptake (low utilization rates), ^{14}N is preferentially taken up by the phytoplankton and the organic matter, which under such conditions will have low $\delta^{15}\text{N}$ values. As nutrients are more efficiently utilized, less isotopic discrimination occurs and the $\delta^{15}\text{N}$ of organic matter shifts towards heavier

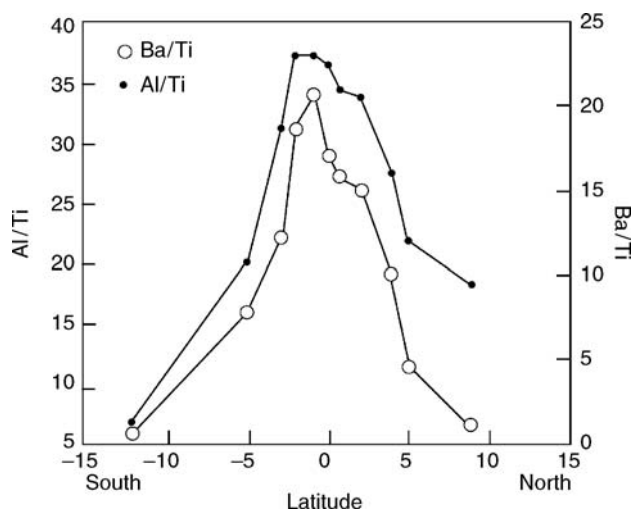


Figure O21 Profiles of Al/Ti and Ba/Ti trace productivity across a meridional transect at 140° W in the central equatorial Pacific Ocean (modified from Murray et al., 2000 and references therein).

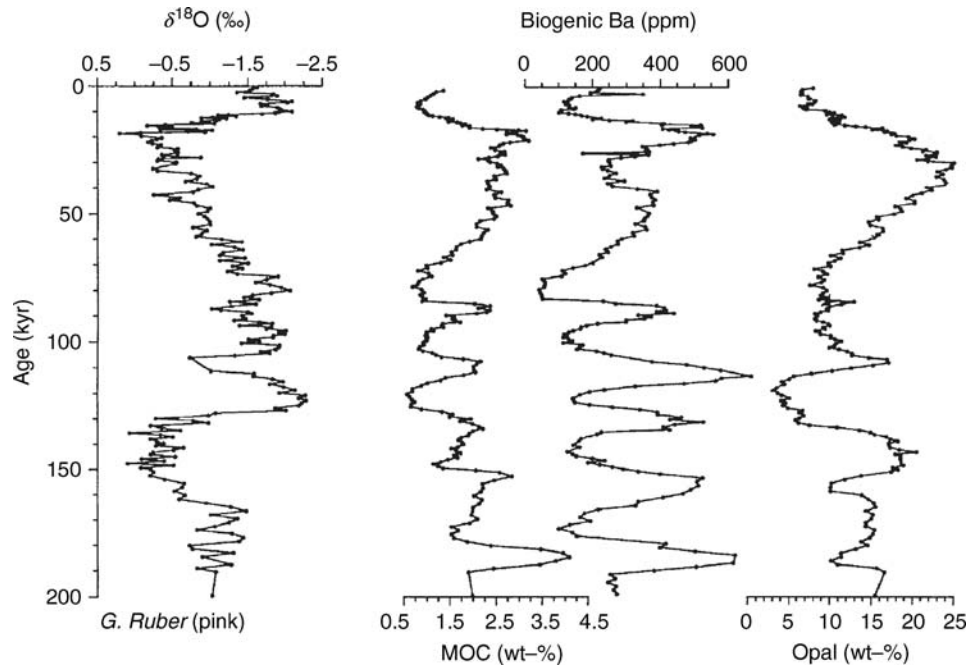


Figure O22 A multi-proxy approach for reconstructing marine productivity. Marine organic carbon (MOC), biogenic Ba, and opal co-vary down-core and show higher values during glacial periods (as indicated by the oxygen isotope record) in core GeoB 1008-3 from the South Atlantic (modified from Schneider et al., 1997).

values. Similar uptake effects result in changes in the $\delta^{32}\text{Si}$ of diatoms and the Cd/Ca ratio in planktonic foraminifera.

It must be kept in mind, however, that the relation between nutrient input and uptake (i.e., utilization) and biological productivity is not straightforward. In addition, changes in the isotope ratio or elemental composition of the bulk oceanic reservoir and post-depositional changes cannot be ruled out and may affect the sedimentary record (Montoya, 1994).

Reconstruction of productivity from organic biomarkers

Algal class structure is intimately related to overall water productivity and nutrients. Knowledge of the phytoplankton community can help distinguish high productivity from low productivity areas.

Marine phytoplankton, zooplankton and bacteria all synthesize a large number of organic compounds, many of which are taxon specific. The relation between the occurrence of certain compounds (biomarkers) and abundance of particular phytoplankton groups has been utilized to distinguish between marine and terrestrial organic matter and, in principle, could be used to reconstruct community structure.

Efforts to develop these proxies are underway; however, diagenesis is a major hurdle for quantitative reconstruction. In addition, the extraction of specific organic compounds from bulk sediment using solvents results in only partial recovery and the resulting extracted fraction may not be necessarily representative of the total organic matter.

Summary

Although ocean productivity is very important for understanding the operation of the global carbon cycle at present and in

the past, reconstruction of past ocean productivity patterns using empirical relations derived from present-day ocean characteristics is not a trivial undertaking. Each one of the proxies (methods) developed so far, although it contributes to our overall knowledge, has important limitations and therefore the best approach is to use multiple proxies (Figure O22). Critical evaluation of the validity of assumptions associated with each existing proxy and development of additional proxies will result in more robust reconstructions of paleoproductivity and understanding of the coupling and feedbacks between productivity, tectonics, and climate.

Adina Paytan

Bibliography

- Altabet, M.A., and Francois, R., 1994. Sedimentary nitrogen isotopic ratio as a recorder for surface ocean nitrate utilization. *Glob. Biogeochem. Cycles*, **8**, 103–116.
- Altenbach, A.V., and Sarnthein, M., 1989. Productivity record in benthic foraminifera. In Berger, W.H., Smetacek, V.S., and Wefer, G. (eds.), *Productivity of the Oceans: Present and Past*. Berlin: Springer, pp. 255–269.
- Anderson, R.F., Bacon, M.P., and Brewer, P.G., 1983. Removal of 230-Th and 231-Pa from the open ocean. *Earth Planet. Sci. Lett.*, **62**, 7–23.
- Arrhenius, G.O.S., 1952. Sediment cores from the East Pacific. *Rep. Swed. Deep. Sea. Exped. 1947–1948*, **5**, 228.
- Bains, S., Norris, R., Corfield, R., and Faul, K., 2000. Termination of global warmth at the Palaeocene/Eocene boundary through productivity feedback. *Nature*, **407**, 171–174.
- Barnola, J.M., Raynaud, D., Korotkevich, Y.S., and Lorius, C., 1987. Vostok ice cores provides 160,000-year record of atmospheric CO₂. *Nature*, **329**, 408–414.
- Berger, W.H., and Herguera, J.C., 1992. Reading the sedimentary record of the ocean's productivity. In Falkowski, P.G., and Woodhead, A.D. (eds.), *Primary Productivity and Biogeochemical Cycles in the Sea*. New York: Plenum Press, pp. 455–486.

- Berger, W.H., Smetacek, V.S., and Wefer, G., 1989. Ocean productivity and paleoproductivity – an overview. In Berger, W., Smetacek, V.S., and Wefer, G. (eds.), *Productivity in the Oceans: Present and Past*. New York: Wiley, pp. 1–34.
- Bishop, J.K.B., 1988. The barite-opal-organic carbon association in oceanic particulate matter. *Nature*, **332**, 341–343.
- Bonn, W.J., Gingele, F.X., Grobe, H., Mackensen, A., and Futterer, D.K., 1998. Palaeoproductivity at the Antarctic continental margin: Opal and barium records for the last 400 ka. *Palaeogeogr. Palaeoclimatol. Palaeoecol.*, **139**, 195–211.
- Calvert, S.E., 1966. Accumulation of diatomaceous silica in the sediment of the Gulf of California. *Geol. Soc. Am. Bull.*, **77**, 569–572.
- Curry, W.B., and Crowley, T.J., 1987. The $\delta^{13}\text{C}$ of equatorial Atlantic surface waters: Implications for ice age pCO_2 levels. *Paleoceanography*, **2**, 489–517.
- Dehairs, F., Chesselet, R., and Jedwab, J., 1980. Discrete suspended particles of barite and the barium cycle in the open ocean. *Earth Planet. Sci. Lett.*, **49**(2), 528–550.
- Delaney, M.L., 1998. Phosphorous accumulation in marine sediments and the oceanic phosphorous cycle. *Glob. Biogeochem. Cycles*, **12**, 563–572.
- De La Rocha, C., Brzezinski, M., DeNiro, M., and Shemesh, A., 1998. Silicon-isotope composition of diatoms as an indicator of past oceanic change. *Nature*, **395**, 680–683.
- DeMaster, D.J., 1981. The supply and accumulation of silica in the marine environment. *Geochim. Cosmochim. Acta*, **45**, 1715–1732.
- Deuser, W.G., Ross, E.H., and Anderson, R.F., 1981. Seasonality in the supply of sediments to the deep Sargasso Sea and implications for the rapid transfer of matter to the deep ocean. *Deep-Sea Res.*, **28A**, 495–505.
- Duplessy, J.C., Shackleton, N.J., Matthews, R.K., Prell, W.L., Ruddiman, W.F., Caralp, M., and Hendy, C., 1984. ^{13}C record of benthic foraminifera in the last interglacial ocean: Implications for the carbon cycle and the global deep water circulation. *Quaternary Res.*, **21**, 225–243.
- Dymond, J., Suess, E., and Lyle, M., 1992. Barium in deep-sea sediment: A geochemical proxy for paleoproductivity. *Paleoceanography*, **7**(2), 163–181.
- Eagle, M., Paytan, A., Arrigo, K., van Dijken, G., and Murray, R., 2003. A comparison between excess barium and barite as indicators of carbon export. *Paleoceanography*, **18**(1), 1021.
- Elderfield, H., and Rickaby, R., 2000. Oceanic Cd/P ratio and nutrient utilization in the glacial Southern Ocean. *Nature*, **405**, 305–310.
- Emerson, S., 1985. Organic carbon preservation in marine sediments. In Sundquist, E.T., and Broecker, W.S. (eds.), *The Carbon Cycle and Atmospheric CO_2 : Natural Variations Archean to Present*. Washington, DC: American Geophysical Union. pp. 78–87.
- Farrell, J.W., Pedersen, T.F., Calvert, S.E., and Nielsen, B., 1995. Glacial-interglacial changes in nutrient utilization in the equatorial Pacific ocean. *Nature*, **377**, pp. 514–516.
- Filippelli, G.M., 2002. The global phosphorus cycle. In Kohn, M.J., Rakovan, J., and Hughes, J.M. (eds.), *Reviews in Mineralogy and Geochemistry*, Vol. 48. Blacksburg, VA: Mineralogical Society of America, pp. 391–425.
- Finney, B.P., Lyle, M.W., and Heath, G.R., 1988. Sedimentation at MANOP Site H (eastern equatorial Pacific) over the past 400,000 years: Climatically induced redox variations and their effect on transition metal cycling. *Paleoceanography*, **3**, 169–189.
- Ganeshram, R., Francois, R., Commeau, J., and Brown-Leger, S., 2003. An experimental investigation of barite formation in seawater. *Geochimica et Cosmochimica Acta*, **67**(14), 2599–2605.
- Goñi, M.A., Ruttner, K.C., and Eglinton, T.I., 1998. A reassessment of the sources and importance of land-derived organic matter in surface sediments from the Gulf of Mexico. *Geochimica et Cosmochimica Acta*, **62**, 3055–3075.
- Herguera, J.C., 2000. Faunal perspectives on paleoproductivity. *Mar. Micropaleontol.*, **40**, 131–134.
- Hutchins, D.A., and Bruland, K.W., 1998. Iron limited diatom growth and Si:N uptake ratios in a coastal upwelling regime. *Nature*, **393**, 561–564.
- Imbrie, J., and Kipp, N.G., 1971. A new micropaleontological method for quantitative paleoclimatology: Application to a Late Pleistocene Caribbean core. In Turekian, K. (ed.), *The Late Cenozoic Glacial Ages*. New Haven, CT: Yale University Press, pp. 71–181.
- Keil, R.G., Tsamakis, E., Fuh, C.B., Giddings, C.A., and Hedges, J., 1994. Mineralogical and textural controls on the organic composition of coastal marine sediments: Hydrodynamic separation using SPLITT-fractionation. *Geochimica et Cosmochimica Acta*, **58**, 879–893.
- Kumar, N., Anderson, R., Mortlock, R., Froelich, P., Kubik, P., Dittrich-Hannen, B., and Suter, M., 1995. Increased biological productivity and export production in the glacial Southern Ocean. *Nature*, **378**, 675–680.
- Loubere, P., 1999. A multiproxy reconstruction of biological productivity and oceanography in the eastern equatorial Pacific for the past 30,000 years. *Mar. Micropaleontol.*, **37**, 173–198.
- Lyle, M., Murray, D., Finney, B., Dymond, J., Robbins, J., and Brooksforce, K., 1988. The record of Late Pleistocene biogenic sedimentation in the eastern tropical Pacific Ocean. *Paleoceanography*, **3**, 39–59.
- Mekik, A.F., Loubere, P., and Archer, D., 2002. Organic carbon flux and organic carbon to calcite flux ratio Recorded in deep sea carbonates: Demonstration and a new proxy. *Glob. Biogeochem. Cycles*, **16**, 1052, doi:10.1029/2001GB001634, 2002.
- Mix, A.C., 1989. Pleistocene paleoproductivity: Evidence from organic carbon and foraminiferal species. In Berger, W.H. et al., (eds), *Productivity of the Ocean, Past and Present*. New York: Wiley, pp. 313–340.
- Montoya, J.P., 1994. Nitrogen isotope fractionation in the modern ocean: Implications for the sedimentary record. In Zahn, R., Pedersen, T.F., Kaminski, M.A., and Labeyrie L. (eds.), *Carbon Cycling in the Glacial Ocean: Constraints on the Ocean's Role in Global Change*. NATO ASI Series, vol. 17, Berlin: Springer pp. 259–279.
- Muller, P.J., and Suess, E., 1979. Productivity, sedimentation rate, and sedimentary organic matter in the oceans. I. Organic carbon preservation. *Deep Sea Res.*, **26**, 1347–1362.
- Murray, R.W., and Leinen, M., 1996. Scavenged excess Al and its relationship to bulk Ti in biogenic sediment from the central equatorial Pacific Ocean. *Geochimica et Cosmochimica Acta*, **60**, 3869–3878.
- Murray, R., Knowlton, C., Leinen, M., Mix, A., and Polsky, C., 2000. Export production and carbonate dissolution in the central equatorial Pacific Ocean over the past 1 Myr. *Paleoceanography*, **15**(6), 570–592.
- Nürnberg, C.C., Bohrmann, G., and Schlüter, M., 1997. Barium accumulation in the Atlantic sector of the Southern Ocean: Results from 190,000-year record. *Paleoceanography*, **12**, 594–603.
- Paytan, A., Kastner, M., and Chavez, F., 1996. Glacial to interglacial fluctuations in productivity in the equatorial Pacific as indicated by marine barite. *Science*, **274**, 1355–1357.
- Pedersen, T.F., 1983. Increased productivity in the eastern equatorial Pacific during the last glacial maximum (19,000 to 14,000 yr B.P.). *Geology*, **11**, 16–19.
- Rowe, G.T., 1983. Biomass and production of the deep-sea macrobenthos. In Rowe, G.T. (ed.), *Deep-sea Biology, The Sea*, vol. 8. New York: Wiley, pp. 97–121.
- Ruhlemann, C., Frank, M., Hale, W., Mangini, A., Mulitza, S., Muller, P.J., and Wefer, G., 1996. Late Quaternary productivity changes in the western equatorial Atlantic: Evidence from ^{230}Th -normalized carbonate and organic carbon accumulation rates. *Mar. Geol.*, **135**, 127–152.
- Rutsch, H., Mangini, A., Bonai, G., Dittrich-Hanen, B., Kubik, P., Suter, M., and Segl, M. 1995. ^{10}Be and Ba concentrations in West African sediments trace productivity in the past. *Earth Planet. Sci. Lett.*, **133**, 129–143.
- Ruttner, K.C., and Berner, A.B., 1993. Authigenic apatite formation and burial in sediments from non-upwelling, continental margin environments. *Geochim. Cosmochim. Acta*, **57**, 991–1007.
- Sarnthein, M., Winn, K., Duplessy, J.-C., and Fontugne, M.R., 1988. Global variations of surface ocean productivity in low and mid latitudes: Influence on CO_2 reservoirs of the deep ocean and the atmosphere during the last 21,000 years. *Paleoceanography*, **3**, 361–399.
- Schneider, R.R., Müller, P.J., and Wefer, G., 1994. Late Quaternary paleoproductivity changes off the Congo deduced from stable carbon isotopes of planktonic foraminifera. *Palaeogeogr. Palaeoclimatol. Palaeoecol.*, **110**, 255–274.
- Schneider, R.R., Price, B., Muller, P.J., Kroon, D., and Alexander, I., 1997. Monsoon related variations in Zaire (Congo) sediment load and influence of fluvial silicate supply on marine productivity in the east equatorial Atlantic during the last 200,000 years. *Paleoceanography*, **12**, 463–481.

- Shackleton, N.J., Hall, M.A., and Shuxi, C., 1983. Carbon isotope data in core V19–30 confirm reduced carbon dioxide concentrations in the ice age atmosphere. *Nature*, **306**, 319–322.
- Shackleton, N.J., and Pisias, N.G., 1985. Atmospheric carbon dioxide, orbital forcing, and climate, in *The Carbon Cycle and Atmospheric CO₂: Natural Variations Archaean to Present*, Geophys. Monogr. Ser., 32, edited by E. Sundquist and W.S. Broecker, pp. 303–317, AGU, Washington, D.C.
- Stoll, H.M., and Schrag, D.P., 2000. Coccolith Sr/Ca as a new indicator of coccolithophorid calcification and growth rate. *Geochim. Geophys. Geosys.*, **1**, 1999GC000015.
- Tappan, H., 1968. Primary production, isotopes, extinctions and the atmosphere. *Paleogeogr. Paleoclimatol. Paleoecol.*, **4**, 187–210.
- Treuger, P., Nelson, D., van Bennekom, A., Demaster, D., Lanaert, A., and Queguiner, B., 1995. The silica balance in the world ocean: A re-estimate. *Science*, **268**, 375–379.
- Walter, H.J., Rutgers, M.M., van der Loeff and Francois, R., 1999. Reliability of ²³¹Pa/²³⁰Th activity ratio as a tracer for bioproductivity of the ocean. In Fischer, G., and Wefer, G. (eds.), *Use of Proxies in Paleoceanography: Examples from the South Atlantic*. Berlin: Springer, pp. 393–408.

Cross-references

Animal Proxies, Invertebrates
 Carbon Cycle
 Carbon Dioxide, Dissolved (Ocean)
 Carbon Isotopes, Stable
 Carbonate Compensation Depth
 Coccoliths
 Diatoms
 Dinoflagellates
 Foraminifera
 Geochemical Proxies (Non-isotopic)
 Iron and Climate Change
 Marine Biogenic Sediments
 Marine Carbon Geochemistry
 Organic Geochemical Proxies
 Paleoclimate Proxies, an Introduction
 Paleoceanography
 Phosphorus Cycle
 Stable Isotope Analysis
 Transfer Functions

OCEAN PALEOTEMPERATURES

Ocean paleotemperatures are the principal characteristics of past ocean scenarios. Over geological time, ocean temperature patterns underwent large changes, responding on long timescales ($\times 10^6$ yr) to different plate tectonical configurations, favoring either circum-equatorial flow and promoting a generally warmer ocean, or circum-polar flow with steep low-to-high latitude temperature gradients. On shorter timescales ($\times 10^4$ – 10^5 yr), ocean temperatures respond to insolation changes controlled by Earth orbital parameters which determine the amount of radiation the Earth's surface receives. High-amplitude, short-term temperature fluctuations are superimposed on decadal-to-millennial time scales and match the short-term temperature fluctuations recorded in Greenland ice cores during glacial times. This is a recent discovery that has immediately focused interest in climate research because of the potential analogy to human-induced climate change.

Because ocean temperatures are a key component of the climate system, deciphering ocean paleotemperatures from “marine climate archives” reflecting the climatic state of the Earth continues to be a longstanding aim. Sea surface temperatures

(SSTs) exert an immediate impact on the atmosphere, driving atmospheric circulation in terms of heat and moisture transport, and oceanic-atmospheric gas exchange. Moreover, aside from salinity, temperature determines the density of surface water, which drives thermohaline deepwater circulation. Thus, paleo-SSTs allow conclusions to be drawn about oceanic and atmospheric circulation. Deepwater temperatures depend on the loci where they are formed by sinking of dense surface waters; paleo-deepwater temperatures reflect the state of thermohaline circulation.

Different concepts are used to reconstruct water temperatures of past times, including micropaleontological, stable isotope, biomarker, and geochemical approaches. Several micropaleontological and geochemical data sets have been calibrated with the aim of yielding quantitative paleotemperature proxies. A variety of studies of past ocean scenarios (e.g., of the Last Glacial Maximum, Cenozoic warm climates), based on paleotemperature proxies, has greatly improved our understanding of the climate system over the last few decades. In particular, ocean paleotemperatures may serve as boundary conditions to initiate and validate climate model calculations that aim to predict the magnitude of future global warming.

History

Geological and paleontological studies aiming to reconstruct Earth's climate are perhaps as old as these disciplines. The oldest paleoclimate records based on marine fossils from land outcrops date back to the late eighteenth and early nineteenth century, when Cretaceous boreal, tropical, and austral provinces were identified in mollusk, ammonite and other faunas and changes in biogeographical distribution patterns were interpreted in terms of climatic change (e.g., Hutton, 1795; Cuvier, 1817).

The earliest climate records aiming for quantitative temperature reconstructions from microfossils were based on the identification of key species in Pleistocene marine sediments; species that could be related to climate zones (e.g., Phleger et al., 1953). However, it was not until the second half of the twentieth Century that an array of studies on the biogeographical distribution of modern planktonic foraminifera in the world ocean and in marine sediments became available, the potential of this species group as a tool for climate studies was discovered (e.g., Bradshaw, 1959; Bé, 1977; and others), and a conceptual framework for quantitative faunal approaches was found (Imbrie and Kipp, 1971).

Stable isotopes began to flourish as a tool in paleoceanography in the mid-twentieth century. Urey (1947) first explored the potential of oxygen isotope fractionation in natural carbonates as a paleotemperature indicator. Epstein et al. (1953) established the first paleotemperature equation based on oxygen isotopes. They found a 0.2‰ decrease in oxygen isotopic composition (expressed as $\delta^{18}\text{O}$) per 1 °C temperature increase for mollusk calcite. Emiliani (1955) published the first “paleotemperature records” based on $\delta^{18}\text{O}$ variations of foraminifera in Caribbean sediment cores, which he interpreted purely in terms of temperature fluctuations of 6–8 °C. However, it was yet not fully recognized to what extent the oxygen isotopic composition of the ocean changes through time. Shackleton (1967) discovered $\delta^{18}\text{O}$ fluctuations of similar amplitude in benthic foraminifera of the deep Pacific where deepwater is continuously close to freezing temperature. Here it became evident that the major portion of the $\delta^{18}\text{O}$ fluctuations observed in deep sea sediments are a result of waxing and waning continental ice

volumes where the light ^{16}O isotope is alternately stored away and released into the ocean. This finding has converted $\delta^{18}\text{O}$ into a stratigraphical tool, and when combined with independent temperature proxies, into a salinity and ice volume proxy.

Since the mid-1980s, alkenones have become established as a sea surface temperature (SST) proxy. The use of this proxy is based on the finding that these lipids, which are produced by marine algae, show a characteristic unsaturation pattern that is linked to growth temperature (Marlowe et al., 1984; Brassell et al., 1986). Over the last 20 years, analytical methods have improved and data sets for calibration that cover wide ocean regions have been established for water column, laboratory cultures, and sediment surface samples. These eventually gave rise to a new proxy that is now widely applied in paleoceanography (Müller et al., 1998).

Knowledge that magnesium contents in carbonates vary with temperature dates back to the early part of the twentieth century (Clarke and Wheeler, 1922). Nevertheless, only the development of precise analytical methods in the last decade of the past century enabled utilization of this trace element in carbonate microfossils as a quantitative proxy for paleotemperature (Nürnberg et al., 1996).

Ongoing work concentrates on: (a) achieving a still more precise calibration of established paleotemperature proxies, in particular for deepwater temperature reconstructions and near the “cold end” of temperature transfer functions, (b) exploring the use of quantitative proxies further back in geological time, and (c) testing new approaches. Questions addressing future warming have focused interest on the temperature reconstruction of former warm periods; (d) Multi-proxy approaches enable comparison of different reconstructions and, moreover, help to identify the influence of different seasons and growth habitats on the SST signal. In this context, reef corals are particularly promising in providing SST records with annual, seasonal, and even monthly time resolution and thus have gained increasing importance in addressing questions of short-term climate change.

Concepts for paleotemperature reconstructions

Most concepts for reconstructing past water temperatures are based on microfossils because of their widespread occurrence in marine sediments. Sea surface waters are inhabited by planktonic microorganisms, some of them bearing shells. In general, marine phyto- and zooplankton occur everywhere in the open ocean. Temperatures range from less than -1.8°C in the polar ice-covered areas up to 30°C in the tropical belt.

As the shells settle to the sea floor and are fossilized in marine sediments they preserve information about the environment in which they once lived. Paleoceanographers take advantage of this ‘climate archive’ to decipher paleotemperatures from microfossils, either from their faunal (or floral) assemblages or by analyzing the stable isotope or trace element composition of the calcareous shells. Most commonly employed microfossil groups are planktonic foraminifera. In addition, coccoliths, dinoflagellate cysts, and siliceous microfossils (radiolaria and diatoms) are used, the latter in particular to reconstruct Southern Ocean environments, where carbonate preservation is poor.

In contrast, deep-water temperatures are far more uniform and are generally near the cold end of transfer functions, ranging from close to freezing temperature to approximately 3°C . This makes them more difficult to assess. Deep-sea benthic foraminifera and ostracoda (little crustaceans bearing a calcareous carapace) living at the seafloor similarly record

deepwater temperatures in the isotopic and geochemical composition of their shells. Benthic assemblage structures, however, are much more complex than those of planktonic foraminifera and are primarily controlled by variables different from temperature.

Transfer functions based on microfossil species assemblages

Planktonic species assemblages are primarily sensitive to temperature, most species showing preference for a certain temperature range to which their vital functions are optimally adjusted. Therefore, planktonic assemblages display an ocean-wide, bipolar, roughly latitudinal distribution pattern, reflecting the occurrence of tropical, subtropical, transitional, subpolar, and polar water masses (Figure O23). Plankton distribution patterns of former times may thus be used to determine SSTs by using so-called transfer functions if evolutionary changes did not affect these patterns – that is, approximately over the last 0.5 million years. Imbrie and Kipp (1971) were the first to apply multivariate statistical methods to census data of planktonic foraminifera in order to derive quantitative SST estimates. Their method commonly consists of subjecting relative species abundances counted in core tops from a specific ocean region to a principal component (Q mode) analysis in order to discriminate factors by correlation between single species. The factors represent statistical assemblages, characterized by an end member species, the distribution pattern of which is related to specific watermass qualities (Figure O23).

Usually 5–6 factors are sufficient to explain $> 90\%$ of total variance in the assemblages. The role of single species grouped in a factor is weighted by factor loadings. Regression analysis (linear or non-linear) of the factors with instrumental temperatures above each station provides a set of equations (transfer functions) which can be used to calculate paleotemperatures from fossil species abundances. The equations have the shape of Equation (1)

$$P_{\text{est}} = k_0 + k_1A + k_2B + k_3C + k_4D \quad (1)$$

Where P is an environmental parameter, k s are predictive coefficients, and A – D are variables. In example (2), by Imbrie and Kipp (1971), T_8 is the summer temperature estimate, and the letters A – D stand for the values of tropical (Figure O24), subtropical, subpolar, and gyre margin assemblages.

$$T_8 = 19.7A + 11.6B + 2.7C + 0.3D + 7.6 \quad (2)$$

The quality of the calculated temperatures may be assessed by the measure of communality. This statistical measure, which is defined as the squared sum of factor loadings calculated for the fossil assemblage, shows how well the fossil assemblage fits into the pattern of modern assemblages.

The most impressive example of temperature reconstructions based on this approach was, without doubt, a global reconstruction of sea surface temperatures for the Last Glacial Maximum (LGM), accomplished by the CLIMAP Project members (1981) in 1976–1981. They applied the “Imbrie and Kipp (I&K) method” to a worldwide set of 700 glacial sediment samples where they used planktonic foraminifera, radiolaria, and coccolith assemblages as a joint base to produce SST maps of the glacial ocean.

A more advanced approach to derive paleotemperatures from faunal assemblages is the Modern Analog Technique

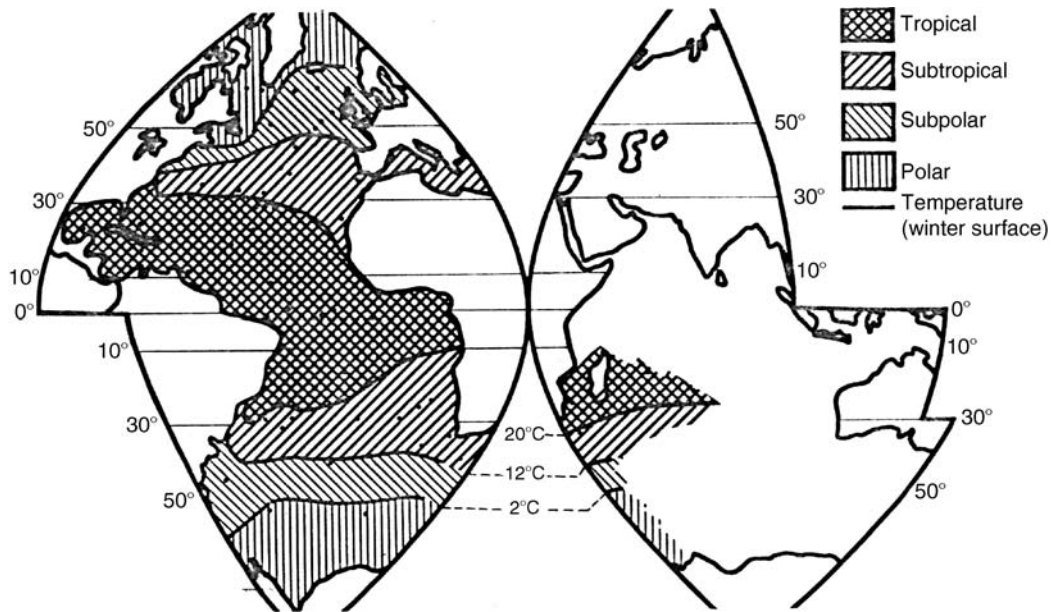


Figure O23 Distribution of core top samples dominated by statistical assemblages defined by Imbrie and Kipp (1971).

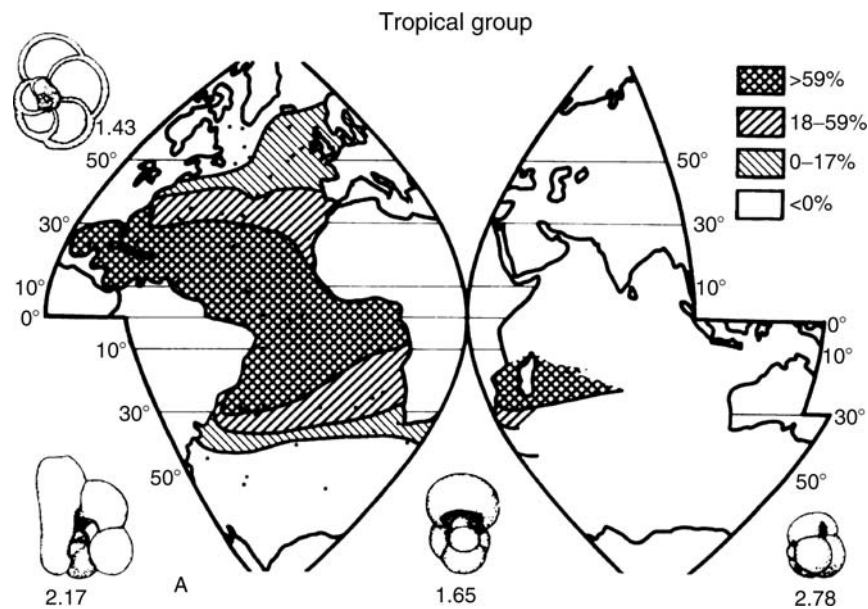


Figure O24 Geographical distribution of the tropical planktonic foraminifera group as defined by the multivariate statistical method. Four dominant species are shown with factor loadings ($\times 10$) (from Imbrie and Kipp, 1971).

(MAT) (Hutson, 1977), relying on the assumption that there is a direct relationship between the distribution of modern faunas and the physical properties of the environment. The method compares any fossil assemblage of planktonic foraminifera or other plankton with a set of census data from modern sediments in an ocean region (calibration data set) and transfers the measured temperatures above the most similar modern samples (= modern analogs) to the site of the fossil fauna. This approach employs a measure of faunal dissimilarity or similarity to identify the best modern analogs in the calibration data

set. The most commonly used dissimilarity coefficient is the squared chord distance (Equation (3)).

$$d_{ij} = \text{Sigma } k(p_{ik}^{1/2} - p_{jk}^{1/2})^2 \quad (3)$$

where d_{ij} is the squared chord distance between two multivariate samples i and j , and p_{ik} is the proportion of species k in a sample. Commonly, 10 modern analogs are selected. Measured sea surface temperatures at the various sample sites selected are averaged to give the paleotemperature. Further

refined variants of the MAT include SIMMAX (“similarity maximum”; Pflaumann et al., 1996, 2003), which weights the modern analog samples according to their geographical distance to the fossil sample, presuming that closer samples are more likely to record accurate temperatures. The Revised Analog Technique (RAM, Waelbroeck et al., 1998) pays tribute to the circumstance that core top samples as modern analogs are not evenly distributed across the ocean and therefore not all temperature settings are equally represented. Therefore, RAM does not use a pre-given number of analogs but defines for each sample the number to include, according to the dissimilarity. Moreover, artificial (interpolated) modern analogs are introduced into the database to strengthen the weight of poorly sampled temperature settings.

The use of Artificial Neural Networks (ANN; Malmgren et al., 2001) presents a more recent innovative approach to employ planktonic faunal data for SST reconstruction. The ANN technique is a computer-intensive method, which is based on an algorithm that has the ability to autonomously “learn” of a relationship between two groups of numbers (e.g., faunal and temperature data). The advantage of ANNs is that they have the ability to overcome problems of fuzzy and nonlinear relationships between sets of input and output variables. Each trained neural network serves as a unique transfer function, yet at the same time, this highly nonlinear and recurrent function is so complicated that it has the ability to simulate a decision algorithm.

To assess the differential quality of the outlined transfer functions, they have been applied to the same calibration data set of Atlantic core tops. Comparison of the resulting SST estimates to measured SST reveals that typical error ranges of transfer functions based on planktonic foraminifera range between $\pm 1^\circ\text{C}$ (SIMMAX; ANN; RAM) to $\pm 1.4^\circ\text{C}$ (I&K) (Malmgren et al., 2001).

The outlined transfer functions have the following general requirements in common: (a) The species composition in core top samples needs to be systematically linked to the environment of the ambient surface water mass; (b) the ecosystem has not undergone fundamental evolutionary changes, meaning that currently occurring species in an ocean basin are the same as those found in the sediments of the past period under investigation; (c) the ecological preferences of species have not changed over time; and (d) differential carbonate dissolution at the deep-sea floor has not significantly affected the species composition in the sediment.

Therefore, transfer functions *sensu strictu* are only valid for the period of time when all modern species have already existed. This applies to planktonic foraminifera of the last 0.5–0.7 million years. However, a number of authors have also tried to extend the use of transfer functions beyond that time limit. Aiming to reconstruct Miocene to Pliocene SSTs, Hooper and Funnell (1986) argued that it was legitimate to replace two species out of some 28, two species that only appeared in the Pleistocene, and the Miocene/Pliocene ancestor species that probably occupied similar ecological niches. Wang (1994) developed a transfer function for the reconstruction of Pliocene SST in the West Pacific. However, these attempts have not convinced the majority of investigators.

Oxygen isotopes

As with all stable isotopes, fractionation (= partitioning of isotopes between substances) of ^{16}O vs. ^{18}O in carbonates is temperature-dependent. The thermodynamic fractionation between

^{16}O and ^{18}O that occurs during carbonate precipitation offsets the $\delta^{18}\text{O}$ values of carbonate minerals relative to seawater by $\sim +30\text{‰}$. The $\delta^{18}\text{O}$ fractionation is a logarithmic function of temperature with a slope of -0.2‰ to -0.25‰ per degree Celsius, which means that a 1°C temperature increase results in an approximately 0.23‰ decrease in carbonate $\delta^{18}\text{O}$. Stable isotopes in carbonates are measured by mass spectrometry by determining the mass ratio in CO_2 gained from the reaction in which the carbonate sample is dissolved with phosphoric acid. Because ^{16}O is very abundant (99.76%) in nature and ^{18}O very rare (0.2%), the ratio between both isotopes is determined relative to a known standard (δ notation) (Equation (4)).

$$\delta^{18}\text{O}_{\text{Sample}} = ({}^{18}\text{O}_{\text{Sample}} / {}^{18}\text{O}_{\text{Standard}}) - 1,000 / {}^{18}\text{O}_{\text{Standard}} \quad (4)$$

In general, carbonate shells of foraminifera, both planktonic and benthic species, provide a fairly robust $\delta^{18}\text{O}$ record of predicted equilibrium. Thus, they allow for reconstructions of both sea surface and deepwater temperatures. However, the $\delta^{18}\text{O}$ signal of some species is offset from predicted equilibrium values by secondary effects related to cell biology, often referred to as vital effects. Several paleotemperature equations have been established for foraminiferal $\delta^{18}\text{O}$, based on calibrations from core-tops (Shackleton, 1974; Ganssen and Kroon, 2000) and laboratory cultures (Erez and Luz, 1983). They fit the polynomial form of equation (5)

$$T = a + b(\delta^{18}\text{O}_{\text{Calcite}} - \delta^{18}\text{O}_{\text{Water}}) + c(\delta^{18}\text{O}_{\text{Calcite}} - \delta^{18}\text{O}_{\text{Water}})^2 \quad (5)$$

Where T = temperature in $^\circ\text{C}$, a = temperature when $\delta^{18}\text{O}_{\text{calcite}} - \delta^{18}\text{O}_{\text{water}} = 0$, b is the slope, and c is the second order polynomial value. Shackleton’s equation (Equation (6)), for example, predicts a 0.23‰ decrease with reference to PDB (= Pee Dee Belemnite calcite) standard in $\delta^{18}\text{O}$ per 1°C increase.

$$T = 16.9 - 4.38(\delta^{18}\text{O}_{\text{Calcite}} - \delta^{18}\text{O}_{\text{Water}}) + 0.1(\delta^{18}\text{O}_{\text{Calcite}} - \delta^{18}\text{O}_{\text{Water}})^2 \quad (6)$$

Measurements of $\delta^{18}\text{O}$ by mass spectrometry are analytically highly precise, yielding an error smaller than 0.1‰ , which would translate into a temperature error as small as $< 0.4\text{--}0.5^\circ\text{C}$, if only temperature was involved. Because $\delta^{18}\text{O}$ in carbonates reflects both temperature fractionation and the $\delta^{18}\text{O}$ of ambient seawater where the carbonate has been precipitated, changes in seawater $\delta^{18}\text{O}$ over time also need to be considered. The global “ice volume effect” depends on the amount of ice accumulated on continents during the time under discussion. Where this ice volume effect is known, the portion of temperature-related fractionation in a $\delta^{18}\text{O}$ carbonate value can be identified.

In addition, $\delta^{18}\text{O}$ values in the ocean vary regionally with changes in the evaporation–precipitation balance, and locally with river and meltwater runoff. Since this “water mass effect” is difficult to assess in past ocean scenarios, it introduces a major portion of uncertainty into paleotemperature estimates from $\delta^{18}\text{O}$. Spatial and temporal variations of seawater $\delta^{18}\text{O}$ thus limit the use $\delta^{18}\text{O}$ in carbonates as a temperature proxy.

However, $\delta^{18}\text{O}$ is still widely used to estimate temperatures of warm climates in the absence of major ice sheets and low-to-high-latitude climatic gradients much smoother than in the Pleistocene; for example, for early Paleogene and Cretaceous times.

In these sediment records, the impact of diagenetic alteration on $\delta^{18}\text{O}$ may have been significant. Pearson et al. (2001) demonstrated from well-preserved planktonic foraminifera that low-latitude SSTs during the Late Cretaceous and Eocene epochs were as warm as 28–32 °C rather than 15–23 °C, as previously estimated. Their study also revealed a strong impact of diagenetic alteration on $\delta^{18}\text{O}$ of old fossil carbonates.

Since many sites in the Southern Ocean contain virtually no carbonate, the use of $\delta^{18}\text{O}$ from diatoms (marine algae bearing opal shells) has also been tested. Unfortunately, the systematics of oxygen isotopes in opal appears to be considerably more complex than for carbonates (Juillet-Leclerc and Labeyrie, 1986; Shemesh et al., 1992).

An innovative stable isotope approach currently under investigation is $\delta^{44}\text{Ca}$, based on the temperature-related fractionation between ^{44}Ca and ^{40}Ca isotopes. Note that the fractionation of Ca isotopes is inverse to that of oxygen isotopes. In culturing experiments with the planktonic foraminifer *Globigerinoides sacculifer*, a 1 °C increase in temperature resulted in a 0.24% increase of $\delta^{44}\text{Ca}$ (Näglér et al., 2000).

Magnesium-calcium ratio

In the ocean, magnesium may largely behave as a conservative tracer. This means that it occurs in a fixed ratio to calcium, displaying a long residence time. This concept, however, has been questioned by Martin et al. (2002), who suggested some glacial-to-interglacial changes in the oceanic Mg balance.

In calcite shells of planktonic foraminifera, this trace element occurs at very low concentrations (about 0.5–5 mmol mol⁻¹), being directly incorporated during calcite precipitation. Cronblad

and Malmgren (1981) published the first study on Quaternary climate cycles based on Mg in planktonic foraminifera. Newly developed high-precision analytical devices (Atomic Absorption Spectrophotometry (AAS); Inductively Coupled Plasma Spectrometry (ICP-MS; ICP-AS; ICP-AES)) facilitated high-precision Mg/Ca analyses of foraminiferal calcite and permitted its potential as a quantitative paleotemperature indicator to be explored. Precise measurements require a complex cleaning process of foraminifera shells, including physical and chemical steps where extraneous phases of Mg are removed, but the Mg content of the shells must not be affected.

The underlying concept for using Mg/Ca as a temperature proxy is based on the endothermic substitution of Mg in calcite, favoring the Mg substitution at higher temperatures. This relationship is not linear but underlies an exponential function. For inorganic calcite precipitates, the van't Hoff equation predicts an exponential Mg/Ca increase by 3% per degree Celsius. Foraminifera shells in general contain 5–10 times less Mg than inorganic calcite precipitates from seawater. The reason for this shift is still unknown. Possibly, lower Mg or higher Ca somehow is favorable for the internal-cell carbon cycle. On the other hand, foraminifera show a stronger response of shell Mg (on average, 9% increase in Mg per degree centigrade Celsius) to temperature than predicted by thermodynamics (Figure O25; Lea et al., 1999). This makes the Mg/Ca ratio of both planktonic and benthic foraminifera shells a very sensitive tool for reconstructing surface and deep-water temperatures.

The Mg substitution in calcite is different for the different foraminifera species, which necessitates a temperature calibration of each single species. Calibrations based on cultured

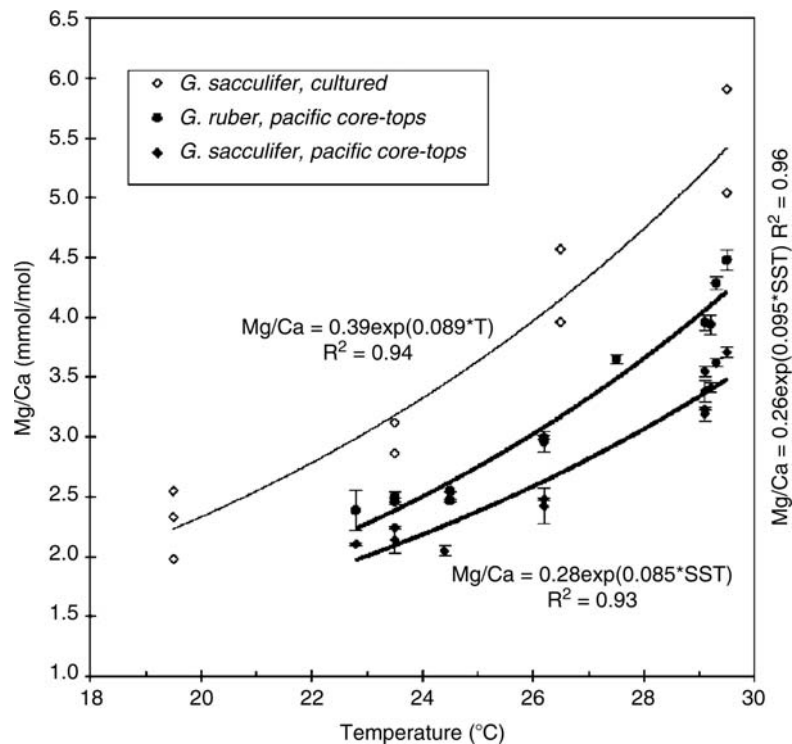


Figure O25 Comparison of exponential fits of Mg/Ca in planktonic foraminifera with temperature from cultured and core top planktonic foraminifera (from Lea et al., 1999).

planktonic foraminifera under controlled temperature conditions and from core tops fit equations of the form

$$\text{Mg/Ca}(\text{mmol mol}^{-1}) = b \cdot e^{mT} \quad (7)$$

where b is the pre-exponential constant (relevant for the absolute temperature, m the exponential constant (relevant for the temperature difference) and T is the temperature (Lea et al., 1999) (Equation (7)). Parallel Mg/Ca measurements on different planktonic foraminifera species that calcify their shells preferentially at different water depths may be used to reconstruct vertical temperature profiles of the water column according to calcification depth.

It is generally more difficult to assess the temperature of cold deep-water masses than warm temperature masses because temperature differences in deep-water masses are generally small. Moreover, the calibration of the slope between temperature and Mg/Ca is still quite uncertain near its “cold end.” To address questions on the evolution of deep-water temperatures, still more precise calibrations of benthic species are required (Martin et al., 2002). Nevertheless, the potential of Mg/Ca in benthic foraminifera has been demonstrated in a recent study of Lear et al. (2000). They suggested an ocean-wide gradual decrease in deep-water temperature of 12 °C over Cenozoic times on the basis of a mixed benthic Mg/Ca record (Figure O26).

Apart from foraminifera, ostracods have also proven useful indicators for bottom water temperatures (Dwyer et al., 1995; Cronin et al., 1996). As opposed to foraminifera, ostracod Mg/Ca ratios are fitted to temperatures through a linear relationship. Dwyer et al. (1995) revealed that a temperature drop of 3 °C in the deep North Atlantic Ocean occurred together with major Northern Hemisphere glaciation during the late Pliocene.

Differential dissolution results in an unwelcome secondary effect on Mg/Ca ratios in carbonate shells because Mg is preferentially removed from the shells, thus falsely suggesting cold paleotemperatures. A major complication arises from the fact that foraminifera shells are composed of carbonate layers containing different Mg concentrations, which are differentially susceptible to dissolution. Also salinity, pH, and, in the long term, changes in the marine Mg reservoir may affect Mg/Ca ratio.

Strontium represents a further trace element with potential for temperature reconstructions, yet has been little exploited

(especially in coral records). Its distribution in planktonic foraminifera is much more uniform (1.2–1.6 mmol mol⁻¹) than Mg, with a slope of approximately 5% per 1 °C.

Long-chain alkenones

Apart from shells, organic remains of marine plankton are also preserved in marine sediments. Proxies based on the composition of organic matter are particularly useful for sediments barren of carbonate, which occur below the carbonate compensation depth. Biomarkers are organic substances in the sediment that preserve sufficient structural characteristics to allow for conclusions on the original biogenic compound, even when modified. Lipids in the cell membranes of phytoplankton may vary in response to environmental stress in molecular chain length and unsaturation and thus record a paleotemperature signal. Notably, unsaturated long-chain ketones (= alkenones) shows a distinct dependency on growth temperature. Alkenones are produced by a few phytoplankton species belonging to the class of Prymnesiophyceae; in Late Quaternary sediments, they are mostly produced by the Coccolithophorid *Emiliana huxleyi*. Their physiological function in the living cells still is unknown, yet it is suspected that the increasing alkenone unsaturation with cooler temperatures compensates for increasing viscosity of the cell membrane (Prahl and Wakeham, 1987). With decreasing temperature, the concentration of 3-fold unsaturated (C37:3) and 4-fold unsaturated (C37:4) alkenones increases. Unsaturation of alkenones is measured by gas chromatography peak area integration. Unsaturation indices U_{37}^k and $U_{37}^{k'}$ (Equations (8) and (9)) express the ratio of (C37:4) (C37:3), and (C37:2) ketones or between 3- and 2-fold unsaturated (C:37) ketones.

$$U_{37}^k = [\text{C37:2}] - [\text{C37:4}] / [\text{C37:2} + \text{C37:3} + \text{C37:4}] \quad (8)$$

$$U_{37}^{k'} = [\text{C37:2}] / [\text{C37:2} + \text{C37:3}] \quad (9)$$

Indeed, the unsaturation indices adopt high values in low latitude warm waters and low values in high latitude cold waters. The role of 4-fold unsaturated alkenones, which only occur at high latitudes, is still debated. Some authors suspect that they are related to low salinity rather than to low SST. Calibrations of the U_{37}^k index versus growth temperature have been

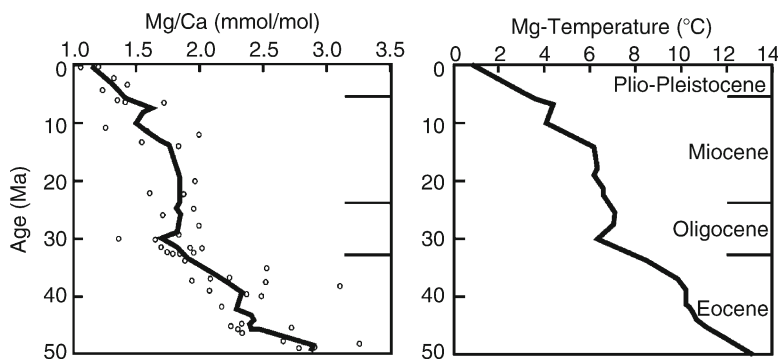


Figure O26 Gradual decrease of bottom water temperatures over Cenozoic times as deduced from Mg/Ca of mixed benthic foraminifera species (Lear et al., 2000).

established based on culturing experiments (Prahl and Wakeham, 1987; Prahl et al., 1988), particulate organic matter from sediment trap samples obtained in the water column (Herbert, 2001), and sediment surface samples (Müller et al., 1998). The calibrations generally fit linear regressions of U_{37}^k with temperature in the form of the example (Equation (10)) by Müller et al.

$$U_{37}^k = 0.033\text{SST} + 0.044 \quad (10)$$

The global calibration of core top samples by Müller et al. (1998) covers the ocean with 456 samples between 60° N and 60° S and a temperature range of 1–29 °C (Figure O27; Equation (10)). The regression does not significantly differ from that obtained by Prahl et al. (1988, 1993) based on culturing experiments. The best overall fit has been shown for average annual temperatures at 10 m water depth (Müller et al., 1998). However, growth depth may vary regionally, as shown for the subtropical gyres, where coccolithophorids tend to live in deeper layers (references in Herbert, 2001).

Strictly speaking, these calibrations are valid for the Late Pleistocene back to 250,000 yBP, when *Emiliana huxleyi* made its first appearance in marine sediments. However, alkenones produced earlier by other Prymnesiophyts may have preserved a comparable temperature signal. Herbert and Schuffert (1998) analyzed alkenones in Miocene to Pliocene samples from ODP site 958 and found a 5 °C temperature drop off Northwest Africa in the Late Pliocene. They argued that as long as alkenones performed a similar (though as yet unknown) biological function, calibrations established for the Late Pleistocene should similarly apply to older alkenone records. Recently, alkenones were also identified in Lower Cretaceous sediments, representing the oldest records of these compounds (Brassell and Dumitescu, 2003).

Summary

As a primary expression of the Earth is past climatic stages, paleotemperatures are a central issue in paleoceanography. Most concepts used to reconstruct ocean paleotemperatures rely on marine microfossils, either on plankton assemblages or on the isotopic or trace metal composition of carbonate shells. Table O1 summarizes the main approaches currently used in paleoceanography to reconstruct paleotemperatures.

Mara Weinelt

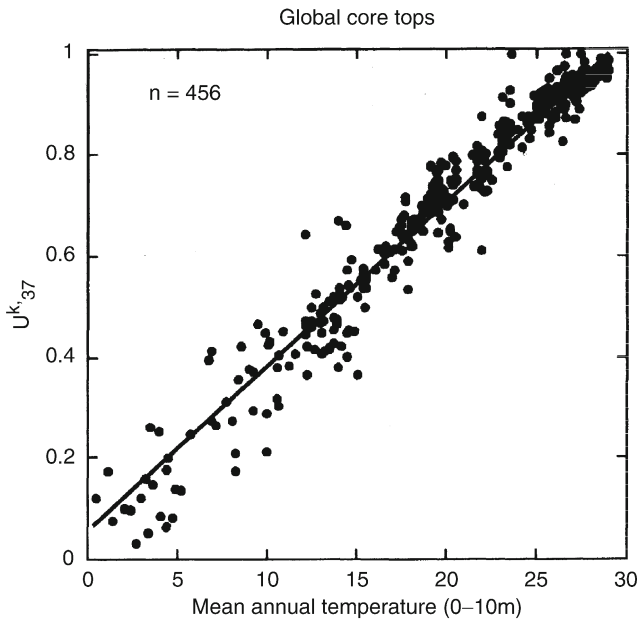


Figure O27 Global calibration of U_{37}^k index versus temperature by Müller et al. (1998).

Table O1 Summary of main approaches currently used to reconstruct ocean paleotemperatures and environment and time period where they are applicable

Approach/method	Reconstruction of	Applicable time
Transfer functions based on plankton assemblages		
I&K method	SST	500,000–700,000 yBP
MAT/SIMMAX/RAM	SST	500,000–700,000 yBP
ANN	SST	500,000–700,000 yBP
Long-chain alkenone Unsaturation indices $\delta^{18}\text{O}$	SST	250,000 yBP Neogene/Cretaceous?
Planktonic foraminifera	Temperature of upper water column (depending on calcification depth of single species)	Lower Cretaceous to present
Siliceous microfossils Benthic foraminifera	SST Deep-water temperature	Unlimited, where $\delta^{18}\text{O}$ of seawater can be assessed
Mg/Ca Planktonic foraminifera	Temperature of upper water column (depending on calcification depth of single species)	Lower Cretaceous to present
Benthic foraminifera Ostracods Reef corals	Deep-water temperature Deep-water temperature	In principle, unlimited In principle, unlimited
Sr/Ca $\delta^{18}\text{O}$	Tropical shallow water temperatures Tropical shallow water temperatures	Historical times, in particular Historical times, in particular

Bibliography

- Bé, A.W.H., 1977. An ecological, zoogeographic and taxonomic review of recent planktonic foraminifera (chapter 1). In Ramsay, A.T.S. (ed.), *Oceanic Micropaleontology*, vol. 1. London: Academic Press, pp. 1–100.
- Bradshaw, J.S., 1959. Ecology of living planktonic foraminifera in the North and Equatorial Pacific Ocean. *Cushman Found. Foraminiferal Res. Contr.*, **10**, 25–64.
- Brassell, S.C., and Dumitrescu, M., (2003). Alkenones in early Aptian organic-rich sediments from Shatsky Rise, ODP Leg 198. *Geophys. Res. Abstr.*, **5**, 13106.
- Brassell, S.C., Eglinton, J., Marlowe, I.T., Pflaumann, U., and Sarnthein, M., 1986. Molecular stratigraphy: A new tool for climatic assessment. *Nature*, **320**, 129–133.
- Clark, F.W., and Wheeler, W.C., 1922. The inorganic constituents of marine invertebrates. US Geological Survey Professional Paper 124, 55pp.
- CLIMAP, 1981. Seasonal reconstructions of the Earth's surface at the last glacial maximum. The Geological Society of America Map and Chart Series MC–36.
- Cronblad, H.G., and Malmgren, B.A., 1981. Climatically controlled variation of Sr and in Quaternary planktonic foraminifera. *Nature*, **291**, 61–64.
- Cronin, T.M., Raymo, M.E., and Kyle, K.P., (1996). Pliocene (3.2–2.4 Ma) ostracode faunal cycles and deep ocean circulation, North Atlantic ocean. *Geology*, **24**, 695–698.
- Cuvier, M., 1817. *Essay on the theory of the Earth*. Edinburgh, New York: Arno Press (reprinted 1978).
- Dwyer, G.S., Cronin, T.M., Baker, P.A., Raymo, M.E., Buzas, J.S., and Corregge, T., 1995. North Atlantic deepwater temperature change during Late Pliocene and Late Quaternary Climate cycles. *Science*, **270**, 1347–1351.
- Emiliani, C., 1955. Pleistocene temperatures. *J. Geol.*, **63**, 538–578.
- Epstein, S., Buchsbaum, R., Lowenstam, H.A., and Urey, H.C., 1953. Revised carbonate-water isotopic temperature scale. *Geol. Soc. Am. Bull.*, **64**, 1315–1325.
- Erez, J., and Luz, B., 1983. Experimental paleotemperature equation for planktonic foraminifera. *Geochim. Cosmochim. Acta*, **47**, 1025–1031.
- Ganssen, G.M., and Kroon, D., 2000. The isotopic signature of planktonic foraminifera from NE Atlantic surface sediments: implications for the reconstruction of past oceanic conditions. *J. Geol. Soc., London*, **157**, 693–699.
- Hemleben, C., Spindler, M., and Anderson, O.R., 1989. *Modern Planktonic Foraminifera*. New York: Springer, 363pp.
- Herbert, T.D., 2001. Review of alkenone calibrations (culture, water column, and sediments). *Geochem. Geophys. Geosyst.*, **2**(2), doi: 2000GC000055.
- Herbert, T.D., and Schuffert, J.D., 1998. Alkenone unsaturation estimates of Late Miocene through Late Pliocene sea surface temperatures at Site 958. In Proceedings of the Ocean Drilling Program, Scientific Results, **159T**, 17–21.
- Hooper, P.W., and Funnell, 1986. Palaeoceanographic significance of Late Miocene to early Pliocene planktonic foraminifera at DSDP Site 609. Initial Reports of the Deep Sea Drilling Project, **94**, 925–934.
- Hutson, W.H., 1977. Transfer functions under no-analog conditions: Experiments with Indian Ocean planktonic foraminifera, *Quaternary Res.*, **8**, 355–367.
- Hutton, J., 1795. *Theory of the Earth*. Edinburgh: Creech, vol. 1: 620pp, vol. 2: 576pp.
- Imbrie, J., and Kipp, N.G., 1971. A new micropaleontological method quantitative paleoclimatology: Application to a late Pleistocene Caribbean core. In Turekian, K. (ed.), *The Late Cenozoic Ice Ages*. New Haven: Yale University Press, pp. 71–181.
- Juillet-Leclerc, A.D., and Labeyrie, L.D., 1986. Temperature dependence of the oxygen isotope fractionation between diatom silica and water. *Earth Planet. Sci. Lett.*, **84**, 69–74.
- Lea, D.W., Mashiotta, T.A., and Spero, H.J., 1999. Controls on magnesium and strontium uptake in planktonic foraminifera determined by live culturing. *Geochim. Cosmochim. Acta*, **63**, 2369–2379.
- Lear, C., Elderfield, H., and Wilson, P.A., 2000. Cenozoic deep-sea temperatures and global ice-volumes from Mg/Ca in benthic foraminiferal calcite. *Science*, **287**, 269–272.
- Malmgren, B.A., Kucera, M., Nyberg, J., and Waelbroeck, C., 2001. Comparison of statistical and artificial neural network techniques for estimating past sea-surface temperatures from planktonic foraminifer census data. *Paleoceanography*, **16**, 520–530.
- Marlowe, I.T., Brassell, S.C., Eglinton, G., and Green, J.C., 1984. Long-chain unsaturated ketones and esters in living algae and marine sediments. *Org. Geochem.*, **6**, 135–141.
- Martin, P.A., Lea, D.W., Rosenthal, Y., Shackleton, N.J., Sarnthein, M., and Papenfuß, T., 2002. Quaternary deep sea temperature histories derived from benthic foraminiferal Mg/Ca. *Earth Planet. Sci. Lett.*, **198**, 193–209.
- Müller, P.J., Kirst, G., Ruhland, G., von Storch, I., and Rosell-Melé, A., 1998. Calibration of the alkenone paleotemperature index Uk³⁷ based on core-tops from the eastern South Atlantic and the global ocean (60° N–60° S). *Geochim. Cosmochim. Acta*, **62**, 1757–1772.
- Nägler, T.F., Eisenhauer, A., Müller, A., Hemleben, C., and Kramers, J., 2000. The $\delta^{44}\text{Ca}$ temperature calibration on fossil and cultured Globigerinoides sacculifer: new tool for reconstruction of past sea surface temperatures. *Geochem., Geophys., Geosys.*, **1**, doi: 2000GC000091.
- Nürnberg, D., Bijma, J., and Hemleben, C., 1996. Assessing the reliability of magnesium in foraminiferal calcite as a proxy for water mass temperatures. *Geochimica et Cosmochimica Acta*, **60**, 803–814.
- Pearson, P.N., Ditchfield, P.W., Singano, J., Harcourt-Brown, K.G., Nicholas, C.J., Olsson, R.K., Shackleton, N.J., and Hall, M.A., 2001. Warm tropical sea surface temperatures in the late Cretaceous and Eocene epochs. *Nature*, **413**, 481–487.
- Pflaumann, U., Duprat, J., Pujol, C., and Labeyrie, L.D., 1996. A modern analog technique to deduce Atlantic sea surface temperatures from planktonic foraminifera in deep-sea sediments, *Paleoceanography*, **11**, 15–35.
- Pflaumann, U., Sarnthein, M., Chapman, M., Duprat, J., Huels, M., Kiefer, T., Maslin, M., Schulz, H., van Kreveld, S., Vogelsang, E., and Weinelt, M., 2003. The Glacial North Atlantic: Sea-surface conditions reconstructed by GLAMAP-2000. *Paleoceanography*, **18**, 1065.
- Phleger, F.B., Parker, F.L., and Peirson, J.F., 1953. North Atlantic core foraminifera. Report of the Swedish Deep-Sea Expedition, 1947–1948, **7**(1), 3–122.
- Prahl, F.G., and Wakeham, S.G., 1987. Calibration of unsaturation patterns in long-chain ketone compositions for paleotemperature assessment. *Nature*, **330**, 367–369.
- Prahl, F.G., Muehlhausen, L.A., and Zahnle, D.L., 1988. Further evaluation of long-chain alkenones as indicators of paleoceanographic conditions. *Geochim. Cosmochim. Acta*, **52**, 2303–2310.
- Prahl, F.G., Collier, R.B., Dymond, J., Lyle, M., and Sparrow, M.A., 1993. A biomarker perspective on Pymnesiophyte productivity in the Northeast Pacific Ocean. *Deep Sea Res. I*, **40**, 2071–2076.
- Shackleton, N.J., 1967. Oxygen isotope analysis and Pleistocene temperatures re-assessed. *Nature*, **215**, 15–17.
- Shackleton, N.J., 1974. Attainment of isotopic equilibrium between ocean water and the benthonic foraminifera genus *Uvigerina*: Isotopic changes in the ocean during the last glacial. *Cent. Nat. Rech. Colloq. Int.*, **219**, 203–209.
- Shemesh, A., Charles, C.D., and Fairbanks, R.G., 1992. Oxygen isotopes in biogenic silica – global changes in ocean temperature and isotopic composition. *Science*, **256**, 1434–1436.
- Urey, H.C., 1947. The thermodynamic properties of isotopic substances. *J. Chem. Soc.*, 562–581.
- Waelbroeck, C., Labeyrie, L., Duplessy, J.-C., Guiot, J., Labracherie, M., Leclaire, H., and Duprat, J., 1998. Improving past surface temperature estimates based on planktonic fossil faunas. *Paleoceanography*, **13**, 272–282.
- Wang, L., 1994. Sea surface temperature history of the low latitude western Pacific during the last 5.3 million years. *Palaeogeogr. Palaeoclimatol. Palaeoecol.*, **108**, 379–436.

Cross-references

Alkenones
 Cenozoic Climate Change
 CLIMAP
 Coccoliths
 COHMAP
 Coral and Coral Reefs
 Cretaceous Warm Climates
 Diatoms

Dinoflagellates
 Foraminifera
 Geochemical Proxies (Non-Isotopic)
 Heat Transport, Oceanic and Atmospheric
 Ice Cores
 Isotope Fractionation
 Last Glacial Maximum
 Marine Biogenic Sediments
 Miocene Climate
 Organic Geochemical Proxies
 Ostracodes
 Oxygen Isotopes
 Paleotemperatures and Proxy Reconstructions
 Pleistocene Climates
 Radiolaria
 Thermohaline Circulation
 Transfer Functions

ORGANIC GEOCHEMICAL PROXIES

Introduction

Organic matter is produced principally by photosynthetic plants, bacteria, and archaea. The amounts and kinds of lipids, carbohydrates, proteins and other biochemical components have varied as the amounts and kinds of plants and microbes have changed over time. Incorporation of organic matter into the sediments of lakes and oceans, which are nature's archives, typically blends components from many sources. Biochemical components of biota are altered to become the geochemical constituents of sediments, first by metabolic utilization by microbes and other biota and later by oxidation-reduction processes. Despite these very early diagenetic changes, sedimentary organic matter retains important information about its origins, and it provides equally important information about how it was delivered and deposited.

Different environments support different biological communities, with the result that geochemical components indicative of changes in the communities exist in sediment horizons deposited at different times. These proxies of paleoclimatic, paleolimnologic, and paleoceanographic histories are provided by the elemental, isotopic, and molecular compositions of sedimentary organic matter.

Organic matter C/N ratios

The proportions of sedimentary organic matter that originate from aquatic as opposed to land sources can be distinguished from compositional differences between algae and vascular land plants. Fresh organic matter from aquatic algae is protein-rich and cellulose-poor and yields molar C/N values that are commonly between 4 and 9. Vascular land plants, which are protein-poor and cellulose-rich, create organic matter that usually has C/N ratios of 20 and greater.

Partial degradation of organic matter during early diagenesis sometimes modifies the initial elemental compositions and hence C/N ratios of organic matter in sediments. C/N ratios of fresh wood samples are generally higher than those of wood that has been buried in sediments (Meyers et al., 1995). This change reflects selective degradation of carbon-rich sugars and lipids in the buried wood. In contrast, the C/N ratio of algal organic matter can increase during sinking and early sedimentation as nitrogen-rich proteins are selectively degraded. When diagenetically

elevated C/N ratios of marine organic matter are found in sediment records, they imply periods of enhanced aquatic paleoproductivity, such as occur in oceanic upwelling systems (Twichell et al., 2002). In most depositional settings, changes in the elemental composition of sedimentary organic matter are minor and do not erase the distinctive C/N differences between the organic matter derived from aquatic algae and land plants.

Organic matter stable isotopic compositions

The carbon and nitrogen stable isotopic compositions of bulk sedimentary organic matter are widely used to reconstruct paleoenvironmental conditions by assessing sources of organic matter in sediment records and past changes in the availability of nutrients in the surface waters of lakes and oceans.

Organic $\delta^{13}\text{C}$ values

Carbon isotopic ratios are useful to distinguish between marine and continental plant sources of sedimentary organic matter and to identify organic matter from different types of land plants. The carbon isotopic compositions of organic matter reflect principally the dynamics of photosynthetic carbon assimilation and the $^{13}\text{C}/^{12}\text{C}$ ratio of the carbon source. Most plants assimilate carbon using the C_3 pathway, which discriminates against ^{13}C to produce a $\delta^{13}\text{C}$ shift of about -20‰ from the source isotopic composition. Some plants use the C_4 pathway, which creates an isotope shift of about -7‰ . All C_4 plants are specialized for warm, dry, land environments.

The distinctive $\delta^{13}\text{C}$ values of C_3 and C_4 plants can be combined with the characteristic C/N values of algal and land-plant tissues to identify the major sources of organic matter in sediments (Figure O28, top). Deviations from the generalized $\delta^{13}\text{C}$ and C/N values occur, which represent natural variations in biochemical compositions, diagenetic modifications of initial compositions, or valuable evidence of paleoenvironmental changes.

The amount of inorganic carbon that is available for assimilation can affect the $\delta^{13}\text{C}$ values of photosynthesized organic matter. Periods of increased primary productivity in lakes and oceans are commonly recorded as increases in the $\delta^{13}\text{C}$ values of the organic matter that becomes buried in the sediment record. Production of algal organic matter selectively removes ^{12}C from photic zone dissolved inorganic carbon reservoirs. As availability of the inorganic carbon becomes less, the $^{13}\text{C}/^{12}\text{C}$ ratio of the remaining inorganic carbon increases and leads to less negative $\delta^{13}\text{C}$ values of subsequently produced organic matter. However, if inorganic carbon concentrations are elevated, then algal photosynthesis selectively assimilates ^{12}C from the replete carbon reservoir to produce organic matter with more negative $\delta^{13}\text{C}$ values. Cretaceous black shales, which record elevated algal production under a CO_2 -rich atmosphere and have $\delta^{13}\text{C}$ values of about -28‰ (Rau et al., 1987), are a classic example of this kind of environment.

$\delta^{15}\text{N}$ values

Nitrogen is a biolimiting nutrient in aquatic systems, and it has multiple oxidation states that have different isotopic compositions. The $\delta^{15}\text{N}$ values of sediment organic matter consequently reflect the paleoenvironmental processes that affect nitrogen biogeochemical cycling. The $\delta^{15}\text{N}$ value of the dissolved NO_3^- that is commonly assimilated by algae is typically $5\text{--}10\text{‰}$, whereas the value of atmospheric N_2 made accessible to land plants by nitrogen-fixing soil bacteria is about 0‰ . This isotopic difference

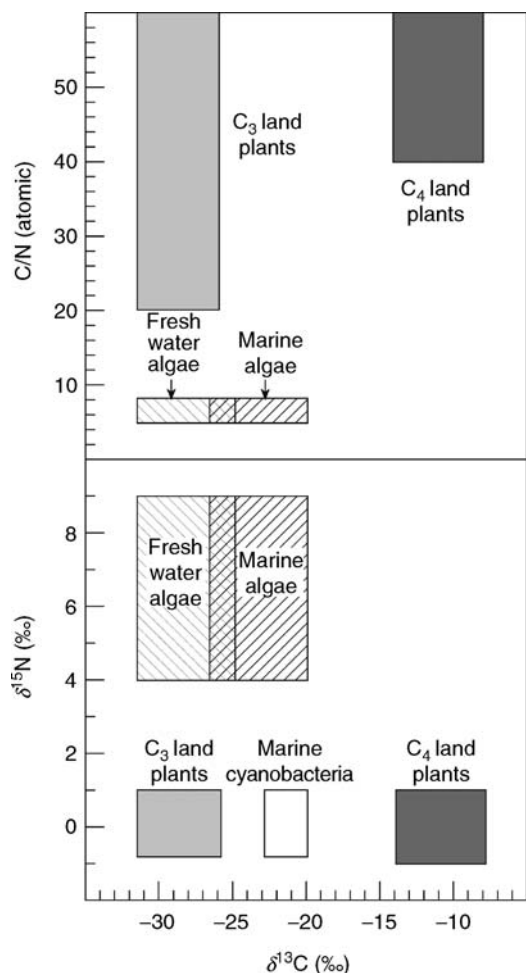


Figure O28 Generalized elemental and carbon isotopic (*top*) and nitrogen and carbon isotopic (*bottom*) compositions of organic matter from marine and freshwater algae, C₃ and C₄ land plants, and cyanobacteria.

is preserved in the $\delta^{15}\text{N}$ values of organic matter from algae and from land plants (Figure O28, *bottom*) because the limited availability of nitrogen discourages much isotopic discrimination.

Denitrification occurs during dysoxic conditions in lakes and oceans and strongly discriminates against ^{15}N to yield N_2 enriched in ^{14}N and residual nitrate enriched in ^{15}N . These conditions accompany the strong stratification that seasonally happens in many lakes and is a permanent feature of some oceanic areas. Subsequent uptake of the residual nitrate by algae leads to organic matter with high (12–14‰) $\delta^{15}\text{N}$ values in the sediment records of these settings. Conversely, good ventilation of the water column is recorded as relatively low (3–4‰) $\delta^{15}\text{N}$ values.

Nitrogen-fixing organisms such as cyanobacteria are autotrophs that convert dissolved N_2 to bioavailable NH_4^+ when anoxia exists within the photic zone of lakes and oceans. Their activity leads to lower $\delta^{15}\text{N}$ values in sedimented organic matter. Evidence of this special environmental condition exists in sediments deposited between 10 to 3.3 ka in Lake Bosumtwi, Ghana, where it records a period of strong stratification in this lake (Talbot and Johannessen, 1992). Suitable conditions for cyanobacterial activity also commonly occur in eutrophic lakes.

Sediments deposited in central Florida lakes display shifts to low (–1 to 3‰) $\delta^{15}\text{N}$ values as eutrophication of these lakes increased (Brenner et al., 1999). The remarkably low (–4 to 0‰) $\delta^{15}\text{N}$ values of Cretaceous black shales (Rau et al., 1987) and of Pliocene-Pleistocene sapropels in the Mediterranean Sea (Struck et al., 2001) imply strong salinity stratification of these marine settings and consequent enhancement of cyanobacterial primary production. As such, these sediment records indicate periods of wetter paleoclimatic conditions that were maintained for multi-thousand-year periods.

Sediment $\delta^{15}\text{N}$ values are also sometimes useful in reconstructing algal paleoproductivity histories, especially in lakes where phosphorus is often more biolimiting than nitrogen. In nitrogen-replete environments, biota discriminate in favor of ^{14}N , and sediment $\delta^{15}\text{N}$ values are relatively low. During times of amplified phosphorus delivery, either from human activities or from climate-enhanced weathering of regolith, increased algal utilization of bioavailable nitrogen and consequent decreased discrimination in favor of ^{14}N appear as shifts to larger $\delta^{15}\text{N}$ values in sediments (Meyers and Lallier-Vergès, 1999).

Biomarker molecules

Biomarker molecules are compounds that characterize biotic sources and that retain their source information after burial in sediments (Table O2). Biomarkers in sediments and rocks are usually diagenetically stabilized derivatives of specific precursor compounds, yet the carbon skeletons of the derived molecules preserve the source-distinctive structures of their precursor compounds. Although biomarkers typically constitute less than 1% of sediment organic matter, they yield important paleoenvironmental information that bulk organic geochemical proxies cannot provide.

Hydrocarbons

Because of their low susceptibility to microbial degradation relative to other types of organic matter, saturated hydrocarbons are generally robust recorders of the origins of organic matter in sediments. The hydrocarbon compositions of many aquatic algae and photosynthetic bacteria are dominated by the C₁₇ *n*-alkane (Cranwell et al., 1987). Vascular land plants contain large proportions of C₂₇, C₂₉, C₃₁, and C₃₃ *n*-alkanes in their waxy coatings, and the biomarker constitutions are indicative of different kinds of plants. The *n*-alkane distributions of grasses and herbs are dominated by C₃₁, birches by C₂₇, and most trees by C₂₉ (Schwark et al., 2002).

Fatty acids

Fatty acids in lake sediments typically originate from multiple sources. The *n*-C₁₆ and *n*-C₁₈ alkanolic and alkenolic acids are ubiquitous components of biota, whereas the even-chain C₂₄–C₃₀ *n*-alkanoic acids originate principally from the waxy coatings of land plants (Cranwell et al., 1987). The long-chain *n*-acid components of organic matter in sediments therefore represent transport of land-derived debris to the depositional setting. Unsaturated *n*-C₁₆ and *n*-C₁₈ acids are major constituents of the lipids of algae, yet they are rapidly degraded by microbes during and after sedimentation. The microbes contribute their own distinctive biomarker acids to the sediments. For example, *normal* and *anteiso* C₁₅ alkanolic acids have been used as indicators of microbial biomass in lake sediments (Goossens et al., 1989), and they represent *in situ* production of secondary lipids at the expense of primary organic matter.

Table O2 Examples of important biomarker molecules and their significance to organic geochemical reconstructions of paleoenvironmental and paleoclimatic histories

Biomarker molecules	Source/significance
Hydrocarbons	
C ₂₇ , C ₂₉ , C ₃₁ and C ₃₃ <i>n</i> -alkanes	Vascular land plant waxes; indicates land-plant organic matter contributions and community compositions
C ₁₅ and C ₁₇ <i>n</i> -alkanes	Aquatic algae; indicates aquatic organic matter
7- and 8-methyl-branched C ₁₇ alkanes	Cyanobacteria; indicates aquatic nitrogen fixation
Pristane	Phytol sidechain of chlorophyll; indicates zooplankton-based food chains
Phytane	Phytol sidechain of chlorophyll; methanogens; halophilic bacteria; indicates anoxic conditions
Botryococcane	Mat-forming freshwater alga <i>Botryococcus braunii</i>
Fichtelite	Conifer resins; indicates reducing depositional conditions
Retene	Conifer resins; indicates oxidizing depositional conditions
Fatty acids	
C ₂₄ , C ₂₆ , and C ₂₈ <i>n</i> -alkanoic acids	Vascular land plant waxes
Iso and anteiso branched acids	Bacteria; evidence of microbial organic matter
Fatty alcohols	
C ₂₄ , C ₂₆ , and C ₂₈ <i>n</i> -alkanols	Vascular land plant waxes
Alkenones	
C ₃₇ , C ₃₈ , and C ₃₉ alkenones	Marine haptophyte algae; proxies for sea surface paleotemperatures
Sterols and sterols	
Dinosterol and derivatives	Dinoflagellate-derived organic matter
4-methyl sterols	Dinoflagellate-derived organic matter
Brassicasterol	Diatom-derived organic matter
C ₂₉ sterols	Land-plant organic matter
C ₂₇ sterols	Marine or freshwater algal organic matter
Pigments	
Fucoxanthin, diadinoxanthin	Diatom-derived organic matter
Peridinin	Dinoflagellate-derived organic matter
Myxoxanthophyll, oscillaxanthin	Cyanobacteria; indicates aquatic nitrogen fixation
Isorenieratene derivatives	Green sulfur bacteria; anoxic conditions in photic zone
Lignin-derived phenols	
Cinnamyl/vanillyl ratio	Proportions of woody and non-woody land-plant tissues
Syringyl/vanillyl ratio	Proportions of gymnosperm and angiosperm land-plant organic matter

Unlike the shorter chain-length fatty acids, the longer chain-length ones survive in sediments and provide evidence of their plant origins.

Fatty alcohols

Fatty alcohols have source patterns roughly similar to those of fatty acids. Epicuticular waxes of land plants contain even-chain *n*-alkanols from C₂₂ to C₃₀ (Rieley et al., 1991). However, unlike fatty acids, *n*-alkanol distributions dominated by the C₁₆ to C₂₂ components generally indicate organic matter derived from aquatic algae and bacteria and not biota in general (Volkman et al., 1999). Individual species of plants can have distinctive chain-length patterns that deviate from these generalized distributions.

Alkenones

Long-chain (*n*-C₃₇, *n*-C₃₈, *n*-C₃₉) methyl and ethyl alkenones are distinctive biomarkers of marine coccolithophores. Their abundance in sedimentary records can be used as a paleoproductivity proxy for these algae, but their special usefulness is as paleotemperature proxies. Alkenone distributions usually consist of a series of homologs having a mixture of 1, 2, 3, and 4 double bonds that is temperature-sensitive. The algae produce proportionally more polyunsaturated homologs as water temperatures decrease in order to maintain cell-wall fluidity. Alkenones also appear in lake sediment records (Zink et al., 2001), but their utility as a paleoenvironmental proxy is not yet established because their origin is unknown.

Sterols and their derivatives

Sterol compositions distinguish aquatic contributions of organic matter in sediments from land-derived material. Cholesterol (C₂₇) is the dominant algal sterol, whereas β -sitosterol (C₂₉) is the major sterol in emergent water plants (Nishimura and Koyama, 1977). Land-plant leaf waxes contain C₂₈ and C₂₉ but not C₂₇ sterols (Rieley et al., 1991). Ternary plots of the C₂₇, C₂₈, and C₂₉ sterol compositions of algae, vascular plants, soils, and sediments identify ecological patterns (Huang and Meinschein, 1979) that can be applied to paleoenvironmental interpretations. Specific sterols are particularly useful to paleoenvironmental reconstructions. Stronger wind-induced upwelling is indicated from increased amounts of dinosterol and C₂₇ + C₂₈ 4-methylsterols, which are dinoflagellate biomarkers, in glacial-age sediments in the equatorial Pacific (Prah et al., 1989).

Pigments

Plants have evolved a variety of photosynthetic pigments that can serve as biomarkers. Chlorophyll *a*, the most common pigment, is non-specific, but aquatic plants and microbes produce distinctive secondary pigments (Table O2) that facilitate photosynthesis in water. Human-induced eutrophication of Esthwaite Water in the English Lake District is recorded as progressive increases in the concentrations of myxoxanthophyll and oscillaxanthin, two carotenoids indicative of cyanophytes and hence conditions of elevated lake productivity (Griffiths, 1978). Climate-induced strong surface stratification of the Mediterranean Sea during times of Pliocene sapropel formation is implied by

isorenieratene derivatives in the sapropel layers but not outside them (Passier et al., 1999). Isorenieratene is a carotenoid that is diagnostic for green sulfur bacteria, which are photosynthetic obligate anaerobes, and their presence means that a near-surface anoxic zone intruded into the photic zone.

Lignin derivatives

Lignins are phenolic polymers that are synthesized by higher plants to construct parts of their vascular and structural systems. Nearly all vascular plants grow on land, and therefore the lignin fraction of sediment organic matter largely records the contribution and preservation of land-plant materials. Gymnosperms and angiosperms synthesize distinctive types of lignin components. Past changes in continental vegetation can therefore be inferred from the kinds of lignin found in sediment records. Molecular analysis of lignin typically begins with an aggressive oxidation step to break down the biopolymer into various phenolic monomeric fragments. The oxidation fragments of lignin have been grouped by Hedges and Mann (1979) as a guide to identifying their plant sources (Table O2). A measure of the relative contributions of woody and non-woody land-plant tissues is given by the C/V (cinnamyl/vanillyl) ratio, which is the sum of *p*-coumaric acid plus ferulic acid concentrations divided by the sum of the three vanillyl phenols. Gymnosperm sources of land-plant residues are distinguished from angiosperm sources by the S/V (syringyl/vanillyl) ratio, which is the sum of the amounts of the three syringyl phenols divided by the sum of the vanillyl phenols.

Compound-specific isotopic compositions

Isotopic analysis of individual biomarker compounds provides a powerful source of paleoclimatic and paleoenvironmental information. Compound-specific stable isotope analysis improves identification of the biological origin of specific components within the complex mixture of materials that constitutes sediment organic matter.

Compound-specific $\delta^{13}\text{C}$ values

Studies of the $\delta^{13}\text{C}$ values of biomarkers have been especially important in tracing the evolution of C_4 plants. A shift to less negative $\delta^{13}\text{C}$ values of individual plant-wax C_{27} to C_{33} *n*-alkanes and C_{24} to C_{30} *n*-alkanols enabled Freeman and Colarusso (2001) to identify a dramatic expansion of C_4 vegetation on the Indian subcontinent between 8 and 6 Ma that has persisted to modern times. This paleoecological change reflects uplift of the Tibetan Plateau and associated growth of regional aridity.

The distinctive isotopic compositions of biomarkers from C_3 and C_4 plants also trace Holocene environmental changes. Sediments of Lake Baikal, Siberia, exhibit a 3‰ shift to more negative bulk organic matter $\delta^{13}\text{C}$ values that might record a shift from glacial-age C_4 to post-glacial C_3 plants. Brincat et al. (2000) show from $\delta^{13}\text{C}$ values of individual C_{27} to C_{31} *n*-alkanes in the sediment record that C_3 plants have remained the dominant vegetation throughout this period. Instead of recording a floral transition, the bulk organic carbon isotopic shift indicates increased fluvial delivery of isotopically light soil-derived carbon to the lake in response to a change to locally wetter post-glacial climate.

Applications of multiple biomarker compound-specific carbon isotopic measurements are especially fruitful for detailed paleoenvironmental reconstructions. Filley et al. (2001) utilize the $\delta^{13}\text{C}$ values of biomarkers from vascular plants (lignin

derivatives, C_{29} and C_{31} *n*-alkanes, C_{26} *n*-alkanol), cyanobacteria (7- and 8-methylheptadecanes), and phytoplankton (C_{17} *n*-alkane) to reconstruct the delivery of sedimentary organic matter in Mud Lake, Florida, over the past five millennia. Originally a land-plant dominated marsh, the lake evolved into a cyanobacteria-dominated system as the regional climate became more humid and the local water table rose.

Compound-specific δD values

Because the hydrogen in most organic matter originates from water, the D/H ratio in aquatic biomarker compounds is a sensitive paleohydrologic proxy. The δD of lake water can be reconstructed within 10‰ from the D/H ratios of sterols derived from phytoplankton (Sauer et al., 2001). The D/H ratios of the C_{23} *n*-alkane that is a biomarker for *Sphagnum* were used by Xie et al. (2000) to reconstruct a multi-century paleoclimatic record for Bolton Fell Moss, Cumbria, England. The δD values increase during times of warmer climate and decrease when climate was cooler as rates of evaporative distillation of bog waters increased or decreased. Similarly, Huang et al. (2002) employed δD variations in *n*-hexadecanoic acid, which is produced principally by lake algae, to reconstruct the post-glacial temperature record preserved in the sediments of Crooked Pond, Massachusetts.

Summary

Sediment organic matter provides a variety of elemental, isotopic, and molecular proxies to reconstruct past climates and ancient environments. C/N ratios identify the general origin of organic matter from aquatic or land plants. Bulk and compound-specific $\delta^{13}\text{C}$ values distinguish proportions of C_3 and C_4 plant organic matter and thereby identify periods of dry climate. Nitrogen cycling is sensitive to various environmental conditions that leave distinctive impacts on $\delta^{15}\text{N}$ values. Biomarker molecules identify organic matter contributions from specific sources, which record different environmental settings, and they provide information about depositional conditions from their alterations from precursor compounds.

Philip A. Meyers

Bibliography

- Brenner, M., Whitmore, T.J., Curtis, J.H., Hodell, D.A., and Schelske, C.L., 1999. Stable isotopes (^{13}C & ^{15}N) signatures of sedimented organic matter as indicators of historic lake trophic state. *J. Paleolimnol.*, **22**, 205–221.
- Brincat, D., Yamada, K., Ishiwatari, R., Uemura, H., and Naraoka, H., 2000. Molecular-isotopic stratigraphy of long-chain *n*-alkanes in Lake Baikal Holocene and glacial age sediments. *Org. Geochem.*, **31**, 287–294.
- Cranwell, P.A., Eglinton, G., and Robinson, N., 1987. Lipids of aquatic organisms as potential contributors to lacustrine sediments – II. *Org. Geochem.*, **11**, 513–527.
- Filley, T.R., Freeman, K.H., Bianchi, T.S., Baskaran, M., Colarusso, L.A., and Hatcher, P.G., 2001. An isotopic biogeochemical assessment of shifts in organic matter input to Holocene sediments from Mud Lake, Florida. *Org. Geochem.*, **32**, 1153–1167.
- Freeman, K.H., and Colarusso, L.A., 2001. Molecular and isotopic records of C_4 grassland expansion in the late Miocene. *Geochim. Cosmochim. Acta*, **65**, 1439–1454.
- Goossens, H., Duren, R.R., de Leeuw, J.W., and Schenck, P.A., 1989. Lipids and their mode of occurrence in bacteria and sediments-II. Lipids in the sediment of a stratified, freshwater lake. *Org. Geochem.*, **14**, 27–41.
- Griffiths, M., 1978. Specific blue-green algal carotenoids in sediments of Esthwaite water. *Limnol. Oceanogr.*, **23**, 777–784.

- Hedges, J.I., and Mann, D.C., 1979. The characterization of plant tissues by their lignin oxidation products. *Geochim. Cosmochim. Acta*, **43**, 1803–1807.
- Huang, W.-Y., and Meinschein, W.G., 1979. Sterols as ecological indicators. *Geochim. Cosmochim. Acta*, **43**, 739–745.
- Huang, Y., Shuman, B., Wang, Y., and Webb, T., 2002. Hydrogen isotope ratios of palmitic acid in lacustrine sediments record late Quaternary climate variations. *Geology*, **30**, 1103–1106.
- Meyers, P.A., and Lallier-Vergès, E., 1999. Lacustrine sedimentary organic matter records of Late Quaternary paleoclimates. *J. Paleolimnol.*, **21**, 345–372.
- Meyers, P.A., Leenheer, M.J., and Bourbonniere, R.A., 1995. Diagenesis of vascular plant organic matter components during burial in lake sediments. *Aquat. Geochem.*, **1**, 35–52.
- Nishimura, M., and Koyama, T., 1977. The occurrence of stanols in various living organisms and the behavior of sterols in contemporary sediments. *Geochim. Cosmochim. Acta*, **41**, 379–385.
- Passier, H.F., Bosch, H.J., Nijenhuis, I.A., Lourens, L.J., Böttcher, M.E., Leenders, A., Sinninghe Damsté, J.S., de Lange, G.J., and de Leeuw, J.W., 1999. Sulphidic Mediterranean surface waters during Pliocene sapropel formation. *Nature*, **397**, 146–149.
- Prahl, F.G., Muehlhasusen, L.A., and Lyle, M.A., 1989. An organic geochemical assessment of oceanographic conditions at MANOP Site C over the past 26,000 years. *Paleoceanography*, **4**, 495–510.
- Rau, G.H., Arthur, M.A., and Dean, W.E., 1987. $^{15}\text{N}/^{14}\text{N}$ variations in Cretaceous Atlantic sedimentary sequences; implication for past changes in marine nitrogen biogeochemistry. *Earth Planet. Sci. Lett.*, **82**, 269–279.
- Rieley, G., Collier, R.J., Jones, D.M., and Eglinton, G., 1991. The biogeochemistry of Ellesmere Lake, U.K. – I: source correlation of leaf wax inputs to the sedimentary record. *Org. Geochem.*, **17**, 901–912.
- Sauer, P.E., Eglinton, T.I., Hayes, J.M., Schimmelmann, A., and Sessions, A.L., 2001. Compound-specific D/H ratios of lipid biomarkers from sediments as a proxy for environmental and climatic conditions. *Geochim. Cosmochim. Acta*, **65**, 213–222.
- Schwark, L., Zink, K., and Lechterbeck, J., 2002. Reconstruction of post-glacial to early Holocene vegetation history in terrestrial Central Europe via cuticular lipid biomarkers and pollen records from lake sediments. *Geology*, **30**, 463–466.
- Struck, U., Emeis, K.C., Voss, M., Krom, M.D., and Rau, G.H., 2001. Biological productivity during sapropel S5 formation in the Eastern Mediterranean Sea: Evidence from stable isotopes on nitrogen and carbon. *Geochim. Cosmochim. Acta*, **65**, 3249–3266.
- Talbot, M.R., and Johannessen, T., 1992. A high resolution palaeoclimatic record for the last 27,500 years in tropical West Africa from the carbon and nitrogen isotopic composition of lacustrine organic matter. *Earth Planet. Sci. Lett.*, **110**, 23–37.
- Twichell, S.C., Meyers, P.A., and Diester-Haass, L., 2002. Significance of high C/N ratios in organic-carbon-rich Neogene sediments under the Benguela Current upwelling system. *Org. Geochem.*, **33**, 715–722.
- Volkman, J.K., Barrett, S.M., and Blackburn, S.I., 1999. Eustigmatophyte microalgae are potential sources of C_{29} sterols, $n\text{-C}_{23}$ – $n\text{-C}_{28}$ n-alkanoles and C_{28} – C_{32} n-alkyl diols in freshwater environments. *Org. Geochem.*, **30**, 307–318.
- Xie, S., Nott, C.J., Avsejs, L.A., Volders, F., Maddy, D., Chambers, F.M., Gledhill, A., Carter, J.F., and Evershed, R.P., 2000. Palaeoclimate records in compound-specific δD values of a lipid biomarker in ombrotrophic peat. *Org. Geochem.*, **31**, 1053–1057.
- Zink, K.-G., Leythaeuser, D., Melkonian, M., and Schwark, L., 2001. Temperature dependency of long-chain alkenone distributions in Recent to fossil limnic sediments and in lake waters. *Geochim. Cosmochim. Acta*, **65**, 253–265.

Cross-references

Alkenones
 Carbon Isotopes, Stable
 Deuterium, Deuterium Excess
 Geochemical Proxies (Non-Isotopic)
 Nitrogen Isotopes
 Paleoceanography
 Paleoclimate Proxies, an Introduction
 Paleolimnology
 Sapropels

OSTRACODES*

Introduction

Ostracodes (also ostracods, Ostracoda) are a class of bivalved, aquatic Crustacea that secrete a small (0.1 to > 2-mm long) calcitic shell (the carapace) that is commonly fossilized. Ostracodes are used widely in paleoclimatology and the reconstruction of marine and non-marine paleoenvironments because of their small size, ecological sensitivity, well-known biology and shell chemistry, long stratigraphic range (Ordovician-present), and occurrence in sediments from lakes, estuaries, bays, and oceans.

There are an estimated 33,000 described living and extinct ostracode species divided into two subclasses, the Myodocopa and Podocopa, and 10 orders distinguished from one another on the basis of appendages and carapace features such as size, shape, muscle scar pattern, pore patterns, and hinge structure. Many Myodocopids are pelagic in habitat; some are non-calcitic and are rarely fossilized. The Podocopa includes the order Podocopida, (Figures O29 and O30), which are the most commonly fossilized ostracode group and the most applicable to paleoclimatology.

Morphology and ecology

The carapace consists of two valves articulated along the dorsal margin, encompasses the living animal, and forms part of the organism's cuticle, which is secreted by the epidermis. Ostracodes grow by molting (ecdysis), during which podocopids produce 8–9 molts or instars. Both adult and juvenile carapaces and valves are commonly fossilized. Most ostracode genera and species can be identified on the basis of external and internal carapace features, although examination of soft parts is necessary to identify species in some groups and recent genetic studies have added considerably to understanding ostracode taxonomy.

Most species are free-living (either benthonic or pelagic), move by crawling or swimming, reproduce sexually (a few are parthenogenic), and disperse passively (there is no planktonic larval stage). They inhabit a full range of aquatic environments from small ephemeral pools of water, groundwater, to all types of lakes, estuaries, bays, rivers, and oceanic environments. Species are adapted to specific microhabitat conditions and physical and chemical factors controlling species distribution include temperature, salinity, light availability, solute chemistry, alkalinity, oxygen and carbon dioxide levels, and food resources.

Application to paleoclimatology and paleoenvironments

The ecological sensitivity of living species has made ostracodes useful for paleoenvironmental reconstruction since the nineteenth Century, especially in studies of Quaternary sediments where living species are often found as fossils. Quantitative analyses of faunal assemblages and indicator species have been used extensively to reconstruct water solute composition and regional atmospheric conditions in lakes, salinity and submerged aquatic vegetation in estuaries, ocean temperatures on continental shelves, dissolved oxygen on continental slopes, and deep water masses in abyssal environments.

During the past decade, the application of ostracode shell chemistry to contemporary issues surrounding climate variability has accelerated rapidly, especially in paleolimnology

*All rights reserved

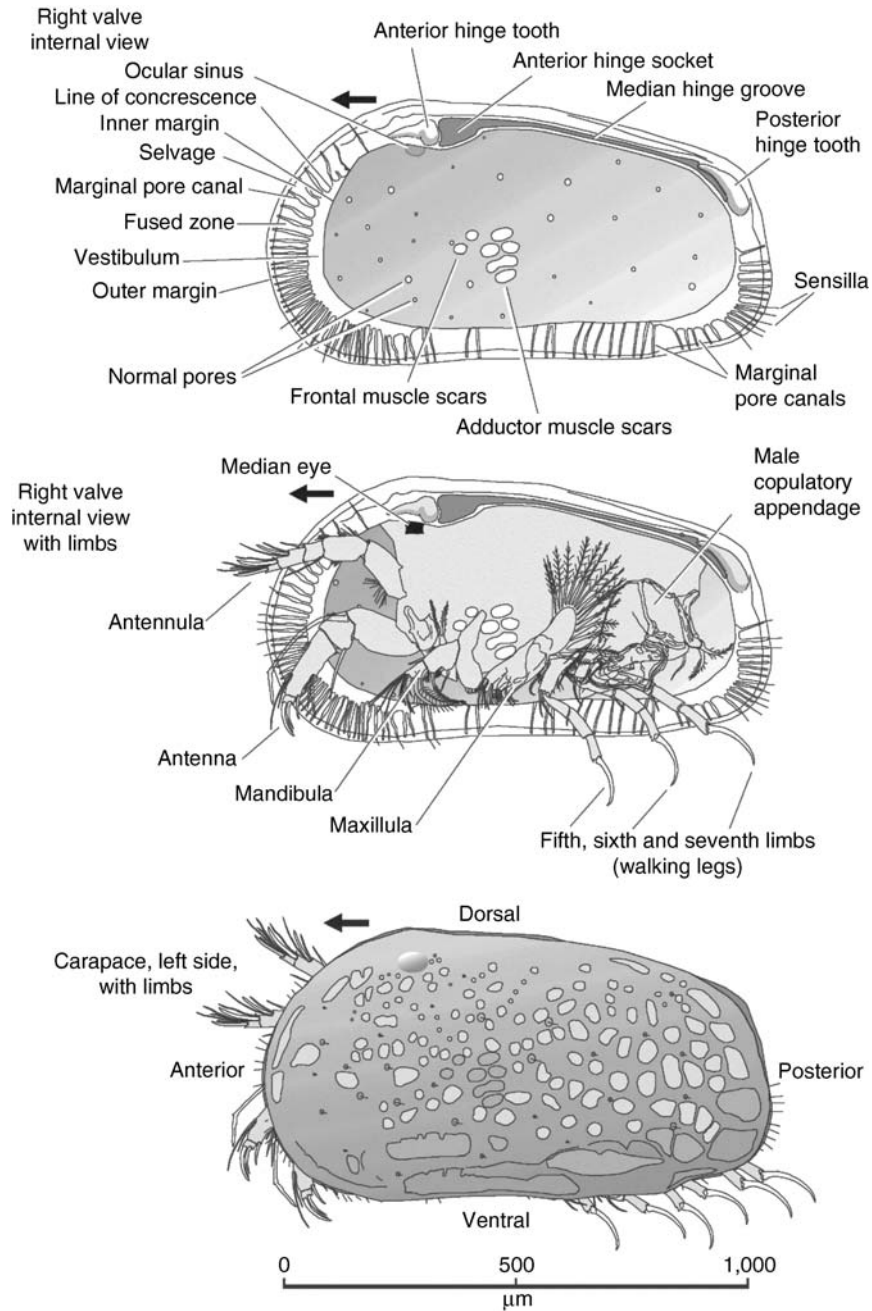


Figure O29 Morphology of Podocopid ostracode *Hemicythere villosa* (courtesy of David J. Horne).

because ostracodes are usually the only calcitic microfossil group. With greatly improved understanding of the factors that control the trace element (magnesium/calcium, strontium/calcium ratios) and stable isotopic (oxygen and carbon) composition of the carapace, ostracode researchers have been able to quantify temporal changes in lake and ocean temperature, atmospheric temperature and precipitation, estuarine and bay salinity, and other climate-related parameters (see review papers in Holmes and Chivas, 2002). For example, in semi-arid to subhumid, hydrologically-closed lakes, precipitation

influences the salinity, solute chemistry and $^{18}\text{O}/^{16}\text{O}$ ratios of the water. Chivas et al. (1993) applied these relationships to infer salinity and evaporation changes in Lake Keilambete, Australia during the late Quaternary using a $\delta^{18}\text{O}$ isotopic record and Sr/Ca ratios for several ostracode species. In deep lakes, ostracode shell chemistry can provide a record of atmospheric temperature. Von Grafenstein et al. (1999) reconstructed decadal scale changes in atmospheric temperature from the $\delta^{18}\text{O}$ record of *Candona* from the Ammersee, Germany for the important glacial, deglacial and Holocene



Figure O30 Scanning electron photo of deep sea ostracode *Bradleya*. Left valve, 1.0 mm long.

interval, and showed a remarkable correspondence to the paleotemperature record from Greenland ice cores. Wansard (1996) also reconstructed summer temperatures from Lake Banyoles, Spain for the interval 30,000–6,000 years ago using Mg/Ca ratios in *Cyprideis*.

Ostracode shell chemistry has also been applied to shallow water paleoclimate records. In the Gulf of Carpentaria, northern Australia, DeDecker et al. (1988) reconstructed the late Quaternary salinity changes caused by changing sea level from Mg/Ca, Sr/Ca and $^{87}\text{Sr}/^{86}\text{Sr}$ ratios of *Cyprideis*. Dwyer et al. (2001) showed that salinity influences Mg/Ca ratios in Florida Bay, which allowed them to reconstruct paleosalinity history controlled by climate processes such as the El Niño–Southern Oscillation. In Chesapeake Bay, eastern North America, water temperature controls the Mg/Ca ratios in *Loxoconcha* and Cronin et al. (2003) reconstructed a 2,200-year bay temperature record. In the deep sea, studies by Dwyer et al. (1995, 2000), Cronin et al. (2000), and Didié and Bauch (2002) provide evidence from ostracode shell chemistry for Pliocene and Quaternary variability in deep-sea temperatures, associating them with orbital and suborbital control of deep-water formation.

Thomas M. Cronin

Bibliography

- Chivas, A.R., De Deckker, P., Cali, J.A., Chapman, A., Kiss, E., and Shelley, J.M.G., 1993. Coupled stable isotope and trace-element measurements of lacustrine carbonates as paleoclimatic indicators. In Swart, P.K., Lohmann, K.C., McKenzie, J., and Savin S. (eds.), *Climate Change in Continental Isotopic Records*, Washington, USA: American Geophysical Union, pp. 113–121.
- Cronin, T.M., Dwyer, G.S., Baker, P.A., Rodriguez-Lazaro, J., and DeMartino, D.M., 2000. Orbital and suborbital variability in North Atlantic bottom water temperature obtained from deep-sea ostracode Mg/Ca ratios. *Palaeogeogr. Palaeoecol. Palaeoclimatol.*, **162**, 45–57.
- Cronin, T.M., Dwyer, G.S., Kamiya, T., Schwede, S., and Willard, D.A., 2003. Medieval warm period, Little Ice Age and 20th century temperature variability from Chesapeake Bay. *Glob. Planet. Change*, **36** (1–2), 17–29.
- DeDeckker, P., Chivas, A.R., Shelley, J.M.G., and Torgersen, T., 1988. Ostracod shell chemistry: A new palaeoenvironmental indicator applied to a regressive/transgressive record from the Gulf of Carpentaria, Australia. *Palaeogeogr. Palaeoclimatol. Palaeoecol.*, **66**, 231–241.
- Didié, C., and Bauch, H.A., 2002. Implications of Upper Quaternary stable isotope records of marine ostracodes and benthic foraminifers for paleoecological and paleoceanographical investigations. In Holmes, J.A., and Chivas, A.R. (eds.), *The Ostracoda: Applications in Quaternary Research*. Washington, USA: American Geophysical Union, pp. 279–299.
- Dwyer, G.S., and Cronin, T.M., 2001. Ostracode shell chemistry as a paleosalinity proxy in Florida Bay. In Wardlaw, B. (ed.), *Bulletins of American Paleontology No. 361*, pp. 249–276.
- Dwyer, G.S., Cronin, T.M., Baker, P.A., Raymo, M.E., Buzas, J., and Corrège, T., 1995. Late Pliocene and Quaternary bottom water temperature change in the deep North Atlantic. *Science*, **270**, 1347–1351.
- Dwyer, G.S., Cronin, T.M., Baker, P.A., and Rodriguez-Lazaro, J., 2000. Changes in North Atlantic deep-sea temperature during climatic fluctuations of the last 25,000 years based on ostracode Mg/Ca ratios. *Geochem. Geophys. Geosyst.*, **1**(12): (doi:10.1029/2000GC000046).
- Holmes, J.A., and Chivas, A.R. (eds.), 2002. *The Ostracoda: Applications in Quaternary Research*. Washington, USA: American Geophysical Union, 313pp.
- Von Grafenstein, U., Erlenkeuser, H., Brauer, A., Jouzel, J., and Johnsen, S.J., 1999. A mid-European decadal isotope-climate record from 15,500 to 5,000 years BP. *Science*, **284**, 1654–1657.
- Wansard, G., 1996. Quantification of paleotemperature changes during isotopic stage 2 in the La Draga continental sequence (NE Spain) based on the Mg/Ca ratio of freshwater ostracods. *Quaternary Sci. Rev.*, **15**, 237–245.

Cross-references

[Geochemical Proxies \(non-isotopic\)](#)
[Oxygen Isotopes](#)
[Paleolimnology](#)
[Paleotemperatures and Proxy Reconstructions](#)
[Strontium Isotopes](#)

OUTWASH PLAINS

Outwash plains are extensive areas of glaciofluvial sediments deposited in the proglacial zone. They occur in topographically unconfined locations, such as the margins of ice sheets or piedmont glaciers, distinct from the valley trains or valley bottom deposits that occur in front of valley glaciers in confined settings. The Icelandic term “Sandur” (plural: Sandar) is often used.

Sediment is deposited primarily by braided meltwater streams that migrate across the surface of the outwash plain. The whole plain is rarely covered all at once except during extreme jökulhlaup floods. During floods, previously deposited sediments may be reworked and redeposited. Outwash deposits can retain sedimentological signatures of long periods of discharge from the glacier, making it possible to judge the relative significance of ablation dominated discharge and discharge related to extraordinary events such as subglacial volcanic eruptions as in Iceland. Outwash plains that are periodically inundated by floods exhibit distinctive sediment structures.

Outwash plains can aggrade to thicknesses of several hundred meters and bury the snout of the glacier from which the meltwater and sediment are derived. Melting of buried ice can then lead to the formation of kettles and pitted outwash surfaces, and rapid retreat of the ice margin can leave a distinctive ice-contact slope at the head of the outwash plain. Fluctuations in meltwater discharge or supply of sediment can cause changes in the rate of aggradation, and incision can occur creating terraces in the outwash surface.

Close to the glacier, sediments are often coarse grained and poorly sorted, with sub-angular clasts. Farther from the glacier sediments are characteristically finer grained and better sorted with more rounded clasts.

Sedimentary structures within the outwash can reveal details of flow regimes and sedimentary processes, can help to reconstruct paleodischarges, and can help to unravel the dynamic history of the glacier from which they are derived Benn and Erans (1998) provide a useful review of this topic.

Peter G. Knight

Bibliography

Benn, D.I., and Evans, D.J.A., 1998. *Glaciers and Glaciation*. London, UK: Arnold, 734pp.

Cross-references

Glacial Geomorphology
Glacial Sediments
Kettles

OXYGEN ISOTOPES

Natural occurrence

Oxygen has three stable isotopes with atomic mass numbers of 16, 17, and 18 (^{16}O , ^{17}O and ^{18}O), which occur naturally in relative proportions of 99.76%, 0.04%, and 0.2%, respectively. Because ^{17}O and ^{18}O fractionate (to a first order) proportionally with respect to ^{16}O , and because of the very small abundance of ^{17}O , the isotopic ratio $^{18}\text{O}/^{16}\text{O}$ ($\sim 1/500$) is most commonly measured in water (e.g., groundwater, ice), carbonate sediments (CaCO_3), oxygen gas (O_2), carbon dioxide (CO_2), and organic matter, in which the $^{18}\text{O}/^{16}\text{O}$ ratio varies by more than 100%.

The $^{18}\text{O}/^{16}\text{O}$ ratio of a sample is measured by mass spectrometry on CO_2 or O_2 . The isotopic composition is usually expressed relative to a standard (which depends on the measured material) and expressed with the δ notation:

$$\delta^{18}\text{O} = \left[\frac{(^{18}\text{O}/^{16}\text{O})_{\text{Sample}}}{(^{18}\text{O}/^{16}\text{O})_{\text{Standard}}} - 1 \right] (\times 1,000, \text{ per mil}) \quad (1)$$

Atmospheric fractionation and local temperature control of the isotopic composition

Isotopic fractionation occurs during water evaporation and condensation (processes 1, 2 and 3 in Figure O31). At equilibrium, the $^{18}\text{O}/^{16}\text{O}$ ratio in the condensed phase (liquid or solid) is higher by approximately 10 per mil as compared to the vapor phase. In the hydrological cycle, water is mostly fractionated in the atmosphere during the net transport of vapor between low to high latitudes, ocean to continents, or low to high elevations, as a result of successive condensation–evaporation stages (Dansgaard, 1964). At each stage, the isotopic enrichment of the condensate depletes the remaining vapor in ^{18}O as compared to ^{16}O (Figure O32, and process 3 in Figure O31), and this results in more depleted precipitation at the next condensation stage. In this process of distillation, the isotopic depletion of the vapor is primarily related to its exhaustion (quantity of remaining vapor compared to the initial quantity). Multivariate analyses of the $^{18}\text{O}/^{16}\text{O}$ ratio in modern precipitation have shown that the main parameters controlling this depletion are the local temperature, the quantity of precipitation, the distance to the coast, and the elevation (Figure O33). The corresponding effects have been coined “temperature effect,” “amount effect,” “continental effect,” and “altitude

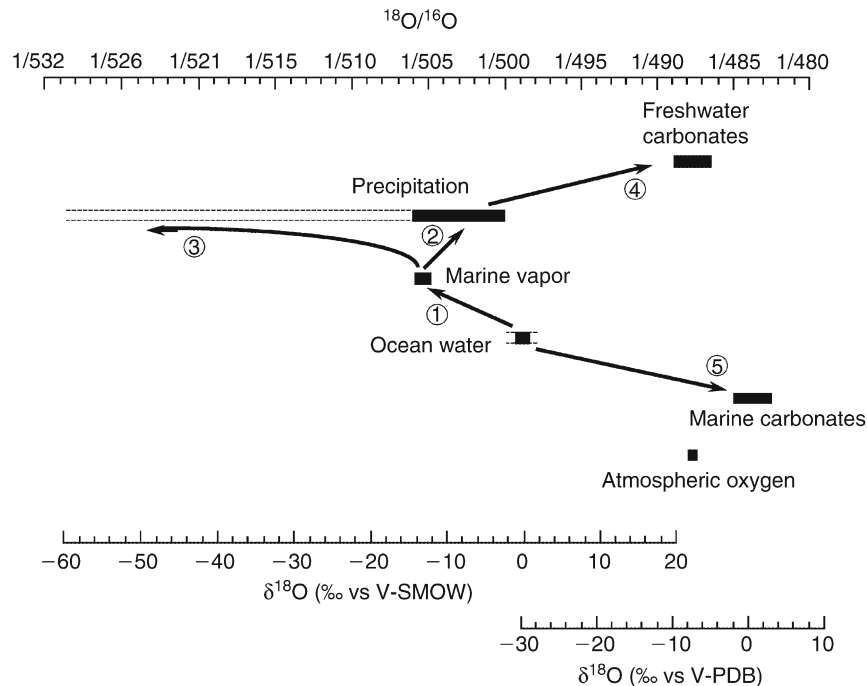


Figure O31 Range of the isotopic composition of oxygen at the surface, and relationships between the different compositions.

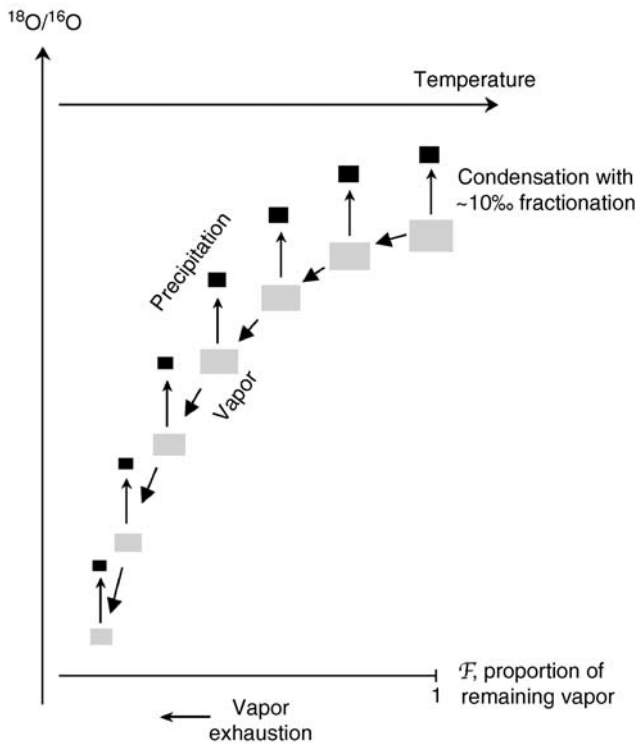


Figure O32 Isotopic evolution of a vapor mass, modeled as a Rayleigh-type distillation: an initial vapor mass is exhausted by successive condensation stages, for instance during an advection to higher latitude. At each stage, the $^{18}\text{O}/^{16}\text{O}$ ratio of the condensate is enriched by $\sim 10\text{‰}$ compared to the vapor ratio, which depletes the remaining vapor. F is the fraction of remaining vapor.

effect.” This isotopic depletion in the atmosphere determines the composition of the water reservoirs on the Earth, from the ocean to the cryosphere. See Mook (2001) for a thorough exposition of the environmental isotopes.

When minerals like carbonate, phosphate, and silica, which constitute sediments, form in water, their $^{18}\text{O}/^{16}\text{O}$ ratios are fractionated with respect to the water ratio, a fractionation mainly controlled by temperature (Epstein et al., 1953). Hence, fossil water, mainly ice and groundwater, as well as sediments, represent potential archives of information regarding past climates and environments.

Precipitation and the isotopic thermometer

The first primary standard for water was the Standard Mean Ocean Water (SMOW; Craig, 1961a,b). Because of problems with its definition, the International Atomic Energy Agency (IAEA) defined the Vienna Standard Mean Ocean Water (V-SMOW), with an isotopic composition very close to SMOW, and prepared in a large amount such that it is still distributed to laboratories today. Its absolute $^{18}\text{O}/^{16}\text{O}$ atomic ratio is $2,005.20 (\pm 0.45) \times 10^{-6}$ (Baertschi, 1976). This composition has been chosen to be very close to the oceanic composition. As such, most precipitation has a much lower $^{18}\text{O}/^{16}\text{O}$ ratio (Figure O31 and O33), and secondary, more depleted, standards are used for their measurements. IAEA now recommends that isotopic measurements on water be expressed with respect to V-SMOW, and normalized on a two-standard scale, V-SMOW and SLAP (Standard Light Antarctic Precipitation), assuming a value $\delta^{18}\text{O} = -55.5\text{‰}$ for SLAP (Coplen, 1995).

The usual measurement technique is to equilibrate a small amount of CO_2 gas with each water sample, and to determine the isotopic composition of this CO_2 by mass spectrometry. This technique requires only a few milliliters of water. The

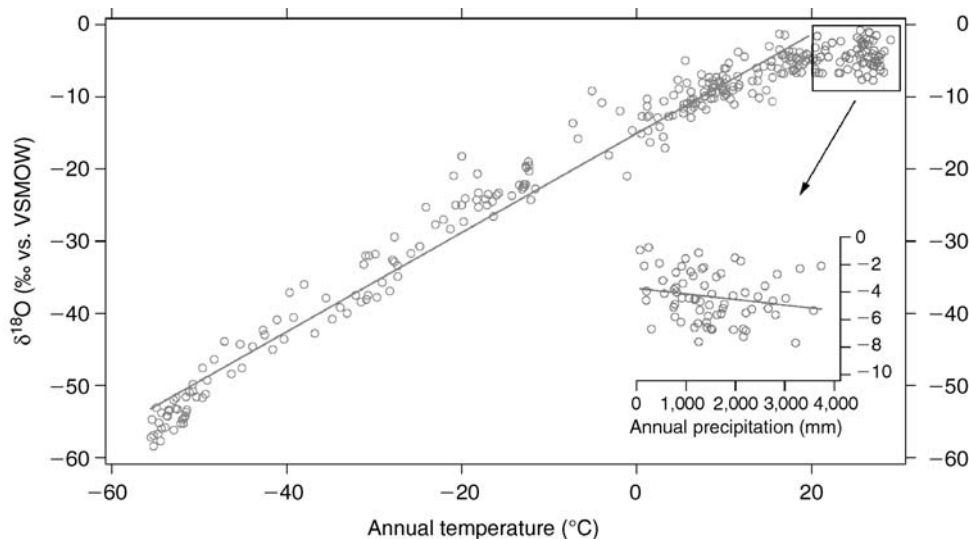


Figure O33 $\delta^{18}\text{O}$ – surface temperature relationship for modern precipitation (annual averages) (data from the GNIP network Rozanski et al., 1993), augmented by some polar data (cf. Figure O34). The linear correlation is calculated for points with an annual temperature $< 20^\circ\text{C}$ ($N = 243$ points, $r = 0.987$). The insert shows the annual $\delta^{18}\text{O}$ – precipitation relationship (“amount effect”) for stations with annual temperature $> 20^\circ\text{C}$.

sample composition is measured with respect to a reference sample, which has been previously calibrated against V-SMOW. Both samples are measured under the same conditions, so that a correction for the gas–water fractionation does not have to be applied. This technique usually achieves a precision better than 0.1‰, but with lower accuracy, as shown from interlaboratory comparisons organized by IAEA. Other techniques have been developed, like water hydrolysis and laser spectrometry.

The isotopic composition of precipitation is imprinted, more or less directly, in many continental records like glacier ice, snow, groundwaters, tree rings, freshwater carbonates, speleothems, etc. The discussion below focuses on ice, but may be extended in a similar way to the other archives (see below).

Isotopic measurements on precipitation have been shown to correlate strongly with surface temperature at mid-to-high latitudes, and with the amount of precipitation at low latitudes, the so-called “amount effect” (Figure O33; Dansgaard, 1964; Rozanski et al., 1993). The isotope–temperature relationship can be described with the vapor exhaustion, as shown by a simple distillation model (batch distillation, also called “Rayleigh distillation”: Figure O32; Dansgaard, 1964). The modeling of this relationship can be improved by considering other secondary parameters, like the proportion of different water phases in the clouds (vapor, liquid, and solid water), evaporation of the falling droplets (especially for the “amount effect”); and kinetic fractionation during the formation of snow (Jouzel and Merlivat, 1984).

The observed correlation between $\delta^{18}\text{O}$ and temperature (Figure O33) is strongest for annual means, and in polar regions (Figure O34). It is based on different stations, and thus a spatial gradient $\Delta\delta^{18}\text{O}/\Delta T$ is defined, where Δ is a variation over space. This gradient is traditionally used to interpret isotopic variations (e.g., in the ice) in terms of past temperature, and has been called the “isotopic paleothermometer” (Figure O34). Yet, a temporal gradient $\Delta\delta^{18}\text{O}/\Delta T$ must be used to interpret past isotopic variations, where Δ is a variation, at one location, over the timescale of the considered climatic variations. In recent years, estimates of temperature variations in Central Greenland

have been achieved independently of $\delta^{18}\text{O}$. They have shown that, over the last glacial period, the isotopic paleothermometer underestimates past temperature variations by a factor of two; that is, the temporal gradient is about half the spatial one (Cuffey et al., 1995; Jouzel, 1999). So far, there is no evidence for such a strong bias in East Antarctica records (Jouzel et al., 2003). The difficulty in interpreting past $\delta^{18}\text{O}$ variations thus consists in determining the relevant temporal $\delta^{18}\text{O}$ –temperature gradient, because a number of climatic parameters can cause this gradient to differ from the spatial gradient. Some of these parameters are briefly described below; a thorough review can be found in Jouzel et al. (1997).

The origin of the temperature–isotope relationship in precipitation has to be determined for each case. The $\delta^{18}\text{O}$ of the condensate is determined by both the vapor $\delta^{18}\text{O}$ and the local temperature at the condensation level, T_c . Over the year, temperatures at the surface (T_s) and at the condensation level (T_c) may well correlate during precipitation events, particularly in polar regions. For Antarctica, a linear relationship $T_c = 0.67 \times T_s - 1.2$ has been observed (Jouzel and Merlivat, 1984). This justifies the use of the surface temperature T_s , rather than T_c , in the paleothermometer, and alternatively may help explain some bias of this thermometer if the correlation between T_s and T_c has not held through climatic changes.

The $\delta^{18}\text{O}$ of the vapor, before condensation, mainly depends on the fraction of remaining vapor (f in Figure O32). To a first order approximation, as shown by simple modeling, this fraction is somehow determined by the difference between the temperature of the remote vapor source and the temperature at the location of precipitation. This is so because the temperature governs the quantity of vapor the air can hold (specific humidity). Thus, interpreting a $\delta^{18}\text{O}$ record in terms of local temperature changes only requires that the remote (source) temperature has remained constant in time. For instance, Aristarain et al. (1986) analyzed snow from the Antarctic Peninsula and showed that, given that the precipitation originates in the Southern Ocean, a covariation of the local and oceanic temperatures can explain a temporal gradient

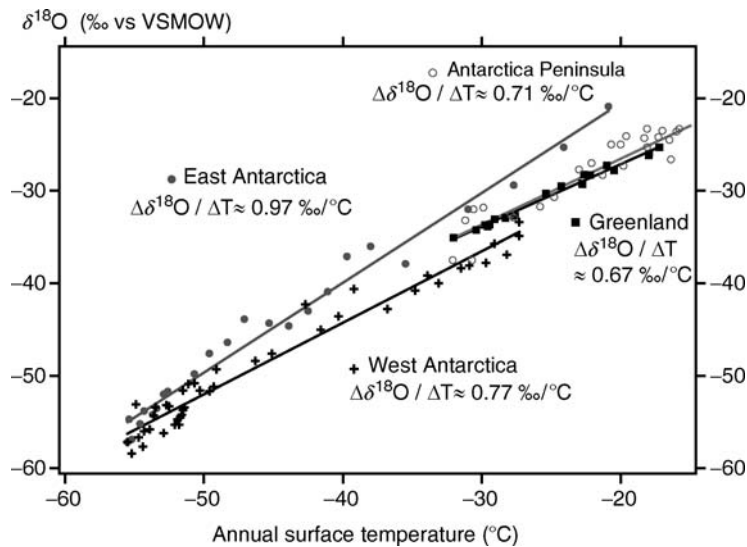


Figure O34 Isotopic paleothermometer for polar stations: data from Dahe et al. (1994) for Antarctica, and Johnsen et al. (1989) for Greenland.

$\Delta\delta^{18}\text{O}/\Delta T$ lower by a factor of two than that of the observed spatial slope. A way to check the temperature stability of the precipitation source is provided by the deuterium-excess, a second-order isotopic parameter measured in precipitation (Jouzel and Merlivat, 1984). To a first order, the isotopic composition of hydrogen in the water (δD , see *Deuterium, deuterium excess*) is linearly related to the composition of oxygen, $\delta^{18}\text{O}$, because both vary similarly with temperature; thus, combining $\delta^{18}\text{O}$ and δD gives access to other climatic parameters.

It is also important to consider that each isotopic measure from an archive results from the accumulation of many precipitation events, and is thus a weighted average, usually over several months or years. If the accumulation is not evenly distributed over the year, the temperature record may be biased towards one particular season. For Central Greenland, modeling studies have shown that the contribution of the warm season to the yearly accumulation may have been more important during glacial periods than today (Krinner et al., 1997). This would bias the glacial $\delta^{18}\text{O}$ signal towards warmer temperature, and may explain why the temporal gradient $\Delta\delta^{18}\text{O}/\Delta T$ is lower than the spatial gradient (cf. supra).

At low latitudes, the $\delta^{18}\text{O}$ depends less on temperature and more on the quantity of precipitation (Figure O33), which is called the “amount effect.” The isotopic signal may be interpreted in terms of hydrologic changes, especially in the monsoon area.

The isotopic record of carbonate sediments

Carbonate isotopic fractionation and the temperature scale

Carbonate is a widely distributed sediment, usually of biogenic origin, and for this reason it is also the most frequently used to retrieve a climatic signal routinely from the ^{18}O composition. The climatic interpretation of the carbonate $\delta^{18}\text{O}$ signal is based on the pioneering work done by Harold C. Urey, Samuel Epstein, Cesare Emiliani, and their colleagues at the University of Chicago. They developed the concept of paleothermometry, and defined the first isotopic reference, a belemnite from the Peedee formation in South Carolina, called PDB. The isotopic ratio is measured with a mass spectrometer directly on the CO_2 degassed by reaction with pure H_3PO_4 (McCrea, 1950). For PDB, this isotopic ratio is $2,067.2 \times 10^{-6}$ (Figure O31). From measurements of the isotopic fractionation between water and carbonate, they demonstrated the potential of fossil carbonate to record environmental parameters (Urey, 1947; McCrea, 1950), especially temperature: newly formed carbonate records the isotopic composition of the water, accounting for an isotopic fractionation that is temperature-dependent. Epstein et al. (1953) calibrated a temperature equation on living mollusks, based on the isotopic composition of the carbonate (δ_c) and of the water (δ_w):

$$t = 16.5 - 4.3 \times (\delta_c - \delta_w) + 0.14 \times (\delta_c - \delta_w)^2 \quad (2)$$

with t in $^\circ\text{C}$ and the δ in per mil with respect to VPDB. Applying this equation to a long marine record, Emiliani (1955) pioneered the use of $\delta^{18}\text{O}$ in paleoceanography. Due to a shortage in PDB, IAEA defined the Vienna Peedee Belemnite (V-PDB) reference with respect to the standard of the National Bureau of Standard NBS-19 as: $\delta^{18}\text{O}_{\text{NBS19}/\text{VPDB}} = -2.2\text{‰}$. The reference material currently distributed to laboratories is NBS-19.

Isotopic records and stratigraphy for the last million years

The paleotemperature equation (Equation 2) is applied to carbonate shells secreted by planktonic or benthic micro-organisms like foraminifera, coccolithophoridae, which are found in marine sediments retrieved by deep sea coring. It is also applied to other organic carbonate found in marine as well as freshwater environments, like corals, mollusks, etc. (Figure O31, processes 4 and 5), and to inorganic carbonates like speleothems. Comparison between inorganically and organically precipitated calcite has shown a fair agreement for the isotopic fractionation of oxygen, suggesting that, to a first order, organic carbonate precipitates close to equilibrium with the surrounding water. Yet, the temperature dependence of this fractionation (Equation 2) has been recalibrated several times on different species to account for small departures from equilibrium (Wefer and Berger, 1991; Bemis et al., 1998). This temperature dependence is approximately -0.25 per mil of δ_c per $^\circ\text{C}$, or -4 $^\circ\text{C}$ per mil of δ_c . Equation 2 also shows that, for a constant temperature, a 1 per mil variation of δ_w is equivalent to a 4 $^\circ\text{C}$ change. Over the last million years, which have been dominated by glacial cycles, both temperature and sea water composition have changed, with similar effects on the isotopic record. The marine glacial cooling of a few degrees has increased fractionation by around 1 per mil, while stocking up water in wide ice sheets has also enriched δ_w (and thus δ_c) by 1 per mil. This amplification of global climatic changes explains the similarity of isotopic records retrieved from different oceanic regions, which underlies the so-called oxygen isotope stratigraphy: periodic $\delta^{18}\text{O}$ up-and-downs are matched between records and numbered, with odd and even numbers corresponding to warm and cold periods, respectively (Figure O35). The SPECMAP group (Imbrie et al., 1984) compiled a global $\delta^{18}\text{O}$ signal by retaining the most significant excursions of different records. The final objective of SPECMAP was to produce a common temporal framework in order to date other records. The absolute dating of this framework has been a difficult task. Magnetic reversals detected in the sediments are widely used, the youngest one being the Brunhes-Matuyama about 780,000 years ago. Sea level markers like coral terraces are also used, since sea level variations are imprinted in the marine isotopic signal. Spectral analysis of the isotopic records have proved their origin in the variations of the Earth orbit (Hays et al., 1976), confirming the astronomical theory of glacial cycles. A dating technique derived from this confirmation, called “orbital tuning,” consists in tuning the age of a record to the orbital configurations, assuming some relationships between them.

The marine $\delta^{18}\text{O}$ signal: temperature and ice volume

The marine carbonates record both variations of water temperature and of water $\delta^{18}\text{O}$. The latter is conceptually divided into a global and a local component. The global component affects the quantity of ^{18}O of the ocean as a whole, on a timescale longer than the ocean mixing time so that it is expected to be homogeneous. This is due to fluctuations of the ice sheet volume, which extract or release isotopically depleted water from or to the oceans (Figure O31). On timescales longer than hundred million years, an imbalance in the ^{18}O oceanic budget is also possible (Lécuyer and Allemand, 1999). The local component affects the spatial distribution of ^{18}O . For the surface, this is mainly due to hydrological

conditions: precipitation-minus-evaporation budget, plus any continental contribution (runoff, iceberg discharge, etc.). Because salinity is also sensitive to this hydrological budget, a good correlation is observed between both tracers (Craig and Gordon, 1965; Figure O36). For this reason, the local component of $\delta^{18}\text{O}$ variation has been coined the “salinity effect,” in addition to the global “ice volume” effect. The $\delta^{18}\text{O}$ distribution is also modified by changes in the ocean circulation, by mixing the different water masses and altering their isotopic fingerprint. Table O3 sums up the different interpretations of a sediment $\delta^{18}\text{O}$ signal.

The “ice volume” effect is related to the decrease of the global oceanic mass M_0 during the growth of ice sheets with

a mean isotopic composition $\delta^{18}\text{O}_i$. At steady state, the conservation of the ^{18}O mass between the remaining oceanic mass M and the additional mass dM of the ice sheets reads:

$$M \times \delta^{18}\text{O}_s + dM \times \delta^{18}\text{O}_i = M_0 \times \delta^{18}\text{O}_{s0}, \quad (3)$$

where the subscripts s and i stand for sea and ice sheet, respectively, and 0 for the time before the growth of ice sheets. dM is expressed relative to ocean mass because it is then comparable to the eustatic sea level change. The global oceanic $\delta^{18}\text{O}$ variation (“ice volume effect”) is then:

$$\delta^{18}\text{O}_s - \delta^{18}\text{O}_{s0} = dM/M \times (\delta^{18}\text{O}_{s0} - \delta^{18}\text{O}_i). \quad (4)$$

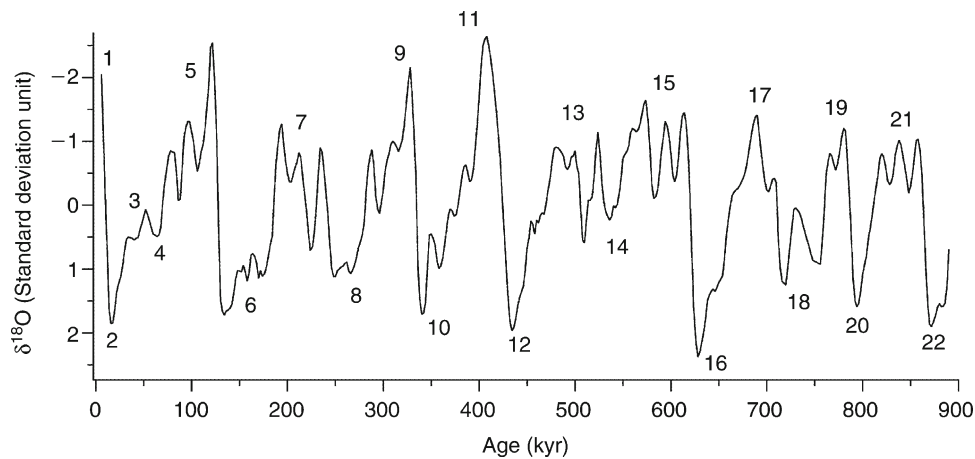


Figure O35 Isotopic stack over the past 900,000 years (after Bassinot et al., 1994), representative of the global ocean variations. Note the usual inverted y-axis, so that an upward excursion corresponds to a warming, and conversely. The $\delta^{18}\text{O}$ values have been scaled so that the record has an average of 0 (centered) and a standard deviation of 1. The marine isotopic stages (MIS) are numbered in *bold*: odd numbers for warm stages, even numbers for cold ones.

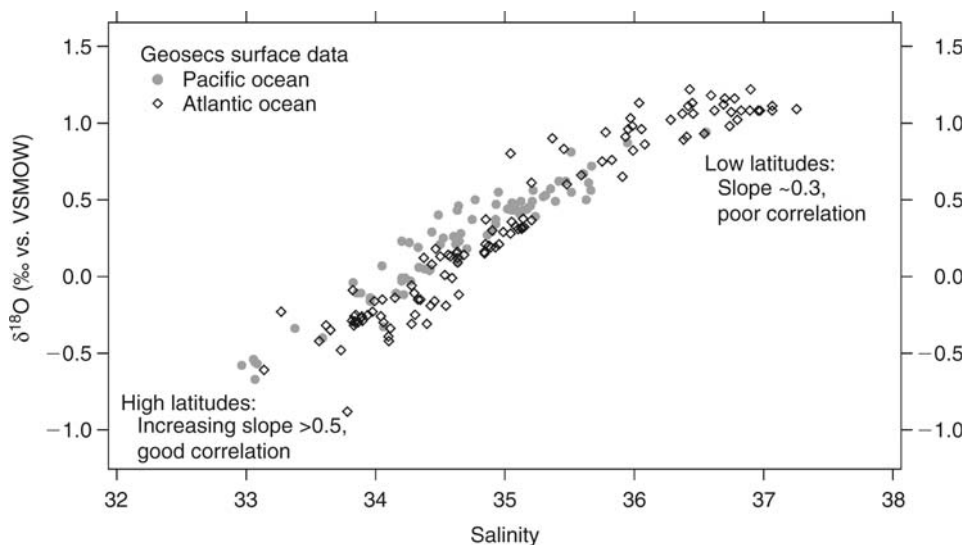


Figure O36 Relationships between surface salinity and water $\delta^{18}\text{O}$ for the Atlantic and Pacific Oceans, due to the common dependence on the hydrological cycle. Note also the highest values in the tropical Atlantic, due to a net transfer of vapor to the Pacific (GEOSECS data from Östlund et al., 1987).

For the Last Glacial Maximum, the variation $\delta^{18}\text{O}_s - \delta^{18}\text{O}_{s0}$ is estimated directly from benthic foraminifera records (Labeyrie et al., 1987) and pore water analyses (Schrag et al., 1996), with a current consensus value ranging between 1 and 1.3‰. Ice sheet growth dM is estimated from changes in coral terrace levels, and from modeling the ice sheet distribution and isostatic rebound. It is equivalent to approximately 120–140 m of sea level (thus, $dM/M \sim 130/4,000$). These values are consistent with a mean ice composition $\delta^{18}\text{O}_i$ between -30 and -50 ‰ (Mix et al., 2001). All these estimates are biased; for instance, the benthic foraminifera record approximates the $\delta^{18}\text{O}_s - \delta^{18}\text{O}_{s0}$ difference because the temperature of their deep environment has changed. Thus, only the combination of these different approaches is able to reduce the uncertainties in each term in Equation 4. Over the Cenozoic, the past 65 million years, the marine $\delta^{18}\text{O}$ record shows a consistent increase of about 5 per mil (Figure O37), an amplitude too large to be interpreted by the waning and waxing of ice sheets. This long positive trend is interpreted as a global ocean cooling by 7°C over the Eocene. Increasing steps around 33 Ma and 15 Ma

ago are interpreted as corresponding to the building up of the Antarctic ice sheet (for a total of about 1.2‰) and the Northern Hemisphere ice sheet around 3 Ma ago (Zachos et al., 2001).

On longer timescales, reliable marine oxygen records are difficult to produce because of the scarcity of sediments, and because the likelihood that the sediments have been altered and re-equilibrated under different environmental conditions increases dramatically. A case study is provided by reconstructions of climatic conditions during the Cretaceous and Early Cenozoic periods. Different proxies, including marine $\delta^{18}\text{O}$, point to a globally warmer climate, consistent with a higher atmospheric CO_2 level, except in the tropics where interpretation of marine $\delta^{18}\text{O}$ records points to temperatures as warm as today or even cooler. This contradiction seems to be due to an alteration of the isotopic signal during diagenesis (Pearson et al., 2001). Over the Paleozoic (timescale of hundreds of millions of years), isotopic data display an increasing isotopic trend of ~ 8 ‰, but its origin could be a long term cooling, a diagenetic alteration, or even an ^{18}O enrichment of the global ocean, among other possibilities (Veizer et al., 1999).

Table O3 Basic interpretation of $\delta^{18}\text{O}$ signal recorded in biogenic sediments

Interpretation	Main origin in variations of	How to isolate it	Original reference
Temperature	Water temperature (also: living depth, etc.)	Subtract the global ice signal, assuming no local seawater change	Shackleton, 1967
Water $\delta^{18}\text{O}$			
Global component	Ice sheet volume	Assume no temperature change (e.g., in benthic foraminifera)	Labeyrie et al., 1987
Local component	Local hydrological balance ("salinity effect") (also: water mass mixing)	Subtract the global ice signal plus an independent estimate of temperature change	Duplessy et al., 1991
Biological bias ("vital effect")	Non-equilibrium biogenic fractionation (also: growth rate, secondary calcification, diagenetic exchange, etc.)	Isotopic measurements on living organisms in known conditions (collection with tows; culture)	Epstein et al., 1953

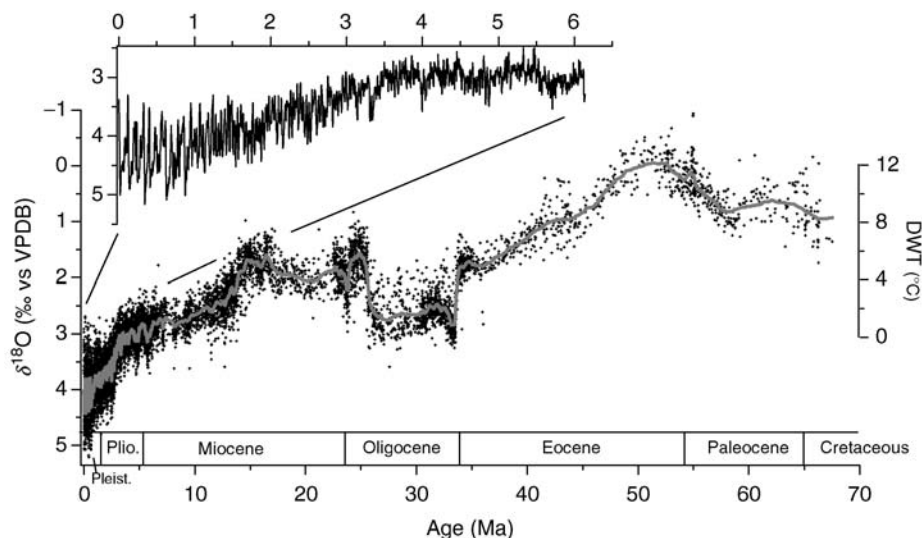


Figure O37 Trend of the deep ocean $\delta^{18}\text{O}$ over the Cenozoic (last 70 Myr), compiled from benthic records (Zachos et al., 2001). The close-up shows the last 6 Myr. The measured $\delta^{18}\text{O}$ values have been adjusted to approximate the water value. The Deep Water Temperature (DWT) scale (right side) has been calculated by considering a marine $\delta^{18}\text{O}$ of -1.2 before the appearance of ice sheets (before ~ 35 Ma).

Still, positive excursions lasting tens of million years have been contemporaneous with periods of cooling or large glaciations, and seem to be of climatic origin.

Bias on the sediment $\delta^{18}\text{O}$ record

Comparisons have been performed between known environmental conditions (temperature and water $\delta^{18}\text{O}$) and the $\delta^{18}\text{O}$ of living shells, from either tow fishing or aquarium cultures. First, some species appear to calcify out of isotopic equilibrium with water, possibly due to kinetic bias. Second, species live at different depths and thus record different environmental conditions. This is especially important for planktonic species living in the mixed layer because of the strong vertical gradient of temperature. In addition, organisms may migrate vertically over several hundreds of meters, on a seasonal or daily basis. Depending when the calcification happens, the exact depth recorded by the $\delta^{18}\text{O}$ may be different to that of the usual living habitat. Thus, interpreting a sediment $\delta^{18}\text{O}$ record requires a precise calibration on modern tests to know which conditions are represented in terms of depth and season. Isotopic corrections have been determined in order to estimate the correct environment; for instance, $\delta^{18}\text{O}$ measured from the foraminifera *C. wuellerstorffi* is usually corrected by 0.64 per mil to be closer to the value in equilibrium with deep water conditions. A good review of these biases is provided by Wefer and Berger (1991).

Diagenesis may also alter the original isotopic signal. This is especially true for aragonitic and high-magnesium calcitic shells, because these minerals are not stable and recrystallize. Low-magnesium calcitic shells, like those of foraminifera, are not free of diagenetic alteration, which must be discarded by a thorough examination and cleaning.

Other records: corals and speleothems

These carbonates, like sediments, record both the temperature and the water $\delta^{18}\text{O}$ composition, with some possible offset to the expected equilibrium value. In addition, they grow with fine laminations that may be annual bands, as for corals, allowing both a high-resolution sampling and a detailed chronology. They can be well dated by counting the annual bands and by ^{14}C and U/Th techniques. Subannual $\delta^{18}\text{O}$ measurements on corals showed that oxygen isotopes record the seasonal temperature, with some offset (Fairbanks and Dodge, 1979), although changes in the isotopic composition of surface water (linked to precipitation or river runoff) may explain part of the variations. In the tropics, reef building species have been shown to be especially useful for documenting ENSO (El Niño-Southern Oscillation) variability in areas where either temperature or precipitation change dominates the isotopic signal (Cole et al., 1993). Because most reef-building corals live in symbiosis with algae (zooxanthellae), they can only grow within a restricted depth range, which makes them reliable records of sea level variations. Speleothems grow from calcite precipitation when CO_2 -supersaturated water degasses. Since this water comes, more or less directly, from precipitation, the calcite $\delta^{18}\text{O}$ is strongly influenced by the factors affecting the $\delta^{18}\text{O}$ of precipitation (see above), including the local temperature. At mid-to-high latitudes, the positive correlation between the $\delta^{18}\text{O}$ of precipitation and temperature (Figure O33) is balanced by the negative effect of the temperature on the isotopic fractionation (Emiliani, 1971, note 23). At low latitudes, if the precipitation $\delta^{18}\text{O}$ is under greater control of the quantity of precipitation (Figure O33), the influence of temperature may be amplified (Neff et al., 2001). Changes in

the marine $\delta^{18}\text{O}$ add to this complexity, making a quantitative interpretation of a speleothem record not that straightforward. Several records, $\delta^{18}\text{O}$, $\delta^{13}\text{C}$, growth rate, trace elements, etc., are usually combined in order to decipher the origin of the signals. One of the longest $\delta^{18}\text{O}$ records, from Devils Hole, Nevada, covers more than half a million years (Winograd et al., 1992).

Global biogenic productivity estimated from oxygen isotopes

Measurements of the isotopic composition of atmospheric oxygen, O_2 , have shown an enrichment as compared to the ocean (Dole, 1935), by 23.5 per mil versus V-SMOW. This enrichment, called the “Dole effect” (see Dole effect), is mainly determined by gross biospheric fluxes, respiration and photosynthesis. Estimation of Dole effect variations from measurements in air bubbles trapped in glacial ice allows one to infer past changes in these fluxes. More recently, Luz et al. (1999) exploited a mass-independent fractionation of oxygen isotopes in the stratosphere to infer the global biospheric productivity (i.e., gross production of O_2 by photosynthesis). Most chemical processes fractionate oxygen isotopes according to their mass, in which case the fractionation of ^{17}O to ^{16}O is around half that of ^{18}O to ^{16}O (0.521, precisely). In contrast, in the stratosphere, a series of reactions involving O_2 , O_3 and CO_2 does not fractionate ^{18}O versus ^{17}O , and thus modifies their proportion in atmospheric CO_2 and O_2 . The extent of this atmospheric anomaly depends on the relative intensities of mass-dependent and mass-independent processes. It is expressed as the deviation towards the mass-dependent relationship between ^{18}O and ^{17}O :

$$\Delta^{17}\text{O} (\times 10^6 \text{ per meg}) \equiv (\delta^{17}\text{O} - 0.521 \times \delta^{18}\text{O}) \quad (5)$$

where $\delta^{17}\text{O}$ and $\delta^{18}\text{O}$ are isotopic compositions with respect to air.

Measurements of oxygen $\Delta^{17}\text{O}$ in air bubbles trapped in Greenland ice core allowed Luz et al. (1999) to infer that the global biospheric productivity did not differ significantly over the last 80,000 years, although it was slightly lower than at present.

Gilles Delaygue

Bibliography

- Aristarain, A.J., Jouzel, J., and Pourchet, M., 1986. Past Antarctic Peninsula climate (1850–1980) deduced from an ice core isotope record. *Clim. Change*, **8**, 69–89.
- Baertschi, P., 1976. Absolute ^{18}O content of standard mean ocean water. *Earth Planet. Sci. Lett.*, **31**, 341–344.
- Bassinot, F.C., Labeyrie, L.D., Vincent, E., Quidelleur, X., Shackleton, N.J., and Lancelot, Y., 1994. The astronomical theory of climate and the age of the Brunhes-Matuyama magnetic reversal. *Earth Planet. Sci. Lett.*, **126**, 91–108.
- Bemis, B.E., Spero, H.J., Bijma, J., and Lea, D.W., 1998. Reevaluation of the oxygen isotopic composition of planktonic foraminifera: Experimental results and revised paleotemperature equations. *Paleoceanography*, **13**, 150–160.
- Cole, J.E., Fairbanks, R.G., and Shen, G.T., 1993. Recent variability in the Southern Oscillation: Isotopic results from a Tarawa Atoll coral. *Science*, **260**, 1,790–1,793.
- Coplen, T.B., 1995. Reporting of stable carbon, hydrogen, and oxygen isotopic abundances. In *Reference and intercomparison materials for stable isotopes of light elements*, Vienna, IAEA TecDoc 825, pp. 31–34 (available online at www.iaea.org).
- Craig, H., 1961a. Isotopic Variations in meteoritic waters. *Science*, **133**, 1,702–1,703.
- Craig, H., 1961b. Standards for reporting concentrations of deuterium and oxygen-18 in natural waters. *Science*, **133**, 1,833–1,834.

- Craig, H., and Gordon, L.I., 1965. Deuterium and oxygen 18 variations in the ocean and the marine atmosphere. In Tongiorgi, E. (ed.), *Stables Isotopes in Oceanographic Studies and Paleotemperatures*. Pisa, Italy: CNR, Lab. di Geologia Nucleare, pp. 9–130.
- Cuffey, K. M., Clow, G.D., Alley, R.B., Stuiver, M., Waddington, E.D., and Saltus, R.W., 1995. Large Arctic temperature change at the Wisconsin-Holocene glacial transition. *Science*, **270**, 455–458.
- Dahe, Q., Petit, J.-R., Jouzel, J., and Stievenard, M., 1994. Distribution of stable isotopes in surface snow along the route of the 1990 International Trans-Antarctica Expedition. *J. Glaciology*, **40**, 107–118.
- Dansgaard, W., 1964. Stable isotopes in precipitation. *Tellus*, **16**, 436–468.
- Dole, M., 1935. The relative atomic weight of oxygen in water and in air. *J. Am. Chem. Soc.*, **57**, 2731.
- Duplessy, J.-C., Labeyrie, L., Juillet-Leclerc, A., Maitre, F., Duprat, J., and Samtheim, M., 1991. Surface salinity reconstruction of the North Atlantic Ocean during the Last Glacial Maximum. *Oceanol. Acta*, **14**, 311–324.
- Emiliani, C., 1955. Pleistocene temperature. *J. Geology*, **63**, 538–578.
- Emiliani, C., 1971. The Last Interglacial: Paleotemperatures and chronology. *Science*, **171**, 571–573.
- Epstein, S., Buchsbaum, R., Lowenstam, H.A., and Urey, H.C., 1953. Revised carbonate-water isotopic temperature scale. *Geol. Soc. Am. Bull.*, **64**, 1,315–1,325.
- Fairbanks, R.G., and Dodge, R.E., 1979. Annual periodicity of the $^{18}\text{O}/^{16}\text{O}$ and $^{13}\text{C}/^{12}\text{C}$ ratios in the coral *Montastrea annularis*. *Geochim. Cosmochim. Acta*, **43**, 1,009–1,020.
- Hays, J.D., Imbrie, J., and Shackleton, N.J., 1976. Variations in the Earth's orbit: pacemaker of the Ice Ages. *Science*, **194**, 1,121–1,132.
- Imbrie, J., Hays, J.D., Martinson, D.G., McIntyre, A., Mix, A.C., Morley, J.J., Pisias, N.G., Prell, W.L., and Shackleton, N.J., 1984. The orbital theory of Pleistocene climate: Support from a revised chronology of the marine $\delta^{18}\text{O}$ record. In Berger, A.L., et al., (eds), *Milankovitch and Climate*. Dordrecht: Reidel, pp. 269–305.
- Johnsen, S.J., Dansgaard, W., and White, J.W.C., 1989. The origin of Arctic precipitation under present and glacial conditions. *Tellus*, **41B**, 452–468.
- Jouzel, J., 1999. Towards a calibration of the isotopic paleothermometer. *Science*, **286**, 910–913.
- Jouzel, J., and Merlivat, L., 1984. Deuterium and oxygen 18 in precipitation: modeling of the isotopic effects during snow formation. *J. Geophys. Res.*, **89**, 11,749–11,757.
- Jouzel, J., 1997. Validity of the temperature reconstruction from water isotopes in ice cores. *J. Geophys. Res.*, **102**, 26,471–26,487.
- Jouzel, J., Vimeux, F., Caillon, N., Delaygue, G., Hoffmann, G., Masson-Delmotte, V., and Parrenin, F., 2003. Magnitude of isotope/temperature scaling for interpretation of central Antarctic ice cores. *J. Geophys. Res.*, **108**, 4,361–4,372.
- Krinner, G., Genthon, C., and Jouzel, J., 1997. GCM analysis of local influences on ice core δ signals. *Geophys. Res. Lett.*, **24**, 2,825–2,828.
- Labeyrie, L.D., Duplessy, J.C., and Blanc, P.L., 1987. Variations in mode of formation and temperature of oceanic deep waters over the past 125,000 years. *Nature*, **327**, 477–482.
- Lécuyer, C., and Allemand, P., 1999. Modelling of the oxygen isotope evolution of seawater: implications for the climate interpretation of the $\delta^{18}\text{O}$ of marine sediments. *Geochim. Cosmochim. Acta*, **63**, 351–361.
- Luz, B., Barkan, E., Bender, M.L., Thieme, M.H., and Boering, K.A., 1999. Triple-isotope composition of atmospheric oxygen as a tracer of biosphere productivity. *Nature*, **400**, 547–550.
- Mix, A.C., Bard, E., and Schneider, R., 2001. Environmental processes of the ice age: Land, oceans, glaciers (EPILOG). *Quaternary Sci. Rev.*, **20**, 627–657.
- McCrea, J.M., 1950. On the isotopic chemistry of carbonates and a paleotemperature scale. *J. Chem. Phys.*, **18**, 849–857.
- Mook, W.G. (ed.), 2001. Environmental Isotopes in the Hydrological Cycle: Principles and Applications. IHP TecDoc **39**, UNESCO/IAEA. Available online at: <http://www.iaea.org/programmes/ripc/ih/volumes/volumes.htm>.
- Neff, U., Burns, S.J., Mangini, A., Mudelsee, M., Fleitmann, D., and Matter, A., 2001. Strong coherence between solar variability and the monsoon in Oman between 9 and 6 kyr ago. *Nature*, **411**, 290–293.
- Östlund, H., Craig, H., Broecker, W.S., and Spenser, D. (eds.), 1987. Shorebased Data and Graphics, in GEOSECS Atlantic, Pacific and Indian Ocean Expeditions, 7, Washington, DC: IDOE NSF.
- Pearson, P.N., Ditchfield, P.W., Singano, J., Harcourt-Brown, K.G., Nicholas, C.J., Olsson, R.K., Shackleton, N.J., and Hall, M.A., 2001. Warm tropical sea surface temperatures in the Late Cretaceous and Eocene epochs. *Nature*, **413**, 481–487.
- Rozanski, K., Araguás-Araguás, L., Gonfiantini, R., 1993. Isotopic patterns in modern global precipitation. In Swart, P.K., Lohmann, K.C., McKenzie J., and Savin S. (eds.), *Climate Change in Continental Isotopic Records*. Washington, DC: AGU, Geophys. Monograph 78, pp. 1–36.
- Shackleton, N.J., 1967. Oxygen isotopic analyses and Pleistocene temperatures re-assessed. *Nature*, **215**, 15–17.
- Schrag, D.P., Hampt, G., and Murray, D.W., 1996. Pore fluids constraints on the temperature and oxygen isotopic composition of the glacial ocean. *Science*, **272**, 1,930–1,932.
- Urey, H.C., 1947. The thermodynamic properties of isotopic substances. *J. Chem. Soc. (London)*, **1947**, 562–581.
- Veizer, J., 1999. $^{87}\text{Sr}/^{86}\text{Sr}$, $\delta^{13}\text{C}$ and $\delta^{18}\text{O}$ evolution of Phanerozoic seawater. *Chem. Geol.*, **161**, 59–88.
- Wefer, G., and Berger, W.H., 1991. Isotope paleontology: growth and composition of extant calcareous species. *Mar. Geol.*, **100**, 207–248.
- Winograd, I.J., Coplen, T.B., Landwehr, J. M., Riggs, A.C., Ludwig, K.R., Szabo, B.J., Kolesar, P.T., and Revesz, K.M., 1992. Continuous 500,000-year climate record from vein calcite in Devils Hole, Nevada. *Science*, **258**, 255–260.
- Zachos, J., Pagani, M., Sloan, L., Thomas, E., and Billups, K., 2001. Trends, rhythms, and aberrations in global climate 65 Ma to present. *Science*, **292**, 686–693.

Cross-references

- Cenozoic Climate Change
- Coral and Coral Reefs
- Deuterium, Deuterium Excess
- Dole Effect
- Ice Cores, Antarctica and Greenland
- Ice Cores, Mountain Glaciers
- Isotope Fractionation
- Ocean Paleotemperatures
- Paleohydrology
- Paleotemperatures and Proxy Reconstructions
- Quaternary Climate Transitions and Cycles
- Sea Level Change, Quaternary
- SPECMAP
- Speleothems
- Stable Isotope Analysis

P

PAGES

The PAGES mission

PAGES (Past Global Changes) is the IGBP (International Geosphere Biosphere Programme) project charged with providing a quantitative understanding of the Earth's past climate and environment. Reliable predictions of global climate change and its environmental impacts in the future require an understanding of processes operating on time scales longer than the short instrumental record. The study of natural archives of past climatic and environmental variability can provide this information.

Why PAGES?

PAGES operates on the principle of subsidiarity, a term borrowed from the European Union. This means that projects within the PAGES umbrella are those that clearly benefit from value added through participation in a coordinated, international, cooperative framework. Although research funding for paleoenvironmental science is almost entirely national, the global nature of the questions involved, the global distribution of proxy archives, and the fact that the community of paleoresearchers is global, requires a globally integrated research strategy. PAGES provides interdisciplinary and international linkages between nationally funded research projects in order to ensure that the combined effort adds to more than the sum of the parts. PAGES synergies lead to community building and the development of integrated research objectives. Tangible products include the website (www.pages-igbp.org), newsletter (*PAGES News*), and numerous books (Markgraf, 2001; Alverson et al., 2002), special issues (Alverson et al., 2000; Clark and Mix, 2002), synthesis papers (Alverson and Kull, 2002), outreach publications (Alverson et al., 2001a), and brochures (Alverson et al., 2001b).

Research program

The PAGES research program is structured to bring researchers from a variety of disciplines and countries together. Thus, no explicit disciplinary or national structures exist within the program. Rather, the program elements are designed to reduce

constraints imposed by geography and artificial disciplinary boundaries such as those that commonly separate physical oceanography from continental paleoecology from archaeology. Although the five foci that make up the core of the PAGES program have been created to group types of research together, they are by no means restrictive, and collaboration between foci is strongly encouraged. The activities of each focus are guided by a chair and a small steering group. PAGES activities are driven by rapidly evolving scientific understanding and are designed to shift focus accordingly. The most recent structure and activities are always readily available on the website; www.pages-issp.org.

Focus 1 – PANASH

The goal of the Paleoclimate and Environments of the Northern and Southern Hemispheres (PANASH) focus is to reconstruct paleoenvironments and paleoclimate along three Pole-Equator-Pole (PEP) terrestrial transects using a multiproxy data and modeling approach. One of the major roles of the PEP transects is to facilitate the development of north-south research partnerships and foster a unified sense of purpose within the diverse international and interdisciplinary community that addresses questions of past global change. The PEP transects have been extremely successful in achieving these goals, as evidenced by the strong community interest in PEP meetings, as well as the peer reviewed synthesis publications that have arisen from each transect (Dodson and Guo, 1998; Markgraf, 2001; Battarbee et al., 2004; Dodson et al., 2004).

In addition to supporting the PEP transects, PANASH as a whole stimulates global exchange of information among marine, atmospheric, and terrestrial scientists, historical ecologists, and environmental archaeologists. Its primary tasks are to:

- document the amplitude, phase, and geographic extent of past climate change in the two hemispheres,
- determine the history of potentially important forcing factors,
- identify the feedbacks that amplify or reduce the influence or the effect of these forcings,
- identify the mechanisms of climatic coupling between the two hemispheres.

The basis of all PANASH activities is a hypothesis-driven approach to understanding modes of climatic and environmental variability through the use of global, multi-proxy based climate and environmental reconstruction. As an example of the wealth of information that must be integrated within PANASH, Figure P1 shows a highly condensed impression of the variety of proxy records of environmental variability available over a range of timescales from around the world.

Focus 2 – The PAGES/CLIVAR intersection

The PAGES/CLIVAR Intersection focus aims to improve the understanding of decadal to century scale climate variability, especially when relevant to improving predictability, through the use of high resolution paleoclimatic data. The activities within this focus are overseen by a joint working group shared between PAGES and the World Climate Research Program (WCRP) Climate Variability and Predictability Program (CLIVAR). The four principal areas of focus, as outlined at the first international CLIVAR conference (Alverson et al., 1999), are:

1. extending the instrumental climate record back in time with quantitative proxy data that can be accurately calibrated against instrumental records,

2. documenting and understanding rapid climate change,
3. documenting and understanding natural climate variability during the Holocene and other interglacial periods with background climatic states similar to those of today,
4. testing the ability of climate models to capture known past climate variability.

Focus 3 – IMAGES

The International Marine Past Global Changes Study (IMAGES) is the marine program shared between PAGES and the Scientific Committee for Ocean Research (SCOR). The principal aim of this program is to understand the mechanisms and consequences of past climate changes involving ocean circulation, salinity, and ventilation as well as the past history of marine ecosystems and carbon cycle dynamics, using oceanic sedimentary records. IMAGES supports a number of working groups, some of which are oriented around cruise planning and others around more general research questions. One major task of IMAGES is to organize international pooling of financial resources and research expertise in order to enable cruises to be carried out throughout the world oceans. All IMAGES activities are carried out with strong input

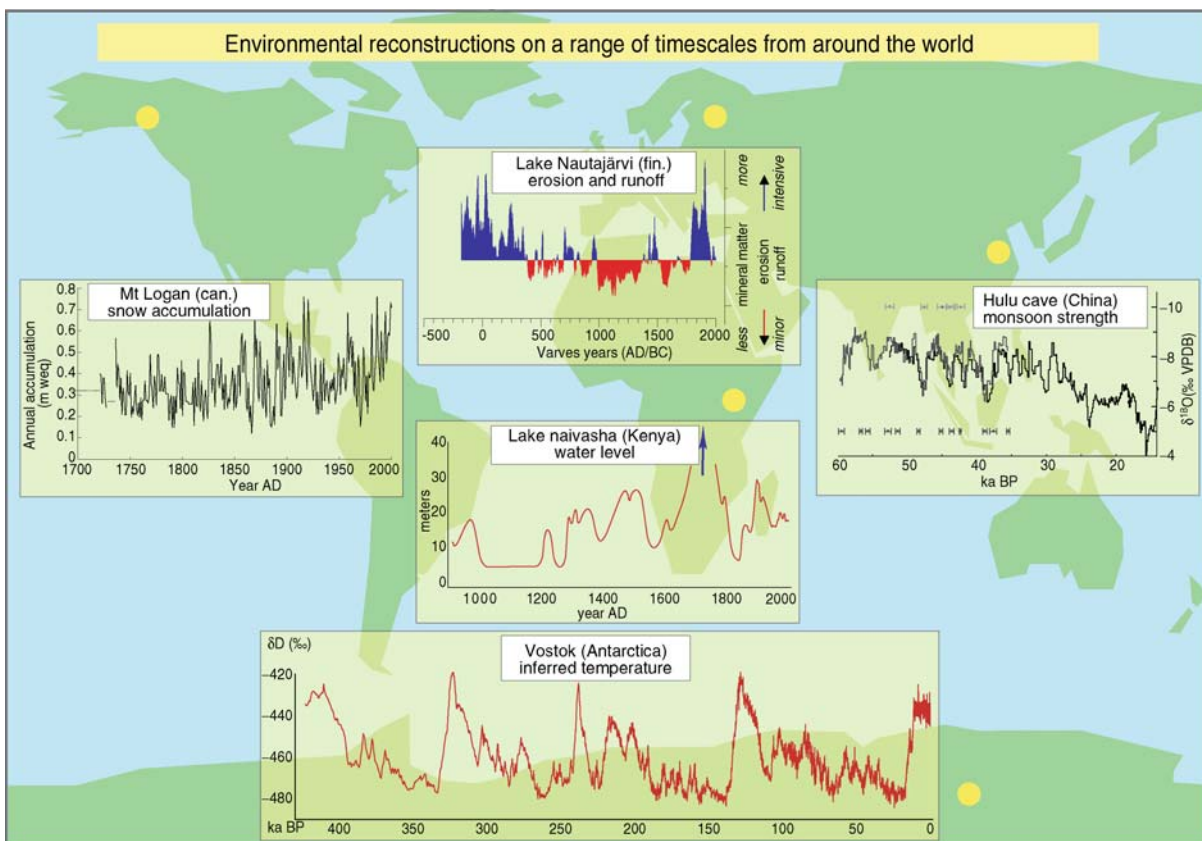


Figure P1 A highly condensed view of the variety of proxy records of Quaternary environmental variability available over a range of timescales from around the world. Yellow dots indicate the location of these records on the underlying global map. The records are: 1. A three hundred year record of snow accumulation, related to the Pacific Decadal Oscillation, from an ice core on Mt. Logan, Canada (Moore et al., 2002). 2. A two thousand year record of runoff intensity, related to the North Atlantic Oscillation, from a Finnish laminated lake sediment core (Ojala, 2001). 3. An oxygen isotope record, as indicator of moisture source and hence monsoon penetration, covering the last glacial period through the Holocene from a speleothem in Eastern China (Wang et al., 2001). 4. A lake level reconstruction from Naivasha, Kenya as an indicator of regional hydrological balance (Verschuren et al., 2000). 5. Isotopically inferred temperature changes over four glacial cycles from the Vostok ice core in Antarctica (Petit et al., 1999).

and interaction from climate modelers, continental scientists, and ice core researchers.

Focus 4 – Polar programs

The focus of the Polar programs is bi-polar. Examples of research within the scope of this focus include the European and US N GRIP ice core programs, EPICA, and the International Trans-Atlantic Scientific Expedition (ITASE), which seeks to map the spatial variability of Antarctic climate over the last millennium. This initiative is shared with the Scientific Committee on Antarctic Research (SCAR). In addition to ice core work, a wealth of other archives in polar regions are employed to provide a robust picture of high latitude environmental change. For example, the ESF-funded Quaternary Environment of the Eurasian North project (QUEEN) concentrates on mapping the extent of the last glaciation, and the CircumArctic Paleo-Environments program (CAPE) facilitates integration of paleoenvironmental research on terrestrial and adjacent margins covering the last few glacial cycles.

Focus 5 – Past ecosystem processes and human environment interactions

The Past Ecosystems and Human-Environment Interactions focus highlights PAGES concern with ecological responses to climate change and past human activities. The research within Focus 5 integrates past human-environment interactions at sub-continental scale with research and modeling based on present-day ecosystems and watersheds. The focus is divided into three main activities: Human Impacts on Terrestrial Ecosystems (HITE), Land Use and Climate Impacts on Fluvial Systems during the Period of Agriculture (LUCIFS), and Human Impact on Lake Ecosystems (LIMPACS). These activities are case-study based and focus on ecosystems made vulnerable to global change through any combination of natural and human-induced stresses. They also explore the basis for the durability of long-sustained ecosystems, and questions of sensitivity, thresholds, and non-linear responses.

Initiatives

In addition to its standing foci, PAGES supports initiatives driven by scientific questions arising within the community. The PAGES Steering committee serves to critically ascertain if proposed initiatives should qualify for PAGES endorsement and support. Successful initiatives develop a clear research and workshop agenda over a 3–5 year period leading to a tangible goal. PAGES support for these initiatives is flexible but can include enhancing the profile of the initiative, advertising it to the international community, and providing partial funding for workshops. One example of a successful initiative is the Environmental Processes of the Ice Age: Land, Oceans, Glaciers (EPILOG) program, which arose in 1999 as a multi-national working group of the PAGES marine program IMAGES. EPILOG received PAGES support, including co-funding for several workshops, and recently published an extensive special issue on ice sheets and sea level of the last glacial maximum (Clark and Mix, 2002). The required qualifications for a PAGES initiative are:

1. A question that seems likely, within a 3–5 year timeframe, to be tractable in the sense of leading to a peer-reviewed product that advances the field.
2. A clear reason why PAGES should be involved, for example to facilitate new international or interdisciplinary bridges and community building.

Program structure

PAGES activities are overseen by an international scientific steering committee (SSC) appointed by the Steering Committee of the IGBP. The sixteen members, who each serve for at most two consecutive three-year terms, are chosen to provide a balance of scientific expertise and national representation. This committee meets once a year to provide guidance for and oversight of the program as a whole. A subset of five committee members serves as an executive committee. As a general guideline, the five member executive committee includes an American and a Swiss by virtue of the fact that these two countries currently provide the bulk of PAGES funding, and at least one member from a less developed country. Under direction of the SSC, the staff of the small International Project Office (IPO) carries out the day to day running of the PAGES program as a whole. These activities include maintaining the PAGES website and database, organizing meetings and workshops, editing and writing PAGES publications, and serving as a liaison with other global change programs. In addition, the office regularly hosts both short-and long-term (sabbatical) visits from paleoscientists around the world.

Links with other international programs

PAGES continues to be primarily concerned with understanding the past operation of the Earth system. The PAGES domain includes the physical climate system, biogeochemical cycles, ecosystem processes and, human dimensions. Thus, PAGES activities are not restricted to IGBP, but overlap substantially with IGBP's sister programs within the "earth system science partnership," the WCRP, the International Human Dimensions Program on Global Environmental Change (IHDP) and Diversitas. Facilitating publicly accessible paleodata access, engaging with the climate modeling community, and strengthening the role of developing countries in PAGES research are the stable tripod upon which the wider PAGES scientific program rests.

PAGES has built bridges with many other international scientific programs. Although only two of the foci are officially shared (Focus 2 with WCRP-CLIVAR and Focus 3 with SCOR), all of them have substantial interactions with other programs. PAGES has launched joint initiatives with all of the other components of the IGBP, including both the core projects of IGBP phase 1. In the newly developing IGBP phase 2, which runs from 2003 to 2013, PAGES is expected to serve in a central synthesizing role, and thereby interact strongly with all of the new IGBP programs (Figure P2). A full listing of PAGES science partnerships is available on the PAGES website; some examples include the Global Network for Isotopes in Precipitation (GNIP), shared with the WCRP and the International Atomic Energy Agency (IAEA), and the International Mountain Research Initiative, co-sponsored by three other IGBP core projects, IHDP, GTOS (Global Terrestrial Observing System), and UNESCO. Through these intersection activities, PAGES provides the historical context for global change programs.

Outreach, communication, and publications

One major task for PAGES is to provide easy access to paleoenvironmental information to active researchers in paleosciences, researchers in other aspects of global change research, and the public. One of the most important communication platforms is the website, www.pages-igbp.org. This site is modified regularly and includes lists of new products, links to paleoenvironmental databases, science highlights, a calendar of upcoming events, and information on how to become involved in PAGES activities.

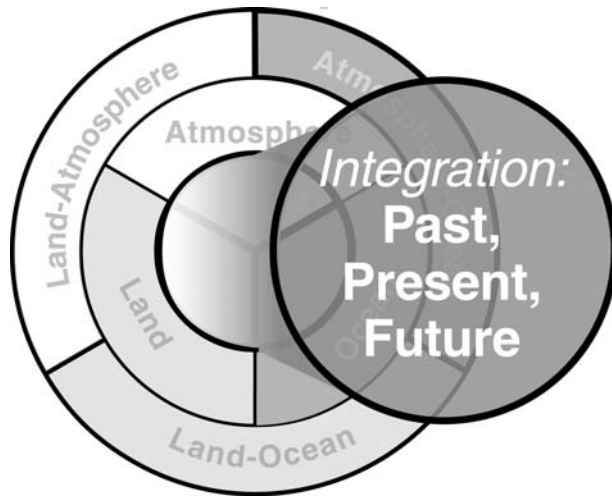


Figure P2 Schematic diagram of the core projects expected to be active in phase 2 of the International Geosphere Biosphere Programme (IGBP), which runs from 2003 to 2013. These new projects are based around the three Earth system components, land, atmosphere, and ocean, and the three interfaces between them. Two further projects, GAIM (AIMES) and PAGES will serve as integrating projects, providing past and future time dimensions to the program. PAGES will play a central, integrating role in the new IGBP structure.

Another important element in the PAGES communication strategy is the newsletter. PAGES NEWS is produced three times a year and sent free of charge to more than 3,000 subscribing scientists in more than 70 countries. All issues are made available as pdf files on the PAGES website. Such wide distribution, coupled with a high degree of proactive submission by the research community, has made the newsletter an important vehicle for the dissemination of research results, workshop reports, and program news, especially in countries with limited access to western journals. Most issues are developed around a specific theme, which might be a PAGES program or a particular paleoarchive. In addition to its newsletter and website, PAGES strongly encourages publications in the peer-reviewed literature as one outcome of all of its scientific activities.

Data archives

Internationally accessible data archives are one of the primary foundations for paleoclimatic research that seeks to go beyond reporting results on a site by site basis. PAGES is committed to ensuring the preservation of all data needed for long-term, global change research and making them openly available. PAGES endorses a number of such data repositories, including the World Data Center for paleoclimatology, Boulder (www.ngdc.noaa.gov/paleo/, appendix B) and PANGAEA (<http://www.pangaea.de>). PAGES supports a data board with a primary responsibility for assuring compatibility and accessibility of available existing paleo-databases. The PAGES data board is open to all interested participants and includes members from most major database centers and focus leaders.

Capacity building – encouraging north-south research partnerships

PAGES has a strong interest in capacity building. The majority of paleo-environmental data are extracted in less developed countries. Recent high profile examples include ice cores from

Kilimanjaro, tree rings and lake sediments from Siberia, loess records in China, tropical tree rings in SE Asia, and speleothems in Oman. Bringing these records together into a synthesis view of past environmental change requires that a global community of independent working scientists matching the diversity of these records also exists. PAGES therefore allocates approximately 20% of its budget directly to activities geared towards building the capacity of scientists residing in developing countries to carry out active participation in paleoenvironmental research. In addition, most PAGES workshop and summer school support is earmarked for participants from developing countries. In addition to finances, PAGES seeks to follow up one-time support wherever possible, by enhancing the number of young scientists from developing countries in the database, nominating outstanding individuals for various awards, and entraining them directly in PAGES major scientific initiatives. PAGES occasionally hosts visits at the PAGES office, usually when tied to academic visits at a department at the nearby University of Bern or the Swiss Climate summer school.

The PAGES Regional, Educational and Infrastructure Efforts (REDIE) project seeks to:

1. enlist scientists and technicians in developing countries in international paleoenvironmental research activities, and
2. promote the development of paleoscience research within developing countries.

Within the REDIE program, a number of approaches are used. Financial support is made available for the attendance of active young scientists at key conferences and summer schools. PAGES publications are made available free of charge to libraries and university laboratories in less-developed countries. Scientists from Asia, Africa, and South America sit on the PAGES Science Committee and act as liaisons with their regional communities. PAGES scientific meetings are regularly organized in developing countries, with ample support and presentation time provided for the attendance of scientists from the region.

Keith Alverson and Christoph Kull

Bibliography

- Alverson, K., and Kull, C., 2002. Understanding Future Climate Change Using Paleorecords. In Rodó X., and Comin F.A. (eds.), *Global Climate: Current research and uncertainties in the climate system*. Springer, pp. 153–185.
- Alverson, K., Duplessy, J.C., Jouzel, J., and Overpeck, J., 1999. The PAGES/CLIVAR Intersection. *World Climate Research Program Report Series*, Venice, Italy, 108, 42–47.
- Alverson, K., Oldfield, F., and Bradley, R. (eds.), 2000. Past Global Changes and Their Significance for the Future. *Quaternary Sci. Rev.*, **19**(1), 391–402.
- Alverson, K., Bradley, R., Briffa, K., Cole, J., Hughes, M., Larocque, I., Pedersen, T., Thompson, L., and Tudhope, S., 2001a. A global paleoclimate observing system. *Science*, **293**(5527), 47–48.
- Alverson, K., Bradley, R., and Pedersen, T., 2001b. *Environmental Variability and Climate Change*. IGBP Science vol. 3. S. Eliott. Stockholm: IGBP Secretariat, 32pp.
- Alverson, K., Bradley, R., and Pedersen, T. (eds.), 2002. *Paleoclimate, Global Change and the Future*. IGBP book Series, Heidelberg, Germany: Springer, 221pp.
- Battarbee, R.W., Gasse, F., and Stickley, C. (eds.), 2004. *Past Climate Variability through Europe and Africa*. Developments in Paleoenvironmental Research, vol. 6, Springer, 638pp.
- Clark, P.U., and Mix, A.C. (eds.), 2002. Ice Sheets and Sea Level of the Last Glacial Maximum. *Quaternary Sci. Rev.*, **21**(1), 1–7.

- Dodson, J.R., and Guo, Z.T., 1998. Past Global Change. *Global and Planetary Change*, **18**(3–4), 202pp.
- Dodson, J.R., Taylor, D., Ono, Y., and Wang, P. (eds.), 2004. Climate, human, and natural systems of the PEP II transect, *Quaternary Int.*, **118/119**, 3–12.
- Markgraf, V. (ed.), 2001. *Interhemispheric Climate Linkages*. San Diego: Academic Press, 454pp.
- Moore, G.W.K., Holdsworth, G., and Alverson, K., 2002. Climate change in the North Pacific region over the last three centuries. *Nature*, **420**, 401–403.
- Ojala, A., 2001. Varved lake sediments in southern and central Finland: long varve chronologies as a basis for Holocene palaeoenvironmental reconstructions, Espoo: Geological Survey of Finland, 41pp.
- Petit, J.R., Jouzel, J., Raynaud, D., Barkov, N.I., Barnola, J.M., Basile, I., Bender, M., Chappellaz, J., Davis, M., Delaygue, G., Delmotte, M., Kotlyakov, V.M., Legrand, M., Lipenkov, V.Y., Lorius, C., Pepin, L., Ritz, C., Saltzman, E., and Stievenard, M., 1999. Climate and atmospheric history of the past 420,000 years from the Vostok ice core, Antarctica. *Nature*, **399**: 429–436.
- Verschuren, D., Laird, K.R., and Cumming, B.F., 2000. Rainfall and drought in equatorial east Africa during the past 1,100 years. *Nature*, **403**, 410–414.
- Wang, Y.J., Cheng, H., Edwards, R.L., An, Z., Wu, J., Shen, C.-C., and Dorale, J.A., 2001. A high-resolution absolute-dated late Pleistocene monsoon record from Hulu Cave, China. *Science*, **294**, 2345–2348.

Cross-references

[Climate Variability and Change, Last 1,000 Years](#)
[Holocene Climates](#)
[Ice Cores, Antarctica and Greenland](#)
[Millennial Climate Variability](#)
[Paleotemperatures and Proxy Reconstructions](#)
[Pleistocene Climates](#)
[Quaternary Climate Transitions and Cycles](#)

PALEOBOTANY

Introduction

Plants are ideally suited as records of, or proxies for, terrestrial climate because they are sessile organisms. As climate changes around them, they must adapt or perish. Over evolutionary time, many aspects of plant growth have been constrained by adaptation to specific climate regimes (e.g., Parkhurst and Loucks, 1972; Chaloner and Creber, 1990; Uhl and Mosbrugger, 1999). The sessile nature of plants combined with the tendency for most plant parts to be preserved relatively close to the site at which they grew means that plant fossils can be used as a record of local paleoclimate (Spicer, 1989; Greenwood and Wing, 1995).

Three main techniques are often used to determine paleoclimate from fossil plants. The first is referred to as the nearest-living-relative technique. The nearest-living-relative technique compares fossil plants to the modern plants to which they are most closely related and assumes that the climatic tolerances for both have remained similar through geologic time. The second technique uses plant structures as vegetation proxies for climate. These methods use various aspects of leaves and wood, such as leaf morphology, tree rings or stomatal index, as proxies to determine the climate in which these plant organs grew. The final technique involves measuring isotopic ratios of plant tissue to determine the climatic surroundings of the plant.

Nearest-living-relative technique

The nearest-living-relative technique is widely used in paleoclimate reconstructions. This technique is taxon based and compares fossil plants to their most closely related modern plants, which are usually determined by finding similar morphological characters in a fossil and in a living taxon. The main assumptions are that the climatic tolerances for both fossil and modern plants are similar and the identifications and relationships proposed between the fossil and living taxa are reliable. Dilcher (1974, 2000) suggests that upwards of 60–75% of taxa identified for Paleogene and Cretaceous fossil angiosperms are incorrect. One advantage to this technique is that it can be used with many different plant organs, including leaves, pollen, wood, fruits and seeds. For some plant assemblages, a combination of different plant organs can be used to establish a more robust determination of paleoclimate. In general, assemblages with fruits and seeds or combinations of plant organs give more accurate results than those that preserve only leaves, as taxonomic affinity is often difficult to determine with leaf material. The best results are obtained when a large number of taxa are used, the taxonomic identifications are correct and the taxonomic identifications are at the species level. Use of this technique assumes that the ecological tolerances of the fossil and extant relatives are similar, and have not changed through time. The more recent the fossil, the more likely it is that the ecological tolerances are similar. Thus Holocene and Neogene climate reconstructions are more likely to be accurate than Paleogene and Mesozoic comparisons. Paleozoic plants are too dissimilar to recent plants to use this technique (Chaloner and Creber, 1990).

Species level comparisons are the most robust, because ecological tolerances of species are often better defined than those of higher taxonomic groups. However, in many instances determination of the fossil can be made only to the genus or family level, especially when using pollen or wood. Some genera and families have similar tolerances throughout the group. For example, palms and gingers have been said to live only in subtropical and tropical areas (Wing and Greenwood, 1993), although palms often grow and reproduce in warm temperate areas of southeastern North America and South America. However, some genera have broad ecological tolerances, (e.g., *Quercus* and *Acer*), and most plant families have an extremely broad ecological range (e.g., *Fabaceae*). This problem is somewhat circumvented by using large numbers of taxa to reconstruct paleoclimate, which reduces the likelihood that one broad-ranging taxon will influence the results.

The nearest-living-relative technique is used both to estimate paleoclimate with absolute values and to determine vegetation or climatic zones. The former method requires knowledge of the climatic tolerances of many different modern species, while the latter relies on determining which combinations of taxa are commonly found together in modern vegetation or climate zones. Absolute climate values can be determined from individual modern taxonomic relatives of fossil taxa, and a range of temperatures or precipitation values may result. However, combining many modern climate ranges should result in a more precise estimate for the fossil assemblage, with the resulting climatic estimate being the range where all of the modern taxa align (Figure P3). Combining many taxonomic ranges decreases the likelihood that a single problem taxon will skew the resulting climate range. One application of this method has been termed the coexistence approach (Mosbrugger and Utescher, 1997) and uses a database of modern ecological tolerances of leaves, fruits and seeds from

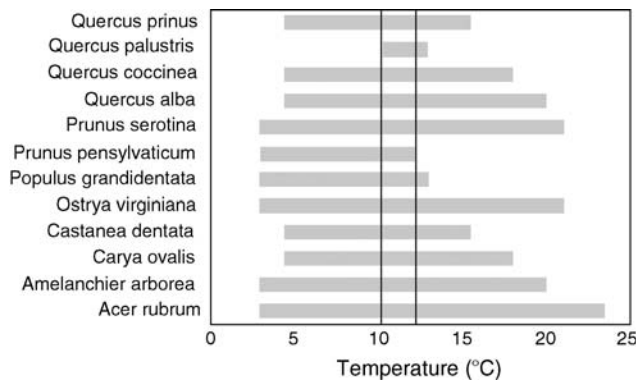


Figure P3 A hypothetical list of modern relatives based on a flora from southern Pennsylvania. If these modern taxa had represented the modern relatives of a fossil flora, the estimated mean annual temperature of the fossil site would be between approximately 10°C and 12°C, the range of overlap between all taxa present.

Europe to apply the nearest-living-relative technique to fossil assemblages. This approach works for Tertiary and younger-aged fossil assemblages and has resulted in temperature estimates with ranges as small as 1–4°C.

Using the nearest-living-relative technique to determine vegetation and climatic zones is more common than finding absolute climate values, as it is the method preferred by palynologists. This application of the method relies on finding similar taxonomic combinations in both modern and fossil assemblages. As with the coexistence approach, using many taxa is preferable in determining a paleovegetation or paleoclimatic zone. This is especially true when using pollen grains, which are often only determined on the genus level and thus may have large individual ecological tolerances, but a smaller tolerance as an assemblage. However, on occasion, the presence of a small number of extremely indicative taxa can constrain the paleovegetation or paleoclimatic zone regardless of the other taxa involved (Martin, 1997). Sinka and Atkinson (1999) have used factor analysis to determine the overlapping climate zones of modern plant assemblages, and then map the unknown fossil ranges onto a “climate space.” This technique is a more objective method of determining climatic zones of fossil assemblages, and eliminates the bias that one taxon may have in the overall zonation.

Plant structure proxies

Similar combinations of wood or leaf characters tend to be common in floras that live in similar climates (Dilcher, 1973; Givnish, 1987; Woodcock and Ignas, 1994), even those that are widely separated spatially and compositionally (Halloy and Mark, 1996). Thus, specific plant characters are emergent properties of a flora living under a specific climate regime. The presence or absence of these characters in a fossil floral assemblage allows for a paleoclimatic determination of the assemblage site. Climatic interpretation is based on modern relationships between climate and specific plant characteristics. Unlike the nearest-living-relative technique, foliar and wood physiognomy approaches do not require specific or correct taxonomic identification, although knowledge of the number of taxa present and some aspects of their morphological or anatomical characters are needed. This can be done using a parataxonomical or morphotype based approach (Woodcock and Ignas, 1994; Davies-Vollum, 1997), which interprets suites of morphologically similar plant

fossils as species groups. Exact taxonomic identification is needed for stomatal indices and leaf venation density methods, as these proxies are species dependent.

Leaves

Angiosperm leaves are often used in paleoclimatic reconstructions, with common proxies including leaf physiognomy, stomatal density or stomatal index, and leaf venation density. Leaf physiognomy is often used to determine annual and seasonal temperature and precipitation. Stomatal density and stomatal index are used to determine paleoCO₂ levels, moisture availability and temperature. Leaf venation density is used to determine transpiration stress.

Leaf physiognomic methods have their basis in numerous qualitative relationships between leaves and climate that have been quantified using modern climatic and floral data from a range of climates and areas. By quantifying the proportions of certain leaf characteristics present in specific modern climates, predictive equations have been formed to determine climate from fossil leaves. The most common equations correlate leaf morphological characters with mean annual temperature and mean annual precipitation, but others have been used to quantify other climatic variables such as growing season precipitation, and cold month or warm month mean temperatures (Wolfe, 1993; Gregory-Wodzicki, 2000; Jacobs, 2002).

Simple linear regression has been shown to be a relatively direct and accurate means of predicting both mean annual temperature and mean annual precipitation. The correlation between leaf margin state (toothed or smooth) and mean annual temperature is robust (Figure P4), and results in a fairly precise and accurate predictive equation. As a consequence, this has been the most studied and refined relationship within leaf physiognomic studies (e.g., Dilcher, 1974; Wilf, 1997; Kowalski and Dilcher, 2003). The resulting mean annual temperature estimates generally have a suggested minimum standard error of 2°C (Wilf, 1997). For precipitation, equations correlating leaf area and mean annual precipitation have shown the most promise, and are slowly being refined by different researchers (e.g., Wilf et al., 1998; Jacobs, 2002). However, most authors have expressed caution in relying on the resulting mean annual precipitation estimates, as the estimates have high standard errors.

Several authors have started using a multi-character approach to climate prediction from leaf morphology, as the morphology of most leaf characters is thought to be the result of the complex interaction of many climate parameters. Multiple regression equations using from two to nine or ten leaf characters have shown some refinement of climate prediction (e.g., Wing and Greenwood, 1993; Gregory-Wodzicki, 2000; Jacobs, 2002), and are often more accurate than simple linear regression equations for paleoclimate prediction (Kowalski, 2002). Wolfe (1993) has compiled a large, worldwide database of modern climate and floral data, called CLAMP, to use with canonical correspondence analysis, a multivariate statistical approach for paleoclimate prediction. His database uses 31 leaf characters to predict numerous climate parameters, including mean annual temperature, growing season temperature and precipitation, enthalpy and range of temperature. Nearest neighbor analysis uses only the sites from the CLAMP database that are closest to the unknown site in multivariate space to form predictive equations for paleoclimate (Stranks and England, 1997). This technique has refined multivariate prediction further by restricting the predictor set to similar floras and often results in smaller estimate error.

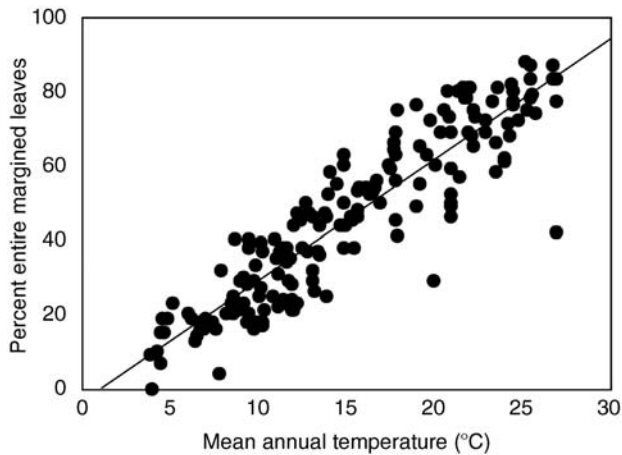


Figure P4 Percentage of entire margined leaves in a flora versus mean annual temperature for 177 sampled floras worldwide. Data from Wolfe (1993); Gregory-Wodzicki (2000); and Kowalski, (personal observation).

Leaf physiognomy predictions are relatively accurate, but several assumptions do exist. The first assumption is that the relationship between leaf morphology and climate has remained constant through time. The second is that taphonomic biases are small, though they are known to exist (Roth and Dilcher, 1978; Greenwood, 1992). The third is that regional differences due to climatic or taxonomic history are not great. Several authors have suggested that it is important to use predictor data sets that are similar geographically, taxonomically or climatically to those likely to be encountered in the fossil assemblage (Stranks and England, 1997; Gregory-Wodzicki, 2000; Jacobs, 2002; Kowalski, 2002). This restriction should reduce the problems that might be encountered by the third assumption above. Leaf physiognomy methods also require a relatively high number of fossil taxa (~20) to reduce paleoclimate estimate errors. Only the leaf characters of woody angiosperms have been shown to correlate with climate, restricting the use of the method to the Cretaceous and Cenozoic.

Both stomatal density (number of stomata per area) and stomatal index (the ratio of the number of epidermal leaf cells to the number of stomata in a defined area, multiplied by 100) can be used to determine atmospheric CO₂ concentrations, temperature or moisture availability. Stomata pores are surrounded by guard cells that control the size of the stomatal opening and thus the gas exchange and water loss from the leaf to the atmosphere. The number of stomata that differentiate is determined at the time of leaf unfolding (Kurschner et al., 1998) when the leaf acts as a biosensor of atmospheric CO₂. Stomatal index is used more often than stomatal density, as it eliminates the effect of leaf size on density counts (large leaves with large cells might have a decreased stomatal density, but not a decreased stomatal index). *Quercus*, *Ginkgo* and *Metasequoia* have been used, among other taxa, to calibrate CO₂-stomatal index curves from which to estimate paleoCO₂ levels (e.g., Kurschner et al., 1998; Royer, 2001; Beerling and Royer, 2002). All species have a stomatal density and stomatal index with a negative relationship to atmospheric carbon concentration. These taxa are broad-ranging temporally (both *Ginkgo* and *Metasequoia* are termed “living fossils”) and can track atmospheric carbon changes over long periods of time.

Like all methods, stomatal index and stomatal density have advantages, but must be used with caution. As CO₂ rises, stomatal index responds non-linearly. Thus, problems arise when estimating paleoCO₂ during periods of higher than modern atmospheric CO₂ concentrations (Kurschner et al., 1998; Beerling and Royer, 2002). Stomatal index decreases as temperature increases, even under the same ambient CO₂ (Beerling and Chaloner, 1993). This can influence atmospheric CO₂ estimates if temperature is not constant over the time period being analyzed. However, temperature can be estimated in combination with other leaf physiognomy methods, which can minimize potential interpretation problems. Stomatal density also appears to correlate, at least qualitatively, with precipitation amount, especially in shade leaves (Sun et al., 2003). Stomatal index does not seem to reflect this correlation and as such is a better measure for atmospheric CO₂ concentration. A major benefit to using stomatal index and stomatal density to estimate CO₂ is that this method can be used from the Paleozoic to the Recent (Chaloner and McElwain, 1997).

Leaf venation density is a method that is more recently being refined as a way to estimate paleomisture parameters. Leaf venation density changes in response to the amount of leaf transpiration, which is due to water availability or temperature (Uhl and Mosbrugger, 1999; Uhl et al., 2002). Leaf venation density is influenced by climate factors during leaf production in one growing season; thus, this method can record small-scale changes that may vary on the order of seasons. However, several problems still exist with this method, including density differences with leaf size dependent on species, how to define density, and differences between sun and shade leaves. However, if these problems are addressed, this method could potentially be used from the Paleozoic to the Recent.

Wood

Several aspects of wood can be used to determine paleoclimate, including wood anatomy, tree rings and charcoal. Wood is often found in fossil environments that are not suited for leaf preservation. Thus, using wood as a climate proxy can increase the number of environments in which paleoclimatic reconstruction is possible from plants.

Paleoclimate reconstruction from wood anatomy is based on cellular level proxies, such as the presence, organization or size of vessel elements, ray cells, axial parenchyma and fiber cells (Wiemann et al., 1999; Woodcock and Ignas, 1994). The relationship between wood anatomy and climate has been demonstrated qualitatively based upon relationships observed between vessel density and diameter with moisture, vessel diameter as a function of temperature, and the presence of ring porosity as an indicator of seasonality. Quantitative equations have been derived, most notably by Wiemann et al. (1998, 2001), that result in numerical climate estimates from these same features. These equations ideally predict temperature to within 5 °C, although equations using differing predictive characters from the same site can differ by almost 6 °C. Temperature correlates fairly well with wood anatomical characters, but precipitation correlates poorly (Wiemann et al., 1998, 2001). These equations need a relatively large number of taxa (~25) to estimate climate in order to reduce error. However, Terral and Mengal (1999) have shown that it is possible to use one species through time to estimate climate, if that species shows variation in anatomical characters with respect to climate. In their study, olive wood was used to estimate Holocene paleoclimate.

Both qualitative and quantitative climate estimates, based upon wood anatomy, work relatively well to distinguish tropical from more temperate or seasonal sites. The cellular anatomy of wood grown in temperate or seasonal climates is more influenced by climate than wood grown in tropical environments. As such, climate reconstruction using wood allows for broad categorical statements about paleoclimate, and can distinguish well between worldwide sites. However, in smaller areas (e.g., eastern North America), taxonomic overlap between sites can result in temperature differences that are not reflected in the wood assemblage (Kowalski, personal observation). In some areas, anatomical characters used in this type of climate reconstruction, such as the presence or absence of spiral thickening, do not vary significantly within species.

Cautions with using wood anatomy to determine paleoclimate are similar to those using leaf methods, such as the assumption that the relationship between climate and anatomy has been constant through time. Ideally, wood anatomy techniques could be used back into the Paleozoic. However, some wood characters used to estimate climate are derived (e.g., vessel characters such as vessel density and ring porosity). These wood characters developed with the evolution of angiosperms in the late Mesozoic (Francis and Poole, 2002), and thus these wood characters cannot be used to estimate the paleoclimate of the Paleozoic and early and middle Mesozoic.

Dendrochronology or tree ring analysis can be used to determine climate over several seasons, as each ring records aspects of moisture and temperature of one growing season. The resulting information details a long series of annual climate and climate changes, with a precision that few other records approach. Most information regarding the response of tree ring characteristics to climate has come from studies of conifers (Francis and Poole, 2002), although angiosperms are occasionally studied as well. A continuous record of annual tree rings has been established in the southwestern USA, extending back nearly 9,000 years. Changes in moisture and temperature of local climates often can be correlated to ancient human habitations and migrations. The presence/absence of tree rings is an indication of seasonality, often related to temperature (Francis and Poole, 2002). Ring presence, as an indicator of seasonality of temperature, is best determined from more than one taxa, as some tropical tree species possess rings and could be confused with temperate species. Tropical tree rings are most likely due to seasonality of precipitation or seasonal leaf loss (Woodcock and Ignas, 1994). Ring width is useful in determining growing conditions, with wide rings the product of warmer and wetter conditions or increased CO₂ (Beerling, 1999), and narrow rings produced under cooler or drier conditions (Francis and Poole, 2002). Occasionally, false rings occur, which can indicate a halt during the growing season due to fire, drought, insect damage or frost. Ring widths are best used for broad floral comparisons, rather than estimating the absolute temperature or humidity of one flora. Mean sensitivity measures the variability of tree rings from year to year, and gives an indication of the constancy of climate regime (Francis and Poole, 2002). Tree ring analyses can be performed on floras from the Recent to the Paleozoic but most applications have documented climate during the last 10,000 years.

Finally, the presence of charcoal in an assemblage can determine whether paleoO₂ levels are within the relatively narrow range associated with charcoal formation. Charcoal can only form within a relatively narrow O₂ range (Chaloner and McElwain, 1997). This area needs more research because plant parts are

frequently charcoaled and found in sediments from the Devonian to the Recent. Such fragments are known as mesofossils and can be used in floristic studies to assign nearest-living-relative climatic relationships.

Chemical signatures

Plants take up carbon, oxygen and hydrogen isotopes from atmospheric CO₂ and water during growth. These isotopes are incorporated into the plant structure. They preserve a record of the atmosphere and climate in which the plant grew. These records can show an individual season's values by looking at leaves or individual tree rings, or can show long-term fine-scale variations by comparing tree ring values over the life of the tree. $\delta^{13}\text{C}$ measurements are used to estimate paleoclimate, but have also been used to match CO₂ records of tree rings with ice core data to determine the exact ages of the trees being measured. ^{13}C is the most commonly measured isotopic ratio used to determine paleoclimate from plants, and is taken into the plant from CO₂ in the atmosphere during growth. In wood, ^{13}C ratios are measured in the cellulose and show a negative relationship with relative humidity and temperature (Edwards et al., 2000). ^{13}C measurements from the leaf cuticle also show a negative correlation between ^{13}C ratios and precipitation or humidity (Sun et al., 2003), (Figure P5).

In addition to ^{13}C , both $\delta^{18}\text{O}$ and $\delta^2\text{H}$ have been measured using wood cellulose and wood nitrite to determine variability in meteoric water, seasonal moisture (relative humidity and precipitation) and precipitation amount (Buhay and Edwards, 1995; Edwards et al., 2000). In addition, $\delta^2\text{H}$ shows a relationship with mean annual and seasonal temperature, though this relationship is best measured in areas where the water supply has a constant isotopic value (Buhay and Edwards, 1995). Because of the complex interaction between precipitation and temperature, climate estimates using measurements from only one isotope may be misleading. Using a combination of $\delta^{13}\text{C}$,

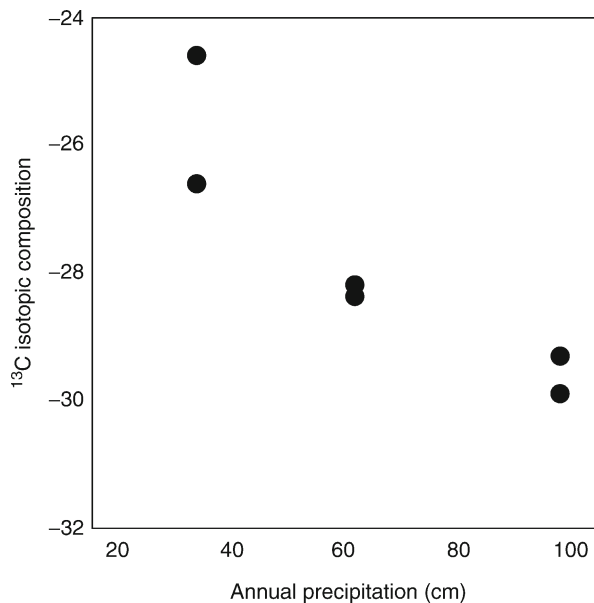


Figure P5 ^{13}C isotopic composition of modern *Ginkgo* leaves versus annual precipitation for three sites in China. Data from Sun et al. (2003).

$\delta^2\text{H}$ and $\delta^{18}\text{O}$ measurements seems to offer the most paleoclimatic information from plants (Edwards et al., 2000).

Elizabeth A. Kowalski and David L. Dilcher

Bibliography

- Beerling, D.J., 1999. Atmospheric carbon dioxide, past climates and the plant fossil record. *Bot. J. Scotl.*, **51**, 49–68.
- Beerling, D.J., and Chaloner, W.G., 1993. The impact of atmospheric CO_2 and temperature change on stomatal density: Observations from *Quercus robur* Lammas leaves. *Ann. Bot.*, **71**, 231–235.
- Beerling, D.J., and Royer, D.L., 2002. Reading a CO_2 signal from fossil stomata. *New Phytol.*, **153**, 387–397.
- Buhay, W.M., and Edwards, T.W.D., 1995. Climate in southwestern Ontario, Canada between AD 1610 and 1885 inferred from oxygen and hydrogen isotopic measurements of wood cellulose from trees in different hydrologic settings. *Quaternary Res.*, **44**, 438–446.
- Chaloner, W.G., and Creber, G.T., 1990. Do fossil plants give a climatic signal? *J. Geol. Soc. London*, **147**, 343–350.
- Chaloner, W.G., and McElwain, J., 1997. The fossil plant record and global climatic change. *Rev. Palaeobot. Palynol.*, **95**, 73–82.
- Davies-Vollum, K.S., 1997. Early Palaeocene palaeoclimatic inferences from fossil floras of the western interior, USA. *Palaeogeogr. Palaeoclimatol. Palaeoecol.*, **136**, 145–164.
- Dilcher, D.L., 1974. Approaches to the identification of fossil leaf remains. *Bot. Rev.*, **40**, 1–157.
- Dilcher, D.S., 1973. A Paleoclimatic interpretation of the Eocene Floras of Southeastern North America. In Graham, A. (eds.), *Vegetation and Vegetational History of Northern Latin America*. Amsterdam: Elsevier. Chapter 2, pp. 39–59.
- Dilcher, D.L., 2000. Toward a new synthesis: Major evolutionary trends in the angiosperm fossil record. *PNAS*, **97**, 7030–7036.
- Edwards, T.W.D., Graf, W., Trimbom, P., Stiehler, W., Lipp, J., and Payer, H.D., 2000. $\delta^{13}\text{C}$ response surface resolves humidity and temperature signals in trees. *Geochim. Cosmochim. Acta*, **64**, 161–167.
- Francis, J.E., and Poole, I., 2002. Cretaceous and early Tertiary climates of Antarctica: Evidence from fossil wood. *Palaeogeogr. Palaeoclimatol. Palaeoecol.*, **182**, 47–64.
- Givnish, T.J., 1987. Comparative studies of leaf form: Assessing the relative roles of selective pressures and phylogenetic constraints. *New Phytol.*, **106**, 131–160.
- Greenwood, D.R., 1992. Taphonomic constraints on foliar physiognomic interpretations of Late Cretaceous and Tertiary paleoclimates. *Rev. Palaeobot. Palynol.*, **71**, 149–190.
- Greenwood, D.R., and Wing, S., 1995. Eocene continental climates and latitudinal temperature gradients. *Geology*, **23**, 1044–1048.
- Gregory-Wodzicki, K.M., 2000. Relationships between leaf morphology and climate, Bolivia: Implications for estimating paleoclimate from fossil floras. *Paleobiology*, **26**, 668–688.
- Halloy, S.R.P., and Mark, A.F., 1996. Comparative leaf morphology spectra of plant communities in New Zealand, the Andes and the European Alps. *J. R. Soc. N. Z.*, **26**, 41–78.
- Jacobs, B.F., 2002. Estimation of low-latitude paleoclimates using fossil angiosperm leaves: Examples from the Miocene Tugen Hills, Kenya. *Paleobiology*, **28**, 399–421.
- Kowalski, E.A., 2002. Mean annual temperature estimation based on leaf morphology: A test from tropical South America. *Palaeogeogr. Palaeoclimatol. Palaeoecol.*, **188**, 141–165.
- Kowalski, E.A., and Dilcher, D.L., 2003. Warmer paleotemperatures for terrestrial ecosystems. *PNAS*, **100**, 167–170.
- Kurschner, W.M., Stulen, I., Wagner, F., and Kuiper, P.J.C., 1998. Comparison of paleobotanical observations with experimental data on the leaf anatomy of Durmast Oak [*Quercus petraea* (Fagaceae)] in response to environmental change. *Ann. Bot.*, **81**, 657–664.
- Martin, H.A., 1997. The use of ecological tolerances for the reconstruction of Tertiary palaeoclimates. *Aust. J. Bot.*, **45**, 475–492.
- Mosbrugger, V., and Utescher, T., 1997. The coexistence approach – a method for quantitative reconstructions of Tertiary terrestrial palaeoclimate data using plant fossils. *Palaeogeogr. Palaeoclimatol. Palaeoecol.*, **134**, 61–86.
- Parkhurst, D.F., and Loucks, O.L., 1972. Optimal leaf size in relation to environment. *J. Ecol.*, **60**, 505–537.
- Roth, J.L., and Dilcher, D.L., 1978. Some considerations in leaf size and leaf margin analysis of fossil leaves. *Cour. Forsch. – Inst. Senckenberg*, **30**, 165–171.
- Royer, D.L., 2001. Stomatal density and stomatal index as indicators of atmospheric CO_2 concentration. *Rev. Palaeobot. Palynol.*, **114**, 1–28.
- Sinka, K.J., and Atkinson, T.C., 1999. A mutual climatic range method for reconstructing palaeoclimate from plant remains. *J. Geol. Soc. London*, **156**, 381–396.
- Spicer, R.A., 1989. The formation and interpretation of plant fossil assemblages. *Adv. Bot. Res.*, **16**, 95–191.
- Stranks, L., and England, P., 1997. The use of a resemblance function in the measurement of climatic parameters from the physiognomy of woody dicotyledons. *Palaeogeogr. Palaeoclimatol. Palaeoecol.*, **131**, 15–28.
- Sun, B., Dilcher, D.L., Beerling, D.J., Zhang, C., Yan, D., and Kowalski, E., 2003. Variation in *Ginkgo biloba* L. leaf characters across a climatic gradient in China. *PNAS*, **100**, 7141–7146.
- Terral, J.-F., and Mengal, X., 1999. Reconstruction of Holocene climate in southern France and eastern Spain using quantitative anatomy of olive wood and archeological charcoal. *Palaeogeogr. Palaeoclimatol. Palaeoecol.*, **153**, 71–92.
- Uhl, D., and Mosbrugger, V., 1999. Leaf venation density as a climate and environmental proxy: A critical review and new data. *Palaeogeogr. Palaeoclimatol. Palaeoecol.*, **149**, 15–26.
- Uhl, D., Walther, H., and Mosbrugger, V., 2002. Leaf venation density in angiosperm leaves as related to climatic and environmental conditions—problems and potential for palaeoclimatology. *N. Jb. Geol. Paläont. Abh.*, **224**, 49–95.
- Wiemann, M.C., Wheeler, E., Manchester, S.R., and Portier, K.M., 1998. Dicotyledonous wood anatomical characters as predictors of climate. *Palaeogeogr. Palaeoclimatol. Palaeoecol.*, **139**, 83–100.
- Wiemann, M.C., Manchester, S.R., and Wheeler, E., 1999. Paleotemperature estimation from dicotyledonous wood anatomical characters. *Palaïos*, **14**, 459–474.
- Wiemann, M.C., Dilcher, D.L., and Manchester, S.R., 2001. Estimation of mean annual temperature from leaf and wood physiognomy. *Forest Sci.*, **47**, 141–149.
- Wilf, P., 1997. When are leaves good thermometers? A new case for leaf margin analysis. *Paleobiology*, **23**, 373–390.
- Wilf, P., Wing, S., Greenwood, D.R., and Greenwood, C.L., 1998. Using fossil leaves as paleoprecipitation indicators: An Eocene example. *Geology*, **26**, 203–206.
- Wing, S., and Greenwood, D.R., 1993. Fossils and fossil climate: The case for equable continental interiors in the Eocene. *Phil. Trans. R. Soc. Lond. B*, **341**, 243–252.
- Wolfe, J.A., 1993. A method of obtaining climatic parameters from leaf assemblages. *USGS Bull.*, **2040**, 71.
- Woodcock, D.W., and Ignas, C.M., 1994. Prevalence of wood characters in eastern North America: What characters are most promising for interpreting climates from fossil wood? *Am. J. Bot.*, **81**, 1243–1251.

Cross-references

[Carbon Isotopes, Stable](#)
[CLAMP](#)
[Dating, Dendrochronology](#)
[Dendroclimatology](#)
[Deuterium, Deuterium Excess](#)
[Nearest-Living-Relative Method](#)
[Oxygen Isotopes](#)
[Paleotemperatures and Proxy Reconstructions](#)
[Palynology](#)

PALEOCEAN MODELING

Introduction

Paleoceanographic (paleocean) modeling is the application of analytic or numerical techniques to predict and understand the ocean's past circulation, biogeochemical interactions, and climate. Paleocean modeling is primarily a tool for exploring

the mechanistic functioning of the ocean and for making concrete predictions testable against paleoenvironmental proxies.

Paleocean modeling may be used to investigate such specific questions as: (a) What was the current structure and tracer distribution of a given past time interval? (b) How sensitive are major oceanographic features, e.g., the Gulf Stream or the meridional overturning circulation (MOC) to boundary condition changes? (c) How might modes of variability, e.g., interannual, interdecadal, and millennial-scale variability change under different conditions? It may also answer some more general questions, such as: (d) What is the role of the ocean in governing the Earth system's response to greenhouse gas (GHG) forcing, and what is the ocean's role in GHG storage and release through Earth's history? (e) To what degree are ocean heat transport (OHT) changes important for understanding climate change, and to what is OHT sensitive: GHGs, gateways, multiple equilibria? Due to recent advances in modeling, answers to these questions are now in the offing, once suitable data and a framework with which to interpret them can be developed.

Conditions are sufficiently close to the present for modeling intervals within the past several million years, such that modern numerical ocean modeling techniques are likely to work as well for the past as they do for modern times. Analytic, "box," and simplified physical models are general enough that they can be applied as readily to paleoceanographic problems. Biogeochemical models are crucial but difficult to extend into the deep past because many ecological and biogeochemical processes that only are moderately understood today are poorly known in the deep past.

This article will focus largely, therefore, on the use of sophisticated numerical models in time periods deep in the past (>3 Ma), before continents and climate had reached their near-modern states – first, on the unique challenges that arise in these periods; and next, on the techniques used to overcome these challenges. These special challenges are balanced by unique opportunities to study the evolution of climate and the Earth system over its full dynamic range. If chosen carefully, i.e., only when the environmental "signal" provided by proxies is much greater than the "noise" inherent in the uncertain physics of models, paleocean modeling answers questions that are impossible to answer within near-modern settings. We conclude with the main results of this young field and discuss some important future directions.

Challenges of paleocean modeling

The ocean is coupled to climate through its surface: via its state, i.e., sea surface temperatures (SSTs), and via fluxes of sunlight, heat, water, and momentum. It is also biogeochemically coupled to the biosphere, through fluxes of sunlight, carbon dioxide, and dust, and traces of organic and inorganic chemicals.

Thus, in order to understand the ocean's dynamics and phenomenology and to predict its role in climate and biogeochemical cycles it is necessary to constrain the state of – and fluxes through – the interface between ocean and atmosphere (Power and Kleeman, 1994; Seager et al., 1995).

Because the ocean is driven, to first order, from its top boundary – the conditions of which are poorly known in the past – paleocean modeling requires that either these surface conditions be quantitatively estimated, or in the best case, objectively prognosed within a coupled ocean-atmosphere model. There are, furthermore, only weak constraints on paleobathymetry, an important boundary condition for paleo-oceanographic modeling (Crowley, 1998), and vertical and horizontal ocean current

velocities that might be used as a test of model predictions are poorly known. Thus, there are two sets of problems – even given a perfect ocean model. How does one: (a) set up the model experiment, given significant sources of uncertainty, and (b) test model predictions if significant mismatches occur between what models predict and what proxies record? We begin with (a).

Setting up deep paleocean model experiments

Beyond the normal challenges associated with ocean modeling (e.g., Gent et al., 1998), deep past paleoceanographic simulations face three challenges: uncertainty introduced by choice of initial conditions, boundary conditions, and model spin up.

Initial conditions. Proxies that might be used as initial conditions for modeling experiments are sparsely distributed in time and space, have inherent uncertainties associated with them, and may not constrain important quantities (e.g., salinity). This challenge is usually overcome by specifying an initial sea surface temperature (SST) distribution derived from proxies or using output from an atmospheric general circulation model (AGCM), which in turn has predicted SSTs, assuming some distribution of oceanic mixed layer depth and heat transport. Surface salinities are normally based on output from such AGCM simulations after assuming an empirical relationship between precipitation minus evaporation (P–E) distributions and surface salinity, or alternatively, a global constant value can be specified as an initial condition. In paleoceanographic simulations carried out with a coupled ocean-atmosphere model, these initial conditions values may strongly deviate as a consequence of the model's evolution. In simulations that are not coupled to an atmospheric model, these distributions are more or less fixed (discussed below). Deep ocean temperatures are normally taken from benthic foraminifera-derived temperature estimates (where available) and salinity is frequently set at the modern global mean value or sometimes set to a different global mean value designed to include past variations in global mean salinity.

Boundary conditions. These include the way in which heat, moisture, and momentum fluxes are passed to the ocean model throughout the simulation as well as static features such as bathymetry. Fluxes have traditionally been handled through the use of so-called Haney restoring (Haney, 1971) of temperature and the specification of net virtual salt fluxes, i.e., mixed boundary conditions. In general, the "weaker" the restoring the more closely this boundary condition mimics atmospheric interaction, but mixed boundary conditions have been shown to be susceptible to spurious multiple equilibria (Weaver and Sarachik, 1991; Zhang et al., 1993; Power and Kleeman, 1993, 1994; Saravanan and McWilliams, 1995). The use of so-called bulk forcing (Brady et al., 1998; Doney et al., 1998), or preferably inclusion of even a simple representation of atmospheric fluxes as in Nong et al. (2000) and Najjar et al. (2002), is best in those cases in which a coupled model is not used. Surface wind stress patterns are normally specified based on modern conditions or a theoretical distribution, or produced by an AGCM.

Since a non-interactive atmosphere – i.e., one in which winds, temperature, and freshwater fluxes cannot adapt to changing ocean conditions – is inherently unrealistic, in most cases a coupled model is preferable to an uncoupled model, even when the focus is strictly oceanographic (Doney et al., 1998). This also allows for a more realistic pattern of surface state and flux variations, and for OHT to be a well-posed prognostic variable, which

it is not if surface temperature patterns are specified (Seager et al., 1995; Nong et al., 2000; Huber et al., 2003).

Ocean bathymetry is a boundary condition that has frequently been a subject of concern in the construction of paleocean modeling experiments (Bice et al., 1998). Some studies have employed a flat bottom configuration, eschewing bathymetric variation altogether (Barron and Peterson, 1991; Bush and Philander, 1997) and dynamical arguments suggest that most ocean current patterns and transports are not sensitive to bathymetric variations (summarized in Bush, 1997). Nevertheless, the details of some currents certainly involve bathymetry (Bice et al., 1998). Perhaps more importantly, the degree of upwelling from the abyss is governed to a large extent by the presence of abyssal bathymetric rises (e.g., geostrophically balanced meridional flows along ocean ridges) and thus some representation is probably important even for the gross features of the ocean circulation (e.g., Toggweiler and Samuels, 1995; Vallis, 2000).

The freshwater (salt) forcing of the ocean is another potentially important variable, with potential issues being the placement of continental runoff into marginal seas and determination of the overall meridional P–E. The former issue is important for determining the exact location of deep water formation (Bice et al., 1997) and the latter is a factor in determining strength of the MOC. However, neither of these issues proves fatal to the study of paleoclimates with ocean models (see below).

Deep ocean spin up procedure. Another difficulty with performing paleocean modeling experiments has been in integrating the entire system, including the deep ocean, to a quasi-steady state. Nevertheless, ocean models – at least the non-eddy resolving models employed in climate and paleoclimate studies – are computationally inexpensive relative to their atmospheric cousins. In ocean-only ocean general circulation model (OGCM) studies, it is now feasible to integrate the model to equilibrium without so-called deep ocean acceleration, although accelerating the deep ocean tracer fields during spin up has been shown to speed equilibration without unduly affecting the final climate state (Danabasoglu et al., 1996, 2004).

However, as described above, a coupled model is preferred for most climate purposes, so that surface temperature, salinity fields, ocean heat, and freshwater transport are fully prognostic. Many coupled models historically display a “drift” of climate away from modern values even under modern conditions, which have precluded them for use in paleoclimatology, but this modeling challenge has been overcome in the recent generation of models. It has not been feasible with existing computational resources to attempt the ideal solution with a coupled general circulation model (CGCM), which is to integrate several multi-millennial simulations. Two options exist: (a) using a simplified coupled model that is computationally less expensive, or (b) using a technique to accelerate convergence of a full CGCM.

Many simplified CGCMs or “intermediate” complexity models now exist, and in general, they are a useful tool in the modeling toolbox (Saravanan and McWilliams, 1995; Poussart et al., 1999; Weaver et al., 2001; Claussen et al., 2002). When these tools are not sufficient, iterative accelerated spin up techniques have been developed to allow several thousand years of deep ocean simulation to be carried out in only several hundred years of surface ocean computation using fully coupled GCMs.

There is a variety of techniques – most draw on two existing procedures: iteration of coupled and uncoupled modeling steps, and deep ocean acceleration. The iteration technique has been used and validated in somewhat different forms by Sausen and Voss (1996), Kutzbach and Liu (1997), Liu et al. (1999),

Vavrus et al. (2000), Huber and Sloan (2001), Otto-Bliesner et al. (2002), and Liu et al. (2004). Shin et al. (2003) describe a different technique that employs deep ocean acceleration directly in the fully coupled integration and this has been shown to produce convergent climates with the iterative technique in the Eocene, thus either family of techniques is a potential candidate for use. There are no guarantees that a given acceleration technique will apply equally well to all time intervals or that it can be generalized for different models or model configurations. Therefore, initial validation of the convergence of a given modeling framework to a reference condition (presumably the present) to some appropriate level of similarity is a primary requirement of any technique.

Minimal tests of model suitability. Although the models used in paleoceanography are usually well-validated for modern day conditions, even a “perfect” model for the present may not be perfect for the correct physical reasons (instead, tuning may be responsible), nor nearly as accurate with less accurate boundary conditions. Our incomplete knowledge of boundary and initial conditions for paleocean modeling, simplification of model physics, and/or use of acceleration techniques introduces errors into the simulation. Therefore, paleocean modeling investigations should be tailored to answering questions that can be answered with the level of detail available for the specified time interval. One method to assess the suitability of a model is a process called “degradation” (Huber and Sloan, 2001). This involves simplifying boundary conditions in the control case (i.e., changing bathymetry) and appropriate “detuning” of the model. A degraded control solution provides a benchmark to determine what model-predicted variables might potentially be robustly determined in the past. Degradation has been shown to provide one (minimum) estimate of the errors introduced into model predictions by misrepresenting multiple aspects of the system (Huber et al., 2003).

Modeling choices. No model is perfect, and many parameterizations and models in existence are better for some purposes than others. Nevertheless, there are some general guidelines, at least with complex, GCM caliber models, that should be considered. Oceanic vertical diffusion is one of the most important and most contentious issues in modern oceanography. It is likely to have been even more important in the past. The absolute “background” value of the diffusivity and the physical processes that increase it above this background value are much debated. While some spread exists for an estimate of this background value, a reasonable observed number is $0.1 \text{ cm}^2 \text{ s}^{-1}$, and values in this range should be the default in paleoceanographic applications. Values 10–100 times greater than this are commonly used even in modern simulations, which highlights the deficiencies in those models. The inclusion of state-of-the-art treatments of diapycnal and isopycnal eddy mixing is important, and currently it appears that a combination of the KPP and Gent-McWilliams treatments of these processes is best from the point of view of the tracer circulation and tracer properties (Gent et al., 1998). There is substantial room for improvement in these parameterizations and ideally several vertical diffusion methods should be tested because the resulting ocean circulations can be fundamentally different (e.g., Nilsson et al., 2003).

Predictions of paleocean modeling

Horizontal ocean currents. These are prognosed by OGCMs as well as a host of simplified models, and are the quantities most directly tied to the well-understood and well-represented

dynamics of the ocean. In general, an OGCM is not necessary to predict velocities. The surface and upper ocean flows largely reflect the driving wind fields, and consequently “shallow water” ocean models, or even analytic calculations such as the “island rule” or the Sverdrup transport allow estimates of the strength, shape, and disposition of gyre circulations as well as the western boundary currents in equilibrium with them for a given wind field (Huber and Nof, 2006; Nof, 2000; Nof and Van Gorder, 2002; see Figure P6). In the deep ocean, OGCM results have mainly reproduced features that were adducible from Stommel-Arons theory (see results in Huber et al., 2003). Such predictions may be verified with records of paleocirculation intensity and direction.

Unfortunately, current directions are weakly constrained and current magnitudes are among the most poorly known features in “deep-time” paleoceanography, since these features are not strongly constrained by direct proxies, and the indirect proxies are qualitative (Carter et al., 1996; McGowran et al., 1997; Watkins and Kennett, 1972). Nevertheless, a substantial amount of work has been done in predicting paleocean current directions and testing these against proxy interpretations. Some notable studies include those in the Permian (Winguth et al., 2002), the Cretaceous Tethyan current regime (Barron and Peterson, 1991; Bush and Philander, 1997), and in the global ocean (Poulsen et al., 1998, 2001), and on a regional scale, in the Turonian seaway (Slingerland et al., 1996). For more recent periods, attempts have been made to understand changes in flow direction between the Atlantic and Pacific, i.e., during the Miocene (Nof and Van Gorder, 2002; Nisancioglu et al., 2003; Omta and Dijkstra, 2003), although explicit model-data comparison has been lacking in these studies. The more widespread use of sediment and biological transport and dispersal models in such investigations would substantially assist in the

comparison to proxy records. Some first steps in that direction have been taken in Huber et al. (2004).

Upwelling and productivity. Upwelling is a feature more closely tied to the proxy record than ocean current direction because it is more directly linked to an observable quantity (productivity and burial). Understanding how upwelling patterns may have changed during the past can provide us with clues to the nature of circulation changes (Toggweiler and Samuels, 1995; Vallis, 2000), primary productivity shifts (Moore et al., 2004), and alterations in global cycling of chemical species that may have occurred. Upwelling predictions may be especially useful for placing constraints on organic carbon burial rates (Handoh et al., 1999, 2003) over these time intervals.

For the purely wind-driven component of upwelling, an OGCM is not particularly necessary; a “shallow water” model is adequate to the task (Handoh et al., 1999, 2003). Calculation of Ekman pumping from the wind fields produces nearly identical results.

Quantitatively tying the upwelling velocity to a sediment accumulation rate involves a deep understanding of many ecological and biogeochemical processes. Currently, our ability to make quantitative predictions on productivity, burial, and the carbon cycle in the past is more limited by our understanding of past biogeochemical cycles and paleoecology than by insights into past physical oceanography (more below).

Deep water formation and MOC

Transformation of surface waters into shallow mode and intermediate and deep waters, and subsequent recycling of these waters into the surface, is an important and complex process. It is fundamental to the redistribution of heat, nutrients, and other tracers in the ocean and is consequently of great interest in paleoceanography.

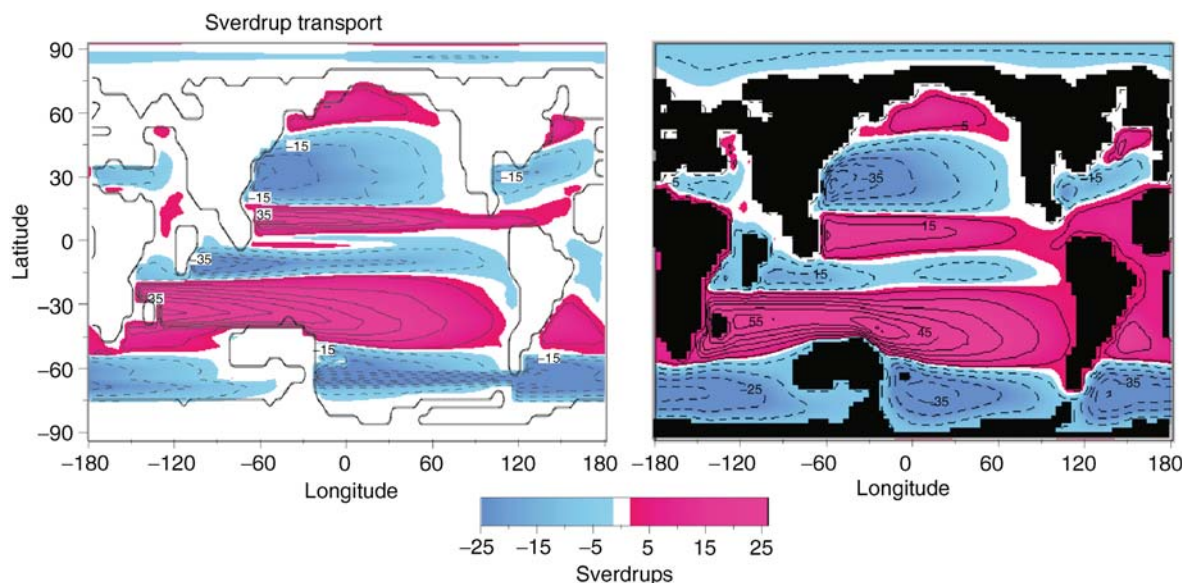


Figure P6 Results from Huber et al. (2004) for the theoretical wind-driven and general circulation model derived ocean circulations. The estimated wind-driven ocean gyre transport in equilibrium with the AGCM-derived winds calculated from the Sverdrup transport driven by the wind stress curl. Theory suggests to first order that barotropic velocities should correspond closely to the Sverdrup transport. Right, this is confirmed by comparison to the barotropic stream function produced by the ocean model. Clockwise gyres are indicated in *blue*, counterclockwise gyres in *red*. The flow is contoured at 10 Sverdrup intervals. The correspondence between the upper ocean velocities shows clearly that – if wind fields are well-known, or simply prescribed – the major ocean current systems will be entirely governed by this distribution.

Just as there are weak data-based constraints on ocean velocity, there are weak constraints on its integral properties, such as the meridional overturning streamfunction. One commonly applied constraint is the calculation of vertical and spatial gradients of $\delta^{13}\text{C}$, which is an isotopic tracer related to nutrient distribution and the carbon cycle (e.g., Corfield and Norris, 1996). Where sufficient $\delta^{13}\text{C}$ gradients exist, the location of regions of deep water formation can be ascertained and bulk flow patterns may be estimated. The use of other water mass tracers, such as neodymium (e.g., Thomas, 2004), is a recent innovation that may add significant detail to the picture that has developed from $\delta^{13}\text{C}$ tracer distributions.

Rates of deep water formation and deep water flow are not currently predictable from these methods, which is unfortunate because these are the quantities that bear directly on the critical paleoceanographic questions, whereas the *location* of deep water formation reveals little, by itself, about the ability of the circulation to transport heat or nutrients.

The rate at which heat is transported by circulation is a function of the velocities, diffusion, and temperature gradients, and analogous balances obtained for the transport of all tracers. Thus the main importance of the location of deep water formation, i.e., whether it occurs at high latitudes or at low latitudes, is indirect, through its relationship with the resulting transport rates and tracer gradients. Some debate exists as to whether true deep water formation at low latitudes was physically possible in the Earth's past – results and interpretations vary from model to model (compare Saravanan and McWilliams, 1995; Bice and Marotzke, 2002; Zhang et al., 2002). In general, even in simulations in which low latitude deep water formation occurs, it is either weak or transient, and is associated with a decrease in OHT (see below).

Proxy records of benthic oxygenation have been employed as constraints on overturning circulation rates in the oceans. These records are difficult to interpret because they involve deconvolution of the competing influences of the supply of organic matter and oxygen to the deep. Both factors may increase as the overturning rate increases – increased oxygen supply occurs as the overturning strengthens, but increased upwelling of nutrient rich waters may enhance export of organics out of the surface and into the deep. For a revealing view of the divergences of interpretation that can occur, compare Zhang et al. (2001) and Hotinski et al. (2001).

Without improvement of our understanding of past biogeochemical cycles and the development of multiple and independent proxies for upwelling, productivity, oxygenation, and deep water formation, it is unlikely that it will be possible to discriminate between different models of the ocean's overturning circulation in the deep past.

Ocean gateways and heat transport

Past climate changes have been frequently attributed to ocean gateway changes – such as the opening of Drake Passage and closing of the Panamanian Gateway (Kennett, 1977; Crowley 1998; Lawver and Gahagan, 1998). This belief finds its support in the approximate correlation between major gateway changes and climatic change (Zachos et al., 2001). A number of modeling studies have demonstrated that the ocean's overturning circulation, heat transport, and resulting temperature distribution are somewhat sensitive to changes in ocean gateways (Mikolajewicz et al., 1993, 1997). There is, furthermore, a strong line of theoretical and modeling evidence that backs

up the theory that wind-driven upwelling of deep water in the Southern Ocean plays a dominant role in modern day ocean circulation (Toggweiler and Samuels, 1995; Nof, 2000) and that past changes in this upwelling may have been especially important at both high latitudes (Toggweiler and Bjornsson, 2000) and low latitudes (Hotinski and Toggweiler, 2003). The most frequently cited example of a direct impact of gateway changes on OHT is due to the creation of the Antarctic Circumpolar Current (ACC). As noted in Toggweiler and Bjornsson (2000), creation of the ACC leads to a cooling of the Southern Hemisphere, and a warming of the Northern Hemisphere, because the flows associated with the ACC “steal” heat across the equator.

While all of the above studies yield similar predictions with respect to the physical oceanographic responses to gateway changes, the surface temperature response, i.e., the climatic impact of this change shows a wide spread. In studies in which a simple representation of coupling of ocean-atmosphere exchanges has been included, opening and closing of Southern Ocean gateways result in Southern Ocean surface temperature changes from a low value of 0.8°C (Mikolajewicz et al., 1993), to a middle range of ~1.5°C (Nong et al., 2000), and a high value of ~3.5°C (Toggweiler and Bjornsson, 2000; Najjar et al., 2002). When a CGCM is used, the resulting change within the Southern Ocean is in the middle of the range of previous estimates (Huber and Sloan, 2001; Huber et al., 2003). The spread of values represents differences in the treatment of the “top” boundary condition, including sea ice feedbacks and damping by the atmosphere, rather than representing an important difference in predicted ocean dynamics behavior.

The mechanism that links gateways to climate change is usually presumed to be ocean heat modifications induced by shifts in ocean currents. The impacts that such ocean current changes have had on ocean productivity and burial and hence global inventories of atmospheric GHGs have received less attention in comparison (Huber et al., 2003).

Some lessons learned

Paleocean modeling has been applied to a suite of paleoclimate problems in Earth's history – mostly, it has focused on the leading role played by changes in greenhouse gas concentrations. Results from this work indicate that, within a sophisticated coupled modeling framework, ocean temperatures in line with proxies for both past “greenhouse” and “icehouse” intervals are generally achievable without major changes in ocean circulation, but are driven by changes in deep water temperatures (Huber and Sloan, 2001; Otto-Bliessner et al., 2002; Poulsen et al., 2002; Shin et al., 2002; Peltier and Solheim, 2004). See Figure P7 for a Cretaceous example.

The main current limitation of physical paleocean modeling in paleoclimatology is the availability and accuracy of data for inclusion in initial and boundary conditions and the need for a suite of proxies sufficient to verify and validate the model predictions. Fully coupled modeling offers the advantage of increasing the range of model predictions testable against proxies (Huber and Caballero, 2003). Modeling of biological, isotopic, ecological, and geochemical processes for the deep past lags behind physical modeling by a significant margin and the current sophistication of these efforts may be considered rudimentary, despite significant efforts to improve the situation (e.g., Heinze and Crowley, 1997). The next main challenge of paleoceanographic modeling is to close the gap

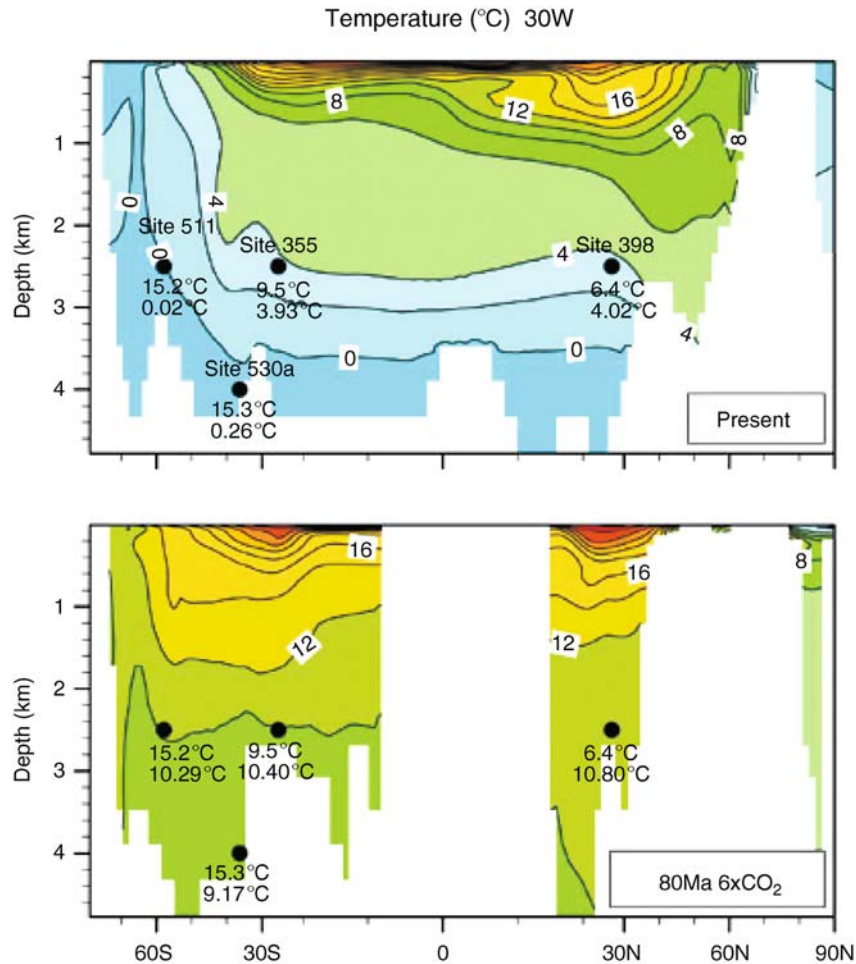


Figure P7 Cretaceous paleotemperature estimates published from ODP and DSDP cores based on deep-dwelling fauna are sparse and exhibit a wide range of values, but point to a much warmer deep ocean. For a transect in the Atlantic Ocean, the NCAR Climate System Model predicts ocean temperatures below 2.5 km depth of approximately 10°C (*bottom values*) compared with proxy estimates of 6–15°C (*top values*). The model simulation indicates that the source of the warmer deep ocean temperatures is sinking of warmer southern polar waters. See Otto-Bliesner et al. (2002) for more details.

between the physics of the ocean and the biology, sedimentology, and chemistry that provides key constraints on the paleoclimatic record as well as being of fundamental importance to paleoclimate itself.

Matthew Huber

Bibliography

- Barron, E.J., and Peterson, W.H., 1991. The Cenozoic ocean circulation based on ocean general circulation model results. *Palaeogeogr. Palaeoclimatol. Palaeoecol.*, **83**, 1–28.
- Bice, K.L., Barron, E.J., and Peterson, W.H., 1997. Continental runoff and early Cenozoic bottom water sources. *Geology*, **25**, 951–954.
- Bice, K.L., Barron, E.J., Peterson, W.H., 1998. Reconstruction of realistic Early Eocene paleobathymetry and ocean GCM sensitivity to specified ocean basin configuration. In Crowley, T.J., and Burke, K.C. (eds.), *Tectonic Boundary Conditions for Climate Reconstructions*. New York: Oxford University Press, pp. 212–226.
- Bice, K.L., and Marotzke, J., 2002. Numerical evidence against reversed thermohaline circulation in the warm Paleocene/Eocene ocean. *J. Geophys. Res.*, **106**, 11529–11542.
- Brady, E.C., DeConto, R.M., and Thompson, S.L., 1998. Deep water formation and poleward ocean heat transport in the warm climate extreme of the Cretaceous (80 Ma). *Geophys. Res. Lett.*, **25**, 4205–4208.
- Bush, A.B.G., and Philander, S.G.H., 1997. The Late Cretaceous: Simulation with a coupled ocean – atmosphere general circulation model. *Paleoceanography*, **12**, 495–516.
- Bush, A.B.G., 1997. Numerical simulation of the Cretaceous Tethys Circumglobal Current. *Science*, **275**, 807–8.
- Carter, R.M., Carter, L., and McCave, I.N., 1996. Current controlled sediment deposition from the shelf to the deep ocean: The Cenozoic evolution of circulation through the SW Pacific gateway. *Geol. Rundsch.*, 438–451.
- Claussen, M., Mysak, L.A., Weaver, A.J., Crucifix, M., Fichefet, T., Loutre, M.F., Weber, S.L., Alcamo, J., Alexeev, V.A., Berger, A., Calov, R., Ganopolsky, A., Goosse, H., Lohman, G., Lunkeit, F., Mohkov, I.I., Petoukhov, V., Stone, P., and Wang, Z., 2002. Earth System Models of Intermediate Complexity: Closing the gap in the spectrum of climate system models. *Clim. Dynam.*, **18**, 579–586.
- Corfield, R., and Norris, R.D., 1996. Deep water circulation in the Paleocene Ocean. In Knox, R.W.O.B., Corfield, R.M., and Dunay, R.E. (eds.), *Correlation of the Early Paleogene in Northwest Europe*. Geological Society Special Publication, pp. 443–456.

- Crowley, T.J., 1998. Significance of tectonic boundary conditions for paleoclimate simulations. In Crowley, T.J., and Burke, K.C. (eds.), *Tectonic Boundary Conditions for Climate Reconstructions*. New York: Oxford University Press, pp. 212–226.
- Danabasoglu, G., 2004. A comparison of global ocean circulation model solutions obtained with synchronous and accelerated integration methods. *Ocean Model.*, **7**, 323–341.
- Danabasoglu, G., McWilliams, J.C., and Large, W.G., 1996. Approach to equilibrium in accelerated global oceanic models. *J. Climate*, **9**, 1092–1110.
- Doney, S.C., Large, W.G., and Bryan, F.O., 1998. Surface ocean fluxes and water-mass transformation rates in the coupled Climate System Model. *J. Climate*, **9**, 1420–1441.
- Gent, P.R., Bryan, F.O., Danabasoglu, G., Doney, S.C., Holland, W.R., Large, W.G., and McWilliams, J.C., 1998. The NCAR Climate System Model global ocean component. *J. Climate*, **11**, 1287–1306.
- Haney, R.L., 1971. Surface thermal boundary condition for ocean circulation models. *J. Phys. Oceanogr.*, **1**, 241–248.
- Handoh, I.C., Bigg, G.R., Jones, E.J.W., and Inoue, M., 1999. An ocean modeling study of the Cenomanian Atlantic: Equatorial paleo-upwelling, organic-rich sediments and the consequences for a connection between the proto-North and South Atlantic. *Geophys. Res. Lett.*, **26**, 223–226.
- Handoh, I.C., Bigg, G.R., and Jones, E.J.W., 2003. Evolution of upwelling in the Atlantic Ocean Basin. *Palaeogeogr. Palaeoclimatol. Palaeoecol.*, **202**, 31–58.
- Heinze, C., and Crowley, T.J., 1997. Sedimentary response to gateway circulation changes. *Paleoceanography*, **12**, 742–754.
- Hotinski, R.M., Bice, K.L., Kump, L.R., Najjar, R.G., and Arthur, M.A., 2001. Ocean stagnation and end-Permian anoxia. *Geology*, **29**, 7–10.
- Hotinski, R.M., and Toggweiler, J.R., 2003. Impact of a Tethyan circum-global passage on ocean heat transport and “equable” climates. *Paleoceanography*, **18**, doi: 10.1029/2001PA000730.
- Huber, M., Brinkhuis, H., Stickley, C.E., Doos, K., Sluijs, A., Warnaar, J., Schellenberg, S.A., and Williams, G.L., 2004. Eocene circulation of the Southern Ocean: Was Antarctica kept warm by subtropical waters. *Paleoceanography*, **19**, PA4026.
- Huber, M., and Caballero, R., 2003. Eocene El Niño: Evidence for robust tropical dynamics in the “hothouse”. *Science*, **299**, 877–881.
- Huber, M., Sloan, L.C., and Shellito, C., 2003. Early Paleogene oceans and climate: A fully coupled modelling approach using NCAR’s CSM. In Wing, S.L., Gingerich, P.D., Schmitz, B., and Thomas, E. (eds.), *Causes and Consequences of Globally Warm Climates in the Early Paleogene*. *Geol. Soc. Amer. Special Paper*, **369**, 25–47.
- Huber, M., and Sloan, L.C., 2001. Heat transport, deep waters, and thermal gradients. *Geophys. Res. Lett.*, **28**, 3481–3484.
- Huber, M., and Nof, D., 2006. The ocean circulation in the Southern Hemisphere and its climatic impacts in the Eocene. *Palaeogeogr. Palaeoclim. Palaeoecol.*, **231**, 9–28.
- Kennett, J.P., 1977. Cenozoic evolution of Antarctic glaciations, the circum-Antarctic ocean and their impact on global paleoceanography. *J. Geophys. Res.*, **82**, 3843–3860.
- Kutzbach, J.E., and Liu, Z., 1997. Response of the African monsoon to orbital forcing and ocean feedbacks in the middle Holocene. *Science*, **278**, 440–443.
- Lawver, L.A., and Gahagan, L.M., 1998. The Initiation of the Antarctic Circumpolar Current and its impact on Cenozoic climate. In Crowley, T., and Burke, K. (eds.), *Tectonic Boundary Conditions for Climate Model Simulations*. New York: Oxford University Press, 213–226.
- Liu, Z.R., Gallimore, G., Kutzbach, J.E., Xu, W., Golubev, Y., Behling, P., and Selin, R., 1999. Coupled modeling of long-term climate change with the equilibrium asynchronous coupling scheme. *Clim. Dyn.*, **15**, 325–240.
- Liu, Z., Lewis, W., and Ganopolski, A., 2004. A coordinated acceleration scheme for the simulation of long term climate evolution. *Clim. Dyn.*, **22**, 771–781.
- McGowan, B., Li, Q., Cann, J., Padley, D., McKirdy, D.M., and Shafik, S., 1997. Biogeographic impact of the Leeuwin Current in southern Australia since the late middle Eocene. *Palaeogeogr. Palaeoclimatol. Palaeoecol.*, **136**, 19–40.
- Mikolajewicz, U., Maierreimer, E., Crowley, T.J., and Kim, K.Y., 1993. Effect of Drake and Panamanian Gateways on the circulation of an ocean model. *Paleoceanography*, **8**, 409–426.
- Mikolajewicz, U., and Crowley, T.J., 1997. Response of a coupled ocean/energy balance model to restricted flow through the Central American isthmus. *Paleoceanography*, **12**, 429–441.
- Moore, T. C. Jr., Backman, J., Raffi, I., Nigrini, C., Sanfilippo, A., Palike, H., and Lyle, M., 2004. Paleogene tropical Pacific: Clues to circulation, productivity, and plate motion. *Paleoceanography*, **19**(3), PA3013.
- Najjar, R.G., Nong, G.T., Seidov, D., and Peterson, W.H., 2002. Modeling geographic impacts on early Eocene ocean temperature. *Geophys. Res. Lett.*, **29**, doi: 10.1029/2001GL014–438.
- Nilsson, J., Broström, G., and Walin, G., 2003. The thermohaline circulation and vertical mixing: does weaker density stratification give stronger overturning? *J. Phys. Oceanogr.*, **33**, 2781–2795.
- Nisancioglu, K.H., Raymo, M.E., and Stone, P.H., 2003. Reorganization of Miocene deep water circulation in response to shoaling of the Central American Seaway. *Paleoceanography*, **18**, doi:10.1029/2002PA000767.
- Nof, D., 2000. Does the wind control the import and export of the South Atlantic? *J. Phys. Oceanogr.*, **30**, 2650–2667.
- Nof, D., and Van Gorder, S., 2002. Did an open Panama Isthmus correspond to an invasion of Pacific water into the Atlantic? *J. Phys. Oceanogr.*, **33**, 1324–1336.
- Nong, G.T., Najjar, R.G., Seidov, D., and Peterson, W.H., 2000. Simulation of ocean temperature change due to the opening of the Drake Passage. *Geophys. Res. Lett.*, **27**, 2689–2692.
- Omta, A.W., and Dijkstra, H.A., 2003. A physical mechanism for the Atlantic-Pacific flow reversal in the early Miocene. *Glob. Planet. Change*, **788**, 1–12.
- Otto-Bliesner, B.L., Brady, E.C., and Shields, C., 2002. Late Cretaceous Ocean: Coupled simulations with the NCAR CSM. *J. Geophys. Res.*, **107**, doi: 10.1029/2001JD000821.
- Peltier, W.R., and Solheim, L.P., 2004. The climate of the Earth at Last Glacial Maximum: statistical equilibrium state and a mode of internal variability. *Quaternary Sci. Rev.*, **23**, 335–357.
- Poulsen, C.J., Seidov, D., Barron, E.J., and Peterson, W.H., 1998. The impact of paleogeographic evolution on the surface oceanic simulation and the marine environment within the mid-Cretaceous Tethys. *Paleoceanography*, **13**, 546–559.
- Poulsen, C.J., Barron, E.J., Arthur, M.A., and Peterson, W.H., 2001. Response of the mid-Cretaceous global oceanic circulation to tectonic and CO₂ forcings. *Paleoceanography*, **16**, 576–592.
- Poulsen, C.J., Jacob, R.L., Pierrehumbert, R.T., and Huynh, T.T., 2002. Testing paleogeographic controls on a Neoproterozoic snowball Earth. *Geophys. Res. Lett.*, **29**, doi: 10.1029/2001GL014352.
- Poussart, P.F., Weaver, A.J., and Barnes, C.R., 1999. Late Ordovician glaciation under high atmospheric CO₂: A coupled model analysis. *Paleoceanography*, **14**, 542–558.
- Power, S.B., and Kleeman, R., 1993. Multiple equilibria in a global ocean general circulation model. *J. Phys. Oceanogr.*, **23**, 1670–1681.
- Power, S.B., and Kleeman, R., 1994. Surface flux parameterisation and the response of OGCMs to high latitude freshening. *Tellus*, **46**, 86–95.
- Saravanan, R., and McWilliams, J.C., 1995. Multiple equilibria, natural variability, and climate transitions in an idealized ocean-atmosphere model. *J. Climate*, **10**, 2296–2323.
- Sausen, R., and Voss, R., 1996. Techniques for asynchronous and periodically synchronous coupling of atmosphere and ocean models. I. General strategy and application to the cyclo-stationary case. *Clim. Dyn.*, **12**, 595–604.
- Seager, R., Kushnir, Y., and Cane, M.A., 1995. On heat flux boundary conditions for ocean models. *J. Phys. Oceanogr.*, **25**, 3219–3230.
- Shin, S.I., Liu, Z., Otto-Bliesner, B., Brady, E.C., Kutzbach, J.E., Harrison, S.P., 2003. A simulation of the last Glacial Maximum Climate using the NCAR-CCSM. *Clim. Dyn.*, **20**, 127–151.
- Slingerland, R., Kump, L.R., Arthur, M.A., Fawcett, P.J., Sageman, B.B., and Barron, E.J., 1996. Estuarine circulation in the Turonian Western Interior seaway of North America. *Geol. Soc. Am. Bull.*, **108**, 941–952.
- Thomas, D.J., 2004. Evidence for production of North Pacific deep waters during the early Cenozoic Greenhouse. *Nature*, **430**, 65–68.
- Toggweiler, J.R., and Samuels, B., 1995. Effect of Drake Passage on the Global Thermohaline Circulation. *Deep Sea Res.*, **42**, 477–500.
- Toggweiler, J.R., and Bjornsson, H., 2000. Drake Passage and paleoclimate. *J. Quatern. Sci.*, **15**, 319–238.

- Watkins, N.D., and Kennett, J.P., 1972. Regional sedimentary discontinuities and upper Cenozoic changes in bottom water velocities between Australia and Antarctica. *Antarct. Res. Ser.*, **19**, 317–334.
- Weaver, A.J., and Sarachik, E.S., 1991. The role of mixed boundary condition in numerical models of ocean's climate. *J. Phys. Oceanogr.*, **21**, 1470–1493.
- Weaver, A.J., Eby, M., Wiebe, E.C., Bitz, C.M., Duffy, P.B., Ewen, T.L., Fanning, A.F., Holland, M.M., MacFadyen, A., Matthews, H.D., Meissner, K.J., Saenko, O., Schmittner, A., Wang, H., and Yoshimori, M., 2001. The UVic Earth System Climate Model: Model description, climatology and application to past, present and future climates. *Atmosphere Ocean*, **39**, 361–428.
- Winguth, A.M.E., Heinze, C., Kutzbach, J.E., Maier-Reimer, E., Mikolajewicz, U., Rowley, D., Rees, A., and Zieger, A.M., 2002. Simulated warm polar currents during the middle Permian. *Paleoceanography*, **17**, 4.
- Vallis, G.K., 2000. Large-scale circulation and production of stratification: Effects of wind, geometry, and diffusion. *J. Phys. Ocean.*, **30**, 933–954.
- Vavrus, S., Gallimore, R., and Liu, Z., 2000. A mixed-flux equilibrium asynchronous coupling scheme for accelerating convergence in ocean-atmosphere models. *Clim. Dyn.*, **16**, 821–831.
- Zachos, J., Pagani, M., Sloan, L.C., Thomas, E., and Billups, K., 2001. Trends, rhythms, and aberrations in global climate 65 Ma to Present. *Science*, **292**, 686–693.
- Zhang, S., Greatbach, R.J., and Lin, C.A., 1993. A reexamination of the polar halocline catastrophe and implications for coupled ocean-atmosphere modeling. *J. Phys. Oceanogr.*, **23**, 287–299.
- Zhang, R., Follows, M., Grotzinger, J.P., and Marshall, J., 2001. Could the late Permian deep ocean have been anoxic? *Paleoceanography*, **16**, 317–329.
- Zhang, R., Follows, M., and Marshall, J., 2002. Mechanisms of thermohaline mode switching with application to warm equable climates. *J. Clim.*, **15**, 2056–2072.

Cross-references

Carbon Isotopes, Stable
Heat Transport, Oceanic and Atmospheric
Ocean Paleocirculation
Ocean Paleotemperatures
Paleoclimate Modeling, Pre-Quaternary
Paleoclimate Modeling, Quaternary
Paleoceanography
Plate Tectonics and Climate Change
Thermohaline Circulation

PALEOCEANOGRAPHY

Introduction

Paleoceanography is the study of the history of the oceans. It encompasses aspects of oceanography, climatology, biology, chemistry and geology. The main sources of information are biogenic and inorganic marine sediments, as well as corals. Biogenic sediment includes planktonic and benthic fossils whereas inorganic sediment includes ice-rafted debris and dust. On land, paleo-shorelines and erosional features as well as outcroppings of paleomarine sediments are the principal sources of proxy data. Glaciological records can also give indirect information about paleoceans. The ocean's high heat capacity and its ability to transport energy and to sequester and release greenhouse gases give it an important role in helping to determine the state of the planet's climate. Thus, paleoceanographic research is also intimately linked to paleoclimatology.

Methods

The reconstruction of paleocean characteristics and dynamics requires climatic detective work. It involves the dating and interpretation of paleoclimatic records as well as the definition of physical and dynamical constraints which specify possible circulation patterns and characteristics.

Reconstructions (Proxy Data)

Direct measurements of the quantities of interest to oceanographers extend only into the relatively recent past and in most cases do not go further back than the mid-nineteenth century. To study the ocean during periods for which there are no direct measurements one must rely on indirect evidence. Historical documents can be used as sources of data. Ship logbooks and sailing times across frequently traveled routes have provided estimates of the directions and strengths of past prevailing winds (Brazdil et al., 2005). The frequency and intensity of El Niño events since the 1500s have been reconstructed based partially on historical accounts of large floods and crop losses (Quinn and Neal, 1987). This type of analysis furnishes qualitative descriptions of the past.

Quantitative reconstructions are possible by proxy, where a quantity which is preserved in a natural archive and can be measured, stands as a surrogate of the parameter of interest. A basic requirement is that the relationship between the proxy parameter and the quantity of interest has to be known. When this is the case, the history of the proxy variable can be converted into the history of the variable of interest by the use of mathematical expressions of the type:

$$Int_t = f(Prx_t) \quad (1)$$

which state that the parameter of interest, Int_t , is a function of the proxy quantity, Prx_t . The t index refers to time. Equations of this kind are commonly called *transfer functions*. The confidence with which Int_t can be estimated will depend on a series of factors, starting with the quality of the proxy measurements. Also relevant, and a common source of uncertainty, is how well f represents the relationship between Prx_t and Int_t .

In most cases, transfer functions are obtained empirically by comparing directly measured values of the quantity of interest to a pertinent set of proxy data. A potential source of error is that the function obtained by this procedure might not be general, but in fact could represent a relationship between Prx_t and Int_t that is peculiar to the data sets used to generate f . This problem can be minimized by expanding the spatial and temporal coverage of the data used to establish the transfer function. Still, even assuming that f is a perfect representation of how the proxy and the quantity of interest are connected to each other in the present, there is no guarantee that the relationship between them was the same in the past.

Another source of error can be easily understood by re-writing Equation (1) so that it expresses the proxy quantity as a function of the variable of interest. It is reasonable to assume (and in many cases it has been demonstrated) that Int_t is not the only factor controlling Prx_t , so that in fact we end up with:

$$Prx_t = f^{-1}(Int_t, E_{1t}, E_{2t}, \dots, E_{nt}) \quad (2)$$

where E_1, E_2, \dots, E_n represent environmental parameters that also influence the proxy variable but are independent of the quantity of interest. An immediate conclusion is that reconstructions of Int_t based on Prx_t will be "contaminated" by other

factors so that part of the variability observed in the proxy quantity is not related to changes in the parameter of interest. Comprehensive analysis of the relationships between proxies and a series of observed parameters can offer some insight into how to remove part of the undesired influence of other factors from the reconstruction.

Given the complexity involved in developing skillful transfer functions as well as in identifying and correcting for potential sources of error, a common strategy is to reconstruct the same parameter of interest using different proxies. Such analyses are known as multi-proxy reconstructions (Fischer and Wefer, 1999).

Types of proxies:

The systematic use of proxies in quantitative reconstructions of past oceanic environments originated in the second half of the twentieth century. Since then, a large number of proxy techniques have been established and more are constantly being developed. Proxies can be grouped in six broad categories, based on the type of direct measurement (Fischer and Wefer, 1999). These are listed below, together with brief descriptions of the main variables of interest associated with each proxy. The following chapters on paleotemperature, paleoproductivity and paleocirculation present in more detail the proxies relevant to each of these fields. Comprehensive discussions of oceanographic proxies can be found in the literature (Bradley, 1999; Fischer and Wefer, 1999; Henderson, 2002).

- *Microfossil assemblages.* The relative abundance of planktonic and benthic species of foraminifera, coccoliths, radiolaria, diatoms and other organisms can be used to estimate past ocean temperature, productivity and sea ice distribution. This proxy type was used for the CLIMAP project, which produced the first global distribution of sea surface temperature for the Last Glacial Maximum (CLIMAP – Project Members, 1976).
- *Stable isotopes* are based on the ratio between different isotopes of an element. The ratios are usually standardized by a reference value and named after the heavier isotope. The ratio between ^{18}O and ^{16}O , for example, is represented by $\delta^{18}\text{O}$. Isotope readings are retrieved mainly from foraminifera skeletons (tests), organic matter or other sources (e.g., water molecules in continental ice sheets). The amount of ^{18}O incorporated by organisms like foraminifera and corals increases as temperature decreases. Continental ice is relatively depleted in ^{18}O compared to sea water. This makes $\delta^{18}\text{O}$ a proxy for both temperature and the extent of continental ice sheets. $\delta^{11}\text{B}$ is used as a proxy for pH. Productivity, nutrient concentration and past circulation can be reconstructed from $\delta^{15}\text{N}$ and $\delta^{13}\text{C}$ (^{12}C is taken up with slight preference to ^{13}C during photosynthesis). Together with microfossil assemblages, $\delta^{18}\text{O}$ and $\delta^{13}\text{C}$ are the paleoceanographic proxies with the most widespread use.
- *Radiogenic isotopes.* The different solubilities of uranium and two products of its naturally occurring decay, thorium (Th) and protactinium (Pa) can be used to estimate the rate of deep water flow and the flux of particles from the water column to the sediments. This flux can also be used as a productivity estimate. ^{14}C preserved in organic matter is used to estimate the age difference between near surface and deep waters and hence, ventilation rates.
- *Biogenic compounds.* The concentrations of some compounds, mainly organic carbon, calcium carbonate and opal,

are used as estimates of past productivity. Calcium carbonate is also an indicator of the calcite compensation depth. Alkenones are long chained organic molecules resistant to degradation. The alkenones produced by some coccolithophors can have two or three double bonds in their structure. The ratio between molecules with two and three double bonds reflect the temperature at the time of synthesis.

- *Elements.* The concentrations and ratios of certain elements in the sediment, organic remains, tests and corals are also used as proxies. The ratios of strontium to calcium (Sr/Ca) and magnesium to calcium (Mg/Ca) in biologically precipitated marine carbonates are temperature dependent. The cadmium to calcium (Cd/Ca) ratio is used for nutrient reconstructions. Barium concentration and the Ba/Ca ratio are proxies for productivity and alkalinity, respectively.
- *Sedimentology.* Grain size distribution can provide qualitative information about bottom current speeds and act as an indicator of ice rafted debris. Information about past tides can be inferred from layered sediments called rhythmites. The mineralogy of the sediments can be used to establish source areas and direction of transport for both water and wind borne sediments.

Conspicuously absent from the quantities of interest listed above is salinity, a fundamental parameter which influences many aspects of the ocean environment. There is, at the moment, no independent proxy for this quantity. As salinity also influences $\delta^{18}\text{O}$, an indirect measurement can be obtained by using independent estimates of temperature (alkenones, for example) to remove the temperature signal from existing $\delta^{18}\text{O}$ series. Attempts have also been made to infer salinity from microfossil assemblages. Unfortunately, both approaches generate errors of ~ 1 psu, very large compared to the range of salinity variability in the oceans (Fischer and Wefer, 1999).

Reconstructions (Models)

The theoretical approach to paleoceanography uses quantitative ocean and climate models to reconstruct paleoconditions of the ocean and interpret observations. A number of different ocean and coupled climate models have been used in the past and we will give a very short overview of the hierarchy and use of these models in the broad research area of paleoceanography.

It is, of course, impossible to build an exact model of the climate system; for the ocean alone, the position and momentum of approximately 5×10^{46} molecules would have to be calculated at each instant of time. As an alternative, the ocean, atmosphere, sea ice, or land surface is split into discrete macroscopic elements with measurable characteristics such as temperature, density, velocity, etc. The state of and exchange between these discrete elements follow physical laws and can therefore be determined with numerical models. Small scale processes within each element can also influence the large scale pattern and therefore have to be parametrized. Existing ocean (and climate) models differ in regards to:

- their temporal and spatial resolution (resolution is defined as the spatial scale which defines the boundary between processes that are resolved by the model and those which are parametrized)
- the nature of processes which are resolved (for example, some models include biogeochemical cycles whereas other models resolve physical processes only)

- the number of subsystems taken into account (for example, an ocean model needs boundary conditions at the surface which can either be provided by data, or by an atmosphere model which is physically interacting with the ocean model)

As the different subsystems (ocean, atmosphere, sea ice, continental ice sheets, vegetation, etc.) of the climate system interact with each other in a complex manner and on a very broad range of timescales, climate modelling reduces to the process of identifying isolable subsystems and processes that are relevant to the problem at hand. While identifying these subsystems and processes, the researcher has also to keep in mind that these processes have to be suitable to be simulated by limited mathematical models and will provide results in a reasonable computational time (Crowley and North, 1991).

The simplest class of climate models includes one-dimensional Energy Balance Models which were first developed by Budyko (1969) and Sellers (1969). It is interesting to note that these simple models yield two stable solutions under present day boundary conditions: the present day climate and a completely frozen Earth (also called “Snowball Earth”).

Today’s physical ocean models can be classified based on the following categories:

- geography (regional models, global models)
- physics (hydrodynamic, thermodynamic or hydro-thermodynamic models)
- surface approximation (free surface, rigid lid)
- vertical discretization (fixed level, isopycnal, sigma-coordinate, semi-spectral)
- density variation (barotropic, baroclinic)

Because the boundary data for paleoclimatic simulations tend to contain large uncertainties, global models are better suited for this research area than regional models. The most comprehensive results are given by global ocean general circulation models (OGCMs). These models can be driven with reconstructed data specifying the boundary conditions. For example, numerous modelling studies restored the ocean surface characteristics to the CLIMAP data set (CLIMAP – Project Members, 1976) for simulations of the Last Glacial Maximum.

A better approach than using ocean-only models is to use coupled ocean-atmosphere models; by computing the surface boundary conditions, one can bypass the data problem. However, coupled ocean-atmosphere GCMs often need flux adjustments. Flux adjustments balance surface fluxes at the ocean-atmosphere interface to avoid a numerical drift of the coupled system. As flux adjustments have been “tuned” to the present day climate, the use of these adjustments to simulate past climates is not very reliable. However, some recent studies use coupled atmosphere-ocean GCMs which do not need artificial flux adjustments (e.g., LeGrande et al., 2006).

Some studies use simple atmosphere models which still provide reasonable boundary conditions for the ocean model (Weaver et al., 2001). Other climate subsystems may also have an important influence on the state of the ocean (continental ice sheets, sea ice and land surface processes for example). The class of Earth System Models has been developed recently and comprise all models which take into account more than two subsystems of the climate system. Today, Earth System Models are widely used for paleoceanographic and paleoclimate simulations. There is also growing evidence that geochemical interactions between the subsystems are more important than initially thought (carbon cycle, nitrogen cycle, methane, etc.) and some initial attempts in integrating these

cycles in Earth System Climate models for paleoclimatic simulations have been made (Crucifix, 2005). The modelling community is continuously integrating new processes and subsystems in their models to obtain a better representation of the climate system dynamics.

Combining models and proxy data

The interpretation of paleoproxy data is an ongoing challenge for paleoclimate scientists. As a striking example, one could compare the studies of Clark et al. (2002) and Bond et al. (2001). Both papers are highly regarded, yet draw opposite conclusions from the atmospheric $\Delta^{14}\text{C}$ record. Whereas Bond et al. (2001) relate the variability of atmospheric $\Delta^{14}\text{C}$ to changes in solar radiation, Clark et al. (2002) interpret the same type of record as a signature of variability in the thermohaline circulation and ocean heat transport. On the other hand, model simulations of past climates depend strongly on boundary conditions, assumptions, and the model used for the study. The simulated climate for a certain time span can be radically different depending on the model and boundary conditions used. Interpretation of measured paleoclimate data is thus urgently needed through collaboration between modellers and observers.

One possible approach to combine proxy data with climate models is that of “data assimilation.” Data assimilation involves the construction of a field that accommodates best the information obtained from paleoproxies with the physical (and dynamical) constraints of the climate system using coupled climate models (e.g., Paul and Schäfer-Neth, 2005).

Another possible approach is to incorporate paleoproxy data (e.g., $\delta^{18}\text{O}$, deuterium excess, $\Delta^{14}\text{C}$, $\delta^{13}\text{C}$, $\delta^{10}\text{Be}$, etc.) as prognostic active tracers in climate models. Perturbations (such as meltwater events or changing solar activity) and other climate states (e.g., the Last Glacial Maximum) can then be simulated and the behaviour of these simulated proxies can be compared to observed proxy data obtained from ice cores, marine sediments and other records. This has been done with uncoupled ocean (or atmosphere) general circulation models (e.g., Schmidt, 1999; Werner et al., 2000; Butzin et al., 2005), vegetation models (Kaplan et al., 2002) and continental ice sheet models (e.g., Clarke et al., 2005). However, the importance of interactions between atmosphere, oceans and other systems such as the biosphere and the cryosphere point to the necessity of using coupled models. To date, there have been only a few studies simulating paleoproxy data with either coupled ocean-atmosphere GCMs or Earth System Models (e.g., Stocker and Wright, 1996; Meissner et al., 2003; Roche et al., 2004; Crucifix, 2005; LeGrande et al., 2006).

A third way to bridge the gap between the modelling and proxy data approach is to find locations of proxy data records of special interest with the use of climate models. A simulation including prognostic paleoproxy tracers can determine the geographical region of greatest impact on a given paleoproxy data during a given climate event.

In conclusion, large amounts of paleoproxy data have been retrieved from various types of archives, but attempts to use numerical models for verification and interpretation of this data are sparse. The science of using three-dimensional climate models to interpret paleo records is still in its infancy.

Processes

In this Section, we give a short overview of the processes and boundary conditions which might have influenced the oceans in the past.

Paleotides

The history of tides over geological time is associated with the evolution of the Earth-Moon system and the shape of ocean basins. Tidal currents generate friction at the bottom of the ocean resulting in the transfer of energy and angular momentum associated with the Earth's rotation to the Moon's orbital motion. This process has been gradually slowing the Earth's spin and increasing the radius of the Moon's orbit. According to some estimates, at ~620 million years ago (Ma), days were approximately 22 h long and the Earth-Moon distance was about 96% of its present day value (Williams, 2000). The main proxy for tidal (and Earth-Moon system) changes over periods of millions of years is based on the analysis of tidal rhythmites, laminated sediments whose deposition is associated with tidal currents (Williams, 2000).

Tidal dissipation depends strongly on the shape of ocean basins. As tectonic processes cause the basins to change, the effects of tidal friction should also change. There are many indications that this is the case. For example, the present rates of dissipation appear to be higher than the average rates over the planet's history (Kagan, 1997; Gills and Ray, 1999).

Over the Quaternary, the shape of ocean basins was altered due to changes in sea level and the presence or absence of ice shelves. Numerical models show that in the Labrador Sea, tidal amplitudes during the last glacial were about twice as large compared to present day conditions. This has led to the suggestion that these higher tides could have destabilized floating ice shelves and caused Heinrich events (Arbic et al., 2004). Another connection between tides and climate relates to a millennial tidal cycle. It has been proposed that very high tides, occurring every 1,800 years, can cause increased mixing and cooling of the sea surface. This cooling would be related to abrupt climate change observed with similar periodicity (Keeling and Whorf, 2000). Some researchers contest this hypothesis, arguing that tidal forcing at these frequencies is very weak (Munk et al., 2001).

Radiation

Incoming short wave radiation from the Sun is the ultimate source of energy for ocean dynamics, the hydrological cycle and life in the oceans. Geographic and seasonal variations in the intensity of insolation result in temperature and pressure gradients which have an important influence on ocean dynamics and the climate system. Although the ocean surface circulation is mostly wind driven, the winds themselves are the result of the uneven distribution of energy on Earth. Density driven currents on the other hand depend strongly on temperature (and thus indirectly on energy distribution) and salinity gradients (which result from precipitation/evaporation patterns and are thus closely linked to the hydrological cycle).

Incoming solar radiation changes over a range of very different timescales. Firstly, the solar luminosity has gradually increased throughout the Earth's lifetime. It is estimated that, during the early days of our planet, the solar luminosity was 25–30% weaker than today's value. According to model results, such a reduction in incoming shortwave radiation should result in a completely frozen planet ("Snowball Earth"). However, even if evidence exists for snowball Earth conditions in early Earth's climate history, there is also counter evidence that during long periods of time the paleoceans were ice-free. Thus, it is inferred that, at these times, greenhouse gas concentrations must have been higher than present day levels in order

to prevent the system from slipping into an icehouse state (see *Faint young Sun paradox*, this volume).

On shorter timescales (order of tens to hundred thousands of years), the incoming solar radiation is modulated by changes in the Earth's orbital parameters which describe the character of the Earth's orbit around the Sun. These three parameters change continuously, causing a variation in the total amount of solar radiation received on Earth as well as the seasonal and latitudinal distribution of insolation. The first parameter, called eccentricity, describes the degree of ellipticity in the Earth's orbit around the Sun and hence the shape of its orbit. The characteristic periods of changes in eccentricity are 95,000, 131,000, 413,000, and 2,100,000 years. Eccentricity is the only parameter which modulates the total global amount of solar energy received at the top of the atmosphere. The change in Earth's axial tilt through time is described by obliquity and has a distinct period of 41,000 years. Finally, the precession of the equinoxes combines the axial precession (wobbling of the axis) and the precession of the ellipse (rotation of the elliptical shape of Earth's orbit) and consists of a strong cycle with a 23,000 year period and a weaker one with a 19,000 year period (Ruddiman, 2000). Precession and obliquity do not alter the total amount of solar radiation received, however, they change the distribution of incoming radiation by latitude and by season. All the frequencies of these parameters can be found in climatological records of the paleocean. Thus, orbital parameters play an important role in driving the climate system and ocean dynamics.

Finally, short-term variability in solar luminosity (which is correlated with changes in the number of sunspots visible on the Sun's surface) acts on timescales of decades to millenia. Over the last hundred years, the global mean temperature has followed a trend similar to the sunspot record. Some climate scientists have hypothesized that periods of global cooling (e.g., the Little Ice Age (~1560–1850)) have been partly caused by a minimum in sunspots (Spörer sunspot minimum (1460–1550) and Maunder sunspot minimum (1645–1715)).

Ocean basin changes

The shape of the ocean basins sets the boundary conditions for the ocean circulation. Different continent configurations result in different flow patterns. Understanding how the boundaries influenced past circulation patterns might offer insight into the dynamics and other important processes of the present day oceans. For example, the existence of an unobstructed low latitude passage in the Tethys Ocean (~160–14 Ma) has been associated with increased poleward heat transport (Hotinski and Toggweiler, 2003). Of course, both reconstructions and simulations of ocean currents this far into the past are subject to many uncertainties. For example, even the existence of a prominent, large scale feature such as the Tethys circum-equatorial current is still not unequivocally accepted (Barron and Peterson, 1989; Bush, 1997; Poulsen et al., 1998; Hotinski and Toggweiler, 2003).

A number of proxy and modelling studies show that the opening and closing of passages between two basins can have a large impact on ocean circulation and climate. The closing of the isthmus of Panama which is the gap between the North and South American continents at ~5–3 Ma is thought to have intensified the Gulf Stream and the associated northward transport of heat and salt into the North Atlantic (Haug and Tiedemann, 1998). The closure of the isthmus of Panama has

also been associated with the onset of Northern Hemisphere glaciation (Keigwin, 1982; Lear et al., 2003; Mudelsee and Raymo, 2005) as well as with changes in water mass properties and the overturning circulation of the North Pacific (Motoi et al., 2005). The opening of the Drake passage between Antarctica and South America (~28–33 Ma) and subsequent establishment of the Antarctic Circumpolar Current is associated with the glaciation of the Antarctic continent (Kennett, 1977; Toggweiler and Bjornsson, 2000). It has been proposed that the relative stability of the Atlantic Meridional Overturning Circulation (MOC) during the Holocene is related to the open connection between the Arctic and Pacific Oceans provided by the Bering Strait (De Boer and Nof, 2004). According to this scenario, low salinity anomalies in the North Atlantic make the MOC unstable when the strait is blocked (as during the last glacial). On the other hand, the flux of low salinity water from the Pacific into the Arctic through a wide open Bering Strait during conditions with higher sea levels (last interglacial, ~115–130 ka BP) has been linked to the more unstable MOC (Shaffer and Bendsten, 1994).

Oscillations in sea level result in changes of the surface's land to ocean ratio which in turn influences the planetary albedo. According to model results, alteration of the planet's albedo caused by a sea level drop of approximately 400 m during the late Ordovician (~455–445 Ma) was one of the factors that could have driven the climate into a cooler state (Herrmann et al., 2004). By submerging vegetated areas or making new land available to plants, changes in sea level can also impact carbon storage. The amount of carbon present on shelves inundated by the rise in sea level since the Last Glacial Maximum appears to be equivalent to the increase in the atmospheric stock of carbon during the same period (Montenegro et al., 2006).

Ice

A gradual cooling over the last 55 million years led to the presence of extensive continental ice sheets in both the Southern and Northern Hemisphere. Intensification of Northern Hemisphere glaciation in Eurasia and North America occurred between 2.7 and 2.5 Ma. With increasing terrestrial ice sheets, sediment records show an intensification of climate oscillations between extreme cold glacial maxima and interglacial warm periods on timescales related to the orbital parameters. The boundary conditions for paleoceans varied dramatically between glacial and interglacial periods. The formation and melting of extensive ice sheets in North America and Eurasia, important variations in atmospheric CO₂ concentrations as well as shifts in the extent of sea ice changed the radiation balance, salinity distribution, dynamical forcing and productivity of the oceans.

Continental ice sheets

Continental ice sheet growth and decay during glacial cycles may have influenced the ocean circulation in several ways:

- Sea level changes due to the storage of freshwater on continents and bedrock depression may have led to different circulation patterns in the ocean.
- Extraction of freshwater from the ocean to build up continental ice sheets led to changes in the global average and distribution of ocean salinity. These changes in salinity (and therefore density) may in turn have influenced the circulation and heat transport (Meissner and Gerdes, 2002).

- Changes in land surface albedo altered the local radiation balance over continental ice sheets, which in turn must have changed sea surface temperatures and circulation.
- Elevation changes in regions of continental ice sheets could also have caused changes in atmospheric circulation (Lehman, 1993) by affecting the atmosphere's stationary wave pattern (Jackson, 2000) and therefore the dynamic forcing of the ocean circulation.
- Changes in global atmospheric temperatures resulting from the presence or absence of ice sheets led to changes in ocean temperatures which may in turn have affected the circulation and heat transport.

Climate variability on millennial time scales has been more important during glacial periods than during interglacials. Dansgaard-Oeschger temperature oscillations, which seem to be part of slow-cooling cycles occurring every 10–15 kyr (Dansgaard et al., 1993), have been related in several studies to changes in the strength of the meridional overturning (MOC, see *Thermohaline Circulation*, this volume). Local sea surface salinity perturbations at high latitudes due to meltwater and/or iceberg discharges (Heinrich Events) may have weakened the MOC (e.g., Rahmstorf, 1995 and references therein) leading to abrupt climate change (Broecker, 1994; Manabe and Stouffer, 1995).

Sea ice

Sea ice regulates exchanges of heat and freshwater between ocean and atmosphere and can change sea surface salinity through melting or freezing (brine rejection). It insulates the relatively warm ocean water from the cold polar atmosphere, changes the surface albedo (and therefore the local radiation balance) dramatically and influences evaporation and therefore local cloud cover and precipitation. By changing the surface characteristics of the oceans, sea ice plays an important role in deep water formation and meridional heat transport in the ocean. The positive ice-albedo climate feedback might have led to a "run away" icehouse feedback in the Precambrian ("Snowball Earth," Hoffman et al., 1998).

Conclusion

Paleoceanography is an exciting research area that unifies specialists with a broad range of backgrounds. Scientists in each of the two classical schools of paleoceanography (reconstructions through proxy data and theoretical quantitative analysis using models) are more and more exchanging expertise and working together for a better understanding of the past oceanographic environment. However, inherent problems associated with the poor spatial and temporal resolution of proxy data as well as uncertainties related to the proxy data themselves make their interpretation difficult and sometimes impossible. At the same time, models are limited by resolved processes, resolution and the quality of boundary conditions. Overall, there is much progress to be made in both fields. In spite of these problems, the geological data as well as model simulations provide a substantial set of results which gives us some insight on how the ocean and the whole climate system functions. This knowledge is of ultimate importance to understand and predict future climate changes due to anthropogenic perturbations.

Katrin J. Meissner, Alvaro Montenegro, and Chris Avis

Bibliography

- Arbic, B.K., Macayeal, D.R., Mitrovica, J.X., and Milne, G.A., 2004. Palaeoclimate – Ocean tides and Heinrich events. *Nature*, **432**, 460–460.
- Barron, E.J., and Peterson, W.H., 1989. Model simulation of the Cretaceous ocean circulation. *Science*, **244**, 684–686.
- Bond, G., Kromer, B., Beer, J., Muscheler, R., Evans, M., Showers, W., Hoffmann, S., Lotti-Bond, R., Hajdas, I., and Bonani, G., 2001. Persistent solar influence on North Atlantic surface circulation during the Holocene. *Science*, **294**, 2130–2136.
- Bradley, R.S., 1999. *Paleoclimatology*. Reconstructing the climates of the Quaternary (2nd edn.), International Geophysics (vol. 64). San Diego: Academic Press.
- Brazdil, R., Pfister, C., Wanner, H., Storch, H.V., and Luterbacher, J., 2005. Historical climatology in Europe – The state of the art. *Clim. Change*, **70**, 363–430.
- Broecker, W.S., 1994. Massive iceberg discharges as triggers for global climate change. *Nature*, **372**, 421–424.
- Budyko, M.I., 1969. The effect of solar radiation variations on the climate of the earth. *Tellus*, **21**, 611–619.
- Bush, A.B.G., 1997. Numerical simulation of the Cretaceous Tethys circumglobal current. *Science*, **275**, 807–810.
- Butzin, M., Prange, M., and Lohmann, G., 2005. Radiocarbon simulations for the glacial ocean: The effects of wind stress, Southern Ocean sea ice and Heinrich events. *Earth Planet. Sci. Lett.*, **235**(1–2), 45–61.
- Clark, P.U., Pisias, N.G., Stocker, T.F., and Weaver, A.J., 2002. The role of the thermohaline circulation in abrupt climate change. *Nature*, **415**, 863–869.
- Clarke, G.K.C., Lhomme, N., and Marshall, S.J., 2005. Tracer transport in the Greenland ice sheet: Three-dimensional isotopic stratigraphy. *Quaternary Sci. Rev.*, **24**, 155–171.
- CLIMAP – Project Members, 1976. The surface of the Ice-Age Earth. *Science*, **191**, 1131–1144.
- Crowley, T.J., and North, G.R., 1991. *Paleoclimatology*. *Oxford Monographs on Geology and Geophysics*, No. 18. New York: Oxford University Press.
- Crucifix, M., 2005. Distribution of carbon isotopes in the glacial ocean: A model study. *Paleoceanography*, **20**, 1–18, PA4020.
- Dansgaard, W., Johnson, S.J., and Clausen, H.B., 1993. Evidence for general instability of past climate from a 250-kyr ice-core record. *Nature*, **364**, 218–222.
- De Boer, A.M., and Nof, D., 2004. The Bering Strait's grip on the northern hemisphere climate. *Deep Sea Res. I*, **51**, 1347–1366.
- Fischer, G., and Wefer, G. (eds.), 1999. *Use of proxies in paleoceanography. Examples from the South Atlantic*. Berlin: Springer.
- Gills, B.G., and Ray, R.D., 1999. Lunar orbital evolution: A synthesis of recent results. *Geophys. Res. Lett.*, **26**(19), 3045–3048.
- Haug, G.H., and Tiedemann, R., 1998. Effect of the formation of the Isthmus of Panama on Atlantic Ocean thermohaline circulation. *Nature*, **393**, 673–676.
- Henderson, G.M., 2002. New proxies for paleoclimate. *Earth Planet. Sci. Lett.*, **203**, 1–13.
- Herrmann, A.D., Haupt, B.D., Patzkowsky, M.E., Seidov, D., and Slingerland, R.L., 2004. Response of Late Ordovician paleoceanography to changes in sea level, continental drift and, atmospheric pCO₂: Potential causes for long-term cooling and glaciation. *Palaeogeogr. Palaeoclimatol. Palaeoecol.*, **210**, 385–401.
- Hoffman, P.F., Kaufman, A.J., Halverson, G.P., and Schrag, D.P., 1998. A neoproterozoic snowball earth. *Science*, **281**(5381), 1342–1346.
- Hotinski, R.M., and Toggweiler, J.R., 2003. Impact of a Tethyan circumglobal passage on ocean heat transport and “equable” climates. *Paleoceanography*, **18**(1), 1007.
- Jackson, C., 2000. Sensitivity of stationary wave amplitude to regional changes in Laurentide ice sheet topography in single-layer models of the atmosphere. *J. Geophys. Res.*, **105**(D19), 24443–24454.
- Kagan, B.A., 1997. Earth-Moon tidal evolution: Model results and observational evidence. *Prog. Oceanogr.*, **40**, 109–124.
- Kaplan, J.O., Prentice, I.C., Knorr, W., and Valdes, P.J., 2002. Modeling the dynamics of terrestrial carbon storage since the Last Glacial Maximum. *Geophys. Res. Lett.*, **29**(22), doi: 10.1029/2002GL015230.
- Keeling, C.D., and Whorf, T.P., 2000. The 1800-year oceanic tidal cycle: A possible cause of rapid climate change. *Proc. Natl. Acad. Sci.*, **97**(8), 3814–3819.
- Keigwin, L., 1982. Isotopic paleoceanography of the Caribbean and East Pacific: Role of Panama uplift in late Neogene time. *Science*, **217**, 350–353.
- Kennett, J.P., 1977. Cenozoic evolution of antarctic glaciation, circum-antarctic ocean, and their impact on global paleoceanography. *J. Geophys. Res.*, **82**(C27), 3843–3860.
- Lear, C.H., Rosenthal, Y., and Wright, J.D., 2003. The closing of a seaway: Ocean water masses and global climate change. *Earth Planet. Sci. Lett.*, **210**, 425–436.
- LeGrande, A.N., Schmidt, G.A., Shindell, D.T., Field, C.V., Miller, R.L., Koch, D.M., Faluvegi, G., and Hoffmann, G., 2006. Consistent simulations of multiple proxy responses to an abrupt climate change event. *Proc. Natl. Acad. Sci.*, **103**(4), 837–842.
- Lehman, S., 1993. Ice sheets, wayward winds, and sea change. *Nature*, **365**, 108–110.
- Manabe, S., and Stouffer, R.J., 1995. Simulation of abrupt climate change induced by freshwater input to the North Atlantic Ocean. *Nature*, **378**, 165–167.
- Meissner, K.J., and Gerdes, R., 2002. Coupled climate modeling of ocean circulation changes during ice age inception. *Clim. Dyn.*, **18**, 455–473.
- Meissner, K.J., Schmittner, A., Weaver, A.J., and Adkins, J.F., 2003. The ventilation of the North Atlantic Ocean during the Last Glacial Maximum – A comparison between simulated and observed radiocarbon ages. *Paleoceanography*, **18**(2), 1023.
- Montenegro, A., Eby, M., Kaplan, J.O., Meissner, K.J., and Weaver, A.J., 2006. Carbon storage on exposed continental shelves during the glacial-interglacial transition. *Geophys. Res. Lett.*, **33**, L08703.
- Motoi, T., Chan, W.L., Minobe, S., and Sumata, H., 2005. North Pacific halocline and cold climate induced by Panamanian Gateway closure in a coupled ocean-atmosphere GCM. *Geophys. Res. Lett.*, **32**, L10618.
- Mudelsee, M., and Raymo, M.E., 2005. Slow dynamics of the Northern Hemisphere glaciation. *Paleoceanography*, **20**, PA4022.
- Munk, W., Dzieciuch, M., and Jayne, S., 2001. Millennial climate variability: Is there a tidal connection? *J. Clim.*, **15**(44), 370–385.
- Paul, A., and Schäfer-Neth, C., 2005. How to combine sparse proxy data and coupled climate models. *Quaternary Sci. Rev.*, **24**, 1095–1107.
- Poulsen, C.J., Seidov, D., Barron, E.J., and Peterson, W.H., 1998. The impact of paleogeographic evolution on the surface oceanic circulation and the marine environment within the mid-Cretaceous tethys. *Paleoceanography*, **13**, 546–559.
- Quinn, W.H., and Neal, V.T., 1987. El Niño over the past four and a half centuries. *J. Geophys. Res.*, **92**(C13), 14449–14461.
- Rahmstorf, S., 1995. Bifurcations of the Atlantic thermohaline circulation in response to changes in the hydrological cycle. *Nature*, **378**, 145–149.
- Roche, D., Paillard, D., Ganopolski, A., and Hoffman, G., 2004. Oceanic oxygen-18 at the present day and LGM: equilibrium simulations with a coupled climate model of intermediate complexity. *Earth Planet. Sci. Lett.*, **218**, 317–330.
- Ruddiman, W.F., 2000. *Earth's climate: Past and future*. New York: W.H. Freeman.
- Schmidt, G.A., 1999. Forward modeling of carbonate proxy data from planktonic foraminifera using oxygen isotope tracers in a global ocean model. *Paleoceanography*, **14**, 482–497.
- Sellers, W.D., 1969. A global climatic model based on the energy balance of the earth-atmosphere system. *J. Appl. Met.*, **8**, 392–400.
- Shaffer, G., and Bendtsen, J., 1994. Role of the Bering strait in controlling North Atlantic ocean circulation and climate. *Nature*, **367**, 354–357.
- Stocker, T.F., and Wright, D.G., 1996. Rapid changes in ocean circulation and atmospheric radiocarbon. *Paleoceanography*, **11**(6), 773–795.
- Toggweiler, J.R., and Bjornsson, H., 2000. Drake Passage and paleoclimate. *J. Quaternary Sci.*, **15**, 319–328.
- Weaver, A.J., Eby, M., Wiebe, E.C., Bitz, C.M., Duffy, P.B., Ewen, T.L., Fanning, A.F., Holland, M.M., MacFadyen, A., Matthews, H.D., Meissner, K.J., Saenko, O., Schmittner, A., Wang, H., and Yoshimori, M., 2001. The UVic Earth System Climate Model: Model description, climatology, and applications to past, present and future climates. *Atmos. Ocean*, **4**, 361–428.
- Werner, M., Mikolajewicz, U., Hoffmann, G., and Heimann, M., 2000. Possible changes of δ¹⁸O in precipitation caused by a meltwater event in the North Atlantic. *J. Geophys. Res.* **105**(D8), 10161–10168.
- Williams, G.E., 2000. Geological constraints on the precambrian history of earth's rotation and the moon's orbit. *Rev. Geophys.*, **38**(1), 37–59.

Cross-references

Alkenones
 Astronomical Theory of Climate Change
 Atmospheric Circulation During the Last Glacial Maximum
 CLIMAP
 Dating, Radiometric Methods
 Eolian Dust, Marine Sediments
 Faint Young Sun Paradox
 Geochemical Proxies (Non-Isotopic)
 Ice-Rafted Debris (IRD)
 Little Ice Age
 Marine Biogenic Sediments
 Maunder Minimum
 Ocean Paleotemperatures
 Organic Geochemical Proxies
 Paleocane Modeling
 Paleoclimate Proxies, an Introduction
 Plate Tectonics and Climate Change
 Quaternary Climate Transitions and Cycles
 Snowball Earth Hypothesis
 Thermohaline Circulation

PALEOCENE-EOCENE THERMAL MAXIMUM

Approximately 55.5 Ma ago in marine and terrestrial sections all around the globe, there was an exceptionally large carbon isotope ($\delta^{13}\text{C}$) excursion (CIE) which is unique in the Tertiary for its size and rapidity of its onset. This event, which was first recognized in multiple cores by Kennett and Stott (1991), is contemporaneous with a significant warm anomaly (and oxygen isotope anomaly) and has thus been named the Paleocene-Eocene Thermal Maximum (PETM) (Figure P8). Due to the singular nature of this perturbation and the ecological, faunal and physical gradients across it, the base of this event is now used to define the boundary of the Paleocene-Eocene transition. The previous definition of the P/E boundary was significantly later (at the base of the Ypresian section in Europe), and thus placed the CIE in the late Paleocene. Previously authors had therefore referred to this event as the Late (or Latest) Paleocene Thermal Maximum (LPTM). Some authors have since referred to it as the Initial Eocene Thermal Maximum (IETM). The CIE is contemporaneous with the Clarkforkian/Wasatchian transition, long accepted as the Paleocene-Eocene boundary in the North American Land Mammal Series.

Full characterization of the event has been handicapped by the number of incomplete sections and frequent hiatuses found near the Paleocene-Eocene transition. The Global Stratigraphic Section and Point (GSSP) for this transition has been defined to be the Dababiya Section, 35 km south of Luxor, on the right bank of the Nile Valley. The event lies within Nano-Plankton zone 9 (NP-9) and reverse-polarity magnetic period Chron 24r. The dating of the PETM is estimated to be around 55.5 Ma, based on the chronology of (1996) using interpolation between well-dated ash layers.

Background

The Paleocene was a time of large shifts in the global environment following the disruptions that occurred at the Cretaceous-Tertiary boundary (65 Ma). Evolutionary increases in diversity, and increasing ocean productivity marked this epoch, leading to the most positive carbon isotope values in the Tertiary.

Temperatures were generally warm, and the polar regions (such as Ellesmere Island) were replete with sub-tropical fauna and flora (crocodiles, ferns etc.). There is no evidence of extensive glacial ice, though evidence for absence of sea ice in high northern latitudes is not as convincing. Tropical temperature estimates do not show as much (if any) change compared to present, but tropical proxies are known to suffer more from diagenetic alteration and the possibly complicating factors relating to the tropical hydrological cycle.

Focusing more specifically on the ≈ 2 Ma late Paleocene to early Eocene transitional period, global temperatures increased (to an estimated 2–4 °C warmer than present day), deep ocean temperatures increased by approximately 3 °C and $\delta^{13}\text{C}$ values

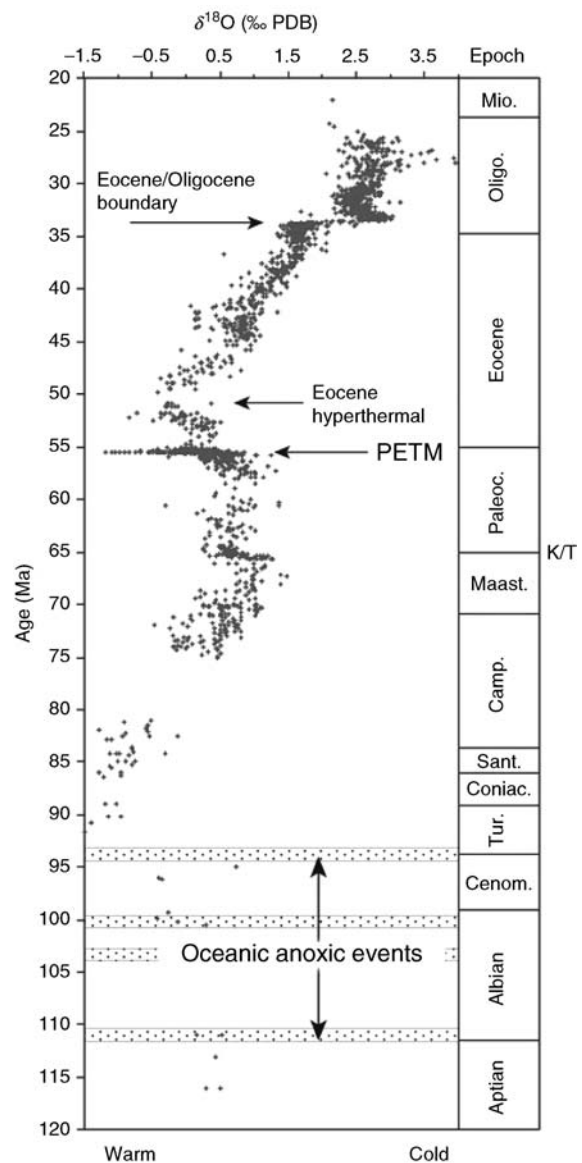


Figure P8 A compilation of $\delta^{18}\text{O}$ values in marine carbonate sediments since the Cretaceous showing the PETM anomaly in the context of Cenozoic variability (after Zachos et al., 2001).

decreased over this long term (Figure P9; Aubry et al., 1998, and references therein). This led to the Eocene Hyperthermal (or early Eocene climatic optimum), the warmest period in the Cenozoic. The collision of the Indian and Asian plates continued throughout this period although a land bridge may have already existed in the late Maastrichtian period. At some point during the late Paleocene, the island arc volcanism at this plate boundary would have ceased. However, the opening of the North Atlantic was perhaps accompanied by increased volcanism along the spreading ridge there. It is likely that a land bridge between North America and Europe was established during this period due to rapid extrusion of lava flows in the Faroe-Rockall area. In the Gulf of Alaska accretionary prism large amounts of sediment were being sequestered (peaking between 65 and 55 Ma) (Hudson and Magoon, 2002). These tectonic processes may have affected climate through the carbon cycle by removing sinks of organic carbon, global temperatures through a limiting of volcanic aerosol input, sea level and possibly ocean circulation through the closing of important gateways (in particular the Tethys ocean and access to the Northern Atlantic). The vegetation over this period was predominantly tropical and sub-tropical with climatic boundaries significantly further poleward than at present. Wetlands have been estimated to be significantly more extensive (Sloan et al., 1992, 1999). Similarities in deep and intermediate water masses point to a single, southern ocean source for deep water for most of this period (Corfield and Norris, 1998).

CO₂ levels have been estimated to be relatively high based on geochemical cycling models, but there are many conflicting lines of evidence from paleosol $\delta^{13}\text{C}$, or leaf-based stomatal density proxies, leaving a consensus elusive (Berner, 1994; Pearson and Palmer, 2001; Royer et al., 2001; Sinha and Stott, 1994). The levels of other radiatively active constituents (CH₄, O₃, volcanic aerosols) are even more highly uncertain. Dustiness appears to have decreased significantly across this interval, possibly indicating a long-term decrease in winds (Rea, 1994). However, the link between changes in radiative forcing and the long term warming, although much discussed, remains speculative.

It must be made clear that changes over the whole Paleocene-Eocene boundary interval (54–57 Ma) were large and significant, but not necessarily connected with the much shorter duration PETM event to which we now turn.

Characterization of the PETM event

The principle and unique definer of the PETM is the carbon isotope excursion (Figure P9). Since this was first recognized it has been found in many deep ocean cores and terrestrial sequences. In the deep ocean the excursion is 3–4‰ and has a very rapid onset (<10,000 years) (Zachos et al., 2000). The initial carbon isotope excursions appear to have been stepped and extremely rapid, occurring in bursts of less than 1 kyr over this interval (Bains et al., 1999; Röhl et al., 2000). The terrestrial excursion is

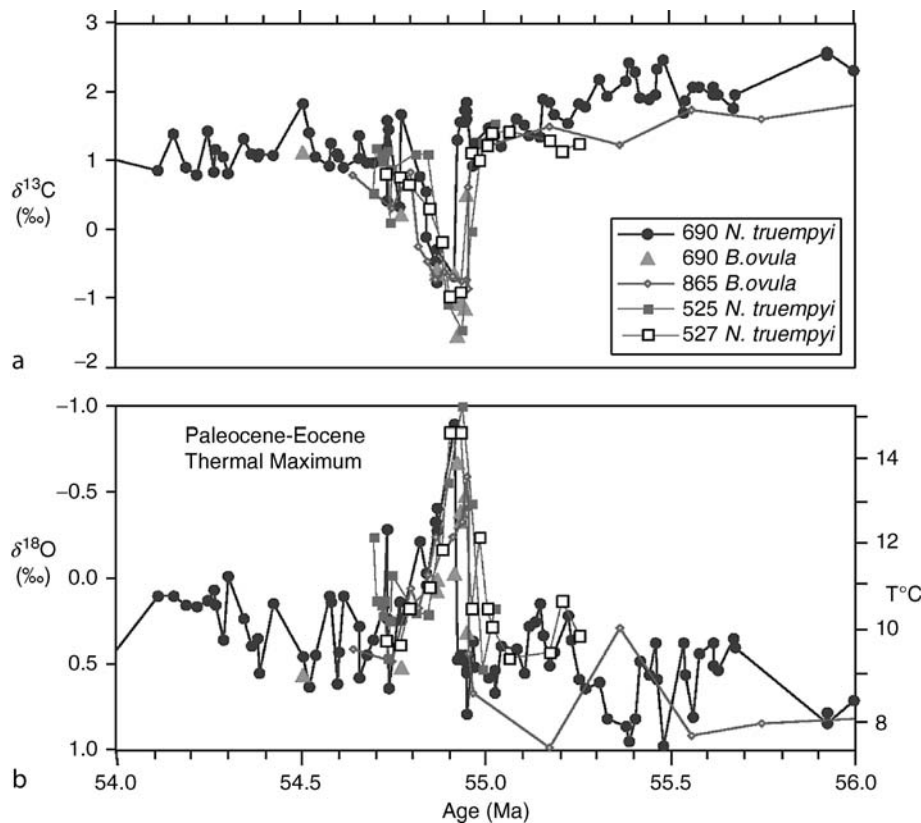


Figure P9 Detailed benthic foraminiferal carbon and oxygen isotopic series across the PETM event (Zachos et al., 2000) from ODP sites 690 (Maud Rise, South Atlantic), 865 (Allison Guyot, Equatorial Pacific), 525 and 527 (Walvis Ridge, South Atlantic).

higher (up to 7‰) measured in both paleosol carbonates and mammalian tooth enamel (hydroxyapatite) (Koch et al., 1992).

Contemporaneous with this excursion, though possibly slightly lagged, is a large increase in deep ocean temperatures (up to 5–7 °C) as indicated by $\delta^{18}\text{O}$ values in carbonate sediments. Isotope signals from upper ocean-dwelling planktonic foraminifera also register a similar change, indicating that the warming occurred over the whole ocean column, particularly at higher latitudes. Tropical temperatures, although more uncertain, may have also increased by 1–2 °C (Bralower et al., 1997). The deep water changes have been hypothesized to have been due to a switch from high latitude deep water production to a tropical source of warm saline bottom water (WSBW), but unequivocal evidence for this is not yet available (Kennett and Stott, 1991).

There also seems to have been a widespread (but not universal) increase in carbonate dissolution at this point, complicating attempts to find continuous sequences across the event. There was an increase in kaolinite clay deposition in coastal locations at the CIE, which indicates increased weathering, or at least, increased transport of weathered material to the ocean (Robert and Kennett, 1994). Some coastal regions saw an increase in the deposition of black shales, indicative of increased productivity. There are widespread discontinuities at the Paleocene-Eocene transition, and evidence of massive slope failures at Blakes Nose, in particular, in the North Atlantic (Katz et al., 1999).

There is a coincident benthic foraminiferal extinction (BFE) event at the onset of the carbon isotope excursion, which saw approximately 50% of the extant benthic species disappear at this time (Thomas and Shackleton, 1996). This extinction has been related to a decrease in dissolved O_2 , increased pH (consistent with the increased carbonate dissolution) and large temperature changes. In addition to foraminifera, other benthic species groups (ostracodes, molluscs) also underwent significant turnover. In particular, there was a widespread expansion of exotic planktonic taxa and dinoflagellates. On land, the CIE marked the final appearance of a number of archaic mammal orders, and the onset of a more “cosmopolitan” range of mammalian fauna in both North America and Eurasia. Large-scale ecological turnover is also indicated at this point.

The duration of any climate event deep in the geological record is particularly difficult to assess. The most useful methods rely upon estimates of Milankovitch cycle variability (mostly precessional cycles ≈ 20 Kyr) in $\delta^{13}\text{C}$ records which can be counted across the event. Other estimates are based on interstellar dust accumulation rates (as measured by $^3\text{He}/^4\text{He}$ ratios). Best estimates for the duration of the event as determined by the $\delta^{13}\text{C}$ excursion are between 90–200 Kyr. These estimates are consistent with present day estimates for the residence time of perturbations to the carbon cycle. Climate perturbations would be shorter than this timescale since the equilibrium of atmospheric and oceanic carbon happens much more quickly than the recycling time for carbon isotopes.

Mechanisms of PETM climate change

The size and rapidity of the PETM CIE serve to usefully eliminate many candidates for a primary cause. A perturbation of up to 4‰ in the global carbon cycle implies a very large input of depleted carbon. Given reasonable estimates of the isotopic signature of terrestrial carbon, the necessary mass of carbon from any source can be estimated. For instance, if the land biosphere were to provide the source, three times the total carbon content of the current biosphere would need to be added, and since no disruption on this kind of scale is observed at this

time, this source can be ruled out. Similarly, the amount of volcanism ($900\times$ present) required would have certainly left other geochemical traces (Dickens et al., 1995). An intriguing alternative is a carbonaceous extraterrestrial bolide impact, for which there is little evidence as yet (Kent et al., 2003).

The most compelling theory to date for the source of this light carbon comes from the large scale dissociation of methane from gas hydrates sequestered on the continental shelf (Dickens et al., 1995). The methane is produced by methanogenic bacteria that live off the organic material in sediment in predominantly anaerobic situations. Methane hydrates (or clathrates) are stable only when cold and under pressure. If the oceans warm, or pressure is reduced, the methane gas can be released. The carbon in such hydrates at present has an approximate value of -60‰ , and approximately 1,500–2,000 Gt (1 Gt = 10^{15} g) of carbon would be required to match the CIE. This amount is significantly less than the present-day known reserves of gas hydrates in the ocean. The maximum in $\delta^{13}\text{C}$ in the mid-Paleocene may be an indication that significantly more methane was sequestered by the late Paleocene. The methane hydrate hypothesis implies carbon additions to the global ocean that are consistent with the widespread carbonate dissolution at this time.

The main issue with this hypothesis is how the dissociation was triggered. Was it caused by a long-term ocean warming that crossed a threshold, a massive slope failure, or an abrupt change of ocean circulation, possibly related to a switch to WSBW formation (Bice and Marotzke, 2002; Katz et al., 1999; Kennett and Stott, 1991)? Was the warming actually caused by the greenhouse effect related to the CH_4 (and its oxidation product CO_2)? All of these possibilities have been tackled in the numerous modeling studies related to the PETM.

Modeling

A hierarchy of models from simple box models of the carbon cycle to full atmospheric and oceanic general circulation models have been applied to the PETM. Box models of the Paleocene carbon cycle have been used to constrain the total amount of depleted carbon required to match the CIE at about 1,500–2,000 Gt of carbon (Dickens, 2001). These models have also been used to assess processes that would eventually remove the excess carbon from the systems by increased organic carbon burial, increased weathering, or a recharging of the methane ‘capacitor’. None of these mechanisms have yet been eliminated as possibilities.

Inputs from methane would have important effects on atmospheric chemistry if emissions went directly into the atmosphere, leading to a reduced oxidation capacity and increased lifetimes for methane, other hydrocarbons (such as isoprene) and CO (Sloan et al., 1999). The radiative effects of these elevated methane (and subsequently CO_2) concentrations are important and have been estimated to be sufficient to have been the cause of the contemporaneous warming (Schmidt and Shindell, 2003). However, uncertainties in timing, background climate state, and Paleocene background emissions make this a tentative conclusion at best. Even more speculative is a possibly increased radiative role for polar stratospheric clouds (due to increased stratospheric water vapour associated with increased methane oxidation in the stratosphere) (Sloan and Pollard, 1998).

The use of full GCMs has necessarily been limited by the lack of well constrained boundary conditions (sea surface temperatures (SSTs), vegetation distributions, continental configurations, etc.); however a series of interesting experiments that

may have implications for the PETM have been published. Simulations using estimates of the varying equator-pole temperature gradient as a forcing function may give insight into the climatic consequences of those changes (Huber and Sloan, 2001). However, models that attempt to predict the SST changes (by using increased greenhouse gases for instance) are not necessarily consistent with these reconstructions (Sloan and Rea, 1995). In particular, whether the main westerly wind belts strengthen or not at the PETM is model dependent (Schmidt and Shindell, 2003; Sloan and Rea, 1995). Ocean-only model results, although limited by the lack of an interactive atmosphere, have been used to: (a) estimate whether hydrates could be destabilized in sufficient quantities by a shift in deep water circulation, or alternately, (b) whether radiatively-forced climate changes are sufficient to match the changes in ocean structure reflected in the benthic and planktonic isotope data (Bice and Marotzke, 2001, 2002). No definitive conclusions have yet been drawn, but no study has yet been able to demonstrate the existence of WSBW. Particular problems for ocean models are the depth of important sills (in the North Atlantic, the Walvis ridge and the Isthmus of Panama, for instance) and finding consistent surface freshwater and heat fluxes. Other ubiquitous problems with GCM simulations of warm climates are also relevant here (e.g., too cold continental interiors and apparently too large tropical warming).

Future studies are likely to yield further insights into possible mechanisms as dynamical oceans are interactively coupled to atmospheric models for this period, and carbon cycle models start to take the methane component (including atmospheric chemistry and subsequent radiative forcing) into account. Some work is also required to better define the vegetation distribution (which has consequence for the albedo, chemical emissions and deposition of other chemical species (such as O₃) which impact the oxidation capacity of the atmosphere (Beerling, 2000)) and also river drainage systems and wetland extent.

Mesozoic analogs

It has been hypothesized that similar CIE have occurred in the past. While none of the other excursions in the Cenozoic period have a documented size and rapidity of the PETM, excursions associated with ocean anoxic events in the Cretaceous, Jurassic, or possibly at the end of the Neoproterozoic glaciations do have similarities. However, the quality of data for these earlier events is significantly poorer, and so these possible analogs will probably remain ambiguous for some time (Hesselbo et al., 2000; Jahren et al., 2001).

Relevance

Estimates of exogenous carbon inputs during the PETM are comparable to the rates of fossil fuel-derived emissions at the present day. Therefore understanding the fate of the carbon during this episode may lead to insights into the eventual fate of anthropogenic carbon.

The PETM is also one of the first short-term climatic events that have been closely studied prior to the Quaternary. It is clear that the high resolution study of deep-time climate events is likely to be an increasingly fruitful line of research in understanding the earth system (Zachos et al., 2000). The singular example of the PETM has already led to re-assessments of the role of methane hydrates in the carbon cycle, the time-scales for carbon recycling, and the importance of atmospheric

chemistry in paleo- (and present day) climate, and it is likely that further insights will be forthcoming as data become more precise and widespread.

Gavin A. Schmidt

Bibliography

- Aubry, M.-P., Berggren, W.A., Stott, L., and Sinha, A., 1996. The upper Paleocene-lower Eocene stratigraphic record and the Paleocene-Eocene boundary carbon isotope excursion: Implications for geochronology. In Knox, R.W.O., Corfield, R.M., and Dunay, R.E. (eds.), *Correlation of the Early Paleogene in Northwest Europe*. London: Geological Society, Special Publication, vol. 101, pp. 353–380.
- Aubry, M.-P., Lucas, S., and Berggren, W.A. (eds.), 1998. *Late Paleocene-early Eocene Biotic and Climatic Events in the Marine and Terrestrial Records*. New York: Columbia University Press.
- Bains, S., Corfield, R.M., and Norris, R.D., 1999. Mechanisms of climate warming at the end of the Paleocene. *Science*, **285**, 724–727.
- Beerling, D., 2000. Increased terrestrial carbon storage across the Paleocene-Eocene boundary. *Palaeogeogr. Palaeoclimatol. Palaeoecol.*, **161**, 395–405.
- Berner, R.A., 1994. 3GEOCARB II: A revised model of atmospheric CO₂ over Phanerozoic time. *Am. J. Sci.*, **294**, 56–91.
- Bice, K.L., and Marotzke, J., 2001. Numerical evidence against reversed thermohaline circulation in the warm Paleocene/Eocene ocean. *J. Geophys. Res.*, **106**, 11529–11542.
- Bice, K.L., and Marotzke, J., 2002. Could changing ocean circulation have destabilized methane hydrate at the Paleocene/Eocene boundary? *Paleoceanography*, **17**(2), 1018, doi: 10.1029/2001PA000678.
- Bralower, T.J., Thomas, D.J., Zachos, J.C., Hirschmann, M.M., Röhl, U., Sigurdsson, H., Thomas, E., and Whitney, D.L., 1997. High-resolution records of the late Paleocene thermal maximum and circum-Caribbean volcanism: Is there a link? *Geology*, **25**, 963–966.
- Corfield, R.M., and Norris, R.D., 1998. The oxygen and carbon isotope context of the Paleocene/Eocene epoch boundary. In Aubry, M.-P., Lucas, S., and Berggren, W.A. (eds.), *Late Paleocene-early Eocene Biotic and Climatic Events in the Marine and Terrestrial Records*, New York: Columbia University Press.
- Dickens, G.R., 2001. Carbon addition and removal during the late Paleocene thermal maximum: Basic theory with a preliminary treatment of the isotope record at Ocean Drilling Program Site 1051, Blake Nose. In Norris, R.D., Kroon, D., and Klaus, A. (eds.), *Western North Atlantic Paleogene and Cretaceous Paleoclimatology*. London: Geological Society, pp. 293–306.
- Dickens, G.R., O'Neil, J.R., Rea, D.K., and Owen, R.M., 1995. Dissociation of oceanic methane hydrate as a cause of the carbon isotope excursion at the end of the Paleocene. *Paleoceanography*, **10**, 965–971.
- Hesselbo, S.P., Grocke, D.R., Jenkyns, H.C., Bjerrum, C.J., Farrimond, P., Morgans-Bell, H.S., and Green, O.R., Massive dissociation of gas hydrate during a Jurassic oceanic anoxic event. *Nature*, **406**, 392–395.
- Huber, M., and Sloan, L.C., 2001. Heat transport, deep waters, and thermal gradients: Coupled simulation of an Eocene greenhouse climate. *Geophys. Res. Lett.*, **28**, 3481–3484.
- Hudson, T.L., and Magoon, L.B., 2002. Tectonic controls on greenhouse gas flux to the Paleogene atmosphere from the Gulf of Alaska accretionary prism. *Geology*, **30**, 547–550.
- Jahren, A.H., Arens, N.C., Sarmiento, G., Guerrero, J., and Amundson, R., 2001. Terrestrial record of methane hydrate dissociation in the Early Cretaceous. *Geology*, **29**, 159–162.
- Katz, M.E., Pak, D.K., Dickens, G.R., and Miller, K.G., 1999. The source and fate of massive carbon input during the latest Paleocene thermal maximum. *Science*, **286**, 1531–1533.
- Kennett, J., and Stott, L.D., 1991. Abrupt deep sea warming, paleoceanographic changes and benthic extinctions at the end of the Paleocene. *Nature*, **353**, 319–322.
- Kent, D.V., Cramer, B.S., Lanci, L., Wang, D., Wright, J.D., and der Voo, R.V., 2003. A case for a comet impact trigger for the Paleocene/Eocene thermal maximum and carbon isotope excursion. *Earth Planet. Sci. Lett.*, **211**, 13–26.
- Koch, P.L., Zachos, J.C., and Gingerich, P., 1992. Correlation between isotope records in marine and continental carbon reservoirs near the Paleocene/Eocene boundary. *Nature*, **358**, 319–322.

- Pearson, P., and Palmer, N., 2001. Atmospheric carbon dioxide concentrations over the past 60 million years. *Nature*, **406**, 695–699.
- Rea, D.K., 1994. The paleoclimatic record provided by eolian deposition in the deep sea: The geologic history of wind. *Rev. Geophys.*, **32**, 159–195.
- Robert, C., and Kennett, J.P., 1994. Antarctic subtropical humid episode at the Paleocene-Eocene boundary: Clay mineral evidence. *Geology*, **22**, 211–214.
- Röhl, U., Bralower, T.J., Norris, R.D., and Wefer, G., 2000. New chronology for the late Paleocene thermal maximum and its environmental implications. *Geology*, **28**, 927–930.
- Royer, D.L., Wing, S.L., Beerling, D.J., Jolley, D.W., Koch, P.L., Hickley, L.J., and Berner, R.A., 2001. Paleobotanical evidence for near present day levels of atmospheric CO₂ during part of the tertiary. *Science*, **292**, 2310–2313.
- Schmidt, G.A., and Shindell, D.T., 2003. Atmospheric composition, radiative forcing and climate change as a consequence of a massive methane release from gas hydrates. *Paleoceanography*, **18**, 1004, doi: 10.1029/2002PA000757.
- Sinha, A., and Stott, L.D., 1994. New atmospheric pCO₂ estimates from paeols during the late Paleocene/early Eocene global warming interval. *Global Planet. Change*, **9**, 297–307.
- Sloan, L.C., and Pollard, D., 1998. Polar stratospheric clouds: A high latitude warming mechanism in an ancient greenhouse world. *Geophys. Res. Lett.*, **25**, 3517–3520.
- Sloan, L.C., and Rea, D.K., 1995. Atmospheric carbon dioxide and early Eocene climate: A general circulation modeling sensitivity study. *Palaeogeogr. Palaeoclimatol. Palaeoecol.*, **119**, 275–292.
- Sloan, L.C., Walker, J.C.G., Moore, T.C., Rea, D.K., and Zachos, J.C., 1992. Possible methane induced warming in the early Eocene. *Nature*, **357**, 320–322.
- Sloan, L.C., Huber, M., and Ewing, A., 1999. Polar stratospheric cloud forcing in a greenhouse world: A climate modeling sensitivity study. In Abrantes F., and Mix A. (eds.), *Reconstructing Ocean History*. New York: Kluwer, pp. 273–293.
- Thomas, E., and Shackleton, N.J., 1996. The Paleocene-Eocene benthic foraminiferal extinction and stable isotope anomalies. In Knox, R.W.O., Corfield, R.M., and Dunay, R.E. (eds.), *Correlation of the Early Paleogene in Northwest Europe*. London: Geological Society, Special Publication, vol. 101, pp. 401–441.
- Zachos, J.C., Pagani, M., Sloan, L., Thomas, E., and Billups, K., 2000. Trends, rhythms, and aberrations in global climate 65 Ma to present. *Science*, **292**, 686–693.
- Zachos, J.C., Thomas, D., Bralower, T., and Thomas, E., 2001. New constraints on the timing and magnitude of the Paleocene-Eocene boundary carbon isotope excursion in marine environments. *Eos. Trans. AGU Fall Meet. Suppl.*, **82**, 767.

Cross-references

[Carbon cycle](#)
[Carbon isotope variations over geologic time](#)
[Carbon isotopes, stable](#)
[Methane hydrates, carbon cycling, and environmental change](#)
[Oxygen isotopes](#)
[Paleoclimate modeling, pre-Quaternary](#)
[Paleogene climates](#)
[Plate tectonics and climate change](#)

PALEOCLIMATE MODELING, PRE-QUATERNARY

Introduction

Pre-Quaternary paleoclimate modeling is the science of simulating climate change over the earliest 99.9% of Earth's history using numerical models of the climate system. The record of pre-Quaternary climate documents enormous climate swings with global ice-covered and ice-free end members. A number

of climate factors shaped Quaternary and pre-Quaternary paleoclimate on timescales ranging from hundreds of thousands to several years. However, in contrast to Quaternary paleoclimate, tectonically-controlled processes (including continental drift, orogenies, and fluctuations in the long-term carbon cycle) and solar evolution were also important controls on pre-Quaternary climate. Understanding how these factors have influenced climate change through the Precambrian, Paleozoic, Mesozoic, and Cenozoic eras, and how they are expressed in the geological record is a principal objective of pre-Quaternary paleoclimate modeling.

The utility of pre-Quaternary paleoclimate modeling has been several-fold. Pre-Quaternary climate modeling has contributed to ocean, atmosphere, and geological sciences by: (a) identifying mechanisms of climate change; (b) quantifying the climate response to a variety of forcing factors; (c) recognizing climatic feedbacks that amplify/dampen climatic forcings; (d) identifying limitations of climate proxies from the geological record; and (e) demonstrating strengths/shortcomings in numerical climate models. Pre-Quaternary paleoclimate modeling has made fundamental contributions to climate science. Among these, the recognition that the Earth's climate has experienced enormous variability on a multitude of temporal and spatial scales as a result of complex interactions between multiple climate factors is one of the most profound.

Methodology

Today, "paleoclimate models" are synonymous with numerical climate models implemented to study past climates. Prior to the wide availability of numerical climate models, paleoclimate models also referred to conceptual models constructed using physically-based rules about the general circulation of the atmosphere and ocean (e.g., Ziegler et al., 1977; Parrish et al., 1982). Numerical climate models are mathematical expressions of the theoretical laws that govern the climate system, approximated and written in computer code for fast, efficient computation. The model domain, frequently global in extent, is discretized into an array of horizontal and vertical grid cells. Not all models incorporate the full suite of governing equations in three dimensions. In fact, a hierarchy of numerical climate models has been used to study past climates. Numerical climate models can range in complexity from zero-dimensional energy balance models (EBMs) that simply express the conservation of energy, to three-dimensional general circulation models (GCMs) of the ocean and atmosphere that predict fluid flow on a rotating sphere heated by solar radiation. Many aspects of the climate system cannot be explicitly calculated, frequently because specific phenomena develop and act on sub-grid cell scale (i.e., over distances that are much smaller than represented by a model grid cell). Clouds provide an instructive example. Cloud motions vary over a horizontal scale of tens to hundreds of meters. Yet, the horizontal resolution of a GCM is typically tens to hundreds of kilometers. In order to represent clouds in GCMs, cloud processes are approximated or parameterized. Many of the differences between common types of numerical climate models (e.g., GCMs) arise from different parameterizations. To date, there are several different classes of GCMs, including atmosphere-only GCMs, ocean-only GCMs, coupled atmosphere-ocean GCMs, and GCMs coupled to models of the biosphere, cryosphere, and lithosphere. Climate models also differ in their horizontal and vertical resolution. As computational speed and efficiency has increased, so has the complexity and resolution of numerical

paleoclimate models. For a more detailed description of numerical climate models, the reader is referred to one of several good texts on the subject (e.g., Washington and Parkinson, 1986; Trenberth, 1992; McGuffie and Henderson-Sellers, 1997).

Most models used in pre-Quaternary climate studies were initially developed and fine-tuned for the modern climate, and then modified for use in pre-Quaternary studies. The modifications for “paleo” use are generally limited to changes in the model’s initial and boundary conditions. Table P1 lists the boundary conditions that have been explored in paleoclimate studies of the pre-Quaternary. A critical aspect of paleoclimate modeling is accurately defining the boundary conditions for a past age. For example, consider the difficulty of reconstructing the Cretaceous sea-surface temperatures (SSTs), continental vegetation, bathymetry, or atmospheric $p\text{CO}_2$. The task of reconstructing past boundary conditions is often made difficult or impossible because: (a) the geological record has been destroyed, incompletely sampled, or was never preserved; (b) the temporal resolution of the proxy is too coarse or too uncertain; (c) the spatial resolution (e.g., a single drill or field site) may be incompatible with the model resolution; or (d) the geological proxy may have lost its original signal through alteration or have an equivocal interpretation. In the absence of a detailed reconstruction of a particular boundary condition, a generalization or simplification has often been made (e.g., specification of globally uniform vegetation type or zonally-averaged SSTs). Numerous studies have demonstrated that differences within the uncertainty of a boundary condition can have regional or global climatic consequences (e.g., Kutzbach and Ziegler, 1993; Otto-Bliesner, 1998; Poulsen et al., 1998; Sewall et al., 2000; Huber and Sloan, 2000). In pre-Quaternary paleoclimate studies, initial conditions have usually been paid little attention for two reasons. First, the initial conditions are unknown. Second, very few pre-Quaternary proxy reconstructions have centennial or better resolution. Consequently, most paleoclimate modeling studies time-average the model results to mask interannual and interdecadal climate variability. Insofar as multiple climate states are possible, initial conditions may be important, and have been examined to a

limited degree (e.g., Bice and Marotzke, 2001; Herrmann et al., 2003).

Pre-Quaternary paleoclimate modeling studies have tended to focus on specific intervals or time slices of Earth’s history (e.g., the mid-Cretaceous), rather than the continuum spanning all or a portion of Earth’s 4.6 billion years. Practical limitations, including the computational costs incurred by long (i.e., greater than a few thousand years) simulations, the relative incompleteness of the paleoclimate proxy records, and the technical complexity of dynamically varying boundary conditions (specifically geography or orography), have motivated this time-slice approach. As these limitations diminish, long climate simulations may be possible, particularly for simpler or coarse-resolution models. The timescales of interest have varied tremendously, ranging from tens of millions of years to only a few years, and are mainly constrained by the resolution of paleoclimate proxy records.

Pre-Quaternary paleoclimate models have been utilized in several fashions. Due to the limitations of boundary condition reconstructions, many paleoclimate modeling studies fall within the category of sensitivity experiments – modeling experiments in which one parameter is varied at a time and compared to a control case. Alternatively, some studies have attempted to “simulate” a particular time interval by specifying the “best” boundary conditions and then comparing the simulation to proxy reconstructions. In practice, many studies mix these two approaches.

Paleoclimate modeling contributions

In this section, progress achieved on a number of pre-Quaternary paleoclimate problems through paleoclimate modeling has been summarized. As much as possible, the types of models used have been described in order to provide a sense of the evolution of the paleoclimate modeling field.

Faint Young Sun paradox

Stellar evolution models indicate that solar luminosity was 25–30% lower during the early Precambrian than today. Yet, the earliest one-dimensional EBMs and atmospheric GCMs predicted that much smaller decreases (2–5%) in solar luminosity would have triggered climate instability once sea ice had reached $\sim 30^\circ$ latitude, leading to a runaway ice-albedo feedback (Budyko, 1969; Sellers, 1969). Subsequent EBM experiments showed that the critical latitude for a runaway ice-albedo feedback was not entirely fixed; increasing the heat transport caused the instability to move to higher latitudes (Held and Suarez, 1974). The prediction of an early Precambrian ice-covered Earth is inconsistent with the presence of sedimentary rocks early in Earth history and evidence of primitive life at 3.5 Ga. Moreover, EBM calculations indicate that the formation of highly reflective CO_2 clouds would have made an ice-covered Earth irreversible (Caldiera and Kasting, 1992). This conflict between climate model predictions and the geological record has become known as the Faint Young Sun paradox.

Several climatic factors have been hypothesized to resolve the Faint Young Sun paradox, including the atmospheric concentration of greenhouse gases, the extent and configuration of continents, and the rotation rate and obliquity of the early Earth. Calculations using one-dimensional radiative-convective models indicate that high concentrations of NH_3 (Sagan and Mullen, 1972), CO_2 (Owen et al., 1979; Kuhn and Kasting, 1983;

Table P1 Common paleoclimate boundary conditions

Continental distribution
Topography
Bathymetry
Land surface characteristics ^a
<i>Vegetation properties</i>
<i>Soil properties</i>
Land ice distribution and height ^a
Solar luminosity
Orbital parameters
<i>Eccentricity</i>
<i>Obliquity</i>
<i>Precession</i>
Atmospheric gases
<i>Carbon dioxide</i>
<i>Methane</i>
<i>Nitrous oxide</i>
<i>CFCs</i>
<i>Ozone</i>
Sea-surface temperatures ^a
Drainage basins or continental runoff

^aIn some studies, boundary condition may not be necessary if the parameter is explicitly calculated. For example, sea-surface temperatures are not necessary if a mixed-layer or fully dynamic ocean model is implemented.

Kasting et al., 1984; Kiehl and Dickinson, 1987) and/or CH₄ (Kiehl and Dickinson, 1987; Pavlov et al., 2000) in the atmosphere could have maintained surface temperatures above freezing by enhancing the Earth's greenhouse effect.

Theories of continental formation suggest that the extent of continental crust was considerably less than today. The small continental area may have affected the Precambrian climate by reducing the Earth's albedo (Henderson-Sellers and Henderson-Sellers, 1989; Kuhn et al., 1989; Gérard et al., 1992; Jenkins et al., 1993), increasing poleward heat transport (Endal and Schatten, 1982), and altering the global cloud fraction (Jenkins et al., 1993; Longdoz and François, 1997). These changes are hypothesized to compensate for the low solar luminosity at least partially, by impeding the equatorward growth of sea ice and increasing the solar radiation captured at the Earth's surface. However, the influence of continental configuration on Precambrian climate is highly model dependant. For example, in response to a global ocean, the cloud coverage decreased in the atmospheric GCM used by Jenkins et al. (1993) due to a shift from non-convective to convective cloud types, which have a smaller cloud fraction. In contrast, cloud coverage increased in the quasi-three-dimensional model used by Longdoz and François (1997) due to a more active hydrological cycle.

The Earth's rotation velocity has decreased through its history, causing day length to increase from 14-h days at 4.0 Ga to 24-h days (Walker and Zahnle, 1986). The dynamical consequences of an enhanced rotation rate during the Precambrian have been studied using EBMs and GCMs (Hunt, 1979; Kuhn et al., 1989; Jenkins et al., 1993). A faster rotation velocity reduces the scale size of synoptic disturbances, leading to a reduction in poleward heat transports, cold high latitude temperatures, and larger meridional temperature gradients (Hunt, 1979). Dynamical changes in eddy and mean motions may also reduce global cloud coverage, causing a 2 °C increase in global average air temperature that potentially compensated for the low Precambrian solar luminosity (Jenkins et al., 1993).

Snowball Earth hypothesis

The late Precambrian witnessed the most severe glaciations in Earth history. Paleomagnetic evidence from South Australia and Northwest Canada confirm the low-latitude (<10°) settings of late Precambrian glacial deposits. Paleoclimate models have been used extensively to evaluate the factors responsible for the low-latitude glaciation, and have examined the influences of paleogeography (Crowley and Baum, 1993; Chandler and Sohl, 2000; Poulsen et al., 2002), atmospheric CO₂ concentrations (Chandler and Sohl, 2000; Hyde et al., 2000; Baum and Crowley, 2001), continental surface characteristics (Baum and Crowley, 2001), ocean heat transport (Chandler and Sohl, 2000; Poulsen et al., 2001b), and ice-sheet dynamics (Hyde et al., 2000; Donnadieu et al., 2003). These modeling studies demonstrate that a combination of climate forcings can produce conditions for low-latitude glaciation (Chandler and Sohl, 2000; Hyde et al., 2000).

The low-latitude glacial deposits, and other sedimentary (deposition of banded iron formations and thick post-glacial carbonates) and geochemical evidence (carbon isotopes from carbonates), has been cited as confirmation that the entire Earth may have been completely ice-covered during the late Precambrian (Kirschvink, 1992; Hoffman et al., 1998). This idea, known as the Snowball Earth hypothesis, has gained support from some climate models. EBMs and atmospheric GCMs have simulated an ice-covered Earth under late Precambrian

conditions (when the solar luminosity was about 6% less than present) (Jenkins and Smith, 1999; Baum and Crowley, 2001; Poulsen et al., 2001). However, this result is highly model dependent. Climate models that explicitly calculate ocean circulation and heat transport do not permit an ice-covered Earth under late Precambrian conditions. The energy released by convection at the sea-ice margin and the large heat capacity of the ocean work against the ice-albedo feedback (Poulsen et al., 2001; Bendtsen, 2002). The extent of late Precambrian ice is critical to the Earth's recovery – escape from an ice-covered state would have required ~300–1,000 × present atmospheric levels (PAL) of CO₂ (Caldiera and Kasting, 1992), while escape from a world with water at the equator would have required as little as 4 × PAL CO₂ (Crowley et al., 2001).

An alternative explanation for low-latitude glaciation is that the Earth's obliquity was substantially greater than at any time in the Phanerozoic (Williams, 1975, 1986). If the obliquity were higher than 54°, the poles would be the warmest region on Earth, and the equator would be the coldest. Atmospheric GCMs confirm that an extreme obliquity (≥60°) would produce freezing temperatures on low-latitude continents while maintaining above freezing conditions at high latitudes (Oglesby and Ogg, 1999; Jenkins, 2000; Donnadieu and Ramstein, 2002). The missing ingredient in this hypothesis is a reasonable physical mechanism for causing large changes in Earth's obliquity.

Ordovician glaciation

Geological evidence exists for a late Ordovician (~440 Ma) glaciation. This short-lived (~1 million year) glaciation (Brenchley et al., 1995, 2003) was remarkable because atmospheric CO₂ levels were high (14 ± 6 × PAL) during the late Ordovician (Yapp and Poeths, 1992). Numerical climate models of increasing complexity have been used to determine the conditions permitting glaciation at high CO₂ levels. Early studies using 2-D EBMs focused on the role of the late Ordovician paleogeography (Crowley et al., 1987; Crowley and Baum, 1991a), and specifically the orientation of Gondwanaland relative to the South Pole. With an edge of Gondwanaland near the South Pole, the thermal inertia of the ocean prevented continental summer temperatures from rising above freezing, thus allowing permanent snow cover (Crowley et al., 1987; Crowley and Baum, 1991a). Subsequent GCM experiments have confirmed the EBM result (Gibbs et al., 2000), but have also shown that the continental configuration of Gondwanaland is not a sufficient condition for glaciation. The influences of additional climatic factors on Ordovician glaciation have since been tested, including atmospheric CO₂, topography, ocean heat transport, orbital parameters, and snow/ice albedo (Crowley and Baum, 1995; Gibbs et al., 1997; Poussart et al., 1999; Herrmann et al., 2003). These studies generally conclude that glaciation is possible with high (8–14 × PAL) atmospheric CO₂ levels given favorable orbital parameters (i.e., a cold Southern Hemisphere summer configuration) and continental topography. With orbital forcing varying from cold-summer to warm-summer configurations, ice-sheet model calculations indicate that CO₂ levels must fall to 8 × PAL to grow a permanent ice sheet (Herrman et al., 2003).

Gondwanan glaciations

Ice sheets on Gondwana persisted for ~55 million year during the Permo-Carboniferous (275–330 Ma), and reached a size

comparable to that of the Pleistocene ice sheets (Crowley and Baum, 1991b). The presence of ice sheets on a supercontinent is surprising since enhanced seasonality would have produced summer temperatures on the Gondwana ice sheet that may have been 15 °C greater than temperatures over the Laurentide Ice Sheet (Crowley, 1994). Two-dimensional EBM calculations indicate that a reduced solar luminosity (~3% less than modern) and favorable orbital parameters could compensate for the supercontinental effect, allowing freezing summer temperatures over the Gondwanan ice sheet (Crowley et al., 1991). Crowley and Baum (1992a) used a series of two-dimensional EBM experiments with a combination of evolving climatic factors (geography, geography + solar luminosity, geography + solar luminosity + CO₂) to simulate the estimated extent of the Gondwanan ice sheet. To simulate both the initiation and demise of the ice sheet, changes in geography, solar luminosity, and, most importantly, CO₂ were required (Crowley and Baum, 1992a).

EBM and GCM modeling of the Permo-Carboniferous glaciation has demonstrated that the onset and growth of the Gondwanan ice sheet may have been highly nonlinear due to a Small Ice Cap Instability (SICI) (Baum and Crowley, 1991; Crowley et al., 1994). A coupled climate-ice sheet model of the Gondwanan ice sheet also shows critical behavior with small changes in solar luminosity (0.0005%) leading to large differences (>10×) in the simulated ice volume (Hyde et al., 1999). The model also exhibits multiple equilibria. The melting of a large ice sheet due to an increase in CO₂ to 2 × PAL results in a small, stable Gondwanan ice sheet. Yet, no ice sheet is simulated given ice-free initial conditions and 2 × PAL CO₂ (Hyde et al., 1999).

Pangean climate

Paleogeography has been recognized as a first-order control on climate. During the late Paleozoic and early Mesozoic, the continents were agglomerated into the supercontinent Pangea. The supercontinental configuration had large consequences for Earth's climate. Typical features simulated by climate models include extreme continentality (i.e., a seasonal temperature range (>45 °C) that surpassed that of modern Eurasia) resulting from the small heat capacity of land (Crowley et al., 1989; Kutzbach and Gallimore, 1989; Kutzbach and Ziegler, 1993; Crowley and Baum, 1994; Wilson et al., 1994; Gibbs et al., 2002), strong monsoonal systems along the Tethyan coast (Kutzbach and Gallimore, 1989; Kutzbach and Ziegler, 1993; Wilson et al., 1994; Gibbs et al., 2002), and intense aridity in continental interiors due to the depletion of atmospheric moisture over the long continental trajectories (Kutzbach and Gallimore, 1989; Kutzbach and Ziegler, 1993; Wilson et al., 1994; Fawcett and Barron, 1998; Gibbs et al., 2002). Two-dimensional EBM calculations predict that Pangean surface temperatures would have been greatly influenced by orbital parameters with a maximum range of ~14–16 °C between maximum and minimum orbital insolation values (as determined from Pleistocene fluctuations) (Crowley and Baum, 1992b). In addition, atmospheric GCM experiments using an idealized Pangean paleogeography indicate that tropical and subtropical precipitation and runoff would have varied by 50% between the extreme phases of the precessional cycle with enhanced hydrology when perihelion (aphelion) occurred in summer (winter) (Kutzbach, 1994).

Mountains and plateaus may have played an important secondary role in controlling Pangean climate. The intensification of radiative heating and cooling over plateaus produced more

extreme high and low pressure systems, which acted with the topography to guide the winds and focus precipitation (Kutzbach and Ziegler, 1993; Otto-Bliesner, 1993, 1998; Wilson et al., 1994; Hay and Wold, 1998). The effects of uplift were greatest in low latitude regions because of the influence of mountains on the position of the Inter-Tropical Convergence Zone (ITCZ) (Otto-Bliesner, 1998; Hay and Wold, 1998). Otto-Bliesner found that the presence of high (1,000–3,000 m) Central Pangean Mountains impeded the seasonal northward migration of the ITCZ, enhancing local precipitation by 68% in July and possibly explaining the extensive occurrence of tropical, late Carboniferous coals.

Considerable effort has been made to evaluate, through comparison with climate proxies, the ability of atmospheric GCMs to simulate elements of the Pangean climate (Kutzbach and Ziegler, 1993; Fawcett et al., 1994; Pollard and Schulz, 1994; Wilson et al., 1994; Rees et al., 1999, 2002; Gibbs et al., 2002). In general, atmospheric GCM simulations tend to do a “fair to good” job of simulating the requisite conditions for lithologic climatic indicators (Pollard and Schulz, 1994; Wilson et al., 1994; Gibbs et al., 2002) and sedimentary structures generated by severe weather (PSUCLIM, 1999a; PSUCLIM, 1999b). In comparison to climate inferred from Permian paleobotanical data, an atmospheric GCM predicts temperatures that are too cold in the high latitudes of the Southern Hemisphere (Rees et al., 1999, 2002). The absence of ocean dynamics (particularly the absence of warm polar currents, upwelling zones, and the explicit calculation of ocean heat transport) and the coarse model resolution (particularly the poor or nonexistent resolution of narrow mountain ranges, lakes, and coastlines) in the atmospheric GCMs have been implicated as potential reasons for the discrepancies between the model predictions and the proxy indicators (Pollard and Schulz, 1994; Rees et al., 1999, 2002; Gibbs et al., 2002).

Several atmospheric GCM studies have focused on the Jurassic (Chandler, 1994; Chandler et al., 1992; Moore et al., 1992; Valdes and Sellwood, 1992; Valdes, 1994), a geological interval that saw the rifting of Pangea. The large continental blocks shared many features with that of Pangea, including high continentality, intense continental aridity, and strong monsoonal systems (Moore et al., 1992). The latter conclude that the Jurassic warmth evidenced by climate proxies may be explained by elevated atmospheric CO₂. In contrast, Chandler et al. (1992) suggested that a Jurassic simulation with specified, warm SSTs was in energy balance without high atmospheric CO₂, implying that a warm Jurassic climate could have been the product of enhanced poleward heat transport through the ocean. However, in a Jurassic experiment with a specified, reduced meridional sea-surface gradient, the implied ocean heat transport was much smaller than in a present-day simulation, suggesting that enhanced ocean heat transport may not be viable for the Jurassic (Valdes, 1994). A comparison of Jurassic climates simulated using different GCMs has confirmed that the treatment of the ocean is an important variable that likely explains model differences in high latitude climate prediction. Furthermore, mixed-layer ocean models without poleward heat transport exaggerate the equator to pole temperature gradient, while specified SSTs may not be sustainable (Valdes, 1994).

Cretaceous greenhouse climate

The Cretaceous was a period of global warmth with ice-free continents and globally averaged surface temperatures 6–14 °C higher than present (Barron, 1983). The focus of

the earliest Cretaceous modeling studies was to understand the factors that led to a warm Cretaceous period. Using a simple planetary albedo model, Thompson and Barron (1981) concluded that reductions in albedo resulting from reduced land area, snow cover, and sea ice, could account for all of the Cretaceous warmth. Subsequent calculations using a one-dimensional EBM (Barron et al., 1981), a mean-annual atmospheric GCM coupled to an energy balance ocean model with no thermal inertia (Barron and Washington, 1982), and an atmospheric GCM with seasonally varying solar insolation and a mixed-layer ocean (Barron et al., 1993a) indicated that the role of continental geography on global-average Cretaceous surface temperature was minor. On the other hand, an increase in atmospheric CO₂ levels (2–10 × PAL) caused substantial global-average warming (Barron and Washington, 1985; Barron et al., 1993) due to a decrease in global albedo resulting from melting of snow/ice and an increase in water vapor. In fact, an increase to 4 × PAL CO₂ levels caused a global-average warming of 3.6–5.5 °C. An additional CO₂ feedback, enhanced high-latitude cloud cover, may further contribute to Cretaceous high-latitude warming (Sellwood and Valdes, 1997).

Ironically, the greenhouse gas solution to Cretaceous global warmth introduced a new climate problem: model-predicted Cretaceous tropical temperatures exceeded the estimates from climate proxies and approached the thermal tolerance of some tropical organisms while high-latitude regions were still too cold (Barron and Washington, 1985; Barron et al., 1993). Efficient poleward heat transport was suggested as a way to reduce the Cretaceous surface thermal gradient (Barron et al., 1981; Barron, 1983), but this flew in the face of classical theories that suggested a reduced thermal gradient would displace large-scale circulation features towards the poles and cause sluggish atmospheric and oceanic circulation. However, early atmospheric and coupled ocean-atmosphere GCM simulations demonstrated that a reduction in the surface thermal gradient did not cause sluggish circulation (Barron and Washington, 1982; Manabe and Bryan, 1985; Bush and Philander, 1997). Rather, the vertically integrated meridional temperature gradient was maintained or slightly increased through compensation by differential latent heating, leading to slightly increased zonal-average wind speeds at many latitudes (Barron and Washington, 1982).

Because of its enormous heat capacity, the ocean was identified as a possible source of enhanced poleward heat transport (Barron et al., 1981; Barron and Washington, 1982, 1985; Schneider et al., 1985; Covey and Barron, 1988; Covey and Thompson, 1989; Rind and Chandler, 1991). The idea of enhanced ocean heat transport was strengthened by atmospheric GCM experiments that demonstrate that an increase in ocean heat transport is only partially compensated by a reduction in atmospheric heat transport (Covey and Thompson, 1989) and could produce substantial global climate warming (Covey and Thompson, 1989; Rind and Chandler, 1991; Barron et al., 1993). Cretaceous atmospheric GCM simulations with enhanced oceanic heat transports predict high-latitude warming and low-latitude cooling, reducing the meridional surface temperature gradient (Barron et al., 1993; Barron et al., 1995; Poulsen et al., 1999). Yet, to date, a mechanism for sustaining high ocean heat transport has not been identified, though some modeling studies suggest the possibility of intensified surface circulation (Bush and Philander, 1997; Hotinski and Toggweiler, 2003).

Despite the specification of elevated atmospheric CO₂ and enhanced ocean heat transport in atmospheric GCMs of

the Cretaceous, mean-annual temperatures in the continental interiors remained subfreezing, and at odds with the paleobotanical and sedimentological evidence (Schneider et al., 1985; Barron et al., 1995). This problem has been markedly ameliorated by including non-uniform vegetation, either by direct specification or by prediction with a vegetation-ecology model, in atmospheric GCM experiments (Otto-Bliesner and Upchurch, 1997; DeConto et al., 1999; Upchurch et al., 1999). The inclusion of high-latitude forest, in particular, produced a large warming effect that contributed to a 2.2 °C increase in global average temperature. These low-albedo forests warmed the high-latitude continents, which then transferred more heat to the high-latitude oceans, impeding sea-ice formation and warming coastal regions (Otto-Bliesner and Upchurch, 1997).

Ocean circulation in a warm Cretaceous climate has received considerable attention, because of the possibility that the thermohaline circulation may have reversed, resulting in subtropical deepwater formation (i.e., warm saline deepwater) and sluggish meridional ocean circulation (Chamberlin, 1906; Brass et al., 1982). Ocean GCM studies have largely undermined the hypothesis that the global thermohaline circulation was completely reversed. Using a coarse 5° × 5° ocean GCM with mean-annual forcing, Barron and Peterson (1990) reported significant subtropical deepwater formation in eastern Tethys with elevated (4 × PAL) CO₂ levels. However, subsequent finer-resolution ocean GCM simulations with seasonal forcing have predicted only limited convection at subtropical sites with most convection occurring at high-latitude Southern Hemisphere locations (Brady et al., 1998; Poulsen et al., 2001). Cretaceous GCM studies also do not support the notion of a sluggish, global meridional circulation; meridional overturning circulation is similar in experiments with different meridional surface temperature gradients (Manabe and Bryan, 1985; Brady et al., 1998).

On the basis of biogeographic and paleogeographic reconstructions, a Tethys circumglobal current has been inferred for the Cretaceous. Ocean GCM results indicate that a Tethys circumglobal current may have driven high rates of upwelling, cooling tropical temperatures and warming northern high latitudes, thereby reducing the Cretaceous meridional thermal gradient (Hotinski and Toggweiler, 2003). However, ocean GCMs have had mixed success simulating a Tethys circumglobal current (Seidov, 1986; Barron and Peterson, 1989; Bush, 1997; Bush and Philander, 1997), because the current is very sensitive to continental geometry (Poulsen et al., 1998). Regional ocean circulation and water properties may also have been highly sensitive to opening/closing of Cretaceous gateways (Poulsen et al., 2001; 2003). In addition to global models of ocean circulation, regional circulation models have been implemented to predict detailed Cretaceous circulation in the Western Interior Seaway of North America (Ericksen and Slingerland, 1990; Kump and Slingerland, 1999).

Warm “equable” Paleocene-Eocene climate

The early Eocene was the warmest interval in the Cenozoic, with global-average surface temperatures 2–4 °C warmer than present (Barron, 1987). Floral and faunal proxies suggest that continental temperatures were warm with a small annual range. Yet, on the basis of perpetual January and July atmospheric GCM simulations with specified SSTs, Sloan and Barron (1990) reported that warm, equable continental interiors could not be maintained in light of the small thermal inertia of land surfaces. Subsequently, a number of studies have attempted to

reconcile the GCM predictions with early Eocene proxy evidence from the continental interiors (Sloan and Barron, 1990, 1992; Sloan and Cirbus, 1994; Sloan and Morrill, 1998; Sloan and Pollard, 1998; Sloan et al., 2001). Several factors have been identified that ameliorate the model-predicted high-latitude continental temperature range, including the presence of a large interior lake (Sloan and Cirbus, 1994), enhanced atmospheric CO₂ levels (Sloan and Cirbus, 1994; Shellito et al., 2003), cold summer-warm winter orbital parameters (Sloan and Morrill, 1998), and the specification of seasonally-varying, warm SSTs (Sloan et al., 2001).

Atmospheric GCM results indicate that elevated atmospheric CO₂ levels (at least 3 × PAL) could explain the Eocene global warmth, but introduce a problem familiar to warm climates – tropical overheating (Sloan and Rea, 1995; Shellito et al., 2003). As in the Cretaceous studies, enhanced oceanic heat transport has been proposed as a possible mechanism for reducing the Eocene meridional surface temperature gradient (Barron, 1987; Covey and Barron, 1988; Rind and Chandler, 1991). Again, a mechanism for enhancing ocean heat transport has not been identified. Using an uncoupled ocean GCM forced by atmospheric GCM fields, Bice et al. (2000) suggest that the distribution of ocean heat transports between the Northern and Southern Hemisphere may be sensitive to the basin configuration. However, a coupled ocean-atmosphere model of the Eocene demonstrated reduced heat transports relative to the modern (Huber and Sloan, 2001). Polar stratospheric clouds, frozen water vapor clouds that form in polar regions, may be a partial solution for producing warm climates with low surface temperature gradients (Sloan and Pollard, 1998). By absorbing outgoing, long-wave radiation, prescribed polar stratospheric clouds in an atmospheric GCM caused warming of the troposphere and melting of sea ice, leading to significant (up to 20 °C) high-latitude warming (Sloan and Pollard, 1998).

Paleoclimate modeling studies have been conducted to determine how the ocean circulated in a warm Eocene climate. Atmospheric GCM experiments with specified SSTs displayed an intensification of the Hadley circulation and associated extremes in equatorial precipitation and subtropical evaporation, leading O'Connell et al. (1996) to suggest that conditions might have been ripe for warm, saline deepwater formation in the eastern Tethys Ocean. Indeed, Eocene ocean GCM experiments support the possibility of limited convection of warm, saline subtropical water (Barron and Peterson, 1991), provided the moisture flux from the atmosphere is favorable (Bice et al., 1997; Bice and Marotzke, 2001). In an attempt to simulate a “haline” mode circulation, Bice and Marotzke (2001) show that large perturbations to the atmospheric moisture flux (evaporation-precipitation) enhance subduction of warm, saline water to the depths, but do not increase subtropical convective mixing (the mechanism controlling deepwater formation). A coupled ocean-atmosphere simulation of the Eocene exhibits sluggish meridional circulation and warm, saline deep water (Huber and Sloan, 2001); however, the published results do not indicate whether the warm, saline water was formed by subduction or convection.

Late Cenozoic climate deterioration

After the warm, ice-free climate of the Cretaceous and early Cenozoic, a long-term cooling trend ensued, punctuated by the development of the Antarctic Ice Sheet near the Eocene/Oligocene boundary, and culminating in the Pleistocene ice age. Several mechanisms have been cited as instigators of the

Cenozoic cooling, including changes in continental distribution, plateau uplift, oceanic gateways, and atmospheric CO₂. Barron (1985) used an annual-average atmospheric GCM to test the hypothesis that the evolution of the distribution and size of continental land masses caused the Cenozoic cooling trend. This model exhibited minor sensitivity to the Cenozoic paleogeographic changes, including changes in topography and continental position, and did not demonstrate a systematic decrease in global-average surface temperature.

Geologic evidence supports a significant increase in uplift rates and absolute elevation in southern Asia (the Tibetan Plateau and Himalayan Mountains) and the American West during the Cenozoic (Ruddiman et al., 1989), though the details of the uplift history remain uncertain. In a series of atmospheric GCM sensitivity experiments testing the influence of mountain elevation on climate, Kutzbach et al. (1989, 1993) showed that progressive uplift in Southern Asia and the American West resulted in largely linear changes in heating rates, vertical motion patterns, and low-level winds over the plateaus. In a similar series of experiments, Manabe and Broccoli (1990) and Broccoli and Manabe (1992) observed that large-amplitude stationary waves occur in response to the plateaus; general subsidence and infrequent storm development upstream of the troughs of these waves contribute to continental aridity. Changes in circulation associated with uplift led to patterns of regional climatic changes (colder winters over Northern Hemisphere continents; drier summers along the American Pacific coast and in the interior of Eurasia; winter drying of the American northern plains and the interior of Asia; and maintenance of warm/wet conditions along the southeast coasts of Asia and the United States), which are consistent with those in the Northern Hemisphere during the last 10 or 15 million years (Ruddiman and Kutzbach, 1989; Manabe and Broccoli, 1990). Atmospheric GCM experiments have also shown that Tibetan uplift and increased summer radiation through orbital changes are also primary controls on monsoon strength (Prell and Kutzbach, 1992). Despite the large regional climate response, plateau uplift contributes little to global cooling, indicating the need for additional climatic forcing to explain the Cenozoic cooling (Ruddiman and Kutzbach, 1989).

Ocean gateways have also been implicated in Cenozoic cooling. Kennett (1977) hypothesized that the opening of the Drake Passage near the Eocene/Oligocene boundary created an Antarctic Circumpolar Current (ACC), which thermally isolated Antarctica, leading to growth of the Antarctic Ice Sheet. Ocean GCMs that test the effect of the Drake Passage predict the formation of an ACC-reduced poleward heat transport in the high-latitude Southern Hemisphere, cooling high-latitude surface temperatures up to several degrees (ranging from 0.8–4 °C), depending on the type of sea-surface boundary conditions (restoring vs. non-restoring) (Mikolajewicz et al., 1993; Toggweiler and Samuels, 1995; Bice et al., 2000; Toggweiler and Bjornsson, 2000). In contrast, atmospheric GCM results indicated that warmer SSTs favor snowfall in the continental interior, promoting Antarctic Ice Sheet growth (Oglesby, 1989). Ocean GCMs also exhibit large circulation changes in response to an open Central American Isthmus, which existed prior to 3–4 Ma (Maier-Reimer et al., 1990; Mikolajewicz et al., 1993). In the open isthmus case, North Atlantic surface water is diluted by low salinity Pacific water, collapsing North Atlantic deepwater production. Because the North Atlantic circulation is an important source of heat in the high latitudes of the North Atlantic, Maier-Reimer et al. (1990) speculate that a

compensating climatic factor must have warmed the region prior to the initiation of Northern Hemisphere Pleistocene glaciation.

Results from an asynchronously coupled ice sheet-atmosphere GCM suggest that Antarctic glaciation was induced primarily by declining atmospheric CO₂ (DeConto and Pollard, 2003). The ice sheet model exhibits highly nonlinear behavior; once an atmospheric CO₂ threshold (between ~3 and 2 × PAL) is crossed, Antarctic ice caps expand rapidly, with large orbital variations. A parameterization of the Drake Passage opening and ACC formation has a modest (and secondary) effect on ice sheet mass balance (DeConto and Pollard, 2003). Vegetation changes may also have contributed to Cenozoic cooling. Using an atmospheric GCM, Dutton and Barron (1997) propose that the evolution of grasslands and tundra in the Miocene may have caused a 1.9 °C global cooling, mainly due to the higher albedos of these vegetation types.

Warm Pliocene climate

The middle Pliocene was the most recent period in Earth history that was significantly warmer than the present. In contrast to other pre-Quaternary intervals, the boundary conditions for the Pliocene are fairly well-known as a result of the concerted efforts of the U.S. Geological Survey's PRISM (Pliocene Research, Interpretations, and Synoptic Mapping) Group. Several modeling groups have utilized the PRISM data sets to simulate the middle Pliocene climate (Chandler et al., 1994; Sloan et al., 1996; Haywood et al., 2000a,b). Despite incremental enhancements to the PRISM data set and the use of different atmospheric GCMs with varying resolution, the Pliocene simulations agree in several respects. As compared with the present, the Pliocene simulations exhibit global warming, a reduction in the equator-to-pole surface temperature gradient and zonal wind strength, and enhanced Northern Hemisphere high-latitude precipitation (Chandler et al., 1994; Sloan et al., 1996; Haywood et al., 2000b). The GCM results support the possibility that enhanced thermohaline circulation and concomitant increases in ocean heat transport could explain the middle Pliocene warmth (Chandler et al., 1994; Sloan et al., 1996). Alternatively, regional intensification of atmospheric and oceanic circulations may have induced greater heat transports from the equatorial region, warming Europe and the Mediterranean (Haywood et al., 2000a). Modeling results indicate that warmer SSTs and reduced ice cover in the Northern Hemisphere gave way to intensification of the Icelandic low-pressure and Azores high-pressure systems in the North Atlantic. The resulting surface pressure gradient increased the annual westerly wind velocity and wind stress, ultimately enhancing the flow of the Gulf Stream and North Atlantic Current as well (Haywood et al., 2000a).

Summary

Pre-Quaternary paleoclimate modeling is the science of simulating Earth's climate prior to the Quaternary using numerical climate models. The pre-Quaternary witnessed climate states that were fundamentally different to those of the Quaternary and the modern day. Since the earliest paleoclimate modeling studies using EBMs, considerable progress has been achieved in understanding the factors that have controlled Earth's past climates. Paleoclimate modeling studies have directly contributed to reshaping and debunking climate hypotheses, recognizing new climatic processes, and quantifying the climate response to various climatic factors. Much of the scientific progress has proceeded hand-in-hand with the development of

increasingly sophisticated climate models. Yet, many outstanding questions remain about the evolution of Earth's climate. Future progress will be realized through further improvement and enhancement of paleoclimate models, the continued documentation of Earth's environmental and climatic history, and the persistent ingenuity of paleoclimate scientists.

Christopher J. Poulsen

Bibliography

- Barron, E.J., 1983. A warm, equable Cretaceous: The Nature of the problem. *Earth Sci. Rev.*, **19**, 305–338.
- Barron, E.J., 1985. Explanations of the Tertiary global cooling trend. *Palaeoogeogr. Palaeoclimatol. Palaeoecol.*, **50**, 45–61.
- Barron, E.J., 1987. Eocene equator-to-pole surface ocean temperatures: A significant climate problem? *Paleoceanography*, **2**, 729–739.
- Barron, E.J., and Peterson, W.H., 1989. Model simulation of the Cretaceous ocean circulation. *Science*, **244**, 684–686.
- Barron, E.J., and Peterson, W.H., 1990. Mid-Cretaceous ocean circulation: Results from model sensitivity studies. *Paleoceanography*, **5**, 319–337.
- Barron, E.J., and Peterson, W.H., 1991. The Cenozoic ocean circulation based on ocean general circulation model results. *Palaeoogeogr. Palaeoclimatol. Palaeoecol.*, **83**, 1–28.
- Barron, E.J., and Washington, W.M., 1982. Cretaceous climate: A comparison of atmospheric simulations with the geologic record. *Palaeoogeogr. Palaeoclimatol. Palaeoecol.*, **40**, 103–133.
- Barron, E.J., and Washington, W.M., 1985. Warm Cretaceous climates: High atmospheric CO₂ as a plausible mechanism. In Sundquist, E.T., and Broecker, W.S. (eds.), *The Carbon Cycle and Atmospheric CO₂: Natural Variations, Archean to Present*. Washington, DC: American Geophysical Union Geophysical Monograph 32, pp. 546–553.
- Barron, E.J., Thompson, S.L., and Schneider, S.H., 1981. An ice-free Cretaceous? Results from climate model simulations. *Science*, **212**, 501–508.
- Barron, E.J., Fawcett, P.J., Pollard, D., and Thompson, S., 1993a. Model simulations of Cretaceous climates: The role of geography and carbon dioxide. *Phil. Trans. R. Soc. Lond.*, **341**, 307–316.
- Barron, E.J., Peterson, W.H., Pollard, D., and Thompson, S., 1993b. Past climate and the role of ocean heat transport: Model simulations for the Cretaceous. *Paleoceanography*, **8**, 785–798.
- Barron, E.J., Fawcett, P.J., Peterson, W.H., Pollard, D., and Thompson, S.L., 1995. A "simulation" of mid-Cretaceous climate. *Paleoceanography*, **10**, 953–962.
- Baum, S.K., and Crowley, T.J., 2001. GCM response to late Precambrian (~590 Ma) ice-covered continents. *Geophys. Res. Lett.*, **28**, 583–586.
- Baum, S.K., and Crowley, T.J., 1991. Seasonal snowline instability in a climate model with realistic geography: Application to Carboniferous (~300 MA) glaciation. *Geophys. Res. Lett.*, **18**, 1719–1722.
- Bendtsen, J., 2002. Climate sensitivity to changes in solar insolation in a simple coupled climate model. *Clim. Dyn.*, **18**, 595–609.
- Bice, K.L., and Marotzke, J., 2001. Numerical evidence against reversed thermohaline circulation in the warm Paleocene/Eocene ocean. *J. Geophys. Res.*, **106**, 11529–11542.
- Bice, K.L., Barron, E.J., and Peterson, W.H., 1997. Continental runoff and early Cenozoic bottom-water sources. *Geology*, **25**, 951–954.
- Bice, K.L., Scotese, C.R., Seidov, D., and Barron, E.J., 2000. Quantifying the role of geographic change in Cenozoic ocean heat transport using uncoupled atmosphere and ocean models. *Palaeoogeogr. Palaeoclimatol. Palaeoecol.*, **161**, 295–310.
- Brady, E.C., DeConto, R.M., and Thompson, S.L., 1998. Deep water formation and poleward ocean heat transport in the warm climate extreme of the Cretaceous (80 Ma). *Geophys. Res. Lett.*, **25**, 4205–4208.
- Brass, G.W., Southam, J.R., and Peterson, W.H., 1982. Warm saline bottom water in the ancient ocean. *Nature*, **296**, 620–623.
- Brenchley, P.J., Carden, G.A.F., and Marshall, J.D., 1995. Environmental changes associated with the "first strike" of the Late Ordovician mass extinction. *Mod. Geol.*, **22**, 69–82.
- Brenchley, P.J., Carden, G.A., Hints, L., Kalijo, D., Marshall, J.D., Martma, T., Meidla, T., and Nolvak, J., 2003. High-resolution stable isotope stratigraphy of Upper Ordovician sequences: Constraints on the timing of bioevents and environmental changes associated with mass extinction and glaciation. *Geol. Soc. Am. Bull.*, **96**, 597–610.

- Broccoli, A.J., and Manabe, S., 1992. The effects of orography on middle latitude northern hemisphere dry climates. *J. Clim.*, **5**, 1181–1201.
- Budyko, M.I., 1969. The effect of solar radiation variations on the climate of the earth. *Tellus*, **21**, 611–619.
- Bush, A.B.G., 1997. Numerical simulation of the Cretaceous Tethys circumglobal current. *Science*, **275**, 807–810.
- Bush, A.B.G., and Philander, S.G.H., 1997. The late Cretaceous: Simulations with a coupled ocean-atmosphere general circulation model. *Paleoceanography*, **12**, 495–516.
- Caldiera, K., and Kasting, J.F., 1992. Susceptibility of the early Earth to irreversible glaciation caused by carbon dioxide clouds. *Nature*, **359**, 226–228.
- Chamberlin, T., 1906. On a possible reversal of deep-sea circulation and its influence on geologic climates. *J. Geol.*, **14**, 363–373.
- Chandler, M.A., 1994. Depiction of modern and Pangean deserts: Evaluation of GCM hydrological diagnostics for paleoclimate studies. In Klein G.D. (ed.), *Pangea: Paleoclimate, Tectonics, and Sedimentation During Accretion, Zenith, and Breakup of a Supercontinent*. Boulder, CO: Geological Society of America Special Paper 288, 117–138.
- Chandler, M.A., Rind, D., and Ruedy, R., 1992. Pangean climate during the Early Jurassic: GCM simulations and the sedimentary record of paleoclimate. *Geol. Soc. Am. Bull.*, **104**, 543–559.
- Chandler, M.A., Rind, D., and Thompson, R., 1994. Joint investigations of the middle Pliocene climate. II. GISS GCM northern hemisphere results. *Global Planet. Change*, **9**, 197–219.
- Chandler, M.A., and Sohl, L.E., 2000. Climate forcings and the initiation of low-latitude ice sheets during the Neoproterozoic Varanger glacial interval. *J. Geophys. Res.*, **105**, 20737–20756.
- Covey, C., and Barron, E., 1988. The role of ocean heat transport in climatic change. *Earth Sci. Rev.*, **24**, 429–445.
- Covey, C., and Thompson, S.L., 1989. Testing the effects of ocean heat transport on climate. *Palaeogeogr. Palaeoclimatol. Palaeoecol.*, **75**, 331–341.
- Crowley, T.J., 1994. Pangean climates. In Klein G.D. (ed.), *Pangea: Paleoclimate, Tectonics, and Sedimentation During Accretion, Zenith, and Breakup of a Supercontinent*. Boulder, CO: Geological Society of America Special Paper 288, 25–39.
- Crowley, T.J., and Baum, S.K., 1991a. Toward reconciliation of Late Ordovician (~440 Ma) glaciation with very high CO₂ levels. *J. Geophys. Res.*, **96**, 22597–22610.
- Crowley, T.J., and Baum, S.K., 1991b. Seasonal snowline instability in a climate model with realistic geography: Application to Carboniferous (~300 Ma) glaciation. *Geophys. Res. Lett.*, **18**, 1719–1722.
- Crowley, T.J., and Baum, S.K., 1992a. Modeling late Paleozoic glaciation. *Geology*, **20**, 507–510.
- Crowley, T.J., and Baum, S.K., 1992b. Milankovitch fluctuations on the supercontinents. *Geophys. Res. Lett.*, **19**, 793–796.
- Crowley, T.J., and Baum, S.K., 1993. Effect of decreased solar luminosity on late Precambrian ice extent. *J. Geophys. Res.*, **98**, 16723–16732.
- Crowley, T.J., and Baum, S.K., 1994. General circulation model study of Late Carboniferous interglacial climates. *Palaeoclimates*, **1**, 3–21.
- Crowley, T.J., and Baum, S.K., 1995. Reconciling Late Ordovician (440 Ma) glaciation with very high (14X) CO₂ levels. *J. Geophys. Res.*, **100**, 1093–1101.
- Crowley, T.J., Mengel, J.G., and Short, D.A., 1987. Gondwanaland's seasonal cycle. *Nature*, **329**, 803–807.
- Crowley, T.J., Hyde, W.T., and Short, D.A., 1989. Seasonal cycle variations on the supercontinent of Pangea. *Geology*, **17**, 457–460.
- Crowley, T.J., Baum, S.K., and Hyde, W.T., 1991. Climate model comparisons of Gondwana and Laurentide glaciations. *J. Geophys. Res.*, **96**, 9217–9226.
- Crowley, T.J., Yip, K.J. J., and Baum, S.K., 1994. Snowline instability in a general circulation model: application to Carboniferous glaciation. *Clim. Dyn.*, **10**, 363–376.
- Crowley, T.J., Hyde, W.T., and Peltier, W.R., 2001. CO₂ levels required for deglaciation of a “Near-Snowball” Earth. *Geophys. Res. Lett.*, **28**, 283–286.
- DeConto, R.M., Hay, W.W., Thompson, S.L., and Bergengren, J., 1999. Late Cretaceous climate and vegetation interactions: Cold continental interior paradox. In Barrera, E., and Johnson, C.C. (eds.), *Evolution of the Cretaceous Ocean-Climate System*. Boulder, CO: Geological Society of America Special Paper 332, 391–406.
- DeConto, R.M., and Pollard, D., 2003. Rapid Cenozoic glaciation of Antarctica induced by declining atmospheric CO₂. *Nature*, **421**, 245–249.
- Donnadieu, Y., Fluteau, F., Ramstein, G., Ritz, C., and Besse, J., 2003. Is there a conflict between the Neoproterozoic glacial deposits and the snowball Earth interpretation: An improved understanding with numerical modeling. *Earth Planet. Sci. Lett.*, **208**, 101–112.
- Donnadieu, Y., and Ramstein, G., 2002. Is high obliquity a plausible cause for Neoproterozoic glaciations? *Geophys. Res. Lett.*, doi: 10.1029/2002GL015902.
- Dutton, J.F., and Barron, E.J., 1997. Miocene to present vegetation changes: A possible piece of the Cenozoic cooling puzzle. *Geology*, **25**, 39–41.
- Endal, A.S., and Schatten, K.H., 1982. The faint young-sun climate paradox: Continental influences. *J. Geophys. Res.*, **87**, 7295–7302.
- Erickson, M.C., and Slingerland, R., 1990. Numerical simulations of tidal and wind-driven circulation in the Cretaceous Interior Seaway of North America. *Geol. Soc. Am. Bull.*, **102**, 1499–1516.
- Fawcett, P.J., and Barron, E.J., 1998. The role of geography and atmospheric CO₂ in long-term climate change: Results from model simulations for the Late Permian to present. In Crowley, T.J., and Burke, K. (eds.), *Tectonic Boundary Conditions for Climate Reconstructions*. New York: Oxford University Press, pp. 21–38.
- Fawcett, P.J., Barron, E.J., Robison, V.D., and Katz, B.J., 1994. The climatic evolution of India and Australia from the Late Permian to mid-Jurassic: A comparison of climate model results with the geological record. In Klein, G.D. (ed.), *Pangea: Paleoclimate, Tectonics, and Sedimentation During Accretion, Zenith, and Breakup of a Supercontinent*. Boulder, CO: Geological Society of America Special Paper 288, 139–157.
- Gérard, J.C., Hauglustaine, D.A., and François, L.M., 1992. The faint young sun climate paradox: A simulation with an interactive seasonal climate-sea ice model. *Palaeogeogr. Palaeoclimatol. Palaeoecol.*, **97**, 133–150.
- Gibbs, M.T., Barron, E.J., and Kump, L.R., 1997. An atmospheric pCO₂ threshold for glaciation in the Late Ordovician. *Geology*, **25**, 447–450.
- Gibbs, M.T., Bice, K.L., Barron, E.J., and Kump, L.R., 2000. Glaciation in the early Paleozoic “greenhouse”: The roles of paleogeography and atmospheric CO₂. In Huber, B.T. et al., (eds), *Warm Climates in Earth History*. Cambridge: Cambridge University Press, pp. 386–422.
- Gibbs, M.T., Rees, P.M., Kutzbach, J.E., Ziegler, A.M., Behling, P.J., and Rowley, D.B., 2002. Simulations of Permian climate and comparisons with climate-sensitive sediments. *J. Geol.*, **110**, 33–55.
- Hay, W.W., and Wold, C.N., 1998. The role of mountains and plateaus in a Triassic climate model. In Crowley, T.J., and Burke, K. (eds.), *Tectonic Boundary Conditions for Climate Reconstructions*. New York: Oxford University Press, pp. 116–143.
- Haywood, A.M., Sellwood, B.W., and Valdes, P.J., 2000a. Regional warming: Pliocene (3 Ma) paleoclimate of Europe and Mediterranean. *Geology*, **28**, 1063–1066.
- Haywood, A.M., Valdes, P.J., and Sellwood, B.W., 2000b. Global scale paleoclimate reconstruction of the middle Pliocene climate using the UKMO GCM: Initial results. *Global Planet. Change*, **25**, 239–256.
- Held, I.M., and Suarez, M.J., 1974. Simple albedo feedback models of the icecaps. *Icarus*, **26**, 613–628.
- Henderson-Sellers, B., and Henderson-Sellers, A., 1989. Modelling the ocean climate for the early Archaean. *Palaeogeogr. Palaeoclimatol. Palaeoecol.*, **75**, 195–221.
- Herrmann, A.D., Patzkowsky, M.E., and Pollard, D., 2003. Obliquity forcing with 8–12 times preindustrial levels of atmospheric pCO₂ during the Late Ordovician glaciation. *Geology*, **31**, 485–488.
- Hoffman, P.F., Kaufman, A.J., Halverson, G.P., and Schrag, D.P., 1998. A Neoproterozoic snowball earth. *Science*, **281**, 1342–1346.
- Hotinski, R.M., and Toggweiler, J.R., 2003. Impact of a Tethyan circumglobal passage on ocean heat transport and “equable” climate. *Paleoceanog.*, doi:10.1029/2001PA000730.
- Huber, M., and Sloan, L.C., 2000. Climatic response to tropical sea surface temperature changes on a “greenhouse” Earth. *Paleoceanography*, **15**, 443–450.
- Huber, M., and Sloan, L.C., 2001. Heat transport, deep waters, and thermal gradients: Coupled simulation of an Eocene greenhouse climate. *Geophys. Res. Lett.*, **28**, 3481–3484.
- Hunt, B.G., 1979. The effects of past variations of the Earth's rotation rate on climate. *Nature*, **281**, 188–191.
- Hyde, W.T., Crowley, T.J., Baum, S.K., and Peltier, W.R., 2000. Neoproterozoic ‘snowball Earth’ simulations with a coupled climate/ice-sheet model. *Nature*, **405**, 425–429.

- Hyde, W.T., Crowley, T.J., Tarasov, L., and Peltier, W.R., 1999. The Pan-gean ice age: Studies with a coupled climate-ice sheet model. *Clim. Dyn.*, **15**, 619–629.
- Jenkins, G.S., 2000. Global climate model high-obliquity solutions to the ancient climate puzzles of the Faint-Young Sun Paradox and low-latitude Proterozoic glaciation. *J. Geophys. Res.*, **105**, 7357–7370.
- Jenkins, G.S., Marshall, H.G., and Kuhn, W.R., 1993. Precambrian climate: The effects of land area and Earth's rotation rate. *J. Geophys. Res.*, **98**, 8785–8791.
- Jenkins, G.S., and Smith, S.R., 1999. GCM simulations of Snowball Earth conditions during the late Proterozoic. *Geophys. Res. Lett.*, **26**, 2263–2266.
- Kasting, J.F., Pollack, J.B., and Crisp, D., 1984. Effects of high CO₂ levels on surface temperatures and atmospheric oxidation state of the early earth. *J. Atmos. Chem.*, **1**, 403–428.
- Kennett, J.P., 1977. Cenozoic evolution of Antarctic glaciation, the circum-Antarctic oceans and their impact on global paleoceanography. *J. Geophys. Res.*, **82**, 3843–3859.
- Kiehl, J.T., and Dickinson, R.E., 1987. A study of the radiative effects of enhanced atmospheric CO₂ and CH₄ on early Earth surface temperatures. *J. Geophys. Res.*, **92**, 2991–2998.
- Kirschvink, J.L., 1992. Late Proterozoic low-latitude global glaciation: The snowball Earth. In Schoff, J.W., and Klein, C. (eds.), *The Proterozoic biosphere*. New York: Cambridge University Press, pp. 51–52.
- Kuhn, W.R., and Kasting, J.F., 1983. Effects of increased CO₂ concentrations on surface temperatures of the early Earth. *Nature*, **301**, 53–55.
- Kuhn, W.R., Walker, J.C.G., and Marshall, H.G., 1989. The effect on Earth's surface temperature from variations in rotation rate, continent formation, solar luminosity, and carbon dioxide. *J. Geophys. Res.*, **94**, 11129–11136.
- Kump, L.R., and Slingerland, R.L., 1999. Circulation and stratification of the early Turonian Western Interior Seaway: Sensitivity to a variety of forcings. In Barrera, E., and Johnson, C.C. (eds.), *Evolution of the Cretaceous Ocean-Climate System*. Boulder, CO: Geological Society of America Special Paper 332, 181–190.
- Kutzbach, J.E., 1994. Idealized Pangean climates: Sensitivity to orbital change. In Klein G.D. (ed.) *Pangea: Paleoclimate, Tectonics, and Sedimentation During Accretion, Zenith, and Breakup of a Supercontinent*. Boulder, CO: Geological Society of America Special Paper 288, 41–55.
- Kutzbach, J.E., and Gallimore, R.G., 1989. Pangaean climates: Megamonsoons of the megacontinent. *J. Geophys. Res.*, **94**, 3341–3357.
- Kutzbach, J.E., and Ziegler, A.M., 1993. Simulation of Permian climate and biomes with an atmosphere-ocean model: Comparisons with observations. *Phil. Trans. R. Soc. Lond.*, **341**, 327–340.
- Kutzbach, J.E., Guetter, P.J., Ruddiman, W.F., and Prell, W.L., 1989. Sensitivity of climate to late Cenozoic uplift in Southern Asia and the American West: Numerical experiments. *J. Geophys. Res.*, **94**, 18393–18407.
- Kutzbach, J.E., Prell, W.L., and Ruddiman, W.F., 1993. Sensitivity of Eurasian climate to surface uplift of the Tibetan Plateau. *J. Geology*, **101**, 177–190.
- Longdoz, B., and Francois, L.M., 1997. The faint young sun climatic paradox: Influence of the continental configuration and of the seasonal cycle on the climatic stability. *Global Planet. Change*, **14**, 97–112.
- Maier-Reimer, E., Mikolajewicz, U., and Crowley, T., 1990. Ocean general circulation model sensitivity experiment with an open Central American Isthmus. *Paleoceanography*, **5**, 349–366.
- Manabe, S., and Broccoli, A.J., 1990. Mountains and arid climates of middle latitudes. *Science*, **247**, 192–195.
- Manabe, S., and Bryan, K. Jr., 1985. CO₂-induced change in a coupled ocean-atmosphere model and its implications. *J. Geophys. Res.*, **90**, 11689–11707.
- McGuffie, K., and Henderson-Sellers 1997. *A Climate Modeling Primer*. New York: Wiley, 253 pp.
- Mikolajewicz, U., Maier-Reimer, E., Crowley, T.J., and Kim, K.Y., 1993. Effect of Drake Passage and Panamanian gateways on the circulation of an ocean model. *Paleoceanography*, **8**, 409–426.
- Moore, G.T., Hayashida, D.N., Ross, C.A., and Jacobson, S.R., 1992. Paleoclimate of the Kimmeridgian/Tithonian (Late Jurassic) world. I. Results using a general circulation model. *Palaeogeogr. Palaeoclimatol. Palaeoecol.*, **93**, 113–150.
- O'Connell, S., Chandler, M.A., and Reudy, R., 1996. Implications for the creation of warm saline deep water: Late Paleocene reconstructions and global climate model simulations. *Geol. Soc. Am. Bull.*, **108**, 270–284.
- Oglesby, R.J., 1989. A GCM study of Antarctic glaciation. *Clim. Dyn.*, **3**, 135–156.
- Oglesby, R.J., and Ogg, J.G., 1999. The effect of large fluctuations in obliquity on climates of the late Proterozoic. *Paleoclimates*, **2**, 293–316.
- Otto-Bliesner, B.L., 1993. Tropical mountains and coal formation: a climate model study of the Westphalian (306 MA). *Geophys. Res. Lett.*, **20**, 1947–1950.
- Otto-Bliesner, B.L., 1998. Effects of tropical mountain elevations on the climate of the Late Carboniferous: Climate model simulations. In Crowley, T.J., and Burke, K. (eds.), *Tectonic Boundary Conditions for Climate Reconstructions*. New York: Oxford University Press, pp. 100–115.
- Otto-Bliesner, B.L., and Upchurch, G.R. Jr., 1997. Vegetation-induced warming of high-latitude regions during the Late Cretaceous period. *Nature*, **385**, 804–807.
- Owen, T., Cess, R.D., and Ramanathan, V., 1979. Enhanced CO₂ greenhouse to compensate for reduced solar luminosity on early Earth. *Nature*, **277**, 640–642.
- Parrish, J.T., Ziegler, A.M., and Scotese, C.R., 1982. Rainfall patterns and the distribution of coals and evaporates in the Mesozoic and Cenozoic. *Palaeogeogr. Palaeoclimatol. Palaeoecol.*, **40**, 67–101.
- Pavlov, A.A., Kasting, J.F., Brown, L.L., Rages, K.A., and Freedman, R., 2000. Greenhouse warming by CH₄ in the atmosphere of early Earth. *J. Geophys. Res.*, **105**, 11981–11990.
- Pollard, D., and Schulz, M., 1994. A model for the potential locations of Triassic evaporate basins driven by paleoclimatic GCM simulations. *Global. Planet. Change*, **9**, 233–249.
- Poulsen, C.J., Seidov, D., Barron, E.J., and Peterson, W.H., 1998. The impact of paleogeographic evolution on the surface oceanic circulation and the marine environment within the mid-Cretaceous Tethys. *Paleoceanography*, **13**, 546–559.
- Poulsen, C.J., Barron, E.J., Johnson, C.C., and Fawcett, P., 1999. Links between major climatic factors and regional oceanic circulation in the mid-Cretaceous. In Barrera, E., and Johnson, C.C. (eds.), *Evolution of the Cretaceous Ocean-Climate System*. Boulder, CO: Geological Society of America Special Paper 332, 73–89.
- Poulsen, C.J., Barron, E.J., Arthur, M.A., and Peterson, W.H., 2001a. Response of the mid-Cretaceous global oceanic circulation to tectonic and CO₂ forcings. *Paleoceanography*, **16**, 576–592.
- Poulsen, C.J., Pierrehumbert, R.T., and Jacob, R.L., 2001b. Impact of ocean dynamics on the simulation of the Neoproterozoic "snowball Earth." *Geophys. Res. Lett.*, **28**, 1575–1578.
- Poulsen, C.J., Jacob, R.L., Pierrehumbert, R.T., and Huynh, T.T., 2002. Testing paleogeographic controls on a Neoproterozoic snowball Earth. *Geophys. Res. Lett.*, doi: 10.1029/2001GL014352.
- Poulsen, C.J., Gendaszek, A.S., and Jacob, R.L., 2003. Did the rifting of the Atlantic Ocean cause the Cretaceous thermal maximum? *Geology*, **31**, 115–118.
- Poussart, P.F., Weaver, A.J., and Barnes, C.R., 1999. Late Ordovician glaciation under high atmospheric CO₂: A coupled model analysis. *Paleoceanography*, **14**, 542–558.
- Prell, W.L., and Kutzbach, J.E., 1992. Sensitivity of the Indian monsoon to forcing parameters and implications for its evolution. *Nature*, **360**, 647–652.
- PSUCLIM 1999a. Storm activity in ancient climates 1. Sensitivity of severe storms to climate forcing factors on geologic timescales. *J. Geophys. Res.*, **104**, 27277–27293.
- PSUCLIM 1999b. Storm activity in ancient climates 2. An analysis using climate simulations and sedimentary structures. *J. Geophys. Res.*, **104**, 27295–27320.
- Rees, P.M., Gibbs, M.T., Ziegler, A.M., Kutzbach, J.E., and Behling, P.J., 1999. Permian climates: Evaluating model predictions using global paleobotanical data. *Geology*, **27**, 891–894.
- Rees, P.M., Ziegler, A.M., Gibbs, M.T., Kutzbach, J.E., Behling, P.J., and Rowley, D.B., 2002. Permian phytogeographic patterns and climate data/model comparisons. *J. Geol.*, **110**, 1–31.
- Rind, D., and Chandler, M., 1991. Increased ocean heat transports and warmer climates. *J. Geophys. Res.*, **96**, 7437–7461.
- Ruddiman, R.F., and Kutzbach, J.E., 1989. Forcing of late Cenozoic northern hemisphere climate by plateau uplift in Southern Asia and the American West. *J. Geophys. Res.*, **94**, 18409–18427.

- Ruddiman, W.F., Prell, W.L., and Raymo, M.E., 1989. Late Cenozoic uplift in Southern Asia and the American West: Rationale for general circulation modeling experiments. *J. Geophys. Res.*, **94**, 18379–18391.
- Sagan, C., and Mullen, G., 1972. Earth and Mars: Evolution of atmospheres and surface temperatures. *Science*, **177**, 52–56.
- Schneider, S.H., Thompson, S.L., and Barron, E.J., 1985. Mid-Cretaceous continental surface temperatures: Are high CO₂ concentrations needed to simulated above-freezing winter conditions? In Sundquist, E.T., and Broecker, W.S. (eds.), *The carbon cycle and atmospheric CO₂: Natural variations, Archean to present*. Washington, DC: American Geophysical Union Geophysical Monograph 32, 546–553.
- Seidov, D.G., 1986. Numerical modeling of the ocean circulation and paleocirculation. In Hsu, K.J. (ed.), *Mesozoic and Cenozoic Oceans*. Washington, DC: Geodynamics Series, American Geophysical Union, 15, 11–26.
- Sellers, W.D., 1969. A global model based on the energy balance of the Earth-Atmosphere system. *J. Appl. Meteorol.*, **8**, 392–300.
- Sellwood, B., and Valdes, P.J., 1997. Geological evaluation of climate General Circulation Models and model implications for Mesozoic cloud cover. *Terra Nova*, **2**, 75–78.
- Sewall, J.O., Sloan, L.C., Huber, M., and Wing, S., 2000. Climate sensitivity to changes in land surface characteristics. *Global. Planet. Change*, **26**, 445–465.
- Shelto, C., Sloan, L., and Huber, M., 2003. Climate model sensitivity to atmospheric CO₂ levels in the Early-Middle Paleogene. *Palaeogeogr. Palaeoclimatol. Palaeoecol.*, **193**, 113–123.
- Sloan, L.C., and Barron, E.J., 1990. “Equable” climates during Earth history? *Geology*, **18**, 489–492.
- Sloan, L.C., and Barron, E.J., 1992. A comparison of Eocene climate model results to quantified paleoclimatic interpretations. *Palaeogeogr. Palaeoclimatol. Palaeoecol.*, **93**, 183–202.
- Sloan, L. Cirbus 1994. Equable climates during the early Eocene: Significance of regional paleogeography for North American climate. *Geology*, **22**, 881–884.
- Sloan, L.C., and Morrill, C., 1998. Orbital forcing and Eocene continental temperatures. *Palaeogeogr. Palaeoclimatol. Palaeoecol.*, **144**, 21–35.
- Sloan, L.C., and Pollard, D., 1998. Polar stratospheric clouds: A high latitude warming mechanism in an ancient greenhouse world. *Geophys. Res. Lett.*, **25**, 3517–3520.
- Sloan, L.C., and Rea, D.K., 1995. Atmospheric carbon dioxide and early Eocene climate: A general circulation modeling sensitivity study. *Palaeogeogr. Palaeoclimatol. Palaeoecol.*, **119**, 275–292.
- Sloan, L.C., Crowley, T.J., and Pollard, D., 1996. Modeling of middle Pliocene climate with the NCAR GENESIS general circulation model. *Mar. Micropaleontol.*, **27**, 51–61.
- Sloan, L.C., Huber, M., Crowley, T.J., Sewall, J.O., and Baum, S., 2001. Effect of sea surface temperature configuration on model simulations of “equable” climate in the Early Eocene. *Palaeogeogr. Palaeoclimatol. Palaeoecol.*, **167**, 321–335.
- Thompson, S.L., and Barron, E.J., 1981. Comparison of Cretaceous and present Earth albedos: Implications for the causes of paleoclimates. *J. Geol.*, **89**, 143–167.
- Toggweiler, J.R., and Bjornsson, H., 2000. Drake Passage and palaeoclimate. *J. Quat. Sci.*, **15**, 319–328.
- Toggweiler, J.R., and Samuels, B., 1995. Effect of Drake Passage on the global thermohaline circulation. *Deep Sea Res. I*, **42**, 477–500.
- Trenberth, K.E., 1992. *Climate system modeling*. New York: Cambridge University Press, 788 pp.
- Upchurch, G.R. Jr., Otto-Bliessner, B.L., and Scotese, C.R., 1999. Terrestrial vegetation and its effects on climate during the latest Cretaceous, In Barrera, E., and Johnson, C.C. (eds.), *Evolution of the Cretaceous Ocean-Climate System*. Boulder, CO: Geological Society of America Special Paper 332, 407–426.
- Valdes, P.J., 1994. Atmospheric general circulation models of the Jurassic. In Allen, J.R.L., Hoskins, B.J., Sellwood, B.W., Spicer, R.A., and Valdes, P.J. (eds.), *Palaeoclimates and Their Modeling: With Special Reference to the Mesozoic Era*. London: Chapman and Hall, pp. 109–118.
- Valdes, P.J., and Sellwood, B.W., 1992. A palaeoclimate model of the Kimmeridgian. *Palaeogeogr. Palaeoclimatol. Palaeoecol.*, **95**, 47–72.
- Walker, J.C.G., and Zahnle, K.J., 1986. Lunar nodal tides and distance to the Moon during the Precambrian. *Nature*, **320**, 600–602.
- Washington, W.M., and Parkinson, C.L., 1986. *An introduction to three-dimensional climate modeling*. New York: University Science Books, 422 pp.
- Williams, G.E., 1975. Late Precambrian glacial climate and the Earth’s obliquity. *Geol. Mag.*, **112**, 441–465.
- Williams, G.E., 1986. Precambrian permafrost horizons as indicators of palaeoclimate. *Precambrian Res.*, **32**, 233–242.
- Wilson, K.M., Pollard, D., Hay, W.W., Thompson, S.L., and Wold, C.N., 1994. General circulation model simulations of Triassic climates: Preliminary results. In Klein, G.D. (ed.), *Pangea: Paleoclimate, Tectonics, and Sedimentation During Accretion, Zenith, and Breakup of a Supercontinent*. Boulder, CO: Geological Society of America Special Paper 288, 91–116.
- Yapp, C.H., and Poets, H., 1992. Ancient atmospheric CO₂ inferred from natural goethites, *Nature*, **355**, 342–344.
- Ziegler, A.M., Hansen, K.S., Johnson, M.E., Kelly, M.A., Scotese, C.R., and Van der Voo, R., 1977. Silurian continental distributions, paleogeography, climatology, and biogeography. *Tectonophysics*, **40**, 13–51.

Cross-references

Carbon Isotope Variations over Geologic Time
 Cenozoic Climate Change
 Climate Change, Causes
 Climate Forcing
 Cretaceous Warm Climates
 Faint Young Sun Paradox
 Early Paleozoic Climates (Cambrian-Devonian)
 Glaciations, Pre-Quaternary
 Heat Transport, Oceanic and Atmospheric
 Late Paleozoic Paleoclimates (Carboniferous-Permian)
 Mesozoic Climates
 Mountain Uplift and Climate Change
 Neogene Climates
 Obliquity
 Paleocene-Eocene Thermal Maximum
 Paleocene Modeling
 Paleogene Climates
 Plate Tectonics and Climate Change
 Snowball Earth Hypothesis

PALEOCLIMATE MODELING, QUATERNARY

Introduction

Climate models have proven to be very powerful tools in the study of past, present, and future climate. Particular emphasis has been placed on paleoclimate modeling of the Quaternary. The Quaternary is conventionally defined as the Pleistocene plus the Holocene. This modeling has served two basic roles. First, it has helped us to understand the forces driving the diverse phenomena that occurred during this geologic period. Second, by understanding how climates of the recent past differed from those of the present-day, we can both shed light on how climate may change in the future and help to validate our models by seeing how well they simulate a different climate, especially one for which considerable proxy data exist that enable climate reconstruction over much of the globe.

While many diverse paleo-modeling studies have been made for the Quaternary, two major foci can be identified. The first concerns the phenomena for which this period is best known – the cyclical appearance and subsequent disappearance of massive continental ice sheets over much of North America and Europe. Topics here include ice sheet inception, interactions between ice sheets and climate at the Last Glacial Maximum (LGM), and simulation of entire ice sheet cycles. The second major focus is simulation of the mid-Holocene climatic optimum at about 8–6 kyr B.P. While these two themes have drawn the most attention, numerous

other facets of Quaternary climate have also been addressed, e.g., the last interglacial at around 120 kyr B.P., the Younger Dryas cold event at around 11–12 kyr B.P., quasi-cyclical Heinrich and Dansgaard-Oeschger events, and the study of past abrupt climate changes in general (e.g., Bradley, 1999). Much attention has recently been paid to climatic changes over the past 2,000 years, for example “mega-droughts” over continental interiors (see *Climate variability and change, last 1,000 years*).

A variety of different types of climate models has been used for these simulations of Quaternary climate. Probably the best-known of these are the so-called “general circulation models,” or GCMs (also popularly known as “global climate models”); indeed these types of models will be the primary (but not sole) focus of this chapter. Originally, these only modeled the atmosphere, with the state of the ocean, land surface, and cryosphere specified. More recently, a major push has occurred toward modeling of the entire climate system, with fully coupled ocean-atmosphere GCMs that frequently also include such features as an interactive land surface (including dynamical vegetation components), explicit simulation of sea ice, and most recently, chemistry of the oceans and atmosphere, with particular emphasis on the carbon cycle. These more comprehensive models are frequently referred to as “earth system models,” or ESMs, though it is important to remember that their core component is still a GCM.

A number of earlier studies used a much simpler climate model known as the “statistical dynamical model” or SDM. In recent years, a new, hybrid model has been developed that combines features of the GCM and SDM into a robust model that can be used to simulate long periods of time; these are known as “earth models of intermediate complexity,” or “EMIC.” Finally, a very different type of model, based on the concepts of low-order dynamical systems, has been used to study long term climate changes, such as the Pleistocene ice sheet cycles. These low order paleoclimate dynamical models, or PDMs, have considered the role of such factors as internal non-linear oscillations and external forcings due to Milankovitch orbital cycles (e.g., Berger, 1977) in explaining the ice sheet cycles (as do EMICS).

In the remainder of this entry, we explore in more depth how different climate models have been applied to key problems of Quaternary climate. Since all of these specific Quaternary issues/problems are explored in some detail in other entries of this encyclopedia, key results are summarized rather than explained in detail. The thrust here is rather to explain how one goes about doing this paleoclimate modeling, using an evolutionary time-frame, and emphasizing strengths and weaknesses of the models.

Model descriptions and evolution

The GCM

The core of the GCM is essentially the same type of model that is used for modern day weather forecasting; the major distinction is in how the model is used. For weather forecasting, the model is started from a set of initial conditions and run forward in time for a few days (usually 10–14). For climate studies, the model is used to generate a climatic state for a given set of boundary conditions and forcings. The model must be spun-up for a period of months to centuries, both to remove the effect of what are now arbitrary initial conditions and to come into quasi-equilibrium with the imposed boundary conditions and forcings. The model run is then continued for a period

ranging from a few years to centuries – the model at this point is generating a series of daily weather patterns, which are then used to generate the desired “climatic statistics” in much the same way that real climate statistics are generated from daily weather observations.

The original GCMs (dating back to the 1970s) were mostly atmosphere-only models; the state of the ocean was prescribed by imposing known (for present-day) or reconstructed (for past times) sea surface temperatures (SST). The state of the land surface was prescribed through very simplistic formulations that specified a surface albedo and a crude representation of water availability (and hence surface evaporation); snow cover was either specified or simulated using simple models. The cryosphere (that is sea ice and continental ice sheets) were imposed, again based on observations or past reconstructions. These early GCMs were constrained both by lack of sufficient physically-based knowledge (especially how to deal with the ocean, cryosphere, and land surface) and, very importantly, by limitations on computational resources to run these computer-intensive models. Over the past four decades, both our understanding of the physics and computational resources have increased tremendously; as of this writing (early 2006) GCMs that contain fully-interactive atmosphere, ocean, ice, and land surface components are in wide use. It is, however, fair to say that the atmosphere component is still the best understood (and hence best modeled), though the other components are rapidly catching up. Furthermore, while the greatly enhanced computational resources we now enjoy mean that the GCM can include all relevant components of the climate system, they still cannot be run for very long time spans (e.g., thousands to tens of thousands of years). See McGuffie and Henderson-Sellers (2005) and Washington and Parkinson (1986) for a more detailed discussion of the GCM.

Other models (SDM; low order dynamical; EMIC)

Around the time that GCMs were first used to address questions of Quaternary climate, the SDM was also in vogue, and used to address the same questions. Unlike the GCM (which is a daily weather model used to generate climate statistics), the SDM attempts to solve the questions by providing appropriate physical quantities on seasonal to annual climatic time-scales. The problem is that key physical processes involved in describing individual weather systems (especially those responsible for rain and snow at mid and high latitudes) must be heavily parameterized, that is, explained in terms of basic quantities like temperature and large-scale circulation (Figure P10). Thus, these models, as such, contributed little to direct understanding of Quaternary climate, though as described below, they did make substantial contributions to low order dynamical models, and, especially, to the recent develop of the EMIC. Saltzman (1978) provides a review of the SDM.

Low order dynamical models differ from the other climate models discussed here in that the major goal is not to simulate a specific climate state, but rather to directly simulate the way in which climate changes over long timescales. These models attempt to define the important feedbacks involved in long-term climate change and then to show how both linear and non-linear interactions, as driven or modulated by external forcings, account for the known record of climate change, especially when the climate changes are expressed as a time series averaged either globally or over key geographic regions. Saltzman (2001) provides an extensive review and discussion of these models; for our present purposes, it suffices to say that they

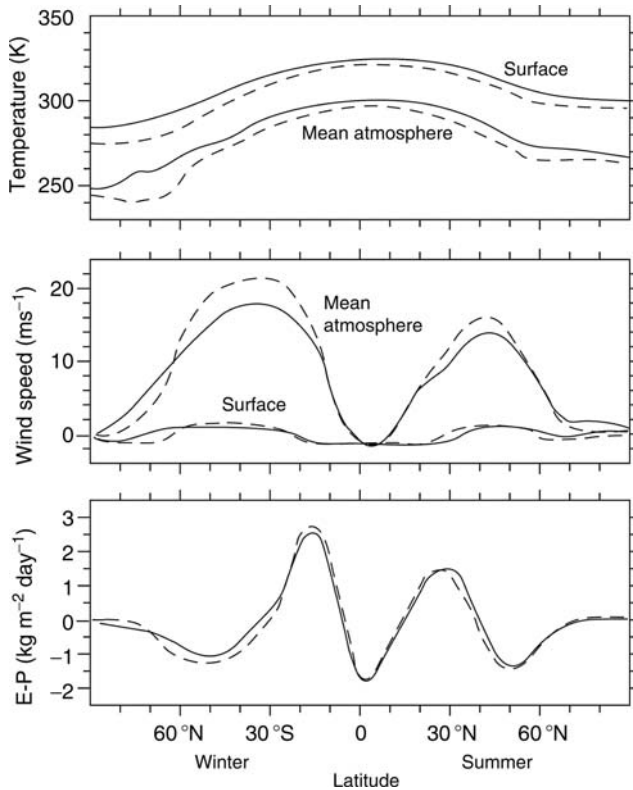


Figure P10 The distribution of zonally-averaged potential temperature (*top panel*), zonal wind (*middle panel*), and evaporation-precipitation difference (*bottom panel*), as simulated by an atmospheric SDM for modern conditions (*full line*) and for 20 ka glacial conditions (*dashed line*) (after Saltzman and Vernekar, 1975).

have demonstrated the important ways in which the state of the oceans, the carbon cycle (i.e., atmospheric carbon dioxide), and the extent and volume of the ice sheets themselves interact non-linearly to describe how the Pleistocene ice ages occur. Furthermore, they show how such key external forcing agents, especially Milankovich orbital cycles, could act as a pace-maker, that is, phase-lock the otherwise arbitrary ice sheet cycles into the specific time frame given by the paleorecords. An additional key feature of these models is that they are computationally very cheap, and therefore can easily be run for thousands or even millions of years.

The most recent addition to the suite of models is the EMIC. This type of model has been developed specifically to address many of the limitations of the above modeling approaches, and therefore draws upon each of them. These models attempt to explain important physical processes with sufficient rigor (drawing upon concepts adapted from both the GCM and SDM), while at the same time being simple enough that, like the low-order dynamical system models, they can be integrated over geologic timescales (at least those spanning thousands of years, Figure P13). Conceptually these models would seem to offer much, and therefore demonstrate considerable promise. However, since they have only been developed over the past few years, the “jury is still out” on how useful they will ultimately prove to be. One key disadvantage of these models is that they have low spatial resolution compared to the GCM (on the other hand this is a key feature that allows very long

runs to be made with them). Claussen et al. (2002) provide an excellent description of one widely used EMIC.

One final modeling approach that has recently been developed and employed is the use of regional climate models (RCM), which have very high spatial resolution (e.g., Giorgi et al., 1990). For many problems, this high resolution is desired or even essential, a good example being the need to resolve mountainous topography (or the full structure of an ice sheet, see Figure P12). Even modern GCMs are typically run for paleoclimate studies at a horizontal resolution no greater than 150 km in latitude and longitude, and many present-day studies are still made with a resolution no greater than 300–400 km. Past studies frequently used even lower resolution GCMs. The drawback to the much higher resolution RCM is inherent in the name; because of computational cost, they can only be run for limited areas, and must be forced at their lateral boundaries, usually from a GCM when conducting paleoclimate studies. Essentially then, the RCM can be thought of as providing a physically based downscaling of GCM results.

With this modeling background developed, focus now shifts to modeling of specific issues of Quaternary climate; emphasizing the use of the GCM, but bringing in other models as appropriate.

Historical development of Quaternary modeling

Some of the earliest GCM and SDM modeling studies involved simulating the impacts of the massive ice sheets of the Last Glacial Maximum (LGM) on the atmosphere (SDM – Saltzman and Vernekar, 1975; GCM – Gates, 1976). Though crude by present-day standards, this work did demonstrate that the climate at the LGM was significantly colder and generally drier than at present, and that orbital forcing played at least some role in accounting for the ice age cycles. Subsequent work generally advanced in two areas: exploration of the physical mechanisms responsible for the relatively cold, dry LGM climate, and snapshot simulations of the climate state every few thousand years from the LGM until the present.

The need to provide specified sea surface temperatures (SST) for the early generation GCM provided the original motivation for the CLIMAP (Climate: Long-range Investigation, Mapping, and Prediction) program, which, in the late 1970s and early 1980s, used all available deep sea core data, especially oxygen isotope data, to develop SST reconstructions for the LGM (CLIMAP group, 1981; Manabe and Broccoli, 1985). These CLIMAP LGM SST became the standard for virtually all GCM work of the LGM, and indeed, with some modification, continue to be used at present. They also engendered considerable controversy when modeling studies using CLIMAP SST yielded significant discrepancies with tropical terrestrial LGM reconstructions from proxy data. Suspicion arose that CLIMAP was flawed over large sections of the tropical Pacific, and much work has gone into resolving this issue, which even at this writing has not been fully resolved (see for example Crowley, 2000; and Toracinta et al., 2004). The controversy does provide an excellent example of the iterative nature by which reconstruction of past environments and paleoclimate modeling work hand in hand.

Another significant development that began in the 1980s was the concept of analyzing GCM time slices through the late Quaternary (especially from the LGM to the present, Figure P11), that is, GCM “snapshots” of simulated climate every few thousand years. The first sets of snapshots

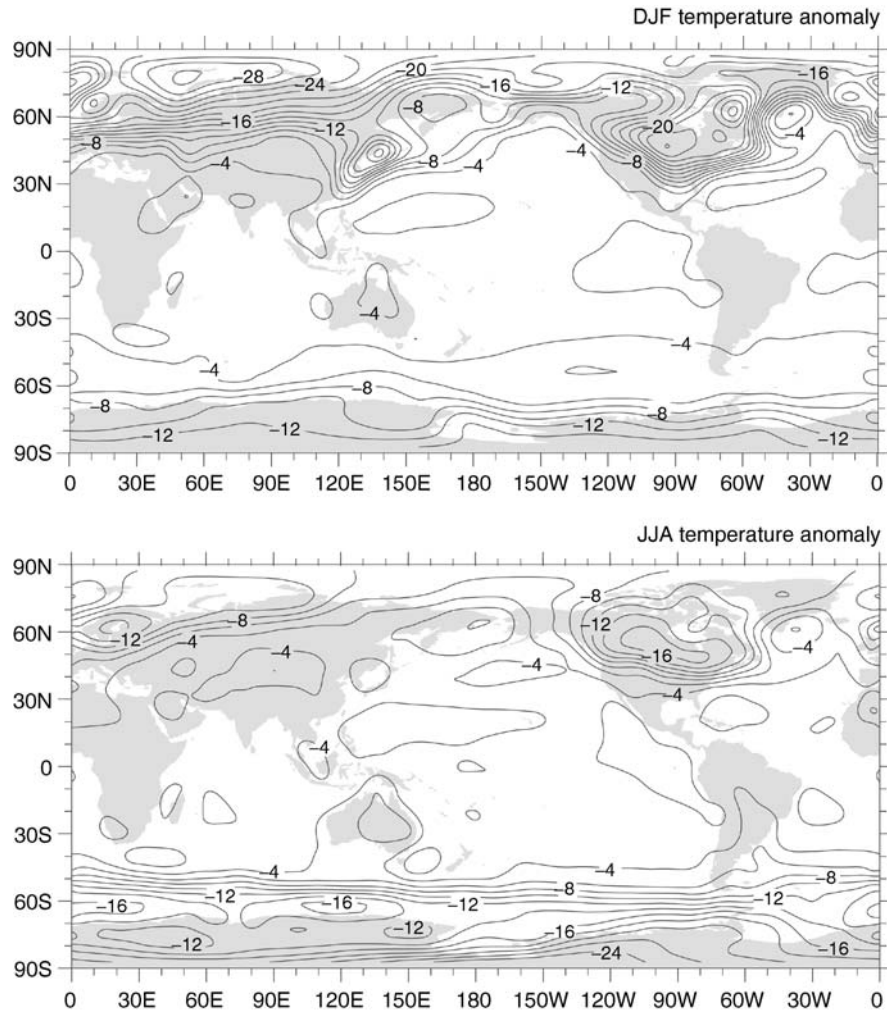


Figure P11 LGM minus present surface temperature anomaly from the NCAR CCSM GCM, averaged over December, January, and February (*top panel*) and averaged over June, July, and August (*bottom panel*). Units are in degrees Celsius (after Shin et al., 2003).

(Kutzbach and Guetter, 1986) were for 18 ka, 15 ka, 12 ka, 9 ka, 6 ka, and 3 ka, or every 3,000 years from what was then thought to be the time of the LGM (18 ka) until the present. Of course, as the difference between “radiocarbon years” and “calibrated years” became known, it was realized that the LGM actually occurred about 21 ka (especially important because it affects the particular configuration of orbital parameters). Thus, subsequent series of model runs had their timings adjusted accordingly. Taken individually, each run of the series can be compared to reconstructions of the Quaternary for that time period. Taken as a group, they can form a description of how climate changed from the LGM to the present, in effect accomplishing, albeit in a different way, a goal similar to that of low order dynamical modeling. These time slice runs have been repeated a number of times, with entirely different models, and with improved versions of the same model. This means that in addition to shedding light on the climate of each of these times, they are also used to describe inter-model differences, and track improvements to individual models.

Related to this time slice approach, the COHMAP (Cooperative Holocene Mapping Project) has focused on reconstructions

and modeling of the Holocene, loosely defined as the time after the ice sheets decayed to a point where they (presumably) had little impact (approximately 9–12 ka depending on research group and specific definitions) (COHMAP, 1988). Much of this attention has been focused on the mid-Holocene so-called “climatic optimum” at 6 ka, when, in the Northern Hemisphere at least, orbital parameters should dictate a relatively warm climate. Particular attention has been paid to changes in Asian, African, and North American monsoonal circulations and effects at 6 ka, as these presumably would have been enhanced. Prell and Kutzbach (1987) have also carefully studied monsoon response in simulations earlier in the Holocene as well as during glacial and interglacial times. Not surprisingly, they found that monsoon circulations tend to be stronger during interglacials than during glacials. In part, this is due to the absence of the ice sheets but it is also because interglacials tend to be times of enhanced orbital insolation.

The above modeling studies were primarily focused on model simulation of the overall climate of specific time periods, and comparison to climates of other times, especially the present-day climate. Quite a number of other studies have

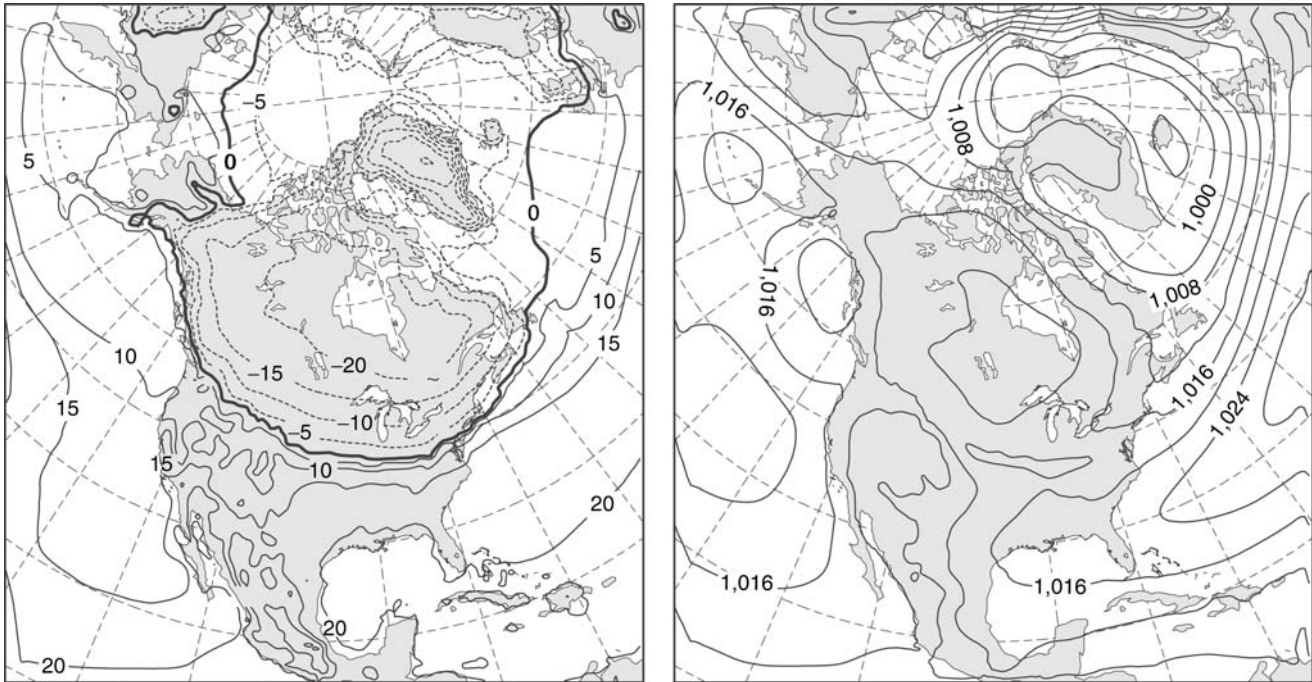


Figure P12 LGM surface temperatures and sea-level pressures as simulated by the PMM5 RCM. *Left panel* is surface temperature averaged over January in degrees Celsius and *right panel* is sea-level pressure averaged over January in hPa (after Bromwich et al., 2004).

addressed how these very different climates have been maintained. These studies fall into two broad categories, the first of which are process-oriented studies for a particular time period. Two key examples here include: (i) the dynamical effects of the ice sheets at the LGM on the circulation of the atmosphere, especially the way in which these very high elevation, white (due to the high albedo of snow and ice) ice sheets impact the circulation (Shinn and Barron, 1989), and (ii) the effect of tropical Pacific SST (especially so-called “permanent La Niña conditions”) on the hydrologic cycle and drought over central North America and northern Africa (Shin et al., 2006).

The second category includes sensitivity studies, in which a series of model simulations is made, spanning a range of values for a particular climate component, boundary condition, or forcing. These can be considered individually, or in concert. Key examples include evaluation of: (i) the sensitivity of climate to ice sheet areal extent, height, and “whiteness” (albedo) and (ii) the relative roles that such factors as atmospheric carbon dioxide (CO_2), orbital forcing, and the ice sheets themselves play in accounting for the cooler climate of the LGM. In the first case, Felzer et al. (1996), for example, demonstrated the importance of thresholds in ice sheet elevation – too low and the atmosphere flows over them, but above a certain height the atmosphere must flow around them instead, yielding a very different regional climate, whose effects in turn can be seen over a much larger portion of the Earth. In the second case, Felzer et al. (1999) showed that the ice sheets and lowered CO_2 played approximately equal roles in accounting for the colder LGM temperatures, with orbital forcing playing a much smaller role.

Recently, considerable attention has focused on extending modeling studies further back in the Quaternary. One particular interest has been 115 ka (sometimes taken as 116 ka), which is

when the last great Pleistocene ice sheet cycle is thought to have begun (Fig. P13). The primary focus of these studies has been on ice sheet inception, that is, how does the climate system change from little or no perennial snow cover to multi-year perennial snow cover and then to growth of ice of sufficient mass that it begins to flow and thereby leaves a trace in the geologic record (Vettoretti and Peltier, 2002)? This is a question yet to be satisfactorily resolved (Dong and Valdes, 1995). Cold temperatures will certainly help preserve snow/ice, but the colder the atmosphere the less moisture it can hold; the warmer the atmosphere the more moisture can precipitate out as snow (assuming surface temperatures not much above freezing). The other time period of interest has been the time around 125 ka, when the last major interglacial occurred. Evidence from the geologic record suggests this interglacial may have been even warmer than the mid-Holocene; orbital forcing was also somewhat larger at this time. Prell and Kutzbach (1987) indeed found in GCM studies that the monsoon at 125 ka was enhanced relative to 6 ka (and hence also to the present).

A few early attempts were made to use regional climate models (RCM) to address some of the above problems, but neither the RCMs nor the GCMs required for the lateral forcings were adequate. This has changed in recent years; regional model simulations of the Laurentide and Fennoscandian Ice Sheets at the LGM have been shown to yield much closer overall agreement with paleo proxy reconstructions than does the GCM used to drive the RCM (Bromwich et al., 2004). In particular, the much higher resolution RCM appears more capable of simulating the highly-variable spatial details of precipitation, and the nuances of topography, land surface type and state, and atmospheric circulation than the low resolution GCM, which all too often can only broad-brush these features. On the other hand, occasionally the RCM will provide surprising results that seem at odds with at least

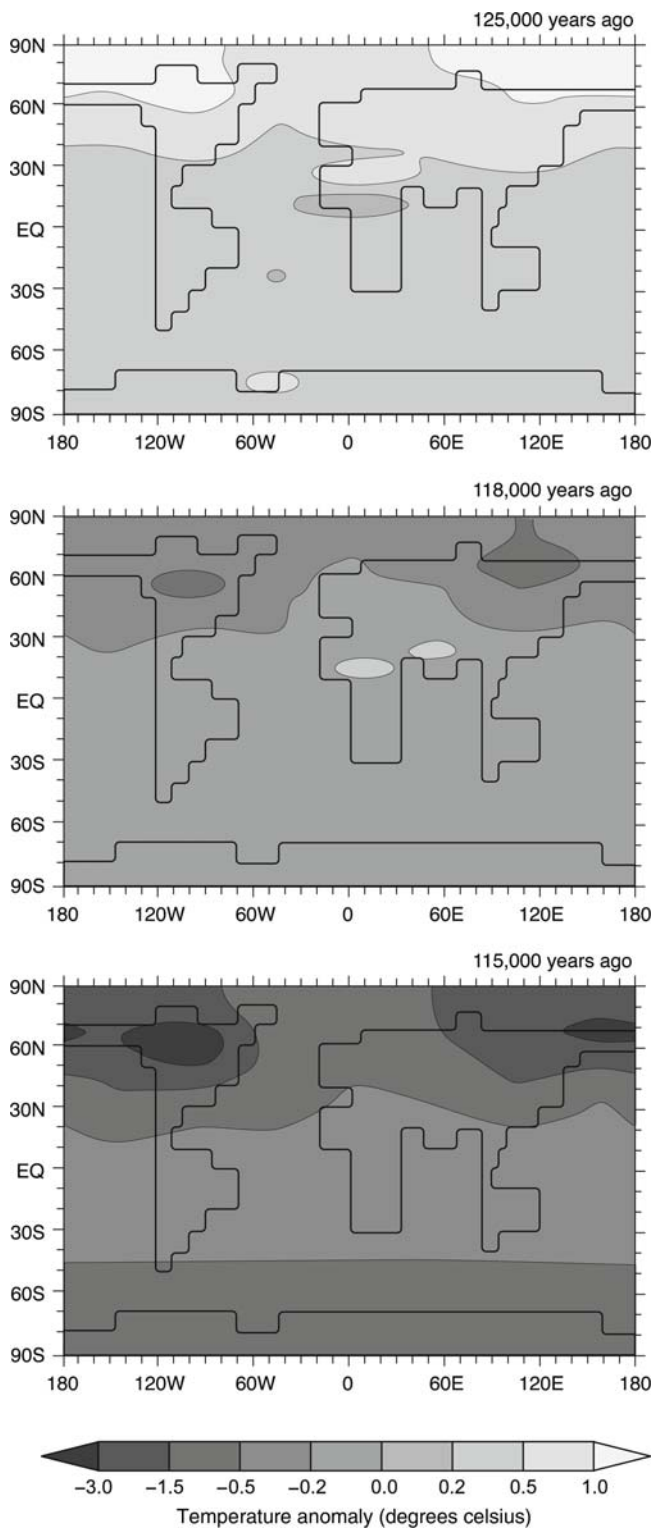


Figure P13 Annually-averaged temperature anomalies, relative to the present, at 125,000 years ago (*top panel*), 118,000 years ago (*middle panel*), and 115,000 years ago (*bottom panel*) from the CLIMBER-2 EMIC. Units are in degrees Celsius. The progression is from full interglacial conditions at 125,000 years ago, to the onset of the next glaciation at 115,000 years ago (after Calov et al., 2005).

the conventional paleo reconstructions. This is yet another example of how models and proxy data together can be used iteratively to provide a much deeper understanding than either one alone. It is likely that GCMs will continue to be used in future paleoclimate studies.

Most recently, the EMIC has been used to address climate problems of the Quaternary. The advantage to these models is that they can be easily integrated over long periods of time. EMICs have been used to simulate changing climate over the past few thousand years (although this is also beginning to be done with GCMs) (Crucifix et al., 2002; Calov et al., 2005). They have also been used to address problems earlier in the Quaternary, e.g., around 400,000 years ago, as well as at the Plio-Pleistocene transition. As described above, it is unclear how informative these models are, largely because of their low spatial resolution (how, for example, can monsoon effects be studied with a model that may only have a 57 degree resolution in longitude?). These models could possibly be considered as an attempt to combine the best of both worlds of low order dynamical models and GCMs; but instead they may actually only capture the worst of both worlds. Again, the jury is still out.

The current state-of-the-art

As climate models continue to evolve, together with our understanding of Quaternary climates, recent efforts have focused on addressing key Quaternary climatic issues with improved models. For GCM studies, this has meant explicitly including other climate components in addition to the atmosphere. Fully-coupled atmosphere-ocean GCMs have been used to simulate the climates of the LGM and the Holocene “climatic optimum” at 6 ka. While somewhat less mature and less well-developed, attention is also being paid to simulating these time periods with interactive vegetation, ice sheet, and biogeochemical cycle components embedded in the GCM (with the model now typically called an ESM). These new, enhanced modeling studies typically have broadly the same results as the more crude earlier models, but do highlight important regional differences and provide new understanding of the relevant physical processes. For example, fully coupled runs at 6 ka have shown the importance of tight atmosphere-ocean coupling in modulating the African and Asian monsoons. This same type of fully-coupled modeling for the LGM-Holocene transition (broadly 9–12 ka) has shown the importance of, and possible bimodality in, the ocean thermohaline circulation, especially the production of North Atlantic Deep Water (NADW). This type of bimodal “switch” or threshold, has profound implications for past climates, and is of potential importance concerning near-term future climate change.

Furthermore, many researchers are now starting to use GCMs not just to study “snapshots” of a particular past time, but instead are actually running the models for periods of thousands of years. A lot of this has already been done for the past 2,000 years, but runs are also underway using a GCM to simulate the past 6,000 years. In addition to the GCM, the EMIC has also been used to perform these simulations through geologic time. By coupling the GCM to high resolution RCMs, models can also commonly be run with local resolutions around 50 km, with as fine as 10–20 km possible. Finally, recovery of higher resolution paleoclimate proxy records in recent years has meant significant improvements in the iterative procedure by which the past reconstructions are used to evaluate the models and, in turn, the model results are used to help understand the implications of the geologic record and guide in the search

for more proxy data. Especially important has been the development of high temporal resolution, well-dated, multi-proxy records from ice cores and lake sediments, which have greatly complemented the more traditional deep-sea cores.

Future directions

One direction that has been discussed for years is the development of a super-model; that is, essentially a super-GCM that has very high spatial resolution, can be run for extended periods of time (at least thousands of years) and that incorporates all relevant climate phenomena, regardless of timescale. In other words, such a model would explicitly simulate the motions of the atmosphere on timescales of minutes, and would simulate the waxing and waning of ice sheets, with timescales of tens of thousands of years. Both the recent development of ESMs and of EMICs can be considered as steps towards the development of such a super-model; however, approaching from opposite ends of the spectrum. That is, the ESM attempts to include as many physical processes as possible at high spatial and temporal resolution (increasing the computer resources needed for long runs severely), while the EMIC, which also attempts to consider as many physical processes as feasible, explicitly uses low temporal and spatial resolution so that long runs can be made. The practical obstacles to developing a super-model are obvious – the need for considerably more computational resources than currently available as well as sharp limitations in our knowledge of the relevant physical processes. In addition, is it not even clear conceptually whether such a model is even possible given the huge range of timescales over which it must be run. Small errors in the short time-scale processes may cascade over longer times, making it impossible to get a satisfactory solution of the long timescale processes.

More use of coupled GCM-RCM studies is likely to be made so that climatic states and phenomena can be studied at much higher resolution. Also, the EMIC could mature as a class of models and continue to provide better ways of making fairly low-resolution but physically-plausible long simulations. Indeed, it may be expected that a “morphing” will continue to take place between the EMIC and low-order dynamical system models. Finally, there will be a continuing need for more and better geologic data to constrain the models, with the models in turn being used to help better understand paleoclimate reconstructions.

Summary and conclusions

The above is intended to provide a concise but necessarily brief and limited overview of how paleoclimate modeling of the Quaternary has developed from the early 1970s until the mid-2000s. Many important problems, concepts, and studies have either been given only a cursory treatment, or even not considered at all. As a glance at the bibliography quickly shows, full treatment of this topic would require at least one, if not several, entire lengthy volumes. All of the issues that have been raised above, as well as those beyond the scope of this discussion, are being actively investigated; none have been satisfactorily “proven,” nor, given the simple fact that we will never know precisely what happened in the past (unless someone eventually constructs a true time machine), will they ever be. Nonetheless, they have taught us many things about how the climate system works, which is perhaps the single most important issue to be addressed via climate modeling of any time period, be it the past, the present, or projected future climate states, as well as the climatic changes required to make them. The interested

reader is strongly encouraged to use this treatment, and especially the papers and books listed in the bibliography, as a starting point for a more in depth study and analysis of this very interesting and important theme.

Robert J. Oglesby and Kirk A. Maasch

Bibliography

- Berger, A., 1977. Long-term variations of the earth's orbital elements. *Celestial Mechanics*, **15**, 53–74.
- Bradley, R.S., 1999. *Paleoclimatology: Reconstructing Climates of the Quaternary, 2nd Edition*. San Diego: Academic Press, 613pp.
- Bromwich, D.H., Toracinta, E.R., Wei, H., Oglesby, R.J., Fastook, J.L., and Hughes, T.J., 2004. Polar MM5 simulations of the winter climate of the Laurentide ice sheet at the LGM. *Journal of Climate*, **17**, 3415–3433.
- Calov, R., Ganopolski, A., Petoukhov, V., Claussen, M., Brokin, V., and Kubatzki, C., 2005. Transient simulation of the last glacial inception. Part II: sensitivity and feedback analysis. *Climate Dynamics*, **24**, 563–576.
- Claussen, M., Mysak, L., Weaver, A., Crucifix, M., Fichet, T., Loutre, M.-F., Weber, S., Alcamo, J., Alexeev, V., Berger, A., Calov, R., Ganopolski, A., Gooze, H., Lohmann, G., Lunkeit, F., Mokhov, I., Petoukhov, V., Stone, P., and Wang, Z., 2002. Earth system models of intermediate complexity: closing the gap in the spectrum of climate system models. *Climate Dynamics*, **18**, 579–586.
- CLIMAP Members, 1981. *Seasonal reconstruction of the earth's surface at the Last Glacial Maximum*. Map and Chart Series, Vol. 36, Geological Society of America, 18pp.
- COHMAP, 1988. Climatic changes of the last 18,000 years: observations and model simulations. *Science*, **241**, 1043–1052.
- Crowley, T.J., 2000. CLIMAP SSTs revisited. *Climate Dynamics*, **16**, 241–255.
- Crowley, T.J., and North, G.R., 1991. *Paleoclimatology*. Oxford Monographs on Geology and Geophysics 18, New York: Oxford University Press, 339pp.
- Crucifix, M., Loutre, M.-F., Tulkens, P., Fichet, T., and Berger, A., 2002. Climate evolution during the Holocene: a study with an Earth system model of intermediate complexity. *Climate Dynamics*, DOI: 10.1007/s00382-001-0208-6 v19, 43–60
- Dong, B., and Valdes, P.J. 1995. Sensitivity Studies of Northern Hemisphere Glaciation Using an Atmospheric General Circulation Model. *Journal of Climate*, **10**, 2471–2496.
- Felzer, B., Oglesby, R.J., Webb, T., III, and Hyman, D.E., 1996. Sensitivity of a general circulation model to changes in northern hemisphere ice sheets. *Journal of Geophysical Research*, **101**, 19,077–19,092.
- Felzer, B., Webb, T., III, and Oglesby, R.J., 1999. Climate model sensitivity to changes in boundary conditions during the last glacial maximum. *Paleoclimates*, **3**, 257–278.
- Gates, W.L., 1976. Modeling the ice-age climate. *Science*, **191**, 1138–1144.
- Giorgi, F., Marinucci, M.R., and Visconti, G., 1990. Use of a limited-area model nested in a general circulation model for regional climate simulation over Europe. *Journal of Geophysical Research*, **95**, 18413–18431.
- Kutzbach, J.E., and Guetter, P.J., 1986. The influence of changing orbital parameters and surface boundary conditions on climate simulations for the past 18,000 years. *Journal of Atmospheric Sciences*, **43**(16), 1726–1759.
- Manabe, S., and Broccoli, A.J., 1985. The influence of continental ice sheets on the climate of an ice age. *Journal of Geophysical Research*, **90**, 2167–2190.
- McGuffie, K., and Henderson-Sellers, A., 2005. *A Climate Modelling Primer, 3rd Edition* Kendal ISBN: 0-470-85750-1 Hardcover 296 pages March 2005.
- Prell, W.L., and Kutzbach, J.E., 1987. Variability of the monsoon over the past 150,000 years: Comparison of observed and simulated paleoclimatic time series. *Journal of Geophysical Research*, **92**, 8411–8425.
- Saltzman, B., 1978. A survey of statistical-dynamical models of the terrestrial climate. *Advances in Geophysics*, **20**, 183–304.
- Saltzman, B., 2001. *Dynamical Paleoclimatology*. International Geophysics Series, 80, San Diego: Academic Press, 350pp.
- Saltzman, B., and Vernekar, A., 1975. A solution for the northern hemisphere climatic zonation during a glacial maximum. *Quaternary Research*, **5**, 307–320.

- Shin, S., Liu, Z., Otto-Bliesner, B., Brady, E.C., Kutzbach, J.E., and Harrison, S.P., 2003. A simulation of the last glacial maximum using the NCAR-CCSM. *Climate Dynamics*, **20**, 127–151.
- Shin, S., Sardeshmukh, P.D., Webb, R.S., Oglesby, R.J., and Barsugli, J.J., 2006. Understanding the mid-Holocene Climate. *Journal of Climate*, in press.
- Shinn, R.A., and Barron, E.J., 1989. Climate sensitivity to continental ice sheet size and configuration. *Journal of Climate*, **2**, 1517–1537.
- Toracinta, E.R., Oglesby, R.J., and Bromwich, D.H., 2004. *Journal of Climate*, **17**, 504–522.
- Vettoretti, G., and Peltier, W.R., 2002. Post-Eemian Glacial Inception. Part I: The Impact of Summer Seasonal Temperature Bias. *Journal of Climate*, **16**, 889–911.
- Washington, W.M., and Parkinson, C.L., 1986. *An Introduction to Three-Dimensional Climate Modeling*. Mill Valley, CA: University Science Books, 422pp.

Cross-references

[Astronomical Theory of Climate Change](#)
[Atmospheric Circulation during the Last Glacial Maximum](#)
[CLIMAP](#)
[Climate Variability and Change, Last 1,000 Years](#)
[COHMAP](#)
[Glaciations, Quaternary](#)
[Holocene Climates](#)
[Last Glacial Maximum](#)
[Last Glacial Termination](#)
[Laurentide Ice Sheet](#)
[Millennial Climate Variability](#)
[Monsoons, Quaternary](#)
[Pleistocene Climates](#)
[Quaternary Climate Transitions and Cycles](#)
[SPECMAP](#)
[Younger Dryas](#)

PALEOCLIMATE PROXIES, AN INTRODUCTION

The Earth's climate has changed dramatically over the eons, as the atmosphere continuously interacts with oceans, lithosphere, and biosphere over a wide range of timescales. Efforts to place recent climate observations into a longer-term context have been stimulated by concern over whether the twentieth century global warming trend is part of natural climate variability or linked to increasing anthropogenic inputs of greenhouse gases into the atmosphere. The ability to decipher past climates has expanded in recent years with an improved understanding of present climatic processes and the development of more sophisticated analytical tools. Instrumental records go back only a century or two. To extend the record beyond the instrumental period, scientists turn to “proxies” or “indicators” that are indirect measures of past climates or environments preserved in natural archives, such as marine and terrestrial sediments, trees, and ice cores, among others. Paleoclimatic or paleoenvironmental proxies are materials that are sensitive to a variety of climatic or environmental parameters. These can be grouped into three major categories: (a) lithological/mineralogical, (b) geochemical, and (c) paleontological (Table P2). The types of information on past climates or environments that can be obtained from these proxies are briefly summarized in Table P2 and below. Additional information is provided in the individual entries listed under *Cross references*.

Lithological/mineralogical indicators

Lithological indicators consist of sedimentary deposits or fossil soils (paleosols) that have originated at or near the Earth's surface under conditions characteristic of a particular climatic regime or environmental setting. The paleoclimatic information yielded by terrestrial lithological indicators comes from interpreting the specific environments under which they formed and their spatiotemporal distribution on local to global scales (see Table P2; Parrish, 1998; *Sedimentary indicators of climate change*). Some lithological or sedimentary indicators point to specific climate conditions, such as glaciation (e.g., tills and tillites, moraines, eskers, kames, kettles), aridity (e.g., eolian dunes, evaporites), or warm, humid climates (e.g., laterites, bauxite) (see *Arid climates and indicators*; *Coal beds, origin and climate*; *Glacial geomorphology*; *Glaciofluvial sediments*; *Glaciomarine sediments*; *Laterites*). Others provide more indirect signs of climate change interpreted from the depositional environments of sediments, using classical geological techniques (see *Encyclopedia of Sedimentology*). Examples of depositional environments include fluvial, deltaic, lacustrine, eolian (wind-borne), near-shore, and deep sea settings (see *Coastal environments*; *Deltaic sediments, climate records*; *Eolian sediments and processes*; *Lacustrine sediments*; *Marine biogenic sediments*). Finely laminated sediments, such as varves, preserve seasonal variations in rainfall, streamflow, ice melt, or chemical precipitation in lakes (see *Varved sediments*). Lithological indicators are also closely linked to biogeochemical phenomena, which create additional paleoclimate proxies (see below).

Major shifts in the environment or climate over longer geologic time periods are marked by pronounced lithologic or compositional changes in the stratigraphic column. A beautiful example can be seen in the well-exposed Carboniferous-Permian strata of the upper half of the Grand Canyon, Arizona, where marine limestones of the Redwall Formation were overlain by intercalated reddish mudstones, sandstones, and calcareous sandstones of the Supai Group deposited in a complex coastal plain setting in which the sea repeatedly advanced and retreated. Eolian features within some sandstone units were likely formed by onshore winds (Beus and Morales, 2003). The Supai strata were succeeded by red beds of the Hermit Formation – siltstones, mudstones and fine-grained sandstones – deposited by rivers, showing cyclical alternations possibly related to climatic fluctuations. Desiccated mudcracks and ripples at the top of the Hermit Shale suggest a climatic aridification, which culminated in the vast accumulation of desert sands represented by the Coconino Sandstone. The seas returned toward the end of the Permian period, as exemplified by the thick marine limestone sequence (Toroweap Formation, Kaibab Limestone).

Minerals that form at or near the Earth's surface reflect ambient conditions at the earth-atmosphere interface and can therefore furnish important clues about former climates (see *Mineral indicators of past climates*). Climate-sensitive minerals can be used to infer past climates and changes over time, to deduce changes in atmospheric composition, to act as mineralogical “markers” in provenance studies, and to serve as “hosts” for stable isotopes and trace elements used in paleoclimate studies. The most direct mineral indicators or proxies are those that are generated under relatively narrow climatic ranges or within restricted environmental settings. Examples include chemical precipitates such as evaporites (e.g., halite, or rock salt), clays formed by intense chemical weathering (e.g., kaolinite, smectite), and chemically-resistant minerals concentrated into eolian

Table P2 Paleoclimatic and paleoenvironmental indicators

Major category	Indicator	Paleoclimate/paleoenvironment parameter(s)
Lithological/mineralogical	Banded iron formations	Atmospheric evolution; ocean paleochemistry
	Bauxite	Tropical, humid climates; paleogeographic reconstructions
	Beachrock	Sea level indicator
	Bedded chert (marine)	Ocean paleoproductivity
	Carbonates, cool water	Cool ocean paleotemperatures
	Chalk	Ocean paleoproductivity, carbonate compensation depth
	Clays (various)	Chemical weathering (humid vs. arid climates)
	Coal	Humid to perhumid climate
	Eolian dust (ice cores; ocean sed.)	Wind strength and direction
	Eolianite (carbonate-rich)	Arid, high wind and wave energy, low relief coasts; interglacial high sea-level stands
	Eskers	Glaciation
	Evaporites	Arid climate
	Dunes	Arid climate; wind direction and strength, atmospheric circulation
	Duricrusts	Warm, seasonally wet/dry climates, semi-arid climates (calcrete)
	Glendonite/ikaite	Cold climate
	Ice-rafted debris	Glaciation
	Kames and kettles	Glaciation
	Lacustrine sediments	Temperature, precipitation, salinity
	Laterite	Tropical, humid climates; paleogeographic reconstructions
	Loess deposits	Periglacial, desert environments, glacial-interglacial variations in wind direction and strength, atmospheric circulation
	Moraines	Glaciation
	Outwash plains	Glaciation
	Paleosols	Precipitation, (temperature–warm, cold), pCO ₂
	Patterned ground	Periglacial environment
	Pingo	Periglacial environment
	Phosphates	Ocean paleoproductivity, wind-driven upwelling zones
	Red beds	Warm, seasonally wet/dry climates
	Roche moutonnée	Glaciation
	Sapropels	Anoxic conditions and/or high paleocean productivity
	Speleothems	Paleotemperature ($\delta^{18}\text{O}$ ratios), vegetation change ($\delta^{13}\text{C}$ ratios), paleoprecipitation
	Tills, tillites	Glaciation
	Varved sediments	Seasonal variations in rainfall or streamflow, glacial or non-glacial sediments; annual dating
	Geochemical	<i>Isotopes</i>
¹⁰ Be		Solar variability, dating
$\delta^{11}\text{B}$		Paleo-ocean pH
¹³ C/ ¹² C		pCO ₂ , C ₃ versus C ₄ plant distributions, ocean paleoproductivity, global organic carbon burial/weathering
¹⁴ C/ ¹² C		Solar variability, dating
² H/ ¹ H		Paleohydrology, paleotemperature
¹⁸ O/ ¹⁶ O		Local atmospheric temperature (in ice), ice volume or sea level (air bubbles in polar ice; benthic foraminifera), paleoprecipitation
¹⁵ N/ ¹⁴ N		Rapid temperature fluctuations (air bubbles in polar ice), stratification in lakes, oceans
⁸⁷ Sr/ ⁸⁶ Sr		Continental weathering, river runoff
³⁴ S/ ³² S		Ocean paleochemistry—changes in sulfate precipitation (evaporites) or sedimentary sulfide burial
<i>Organic matter</i>		
Alkenones		Ocean paleotemperature
Carbon accumulation rates		Ocean paleoproductivity
<i>Trace elements</i>		
Barium (barite)		Ocean paleoproductivity
Boron (as B(OH) ₄ ⁻)		Paleo-ocean pH
Cadmium		Ocean nutrients (in planktonic forams, coccoliths), proxy for PO ₄ ³⁻
Magnesium		Ocean paleotemperature
Phosphorus		Ocean paleoproductivity
Iron		Ocean nutrient
Mn, Co, Ni, Zn, Cu	Ocean nutrients	
Strontium	Ocean paleotemperature	
Geophysical	Electrical conductivity	Variations in ice core acidity, volcanic activity, rapid climate oscillations
	Paleomagnetism	Paleolatitude, dating
Paleontological	Animals, invertebrates	Marine facies, cool versus warm climate, paleolatitude
	Animals, vertebrates	Paleotemperature, biogeography

Table P2 (Continued)

Major category	Indicator	Paleoclimate/paleoenvironment parameter(s)
	Beetles	Paleotemperature
	Coccoliths	Ocean paleoproductivity, biostratigraphy
	Corals, coral reefs	Tropical to subtropical shallow water temperatures
	Diatoms	Ocean paleoproductivity, temperature, salinity, pH
	Dinoflagellates	Ocean paleotemperature, salinity, productivity, sea-ice cover extent
	Foraminifera	
	Benthic	Ice volume, sea level ($\delta^{18}\text{O}$ ratios), ocean paleoproductivity
	Planktonic	Ocean paleotemperature, paleoproductivity
	Ostracodes	Ocean and lacustrine paleotemperature, salinity, precipitation
	Plants	
	Leaf morphology	Paleoaltitude, seasonal and mean annual temperature, precipitation
	Stomatal index	pCO ₂ , temperature, moisture availability
	Tree rings	Temperature, precipitation, interannual variability, annual dating
	Plant assemblages	Paleoecology, paleoclimate
	Pollen	Paleoecology, paleotemperature, paleoprecipitation
	Treeline fluctuations	Growing season temperature variations
	Radiolaria	Paleocean temperature, ocean paleoproductivity

sand (sandstone) deposits (e.g., quartz). Iron-bearing minerals sensitive to oxidation (e.g., pyrite, siderite) may provide information about past atmospheric composition. Hematite-stained quartz and feldspar grains help track the sources of ice-rafted debris in the North Atlantic during the late Pleistocene. Records of oscillations in late Quaternary East African rainfall and in eolian dust transport have been recorded by variations in tracer mineral composition. Minerals such as calcite or aragonite in speleothems, corals, or shells of foraminifera house vital paleoclimatic oxygen isotope data.

Although lithological and mineralogical indicators extend back to the oldest sedimentary rock record almost 4 billion years ago, they are generally qualitative and incomplete. Preservation may have been selective and affected by climate-influenced processes such as erosion, weathering, and deposition. While terrestrial sedimentary deposits or soils have developed in contact with the atmosphere and hydrosphere, their development can also be strongly controlled by other non-climatic processes, such as tectonics. Marine sediments are derived from a combination of terrestrial sources (fluvial, eolian, glacial), biogenic deposition (calcareous and siliceous oozes, bedded cherts, phosphorites, etc.), and authigenic mineralization (see *Carbonates, warm water; Carbonates, cool water; Marine biogenic sediments; Phosphorites*). Ocean sedimentation patterns are products of continental weathering, water temperatures, and ocean circulation, all of which are influenced by climate on regional to global scales. However, marine sediments contain a major archive of climate change, including evidence for rapid climate shifts. Mineralogical, geochemical, and paleontological signals enclosed in these sediments hold important keys to understanding the causes of climate change (see below).

Geochemical indicators

More detailed, quantitative information can be gleaned from geochemical markers contained in sediments. These proxies include isotopic ratios, trace elements, and organic molecules.

Isotope ratios. Most chemical elements have several isotopes, which differ only in atomic weight. Isotope ratios are reported in terms of the notation:

$$\delta^{\text{B}} = (R_{\text{sample}}/R_{\text{standard}} - 1) \times 1,000$$

where a is the atomic weight of the heavier isotope, B is the element, and R is the isotope ratio (heavy to light) in the sample and in a standard reference material, and values of δ are given in parts per thousand (‰). Positive δ values occur when $R_{\text{sample}} > R_{\text{standard}}$; conversely, negative δ values result when $R_{\text{sample}} < R_{\text{standard}}$. The most widely used isotope ratios in paleoclimatology are $^{18}\text{O}/^{16}\text{O}$, $^{13}\text{C}/^{12}\text{C}$, $^2\text{H}/^1\text{H}$, and to a lesser extent $^{15}\text{N}/^{14}\text{N}$ (see *Carbon isotopes, stable; Oxygen isotopes; Deuterium, deuterium excess; Nitrogen isotopes*). A broad array of geological and biological materials can be analyzed for their oxygen, carbon isotope, or hydrogen composition, including the shells of foraminifera, corals, speleothems, tree wood, and ice, to name just a few.

A number of geochemical and biogenic processes cause the ratios of stable (i.e., non-radiogenic) isotopes to vary in nature (see *Stable isotope analysis*). Several of these are related to climate variables, such as atmospheric and ocean temperatures, ice volume, and precipitation. Lighter isotopes of an element are usually more mobile and react faster chemically than heavier ones. The lighter isotopes of hydrogen and oxygen (^1H and ^{16}O) in water, for example, evaporate more rapidly and therefore are preferentially incorporated into water vapor. During condensation, the lighter isotopes remain in the cloud, while the heavier isotopes (^2H and ^{18}O) precipitate out in rainwater (see *Oxygen isotopes; Deuterium, deuterium excess*). Over successive cycles of evaporation and condensation, rainwater becomes progressively enriched in the lighter isotopes, as air masses travel landward and poleward. Thus, snow falling at the poles, which eventually turns to ice, is isotopically lighter. Conversely, ocean water becomes more depleted in the lighter isotopes. The partitioning (or fractionation) of isotopes is also temperature-dependent. The isotopic composition of a mineral, carbonate shell, or snow reflects that of the fluid from which it formed, which largely depends on temperature. In general, as temperature increases, the isotopic ratio of the resulting mineral, shell, or snow becomes progressively lighter. Thus, for example, variations in the oxygen and hydrogen isotope ratios in polar ice can be related to the local atmospheric temperatures from which the snow precipitated. The ice cores can therefore provide a record of temperature variations over glacial-interglacial cycles (see *Ice cores, Antarctica and Greenland*).

During glacial periods, large volumes of water were locked up in polar ice sheets, leaving the oceans relatively enriched in the heavier isotope, ^{18}O . Carbonate shells of benthic foraminifera (which are less influenced by local surface ocean temperature variations than planktonic forams) record deep sea isotope variations that correspond to major global climate changes. The $\delta^{18}\text{O}$ values of these shells were heavier during glacial periods than during interglacials, due in large part to the greater ice sheet volume and lower sea level. However, during globally warm climate periods (i.e., “greenhouse” climates) when polar ice sheets were small or even absent (e.g., the Cretaceous and Paleogene periods), variations in marine $\delta^{18}\text{O}$ values have been attributed mainly to water temperature variations. A number of other factors, however, influence the correlation between oxygen isotope ratios in ocean water and foraminifera, including the species and its preferred temperature range, mean annual and seasonal water temperature, and ocean salinity.

Biological processes also lead to isotopic fractionation that tends to enhance the lighter isotope. For example, $^{13}\text{C}/^{12}\text{C}$ ratios are lower in biologically-produced organic matter than in atmospheric CO_2 or in marine carbonates. Plants take up ^{12}C more readily than ^{13}C . Furthermore, plants utilizing the C_3 photosynthetic pathway show ever greater carbon isotope depletions than those following the C_4 photosynthetic pathway. Variations in $^{13}\text{C}/^{12}\text{C}$ ratios during the Phanerozoic Eon have been interpreted in terms of major changes in organic versus inorganic terrestrial carbon reservoirs (e.g., see *Carbon cycle*). In general, higher $\delta^{13}\text{C}$ values in carbonates imply a greater rate of storage of organic matter enriched in ^{12}C relative to ^{13}C (leaving the inorganic C reservoirs depleted in the lighter carbon isotope).

Trace elements. Trace metals in the hard parts of marine fossils also provide useful proxies of past temperatures and ocean biogeochemistry. Ratios of Mg/Ca , and to a lesser extent Sr/Ca , in foraminifera show temperature-dependent variations. Ba/Ca , Cd/Ca , and Si/Al ratios have been linked to nutrient concentrations and productivity, as have phosphorus and iron. The Mg/Ca paleotemperature proxy is based upon the observation that substitution of Mg for Ca in calcite of foraminifera and ostracodes increases with rising temperatures (see *Ocean paleotemperatures*). Mg/Ca temperature reconstructions can be paired with $\delta^{18}\text{O}$ measurements on the same sample, providing an independent estimate of temperature. However, Mg/Ca ratios are sensitive to differential solution effects as well as changes in ocean pH and salinity.

Organic biomarkers. A number of organic molecules produced through biological activity can serve as paleoclimate or paleoenvironmental proxies. In order to be useful, an organic biomarker should be geochemically stable and well-preserved in the sedimentary record. Furthermore, it should derive from a particular organism or group of organisms, within a restricted environment, and have modern analogs. It should also be fairly widespread in occurrence, over extended geological time periods. A number of organic biomarker molecules have been used as paleoclimate proxies, including hydrocarbons, fatty acids, alkenones, sterols, pigments (e.g., chlorophyll), and lignin derivatives (see *Organic geochemical proxies; Geochemical proxies (non-isotopic)*). Of these, alkenones are probably the most widely used (see *Alkenones*). Alkenones are long-chain ketones produced by marine coccolithophores (see *Coccoliths*), particularly the species *Emiliani huxleyi*. They extend as far back in time as the Cretaceous. The alkenone unsaturation

index, U_{37}^k , expresses the relation of alkenone composition to sea surface temperature. This index increases with increasing ocean temperatures.

Paleontological indicators

Fossils can serve as useful paleoclimate indicators, since plants and animals are often quite sensitive to their environment and to climate. A useful fossil species is one that responds rapidly to climate shifts, spans a range of time without significant evolutionary change, is relatively abundant and widespread in the geological record, and can be well-preserved without subsequent alteration. In some cases, important insights into paleoclimate can be gained if the morphology reflects the organism's adaptation to its environment. For example, plant leaf morphology has been used to interpret paleoclimate by comparing specific leaf characteristics, such as size, thickness, stomatal density, shape, and margin types in living plants to present-day climate (Parrish, 1998; see *CLAMP; Paleobotany*). Leaf physiognomy reflects annual and seasonal temperature and precipitation, whereas stomatal density is more closely related to CO_2 levels and water availability. These characteristics are responses to particular climate regimes and are often independent of taxonomic classification. The climate signal encoded in leaf morphology can be extracted using multivariate statistical methods, such as CLAMP. Leaf physiognomy is calibrated using a reference database with climatic information on modern vegetation. The CLAMP method has been applied to woody dicotyledons, spanning the late Tertiary and Quaternary periods.

Another widely-used approach is the nearest-living-relative (NLR) method. The NLR approach assumes that the fossil had the same environmental tolerances of its closest living relatives and that these tolerances have remained constant over time (for example, the presence of fossilized palm fronds might indicate mild or tropical climates; ancient mangroves would indicate intertidal zones or paleoshorelines). The NLR technique is limited to relatively young fossil assemblages (preferably Neogene and younger).

Statistical methods, such as transfer functions, are employed to quantify links between the modern distributions of species and specific climate parameters (see *Transfer functions*). The transfer function approach was used with certain species of planktonic foraminifera, radiolarians, and coccolithophorids to establish sea-surface temperatures during the Last Glacial Maximum, 18,000 years BP (e.g., CLIMAP Project Members, 1976). In the CLIMAP project, the geographic distributions of modern planktonic assemblages were sampled by collecting core-top material and living specimens from sediment traps. Correlations between the spatial distributions of the modern species and sea-surface temperatures were then established by multivariate regression analysis (e.g., Imbrie and Kipp, 1971). The abundance of the planktonic foram *Neogloboquadrina pachyderma*, for example, varies inversely with sea-surface temperature, making it an excellent high latitude, cold climate indicator. The geographic ranges of the modern species were then compared with their fossil counterparts and the resulting data used to construct boundary sea-surface temperatures for the last ice age (see *CLIMAP*).

The study of pollen and spores produced by plants and preserved in sediments reveals evidence of past ecological and climate changes (see *Pollen analysis*). The shape and texture of the outer layer of the pollen grain, when magnified, is characteristic of a given family, genus, and sometimes even species. Pollen is dispersed by wind, insects, or birds. The grains are

resistant to decay, especially under anaerobic conditions in lakes or peat bogs. Any shifts in pollen abundances over time observed in the sediment column represent changes in vegetation, caused by ecological or climatic factors. As with other biotic proxies, it is assumed that modern analogs exist, that the environmental factors affecting the plants have not changed over time, that their climatic tolerances are known, and that the pollen can be identified at some meaningful level. Biases can be introduced by dispersal mode or differential preservation. To overcome potential biases, palynologists may exclude certain local pollen types that tend to be over-represented. They may also count absolute numbers of grains per cm³ of sediment. Fossil pollen assemblages are interpreted in two principal ways: first by comparing the pollen assemblage at a given site with the surrounding vegetation (modern analog method), and second, by using an indicator species, whose habitat is narrowly defined by ecological or climatic factors that have remained constant. Although pollen analysis could, in principle, be extended much further back in geologic time, in practice this method has generally been applied to Quaternary and Recent vegetation, which have much closer living relatives.

Tree rings provide another important climate archive (e.g., Fritts, 1976; Cook, 1995; Stokes and Smiley, 1996). Trees that grow in seasonal climates, such as mid-latitude temperate or low-latitude monsoonal climates, generally produce discrete annual growth rings – wider during the growing season and narrower during the dormant period. Some useful characteristics include mean ring width, relative width of early to late wood, and ring density. The development of rings, however, depends on many environmental factors, among which are temperature and precipitation. The strongest climate signals come from trees living where sensitivity to some limiting factor, such as rainfall or temperature, is greatest, e.g., at the limits of their ranges. Because of the complex interactions among factors affecting tree growth, the climate response is inferred indirectly through semi-empirical relationships, using multivariate statistical analyses. Standardized tree ring indices are calibrated against long-term meteorological data from the nearest available stations. Additional information on the methodology of tree ring analysis, its application to paleoclimatology, and its limitations is summarized under *Dendroclimatology*.

Multiple proxies

The information provided by any single proxy is limited in its relation to a specific climate variable, or in its initial spatiotemporal distribution. Furthermore, the effects of preservation or subsequent alteration can lead to a certain ambiguity in interpretation. One way of increasing the reliability of paleoclimate reconstructions is by the use of multiple proxies. More confidence can be placed on consistent results obtained from several different proxies. Recent paleoclimate reconstructions often use multiple proxies. For example, a temperature curve of the last millennium has been derived from a combination of tree ring, coral, foraminiferal, δO^{18} , borehole, and ice core data (e.g., Mann et al., 1998; Moberg et al., 2005). A long-term record of global sea-level change has been pieced together, using stratigraphic data, oxygen isotope variations, and marine fossil assemblages (Miller et al., 2005).

Ice cores offer a multitude of paleoclimate proxies from a single source (see *Ice cores, Antarctica and Greenland*). These include concentrations of CO₂, CH₄, and N₂O in trapped gas bubbles, δO^{18} and δd in ice, and stable isotope composition of included gases, dust, and sulfate levels. These proxies

provide insights into glacial-interglacial changes in atmospheric composition and circulation, temperature, ice volume, volcanic activity, and global biogeochemical cycles, among others. The ice core record in Antarctica now extends to 8 glacial cycles (EPICA, 2004).

In summary, climate “proxies” or indicators preserved in sediments, ice sheets and glaciers, caves, corals, and trees provide indirect measures of former climates for geological periods when no instrumental data existed. Many different types of proxies exist (Table P2), which offer qualitative or quantitative information on a number of climatological or environmental parameters, such as paleotemperature, atmospheric composition, ocean and atmospheric circulation, glaciation, or paleoprecipitation. A more complete synthesis of paleoclimate is available through the integration of data from multiple proxies.

Vivien Gornitz

Bibliography

- Beus, S.S., and Morales, M., (eds.), 2003. *Grand Canyon Geology*, 2nd edn. New York, NY: Oxford University Press, 432p.
- CLIMAP Project Members, 1976. The surface of the ice-age Earth. *Science*, **191**, 1131–1137.
- Cook, E.R., 1995. Temperature history from tree rings and corals. *Clim. Dyn.*, **11**, 211–222.
- EPICA Community Members, 2004. Eight glacial cycles from an Antarctic ice core. *Nature*, **429**, 623–628.
- Fritts, H.C., 1976. *Tree Rings and Climate*. London: Academic Press.
- Imbrie, J., and Kipp, N.G., 1971. A new micropaleontological method for quantitative micropaleontology: Application to a late Pleistocene Caribbean core. In Turekian, K.K. (ed.), *Late Cenozoic Ice Ages*. New Haven, CT: Yale University Press, pp. 71–181.
- Mann, M.E., Bradley, R.S., and Hughes, M.K., 1998. Global-scale temperature patterns and climate forcing over the past six centuries. *Nature*, **392**, 779–787.
- Miller, K.G., Kominz, M.A., Browning, J.V., Wright, J.D., Mountain, G.S., Katz, M.E., Sugarman, P.J., Cramer, B.S., Christie-Blick, N., and Pekar, S.F., 2005. The Phanerozoic record of sea-level change. *Science*, **310**, 1293–1298.
- Moberg, A., Sonechkin, D.M., Holmgren, K., Dasenko, N.M., and Karlen, W., 2005. Highly variable Northern Hemisphere temperatures reconstructed from low- and high-resolution proxy data. *Nature*, **433**, 613–617.
- Parrish, J.T., 1998. *Interpreting Pre-Quaternary Climate from the Geologic Record*. New York, NY: Columbia University Press, 338p.
- Stokes, M.A., and Smiley, T.L., 1996. *An Introduction to Tree-ring Dating*. Tucson, AZ: University of Arizona Press.

Cross-references

- [Alkenones](#)
- [Animal Proxies, Invertebrates](#)
- [Animal Proxies, Vertebrates](#)
- [Arid Climates and Indicators](#)
- [Banded Iron Formations and the Early Atmosphere](#)
- [Carbon Cycle](#)
- [Carbon Isotopes, Stable](#)
- [Carbonates, Cool Water](#)
- [Carbonates, Warm Water](#)
- [CLAMP](#)
- [CLIMAP](#)
- [Coal Beds, Origin and Climate](#)
- [Coastal Environments](#)
- [Coccoliths](#)
- [Continental Sediments](#)
- [Coral and Coral Reefs](#)
- [Dendroclimatology](#)
- [Deuterium, Deuterium Excess](#)
- [Diatoms](#)
- [Dinoflagellates](#)
- [Deltaic Sediments, Climate Records](#)

Dendroclimatology
 Eolian Sediments and Processes
 Eolianite
 Geochemical Proxies (non-isotopic)
 Glacial Geomorphology
 Glaciofluvial Sediments
 Glaciomarine Sediments
 Glendonite/ikaite
 Ice Cores, Antarctica and Greenland
 Lacustrine Sediments
 Laterite
 Loess Deposits
 Marine Biogenic Sediments
 Mineral Indicators of Past Climates
 Nearest-Living-Relative Method
 Nitrogen Isotopes
 Ocean Paleoproductivity
 Ocean Paleotemperatures
 Organic Geochemical Proxies
 Ostracodes
 Oxygen Isotopes
 Paleobotany
 Paleo-Ocean pH Indicators
 Paleosols, Pre-Quaternary
 Paleosols, Quaternary
 Paleotemperatures and Proxy Reconstructions
 Periglacial Geomorphology
 Phosphorites
 Pollen Analysis
 Radiolaria
 Red Beds
 Sedimentary Indicators of Climate Change
 Stable Isotope Analysis
 Strontium Isotopes
 Sulfur Isotopes
 Transfer Functions
 Varved Sediments

PALEO-EL NIÑO-SOUTHERN OSCILLATION (ENSO) RECORDS

Introduction

The El Niño-Southern Oscillation (ENSO) phenomenon involves two extreme states, El Niño and La Niña, and their connection with the atmosphere through the Southern Oscillation. The term El Niño (or “the boy child”) was originally used by Peruvian fisherman in the 19th century to refer to a Christmas-time warming of coastal sea surface temperature (SST), often associated with a decrease in the productivity of local fisheries. Today, El Niño refers to the well known, large-scale warming and deepening of the thermocline across the eastern equatorial Pacific affecting climate over much of the globe. In the mid to late 1980s, Philander (1990) coined the term La Niña (“the girl child”) for the opposite oceanic conditions to El Niño – large-scale cooling across the tropical Pacific. The Southern Oscillation (SO) portion of ENSO describes the global-scale surface pressure oscillation documented by workers around the turn of the century, and first studied by Sir Gilbert Walker. Subsequently, the normalized sea level pressure anomaly records from Tahiti and Darwin, Australia, have been widely used to index the atmospheric pressure gradient across the tropical Pacific basin.

The early physical explanations for ocean-atmosphere interactions at the heart of the ENSO phenomenon deduced by Jacob Bjerknes, and the subsequent oceanographic

contributions by Klaus Wyrtki, have formed the basis for much of what is known about ENSO. The term ENSO was first used by Rasmusson and Carpenter (1982) to describe the interaction of the oceanic El Niño with the negative phase of the Southern Oscillation phenomenon. Bjerknes (1969) popularized the word *teleconnections* to describe the complex of overturning cells consisting of the Hadley (north-south) and Walker (east-west) circulations that direct mass and energy from the equatorial Pacific to other regions of the globe. Thorough reviews of the historical development and our modern understanding of the ENSO climate system are presented by Philander (1990) and Allan et al. (1996).

On interannual time scales, ENSO and its teleconnections generate impacts in both marine and terrestrial environments over a large part of the globe (Rasmusson and Carpenter, 1982; Ropelewski and Halpert, 1987). During the El Niño phase, anomalous cloudiness and convection are generated over the band of unusually warm water that develops across the central to eastern equatorial Pacific. This coincides with lower than normal atmospheric pressure occurring in the eastern Pacific and higher than normal atmospheric pressure in the Australasian region. These patterns cause widespread drought across many parts of Australia, southern Africa, northern India, Sahelian Africa, Indonesia and Southeast Asia (Ropelewski and Halpert, 1987). During the La Niña phase, impacts are generally the opposite of those described above. ENSO also influences high-latitude processes, including North American air temperature, Antarctic sea ice extent and ice chemistry, as well as aspects of Atlantic hydrography relevant to thermohaline circulation (Philander, 1990; Allan et al., 1996).

One of the most significant contributions to the longer-term record of El Niño events was made during the 1970s–1980s by William Quinn, who compiled historical evidence of meteorological anomalies in Peru and adjacent countries back to A.D. 1525 (Quinn et al., 1987). According to this chronology, moderate to strong El Niño events occur at irregular intervals and may appear two years in succession and then not appear for another 3–12 years. An average period of 3.8 years between El Niños was arrived at by considering all events (moderate to very strong) over the period 1803 to 1987. However, these events were not always representative of the wider ENSO phenomenon across the Indo-Pacific basin. As a consequence, Quinn (1992) looked at evidence for responses to large-scale ENSO events, such as droughts in India, Australia and Indonesia, and weak Nile River floods.

Changes in the magnitude and frequency of ENSO events observed in instrumental records since the 1970s have generated considerable debate about recent ENSO behavior, and the possibility that it may be responding to global warming. There is also a growing body of evidence indicating that the near-global influence of ENSO teleconnections can wax and wane on decadal time scales. Decadal variations in ENSO frequency, strength and teleconnections are suggested by 20th century instrumental records. For example, the well-known link between ENSO and the Indian monsoon has virtually disappeared since 1976, in parallel with a recent shift in 1976 to warmer and wetter (El Niño-like) conditions in the tropical Pacific. Another style of decadal ENSO variability consists of modulating the frequency of extreme events; some decades have stronger interannual variability than others do. Fluctuations in ENSO and its teleconnection patterns are probably caused by changes in the frequency, magnitude and spatial characteristics of ENSO events between different climate epochs.

Paleo-ENSO reconstruction

Concerns about the future behavior of the ENSO, and its potential far-reaching effects on societies, have promoted research into its long-term history via proxy records. There is intense interest in documenting ENSO variability in the past, during times when Earth's climate was different from today. Documenting ENSO behavior during intervals when climate boundary conditions (e.g., orbitally determined seasonal insolation, global ice cover, sea level, aerosols) were markedly different from those of today is particularly important. Proxy records can be used to answer specific questions, such as how long has ENSO been operating in its present form and how robust is the ENSO phenomenon during the major climate changes accompanying glacial-interglacial cycles? Furthermore, is ENSO an unstable oscillation that can switch between being "El Niño-like," or permanently "La Niña-like"?

The paleoclimate record can be used to understand both high- and low-resolution changes in the ENSO phenomenon. The ideal situation would be to have a suite of paleo-ENSO records from the tropics that record both the oceanic and atmospheric components of the phenomenon at seasonal time scales. However, with the exception of records of SST and changes in surface-ocean salinity extracted from annually banded corals, no such records exist. High-resolution records, such as tree rings, fire scars, varved sediments and ice cores, register the effects of droughts, fires, floods and air temperature fluctuations that can be attributed to single ENSO events. Nevertheless, high-resolution records for long time periods are still rare.

On the other hand, low-resolution records can also be used, but these need to be interpreted with caution. Former impacts of the ENSO phenomenon can be recorded by riverine deposits, pollen assemblages in lake deposits, beach ridge sequences, marine sediments and geoarchaeological remains. Low-resolution studies of ENSO rely on networks of sites, especially from regions known for their sensitivity to ENSO. Multi-proxy analyses dramatically reduce the possibility that a non-ENSO environmental factor was responsible for ENSO-like changes in climatic patterns. Utilizing networks of sites and a multi-proxy approach is particularly useful when studying the distant past, when climate boundary conditions and ENSO teleconnection patterns may have been vastly different from those observed today.

Evidence for Plio-Pleistocene onset

How old is the ENSO? ENSO-like phenomena, both oceanic and atmospheric, have probably existed since the separation of the eastern Pacific Ocean from the western Atlantic Ocean. During the course of the mountain building process that produced the Andes and Central American chains, and the formation of the land bridge between North and South America, exchanges of seawater between the tropical Pacific and Atlantic Oceans ended. On paleogeographical grounds, the modern oceanic circulation of the Pacific basin has probably existed for about the last three million years (since the late Pliocene), following the final closure of the Isthmus of Panama (Keigwin, 1978). At this time, anticyclonic ocean circulation and high-pressure cells were established in the Pacific Ocean leading to the thermal gradients across the Pacific (cold in the east, warm in the west) that are essential for the development of ENSO events (Romine, 1982). However, the existence of Pliocene ENSO activity awaits confirmation with high-resolution sedimentary records.

Nicholls (1989) argued that ENSO must have persisted continuously throughout the Cenozoic because the fauna and flora of Australia are highly adapted to precipitation variability. Rainfall variability tends to be 30–50% greater in areas affected by the ENSO, such as Australia, compared with areas of similar mean rainfall. Therefore, marked adaptation of the fauna and flora to high precipitation variability in ENSO-affected areas may indicate that ENSO has been operating long enough for these characteristics to have evolved. The Australian red kangaroo, long-haired rat and several species of bird, for example, have all developed opportunistic life-history strategies tuned to erratic rainfall (Nicholls, 1989). These adaptations cannot be attributed to the arid or semi-arid Australian environment alone because they are absent in other arid regions. However, this theory of an ancient ENSO may underestimate the potential range of climatic conditions to which plants and animals can adapt. Comparative studies of adaptations to high rainfall variability in other ENSO-sensitive regions of the world are necessary in order to conclude that ENSO has helped shape the evolutionary paths of fauna and flora.

Pleistocene glacial-interglacial cycles

Low-resolution records

How did the ENSO respond to changes in background climate during glacial-interglacial cycles? One of the first discussions of the past expression of ENSO under an altered glacial climate state was presented by Quinn (1971). Quinn suggested that the paleoenvironmental evidence for enhanced upwelling in the east Pacific during the late Pleistocene, indicating permanently enhanced trade winds, would imply that ENSO was locked in the La Niña state. Anderson et al. (1990) came to a similar conclusion based on high-resolution analysis of late Quaternary marine varves indicating high biological productivity in response to enhanced upwelling along the coast of California. More recently, studies of the Mg/Ca paleothermometer in the surface-dwelling foraminifer, *Globigerinoides ruber*, from the equatorial Pacific Ocean showed that glacial intervals (marine oxygen isotope stages 2, 4, 6, 8, 10) were characterized by markedly stronger upwelling, suggesting enhanced Pacific trade winds and a La Niña-like state for the mean climate (Lea et al., 2000).

In contrast to marine proxies, terrestrial paleoclimate evidence for the last full glacial cycle from Australasia and South America does not show patterns that resemble modern La Niña teleconnection patterns (Markgraf and Diaz, 2000). Paleovegetation records from Java, Papua New Guinea, north-eastern Australia and South America invariably show colder and drier conditions during the last glacial. A high-altitude tropical ice core record from Huascarán, Peru, also shows cooler and drier conditions during the Last Glacial Maximum (LGM; Thompson et al., 1995). If, as suggested by the marine records, La Niña conditions had become a permanent mode, northern Australia and the western Pacific should have experienced high levels of precipitation, and only north-eastern South America should have become arid.

One explanation for this apparent discrepancy between marine and terrestrial records could be that a 3–4 °C reduction in SST in the warm equatorial western Pacific would result in weaker atmospheric convection and an overall reduction in precipitation over both the western Pacific and adjacent land areas. Furthermore, the most recent SST reconstructions, based on Mg/Ca paleothermometry using surface-dwelling foraminifera, suggest that the Pacific was in an El Niño-like state during the

LGM (Koutavas et al., 2002, Stott et al., 2002). An El Niño-like state for Pacific SSTs would help explain the precipitation patterns indicated by the circum-Pacific terrestrial paleoclimate records for the LGM. However, until we have high-resolution paleo-ENSO records from the equatorial Pacific “center of action,” ENSO reconstructions based on teleconnected precipitation patterns during glacial periods should be interpreted with caution because it is likely that ENSO teleconnections do not remain stationary as the background climate changes.

High-resolution records

The best high-resolution paleo-ENSO records for the Last Interglacial epoch (~128–118 kyr B.P.) come from massive corals from the tropical Pacific region. Spectral analysis of time-series of skeletal Sr/Ca and $^{18}\text{O}/^{16}\text{O}$ ratios extracted from annually banded fossil corals from Indonesia (Hughen et al., 1999) and

Papua New Guinea (Tudhope et al., 2001) reveals power at periods of 3–6 years during the Last Interglacial. Hughen et al. (1999) showed that the periodicity of the Last Interglacial ENSO was similar to that for the period 1856–1960, but different from that of 1960–1998. Thus it appears that interannual rainfall and SST variability in the western Pacific region was forced by ENSO during the Last Interglacial, when the background climate was similar to, or slightly warmer than, the modern climate.

The most complete study of past ENSO variability to date used a suite of coral records from Papua New Guinea to examine the behavior of ENSO over the last glacial-interglacial cycle (Tudhope et al., 2001). Multi-decadal sections of annually banded coral analyzed at near-monthly resolution showed that ENSO interannual variability is a common feature of the climate system over the past 130 kyr (Figure P14). While none

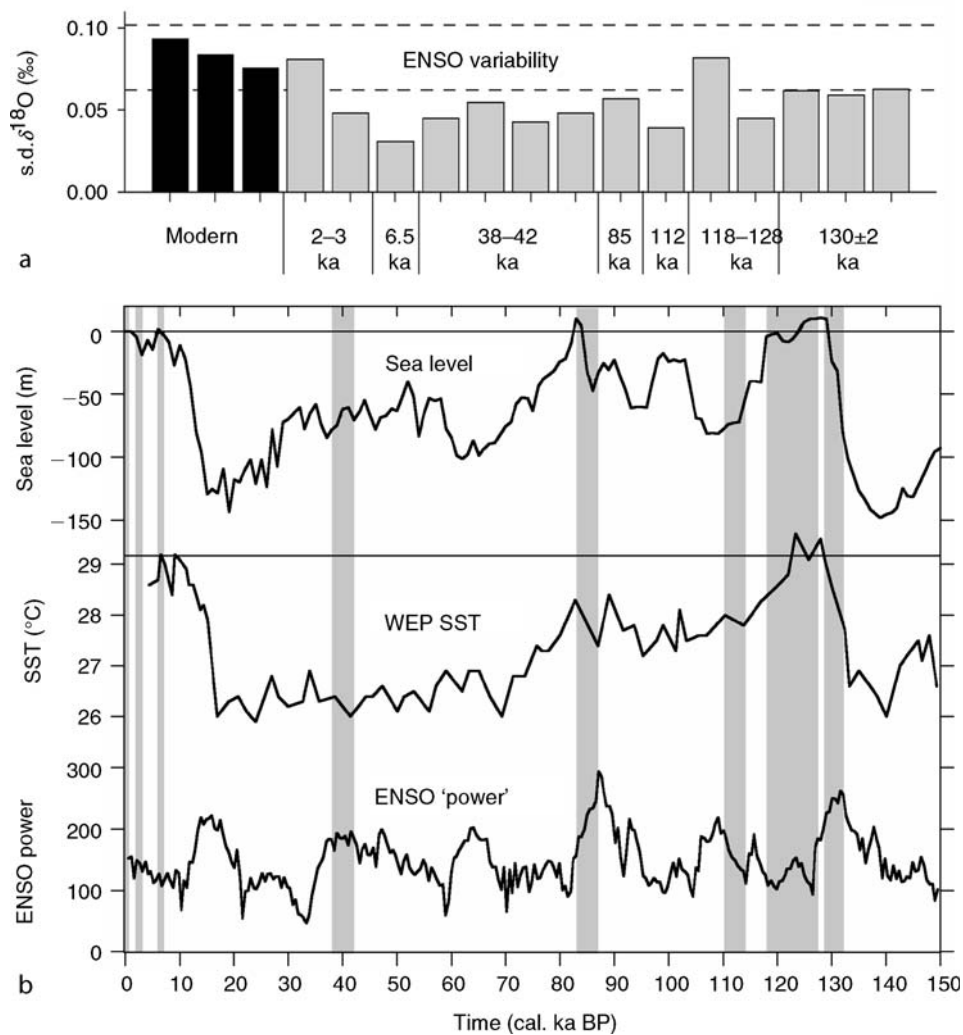


Figure P14 Comparison of paleo-ENSO variability in fossil coral oxygen isotope ($\delta^{18}\text{O}$) records from Papua New Guinea and climate parameters over the past 130 kyr (after Tudhope et al., 2001). **a** Standard deviation of the 2.5–7 year (ENSO) filtered $\delta^{18}\text{O}$ records for modern (black bars) and fossil (grey bars) corals. Dashed lines show the maximum and minimum standard deviations for sliding 30-year periods in the modern coral records. **b** Global sea level (Shackleton, 2000); sea surface temperature (SST) for the western equatorial Pacific (Lea et al., 2000); and changes in ENSO power forced by changing orbital parameters (Clement et al., 1999). Shading marks the eight time periods covered by the coral records.

of the coral specimens dated to the LGM, all the records showed ENSO variability in the characteristic 2.5–7 year band. However, the amplitude of ENSO variability was weaker, relative to modern ENSO variability, during the time intervals examined (130, 128–118, 112, 85, 40, 6.5, 2.5 kyr B.P.).

Paleo-ENSO forcing mechanisms

Three possible mechanisms could lead to weakening of ENSO activity during glacial periods. During glacial sea-level low stands and periods of cooler tropical SSTs, weaker ocean-atmosphere interactions may have dampened ENSO variability (Quinn, 1971). Secondly, shallow continental shelves exposed by lower sea level in the Indonesian Maritime Continent may also have stabilized ENSO variability by anchoring the Indonesian Low convection system. Finally, precessional forcing of the seasonal distribution of insolation in the tropics on ~21,000 year cycles may also contribute to suppressing ENSO variability. A numerical model of the equatorial Pacific Ocean and atmosphere shows that seasonal insolation changes associated with precession of the Earth's equinoxes influence the seasonal strength of the Pacific trade winds (Clement et al., 1999). When perihelion (the time that Earth is closest to the Sun) falls in the boreal summer/fall, stronger trade winds in that season inhibit the development of warm El Niño anomalies in the eastern-central equatorial Pacific. This response may be sufficient to have generated significant changes in ENSO frequency and recurrence over the late Quaternary (Clement et al., 1999).

LGM to early Holocene transition

Paleo-ENSO records

There have not been sufficient paleo-ENSO records to evaluate ENSO behavior during the postglacial to early Holocene transition until recently. Although late-glacial paleo-ENSO records are still scarce, the overall early Holocene trend exhibited in the records includes a low frequency and amplitude of events. Several studies have investigated the paleo-ENSO in north-western South America where torrential rain, floods and erosion occur along the normally arid coast of Peru during strong El Niño events. Based on the analysis of flood deposits from coastal Peru, Wells (1987) estimated that about 100 El Niño events had occurred over the last 40,000 years. Sediment profiles from archaeological sites along the coast of Peru indicate a lack of strong flood events (interpreted as El Niños) between 12–5.7 kyr B.P. at Quebrada Tacahuay (Keefer et al., 1998) and between 8.9–3.4 kyr B.P. at nearby Quebrada de los Burros (Fontugne et al., 1999). Nevertheless, a debris flow in northern Peru, dated at 7.5 kyr B.P. (Wells, 1990), has been interpreted to reflect a major El Niño event, suggesting that ENSO may have operated at that time. The most continuous, high-resolution record for the postglacial transition period comes from laminated clastic deposits in a high-altitude lake, Laguna Pallcacocha, in Ecuador (Rodbell et al., 1999). Today, such clastic laminae are associated with anomalously high rainfall during El Niño events. The sedimentary record shows a clear suppression of ENSO variability, with periodicities of ~15 years, between 12 kyr B.P. (the beginning of the record) and 7 kyr B.P.

Terrestrial paleo-ENSO records from outside the core ENSO impact area rely on the interpretation of teleconnection patterns. A late-glacial varve chronology from New England, USA, spanning 17.5 to 13.5 kyr B.P., shows a distinct

interannual band (3–5 years) of variability suggestive of ENSO teleconnections into North America (Rittenour et al., 2000). The interannual variability largely disappears by 13.5 kyr B.P., with only the highest frequency components persisting. Pollen records from South America, New Zealand and Australia indicate that early Holocene vegetation did not include types adapted to the periodic droughts associated with the ENSO (McGlone et al., 1992; Markgraf and Diaz, 2000). By comparing early Holocene vegetation, lake level and fire history records from these regions, McGlone et al. (1992) concluded that the circum-Pacific precipitation patterns, reduced environmental variability and absence of fire all suggest the suppression of ENSO between 10–8 kyr B.P.

Marine records of the paleo-ENSO during the postglacial transition are more sparse than terrestrial records. Nevertheless, the character and intensity of major El Niños has been traced back to 17 kyr B.P., based on evidence from the pollen of conifer and oak species in marine sediments from the Santa Barbara basin, California (Heusser and Sirocko, 1997). High-resolution marine records during postglacial sea-level low stands are also rare, but coral reconstructions of the paleo-ENSO exist for the end of the deglaciation, when sea levels reached near-modern positions. Coral records from Papua New Guinea indicate that ENSO variability was ~60% weaker at 6.5 kyr B.P. than during the 20th century (Tudhope et al., 2001). ENSO-related interannual variability was also weaker in a coral record from the Great Barrier Reef, Australia, for 6.2 kyr B.P. (Gagan et al., 1998). However, mid-Holocene reconstructions of SST variability in the tropical south-western Pacific suggest there is a significant mismatch between strong El Niño SST variability and weak precipitation variability, indicating some degree of decoupling of ENSO ocean-atmosphere interactions during this period (Gagan et al., 2004). These observations agree with results from a coupled climate system model (Otto-Bliesner, 1999), which indicate that ENSO teleconnections may have differed from modern patterns at 6 kyr B.P. because of the overriding influence of regional climate changes.

Models of insolation forcing of ENSO

A recent modeling study of orbitally-induced changes in insolation in the tropical Pacific reproduced the observed reduction in ENSO amplitude and frequency during the early Holocene (Clement et al., 1999). The authors attributed the reduced early Holocene ENSO to the peak in boreal summer/fall insolation brought about by precession of the Earth's equinoxes. According to the numerical model, the additional heating of equatorial Pacific surface waters in the early Holocene produced an easterly wind anomaly that suppressed the development of El Niño events. Ocean-atmosphere feedbacks drive the ENSO system towards a La Niña state by increasing SST and pressure gradients across the Pacific, in good agreement with the paleoclimate records. A similar effect has been observed in a global coupled ocean-atmosphere model, whereby the intensified Asian monsoon during the early Holocene further enhances Pacific trade winds, thus cooling the eastern equatorial Pacific and reducing ENSO interannual variability (Liu et al., 2000).

Mid-Holocene onset

Several lines of paleoclimate evidence suggest that the onset of modern ENSO variability occurred between 7 and 4 kyr B.P. Evidence for the demise of the period of weakened ENSO activity during the early Holocene is most clear in the tropical

eastern Pacific and northern South America. Spectral analysis of the 15,000-year high-resolution record of storm-derived clastic sedimentation in Laguna Pallcacocha, Ecuador (Rodbell et al., 1999; Moy et al., 2002) shows that the transition to modern ENSO periodicities (2–8 yr) began ~ 7 –5 kyr B.P. (Figure P15). A similar conclusion was reached by Sandweiss et al. (1996, 2001), based on their analysis of fossil mollusk assemblages and geochronological evidence from coastal Peru. There, the onset of El Niño events at 5.8 kyr B.P. is indicated by the demise of thermally anomalous molluscan assemblages. The beginning of monumental temple construction on the Peruvian coast at 5.8 kyr B.P. is thought to reflect the end of early Holocene hyperaridity brought about by the resurgence of El Niño activity (Sandweiss et al., 2001). More indirect evidence of Holocene ENSO variability is provided by titanium concentrations in sediment from ODP site 1002 in the Cariaco Basin, off northern Venezuela (Haug et al., 2001), which reflect variations in runoff associated with shifts in the position of the Intertropical Convergence Zone (ITCZ). Enhanced runoff variability beginning at 3.8 kyr B.P. indicates a mean southward shift in the position of the ITCZ, thought to be linked to the strengthening of El Niño events.

On the western side of the Pacific basin, pollen records from northern Australia yield a slightly later time for ENSO onset. The first occurrence of drought-adapted pollen taxa in lake sediment cores from tropical northern Australia indicates ENSO onset at ~ 4 kyr B.P. (Shulmeister and Lees, 1995). A composite charcoal abundance record derived from 10 lake and wetland records from eastern Indonesia and Papua New Guinea reflects changes in the pattern of regional burning from the LGM to the present (Haberle et al., 2001). Higher charcoal concentrations from the middle to late Holocene (5 kyr B.P. to the present) are interpreted to reflect higher precipitation variability associated with the onset of modern ENSO variability.

Late Holocene ENSO variability

The picture emerging for the most recent 5,000 years of ENSO history indicates that it began to operate as it does now, but

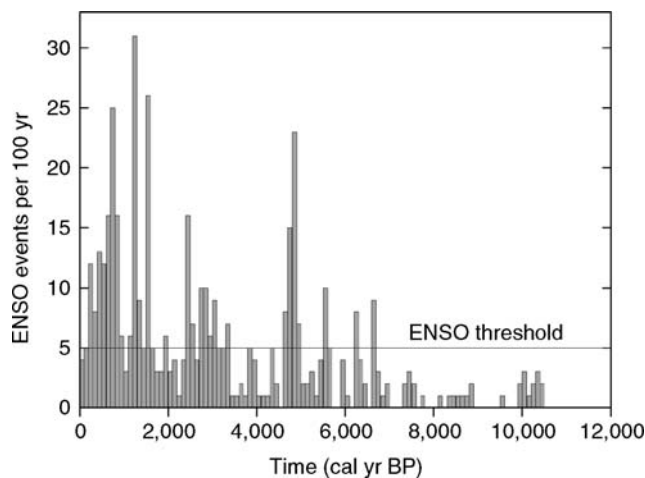


Figure P15 Number of El Niño events in 100 year intervals since 12,000 cal. yr B.P., based on the analysis of clastic laminae in Laguna Pallcacocha, Ecuador (after Moy et al., 2002). Line indicates the minimum number of events (~ 5) required to produce ENSO-band variance.

with variability on millennial timescales and a peak in ENSO frequency and magnitude at ~ 1.8 –1.2 kyr B.P. (Figure P15). The record of clastic sedimentation from Laguna Pallcacocha, Ecuador shows that El Niño events became more frequent over the Holocene until about 1.2 kyr B.P., and then declined towards the present (Moy et al., 2002). Superimposed on this long-term trend are periods of relatively high and low ENSO activity, alternating at a time scale of about 2,000 years. Geochronological evidence from the coast of Peru also indicates an increase in ENSO event frequency after 3.2–2.8 kyr B.P. (Sandweiss et al., 2001). Titanium concentrations in sediment from the Cariaco Basin (Haug et al., 2001) also show enhanced runoff variability after 3.8–2.8 kyr B.P., which is thought to be linked to a southward shift in the ITCZ related to warming of equatorial eastern Pacific SSTs in response to more frequent El Niño events.

Coral $^{18}\text{O}/^{16}\text{O}$ records from massive fossil *Porites* micro-atolls at Christmas Island in the central equatorial Pacific record the migration of warm SSTs and convective rainfall during El Niño events (Woodroffe et al., 2003). Three multi-decadal records from this locality indicate that ENSO amplitudes were 20–40% weaker than modern values during the period 3.6–2.9 kyr B.P., in good agreement with terrestrial paleo-ENSO records from tropical South America. The coral records from Christmas Island, like the Ecuadorian lake record, indicate that ENSO variability reached, or exceeded, modern values from 2.5–1.7 kyr B.P.

Coupled ocean-atmosphere model simulations forced by precessional changes in the seasonal cycle of insolation generally agree with paleo-ENSO records showing an increase in large El Niño events during the Holocene, with a peak ~ 3.1 –1.0 kyr B.P. However, according to the paleo-ENSO records, the abrupt onset of ENSO and millennial-scale variability was more complex than that predicted by the models, suggesting that factors other than insolation forcing may be at work. It has been suggested that the millennial variability in ENSO observed at Laguna Pallcacocha may be due to internal ENSO dynamics. Another possibility is that since ~ 3 kyr B.P., tighter coupling in the Pacific between the more southerly ITCZ and the Southern Oscillation (Haug et al., 2001) has served to amplify ENSO precipitation variability and associated teleconnections (Woodroffe et al., 2003). Such a scenario is consistent with terrestrial paleoclimate records indicating a marked increase in El Niño activity since ~ 3 kyr B.P.

The last millennium

Evidence for the behavior of ENSO over the last millennium comes from historical records, tropical ice cores, subtropical to mid-latitude tree rings, and corals from the Pacific basin. Historical records of Nile River flood level from as early as A.D. 622 (Quinn, 1992; Kondrashov et al., 2005) record the effects of summer monsoon (June–September) rainfall over the highlands of Ethiopia, the major source region for the Nile where El Niño events produce below-average flood levels at Cairo. At the start of the last millennium, during the Medieval Warm Period, the percentage of weak Nile floods from A.D. 1000–1290 was low (8% of years), suggesting that a La Niña-like climate mode operated when the climate of the Northern Hemisphere was warmer. In contrast, the period 1694–1899, spanning the latter part of the Little Ice Age, shows more frequent occurrences of weak Nile floods (35% of years), indicating that El Niño-induced droughts were common.

Analysis of drill cores from the Quelccaya ice cap in the high Andes of southern Peru has provided a record of ENSO variability back to about A.D. 1450 (Thompson et al., 1992). In contrast to the Nile River flood record, El Niño events were rare at Quelccaya during the Little Ice Age (~1550–1850), suggesting that the spatial signature of ENSO may have been different under the altered background climate at that time. Annually laminated ice cores from Dasuopu Glacier, on the southern Tibetan Plateau, allow examination of the teleconnections between El Niño events and the Asian monsoon (Figure P16). At Dasuopu, fluctuations in $\delta^{18}\text{O}$, dust and chloride concentrations are associated with major monsoon failures (e.g., 1790–1796, 1876–1877) during very strong El Niño events. The ~560-year record also shows rare, but large, monsoon failures associated with El Niño-induced drought in the region (Thompson et al., 2000). The full Dasuopu ice core record (not shown) reveals earlier moderate monsoon failures in the 1230s, 1280s, 1330s, 1530s, 1590s and 1640s.

Studies of tree rings have the potential to provide annual and even seasonal data from which the long-term behavior of ENSO may be derived (Cook et al., 2000). However, tree-ring analysis of tropical trees has been problematic due to a paucity of long-lived species and a lack of annual growth rings. Alternatively, Lough and Fritts (1985) developed a network of tree-ring width series back to A.D. 1660 based on the connection between precipitation anomalies and ENSO in western North America, particularly moisture limitation and its effect on tree growth during El Niño events. The result was a series of annual

maps of seasonal climate features such as temperature, precipitation and sea-level pressure indicative of ENSO variability in North America. Stahle et al. (1998) developed a 272-year (1706–1997) reconstruction of the Southern Oscillation Index based on drought-sensitive tree-ring chronologies (Figure P17). The proxy data set comprises 20 sub-tropical tree-ring chronologies from the southern United States and Mexico, and a single tropical teak chronology from Java. This index targets the Northern Hemisphere cool season (October–March), when El Niño and La Niña events typically mature in the equatorial Pacific. Their reconstruction indicates stronger interannual ENSO variance in the late 19th and 20th centuries as compared to earlier periods. However, a network of drought reconstructions over the continental USA shows that, although the ENSO-drought link in the southwest is relatively robust, drought in other regions (the Atlantic region) shows a more variable connection to tropical Pacific climate variability (Cole and Cook, 1998).

Coral records from the tropical Pacific clearly show that the characteristic timescale of ENSO variability has changed over the past four centuries (Dunbar et al., 1994; Urban et al., 2000). A 400-year long coral record from the Galapagos Islands, in the eastern equatorial Pacific, reveals that decadal SST variability and ENSO change in strength simultaneously (Dunbar et al., 1994). The Galapagos record indicates that the dominant oscillatory ENSO mode shifted from 6 years to 4.6 years by A.D. 1700, and to 3.4 years after A.D. 1850. Another coral record from Maiana Atoll, in the central equatorial Pacific, registers a long-term trend from cooler/drier to warmer/wetter conditions that is associated with changes in ENSO variance since A.D. 1840 (Urban et al., 2000). When the background climate was cooler/drier during the 19th century, ENSO variability occurred on a decadal time scale, in contrast to the shorter, dominantly interannual variance of the 20th century (Figure P18).

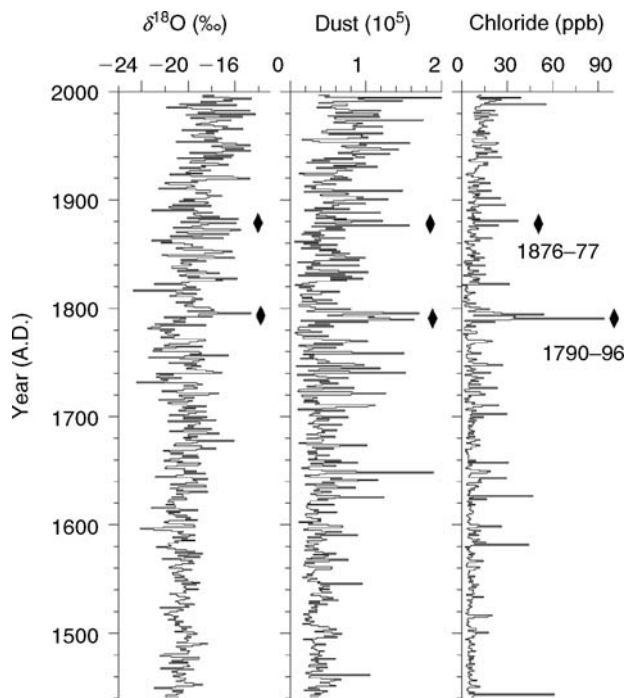


Figure P16 Annual averages of oxygen isotopes ($\delta^{18}\text{O}$), insoluble dust and chloride in ice from the high-altitude (7,200 m a.s.l.) Dasuopu Glacier in southern Tibet since A.D. 1440 (after Thompson et al., 2000). Dust concentrations are per milliliter of melted ice. El Niño events (low monsoon precipitation) are indicated by higher $\delta^{18}\text{O}$ values, dust and chloride concentrations in the ice. *Diamonds* mark very strong El Niño events (monsoon failures) in 1876–1877 and 1790–1796.

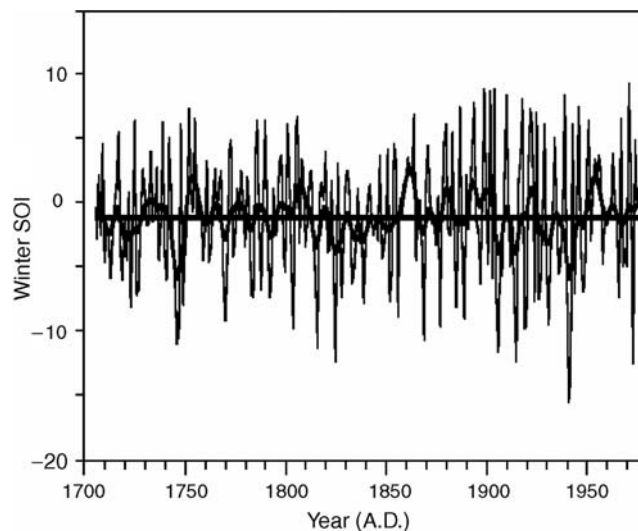


Figure P17 Boreal winter (October–March) Southern Oscillation Index (SOI) reconstructed using tree-ring data from Mexico, the southwestern USA and Indonesia (after Stahle et al., 1998). The tree-ring reconstruction indicates a significant increase in the interannual variability of the winter SOI, and more La Niña events, beginning in the mid-19th century.

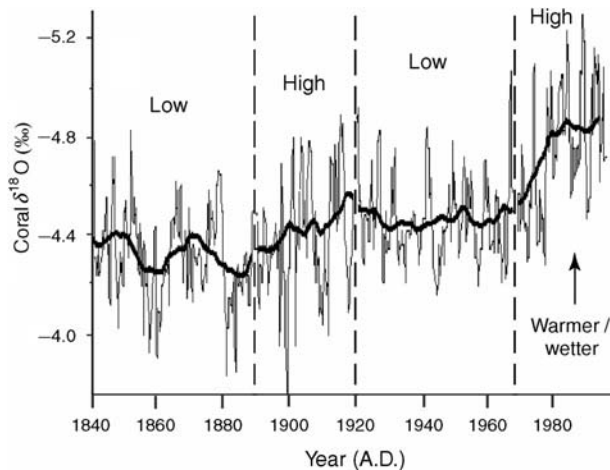


Figure P18 Bimonthly coral oxygen isotope ($\delta^{18}\text{O}$) record from Maiana Atoll, central equatorial Pacific (after Urban et al., 2000). The 21-yr running mean (thick line) shows a long-term trend towards warmer/wetter conditions. Decadal variance in ENSO (low frequency) prevailed during the cooler/drier conditions of the 19th century. Interannual ENSO variance (high frequency) dominated the transitions to warmer/wetter conditions at the beginning and end of the 20th century.

A composite record of ENSO-related rainfall and river runoff variability since A.D. 1615, compiled from eight multi-century coral cores from the Great Barrier Reef, Australia (Hendy et al., 2003), shows strong anti-correlations with SSTs in the equatorial eastern Pacific during the mid-17th to late 18th centuries. This suggests similar, strong ENSO-related teleconnections occurred then as in recent decades. However, disappearance of the anti-correlation between the eastern and western Pacific for most of the period from the 1800s to 1870s suggests that ENSO-related teleconnections with northeast Australian rainfall were not operating during much of the 19th century. During this period both interdecadal and interannual variability were suppressed, in good agreement with other coral and tree-ring records. The late 20th century increase in ENSO variability and the strength of ENSO teleconnections are, therefore, not solely recent phenomena.

Conclusions

In summary, significant progress has been made in our understanding of past ENSO behavior. However, well-calibrated records from the tropical Pacific region of strongest ENSO influence are still sparse. A full understanding of the paleo-ENSO will require the comparison of El Niño temperature forcing in the Pacific with rainfall perturbations that may be modulated under the influence of what is potentially an evolving ocean-atmosphere system.

Michael K. Gagan

Bibliography

- Allan, R.J., Lindesay, J., and Parker, D., 1996. *El Niño Southern Oscillation and Climatic Variability*. Collingwood, Australia: CSIRO Publishing, 405pp.
- Anderson, R.Y., Linsley, B.K., and Gardner, J.V., 1990. Expression of seasonal and ENSO forcing in climatic variability at lower than ENSO frequencies: evidence from Pleistocene marine varves off California. *Palaeogeogr., Palaeoclimatol., Palaeoecol.*, **78**, 287–300.

- Bjerknes, J., 1969. Atmospheric teleconnections from the equatorial Pacific. *Month. Weather. Rev.*, **97**, 163–172.
- Clement, A.C., Seager, R., and Cane, M.A., 1999. Orbital controls on the El Niño/Southern Oscillation and the tropical climate. *Paleoceanography*, **14**, 441–456.
- Cole, J.E., and Cook, E.R., 1998. The changing relationship between ENSO variability and moisture balance in the continental United States. *Geophys. Res. Lett.*, **25**, 4529–2532.
- Cook, E.R., D'Arrigo, R.D., Cole, J.E., Stahle, D.W., and Villalba, R., 2000. Tree-ring records of past ENSO variability and forcing. In Diaz, H.F., and Markgraf, V. (eds.), *El Niño and the Southern Oscillation: Multiscale Variability and Global and Regional Impacts*. Cambridge, UK: Cambridge University Press, pp. 297–324.
- Dunbar, R.B., Wellington, G.M., Colgan, M.W., and Glynn, P.W., 1994. Eastern Pacific sea surface temperature since 1600 A.D.: the $\delta^{18}\text{O}$ record of climate variability in Galápagos corals. *Paleoceanography*, **9**, 291–315.
- Fontugne, M., Usselman, P., Lavallee, D., Julien, M., and Hatte, C., 1999. El Niño variability in the coastal desert of southern Peru during the mid-Holocene. *Quat. Res.*, **52**, 171–179.
- Gagan, M.K., Ayliffe, L.K., Hopley, D., Cali, J.A., Mortimer, G.E., Chappell, J., McCulloch, M.T., and Head, M.J., 1998. Temperature and surface-ocean water balance of the mid-Holocene tropical western Pacific. *Science*, **279**, 1014–1018.
- Gagan, M.K., Hendy, E.J., Haberle, S.G., and Hantoro, W.S., 2004. Post-glacial evolution of the Indo-Pacific Warm Pool and El Niño-Southern Oscillation. *Quat. Intl.*, **118–119**, 127–143.
- Haberle, S.G., Hope, G.S., and van der Kaars, S., 2001. Biomass burning in Indonesia and Papua New Guinea: natural and human induced fire events in the fossil record. *Palaeogeogr., Palaeoclimatol., Palaeoecol.*, **171**, 259–268.
- Haug, G.H., Hughen, K.A., Sigman, D.M., Peterson, L.C., and Rohl, U., 2001. Southward migration of the intertropical convergence zone through the Holocene. *Science*, **293**, 1304–1308.
- Hendy, E.J., Gagan, M.K., and Lough, J.M., 2003. Chronological control of coral records using luminescent lines and evidence for non-stationary ENSO teleconnections in northeast Australia. *The Holocene*, **13**, 187–199.
- Heusser, L.E., and Sirocko, F., 1997. Millennial pulsing of environmental change in southern California from the past 24 k.y.: A record of Indo-Pacific ENSO events? *Geology*, **25**, 243–246.
- Hughen, K.A., Schrag, D.P., Jacobsen, S.B., and Hantoro, W.S., 1999. El Niño during the last interglacial period recorded by a fossil coral from Indonesia. *Geophys. Res. Lett.*, **26**, 3129–3132.
- Keefer, D.K., deFrance, S.D., Moseley, M.E., Richardson III, J.B., Satterlee, D.R., and Day-Lewis, A., 1998. Early maritime economy and El Niño events at Quebrada Tacahuay, Peru. *Science*, **281**, 1833–1835.
- Keigwin, L.D., 1978. Pliocene closing of the Isthmus of Panama based on biostratigraphic evidence from nearby Pacific Ocean and Caribbean Sea cores. *Geology*, **6**, 630–634.
- Kondrashov, D., Feliks, Y., and Ghil, M., 2005: Oscillatory modes of extended Nile River records (A.D. 622–1922). *Geophys. Research Letters*, **32**, L10702, p. 1–4.
- Koutavas, A., Lynch-Stieglitz, J., Marchitto T.M., Jr., and Sachs, J.P., 2002. El Niño-like pattern in ice age tropical Pacific sea surface temperature. *Science*, **297**, 226–230.
- Lea, D.W., Pak, D.K., and Spero, H.J., 2000. Climate impact of late Quaternary equatorial Pacific sea surface temperature variations. *Science*, **289**, 1719–1724.
- Liu, Z., Kutzbach, J., and Wu, L., 2000. Modeling climate shift of El Niño variability in the Holocene. *Geophys. Res. Lett.*, **27**, 2265–2268.
- Lough, J.M., and Fritts, H.C., 1985. The Southern Oscillation and tree-rings: 1660–1961. *J. Clim. App. Meteorol.*, **24**, 952–965.
- Markgraf, V., and Diaz, H.F., 2000. The past ENSO record: a synthesis. In Diaz, H.F., and Markgraf, V. (eds.), *El Niño and the Southern Oscillation: Multiscale Variability and Global and Regional Impacts*. Cambridge, UK: Cambridge University Press, pp. 465–488.
- McGlone, M.S., Kershaw, A.P., and Markgraf, V., 1992. El Niño/Southern Oscillation climatic variability in Australasian and South American palaeoenvironmental records. In Diaz, H.F., and Markgraf, V. (eds.), *El Niño and the Southern Oscillation: Multiscale Variability and Global and Regional Impacts*. Cambridge, UK: Cambridge University Press, pp. 435–462.

- Moy, C.M., Seltzer, G.O., Rodbell, D.T., and Anderson, D.M., 2002. Variability of El Niño/Southern Oscillation activity at millennial timescales during the Holocene epoch. *Nature*, **420**, 162–165.
- Nicholls, N., 1989. How old is ENSO? *Climatic Change*, **14**, 111–115.
- Otto-Bliessner, B.L., 1999. El Niño/La Niña and Sahel precipitation during the middle Holocene. *Geophys. Res. Lett.*, **26**, 87–90.
- Philander, S.G.H., 1990. *El Niño, La Niña, and the Southern Oscillation*. New York: Academic Press, 293pp.
- Quinn, W.H., 1971. Late Quaternary meteorological and oceanographic developments in the equatorial Pacific. *Nature*, **229**, 330–332.
- Quinn, W.H., 1992. A study of Southern Oscillation-related climatic activity for A.D. 622–1900 incorporating Nile River flood data. In Diaz, H.F., and Markgraf, V. (eds.), *El Niño and the Southern Oscillation: Multiscale Variability and Global and Regional Impacts*. Cambridge, UK: Cambridge University Press, pp. 119–149.
- Quinn, W.H., Neal, V.T., and Antunez de Mayolo, S., 1987. El Niño occurrences over the past four and a half centuries. *J. Geophys. Res.*, **92**, 14449–14461.
- Rasmusson, E.M., and Carpenter, T.H., 1982. Variations in tropical sea surface temperature and surface wind fields associated with the El Niño/Southern Oscillation. *Month. Weather Rev.*, **110**, 354–384.
- Rittenour, T.M., Brigham-Grette, J., and Mann, M.E., 2000. El Niño-like teleconnections in New England during the Late Pleistocene. *Science*, **288**, 1039–1042.
- Rodbell, D.T., Seltzer, G.O., Anderson, D.M., Abbott, M.B., Enfield, D.B., and Newman, J.H., 1999. An ~15,000-year record of El Niño-driven alluviation in southwestern Ecuador. *Science*, **283**, 516–520.
- Romine, K., 1982. Late Quaternary history of atmospheric and oceanic circulation in the eastern equatorial Pacific. *Mar. Micropaleontol.*, **7**, 163–187.
- Ropelewski, C.F., and Halpert, M.S., 1987. Global and regional scale precipitation patterns associated with the El Niño/Southern Oscillation. *Month. Weather Rev.*, **115**, 1606–1626.
- Sandweiss, D.H., Richardson, J.B. III, Reitz, E.J., Rollins, H.B., and Maasch, K.A., 1996. Geoarchaeological evidence from Peru for a 5000 B.P. onset of El Niño. *Science*, **273**, 1531–1533.
- Sandweiss, D.H., Maasch, K.A., Burger, R.L., Richardson, J.B., Rollins, H.B., and Clement, A.C., 2001. Variation in Holocene El Niño frequencies: Climate records and cultural consequences in ancient Peru. *Geology*, **29**, 603–606.
- Shackleton, N.J., 2000. The 100,000-year ice age cycle identified and found to lag temperature, carbon dioxide and orbital eccentricity. *Science*, **289**, 1897–1902.
- Shulmeister, J., and Lees, B.G., 1995. Pollen evidence from tropical Australia for the onset of an ENSO-dominated climate at c. 4000 BP. *The Holocene*, **5**, 10–18.
- Stahle, D.W., D'Arrigo, R.D., Krusic, P.J., Cleaveland, M.K., Cook, E.R., Allan, R.J., Cole, J.E., Dunbar, R.B., Therrell, M.D., Gay, D.A., Moore, M.D., Stokes, M.A., Burns, B.T., Villanueva-Diaz, J., and Thompson, L.G., 1998. Experimental dendroclimatic reconstruction of the Southern Oscillation. *Bull. Amer. Meteorol. Soc.*, **79**, 2137–2152.
- Stott, L., Poulsen, C., Lund, S., and Thunell, R., 2002. Super ENSO and global climate oscillations at millennial time scales. *Science*, **297**, 222–226.
- Thompson, L.G., Mosley-Thompson, E., and Thompson, P.A., 1992. Reconstructing interannual climate variability from tropical and subtropical ice-core records. In Diaz, H.F., and Markgraf, V. (eds.), *El Niño: Historical and Paleoclimatic Aspects of the Southern Oscillation*. Cambridge, UK: Cambridge University Press, pp. 295–322.
- Thompson, L.G., Mosley-Thompson, E., Davis, M.E., Lin, P.-N., Henderson, K.A., Cole-Dai, J., Bolzan, J.F., and Liu, K.-b., 1995. Late glacial stage and Holocene tropical ice core records from Huascarán, Peru. *Science*, **269**, 46–50.
- Thompson, L.G., Yao, T., Mosley-Thompson, E., Davis, M.E., Henderson, K.A., and Lin, P.-N., 2000. A high-resolution millennial record of the South Asian Monsoon from Himalayan ice cores. *Science*, **289**, 1916–1919.
- Tudhope, A.W., Chilcott, C.P., McCulloch, M.T., Cook, E., Chappell, J., Ellam, R.M., Lea, D.W., Lough, J.M., and Shimmield, G.B., 2001. Variability in the El Niño-Southern Oscillation through a glacial-interglacial cycle. *Science*, **291**, 1511–1517.
- Urban, F.E., Cole, J.E., and Overpeck, J.T., 2000. Influence of mean climate change on climate variability from a 155-year tropical Pacific coral record. *Nature*, **407**, 989–993.
- Wells, L.E., 1987. An alluvial record of El Niño events from northern coastal Peru. *J. Geophys. Res.*, **92**, 14463–14470.
- Wells, L.E., 1990. Holocene history of the El Niño phenomenon as recorded in flood sediments of northern coastal Peru. *Geology*, **18**, 1134–1137.
- Woodroffe, C.D., Beech, M., and Gagan, M.K., 2003. Mid-late Holocene El Niño variability in the equatorial Pacific from coral microatolls. *Geophys. Res. Lett.*, **30**, 1358, doi:10.1029/2002GL015868.

Cross-references

[Ancient Cultures and Climate Change](#)
[Atmospheric Circulation during the Last Glacial Maximum](#)
[Climate Variability and Change, Last 1,000 Years](#)
[Coral and Coral Reefs](#)
[Dendroclimatology](#)
[Holocene Climates](#)
[Ice Cores, Mountain Glaciers](#)
[Last Glacial Maximum](#)
[Little Ice Age](#)
[Medieval Warm Period](#)
[Monsoons, Quaternary](#)
[Ocean Paleotemperatures](#)
[Paleoclimate Modeling, Quaternary](#)
[Paleoclimate Proxies, an Introduction](#)
[Paleoceanography](#)
[Paleotemperatures and Proxy Reconstructions](#)
[Paleotempestology, the Sedimentary Record of Intense Hurricanes](#)
[Pleistocene Climates](#)
[Quaternary Climate Transitions and Cycles](#)
[Teleconnections \(see Encyclopedia of World Climatology\)](#)
[Time Series Analysis](#)
[Varved Sediments](#)

PALEOGENE CLIMATES

Introduction

The Paleogene spans the first half of the Cenozoic era, from 65 to 23 million years ago. It includes the Paleocene epoch (65–55 million year ago), the Eocene epoch (55–34 million years ago), and the Oligocene epoch (34–23 million years ago). The Paleogene marked an important transformation in the climatic history of the Earth, from the “greenhouse” world of the Mesozoic (which persisted into the early Eocene), through the climatic deterioration to form the “doubthouse” world of the middle and late Eocene, to the Antarctic glaciation of the early Oligocene, producing the “icehouse” world that we are still experiencing today (Miller et al., 1987, 1991; Miller, 1992; Zachos et al., 1993, 1994; Prothero and Berggren, 1992; Prothero, 1994; Prothero et al., 2003).

The overall history of Paleogene climates is shown in [Figure P19](#). Our best proxy of global paleotemperature is the record of oxygen isotopes in the shells of microfossils from the deep oceans around the world (see *Oxygen isotopes*). Other indicators are used as well, such as the known paleoclimatic preferences of certain fossils, and the presence of certain sediments that are climatically informative. For example, in deep-sea cores, the presence of coarse sediments rafted by icebergs a long way from the continent and dropped into deep ocean muds is considered an excellent indicator of the growth of ice sheets and the calving of icebergs (see *Ice-rafted debris (IRD)*).

In addition to these important marine signals, there are many climatic indicators on land. Perhaps the most useful is the record of land plants, which are highly sensitive to climate and other changes in their growing conditions. The most

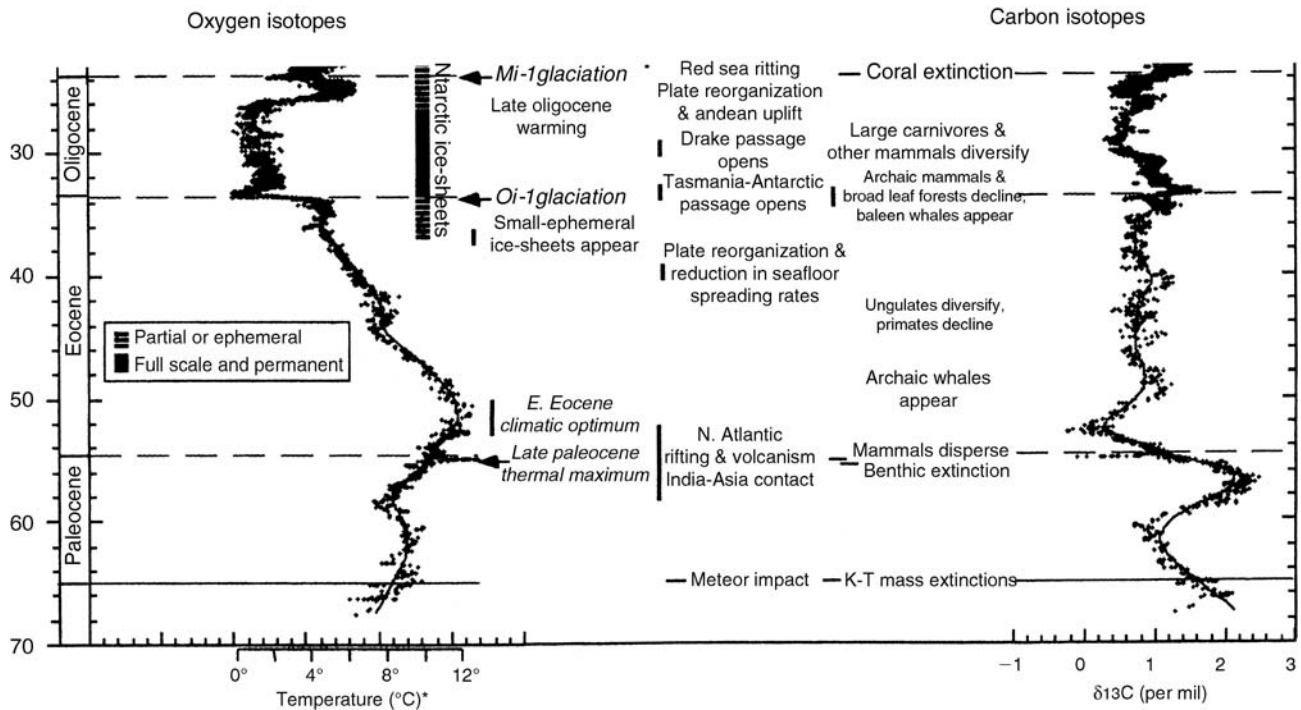


Figure P19 Climatic history, global deep-sea oxygen, and carbon isotope record correlated with major oceanographic and climatic events from 70 to 23 million years ago (modified from Zachos et al., 2001).

straightforward such index is the shape of leaves (Wolfe, 1978, 1994 see *Paleobotany*). Other terrestrial indicators, such as the presence of dune sands and evaporites indicating deserts, or thick coal deposits, indicating swampy conditions, are also used. Finally, certain types of terrestrial organisms, such as turtles and crocodylians (Markwick, 1994), and some kinds of land snails, are highly sensitive to climatic changes, and can also be used as constraints on the paleoclimate of a region (see *Animal proxies, invertebrates; Animal proxies, vertebrates*).

The Paleocene to early Eocene “greenhouse” world

The Paleocene epoch was the 11-million-year period of recovery from the great extinction at the end of the Cretaceous that wiped out the dinosaurs, ammonites, marine reptiles, and many other typically Mesozoic groups. Some groups that had been decimated by the extinction event, such as the foraminifera and mollusks, recovered and radiated in the Paleocene. Other groups, such as the mammals, had lived as tiny animals overshadowed by the dinosaurs during the entire Mesozoic. Once the dinosaurs were gone, mammals underwent an explosive adaptive radiation in the Paleocene, and evolved from a handful of rat-sized animals at the beginning of the Paleocene to over two dozen different orders by the early Eocene, including all the living orders of mammals. They soon occupied most of the terrestrial niches, from the tiny insectivore or seed eater, to the large and small carnivore, and even the huge herbivorous land animal niche as well. By the middle Eocene, there were also mammals in the seas (early whales) and the air (bats).

Although there were some perturbations of the oceans and atmospheres as a result of the end-Cretaceous extinctions, climate soon returned to the “greenhouse” state that had occurred through most of the later Mesozoic. Paleocene and early Eocene rocks

above the Arctic Circle and in Antarctica yield temperate-zone plants, and tropical plants, such as palms and cycads, occurred as far as 60°N latitude. Alligators and tortoises also lived above 77°N latitude in a region that today experiences 6 months of darkness and has only freezing climates and tundra vegetation. Calculations from oxygen isotopes suggest that tropical temperatures were much like those of today (Pearson et al., 2001), but polar waters (which are now at or below freezing) were as warm as 10–12°C in the late Paleocene, and 15°C in the early Eocene. To explain this puzzle, some scientists have suggested that the Arctic Circle would be much smaller if the Earth’s tilt on its rotational axis was much less than its present angle of 23.5°. However, such a major change in the Earth’s tilt creates all sorts of geophysical problems, and some climatic models of an Earth with a shallower tilt create colder, not warmer, polar regions. The consensus of scientists is that these polar animals and plants were capable of living for 6 months in a near-dark world as long as temperatures remained warm and mild even in the months of darkness.

Such conditions require that the entire Earth be much warmer than today on average, and that there was a lot of heat transport from the equators to the poles, so that the difference between their temperatures was much less than today. Most scientists agree that a higher level of greenhouse gases (such as carbon dioxide and methane) was largely responsible for the overall level of warmth in the early Cenozoic. Although some scientists point primarily to carbon dioxide (De Conto and Pollard, 2003), others have shown that the plant record does not support unusually high levels of this gas (Royer et al., 2001). Estimates from the geochemistry of carbonate (Pearson and Palmer, 1999) and climatic modeling (Sloan and Rea, 1995) also indicate that atmospheric carbon dioxide levels were

not much higher than present. Instead, Sloan et al. (1992) argue that methane might have been a more effective greenhouse gas, consistent with all the geochemical evidence.

However, plate tectonics and oceanic circulation must have been important factors as well. To explain the shallow gradient in temperature between poles and equator, there must be oceanic circulation that allows warm waters from the equator to mix with temperate and polar waters, transferring the heat to the poles. Oceanic circulation models with early Cenozoic continental positions show that a key factor is the connection of Antarctica to both Australia and South America. Today, Antarctica is isolated from these continents, producing the Circum-Antarctic Current, which circulates in a clockwise direction around the Antarctic. This shallow-water current is one of the most voluminous in the ocean, with a velocity of 25 cm s^{-1} , and a volume of 233 million cubic m s^{-1} , more than 1,000 times the flow of the Amazon River. The Circum-Antarctic Current acts as a “refrigerator door” that locks in the cold around the Antarctic continent, and promotes the growth of polar ice caps. It also promotes upwelling of deep waters from the Antarctic margin, which rise, chill, and then sink to generate the cold Antarctic bottom waters. These cold, oxygenated currents make up 59% of the world’s marine waters, and flow from the surface of the Southern Ocean to the bottoms of the deep oceans all the way to the Northern Hemisphere as far as 50° north latitude in the Atlantic.

For over 30 years now, geologists have known that this current and its effects could not have existed in the Paleocene and Eocene, as long as the connection between Antarctica and both South America and Australia blocked its path. Instead, models of Paleocene and Eocene oceanic circulation show that the tropical currents mixed with temperate and polar currents, warming the poles. In some models (Kennett and Stott, 1990a), the modern circulation pattern dominated by cold Antarctic bottom waters is replaced by a different kind of ocean, where warm saline waters are generated in the tropics by evaporation, and then sink (due to increased salinity) to form warm saline deep waters, which traveled along the ocean bottom all the way to the poles. These ideas are still controversial, but clearly warm tropical currents were reaching the poles and transferring heat to this region to keep it so balmy.

The late Paleocene thermal maximum

On top of the overall warm “greenhouse” climates of the Paleocene and Eocene, there are short-term events that cannot be explained by slow-moving causes such as changes in atmospheric gases or oceanic circulation. The most remarkable of these is the Late Paleocene Thermal Maximum (LPTM) at 55.6 million years ago, when deep-sea temperatures warmed 5°C , and sea surface temperatures warmed by $4\text{--}8^\circ\text{C}$ in less than 200,000 years (Röhl et al., 2000). Carbon isotope values show a dramatic negative excursion over the same short interval of time (Kennett and Stott, 1990b; Zachos et al., 1993), and this carbon isotope signal is even apparent in the teeth of land mammals and in ancient soil carbonates (Koch et al., 1992). In addition, there was a major mass extinction in the benthic foraminifera that live on the ocean bottom, and rapid diversification in the planktonic foraminifera and blooms of dinoflagellates. An evolutionary radiation in land mammals occurred and they freely migrated over the polar routes from Eurasia to North America in the early Eocene, and even lived above the Arctic Circle (papers in Aubry et al., 1998).

The extraordinary rapidity and the peculiarity of the warming of deep ocean waters led to another explanation of the LPTM (Dickens et al., 1995, 1997; Thomas et al., 2002).

The most striking evidence comes from the ratio of ^{12}C (the common isotope of carbon) to ^{13}C (a rare isotope of carbon). In two short pulses, each less than a thousand years in duration, the oceans became extremely rich in ^{12}C , suggesting that some source had released enormous amounts of biogenic carbon in a geologic instant. This rules out the slow oceanographic or plate tectonic changes discussed above. Instead, many scientists now think that methane (CH_4 , or natural gas) was trapped in a chemical form known as methane hydrate (methane combined with water in complex cage-like, icy compounds). These compounds can form huge volumes of trapped carbon, frozen on the ocean floor. According to the late Paleocene scenario, as much as $1.12 \times 10^{18} \text{ g}$ of CH_4 was locked up on the sea bottom. When the methane hydrates broke down and their methane was released, that flooded the deep ocean with excess methane and carbon dioxide (hypercapnia). This carbon-rich water nearly wiped out many of the bottom-dwelling organisms (especially the benthic foraminifera). Eventually this methane escaped to the atmosphere to produce a warm “super-greenhouse.” Although some of the carbon was eventually returned to the crust in the form of carbonates and coals, much remained throughout the early Eocene, and was responsible for the extraordinary global warming.

The Eocene climatic deterioration and the “doubthouse”

The warm, balmy world of the early Eocene began to deteriorate by the early part of the middle Eocene. Over the course of the 12 million years of the middle Eocene (49–37 million years ago), and the 3 million years of the late Eocene (37–34 million years ago), this climatic deterioration continued so that by the early Oligocene, glacial ice returned to Antarctica. From the beginning of the middle Eocene, mean global temperature declined by more than 10°C , more than during any ice age cycle (Figure P19). In North America, the land plants suggest $13\text{--}15^\circ\text{C}$ of cooling over the same interval. This climatic transformation was gradual during the entire middle Eocene, although there was an abrupt cooling episode (causing temperatures to drop 5°C globally) at the end of the middle Eocene (37 million years ago).

During the three million years of the late Eocene (37–33 million years ago), there was a slight warming and recovery from the long-term cooling trend. At least three major impacts struck the Earth in the middle of the late Eocene (35.5–36.0 million years ago), but they caused no significant changes in climate, nor any extinction of importance.

In addition to the isotopic and leaf-margin climatic signals, there are other indicators of cooling climate. Antarctic glacial deposits overlain by a lava flow dated at 49.4 million years old have been reported (Birkenmajer, 1987); although most scientists do not think that there was significant Antarctic glacial ice this early. Gradual changes in the oceanic circulation patterns are also seen during the middle Eocene (Boersma et al., 1987), although nothing as dramatic as the inception of Antarctic bottom waters in the early Oligocene. To many scientists, the middle-late Eocene is the “doubthouse” world (Miller et al., 1991): a time of transition between better known “greenhouse” and “icehouse” conditions, where there are few modern analogues and it is difficult to describe how the oceans and atmospheres worked during this time.

The causes of this middle-late Eocene climatic change are still unclear. As discussed above, some scientists argue that the climate was changed by addition or withdrawal of greenhouse gases, but it is not clear that carbon dioxide was the main

culprit. More importantly, it is difficult to say where all the carbon from those gases has gone if it has been locked up in the crustal reservoirs and withdrawn from the atmosphere. There are limited coal deposits of middle-late Eocene age, but none on the scale of the Carboniferous coals that locked up the greenhouse gases and shifted the late Carboniferous world from greenhouse to icehouse. The volume of carbonate precipitation in the middle Eocene is insufficient to serve as the chief reservoir, either. Some have suggested that these gases are locked up in methane hydrates on the seafloor (as discussed above), but so far there is no way to test this hypothesis.

The Oligocene

The Eocene-Oligocene boundary is formally recognized by the extinction of the hantkeninid foraminifera, although no other major climatic or extinction events occurred at this time. This invalidates the old idea from the 1970s and 1980s that a “Terminal Eocene Event,” comparable to the event that ended the Cretaceous, marked the end of the Eocene.

The most significant climatic event occurred in the earliest Oligocene (as currently defined, using the hantkeninid criterion), about 33 million years ago (now known as the “Oil event”). In the marine record from both benthic and planktonic foraminifera, the oxygen isotopes show about a 1.3‰ increase. Miller (1992) calculated that about 0.3–0.4‰ of the change was due to a major expansion of Antarctic ice sheets, which lowered global sea level by at least 30 m. The remaining 0.9–1.0‰ is explained by global cooling of about 5–6°C, which lowered global mean temperature from as high as 13°C in the early Eocene and 7°C in the latest Eocene to values just a few degrees above freezing (as a global average – the poles were well below freezing for the first time, while the tropics remained relatively unchanged).

Abundant evidence suggests that this global cooling event was largely due to the growth of the first major Antarctic ice sheet since the Permian, over 250 million years ago. Drilling on the margin of the Antarctic continent and in oceanic plateaus in the Southern Ocean (such as Maud Rise and the Kerguelen Plateau) has produced abundant evidence of the growth of the Antarctic ice sheet. Not only do the isotopic records show its effect, many of the sediments drilled from the Antarctic margin are glacial in origin, and even well out into the Southern Ocean where there are sediments dropped by melting icebergs.

What caused this global cooling and the extinctions in the early Oligocene? A few geologists have suggested that the late Eocene impact events or major volcanic eruptions in the Ethiopian Plateau might have had an effect, but these ideas are contradicted by the geological record. As noted above, the impacts occurred in the middle of the late Eocene, about 2 million years before the early Oligocene cooling, and 2 million years after the end-middle Eocene cooling. Likewise, the Ethiopian traps are now dated in the late Oligocene, when no significant extinctions are recorded. As discussed above, the primary culprit has been identified as the development of the Circum-Antarctic Current.

So what triggered the growth of this current? The most obvious factor is plate tectonics. In the late Cretaceous, Australia and South America were still attached to Antarctica as remnants of the ancient Gondwana supercontinent. As noted above, this caused the tropical currents to mix with polar currents and moderated global temperatures, since there were barriers

between the Atlantic, Pacific, and Indian Oceans, and there was not yet a global Southern Ocean. Geophysical evidence shows that these three southern continents began their separation in the latest Cretaceous, but they were not far apart enough to allow ocean currents to pass through until the latest Eocene or early Oligocene (Exon et al., 2002). By the early Oligocene, deep-sea cores south of New Zealand reveal that a blast of cold water was passing between Australia and East Antarctica. As the Oligocene progressed, the separation grew wider, and larger and more powerful cold-water currents developed. Originally, geologists thought that the separation between the tip of South America and the Antarctic Peninsula did not occur until the end of the Oligocene, but recent evidence (Diester-Haass and Zahn, 1996) has suggested that it was also occurring in the early Oligocene, so the entire Circum-Antarctic Current developed in a short period of time.

In addition to these important currents, it is also thought that another body of water, the North Atlantic Deep Water, which flows out of the Arctic Ocean past Greenland into the bottom of the North Atlantic, originated sometime in the Oligocene (Davies et al., 2001). Thus, the global “icehouse” conditions of the Oligocene can be largely attributed to the development of modern oceanic stratification and circulation patterns.

The effects of these global changes in oceanic temperatures are critical, not only to marine climates and organisms but also to land climates. The most complete record comes from the North American continent, where paleobotanical records (Wolfe, 1978, 1994) show that mean annual terrestrial temperatures dropped 7–11°C in the earliest Oligocene. This is true of floral records all the way from Alaska and the Pacific Northwest to the Gulf Coast. In addition to this rapid cooling, the record of ancient plants and soils also suggests that the continent underwent significant drying, with much more seasonal, drought-prone climates. In the Big Badlands of South Dakota, late Eocene paleosols suggest over a meter of annual rainfall, supporting a dense forest (Retallack, 1983). By contrast, in the early Oligocene, mean annual rainfall was less than half a meter and the vegetation was patchy scrubland with limited riparian forests. The land snails from the Badlands also change, from late Eocene forms like those found today in tropical Central America, to early Oligocene forms, which are smaller and more drought-tolerant, and found today in Baja California. In addition, the late Eocene reptilian fauna that was dominated by crocodylians and pond turtles was replaced by dry land tortoises in the early Oligocene.

Once the early Oligocene climatic deterioration was completed, the earth remained in this “icehouse” mode through the rest of the Oligocene. The other significant event was several pulses of glaciation during the middle part of the Oligocene, about 30 million years ago (the “Oi2” event). Thick, extensive mid-Oligocene glacial deposits are found throughout the Antarctic region, and benthic foraminiferal oxygen isotopes shifted by 1.6‰, suggesting another increase in ice volume and drop in global temperatures. As these ice sheets grew, they pulled water out of the oceans, resulting in the largest drop of sea level in the past 100 million years. Originally, it was suggested that sea level dropped almost 150 m, although more recent estimates suggest it was only about half that much. Whatever its magnitude, it had a major effect on the shallow marine realm, causing the continental shelves to be deeply incised once they were exposed to the aerial erosion, and producing huge mid-Oligocene unconformities in most marine rocks around the world.

The effect of the middle Oligocene cooling and regression on land climates was less obvious. The sensitive tropical floral elements were already gone by the mid-Oligocene, so the land plant record shows only minor cooling effects. The record of ancient soils from the Big Badlands of South Dakota shows that, as the climate became cooler and much drier, sand dune deposits became common in the mid-western United States in the late Oligocene (Retallack, 1983). These same soils suggest that vegetation was a mixture of scrublands and grasses, with few trees, by the late Oligocene.

As the climatic deterioration of the Eocene and Oligocene began, the total diversity of land mammals or marine organisms decreased significantly from Eocene levels, reaching an all-time low in the late Oligocene. The forests and jungles of the early Eocene were rapidly disappearing by the late Eocene, so that by the Oligocene most of the temperate latitudes were covered by a mixture of forest and scrubland vegetation. Along with the change in vegetation triggered by this cooling and drying was a major change in many of the land organisms. In this realm lived a land mammal fauna dominated by primitive members of mostly living families. These included three-toed horses (which began to radiate into multiple lineages by the late Oligocene), three different lineages of rhinos, early camels, deer, and peccaries, as well as a handful of archaic groups left over from the Eocene. Numerous modern carnivorous groups (especially early dogs, and the catlike nimravids, as well as primitive members of the bear, weasel, and raccoon families) became the dominant predators as the last of the archaic carnivorous mammals straggled on. On all the northern continents and Africa, rodents and rabbits both underwent a huge diversification as the niches for ground-dwelling seed-eaters increased, and the habitat for squirrel-like nut and fruit eaters diminished.

In Eurasia, many of the same trends were apparent. In the early Oligocene, the Turgai Strait across the Obik Sea between Europe and Asia opened up, allowing Asian mammals (such as rhinos and ruminants) to immigrate to Europe and drive many of the endemic natives to extinction. This early Oligocene event is known as the Grande Coupure. However, there was only limited migration between Asia and North America via the Bering Strait. In Eurasia, the Oligocene saw a similar diversification of rhinos (including one group, the giant indricotheres of Mongolia and Pakistan, which reached 6 m at the shoulder and weighed 20 tonnes), plus some of the earliest members of the deer, giraffe, pig, and cattle families. Tree-dwelling mammals became much less common and vanished from many continents. For example, primates once dominated all the northern continents during the early and middle Eocene, but became restricted to Africa and South America, where they evolved into Old World and New World monkeys, respectively. The rest of the African fauna was also endemic to this island continent, which was not connected to Eurasia at the Arabian Peninsula until the early Miocene. Instead, Africa had a fauna populated by archaic mastodonts, a wide diversity of hyraxes, and other peculiar endemic forms, such as the horned arsinotheres. South America and Australia were also island continents, unconnected to the rest of the world, and each developed their own endemic faunas.

In the marine realm, the early Oligocene extinctions triggered by global cooling were severe, causing major extinction in the planktonic and benthic foraminifera, and even in the planktonic algae such as diatoms and coccolithophores. In the Gulf Coast of the United States, 97% of the marine snail species and 89% of the clam species found in the late Eocene did not survive into

the late early Oligocene, and over 50% of the sea urchins and sand dollars went extinct as well. However, the overall taxonomic composition of the marine fauna remained essentially the same, with new species of clams, snails, and sea urchins replacing the extinct species (but at lower diversity), and making up the bulk of the fossilizable organisms in the Oligocene. By the end of the early Oligocene, diversity was at an all-time low. Marine faunas were dominated by groups tolerant of the cooler waters that began in the Oligocene. This is true especially in the mollusks of the Pacific Rim, which are mostly cold-water tolerant forms that migrated south to California from Alaska and Siberia during the Oligocene. Planktonic organisms were not only low in diversity, but occupied relatively few, simple biogeographic realms (since the area of the tropics had decreased), and evolved relatively slowly during the Oligocene.

Summary and conclusions

The Paleogene (from 65 to 23 million years ago) marked the global transition from "greenhouse" climates that had persisted from the Mesozoic to the modern "icehouse" world with glaciers on the poles. "Greenhouse" conditions persisted from 65 to 50 million years ago, with a "super-greenhouse" short-term warming event at 55.6 million years ago. The causes of this global warming are still controversial, although some combination of greenhouse gases, such as carbon dioxide and methane, are usually implicated. In addition, the circulation and mixing of polar waters with tropical waters prevented the poles from freezing, and allowed alligators and temperate plants to live above the Arctic Circle. This "greenhouse" world began a slow cooling from 49 to 33 million years ago, with the first signs of Antarctic ice appearing at 49 million years ago. At 33 million years ago, the Antarctic ice cap appeared, possibly due to the separation of Antarctica from Australia and South America to form the Circum-Antarctic Current, which generated cold bottom waters and began modern oceanic circulation patterns. Since that time, the Antarctic ice cap has waxed and waned, but the Earth continues in the "icehouse" state that began 33 million years ago.

Donald R. Prothero

Bibliography

- Aubry, M.-P., Lucas, S., and Berggren, W.A. (eds.), 1998. *Late Paleocene-Early Eocene Biotic and Climatic Events in the Marine and Terrestrial Records*. New York: Columbia University Press, 513pp.
- Birkenmajer, K., 1987. Tertiary glacial and interglacial deposits, south Shetland Islands, Antarctica: Geochronology versus biostratigraphy (a progress report). *Bulletin of the Polish Academy Science, Earth Science*, **36**, pp. 133–145.
- Boersma, A., Premoli-Silva, I., and Shackleton, N.J., 1987. Atlantic Eocene planktonic foraminiferal paleohydrographic indicators and stable isotope paleoceanography. *Paleoceanography*, **2**, 287–331.
- Davies, R., Cartwright, J., Pike, J., and Line, C., 2001. Early Oligocene initiation of North Atlantic deep water formation. *Nature*, **410**, 917–920.
- DeConto, R.M., and Pollard, D., 2003. Rapid Cenozoic glaciation of Antarctica induced by declining atmospheric CO₂. *Nature*, **421**, 245–249.
- Dickens, G.R., O'Neill, J.R., Rea, D.K., and Owen, R.M., 1995. Dissociation of oceanic methane hydrate as a cause of the carbon isotope excursion at the end of the Paleocene. *Paleoceanography*, **10**, 965–971.
- Dickens, G.R., Castillo, M.M., and Walker, J.C.G., 1997. A blast of gas in the latest Paleocene: Simulating first-order effects of massive dissociation of oceanic methane hydrate. *Geology*, **25**, 259–262.
- Diester-Haass, L., and Zahn, R., 1996. The Eocene-Oligocene transition in the Southern Ocean: History of water masses, circulation, and biological productivity inferred from high resolution records of stable

- isotopes and benthic foraminiferal abundances (ODP Site 689). *Geology*, **24**, 16–20.
- Exon, N., and 20 others, 2002. Drilling reveals climatic consequences of Tasmanian gateway opening. *EOS*, **83**, 253–259.
- Kennett, J.P., and Stott, L.D., 1990a. Proteus and Proto-Oceanus: Ancestral Paleogene oceans as revealed from Antarctic stable isotope results. *Proceedings of the Ocean Drilling Program, Scientific Results*, vol. 113, pp. 865–880. College Station, TX: Ocean Drilling Program.
- Kennett, J.P., and Stott, L.D., 1990b. Abrupt deep-sea warming, palaeoceanographic changes and benthic extinctions at the end of the Palaeocene. *Nature*, **353**, 225–229.
- Koch, P.L., Zachos, J.C., and Gingerich, P.D., 1992. Correlation between isotopic records in marine and continental carbon reservoirs near the Palaeocene/Eocene boundary. *Nature*, **358**, 319–322.
- Markwick, P.J., 1994. “Equability,” continentality, and Tertiary “climate”: The crocodylian perspective. *Geology*, **22**, 613–616.
- Miller, K.G., 1992. Middle Eocene to Oligocene stable isotopes, climate, and deep-water history: The Terminal Eocene Event? In Prothero, D.R., and Berggren, W.A. (eds.), *Eocene-Oligocene Climatic and Biotic Evolution*. Princeton, NJ: Princeton University Press, pp. 160–177.
- Miller, K.G., Fairbanks, R.G., and Mountain, G.S., 1987. Tertiary oxygen isotope synthesis, sea level history, and continental margin erosion. *Paleoceanography*, **2**, 1–19.
- Miller, K.G., Wright, J.D., and Fairbanks, R.G., 1991. Unlocking the Ice House: Oligocene-Miocene oxygen isotopes, eustasy, and margin erosion. *J. Geophys. Res.*, **96**, 6829–6848.
- Pearson, P.N., and Palmer, M.R., 1999. Middle Eocene seawater pH and atmospheric carbon dioxide concentrations. *Science*, **284**, 1824–1826.
- Pearson, P.N., Ditchfield, P.W., Singano, J., Harcourt-Brown, K.G., Nicholas, C.J., Olsson, R.K., Shackleton, N.J., and Hall, M.A., 2001. Warm tropical sea surface temperature in the Late Cretaceous and Eocene epochs. *Nature*, **413**, 481–487.
- Prothero, D.R., 1994. *The Eocene-Oligocene Transition: Paradise Lost*. New York: Columbia University Press, 291pp.
- Prothero, D.R., and Berggren, W.A. (eds.), 1992. *Eocene-Oligocene Climatic and Biotic Evolution*. Princeton, NJ: Princeton University Press, 568pp.
- Prothero, D.R., Ivany, L.C., and Nesbitt, E.A. (eds.), 2003. *From Greenhouse to Icehouse: The Marine Eocene-Oligocene Transition*. New York: Columbia University Press, 541pp.
- Retallack, G.J., 1983. *Late Eocene and Oligocene Palesols from Badlands National Park, South Dakota*, GSA Special Paper 193. Boulder, CO: Geological Society of America.
- Röhl, U., Bralower, T.J., Norris, R.D., and Wefer, G., 2000. New chronology for the late Paleocene thermal maximum and its environmental implications. *Geology*, **28**, 927–930.
- Royer, D.L., Wing, S.L., Beerling, D.J., Jolley, D.W., Koch, P.L., Hickey, L.J., and Berner, R.A., 2001. Paleobotanical evidence for near present-day levels of atmospheric CO₂ during part of the Tertiary. *Science*, **292**, 2310–2313.
- Sloan, L.C., and Rea, D.K., 1995. Atmospheric carbon dioxide and early Eocene climate: A general circulation modeling sensitivity study. *Palaeoogeogr. Palaeoclimatol. Palaeoecol.*, **119**, 275–292.
- Sloan, L.C., Walker, J.C.G., Moore, T.C. Jr., Rea, D.K., and Zachos, J.C., 1992. Possible methane-induced polar warming in the early Eocene. *Nature*, **357**, 320–322.
- Thomas, D.J., Zachos, J.C., Bralower, T.J., Thomas, E., and Bohaty, S., 2002. Warming the fuel for the fire: Evidence for the thermal dissociation of methane hydrate during the Paleocene-Eocene thermal maximum. *Geology*, **30**, 1067–1070.
- Wolfe, J.A., 1978. A paleobotanical interpretation of Tertiary climates in the Northern Hemisphere. *Am. Sci.*, **66**, 694–703.
- Wolfe, J.A., 1994. Tertiary climatic changes at middle latitudes of western North America. *Palaeoogeogr. Palaeoclimatol. Palaeoecol.*, **105**, 195–205.
- Zachos, J.C., Lohmann, K.C., Walker, J.C.G., and Wise, S.W., 1993. Abrupt climate change and transient climates during the Paleogene: A marine perspective. *J. Geol.*, **101**, 191–213.
- Zachos, J.C., Stott, L.D., and Lohmann, K.C., 1994. Evolution of early Cenozoic marine temperatures. *Paleoceanography*, **9**, 353–387.
- Zachos, J., Pagani, M., Sloan, L., Thomas, E., and Billups, K., 2001. Trends, rhythms, and aberrations in global climate 65 Ma to present. *Science*, **292**, 686–693.

Cross-references

Animal Proxies, Invertebrates
 Animal Proxies, Vertebrates
 Antarctic Bottom Water and Climate Change
 Antarctic Glaciation History
 Carbon Isotope Variations over Geologic Time
 Carbon Isotopes, Stable
 Cenozoic Climate Change
 Deep Sea Drilling Project (DSDP)
 Evolution and Climate Change
 Foraminifera
 Glaciations, Pre-Quaternary
 “Greenhouse” (warm) Climates
 Ice-Rafted Debris (IRD)
 “Icehouse” (cold) Climates
 Methane Hydrates, Carbon Cycling, and Environmental Change
 North Atlantic Deep Water and Climate Change
 Obliquity
 Ocean Drilling Program (ODP)
 Ocean Paleocirculation
 Oxygen Isotopes
 Paleobotany
 Paleocene Modeling
 Paleocene-Eocene Thermal Maximum
 Paleoclimate Modeling, Pre-Quaternary
 Paleoclimate Proxies, an Introduction
 Plate Tectonics and Climate Change

PALEOHYDROLOGY

Introduction

Ecosystems, human life, economic activities, . . . , all life on the continents depends on the availability of liquid fresh water.

Today, the hydrosphere (about $1,400 \times 10^6 \text{ km}^3$) contains 2.5% of fresh water, of which 2/3 is stored as ice and permanent snow, 1/3 as groundwater, and only 0.3% is found in lake, wetland, soil, and river systems (Shiklomanov, 1998). The “global hydrological cycle” – the overturning of water from the Earth’s surface to the sky and back – recycles an amount of water equivalent to the world’s ocean in 3,000 years. With highly variable delays, precipitation falling on land surface (about $0.111 \times 10^6 \text{ km}^3 \text{ yr}^{-1}$) returns to the sea through overland, subterranean, and partly atmospheric paths.

Earth’s water distribution varies through space and time. The dramatic floods of August 2002 in central Europe and the 1970–1980s Sahel drought caused substantial damage but hydrological changes of much larger amplitude and duration have occurred in the past. From ~10 to 5 kyr ago, the Sahara was a verdant landscape with numerous lakes, supporting Neolithic populations; and 21 kyr ago, the sea level was ~120 m lower and the Northern Hemisphere continental ice volume was 20 times greater than today. Hydrological changes occur on all timescales (Figure P20).

Paleohydrology aims at reconstructing the timing, frequency, and magnitude of changes in water storage and quality, in moisture sources and trajectories, and understanding their causes and mechanisms. To represent the full range of natural variability, it has to go back in time far beyond the instrumental period, i.e., at most the past 200 years. Practically, paleohydrology studies the land-based portion of the hydrological cycle and focuses on its liquid phase; other components of the hydrosphere (atmosphere, vegetation, ocean, ice) are

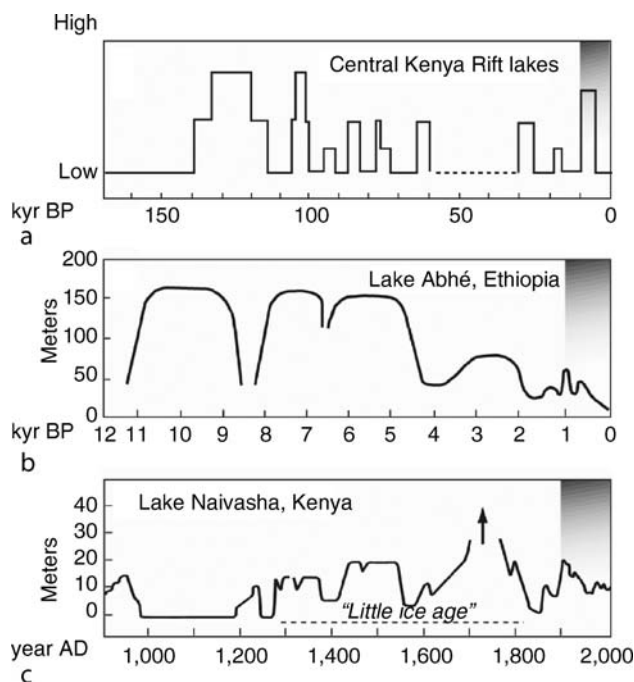


Figure P20 Hydrological variability on different timescales: lake-level changes in East Africa, reflecting changes in the Precipitation minus Evaporation balance in the lake catchment are; (a) after Trauth et al. (2003); (b) after Gasse (2000); (c) after Verschuren et al. (2000).

considered because of their relationships with liquid inland water bodies. The present dating techniques mainly allow coverage of the late Quaternary period.

Major concepts

Inland water systems

The irregular distribution of inland water bodies results from the global climate zonal belts, the regional climate, geological patterns, and topography. The latter provides a natural partitioning of land into drainage basins or catchment areas, also called “watersheds.” In an “exoreic” basin, water falling within its divides gathers to the same outlet toward the sea; an “endoreic” basin is a land-locked, inland drainage system.

Hydrological systems range from small ponds < 0.1 km² to the largest water bodies, e.g., the Caspian Sea (371,000 km²; 78,200 km²). They also differ in lifetime, from a few weeks for ephemeral floodplains to millions of years for subsident tectonic lake basins or deep aquifers.

The time of complete water renewal, or residence time, ranges in average from tens of days in rivers, to tens of years in lakes and 10³ years in groundwater reservoirs and mountain glaciers. It may reach up to 10⁶ years in deep groundwater systems, especially in endoreic basins of arid zones.

Hydrological variability

The major cause of hydrological fluctuations is climate variability. Human activities and geological events (e.g., landslides, lava flow dams) can also modify hydrological systems locally or regionally.

The variation of the amount of stored water in a time interval, ΔS , is the difference between total inflow and outflow, which can further break down as:

$$\Delta S = (P + R_i + G_i) - (E + R_o + G_o) \quad (1)$$

where P is precipitation, R_i and G_i are the surface and ground water inflows, respectively, E is evaporation + evapotranspiration, and R_o and G_o the surface and ground water outflows, respectively, during that interval. The terms P and E of this water-balance equation depend on climate, while R , G , and part of E are related to watershed specific factors, i.e., hydraulic properties, river bed geometry, soil and vegetation cover, and man-controlled water diversion.

Since Equation (1) expresses the conservation of matter, it is equally applicable to solutes, isotopes, dissolved substances, and solid particles.

Processes that relate hydrological variations to changes in climate and human activities need further research, e.g., how are the different surface and subsurface compartments physically and chemically interconnected? How do they respond to natural or human-induced disturbances? What is their individual response time? Although many paleohydrological records are still qualitative, emphasis is now placed on exchange processes and rates between water pools, on quantification of past hydrological conditions, and on periodicities and probability distributions of hydrological events. Crucial to any paleohydrology study is the establishment of a reliable and accurate chronology.

History

Paleohydrology sprang from several branches with their own techniques and methods, e.g., fluvial paleohydrology, paleolimnology. It emerged as an earth science of its own over the past decades (Schumm, 1965; Gregory et al., 1995). Integration of groundwaters as paleohydroclimatic archives is even more recent. This emergence was triggered by the urgent issue of predicting water resource evolution at global, regional, and local scales, in response to climatic and societal stress. It was favored by the development of new dating techniques, new methods for inferring past hydrological conditions, and computing facilities for data storage and modeling approaches.

Methods and techniques

Paleohydrological analysis of water systems usually begins at the watershed level, with a field observations and measurements, material collection and laboratory analyses (Stage 1). Dating is a major step (Stage 2). Then, primary data are converted into time series of hydrological parameters (Stage 3). The last stage analyzes the observed and inferred data through statistics and/or modeling (Stage 4), putting the findings into broader perspective, and eventually linking them with known geological, climatic, or human facts.

Archives and proxies (Stage 1)

Documentary records provide direct information over many centuries in Europe or China, for example on major floods or droughts, advance and retreat of mountain glaciers, or land-use changes.

Beyond instrumental and historical data, paleohydrology resorts to indirect indicators of past conditions, the proxies,

archived in the geomorphic features and sediments of ancient water bodies (Figure P21), and in fossil water trapped in aquifers and glaciers.

In river systems, the past stream regime and discharge are primarily inferred from geomorphic and hydraulic properties of the drainage network, the channel geometry (terraces, bankfull width, cross-sections, depth, slope, meander wavelength, . . .), the characteristics of channel sediments (particle sizes), botanic evidence, and indicators of past flood levels, e.g., slack-water or bouldery flood-bar deposits. Dead paleochannels can be detected through remote sensing and field observations.

Changes in lake and swamp water area, depth, and volume, as well as chemistry and biology, are reconstructed from geomorphology (ancient shorelines, ancient tributaries or outflow, spatial sediment distribution), and from the analysis of sediments collected from drillings and outcrops. The most widely used proxies derived from sediments are stratigraphic features, mineralogy and chemistry of the allochthonous (detrital) and endogenic fractions, stable isotopes of organic matter, primary carbonates, biogenic silica . . ., and biological remains (e.g., diatoms, ostracods, insects, pollen macrofossils . . .).

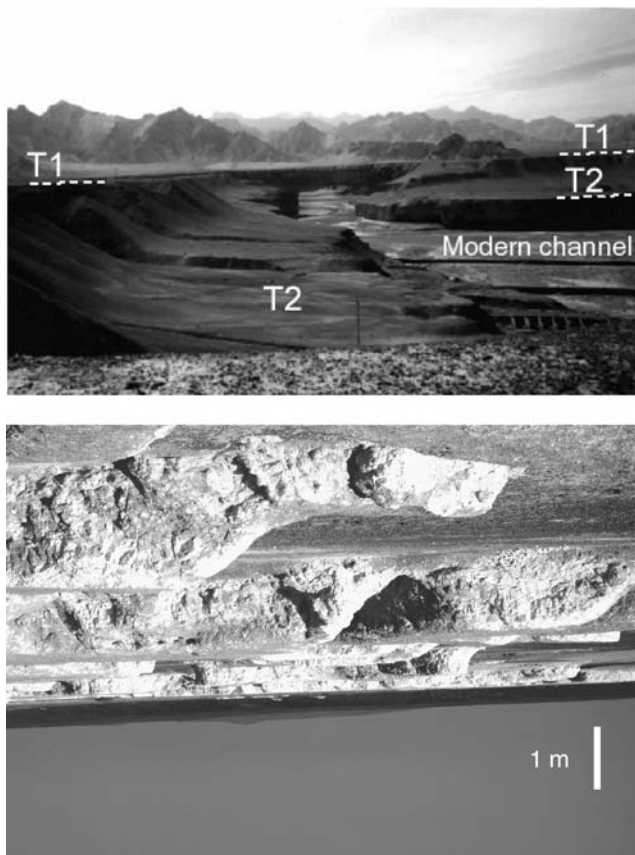


Figure P21 Examples of proxy sources. *Upper panel:* fluvial terraces (*T1*, *T2*) abandoned during phases of river entrenchment (Dang River, central China). *Lower panel:* early Holocene sediments of Paleolake Abhé (6,000 km², 160 m deep; see Figure P20), Afar desert (Ethiopia).

With speleothems (cave deposits), the annual growth layers and the carbonate stable isotope composition can inform on past precipitation and temperature.

The use of groundwater as a paleohydrological archive requires knowledge of the hydraulic conductivity, porosity, and geological structure of the system. Aquifer water is sampled from wells and boreholes, or springs in the discharge zones. The water isotopic composition, atmospheric noble gases, nitrates, chloride contents, and bromide/chloride ratio are the major indicators on input conditions (isotopic composition of paleoprecipitation, ground temperature, vegetation cover).

Dating (Stage 2)

Besides instrumental and historical records, a few archives deliver calendar ages intrinsically through annual layer counting: varved sediments, glacier ice, and tree rings. ¹⁴C dating is most widely used today when aerial plant remains are found; it is also applied to groundwater-dissolved carbon. It covers the last 40 kyr. Other radiometric methods are now available for different time-scales, which cover up to 10⁶ years: e.g., ²¹⁰Pb (0–200 yr) in lake sediments, ²³⁰Th/²³⁴U in carbonates and organic matter, ¹⁰Be to date geomorphic surfaces (fluvial terraces, lake shorelines) or sediments, and K-Ar and ³⁹Ar/⁴⁰Ar in volcanic interbedded materials. Dating methods also include luminescence, tephrochronology, and paleomagnetism for long continuous stratigraphic profiles.

The time resolution depends on the archive and on the dating method. Laminated deposits can provide annual resolution in best cases. Conversely, uncertainty on groundwater chronology can reach as much as thousands of years, due to the inherent characteristics of subsurface flow and the long residence time. However, groundwaters register the average magnitude of long-term climate change since the signal of local effects or short-term extremes is smoothed out.

Proxy calibration (Stage 3)

Data derived from the initial proxy analyses translate into hydro-climatic parameters, assuming that the relations between a proxy and its environment are similar to present. Calibration functions, also called transfer functions, can be established through statistical techniques, using a training set including modern observations on the proxies and measured parameters, e.g., diatom-inferred lake water salinity, or pollen-inferred rainfall amount and seasonality. They can also result from the study of the physical processes that control, retain, and modify the hydrological signal archiving, e.g., precipitation inferred from oxygen isotopes in speleothem calcite; these require quantitative adjustment against measured parameters. Because of uncertainties in all methods, multiple proxies and techniques are desirable for cross-checking. Calibrated data provide a record of hydrological variations through time at a particular location. Their synthesis can be conducted at a watershed-scale or wider, provided more local factors are identified.

Time-series analyses, hydrological modeling (Stage 4)

Spatial patterns of paleohydrological estimates through time can sometimes be transformed into statistical syntheses. Periodicities can be identified through spectral analyses. The distribution of discrete events, e.g., flood-frequency distribution, can be assessed through a variety of distribution functions.

Understanding the dynamics of hydrological changes often requires modeling of the investigated system, and calls for data beyond those derived from paleohydrological archives. For example, in a paleolake of known ΔS (Equation (1)), why and how have the water balance terms fluctuated? Evaporation and runoff rates are affected by solar radiation, wind speed, temperature, vegetation cover, etc. The evaluation of such factors comes from astronomical data, botanic evidence, or from outputs of Global Circulation Model (GCM) simulations, although the low GCM spatial resolution is usually inappropriate to the regional or local problem at hand. Models depend on the proxy source, the variable estimated, and the spatial scale under consideration. They greatly differ in complexity and accuracy. Once calibrated and validated on instrumental data, models can simulate past hydrological parameters, e.g., P , E or R (Equation (1)) using lake water, water-energy, water-isotope, or water-salt balance models. They also can predict hydrological changes in response to varying climate or land-use.

Time-series analyses and modeling represent the upper level of paleohydrological reconstruction and provide the greatest insight into the mechanisms and potential causes of hydrological changes.

Applications

Paleohydrology and paleoclimatology

Hydrological fluctuations are intrinsically linked to changes in climatic forcing factors; in turn, they have acted on climate through varying evaporative fluxes from the continental surfaces, and energy exchanges as water undergoes phase changes. While GCM simulations of past climatic conditions help understand the mechanisms of observed hydrological changes, conversely paleohydrological data are used to validate the climatic models: quantitative estimates of hydrological variables are then essential.

At the orbital time-scale, records primarily reflect the glacial/interglacial cycles and the smooth, long-term variations of the Earth's orbit. For example, over the past 70 kyr, changes in level of Lake Lisan (the precursor of the Dead Sea which extend along the Dead Sea-Jordan Valley Dead) correlates with temperature changes inferred from isotopic data in polar ice cores: high/low levels generally coincide with colder/warmer global climate intervals, respectively (Figure P22). Tropical hydrological changes are initially driven by the impact of the orbital precession cycle on monsoon strength; the spectacular early-mid Holocene wetting in the northern tropics (e.g., Figure P20b; Gasse and Roberts, 2004) is an example, although orbital forcing was modified by feedbacks from sea surface temperatures, vegetation, and moisture recycling from soils and large land waterbodies.

At shorter time-scales, subtle disturbances in the climate systems generate, abrupt hydrological changes. Sudden injections of large amounts of continental freshwater in the North Atlantic Ocean have generated remote rainfall anomalies, such as catastrophic droughts in the eastern Mediterranean region coeval with Heinrich events (Figure P22), as shown by abrupt decreases in the Lake Lisan level (Figure P22); the outbreak of Lake Agassiz in the Laurentide at 8.2 kyr BP may have had a widespread impact on rainfall. Holocene abrupt changes are commonly attributed to shift in total solar irradiance or injections of volcanic aerosols in the atmosphere. The Little Ice Age, a cold event in northern high-mid latitudes, is expressed as a wet episode in equatorial East African lakes

(Fig. P20C) but as a dry period in tropical East African and South American records, suggesting persistent El Niño-like conditions (Brown and Johnson, 2006). Despite significant progress in paleohydrological reconstructions during the past decades, further work is needed to quantify hydrological changes, to fill geographical gaps in data coverage, and to analyse changes in seasonality, in order to turn paleohydrology into a more accurate paleoclimatic tool.

Paleohydrology and landscape evolution

Changes in water routing induced by geological events or climate changes may drastically affect the regional geographic features. For instance, ~90 kyr ago, an ice sheet over northern Eurasia dammed the large rivers flowing north to the Arctic Ocean; and huge lakes developed between the sheet and the water divides to the South, and overflowed towards the Aral, Caspian, and Black Seas, and ultimately the Mediterranean, draining large, now endoreic, areas to the sea. The drainage direction of major catchments in Europe and western Siberia was reversed, with considerable impact on both continental and sea hydrology (Mangerud et al., 2001).

Paleohydrology allows quantification of such processes as erosion or river incision rate under varying climatic conditions. For instance, over the past 12,000 years, the northern alluvial piedmont of the Tian Shan in central Asia has been incised as much as 300 m by the rivers flowing from the mountain. Changes in hydrological regime were inferred from the geomorphic survey of one of them and from a model of alluvial stream erosion based on a transport-limit erosion law (Poisson and Avouac, 2004). The estimated incision rate increased markedly at the transition from the generally wet early Holocene conditions to a rather arid climate with enhanced seasonal contrasts around 6,000 years ago.

Paleohydrology and human societies in the past

Several studies suggest relationships between past natural hydrological variability and societal changes. A striking example is that of the Holocene occupation in the Sahara controlled by changes in water availability (Kuper and Kröpelin, 2006), as illustrated in Figure P23. The history of droughts evident in the 1,000-year hydrological reconstruction in Lake Naivasha, Kenya (Figure P20c, is in line with the cultural history of the region; prosperity during the wettest episode (the Little Ice Age).

Paleohydrology can also detect human impacts on hydrological systems. Increased erosion rate induced by forest clearance is fingerprinted in lake sediment magnetic properties. Atmospheric pollution (e.g., from lead in Roman times or acid rains in recent times) and eutrophication has been recorded in lake sediment chemistry and lake-water pH.

Water resource implications and hydrological risk-assessment

Groundwater is a crucial source of freshwater throughout the world. Paleohydrology shows that, in many areas, exploited groundwater is "fossil" and dates from periods of greater moisture availability thousands of years ago or more. Groundwater is often being mined at a rate vastly exceeding that of possible recharge under current climatic conditions, leading to a swift water resource decline.

Ice melting water is the prime water resource and hydroelectric power supply in several areas, e.g., the Andean countries of

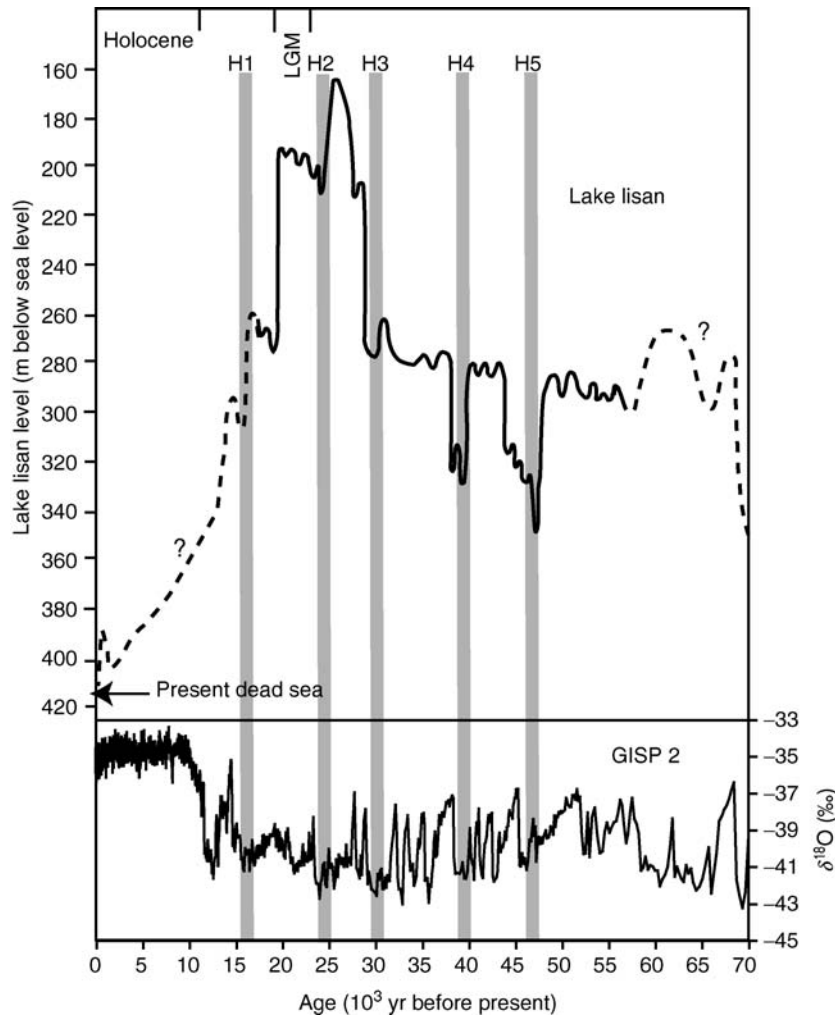


Figure P22 Correlations between levels of Lake Lisan and oxygen isotope records from GISP 2 (The Greenland Ice Sheet Project 2, 1997). After Bartov et al., 2003.

South America. The current global warming induced a rapid decay of mountain glaciers, especially in the tropics. Has such a decay an equivalent in the past? This question is approached through study of the glacier history and the dependent river and lake systems.

The risk of extreme floods and droughts is of critical concern for societies. It must be assessed for selecting the location of equipment, such as dams. Streamflow-gauging records are too short to provide realistic probabilities of the heavy flow magnitude and frequency distribution. Paleoflood data can be incorporated into flood-frequency analyses to extend the records, as exemplified by the regional Holocene paleoflood approach performed in northwestern Colorado (Jarrett and Thomlison, 2000). This study could estimate the peak discharge at recurrence intervals ranging from 10 yr to 10 kyr.

The suitability of potential repositories of chemical and radioactive waste also refers to paleohydrology. Estimating groundwater flow paths and fluxes through rocks of low permeability under past and current climates is necessary to assess future risk.

Conclusions

Paleohydrological research unveils an enormous natural variability in inland water quality and availability, primarily driven by climate change, at least over the Quaternary period. Superimposed on the natural variability, human activities affect the global climate and individual hydrological systems. Knowledge of hydrological changes in the absence of any significant human impact is key to disentangle natural and anthropogenic factors.

Paleohydrology is concerned with very practical applications, from changes in the hydrological cycle at a continental scale to local water resource management.

The anticipated global warming is expected to cause the hydrological cycle to churn more vigorously, putting more moisture into the atmosphere, generating a stormier climate in some regions and drier conditions elsewhere, and higher frequency and amplitude of extreme hydrological events (IPCC, 2007). However, even the most sophisticated numerical climate models do not yet provide a realistic representation of



Figure P23 Late Neolithic rock engraving in central Sahara (Temet, Aïr, Northern Niger).

precipitation patterns or amounts at regional scales. Better documenting and understanding of the full range of climate driven hydrological variability is a most urgent and significant tasks in paleoscience.

Françoise Gasse

Bibliography

- Bartov, Y., Goldstein, S.L., Stein, M., Enzel, Y., 2003. Catastrophic arid episodes in the Eastern Mediterranean linked with the North Atlantic Heinrich events. *Geology*, **31**(5), 439–442.
- Brown, E.T., and Johnson, T.C., 2005. Coherence between tropical East African and South American records of the Little Ice Age. *Geochemistry, Geophysics, Geosystems*, **6** (12) doi:10.1029/2005GC000959.
- Gasse, 2000. Hydrological changes in the African tropics since the Last Glacial Maximum. *Quaternary Sci. Rev.*, **19**, 189–211.
- Gasse, F., and Roberts, C.N., 2004. Late Quaternary hydrologic changes in the arid and semiarid belt of northern Africa. Implications for past atmospheric circulation. In “*The Hadley Circulation: Present, Past and Future.*” (Diaz H.F., and Bradley R.S., Eds.), Kluwer Ac. Pub., Dordrecht. pp. 313–345.
- Gregory, K.J., Starkel, L., and Baker, V.R. (eds.), 1995. *Global Continental Paleohydrology*. Chichester: Wiley, 334pp. IPCC (Intergovernmental Panel on Climate Change), 2007. Fourth Assessment report, WMO, UNEP.
- Jarrett, R.D., and Tomlison, E.M., 2000. Regional interdisciplinary paleoflood to assess extreme flood potential. *Water Resour. Res.*, **36**(10), 2957–2984.
- Kuper, R., and Kröpelin, S., 2006. Climate controlled Holocene occupation in the Sahara. *Science*, **313**, 803–807.
- Mangerud, J., Astakhov, V., Jakobson, M., and Svendsen, J.I., 2001. Huge Ice-age lakes in Russia. *J. Quaternary Sci.*, **16**(8), 773–777.
- Poisson, B., and Avouac, J.P., 2004. Holocene hydrological changes inferred from alluvial stream entrenchment in North Tian Shan (Northwestern China). *J. Geol.* **112**, 231–249.
- Schumm, S.A., 1965. Quaternary paleohydrology. In Wright, H.E., and Fret, D.G. (eds.), *The Quaternary of the United States*. Princeton: Princeton University Press, 783–794.

Shiklomanov, I.A., 1998. World Water Resources: A new appraisal and assessment for the 21th century. Executive summary for World Water Resources Monograph. Paris: UNESCO-IHP.

The Greenland Summit Ice Cores CD-ROM, 1997. Available from the National Snow and Ice Data Center, University of Colorado at Boulder, and the World Data Center-A for Paleoclimatology, National Geophysical Data Center, Boulder, Colorado.

Trauth, M.H., Deino, A.L., Bergner, A.G.N., and Strecker, M.R., 2003. East African climate change and orbital forcing during the last 175 kyrBP. *Earth Planet. Sci. Lett.*, **206**, 297–313.

Verschuren, D., Laird, K.R., and Cumming, B.F., 2000. Rainfall and drought in equatorial East Africa during the past 1,100 years. *Nature*, **403**, 410–414.

Cross-references

[Continental Sediments](#)
[Dating, Dendrochronology](#)
[Dating, Magnetostratigraphy](#)
[Dating, Radiometric Methods](#)
[Glacial Megalakes](#)
[Lacustrine Sediments](#)
[Lake Level Fluctuations](#)
[Little Ice Age](#)
[Millennial Climate Variability](#)
[Mountain Glaciers](#)
[Ostracodes](#)
[Paleoclimate Proxies, an Introduction](#)
[Paleotemperatures and Proxy Reconstructions](#)
[Paleolimnology](#)
[Speleothems](#)
[Stable Isotope Analysis](#)
[Time-Series Analysis of Paleoclimate Data](#)
[Transfer Functions](#)

PALEOLIMNOLOGY

Paleolimnology is the multidisciplinary science that studies past environmental conditions from the evidence preserved in lake sediments. It addresses a very broad range of issues relating to former ecosystem composition and development, lake ontogeny, the variability of catchment and land use processes, climate change, water quality trends, pollution studies, and even the hydrocarbon potential of ancient lake sediments. Such diversity has led to the emergence of at least three major traditions within the subject. The first deals with trends in extant lakes, often investigating relatively short time scales (10–200 years) and allied to work by the limnological community. A second strand studies ancient lake basins, an area merging with the sub-discipline of limnogeology, and usually the realm of sedimentology. The third tradition considers the evidence of climate change preserved by lakes, usually with a recent or Quaternary perspective, using tools that bridge the aforementioned areas of paleolimnology. A convergence of methodologies, shared principles, and assumptions unifies paleolimnology as a discipline and these will form the initial part of this discussion. Given the focus of this encyclopedia, emphasis will then be placed on the application of paleolimnology to studies of past climates and climate change.

Principles, assumptions, and chronologies

Lakes are temporary stores of sediment in the drainage basin and have been described as an ecosystem’s memory (Smol, 2002). The length of the memory depends on the age of the lake and on the sedimentation rate. Since lakes accumulate

sediments faster than equivalent marine environments, they are often well-equipped to furnish high-resolution records. Some lakes are very young, for example those in recent volcanic craters or man-made reservoirs; others in formerly glaciated regions were formed after the retreat of the last ice sheet that covered the region and are typically less than $\sim 16,000$ years old. A further group of lakes, including the large rift lakes of East Africa and Lake Baikal, are extremely old and have been accumulating sediment for millions of years (Cohen, 2003).

The diversity of lakes matches the range of studies undertaken by paleolimnologists, but commonalities in approach and methods are evident. Paleolimnological studies exploit the fact that sediment accumulates in lake basins from different sources, sometimes arriving from great distances, as is the case in airborne deposition of fly ash, although more immediate and important sources are the lake catchment and materials produced within the lake itself (Figure P24). Allochthonous materials are those introduced from catchments including sediments derived from eroding soils, weathered materials, and vegetation. Some allochthonous components have origins outside the immediate catchment, for example long distance transport of pollen, volcanic ash, and airborne industrial pollutants. Identifying the source and flux of allochthonous materials is a major goal of many paleolimnological investigations as these can give clues about changing catchment conditions and regional processes. Autochthonous materials, or those living or produced within the lake, constitute the other major components of the sediments. The remains of algae, higher plants, fish, invertebrate animals, etc. that once lived within the lake, together

with chemical precipitates including salt deposits are all termed autochthonous. Diagenetic minerals that form *in situ* from previously deposited sediments would also contribute to this autochthonous group.

One key assumption of the paleolimnologist is the law of superposition. In collecting material from lakes it is usually reasonable to assume that more recent sediments overlie older materials, making them especially suited to temporal studies, and giving lakes an advantage in this respect over other sediment stores. However, there are instances when this assumption does not hold and the stratigraphy is disturbed or even inverted. All lakes experience some sediment focusing, a process that is a function of their bathymetry, catchment topography, river inputs, and internal water movements, creating uneven sedimentation patterns within a basin. Even in simple lakes some fining of deposits takes place, so that the representation of a particular indicator may be skewed, and therefore not all sampling sites are equally representative. Problems frequently occur in nearshore areas where the sedimentation may be erratic, leading to slumps or hiatuses, or in deltaic areas where variability in discharge may be important. Once deposited, sediments can be ruptured and faulted by tectonic movements, and localized slumps are common on slopes with even relatively shallow angles. In deep lakes, turbidity currents are common and these can intersperse the stratigraphy with homogeneous turbidite layers. To offset the problems posed by post-depositional deformation, a number of paleolimnologists have used seismic profiling to identify undisturbed coring sites. Excellent examples of this approach come from the large lakes

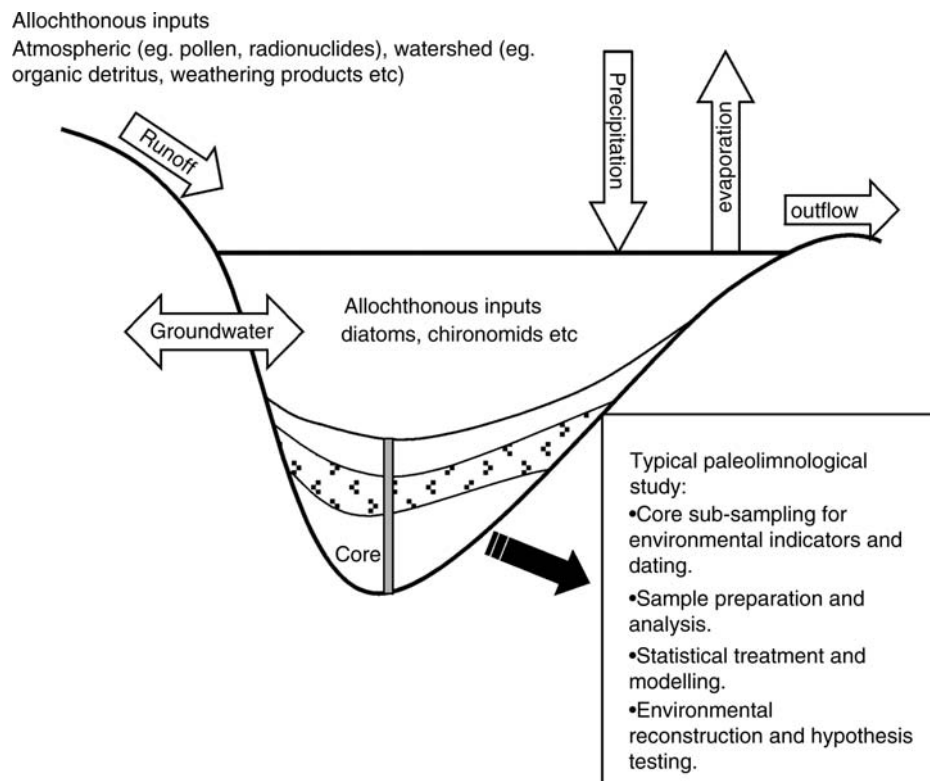


Figure P24 Principles of paleolimnology. The key sources of water and sediment to a typical lake are indicated. The core location is important to sample the most complete sequence of sediments. Major stages in a palaeolimnological investigation are listed.

of East Africa where deep-drilling operations need to be sure of collecting undisturbed sediment cores (Cohen, 2003).

In general, paleolimnology is more successful in small, deep lakes within sheltered catchments such as volcanic craters, rather than large shallow lakes that are more prone to wind stress and sediment mixing from wind-induced turbulence. Eddies can reach the sediment, causing remobilization of recently deposited sediment and smoothing of the stratigraphic record. A problem common to all paleolimnological studies is that of bioturbation. Burrowing benthic organisms tunnel into the sediments, once again smoothing the stratigraphy and limiting the temporal resolution possible. Extreme examples of bioturbation include fish mounds and even mixing by mammals using the lake as a watering hole. Bioturbation is less of a problem in anoxic deepwater sediments, out of the range of wading animals and often with a limited benthic fauna. The discussion above demonstrates the unique nature of lakes. While it is possible to generalize, each basin has to be treated differently. In extant lakes, the paleolimnologist can rigorously apply uniformitarian principles. By fully understanding present-day limnology, sedimentation, patterns, and responses of the lake to external forcing, interpretation of the sediment record becomes comprehensible.

Sampling the sediments of extant lakes usually requires the collection of sediment cores from a boat or other platform. The method selected depends on the length of core required and the nature of the study. If the aim is to investigate recent high-resolution changes, the collection of the mud-water interface is vital and sampling devices such as the Glue corer or Hongve sampler should be used to get short, <50 cm, gravity cores (see Smol, 2002). Both work by lowering a tube into the sediment and triggering a bung that seals the tube and enables it to be raised. A better, but more complicated system for taking high resolution short cores is freeze-coring, where dry ice or liquid nitrogen freezes the sediments and avoids deformation during the coring process. It has even been successfully deployed in warm tropical waters. Freeze-coring is particularly important in the recovery of sediment structures such as laminations.

Probably the most common coring system used by paleolimnologists is the 1 m Mackereth corer, which consists of a column of fixed height, containing a piston and a sampling tube, mounted on a large drum. During its operation, the Mackereth corer is lowered to the bottom of the lake, taking care to preserve verticality. The sampling tube is then forced into the sediments using compressed air, which when fully extended allows the air to fill a drum; this creates buoyancy to recover the corer. This system works well in many lakes, providing that sediments are sufficiently cohesive to remain within the tube, neither too sandy nor excessively consolidated. Mackereth corers are available in a range of fixed lengths up to 12 m.

A more flexible system is the Livingstone corer and its modified version, the Wright corer. These work by fixed rods that are used to collect 1–1.5 m of material at a time. The corer consists of a barrel, a piston, and sometimes a plastic inner tube that can be used to store the core. The corer is lowered in closed position and then the piston is raised using a cable before it is forced into the sediments. The operation is repeated for consecutive sections until an impenetrable barrier is reached or all the rods are deployed. Typical cores gathered using this method are 10–15 m long, but much longer (50–60 m) cores have also been taken. Locating the core hole after each drive is problematic in all but very shallow water and a core-hole

liner is often used both to facilitate relocating the hole and preventing materials falling into it. Good practice involves taking parallel cores with one offset to cover gaps between drives. The mud-water interface is rarely recovered intact with a Livingstone-type corer and has to be taken separately with a short coring system. Some recent work on large lakes has been undertaken using the GLAD800 coring rig, a system capable of reaching combined water-sediment depths of 800 m (Cohen, 2003). The technology involved here is broadly analogous to that used in the offshore oil and gas industries.

Not all paleolimnological work is from extant lakes. Some studies have used modified versions of the Wright and Livingstone corers to obtain cores from former lake beds or seasonally drained lakes without the need for a boat. While these cores will not be continuous, the extra stability gained by working in a relatively dry environment can be advantageous in ensuring precision. Other workers have sampled exposures of lake deposits, giving them the advantage of unlimited material to study, ready inspection of deformation features, and no distortion due to coring. Such exposed deposits are rarely as continuous in time as cored sediments and can be more prone to sub-aerial weathering. The study of fossil shorelines is frequently allied to core studies, as these give precise indications of former lake level and hence lake volume and surface area (important in paleoclimate climate modeling), but these only mark highstands and do not offer continuous sequences to investigate rates or directions of change, or information about lower lake stages.

All paleolimnological studies need to establish a chronology to understand the rate of change or the timing of an event. A precise method available in some lakes is the counting of annual varves (Lamoureux, 2001). A varve, in de Geers's original usage, is a couplet of sediments of contrasting size fractions caused by seasonal melting of glacier ice. Not all laminations are of glacial origin; in temperate regions, the regular seasonal cycle of diatom blooms in spring (and less strongly in autumn) can create a lightly colored layer contrasting with darker organic material deposited during the productive summer months. By counting the couplets, an absolute chronology can be established, as long as the mud-water interface is known or some other clearly identified dating horizon is present, such as the tephra from a known volcanic eruption. An exceptional series of varves has formed in Baldeggersee, an alpine lake showing evidence of recent eutrophication (Lotter, 1998). These have been used to tie trophic changes inferred using paleolimnological methods to a series of instrumental measurements. Sites like these help test the assumptions implicit in paleolimnology and the strength, or otherwise, of the methods. In areas of strong seasonality, such as parts of the tropics, the precipitation of salts during dry seasons often can create a distinct horizon, or a characteristic bloom of algae may occur on a seasonal basis. According to independent bracketing dates, it has been shown that laminations are not always annual, and a range of cyclical climate forcing mechanisms has been proposed to explain their origin. Some laminations are too fine to be easily visible and are difficult to enumerate without magnification or improved contrast. In these cases, x-ray images can help as they can be digitally counted using image analysis software. Similarly, gray-scale imaging can sometimes help decipher laminations, although difficulties can persist (Dean et al., 2002).

Unfortunately, annually laminated sediments are rare, and most paleolimnologists have to use either marker horizons of known date, or more often radiometric methods, to obtain a chronology. The most commonly used markers are volcanic

tephra layers, and tephrochronologies have become established for several volcanic regions (Turney and Lowe, 2001). Tephrochronology enables correlation between lakes, providing the tephra layers have distinctive chemical characteristics that enable them to be tied to a particular eruption. Paleomagnetic properties including field reversals and secular variations have been used in some localities to give chronologies, but the widespread use of paleomagnetism as an independent dating tool for recent lake sediments is not common. Magnetic measurements have been more extensively used to correlate cores from the same basin and to trace catchment erosion (Maher and Thompson, 1999). In recent studies, the use of spheroidal carbonaceous particles (SCPs) from high temperature combustion processes have been useful in giving a marker horizon, providing the history of industrialization in the region is known (Smol, 2002).

Virtually all published paleolimnological studies use a chronology derived from radiometric methods. Various radionuclides with different half-lives are routinely used, and choice is dependent on the temporal scale of the study and the materials present within the sediments. Recent paleolimnology relies heavily on ^{210}Pb that has a half life of ~ 22 years and is suitable for dating the last 150–200 years. It is usually partnered with ^{137}Cs , as this artificial radionuclide has distinctive peaks in the early 1960s and 1986, relating to the testing of atomic weapons and the Chernobyl nuclear accident, respectively. Studies of the last $\sim 40,000$ years make extensive use of ^{14}C measurements to produce a chronological framework. Radiocarbon measurements from lake sediments can be made on bulk organic material, charcoal, or plant macrofossils. The latter are preferred as terrestrial plants are more likely to be in equilibrium with the atmosphere and therefore give a more reliable date. Some lakes in karst terrains are difficult to date using ^{14}C because lake biota can incorporate old dissolved carbonate leading to ^{14}C dates that are too old. An alternative method is U/Th dating on carbonates or occasionally on silicates. U/Th has great potential in the dating of lake sediments up to 250,000 years old and is increasingly used by paleolimnologists.

Paleolimnology and climate change

Lakes have been referred to as “natural archives,” since like libraries they contain information that can be “read” if the “language” of the particular proxy indicator is known. To continue the literary analogy, the evidence contained in lake sediments is like an incomplete collection of books, with some pages missing, written in an unfamiliar language, and all with different perspectives on the question under consideration. Therefore, interpreting different environmental indicators is problematic, as they are rarely responsive to a single variable, they are frequently incomplete reflections of former ecosystems, and are often prone to diagenesis or other corruption. Moreover, few indicators can be used to directly reconstruct former climate variables such as precipitation or temperature, and a surrogate measure of climate such as lake water salinity is often used. With these caveats this discussion will now briefly consider the types of evidence used by paleolimnologists. It is not possible to review the full range of indicators used here, but some of the most common techniques will be introduced.

The water balance of a closed basin lake is determined by precipitation inputs, evaporation losses, and the net exchange with groundwater. Open systems also lose water through fluvial outflows. In theory then, it is possible to reconstruct precipitation minus evaporation (P-E) from the lake water volume, usually calculated from the lake level, providing groundwater

flux and any outflow component can be estimated. Fossil shorelines provide the only absolute method of reconstructing lake level, but paleolimnological indicators can at least show relative changes in P-E. An indirect measure of P-E is offered by salinity changes, since, as the volume contracts in a closed basin, the salt concentration should increase, assuming other variables are constant. This relationship is complicated by several factors, including changes in brine evolution since different salts precipitate at different stages of concentration, (see Cohen, 2003), and hysteresis as salt precipitates are redissolved during lake water dilution.

Diatoms, unicellular algae with silica shells (frustules), are one of the most ubiquitous autochthonous components preserved in lake sediments and have a great number of uses in paleolimnology (Stoermer and Smol, 1999). Diatoms are sensitive to changes in pH, nutrient levels, and salinity. The latter variable is especially useful in paleolimnological studies of climate change from closed basin lakes where salinity can approximate P-E providing local hydrological factors are understood. In the salt lakes of East Africa, diatoms have revealed long records of salinity change linked to climate fluctuations. One of the best comes from Lake Abhé, a closed basin lake in the Afar depression of Djibouti, where changes in the diatom community are indicative of monsoon strength and orbital forcing of palaeoclimate during the past 70,000 years (see Gasse et al., 1997). The interpretation of climate from diatom records is indirect and has to consider a range of taphonomic and diagenetic changes (Gasse et al., 1997). Similar data can be obtained using ostracods, millimeter-sized animals with carbonate shells or carapaces. Ostracods are often abundant in carbonate-rich lakes where statistical inference models can, as for diatoms, be used to predict past salinities from their assemblage composition (Holmes, 2001). Often, ostracods are found in sediments devoid of diatoms and vice versa. Ostracods also provide an alternative geochemical approach to salinity reconstruction, from the ratio of Ca/Sr and Mg/Sr in their carapaces.

Further insights into P-E can be obtained using oxygen isotopes. In closed basin lakes, oxygen isotope analysis, the ratio between ^{18}O and ^{16}O levels ($\delta^{18}\text{O}$), can be used to infer shifts in P-E (Cohen, 2003). In its simplest form, the lighter oxygen is preferentially evaporated under relatively dry climates, leaving waters enriched in the heavier isotope. Source area, water temperature, and precipitation amount all influence the $\delta^{18}\text{O}$ of lake waters, and a modeling approach is required to get quantitative climate estimates (Gat, 1995). The isotope ratios are derived from authigenic carbonates and the shells of organisms such as molluscs and ostracods. Until recently, this method was not applicable to the large number of lakes where carbonate was absent, but it is now possible to get reliable measurements from silica such as diatoms, and plant cellulose (see discussion in Cohen, 2003). More development work is necessary to establish fractionation processes and sources of error in oxygen isotope analysis from non-carbonate hosts but results do appear promising.

Distinguishing between the major climate variables of precipitation and temperature using paleolimnological indicators is difficult but can be achievable in some situations. Pollen analysis is one of the best known methods of environmental reconstruction, including quantitative estimates of climate variables, and it is usually abundant in anaerobic lake sediments (Bennett and Willis, 2001). In some cases it is possible to calibrate pollen records to reconstruct former precipitation and temperature values using transfer functions (Bonnefille et al., 1990). It is not always possible to confidently identify the contribution of

each of these variables, or to exclude the influence of edaphic conditions, ecological competition, and human agency on vegetation. Another widely used method of temperature reconstruction comes from chironomids (midges). These are extremely good indicators of temperatures, at least in high latitude regions. Fossil chironomid larvae in lake sediments can be used to reconstruct paleotemperatures providing temperature is the dominant variable in the region being investigated (Brooks and Birks, 2001). The greater abundance and ubiquity of chironomid remains in lake sediments gives them an advantage over coleoptera, although beetle remains have also yielded excellent temperature reconstruction.

Changing nutrient cycles in lakes can be reconstructed by paleolimnologists to better understand ecosystem changes and also to give insights into climate processes. Carbon isotope analysis ($^{13}\text{C}/^{12}\text{C}$, usually $\delta^{13}\text{C}_{\text{PDB}}$) of bulk lake sediments measures changes in lake productivity and shifts in the source of organic materials to the lakes. On Mt. Kenya, Street-Perrott et al. (1997), demonstrated how more positive $\delta^{13}\text{C}$ values occurred in the bulk organic matter of glacial age sediments because of materials derived from C_4 plants. Plants using the C_4 and CAM photosynthetic pathway are adapted to moisture and CO_2 stress, as would occur under relatively arid climates with low $p\text{CO}_2$. Conversely, in Holocene sediments, the $\delta^{13}\text{C}$ values became more negative as plants using the C_3 pathway increased, replacing the C_4 species; thereby indicating greater moisture and CO_2 availability. The analysis has been taken further by measuring compound specific isotope ratios, enabling the distinction of materials originating from algae, aquatic macrophytes, and terrestrial plants (Cohen, 2003). At the glacial-interglacial scale, paleolimnological research has shown that changes in the biogeochemical cycling of carbon is coupled with major climate shifts.

The cycling of nitrogen within lakes is also of interest to paleolimnologists given the importance of this element to aquatic productivity, where along with phosphorus it is often a limiting nutrient. Analysis of the ^{15}N to ^{14}N ratio ($\delta^{15}\text{N}_{\text{AIR}}$) helps determine the origin of organic materials (i.e., algae or higher plants), N-fixation and limitation, NH_3 volatilisation under high pH, flushing rates of soil N, dissolved inorganic N abundance, and the stratification regime (Talbot, 2001). Nitrogen isotopes have been successfully used by paleolimnologists, with one of the best examples being from Lake Bosumtwi, Ghana. Here a multidisciplinary study of bulk organic properties, $\delta^{13}\text{C}$ and $\delta^{15}\text{N}$ has shown limnological changes linked to regional climatic variability (Cohen, 2003).

Biological and geochemical indicators are most common in paleolimnological studies of climate change. Physical parameters can also be used as a proxy of catchment changes that may be indirectly linked to climate. Probably the most useful methods in this respect are a cluster of related magnetic techniques that can discriminate between particular minerals that are indicative of provenance. Some of these minerals are derived from topsoil, others from subsoil, and some from weathering of bedrock. It is possible to identify the nature and rate of the material being eroded and also the area supplying the major sources of sediment in catchments of mixed geology. These data are useful in a range of environmental management applications as well as for sediment tracing experiments (Maher and Thompson, 1999).

Conclusions and perspective

Paleolimnology has provided limnologists with time series data beyond the scope of ecological studies, and has answered questions about lake ontogeny and ecosystem response to climate that

would not have otherwise been possible. Furthermore, some of the longest, highest resolution sequences of environmental change are from the sediments of lakes. Paleolimnological investigations of climate change have been conducted worldwide, but a particular contribution has been made in low latitude regions where other hosts of paleoclimate data are either limited or have proven difficult to exploit.

Over the last decade, the number of publications in paleolimnology has risen enormously (i.e., in the *Journal of Paleolimnology*). Recent developments include high resolution automated techniques, greater accuracy, and more focused scientific questions. There is also a trend toward analysis of specific sedimentary components (e.g., biomarkers) rather than bulk samples, thereby achieving greater precision in reconstructions. Numerical modeling has further improved the importance and application of paleolimnology to climate change.

Philip Barker

Bibliography

- Bennett, K.D., and Willis, K.J., 2001. Pollen. In Smol, J.P., Birks, H.J.B., and Last, W.M. (eds.), *Tracking Environmental Change Using Lake Sediments. Terrestrial, Algal and Siliceous Indicators*. Developments in Paleoenvironmental Research. Dordrecht, The Netherlands: Kluwer, pp. 5–32.
- Bonnefille, R., Roeland, J.C., and Guiot, J., 1990. Temperature and rainfall estimates for the past ca.40,000 years in equatorial Africa. *Nature*, **346**, 347–349.
- Brooks, S.J., and Birks, H.J.B., 2001. Chironomid-inferred air temperatures from Lateglacial and Holocene sites in north-west Europe: Progress and problems. *Quat. Sci. Rev.*, **20**, 1723–1741.
- Cohen, A.S., 2003. *Paleolimnology. The History and Evolution of Lake Systems*. New York: Oxford University Press, p. 500.
- Dean, W., Anderson, R., Bradbury, J.P., and Anderson, D., 2002. A 1500-year record of climatic and environmental change in Elk Lake, Minnesota. I. Varve thickness and gray-scale density. *J. Paleolimnol.*, **27**, 287–299.
- Gasse, F., Barker, P., Gell, P.A., Fritz, S.C., and Chalié, F., 1997. Diatom-inferred salinity in palaeolakes: An indirect tracer of climatic change. *Quaternary Sci. Rev.*, **16**, 547–563.
- Gat, J.R., 1995. Stable isotopes of fresh and saline lakes. In Lerman, L., Imboden, D.M., and Gat, J.R. (eds.), *Physics and Chemistry of Lakes*. Berlin: Springer, p. 334.
- Holmes, J.A., 2001. Ostracoda. In Smol, J.P., Birks, H.J.B., and Last, W.M. (eds.), *Tracking Environmental Change Using Lake Sediments. Zoological Indicators*, vol 4. Dordrecht, The Netherlands: Kluwer, pp. 125–151.
- Lamoureux, S., 2001. Varve chronology techniques. In Last, W.M., and Smol, J.P. (eds.), *Tracking Environmental Change Using Lake Sediments. Basin Analysis, Coring, and Chronological Techniques*. Developments in Paleoenvironmental Research. Dordrecht, The Netherlands: Kluwer, pp. 247–260.
- Lotter, A.F., 1998. The recent eutrophication of Baldeggersee (Switzerland) as assessed by fossil diatom assemblages. *Holocene*, **8**, 395–405.
- Maher, B.A., and Thompson, R., 1999. *Quaternary Climates, Environments and Magnetism*. Cambridge: Cambridge University Press, p. 328.
- Smol, J.P., 2002. *Pollution of Lakes and Rivers. A Paleoenvironmental Perspective*. London: Arnold, p. 280.
- Stoermer, E.F., and Smol, J.P., 1999. *The Diatoms: Applications for the Environmental and Earth Sciences*. Cambridge: Cambridge University Press, p. 469.
- Street-Perrott, F.A., Huang, Y., Perrott, R.A., Eglinton, G., Barker, P., Ben Khelifa, L., Harkness, D.A., and Olago, D. 1997. Impact of lower atmospheric CO_2 on tropical mountain ecosystems: Carbon-isotope evidence. *Science*, **278**, 1422–1426.
- Talbot, M.R., 2001. Nitrogen isotopes in palaeolimnology. In Last, W.M., and Smol, J.P. (eds.), *Tracking Environmental Change Using Lake Sediments. Physical and Geochemical methods*. Dordrecht, The Netherlands: Kluwer, Developments in Paleoenvironmental Research. pp. 401–439.

Turney, C.S.M., and Lowe, J.J., 2001. Tephrochronology. In Last, W.M., and Smol, J.P. (eds), *Tracking Environmental Change Using Lake Sediments. Basin Analysis, Coring, and Chronological Techniques*. Developments in Paleoenvironmental Research. Dordrecht, The Netherlands: Kluwer, pp. 451–471.

Cross-references

Beetles as Quaternary and Late Tertiary Climate Indicators
Carbon Isotopes, Stable
Dating, Magnetostratigraphy
Dating, Radiometric Methods
Diatoms
Glacial Megalakes
Lacustrine Sediments
Lake Level Fluctuations
Nitrogen Isotopes
Ostracodes
Oxygen Isotopes
Palynology
Pollen Analysis
Radiocarbon Dating
Tephrochronology
Uranium-Series Dating
Varved Sediments

PALEO-OCEAN pH

Before discussing past variations in the pH of the oceans, it is first necessary to understand what controls the present distribution of pH in seawater. Along with alkalinity, total dissolved inorganic carbon (Σ_{DIC}) and the partial pressure of carbon dioxide ($p\text{CO}_2$), pH is one of the four key variables of the seawater dissolved carbonate system. If any two of these four variables are specified, then the values of the other two are fixed. For those areas of the modern oceans that are in equilibrium with the CO_2 content of the atmosphere, their pH is set at a value of ~ 8.2 (depending on the temperature of the surface ocean). An increase in atmospheric CO_2 (for a given value of alkalinity or Σ_{DIC}) will result in a decrease in the pH of surface waters. For example, increasing atmospheric $p\text{CO}_2$ from the pre-industrial value of 280 ppmv (parts per million by volume) to its present day value of ~ 370 ppmv would result in a decrease in pH from 8.18 to 8.08. Similarly, the rise in atmospheric CO_2 values from ~ 180 ppmv at the height of the last glacial interval to 280 ppmv would have resulted in a decrease in pH from 8.32 to 8.18.

Higher pH values are also seen in areas of the modern oceans where there is significant uptake of dissolved CO_2 by biological activity and downwelling of the surface waters before equilibrium with the atmosphere can be re-established. In the modern oceans, this process is mainly operating in the North Atlantic Ocean and in the southern oceans around Antarctica, and results in these areas acting as sinks for atmospheric CO_2 . Deeper waters have higher CO_2 concentrations and lower pH than surface waters (see below). Hence, areas of the oceans where there are strong upwelling currents (mainly the eastern equatorial Pacific and the Arabian Sea) have much lower pH values than would otherwise be expected. These areas of the oceans act as the Earth's largest natural source of CO_2 to the atmosphere.

The pH of the oceans also varies with depth. In the surface oceans, phytoplankton incorporate dissolved CO_2 to form

organic carbon and, in the case of coccoliths, they also form calcium carbonate shells. The former process acts to increase the pH of the surface water, while the latter acts to decrease it. In either case, the pH of the surface waters generally remains buffered at a constant value by exchange of CO_2 with the atmosphere. Once the phytoplankton and other organisms die, their remains sink through the water column. The organic matter is rapidly oxidized to CO_2 by microbiological activity, such that the pH of seawater decreases below the mixed layer, to reach a minimum value of between ~ 7.6 and 7.8 at depths of ~ 200 – 600 m. The precise depth and magnitude of the pH minimum depend on the rate of supply of organic matter from the surface (essentially a function of primary productivity) and the physical oceanography of the water column. At even greater depths, first aragonite shells and then calcite shells start to undergo dissolution, resulting in an increase in pH, such that the deepest waters of the ocean have similar pH to surface waters. The net result of all these processes is a water column pH profile similar to that shown in Figure P25.

It is apparent, therefore, that if we were able to generate a record of past variations in the pH of the oceans, we could glean much information about processes such as the history of atmospheric CO_2 , the spatial distribution of oceanic CO_2 sinks and sources, and the spatial and temporal history of oceanic primary production. Recent developments in boron isotope geochemistry have provided us with the first opportunity to address these problems.

In seawater, boron is a conservative element with an oceanic residence time of ~ 20 million years. Although the boron/salinity ratio is constant throughout the oceans, dissolved boron can exist as $\text{B}(\text{OH})_3$ or $\text{B}(\text{OH})_4^-$, with the former species being dominant at lower pH and vice versa. The boron isotope composition of seawater is also constant throughout the oceans at a $\delta^{11}\text{B}$ value of $+40\%$. However, the boron isotope systematics are such that the light isotope, ^{10}B , is preferentially partitioned into $\text{B}(\text{OH})_4^-$. The magnitude of this isotope fractionation is temperature dependent, but is of the order of 20% at 20°C . The relative proportions of $\text{B}(\text{OH})_3$ and $\text{B}(\text{OH})_4^-$ are pH dependent, but the boron isotope fractionation between them is constant, so the absolute $\delta^{11}\text{B}$ value of both species is also pH dependent (Figure P26).

Empirical studies and culture experiments have shown that when foraminifera form their calcite shells they incorporate

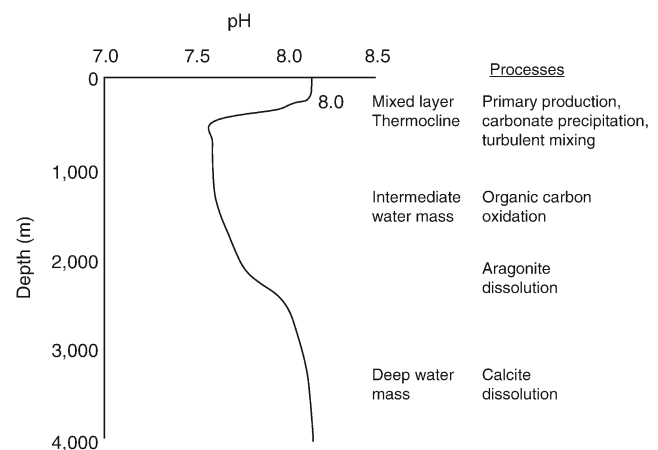


Figure P25 Schematic pH-depth profile in the ocean.

~10 ppm boron. This boron is exclusively derived from the dissolved $B(OH)_4^-$ in seawater and it is incorporated without significant fractionation of the $\delta^{11}B$ value of this species (Sanyal et al., 1996). Hence, measurements of the $\delta^{11}B$ of foraminiferal calcite can be used to reconstruct the pH of the waters from which they precipitated their shells. As with measurements of any other paleo-oceanographic proxy, care must be taken to ensure that the shells have not been altered (e.g., recrystallized or partially dissolved) since they were first

formed, and the foraminiferal calcite must be cleansed of any potential contaminant phases (such as clays and coccoliths) before it is analyzed. In addition, the analytical methods required for determining the $\delta^{11}B$ value of the small quantities of boron present (~1 ng) in the typical sample sizes available (20–50 shells) are not simple and much effort is required to obtain reliable data. Nevertheless, important results have emerged from this technique.

The utility of this approach in reconstructing the past pH of the oceans was provided by a study of the boron isotope composition of well-preserved foraminifera from sediments recovered from the Ontong-Java Plateau in the western equatorial Pacific by the Ocean Drilling Project (ODP) (Palmer et al., 1998). Samples of sediment deposited at five different times from 85 thousand years ago (ka) to 15.7 million years ago (Ma) were hand picked to separate individual species of foraminifera. This is important as different species of foraminifera precipitate their shells at different depths within the water column. For example, *Globigerinoides sacculifer* precipitates its shell within the mixed layer of the surface ocean that is in approximate equilibrium with atmospheric CO_2 , whereas *Globorotalia crassaformis* calcifies its test at depths of 200–400 m. Foraminifera from deeper waters would be expected to record $\delta^{11}B$ values indicating that they precipitated their shells in lower pH water than those that lived near the surface. Indeed, Figure P27 demonstrates that in the five time slices considered the foraminifera recorded pH values that yielded similar pH-depth profiles to that observed in the modern ocean at this site.

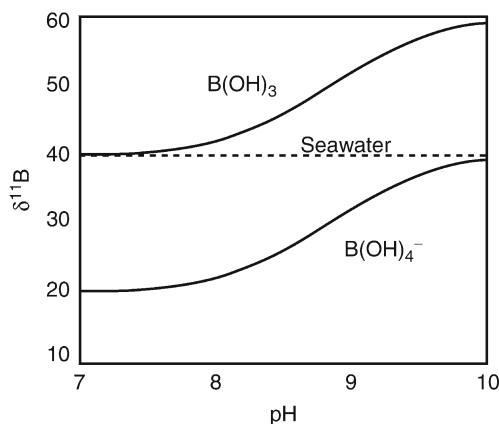


Figure P26 Boron isotope composition of dissolved boron species in seawater.

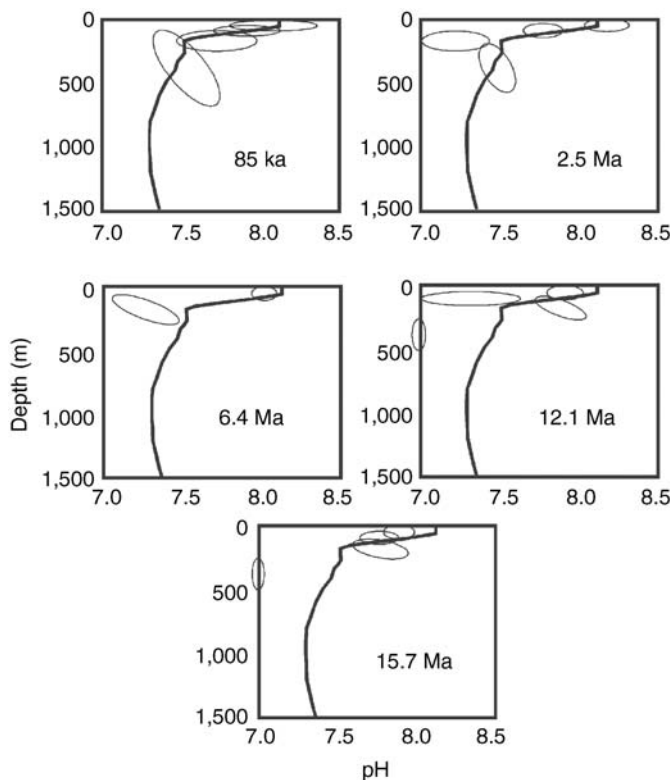


Figure P27 pH depth profiles for various time slices in the Neogene (ellipses define pH values calculated from the $\delta^{11}B$ of foraminifera; solid lines are present day pH-depth curve).

This technique of reconstructing pH-depth profiles was applied to foraminifera from the middle Eocene (~43 Ma) (Pearson and Palmer, 1999). At that time, the global climate was considerably warmer than today, such that polar ice caps were either absent entirely, or very much smaller than those of today. The warmer climate of the Eocene has been variously ascribed to higher atmospheric CO₂ levels or different ocean circulation patterns that resulted from the position of the continents at that time. Although boron has a very long oceanic residence time, which means that its isotopic composition will not change over periods of thousands of years, it is likely that there will have been changes in the $\delta^{11}\text{B}$ value of seawater over millions of years. Hence, any changes that are observed in the $\delta^{11}\text{B}$ of ancient foraminiferal calcite could arise from changes in the boron isotope ratio of seawater as well as changes in the pH of the seawater. Fortunately, this problem can be addressed by analyzing the $\delta^{11}\text{B}$ of foraminifera that precipitated their shells at different depths. As noted above, the decrease in pH from surface to intermediate depth waters is a result of the oxidation of organic carbon. This process utilizes dissolved oxygen in the water column and thus provides two constraints on the minimum pH that can be calculated for deeper waters. Firstly, the pH cannot have been so low as to inhibit

the calcification of the deepest dwelling foraminifera. Second, the change in pH from surface to deep waters cannot have been so great as to completely deplete the seawater of dissolved oxygen, as foraminifera cannot live in anoxic waters. Using these constraints Pearson and Palmer (1999) were able to calculate that the $\delta^{11}\text{B}$ of mid-Eocene waters lay between +41 and +38 (best estimate of +39.4) and that the pH of surface waters was between 7.91 and 8.33, with a best estimate of 8.05. This in turn implied that the CO₂ of the atmosphere at that time was similar to that of today or only slightly higher.

By using the boron isotope composition of surface dwelling foraminifera from the past 60 million years, Pearson and Palmer (2000) were able to provide a record of surface water pH over this time period (Figure P28a). This study showed that surface water pH values were roughly similar to present day values over the past 20 Ma, but that they were considerably lower during the late Paleocene thermal maximum (LPTM) and for much of the Eocene. By making certain assumptions concerning the past alkalinity of the oceans, it was also possible to reconstruct a record of atmospheric CO₂ levels since this time (Figure P28b). As might be expected, the uncertainties in the calculated pH and CO₂ values become greater further back in time. This uncertainty arises from some of the assumptions that have to be made concerning the past $\delta^{11}\text{B}$ -pH and alkalinity of the oceans, but the increased uncertainties in pH and CO₂ also arises from the fact that the $\delta^{11}\text{B}$ relationship illustrated in Figure P26 is not linear. Hence, at low pH values the same analytical error in measured $\delta^{11}\text{B}$ as was observed at higher pH results in a larger error in the calculated pH and

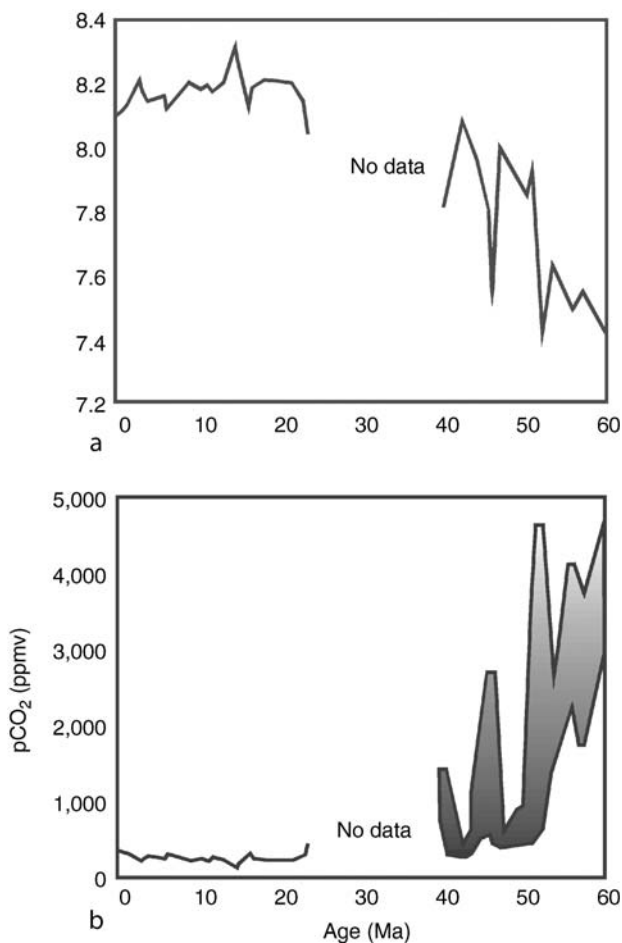


Figure P28 (a) Sea surface pH for the past 60 Ma; (b) Atmospheric CO₂ for the past 60 Ma.

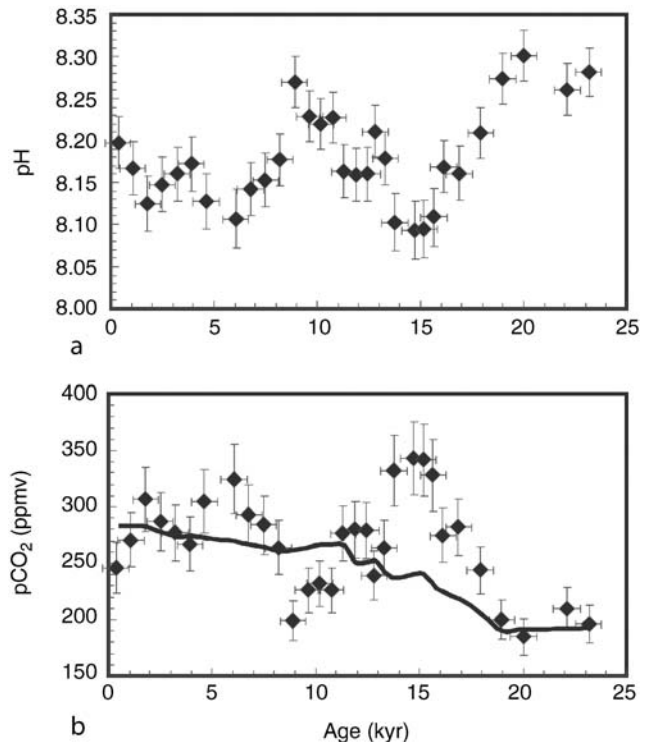


Figure P29 (a) pH of surface waters from the western equatorial Pacific Ocean; (b) pCO₂ of surface waters from the western equatorial Pacific Ocean – solid line gives contemporaneous atmospheric CO₂ levels.

CO₂ values. Despite these uncertainties, this study lends support to the theory that the very warm climate of the LPTM was due to high atmospheric CO₂ levels that also resulted in low surface water pH values.

More recently, Palmer and Pearson (2003) measured the $\delta^{11}\text{B}$ values of *G. sacculifer* to determine the change in pH and CO₂ of surface waters from the western equatorial Pacific (Figure P29a). By comparison with the record of atmospheric CO₂ preserved in ice cores, they were able to show that surface waters from this area were in equilibrium with the atmosphere during most of the Holocene and at the height of the last glaciation, but that they had much higher pCO₂ values during the transition from glacial to interglacial periods (Figure P29b). This study suggests that increased upwelling in the eastern equatorial Pacific may have played an important role in the increase in atmospheric CO₂ levels from glacial to interglacial times.

Although still very much in its infancy, it is apparent that the reconstruction of the paleo-pH of the oceans is a powerful tool with which to investigate some of the fundamental processes that have controlled the Earth's climate. With improvements in analytical techniques, it can be anticipated that we will be able to reconstruct increasingly detailed records of the spatial and temporal variation of seawater pH in the ancient oceans.

Martin R. Palmer

Bibliography

- Palmer, M.R., and Pearson, P.N., 2003. A 23,000 year record of surface water pH and pCO₂ in the western equatorial Pacific. *Science*, **300** (5618), 480–482.
- Palmer, M.R., Pearson, P.N., and Cobb, S.J., 1998. Reconstructing past ocean pH-depth profiles. *Science*, **282**, 1468–1471.
- Pearson, P.N., and Palmer, M.R., 1999. Middle Eocene seawater pH and atmospheric carbon dioxide concentrations. *Science*, **284**, 1824–1826.
- Pearson, P.N., and Palmer, M.R., 2000. Atmospheric carbon dioxide concentrations over the past 60 million years. *Nature*, **406**, 695–699.
- Sanyal, A., Hemming, N.G., Broecker, W.S., Lea, D.W., Spero, H.J., and Hanson, G.N., 1996. Oceanic pH control on the boron isotope composition of foraminifera: Evidence from culture experiments. *Palaeogeography*, **11**, 513–517.

Cross-references

Atmospheric Evolution, Earth
 Carbon Dioxide and Methane, Quaternary Variations
 Carbon Dioxide, Dissolved (Ocean)
 Carbon Isotope Variations Over Geologic Time
 Foraminifera
 Marine Carbon Geochemistry
 Paleocene-Eocene Thermal Maximum
 Paleogene Climates
 Quaternary Climate Transitions and Cycles
 Stable Isotope Analysis

PALEO-PRECIPIATION INDICATORS

Introduction

Precipitation is one of the most important elements of the climate and the variability of precipitation affects much of life on Earth. Instrumental records of precipitation (and related measurements such as riverine discharge, lake-level change, outgoing longwave radiation, and others) exist for many parts of

the Earth, but rarely exceed one century in duration. In order to extend knowledge of precipitation variability further back in time, the use of paleo-precipitation indicators, also known as “proxies,” is required. There are no perfect proxies for past precipitation amount and Mann (2002) has argued persuasively that accurate paleoclimatic reconstructions are best achieved through application of multi-proxy approaches.

Natural archives of paleo-precipitation

The most important paleoclimatic archives are historical documentary records, lacustrine and marine sediments, mountain and continental glacial ice, tree rings, reef corals, speleothems (cave deposits), and loess (e.g., Bradley, 1999). Each archive has its own characteristic rate of formation and fidelity of preservation; both factors constrain the ultimate temporal resolution of sampling. For example, snow may accumulate on a mountaintop at a rate of centimeters to meters each year (a potential record of precipitation amount on a sub-annual timescale), but some of this snow may be subsequently lost by sublimation, melting, or wind erosion. The snow that remains is eventually buried, compacted, and recrystallized to ice; a portion of it may flow laterally under the force of gravity. All of these processes, which collectively may be called “diagenesis” (changes happening to materials after their initial formation), introduce complications for the interpretation of proxy measurements from glacial ice cores (for a thorough, but non-technical account of all aspects of ice cores see Alley, 2002). Similar diagenetic alteration may also impact proxy measurements made on sediments, corals, and speleothems.

Lacustrine indicators of paleo-precipitation

Lakes, especially lakes with no outlets, may effectively behave as very large rain gauges. Precipitation (plus runoff into the lake, minus any outflow from the lake) is recorded as changes in lake level, changes that are also dependent upon temperature-controlled evaporation, although several other climatic elements (e.g., humidity and wind speed) also influence evaporation rates. There are many published studies that attempt to quantitatively reconstruct precipitation history from a history of lake level (e.g., Blodgett et al., 1997; Cross et al., 2001). Lacustrine sediments contain many components that are useful in reconstructing lake level or related variables such as salinity. Pollen grains and spores commonly accumulate in lakes and wetlands. The analysis of pollen in sediments, the field of palynology, enables a regional reconstruction of the vegetation cover in the watershed of the lake (or beyond). Plant growth is dependent on precipitation as well as other variables such as temperature, light, and nutrients (atmospheric carbon dioxide). Because each may vary independently, multivariate statistical analysis is an important methodology that can sometimes permit the deduction of past precipitation. As a simple example, the ratio of non-arboreal pollen to arboreal pollen is sometimes utilized as a qualitative indicator of aridity (e.g., Maley, 1996). Diatoms are unicellular algae that inhabit rivers, lakes, and the ocean. Some diatom taxa are planktonic and some are benthic (shallow water). The ratio of benthic-to-planktonic diatoms in a sediment sample is often used as a qualitative measure of lake level (e.g., Gasse et al., 1997). Some diatom taxa are restricted to specific ranges of salinity, hence can also be useful indicators of lacustrine water balance (precipitation minus evaporation). The mineralogy, trace element composition, and especially the stable oxygen isotopic composition of calcium carbonate components of lacustrine sediments can all be useful measures of water balance. Most often, the carbonate components used in such studies are the shells of organisms such as ostracodes, gastropods, or

bivalves (e.g., Schwab, 2003). Less ideally, the isotopic analysis can be performed on the bulk carbonate fraction that may consist of shell fragments, carbonate precipitated by macrophytes or microorganisms, or apparently abiogenic carbonate precipitates. When calcium carbonate is absent, stable oxygen isotopic analysis of siliceous microfossils, such as diatoms, is also possible (e.g., Hu and Shemesh, 2003). Stable oxygen or hydrogen isotopic studies are increasingly being performed on specific organic compounds found in lacustrine sediments, such as cellulose, *n*-alkanes, or palmitic acid (Huang et al., 2004). The stable isotopic composition of all of these compounds is dependent not only upon the precipitation amount, but also upon the isotopic composition of the lake water (and in some cases the temperature of formation of the compound). This, in turn, is determined by the isotopic composition of the source precipitation and inflow as well as the amount of evaporative concentration of lake water. In many cases, variation of the isotopic composition of the source water (precipitation and inflow) is the dominant source of variation. The lack of knowledge of the temporal variability of the isotopic composition of precipitation and inflow is a common limit to quantitative application of this method, although in exceptional cases the isotopic composition of source precipitation may be known (e.g., Seltzer et al., 2000).

Marine sedimentary indicators of paleo-precipitation

Most open-marine (pelagic) sediments contain few indicators of paleo-precipitation. However, in marginal marine environments, sediments derived from adjacent land masses can be useful indicators of terrestrial runoff (precipitation minus evaporation). For example, color reflectance (Peterson et al., 2000) and Ti/Al ratios (Haug et al., 2001) of marine sediments from the Cariaco Basin just offshore of Venezuela were used to deduce the runoff from the adjacent continent. These studies demonstrated that northern South America was relatively dry during the Little Ice Age, the Younger Dryas, and the Last Glacial Maximum. DeMenocal et al. (2000) concluded that a rapid increase of wind-blown lacustrine diatoms and other terrestrial sediments in marine sediments off the coast of northwest Africa indicated an abrupt drying in the Sahara Desert at about 4,000 yBP. Pollen grains can also be transported by wind or runoff and deposited in marine sediments where they can provide important information about past precipitation amounts on the adjacent continent. In the marine sediments of the Amazon fan, analyses of pollen (Haberle and Maslin, 1999), iron-oxide minerals (Harris and Mix, 1999), oxygen isotopes in marine calcareous organisms (Maslin and Burns, 2000), and organic biomarkers of rain forest vegetation (Kastner and Goni, 2003) have all been related to past precipitation amount in the adjacent Amazon basin.

Ice cores as recorders of snow accumulation

Ice cores record many aspects of past climates. It is usually possible to detect annual layers in the upper portions of ice cores. These annual layers are due to summer melting and re-freezing (in high latitude ice cores) or to dry-season dust accumulation (in low-latitude ice cores). The annual precipitation amount can be calculated (as water equivalent) from the thickness of the annual layer and the snow/ice density. Unfortunately, wind erosion, melting, sublimation, and lateral flow are often significant and such direct deduction of past precipitation amount is limited to the upper portion of ice cores. In tropical ice cores, it is possible to reconstruct paleo-precipitation from the oxygen (or hydrogen) stable isotopic composition of the ice (Hoffmann et al., 2003). This

method of reconstruction (although not universally accepted) relies upon the observation that there is a significant correlation between precipitation amount and $\delta^{18}\text{O}$ (or δD) of the precipitation (e.g., Rozanski et al., 1993) in tropical latitudes and that this relationship has held through time.

Glacial mass balance (accumulation minus ablation), like the water balance of lakes, is dependent upon precipitation amount (as well as temperature). Reconstructions of snowline elevation in arid mountain regions can provide useful estimates of past levels of precipitation (Kull and Grosjean, 2000).

Speleothems as recorders of paleo-precipitation

Speleothems are calcium carbonate deposits, including stalagmites and stalactites, that are deposited from carbon dioxide dissolved in groundwater that seeps into caves. These deposits are increasingly being used for high-resolution reconstruction of precipitation. Rates of growth of the cave deposits may be related to precipitation amount, with more rapid deposition of calcium carbonate occurring in wetter periods. In rare cases, cave deposits may form annual layers, whose thickness can be related to annual precipitation amount. Oxygen isotopic composition of the speleothem calcite is determined by its temperature of formation and the isotopic composition of groundwater. If mean annual temperature changes are relatively small through time, then changes in $\delta^{18}\text{O}$ of the calcite are largely controlled by changes in the isotopic composition of groundwater, which is most often nearly the same as the isotopic composition of regional precipitation. As mentioned previously, in the tropics, $\delta^{18}\text{O}$ of rainwater is correlated with precipitation amount, thus, within accepted bounds, the isotopic composition of tropical cave deposits is a reliable indicator of past precipitation (e.g., Fleitmann et al., 2003). Because cave deposits can be precisely dated by the U/Th method, this method of precipitation reconstruction is of great utility for the past few hundred thousand years. Furthermore, if the hydrogen isotopic composition of fluid inclusions in the cave deposit is measured along with the oxygen isotopic composition of the host calcite, paleotemperatures can be directly calculated (e.g., Schwarcz and Yonge, 1983).

Other recorders of paleo-precipitation

Many other proxies have been used as recorders of paleo-precipitation. In semi-arid environments, tree growth is particularly dependent upon water availability and annual extension (tree-ring width) may be a reliable indicator of past precipitation amount (e.g., Villalba et al., 1998). The magnetic susceptibility of loess sequences in China has been utilized as a paleo-precipitation indicator (Maher and Thompson, 1995). The oxygen isotopic composition of the calcium carbonate precipitated by reef-building corals is controlled by both temperature and isotopic composition of surface seawater, itself partly dependent on precipitation amount, thus if temperature can be independently determined (for example, using the strontium/calcium ratio of the coral aragonite), then it may be possible to reconstruct paleo-precipitation (McCulloch et al., 1994).

Paul A. Baker

Bibliography

Alley, R.B., 2002. *The Two-Mile Time Machine: Ice Cores, Abrupt Climate Change, and Our Future*. Princeton, NJ: Princeton University Press, 229pp.

- Blodgett, T.A., Lenters, J.D., and Isacks, B.L., 1997. Constraints on the origin of paleolake expansions in the central Andes. *Earth Interactions*, **1**, 1–28.
- Bradley, R.S., 1999. *Paleoclimatology*. San Diego, CA: Academic Press, 613pp.
- Cross, S.L., Baker, P.A., Seltzer, G.O., Fritz, S.C., Dunbar, R.B., 2001. Late Quaternary climate and hydrology of tropical South America inferred from an isotopic and chemical model of Lake Titicaca, Bolivia and Peru. *Quaternary Res.*, **56**, 1–9.
- DeMenocal, P., Ortiz, J., Guilderson, T., Sarnthein, M., 2000. Coherent high- and low-latitude climate variability during the Holocene warm period. *Science*, **288**, 2198–2202.
- Fleitmann, D., Burns, S., Mudelsee, M., Neff, U., Kramers, J., Mangini, A., and Matter, A., 2003. Holocene forcing of the Indian monsoon recorded in a stalagmite from Southern Oman. *Science*, **300**, 1737–1739.
- Gasse, F., Barker, P., Gell, P.A., Fritz, S.C., Chalie, F., 1997. Diatom-inferred salinity in palaeolakes: An indirect tracer of climate change. *Quaternary Sci. Rev.*, **16**, 547–563.
- Haberle, S., and Maslin, M., 1999. Late Quaternary vegetation and climate changes in the Amazon basin based on a 50,000 year pollen record from the Amazon Fan ODP Site 932. *Quaternary Res.*, **51**, 27–38.
- Harris, S.E., Mix, A.C., 1999. Pleistocene precipitation balance in the Amazon Basin recorded in deep sea sediments. *Quaternary Res.*, **51**, 14–26.
- Haug, G., Hughen, K., Sigman, D., Peterson, L., Rohl, U., 2001. Southward migration of the Intertropical Convergence Zone through the Holocene. *Science*, **293**, 1304–1308.
- Hoffmann, G., et al., 2003. Coherent isotope history of Andean ice cores over the last century. *Geophys. Res. Lett.*, **30**, 10.1029/2002GL014870.
- Hu, F.S., and Shemesh, A., 2003. A biogenic-silica delta O-18 record of climatic change during the last glacial-interglacial transition in southwestern Alaska. *Quaternary Res.*, **59**, 379–385.
- Huang, Y., Shuman, B., Wang, Y., and Webb, III, T., 2004. Hydrogen isotope ratios of individual lipids in lake sediments as novel tracers of climatic and environmental change: A surface sediment test. *J. Paleolimnol.*, **31**, 363–375.
- Kastner, T.P., and Goñi, M.A., 2003. Constancy in the vegetation of the Amazon Basin during the Late Pleistocene: Evidence from the organic matter composition of Amazon Deep Sea Fan sediments. *Geology*, **31**, 291–294.
- Kull, C., and Grosjean, M., 2000. Late Pleistocene climate conditions in the north Chilean Andes drawn from a climate-glacier model. *J. Glaciol.*, **46**, 622–632.
- Maher, B.A., and Thompson, R., 1995. Paleorainfall reconstructions from pedogenic magnetic susceptibility variations in Chinese loess. *Quaternary Res.*, **44**, 383–391.
- Maley, J., 1996. The African rainforest – main characteristics of changes in vegetation and climate from the Upper Cretaceous to the Quaternary. *Proc. R. Soc. Edinb.*, **104B**, 31–73.
- Mann, M.E., 2002. The value of multiple proxies. *Science*, **297**, 1481–1482.
- Maslin, M.A., and Burns, S.J., 2000. Reconstruction of the Amazon basin effective moisture availability over the past 14,000 years. *Science*, **290**, 2285–2287.
- McCulloch, M.T., Gagan, M.K., Mortimer, G.E., Chivas, A.R., and Isdale, P.J., 1994. A high resolution Sr/Ca and $\delta^{18}\text{O}$ coral record from the Great Barrier Reef, Australia, and the 1982–83 El Niño. *Geochim. Cosmochim. Acta*, **58**, 2747–2754.
- Peterson, L., Haug, G., Hughen, K., and Rohl, U., 2000. Rapid changes in the hydrologic cycle of the tropical Atlantic during the last glacial. *Science*, **290**, 1947–1951.
- Rozanski, K., Araguas-Araguas, L., and Gonfiantini, R., 1993. Isotopic patterns in modern global precipitation. In Swart, P.K., Lohmann, K.C., MacKenzie, J., and Savin, S. (eds.), *Climate Change in Continental Isotopic Records*. Washington D.C: American Geophysical Union. AGU Monograph series, no. 78, pp. 1–37.
- Schwalb, A., 2003. Lacustrine ostracodes as stable isotope recorders of late-glacial and Holocene environmental dynamics and climate. *J. Paleolimnol.*, **29**, 265–351.
- Schwarz, H., and Yonge, C., 1983. Isotopic composition of palaeowaters as inferred from speleothem and its fluid inclusions. In anon. (ed.), *Palaeclimates and Palaeowaters; a Collection of Environmental Isotope Studies*. Vienna, Austria: International Atomic Energy Agency, pp. 115–133.
- Seltzer, G., Rodbell, D., and Burns, S., 2000. Isotopic evidence for late Quaternary climatic change in tropical South America. *Geology*, **28**, 35–38.
- Villalba, R., Grau, H.R., Boninsegna, J.A., Jacoby, G.C., and Ripalta, A., 1998. Tree-ring evidence for long-term precipitation changes in subtropical South America. *Int. J. Climatol.*, **18**, 1463–1478.

Cross-references

[Dendroclimatology](#)
[Diatoms](#)
[Ice Cores, Mountain Glaciers](#)
[Lacustrine Sediments](#)
[Lake Level Fluctuations](#)
[Loess Deposits](#)
[Ostracodes](#)
[Paleoclimate Proxies, an Introduction](#)
[Paleosols, Pre-Quaternary](#)
[Pollen Analysis](#)
[Stable Isotope Analysis](#)
[Speleothems](#)
[Uranium-Series Dating](#)

PALEOSOLS, PRE-QUATERNARY

Introduction and definitions

Paleopedology is the study of the genesis, properties, climate, and landscape records of fossil soils, or paleosols. Pre-Quaternary paleosols are buried, “fossilized” soil horizons, which are older than 2 Ma; they are also commonly lithified, i.e., converted from soil into rock by the geological processes of burial diagenesis (Retallack, 1991). Unlike the more rigid definition used by soil scientists, who consider a soil to be a body of geologic material that supports plant life, geoscientists interpret pre-Quaternary paleosols as any former subaerially exposed surfaces or layers of earth material that have been affected by physical, chemical, and biological weathering processes. However, evidence for the presence of plants is not considered a prerequisite for identification of a fossil soil (Retallack, 2001). This broader geological definition allows for greater flexibility in examining parts of Earth history during which terrestrial plants were not present.

Paleosol features

Impetus for the study of pre-Quaternary paleosols largely originated with Dr. Gregory Retallack at the University of Oregon, who has published a widely used textbook on paleopedology (Retallack, 2001). In a 1985 Geological Society of America Penrose Conference on paleosols (organized by Dr. Retallack), geoscientists, for the first time, began to think about soils of the past set in the backdrop of “deep” geologic time. Recognition and interpretation of pre-Quaternary paleosols requires the use of multidisciplinary approaches that involve integration of field morphological, microscopic, and geochemical data, as well as an appreciation for evolutionary changes in terrestrial biota and flora that have occurred over time (Mora and Driese, 1999). Field morphological features such as plant root traces (in post-Silurian paleosols), soil horizons, and soil structures (especially peds or natural soil aggregates), are very diagnostic for pre-Quaternary paleosol identification (Figure P30a; Retallack, 1988). Micromorphological (thin section) features are commonly well preserved in

paleosols and include root and soil animal traces, peds, and concentrations (or evidence for removal) of soil constituents such as clays, carbonates, Fe-Mn oxides, etc. (Figure P30b; Driese and Foreman, 1992; Mora and Driese, 1999). Geochemical patterns related to weathering and element translocation, including molecular ratios of oxides or elements (e.g., Figure P30c; Retallack, 2001), concentration ratios (molecular ratios normalized to an assumed immobile element such as Ti; Driese and Foreman, 1992), and mass balance (residual enrichment, volume change during weathering, and mass transport, normalized to an immobile element such as Ti or Zr; Driese et al., 2000), provide supporting evidence for interpretations of paleosols. Stable isotopes, especially $\delta^{13}\text{C}$ values of paleosol organic matter and pedogenic carbonate, are useful in identifying terrestrial sources of organic matter and ecosystem types (Cerling, 1991). Most plant communities during the Paleozoic and Mesozoic eras were C3 (Calvin cycle), with $\delta^{13}\text{C}$ values of soil organic matter averaging -26‰ PDB and pedogenic carbonate values ranging from -5 to -12‰ PDB (Mora et al., 1996; Mora and Driese, 1999). The $\delta^{18}\text{O}$ values

of pedogenic carbonate, if not diagenetically altered, can be used as proxies for meteoric water compositions and paleotemperatures (Cerling, 1984), but most values measured for Paleozoic pedogenic carbonates have been apparently reset during burial diagenesis (Mora and Driese, 1999).

Problems in recognition and interpretation of paleoclimates from pre-Quaternary paleosols include extensive burial diagenetic alteration (Retallack, 1991). Common diagenetic alteration processes include physical compaction and consequent modifications of original soil thickness and morphology, oxidation of soil organic matter, burial gleization (Fe loss, largely through microbial reduction), color modifications (intensification) related to dehydration and recrystallization of hydrous mineral phases (such as FeOOH), recrystallization of soil smectites to illites (or even to metamorphic mineral assemblages; Table P3), and exchange of oxygen isotopes between burial fluids and pedogenic carbonates and clays (Mora and Driese, 1999). Mack et al. (1993) proposed an alternative paleosol classification, because of burial diagenetic alteration and associated lack of preservation of

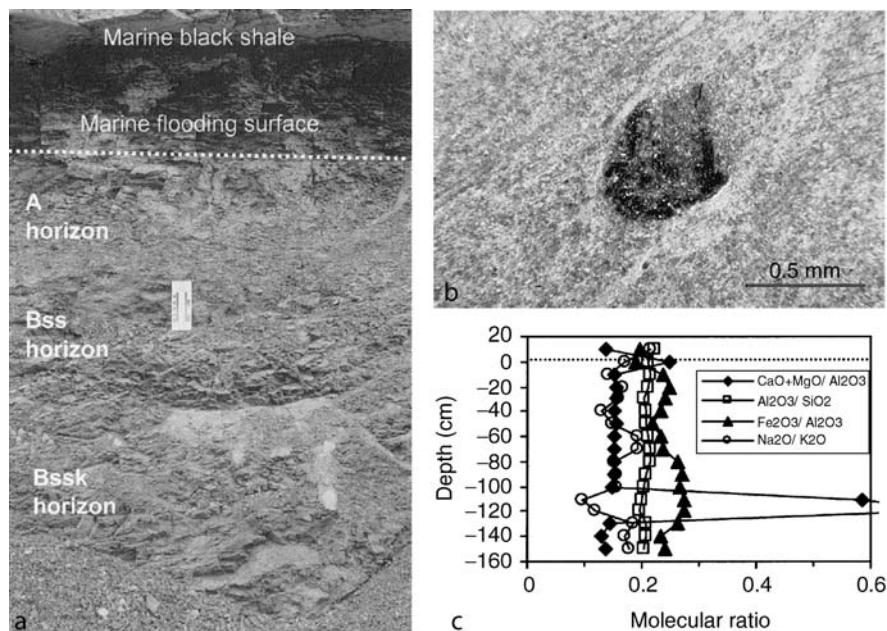


Figure P30 Pennington Formation (325 Ma, late Mississippian), Tennessee, USA paleosol. (a) Field photograph: A (surface), Bss (slickensided B) and Bks (slickensided B with pedogenic carbonate) refer to paleosol horizons. Note angular blocky ped structure in outcrop (scale card is 15 cm long). (b) Thin-section photomicrograph of paleosol shown in (a), which exhibits oriented bright clay microfabric related to seasonal cycles of wetting and drying and associated clay shrinking and swelling, as well as dark-colored Fe-Mn oxide nodule (cross-polarized light). (c) Molecular ratios for paleosol profile depicted in (a), including calcification ($\text{CaO} + \text{MgO}/\text{Al}_2\text{O}_3$), clay accumulation ($\text{Al}_2\text{O}_3/\text{SiO}_2$), Fe accumulation ($\text{Fe}_2\text{O}_3/\text{Al}_2\text{O}_3$), and salinization ($\text{Na}_2\text{O}/\text{K}_2\text{O}$). Note carbonate and Fe accumulation in deeper portion of paleosol, but relatively uniform clay content and salinization.

Table P3 Diagenetic alteration of paleo-Vertisols (high clay-content paleosols with extensive shrink-swell features such as slickensides) compared with a modern soil analog (Houston Black series), as a function of increasing burial depth, temperature, and time (Driese et al., 2000; Rye and Holland, 2000)

Name, Geologic age	Burial depth (km)	Burial temperature ($^{\circ}\text{C}$)	Clay mineral assemblage	wt% K_2O
Houston Black (modern)	Surface	22 (mean annual temperature).	Na-smectite	1.29
Pennington (325 Ma)	2–3	60–90	Illite (+ kaolinite + chlorite)	4.61
Hekpoort (2.25 Ga)	12–15	350	Sericite – muscovite – chlorite	9.50

features necessary for rigorous application of USDA Soil Taxonomy (Figure P31). Evolutionary changes in terrestrial plant and animal communities over time also create difficulties in paleosol interpretations because of attendant changes in morphological features such as root traces, which are: (a) not present in Ordovician paleosols; (b) rhizomatous and fine in Silurian paleosols; and (c) larger, deeper, and more “modern” in Devonian and post-Devonian paleosols (Driese and Mora, 2001).

Paleosols as paleoclimate proxies research

Current research on pre-Quaternary paleosols no longer concerns simple identification of paleosols in the geologic record, but instead focuses on the use of paleosols as proxies for reconstructions of paleoclimate, paleolandscape evolution, and paleoatmospheric chemistry. Paleoclimate reconstructions primarily emphasize the determination of estimates of mean annual precipitation (MAP) by using a variety of proxy measures, including: (a) the depth to pedogenic carbonate (Bkss) horizon used by Caudill et al. (1996) to estimate mean annual paleoprecipitation (MAP) of $648 \pm 141 \text{ mm yr}^{-1}$ (after Retallack, 2001;

Figure P30a), (b) Fe content of pedogenic Fe-Mn nodules and concretions (Figures P30b and P32a), which was used by Stiles et al. (2001) to estimate MAP of 989 mm based on wt% Fe content; (c) chemical indices of weathering based on bulk geochemistry (Figures P30c and P32b; e.g., Chemical Index of Alteration minus Potash or CIA-K, Sheldon et al., 2002); and (d) total element mass-flux and mass-balance calculations (Stiles et al., 2003). Paleolandscape reconstructions in which topography or hydrology are important variables (interpretation of paleocatenas) are commonly conducted at both local and more regional scales. Reconstructions of Phanerozoic $p\text{CO}_2$ employ the CO_2 -carbonate paleobarometer of Cerling (1991) to interpret Paleozoic (Mora et al., 1996; Mora and Driese, 1999) and Mesozoic paleoatmospheres. This technique utilizes the $\delta^{13}\text{C}$ values measured from pedogenic carbonates, measurements of $\delta^{13}\text{C}$ values of paleosol organic matter (or an estimate based on marine proxy records), and assumptions of soil productivity to infer paleoatmospheric $p\text{CO}_2$. These results are in good agreement with $p\text{CO}_2$ estimates based on long-term mass-balance carbon models (Figure P33). Studies of oxygen levels of Precambrian atmospheres focus on

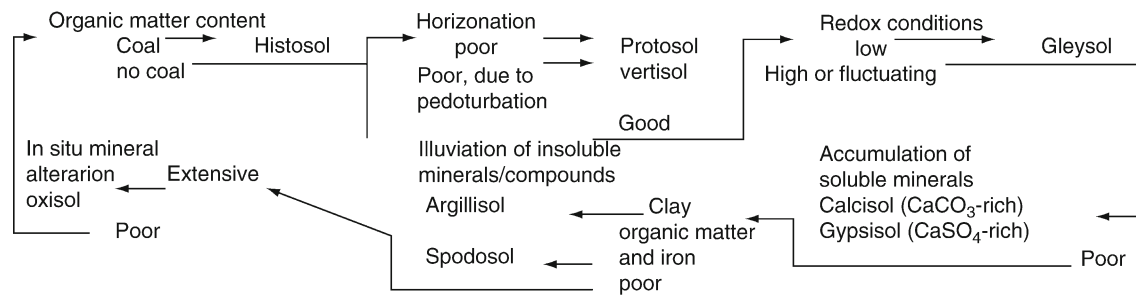


Figure P31 Classification for paleosols (Mack et al., 1993).

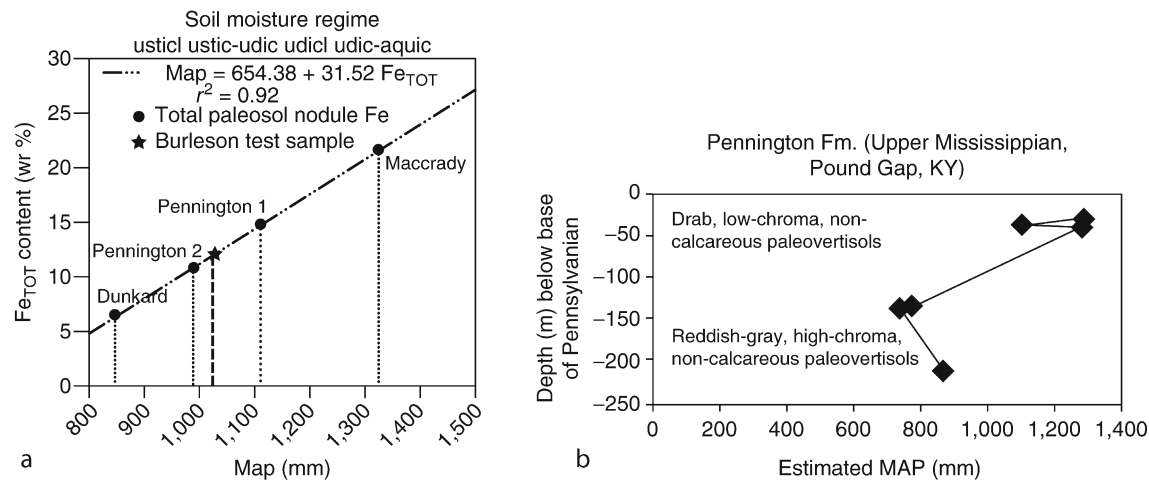


Figure P32 Geochemical climate proxies derived from pre-Quaternary paleosols. (a) Paleoprecipitation (MAP) for mid-Mississippian (Maccrady), late Mississippian (Pennington), and early Permian (Dunkard) Appalachian basin paleo-vertisols based on measured Fe content of paleosol Fe-Mn nodules and regression equation of Stiles et al. (2001) for total Fe content of Fe-Mn nodules in modern soil analogs in Texas, USA. Estimated MAP ranges from 850 to 1,310 mm yr^{-1} . (From Stiles et al., 2001, used with permission). (b) Mean annual precipitation (MAP) for six Appalachian basin paleo-Vertisols derived from bulk chemistry and regression equation of Sheldon et al. (2002) that relates MAP to Chemical Index of Alteration minus Potash (CIA-K = molar ratio of $\text{Al}_2\text{O}_3 / (\text{Al}_2\text{O}_3 + \text{Na}_2\text{O} + \text{CaO}) \times 100$, $P = 14.265(\text{CIA-K}) - 37.632$, where $P = \text{MAP}$ in mm yr^{-1} , $r^2 = 0.73$), which increases by 400–500 mm MAP during latest Mississippian time in southeastern Kentucky, USA.

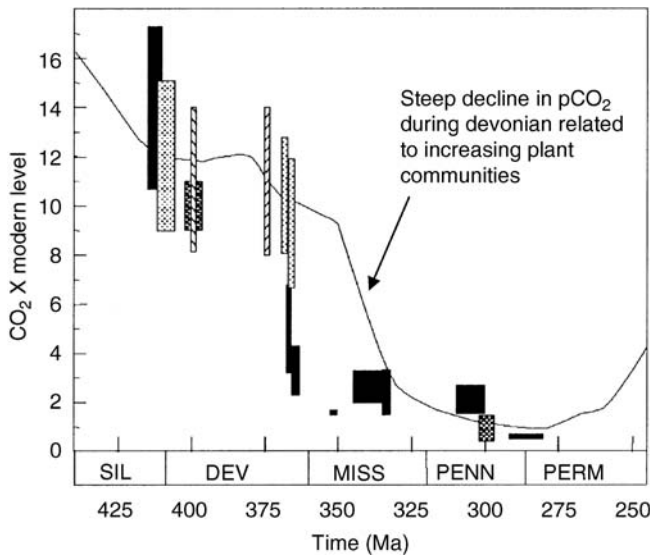


Figure P33 Estimates of middle to late Paleozoic atmospheric CO_2 levels (expressed as times present atmospheric level) derived from Appalachian basin paleosols (closed symbols from Mora et al., 1996; other sources (patterned symbols) of pedogenic carbonate-based estimates cited in Driese and Mora, 2001), calculated using the soil carbonate carbon isotope paleobarometer (Cerling, 1991). Other proxy-based estimates include stomatal density (open symbols) and carbon mass-balance model (line; see discussion in Driese and Mora (2001)).

measuring Fe contents and Fe losses during weathering of Precambrian paleosols. These investigations have been further expanded to include other redox-sensitive elements, as well as the ratio of oxygen demand to demand for CO_2 during weathering (Rye and Holland, 2000). Other research directions include systematic studies of root diameter, depth, and density in paleosols, using root traces, and relating these changes to development of soil morphology (Driese and Mora, 2001), widespread deposition of black shales, and carbon sequestration.

New research directions on pre-quaternary paleosols

Study of pre-Quaternary paleosols appears to be heading in many future directions. One important research area involves studies of soil chronosequences (a suite of related soils in which all soil-forming factors are held constant except for the time duration of pedogenesis) in order to interpret the time significance of paleosols in the geologic record (Stiles et al., 2003). Because paleosols represent unconformities within otherwise conformable stratigraphic successions, the ability to resolve time in paleosols is extremely important in terms of interpreting earth history. U-Pb age-dating of pedogenic carbonates offers a promise of improved chronology of pre-Quaternary paleosols, whose ages place them beyond the limits of ^{14}C or other dating methods commonly used for Quaternary paleosols. Applications of paleosol research to interpretations of sequence stratigraphy will help to connect time and sea level-base level relationships between marine and terrestrial stratigraphic sections. Careful documentation of continental traces of invertebrate animals (paleoichnological studies), especially those relating soil animals and their relationships to soil

forming-processes in the past, is yet another area that is currently developing.

Steven G. Driese

Bibliography

- Caudill, M.R., Driese, S.G., and Mora, C.I., 1996. Preservation of a paleo-Vertisol and an estimate of Late Mississippian paleoprecipitation. *Jour. Sed. Res.*, **66**, 58–70.
- Cerling, T.E., 1984. The stable isotopic composition of modern soil carbonate and its relationship to climate. *Earth Planet. Sci. Letters*, **71**, 229–240.
- Cerling, T.E., 1991. Carbon dioxide in the atmosphere: Evidence from Cenozoic and Mesozoic paleosols. *Am. J. Sci.*, **291**, 377–400.
- Driese, S.G., and Foreman, J.L., 1992. Paleopedology and paleoclimatic implications of Late Ordovician vertic paleosols, southern Appalachians. *J. Sed. Petrol.*, **62**, 71–83.
- Driese, S.G., and Mora, C.I., 2001. Diversification of Siluro-Devonian plant traces in paleosols and influence on estimates of paleoatmospheric CO_2 levels. In Gensel, P.G., and Edwards, D. (eds.), *Plants invade the Land: Evolutionary and Environmental Perspectives*. New York: Columbia University Press, pp. 237–253.
- Driese, S.G., Mora, C.I., Stiles, C.A., Joeckel, R.M., and Nordt, L.C., 2000. Mass-balance reconstruction of a modern Vertisol: Implications for interpretations of geochemistry and burial alteration of paleo Vertisols. *Geoderma*, **95**, 179–204.
- Mack, G.H., James, W.C., and Monger, H.C., 1993. Classification of paleosols. *Geol. Soc. Am. Bull.*, **105**, 129–136.
- Mora, C.I., Driese, S.G., and Colarusso, L.A., 1996. Middle to Late Paleozoic atmospheric CO_2 from soil carbonate and organic matter. *Science*, **271**, 1105–1107.
- Mora, C.I., and Driese, S.G., 1999. Palaeoclimatic significance and stable carbon isotopes of Palaeozoic red bed paleosols, Appalachian Basin, USA and Canada. In Thiry, M., and Simon-Coinçon, R. (eds.), *Palaeo-weathering, Palaeosurfaces and related Continental Deposits*. International Association of Sedimentologists Special Publication No. 27, pp. 61–84.
- Retallack, G.J., 1988. Field recognition of paleosols. In Reinhardt, J., and Sigleo, W.R. (eds.), *Paleosols and Weathering Through Geologic Time*. Boulder, CO: Geological Society of America. GSA Special Paper **216**, pp. 1–20.
- Retallack, G.J., 1991. Untangling the effects of burial alteration and ancient soil formation. *Ann. Rev. Earth Planet. Sci.*, **19**, 183–206.
- Retallack, G.J., 2001. *Soils of the Past: An Introduction to Paleopedology*, (2nd ed.). Oxford: Blackwell Science, 416pp.
- Rye, R., and Holland, H.D., 2000. Geology and geochemistry of paleosols developed on the Hekpoort Basalt, Pretoria Group, South Africa. *Am. J. Sci.*, **300**, 85–141.
- Sheldon, N.D., Retallack, G.J., and Tanaka, S., 2002. Geochemical climofunctions from North American soils and application to paleosols across the Eocene-Oligocene Boundary in Oregon. *J. Geol.*, **110**, 687–696.
- Stiles, C.A., Mora, C.I., and Driese, S.G., 2001. Pedogenic iron-manganese nodules in Vertisols: A new proxy for paleoprecipitation? *Geology*, **29**, 943–946.
- Stiles, C.A., Mora, C.I., Driese, S.G., and Robinson, A.C., 2003. Distinguishing climate and time in the soil record: Mass-balance trends in Vertisols from the Texas Gulf Coastal Prairie. *Geology*, **31**, 331–334.

Cross-references

- [Atmospheric Evolution, Earth](#)
- [Carbon isotope Variations Over Geologic Time](#)
- [Carbon Isotopes, Stable](#)
- [Early Paleozoic Climates \(Cambrian-Devonian\)](#)
- [Geochemical Proxies \(non-isotopic\)](#)
- [Late Paleozoic Paleoclimates \(Carboniferous-Permian\)](#)
- [Mesozoic Climates](#)
- [Mineral Indicators of Past Climates](#)
- [Oxygen Isotopes](#)
- [Paleoclimate Proxies, an Introduction](#)
- [Paleo-Precipitation Indicators](#)
- [Paleosols-Quaternary](#)
- [Stable Isotope Analysis](#)

PALEOSOLS, QUATERNARY

Introduction

Paleosols, the remains of former soil covers of the Earth now buried under younger deposits, are an important testimony of the environmental conditions of ancient epochs. Paleosols occur in sediment sequences of various origins, such as alluvial sediments of river terraces, and in shallow marine (lagoon), volcanic, and even glacial deposits. However, the most widespread and best-preserved paleosols occur in loess deposits. The buried soils are detected on all continents except for the Antarctic. The first half of the twentieth century was the period of upbuilding data about paleosols in loess sequences. It was established that paleosols contain very important information on chronostratigraphy and paleogeography.

Paleosols as a chronostratigraphic component of the Pleistocene

The horizons of paleosols are widely used as key horizons for the stratigraphic subdivision of continental sedimentary series. Frequently located in the periglacial zone and occupying an intermediate position between regions of moraine distribution on the one hand, and marine deposits on the other hand, horizons of buried soils represent an important link in a system of general correlation of events in glacial, periglacial, and maritime areas.

The reliability of usage of paleopedologic data has increased, especially with the development of methods of absolute and relative dating: radiocarbon, thermoluminescent, paleomagnetic, amino acid, and paleontological (palynological and paleofaunistic). The use of paleosols as components of the stratigraphic record has increased, especially after paleosols morphotypical features of different ages were studied (Figure P34).

Paleosols in various sediment sections were once compound units of soil covers of different ages. The possibility of their use as a reliable tool for chronostratigraphic subdivision and correlation is based upon the fact that each of the interglacial epochs of the Quaternary soil formation was characterized by intrinsic features of pedogenesis, combinations of paleosols in automorphic conditions, and specific features of their geographic distribution. These include, for example, soil complexes that belong to the late Pleistocene (Sangamon) interglacial in North America, to the Eemian interglacial in West Europe, to the Mikulino (East Europe), and to the Kazantsevo interglacial in Siberia. Such paleosols were named "soil stratigraphic units" or "pedostratigraphic units" (Catt, 1990). For these, R. Morrison (1967) has suggested the term "geosol." Not only interglacial soils can be used as stratigraphic markers. Interstadial Pleistocene soils having regional names (e.g., Kesselt, Gleina, Stilfrid B, and Mende F in West Europe; the Bryansk soil in East Europe; Farmdale in North America) with established genetic connections and age control based on radiocarbon dating (32–24 kyrBP) can also be used for distant correlations.

		Glaciations, interglacials (Northern Europe)	Glaciations, interglacials (Russian stratigraphic scheme)	Loess and paleosols		
Holocene						
Holocene soil						
Pleistocene	Upper	Late weichselian	Late valdai glaciation	Altynovo loess III		
		Denekamp interstadial	Bryansk (Dunaevo) interstadial	Trubchevsk soil		
			Early valdai glaciation	Desna loess II		
		Brorup	Verkhevolzhsky interstadial	Bryansk soil		
		Early weichsel	Cold stage	Khotylevo loess I		
		Eemian interglacial	Mikulino interglacial	Mezin soil complex		
	Middle	Warthe stage	Dnieper glaciation	Moscow stage	Krutitsa soil	
		Treene interstadial		Interstadial	Sevsk loess	
		Drenthe stage		Cold stage	Dnieper stage	Salny soil
				Warming (Romny)		Moscow loess
			Cold stage		Kursk soil	
		Demnits interglacial		Kamenka interglacial	Dnieper loess	
	Lower	Fuhne glaciation		Pechora glaciation	Romny soil	
		Holstein interglacial		Likhvin interglacial	Orchik loess	
		Elster glaciation		Oka glaciation	Kamenka soil complex	
		Cromerian complex			Muchkap interglacial	Borisoglebsk loess
					Don glaciation	Inzhavino soil complex
					Okatovo interglacial	Korosteleva loess
			Setun glaciation	Vorona soil complex		
		Akulovo interglacial	Don loess			
			Rzhaksa soil			
			Bobrov loess			
			Balashov soil			

Figure P34 The Pleistocene sequence of the East European Plain.

Diagnostic methods of paleosol genesis

The main aim of paleopedological studies is to reconstruct genetic paleosol profiles and to identify the soil formation factors. The structure of a soil profile can therefore be used for paleopedologic reconstructions.

Consequently, analysis of a paleosol in the field starts with a detailed description of its genetic profile on well-cleaned walls of natural exposures – those of open pits, ravines, river banks, marine coasts, and others.

Paleosols contain much more information on the relevant processes, which occurred at different times and affected not only the formation of the soil profiles, as such, but also their preservation. We can distinguish the following main processes responsible for the formation of the buried soils observed in loess-paleosol formations (where the best preserved paleosols are found):

1. Processes of soil formation, which took place during periods of intensive pedogenesis in warm semicycles of glacial-interglacial cycles. Their direction and intensity changed in response to different environmental-climatic conditions.
2. Processes specific to transitional stages to cold semicycles and to glacial ones. These specific processes, which took place at the end of or at the completion of soil formation during warm semicycles, greatly affected the preservation of soil of profiles, especially their upper parts that were marginal to the overlapping loess horizons. Cryogenic processes that contributed to distortion of soil horizons include processes of sedimentation

intensification, when intermediate deposits transitional from fossil soils to loess horizons were formed between loess and soil, and removal and re-deposition processes that affected materials in the upper parts of fossil soils located on slopes (formation of so-called pedosediments).

3. Pedometamorphic (after Gerasimov, 1971) or diagenetic processes that transformed the buried fossil soils. As a result of these processes, fossil soils lost their indices of low stability and acquired new secondary ones.

In studying the genesis of fossil soils, the greatest attention is naturally paid to indices of pedogenesis stages, which reflect conditions extant when the soils proper were formed. These processes lie at the base of paleopedologic reconstructions. However, study of the different forms of disturbances of the soil profile and of pedometamorphic changes in their properties is also very important.

The set of analytic methods that we use in our studies depends on the preservation of the most stable indices of soil formation. They include the following:

Analytical methods for studying the mineral components of soils

Data from chemical and physical-chemical analyses, including particle-size (granulometric) analysis, total chemical composition, clay minerals, and others can be used for diagnostic purposes (Figure P35a and P36a). In a number of cases, however, when fossil soils have been subjected to the impact of secondary

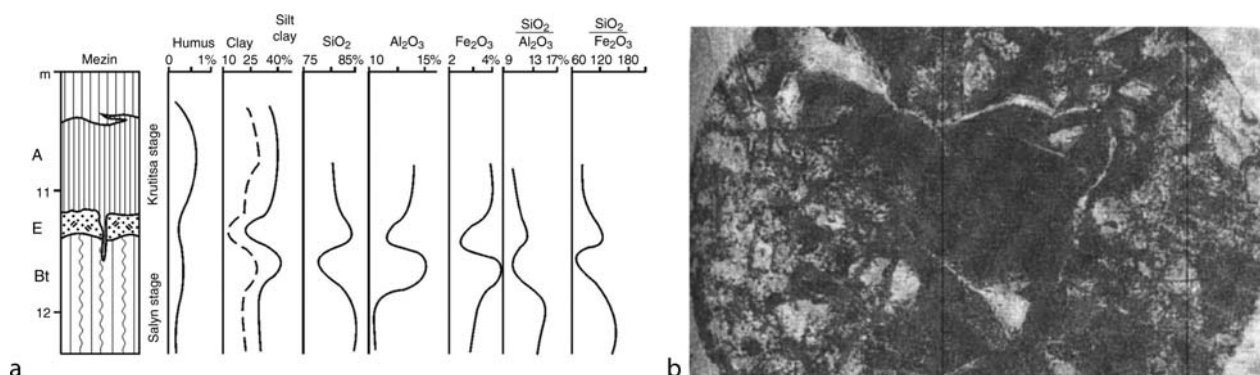


Figure P35 (a) Analytical data of Mezin paleosol complex, Mezin section, Dnieper basin; (b) Clay illuviation coating in Bt horizon.

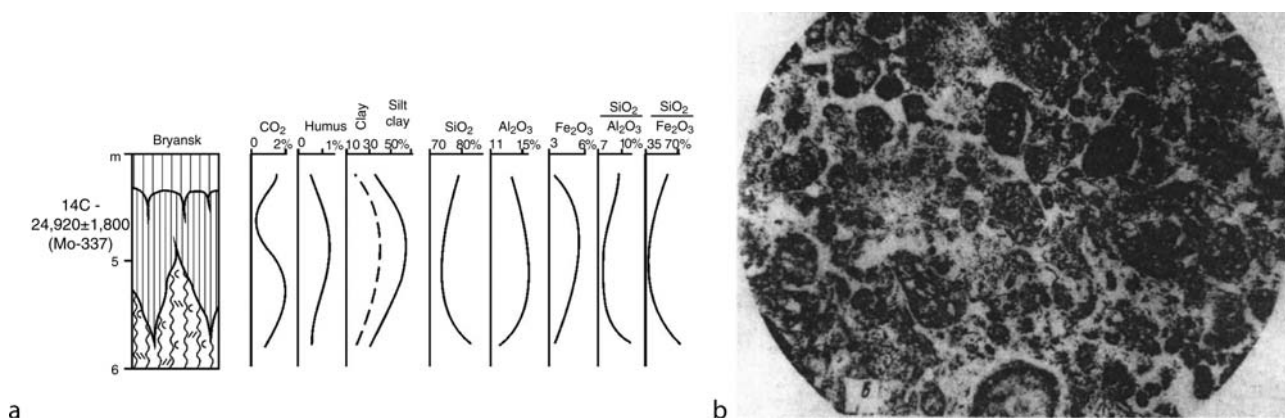


Figure P36 (a) Analytical data of the Bryansk interstadial paleosol, Bryansk section, Dnieper basin; (b) Ooid type of microstructure (humus horizon).

cryogenesis and fracturing, their genetic horizons may appear to be mixed, and the data of the distribution of mineral components along their profiles may be greatly distorted.

Analytical methods for investigating organic matter

The composition and characteristics of organic matter in the soil are the most important diagnostic criteria of soil formation processes. Soils show differences in their humus content depending on natural climatic conditions. The fractional composition of soils, the properties of their humic acids, and the regularities of humus distribution along this profile all change as well.

When the soil is buried, the amount of organic matter it contains decreases noticeably in spite of the fact that the soil preserves its dark color. Analyses of radiocarbon data on the ages of different fractions of humus indicate that fractions of the humic acids proper and the humic acids of humins are the most of stable and the least subject to pedometamorphic transformation (Gerasimov and Chichagova, 1971). Numerous studies have confirmed the hypothesis, first advanced by I. P. Gerasimov, who suggested that the correlation of the main groups of humic matters (humic and fulvic acids, humins) in fossil soils generally reflects two main directions in the formation of paleosols: the forest and steppe types.

The data on some properties of humic acids (optical density, stability to electrolytes) are also used as diagnostic indicators of former pedogenesis. This was demonstrated for the first time in the study of humic acids in soils of the Bryansk interval and of the Mikulino interglacial (Morozova and Chichagova, 1979).

Micromorphological method

This method, developed by W. L. Kubiena (1970), is widely used for the study of fossil soils in different countries (Fedoroff, 1971; Bronger, 1972; Smolikova, 1972; Konecka-Betley, 1979; Morozova, 1981; Matviishina, 1982; Mucher and Morozova, 1983; Catt, 1990; and others). The micromorphological method permits us to study those details of the soil profile that contain the basic information both on processes of the old pedogenesis, and on those that resulted from soil fossilization and that disturbed its overall structure.

As micromorphological diagnostics of soils, the following are used: data about microstructure (aggregation and voids), grade of pedality (degree of aggregation; Bullock et al., 1985), ground-mass (b-fabric), pedofeatures, and other features (Figure P35b and P36b).

To define paleosols, the paleoactualistic principle is applied: paleosol properties are compared to the properties of modern soils, and their genesis is inferred on the basis of their commonality. Micromorphological research using these materials is presented in the works of Kubiena (1970) and Bullock et al. (1985). Genetic types of paleosols are named according to International (FAO) system and its correlation with the Russian system of soil classification (Gerasimova et al., 1996).

Evolution of soil formation in the Quaternary period

Quaternary types of soil formation epochs

The difference in heat and moisture supply between phases of the climatic macrocycles of the Pleistocene controlled succession of soil formation types, and various patterns of soil zonation, under changing conditions of sedimentation and lithogenesis through macrocycles.

Interglacial soil formation. This soil type developed during the thermal optimum of the climatic macrocycle. Interglacial paleosols either corresponded by their genesis to modern soils in

the considered territory or were formed against the background of a warmer and wetter climate. At temperate latitudes, over the vast spaces of large watersheds, a latitudinal soil zonation was developed. In the late and middle Pleistocene, cambisols, luvisols, luvisols, phaeozems, and chernozems were formed. During the early Pleistocene warm epoch (Cromer), paleosols with subtropical features of pedogenesis were formed.

Interstadial soil formation. During the cold semicycle, drastic landscape-climatic changes occurred. These were accompanied by climatic oscillations of heat and moisture supply, both of a stadial and interstadial nature, as reflected in the processes of soil formation and sedimentation.

Interstadial soil formation was characterized by two main types of paleosols. The first was typified by predominance of paleosols of the cryo-gley genesis (gelic gleysols). For example, in the Bryansk (Farndale) epoch, the gleyezems were widespread in west and middle Europe, on the southwestern margins of the East European Plain, and in some regions of North America. Gleyezems were characterized by the development of gleyization processes (i.e., water logged, anaerobic conditions), weakly developed pedality, and massive microstructures. Paleosols with aggregates of ooid type have been identified in the central regions of the East European Plain.

The second type differed from the interglacial paleosols by greater uniformity in the manifestation of soil-forming processes, with humus accumulation predominant among them. Pedality was moderately developed, with aggregation and plasma clay-humus. The latitudinal zonation was then essentially simplified, becoming nearly hyperzonal. Interstadial soils of early glacial stages (such as the Krutitsa soil of the Mezin complex) belong to that type.

Pleniglacial soil formation corresponded to the maximum of the cold phase of a semicycle. During this time, permafrost was widespread beyond the ice-sheet in the periglacial zone. Sedimentation was dominant over pedogenesis. Overall, the biogeochemical processes of rock breakdown were overwhelmed, and specific synlithogenic paleosols (loesses) were formed. These processes can be compared to those characteristic for the gray soils of semideserts, to some extent. Very low-intensity soil formation occurred during slightly wetter phases; it was manifested in the processes of gleyization, segregation of ferric hydroxides, and discrete humification.

General features of the pedogenesis in the Quaternary period

The nature of soil formation did not repeat itself, but changed consistently due to the overall trend of climatic changes. In general, interglacial soil formation within the middle latitudes of the Northern Hemisphere (the present-day temperate belt) changed from subtropical (Mediterranean) in the early stages of the Pleistocene up to subboreal (boreal) at its termination. These changes have been established based on genetic types of the interglacial paleosols known from the loess sections of North America, Europe, and Asia (West Siberia, and China).

Evolution of soil formation processes in the Quaternary and their climatic interpretation (based on the example of the central East European Plain)

At present, soddy podzols and gray forest soils in combination with leached chernozems of the meadow steppe occur in the central regions of the East European Plain. The main climatic parameters of this territory are: $t_1 = -10^\circ\text{C}$, $t_7 = +18^\circ\text{C}$,

$t_{yr} = +8^{\circ}\text{C}$, $P_{yr} = 550\text{--}600$ mm, where t_1 = average January temperature, t_7 = average July temperature, t_{yr} = annual mean temperature, and P_{yr} = annual mean precipitation.

The loess-soil series in this region are the most studied (Figure P37). Here, it is possible to observe changes in interglacial soil formation during the last million years. The earliest known interglacial soils are the paleosols of two climatic macrocycles prior to the Brunhes-Matuyama (780 kyBP) paleomagnetic boundary.

During the period when the oldest fossil soils studied were formed (the Balashovskaya paleosol, in the Matuyama zone), the type of pedogenesis with well-expressed subtropical features dominated. For this time, two types of paleosol profiles are established. One of them corresponded to wet subtropical conditions due to a texture-differentiated structure of the profile and presence of braunlehm plasma (containing fragments of illustrated coatings in finely dispersed clay; Kubiena, 1970) in the Bt horizon. In the second type, the features of rubefication

and ferruginization (reddening of soil due to iron oxide accumulation) of the soil plasma are established.

During the Okatovo interglacial, when the Rzhaksa soil formed, phaeozems appeared in this region (Figure P34). The Vorona (Muchkap) interglacial (the late Cromer) had set in after the Don glaciation. Polygenetic soils from less than two contiguous paleosols were detected in the soil cover. The soils of the main stage of soil formation were represented by phaeozems in combination with luvic cambisols. For this stage, the following climatic parameters (average values) have been reconstructed based on soil types: $t_1 = 0^{\circ}\text{C}$, $t_7 = +23^{\circ}\text{C}$, $t_{yr} = +12^{\circ}\text{C}$, $P_{yr} = 800\text{--}900$ mm.

During the main phase of the Inzhavino epoch of soil formation, corresponding to the Likhvin (Holstein) interglacial, pedogenesis occurred under conditions of the subboreal forest zone. The forest soils that had a genetically differentiated profile of eluvial-illuvial type, with traces of surface gleyization, were widespread (luvic cambisols, with participation of stagnic

Age, K yr	Soil unit		Modern soil type analogs							
			I	II	III	IV	V	VI	VII	
32 - 23	Bryansk	Late stage	1							
98	Mezin complex	Krutitsa stage		2						
125		Salyn stage interglacial (Mikulino)			3					
260	Romny		4							
290	Kamenka complex	Late stage		5						
330		Main stage interglacial				6				
390	Inzhavino complex	Late stage		7						
410	Likhvin	Main stage interglacial (Likhvin)						8		
	Vorona complex	Late stage		9						
480		Main stage interglacial (Muchkap)								10

Figure P37 Quaternary evolution of central part of East European Plain. Modern soil type analogs: I – gelic gleysols, gelic podzoluvisols; II – chernozem-like sols of cold steppe and forest steppe; III – luvisols; IV – luvisols with participation cambisols; V–VI – cambisols with participation of luvisols and stagnic podzoluvisols; VII – phaeozems with participation of cambisols. Area of distribution of modern soil type analogs: 1 – upstream basin of Lena river; 2, 5, 7, 9 – intermountain depressions of Central Altay; 3 – northern part of West and Central Europe; 4 – North of western Siberia; 6 – upstream basin of Visla river; 8 – upstream basins of Rhine and Danube rivers; 10 – intermountain depression of Danube midstream.

podzoluvisols). The modern analogs of these fossil soils are now widespread in West Europe, in the upper reaches of the Rhine and Danube rivers. The reconstructed climatic parameters for the Likhvin interglacial based on the paleopedologic data are: $t_1 = 0^\circ\text{C}$, $t_7 = +21^\circ\text{C}$, $t_{yr} = 10^\circ\text{C}$, $P_{yr} = -700$ to 750 mm.

During the main phase of the Kamenka (Demnitz) interglacial period of soil formation, the forest soils dominated. These soils can be attributed to luvisols and cambisols. Similar forest soils are now widespread in West Europe and in the south of central Europe, in particular, in the upper reaches of the Vistula River. For the Kamenka interglacial, the following climatic parameters are reconstructed: $t_1 = -1^\circ\text{C}$, $t_7 = +21^\circ\text{C}$, $t_{yr} = +9^\circ\text{C}$, $P_{yr} = 600$ – 700 mm.

Apparently, it is possible to consider the tundra-gley soil or gelic gleysols as a modern analog of soils of the Romny interval (Dnieper glaciation; Figure P32). The soils have a profile A1g-Cg. Near the upper contact of the Romny soil, the festoon-like cryogenic deformations are described. Their analogs can be found in similar formations of the modern active layer of permafrost in the western Yamal Peninsula. It is possible to assume that the modern analogs of the Romny interstadial paleosols lay within the limits of the West Siberian tundra. The climatic parameters of this interstadial based on paleopedologic data average: $t_1 = -26^\circ\text{C}$, $t_7 = +13^\circ\text{C}$, $t_{yr} = -6^\circ\text{C}$, $P_{yr} = 250$ – 350 mm.

At the base of the late Pleistocene loess-soil series, the polygenetic Mezin complex occurs. Its early phase (Salyn) corresponds to the Mikulino (Eemian, Sangamon) interglacial, the late phase to the Krutitsy (Brorup) interstadial. The soils of the Mikulino (Eemian) interglacial were formed in conditions corresponding to the forest zone of the subboreal belt.

They are represented by paleosols with the distinct texture-differentiated profile A-E-Bt-C. The Bt horizon is characterized by abundance of illuviation coatings, testifying to participation of inwashing processes (illuviation of clay) in the soil formation. As modern analogs of the Mikulino interglacial soils, one can consider luvisols, which comprise the present soil cover in the north of central and middle Europe. Climatic parameters of the Mikulino interglacial based on the paleopedological data are as follows: $t_1 = +1^\circ\text{C}$, $t_7 = +17^\circ\text{C}$, $t_{yr} = +9^\circ\text{C}$, $P_{yr} = 600$ – 650 mm. For this interglacial, small-scale maps of the soil cover of Europe and of the East European Plain were compiled (Figure P38).

Soils of the Krutitsy interstadial had a genetic profile A1-AB-C. The chernozem-like soils under the meadow-steppe vegetation or open larch woodlands in the intermountain depressions of Central Altai can be considered as their modern analogs. The reconstructed climatic parameters are: $t_1 = -7^\circ\text{C}$, $t_7 = +15^\circ\text{C}$, $t_{yr} = -0.5^\circ\text{C}$, $P_{yr} = 220$ – 450 mm.

It is necessary to note that the interglacial soil formation of the middle and, probably early Pleistocene, apparently included the concluding phases of interstadials of subsequent glaciations, when the soils, similar to those of the Krutitsy interstadial, were formed.

In the concluding phase of the Bryansk interstadial (correlated with the middle Valdai, Denekamp interstadial) soil formation took place under the conditions of the polar belt. The soils are identified as tundra-gley (gelic gleysols), with characteristic features of these paleosols being strong gleyzation of the entire profile (Ag-Bg-Cg), and a particular ooid aggregation. An area of modern analogs of these paleosols lies within the upper Lena River basin. The reconstructed climatic

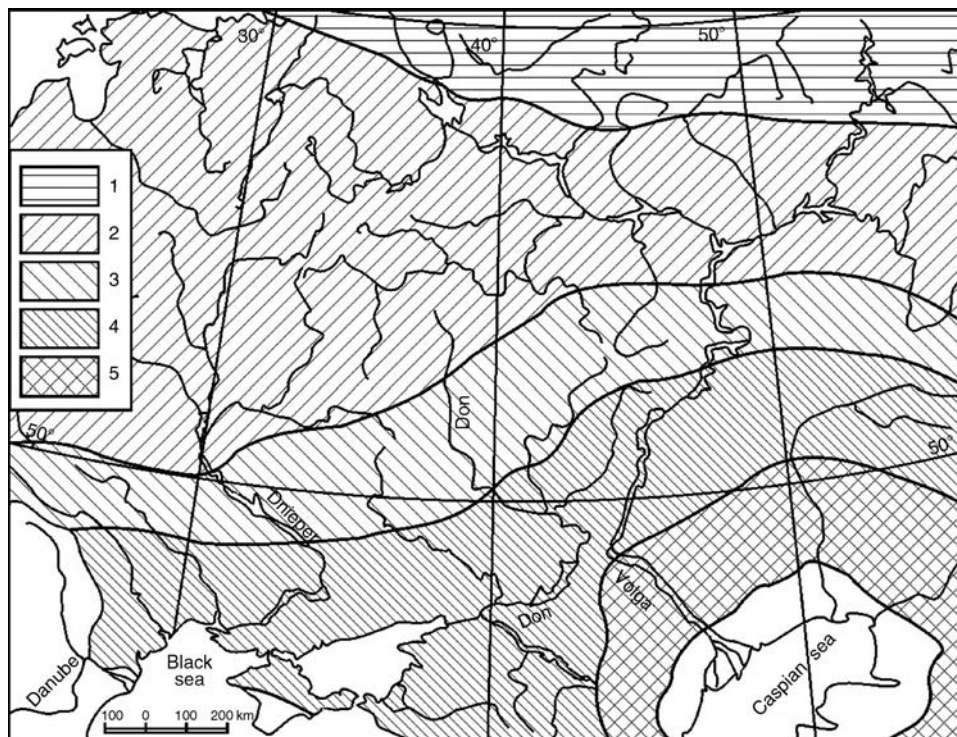


Figure P38 Mikulino interglacial soil map of East European Plain (central and south part); 1 – podzoluvisols; 2 – luvisols of broadleaf forests; 3 – luvisols and gleyic chernozems of forest-steppe; 4 – chernozems of grass steppe; 5 – kastanozems of grass steppe.

parameters of the Bryansk interstadial (average values) are: $t_1 = -23^\circ\text{C}$, $t_7 = +13^\circ\text{C}$, $t_{yr} = -6^\circ\text{C}$, $P_{yr} = 150\text{--}250\text{ mm}$.

The peak of the late Valdai glaciation (20–18 kyBP), corresponding to the Last Glacial Maximum, was the main climatic minimum of the Cenozoic (Velichko, 1973). At this time, a vast periglacial zone stretched. Beyond the Scandinavian Ice Sheet, a considerable portion of this zone (up to 47–48%) was occupied by permafrost (Velichko, 1982). In this region, peculiar synlithogenic paleosols of pleniglacial type occurred. These were characterized by slow humus accumulation, microaggregation, and accumulation and re-distribution of secondary carbonates without their leaching. The reconstructed climatic parameters inferred from paleocryogenic structures of this time are: $t_1 = -25$ to 30°C , $t_7 = +12^\circ\text{C}$, $t_{yr} = -9^\circ\text{C}$, $P_{yr} = 250\text{--}300\text{ mm}$.

At the Pleistocene/Holocene transition, the permafrost boundary retreated to 54–55° N. Within the loess periglacial regions, thermokarst processes of the ground ice melting took place, along with formation of a specific complex of landforms – the relic cryogenic microrelief (RCM) (Velichko, 1973). RCM strongly influenced the structure of the Holocene soil cover. Within the range of the light-gray and soddy podzolic soils of the central Russian Plain, the small-contour differentiation of soils is represented by the combination of the eroded hummocky soils in place of polygonal blocks, and the meadow soils in the troughs and depressions in place of the melted out ice-veins of the Yaroslavl' cryogenic stage. The meadow soils were formed during the optimum phase of the Holocene and were preserved in the form of the relic second humus horizon in genetic profiles of modern soddy-podzolic and gray forest soils (Velichko et al., 1996).

Conclusion

During the Quaternary, abrupt changes took place in the direction and intensity of pedogenesis, corresponding to glacial-interglacial climate cycles and general trend. According to these changes, three main types of soil-formation epochs are distinguished: interglacial, interstadial, and pleniglacial (glacial). Within the macrocycles, all three types of pedogenesis occur. Due to the general trend of climate change, the soil formation process changed from subtropical type in the early phases of the Pleistocene to polar types in its final stages.

Tatiana D. Morozova and Andrei A. Velichko

Bibliography

- Bronger, A., 1972. Zur Mikromorphologie und Palaoboden aus Loss in Karpatenbecken. In St. Kowalinsky (ed.), *Soil Micromorphology*. Warszawa, Poland: Naukowe, pp. 607–615.
- Bullock, P., Fedoroff, N., Jongerius, A., Stoops, G., and Tursina, T.V., 1985. *Handbook for Soil Thin Sections Description*. Wolverhampton, UK: Waive Research Publications, 152pp.
- Catt, J. (ed.), 1990. Paleopedological manual. *Quaternary Int.*, **6**, 1–95.
- Fedoroff, N., 1971. The usefulness of micromorphology in paleopedology. In Vaalon, D.R. (ed.), *Paleopedology. Origin, Nature and Dating of Paleosols*. Jerusalem, Israel: Israel University Press, pp. 156–160.
- Gerasimov, I.P., 1971. Nature and originality of paleosol. In Vaalon D.R. (ed.), *Paleopedology. Origin, Nature and Dating of Paleosols*. Jerusalem, Israel: Israel University Press, pp. 15–27.
- Gerasimov, I.P., and Chichagova, O.A., 1971. Nekotarie voprosy radiouglerodnogo datirovaniya gumusa. In *Pochvovedenie*, vol. 10. pp. 3–11.
- Gerasimova, M.I., Gubin, S.V., and Shoba, S.A., 1996. *Soil of Russia and Adjacent Countries*. In Suiedema R., (ed.), *Geography and Micromorphology*. Moskow-Wagenningen, 204pp.

- Konecka-Betley, K., 1979. Reliktowe procesy glebotworcze w glebach wspolczesnych wytworzonych z gleny zwalowej. *Zeszyty Naukowe Szkoły Głownej Gospodarstwa Wiejskiego Akademii Rolniczej w Warszawie. Rolnictwo*, **18**, pp. 78–97.
- Kubiena, W.L., 1970. *Micromorphological Features of Soil Geography*. New Brunswick, NJ: Rutgers University Press, 255pp.
- Matviushina, Zh.N., 1982. *Micromorfology of Pleistocene Soils of the Ukraine*. Kiev, Ukraine: Naukova Dumka, p. 174.
- Morozova, T.D., 1981. *Razvitie Pochvennogo Pokrova Evropy v Pozdnem Pleistotsene*. Moscow, Russia: Nauka, p. 231.
- Morozova, T.D., and Chichagova, O.A., 1979. Peculiarities of organoc matter of fossil soils in connection with genesis and diagenesis. In: Vassoevich, N., (ed.), *Organicheskoe vesthestvo v sovremennyh I iskopoemyh osadkah (sedikakhity)*, Moscow, Russia: Izd. Mosk. Univ., pp. 68–69.
- Morrison, R.B., 1967. Principles soil of Quaternary stratigraphic. In Morrison, R.B., and Wright, H.E. (eds.), *Quaternary Soils. Proc. VII INQUA Congress*, vol. 9, Denvez, Colozado, USA. pp. 1–69.
- Mucher, H.I., and Morozova, T.D., 1983. The application of soil micromorphology in Quaternary geology and geomorphology. In Bullock and Murphy, G.P. (eds.), *Soil Micromorphology*, vol. 1. Berkamsted, UK: A.B. Acad. Publ., pp. 151–194.
- Smolikova, L., 1972. The significance of soil micromorphology for the solutions of soil evolution in the geology of quaternary. In St. Kowalinsky, (ed.), *Soil Micromorphology*. Warszawa, Poland: Naukowe, pp. 543–557.
- Velichko, A.A., 1973. *Prirodnyi Process v Pleistitsene*. Moskow, Russia: Nauka, p. 265.
- Velichko, A.A., 1982. Main features of the last climatic macrocycle and the present state of environments. In Gerasimov, I.P., and Velichko, A.A. (eds.), *Paleogeography of Europe during the last hundred thousand years (Atlas-Monograph)*. Moscow, Russia: Nauka Press, pp. 139–144.
- Velichko, A.A., Morozova, T.D., Nechaev, V.P., Poroshnyakova, O.M., 1996. *Paleogenesis, Soil Cover and Agriculture*. Moscow, Russia: Nauka Press, p. 151.

Cross-references

- [Eemian \(Sangamonian\) Interglacial](#)
[Encyclopedia of Soil Science and Technology](#)
[Interstadials](#)
[Last Glacial Maximum](#)
[Loess Deposits](#)
[Pleistocene Climates](#)
[Quaternary Climate Transitions and Cycles](#)
[Wisconsinan \(Weichselian, Würm\) Glaciation](#)

PALEOTEMPERATURES AND PROXY RECONSTRUCTIONS

Introduction

Earth's global temperature is mainly a function of energy derived from incoming solar radiation (insolation) of varying wavelengths, with a very minor energy input coming from geothermal processes. About 28% of the total incoming insolation is reflected back to space by clouds, particles and molecules in the atmosphere, about 25% is absorbed in the atmosphere by ozone, clouds and water vapor, and about 47% is absorbed at the Earth's surface. Of this 47%, about 18% is reflected to back to space, while the remainder heats the atmosphere through latent heating (conversion of water to water vapor), convection, and absorption of infrared radiation by greenhouse gases. This trapping of solar energy by the atmosphere is why the Earth's mean annual temperature is ~33°C warmer than it would be otherwise and the main reason there is concern about future global warming caused by anthropogenic greenhouse gas emissions.

Earth's temperature, however, is not stable. It is governed by many external and internal processes operating over different spatial and temporal scales. Changes in the output of energy by the Sun, in the seasonal and geographic distribution of insolation due to changes in Earth's orbital configuration (axial tilt, precession and the eccentricity of its orbit), and in physical (wind-blown dust, volcanic emissions) and chemical (radiatively-active gas concentrations) characteristics of the atmosphere, as well as tectonic processes altering the continental distribution and oceanic circulation, all serve to influence temperature. For example, the oxygen isotopic record of ocean foraminifera (Figure P39) provides a vivid picture of the progressive cooling

in climate over the past 100 million years, due mainly to the influence of long-term changes in ocean basin and continental configurations, atmospheric composition and other factors (Miller et al., 1987).

Historical and instrumental temperature records are far too short to understand these and other complex patterns of Earth's temperature variability over different timescales, or to serve as a baseline against which to evaluate current global temperature trends and human influence on climate. Therefore, one of the most actively researched topics in paleoclimatology is the reconstruction and interpretation of past atmospheric and ocean temperatures. This entry deals with general aspects of Earth's temperature history, mainly atmospheric temperature; see also *Ocean paleotemperatures* for methods of estimating oceanic temperatures.

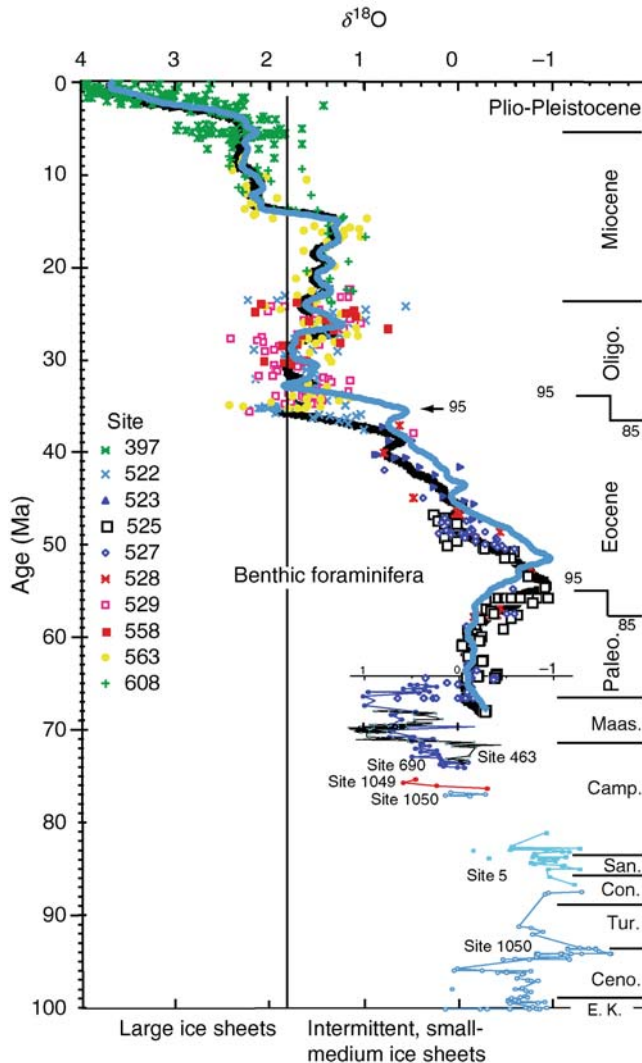


Figure P39 Progressive cooling of global climate is illustrated by changes in the isotopic composition of foraminifera from deep-sea cores. More negative $\delta^{18}\text{O}$ values characterize the Cretaceous and Eocene periods of global warmth and minimal polar ice volume; more positive values during the Oligocene through Quaternary signify gradual cooling and the build-up of polar ice caps. Modified from Miller et al. (1987); Cretaceous data from Huber et al. (2002). Courtesy of Kenneth G. Miller, Rutgers University, Brian Huber, Smithsonian Institution.

Methods of paleotemperature reconstruction

Paleoclimatologists use a wide variety of temperature “proxies” preserved in natural archives such as tree rings, ocean and lake sediments, glaciers and ice sheets (ice cores), speleothems (precipitated calcite), ancient soils (paleosols), corals and other mineralized organisms, and geological and geomorphological features to estimate past changes in temperature (Table P4). Paleotemperature reconstructions can be qualitative or quantitative, depending on the proxy method used; however, all methods carry a certain error bar due to analytical uncertainty, incomplete knowledge of processes governing organic and biogeochemical systems, and the influence of factors other than temperature. Uncertainties notwithstanding, paleotemperature estimates have improved markedly in their accuracy and reliability over the past few decades, and some of the more important applications to reconstruct past atmospheric temperatures are discussed here.

Tree rings

The study of tree rings, or dendroclimatology (Fritts, 1976; Schweingruber, 1988), relies on the influence that temperature and precipitation have on the growth of trees and is most useful in the study of climate variability over the past millennium. Tree rings consist of couplets of alternating light and dark layers of earlywood and latewood growth, respectively, forming seasonal growth patterns that vary year-to-year depending on environmental conditions, soil, the age of the tree, and other factors. Tree ring width, density (a function of several aspects of cell and wood morphology), and the isotopic (carbon, oxygen and hydrogen) composition of the wood are commonly used to reconstruct climate history especially in middle to high latitudes. Summer temperature is a particularly important influence on latewood density in boreal trees. The success of dendroclimatology hinges on careful selection of sites and trees, sophisticated statistical analyses to calibrate tree ring characteristics to climatic parameters, extensive cross-calibration of multiple trees for chronological control, and an understanding of the ecology and growth of various tree genera. For example, ring widths have been used to produce annual temperatures in northern parts of North America for the past few centuries (D'Arrigo and Jacoby, 1992). Longer temperature records are available from carbon isotopes in the case of a 2,000-year record of temperature developed from conifer trees from the western United States (Stuiver and Braziunas, 1987).

In recent years, researchers have produced extensive networks of tree ring records of temperature and other climate parameters such as sea level pressure in North America, Europe, and Asia (Briffa and Matthews, 2002; Cook et al., 2002), with more

Table P4 Summary of methods used to reconstruct atmospheric temperatures

Paleoclimate archive ^a	Proxy method for temperature	Comments and complications	Reference ^b
Ice Sheets & Glaciers (ice cores)	Oxygen and hydrogen isotopes	Changes in moisture source and seasonal precipitation	Jouzel et al. (1997); Grootes et al. (1993)
	Deuterium excess Melt layers	Summer only	Bradley (1999)
Lake Sediments and Peats	Insects (mainly beetles)		Elias and Coope (1994)
	Fossil pollen		Prentice et al. (1991), Guiot et al. (1989)
	Ostracode shell isotopic composition		Von Grafenstein et al. (1999)
	Ostracode shell trace element composition		Holmes and Chivas (2002)
Speleothems (stalagmites, stalagmites, vein calcite)	Oxygen isotopes	Temperature effects during calcite (aragonite) deposition; composition of regional precipitation	McDermott et al. (2001), Winograd et al. (1992), see text
	Tree rings (dendroclimatology)	Ring density and ring width	Usually <1,000 years; standardization due to growth (1988)
Geological & Geomorphological features	Carbon, oxygen, hydrogen isotopic composition	Precipitation and other factors important; complex hydrological and biological processes during wood growth	Briffa and Matthews (2002), Mann et al. (1999), Mann and Jones (2003)
	Paleosols (fossil soils)	Rainfall has strong influence	Retallak (1990)
<i>Other</i>	Glacial sediments	High latitudes, elevations	Washburn (1979)
	Periglacial sediments	Only near glacial margins	
Tree lines, elevation changes	Lithology & mineralogical associations	Qualitative	Parrish (1998)
	Tree lines, elevation changes	Pollen, macroflora from packrat middens	Discontinuous, mainly glacial-interglacial timescales
Tree lines, geographic changes	Pollen	Mainly used in Arctic region	Betancourt et al. (1990)
Plant macrofossils	Plant associations, leaf morphology		

^aGeneral Paleoclimatology texts with discussion of paleotemperature reconstruction include Crowley and North (1991), Parrish (1998), Bradley (1999), Cronin (1999).

^bThese are either comprehensive texts on the proxy method or important applications.

limited data from the Southern Hemisphere. By combining tree ring data with other temperature proxy records (i.e., ice cores, lakes) and splicing the proxy records with instrumental records dating back to the nineteenth century, mean annual hemispheric and global temperature anomalies and climate variability can be estimated for the past 2,000 years (Mann and Jones, 2003, Figure P40). These studies provide convincing evidence that Northern Hemisphere twentieth century temperatures are among the warmest in the last 1,000 years, although the density of Southern Hemisphere sites is too sparse to make conclusions about that region. These and other studies also suggest that the interannual and decadal climate variability during the twentieth century exhibits patterns consistent with the hypothesis that anthropogenic greenhouse gases have influenced global climate. They also demonstrate the importance of integrating temperature records derived from multiple proxy indicators to achieve hemispheric and global scale atmospheric temperature reconstructions.

Ice core studies of ice sheets and glaciers

Water trapped as ice in glaciers and continental ice sheets provides a wealth of information on temperature history of high latitudes and high elevation regions because the isotopic composition of the water is heavily dependent on the atmospheric temperature at time of precipitation. Ice cores from Greenland

and Antarctica recovered paleotemperature records dating back about 110,000 and 700,000 years, respectively. Of the dozens of paleoclimate proxies recovered from ice cores, the most widely used to reconstruct past atmospheric temperatures are the oxygen ($^{18}\text{O}/^{16}\text{O}$ ratio) and hydrogen (deuterium = ^2H) isotopic composition of the ice. Due to the lower vapor pressures of water molecules containing heavy isotopes of H (D) and O (^{18}O), water condensed from vapor is preferentially enriched in heavier isotopes. At cooler temperatures, there is progressively less enrichment in condensation. The relationship between $\delta^{18}\text{O}$ of precipitation and atmospheric temperature has been expressed in a number of equations depending on geographic location and other climatic factors (Jouzel et al., 1987; Rozanski et al., 1993; Bradley, 1999).

Complications with the ^{18}O -temperature relationship arise due to changing moisture source and seasonal variability in precipitation, which can also influence the oxygen isotopic composition of the water. These processes are particularly important over longer timescales and researchers must devise means to sort them out to obtain paleotemperature curves. One approach is to exploit the relationship between differential fractionation of hydrogen and oxygen during precipitation, known as the deuterium excess, or d. During precipitation, a global relationship exists between hydrogen and oxygen expressed as $\delta\text{D} = 8 \delta^{18}\text{O} + 10$. The value + 10 represents an offset between the hydrogen and oxygen

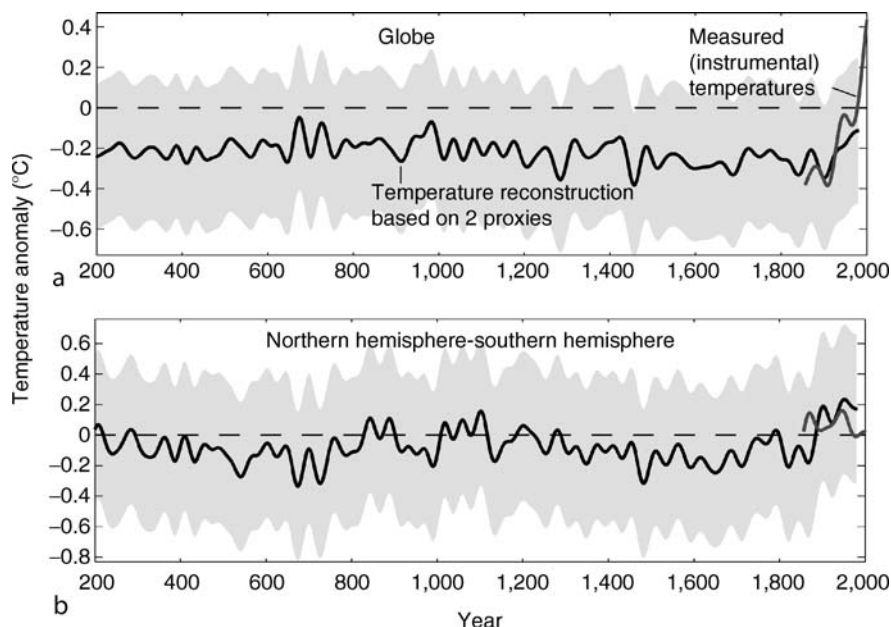


Figure P40 Reconstructed and measured global mean temperatures averaged from tree rings, polar and alpine ice cores, and lake and estuarine sediments for the last 1,800 years. (a) Reconstructed temperatures combining Northern and Southern Hemisphere records. Alternative temperature reconstructions based on different weighting methods given in Mann and Jones (2003) and references therein. (b) Hemispheric temperature difference based on same reconstructed and instrumental temperature curves. From Mann and Jones (2003); Courtesy of Michael E. Mann, Pennsylvania State University.

isotopes and is known as d . As atmospheric conditions vary over time, the value for d also changes and by measuring both $\delta^{18}\text{O}$ and δD in ice cores, a measure of d through time is obtained. The influence of kinetic processes during both evaporation and condensation, changing moisture sources and temperature of the water are complex and need to be sorted out for application of d to the study of paleotemperature.

Despite these and other complexities, some of the most important discoveries about Earth's climate history have come from oxygen and hydrogen isotopic records from Greenland, Antarctica, and low latitude alpine glaciers. At the Summit region of Greenland (mean annual temperature = -31°C), two large research projects carried out under the auspices of the European research program called GRIP (Greenland Ice Core Project), and its American counterpart, GISP II (Greenland Ice Sheet Project II), have provided excellent isotopic records of past temperature variability (Dansgaard et al., 1993; Grootes et al., 1993) that have become a standard against which all late Quaternary climate records are compared. Figure P41 depicts the GRIP oxygen isotopic record for the past 100,000 years, indicating extreme temperature-related isotopic stability during the Holocene (10,000 years to present) and the existence of more than 20 millennial-scale climatic oscillations between $\sim 100,000$ and 15,000 years ago. These events, known as Dansgaard-Oeschger events, reflect extreme climate instability during the last glacial period, and they are also recognized in the GISP II core and many paleoclimate records from around the world. Since the Greenland ice core isotopic fluctuations were first described, the interpretation of the temporal variability of the Greenland $\delta^{18}\text{O}$ -temperature relationship has been improved based on borehole calibration and other means (Cuffey et al.,

1995; Johnsen et al., 1995; Jouzel et al., 1997) and suggest a glacial to interglacial temperature difference of as much as 15°C .

Speleothems and precipitated calcite

Speleothems are rocks deposited when calcite or aragonite precipitate from groundwater, often forming stalactites and stalagmites. Vein calcite is a type of low temperature ($\sim 34^\circ\text{C}$) hydrothermal deposit precipitated from groundwater. Speleothems and vein calcite, when sampled at fine sub-millimeter-scale intervals, can yield important paleoclimate information because oxygen fractionation that occurs during deposition of the calcitic rock is dependent on surface temperature. However, precipitation of source water is itself temperature dependent and also varies due to kinetic processes, such that the interpretation of speleothem oxygen isotope records must be carried out carefully, on a case-by-case basis. For example, in an excellent centennial-scale speleothem record from Ireland, McDermott et al. (2001) were able to detect rapid climate shifts in the regional climate, which they attributed to both the effects of temperature and changes in water vapor sources.

In a series of studies of vein calcite at Devils Hole (DH), Nevada, Winograd, Landwehr and colleagues (Winograd et al., 1992, 1997; Landwehr et al., 1997; Landwehr and Winograd, 2001) provided an important, but controversial late Quaternary paleotemperature record reflecting mainly eastern Pacific sea surface and western United States atmospheric temperatures (Figure P42). The DH record is unique because, in contrast to marine records covering the past 400,000 years, DH is directly dated by the uranium-series methods, and thus yielded a test of the Milankovitch theory of climate (see *Astronomical theory of climate change*). The DH temperature record shows remarkable

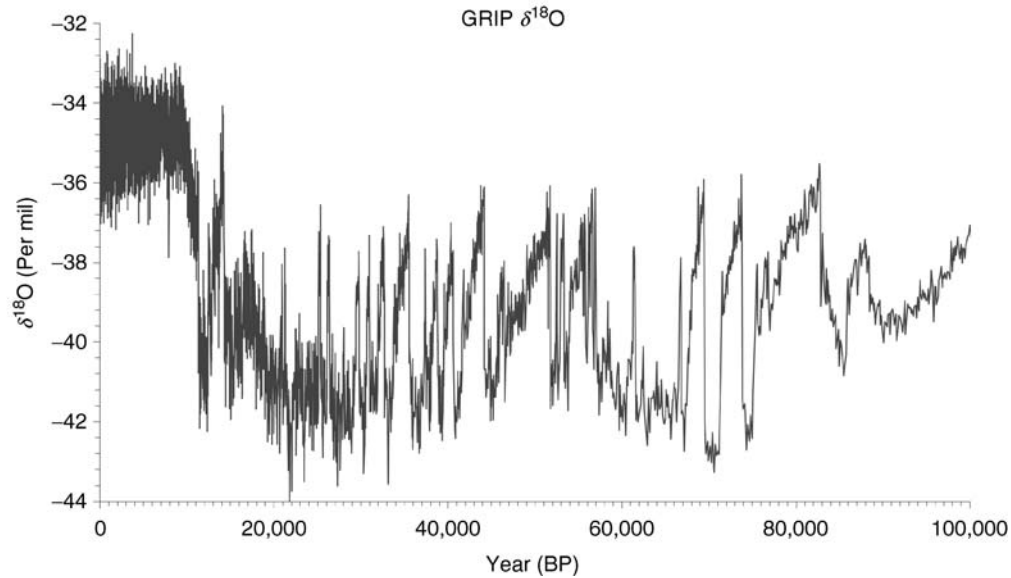


Figure P41 Isotopic record from the GRIP ice core, Summit, Greenland for the past 100,000 years. Oxygen isotopes are 55 cm averages in parts per mil. Isotopic excursions between 90,000 and 15,000 yBP represent Dansgaard-Oeschger millennial climate events when rapid atmospheric warming and cooling occurred over Greenland and many other parts of the world. Isotopic data from Dansgaard et al. (1993), GRIP Project members (1993), obtained from World Data Center for Paleoclimatology.

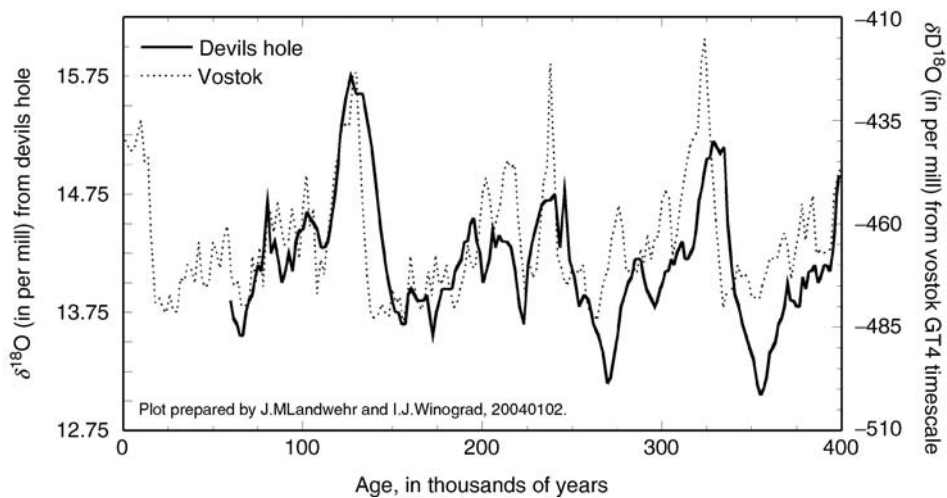


Figure P42 The Devils Hole, Nevada, core DH-11 vein calcite oxygen-18 and the Vostok, Antarctica, ice core deuterium time series for the past 400,000 years. These sites are separated by 114 degrees of latitude: the Devils Hole record reflects northeast Pacific sea surface temperatures and the Vostok deuterium record reflects East Antarctic regional temperatures. The Devils Hole data are from Landwehr et al. (1997); detailed discussions of these time series appears in Landwehr and Winograd (2001), Winograd et al. (1992, 1997) and Petit et al. (1999).

similarities to many other climate records in its clear pattern of 100,000-year eccentricity cycles. For example, Figure P42 compares the DH isotope record to the deuterium records from the Vostok, Antarctica, ice core (Petit et al., 1999). Controversy has arisen, however, because the Devils Hole record indicates that climate warming at the inception of the last interglacial period began about 135,000 years ago, about 8,000–10,000 years earlier than predicted by the Milankovitch theory of climate. This early age for the penultimate interglacial remains an unresolved challenge to the Milankovitch theory.

Lake records of temperature

Several floral, faunal and geochemical proxies have been used to reconstruct atmospheric temperatures from lake sediment cores. Fossil pollen assemblages are commonly used to infer past temperatures (and precipitation) using a variety of quantitative statistical techniques. The modern analog technique (MAT) compares fossil assemblages to a large modern pollen database linked to winter and summer climate parameters. Except during time of rapid climate change, when forest and pollen assemblages

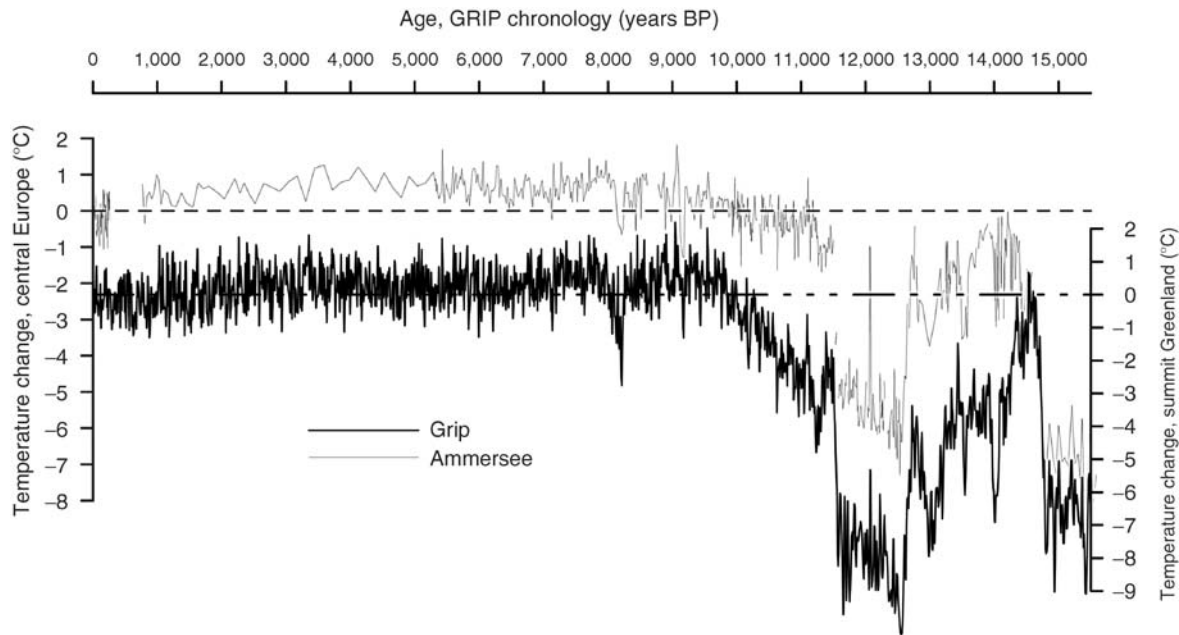


Figure P43 Comparison of temperature changes at Summit, Greenland GRIP ice core reconstructed from oxygen isotopes (*thick line, bottom*) and central European temperatures reconstructed from ostracode oxygen isotopes from Ammersee (*thin line, top*). Modified from Von Grafenstein et al. (1999), GRIP record of Dansgaard et al. (1993); Courtesy of U. Von Grafenstein, Laboratoire des Sciences du Climat et de l'Environnement, Commissariat à l'Énergie Atomique and Centre National de Recherche Scientifique, Gif-sur-Yvette, France.

sometimes had no modern analogs, the MAT method has provided excellent temperature history for North America during the past 15,000 years (Prentice et al., 1991). In Europe, using a slightly different statistical approach to fossil pollen, Guiot et al. (1989) reconstructed a 140,000-year long temperature record from La Grande Pile and Les Echets in France. These studies show that mean annual temperature in France varied from as low as -12 to -13°C during peak glacial conditions, to $+2$ to 4°C during the Eemian interglacial compared to today.

Geochemical methods applied to fossil lacustrine ostracodes recovered from lake cores also provide quantitative estimates of aquatic and atmospheric temperatures (Curtis and Hodell, 1993; Holmes and Chivas, 2002). Von Grafenstein et al. (1999) applied the relationship between mid-European oxygen isotopic composition of precipitation and atmospheric temperatures to reconstruct a 15,500-year temperature record from the $\delta^{18}\text{O}$ of fossil ostracodes from Lake Ammersee, Germany (Figure P43). This decadal resolution achieved at Ammersee allowed the researchers to correlate fine-scale European temperature changes during the deglacial period with the record from Greenland.

Other methods

A wide variety of methods have used qualitative (i.e., relatively warm, cool) and semi-quantitative (i.e., $< 4^{\circ}\text{C}$, between 15 and 20°C) interpretations of paleotemperature from the geological record (Table P4; see Frakes et al., 1992; Parrish, 1998; Bradley, 1999). These approaches rely on expert interpretation of glacial and periglacial sediments and geomorphological features, lithologic types (i.e., gypsum, peat) and paleogeographic distribution, fossil plant associations and morphologies (leaf shape), ancient soils (paleosols), ancient snowline and treeline positions, among others. As is the case with more quantitative

methods, some of these indicators are influenced as much by precipitation and other climatic factors as they are by temperature. Even when firm estimates of temperature can be obtained, for example, in the case of fossil insects (Coope, 1994; Elias and Coope, 1994), many of these records are temporally and spatially discontinuous, making it difficult to achieve interregional paleotemperature correlations and to infer causal factors. Nonetheless, for many regions of the world, these methods provide a rich and valuable literature providing local and regional information on mean annual or seasonal temperature conditions for many periods in the geological past.

Thomas M. Cronin

Bibliography

- Betancourt, J.L., Van Devender, T.R., and Martin, P.S. (eds.), 1990. *Packrat Middens: The Last 40,000 years of Biotic Change*. Tucson, AZ: University of Arizona Press, 467pp.
- Bradley, R.S., 1999. *Paleoclimatology, Reconstructing Climates of the Quaternary* (2nd edn.). San Diego, CA: Academic Press, 613pp.
- Briffa, K.R., and Matthews, J.A., 2002. Analysis of dendrochronological variability and associated natural climates in Eurasia (ADVANCE-10k). *The Holocene*, **12**(6), 639–796.
- Cook, E.R., D'Arrigo, R.D., and Mann, M.E., 2002. A well-verified, proxy reconstruction of the winter North Atlantic Oscillation index since AD 1400. *J. Clim.*, **15**, 1754–1764.
- Coope, G.R., 1994. The response of insect faunas to glacial-interglacial climatic fluctuation. *Philos. Trans. R. Soc. Lond.*, **344B**, 19–26.
- Cronin, T.M., 1999. *Principles of Paleoclimatology*. New York: Columbia University Press, 560pp.
- Crowley T.J., and North, G.R., 1991. *Paleoclimatology*. New York: Oxford University Press, 339pp.
- Cuffey, K.M., Clow, G.D., Alley, R.B., Stuiver, M., Waddington, E.D., and Saltus, R.W., 1995. Large Arctic temperature change at the Wisconsin-Holocene transition. *Science*, **270**, 455–458.

- Curtis, J.H., and Hodell, D.A., 1993. An isotopic and trace element study of ostracodes from Lake Miragone, Haiti: A 10,500 year record of paleosalinity and paleotemperature changes in the Caribbean. In Swart, P.K., Lohman, K.C., McKenzie, J., and Savin, S. (eds.), *Climate Change in Isotopic Records*. Washington, DC: American Geophysical Union. Geophysical Monograph 78, pp. 135–152.
- Dansgaard, W., Johnsen, S.J., Clausen, H.B., Dahl-Jensen, D., Gundestrup, N.S., Hammer, C.U., Hvidberg, C.S., Steffensen, J.P., Sveinbjornsdottir, A.E., Jouzel, J., and Bond, G., 1993. Evidence for general instability of past climate from a 250-kyr ice-core record. *Nature*, **364**, 218–220.
- D'Arrigo, R.D., and Jacoby, G., 1992. Dendroclimatic evidence from North American. In Bradley, R.S., and Jones, P.D. (eds.), *Climate Since AD 1500*. London: Routledge, pp. 296–311.
- Elias, S.A., and Coope, G.R., 1994. *Quaternary Insects and Their Environments*. Washington, DC: Smithsonian Institution Press, 256pp.
- Frakes, L.A., Francis, J.E., and Syktus, J.I., 1992. *Climate Modes of the Phanerozoic*. Cambridge, UK: Cambridge University Press, 286pp.
- Fritts, H.C., 1976. *Tree Rings and Climate*. London: Academic Press, 567pp.
- GRIP Project Members, 1993. Climate instability during the last interglacial period recorded in the GRIP ice core. *Nature*, **364**, 203–207.
- Groote, P.M., Stuiver, M., White, J.W.C., Johnsen, S., and Jouzel, J., 1993. Comparison of oxygen isotope records from the GISP2 and GRIP Greenland ice cores. *Nature*, **366**, 552–554.
- Guiot, J., Pons, A., de Beaulieu, J.-L., and Reille, M., 1989. A 140,000-year continental climate reconstruction from two European pollen records. *Nature*, **338**, 309–313.
- Holmes, J.A., and Chivas, A.R. (eds.), 2002. *The Ostracoda: Applications in Quaternary Research*, Geophysical Monograph Series, vol. 131. Washington, DC: American Geophysical Union.
- Huber, B.T., Norris, R.D., and MacLeod, K.G., 2002. Deep sea paleotemperature record of extreme warmth during the Cretaceous. *Geology*, **30**, 123–126.
- Johnsen, S.J., Dahl-Jensen, D., Dansgaard, W., and Gundestrup, N.S., 1995. Greenland palaeotemperatures derived from GRIP borehole temperature and ice core isotope profiles. *Tellus*, **47B**, 624–629.
- Jouzel, J., Lorius, C., Petit, J.R., Genthon, C., Barkov, N.I., Kotlyakov, V.M., and Petrov, V.N., 1987. Vostok ice core: A continuous isotopic temperature record over the last climatic cycle (160,000 years). *Nature*, **329**, 403–408.
- Jouzel, J., Alley, R.B., Cuffey, K.M., Dansgaard, W., Groote, P., Hoffmann, G., Johnsen, S.J., Koster, R.D., Peel, D., Shuman, C.A., Stievenard, M., Stuiver, M., and White, J., 1997. Validity of the temperature reconstruction from water isotopes in ice cores. *J. Geophys. Res.*, **102**, 26471–26487.
- Landwehr, J.M., and Winograd, I.J., 2001. Dating the Vostok ice core record by importing the Devils Hole chronology. *J. Geophys. Res.*, **106**(D23), 31853–31861.
- Landwehr, J.M., Coplen, T.B., Ludwig, K.R., Winograd, I.J., and Riggs, A.C., 1997. Data from Devils Hole core DH-11. *U. S. Geol. Survey Open-File Report 97-792*, 8pp.
- Mann, M.E., and Jones, P.D., 2003. Global surface temperature over the past two millennia. *Geophys. Res. Lett.*, **30**(15), 1820.
- Mann, M.E., Bradley, R.S., and Hughes, M., 1999. Northern Hemisphere temperatures during the millennium: Inferences, uncertainties, and limitations. *Geophys. Res. Lett.*, **26**, 759–762.
- McDermott, F., Mathey, D.P., and Hawkesworth, C., 2001. Centennial-scale Holocene climate variability revealed by a high-resolution speleothem $\delta^{18}\text{O}$ record from SW Ireland. *Science*, **294**, 1328–1331.
- Miller, K.G., Fairbanks, R.K., and Mountain, G.S., 1987. Tertiary oxygen isotope synthesis, sea level and continental margin erosion. *Paleoceanography*, **2**, 1–19.
- Parrish, J.T., 1998. *Interpreting Pre-Quaternary Climate from the Geologic Record*. New York: Columbia University Press, 338pp.
- Petit, J.R., Jouzel, J., Raynaud, D., Barkov, N.I., Barnola, J.-M., Basile, I., Bender, M., Chappellaz, J., Davis, M., Delaygue, G., Delmotte, M., Kotlyakov, V.M., Legrand, M., Lipenkov, V.Y., Lorius, C., Pepin, L., Ritz, C., Saltzman, E., and Stievenard, M., 1999. Climate and atmospheric history of the past 420,000 years from the Vostok ice core, Antarctica. *Nature*, **399**, 429–436. Data available from NOAA at <http://www.ngdc.noaa.gov>.
- Prentice, I.C., Bartlein, P.J., and Webb, T.W. III., 1991. Vegetation and climate in eastern North America since the last glacial maximum. *Ecology*, **72**, 2038–2056.
- Retallack, G.J., 1990. *Soils of the Past*. Boston, MA: Unwin Hyman, 512pp.
- Rozanski, K., Araguás, L., and Gofiantini, R., 1993. Isotopic patterns in modern global precipitation. In Swart, P.K., Lohman, K.C., McKenzie, J., and Savin, S. (eds.), *Climate Change in Continental Isotopic Records*. Washington, DC: American Geophysical Union. Geophysical Monograph 78, pp. 1–36.
- Schweingruber, F.H., 1988. *Tree Rings. Basics and Applications of Dendrochronology*. Dordrecht: D. Reidel, 276pp.
- Stuiver, M., and Braziunas, T.F., 1987. Tree cellulose $^{13}\text{C}/^{12}\text{C}$ isotopic ratios and climate change. *Nature*, **328**, 58–60.
- Von Grafenstein, U., Erlenkeuser, H., Brauer, A., Jouzel, J., and Johnsen, S.J., 1999. A mid-European decadal isotope-climate record from 15,500 to 5,000 years BP. *Science*, **284**, 1654–1657.
- Washburn, A.L., 1979. *Geocryology*. London: Arnold, 406pp.
- Winograd, I.J., Coplen, T.B., Landwehr, J.M., Riggs, A.C., Ludwig, K.R., Szabo, B., Kolesar, P.T., and Revesz, K.M., 1992. Continuous 500,000 year climate record from vein calcite in Devils Hole, Nevada. *Science*, **258**, 255–260.
- Winograd, I.J., Landwehr, J.M., Ludwig, K.R., Coplen, T.B., and Riggs, A.C., 1997. Duration and duration of the past four interglaciations. *Quaternary Res.*, **48**, 141–154.

Cross-references

[Astronomical Theory of Climate Change](#)
[Beetles as Quaternary and Late Tertiary Climate Indicators](#)
[Climate Change, Causes](#)
[Climate Variability and Change, Last 1,000 years](#)
[Dansgaard-Oeschger Cycles](#)
[Dendroclimatology](#)
[Glacial Geomorphology](#)
[Ice Cores, Antarctica and Greenland](#)
[Ice Cores, Mountain Glaciers](#)
[Lacustrine Sediments](#)
[Mineral Indicators of Past Climates](#)
[Ocean Paleotemperatures](#)
[Ostracodes](#)
[Paleobotany](#)
[Paleolimnology](#)
[Paleosols, Pre-Quaternary](#)
[Paleosols, Quaternary](#)
[Palynology](#)
[Sedimentary Indicators of Climate Change](#)
[Speleothems](#)
[Stable Isotope Analysis](#)

PALEOTEMPESTOLOGY, THE SEDIMENTARY RECORD OF INTENSE HURRICANES

Introduction

Intense storms can modify landforms, and in appropriate depositional settings a geologic record can be preserved (e.g., Liu and Fearn, 2000; Donnelly et al., 2001a, b). Due to the relatively short period of reliable instrumental and historic records, little is known about past intense hurricane landfalls and tropical cyclone activity in general, and the processes that govern the formation, intensity, and track of tropical cyclones are poorly understood (Goldenberg et al., 2001). Reliable records of Atlantic tropical cyclones maintained by the National Oceanic and Atmospheric Administration (NOAA) only extend back to the mid-nineteenth century. An often incomplete historical record of North Atlantic hurricanes dates back several hundred years.

Given the potential for changes in the intensity and frequency of storms due to anthropogenic warming of the global

climate system, decision makers, scientists and the general public have become increasingly concerned about potential risks to coastal populations. Gaining an understanding of how changes in hurricane activity may link to changes in climate is important in order to forecast future changes and possibly mitigate socio-economic impacts. Potential connections between the frequency and intensity of hurricanes and changes in the Earth's climate system can be examined if long-term records of hurricane activity can be developed.

Hurricanes and climate

Some studies have suggested that the intensity and frequency of hurricanes may increase in a warmer climate. In a case study from the western Pacific, model results suggest a 5–12% increase in hurricane intensity with a 2.2 °C increase in sea-surface temperatures (SSTs) (Knutson et al., 1998). Globally SSTs increased by 0.31 °C in the last half of the twentieth century, possibly as a result of anthropogenic greenhouse gas emissions (Levitus et al., 2001). Goldenberg et al. (2001) attribute the recent increase in North Atlantic hurricane activity to increasing SSTs and lower amounts of vertical wind shear. Long-term records of SSTs derived from oxygen isotope data (e.g., Keigwin, 1996) and faunal data (deMenocal et al., 2000) document centennial- to millennial-scale fluctuations in SST in the North Atlantic. These records indicate that SSTs were as much as 1 °C greater than present during the Medieval Warm Period about 1,500–900 years ago and again for a brief interval, interrupting the Little Ice Age, about 500–600 years ago.

Recently numerous researchers have postulated links between changing modes of interannual climate variability, like El Niño-Southern Oscillation (ENSO) and the North Atlantic Oscillation (NAO), and patterns of tropical cyclone activity. Studies relying on recent climatology indicate that North Atlantic hurricane activity is greater during strong La Niña years and suppressed during strong El Niño years (Bove et al., 1998). In strong El Niño years, increased vertical wind shear associated with a strengthening of the subtropical jet over the tropical North Atlantic hinders tropical cyclone development. Several reconstructions of past ENSO variability have been published in recent years. For example, Moy et al. (2002) reconstructed a 12,000-year sedimentary record of ENSO variability from southern Ecuador. Significant millennial and sub-millennial scale ENSO variability is evident in this record. Warm ENSO (El Niño) events became more frequent in the Holocene. Approximately 1,200 years ago, a trend of decreasing frequency of warm ENSO events began. Several intervals in the last 2,000 years had notably few warm ENSO events. Given that warm ENSO phases are thought to diminish North Atlantic tropical cyclone activity, including intense hurricanes, more North Atlantic hurricanes may have occurred in intervals with relatively few warm ENSO events.

Elsner et al. (2000a) propose a possible link between a weak NAO and increased intense hurricanes in the North Atlantic, possibly related to the strength of the trade winds. Using sandy washovers preserved in a coastal lake from the Florida Panhandle, Liu and Fearn (2000) inferred two intervals of intense hurricane activity in the Gulf of Mexico from present day to 1,000 and 3,400–5,000 years ago. They suggest that this millennial-scale variability may be associated with changes in the position of the Bermuda High that may alternately focus hurricanes into the Gulf Coast and East Coast of the USA. Elsner et al. (2000b) document this kind of see-saw pattern in Atlantic hurricane tracks associated with the position of the Bermuda High and NAO intensity over the last

two centuries, where the Gulf Coast experiences more hurricane activity during a weak NAO and the U.S. East Coast experiences more activity during a strong NAO.

Storm-induced deposits

Washovers (overwash deposits) occur when wave energy combined with high water levels (storm surge) overtop or breach barrier beaches and transport nearshore and barrier sediments into the backbarrier environment. If the barrier is breached, a lobate fan will form at the terminus of the breach. If multiple breaches occur close together, these lobes may coalesce. When the entire barrier is overtopped by storm surge, sheet washovers that extend the length of the barrier are deposited. In a regime of rising sea level, low-energy estuarine deposits are typically deposited over washovers between overwash events. If these deposits are not reworked during subsequent storms, the overwash fans will be preserved as laterally continuous horizons of sand within backbarrier sediments and provide a record of past storm surge (Figure P44).

Washovers are composed of locally-derived material from the foredune, beach and nearshore environments and are typically well- to poorly-sorted, fine- to coarse sand. The mean grain-size within overwash deposits generally decreases as a function of distance from the barrier (Hennessy and Zarillo, 1987). Washovers often exhibit horizontal stratification, and if the deposit terminates in a coastal pond or lagoon they can exhibit medium- to small-scale delta foreset stratification (Schwartz, 1975). However some washovers can also lack stratification. Cores from backbarrier environments in southern Rhode Island contain washovers with little or no horizontal stratification (Donnelly et al., 2001a). In some cases post-depositional processes like ice scour and bioturbation may eradicate laminations.

Another characteristic of washovers preserved in backbarrier environments is the abrupt nature of the contact with the underlying peat or estuarine mud (Donnelly et al., 2001a, b). Evidence of soft-sediment deformation is common where a washover is deposited over saturated, fine-grained sediments (Klein, 1986). In addition, rip-up clasts are frequently encountered at the basal contact of washovers and are indicative of high-velocity currents associated with overwash deposition.

Washovers preserved in coastal sediments have provided the basis for constructing prehistoric records of intense-hurricane strikes in Alabama, Florida, Rhode Island, and New Jersey (Liu and Fearn, 2000; Donnelly et al., 2001a,b). In Alabama and Florida, sand deposited in coastal lakes provided evidence of apparent intense-hurricane strikes dating back several

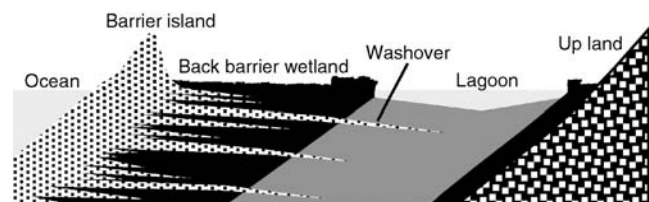


Figure P44 Cross-section of conceptual model of overwash deposition and the landward translocation of the barrier-marsh system in a regime of rising sea level. Overtopping of the barrier beach by storm surge results in washover deposition across backbarrier marshes. Washover fans are preserved as sea level increases and they are covered with marsh deposits. Vertical exaggeration = approximately 100 to 500×.

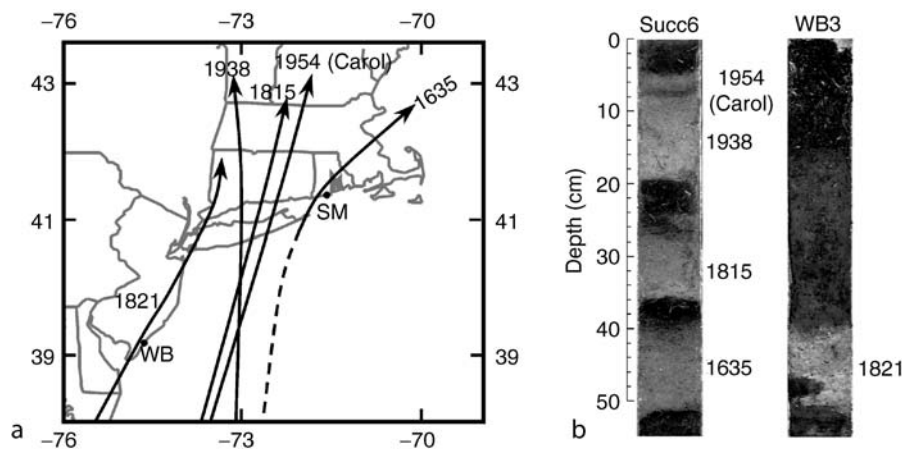


Figure P45 (a) Tracks of historic hurricanes resulting in over 3 meters of storm surge in the northeastern U.S. and the location of Succotash Marsh, RI (SM) and Whale Beach, NJ (WB). (b) Photographs of sandy washovers (light layers) interbedded with backbarrier marsh sediments (dark layers) at Succotash Marsh, RI (Succ6; Donnelly et al., 2001a) and Whale Beach, NJ (WB3; Donnelly et al., 2001b). (Note: the rip-up clast 46–50 cm in WB3).

thousand years (Liu and Fearn, 2000). Higher-resolution records obtained from backbarrier marshes in Rhode Island (Donnelly et al., 2001a) and New Jersey (Donnelly et al., 2001b) contain evidence of intense-hurricane strikes dating back approximately 700 years.

Succotash Marsh in Rhode Island contains six distinct washovers dating back to A.D. 1300 (Donnelly et al., 2001a). Four of these deposits (Figure P45) date to the historic period and the ages are consistent with known hurricane strikes (A.D. 1954, 1938, 1815, and 1635) that resulted in significant levels of storm surge (>3 m). Two additional washovers at Succotash Marsh date to A.D. 1411–1446 and A.D. 1295–1446 and were probably deposited during prehistoric hurricane strikes. At Whale Beach, NJ, a large-scale washover is attributed to an intense-hurricane strike in A.D. 1821 (Donnelly et al., 2001b). An earlier land-falling hurricane probably deposited an older, larger-scale washover at Whale Beach dated to between A.D. 1278 and 1434.

Conclusions

Faced with expectations of a potentially rapidly changing global climate system, concern has increased about potential risks to coastal communities and ecosystems from possible increased tropical cyclone activity. An improved understanding of the relationship between changes in tropical cyclone activity and changes in climate will help to anticipate future changes and possibly mitigate socio-economic impacts. Long-term records of these events can show how hurricane activity has varied in the past as the Earth's climate has changed. The relatively new field of paleotempestology is focused on extending the limited instrumental and historic records of intense storms by recovering and quantifying natural archives of storm occurrence.

Backbarrier wetlands, lagoons, and coastal ponds are often well situated to receive allocthonous sediments during intense hurricane landfalls. These normally low-energy environments are dominated by fine-grained highly organic sediments, with the exception of episodic deposition of coarser-grained mineral sediments from the beach and near-shore environment during extreme storms. Results from the northeast and Gulf coasts of the United States indicate that intense hurricane strikes produce

a distinctive sedimentary signature that can be used to reconstruct long-term records of these events.

Jeffrey P. Donnelly

Bibliography

- Bove, M.C., Elsner, J.B., Landsea, C.W., Niu, X., and O'Brien, J.J., 1998: Effect of El Niño on U.S. landfalling hurricanes, revisited: *Bulletin of the American Meteorol. Soc.*, **79**, 2477–2482.
- DeMenocal, P., Ortiz, J., Guilderson, T., and Samthein, M., 2000. Coherent high- and low-latitude climate variability during the Holocene warm period. *Science*, **288**, 2198–2202.
- Donnelly, J.P., Bryant, S.S., Butler, J., Dowling, J., Fan, L., Hausmann, N., Newby, P.N., Shuman, B., Stern, J., Westover, K., and Webb, T., III, 2001a. A 700-year sedimentary record of intense hurricane landfalls in southern New England. *Geol. Soc. Am. Bull.*, **113**, 714–727.
- Donnelly, J.P., Roll, S., Wengren, M., Butler, J., Lederer, R., and Webb, T., III, 2001b. Sedimentary evidence of intense hurricane strikes from New Jersey. *Geology*, **29**, 615–618.
- Elsner, J.B., and Jagger, T., and Niu, X., 2000a. Changes in the rates of North Atlantic major hurricane activity during the 20th Century. *Geophys. Res. Lett.*, **27**, 1743–1746.
- Elsner, J.B., Liu, K., and Kocher, B., 2000b. Spatial Variations in Major U.S. Hurricane Activity: Statistics and a Physical Mechanism. *J. Clim.*, **13**, 2293–2305.
- Goldenberg, S.B., Landsea, C.W., Mestas-Nunez, A.M., and Gray, W.M., 2001. The recent increase in Atlantic hurricane activity: causes and implications. *Science*, **293**, 474–479.
- Hennessy, J.T., and Zarillo, G.A., 1987. The interrelation and distinction between flood-tidal delta and washover deposits in a transgressive barrier island. *Mar. Geol.*, **78**, 35–56.
- Keigwin, L.D., 1996. The little ice age and medieval warm period in the Sargasso Sea. *Science*, **274**, 1504–1508.
- Klein, G., 1986. Intertidal flats and intertidal sand bodies. In Davis, R.A. (ed.), *Coastal Sedimentary Environments*. New York, NY: Springer, pp. 187–224.
- Knutson, T.R., Tuleya, R.E., and Kurihara, Y., 1998. Simulated increase in hurricane intensities in a CO₂-warmed climate. *Science*, **279**, 1018–1020.
- Levitov, S., Antonov, J.I., Wang, J., Delworth, T.L., Dixon, K.W., and Broccoli, A.J., 2001. Anthropogenic warming of the Earth's climate system. *Science*, **292**, 267–270.
- Liu, K., and Fearn, M.L., 2000. Reconstruction of prehistoric landfall frequencies of catastrophic hurricanes in northwestern Florida from lake sediment records. *Quaternary Res.*, **54**, 238–245.

- Moy, C.M., Seltzer, G.O., Rodbell, D.T., and Anderson, D.M., 2002. Variability of El Niño/Southern Oscillation activity at millennial timescales during the Holocene epoch. *Nature*, **420**, 162–165.
- Schwartz, R.K., 1975. Nature and Genesis of Some Washover Deposits. United States Army Coastal Engineering Research Center, Technical Memo No. 61, 69pp.

Cross-references

Coastal Environments
 Little Ice Age
 Medieval Warm Period
 North Atlantic Oscillation (NAO) Records
 Paleo-El Niño-Southern Oscillation (ENSO) Records

PALYNOLOGY

Palynology is the study of microorganisms, and microscopic fragments of mega-organisms, that occur in sediments. “Palynomorph” is a broad term for a variety of acid-resistant microfossils produced by plants, animals, or Protista that have existed since the late Proterozoic (approximately one billion years ago). The oldest known palynomorphs are arcritarchs (Figure P46), which are likely marine algal bodies that appeared in the Proterozoic eon. Other palynomorphs that appeared in the Paleozoic and are frequently studied are chitinozoans (marine fossils of uncertain origin); scolecodonts (annelid worm jaws); microscopic colonial algae; embryophyte spores; megaspores; pollen (Figures P47–P51); and dinoflagellates. All of these are still present except the chitinozoans. Chitinous fungal spores are first found in Jurassic rocks, and microforaminiferal inner tests can be dated to the Lower Cretaceous (Traverse, 1988). Fragments of wood and cuticle are additional acid-resistant plant materials that may be present in palynological preparations and are frequently studied in

conjunction with palynomorphs. Palynomorphs range in size from 5 to 500 microns. Identification to the specific, generic, or higher taxonomic rank requires study with a light microscope. With few exceptions, palynomorphs are at least partly composed of sporopollenin, chitin, or pseudochitin; resistant organic molecules that survive the standard laboratory treatments with hydrofluoric and hydrochloric acids (Traverse, 1988). Thus neither siliceous microorganisms (e.g., diatoms and radiolarians), nor

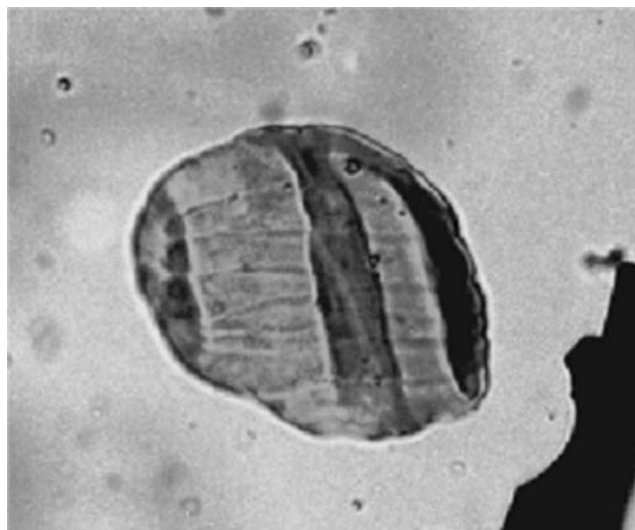


Figure P47 The pollen grain *Vittatina costabilis* Wilson, 1962, identified from 7.1 meters below the Carboniferous-Permian boundary stratotype section at Aidaralash Creek, Ural Mountains, Kazakhstan (Dunn, 2001). This grain is striate (deep parallel grooves) and slightly saccate. The palynomorph was well-established in the late Carboniferous and early Permian and has been referred to the Gnetales order by some authors, and conifers by others (Traverse, 1988). Photo courtesy of M. Dunn.

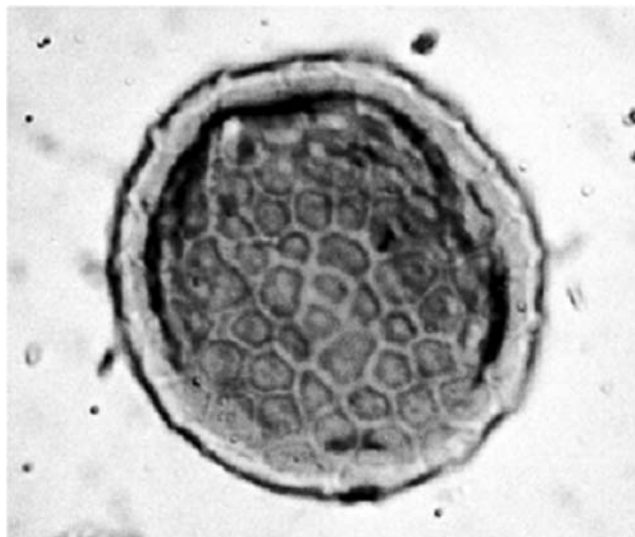


Figure P46 The arcritarchs *Inderites* spp. This example occurs 5.8 meters above the Carboniferous-Permian boundary stratotype section at Aidaralash Creek, Ural Mountains, Kazakhstan (Dunn, 2001). Photo courtesy of M. Dunn.

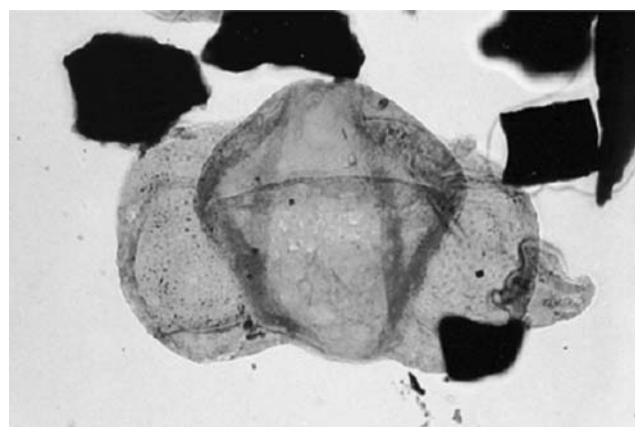


Figure P48 The pollen grain *Limitisporites monstruosus* Lyuber and Val'ts, from 7.4 meters above the Carboniferous-Permian boundary stratotype section at Aidaralash Creek, Ural Mountains, Kazakhstan (Dunn, 2001). This pollen grain has a bisaccate form. Bisaccate pollen with residual three-rayed slits (called trilete) may be intermediate forms between ancestral trilete spores and the modern bisaccate conifer pollen, which have no slits. Photo courtesy of M. Dunn.

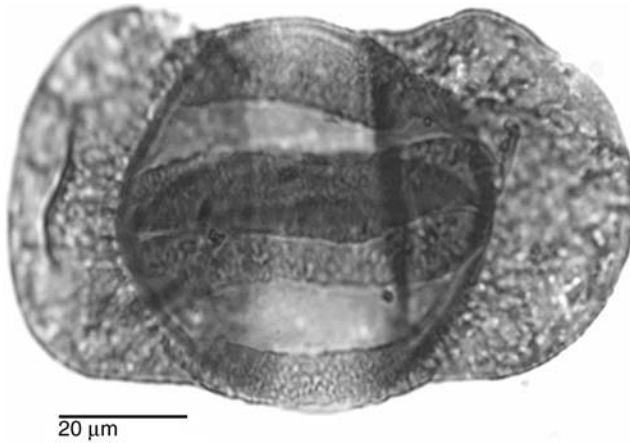


Figure P49 *Lunatisporites* sp. (Upper Permian, UK) pollen. This is a pollen grain that is bisaccate in form, with a striate sculpture consisting of parallel grooves and/or thickenings on the main body (corpus). Striate bisaccates, which appeared during the Carboniferous and flourished during the late Permian and early Triassic, were produced by coniferous and glossopterid gymnosperms, which have since vanished from the paleobotanical record. However, striate, non-saccate pollen is known from the extant gnetalean gymnosperms *Ephedra* and *Welwitschia* (Traverse, 1988). Photo courtesy of S. Fowell.

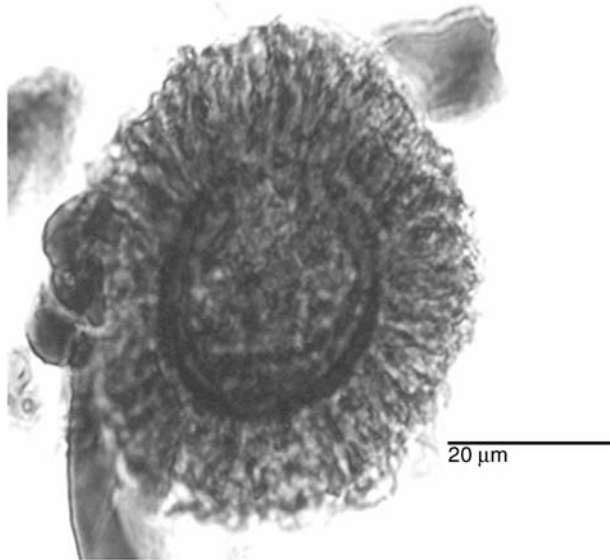


Figure P50 An example of a pollen grain, *Patinasporites densus*, Leschik, 1955 (Upper Triassic, North America), which is monosaccate in form. Monosaccate pollen appeared during the Carboniferous and proliferated during the Lower Permian. Transitional forms between monosaccate and bisaccate grains suggest that at least some bisaccate pollen types originate by modification of the monosaccate condition. *P. densus* has been recovered from Triassic conifer cones (Cornet, 1977). Abundant in Upper Triassic rocks, *P. densus* disappears at the Triassic-Jurassic boundary. Monosaccate pollen is still produced by modern conifers such as *Tsuga* (hemlock). Photo courtesy of S. Fowell.

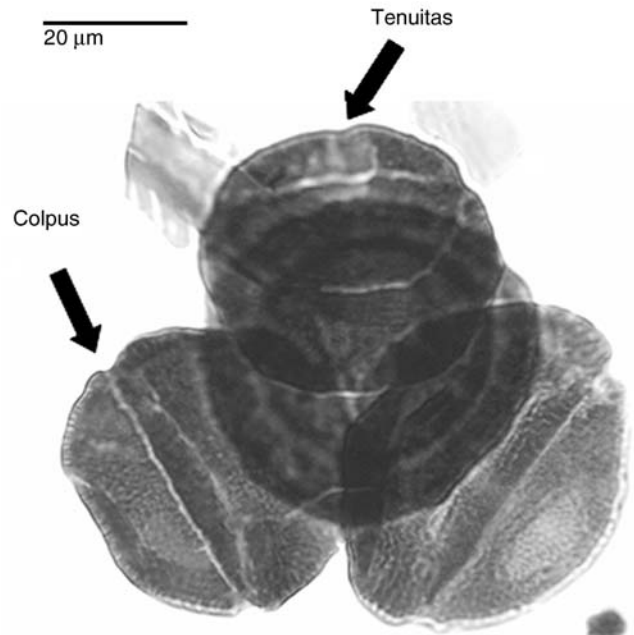


Figure P51 *Corollina torosa* (Reissinger, 1950) Klaus, 1960 emend. Cornet and Traverse, 1975 (Lower Jurassic, North America) pollen. The palynomorph is found as a tetrahedral tetrad, as shown here, or as a single grain, monad. The pore-like thinning, or tenuitas, and the encircling colpus of the *Corollina* genus are features generally associated with angiosperms. However, pollen grains of *Corollina* have been extracted from Mesozoic conifer cones of the family Cheirolepidaceae. *C. torosa* appears in the late Triassic and becomes extremely abundant in early Jurassic assemblages. In North America, the acme zone of *Corollina* spp. can be used to distinguish basal Jurassic palynofloras from those of latest Triassic age. Photos courtesy of S. Fowell.

calcareous microorganisms (e.g., foraminifera and coccolithophores) are palynomorphs.

Modern palynology addresses the morphology and biochemistry of the microorganisms, and their production and distribution within the present environment. Palynological studies are used in plant taxonomy, plant pathology, phytogeography, ecology, forensics, medicine (allergies), entomology, melissopalynology (study of honey), and archeology. An extant palynomorph's environmental preferences can help define the ecological preferences of the same (or possibly similar) palynomorph in the geological record; this is the "modern analogue" interpretive technique, which is applied to paleopalynology. Recently, some palynomorphs have been increasingly utilized for environmental monitoring (e.g., algal blooms, including the "red tide" phenomena).

Palynomorphs may be found in consolidated or unconsolidated marine and terrestrial sediments of siliclastic or carbonate composition. Fossil palynomorphs are typically studied from small samples (even 10 grams) of fine-grained sediments or sedimentary rock, such as siltstone retrieved from sediment cores, drill cores, or rock outcrops. The age of the sedimentary matrix will determine the geological age of the constituent palynomorphs.

Paleopalynology is utilized in biostratigraphy, geochronology, and in paleoenvironmental studies (Traverse, 1988). Biostratigraphy involves dating and correlation of spatially distant rock strata, based upon assemblages of palynomorphs found within the sedimentary matrix. Geochronology, or relative age dating, is based

on correlation of palynomorph taxa from a sedimentary rock of unknown age with established palynomorph reference sequences. Paleopalynology is also utilized in paleoecological studies, since many palynomorphs are indicative of specific environments. Pollen and spores in particular are sensitive indicators of terrestrial environments and thus have been used in terrestrial paleoenvironmental studies (Traverse, 1988). Palynomorphs have been used extensively in exploration geology and hydrocarbon studies, because the color of constituent pollen and spores reflects the thermal maturity of the rock. Regional studies can elucidate paleogeographic patterns, biodiversity, phylogeny, taxonomy, and ecology of the plant or animal group under examination.

The scientific issues addressed by palynological studies vary considerably, dependent on the organism and time period analyzed. In Pliocene to Holocene studies, the ecological and climatic range of the vascular plant taxa that produced the fossil pollen (or spore) is almost always considered relevant to the scientific interpretation. Thus, studies of Pliocene to Holocene fossil pollen will often have a strong ecological component. Similarly, marine dinoflagellate species are distributed according to distinct environments (e.g., temperature, salinity, nutrients). Thus a paleoenvironment may be interpreted based upon the present-day environmental affinity of a taxon. Palynological studies of Proterozoic to middle Miocene strata are generally conducted in order to resolve biostratigraphic and geochronologic questions, to provide information regarding the past distribution of organisms, or to place broad constraints on past climatic conditions.

The application of palynomorphs to biostratigraphy is exemplified by a study of the Carboniferous-Permian boundary stratotype section at Aidaralash Creek, in the southern Ural Mountains of Kazakhstan (Dunn, 2001). The Lower Permian boundary has already been established based upon conodont biostratigraphy. Palynomorphs found in this stratotype section include abundant and diverse species of the pollen genus *Vittatina*, *Limitisporites monstruosus* pollen, and the acritarch *Inderites* (Figures P46–P48). Documentation of the palynomorph assemblages may help determine which microfossils can be correlated from the stratotype section to other palynomorph-bearing Permian sections and permits correlation with stratigraphic sections where the conodonts (other marine invertebrates) are rare or absent (Dunn, 2001). In North America, identification of *Corollina* spp. pollen grains (Figure P51) has biostratigraphic and evolutionary plant taxonomy implications. The *Corollina* pollen grains were apparently produced by conifers, yet show morphology characteristics usually unique to angiosperms (Cornet, 1977). The acme zone of *Corollina* spp. can be used to distinguish basal Jurassic palynofloras from those of latest Triassic age.

Margaret Kneller and Sarah Fowell

Bibliography

- Cornet, B., 1977. *The Palynology and Age of the Newark Supergroup*. Unpublished PhD thesis, Pennsylvania State University.
- Dunn, M.T., 2001. Palynology of the Carboniferous-Permian boundary stratotype, Aidaralash Creek, Kazakhstan. *Rev. Palaeobot. Palynol.*, **116**, 175–194.
- Traverse, A., 1988. *Paleopalynology*. Winchester, MA: Allen & Unwin Inc., 600pp.

Cross-references

Dating, Biostratigraphic Methods
 Dinoflagellates
 Pollen Analysis

PATTERNED GROUND

Patterned ground occurs in a variety of different geographical environments, but is perhaps best developed within soils subject to regular freeze-thaw cycles. It provides a good example of self-organization within a geomorphological system (Hallet, 1990a). The term-patterned ground is used to describe a plethora of different phenomena with a variety of characteristics and sizes. On horizontal surfaces, patterned ground usually consists of isolated circles, polygonal nets, or closely spaced mounds, while on slopes it commonly occurs as either transverse steps or down-slope stripes. The most spectacular forms of pattern ground involve size sorting (Figure P52a, b). The formation of patterned ground has been the subject of considerable debate ever since earlier explorers of Arctic regions marveled at its regularity. It is now clear that there is no single mechanism to explain all examples of patterned ground, most types are polygenetic, and several different processes may result in very similar forms (Washburn, 1979). Three suites of processes are required to give the range of forms observed (Figure P53). Firstly, a sorting process (or processes) is required that can separate and concentrate particles of different sizes. Secondly, a process (or processes) is needed that can give rise to the regular patterns and spacing observed. Finally, it is clear, as one would expect, that gravity must play an important role in modifying the patterning and sorting processes on slopes. Of these three process suites, it is sorting and patterning that provides the greatest challenge and remains controversial despite considerable research (French, 1996).

It is possible to provide a size sorting mechanism by examining the behavior of a soil of mixed grain size subject to repeated freeze-thaw cycles (Mackay, 1984; French, 1996). As a soil freezes, it expands as the water within it changes phase. As the freezing front (0 °C isotherm) descends through the soil, the upper part of a large stone is likely to freeze firmly to the adjacent soil before the lower part. Subsequent ice growth and expansion will tend to raise each stone relative to the surrounding unfrozen soil beneath it. Most of this relative motion will be lost during a thaw, as the stone settles. However, the reversal is unlikely to be complete as finer particles will tend settle and work beneath the larger ones. The net result of this process after successive freeze-thaw events is the upward movement of larger stones with respect to the finer matrix. The movement of these stones will parallel the direction of maximum heat flow (Hallet, 1990b). If the freezing front descends parallel to the surface, movement will occur perpendicular to it. However, given slight heterogeneities in natural terrain due to local relief, cracks, varying soil texture, or vegetation cover, the freezing front may not be a planar surface. The consequence of this is that stones will be drawn towards certain areas on the ground surface. For example, freezing is likely to be slowest in finer grained soils, in part because they retain more moisture and hence release more latent heat upon freezing than coarser soils (Hallet, 1990b). The freezing front will therefore propagate faster in areas of coarser texture and will be lowered in these regions with respect to areas of finer texture. The heat flow vectors will therefore be directed towards areas of coarser soil, and consequently coarser particles within the soil will tend to move towards these areas during repeated freeze-thaw cycles, thereby reinforcing the textural inhomogeneities present. This provides not only a vertical but also a lateral sorting mechanism.

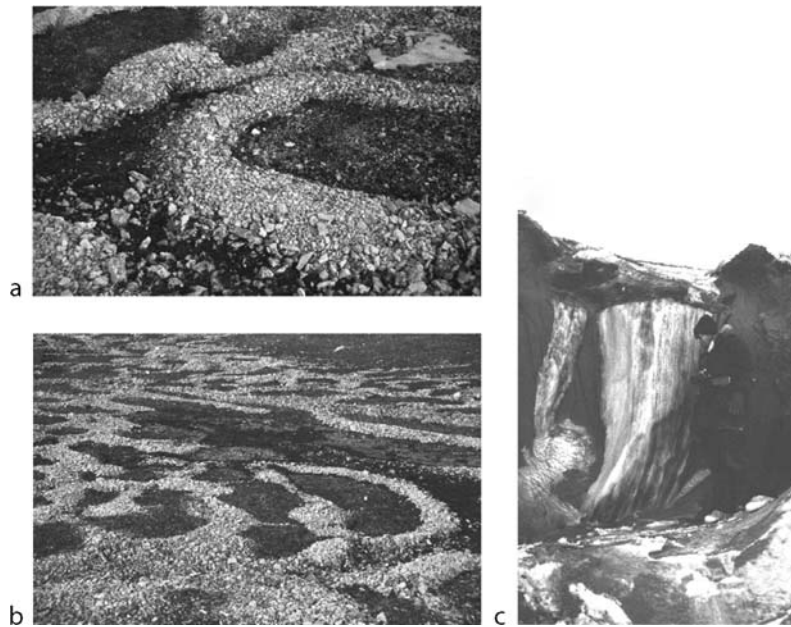


Figure P52 (a, b) Sorted circles and nets, Brøggerhalvoya (Photo: M. R. Bennett); (c) ice wedge below polygonal patterned ground, Tuktoyaktut, MWT Canada (Photo: R. I. Waller).

The next issue to consider is the range of possible patterning processes. The simplest of these processes is contraction cracking of frozen ground and the formation of polygonal nets (Washburn, 1979). These result from horizontal tension within the soil associated with a decrease in volume caused by thermal contraction, and resemble patterned ground produced in arid regions by the desiccation of surface soils. The size and configuration of the polygons depends on the rheological behavior of the soil and the nature of the volume change, which is in part determined by the climatic regime. In permafrost areas, the cracks become ice-filled and demarcated by ice wedges (Figure P52c; French, 1996). Thermal contraction does not explain all patterned ground and additional patterning processes are required. Research in recent years has concentrated on the presence of convective systems within soils subject to regular freeze-thaw cycles (Hallet, 1990b). There are two main types of convective systems. The first of these involves the movement of water through porous soils (Gleason et al., 1986; Krantz, 1990). This process operates during summer months when the temperature near the ground surface is a few degrees above 0°C , while at depth it remains at 0°C along the thaw surface. In the case of permafrozen soils, this corresponds to the top of the permafrost table. Water reaches its maximum density at 4°C and consequently the warmer surface waters are denser than the water at the thaw front, leading to a density-driven water circulation through the soil pore network. This circulation will result in the movement of heat, and therefore variations in the rate of thawing at different depths within the soil. Irregularities in the downward propagation of the thaw front may develop, producing patterns that are dictated by the size and geometry of the circulation cells. Although water movements have been observed and the theoretical geometry of the cells corresponds well with the scale of observed patterning, problems remain in understanding how this process controls the long-term formation and maintenance of patterned ground (Hallet, 1990b; French, 1996). The alternative

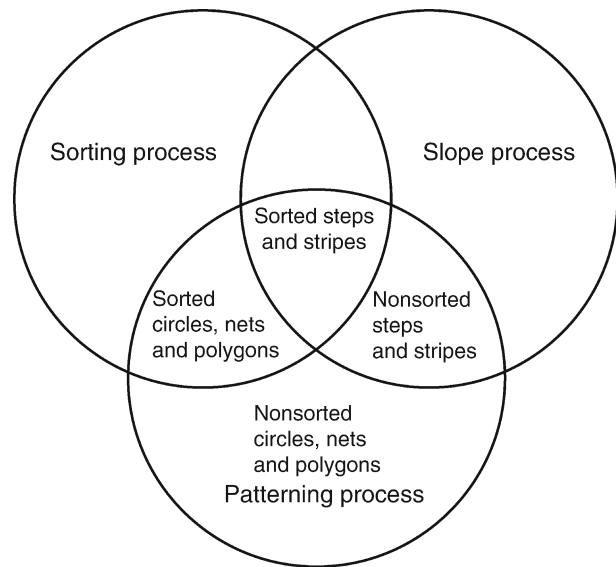


Figure P53 Processes involved in the formation of patterned ground (after Washburn, 1979, fig. 5.41, p. 160).

view involves the convective movement of soil. Again, theoretical considerations suggest that potential cell dimensions correspond well with the scale of patterned ground, and soil movement has been observed at rates of 1 cm per year, but the mechanism that drives this circulation remains elusive (Hallet et al., 1988; Washburn, 1989). Research is underway to observe and model potential convective movement of soil and water and to relate this movement to the formation and maintenance of patterned ground.

Irrespective of the lack of consensus about the formation of patterned ground, it remains one of the most spectacular examples of self-organization within a geomorphological system.

Matthew R. Bennett

Bibliography

- French, H.M., 1996. *The Periglacial Environment*. Harlow, UK: Longman, 341pp.
- Gleason, K.J., Krantz, W.B., Caine, N., George, J.H., and Gunn, R.D., 1986. Geometrical aspects of sorted patterned ground in recurrently frozen soil. *Sciences*, **232**, 216–220.
- Hallet, B., 1990a. Spatial self-organization in geomorphology: From periodic bedforms and patterned ground to scale-invariant topography. *Earth Sci. Rev.*, **29**, 57–75.
- Hallet, B., 1990b. Self-organization in freezing soils: From microscopic ice lenses to patterned ground. *Can. J. Phys.*, **28**, 842–852.
- Hallet, B., Anderson, S.P., Stubbs, C.W., and Gregory, E.C., 1988. Surface soil displacements in sorted circles, Western Spitsbergen. In *Proceedings, Fifth International Conference on Permafrost*, vol. 1, Trondheim, Norway, Tapir Publishers, pp. 770–775.
- Krantz, W.B., 1990. Self-organization manifest as patterned ground in recurrently frozen soils. *Earth Sci. Rev.*, **29**, 117–130.
- Mackay, J.R., 1984. The frost heave of stones in the active layer above permafrost within downward and upward freezing. *Arct. Alp. Res.*, **16**, 439–446.
- Washburn, A.L., 1979. *Geocryology: A Survey of Periglacial Processes and Environments*. London, UK: Edward Arnold, 406pp.
- Washburn, A.L., 1989. Near-surface soil displacement in sorted circles, Resolute Area, Cornwallis Island, Canadian High Arctic. *Can. J. Earth Sci.*, **25**, 941–955.

Cross-references

Cryosphere
Periglacial Geomorphology

PERIGLACIAL GEOMORPHOLOGY

Definition

The periglacial system is characteristic of cold morphogenetic regions at both high latitudes and high altitudes. It is specific to cold regions, both in the vicinity of glaciers and not. In periglacial areas, ice can modify the landscape by two ways. The dominant process is through landforms associated with freezing and thawing on an annual or shorter-term basis, the *seasonal frost*. The second is through landforms associated with *permafrost* or permanently frozen ground that melts only superficially in summer. As cold climates imply cold temperatures, at least in winter, water is present during part of the year in the form of snow or of ice. As ice is needed for most of the specific mechanisms, water is the sine qua non condition of frost activity (Washburn, 1979). Frost also implies desiccation, as the vapor tension is low at temperatures below freezing. Other processes such as alluvial and eolian also act specifically in this environment. For these reasons, the present-day periglacial landscape preserves morphologies surviving from Tertiary climates. The periglacial transformation of the landscape is limited at depth.

History

The term “peri-glacial” was introduced in 1909 by W. Lozinski and has been used since the beginning of the twentieth century to describe cold Pleistocene landscapes of non-glacial origin.

Permafrost

Permafrost is a part of the subsoil that remains frozen ($T < 0^{\circ}\text{C}$) during at least two successive years. The upper part of the soil melts each summer; it is the *active layer*. The depth of the active layer is controlled by climate and moisture content, being deeper in drained terrains and shallower in poorly drained soils. The upper part of the permanently frozen ground is called the *permafrost table*. It is often rich in ice accumulation for the first 10 m of the soil in interglacial conditions, with much poorer ice accumulation during glacial events. Permafrost records the thermal deficit induced by climate, especially in summer on a long time span (10^3 years). We can distinguish:

- *Continuous permafrost*. It covers more than 80% of the topography. Mean Annual Air Temperature (MAAT) is $< -7^{\circ}\text{C}$, Mean Annual Soil Temperature (MAST) is $< -3^{\circ}\text{C}$, varying with the dynamic of the snow cover.
- *Discontinuous permafrost*. It covers less than 80% of the landscape. MAAT mostly ranges from -3 to -7°C , MAST from 0 to -3°C , controlled by the snow cover. The depth of the lower boundary of the permafrost ranges from 20 m to about 60 m.
- *Sporadic permafrost*. Patchy permafrost located only in peat bogs or on north-facing slopes. It covers less than 30% of the landscape. MAAT is $> -3^{\circ}\text{C}$, MAST is close to 0°C . The permafrost reaches a thickness of about 20–30 m.

Thermal and hydrological impacts of permafrost on the substratum

The permafrost table creates a summer barrier for surface waters. Its lower boundary is in equilibrium with the long-term climate (10^3 years) and the local geothermal gradient. The occurrence of permafrost has an impact on the hydraulic functioning of the subsoil. Fluids migrate from the subsoil to the coldest part of this horizon, at a depth of about 10–20 m, which corresponds to that of penetration of the annual thermal fluctuations (Williams & Smith, 1989).

Present extent

At low altitudes, permafrost extends today between 57°N on the eastern sides of continents and 70°N on the western sides. Its thickness varies from 20 m in the south, reaching about 300 m in the deglaciated regions, and more than 600 m in the continental never-glaciated regions such as Siberia. The deepest record is more than 1,000 m in the Verkoyansk Mountains, in eastern Siberia.

Permafrost in polar and middle latitude regions

Antarctic permafrost is very old; it probably occurred prior to the onset of the Cenozoic glaciations (38 Ma). Arctic permafrost is a little younger, but still as old as the late Miocene (7–5 Ma). It has probably spread since 20 Ma. Its thermal inertia allowed its preservation at depth, as well as during the lower Pliocene warming, and during the warmest interglacials of the Quaternary. Its extent over geological time has been controlled at polar latitudes by the same parameters as glaciations: the massiveness of continents, orbital parameters (obliquity and precession), and eustatic lows. At middle latitudes, permafrost developed during periods with a depleted summer input in solar energy without being necessarily linked to large ice sheets. Its occurrence is a recent feature in Western Europe and temperate North America (<1 Ma) (Van Vliet and Hallégouët, 2001).

Interglacial-glacial extent of permafrost

The extent of permafrost reached an average 44° N latitude at low altitude during the Late Glacial Maximum (LGM). Its extent during the Holocene Optimum is restricted to 50° N along the east side of continents (Bering Strait) and to 65–70° N on the western sides. Its maximal extent, during the coldest episodes of the Quaternary, was not more significant than those of the LGM, due to the landmass configuration. During the Holocene Optimum, permafrost extent was restricted within the polar circle in the North. As a result of the lowering of the solar summer energy input during the second half of the Holocene, the southern re-expansion of permafrost today reaches about one-third of its LGM extent.

Thermal cracking

Thermal cracking occurs when temperature drops around 15 °C in a dozen hours, such as from 0 to –15 °C and from –15 to –30 °C (Mackay, 1990). The efficiency of the thermal contraction is controlled directly by the ice content of the ground, even in peat, because the ice retraction coefficient is much larger than that of most of the rocks or sediments. This is not specific to the permafrost environment. The crack may be shallow or many meters deep. It develops either as an isolated event or in polygonal nets with a 1–40 m mesh, even on rather steep slopes (up to 22°) (Figure P54). The net is usually pentagonal

or hexagonal in poorly-stratified material. In alluvial plains, it is often square. When weaknesses such as tension faults pre-exist, they control the development of the net. In the High Arctic today or in pleniglacial deposits, thermal cracking is located only in waterlogged sites (oasis in the cold desert).

When thermal cracking occurs in frost-susceptible grounds, *soil wedges* form by percolating soil suspension into the open fissure in spring. In gravel, when the crack opens, gravel and stones may fall into the furrow.

When permafrost exists, the crack that opens in winter is filled up by impure melt water (from snow and active layer), which is preserved in the form of refrozen ice, forming an *ice vein*. Year by year, as the thermal contraction follows pre-existing weaknesses, the accumulation of successive ice veins leads to the development of *ice wedges* from about 20 cm wide for recent forms up to 30 m for very old forms. The ice wedge develops exclusively in the upper permafrost horizons and the ice is vertically foliated.

In a very dry climatic context, eolian sand replaces most of the ice, leading to *sand wedges* with vertically laminated infill. Usually, lateral stresses deform the permafrost horizon with upturning of the adjacent strata. In the active layer, deformations are linked with the width of the ice wedge, and the rheology of the unfrozen material and its climatological history. Cryoturbation and thermal cracking may be synchronous.

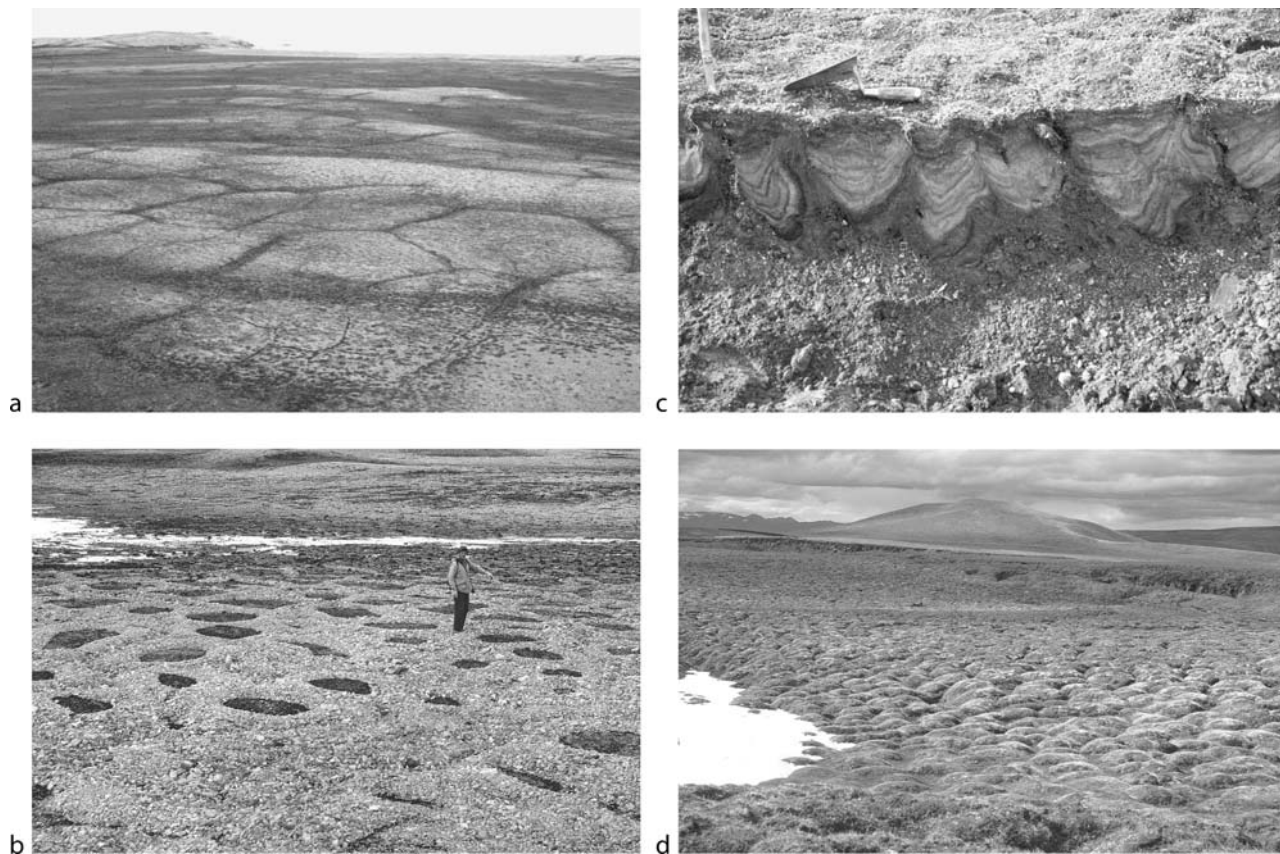


Figure P54 Examples of periglacial land forms; (a) thermal cracking, NW Svalbard, average width of polygons ~30 m; (b) patterned ground (sorted circles), NW Svalbard; (c) cryoturbation (Gåsebu, Svalbard); (d) thufur or hummocks, Northern Iceland.

These forms are further deformed by thermokarst and differential frost heave, according to the lithology and ice content of the infill when thaw occurs.

The significance of thermal cracking is limited; ice wedges reveal very short but abrupt cooling events in a continuous permafrost context. Fully vertically stratified sand wedges trace thermal cracking in dry climate with continuous permafrost (Romanovskii, 1985).

Patterned ground

These forms are the most spectacular and beautiful of the periglacial landscape (Figure P54).

Ground ice and differential frost heave

Frost may be considered as a peculiar type of thermally induced desiccation. This means that most of the cryogenic (micro) fabrics may be linked to shrinkage related to desiccation induced by low vapor tension and crystallization, *frost heave* pressure or frost induced swelling, and gravitational movements during thaw consolidation (sliding or setting). This heave is due to ice segregating in the soil as lenses and reticulated crystallizations.

Ice can nucleate at the surface of a wet soil during quick cooling and form pipekrake or *needle ice*, which lifts stones, or at depth in desiccation fissures or nets, segregating *ice lenses* or *reticulate ice*. Ice segregations cut the sediment in aggregates and generate the *cryogenic fabric*.

Frost heave is controlled by: (a) a moisture content that is optimal at the field capacity and the maximal water retention in drained conditions, (b) a thermal gradient leading to a coldward water suction, and (c) the particle size distribution (hydraulic conductivity) of the sediments. Local differences in temperature, porosity, specific surface of the mineral/organic matter fraction in connection with the particle size, and vegetation cover lead to *differential frost heaving*. Soil horizons with low water retention freeze first and those richer in fine particles freeze later because of their higher water retention. They heave more intensely because of a longer and a more efficient suction driving migration of capillary water to the growing ice segregation. Soils that easily develop a high content in segregated ice are called *frost susceptible*. Very small differences in water retention or permeability can lead to differential frost heave and *frost susceptibility gradients* (Van Vliet, 1998). Deformations known as *cryoturbations* develop by differential heave where sediments are stratified or translocated. An upward or downward *gradient of frost susceptibility* controls the geometry of the deformations. A regular network of fissures (thermal or desiccation net) assists the cryoturbation. Deformations develop both in waterlogged and drained sites. These are noticeable on flat land surfaces as well as on slopes, irrespective of density gradients. Deformations evolve in morphology along a topographic catena; the deformation morphology and its evolution with ageing will be ruled by the drainage quality and its evolution with time.

Desiccation cracking, pattern ground and hummocks

Because of the ice segregation process, all the soils are wetter on the surface from the onset of thaw. Every year, by late fall, the active layer or the seasonally frozen ground starts freezing both from the soil surface and from the permafrost table. The following spring, the soil drains progressively from the onset of thaw, leading to shrinkage pattern expression. In more

or less frost-susceptible material, desiccation cracks develop further with drainage, creating small polygonal forms up to 1 m in diameter. Frost fissures or desiccation fissures are the most common features associated with downward bending of the stratification. These fissures are at the starting point for most periglacial deformations.

Polygonal forms evolve from flat microtopography in waterlogged sites to hummocky or raised small mounds in drained conditions (Tedrow, 1977). Mounds vary from purely mineral to holorganic. They can be associated with cryoturbation, with stone jacking, and with solifluction. In this case, the material is stretched and forms sorted stripes.

Polygonal forms do not necessarily imply permafrost. Nevertheless, permafrost induces a high water table and enhances frost heave and frost jacking of stones. Polygons and hummocks develop during a cooling event such as a Heinrich event. Further warming, by enhancing the drainage, favors raised hummocky forms, leading sometimes to pseudo-convective forms.

Cryoturbation induces deformation similar to gilgai, produced by differential swelling by hydration. Cryoturbations are often confused with loading or explained by "thermal convection" not compatible with the hydrothermal regime of permafrost soils. This is related to the high frequency of cryoturbations in the same regions as tremors during the onset of deglaciations.

Stone jacking

Frost jacking is the traction of stone towards the soil surface by frost heave. This process is very fast and leads to vertically oriented stones and to loose gravel accumulation at the soil surface. This process is assisted by *needle ice*, which allows displacement of the lifted stones downslope. When the soil develops a polygonal pattern of various sizes, stones are accumulated in the furrow at the top of the fissure: the form becomes *sorted*. Similarly, if the fissure reaches a level of frost-shattered rocks at depth, differential frost heave leads to an upward migration of stones. Both processes generate *sorted polygons*. When frost susceptible material rises to the surface and pushes the superficial gravel laterally, it forms *sorted circles*. The morphological shaping induced by drainage is also valid in this case, with low and raised forms. When the stone circles are deformed by frost creep on slopes, they evolve into sorted stripes. These forms do not necessarily imply permafrost. Their climatic signature is similar to that of the normal patterned grounds.

Slope deformation

Periglacial solifluction is mass movement controlled by soil creep, which results from a combination of thaw settlement and sliding on slopes under gravity; it is directly related to the content of ice and to the water supply during thaw. It is at least ten times more efficient than common soil creep (thermo-hydric creep) (Figure P55).

Permafrost creep and rock glacier

Soils rich in segregated ice, or regolith rich in ice, flow down at a very low annual rate in relation to the ice plasticity, just as in glaciers. The origin of the ice may be segregated, refrozen meteoric water, or buried snow or ice. Scree and rock falls present a glacier-like mobility when ice-saturated. The rock glacier is a peculiar type, intermediate between a mobile scree and a decaying glacier.

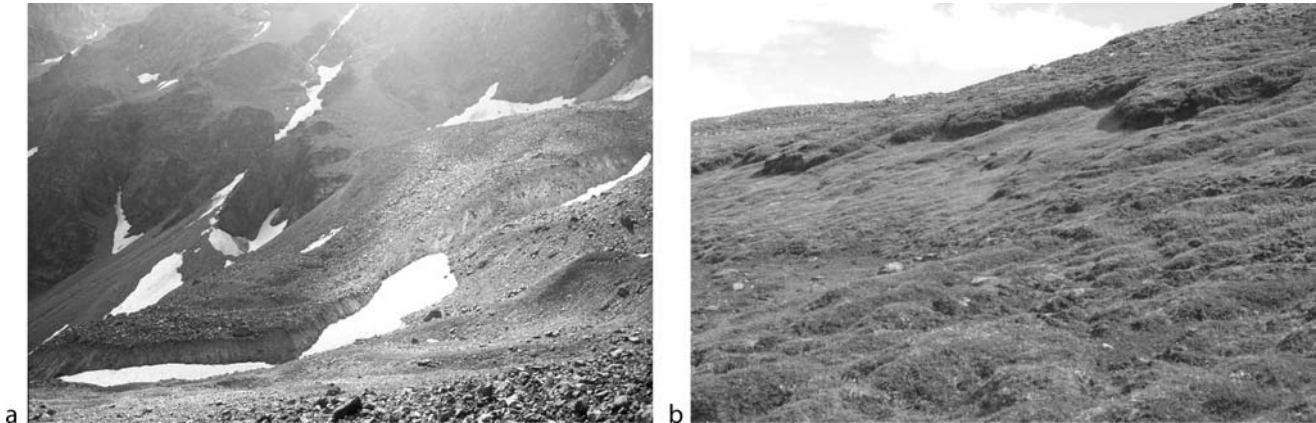


Figure P55 Examples of slope deformation in a periglacial environment; (a) rock glacier (Chambeyron, French Alps); (b) solifluction lobes (Northeast Iceland).

Mobile screes and rock glaciers are representative of dry, precipitation-starved environments, usually in discontinuous to continuous permafrost zones. They usually develop during cooling events, following a deglaciation.

Frost creep, gelifluction, and mud flow

Specific versions of solifluction in periglacial system are enhanced by soil freezing. *Frost creep* is a slow laminar flow of about 1cm per freezing cycle. In soil that is frost heaved orthogonally to the slope, frost creep develops from the onset of thaw, starting on very low angle slopes ($2-22^\circ$). The displacement is the summation of a gravity collapse by thaw consolidation, of a lateral sliding on the roof of the successive sheets of ice lenses, and of shrinking that results from drainage. The more abundant that water is during thaw, the more important the sliding component is. Below a snow patch or in a down slope position, this is fulfilled by oblique seepage. This process is common in deep seasonal frozen soils as well as in the active layer of permafrost (Harris, 1988). Frost creep is syngenetic with frost jacking, cryoturbation, and particle translocation.

Gelifluction is an accelerated form, characterized by a turbulent flow on a centimeter scale even if the total mass flows in a laminar mode. It is linked with more abundant seepage, and is more frequent on permafrost. The permafrost table restricts the water flow to the active layer only. In that case, the cryogenic fabric is stable and the form is drained when thaw proceeds: oversaturation is never reached.

When the cryogenic fabric is unstable, it collapses at thaw and the excess water cannot be evacuated: oversaturation is raised, leading to hydrostatic instability and *mud flow*. This is also common in *thermokarst* conditions.

Common deformations are terminal curvature of beds and solifluction deforming by buckling and stretching the strata, sometimes with syngenetic cryoturbation (permafrost). They are usually shallow (<1 m max) and tend to diminish and vanish with depth. Deformations and clast alignments are related to ice content and moisture supplied during thaw: flat lying clasts with their long axes oriented down slope indicate excess moisture from snow melt; vertical clasts indicate dominant frost heave. The morphology is commonly lobbed or elongated parallel to the slope. It occurs in pure mineral soils as well as in organic material. Vegetation, as shrubs or grassy mats, and

frost-jacked gravel accumulations may support the fronts of some features, leading to terraces or lobate morphology.

Frost creep has no specific climatic association as only frost is needed. It occurs from subtropical to high latitude or altitude, and on permafrost as well as in seasonally frozen ground. The presence of permafrost is indicated by a regionally higher frequency of gelifluction.

Frost shattering

Frost shattering is controlled by the porosity of the rock, especially the closed porosity and the pre-existing fissility. It can result from three mechanisms: the change of the pore water volume by freezing, acting like a wedge; induced hydrofracturation of the rock or water expulsion; and ice growth by segregation in fissures when some accumulated debris or organic matter (in situ or by translocation) induces water retention – mechanisms are similar to those in soil. The efficiency of the shattering is linked with the rapidity of frost, allowing trapping of water into the porosity and a sudden rise in pressure.

In the field, paleo-weathering or hydrothermal activity, tectonism, and previous thermal and hydric (dilation) shattering commonly enhance frost shattering. Frost shattering fragments the rock into blocks, flakes, shards, and particles, down to sandy or loamy size following the lithology. The sorting is normally poor except for some isograined lithologies (Lautridou and Ozouf, 1982). In situ frost shattering and cliff frost shattering produce screes, stratified slope deposits (“grèzes litées,” “heads”), and debris flows. Snow patches may locally enhance the frost shattering and permit the formation of nivation *benches* or *terraces*. Salt can emphasize the process, by lowering the freezing point. This is common on the coast. Along lakes or seashore, frost shattering, associated with the action of drift ice, facilitates the formation of *abrasion surfaces* and *littoral notches*. Normally, frost shattering is associated with moisture and the speed of frost penetration. It is inactivated within permafrost as in frozen caves. Climatic significance is thus limited.

Thermokarst

When the ground contains an excess of ice (ground ice, injected ice, or buried ice of various origins), thawing leads to subsidence, which results in sink-holes or retrogressive sliding. Simple subsidence of 8–25 m of an important portion of

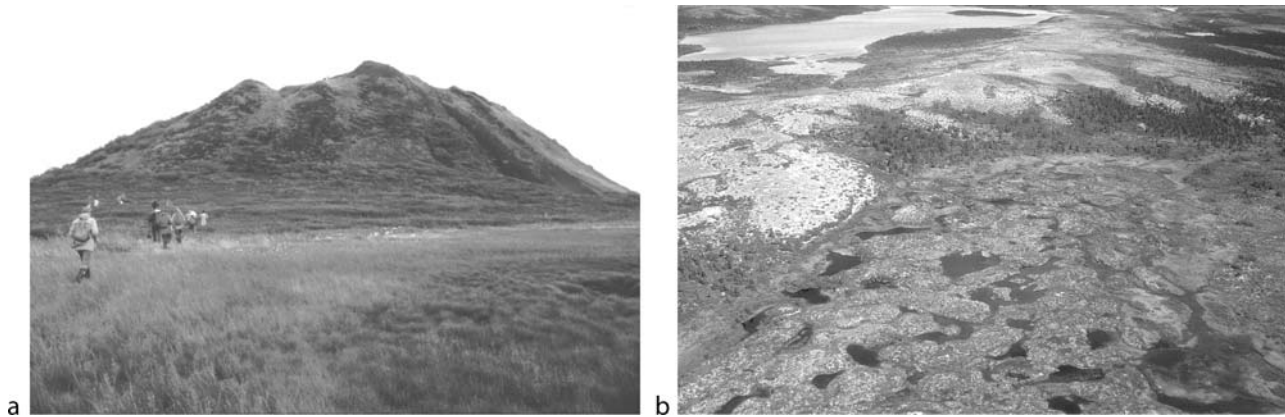


Figure P56 Examples of periglacial mounds; (a) Pingo (Mackenzie delta, Canada); (b) Palsa field (Ungava, Canada).

the ground allows the formation of *sink-holes*, often associated with *normal faulting*. The hollows are commonly occupied by a circular lake, which is further extended by the undercutting of waves. It results in a landscape of *oriented lakes*. In the presence of a polygonal network of ice wedges, thermokarst activity develops firstly polygonal furrows occupied by water and later, when drained, a specific hilly morphology called “*bad-jarak*” by the Russian authors (Solovyev, 1973). As the drainage is modified, melting progresses retrogressively upwards. On a slope, a modification of the thaw depth and drainage may induce the thawing of the ice-rich upper horizon of the permafrost, allowing downward collapse and slumping of water-saturated sediments. Mud flows can be generated. As the drainage is modified, melting progresses *retrogressively upwards* with *slumps* (MacRoberts, 1978). This process may lead to a cyclic landscape rejuvenation, as in the high Arctic.

Thermokarst is generated by various disturbances: (a) by warming, such as during the late glacial and the early Holocene; (b) by fire modifying the local energy budget, by destroying the vegetation cover; (c) by river incision, which alters the drainage and allows a deeper thaw; and (d) by anthropogenic perturbations or global warming, which like fire can modify the energy budget (Burn, 1997).

Periglacial mounds

Two main types exist: the pingo and the palsa. The fossil traces are similar except for size and some specific details (Figure P56).

Pingo

These are the largest forms, often more than 50 m in diameter (they can be several hundred meters in diameter) and up to 60 m high. They generally occur isolated. They are specifically linked to the growth of a hydrolaccolith (injected massive ice), to permafrost aggradation squeezing a water table in a former lacustrine depression, or to lateral seepage from a slope talik or unfrozen volume in the permafrost. This form lifts up sediments until the pressure of the water balances the overburden pressure. Tension fissures may open at its top. The basal layer is porous or fractured, allowing water circulation.

During the growth and the decay phases, solifluction develops on the sides. After the melting, a circular lake remains in a sink-hole surrounded by a rather high, residual circular rim. Upturned layers dipping towards the outer part of the structure exist in the rim and at depth, with a “cone-in-cone”

collapsed structure (thermokarst) (De Gans, 1988). Lacustrine deposition and peat formation occur in the lake. These mounds are specific to a continuous permafrost environment and indicative of a cooling trend during the end of an interstadial or an interglacial.

Palsa

These forms range from rather small sizes (1–5 m high) up to rather large forms, reaching up to 15 m high and 50 m wide. They develop in waterlogged depressions (mire) by segregation of ice in peat or sediments, usually when the wind drift in winter reduces the thermal insulation by the snow cover (Seppälä, 1988). The surficial layer is desiccated when uplifted, and acts as a thermal insulation in summer. Some palsas are purely mineral soils. The mounds occur in clusters, often forming oriented plateaus, sometimes affected by thermal cracking. The ice segregation is reticulated in lacustrine or glacio-marine deposits, or forms ice lenses in sectors affected by impeded drainage connected with climate cooling.

During the growth and decay phase, solifluction develops on the sides. The decay is not necessarily linked to a warming: the drainage of the peat allows its fracturing and warmth penetration, and solifluction develops on the sides, stretching the peat layer; wind abrasion may also destroy the peat cover and favor the thermokarst collapse. After the melting, a circular lake subsists in a sink-hole surrounded by a residual, circular rim. Upturned (peat) layers dipping towards the outer part of the structure exist in the rim (Pissart, 1983) with no peculiar organization at depth (thermokarst). Lacustrine deposition and peat formation occur in the thaw lake.

These mounds are specific to sporadic to discontinuous permafrost zones. Their development is specifically epigenetic during a cooling trend that follows a long, humid period such as an interstadial or an interglacial. Syngenetic forms develop in a rather stabilized climate.

Brigitte Van Vliet-Lanoë

Bibliography

- Burn, C., 1997. Cryostratigraphy, paleogeography and climate change during the early Holocene warm interval, western Arctic coast, Canada. *Can. J. Earth Sc.*, **34**, 912–925.
- De Gans, W., 1988. Pingo scars and their identification. In Clark, M.J. (ed.), *Advances in Periglacial Geomorphology*, Chichester: Wiley, pp. 299–322.

- Harris, C., 1988. Mechanisms of mass movement in periglacial environments. In Anderson, M.G., and Richards, K.S. (eds.), *Slope Stability*. Chichester: Wiley, pp. 531–559.
- Lautridou, J.P., and Ozouf, J.C., 1982. Experimental frost shattering. 25 years of research at the Centre de Géomorphologie du CNRS. *Prog. Phys. Geogr.*, **6**(2), 215–232.
- Mackay, J.R., 1990. Some observations on the growth and deformation of epigenetic, syngenetic and anti-syngenetic ice wedges. *Permafrost Periglacial Proc.*, **1**:15–29
- MacRoberts, E.C., 1978. Slope Stability in cold regions. In Andersland, O.B., and Anderson, D.M. (eds.), *Geotechnical Engineering for Cold Regions*. New York: McGraw Hill, pp. 363–404.
- Pissart, A., 1983. Remnants of periglacial mounds in the Hautes fagnes (Belgique); structure and age of the ramparts. *Geologie en Mijnbouw*, **62**(4), 551–555.
- Romanovskii, N.N., 1985. Distribution of recently active ice and soil wedges in the USSR. In Church, M., and Slaymaker, O. (eds), *Field and Theory – Lectures in Geocryology*. Vancouver: University of British Columbia Press, pp. 154–165.
- Seppälä, M., 1988. Palsas and related forms. In Clark, M.J. (ed.), *Advances in Periglacial Geomorphology*. Chichester: Wiley, 247–278.
- Solovyev, P.A., 1973. Thermokarst phenomena and landforms due to frost heaving in Central Yakoutia. *Biuletyn Peryglacjalny*, **23**, 135–155.
- Tedrow, J.C.F., 1977. *Soils of the Polar Landscape*. New Brunswick, NJ: Rutgers University Press, 638pp.
- Van Vliet-Lanoë, B., 1998. Frost and soils: Implications for paleosols, paleo-climates and stratigraphy. *Catena*, **34**, 157–183.
- Van Vliet-Lanoë, B., and Hallégouët, B., 2001. European permafrost at the LGM and at its maximal extent. The Geological Approach, 1999. In Paepe, R., and Melnikov, V. (eds), *Permafrost Response on Economic Development, Environmental Security and Natural Resources*, Dordrecht: Kluwer, pp. 195–213.
- Washburn, A.L., 1979. *Geocryology. A Survey of Periglacial Processes and Environment*. London: Edward Arnold publications, 406pp.
- Williams, P.J., and Smith, M.W., 1989. *The Frozen Earth. Fundamentals of Geocryology. Studies in Polar Research*, Cambridge: Cambridge University Press, 306pp.

Cross-references

Astronomical Theory of Climate Change
 Cenozoic Climate Change
 Cryosphere
 Glacial Eustasy
 Glacial Geomorphology
 Glacial Sediments
 Heinrich Events
 Last Glacial Maximum
 Loess Deposits
 Millennial Climate Variability
 Orbital Variation and Climate
 Paleosols–Quaternary
 Patterned Ground
 Pingos
 Pleistocene Climates

PHOSPHORITE

Phosphorite (often referred to as phosphate rock) is a sedimentary rock of which the main mineralogical constituent is francolite (carbonate-fluor-apatite, CFA). The above definition excludes igneous phosphate-rich rocks as well as continental deposits (e.g., guano; a few lacustrine deposits) Whereas most sedimentary rocks contain less than 1% of P₂O₅, its content in phosphorites is above 18%, (>50% in francolite) and may reach values as high as 37%. Usually phosphorus content is expressed as P₂O₅ percentage. An alternative unit is BPL (bone phosphate of lime or tricalcium phosphate), where BPL = 2.185 × %P₂O₅.

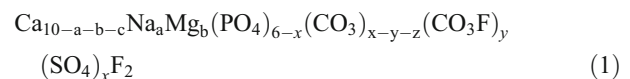
Since antiquity have farmers applied lime-treated bones to soil as a means of improving soil fertility. However it was only in the mid 19th century that J. von Liebig suggested the use of phosphorite as a fertilizer, and J. Lawes (1842) invented the dissolution of phosphorite in sulfuric acid to produce a more soluble and efficient fertilizer. The study of phosphorites received much attention beginning with the late thirties of the 20th century, when the demand for fertilizers increased dramatically. Research boomed after WW II, and the last decades of the previous century saw several comprehensive reviews of the subject in the literature (Cook, 1976; Bentor, 1980; Kolodny, 1981; Sheldon, 1980; Notholt and Jarvis, 1990; Föllmi, 1996, Burnett and Froehlich, 1988). The three volumes of “Phosphate Deposits of the World” were the fruits of a concentrated effort of an international research program (IGCP156) between 1977 and 1984 (Cook and Shergold, 1986; Notholt et al. 1989; Burnett and Riggs, 1990). The three multi-authored volumes are a comprehensive summary of all important phosphorite deposits of the world.

Distribution

Phosphorites are found in marine deposits of all ages, from the Proterozoic to the Recent seafloor (Burnett and Riggs, 1990, Cook and Shergold., 1986, Notholt et al., 1989, [Figures P57, P57](#)). Phosphorites have been found on all continents except Antarctica. Cook and McElhinny (1979) ([Figure P57](#)) have shown that the distribution of phosphorites in the record is uneven: “phosphate giants” dominate geological history with peaks in the Cambrian, Permian, and Mio-Pliocene. The young and Recent phosphorites on the shelves around America, the western coast of Africa, and surrounding Australia ([Figure P58](#)) were the object of intensive study since their discovery by Murray and Renard in 1891, especially since the identification of localities of present phosphogenesis by Baturin in 1971 (Baturin, 1981). The most common lithological association is that of phosphorites with cherts and black shales (reflecting the geochemical nutrient trinity of P-Si-C). This is the association typical of many phosphorite “giants” such as the Permian Phosphoria Formation of the western United States, the Cretaceous-Eocene phosphorites of the southern Tethys, and the Karatau (Kazakhstan) and Khubsugul (Mongolia) Cambrian deposits. In contrast to this “West Coast” type association, an assemblage of phosphorites with carbonates and siliciclastic rocks has been described from the Neogene of the East Coast of the US. Surface weathering of primary marine phosphates may result in residual type deposits such as the Holocene brown-rock weathering products of Ordovician phosphatic limestones in Tennessee. Various authors (e.g., Bentor, 1980) have mentioned evaporites, dolomite, Mg-rich clays (e.g., palygorskite), and glauconite as being paragenetically related to phosphorites.

Mineralogy and petrology

The chemical formula of francolite, the major phase in phosphorite, can be approximated by



where $x = y + a + 2c$, x varies from near zero to 1.5, $y = 0.4x$ on average, and $b = 0.4a$. c is the number of Ca vacancies (Nathan, 1984). The key substitution seems to be that of a planar $(\text{CO}_3)^{2-}$ triangle replacing a tetrahedral $(\text{PO}_4)^{3-}$ ion.

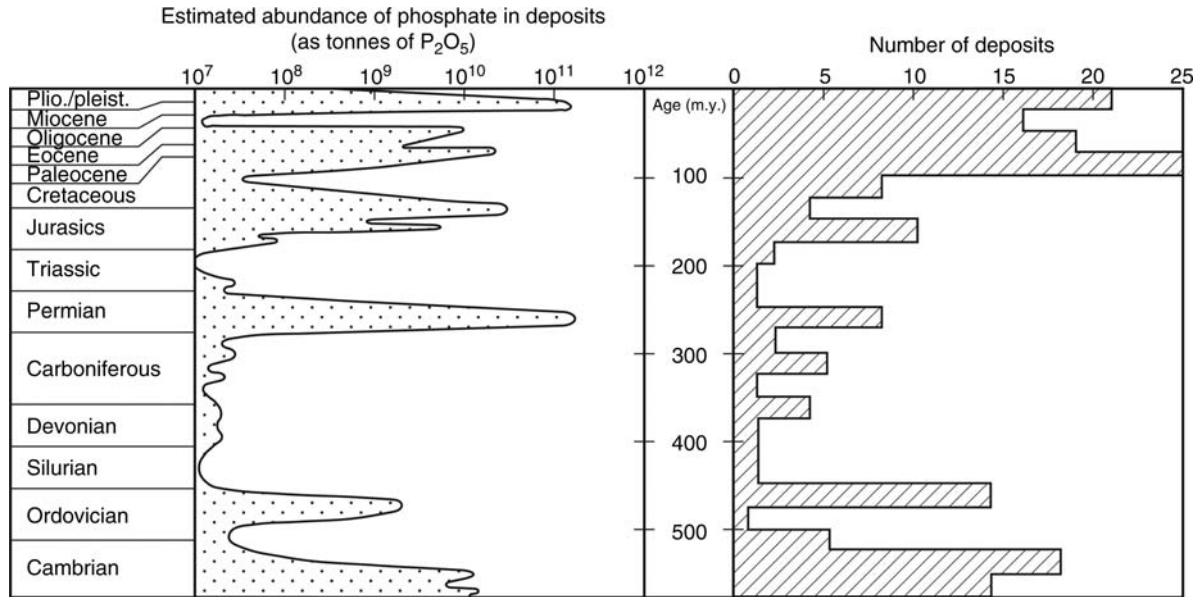


Figure P57 Estimated abundance of phosphorite deposits and P₂O₅ tonnage in Phanerozoic sediments (from Cook and McElhinny, 1979).

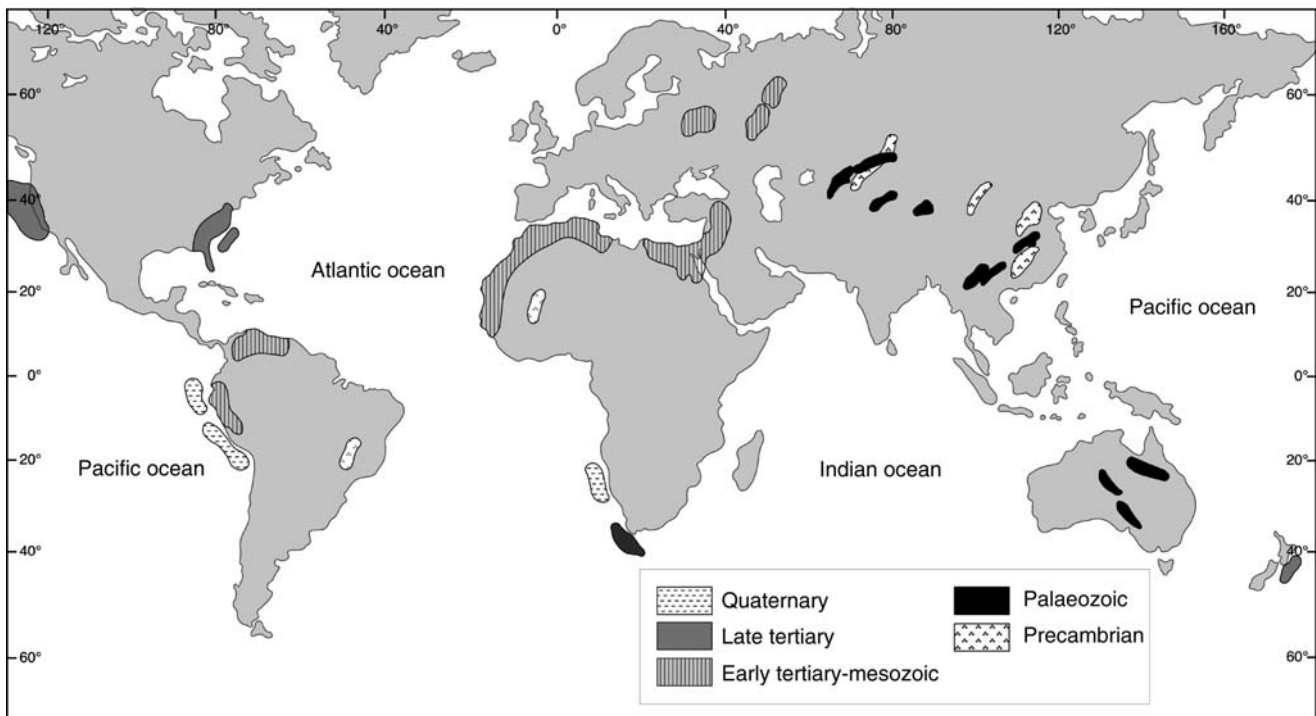


Figure P58 Distribution of major and important sedimentary phosphorite deposits. The symbols mark the age of the deposit. Note the South-Tethyan Mesozoic belt that extends from Turkey via Morocco to Mauritania and Senegal; it extends across the Atlantic to Venezuela and Colombia (after Cook, 1976).

Figure P59 summarizes only the most important substitutions in the very “open” apatite structure.

Phosphorites may be texturally classified into: (a) bedded phosphorites, (b) bioclastic phosphorites, (c) nodular phosphorites, and (d) pebble-bed phosphorites. Francolite occurs in

phosphorites as laminae, pellets, ooids, crusts, nodules of various irregular shapes, skeletal shell and bone fragments, and cements. Phosphorite types may range from predominantly pelletal to purely bioclastic – or “bone beds.” Glenn et al. (1994), distinguished between *pristine* phosphate-bearing deposits,

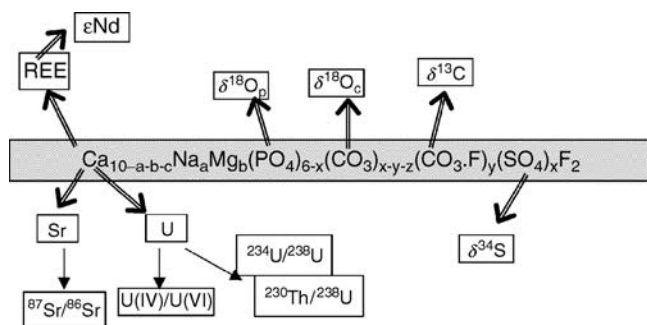


Figure P59 Scheme of possible substitutions and of the isotopic tracers that are commonly analyzed in francolite. Note that whereas the light stable isotopes (of C, O, S) are major anions in CFA, the heavy isotopes (of Sr, Nd and U) substitute for Ca in the lattice (after Kolodny and Luz, 1992).

which lack any sign of reworking, *condensed* phosphatic laminae in which particles were concentrated by winnowing, and *allochthonous* redeposited particles.

The weathering zone of phosphorites often includes several Al- and Fe-phosphates such as wavellite and millisite.

Geochemistry

The large amount of substitutions in francolite makes it a most sensitive recorder of the environments in which it forms.

Major elements

Most unweathered seafloor francolites contain about 6.3% CO₂ and between 3 and 4% F. Carbonate and fluorine concentrations are correlated, probably reflecting the coupled substitution of (CO₃F)³⁻ for phosphate. Several interpretations have been offered for this variability: (a) temperature variation of the depositional basin, causing variable degrees of CO₂ saturation; (b) late diagenetic burial effects, metamorphism and weathering; and (c) CO₃²⁻ content of the interstitial water, i.e., carbonate alkalinity.

Trace elements

Phosphorites are enriched in a large number of trace elements. Many of these enrichment factors can actually be attributed to the organic matter associated with the phosphorites rather than to the francolite itself. Still, after accounting for the organic matter, a strong enrichment in Cd, Ag, Mo, Se, U, Y, Zn, REE, and V is probably related to apatite. Some of these have been studied for their importance as valuable by-products (U, REE), others because of their toxicity, which requires their removal from the marketable product (Cd and U in production of phosphogypsum). We shall consider here only those from which paleo-environmental information has been retrieved.

REE. The rare-earth elements (La–Lu) and Y apparently substitute for Ca²⁺ in the francolite lattice. Both total REE concentration and the relative abundance of the different REE in phosphorites vary. It is customary to consider such abundances on a shale- (or chondrite-) normalized distribution graph, with atomic number as the abscissa and log (normalized abundance) as the ordinate. In such space, “anomalies” can be conveniently expressed. Thus a Ce anomaly (Ce*) in a rock is defined as

$$Ce^* = \log(3Ce_{SN}/(2La_{SN} + Nd_{SN})) \quad (2)$$

where the subscript SN denotes a shale-normalized concentration. Many phosphorites display a typical “seawater pattern”:

they are strongly depleted in Ce and enriched in the heavy REE (HREE; Ho–Lu). These include the western US Permian Phosphoria Formation, as well as many of the Mesozoic Tethys belt deposits: Morocco, Egypt, Jordan (Jarvis et al., 1994). On the other hand, numerous deposits (offshore Namibia, Agulhas Bank, off Peru, Karatau, Kazakhstan) have shale-like (flat) patterns with no Ce anomaly. The Ce anomaly has been attributed to the oxidation of Ce³⁺ in the deep sea to Ce⁴⁺, which is then sequestered from seawater by ferromanganese oxides. Indeed modern coastal and surface seawater display little or no Ce* and little HREE enrichment. Numerous attempts have been made to interpret REE patterns in phosphorites as reflecting depositional environment, specifically depositional oxygenation levels. The very low content of REE in apatitic skeletal elements of living organisms (e.g., fish bones) compared to their higher concentration in fossils suggests, however, that at least a large part of the REE is introduced into francolite during early diagenesis.

Uranium. Phosphorite typically contains between 50 and 200 ppm U, though numerous deposits (Proterozoic-Cambrian of Karatau and Khubsugul) contain as little as 2 ppm whereas others (Eocene of the Central African Republic) may reach levels of 5,600 ppm. Uranium in phosphorites occurs both as U(IV) and U(VI), both apparently substituting for Ca in francolite. U(IV) content varies between zero and almost 90%. That variation in conjunction with petrography and other geochemical parameters has been successfully used for the reconstruction of marine paleo-redox conditions.

Uranium and uranium series daughter isotopes (specifically ²³⁴U/²³⁸U, ²³⁰Th/²³⁴U, ²³¹Pa/²³⁵U) have been successfully used as dating clocks of young phosphogenesis in the ocean (Baturin, 1981; Jarvis et al., 1994; Kolodny and Kaplan, 1971; see also summary in Kolodny and Luz, 1992). Dating was instrumental in demonstrating that: (a) most sites of seafloor phosphorite nodule occurrence are *not* sites of present-day phosphogenesis, and (b) phosphorites *have* formed recently off the coasts of Peru-Chile, Namibia, western South Africa, and East Australia. Applying these techniques, the episodic nature of phosphogenesis – confined to periods of high eustatic sea level – has been demonstrated for the region off Peru-Chile and western South Africa.

Sr and Nd isotopes (Jarvis et al., 1994; Kolodny and Luz, 1992). Since the 1970s, it has been demonstrated that the ratio of ⁸⁷Sr/⁸⁶Sr in the world ocean can be described by the ⁸⁷Sr/⁸⁶Sr reference curve (see *Strontium isotopes*). The high Sr content of francolite makes it potentially possible (within reasonable assumptions) to date phosphorite formation by measuring this ratio and comparing it to the reference curve. Thus, episodes of Neogene phosphogenesis, grain concentration, and reworking of phosphatic sediments have been established for the phosphorites of Florida and the North Carolina shelf by Glenn et al. (1994), as well as by P. Stille and his coworkers.

Unlike Sr, the much shorter residence time of Nd (*see Dating, radiometric methods*) in the ocean (about 2 kyr) results in a heterogeneity of the ¹⁴³Nd/¹⁴⁴Nd ratio in seawater: each major ocean yields a different Nd-isotope evolution curve. Measurements of εNd in sedimentary apatites showed that the present day Pacific-Atlantic provincialism is about 50 Ma old. Prior to that, a single Panthalassa Ocean seems to have existed for about 400 Ma. Prior to 450 Ma, two separate water masses can again be distinguished – the South and North Iapetus Oceans.

Stable isotopes (Jarvis et al., 1994; Kolodny and Luz, 1992)

Significant information on the nature of phosphogenesis has been acquired from the study of the stable isotopes of oxygen, carbon, and sulfur.

Oxygen. Francolite has the unique property of containing oxygen in two distinct sites, which are rather simply analytically separated. These are oxygen in the carbonate – $\delta^{18}\text{O}_c$ and oxygen in phosphate – $\delta^{18}\text{O}_p$ (Figure P59; see *Stable isotope analysis* for definitions of the δ notation used here). It is assumed that oxygen (and carbon) isotope fractionation in the carbonate follows the carbonate paleotemperature equation (Epstein et al., 1953, see *Paleotemperatures, proxy reconstructions*)

$$T(^{\circ}\text{C}) = 16.5 - 4.3(\delta^{18}\text{O}_c - \delta^{18}\text{O}_w) + 0.14(\delta^{18}\text{O}_c - \delta^{18}\text{O}_w)^2 \quad (3)$$

and $\delta^{18}\text{O}_p$ is governed by (Kolodny and Luz, 1992; Longinelli and Nuti, 1973)

$$T(^{\circ}\text{C}) = 111.4 - 4.3(\delta^{18}\text{O}_p - \delta^{18}\text{O}_w) \quad (4)$$

In Equation (3), $\delta^{18}\text{O}_c$ is for all practical purposes equal to $\delta^{18}\text{O}$ of the CO_2 extracted with phosphoric acid and measured vs. PDB, $\delta^{18}\text{O}_p$ in Equation (4) is the $\delta^{18}\text{O}$ value (vs. SMOW) of the oxygen of the francolite phosphate, and $\delta^{18}\text{O}_w$ in both equations is the $\delta^{18}\text{O}$ value of the water with which the francolite equilibrated. T is the temperature of formation of the francolite. It was initially hoped that $\delta^{18}\text{O}_p$ might be a sensitive recorder of environmental temperature and water composition, and a robust preserver of such records. It turned out, however, that although $\delta^{18}\text{O}_c$ is more susceptible to alteration than $\delta^{18}\text{O}_p$, both oxygen sites are prone to post depositional exchange. Indeed $\delta^{18}\text{O}_p$ and $\delta^{18}\text{O}_c$ in phosphorites that span the time range of the last 10^9 years are very well correlated. $\delta^{18}\text{O}_p$ and $\delta^{18}\text{O}_c$ in phosphorites vary with time in a roughly parallel pattern, both decreasing with increasing age, the greatest changes occurring within samples of the last 100 Myr. A similar trend has been observed before for several other sedimentary phases: carbonates, cherts, and glauconites. The question whether these trends record changing temperature, change in $\delta^{18}\text{O}$ of seawater, or increasing alteration has not yet been resolved. Several attempts were made to use $\delta^{18}\text{O}$ in phosphorites for paleotemperature reconstruction: Karhu and Epstein, 1986 (see also Kolodny and Luz, 1992) deduced high pre-Cambrian temperatures from the phosphate-chert oxygen isotopic fractionation. Shemesh and Kolodny (1988) concluded from the stratigraphic variation in $\delta^{18}\text{O}_p$ of Tethyan phosphorites that the phosphogenic event was associated with a cool-water upwelling. In many phosphorites (e.g., Miocene Monterey Formation of California, Cambrian Georgina basin in Australia), $\delta^{18}\text{O}_p$ values are much too low to represent marine temperatures. Thus, the interpretation of such results is still problematic.

Carbon. The carbonate ion in francolite (CFA) can also be analyzed for $\delta^{13}\text{C}$. Such measurements lead to the conclusion that not all carbonate enters the CFA lattice at the time of precipitation; usually such carbonate is in equilibrium with interstitial water rather than with seawater. McArthur et al. (1986) have demonstrated that organic matter-derived (low $\delta^{13}\text{C}$) carbon was to some degree involved in the diagenesis of francolites. $\delta^{13}\text{C}$ is negatively correlated with the CO_2

content of CFA. These studies led to the realization that most phosphorites formed in dominantly suboxic conditions; some (e.g., the Blake Plateau) were formed in a clearly oxic environment, others (Morocco) have been in contact with anoxic pore waters.

Sulfur. The sulfate ion substitutes for phosphate in CFA. $\delta^{34}\text{S}$ varies in phosphorites between values equal to those of coeval seawater sulfate and much higher values (by as much as 10‰). The former apparently reflects seawater sulfate incorporation, whereas the heavier sulfur reflects the residual sulfate after partial reduction. Such “Rayleigh distillation” in a closed system results in a negative correlation between SO_4^{2-} and $\delta^{34}\text{S}$, as observed in francolites of the Phosphoria Formation (Piper and Kolodny, 1987).

Origin and paleoclimatology

Three closely related observations influence strongly all thinking on the genesis of phosphorites: (a) Though phosphorites were deposited in a variety of settings, on seamounts, continental margins, and epeiric seas, all were related to high organic productivity and nearly all to upwelling. This is evidenced by the very nature of phosphorus as a biolimiting element and by the ocean being the major phosphorus reservoir, as well as by the abundance of phosphatic skeletal fragments in phosphorite deposits. (b) Though most phosphorites on the seafloor were proven to be relict (see Kolodny and Luz, 1992), all modern phosphorites are found in areas of oceanic upwelling. (c) The strong association of phosphorites with chert and black shales (P-Si-C) in the geological record further points to such an association. In a series of studies, J. Parrish and coworkers (see Parrish, 1998 for summary and references) concluded that “the distribution of phosphorites is mostly simply dependent on the distribution of upwelling zones over continental shelves for much of the Phanerozoic.” She then used phosphorite distribution as a tool for mapping upwelling zones of the past. Cook and McElhinny (1979) stressed the low paleolatitude distribution of ancient phosphorites and their association with evaporates.

Thus, the explanation of the formation of phosphorite deposits amounts to pointing to a suggested break (sink) in the chain: river input \rightarrow dissolved phosphate \rightarrow organic matter formation \rightarrow dissolved phosphate. In about two centuries of research, almost all possible breaks in the chain were offered in addition to suggestions of additional sources such as volcanism (see Bentor, 1980; Cook et al., 1990; Glenn et al., 1994; Kolodny, 1981). Of seminal importance was the publication of Kazakov’s paper in 1937, in which he linked phosphogenesis to oceanic upwelling, warming of the rising cold water, CO_2 release, and francolite precipitation. Kazakov’s idea, though ultimately rejected in its original form, became the basis of most variants of modern theories of phosphogenesis. Most researchers today agree that francolite is primarily precipitated interstitially in sediments, either chemically or biochemically. In many cases, an association between microbial activity with both mobilization and precipitation of CFA has been documented. Apatitic microbial structures were identified in phosphorite deposits (e.g., Krajewski et al., 1994; Soudry and Champetier, 1983). It is not clear whether the role of microbial mats in phosphogenesis was active, passive, or in-between these extremes. Apatite was also formed bacterially in the laboratory by J. Lucas and L. Prevot (see also Krajewski et al., 1994).

Although seawater is oversaturated with respect to CFA, the slow kinetics of its nucleation and crystallization at the sediment water interface cause the principal formation site to be a

few centimeters inside the sediment, and associated with surfaces of non-deposition or slow sedimentation rates. Whatever the process of primary francolite formation is, the achievement of a high-grade phosphorite requires an additional step of concentration, most likely by mechanical re-working and winnowing (Baturin, 1981). It has been stressed by Föllmi (1994) that no exceptionally long times were required to form even the very large phosphorite deposits. Thus, he estimates that assuming an efficient P supply, only about 12 kyr were required to form the southern Tethyan Paleocene-Eocene province, and only 240 kyr of similar conditions for the formation of the Permian Phosphoria deposit in the Western US. Filippelli and Delaney (1992) showed that phosphorus accumulation and burial rates of major phosphorite deposits are comparable to those of the modern Peru margin.

Following the different models of phosphogenesis, various authors chose to interpret the occurrence of “phosphate giants” in the sedimentary record. These were cited as evidence for times of warm climate (Fisher and Arthur, 1977), as well as times of glaciation (Sheldon, 1980), times when continents drifted into low latitudes (Cook and McElhinny, 1979), major transgressions leading to major anoxia (Arthur and Jenkyns, 1981), or increased continental weathering. The broad spectrum of causes cited above probably shows that no single cause could be regarded as *the* cause for phosphogenesis. Upwelling may be an exception, it seemingly being related to most large phosphorite deposits.

Economics

Phosphorites account for about 85% of the world's phosphate consumption (the rest is supplied from igneous and guano ores). Mineral fertilizers account for approximately 80% of phosphate use, with the balance divided between detergents (12%), animal feeds (5%) and specialty applications (3%), e.g. food grade, metal treatment etc. The production of phosphate rock peaked in 1988 at a level of 166 million tons product, falling to 125 million tons in 2001, and rebounding to 147 million tons in 2007. Over 30 countries are currently producing phosphate rock for use in domestic markets and/or international trade. However, the world's top 12 producing countries account for nearly 95% of the world's total phosphate production. The main producers are the USA, China, Morocco, Russia and the Middle East.

In 2002 the US Geological Survey estimated that world phosphate rock reserves amounted to about 12 billion tons, with a larger reserve base of about 47 billion tons. Of these reserves the lion's share is concentrated in Morocco. The last two decades of the twentieth century have seen a sharp decrease in the demand for phosphate, primarily due to an economic slowdown in developing countries. In 2008 the price of phosphate rock reached \$200/ton after several years of a stable price of \$50/ton. The expected growth is based on the demand for more food by a growing and more affluent population, especially in the developing countries. It also is a reflection of the fact that there is no substitute for phosphorus in agriculture.

Yehoshua Kolodny

Bibliography

Arthur, M.A., and Jenkyns, H.C., 1981. Phosphorites and paleoceanography. *Oceanologica Acta*, Proceedings of 26th International Geological Congress, Geology of Oceans Symposium, Paris, 1981, pp. 83–96.
 Baturin, G.N. (1981). Phosphorites on the Sea Floor. *Developments in Sedimentology*, 33. Amsterdam: Elsevier, 343pp.

Bentor, Y.K. (ed.), 1980. *Phosphorites – the unsolved problems*. Tulsa: Society Economic Paleontology Mineralogy (SEPM) Special Publication No. 29, pp. 3–18.
 Burnett, W.C., and Riggs, S.R. (eds.), 1990. *Phosphate Deposits of the World, Vol. 3: Neogene to Modern Phosphorites*, Cambridge: Cambridge University Press, 464pp.
 Cook, P.J., 1976. Sedimentary phosphate deposits. In Wolf, K.H. (ed.), *Handbook of Strata-Bound and Stratiform Ore Deposits*, Vol. 7, Amsterdam: Elsevier, pp. 505–535.
 Cook, P.J., and McElhinny, M.W., 1979. A reevaluation of the spatial and temporal distribution of sedimentary phosphate deposits in the light of plate tectonics. *Econ. Geol.*, **74**, 315–330.
 Cook, P.J., and Shergold, J.H. (eds.), 1986. *Phosphate Deposits of the World, Vol. 1: Proterozoic and Cambrian Phosphorites*. Cambridge: Cambridge University Press. 386pp.
 Cook, P.J., Shergold, J.H., Burnett, W.C., and Riggs, S.R., 1990. Phosphorite research: A historical overview. In Notholt, A.J.G., and Jarvis, I. (eds.), *Phosphorite Research and Development*. London: Geological Society, Special Publication 52, pp. 1–22.
 Epstein, S., Buchsbaum, R., Lowenstam, H.A., and Urey, H.C., 1953. Revised carbonate-water isotopic temperature scale. *Bull. Geol. Soc. Am.*, **64**(11), 1315–1326.
 Filippelli, G.M., and Delaney, M.L., 1992. Similar phosphorus fluxes in ancient phosphorite deposits and a modern phosphogenic environment. *Geology*, **20**(8), 709–712.
 Fisher, A.G., and Arthur, M.A. 1977. Secular variations in the pelagic realm. In: Cook, H.E and Enos, P. (eds.), *Deep-Water Carbonate Environments*. Tulsa: Society Economic Paleontology Mineral (SEPM), Special Publication No. 25, pp. 19–50.
 Föllmi, K.B. (ed.), 1994. Concepts and controversies in phosphogenesis. *Eclogae Geol. Helv.*, **87**(3): 639–641.
 Föllmi, K.B., 1996. The phosphorus cycle, phosphogenesis and marine phosphate rich deposits. *Earth Sci. Rev.*, **40**, 55–124.
 Glenn, C.R., Föllmi, K.B., Riggs, S.R., Baturin, G.N., Grimm, K.A., Trappe, J., Abed, A.M., Galliolivier, C., Garrison, R.E., Ilyin, A.V., Jehl, C., Rohrllich, V., Sadaqah, R.M.Y., Schidlowski, M., Sheldon, R.E., and Siegmund, H., 1994. Phosphorus and phosphorites – Sedimentology and environments of formation. *Eclogae Geol. Helv.*, **87**(3), 747–788.
 Jarvis, I., Burnett, W.C., Nathan, Y., Almbaydin, F.S.M., Attia, A.K.M., Castro, L.N., Flicoteaux, R., Hilmy, M.E., Husain, V., Qatwanah, A.A., Serjani, A., and Zanin, Y.N., 1994. Phosphorite geochemistry – state-of-the-art and environmental concerns. *Eclogae Geol. Helv.*, **87**(3), 643–700.
 Karhu, J., and Epstein, S., 1986. The implication of the oxygen isotope records in coexisting cherts and phosphates. *Geochimica et Cosmochimica Acta*, **50**, 1745–1756.
 Kolodny, Y., 1981. Phosphorites (Chapter 11.3). In Emiliani, C. (ed.), *The Sea*, vol. 7. New York: Wiley, pp. 981–1023.
 Kolodny, Y., and Kaplan, I.R., 1971. C and O isotopes in apatite CO₂ and coexisting calcite from sedimentary phosphorite. *J. Sed. Pet.*, **3**, 954–959.
 Kolodny, Y., and Luz, B., 1992. Phosphate deposits, formation and diagenetic history. In Clauer N., and Chaudhuri, S. (eds.), *Isotopic Signatures and Sedimentary Records*. New York: Springer, 69–122.
 Krajewski, K.P., Vancappellen, P., Trichet, J., Kuhn, O., Lucas, J., Martinalgara, A., Prevot, L., Tewari, V.C., Gaspar, L., Knight, R.I., and Lamboy, M., 1994. Biological processes and apatite formation in sedimentary environments. *Eclogae Geol. Helv.*, **87**(3), 701–745.
 Longinelli, A., and Nuti, S., 1973. Revised phosphate-water isotopic temperature scale. *Earth Planet. Sci. Lett.*, **20**, 337–340.
 McArthur, J.M., Benmore, R.A., Coleman, M.L., Soldi, C., Yeh, H.W., and Obrien, G.W., 1986. Stable isotopic characterization of francolite formation. *Earth Planet. Sci. Lett.*, **77**(1), 20–34.
 Nathan, Y., 1984. The mineralogy and geochemistry of phosphorites. In Nriagu, J.O., and More, P.B. (eds.), *Phosphate Minerals*, Berlin: Springer, 275–291.
 Notholt, A.J.G., Sheldon, R.P., and Davidson, D.F. (eds.), 1989. *Phosphate Deposits of the World, Vol. 2: Phosphate Rock Resources*. Cambridge: Cambridge University Press, 566pp.
 Parrish, J.T., 1998. *Interpreting Pre-Quaternary Climate from the Geologic Record*. New York: Columbia University Press, 338pp.
 Piper, D.Z., and Kolodny, Y., 1987. The stable isotopic composition of a phosphorite deposit, $\delta^{13}\text{C}$, $\delta^{34}\text{S}$ and $\delta^{18}\text{O}$. *Deep Sea Res.*, **34**, 897–911.

Sheldon, R.P., 1980. Ancient marine phosphorites. *Annu. Rev. Earth Planet. Sci.*, **9**, 251–284.

Shemesh, A., and Kolodny, Y., 1988. Oxygen isotope variations in phosphorites from the southeastern Tethys. *Isr. J. Earth Sci.*, **37**, 1–15.

Soudry, D., and Champetier, Y., 1983. Microbial processes in the Negev phosphorites (southern Israel). *Sedimentology*, **30**, 411–423.

Cross-references

Carbon Isotopes, Stable
 Dating, Radiometric Methods
 Geochemical Proxies (Non-Isotopic)
 Mineral Indicators of Past Climates
 Oxygen Isotopes
 Paleotemperatures and Proxy Reconstructions
 Phosphorus Cycle
 Stable Isotope Analysis
 Strontium Isotopes
 Sulfur Isotopes
 Uranium-Series Dating

PHOSPHORUS CYCLE

Introduction

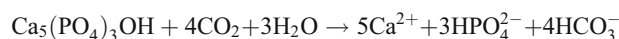
Phosphorus (P) is a limiting nutrient for terrestrial biological productivity, and thus it commonly plays a key role in net carbon uptake in terrestrial ecosystems. Unlike nitrogen (another limiting nutrient but one with an abundant atmospheric pool), the availability of “new” P in ecosystems is restricted by its rate of release during soil weathering. The release of P places a limit on ecosystem productivity (Schlesinger, 1997), which in turn is critical to terrestrial carbon balances. Furthermore, the weathering of P and transport by rivers is the only appreciable source of P to the oceans. On longer time scales, this supply of P limits total primary production in the ocean (Smith, 1984). Thus, understanding the controls on P cycling is one key element of elucidating biogeochemical responses to and forcing of paleoclimate.

Natural Phosphorus Cycle

The human impact on the global P cycle has been substantial over the last 150 years. Because this anthropogenic modification began well before scientific efforts to quantify the cycle of P, we can only guess at the “pre-anthropogenic” mass balance of P. Several aspects of the P cycle are well-constrained (Figure P60). Phosphorus is initially solubilized, mainly from apatite minerals, by chemical weathering during soil development. Physical weathering also plays a role by producing fine materials with extremely high surface area/mass ratios, which enhances chemical weathering in continental environments (i.e., floodplains, delta systems).

Phosphorus cycling in soils

The cycling of P in soils has received much attention, in terms of both fertilization and the natural development of ecosystems. Of the approximately 122,600 Tg P within the soil/biota system on the continents, nearly 98% is held in soils in a variety of forms. The exchange of P between biota and soils is relatively rapid, with an average residence time of 13 years, whereas the average residence time of P in soils is 600 years (Figure P60). The most significant weathering source for phosphorus in soils are apatite minerals. These minerals can be congruently weathered as a result of reaction with dissolved carbon dioxide:



In soils, P is released from mineral grains by several processes. First, the reduced pH produced from respiration-related CO_2 in the vicinity of both degrading organic matter and root hairs dissolves P-bearing minerals (mainly apatites) and releases P to root pore spaces. Second, organic acids released by plant roots also can dissolve apatite minerals and release P to soil pore spaces (Jurinak et al., 1986). Phosphorus is very immobile in most soils, and its slow rate of diffusion from dissolved form in pore spaces strongly limits its supply to rootlet surfaces. Furthermore, much of the available P in soils is in organic matter, which is not directly accessible for plant nutrition. Plants have developed two specific tactics to increase the supply of P to roots. Phosphatase, an enzyme that can release bioavailable inorganic P from organic matter, is often excreted

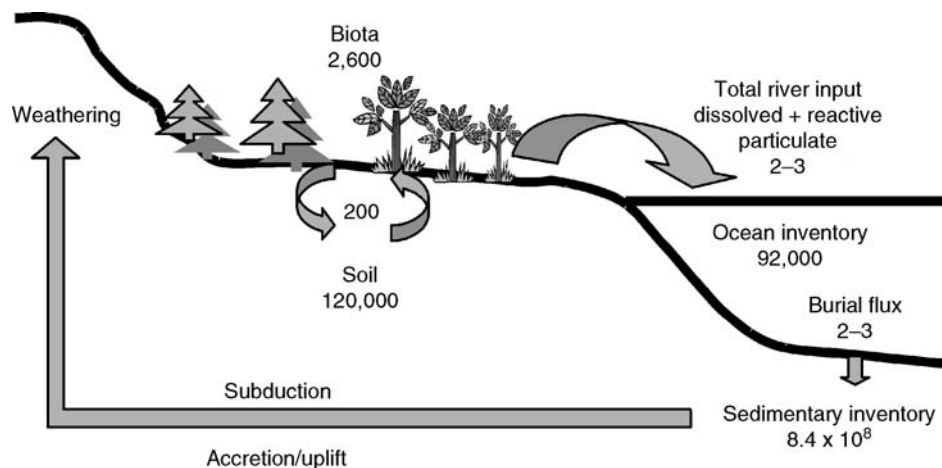


Figure P60 The natural (pre-human) phosphorus cycle, showing reservoirs (in Tg P, where Tg = 10^{12} g) and fluxes (denoted by arrows, in Tg P yr⁻¹) in the P mass balance (after Filippelli, 2002).

by plants and soil microbes, and the symbiotic fungi *Mycorrhizae* can coat plant rootlets, excreting phosphatase and organic acids to release P and providing an active uptake site for rapid diffusion of P from soil pore spaces to root surfaces (e.g., Schlesinger, 1997).

Phosphorus in soils is present in a variety of forms, and the distribution of P between these forms changes dramatically with time and soil development. The forms of soil P can be grouped into refractory (not readily bioavailable) and labile (readily bioavailable). The refractory forms include P in apatite minerals and P co-precipitated with and/or adsorbed onto iron and manganese oxyhydroxides (termed “occluded” P). The reducible oxyhydroxides have large binding capacities for phosphate, due to their immense surface area and numerous delocalized positively charged sites (e.g., Froelich, 1988). The labile forms include P in soil pore spaces (as dissolved phosphate ion) and adsorbed onto soil particle surfaces (these forms are termed “nonoccluded” P), as well as P incorporated in soil organic matter. On a newly-exposed lithic surface, nearly all of the P is present as P in apatite. With time and soil development, however, P is increasingly released from this form and incorporated in the others (Figure P61). Over time, the total amount of P available in the soil profile decreases, as soil P is lost through surface and subsurface runoff. Eventually, the soil reaches a terminal steady state, when soil P is heavily recycled and any P lost through runoff is slowly replaced by new P weathered from apatite minerals at the base of the soil column.

Riverine transport of particulate and dissolved phosphorus

The eventual erosion of soil material and transport by rivers delivers P to the oceans. Riverine P occurs in two main forms: particulate and dissolved. Most of the P contained in the particulate load of rivers is held within mineral lattices and never participated in the active biogenic cycle of P. This will also be its fate once it is delivered to the oceans, because dissolution rates in the high pH and heavily buffered waters of the sea are exceedingly low. Thus, much of the net

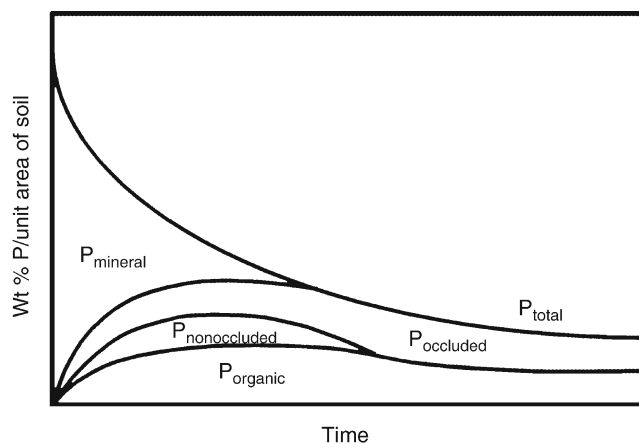


Figure P61 Modeled changes in soil phosphorus geochemistry over time (based on Walker and Syers, 1976), showing transformation of mineral phosphorus into non-occluded and organic forms before eventual dominance of occluded (oxide-bound) and organic forms. The relative bio-reactivity of phosphorus increases from mineral to occluded to organic forms of phosphorus. Note the continual loss of total phosphorus from system.

P physically eroded from continents is delivered relatively unaltered to the oceans, where it is sedimented on continental margins and in the deep sea, until subduction or accretion eventually returns P to be exposed on land again. Some of the particulate P is adsorbed onto soil surfaces, held within soil oxide, and incorporated into particulate organic matter. This P likely interacted with the biotic P cycle on land, and its fate upon transfer to the ocean is poorly understood. For example, P adsorbed onto soil surfaces may be effectively displaced by the high ionic strength of ocean water, providing an additional source of P into the ocean. Furthermore, a small amount of the P incorporated into terrestrial organic matter may be released in certain environments during bacterial oxidation after sediment burial. Finally, some sedimentary environments along continental margins are suboxic or even anoxic, conditions favorable for oxide dissolution and release of the incorporated P. The net pre-human flux of dissolved P to the oceans is $\sim 1 \text{ Tg P yr}^{-1}$, with an additional $1\text{--}2 \text{ Tg P yr}^{-1}$ of potentially soluble P, bringing the total to about $2\text{--}3 \text{ Tg P yr}^{-1}$. Thus, the residence time of biologically available P on land is about 40–60 kyr with respect to export to the oceans. That this residence time is of a glacial time-scale may be no coincidence, and is likely tied to variable inputs from continental weathering and output sinks driven by sea level variations. However, the interaction between biologically available P on land and loss of this P to the oceans is clearly relatively dynamic and suggests the relatively rapid cycling of P on land.

Marine sedimentation

Once in the marine system, dissolved P acts as the critical long-term nutrient limiting biological productivity. Phosphate concentrations are near zero in most surface waters, as this element is taken up by phytoplankton as a vital component of their photosystems (phosphate forms the base for ATP and ADP, required for photosynthetic energy transfer) and their cells (cell walls are comprised of phospholipids). Dissolved P has a nutrient profile in the ocean, with a surface depletion and a deep enrichment. Furthermore, deep phosphate concentrations increase with the age of deep water, and thus values in young deep waters of the Atlantic are typically $\sim 1.5 \mu\text{M}$ whereas those in the older Pacific are $\sim 2.5 \mu\text{M}$. Once incorporated into plant material, P roughly follows the organic matter loop, undergoing active recycling in the water column and at the sediment/water interface.

Phosphorus input and output are driven to steady state mass balance in the ocean by biological productivity. As mentioned previously, one of the difficulties with accurately determining the pre-anthropogenic residence time of P in the ocean is that input has been nearly doubled due to anthropogenic activities, and thus we must resort to estimating the burial output of P, a technique plagued by site-to-site variability in deposition rates and poor age control. Estimates of P burial rates have been performed by a variety of methods, including determination via P sedimentary sinks and riverine suspended matter fluxes calibrated to the P geochemistry of those fluxes. An areal approach is a more direct route to quantifying the burial terms in the P mass balance, and indicates that reactive P burial in continental margin sediments accounts for about 60% of the oceanic output, with deep sea sediments nearly equivalent as a sink (Filippelli and Delaney, 1996). Although continental margins comprise less than 10% of ocean surface area, high burial rates in these settings are linked to high bulk sedimentation rates, which ultimately drive P accumulation rates in marine sediments (Filippelli, 1997).

Impact of climate change on the terrestrial phosphorus cycle

The effect of climate and soil development on P availability has been a focus of several excellent papers (e.g., Chadwick et al., 1999). For the most part, these studies have used P extraction techniques to determine the biogeochemical forms of P within soils (e.g., Figure P61). The extraction techniques have been applied to depth and age profiles in soils, and to assessment of the rate of soil P transformations, the role of climate on these processes, the bioavailability of P in these systems, and the limiting controls on plant productivity. As the current geochemical state of a given soil is an integration of all conditions acting since soil development, most efforts have focused on settings in which climate is likely to have been constant (i.e., tropical settings), and the beginning state of the system and its age are very well known (i.e., soil developing on lava flows). These studies have thus made the classic substitution of space for time, with all the inherent assumptions of constancy in climate and landscape history.

Another approach to assessing terrestrial P cycling is to examine P geochemistry in lake sediments, using the same extraction techniques as the soil studies. This technique adds several dimensions to the soil work outlined above. First, lake sediment records allow us to examine an integrated record of watershed-scale processes associated with P cycling on the landscape. Second, it allows discrete temporal resolution at a given site, providing an actual record of local processes including landscape stability, soil development, and ecosystem development. Third, it extends our understanding of terrestrial P cycling to alpine and glaciated systems. The soil chronosequence approach is not likely to be successful here because of the climatic and slope variability between various sites (i.e., no substitution of space for time is possible). This third dimension is perhaps the most critical in terms of

the P mass balance, as the greatest degree of variations in climate has occurred in these settings, and thus they hold the key to understanding the terrestrial P cycle on glacial/interglacial timescales.

Example of the lake history approach to terrestrial P cycling

The lake sediment approach described above has been applied to several settings, revealing the impact of paleoclimatic variations on the terrestrial P cycle (Filippelli and Souch, 1999). One example of this application is a ~20,000 year record from two small lakes (Jackson and Anderson Ponds) in the western Appalachian Plateau. Paleoclimatic variations have strongly affected the ecological development of this region (Wilkins et al., 1991), although neither lake was directly glaciated. The geochemical profile for Jackson Pond reveals extreme changes in P cycling through time (Figure P62). In the early part of the record, marked by full glacial conditions, mineralized P was the dominant form entering the lake, with occluded and organic forms of lesser importance. During this interval, the landscape was marked by thin soils, high surface runoff, and closed boreal forests (Wilkins et al., 1991). With landscape stabilization and the onset of soil development (17–10 ka), the dominant forms of P entering the lake changed significantly, marked by a decline in the proportion of mineralized P and an increase in organic P (occluded P varied but exhibited no clear trend with age during this interval). In this interval, the closed boreal forests gave way to more open boreal woodland and a rapidly thickening soil cover. From the early mid-Holocene to the present, the concentration of mineral P shows little variation, while that of organic P and occluded P increased. Meanwhile, the ecosystem became dominated by deciduous hardwood forests and grasses, and a thick, stable soil existed. In terms of the percent of total P reflected by each fraction, the

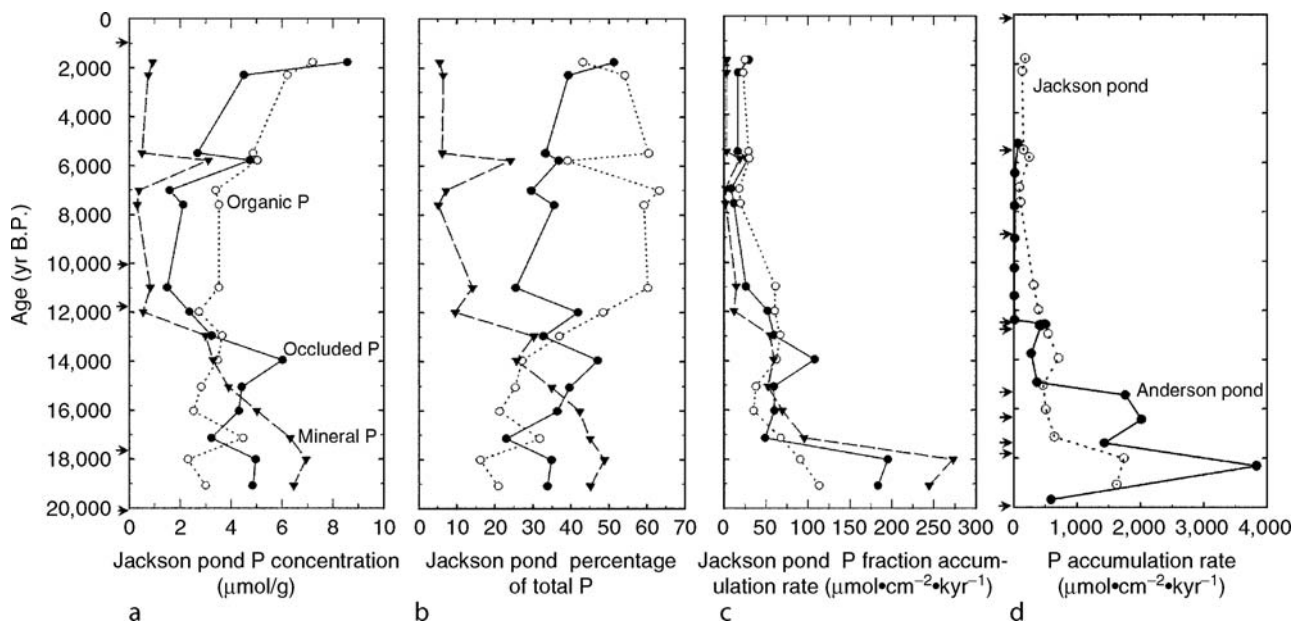


Figure P62 (a) P concentration, (b) percent of total P for each P-bearing fraction in sediments, and (c) accumulation rate of P fractions at Jackson Pond, (d) Total P accumulation rate at Anderson and Jackson Ponds. ¹⁴C age-control points for Jackson Pond (Wilkins et al., 1991) are shown as arrows on age axis in a. Lowermost point is 20,330 yr. ¹⁴C age-control points are also shown for Anderson Pond as arrows in d (after Filippelli and Souch, 1999).

early Holocene marks a stabilization of the system to one dominated by organic and occluded P.

Large changes in the accumulation rate of P over time are reflected in the lake records. These accumulation rate changes are driven partly by changes in bulk sedimentation rate, but several of the rapid shifts in P accumulation occur between age control points and are thus not just driven by rates of sedimentation. The two western Appalachian sites reveal a rapid pulse of P input during the glacial and initial deglacial interval (Figure P62), a period of enhanced colluvial activity when soil development was just commencing. Upon landscape and soil stability (by 10 ka), P inputs had decreased 10–40 fold, and remained low and constant to the top of the record (2 ka). In the case of dissolved phosphate, we can infer that the initial stage of soil development, marked by high solid-phase loss (reflected by the accumulation rate record) also likely leads to a relatively poor recycling of the dissolved phase (from a lack of oxide-bound occluded pools), a so-called ‘leaky ecosystem.’

The lake sediment records presented here indicate a terrestrial P mass balance that is not near steady state on glacial/interglacial time-scales, with important implications for the functioning of terrestrial and oceanic systems. Coupling these records of solid-phase P changes over time with oceanic records of dissolved inputs from rivers will eventually provide important constraints for the influence of climate on chemical weathering and the global P cycle.

Gabriel M. Filippelli

Bibliography

- Chadwick, O.A., Derry, L.A., Vitousek, P.M., Huebert, B.J., and Hedin, L.O., 1999. Changing sources of nutrients during four millions years of ecosystem development. *Nature*, **397**, 491–497.
- Filippelli, G.M., 1997. Controls on phosphorus concentration and accumulation in oceanic sediments. *Mar. Geol.*, **139**, 231–240.
- Filippelli, G.M., 2002. The global phosphorus cycle. *Rev. Mineral. Geochem.*, **48**, 391–425.
- Filippelli, G.M., and Delaney, M.L., 1996. Phosphorus geochemistry of equatorial Pacific sediments. *Geochim. Cosmochim. Acta*, **60**, 1479–1495.
- Filippelli, G.M., and Souch, C., 1999. Effects of climate and landscape development on the terrestrial phosphorus cycle. *Geology*, **27**, 171–174.
- Froelich, P.N., 1988. Kinetic controls of dissolved phosphate in natural rivers and estuaries: A primer on the phosphate buffer mechanism. *Limnol. Oceanogr.*, **33**, 649–668.
- Jurinak, J.J., Dudley, L.M., Allen, M.F., and Knight, W.G., 1986. The role of calcium oxalate in the availability of phosphorus in soils of semiarid regions: A thermodynamic study. *Soil Sci.*, **142**, 255–261.
- Schlesinger, W.H., 1997. *Biogeochemistry: An Analysis of Global Change*. San Diego, USA: Academic Press, 588pp.
- Smith, S.V., 1984. Phosphorus versus nitrogen limitation in the marine environment. *Limnol. Oceanogr.*, **29**, 1149–1160.
- Walker, T.W., and Syers, J.K., 1976. The fate of phosphorus during pedogenesis. *Geoderma*, **15**, 1–19.
- Wilkins, G.R., Delcourt, P.A., Delcourt, H.R., Harrison, F.W., and Turner, M.R., 1991. Paleocology of central Kentucky since the last glacial maximum. *Quat. Res.*, **36**, 224–239.

Cross-references

Carbon Cycle
 Climate Forcing
 Continental Sediments
 Lacustrine Sediments
 Ocean Paleoproductivity
 Paleosols, Pre-Quaternary
 Paleosols–Quaternary
 Phosphorites
 Sedimentary Indicators of Climate Change
 Weathering and Climate

PINGOS

Pingos are ice-cored hills (Figure P63), typically conical in shape, covered by soil and vegetation with a core of massive ice produced primarily by the injection of water to the base of aggrading permafrost. They grow and persist only in a permafrost environment. Porsild (1938) first proposed the term pingo, which is a local Inuit word for an ice-cored conical hill in the Mackenzie Delta. In Siberia, similar forms are referred to as bulgannyakh. Pingos vary considerably in size (anywhere from 2 to 50 m high) and active examples show steady increases in height during their lifetime.

Perhaps the greatest concentration of pingos occurs in the Tuktoyaktuk Peninsula to the west of the Mackenzie Delta in the North West Territories of Canada, where over 1,350 examples have been identified. This is a significant concentration given that the number of active pingos world-wide is estimated at around 5,000, with examples occurring in the Yukon, Alaska, Svalbard, Greenland, Siberia, Mongolia and at altitude on the Tibetan Plateau (Mackay, 1998). There are two basic types of pingos, they are:

1. *Open (hydraulic) system pingos*. These occur in hydraulic systems where intra- or sub-permafrost groundwater flows under a hydraulic gradient to the pingo site and maintains a sub-pingo water lens that freezes to form a body of injection ice (hydrolaccolith) that uplifts the surface permafrost to form a conical hill (Figure P64). The key element in this process is the presence of artesian water pressures, which maintain a steady but slow supply of groundwater to the growing ice mound. Open system pingos tend therefore to be concentrated in high relief areas, such as on lower hill-slopes, at the base of alluvial fans, in alluvial valley bottoms or in front of glaciers where subglacial groundwater rise beneath proglacial permafrost. The hydrology of these systems is poorly understood, and other growth mechanism may be involved. In particular, their formation appears to require a delicate balance between three variables all of which may be subject to seasonal or annual oscillations (French, 1996), namely water pressure, overburden or permafrost strength, and the rate of freezing. If water is injected



Figure P63 Closed system pingo from the Tuktoyaktuk, NWT Canada (photo: R.I. Waller).

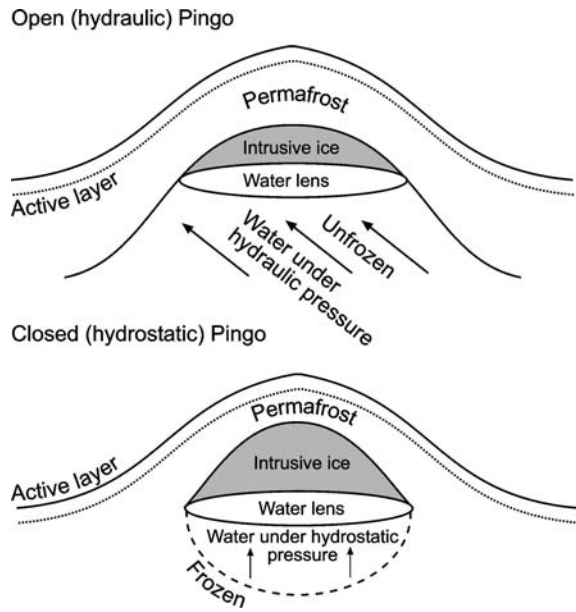


Figure P64 Two main types of pingo.

toward the base of the growing pingo too fast, water pressure will rise until the pingo ruptures and a surface spring is formed. Alternatively, if the water is injected too slowly then the sub-pingo water lens will freeze and the pingo will cease to grow. These variables are unlikely to remain in perfect balance for long and consequently other mechanisms may be involved in sustaining the growth of the ice-core, such as the formation of segregation ice.

2. *Closed (hydrostatic) system pingos.* In this case, the groundwater flow necessary to maintain the growth of the ice core results from pore water exclusion caused by permafrost aggradation within saturated sands found beneath drained lakes or in areas of permafrost talik (Figure P64). Hydrostatic pingos tend to occur in regions where thaw lakes, in areas of permafrost, are drained catastrophically via either coastal retreat or the headward erosion of rivers. Closed system pingos have been widely studied and perhaps the most comprehensive data set exists for those examples on Tuktoyaktuk Peninsula (Mackay, 1998).

Relict pingos occur extensively within areas of former permafrost, and consist of a circular rampart surrounding a shallow depression. Relict examples are considered by many to provide good evidence of former extent of permafrost in the past and Pleistocene examples have been described from across Northwest Europe (Watson, 1977; De Gans, 1988), and North America (Bik, 1969). In addition, fossil examples have been recorded from glacial deposits of late Ordovician age in Jordan (Abed et al., 1993).

Matthew R. Bennett

Bibliography

- Abed, A.M., Makhlof, I.M., Amireh, B.S., and Khalil, B., 1993. Upper Ordovician glacial deposits in southern Jordan. *Episodes*, **16**, 316–328.
 Bik, M.J.J., 1969. The origin and age of prairie mounds of southern Alberta, Canada. *Biuletyn Peryglacjajny*, **19**, 85–130.

De Gans, W., 1988. Pingo scars and their identification. In Clark, M.J. (ed.), *Advances in periglacial Geomorphology*. Chichester, UK: Wiley, pp. 299–322.

French, H.M., 1996. *The Periglacial Environment*. Harlow, UK: Longman, 341pp.

Mackay, J.R., 1998. Pingo growth and collapse, Tuktoyaktuk Peninsula Area, Western Arctic Coast, Canada: a long-term field study. *Géographie Physique et Quaternaire*, **52**, 271–323.

Porsild, A.E., 1938. Earth mounds in unglaciated Arctic northwestern America. *Geograph. Rev.*, **28**, 46–58.

Watson, E., 1977. The periglacial environment of Great Britain during the Devensian. *Philos. Trans. R. Soc. Lond.*, **B280**, 183–198.

Cross-references

Cryosphere

Periglacial Geomorphology

PLATE TECTONICS AND CLIMATE CHANGE

The horizontal and vertical displacements associated with plate tectonics play a fundamental role in climate change over a wide range of timescales. The solid-earth surface is in direct contact with the atmosphere and oceans and its evolving character affects balances of incoming and outgoing radiation, atmospheric circulation, ocean currents, and the location of elevated terrain suitable for glaciers and ice sheets. Tectonic processes also have important indirect climatic effects through their control on geochemical cycling and the composition of the atmosphere and ocean. This entry provides an introduction to the more direct, physical effects of tectonics on the climate system. While touched on briefly, the less direct climatic effects of volcanism and chemical processes are left to other entries in this volume. For a historical perspective on many of the ideas presented here, the interested reader should refer to the comprehensive survey by Hay (1996). Other excellent resources include an in-depth discussion of climate forcing mechanisms and climate modeling strategies relevant to tectonic timescales (Crowley and North, 1996), and edited volumes focusing on the climatic and geochemical effects of mountain uplift (Ruddiman, 1997) and uncertainties related to tectonic reconstructions and climate forcing (Crowley and Burke, 1998).

Shifting continents

While the German astronomer and climatologist Alfred Wegener (1880–1930) is usually credited with founding the modern theory of plate tectonics, the concept of a fundamental link between climate and the changing distribution of continents and oceans dates back at least to Lyell (Hay, 1996). He speculated that a concentration of polar land area should cool the Earth and that changing land distributions were somehow responsible for the deposition of Carboniferous coal beds and the obvious differences between Mesozoic and Cenozoic fossil assemblages (Lyell, 1830). Today, we acknowledge that tectonic processes can indeed have local to global-scale climatic impacts. Those impacts can be direct or indirect, and can be the result of horizontal displacements, vertical displacements, or both.

Perhaps the most fundamental, direct link between plate tectonics and climate comes from the slowly evolving global distribution of continental blocks and fragments (Figure P65). As tectonic plates move, so do the subaerial continents and

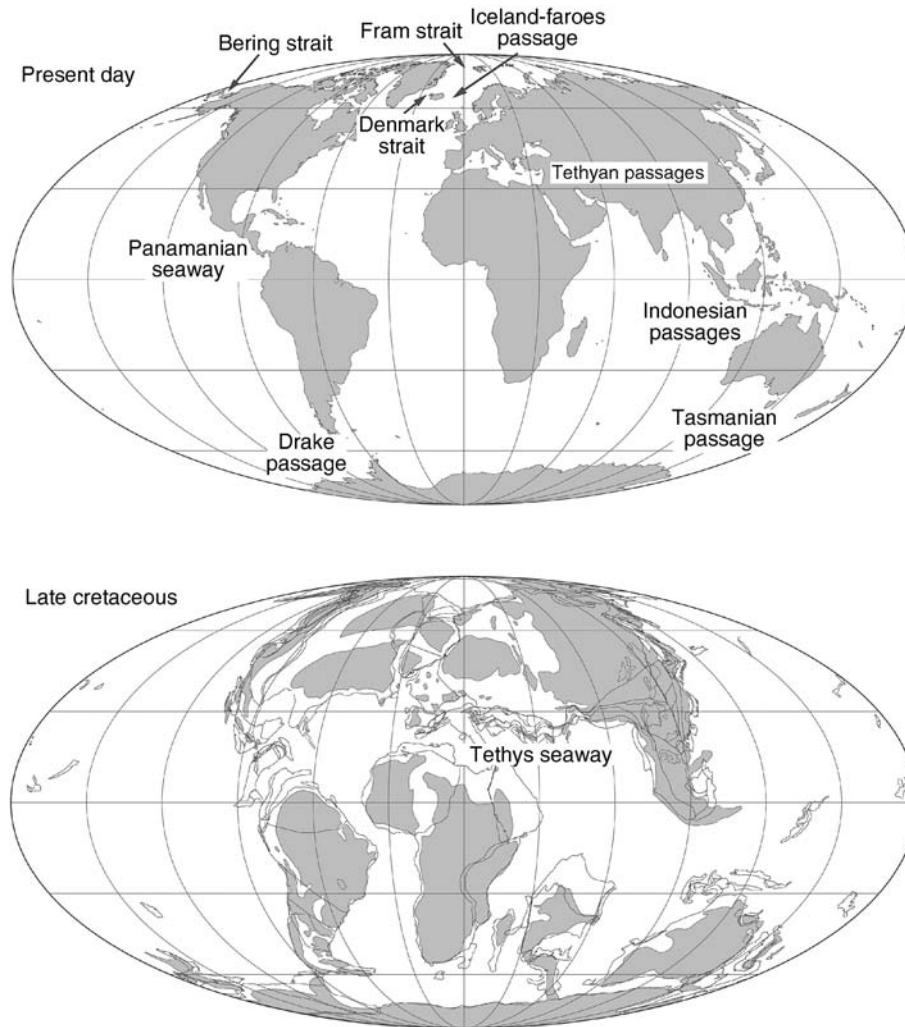


Figure P65 A comparison of modern and late Cretaceous (80 Ma) geography (after Hay, 1996; DeConto et al., 1999; Hay et al., 1999). The approximate locations of Cenozoic gateways discussed in the text are shown on the present day map (*top*). The outlines of tectonic blocks and subaerial land areas (*shaded*) are shown on the Late Cretaceous map (*bottom*). Note the low latitude, circum-global ocean passage (Tethys Seaway), closed Southern Ocean gateways, narrow Atlantic Basin, and flooded continental interiors characteristic of the mostly ice-free Cretaceous and early Cenozoic.

this redistribution of landmass has an important effect on the spatial heterogeneity of the Earth's energy balance via differences in the albedos (reflectivities) and thermal properties of land versus ocean.

Albedo and thermal properties of land and sea

As a whole, the albedo of today's Earth is ~ 0.31 , with the atmosphere and clouds responsible for most (about 85%) of the energy reflected back to space. While the atmosphere and clouds dominate planetary albedo (see entry on *Albedo feedback*), the surface is the dominant absorber of solar energy, responsible for $\sim 65\%$ of the total absorbed solar radiation and for transferring energy to the atmosphere through long-wave radiation, and fluxes of sensible and latent heat. Consequently, variations in surface albedo have important effects on atmospheric dynamics and climate. This is particularly true in mostly cloud-free regions and polar latitudes, which on today's

Earth are covered by highly reflective snow and ice. Surface albedos over open, ice-free ocean are generally much lower than those over land (Table P5). Thus, at the global scale, changes in the latitudinal distribution of land can have a significant effect on zonally-averaged net radiation balance. For example, an Earth with polar continents covered by perennial snow and ice will have higher surface albedo than an Earth with a polar geography dominated by open water. Because the need for poleward heat transport (the ultimate driver of winds and ocean currents) is determined by the latitudinal net radiation gradient, major changes in the distribution of continents are likely to have significant climatic consequences.

Like albedo, the thermal properties of open water are also very different from those of land. Water has very high specific heat (about five times greater than soil and rock) and the upper $\sim 10\text{--}150$ m of the oceans are well mixed by winds and convection. This allows seasonal temperature changes to

Table P5 Albedos of different cloud and surface types

Cloud/surface type	Range of values	Typical values
Cumulonimbus clouds		0.9
Stratocumulus clouds		0.6
Cirrus clouds	0.4–0.5	0.45
*Water (low wind)	0.02–0.12	0.07
Water (high wind)	0.10–0.20	0.12
<i>Bare land surfaces</i>		
Moist dark soil	0.05–0.15	0.10
Moist gray soil	0.10	0.15
Dry soil	0.20–0.35	0.20
Wet sand	0.20–0.30	0.25
Dry light sand	0.30–0.40	0.35
<i>Vegetation</i>		
Low canopy vegetation	0.10–0.20	0.17
Dry vegetation	0.20–0.30	0.25
Evergreen forest	0.10–0.20	0.12
Deciduous forest	0.15–0.25	0.17
Forest with snow cover	0.20–0.35	0.25
Sea ice	0.25–0.40	0.30
Sea ice (snow covered)	0.40–0.90	0.70
Old, wet snow	0.40–0.65	0.50
Old, dry snow	0.60–0.75	0.70
Fresh, dry snow	0.70–0.90	0.80

Source: Compiled from Barry and Chorley (1998); Hartmann (1994); Houghton (1985).

*At the low solar zenith angles typical of tropical latitudes, the albedo of calm water can be as low as ~ 0.02 , much lower than typical land-surface albedos. Albedos over open water increase sharply as solar zenith angles approach 90° .

penetrate much deeper into the ocean (tens to hundreds of meters) than into immobile soil and rock on land (~ 1 m, by conduction). Consequently, sea surface temperatures (SSTs) are relatively slow to respond to seasonal changes in insolation. In the hemisphere experiencing winter, relatively warm surface waters suppress extreme temperature swings and provide the atmosphere with a source of moisture and diabatic heating. In contrast, the smaller heat capacity of land combined with relatively high albedo allows much greater seasonality, particularly in the interiors of the larger continents (Figure P66).

Monsoons and the intertropical convergence zone (ITCZ)

The seasonal thermal contrast between land and ocean mentioned above is generally considered to be responsible for the well-known monsoonal circulation systems driven by seasonally alternating low-level pressure patterns over land and sea. The best example on today's Earth is the Asian monsoon system (Figure P66). Over central Asia, seasonal mean temperature differences can exceed 50°C . During boreal winter, cold (dense), sinking air contributes to high atmospheric surface pressure (the Siberian High). Lower atmospheric pressure over the warmer Indian Ocean produces a meridional pressure gradient and northeasterly flow over southeastern Asia, Indonesia and the northern Indian Ocean. During the summer months, continental heating reverses the pressure gradient and the regional wind field. The resulting southwesterly winds (Southwest Monsoon) bring moisture-laden air and rain northward across India, the foothills of the Himalaya, and parts of China and Indonesia. This seasonal reversal of the wind field also produces dramatic changes in the dominant Indian Ocean currents. For example, during boreal summer, a strong low-level atmospheric jet, in part deflected northeastward by east African highlands, drives the northeastward flowing Somali Current, vigorous coastal upwelling, and high

ocean productivity along the coasts of Somalia and Oman. During the Northeast Monsoon, the Somali Current reverses, primary productivity in the Arabian Sea slows, and the entire Indian Ocean equatorial current system reorganizes.

While definitions of the monsoons and the ITCZ are somewhat intertwined, the ITCZ is traditionally considered to be the region of low-level convergence and convective precipitation near the equator, where the trade winds meet. As the seasons progress, uneven interhemispheric heating moves the mean latitudinal position of the ITCZ into the hemisphere experiencing summer (Figure P66). This seasonal shift in the ITCZ is exaggerated over the continents. On today's Earth, the Northern Hemisphere contains a greater fraction of total land area, which contributes to the average position of the ITCZ being several degrees north of the equator, as does the orientation of the coastlines of western tropical Africa and South America (Philander et al., 1996). Because the northeast and southeast trade winds generally converge north of the equator, the Southeast Trades can cross the equator where the effects of the Earth's rotation are minimal. This has important consequences for the latitudinal position of the major zonal equatorial ocean currents and zones of oceanic convergence, divergence, and upwelling, which, like the winds, are also asymmetric with respect to the equator (Gill, 1982).

Alternatively, monsoons have been described as convergence zones more than 10° away from the equator that do not necessarily require a strong land-sea thermal contrast (Chao and Chen, 2001). In this interpretation, the Earth's rotation is considered the primary cause of the monsoons, with land-sea contrast playing a lesser, modifying role. This notion is supported by numerical climate modeling studies showing the existence of monsoons even in the absence of continents. In simulations with the Asian and Australian continents, which are replaced by open ocean, monsoonal circulation patterns still develop over roughly the same regions as today's Asian, Indian and Australian monsoons occur. Land-sea contrast appears to play a more fundamental role in monsoons over Africa, South America and Mexico, however (Chao and Chen, 2001).

Continentality

At times in the geologic past, episodic convergence of major continental plates formed giant supercontinents (e.g., Rodinia, Pangea, Gondwana, and Laurasia). Enhanced *continentality* likely produced extreme seasonal temperature swings and aridity in the continental interiors, and invigorated monsoonal circulation patterns in many coastal locations (Crowley et al., 1989; Kutzbach and Gallimore, 1989). The Permo-Triassic convergence of Laurasia and Gondwana provides a well-known example of a single supercontinent, *Pangea*, and a giant *Panthalasia Ocean*. In central *Pangea*, mean summer temperatures were at least $6\text{--}10^\circ\text{C}$ warmer than today's continental interiors, with daytime high temperatures reaching 50°C in some locations (Crowley and North, 1996). Extreme aridity dominated the continental interiors because most atmospheric water vapor would have been lost to precipitation near the continental margins and because high summer temperatures would have increased evaporation. This continental aridity effect would have been exacerbated downwind of mountain ranges (see *Rain shadows* below). Estimates of net precipitation minus evaporation over *Pangea* are only about half that of modern land areas and these conditions must have played an important role in the distribution of terrestrial ecosystems (Crowley and North, 1996).

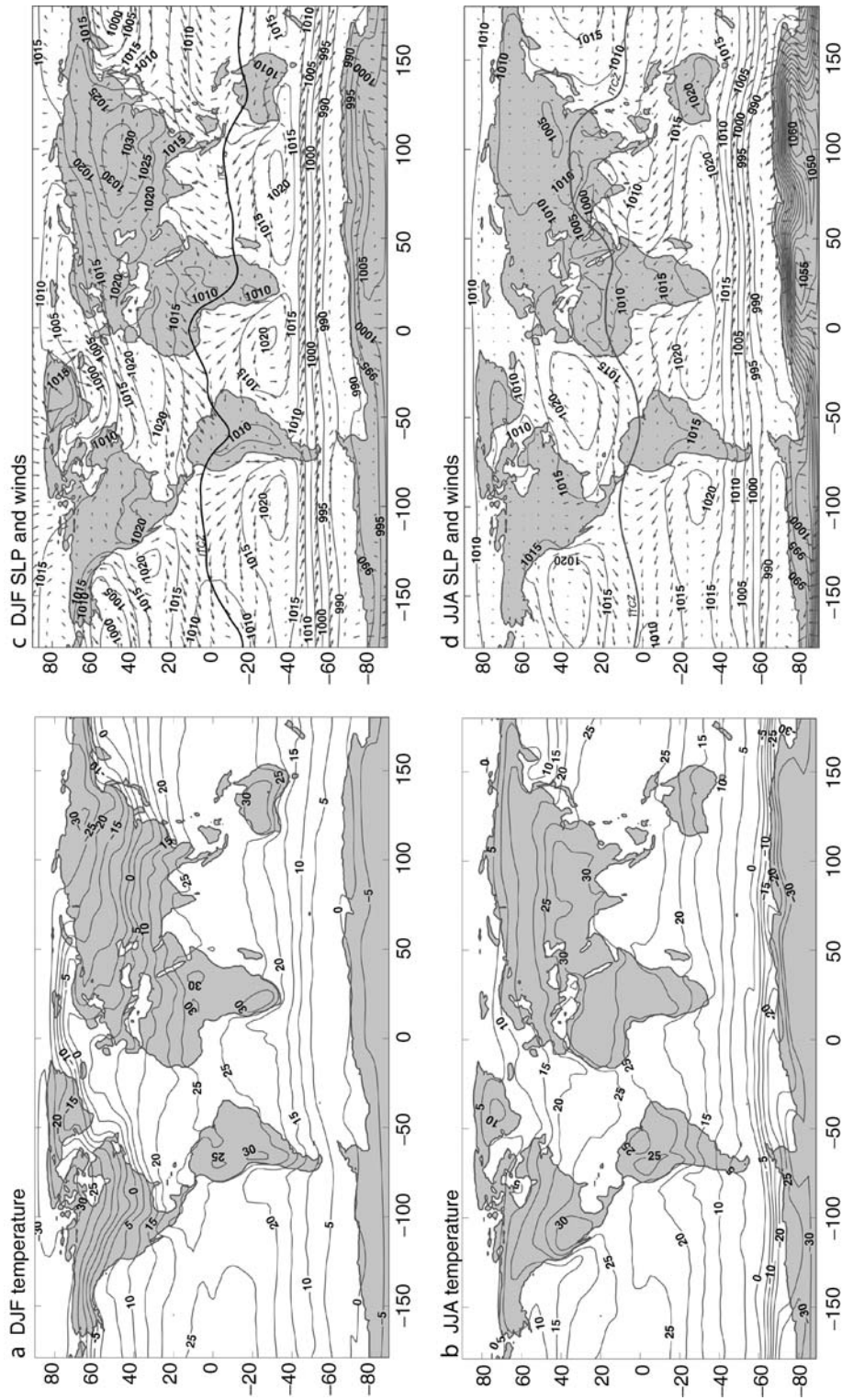


Figure P66 Seasonal surface air temperature (a and b), sea level pressure, and winds (c, d). Modern DJF (December, January, February) and JJA (June, July, August) averages are calculated from 1971–2000 NCEP/NCAR reanalysis data. Seasonal temperatures (a, b) are shown in °C with 5 °C contours. Sea level pressure (c, d) is shown in hPa with 5 hPa contours. The *thick black line* (c, d) shows the approximate seasonal location of the ITCZ (see text for discussion). Vectors show wind velocity, with the longest vectors representing winds of $\sim 13 \text{ m s}^{-1}$.

Pangean climate simulations using global climate models (GCMs) exhibit enhanced land-ocean pressure gradients, resulting in “mega-monsoons” (Kutzbach and Gallimore, 1989) analogous to today’s Asian monsoon system described above, albeit more severe. Such mega-monsoons were likely strongest in the hemisphere with more land area in the subtropics (Gibbs and Kump, 1994) and would have been highly sensitive to the location of mountains and high plateaus (Hay and Wold, 1998). Monsoonal circulation systems have also been shown to be sensitive to orbital forcing (see *Astronomical theory of climate change*), with the summer monsoon becoming invigorated in the hemisphere experiencing increased insolation (Kutzbach and Liu, 1997). This sensitivity was likely enhanced over the largest continents and may account for some of the rhythmic sedimentary sequences (cyclothem) seen in the late Paleozoic and early Mesozoic sedimentary record.

Extreme seasonality associated with large continents also affects the potential for widespread glaciation. While extreme cold winters provide many opportunities for winter snow accumulation, summer ablation is the critical factor in maintaining perennial snow cover leading to the growth of ice sheets. Increased seasonality and a lack of precipitation in the interior of ancient supercontinents would have been generally unfavorable for the growth of continental-scale ice sheets in mid-high latitudes (Crowley et al., 1989), unless accompanied by global cooling and/or uplift. For example, the Carboniferous glaciation of the Gondwanan supercontinent is thought to coincide with a time of broad epeirogenic uplift (Gonzalez-Bonorino and Eyles, 1995) combined with relatively low levels of atmospheric CO₂ (Berner and Kothavala, 2001), an important contributor to the heat-trapping greenhouse effect. In more recent times, the Cenozoic separation of Southern Hemisphere continents and associated reductions in continentality and seasonality, along with declining CO₂, may have contributed to the summer cooling requisite for the first extensive glaciation of Antarctica in the Paleogene (DeConto and Pollard, 2003a,b; Oglesby, 1991).

The polar latitudes’ sensitivity to geography is clearly illustrated by the very different climatic regimes of today’s north versus south polar regions. Increasing concentration of land area in high northern latitudes has long been considered a

contributor to the overall global cooling trend through the Cenozoic, eventually culminating in Northern Hemisphere glaciation (Crowell and Frakes, 1970; Donn and Shaw, 1977). A number of early paleoclimate modeling studies using GCMs explored the potential global impacts of latitudinal shifts in land area (Barron et al., 1984; Hay et al., 1990a). Like the simulations shown in Figure P67, these studies showed that an Earth with a concentration of equatorial continents and open polar oceans is indeed warmer and has lower equator-to-pole temperature gradients than an Earth with a concentration of polar continents and an equatorial ocean (Figure P67). Subsequent modeling studies focusing on the extreme warmth of the Cretaceous period (Barron et al., 1993) showed that the effect of paleogeography alone does not account for all of the warmth characteristic of much of the Mesozoic and early Cenozoic. This work concluded that some other climate forcing factor in addition to paleogeography (probably elevated concentrations of atmospheric CO₂) must have contributed to the warmth of the Cretaceous and other warm periods in Earth history, as speculated a century earlier (Arrhenius, 1896). While the models used in these studies were crude by current standards, they showed that changes in continental configuration could produce significant climate change, albeit smaller than the full range of climate variability recognized in the geologic record. They also showed that small tectonic changes associated with the movement of individual continental blocks and fragments have only limited, local effects (Hay, 1996) and could only produce major climatic change if combined with amplifying feedbacks.

In addition to latitudinal displacements, the evolving zonal (east-west) distribution of land can also have important climatic consequences. In tropical latitudes, the modern pan-Pacific atmospheric pressure pattern is dominated by the *Walker Circulation*. The Walker Circulation is driven by the longitudinal distribution of diabatic heating over land and sea, with Africa, South America, and the warm waters surrounding Indonesia providing sources of heating. On today’s Earth, easterly trade winds drive warm surface waters westward, forming the Western Pacific Warm Pool, where surface waters “pile-up” against the Indonesian archipelago. Consequently, the equatorial thermocline (the layer in the ocean below the surface mixed

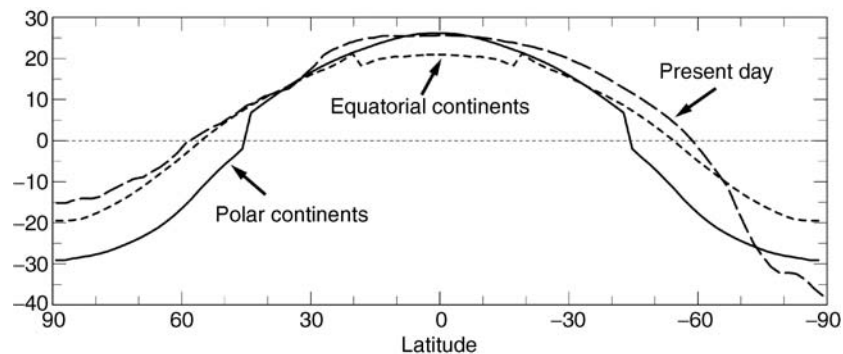


Figure P67 Zonally-averaged, mean annual surface air temperature over the modern Earth (*long dashes*) compared with GCM simulations of a planet with two polar continents (*solid line*) and a planet with a single equatorial supercontinent (*short dashes*). The climate simulations used the current (2008) version of the GENESIS V.3 GCM (Thompson and Pollard, 1997), preindustrial CO₂ (280 ppmv), and a mean orbital configuration (zero eccentricity and an obliquity of 23.5°). Total land areas in the polar and equatorial geographies are equal and close to modern. All land points were assigned an elevation of 800 m and a generic (mixed deciduous and evergreen) vegetation. Note the similarity of north polar temperatures in the modern versus equatorial continent (polar ocean) scenarios, and south polar temperatures in the modern versus polar continents scenarios.

layer where temperature decreases rapidly with depth) slopes down toward the west and shoals on the eastern margin of the basin to produce the $\sim 5^{\circ}\text{C}$ zonal SST difference across the Pacific. On the warmer, Indonesian side of the Pacific, latent and diabatic heating contributes to convection, low surface pressure, low-level convergence, and high pressure aloft. The upper-level, westerly pressure gradient is balanced by a sinking branch of the *Walker Circulation* and corresponding high surface pressure near the west coast of South America – a region typically dominated by upwelling and relatively cool sea surface temperatures.

Thus, the distribution of landmasses and restriction between the Pacific and Indian Oceans provided the basic framework for the *Walker Circulation* and related atmosphere-ocean dynamics like ENSO (El Niño Southern Oscillation – the dominant mode of modern Pacific climate variability). During an El Niño event, the western tropical Pacific cools and the core of warmest surface waters moves eastward, inhibiting upwelling along the west coast of South America. This zonal redistribution of SSTs perturbs the *Walker Circulation* and this is reinforced by atmosphere-ocean feedbacks involving the trade winds (Bjerknes, 1969). The 2–7-year quasi-periodicity of the modern ENSO cycle is, in part, modulated by equatorially-bound Kelvin waves in the ocean's interior, propagating from west to east in the upper thermocline, and westward traveling Rossby waves. On the eastern side of the basin, where the thermocline is already near the surface, these long waves can have a significant impact on SSTs and hence the atmosphere (Battisti and Hirst, 1989).

The long-term evolution of the Warm Pool has likely been influenced by the progressive closure of the eastern Tethys Sea (Figure P65) and restriction of the Indonesian Seaway through the Neogene (Cane and Molnar, 2001). While the character and timing of long wave-modulated atmosphere-ocean dynamics are expected to be different in a world with a wider Pacific basin, climate model simulations and geological evidence show the presence of ENSO-like variability as early as the Eocene (Huber and Caballero, 2003). This would suggest atmosphere-ocean oscillations like ENSO are robust features of the climate system that operate over a wide range of paleogeographic boundary conditions.

Eustasy

Tectonically-driven changes in global mean sea level (eustasy) and the associated flooding or exposure of low-lying continental areas also have important climatic consequences. The effects mainly stem from the changes in albedo and surface-atmospheric heat and moisture exchange associated with sub-aerial versus water-covered surfaces, although indirect effects on the marine carbon cycle and atmospheric CO_2 may also be important (Gibbs and Kump, 1994). Over 10^6 -year and longer time scales, eustasy is thought to be dominated by tectonic influences on the volume of the ocean basins (Hays and Pitman, 1973). Increases in the total length of mid-ocean ridges, high sea floor spreading rates producing warm, lower-density ocean crust, and the emplacement of Large Igneous Provinces (LIPs) can all displace ocean water and raise sea level (Kominz, 1984). Increased spreading rates have also been associated with increased volcanic outgassing and high levels of atmospheric CO_2 (Larson and Erba, 1999), although the linkages between sea floor spreading and atmospheric composition remain equivocal (Conrad and Lithgow-Bertelloni, 2007; Rowley, 2002).

The Cretaceous period offers one of the best examples of a warm “greenhouse” climate during a time of high sea level, when a combination of mostly ice-free poles and high sea floor spreading rates produced sea levels ~ 100 m higher than today (Haq et al., 1987; Larson, 1991). More than 20% of the continents were flooded (Figure P65), forming vast epicontinental seas (Hay et al., 1999). Climate modeling studies (Barron et al., 1993; DeConto et al., 1999; Otto-Bliesner et al., 2002) have shown that the combination of high greenhouse gas concentrations, continental positions, and high sea levels all contributed to the overall warmth of the Cretaceous. The ameliorating effects of open water in epicontinental seas and inland lakes likely reduced seasonality and contributed to the apparent winter-warmth of many continental locations (Sloan, 1994; Valdes et al., 1996). As discussed below, however, a satisfactory explanation for the extreme warmth of the polar regions during the Cretaceous and other warm climate intervals remains elusive.

Ocean gateways

The oceans transport vast amounts of water, heat, and salt across entire ocean basins and from low to high latitudes. As the ocean basins and the *gateways* between them evolve over tectonic timescales, so does ocean circulation. These tectonically-forced changes in ocean circulation have long been thought to play a key role in some of the major climatic events and transitions recognized in the geological record. While the timing of some tectonic gateway events broadly correspond with major paleoenvironmental changes (e.g., the ocean anoxic events (OAEs) of the Cretaceous (Leckie et al., 2002), the onset of Antarctic glaciation in the earliest Oligocene (Kennett, 1977; Livermore et al., 2004), and the onset of Northern Hemisphere glacial cycles in the Pliocene (Haug and Tiedemann, 1998)), the actual role of the ocean in these changes remains equivocal and likely involves a complex web of both direct and indirect effects.

Ocean heat transport

The link between tectonically forced changes in ocean circulation and global climate is usually attributed to changes in the ocean's contribution to poleward heat transport (Covey and Barron, 1988; Rind and Chandler, 1991). While modern estimates of atmospheric and oceanic heat transport remain poorly constrained, it is generally believed the oceans contribute about half of the total heat transport required to maintain the Earth's meridional energy balance. Because of the large equatorward latent heat flux associated with the lower limb of the Hadley circulation, the atmosphere contributes little heat transport out of the tropics, where the oceans do most of the work (maximum poleward ocean heat transport of about 2×10^{15} watts occurs at about $20\text{--}25^{\circ}$ North and South (Peixoto and Oort, 1992; Trenberth and Solomon, 1994)). While ocean circulation contributes little direct poleward heat transport in high latitudes, it plays an important role in polar climate via its influence on atmospheric teleconnections to the tropics (Cane and Evans, 2000) and its control on seasonal distributions of sea ice, which affects albedo and energy transfer between the ocean and atmosphere (Rind et al., 1995).

Because changes in the physiognomy of ocean basins and/or the opening or closure of gateways alters both the wind-driven (surface) and density-driven (deep) components of the ocean's meridional overturning (Bice et al., 1998; Poulsen et al., 2001), it may be reasonable to assume that tectonically-forced changes in ocean circulation can have profound climatic consequences (Covey and Barron, 1988). Conversely, theoretical

arguments suggest the potential effects of ocean circulation on total poleward heat transport are inherently limited. It has been hypothesized that the total energy transport by the atmosphere-ocean system remains roughly unchanged, so if the efficiency of either the atmosphere or ocean is reduced, the other compensates (Stone, 1978). Furthermore, ocean heat transport is proportional to the product of the temperature change and mass transport of water advected into a given region. Thus, the ocean's potential to transport heat would have been limited during times in the past when the temperature difference between low and high latitudes (and surface and deep waters) was much smaller than today, such as during the Cretaceous and early Eocene (Hay and DeConto, 1999; Sloan et al., 1995).

The limited potential of the oceans to maintain the warm, ice free polar conditions characteristic of most of the Phanerozoic is generally supported by numerical climate model simulations of paleoclimates using Mesozoic and early Cenozoic paleogeographies and high greenhouse gas concentrations (Brady et al., 1998; Huber and Sloan, 2001; Otto-Bliesner et al., 2002). While these simulations do produce relatively warm climates with somewhat reduced equator-to-pole temperature gradients relative to today, they fail to produce the dramatic increases in ocean heat transport required to explain all of the polar warmth of these intervals, provided the oceans were the primary mechanism for polar warming (Lyle, 1997). Several alternative mechanisms have been proposed to account for extreme polar warmth during these periods, including increased atmospheric latent heat transport (Hay and DeConto, 1999), increased tropical cyclone activity (Emanuel, 2001) and polar stratospheric clouds (Sloan and Pollard, 1998), although the potential climatic effects of these mechanisms are speculative. The underestimation of polar warmth in model simulations of these ancient climates remains an important problem, because it implies that climate model simulations of future climates may be underestimating future polar warming in response to anthropogenic increases in greenhouse gas concentrations.

While the global-scale impact of tectonically forced changes in ocean circulation is debatable, the breakup of Pangea certainly had profound effects on both the wind-driven current system and location(s) of deepwater formation. Such changes likely had important regional climatic effects that could have triggered indirect forcing mechanisms with global consequences. For example, tectonically forced changes in ocean circulation can impact atmospheric CO₂ via changes in ocean overturning, primary productivity, and the biological pump. Furthermore, changes in ocean circulation contributing to deep sea warming have the potential to trigger the release of methane (another important greenhouse gas that oxidizes to form CO₂) from frozen, temperature-sensitive gas hydrates (clathrates) stored in deep sea sediments. Such a feedback mechanism has been proposed to have contributed to the dramatic global warming event known as the Paleocene-Eocene Thermal Maximum (Dickens et al., 1997).

The oldest surviving ocean crust is less than 200 million years old and detailed paleogeographic reconstructions become increasingly difficult to assemble with increasing age (Crowley and Burke, 1998). Despite the inherent limitations, the timing of major late Mesozoic and Cenozoic gateway events are becoming better constrained, including the opening of the North and South Atlantic basins, the closure of the ancient Tethys Ocean, the opening of the Southern Ocean gateways, the restriction of the Indonesian Seaway, and the closure of the Panamanian Isthmus (Figure P65). Among these, the closure of the Tethys and the

opening of the Southern Ocean may be the most profound because they produced the late Cenozoic world as we know it today – with a single high-latitude circum-global passage (Southern Ocean) rather than a tropical circum-global passage (Tethys Ocean) as existed during the relative global warmth of the late Mesozoic and early Cenozoic.

Tethys Ocean

The Tethys (Figure P65) formed sometime in the late Jurassic, reached its zenith during the Cretaceous, and remained at least partially open until the Miocene (Hay et al., 1999). The modern Mediterranean Basin is the last remaining expression of the ancient Tethys, which both reduced Eurasian continentality and provided a low latitude ocean passage between the Indian and Atlantic Ocean basins. The Cenozoic retreat of the Tethys and Paratethys Seas, and the associated increase in Eurasian continentality and aridity, may have had climatic effects comparable in magnitude to the uplift of the Himalaya and Tibetan Plateau (Ramstein et al., 1997).

Like the modern Mediterranean, Tethyan (sub-tropical) latitudes were likely dry and dominated by strong net evaporation. Relatively warm and saline (high density) deep-water masses could have formed there. Given the size of the ancient Tethys, such water masses have been proposed to have driven a thermohaline circulation system essentially the opposite of today's, with warm, but dense (high salinity) deep waters sinking in low latitudes and flowing polewards (Brass et al., 1982; Chamberlin, 1906). The potential climatic impacts of warm saline deep and bottom water formation remains equivocal, however. Numerical ocean models have not been able to maintain a stable mode of circulation with deep convection in low latitudes (Bice, 1997; Brady et al., 1998). Furthermore, even if such a mode of circulation did persist, it is unlikely that a reversal of the thermohaline component of the meridional overturning circulation would significantly increase ocean heat transport on an Earth with warm polar temperatures already in place.

While the global importance of Tethyan deepwater formation is debatable, closure of the Tethys likely did have a number of important impacts on the evolution of Cenozoic oceans and climate. For example, a recent modeling study of Cenozoic ocean circulation (von der Heydt and Dijkstra, 2006) showed that the opening of Southern Ocean gateways combined with progressive closure of the Tethys could have induced a flow reversal (from westward to eastward) between the Atlantic and Pacific oceans through the Central American Seaway. Today, net fresh water flux out of the Atlantic basin maintains a relatively saline Atlantic and fresh Pacific. In turn, dominant sources of deepwater formation are limited to the Atlantic. Prior to the closure of the Tethyan and Panamanian seaways, inter-basin connectivity would have reduced this salinity contrast, possibly allowing locations of major deepwater formation in both the North Atlantic and North Pacific. Another ocean modeling study of an open versus closed circum-equatorial passage suggest an open Tethys would have increased upwelling of cold deepwaters in low latitudes, possibly helping to moderate tropical temperatures during warmer Mesozoic and early Cenozoic climate intervals (Hotinski and Toggweiler, 2003).

While the actual global climatic effects of these changes in the ocean remain unconstrained, the final closure of the eastern Tethys, ongoing Cenozoic restriction of Indonesia throughflow, and final closure of the Panamanian Isthmus in the Pliocene all contributed to forming the thermal structure of the oceans

as we know them today. This includes a trade wind-driven Western Pacific Warm Pool (WPWP), westward dipping thermoclines in the major ocean basins, and cool eastern Pacific tropical SSTs – the essential components of the modern ENSO system (Philander, 1999). Differentiation of the ocean basins during the Cenozoic also influenced the partitioning of salt in the oceans, with fundamental consequences for the location of deepwater formation and ocean circulation in general.

Southern Ocean gateways

The opening of the Southern Ocean passages between Antarctica and Australia (Tasmanian Passage) and Antarctica and South America (Drake Passage) and Antarctic glaciation in the earliest Oligocene is an often-cited example of ocean gateways causing a specific climatic event. As these passages widened and deepened and the Antarctic Circumpolar Current and Polar Frontal Zone developed, reduced poleward ocean heat transport and cooler Southern Ocean temperatures are thought to have cooled Antarctica enough to allow continental glaciation (Kennett, 1977; Robert et al., 2001). While the earliest Oligocene glaciation of East Antarctica broadly coincides with the timing of Tasmanian gateway development (Stickley et al., 2004), estimates of the opening of Drake Passage range between about 45 and 22 Ma (Barker and Burrell, 1977; Lawver and Gahagan, 1998; Scher and Martin, 2006), clouding the direct cause and effect relationship between the gateways, cooling, and glaciation.

Several ocean modeling studies (Mikolajewicz et al., 1993; Toggweiler and Bjornsson, 2000) have reported reductions in Southern Ocean heat transport and cooler SSTs ($\sim 1\text{--}4^\circ\text{C}$) in response to opening Southern Ocean gateways. In contrast, a recent study using a fully coupled atmosphere-ocean GCM showed little change in ocean heat transport or the climate of the Antarctic interior associated with the opening of the Tasmanian gateway (Huber et al., 2004). Even when forced with an unrealistically large (25%) change in southward ocean heat transport, a coupled GCM-ice sheet model showed that the effect on the timing of Antarctic glaciation caused by the gateways is small (DeConto and Pollard, 2003b) relative to the effects of declining Cenozoic CO_2 (Pagani et al., 2005). When considered together, these results suggest some other forcing mechanisms and/or feedbacks, perhaps related to the carbon cycle, may bear greater responsibility for Antarctic cooling and glaciation than the direct physical effects of the gateways on the oceans (Zachos and Kump, 2005).

The importance of atmospheric CO_2 concentrations relative to ocean gateways has also been recognized in modeling studies of other periods. For example, in ocean simulations testing the effects of the mid-Cretaceous opening of the gateway between the North and South Atlantic (Poulsen et al., 2001), very warm, saline conditions dominate the North Atlantic prior to the opening. While connecting these basins produces significant changes in regional ocean circulation, no fundamental change in the mode of thermohaline circulation occurs, and globally averaged SSTs change only by $\sim 0.2^\circ\text{C}$, which is insignificant relative to the warming caused by the levels of greenhouse concentrations presumed to have existed at that time.

Central American passage and Indonesian Seaway

The Neogene closure of the Central American passage and ongoing restriction of the Indonesian Seaway have also been implicated in climate change, including the onset of Northern Hemisphere glaciation and African aridification (Cane and

Molnar, 2001; Mikolajewicz et al., 1993). In the case of the Panamanian Seaway, restricted inter-basin water mass exchange was thought to have invigorated the Gulf Stream component of the North Atlantic subtropical gyre, increasing the moisture available for advection to high latitudes and growing ice sheets (Keigwin, 1982). More recent studies, however, have shown that closure of the Isthmus of Panama likely predates the onset of Northern Hemisphere glaciation, pointing to other possible forcing mechanisms (Haug et al., 2005).

Between the Pacific and Indian Oceans, the northward movement of Australia and New Guinea through the Cenozoic, combined with the emergence of individual volcanic islands, has led to the progressive restriction of Indonesian throughflow and a change in the source of surface waters entering the Indian Ocean from predominantly warm South Pacific waters to cooler North Pacific waters. The resulting cooling of the Indian Ocean has been implicated in African aridification $\sim 3\text{--}5$ Ma, with possible impacts on Hominid evolution. Furthermore, the restriction would have increased the zonal temperature gradient across the Pacific, with potentially important teleconnections to high northern latitudes (Cane and Molnar, 2001).

Other significant gateway events during the Cenozoic include the opening of Fram Strait, which has allowed a deep water passage between the Arctic and North Atlantic basins since sometime in the late Miocene (Kristoffersen, 1990), and the Oligocene-Miocene deepening of the Denmark Strait and Iceland-Faeroes passages (Wold et al., 1993). The Denmark Strait and Iceland-Faeroes passages are of particular importance because they allow the outflow of deep waters formed in the Greenland and Norwegian Seas to flow into the North Atlantic, then becoming North Atlantic Deep Water – an important component of the so-called “global ocean conveyor” (Broecker, 1991).

The relatively narrow and shallow (< 50 m) Bering Strait provides the only modern connection between the Arctic and the Pacific. While the gateway lies on continental crust, the low elevation of the area is attributed to regional extension and faulting associated with subduction of the Pacific Plate and rotation of the Bering Block (Mackey et al., 1997). The Bering Strait has allowed an intermittent shallow-water connection between the Arctic and Pacific basins since the late Miocene, with the Strait and surrounding area becoming subaerial during glacial periods. Today, only about 1 Sv ($10^6\text{ m}^3\text{ s}^{-1}$) of water passes through the strait into the Arctic basin; however, it has had an important impact on Plio-Pleistocene climate via its influence on North Pacific and Arctic salinity, sea ice, and the effect of repeated flooding/exposure of the Bering and Chukchi shelves on regional albedo and moisture availability for Beringian ice sheets (Brigham-Grette, 2001).

While the global effects of tectonically forced changes in ocean circulation remain equivocal, numerous ocean modeling studies have indeed shown that changes in ocean circulation in response to evolving basin configuration do have important regional impacts. Indeed, ocean currents are often attributed to the maintenance of specific terrestrial climate patterns, especially in maritime locations. Perhaps the most obvious example is the transport of warm subtropical surface waters in the North Atlantic Subtropical Gyre (via the Gulf Stream and North Atlantic Current), which warms the waters adjacent to northwestern Europe. The advection of warm waters into this region, in part driven by the North Atlantic Deep Water formation noted above, has long been presumed to be the primary reason for Northern Europe's equability relative to North

American climates at the same latitude. This paradigm has recently been challenged, however, with the role of topographically-forced atmospheric planetary waves (see below) and prevailing North Atlantic wind patterns possibly being more important in the transport of heat to Northern Europe (via the atmospheric transport of heat stored seasonally in North Atlantic surface waters) than previously considered (Seager et al., 2002).

Mountain uplift

Tectonic uplift is often cited as an important contributor to long-term climatic change (Birchfield et al., 1982; Raymo and Ruddiman, 1992; Ruddiman and Kutzbach, 1991). Because modern orography appears to be anomalously high relative to the warmer climatic intervals that dominated the Mesozoic and early Cenozoic, relatively recent mountain building events, like the collision of India with Asia that formed the Himalayas beginning ~ 40 Ma, are often implicated as primary contributors to Cenozoic cooling and Northern Hemispheric glaciation. In fact, a number of the world's mountainous regions have been described as having undergone significant uplift during the late Cenozoic (see Hay et al., 2002 and references therein) and speculated linkages between those uplifts and Cenozoic cooling date as far back as the nineteenth century (Dana, 1856).

With the exception of the ice sheets covering Greenland and Antarctica, the most prominent topographic feature on today's Earth is the Himalayan-Tibetan plateau, covering a vast area (4×10^6 km²) at an elevation averaging ~ 5 km. The only geological intervals known to have had comparable orographic features occurred as a result of the continental collisions that formed Pangea about 320 and 240 Ma (see Ruddiman, 1997). The climatic effects of such features are multifaceted and complex. In addition to providing a barrier to atmospheric flow, mountains and high plateaus produce rain shadows on their leeward slopes and can have important effects on albedo and energy balance. Tectonic setting, including the orientation of land surface slope and the presence of bare soil and/or rock can influence albedo directly and through its control on vegetation. Vegetation is of particular importance because it affects land surface roughness, atmospheric moisture, and the partitioning of sensible and latent heat fluxes between the surface and atmosphere (Dickinson and Henderson-Sellers, 1988). Areas dominated by evergreen vegetation are also likely to maintain much lower albedo and warmer temperatures than bare soil or tundra, which are easily covered by winter snow (Bonan et al., 1992). Because tropospheric temperatures generally decrease with increasing altitude (the globally averaged tropospheric lapse rate is about $6.5^\circ\text{C km}^{-1}$), high terrain is more likely to maintain perennial snow cover and glacial ice with high albedos (0.6–0.8).

Uplift and glaciation

In addition to the latitudinal position of continents, epeirogenic uplift is a critical factor in glaciation (Birchfield et al., 1982). This is mainly due to the dependence of both temperature and orographic effects on snowfall. On local to regional scales, glaciers are found where winter snowfall is high and summer temperatures remain cold enough to limit ablation. Conversely, the termination zones of glaciers often occur in low-lying valleys, where temperatures are warmer and summer ablation outpaces winter accumulation. The slope of the land surface also has a mechanical effect on ice flow, although the relative importance of snowline elevation versus flow

effects is likely to depend on the amplitude and spacing of individual mountain peaks and troughs (Marshall and Clarke, 2000; Oerlemans, 2002).

Theoretical and numerical modeling studies have shown that tectonic uplift of widespread land areas above the equilibrium snowline can lead to the sudden, non-linear growth of glaciers and ice sheets, possibly leading to continental-scale glaciation. The rapid non-linear response is caused by albedo and height-mass balance feedbacks (North et al., 1983; Weertman, 1961) associated with the high reflectivity of snow and ice and the geometrical effect of a growing ice cap and its rapidly expanding net accumulation zone. The spatial scale of uplift appears to be a key factor in the potential response. For example, climate-ice sheet modeling studies have shown that broad uplift of an initially ice-free Antarctic interior can trigger sudden glaciation, provided the continent is already near a glaciation threshold (DeConto and Pollard, 2003b). In contrast, ice modeling studies of the effects of the Transantarctic Mountains on the East Antarctic Ice Sheet have shown that the uplift of individual mountains or the development of mountain troughs has limited influence (Kerr and Huybrechts, 1999).

Mountains, high plateaus, and atmospheric planetary waves

In mid-latitudes, zonal distributions of major landmasses and sea surface temperatures contribute to the position of standing atmospheric planetary waves via their influence on dominant low-level pressure patterns. Large mountains belts (Himalaya and Rocky Mountains) and high plateaus also provide direct physical barriers to atmospheric flow, which induce these long planetary Rossby waves in the upper-level westerlies, recognizable by the well-known meridional meanders in the polar and sub-tropical jet streams. Rossby waves form as a consequence of the conservation of absolute vorticity. When a parcel of air (or water) is displaced from its original latitude or changes its thickness as it passes over a mountain range, it responds by changing its latitude (planetary vorticity) and/or its relative vorticity (tendency to rotate). The resulting oscillations in the mean flow about a given latitude produce long planetary waves which move westward relative to the flow. In the fast flow of the upper troposphere, the waves appear to move slowly eastward relative to the Earth's surface. In the Northern Hemisphere, the longest of these waves tend to become stationary or *locked* relative to major orographic features. Wave crests (ridges) form over the Rocky Mountains and Tibet where the westerlies are displaced poleward before turning equatorward in the lee of the mountains, forming atmospheric troughs at $\sim 70^\circ\text{W}$ and $\sim 150^\circ\text{E}$ (Figure P68). While the amplitude of the long waves is highly variable, higher elevations tend to increase the meridional component of flow (Nigam et al., 1988). Thus, atmospheric planetary waves in the Northern Hemisphere tend to exhibit higher amplitudes than those in the ocean-dominated Southern Hemisphere, where the upper-level flow is more zonal.

Because vorticity associated with curvature in the waveform produces convergence downwind of the wave's crest (ridge) and divergence downwind of the trough, high pressure and generally fair conditions tend to be maintained eastward of the ridge. Conversely, cyclonic flow, low pressure, and storminess are found east of the trough. Thus, the time-averaged position of the waves has a fundamental effect on regional climates, storm tracks, and precipitation patterns. For example, the general aridity of the American interior and storminess of the

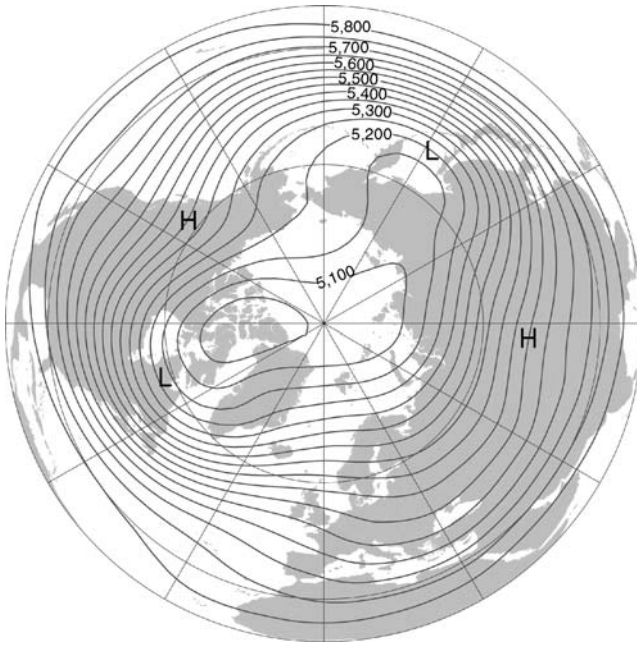


Figure P68 Seasonally averaged (DJF) 500 hPa geopotential heights over the Northern Hemisphere. Heights (shown in meters with 100 m contours) are calculated from 1971–2000 NCEP/NCAR reanalysis data, showing the time-averaged position of the dominant planetary wave pattern (see text for discussion).

U.S. East Coast can, at least in part, be attributed to the effect of the Rocky Mountains on the planetary wave pattern (Manabe and Broccoli, 1990). Further downstream, some of Western Europe's winter warmth can be attributed to the generally southwesterly flow over the relatively warm eastern North Atlantic, which is ultimately controlled by the standing wave pattern fixed by the Rockies (Seager et al., 2002). The standing wave pattern forced by the Rockies and Himalayas has also been implicated in establishing the conditions necessary for the onset of Northern Hemisphere glacial cycles in the Pliocene by allowing increased moisture advection from the warmth of the Gulf of Mexico and the western Atlantic to sites of Laurentide and Scandinavian Ice Sheet nucleation (Ruddiman and Kutzbach, 1989).

Uplift and monsoons

In addition to their effect on zonal airflow, the lower air densities associated with high elevations amplify seasonal temperature changes and vertical motions associated with monsoonal systems (rising and sinking air in summer and winter, respectively). This effect is thought to be largely responsible for the strength of the modern Asian-Indian monsoon system (Prell and Kutzbach, 1992) and modeling studies have shown that elevations roughly equal to half those of the modern Himalayan-Tibetan elevation are required to produce the strength of the southeast summer monsoon over India (Kutzbach et al., 1993). The Himalayan and Tibetan plateaus have also been implicated as an amplifier of orbital (Milankovitch) variability, whereby a combination of enhanced condensational heating over South Asia and dynamical effects associated with planetary waves significantly increases the monsoon's sensitivity to orbital forcing (Liu et al., 2003).

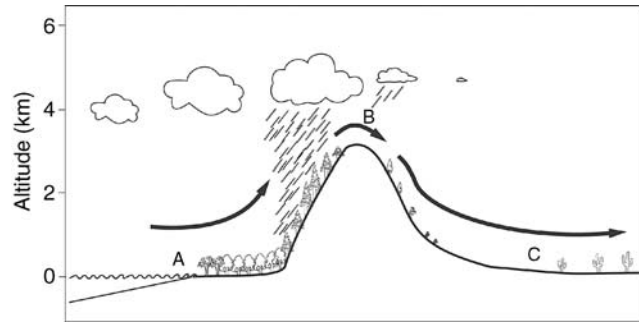


Figure P69 A schematic diagram showing the orographic precipitation and rain shadow effects of a mountain range. The *black arrow* represents air flow. Relationships between altitude, pressure, temperature, and absolute humidity control the distribution of precipitation, temperature and humidity on the windward and leeward side of the mountains. Typical temperatures and relative humidities of air at locations A, B, and C are $\sim 28^\circ\text{C}$ and 70%, 8°C and 100%, and 38°C and 25%, respectively (redrawn from Hay, 1996).

Rain shadows

In addition to their widespread radiative and dynamical effects, mountains can have important regional impacts – especially on precipitation. When air is forced upward as it passes over a mountain range, adiabatic cooling induces condensation of available water vapor, resulting in clouds and precipitation (Figure P69). Having lost some of its available water, sinking, dry air on the leeward flanks of a mountain range is adiabatically warmed, which is why arid and warm conditions tend to prevail downwind of mountain ranges. This *rain shadow* effect can extend hundreds of kilometers, with obvious implications for the distribution of vegetation and the formation of climate sensitive sediments, such as evaporites. This drying effect is strongest where air can descend back to (or below) its initial altitude after passing over a mountain range, as can occur in rift valleys. Due to the non-linear relationships between temperature, saturation vapor pressure, and air pressure, an air mass passing over a second mountain range (out of a rift valley, for example) will be warmer and capable of carrying more water vapor than it was before it entered the basin. The resulting net export of fresh water out of rift valleys may account for the wide latitudinal distribution of Phanerozoic evaporite deposits, which extends far outside the subtropical arid zones (see Hay, 1996).

The modern Andes provide an excellent example of the importance of orographic effects on regional precipitation. In mid latitudes dominated by the westerlies, precipitation is enhanced on the western side of the mountain range, while the Patagonian Desert lies to the east. In tropical South America, where the winds are generally easterly, the opposite pattern is found, with enhanced precipitation over the rainforests of the Amazon Basin and dry conditions along the coastal margin of the Andes. For example, the high altitude Atacama Desert in northern Chile, one of the driest places on Earth, lies between the Pacific Ocean and the foothills of the Andes at a latitude of about 20°S and within the influence of the easterlies.

Similar rain shadow effects may have been even more profound on ancient supercontinents, with large seasonal cycles and arid interiors already in place. In GCM simulations using a single, idealized supercontinent extending from the north to south poles and with meridionally-oriented coastal mountain

ranges running along the eastern continental margin, tropical precipitation associated with the trade winds and the ITCZ is intercepted on the seaward (eastern) flanks of the mountains (Figure P70). In a simulation with mountains running along the west coast of the supercontinent, continental precipitation is increased in tropical latitudes, while precipitation associated with cyclonic systems embedded in the westerlies falls mainly on the western slopes of the mountains (Hay et al., 1990b).

Mountain uplift or climate change?

In addition to tectonic, geomorphological, and structural studies, evidence of mountain uplift comes from records of continental denudation found in sediment accumulation rates (Hay, 1988) and marine records of $^{87}\text{Sr}/^{86}\text{Sr}$ (an indicator of chemical weathering (Richter et al., 1992)). Other techniques rely on the physiognomy of fossil vegetation (Royer, 2001), and oxygen isotopes in carbonate rocks (Garzzone et al., 2004) to constrain the ancient elevations of specific locations. It should be noted that the term “uplift” can be used to describe the uplift of a region of the Earth’s surface (with respect to the geoid) or the uplift of rocks (with respect to the surface). Depending on erosion rates, the uplift of rocks relative to the local surface, sometimes referred to as “exhumation” (England and Molnar, 1990), can be much greater than the uplift relative to the geoid. Erosion and the removal of mass from mountain valleys can actually raise the surrounding peaks through isostasy (Molnar and England, 1990). In the Alps and Himalayas, loss of mass in deep fluvial and glacial valleys has been estimated to account for up to 25% of the elevation of the highest mountains (Hay et al., 2002; Montgomery, 1994). Because chemical and

physical erosion rates are ultimately controlled by the combined effects of surface relief and climatic parameters such as seasonality, precipitation, and glaciation, observed increases in the delivery of sediment to basins and continental margins can be attributed to climate change, mountain uplift, or both. The paradigm of Cenozoic uplift causing global cooling and Northern Hemisphere glaciation was challenged by Molnar and England (1990), who argued that the appearance of recent uplift in a number of disparate mountain ranges may be an artifact of Cenozoic climate change rather than the cause of the cooling (see also *Mountain uplift and climate change*).

Can the atmosphere drive tectonic processes?

The potential for the atmosphere to be a driver of tectonic processes has only recently begun to be appreciated. In addition to the processes mentioned above, whereby erosion in mountain valleys can raise mountain peaks, differential erosion rates on the windward (wet) versus leeward (dry) flanks of mountains and latitudinal climate gradients can cause structural asymmetries that influence the morphological evolution of entire mountain ranges. This effect has been proposed for the Andes (Montgomery et al., 2001), where structural asymmetries and latitudinal changes in crustal thickness correlate with climatically-controlled erosion patterns. Furthermore, progressive Cenozoic cooling and associated increases in wind stress, upwelling intensity, and cooler sea surface temperatures along the South American margin may be enhancing rain shadow aridity along the Chilean and Peruvian margin. The resulting decrease in precipitation and runoff is thought to be starving the adjacent convergent plate boundary (subduction zone) of lubricating sediment, thus contributing to the stresses supporting the high Andes (Lamb and Davis, 2003).

Plate tectonics and the global carbon cycle

While not the focus of this entry, the effects of tectonic processes on geochemical cycling and atmospheric greenhouse gas concentrations should be considered in any discussion of plate tectonics and climate change. Primary inputs of CO_2 include mantle outgassing at sea floor spreading centers and volcanoes, metamorphism of carbonate rocks along subduction zones, and respiration and burning of organic matter. Long-term sinks for CO_2 are controlled by the burial of organic matter and by the weathering of silicate rocks to form carbonates (Berner and Kothavala, 2001). Cenozoic mountain building, particularly the uplift of the Himalayan-Tibetan Plateau, has been related to CO_2 drawdown, cooling, and glaciation via increased weathering rates and the effects of increased nutrient delivery on ocean productivity and organic carbon burial (Chamberlin, 1899; Filipelli, 1997; Raymo et al., 1988). While the actual mechanisms responsible for CO_2 drawdown on tectonic timescales are complex and continue to be debated, geochemical reconstructions of Cenozoic CO_2 levels do show a dramatic decrease in atmospheric mixing ratios from more than three times present day levels during the warmth of the Eocene, to near modern levels by the early Miocene (Pagani et al., 2005).

Volcanism and large igneous provinces

Volcanism, often associated with tectonic processes, can also play an important role in climatic change. In addition to outgassing CO_2 , an important greenhouse gas with the potential to raise global temperatures, magma can be rich in SO_2 , which can lead to the production of sulfuric acid (H_2SO_4) aerosols in the atmosphere. When injected into the stratosphere via

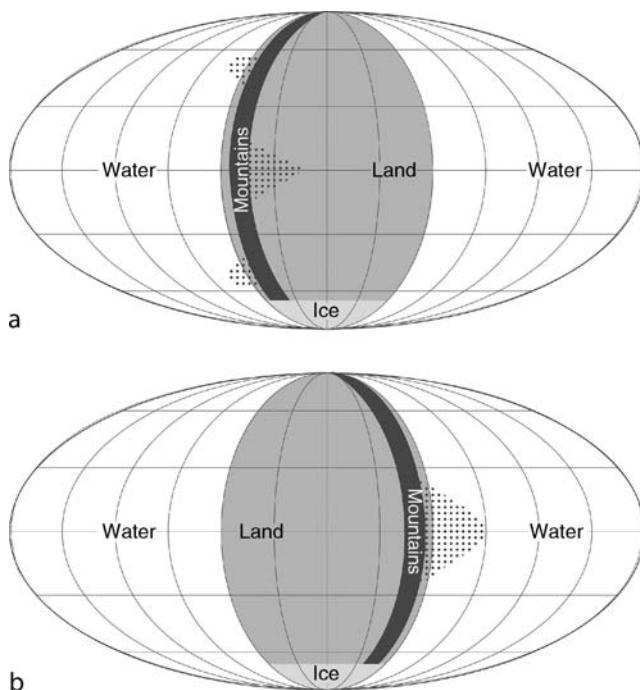


Figure P70 The distribution of maximum precipitation rate (stippling) in GCM simulations of a planet with a single supercontinent and a meridional mountain range oriented on either the western (a) or eastern (b) continental margin (redrawn from Hay, 1996 and based on GCM simulations described in Hay et al., 1990a).

energetic volcanism, sulfur aerosols are highly reflective to incoming short wave radiation from the Sun, providing a cooling effect on the troposphere and Earth's surface. In 1991, the SO₂-rich eruption of Mt. Pinutubo in the Philippines cooled the Northern Hemisphere by 0.5–0.6 °C (Hansen et al., 1996) and the recent frequency of volcanic events may account for some of the variability recognized in highly resolved climate reconstructions of the Holocene (Mann et al., 1999). Global cooling associated with each injection of stratospheric aerosols is generally limited to a few years. On longer timescales, the atmospheric CO₂ loading associated with pervasive volcanism could have a net warming effect, complicating estimates of the net global environmental impacts of the larger and most long-lived volcanic events in Earth history.

The prolonged, effusive emplacement of mafic magmas to form large igneous provinces (LIPs) is usually associated with plate tectonic processes including uplift and continental rifting. LIPs can be continental or oceanic, and large oceanic LIPs, such as the Ontong Java Plateau in the western Pacific, can contain more than 50 million km³ of volcanic and plutonic rocks. The episodic emplacement of LIPs has occurred throughout Earth history; although most surviving examples of continental and oceanic flood basalts are Mesozoic and Cenozoic in age (see *Flood basalts, climatic implications*). While the timing of some emplacement events has been directly associated with climate change (Mahoney and Coffin, 1997), LIP-climate connections are highly complex. In addition to their effect on sea level, LIP and mid-ocean ridge volcanism can release CO₂, SO₂, Cl, F, and H₂O into the atmosphere with significant climatic consequences. For example, the overall warmth of the Cretaceous period has been attributed, at least in part, to a combination of high atmospheric CO₂ and high sea level, with times of peak warmth and ocean anoxia associated with LIP emplacement (Larson and Erba, 1999; Leckie et al., 2002). While a number of studies have related LIP emplacement to extinction events (Rampino and Caldeira, 1993), the specific mechanisms causing environmental stress are difficult to tease apart and may be due to the direct effects of LIPs on climate, the biotic effects of toxic atmospheric fallout (i.e., acid rain), or some combination of the two.

The Neoproterozoic *Snowball Earth* provides another example of indirect tectonic-climate linkages through volcanism. Between ~750 and 580 Ma, the Earth is thought to have been episodically completely covered by ice, with some glaciations lasting for millions to tens of millions of years (Hoffman et al., 1998). While the evidence of significant ice at the equator remains controversial, tectonic processes (largely through volcanism's contribution to atmospheric CO₂) play a central role in most theoretical models of both the onset and demise of the snowball. First, a prolonged period of tectonic quiescence and minimal outgassing is thought to have allowed CO₂ concentrations to drop below some critical threshold, initiating a powerful ice-albedo cooling feedback (Schrage et al., 2002). The continental breakup of Rodinia (a Proterozoic supercontinent), and associated changes in runoff and weathering have also been linked with a decline in CO₂ around this time (Donnadieu et al., 2004). As the Earth cooled, expanding ice sheets and sea ice would have increased planetary albedo. As shown in simple energy balance model (EBM) experiments, the ice-albedo feedback becomes unstable once snow and ice reach ~30° North and South, resulting in the sudden expansion of ice to the equator (Budyko, 1968). Once the Earth was completely covered by ice, continental weathering of silicate rocks,

a long-term sink for CO₂, would have been greatly reduced. This would have allowed atmospheric CO₂ to accumulate to levels sufficient to cause significant warming, although additional warming mechanisms including the presence of other greenhouse gases and/or other feedbacks may have been necessary to trigger deglaciation (Pierrehumbert, 2004).

Summary

A number of tectonic processes are linked both directly and indirectly to a wide range of climate forcings, so the direct role of plate tectonics in specific ancient climate events is often difficult to decipher. In addition to the direct climatic effects of horizontal and vertical tectonics discussed here, paleogeography strongly influences the climate system's sensitivity to external forcing and provides the basic framework for studying ancient climate change over geological timescales.

While the relative contributions of greenhouse gas concentrations and plate tectonics in the evolution of the Earth's climate continues to be debated, tectonic processes influence the composition of the atmosphere, so the two cannot be entirely separated. Tectonically forced changes in ocean and atmospheric circulation have greatly influenced the evolution of specific regional climates; however, their potential to produce the full range of global climatic variability recognized in the geological record may not be as great as once suspected.

Lastly, while tectonic processes are usually associated with slowly evolving environmental change, there are important exceptions. Volcanism's essentially instantaneous effect on the atmosphere provides one example. Less obvious is the climate system's potential to respond non-linearly to the most gradual tectonic forcing, with sometimes sudden and extreme consequences. Thus, plate tectonic processes should be considered a potential climate forcing mechanism on all timescales.

Robert M. DeConto

Bibliography

- Arrhenius, S., 1896. On the influence of carbonic acid in the air upon the temperature of the ground. *Phil. Mag.*, **41**, 237–275.
- Barker, P.F., and Burrell, J., 1977. The opening of Drake Passage. *Mar. Geol.*, **25**, 15–34.
- Barron, E.J., Fawcett, P.J., Pollard, D., and Thompson, S.L., 1993. Model simulations of Cretaceous climates: the role of geography and carbon dioxide. *Phil. Trans. R. Soc. Lond.*, **341**, 307–316.
- Barron, E.J., Thompson, S.L., and Hay, W.W., 1984. Continental distribution as a forcing factor for global scale temperature. *Nature*, **310**, 574–575.
- Barry, R.G., and Chorley, R.J., 1998. *Atmosphere, Weather, and Climate*, 7th edn. London: Routledge, 409pp.
- Battisti, D.S., and Hirst, A.C., 1989. Interannual Variability in the Tropical Atmosphere-Ocean System: Influences of the Basic State, Ocean Geometry and Nonlinearity. *J. Atmos. Sci.*, **46**, 1687–1712.
- Berner, R.A., and Kothavala, Z., 2001. Geocarb III: A revised model of atmospheric CO₂ over phanerozoic time. *Am. J. Sci.*, **301**, 182–204.
- Bice, K.L., 1997. An investigation of early Eocene deep water warmth using uncoupled atmosphere and ocean general circulation models: Model sensitivity to geography, initial temperatures, atmospheric forcing and continental runoff, Ph.D. Thesis, The Pennsylvania State University, University Park.
- Bice, K.L., Barron, E.J., and Peterson, W.H., 1998. Reconstruction of realistic early Eocene paleobathymetry and ocean GCM sensitivity to specified basin configuration. In Crowley, T., and Burke, K. (eds.), *Tectonic Boundary Conditions for Climate Reconstructions*. New York: Oxford University Press, pp. 227–247.
- Birchfield, G.E., Weertman, J., and Lunde, A.T., 1982. A model study of the role of high latitude topography in the climatic response to orbital insolation anomalies. *J. Atmos. Sci.*, **39**, 71–87.

- Bjerknes, J., 1969. Atmospheric teleconnections from the equatorial Pacific. *Mon. Weather Rev.*, **97**, 163–172.
- Bonan, G.B., Pollard, D., and Thompson, S.L., 1992. Effects of boreal forest vegetation on global climate. *Nature*, **359**, 716–718.
- Brady, E.C., DeConto, R.M., and Thompson, S.L., 1998. Deep water formation and Poleward ocean heat transport in the warm climate extreme of the Cretaceous (80 Ma). *Geophys. Res. Lett.*, **25**, 4205–4208.
- Brass, G.W., Southam, J.R., and Peterson, W.H., 1982. Warm saline bottom waters in the ancient ocean. *Nature*, **296**, 620–623.
- Brigham-Grette, J., 2001. New perspectives on Beringian Quaternary paleogeography, stratigraphy, and glacial history. *Quaternary Sci. Rev.*, **20**, 15–24.
- Broecker, W.S., 1991. The great ocean conveyor. *Oceanography*, **4**, 79–89.
- Budyko, M.I., 1968. O proischozhdenii ledinkovi'ch epoch (On the origin of glacial epochs). *Meteorologia i Hidrologia*, **11**, 3–12.
- Cane, M.A., and Evans, M., 2000. Climate variability – Do the tropics rule? *Science*, **290**, 1107–1108.
- Cane, M.A., and Molnar, P., 2001. Closing of the Indonesian seaway as a precursor to East African aridification around 3–4 million years ago. *Nature*, **411**, 157–162.
- Chamberlin, T.C., 1899. An attempt to frame a working hypothesis of the cause of glacial periods on an atmospheric basis. *J. Geol.*, **7**, 545–584, 667–685, 751–787.
- Chamberlin, T.C., 1906. On a possible reversal of deep sea circulation and its influence on geologic climates. *J. Geol.*, **14**, 363–373.
- Chao, W.C., and Chen, B., 2001. The origin of monsoons. *J. Atmos. Sci.*, **58**, 3497–3507.
- Conrad, C.P., and Lithgow-Bertelloni, C., 2007. Faster seafloor spreading and lithosphere production during the mid-Cenozoic. *Geology*, **35**, 29–32, doi: 10.1130/G22759A.22751.
- Covey, C., and Barron, E.J., 1988. The role of ocean heat transport in climatic change. *Earth Sci. Rev.*, **24**, 429–445.
- Crowell, J.C., and Frakes, L.A., 1970. Phanerozoic glaciations and the causes of ice ages. *Am. J. Sci.*, **268**, 193–224.
- Crowley, T.J., and Burke, K., (eds.), 1998. *Tectonic Boundary Conditions for Climate Reconstructions*. New York: Oxford University Press.
- Crowley, T.J., Hyde, W.T., and Short, D.A., 1989. Seasonal Cycle Variations on the Supercontinent of Pangaea. *Geology*, **17**, 457–460.
- Crowley, T.J., and North, G.R., 1996. *Paleoclimatology*. New York: Oxford University Press, 360pp.
- Dana, J.D., 1856. On American geological history. *Am. J. Sci.*, **22**, 305–344.
- DeConto, R.M., Hay, W.W., Thompson, S.L., and Bergengren, J.C., 1999. Late Cretaceous climate and vegetation interactions: The cold continental interior paradox. In Barrera, E., and Johnson, C. (eds.), *The Evolution of Cretaceous Ocean/Climate Systems*. Boulder, CO: Geological Society of America, pp. 391–406.
- DeConto, R.M., and Pollard, D., 2003a. Rapid Cenozoic glaciation of Antarctica induced by declining atmospheric CO₂. *Nature*, **421**, 245–249.
- DeConto, R.M., and Pollard, D., 2003b. A coupled climate-ice sheet modeling approach to the early Cenozoic history of the Antarctic ice sheet. *Palaeogeogr. Palaeoclimatol. Palaeoecol.*, **198**, 39–53.
- Dickens, G.R., Castillo, M.M., and Walker, J.C.G., 1997. A blast of gas in the latest Paleocene: Simulating first-order effects of massive dissociation of oceanic methane hydrate. *Geology*, **25**, 259–264.
- Dickinson, R.E., and Henderson-Sellers, A., 1988. Modelling tropical deforestation: A study of GCM land-surface parameterizations. *Q. J. R. Meteorol. Soc.*, **114**, 439–462.
- Donn, W.L., and Shaw, D.M., 1977. Model of climate evolution based on continental drift and polar wandering. *Geol. Soc. Am. Bull.*, **88**, 390–396.
- Donnadieu, Y., Godderis, Y., Ramstein, G., Nedelec, A., and Meert, J., 2004. A 'snowball Earth' climate triggered by continental break-up through changes in runoff. *Nature*, **428**, 303–306.
- Emanuel, K., 2001. Contributions of tropical cyclones to meridional heat transport by the oceans. *J. Geophys. Res.*, **D14**, 14771–14781.
- England, P., and Molnar, P., 1990. Surface uplift, uplift of rocks, and exhumation of rocks. *Geology*, **18**, 1173–1177.
- Filipelli, G.M., 1997. Intensification of the Asian monsoon and a chemical weathering event in the late Miocene-early Pliocene: Implications for late Neogene climate change. *Geology*, **25**, 27–30.
- Garzzone, C.N., Dettman, D.L., and Horton, B.K., 2004. Carbonate oxygen isotope paleoaltimetry: Evaluating the effect of diagenesis on estimates of paleoelevation in Tibetan plateau basins. *Palaeogeogr. Palaeoclimatol. Palaeoecol.*, **212**, 219–240.
- Gibbs, M.T., and Kump, L.R., 1994. Global chemical erosion during the last glacial maximum and the present: Sensitivity to changes in lithology and hydrology. *Paleoceanography*, **9**, 529–543.
- Gill, A., 1982. *Atmosphere-Ocean Dynamics*. San Diego: Academic Press, 662pp.
- Gonzalez-Bonorino, G., and Eyles, N., 1995. Inverse Relation between Ice Extent and the Late Paleozoic Glacial Record of Gondwana. *Geology*, **23**, 1015–1018.
- Hansen, J., Sato, M., Ruedy, R., Lacis, A., Asamoah, K., Borenstein, S., Brown, E., Cairns, B., Caliri, G., Campbell, M., Curran, B., de Castro, S., Druryan, L., Fox, M., Johnson, C., Lerner, J., McCormick, M.P., Miller, R.L., Minnis, P., Morrison, A., Pandolfo, L., Ramberan, I., Zaucker, F., Robinson, M., Russell, P., Shah, K., Stone, P., Tegen, I., Thomason, L., Wilder, J., and Wilson, H., 1996. A Pinatubo climate modeling investigation. In Fiocco, G., Fua, D., and Visconti, G. (eds.), *The Mount Pinatubo Eruption: Effects on the Atmosphere and Climate*. Heidelberg, Germany: Springer-Verlag, pp. 233–272.
- Haq, B.U., Hardenbol, J., and Vail, P.R., 1987. Chronology of fluctuating sea-levels since the Triassic. *Science*, **235**, 1156–1166.
- Hartmann, D., 1994. *Global Physical Climatology*. San Diego: Academic Press, 411pp.
- Haug, G., and Tiedemann, R., 1998. Effect of the Isthmus of Panama on Atlantic Ocean thermohaline circulation. *Nature*, **393**, 673–676.
- Haug, G.H., Ganopolski, A., Sigman, D.M., Rosell-Mele, A., Swann, G.E.A., Tiedemann, R., Jaccard, S.L., Bollmann, J., Maslin, M.A., Leng, M.J., and Eglinton, G., 2005. North Pacific seasonality and the glaciation of North America 2.7 million years ago. *Nature*, **433**, 821–825.
- Hay, W.W., 1988. Detrital sediment fluxes from the continents to the oceans. *Chem. Geol.*, **145**, 287–323.
- Hay, W.W., 1996. Tectonics and climate. *Geol. Rundsch.*, **85**, 409–437.
- Hay, W.W., and DeConto, R.M., 1999. Comparison of modern and Late Cretaceous meridional energy transport and oceanology. In Barrera, E., and Johnson, C.C. (eds.), *Evolution of the Cretaceous Ocean-Climate System*. Boulder: Geological Society of America, pp. 283–300.
- Hay, W.W., and Wold, C.N., 1998. The role of mountains and plateaus in a Triassic climate model. In Crowley, T.J., and Burke, K. (eds.), *Tectonic Boundary Conditions for Climate Reconstructions*. New York: Oxford University Press, pp. 116–146.
- Hay, W.W., Barron, E.J., and Thompson, S.L., 1990a. Global atmospheric circulation experiments on an earth with a meridional pole-to-pole continent. *J. Geol. Soc. Lond.*, **147**, 385–392.
- Hay, W.W., Barron, E.J., and Thompson, S.L., 1990b. Global atmospheric circulation experiments on an earth with polar and tropical continents. *J. Geol. Soc. Lond.*, **147**, 749–757.
- Hay, W.W., DeConto, R.M., Wold, C.N., Wilson, K.M., Voigt, S., Schulz, M., Wold-Rosby, A., Dullo, W.-C., Ronov, A.B., Balukhovskiy, A.N., and S.E., 1999. An alternative global Cretaceous paleogeography. In Barrera, E., and Johnson, C. (eds.), *The Evolution of Cretaceous/Ocean Climate Systems*. Boulder: Geological Society of America, pp. 1–48.
- Hay, W.W., Soeding, E., DeConto, R.M., and Wold, C.N., 2002. The Late Cenozoic uplift – climate paradox. *Int. J. Earth Sci.*, **91**, 746–774.
- Hays, J.D., and Pitman, W.C., 1973. Lithospheric plate motion, sea level changes, and climatic and ecological consequences. *Nature*, **246**, 18–22.
- Hoffman, P.F., Kaufman, A.J., Halverson, G.P., and Schrag, D.P., 1998. A Neoproterozoic snowball earth. *Science*, **281**, 1342–1346.
- Hotinski, R.M., and Toggweiler, J.R., 2003. Impact of a Tethyan circum-global passage on ocean heat transport and "equable" climates. *Paleoceanography*, **18**, 1007.
- Houghton, H.G., 1985. *Physical Meteorology*. Cambridge, MA: MIT, 442pp.
- Huber, M., and Caballero, R., 2003. Eocene El Niño: Evidence for robust tropical dynamics in the "hothouse." *Science*, **299**, 877–881.
- Huber, M., and Sloan, L.C., 2001. Heat transport, deep waters, and thermal gradients: Coupled simulation of an Eocene Greenhouse Climate. *Geophys. Res. Lett.*, **28**, 3481–3484.

- Huber, M., Brinkhuis, H., Stickley, C.E., Doos, K., Sluijs, A., Warnaar, J., Schellenberg, S.A., and Williams, G.L., 2004. Eocene circulation of the Southern Ocean: Was Antarctica kept warm by subtropical waters? *Paleoceanography*, **19**, doi:10.1029/2004PA001014.
- Keigwin, L., 1982. Isotope paleoceanography of the Caribbean and east Pacific: Role of Panama Uplift in late Neogene time. *Science*, **217**, 350–353.
- Kennett, J.P., 1977. Cenozoic evolution of Antarctic glaciation, the circum-Antarctic oceans and their impact on global paleoceanography. *J. Geophys. Res.*, **82**, 3843–3859.
- Kerr, A., and Huybrechts, P., 1999. The response of the East Antarctic ice-sheet to the evolving tectonic configuration of the Transantarctic Mountains. *Global Planet. Change*, **23**, 213–299.
- Kominz, M., 1984. Oceanic ridge volumes and sea level change—An error analysis. In Schlee, J. (ed.), *Interregional Unconformities and Hydrocarbon Accumulation*. American Association of Petroleum Geologists Memoir 36, pp. 109–127.
- Kristoffersen, Y., 1990. On the tectonic evolution and paleoceanographic significance of the Fram Strait gateway. In Bleil, U., and Theide, J. (eds.), *Geological History of the Polar Oceans: Arctic Versus Antarctic*. Dordrecht: Kluwer, pp. 63–76.
- Kutzbach, J.E., and Gallimore, R.G., 1989. Pangaeon Climates – Megamonsoons of the Megacontinent. *J. Geophys. Res. Atmos.*, **94**, 3341–3357.
- Kutzbach, J.E., and Liu, Z., 1997. Response of the African monsoon to orbital forcing and ocean feedbacks in the middle Holocene. *Science*, **278**, 440–442.
- Kutzbach, J.E., Prell, W.L., and Ruddiman, W.F., 1993. Sensitivity of Eurasian climate to surface uplift of the Tibetan Plateau. *J. Geol.*, **101**, 177–190.
- Lamb, S., and Davis, P., 2003. Cenozoic climate change as a possible cause for the rise of the Andes. *Nature*, **425**, 792–797.
- Larson, R.L., 1991. Geological Consequences of Superplumes. *Geology*, **19**, 963–966.
- Larson, R.L., and Erba, E., 1999. Onset of the mid-Cretaceous greenhouse in the Barremian-Aptian: Igneous events and the biological, sedimentary, and geochemical responses. *Paleoceanography*, **14**, 663–678.
- Lawver, L.A., and Gahagan, L.M., 1998. Opening of Drake passage and its impact on Cenozoic ocean circulation. In Crowley, T.J., and Burke, K.C. (eds.), *Tectonic Boundary Conditions for Climate Reconstructions*. New York: Oxford University Press, pp. 212–223.
- Leckie, R.M., Bralower, T., and Cashman, R., 2002. Oceanic Anoxic Events and plankton evolution: Exploring biocomplexity in the mid-Cretaceous. *Paleoceanography*, **17**, doi: 10.1029/2000PA000572.
- Liu, X.D., Kutzbach, J.E., Liu, Z.Y., An, Z.S., and Li, L., 2003. The Tibetan Plateau as amplifier of orbital-scale variability of the East Asian monsoon. *Geophys. Res. Lett.*, **30**, 1839.
- Livermore, R., Eagles, G., Morris, P., and Maldonado, A., 2004. Shackleton Fracture Zone: No barrier to early circumpolar ocean circulation. *Geology*, **32**, 797–800.
- Lyell, C., 1830. *Principles of Geology, Being an Attempt to Explain the Former Changes of the Earth's Surface by Reference to Causes Now in Operation*. London: John Murray.
- Lyle, M., 1997. Could early Cenozoic thermohaline circulation have warmed the poles? *Paleoceanography*, **12**, 161–167.
- Mackey, K.G., Fujita, K., Gunbina, L.V., Kovalev, V.N., Imaev, V. S., Koz'min, B.M., and Imaeva, L.P., 1997. Seismicity of the Bering Strait region: Evidence for a Bering Block. *Geology*, **25**, 979–982.
- Mahoney, J.J., and Coffin, M.F. (eds.), 1997. *Large Igneous Provinces: Continental, Oceanic, and Planetary Flood Volcanism*. Washington, DC: American Geophysical Union, 438pp.
- Manabe, S., and Broccoli, A.J., 1990. Mountains and arid climates of middle latitudes. *Science*, **247**, 192–194.
- Mann, M.E., Bradley, R.S., and Hughes, M.K., 1999. Northern hemisphere temperatures during the past millennium: Inferences, uncertainties, and limitations. *Geophys. Res. Lett.*, **26**, 759–762.
- Marshall, S.J., and Clarke, G.K.C., 2000. Ice sheet inception: Subgrid hypsometric parameterization of mass balance in an ice sheet model (**15**, 533, 1999). *Clim. Dyn.*, **16**, 319–319.
- Mikolajewicz, U., Maier-Reimer, E., Crowley, T.J., and Kim, K.-Y., 1993. Effect of Drake and Panamanian gateways on the circulation of an ocean model. *Paleoceanography*, **8**, 409–426.
- Molnar, P., and England, P., 1990. Late Cenozoic uplift of mountain ranges and global climate change: chicken or egg? *Nature*, **346**, 29–34.
- Montgomery, D.R., 1994. Valley incision and the uplift of mountain peaks. *J. Geophys. Res. Solid Earth*, **99**, 13913–13921.
- Montgomery, D.R., Balco, G., and Willett, S.D., 2001. Climate, tectonics, and the morphology of the Andes. *Geology*, **29**, 579–582.
- Nigam, S., Held, I.M., and Lyons, S.W., 1988. Linear simulation of the stationary eddies in a GCM. Part II: The “mountain” model. *J. Atmos. Sci.*, **45**, 1433–1452.
- North, G.R., Mengel, J.G., and Short, D.A., 1983. Simple energy balance model resolving the seasons and the continents: Application to the astronomical theory of the ice ages. *J. Geophys. Res.*, **88**, 6576–6586.
- Oerlemans, J., 2002. On glacial inception and orography. *Quaternary Int.*, **95–96**, 5–10.
- Oglesby, R.J., 1991. Joining Australia to Antarctica: GCM implications for the Cenozoic record of Antarctic Glaciation. *Clim. Dyn.*, **6**, 13–22.
- Otto-Bliesner, B.L., Brady, E.C., and Shields, C., 2002. Late cretaceous ocean: Coupled simulations with the national center for atmospheric research climate system model. *J. Geophys. Res. Atmos.*, **107**, 4019.
- Pagani, M., Zachos, J.C., Freeman, K.H., Tipler, B., and Bohaty, S.M., 2005. Marked decline in atmospheric carbon dioxide concentrations during the Paleogene. *Science*, **309**, 600–603.
- Peixoto, J.P., and Oort, A.H., 1992. *Physics of Climate*. New York: American Institute of Physics, 520pp.
- Philander, S.G., 1999. A review of tropical ocean-atmosphere interactions. *Tellus Dyn. Meteorol. Oceanogr.*, **51**, 71–90.
- Philander, S.G.H., Gu, D., Halpern, D., Lambert, G., Lau, N.C., Li, T., and Pacanowski, R.C., 1996. Why the ITCZ is mostly north of the equator. *J. Clim.*, **9**, 2958–2972.
- Pierrehumbert, R.T., 2004. High levels of atmospheric carbon dioxide necessary for the termination of global glaciation. *Nature*, **429**, 646–649.
- Poulsen, C.J., Barron, E.J., Arthur, M.A., and Peterson, W.H., 2001. Response of the mid-Cretaceous global oceanic circulation to tectonic and CO₂ forcings. *Paleoceanography*, **16**, 576–592.
- Prell, W., and Kutzbach, J.E., 1992. Sensitivity of the Indian monsoon to forcing parameters and implications for its evolution. *Nature*, **360**, 647–652.
- Rampino, M.R., and Caldeira, K., 1993. Major episodes of geologic change: Correlations, time structure and possible causes. *Earth Planet. Sci. Lett.*, **114**, 215–227.
- Ramstein, G., Fluteau, F., Besse, J., and Joussaume, S., 1997. Effect of orogeny, plate motion and land sea distribution on Eurasian climate change over the past 30 million years. *Nature*, **386**, 788–795.
- Raymo, M.E., and Ruddiman, W.F., 1992. Tectonic Forcing of late Cenozoic climate. *Nature*, **359**, 117–122.
- Raymo, M.E., Ruddiman, W.F., and Froelich, P.N., 1988. Influence of late Cenozoic mountain building on ocean geochemical cycles. *Geology*, **16**, 649–653.
- Richter, F.M., Rowley, D.B., and Depaolo, D.J., 1992. Sr isotope evolution of seawater – the role of tectonics. *Earth Planet. Sci. Lett.*, **109**, 11–23.
- Rind, D., and Chandler, M., 1991. Increased ocean heat transports and warmer climate. *J. Geophys. Res.*, **96**, 7437–7461.
- Rind, D., Healy, R., Parkinson, C., and Martinson, D., 1995. The role of sea ice in 2xCO₂ climate model sensitivity. I. The total influence of sea-ice thickness and extent. *J. Clim.*, **8**, 379–389.
- Robert, C.M., Exon, N.F., Kennett, J.P., Malone, M.J., Brinkhuis, H., Chaproniere, G.C.H., Ennyu, A., Fothergill, P., Fuller, M.D., Grauert, M., Hill, P.J., Janecsek, T.R., Kelly, D.C., Latimer, J.C., Roessig, K.M., Nees, S., Ninnemann, U.S., Nurnberg, D., Pekar, S.F., Pellaton, C.C., Pfuhl, H.A., Rohl, U., Schellenberg, S.A., Shevenell, A.E., Stickley, C.E., Suzuki, N., Touchard, Y., Wei, W.C., and White, T.S., 2001. Palaeogene ocean opening south of Tasmania, and palaeoceanographic implications: Preliminary results of clay mineral analyses (ODP Leg 189). *Compt Rendus Acad. Sci. Fascicule a-Sci. Terre Des Planet.*, **332**, 323–329.
- Rowley, D.B., 2002. Rate of plate creation and destruction: 180 Ma to present. *GSA Bull.*, **114**, 927–933.
- Royer, D.L., 2001. Stomatal density and stomatal index as indicators of paleoatmospheric CO₂ concentration. *Rev. Palaeobot. Palynol.*, **114**, 1–28.
- Ruddiman, W.F. (ed.), 1997. *Tectonic Uplift and Climate Change*. Plenum Press, New York.

- Ruddiman, W.F., and Kutzbach, J.E., 1989. Forcing of Late Cenozoic Northern Hemisphere Climate by Plateau Uplift in Southern Asia and the American West. *J. Geophys. Res. Atmos.*, **94**, 18409–18427.
- Ruddiman, W.F., and Kutzbach, J.E., 1991. Plateau uplift and climatic-change. *Sci. Am.*, **264**, 66–75.
- Scher, H.D., and Martin, E.E., 2006. Timing and climatic consequences of the opening of drake passage. *Science*, **312**, 428–430.
- Schrag, D.P., Berner, R.A., Hoffman, P.F., and Halverson, G.P., 2002. On the initiation of a snowball Earth. *Geochem. Geophys. Geosyst.*, **3**, 1036.
- Seager, R., Battisti, D.S., Yin, J., Gordon, N., Naik, N., Clement, A.C., and Cane, M.A., 2002. Is the Gulf Stream responsible for Europe's mild winters? *Q. J. R. Meteorol. Soc.*, **128**, 2563–2586.
- Sloan, L.C., 1994. Equable climate during the early Eocene: Significance of regional paleogeography for North American climate. *Geology*, **22**, 881–884.
- Sloan, L.C., and Pollard, D., 1998. Polar stratospheric clouds: A high latitude warming mechanism in an ancient greenhouse world. *Geophys. Res. Lett.*, **25**, 3517–3520.
- Sloan, L.C., James, C.G., and Moore, T.C.J., 1995. Possible role of ocean heat transport in Early Eocene climate. *Paleoceanography*, **10**, 347–356.
- Stickley, C.E., Brinkhuis, H., Schellenberg, S.A., Sluijs, A., Röhl, U., Fuller, M., Grauert, M., Huber, M., Warnaar, J., and Williams, G.L., 2004. Timing and nature of the deepening of the Tasmanian Gateway. *Paleoceanography*, **19**; PA4027, doi:10.1029/2004PA001022.
- Stone, P.H., 1978. Constraints on dynamical transports of energy on a spherical planet. *Dyn. Atmos. Oceans*, **2**, 123–139.
- Thompson, S.L., and Pollard, D., 1997. Greenland and Antarctic mass balances for present and doubled atmospheric CO₂ from the GENESIS Version-2 Global Climate Model. *J. Clim.*, **10**, 871–900.
- Toggweiler, J.R., and Bjornsson, H., 2000. Drake Passage and paleoclimate. *J. Q. Sci.*, **15**, 319–328.
- Trenberth, K.E., and Solomon, A., 1994. The global heat balance: heat transports in the atmosphere and ocean. *Clim. Dyn.*, **10**, 107–134.
- Valdes, P.J., Sellwood, B.W., and Price, G.D. 1996. Evaluating concepts of Cretaceous equability. *Paleoclimates*, **2**, 139–158.
- von der Heydt, A., and Dijkstra, H.A., 2006. Effect of ocean gateways on the global ocean circulation in the late Oligocene and early Miocene. *Paleoceanography*, **21**, PA 10111, doi:10.1029/12005PA001149.
- Weertman, H., 1961. Stability of ice-age ice sheets. *J. Geophys. Res.*, **66**, 3783–3792.
- Wold, C.N., Hay, W.W., Dullo, E., Wolf, T.C., and Bruns, P., 1993. Oligozäne Paläo-Ozeanographie des Grönland-Schottland Rückens. *Geowissenschaften*, **11**, 353–359.
- Zachos, J., and Kump, L., 2005. Carbon cycle feedbacks and the initiation of Antarctic glaciation in the earliest Oligocene. *Global Planet. Change*, **47**, 51–66.

Cross-references

Albedo Feedbacks
 Astronomical Theory of Climate Change
 Carbon Cycle
 Carbon Isotope Variations over Geologic Time
 Cenozoic Climate Change
 Climate Change, Causes
 Flood Basalts: Climatic Implications
 Heat Transport, Oceanic and Atmospheric
 Monsoons, Pre-Quaternary
 Monsoons, Quaternary
 Mountain Glaciers
 Mountain Uplift and Climate Change
 Ocean Anoxic Events
 Ocean Paleocirculation
 Paleoclimate Modeling, Pre-Quaternary
 Paleoclimate Modeling, Quaternary
 Paleocene-Eocene Thermal Maximum
 Paleo-El Niño-Southern Oscillation (ENSO) Records
 Snowball Earth Hypothesis
 Thermohaline Circulation
 Volcanic Eruptions and Climate Change
 Walker Circulation, in *Encyclopedia of World Climatology*
 Weathering and Climate

PLEISTOCENE CLIMATES

Introduction

In the search to understand Pleistocene climates, it is necessary to reconstruct “horizontal” time slices representing the surface of the Earth from which the prevailing climate may be inferred, and to mesh them with “vertical” time-series data, primarily from ocean, ice and lake cores, to understand processes involved. These include forcing functions and their consequential fluxes of heat and moisture as they are propagated through the complex systems of the atmosphere, oceans and biosphere. Ultimately, it will be a meshing together of these two thrusts that may bring about a more comprehensive understanding. The past decade has witnessed major advances in the field, especially in greater understanding of lateral connections and phase relationships. However, modeling of climates has lagged behind other advances and no model has yet simulated the millennial variability of Pleistocene climates as inferred from high-resolution records.

Pleistocene climates have varied in time and space and are inferred from a wide range of evidence on the continents and in the oceans. They reflect the evolution of the climate system over the last 2.4–2.5 Ma, more or less under the same boundary conditions as today with regard to the present configuration of continents and oceans, location of mountain ranges, high plateaus, and ocean seaways. The major prelude to the Pleistocene epoch, around 3 million years ago, was a transition from relatively milder Pliocene climates to cooler ones, strongly affected by the closure of the Straits of Panama (Figure P71). This changed a zonal circulation of ocean surface water into a meridional one, thus providing precipitation to nourish the high latitude ice growth that duly followed (Figure P71). The earlier part of the Pleistocene, until about a million years ago, was dominated by ice age cycles of low amplitude but relatively high frequency at 41,000 years (obliquity – see below), whereas since that time the climate has been dominated by high amplitude cycles of longer, 100,000 year, frequency (eccentricity – see below). The cause of the change in climate pacing is still uncertain: the role of large mid-latitude ice sheets, such as the Laurentide, may have had a role in affecting the circulation of the atmosphere; or there may have been a long term trend in decreasing atmospheric carbon dioxide.

The latest findings show that in order to understand Pleistocene climates it is necessary to examine them in relation to the forcing associated with several interacting timescales, from orbital to millennial to interannual (Cronin, 1999).

No significant speciation occurred during the Pleistocene because of the rapid reversals in climate, although a major exception was hominid speciation in Africa that may have been a response to intensified Northern Hemisphere glaciation and the rigors of repeated and enhanced aridity in tropical Africa (deMenocal, 1995) (Figure P71).

History

Traditional appreciation of Pleistocene climates involved a concept of four major ice ages (glacials) when ice sheets grew at middle latitudes of the Northern Hemisphere. “Interglacial” climates in between them were similar to that of the present. During the ice ages, the snowline dropped spectacularly (Figure P72),

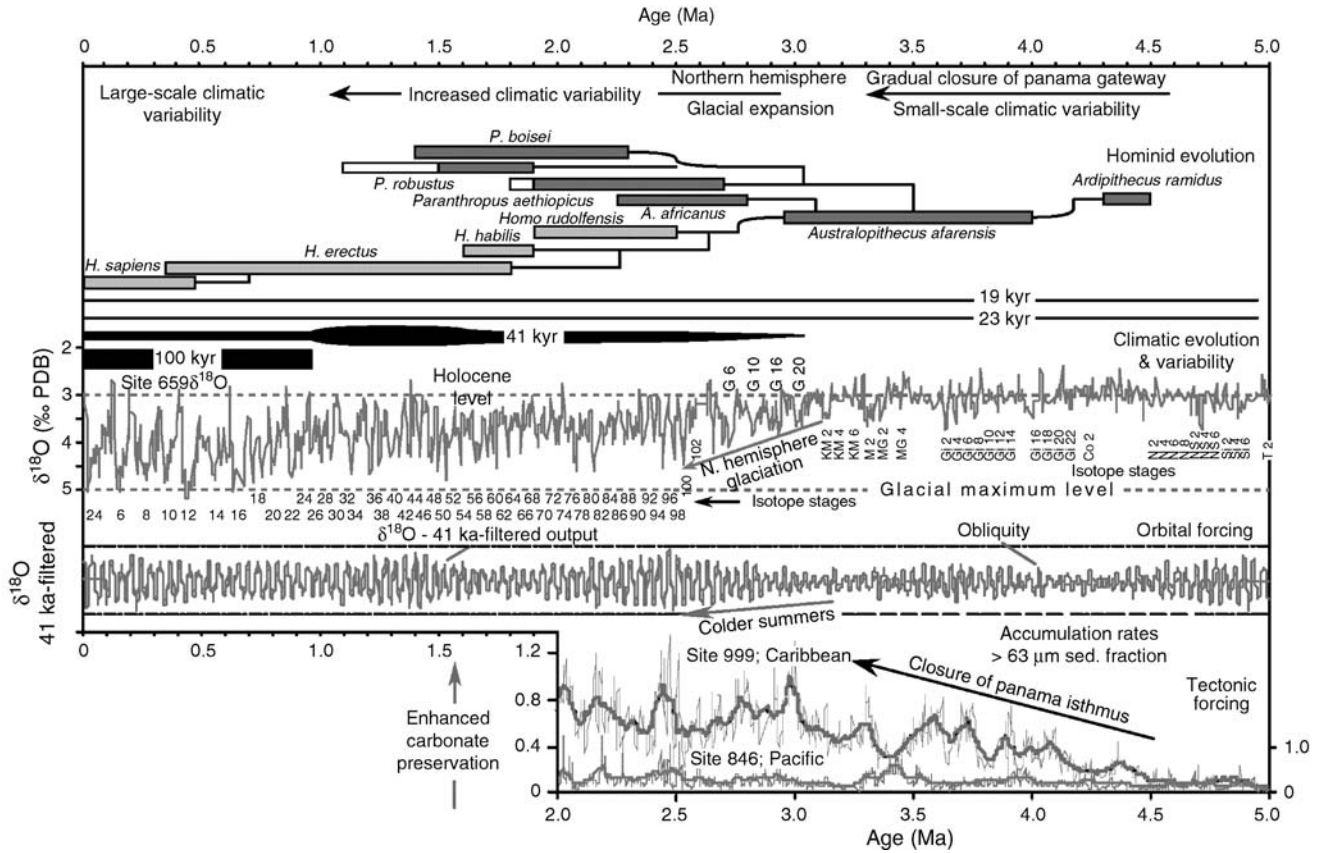


Figure P71 Evolution of climate over the past 5 million years. *Top panel* shows hominid speciation in Africa and its possible relationship to major climate events. *Middle panel* shows the detailed climate record from deep ocean core ODP 659 (offshore from northwest Africa) inferred from oxygen isotope measurements on benthic foraminifera, which shows coherence with orbital forcing frequencies of axial tilt (41,000 years), precession (23,000 years) and eccentricity of the orbit (100,000 years). Stages are oxygen isotope stages numbered backwards in time: even numbers are glacials and odd numbers interglacials. *Bottom panel* shows the effect of the closure of the Straits of Panama on calcium carbonate preservation (Zahn, 2002).

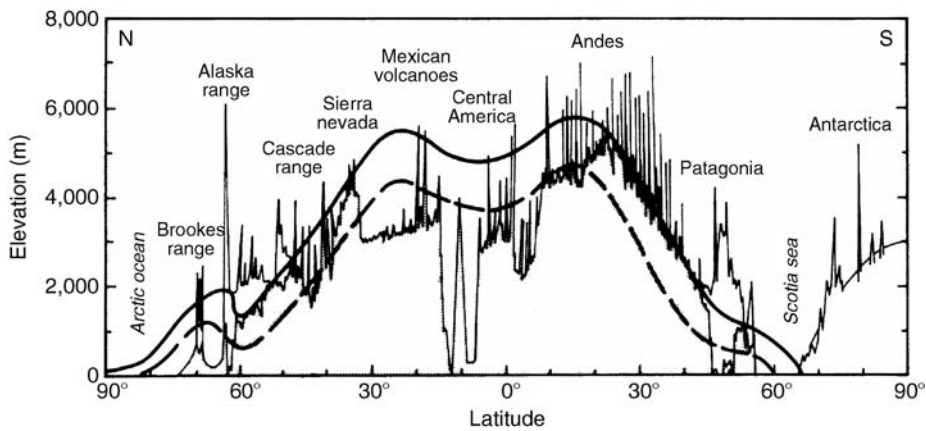


Figure P72 Meridional transect along the cordillera of the Americas (Broecker and Denton, 1989). The present snowline is shown by the *heavy line* above which are present glaciers. During the Last Glacial Maximum the snowline was depressed (*dashed line*) and the area occupied by ice correspondingly increased.

the albedo of the Earth increased strongly, and vegetation and climatic zones were telescoped between continental ice sheets in the north and wetter ("pluvial") conditions in the near tropics and tropics.

Conceptual reconstructions or climate schema were zonal in character: southward of the ice sheets in Europe were climate zones corresponding to tundra, loess steppe and evergreen forest. Some mixed oak deciduous forest occurred in the Mediterranean area or in favorable areas called "refugia." At lower latitudes, wetter, "pluvial" climates appeared as the tropics contracted. However, in North America, where moist tropical maritime air from the Gulf of Mexico was channeled northwards between the Appalachians and the western Cordilleran mountain system, a more complicated mosaic pattern of vegetation prevailed. Thus, the existence of large, high domed ice sheets not only influenced the Earth's albedo, but maintained quasi-permanent anticyclones, which influenced the circulation of the atmosphere and contracted the zonal climatic belts.

Interglacials, when ice sheets melted and sea level rose, witnessed a return to climates not greatly unlike that of the present (Holocene) interglacial. Although the characteristics of successive interglacials have yet to be established definitively, it is assumed that vegetation zones were similar to the present.

The four-fold ice ages concept, together with some indications of earlier Pleistocene complexity, was based on geologic evidence in Europe and North America for major expansions of continental ice sheets marked by moraines and outwash terraces. Interglacials were inferred from temperate vegetation provided by pollen analysis in Europe or from paleosols in America that evolved under deep chemical weathering. These ideas dominated thinking during the twentieth century up until the 1970s. All evidence for climate and climate change was pigeonholed into what came to be seen as a straitjacketed classification of Pleistocene climates. Even contrary indications from back-calculated variations in the orbital configuration of the Earth, and evidence from the earliest ocean cores, was forced into the prevailing classification.

Techniques

Technological advances in obtaining long cores through oceans sediments, ice sheets and lake basins, together with new analytical techniques, have revolutionized the field since the early 1970s (Cronin, 1999). Geochemical measurements have elucidated the record preserved in deep ocean sediments: oxygen isotope measurements ($^{18}\text{O}/^{16}\text{O}$) on benthic and planktic microfossils (mostly foraminifera) have allowed inferences to be drawn about the isotopic composition of the ocean that is directly related to the volume of isotopically lighter ice on the continents, and indirectly to sea level fluctuations. Carbon isotopes in fossil shells (^{13}C) reveal patterns of productivity in the oceans and the strength and direction of intermediate and bottom ocean circulation. Nitrogen isotopes indicate nutrient inventories. Surface or near-surface dwelling plankton provide estimates of former sea surface temperatures (SSTs) using transfer functions that compare the fossil record with core top faunas assumed to represent the present day. This, however, is being superseded by the use of SST temperature-dependent Mg/Ca ratios fixed in the shell during life. A further developing tool is alkenone thermometry derived from fossil phytoplankton from sediment cores. This provides not only information about sea surface temperatures, but also regarding primary productivity and atmospheric carbon dioxide levels in the past. Finally, sedimentological techniques indicate current

speeds as well as the provenance of ice-rafted debris and other sediment derived from the continents.

Oxygen isotope ($\delta^{18}\text{O}$) measurements on layers of ice from ice cores reveal the temperature of snow deposition; greenhouse gas concentrations are measured from bubbles of air within the ice, and the nature and derivation of various aerosols provide insight into wind direction and intensity (Alley, 2000).

Continental data are obtained from the fossil record of flora and fauna preserved in different environments such as peat, lake, and cave sediments. Because of the relative lack of speciation, most of the fossil record is used for paleoecologic reconstruction. Such reconstructions of Pleistocene environments as time slices across major areas provide a broad-brush reflection of the prevailing climate.

Common to all evidence is the need for a precise geochronology to determine the age of isolated pieces of evidence as well as for dating continuous sequences of change. Most methods, however, have inherent uncertainties, limited age ranges and, sometimes, spatial limitations (Cronin, 1999).

Orbital cycles

The most fundamental change in understanding of the last thirty years or so has been the result of $\delta^{18}\text{O}$ measurements on benthic and planktonic fossils from ocean cores, interpreted as showing major changes in ice volume on the continents, and a more complex evolution of the climate system than was suggested by classical concepts of the Pleistocene.

Essentially, such measurements in all ocean basins showed that some 50 ice ages and interglacials had occurred over the last 2.5 Ma or so (Figure P71). This alone shows that rates of climate change were much more rapid than previously thought. This has compelled a re-thinking of the climate system and what forced it, and in 1976 it was shown that back-calculations of variations in the Earth's orbit matched the deep-sea evidence for ice ages (Imbrie and Imbrie, 1979). This study marked a turning point and evidence of all kinds became interpreted in terms of the 100,000 eccentricity, the 41,000 obliquity and the 23,000 and 19,000 precessional paces of the Earth's orbital parameters (Figure P71). Precise dating of the marine isotopic record is still hindered by an insufficient number of age markers. Those provided by paleomagnetic reversals serve to subdivide the record but on a relatively crude scale: for example, the Matuyama-Brunhes reversal at 790,000 years B.P. occurs in oxygen isotope stage 19, but ages for subsequent ice ages and interglacials are provided only by assuming constant sedimentation and/or the "tuning" of the sedimentary record with orbital parameters using theoretical phase relationships between the timing of insolation changes and oxygen isotope (ice volume) response (e.g., see *SPECMAP*). In the absence of adequate dating controls, debate continues, for example, on the age of the last interglacial, despite its high sea level on global coastlines, especially in the low latitude coral belt where orbitally-tuned ages suggest an age between 128,000 and 118,000 years. On the other hand, many uranium series ages suggest it occurred between 135,000 and 116,000 or even 113,000 years. The latter corresponds with a chronology for the last interglacial from earlier ice flow models from the Vostok ice core, but also from the Devil's Hole calcite vein in Nevada.

The stratigraphic framework provided by oxygen isotope stratigraphy led to attempts to map the surface of the ice age Earth at the Last Glacial Maximum (LGM) by the CLIMAP group

(Imbrie and Imbrie, 1979). One of the findings of the CLIMAP ocean reconstructions was that ice age tropical SSTs did not fall greatly relative to the present. However, since then it has been shown that tropical SSTs were considerably cooler than at present. Continental reconstructions, however, lagged behind because of the fragmental nature of the record, often of insufficiently high quality. Indeed, land-sea correlations remain as one of the greatest challenges.

Some of the earliest land-sea correlations were between marine oxygen isotope stratigraphy and the loess sequences of Central Europe and China. Ice ages were indicated by loess deposition in arid environments and interglacials were indicated by soil development. The long loess sequences in China, as well as those offshore in the North Pacific, show that atmospheric dust was an important component of the changing climate system.

Better and longer pollen sequences on the continents questioned earlier precepts: for example, it was shown that temperate forest did not exist during the last ice age in the Mediterranean but instead steppic plant communities were extensive, with temperate forest survival in Balkan and Greek plant refugia. More significantly, much of the tropics and sub-tropical regions were shown to be arid rather than, as previously thought, wetter places. This compelled a review of the climate system and the role of the Hadley-Walker cells, the trade winds and Intertropical Convergence Zone (ITCZ) in a drier and cooler ice age world. The pollen record from some long lake sequences, for example in Greece, Colombia and Lake Baikal in Asia, matched the deep sea record and confirmed that Pleistocene vegetation patterns pulsed primarily to the orbital beat as the result of changing seasonality and insolation. The 41,000-year obliquity forcing was dominant at mid to

high latitudes, especially in influencing ice sheet growth and decay, whereas precession (23,000 and 19,000 years) was dominant at lower latitudes.

Although much is now known about the last glacial cycle, aided to a large extent by the availability of ^{14}C ages for the past $\sim 40,000$ years, relatively little is known in detail before the last interglacial (oxygen isotope sub-stage 5e or event 5.5 of the marine record). Currently some emphasis is placed on oxygen isotope stage 11, the interglacial some 400,000 years ago, because of its orbitally similar configuration to the current (Holocene) interglacial (Droxler et al., 2003). However, relatively little is known about major continental areas during other ice ages and interglacials.

Millennial cycles

Although the evidence for sub-orbital pacings had been long available from the Camp Century drill hole in Greenland (Dansgaard et al., 1969), it was not until additional ice cores were recovered that their millennial time scale records were appreciated, especially the 1,450 or 1,500 year pacing (Alley, 2000; Bond et al., 2001). These Dansgaard-Oeschger (D-O) cycles, with the warmer events called interstadials and colder ones stadials, are grouped into saw-toothed packages of increasing cold that are terminated by rapid warming events. Rapid changes in temperatures at the surface of the ice sheets occurred in less than a decade. The pattern of square-wave climate changes shown by the ice core records is matched by evidence from high sedimentation cores in the North Atlantic of SSTs inferred from the polar-dwelling foraminifer *Neogloboquadrina pachyderma* (s.) and oxygen isotope variability (Bond and Lotti, 1995). The evolution of these cycles has been

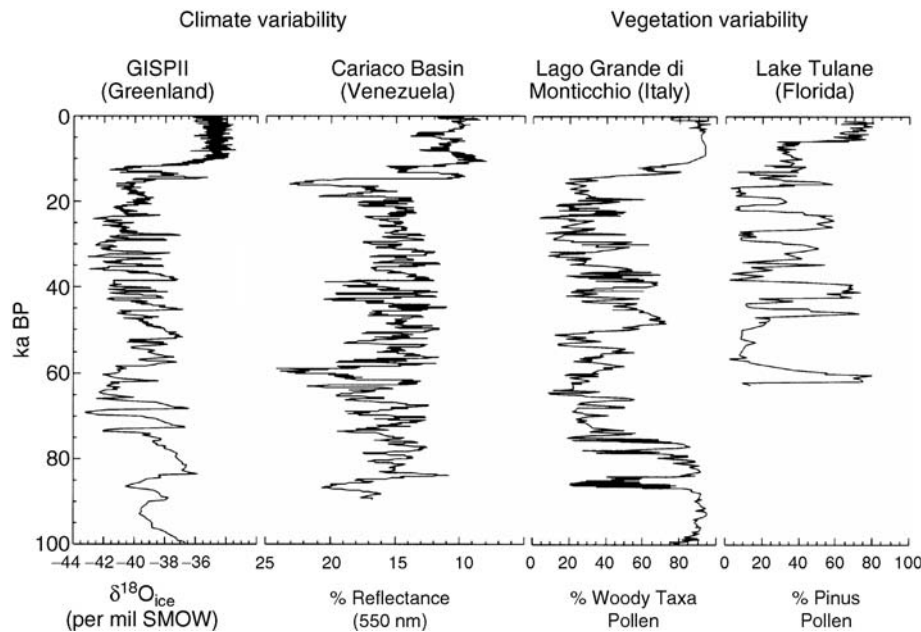


Figure P73 Four records showing millennial time scale variability over the last glacial cycle. The Greenland record of oxygen isotope variability shows the last 10,000 years of the present (Holocene) interglacial with which the warmer climates of the last glacial cycle (interstadials) alternate with colder ones (stadials). The offshore Cariaco Basin records influxes of minerals (high reflectance) from South America during stadials. In Italy and Florida, the changing vegetation, inferred from the fossil pollen record, shows similar variability, including cooler climates during Heinrich events (Overpeck et al., 2003).

attributed to oscillations in the strength of heat delivery by the Atlantic thermohaline circulation that caused changing temperatures at the ice sheet surface (Alley, 2000). Others have pointed to a solar connection because oxygen isotope variability in ice cores corresponds with similar variability in the concentration of the cosmogenic isotope ^{10}Be , which indicates changes in solar irradiance (Rind, 2002). Corresponding with the rapid warming at the end of Bond Cycles (Bond and Lotti, 1995), layers of ice-rafted debris (IRD), representing “Heinrich events” occur in marine cores. Deposited from “armadas” of icebergs discharged into the North Atlantic (Broecker, 1994; Bond and Lotti, 1995), IRDs indicate collapse and surging of ice sheets into the tidewater zone. Because they do not correspond with every D-O package of events, it is likely they were partly forced by climate, but only occurred when appropriate glaciological conditions for collapse and surging existed.

Greenland and Antarctic ice cores contain bubbles of air from which the near-contemporary concentrations of atmospheric greenhouse gases (CO_2 and CH_4) can be measured (Alley, 2000). Spikes of CH_4 provide a means of correlation of the oxygen isotope temperature record between Greenland and Antarctica and allow phase relationships between the

Northern and Southern Hemisphere polar regions to be explored. The pattern of greenhouse gas variability pulsed on both orbital and millennial time scales. When correlated with other evidence, they confirm previous inferences of a cooler and more arid Earth during the ice ages, with relatively lower atmospheric concentrations (~ 180 ppm) of carbon dioxide, and warmer interglacial conditions with relatively higher (~ 280 ppm) concentrations.

Further evidence that all the Earth’s systems pulsed at millennial timescales is available from a wide range of environments that show that atmospheric patterns changed rapidly: for example, in the lake systems of western North America, and monsoonal climates in India, Asia and South America (Clark et al., 2001). Figure P73 (Overpeck et al., 2003) shows the GISP2 (Greenland Ice Sheet Project 2) $\delta^{18}\text{O}$ temperature signal with packages of D-O pacings that end with a rapid warming. These pacings at 1,450 years continue, with reduced amplitude, into the present (Holocene) interglacial (Bond et al., 2001). The reflectance characteristics of sediments from the Cariaco Basin, offshore of Venezuela, record major changes in the hydrologic systems of the tropical Atlantic. Increased precipitation and river discharge from northern South America

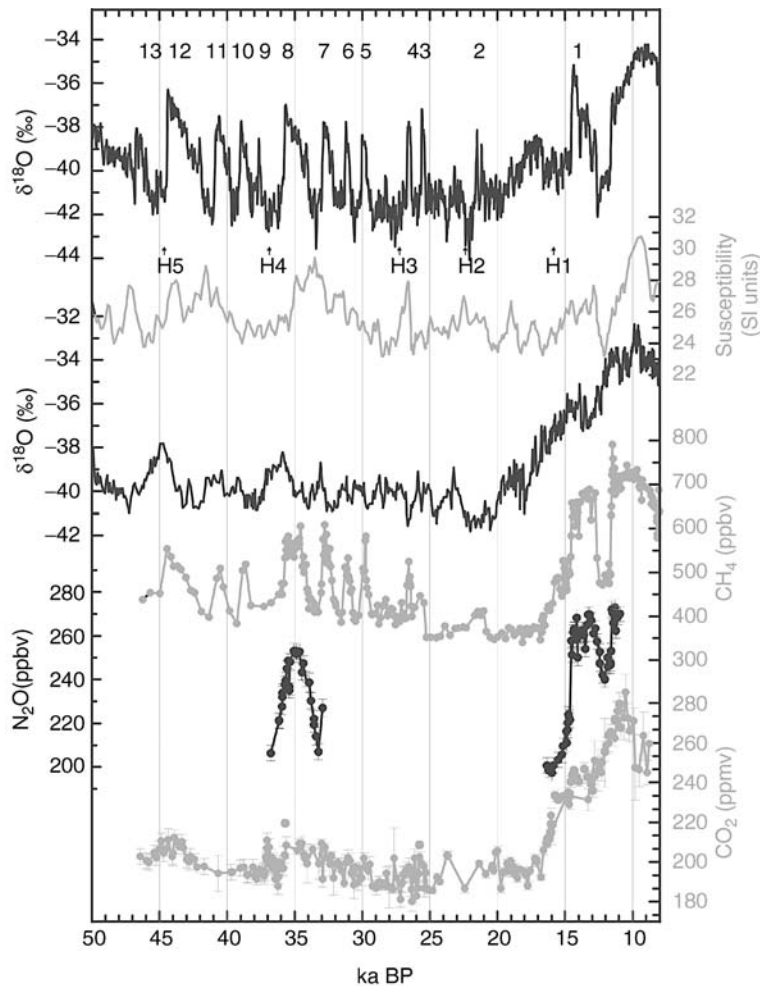


Figure P74 Greenland and Antarctic ice core records and Loess in China show millennial pacing for variability in temperature, carbon dioxide, methane, nitrous oxide and the East Asian monsoonal over the past 50,000 years (from Raynaud et al., 2003).

correspond with interstadial (warmer) events, which suggests higher moisture fluxes from the Atlantic to the Pacific, interspersed with lower precipitation (light colored sediments) as the Intertropical Convergence Zone migrates south during colder stadials. Note the rapid changes in vegetational stability in Italy and Florida that are correlated with D-O events.

Figure P74 shows millennial scale changes from different sources (Raynaud et al., 2003). From top to bottom: temperature variability as shown by the Greenland (GRIP) oxygen isotopic record; record of the Asian summer monsoon from magnetic susceptibility of Chinese loess, peaks indicate times of strong monsoons; temperature variability as shown by the Antarctic (Byrd station) oxygen isotope record; the methane record from Greenland; the N₂O record from Greenland; and the CO₂ record from Antarctica (Byrd station). Note that the Greenland and Antarctic records have been correlated by global methane spikes. Numbers 1–13 indicate Dansgaard-Oeschger (D-O) events in the Greenland record, while H1–H5 indicate Heinrich events.

Clearly, different sub-systems that were widely separated pulsed at the 1,450 pacing. Millennial variability at a global scale shows that climate signals are transmitted rapidly throughout the entire system. However, is this compatible with heat distribution by ocean thermohaline circulation? To what extent does the atmosphere play a role in the advection of heat and moisture from low latitude tropical oceans, notably the Pacific Ocean (Cane and Clement, 1999)?

Sub-millennial changes

Some of the answers to the questions raised above may come from records of sub-millennial changes in climate on inter-decadal or inter-annual timescales of physical annular modes of variability. These include records of the transfer of heat and moisture by Indian, African and Asian monsoons, El Niño (ENSO), North Atlantic Oscillations (NAO), Arctic Oscillation and Antarctic Oscillation. These are all interconnected in transporting heat from tropical oceans to higher latitudes. Their teleconnections are complex and may be driven in part by variability in solar irradiance as well as eccentricity-modulated precession. Cane and Clement (1999) have suggested that scaling El Niño (ENSO) events may well provide explanations for variability in large-scale Pleistocene climates. This may also account for the “stage 11 problem,” the apparently disproportionate response of the climate system to weak eccentricity forcing. Perhaps low eccentricity may dampen precessional variability and concentrates heat in the low latitude tropical belt from where it is advected polewards.

Although there seems little doubt that discharges of freshwater from the Laurentide Ice Sheet influenced thermohaline activity in the North Atlantic Ocean during ice ages (Clark et al., 2001), it is otherwise undeniable that the concept of the North Atlantic, Greenland and Norwegian Seas’ thermohaline influence in redistributing heat is under challenge from the tropical Pacific as the main source of heat and moisture. Thus, 65° N, the “critical latitude” of Milutin Milankovitch, and the ocean thermohaline circulation climate signal carrier is challenged by data from the tropical Pacific Ocean.

This debate has rejuvenated the climatologic-paleoclimate link in the search for mechanisms of abrupt and rapid change for Pleistocene climates. Increasing interest in solar irradiance variability is the result of ongoing physical measurements as well as the record of variability inferred from cosmogenic isotope abundances in ice cores. The not-unrelated role of cosmic

particles may also have a bearing on the elusive role of cloud and water vapor in climate variability on different timescales. Concepts of Pleistocene climates have been revolutionized in less than half a century and, while the Pleistocene past may hold a key to the present and future, its reciprocal, of the present being the key to the past, remains undiminished.

David Q. Bowen

Bibliography

- Alley, R.B., 2000. *The Two-Mile Time Machine: ice cores, abrupt climate change, and our future*. Princeton: Princeton University Press, 229pp.
- Bond, G.C., and Lotti, R., 1995. Iceberg discharges into the North Atlantic on millennial timescales during the last glaciation. *Science*, **267**, 1005–1010.
- Bond, G., Kromer, B., Beer, J., Muscheler, R., Evans, M.N., Showers, W., Hoffmann, S., Lotti-Bond, R., Hajdas, I., and Bonani, G., 2001. Persistent solar influence on North Atlantic climate during the Holocene. *Science*, **294**, 2130–2136.
- Broecker, W.S., 1994. Massive iceberg discharges as triggers for global climate change. *Nature*, **372**, 421–424.
- Broecker, W.S., and Denton, G.H., 1989. The role of ocean-atmosphere reorganizations in glacial cycles. *Geochim. Cosmochim. Acta*, **53**, 2465–2501.
- Cane, M., and Clement, A.C., 1999. A role for the Tropical Pacific Coupled Ocean-Atmosphere System on Milankovitch and Millennial Timescales: Part II: Global Impacts. In Clark, P.U., Webb, R.S., and Keigwin, L.D. (eds.), *Mechanisms of Global Climate Change at Millennial Time Scales*. Washington, DC: American Geophysical Union, pp. 373–384.
- Clark, P.U., Marshall, S.J., Clarke, G.K.C., Hostetler, S.W., Licciardi, J.M., and Teller, J.T., 2001. Reshwater forcing of abrupt climate change during the last glaciation. *Science*, **293**, 283–287.
- Cronin, T. M., 1999. *Principles of Paleoclimatology*, New York: Columbia University Press, 560pp.
- Dansgaard, W.S., Johnsen, S.J., Møller, J., and Langway, C.C., 1969. One thousand centuries of climatic record from Camp century on the Greenland Ice Sheet. *Science*, **166**, 377–380.
- deMenocal, P., 1995. Plio-Pleistocene African climate. *Science*, **270**, 53–59.
- Droxler, A., Poore, R.Z., and Burkle, L.H., 2003. *Earth's Climate and Orbital Eccentricity: The Marine Isotope Stage 11*. Washington, DC: Geophysical Monograph, American Geophysical Union.
- Imbrie, J., and Imbrie, K.P., 1979. *Ice Ages: Solving the Mystery*. London: Macmillan, 224pp.
- Overpeck, J.T., Whitlock, C., and Huntley, B., 2003. Terrestrial biosphere dynamics in the climate system: Past and future. In Alverson, K.D., Bradley, R.S., and Pederson, T.F. (eds.), *Paleoclimate, Global Change and the Future*. Berlin: Springer, pp. 82–103.
- Rind, D., 2002. The Sun's Role in Climate Change. *Science*, **296**, 673–677.
- Raynaud, D., Blunier, T., Ono, Y., Delmas, R., Barnola J.M., Joos, F., Petit, J.R., and Spahni, R., 2003. The late Quaternary history of atmospheric trace gases and aerosols: Interactions between climate and biogeochemical cycles. In Alverson, K.D., Bradley, R.S., and Petersen, T.F. (eds.), *Paleoclimate, Global Change and the Future*. Berlin: Springer, 13–32.
- Zahn, R., 2002. Milankovitch and Climate: the Orbital Code of Climate Change. *JOIDES J. (Special Issue)*, **28**, 17–22.

Cross-references

- [Aerosol \(mineral\)](#)
- [Albedo Feedbacks](#)
- [Alkenones](#)
- [Arid Climates and Indicators](#)
- [Astronomical Theory of Climate Change](#)
- [Atmospheric Circulation During the Last Glacial Maximum](#)
- [CLIMAP](#)
- [Climate Change, Causes](#)
- [Cosmogenic Radionuclides](#)
- [Dansgaard-Oeschger Cycles](#)
- [Eccentricity](#)

Foraminifera
 Glaciations, Quaternary
 Heat Transport, Oceanic and Atmospheric
 Heinrich Events
 Human Evolution and Climate Change
 Ice Cores, Antarctica and Greenland
 Ice-Rafted Debris (IRD)
 Interstadials
 Lake Level Variations
 Last Glacial Maximum
 Laurentide Ice Sheet
 Little Ice Age
 Loess Deposits
 Millennial Climate Variability
 Moraines
 Monsoons, Quaternary
 North Atlantic Deep Water and Climate Change
 North Atlantic Oscillation (NAO) Records
 Obliquity
 Ocean Paleotemperatures
 Oxygen Isotopes
 Paleo-El Niño-Southern Oscillation (ENSO) Records
 Paleoceanography
 Paleotemperatures and Proxy Reconstructions
 Pliocene Climates
 Pollen Analysis
 Precession, Climatic
 Quaternary Climate Transitions and Cycles
 Quaternary Vegetation Distribution
 Sea Level Change, Quaternary
 SPECMAP
 Stable Isotope Analysis
 Sun-Climate Connections
 Thermohaline Circulation
 Time-Series Analysis of Paleoclimate Data
 Transfer Functions
 Uranium-Series Dating
 Wisconsinan (Weichselian, Würm) Glaciation

PLIOCENE CLIMATES

Introduction

The Pliocene (*Plio More – Cene Recent*) epoch represents the uppermost sub-division of the Tertiary period. It spans a time-frame from 5.3 to 1.8 million years before present, according to the geological timescale of Berggren et al. (1995). The epoch incorporates the time interval in which Earth experienced a transition from relatively warm climates to the prevailing cooler climates of the Quaternary period.

Climatically, the Pliocene can be crudely divided into three phases, (a) an Early Pliocene warm period, (b) a relatively short-lived ‘warm blip’ during the middle part of the Pliocene (centered around 3 million years before present), and (c) a climatic deterioration during the late Pliocene. It is important to realize that available higher resolution climate records for this time (e.g., Leroy and Dupont, 1994) suggest that even relatively short subdivisions of the epoch were characterized by almost continuous changes in precipitation and temperature, occurring on the timescale of several thousand years. This climatic variability is poorly resolved in terms of magnitude (Haywood et al., 2002a) but often occurred with detectable periodicities of 41,000 and 19,000, 21,000 and 23,000 years, linked to obliquity and precessional Milankovitch cycles (cyclic variations of the Earth’s orbital position; obliquity is the angle of Earth’s axial tilt as measured against the plane of the

ecliptic; precession is the degree of wobble of the Earth on its axis, which is caused by the gravitational pull of the Sun and the Moon). It is likely that many abrupt, short timescale climate events currently remain undetected due to the lack of high resolution and long paleoclimatic records, thus making the process of generalization regarding the climate of the Pliocene extremely hazardous.

Even though a progressive cooling was occurring during the Tertiary, the Pliocene world appears to have been, for the most part, warmer than at present. The ancient distribution of planktonic (free-floating marine organisms) and benthic (bottom-dwellers) foraminifer (minute aquatic organisms that consist of a single cell or a colonial aggregate of cells without differentiation of function) along with terrestrial fossil fauna and flora, indicates that mean annual temperatures in the mid-latitudes were often several degrees higher (3 °C to 5 °C) than at present (e.g., Thompson, 1991; Dowsett et al., 1996). The greatest warming appears to have been in the high latitudes and polar regions, where temperatures were often warm enough to allow species of animals and plants to exist at higher latitudes than their nearest modern relatives (Adam, 1994).

The recognition that significant warming took place at high latitudes and at the poles has interesting implications for the behavior and extent of sea ice, the major terrestrial ice sheets of Greenland and Antarctica, and for Pliocene sea levels.

Sea ice

Diatom (see *Diatoms*) data from the Southern Ocean (Barron, 1996), and foraminifer, ostracod (see *Ostracodes*) and mollusk (invertebrate of the phylum Mollusca) data (Cronin et al., 1993) suggest that sea ice extents were greatly reduced at approximately 3 million years before present, with modern summer sea-ice limits similar to Pliocene winter sea-ice cover and the possibility that the Arctic Ocean was seasonally sea-ice free (Cronin et al., 1993).

Ice sheets

Significant debate has centered on the nature of the terrestrial ice sheets of Greenland and Antarctica during the Pliocene. The consensus view, through examination of ice-rafted detritus (IRD) in marine sediment cores (e.g., Kleiven et al., 2002), is that the initiation of significant Northern Hemisphere glaciation began during the middle to late Pliocene. However, there may have been many false starts to this glaciation, with evidence existing for glacial activity on Greenland as far back as the late Miocene. Total ice volume on Greenland may have remained significantly less than at present even during the latter parts of the Pliocene epoch.

With regard to Antarctica, two contrasting viewpoints exist. The first, based on evidence derived from Pliocene marine diatoms (Harwood and Webb, 1986) and the remains of *Nothofagus* (Southern Beech) in the Sirius Group glacial sediments along the Transantarctic Mountain Range (Francis and Hill, 1996), suggests that the East Antarctic Ice Sheet (EAIS) may have been significantly reduced in size (by a maximum of one-third). The second, based on geomorphic investigations of the landscape in the Dry Valleys region, suggests that stable polar conditions have persisted for at least the last 14 million years (Denton et al., 1993). The dating of a variety of landforms including superficial till sheets, old desert pavements, avalanche deposits and volcanic ash layers that span the Miocene and Pliocene apparently testify to remarkably slow

rates of weathering and erosion in the Dry Valleys (Marchant et al., 1993). If the EAIS did behave in a dynamic manner, it is unlikely that such geomorphic features, if truly Miocene or Pliocene in age, would have survived.

Sea level

If terrestrial ice cover was reduced during the Pliocene, then global sea levels should also have been higher than at present. Evidence exists which indicates that sea levels were higher, although the potential errors in the data make it difficult to assess the true magnitude of sea-level change. Based on sequence stratigraphic techniques, sea-level highstands of up to 60 m were reported by Haq et al. (1987). Dowsett and Cronin (1990) used the presence of the Orangeburg Scarp (an extensive paleoshoreline from the southeastern U.S. Atlantic Coastal Plain) combined with micropaleontological evidence to suggest that a sea-level highstand of approximately 35 ± 18 m higher than present existed between 3.5 and 3.0 million years before present. The stratigraphic distribution of disconformities (type of unconformity where the buried erosion surface lies between two series of strata that are parallel on a large scale) at Enewetak Atoll suggests a Pliocene sea level 36 m higher than today's (Wardlaw and Quinn, 1991). Through the analysis and correlation of Atlantic Coastal Plain sediments with $\delta^{18}\text{O}$ (see *Oxygen isotopes*) isotopic records from deep-sea cores, sea levels between 4.0 to 3.5 million years ago and 3.0 million years ago have been estimated as 30–35 and 25 m higher than modern, respectively (Krantz, 1991). These sea-level changes appear to have been driven by glacio-eustatic events (see *Glacial eustasy*), but their precise correlation to changes in the polar regions remains unclear (Dowsett et al., 1996).

Climate dynamics and climate modeling

The use of numerical climate models, or General Circulation Models (GCMs), is one of the most powerful tools at our

disposal for the investigation of past climate dynamics. Numerous climate modeling studies have been conducted for the Pliocene using a host of different models of varying sophistication (see *Mid-Pliocene warming* this volume; Chandler et al., 1994; Sloan et al., 1996; Haywood et al., 2000a,b; Kim and Crowley, 2000; Haywood, 2001; Haywood et al., 2001; Haywood et al., 2002a,b,c; Haywood and Valdes, 2004). The focus of these modeling studies has been on the period of warming which occurred around 3 million years before present. This is primarily due to the wealth of geological and boundary condition data sets (necessary for the initiation of the climate model experiments) that exist for this period (see Dowsett et al., 1999).

Climate modeling – surface temperature ($^{\circ}\text{C}$)

Atmosphere-only climate model studies (experiments that do not include an interactive ocean model in any form) suggest that the climate of 3 million years before present was, as a global annual average, 2 to 5 $^{\circ}\text{C}$ warmer than at present (Sloan et al., 1996; Haywood et al., 2000a; see Figure P75). Three zones of temperature change were predicted in the climate modeling study of Haywood et al. (2000a). Between 10 $^{\circ}$ and 30 $^{\circ}$ North and South of the equator, the predicted warming was a modest 1 to 4 $^{\circ}\text{C}$. Between 30 $^{\circ}$ and 50 $^{\circ}$ in the Northern Hemisphere, temperatures warmed by 4–8 $^{\circ}\text{C}$. This pattern was not duplicated in the Southern Hemisphere, where the temperature rise was 0–4 $^{\circ}\text{C}$. By far the greatest relative warming was indicated at latitudes above 70 $^{\circ}$ in both hemispheres (Figure P76). Temperature changes relative to present in high latitude areas of the Northern Hemisphere during the winter period (December, January and February; DJF) ranged from 16–20 $^{\circ}\text{C}$ in Greenland to 20–28 $^{\circ}\text{C}$ in the Arctic. During DJF (Southern Hemisphere summer), dramatic warming in parts of west and east Antarctica (~32–36 $^{\circ}\text{C}$) was predicted. During June, July and August (JJA), Antarctica warmed in a

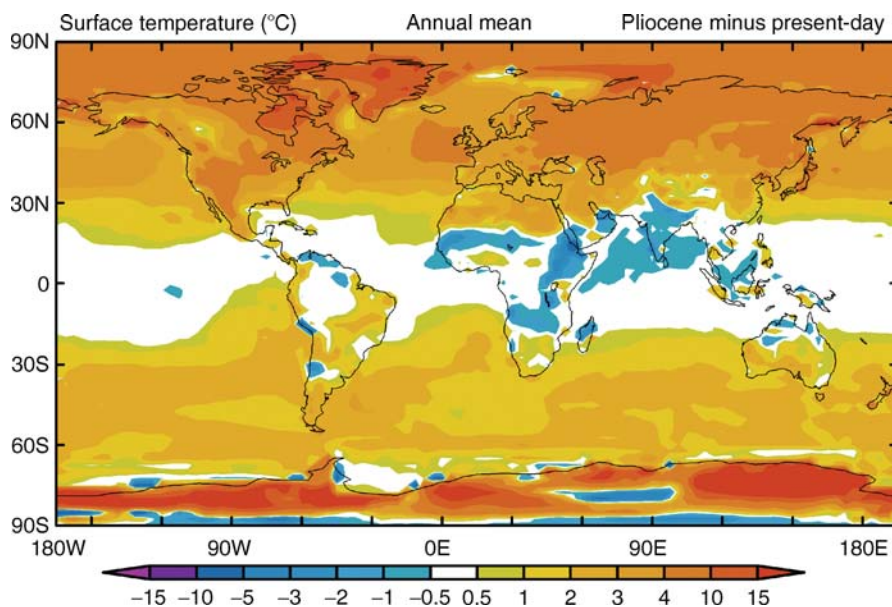


Figure P75 Climate model prediction: difference between simulated Pliocene (3 million years before present) and present-day surface temperature ($^{\circ}\text{C}$) as an annual mean (redrawn from Haywood et al., 2000a; Haywood, 2001). Model used was the Hadley Center Atmospheric Climate Model Version 3 (HadAM3), boundary conditions specified from the PRISM2 data set (Dowsett et al., 1999).

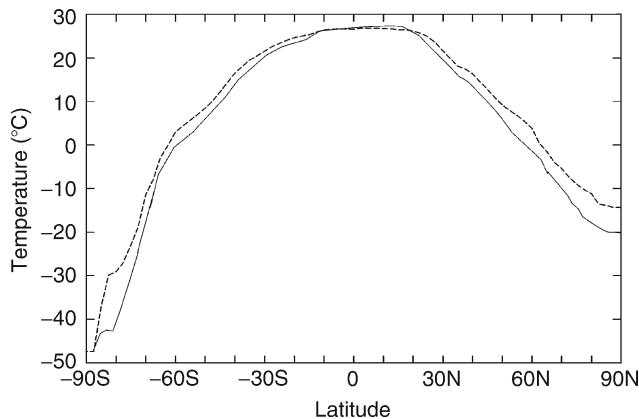


Figure P76 Model-predicted Pliocene (*dashed line*) and present-day (*solid line*) mean annual surface temperatures ($^{\circ}\text{C}$) plotted as a function of latitude. This plot indicates a surface temperature regime with reduced seasonality and greater equability during the Pliocene compared to present-day (Haywood, 2001).

comparable fashion to the DJF period ($20\text{--}32^{\circ}\text{C}$). However, the warming occurred over a significantly wider area of the continent.

The pattern of temperature change was not spatially uniform. During DJF, a zone of discontinuous cooling (maximum of 4°C) was predicted from 10° North to 10° South of the equator; this extended over parts of northern Australia and South America. During JJA, the equatorial/low latitude belt of cooling became more continuous, especially over parts of Africa and southern Asia. Temperatures in parts of Africa at 10° North of the equator cooled by 4 and 8°C as compared to the present.

The predicted high latitude warming ($>70^{\circ}$ North and South) can be attributed to a reduction of ice cover in both oceanic and terrestrial settings during the Pliocene and to the prescribed warmer high latitude sea surface temperatures (SSTs). Furthermore, the significance of a higher Pliocene sea level should not be underestimated. Oceans cool less than land when exposed to cold conditions, so higher sea levels act as a positive feedback mechanism for temperature, especially in the high latitudes (Sloan et al., 1996). The equatorial and low latitude cooling is due to more than one contributing factor. SST values for the oceans in equatorial and low latitudes are likely to have an effect, as are variations in cloud cover and vegetation in these areas. Increased precipitation promoting greater evaporation in this region acts as a cooling feedback. This is probably the main cause of the tropical cooling observed over Africa.

The GCM indicated that the greatest degree of warming occurred in the Northern and Southern Hemisphere during their respective winter seasons. This is attributable to the warmer SSTs in the mid to high latitudes, with associated changes in snow and ice cover.

Climate modeling – total precipitation rate (mm day^{-1})

The distribution of total precipitation during the Pliocene was simulated in Haywood et al. (2000a) and Haywood (2001) to be broadly similar to present (Figure P77). A general but modest increase, of between 0 and 2 mm day^{-1} , was predicted in both hemispheres during DJF and JJA. Although sporadic pockets of less rainfall (-2 mm day^{-1}) were common, especially during JJA, they were frequently not statistically significant. Annual mean precipitation during the Pliocene was $34.65\text{ cm year}^{-1}$,

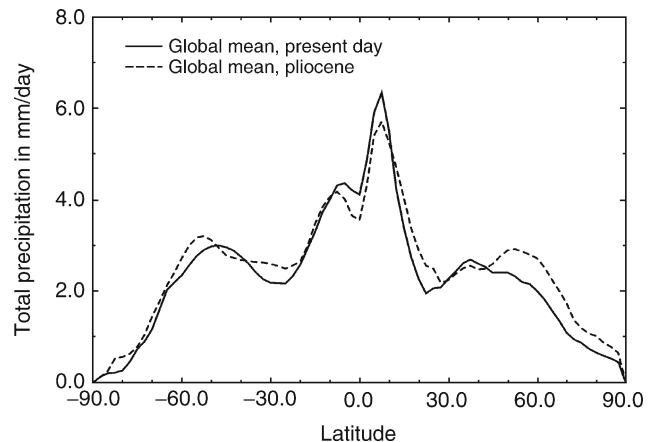


Figure P77 Annual mean total precipitation rate as a function of latitude for present-day and the Pliocene in mm day^{-1} (redrawn from Haywood et al., 2000a; Haywood, 2001).

2 cm higher than at present ($32.84\text{ cm year}^{-1}$), representing a 6% increase relative to modern values (Figure P77). During DJF in the Northern Hemisphere ($10^{\circ}\text{--}70^{\circ}$ North), areas of enhanced precipitation were noted (Figure P78). These areas include the Indian Ocean, the Caribbean, the North Atlantic and northwestern North America, where precipitation was enhanced by $2\text{--}8\text{ mm day}^{-1}$. The increase in mid-latitude precipitation in the Northern Hemisphere was associated with the warmer surface temperatures.

Increases in precipitation during JJA were seen to occur in a narrow belt at equatorial and low latitudes. India, Arabia, Central and West Africa, the Caribbean and the West Coast of Central and Latin America all showed an increase in precipitation of between 2 and 10 mm day^{-1} (Figure P78). The model indicated that the southern limit of the Hadley Cell (atmospheric cell which transports heat and momentum in the atmosphere at low-latitudes) was in approximately the same position as at present. However, the northern limit was shifted further to the North by 5° of latitude. The result was a net ‘broadening’ of the Hadley Cell in the Pliocene, which allowed more precipitation to fall over a larger geographical area. This change in the Hadley Cell was caused by the simulated reduction in the equator-to-pole temperature gradient (by 6°C). Broadening of the Hadley Cell explained several of the model’s responses observed at equatorial and low latitudes, such as increased precipitation, evaporation and subsequent reduction of surface temperatures.

Over Greenland, a statistically significant increase in precipitation was predicted, except over the southern tip of Greenland where precipitation decreased. This decrease was related to a shift in the position of the Atlantic storm track.

Climate modeling – wind (m s^{-1}) and surface pressure (hPa)

As a global annual average, surface wind strength decreased in the Pliocene experiment compared to the present. This response was consistent with the model-predicted reduction in the equator-to-pole temperature gradient of 6°C , which diminished the general circulation of the atmosphere. Most variations in wind dynamics were observed in the westerly component.

In the simulation, Pliocene wind directions were broadly similar to the present. Increases in wind speed were observed

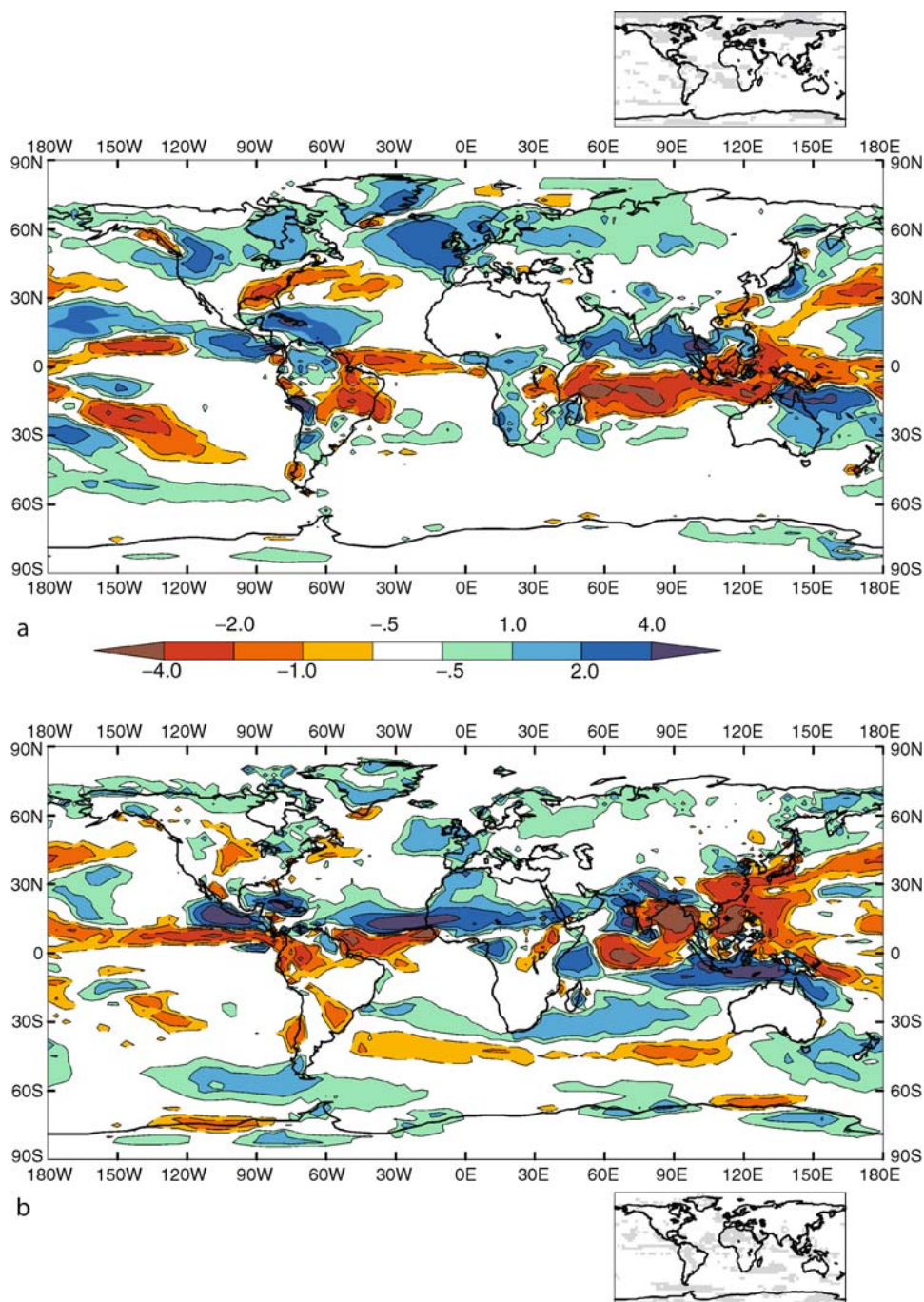


Figure P78 Model-predicted difference in mean total precipitation rate (mm day^{-1}) between the Pliocene and present-day for (a) DJF and (b) JJA. Note that the contour interval is not equally spaced and regions where precipitation change is less than 0.5 mm day^{-1} are unshaded. The grey shading in accompanying mini-boxes shows the geographical areas in which the difference in precipitation rate is significant to a 95% statistical significance level (redrawn from Haywood et al., 2000a; Haywood, 2001).

over areas of North America, Siberia and the Tibetan Plateau. This was a function of the altered land cover and surface heating characteristics of the Pliocene simulation as compared to the modern one. Wind strengths over the oceans exhibited a more dramatic change in the Pliocene scenario. Wind speeds increased by a maximum of 6 m s^{-1} during DJF in areas

affected by the Icelandic and Aleutian low-pressure systems. These pressure systems deepened in the Pliocene simulation as compared to the present (Figure P79).

Analysis of wind strength fields at 200 mbs indicated that the strength of the mid-latitude jet streams was enhanced in the Pliocene experiment. Increases in wind speeds in other locations

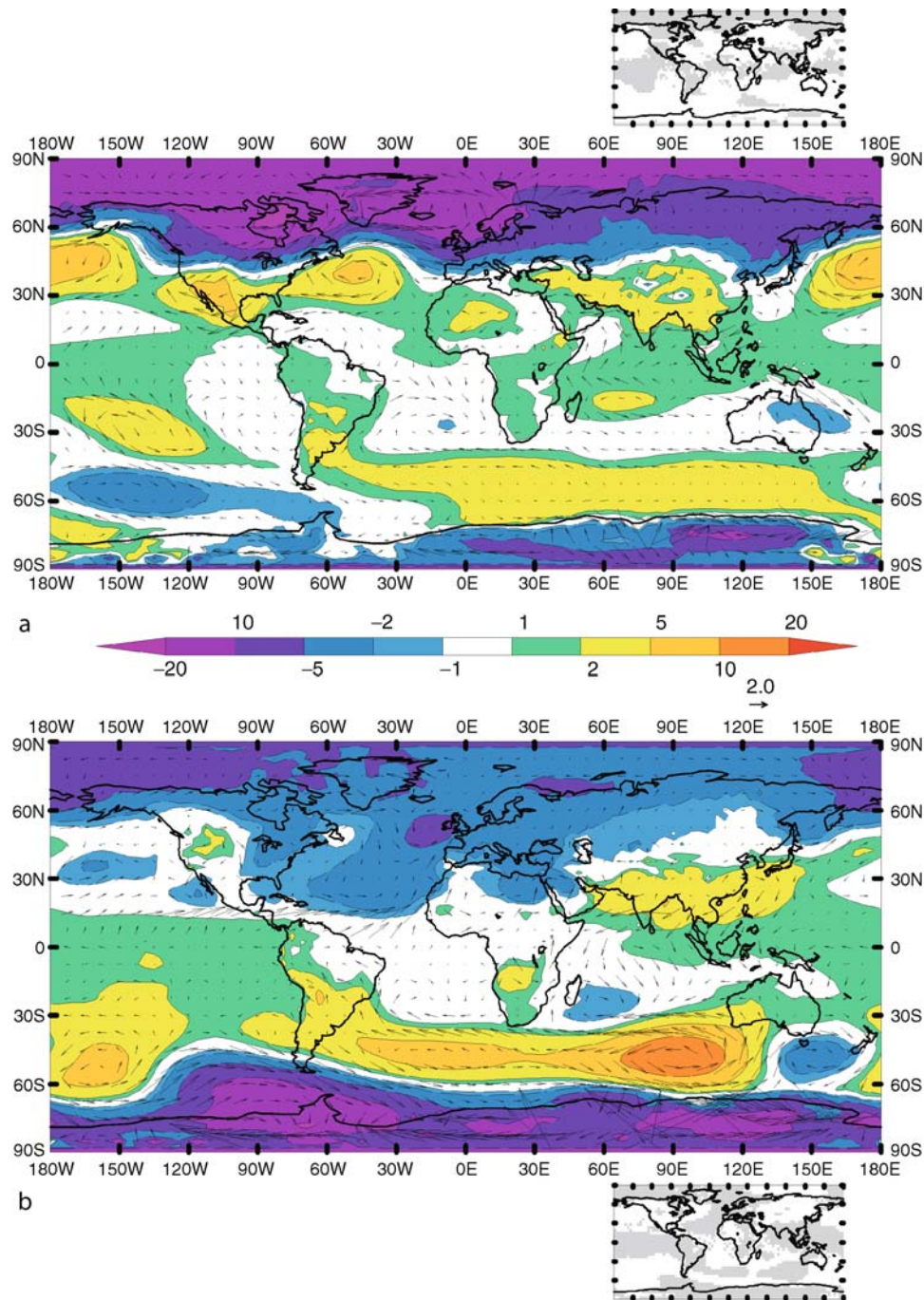


Figure P79 Model-predicted difference in surface pressure (hPa) between the Pliocene and present-day for (a) DJF and (b) JJA: Vector surface mean winds are also shown. The *grey shading* in accompanying mini-boxes shows the geographical areas in which the difference in precipitation rate is significant to a 95% statistical significance level (redrawn from Haywood et al., 2000a; Haywood, 2001).

were accounted for by the enhancement of high-pressure zones over subtropical ocean regions. A strong high-pressure anomaly was observed in the Southern Ocean west of Australia during DJF and JJA (Figure P79). This was related to alterations in Rossby wave (planetary wave) propagation caused by changes in the Antarctic orography in the Pliocene simulation. The

strength of JJA monsoon circulation in the Indian Ocean was weakened in the Pliocene experiment.

Climate modeling summary

The results of the modeling study by Haywood et al. (2000a) and Haywood (2001) are closely linked to, and dependent

on, the specified model boundary conditions. From analysis of the model simulation and from sensitivity experiments (Haywood, 2001), it is clear that alterations in SSTs combined with sea and land ice volumes within the model boundary conditions are primarily responsible for the observed variations between Pliocene and present-day climates. The variations in climate are caused by the alteration of processes, including the release of sensible and latent heat (SST driven) and by variations in heat exchange between the ocean and atmosphere that are also caused by differences in sea ice.

The warmer SSTs are responsible for the majority of model-predicted annual mean increase in surface temperatures and precipitation for the Pliocene. However, changes in high latitude surface temperatures and precipitation rate are also closely linked to the altered configuration of terrestrial ice sheets and sea-ice extents specified within the model boundary conditions. The enhancements of the mid-latitude jet streams and surface westerly winds predicted in the Pliocene experiment are primarily linked with changes in atmospheric pressure systems, which are themselves generated by reduced high latitude terrestrial and sea-ice cover. The role of altered jet stream flow, in response to the altered orography of the western cordillera of North America, may also be important in generating the enhancements in westerly wind strength observed in the Pliocene simulation.

Causes of pliocene climate change

Climatic warmth

The causes of Pliocene climate change have been widely discussed (e.g., Raymo et al., 1996). The applicability and scientific usefulness of the question “what was the cause of Pliocene warmth?” is arguable. This is because of (a) the multiple interactions of different components of the Earth’s climate system, (b) equifinality (different climate forcing mechanisms leading to the production of a similar response in climate), and (c) climatic memory effects (the existence of a global climate regime at any one time depends not only on forcing mechanisms in operation during the said regime but also those which occurred previously). A more scientifically useful question to pose might be “what were the processes that helped promote, sustain and ultimately terminate the climates of the Pliocene?”. Such an approach has the advantage of being process rather than causation driven, which increases the usefulness of studying past warm periods in our quest to better understand future climate change.

Atmospheric CO₂

Estimates of atmospheric CO₂ levels have been derived from analyses of the stomatal density of fossil leaves (stomata are small pores on a leaf surface that allow carbon dioxide to enter the leaf and oxygen to escape, thereby facilitating photosynthesis; Kürschner et al., 1996), through analyses of $\delta^{13}\text{C}$ ratios of marine organic carbon (Raymo and Rau, 1992) and through measurement of the differences between the carbon isotope composition of surface and deep waters (Shackleton et al., 1992). Use of all of these proxy methods suggests that absolute CO₂ levels during the epoch ranged from 360 to 400 ppmv, compared to mid-nineteenth century levels of approximately 280 ppmv and modern concentrations of 375 ppmv. The cause for this higher Pliocene concentration is not well understood and may be attributable to the long-term trend of CO₂ change throughout the Tertiary (Berner, 1990). Alternatively, feedbacks between climate and the carbon cycle (the cycling of

carbon in the form of carbon dioxide, carbonates, organic compounds, etc. between various reservoirs, e.g., the atmosphere, the oceans, land and marine biota and, on geological time scales, sediments and rocks) may also have been important.

The modest CO₂ increase reconstructed for the Pliocene would produce a radiative forcing of approximately 2 W m^{-2} . This may be sufficient to explain the warmth of the Pliocene globally, depending on the chosen climate sensitivity parameter, and whether there are any significant changes in other aspects of the radiative forcing. It cannot explain the regional changes in reconstructed SSTs, which apparently display no warming trend relative to present day in the tropics (Dowsett et al., 1996). Therefore, an additional mechanism (or mechanisms) working independently or combined with variations in CO₂ concentrations in the atmosphere would have been required to drive and maintain the warmer climates reconstructed for the Pliocene.

Ocean heat transport

A likely additional factor is a change in the heat transport of the oceans. This could be achieved through an increase in thermohaline or surface gyre circulation. This possibility was highlighted in early modeling studies (e.g., Rind and Chandler, 1991), but many difficulties and unexplained issues remain. Paradoxically, a reduced latitudinal SST gradient implies weaker atmospheric forcing of surface oceanic circulation, and hence weaker oceanic heat transport from equator to higher latitudes. This is a common problem associated with past warm climate dynamics. Problems exist in any explanation of Pliocene warmth that is based solely upon strengthening of the thermohaline circulation as it is, (a) difficult to ascribe a thermohaline coupling argument to all ocean basins and, (b) difficult to generate the correct reconstructed hemispheric temperature distribution (Crowley, 1996).

The arguments above are largely based on a consideration of global scale energetics. The importance of specific regional aspects, such as changes in surface wind strength and wind stress over different ocean basins, has only recently been considered in detail. Climate modeling results presented in Figure P79 indicate an increase in westerly component winds at mid to high latitudes in both hemispheres. This is a direct response to less ice cover and warmer surface temperatures over Greenland, the Arctic, Southern Ocean and Antarctica and to warmer sea-surface temperatures in the North and South Atlantic Oceans during the Pliocene. Conversely, sub-tropical high-pressure systems in both hemispheres are also enhanced. Therefore, regional pressure gradients in the mid to high latitudes of both hemispheres may have been intensified during the Pliocene. This has the potential, when combined with warmer SSTs, to increase the atmospheric transport of heat and moisture to the high latitudes (Figure P80). Increasing westerly wind strength applies greater wind stress (maximum 20 N m^{-2} on the basis of modeling experiments) to the surface of the oceans, thus potentially strengthening the flow of heat-transporting surface ocean currents such as the Gulf Stream (Figure P81).

These interpretations, based upon modeling studies (e.g., Haywood et al., 2000b), support paleoceanographical evidence for enhanced oceanic heat transports (e.g., Dowsett et al., 1996). Enhanced carbonate accumulation and upwelling from the California margin during the Pliocene relates to increased wind stress (Ravelo et al., 1997). Results from a study of marine ostracodes (Cronin, 1991) suggest that: (a) North Atlantic circulation may have been intensified, and (b) reconstructed

cooler ocean temperatures off the southeastern and mid-Atlantic coast of the USA during the Pliocene were a result of enhanced upwelling driven by the Gulf Stream. Billups et al. (1998) speculated that positive feedbacks involving Southern Hemisphere atmospheric circulation and Northern Hemisphere poleward heat transport, together with sea-ice feedbacks, might have played an important role in maintaining the climatic warmth of the Pliocene.

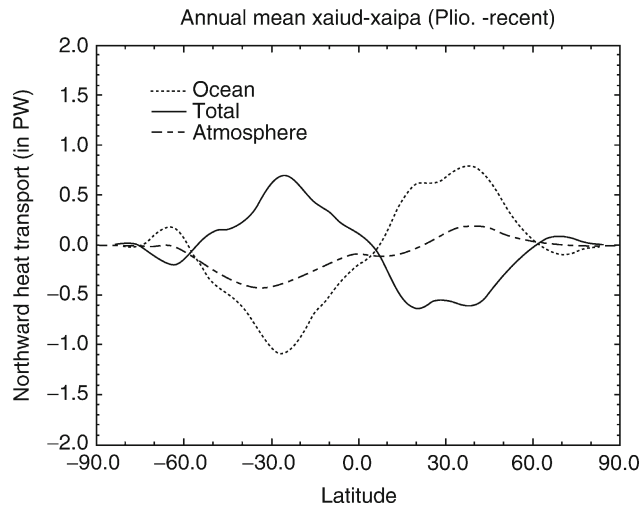


Figure P80 Model prediction of the difference in total poleward heat transport (in PW), by atmosphere and oceans between the Pliocene climate modeling experiment of Haywood et al. (2000a) and the present-day (*xaiud* = mid-Pliocene simulation; *xajpa* = present-day simulation).

Ocean heat transport – difficulties

The mechanism of enhanced ocean heat transport may have been important in helping to maintain greater mid to high latitude warmth during the Pliocene. However, the oceans act, to a first approximation, as a feedback mechanism rather than a direct forcing on climate. In other words, if we invoke greater oceanic transport of heat to help explain the warmth of the Pliocene then we must deal with the following question “what were the factors responsible for forcing a change in oceanic circulation and heat transports?”. Rind and Chandler (1991) postulated that changes in poleward ocean heat transport might be related to changes in orography, which would affect the planetary wind-driven circulation. However, it is unknown whether changes in orography are capable of affecting wind-driven circulation on anything more than a regional scale (Crowley, 1991). Climate modeling sensitivity experiments conducted by Haywood (2001) indicate that lowering the elevation of the western cordillera of North America, for example, does have an impact on the surface circulation across North America and into the Atlantic sector. However, alterations in high latitude low-pressure and sub-tropical high-pressure cells, as a result of reduced ice cover and altered SST gradients, are required to sustain the changes in circulation over the European and other sectors. Hence, whilst changes in orography may have been an important contributing factor in forcing changes in the wind-driven circulation, other mechanisms must have been in operation to drive larger-scale alterations in oceanic circulation, for the Pliocene at least.

The potential influence of changing terrestrial ice cover on oceanic circulation should not be forgotten. Although the direct effect of reduced high latitude ice cover on surface temperatures may only be observed over a couple of thousand kilometers away from the ice edge, it can have a significant impact on atmospheric pressure systems in the mid to high

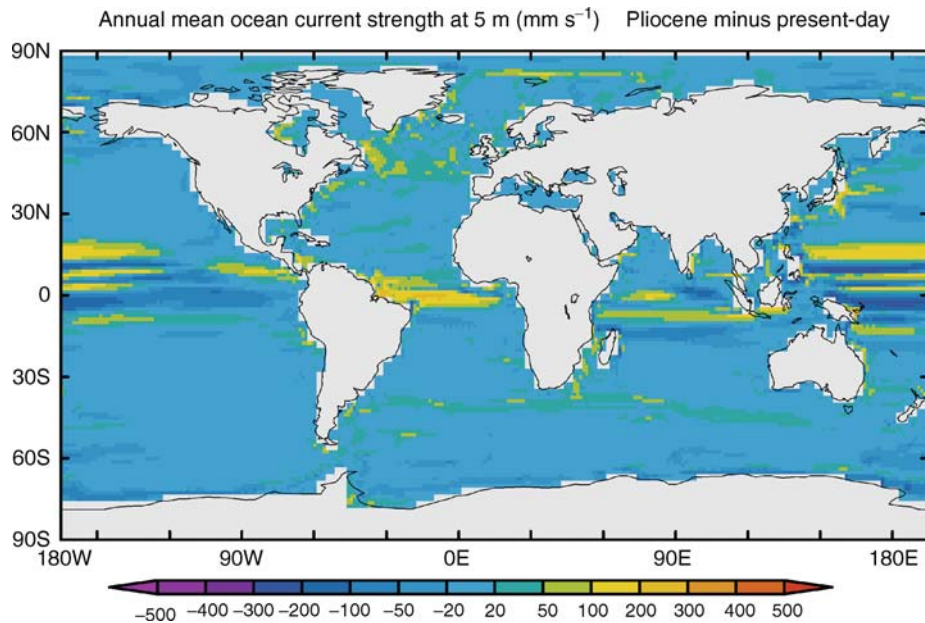


Figure P81 Coupled ocean-atmosphere model prediction of the difference in ocean current strength (mm s^{-1}) at 5 m between the Pliocene and present-day. Note the increase in the strength of the Gulf Stream and North Atlantic Drift currents in the North Atlantic (redrawn from Haywood and Valdes, 2004).

latitudes. This can affect atmospheric circulation and hence the wind-driven circulation of the ocean surface (Haywood et al., 2000b), thus providing a mechanism for forcing changes in oceanic heat transport. The key to understanding Pliocene warmth may therefore be as simple as knowing why the global coverage of ice was reduced compared to the present. This of course assumes that ice sheets of greater size than those of the Pliocene existed before that epoch.

One tectonically-driven process that may have had a significant impact on oceanic circulation during the Pliocene is the closing of ocean gateways and changes in the character of ocean sills. The sill depth of the Central American Seaway (CAS) decreased from approximately 1,000 m during the Miocene to near breaching of the sea surface during the early Pliocene. This may have had the effect of redirecting the flow of warm and salty water to the North within the Atlantic (e.g., Haug and Tiedemann, 1998). The sill depth between the North Atlantic and Norwegian-Greenland seas may have been lower during the Pliocene. This would have allowed the overflow of Arctic waters into the North Atlantic, thereby stimulating North Atlantic Deep Water (NADW) Formation (Wright and Miller, 1996). Changes in the depth of the Indonesian throughflow between 5 and 3 million years before present may have enhanced oceanic heat transports away from the tropics (Cane and Molnar, 2001). Finally, the first opening of the Bering Strait was an oceanographic event of global importance. Stratigraphic information suggests that the minimum age range for the strait's first opening was between 4.8 and 7.3–7.4 million years before present (Marincovich and Gladenkov, 1999). The fact that many more Pacific invertebrates invaded the Arctic Ocean than the reverse (Fyles et al., 1991) suggests that the main current flow was to the North. Heat transfer through the strait represents only a small part of the Arctic energy budget but the event may have warmed and moderated the Pliocene climate of the Arctic (White et al., 1997).

Climatic deterioration

Explanations for the climatic deterioration that occurred during the late Pliocene have centered on the effects of tectonics, alterations in atmospheric composition and the effect of changing orbital forcing on ice-sheet growth. The onset of Northern Hemisphere glaciation may be related to the progressive uplift of the Tibetan-Himalayan and Sierran/Coloradan regions (e.g., Ruddiman and Raymo, 1988). It is possible that the uplift in these two regions altered the circulation of atmospheric planetary waves so that summer ablation was decreased, allowing for the progressive build up of snow and ice in the Northern Hemisphere. The coincidence of Tibetan-Himalayan uplift and the sudden climatic deterioration during the late Pliocene remains to be confirmed; Copeland et al. (1987) and Spicer et al. (2003) have suggested that the majority of Himalayan uplift was completed between 20 and 15 million years before present and not during the mid-Pliocene as suggested by paleobotanical studies (Mercier et al., 1987). Until the dating of Tibetan-Himalayan uplift has been established it will be difficult to assess the true significance of this mechanism in forcing the climatic deterioration of the late Pliocene.

The Tibetan-Himalayan debate has broadened to include the impact that such uplift could have on atmospheric concentration of CO₂. Raymo (1991) discussed how Himalayan uplift might have increased chemical weathering rates during the late Cenozoic (see *Weathering and climate*). Weak carbonic acid

(rainwater) weathers rocks via hydrolysis. The chemical weathering of carbonate rocks returns CO₂ to the atmosphere. However, the weathering of silicate rocks has the potential to reduce atmospheric concentrations of CO₂. During chemical weathering of silicate rocks, bicarbonate (HCO₃⁻) is produced as a bi-product. The bicarbonate is metabolized by marine plankton upon reaching the oceans and converted into calcium carbonate (CaCO₃). The calcite skeletons of the marine plankton are ultimately deposited as deep-sea sediments which lock up the stored CO₂ in the calcium carbonate for the lifespan of the oceanic crust on which they were deposited. This process continually removes CO₂ from the atmosphere, cools global climate and hence could have initiated Northern Hemisphere glaciation. If left unchecked, this mechanism would very quickly deplete the entire atmospheric CO₂ reservoir (Berner, 1994). However, subduction-related volcanism would release CO₂ back into the atmosphere. Resolution of this problem awaits our improved understanding of the global carbon cycle for the Cenozoic.

The closing of the CAS is also considered to be a potentially important event in forcing the build up of substantial ice sheets in the Northern Hemisphere. At present, it is not known if the closing of the CAS and the abrupt shift in climate of the late Pliocene are coincident. Furthermore, the current scientific understanding of whether the closing of the CAS would have helped or hindered the intensification of Northern Hemisphere glaciation is incomplete. One theory is that the closing of the CAS would have increased the salinity of the Caribbean, which would have increased the salinity and strength of the Gulf Stream and ultimately NADW formation. Mikolajewicz et al. (1993) argued that an increase in the Gulf Stream and NADW formation brought about through the closure of the CAS would have worked against the progress of Northern Hemisphere glaciation since the oceanic heat transport to the high latitudes would be enhanced. In contrast Haug and Tiedemann (1998) argued that enhanced Gulf Stream flow would have brought more moisture as well as heat to the higher latitudes. The increased flux of moisture may have promoted the growth of the Greenland Ice Sheet.

Changes in orbital forcing have been suggested as an important mechanism contributing towards the global cooling of the late Pliocene. Maslin et al. (1995) suggested that the observed increase in the amplitude of the orbital obliquity cycles from 3.2 million years before present increased the seasonality of the Northern Hemisphere, thus initiating the long-term global cooling trend. Furthermore, the rise in amplitude of precession and variation of insolation between 2.8 and 2.55 million years before present may have forced the rapid glaciation of the Northern Hemisphere. Inevitably, like the warmth that preceded it, the climatic deterioration that characterizes the late Pliocene is likely to have more than one origin. Tectonic changes might have brought the global climate to a critical threshold with relatively rapid variations in the Earth's orbital parameters triggering the intensification of Northern Hemisphere glaciation.

Summary

The 3.5 million year long Pliocene epoch appears to have been generally warmer than at present, particularly at mid to high latitudes. This greater warmth may have been generated and/or sustained by a number of forcing mechanisms working concurrently. These include enhanced levels of atmospheric CO₂, enhanced

oceanic heat transports, and ice-albedo feedbacks. Climatic variability occurred during the epoch on Milankovitch periodicities. A climatic deterioration occurred during the late Pliocene which saw the initiation of significant Northern Hemisphere glaciation. This downturn, like the warm period that preceded it, is likely to have a complex origin. Current hypotheses include the effect of tectonic uplift, drawdown of atmospheric CO₂, and changes in oceanic circulation, heat transports and orbital forcing.

Alan M. Haywood

Bibliography

- Adam, D.P., 1994. Pliocene pollen data set dynamics: Tulelake, California and Lost Chicken Mine, Alaska. In Thompson, R.S. (ed.), *Pliocene Terrestrial Environments and Data/Model Comparisons*. U.S. Geological Survey Open-File Report 94-23, pp. 6-10.
- Barron, J.A., 1996. Diatom constraints on the position of the Antarctic Polar Front in the middle part of the Pliocene. *Mar. Micropaleontol.*, **27**, 195-213.
- Berggren, W.A., Kent, D.V., Swisher, C.C., and Aubry, M.P., 1995. A revised Cenozoic geochronology and chronostratigraphy. In Berggren, W.A., Kent, Aubry, M.P. and Hardenbol, J. (eds.), *Geochronology, Time Scales and Global Stratigraphic Correlation*. Tulsa, OK: Society for Sedimentary Geology. Special Publication 54, pp. 129-212.
- Berner, R.A., 1990. Atmospheric carbon dioxide over Phanerozoic time. *Science*, **249**, 1382-1386.
- Berner, R.A., 1994. Geocarb II: A revised model of atmospheric CO₂ over the Phanerozoic time. *Am. J. Sci.*, **294**, 56-91.
- Billups, K., Ravelo, A.C., Zachos, J.C., 1998. Early Pliocene climate: A perspective from the western equatorial Atlantic warm pool. *Paleoceanography*, **13**(5), 459-470.
- Cane, M.A., and Molnar, P., 2001. Closing of the Indonesian sea-way as a precursor to east African aridification around 3-4 million years ago. *Nature*, **411**, 157-162.
- Chandler, M., Rind, D., and Thompson, R., 1994. Joint investigations of the middle Pliocene climate II: GISS GCM Northern Hemisphere results. *Glob. Planet. Change*, **9**, 197-219.
- Copeland, P., Harrison, T.M., Kidd, W.S.F., Ronghua, X., and Yuquan, Z., 1987. Rapid early Miocene acceleration of uplift of the Gagedese Belt, Xizang (southern Tibet), and its bearing on accommodation mechanisms of the India-Asia collision. *Earth Planet. Sci. Lett.*, **86**, 240-252.
- Cronin, T.M., 1991. Pliocene shallow water paleoceanography of the North Atlantic Ocean based on marine ostracodes. *Quaternary Sci. Rev.*, **10**(2/3), 175-188.
- Cronin, T.M., Whatley, R.C., Wood, A., Tsukagoshi, A., Ikeya, N., Brouwers, E.M., and Briggs, W.M., 1993. Microfaunal evidence for elevated mid-Pliocene temperatures in the Arctic Ocean. *Paleoceanography*, **8**, 161-173.
- Crowley, T.J., 1991. Modeling Pliocene warmth. *Quaternary Sci. Rev.*, **10**, 272-282.
- Crowley, T.J., 1996. Pliocene climates: The nature of the problem. *Mar. Micropaleontol.*, **27**(1-4), 3-12.
- Denton, G.H., Sugden, D.E., Marchant, D.R., Hall, B.L., and Wilch, T.I., 1993. East Antarctic ice sheet sensitivity to Pliocene climatic change from a Dry Valleys perspective. *Geografiska Annaler*, **75A**, 155-204.
- Dowsett, H.J., and Cronin, T.M., 1990. High eustatic sea level during the Middle Pliocene: Evidence from the southeastern U.S. Atlantic Coastal Plain. *Geology*, **18**, 435-438.
- Dowsett, H., Barron, J., and Poore, R., 1996. Middle Pliocene sea surface temperatures: A global reconstruction. *Mar. Micropaleontol.*, **27**(1-4), 13-26.
- Dowsett, H.J., Barron, J.A., Poore, R.Z., Thompson, R.S., Cronin, T.M., Ishman, S.E., and Willard, D.A., 1999. Middle Pliocene paleoenvironmental reconstruction: PRISM2. USGS Open File Report 99-535, <http://pubs.usgs.gov/openfile/of/99-535>.
- Francis, J.E., and Hill, R.S., 1996. Fossil plants from the Pliocene sirius group, Transantarctic mountains: Evidence for climate from growth rings and fossil leaves. *Palaos*, **11**, 389-396.
- Fyles, J.G., Marincovich, L., Matthews, J.V., and Barrendrest, R., 1991. Unique mollusk find in the Beaufort formation (Pliocene) Meighen Island, arctic Canada. *Curr. Res. Part B*, Geological Survey Paper, **91**, 105-112.
- Haq, B.H., Hardenbol, J., and Vail, P.R., 1987. The new chronostratigraphic basis of Cenozoic and Mesozoic sea level cycles. *Cush. Found. Foram. Res.*, Special Publication, **24**, 7-13.
- Harwood, D.M., and Webb, P.N., 1986. Recycled marine microfossils from basal debris-ice in ice-free valleys of southern Victoria Land. *Antarct. J. US.*, **21**(5), 87-88.
- Haug, G.H., and Tiedemann, R., 1998. Effect of the formation of the Isthmus of Panama on Atlantic Ocean thermohaline circulation. *Nature*, **393**, 673-676.
- Haywood, A.M., 2001. Evaluating general circulation climate model reliability against the Pliocene geological record. Ph.D. Thesis, Reading University, Reading, Berkshire, 295pp.
- Haywood, A.M., and Valdes, P.J., 2004. Modelling Pliocene warmth: Contribution of atmosphere, oceans and cryosphere. *Earth Planet. Sci. Lett.*, **218**, 363-377.
- Haywood, A.M., Valdes, P.J., Sellwood, B.W., 2000a. Global scale palaeoclimate reconstruction of the middle Pliocene climate using the UKMO GCM: Initial results. *Glob. Planet. Change*, **25**(1-3), 239-256.
- Haywood, A.M., Sellwood, B.W., Valdes, P.J., 2000b. Regional warming: Pliocene (3 Ma) paleoclimate of Europe and the Mediterranean. *Geology*, **28**(12), 1063-1066.
- Haywood, A.M., Valdes, P.J., Sellwood, B.W., Kaplan, J.O., and Dowsett, H.J., 2001. Modeling middle Pliocene warm climates environments of the U.S.A. *Palaeontologia Electronica*, **4**(1), http://palaeo-electronica.org/2001_1/climate/issue1_01.htm.
- Haywood, A.M., Valdes, P.J., and Sellwood, B.W., 2002a. Magnitude of climate variability during middle Pliocene warmth: A palaeoclimate modeling study. *Palaeogeogr. Palaeoclimatol. Palaeoecol.*, **188**, 1-24.
- Haywood, A.M., Valdes, P.J., Sellwood, B.W., and Kaplan, J.O., 2002b. Antarctic climate during the middle Pliocene: Model sensitivity to ice sheet variation. *Palaeogeogr. Palaeoclimatol. Palaeoecol.*, **182**, 93-115.
- Haywood, A.M., Valdes, P.J., Francis, J.E., and Sellwood, B.W., 2002c. Global middle Pliocene biome reconstruction: A data/model synthesis. *Geochim. Geophys., Geosyst.*, **3**(1), December 2002.
- Kim, S.J., and Crowley, T.J., 2000. Increased Pliocene North Atlantic Deep Water: Cause or consequence of Pliocene warming. *Paleoceanography*, **15**, 451-455.
- Kleiven, H.F., Janssen, E., Fronval, T., and Smith, T.M., 2002. Intensification of Northern Hemisphere glaciations in the circum Atlantic region (3.5-2.4 Ma) - Ice-rafted detritus evidence. *Palaeogeogr. Palaeoclimatol. Palaeoecol.*, **184**(3-4), 213-223.
- Krantz, D.E., 1991. A chronology of Pliocene sea level fluctuations: The U.S. middle Atlantic Coastal Plain record. *Quaternary Sci. Rev.*, **10**, 163-174.
- Kürschner, W.M., Van der Burgh, J., Visscher, H., and Dilcher, D.L., 1996. Oak leaves as biosensors of late Neogene and early Pleistocene paleoatmospheric CO₂ concentrations. *Mar. Micropaleontol.*, **27**(1-4), 299-312.
- Leroy, S., and Dupont, L., 1994. Development of vegetation and continental aridity in northwestern Africa during the Late Pliocene: The pollen record of ODP Site 658. *Palaeogeogr. Palaeoclimatol. Palaeoecol.*, **109**, 295-316.
- Marchant, D.R., Swisher, C.C. III., Lux, D.R., West, D.P. Jr., and Denton, G.H., 1993. Pliocene paleoclimate and East Antarctic Ice-Sheet history from surficial ash deposits. *Science*, **260**, 667-670.
- Marincovich, L. Jr., and Gladenkov A. Yu., 1999. Evidence for an early opening of the Bering Strait. *Nature*, **397**, 149-151.
- Maslin, M.A., Haug, G.H., Sarnthein, M., Tiedemann, R., Erlenkeuser, H., and Stax, R., 1995. Northwest Pacific Site 882: The initiation of Northern Hemisphere Glaciation. Ocean Drilling Program. College Station, TX. In *Proceedings of the Ocean Drilling Program Scientific Reports*. **145**, 315-329.
- Mercier, J.L., Armijo, R., Tapponnier, P., Carey-Gailhrdis, E., and Lin, T., 1987. Change from late Tertiary compression to Quaternary extension in Southern Tibet during the India-Asia collision. *Tectonics*, **6**, 275-304.
- Mikolajewicz, U., Maier-Reiner, F., Crowley, T.J., and Kim, K.Y., 1993. Effect of Drake and Panamanian gateways on the circulation of an ocean model. *Paleoceanography*, **8**, 409-427.

- Ravelo, A.C., Lyle, M., Koizumi, I., Caulet, J.P., Fornaciari, E., Hayashida, A., Heider, F., Hood, J., Hovan, S., Janecek, T., Janik, A., Stax, R., Yamamoto, M., and the ODP Leg 167 Shipboard Scientific Party. 1997. Pliocene carbonate accumulation along the Californian margin. *Paleoceanography*, **12**, 729–741.
- Raymo, M.E., 1991. Geochemical evidence supporting T.C. Chamberlin's theory of glaciation. *Geology*, **19**, 344–347.
- Raymo, M.E., and Rau, G.H., 1992. Plio-Pleistocene atmospheric CO₂ levels inferred from POM d13C at DSDP Site 607. *EOS, Transactions of the American Geophysical Union*, Spring Meeting 73 (Suppl.).
- Raymo, M.E., Grant, B., Horowitz, M., and Rau, G.H., 1996. Mid-Pliocene warmth: Stronger greenhouse and stronger conveyor. *Mar. Micropaleontol.*, **27**(1–4), 313–326.
- Rind, D., and Chandler, M., 1991. Increased ocean heat transports and warmer climate. *J. Geophys. Res.*, **96**, 7437–7461.
- Ruddiman, W.F., and Raymo, M.E., 1988. Northern Hemisphere climate regimes during the past 3 Ma: Possible tectonic connections. *Philos. Trans. R. Soc. Lond. B*, **318**, 411–430.
- Shackleton, N.J., Le, J., Mix, A., and Hall, M.A., 1992. Carbon isotope records from Pacific surface waters and atmospheric carbon dioxide. *Quaternary Sci. Rev.*, **11**, 387–400.
- Sloan, L.C., Crowley, T.J., and Pollard, D., 1996. Modeling of middle Pliocene climate with the NCAR GENESIS general circulation model. *Mar. Micropaleontol.*, **27**(1–4), 51–61.
- Spicer, R.A., Harris, N.B.W., Widdowson, M., Herman, A.B., Guo, S., Valdes, P.J., Wolfe, J.A., and Kelley, S.P., 2003. Constant elevation of southern Tibet over the past 15 million years. *Nature*, **421**, 622–624.
- Thompson, R.S., 1991. Pliocene environments and climates in the western United States. *Quaternary Sci. Rev.*, **10**(2/3), 115–132.
- Wardlaw, B.R., and Quinn, T.M., 1991. The record of Pliocene sea-level changes at Enewetak Atoll. *Quaternary Sci. Rev.*, **10**, 247–258.
- White, J.M., Ager, T.A., Adam, D.P., Leopold, E.B., Liu, G., Jette, H., and Schweger, C.E., 1997. An 18 million year record of vegetation and climate change in northwestern Canada and Alaska: Tectonic and global climatic correlates. *Palaeoogeogr. Palaeoclimatol. Palaeoecol.*, **130**(1–4), 293–306.
- Wright, J.D., and Miller, K.G., 1996. Control of North Atlantic Deep Water circulation by the Greenland Scotland Ridge. *Paleoceanography*, **11**, 157–170.

Cross-references

Albedo Feedbacks
 Antarctic Glaciation History
 Astronomical Theory of Climate Change
 Atmospheric Circulation During the Last Glacial Maximum
 Carbon Isotope Variations over Geologic Time
 Cenozoic Climate Change
 Climate Change, Causes
 Climate Forcing
 Cryosphere
 Diatoms
 Foraminifera
 Glacial Eustasy
 Heat Transport, Oceanic and Atmospheric
 Marine Biogenic Sediments
 Mid-Pliocene Warming
 Mountain Uplift and Climate Change
 Neogene Climates
 North Atlantic Deep Water and Climate Change
 Obliquity
 Ocean Paleocirculation
 Ocean Paleotemperatures
 Ostracodes
 Oxygen Isotopes
 Paleobotany
 Paleocene Modeling
 Paleoclimate Modeling, Pre-Quaternary
 Paleotemperatures and Proxy Reconstructions
 Plate Tectonics and Climate Change
 Sea Level Change, Quaternary
 Thermohaline Circulation
 Weathering and Climate

PMIP

Objectives and project design

The Paleoclimate Modeling Intercomparison Project (PMIP), initiated in 1992, is an international undertaking designed to evaluate the performance and reliability of global atmospheric general circulation models by comparing past climates for periods that had significantly different external forcings from the modern climate. This initiative has been endorsed by the World Climate Research Programme (WCRP) and the International Geosphere-Biosphere Programme (IGBP). The first phase of this project (PMIP 1) initially focused on simulations of the Last Glacial Maximum (LGM, 21,000 yBP) and the mid-Holocene (6,000 yBP). The LGM was selected to assess the models' ability to simulate conditions characterized by extensive ice sheets, cold oceans, and reduced atmospheric CO₂ levels. Boundary conditions for the LGM experiment included specification of the ice sheet extent and height with lower ice elevations (Peltier, 1994) than those used in CLIMAP (1981) and an atmospheric CO₂ concentration of 200 ppm (as compared to a modern pre-industrial level of 280 ppm). Two different ocean scenarios were specified: the first employing fixed sea surface temperatures (SSTs) based on CLIMAP (1981), and the second computing SSTs from coupled atmosphere-mixed layer ocean models, assuming the same ocean heat transports as today (Joussau and Taylor, 2000). Earth's orbital parameters were also adjusted to correspond to their values 21,000 years ago (see *Eccentricity, Obliquity, and Precession, climatic*, this volume). For the mid-Holocene experiment, only two factors differed from those of the control run: the atmospheric CO₂ concentration was reduced to a pre-industrial level of 280 ppm and orbital parameters were adjusted to their 6,000 yBP values. The difference in obliquity 6,000 years ago induces only minor changes in low- to mid-latitude annual mean insolation from that of the present, but the change in precession causes an intensified Northern (and lessened Southern) Hemisphere seasonal cycle (see *Astronomical theory of climate change; Precession, climatic*, this volume). SSTs were assumed to be the same as at present; land-surface characteristics were also assumed to remain unaltered.

Simulations were compared with observations using inverse and forward-modeling techniques (Harrison, 2000). The inverse technique derives climate-related parameters by means of statistical techniques such as transfer functions, modern analog analyses, or response surfaces (see *Transfer functions, Paleobotany, Nearest living relative method*, this volume). Correlations are established between modern distributions of species and specific climate parameters, from which past climates are inferred, based on the paleodata. The forward modeling approach predicts the response of the paleoclimate proxy to the simulated climate change by means of process-based models. The predicted response is then compared with the original paleoclimate record. In PMIP, this approach has enabled closer comparisons between terrestrial vegetation and lacustrine data sets.

Model performance was evaluated using paleoenvironmental data bases (Harrison, 2000), including: (a) the Global Lake Status Data Base – a compilation of geomorphological and biostratigraphic data relating to changes in lake level, area, or volume; (b) BIOME 6000 – global paleovegetation data sets

for the LGM and mid-Holocene (Prentice and Webb, 1998; Prentice et al., 2000); and (c) the 21 ka Tropical Terrestrial Data Synthesis – a compilation of data for sites between 32°N and 33°S from diverse land-based paleoclimate proxies (e.g., pollen, lake level records, speleothems, etc.). These enable derivation of several climate-related parameters (e.g., mean temperature of the coldest month (MTCO), mean annual ground temperature (MAT), plant-available moisture (PAM), and stream runoff (precipitation minus evapotranspiration, P-E)).

More recent experiments initiated under PMIP 2, and which started in 2002, were designed to address several shortcomings identified in the initial simulations, such as a need for improved representation of ocean and vegetation feedbacks and the role of freshwater fluxes, using fully coupled ocean-atmosphere (OAGCM) and ocean-atmosphere-vegetation (OAVGCM) models. A more realistic recreation of ocean-vegetation interactions is necessary in order to account for discrepancies between climate models and land surface proxies identified in earlier experiments (e.g., in mid-Holocene monsoon intensity, Joussaume et al., 1999). Several more time periods have been added (Harrison et al., 2002; Crucifix et al., 2005). Time slices investigated in PMIP 2 now include the “glacial inception” (115,000 yBP), the early Holocene (10,000–9,000 yBP), the Younger Dryas (12,700–11,700 yBP) and the abrupt cooling event (8,200 yBP), in addition to the LGM and mid-Holocene, which were examined previously (Crucifix et al., 2005). The glacial inception experiment examines the role of vegetation and ocean feedbacks on interannual snow accumulation in northeastern North America at the end of the last interglacial period in order to better understand how an ice age is initiated. The early Holocene experiment explores the way in which climate reacts to changes in insolation and ice sheet coverage. The Younger Dryas and 8,200 year experiments examine the effects of meltwater additions on thermohaline circulation and their role in abrupt climate change.

Revised boundary conditions for the LGM under PMIP 2 include new estimates of ice sheet extent and height. In the latest reconstruction (ICE-5G), the thickness of the central Greenland ice sheet at the LGM has been reduced from that used in PMIP 1, but is still ~100–300 m thicker than at present (Peltier, 2004). Antarctica remains approximately the same, whereas the Laurentide Ice Sheet has increased in thickness relative to the earlier reconstruction. Paleoclimate databases used to define and constrain initial boundary conditions have been updated, including additional pollen and macrofossil data, revised ice sheet extent, and a river routing scheme that provides a more naturalistic representation of the hydrological cycle (Crucifix et al., 2005). A series of experiments probe the role of major feedback loops, by successively shutting off the contribution of oceans or vegetation singly, and ocean/vegetation in combination (Harrison et al., 2002). Another set of experiments simulate climate responses to 6,000 kyr BP changes in solar insolation and removal of ice sheets.

Results

The PMIP 1 LGM model runs forced by CLIMAP SSTs produced a global mean cooling of 4 °C, which was stronger over Northern Hemisphere ice sheets and landmasses, especially around the North Atlantic (Joussaume and Taylor, 2000). Computed SSTs yielded a wider range of cooling, from 2 to 6 °C below present, as well as a sharper hemispheric temperature gradient. Both types of simulations found greater LGM aridity over most northern continents and tropics. The relatively warm

CLIMAP-specified tropical SSTs led to higher land temperatures than suggested by paleotemperature proxies, except for equatorial Africa. Slab ocean models, on the other hand, generated a range of land cooling, related to the intensity of tropical ocean cooling, which in some cases was much too high. Regionally, the Afro-Asian monsoon was reduced in strength and intertropical aridity increased. The presence of ice sheets modified mid-latitude atmospheric circulation by inducing anticyclonic circulation over the ice and intensifying planetary waves. However, splitting of the jet stream (e.g., COHMAP, 1988) was not clearly seen in PMIP 1. Increased meridional temperature gradients due to the presence of ice sheets enhanced baroclinicity and shifted storm tracks eastward, particularly over the North Atlantic. While all models displayed an increase in the summer monsoon over Africa during the mid-Holocene, they tended to underestimate its intensity relative to that suggested by pollen data and lake models (Joussaume et al., 1999). The models also missed some important features, such as a colder/wetter Mediterranean growing season than at present, as implied by lake level data.

Initial PMIP 2 results show that global mean temperatures at the LGM are 3–6 °C below present, with a median value of –4 °C (Masson-Delmotte et al., 2006). Polar amplification (ratio of polar to global annual mean temperature change) at the LGM ranges between 2.1 and 2.6 for Greenland, but only 1.2–1.9 for central Antarctica. However, the models underestimate the extent of glacial cooling for Greenland, whereas the polar amplification is realistically simulated for Antarctica. PMIP 2 simulations find mid-Holocene global mean temperatures close to present values (Masson-Delmotte et al., 2006). Temperatures are 0.35°–0.9° C higher in central Greenland during the mid-Holocene, and 0.1°–0.7° C warmer in Antarctica. The OAGCMs reproduce mid-Holocene seasonal cycle and regional changes, such as higher mid-latitude summer temperatures in many regions, which stem from the altered precessional parameters (Zhao et al., 2005). They produce consistent changes in summer monsoon behavior, such as increased precipitation over northern India and Sahelian Africa, and strengthened monsoon flow from the western Pacific warm pool to the Indian Ocean, although the areal extent and magnitude of the monsoons appears model-dependent. The changes in monsoonal flow appear to be associated with a reduction in Hadley-style circulation and a westward shift in Walker-type circulation from the Pacific to Indian Oceans (Zhao et al., 2005).

Illuminating insights have emerged from new paleodata used to validate the PMIP 2 climate models. For example, pollen and macrofossil data reveal that the warmest period during the Holocene (see *Hypsithermal*, this volume) varied sharply over time in different regions, beginning as early as 10,000 years ago in Alaska-eastern Siberia, and ending less than 6,000 years ago in northeastern North America. This was in part related to lingering remnants of the Laurentide Ice Sheet (Crucifix et al., 2005). New information about ice sheet history also contributes to the climate modeling efforts. For example, catastrophic outflow from Glacial Lake Agassiz had long been considered to be the main source of freshwater outflow that led to a decrease in rate of North Atlantic Deep Water Formation, presumably triggering the Younger Dryas cooling. Recent dating of glacial landforms suggests, instead, that ice retreat around southern and western Hudson Bay occurred approximately 1,000 years after the start of the Younger Dryas (Lowell et al., 2005), casting doubt on the role played by Lake Agassiz. Moreover, detailed geophysical models of the Laurentide Ice

Sheet retreat, constrained by ^{14}C -dated geomorphological features, relative sea level data, and geodetic measurements point to large meltwater influxes via the Arctic Ocean, Fram Strait, into the North Atlantic Ocean during the Younger Dryas (12,700–11,700 yBP) (Tarasov and Peltier, 2005). Freshwater input via this route rather than outflow from Lake Agassiz may have led to the abrupt Younger Dryas cooling.

Conclusions

PMIP, by comparing and contrasting results from a number of general circulation models under climate regimes that differ significantly from the present, enables one to test the ability of these models to reproduce key elements of climate, such as temperature, precipitation, atmospheric dynamics, and seasonal and regional variations. Results to date point to the importance of using fully coupled ocean-atmosphere models and the role played by vegetation. The sensitivity of various climate features, such as changes in the North Atlantic Oscillation or the role of tropical SSTs, to altered global conditions is also best evaluated with a “super-ensemble” of models. Concomitant with the PMIP modeling program is the growth and expansion of supporting paleoclimate databases that are used to validate these models.

Vivien Gornitz

Bibliography

- CLIMAP Project Members, 1981. The surface of the ice-age earth. *Science*, **191**, 1131–1137.
- COHMAP Members, 1988. Climatic changes of the last 18,000 years: Observations and model simulations. *Science*, **241**, 1043–1052.
- Crucifix, M., Braconnot, P., Harrison, S.P., and Otto-Bliesner, B., 2005. Second phase of Paleoclimate Modelling Intercomparison Project. *EOS*, **86**(12), 264–265.
- Harrison, S.P., 2000. Palaeoenvironmental data sets and model evaluation in PMIP. In Braconnot, P. (ed.), Proceedings of the Third PMIP Workshop, 1999. WCRP-111 WMO/TD-1007.
- Harrison, S.P., Braconnot, P., Joussaume, S., Hewitt, C., and Stouffer, R.J., 2002. Comparison of paleoclimate simulations enhances confidence in models. *EOS*, **83**(40), 447–448.
- Joussaume, S. et al., 1999. Monsoon changes for 6000 years ago: Results of 18 simulations from the Paleoclimate Modeling Intercomparison Project (PMIP). *Geophys. Res. Lett.*, **26**, 859–862.
- Joussaume, S., and Taylor, K.E., 2000. The Paleoclimate Modeling Intercomparison Project. In Braconnot, P. (ed.), Proceedings of the Third PMIP Workshop, 1999. WCRP-111 WMO/TD-1007.
- Lowell, T.V., Fisher, T.G., Comer, G.C., Hadjas, I., Waterson, N., Glover, K., Loope, H.M., Schaeffer, J.M., Rinterknecht, V., Broecker, W., Denton, G., and Teller, J.T., 2005. Testing the Lake Agassiz meltwater trigger for the Younger Dryas. *EOS*, **86** (40), pp. 365, 372.
- Masson-Delmotte, V. et al., 2006. Past and future polar amplification of climate change: Climate model intercomparisons and ice-core constraints. *Clim. Dyn.*, **26**, 513–529.
- Peltier, W.R., 2004. Global glacial isostasy and the surface of the ice-age Earth: The ICE-5G (VM2) model and Grace. *Ann. Rev. Earth Planet. Sci.* **32**, 111–149.
- Peltier, W.R., 1994. Ice age paleotopography. *Science*, **265**, 195–201.
- Prentice, I.C., and Webb, T. III, 1998. BIOME 6000: Reconstructing global mid-Holocene vegetation patterns from palaeoecological records. *J. Biogeogr.*, **25**, 997–1005.
- Prentice, I.C., Jolly, D., and BIOME 6000 participants, 2000. Mid-Holocene and glacial-maximum vegetation geography of the northern continents and Africa. *J. Biogeogr.*, **27**, 507–519.
- Tarasov, L., and Peltier, W.R., 2005. Arctic freshwater forcing of the Younger Dryas cold reversal. *Nature*, **435**, 662–665.
- Zhao, Y., Braconnot, P., Marti, O., Harrison, S.P., Hewitt, C., Kitoh, A., Liu, Z., Mikolajewicz, U., Otto-Bliesner, B., and Weber, S.L., 2005. A multi-model analysis of the role of the ocean on the African and Indian monsoon during the mid-Holocene. *Clim. Dyn.*, **25**, 777–800.

Cross-references

Astronomical Theory of Climate Change
 CLIMAP
 COHMAP
 Eccentricity
 Holocene Climates
 Hypsithermal
 Last Glacial Maximum
 Late Quaternary-Holocene Vegetation Modeling
 Nearest-Living-Relative Method
 Obliquity
 Paleobotany
 Paleoclimate Proxies, an Introduction
 Precession, Climatic
 Paleoclimate Modeling, Quaternary
 Quaternary Climate Transitions and Cycles
 Transfer Functions
 The 8200-year BP Event
 Younger Dryas

POLLEN ANALYSIS

Introduction

Pollen analysis is a scientific method that can reveal evidence of past ecological and climate changes: it combines the principles of stratigraphy with observations of actual (modern) pollen-vegetation relationships in order to reconstruct the terrestrial vegetation of the past.

Early history

Pollen analysis plays a critical role in climate change studies during the Quaternary (Fægri and Iversen, 1975) and is the single most important branch of paleoecology for the late Pleistocene and Holocene (Roberts, 1998). Its scientific scope is broad since it encompasses knowledge from many disciplines including botany, geology, ecology, climatology and archeology. The extent to which a pollen analysis study may be slanted toward botanical, ecological or geological questions will depend on the sedimentary deposits analyzed and the researcher's background. Pollen analysis may be utilized for the evaluation of vegetation changes occurring as recently as the Holocene. It may also be applied as far back as the late Devonian, when the first seed plants evolved, although presumably not until the Pennsylvanian or later did distal germination of the pollen evolve in the early gymnosperms (Traverse, 1988, p. 163).

A brief summary of key historical developments shows how pollen analysis evolved as a methodology, and how distinct disciplinary characteristics have been imprinted upon it. An early history of pollen analysis is found in the book entitled “An Introduction to Pollen Analysis,” written by G. Erdtman (1943). Erdtman recounts how European scientists had laid the groundwork for pollen analytical studies in the late nineteenth and early twentieth centuries. The Swiss geologist, J. Früh had identified many of the common tree and herb pollen types, and spores from ferns and mosses, found in the regional environment, in an 1885 paper. The Swedish geologist F. Trybom, in 1888 showed that pine and spruce pollen grains were found in sediment samples from the bottoms of Swedish lakes. The microscopist G. Lagerheim introduced a quantitative aspect: he and N. O. Holst published a paper in the Geological

Survey of Sweden, in 1909, entitled, “*Postglaciala tidsbestämningar*.” In this paper, common northern European tree genera pollen had been identified (i.e., *Pinus* (pine), *Betula* (birch), *Alnus* (alder), *Ulmus* (elm), *Corylus* (hazel), *Fraxinus* (ash), *Quercus* (oak), and *Tilia* (basswood)) from different levels of lacustrine sediment layers within Kallsjö bog in southern Sweden. Lagerheim identified pollen within the layers, and presented the quantity of each genus as a percentage of all pollen; furthermore, he examined the shifts in these pollen percentages from layer to layer. Lagerheim (as translated by Erdtman, 1943, p. 4) concluded that the varying pollen frequencies are “a reliable method with which to follow, step by step, from one layer to another, the immigration of all plants whose pollen or spores are preserved as fossils as well as the relative frequency of these species.” A decrease in the percentage of pine pollen from the lower to the upper layers caused Holst to speculate that, “the pine disappeared from southernmost Sweden in historical times, exterminated probably by the activity of man.”

Lennart von Post (a pupil of Lagerheim at the University College of Stockholm) transformed pollen analysis into a refined method in Quaternary geology, he “indicated how pollen analysis should be applied in order to give information on problems related to Quaternary geology and paleontology (Erdtman, 1943).” Von Post drew the first pollen diagrams and defined distinctive tree pollen “horizons” and “limits” in 1909. A “spruce pollen limit” or “spruce horizon” could be used as a datum line to trace time synchronous horizons in different bogs within a small area. In 1916, von Post presented a paper with many pollen diagrams at the Sixteenth Meeting of Scandinavian Naturalists in Oslo, examining the pollen of forest trees in bogs in southern Sweden (von Post, 1967 [1916]). His presentation is considered the realization of pollen analysis as a science.

Thus by the early 1900s, the basic principles underlying pollen analysis were already in place. Plants produce pollen grains, which are dispersed and then preserved in sediments for thousands and exceptionally even millions of years. Then, samples taken from a column of sediment will show shifts in pollen occurring over time, assuming that the original stratigraphy has been maintained. Any apparent shifts may be interpreted as due to changes in vegetation, perhaps forced by climatic, geological, or ecological factors.

Subsequently, the number of pollen studies vastly expanded to include other geographical regions and other geological time periods. The advent of radiocarbon dating and its extensive application in the late 1900s allowed relatively firmer chronologies to be developed from the late Quaternary. Extensive research of pre-Pleistocene deposits is also carried out by geologists (Traverse, 1988). Pollen analysis has also evolved with the increasingly interdisciplinary aspect of many sciences (including geology and ecology), as results from pollen analysis are now interpreted with respect to site data of a limnological, isotopic, or microfaunal nature, to name just a few.

Theory of pollen analysis: the pollen-vegetation relationship

The basic theory of pollen analysis is that pollen is released by plants, transported through the air, and then deposited uniformly upon the Earth’s surface. In fact, the pollen represents the actual surface vegetation growing over an area (the area to be defined by the researcher). The pollen that is transported in the air is called *pollen rain*. The pollen rain may be deposited over land or any water body. The pollen that is deposited

in lakes or other water bodies (such as bogs and marshes) sinks to the bottom of the basin and becomes part of the accumulating lacustrine or peat sediment. When pollen is deposited in water, the pollen’s outer layer may remain practically intact for thousands and perhaps even millions of years. Thus, the pollen becomes part of the fossil record. This fossilized representation of the terrestrial vegetation may then be used to interpret the vegetation, or plant geography, which existed in the past. Furthermore, since climate is one of the key determinants of the plant taxa growing at any place on the Earth’s surface, the fossil pollen may be used to interpret past climates. This is highly useful when attempting to reconstruct the Earth’s climate and ecology, as it existed before any instrumental records or observations made by humans.

A fundamental operating assumption is that the pollen-vegetation and vegetation-climate relationships that can be observed now also operated in the past (Roberts, 1998). This is the principle of *uniformitarianism*, which is applied in many disciplines related to Earth history. Paraphrasing from Roberts (1998, p. 29) and applying to the field of pollen analysis, the uniformitarian assumptions are: (a) the environmental factors affecting present-day vegetation are understood, (b) a species’ natural history has not changed over time, (c) the vegetation was in equilibrium with its environment (this means that the environment remained unchanged during the plant’s lifespan), (d) modern analogs exist, (e) the origin (taphonomy) of the fossil pollen assemblage can be established, (f) the pollen assemblage has not been biased by contamination (from outside the sample) or differential preservation, and (g) the pollen can be identified to a meaningful taxonomic level.

In practice, all these assumptions are never perfectly met. In fact, pollen analysis as applied to the fields of paleoclimatology and paleoecology exemplifies the concept succinctly phrased by the ecologist Edward Deevey (1969), “coaxing history to conduct experiments.” Essentially, the sciences of paleoecology and paleoclimatology do not utilize data from controlled experiments conducted in an artificial laboratory. Instead, the experiment has been conducted by nature, in the natural environment, in the geological past. The data, or evidence, from these experiments remains within the natural environment, waiting to be retrieved and interpreted by the discerning researcher via a variety of tools.

Pollen production and dispersal

Pollen and spores are produced by green plants (Viridophytae) (taxonomy according to Pennisi, 2003). What is commonly called “pollen” comes from the conifers (sometimes referred to as gymnosperms) and angiosperms. Green plants that are neither angiosperms nor conifers produce what are commonly called “spores.” Mosses, lycophytes, and ferns are green plants that produce spores. Both pollen and spores are typically identified by the researcher conducting the pollen analysis.

Pollen is produced in a flower’s anthers (microsporangia or pollen sacs). It is the haploid microgametophyte, male partner, in sexual reproduction. Pollen grains germinate on the female (stigma) surface by forming a pollen tube, which emerges through one of the apertures in the pollen grain wall (Twell, 2000). In pollen analysis, the scientist studies those pollen grains that have been dispersed, but rather than germinating, have accumulated as sediment. This is because the pollen shape and surface texture, which is called morphology, is highly distinctive when magnified.

The most striking structural feature of the pollen or spore grain is the tough, resistant outer coat, called the exine, which protects the reproductive cells from environmental injury. Beneath the exine is a second major layer surrounding the pollen grain protoplasm, called the intine. The exine is composed of a material called sporopollenin, which is a very inert C–H–O compound (Traverse, 1988). Sporopollenin has been identified in acritarchs in Precambrian rocks, and is a component of many higher green plants. What is unique about sporopollenin is its ability to withstand desiccation and oxidation. Sporopollenin within a sediment matrix is able to survive for extended time periods, even as the other components of the pollen or spore degrade. Oxidizing, highly alkaline, and high temperatures environments are likely to accelerate sporopollenin's degradation. In short, the accumulating sediment within a water body is an ideal place to store the exine of pollen and spores. This exine may survive for thousands to even millions of years in a non-oxidizing environment, and thus becomes the fossil utilized in pollen analysis.

The pollen of different plant taxa manifest considerable variation in size, shape and surface characteristics. To the naked eye, it is a fine granular or powdery substance. Pollen grains may vary in length from 5 µm in *Myosotis* to more than 200 µm in the *Curcubitaceae*; the shape varies from spherical to elliptical to more unusually and irregularly shaped objects. The exine has a three-dimensional patterned surface, several microns deep, called sculpturing, which helps the grain adhere to insect pollinators and the stigma. The exine does not develop over certain regions; these define the positions of the germination apertures. Apertures also show wide variation in shape, ranging from elongated furrows to circular pores, and combinations of furrows and pores. The pollen's shape, aperture number and position, and exine sculpturing are unique taxonomic features that allow the identification of species, genus, or family (Twell, 2000).

The dispersal of the pollen strongly conditions the pollen-analytical studies. Fægri and Iverson (1975) describe the different means of pollen production and dispersal. Those plants that are pollinated by wind-carried pollen, called anemophilous, produce the greatest quantities of pollen. In zoophilous plants, the pollen is carried from the anther of one flower to the stigma of another by an animal vector such as insects, birds or bats; these plants produce relatively less pollen. Hyp-hydrogamous (pollination under water) and obligate autogamous plants produce very little pollen and are rarely analyzed. The earliest pollen studies involved the anemophilous species and even now, wind pollinated species are those most commonly addressed. Because of the larger quantities of pollen dispersed, the anemophilous species are more likely to leave pollen deposited within the sediment. Typical quantities of pollen produced by mid-latitude forest tree species are: 10,000 pollen grains in a single *Betula* anther, 28 million pollen grains produced by 10-year old *Betula* branch system, up to 350 million pollen grains produced by a 10-year old *Pinus* branch system (Fægri and Iverson, 1975). A common mid-latitude zoophilous tree, *Acer* (maple), may have only 1,000 pollen grains per anther. Generally, those trees reaching the upper canopy will produce the most pollen, while the shrub and herb plants under the canopy will produce less. Zoophilous species are usually more frequent in the lower strata. Pollen production will also vary seasonally and even annually.

Pollen analysis is based upon the assumption of uniform dispersal of this great quantity of pollen grains (Fægri and

Iverson, 1975). The pollen of wind-pollinated species should be dispersed by the wind, then settle out and be deposited over a region, including any lakes and bogs, in which strata they will remain, until finally being retrieved by the researcher.

All aspects of pollen production and dispersal continue to be studied by botanists and ecologists, more detailed information may be found in the specialist literature. Since the earliest pollen studies were based in the temperate northern European forests, the earlier methodologies were constructed around the life history of the local, predominantly anemophilous species. Newer studies also address the tropical and even high-latitude habitats. Understanding key species in pollen production in tropical habitats is especially challenging as the number of species composing the local vegetation formations is high, and many are zoophilous.

Pleistocene palynology

Living organisms evolve over time. The assumption that the ecological and climatological affinities of extant vegetation have the same paleoecological and paleoclimatological affinities as paleovegetation (interpreted via pollen), is accepted as generally holding true for the Pleistocene, that is the most recent 1.8 million years. This conclusion is based on the studies of Neogene fossil flora remains, both megafossils and microfossils. Fossil pollen are usually identified by genus, although sometimes a species identification is possible. Some pollen can only be identified to its taxonomic family, a good example being the grasses (*Poaceae*) and sedges (*Cyperaceae*). By the beginning of the Pleistocene, nearly 100% of flora species recognized are still extant. Nearly 100% of extant plant genera are present by 10 million years ago; by 20 million years ago, practically all angiosperm remains are referable to extant families (Traverse, 1988). Thus, as one moves from the distant geological past to the present, the precision with which a researcher can link the pollen fossil to an extant plant, and hence that plant's natural history, improves. Thus returning to the uniformitarian assumptions given by Roberts (1998), we see that at least the first two assumptions (the environmental factors are understood, a species natural history has not changed over time) can be applied with greater certainty to the most recent geological time – the Pleistocene and the Holocene. Hence, pollen analysis applied to Pleistocene and Holocene sediments may aim for relatively precise determinations of climate and environment. Pollen analysis applied to fossils of the last 10 million years may still yield information relevant to climate and ecology, since most of the plant genera were extant, but the questions will have more of a geological flavor (Traverse, 1988).

The sample site and laboratory technique

Field sites

Determining which site was a suitable pollen collection basin will have a decisive impact upon the relevance of the final results. Equipment and the natural landscape are major limiting factors. Ideally the basin should have accumulated sediment continuously over time, thus its geological origins should be clear. From an ecological perspective, one wishes to know the distance of the pollen from the source vegetation.

The aim of the field work is to collect uncontaminated samples, to define as precisely as possible the conditions under which the samples were taken, and to characterize the sediments and stratigraphy (Fægri and Iverson, 1975). The investigator must evaluate and balance two (sometimes competing)

factors: the field sites actually available, and the spatial scale which the pollen analysis will address. Most frequently, the investigator is seeking to reconstruct changes in the natural undisturbed vegetation – present day vegetation is frequently altered by human activity and undisturbed sites are usually kilometers to hundred of kilometers from roads. In addition, pollen is best preserved under anaerobic conditions – those at the bottom of a peat bog or lake.

Given the historical roots of pollen analyses in the northern temperate latitudes, the ideal sedimentary basin is a lake or bog of roughly 5,000 m² which collects windblown pollen (Fægri and Iverson, 1975). The pollen sources are defined as local, regional, and extra-regional (Fægri et al., 1989) – these divisions are usually only qualitative (Figure P82). The researcher usually wishes to describe the “regional” vegetation; very approximately, the vegetation within one kilometer of the basin’s center. The relatively small basins allow this interpretation of a “regional pollen signal.” Since the pollen deposited should be transported by wind, input to the basin from streams must be avoided – this would bring in pollen from outside the “region,” and also pollen eroded from older sediments.

In the first pollen studies conducted in northern Europe and Scandinavia, a single person might have cut samples from exposed peat deposits. Peat sediments were easy to examine, pollen was frequently well preserved within the peat and mud matrix, and continuous sedimentation was possible for approximately 10,000 years; that is, since the last deglaciation.

Pollen analyses have expanded in their scientific and geographic scope. The ideal 5,000 m² size catchment basin is simply unavailable in the lower latitudes and tropics, thus other catchments may be utilized. Small basins also effectively limit the geological time span of the sediment, since they are almost always the by-product of a geomorphological regime occurring after the last glaciation. Hence, large basins are studied: wind-blown pollen is collected from a much larger “region,” yet sediment cores may be longer and hence encompass more time. Pollen accumulated in marine sediments may be very useful in paleoclimatological studies. Rat middens and cave deposits have been frequently utilized in the arid southwest of North America. Archeological sites also contain pollen. These

sedimentary accumulations have the disadvantage of being relatively stratigraphically discontinuous; however, in more arid regions they still provide valuable information.

Sampling methods have also advanced. Piston corers of varying degrees of sophistication are now often utilized: they consist of drill bit that can bore into the ground, a sampling tube into which the sediment slides, a piston which maintains a vacuum inside the tube, and extension rods connecting the sampling tube to the piston, allowing the entire apparatus to be taken in and out of the ground. A typical sediment core is 5–10 cm in diameter and from 1 to more than 10 meters in length, the core is retrieved in sections of usually a meter’s length or less. The coring operation may be conducted on dry land or on water. In the latter case, the machinery and people operating the coring equipment must utilize a dry and level platform: the platform may range from portable wooden planks, to the drilling rigs aboard modern research sea vessels, even to the ice covering a lake. The goal is always to reach the deepest depths, while retrieving the most continuous sections of sediment to the surface. The depths achieved, and the continuity of the core, depend mostly on the types of sediment cored and the equipment being used. Marine sediments, usually composed of clays and silts, are easier to penetrate and may yield cores in the range of tens to hundreds of meters. Lacustrine cores may exceptionally exceed ten meters in depth, peat and lake sediments are relatively soft and easy to penetrate. However, changes in the climatic or geomorphological regime must be expected as one proceeds deeper into any sediment, essentially going back in time, and thus coarser sediments such as sands, gravels, and even bedrock may be encountered at the bottoms of the collecting basins. Indurated or coarse sediments, or bedrock, effectively stop the drilling equipment.

Laboratory techniques

The laboratory work comprises the separation of pollen grains from their sediment matrix, and then identification of the pollen grains. Work in the laboratory is the most time consuming aspect of pollen analyses, and the identification of the pollen is the most beautiful aspect of the study. The sediment (in cores, blocks, or even sub-samples taken from other studies) retrieved during field work must be described, evaluated for any possible lack of stratigraphic continuity, and then sub-sampled. Sub-samples are taken from the cores or sediment blocks, the researcher must decide at what distance interval to sample. A closer sampling interval usually increases the time resolution of the study.

The description of the sediment combined with any geological study of the sampling site should allow a geological reconstruction of the site’s genesis over time. Furthermore, a correct interpretation of the changing vegetation or climate based upon the pollen data requires knowledge of the depositional environment. The description of sediment may follow geological or soil classification schemes. Two commonly utilized classification schemes are the “Fægri and Gams” and the “Troels-Smith” descriptions. “Fægri and Gams” is a synthetic-interpretive approach in which the sediment’s description implies its genesis. The “Troels-Smith” scheme is an analytic-descriptive approach. A referenced system of notation and graphic symbols (called *signatures*) exists for each system, the signatures are usually presented in the final pollen diagram. Fægri et al. (1989) emphasized that classification should include the identification of deposit-forming vegetation (e.g., sedges, mosses, wood), degree of humification, mineral content and grain size. Basins formed by glacial action in the temperate

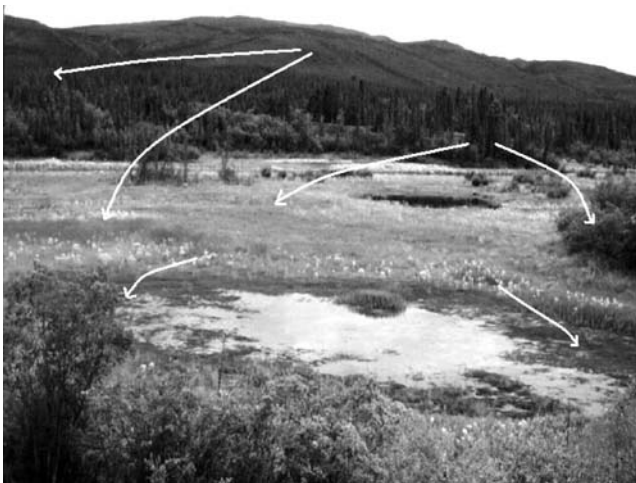


Figure P82 Schematic representation of wind deposition of pollen from local, regional, and extra-regional sources.

mid-latitudes, used in early pollen studies, typically show a change (over several thousand years) from minerogenic sediment to organic muds or gyttja – this change is a response to the gradual development of soil and vegetative cover. In the tropical basins, the more dramatic changes in the sedimentary matrix are usually linked to fluctuations in water level.

Fossil pollen is separated from the sediment matrix in a laboratory. Essentially, the extraneous, non-pollen material must be removed from the sediment samples so that the final preparation contains only the pollen, which will be easily visible and unobscured when viewed under magnification. The laboratory and all air, water and supplies that enter the room must be pollen-free, only the samples themselves should contain pollen. A typical pollen laboratory is furnished with a fume hood, centrifuge and water baths.

The quantity of sediment needed for a single sample is usually small, approximately 1 cubic centimeter for lacustrine sediments, and 10 cubic centimeters or more for marine sediments – hundreds to thousands of pollen grains may be hidden within. To allow the absolute pollen frequency count or the density of the individual pollen taxa in the sediment to be determined, a known quantity of a *marker* is commonly added to the sample. Common markers are polystyrene spheres or a pollen taxon that is clearly foreign to the native vegetation.

Filters and chemicals are used to remove the extraneous material. The large majority of pollen grains have a minimum diameter between 7 and 125 microns, while the supporting sediment matrix ranges from finer-grained clays to coarser-grained sands. Filters or sieves can be used to separate these fine and coarse materials from the pollen containing sediment; the researcher decides which filter sizes to utilize. The basic chemical processing steps applied to a measured quantity of sediment are the addition of alkalis (KOH or NaOH solution) to remove and deflocculate humic acids (associated with peat and organic matter), and acid baths to chemically remove the silt and fine sand. Hydrochloric acid removes the calcium carbonate components. Siliceous sediments are dissolved by hydrofluoric acid. Gravity separation, utilizing what are known as “heavy liquids” (e.g., bromoform, stannic chloride, or zinc chloride) may be used as alternatives to the hydrofluoric acid treatments. Both the acids and heavy liquids are noxious and must be carefully handled. Excessive use of acids may degrade the pollen exine. Different samples will react quite differently to the same treatments; the researcher must adjust methods to fit the nature of the sediment. It is important that no pollen should be lost during this processing, and the pollen types must not respond differentially to the physical and chemical treatments (Traverse, 1988; Fægri et al., 1989).

The prepared samples containing only pollen may be stained in order to increase contrast in the exine’s features. The sample is mounted on a microscope slide; common mounts are glycerol and silicone oil. It is crucial that the grains can be turned within a liquid medium so that all sides are visible.

The next step is to make a taxonomic identification of each pollen grain, and an absolute count of frequency. The researcher is aiming to define two quantities: *percentage* of total pollen for each pollen type found; and *pollen concentration*, which is expressed as the number of pollen grains per unit volume of the sediment. These two quantities, combined with the eventual determination of the rate of sedimentation, allow the calculation of two additional variables: the *sediment matrix accumulation rate*, expressed as thickness of sediment accumulated per unit of time; and *pollen deposition rate* (also called

pollen accumulation rate, or *pollen influx*), which is expressed as number of grains accumulated per unit area of sediment per unit time (Davis, 1969). It is the *pollen percentages* of the taxa of interest, usually graphically presented on a single page, that are considered the main result of the field work and laboratory analysis.

The brief description here cannot do justice to the time intensive aspect of the pollen analyses. Most identification is done with an optical microscope; the magnification necessary ranges from 250× to 1,000×. This is the resolution needed to evaluate the three-dimensional shape of the pollen grain, the number and shape of the apertures, and exine structure and sculpturing (examples in Figure P83). Identification is based upon a combination of modern samples in a pollen herbarium, and pollen and spore identification keys. A “pollen herbarium” is essential for learning to identify a plant taxon by its pollen. Herbariums are usually created by individual researchers, or members of a research institution: at their smallest, they may be composed of only the key vegetation relevant to the studied region, while at their largest they may contain multiple exemplars of pollen collected from different individuals, and include both common wind-pollinated and rare insect-pollinated species. Identification keys are usually composed for the native flora of a specified geographic region: the “Identification Key for Northwest European Pollen Flora” compiled primarily by Fægri and Iversen (1975), and the “Key to the Quaternary Pollen and Spore of the Great Lakes Region,” by McAndrews et al. (1973) are examples of pollen keys that are utilized extensively for research in the appropriate geographic regions. In these keys, most grains are identified to the taxonomic level of genus, others to species, and a few only to family. There have been many recent efforts to compile pollen keys for other geographic regions including tropical, Southern Hemisphere, African and Asian flora.

The shape of the pollen or grain, and the arrangement of the apertures, can be classified into “morphological types (Traverse, 1988)” or “pollen classes (Fægri and Iversen, 1975).” The exine morphology also has its own vocabulary. However, morphology terminology has been, and still to a great extent is, a controversial and even chaotic subject (Fægri et al., 1989). The morphological reference the researcher utilizes will depend on the area and geologic age of the samples being studied. It can be difficult to discern the features of a fossil pollen grain even at high magnification. The identification and counting of pollen grains has still not been successfully automated. A sample that contains only pollen grains, all of which are in perfect form, may lend itself to computerized image recognition. In reality, most samples still contain extraneous material (ranging from charcoal to mineral dust) and pollen grains that have been folded and broken – the trained human eye still making the more definitive identification.

The pollen record

Typically, the researcher takes a few hours to examine the pollen from a single sediment sample. A minimum number of pollen grains, the *pollen sum*, must be counted in order to ensure the statistical robustness of the pollen percentages; this number varies from approximately 300 to 1,000 grains. The number counted will depend on the pollination characteristics of the vegetation; for example, pine trees produce greater quantities of pollen than other typical North American deciduous genera (such as beech and elm) and therefore pine pollen is said to “swamp” the pollen counts. A large pollen sum may

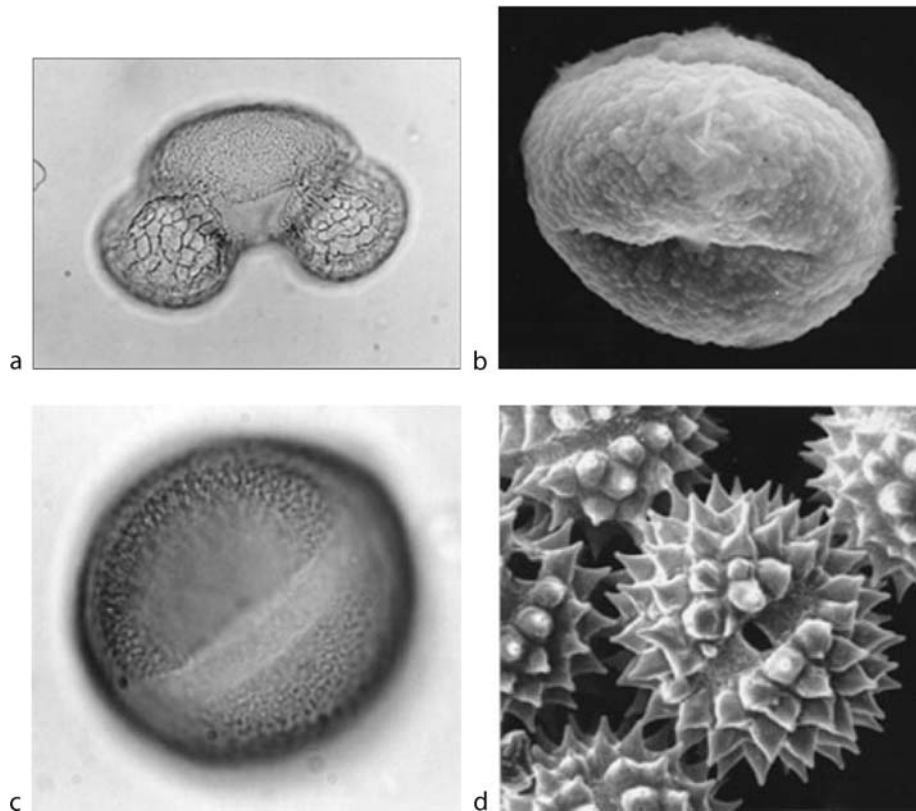


Figure P83 (a) Light micrograph of *Pinus palustris* P. Miller. *Pinus* is a vesiculate pollen grain, the two hemispheric bladders show reticulate sculpturing; the cap of the body (proximal surface) shows verrucate sculpturing (terminology follows Faegri and Iversen, 1975). Courtesy of Gretchen D. Jones, USDA-ARS, APMRU. (b) Scanning electron micrograph of *Quercus alba* L. *Quercus* pollen often has three furrowed apertures called colpi, this grain is tricolpate, the sculpturing is verrucate (terminology follows Faegri and Iversen, 1975). Courtesy of Gretchen D. Jones, USDA-ARS, APMRU. (c) Light micrograph of *Acer saccharum* H. Marshall var. *saccharum*. *Acer* pollen is tricolpate, the exine is relatively thick with spines, echinate sculpturing (terminology follows Faegri and Iversen, 1975). Courtesy of Gretchen D. Jones, USDA-ARS, APMRU. (d) Scanning electron micrograph of *Aster sericeus*. *Aster* pollen, and many genera in the Asteraceae family, have three colpi, each with a pore; this grain is tricolporate, the sculpturing is reticulate (terminology follows Faegri and Iversen, 1975). Courtesy of Gretchen D. Jones, USDA-ARS, APMRU.

be used in order to discern abundance patterns of less-prolific pollen producers. It is also common to exclude some pollen taxa from the pollen sum: grains commonly excluded are those from aquatic plants, ferns, or all non-arboreal plants. The end result of the pollen analysis is a *pollen record* (Faegri et al., 1989), or a numerical matrix of pollen taxa identified per depth sample.

Commonly, after the pollen record has been compiled, the various types of pollen and spores encountered are calculated as percentages of the pollen sum. Admittedly, “percentage data have a built in bias, because the percentages must total 100%, and the percentage of pollen ‘A’ therefore influences the percentage of pollen ‘B’” (Traverse, 1988). Nevertheless, a *pollen diagram*, which presents the percentages in a simple graphic form, continues to provide easily readable information, relevant to further ecological or climatological interpretation. If the researcher has sufficient chronological control to calculate sedimentation rates, then pollen deposition rates may also be calculated and graphed. The graphical format of pollen deposition rates is similar to the pollen percentage diagrams graphs, although usually only a few key taxa are presented.

Ideally, the pollen percentage diagram should contain chronostratigraphic, lithostratigraphic, and biostratigraphic data

(Faegri et al., 1989). The chronostratigraphic element, on the ordinate axis, is composed of the depth scale, radiometric or relative dates, and any geological age assignments. The lithostratigraphy is usually a single column utilizing symbols, with accompanying legend, which conveys sediment information. The biostratigraphy is the heart of the pollen diagram: the *pollen spectrum*, which are the relative frequencies (percentages) of the various types of pollen per single sample, on the abscissa. Graphically the spectrum are shown as histograms, or as points which connect from depth to depth forming a “sawblade.” A variety of diagram types is found (see Figures P84 and P85). The most common diagram type presently constructed is termed the *resolved diagram* (Faegri et al., 1989); the varying percentages of many taxa are displayed, side by side.

The pollen percentage diagrams may contain any number of depth points, and their respective pollen spectra. The more spectra a diagram contains, the more it becomes practical to sub-divide the biostratigraphic portion of the diagram into pollen zones. A “zone is a common, usually informal, term for a minor stratigraphic interval in any category of stratigraphic classification (Hedberg, 1972 in Faegri et al., 1989).” Zones may be defined by presence/absence relations or by percentage variations of key pollen taxa. Pollen assemblage zones have

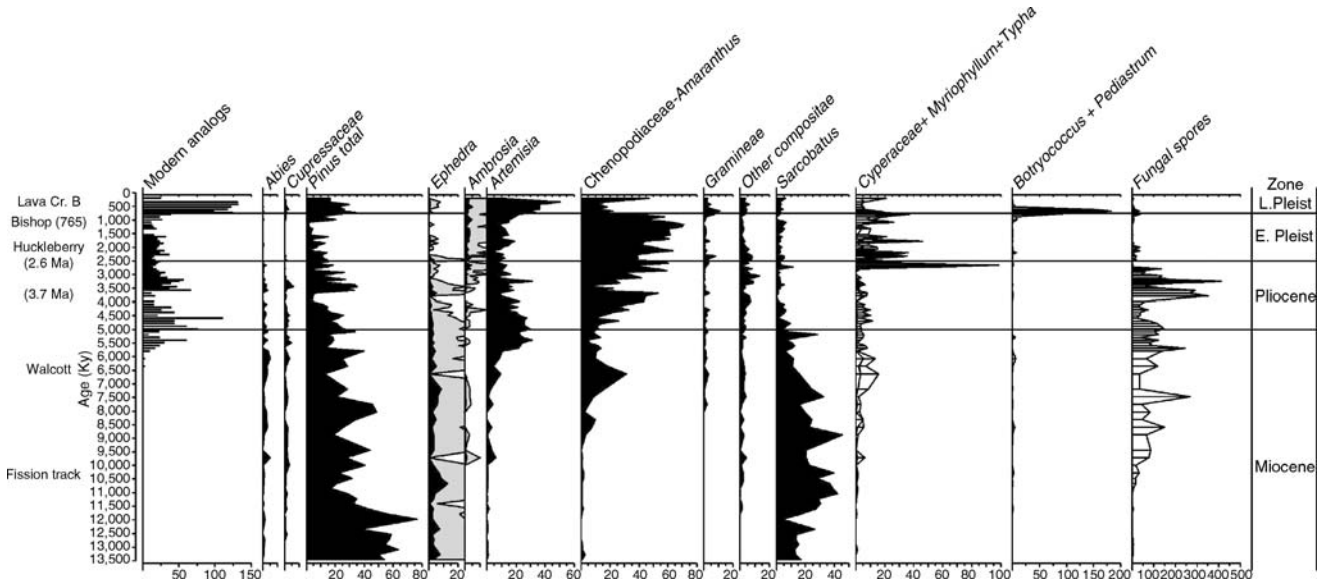


Figure P84 Percentage pollen diagram from Amoco Production Company's Bridge well, Great Salt Lake. The volcanic ashes utilized for age control are at the far left, along with a chronostratigraphic ordinate axis. The modern analog index has been plotted, along with ten common pollen taxa utilized in the pollen sum. The shaded sawtooth curve for "Ephedra and Artemisia" represents a 10× exaggeration of the percentages. "Cyperaceae + Myriophyllum + Typha" are wetland plants. "Botryococcus + Pediastrum" are algae. Geological time periods appear to the far right (from Davis and Moutoux, 1998). Reproduced with permission from the author.

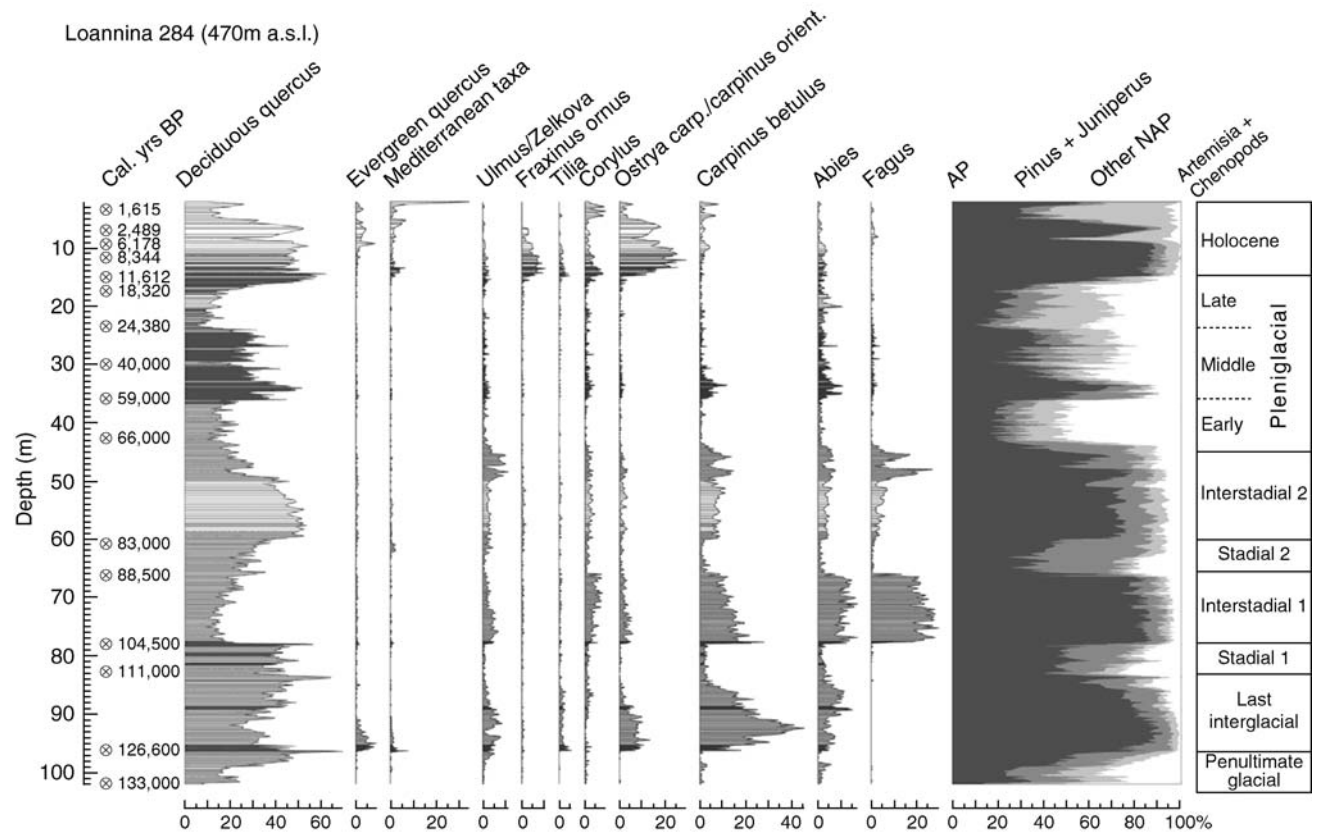


Figure P85 Pollen percentage diagram from borehole loannina 284. The spectra are presented as histograms connected by a sawtooth curve. Depth is on the ordinate axis. Ages are given for specific points: the upper seven ages are calibrated radiocarbon ages, the lower ages are based on astronomical calibration of pollen-vegetation abundance patterns (Tzedakis et al., 2002). Reprinted with permission from Tzedakis et al., 2002. Copyright 2002 AAAS.

often been used as biostratigraphic tools. The correlation of zones amongst sites is a frequent point of discussion and controversy in post-glacial pollen analysis, especially in Western Europe. The recent increased utilization of radiometric dating, most commonly radiocarbon applied to late Quaternary sediments, has somewhat replaced the reliance on zones for site-to-site correlation.

Interpretation

The researcher is striving to interpret pollen assemblages and their changes over time, or from one locale to another, as changes in vegetation. "The vegetation is the central object in pollen-analytic investigations" . . . and yet there is "no one-to-one correlation between the representation of a species in the vegetation cover and in the pollen spectrum (Fægri et al., 1989, p. 129)." Therefore, the soundest interpretations will depend on the researcher's knowledge of all the ecological and geological factors that have affected the final pollen record. The knowledge and skills required making a reasonable interpretation of past vegetation and climate based upon a pollen record will vary as greatly as the vegetation formations and geological regimes encompassed by the pollen record.

Two common methodologies utilized to interpret the pollen assemblages are the "modern analog" and the "indicator species" methods. The modern analog method seeks to elucidate the relationship between the vegetation that covers an area and the *pollen assemblage* found at a point within that area. Much field work has involved the collecting of small surface sediment samples from within different types of vegetation formations: the pollen are separated from the sediment, identified with a microscope, and a spectrum of the identified pollen taxa is produced; the surrounding vegetation is also identified and classified. With sufficient samples, one can at least qualitatively correlate a pollen spectrum with a vegetation formation. Several complications arise: the existing array of pollen surface samples is extensive in some vegetation types and not others, the pollen surface samples are useful only insofar as the vegetation (which produced the pollen) is in a state of equilibrium with the environment (in all aspects), some important geographical regions can yield no information on the modern pollen-vegetation relationships since anthropogenic activity has eliminated all the natural vegetation, and not all pollen assemblages in the geological record have a modern analog. However, in areas with adequate pollen surface samples, quantitative relationships between climate and pollen may be attempted and the specialist literature contains examples of these (for a more detailed introduction see Bradley, 1999).

The indicator species method relies on the ecological or climatological preferences of one (or a few) key taxa. If a taxon's habitat is highly specific, ecologically or climatologically, then the presence of that single taxon may indicate the habitat, even in the past. Alternatively, several taxa might be used to narrow the climatic or ecological range of the spectrum. The indicator species method is valid only if the fossil pollen truly indicates the presence of the plant in the immediate vicinity of the sampled site. Thus, application of this method should also utilize modern pollen distribution studies showing correlations between actual presence of a taxon, and a numerical pollen percentage threshold. The identification of plant macrofossils (seeds, leaves, etc.) can substantiate a specific taxon's presence, which may be doubtful if based on pollen percentages alone.

Conclusions: examples of pollen records

The following examples show pollen analysis applied to late Cenozoic sediments. The pollen taxa identified belong to extant genera (or families) and hence interpretation may be based on modern analogs and indicator species. Chronological resolution varies with the basin cored; chronological control also varies, from volcanic ashes to radiocarbon dates and to correlation with marine records.

The longest continuous terrestrial sediment cores in North America on which pollen analysis have been conducted come from the Great Salt Lake, northern Bonneville Basin region (northwest Utah; Davis and Moutoux, 1998; Davis, 2002). Pollen analysis was conducted from sediment cuttings (which integrate sediment from a range of depths) retrieved during drilling conducted for geophysical exploration. The wells are exceptionally deep, exceeding 3 km. The sampling interval is from 3 to 30 m, and thus chronological resolution ranges from 8 to 23 kyr. The Bridge well (Figure P84) contains the longest accumulation of pollen and sediments. The interpretation of the relationship between vegetation and pollen spectra is based on modern analogs; the fossil pollen samples were compared to 1,367 modern pollen samples from the western United States. The squared chord distance metric statistical method, also called square chord distance, was used to determine the analogy between modern and the fossil pollen samples quantitatively. The environmental development of the Great Basin can be interpreted from these pollen diagrams. Since the pollen spectra were dominated by xerophytic vegetation, *Sarcobatus* and *Ephedra*, from >5 Ma ago to the present, the region's present-day desert vegetation is interpreted to have existed since the late Miocene. In addition, the poor pollen preservation and scarce pollen of wetland plants indicates that lakes and marshes in the Great Salt Lake basin were shallow and intermittent before 2.6 Ma. Between 5 and 0.75 Ma, the *Sarcobatus* and *Ephedra* pollen are replaced by pollen from the wetland plants, "Chenopodiaceae + *Amaranthus*" (these pollen types are indicative of greasewood steppe vegetation), and *Artemisia* (sagebrush), which indicates a regional cooling and increase in moisture. After 0.75 Ma, *Artemisia* and *Pinus* pollen predominate, which is interpreted as downward displacement of vegetation zones by approximately 500 m in elevation, and the replacement of the greasewood steppe by sagebrush steppe in the intermountain basins (Davis, 2002).

The Ioannina basin, Pindus Mountain Range, Greece, contains a 430,000 year record of pollen in which fluctuating percentages can be used to understand the Quaternary climate cycles and the reactions of tree populations (Tzedakis, 1993). It provides a rare combination of stratigraphic continuity, and high sedimentation accumulation rates for the late Quaternary. Several lacustrine cores have been taken from the basin: the increasing detail of the pollen analysis is evident, as the results have been published. The first analysis shows the pollen spectra alternating between forest and open vegetation communities, reflecting the interglacial and glacial climate, respectively. Four cycles are evident, and they are correlated with glacial-interglacial changes registered in other southern European pollen records. However, a unique feature of the Ioannina cores is the continuous presence of *Quercus* and *Abies*, followed by *Pinus*, *Ulmus/Zelkova* and, to a certain extent, *Corylus*: these are temperate trees (Tzedakis, 1993). These temperate tree populations persist even during glacial periods. This record of the continuous presence of temperate tree

pollen is used to support the ecological hypothesis that these mountains provided long-term refugia for the temperate taxa (Tzedakis, 1993).

Increased detail is apparent in the pollen analysis conducted on a borehole called Ioannina 284 (Figure P85) (Tzedakis et al., 2002, 2003). The mean sampling interval has been increased to approximately 225 years. Because of the increased temporal resolution of the record, greater detail within a single glacial or interglacial becomes evident. The onset of the last interglacial has been defined by the authors as occurring when tree pollen consistently rises above 50% frequency, and when tree pollen concentration exceeds 200,000 grains per cm³; the onset of the ensuing colder stadial occurs when tree pollen consistently drops below 50%. Thus, the Last Interglacial is represented in the interval from 96.7 to 83.4 cm depth, or approximately 127.3–111.7 kyr ago (Tzedakis et al., 2003). After the chronology has been determined, the pollen changes in Ioannina 284 are compared with other climatic data from the North Atlantic region. The data indicate that the millennial-scale expansions and contractions of tree populations may be in phase with climate events in the North Atlantic region and Greenland regions. However, sufficient moisture to maintain refugial temperate tree populations is proposed to be linked to the topographic variability of the Pindus Mountains (Tzedakis et al., 2002).

The pollen analyses from these two sites show how both paleoclimatological and paleoecological interpretations may be extracted from the studies. Furthermore, the means of chronological control will vary with the age of the sediments. With basins that encompass the Holocene epoch, laminated sediments may allow high temporal resolution. For older basins (including marine sediments), age may be based on biostratigraphic correlations. Regionally significant climate changes usually cannot be derived from a single pollen record: several fossil pollen records together from a user-defined region are necessary in order to confirm that patterns in pollen spectrum have significance beyond the single site examined.

Margaret Kneller

Bibliography

- Bradley, R.S., 1999. *Paleoclimatology, Reconstructing Climates of the Quaternary*. Burlington, MA: Harcourt/Academic Press, 613pp.
- Davis, M., 1969. Climatic changes in southern Connecticut recorded by pollen deposition at Rogers Lake. *Ecology*, **50**, 409–422.
- Davis, O.K., 2002. Late Neogene environmental history of the Northern Bonneville Basin: A review of palynological studies. In Hershler, R., Madsen, D.B., and Currey, D.R. (eds.), *Great Basin Aquatic Systems History*. Washington, D.C.: Smithsonian Institution, pp. 295–307.
- Davis, O.K., and Moutoux, T.E., 1998. Tertiary and Quaternary vegetation history of the Great Salt Lake, Utah, USA. *J. Paleolimnol.*, **19**, 417–427.
- Deevey, E.S., 1969. Coaxing history to conduct experiments. *Bioscience*, **19**, 40–43.
- Erdtman, G., 1943. *An Introduction to Pollen Analysis*. Waltham, MA: Chronica Botanica Company, 239pp.
- Fægri, K., and Iversen, J., 1975. *Textbook of Pollen Analysis, third revised edition*. New York: Hafner Press, 295pp.
- Fægri, K., Kaland, P.E., and Krzywinski, K., 1989. *Textbook of Pollen Analysis, by Knut Fægri and Johs. Iversen*. Caldwell, NJ: The Blackburn Press, 328pp.
- McAndrews, J.H., Berti, B., and Norris, G., 1973. *Key to the Quaternary Pollen and Spores of the Great Lakes Region*. Toronto, ON: The Royal Ontario Museum, 64pp.
- Pennisi, E., 2003. Modernizing the Tree of Life. *Science*, **300**, 1692–1697.
- Roberts, N., 1998. *The Holocene: An Environmental History*, 2nd edn. Oxford, UK: Blackwell Publishers Ltd, 316pp.
- Traverse, A., 1988. *Paleopalynology*. Winchester, MA: Allen & Unwin Inc., 600pp.
- Twell, D., 2000. Pollen: Structure, Development and Function. In *Nature Encyclopedia of Life Sciences*. London, UK: Nature Publishing Group. [http://80-www.els.net.osiyou.cc.columbia.edu:2048/\[doi:10.1038/npg.els.0002039\]](http://80-www.els.net.osiyou.cc.columbia.edu:2048/[doi:10.1038/npg.els.0002039]).
- Tzedakis, P.C., 1993. Long-term tree populations in northwest Greece through multiple Quaternary climatic cycles. *Nature*, **364**, 437–440.
- Tzedakis, P.C., Lawson, I.T., Frogley, M.R., Hewitt, G.M., and Preece, R.C., 2002. Buffered tree population changes in a Quaternary refugium: Evolutionary implications. *Science*, **297**, 2044–2047.
- Tzedakis, P.C., Frogley, M.R., and Heaton, T.H.E., 2003. Late Interglacial conditions in southern Europe: Evidence from Ioannina, northwest Greece. *Glob Planet. Change*, **367**, 157–170.
- von Post, L., 1967 [1916]. Forest tree pollen in south Swedish peat bog deposits, a translation by M.B. Davis and K. Fægri of *Om skogstradspollen i sydsvenska torfmosselagerföljder (foredragsreferat)* (Geologiska Föreningen i Skockholm. Föreläsningar 38:384), with an introduction by Knut Fægri and Johs. Iversen. *Pollen et Spores*, **9**, 378–401.

Cross-references

- Dating, Biostratigraphic Methods
- Late Quaternary-Holocene Vegetation Modeling
- Paleobotany
- Palynology
- Quaternary Vegetation Distribution

POTASSIUM-ARGON/ARGON-ARGON DATING

General principles

The K-Ar dating method utilizes the decay of the naturally-occurring radioactive isotope of potassium, ⁴⁰K, into an isotope of the noble gas, argon (i.e., ⁴⁰Ar). ⁴⁰K decays into two different daughter products: the most common path (89.5%) is via beta decay into ⁴⁰Ca; the remainder of the decay paths arrive at ⁴⁰Ar, mostly via electron capture, but also rarely via positive beta (positron emission) decay. The total decay half life for ⁴⁰K is about 1.25 billion years, which means that there is still some of the isotope remaining from the formation of the solar system. Because of the branching decay scheme, the standard radiometric age equation needs to be modified as follows:

$$t = \frac{1}{\lambda} \ln \left(1 + \frac{\lambda}{\lambda_e} \frac{{}^{40}\text{Ar}}{{}^{40}\text{K}} \right) \quad (1)$$

where λ_e is the decay constant leading to ⁴⁰Ar ($0.581 \times 10^{-10} \text{ yr}^{-1}$) and λ is the total decay constant for both branches ($5.543 \times 10^{-10} \text{ yr}^{-1}$).

Much of the natural radioactivity surrounding us is due to ⁴⁰K, but fortunately, it is a quite rare isotope, only accounting for about one atom in 8,570 atoms of potassium. Despite the rarity of ⁴⁰K and the fact that only about one atom in ten decays into ⁴⁰Ar, the K-Ar system is arguably the most versatile of the long-lived decay scheme dating methods. It is nearly an ideal chronometer because K is a major element present in almost all rocks and minerals, but the act of mineral formation is usually exceptionally efficient at excluding atmospheric argon from the mineral's crystal structure. Radiogenic ⁴⁰Ar is well

accommodated in many minerals, which can often quantitatively retain their Ar to temperatures of 300–400 °C or higher. Therefore, K-Ar dating usually has a very clear-cut resetting of the radiometric clock and the clock can faithfully record geological time for durations ranging from thousands to billions of years. Indeed, K-Ar and its cousin Ar-Ar dating have been used successfully to calibrate all of the geomagnetic reversal time scale, much of the history of early humanity, and most of the Phanerozoic timescale, plus ancient samples from Earth, the Moon and Mars.

K-Ar method

In the conventional K-Ar dating method, a part of the sample is analyzed via wet chemistry techniques for K concentration; the remainder of the sample is placed into an ultra-high vacuum system and fused to release all of its trapped gases. The released water vapor is usually trapped in a “cold trap” at dry ice or liquid N₂ temperatures, and the remaining active gases are removed using a “getter” pump, which consists of a highly reactive metal alloy kept at an elevated temperature. The getter removes O₂, N₂, CO₂, CH₄, etc., but leaves the Ar untouched. The remaining “cleaned” Ar sample is usually mixed with a known quantity of the rare argon isotope ³⁸Ar so that the concentration of ⁴⁰Ar can be estimated from the ⁴⁰Ar/³⁸Ar ratio (i.e., isotope dilution). The combined Ar sample is then admitted to a noble gas mass spectrometer. The presence of any atmospheric Ar is corrected by monitoring the ³⁶Ar signal and subtracting an amount 295.5 times larger from the ⁴⁰Ar peak (i.e., the ⁴⁰Ar/³⁶Ar ratio of the atmosphere).

The precision of the K-Ar method is limited by the errors associated with the isotope dilution technique, weighing errors, and the precision of the chemical measurement of K concentration. Typical error estimates are about 1–2% for this method. Accuracy and the reliability of K-Ar ages are further hampered by so-called “nugget effects,” where there may be unusual phases in either the K or Ar sample split. This possibility and the requirement for two separate measurements limit the use of the technique to relatively large and homogeneous samples.

Ar-Ar or the ⁴⁰Ar/³⁹Ar method

In 1966, the team of Merrihue and Turner, working in John Reynold’s laboratory, devised a remarkable enhancement of the K-Ar method that has greatly increased its scope and power (Merrihue and Turner, 1966). In the ⁴⁰Ar/³⁹Ar (or Ar-Ar) dating method, a single split of the sample is sent to a nuclear reactor and irradiated with high-energy neutrons. Some of the most common isotope of potassium, the stable isotope ³⁹K, undergoes a reaction where it briefly absorbs a neutron and expels a proton, thereby transforming into ³⁹Ar. This isotope of argon is radioactive and is not present in the atmosphere in appreciable quantities since it has a half-life of only ca. 270 years. The sample now has both its original radiogenic ⁴⁰Ar and another argon isotope, which can effectively be used as a proxy for potassium. It is possible to measure the ⁴⁰Ar/³⁹Ar ratio, which is proportional to the ⁴⁰Ar/K ratio, which is in turn proportional to the ⁴⁰Ar/³⁹K ratio. The proportionality constant is estimated by analyzing a standard mineral of known K-Ar apparent age during the same neutron irradiation as the sample. The ⁴⁰Ar/³⁹Ar age equation can be written as:

$$t = \frac{1}{\lambda} \ln \left(1 + J \frac{{}^{40}\text{Ar}^*}{{}^{39}\text{Ar}_K} \right) \quad (2)$$

The superscript * denotes radiogenic ⁴⁰Ar. *J* is calculated as:

$$J = \frac{e^{\lambda t_{\text{standard}}} - 1}{({}^{40}\text{Ar}^*/{}^{39}\text{Ar}_K)_{\text{standard}}} \quad (3)$$

The suffix “K” is put on ³⁹Ar to indicate that only the component from potassium is used. There are interfering nuclear reactions, usually from Ca, which produce small amounts of ³⁶Ar and ³⁹Ar, but these can be corrected by calibration analyses of pure Ca salts. Ca also produces significant quantities of the radioactive isotope ³⁷Ar and it is possible to infer the relative concentrations of Ca, Cl, and K by the enhanced abundances of ³⁷Ar, ³⁸Ar, and ³⁹Ar, respectively.

The ⁴⁰Ar/³⁹Ar method eliminates the problem of sample heterogeneity and it has significantly better precision relative to K-Ar dating because all of the measurements are based on isotope ratio measurements, not absolute concentration estimates, and mass spectrometers are much more accurate with the former style of measurement. Age estimates that are precise to within a few tenths of a percent are commonplace, but even more important than laboratory precision are the extra interpretation capabilities of the technique, which lead to more accurate age estimates.

Since age information comes from Ar isotope ratios, it is possible to step-heat a sample in gradually increasing temperature steps and calculate an apparent age for each gas fraction. The sequence of apparent ages is plotted as an “age spectrum,” which can be extremely useful in testing whether or not the sample has remained a closed system during its lifetime. Ideally, the age spectrum will yield a flat sequence of ages or a perfect “plateau age” which can be used with much greater confidence than a comparable single K-Ar age. Alternatively, there are other typical age spectral patterns such as that expected from diffusive loss of Ar or the so-called “saddle shaped” spectrum, which is diagnostic for the presence of excess ⁴⁰Ar. Sometimes it is possible to derive useful age information event from these disturbed age spectra (e.g., Snyder et al., 1996), but at the very least a disturbed age spectrum is a red flag indicating that the data need to be interpreted with care.

⁴⁰Ar/³⁹Ar step-heating also makes it possible to do an isochron style analysis on a single sample, which was impossible with the K-Ar method. Usually in an argon isochron diagram, the ³⁶Ar/⁴⁰Ar ratio is plotted against the ³⁹Ar/⁴⁰Ar ratio, and the intercepts of the fitted line indicate the sample’s initial ³⁶Ar/⁴⁰Ar ratio and apparent age. This kind of analysis is particularly useful for young samples (a few Ma) where the usual assumption of atmospheric composition initial Ar can be rigorously tested.

Finally, the combination of ⁴⁰Ar/³⁹Ar dating with a new generation of low-blank laser fusion systems (York et al., 1981) and high sensitivity mass spectrometers has led to a whole generation of highly automated laboratories capable of routinely analyzing extremely small and extremely young samples. A crucial application has been to revolutionize the dating of volcanic tephra (Lo Bello et al., 1987) by enabling the researcher to date single crystals of volcanic feldspar, thereby eliminating contamination problems, which had long plagued bulk sample analyses. This in turn has allowed for extremely accurate ages for studies ranging from calibrating the geomagnetic reversal timescale to dating early human specimens. For a more complete description of the ⁴⁰Ar/³⁹Ar method, see McDougall and Harrison (1999).

Chris M. Hall

Bibliography

- Lo Bello, P., Fraud, G., Hall, C.M., York, D., Lavina, P., and Bernat, M., 1987. $^{40}\text{Ar}/^{39}\text{Ar}$ step-heating and laser fusion dating of a Quaternary volcanic from Neschers, Massif Central, France: The defeat of xenocrystic contamination. *Chem. Geol. (Isotope Geosci.)*, **66**, 61–71.
- McDougall, I., and Harrison, T.M., 1999. *Geochronology and thermochronology by the $^{40}\text{Ar}/^{39}\text{Ar}$ method*. New York: Oxford University Press, 269pp.
- Merrihue, C., and Turner, G., 1966. Potassium-argon dating by activation with fast neutrons. *J. Geophys. Res.*, **71**, 2852–2859.
- Snyder, G.A., Hall, C.M., Lee, D.-C., Taylor, L.A., and Halliday, A.N., 1996. Earliest high-Ti volcanism on the moon: ^{40}Ar - ^{39}Ar , Sm-Nd and Rb-Sr isotopic studies of Group D basalts from the Apollo 11 landing site. *Meteoritics*, **31**, 328–334.
- York, D., Hall, C.M., Yanase, Y., Hanes, J.A., and Kenyon, W.J., 1981. $^{40}\text{Ar}/^{39}\text{Ar}$ dating of terrestrial minerals with a continuous laser. *Geophys. Res. Lett.*, **8**(11), 1136–1138.

Cross-reference

Dating, Radiometric Methods

PRECESSION, CLIMATIC

The celestial equator intersects the ecliptic in two points. The vernal equinox is the one at which the Sun in its apparent annual motion crosses from South to North of the equator. The vernal equinox can be used as a reference point to define the celestial longitude locating the Earth along its orbit during the year. The longitude of the perihelion (ϖ) represents the angular position of the perihelion of the orbit from the vernal equinox. This angle gives the position of the Earth on its orbit at the spring equinox. Knowing the longitude of the perihelion, it is possible to determine the Earth-Sun distance at any time in the year. Climatic precession ($e \sin \varpi$) is usually used instead of the longitude of the perihelion. It is the main factor driving the 24 h-mean irradiance.

Astronomers of old civilizations kept records of the direction of the Earth's axis of rotation in the sky. Five thousand years ago, stars circled around α -Draco's in the night sky, while it is now around α Ursa Minor (polaris). Indeed the Earth's axis of rotation does not point towards a fixed direction through time but describes a clockwise circle in space. This happens because the torque of the Moon and the Sun on the Earth's equatorial bulge causes the axis of rotation to wobble (the Earth's equatorial radius is close to 6,375 km while its polar radius is only 6,355 km). This motion of the Earth's axis of rotation, called astronomical precession, is similar to the

precession of a tilted top and it induces the motion of the vernal equinox, with a period of 25,700 years. However, from a paleoclimatic point of view, the situation is not so simple. Indeed, the ecliptic is not fixed in time either, leading to an anticlockwise motion of the perihelion. Consequently the climatic precession, which describes the position of the perihelion with respect to the vernal equinox, varies with a quasi-period of 21,000 years, resulting from the combination of several periods, the most important being around 23,000 and 19,000 years (Berger, 1978; Berger and Loutre, 1991) (Figure P86).

The present-day value of the longitude of the perihelion is $\varpi = 102.04^\circ$, which gives a climatic precession of $e \sin \varpi = 0.01636$. In this situation the Earth is at the closest distance to the Sun in early January (Berger and Loutre, 1994). Therefore the mean solar irradiance received during the southern summer in the Southern Hemisphere is larger than the mean solar irradiance received during the boreal summer in the Northern Hemisphere. Some 11,000 years ago, the Earth was at the closest distance to the Sun around the June solstice. This increased the solar irradiance received during boreal summer and reduced it during Southern Hemisphere summer. The climatic precession therefore plays opposite roles in both hemispheres. Any insolation change in one hemisphere due solely to a variation in climatic precession corresponds to an insolation change of opposite sign and same amplitude in the other hemisphere six months later (Figure P87).

Moreover, the length of the seasons, which vary in time according to Kepler's law, is also strongly dependent on the climatic precession (Berger and Loutre, 1994). Presently the length of the Northern Hemisphere seasons is respectively 92.8 days for spring, 93.6 days for summer, 89.8 days for autumn, and 89 days for winter. In about 4,500 years from now, the Northern Hemisphere spring and winter will have about the same short duration (89.6 days), and summer and fall will also be equally long (93.0 days).

Marie-France Loutre

Bibliography

- Berger, A.L., 1978. Long-term variations of daily insolation and Quaternary climatic changes. *J. Atmos. Sci.*, **35**(12), 2362–2367.
- Berger, A., and Loutre, M.F., 1991. Insolation values for the climate of the last 10 million years. *Quaternary Sci. Rev.*, **10**, 297–317.
- Berger, A., and Loutre, M.F., 1994. Precession, eccentricity, obliquity, insolation and paleoclimates. In Duplessy, J.C., and Spyridakis, M.-T. (eds.), *Long Term Climatic Variations, Data and Modelling*, vol. 22. Nato ASI series, Serie I: Global Environmental Change, Berlin: Springer, pp. 107–151.

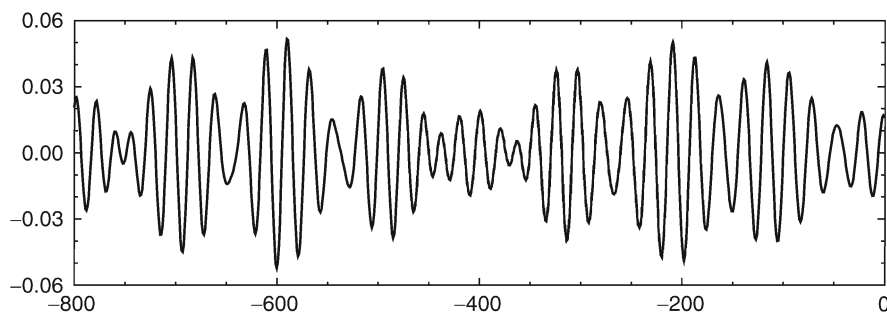


Figure P86 Long-term variations of the climatic precession over the last 800,000 years.

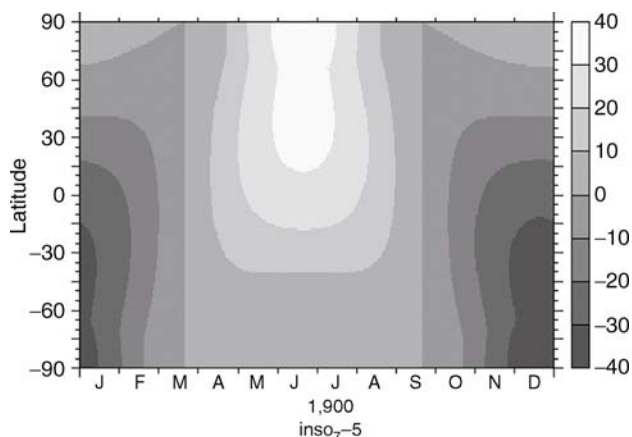


Figure P87 Variation of the mean irradiance ($W m^{-2}$) following a change in the climatic precession from perihelion at winter solstice to perihelion at summer solstice (at present-day eccentricity, $e = 0.0167$ and obliquity, $\varepsilon 23.446^\circ$).

Cross-references

[Astronomical Theory of Climate Change](#)
[Climate Forcing](#)
[Eccentricity](#)
[Obliquity](#)
[Pre-Quaternary Milankovitch Cycles and Climate Variability](#)
[Quaternary Climate Transitions and Cycles](#)
[SPECMAP](#)

PRE-QUATERNARY MILANKOVITCH CYCLES AND CLIMATE VARIABILITY

Introduction

Cyclic variations in insolation, caused by the precession and obliquity of Earth's spin axis and variations in the eccentricity of Earth's orbit, have been stressed as a driver of Quaternary climate since Hays et al. (1976). The Quaternary, however, comprises only 0.4% of Earth history, and is characterized by unusual "ice house" conditions. In addition, neither the mechanism through which ice house conditions were initiated, nor the mechanism whereby the 100 kyr cycle has come to dominate glacial oscillations are understood (see Muller and MacDonald, 2000). Analysis of pre-Quaternary Milankovitch cycles provides a more synoptic view of the role of astronomically controlled climate change, a context for understanding the present state of the Earth system and anthropogenic modifications, a mechanism for producing high-resolution timescales, and data for calibrating the dynamic evolution of the solar system (see reviews by Berger et al., 1989; Fischer et al., 1991; Schwarzacher, 1993; Weedon, 1993, 2003; Hinnov, 2000, 2005).

Methods

Two fundamentally different, although mutually illuminating, approaches to the analysis of pre-Quaternary Milankovitch cyclicity have been developed. The first, cycle counting, predates acceptance of the Milankovitch theory for Quaternary climate change by nearly a century (e.g., Gilbert, 1895)

(Figure P88). Cycle counting is an inherently typological approach requiring both identification of each sedimentary or proxy cycle and its boundaries within a section and a timescale to determine cycle duration. Bundles of cycles of variable thickness allow recognition of the characteristic Milankovitch cycle hierarchy based on the thickness ratio of short to long cycles, assuming the highest frequency cycles have been correctly identified. A variant of the cycle counting approach is named for Fischer's (1964) analysis of the Triassic asymmetric carbonate Lofer cycles (Figure P89). These so-called Fischer plots are graphs of cumulative departure from average cycle thickness plotted against cycle number, assuming a uniform period for each cycle and modified for assumed constant subsidence during each cycle (see Sadler et al., 1993; Boss and Rasmussen, 1995 for criticism). While the typological cycle counting method allows easy visualization of sedimentological patterns and cycle identification in the field, the numerous ad hoc assumptions that must be made about the variability of the cyclicity makes its practical use treacherous unless there is a known target pattern for correlation, such as an age-appropriate and accurate insolation curve. Additionally, often used as a measure of relative sea-level change, Fischer plots appear to be a poor predictor for Quaternary examples where sea-level change is well understood (e.g., Boss and Rasmussen, 1995).

The second approach, time series analysis, is commonly used in Quaternary analyses and was inspired by the pivotal paper by Hays et al. (1976) that established Milankovitch cyclicity as the "Pacemaker of the Ice Ages," although there were earlier applications. Here, a variable (lithological or climate proxy) is plotted against thickness or time, and Fourier or other quantitative methods are used to determine the frequency properties of the data that can then be compared to a hypothesis of orbital forcing (Figure P90). This method dispenses with the need to identify the cycle type, has the advantage of not requiring variability in the data to be discarded, and thus does not presume the mode of cyclicity (i.e., precession vs. obliquity). The disadvantage is that the variable must have a unimodal relationship to climate or a precise timescale must be available; these become progressively much less common in more ancient deposits. Sequences have typically been analyzed by Fourier methods with the data transformed from the depth or time domain to the frequency domain. The results are usually expressed as a periodogram (a graph of frequency against a measure of the importance of that frequency, such as power). This method, however, presumes little variation in accumulation rate; that is, the frequencies are stationary with respect to the depth scale. This assumption can be considerably relaxed with use of evolutive or depth-frequency analysis. Here, the frequency properties of the section are analyzed by use of a moving window and are plotted with respect to depth (Figure P91). A plethora of techniques is available in which accumulation rate changes can be determined directly from the internal frequency properties of the data.

Timescales

Both cycle counting and time series methods require a timescale to help assess accumulation rates. Accumulation rates are quantified by relying largely on direct dating by annual rhythms (varves) and radiometric methods, indirect dating by correlation to other well established timescales, such as $\delta^{18}O$ curves or magnetic polarity transitions, and tuning to insolation curves based on celestial mechanics. In older stratigraphic

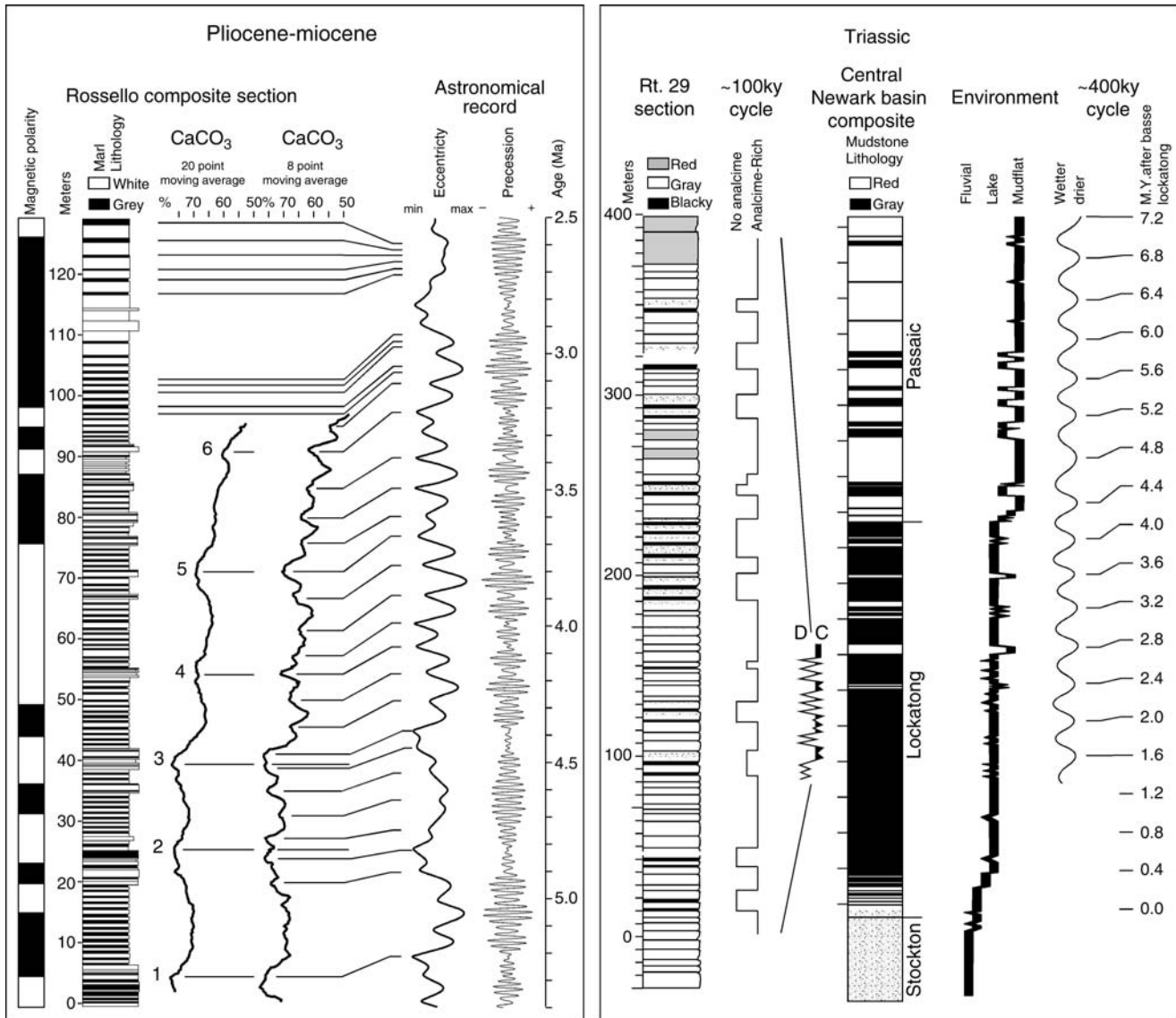


Figure P88 Cycle counting and matching to an astronomical record; *left*: marine Pliocene-Miocene example with astronomical calibration from Sicily modified from Hilgen (1991b); *right*: lacustrine Triassic example, modified from Van Houten (1964) with 400 kyr cycle added.

records, it becomes progressively harder to apply these proxies and dating methods successfully and other, more inferential, methods must be used.

Varves are annual rhythms that can be marine or non-marine and generally consist of couplets or, more rarely, of triplets of heterogeneous laminae (see review by Anderson, 1964; Anderson and Dean, 1988). It is usually assumed that a single couplet or lamina series represents one year, corresponding to summer and winter or wet and dry seasons, although some lacustrine environments could theoretically possess two couplets of laminae series per year, and there can be confusion with tidal banding. Although varve calibration provides direct and very high-resolution records of accumulation rates, varved sequences are rare and when present often constitute only a small part of the sedimentary column.

Radiometric dates provide another direct way to calibrate accumulation rates and a basis for a timescale. To be useful, there must be several dates in a section separated in time sufficiently to exceed error limits, and they must be geologically accurate. Very few sections meet these criteria. It is possible to obtain paleontological or other time-correlative means to tie radiometric dates to sections under analysis. Possible difficulties are exemplified by debates on the Triassic Latemar and the Eocene Green River Formation (Hinnov and Goldhammer, 1991; Brack et al., 1996; Pietras et al., 2003; Machlus et al., 2004, 2008).

As is true for Quaternary records, the relatively well-established marine $\delta^{18}\text{O}$ record provides a powerful tie to published timescales for older Neogene marine sections (e.g., Miller et al., 1987). The temporal accuracy, however, of correlations to the

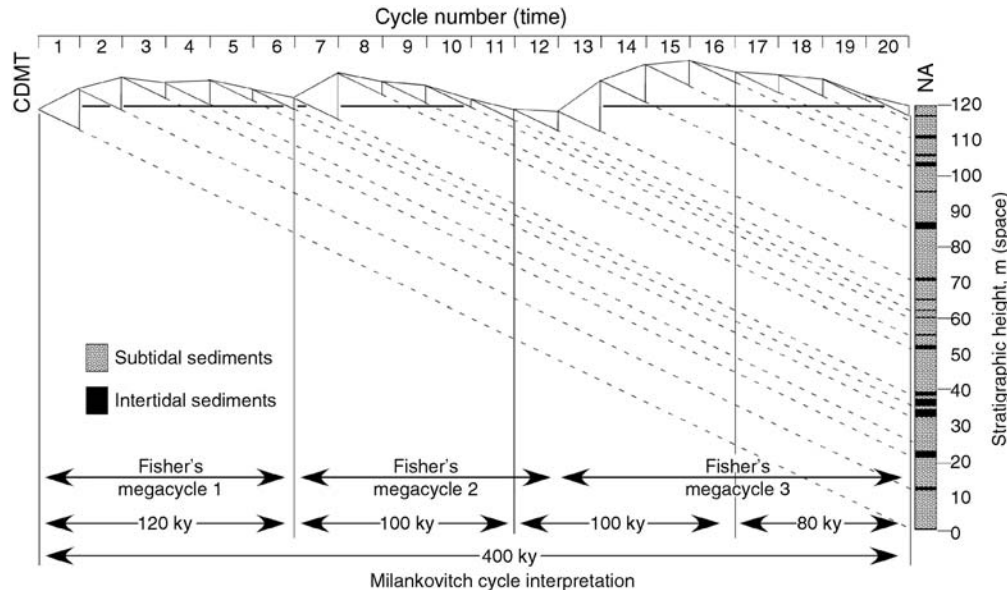


Figure P89 Fischer plot of Fischer's example of Triassic Lofers cycles in marine Triassic carbonates of Austria (modified from Fischer, 1964) with a modern Milankovitch cycle interpretation overlain.

$\delta^{18}\text{O}$ record can be no better than the accuracy of the $\delta^{18}\text{O}$ record itself, which is undergoing significant modifications. Using this technique for accumulation rate calibration, only open marine sections can be meaningfully correlated, and the section being correlated needs sufficient temporal scope to encompass enough of the character of the $\delta^{18}\text{O}$ curve.

Correlation and tuning to insolation curves has been extensively used in strata of Neogene age, but less commonly in the Paleogene (e.g., Hilgen, 1991a,b; Shackleton et al., 2000), and not at all in the Mesozoic and older strata (Figure P88). The production of insolation curves to which ancient proxy curves can be matched is limited by uncertainties in observations, chaotic behavior of the planets, lack of knowledge of the evolution of the Earth-Moon system, and dynamic aspects of mass distribution within the Earth. Insolation curves for the higher frequency climatic precession and obliquity cycles are accurate to 40–50 Ma, and the 405 kyr cycle to 250 Ma. The variations of the 405 kyr cycle beyond 250 Ma are relatively small, and could be used, recognizing the larger uncertainties, back to the age of the Earth (see Laskar, 1990, 1999; Berger et al., 1992; Laskar et al., 1993, 2004; Palike et al., 2004). If the 405 kyr cycle can be identified, it can be used to calibrate average accumulation rate and hence provide a mechanism to establish the period of higher frequency cycles independent of their drift through deep time (e.g., Olsen and Kent, 1999).

For the late Jurassic through Neogene, the well-established marine magnetic anomaly timescale (Cande and Kent, 1995) establishes broad constraints for sections with internal polarity data. Although the average duration of a chron is ~ 0.25 million years (Lowrie and Kent, 2004), correlation to the marine magnetic anomaly timescale is useful only for sections involving millions of years. As there is no marine magnetic anomaly timescale for strata older than late Jurassic, Milankovitch cycles have proved more useful for calibrating the magnetic polarity record than vice versa (e.g., Kent and Olsen, 1999).

One of the most powerful methods of calibrating accumulation rate is via the internal frequency structure of the data series itself, and this takes two basic forms. First, the celestial mechanical theory predicts a very specific relationship between the higher and lower frequencies present in data. The lower frequencies are beat cycles of the higher frequencies within the precession-related bands or the obliquity-related bands. The frequencies of the ~ 100 kyr eccentricity cycles are equal to the differences between the frequencies of the climatic precession cycles because these cycles result from the interaction of the Earth's precession and the gravitational attraction of the planets and the eccentricity cycles result from the gravitational interaction of the very same planets. At present, the main periods that can be recognized in climatic precession are about 19, 23, and 24 kyr. The periods of the linear combinations of differences of the frequencies of these periods are about 93, 125, and 405 kyr (calculated using appropriate precision). This is a mathematical relationship that holds regardless of changes in the value of the precession constant in the deep past (due to the Earth-Moon system evolution or mass distribution within the Earth), or chaotic changes in planetary orbits. The same relationship is maintained for the obliquity-related cycles. However, only the most high-fidelity records (e.g., Triassic Lofertong Formation; Olsen and Kent, 1996; Hinnov, 2005) have this level of detail (Figure P89). The second, more widely used concept is that the ratio of the shorter to the longer periods within the Milankovitch bands, such as precession to eccentricity, changes very slowly through Earth history, presently there is a 1:5:20 ratio of precession (~ 20 kyr) to short (~ 100 kyr) and long (~ 400 kyr) eccentricity cycles. This change is theoretically a steady decrease in the precession period due to tidal friction that should increase the ratio of climatic precession to eccentricity cycles (Figure P92). The same effect is seen in obliquity. The actual change in precession, however, may be more complicated due to other factors, especially the changing dynamic

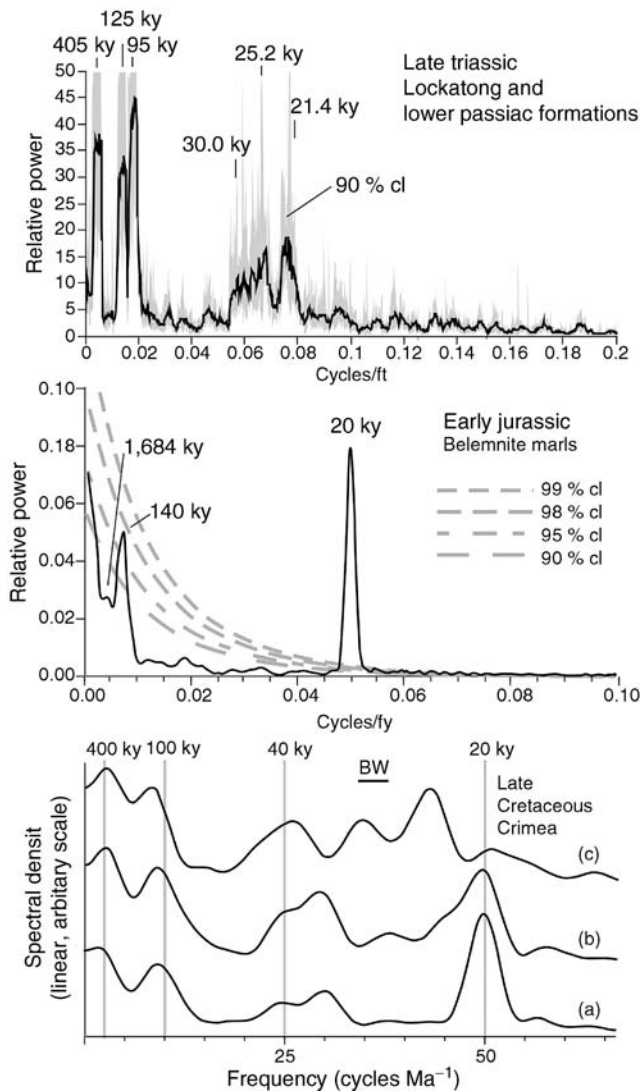


Figure P90 Power spectra of pre-Quaternary paleoclimate proxy time series. *Top*: Thompson multitaper spectral estimate of 3 million year of Triassic lake level data (depth ranks) from New Jersey, USA, modified from Olsen and Kent (1996), shaded area is 90% confidence limits; *middle*: discrete Fourier transform power spectrum of 1.7 million year of wt% CaCO_3 data from the marine Belemnite Marls, England (modified from Weedon et al., 1999); *bottom*: linear Blackman Tukey spectral analysis of grey scale reflectance of a 720 kyr section of Cretaceous marine strata from the Crimea, Ukraine (from Gale et al., 1999).

ellipticity of the Earth caused by movement of continents, mantle, or ice sheets. There should be little measurable change caused by the chaotic diffusion of the planetary orbits for the typically cited 405 kyr and 100 kyr eccentricity periods, and thus the main observable secular change in orbital frequencies should be in precession.

Many authors have used the canonical 1:5:20 ratio of the shorter to longer cycles as strong evidence of the Milankovitch origin of pre-Quaternary cycles, despite uncertainty in the actual ratio, especially in strata hundreds of millions of years old. In the absence of any other time constraints, these ratios may not

be unique (e.g., Latemar controversy, see below). Presuming that the average ratios are broadly consistent with available constraints, and the section covers millions of years, evolutive depth-frequency analysis (as opposed to time-frequency) can reveal shifts in the absolute values of frequencies through a section, while maintaining the ratios of the higher to lower frequencies. Only Milankovitch theory predicts constancy of those frequencies independent of actual accumulation rate. The advantage to this analysis is that the changes in accumulation rate can be derived directly from the spectrogram. At present, only a few sections have been examined this way (e.g., see Olsen and Kent, 1999; Preto et al., 2001; Weedon, 2003).

The interaction of climatic and sedimentological processes should produce a distortion of accumulation rates, resulting in periodograms and time- or depth-frequency spectrograms that are noisy or distorted beyond interpretation. Two techniques, gamma analysis (Kominz and Bond, 1990) and frequency modulation (FM) analysis (Hinnov and Park, 1998) were developed to deal with a situation in which accumulation rate may be a function of Milankovitch cycles themselves. Both involve a version of cycle counting. In gamma analysis, an approximate solution to the relationship between time and facies is found for a succession of sedimentary cycles. Individual facies specific to certain environments are identified within a section and measured in thickness. Assuming that each cycle is of constant duration and each facies is characterized by a specific effective accumulation rate (γ), an approximation of the accumulation rate of each facies can be found by solving a series of simultaneous equations representing the cumulative time of the different facies within each cycle. The fit of these approximations is assessed by an inverse method using the accumulation rates derived from the measured section and Fourier analysis of the resulting time series. If the accumulation rates are identified correctly and the sequence is of Milankovitch origin, the Fourier spectrum should reflect a better fit to the expectations of Milankovitch theory than the original data. Although this method incorrectly assumes a constant duration for the precessional cycles, it might reveal the presence of another cycle to which the section could be tuned, such as the 40 kyr obliquity cycle of relatively constant frequency. This method has been applied to Cambrian marine, and Triassic and Jurassic lacustrine sequences, significantly improving the spectral properties of the data.

FM analysis begins with the identification of the presumed geological expression of precessional (or obliquity) cycles and estimation of the length of each cycle, creating a new time series of depth against cycle thickness. Fourier analysis of this new time series reveals the FM modulating cycles. Since the precession cycle is frequency modulated by the “eccentricity” cycles, FM analysis of a real insolation curve reveals the eccentricity cycles (see Hinnov, 2000). FM analysis of the data curve also has this characteristic shape if it is the result of Milankovitch processes. A tacit assumption of this method is that there is a strong and amplified link between the frequency modulators of accumulation rate and the eccentricity cycles themselves. A major disadvantage to this method is that the higher frequency cycles must be identified, which is nearly impossible in noisy, low amplitude, or clipped records. In addition, the Fourier FM spectral pattern may not be unique to the frequency band characterized by the “usual” Milankovitch frequencies; it may be shared with sub-Milankovitch, yet still quasiperiodic, climatic processes.

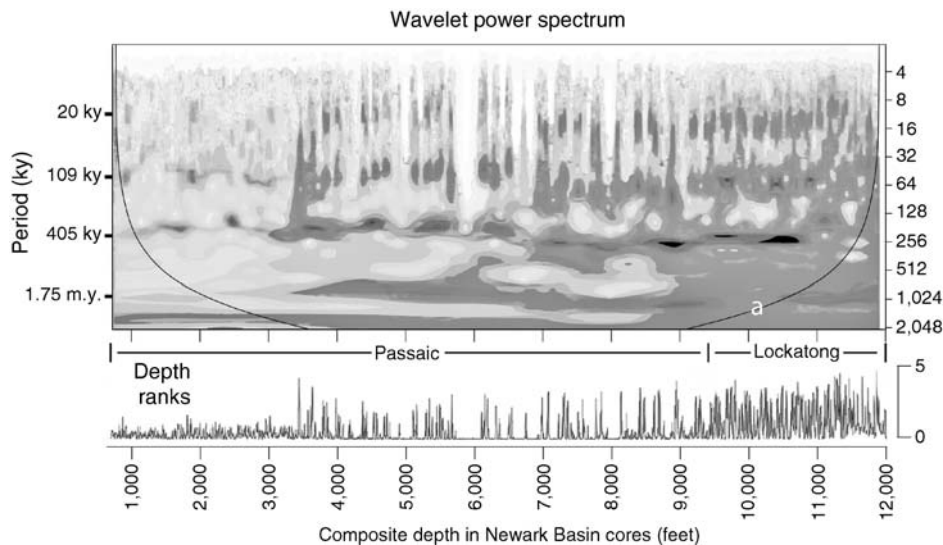


Figure P91 Evolutive spectral analysis of 22 million year of lake level (depth rank) data from the continuously cored Late Triassic age lacustrine Lockatong and Passaic formations of the Newark Rift basin, New Jersey, USA. Above: continuous wavelet transform of lake level data (wavelet provided by C. Torrence and G. Compo; <http://paos.colorado.edu/research/wavelets/run> by M. Machlus); bottom: depth rank data in depth domain (from Olsen and Kent, 1996).

Proxies

Since climate parameters cannot be measured in sedimentary strata, a reasonably direct recorder of a response to climate change, or climate proxy, is necessary. For Quaternary sequences, a vast array of possible climate proxies can be reasonably calibrated because neither the tectonic plate configuration nor species composition has changed much over the last 2 million years. These proxies include $\delta^{18}\text{O}$, a proxy mostly for ice volume (e.g., Hays et al., 1976), eolian dust, a proxy mainly for aridity and wind intensity, and pollen and spores, a reflection of climate-related changes in plant species distributions. Deeper in time these proxies can be affected by diagenesis, lithification, and lack of extant taxa that can be calibrated. Proxies less prone to time-related processes range from sedimentary facies classifications sensitive to water depth (e.g., Olsen, 1986) to geochemical proxies such as $\delta^{13}\text{C}$ of organic matter, carbonate sensitive to climate-related oceanographic processes, and oil-shale yield, related to water depth (e.g., Bradley, 1929).

Examples of pre-Quaternary Milankovitch cycles

Neogene

Largely circum-Mediterranean and deep sea core sections are the basis of a high resolution Miocene to Quaternary Milankovitch-cycle-calibrated timescale (Shackleton et al., 1990; Hilgen, 1991b; Hilgen et al., 1995, 1997). The Mediterranean marine sections exhibit the marl-sapropel cyclicity originally described from Mediterranean cores. The largest-scale bundles of cycles visible are matched to the 400 kyr of a precession-dominated isolation curve, in a portion of the section that is already well dated. Progressively smaller bundles are matched to the insolation curve, followed by precession-related individual marl-sapropel cycles (Figure P88). Older sections are then spliced. The hierarchical nature of both the bundling and the insolation curve limits potential miscorrelations. Radiometric dates have been used to test the timescale. The astronomical calibration is so robust that it has allowed for a recalibration of the ^{40}K decay

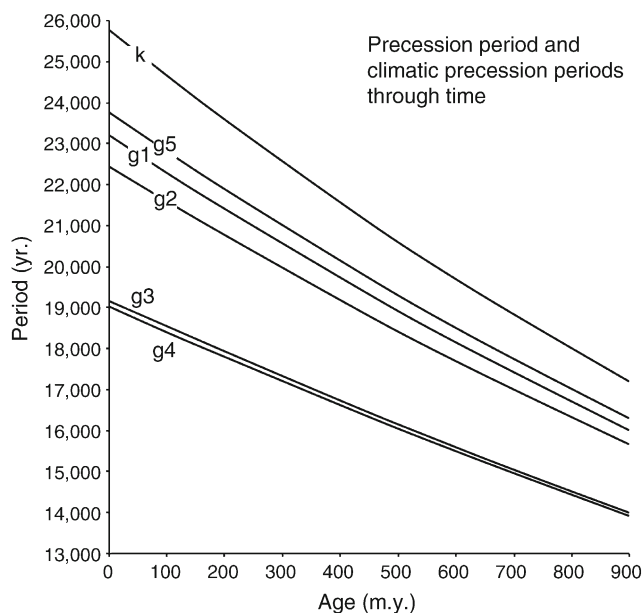


Figure P92 Change in the period of the Earth's axial precession due to tidal friction over the last 900 million years, and the expected changes in climatic precessional cycles. The sum of the frequency of axial precession, k , and the various fundamental frequencies of the planets, g_1 – g_5 (only the most important 5 shown here) is equal to the frequency of climatic precession. For the present day, there is a cluster of 3 periods around 23 kyr and another 2 periods around 19 kyr. Derived from Berger et al. (1992).

constant, itself (Hilgen et al., 1999) now widely adopted. Hilgen's method has also been extended to non-marine strata, particularly in the Miocene (Aziz et al., 2003).

Shackleton et al. (1999, 2000), Palike et al. (2004), and Billups et al. (2004) have used marine cores showing strong

obliquity forcing to produce an astronomical calibration of the Oligocene, Miocene and Neogene. These cores exhibit the usual Milankovitch frequencies and modulation by longer cycles, notably the 1.2 million year cycle of obliquity modulation, and show that the resonance of the orbits of Earth and Mars has not changed state for the last 30 million years.

Paleogene

The description by Bradley (1929) of lacustrine cycles in the Eocene Green River Formation in Colorado and Utah is the classic example of pre-Quaternary Milankovitch cycles. Assuming the relationship between oil shale yield and accumulation rate within each facies to be constant, Bradley used oil shale yield as a proxy for accumulation rate within several sections of a few cycles each. The duration of each cycle was estimated at an average ~21 kyr using the accumulation rates derived from varve calibration. Recently, $^{40}\text{Ar}/^{39}\text{Ar}$ dates from tuffs within the Green River Formation and cycle counting (without quantitative time-series analysis) have been used to argue that the accumulation rate of the strata was too slow for the individual cycles to average 21 kyr (e.g., Pietras et al., 2003; countered by Machlus et al., 2004, 2008).

Cretaceous

One of the first quantitative applications of the astronomical theory of climate change was by Gilbert (1895) who hypothesized that the marine limestone-shale bedding rhythms of the late Cretaceous of Colorado were of precessional origin. Based on extrapolation from admittedly very limited outcrops, he estimated the duration of the late Cretaceous to be between 20 and 40 million year, favoring 20 million year. Current estimates place the duration of that epoch to be ~34 million year. More recent analysis shows that Gilbert's hypothesis is largely correct and that obliquity and eccentricity cycles are also important (Figure P90). There are many other modern treatments of Cretaceous marine cyclicity (see Hinnov, 2005). Herbert and D'Hondt (1990) used the Milankovitch cyclicity of the latest Cretaceous and earliest Cenozoic (Maastrichtian and Danian) cores from the South Atlantic to estimate accumulation rates across the Cretaceous-Tertiary boundary and found an essentially stepwise decrease in accumulation rates consistent with an abrupt boundary event.

Jurassic

Among the first to recognize cyclicity attributable to Milankovitch processes, Schwarzscher (1964) recognized that the Alpine Jurassic carbonate cycles attributed to ~20 kyr precession were bundling into ~100 kyr eccentricity cycles. According to Weedon (2003), the European Tethyan marine sequences are dominated by obliquity-forced cycles in the Hettangian and Sinemurian age parts of the sections, precession in the Pliensbachian (Figure P90), and a mixture of precession and obliquity in the Kimmeridgian (see Hinnov, 2005 for additional references). In eastern North America, Olsen et al. (1996) and Whiteside et al. (2007) described lacustrine cyclicity ascribed to precession and eccentricity forcing, and used it to constrain the duration of the Central Atlantic Magmatic Province (~600 kyr), the most geographically-extensive continental flood basalt province on Earth. Olsen et al. (2002) also used the Milankovitch cyclostratigraphy of the latest Triassic and earliest Jurassic to determine the duration of the Triassic-Jurassic boundary events.

Triassic

Schwarzscher (1948, 1954) and Fischer (1964, 1991) recognized a hierarchy of cycles, termed Lofer cycles, within late Triassic age carbonates of the Italian Alps (Norian-Rhaetian), attributing them to the precession and the ~100 and 405 kyr eccentricity cycles (Figure P89). Van Houten (1964) likewise recognized a hierarchy of lake level cycles within the continental late Triassic Newark Supergroup of the Newark rift basin of New York, New Jersey and Pennsylvania using varve calibration and constraints imposed by the duration of the late Triassic itself (Figure P88). This work has been fully supported by later work (e.g., Figure P90), and led to the Newark Basin Coring Project that continuously cored virtually the entire Newark basin sedimentary record (Figure P93). The lacustrine portion of the core record spans 25 million years (Norian-Hettangian) and is characterized by a continuous Milankovitch pattern of lacustrine cycles revealing the full spectrum of precessional and eccentricity frequencies including the longest frequency cycle with periods of 1.75 and 3.5 million year, corresponding to today's 2.4 and 4.8 million year eccentricity cycles (Figure P91). The difference is attributed to chaotic drift in the fundamental orbital frequencies of Earth and Mars (g_3 and g_4 of Laskar, 1990; Olsen and Kent, 1999). The 405 kyr eccentricity cycle is very clear in this record and provides the basis for an astronomically tuned geomagnetic polarity timescale (Kent and Olsen, 1999, 2000) for the late Triassic that has been recently correlated in detail with Tethyan marine records at the sub-stage level (e.g., Muttoni et al., 2004) (Figure P93).

One of the most contentious debates in pre-Quaternary Milankovitch cyclicity is the Latemar controversy. Middle Triassic age cyclical marine carbonate cycles are well exposed in the northern Italian Alps. Originally, Fischer-plot analysis of this section by Goldhammer et al. (1987) suggested a Milankovitch origin of the cyclicity. Buttressed in their interpretation by Fourier and other numerical analyses, Hinnov and Goldhammer (1991) counted ~600 cycles in ~470 m of section that they attributed to precession cycle forcing of sea level over a period of 12 million year (Hinnov, 2000; Preto et al., 2001). This interpretation is directly challenged by radiometric age data from interbedded and correlative tuffs that imply a duration of 0.5–2 million year for this same interval and by the presence of only two magnetic polarity zones (Brack et al., 1996; Kent et al., 2004). This led to the alternative, perhaps in some ways more interesting, interpretation that what were thought to be precessional cycles are in fact very short, sub-Milankovitch cycles imbedded within much thicker precessional cycles (Kent et al., 2004), highlighting the non-uniqueness of the frequency ratios when order of magnitude differences in the possible timescale are involved.

Paleozoic

There are far fewer convincing examples of Milankovitch cyclicity in Paleozoic records because they tend to be shorter and more poorly temporally constrained (see Hinnov, 2005). Using varves in evaporites, Anderson et al. (1972) calibrated accumulation rates of the Permian Castile Formation of New Mexico and recognized the cycle of climatic precession, sub-Milankovitch cycles that he attributed to sun spot cycles, and other periodicities. Rampino et al. (2000) used evolutive Fourier analysis to determine the duration of Permo-Triassic boundary events.

Carboniferous age, often coal-bearing cycles, termed cyclothem, may have a Milankovitch origin (Fischer, 1986). The Carboniferous was a glacial period and glacio-eustatic

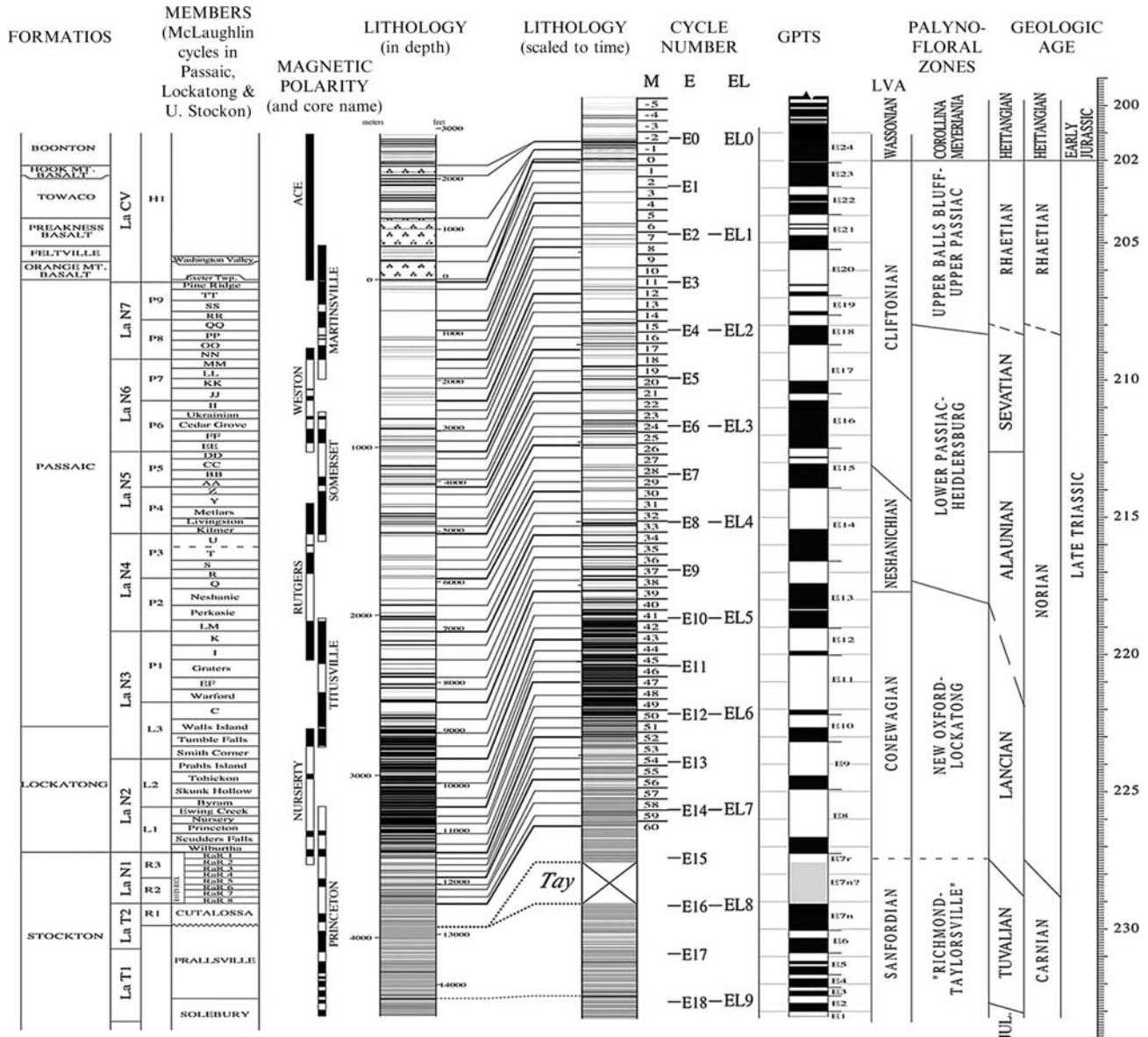


Figure P93 Opposite. Late Triassic and earliest Jurassic astronomically calibrated geomagnetic polarity time scale based on lacustrine strata from the Newark basin and correlation with marine stages and substages (derived from Kent and Olsen, 1999; Olsen and Kent, 1999; Muttoni et al., 2004).

cycles paced in some way by orbital cycles were presumably present. As yet, neither detailed evolutionary techniques nor robust dating techniques have been available to determine the periodicity of these cycles. A similar problem exists for Devonian marine carbonate cycles that have been described in abundance (e.g., Goodwin and Anderson, 1985; Goldhammer et al., 1991; Maynard and Leeder, 1992; Wilkinson et al., 1998; Miller and Eriksson, 1999).

Cyclical lacustrine strata very similar to those present in the Triassic and Jurassic of eastern North America crop out in the Orcadian basin, Scotland (Donovan et al., 1974; Donovan, 1980). Astin (1990) has demonstrated that these strata appear to possess a hierarchy of cycles compatible with a Milankovitch origin.

Older documented Paleozoic examples of Milankovitch cyclicity are much less common, but some convincing examples include the Cambro-Ordovician Aisha-Bibi carbonate seamount (Kazakhstan; Hinnov, 2005) and Cambrian limestones of the Wah Wah range of Utah (Bond et al., 1991). These studies show that the cyclicity is consistent with the estimate of Berger et al. (1989) for the Cambrian precessional frequency.

Precambrian

Precambrian examples of Milankovitch forcing are even less well documented. The best-known example is the 2.2 billion year of cyclicity in the Proterozoic Rocknest Formation of the Wopmay Orogen, N.W.T., Canada (Grotzinger, 1986). The sequence

consists of asymmetrical carbonate cycles analyzed using Fischer plots. Hofmann et al. (2004) used Markov chain analysis and Fischer plots to examine Archean carbonate cyclicity in the Belingwe Greenstone Belt of Zimbabwe. They pointed out a strong correspondence between the bundling of 7–11 short cycles per long cycle and the predicted ratio by Berger et al. (1989) between precession and short eccentricity cycles.

Challenges

Milankovitch cycles result from the combined gravitational effects of the other bodies in the solar system upon the Earth's spin axis and orbit, and similar effects are thought to be present on other planets (e.g., Kieffer and Zent, 1992; Correia and Laskar, 2001). It is not surprising that orbital cycles have affected the climate and the resulting sedimentary record through Earth's history, and thus the discovery of past Milankovitch cyclicity is less interesting for itself than for its possible uses. Four main challenges facing future work on pre-Quaternary Milankovitch cyclicity can be identified: (a) continued documentation of the orbital cyclicity into older strata with sufficient precession to discriminate deviations from the existing simple models of the secular evolution of the Earth's axial and orbital dynamics, (b) analysis of very long records (10s of millions of years) from various parts of Earth's history to calibrate the chaotic drift in the fundamental frequencies of the solar system (e.g., Olsen and Kent, 1999; Palike et al., 2004) with the ultimate goal of producing insolation curves for any arbitrary time in Earth history, (c) using Milankovitch cycles as a tool for high-resolution correlation and the calibration of other processes in truly ancient sequences, and (d) understanding the mechanisms by which insolation changes result in changes in Earth system processes and the resulting geological record.

Paul E. Olsen and Jessica H. Whiteside

Bibliography

- Anderson, R.Y., 1964. Varve calibration of stratification. *Kansas Geological Survey Bulletin* **169**, 1–20.
- Anderson, R.Y., and Dean, W.E., 1988. Lacustrine varve formation through time. *Palaeogeogr. Palaeoclimatol. Palaeoecol.*, **62**, 215–235.
- Anderson, R.Y., Dean, W.E., Kirkland, D.W., and Snyder, H.I., 1972. Permian Castile varved evaporite sequence, West Texas and New Mexico. *Geol. Soc. Am. Bull.*, **83**, 59–86.
- Astin, T.R., 1990. The Devonian lacustrine sediments of Orkney, Scotland; implications for climate cyclicity, basin structure and maturation history. *J. Geol. Soc., London*, **147**, 141–151.
- Aziz, A.H., Hilgen, F.J., Wilson, D.S., Krijgsman, W., and Calvo, J.P., 2003. An astronomical polarity timescale for the middle Miocene based on continental sequences. *J. Geophys. Res.*, **108**, 2159.
- Berger, A., Loutre, M.F., and Dehant, V., 1989. Pre-Quaternary Milankovitch frequencies. *Nature*, **342**, 133.
- Berger, A.M., Loutre, M., and Laskar, J., 1992. Stability of the astronomical frequencies over the Earth's history for paleoclimate studies. *Science*, **255**, 260–266.
- Billups, K., Palike, H., Channell, J., Zachos, J., and Shackleton, N., 2004. Astronomical calibration of the Late Oligocene through Early Miocene geomagnetic polarity time scale. *Earth Planet. Sci. Lett.*, **224**, 33–44.
- Bond, G.C., Kominz, M.A., and Beavan, J., 1991. Evidence for orbital forcing of Middle Cambrian peritidal cycles: Wah Wah Range, south-central Utah. In Watney, L., Franseen, E., Kendall, C., and Ross, W. (eds.), *Sedimentary Modeling: Computer Simulations and Methods for Improved Parameter Definition*. Kansas Geological Survey Bulletin 233, pp. 293–318.
- Boss, S.K., and Rasmussen, K.A., 1995. Misuse of Fisher plots as sea-level curves. *Geology*, **23**, 221–224.
- Brack, P., Mundil, R., Meier, M., Oberli, F., and Rieber, H., 1996. Biostratigraphic and radiometric age data question the Milankovitch characteristics of the Latemar cycles (Southern Alps, Italy). *Geology*, **24**, 371–375.
- Bradley, W.H., 1929. The varves and climate of the Green River epoch. *U.S. Geological Survey Professional Paper*, **158**, 87–110.
- Cande, S.C., and Kent, D.V., 1995. Revised calibration of the geomagnetic polarity timescale for the late Cretaceous and Cenozoic. *J. Geophys. Res.*, **100**, 6093–6095.
- Correia, A.C., and Laskar, J., 2001. The four final rotation states of Venus. *Nature*, **411**, 767–770.
- Donovan, R.N., 1980. The lacustrine cycles, fish ecology and stratigraphic zonation in the middle Devonian of Caithness. *Scott. J. Geol.*, **16**, 35–50.
- Donovan, R.N., Foster, R.J., and Westoll, T.S., 1974. A stratigraphical revision of the Old Red Sandstone of northeastern Caithness. *Trans. R. Soc. Edinb.*, **69**, 171–205.
- Fischer, A.G., 1964. The Lofers cyclothem of the Alpine Triassic. *Kansas Geological Survey Bulletin* **169**, 107–149.
- Fischer, A.G., 1986. Climatic Rhythms Recorded in Strata. *Annu. Rev. Earth Planet. Sci.*, **14**, 351–376.
- Fischer, A.G., 1991. Orbital cyclicity in Mesozoic strata. In Einsele, G., Ricken, W., and Seilacher, A. (eds.), *Cycles and Events in Stratigraphy*. Berlin: Springer, pp. 48–62.
- Fischer, A.G., Herbert, T.D., Napoleone, G., Premoli Silva, I., and Ripepe, M., 1991. Albian pelagic rhythms (Piobbico Core). *J. Sediment. Res.*, **61**, 1164–1172.
- Gale, A.S., Young, J.R., Shackleton, N.J., Crowhurst, S.J., and Wray, D.S., 1999. Orbital tuning of Cenomanian marly chalk successions: Towards a Milankovitch time-scale for the Late Cretaceous. *Philos. Trans. R. Soc. London, Math. Phys. Eng. Sci.*, **357**, 1815–1829.
- Gilbert, G.K., 1895. Sedimentary measurement of Cretaceous time. *J. Geol.*, **3**, 121–127.
- Goldhammer, R.K., Dunn, P.A., and Hardie, L.A., 1987. High frequency glacio-eustatic oscillations with Milankovitch characteristics recorded in northern Italy. *Am. J. Sci.*, **287**, 853–892.
- Goldhammer, R.K., Oswald, E.J., and Dunn, P.A., 1991. Hierarchy of stratigraphic forcing – example from Middle Pennsylvanian shelf carbonates of the Paradox basin. In Franseen, E.K., Watney, W.L., Kendall, C.G. St. C., and Ross, W. (eds.), *Sedimentary Modeling: Computer Simulations and Methods for Improved Parameter Definition*. Kansas Geological Survey Bulletin 233, pp. 361–413.
- Goodwin, P.W., and Anderson, E.J., 1985. Punctuated Aggradational Cycles: A General Model of Stratigraphic Accumulation. *J. Geol.*, **93**, 515–534.
- Grotzinger, J.P., 1986. Upward shallowing platform cycles: A response to 2.2 billion years of low-amplitude, high-frequency (Milankovitch band) sea level oscillations. *Paleoceanography*, **1**, 403–416.
- Hays, J.D., Imbrie, J., and Shackleton, N.J., 1976. Variations in the Earth's orbit: Pacemaker of the ice ages. *Science*, **194**, 1131–1133.
- Herbert, T.D., and D'Hondt, S.L., 1990. Precessional climate cyclicity in Late Cretaceous-Early Tertiary marine sediments: A high resolution chronometer of Cretaceous-Tertiary boundary events. *Earth Planet. Sci. Lett.*, **99**, 263–275.
- Hilgen, F.J., 1991a. Astronomical calibration of Gauss to Matuyama sapropels in the Mediterranean and implications for the Geomagnetic Polarity Scale. *Earth Planet. Sci. Lett.*, **104**, 226–244.
- Hilgen, F.J., 1991b. Extension of the astronomically calibrated (polarity) timescale to the Miocene/Pliocene boundary. *Earth Planet. Sci. Lett.*, **107**, 349–368.
- Hilgen, F.J., Krijgsman, W., Langereis, C.G., Lourens, L.J., Santarelli, A., and Zachariasse, W.J., 1995. Extending the astronomical (polarity) timescale into the Miocene. *Earth Planet. Sci. Lett.*, **136**, 495.
- Hilgen, F.J., Krijgsman, W., Langereis, C.G., and Lourens, L.J., 1997. Breakthrough made in dating of the geological record. *Eos*, **78**, 285, 288–289.
- Hilgen, F.J., Abdul Aziz, H., Krijgsman, W., Langereis, C.G., Lourens, L.J., Meulenkamp, J.E., Raffi, I., Steenbrink, J., Turco, E., and van Vugt, N., 1999. Present status of the astronomical (polarity) time-scale for the Mediterranean Late Neogene. *Philos. Trans. R. Soc. London (series A)*, **357**, 1931–1947.
- Hinnov, L.A., 2000. New perspectives on orbitally forced stratigraphy. *Annu. Rev. Earth Planet. Sci.*, **28**, 419–475.
- Hinnov, L.A., 2005. Astronomical signals from Pre-Cenozoic eras. In Berger, A., and Ercegovac, M. (eds.), *Milutin Milankovitch 125th*

- Anniversary Symposium: Paleoclimate and the Earth Climate System, Proceedings of the Serbian Academy of Sciences and Arts, Serbia, Belgrade.*
- Hinnov, L.A., and Goldhammer, R.K., 1991. Spectral analysis of the Middle Triassic Latemar Limestone. *J. Sediment. Petrol.*, **61**, 1173–1193.
- Hinnov, L.A., and Park, J., 1998. Detection of astronomical cycles in the sedimentary record by frequency modulation (FM) analysis. *J. Geophys. Res.*, **68**, 524–539.
- Hofmann, A., Dirks, P.H.G.M., and Jelsma, H.A., 2004. Shallowing-upward carbonate cycles in the Belingwe Greenstone Belt, Zimbabwe: A record of Archean sea-level oscillations. *J. Sediment. Res.*, **74**, 64–81.
- Kent, D.V., and Olsen, P.E., 1999. Astronomically tuned geomagnetic polarity timescale for the Late Triassic. *J. Geophys. Res.*, **104**, 12831–12841.
- Kent, D.V., and Olsen, P.E., 2000. Implications of a new astronomical time scale for the Late Triassic. In Bachmann, G., and Lerche, I. (eds.), *Epicontinental Triassic*, vol 3, Zentralblatt fur Geologie und Palaontologie, VIII, pp. 1463–1474.
- Kent, D.V., Muttoni, G., and Brack, P., 2004. Magnetostratigraphic confirmation of a much faster tempo for sea-level change for the Middle Triassic Latemar platform carbonates. *Earth Planet. Sci. Lett.*, **228**, 369–377.
- Kieffer, H.H., and Zent, A.P., 1992. Quasi-periodic climate change on Mars. In Kieffer, H.H., Jakosky, B.M., Snyder, C.W., and Matthews, M.S. (eds.), *Mars*, Space Science Series. Tucson, AZ: University of Arizona Press, pp. 1180–1218.
- Kominz, M.A., and Bond, G.C., 1990. A new method of testing periodicity in cyclic sediment: Application to the Newark Supergroup. *Earth Planet. Sci. Lett.*, **98**, 233–244.
- Laskar, J., 1990. The chaotic motion of the solar system: A numerical estimate of the size of the chaotic zones. *Icarus*, **88**, 266–291.
- Laskar, J., 1999. The limits of Earth orbital calculations for geological time-scale use. *Philos. Trans. R. Soc. London, A*, **357**, 1735–1759.
- Laskar, J., Joutel, F., and Boudin, F., 1993. Orbital, precessional, and insolation quantities for the Earth from -20 myr to +10 myr. *Astron. Astrophys.*, **270**, 522–533.
- Laskar, J., Robutel, P., Joutel, F., Gastineau, M., Correia, A.C.M., and Levrard, B., 2004. A long term numerical solution for the insolation quantities of the Earth. *Astron. Astrophys.*, **428**, 261–285.
- Lowrie, W., and Kent, D.V., 2004. Geomagnetic polarity timescales and reversal frequency regimes. In Channell, J.E.T., Kent, D.V., Lowrie, W., and Meert, J. (eds.), *Timescales of the Paleomagnetic Field, AGU Geophysical Monograph 145*. Washington, DC: American Geophysical Union, pp. 117–129.
- Machlus, M., Hemming, S.R., Olsen, P.E., and Christie-Blick, N., 2004. Eocene calibration of geomagnetic polarity timescale reevaluated: Evidence from the Green River Formation of Wyoming. *Geology*, **32**, 137–140.
- Machlus, M., Olsen, P.E., Christie-Blick, N., and Hemming, S.R., 2008. Spectral Analysis of the Lower Eocene Wilkins Peak Member, Green River Formation, Wyoming: Support for Milankovitch Cyclicity. *Earth Planet. Sci. Lett.*, **286**, 64–75.
- Maynard, J.R., and Leeder, M.R., 1992. On the periodicity and magnitude of Late Carboniferous glacio-eustatic sea-level changes. *J. Geol. Soc.*, **149**, 303–311.
- Miller, D.J., and Eriksson, K.A., 1999. Linked sequence development and global climate change: The upper Mississippian record in the Appalachian basin. *Geology*, **27**, 35–38.
- Miller, K.G., Fairbanks, R.G., and Mountain, G.S., 1987. Tertiary oxygen isotope synthesis, sea level history, and continental margin erosion. *Paleoceanography*, **2**, 1–19.
- Muller, R., and MacDonald, G., 2000. *Ice Ages and Astronomical Causes: Data, Spectral Analysis, and Mechanisms*. London: Springer-Praxis, 318pp.
- Muttoni, G., Kent, D.V., Olsen, P.E., DiStefano, P., Lowrie, W., Bernasconi, S., and Hernandez, F.M., 2004. Tethyan magnetostratigraphy from Pizzi Mondello (Sicily) and correlation to the Late Triassic Newark astrochronological polarity time scale. *Geol. Soc. Am. Bull.*, **116**, 1043–1058.
- Olsen, P.E., 1986. A 40-million-year lake record of early Mesozoic climatic forcing. *Science*, **234**, 842–848.
- Olsen, P.E., and Kent, D.V., 1996. Milankovitch climate forcing in the tropics of Pangea during the Late Triassic. *Palaeogeogr. Palaeoclimatol. Palaeoecol.*, **122**, 1–26.
- Olsen, P.E., and Kent, D.V., 1999. Long-period Milankovitch cycles from the Late Triassic and Early Jurassic of eastern North America and their implications for the calibration of the early Mesozoic time scale and the long-term behavior of the planets. *Philos. Trans. R. Soc. London (series A)*, **357**, 1761–1787.
- Olsen, P.E., Schlichte, R.W., and Fedosh, M.S., 1996. 580 ky duration of the Early Jurassic flood basalt event in eastern North America estimated using Milankovitch cyclostratigraphy. In Morales, M. (ed.), *The Continental Jurassic*. Flagstaff, AZ: Museum of Northern Arizona. Museum of Northern Arizona Bulletin 60, pp. 11–22.
- Olsen, P.E., Kent, D.V., Sues, H.-D., Koeberl, C., Huber, H., Montanari, A., Rainforth, E.C., Fowell, S.J., Szajna, M.J., and Hartline, B.W., 2002. Ascent of dinosaurs linked to an iridium anomaly at the Triassic-Jurassic boundary. *Science*, **296**, 1305–1307.
- Palike, H., Laskar, J., and Shackleton, N.J., 2004. Geologic constraints on the chaotic diffusion of the solar system. *Geology*, **32**, 929–932.
- Pietras, J.T., Carroll, A.R., Singer, B.S., and Smith, M.E., 2003. 10 k.y. depositional cyclicity in the early Eocene: Stratigraphic and ⁴⁰Ar/³⁹Ar evidence from the lacustrine Green River Formation. *Geology*, **31**, 593–596.
- Preto, N., Hinnov, L.A., Hardie, L.A., and De Zanche, V., 2001. A Middle Triassic orbital signal recorded in the shallow marine Latemar carbonate buildup (Dolomites, Italy). *Geology*, **29**, 1123–1128.
- Rampino, M.R., Prokoph, A., and Adler, A., 2000. Tempo of the end-Permian event: High-resolution cyclostratigraphy at the Permian-Triassic boundary. *Geology*, **28**, 643–646.
- Sadler, P.M., Osleger, D.A., and Montañez, I.P., 1993. On the labelling, length and objective basis of Fischer plots. *J. Sediment. Petrol.*, **63**, 360–368.
- Schwarzacher, W., 1948. Sedimentpetrographische Untersuchungen kalkalpiner Gesteine; hallstaetterkalke von Hallstatt und Ischl. *Jahrbuch der Geologischen Bundesanstalt Wien*, **91**, 1–48.
- Schwarzacher, W., 1954. Die Grossrhythmik des Dachsteinkalkes von Lofer. *Tschermak's Mineralogische und Petrographische Mitteilungen*, **4**(1–4), 44–54.
- Schwarzacher, W., 1964. An application of statistical time-series analysis of a limestone/shale sequence. *J. Geol.*, **72**, 195–213.
- Schwarzacher, W., 1993. Milankovitch cycles in the pre-Pleistocene stratigraphic record; a review. In Hailwood, E.A., and Kidd, R.B. (eds.), *High Resolution Stratigraphy*. Geological Society Special Publications 70, pp. 187–194.
- Shackleton, N.J., Berger, A., and Peltier, W.R., 1990. An alternative astronomical calibration of the lower Pleistocene timescale based on ODP Site 677. *Trans. R. Soc. Edinb. Earth Sci.*, **81**, 251.
- Shackleton, N.J., Crowhurst, S.J., Weedon, G., and Laskar, L., 1999. Astronomical calibration of Oligocene-Miocene time. *R. Soc. London, Philos. Trans. series A*, **357**, 1909–1927.
- Shackleton, N.J., Hall, M.A., Raffi, I., Tauxe, L., and Zachos, J., 2000. Astronomical calibration age for the Oligocene-Miocene boundary. *Geology*, **28**, 447–450.
- Van Houten, F.B., 1964. Cyclic lacustrine sedimentation, Upper Triassic Lockatong Formation, central New Jersey and adjacent Pennsylvania. In Mermaid, O.F. (ed.), *Symposium on Cyclic Sedimentation*. Kansas Geological Survey Bulletin 169, 497–531.
- Weedon, G.P., 1993. The recognition and stratigraphic implications of orbital-forcing of climate and sedimentary cycles. In Wright, V.P. (ed.), *Sedimentology Review/1*. Oxford, UK: Blackwell Scientific Publications, pp.31–50.
- Weedon, G.P., 2003. *Time-series Analysis and Cyclostratigraphy-Examining Stratigraphic Records of Environmental Cycles*. Cambridge, UK: Cambridge University Press, 259pp.
- Weedon, G.P., Jenkyns, H.C., Coe, A.L., and Hesselbo, S.P., 1999. Astronomical calibration of the Jurassic time-scale from cyclostratigraphy in British mudrock formations. *Philos. Trans.: Math. Phys. Eng. Sci.*, **357**, 1787–1813.
- Whiteside, J.H., Olsen, P.E., Kent, D.V., Fowell, S.J., and Et-Touhami, M., 2007. Synchrony between the CAMP and the Triassic-Jurassic mass-extinction event? *Palaeogeogr. Palaeoclimatol. Palaeoecol.*, **244**, 345–367.
- Wilkinson, B.H., Diedrich, N.W., Drummond, C.N., and Rothman, E.D., 1998. Michigan hockey, meteoric precipitation, and carbonate accumulation on peritidal carbonate platforms. *Bulletin of the Geological Society of America*, **110**, 1075–1093.

Cross-references

Astronomical Theory of Climate Change
 Atmospheric Evolution, Mars
 Cyclic Sedimentation (cyclothem)
 Dating, Radiometric Methods
 Eccentricity
 Monsoons, Pre-Quaternary
 Monsoons, Quaternary
 Obliquity
 Oxygen Isotopes
 Precession, Climatic
 Quaternary Climate Transitions and Cycles
 SPECMAP
 Time-Series Analysis of Paleoclimate Data
 Varved Sediments

PROGLACIAL LACUSTRINE SEDIMENTS

Proglacial lacustrine sediments reflect changes in the size of glaciers. Because the size of a glacier depends on its mass balance (e.g., the balance between the amount of solid precipitation and temperature during the ablation season), lacustrine sediments can contribute to our knowledge about climatic change. Proglacial lacustrine sediments will yield information integrating the data on both temperature during the melting season and precipitation during the cold season. In general it is difficult to separate the extent of the contribution of these two factors to changes in mass balance.

Abundant snowfall and/or reduced ablation will yield a positive glacier mass balance; the glacier will respond to these factors by increasing its thickness, surface gradient, flow rate, and surface area (Menzies, 1995). This allows wet-based and polythermal (sub-polar) glaciers to erode the substrate more efficiently, i.e., produce more glacial silt, which will lead to a higher transport of silt in meltwater streams and an increased sedimentation rate in proglacial lakes. There are no streams flowing under cold-based (polar) glaciers, and therefore proglacial lacustrine sediments in these localities do not reflect changes in glacier size but only the fluvial erosion outside of the glaciated area.

Glacial meltwater streams carry the sediment washed out from beneath the glacial. The transport of glacier silt may not be directly related to the temporary glacier size because the streams may also carry sediments that had been previously eroded and trapped beneath the glacier or deposited in front of it. However, variations over periods of centuries are more likely to reflect glacier size. The sediment load can vary considerably and often the color of a glacial meltwater stream is grey or whitish during the melting season.

When glacial meltwater is loaded with sediment, the ratio of the inorganic component of the sediments in a proglacial lake (basically within the silt fraction) increases in comparison to the organic component. The silt content is therefore relatively large during periods with active glaciers; in addition, the rate of deposition of lacustrine sediment is slightly greater than it is during periods of reduced glacier size. Only rarely have annual laminations (varves) been observed in lakes with a high rate of sedimentation (Leonard, 1986).

Even if the influx of glacial silt can vary considerably over time, sediments typically have a relatively homogenous color. Therefore, visual stratigraphic descriptions do not necessarily reveal information about variations in glacier size. Variations in silt

content can be observed as a change in organic content (weight loss at ignition or by using a carbon analyzer). In addition, as silt content affects the penetration of X-ray radiation, even relatively subtle changes in glacial silt content can be detected by X-ray photography. This technique, when applied to thin slabs of sediment, permits the determination of the fine lamination not discernable when only the "weight loss at ignition technique" is applied. The density of an X-ray film will be proportional to the organic/inorganic sediment content. Thus, digitizing the film density will permit a semi-quantitative estimate of sediment influx (Karlen et al., 2002).

Non-glacier processes, such as land slides, avalanches and other rapid slope processes, can also produce high-density stratigraphic units (Rubensdotter, 2002). In non-glacial environments, these units are often distinct and easy to distinguish. The origin of such units can be less obvious in proglacial lacustrine sediments, because of the high inorganic background component and the similarity between units formed due to increased glacial erosion and to rapid slope processes. However, when considered together in combination, the presence of a distinct lower boundary of the unit, as well as a grain size distribution deviating from that of the relatively homogenous deposits of glacial silt facilitates classification. Changes in precipitation and possibly also major changes in vegetation cover can yield a lacustrine sediment signal similar to the one created by a glacial meltwater influx. However, this signal will be markedly weaker.

Information from a proglacial lake is of limited value until a chronology has been established. The most common method is ^{14}C dating of macrofossils or of organic-rich layers (AMS, accelerator mass spectrometry). Additional methods include ^{210}Pb , ^{137}Cs and the recognition of volcanic ashes of known age.

Proglacial sediments yield, in contrast to several other techniques, a continuous record of glacier size variations. These proglacial records can confirm results of studies that yield dates on single events and can also add important details. The sediment record, as well as other records, such as dendrochronology, indicates a frequently fluctuating climate during the Holocene. However, glaciers in many areas, particularly in those areas that are at present marginal, vanished during the early and mid-Holocene, a period well known to have been slightly warmer than the present time.

Wibjörn Karlén

Bibliography

- Karlen, W., Odada, E., and Svanered, O., 2002. Organic content and X-ray density of lacustrine sediments from Hausberg Tarn, Mount Kenya. In Odada, E., and Olago, O. (eds.), *The East African Great Lakes: Limnology, Paleolimnology and Biodiversity*. Dordrecht: Kluwer, pp. 525–533.
- Leonard, E.M., 1986. Varve studies at Hector Lake, Alberta, Canada, and the relationship between glacial activity and sedimentation. *Quaternary Res.*, **25**, 199–214.
- Menzies, J., 1995. Glaciers and ice sheets. In Menzies, J. (ed.), *Modern Glacial Environments: Processes, Dynamics and Sediments*. Oxford: Butterworth-Heinemann, pp. 101–138.
- Rubensdotter, L., 2002. Detailed geomorphological survey of a small mountain drainage area, Abisko, northern Swedish Lapland. *Geogr. Ann.*, **84A**(3–4), 267–273.

Cross-references

Dating, Radiometric Methods
 Dendroclimatology
 Glacial Geomorphology

Glacial Megalakes
 Holocene Climates
 Hypsithermal
 Lacustrine Sediments
 Little Ice Age
 Millennial Climate Variability
 Paleotemperatures and Proxy Reconstructions
 Radiocarbon Dating
 Varved Sediments

PROTEROZOIC CLIMATES

The Proterozoic eon is a subdivision of geologic time (Figure P94). It extends from the end of the Archean eon at 2.5 billion years ago (Ga) to the beginning of the Phanerozoic eon/Cambrian period at 542 million years ago (Ma). This long period, encompassing almost half of the Earth's history, has been divided into three parts: the Paleoproterozoic, Mesoproterozoic and Neoproterozoic eras (Figure P94). This brief summary will emphasize some highlights of Proterozoic paleoclimatology.

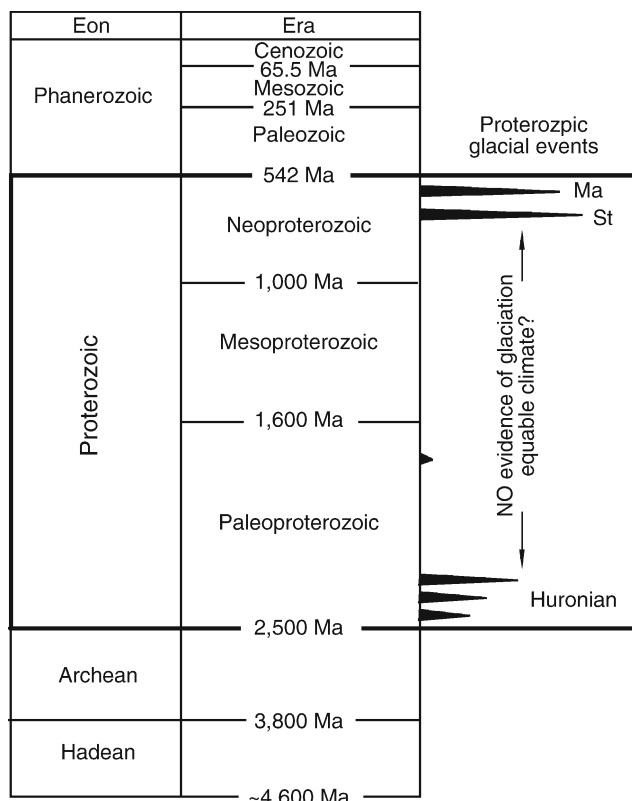


Figure P94 Subdivisions of geologic time to show the occurrence of glaciogenic rocks near the beginning and end of the Proterozoic eon. Three glacial episodes are recorded in the Huronian in North America. *St*, Sturtian; *Ma*, Marinoan. Note there may be more glacial episodes in the Neoproterozoic.

Problems in interpretation of Proterozoic paleoclimates

Interpretation of ancient climatic conditions is based mainly on investigation of sedimentary rocks, but the study of Proterozoic rocks is more difficult than that of younger (Phanerozoic) rocks for several reasons. Fossils of life forms such as land plants and complex animals (metazoans) often play an important role in interpretation of Phanerozoic rocks because many organisms are climatically sensitive, but such fossils are scarce to absent from the Proterozoic record. Some evaporitic minerals, such as sulfate and chloride salts, provide paleoclimatic clues in younger rock sequences but are rare in the Paleoproterozoic. The dearth of evaporitic rocks could be related to a lack of certain solutes (such as sulfate) in ocean waters and/or could be due to the susceptibility of such soluble materials to loss by subsequent dissolution.

One of the great problems in Precambrian paleoclimatology has been the “faint young Sun paradox.” Based on the known life histories of stars, astrophysicists have proposed that the early or “young” Sun must have been considerably less luminous than at present. The figure of ~30% less radiation is commonly used for about 2.5 Ga, the beginning of the Proterozoic. The paradox arises because, with the present atmosphere, it has been calculated that the early Earth's surface should have been entirely frozen but evidence from abundant waterlain Archean sedimentary rocks clearly contradicts this. The solution to the faint young Sun paradox has revolved around the idea that the Earth's atmosphere was different during its early history. Specifically, it has been suggested that liquid water was maintained on the Earth's surface as a result of enhanced atmospheric content of greenhouse gases (carbon dioxide, methane, etc.). If these interpretations are correct, then rocks with a highly “weathered” chemical signature could have been produced under relatively cool conditions (because of the high CO₂ content of the atmosphere, giving rise to extremely acid rains). Likewise, the occurrence of three glacial episodes in Huronian times may be explained by fluctuations in the greenhouse gas content (especially CO₂) of the atmosphere. Descent of the Earth into frigid episodes would have occurred more readily in Paleoproterozoic times because of reduced solar luminosity.

Paleolatitude and paleoclimate

In Phanerozoic (<542 Ma) sedimentary successions (Figure P94), there is some correspondence between ancient latitude (paleolatitude) and climate, as is observed today. Paleomagnetic interpretations are based on the assumption that the magnetic field of the ancient Earth was dipolar and that the orientation of the Earth's magnetic axis was similar to that of its rotational axis. In an attempt to explain the apparent occurrence of Proterozoic glacial deposits in equatorial paleolatitudes, it has been suggested (Williams, 1993) that, prior to the Cambrian, the obliquity of the ecliptic may have exceeded 54°.

Proterozoic glaciations

By far the most striking aspect of Proterozoic paleoclimatology is the evidence of widespread glaciations near the beginning and end of that eon (Young, 2003). The near-absence of such evidence during the long intervening period (spanning about 1.5 Ga) is, however, perhaps even more remarkable. Cold periods in Earth's history, such as that of the Paleoproterozoic, are easily identified from field observations, including the following:

1. Diamicrites are sedimentary rocks that consist of large rock fragments (clasts) “floating” in a finer grained matrix.

Since such sedimentary rocks can form by a variety of sedimentary processes, additional criteria are necessary to confirm their glaciogenic nature, such as the presence of faceted and/or striated clasts, for example.

2. The presence of a scratched or striated substrate, commonly developed beneath a diamictite. Striated “pavements” are a good criterion of glacial activity. They are formed by erosive action of rock fragments carried in glacier ice as it advances over a substrate.
3. Dropstones are isolated rock fragments in laminated or finely bedded sedimentary rocks, generally believed to have been transported by glacial ice that, on reaching a body of water, calved off icebergs that melted, freeing the stones.
4. The occurrence of rhythmic alternations of thin beds and laminae of siltstone and claystone (varves). Such couplets are thought to represent annual accumulations of sediment in proglacial lakes, the coarser layer representing accumulation during the summer months when there was more melt-water available and the finer material being deposited (largely from suspension) during winter.

Paleoproterozoic paleoclimates

The majority of Paleoproterozoic glacial deposits have been documented in North America but similar glaciogenic rocks have also been identified in NW Europe, in South Africa and in Western Australia. The earliest recognized and best known early Proterozoic glaciogenic rocks occur in the Huronian Supergroup, which is a thick succession (up to about 11 km) of mainly sedimentary rocks in Ontario, Canada. Glacial diamictites and associated sedimentary rocks occur at three different levels within the Huronian Supergroup but the thickest and most widespread of these is the Gowganda Formation. This unit is considered to be approximately correlative with similar deposits of similar age (~2.3 Ga) in several places in North America and, less certainly, around the world.

One unusual aspect of the Paleoproterozoic glaciogenic deposits is that they are commonly associated with other sedimentary rocks containing geochemical and other evidence that they were deposited under conditions of relatively intense weathering (Nesbitt and Young, 1982). By calculating a chemical index of alteration (*CIA*), major elements can be used to quantify the degree of chemical weathering to which sedimentary materials have been subjected (Nesbitt et al., 1996). The *CIA* is calculated according to the formula:

$$CIA = (Al_2O_3 / (Al_2O_3 + CaO^* + Na_2O + K_2O)) \times 100 \quad (1)$$

This calculation quantifies the ratio of secondary aluminous clay minerals formed during the weathering process to primary minerals (mainly feldspars). CaO^* means CaO that occurs in silicate minerals, as opposed to that in carbonates and phosphates. The *CIA* formula yields a number that ranges between about 50 (fresh rocks) and 100 (extremely weathered materials). In applying this technique to sedimentary successions, care must be taken to compare values from rocks of similar grain size because clay minerals tend to be smaller than primary minerals such as feldspar and quartz. During natural sorting of weathered materials, the fine grained sediments will tend to have a high proportion of clay minerals, which will yield higher *CIA* values than associated sandy materials. *CIA* values of ancient sedimentary and other materials (e.g., ancient weathering profiles or paleosols) can be modified by metasomatic introduction of elements such as K and Na. Such

alterations can, however, be detected by judicious use of the *CIA* and, in particular by illustrating the data on a triangular plot with Al_2O_3 , $CaO^* + Na_2O$ and K_2O at its apices. For details of this and other aspects of the application of this technique, see Fedo et al. (1995).

Whereas it must be recognized that the *CIA* is not simply controlled by climatic conditions (other factors include tectonism, diagenesis and metasomatic alteration), when judiciously applied, it provides a useful tool for obtaining insight into weathering intensity, which is, in turn, controlled by temperature and rainfall. It can thus provide a powerful proxy for paleoclimate.

In the case of the Paleoproterozoic Huronian Supergroup, *CIA* values from mudstones throughout this thick succession have shown that the three glacial episodes were superimposed on a regime that was characterized by relatively strong weathering (high *CIA* values). This paleoclimatic conundrum – the juxtaposition of deposits formed in a frigid regime with those resembling sediments formed in warm humid regions of the Earth today – may be resolved by invoking differences in atmospheric composition. Various lines of geological evidence from the Huronian Supergroup and similar successions elsewhere also suggest that the early atmosphere was oxygen-deficient before about 2.5 Ga and that during deposition of the Huronian at least some free oxygen accumulated. By about 2.3 Ga, the presence of red beds (clastic sediments that contain red pigmentation, related to the presence of disseminated hematite) suggests that some free oxygen was available in the atmosphere.

The Mesoproterozoic equable interval

Following the glacial episodes of the Huronian and their equivalents elsewhere, the Earth appears to have entered a long period during which equable climates predominated. Stable isotopes of carbon preserved in sedimentary rocks suggest that the oxygen content of the atmosphere may have peaked at about 2.1 Ga and then diminished and remained low until the Neoproterozoic, when the first complex animals made their appearance. This decrease in atmospheric oxygen may have been accompanied by an increase in CO_2 , which, together with strengthening of the Sun's radiative signal, may explain the equable climates that appear to typify this long period of geological history (from about 2.2 Ga to about 750 Ma). However, recently Williams (2005) has described glaciogenic rocks dated at about 1,800 Ma from Western Australia. The widespread development of stromatolitic carbonates and common preservation of red beds have been cited as evidence of warm climatic conditions during the Mesoproterozoic but interpretation of such features is not always certain. Examples of cold water stromatolites have been described from the literature and these organo-sedimentary structures may have proliferated in much more varied environments than at present because of the absence of predatory metazoans. Likewise, red beds are more indicative of the presence of free oxygen in the atmosphere than of ambient temperatures at the time of their formation.

The Neoproterozoic climatic convulsions

Following the enormously long and paleoclimatologically “quiet” period of the Mesoproterozoic, the latter half of the Neoproterozoic (from about 750 Ma to the beginning of the Cambrian period at 542 Ma) was characterized by some of the most extremely cold climatic episodes that the Earth has ever known. These events are inferred from extremely widespread and convincing

evidence (on every continent) of glacial depositional processes. The exact number and extent of glacial episodes remain unresolved but they appear to have ended by the beginning of the Cambrian, which saw a return to relatively warm climatic conditions and a burgeoning in the Earth's population of complex animals (metazoans). Some have suggested that there were two major glacial episodes, known as the Sturtian (~750–720 Ma) and the Marinoan (~620–600 Ma).

When reliable physical criteria for the recognition of ancient glacial deposits were developed, it was realized that Neoproterozoic glaciogenic rocks were extremely widespread. As far back as the 1940s, it was suggested that the Earth may have experienced a glaciation (or glaciations) so severe that its entire surface was frozen (Mawson, 1949). With the development of sedimentological and paleomagnetic techniques, it was also claimed that many of these ancient glaciers had descended to sea level in equatorial latitudes. Although glaciers exist today in low latitude regions (e.g., on Mount Kilimanjaro, which is about 3 degrees south of the equator), they are present only on high mountain tops and melt before they can descend to sea level, because of elevated temperatures. These paleomagnetic findings lent fuel to the concept of a frozen planet.

In recent years another element was added, namely the discovery that there are significant fluctuations in the isotopic ratios of carbon (and oxygen) in carbonate rocks beneath and above many Neoproterozoic glacial successions. The lows and highs in carbon isotopic ratios were interpreted to reflect the near-extirpation and blooms of marine photosynthetic microorganisms, respectively. The photosynthetic metabolic pathways of many marine microorganisms lead to sequestering of the light isotope of carbon (^{12}C), which, in turn, leads to an ocean enriched in the heavier isotope (^{13}C). High $\delta^{13}\text{C}$ values tend to occur during organic blooms. Thus, if seawater and carbonates derived there from exhibit low values of the carbon isotopic ratio ($\delta^{13}\text{C}$), this suggests a dearth of organic activity. Low $\delta^{13}\text{C}$ values were reported from carbonates below and above some glacial deposits and were interpreted to mean the near-extirpation of life during world-encircling glacial episodes (Hoffman et al., 1998). Subsequently it has been shown that many photosynthetic microorganisms survived through the Neoproterozoic glacial episodes and several alternative explanations for the carbon isotopic anomalies have been suggested (e.g., Kennedy et al., 2001). These anomalous geochemical signatures are therefore poorly understood.

The sum of evidence for widespread Neoproterozoic glaciations led to coining of the term, "Snowball Earth Hypothesis" (Kirschvink, 1992; Hoffman et al., 1998). This controversial theory proposed that the Neoproterozoic glaciations were so severe that the entire surface of the planet was frozen. Such global glaciation was explained by a "runaway albedo" effect – when icecaps extend to middle latitudes, it is hypothesized that the amount of solar energy reflected (lost) from the ice is sufficient to promote rapid glacial advance. Escape from such a condition was attributed to gradual build-up of CO_2 in the atmosphere by volcanic activity related to on-going plate tectonics. According to the hypothesis, destruction of the ice cover would be extremely rapid, followed by establishment of very warm conditions and extreme weathering that would flush the oceans with weathering products that gave rise to post-glacial carbonates, the so-called "cap carbonates." This version of the Snowball Earth Hypothesis remains controversial. New evidence for a series of geomagnetic reversals in the cap carbonates suggests that deglaciation was a long process and not a catastrophic event.

Problems with the Snowball Earth Hypothesis

There are many problems associated with the Snowball Earth Hypothesis. A few are discussed briefly below. Many Neoproterozoic glacial successions are very thick (several km). Such abundant glacial sediments are unlikely under the Snowball Earth Hypothesis, for the hydrological cycle would have been essentially cut off. Neoproterozoic glacial deposits that formed at sea level in low latitudes contain evidence of strong seasonality (varved deposits, fossil ice-wedge structures) not seen in tropical regions at present. One possible explanation is that the obliquity of the ecliptic (tilt of the Earth) was much greater (Williams, 1993), leading to low latitude glaciation. It has, however, been suggested by some (e.g., Pais et al., 1999) that the high obliquity hypothesis does not account well for the Neoproterozoic glaciation. Another major problem is that paleontological studies of a number of Neoproterozoic successions appear to show that many life forms survived through the Neoproterozoic glaciations so that the proposed "near-extirpation" of life, proposed as a possible explanation of the C-isotope excursions in associated carbonate rocks, does not seem to have occurred. In any event, the Neoproterozoic was a time when the planet underwent extreme climatic variations. Associated dramatic environmental changes could have been a major factor in promoting evolution of the diverse assemblage of complex life forms that characterizes the remainder of geologic time.

Conclusions

Paleoclimatological studies of the Proterozoic are rendered difficult by the dearth of fossil remains of environmentally-sensitive organisms and the rarity of some rock types (such as coals and evaporites) that facilitate climatological interpretations. Most Proterozoic sedimentary rocks lack evidence of glaciation, suggesting that the typical world temperatures were moderate. Near the beginning and end of the Proterozoic, however, there is abundant evidence of multiple widespread glaciations. Neoproterozoic glaciogenic sediments are the most extensive in the world and provide evidence of tremendous climatic upheaval, but whether the entire surface of the planet was frozen (Snowball Earth Hypothesis) at any one time remains unknown. The dramatic paleoclimatic events at the end of the Proterozoic may have played a significant role in the emergence and proliferation of metazoans at the beginning of the Phanerozoic eon.

Grant M. Young

Bibliography

- Fedo, C.M., Nesbitt, H.W., and Young, G.M., 1995. Unraveling the effects of potassium metasomatism in sedimentary rocks and paleosols, with implications for paleoweathering conditions and provenance. *Geology*, **23**, 921–924.
- Hoffman, P.F., Kaufman, A.J., Halverson, G.P., and Schrag, D.P., 1998. A Neoproterozoic Snowball Earth. *Science*, **281**, 1342–1346.
- Kennedy, M.J., Christie-Blick, N., and Prave, A.R., 2001. Carbon isotopic composition of Neoproterozoic glacial carbonates as a test of paleoceanographic models for Snowball Earth phenomema. *Geology*, **29**, 1135–1138.
- Kirschvink, J.L., 1992. Late Proterozoic low-latitude glaciation: The snowball Earth. In Schopf, J.W., and Klein, C. (eds.), *The Proterozoic Biosphere: A Multidisciplinary Study*. Cambridge: Cambridge University Press, 51–52.
- Mawson, D., 1949. The late Precambrian ice age and glacial record of the Bibliando Dome. *J. Proc. R. Soc. New S. Wales*, **82**, 150–174.

- Nesbitt, H.W., and Young, G.M., 1982. Early Proterozoic climates and plate motions inferred from major element chemistry of lutites. *Nature*, **299**, 715–717.
- Nesbitt, H.W., Young, G.M., McLennan, S.M., and Keays, R.R., 1996. Effects of chemical weathering and sorting on the petrogenesis of siliciclastic sediments, with implications for provenance studies. *J. Geol.*, **104**, 525–542.
- Pais, M.A., Le Mouel, J.L., Lambeck, K., and Poirier, J.P., 1999. Late Precambrian paradoxical glaciation and obliquity of the Earth—a discussion of dynamical constraints. *Earth Planet. Sci. Lett.*, **174**, 155–171.
- Williams, G.E., 1993. History of Earth's obliquity. *Earth Sci. Rev.*, **34**, 1–45.
- Williams, G.E., 2005. Subglacial meltwater channels and glaciofluvial deposits in the Kimberley Basin, Western Australia: 1.8 Ga low latitude glaciation coeval with continental assembly. *J. Geol. Soc. Lond.*, **162**, 111–124.
- Young, G.M., 2003. Stratigraphic and tectonic settings of Proterozoic glaciogenic rocks and banded iron-formations: Relevance to the snowball Earth debate. *J. Afr. Earth Sci.*, **34**, 451–466.

Cross-references

Albedo Feedbacks
Archean Environments
Atmospheric Evolution, Earth
Carbon isotopes, Stable
Diamicton
Faint Young Sun Paradox
Ice-rafted Debris (IRD)
Obliquity
Oxygen isotopes
Paleosols, Pre-Quaternary
Sedimentary Indicators of Climate Change
Snowball Earth Hypothesis
Stable Isotope Analysis
Varved Sediments
Weathering and Climate

Q

QUATERNARY CLIMATE TRANSITIONS AND CYCLES

Introduction

The last few million years have been punctuated by many abrupt climate transitions, many of them occurring on time scales of centuries or even decades. These sudden stepwise climate transitions provide a disturbing scenario in terms of possible human effects on the present climate system through global warming. In order to gain a better understanding of our current climate system, we need to comprehend the causes of past climate transitions and cycles. This paper examines key climate transitions in the Quaternary period identified as: (a) the Intensification of Northern Hemisphere Glaciation (INHG), which heralded the start of the Quaternary period; (b) the intensification of the Walker Circulation; (c) glacial-interglacial cycles; (d) the Mid-Pleistocene Revolution (MPR); (e) Heinrich events and glacial Dansgaard-Oeschger (D-O) cycles; and (f) the last glacial-interglacial transition (LGIT) including the Younger Dryas. For each key climate transition, the current theories of causation are examined in terms of external and/or internal forcing factors.

Modes of climate change

Until a few decades ago, it was generally thought that significant large-scale global and regional climate changes occurred gradually over many centuries or millennia. Hence, the climate shifts were assumed scarcely perceptible during a human lifetime. The tendency of climate to change abruptly throughout the Quaternary period (last 2.5 million years) has been one of the most surprising outcomes of the study of Earth history. Some of these observed regional changes involve a shift in the mean annual temperature of several degrees Celsius within a few decades. These sudden stepwise climate transitions illustrate disturbing scenarios in terms of potential anthropogenic effects on the climate system through greenhouse gas emissions (Maslin, 2004a). Global climate variability in the Quaternary

can be divided into individual transitions; for example, the intensification of glaciation in the Northern Hemisphere is a good example of the global climate system shifting to a new equilibrium. Tied transitions are part of regular or quasi-cyclic climate changes; for example, the waxing and waning of the Ice Ages (or glacial period) which characterize the Quaternary period. Each transition, however, is a response to external and/or internal forcing mechanisms. A good example of an external forcing mechanism is the changing orbital parameters that alter the net radiation budget of the Earth, while an example of an internal forcing mechanism is the carbon dioxide content of the atmosphere, which modulates the greenhouse effect (Maslin, 2004a). We can abstract the way the global climate system responds to an internal or external forcing agent by examining four different scenarios:

1. Linear and synchronous response (Figure Q1a). In this case, the forcing produces a direct response in the climate system with a magnitude that is in proportion to the forcing.
2. Muted or limited response (Figure Q1b). In this case, the forcing may be extremely strong, but the climate system is buffered and therefore has very little response.
3. Delayed or non-linear response (Figure Q1c). In this case, the climate system may have an initial slow response to the forcing. The climate system response may then accelerate in a non-linear way until it overshoots the forcing effect and then drops back in an attempt to reach equilibrium with the forcing.
4. Threshold response (Figure Q1d). In this case, there is initially no or very little response in the climate system to the forcing; however, all the response takes place in a very short period of time in one large step or threshold. In many cases, the response may be much larger than one would expect from the size of the forcing and this can be referred to as a response overshoot.

Although these are purely theoretical models of how the climate system can respond, they are important to keep in mind when trying to understand Quaternary climate transitions. An added complication when assessing the causes of climate transitions is the possibility that climate thresholds contain

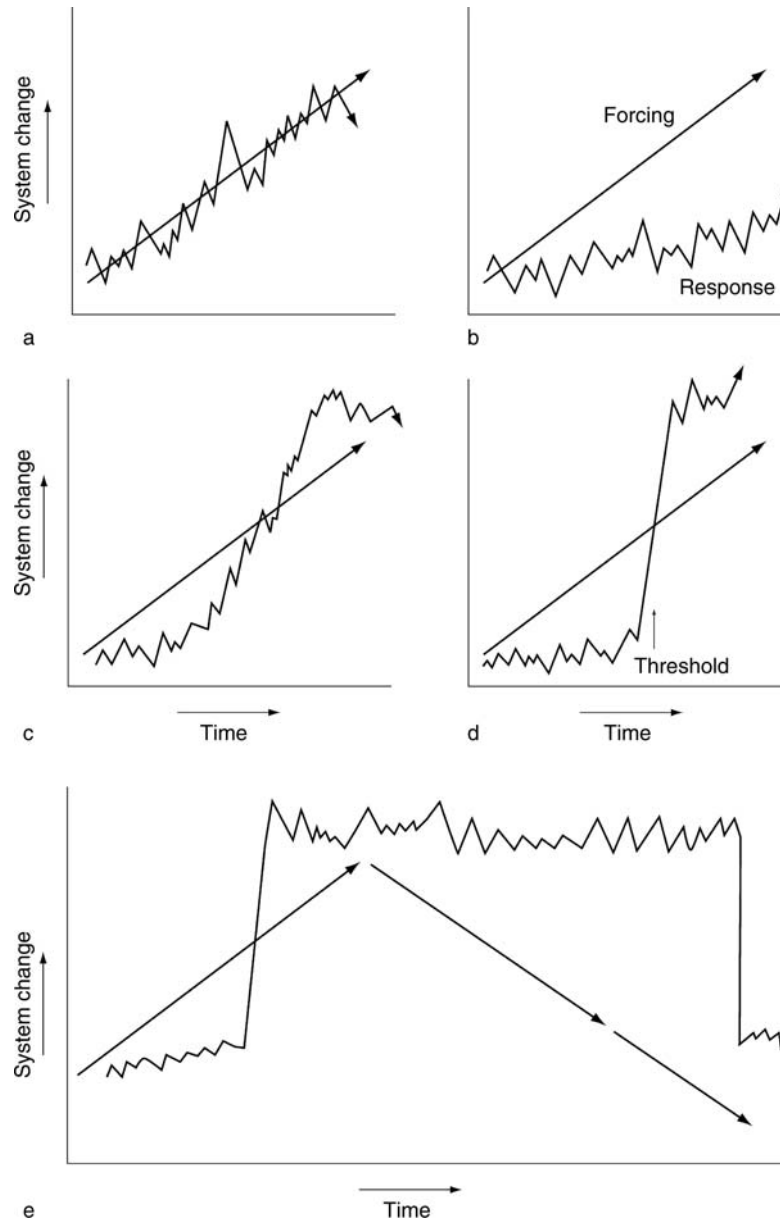


Figure Q1 Schematic diagram of the four alternative responses of the global climate system to internal or external forcing: (a) Linear and synchronous response: forcing produces a direct response with a magnitude that is proportional to the forcing. (b) Muted or limited response: forcing may be extremely strong, but the climate system is in some way buffered and therefore has very little response. (c) Delayed or non-linear response: the climate system may respond slowly to the forcing or is in some way buffered initially, but then responds to the forcing in a non-linear way. (d) Threshold response: very little or no response to the forcing initially, however all the response then takes place in a very short period in one large step or threshold. In many cases, the response may be much larger than expected from the size of the forcing, leading to a response over-shoot. (e) Bifurcation. Similar to the threshold response except that reversing the forcing does not reverse the climate response, see Figure Q2.

bifurcations (Figure Q1e). This means the forcing required to cause a climate transition is different from that needed to reverse it. This bifurcation of the climate system has been inferred from ocean models which mimic the impact of fresh-water (control variable) on deep-water formation in the North Atlantic (climate variable) (e.g., Rahmstorf, 1995). However, a bifurcation relationship could be applied to many forcing mechanisms and the corresponding responses of the global

climate system. For example, Maslin (2004b) applied it to rainfall control on rainforest versus savannah vegetation in the tropics. Figure Q2 demonstrates this bifurcation of the climate system and shows that different relationships exist between climate and forcing mechanism, depending on the direction of the threshold. This is very common in natural systems, for example in cases where inertia or the shift between different states of matter need to be overcome. Figure Q2 shows that

in cases A and B, the system is reversible, but in case C, it is not. Figure Q1e shows how case C would manifest itself if the outcome were plotted on a forcing-response diagram.

In this paper, current theories on major transitions and cycles within the Quaternary period are reviewed, always considering the modes of climate changed discussed above. These include the Intensification of Northern Hemisphere Glaciation (~2.5 Ma), intensification of the Walker Circulation (~1.9 Ma), glacial-interglacial cycles, Mid-Pleistocene Revolution (~1 Ma), quasi-periodic millennial climate cycles and the last glacial-Holocene transition (Figure Q3).

Onset and intensification of Northern Hemisphere glaciation

Heralding the start of the Quaternary period

The earliest recorded onset of significant global glaciation during the last 100 Ma was the widespread continental glaciation of Antarctica at about 34 Ma (e.g., Zachos et al., 2001). Records indicate that ice rafting started in the Arctic as early as 46 Ma (Eldrett et al., 2007) but major glaciation did not occur until 14–6 Ma (Thiede et al., 1998). Marked expansion of continental ice sheets in the Northern Hemisphere was the culmination of a

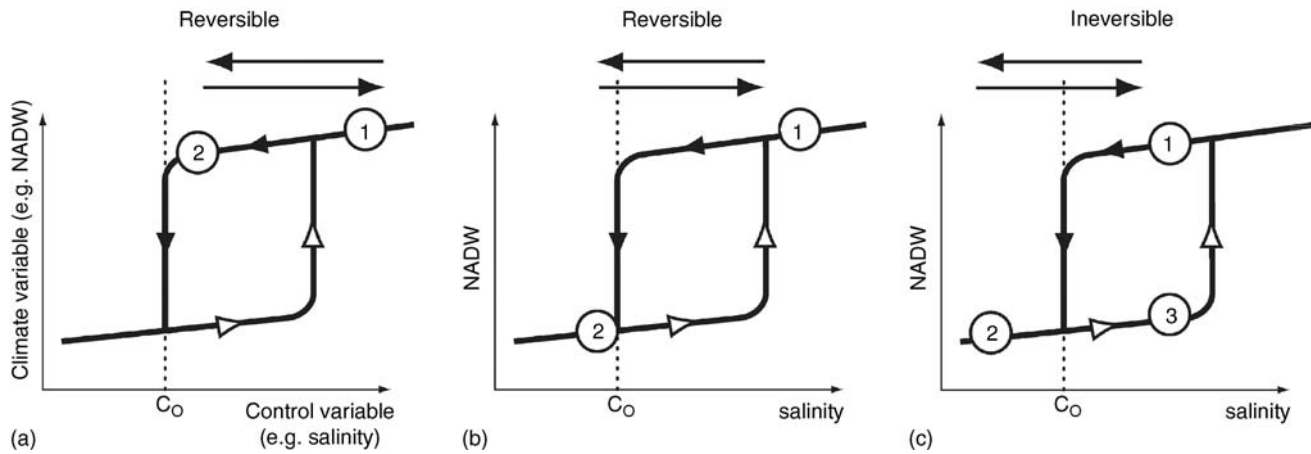


Figure Q2 Bifurcation of the global climate system. For example, the control variable could be North Atlantic salinity and the climate variable could be production of NADW. (a) An insensitive system in which the climate variable does not vary greatly with large changes in the control variable. (b) The control variable drops beneath the critical threshold point C_0 (point 2), causing a major change in the climate variable; however, by returning the control variable to its original state, the system is reversible and the climate variable returns to its original point 1. (c) The control variable drops beneath the critical threshold point C_0 (point 2); however, returning the control variable to its original state does not reverse the change and the climate variable remains at point 3. An additional change to the control variable is required to overcome the bifurcation and return the climate variable back to point 1. If this change cannot occur, then the threshold becomes irreversible. Note that returning the system back to its initial boundary conditions by going beyond point 3 may take the system to a new state of equilibrium that differs from the initial state.

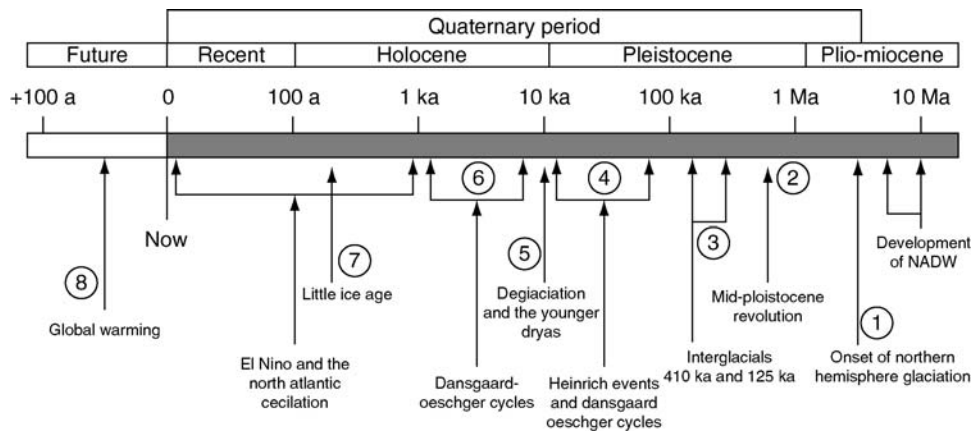


Figure Q3 Schematic diagram (logarithmic timescale) illustrating the most important climate events in the Quaternary period discussed in this entry. (1) Intensification of Northern Hemisphere glaciation (3.2–2.5 Ma), inducing the strong glacial-interglacial cycles characteristic of the Quaternary period. Also in this period is the intensification of the Walker Circulation in the tropics at about 1.9 Ma. (2) Mid-Pleistocene Revolution when the periodicity of glacial-interglacial cycles switched from 41 ka to every 100 ka. (3) Glacial-interglacial cycles (of particular importance are oxygen isotope stages 5 and 11 which may have characteristics similar to the current Holocene interglacial). (4) Heinrich events and Dansgaard-Oeschger cycles. (5) Deglaciation and the Younger Dryas events. (6) Holocene Dansgaard-Oeschger cycles. (7) Little Ice Age, the most recent example of the Holocene D-O cycles. (8) The future and global warming.

longer term, high latitude cooling, which began with the late Miocene glaciation of Greenland and the Arctic and continued through to the major increase in global ice volume around 3.6 Ma (Mudelsee and Raymo, 2005). It has been suggested there were three key steps in this climate transition: (a) Eurasian Arctic, Northeast Asia and North America glaciated at approximately 2.74 Ma, (b) Alaska glaciation occurred at 2.70 Ma, and (c) a significant increase in the glaciation of the North East American continent occurred at 2.54 Ma (Maslin et al., 1998; Kleiven et al., 2002).

Possible causes of the intensification of Northern Hemisphere glaciation

The predominant theories to explain the Intensification of Northern Hemisphere Glaciation (INHG) have focused on major tectonic events and their modification of both atmospheric and ocean circulation (Hay, 1992; Maslin et al., 1998). For example, the uplift and erosion of the Tibetan-Himalayan Plateau, the deepening of the Bering Straits and/or the Greenland-Scotland Ridge, and emergence of the Panama Isthmus have all been suggested.

Ruddiman and Raymo (1988) suggested that the initiation of Northern Hemisphere glaciation was caused by progressive uplift of the Tibetan-Himalayan and Sierran-Coloradan regions. This may have altered the circulation of atmospheric planetary waves such that summer ablation was decreased, allowing snow and ice to build-up in the Northern Hemisphere. However, most of the Himalayan uplift occurred much earlier, between 20 and 17 Ma, and thus is too early to have been the direct cause of the INHG. It was then suggested that uplift caused a massive increase in tectonically-driven chemical weathering in the late Cenozoic. Raymo (1994) argue that carbonation of rainwater removes CO₂ from the atmosphere and forms a weak carbonic acid solution, with dissociated H⁺ ions in the acidified rainwater caused by hydrolysis leading to enhanced chemical weathering of rocks. Only weathering of silicate minerals makes a difference to atmospheric CO₂ levels, as weathering of carbonate rocks by carbonic acid returns CO₂ to the atmosphere. By-products of hydrolysis reactions affecting silicate minerals are bicarbonate (HCO₃⁻) anions and calcium cations. These, when washed into the oceans, are metabolized by marine plankton and are converted to calcium carbonate. The calcite skeletal remains of the marine biota are ultimately deposited as deep-sea sediments and hence lost from the global biogeochemical carbon cycle for the duration of the life cycle of the oceanic crust on which they were deposited. Consequently, atmospheric CO₂ could have been depleted, causing a cooling of the global climate and thus the INHG. This theory, however, suffers from a number of major draw-backs: (a) there is debate whether strontium (Sr) isotope data can be used as evidence of continental weathering, (b) there seems to be no obvious negative feedback mechanism to prevent a complete depletion of the relatively small reservoir of atmospheric CO₂, and (c) there is now evidence that suggest that there was no decrease in atmospheric carbon dioxide during the Miocene.

A second key tectonic control invoked as a trigger for the INHG is the closure of the Pacific-Caribbean gateway. Haug and Tiedemann (1998) suggest it began to emerge at 4.6 Ma and finally closed at 1.8 Ma. The closure of the Panama gateway, however, causes a paradox (Berger and Wefer, 1996) as it would have both helped and hindered the intensification of North Hemisphere glaciation. The reduced inflow of Pacific

surface water to the Caribbean would have increased the salinity of the Caribbean, increasing the salinity of water carried northward by the Gulf Stream and North Atlantic Current, and thus enhancing deepwater formation. Increased deep-water formation could have worked against the initiation of Northern Hemisphere glaciation as it enhances the oceanic heat transport to the high latitudes and would have opposed ice sheet formation (see Figure Q4). This enhanced Gulf Stream would also have pumped more moisture northward, stimulating the formation of ice sheets.

Tectonic forcing alone cannot explain the fast changes of both the intensity of glacial-interglacial cycles and mean global ice volume. It has therefore been suggested that changes in orbital forcing may have been an important mechanism contributing to gradual global cooling and the subsequent rapid intensification of Northern Hemisphere glaciation (Haug and Tiedemann, 1998; Maslin et al., 1998). The observed increase in the amplitude of orbital obliquity cycles from 3.2 Ma onwards may have increased the seasonality of the Northern Hemisphere, thus initiating the long-term global cooling trend (Figure Q4). The subsequent sharp rise in the amplitude of precession and consequently in insolation at 60° N between 2.8 and 2.55 Ma may have forced the rapid glaciation of the Northern Hemisphere. This theory is supported by model simulation of the Northern Hemisphere ice-sheet volume variation (Li et al., 1998; Raymo et al., 2006).

We still do not know what caused the climate transition that induced the Northern Hemisphere to glaciates some two and half million years ago. A plausible theory could be that the Tibetan uplift caused long term cooling during the late Cenozoic. The closure of the Panama Isthmus may then have delayed the Intensification of Northern Hemisphere Glaciation but ultimately provided the moisture which allowed intensive glaciation to develop at warmer high latitude temperatures (Figure Q4). However, Huybers and Molnar (2007) suggest cooling in the Pacific Ocean may also have contributed to the timing of the INHG. The global climate system seems to have reached a threshold at about 3 Ma, when orbital configurations became more influential, leading to building of all the major Northern Hemisphere ice sheets in little over 200 kyr.

Intensification of the Walker circulation

The onset and intensification of Northern Hemisphere glaciation may be seen as a continual cooling of the global climate during the late Cenozoic, which intensified over the last 5 million years. The so-called onset at about 3.2–2.5 Ma may be seen to have occurred as one step in this global transition. Ravelo et al. (2004) have suggested that another step occurred between 2 and 1.5 Ma. They have observed that prior to 1.9 Ma there was no, or very little, East-West sea surface temperature (SST) gradient in the Pacific Ocean. After 1.9 Ma there was a significant East-West Pacific SST gradient which Ravelo et al. (2004) and McClymont and Rosel-Mele (2005) interpret as a switch in the tropics and subtropics to a modern mode of circulation with relatively strong Walker Circulation and cool subtropical temperatures. This major switch at about 1.9 Ma has also been observed in the lake records of East Africa (Trauth et al., 2005; 2007 and Maslin and Christensen, 2007), again indicating a significant shift and intensification in Walker Circulation. If these climate changes are part of the long-term transition to a cooler global climate, then the major step of this intensification of Northern Hemisphere glaciation is the Mid-Pleistocene Revolution, which occurred about 1–0.6 Ma and is discussed in greater detail below.

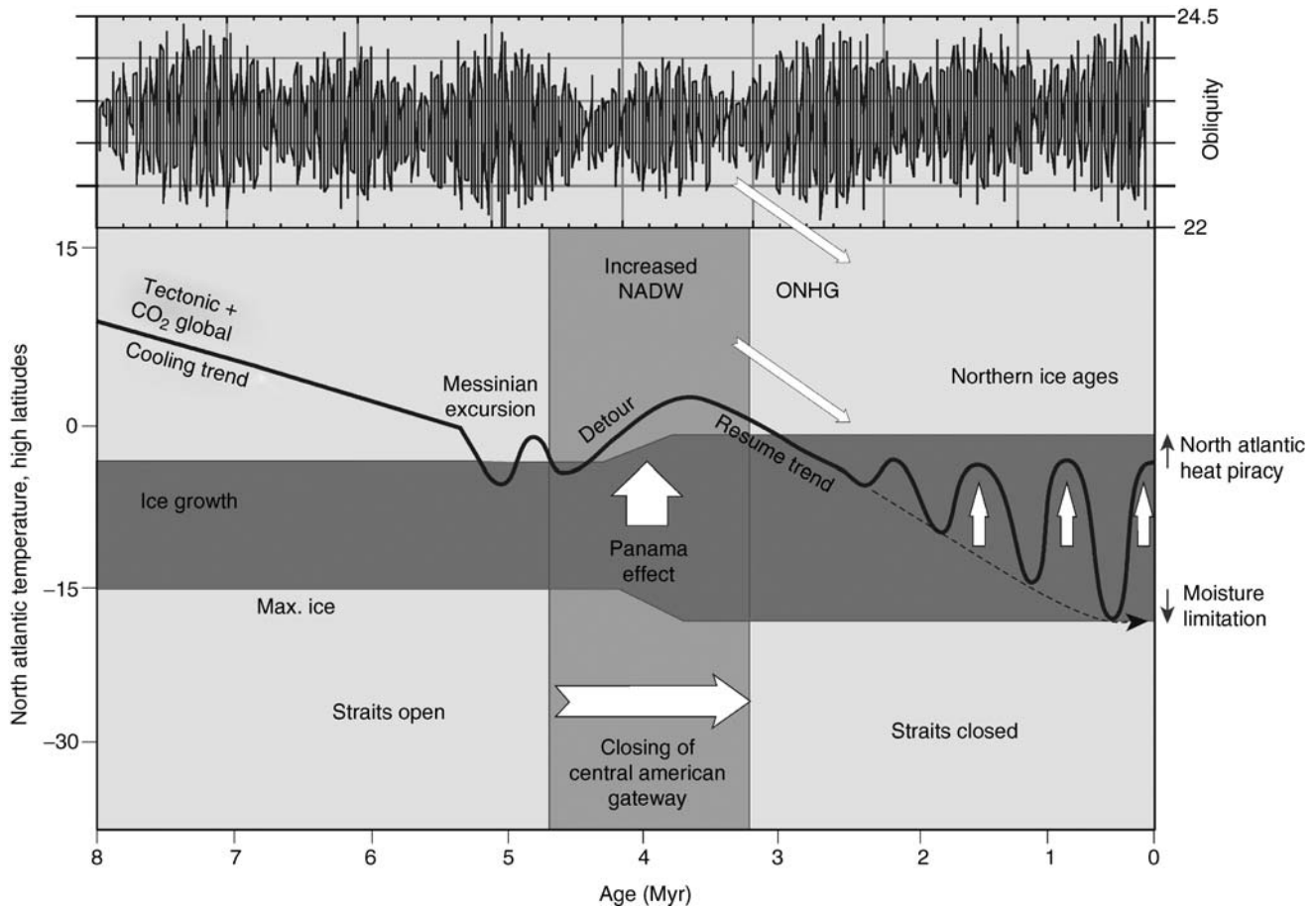


Figure Q4 Summary of the causes of the Intensification of Northern Hemisphere Glaciation (INHG). Note the detour of the cooling trend and the expansion of the temperature range of ice growth caused by the closure of the Central American gateway. Note also the kick in obliquity that occurs between 3.2 and 2.5 Ma and drives the continued cooling of the climate system and the INHG (adapted from Berger and Wefer, 1996).

Glacial-interglacial cycles

Orbital forcing

The most fundamental characteristic of the Quaternary period are the glacial-interglacial cycles. These cycles are believed to be primarily forced by changes in the Earth's orbital parameters. However, these cycles are not caused by Earth's orbital parameters alone, but rather by the Earth's climate system feedback mechanisms, which translate relatively small changes in regional insolation into major climatic variability. An illustration of this is that the insolation received at the critical 65° N was the same level, 18,000, during the Last Glacial Maximum (LGM) and today (Laskar, 1990; Berger and Loutre, 1991). There are three main orbital parameters, eccentricity (96 ka, 125 ka, 413 ka), obliquity or tilt (41 ka), and precession (19 ka, 23 ka) (see individual articles in this volume for greater detail).

Combining the effects of eccentricity, obliquity and precession provides the means of calculating the insolation for any latitude back through time (e.g., Berger and Loutre, 1991). Milankovitch (1949) suggested that summer insolation at 65° N was critical in controlling glacial-interglacial cycles. He argued that if this summer insolation was reduced enough then ice could survive through the summer and thus start to buildup, eventually producing an ice sheet. Orbital forcing does

have a large influence on this summer insolation. The maximum change in solar radiation in the last 600 ka is equivalent to reducing the amount of summer radiation received today at 65° N to that received now at 77° N, over 550 km to the north (Wilson et al., 2000). In simplistic terms, this brings the current glacial limit in mid-Norway down to the latitude of Scotland. These lows in 65° N insolation are caused by eccentricity elongating the summer Earth-Sun distance, obliquity being shallow, and precession placing the summer season at the longest Earth-Sun distance produced by eccentricity. It must also be noted that each of the orbital parameters has a different effect with changing latitude. For example, obliquity has increasing influence the higher the latitude, while precession has its largest influence in the tropics. This is important when investigating different forcing functions (see *Astronomical theory of climate change*).

Feedback mechanisms

Orbital forcing in itself does not cause glacial-interglacial cycles, rather, the climate system must be predisposed to amplify these effects through feedback mechanisms. The insolation changes received by the Northern Hemisphere temperate zone are thought to be critical for driving glacial-interglacial

cycles. This is because the Southern Hemisphere is limited in its response as the expansion of the ice sheets is curtailed by the Southern Ocean around Antarctica. It was initially suggested by Milankovitch (1949) that the critical factor is total summer insolation at about 65° N, as the ice sheets must survive the summer melting. The conventional view of glaciation is that low summer insolation in the temperate North Hemisphere

allowed ice to survive summer and thus start to buildup on the northern continents (Hays et al., 1976). At some point, this expansion allowed the ice sheet to produce its own sustainable environment, primarily by increasing the albedo, and thereby promoting the accumulation of more ice (Figure Q5). The next critical stage occurred when the ice sheets, particularly the Laurentide Ice Sheet on North America, become big enough

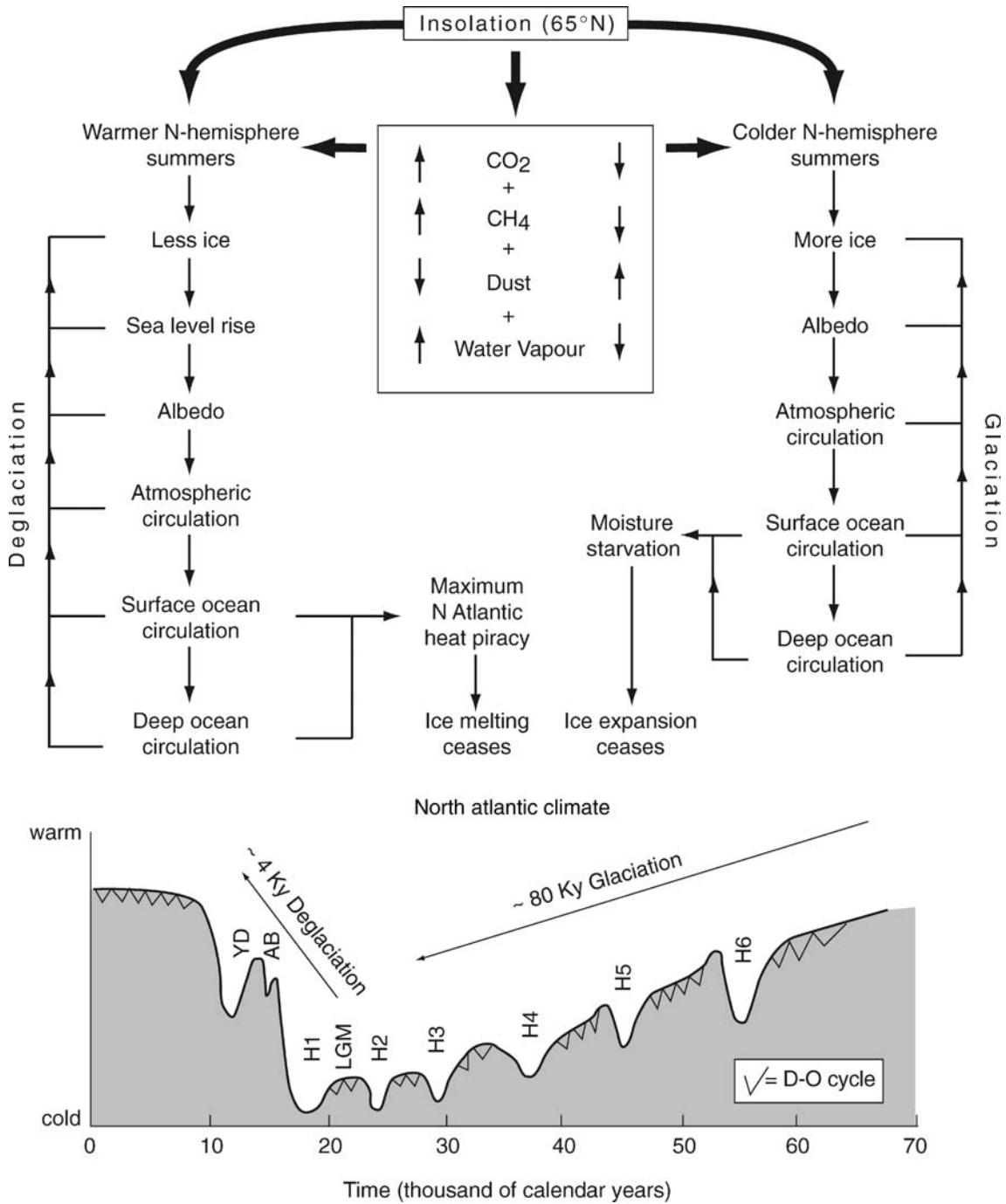


Figure Q5 Summary of the feedback mechanisms forced by insolation at 65° N that drive glaciation and deglaciation. H: Heinrich events, LGM: Last Glacial Maximum, AB: Allerød Bølling Interstadial, YD: Younger Dryas Stadial and D-O: Dansgaard-Oeschger cycles.

to deflect atmospheric planetary waves (Huybers and Tziperman, 2007). This changed the storm path across the North Atlantic Ocean and prevented Gulf Stream penetration as far north as today. This surface ocean change and increased melt-water in the Nordic Seas and Atlantic Ocean ultimately reduced the production of deepwater. This in turn reduced the amount of warm water pulled northwards. All of these led to increased cooling in the Northern Hemisphere and expansion of the ice sheets.

There are other feedback mechanisms that also helped drive the system towards maximum possible glacial conditions (Raymo and Huybers, 2008). These include changes in the carbon cycle that reduced both atmospheric carbon dioxide and methane. Ridgwell et al. (2003) discuss the main controls on the carbon cycle and the possible causes of reduced glacial atmospheric carbon dioxide. They speculate that glacial-interglacial changes in atmospheric carbon dioxide may be primarily driven by changes in oceanography in the Southern Ocean. This could have altered the nutrient supply to the surface waters, and hence surface water productivity. Dust-stimulated increased glacial surface water productivity would have drawn down atmospheric carbon dioxide into the surface water to produce organic matter through photosynthesis. However, the controls on the glacial-interglacial carbon cycle are still very poorly understood. Glacial periods are also by their very nature drier, which reduces atmospheric water vapor. For example, Lea et al. (2000) provide clear evidence that the water vapor production of the equatorial Pacific zone was greatly curtailed during the last five glacial periods. CO₂, CH₄ and water vapor are all crucial greenhouse gases and any reduction in them leads to general global cooling (Figure Q5), which in turn furthers glaciation.

These feedbacks are prevented from becoming a runaway effect by “moisture limitation.” As warm surface water is forced further and further south, the moisture supply that is required to build ice sheets decreases. Moreover, it is very clear that ice sheets are naturally unstable and these feedbacks are constantly altering direction during the whole glacial period, hence it takes 80 ka to achieve the maximum ice extent during the LGM and that period is characterized by rapid oscillations such as Heinrich events and D-O cycles (see below).

The natural instability of ice sheets means that deglaciation is much quicker than glaciation. For example, the last deglaciation or Termination I, endured a maximum of 4 ka including the brief return to glacial conditions called the Younger Dryas period. The increase in summer 65° N insolation (e.g., Imbrie et al., 1993) led to the initial melting of the northern ice sheets. The resultant raised sea level then undercut the ice sheets adjacent to the oceans, which in turn increased sea level. This sea level feedback mechanism was extremely rapid. Once the ice sheets retreated then the other feedback mechanisms discussed for glaciation reversed (see Figure Q5), leading to a massive increase in the greenhouse gases CO₂, CH₄ and water vapor. These feedbacks were prevented from creating a runaway effect by the limit of how much heat the North Atlantic could steal from the South Atlantic to maintain the interglacial deep-water overturning rate.

The latest data concerning the link between orbital forcing and these feedbacks suggests that changes in the carbon cycle lead to changes in global ice volume (Shackleton, 2000; Ridgwell et al., 2003; Ruddiman and Raymo, 2003; Pagani et al., 2005; Raymo and Huybers, 2008). This suggests that orbital forcing has a direct effect on atmospheric carbon dioxide and methane,

which may drive global temperatures, and in turn change global ice volume. Thus, the carbon cycle, instead of being a response to glacial-interglacial cycles, could indeed be one of the key driving forces (see Figure Q5).

The Mid-Pleistocene revolution

Debunking the eccentricity myth?

The Mid-Pleistocene Revolution (MPR) is the term used to denote the marked prolongation and intensification of the global glacial-interglacial climate cycles which occurred between 900 and 650 ka (Berger and Jansen, 1994). Prior to the MPR, since at least the intensification of Northern Hemisphere glaciation (~2.75 Ma), global climate appears to have responded to obliquity variations (Imbrie et al., 1992), i.e., the glacial-interglacial cycles occurred with a frequency of 41 kyr. After about 800 ka, glacial-interglacial cycles became more pronounced and occurred with a frequency of approximately 100 ka. The MPR, therefore, marks a dramatic sharpening of the contrast between warm and cold periods. Mudelsee and Stettger (1997) used advanced methods of time-series analysis to review the deep-sea evidence spanning the MPR and summarized the salient features (Figure Q6). The first transition occurred between 942 and 892 ka when global ice volume significantly increased. However, the 41 ka climate forcing continued. This situation persisted until about 650–725 ka when the climate system entered a bi-modal phase and the strong 100 ka climate cycles began (Mudelsee and Stettger, 1997).

Imbrie et al. (1993) called the MPR the “100 ka problem,” as the eccentricity signal is by far the weakest of the orbital parameters. Hence, it has been assumed that there must have been a change from a linearly to a non-linearly forced climate system (Imbrie et al., 1992, 1993). Many different theories have thus been postulated to produce this critical non-linear transition, including: critical size of the Northern Hemisphere ice sheets, global cooling trend, erosion of regolith beneath the Laurentide Ice Sheet, orbital inclination, Greenland-Scotland submarine ridge and carbon cycle and atmospheric CO₂ (see Maslin and Ridgwell, 2005 for detailed references).

There are a number of problems with associating the 100 ka cycles with eccentricity. The first is that eccentricity has spectral peaks at 95 ka, 125 ka and 400 ka. The spectral analysis of benthic foraminifera oxygen isotopes (SPECMAP) – a proxy for global ice volume – shows a consistent single peak of 100 ka (Maslin and Ridgwell, 2005). However, the lengths of the last 8 glacial-interglacial cycles vary from 87 to 119 ka, averaging about 100 ka. Ridgwell et al. (1999) demonstrated that this strong 100 ka peak could not be produced by eccentricity, but rather by a simple saw-tooth pattern based on a long glaciation period followed by a short deglaciation (Figure Q7). This suggests that the 100 ka cycle seen in the ice volume records is dominated by deglaciations that occur every 100 ka after the MPR, on average. Note that summer insolation at 65° N is also strongly influenced by precession; hence, the saw-toothed pattern of rapid deglaciation occurs every fourth or fifth precessional cycle over the last 600 ka. A similar saw-tooth pattern can be produced from obliquity using every second or third cycle (Ridgwell et al., 1999; Huybers and Wunsch, 2005; Raymo et al., 2006; Raymo and Huybers, 2008), but the spectral analysis does not match the global ice volume signal as well (Ridgwell et al., 1999; Maslin and Ridgwell, 2005). Models have also been used to re-create the 100 ka cycle and the most successful is the LLN 2D model,

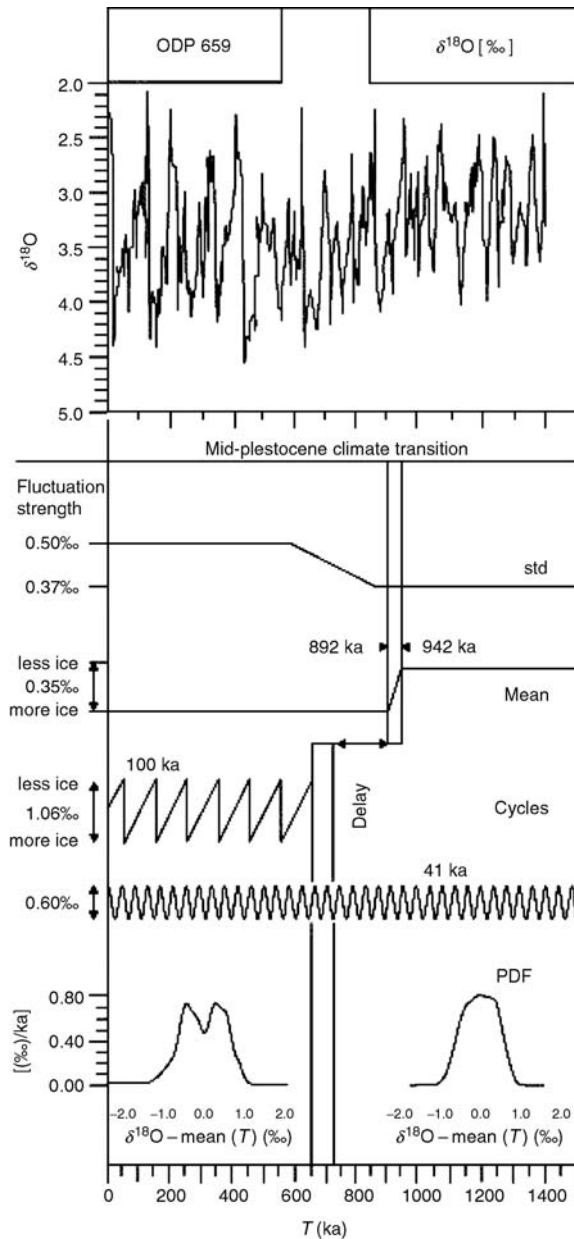


Figure Q6 Detailed breakdown of the Mid-Pleistocene Revolution (after Mudelsee and Statterger, 1997), demonstrating a delay of 200 ka between the significant increase in global ice volume and the start of the 100 ka glacial-interglacial cycles.

which combines orbital forcing with atmospheric carbon dioxide. Hence, the keys to the MPR are precession and atmospheric carbon dioxide. Ridgwell et al (1999) suggested that the episodic occurrence of unusually low maxima in Northern Hemisphere summer insolation is the critical factor controlling subsequent deglaciation. Ruddiman (2003) furthermore suggests that both precession and obliquity affect the concentration of the greenhouse gases carbon dioxide and methane, and this combined influence results in the strong 100 ka cycle. This means that all three orbital periodicities are involved and the

MPR is not a simple non-linear amplification of eccentricity. In effect, this new research from the study of the MPR suggests that it is very hard to get the global climate system out of a glacial or near-glacial condition. Deglaciation can only occur when the climate system has been allowed to reach maximum glaciation by the previous low maxima in Northern Hemisphere summer insolation, for example during the LGM. The following precessionally driven summer maxima pushes the climate system too far and it overshoots the mild glacial (e.g., oxygen isotope stage 3 to 5a) type climate, entering an interglacial period.

The dominance of precession leads to another problem, the assumption of a linear response of the climate system to obliquity prior to MPR (Imbrie et al., 1992), as the insolation records for 2.5–1 Ma for the temperate regions are very similar to the period after 1 Ma, i.e., dominated by precession. Raymo and Nisancioglu (2003) suggest another solution to the obliquity problem: the MPR is a switch from an obliquity-driven latitudinal heat gradient system to a precessional-driven deglacial system. In contrast Raymo et al. (2006) and Raymo and Huybers (2008) suggested that prior to the MPR both the Northern Hemisphere and Antarctic ice sheets are responding to precession; but because they are 180° out of phase the precessional component cancels out leaving a dominant obliquity signal. After the MPR the dominance of the Northern Hemisphere ice sheet is such that Northern Hemisphere precession dominates global climate.

Millennial-climate cycles

Heinrich events

Heinrich events are intense and quasi-periodic ice-rafting pulses that are thought to originate primarily from the Laurentide Ice Sheet (e.g., Ruddiman, 1977; Heinrich, 1988; Bond et al., 1992; Maslin et al., 1995). These events occurred against the general background of unstable glacial climate, and represent the brief expression of the most extreme glacial conditions around the North Atlantic. Heinrich events are evident in the Greenland ice cores as a further 3–6 °C drop in temperature from the already cold glacial climate (Bond et al., 1993; Dansgaard et al., 1993). These events have been found to have a global impact with evidence for coeval climate changes from as far a field as: South America, North Pacific, Santa Barbara Basin, Arabian Sea, China, South China Sea, and Sea of Japan (e.g., reviewed in Maslin et al., 2001). Around the North Atlantic, much colder conditions prevailed in both North America and Europe, while huge armadas of melting icebergs reduced sea surface temperatures in the North Atlantic Ocean by another 1–2 °C and reduced the surface salinity by up to 4‰ (Chapman and Maslin, 1999; Rashid and Boyle, 2007).

Detailed studies of the sequence of events in ocean sediments and ice cores show that Heinrich events occurred on an average of $7,200 \pm 2,400$ calendar years in the time interval between about 70 and 10.5 ka. In between the Heinrich events, much higher frequency, smaller amplitude events occurred about every 1,500 years, which are referred to as Dansgaard-Oeschger events or cycles (Dansgaard et al., 1993; Bond et al., 1997). Heinrich events may in fact be just super Dansgaard-Oeschger events. (see *Dansgaard-Oeschger cycles*; *Heinrich events*).

Dansgaard-Oeschger cycles

Dansgaard-Oeschger (D-O) cycles were first identified in the Greenland ice core records (Dansgaard et al., 1993). A succession

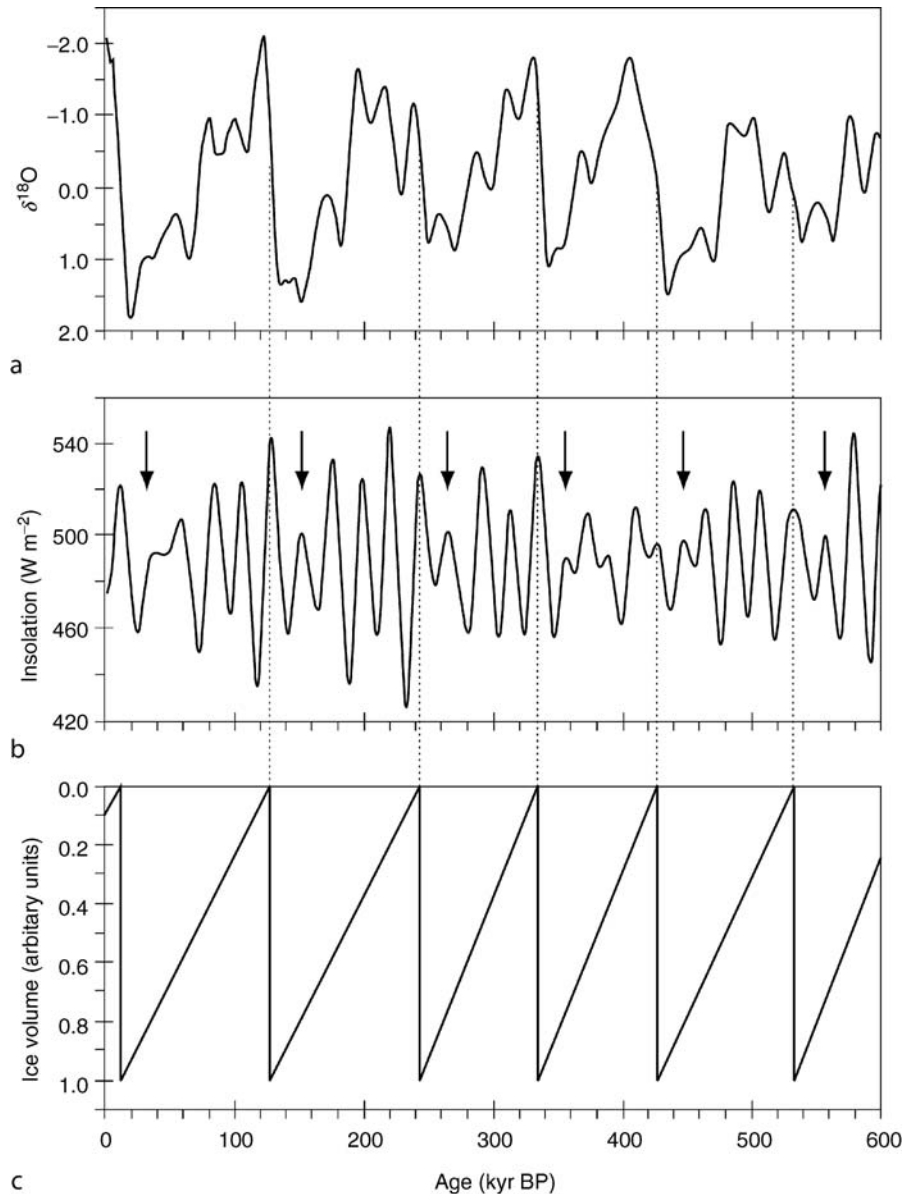


Figure Q7 (a) SPECMAP stacked $\delta^{18}\text{O}$ composite, (b) insolation for June 21 65°N showing the quasi-periodic insolation maxima of unusually low strength (shown by arrows) preceding glacial-interglacial terminations by one precessional cycle in each case and (c) sawtooth artificial ice volume signal.

of short lived “warm” events or Greenland interstadials (GIS) characterize the ice core records of the last glacial episode and are numbered down from the “Bølling” as GIS 1 to GIS 24 at 105 ka. The D-O stadials or cold sections of the D-O cycle have been found in the ice rafting records of the North Atlantic (e.g., Bond and Lotti, 1995). These stadials are characterized by increased meltwater and ice-rafted debris originating from Iceland and East Greenland. These D-O cycles have a frequency of $1,479 \pm 532$ years, and seem to persist into the Holocene interglacial as well as occurring during earlier glacial and interglacial stages (Bond et al., 2001). A precise time-scale for the duration and sequence of these millennial-scale climate events is uncertain, though the events themselves do

not appear to have lasted longer than a few centuries. Furthermore, the transitions marking the beginnings and ends of each Heinrich and D-O event are particularly rapid, probably lasting no more than a few decades, indicating that climate responded in a step-like series of jumps to whatever driving mechanism initiated them.

Possible causes of the Heinrich events and Dansgaard-Oeschger cycles

There are a number of possible causes suggested for these millennial climate cycles, including the theory that they are due to stochastic resonance (Alley et al., 2001). Although none

of these theories is conclusive, the major ones are summarized below.

Internal ice sheet failure

MacAyeal (1993a,b) suggested that the Heinrich event iceberg surges were caused by internal instabilities of the Laurentide Ice Sheet. This ice sheet rested on a bed of soft unconsolidated sediment, which, when it was frozen, did not deform and behaved like concrete, so that it would have been able to support the weight of the growing ice sheet. As the ice sheet expanded, the geothermal heat from within the Earth's crust, together with heat released from friction of ice moving over ice was trapped by the insulating effect of the overlying ice. This "duvet" effect allowed the temperature of the sediment to increase until a critical point when it thawed. When this occurred, the sediment became soft, and thus lubricated the base of the ice sheet, causing a massive outflow of ice through the Hudson Strait into the North Atlantic. This, in turn, led to sudden loss of ice mass, which then reduced the insulating effect and led to re-freezing of the basal ice and sediment bed, at which point the ice reverted to a slower build-up and outward movement. According to MacAyeal (1993a,b), this system of progressive ice build-up, melting and surge, followed by renewed build-up, has an approximate periodicity of 7,000 years, which compares well with the interval between the last six Heinrich events, which is on average $7,200 \pm 2,400$ calendar years. However, different ice sheets may have had different binge-purge times, thus the Fenno-Scandinavian, Greenland and Icelandic Ice Sheets would have surged with different periodicities. An alternative suggestion is that D-O events are caused by the more frequent regular failure of the European and Greenland Ice Sheet, while the larger, more infrequent Heinrich events are caused by collapse of the Laurentide Ice Sheet.

Sea level connection between Heinrich and D-O events

The second theory is that sea level rises induced by the 1,500-year D-O cycles undercuts and thus destabilizes the Laurentide Ice Sheets, triggering a much larger Heinrich event. The periodicities are such that a Heinrich event occurs for every fifth D-O cycle. Support for this theory comes from the detailed analysis of the sources of ice-rafted material in the Heinrich layers. From the detailed breakdown of H1, H2, H4 and H5, it has been shown that European ice-rafted debris was deposited in the North Atlantic up to 1,500 years before the Laurentide material (e.g., Grousset et al., 2000). This theory, however, does not explain what causes the Dansgaard-Oeschger cycles, since they occur with a similar frequency during both glacial and interglacial periods.

Bipolar climate seesaw

Ice core data from Greenland and Antarctica show an out-of-phase relationship in glacial millennial-scale climate cycles for the North and Southern Hemisphere (Blunier et al., 1998), see Figure Q8. It has been suggested that this so-called bipolar climate seesaw can be explained by alternating meltwater events in the North Atlantic and Southern Ocean. Each meltwater event would change the relative amount of deepwater formation in the two hemispheres and the resulting direction of inter-hemispheric "heat piracy" (Figure Q8; Seidov and Maslin, 2001; Seidov et al., 2001; see *Thermohaline circulation*). The

bipolar seesaw model suggested by Maslin et al. (2001) could be self-sustaining with meltwater events in either hemisphere triggering a chain of climate changes that eventually causes a meltwater event in the opposite hemisphere by switching the direction of the hemispheric heat exchange (Figure Q9). The advantage of this theory is that it can explain D-O cycles during both glacial and interglacial periods.

External forcing

Heinrich (1988) originally suggested that ice-rafting events could be forced by harmonics of orbital parameters, as their quasi-cyclicity is on the order of 10 kyr. However, it now seems that the periodicity shortens through a glacial period starting at 13 ka and decreasing to 7 ka. With the discovery that Heinrich events were part of the more frequent D-O cycles and that both hemispheres respond asynchronously, it is unlikely that longer-term orbital forcing (minimum 10 kyr) could be the cause. Hence, until recently it was thought these millennial events were internally and not externally, forced. The latest development in this area is a study showing a significant correlation between drift-ice deposited material in the North Atlantic and the production of both ^{14}C and ^{10}Be in the atmosphere over the last 12,000 years (Bond et al., 2001). Bond et al. suggest that the production of both ^{14}C and ^{10}Be indicates millennial-scale variations in solar output, which may have caused the D-O climate cycles. They further postulate that amplification of relatively weak solar changes was due to the Arctic-Nordic Sea's sensitivity to changes in surface-water salinity. Hence, increased freshening of this region would reduce the North Atlantic Deep Water (NADW) and thus transmit the solar influence globally. However, a number of problems remain with the millennial-scale solar output theory, the most important being how the extremely small solar output variations are translated into regional and global climate changes of over 2°C . The debate about solar forcing on Holocene climate records and its application to glacial periods continues (e.g., Braun et al., 2005; *Holocene climates*).

Last glacial-interglacial transition (LGIT)

The nature of the LGIT

The last glacial-interglacial transition (LGIT, ca. 14–9 ^{14}C kyrBP) was characterized by a series of extremely abrupt climatic changes (e.g., Alley and Clark, 1999; Lowe and Walker, 2000; Stocker, 2003). These abrupt climate shifts are found in earlier glacial terminations and therefore seem to be part of the natural climate variability associated with this type of transition. The two most prominent features are rapid warming at 14.7 k GRIP ice-core years BP (the start of the "Bølling" episode) and the well-known period of severe cooling referred to as the Younger Dryas Stadial, dated to between 12.7 and 11.5 ka BP in GRIP ice-core years. These features are easily recognizable in a wide range of proxy records from sites throughout the Northern Hemisphere (e.g., Alley and Clark, 1999). There is also a growing body of evidence that suggests that parts of the Southern Hemisphere may have experienced a broadly similar sequence of climatic events, including parts of South America and New Zealand.

According to the GRIP and GISP2 ice-core records (e.g., Dansgaard et al., 1993; Alley and Clark, 1999), the sequence of events during the last glacial-interglacial transition were far more abrupt than had been assumed from prior interpretations based on continental and marine stratigraphical records.

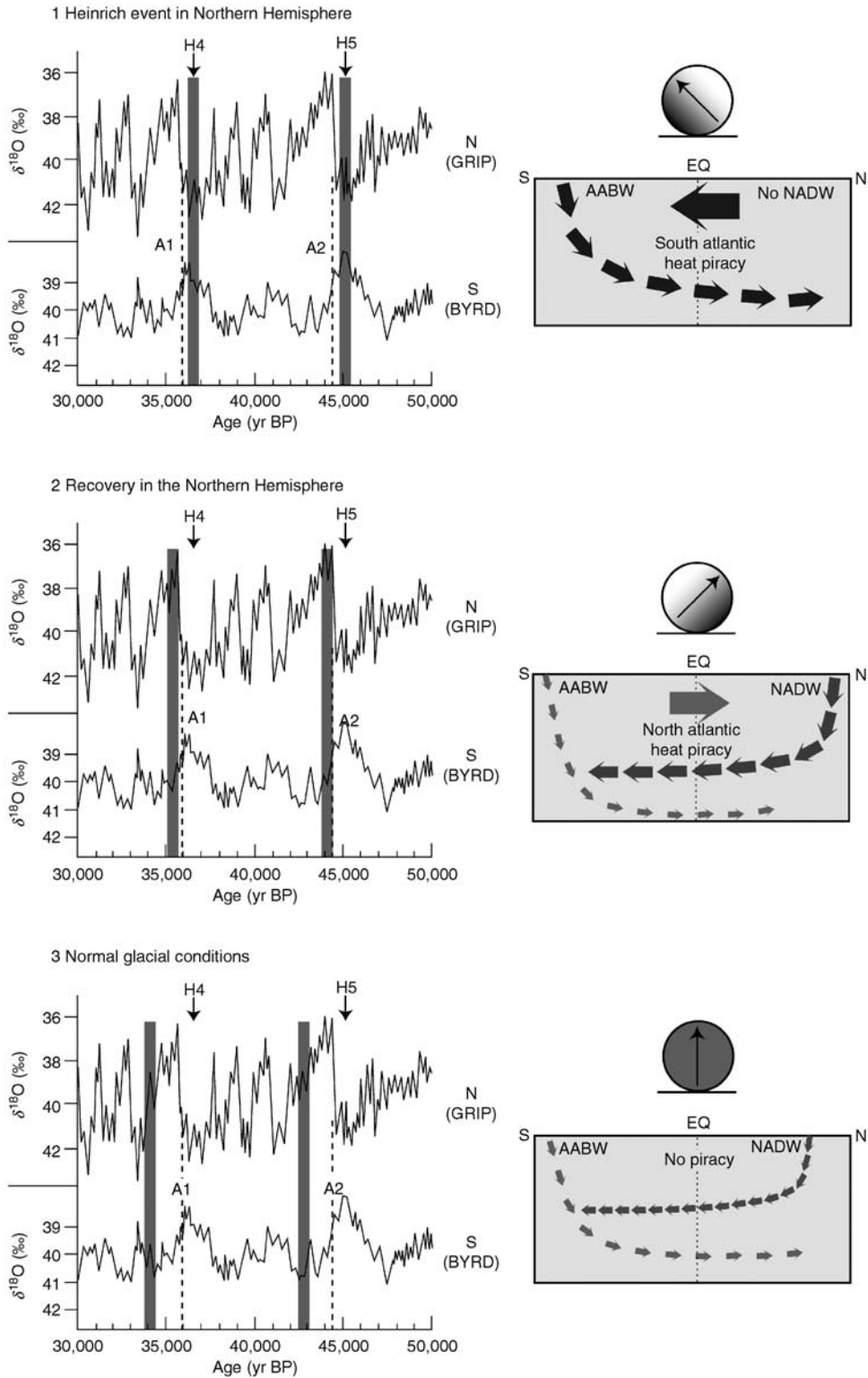


Figure Q8 Left: Greenland (GRIP) and Antarctic (Byrd) ice core $\delta^{18}\text{O}$ temperature proxy records on the age models generated by Blunier et al. (1998). Three time slices are illustrated with *solid bars*; (1) Heinrich event, (2) Northern Hemisphere climate recovery post-Heinrich event, and (3) Normal glacial conditions. Right: Schematic view of oscillating meridional ocean overturning and associated regimes of heat transport in the Atlantic Ocean, showing which hemisphere controls deepwater circulation and thus inter-hemispheric heat transport (adapted from Maslin et al., 2001 and Seidov et al., 2001).

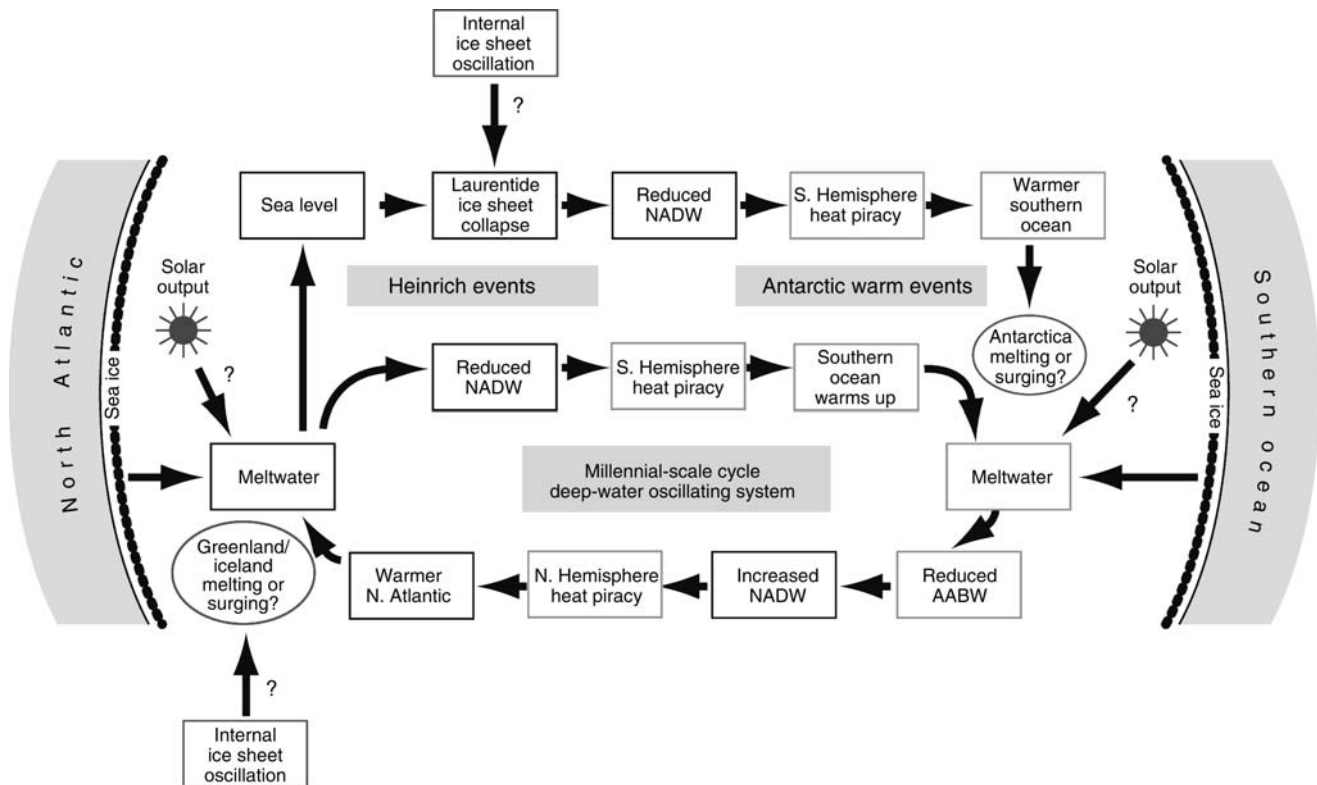


Figure Q9 Possible “deep-water oscillatory system” explaining glacial and interglacial Dansgaard-Oeschger cycles (adapted from Maslin et al., 2001). Meltwater in either the North Atlantic or Southern ocean can start the system. The meltwater caps the sites of deep water formation in that particular hemisphere and reduces the deepwater formation. This increases heat piracy to the other hemisphere, warming that hemisphere, which instigates ice sheet melting after hundreds or thousands of years, thus reversing the whole process. The system is quasi-periodic because of its oscillatory nature. The stochastic element observed in the records (Alley et al., 2001) comes from the different internal dynamics of each ice sheet. The link between the Dansgaard-Oeschger $\sim 1,500$ year cycles and the Heinrich events is through their successive effect on sea level. At a certain point, sea level has risen enough to undercut the Laurentide Ice Sheet and precipitate a full Heinrich event.

For example, a detailed study of the Greenland ice-core records (Taylor et al., 1997) suggests that the transition from the end of the Younger Dryas to the Holocene warm period may have been completed in a series of warming steps lasting no more than a few decades, most probably in less than 50 years (Alley and Clark, 1999). About half of the warming was concentrated into a single short step that lasted no more than 15 years. In contrast to the abrupt warming at the start of the “Bølling,” the cooling from the warm “Bølling” to the Younger Dryas appears to have been a more gradual process, involving a series of steps and minor climatic oscillations extending over a period in excess of 1,500 years.

The extent to which abrupt climate shifts during the LGIT were globally synchronous, or not, is pivotal to our understanding of global climate mechanisms. Detailed comparisons between the Antarctic and Greenland ice cores show that Antarctic climate changes were significantly out of step with those in the North Atlantic (Figure Q10) and provide another example of the bipolar climate seesaw described above. The data suggest that cooling (the Antarctic Cold Reversal) occurred in Antarctica during the period of warming in the North Atlantic region referred to as the “Bølling-Allerød Interstadial.” They also suggest that the severely cold Younger Dryas Stadial was a period of rapid

warming in Antarctica. In addition, Ridgwell et al. (2003) have shown that the majority of the changes in atmospheric carbon dioxide occurred in three major pulses that are synchronous with rapid warming in Antarctica (Figure Q10).

Possible causes of abrupt climate oscillations during the LGIT

It is believed that deglaciations were dominated by orbitally-induced ice sheet and associated climatic changes. The colder episodes, especially the very pronounced Younger Dryas cooling (Dansgaard et al., 1993), are periods imprinted on this trend of warmer interglacial conditions. For example, marine records from all parts of the North Atlantic during the Younger Dryas show significant increases in freshwater and ice-rafted debris input. This has led to the suggestion that the Younger Dryas was caused by a sudden influx of cold fresh meltwater from the North American and European Ice Sheets, which was sufficient to cap deepwater formation in the North Atlantic. Another suggestion is that meltwater diverted through the Gulf of St. Lawrence was enough to stop deepwater formation (Berger and Jansen, 1995; Clark et al., 2001; Carlson et al., 2007; Carlson, 2008). It seems almost axiomatic that the driving

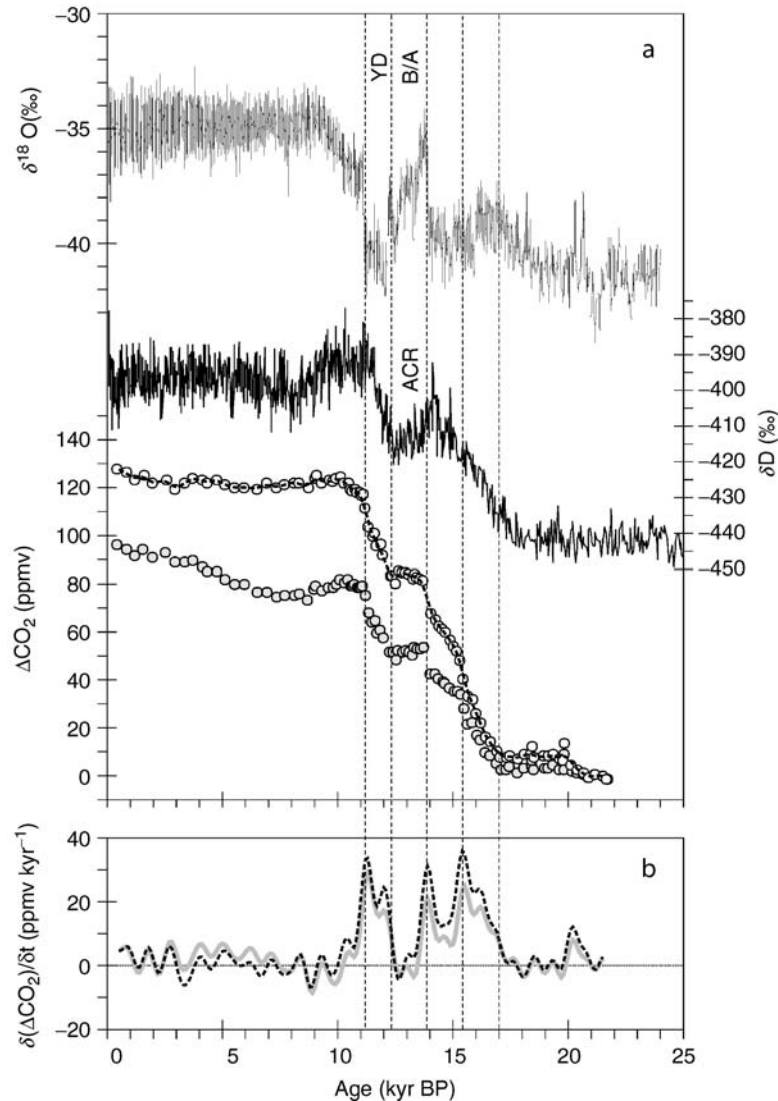


Figure Q10 (a) GRIP $\delta^{18}\text{O}$ “temperature proxy” showing timing of the Bølling/Allerød (B/A), and Younger Dryas (YD) intervals, the Antarctic Dome C δD “temperature proxy” record highlighting the relative timing of the Antarctic Cold Reversal (ACR), and observed atmospheric CO_2 changes as gray-filled circles, and the “residual” CO_2 record as empty circles, formed by subtracting the effects of re-growth of the terrestrial biosphere, sea level and reef buildup (see Ridgwell et al., 2003). Both data sets are now plotted as change relative to LGM values. (b) Rate of change of observed (thick gray line) and “residual” (dashed red line) CO_2 since the LGM. The timing of the sharp spikes corresponds to discernable “jumps” in the observed CO_2 record and correlates with significant warming in Antarctica (adapted from Ridgwell et al., 2003).

mechanism for the Younger Dryas episode, for example, must be some form of internal mechanism, such as oceanic circulation change, since this episode of very pronounced cooling occurred at a time of summer radiation maximum in Milankovitch calculations. There is also a new theory that suggest an asteroid impact may have caused the Younger Dryas event (Firestone et al., 2007) and this may explain why a Younger Dryas event is not seen at other earlier Terminations (Carlson, 2008).

On top of this are climate records of Greenland and Antarctic ice cores showing an anti-phase between the North and Southern Hemispheres through the LGIT. Prominent among the emerging ideas is Broecker’s (1998) suggestion of a “bipolar seesaw behavior in thermohaline circulation” as a mechanism

that explains this anti-phase relationship, as discussed above. Recent modeling work has shown that the anti-phase hemispheric climate during the LGIT can be produced from simple alternation of the deep ocean circulation driven by the Younger Dryas meltwater event in the North Atlantic (Knorr and Lohmann, 2003; Stocker, 2003; Weaver et al., 2003; Carlson, 2008).

Conclusions

Based on our present understanding of Quaternary climate change, large climatic transitions have occurred on the timescale of individual human lifetimes, for example, the end of the Younger Dryas and various D-O cold events. Many other substantial shifts in

climate took at most a few decades or centuries e.g., Heinrich events and events during the LGIT. Despite a huge amount of data, many problems remain in understanding the mechanisms controlling these rapid climate changes. Both external and internal forcing play a part. Of fundamental importance, however, is the discovery of the central role of the deepwater system in controlling past rapid global climatic changes (Stocker, 2003) and this should be of central concern in possible future climate change (Maslin, 2004a).

Mark Maslin

Bibliography

- Alley, R.B., and Clark, P.U., 1999. The deglaciation of the Northern Hemisphere. *Annu. Rev. Earth Planet. Sci.*, **27**, 149–182.
- Alley, R.B., Anandakrishnan, S., Jung, P., and Clough, A., 2001. Stochastic resonance in the North Atlantic: Further insights. In Seidov, Haupt, and Maslin (eds.), *The Oceans and Rapid Climate Change: Past, Present and Future*. Washington, DC: American Geophysical Union. Geophysical Monograph Series, vol. 126, pp. 57–68.
- Berger, A., and Loutre, M.F., 1991. Insolation values for the climate of the last 10 million years. *Quaternary Sci. Rev.*, **10**, 297–317.
- Berger, W.H., and Jansen, E., 1994. Mid-Pleistocene climate shift: The Nansen connection. In Johannessen et al., (eds), *The Polar Oceans and Their role in Shaping the Global Environment*. Washington, DC: American Geophysical Union. Geophysical Monograph, vol. 85, pp. 295–311.
- Berger, W.H., and Jansen, E., 1995. Younger Dryas episode: Ice collapse and super-fjord heat pump. In Troelstra, S.R., van Hinte, J.E., and Ganssen, G.M. (eds.), *The Younger Dryas*. Koninklijke Nederlandse Akademie van Wetenschappen, Afdeling Natuurkunde, Eerste Reeks, **44**, 61–105.
- Berger, W.H., and Wefer, G., 1996. Expeditions into the Past: Paleoceanographic studies in the South Atlantic. In Wefer et al., (eds), *The South Atlantic: Present and Past Circulation*. Berlin: Springer, pp. 363–410.
- Blunier, T., Chappellaz, J., Schwander, J., Dällenbach, A., Stauffer, B., Stocker, T.F., Raynaud, D., Jouzel, J., Clausen, H.B., Hammer, C.U., and Johnsen, S.J., 1998. Asynchrony of Antarctic and Greenland climate change during the last glacial period. *Nature*, **384**, 739–743.
- Bond, G.C., and Lotti, R., 1995. Iceberg discharges into the North Atlantic on millennial time scales during the last deglaciation. *Science*, **267**, 1005–1010.
- Bond, G., Heinrich, H., Broecker, W., Labeyrie, L., McManus, J., Andrews, J., Huon, S., Jantschik, R., Clasen, S., Simet, C., Tedesco, K., Klas, M., Bonani, G., and Ivy, S., 1992. Evidence for massive discharges of icebergs into the North Atlantic Ocean during the last glacial period. *Nature*, **360**, 245–249.
- Bond, G.C., Broecker, W., Johnsen, S., McManus, J., Labeyrie, L., Jouzel, J., and Bonani, G., 1993. Correlations between climate records from North Atlantic sediments and Greenland ice. *Nature*, **365**, 143–147.
- Bond, G., Showers, W., Cheseby, M., Lotti, R., Almasi, P., deMenocal, P., Priore, P., Cullen, H., Hajdas, I., and Bonani, G., 1997. A pervasive millennial-scale cycle in North Atlantic Holocene and glacial climates. *Science*, **278**, 1257–1265.
- Bond, G., et al. 2001. Persistent solar influence on North Atlantic climate during the Holocene. *Science*, **294**, 2130–2136.
- Braun, H., Christl, M., Rahmstorf, S., Ganopolski, A., Mangini, A., Kubatzki, C., Roth, K., and Kromer, B., 2005. Possible solar origin of the glacial 1,470-year climate cycle demonstrated in a coupled model. *Nature*, **438**, 208–211.
- Broecker, W., 1998. Paleocean circulation during the last deglaciation: A bipolar seesaw? *Paleoceanography*, **13**, 119–121.
- Chapman, M., and Maslin, M.A., 1999. Low latitude forcing of meridional temperature and salinity gradients in the North Atlantic and the growth of glacial ice sheets. *Geology*, **27**, 875–878.
- Clark, P.U., Marshall, S.J., Clarke, G.K.C., Hostetler, S.W., Licciardi, J.M., and Teller, J.T., 2001. Freshwater forcing of abrupt climate change during the last glacial period. *Science*, **293**, 283–287.
- Carlson, A.E., 2008. Why there was not a Younger Dryas-like event during the Penultimate Deglaciation, *Quaternary Science Reviews*, **Volume 27**, Issues 9-10, Pages 882–887.
- Carlson, A.E., Clark, P.U., Halsey, B.A., Klinkhammer, G.P., Simmons, K., Brook, E.J., and Meissner, K.J., 2007. Geochemical proxies of North American freshwater routing during the Younger Dryas cold event. *Proceedings of the National Academy of Sciences*, **104**, pp. 6556–6561.
- Dansgaard, W., Johnson, S.J., Clausen, H.B., Dahl-Jensen, D., Gundenstrup, N.S., Hammer, C.U., Hvidberg, C.S., Steffensen, J.P., 1993. Sveinbjörnsdóttir, Evidence for general instability of past climate from a 250-kyr ice-core record. *Nature*, **364**, 218–220.
- Eldrett, J.S., Harding, I.C., Wilson, P.A., Butler, E., and Roberts A.P., 2007. *Continental ice in Greenland during the Eocene and Oligocene* *Nature* **446**, 176–179.
- Firestone, R.B., West, A., Kennett, Becker, L., Bunch, T.E., Revay, Z.S., Schultz, P.H., Belgia, T., Kennett, D.J., Erlandson, J.M., Dickenson, O.J., Goodyear, A.C., Harris, R.S., Howard G.A., Kloosterman, J.B., Lechler, Mayewski, P.A., Montgomery, J., Poreda, R., Darrah, T., Que Hee, S.S., Smith, A.R., Stich, A., Topping, W., Wittke J.H., and Wolbach, W.S., 2007. Evidence for an extraterrestrial impact 12,900 years ago that contributed to the megafaunal extinctions and the Younger Dryas cooling. *Proceedings of the National Academy of Sciences*, **104**, pp. 16016–16021.
- Grousset, F.E., Pujol, C., Labeyrie, L., Auffret, G., Boelaert, A., 2000. Were the North Atlantic Heinrich Events triggered by the behavior of the European Ice Sheets? *Geology*, **28**(2), 123–126.
- Haug, G.H., and Tiedemann, R., 1998. Effect of the formation of the Isthmus of Panama on Atlantic Ocean thermohaline circulation. *Nature*, **393**, 673–675.
- Hay, W., 1992. The cause of the late Cenozoic Northern Hemisphere Glaciations: A climate change enigma. *Terra Nova*, **4**, 305–311.
- Hays, J.D., Imbrie, J., Shackleton, N.J., 1976. Variations in the Earth's orbit: Pacemaker of the Ice Ages. *Science*, **194**, 1121–1132.
- Heinrich, H., 1988. Origin and consequences of cyclic ice rafting in the northeast Atlantic Ocean during the past 130,000 years. *Quaternary Res.*, **29**, 142–152.
- Huybers and Molnar, Tropical cooling and the onset of North American glaciation, *Climate of the Past*, 2007.
- Huybers and Tziperman, Integrated summer insolation forcing and 40,000 year glacial cycles: the perspective from an icesheet/energy-balance model, *Paleoceanography*, 2008. pdf and code.
- Huybers, P., and Wunsch, C., 2005. Obliquity pacing of the late Pleistocene glacial terminations. *Nature*, **434**, 491–494.
- Imbrie, J., Boyle, E., Clemens, S., Duffy, A., Howard, W., Kukla, G., Kutzbach, J., Martinson, D., McIntyre, A., Mix, A., Molfino, B., Morley, J., Peterson, L., Pisias, N., Prell, W., Raymo, M., Shackleton, N., and Toggweiler, J., 1992. One the structure and origin of major glacial cycles. 1. Linear responses to Milankovitch forcing. *Paleoceanography*, **7**, 701–738.
- Imbrie, J., Berger, A., Boyle, E.A., Clemens, S.C., Duffy, A., Howard, W.A., Kukla, G., Kutzbach, J., Martinson, D.G., McIntyre, A., Mix, A.C., Molfino, B., Morley, J.J., Peterson, L.C., Pisias, N.G., Prell, W.G., Raymo, M.E., Shackleton, N.J., and Toggweiler, J.R., 1993. On the structure and origin of major glacial cycles. 2. The 100,000 year cycle. *Paleoceanography*, **8**, 699–735.
- Kleiven, H.F., Jansen, E., Fronval, T., and Smith, T.M., 2002. Intensification of Northern Hemisphere glaciations in the circum Atlantic region (3.5–2.4 Ma). *Palaeogeogr. Palaeoclimatol. Palaeoecol.*, **184**, 213–223.
- Knorr, G., and Lohmann, G., 2003. Southern Ocean origin for the resumption of Atlantic thermohaline circulation during deglaciation. *Nature*, **424**, 532–534.
- Laskar, J., 1990. The chaotic motion of the solar system: A numerical estimate of the chaotic zones. *Icarus*, **88**, 266–291.
- Lea, D.W., Pak, D.K., and Spero, H.J., 2000. Climate impact of late Quaternary equatorial Pacific sea surface temperature variations. *Science*, **289**, 1719–1724.
- Li, X.S., Berger, A., Loutre, M.F., Maslin, M.A., Haug, G.H., and Tiedemann, R., 1998. Simulating late Pliocene Northern Hemisphere climate with the LLN 2-D model. *Geophys. Res. Lett.*, **25**, 915–918.
- Lisiecki, L., and Raymo, M.E., 2007. Plio-Pleistocene climate evolution: trends in obliquity and precession responses, *Quat Sci Revs.*, **v. 26**, p. 56–69.
- Lowe, J.J., and Walker, M.J.C., 2000. Radiocarbon dating the last glacial interglacial transition (ca. 14–9 ¹⁴C ka BP) in terrestrial and marine records: The need for new quality assurance protocols. *Radiocarbon*, **42**, 53–68.
- MacAyeal, D.R., 1993a. A low-order model of the Heinrich Event cycle. *Paleoceanography*, **8**, 767–773.

- MacAyeal, D.R., 1993b. Binge/Purge oscillations of the Laurentide Ice Sheet as a cause of the North Atlantic's Heinrich Events. *Paleoceanography*, **8**, 775–784.
- Maslin, M., 2004a. *Global Warming, A Very Short Introduction*. Oxford, UK: Oxford University Press, p. 162. ISBN 0-19-284097-5.
- Maslin, M.A., 2004b. Ecological verses climatic thresholds. *Science*, **306**, 2197–2198.
- Maslin, M.A., and Christensen, B., 2007. Tectonics, orbital forcing, global climate change, and human evolution in Africa. *Journal of Human Evolution* **Volume 53**, Issue 5, p. 443–464.
- Maslin, M.A., and Ridgwell, A., 2005. *Mid-Pleistocene Revolution and the Excentricity Myth*. Piccadilly, London: Geological Society of London. Special Publication of the Geological Society of London, vol. 247, pp. 19–34.
- Maslin, M.A., Shackleton, N.J., and Pflaumann, U., 1995. Temperature, salinity and density changes in the Northeast Atlantic during the last 45,000 years: Heinrich events, deep water formation and climatic rebounds. *Paleoceanography*, **10**, 527–544.
- Maslin, M.A., Li, X-S., Loutre, M-F., and Berger, A., 1998. “The contribution of orbital forcing to the progressive intensification of Northern Hemisphere Glaciation.” *Quaternary Sci. Rev.*, **17**(4–5), 411–426.
- Maslin, M.A., Seidov, D., and Lowe, J., 2001. Synthesis of the nature and causes of sudden climate transitions during the Quaternary. In Seidov, Haupt, and Maslin (eds.), *The Oceans and Rapid Climate Change: Past, Present and Future*. Washington, DC: American Geophysical Union. Geophysical Monograph Series, vol. 126, pp. 9–52.
- Milankovitch, M.M., 1949. *Kanon der Erdbestrahlung und seine Anwendung auf das Eiszeitenproblem*. Royal Serbian Sciences, Spec. pub. 132, Section of Mathematical and Natural Sciences, 33, Belgrade, pp.633 (Canon of Insolation and the Ice Age Problem, English translation by Israel Program for Scientific Translation and published for the U.S. Department of Commerce and the National Science Foundation, Washington D.C., 1969).
- Mudelsee, M., and Raymo, M.E., 2005. Slow dynamics of the Northern Hemisphere glaciation. *PALEOCEANOGRAPHY*, **VOL. 20**, PA4022, doi:10.1029/2005PA001153.
- Mudelsee, M., and Statterger, K., 1997. Exploring the structure of the mid-Pleistocene revolution with advance methods of time-series analysis. *Geol. Rundsch.*, **86**, 499–511.
- Pagani, M., Zachos, J.C., Freeman, K.H., Tipple, B., Bohaty, S., 2005. Marked Decline in Atmospheric Carbon Dioxide Concentrations During the Paleogene. *Science*, **Vol. 309**, no. 5734, pp. 600–603. DOI: 10.1126/science.1110063.
- Rahmstorf, S., 1995. Bifurcations of the Atlantic thermohaline circulation in response to changes in the hydrological cycle. *Nature*, **378**, 145–149.
- Rashid H., and Boyle, E.A., 2007. Mixed-Layer Deepening During Heinrich Events: A Multi-Planktonic Foraminiferal $\delta^{18}O$ Approach. *Science*, **Vol. 318**, no. 5849, pp. 439–441. DOI: 10.1126/science.1146138.
- Ravelo, A.C., Andreasen, D.H., Lyle, M., Lyle, A.O., and Wara, M.W., 2004. Regional climate shifts caused by gradual global cooling in the Pliocene epoch. *Nature*, **429**, 263–266.
- Raymo, M.E., 1994. The initiation of Northern Hemisphere glaciation. *Annu. Rev. Earth Planet. Sci.*, **22**, 353–383.
- Raymo, M.E., and Nisancioglu, K., 2003. The 41 ka world: Milankovitch's other unsolved mystery. *Paleoceanography*, **18**, doi: 10.1029/2002PA000791.
- Raymo, M.E., and Huybers, P., 2008. Unlocking the mysteries of the Ice Ages. *Nature*, **v. 451**, p. 284–285.
- Raymo, M.E., Lisiecki, L., and Nisancioglu, K., 2006. Plio-Pleistocene ice volume, Antarctic climate, and the global $\delta^{18}O$ record. *Science*, **v. 313**, p. 492, doi: 10.1126/science.1123296.
- Ridgwell, A., Watson, A., and Raymo, M., 1999. Is the spectral signature of the 100 kyr glacial cycle consistent with a Milankovitch origin. *Paleoceanography*, **14**, 437–440.
- Ridgwell, A.J., Watson, A.J., Maslin, M.A., Kaplan, J.O., 2003. Implications of coral reef build-up for controls on atmospheric CO₂ since the Last Glacial Maximum. *Palaeoceanography*, **18**(4), 1083. doi: 10.1029/2003PA000893.
- Ruddiman, W.F., 1977. Late Quaternary deposition of ice-rafted sand in the subpolar North Atlantic (lat. 40° to 65° N). *Geol. Soc. Am. Bull.*, **88**, 1813–1827.
- Ruddiman, W.F., 2003. Orbital insolation, ice volume, and greenhouse gases. *Quaternary Sci. Rev.*, **22**, 1597–1629.
- Ruddiman, W.F., and Raymo, M.E., 1988. Northern Hemisphere climate regimes during the past 3 Ma: Possible tectonic connections. *Phil. Trans. R. Soc. Lond.*, **B 318**, 411–430.
- Ruddiman, W.F., and Raymo, M.E., 2003. A methane based time scale for Vostok ice. *QSR*, **22**, 141–155.
- Seidov, D., and Maslin, M.A., 2001. “Atlantic Ocean heat piracy and the bipolar climate seesaw during Heinrich and Dansgaard-Oeschger events.” *J. Quaternary Sci.*, **16**, 321–328.
- Seidov, D., Barron, E., Haupt, B.J., and Maslin, M.A., 2001. “Ocean bi-polar seesaw and climate: Southern versus Northern meltwater impacts.” In Seidov, D., Haupt, B.J., and Maslin, M.A. (eds.), *The Oceans and Rapid Climate Change: Past, Present and Future*. Washington, DC: American Geophysical Union. Geophysical Monograph Series, vol. 126, pp. 147–167.
- Shackleton, N.J., 2000. The 100,000 year Ice Age cycle identified and found to lag temperature, carbon dioxide and orbital excentricity. *Science*, **289**, 1989–1992.
- Stocker, T.F., 2003. South dials north. *Nature*, **424**, 496–498.
- Taylor, K.C., Mayewski, P.A., Alley, R.B., Brook, E.J., Gow, A.J., Grootes, P.M., Meese, D.A., Saltzman, E.S., Severinghaus, J.P., Twickler, M.S., White, J.W.C., Whitlow, S., Zielinski, G.A., 1997. The Holocene-younger dryas transition recorded at summit, Greenland. *Science*, **278**, 825–827.
- Thiede, J., Winkler, A., Wolf-Welling, T., Eldholm, O., Myhre, A., Baumann, K-H., Henrich, R., Steind, R. (1998) Late Cenozoic history of the Polar North Atlantic: results from ocean drilling. *Quaternary Science Reviews*, **Volume 17**, Issues 1-3, Pages 185–208.
- Trauth, M.H., Maslin, M.A., Deino, A., Bergner, A., Strecker M. (2007) “High and low latitude controls and East African climate and early human evolution” *Journal of Human Evolution*, **Volume 53**, Issue 5, p.475–486.
- Trauth, M., Maslin, M.A., Deino, A., Strecker, M., 2005. Late Cenozoic moisture history of East Africa and its implication for human evolution. *Science*, **309**, 2051–2053.
- Weaver, A.J., Saenko, O.A., Clark, P.U., and Mitrovica, J.X., 2003. Meltwater pulse 1A from Antarctica as a trigger of the Bolling-Allerod warm interval. *Science*, **299**, 1709–1713.
- Wilson, R.C.L., Drury, S.A., Chapman, J.A., 2000. *The Great Ice Age; Climate Change and Life*. London: Routledge, 288pp.
- Zachos, J.C., Pagani, M., Sloan, L., Thomas, E., and Billups, K., 2001. Trends, rhythms and aberrations in global climate 65 Ma to present. *Science*, **292**, 686–690.

Cross-references

[Albedo Feedbacks](#)
[Antarctic Bottom Water and Climate Change](#)
[Astronomical Theory of Climate Change](#)
[Binge-Purge Cycles of Ice Sheet Dynamics](#)
[Carbon Dioxide and Methane, Quaternary Variations](#)
[Climate Change, Causes](#)
[Climate Forcing](#)
[Dansgaard-Oeschger Cycles](#)
[Eccentricity](#)
[Glaciations, Quaternary](#)
[Heinrich Events](#)
[Holocene Climates](#)
[Ice cores, Antarctica and Greenland](#)
[Last Glacial Maximum](#)
[Last Glacial Termination](#)
[Millennial Climate Variability](#)
[Mountain Uplift and Climate Change](#)
[North Atlantic Deep Water and Climate Change](#)
[Obliquity](#)
[Plate Tectonics and Climate Change](#)
[Precession, Climatic](#)
[SPECMAP](#)
[Sun-Climate Connections](#)
[Thermohaline Circulation](#)
[Weathering and Climate](#)
[Younger Dryas](#)

QUATERNARY VEGETATION DISTRIBUTION

Introduction

All aspects of Quaternary vegetation distributions, from the range and abundance of individual species, to the global position, extent, and composition of biomes, have changed extensively and repeatedly in response to the orbitally-paced oscillations in climate, atmospheric CO₂, and ice extent that are characteristic of the Quaternary. At centennial and longer timescales, the distribution and abundance of plant species closely track shifts in climate, despite the rooted habit of individual plants, via the dispersal of propagules to newly favorable regions, local changes in population abundances, and the dying out of populations in unfavorable locations. Distributions of vegetation formations and biomes emerge from these species-level responses. The history of Quaternary vegetation distributions is thus indirectly a history of global and regional climate change, and paleo-vegetational records are an important source of information about Quaternary environments. As an active component of the Earth system, shifts in the global vegetation affect the biogeochemical and biogeophysical fluxes between the land surface and atmosphere as well as the functioning of the global carbon cycle. Moreover, the present genetic structure and distribution of populations, species, and communities is in part a legacy of late-Quaternary species migrations and colonization history.

Primary sources of information for Quaternary vegetation history are the fossil pollen records collected from lake, wetland, and near-shore marine sediments, supplemented extensively by plant macrofossil, phytolith, and stable carbon isotope records. The present genetic structure of plant populations provides additional information about colonization routes and refugia. Detailed information about Quaternary vegetation distributions is mainly limited to the past 25,000 years, due to the limited length of most terrestrial records and because radiocarbon dating, the primary source of age estimates for late-Quaternary organic sediments, becomes increasingly uncertain after 40,000 years as radioactivity declines to background levels. The accuracy of radiocarbon ages varies over time, due to secular variations in atmospheric radiocarbon concentrations; all radiocarbon ages here have been converted to calendar years unless otherwise indicated. The past 40,000 years include the Last Glacial Maximum, last glacial-interglacial transition, and current interglacial and so may serve as a model for vegetation distributions during previous glacial-interglacial sequences. Individual records can span one million years or more, allowing longer-term reconstructions of vegetation history for certain locales.

Vegetation processes and dynamics

At Quaternary time scales (10²–10⁵ years), vegetation dynamics are mainly forced by climate change, and plant taxa have primarily accommodated late-Quaternary climate change via local changes in abundance and regional to continental shifts in distribution (Huntley and Webb, 1989). These biogeographic shifts can be dramatic: for example, *Picea* (spruce), which today is abundant in boreal and alpine regions, at the Last Glacial Maximum was apparently most abundant in the eastern interior of the USA (Figure Q11), a geographic shift of approximately 2,000 km. The maps of spruce also illustrate

that although migration is an important component of Quaternary vegetation dynamics, within-range changes in abundance are equally significant. The range of spruce (approximated by the 5% pollen contour in Figure Q11) has been relatively stable during the middle to late Holocene, but the area of highest abundance has shifted from western to eastern Canada (Figure Q11). These internal shifts in abundances are the result of changing rates of reproduction, growth, and mortality within and among populations, mediated by climate and disturbance regimes. The changes in extent and abundance differ among plant taxa, and the associations among taxa have changed with time. Species such as *Fagus grandifolia* (American beech) and *Tsuga canadensis* (eastern hemlock) that today are closely associated, had differing late-glacial distributions and migration histories (Figure Q11). Conversely, plant associations existed in the past that no longer exist today (indicated by high dissimilarities in Figure Q11), and may have grown under climatic conditions unlike any found today (Williams et al., 2001). Species movements along altitudinal gradients in response to climate change also display individualistic behavior, rather than wholesale shifts in vegetation zones.

The available evidence indicates that vegetation is in dynamic equilibrium with climate at millennial time scales (Webb, 1986). Climatic reconstructions based on pollen-response surfaces are generally consistent with other climatic proxies and general circulation model simulations and can successfully predict pollen abundances for other plant taxa (Prentice et al., 1991). Multi-proxy sediment records with evidence of abrupt climate change typically show that terrestrial vegetation composition responded to such changes with response times on the order of decades to a century (Tinner and Lotter, 2001). Holocene migration rates based upon pollen data range from 10 to 1,000 m yr⁻¹. However, these migration rates are at the edge of or beyond those predicted by current dispersal theory (Clark et al., 2001), and may be over-estimates in cases where outlier populations invisible to the pollen record are nucleating range expansions. Disturbance agents (fire, flood, windthrow, extreme climate events) contribute to and accelerate vegetation change by increasing plant mortality and opening up gaps for colonization.

At subcontinental to global scales, the individualistic responses of plant taxa to climate change cause the position, extent, and species composition of plant functional types (PFTs) and biomes to change over time. PFTs and biomes are useful units of vegetation at global scales, because they are based upon structural features of the vegetation and so are not constrained by intercontinental differences in evolutionary history and floristic lists (Prentice et al., 2000). Moreover, the number of plant morphological and functional types is limited relative to the number of species, so biomes can persist despite individualistic species behavior.

Vegetation history

Plio-Pleistocene transition to the last glacial maximum (ca. 2.5 million to 21,000 yBP)

The major floristic elements of the Quaternary vegetation were in place by the end of the Tertiary, with few new species or morphological changes apparent in the fossil record. Vegetation distributions during the Plio-Pleistocene transition changed in response to the onset of widespread glaciation in the Northern Hemisphere at ca. 2.45 million yBP, decreased global mean temperatures, and increased climate variability. Vegetation change

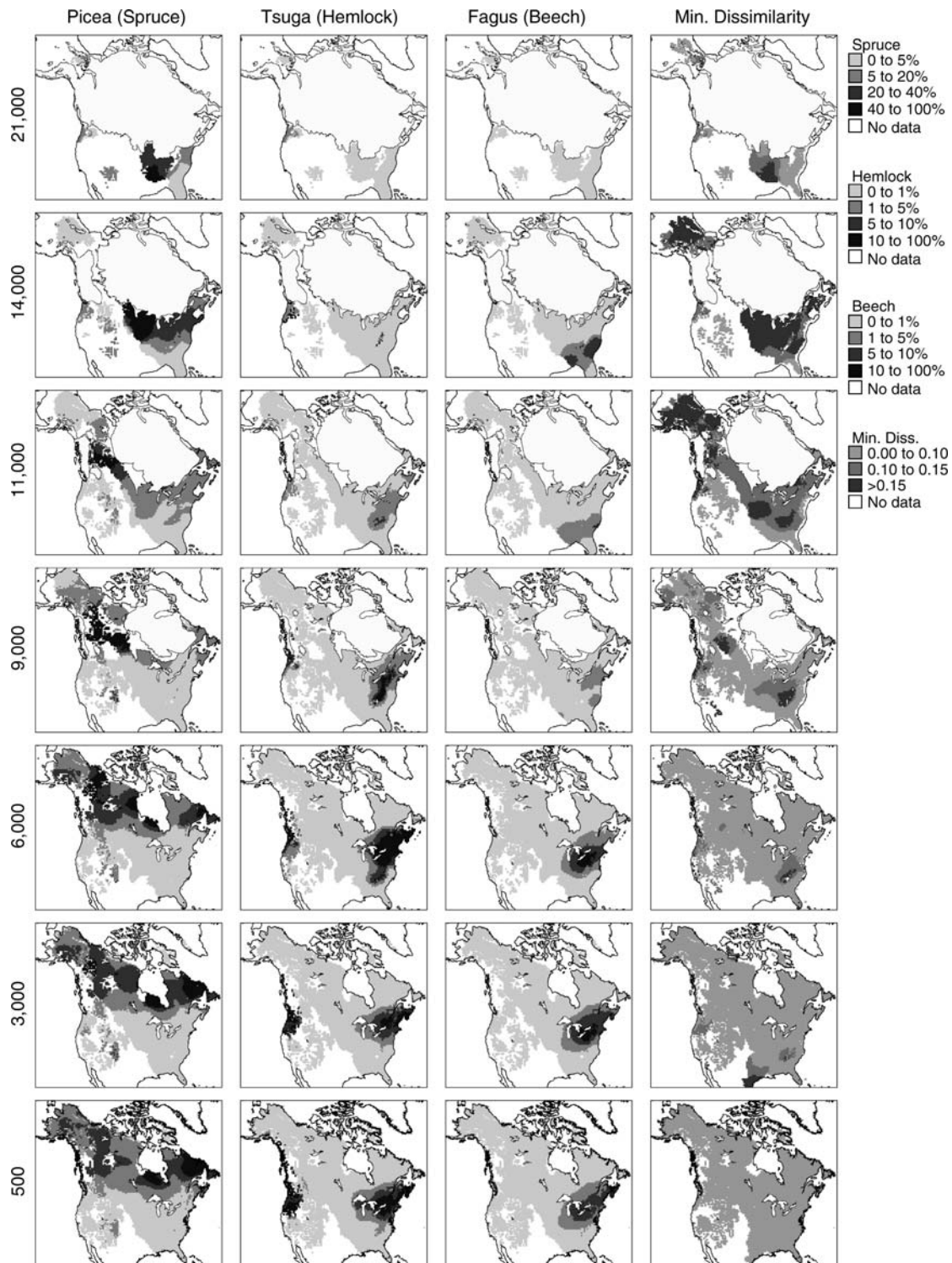


Figure Q11 Rows 1–3: Mapped pollen percentages for spruce (*Picea*), hemlock (*Tsuga*), and beech (*Fagus*) in northern and eastern North America for selected 1,000-year time periods since the Last Glacial Maximum. Each row header indicates the age in yrBP. Maps are based upon fossil pollen records from the North American Pollen Database, and consist of percent pollen abundances calculated relative to a summed pollen count and interpolated to a 50-km grid. Such maps are widely interpreted to represent past shifts of plant distributions, and analyses of modern pollen-vegetation relationships have shown that such maps capture contemporary patterns of plant abundances. Row 4: Mapped dissimilarities between fossil pollen assemblages and a dataset of modern and 500-yrBP pollen samples. High dissimilarities indicate that the fossil pollen assemblage has no close counterpart among modern pollen samples, and is interpreted to indicate plant communities unlike any today.

was most pronounced at high latitudes, where during the relatively warm Middle Pliocene, coniferous forests had grown to the Arctic coast in regions today occupied by tundra; while in the Southern Hemisphere, beech grew in coastal areas of Antarctica (Thompson and Fleming, 1996). Despite the drastic climate changes during the Plio-Pleistocene transition, there is little evidence of significant global plant extinctions, although local extinctions were widespread (Watts, 1988).

For the past 700,000 years, vegetation history has been paced by the pronounced 100,000-year cycle in climate, atmospheric CO₂, and global ice volume. Vegetation distributions at previous interglacials are broadly similar to the current interglacial, with expansions in the abundance and range of thermophilous taxa, but just as climates differed among interglacials, so too did the distribution and composition of the vegetation. The Eemian Interglacial in Europe (130–107 thousand yBP), which is the last interglacial prior to the current one and is particularly well documented, is characterized by high pollen abundances of oak (*Quercus*), hazel (*Corylus*), alder (*Alnus*), beech (*Fagus*), hornbeam (*Carpinus*), and other temperate woody taxa, with differences among sites likely reflecting interregional differences in Eemian climates. After the last interglacial ended, the proportion of treeless vegetation increased, with high pollen abundances of grass (Poaceae), sagebrush (*Artemisia*), chenopods (Chenopodiaceae), pine (*Pinus*), and juniper (*Juniperus*) reported from records spanning the last glacial period (Allen et al., 1999). On both sides of the North Atlantic, the proportion of woody vegetation increased during Heinrich events and interstadials (Grimm et al., 1993). In western North America, high abundances of oak, willow (*Salix*), and alder pollen during interglacials alternated with high abundances of fir (*Abies*), pine, and Taxaceae/Cupressaceae/Taxodiaceae (key taxa include redwood, cedar, and cypress) pollen during glacial periods (Adam, 1988; Heusser, 2000).

Last Glacial Maximum (LGM; 21,000 yBP)

By the last glacial maximum (LGM), enough well-dated paleovegetation records are available to systematically map global vegetation distributions, although tropical regions remain underrepresented. LGM vegetation distributions (Figure Q12a) formed in response to climates that were colder and drier than present. Atmospheric CO₂ concentrations that were 80 ppm lower than pre-industrial levels may have amplified the ecological impact of decreased moisture availability. Treeless conditions predominated in high-latitude regions not buried by ice, with tundra intergrading into steppe in central Asia and China (Figure Q11a) and steppe vegetation in North America along the margin of the Cordilleran and Laurentide Ice Sheets, in southern Europe and Northern Africa, in southern Africa, and in Australasia. Deserts extended to the east coast of China in now-forested regions. In contrast, lake level records from the western interior of North America indicate that full-glacial climates were wetter than present, and conifer woodlands grew widely in areas that today are desert or shrubland-steppe (Thompson and Anderson, 2000). Northern Hemisphere temperate and boreal forests were mainly confined to the southeastern USA, southeastern China, and Japan, and included a large component of cold-tolerant evergreen taxa.

The difference between LGM and modern climate and vegetation in the tropics is less pronounced than in higher latitudes, but neither tropical climates nor vegetation were stable during the late Quaternary (Bush et al., 2001). Tropical lowland

rain forests were somewhat diminished in extent, although the extent of the decrease and degree of fragmentation has been controversial. In Africa, tropical rain forest was partially replaced by tropical seasonal forest, whereas in southern Amazonia and Australasia, grasslands and savanna encroached on areas today occupied by tropical rain forest, subtropical forest, and savanna (Kershaw, 1988; Behling, 2002). The upper treeline was as much as 1,000 m lower than present, as the elevational ranges of upland types moved downslope, and upland evergreen forests were replaced by steppe and sclerophyll shrubland.

Recent explanations for LGM tropical treeline depressions have focused upon the effects of increased aridity and low CO₂ concentrations in addition to lowered temperatures (Jolly and Haxeltine, 1997). Tropical plant communities above treeline are dominated by plants utilizing the C₄ photosynthetic pathway, which enables maintenance of high intracellular CO₂ concentrations despite low ambient CO₂ concentrations. C₃ plants, conversely, are adversely affected by increased photorespiration and decreased water-use efficiency under low ambient CO₂ concentrations and the resulting competitive disadvantage may have depressed tropical treelines. In some areas, however, full-glacial C₃ communities were replaced by C₄ communities during deglaciation, indicating that the physiological effects of varying CO₂ concentrations can be overridden by local climatic controls (Huang et al., 2001). The importance of varying CO₂ concentrations for Quaternary vegetation dynamics remains under debate.

Deglaciation (14,000–8,000 yBP)

Global vegetation distributions were fundamentally transformed during deglaciation as glacial climates warmed to interglacial conditions during a period of higher-than-present seasonal contrasts in insolation. Forest cover increased, thermophilous taxa expanded upslope and northwards, and vegetation formations characteristic of the Holocene (e.g., taiga) emerged from the reshuffling of species distributions. In northwestern Canada and northern Eurasia, the northern treeline reached its northernmost position during the early Holocene, advancing near to the Arctic coastline. It then retreated to its present position by 4,000–3,000 yBP (MacDonald et al., 2000). Montane forest developed in central Africa by 10,000 yBP (Jolly et al., 1997) and podocarp forests in New Zealand by 13,000 yBP (McGlone, 1988). In Europe and eastern North America, thermophilous plant taxa began migrating north between 14,000 and 13,000 yBP. In Africa, C₄ plants diminished in abundance (Street-Perrott et al., 1997).

This period is further marked by abrupt changes in atmospheric and oceanic circulation that were superimposed upon the general transition from glacial to interglacial climates, and vegetation distributions closely tracked these rapid climate events. During the Younger Dryas Chronozone (12,900–11,600 yBP), plant communities adjacent to the North Atlantic reverted to cold-tolerant assemblages, switching to tundra in the European Alps and to alder shrublands in Maritime Canada (Mayle et al., 1993; Ammann et al., 2000). Vegetation changes consistent with a reversion to lower temperatures have been reported in Alaska, the Pacific Northwest, and at individual sites in South America and the Indo-Pacific region (Petee, 1995). In other regions, vegetation shifts coincident with the Younger Dryas suggest variations in moisture balance rather than temperature. In eastern North America, pine rapidly

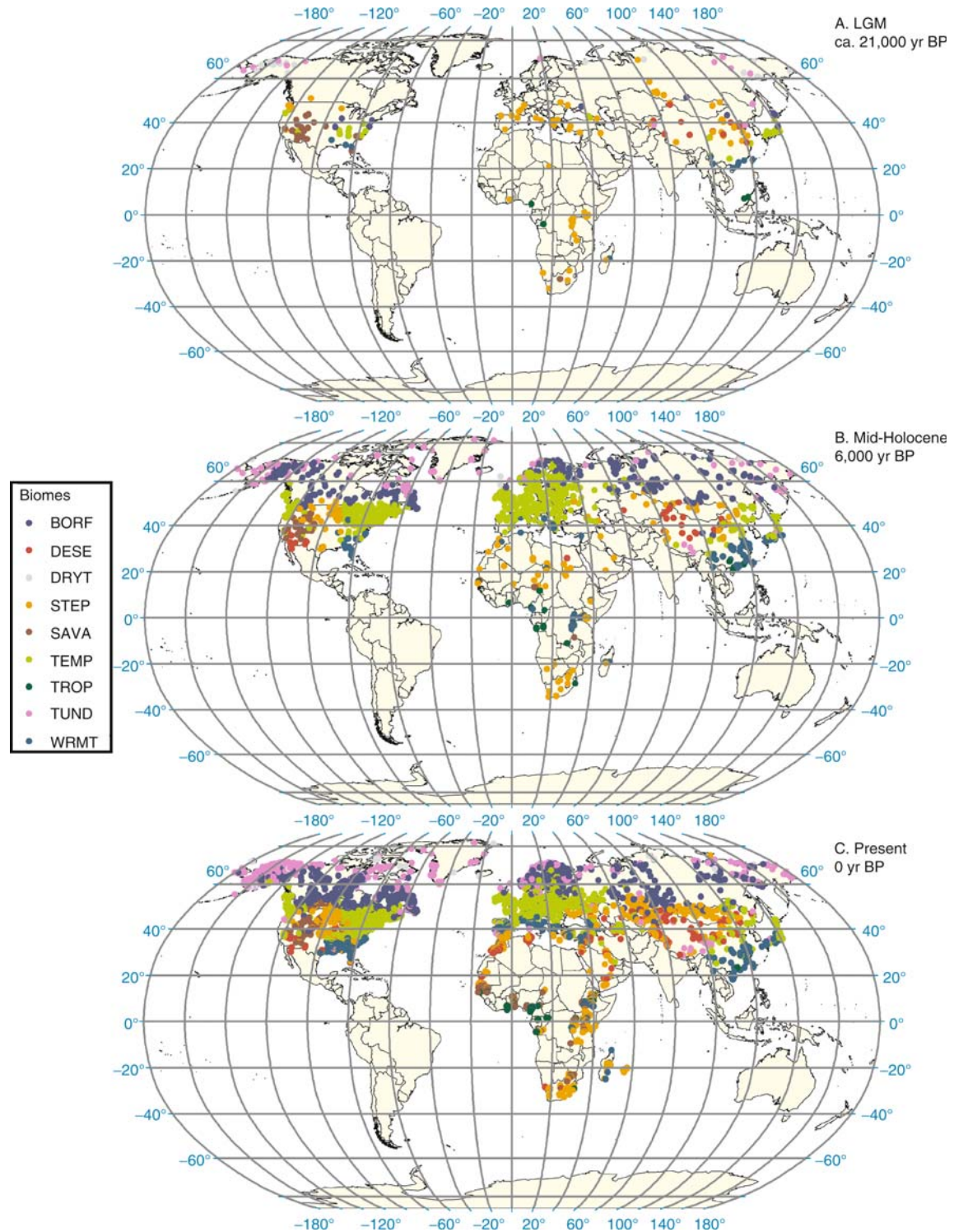


Figure Q12 Global vegetation maps produced by the Biome 6000 working group (Prentice et al., 2000; Bigelow et al., 2003), version 4.1 for the Last Glacial Maximum (18,000 radiocarbon yBP; ca. 21,000 calendar yBP), mid-Holocene (6,000 yBP), and present (0 yBP), based upon systematic application of a standardized classification algorithm to pollen and macrofossil data. The present-day vegetation reconstructions closely agree with independent maps of the vegetation. Ice sheet extent and changes in sea level are not shown. Paleovegetational reconstructions for India, the Indo-Pacific, South America, and Australia will be included in future versions of the Biome 6,000 synthesis. Biome codes: *BORF*, Boreal Forest; *DESE*, Desert; *DRYT*, Dry Tundra; *STEP*, Steppe/Grassland/Dry Shrubland; *SAVA*, Savanna and Open Woodland; *TEMP*, Temperate Forest; *TROP*, Tropical Forest; *TUND*, Tundra; *WRMT*, Warm Temperate Forest.

migrated westwards into the Great Lakes region, and spruce abundances declined (Shuman et al., 2002). Tropical African pollen records indicate that the Younger Dryas coincided with increased aridity. Vegetation distribution shifts during the Younger Dryas thus appear to have varied in direction among regions and continents as changes in climate varied among these regions.

Middle Holocene (7,000–4,000 yBP)

Global vegetation distributions during the mid-Holocene were similar to present, although differences persisted regionally (Figure Q11b). The position of the northern treeline was asymmetric relative to its present position, approximately 25 km north in northwestern Canada, 200–300 km north in central Siberia, and up to 200 km south in eastern Canada (Prentice et al., 2000; Bigelow et al., 2003). Temperate forests in eastern North America, Europe, and China were poleward of their present position, with shifts on the order of 100 km and as much as 800 km in northeastern China. In New Zealand, southern beech (*Nothofagus*) forests expanded (McGlone, 1988). These patterns suggest warmer-than-present temperatures in middle and upper latitudes.

Other distributional differences between the mid-Holocene and present vegetation were likely due to interregional variations in moisture balance. These differences are greatest in northern Africa, where steppe, xerophytic woodlands, and even warm mixed forest grew across a broad area now occupied by Saharan desert (Figure Q12b). Lake level highstands and modeling studies show that the African monsoon was enhanced relative to present (COHMAP Members, 1988). In the Columbian Andes, xeric vegetation types increased in extent during the middle Holocene although vegetation distributions in Chile suggest wetter-than-present conditions (Marchant et al., 2002). Steppe expanded at the expense of forest in the northern Midwest but was reduced in central Asia relative to present.

Consequences of Quaternary vegetation change

Earth system effects and feedbacks

The terrestrial biosphere is an integral component of the Earth system, and changes in vegetation distributions likely affected atmospheric circulation and the functioning of global energy and biogeochemical cycles. At high latitudes, changes in surface albedo associated with shifts in treeline may have amplified the orbitally-induced variations in temperature (Foley et al., 1994). In Northern Africa, the mid-Holocene expansion of steppe at the expense of desert may have enhanced monsoonal strength by increasing rates of evapotranspiration (Kutzbach et al., 1996). At the LGM, decreased vegetation cover in mid- and high-latitudes may have amplified cooling, due to an albedo feedback, whereas decreased evapotranspiration and a weakened hydrological cycle may have enhanced tropical aridity in the tropics (Levis et al., 1999). Furthermore, the LGM decrease in vegetation cover may have increased the source area for dust emissions and increased atmospheric LGM dust loadings (Harrison et al., 2001), thereby indirectly affecting the Earth's radiative budget and increasing rates of nutrient transport. The effects of vegetation change upon glacial-interglacial carbon budgets are large but uncertain, with recent estimates ranging from 500 to 1,100 Pg carbon lost from the terrestrial biosphere at the LGM, compared to present-day stocks of 2,000 Pg C. (Maslin, 2003). Increases in atmospheric methane concentrations from 350 ppbv at the LGM to 700 ppbv at the beginning of the Holocene may be due to expansion in tropical and boreal wetlands, or increased

rates of wetland CH₄ emissions due to increased CO₂ levels (Kaplan, 2002).

Evolutionary and genetic impacts

The close similarities between late Tertiary and Pleistocene faunas and the corresponding lack of widespread extinction and macroevolutionary change during the Quaternary is somewhat surprising given that the signal feature of the Quaternary is its extensive and repeated large climatic fluctuations. Apparently, plant taxa have accommodated Quaternary climate change primarily by ecological rather than evolutionary processes. Bennett (1997) has argued that individualistic species behavior effectively decouples microevolutionary and macroevolutionary processes, as orbitally-paced reorganizations of species associations remove coevolutionary adaptations.

Nevertheless, the repeated range shifts characteristic of the Quaternary are highly likely to have affected species' genetic structure, as individual populations have propagated or gone extinct (Davis and Shaw, 2001). Whether Quaternary vegetation dynamics tended to foster increased or decreased genetic diversity is not yet known. The genetic structure observed in present populations and species is in part a legacy of the biogeographic responses to the last deglaciation. For example, haplotype distributions within European white oaks (*Quercus* spp., subgenus *Lepidobalanus*) and North American whitebark pines have been convincingly related to likely colonization routes and glacial population distributions (Petit et al., 2002; Richardson et al., 2002). Differences in genetic structures among modern populations thus may help refine inferences about vegetation history.

Quaternary environmental variability may have helped shape the modern latitudinal gradient in species richness and other biogeographic patterns of species diversity. Historical explanations for high levels of tropical species diversity include focused upon two contrasting hypotheses: (a) long-term stability of tropical climates encouraging persistence of tropical rainforests and low rates of extinction versus (b) high levels of endemism caused by repeated fragmentation of rainforests during glacial periods (Hooghiemstra and van der Hammen, 1998). The extent of Amazonian rain forest fragmentation remains controversial, but lowland rainforests appear to have persisted as intact, albeit diminished, bodies of vegetation (Colinvaux et al., 2000), weakening the endemism hypotheses.

John Jack W. Williams

Bibliography

- Adam, D.P., 1988. Palynology of two upper Quaternary cores from Clear Lake, Lake County, California. US Geological Survey, Washington, DC. Professional Paper 1363.
- Allen, J.R.M., Brandt, U., Brauer, A., Hubberten, H.-W., Huntley, B., Keller, J., Kraml, M., Mackensen, A., Mingram, J., Negendank, J.F.W., Nowaczyk, N.R., Oberhänsli, H., Watts, W.A., Wulf, S., and Zolitschka, B., 1999. Rapid environmental changes in southern Europe during the last glacial period. *Nature*, **400**, 740–743.
- Ammann, B., Birks, H.J.B., Brooks, S.J., Eicher, U., von Grafenstein, U., Hofmann, W., Lemdahl, G., Schwander, J., Tobolski, K., and Wick, L., 2000. Quantification of biotic responses to rapid climatic changes around the Younger Dryas – A synthesis. *Palaeogeogr. Palaeoclimatol. Palaeoecol.*, **159**, 313–347.
- Behling, H., 2002. South and southeastern Brazilian grasslands during Late Quaternary times: A synthesis. *Palaeogeogr. Palaeoclimatol. Palaeoecol.*, **177**, 19–27.
- Bennett, K.D., 1997. *Evolution and Ecology: The Pace of Life*. Cambridge: Cambridge University Press, 241pp.
- Bigelow, N.H., Brubaker, L.B., Edwards, M.E., Harrison, S.P., Prentice, I.C., Anderson, P.M., Andreev, A.A., Bartlein, P.J., Christensen, T.R.,

- Cramer, W., Kaplan, J.O., Lozhkin, A.V., Matveyeva, N.V., Murray, D.F., McGuire, A.D., Razzhivin, V.Y., Ritchie, J.C., Smith, B., Walker, D.A., Gajewski, K., Wolf, V., Holmqvist, B., Igarashi, U., Kremenetskii, K., Paus, A., Pissari, M.F.J., and Volkova, V.S., 2003. Climate change and Arctic ecosystems I: Vegetation changes north of 55° N between the Last Glacial Maximum, mid-Holocene and present. *J. Geophys. Res. Atmos.*, **108**(D19), 8170.
- Bush, M.B., Stute, M., Ledru, M.-P., Behling, H., Colinvaux, P.A., De Oliveira, P.E., Grimm, E.C., Hooghiemstra, H., Haberle, S., Leyden, B.W., Salgado-Labouriau, M.-L., and Webb, R., 2001. Paleotemperature estimates for the lowland Americas between 30° S and 30° N at the Last Glacial Maximum. In Markgraf, V. (ed.), *Interhemispheric Climate Linkages*. San Diego: Academic Press, pp. 293–306.
- Clark, J.S., Lewis, M., and Horvath, L., 2001. Invasion by extremes: variation in dispersal and reproduction retards population spread. *Am. Naturalist*, **157**, 537–554.
- COHMAP Members, 1988. Climatic changes of the last 18,000 years: observations and model simulations. *Science*, **24**, 1043–1052.
- Colinvaux, P.A., De Oliveira, P.E., and Bush, M.B., 2000. Amazonian and neotropical plant communities on glacial time-scales: The failure of the aridity and refuge hypotheses. *Quaternary Sci. Rev.*, **19**, 141–169.
- Davis, M.B., and Shaw, R.G., 2001. Range shifts and adaptive responses to Quaternary climate change. *Science*, **292**, 673–679.
- Foley, J.A., Kutzbach, J.E., Coe, M.T., and Levis, S., 1994. Feedbacks between climate and boreal forests during the Holocene epoch. *Nature*, **371**, 52–54.
- Grimm, E.C., Jacobson, G.L. Jr., Watts, W.A., Hansen, B.C.S., and Maasch, K.A., 1993. A 50,000-year record of climate oscillations from Florida and its temporal correlation with the Heinrich events. *Science*, **261**, 198–200.
- Harrison, S.P., Kohfeld, K.E., Roelandt, C., and Claquin, T., 2001. The role of dust in climate changes today, at the Last Glacial Maximum and in the future. *Earth Sci. Rev.*, **54**, 43–80.
- Heusser, L.E., 2000. Rapid oscillations in western North America vegetation and climate during oxygen isotope stage 5 inferred from pollen data from Santa Barbara Basin (Hole 893A). *Palaeogeogr. Palaeoclimatol. Palaeoecol.*, **161**, 407–421.
- Hooghiemstra, H., and van der Hammen, T., 1998. Neogene and Quaternary development of the neotropical rain forest: the forest refugia hypothesis, and a literature overview. *Earth Sci. Rev.*, **44**, 147–183.
- Huang, Y., Street-Perrott, F.A., Metcalfe, S.E., Brenner, M., Moreland, M., and Freeman, K.H., 2001. Climate change as the dominant control on glacial-interglacial variations in C₃ and C₄ plant abundance. *Science*, **293**, 1647–1651.
- Huntley, B., and Webb, T. III, 1989. Migration: Species' response to climatic variations caused by changes in the Earth's orbit. *J. Biogeogr.*, **16**, 5–19.
- Jolly, D., and Haxeltine, A., 1997. Effect of low glacial atmospheric CO₂ on tropical African montane vegetation. *Science*, **276**, 786–788.
- Jolly, D., Taylor, D., Marchant, R., Hamilton, A., Bonnefille, R., Buchet, G., and Riollet, G., 1997. Vegetation dynamics in central Africa since 18,000 ybp: Pollen records from the interlacustrine highlands of Burundi, Rwanda, and western Uganda. *J. Biogeogr.*, **24**, 495–512.
- Kaplan, J.O., 2002. Wetlands at the Last Glacial Maximum: Distribution and methane emissions. *Geophys. Res. Lett.*, **29**, 1–4.
- Kershaw, A.P., 1988. Late-Tertiary and Pleistocene vegetation history: Australasia. In Huntley, B., and Webb, T. III. (eds.), *Vegetation History*. Dordrecht: Kluwer, pp. 237–306.
- Kutzbach, J., Bonan, G., Foley, J., and Harrison, S.P., 1996. Vegetation and soil feedbacks on the response of the African monsoon to orbital forcing in the early to middle Holocene. *Nature*, **384**, 623–626.
- Levis, S., Foley, J., and Pollard, D., 1999. CO₂, climate, and vegetation feedbacks at the Last Glacial Maximum. *J. Geophys. Res.*, **104**(ND24), 31191–31198.
- MacDonald, G.M., Velichko, A.A., Kremenetski, C.V., Borisova, O.K., Goleva, A.A., Andreev, A.A., Cwynar, L.C., Riding, R.T., Forman, S.L., Edwards, T.W.D., Aravena, R., Hammarlund, D., Szeicz, J.M., and Gattaulin, V.N., 2000. Holocene treeline history and climate change across northern Eurasia. *Quaternary Res.*, **53**, 302–311.
- Marchant, R., Behling, H., Berrio, J.C., Cleef, A., Duijvenvoorden, J., Hooghiemstra, H., Kuhry, P., Melief, B., Schreve-Brinkman, E., Van Geel, B., Van Der Hammen, T., Van Reenen, G., and Wille, M., 2002. Pollen-based biome reconstructions for Colombia at 3,000, 6,000, 9,000, 12,000, 15,000, and 18,000 ¹⁴C year ago: Late Quaternary tropical vegetation dynamics. *J. Quaternary Sci.*, **17**, 113–129.
- Maslin, M.A., and Thomas, E., 2003. Balancing the deglacial global carbon budget: The hydrate factor. *Quaternary Sci. Rev.*, **22**, 1729–1736.
- Mayle, F.E., Levesque, A.J., and Cwynar, L.C., 1993. *Alnus* as an indicator taxon of the Younger Dryas cooling in eastern North America. *Quaternary Sci. Rev.*, **12**, 295–305.
- McGlone, M.S., 1988. Glacial and Holocene vegetation history – 20 kyr to present: New Zealand. In Huntley, B., and Webb, T. III, (eds.), *Vegetation History*. Dordrecht: Kluwer, pp. 557–599.
- Peteet, D., 1995. Global Younger Dryas? *Quaternary Int.*, **28**, 93–104.
- Petit, R.J., Brewer, S., Bordács, S., Burg, K., Cheddadi, R., Coart, E., Cottrell, J., Csai, U.M., van Dam, B., Deans, J.D., Espinel, S., Fineschi, S., Finkeldey, R., Glaz, I., Goicoechea, P.G., Jensen, J.S., König, A.O., Lowe, A.J., Madsen, S.F., Mátyás, G., Munro, R.C., Popescu, F., Slade, D., Tabbener, H., de Vries, S.G.M., Ziegenhagen, B., de Beaulieu, J.-L., and Kremer, A., 2002. Identification of refugia and post-glacial colonization routes of European white oaks based on chloroplast DNA and fossil pollen evidence. *Forest Ecol. Manag.*, **156**, 49–74.
- Prentice, I.C., Bartlein, P.J., and Webb, T. III, 1991. Vegetation and climate changes in eastern North America since the Last Glacial Maximum: A response to continuous climatic forcing. *Ecology*, **72**, 2038–2056.
- Prentice, I.C., Jolly, D., and BIOME 6,000 participants, 2000. Mid-Holocene and glacial-maximum vegetation geography of the northern continents and Africa. *J. Biogeogr.*, **27**, 507–519.
- Richardson, B.A., Brunsfeld, S.J., and Klopfenstein, N.B., 2002. DNA from bird-dispersed seed and wind-disseminated pollen provides insights into postglacial colonization and population genetic structure of whitebark pine (*Pinus albicaulis*). *Mol. Ecol.*, **11**, 215–227.
- Shuman, B.N., Webb, T. III, Bartlein, P.J., and Williams, J.W., 2002. The anatomy of a climatic oscillation: Vegetation change in eastern North America during the Younger Dryas chronozone. *Quaternary Sci. Rev.*, **21**, 1777–1791.
- Street-Perrott, F.A., Huang, Y., Perrott, R.A., Eglinton, G., Barker, P., Khelifa, L.B., Harkness, D.D., and Olago, D.O., 1997. Impact of lower atmospheric carbon dioxide on tropical mountain ecosystems. *Science*, **278**, 1422–1426.
- Thompson, R.S., and Anderson, K.H., 2000. Biomes of western North America at 18,000, 6000 and 0 ¹⁴C ybp reconstructed from pollen and packrat midden data. *J. Biogeogr.*, **27**, 555–584.
- Thompson, R.S., and Fleming, R.F., 1996. Middle Pliocene vegetation: Reconstructions, paleoclimatic inferences, and boundary conditions for climate modeling. *Mar. Micropaleontol.*, **27**, 27–49.
- Tinner, W., and Lotter, A.F., 2001. Central European vegetation response to abrupt climate change at 8.2 ka. *Geology*, **29**, 551–554.
- Watts, W.A., 1988. Late-Tertiary and Pleistocene vegetation history: Europe. In Huntley, B., and Webb, T. III, (eds.), *Vegetation History*. Dordrecht: Kluwer, pp. 155–192.
- Webb, T. III, 1986. Is vegetation in equilibrium with climate? How to interpret late-Quaternary pollen data. *Vegetatio*, **67**, 75–91.
- Williams, J.W., Shuman, B.N., and Webb, T. III, 2001. Dissimilarity analyses of late-Quaternary vegetation and climate in eastern North America. *Ecology*, **82**, 3346–3362.

Cross-references

[Carbon Dioxide and Methane, Quaternary Variations](#)
[Carbon Isotopes, Stable](#)
[Holocene Climates](#)
[Holocene Treeline Fluctuations](#)
[Last Glacial Maximum](#)
[Last Glacial Termination](#)
[Late Quaternary-Holocene Vegetation Modeling](#)
[Monsoons, Quaternary](#)
[Paleobotany](#)
[Palynology](#)
[Pollen Analysis](#)
[Quaternary Climate Transitions and Cycles](#)
[Younger Dryas](#)

R

RADIOCARBON DATING

Radiocarbon (^{14}C) dating, now in its fifth decade of routine use, remains the most widely employed method of inferring chronometric age for organic materials from the late Pleistocene and Holocene. It provides the principal time scale for reconstruction of the history of late Quaternary environments, including the temporal scale for climate proxy records, and documents chronometric relationships for prehistoric human cultures on a world-wide basis.

Radiocarbon dating model

The natural production of ^{14}C is a secondary effect of cosmic-ray interactions with atmospheric gas molecules, with the resultant production of neutrons (Figure R1). Most ^{14}C is formed by the reaction of neutrons with ^{14}N . It is then rapidly oxidized to form $^{14}\text{CO}_2$. In this form, ^{14}C is distributed throughout the Earth's atmosphere by stratospheric winds, becoming generally well-mixed by the time ^{14}C -tagged CO_2 molecules reach the Earth's surface. Most ^{14}C is absorbed in the oceans, while 1–2% becomes part of the terrestrial biosphere, primarily by means of photosynthesis. Plant materials and animals that are, directly or indirectly, dependent on plants, are thus all labeled with ^{14}C .

Metabolic processes in living organisms maintain the ^{14}C content in approximate equilibrium with atmospheric ^{14}C concentrations. While ^{14}C decays in living tissue, it is continually replaced through the biochemical processing of plant or animal tissue. Once metabolic processes cease, as at the death of an animal or plant, the amount of ^{14}C begins to decrease by radioactive decay – in the case of ^{14}C , by beta decay – at a rate measured by the ^{14}C half-life (Taylor, 1987, 1997a).

The radiocarbon age of a sample is based on a measurement of its residual ^{14}C content. For the ^{14}C age of a sample to be equivalent to its true or solar/calendar age at a reasonable level of precision, a set of assumptions needs to be satisfied. These assumptions are that: (a) the $^{14}\text{C}/^{12}\text{C}$ ratio in materials of zero age in each carbon reservoir has remained essentially constant

over the entire ^{14}C time scale, (b) complete and rapid mixing of ^{14}C occurs throughout the various carbon reservoirs on a worldwide basis, (c) carbon isotope ratios (e.g., $^{13}\text{C}/^{12}\text{C}$ as well as $^{14}\text{C}/^{12}\text{C}$) in samples have not been altered except by ^{14}C decay since the death of an organism, (d) the half-life of ^{14}C is accurately known with reasonable precision, and (e) natural levels of ^{14}C can be measured to appropriate levels of accuracy and precision (Taylor, 1996).

A significant portion of contemporary ^{14}C studies involves two major types of efforts. First, there are investigations designed to examine and compensate for the effects of violations of the primary assumptions as applied to specific sample types or portions of the carbon reservoirs. Second, there are efforts to document explicitly the physical association between the organic sample on which a ^{14}C age estimate is obtained and the object, feature, or geological context for which an age determination is desired.

Radiocarbon age estimates are generally expressed in terms of a set of characteristic parameters that define a conventional radiocarbon age. These parameters, introduced in the mid-1970s and explicitly defined by Stuiver and Polach (1977), include (a) the use of 5,568 (± 30) years as the ^{14}C half-life (8,033 year mean life) used to calculate age, although the actual half-life value is probably closer to 5,730 (± 40) years; (b) the use of one of the United States National Institute of Standards and Technology (formerly U.S. National Bureau of Standards, NBS)-distributed oxalic acid preparations – or a secondary standard with a known relationship to the primary standard – as a contemporary or modern reference standard to define a “zero” ^{14}C age; (c) the use of AD 1950 as the zero point from which to measure ^{14}C time; (d) to account for fractionation effects, a normalization of the measured ^{14}C content in all samples to a common $^{13}\text{C}/^{12}\text{C}$ ($\delta^{13}\text{C}$) value of -25‰ (wrt PDB standard); and, finally, (e), an assumption that $^{14}\text{C}/^{12}\text{C}$ ratios in all reservoirs have remained constant over the ^{14}C time scale. In addition, each ^{14}C determination is expected to be accompanied by an expression that provides an accurate estimate of the overall experimental or analytical uncertainty. Since counting statistics associated with the measurement of ^{14}C concentrations in samples are usually the dominant component of the analytical uncertainty, this value is informally referred to as the “statistical error.”

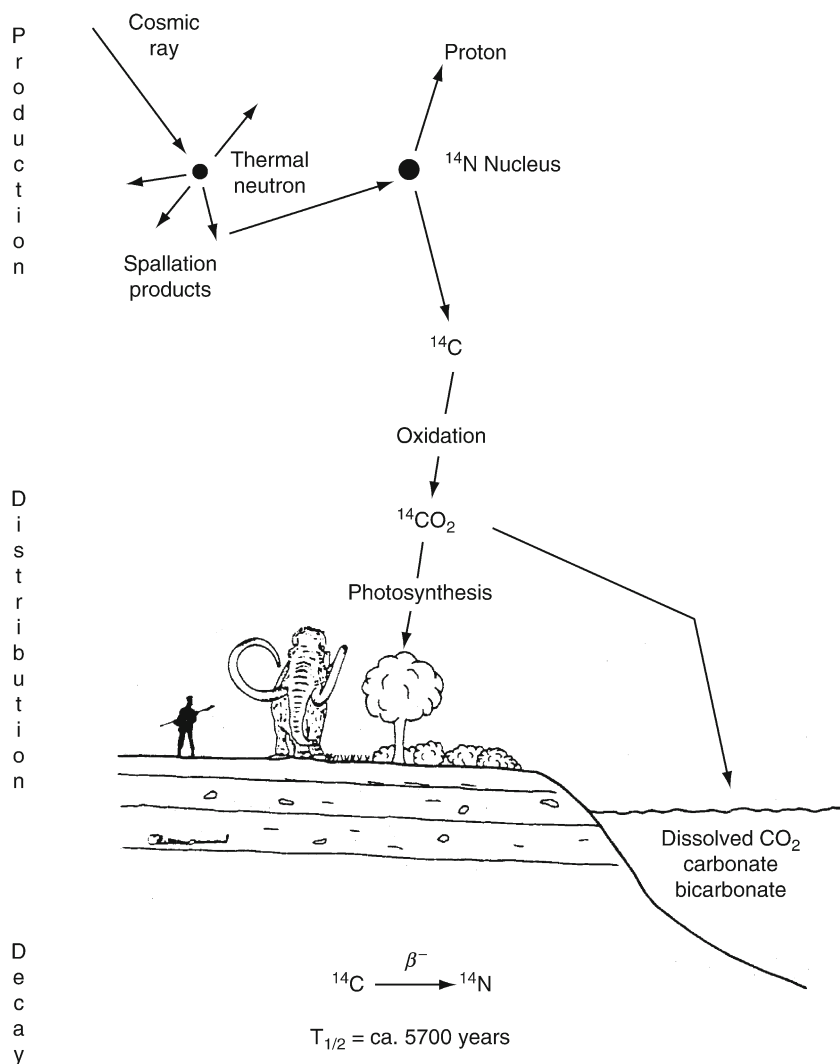


Figure R1 Radiocarbon dating model: production, distribution, and decay of ^{14}C . Figure adapted from Taylor (1997a: Fig. 3.1).

This “ \pm ” term is suffixed to all appropriately documented ^{14}C age estimates and is typically expressed as \pm one standard deviation ($\pm 1 \sigma$).

For samples from some carbon reservoirs, conventional contemporary standards may not define a zero ^{14}C age. A reservoir corrected radiocarbon age can sometimes be calculated by documenting the apparent age exhibited in control samples and correcting for the observed deviation. Reservoir effects are most often observed in samples from fresh water lakes and marine environments. A calibrated radiocarbon age takes into consideration the fact that ^{14}C activity in living organisms, which in most cases directly reflects atmospheric ^{14}C levels, has not remained constant over the ^{14}C time scale because of changes in ^{14}C production rates or reservoir mixing parameters of the carbon cycle. The study of the various factors responsible for the variability in ^{14}C production rates and changes in the world-wide distribution of ^{14}C in various carbon reservoirs over the late Pleistocene and Holocene has occupied the attention of many in the ^{14}C research community for over four

decades (Taylor, 2001). The various issues raised by the nature of the variability over time in the ^{14}C time scale – with the documentation of this variability now extended into the late Pleistocene – will be discussed in greater detail in the next section.

In the current nomenclature of the journal *Radiocarbon* “ ^{14}C years BP” is expressed only as “BP” with the “ ^{14}C years” implied (e.g., $2,510 \pm 50 \text{ BP}$). Calibrated ages, i.e., calendar or solar years, are expressed with only the “cal” (calibrated) designation attached (e.g., cal AD 1520, 3,720 cal BC), with the “years” implied. The journal *American Antiquity* adopted the nomenclature of *Radiocarbon* except for punctuation (B.P. rather than BP). In the early 1970s, the journal *Antiquity* adopted a terminology which distinguished conventional (uncalibrated) and calibrated ^{14}C values whereby “bp” and “ad/bc” are employed to designate conventional ^{14}C values while “BP” and “AD/BC” are used to designate calibrated ^{14}C values.

The ^{14}C time scale now extends from about 300 years to between 40,000 and 60,000 years. The limitations of using

the ^{14}C time scale over the last few hundred years are a consequence of the complex interplay of various recent natural deviations in ^{14}C content (informally referred to variously as “warps” or “wiggles” or more formally as “de Vries effects,” see below) and recent anthropogenic (e.g., “fossil fuel” and “bomb” ^{14}C) effects that have also caused recent deviations in ^{14}C content. The maximum ^{14}C ages that can be inferred using decay counting technology depend on characteristics of different laboratory instrumentation and experimental configurations – e.g., background and sample blank values, counter size, length of counting – and, to some degree, the amount of sample available for analysis. Currently, for laboratories with counters designed to work with older samples, routine upper limits using moderate sample sizes (3–5 grams of carbon) range upward to about 55,000 years. Employing relatively large sample sizes (>15 grams of carbon), a few laboratories have developed the capability to obtain age estimates up to about 70,000 years. With isotopic enrichment – again using relatively large sample amounts – ages up to 75,000 years have been reported on a small number of samples (Grootes et al., 1975; Erlenkeuser, 1979). There are efforts now underway to exploit accelerator mass spectrometry (AMS) technology (see below) to extend the ^{14}C time scale to as much as 70,000–90,000 years using sample weights of less than a gram of carbon.

Development of radiocarbon dating studies

Stages in the history of the development of ^{14}C dating can be distinguished partly by the type of detection technology employed and, partly, on understandings concerning the relationship between radiocarbon and “real” or solar/calendar time. The first generation of ^{14}C studies began with the appearance of the first ^{14}C date list in 1950. In the early 1970s, second generation studies began with the recognition of the existence of systematic temporal offsets in the ^{14}C time scale (Suess, 1970). In the late 1970s, third generation ^{14}C studies were ushered in by a proposal (Muller, 1977) to develop a new approach to ^{14}C measurement by AMS, although routine operation of AMS technology was not achieved until the mid-1980s (Linick et al., 1989).

Several recent technical and methodological advances have provided contexts for a series of significant applications of the ^{14}C method in a number of different disciplines. In addition to the application of AMS technology, these include the extension of the calibrated ^{14}C time scale into the late Pleistocene and a more detailed characterization of Holocene de Vries effects where relatively rapid changes in atmospheric ^{14}C concentrations complicate the inherent precision with which ^{14}C content can be converted into inferred age. The extension of the calibration of the ^{14}C time scale beyond that provided with tree ring data has been accomplished primarily by the use of AMS-based ^{14}C and TIMS (thermal ionization mass spectrometry)-based uranium-thorium (U-series) measurements on marine coral samples.

Extending the calibration of the ^{14}C time scale

Comparisons of ^{14}C with dendrochronological data based on Irish oak and German oak and pine for the earliest portion and Douglas fir, sequoia and bristlecone pine for later periods now document about 12,000 years of solar time (cal BP) (Stuiver et al., 1998a; Reimer et al., 2002). Most of the ^{14}C measurements comprising these data sets are characterized as “high-precision,” referring to carefully measured counting

uncertainties typically at the $\pm 1\sigma$ level of <20 years for the ^{14}C values used to provide the dendrochronologically-based calibration data. The validity of the stated uncertainties has been extensively examined by detailed interlaboratory comparisons among a number of the laboratories producing the calibration data (e.g., Scott et al., 1990). For the period before dendrochronological controls were available, paired uranium/thorium ($^{234}\text{U}/^{230}\text{Th}$) and ^{14}C samples from cores drilled into coral formations (Bard, 1998; Edwards et al., 1993) provide the principal data on which a late Pleistocene ^{14}C calibration curve has been provisionally extended to 24,000 cal BP or, as expressed in ^{14}C time, to 20,300 BP (Bard et al., 1998).

With the extension of the ^{14}C calibration framework using the uranium-series data on corals, it has now become apparent that what was first thought to be a “sine-wave”-like characterization of the Holocene ^{14}C calibration curve was an artifact of the limited time frame documented by the original middle and late Holocene tree-ring/ ^{14}C data set. Figure R2 represents a plot of the off-set between ^{14}C and assumed “true” ages out to about 30,000 years based primarily on the most current combined dendrochronological/ ^{14}C and coral uranium-series/ ^{14}C data, as presented in the INTCAL98 data set (Stuiver et al., 1998b). Based on the expanded calibration data, it now appears that the long-term secular variation ^{14}C anomaly over this period can be characterized as representing a slow-decay function on which has been superimposed middle- and short-term de Vries effects perturbations.

For the period before about 30,000 cal BP, age estimates obtained from ^{14}C and other Quaternary dating methods applied to samples obtained from a variety of contexts are, to varying degrees, inconsistent with regard to indications of the magnitude of the ^{14}C age offsets. For example, comparisons between ^{14}C values (adjusted by 3% to take into consideration the most likely ^{14}C half-life) and thermoluminescence age estimates on materials from hearths at Lake Mungo, Australia suggest deviations in the range of 3,500–5,000 years between 27,000 and 31,000 BP (Bell, 1991). Studies of variations in the intensity of the Earth’s dipole magnetic field – a major cause of the long-term ^{14}C secular variation trend – as well as comparisons of precisely determined ^{14}C and associated $^{40}\text{Ar}/^{39}\text{Ar}$ values from volcanic deposits, suggest somewhat lower age offsets for this period. However, the geomagnetic data suggest an increasing ^{14}C /solar time offset in the range of 1,500–2,700 years between 25,000 and 40,000 years but predict that there will be good agreement between ^{14}C and solar time at about 45,000–50,000 years (Mazaud et al., 1992; Southon et al., 1995). In addition, there also may have been a major “spike” in atmospheric ^{14}C concentrations between 30,000 and 35,000 BP (Voelker et al., 1998: Fig. 6). Further detailed studies will be necessary to clarify the magnitude of the offsets in ^{14}C activity for this period (Geyh and Schlüchter, 1998; Reimer et al., 2002).

Holocene de Vries effects

A fuller rendering of the entire Holocene ^{14}C time scale permits researchers to review more precisely the timing and characteristics of the de Vries effect “wiggles” over the last ten millennia. Figure R3 plots the series of defined Holocene “time warps” reflecting the time ranges of the de Vries effect perturbations in the calibration curve (Taylor et al., 1996: Figs. 3A and 3B). The top panel of Figure R3 represents 0–5,000 BP and the bottom panel the 5,000–10,000 BP period in ^{14}C years.

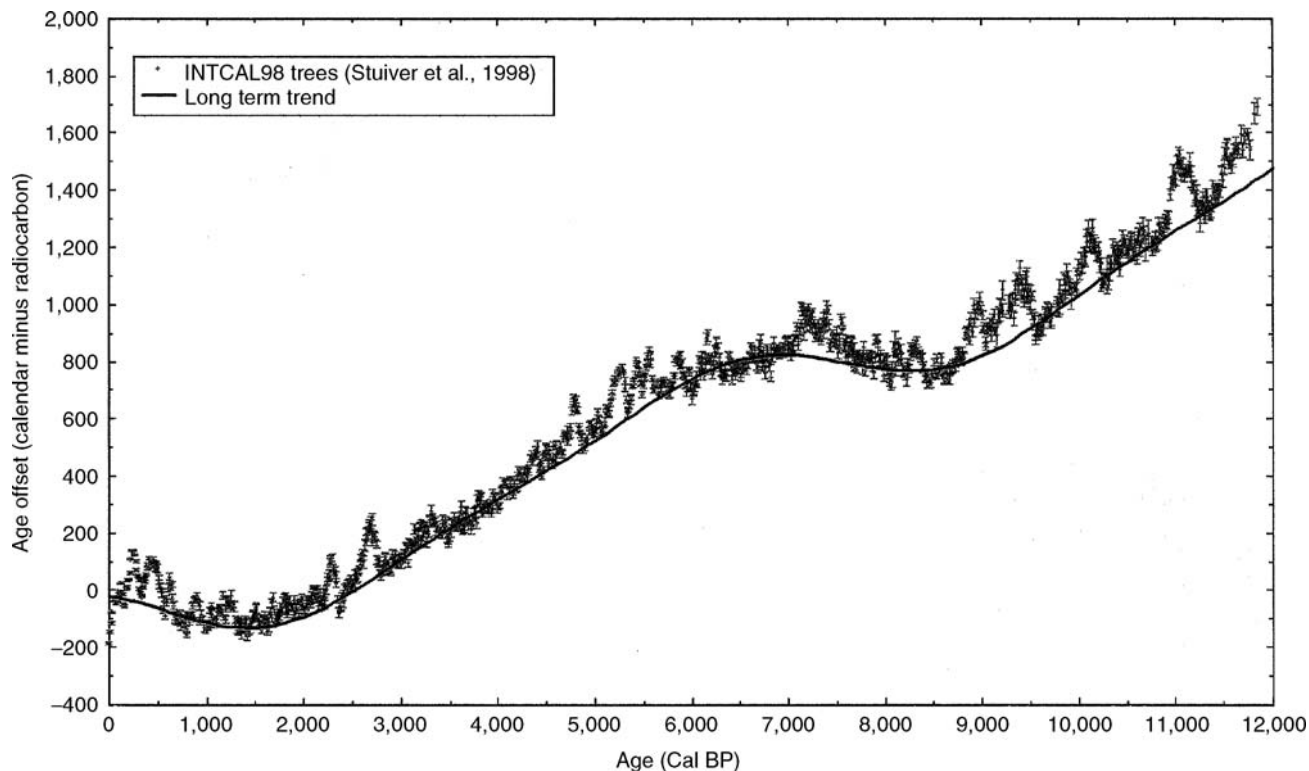


Figure R2 Late Pleistocene and Holocene deviation of ^{14}C from dendrochronological-, uranium-series-, and varve counted marine sediment-based age data (Data from Stuiver et al., 1998a; figure adapted from Taylor 2001: Fig. 2.2).

The inherent uncertainties and fluctuations in the calibration curve cause discrete calibrated ages to broaden into ranges, even when, as in this figure, the ^{14}C ages are plotted with a hypothetical zero variance. Thus, ^{14}C age determinations deriving from time periods with larger calibration range values will be inherently less precise. For example, on average, calibrated age values for 8,000–10,000 BP are inherently much less precise than those in the 0–2500 BP period because of the large ^{14}C de Vries effect “time warps” occurring during in those periods.

In Figure R3, 12 major and 5 intermediate de Vries effect perturbations can be identified. Major de Vries effects have been defined as “time warps” exceeding 250 cal years; intermediate de Vries effects are those that exhibit ranges in excess of 140 cal years, and minor de Vries effects have ranges of less than 140 cal year. The 17 major and intermediate de Vries perturbations have been assigned Roman numeral and letter combinations. Roman numerals identify the ^{14}C millennium, i.e., I = 0–1,000 BP, II = 1,000–2,000 BP, while lower case letters identify the perturbation in chronological order within each ^{14}C millennial period. It should be noted that the INTCAL98 calibration data set shifts the time scale for early Holocene ^{14}C time warps slightly but does not affect their magnitude.

Various strategies to increase the precision of ^{14}C -based age inferences in light of the variable effects of de Vries-type secular variations include the use of Bayesian statistical approaches to calibration procedures (Buck and Christen, 1998) and “wigggle-matching,” in which the known pattern of the de Vries perturbations are matched on an unknown sample of wood

containing a sequence of tree rings by measuring ^{14}C activity in a set of adjacent tree rings in that sample and matching that pattern with the known de Vries pattern. An example of the latter approach includes the determination of a cutting date for a timber from a Japanese tomb to AD 320 with a precision of ± 5 years (Kojo et al., 1994). When precision at the level of $< \pm 30$ years can be statistically justified, concerns about latitude-dependent differences in ^{14}C atmospheric concentrations become relevant. Suggestions of the magnitude of the offset between Northern and Southern Hemispheric samples currently range between 24 ± 3 (Stuiver et al., 1998b) to 40 ± 13 ^{14}C years (Hogg et al., 2002).

Accelerator mass spectrometry

From the initiation of ^{14}C studies until the late 1970s, the basis of inferring ^{14}C concentrations, and thus the ^{14}C age of samples, exclusively employed decay counting technology. In decay counting, isotopic concentrations are measured by counting decay events in an ionization or scintillation detector and comparing the count rate observed in an unknown-age sample to that exhibited by appropriate standards under a common set of experimental conditions. For ^{14}C , this involves counting beta particles, i.e., negatively charged electrons emitted from the ^{14}C nucleus. In decay counting, a relatively small fraction of the ^{14}C atoms present in a carbon sample are actually detected over the course of measurement. While there are approximately 5.9×10^{10} atoms of ^{14}C in 1 gram of modern “pre-bomb” carbon, on average, over a one-minute period, less than 14 of these atoms will decay and be available for

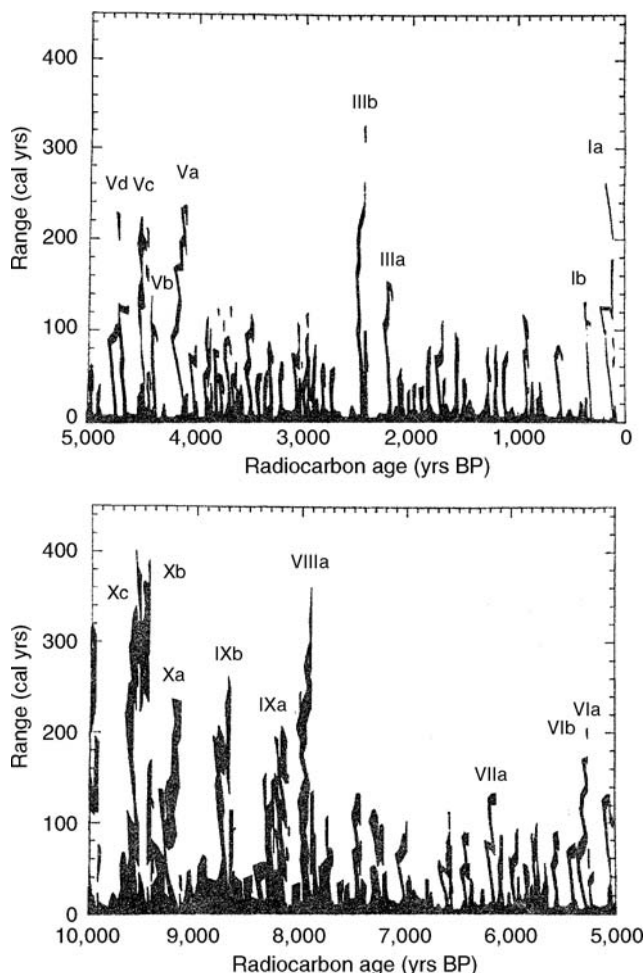


Figure R3 Holocene de Vries effects: Ranges (“time warps”) in calibrated years (cal yr) obtained from the calibration of conventional ^{14}C ages. Figure taken from Taylor et al. (1996) based on data from Stuiver and Reiner (1993: Figs. 3A–3D). Upper panel represents 0–5,000 BP and the lower panel represents 5,000–10,000 BP. Ranges produced for ideal hypothetical samples with zero ^{14}C sample standard deviation that had been formed during a 20-year or shorter interval and with the youngest calibrated age obtained for each ^{14}C age set at zero.

detection. In large part, it was this inherent inefficiency in decay counting that gave impetus to efforts to develop direct or ion counting technology using a form of mass spectrometry.

Within a year of the initial publication of the concept underlying AMS technology, the first published AMS-based ^{14}C determination was obtained using the 88-inch (224-cm) cyclotron at the University of California Lawrence Berkeley Laboratory (Muller, 1977). Because of technical problems with using cyclotron-based AMS systems for natural level measurements, most routine AMS measurements are currently undertaken on another type of particle accelerator, an electrostatic tandem accelerator. Although initially HEMS (high energy mass spectrometry) was used to refer to this technology, typically, TAMS (tandem accelerator mass spectrometry) is now used. “Tandem” here refers to the fact that particle acceleration in

electrostatic systems is accomplished in a two-step “pull-push” process. The TAMS approach proved to be a practical AMS technology for a wide range of rare, cosmogenic isotopes including ^{14}C and, to date, most AMS ^{14}C age determinations have been obtained on a TAMS instrument. By way of a historical footnote, the question of who first conceived the idea that led directly to the development of AMS technology is the subject of continuing discussion (Gove, 1996; 1999; Taylor, 1997b).

Three advantages of AMS technology in the measurement of ^{14}C were anticipated as a result of the greatly enhanced detection efficiency. First, major reductions in sample sizes would be possible – from gram amounts of carbon to milligram amounts and, with additional efforts, to the level of less than 100 micrograms. Second, major reductions in counting times would be possible. Reductions from several days for conventional systems and even weeks and months with micro- and mini-decay counting system could be achieved with several minutes of counting for AMS systems to achieve $\pm 1\%$ counting statistics. Finally, it was anticipated that significant increases in the applicable dating time frame would be possible – from the currently routine 40,000–50,000 years to as many as 100,000 years (Muller, 1977; Gove, 1992).

The first two of the three originally-anticipated benefits of AMS technology – major reductions in sample size and counting times – have been fully realized over the last decade (Taylor et al., 1984; Taylor, 1991; Hedges, 1995). For both sample sizes and counting times, order-of-magnitude reductions have been made possible on a routine basis. However, the projected third advance has not occurred due to the inability, at present, to exclude microcontamination of samples during sample preparation. The source of a significant portion of this contamination results from the current requirement in most laboratories that samples must be converted to graphitic carbon for use in the ion source of an AMS system. Parts per million of modern carbon contamination translates into background levels which generally limit the maximum ages that can be resolved to between 40,000 and 50,000 years. One laboratory has developed a CO_2 gas source but reports similar background values (Bronk and Hedges, 1987). To date, the oldest age reported on a graphitized background blank (Pliocene wood) is 60,500 BP (Kirner et al., 1997).

The development of AMS technology has provided the technical means by which very low organic carbon content sample types, such as organic extracts from bone and ceramics, along with microsample materials such as single seeds and small amounts of hair, can now be routinely dated by ^{14}C . It should be emphasized that AMS-based ^{14}C age determinations are not necessarily more or less accurate or precise than decay counting. Currently, the principal advantage of AMS technology for ^{14}C applications is the ability to obtain meaningful dates with samples containing microgram amounts of carbon (e.g., Kirner et al., 1995).

Applications

Over the last decade, the expanding use of AMS-based ^{14}C analysis has continued to create new and expanded areas of research where ^{14}C data have yielded important new understandings that would not have been possible or practical with decay counting. There have been several issues and topics that have been significantly impacted by the new capability to obtain ^{14}C measurements on milligram amounts of sample.

Hedges (1995) has noted that the advantages of microsample ^{14}C analysis include the ability to increase the reliability of ^{14}C -inferred age estimates as well as the generation of new chronological information. With regard to the former, the capability of remeasuring problematical dating results, the feasibility of undertaking highly selective chemical pretreatment strategies, and the ability to compare different chemical fractions of the same sample and select the most relevant sample material have been made routinely feasible as the result of the development of AMS-based ^{14}C analyses.

Some AMS-based ^{14}C values have been obtained in situations where larger amounts of sample were available. However, those having responsibility for the unique historical object would consent to the removal of only a small portion of the larger sample. Such was the case with the AMS ^{14}C dating of the Shroud of Turin, now perhaps the most widely known sample dated by the ^{14}C dating method. This 4.3 by 1 m rectangular-shaped linen cloth housed in the Cathedral of St. John the Baptist in Turin, Italy has been alleged to have been the burial sheet of Jesus of Nazareth since 1353 when its existence was first documented. The calibrated ^{14}C age of this sample measured by three AMS laboratories indicates that the flax from which the linen was fabricated was most probably growing sometime during the later part of the thirteenth or the fourteenth century AD, exactly the period during which the shroud was first historically documented (Damon et al., 1989). Arguments that ^{14}C activity in portions of the shroud could have been altered by exchange of atmospheric CO_2 with the linen as the result of high temperature effects ("scorching") or other purported chemical reactions have been refuted by experiments specifically designed to test the validity of the hypothetical mechanisms (Jull et al., 1996; Long, 1998).

A good illustration of the effect of being able to target the most relevant sample is illustrated by a study of maize specimens excavated from two rock shelters in the Tehuacan Valley, Mexico. Samples of *Zea mays* from these sites had been regarded as the earliest example of domesticated maize – the most important New World domesticated plant. In the early 1970s, their age had been estimated on the basis of conventional (decay counting) ^{14}C determinations obtained on charcoal assumed to be stratigraphically associated with the maize samples in the Tehuacan Valley sites. In contrast to the 5,350–7,000 BP values on the associated charcoal, the range in ^{14}C values directly obtained on milligram amounts of maize samples using AMS-based ^{14}C analysis was 1,560–4,700 BP for the samples from San Marcos Cave and 450–4,090 BP for the specimens from Coxcatlan Cave (Long et al., 1989). The significantly later occurrence of maize at Tehuacan raised questions concerning assumptions about where the center(s) of maize domestication in the New World may have been and thus the timing of the spread of domestication of this plant in the Western Hemisphere.

Conclusion

The impact of ^{14}C dating on the conduct of research in a number of disciplines has been, in some aspects, clear and explicit and, in others, subtle. In addition to providing a common chronometric time scale for the entire late Quaternary, an important contribution of the ^{14}C method is that the technique provides a means of providing a chronometric time scale using means independent of any assumptions about environmental physical parameters other than radioactive decay, carbon reservoir source, and geochemical conditions.

Radiocarbon data continues to provide the foundation on which most of the most secure chronometric time scales in most areas of the world for the last 40,000–50,000 years are constructed, directly or indirectly, particularly in contexts and areas lacking historical or textual documentation. While currently not often stressed, the influence of ^{14}C data on the pursuit of paleoenvironmental and archaeological studies continues to be profound and pervasive.

R. Ervin Taylor

Bibliography

- Bard, E., 1998. Geochemical and geophysical implications of the radiocarbon calibration. *Geochimica et Cosmochimica Acta*, **62**, 2025–2038.
- Bard, E., Arnold, M., Hamelin, B., Tisnerat-Laborde, N., and Cabioch, G., 1998. Radiocarbon calibration by means of mass spectrometric ^{230}Th - ^{234}U and ^{14}C ages of on corals. *Radiocarbon*, **40**, 1085–1092.
- Bell, W.T., 1991. Thermoluminescence dates for the Lake Mungo aboriginal fireplaces and the implication for the radiocarbon time scale. *Archaeometry*, **33**, 43–50.
- Bronk, C.R., and Hedges, R.E.M., 1987. A gas ion source for radiocarbon dating. *Nucl. Instrum. Methods*, **B29**, 45–49.
- Buck, C.E., and Christen, J.A., 1998. A novel approach to selecting samples for radiocarbon dating. *J. Archaeol. Sci.*, **24**, 303–310.
- Damon, P.E., Donahue, D.J., Gord, B.H., Hatheway, A.L., Jull, A.J.T., Linick, T.W., Sercelo, P.J., Toolin, L.J., Bronk, C.R., Hall, E.T., Hedges, R.E.M., Housley, R., Law, I.A., Perry, C., Bonani, G., Trumbore, S., Wolfli, W., Ambers, J.C., Bowman, S.G.E., Leese, M.N., and Tite, M.S., 1989. Radiocarbon dating the shroud of Turin. *Nature*, **337**, 611–615.
- Edwards, R.L., Beck, J.W., Burr, G.S., Donahue, D.J., Chappell, J.M.A., Bloom, A.L., Druffel, E.R.M., and Taylor, F.W., 1993. A large drop in atmospheric $^{14}\text{C}/^{12}\text{C}$ and reduced melting in the Younger Dryas, documented with ^{230}Th ages of corals. *Science*, **260**, 962–968.
- Erlenkeuser, H., 1979. A thermal diffusion plan for radiocarbon isotope enrichment from natural samples. In Berger, R., and Suess, H.E. (eds.), *Radiocarbon Dating*. Berkeley, CA: University of California Press, pp. 216–237.
- Geyh, M.A., and Schlüchter, C., 1998. Calibration of the ^{14}C time scale beyond 22,000 BP. *Radiocarbon*, **40**, 475–482.
- Gove, H.E., 1992. The history of AMS, its advantages over decay counting: Applications and Prospects. In Taylor, R.E., Long, A., and Kra, R.S. (eds.), *Radiocarbon after Four Decades an Interdisciplinary Perspective*. New York: Springer, pp. 214–229.
- Gove, H., 1996. *Relic, Icon, or Hoax? Carbon Dating the Turin Shroud*. Bristol: Institute of Physics.
- Gove, H., 1999. *From Hiroshima to the Iceman: The Development and Applications of Accelerator Mass Spectrometry*. Bristol: Institute of Physics.
- Grootes, P.M., Mook, W.G., Vogel, J.C., de Vries, A.E., Haring, A., and Kismaker, J., 1975. Enrichment of radiocarbon for dating samples up to 75,000 years. *Zeitschrift für Naturforschung*, **30A**, 1–14.
- Hedges, R.E.M., 1995. Radiocarbon dating by accelerator mass spectrometry. *Am. J. Archaeol.*, **99**, 105–108.
- Hogg, A.G., McCormac, F.G., Higham, T.F.G., Reimer, P.J., Baillie, M.G.I., and Palmer, J.G., 2002. High-precision radiocarbon measurements of contemporaneous tree-ring dated wood from the British Isles and New Zealand: AD 1850–950. *Radiocarbon*, **44**, 633–640.
- Jull, A.J.T., Donahue, D.J., and Damon, P.E., 1996. Factors affecting the apparent radiocarbon age of textiles: A comment on "Effects of fires and biograftation of carbon isotopes on results of radiocarbon dating of old textiles: The Shroud of Turin." *J. Archaeol. Sci.*, **23**, 109–121.
- Kirner, D., Taylor, R.E., and Southon, J.R., 1995. Reduction in backgrounds of microsamples for AMS ^{14}C dating. *Radiocarbon*, **37**, 697–704.
- Kirner, D., Burky, R., Taylor, R.E., and Southon, J.R., 1997. Radiocarbon dating organic residues at the microgram level. *Nucl. Instrum. Methods Phys. Res.*, **B123**, 214–217.
- Kojo, Y., Kalin, R.M., and Long, A., 1994. High-precision 'wiggles-matching' in radiocarbon dating. *J. Archaeol. Sci.*, **21**, 475–479.
- Linick, T.W., Damon, P.E., Donahue, D.J., and Jull, A.J.T., 1989. Accelerator mass spectrometry: The new revolution in radiocarbon dating. *Quaternary Int.*, **1**, 1–6.

- Long, A., 1998. Attempt to affect the apparent ^{14}C age of cotton by scorching in a CO_2 environment. *Radiocarbon*, **40**, 57–58.
- Long, A., Benz, B.F., Donahue, D.J., Jull, A.J.T., and Toolin, L.J., 1989. First direct AMS dates on early maize from Tehuacan, Mexico. *Radiocarbon*, **31**, 1035–1040.
- Mazaud, A., Laj, C., Bard, E., Arnold, M., and Tric, E., 1992. A geomagnetic calibration of the radiocarbon time-scale. In Bard, E., and Broecker, W.S. (eds.), *The Last Deglaciation: Absolute and Radiocarbon Chronologies*. Berlin: Springer, pp. 163–169.
- Muller, R.A., 1977. Radioisotope dating with a cyclotron. *Science*, **196**, 489–494.
- Reimer, P.J., Hughen, K.A., Guilderson, T.P., McCormac, G., Baille, M.G.L., Bard, Ed. Barratt, P., Beck, J.W., Buck, C.E., Damon, P.E., Friedrich, M., Kromer, B., Ramsey, C.B., Reimer, R.W., Remmele, S., Southon, J.R., Stuiver, M., van der Plicht, J., 2002. Preliminary report of the first workshop of the INTCAL04 radiocarbon calibration/comparison working group. *Radiocarbon*, **44**, 653–661.
- Scott, E.M., Long, A., and Kra, R., (eds.) 1990. Proceedings of the International Workshop on Intercomparison of Radiocarbon Laboratories. *Radiocarbon*, **32**(3), 253–397.
- Southon, J.R., Deino, A.L., Orsi, G., Terrasi, R., and Campajola, L., 1995. Calibration of the radiocarbon time scale at 37KA BP. *Abstract of Papers*, 209th American Chemical Society National Meeting, Part 2, p. 10.
- Stuiver, M., and Polach, H.A., 1977. Discussion: Reporting of ^{14}C data. *Radiocarbon*, **19**, 355–363.
- Stuiver, M., and Reimer, P.J., 1993. Extended ^{14}C data base and revised CALIB 3.0 ^{14}C age calibration program. *Radiocarbon*, **35**, 215–230.
- Stuiver, M., Long, A., and Kra, R.S., (eds.) 1998a. INTCAL 98: Calibration Issue. *Radiocarbon*, **40**, 1041–1159.
- Stuiver, M., Reimer, P.J., Bard, E., Beck, J.W., Burr, G.S., Hughen, K.A., Kromer, B., McCormac, G., van der Plicht, J., and Spurk, M., 1998b. INTCAL98 Radiocarbon age calibration 24,000–0 cal BP. *Radiocarbon*, **40**, 1041–1083.
- Suess, H.E., 1970. Bristlecone-pine calibration of radiocarbon time 5200 BC to present. In Olsson, I.U. (ed.), *Radiocarbon Variations and Absolute Chronology*. Stockholm: Almqvist & Wiksell, pp. 303–312.
- Taylor, R.E., 1987. *Radiocarbon Dating An Archaeological Perspective*. San Diego, CA: Academic Press.
- Taylor, R.E., 1991. Radioisotope dating by accelerator mass spectrometry: Archaeological and paleoanthropological perspectives. In Göksu, H.Y., Oberhofer, M., and Regulioi, D. (eds.), *Scientific Dating Methods*. Dordrecht (Netherlands): Kluwer, pp. 37–54.
- Taylor, R.E., 1996. Radiocarbon dating: The continuing revolution. *Evol. Anthropol.*, **4**, 169–181.
- Taylor, R.E., 1997a. Radiocarbon dating. In Taylor, R.E., and Aitken, M.J. (eds.), *Chronometric Dating in Archaeology*. New York: Plenum, pp. 65–96.
- Taylor, R.E., 1997b. Review of H.E. Gove, Relic, Icon or Hoax? Carbon Dating the Turin Shroud. *Radiocarbon* **39**, 115–117.
- Taylor, R.E., 2001. Radiocarbon dating. In Brothwell, D.R., and Pollard, A.M. (eds.), *Handbook of Archaeological Sciences*. New York: Wiley, pp. 23–34.
- Taylor, R.E., Donahue, D.J., Zabel, T.H., Damon, P.E., and Jull, A.T.J., 1984. Radiocarbon dating by particle accelerators: An archaeological perspective. In Lambert, J.B. (ed.), *Archaeological Chemistry III*. Washington, DC: American Chemical Society, pp. 333–356.
- Taylor, R.E., Stuiver, M., and Reimer, P.J., 1996. Development and extension of the calibration of the radiocarbon time scale: Archaeological applications. *Quaternary Sci. Rev.*, **15**, 655–668.
- Voelker, A.H.L., Sarnthein, M., Grootes, P.M., Erlenkeuser, H., Laj, C., Mazaud, A., Nadeau, M.-J., and Schleicher, M., 1998. Correlation of marine ^{14}C ages from the Nordic seas with the GISP2 isotope record: implications for ^{14}C calibration beyond 25 ka BP. *Radiocarbon*, **40**, 517–534.

Cross-references

Carbon Isotopes, Stable
 Dating, Dendrochronology
 Dating, Radiometric Methods
 Isotope Fractionation
 Uranium-Series Dating

RADIOLARIA

Radiolarians are marine protozoa with a geological record ranging from Precambrian to Present. Radiolarians are exclusively marine and are found in all the oceans, in all temperature zones and at all depths. They are also neritic in their distribution, being found in Norwegian fjords, in the plankton (9,000 specimens m^{-3}), more abundantly in the tropics (18,000 specimens m^{-3}), and rarely in the polar oceans. The highest numbers of Radiolaria are found in the upper 50–200 m of the water column. Those radiolarians possessing a skeleton may contribute significantly to the deep sea eupelagic sediments, the so-called radiolarian ooze, which are found deposited in the central parts of the Pacific and Indian Oceans.

Evolution of this group has resulted in a high diversity of both extinct and extant species. Their opal skeleton is characteristic and in many cases is radial, from which the name Radiolaria is derived. Some, however, possess a bilateral skeleton, whilst others have no skeleton at all. The inner part of the protoplasm (endoplasm) houses the nucleus (reproduction), organelles such as mitochondria (respiration) and Golgi bodies (secretion), as well as lipid droplets and vacuoles, all enveloped by an organic central capsule. The outer part of the protoplasm (ectoplasm), the calymma, communicates through openings, or pores, in the central capsular wall (Figure R4). The calymma is a frothy or bubble-like body, which is interpreted as a floating device, besides housing algal symbionts (zooxanthellae), vacuoles, and mitochondria. The outer margin of the protoplasm is characterized by a network of anastomosing

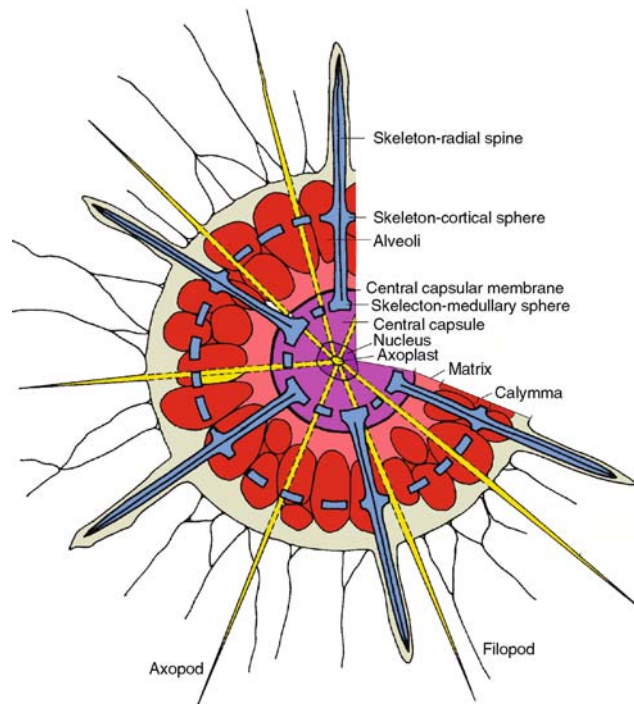


Figure R4 Principal structure of a polycystine radiolarian, showing soft and hard body features (Modified after Kling, 1978).

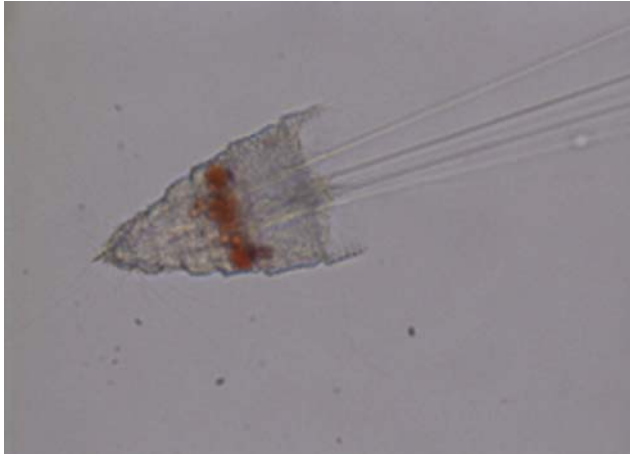


Figure R5 *Spirocyrtis scalaris* Haeckel, a living nassellarian radiolaria taken from the surface water near Okinawa Island, Japan. Photograph provided by Dr. Atsushi Matsuoka.

pseudopodia as well as different irregular rhizopodia, long and stiff radial axopodia (Figure R4), which are clearly seen as a bundle of long, straight spines in the living specimen of *Spirocyrtis scalaris* (Figure R5), and delicate filipodia (Figure R4). The skeletal spines are enveloped by the protoplasm, and therefore protected from being dissolved by seawater. Prey is captured by the pseudopodia and digested in the ectoplasm.

Radiolarian taxonomy was essentially established by Ernst Haeckel when he published an extensive monograph in 1887, based on material collected on the Challenger Expedition (1873–1876) that circumnavigated the world's oceans. This is not a natural taxonomic system, but a useful system to group similar morphotypes. Radiolarian taxonomic studies were initiated in Germany, but subsequent schools developed in France, Russia, and the U.S.A., where taxonomy was based predominantly on intricate skeletal morphologies, as shown in *Callimitra carolotae* (Figure R6), with the exception of the French group who in addition based their taxonomy on microscopic cellular structures. There is no consensus on the higher rank taxonomy within the radiolarians, but the following is often used:

Kingdom PROTISTA Haeckel, 1866
 Phylum SARCODINA Hertwig, 1876
 Class ACTINOPODA Calkins, 1910
 Subclass RADIOLAIRA Müller, 1858
 Superorder PHAEODARIA Haeckel, 1879
 Superorder POLYCYSTINA Ehrenberg, 1838, emend. Riedel, 1967
 Order SPUMELLARIA Ehrenberg, 1875
 Order NASSELLARIA Ehreneberg, 1875

Recent work on radiolarian DNA suggests another relationship of the main Radiolaria groups, in addition to that proposed by Haeckel (1887), above. Yuasa et al. (2003) showed that the Phaeodaria made a separate clade, while the Acantharia, Spumellaria and Nassellaria made another clade. The latter made two subclades where solitary Spumellaria grouped with the Acantharia and the colonial Spumellaria grouped with the

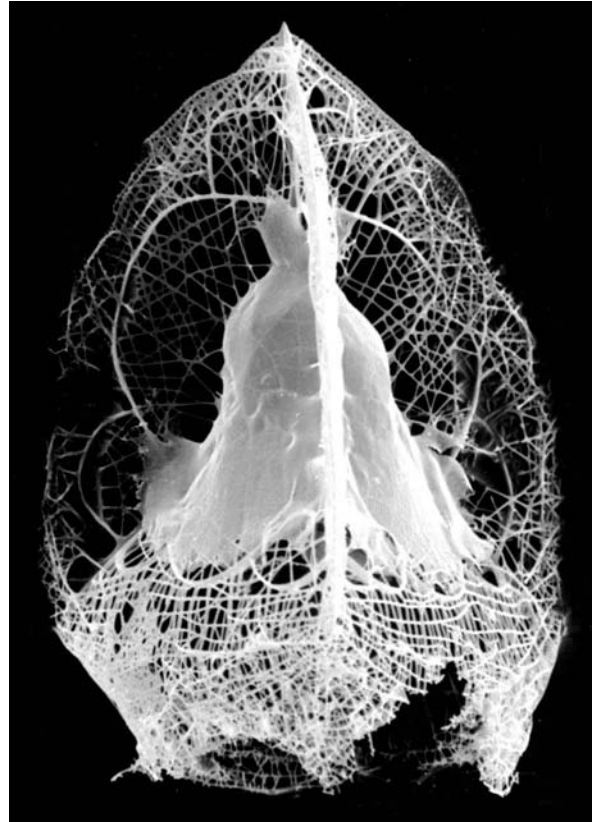


Figure R6 *Callimitra carolotae* Haeckel. Recent, from surface sediments in the Orca Basin, Gulf of Mexico. Photograph by K. R. Bjørklund and R. M. Goll.

Nassellaria. This is supported by other DNA studies (Polet et al., 2004).

The diversity and relatively rapid rate of evolution of Radiolaria through time makes this group very important in Tertiary and Quaternary biostratigraphy, especially in deep-sea sediments where carbonate fossils are dissolved. Levine (1963) calculated the total number of living and fossil radiolarians to be 4,791 and 2,389, respectively. Goll and Merinfeld (1979) concluded that these numbers are inflated by unwarranted taxonomic splitting and suggested numbers that are more conservative: about 200 Acantharia, more than 600 Phaeodarians, and about 1,500 extant and extinct polycystine radiolarians, the latter number is very uncertain.

Polycystine radiolarians are important in deep sea stratigraphy. The Cenozoic is divided into 32 biozones (Recent through Eocene, Paleocene is still unzoned). Radiolarians are also important for paleotemperature proxy data, and estimates for the last ca 13,400 ^{14}C years BP have been successfully applied in the Norwegian Sea (Dolven et al., 2002). Here, the calculations show an average temperature of $12 \pm 1^\circ\text{C}$ during the Holocene (the last 10,000 ^{14}C years). During the Younger Dryas (10,000–11,000 ^{14}C years BP), the temperature decreased to about 7°C in only a few centuries. In the Holocene, the “8,200-year event,” as observed in the GISP2 ice core, is also

observed in the radiolarian paleotemperature estimates, with a temperature drop of ca. 3 °C. The associated radiolarian assemblages changed during this time interval with a relative abundance minimum of the warm water species *Lithomelissa setosa* and *Pseudodictyophimus gracilipes*, while *Stylodictya validispina* displayed an absolute maximum (26%). This evidence proves that radiolarians are a sensitive and powerful paleoclimatic tool.

Adolfo Molina-Cruz and Kjell R. Björklund

Bibliography

- Calkins, G.N., 1910. *Protozoölogy*. London: Bailliere, Tidal and Cox, 349pp.
- Dolven, J.K., Cortese, G., and Björklund, K.R., 2002. A high-resolution radiolarian-derived paleotemperature record for the Late Pleistocene-Holocene in the Norwegian Sea. *Paleoceanography*, **17**(4), 1072, doi:10.1029/2002PA000780,2002. (Electronic journal).
- Ehrenberg, C.G., 1838. Über die Bildung der Kreidefelsen und des Kreidemergels durch unsichtbare Organismen. *Königliche Akademie der Wissenschaften zu Berlin, Abhandlungen, Jahre 1838*, 59–147.
- Ehrenberg, C.G., 1875. Fortsetzung der mikogeologischen Studien als Gesamt-Uebersicht der mikroskopischen Palaontologie gleichartig analysirter Gebirgsarten der Erde, mit specieller Rücksicht auf den Polycystinen-Mergel von Barbados. *Königliche Akademie der Wissenschaften zu Berlin, Abhandlungen, Jahre 1875*, 1–225.
- Goll, R.M., and Merinfeld, G., 1979. Radiolaria. In Fairbridge, R.W., and Jablonski, D. (eds.), *The Encyclopedia of Paleontology*. Encyclopedia of Earth Sciences, vol. VII. Stroudsburg, PA: Dowden, Hutchinson & Ross, pp. 673–684.
- Haeckel, E., 1866. *Generelle Morphologie der Organismen. Teil II. Allgemeine Entwicklungsgeschichte der Organismen*. Berlin: Reimer, pp. 1–462.
- Haeckel, E., 1879. Ueber die Phaeodarien, eine neue Gruppe kieselschaliger mariner Rhizopoden. *Jenaische Zeitschrift für Naturwissenschaft*, **14**, 151–157.
- Haeckel, E., 1887. Report on the Radiolaria collected by the H.M.S. Challenger during the Years 1873–1876. *Report on the Scientific Results of the Voyage of the H.M.S. Challenger, Zoology*, vol. **18**, 1803pp.
- Hertwig, R., 1876. *Zur Histologie der Radiolarien. Untersuchungen über den Bau und die Entwicklung der Sphaerozoiden und Thalassicolliden*. W. Engelmann, Leipzig, Germany, 91+ errata.
- Kling, S.A., 1978. Radiolaria. In Haq, B.U., and Boersma, A. (eds.), *Introduction to Marine Micropaleontology*. New York: Elsevier, pp. 203–244.
- Levine, N.D., 1963. Protozoology today. In *Progress in Protozoology*. New York: Academic Press, pp. 39–40.
- Müller, J., 1858. Über die Thalassicollen, Polycystinen und Acanthometren des Mittelmeeres. *Königliche Preussische Akademie der Wissenschaften zu Berlin, Abhandlungen, Jahre 1858*, 1–62.
- Polet, S., Berny, C., Fahrni, J., and Pawlovski, J., 2004. Small-subunit ribosomal RNA gene sequences of Phaeodarea challenge the monophyly of Haeckel's Radiolaria. *Protist*, **155**, 53–63 (<http://www.elsevier-deutschland.de/protist>).
- Riedel, W.R., 1967. Subclass Radiolaria. In Harland, W.B., et al., (eds.), (eds.), *The Fossil Record*. London, UK: Geological Society of London, pp. 291–298.
- Yuasa, T., Takahashi, O., and Mayama, S., 2003. Molecular Phylogeny of the solitary shell-bearing Polycystinea. In Diserens, M.-O., and Jackett, S.-J. (eds.), *Tenth Meeting of the International Association of Radiolarian Palaeontologists, University of Lausanne, September 8–12, 2003, Abstract and Program*: p. 118.

Cross-references

Marine Biogenic Sediments
 Radiocarbon Dating
 The 8,200-Year bp Event
 Younger Dryas

RED BEDS

Red beds are red-colored clastic sedimentary deposits (Figure R7). The term is widespread in the literature and has been used to describe both marine and non-marine rocks, so it is non-genetic. The presence of oxidized (ferric) iron (usually as fine-grained hematite) disseminated throughout the matrix of the deposits is the unifying feature of red beds. Reddening typically forms as a result of the post-depositional dehydration of oxyhydroxides such as goethite to hematite and indicates +D (positive) Eh conditions. Rocks previously called red beds include paleosols (including laterites), banded iron formations, sandstones, siltstones, conglomerates, and deep sea shales. Marine red beds are rare and form only in areas with little organic matter and slow sedimentation rates that allow all of the organic matter to be broken down prior to burial. Only red bed sequences containing or composed of paleosols or evaporites are useful for paleoclimatic reconstructions.

Paleosols in red bed sequences

Red beds have been interpreted as desert deposits by analogy with modern deserts, which are often red (Walker, 1967), but subsequently it was recognized that the modern red deserts are associated with ancient red beds (e.g., the Simpson Desert of Australia where Folk (1976) showed that the red color of the modern dunes was due to prior laterite formation). More recent work has emphasized a role for strongly seasonal climates (Dubiel and Smoot, 1994), such as monsoons with short wet seasons between long dry seasons during which the soils could dry out substantially, promoting formation of iron oxyhydroxides and a high degree of aeration. However, it should be noted that any well-drained soil has the same aerated conditions, and well-drained soils can form in a variety of climatic settings other than in monsoonal belts (Sheldon, 2005). Diagnostic features of monsoonal settings include concentrically layered carbonate or iron oxide concretions (Retallack, 1991; Table R1), dispersed calcium carbonate throughout the deposits (Retallack, 1991; Table R1), and soil types including Vertisols



Figure R7 Eocene red beds from the Wasatch Formation of Wyoming, US.

Table R1 Some features of red bed sequences useful for paleoenvironmental reconstructions

Feature type	Diagnosis
<i>Soil characteristics:</i>	
1. Gilgai (small-scale anticlinal relief)	1. Pronounced wet-dry seasonality
2. Slickensides, ped morphology, relict bedding	2. Relative weathering intensity
3. Horizon thickness and color	3. Duration of weathering
4. Mottling associated with organic matter (roots)	4. Micro-reducing conditions within the soil
<i>Diagnostic soil types:</i>	
5. Caliche/calcrete soils	5. Sub-humid to arid climatic conditions
6. Duripan/silcrete soils	6. Semi-arid to arid climatic conditions
7. Vertisols	7. Pronounced wet-dry seasonality
8. Laterites	8. Tropical conditions
<i>Soil nodules:</i>	
9. Size	9. Large imply longer formation times
10. Distribution	10. Disbursed implies strong seasonality
11. Concentric growth and alternating carbonate and oxide layers indicate	11. Strong seasonality and/or monsoonal climatic conditions
<i>Evaporites</i>	
12. Gypsum and halite	12. Arid conditions
<i>Eolian deposits</i>	
13. Proportion of silt in thin section point counts conditions	13. Semi-arid to arid climatic
<i>Frost wedges</i>	
14. Clastic dikes	14. Cold (taiga or tundra) climatic conditions
<i>Water table characteristics:</i>	
15. Rooting depth	15. Deeply penetrating implies well-drained
16. Burrowing depth	16. Deeply penetrating implies well-drained
17. Density and tiering of ichnofabrics	17. High density implies low flood frequency
<i>Invertebrate fossils with modern analogs</i>	Depends on the modern analog
<i>Vertebrate fossils with modern analogs</i>	Depends on the modern analog

Information after Birkeland (1999), Dubiel and Smoot (1994), and Retallack (2001).

with their characteristic deep cracking due to seasonal shrinking and swelling of clays, or Mollisols with crumb peds. All of these features are also preserved in paleosols. Model results indicate monsoon-like climatic circulation patterns for the Pangean supercontinent (Kutzbach and Gallimore, 1989), but so far insufficient field work has been performed to confirm monsoonal features in either the sediments or paleosols preserved in the Pangean red bed sequences.

Paleosols are fossil soils, typically buried by subsequent deposition. Many sequences of terrestrial fluvial red beds preserve paleosols that developed on flood deposits, but other preservational settings include sequences of lava flows, and lagoonal, lake, and ocean margins. Each paleosol represents a significant hiatus in deposition ranging in duration from perhaps one hundred years up to millions of years in the case of ultisols, oxisols, and laterites. Because paleosols form in direct contact with the atmosphere, they record both paleoenvironmental and paleoclimatic conditions. Identification of paleosols within a sequence of red beds is made on the basis of a number of morphological features (Table R1). Some of the features of individual paleosols also give information about the depth of the paleo-water table beneath the surface of the paleosol, and by extension, information about how well-drained the paleosol was. In addition to gaining this paleohydrological information about the depositional setting of the red bed sequence, a number of other features of paleosols are quantitatively useful as paleoclimatic indicators. Mean annual precipitation may be estimated from the degree of chemical weathering (Sheldon et al., 2002) or from the depth to a Bk (carbonate-bearing) horizon in a paleosol (Retallack, 1994), and atmospheric pCO₂ can be estimated by measuring the isotopic composition of carbonate nodules (Cerling et al., 1989) or pedogenic goethites (Yapp and Poths, 1992).

Geologic record of red beds

Because the red color in red bed forms is due to oxidized iron, the geologic record of red beds reflects the Precambrian rise of atmospheric oxygen levels. The oldest universally agreed upon red beds are red sandstones, siltstones, and mudstones of South Africa, immediately overlying the so-called Hekpoort Paleosol, which has been dated to about 2.2 Ga before present. Red beds have been common in the geologic record ever since, with their greatest extent in the Phanerozoic, especially during the Paleozoic-Mesozoic transition during which red beds are one of the characteristic depositional facies of the Pangean supercontinent.

Nathan D. Sheldon

Bibliography

- Birkeland, P.W., 1999. *Soils and Geomorphology*, 3rd edn. New York: Oxford University Press, 430pp.
- Cerling, T.E., Quade, J., Wang, W., and Bowman, J.R., 1989. Carbon isotopes in soils and palaeosols as ecology and palaeoecology indicators. *Nature*, **341**, 138–139.
- Dubiel, R.F., and Smoot, J.P., 1994. Criteria for interpreting paleoclimate from red beds – a tool for Pangean reconstructions. In Embry, A.F., Beauchamp, B., and Glass, D.J. (eds.), *Pangea: Global Environments and Resources*. Calgary, AB: Canadian Society of Petroleum Geologists, Memoir 17, pp. 295–311.
- Folk, R.L., 1976. Reddening of desert sands: Simpson Desert, N.T., Australia. *J. Sediment. Petrol.*, **46**, 604–615.
- Kutzbach, J.E., and Gallimore, R.G., 1989. Pangean climates: Megamonsoons of the megacontinent. *J. Geophys. Res.*, **94**, 3341–3357.
- Retallack, G.J., 1991. *Miocene Paleosols and Ape Habitats of Pakistan and Kenya*. Oxford, UK: Oxford University Press. Oxford Monographs on Geology and Geophysics, no. 19, 346pp.
- Retallack, G.J., 1994. The environmental factor approach to the interpretation of paleosols. *Soil Sci. Soc. Am.* Special Publication Number, **33**, 31–64.

- Retallack, G.J., 2001. *Soils of the Past: An Introduction to Paleopedology*, 2nd edn. London, UK: Blackwell Science Ltd, 404pp.
- Sheldon, N.D., Retallack, G.J., and Tanaka, S., 2002. Geochemical climofunctions from North American soils and application to paleosols across the Eocene-Oligocene boundary in Oregon. *J. Geol.*, **110**, 687–696.
- Sheldon, N.D., 2005. Do red beds indicate paleoclimatic conditions?: A Permian case study. *Paleogeography, Palaeoclimatology, Palaeogeography*, **228**, 305–319.
- Walker, T.R., 1967. Formation of red beds in modern and ancient deserts. *Bull. Geol. Soc. Am.*, **78**, 353–368.
- Yapp, C.J., and Poths, H., 1992. Ancient atmospheric CO₂ pressures inferred from natural goethites. *Nature*, **355**, 342–344.

Cross-references

[Arid Climates and Indicators](#)
[Atmospheric Evolution, Earth](#)
[Banded Iron Formations and the Early Atmosphere](#)
[Continental Sediments](#)
[Evaporites](#)
[Laterite](#)
[Mineral Indicators of Past Climates](#)
[Paleoclimate Proxies, an Introduction](#)
[Paleosols, Pre-Quaternary](#)
[Paleosols, Quaternary](#)
[Paleo-Precipitation Indicators](#)
[Sedimentary Indicators of Climate Change](#)

ROCHES MOUTONNÉES

Roches moutonnées are classic landforms of glacial erosion (Bennett and Glasser, 1996). They are giant stoss and lee forms carved from bedrock, with smoothly abraded up-ice or stoss faces and roughly quarried/plucked down-ice lee faces. They can occur as isolated forms, can be superimposed on larger asymmetric landforms, or occur as part of erosional landscapes subject to regional scour. Individual forms vary in size from less than 1 m to several hundred meters or even kilometers in diameter (Rastas and Seppälä, 1981). In Sweden, for example, large asymmetric hills (Flyggbergs) exceed 1 kilometer in length; however, most roches moutonnées are much smaller.

Roches moutonnées are the product of both glacial abrasion and glacial quarrying and it is this combination of processes that results in the asymmetric profile. Glacial abrasion occurs on the up-ice or stoss face of the landform, while glacial

quarrying occurs on the lee. Glacial quarrying involves two processes, firstly the exploitation and propagation of rock fractures such as joints and discontinuities, and secondly, the entrainment and removal of bedrock blocks by ice. The characteristics of the rock mass, therefore, are critical to quarrying: the more fractured the rock mass, the more easily it can be plucked by ice. In turn, this means that the morphology of roches moutonnées is closely linked to the depth, orientation and spacing of joints or discontinuities within the rock mass (Gordon, 1981; Rastas and Seppälä, 1981). The exploitation and propagation of joints is assisted by fluctuations in subglacial water pressure (Röthlisberger and Iken, 1981; Iverson, 1991). In addition, the formation of a lee-side cavity between the ice sole and the bed increases the stress gradients imposed on the bedrock hummock by the overriding ice, which again favors fracture propagation. Block entrainment may occur by a variety of processes, not least of which is the regular closure of the lee-cavity, causing the debris within it to be swept clear. Therefore, roches moutonnées are indicative of subglacial conditions in which there is high effective normal pressure on the stoss side of a bedrock bump, but where this pressure is sufficiently low on the down-ice side to allow a cavity to form. Consequently, the up-ice side experiences glacial abrasion, while the down-ice side experiences glacial quarrying. Roches moutonnées tend, therefore, to form in areas of thin, fast-flowing ice and in situations with abundant meltwater. They may also be used as crude indicators of the direction of ice flow.

Matthew R. Bennett

Bibliography

- Bennett, M.R., and Glasser, N.F., 1996. *Glacial Geology: Ice sheets and Landforms*. Chichester, UK: Wiley, 364pp.
- Gordon, J.E., 1981. Ice-scoured topography and its relationship to bedrock structure and ice movement in parts of northern Scotland and West Greenland. *Geografiska Annaler*, **63A**, 55–65.
- Iverson, N.R., 1991. Potential effects of subglacial water pressure fluctuations on quarrying. *J. Glaciol.*, **37**, 27–36.
- Rastas, J., and Seppälä, M., 1981. Rock jointing and abrasion forms on roches moutonnées, SW Finland. *Ann. Glaciol.*, **2**, 159–163.
- Röthlisberger, H., and Iken, A., 1981. Plucking as an effect of water-pressure variations at the glacier bed. *Ann. Glaciology*, **2**, 57–62.

Cross-reference

[Glacial Geomorphology](#)

S

SAPROPELS

The term sapropel is used in a generic sense to describe fine-grained and unconsolidated sediments rich in organic matter that have been deposited under water; in coal petrology, sapropelic coals are those that formed from algal material deposited in aquatic environments. The term sapropel is also often used as a generic term for distinct dark-colored, organic carbon-enriched sediment layers that are found in organic-carbon-poor host sediments. In the Holocene sediment record of several silled basins (e.g., the Baltic Sea, the Black Sea, the Marmara Sea) an organic carbon-enriched sediment layer – often termed sapropel – marks the change in depositional environment and in biological production coincident with the post-glacial transgression.

In a stricter sense, the term stands for a sedimentary feature of the Mediterranean (and Red) Sea with specific connotations regarding the origin: sediment cores and land exposures from the Mediterranean Sea contain rhythmic series of sapropel layers (cm to m thick) sandwiched in carbonate-rich and organic carbon-poor hemipelagic sediments. These sapropels are rich in organic carbon (up to 30% by weight), devoid of benthic organisms and often laminated, and were deposited during periods when the deep waters of the marine basins were anoxic (Comas et al., 1996; Kidd et al., 1978; Emeis et al., 2000). The duration of the numerous anoxic events in the Mediterranean Sea was from a few hundred up to 7,000 years, and the most recent sapropel was deposited between 10,000 and 7,000 years ago. The observed temporal pattern of sapropel deposition is clearly paced by the orbital rhythms of precession, tilt and eccentricity and implies a causal link with orbitally-induced climate change that resulted in changes of the Mediterranean water balance (Cita et al., 1977; Rossignol-Strick, 1983). The link between insolation and sapropel deposition in the eastern Mediterranean Sea is very robust for the last 5.33 million years and the astronomically-tuned stratigraphy established here has set a standard for Pliocene and Quaternary chronostratigraphy world-wide (Hilgen, 1991).

The close link between climate and sapropel formation is firmly established, and a hydrological trigger for sapropel formation is widely agreed. Sapropel periods were preceded by and coincided with changes in surface and deep water circulation that restricted the oxygen supply to the seafloor in the deep basins of the Mediterranean Sea. At present, the deep basins of the Mediterranean Sea are flushed by cold, oxygen-rich waters that are generated during winters in the northern sub-basins – the Gulf of Lyons, the Aegean, and the Adriatic Seas. One prerequisite for anoxic conditions during periods of sapropel formation was a decrease in surface water density (relative to that of deepwater masses) that prevented sinking of oxygenated surface water into the deep basins. Both freshening (indicated by decreasing ratios of stable oxygen isotopes in the tests of planktonic foraminifers and changes in microfossil assemblages) and increasing sea surface temperature (based on evaluation of faunal assemblages and biomarkers) of surface water preceded and accompanied all sapropel events. Because oxygen demand for the mineralization of organic matter that sank from the surface ocean to the deepwater masses continued, the dissolved oxygen in the denser and aging deepwater eventually was depleted. The origin of fresh waters is less clear. The original hypothesis (Olausson, 1961) was that meltwater from the northern catchment (via the Black Sea) prevented deepwater formation. Alternatively, the northern catchment of the eastern Mediterranean Sea may have received increased precipitation during maximum insolation, leading to decreased salinity in the deepwater formation areas of the Mediterranean Sea (Rohling and Gieskes, 1989). However, since approximately 600,000 years ago, sapropels were deposited under fully interglacial, fully glacial, and intermediate climatic conditions.

Because conditions during glacials or cold stadials were as unfavorable for runoff from the northern catchment as for water-column stratification due to warming of the surface layer, sapropel formation even under glacial conditions is a strong argument for a source of freshwater in the monsoon system that influences mainly the southern catchment. According to this hypothesis, sapropel formation would be closely linked to tropical and even Southern Hemisphere climate. A systematic correlation has been observed between the

distribution of sapropels and maxima of the so-called orbital insolation monsoon index (Rossignol-Strick, 1983). Maxima in the monsoon index point to an intensified African summer monsoon, which may have led to enhanced continental humidity in tropical Africa and ultimately enhanced discharge rates of the Nile River. Alternatively, enhanced northward migration of the Intertropical Convergence Zone (the meteorological equator) into Northern Africa has been proposed for sapropel periods; this would have channeled equatorial rainfall into the Mediterranean Sea through what is now the Sahara Desert. A further possible source of freshwater is the Mediterranean Sea itself: virtually all sapropels coincide with significant warming of surface waters at the transition from cold to warm climatic periods. This warming would on the one hand enhance the stratification of water masses and would on the other hand result in increased evaporation and rainfall in the Mediterranean catchment, effectively pooling fresh and warm waters at the sea surface and impeding deepwater formation. It is very likely that all of these sources contributed in succession and in concert to prevent deep convection over several thousands of years.

The immediate reason for the enrichment of organic matter in sapropels is very much open to discussion. Oxygen conditions at the seafloor, biological productivity at the sea surface, and dilution by other sedimentary components are the primary factors controlling concentration and accumulation of organic carbon in marine sediments. Because the rates of sedimentation did not change significantly, the scientific discussion focused on the roles of bottom-water anoxia and biological productivity changes in the formation of organic carbon-rich sediments ("productivity versus preservation"). Much of the data gathered support the hypothesis of anoxic conditions paired with (or possibly accelerated and in part caused by) an increase in biological productivity during sapropel formation. In line with this, many indicators suggest enhanced productivity (assemblages of planktonic and – before and after the sapropel events – benthic foraminifers, the accumulation rates of barium). However, other authors see evidence that the eastern Mediterranean Sea remained nutrient-limited (oligotrophic) and that productivity patterns either shifted to a different type, or were as low as today. A severe obstacle for environmental reconstructions here as elsewhere is diagenesis that erases many indicators after deposition and re-oxygenation of deepwaters.

Detailed investigation of diatom assemblages in one unusually thick sapropel in which biogenic silica was preserved (in the carbonate oozes and in almost all other sapropels, this opal is lost to dissolution) showed that the original sapropel sequence was rich in diatoms that formed a pronounced sequence of laminations, including possible annual bloom layers. The flora consisted of fragile mats of diatoms indicative of stratified, oligotrophic conditions found in association with hydrographic frontal systems. Collecting near the interface between upper and lower water mass in the frontal system, the disintegration of slowly grown mats with large biomass may sporadically have resulted in large flux rates of opal and organic matter to the seafloor (Kemp et al., 1999). Other authors (Sachs and Repeta, 1999) proposed that the productivity level remained similar to the present ultra-oligotrophic nutrient desert during sapropel formation, because cyanobacterial nitrogen fixation then as today apparently was a significant source of the essential plant nutrient nitrate in the water column. In this scenario, anoxia alone was responsible for greatly improved preservation of the sparse rain of organic matter to the seafloor. More recently, the role of phosphate liberated from anoxic sediments as a fuel

for enhanced fixation of atmospheric nitrogen by cyanobacteria has been stressed (Struck et al., 2001; Slomp et al., 2002). In this view, the eastern Mediterranean Sea was fertilized by phosphate diffusing out of suboxic and anoxic sediments. This additional phosphate may have been transported to the surface ocean by ongoing shallow seasonal convection. It may thus have created conditions conducive for massive nitrogen fixation from the atmosphere that added nitrate, and initiated a positive feedback between anoxia at the seafloor and biological productivity in the euphotic zone. The anoxic and fertile sapropel periods ended with the waning of freshwater inputs and warming, and renewed flushing of the deep basins with oxygenated waters. In many cases, the sapropel preceding this flushing was erased by oxygen penetrating into the sediment, burning down the organic matter, and leaving so-called ghost sapropels.

Conclusion

Formation of the Mediterranean sapropels is the result of a combination of factors that include paleoclimate, paleoceanography, and the reactions of marine biogeochemical cycles to changed boundary conditions. Whereas the mechanism of sedimentation and carbon burial can be linked to changes within the depositional environment, these very changes are likely to be forced by processes outside the basin. External forcing is evident from the synchronicity of sapropel deposition in the entire (eastern) Mediterranean. Moreover, the rhythmic recurrence of environmental conditions that produce sapropels on schedules of precessional cycles points to a climatically driven chain of events culminating in sapropel deposition. A tentative chain of events postulates that carbon burial may have been promoted by enhanced rates of marine productivity, fuelled by an as yet contested source of new nutrients, a corresponding increase in oxygen utilization in deep water, and a weakening of deepwater oxygen recharge which all occur at the same time and are driven by the same external motor.

Kay-Christian Emeis

Bibliography

- Cita, M.B., et al., 1977. Paleoclimatic record of a long deep-sea core from the eastern Mediterranean. *Quaternary Res.*, **8**, 205–235.
- Comas, M.C., Zahn, R., Klaus, A., et al., (eds), 1996. *Proceedings ODP, Initial Results*, Vol. 161. College Station, TX: Ocean Drilling Program, 1023 pp.
- Emeis, K.-C., Sakamoto, T., Wehausen, R., and Brumsack, H.-J., 2000. The sapropel record of the Eastern Mediterranean Sea – Results of Ocean Drilling Program Leg 160. *Palaeoogeogr. Palaeoecol.*, **158**, 259–280.
- Hilgen, F.J., 1991. Astronomical calibration of Gauss to Matuyama sapropels in the Mediterranean and implication for the Geomagnetic Polarity Time Scale. *Earth Planet. Sci. Lett.*, **107**, 226–244.
- Kemp, A.E., Pearce, R.B., Koizumi, I., Pike, J., and Rance, J., 1999. The role of mat-forming diatoms in the formation of Mediterranean sapropels. *Nature*, **398**, 57–61.
- Kidd, R.B., Cita, M.B., and Ryan, W.B.F., 1978. Stratigraphy of eastern Mediterranean sapropel sequences recovered during Leg 42A and their paleoenvironmental significance. In Hsü K., and Montadert, J.L. (eds.), *Initial Reports of DSDP*. Washington, US: Govt. Printing Office, pp. 421–443.
- Olausson, E., 1961. Studies in deep-sea cores. *Rep. Swed. Deep Sea Exped.*, **8**, 337–391.
- Rohling, E.J., and Gieskes, W.W.C., 1989. Late Quaternary changes in Mediterranean intermediate water density and formation rate. *Paleoceanography*, **4**(5), 531–545.
- Rossignol-Strick, M., 1983. African monsoons, an immediate climate response to orbital insolation. *Nature*, **304**, 46–49.

- Sachs, J.P., and Repeta, D.J., 1999. Oligotrophy and nitrogen fixation during Eastern Mediterranean sapropel events. *Science*, **286**, 2485–2488.
- Slomp, C.P., Thomson, J., and deLange, G.J., 2002. Enhanced regeneration of phosphorus during formation of the most recent eastern Mediterranean sapropel (S1). *Geochim. Cosmochim. Acta*, **66**(7), 1171–1184.
- Struck, U., Emeis, K.-C., Rau, G.H., Voss, M., and Krom, M., 2001. Biological productivity during sapropel S5 formation in the eastern Mediterranean Sea – Evidence from stable isotopes of nitrogen and carbon. *Geochim. Cosmochim. Acta*, **65**(19), 3241–3258.

Cross-references

Coal Beds, Origin and Climate
 Diatoms
 Eccentricity
 Intertropical Convergence Zone (ITCZ) (see *Encyclopedia of World Climatology*)
 Monsoons, Quaternary
 Obliquity
 Ocean Anoxic Events
 Precession, Climatic

SCANDINAVIAN ICE SHEET

The Scandinavian and adjacent ice sheets

The Scandinavian Ice Sheet is the most commonly used name for an ice sheet that developed over Scandinavia many times during the Quaternary period. It is sometimes called the Fennoscandian Ice Sheet (Fenno = Finland), but as it expanded from the Scandinavian mountains and did not always reach Finland, the Scandinavian Ice Sheet is the most proper name. At its maximum extent, it covered northwestern Europe as far south as the Netherlands (Figure S1). In Eastern Europe it almost reached the Black Sea in southern Ukraine.

During some periods of maximum development, the Scandinavian Ice Sheet coalesced with the Barents-Kara Ice

Sheet, which was centered over the Barents and Kara Seas, and expanded southwards onto Northern Russia and Siberia (Figure S1). At such times, there was a contiguous ice sheet stretching from north of Spitsbergen to the Netherlands and from the Norwegian Sea to the Taimyr Peninsula in Siberia. The Scandinavian Ice Sheet also occasionally met the British Ice Sheet in the North Sea, but these two ice sheets were topographically and dynamically more clearly separated than those discussed above.

The older Scandinavian Ice Sheets

The strong glacial erosion associated with the last ice sheets has removed most of the deposits of the older glacials and interglacials. Glacial erosion also transformed the landscape so that deep U-shaped valleys and fjords now are common, especially in western Norway where vertical erosion of 1,900 m is inferred for part of Sognefjorden (Andersen and Nesje, 1992). The main record of older glaciations is the ice-rafted debris (IRD) found in cores collected from the floor of the deep Norwegian Sea. IRD indicates that the first ice sheets formed in Scandinavia as early as 11 million years ago, whereas the largest ice sheets grew after about 2.7 million years ago (Jansen and Sjøholm, 1991; Mangerud et al., 1996).

It is not known how many times the ice sheet expanded south of Scandinavia. In Germany, there are tills from only three glaciations, the Elsterian, Saalian and Weichselian (Ehlers, 1996). Thus, the classical view is that only at these times did the ice sheet reach this far south. However, Scandinavian erratics found in the Netherlands and glacial deposits in the North Sea indicate that such expansion also happened before the Elsterian (Mangerud et al., 1996).

The last ice age – the Weichselian

The last ice age in Northern Europe is named the Weichselian from the German name of the Vistula River in Poland, where glacial deposits from the Scandinavian Ice Sheet were

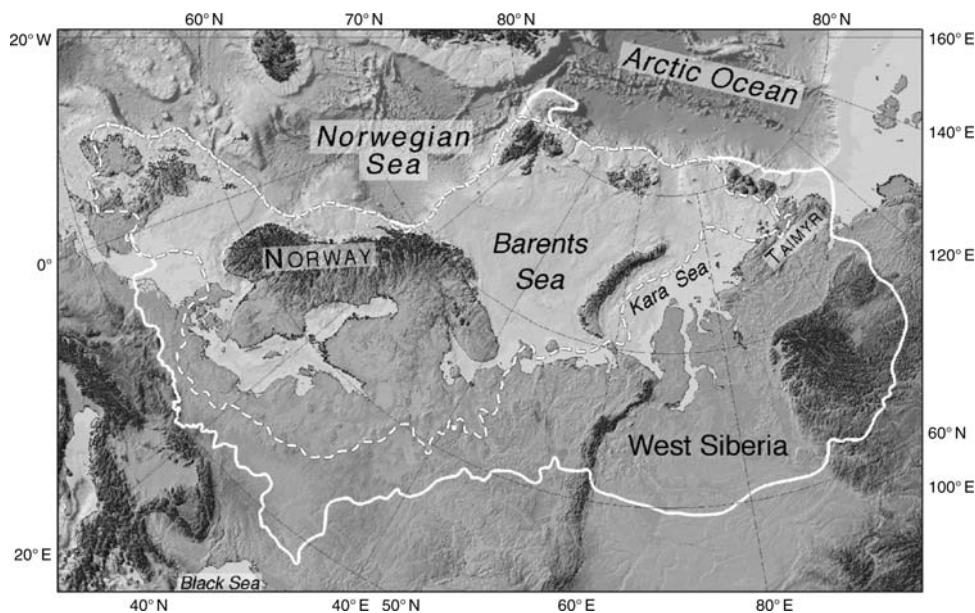


Figure S1 Map showing the extent of the Scandinavian, Barents-Kara and British Ice Sheets during two periods. Full line shows the Saalian glaciation and stippled line the Late Weichselian glaciation. (Modified from Svendsen et al., 2004.)

described by German geologists shortly after 1900 (Ehlers, 1996). We now know that these deposits were formed late during the last ice age, about 20,000 years ago. However, the name Weichselian is accepted for the entire cold period following the last interglacial in Europe, the Eemian. The subdivision and time scale for the Weichselian is shown in Figure S2.

The growth and decay of the Scandinavian and adjacent ice sheets is obviously much better known for the Weichselian than for older glaciations (Ehlers and Gibbard, 2004). However, in most areas, the ice sheets were larger during the Late Weichselian (about 20,000 years ago) than during earlier phases of the Weichselian. Therefore, our knowledge of the first 90,000 years of the Weichselian is limited.

Figure S2 shows a glaciation curve for western Norway for the entire Weichselian (Mangerud, 2004). During the last interglacial, the Eemian, the climate was warmer than at present, and no glacier existed. The first ice advance (Gulstein) almost reached the coast as early as 110,000 years ago.

Subsequently the ice front retreated during the Brørup interstadial when open forests were established over much of Scandinavia (Lundqvist, 1992). As seen from the curve, the ice margin subsequently advanced and retreated several times during the Weichselian. There were probably several more fluctuations than so far identified, although the record of ice rafted detritus in cores from the Norwegian Sea supports the main picture (Figure S2).

It is worth noting that the coast and probably much of the interior of Scandinavia was ice free during and possibly even after the Ålesund interstadial, which ended about 34,000 years ago (Olsen et al., 2002; Mangerud et al., 2003). This means that the ice sheet grew rapidly after this interstadial, until it reached its maximum size about 24,000 years ago.

The extent of the Late Weichselian Ice Sheet is shown in Figure S1. In Denmark, Germany and Poland, the limit of this ice sheet has been known for more than a century (Ehlers, 1996). However, it is still debated whether the British and

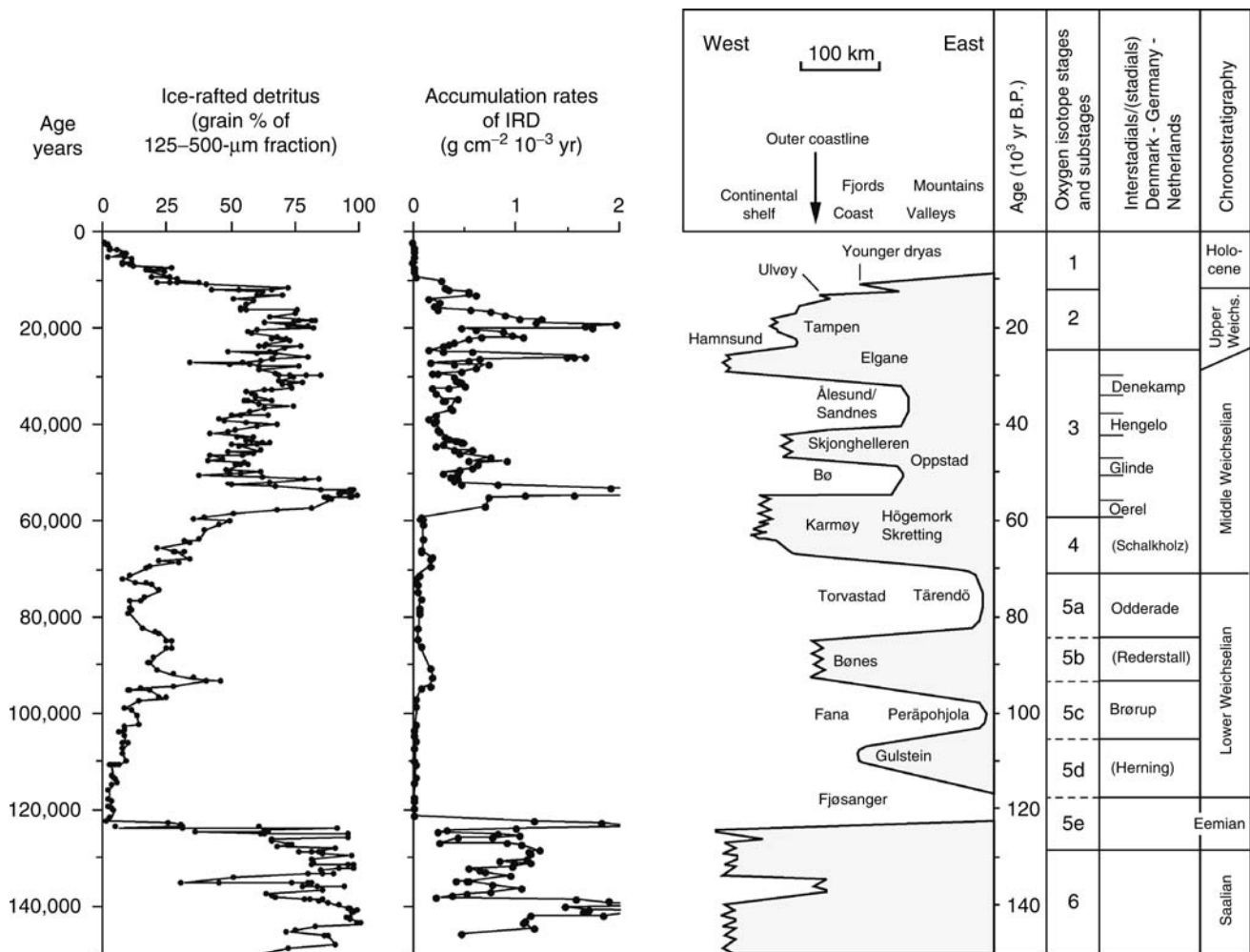


Figure S2 The right hand curve shows fluctuations of the western margin of the Scandinavian Ice Sheet. The lower part of the curve, when the ice front ended at the margin of the continental shelf corresponds with the Saalian ice limit in Figure S1. During the Eemian, the ice sheet disappeared. During the Weichselian, the extent of the ice sheet fluctuated strongly, but about 24,000 years ago it again reached the margin of the continental shelf, as shown in Figure S1. To the left are curves showing the number of ice rafted sand grains and their accumulation rates in cores from the Norwegian Sea (Mangerud, 2004).

Scandinavian Ice Sheets met in the North Sea, although that is assumed on the map. Furthermore, the limit of the ice sheet in Northern Russia has been much debated. A serious problem there is that permafrost with buried glacial ice melted at the end of the Weichselian and created fresh glacial landscapes, even though it had been deglaciated for tens of thousands of years (Svendsen et al., 2004).

The Barents-Kara Ice Sheet

The Barents Sea is located immediately north of Scandinavia, but the Scandinavian and Barents-Kara Ice Sheets did not always react in concert. The Barents-Kara Ice Sheet was much larger during the Early (about 90,000 years ago) and Middle Weichselian (60,000–50,000 years ago) than during the Late Weichselian, in contrast to the Scandinavian and the North American Ice Sheets (Svendsen et al., 2004). During both these periods, the Barents-Kara Ice Sheet moved onto land in Northern Russia, whereas during the Late Weichselian it terminated in the sea (Figure S1). During the Early Weichselian, the northbound rivers in Northern Russia were blocked by the ice sheet and large ice-dammed lakes formed between the ice-sheet and the continental watershed to the south.

Jan Mangerud

Bibliography

- Andersen, B.G., and Nesje, A., 1992. Quantification of Late Cenozoic glacial erosion in a fjord landscape. *Sveriges Geologiska Undersökning* Sr. **81**, 15–20.
- Ehlers, J., 1996. *“Quaternary and glacial geology.”* Chichester, UK: Wiley.
- Ehlers, J., and Gibbard, P. (eds.), 2004. *“Quaternary Glaciations – Extent and Chronology. Part 1: Europe.”* Amsterdam: Elsevier.
- Jansen, E., and Sjøholm, J., 1991. Reconstruction of glaciation over the past 6 million years from ice-borne deposits in the Norwegian Sea. *Nature*, **349**, 600–604.
- Lundqvist, J., 1992. *Glacial Stratigraphy in Sweden.* Geological Survey of Finland Special paper 15, pp. 43–59.
- Mangerud, J., 2004. Ice sheet limits on Norway and the Norwegian continental shelf. In Ehlers, J., and Gibbard, P. (eds.), *“Quaternary Glaciations – Extent and Chronology. Part 1: Europe.”* Amsterdam: Elsevier.
- Mangerud, J., Jansen, E., and Landvik, J., 1996. Late Cenozoic history of the Scandinavian and Barents Sea ice sheets. *Glob. Planet. Change*, **12**, 11–26.
- Mangerud, J., Løvlie, R., Gulliksen, S., Hufthammer, A.-K., Larsen, E., and Valen, V., 2003. Paleomagnetic correlations between Scandinavian Ice-Sheet fluctuations and Greenland Dansgaard-Oeschger Events, 45,000–25,000 ybp. *Quaternary Res.*, **59**, 211–220.
- Olsen, L., Svein, H., van der Borg, K., Bergström, B., and Broekmans, M., 2002. Rapid and rhythmic ice sheet fluctuations in western Scandinavia 15–40 Kya – a review. *Polar Res.*, **21**, 235–242.
- Svendsen, J., Alexanderson, H., Astakhov, V., Demidov, I., Dowdeswell, J., Funder, S., Gataullin, V., Henriksen, M., Hjort, C., Houmark-Nielsen, M., Hubberten, H., Ingólfson, O., Jakobsson, M., Kjær, K., Larsen, E., Lokrantz, H., Lunkka, J., Lyså, A., Mangerud, J., Matiouchkov, A., Murray, A., Möller, P., Niessen, F., Nikolskaya, O., Polyak, P., Saarnisto, M., Siegert, C., Siegert, M., Spielhagen, R., and Stein, R., 2004. Late Quaternary ice sheet history of Northern Eurasia. *Quaternary Sci. Rev.*, **23**, 1229–1271.

Cross-references

Eemian (Sangamonian) Interglacial
 Glaciations, Quaternary
 Ice-Rafted Debris (IRD)
 Interstadials
 Last Glacial Maximum
 Wisconsinan (Weichselian, Würm) Glaciation

SEA LEVEL CHANGE, LAST 250 MILLION YEARS

Introduction

One of the most fundamental geological observations has been that the seas once inundated large areas of the Earth's surface that are now exposed on land. Early observers attributed these marine incursions to one or multiple “Noachian” floods, but empirical science prevailed as uniformitarian concepts were applied to the stratigraphic record. Charles Lyell (1830) recognized that changes in sea level due to volcanic activity were responsible for the submergence and subsequent emergence of the temple at Serapis near Naples, Italy (see discussion by Gould, 1999). Observing cycles of shallow-water sedimentation across Europe, Lyell reasoned that apparent rises in sea level could explain the flooding of the continents (geologists call these “transgressions”) and the subsequent retreat of the seas (called “regressions”). For over a century after Lyell's work, geologists mapped these advances and retreats of the sea, noting that during intervals such as the middle Cretaceous (ca. 80 MyBP), much of the continents were inundated, whereas at other times, such as today, sea level was much lower. Geologists have equated these transgressions and regressions with global sea level (or “eustatic”) changes.

Transgressions and regressions may be related to eustatic sea level changes, but they also are caused by processes of subsidence or uplift, and changes in sediment supply. These processes are revealed by 20th century tide gauge data that indicate a global sea-level rise of $\sim 1.5\text{--}2\text{ mm yr}^{-1}$ (Church et al., 2001), due to the effects of ocean warming and melting of glaciers. However, tide gauge data for the mid-Atlantic United States uniformly show a rise of greater than 3 mm yr^{-1} , in part due to regional subsidence (Psuty and Collins, 1986). Although sea level is rising globally, *relative sea level* (in this region a term encompassing both the effects of subsidence/uplift and eustatic change) is rising much faster. High sediment supply can cause regression even during a relative sea level rise. For example, relative sea level is rising rapidly in the Mississippi Delta region due to the effects of global sea-level rise and rapid regional subsidence. Consequently, this region is generally experiencing a rapid transgression. However, near the mouth of the Mississippi, the high supply of sediments results in regression as the delta builds upward and into the Gulf. These modern examples illustrate the differences between a eustatic rise, a relative rise in sea level, and a marine transgression.

Global sea level has risen and fallen many times in response to growth and decay of the Northern Hemisphere Ice Sheets that have dominated the last 2.5 Myr (“the Ice Ages”). Drilling of submerged reef terrace records off Barbados (Figure S3) and Tahiti provided Rosetta Stone, which showed a 120 m lower sea level than present during the Last Glacial Maximum (Fairbanks, 1989; Bard et al., 1996). Uplifted reef terrace records (corrected for long-term uplift) have extended global sea-level estimates back to 130,000 years ago (Fairbanks and Matthews, 1978; Chappell et al., 1996); however, it has proven difficult to firmly extend reef terrace records further back in time due to dating problems.

Pre-Quaternary sea level change

Oxygen isotope ratios ($\delta^{18}\text{O}$) provide a potential means for reconstructing sea-level change over the past 100 Myr. $\delta^{18}\text{O}$

values reflect the effects of temperature and ice-volume (hence sea level) changes in the shells of single-celled organisms called foraminifera. By calibrating foraminiferal $\delta^{18}\text{O}$ variations to the reef terrace record, geologists can make an estimate of global sea-level changes (Figure S3). However, it is difficult to extend oxygen isotopic sea-level estimates beyond the past million years because the temperature history of the planet prior to this is less well known. In addition, diagenetic alteration potentially overprints Late Cretaceous to early Tertiary $\delta^{18}\text{O}$ values (ca. 100–25 MyBP), whereas records older than 100 Myr are typically altered.

Our primary information on sea-level change prior to the Quaternary (>2 MyBP) is derived from stratigraphic records of continental inundation. Transgressions have flooded the continents on roughly 100-Myr timescales (e.g., Sloss, 1963), reflecting changes in the rates of ocean crust production. Finer-scale cycles (1–10 Myr) have been attributed either to sea-level change (Suess, 1885) or to tectonic controls (Sloss, 1963; Stille, 1924; Grabau, 1936). These cycles are observed in the sediment and rock record with deeper water environments representing transgressions and shallower water environments representing regressions.

Studies at Exxon Production Research Company (EPR) revolutionized our view of the stratigraphic record of sea-level change. Sea level falls and tectonic changes both produce erosion surfaces termed “unconformities”; packages of sediments on continental margins bracketed by unconformities are called “sequences.” Researchers at EPR made a revolutionary breakthrough in using seismic reflection profiles to identify sequences and then using these sequences to estimate the ages and magnitudes of past sea level changes (Figure S4; Haq et al., 1987; Vail et al., 1977). These estimates proved highly controversial, in part because of the proprietary nature of the data used to construct them and in part because of flaws in the method used to estimate the amplitudes of sea-level change. Nevertheless, more than a decade of studies, described below, have been carried out, validating the general number and timing of eustatic events published by EPR – a landmark achievement. However, estimation of eustatic amplitudes remains one of the thorniest problems in geology.

A large mid-Oligocene (ca. 30–32 MyBP) sea level lowering illustrates problems with estimating amplitudes. Vail et al. (1977) initially concluded that this event comprised over

400 m of global sea level lowering, a remarkably large drop. Geophysical studies showed that the methodology employed in these estimates did not properly account for the effects of basin subsidence and water depth and thus grossly overestimated the amplitudes (see summary in Christie-Blick et al., 1990). A further decade of study by EPR scientists provided an estimate of ~160 m of lowering for this mid-Oligocene event (Figure S5), an amplitude that still strained credulity. Stable isotopic studies have long suggested amplitudes closer to 30–60 m for this event (e.g., Miller et al., 1985, 1998). Rigorous studies of borehole transects on the New Jersey margin yield an estimate for this event of 50 m (Kominz and Pekar, 2001) using a method called backstripping (see below for definition), and this estimate is probably correct within ± 10 m. Despite these recent studies, the amplitude of sea-level change remains one of the poorest constrained boundary conditions of the Earth.

Recognizing that it had the unique ability to provide a global dataset, the international Ocean Drilling Program (ODP), operator of the drillship *JOIDES Resolution*, entered into sea-level research in the 1990s. ODP identified four major goals in sea-level research: (a) test the synchrony of sea-level events in widely separated locations; (b) estimate the amplitude of sea-level changes; (c) evaluate various models that seek to explain the stratigraphic response to sea-level oscillations; and (d) determine the mechanisms that control sea level. To accomplish these goals, a strategy of drilling transects of boreholes on passive margins was adopted.

The New Jersey sea level transect

The New Jersey margin was selected by ODP as an ideal location to begin the investigation of the Late Cretaceous to Cenozoic history of sea-level change because of its rapid sedimentation, tectonic stability, good chronostratigraphic control, and abundant seismic well log and borehole data (Miller and Mountain, 1994). To evaluate sequences and sea-level changes, the “New Jersey Sea-Level Transect” was designed as a series of boreholes from the onshore New Jersey Coastal Plain across the continental shelf to the slope and rise (Figure S5). The transect initially focused on the past 34 Myr (Oligocene-Recent; Miller and Mountain, 1996), a time when large ice sheets waxed and waned, potentially changing sea level by up to 100 m. More recent studies

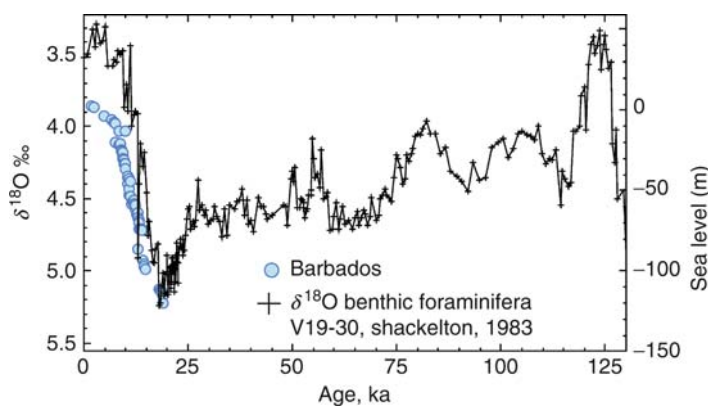
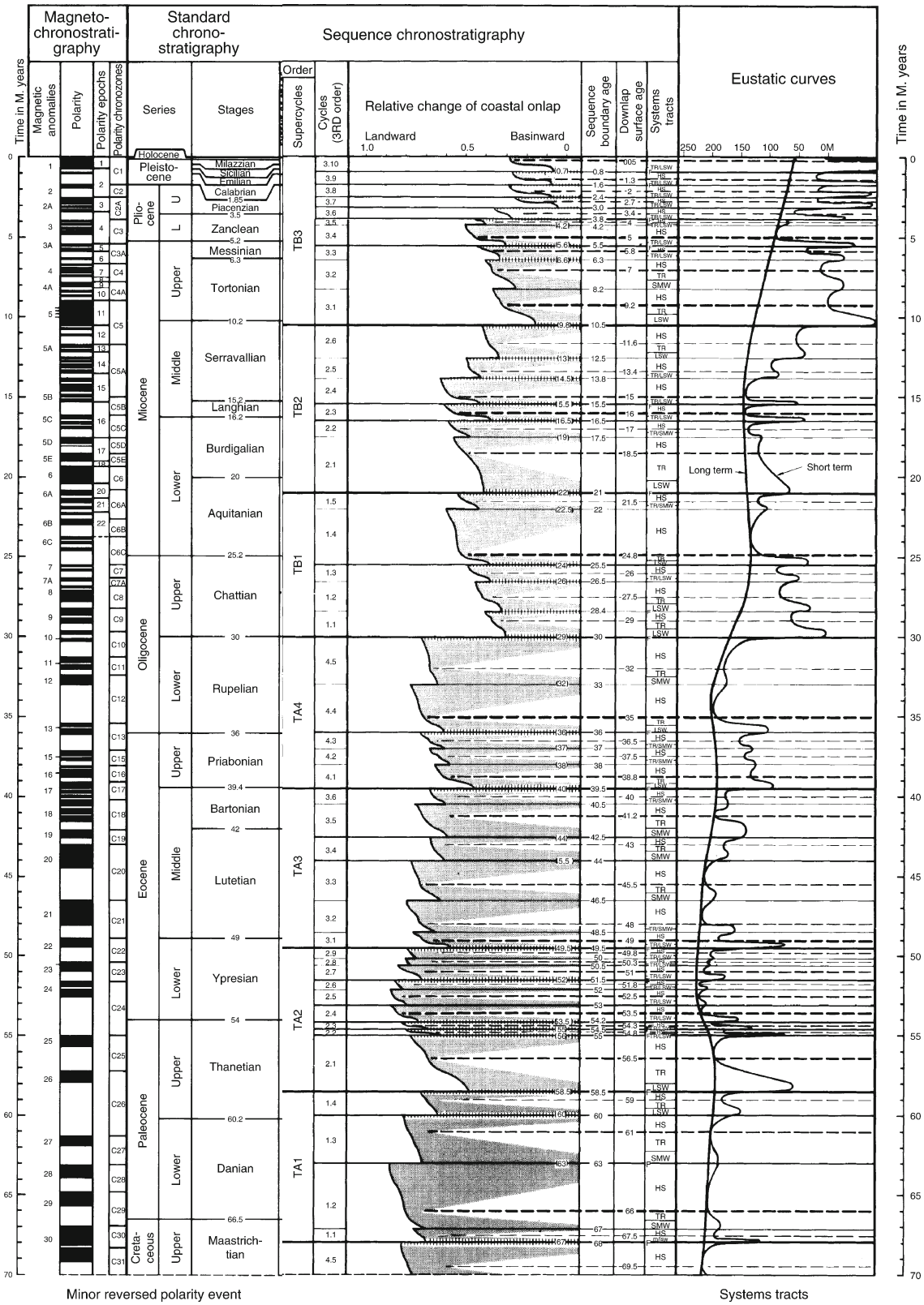


Figure S3 Comparison of the global estimate for sea-level derived from Barbados terraces (Fairbanks, 1989) with deep-sea benthic foraminiferal $\delta^{18}\text{O}$ values from Pacific core V19-30 scaled to sea-level assuming $0.11\text{‰}/10\text{ m}$ of sea-level change (Fairbanks and Matthews, 1978) (Wright, Miller, Sheridan, unpublished).



Minor reversed polarity event

Systems tracts

Figure S4 Cenozoic portion of the Haq et al. (1987) sea-level record.

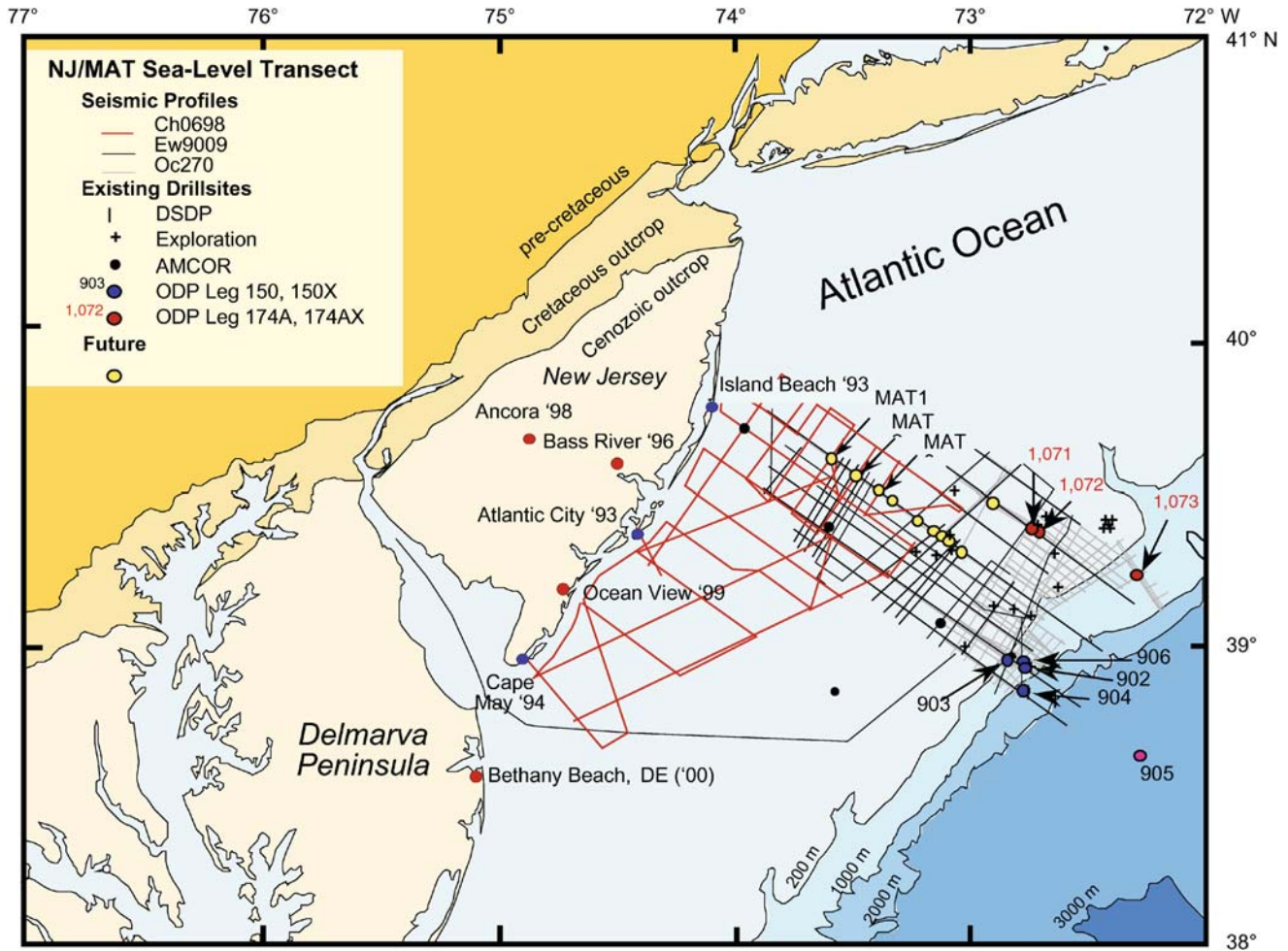


Figure S5 Map showing seismic profiles and boreholes, New Jersey sea-level transect.

have extended back to 100 MyBP (Late Cretaceous; Miller et al., 2003).

Seismic profiles provide a means of imaging strata like a sonogram images structures within the human body. Seismic profiles exhibit stratigraphic geometries resulting from erosion, potentially due to sea-level lowerings ("sequence boundaries"). The seismic surfaces reveal themselves in borehole sediments as erosion surfaces. The New Jersey Transect dated these sequence boundaries by drilling in relatively deep water (400–1,400 m) on the continental slope and rise and using various tools for age control (fossils, magnetostratigraphy, Sr-isotopic stratigraphy). Drilling onshore in New Jersey also dated these sequences in a more proximal nearshore to paleo-shelf setting, where time gaps or hiatuses were longer. Nevertheless, the onshore hiatuses (white gaps between blue boxes; Figure S6) correlate remarkably well with offshore sequence boundaries (m1, m2, etc. on Figure S6). This establishes a regional correlation between these hiatuses and associated sequence boundaries, and a relation to at least regional-scale sea-level lowerings.

Comparison of the New Jersey sequence stratigraphic record with oxygen isotopes provides a link between regional

sea-level lowerings and global changes in ice volume (hence sea level) for the past 34 Ma (Figure S6). Oxygen isotopic ($\delta^{18}\text{O}$) increases in deep-sea Atlantic cores correlate with the sea-level lowerings in New Jersey (Figure S6). This demonstrates that a significant portion of oxygen isotopic changes must be attributed to changes in ice volume. Still, we cannot precisely determine the extent of the role of ice growth versus cooling of bottom waters on any individual $\delta^{18}\text{O}$ increase. For example, a large $\delta^{18}\text{O}$ increase occurred across the Oligocene/Miocene boundary (ca. 23 Ma), correlating with the m6 continental slope and the O6/Kw0 onshore sequence boundaries (Figure S6). If this were attributed entirely to ice volume (presumably from Antarctic ice, because Northern Hemisphere Ice Sheets did not begin to grow until late Miocene to Pliocene), this change would be equivalent to a 90 m eustatic sea level drop. It is likely however, that bottom waters cooled at the same time as the glaciation; during the Quaternary, about two-third of the $\delta^{18}\text{O}$ signal is controlled by ice volume and one-third by temperature (Fairbanks, 1989). Applying this rule of thumb to the older record indicates about 60 m, not 90 m, of eustatic lowering; however, it is still possible that the temperature effects were larger and sea level change would have been correspondingly less.

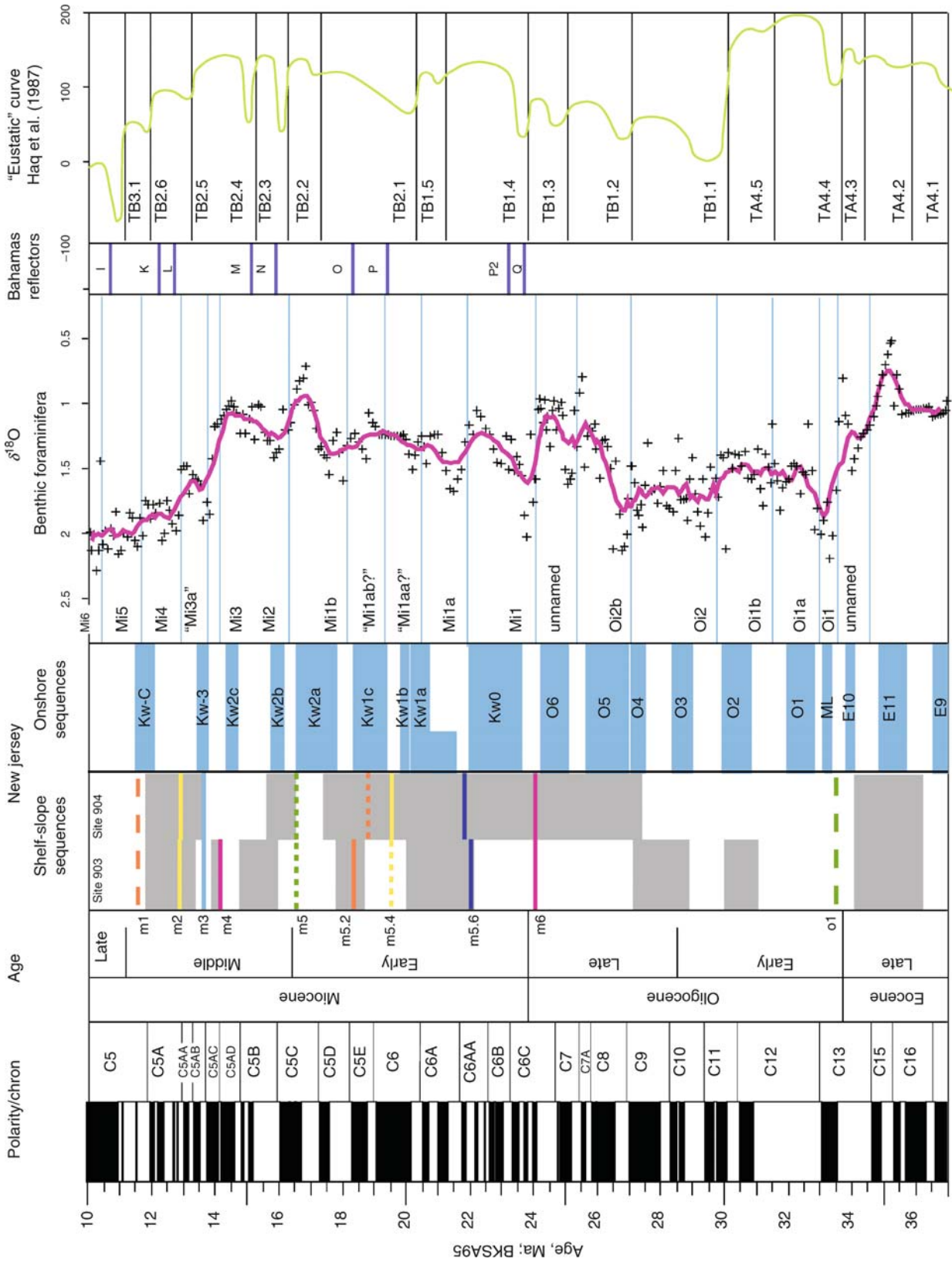


Figure S6 Comparison of offshore New Jersey, onshore New Jersey, global oxygen isotopes, ages of Bahamas reflections, and Haq et al. (1987) sea-level record (Miller et al., 1998). I approximate age error

The above example illustrates the hazards of trying to estimate eustatic amplitudes from oxygen isotopic records. Though continental margin stratigraphic records are complicated by changes in subsidence, it is possible to evaluate subsidence histories using a method called backstripping. This method progressively removes the effects of compaction, sediment loading, and thermal subsidence; the residual provides an estimate of eustatic sea level (e.g., Kominz et al., 1998; Watts and Steckler, 1979). Backstripping requires estimates of age, sediment type (for decompaction), and paleowater depth; the latter is obtained from benthic foraminifera and lithologic data and is the greatest source of uncertainty. Kominz et al. (1998) and Van Sickle et al. (2004) backstripped individual onshore New Jersey boreholes ("1-dimensional" backstripping) and found amplitudes of 20–40 m. Two-dimensional backstripping (backstripping an entire profile using several boreholes) of ten latest Eocene to earliest Miocene sequences provided estimates of ~20–60 m eustatic lowerings (Kominz and Pekar, 2001). Both one and two dimensional backstripping yielded Oligocene-Miocene eustatic estimates that are lower than those published by the EPR group (e.g., Haq et al., 1987) by a factor of two or more (Kominz and Pekar, 2001; Van Sickle et al., 2004).

Studies of sea-level change must be global in scope and ODP has drilled on the Australian margin (Legs 133, 182, and 194) and the Bahamas (Leg 166). Despite the fundamental difference in sedimentation style between carbonate and siliciclastic margins, ODP drilling documented similar-Miocene unconformities in these diverse settings (Figure S6). Drilling in the Bahamas showed that the flanks of a carbonate bank environment develop sequences that are remarkably similar in character to those of siliciclastic margins (Eberli et al., 1997). Though tectonic effects (e.g., rapid subsidence) influence much of the northeast Australian region (Davies et al., 1993), consequences of global sea-level change on the evolution of the Marion Plateau and the Great Barrier Reef were evaluated. Drilling on the Australian margin by Leg 194 (Isern et al., 2002) provided an estimate of a major late middle Miocene eustatic lowering of 33 ± 12 m based on Airy (point) loading to 85 ± 30 assuming rigid crust (flexural loading). These wide ranges again illustrate the difficulty in estimating global sea-level amplitudes.

Causes of sea level change

Drilling on the New Jersey, Bahamas, and Australian margins have firmly demonstrated that ice-volume changes have been one of the primary controls on sea-level change during the Icehouse world of the past 34 Myr. It is not surprising that this is true because ice-volume changes are the only known mechanism for causing the large (>10s m), rapid changes in sea level reported for this time interval. The close correspondence between the oxygen isotopic and continental margin records is testament to this linkage (Figure S6). However, what about the vast amounts of geologic time in which the Earth was presumably ice-free?

Sea level during the Cretaceous (144–65 Ma) was much higher than at present because of long-term changes in sea level. These long-term (10–100 Myr scale) sea-level changes have been largely controlled by tectonics. For example, during the warm interval of the middle Cretaceous (ca. 80–90 Ma), global sea level was between 100 (Miller et al., 2005) and 170 m (Müller et al., 2008) higher than today. However, such high sea levels cannot be explained by a warmer planet and

the absence of ice sheets: even if all of the modern ice sheets were melted (an "ice-free Greenhouse world"), then sea-level would be only 73 m higher than today. Although the Cretaceous oceans were 10–12 °C warmer than today, thermal expansion could only account for another 10–13 m of rise. The generally accepted explanation for the high mid-Cretaceous sea levels is high sea-floor spreading rates; higher rates mean hotter crust, which expands, displacing seawater and causing long-term flooding of the continents (Hays and Pitman, 1973; Kominz, 1984). This pulse of mid-Cretaceous high seafloor spreading has been recently disputed (Rowley, 2002), though various stratigraphic data unequivocally show that relative to the continents, sea level was 100–250 m higher, based on backstripping in the former case (Watts and Steckler, 1979) and continental flooding in the latter (Sahagian et al., 1996). If not caused by high-sea floor spreading rates, the long-term flooding and subsequent retreat of the sea over the past 180 Myr could have been the result of the breakup of the supercontinent Pangea, beginning at 180 Ma, which may have led to overall subsidence of continents relative to the oceans during the Jurassic to mid-Cretaceous.

Even more puzzling than the long-term record is the observation that large (10s to 100 m), rapid (less than 1 Myr) sea-level changes occurred during the Triassic to middle Eocene (ca. 250–50 Ma), a time considered to be an ice-free Greenhouse (Haq et al., 1987; Hallam, 1992). Ice-volume changes (glacioeustasy) are the only known mechanism for producing large, rapid sea-level change (Pitman and Golovchenko, 1983). Although it has been believed in general that there were no significant ice sheets prior to the middle Eocene, Haq et al. (1987) delineated numerous Cretaceous to early Eocene sequence boundaries with associated large (>50 m), rapid (<1 Myr) sea-level lowerings. There are four explanations for this apparent paradox (Browning et al., 1996): (a) the Cretaceous to early Eocene sequences summarized by Haq et al. (1987) were restricted to local basin(s) and do not reflect eustasy (this is unlikely considering that many have been widely recognized; e.g., Aubry, 1985; Mancini and Tew, 1991, 1995; Olsson, 1991); (b) the sequences were controlled by low-amplitude sea-level changes (e.g., 10 m of lowering in 1 Myr can be explained by numerous mechanisms; Donovan and Jones, 1979); (c) mechanisms of sea-level change are not fully understood; and (d) there were ice sheets throughout much of the Cretaceous to early Eocene (e.g., Stoll and Schrag, 1996).

Drilling in New Jersey has recently provided a record of sea-level changes during the warm Late Cretaceous. These studies firmly document that large (>25 m), rapid (<<1 Myr) eustatic variations occurred in the Late Cretaceous, hinting at the presence of ice sheets in this supposedly ice-free Greenhouse world (Figure S7). Continuous coring recovered 11–14 Upper Cretaceous sequences at Bass River and Ancora, New Jersey that were dated by integrating Sr-isotopic and biostratigraphic data (age resolution ± 0.5 Myr) and subsequently backstripped taking into account sediment loading, compaction, paleodepth, and thermo-flexural subsidence, providing a new sea-level estimate. The timing of Late Cretaceous sequence boundaries in New Jersey is similar to sea-level lowerings found by EPR (Haq et al., 1987), NW European sections (Hancock, 1993), and Russian sections (Sahagian et al., 1996), indicating a global cause (Figure S7). However, New Jersey and Russian Platform eustatic estimates are half of the EPR amplitude; the EPR record also differs in shape from the backstripped estimates. The use of the EPR record for the Late

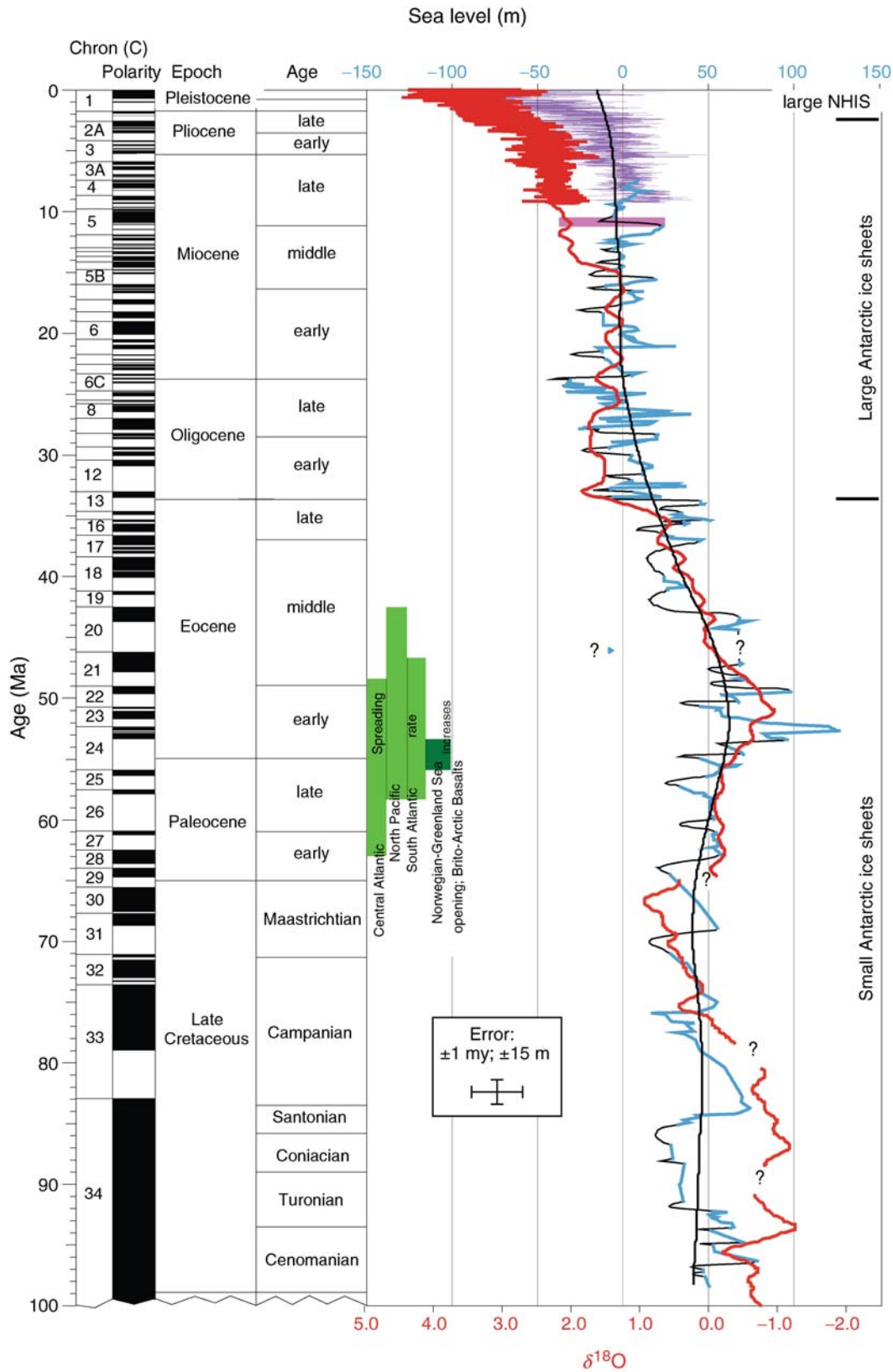


Figure S7 Comparison of Late Cretaceous deep-sea benthic foraminiferal $\delta^{18}\text{O}$ records, New Jersey composite sequences, relative sea level from NW Europe (Hancock, 1993), backstripped Russian platform record (Sahagian et al., 1996), the EPR eustatic estimate for Bass River (Haq et al., 1987), backstripped R2 eustatic estimates for Bass River (black) and Ancora (gray) and our best estimate of eustatic changes (heavy black line constrained by data, dashed inferred). Pink arrows indicate positive $\delta^{18}\text{O}$ inflections (inferred cooling and/or ice volume increases) (after Miller et al., 2004).

Cretaceous should be abandoned; the New Jersey backstripped records provide the best substitute at this time.

The firm documentation of large (>25 m), rapid (<Myr) sea-level changes (Figure S7) indicates some glacioeustatic control during the Late Cretaceous. The apparent inconsistency with evidence for warm high latitudes during the Late Cretaceous can be explained by ephemeral (i.e., lasting $\ll 1$ Myr) ice sheets (presumably in East Antarctica (EAIS)) with volumes approaching one-third to one-half of the modern EAIS (Miller et al., 1999) and intervening warm, ice-free intervals (Miller et al., 2003).

Oxygen isotopic comparisons with Late Cretaceous sequence boundaries have not attained the resolution needed to link the two datasets unequivocally, as has been done for the past 42 Myr (Miller et al., 1998a). Nevertheless, comparisons between Late Cretaceous sequence stratigraphy and $\delta^{18}\text{O}$ records are intriguing (Figure S7), further suggesting small ice sheets in this alleged Greenhouse World: (a) a major mid-Cenomanian sequence boundary (hiatus ca. 96–97 Myr ago) (see also Gale et al., 2002) correlates with a major (>1‰) $\delta^{18}\text{O}$ increase; (b) two minor $\delta^{18}\text{O}$ increases spanning the Cenomanian/Turonian boundary may correlate with sequence boundaries; (c) a mid-Turonian sea-level lowering (91.5–92 Ma) may correlate with a major increase in benthic foraminiferal $\delta^{18}\text{O}$ values ($\sim 1.0\%$), although additional data are needed to determine the precise timing of the increase (Figure S7). Several other Coniacian-Campanian $\delta^{18}\text{O}$ increases (dashed arrows, Figure S7) may be related to sequence boundaries, but the data are too sparse to provide a firm correlation.

The EPR sea-level records (Vail et al., 1977; Haq et al., 1987) are major achievements for the Earth sciences. However, it is not surprising after 15–25 years, that we conclude that these previous sea-level estimates are not entirely correct in their shape and amplitudes. Methods for extracting sea level from stratigraphic data have advanced during this period and the scientific community has begun to document amplitudes of sea-level change with increased precision. Despite their limitations, the EPR curves stand the test of time as an approximate chronology (± 1 Myr) of eustatic lowerings. Studies on the New Jersey and other continental margins have generally confirmed the number and approximate ages of sea-level lowerings of Haq et al. (1987) for the past 100 Myr (Figures S6, S7). In the absence of other datasets for the Triassic-Early Cretaceous, the Haq et al. (1987) record still provides the best estimate for the timing of eustatic lowerings. Although the timing can be estimated, the amplitudes of sea-level change during the Triassic-Early Cretaceous remain poorly constrained and the causal mechanisms for the large, rapid sea-level changes for this interval can only be explained by glacioeustasy. Is our understanding of causal mechanisms for global sea-level change flawed, or is our interpretation of a largely ice-free planet prior to 42 Ma incorrect?

ODP drilling has determined ages of sequence boundaries on continental margins to better than ± 0.5 Myr and provided a chronology of eustatic lowering for the past 42 Myr (Figure S6). ODP has also validated the transect approach of drilling passive continental margins and carbonate platforms (onshore, shelf, slope). Additional integrated geological and geophysical studies of transects of margins are needed to address the history magnitude, and mechanisms of global sea level change over the past 250 Myr.

Kenneth G. Miller

Bibliography

- Aubry, M.-P., 1985. Northern European Paleogene magnetostratigraphy, biostratigraphy and paleogeography: Calcareous nannofossil evidence. *Geology*, **13**, 198–202.
- Bard, E., Hamelin, B., Arnold, M., Montaggioni, L.F., Cabioch, G., Faure, G., and Rougerie, F., 1996. Deglacial sea-level record from Tahiti corals and the timing of global meltwater discharge. *Nature*, **382**, 1996.
- Browning, J.V., Miller, K.G., and Pak, D.K., 1996. Global implications of Eocene greenhouse and doobhouse sequences on the New Jersey coastal plain – The icehouse cometh. *Geology*, **24**, 639–642.
- Chappell, J., Omura, A., Esat, T., McMulloch, M., Pandelfi, J., Ota, Y., and Pillans, B., 1996. Reconciliation of late Quaternary sea levels derived from coral terraces at Huon Peninsula with deep sea oxygen isotope records. *Earth Planet. Sci. Lett.*, **141**, 227–236.
- Christie-Blick, N., Mountain, G.S., and Miller, K.G., 1990. Seismic stratigraphic record of sea-level change. In *Sea-level Change*. Washington, D.C.: National Academy Press, pp. 116–140.
- Church, J.A., Gregory, J.M., Huybrechts, P., et al., 2001. Changes in sea level. In Houghton, J.T., Ding, Y., Griggs, D.J., et al. (eds), *Climate Change 2001: The Scientific Basis*. Cambridge: Cambridge University Press, pp. 639–693.
- Davies, K.A., McKenzie, P.J., Palmer-Julson, A., et al., 1993. In Proceedings of the Ocean Drilling Program, Scientific Results, vol. 133: College Station, TX.
- Donovan, D.T., and Jones, E.J.W., 1979. Causes of world-wide changes in sea level. *J. Geol. Soc. Lond.*, **136**, 187–192.
- Eberli, G.P., Swart, P.K., Malone, M.J., et al., 1997. In *Proceedings of the Ocean Drilling Program, Initial Reports*, vol. 166, College Station, TX.
- Fairbanks, R.G., 1989. A 17,000-year glacio-eustatic sea level record: Influence of glacial melting rates on the Younger Dryas event and deep-ocean circulation. *Nature*, **342**, 637–642.
- Fairbanks, R.G., and Matthews, R.K., 1978. The marine oxygen isotopic record in Pleistocene coral, Barbados, West Indies. *Quaternary Res.*, **10**, 181–196.
- Gale, A.S., Hardenbol, J., Hathaway, B., Kennedy, W.J., Young, J.R., and Phansalkar, V., 2002. Global correlation of Cenomanian (Upper Cretaceous) sequences: Evidence for Milankovitch control on sea level. *Geology*, **30**, 291–294.
- Grabau, A.W., 1936. Oscillation of pulsation. Report of the XVI session, International Geological Congress, Washington, 1933, vol. 1, pp. 539–553.
- Gould, S.J., 1999. Pozzuoli's pillars revisited. *Nat. Hist.*, **24**, 81–91.
- Hallam, A., 1992. *Phanerozoic Sea-level Changes*. New York: Columbia University Press, 266pp.
- Hancock, J.M., 1993. Transatlantic correlations in the Campanian-Maastrichtian stages by eustatic changes of sea-level. In Hailwood, E.A., and Kidd, R.B. (eds.), *High resolution stratigraphy*. London: Geological Society, pp. 241–256.
- Haq, B.U., Hardenbol, J., and Vail, P.R., 1987. Chronology of fluctuating sea levels since the Triassic (250 million years ago to present). *Science*, **235**, 1156–1167.
- Hays, J.D., and Pitman, W.C. III., 1973. Lithospheric plate motion, sea level changes, and climatic and ecological consequences. *Nature*, **246**, 18–22.
- Isem, A.R., Anselmetti, F.S., Blum, P., et al., 2002. Proceedings of the Ocean Drilling Program, Initial Reports, vol. 194, College Station, TX. Available at: http://www-odp.tamu.edu/publications/194_IR/194ir.htm.
- Kominz, M.A., 1984. Oceanic ridge volumes and sea-level change – An error analysis. In Schlee, J.S. (ed.), *Interregional Unconformities and Hydrocarbon Accumulation*. *Am. Assoc. Petrol. Geol., Memoir*, **36**, pp. 108–127.
- Kominz, M.A., and Pekar, S.F., 2001. Oligocene eustasy from two-dimensional sequence stratigraphic backstripping. *Geol. Soc. Am. Bull.*, **113**, 291–304.
- Kominz, M.A., Miller, K.G., and Browning, J.V., 1998. Long-term and short-term global Cenozoic sea-level estimates. *Geology*, **26**, 311–314.
- Lyell, C., 1830. *Principles of Geology: Being an attempt to explain the former changes of the Earth's surface, by reference to causes now in operation*, London: John Murray.
- Mancini, E.A., and Tew, B.H., 1991. Relationships of Paleogene stages and planktonic foraminiferal zone boundaries to lithostratigraphic and allostrostratigraphic contacts in the eastern Gulf Coastal Plain. *J. Foraminiferal Res.*, **21**, 48–66.

- Mancini, E.A., and Tew, B.H., 1995. Geochronology, biostratigraphy and sequence stratigraphy of a marginal marine to marine shelf stratigraphic succession: Upper Paleocene and lower Eocene, Wilcox Group, eastern Gulf Coastal Plain, USA. In Berggren, W.A., Kent, D.V., Aubry, M.-P., Hard Enbol, J. (eds.), *Geochronology, Time Scales and Global Stratigraphic Correlation*. Society of Economic Paleontology and Mineralogy (SEPM) Special publication 54, pp. 281–293.
- Miller, K.G., and Mountain, G.S., 1994. Global sea-level change and the New Jersey margin. Proceedings of the Ocean Drilling Program, Initial Reports, vol. 150, College Station, TX, pp. 11–20.
- Miller, K.G., Mountain, G.S., the Leg 150 Shipboard Party, and Members of the New Jersey Coastal Plain Drilling Project, 1996, drilling and dating New Jersey Oligocene-Miocene sequences: Ice volume, global sea level, and Exxon records. *Science*, **271**, 1092–1094.
- Miller, K.G., Mountain, G.S., and Tucholke, B.E., 1985. Oligocene glacioeustasy and erosion on the margins of the North Atlantic. *Geology*, **13**, 1–13.
- Miller, K.G., Mountain, G.S., Browning, J.V., Kominz, M., Sugarman, P.J., Christie-Blick, N., Katz, M.E., and Wright, J.D., 1998. Cenozoic global sea level, sequences, and the New Jersey transect: Results from coastal plain and continental slope drilling. *Rev. Geophys.*, **36**, 569–601.
- Miller, K.G., Barrera, E., Olsson, R.K., Sugarman, P.J., and Savin, S.M., 1999. Does ice drive early Maastrichtian eustasy? Global $\delta^{18}\text{O}$ and New Jersey sequences. *Geology*, **27**, 783–786.
- Miller, K.G., Sugarman, P.J., Browning, J.V., Kominz, M.A., Hernández, J.C., Olsson, R.K., Wright, J.D., Feigenson, M.D., and Van Sickel, W., 2003. A Late Cretaceous chronology of large, rapid sea-level changes: Glacioeustasy during the greenhouse world. *Geology*, **31**, 585–588.
- Miller, K.G., Sugarman, P.J., Browning, J.V., Kominz, M.A., Olsson, R.K., Feigenson, M.D., and Hernandez, J.C., 2004. Upper Cretaceous sequences and sea level history, New Jersey coastal plain: Chronology, facies, and sea level. *GSA Bull.*, **116**, 368–393.
- Miller, K.G., Kominz, M.A., Browning, J.V., Wright, J.D., Mountain, G.S., Katz, M.E., Sugarman, P.J., Cramer, B.S., Christie-Blick, N., and Pekar, S.F., 2005. The Phanerozoic record of global sea-level change: Science, v. 310, p. 1293–1298.
- Olsson, R.K., 1991. Cretaceous to Eocene sea-level fluctuations on the New Jersey margin. *Sediment. Geol.*, **70**, 195–208.
- Pitman, W.C. III, and Golovchenko, X., 1983. *The effect of sea-level change on the shelf edge and slope of passive margins*. Society of Economic Paleontology and Mineralogy (SEPM) Special publication 33, pp. 41–58.
- Psuty, N.P., and Collins, M., 1986. Holocene sea level in New Jersey. *Phys. Geogr.*, **7**, 156–167.
- Rowley, D.B., 2002. Rate of plate creation and destruction: 180 Ma to present. *Geol. Soc. Am. Bull.*, **114**(8), 927–933.
- Sahagian, D., Pinous, O., Olfieriev, A., Zakaharov, V., and Beisel, A., 1996. Eustatic curve for the middle Jurassic-Cretaceous based on Russian platform and Siberian stratigraphy: Zonal resolution. *Am. Assoc. Petrol. Geol. Bull.*, **80**, 1433–1458.
- Sloss, L.L., 1963. Sequences in the cratonic interior of North America. *Geol. Soc. Am. Bull.*, **74**, 93–114.
- Stille, H., 1924. *Grundfragen der Vergleichenden Tektonik*. Berlin: Borntraeger.
- Stoll, H.M., and Schrag, D.P., 1996. Evidence for glacial control of rapid sea level changes in the early Cretaceous. *Science*, **272**, 1771–1774.
- Suess, E., 1885. *Da Antlitz de Erde, I*. Prague: F. Tempsky.
- Vail, P.R., Mitchum, R.M. Jr., Todd, R.G., Widmier, J.M., Thompson, S. III., Sangree, J.B., Bub, J.N., and Hatlelid, W.G., 1977. Seismic stratigraphy and global changes of sea level. In Payton, C.E. (ed.), *Seismic Stratigraphy – Applications to Hydrocarbon Exploration*. *Am. Assoc. Petrol. Geol. Mem.*, **26**, 49–212.
- Van Sickel, W.A., Kominz, M.A., Miller, K.G., and Browning, J.V., 2004. Late Cretaceous and Cenozoic sea-level estimates backstripping analysis of borehole data, onshore New Jersey. *Basin Res.*, **16**, 451–465.
- Watts, A.B., and Steckler, M.S., 1979. Subsidence and eustasy at the continental margin of eastern North America. *AGU Maurice Ewing Ser.*, **3**, 218–234.

Cross-references

Cenozoic Climate Change
Foraminifera
Glacial Eustasy

Greenhouse (Warm) Climates
Icehouse (Cold) Climates
Ocean Drilling Program (ODP)
Oxygen Isotopes
Sea Level Change, Post-Glacial
Sea Level Change, Quaternary
Sea Level Rise, in *Encyclopedia of World Climatology*

SEA LEVEL CHANGE, POST-GLACIAL

The late Quaternary glacial period was characterized by massive ice sheets that covered parts of North America, northern Europe, and several other high latitude and high altitude regions. This volume of ice was sufficient to lower global sea level by over 100 m. As the ice sheets began to melt and retreat over 20,000 years ago, sea level rose rapidly. However, the time history and magnitude of sea level rise were widely debated, as data from radiocarbon-dated paleosea level indicators began to accumulate in the 1950s and 1960s. A major point of discussion at that time centered on whether or not the post-glacial marine transgression followed a smooth versus a fluctuating curve that reflected world-wide sea level changes (e.g., Shepard and Suess, 1956; Fairbridge, 1961, 1976). Support for both points of view could be found as recently as 1991 in a compilation of Holocene sea level curves (Pirazzoli, 1991). The acquisition of more accurately dated sea level data and development of a theoretical framework to account for interactions among various geophysical and climatological processes has led to a much clearer understanding of post-glacial sea level rise (SLR) within the last 30 years. The deglaciation was accompanied by a global increase in sea level of ~120 m. Post-glacial sea level did not rise smoothly, but instead jumped in several sharp and rapid spikes, termed “melt-water pulses” (Fairbanks, 1989). However, the exact number, timing, and magnitude of these major pulses, and their relation to paleoclimate events have yet to be resolved. The extent and significance of minor Holocene sea level oscillations also needs further investigation.

Processes affecting sea level

Sea level integrates the effects of diverse geological and climatological phenomena that operate over a wide range of spatial and temporal scales. The dominant processes that have affected post-glacial sea level involve changes in ocean water volume caused by melting of ice sheets (*glacial eustasy*) and changes in ocean basin volume due to re-adjustment of the lithosphere in response to removal of the ice load (*glacial isostasy*) and glacial meltwater loading of ocean basins (*hydro-isostasy*). While of lesser importance during this period, major factors controlling global sea level over geologic timescales (10^7 – 10^8 years) include changes in volume of ocean basins due to variations in rates of seafloor spreading and subsidence of cooler, oceanic crust away from spreading centers (*tectono-eustasy*). Changes in ocean water density, caused by changes in temperature or salinity (*steric changes*) become more significant contributors to sea level on much shorter timescales (10 – 10^3 years). A twentieth century global sea level rise of ~1.7–1.8 mm yr⁻¹ (Church et al., 2004; Holgate and Woodworth, 2004) appears to be related to recent climatic warming, which has been attributed to anthropogenic additions of

greenhouse gases into the atmosphere (e.g., Church et al., 2001, IPCC, 2007). Around 0.4 mm yr^{-1} , or 22–24%, derives from penetration of this atmospheric heat signal into the oceans and the consequent thermal expansion (Antonov et al., 2005); the balance is due to melting of mountain glaciers and ice sheets.

The relative magnitudes of the processes influencing sea level vary from place to place, thus tending to obscure any globally coherent sea level signal. Therefore, the derivation of a eustatic sea level curve requires an ability to decouple the effects of land motions (uplift/subsidence) from processes related to changes in continental ice extent or ocean water volume. Away from convergent plate margins, the main cause of long-wavelength elevation differences during the Holocene is related to changes in ice and water loading. Geophysical models of glacial isostatic adjustment (GIA) account for time-varying gravitational interactions among ice sheets, land, and ocean (Peltier, 2001, 2002, 2004; Lambeck et al., 2002; Mitrovica and Milne, 2002). GIA models calculate the observed sea level change over time at any given location as a function of the volumetric addition of glacial meltwater and contributions from both glacial isostasy and hydro-isostasy. Input parameters include values for maximum ice sheet thickness and extent, a history of ice sheet retreat, and mantle viscosity profiles. The GIA models are “tuned” by fitting the results to radiocarbon-dated sea level records (see *Sea level indicators*) and adjusting the mantle viscosity (Peltier, 2001, 2002, 2004; Lambeck et al., 2002). GIA models predict several zones that display similar sea level patterns (Figures S8–S9). In areas formerly covered by ice that are isostatically rebounding, sea level falls continuously (Figure S8a). Areas marginal to ice sheets that had been upwarped during glaciation (the “peripheral forebulge”) subside following removal of the ice load (Figure S8b). Sea level rises continuously in this zone. Transitional zones between glacial rebound and collapse experience a more complex history of sea level fall followed by a rise (Figure S8c). On mid-ocean islands far removed from former ice sheets (the “far field”), after attaining its maximal height, sea level drops once deglaciation has ceased in the mid-Holocene due to “siphoning” of water toward subsiding forebulges (Figure S9a). Finally, far field continental coastlines show regions of sea-level fall, with rising ocean levels further offshore (due to “continental levering,” see below; Mitrovica and Milne, 2002; Figure S9b). Thus, the observed sea level trend at any given locality depends on the interplay between the effects of glacial eustasy and glacial isostasy. The composite eustatic sea level curve (Figure S10) is based on careful selection of sites where glacial isostatic effects are minimal.

Sea level rise after the last glaciation

A composite curve of post-glacial sea level (Figure S10a) has been derived from radiocarbon- and $^{230}\text{Th}/^{234}\text{U}$ -dated sea level indicators, including corals, plant material, foraminifera, and mollusks from a number of regions with minimal glacial isostatic influence. Figure S10b shows the late Quaternary–Holocene sea level curve calculated from the ICE-5G (VM2) GIA model together with Th-U-dated corals from Barbados (after Peltier and Fairbanks, 2006). Note that the coral data suggest a minimum sea level close to 26,000 years before present, significantly older than the commonly accepted date of ~20,000 BP (Table S1).

The post-glacial eustatic sea level rise, although continuous, was punctuated by several periods of more rapid transgression,

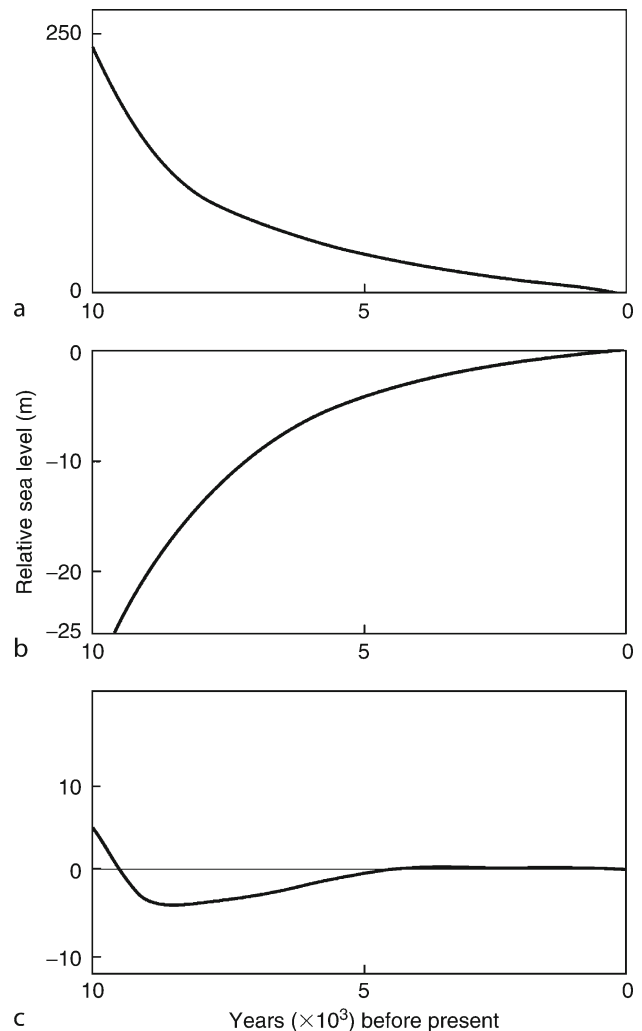


Figure S8 Schematic near field Holocene sea level curves from different zones of glacial isostatic adjustment. The vertical scale represents relative sea level change in meters (negative values are below present sea level, positive values above). These generalized curves do not represent specific localities. (a) Former ice-covered regions—continuous sea level fall (land emergence); e.g., Scandinavia; Canada. (b) Collapsed peripheral bulge—continuous sea level rise (land subsidence); e.g., the Netherlands, Belgium, southern England, East Coast, USA, south of New York. (c) Transitional zone—early Holocene sea level fall followed by sea level rise; e.g., Maine, Canadian Maritimes.

or meltwater pulses. While the exact number and timing of these events has been debated, recent studies support the proposition that rates of sea level rise have varied over this period (see Table S1). Sea level stood close to 120 m below present at the Last Glacial Maximum (LGM) (Table S1). An initial pulse of rapid SLR may have started ~19,000 years ago, at which time ocean levels rose 10–15 m within ≤ 500 year, herein referred to as “meltwater pulse 1A₀” (Yokoyama et al., 2000; Clark et al., 2004). However, this meltwater pulse does not appear in all records (e.g., Hanebuth et al., 2000; Peltier and Fairbanks, 2006), although other paleoclimate proxies suggest a sudden influx of meltwater with accompanying changes in ocean circulation at around this time (Clark et al., 2004). Other

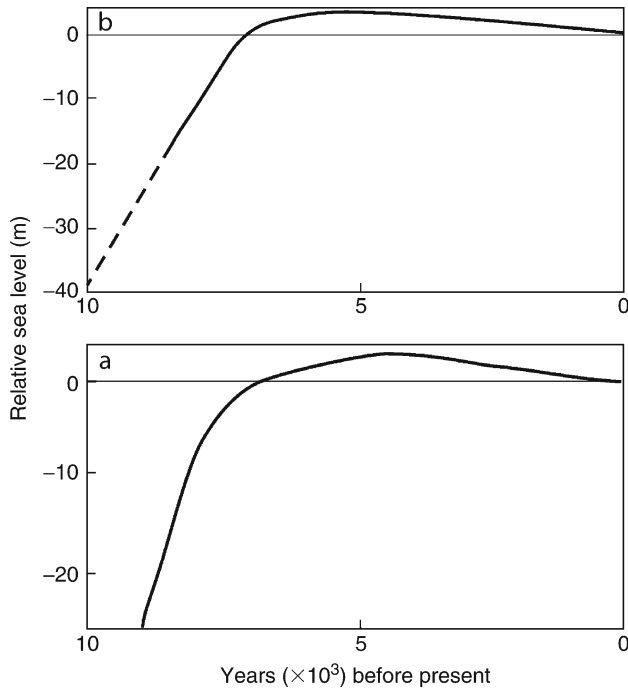


Figure S9 Schematic far field Holocene sea level curves, showing mid-Holocene land emergence. These generalized curves do not represent specific localities. (a) Equatorial ocean islands; e.g., Cocos (Keeling) Islands, Indian Ocean; Fiji Islands, Pacific Ocean. (b) Continental coastlines; e.g., eastern Australia, New Zealand, Brazil, West Africa.

data and theoretical models suggest instead that the post-glacial marine transgression may have begun as early as 26,000 years ago (Figure S10b; Peltier and Fairbanks, 2006).

Another accelerated phase of SLR occurred between 14,600 and 13,500 yBP (meltwater pulse 1A; Table S1), when sea level increased by some 16–24 m (Fairbanks, 1989; Hanebuth, 2000). Depending on its exact timing, this event has been variously associated with the first cold phase during the Bølling-Allerød interstadial or the Older Dryas (Bard et al., 1996), the Bølling warming (Kienast et al., 2003; Peltier, 2005), or the end of the Bølling (Hanebuth et al., 2000; Liu and Milliman, 2004). Kienast et al. (2003), for example, connect a sharp drop in terrigenous organic matter delivered to the South China Sea, a rapid marine incursion, and synchronous rise in ocean temperatures between $\sim 14,600$ and 14,300 yBP with the Bølling warming.

The rate of sea level rise slowed between 14,000 and 12,000 yBP during the Younger Dryas cold period. It was succeeded by a faster phase (meltwater pulse 1B) between 11,500 and 11,000 years ago. Fairbanks (1989) initially estimated that sea level jumped by ~ 28 m during meltwater pulse 1B, but subsequent studies suggest a significantly more modest increase, if at all (Bard et al., 1996; Lambeck et al., 2002).

A fourth surge of rapid sea level rise, herein referred to as “meltwater pulse 1C” has been proposed, but is less firmly established. This meltwater pulse was first identified by a hiatus in coral growth in the Caribbean at $\sim 7,600$ yBP (Blanchon and Shaw, 1995), but neither Bard et al. (1996) nor Lambeck et al. (2002) detected any noticeable increase in sea level at

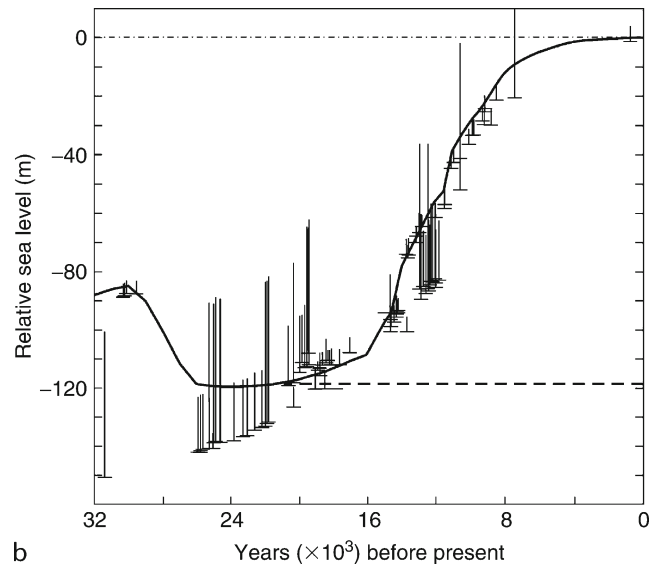
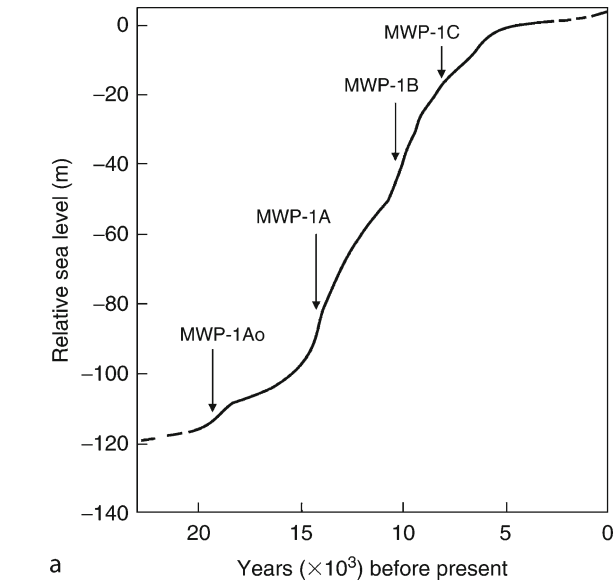


Figure S10 (a) Generalized post-glacial eustatic sea level curve (based on Fairbanks, 1989; Bard et al., 1990, 1996; Hanebuth et al., 2000; Yokoyama et al., 2000). (b) Eustatic sea level curve for the last 32 Kyr corrected for glacial isostatic adjustments using the ICE-5G (VM2) model (smooth curve). Coral data from Barbados are shown by error bars. Horizontal bars indicate depth of coral sample. Vertical bars represent the range with respect to sea level in which the coral species could live. The shortest bars (5 m) correspond to *Acropora palmata*; the intermediate bars (20 m) to *Monasteria annularis*; longer bars to either *Asteroides* or *Diploria* (modified from Peltier and Fairbanks, 2006). The latter species provide only a lower limit of relative sea level.

that time. Nevertheless, findings from diverse locations hint at a possible sudden sea level jump around 8,000 yBP. Data from Chesapeake Bay show a relatively stable period of sea level between 9,200 and 7,900 yBP, followed by a short and rapid spurt of SLR between $\sim 7,900$ and 7,600 yBP (Cronin et al., 2002). Dates on sediment cores from the Mississippi River delta constrain the episode of abrupt SLR to between $\sim 8.5 \pm 0.3$

Table S1 A review of major events associated with post-glacial sea level rise

Sea level at LGM

–121 ± 5 m (Barbados; Fairbanks, 1989)
 –118 m (Barbados; Bard et al., 1990)
 –115 ± 1 m (Sunda Shelf; Hanebuth et al., 2000)
 –125 to –121 m; –135 to –130 m (Bonaparte Gulf, Australia; corrected for glacial isostasy; Yokoyama et al., 2000)
 –123 to –119 m (Barbados; Peltier and Fairbanks, 2006)

Onset of post-glacial sea level rise

18,000 yBP (Barbados; Fairbanks, 1989)
 >19,000–18,000 yBP (Barbados; Bard et al., 1990)
 21,000–19,000 yBP (Sunda Shelf; Hanebuth et al., 2000)
 22,000–19,000 yBP (Bonaparte Gulf; Yokoyama et al., 2000)
 ≥20,000 yBP (Irish Sea; Clark et al., 2004)
 ~26,000 yBP (Barbados; Peltier and Fairbanks, 2006)

Meltwater pulse 1A₀

~19,000 yBP; rate of SLR ~33.3–50 mm yr⁻¹ (Yokoyama et al., 2000)
 19,120 ± 180 yBP; rate of SLR ~20 mm yr⁻¹ (Clark et al., 2004)

Meltwater pulse 1A

~13,000 yBP; rate of SLR, ~39 mm yr⁻¹ (Barbados; Fairbanks, 1989)
 ~13,500 yBP; ~37 mm yr⁻¹ (Barbados; Bard et al., 1990)
 ~14,000 yBP (Tahiti; Bard et al., 1996)
 14,600–14,300 yBP; rate of SLR, 53.3 mm yr⁻¹ (Sunda Shelf; Hanebuth et al., 2000; South China Sea, Kienast et al., 2003)
 14,300–14,000 yBP; rate of SLR, 65 ± 10 mm yr⁻¹ (Liu and Milliman, 2004)

Meltwater pulse 1B

~10,500 yBP; rate of SLR, 26.4 mm yr⁻¹ (Barbados; Fairbanks, 1989)
 11,000 yBP; ~25 mm yr⁻¹ (Barbados; Bard et al., 1990)
 11,300 yBP (Tahiti; Bard et al., 1996)
 11,500–11,200 yBP; rate of SLR ~40 mm yr⁻¹ (Liu and Milliman, 2004)

Meltwater pulse 1C

~7,600 yBP (Caribbean Sea; Blanchon and Shaw, 1995)
 ~8,200 yBP (Mississippi Delta; Törnqvist et al., 2004)
 ~8,000–7,000 yBP (Yellow River Delta, China; their “meltwater pulse 1D,” Liu et al., 2004)
 ~7,900–7,600 yBP; rate of SLR ~40 mm yr⁻¹ (Chesapeake Bay; Cronin et al., 2002)

Other periods of rapid sea level rise

~9,800–9,000 yBP; rate of SLR ~45 mm yr⁻¹ (their “meltwater pulse 1C”; Liu et al., 2004)

and 8.1 ± 0.1 kyBP (Törnqvist et al., 2004). Stratigraphic data from the subaqueous delta of the Yellow River, China (Liu et al., 2004), coastal Lancashire, England and Limfjord, northwestern Denmark (Tooley, 1989) also point to a more rapid marine transgression at around 8,000 yBP. Meltwater pulse 1C has been linked to the 8,200-yBP cold event (Cronin et al., 2002; Törnqvist et al., 2004), which resulted from the catastrophic drainage of proglacial Lakes Agassiz and Ojibway (Barber et al., 1999; Clarke et al., 2004).

Sources of meltwater

Among the proposed episodes of accelerated post-glacial SLR, evidence for meltwater pulse 1A is probably the strongest. This event occurred during a period of maximal ice sheet retreat. Yet, the origin of the meltwater has remained elusive. Meltwater from the breakup of the Laurentide Ice Sheet has generally been assumed to be the main contributor to the rapid SLR, mainly because of its large extent. Geophysical models suggest that sea level changes accompanying rapid melting (or growth) of an ice mass should lead to a spatially non-uniform distribution of sea level change, not only because of ice loading, but also due to gravitational attraction between the ice sheet and ocean water (Clark et al., 2002). As the ice

sheet shrinks, its gravitational attraction on ocean water will diminish and water will flow away from the edge of the ice. Therefore, different sources of meltwater (e.g., the Laurentide, Antarctic, or Barents Sea Ice Sheets) should give rise to different geographic patterns of sea level rise. The closest match between observed sea level records from various parts of the world and model predictions was found when Antarctica made a substantial contribution to meltwater pulse 1A and, in addition, a relatively high value for lower mantle viscosity was assumed (Clark et al., 2002; Bassett et al., 2005). However, from a new reconstruction of ice sheet retreat (Peltier, 2004) based on a glacial systems model that was calibrated by ¹⁴C-dated relative sea level records, geodetic measurements, and geomorphological data, Tarasov and Peltier (2005) determined instead that this meltwater pulse derived largely from North American sources. Furthermore, varved sediments containing diatomaceous ooze from fiords in East Antarctica record the onset of ice sheet recession there at 11,500–10,500 yBP, long after meltwater pulse 1A (Leventer et al., 2006). Thus, Antarctica was not a likely contributor to this meltwater surge. In addition, comparison of relative sea level data from Barbados and the Sunda Shelf, off Indonesia, reveals differences in magnitude of the meltwater pulse 1A at these two far field locations that are much too small to attribute to a specific geographical source (Peltier, 2005).

The signals for meltwater pulse 1B and meltwater pulse 1C are less distinct than that of meltwater pulse 1A. Meltwater from glacial Lake Agassiz has long been thought to have triggered thermohaline circulation changes that led to the Younger Dryas cold period (12,800–11,600 yBP), just prior to meltwater pulse 1B. However, new dates on moraine deposits show that regional deglaciation occurred nearly 1,000 radiocarbon years later than the Younger Dryas (Lowell et al., 2005), and hence Lake Agassiz was not the likely source of meltwater pulse 1B. Instead, glacial models show a period of increased meltwater discharge between 12,900 and 12,800 yBP, originating from outflow into the Arctic Ocean, the Fram Strait, and ultimately the eastern North Atlantic (Tarasov and Peltier, 2005). They suggest that this event may have triggered the Younger Dryas cold reversal, although it has not left a discernable sea level record. On the other hand, the timing of deglaciation in eastern Antarctica roughly coincides with the onset of meltwater pulse 1B (Leventer et al., 2006).

As noted above, meltwater pulse 1C can be identified in a number of widely separated geologic records. This meltwater pulse has been attributed to the catastrophic drainage of proglacial Lakes Agassiz and Ojibway around 8,400 year ago (Barber et al., 1999; Clarke, et al., 2004). The volume released by the sudden outburst flood was ~10⁵ km³ within a few years, or even less. Although this enormous influx of freshwater to the world's oceans probably triggered the 8.2 kyr cold event (see Alley and Ágústsdóttir, 2005; *the 8,200-yBP event*, this volume), the effects on global sea level appear to have been relatively modest. The resulting increase in sea level (assuming an even distribution of this volume over the world's oceans) was only on the order of 1 m or less (Barber et al., 1999; Clarke et al., 2004; Törnqvist et al., 2004). Nevertheless, this minor change in sea level left an imprint in the stratigraphic record.

Middle to late Holocene sea level

By the mid-Holocene, ~6,000–5,000 yBP, glacial melting had essentially ceased. However, glacial isostatic and hydro-isostatic adjustments persisted, although at decreasing amplitudes over

time. Therefore, sea level continued to lower in formerly glaciated regions and rise in areas of the collapsing forebulge. At many equatorial far field ocean island sites, sea level stood several meters higher than present during the mid-Holocene, ~6,000–4,000 yBP, and has been falling slowly ever since (e.g., Dickinson, 2001). This phenomenon has been explained to be a consequence of lithospheric responses due to changes in ice and water loading (Mitrovica and Peltier, 1991; Mitrovica and Milne, 2002). Water is “siphoned” away from the central equatorial ocean basins into nearshore depressions left by the collapse of peripheral forebulges. In addition, the oceanward tilting of far field continental coastlines (“continental levering”) because of hydro-isostasy also leads to migration of ocean water away from central equatorial ocean basins toward the continents (Figure S11). Mid-Holocene sea level high-stands have also been interpreted as eustatic in origin, likely related to minor climate fluctuations. Support for this view comes from well-dated sessile intertidal tubeworms from Western Australia, which show several episodes of higher than present sea level, ranging between 6,000 and 2,000 yBP (Baker et al., 2005). These events are also detected in Antarctic ice cores and several paleosea level proxies elsewhere.

The sea level record of the last 4,000–3,000 years is less-well constrained, in spite of its importance as a baseline for understanding contemporary sea level trends. In part, this arises from a paucity in accurately-dated high resolution sea level proxies, as well as difficulty in extracting a global climatic signal from low-amplitude oscillations. Minor sea level fluctuations of 1–2 m have been reported in a number of records (e.g., Finkl, 1995; Scott et al., 1995a,b; Varekamp and Thomas, 1998). These

probably record local to regional climate-related processes, such as variations in river discharge, storm deposition, or coastal sedimentation, rather than true eustatic changes in sea level.

Recent sea level rise

Twentieth century mean global sea level, determined from tide gauges in coastal harbors, has been increasing by 1.7–1.8 mm yr⁻¹ (Figure S12; Church et al., 2004; Holgate and Woodworth, 2004; Church and White, 2006), apparently related to the recent climatic warming trend (Church et al., 2001, IPCC, 2007). An even higher sea level trend of ~2.8 mm yr⁻¹ has been obtained from the TOPEX/POSEIDON satellite altimeter, since 1993 – a period strongly influenced by major El Niño-Southern Oscillation (ENSO) events, when sea surface temperatures and hence thermal expansion were higher than normal over large portions of the oceans. Nevertheless, analysis of tide-gauge data over a longer period, from 1870 to 2004, shows a twentieth century acceleration in global sea level of 0.013 ± 0.006 mm yr⁻² (Church and White, 2006).

The twentieth century sea level trends are substantially higher than those of the last few thousand years, derived from geological data (Shennan and Woodworth, 1992; Gornitz, 1995; Varekamp and Thomas, 1998; Donnelly et al., 2004). The exact timing for the onset of the current accelerated phase is uncertain because of limited instrumental data prior to the 1850s and lack of high resolution proxy sea level data for the last few thousand years. Although Varekamp and Thomas (1998) claim that the acceleration began at least 200 years ago, other studies point to a mid-late nineteenth century to early twentieth century onset (e.g., Donnelly et al., 2004; Gehrels et al., 2005; Church and White, 2006).

Summary and conclusions

The melting of the ice sheets at the end of the last glaciation, beginning at least 20,000 and possibly as early as 26,000 years ago, produced a rapid rise in sea level of some 120 m, spanning a period of 13,000 years. The post-glacial sea level rise was temporally non-uniform and several periods of more rapid rise may have occurred: ~19,000 yBP (meltwater pulse 1A₀); 14,600–13,500 yBP (meltwater pulse 1A); 11,500–11,000 yBP (meltwater pulse 1B); and 8,200–7,600 yBP (meltwater pulse 1C). However, evidence for some episodes (e.g., meltwater

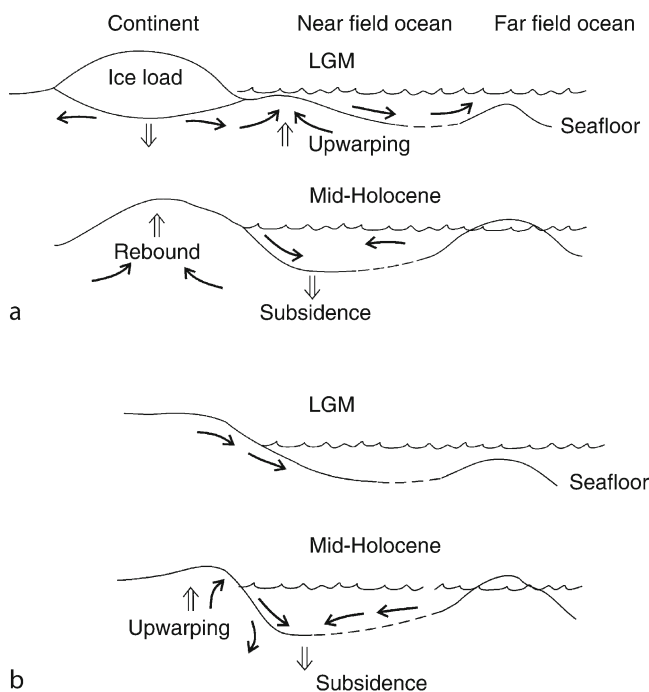


Figure S11 Schematic diagram illustrating processes contributing to mid-Holocene sea level maximum, and subsequent fall, at far field sites (not drawn to scale). (a) Ocean “siphoning” due to flow of water from far field oceans toward collapsed forebulge. (b) “Continental levering” due to ocean loading by meltwater.

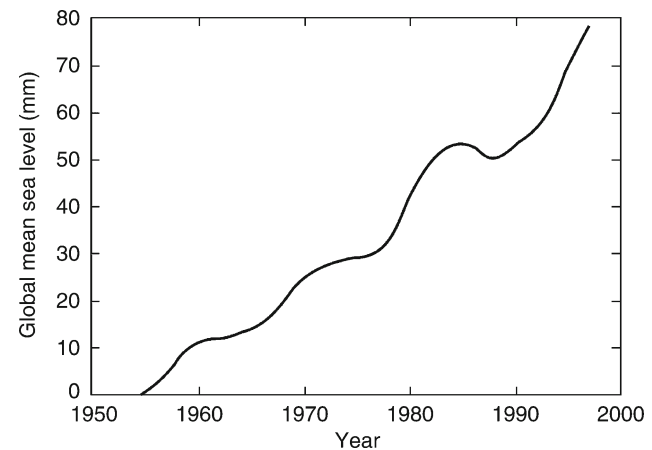


Figure S12 Recent global sea level rise, 1948–2002, from tide gauge data corrected for the effects of glacial isostatic adjustments (after Holgate and Woodworth, 2004).

pulse 1A) is stronger than for others (e.g., meltwater pulses 1A₀, 1C) and further research is needed to confirm dates and magnitudes. During the last 6,000–5,000 years, eustatic sea level changes have been relatively minor after melting of major ice sheets essentially ceased; however, crustal adjustments to glacial and hydro-isostasy have continued, although at diminishing rates, leading to variations in long-term sea level change at different localities. The mid to late Holocene emergence (i.e., apparent sea level fall) of many tropical ocean islands and shorelines has generally been attributed to ocean “siphoning” and continental “levering.” Evidence for low-amplitude Holocene sea level oscillations has been reported from a number of localities, but it remains to be determined whether these represent true eustatic (i.e., global) events or regional to local variability. A recent acceleration in the rate of sea level rise (~1–2 mm yr⁻¹) began within the last 150–100 years and appears to be related to recent global warming (Church et al., 2001, IPCC, 2007).

Vivien Gornitz

Bibliography

- Alley, R.B., and Ágústsdóttir, A.M., 2005. The 8k event: Cause and consequences of a major Holocene abrupt climate change. *Quaternary Sci. Rev.*, **24**, 1123–1149.
- Antonov, J.I., Levitus, S., and Boyer, T.P., 2005. Thermohaline sea level rise, 1955–2003. *Geophys. Res. Lett.*, **32**, L12602, doi:10.1029/2005GL023112.
- Baker, R.G.V., Haworth, R.J., and Flood, P.G., 2005. An oscillating Holocene sea-level? Revisiting Rottneest Island, Western Australia, and the Fairbridge eustatic hypothesis. *J. Coast. Res.*, Special Issue 42, 3–14.
- Barber, D.C., Dyke, A., Hillaire-Marcel, C., Jennings, A.E., Andrews, J.T., Kerwin, M.W., Bilodeau, G., McNeely, R., Southon, J., Morehead, M. D., and Gagnon, J.-M., 1999. Forcing of the cold event of 8,200 years ago by catastrophic drainage of Laurentide lakes. *Nature*, **400**, 344–348.
- Bard, E., Hamelin, B., and Fairbanks, R.G., 1990. U-Th ages obtained by mass spectrometry in corals from Barbados: sea level during the past 130,000 years. *Nature*, **346**, 456–458.
- Bard, E., Hamelin, B., Arnold, M., Montaggioni, L., Cabioch, G., Faure, G., and Rougerie, F., 1996. Deglacial sea-level record from Tahiti corals and the timing of global meltwater discharge. *Nature*, **382**, 241–244.
- Bassett, S.E., Bassett Milne, G.A., Mitrovica, J.X., and Clark, P.U., 2005. Ice sheet and solid Earth influences on far-field sea-level histories. *Science*, **309**, 925–928.
- Blanchon, P., and Shaw, J., 1995. Reef drowning during the last deglaciation: Evidence for catastrophic sea-level rise and ice-sheet collapse. *Geology*, **23**, 4–8.
- Church, J.A., and White, N.J., 2006. A 20th century acceleration in global sea-level rise. *Geophys. Res. Lett.*, **33**, L01602, doi:10.1029/2005GL024826.
- Church, J.A., White, N.J., Coleman, R., Lambeck, K., and Mitrovica, J.X., 2004. Estimates of the regional distribution of sea level rise over the 1950–2000 period. *J. Clim.*, **17**, 2609–2625.
- Church, J.A., Gregory, J.M., Huybrechts, P. et al., 2001. Changes in sea level. In Houghton, J.T., Ding, Y., Griggs, D.J., et al., (eds) *Climate Change 2001: The scientific basis*. Cambridge, UK: Cambridge University Press, pp. 639–693.
- Clark, P.U., Mitrovica, J.X., Milne, G.A., and Tamisiea, M.E., 2002. Sea-level fingerprinting as a direct test for the source of global meltwater pulse 1A. *Science*, **295**, 2438–2441.
- Clark, P.U., McCabe, A.M., Mix, A.C., and Weaver, A.J., 2004. Rapid rise of sea level 19,000 years ago and its global implications. *Science*, **304**, 1141–1144.
- Clarke, G.K.C., Leverington, D.W., Teller, J.T., and Dyke, A.S., 2004. Paleohydraulics of the last outburst flood from glacial Lake Agassiz and the 8,200 BP cold event. *Quaternary Sci. Rev.*, **23**, 389–407.
- Cronin, T.M., Vogt, P.R., and Willard, D.A., 2002. Rapid sea-level rise at 8.0–7.5 ka and Antarctic ice sheet thinning. *EOS, Transactions of the American Geophysical Union*, **83** (47), Fall Meeting Supplement, Abstract # OS71D-0324.
- Dickinson, W.R., 2001. Paleoshoreline record of relative Holocene sea levels on Pacific islands. *Earth Sci. Rev.*, **55**, 191–234.
- Donnelly, J.P., Cleary, P., Newby, P., and Ettinger, R., 2004. Coupling instrumental and geological records of sea-level change: Evidence from southern New England of an increase in the rate sea-level rise in the late 19th century. *Geophys. Res. Lett.*, **31**, L05203, doi:10.1029/2003GL018933.
- Fairbanks, R.G., 1989. 17,000-year glacio-eustatic sea level record: Influence of glacial melting rates on the Younger Dryas event and deep-ocean circulation. *Nature*, **342**, 637–642.
- Fairbridge, R.W., 1961. Eustatic changes in sea-level. *Phys. Chem. Earth*, **4**, 99–185.
- Fairbridge, R.W., 1976. Shellfish-eating pre-ceramic Indians in coastal Brazil. *Science*, **191**, 353–359.
- Finkl, C.W. Jr. (ed.), 1995. Holocene Cycles: Climate, Sea Levels, and Sedimentation. *J. Coast. Res.*, Special Issue No. 17, 402pp.
- Gehrels, W.R., Kirby, J.R., Prokoph, A., Newham, R.M., Achterberg, E.P., Evans, H., Black, S., and Scott, D.B., 2005. Onset of recent rapid sea-level rise in the western Atlantic Ocean. *Quaternary Sci. Rev.*, **24**, 2083–2100.
- Gornitz, V., 1995. A comparison of differences between recent and late Holocene sea-level trends from eastern North America and other selected regions. *J. Coast. Res.*, Special Issue No. 17, 287–297.
- Hanebuth, T., Statterger, K., and Grootes, P.M., 2000. Rapid flooding of the Sunda Shelf: A late-glacial sea-level record. *Science*, **288**, 1033–1035.
- Holgate, S.J., and Woodworth, P.L., 2004. Evidence for enhanced coastal sea level rise during the 1990s. *Geophys. Res. Lett.*, **31**, L07305, doi: 10.1029/2004GL019626.
- IPCC, 2007. Climate Change 2007. The Physical Science Basis. Contribution of Working Group I to the Fourth Assessment Report of the Intergovernmental Panel on Climate Change (Soloman, S.D., Qin, D., Manning, M., Chen, Z., Marquis, M., Averyt, K.B., Tignor, M. and H.L. Miller (eds). Cambridge University Press, Cambridge U.K. and New York, NY, USA, 996pp.
- Kienast, M., Hanebuth, T.J.J., Pelejero, C., and Steinke, S., 2003. Synchronicity of meltwater pulse 1a and the Bølling warming: Evidence from the South China Sea. *Geology*, **31**, 67–70.
- Lambeck, K., Yokoyama, Y., and Purcell, T., 2002. Into and out of the Last Glacial Maximum: Sea-level change during Oxygen Isotope Stages 3 and 2. *Quaternary Sci. Rev.*, **21**, 343–360.
- Leventer, A., Domack, E., Dunbar, R., Pike, J., Stickley, C., Maddison, E., Brachfeld, S., Manley, P., and McClennan, C., 2006. Marine sediment record from the East Antarctic margin reveals dynamics of ice sheet recession. *GSA Today*, **16**(12), 4–10.
- Liu, J.P., and Milliman, J.D., 2004. Reconsidering melt-water pulses 1A and 1B: Global impacts of rapid sea-level rise. *J. Ocean Univ. China*, **3**(2), 183–190.
- Liu, J.P., Milliman, J.D., Gao, S., and Cheng, P., 2004. Holocene development of the Yellow River's subaqueous delta, North Yellow Sea. *Mar. Geol.*, **209**, 45–67.
- Lowell, T.V., Fisher, T.G., Comer, G.C., Hajdas, I., Waterson, N., Glover, K., Loope, H.M., Schaefer, J.M., Rinterknecht, V., Broecker, W., Denton, G., and Teller, J.T., 2005. Testing the Lake Agassiz meltwater trigger for the Younger Dryas. *EOS, Transactions of the American Geophysical Union*, **86**, 365, 372.
- Mitrovica, J.X., and Milne, G.A., 2002. On the origin of late Holocene sea-level highstands within equatorial ocean basins. *Quaternary Sci. Rev.*, **21**, 2179–2190.
- Mitrovica, J.X., and Peltier, W.R., 1991. On postglacial sea level geoid subsidence over the equatorial oceans. *J. Geophys. Res.*, **96**, 20053–20071.
- Peltier, W.R., 2001. Global isostatic adjustment and modern instrumental records of relative sea level history. In Douglas, B.C., Kearney, M.S., and Leatherman, S.P. (eds.), *Sea Level Rise-History and Consequences*. San Diego, CA: Academic Press, pp. 65–95.
- Peltier, W.R., 2002. On eustatic sea level history: Last Glacial Maximum to Holocene. *Quaternary Sci. Rev.*, **21**, 377–396.
- Peltier, W.R., 2004. Global glacial isostasy and the surface of the ice-age Earth: The ICE-5G (VM2) model and GRACE. *Annu. Rev. Earth Planet. Sci.*, **32**, 111–149.
- Peltier, W.R., 2005. On the hemispheric origins of meltwater pulse 1a. *Quaternary Sci. Rev.*, **24**, 1655–1671.
- Peltier, W.R., and Fairbanks, R.G., 2006. Global glacial ice volume and Last Glacial Maximum duration from an extended Barbados sea level record. *Quaternary Sci. Rev.*, **25**, 3322–3337.

- Pirazzoli, P.A., 1991. *World Atlas of Holocene Sea-Level Changes*. Amsterdam: Elsevier, 300pp.
- Scott, D.B., Brown, K., Collins, E.S., and Medioli, F.S., 1995a. A new sea-level curve from Nova Scotia: Evidence for a rapid acceleration of sea-level rise in the late mid-Holocene. *Can. J. Earth Sci.*, **32**, 2071–2080.
- Scott, D.B., Gayes, P.T., and Collins, E.S., 1995b. Mid-Holocene precedent for a future rise in sea level along the Atlantic coast of North America. *J. Coast. Res.*, **11**, 615–622.
- Shennan, I., and Woodworth, P.L., 1992. A comparison of late Holocene and twentieth-century sea level trends from the UK and North Sea region. *Geophys. J. Int.*, **106**, 96–105.
- Shepard, F.P., and Suess, H.E., 1956. Rate of postglacial rise of sea level. *Science*, **123**, 1082–1083.
- Tarasov, L., and Peltier, W.R., 2005. Arctic freshwater forcing of the Younger Dryas cold reversal. *Nature*, **435**, 662–665.
- Tooley, M.J., 1989. Floodwaters mark sudden rise. *Nature*, **342**, 20–21.
- Törnqvist, T.E., Bick, S.J., Gonzalez, J.L., van der Borg, K., and de Jong, A.F.M., 2004. Tracking the sea-level signature of the 8.2 ka cooling event: New constraints from the Mississippi Delta. *Geophys. Res. Lett.*, **31**, L23309, doi: 10.1029/2004GL021429.
- Varekamp, J.C., and Thomas, E., 1998. Climate change and the rise and fall of sea level over the millennium. *EOS, Transactions of the American Geophysical Union*, **79**, p. 69, 74–75.
- Yokoyama, Y., Lambeck, K., De Deckker, P., Johnston, P., and Fifield, L.K., 2000. Timing of the Last Glacial Maximum from observed sea-level minima. *Nature*, **406**, 713–716.

Cross-references

Bølling-Allerød Interstadial
 Glacial Eustasy
 Glacial Isostasy
 Glacial Megalakes
 Hypsithermal
 Last Glacial Maximum
 Last Glacial Termination
 Radiocarbon Dating
 Sea Level Change, Quaternary
 Sea Level Indicators
 Sea Level Rise, in *Encyclopedia of World Climatology*
 The 8,200-Year bp Event
 Uranium-Series Dating
 Varved Sediments
 Younger Dryas

SEA LEVEL CHANGE, QUATERNARY

Relative to the land-masses, the position of sea level has fluctuated throughout the geologic past, owing to changes in both the quantity of ocean water and the geometry of the ocean basins. The total volume in the hydrosphere (water plus ice) appears to have been constant but the fractions held in land reservoirs – glaciers, lakes, groundwater and, in particular, continental ice sheets – fluctuated significantly. For example, if the present Antarctic Ice Sheet were to melt, sea level would rise by about 55 m; at the height of the last ice age, sea level was about 120–130 m below its present position.

The proportions of land and sea are basically determined by the fact that continents, being composed of rock lighter than oceanic crust, stand about 4.5 km above the ocean floor. However, owing largely to slow variations in the rates of sea floor spreading and plate tectonics, the average depth of the ocean basins has varied throughout geological time and shorelines have periodically advanced and retreated across the continental shelves. [Figure S13](#) illustrates examples of observed sea level change on time scales from about 10⁴ to 10⁸ years. On the

longer timescale, sea level changed globally with amplitudes up to several hundred meters, largely owing to plate-tectonic changes in ocean basin geometry ([Figure S13a](#)). During the Quaternary Era, periodic exchanges of mass between the ice sheets and oceans caused sea level changes of tens to over a hundred meters in amplitude, on time scales of tens to hundreds of thousands of years ([Figure S13b](#)).

Global changes of sea level caused by changes in the volumes of seawater or the ocean basins are referred to as eustatic. Superimposed on these global signals are more regional and local changes, where the relative positions of land and sea are affected by uplift or subsidence of the coastal zone. Observations vary substantially from site to site, even over relatively short distances such as in northwestern Europe, where sea level at Ångerman has fallen nearly 200 m in the past 9,000 years, while at Andøya the level 9,000 years ago was near its present position and in southern England was about 35 m below the present shoreline ([Figure S14](#)).

Several interlinked factors contribute to changes in sea level. When ice sheets melt, the resulting sea level change is spatially variable because the Earth's surface deforms under the changing ice and water load, and the gravitational potential of the Earth-ocean-ice system also changes. The combined deformation-gravitational effects are referred to as glacio-hydro-isostatic contributions to sea level, and it is these effects that cause the spatial variability illustrated in [Figure S14](#). Isostatic warping and subsidence also occur in sedimentary basins, in response to the accumulation of sediments many kilometers deep over millions of years. Furthermore, *tectonic* movements drive mountain uplift, enhancing landscape denudation and leading to rapid accumulation in sedimentary basins; they also contribute to changes of relative sea level through coastal uplift or subsidence.

Knowledge of the complex history of Quaternary changes of sea level is relevant in diverse fields, including the understanding of climate changes, and the determination of deep-earth properties such as the viscosity of the Earth's mantle. Once comprehensive sea level models are developed, it becomes possible to test hypotheses about Quaternary migrations of flora and fauna across shallow seas that are now covered by ocean. Moreover, to understand future sea level rise under atmospheric greenhouse conditions, the background “natural” signal must be known. The success of sea level studies depends very much on the ability to separate the different contributions – eustatic, isostatic and tectonic – in the observational record.

Observational evidence

Direct evidence for Quaternary sea level changes occurs mostly in the form of sediments and biohermal reefs that were formed in coastal and nearshore situations. Upper Quaternary sea level changes are usually pieced together from raised or submerged shoreline features, including shallow-water coral reefs ([Figure S15](#)). Further back in time, relative sea level changes can be deduced from sedimentary basins, in which eustatic variations are registered in cyclic sediments (cyclothem) that show alternating transgressions and regressions of the sea ([Figure S16](#)). Using evidence from seismic, drill-hole and outcrop data, the locus of coastal-zone sedimentation can be traced throughout a given basin sequence, allowing the course of sea level changes relative to the basin to be identified (Hallam, 1992).

A relative sea level curve for a given area can be established from age-height data for a series of ancient shorelines, or other indicator deposits such as shallow marine sediments for which

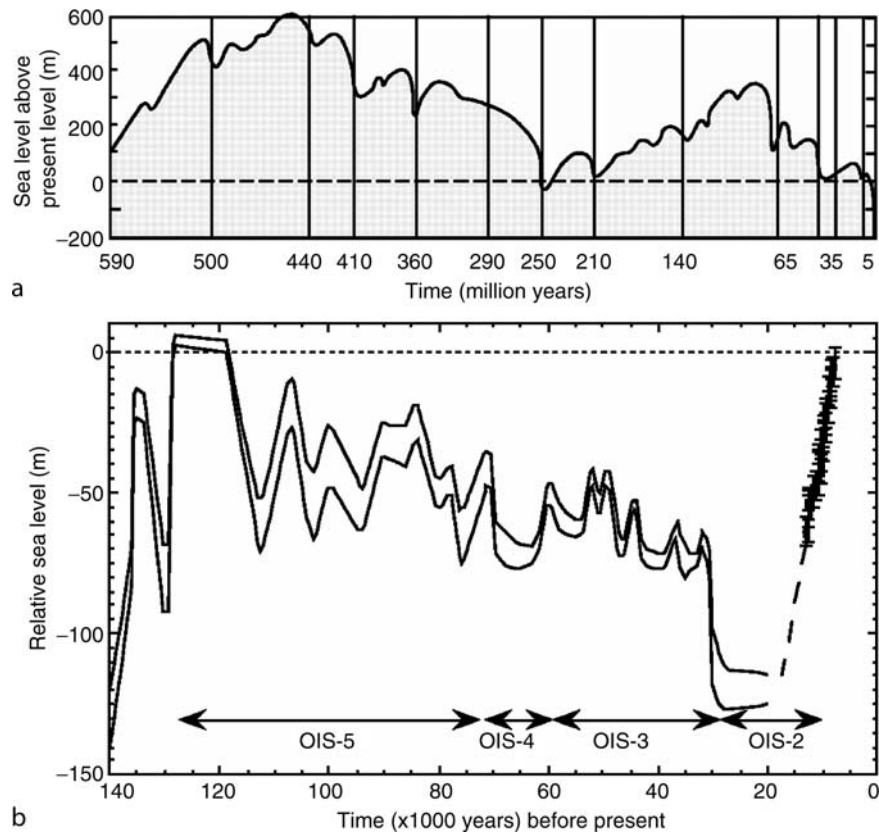


Figure S13 Sea level variation at two time scales. (a) $\sim 10^8$ years, inferred from seismic sequence stratigraphy (Haq et al., 1987; Hallam, 1992). The higher frequency changes reflect both global and local effects; the large, slow changes reflect continental breakup and changes of ocean ridge systems. (b) $\sim 10^5$ years of relative sea level at Huon Peninsula (HP), Papua New Guinea, driven by changes in northern continental ice sheets. Bars show marine oxygen isotope stages (OIS) discussed in text (from Lambeck and Chappell, 2001).

the depth of deposition relative to sea level is determinable. Terrestrial deposits within a sequence, such as peats and floodplain sediments, may usefully indicate levels not reached by the sea. Various methods are used to establish the ages. For deposits less than $\sim 40,000$ years old, radiocarbon dating is used widely, although uranium-series dating is preferable in the case of coral formations and has a time range that extends to ~ 0.5 Myr. Thermoluminescence (TL) and optically-stimulated luminescence (OSL) methods are increasingly used for dating Upper Quaternary shoreline deposits, and amino acid racemization has proven to be useful despite its low precision. Sea level indicator deposits also are correlated to marine oxygen isotope records, described later, that have a chronology based on slow variations in the Earth's orbit, which affect the seasonal receipts of solar radiation and acted as an ice-age pacemaker. Orbital chronology rests on astronomical observations and has been extrapolated several million years into the past. Wherever possible, the dating of older Quaternary and pre-Quaternary deposits is tied to geomagnetic reversal chronology, which in turn is secured by potassium-argon dating methods.

Separation of eustatic, isostatic and tectonic components

Raw separation of uniform uplift or subsidence

A first step towards separation of the tectonic, isostatic and eustatic contributions is subtraction of any obvious vertical

crustal movements from a relative sea level curve. More often than not, this is done by assuming that the sea level for some reference deposit in the record is known and that the rate of uplift (or subsidence) was constant throughout the duration of the record. With these assumptions, the local sea level S represented by a deposit of age t that accumulated at depth d below sea level and now is height H above present sea level, is given by

$$S = H + d - Ut, \text{ with } U = (S_r - H_r + d_r)/t_r \quad (1)$$

where H_r , d_r and t_r are height, depositional depth and age of the reference deposit, and S_r is the sea level at its time of formation. For Upper Quaternary studies, the local height of the Last Interglacial shoreline is widely used to determine uplift rate U , as evidence at tectonically stable sites indicates that the Last Interglacial sea level was 5 ± 2 m above present level, 120,000–127,000 years ago (Chappell et al., 1996). However, for every study, each variable in Equation 1 has an error term arising from dating errors and uncertainties in field relationships. Moreover, in assuming a constant rate of uplift, this approach neglects reversing vertical movements that arise from the global glacio-hydro-isostatic response to advancing and retreating ice sheets. Figure S13b shows the “uplift-free” sea level curve derived by this method from the coral terraces illustrated in Figure S15.

Similar principles are used to derive sea level changes from sedimentary basin sequences, although here the vertical

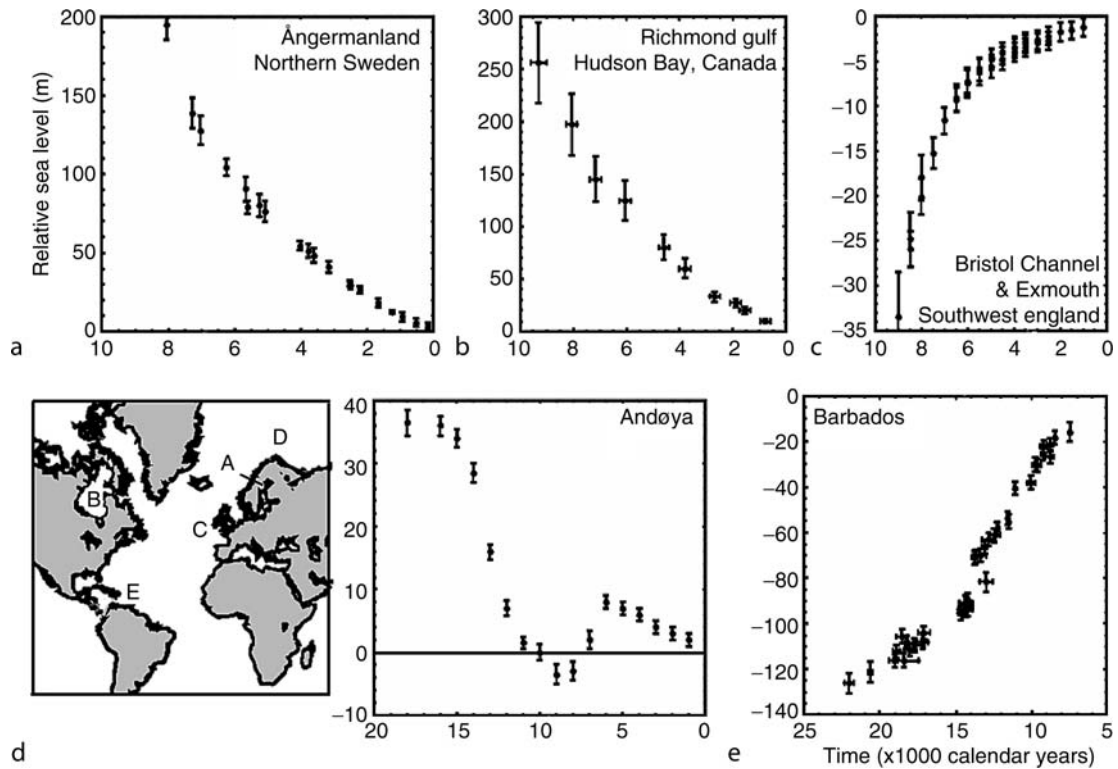


Figure S14 Observed variability of sea level change. Graphs a–c show sea level over the last 10,000 years relative to Ångerman, Gulf of Bothnia, Sweden; Richmond Gulf, Hudson Bay, Canada, and southwest England. Sites A and B were formerly covered by ice sheets and the fall of relative sea level largely reflects isostatic uplift of the land since the ice melted, whereas southwest England lay outside the ice-covered region and rising sea level in this area largely reflects the influx of ice meltwater to the oceans. The counteracting effects of isostatic uplift and ocean increase are reflected in complex sea level changes over the last 20,000 years at Andøya in Norway (d), whereas the ocean increase dominates at sites remote from the former ice sheets, such as Barbados (e) (data sources given in Lambeck and Chappell, 2001).

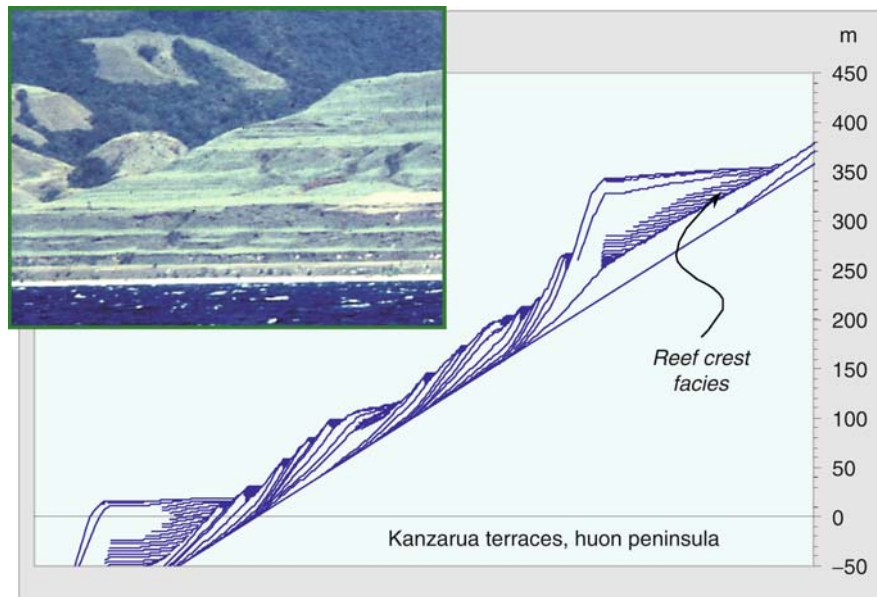


Figure S15 Typical expression of Late Quaternary sea level changes superimposed on tectonically rising terrain: coral terraces Huon Peninsula, Papua New Guinea. The top terrace at right of the inset photo is 350 m a.s.l. and formed at the beginning of the Last Interglacial, ~127,000 years ago. Each of the smaller reef structures within the downstepping stratigraphic sequence was formed during a sea level oscillation within the last glacial cycle. Subtracting the effect of uplift yields the sea level curve shown in Figure S13b.

movement is downwards. In terms of sedimentary facies, individual cyclothem sequences often are very similar from bottom to top of a thick cyclothem sequence (Figure S16), implying fairly uniform subsidence of the basin.

Glacio-hydro-isostasy

When ice sheets melt, to a first approximation the sea level rises by an amount $\Delta\zeta_e(t)$ related to the land-based ice volume V_i (using the notation of K. Lambeck: see Lambeck and Chappell, 2001),

$$\Delta\zeta_e(t) = -(\rho_i/\rho_o) \int (1/A_o(t)dV_i/dt)dt \quad (2)$$

where $A_o(t)$ is the ocean surface area (which changes as sea level rises or falls) and ρ_i , ρ_o are the average densities of ice and ocean water, respectively. $\Delta\zeta_e(t)$ is the ice-volume equivalent sea level change (or equivalent sea level change), which equals eustatic change if no other factors contribute to changes in ocean volume. The relative sea level change $\Delta\zeta_{\text{rsl}}(\varphi, t)$ at position and time t , ignoring tectonic displacements, is

$$\Delta\zeta_{\text{rsl}}(\varphi, t) = \Delta\zeta_e(t) + \Delta\zeta_i(\varphi, t) + \Delta\zeta_w(\varphi, t) \quad (3)$$

where $\Delta\zeta_i$ and $\Delta\zeta_w$ are the glacio- and hydro-isostatic contributions. Both are functions of position and time. The water depth or terrain height, expressed relative to coeval sea level, is

$$h(\varphi, t) = h(\varphi, t_0) - \Delta\zeta_{\text{rsl}}(\varphi, t) \quad (4)$$

where $h(t_0)$ is the present-day (t_0) bathymetry or topography at φ . Both isostatic terms in Equation 3 are functions of Earth rheology as well as of fluctuations in the ice sheets over time.

In formerly glaciated areas, the glacio-isostatic term $\Delta\zeta_i(\varphi, t)$ dominates during and after deglaciation, and leads to uplift at a rate that can exceed the global eustatic rise, so that sea level locally falls (the Ångerman result: Figure S14). Rebound is smaller near the ice margin and although it may dominate initially, the global sea level rise becomes important later. When all melting has ceased, the residual rebound leads to falling local sea level (the Andøya result: Figure S14). During ice sheet growth, mantle material beneath the loaded area is displaced outward and broad bulges develop around the perimeter, which subside when the ice melts, leading to local sea level that slowly rises after melting has ceased. Much further from the ice, the water load becomes the dominant cause of planetary deformation (the hydro-isostatic contribution $\Delta\zeta_w(\varphi, t)$), producing subsidence of the sea floor and adjacent margins. The effect is most pronounced at continental margins far from the ice sheets, such as the Australian coast, and once melting has ceased, sea levels continue to fall at a slow but perceptible rate. The amplitude of this postglacial “highstand” effect can vary by several meters from site to site.

Isostatic corrections and a global eustatic curve can be derived from local sea level curves, using a rheologically appropriate earth model to predict surface deformation in response to changing ice and water loads, with the ocean surface remaining a gravitational equipotential surface at all times. The sea level signal at sites far from the former ice margins approximates the equivalent sea level function to about 10–15% and the isostatic contribution is mainly from water loading, which is insensitive to the details of the ice sheets, provided that the total ice volumes are correct to within about 10–20%. Hence, through an iterative procedure, it becomes possible to estimate

changes in ice volumes V_i from observed sea level changes $\Delta\zeta_{\text{rsl}}(\text{obs})$, using Equations 2 and 5:

$$\Delta\zeta_{\text{rsl}} = \Delta\zeta_{\text{rsl}(\text{obs})} - (\Delta\zeta_i + \Delta\zeta_w) \quad (5)$$

The use of local sea level curves from widely separated places allows earth rheology parameters and models of ice distribution to be evaluated. Recent models include deformation of the basins over time, movement of grounded ice across the shelves, modification of sea level by the time-dependent gravitational attraction between the solid earth, ocean, and ice, and the effect of glacially induced changes in earth rotation on sea level.

Sea level through the Last Glacial Cycle

Sea level data for the last glacial cycle are more plentiful than for earlier periods and at Huon Peninsula, Papua New Guinea provide a near-complete relative sea level curve (Figure S13b), which has been used for reconstructing ice-equivalent sea level for the past 140,000 years (Lambeck and Chappell, 2001). Results indicate that ice melting has varied since the Last Glacial Maximum, with two periods of rapid sea level rise from ~16,000 to 12,500 and from 11,500 to 8,000 years ago, separated by the Younger Dryas cold episode when sea level seems to have risen less rapidly. By 7,000 years ago, the northern ice sheets except for Greenland had gone and ocean volume approached its present level, but Antarctic ice melting may have since contributed a few meters of equivalent sea level.

The Last Interglacial, when sea level was similar to the present, ended about 118,000 years ago with rapidly falling sea level, associated with the growth of northern continental ice. Cyclic sea level changes from 118,000 to ~60,000 years ago reflect the effect of the 20,000-year orbital precession cycle on the ice sheets, although other fluctuations also appear. These occur repeatedly about every 6,000 years from ~60,000 to 30,000 years ago, with amplitudes of 10–15 m, and each rise apparently coincides with a major episode of ice-rafted sediment deposition recorded in the North Atlantic, suggesting that the rise was caused by a large, rapid discharge of continental ice (Chappell, 2002).

Oxygen isotopes and long sea level records

Long, continuous records of oxygen isotopes in calcareous foraminifera preserved in deep-sea sediments have become standard records of Quaternary sea level and temperature changes. The oxygen isotope ratio in foraminifera, conventionally expressed as $\delta^{18}\text{O}$ (the ‰ difference of $^{18}\text{O}/^{16}\text{O}$ in a sample from an international standard), depends on the temperature and isotope ratio of the seawater in which they lived. Furthermore, the seawater isotopic ratio is related to the size of polar ice sheets, because ^{18}O is preferentially removed from atmospheric water vapor as it makes its way poleward, causing the icecaps to be depleted in ^{18}O relative to seawater by ~25–55‰, varying with atmospheric temperature. Thus, foraminiferal isotopes $\Delta\delta^{18}\text{O}_f$ respond to ice volume changes ΔV_i according to

$$\Delta\delta^{18}\text{O}_f \approx \delta^{18}\text{O}_i \Delta V_i / V_w + C_T \Delta T + \varepsilon \quad (6)$$

where ΔV_i is relative to present day V_i , V_w is the present volume of seawater (mean $\delta^{18}\text{O}$ of modern seawater = 0‰_{SMOW}), C_T

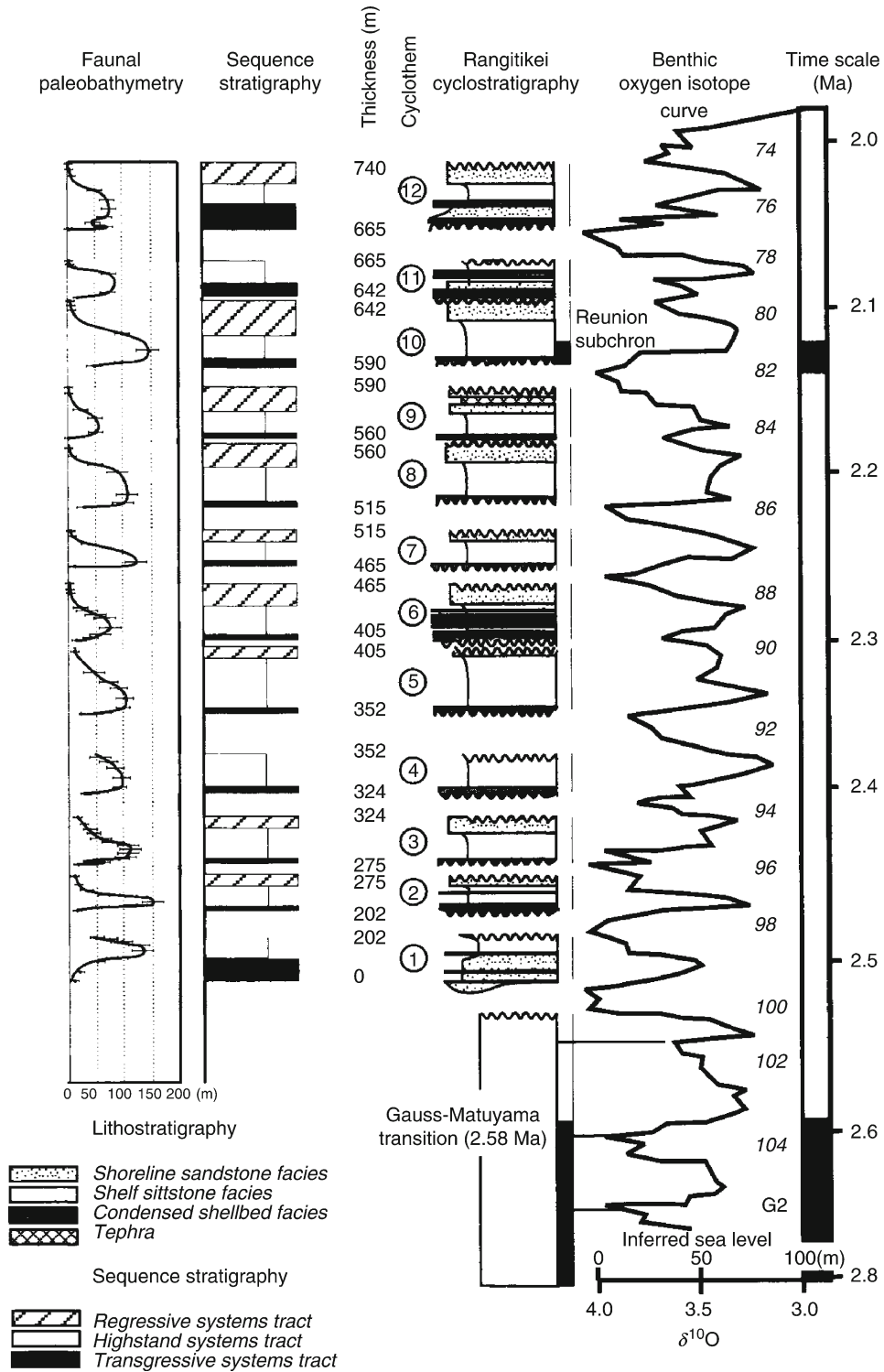


Figure S16 Late Pliocene sea level changes inferred from shallow marine cyclothem in New Zealand. Centre columns show 12 sedimentary cycles; left column shows cyclic variations of water depth at the site of sedimentation, inferred from fossil marine invertebrates. Correlations to global marine oxygen isotope cycles (Shackleton et al., 1995) are shown to the right, tied to magnetic reversal chronology (from Pillans et al., 1998).

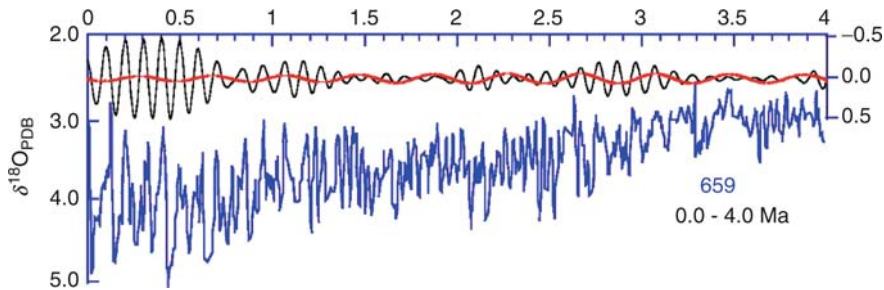


Figure S17 Marine oxygen isotope variations for last 4 Myr indicate sea level changes associated with glacial cycles. The first cycle at the left represents the general curve for the last glacial cycle, shown in detail in Figure S13b. The increase of amplitude in $\delta^{18}\text{O}$ cycles around 2.6 Myr represents the onset of large fluctuations of ice sheets and sea level, which become even more pronounced around 1 Myr, when they adopt a characteristic period of $\sim 100,000$ years. The upper curve shows the changing amplitude of the 100,000 year cycle (after Zachos et al., 2001).

is the coefficient of temperature-dependent isotope fractionation for calcite ($-0.23\text{‰ } ^\circ\text{C}^{-1}$), ΔT is temperature change, and ε represents any local change of seawater $\delta^{18}\text{O}$ not related to ΔV_i . (Equation 6 is approximate because the mean isotopic composition of the ice sheets $\delta^{18}\text{O}_i$ is assumed constant, but the uncertainty here probably is smaller than the effects of ice volume and temperature). Finally, the first term on the right hand side of Equation 6 can be expressed in terms of equivalent sea level $\Delta\zeta_e$: comparison of isotopes and sea levels for the last glacial cycle indicates that $\Delta\delta^{18}\text{O}_w/\Delta\zeta_e \sim -0.009\text{‰ m}^{-1}$.

The numerical value of $\delta^{18}\text{O}_f$ becomes increasingly positive under a fall of both sea level and temperature. Thus, the isotopic affect of temperature and ice-volume changes are additive and the two factors can be decoupled if one or the other is known. After removing the temperature effect, isotopic sea levels for the last glacial cycle derived by Shackleton (1987) compare favorably with Figure S13b. Comparisons further back in time are also encouraging: for example, Figure S14 illustrates typically close correspondence between sea level and isotopic cycles in Late Pliocene times. Thus, oxygen isotopes in continuous deep-sea cores provide proxy records of equivalent sea level (ice volume) changes through and beyond the Quaternary that reveal both progressive global cooling and the onset of ice-driven sea level cycles in the Pliocene (Figure S17). As the history of ocean temperature becomes increasingly well determined, through trace-element analysis of microfossils and other techniques, the sea level contribution in long isotope records is now being isolated (see Zachos et al., 2001).

Shoreline reconstructions and geomorphologic effects

Once a global eustatic curve $\zeta_e(t)$ is established, the course of shoreline changes through time can be predicted. Provided that the present-day shallow water bathymetry is known with high resolution, water depths for any region at any time within the range of the eustatic curve follow from Equation 4, and the paleo-shorelines at time t correspond to the contours $h(\varphi, t) = 0$. Thus, it becomes possible to examine the migrations of shorelines through time for intervals for which sufficient observational data exist to constrain the isostatic variables. Predictions of shorelines since the time of the Last Glacial Maximum have been published for both global and regional reconstructions, which can provide useful insights into the interpretation of prehistoric sites. As Lambeck (1996) has shown, for example, the interpretation of post-Palaeolithic archaeology of the Aegean is intimately linked to reconstructions of shoreline changes, which were a powerful factor in trade and changing human activities in the region.

Rising sea level since the Last Glacial Maximum led to widespread changes in coastal regions. Under the influence of ice-age low sea levels, today's coastal valleys tended to become incised well below present sea level and then became traps for floodplain aggradation when sea level rose, as ice sheets retreated. The alternation of incision and aggradation doubtless was repeated in each glacial cycle throughout the Quaternary, leading to development of broad floodplains on thick sediment valley-fills, which in tectonically stable regions often extend hundreds of kilometers inland. Near-coastal limestone regions under the influence of low sea levels developed vadose karst systems below present sea level, including stream passages and speleothem formations. At coastlines, a range of landforms from drowned valleys through sand-barrier basins to estuarine and deltaic plains were the result of the post-glacial sea level rise, the particular form depending on sediment supply, tidal range and wave energy. In tropical seas, coral reefs were re-established after being reduced by subaerial erosion during glacial-age lowstands.

In tectonically stable terrain, the geomorphic expression of any given Quaternary sea level cycle tends to overprint the record of earlier cycles. In contrast, tectonic uplift results in flights of coastal terraces built at times of high relative sea level (e.g., Figure S15) that often pass inland into flights of river terraces. However, even though a terraced river-valley may grade to present sea level, not all its terraces necessarily relate to sea level highstands. Where continental shelves are broad, a river carrying sufficient fluvial sediment, when sea level was low and the coast far seawards of its present position, may have aggraded to a level higher than the recent floodplain, which thus becomes inset below a Pleistocene lowstand terrace. Given the tendency for all such features to become degraded and overprinted, the geomorphic legacy of past sea levels – while very sharp for recent events – becomes increasingly blurred with time. From this fact springs the irony that, beyond the last glacial cycle, Quaternary sea level changes have become better determined from isotope records in deep sea sediments than from ancient coastal features themselves.

John M. Chappell

Bibliography

- Chappell, J., 2002. "Sea level changes forced ice breakouts in the last glacial cycle: New results from coral terraces." *Quaternary Sci. Rev.*, **21**, 1229–1240.
- Chappell, J., Omura, A., Esat, T., McCulloch, M., Pandolfi, J., Ota, Y., and Pillans, B., 1996. Reconciliation of late Quaternary sea levels derived

- from coral terraces at Huon Peninsula with deep-sea oxygen isotope records. *Earth Planet. Sci. Lett.*, **141**, 227–236.
- Hallam, A.J., 1992. *Phanerozoic Sea-level Changes*. New York: Columbia University Press.
- Haq, B.U., Hardenbol, J., and Vail, P.R., 1987. “Chronology of fluctuating sea levels since the Triassic.” *Science*, **235**, 1156–1167.
- Lambeck, K., 1996. “Sea-level change and shore-line evolution in Aegean Greece since Upper Palaeolithic time.” *Antiquity*, **70**, 588–611.
- Lambeck, K., and Chappell, J., 2001. “Sea level change through the last glacial cycle.” *Science*, **292**, 679–686.
- Pillans, B., Chappell, J., and Naish, T., 1998. “A review of the Milankovitch beat: Template for Plio-Pleistocene sea-level changes and sequence stratigraphy.” *Sediment. Geol.*, **122**, 5–21.
- Shackleton, N.J., 1987. “Oxygen isotopes, ice volume and sea level.” *Quaternary Sci. Rev.*, **6**, 183–190.
- Shackleton, N.J., Hall, M.A., and Pate, D., 1995. “Pliocene stable isotope stratigraphy of ODP site 846,” in Proceedings of ODP, Science Results **138**. College Station, TX: Ocean Drilling Program, pp. 337–353.
- Zachos, J., Pagani, M., Sloan, L., Thomas, E., and Billups, K., 2001. “Trends, rhythms, and aberrations in Global Climate 65 Ma to Present.” *Science*, **292**, 686–693.

Cross-references

Cyclic Sedimentation (Cyclothem)
 Dating, Amino Acid Geochronology
 Dating, Luminescence Techniques
 Dating, Magnetostratigraphy
 Glacial Eustasy
 Glacial Isostasy
 Oxygen Isotopes
 Sea Level Change, Last 250 Million Years
 Sea Level Change, Post-Glacial

SEA LEVEL INDICATORS

Indicators for sea level change encompass direct instrumental evidence of recent changes in sea level at local and global scales to proxy indicators for former sea level variations over the past millennia. The evidence for sea level changes since the late nineteenth century has been mostly derived from tide gauges. However, our knowledge of the sea level record prior to this has been drawn from sources as disparate as former shoreline positions to geochemical and paleoecological data reflecting past changes in local mean tide levels. Considering the variety of indicators, differing widely in timescale, spatial coverage, and accuracy, it is not surprising that they pose considerable problems for the researcher attempting to reconstruct and understand the sea level record.

Instrumental records

Instrumental records for sea level change first appeared in the late seventeenth century in Western Europe. Until the advent of satellites capable of measuring global changes in the ocean surface, instrumental indicators for sea level change – the precision and reliability of the instruments changing with improvements in technology – actually recorded changes in tidal levels over time; variations in mean sea level for an area could be deduced from these data. Because such records are *site-specific*, there has been considerable discussion concerning how such an inherently local nature for sea level change relates to global and even regional sea level trends. In some cases, depending on how the instrument was deployed and monitored, the tidal records derived – and the changes in mean sea level

inferred from them – may have very little to do with the regional sea level history of an area. Historically, many of the instruments for delineating changes in tidal levels were located in ports to aid navigation. Later changes in harbor tidal hydrography from port construction and modification, and even the sinking of docks upon which the instruments were placed into soft, unconsolidated sediments, often introduced considerable errors. Methods (largely statistical) exist for highlighting potential errors in instrument records. These can be augmented by archival evidence for port construction and modification. In particular, comparable instrumental records for sites elsewhere in the region can be very useful in identifying discrepancies. However, such methods may not always be able to pinpoint smaller, but still cumulatively significant, errors due to human activities. Generally, the more recent the instrumental records, the more they are likely to be reliable and free of error – older records should always be approached with caution.

The first instrumental records were derived from a very simple instrument, the tide staff, or graduated staff or rod anchored along a shoreline or dock. Unless monitored throughout the course of the tidal cycle, most early tide staff records were often records of changes in the mean high water mark, the evidence being the highest wetted mark left on the staff. Depending on whether the staff was protected from wave activity, reading the mean high water level accurately as waves rose and fell could be challenging, and making judgment of actual water levels was difficult. Nonetheless, tide staff records comprise the oldest instrumental records of sea level change available; and in the case of the Amsterdam record (Mörner, 1973), extend back to the late seventeenth century, one of the coldest periods of the Little Ice Age.

Since the late nineteenth century, modern tide gauges (mareographs) have provided detailed evidence on tidal variations as indicators of sea level variation. Although problems reflecting such effects as port construction and harbor dredging on tidal hydrography (and the sea level signal) plague many early tide gauge records, modern tide gauges – protected from the “noise” of waves on the tidal signal by stilling wells – yield high precision measurements of daily, monthly and annual tidal variations at a locality. Increasingly automated and capable of downloading tidal data by telemetry, tide gauges are the source for much of what is known about twentieth century sea level rise. They have also revealed considerable information on seasonal (intra-annual), yearly (inter-annual) and longer-term (decadal) fluctuations in regional and global sea level trends (Douglas, 2001). Little progress would have been made in the last two decades toward understanding the linkages between global climatic fluctuations and sea level changes without tide gauge data, though the worldwide rate of sea level rise documented by these records has proved remarkably amenable to interpretation (see Douglas, 1991).

Perhaps the greatest limitations confronting the use of tide gauge records as sea level indicators are the often-short lengths of record available for many areas (especially for developing countries) and the concentration of some of the longest and most continuous archives for the Northern Hemisphere (especially, Northern Europe and Eastern North America). With respect to length of record, 60 years is now recognized as the minimum timescale for which reliable determination of average rates of sea level rise may be made from tide gauge records (Douglas, 2001). The latter problem concerns the lingering effects of glacio-isostasy associated with the Laurentide (North America) and Fenno-Scandinavian (Northern Europe) Ice sheets,

which complicate the delineation of purely eustatic trends in tidal records. Rheological models (e.g., Peltier, 2001) allow for some correction (“detrending”; Douglas, 1991) of northern hemisphere tide gauge records for the phenomena of postglacial rebound and forebulge collapse (for the Atlantic Coast of North America, the hingeline between the two is approximately in the region of the Hudson River estuary). Ultimately, satellite altimetry (e.g., Topex/Poseidon), showing the ocean surface model, should address the spatial limitations of tide gauge data. A recent attempt has been made to reconcile tide gauge data with the ocean surface changes observed from the Topex/Poseidon satellite (Cabanès et al., 2001).

Shoreline features

Ancient shorelines above mean sea level have long been viewed as one of the more persuasive indicators of sea level change. In the last several decades, technological advances like high-resolution seismic stratigraphy (in particular, bottom profilers) have extended the search for evidence of former shorelines to the inner continental shelves of many areas. Nonetheless, though the potential suite of ancient shorelines to be investigated is no longer limited to subaerial features, controversies surrounding whether some fossil shorelines have anything really to do with global sea level trends have not abated. No one argues that former shorelines do not represent a change in mean tide level locally for a sustained period (in some cases, even this argument has been hard to make); rather, the argument centers on whether the change in the elevation of tidal frame was driven by global (i.e., climatic) fluctuations, or was the result of tectonics or possibly even coastal storms. The answer generally lies in the type of feature observed.

Ancient reefs

In the warm tropical waters where ambient temperatures average about 26 °C, coral polyps are able to construct reefs, which over time can build large reef complexes exemplified by the Great Barrier Reef (about 18 million years old). Some of the strongest evidence for global sea level (and climatic with respect to Milankovitch cycles) changes during the Quaternary comes from fossil reefs in Barbados (Mesoletta et al., 1969) and New Guinea (Bloom et al., 1974; Chappell and Shackleton, 1986). The interpretation of fossil reefs as evidence of sea level change must confront the issue of what the relationship of the reef is to modern sea level. For Pleistocene age reefs, the impacts of tectonics are important, as many of the reported reef complexes (e.g., New Guinea) have undergone considerable uplift. Fortunately, in most instances, the rate of long-term uplift appears to have been constant throughout the Quaternary, and adjustment of the elevation of the reef to former sea level (and modern sea level) can be accommodated.

In reefs of late Holocene age (ca. 5,000 BP to present), the species of coral becomes critical to determining the relationship of the reef to former sea level. In areas where the rate of tectonic uplift is very slow, a fossil reef dating from within the last few millennia may be only slightly above present mean sea level. In other instances where tectonism or other crustal movements have been absent, only a few meters may submerge a recent, subfossil reef that is no longer active. Coral species differ significantly in their occurrence with depth of water. Some species (e.g., *Acropora palmata*, or elkhorn coral) grow in very shallow waters, often becoming exposed at low tide. Others, like several brain and head corals (e.g., *Montastrea*),

thrive best in water depths of 5–6 m (Blatt et al., 1972). With the magnitude of sea level changes during the late Holocene amounting to <10 m even along the subsiding US middle Atlantic Coast (Kearney, 2001), the error imparted to a sea level reconstruction by not accounting for the dominant coral species – and relation to former mean sea level – composing a fossil reef could be significant.

“Raised beaches”: berms, strandlines and wave-cut scarps

Apparent beach features occurring above the present limits of the tides (supertidal) have been widely reported as evidence of former sea level high stands. Some of the features undeniably document past sea level highs – whether in response to regional tectonics or possible eustatic events – while others are more ambiguous in the interpretation of their relationship to actual sea level changes.

Along many sandy coasts, like the Florida Panhandle (Stapor, 1973), beach-like features a few meters above present mean sea level have been reported as marking significant transgressive episodes during the late Holocene. These features can be either erosional (scarps) or depositional (berms), but in most cases are relatively small-scale forms (a few meters high at most in height). A common criticism, given their small size, is that these features originated from the penetration of large waves above former tidal limits – perhaps abetted by storm surges – and not from eustatic sea level changes. Certainly, scarps and berms can be observed to have formed after large coastal storms that produced significant storm surges and wave setup. Moreover, some of the most widely cited examples of wave-cut scarps and berms touted as associated with past high stands occur in regions of considerable tropical storm (i.e., hurricane) activity, like the Gulf of Mexico, a coincidence not lost on those who argue that they are largely storm phenomena.

On the other hand, the similar elevation above mean sea level of equivalent-age supertidal scarps and berms over relatively large coastal areas is hard to reconcile with an origin other than a rise in sea level. Wave approach, setup, and similar characteristics from any storm differ across a region, with concomitant changes in the landward penetration of storm waves and the elevation of supertidal forms they create. Assessment, then, of “raised beach” features as sea level indicators is likely to remain contentious.

Wave-cut notches

Wave-cut notches, a phenomenon of rocky cliff coasts, are erosional features produced from abrasion by wave-carried debris at the base of cliffs. Although rock hardness varies, especially comparing relatively soft carbonates to volcanic materials like basalt, wave-produced abrasion is generally a slow process in most rocks. Hence, a significant wave-cut, particularly in hard rocks, indicates a long period of wave impacts against the same spot on the cliff. Most reported wave-cut notches are above present mean sea level, but submerged wave-cut notches marking sea level high stands immediately following deglaciation occur at 60 m depth in areas of Hawaii (cf. Fletcher and Sherman, 1995).

Marine terraces

Marine terraces are former wave-cut platforms that have undergone uplift. Wave-cut platforms typically slope gently seaward,

marking the mean low water level (seaward) and high water level (landward). These features typically characterize rocky cliff coasts. A spectacular flight of marine terraces (>20) fringes parts of San Clemente Island off California. Along the California coast, some of the youngest subaerial terraces date from 100,000 BP, or approximately isotopic Stage 5c. The oldest marine terrace in the Palos Verde Hills of Los Angeles, California rises 394 m above present mean sea level, and is 600,000 years old.

Because they originate as wave-cut platforms, requiring decades or more of corrasion to create, depending on rock hardness, marine terraces clearly represent a considerable period of slow transgression or stable sea level. Thus, if the long-term rate of uplift was known, the original elevation of the terrace – as a proxy for the approximate former sea level position – could be determined. However, coseismic activity is not uniform along long reaches of coast, and deformation of Wisconsinan-age terraces by synclinal and anticlinal folding has been reported for the Santa Barbara area in California (Gurrola and Keller, 1997). Moreover, surface erosion and mass wasting of older Pleistocene terraces can affect their absolute elevation relative to past sea levels, even if corrected for uplift. The determination of sea level position from Pleistocene marine terraces can thus be subject to some error, especially in low terraces of late Sangamonian age (ca. 80–90 ka).

Biological indicators

Biological indicators encompass a great variety of fossil and microfossil animal and plant materials that have been used to reconstruct past sea level changes. Not all are equally useful, and often the accuracy of interpretations of former sea level position derived from many of these indicators is open to question. The keys to using biological indicators are: (a) reliable and precise knowledge of where the organism lives in relation to modern mean sea level, and (b) some certainty that the occurrence of the remains of the organism in the sedimentological record are *in situ*, and have not been subject to post-mortem transport and deposition.

Shells and sponge spicules

Shells of pelecypods, like clams (e.g., *Mercenaria mercenaria*) and oysters (e.g., *Crassostera virginica*), commonly can be found along most coasts. Many of these animals clearly inhabit relatively shallow waters, generally within 5 m or less of mean tide level. Thus, the finding of these shells (if they can be assumed to have buried where the organism lived) can be indicative of relatively shallow water conditions, a particularly useful indicator of former sea level position in long cores of littoral sediments spanning millennia. Nonetheless, because many species of pelecypods can inhabit a range of water depths (e.g., between 3–10 m for *Mytilus edulis*), the usefulness of their shells in littoral sediments of late Holocene age (when the total variation in sea levels was generally <10 m in many areas of the US Atlantic Coast; Kearney, 2001) is substantially limited.

Similar criticisms can be made of employing the occurrence of spicules of shallow water sponges in sediment records as sea level indicators. An additional problem is that these small generally siliceous needles can be widely scattered across the ocean floor after the death of the organism (without breakage and indication of post-mortem transport, necessarily) and, therefore, are often not found *in situ*.

Tree stumps

The finding of rooted fossil tree stumps now submerged in the lower shoreface has been interpreted as marking past sea levels (e.g., Kearney, 1996). However, reconstruction of former sea level position employing submerged tree stumps can be fraught with considerable error, as many riparian or fastland tree species can often occur in strictly upland forests, rendering questionable what the elevation of the tree was to mean tide level at the time of death. Again, this is less of a problem in early Holocene or Pleistocene sea level reconstructions, where the range of total elevational change encompassed in these records is tens of meters. In these instances, they clearly function as dramatic evidence of a substantial change in sea level, despite their limitations in precision.

Intertidal deposits: coastal marshes

The influence of sea level rise on the upward growth (vertical accretion) and overall development of coastal marshes is well-recognized (Stevenson et al., 1986). Theoretically, since the elevation of the marsh surface adjusts to changes in mean tide level, older marsh sediments below the substrate must record similar relationships to ancient tidal levels, and thereby to sea level. Unfortunately, this reasonable assumption was undermined by findings some time ago that older marsh sediments can undergo considerable loss in volume upon burial, initially from dewatering (Kearney and Ward, 1986), and later, by auto-compaction (the collapse of old buried peats under their own weight and that of younger sediments; Kaye and Barghoorn, 1964). These phenomena result in peat sediments sinking below the level at which they were originally deposited in relation to mean tide level, making reliable reconstruction of age-depth relations in long marsh sedimentary records problematic. They also affect the use of geochemical (Varekamp et al., 1992) and faunal indicators of changes in sea level archived in marsh sediments, though these data are typically used for more relative interpretations of the magnitude of past transgressions and regressions. Scott and Medioli (1978) nonetheless have shown that accurate reconstructions of former sea levels are still possible by delineating vertical zonations of marsh foraminifera in marsh cores.

The present use of marsh sediment records as sea level indicators generally is in collection of radiocarbon-dated marsh basal peats. Basal peats are assumed to record the initial conversion of the former upland surfaces to marsh by rising sea (a phenomenon termed marsh lateral accretion). Since the pre-existing surfaces of marshes are typically compacted, dense muds, dates collected from basal peats in contact with these sediments are more likely to be at their original elevation and not to have undergone any auto-compaction. Thus, a more reliable reconstruction of time-depth relationships for sea level change is possible. The only limitation of such indicators is that they are most suited to documenting past rises (transgressions) in sea level, as new marsh covered existing fastlands, and are not suited to documenting significant falls in sea level (regressions), when the marsh may have disappeared with the seaward drop in the elevation of the tides.

Archaeological evidence

Evidence for sea level change drawn from the world archaeological record spans shell middens from Woodland and earlier fishing communities in various sites in North America (see Fairbridge, 1976) to Medieval through Neolithic-age sites

across Mediterranean and Europe (Kearney, 2001). The wealth of archaeological data that has been applied as sea level indicators is so large that it defies easy description. However, archaeological material that is truly useful in sea level reconstruction must fulfill the same criteria as other sea level indicators: (a) the relationship to mean sea level at the time of construction and/or burial can be determined, (b) the material must be *in situ*, and (c) in terms of structures, later modifications of either the structure or the surrounding site must not have changed the initial relationship to mean sea level. The last criterion is especially critical regarding ancient harbor and port facilities that were used for long periods of time. For example, subsequent harbor construction – often many centuries later – to meet demands of increased shipping or better defense, often involved extensive modifications (if not their replacement) of original structures like docks that changed initial relationships to mean sea level in ways that may be not readily discernible. For example, the Port of Alexandria, Egypt, underwent substantial modification over the centuries since Hellenistic times, as waves of conquerors from the Romans to the Mamelukes came and went.

Even when acknowledging the potential problems inherent in the use of archaeological materials, it is not surprising that such evidence is still regarded as highly suspect by many sea level researchers. Nonetheless, the evidence often has the undeniable advantage of being able to be dated to within a decade, even a particular year, especially in the case of Roman (empire) materials. Moreover, in some instances, the relationship to former mean sea level can be deduced with a high degree of precision that similar-age biological materials would never allow.

Michael S. Kearney

Bibliography

- Blatt, H., Middleton, G., and Murray, R., 1972. *Origin of Sedimentary Rocks*. Englewood Cliffs, NJ: Prentice-Hall, 634pp.
- Bloom, A.L., Broecker, W.S., Chappell, J., Mathews, R.K., and Mesolella, K.J., 1974. Quaternary sea level fluctuations on a tectonic coast: new $^{230}\text{Th}/^{234}\text{U}$ dates from the Huon Peninsula. *Quaternary Res.*, **4**, 185–205.
- Cabanes C., Cazenave A., and Le Provost C., 2001. Sea level rise during past 40 years from satellite and *in situ* observations. *Science*, **294**, 840–842.
- Chappell, J.M., and Shackleton, N.J., 1986. Oxygen isotopes and sea level. *Nature*, **324**, 137–138.
- Douglas, B.C., 1991. Global sea level rise. *J. Geophys. Res.*, **96** (C4), 6981–6992.
- Douglas, B.C., 2001. Sea level change in the era of the recording tide gauge. In Douglas, B., Kearney, M.S., and Leatherman S.P. (eds.), *Sea Level Rise: History and Consequences*. New York: Academic Press, pp. 37–62.
- Fairbridge, R.W., 1976. Shellfish-eating preceramic Indians in coastal Brazil. *Science*, **191**, 353–359.
- Fletcher, C.H., and Sherman, C., 1995. Submerged shorelines on Oahu, Hawaii: Archive of episodic transgression during deglaciation? *J. Coast. Res.*, **17**, Special Issue: Holocene cycles: Climate, sea level, and sediment, pp. 141–152.
- Gurrola, L.D., and Keller, E.A., 1997. Tectonic geomorphology of the Santa Barbara Fold Belt, Western Transverse Ranges, California. *Geol. Soc. Am. Abs.*, **29**(6), 344.
- Kaye, C.A., and Barghoorn, E.S., 1964. Late Quaternary sea-level change and crustal rise at Boston, Massachusetts, with notes on the autocompaction of peat. *Geol. Soc. Am. Bull.*, **75**(2), 63–80.
- Kearney, M.S., 1996. Sea-level change during the last thousand years in Chesapeake Bay. *J. Coast. Res.*, **12**, 977–983.
- Kearney, M.S., 2001. Late Holocene sea level variation. In Douglas, B., Kearney, M.S., and Leatherman S.P. (eds.), *Sea Level Rise: History and Consequences*. New York: Academic Press, pp. 13–36.
- Kearney, M.S., and Ward, L.G., 1986. Accretion rates in brackish marshes of a Chesapeake Bay estuarine tributary. *Geo-Mar. Lett.*, **6**, 41–49.
- Mesolella, K.J., Mathews, R.K., Broecker, W.S., and Thurber, D.L., 1969. The astronomical theory of climatic change: Barbados data. *J. Geol.*, **77**, 250–274.
- Mörner, N.-A., 1973. Eustatic changes during the last 300 years. *Palaeogeogr. Palaeoclim. Palaeoceanogr.*, **13**, 1–14.
- Peltier, W.R., 2001. Global glacial isostatic adjustment and modern instrumental records of relative sea level history. In Douglas, B., Kearney, M.S., and Leatherman S.P. (eds.), *Sea Level Rise: History and Consequences*. New York: Academic Press, pp. 65–86.
- Scott, D.B., and Medioli, F.S., 1978. Vertical zonations of marsh foraminifera as accurate indicators of former sea levels. *Nature*, **272**, 528–531.
- Stapor, F.W. Jr., 1973. Coastal Sand Budgets and Holocene Beach Ridge Plain Development, Northwest Florida. Ph.D. thesis, Florida State University, Tallahassee.
- Stevenson, J.C., Ward, L.G., and Kearney, M.S., 1986. Vertical Accretion in marshes with varying rates of sea level rise. In Wolf D. (ed.), *Estuarine Variability*. New York: Academic Press, pp. 241–259.
- Varekamp, J.C., Thomas, E., and van de Plassche, O., 1992. Relative sea level rise and climate change over the last 1,500 years. *Terra Nova*, **4**, 293–304.

Cross-references

[Ancient Cultures and Climate Change](#)
[Beachrock](#)
[Coastal Environments](#)
[Coral and Coral Reefs](#)
[Glacial Isostasy](#)
[Radiocarbon Dating](#)
[Sea Level Change, Post-Glacial](#)
[Sea Level Change, Quaternary](#)

SEDIMENTARY INDICATORS OF CLIMATE CHANGE

Introduction

Innumerable publications deal with the sedimentary record of past climates (e.g., Nairn, 1961, 1963; Schwarzbach, 1963; Frakes, 1979; Parrish, 1998; and Cecil and Edgar, 2003). Earlier paleoclimatic studies concentrated on identifying paleolatitudes and their shifts in response to plate tectonic movements on timescales of millions of years. Spurred by advances in the understanding of Pleistocene and Holocene climate records, more recent studies have focused on climate changes in response to orbital parameters on the timescale of tens of thousands of years and even shorter time frame variability. The sedimentary indicators of climate change are inextricably linked to biological and chemical criteria, which are typically recorded in sediments. The sedimentary indicators of climate change consist of two broad groupings: (a) sedimentary features that directly relate to climatic parameters such as rainfall or temperature, and (b) successions of sedimentary strata that indirectly reflect relative changes in these parameters. In both cases, the link to climate is the regional distribution and stratigraphic coherency of indicators. Many studies now assume a climate driver for variability unless other mechanisms can be identified.

Sedimentary features directly reflecting climatic conditions

Some sedimentary features reflect conditions of temperature or rainfall, and can be used to reconstruct past climate conditions. However, even the best indicators need to be used in

context of their regional setting and associations. Furthermore, some of the features may be confused with other types of deposits that do not have the same climatic constraints.

Extended periods of cold weather are necessary to produce glaciers and their deposits. Striated boulders and tills are excellent indicators of past glaciers. These, however, may be confused with other boulder deposits such as alluvial fans, talus cones, or debris flows in the geologic record. The mechanical grinding of bedrock to clay-sized sediment (rock flour) by glaciers can be recognized in till deposits and other environments well removed from the glaciers. The re-sedimentation of glacial deposits long after the glaciers have retreated may be misconstrued as evidence of colder conditions. Associated glacial features such as eskers, outwash, and dropstones (Figure S18a) are even less easily distinguished from non-glacial deposits in the rock record. Features formed by ground ice such as solifluction lobes, pingos, and ice wedges are good indicators of cold climates (i.e., Washburn, 1980). Some mineral phases are more stable at low temperatures such as ikaite ($\text{CaCO}_3 \cdot 6\text{H}_2\text{O}$) (Figure S18f), mirabilite ($\text{Na}_2\text{SO}_4 \cdot 10\text{H}_2\text{O}$), natron ($\text{Na}_2\text{CO}_3 \cdot 10\text{H}_2\text{O}$) and hydrohalite ($\text{NaCl} \cdot 2\text{H}_2\text{O}$). Within the proper context, these are strong indicators of cold conditions.

Indications of warm or hot climate are less clear. In marine settings, warm tropical waters favor growth of coral reefs and precipitation of carbonate minerals. The biological component of carbonate buildups in the geological record is less certain, particularly with documented "cool-water" carbonate deposits forming at higher latitudes (see James and Clarke, 1997). There is no clear correlation between accumulations of lacustrine carbonates and temperature.

Continuous growth of vegetation to produce thick accumulations of peat is best developed in rainy climates, as are coal and lignite deposits (Figure S18b). Even in areas of moderate rainfall, well-developed root structures are common in soils. The presence of coal or lignite is not unequivocal evidence of rainy conditions, however, because plants will grow in abundance wherever there is enough water, even in an arid climate. Similarly, perennial rivers, lakes, and swamps may all exist in areas of low rainfall, if the source of water is sufficient. Chemical weathering is best developed in wet, rainy, and warm climates, whereas mechanical weathering is best developed in dry and/or cold climates. The production of high-aluminum or lateritic clays and the removal of labile minerals from sands are good indications of prolonged chemical weathering. Even marine units that are dominated by these sediments may be correlated with rainy paleoclimates if regional and stratigraphic constraints are considered. The absence of these features, however, does not eliminate rainy climates since other factors such as relief, sediment transport, and diagenesis are also important.

Indicators of aridity include saline minerals, eolian sand deposits, ephemeral stream deposits, closed-basin lakes, and dry mudflats. Both marine and non-marine syndepositional saline minerals (Figure S18e) require evaporation to exceed water supply in order to concentrate solutes. The environment of formation, however, may reflect only local dryness or the evaporites may be superimposed on materials originally deposited in a wetter climate. Extensive eolian sand seas (Figure S18c) form where vegetation is sparse in dry climates. Local eolian sand deposits may form in a variety of climatic conditions. River and stream channels may remain completely dry for prolonged periods in areas of low rainfall. Ephemeral streams deposits, however, may be very similar to the deposits of perennial

streams. Dry channels may also reflect local phenomena such as channel switching or small drainage areas. Closed-basin lakes are maintained by evaporation exceeding inflow. The criteria for recognizing closed-basin lakes, which include frequent shifts in depth indicators and accumulation of soluble minerals, are not unique or easily recognized in the rock record. Furthermore, closed-basin lakes may form at a small scale in a range of climates under local conditions. Dry mudflats, which are dominated by desiccation cracks and vesicles, require a depressed groundwater table. The criteria for their recognition are still being developed. The predominance of mechanical weathering in both cold and hot arid settings suggests a mineralogical indication of paleoclimate. The abundance of immature sands such as arkoses or lithic arenites has been used as climate indicators. Red sedimentary deposits, stained by iron oxides, have also been cited as indicators of aridity. The mounting evidence suggests that these are unreliable indicators of paleoclimate. Immature sands appear to reflect relief and rate of transport more than climate, and redbeds are diagenetic overprints that are independent of the depositional climate.

The most promising sedimentary features indicative of climate change are soils (for instance, Retallack, 2001). Modern soils show a strong relationship with both local and regional climate as should their fossil counterparts. Some of the features already mentioned are incorporated into the soil classification, such as aridisol (saline minerals or mudcracks and vesicles), histosol (coal or peat), or gelisol (ground ice features). The climatic divisions, however, can be much finer based upon abundance and depth of mineral horizons (such as carbonate, aluminum, or iron), eluviation features, parting textures (peds), and vegetation overprint. Bauxitic and lateritic soils are good indicators of high rainfall. Vertisols (soils with abundant sticky or swelling clay) and calcisols require at least seasonal desiccation or dryness (Figure S18d). Thick eluviated clay B horizons with abundant roots and no soluble minerals, such as in spodosols (soils with a subsurface horizon containing organic matter, iron, and/or aluminum) or ultisols (soils with a well-developed argillic (clay) horizon and low level of exchangeable base metal cations) (Figure S18b), reflect rainier climates that support vegetation and remove soluble minerals. The drawbacks to using paleosols include the difficulty in recognizing fossil counterparts due to diagenetic changes in color and composition, similar features in different soils, and restriction to subaerial conditions.

Sedimentary features that indirectly reflect climate change

Relative changes in the world climate may be indicated by the changing character of sedimentary environments. Shifts in net precipitation are reflected in certain continental or nearshore settings by relative indicators of wetness or dryness. Relative shifts in temperature are usually more difficult to assess from sedimentary criteria. The problem with indirect climatic indicators is that not all environments react the same way to similar climatic changes and the degree of preservation of these changes is highly variable. In the best cases, relative climatic change is recorded at the millennial or centennial scale of resolution or even finer (for instance Fischer, 1986). More often, the patterns of climate change are coarsely preserved, with numerous gaps or uncertainties. Laminated sediment from lakes or deep marine settings often shows variations in mineralogy, sediment type, or thickness that reflect changes in temperature or precipitation (Figure S19). In some circumstances, these can be documented as annual layers that provide incredible

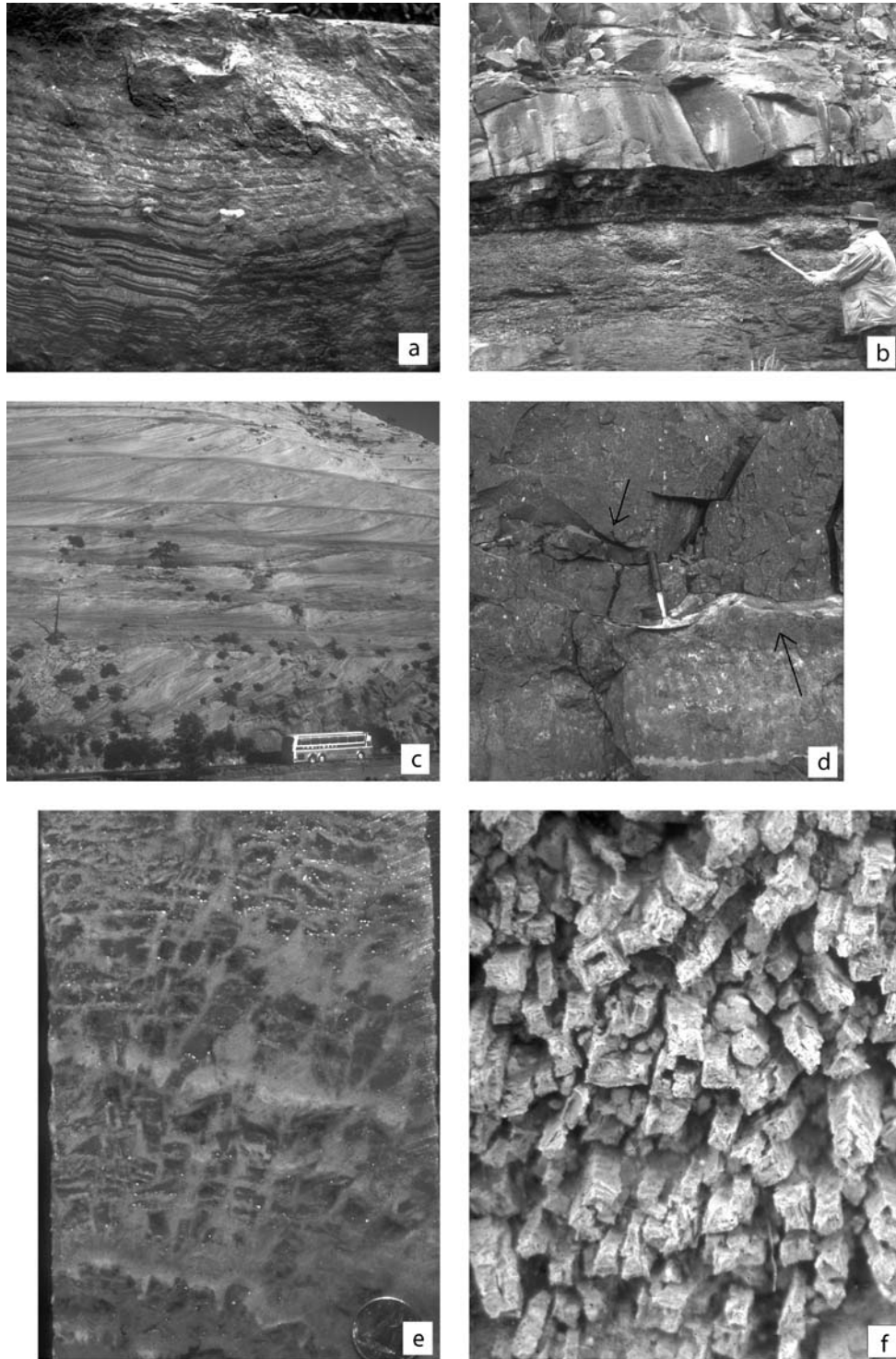


Figure S18 (a) Glacial varves with dropstones, Proterozoic Gowganda Formation near Ontario (thickness shown is about 40 cm). (b) Coal bed (*dark*) in West Virginia overlying an aluminous, blocky, claystone with abundant root casts interpreted as an ultisol. The coal bed is overlain by fluvial sandstone. Pennsylvanian Kanawha Formation, West Virginia. Man is about 1.75 m tall. (c) Eolian cross-bedding formed by migration of large dunes in a sand sea. The Jurassic Navajo Sandstone in Utah. Section shown is about 40 m high. (d) Mudstone with abundant root casts, carbonate nodules (*light blebs*) and curved slickensided planes (*arrows*) interpreted as a vertisol. Silurian Bloomsburg Formation, Pennsylvania. Hammer is about 35 cm long. (e) Gypsum crystals (*dark*) that grew upward from the sediment floor in a standing brine, now replaced by halite (pseudomorphs). Pennsylvanian Paradox Formation, Utah. Section shown is about 14 cm thick. (f) Basal view of pseudomorphs after ikaite ($\text{CaCO}_3 \cdot 6\text{H}_2\text{O}$) now composed of calcite. Pleistocene deposits of Lake Lahontan, Nevada. Section shown is about 30 cm wide.

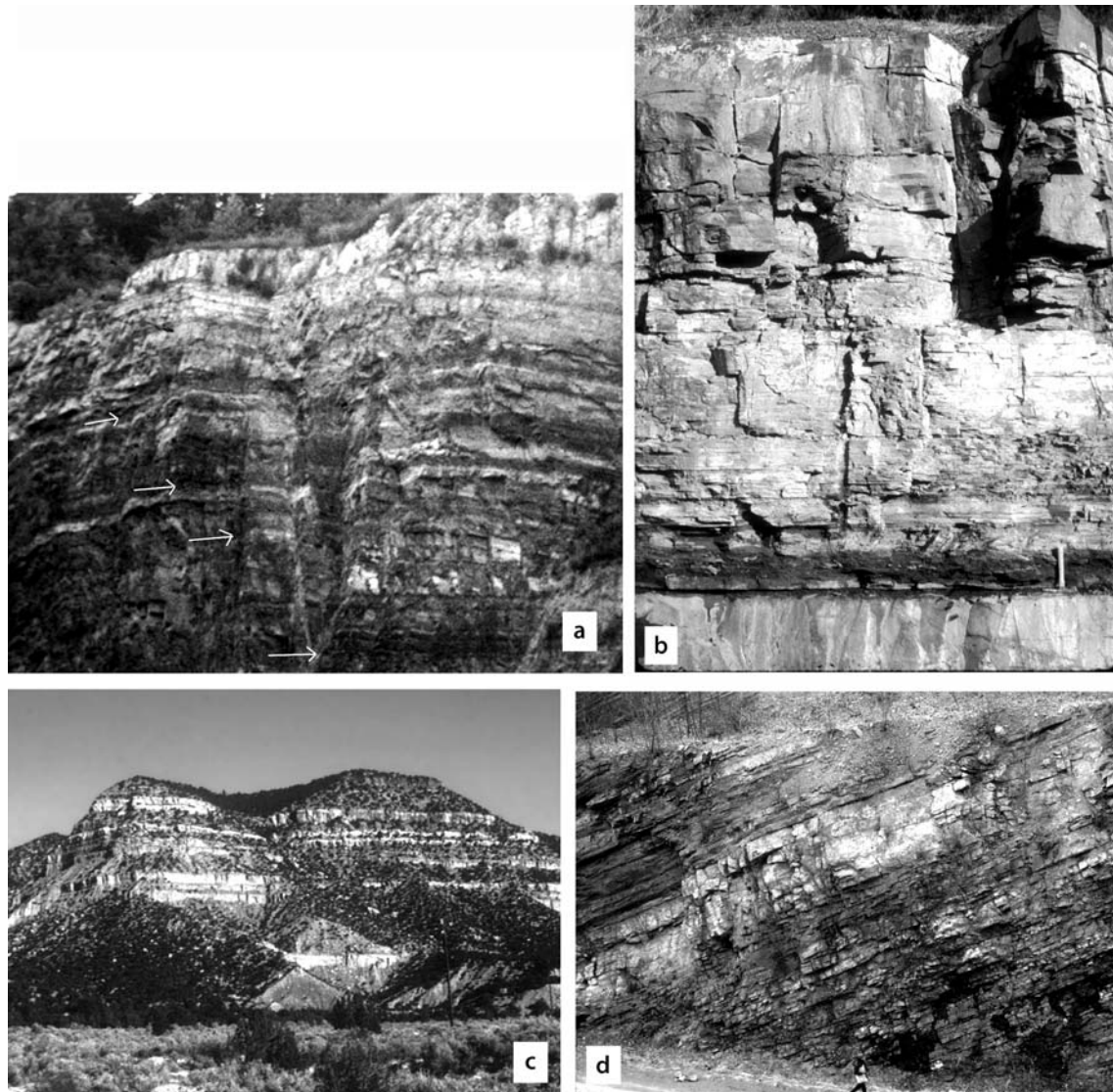


Figure S20 (a) Outcrop of cyclic lacustrine mudstone. The base of four cycles (marked by *arrows*) consists of laminated gray shale that grades upward into unbedded mudstone with abundant desiccation cracks. Triassic Lockatong Formation, New Jersey. Thickness shown is about 15 m. (b) Detail of lake cycle showing black laminated shale (*dark*), representing a deep lake sharply overlying a massive mudstone. Gradual upward transition to massive mudstone (*light*) includes increasing frequency of desiccation features, vertebrate tracks, and root structures that indicate shallowing of water. Triassic Bull Run Formation, Virginia. Thickness shown is about 4 m. (c) Large scale exposure of repeated alternations of wave-dominated shoreline sandstone (*light ledges*) and deep water marine shales (*vegetated slopes*) attributed to rise and fall of sea level. Cretaceous Book Cliffs Formation, Utah. View shown is about 50 m high. (d) Outcrop of deepwater marine shale (*dark*) grading upward to shallow-water sandstone with tidal influence (*light*) interpreted as an indication of sea level change. Devonian Mahantango Formation, Pennsylvania. Outcrop is about 18 m high.

Recent sedimentary settings suggests that a climatic effect on sedimentation should be expected. The significance of this sedimentary impact depends upon the depositional setting and the reliability of direct or relative indicators of climate change.

Joseph P. Smoot

Bibliography

Blum, M.D., and Tornquist, T.E., 2000. Fluvial responses to climate and sea-level change: A review. *Sedimentology*, 47(Supplement), 2–48.

Cecil, C.B., and Edgar, N.T. (eds.) 2003. *Climate Controls on Stratigraphy*. Tulsa, OK: SEPM (Society for Sedimentary Geology). SEPM Special Publication No. 77, 275pp.

Fischer, A.G., 1986. Climatic rhythms recorded in strata. *Annu. Rev. Earth Planet. Sci.*, 14, 351–376.

Frakes, L.A., 1979. *Climates Through Geologic Time*. New York: Elsevier, 310pp.

James, N.P., and Clarke, A.D. (eds.) 1997. *Cool Water Carbonates*. Tulsa, OK: SEPM (Society for Sedimentary Geology). SEPM Special Publication 56, 440pp.

Naim, A.E.M., 1961. *Descriptive Paleoclimatology*. New York: Intersciences Publishers, 380pp.

- Nairn, A.E.M. (ed.) 1963. *Problems in Palaeoclimatology*. London: Interscience Publishers, 705pp.
- Nanson, G.E., and Tooth, S., 1999. Arid-zone rivers as indicators of climate change. In Singhvi, A.K., and Derbyshire, E. (eds.), *Paleoenvironmental Reconstructions in Arid Lands*. Rotterdam: A.A. Balkema, pp. 175–216.
- Parrish, J.T., 1998. *Interpreting Pre-Quaternary Climate from the Geologic Record*. New York: Columbia University Press, 338pp.
- Perlmutter, M.A., and Mathews, M.D., 1989. Global cyclostratigraphy, a model. In Cross, T. (ed.), *Quantitative Dynamic Stratigraphy*. Englewood Cliffs, NJ: Prentice Hall, pp. 233–260.
- Retallack, G.J., 2001. *Soils of the Past*. Oxford: Blackwell Science, 404pp.
- Schwarzbach, M., 1963. *Climates of the Past*. London: D. Van Nostrand Company, 328pp.
- Vail, P.R., Mitchum, R.M., and Thompson, S. III., 1977. Seismic stratigraphy and global changes of sea-level, part 4: global cycles of relative changes in sea-level. In Payton, C.E. (ed.), *Seismic Stratigraphy – Applications to Hydrocarbon Exploration*. Tulsa, OK: American Association of Petroleum Geologists. AAPG Memoir 26, pp. 83–97.
- Washburn, A.L., 1980. *Geocryology*. New York: Wiley, 406pp.

Cross-references

Arid Climates and Indicators
 Carbonates, Cool Water
 Carbonates, Warm Water
 Coal Beds, Origin and Climate
 Coastal Environments
 Continental Sediments
 Cyclic Sedimentation (cyclothems)
 Eolian Sediments and Processes
 Evaporites
 Glacial Sediments
 Glendonite/Ikaite
 Mineral Indicators of Past Climates
 Paleosols, Pre-Quaternary
 Paleosols, Quaternary
 Periglacial Geomorphology

SNOWBALL EARTH HYPOTHESIS

The hypothesis

The snowball Earth hypothesis (SEH) suggests that the Earth experienced surface temperatures so low that virtually its entire surface was covered by glaciers and/or thick sea ice periodically during its early history. Such a condition has been hypothesized for parts of the Neoproterozoic Era from about 750 million years ago (Ma) to about 600 Ma (Figure S21). A similar frozen state has been proposed during the early part of the Paleoproterozoic Era at about 2,300 Ma. There is little evidence of glaciation in the long intervening period but recently Williams (2005) presented evidence for glaciation in the Kimberley region of Western Australia at around 1,800 Ma.

The evidence

Support for this hypothesis comes primarily from field evidence, including the widespread preservation of diamictites, which are conglomerates containing large rock fragments separated by abundant fine grained matrix materials in which they appear to “float.” Included rock fragments commonly have scratched or striated surfaces. Rock fragments with planar surfaces are said to be “faceted.” The presence of many faceted and striated clasts in a diamictite suggests a glacial origin. Another glacial indicator is the preservation of large scale

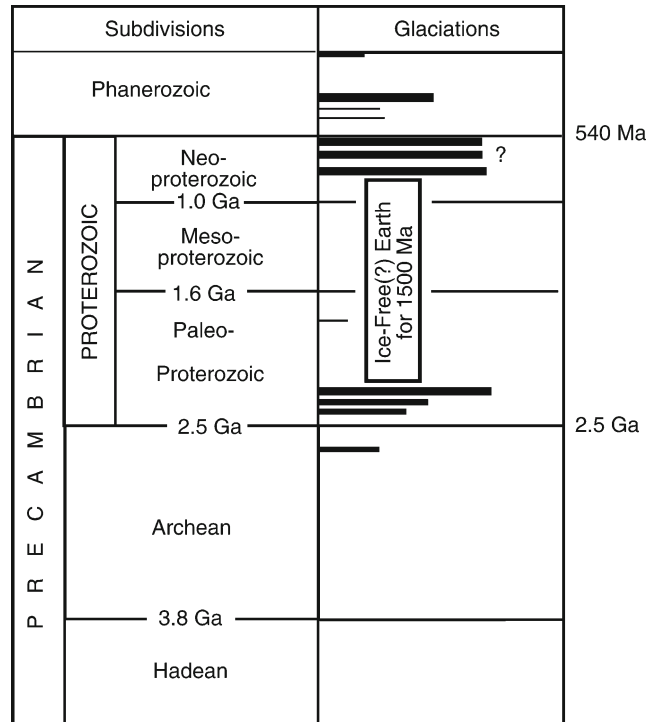


Figure S21 Distribution of glaciations throughout geologic time. Note the large gap between the Paleo- and Neoproterozoic glaciations. Question mark indicates uncertainty concerning the number of Neoproterozoic glacial episodes.

striated or furrowed rock surfaces that are thought to have formed by grinding action as rock-charged glaciers moved over older rocks or penecontemporaneously deposited sediments. Glacial activity is also indicated by the presence of finely bedded (laminated) sedimentary rocks that contain isolated large rock fragments. These fragments commonly show evidence of vertical emplacement in the form of downward penetration of the clast into enclosing sedimentary layers or as “splash up” structures – upfolding of the finely laminated sedimentary rocks on the sides of the fragment. Such rocks are called “dropstones” and are thought to have been released from melting icebergs.

These kinds of evidence have been found in Neoproterozoic rocks on all of Earth’s continents. Rocks with similar glaciogenic characteristics have also been described from older (~2,300 Ma) successions on several continents. The older glacial deposits are best known from North America, where they occur in the Huronian Supergroup on the north shore of Lake Huron in Ontario, Canada. Similar rocks occur in Michigan and bordering states, in SE Wyoming, on the west side of Hudson Bay and in the Chibougamau area of Quebec. Paleoproterozoic glaciogenic rocks also occur in NW Europe, South Africa and Western Australia. Although preserved on four continents, evidence of Paleoproterozoic glaciation is much less widespread than for the younger Neoproterozoic occurrences. It is not known whether this reflects an originally restricted distribution or whether much of the older rock record has been lost as a result of subsequent erosion.

Discovery of the wide distribution of Neoproterozoic glaciogenic rocks led Mawson (1949) and Harland (1964) to suggest

that the surface of the entire planet may have been frozen during parts of the Neoproterozoic. This concept was crystallized in the phrase “snowball Earth” by Kirschvink (1992), who proposed a genetic relationship among Neoproterozoic glaciogenic rocks, banded iron-formations (BIFs), and the snowball Earth state. Banded iron formations are thought to be chemically precipitated sediments that typically consist of finely interbedded (or “banded”) layers of siliceous material (chert and jasper) and iron oxides and other iron-rich minerals. Banded iron formations are common in Late Archean to Palaeoproterozoic successions (2,500 Ma to ~1,800 Ma) but are rare-to-absent from most sedimentary successions deposited in the next billion years. Deposition of the Paleoproterozoic BIF has been attributed to the onset of the oxygenation of Earth’s atmosphere, beginning at about 2,300 Ma. Extensive bodies of younger Fe-rich sedimentary rocks are unlikely because, following oxygenation of the Earth’s atmosphere, large amounts of Fe could not have accumulated in the world’s oceans, since Fe (as Fe^{+3}) is virtually insoluble under oxidizing conditions. Alternatively, the deep oceans were not oxygenated during the period from about 2.3 Ga to 800 Ma but rather were rich in sulfide, which would have reacted with any dissolved iron to precipitate iron sulfides (Anbar and Knoll, 2002). Both scenarios predict a dearth of Fe-oxide-rich chemical sedimentary rocks. The fact that some widespread BIFs, such as those in the Hamersley Basin of Western Australia, appear to pre-date the oxygenation of the atmosphere as indicated by various parameters in the Huronian Supergroup, suggests that deposition of these iron formations was also controlled by other (tectonic?) factors. Kirschvink (1992), however, linked the Neoproterozoic BIFs to the snowball Earth hypothesis. He considered that isolation of the atmosphere (oxygenated) and oceans by ice would have led to the buildup of dissolved Fe in the oceans as the result of on-going hydrothermal activity at subaqueous mid-ocean ridges and other volcanic centers. Once oxygen was re-introduced to the oceans at the termination of the world-encircling glaciation, iron would have precipitated.

Another line of evidence, proposed by Hoffman et al. (1998), involves low $\delta^{13}\text{C}$ values from carbonate rocks both below and above Neoproterozoic glaciogenic diamictites in Namibia. They attributed these unusually low $\delta^{13}\text{C}$ values to the near-cessation of photosynthetic activity in the world oceans, due to the inferred widespread climatic deterioration and development of world-encircling ice sheets and sea ice. Carbonate rocks precipitated from the oceans inherit many of their stable isotopic characteristics from sea water. Many photosynthetic micro-organisms preferentially secrete the lighter isotope of carbon (^{12}C) so that during periods of high biological productivity the oceans are correspondingly enriched in the heavier isotope (^{13}C). Thus, $\delta^{13}\text{C}$ values of carbonates formed in such organic-rich periods would be relatively high, and conversely these values would be low if photosynthetic activity significantly decreased, as might be expected during a global glaciation. Because little evidence exists to support a significant decrease in photosynthetic activity in the Neoproterozoic, Hoffman and Schrag (2002) subsequently suggested that the low $\delta^{13}\text{C}$ values commonly found in post-glacial carbonate rocks (so-called “cap carbonates”) are due to rapid introduction of large amounts of CO_2 to the oceans from the atmosphere, rather than due to a biological catastrophe. The ultimate source of this CO_2 may have been dissociation of oceanic methane hydrate during deglaciation, followed by oxidation to CO_2 (Jiang et al., 2003).

Low latitude glaciation

The angle of inclination of the Earth’s magnetic field to the planet’s surface varies systematically with latitude. The field is steeply inclined in polar regions whereas it is nearly parallel to the Earth’s surface at low latitudes. Thus, if the magnetic field direction is “frozen” into sedimentary rocks at or close to the time of their deposition then the paleolatitude can readily be determined. There are several reports of low (tropical to subtropical) paleolatitudes from both Neoproterozoic and Paleoproterozoic glaciogenic rocks. In some cases, it has been shown that these low latitude glacial deposits were laid down close to sea level. This is very important as some glaciers occur in tropical latitudes (e.g., on Mt. Kilimanjaro) at present but they can exist only above the snowline – at very high altitudes. The widespread nature of low paleolatitude magnetic signals from Neoproterozoic glacial deposits in SE Australia has been demonstrated. This condition was probably long-lived, for it has been shown that it spanned times of magnetic reversals (periods when the Earth’s magnetic field spontaneously reverses direction, so that the north pole becomes the south). Similar low paleolatitudes are also claimed for some Paleoproterozoic glaciogenic rocks in North America and South Africa. These indications of ice at sea level in tropical latitudes have been considered to provide support for the idea of global glaciation – the snowball Earth hypothesis. Even before such paleomagnetic evidence was widely available, Williams (1975) suggested that the unusual rock associations in Neoproterozoic sedimentary successions might be explained as a result of differences in the tilt angle of the Earth’s spin axis. He proposed that there was a significant increase in the obliquity of the Earth’s ecliptic in the Precambrian. He noted that, with a high obliquity (greater than 54°), tropical regions would receive less insolation than polar regions in a given year. If the Earth underwent cooling, the effect would have been greater at low latitudes so that glaciation would have occurred preferentially near the equator. Such a high obliquity would also tend to accentuate seasonal differences throughout the globe and might provide an explanation for evidence of seasonality in some glaciogenic rocks that apparently formed at low latitude (see following section).

Evidence of seasonality at low paleolatitudes

At present, strong seasonality is not observed at low latitudes. In both Pale- and Neoproterozoic glaciogenic successions, however, there is evidence of seasonality in sedimentary rocks that, according to paleomagnetic results, formed in tropical regions. This is manifested by the preservation of laminated sedimentary rocks that closely resemble varves in younger (Pleistocene) glacial sediments formed at high-to-intermediate latitudes. These sediments are organized into couplets, each of which comprises a relatively coarse and fine layer. The fine laminae are thought to represent cold winter conditions when little water or sediment entered the depositional basin and fine material in suspension settled from the water column. The coarse layers formed during summer months when there was abundant sediment-charged meltwater. Many Pleistocene varves contain isolated dropstones. Such clasts are also common in Proterozoic laminated sequences and lend credence to their interpretation as annual deposits formed by significant seasonal temperature changes.

Evidence of strong seasonality in Proterozoic glacial deposits is also provided by large structures that, in plan view, are polygonal and in sectional view take the form of downward-tapering wedges. These structures are typically filled with

sand that exhibits laminations sub-parallel to the edges of the structure. These structures have been described from a number of Neoproterozoic glacial successions, including some that formed at low paleolatitudes. They are interpreted as fossil ice-wedge structures, which are typical of permafrost regions today. They form as a result of thermal contraction and expansion cycles and indicate strong seasonal fluctuations in surface temperature over long periods of time. Although attempts have been made to explain these structures as a result of other phenomena (such as rapid advance-retreat cycles of surging glaciers), the modern and Pleistocene permafrost examples provide the best analog.

Problems with the snowball Earth hypothesis

Lack of precise age control

The ages of Proterozoic glaciations are largely unknown. There is stratigraphic evidence (i.e., one glaciogenic formation occurring on top of another) of several glacial episodes in some areas in both the Paleo- and Neoproterozoic, but the number of glaciations is still under debate. Contemporaneous glaciation of huge areas of the planet is a *sine qua non* for the snowball Earth hypothesis but it has yet to be demonstrated. Part of the problem lies in the fact that most sedimentary rocks (including glaciogenic deposits) cannot be dated using currently available geochronological techniques although some dates are available from contemporaneous volcanic rocks.

Inconsistent geochemical trends

Many diamictite-bearing glaciogenic successions are overlain by carbonate rocks (commonly dolostones). According to Hoffman et al., (1998), the cap carbonates are thought to be the products of extreme alkalization of the oceans brought about by reaction between the abundant CO₂ (that caused destruction of the global ice cover) and fine grained material (rock flour) produced by the grinding of rocks in the glaciers. If this theory is correct then any sediment formed from the residue of the putative extreme alteration should carry chemical evidence of very strong weathering, followed by an upward decrease in weathering intensity as the CO₂ content of the atmosphere diminished. A method of quantifying the degree of weathering of sediments and sedimentary rocks, known as the Chemical Index of Alteration (CIA) was used by Nesbitt and Young, (1982) to study post-glacial sedimentary rocks of the Paleoproterozoic Gowganda Formation in Ontario. This study showed the opposite trend to that predicted by the SEH, i.e., upward-increasing CIA values following the end of glaciation. Similar studies have not been carried out on post-glacial siliciclastic sediments of Neoproterozoic age, but in many cases there could be problems in interpreting such data because of the high proportion of recycled materials (older sedimentary rocks that have been through a previous weathering cycle) and carbonate rocks (which affect the CIA).

Great stratigraphic thicknesses of Proterozoic glaciogenic deposits

Under the snowball Earth hypothesis, it is difficult to envisage accumulation of a thick succession of glaciogenic sedimentary rocks, especially at low latitudes. For glaciation to reach low latitudes, the SEH predicts a totally frozen condition, preceded by rapid onset and followed by abrupt disappearance of glacial ice (Figure S22). On an Earth whose surface was completely frozen, the hydrologic cycle would virtually stop, so that the

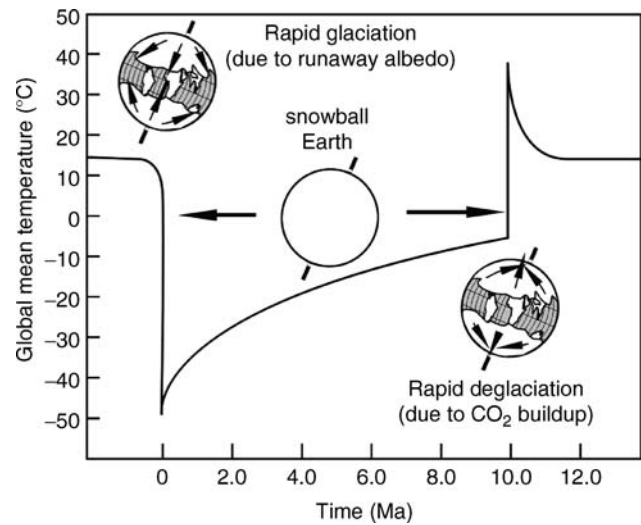


Figure S22 Proposed relationships between geologic time and surface temperature during a snowball Earth period (modified from Hoffman, 2000). Note the rapid growth and destruction of ice sheets.

great ice masses and large-scale ice movements required for production of thick sedimentary successions are unlikely. Many glaciogenic successions, in both the Paleo- and Neoproterozoic, are several km in thickness. It has been suggested by proponents of the SEH that ablation of ice at low paleolatitudes might provide sufficient hydrologic activity but without access to a huge reservoir of water (such as the world oceans). The production of great volumes of glacial sediments remains problematic. It is further hypothesized that much of the continental lithosphere was situated at low paleolatitudes so that in tropical regions, where most ablation would have occurred, there should only have been a thin ice cover and therefore limited ablation (as opposed to having the entire ocean as a moisture source). However, a low paleolatitudinal distribution of continents may not have existed for all snowball Earth glaciations.

Rapid onset and demise of snowball glaciations

Onset of the “snowball Earth” condition has been explained as the result of a “runaway albedo” feedback. If glaciation initiates at the poles and gradually descends to lower latitudes, a threshold occurs beyond which there is rapid lowering of surface temperatures and the entire surface of the planet becomes frozen, due to a positive feedback mechanism. Ice reflects solar energy more efficiently than land or water; therefore, as more of the Earth’s surface becomes ice-covered, it becomes progressively cooler until ice spreads rapidly to cover even low latitude regions of the planet (Hoffman, 2000). Once the entire planetary surface is frozen, the problem becomes one of finding a mechanism to release it from its frozen state. It was proposed (Kirschvink, 1992; Hoffman et al., 1998) that the Earth’s surface was re-warmed through buildup of atmospheric CO₂ from ongoing volcanic eruptions. This would have been accentuated by the absence of normal CO₂ drawdown from rock weathering, which would have ceased during the snowball state because of the widespread ice cover and low temperatures. Thus, the SEH invokes sudden (a few thousand years) onset and demise of glaciations, separated by much longer (several millions of years) glacial periods (Figure S22).

In the Paleoproterozoic Huronian Supergroup, however, there is sedimentological and geochemical evidence that the formations both below and above widespread glaciogenic rocks of the Gowganda Formation testify to a very gradual deterioration of climate before the glaciation and slow amelioration at the end. Likewise, in the Neoproterozoic of the Adelaide geosyncline in South Australia, Sturtian glaciogenic successions are overlain by thick (up to 1 km) accumulations of mudstone with abundant dropstones (Young and Gostin, 1989). Such occurrences testify to a long-lived, gradual amelioration of climate, with abundant floating glacial ice, in contradiction to the rapid amelioration implicit in the SEH. A less-than-catastrophic end to glaciation is also supported by recent evidence for multiple geomagnetic reversals within a cap carbonate, over a span of at least hundreds of thousands of years.

Origin of banded iron-formations associated with Proterozoic glaciogenic deposits

As noted above, the association of banded iron formations (BIFs) with some Neoproterozoic glaciogenic deposits led Kirschvink (1992) and others to propose that there was a genetic link with the snowball Earth condition, with BIFs depositing once deglaciation began. This relationship has also been proposed for the Paleoproterozoic but in the best-known basins, such as the Huronian of Ontario, glaciogenic rocks and Superior-type BIF are separated by about 300 Ma. Likewise, in the Hamersley basin of Western Australia, glacial deposits formed after deposition of major BIF, and not before, as predicted by the SEH. In contrast, there is a much more intimate association between BIF and glacial deposits in the Neoproterozoic. For example, ice-rafted dropstones are present in some laminated iron-formations, clearly attesting to the contemporaneity of glaciation and deposition of iron-formation. This relationship was attributed by some to precipitation of Fe concentrated in the world's oceans as a result of isolation of the atmosphere from the oceans during a snowball Earth period. There are, however, problems with this interpretation. The distribution of Neoproterozoic BIF is much more sporadic than that of the glaciogenic rocks. If deposition of the BIF were the result of global processes in the oceans, they should be much more common. In some cases (e.g., in the Rapitan Group of the northern Cordilleran region of North America), huge deposits of BIF occur below rather than above the glaciogenic diamictites. This is significant because the theory predicts that Fe should be released after the destruction of the oceans' ice cover. Many of the Neoproterozoic BIF occurrences formed in rift basins. This is shown by the presence of strong facies and thickness changes (Yeo, 1981; Young and Gostin, 1989) in the glaciogenic successions and the association, in some basins, with volcanic rocks. Furthermore, the geochemistry of the BIF supports a hydrothermal origin, which is compatible with the glaciated rift hypothesis for their origin (Yeo, 1981). This theory proposes that the iron was produced by hydrothermal circulation of seawater in restricted Red Sea-type rift basins. Iron-charged brines were moved and mixed with "normal" seawater and meltwater as a result of overturn caused by water movements related to release of meltwaters from glaciers that debouched into the basin from surrounding rift shoulders. Experimental studies show that such dilution and oxidation could lead to precipitation of dissolved metals such as Fe. This mechanism provides explanations for the hydrothermal nature of the BIF, their relatively restricted occurrence, fault-related facies and thickness changes and the intimate relationship with glaciogenic deposits.

Conclusions

Glaciogenic rocks are widely preserved in supracrustal successions of early Paleoproterozoic and late Neoproterozoic age and sparse in the long (~1,500 Ma) intervening interval of geologic time. This evidence suggests that the Earth went through significant climatic perturbations near to the beginning and end of the Proterozoic Eon. These perturbations in the Earth's surficial environments may have provided the impetus for significant evolutionary changes in the biosphere, especially near the end of the Proterozoic Eon when the first animals emerged. Whether the Earth's surface achieved a totally frozen condition (the snowball Earth hypothesis) during the great Proterozoic ice ages remains a possibility but currently available evidence is by no means conclusive.

Grant M. Young

Bibliography

- Anbar, A.D., and Knoll, A.H., 2002. Proterozoic ocean chemistry and evolution: A bioinorganic bridge? *Science*, **297**, 137–141.
- Harland, W.B., 1964. Critical evidence for a great Infra-Cambrian glaciation. *Geologische Rundschau*, **54**, 45–61.
- Hoffman, P.F., 2000. Discussion: Vreeland Diamictites – Neoproterozoic glaciogenic slope deposits, Rocky Mountains, southeast British Columbia. *Bull. Can. Pet. Geol.*, **48**, 360–363.
- Hoffman, P.F., and Schrag, D.P., 2002. The snowball Earth hypothesis: Testing the limits of global change. *Terra Nova*, **14**, 129–155.
- Hoffman, P.F., Kaufman, A.J., Halverson, G.P., and Schrag, D.P., 1998. A Neoproterozoic Snowball Earth. *Science*, **281**, 1342–1346.
- Jiang, G., Kennedy, M.J., and Christie-Blick, N., 2003. Stable isotopic evidence for methane seeps in Neoproterozoic postglacial cap carbonates. *Nature*, **426**, 822–825.
- Kirschvink, J.L., 1992. Late Proterozoic low-latitude global glaciation: The snowball Earth. In Schopf, J.W., and Klein, C. (eds.), *The Proterozoic Biosphere: A Multidisciplinary Study*. Cambridge, UK: Cambridge University Press, pp. 51–52.
- Mawson, D., 1949. The Late Precambrian ice age and glacial record of the Bibliando dome. *J. Proc. R. Soc. N.S.W.*, **82**, 150–174.
- Nesbitt, H.W., and Young, G.M., 1982. Early Proterozoic climates and plate motions inferred from major element chemistry of lutites. *Nature*, **299**, 715–717.
- Williams, G.E., 1975. Late Precambrian glacial climate and the Earth's obliquity. *Geol. Mag.*, **112**, 441–465.
- Williams, G.E., 2005. Subglacial meltwater channels and glaciofluvial deposits in the Kimberley Basin, Western Australia: 1.8 Ga low latitude glaciation coeval with continental assembly. *J. Geol. Soc. London*, **162**, 111–124.
- Yeo, G.M., 1981. The Late Proterozoic Rapitan glaciation in the northern Cordillera. In Campbell, F.H.A. (ed.), *Proterozoic Basins of Canada*. Ottawa, ON: Geological Survey of Canada. Paper 81-10, pp. 25–46.
- Young, G.M., and Gostin, V.A., 1989. An exceptionally thick upper Proterozoic (Sturtian) glacial succession in the Mount Painter area, South Australia. *Geol. Soc. Am. Bull.*, **101**, 834–845.

Cross-references

Albedo Feedbacks
 Atmospheric Evolution, Earth
 Banded Iron Formations and the Early Atmosphere
 Carbon Isotopes, Stable
 Carbonates, Cool Water
 Diamiction
 Glacial Sediments
 Glaciations, Pre-Quaternary
 Ice-Rafted Debris (IRD)
 Obliquity
 Periglacial Geomorphology
 Proterozoic Climates
 Varved Sediments
 Weathering and Climate

SPECMAP

SPECMAP – major goals and achievements

In the 1980s, the international SPECMAP project (SPECTral MApping Project) was launched with the aim of producing continuous time series of Ice Age climate recorded in deep-sea sediments, and studying their spectral properties. One of SPECMAP's first, and most referenced, achievements was to publish an astronomical time-scale for the upper Pleistocene (last 780 ka) based on an oxygen isotope reference curve constructed from stacking five planktonic foraminifer isotopic records from low- and mid-latitudes (Imbrie et al., 1984). This stacked curve, phase-locked (tuned) to obliquity and precession orbital oscillations, provided a continuous geological time scale for the upper Pleistocene, accurate to within 5 kyr. A few years later, Martinson et al. (1987) developed a 0–300 ka astronomical time scale transferred to a high-resolution oxygen stable isotope reference curve constructed from stacking benthic foraminifer records (Pisias et al., 1984). Four different tuning procedure approaches were followed, each of which was based upon different assumptions concerning the response of the orbital signal recorded in the data. The final chronology has an average error of ± 5 kyr.

The SPECMAP *astronomical time scale* based on stable oxygen reference curves provided a powerful stratigraphic tool to tie deep-sea climatic records within a common temporal framework with the precision needed to analyze the response of the Earth external system to orbital cyclic modulation of solar radiative forcing. For the first time, amplitude and phase of cycles in different climatic proxy records could be compared at different sites with the geographic pattern of insolation changes. This information provided insight into processes responsible for climate change on glacial-interglacial time scales (i.e., Imbrie et al., 1989).

Background: the astronomical theory of Ice Age

About 2.6 million years ago, Earth climate entered the so-called Ice Age, with its large amplitude glacial-interglacial cycles characterized by the quasi-periodical waxing and waning of large continental ice sheets from the Northern Hemisphere. In the beginning of the nineteenth century, the first geological evidence of these major Quaternary glacial episodes came from observations by Louis Agassiz of sediment deposits (moraine) and erosion features attributed to ancient glaciers in the Jura mountains of western Europe. By the middle of the nineteenth century, the French mathematician Joseph Adhémar and the Scottish geologist James Croll had suggested that past climates might have responded to cyclic changes in the orbital parameters of the Earth. In the 1920s and 1930s, the Serbian mathematician Milutin Milankovich produced time-series of the amount of solar energy received by the Earth at different latitudes and different seasons. Based on these data, he proposed an orbital theory of Ice Age in which changes in the intensity of the seasons in the Northern Hemisphere controlled the waxing and waning of northern high latitude ice sheets. In his astronomical theory of climate, the Northern Hemisphere high latitude summer temperatures hold the key to the onset of glaciations.

Within a few decades, however, the astronomical theory of climate was largely disputed, with discussion based on fragmentary geological records supported by incomplete and

frequently incorrect radiometric age data. From the 1960s onwards, access to continuous and longer oceanic records revealed many more than the four glacial periods recognized from the terrestrial record in Europe, providing more support for the astronomical theory of climate. In 1976, Hays and co-authors published a landmark paper in which they convincingly demonstrated that all the orbital frequencies predicted by the astronomical theory of climate could be found through spectral analysis of climate sensitive indicators from deep-sea records (Hays et al., 1976).

The SPECMAP astronomically derived timescale

In order to analyze the geographical propagation and time-dependence (lead/lag) of various climatic responses to seasonal and latitudinal insolation changes, age-models developed from a few, radiometrically-controlled stratigraphic tie-points are not precise enough. With the convincing validation of the astronomical theory of climate by Hays et al. in 1976, Earth sciences were in need of continuous timescales that would allow cross-correlation and aging of deep-sea sedimentary records to be performed with a precision better than a fraction of Earth's orbital periods. To achieve such a precision, various authors suggested that a timescale could be developed from deep-sea sedimentary records by using orbitally-related oscillations of paleoclimatic proxies as internal "pacemakers" (i.e., Morley and Hays, 1981). The so-called astronomical (or orbital) "tuning" approach for developing timescales rests upon the phase-locking of those orbitally-related oscillations in sedimentary records to primary orbital oscillations, namely the climatic precession (with periods of 19–23 kyr) and the obliquity of the Earth's axis (with a main period of 41 kyr).

To get a global, marine stratigraphic framework on which to develop an upper Pleistocene astronomical time scale, Imbrie et al. (1984) selected five planktonic foraminifer oxygen isotopic records from low- and mid-latitudes in which globally persistent isotopic excursions could be graphically correlated. Over the Ice Age glacial-interglacial cycles, global sea water oxygen isotopic excursions recorded in the foraminifer calcite reflect the waxing and waning of continental ice sheets, enriched in the light ^{16}O isotope relative to seawater. The general circulation of the world ocean (the so-called *Great Conveyor Belt* depicted by Broecker in 1987) insures that isotopic changes related to variations in ice-sheet volume are spread globally over the world's ocean water masses within a few hundred years.

An initial, radiometrically-controlled age-model was developed for each of the five isotopic records, using few stratigraphic levels: core tops (with a \sim zero age); two isotopic events in stage 2 with ^{14}C ages of 18 and 21 ka; the 6.0 isotopic state boundary, taken as 127 ka; and the Brunhes-Matuyama magnetic reversal, taken as 730 ka. The astronomical tuning procedure applied by Imbrie et al. (1984) iteratively modified the initial depth-age models to increase the coherency and phase lock between filtered 19–23 kyr $^{-1}$ and 41 kyr $^{-1}$ oscillations of the oxygen isotopic records on the one hand, and the precession and obliquity components of the Earth's orbital variations on the other. Such an orbital tuning approach assumes constant phase lags at the primary Milankovitch frequencies between the marine oxygen isotopic variations and Earth's orbital changes. Those phase lags had been determined in an earlier paper (Imbrie and Imbrie, 1980) by adjusting the parameterization of a nonlinear (exponential) climatic model predicting ice volume variations, so that the model output would match a radiometrically-dated 130 kyr long isotopic record.

The five astronomically-dated isotopic records were finally normalized and stacked, and the resulting curve smoothed with a 9-point Gaussian filter to produce a reference stratigraphic record (Figure S23). The rationale for the stacking approach

is that global isotopic changes related to ice sheet waxing/waning would be enhanced in the resulting composite curve, whereas local or regional isotopic variations would tend to cancel out. Figure S24 shows the comparison of filtered

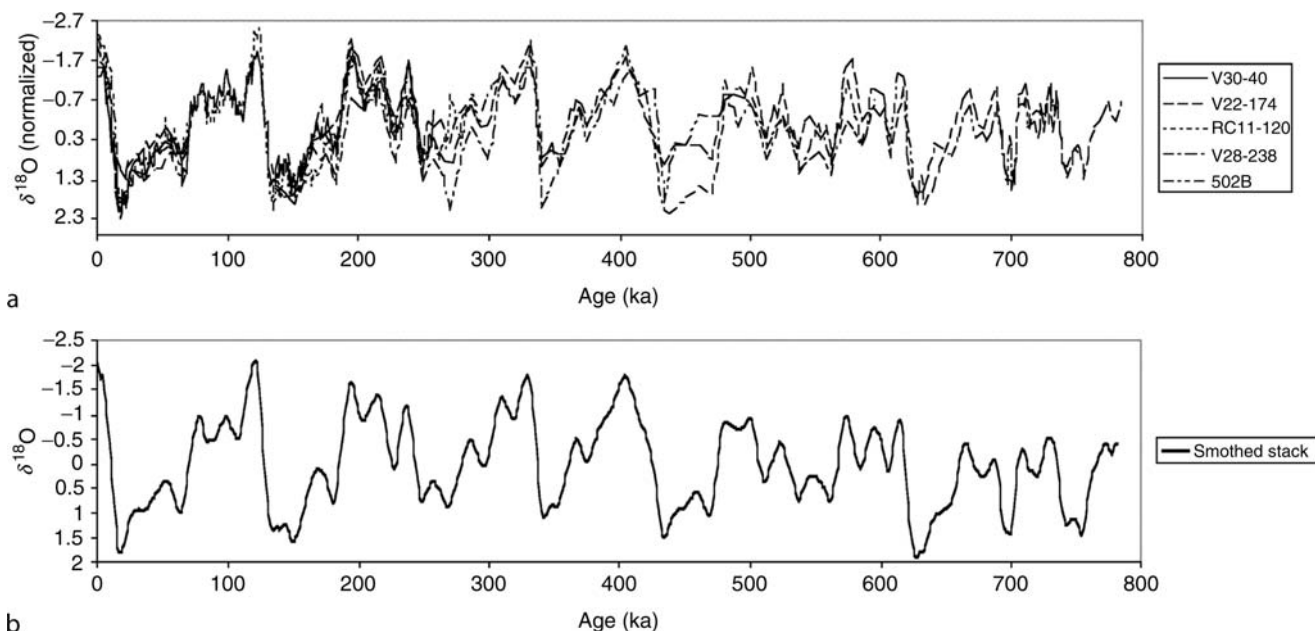


Figure S23 (a) Normalized variations in $\delta^{18}\text{O}$ as a function of astronomically-tuned ages in the five deep-sea cores used to develop the SPECMAP reference curve. (b) Resulting oxygen isotopic reference curve obtained after stacking the 5 records and smoothing the resulting record using a 9-point Gaussian filter (figure modified from Imbrie et al., 1984).

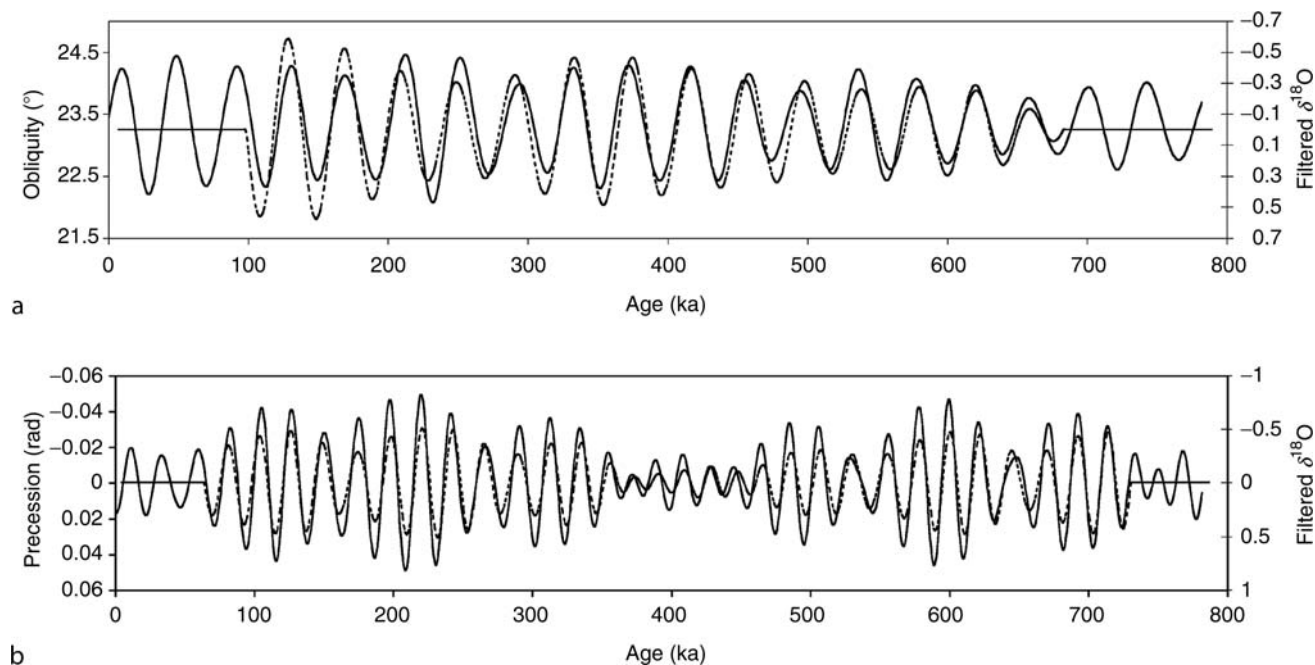


Figure S24 Solid lines show variations in obliquity (a) and precession (b) and the corresponding frequency components extracted by band-filtering the $\delta^{18}\text{O}$ stack record (dashed line) over the past 780 kyr (figure modified from Imbrie et al., 1984).

precession- and obliquity-related oscillations from the stacked isotopic record with obliquity (upper panel) and precession (lower panel) orbital oscillations.

The geological timescale obtained by Imbrie and co-workers for the upper Pleistocene is accurate to within 5 kyr (Imbrie et al., 1984). Since its publication, the orbitally-dated isotopic stacked record has been used in hundreds of paleoceanographic studies as a reference curve for developing age-models and tying marine sedimentary records into a common stratigraphic framework.

Three years after the landmark paper by Imbrie et al. (1984), Martinson et al. (1987) developed an orbital timescale for the last 300 ka that they transferred to the stacked, benthic oxygen-isotope stratigraphy from Pisias et al. (1984; Figure S25). Martinson et al. (1987) followed four different tuning strategies. This made it possible to test the robustness and accuracy of astronomical tuning for developing an upper Pleistocene time scale. The error measured by the standard deviation about the average of their four chronologies has an average magnitude of 2.5 kyr. Transferring the final chronology to the stacked isotopic record of Pisias et al. (1984) leads to additional errors. The final chronology has an average error of ± 5 kyr. Comparison of the younger portion of the chronology of Imbrie et al. and the 300-kyr chronology of Martinson et al. shows that ages of isotopic events agree to within the error bars.

Following the initial SPECMAP effort, astronomical timescales were developed for the Middle and Early Pleistocene periods (Raymo et al., 1989; Ruddiman et al., 1989). It also became increasingly clear that orbital control of climate was not restricted to the Ice Age. This allowed the astronomical tuning approach to be applied to older periods of the Earth history, reaching back to the Neogene (Shackleton et al., 1999).

Limits of the astronomical calibration approach

Orbital tuning provides a global reference standard for dating long, continuous sediment records. However, the approach is not without its problems. Subsequent revisions of the 0–780 ka SPECMAP timescale showed, for instance, that several oscillations predicted by the astronomical theory of climate (in isotopic stages 17 and 18) were apparently missing in the stacked record (Bassilot et al., 1994). Their absence is related

(a) to the incompleteness of some of the isotopic records that reached those stages, and (b) to an erroneous Brunhes-Matuyama (BM) magnetic reversal age assignment in the age-model developed at the first step of the Imbrie et al., 1984 tuning approach. $^{40}\text{Ar}/^{39}\text{Ar}$ radiometric dating of the Brunhes-Matuyama magnetic boundary gives an age of about 780 ka (Baksi et al., 1992), significantly older than the K/Ar age (730 ka) available in the early 1980s, and used by Imbrie et al. (1984) to constrain their initial age-model. Although the time constraint at the B/M boundary was removed midway in the orbital tuning approach of Imbrie et al., it is quite clear that the final age-model suffered from this erroneous tie-point.

Applying astronomical tuning strategies with a higher degree of freedom (i.e., no initial age assignment to the B/M boundary) on carefully selected, high-resolution isotopic records, Shackleton et al. (1990) and Bassilot et al. (1994) obtained astronomical ages for the Brunhes-Matuyama magnetic reversal that are in good agreement with $^{40}\text{Ar}/^{39}\text{Ar}$ radiometric ages. This example illustrates the fact that theoretical precision of astronomical time scales (usually a few thousand years) may actually mask potential, larger uncertainties related to the tuning strategy and/or to incompleteness of paleoclimatic records used to provide the stratigraphic framework on which the astronomical tuning is conducted.

Analyzing the Ice Age record within the framework of the SPECMAP time scale

Using their astronomically dated oxygen isotopic stratigraphy, the SPECMAP group produced a research effort to determine how orbital signals are transferred into climatic responses during the upper Pleistocene part of the Ice Age. The rigorous and robust strategy they developed was based upon partitioning the climatic response at different locations of the world ocean into its frequency components (Imbrie et al., 1989). This strategy allows analysis of three major aspects of the Earth's climatic response to orbital changes in insolation forcing:

1. Examination of climate spectra makes it possible to separate between linear and nonlinear responses to radiative forcing. Many paleoclimatic records indicate that there exist direct, linear responses of Earth's climatic sub-systems to insolation forcing in the precession and obliquity bands (Imbrie

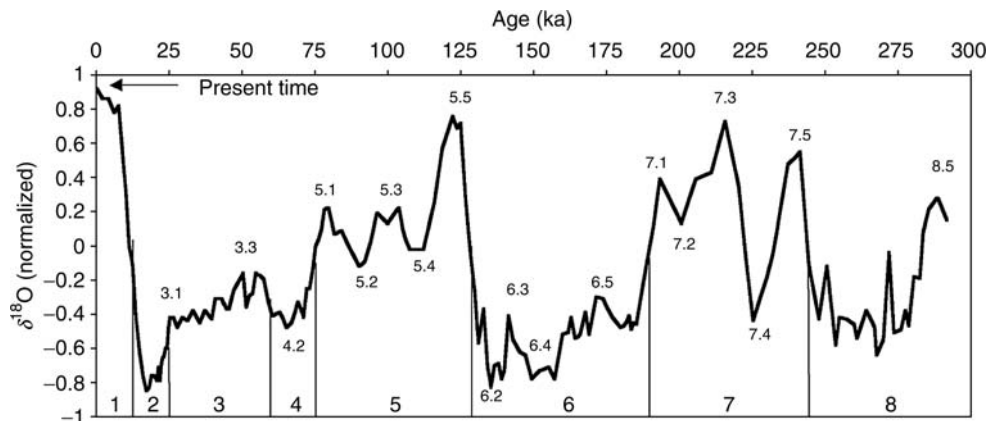


Figure S25 The 0–300 ka time scale developed by Martinson et al. (1987) and transferred to the stacked, benthic oxygen isotopic reference curve of Pisias et al. (1984). Isotopic stages are indicated on the bottom of the figure. Major isotopic events are shown along the isotopic curve, following definition by Pisias et al. (1984) (figure modified from Martinson et al., 1987).

et al., 1992). The dominance of the 100-kyr periodicity in glacial-interglacial oscillations of the last million years, on the other hand, is not easily accounted for by the astronomical theory of climate since eccentricity variations of the Earth's orbit lead to only minor changes in the insolation budget. Non-linear responses to insolation changes have been proposed – amongst several other possible mechanisms – to deal with the puzzling 100-kyr oscillations of the Earth's climate (Imbrie et al., 1993).

2. Analysis of phase relationships provides information about the response time of different oceanic and climate components (i.e., sea surface and deep water hydrology (T, S), surface productivity, wind forcing, etc.) and their causal relationships (e.g., leads/lags indicating which changes might be forcing others).
3. Analysis of geographic distribution of the response provides information about which regions play critical roles in climate changes.

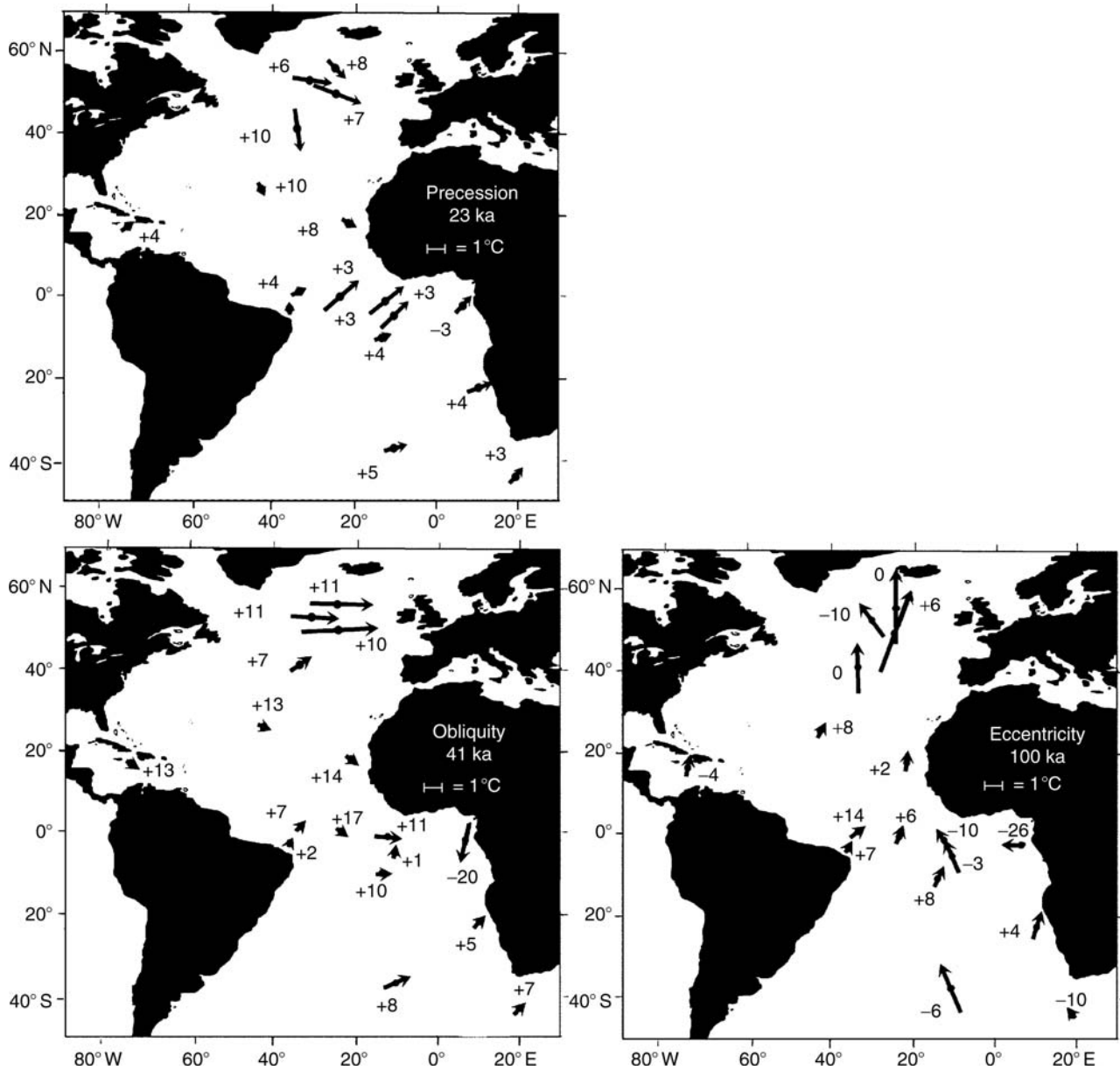


Figure S26 SPECMAP analysis of cold-season SST (Sea Surface Temperature) variations at 17 Atlantic sites in the precession, obliquity and eccentricity frequency bands. Cyclic changes in SST are analyzed relative to $\delta^{18}\text{O}$ oscillations. Phase-relationships between these two signals are displayed as arrows following the so-called “phase wheel” representation, with $\delta^{18}\text{O}$ being set at the “zero phase” (= vertical). The leads/lags (in ka) between $\delta^{18}\text{O}$ and SST are also indicated next to each arrow (a *negative* value indicates that $\delta^{18}\text{O}$ changes *lag* SST changes, whereas a *positive* value indicates that $\delta^{18}\text{O}$ variations *lead* SST changes). The length of each arrow is proportional to the coherent amplitude of the SST cyclic change (see the 1°C reference scale shown in each panel) (figure modified from Imbrie et al., 1989).

Figure S26 shows the amplitude of Atlantic Sea Surface Temperature (SST) oscillations at 17 sites in the precession, obliquity and eccentricity bands, and their phase relationships relative to $\delta^{18}\text{O}$ changes. The largest SST changes (longest arrows) occur generally near 50°N in the North Atlantic and reflect oscillations of the Gulf Stream and North Atlantic polar front in response to changes affecting the nearby continental ice sheets. In this area, SPECMAP results indicate large amplitude SST changes in the obliquity band (Figure S26, lower left panel), a result consistent with the strong influence of Earth's axis tilt oscillations on high-latitude insolation changes. South of about 45°N , the obliquity forcing drops down, as shown by the weak amplitude of SST changes. In contrast, the precession signal keeps its strength closer to the low-latitudes (Figure S26, upper left panel). Major climatic features at low-latitudes – such as monsoons – generally show strong precession variability.

In the eccentricity band, there is a suggestion of a phase shift across the equator: in the South Atlantic, temperature changes generally lead oxygen isotopes, whereas in the North Atlantic the SST changes either are in phase or lag $\delta^{18}\text{O}$ changes (Figure S26, lower right panel). This early response of Southern Hemisphere SST suggests a drawback in Milankovitch's theory of climate changes. Milankovitch proposed that insolation changes in the high-latitudes of the Northern Hemisphere are the key to controlling glacial-interglacial variations. SPECMAP data show that the insolation over the Southern Hemisphere (and inter-hemispheric heat transport) has to be taken into account in scenarios dealing with astronomical control of global Earth's climate.

Conclusion

The SPECMAP project launched in the 1980s radically improved our understanding of how the Ice Age climate responded to changes in latitudinal and seasonal distribution of solar energy controlled by variations in the orbital parameters of the Earth. The development of a high-resolution time frame for the upper Pleistocene made it possible to compare climatic proxy records from sedimentary series at different oceanic sites to the geographic pattern of insolation changes with an unprecedented time precision.

The SPECMAP group also proved to be extremely effective in pointing out some weaknesses of the astronomical theory of climate (i.e., the puzzling 100-kyr cycle that dominates global climate changes over the last million years) and called for more complex mechanisms than those that were originally proposed by pioneers such as Milutin Milankovitch. For instance, the fact that Southern Hemisphere sea surface temperatures seem to lead changes in Northern Hemisphere ice sheets showed the limits of Milankovitch's hypothesis which puts emphasis on insolation changes at about 65°N . Amongst important key players for climate changes that were not taken into account by astronomical theory of climate are greenhouse gases such as CO_2 . Long records of atmospheric composition obtained from bubbles trapped in Antarctica and Greenland ice cores indicate that the $p\text{CO}_2$ of the atmosphere showed large amplitude variations associated with glacial-interglacial global climate oscillations. During the last glacial terminations, the atmospheric $p\text{CO}_2$ rise led the melting of ice sheets by a few thousand years (Broecker and Henderson, 1998). This clearly indicates that atmospheric $p\text{CO}_2$, which is ultimately controlled by changes taking place in the ocean, is an important primary driver of the Earth's climate and that Ice Age

oscillations cannot be fully explained through insolation control on Northern Hemisphere ice sheets.

Franck C. Bassinot

Bibliography

- Baksi, A.K., Hsu, V., McWilliams, M.O., and Farrer, E., 1992. $^{40}\text{Ar}/^{39}\text{Ar}$ dating of the Brunhes-Matuyama geomagnetic field reversal. *Science*, **256**, 356–357.
- Bassinot, F.C., Labeyrie, L.D., Vincent, E., Quidelleur, X., Shackleton, N.J., and Lancelot, Y., 1994. The astronomical theory of climate and the age of the Brunhes-Matuyama magnetic reversal. *Earth Planet. Sci. Lett.*, **126**, 91–108.
- Broecker, W.S., 1987. The biggest chill. *Nat. Hist.*, **96**, 74–82.
- Broecker, W.S., and Henderson, G., 1998. The sequence of events surrounding Termination II and their implications for the cause of glacial-interglacial CO_2 changes. *Paleoceanography*, **13**, 352–364.
- Hays, J.D., Imbrie, J., and Shackleton, N.J., 1976. Variations in the Earth's orbit: Pacemaker of the Ice Ages. *Science*, **194**, 1121–1132.
- Imbrie, J., and Imbrie, J.Z., 1980. Modelling the climatic response to orbital variations. *Science*, **207**, 942–953.
- Imbrie, J., Hays, J.D., Martinson, D.G., McIntyre, A., Mix, A.C., Morley, J.J., Pisias, N.G., Prell, W.L., and Shackleton, N.J., 1984. The orbital theory of Pleistocene climate: Support from a revised chronology of the marine $\delta^{18}\text{O}$ record. In Berger, A., et al. (eds), *Milankovitch and Climate*. Hingham, MA: D. Reidel, pp. 269–305.
- Imbrie, J., McIntyre, A., and Mix, A., 1989. Oceanic response to orbital forcing in the late Quaternary: Observational and experimental strategies. In Berger, A., et al. (eds), *Climate and Geo-Sciences*. Dordrecht: Kluwer. pp. 121–164.
- Imbrie, J., Boyle, E.A., Clemens, S.C., Duffy, A., Howard, W.R., Kukla, G., Kutzbach, J., Martinson, D.G., McIntyre, A., Mix, A.C., Molfino, B., Morley, J.J., Peterson, L.C., Pisias, N.G., Prell, W.L., Raymo, M.E., Shackleton, N.J., and Toggweiler, J.R., 1992. On the structure and origin of major glaciation cycles. 1. Linear responses to Milankovitch forcing. *Paleoceanography*, **7**, 701–738.
- Imbrie, J., Boyle, E.A., Clemens, S.C., Duffy, A., Howard, W.R., Kukla, G., Kutzbach, J., Martinson, D.G., McIntyre, A., Mix, A.C., Molfino, B., Morley, J.J., Peterson, L.C., Pisias, N.G., Prell, W.L., Raymo, M.E., Shackleton, N.J., and Toggweiler, J.R., 1993. On the structure and origin of major glaciation cycles. 2. The 100,000-year cycle. *Paleoceanography*, **8**, 699–735.
- Martinson, D.G., Pisias, N.G., Hays, J.D., Imbrie, J., Moore, T.C., and Shackleton, N.J., 1987. Age dating and the orbital theory of the ice ages: Development of a high-resolution 0 to 300,000 year chronostratigraphy. *Quaternary Res.*, **27**, 1–29.
- Morley, J.J., and Hays, J.D., 1981. Towards a high-resolution, global, deep-sea chronology for the last 750,000 years. *Earth Planet. Sci. Lett.*, **53**, 279–295.
- Pisias, N.G., Martinson, D.G., Moore, T.C., Shackleton, N.J., Prell, W., Hays, J., and Boden, G., 1984. High resolution stratigraphic correlation of benthic oxygen isotopic records spanning the last 300,000 years. *Mar. Geol.*, **56**, 119–136.
- Raymo, M.E., Ruddiman, W.F., Backman, J., Clement, B.M., and Martinson, D.G., 1989. Late Pliocene variations in Northern Hemisphere ice sheets and North Atlantic deep water circulation. *Paleoceanography*, **4**, 413–446.
- Ruddiman, W.F., Raymo, M.E., Martinson, D.G., Clement, B.M., and Backman, J., 1989. Pleistocene evolution: Northern Hemisphere ice sheets and North Atlantic Ocean. *Paleoceanography*, **4**, 353–412.
- Shackleton, N.J., Berger, A., and Peltier, W.R., 1990. An alternative astronomical calibration of the lower Pleistocene timescale based on ODP Site 677. *Trans. R. Soc. Edinb. Earth Sci.*, **81**, 251–261.
- Shackleton, N.J., McCave, I.N., and Weedon, G.P., 1999. Astronomical (Milankovitch) calibration of the geological time-scale. *Philos. Trans. R. Soc. London A*, **357**, 1731–2007.

Cross-references

Astronomical Theory of Climate Change
Carbon Dioxide and Methane, Quaternary Variations

Glaciations, Quaternary
 History of Paleoclimatology
 Ice cores, Antarctica and Greenland
 Obliquity
 Oxygen Isotopes
 Precession, Climatic
 Pleistocene Climates
 Quaternary Climate Transitions and Cycles
 Time-Series Analysis of Paleoclimate Data

SPELEOTHEMS

Speleothems, from the Greek *speilaion* (cave) and *thema* (deposit), are chemical deposits formed in caves. Although close to 200 minerals have been identified as secondary minerals in caves, the bulk of formations that occur in caves consist of carbonates. Dripstones, such as stalagmites (Figure S27a) and stalactites (Figure S27b), and flowstones are types of speleothems. Stalactites grow downward from the ceiling, while stalagmites are their counterparts that grow upwards from the floor. Flowstones, as the name implies, form from flowing water. There are numerous varieties of speleothems that form in the cave environment but carbonate dripstones and flowstones are the most common and voluminous.

The chemical evolution that results in the formation of speleothem calcite (CaCO_3) starts by water absorbing carbon dioxide (CO_2), from the overlying soil to form carbonic acid (H_2CO_3) (Reaction 1). CO_2 levels in soil can reach up to two orders of magnitude higher than the atmospheric value of about 370 ppm due to plant respiration and decay of organic matter (Hendy, 1971). As the carbonic acid containing water percolates down, it dissolves calcium carbonate (Reaction 2). Once the carbonate-rich water is exposed to the CO_2 -poor cave

atmosphere, it releases CO_2 , resulting in the precipitation of calcite or aragonite (Reaction 3).



Speleothems are typically made of calcite (CaCO_3), and to a lesser extent of aragonite, another polymorph (same chemical composition but different crystal type) of CaCO_3 . Calcite forms hexagonal crystals, while aragonite forms orthorhombic crystals; which form crystallizes depends on the degree of saturation of the solution. Highly saturated solutions in warm climates tend to crystallize aragonite, this is especially true in caves formed from dolomite [$\text{CaMg}(\text{CO}_3)_2$], because high Mg concentration from the dissolution of dolomite inhibits calcite formation. The occurrence of alternating calcite and aragonite in stalagmites has been interpreted to indicate differences in the severity of aridity in the region where the speleothems are collected (Denniston et al., 2000a; Polyak and Asmerom, 2001).

Growth layering in speleothems

Speleothem growth can vary widely, depending on the cave environment, and in some cases it can preserve annual-scale layering, especially in stalagmites, where growth layering is simple surface addition. Figure S28 shows a photomicrograph of annual growth banding in a stalagmite from a cave close to Carlsbad Caver, New Mexico. Each layer, around 20 microns thick, represents a single year's growth. Annual banding in speleothems was recognized very early (e.g., Broecker et al., 1960), and has been reported from a variety of settings (e.g., Genty and Quinif, 1996; Brook et al., 1999; Polyak and Asmerom, 2001; Hou et al., 2003). Annual banding

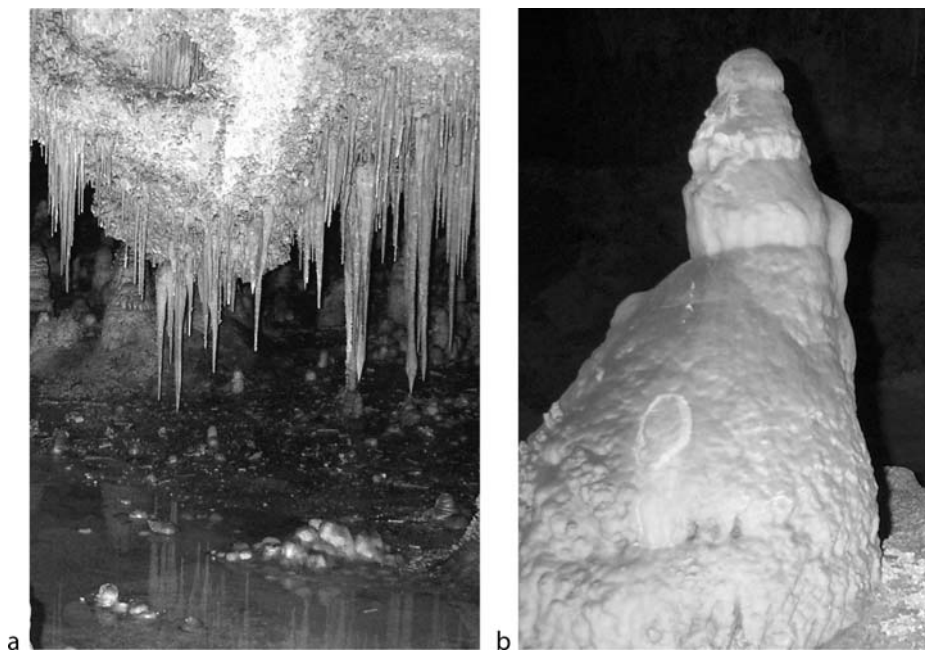


Figure S27 (a) Stalactites hanging from a low ceiling, Slaughter Canyon Cave, Carlsbad Caverns National Park, New Mexico, USA (photo: Yemane Asmerom). (b) Giant Stalagmites, Carlsbad Caverns, Carlsbad Caverns National Park, New Mexico, USA (photo: Yemane Asmerom).

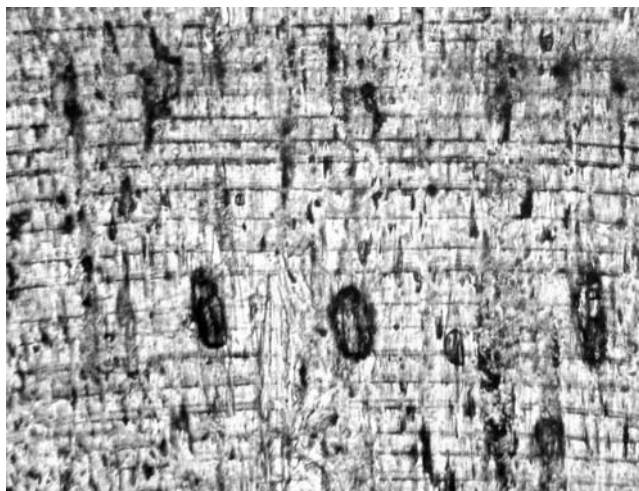


Figure S28 A photomicrograph of annual banding, representing about 17 years of growth in an aragonite stalagmite from Carlsbad Caverns, Carlsbad National Park, New Mexico USA (photo: Victor Polyak and Yemane Asmerom).

can also be expressed in a variety of other ways, including luminescence banding of organic matter (Baker et al., 1993), and in variation of trace elements (e.g., Fairchild et al., 2001; Huang et al., 2001).

Climate and environmental changes from speleothem data

Speleothems contain a wide-range of chemical and physical proxies of past climate in continents that may be resolved at an annual scale, given annual-scale banding and the ability to date them using uranium-series (U-series) isotopic techniques. The method is based on measurement of the decay isotopes of uranium, especially the decay of ^{238}U to ^{234}U , which in turn decays to 230-Thorium. Uranium is soluble in the solution that forms speleothems, while thorium is not. Thus, the amount of ^{230}Th is a measure of the age of the sample and the concentration of ^{238}U and ^{234}U . With the development of modern mass spectrometric techniques for measuring U-series isotopes (Chen et al., 1986; Edwards et al., 1987), it is possible to obtain very precise ages on small amounts, using less than 200 mg of speleothem powder, yielding typical age uncertainties of less than 0.5% ($2-\sigma$) (Dorale et al., 2001).

One of the earliest areas of studies of past climate was looking at the isotopic variations of oxygen (O) and carbon (C) of speleothem calcite. Hendy (1971) outlined the methodology and rationale for the approach. Oxygen has two major (^{16}O , ^{18}O) and one minor (^{17}O) isotopes, while carbon has two stable isotopes, ^{12}C and ^{13}C . The O isotope variations of speleothems reflect processes active in the source and atmosphere meteoric water and the fractionation (one isotope favored another) that occurs when calcite crystallized from drip water. If the O isotope composition of the water is known, either from fluids trapped in the crystal (Matthews et al., 2001) or known independently, and, if the calcite formed in equilibrium with the water, then changes in O isotopes may be related to changes in temperature. In deep enough caves, this generally reflects the mean annual temperature. Variations in O isotopic composition may also indicate changes in the

moisture source of the meteoric water from which the drip water was derived. Such information can give insight into large-scale changes in ocean-atmospheric interactions, such as monsoon intensity (e.g., Wang et al., 2001).

The carbon isotopic composition of speleothems primary reflects: (a) the C isotopic composition of the soil CO_2 , derived from oxidation of local organic matter that dissolves into the drip water; (b) the C isotopic composition of the bedrock, which is constant for a given site; and (c) isotopic fractionation during calcite formation (Hendy, 1971). Carbon isotopes in speleothems have been used to observe the change between plants that utilize the C_3 photosynthetic pathway and plants that use the C_4 pathway. C_4 plants are adapted to an arid, high temperature climate, although it has been suggested that they also evolved to deal with lower atmospheric CO_2 in the Cenozoic (Cerling et al., 1998). C_3 plants have a stronger preference for ^{12}C over ^{13}C , as compared to C_4 plants. Thus, variations in $^{13}\text{C}/^{12}\text{C}$ ratios may indicate variations in C_3 and C_4 plant cover (e.g., Dorale et al., 1998; Denniston et al., 2000b).

A number of other studies have used variations in the growth banding of annually-banded speleothems (Asmerom and Polyak, 2004) as an indicator of changes in precipitation through time. For example, Polyak and Asmerom (2001) reconstructed climate change over the past 4,000 years for the southwestern USA and correlated it with cultural changes over the same time period. Changes in mineralogy of speleothems (aragonite = arid, calcite = wet) have been used to study the relative intensity of the monsoon in Nepal (Denniston et al., 2000a).

The above is a small sampling of the rich-variety of climatic, cultural and environmental studies that are being conducted using speleothem isotopic, chemical and physical data. Above all, speleothems are some of the most beautiful sculptures of nature, worthy of the highest stewardship. A great deal can be learned using speleothems and every effort should be put towards preserving these natural wonders.

Yemane Asmerom

Bibliography

- Asmerom, Y., and Polyak, J.V., 2004. Comment on Betancourt et al. 2002: "A test of annual resolution in stalagmites using tree rings." *Quaternary Res.*, **61**, 119–121.
- Baker, A., Smart, P.L., Edwards, R.L., and Richards, D.A., 1993. Annual growth banding in a cave stalagmite. *Nature* **364**, 518–520.
- Broecker, W.S., Olson, E.A., and Orr, P.C., 1960. Radiocarbon measurements and annual rings in cave formations. *Nature*, **185**, 93–94.
- Brook, G.A., Rafter, M.A., Railsback, L.B., Sheen, S., and Lundberg, J., 1999. A high-resolution proxy record of rainfall and ENSO since AD1550 from layering in stalagmites from Anjohibe Cave, Madagascar. *The Holocene*, **9**, 695–705.
- Cerling, T.E., Ehleringer, J.R., and Harris, J.M., 1998. Carbon dioxide starvation, the development of C-4 ecosystems, and mammalian evolution. *Philos. Trans. R. Soc. Lond. Ser. B Biol. Sci.*, **353**, 159–170.
- Chen, J.H., Edwards, R.L., and Wasserburg, G.L., 1986. ^{238}U , ^{234}U and ^{232}Th in seawater. *Earth Planet. Sci. Lett.*, **80**, 241–251.
- Denniston, R.F., González, L.A., Asmerom, Y., Sharma, R.H., and Reagan, M.K., 2000a. Speleothem evidence for changes in Indian summer monsoon precipitation over the last 2,300 years. *Quaternary Res.*, **53**, 196–202.
- Denniston, R.F., González, L.A., Asmerom, Y., and Reagan, M.K., 2000b. Speleothem records of early and late Holocene vegetation dynamics in the Ozark Highlands, USA. *Quaternary Int.*, **67**, 21–27.
- Dorale, J.A., Edwards, R.L., Ito, E., and González, L.A., 1998. Climate and vegetation history of the midcontinent from 75 to 25 ka. A speleothem record from Crevice Cave, Missouri, USA. *Science*, **282**, 1871–1874.

- Dorale, J.A., Edwards, R.L., Alexander, E.C. Jr., Shen, C.C., Richards, D.A., and Cheng, H., 2001. Uranium-series dating of speleothems: Current techniques, limits, and applications. In Mylroic, J., and Sasowsky, I.D. (eds.), *Studies of Cave Sediments*. New York: Kluwer/Plenum.
- Edwards, R.L., Chen, J.H., and Wasserburg, G.L., 1987. ^{238}U - ^{234}U - ^{230}Th - ^{232}Th systematics and the precise measurement of time over the past 500,000 y. *Earth Planet. Sci. Lett.*, **81**, 175–192.
- Fairchild, I.J., Baker, A., Borsato, A., Frisia, S., Hinton, R.W., McDermott, F., and Tooth, A.F., 2001. Annual to sub-annual resolution of multiple trace-element trends in speleothems. *J. Geol. Soc. London*, **158**, 831–841.
- Genty, D., and Quinif, Y., 1996. Annually laminated sequences in the internal structure of some Belgian stalagmites – importance for paleoclimatology. *J. Sediment. Res.*, **66**, 275–288.
- Hendy, C.H., 1971. The isotopic geochemistry of speleothems, I. The calculation of the effects of different modes of formation on the isotopic composition of speleothems and their applicability as paleoclimatic indicators. *Geochemica et Cosmochimica Acta*, **35**, 801–824.
- Hou, J.Z., Tan, M., Cheng, H., and Liu, T.S., 2003. Stable isotope records of plant cover change and monsoon variation in the past 2,200 years: Evidence from laminated stalagmites in Beijing, China. *Boreas*, **32**, 304–313.
- Huang, Y., Fairchild, I.J., Borsato, A., Frisia, S., Cassidy, N.J., McDermott, F., and Hawkesworth, C.J., 2001. Seasonal variations in Sr, Mg, and P in modern speleothems (Grotta di Ernesto, Italy). *Chem. Geol.*, **175**, 429–448.
- Matthews, A., Ayalon, A., and Bar-Matthews, M., 2001. D/H ratios of fluid inclusions of Soreq Cave (Israel) speleothems as a guide to the eastern Mediterranean meteoric line relationships in the last 120 ky. *Chem. Geol.*, **166**, 183–191.
- Polyak, V.J., and Asmerom, Y., 2001. Late Holocene climate and cultural changes in the southwestern United States. *Science*, **294**, 148–151.
- Wang, Y.G., Cheng, H., Edwards, R.L., An, Z.S., Wu, J.Y., Shen, C.-C., and Dorale, J.A., 2001. A high-resolution absolute-dated late Pleistocene monsoon record from Hulu Cave, China. *Science*, **294**, 2345–2348.

Cross-references

[Carbon Isotopes, Stable Isotope Fractionation](#)
[Mineral Indicators of Past Climates](#)
[Oxygen Isotopes](#)
[Uranium-Series Dating](#)

STABLE ISOTOPE ANALYSIS

Background

Atoms of an element always have the same number of electrons as protons (atomic number), but may differ in the number of neutrons in the nucleus, producing slight differences in atomic mass. These are referred to as isotopes. Few elements consist of just one isotope; most elements in nature have more than two isotopes. Whereas most of these atoms are naturally stable, some isotopes are naturally unstable (radiogenic), spontaneously releasing energy and transforming into more stable atoms. Stable isotopes with low atomic number – the light stable isotopes – are the major focus of paleoclimate research. These isotopes include those of oxygen (^{18}O , ^{16}O), hydrogen (^1H , $^2\text{H} = \text{D}$), carbon (^{13}C , ^{12}C), nitrogen (^{15}N , ^{14}N), and sulfur (^{32}S , ^{34}S).

Notation

Stable isotopes with lower atomic mass are typically more abundant than their larger counterparts (Table S2), and their

Table S2 Abundance of light stable isotopes

Element	Isotope	Abundance (%)
Hydrogen	^1H	99.985
	$^2\text{H} = \text{D}^*$	0.015
Carbon	^{12}C	98.98
	^{13}C	1.11
Nitrogen	^{14}N	99.63
	^{15}N	0.37
Oxygen	^{16}O	99.959
	^{17}O	0.037
	^{18}O	0.204
Sulfur	^{32}S	95.00
	^{33}S	0.76
	^{34}S	4.22

* ^2H is also called deuterium (D). Although ^{17}O and ^{33}S are stable isotopes, they are not currently used for paleoclimatic studies because reproducible analyses of their abundances in natural materials have only been recently achieved.

abundances in natural materials are reported in relative terms as the ratio of the heavier (rare) and lighter (abundant) isotopes:

$$R = \frac{\text{Abundance of rare isotope}}{\text{Abundance of abundant isotope}} \quad (1)$$

Absolute stable isotope ratios are, however, rarely reported because current analytical instrumentation has a relatively low sensitivity that makes it unsuitable for detecting very small natural variations of stable isotopes. Absolute isotope ratios generally possess poor reproducibility. In paleoclimatic studies, changes in stable isotope ratios are therefore more relevant than the absolute isotope ratios. Thus, it is preferable to use an international reference material with which to compare the samples. This standard can provide information about changes in the ratio of rare and abundant isotopes in the sample relative to the ratio in the standard. Since these variations are less than one and are reported to at least five or six significant figures, the delta (δ) notation is used to represent parts per thousand (per mil) deviation of the isotope ratio of the sample relative to that of the reference material (Equation (2)).

$$\delta_{A/B} = \left(\frac{R_{\text{Sample}}}{R_{\text{Standard}}} - 1 \right) 1,000 \quad (2)$$

where R is the isotope ratio, and the values of δ are given in per mil (‰). Equation (2) indicates that an enrichment of the rare (heavy) isotope in the sample relative to the reference material (standard) produces higher δ values. Positive δ values, then, result when $R_{\text{Sample}} \gg R_{\text{Standard}}$, whereas negative δ values result when $R_{\text{Sample}} < R_{\text{Standard}}$.

Standards

Table S3 lists the internationally accepted reference standards and their absolute isotope ratios. By definition (Equation (2)), the δ value of an absolute standard is 0‰. Since absolute reference materials are currently either exhausted or available in small quantities, laboratories routinely employ internal standards that are calibrated against the absolute standards. These calibrations are needed to convert δ values obtained from internal standards into δ values based on absolute standards (Craig, 1957).

Table S3 Absolute reference material

Standard	Isotope ratio	Abundance
V-SMOW	D/H	1.5575×10^{-4}
V-PDB	$^{12}\text{C}/^{13}\text{C}$	1.1237×10^{-3}
Air	$^{15}\text{N}/^{14}\text{N}$	3.677×10^{-3}
V-SMOW	$^{18}\text{O}/^{16}\text{O}$	2.0052×10^{-3}
V-PDB	$^{18}\text{O}/^{16}\text{O}$	2.0672×10^{-3}
CDT	$^{34}\text{S}/^{32}\text{S}$	4.5005×10^{-2}

Note: *V-SMOW*, Vienna-Standard Meteoric Ocean Water; *V-PDB*, Vienna-PeeDee Belemnite; and *CDT*, Canyon Diablo Troilite.

Fractionation effects

Despite having the same number of electrons and protons, isotopes of the same element behave differently during chemical and physical processes which results in a dissimilar distribution of isotopes among reactants and products. This partitioning of isotopes is referred to as isotope fractionation. There are fundamentally two phenomena that cause isotope fractionation: lower mobility of heavier isotope molecules and lower binding energies of lighter isotope molecules. The former produces lower diffusion rates relative to those of their lighter counterparts. Lower mobility also produces a reduction in collision frequency with other molecules during chemical reactions, leading to slower rates of chemical reaction for heavier molecules. In addition to higher mobility, faster reaction rates occur with lighter isotope molecules due to their lower binding energies. These two phenomena (i.e., mobility and binding energy) cause, for example, heavier water molecules ($^1\text{H}_2^3\text{O}$ and $^1\text{H}^2\text{H}^1\text{O}$) to evaporate at a slower rate than their lighter counterpart ($^1\text{H}_2^1\text{O}$).

The partitioning of isotopes between substances A and B (either two different chemical compounds or two phases of the same compound) can be represented as:

$$\alpha_{A-B} = \frac{R_A}{R_B} \quad (3)$$

where R is the isotope ratio, and α is referred to as the fractionation factor. The partitioning of isotopes between substances A and B as represented by Equation (3) can be equated to the more familiar equilibrium constant (K) of a reaction by the following equation:

$$\alpha_{A-B} = K^{1/n} \quad (4)$$

where n is the number of atoms exchanged. The magnitude of the fractionation factor depends on temperature, as indicated by the pioneer work of H. Urey (1947). A general expression that relates temperature and α is of the form:

$$\alpha_{A-B} = N e^{M/T} \quad (5)$$

where N and M are temperature-independent coefficients, and T is temperature. Theoretical, semi-empirical, experimental, and observational calculations of the magnitude of α with temperature exist for different chemical reactions, isotope exchange reactions, and phase changes of compounds. These relationships are typically expressed as the power series solution of the natural logarithm of Equation (5):

$$\ln \alpha_{A-B} = C_1 + \frac{C_2}{T} + \frac{C_3}{T^2} \quad (6)$$

where C_1 , C_2 , C_3 are constants, and T is temperature (in Kelvin).

Urey (1947) was the first to predict the paleoclimatic potential of the dependence of the partitioning of isotopes on temperature. His pioneering work focused on thermodynamic equations that describe the partitioning of isotopes between water and calcium carbonate. Based on these equations, Urey argued that the stable-oxygen isotopic composition of carbonate minerals provides information about past temperatures. To assess the temperature-dependent relationship between isotope ratios of calcium carbonate and water, mollusks were grown in water of known isotopic composition at different temperatures (Epstein et al., 1953). The obtained experimental relationship was in close agreement with Urey's theoretical determinations, providing support for the idea that stable-oxygen isotopes can be used for paleoclimatologic research.

Probably the first most significant use of stable isotopes in paleoclimatology was the work of Emiliani (1955). He determined the oxygen-isotopic composition ($\delta^{18}\text{O}$) of foraminiferal shells from cores retrieved around different ocean basins and found numerous fluctuations in ($\delta^{18}\text{O}$) values that he equated with glacial/interglacial cycles. As indicated by Equations (3), (5), and (6), $\delta^{18}\text{O}$ values of foraminifera depend on seawater $\delta^{18}\text{O}$ values and temperature. Paleotemperatures can only be determined when seawater $\delta^{18}\text{O}$ values are known. Emiliani (1955) realized that seawater $\delta^{18}\text{O}$ values have changed through time due to different volumes of continental ice caps. Employing simple assumptions, Emiliani estimated that glacial-related shifts in $\delta^{18}\text{O}$ values of seawater produce less than 20% of the changes observed in foraminifera $\delta^{18}\text{O}$ values, and the remaining effect was due to temperature. However, subsequent work by Shackleton and Opdyke (1973) strongly suggests that changes in $\delta^{18}\text{O}$ values of seawater are the main parameter controlling $\delta^{18}\text{O}$ values of foraminifera.

Although Urey's pioneer work showed that stable isotopes can be used as temperature proxies, the work by Emiliani (1955) and Shackleton and Opdyke (1973) illustrate the most important factors constraining paleoenvironmental interpretations based on stable isotope data. These factors include temperature and the isotopic composition of water.

Stable isotopes in paleothermometry

If the isotopic composition of water is known or is assumed to have remained constant over the time period of interest, past changes in temperature can be estimated from stable isotope data. This approach has primarily been employed on carbonate substrates precipitated in marine settings. For instance, changes in carbonate $\delta^{18}\text{O}$ values of Holocene corals and marine bivalves have been interpreted to indicate changes in seawater temperature, where a decrease in water temperature results in elevated shell $\delta^{18}\text{O}$ values. Corals in particular offer one of the highest resolution (seasonal to century-scale) paleoclimatic archives of the tropics, commonly encompassing the last 400 yr. A strong relationship ($r^2 = 0.92$) has been found between sea-surface temperature and the oxygen isotopic composition of corals (Quinn et al., 1996; Fairbanks et al., 1997). Although the relationship between temperature and the extent of ^{18}O -enrichment in carbonates (Equations (3)–(5)) has been established at equilibrium conditions (e.g., Epstein et al., 1953), $\delta^{18}\text{O}$ values of modern biogenic carbonate in marine settings exhibit a systematic offset from the values expected at equilibrium. For instance, direct measurements of sea-surface

temperature and $\delta^{18}\text{O}$ values of corals indicate a significant (up to 0.5‰) deviation from the value expected at equilibrium; this difference points to a kinetic and/or biological effect during carbonate secretion (“vital effect”). Fortunately, the isotope offset resulting from the biological secretion of carbonate appears to be constant among specimens of the same species, but different among individuals of different taxa. Constant vital isotope effects in corals and bivalves make their $\delta^{18}\text{O}$ values sensitive indicators for paleoclimate because a simple correction factor can be applied to convert biogenic carbonate $\delta^{18}\text{O}$ values into temperature.

Whereas the isotopic composition of seawater can be assumed to remain constant (~ 0 –1‰) in certain locations for at least the late Holocene, the isotopic composition of water on land is extremely variable (from about 0‰ to -35 ‰ for $\delta^{18}\text{O}$). As a result, it is important to distinguish the effect of temperature from changing $\delta^{18}\text{O}$ values of water to make accurate paleoclimatic reconstructions. An extreme situation occurs when the range of variability of water $\delta^{18}\text{O}$ values far exceeds the temperature effect on shell $\delta^{18}\text{O}$ values. Under this scenario, it still might be possible to obtain paleotemperature assessments from changes in shell $\delta^{18}\text{O}$ values as a result of the strong covariance found between surface temperature and the isotopic composition of meteoric water.

Stable isotope ratios in meteoric water

The basis for the use of hydrogen (δD) and oxygen isotopic composition ($\delta^{18}\text{O}$) of meteoric water comes from observations of modern precipitation in mid- and high-latitudes showing a strong ($r^2 = 0.78$) correspondence between temperature and values of δD and $\delta^{18}\text{O}$ of meteoric water. This strong relationship has been found to occur on seasonal, interannual, and multiannual comparisons (Dansgaard, 1964; Rozanski et al., 1992; Fricke and O’Neil, 1999).

The isotopic composition of rainwater chiefly depends on two processes: evaporation and condensation. During evaporation, the lighter isotopes are preferentially incorporated into the gas phase as a result of their higher mobility. Most evaporation in the world occurs at low- and mid-latitudes, and to a lesser

extent from vegetation and lakes. During condensation, the lighter isotopes preferentially remain in the vapor phase due to their higher vapor pressure relative to that of their heavier counterparts. Removal of heavier isotopes during condensation enriches the lighter isotopes in the cloud. Subsequent condensation events produce a further enrichment of lighter isotopes in the cloud, resulting in progressively lower $\delta^{18}\text{O}$ and δD values of rainwater. This progressive depletion of heavier isotopes due to partial rainout is observed when air masses travel landward and poleward. For instance, rainwater at maritime and coastal sites exhibits higher $\delta^{18}\text{O}$ and δD values than rainwater falling in continental interiors (Figure S29). Similarly, rainwater of tropical regions shows higher $\delta^{18}\text{O}$ and δD values in relation to rainwater falling at higher latitudes (Figure S30). Isotope data of meteoric water collected around the world verifies the gradual decrease in $\delta^{18}\text{O}$ and δD values by showing a gradient towards lower $\delta^{18}\text{O}$ and δD values of rainwater with increasing latitude and continentality.

The extent of incorporation of heavier isotopes in condensates (i.e., fractionation between gas and liquid phase) depends on the prevailing temperature at the cloud base (Gat, 1996). This dependence appears to be the source of the strong relationship found between temperature and the isotopic composition of rainwater in mid-latitudes and polar regions (Figure S31).

The dependence of $\delta^{18}\text{O}$ values of meteoric water on temperature has been used in terrestrial records, primarily in ice-core studies, to reconstruct past changes in temperature. In fact, the covariance between temperature and $\delta^{18}\text{O}$ values has independently been confirmed via bore-hole measurements in Central Greenland (Johnsen et al., 1995), validating the accuracy of paleotemperature estimations deduced from isotope data. Using $\delta^{18}\text{O}$ data, Greenland ice records have revealed exceptionally large and abrupt changes in climate during the most recent glacial interval (Dansgaard et al., 1993). These results suggest that climate is highly variable, showing very rapid transitions from “cold” to “warm” modes. In Antarctica, temperature estimates inferred from isotope data reveal a dramatic 10°C temperature variation between glacial and interglacial intervals. Similar to Greenland records, the conversion

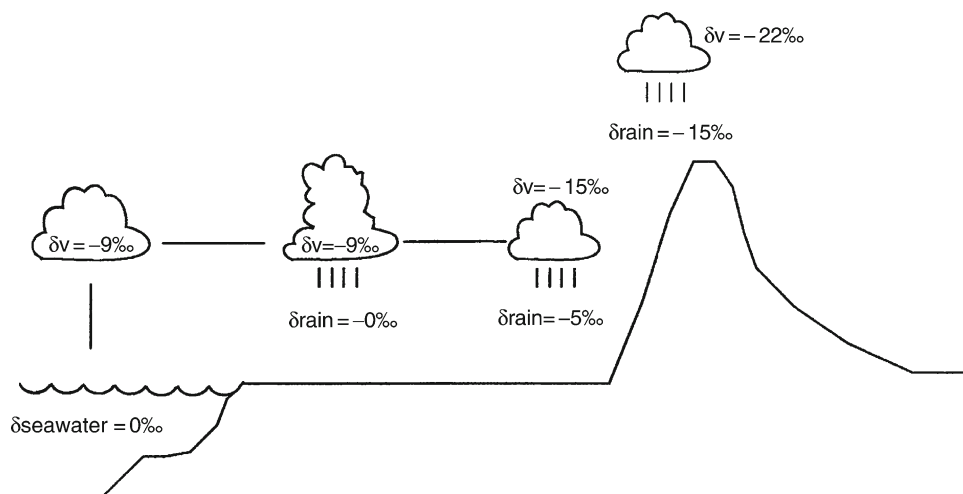


Figure S29 Changes in isotopic composition of air masses as they travel inside continents. Values depicted in the figure correspond to oxygen isotope ratios.

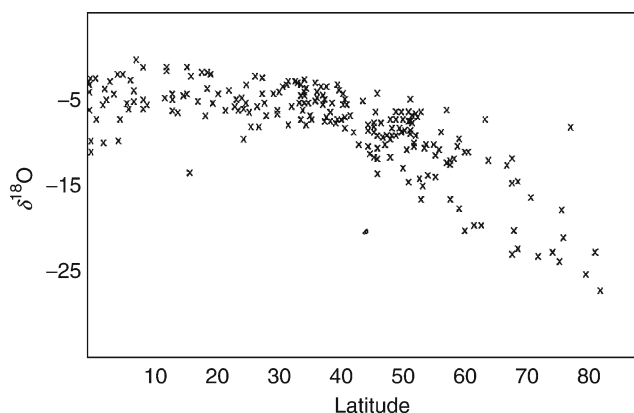


Figure S30 Variation of latitude and the oxygen isotopic composition ($\delta^{18}\text{O}$) of meteoric water. Notice that lower $\delta^{18}\text{O}$ values occur in polar regions.

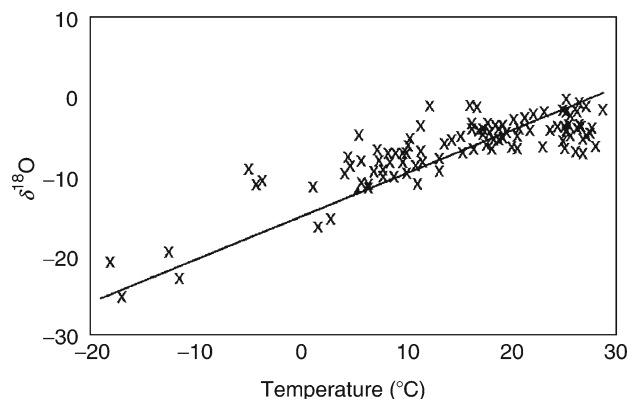


Figure S31 Variation of temperature and the oxygen isotopic composition ($\delta^{18}\text{O}$) of meteoric water.

of temperature from isotope data is based on modern calibration studies of Antarctic snow. It is important to indicate, however, that these modern calibrations might not be directly applicable to snow or ice accumulated during glacial intervals because atmospheric and oceanic processes were different from those operating today. As a result, the isotopic composition of water in clouds, seawater, and rainwater was likely different in glacial times with respect to modern (interglacial) intervals.

Although the strong relationship between surface temperature and $\delta^{18}\text{O}$ values of meteoric water in temperate and polar regions can be used to reconstruct past temperatures, there are a number of confounding factors that also control the isotopic composition of rainwater at a given locality. One of these factors is the so-called “amount effect” (Dansgaard, 1964). Large rain events tend to be associated with an anomalous enrichment of lighter isotopes, leading to lower $\delta^{18}\text{O}$ and δD values of meteoric water. This “amount effect,” characteristic of tropical settings, typically overprints any temperature-dependent isotope fractionation. As a result, tropical regions exhibit a weak relationship between temperature and the isotopic composition of meteoric water.

Another confounding factor is related to the complexity of cloud formation.

Isotopic and thermal equilibrium must exist during condensation in order to use the isotopic composition of meteoric water as a temperature proxy. Non-equilibrium conditions exist in clouds during ice formation or during super saturation events. Moreover, evaporation during travel from the cloud to the ground could result in the removal of lighter isotopes. This evaporation process can also weaken the correlation between temperature and the isotopic composition of meteoric water.

Another potential significant source of error in correlating temperature and the isotopic composition of meteoric water is the mixture of moisture from different sources. For instance, precipitation in North America results from the interplay of air masses coming from the Gulf of Mexico, the Pacific Ocean, and the Arctic region. Because of different evaporation/condensation histories, moisture derived from these masses has distinct isotopic composition. Consequently, the superimposition of moisture from different sources weakens the correlation between temperature and isotope data of meteoric water. This weakening is further enhanced when evapo-transpiration returns significant amounts of moisture to the atmosphere. A typical example of this process includes the Amazon Basin, where about 30% of the precipitation originates from significant evapo-transpiration of rain forests (Gat, 1996). Although the interplay of different air masses and evapo-transpiration affects the relationship between mid-latitude temperature and rainwater $\delta^{18}\text{O}$ values, isotope data from sites where these processes are pronounced can be used to assess the intensity of these processes. In these places, isotope data can consequently be used to assess variations in atmospheric circulation that either shift storm tracks or enhance/suppress evapo-transpiration.

Evaporation/precipitation ratios

The partitioning of stable isotopes that occurs during evaporation has been used as an indicator of the balance of evaporation and precipitation (E/P) in a region. The best systems to assess E/P ratios include relatively closed aquatic systems, where the main source of water is meteoric water. In this setting, the oxygen and hydrogen isotopic composition of the closed aquatic system corresponds to the isotopic composition of meteoric water plus the fractionation effect related to evaporation. One of the substrates employed to reconstruct past E/P ratios include carbonates precipitated in lakes. Since evaporation favors the incorporation of lighter isotopes in the gas phase, carbonates in closed aquatic systems experiencing high evaporation rates (high E/P ratios) exhibit elevated $\delta^{18}\text{O}$ values. The carbonates analyzed for E/P studies primarily come from ostracod shells and lacustrine marls. Isotope analyses on bulk marls in lakes are relatively easy to perform, allowing the possibility of performing high-resolution studies. The disadvantage of lacustrine marl deposits is that bulk carbonates represent a heterogeneous mixture of authigenic, biogenic, and detrital components. Moreover, precipitation of these components could occur under the influence of discrete processes operating at different places, lake depths, and time. In contrast, isotope analyses of biogenic carbonates offer an opportunity to minimize uncertainties related to spatial and temporal heterogeneity.

Whereas lacustrine marls tend to precipitate at steady-state conditions, a number of studies have documented a systematic offset between $\delta^{18}\text{O}$ values of ostracod carbonate relative to expected theoretical calcite $\delta^{18}\text{O}$ values formed at equilibrium (Epstein et al., 1953). This offset (“vital effect”) appears to be constant within a given species, but it is variable among

species, yielding values as low as 0.5‰ to as high as 2‰. Because the offset of ostracod $\delta^{18}\text{O}$ values from those expected at equilibrium is constant, ostracod isotope data have successfully been used to reconstruct past E/P ratios. For example, ostracod isotope data from lakes in the Yucatan Peninsula indicate that the collapse of the Mayan culture coincided with a period of extensive aridity in Meso-America (Hodell et al., 1995).

As indicated before, assessments of E/P ratios from carbonate $\delta^{18}\text{O}$ values can be achieved in closed-basin lakes where rainfall is the main component in the isotopic hydrological balance of lakes. Most lakes, however, are not closed because outlets and groundwater inflow and outflow exist. In these cases, additional information regarding the hydrological isotope balance of the basin is needed to perform accurate interpretations of past changes in E/P ratios from carbonate isotope data. Although groundwater fluxes are difficult to estimate among the different hydrological components, coarse assessments of these fluxes can be achieved from surveys of the isotopic composition of lake-, stream-, and rain-water during the dry and wet seasons. These isotopic data combined with information about rainfall amount, stream flow, and runoff can be used to estimate the influence of groundwater systems into a lake. Although these studies provide only a coarse indication of groundwater fluxes, they are useful to constrain any paleoclimatic interpretation from authigenic and biogenic carbonates in lakes.

A special case is open-basin lakes with short residence times (i.e., low ratios of lake/watershed area) because these lakes tend to exhibit $\delta^{18}\text{O}$ values of lake water close to those of recharging water. Isotopic analyses of lacustrine carbonates formed in these lakes can then provide information about temporal changes in the watershed's hydrology. Although recharge varies from lake to lake, it reflects the balance of precipitation, runoff, evaporation, and groundwater inflow and outflow (Talbot, 1990).

A potential source of uncertainty in assessing P/E ratios is the effect of temperature. Because $\delta^{18}\text{O}$ values of carbonates decrease by about 0.23‰ per + 1 °C, changes in P/E can only be detected in lake carbonates when the effect of evaporation is larger than that of temperature, which is the case for lakes with relatively large surface area and small volume. In contrast, seasonal changes in P/E ratios in large lakes produce a relatively small range of variability in lake water $\delta^{18}\text{O}$ values. This small variability in $\delta^{18}\text{O}$ values can be comparable to the range caused by seasonal changes in temperature, thereby making carbonate $\delta^{18}\text{O}$ values unsuitable for evaluating past P/E ratios unless an independent temperature proxy is utilized.

In addition to lakes, inference of E/P ratios from carbonate isotope data has successfully been employed in corals to assess changes in the balance of evaporation and precipitation in regions where seawater $\delta^{18}\text{O}$ values are sensitive to changes in the balance of precipitation and evaporation. Lindsley et al. (1994), for instance, found decadal changes in $\delta^{18}\text{O}$ values in ~300 year coral record from Gulf Chiriqui, Panama. Because the oxygen isotopic composition of seawater at this site is sensitive to rainfall amount, these changes were interpreted to reflect decadal changes in the strength or position of the Intertropical Convergence Zone.

Carbon isotopes of organic matter

There are two main approaches employed in reconstructing paleoenvironments using stable carbon isotopes. The first approach consists in determining changes in the distribution

of two isotopically distinct groups of vascular plants: C_3 and C_4 . In this approach, increased abundance of C_4 plants reflects increased aridity. The second approach is to infer changes in humidity from the carbon isotopic composition of tree-rings. In this approach, elevated $\delta^{13}\text{C}$ values indicate decreased humidity.

C_3 and C_4 plants possess different photosynthetic mechanisms that produce distinct carbon isotope signatures. The C_4 photosynthetic pathway is an efficient CO_2 concentrating mechanism (Leegood, 1999) that provides C_4 plants with higher water use efficiency. As a result, most C_4 grasses are found today in hot (>22 °C) and relatively dry places (Ehleringer, 1997; Collatz et al., 1998). C_4 plants are common in the monocot families Cyperaceae (sedges) and Poaceae (grasses). Almost 50% of all grasses are C_4 , inhabiting tropical to temperate regions with abundant warm-season precipitation. The C_4 photosynthetic pathway also causes C_4 plants to show $\delta^{13}\text{C}$ values that vary from -9‰ to -16‰. In contrast, C_3 plants exhibit $\delta^{13}\text{C}$ values that range from -21‰ to -30‰. The nonoverlapping $\delta^{13}\text{C}$ values of these two classes of plants produce a distinct isotopic signature that can be identified in past environments, provided that sufficient terrestrial organic matter persists in the geologic record. Changes in the distribution of C_3 and C_4 plant communities have been inferred from stable carbon isotopic composition of soil organic matter, lake deposits, and coastal and marine sediments. In this context, increased abundance of C_4 plants inferred from elevated $\delta^{13}\text{C}$ values has been interpreted to correspond to periods of increased aridity. In addition to widespread aridity, it has been argued that C_4 grasses can out-compete the more abundant C_3 plants under low concentrations of atmospheric carbon dioxide, even under relatively wet conditions. The role of aridity and CO_2 concentrations on expansions of C_4 plants in the geologic record is still unresolved.

Another application of stable carbon isotopes in paleoclimate research consists of inferring changes in relative humidity from changes in the stable carbon isotopic composition of tree-rings. This approach relies on the extent of the biological fractionation effect that occurs during photosynthesis by C_3 trees. The carbon-isotopic composition of a C_3 plant can be expressed by the following equation (Farquhar et al., 1988):

$$\delta^{13}\text{C}_{\text{Plant}} = \delta^{13}\text{C}_{\text{Air}} - a - (b - a)C_i/C_a \quad (7)$$

where a is the fractionation effect of 4.4‰ that occurs during the diffusion of CO_2 through stomata, and b is the biological fractionation effect of 28‰ that results during CO_2 fixation. C_i and C_a represent the concentration of CO_2 inside and outside of the leaf, respectively. $\delta^{13}\text{C}_{\text{Air}}$ is constant for relatively long time-scales because the troposphere is relatively well mixed. Consequently, the only variable actively determining $\delta^{13}\text{C}_{\text{Plant}}$ in Equation (7) is the C_i/C_a ratio. Field observations and laboratory experiments indicate that different plant species could exhibit different C_i/C_a ratios under the same environmental conditions, pointing to a species-specific effect. As indicated before, the natural range of $\delta^{13}\text{C}$ values for C_3 plants is between -21‰ and -30‰, which translates to C_i/C_a ratios of about 0.4–0.8. Elevated $\delta^{13}\text{C}_{\text{Plant}}$ values occur with relatively low C_i/C_a ratios that result when stomata are partially closed. Experimental studies indicate that plants tend to close their stomata under low values of relative humidity in order to suppress water loss associated with transpiration, resulting in elevated $\delta^{13}\text{C}$ values (Farquhar and Richards, 1984). In

addition to humidity, other factors, including light conditions, nutrient levels, and plant maturity, among others, also influence the extent of discrimination against ^{13}C that occurs during photosynthesis in C_3 plants. Despite these complexities, field studies (e.g., Hemming et al., 1998; Edwards et al., 2000) have concluded that a strong correlation exists between relative humidity and $\delta^{13}\text{C}$ values in angiosperm and gymnosperm trees. This covariance is the basis for the use of carbon-stable isotope data in paleoclimate research. The carbon-isotopic composition of tree-rings offer the best substrate for paleoclimate research because a number of confounding factors that affect $\delta^{13}\text{C}$ values in trees are constrained. On the other hand, bulk organic matter appears to be an unreliable substrate because the range of $\delta^{13}\text{C}$ values caused by changes in relative humidity is on the same order of magnitude as that caused by species-specific effects, diagenesis, and admixture of organic matter from different sources.

Summary

Temperature estimations from stable isotope data fall into two categories: (a) those based on fractionation effects related to carbonate formation from water with known or estimated $\delta^{18}\text{O}$ values, and (b) those based on the modern relationship between the isotopic composition of meteoric water and temperature in temperate and polar regions. The isotopic composition of meteoric water in these regions can be assessed from that of a number of substrates including ice, fluid inclusions, groundwater, pedogenic minerals, bones, and organic matter, among others.

Assessments of water balance inferred from stable isotope data can be achieved either through $\delta^{18}\text{O}$ and/or δD at sites sensitive to changes in precipitation and evaporation (such as closed-basin lakes) or via changes in C_3 and C_4 plant communities at sites sensitive to the colonization of these taxa.

Germán Mora

Bibliography

- Collatz, G.J., Berry, J.A., and Clark, J.S., 1998. Effects of climate and atmospheric CO_2 partial pressure on the global distribution of C_4 grasses: Present, past, and future. *Oecologia*, **114**, 441–454.
- Craig, H., 1957. Isotopic standards for carbon and oxygen and correction factors for mass-spectrometric analysis of carbon dioxide. *Geochim. Cosmochim. Acta*, **12**, 133–149.
- Dansgaard, W., 1964. Stable isotopes in precipitation. *Tellus*, **16**, 436–468.
- Dansgaard, W., Johnsen, S.J., Clausen, H.B., Dahl-Jensen, D., Gundestrup, N.S., Hammer, C.U., Hvidberg, C.S., Steffensen, J.P., Sveinbjornsdottir, A.E., Jouzel, J., and Bond, G., 1993. Evidence for general instability in the past climate from a 250-kyr ice-core record. *Nature*, **364**, 218–220.
- Edwards, T.W.D., Graf W., Trimbom, P., Stichler, W., Lipp, J., and Payer, H.D., 2000. $\delta^{13}\text{C}$ response surface resolves humidity and temperature signals in trees. *Geochim. Cosmochim. Acta*, **64**, 161–167.
- Ehleringer, J.R., 1997. C_4 photosynthesis, atmospheric CO_2 , and climate. *Oecologia*, **112**, 285–299.
- Emiliani, C., 1955. Pleistocene temperatures. *J. Geol.*, **63**, 538–578.
- Epstein, S., Buchsbaum, R., Lowenstam, H.A., and Urey, H.C., 1953. Revised carbonate-water isotopic temperature scale. *Geol. Soc. Am. Bull.*, **64**, 1315–1326.
- Fairbanks, R.G., Evans, M.N., Rubenstone, J.L., Mortlock, R.A., Broad, K., Moore, M.D., and Charles, C.D., 1997. Evaluating climate indices and their geochemical proxies measured in corals. *Coral Reefs*, **16**, 93–100.
- Farquhar, G.D., and Richards, R.A., 1984. Isotopic composition of plant carbon correlates with water-use efficiency of wheat genotypes. *Austr. J. Plant Physiol.*, **11**, 539–552.
- Farquhar, G.D., Hubick, K.T., Condon, A.G., and Richards, R.A., 1988. Carbon isotope fractionation and plant water use efficiency. In Rungel,

- P.W., Ehleringer, J.R., and Nagy, K.A. (eds.), *Stable Isotopes in Ecological Research*. Berlin: Springer, pp. 21–40.
- Fricke, H.C., and O'Neil, J.R., 1999. The correlation between $^{18}\text{O}/^{16}\text{O}$ ratios of meteoric water and surface temperature: Its use in investigating terrestrial climate change over geologic time. *Earth Planet. Sci. Lett.*, **170**, 181–196.
- Gat, J.R., 1996. Oxygen and hydrogen isotopes in the hydrologic cycle. *Ann. Rev. Earth Planet. Sci.*, **24**, 225–262.
- Hemming, D.L., Carter, A.H.C., Switsur, V.R., Waterhouse, J.S., and Heaton, T.H.E., 1998. Climate variation and the stable carbon isotope composition of tree-ring cellulose: an intercomparison of *Quercus robur*, *Fagus sylvatica*, and *Pinus silvestris*. *Tellus*, **50B**, 25–33.
- Hodell, D.A., Curtis, J.H., and Brenner, M., 1995. Possible role of climate in the collapse of Classic Maya civilization. *Nature*, **375**, 391–394.
- Johnsen, S.J., Dahl-Jensen, D., Dansgaard, W., and Gundestrup, N., 1995. Greenland paleotemperature derived from GRIP borehole temperatures and ice core isotope profiles. *Tellus*, **47B**, 624–629.
- Leegood, R.C., 1999. Carbon dioxide – Concentrating mechanisms. In Lea, P.J., and Leegood, R.C. (eds.), *Plant Biochemistry and Molecular Biology*, 2nd edn. Chichester: Wiley, pp. 51–79.
- Lindsley, B.K., Dunbar, R.B., Wellington, G.M., and Mucciarone, D.A., 1994. A coral-based reconstruction of intertropical convergence zone variability over Central America since 1707. *J. Geophys. Res.*, **99**, 9977–9994.
- Quinn, T.M., Taylor, F.W., Crowley, T.J., and Link, S.M., 1996. Evaluation of sampling resolution in coral stable isotope records: a case study using records from New Caledonia and Tarawa. *Paleoceanography*, **11**, 529–542.
- Rozanski, K., Araguas-Araguas, L., and Gonfiantini, R., 1992. Relation between long-term trends of oxygen-18 isotope composition of precipitation and climate. *Science*, **258**, 981–985.
- Shackleton, N.J., and Opdyke, N.D., 1973. Oxygen isotope and paleomagnetic stratigraphy of an equatorial Pacific core V28–238: oxygen isotope temperatures and ice volumes on a 10^5 and 10^6 year time scale. *Quaternary Res.*, **3**, 39–55.
- Talbot, M.R., 1990. A review of the palaeohydrological interpretation of carbon and oxygen ratios in primary lacustrine carbonates. *Chern. Geol.*, **80**, 261–279.
- Urey, H.C., 1947. The thermodynamic properties of isotopic substances. *J. Chem. Soc. (Lond.)*, 562–581.

Cross-references

Carbon Isotopes, Stable
 Coral and Coral Reefs
 Dendroclimatology
 Deuterium, Deuterium Excess
 Foraminifera
 Ice Cores, Antarctica and Greenland
 Nitrogen Isotopes
 Ocean Paleotemperatures
 Ostracodes
 Oxygen Isotopes
 Paleoclimate Proxies, An Introduction
 Paleolimnology
 Paleoprecipitation Indicators
 Paleotemperatures and Proxy Reconstructions
 Sea-Surface Temperatures
 Strontium Isotopes
 Sulfur Isotopes

STRONTIUM ISOTOPES

Strontium isotope systematics

The element with atomic number 38, strontium, has four isotopes 84, 86, 87 and 88 with approximate proportions of 0.56: 9.87: 7.04: 82.53 (Faure, 1986). Geologically short-lived nuclides (e.g., ^{90}Sr) are not considered in this contribution. The

proportion of ^{87}Sr is somewhat variable because it is a decay product of ^{87}Rb . The decay constant λ for ^{87}Rb is $1.42 \times 10^{-11} \text{ a}^{-1}$, resulting in a half-life T of 48.8 billion years (Ga).

The present-day quantity of isotope 87 ($^{87}\text{Sr}_p$) depends on the initial stock ($^{87}\text{Sr}_0$) and the amount of radiogenic Sr generated by decay of ^{87}Rb over time t

$$^{87}\text{Sr}_p = ^{87}\text{Sr}_0 + ^{87}\text{Rb}(e^{\lambda t} - 1) \quad (1)$$

Because of the design of mass spectrometers, the above quantities are measured as a ratio to the stable isotope ^{86}Sr

$$\left(\frac{^{87}\text{Sr}}{^{86}\text{Sr}}\right)_p = \left(\frac{^{87}\text{Sr}}{^{86}\text{Sr}}\right)_0 + \left(\frac{^{87}\text{Rb}}{^{86}\text{Sr}}\right)(e^{\lambda t} - 1) \quad (2)$$

The young Earth, at the time of its formation ~ 4.55 Ga ago, inherited the $(^{87}\text{Sr}/^{86}\text{Sr})_0$ ratio of 0.699 from its chondritic meteorite building blocks.

From Equation 2, it is evident that the term $(^{87}\text{Sr}/^{86}\text{Sr})_p$ for coeval rocks that originate from the same source and inherit the same $(^{87}\text{Sr}/^{86}\text{Sr})_0$ ratio depends only on their Rb/Sr ratio. The latter is about six times larger for the fractionated rocks that form the continents than for the basalts of the oceanic crust (~ 0.15 vs. 0.027). As a consequence, the average $(^{87}\text{Sr}/^{86}\text{Sr})_p$ for continents is about 0.720 while for the basalts of the oceanic crust it is ~ 0.703 (Figure S32). The temporal evolution of these two geologic entities is the principal control of chemical and isotopic composition of seawater, reflecting the relative inputs from rivers and submarine hydrothermal circulation, respectively.

Strontium isotopic evolution of seawater

The present day $^{87}\text{Sr}/^{86}\text{Sr}$ ratio of seawater is 0.7092 and is uniform worldwide. This is because the average time that an atom of Sr spends in seawater, the so-called residence time, is somewhere between 2 and 5 million years, while the mixing rate of the oceans is only thousands of years. Thus, from the point of view of Sr, the seawater at any given time is well mixed. Even marginal marine basins, such as the almost brackish Hudson Bay of northern Canada, have a Sr isotopic composition identical to that of the open sea. This is because

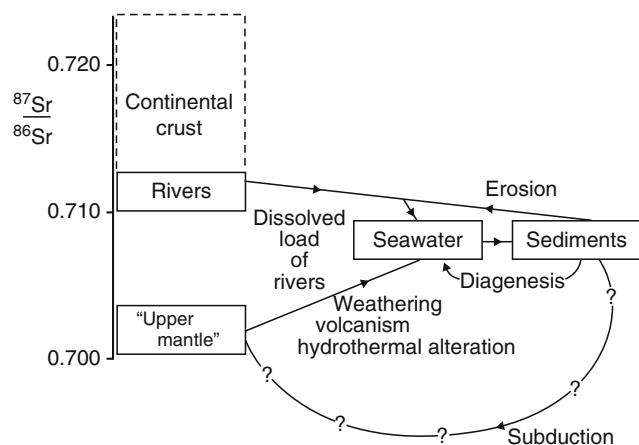


Figure S32 Schematic presentation of Sr isotopic surficial cycle (modified after Wadleigh, 1982).

the Sr concentrations in riverine waters are 2–3 orders of magnitude less than that of seawater, at ~ 8 ppm, and any dilution by river water, while lowering the Sr concentration, will not impact the $^{87}\text{Sr}/^{86}\text{Sr}$ ratio because almost the entire Sr load originates from seawater.

Note that the $^{87}\text{Sr}/^{86}\text{Sr}$ ratio of modern seawater is only about 1/3 of the way up the scale between that of oceanic and continental crust (Figure S32), despite the fact that modern river input of Sr is about 6.5 times larger than its hydrothermal flux (2.73 vs. $0.42 \times 10^{12} \text{ g a}^{-1}$), and therefore dominates the oceanic budget. This is because the average $^{87}\text{Sr}/^{86}\text{Sr}$ of river water, at ~ 0.711 , is much less radiogenic than that of the average continental crust. The discrepancy is a reflection of the fact that carbonate rocks almost always account for a substantial proportion of the lithology in the watersheds of major rivers. Carbonate rocks, being marine sediments, inherit the Sr isotopic composition of seawater at the time of their formation. The oceanic, and particularly the continental crust, was less radiogenic in the early history of the Earth (Figure S33) and this was reflected in the contemporaneous seawater and in the sediments that precipitated from it. Subsequently, weathering of ancient marine carbonates, their redeposition in the sea and renewed uplift and erosion resulted in perpetual recycling of this “ancient” Sr, thus “retarding” the $^{87}\text{Sr}/^{86}\text{Sr}$ signal of seawater relative to the development of the continental crust.

Unfortunately, we do not have samples of past seawater that would enable us to measure directly its past chemical and isotopic composition. On the other hand, we do have sediments that precipitated from seawater, either directly (salts, gypsum) or with the help of biological intermediaries that precipitated carbonate (phosphate, siliceous) minerals as shells or crystallites. We can therefore utilize shells for about 540 Ma and carbonate rocks (limestones, dolostones) for almost 4 Ga to decipher the Sr isotopic composition of ancient seawater. The matter is complicated by the fact that many of these shells and rocks were post-depositionally (diagenetically) altered and this often results in alteration of the $^{87}\text{Sr}/^{86}\text{Sr}$ signal. Techniques do exist for at least partial evaluation of the degree of such alteration, but none is foolproof. Usually, the alteration process shifts the $^{87}\text{Sr}/^{86}\text{Sr}$ values upwards and it is common practice to accept the lowest measured value for any suite of samples as the best approximation of the $^{87}\text{Sr}/^{86}\text{Sr}$ ratio of the coeval ocean.

In the early stages of isotope geology it was believed that the $^{87}\text{Sr}/^{86}\text{Sr}$ of seawater evolved linearly during geologic history (Wickman, 1948) and it was hoped that such a linear trend could be utilized for dating of (bio)chemical marine sediments. Due to the low sensitivity of early mass spectrometers, this proposition could only be tested some 20 years later, when it was realized that we were dealing with a widely oscillating signal (Peterman et al., 1970). This was subsequently documented by Veizer and Compston (1974, 1976) and Burke et al. (1982). The latest editions of these curves for the entire 4 Ga of Earth history were published by Shields and Veizer (2002) (Figure S33) and for the Phanerozoic by Veizer et al. (1999) (Figure S34).

The most important features of the billion-year trend in $^{87}\text{Sr}/^{86}\text{Sr}$ (Figure S33) are the departure of seawater from mantle values somewhere around the Archean/Proterozoic transition, ~ 2.5 Ga ago; the relatively sharp rise until about 1.8 Ga ago; the flat trend to ~ 900 Ma ago; and another steep rise during the Neoproterozoic, followed by a trough-like structure during the Phanerozoic. The Precambrian portion of the

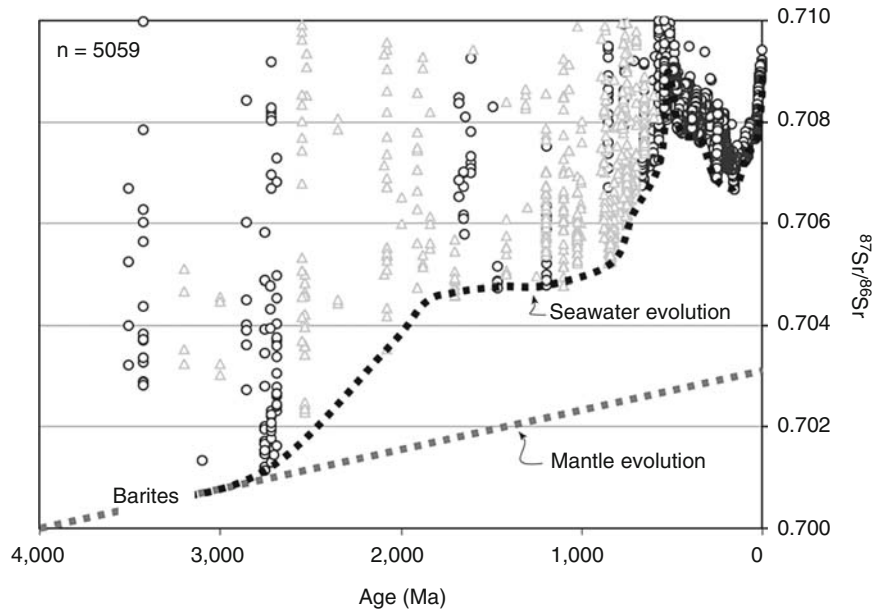


Figure S33 Strontium isotope record of carbonate rocks (seawater) during geologic history. *Full symbols*: chronologically well constrained; *empty symbols*: poorly constrained samples (reproduced from Shields and Veizer, 2002).

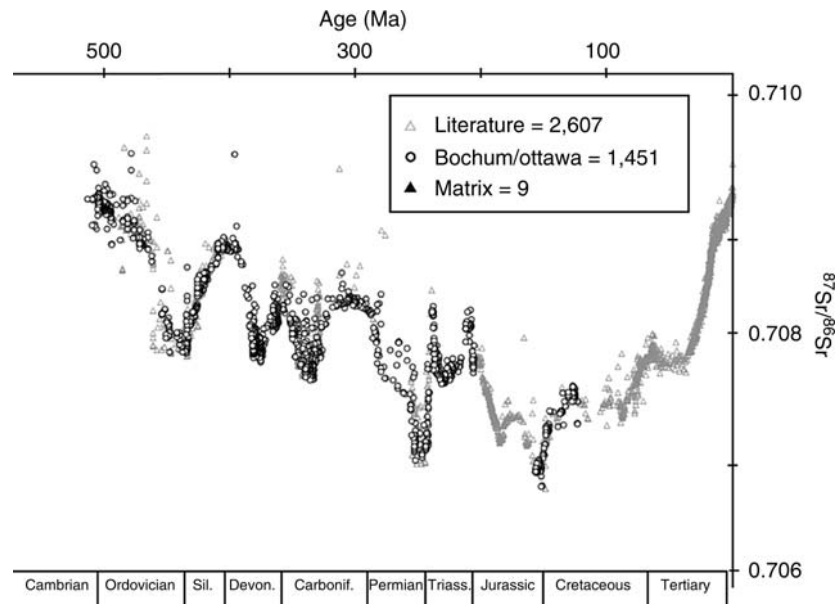


Figure S34 Sr isotope record for Phanerozoic seawater based on 4,055 samples of calcite shells (reproduced from Veizer et al., 1999).

curve is in all likelihood composed of higher order oscillations similar to those of the Phanerozoic, but we do not yet have the geochronological resolution to decipher it. For this reason, we can discuss only the lower bound of the trend. The mantle-like values of seawater during the early Archean indicate that either the river input was negligible, or the hydrothermal flux was much stronger than today, or both. The geological interpretation is that the continents could have been much smaller

and seawater circulation via submarine hydrothermal systems (in order to dissipate heat from the hotter mantle) more vigorous. This was followed by the major interval of generation of continental crust, between ~ 2.7 and 1.8 Ga ago, the cumulative size of continents reached near-modern extent towards the end of this time interval. Simultaneously, the chemical and isotopic composition of the oceans evolved from being “mantle-buffered” to “river-buffered,” and this development

may also have been the cause of other contemporary phenomena, such as the transition from oxygen-poor to oxygen-rich atmospheric composition. The steep rise in $^{87}\text{Sr}/^{86}\text{Sr}$ in the Neoproterozoic may be related to another pronounced phase of continent formation, the Pan African orogeny.

The origin of the trough-like Phanerozoic structure (Figure S34) with its superimposed oscillations is at this stage enigmatic. Attempts to correlate the details of this structure with tectonic development of the Earth have not led to any unequivocal conclusions. A great deal of attention was paid particularly to the steep Tertiary rise of $^{87}\text{Sr}/^{86}\text{Sr}$ values, that was assumed to be a reflection of the collision between India and Asia, with the resulting uplift of the Himalayas. The corollary of such an interpretation was a potential role that this uplift could have played in increased global erosion that, in turn, would have resulted in atmospheric CO_2 drawdown and the overall Tertiary cooling of the globe (Ruddiman, 1997). However, the modeling simulations do not appear to support the validity of such a scenario.

Isotope stratigraphy

Despite the fact that the $^{87}\text{Sr}/^{86}\text{Sr}$ trend for seawater is not linear, the sections of this oscillating trend that show a particularly steep slope can be utilized for dating and correlation of marine (bio)chemical sediments, the approach known as isotope stratigraphy (McArthur, 1994). In particular, the Cenozoic portion of the trend (Figure S34) enabled correlations at levels comparable to biostratigraphic techniques.

Ján Veizer

Bibliography

- Burke, W.H., Denison, R.E., Hetherington, E.A., Koepnick, R.B., Nelson, H.F., and Otto, J.B., 1982. Variation of seawater $^{87}\text{Sr}/^{86}\text{Sr}$ throughout Phanerozoic time. *Geology*, **10**, 516–519.
- Faure, G., 1986. *Principles of Isotope Geology*. New York: Wiley, 589pp.
- McArthur, J.M., 1994. Recent trends in strontium isotope stratigraphy. *Terra Nova*, **6**, 331–358.
- Peterman, Z.E., Hedge, C.E., and Tourtelot, H.A., 1970. Isotopic composition of strontium in seawater throughout Phanerozoic time. *Geochim. Cosmochim. Acta*, **34**, 105–120.
- Ruddiman, W.F., 1997. *Tectonic Uplift and Climate Change*. New York: Plenum Press, 535pp.
- Shields, G., and Veizer, J., 2002. Precambrian marine carbonate isotope database: Version 1.1. *Geochem. Geophys. Geosyst.*, **3**(6), 12 (<http://g-cubed.org/gc2002/2001GC000266>).
- Veizer, J., and Compston, W., 1974. $^{87}\text{Sr}/^{86}\text{Sr}$ composition of seawater during the Phanerozoic. *Geochim. Cosmochim. Acta*, **38**, 1461–1484.
- Veizer, J., and Compston, W., 1976. $^{87}\text{Sr}/^{86}\text{Sr}$ in Precambrian carbonates as an index of crustal evolution. *Geochim. Cosmochim. Acta*, **40**, 905–914.
- Veizer, J., Ala, D., Azmy, K., Bruckschen, P., Buhl, D., Bruhn, F., Carden, G.A.F., Diener, A., Ebner, S., Goddérís, Y., Jasper, T., Korte, C., Pawellek, F., Podlaha, O.G., and Strauss, H., 1999. $^{87}\text{Sr}/^{86}\text{Sr}$, $\delta^{13}\text{C}$ and $\delta^{18}\text{O}$ evolution of Phanerozoic seawater. *Chem. Geol.*, **161**, 59–88.
- Wadleigh, M.A., 1982. *Marine Geochemical Cycle of Strontium*. M.Sc. Thesis, University of Ottawa, ON, 187pp.
- Wickman, P.E., 1948. Isotope ratios: A clue to the age of certain marine sediments. *J. Geol.*, **56**, 61–66.

Cross-references

Atmospheric Evolution, Earth
Mountain Uplift and Climate Change
Stable Isotope Analysis

SULFUR ISOTOPES

Sulfur isotope systematics

The element sulfur has four stable isotopes ^{32}S , ^{33}S , ^{34}S and ^{36}S with the following natural abundances: 95.02%, 0.75%, 4.21%, and 0.02% (Hoefs, 1997). Most commonly, the two major isotopes (^{32}S , ^{34}S) are being measured and results expressed as $\delta^{34}\text{S}$, defined by the following equation

$$\delta^{34}\text{S}[\text{‰}] = \left(\frac{\left(\frac{^{34}\text{S}}{^{32}\text{S}} \right)_{\text{Sample}}}{\left(\frac{^{34}\text{S}}{^{32}\text{S}} \right)_{\text{Standard}}} - 1 \right) 1,000 \quad (1)$$

and reported as per mil difference with respect to the V-CDT-standard (defining the Zero-Point of the sulfur isotope scale). Due to analytical improvements, the minor sulfur isotopes ^{33}S and ^{36}S can now be measured routinely with their delta values defined analogous to equation 1.

Sulfur is present in the atmosphere, hydrosphere, biosphere and lithosphere (Figure S35). In addition to natural processes, the present day sulfur cycle is strongly affected by anthropogenic sulfur inputs. The transfer of sulfur between the different reservoirs is mediated through abiological and biological processes. Such processes are generally associated with a change in the redox state and an isotopic fractionation of variable magnitude, depending on the mode of isotope exchange (i.e., equilibrium vs. kinetic isotope effect). From the geological perspective, research focuses on sulfate as the most oxidized and sulfide as the most reduced form of sulfur. Respective processes are the precipitation of evaporitic sulfate from seawater and the bacterial cycling of sulfur in sediments.

The pure precipitation of sulfate minerals from evaporating seawater is only associated with a small, almost negligible isotope effect (Claypool et al., 1980). As a consequence, marine evaporites and sulfate incorporated into marine chemical and biological precipitates are regarded as proxy signals for the isotopic composition of seawater sulfate (e.g., Strauss, 1999; Kampschulte and Strauss, 2003).

In contrast, variable but generally substantial isotopic fractionation occurs during bacterial sulfate reduction (e.g., Canfield, 2001). At the expense of sedimentary organic matter, sulfate is reduced to hydrogen sulfide, which subsequently reacts with

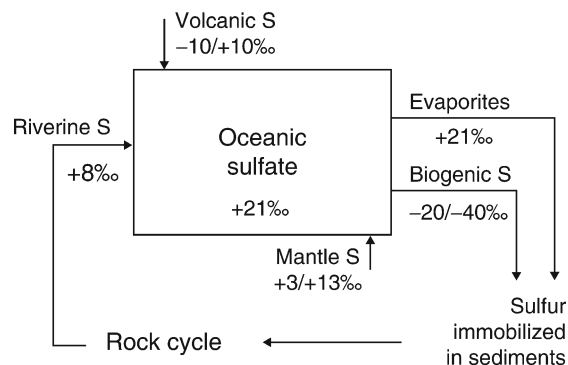


Figure S35 Schematic view of the sulfur cycle showing $\delta^{34}\text{S}$ values for modern reservoirs.

Fe to form sedimentary pyrite (FeS_2). The resulting sulfide is depleted in ^{34}S with respect to ambient sulfate due to the preferential utilization of ^{32}S by sulfate-reducing bacteria. The size of this isotope effect is dependent on the type of organism, the reaction rate, and the availability of sulfate and reactive organic matter (Canfield, 2001). Experimental data from pure cultures indicate an isotopic fractionation of 2–42‰ (e.g., Detmers et al., 2001), whereas natural populations display an isotope effect of 19–43‰ (Habicht and Canfield, 2001). For modern marine sediments, however, the isotope difference between porewater sulfate and sedimentary pyrite amounts to 31–56‰ (Habicht and Canfield, 2001). This additional isotopic fractionation accompanies the disproportionation of partly oxidized intermediate sulfur compounds: elemental sulfur, thiosulfate, and sulfite (e.g., Canfield and Thamdrup, 1994; Habicht et al., 1998). Measurements in recent marine sediments indicate that 41–85% of the apparent isotopic fractionation between seawater sulfate and sedimentary sulfide are the result of bacterial sulfate reduction, with the remaining part being due to disproportionation reactions (Habicht and Canfield, 2001).

Progressive bacterial sulfate reduction under sulfate-limiting conditions (e.g., porewaters in deep sediments) results in a continuous depletion of ^{32}S . As a consequence, the $\delta^{34}\text{S}$ becomes increasingly more positive. This explains part of the sulfur isotope record for reduced sedimentary sulfur.

The oxidative weathering of sulfur-bearing minerals and subsequent riverine delivery as dissolved sulfate from the continents to the ocean is not associated with an isotope effect.

The long-term evolution of the global sulfur cycle can be evaluated via simple isotope mass balance calculations. Considering the two principal output functions as oxidized (sulfate) and reduced (sulfide) sulfur (see Figure S35), this mass balance is defined as:

$$\delta_{\text{Input}} = f_{\text{Sulfide}}\delta_{\text{Sulfide}} - (1 - f_{\text{Sulfide}})\delta_{\text{Sulfate}} \quad (2)$$

with δ_{Input} representing the average isotopic composition of crustal sulfur (assumed constant at +2‰, Holser et al., 1988) and $f_{\text{Sulfide}}\delta_{\text{Sulfide}}$ and $(1 - f_{\text{Sulfide}})\delta_{\text{Sulfate}}$ being the fraction and isotopic composition of sulfide and sulfate sulfur. Fluctuations in the sulfur isotopic composition of seawater sulfate can then

be interpreted as a consequence of temporal variations in the fractional burial of reduced (sulfide) sulfur.

Sulfur isotopic evolution of seawater

The average sulfur isotopic composition of dissolved oceanic sulfate lies at +21‰ (e.g., Rees et al., 1978). Lateral and vertical homogeneity of this value is a consequence of a long residence time for sulfur in the ocean (3 million years) in comparison to the short mixing time for the ocean (1,000 years). Only marginal seas, such as the eastern Mediterranean or the Baltic Sea, represent exceptions. Their isotopic composition is more strongly affected by the riverine input of dissolved sulfate (on average +8 to +10‰). However, part of this input stems from anthropogenic sources (e.g., Grinenko and Krouse, 1992).

Despite its homogeneity at any given point in time (e.g., Nielsen, 1989), empirical data clearly show that the sulfur isotopic composition of seawater sulfate has fluctuated widely throughout four billion years of Earth's history (e.g., Strauss, 2002). However, the existing isotope record is highly variable in its temporal resolution and becomes increasingly fragmentary for the early part of Earth's history (Figure S36).

Early Archean (3.5 billion years ago) barite occurrences from Australia, South Africa and India constrain our knowledge about the sulfur isotopic composition of seawater sulfate from the early part of Earth's history at a value around +4‰ (Strauss, 2002). Sulfate abundance in the global ocean is considered to have been very low (<1 mM, Canfield et al., 2000). This interpretation is supported by a lack of substantial sulfur isotopic fractionation between sulfate and sedimentary sulfide (e.g., Strauss, 2002). Still, contrasting views of an Archean high-sulfate ocean have been proposed (e.g., Ohmoto, 1997).

The sulfur isotopic composition of seawater sulfate increases throughout the Precambrian. Due to the fragmentary record, it is unclear whether this increase is linear or episodic. A significant the sulfur isotopic composition of seawater sulfate is considered to occur between 2.4 and 2.2 billion years ago. It is thought to coincide with a substantial increase in the oxygen abundance in the atmosphere, termed the Great Oxidation Event (Holland, 2002). This would have initiated

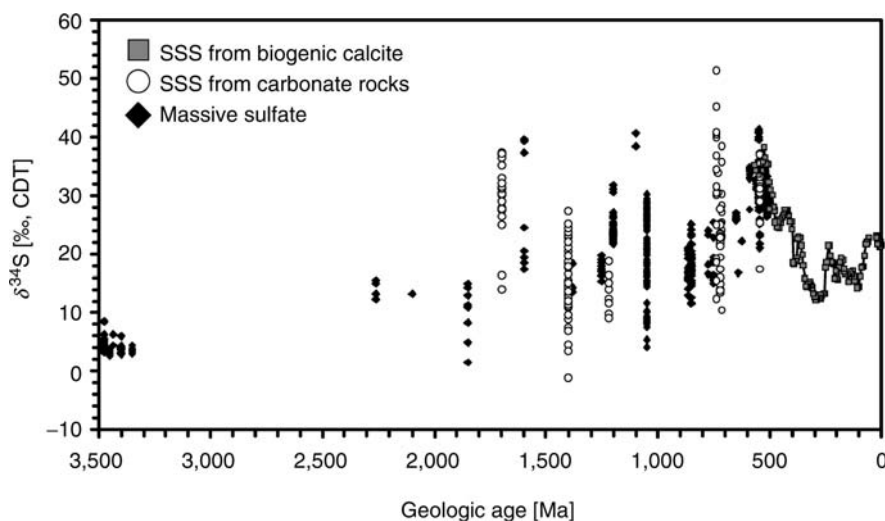


Figure S36 Sulfur isotopic evolution of seawater sulfate.

the oxidative weathering on the continents, delivering dissolved sulfate to the ocean.

The resulting increase in oceanic sulfate abundance would have triggered an increase in sulfur cycling via bacterial sulfate reduction (Canfield and Raiswell, 1999). Supporting evidence stems from the observation that large sulfur isotopic fractionations between sulfate and sedimentary sulfide commence at that time (e.g., Strauss, 2002). These are comparable in size to those recorded from younger times and modern marine sediments.

Towards the end of the Precambrian (600–500 million years ago), the average sulfur isotopic composition of seawater sulfate reaches its all-time maximum at + 35‰. This high $\delta^{34}\text{S}$ value continues into the Phanerozoic.

Substantial fluctuations in the sulfur isotopic composition of seawater sulfate characterize the Phanerozoic (the last 545 million years). The high $\delta^{34}\text{S}$ values at the beginning of this era are followed by a long-term decrease to a minimum value of + 11‰ in the Permian (some 250 million years ago) and a subsequent rise to the present day value. A detailed isotope record with good temporal resolution, based on structurally substituted sulfate (SSS) in biogenic carbonates, reveals additional higher order oscillations (Kampschulte and Strauss, 2003).

Following the simple isotope mass balance (Equation (2)) these temporal variations in $\delta^{34}\text{S}$ of seawater sulfate reflect variations in the fractional burial of reduced sedimentary sulfur. Potential causes for such variations include habitat size (near shore shelf area) and availability of reactive organic matter.

Evolution of biological sulfur cycling

The observation of a large sulfur isotope effect associated with bacterial sulfate reduction has prompted researchers to utilize this as a proxy for biogenicity in their studies of sedimentary pyrite. The resulting sulfur isotope record (Figure S37) reveals a temporal evolution that parallels the evolution of seawater sulfate in many respects.

Early Archean sedimentary pyrite generally displays a very limited variation in $\delta^{34}\text{S}$ near 0‰ and only a small difference to the sulfur isotopic composition of barite sulfur (e.g., Strauss, 2002). Lack of a large isotope effect suggests that bacterial sulfur cycling played only a minor role in sedimentary systems.

Starting in the late Archean/early Proterozoic (about 2.8–2.4 billion years ago) a substantial spread in $\delta^{34}\text{S}$ for sedimentary sulfide indicates sizeable sulfur isotopic fractionations. These are attributed to the activity of sulfate-reducing bacteria. Throughout the Proterozoic (2.5–0.5 billion years ago), the sulfur isotopic composition of sedimentary pyrite remains highly variable. Maximum isotopic fractionation between oceanic sulfate and sedimentary pyrite ranges between 30 and 40‰, reflecting bacterial sulfate reduction. The Neoproterozoic (1,000–545 million years ago) witnesses not only large spreads in $\delta^{34}\text{S}$ but also strongly positive, ^{34}S enriched sulfur isotope values for sedimentary sulfide. Considering minimum $\delta^{34}\text{S}$ values for sedimentary pyrite and $\delta^{34}\text{S}$ values of + 35‰ for Neoproterozoic seawater sulfate results in a maximum isotopic fractionation of 60‰. Such a large apparent isotope fractionation reflects the isotope effect associated with disproportionation reactions in addition to bacterial sulfate reduction.

The Phanerozoic (the last 545 million years) sulfur isotope record for sedimentary sulfur displays comparable large variations in $\delta^{34}\text{S}$ and an apparent isotopic fractionation that reflects sulfate reduction and disproportionation. The sulfur isotope record for reduced sulfur parallels roughly the respective record for seawater sulfate (Figure S36): high $\delta^{34}\text{S}$ values in the early Phanerozoic, followed by a decrease towards the Permian and a subsequent rise during Mesozoic and Cenozoic. The comparable temporal evolution of both sulfur isotope records at least during the last 600 million years suggests that bacterial sulfate reduction and disproportionation of intermediate sulfur compounds have been the key processes in biological sulfur cycling in sedimentary environments.

Multiple sulfur isotopic evidence for an atmospheric impact on the early sulfur cycle

The measurement of multiple sulfur isotopes (^{32}S , ^{33}S , ^{34}S , ^{36}S) reveal that all physical, chemical and biological processes on Earth result in mass-dependent fractionation (MDF) of these isotopes. Hence, mass-dependent relations can be defined as:

$$\delta^{33}\text{S}_{\text{TFL}} = 0.515 \times \delta^{34}\text{S} \quad (3)$$

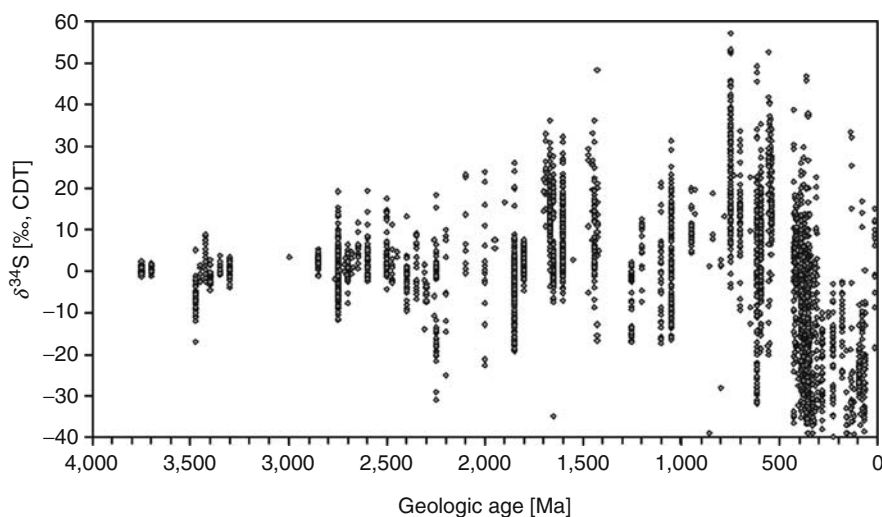


Figure S37 Sulfur isotopic composition of reduced sedimentary sulfur.

$$\delta^{36}\text{S}_{\text{TFL}} = 1.9 \times \delta^{34}\text{S} \quad (4)$$

with data falling on a respective Terrestrial Fractionation Line (TFL) in a three-isotope-plot. Multiple sulfur isotope analyses of sedimentary sulfide and sulfate of Archean and early Paleoproterozoic age (>2350 million years) yielded clear deviations from these mass-dependent relationships (e.g., Farquhar et al., 2000). Such mass-independent fractionation (MIF) in a measured sample can be quantified as:

$$\Delta^{33}\text{S} = \delta^{33}\text{S}_{\text{measured}} - \delta^{33}\text{S}_{\text{TFL}} \quad (5)$$

$$\Delta^{36}\text{S} = \delta^{36}\text{S}_{\text{measured}} - \delta^{36}\text{S}_{\text{TFL}} \quad (6)$$

Based on experimental and modelling data, this mass-independent isotope fractionation is believed to result from photochemical reactions in the atmosphere involving gaseous sulfur species, in particular sulfur dioxide. Furthermore, respective reactions require the absence of an effective UV shield (like ozone). Consequently, the presence of MIF-S has been taken as evidence for the absence of free oxygen in the Archean and early Paleoproterozoic atmosphere (e.g., Farquhar et al., 2000; 2007). Modelling evidence suggests that the maximum concentration of atmospheric oxygen had to be $<10^{-5}$ of the present atmospheric level (PAL) in order to yield MIF-S. Sedimentary sulfur younger than 2350 million years displays only mass-dependent sulfur isotopic fractionation, indicating that the atmospheric oxygen level had increased to $>10^{-2}$ PAL (e.g., Pavlov and Kasting, 2002).

Harald Strauss and Ján Veizer

Bibliography

- Canfield, D.E., 2001. Biogeochemistry of sulfur isotopes. In Valley, J.W., and Cole, D.R. (eds.), *Stable Isotope Geochemistry. Rev. Mineral. Geochem.*, **43**, 607–636.
- Canfield, D.E., and Raiswell, R., 1999. The evolution of the sulfur cycle. *Am. J. Sci.*, **299**, 697–723.
- Canfield, D.E., and Thamdrup, B., 1994. The production of ^{34}S -depleted sulphide during bacterial disproportionation of elemental sulphur. *Science*, **266**, 1973–1975.
- Canfield, D.E., Habicht, K.S., and Thamdrup, B., 2000. The Archean sulfur cycle and the early history of atmospheric oxygen. *Science*, **288**, 658–661.
- Clark, I., and Fritz, P., 1997. *Environmental Isotopes in Hydrogeology*. Boca Raton, FL: CRC Press, 328pp.
- Claypool, G.E., Holser, W.T., Kaplan, I.R., Sakai, H., and Zak, I., 1980. The age curve of sulfur and oxygen isotopes in marine sulfate and their mutual interpretation. *Chem. Geol.*, **28**, 190–260.
- Detmers, J., Brüchert, V., Habicht, K. S., and Kuever, J., 2001. Diversity of sulphur isotope fractionations by sulphate-reducing prokaryotes. *Appl. Environ. Microbiol.*, **67**, 888–894.
- Farquhar, J., Bao, H. M., and Thiemens, M., 2000. Atmospheric influence of Earth's earliest sulfur cycle. *Science*, **289**, 756–758.
- Farquhar, J., Peters, M., Johnston, D.T., Strauss, H., Masterson, A., Wiechert, U., and Kaufman, A.J., 2007. Isotopic evidence for Mesoarchaean anoxia and changing atmospheric sulphur chemistry. *Nature*, **449**, 706–709.
- Grinenko, V., and Krouse, H.R., 1992. Isotope data on the nature of riverine sulfates. *Mitt. Geol.-Paläont. Inst. Univ. Hamburg*, **72**, 9–18.
- Habicht, K.S., and Canfield, D.E., 2001. Isotope fractionation by sulphate-reducing natural populations and the isotopic composition of sulphides in marine sediments. *Geology*, **29**, 555–558.
- Habicht, K.S., Canfield, D.E., and Rethmeier, J., 1998. Sulphur isotope fractionation during bacterial sulphate reduction and disproportionation of thiosulphate and sulfite. *Geochim. Cosmochim. Acta*, **62**, 2585–2595.
- Hoefs, J., 1997. *Stable Isotope Geochemistry*. Berlin: Springer, 201pp.

- Holland, H.D., 2002. Volcanic gases, black smokers, and the great oxidation event. *Geochim. Cosmochim. Acta*, **66**, 3811–3826.
- Holser, W.T., Schidlowski, M., Mackenzie, F.T., and Maynard, J.B., 1988. Geochemical cycles of carbon and sulfur. In Gregor, C.B., Garrels, R.M., Mackenzie, F.T., and Maynard, J.B. (eds.), *Chemical Cycles in the Evolution of the Earth*. New York: Wiley, pp. 105–173.
- Kampschulte, A., and Strauss, H., 2003. The sulphur isotopic evolution of Phanerozoic seawater based on the analysis of structurally substituted sulphate in carbonates. *Chem. Geol.*, **204**(3–4), 255–286.
- Nielsen, H., 1989. Local and global aspects of the sulphur isotope age curve of oceanic sulphate. In Brimblecombe, P., and Lein, A.Y. (eds.), *Evolution of the Global Biogeochemical Sulphur Cycle*. New York: Wiley, pp. 57–64.
- Ohmoto, H., 1997. When did the Earth's atmosphere become oxic? *The Geochemical News*, **93-Fall**, 12–28.
- Pavlov, A.A., Kasting, J.F., 2002. Mass-independent fractionation of sulfur isotopes in Archean sediments: Strong evidence for an anoxic Archean atmosphere. *Astrobiology*, **2**, 27–41.
- Rees, C.E., Jenkins, W.J., and Monster, J., 1978. The sulphur isotopic composition of ocean water sulphate. *Geochim. Cosmochim. Acta*, **42**, 377–381.
- Strauss, H., 1999. Geological evolution from isotope proxy signals – sulphur. *Chem. Geol.*, **161**, 89–101.
- Strauss, H., 2002. The isotopic composition of Precambrian sulphides – seawater chemistry and biological evolution. *Spec. Publ. Int. Assoc. Sediment.*, **33**, 67–105.

Cross-references

[Atmospheric Evolution, Earth](#)
[Carbon Isotope Variations over Geologic Time](#)
[Isotope Fractionation](#)
[Stable Isotope Analysis](#)

SUN-CLIMATE CONNECTIONS

Introduction

All energy distributed in the climate system originates from the Sun. Earth's surface temperature is maintained by a balance between incoming and outgoing radiation. Irradiance is the most important parameter related to solar variability, as the relationship between irradiance and climate in radiative balance is simple and direct. The Earth currently receives an average of $1,367 \text{ W m}^{-2}$, integrated over all wavelengths. Climate variability directly associated with the radiative imbalance caused by changes in solar radiation is “solar forced.” In contrast, a “solar influenced” or “solar triggered” climate change depends mostly on atmospheric or oceanic feedback mechanisms for the effect.

The Sun also generates strong magnetic fields. Through their interaction with Earth's magnetic field and charged particles such as cosmic rays, magnetic fields are central to both observational and proxy records establishing solar variability. A current challenge in Sun-climate research is the interpretation of long-term proxy records related to the Sun's magnetic activity. It will only be possible to confirm a Sun-climate connection for past climates when the innermost workings of the Sun are understood well enough to quantify the relation between magnetic proxies and irradiance.

On millennial and shorter time scales, there is evidence that small changes in irradiance affect climate. It has proven difficult to identify the physical mechanisms by which small observed and reconstructed irradiance changes (a few tenths of a percent) could produce observed and reconstructed climate changes, up to 2°C within 50 years (Bond et al., 2001). Over

the past ten years, researchers have discovered that the atmosphere and ocean can undergo abrupt re-organizations when perturbed only slightly. This can cause large regional climate change while global average changes are small. Positive feedback systems have been proposed involving the upper and lower atmosphere, oceans, and polar ice. These can amplify the effects of small irradiance changes, and are likely critical for Sun-climate connections unless past solar variability was much larger than present estimates.

Solar variability

Solar cycles and sunspots

Perhaps the best-known indirect index of solar variability is the 11-year sunspot cycle. Over this cycle, the number of dark spots visible on the Sun's surface ranges from 0 to over 200. Sunspots are associated with strong local magnetic activity inhibiting surface convection, leading to cooling and darkening relative to the rest of the visible solar surface. Bright regions called faculae surround sunspots, causing a net increase in total solar irradiance (TSI) of about 0.1% during sunspot peaks relative to sunspot minima. Sunspot numbers from 1610 to present

are shown in [Figure S38](#), with the relationship to TSI measured by satellites since 1978 shown in [Figure S39](#).

Though measured irradiance and sunspot number are highly correlated, direct comparison is only possible for the past three solar cycles. The relation between long-term trends in sunspot numbers ([Figure S38](#)) and irradiance is unclear. Sunspot numbers return nearly to 0 during cycle minima, while during the Maunder Minimum, from 1645–1715, hardly any sunspots were observed in 50 years. If irradiance varied over this period, it must be reconstructed from records of solar activity other than sunspot numbers.

Solar magnetic activity and the geomagnetic field

Solar magnetic activity is evident on Earth due to interaction with the geomagnetic field. The *aa* index ([Figure S40](#)) is a measure of the Earth's magnetic field constructed from surface magnetometers.

A portion of the solar magnetic field is carried through the solar system and beyond by the solar wind. This is the interplanetary magnetic field (IMF), which influences Earth's magnetic field. Increasing IMF strength over the past 100 years

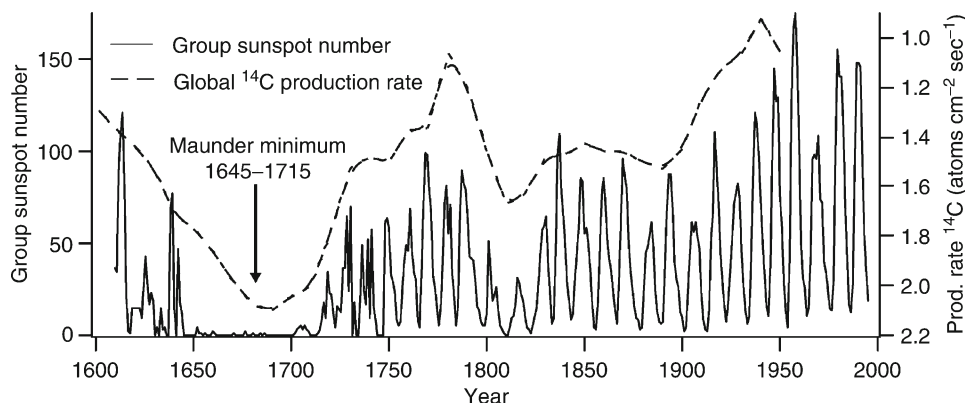


Figure S38 Sunspot numbers and global radiocarbon production rate show coherent variability. Carbon-14 production from nuclear weapons testing limits comparison with sunspots to before 1950. Note the lack of sunspots during the Maunder Minimum, and the increasing amplitudes of the solar cycles (data from National Geophysical Data Center, USA).

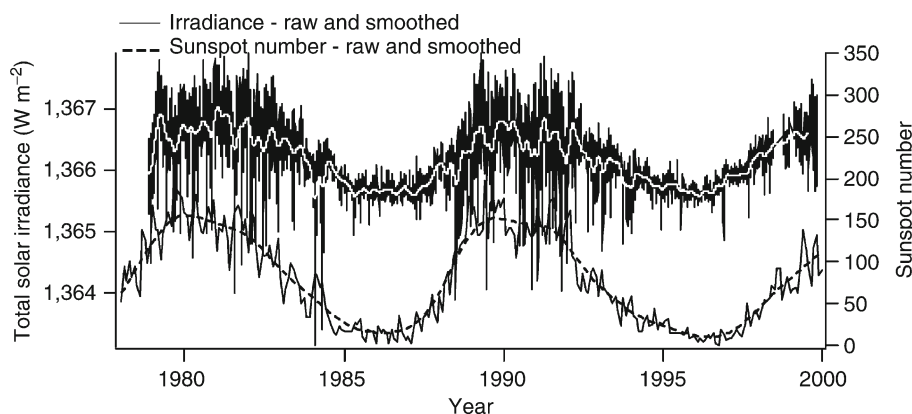


Figure S39 Total solar irradiance and sunspots are closely associated for the past three solar cycles (data from National Geophysical Data Center, USA).

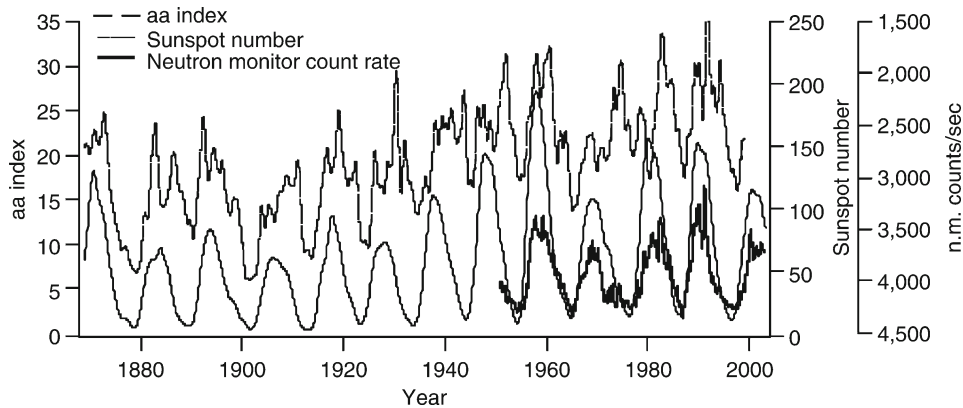


Figure S40 The geomagnetic *aa* index, neutron monitor count rate, and sunspot numbers demonstrate the influence of solar magnetic variability on the geomagnetic field. Cosmic ray flux is lower during solar-geomagnetic maxima (data from National Geophysical Data Center, USA).

is responsible for the long-term upward trend of the *aa* index (Lockwood et al., 1998). Though there is an 11-year cycle in *aa* in addition to the long-term trend, it is not directly convertible to irradiance because the IMF has a different origin from magnetic activity associated with sunspots (Lean et al., 2002).

Solar variability and cosmogenic isotopes

The Earth is continually being bombarded by galactic cosmic radiation (GCR): high-energy charged particles originating mostly from outside the solar system. The charge on cosmic ray particles subjects them to deflection by solar and terrestrial magnetic fields. The partial shielding of Earth by the coupled solar and geomagnetic fields is modulated by variability in those fields. This is clear from cosmic ray neutron monitor measurements taken since the 1950s. Figure S40 shows the neutron monitor counting rate (GCR flux) from Climax, Colorado, USA, which varies inversely with sunspot number.

Cosmic rays interact with Earth materials to produce cosmogenic isotopes, both in the atmosphere and in geologic materials. Two atmospherically produced cosmogenic isotopes, ^{14}C and ^{10}Be , are among the most useful proxy records for solar modulation of cosmic rays. Carbon-14 is produced from cosmic ray neutron reactions with nitrogen. It is rapidly oxidized to $^{14}\text{CO}_2$, and mixed throughout the atmosphere within about one year. Living trees incorporate ^{14}C in their tissues during photosynthesis. Measurements of ^{14}C in German oak tree rings provide a continuous record of atmospheric ^{14}C concentration back to almost 12,000 years. One complication in using atmospheric ^{14}C as a proxy for solar variability is its sensitivity to cycling of carbon in the ocean (Stuiver, 1994). In some ocean basins, surface water is transported to the deep ocean via thermohaline circulation (THC), where it may reside for more than 1,000 years before returning to the surface. Rapid changes in THC can affect atmospheric $^{14}\text{CO}_2$ concentration independently of its production. By increasing THC, more $^{14}\text{CO}_2$ -equilibrated water is sequestered in the ocean, drawing down atmospheric ^{14}C . Atmosphere-ocean carbon cycling effects in tree ring records may be evaluated by comparison with records of other, non-cycling cosmogenic isotopes, such as ^{10}Be .

Beryllium-10 is produced from oxygen and nitrogen in the atmosphere, rapidly sorbed to suspended aerosols, and flushed out in precipitation. The highest quality ^{10}Be records are found in polar ice cores. While ocean circulation changes cannot

directly affect ^{10}Be flux, the ocean can influence polar climate, changing ice-core accumulation rates. Beryllium-10 concentration in the ice is directly convertible to ^{10}Be flux if ice-core accumulation rates are known. Holocene ice-core accumulation rates are believed to have been constant, allowing ^{10}Be variations to reflect changes in production. Figure S41 shows ^{14}C and ^{10}Be production rates for the past 11,000 years.

Ca II emission of sun-like stars

Conversion of the cosmogenic production rates to irradiance remains a major challenge. One approach is to construct an estimate of irradiance for some point in the record, which is then used to scale back from modern irradiance. The most widely cited estimates of irradiance beyond the observed record come from observations of Sun-like stars at wavelengths associated with brightness variations, such as singly ionized calcium (Ca II) (Radick, 2003). Non-cycling stars are observed to be dimmer than those with 8–15 year periods in Ca II emission. Such observations suggest that the Sun was around 0.25% dimmer during the Maunder Minimum, when sunspot cycles ceased (Lean et al., 1995, 1998; Figure S42).

A critical assumption remains unverified, that non-cycling Sun-like stars are in a period of Maunder-type inactivity. None of the non-cycling Sun-like stars observed over the past two decades have resumed cycling. Given this uncertainty, true irradiance change during the Maunder Minimum could be either larger or equal to that during an 11-year cycle.

Correlations between solar variability and climate

In a landmark paper, Eddy (1976) presented evidence suggesting solar influence on climate for periods longer than the 11-year cycle. He noted that the Maunder Minimum corresponded to the coldest years of the Little Ice Age, a period of European history known for its climatic extremes. Eddy described the striking correspondence between minima in sunspot observations and maxima in the tree-ring record of cosmogenic ^{14}C (Figure S38), suggesting that cold years during the Maunder Minimum were linked in some way to reduced solar activity.

In the modern observational record, there have been many attempts to correlate the last three solar cycles with climate-related variables. While some correlations appear convincing, the observational records are typically too short for statistical

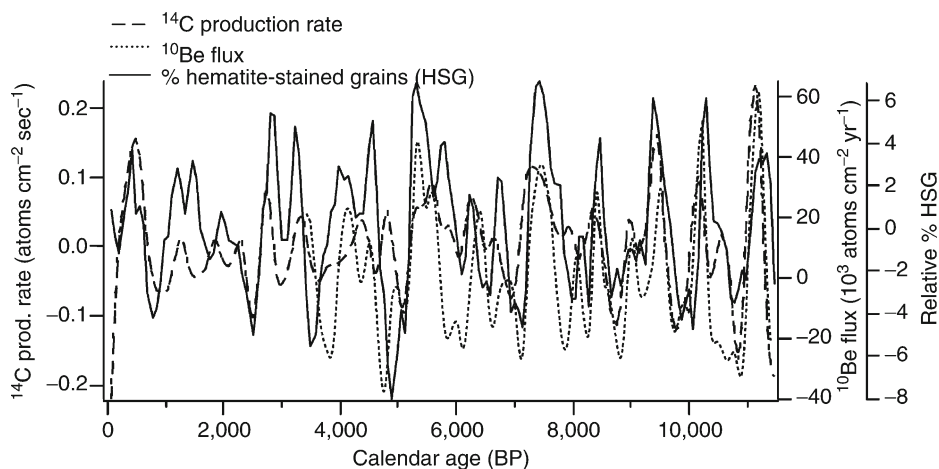


Figure S41 Percentage of hematite-stained quartz grains increases during Holocene cosmogenic isotope maxima, indicating North Atlantic cooling during solar minima. The most recent cold phase corresponds to the Little Ice Age in Europe (data from Bond et al., 2001).

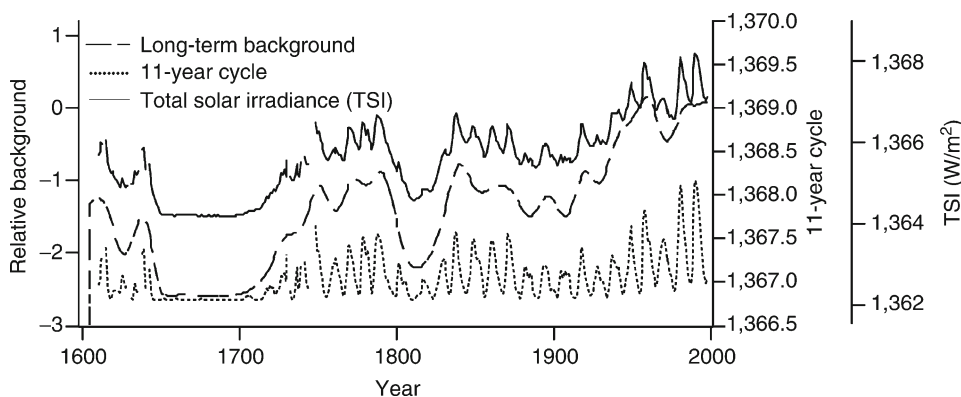


Figure S42 Two components of solar irradiance variability, background and the 11-year cycle, are summed to provide an estimate of total solar irradiance (TSI) since 1610 (data from Lean et al., 1998).

significance (Lean and Rind, 1999). The reviews of Lockwood (2002), Solanki and Fligge (2002), and Haigh (2003) provide excellent summaries of recent Sun-climate correlations using observational records. One example is a study of irradiance correlated with stratospheric temperature by Labitzke and Matthes (2003; Figure S43).

Some correlations imply a physical mechanism other than direct radiative forcing. For example, Marsh and Svensmark (2000) correlated cosmic ray intensity with North Atlantic regional cloud cover. Cloud cover is a potentially powerful climate feedback, critically important in defining climate sensitivity to external forcing in models. The authors suggest a direct link between atmospheric ionization by cosmic rays and cloud nucleation processes. Sun and Bradley (2002) argue that these correlations do not hold using updated data sets. Furthermore, large increases in cosmogenic isotope production such as the Laschamp event around 40 ka appear unassociated with climate. Carlsaw (2002) has reviewed the mechanisms of cloud response to cosmic rays in detail.

Paleoclimate and solar variability

Ocean sediment cores with high accumulation rates ($>20 \text{ cm ka}^{-1}$) can provide paleoclimate records with up to multi-centennial

resolution, currently limited by the accuracy of accelerator mass spectrometer radiocarbon dating. Bond et al. (2001) presented Holocene records of North Atlantic ice rafted detritus (IRD), together with ^{10}Be flux and ^{14}C production rate (Figure S41). IRD consists of mineral grains once frozen in drifting glacier or sea ice. Its occurrence in ocean sediment is evidence of enhanced ice production or survivability, i.e., a cold period. Though climate change could possibly influence ice core ^{10}Be and ocean circulation may influence atmospheric ^{14}C , it is unlikely the agreement between nuclides with different production and transport chemistries could be produced independent of solar variability. The complex patterns of the co-varying IRD and cosmogenic cycles make a strong argument for solar influence on North Atlantic climate.

The Asian monsoon is a climate response to intense summer heating of the Tibetan Plateau, leading to rising of air and low pressure. This low pressure reverses the direction of prevailing winds during summer to bring Indian Ocean moisture onshore. A proxy record for upwelling of deep ocean water from a sediment core off the coast of Oman indicates that during the centennial to millennial coolings in the North Atlantic, winds associated with the summer monsoon were weaker (Gupta et al., 2003; Figure S44).

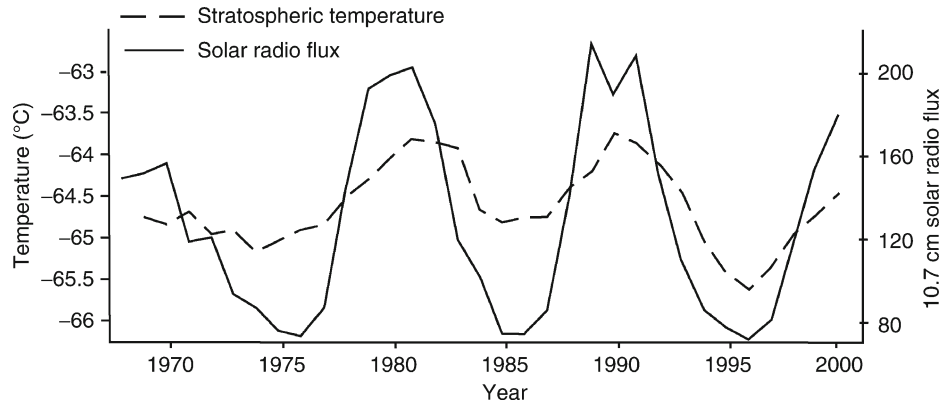


Figure S43 Stratospheric (70 hPa) temperatures at a point 30° N/136° W are correlated with solar radio emission, a proxy for irradiance. The consequences for surface climate depend on uncertain mechanisms of stratosphere-troposphere interaction (adapted from Labitzke and Matthes, 2003).

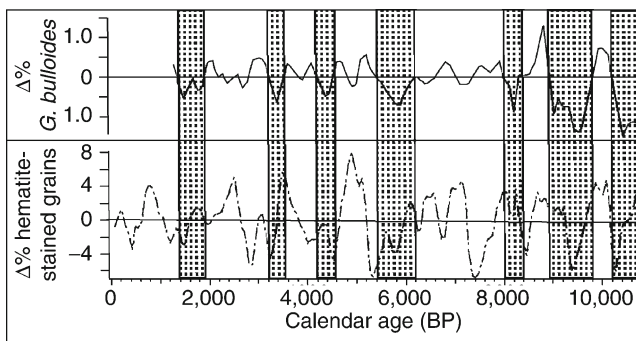


Figure S44 Weak monsoon wind strength results in less nutrient-rich water upwelling off the coast of Oman. This reduces abundance of *G. bullioides*, a hard-shelled plankton whose skeletons may be found in sediment cores. Periods of weak monsoon winds (shaded) correspond to North Atlantic coolings (adapted from Gupta et al., 2003).

Carbon isotope indicators of humidity from lake sediments (Hong et al., 2003) show drier conditions during North Atlantic coolings. Furthermore, Neff et al. (2001) found that rainfall intensity was weaker during solar minima based on a record of oxygen isotopes in Oman cave calcite. These three components of monsoon climate: winds, humidity, and rainfall, all point to a weaker monsoon during periods of reduced solar magnetic activity. Whether it is a direct response, as would be expected only for a large irradiance change, or a response to the solar-influenced climate of the North Atlantic is not yet known.

Amplification of solar influence

The direct radiative temperature response to solar variability is extremely small, around 0.06 °C for a typical solar cycle irradiance change of 0.1%. A measurable climate response therefore requires amplifying mechanisms. One of the simplest amplifiers yet proposed may be the climate system responding with stochastic resonance (Benzi et al., 1982). According to this model, a small signal (solar forcing) by itself would not produce climate change, but once added to a background level of climate system “noise,” the signal crosses a response threshold and is detectable. One candidate for climate noise may be the

El Niño, which has a recurrence interval (2–7 years) well suited to amplifying 11-year solar variability. Modeling has shown that El Niño noise may amplify the solar cycle into decadal variability of climate-related atmospheric anomalies, such as the Pacific North American pattern (Ruzmaikin, 1999).

Another possible amplifier is stratospheric ozone. Irradiance changes in ultraviolet (UV) wavelengths are up to ten times larger over the course of the solar cycle relative to total irradiance change (Lean, 2000). The resulting stratospheric heating due to UV absorption can change ozone concentrations, either amplifying or damping the initial radiative forcing depending on the altitude of ozone change. Aerosols from volcanic eruptions may have affected observational data for the last two solar cycles, so the actual ozone response to the solar cycle is still unclear (Haigh, 2003).

Shindell et al. (2001) simulated climate of the Maunder Minimum assuming a TSI reduction of 0.25%. Ozone concentrations were allowed to vary in response to the larger UV reduction of spectrally resolved irradiance. In the model, the irradiance decrease resulted in Maunder Minimum cooling via two interacting mechanisms. First, stratospheric ozone changed such that the initial negative radiative forcing was amplified. Second, there was a dynamical response resulting in a surface atmospheric pressure pattern resembling the negative phase of the Arctic Oscillation/North Atlantic Oscillation (AO/NAO). The modeled negative AO/NAO was associated with a cooling of nearly 1–2 °C during winter in Northern Europe, consistent with estimates of the coldest Little Ice Age temperatures. Globally, modeled cooling was only around 0.35 °C, emphasizing the role of this amplification mechanism in producing regional climate responses to solar variability.

IRD data of Bond et al. (2001) indicate that for the Little Ice Age, the most recent of the Holocene millennial cycles, the North Atlantic did not cool in the typical dipole pattern of the AO/NAO. Instead, cooling appeared basin-wide. Basin-wide cooling during the Holocene could be achieved via a reduction in thermohaline circulation. Thermohaline circulation transports heat to the North Atlantic region by surface ocean flow from the tropics. It is sensitive to transport of fresher (lighter) water into regions of density-driven convection. If solar influence results in an atmospheric response capable of affecting North Atlantic THC, the regional climate effect could be substantially amplified. A persistent negative phase of the AO/NAO may

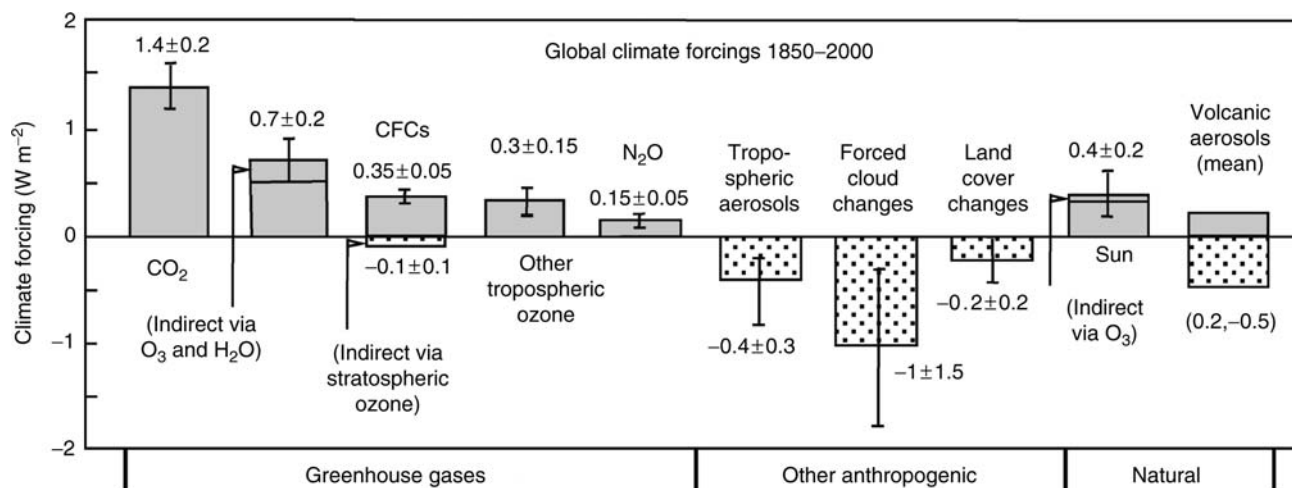


Figure S45 Anthropogenic emissions exert a radiative influence on climate larger than that expected for solar irradiance variability. Solar variability is dominant among natural forcing on decadal and longer time scales (adapted from Hansen, 2000).

be capable of affecting North Atlantic fresh water balance and thus THC. Therefore, the disagreement between the model and paleoclimate data could be a result of differences in the timescale of investigation (i.e., decadal vs. millennial).

Solar forcing and future climate

It has been difficult to confirm solar influence in decadal climate variability, possibly because irradiance records are too short and proxy reconstructions contain much uncertainty. Another reason may be anthropogenic climate forcing obscuring the solar influence. In the future, greenhouse gases (GHG) and tropospheric aerosols such as sulfates and dust could alter Earth's radiative balance with comparable, if not larger magnitudes than solar forcing (Figure S45; Hansen, 2000).

The role of solar forcing therefore depends on future anthropogenic emissions. If efforts to reduce CH₄ and CO₂ emission are implemented, solar forcing may re-emerge as the dominant climate influence on centennial to millennial timescales (Hansen, 2000).

Summary and conclusions

The Sun is a variable star, and from satellite measurements, total solar irradiance varies by 0.1%. Observational records of sunspots, geomagnetic activity, and cosmic ray flux are used as proxies for irradiance variability, though the relationship with irradiance is largely correlational rather than physical. Observations of Sun-like stars, if applicable to our Sun during the Maunder Minimum, suggest an irradiance reduction of around 0.25% relative to today, though key assumptions with this method have not been validated.

Cosmogenic isotopes such as ¹⁰Be and ¹⁴C are among the best records of solar magnetic activity, as they are available for the entire Holocene at high resolution. While the records are subject to complications of accumulation rate variations (ice cores) or changes in deep ocean circulation (atmospheric ¹⁴C), their agreement despite large differences in production and transport chemistry supports their use as proxies for solar variability.

Holocene climate change in the North Atlantic region is influenced by solar variability based on correlations between

cosmogenic isotopes and ice-rafted detritus from sediment cores. The Little Ice Age appears to have been the most recent cold phase of this centennial to millennial cycle. Additionally, several Holocene records of Asian monsoon strength consistently indicate a weaker monsoon during solar minima.

General circulation model simulations suggest a global cooling of around 0.35 °C given an irradiance forcing of 0.25%. North Atlantic paleoclimate records suggest larger regional changes, implying amplification mechanisms such as ozone photochemistry, stochastic resonance, and atmosphere-ocean dynamical responses. Dynamical responses can change climate by affecting the advection of air or water from warmer or colder regions in the absence of large changes in global mean temperature.

Efforts to establish the importance of solar forcing on decadal time scales for recent past climates and the future may be hampered by the growing contribution of anthropogenic forcing. If efforts to curtail emissions are implemented, solar variability may continue to dominate climate change.

Peter F. Almasi and Gerard C. Bond

Bibliography

- Benzi, R., Parisi, G., Sutera, A., and Vulpiani, A. 1982. Stochastic resonance in climatic change. *Tellus*, **34**, 10–16.
- Bond, G., Kromer, B., Beer, J., Muscheler, R., Evans, M.N., Showers, W., Hoffmann, S., Lotti-Bond, R., Hajdas, I., and Bonani, G. 2001. Persistent solar influence on North Atlantic climate during the Holocene. *Science*, **294**, 2130–2136.
- Carslaw, K.S., Harrison, R.G., and Kirkby, J., 2002. Cosmic rays, clouds, and climate. *Science*, **298**, 1732–1737.
- Eddy, J.A., 1976. The Maunder Minimum. *Science*, **192**, 1189–1202.
- Gupta, A.K., Anderson, D.M., and Overpeck, J., 2003. Abrupt changes in the Asian southwest monsoon during the Holocene and their links to the North Atlantic Ocean. *Nature*, **421**, 354–357.
- Hansen, J.E., 2000. The Sun's role in climate change. *Space Sci. Rev.*, **94**, 349–356.
- Haigh, J.D., 2003. The effects of solar variability on the Earth's climate. *Philos. Trans. Roy. Soc. Lond. A*, **365**, 95–111.
- Hong, Y.T., Hong, B., Lin, Q.H., Zhu, Y.X., Shibata, Y., Hirota, M., Uchida, M., Leng, X.T., Jiang, H.B., Xu, H., Wang, H., and Li, L., 2003. Correlation between Indian Ocean summer monsoon and North Atlantic climate during the Holocene. *Earth Planet. Sci. Lett.*, **211**, 371–380.

- Labitzke, K., and Matthes, K., 2003. Eleven-year solar cycle variations in the atmosphere: observations, mechanisms, and models. *Holocene*, **13**, 311–317.
- Lean, J., 2000. Evolution of the Sun's spectral irradiance since the Maunder Minimum. *Geophys. Res. Lett.*, **27**, 2425–2428.
- Lean, J., 2002. The effect of increasing solar activity on the Sun's total and open magnetic flux during multiple cycles: implications for solar forcing of climate. *Geophys. Res. Lett.*, **29**, doi: 10.1029/2002GL015880.
- Lean, J., and Rind, D., 1999. Evaluating Sun-climate relationships since the Little Ice Age. *J. Atmos. Sol. Terr. Phys.*, **61**, 25–36.
- Lean, J., Beer, J., and Bradley, R., 1995. Reconstruction of solar irradiance since 1610: Implications for climate change. *Geophys. Res. Lett.*, **22**, 3195–3198.
- Lean, J., Beer, J., and Bradley, R., 1998. Reconstructed solar irradiance data. IGBP PAGES/World Data Center for Paleoclimatology. Data Contribution Series # 1998–028. NOAA/NGDC Paleoclimatology Program, Boulder CO, USA.
- Lockwood, M., 2002. An evaluation of the correlation between open solar flux and total solar irradiance. *Astron. Astrophys.*, **382**, 678–687.
- Lockwood, M., Stamper, R., and Wild, N.M., 1998. A doubling of the Sun's coronal magnetic field during the past 100 years. *Nature*, **399**, 437–439.
- Marsh, N.D., and Svensmark, H., 2000. Low cloud properties influenced by cosmic rays. *Phys. Rev. Lett.*, **85**, 5004–5007.
- Neff, U., Burns, S.J., Mangini, A., Mudelsee, M., Fleitman, D., and Matter, A. 2001. Strong coherence between solar variability and the monsoon in Oman between 9 and 6 kyr ago. *Nature*, **411**, 290–293.
- Radick, R.R., 2003. Variability of Sun-like stars. *J. Atmos. Sol. Terr. Phys.*, **65**, 105–112.
- Ruzmaikin, A., 1999. Can El Niño amplify the solar forcing of climate? *Geophys. Res. Lett.*, **26**, 2255–2258.
- Shindell, D.T., Schmidt, G.A., Mann, M., Rind, D., and Waple, A. 2001. Solar forcing of regional climate change during the Maunder Minimum. *Science*, **294**, 2149–2152.
- Solanki, S.K., and Fligge, M., 2002. Solar irradiance variations and climate. *J. Atmos. Sol. Terr. Phys.*, **64**, 677–685.
- Stuiver, M., 1994. Atmospheric ^{14}C as a proxy of solar and climatic change. In *The solar engine and its influence on terrestrial atmosphere and climate* (NATO ASI Series). Berlin, Heidelberg: Springer.
- Sun, B., and Bradley, R., 2002. Solar influences on cosmic rays and cloud formation: A reassessment. *J. Geophys. Res.*, **104**, doi: 10.1029/2001JD000560.

Cross-references

[Astronomical Theory of Climate Change](#)
[Beryllium-10](#)
[Cosmogenic Radionuclides](#)
[Dendroclimatology](#)
[Ice-Rafted Debris \(IRD\)](#)
[Little Ice Age](#)
[Maunder Minimum](#)
[Monsoons, Quaternary](#)
[North Atlantic Deep Water and Climate Change](#)
[North Atlantic Oscillation \(NAO\) records](#)
[Thermohaline Circulation](#)

T

TEPHROCHRONOLOGY

Introduction

Tephrochronology is a dating method based on the identification, correlation and dating of tephra layers (Thórarinnsson, 1944; Thórarinnsson, 1981). It is important because it can give unusually precise and accurate dating control and may be applied over large areas of both land and sea. As a compound word “tephrochronology” follows the spelling conventions for the use of Greek loanwords in English where the “a” is replaced by an “o.”

Tephra

Tephra is a “catch-all” term to describe essentially unconsolidated pyroclastic material produced by a volcanic eruption. The term tephra is derived from the Greek word τέφρα, and was introduced as a modern scientific term by Sigurdur Thórarinnsson in his 1944 doctoral thesis. Thórarinnsson wanted a general term for pyroclastic ejecta, a definition that could not be satisfied by existing terms such as “volcanic ash”, “lapilli” and “bombs” which described very specific types of volcanic products. He proposed using tephra, noting how it complemented the use of other Greek loanwords “magma” and “lava” already in use in geology. There has been debate as to what is, or is not, strictly defined as tephra. Its scope may be clarified by considering what it is not: tephra does not include volcanic gases (yet tephra can be an aerosol); it is not a consolidated rock (yet tephra can become one); it is not a liquid (although tephra is formed from molten rock). Tephra is often composed of glass particles formed by the rapid chilling of droplets of magma. These grains may be vesicular or composed of solid fragments or plate-like bubble walls. Tephra can also include varying proportions of crystal and mineral components derived from either magma or the walls of the vent. Violent eruptions may result in the incorporation of significant fractions of lithic fragments either from the vent or, in the case of large-scale eruptions, the edifice of the volcano. As the density of these different fractions varies, their relative abundance will vary with distance from source, due to gravitational sorting. Originally, an “airborne” qualification

was considered in the definition of tephra, but in practice, this condition has been dropped so that the term may be robustly applied to essentially all unconsolidated deposits. This applies whether or not they have ever been truly airborne (as in a volcanic plume), or transported at the ground surface in a flow (as in co-ignimbrite ashes, pyroclastic flows or surges), or generated and transported in water (as in the products of sub-marine, sub-glacial or other sub-aqueous volcanic eruptions). This wide-ranging, inclusive definition of tephra is important when it comes to the use of tephrochronology because it removes any need to consider the exact mode of formation and, the wider the definition of tephra, the wider the applications of tephrochronology.

Characterization

The fundamental properties of tephra that underpin tephrochronology are its potentially rapid and widespread dispersal and distinctive physical and chemical characteristics. Atmospheric dispersal in a volcanic plume may be considered effectively instantaneous. As a result, tephra deposits may be used to define “isochrons”, or horizons of the same age, which are most precisely defined by the basal surface of the tephra deposit. This horizon may be used to define an area of environment at a “moment” in time. The destruction of the Roman cities of Pompeii and Herculaneum by tephra from the AD 79 eruption of Vesuvius defines an isochron and has been used to study cityscapes frozen at one point in time. Likewise tephra horizons may be used to study the characteristics and spatial patterns of other past environments, be they peat bogs, glacier forelands or ocean floors. They can be employed for precise correlation of contemporaneous records from radically different environments.

Significant temporal patterns caused by changing winds can occur within the horizon defined by a single tephra unit. For example, an early stage of an eruption may produce different types of tephra than a later stage, and may inject material into different levels of the atmosphere, where it will be affected by different types of wind. The result can be different dispersal patterns for contrasting stages during the formation of tephra. In this case, one should recognize that somewhat different tephra deposits could record a single event and that associated

deposits could be contemporaneous. Characterization of tephra deposits is best achieved by combining a variety of data and utilizing physical characteristics of the layers as a whole, such as: layer thickness; particle size ranges and particle shapes; composition in terms of glass shard, crystal mineral or lithic content; layer color (although this may be significantly affected by the nature of the enclosing strata); stratigraphic location and stratigraphic relationships. Bulk chemistry has been used to characterize tephra layers, but this has been superseded by discrete grain analyses, generally undertaken by electron probe microanalysis and capable of accurately determining major (and minor) element abundances. Where tephra layers are invisible to the naked eye ("micro" or crypto tephra), the approach has to be modified and generally focuses on the physical and chemical properties of separate grains and stratigraphic data. Collectively, these data may be used to determine characteristics best conceived as "signatures" rather than "fingerprints"; while chemical compositions may be distinctive, they are too frequently similar to be described as a "fingerprint." Examples of this similarity may be found for a wide range of tephra compositions from different eruptions, both silicic and basic (Larsen et al., 1999, 2001). One unambiguously unique characteristic is age. This in combination with the consequential differences, such as dispersal pattern and stratigraphic location, can be used to achieve unambiguous identifications and so correlate widely separated deposits of the same tephra.

Tephra dispersal may follow a series of different environmental pathways leading to distinctively time-transgressive characteristics for the deposit as a whole. For example, fallout from the volcanic plumes of Late Glacial eruptions in Iceland has produced extensive isochronous deposits, but tephra fallout also occurred on sea ice that, through time, has transported the tephra to new locations where the ice melted, releasing the tephra to fall to the seabed. Other more lengthy dispersal routes have resulted from tephra fall onto glaciers, incorporation into glacier ice, transport within the glacier system and later deposition at the ice margin. As another twist, ice calving can result in deposition from melting icebergs long after the formation of the tephra and far from the source volcano. In this case, tephra can form horizons within strata that were not necessarily produced at the same time as the volcanic eruption. This is not, however, a problem, as tephrochronology can be used to determine the time taken for movement through these contrasting environmental pathways, and so it can be used to constrain assessments of environmental process. This may be considered to be "tracer" tephrochronology.

An important aspect of the application of tephrochronology is the use of multiple tephra horizons to constrain periods of time. This may be crucial for the effective integration of some types of environmental data. For example, sediment accumulation rates are best compared over clearly defined time periods rather than in reference to a single moment or "spot" date. If tephrochronology (based on the same tephra layers) is used, then the intervals of time considered at different sites will be precisely comparable.

Chronology

Tephrochronology is indivisible from volcanic history but forms a subset of it, inasmuch as some key aspects of volcanic history (such as lava production) may not be associated with tephra production. Dating tephra layers can harness the full range of chronological methods available to earth science. The age of tephra may be determined either directly or indirectly: direct dating of tephra may come from historical records

or dating the tephra itself. Depending on age and composition, these direct dating methods may include K/Ar, Ar/Ar, fission track, U-series or luminescence dating.

Frequently, tephra are dated by the analysis of related material in which the tephra is found. In this case, depending on the age and location, these indirect dating methods may include ice core, varve, radiocarbon dating and dendrochronology. Crucially, the extensive dispersal of tephra layers means that dating may be optimized by finding the best place within the overall distribution to apply any particular dating method. This has the added benefit that dating specific to one environment (such as ocean core isotope stages) may be applied in another (the distribution of the Toba tephra across India).

Tephrochronologies

Parts of the world where tephrochronologies have been successfully developed and are now an integral part of paleoenvironmental research include the British Isles (Dugmore et al., 1995); Iceland (Thórarinnsson, 1981); Japan (Machida, 1999); New Zealand (Shane, 2000); Mexico (Newton and Metcalfe, 1999); and Alaska (Carson et al., 2002).

Andrew J. Dugmore and Anthony Newton

Bibliography

- Carson, E.C., Fournelle, J.H., Miller, T.P., and Mickelson, D.M., 2002. Holocene tephrochronology of the Cold Bay area, southwest Alaska Peninsula. *Quaternary Sci. Rev.*, **21**, 2213–2228.
- Dugmore, A.J., Larsen, G., and Newton, A.J., 1995. Seven tephra isochrones in Scotland. *The Holocene*, **5**(3), 257–266.
- Larsen, G., Dugmore, A.J., and Newton, A.J., 1999. Geochemistry of historic silicic tephra in Iceland. *The Holocene*, **9**(4), 463–471.
- Larsen, G., Newton, A.J., Dugmore, A.J., and Vilmundardóttir, E., 2001. Geochemistry, dispersal, volumes and chronology of Holocene silicic tephra layers from the Katla volcanic system, Iceland. *J. Quaternary Sci.*, **16**(2), 119–132.
- Machida, H., 1999. The stratigraphy, chronology and distribution of distal marker-tephras in and around Japan. *Glob. Planet. Change*, **21**, 71–94.
- Newton, A.J., and Metcalfe, S.E., 1999. Tephrochronology of the Toluca Basin, central Mexico. *Quaternary Sci. Rev.*, **18**, 1039–1059.
- Shane, P., 2000. Tephrochronology: A New Zealand case study. *Earth-Sci. Rev.*, **49**(1–4), 223–259.
- Thórarinnsson, S., 1944. Tefrokronologiska studier på Island. (Tephrochronological studies in Iceland). *Geogr. Ann.*, **26**, 395–398.
- Thórarinnsson, S., 1981. The application of tephrochronology in Iceland. In Self, S., and Sparks, R.S.J. (eds.), *Tephra Studies*. Dordrecht: D. Reidel. pp. 109–134.

Cross-references

- Dating, Fission-Tracks
 Dating, Luminescence Techniques
 Potassium-Argon/Argon-Argon Dating
 Uranium-Series Dating
 Volcanic Eruptions and Climate Change

THE 8,200-YEAR BP EVENT

Overview

The 8,200 year event, alternatively called the 8.2 kyr event or more simply the 8k event, refers to the last major abrupt climate change, a Northern Hemisphere cooling event that occurred approximately 8,200 years before the present (BP). The 8.2 kyr event is the largest anomaly in the Greenland ice

cores during the Holocene (see *Holocene climates*), a period otherwise marked by a relatively stable climate. Paleoclimate records from Europe, North America, South America, and Africa indicate an abrupt cooling event in the Northern Hemisphere. Separate geologic evidence documents the collapse of the remnants of the Hudson Bay ice dome dam and subsequent catastrophic final drainage of glacial Lakes Agassiz and Ojibway into the Hudson Bay, at approximately the same time. These lakes once occupied northern portions of the Canadian provinces of Manitoba and Ontario, respectively.

A potential atmospheric link between the disappearance of the glacial lakes and the far-field climate events was pointed out first by Hillaire-Marcel and de Vernal (1995). Further evidence for cooling and speculation on the connection to drainage of the glacial lakes was presented by de Vernal et al. (1997) and von Grafenstein et al. (1998). Barber et al. (1999) provided stronger evidence for the connection between the cooling event in Greenland and the disappearance of glacial Lakes Agassiz and Ojibway through improved interpretation of dates derived from the geologic evidence. Dating suggests the disappearance of the glacial lakes and drainage occurred at ~ 7.6 ^{14}C BP, while the anomaly in Greenland ice cores, dated using layer counts, occurred about 8,200 calendar years ago. Reasons for the difference between the calendar date and the ^{14}C date include changes in the production of ^{14}C through time as well as “reservoir age” corrections (see *Radiocarbon dating*).

The pattern of cooling around the North Atlantic basin and related changes in precipitation patterns from paleoclimate studies of the 8.2 kyr event is consistent with a decrease in Atlantic thermohaline circulation (THC, see *Thermohaline circulation*). This outpouring of glacial freshwater in a meltwater pulse (MWP) has been widely hypothesized as a mechanism for abrupt climate change (Broecker et al., 1985). Additional freshwater input into the North Atlantic decreases the density of surface waters and thus the formation of North Atlantic Deep Water (NADW, see *North Atlantic Deepwater and climate change*); this decreased THC reduces the amount of heat transported by the Atlantic Ocean and causes widespread cooling. However, the 8.2 kyr event is thus far the only well-established example of coincident cause and effect.

The well-quantified cause and climate changes of the 8.2 kyr event provide an opportunity to evaluate the effectiveness of global climate models. The ability of climate models to simulate this past abrupt climate change improves confidence in simulating future climates (Schmidt and LeGrande, 2005). In particular, modelers need to be able to evaluate their models’ ocean responses to climate change. The spread in model projections for the North Atlantic THC as a function of increasing greenhouse gases is extremely large, ranging from an almost 50% decrease to a small increase by 2,100. In part, this uncertainty stems from tuning the models for the existence of a stable North Atlantic circulation, but not being able to tune for its sensitivity because of the lack of appropriate data. The 8.2 kyr event thus provides an excellent opportunity to test the ability of the models (“model skill”) to simulate the oceans’ response to freshwater forcing (Schmidt and LeGrande, 2005). A successful model simulation of this last major abrupt climate change will improve confidence in the model’s accuracy, including its ability to simulate future climate changes.

Long term changes versus the abrupt 8.2 kyr event

Naming the “8.2 kyr event” for its occurrence in time lends itself to confusion – an anomaly that occurred around 8.2 kyr

ago need not be an expression of the “8.2 kyr event.” Orbital, orographic, and potentially solar-forced climate changes during the early to mid Holocene may be distinct from the 8.2 kyr event that was likely caused by the final drainage of glacial Lakes Agassiz and Ojibway.

The 8.2 kyr event appears to overlay a strong quasi-millennial-scale oscillation that is potentially linked to small changes in solar forcing (see *Sun-climate connections*; Bond et al., 2001). The production of cosmogenic isotopes (^{10}Be and ^{36}Cl from ice cores and ^{14}C from tree-ring records) is related to solar activity. An increase in Greenland ^{10}Be flux in the GRIP ice core around 8.2 kyr could be interpreted as a decrease in solar activity (Yiou et al., 1997). However, this increased flux is not unique – several such events occur throughout the Holocene, suggesting that solar activity changes are not responsible for the 8.2 kyr event (Muscheler et al., 2004; Field et al., 2006), though they might be responsible for century to millennial scale oscillations during the Holocene.

Another potential confusion results from orographic changes, or changes that occurred as a result of the retreat of the Laurentide Ice Sheet. In North America at roughly $\sim 8,000$ yBP, the shift in atmospheric circulation towards more westerly flow became more pronounced (e.g., Dean et al., 2002) – in archeological records, the subsequent mid-Holocene period is referred to as the “Altitheimal,” or “Hypsithermal” period (see *Hypsithermal*). Ancillary to the orographic changes could be long term shifts in meltwater and precipitation run-off from the Laurentian Ice Sheet. Although these climate shifts are also related to the collapse of the Hudson Bay ice dome dam, they are more generally related to the retreat of the Laurentide ice sheet and thus may be distinct from the abrupt 8.2 kyr event.

Orbital forcing of the Northern Hemisphere was stronger during the early Holocene, and many records document a “Holocene Thermal Optimum” in the early to mid-Holocene (see *Hypsithermal*) that is distinct from the 8.2 kyr event. The timing of the retreat of the ice sheet is tied to these long term changes, but the 8.2 kyr event is ostensibly linked to the climate changes that resulted from the outburst flooding.

The 8.2 kyr event thus refers to Greenland ice core and other records that document an abrupt (less than a few centuries) Northern Hemisphere cooling event that likely resulted from the collapse of the Hudson Bay ice dome dam and subsequent drainage of the glacial freshwater lakes and perturbation of THC in the North Atlantic. Simple “anomaly hunting” for events around 8,200 years ago is insufficient. Since the 8.2 kyr event is extremely abrupt, only high resolution records with excellent chronologies can be confidently correlated with the ice core event – extreme caution should be applied before linking any single anomaly in a record to the 8.2 kyr event (Morrill and Jacobsen, 2005).

Geology of the flood

During the final stage of Lake Agassiz, it was combined on its eastern edge with Lake Ojibway (thus called the “Ojibway Phase”), and the total surface area of these lakes is estimated at 841,000 km², corresponding to a volume of 163,000 km³ (Leverington et al., 2002). Subglacial outflow (run-off beneath the ice sheet), similar to modern Icelandic jökulhlaups, likely initiated the collapse of the ice sheet dam and allowed rapid drainage of these combined lakes into the proto-Hudson Bay (called the Tyrrell Sea) down to the Kinojévis level (also referred to as the Ponton Level for Lake Agassiz) (Teller et al., 2002; Clarke et al., 2004). Complicating this simple drainage

scenario is the Fidler beach level (Klassen, 1983) which lies below the Kinojévis level, possibly suggesting a two-stage drainage of the glacial lakes – first Lake Ojibway and some of Lake Agassiz, followed shortly by the remnants of Lake Agassiz (Teller et al., 2002). Either way, this final drainage of the two lakes exceeded any previous drainage of Lake Agassiz by an order of magnitude (Dyke, 2004).

Scours along the Hudson Bay sea floor, as well as other geomorphic evidence of the quick movement of icebergs, point to a rapid, large flood event along the western edge of the Hudson Bay (Josenhans and Zevenhuizen, 1990). Kerwin (1996) identified a red, hematite-rich, clay layer through the Hudson Strait, deposited at approximately 8,000 ^{14}C yBP that was likely deposited as material fell out of the Agassiz-Ojibway MWP. From the Hudson Strait, the waters traveled through the Labrador Sea and into the North Atlantic Ocean.

Paleo-hydraulic modeling studies (Clarke et al., 2004), or studies that take into account the geometry of the lake basins as well as the estimated volumes and rates of discharge, have constrained the magnitude and length of the event to approximately 5 Sv (1 Sv = 10^6 m s^{-1}) for 0.5–1 year; this is equivalent to $0.79 \times 10^{14} \text{ m}^3$ – $1.58 \times 10^{14} \text{ m}^3$ or 22–44 cm of sea level given the current surface area of the ocean. Alternatively, the best guess for the volumes and rates of a two-phase event are an initial drainage of about 3.6 Sv for 1 year, followed shortly (decades) by 1.6 Sv for 1 year (Teller et al., 2002). The volumes in these estimates are smaller than the upper boundary of 1.2 m of sea level rise indicated by Mississippi delta sediments (Törnqvist et al., 2004).

The link between the geologic evidence of a drainage event and paleoclimate records of an abrupt climate change was initially stymied because the initial dating of the geologic evidence indicated that the large MWP that followed the drainage of the glacial lakes pre-dated the ice core and other paleoclimate records by several centuries. Barber et al. (1999) determined that an additional marine reservoir age correction (see Radiocarbon dating) to the ^{14}C dates was required, and they established that the two events were close enough in time – both around $8,400 \pm 100$ yBP – for the MWP to be the catalyst that caused the abrupt climate cooling events in the paleoclimate records.

Ice cores and important records of the 8.2 kyr event

The largest Holocene abrupt climate change in the GISP2, GRIP, and NGRIP Greenland ice core records occurs from 8,200 until 8,000 years ago (Dansgaard, 1987; Alley et al., 1997). An approximate negative 2‰ excursion in the oxygen isotopic composition of Greenland ice cores indicates that temperatures may have been as much as 6 °C cooler for approximately 200 years at about 8.2 kyr (Cuffey et al., 1995; Alley et al., 1997); although some estimates for the cooling suggest cooling of up to 11 °C (Leuenberger et al., 1999). Paired with this abrupt cooling is decreased snow accumulation (Alley et al., 1993; Spinelli, 1996) and increased deposition of aerosols – e.g., salt, dust, sulfates (and associated cosmogenic isotope ^{10}Be) – characteristic of a cooler, drier regional climate (O'Brien et al., 1995; Muscheler et al., 2004). The approximate 75 ppbv abrupt decrease in methane concentration in bubbles in the Greenland ice cores at 8.2 kyr (Chappellaz et al., 1993; Brook et al., 2000) indicates a hemisphere-wide cooling and drying, since this concentration change would most likely have resulted from decreased wetland methane emissions that were the dominant pre-Industrial source for methane emissions (Houweling et al., 1999). Many records corroborate this indication of cooling and drying in both boreal (Northern

Hemisphere) as well as tropical regions, and an extensive review is available in Alley and Ágústsdóttir (2005). Here, the focus is on records with high resolution and a clear 8.2 kyr event or on records that directly correlate to records with high resolution and a clear 8.2 kyr event.

Glaciers in Scandinavia advanced and quickly retreated roughly synchronously with the 8.2 kyr event; this advance in southern Norway is called the “Finse Event” (Dahl and Nesje, 1994). Tree-ring thickness changes and alterations in the oxygen isotopic composition of a lake from Germany reflect a cooling of 1–2 °C (Klitgaard-Kristensen et al., 1998; von Grafenstein et al., 1998).

Ocean sediment core records off the south-western coast of Norway document an increase in abundance of the cold water planktonic foraminifera species, *Neogloboquadrina pachyderma* (left) (Klitgaard-Kristensen et al., 1998), but no change in its oxygen isotopic composition of planktonic foraminifera (Klitgaard-Kristensen et al., 2001). However, further north in the East Norwegian Sea, the oxygen isotopic composition of *N. pachyderma* (left) does become enriched by 0.7‰, indicating a cooling of 3–4 °C (Risebrobakken et al., 2003).

Interestingly, many Labrador Sea sediment core records do not show a significant change in the oxygen isotopic composition of foraminifera at this time (Hillaire-Marcel et al., 1994). Keigwin et al. (2005) suggest that the MWP may have traveled southward along the coast of North America as a boundary current, thus preventing a significant oxygen isotope signal within the Labrador Sea.

Deep Lake, Minnesota (USA) records a spike in varve thickness, interpreted as an increase in aeolian deposition, at around 8.2 kyr (Hu et al., 1999). A spike in montane conifers in Virginia indicates a short-lived cooling period approximately synchronous with the 8.2 kyr event (Kneller and Peteet, 1999).

Model studies consistently indicate that when the Northern Hemisphere cools, the inter-tropical convergence zone (ITCZ) shifts south (Stouffer et al., in press). The ITCZ is essentially a tropical rain “belt” that generally occurs along the zone of highest sea surface temperature. Hughen et al. (1996) and Haug et al. (2001) used a gray-scale record from an ocean sediment core in the Cariaco Basin, off the Venezuelan coast to infer a southward shift of the Atlantic ITCZ roughly synchronous with the 8.2 kyr event. Brazilian speleothems (stalagmites) suggest a southward shift in the ITCZ as well (Wang et al., 2005). Tropical ice cores from Kilimanjaro, Africa show a dramatic increase in dust deposition, suggesting a drop in African lake levels (Thompson et al., 2002) that could be associated with this southward migration of the ITCZ. Lake records from Africa indicate a dry spell around the same time (e.g., Gasse and Van Campo, 1994), but they lack the resolution to be definitively tied to the 8.2 kyr event.

At about the same time, the ice core record of δD in Vostok, Antarctica shows a negative 22‰ excursion, indicating a warming of approximately 2.5 °C (Petit et al., 1999); however, the dating of the ice core is sufficiently uncertain (± 500 years) to question the link with the 8.2 kyr event of the Northern Hemisphere. Furthermore, not all Antarctic ice cores indicate such an oscillation (Masson et al., 2000). This implied warming Southern Hemisphere coupled with the colder Northern Hemisphere might be an expression of the bi-polar seesaw (Broecker, 1998).

The evidence outlined thus far makes a clear case for cooling in the Northern Hemisphere at around 8.2 kyr ago, but it does not indicate the cause of the abrupt cooling. McManus

et al. (2004) use $^{230}\text{Pa}/^{231}\text{Th}$ (protactinium-thorium) in an ocean sediment core from the Bermuda rise as an indicator of changes in NADW; higher resolution examination of this same record indicates a decades to century long slow-down of Atlantic THC at around 8.2 kyr. The dissolution of aragonite index in an ocean sediment core off the north-eastern coast of Brazil also implies a reduction of the NADW at approximately 8.2 kyr (Arz et al., 2001).

Modeling of the 8.2 kyr event

The 8.2 kyr event particularly lends itself to paleoclimate model simulation for proxy data comparisons (Schmidt and LeGrande, 2005). The outburst flood from the drainage of Lakes Agassiz and Ojibway into the Hudson Bay provides a plausible and interesting hypothesis for the forcing. Geologic evidence paired with modeling efforts has provided specific constraints for the volume and duration of the event (Clarke et al., 2004). Abundant, widespread, and clear proxy data of the climate response provides multiple opportunities for comparing model results to the paleoclimate record (Alley and Ágústsdóttir, 2005). The magnitude of the climate response implies an intermediate THC response (e.g., not “on” or “off,” rather “in between”). It has several more features that make it an especially desirable event to model using fully coupled (atmosphere-ocean-sea ice) general circulation models (GCMs) – the boundary conditions for the 8.2 kyr event are relatively similar to today, and its length is relatively short, an important characteristic since coupled GCMs can take many months to simulate 1,000 years of climate (Schmidt and LeGrande, 2005).

LeGrande et al. (2006) simulated the 8.2 kyr event using the Goddard Institute of Space Studies ModelE-R by adding freshwater to the Hudson Bay at the rate and duration suggested by Clarke et al. (2004). This coupled GCM also tracks water isotopes throughout the hydrologic cycle, and the atmosphere component tracks changes in wetland methane emissions and aerosol deposition. Temperatures over much of the North Atlantic cooled by up to 2°C, while Europe, Asia, and parts of North America cooled by 0.5–1°C. Temperatures in the South Atlantic and Southern Ocean warmed by ~ 0.5°C, which is an expression of the bi-polar seesaw (Broecker, 1998). Storm tracks in the Atlantic became more zonal, and the ITCZ shifted southward. This pattern of climate change is typical for GCM experiments of reduced THC in the North Atlantic, though the magnitude of the climate change is smaller than “hosing” experiments that apply a larger volume of freshwater over a longer period of time and shut down NADW (e.g., Stouffer et al., 2006).

LeGrande et al. (2006) directly compared model tracers to the paleoclimate proxy record and found that the freshwater forcing is a viable cause for the climate anomalies recorded in the Greenland ice cores and elsewhere. Generally, water isotopes in precipitation became more depleted with colder or wetter conditions. Their simulations showed that the water isotopes in precipitation over much of the North Atlantic, Greenland, and Europe became depleted. In addition, bands of enriched and depleted water isotopes in precipitation occurred north and south of the equator, reflecting the southward migration of the ITCZ.

The drier atmosphere over Greenland caused an increase in dust and ^{10}Be deposition (LeGrande et al., 2006). Both wet and dry ^{10}Be deposition over Summit, Greenland increased, implying that ^{10}Be flux (important for inferring changes in solar

activity) cannot be estimated using the ^{10}Be concentration and snow accumulation alone (Field et al., 2006). The cooling and drying of boreal (Northern Hemisphere) areas caused a decrease in wetland methane emissions that resulted in an approximate 60 ppbv shift in atmospheric methane concentration.

The LeGrande et al. (2006) results indicate that the lack of evidence for the 8.2 kyr event in the oxygen isotopic composition of foraminifera from many ocean sediment core records may be due to “canceling” effects in the proxy record – in this case, depleted seawater oxygen isotopes and colder ocean temperatures.

Two Earth system intermediate complexity models (EMICs) have studied the 8.2 kyr event by applying freshwater forcing to “8k appropriate” simulations that include orbital and greenhouse gas forcing. Renssen et al. (2001, 2002) simulated the addition of $4.67 \times 10^{14} \text{ m}^3$ of freshwater to the Labrador Sea at a range of rates (1.5 Sv for 10 years, 0.75 Sv for 20 years, and 0.3 Sv for 50 years) using the ECBilt-CLIO model. They found that the model THC response varied greatly and that the length of the simulated climate event ranged from a few hundred to a few thousand years, suggesting that the climate response to freshwater forcing is strongly dependent on non-linear dynamics within the climate system. Using another EMIC model (CLIMBER-2), Bauer et al. (2004) simulated the addition of 2.6 Sv freshwater for 2 years ($1.6 \times 10^{14} \text{ m}^3$) to a band of the Atlantic Ocean between 50 and 70° N, and also introduced “white noise” to the climate system in the form of small (0.01–0.1 Sv), random inputs of freshwater in this same band. They also found a large range of model responses to the same freshwater forcing, and suggested that “chance” played a role in the temporal evolution of the 8.2 kyr event.

Ágústsdóttir (1998) simulated the 8.2 kyr event using the GENESIS climate model. This model is an atmosphere GCM coupled to a slab (e.g., 50 m thick) ocean; thus, the event was simulated through (a) specifying 8k appropriate greenhouse gas, orbital, and ice sheet forcing; and (b) changing the heat convergence in the Norwegian Sea, where the convection associated with THC occurs, not through freshwater forcing. They found the “typical” pattern of THC perturbation: cooling over the North Atlantic, zonal shift in precipitation bands, and southward migration of the ITCZ.

Summary

Around 8,200 years before the present, Greenland ice core records document the last major, abrupt climate change. Multiple paleoclimate records elsewhere in the Northern Hemisphere provide other evidence for a short-lived (about 200 year) cooling event (Alley and Ágústsdóttir, 2005). Geologic evidence indicates the final drainage of glacial Lakes Agassiz and Ojibway into the Hudson Bay occurred at about the same time (Teller et al., 2002). The coincidence of these two effects suggests that the additional freshwater from the drainage of these lakes may have been the catalyst for this abrupt climate change (Barber et al., 1999).

The theory for the cause of the abrupt climate change is that the drainage of the glacial lakes caused changes in thermohaline circulation, also called meridional overturning circulation (e.g., Broecker et al., 1985). The drainage of the glacial lakes decreased the surface density of the North Atlantic Ocean, causing a decrease in the formation of North Atlantic Deep Water. This “slowdown” of the so-called global conveyor belt caused cooling of around 1–2°C around the North Atlantic

Ocean and surrounding land masses, and perhaps up to 6 °C of cooling in Greenland.

The 8.2 kyr event is well documented in the paleoclimate record, and it has an interesting viable cause, or trigger, for the abrupt cooling. These two properties in addition to its short length make it an excellent candidate for simulation using GCMs (Schmidt and LeGrande, 2005). Modeling studies of the 8.2 kyr event support this theory of abrupt climate change (LeGrande et al., 2006). Conversely, the match between model simulations and paleoclimate record provides a means to evaluate the skill of climate models.

Allegra N. LeGrande

Bibliography

- Ágústsdóttir, A.M., 1998. Abrupt climate changes and the effects of North Atlantic deepwater formation: Results from the GENESIS global climate model and comparison with data from the Younger Dryas event and the event at 8200 yBP and the present. PhD Thesis, Pennsylvania, USA, The Pennsylvania State University, University Park.
- Alley, R., and Ágústsdóttir, A.M., 2005. The 8k event: Cause and consequences of a major Holocene abrupt climate change. *Quaternary Sci. Rev.*, **24**, 1123–1149.
- Alley, R.B., Mayewski, P.A., Sowers, T., Stuiver, M., Taylor, K.C., and Clark, P.U., 1997. Holocene climatic instability: A prominent, widespread event 8200 years ago. *Geology*, **25**, 483–486.
- Alley, R.B., Meese, D.A., Shuman, C.A., Gow, A.J., Taylor, K.C., Grootes, P.M., White, J.W.C., Ram, M., Waddington, E.D., Mayewski, P.A., and Zielinski, G.A., 1993. Abrupt increase in snow accumulation at the end of the Younger Dryas event. *Nature*, **362**, 527–529.
- Arz, H.W., Gerhardt, S., Pätzold, J., and Röhl, U., 2001. Millennial-scale changes of surface- and deep-water flow in the western tropical Atlantic linked to Northern Hemisphere high-latitude climate during the Holocene. *Geology*, **29**(3), 239–242.
- Barber, D.C., Dyke, A., Hillaire-Marcel, C., Jennings, A.E., Andrews, J.T., Kerwin, M.W., Bilodeau, G., McNeely, R., Souhon, J., Morehead, M.D., and Gagnon, J.-M., 1999. Forcing of the cold event of 8,200 years ago by catastrophic drainage of Laurentide lakes. *Nature*, **400**, 344–348.
- Bauer, E., Ganopolski, A., and Montoya, M., 2004. Simulation of the cold climate event 8,299 years ago by meltwater outburst from Lake Agassiz. *Paleoceanography*, **19**, PA3014.
- Bond, G., Kromer, B., Beer, J., Muscheler, R., Evans, M.N., Showers, W., Hoffmann, S., Lott-Bond, R., Hajdas, I., and Bonani, G., 2001. Persistent solar influence on North Atlantic climate during the Holocene. *Science*, **294**, 2130–2136.
- Broecker, W.S., Peteet, D.M., and Rind, D., 1985. Does the ocean-atmosphere system have more than one stable mode of operation? *Nature*, **315**(2), 21–26.
- Broecker, W.S., 1998. Paleoocean circulation during the last deglaciation: A bipolar seesaw? *Paleoceanography*, **13**(2), 119–121.
- Brook, E.J., Harder, S., Severinghaus, J.P., Steig, E.J., and Sucher, C.M., 2000. On the origin and timing of rapid changes in atmospheric methane during the last glacial period. *Glob. Biogeochem. Cycles*, **14**, 559–572.
- Chappellaz, J., Blunier, T., Raynaud, D., Barnola, J.M., Schwander, J., and Stauffer, B., 1993. Synchronous changes in atmospheric CH₄ and Greenland climate between 40 and 8 kyr BP. *Nature*, **366**, 443–445.
- Clarke, G.K.C., Leverington, D.W., Teller, J.T., and Dyke, A.S., 2004. Paleohydraulics of the last outburst flood from glacial Lake Agassiz and the 8200 BP cold event. *Quaternary Sci. Rev.*, **23**, 389–407.
- Cuffey, K.M., Clow, G.D., Alley, R.B., Stuiver, M., Waddington, E.D., and Saltus, R.W., 1995. Large Arctic temperature change at the glacial-Holocene transition. *Science*, **270**, 455–458.
- Dahl, S.O., and Nesje, A., 1994. Holocene glacier fluctuations at Hardangerjøkulen, central-southern Norway: A high-resolution composite chronology from lacustrine and terrestrial deposits. *The Holocene*, **4**, 269–277.
- Dansgaard, W., 1987. Ice core evidence of abrupt climatic changes. In Berger, W.J., and Labeyrie, L.D. (eds.), *Abrupt Climatic Change: Evidence and Implications*. Dordrecht, The Netherlands: Reidel, pp. 223–233.
- Dean, W.E., Forester, R.M., and Bradbury, J.P., 2002. Early Holocene change in atmospheric circulation in the Northern Great Plains: an upstream view of the 8.2 ka cold event. *Quaternary Sci. Rev.*, **21**, 1763–1775.
- De Vernal, A., Hillaire-Marcel, C., von Grafenstein, U., and Barber, D., 1997. Researchers Look for Links Among Paleoclimate Events. *EOS, Transactions of the American Geophysical Union*, vol. **78**, pp. 247–249.
- Dyke, A.S., 2004. An outline of North American Deglaciation with emphasis on central and northern Canada. In Ehlers, J., and Gibbard, P.L. (eds.), *Quaternary Glaciations – Extent and Chronology, Part II: North America*. Amsterdam: Elsevier, pp. 371–406.
- Field, C.V., Schmidt, G.A., Koch, D.M., and Salyk, C., 2006. Modeling production and climate-related impacts on 10Be concentration in ice cores. *J. Geophys. Res. – Atmos.*, **111**, D15107, doi: 10.1029/2005JD006410.
- Gasse, F., and Van Campo, E., 1994. Abrupt postglacial climate events in West Asia and North-Africa monsoon domains. *Earth Planet. Sci. Lett.*, **126**, 435–456.
- Haug, G.H., Hughen, K.A., Sigman, D.M., Peterson, L.C., and Röhl, U., 2001. Southward migration of the inter-tropical convergence zone through the Holocene. *Science*, **293**, 1304–1308.
- Hillaire-Marcel, C., de Vernal, A., Bilodeau, G., and Wu, G., 1994. Isotope stratigraphy, sedimentation rates, deep circulation, and carbonate events in the Labrador Sea during the last ~200 ka. *Can. J. Earth Sci.*, **31**, 63–89.
- Hillaire-Marcel, C., and de Vernal, A., 1995. Mais que s'est-il donc passé vers 8,000 ans BP? *Association Québec Etude Quaternary*, Annual meeting, University of Montreal, Abstracts volume, 16.
- Houweling, S., Kaminski, T., Dentener, F., Lelieveld, J., and Heimann, M., 1999. Inverse modeling of methane sources and sinks using the adjoint of a global transport model. *J. Geophys. Res.*, **104**, 26137–26160.
- Hu, F.S., Slawinski, D., Wright, H.E. Jr., Ito, E., Johnson, R.B., Kelts, K.R., McEwan, R.F., and Boedigheimer, A., 1999. Abrupt changes in North American climate during the early Holocene times. *Nature*, **400**, 437–440.
- Hughen, K.A., Overpeck, J.T., Peterson, L.C., and Trumbore, S., 1996. Rapid climate changes in the tropical Atlantic region during the last deglaciation. *Nature*, **380**, 51–54.
- Josenhans, H.W., and Zevenhuizen, J., 1990. Dynamics of the Laurentide Ice Sheet in Hudson Bay, Canada. *Mar. Geol.*, **92**, 1–26.
- Keigwin, L.D., Sachs, J.P., Rosenthal, Y., and Boyle, E.A., 2005. The 8200 yBP event in the slope water system, western subpolar North Atlantic. *Paleoceanography*, **20**, PA2003.
- Kerwin, M.W., 1996. A Regional Stratigraphic Isochron (ca. 8000 ¹⁴C yBP) from Final Deglaciation of Hudson Strait. *Quaternary Res.*, **46**, 89–98.
- Klassen, R.W., 1983. Lake Agassiz and the late glacial history of northern Manitoba. In Teller, J.T., and Clayton, L. (eds.), *Glacial Lake Agassiz*. St. John's, NL: Geological Association of Canada. GAC Special Paper 26, pp. 97–115.
- Klitgaard-Kristensen, D., Sejrup, H.P., Hafliðason, H., Johnsen, S., and Spurk, M., 1998. A regional 8200 cal yBP cooling event in northwest Europe, induced by final stages of the Laurentide ice sheet deglaciation? *Journal of Quaternary Science*, **13**, 165–169.
- Klitgaard-Kristensen, D., Sejrup, H.P., and Hafliðason, H., 2001. The last 18 kyr fluctuations in Norwegian Sea surface conditions and implications for the magnitude of climatic change: Evidence from the North Sea. *Paleoceanography*, **15**(5), 455–467.
- Kneller, M., and Peteet, D., 1999. Late-glacial to early Holocene climate changes from a central Appalachian pollen and macrofossil record. *Quaternary Res.*, **51**, 133–147.
- LeGrande, A.N., Schmidt, G.A., Shindell, D.T., Field, C.V., Miller, R.L., Koch, D.M., Faluvegi, G., and Hoffmann, G., 2006. Consistent simulations of multiple proxy responses to an abrupt climate change event. *Proc. Natl. Acad. Sci.*, **104**(3), 837–842.
- Leuenberger, M.C., Lang, C., and Schwander, J., 1999. δ¹⁵N measurements as a calibration tool for the paleothermometer and gas-ice age differences: A case study for the 8200 BP event on GRIP ice. *J. Geophys. Res.*, **104D**, 22163–22170.
- Leverington, D.W., Mann, J.D., and Teller, J.T., 2002. Changes in the bathymetry and volume of glacial Lake Agassiz between 9200 and 7600 ¹⁴C yBP. *Quaternary Res.*, **57**, 244–252.
- Masson, V., Vimeux, F., Jouzel, J., Morgan, V., Delmotte, M. et al., 2000. Holocene Climate Variability in Antarctica Based on 11 Ice-Core Isotopic Records. *Quaternary Res.*, **54**, 348–358.

- McManus, J.F., Francois, R., Gherardi, J.M., Keigwin, L.D., and Brown-Leger, S., 2004. Collapse and rapid resumption of Atlantic meridional circulation linked to deglacial climate changes. *Nature*, **428**, 834–837.
- Morrill, C., and Jacobsen, R.M., 2005. How widespread were climate anomalies 8200 years ago? *Geophys. Res. Lett.*, **32**, L19701, doi: 10.1029/2005GL023536.
- Muscheler, R., Beer, J., and Vonmoos, M., 2004. Causes and timing of the 8200 yBP event inferred from the comparison of the GRIP ^{10}Be and the tree ring $\Delta^{14}\text{C}$ record. *Quaternary Sci. Rev.*, **23**, 2101–2111.
- O'Brien, S.M., Mayewski, P.A., Meeker, L.D., Meese, D.A., Twickler, M.S., and Whitlow, S.I., 1995. Complexity of Holocene climate as reconstructed from a Greenland ice core. *Science*, **270**, 1962–1964.
- Petit, J.R., Jouzel, J., Raynaud, D., et al., 1999. Climate and atmospheric history of the past 420,000 years from the Vostok ice core, Antarctica. *Nature*, **399**, 429–436.
- Renssen, H., Goosse, H., Fichefet, T., and Campin, J.M., 2001. The 8.2 kyrBP event simulated by a global atmosphere–sea–ice–ocean model. *Geophys. Res. Lett.*, **28**, 1567–1570.
- Renssen, H., Goosse, H., and Fichefet, T., 2002. Modeling the effect of freshwater pulses on the early Holocene climate: The influence of high-frequency climate variability. *Paleoceanography*, **17**, PA1020.
- Risebrobakken, B., Jansen, E., Andersson, C., Mjelde, E., and Hevroy, K., 2003. A high-resolution study of Holocene paleoclimatic and paleoceanographic changes in the Nordic Seas. *Paleoceanography*, **18**, PA1017.
- Schmidt, G.A., and LeGrande, A.N., 2005. The Goldilocks abrupt climate change event. *Quaternary Sci. Rev.*, **24**, 1109–1110.
- Spinelli, G., 1996. A statistical analysis of ice-accumulation level and variability in the GISP2 ice core and a reexamination of the age of the termination of the Younger Dryas cooling episode. University Park, Pennsylvania State University, Earth System Science Center Technical Report No. 96-001, pp. 1–36.
- Stouffer, R.J., Yin, J., Gregory, J.M., et al., 2006. Investigating the Causes of the Response of the Thermohaline Circulation to Past and Future Climate Changes. *J. Clim.*, **19**, 1365–1387.
- Teller, J.T., Leverington, D.W., and Mann, J.D., 2002. Freshwater outbursts to the oceans from glacial Lake Agassiz and their role in climate change during the last deglaciation. *Quaternary Sci. Rev.*, **21**, 879–887.
- Thompson, L.G., Mosley-Thompson, E., Davis, M.E., Henderson, K.A., Brecher, H.H., Zagorodnov, V.S., Mashiotta, T.A., Lin, P.N., Mikhaleenko, V.N., Hardy, D.R., and Beer, J., 2002. Kilimanjaro ice core records: Evidence of Holocene climate change in tropical Africa. *Science*, **298**, 589–593.
- Törnqvist, T.E., Bick, S.J., Gonzalez, J.L., van der Borg, K., and de Jong, A.F.M., 2004. Tracking the sea-level signature of the 8.2 ka cooling event: New constraints from the Mississippi Delta. *Geophys. Res. Lett.*, **31**, L23309.
- von Grafenstein, U., Erlenkeuser, H., Müller, J., Jouzel, J., and Johnsen, S., 1998. The cold event 8200 years ago documented in oxygen isotope records of precipitation in Europe and Greenland. *Clim. Dyn.*, **14**, 73–81.
- Wang, X., Auler, A.S., Edwards, R.L., Cheng, H., Ito, E., and Solheid, M., 2005. Inter-hemispheric Anti-phased Climate Changes During the Last Deglaciation. *Eos Trans., AGU*, **86**(52), Fall Meeting Supplement, Abstract PP13B-1493.
- Yiou, F., Raisbeck, G.M., Baumgartner, S., Beer, J., Hammer, C., Johnsen, S., Jouzel, J., Kubik, P.W., Lestringuez, J., Stievenard, M., Suter, M., and Yiou, P., 1997. Beryllium-10 in the Greenland Ice Core Project ice core at Summit, Greenland. *J. Geophys. Res. – Oceans*, **102**, 26783–26794.

Cross-references

[Cosmogenic Radionuclides](#)
[Foraminifera](#)
[Glacial Megalakes](#)
[Holocene Climates](#)
[Hypsithermal](#)
[Ice cores, Antarctica and Greenland](#)
[North Atlantic Deep Water and Climate Change](#)
[Oxygen Isotopes](#)
[Paleoclimate Modeling, Quaternary](#)
[Radiocarbon Dating](#)
[Sea Level Change, Post-Glacial](#)
[Sun-Climate Connections](#)
[Thermohaline Circulation](#)

THERMOHALINE CIRCULATION

Definition

Formally defining thermohaline circulation is difficult and numerous definitions exist within the literature. Historically, thermohaline circulation has been defined as the component of oceanic circulation driven by fluxes of heat and freshwater (sometimes combined into a buoyancy flux) through the ocean's surface. This particular definition of thermohaline circulation is prevalent among ocean modelers, wherein ocean models driven exclusively by boundary conditions on heat and freshwater, with wind forcing set to zero, lead to a global-scale meridional overturning.

However, in many cases, anomalies of the surface buoyancy flux, and particularly its thermal component, strongly depend on the thermohaline circulation itself. For example, an intensified meridional overturning cell would lead to stronger poleward heat transport in the ocean. At steady state, this heat transport anomaly must be balanced by more heat loss to the atmosphere over the regions towards which the heat is being transported, and by more heat gain by the ocean over regions from which the heat is being transported (Figure T1).

A further problem with the above definition arises when one tries to separate the thermohaline ocean circulation from the wind-driven circulation. For example, turbulent fluxes (latent and sensible heat fluxes) represent a sizable part of the net heat flux and are highly dependent on the near surface wind speed. Furthermore, evaporation, which represents a negative part of the total freshwater flux into the ocean is essentially given by the latent heat loss, and hence is also proportional to the strength of surface winds. In addition, ocean models and the ocean component of coupled models typically specify a fixed value of diapycnal mixing (mixing of heat and

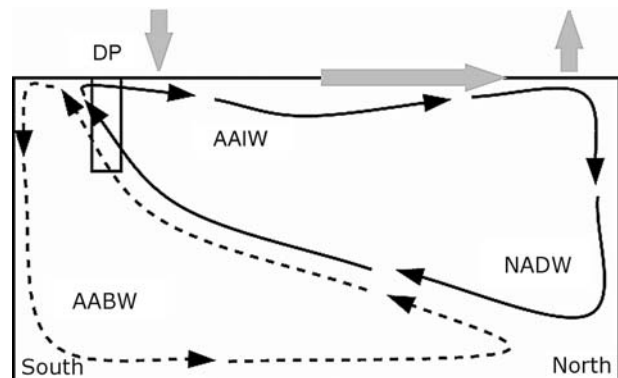


Figure T1 A sketch of the two main cells of the meridional overturning circulation (MOC). One cell is associated with the formation of the North Atlantic Deep Water (NADW) in the North Atlantic, its upwelling in the Southern Ocean, around Drake Passage (DP) and its return flow as a lighter Antarctic Intermediate Water (AAIW); this cell essentially represents the Atlantic Meridional Overturning (AMO). The second cell is associated with the formation of Antarctic Bottom Water (AABW) in high southern latitudes, its spread northward, mixing with NADW, and its return to the Southern Ocean. Arrows illustrate the notion that an intensified (weakened) AMO cell would lead to a stronger (weaker) northward oceanic heat transport in the Atlantic. This would have to be balanced by stronger (weaker) heat loss in the north and by stronger (weaker) heat gain in the south.

salt across surfaces of constant density in the ocean). This representation of diapycnal mixing is a parametrization of internal wave breaking which in turn originates from wind (and tidal) forcing.

Thermohaline circulation is also defined as the density-driven global-scale oceanic circulation. This too has serious shortcomings, as density gradients in the ocean are largely set up by the winds. In particular, the density structure in subtropical and subpolar gyres is determined by Ekman dynamics. The wind stress anomalies themselves are functions of sea surface temperature. Finally, in the ocean, which is typically in geostrophic balance over the spatial and temporal scales of interest to climate and paleoclimate researchers (100s of km and years, respectively) one cannot separate the existence of the density gradients from the existence of the currents.

Wunsch (2002) defined the thermohaline circulation as the circulation of temperature and salt. This definition, however, is not one that is readily accessible to paleoclimatologists. A more practical approach is to move away from the use of the term thermohaline circulation and to focus on the three dimensional (3D) global overturning circulation (GOC). For many paleoclimatological applications, a sufficient representation of the GOC is in terms of the meridional overturning circulation (MOC) and its manifestation in the Atlantic as the Atlantic meridional overturning (AMO), which represent mass transport in the 2D meridional/vertical plane (Figure T1). Inherent in this approach is the acknowledgement that wind and buoyancy forcing are inseparable, and that wind and tidal forcing play a fundamental role in diapycnal mixing within the ocean.

Here, we focus our discussion on the MOC as a fundamental diagnostic in understanding the role of the ocean in past, present and future climate change. Furthermore, sudden changes in the strength of the MOC, and in particular the AMO, are associated with the abrupt climate change prevalent in high resolution proxy records over the last glacial cycle. The importance of the AMO to climate lies in its association with much of the total oceanic poleward heat transport in the present-day Atlantic, peaking at about 1.2 ± 0.3 PW (1 PW equals 10^{15} Watts) at 24° N. Since the MOC represents the ocean circulation in the meridional-vertical plane, its existence and structure is fundamentally connected with the locations of deep water formation in the ocean.

Locations of deep water formation

Two distinct forms of deep water formation occur: near-continent and open ocean. The former involves one of two simple processes: evaporation, or more typically brine rejection, above a continental shelf produces dense heavy water which sinks down and along the slope under the combined forces of gravity, friction and the Coriolis force (Killworth, 1983); alternatively supercooled water may be formed at the base of a thick ice shelf during freezing or melting and this dense water may in turn flow down-slope. By contrast, open ocean convection is observed in areas remote from land and is characterized by a large-scale cyclonic mean circulation which causes a doming of the isopycnals and weakens the static stability over an area tens of kilometers wide. The convection itself is short-lived, is restricted to a narrow circumference and is typically driven through intense surface cooling. These narrow convective chimneys are almost purely vertical and usually do not entrain large volumes of surrounding water as in near-continent convection.

The two main constituent water masses of the deep North Atlantic Ocean – North Atlantic Deep Water at the bottom and Labrador Sea Water at an intermediate level – are currently formed in the Greenland-Iceland-Norwegian Seas and the Labrador Sea, respectively. Deep convection also occurs at a number of locations around Antarctica (Adéle Coast, Amery Ice Shelf, Ross Sea, and Weddell Sea), but the dense bottom water is susceptible to being trapped by topographic sills (as in the Bransfield Strait), or by local circulation patterns (not excluding the Antarctic Circumpolar Current – ACC). In the Southern Ocean, around the southern tip of South America, an enhanced formation of low salinity Antarctic Intermediate Water (AAIW) also occurs.

In today's climate, there are no sources of deep water in the North Pacific Ocean, although North Pacific Intermediate Water (NPIW), characterized by a salinity minimum in the subtropical gyre at depths of 300–800 m within a narrow density range, is locally produced. This water mass is mainly constrained to the subtropical gyre, unlike the Labrador Sea intermediate water mass which is largely confined to the subpolar gyre of the North Atlantic. The original source water for NPIW is thought to be sinking in the Sea of Okhotsk.

Deep convection also occurs in the Mediterranean Sea, but the dense salty outflow that exits into the Atlantic gains buoyancy by mixing with lighter environmental water and spreads out at mid-depth rather than sinking to the bottom. Similar, but weaker, saline outflows have been detected issuing at mid-depth from the Red Sea and Persian Gulf.

In summary, two main bottom water masses exist whose trajectories can be traced by their temperature and salinity characteristics throughout the rest of the world ocean. These are (see Figure T1): (a) the component of Antarctic Bottom Water (AABW) which is largely produced in the Weddell Sea before mixing with Circumpolar Deep Water in the ACC and then flowing into the major ocean basins; (b) North Atlantic Deep Water (NADW), which lies above the AABW at all latitudes except north of 40° N in the North Atlantic. The North Pacific Ocean, although a source of North Pacific Intermediate Water is not a source of bottom water.

In addition, as discussed below, AAIW plays a critical role in linking the Pacific and Atlantic Oceans and in particular on the stability of the AMO. In the present climate, about 13 Sv ($1\text{ Sv} = 10^6 \text{ m}^3 \text{ s}^{-1}$) of cold, fresh Antarctic Intermediate Water (AAIW) flows into the South Atlantic, about 8 Sv of which is converted into thermocline water through mixing by 32° S (Rintoul, 1991). Further mixing converts the remaining 5 Sv of AAIW into thermocline water as it approaches the equator (Schmitz and McCartney, 1993; Table T1). At 24° N there is about 13 Sv of thermocline water which flows northward into the high northern North Atlantic where it is converted into NADW. AABW flows into the South and North Atlantic where it is modified into and exported as NADW into the Southern Ocean.

Table T1 Transport (in Sv) summary from Schmitz and McCartney (1993)

Water type	32° S	24° N
Thermocline water	8	13
Intermediate water (AAIW)	5	–
Deep water (NADW)	–17	–18
Bottom water (AABW)	4	5

Hysteresis behavior of the MOC

Sea water density is a function of not only temperature, but also salinity. Furthermore, at low temperatures, such as those that exist in the deep water formation regions, the density of sea water is more sensitive to changes in salinity than to changes in temperature. In addition, throughout the Quaternary, large quantities of freshwater have been periodically stored on land at middle to high latitudes in the form of continental ice sheets. During the growth or melt of these continental ice sheets, tens of meters of sea level equivalent freshwater have been taken from or released back to the ocean. As a consequence, numerous studies have been conducted in an attempt to understand the role of freshwater perturbations on the stability of the MOC.

The dependence of sea water density on salinity is a key player in what is now known as a hysteresis behavior of the AMO. Recently it has been discovered that the AMO behaves like a “see-saw,” with relatively warm surface conditions in the North Atlantic and relatively cool surface conditions in the South Atlantic occurring when NADW formation is active, and conversely, with relatively cool surface conditions in the North Atlantic and relatively warm surface conditions in the South Atlantic occurring when NADW formation is inactive (Figure T2). Such a finding is supported by both modeling studies, proxy records, and from combined model/proxy record studies. More recently still, it has been realized that the “see-saw” nature of the AMO is fundamentally linked to a coupling between the strength of AAIW formation and the strength of NADW formation (Figure T3).

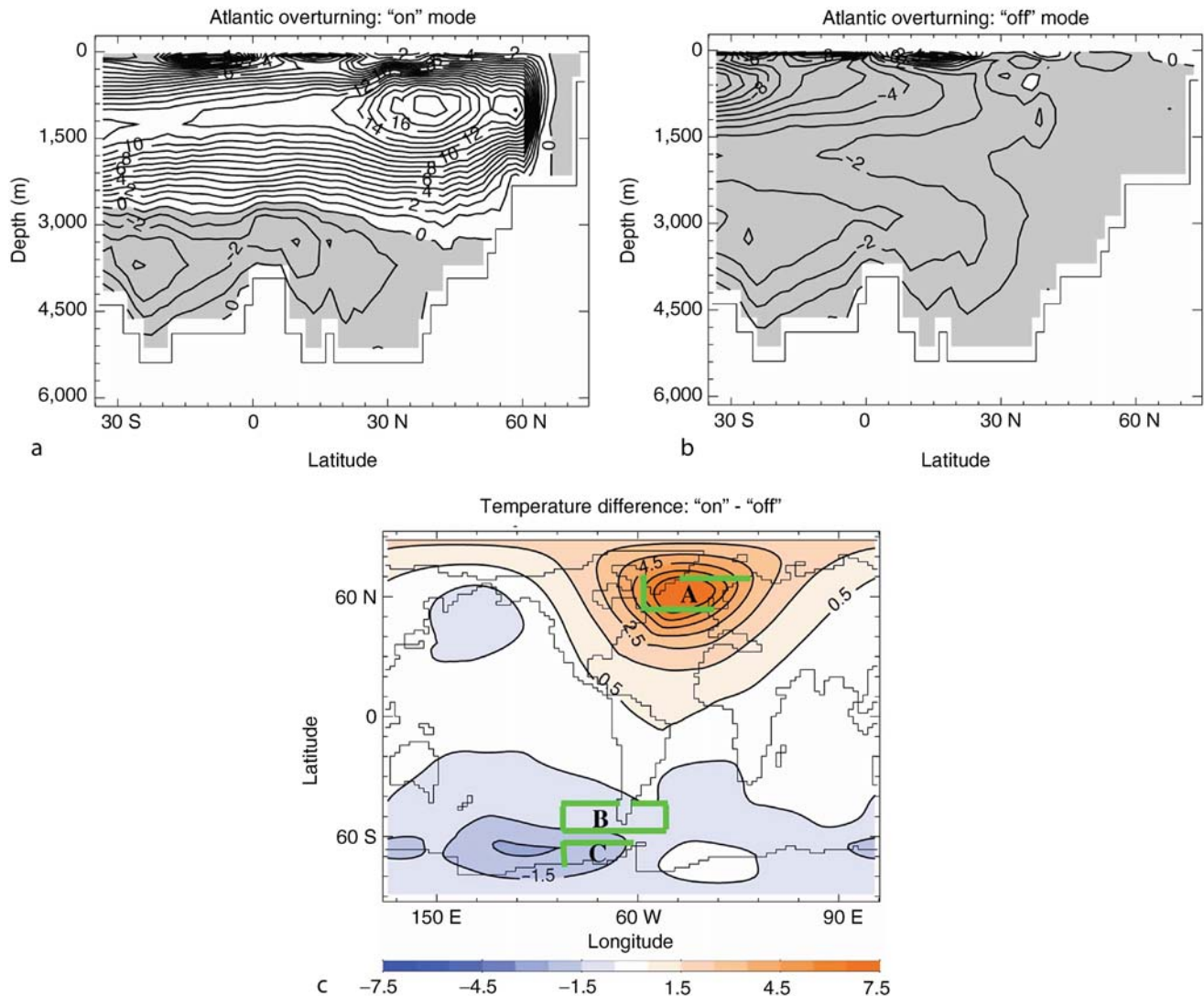


Figure T2 Atlantic meridional overturning circulation (Sv) for: (a) the stable active mode of NADW formation; (b) the stable inactive mode of NADW formation. The inactive mode (b) was obtained by adding freshwater (100 Sv years) to region A. Notice the enhanced intrusion of AAIW and the absence of NADW in (b). (c) Surface air temperature (°C) difference between the climatic states represented by (a) and (b). Region B in (c) is where freshwater is added to get the hysteresis of Figure T3, although similar results are found when freshwater is added to region C. Taken from Weaver et al. (2003).

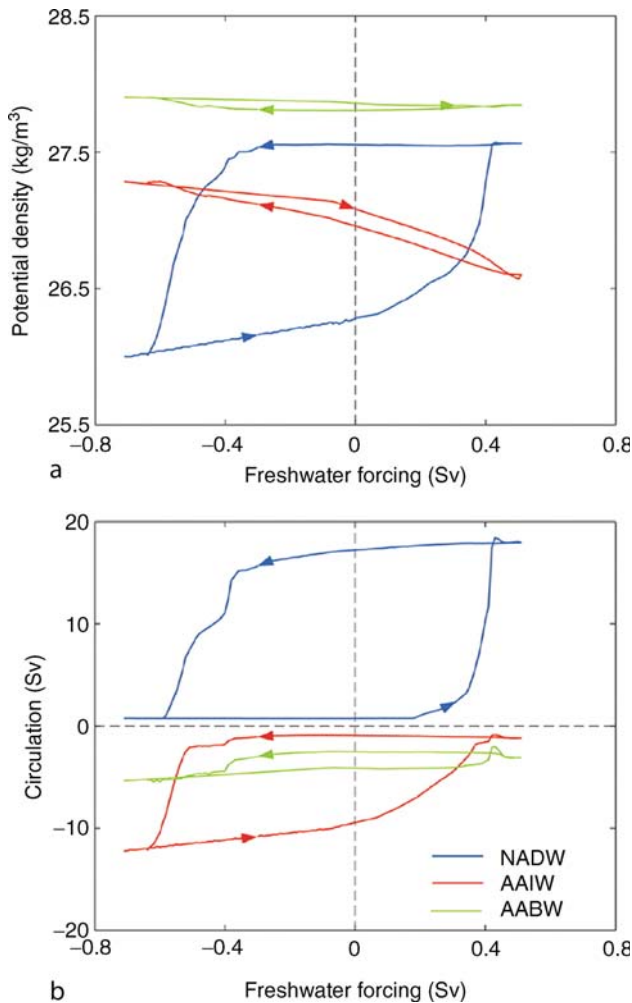


Figure T3 The UVic Earth System Climate Model (Weaver et al., 2001) hysteresis of NADW (blue), AAIW (red), and AABW (green), showing: (a) surface densities in the source regions of these water masses; (b) maximum (or minimum) MOC cells associated with these water masses. The model was started from a mode with no NADW formation with zero externally imposed freshwater flux. A freshwater perturbation was then applied to the AAIW formation region with a linearly-increasing rate of 0.2 Sv/1,000 years. This rate was small enough to ensure a nearly steady-state system, except for abrupt transitional events. Upon transition to a mode with active NADW formation, the freshwater perturbation was reduced at the same rate back to zero, and then to negative values, in order to trigger a transition from the active to the inactive mode of NADW formation. To complete the whole hysteresis loop, the model was integrated for more than 11,000 years. Transitions between the active and inactive modes of NADW formation occur when the surface densities at the site of AAIW and NADW formation cross. Taken from Saenko et al. (2003).

The meridional overturning circulation and Quaternary climate change

Early ice core records for the last glaciation have revealed large amplitude variability on the millennial timescale characterized by abrupt warming events (interstadials) lasting from several hundred to several thousand years. These oscillations (Figure T4 and T5), known as Dansgaard-Oeschger (D-O) oscillations, also appear in North Atlantic sediment records suggesting a

role or response of the ocean. Evidence from the Santa Barbara basin and the Northeast Pacific suggests that a signature of these D-O oscillations is also present in the Pacific Ocean, while further recent sediment analyses suggest they may be an inherent part of late and early Pleistocene climate.

In an attempt to provide a mechanism for the observed D-O variability, it was initially proposed that a stable AMO was not possible during glacial times, when the northern end of the Atlantic Ocean was surrounded by ice sheets. Furthermore, when the AMO was weakened or shut down and ice sheets were growing, there was little oceanic salt export from the Atlantic to the other ocean basins. Assuming a net evaporation over the North Atlantic, its salinity continued to increase as moisture was deposited on land as snow, thereby expanding the ice sheets. Upon reaching a critical salinity, deep convection, and subsequently the AMO, turned on, transporting and releasing heat to the North Atlantic and thereby melting back the ice sheets. The fresh water flux into the North Atlantic from the melting ice sheets (or enhanced iceberg calving) eventually reduced or shut off the AMO, causing the process to begin anew. This hypothesis fundamentally assumed that most of the evaporation from the Atlantic basin was balanced by a net freshwater transport into the Atlantic associated with an active AMO. While this in itself has not yet been established, it could be true for a climate with an active AMO. However, it is clear that the weakening of the AMO would trigger a reorganization of the circulation in the South Atlantic, but it is not clear whether this reorganized circulation would be able to balance the required Atlantic evaporation.

Recent models, including an interactive continental ice sheet, showed that the earlier mechanism for D-O oscillations was in fact opposite to what actually occurred within the coupled system. During the cold, glacial climate, when the AMO was *still* active, the mass balance over continental ice sheets was positive. That is, rather than melting the ice sheets when the AMO was active, they grew, since the warmer atmosphere allowed greater precipitation (in the form of snow). The models also found a mechanism for D-O oscillations that involved an interaction between the AMO and the adjacent continental ice sheets, by assuming that the rate of iceberg calving into the North Atlantic was not constant in time, which is consistent with observations of ice-rafted debris. It was shown that after a delay of several hundred years following a major surging event and a reduction of the iceberg calving rate, the AMO intensified and the North Atlantic experienced an abrupt shift to a much warmer climate. This mechanism appears to be more intuitively appealing than a competing hypothesis involving stochastic resonance of the AMO, which relies upon the existence of an unknown 1,500 year external periodic forcing.

Heinrich (1988), in analyzing marine sediments in three cores from the North Atlantic, noted the presence of six anomalous concentrations of lithic fragments over the last glaciation. Since the source for these fragments was the land (and in particular Canada), he argued that this provided evidence for six anomalous surges of icebergs into the North Atlantic (Figure T5). The so-called Heinrich events (H) were even more striking when expressed in terms of the ratio of lithic fragments to the sum of lithic fragments and foraminiferal shells, due to the low foraminiferal counts in the Heinrich sediment layers. A simple model illustrates the mechanism for Laurentide Ice Sheet instability, which ultimately gives rise to an ice-sheet surge and a Heinrich event. It has been argued that the Heinrich

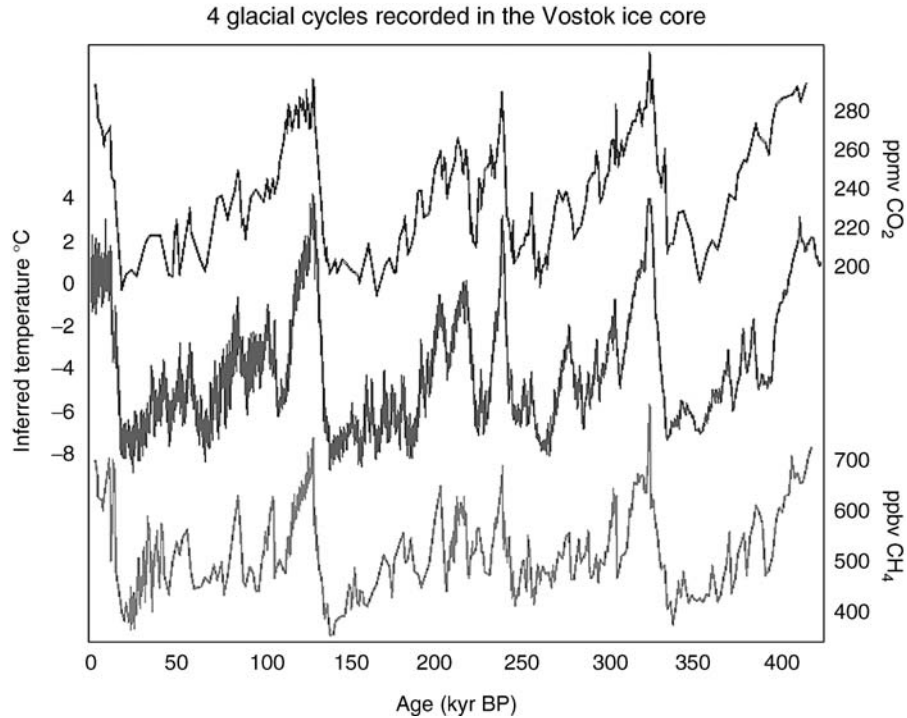


Figure T4 Variations in local Antarctic atmospheric temperature, as derived from oxygen isotope data, as well as concentrations of atmospheric CO_2 and CH_4 from Vostok, Antarctica ice core records over the last four glacial cycles. The rapid oscillations represent Dansgaard-Oeschger cycles. Figure redrawn from Petit et al. (1999).

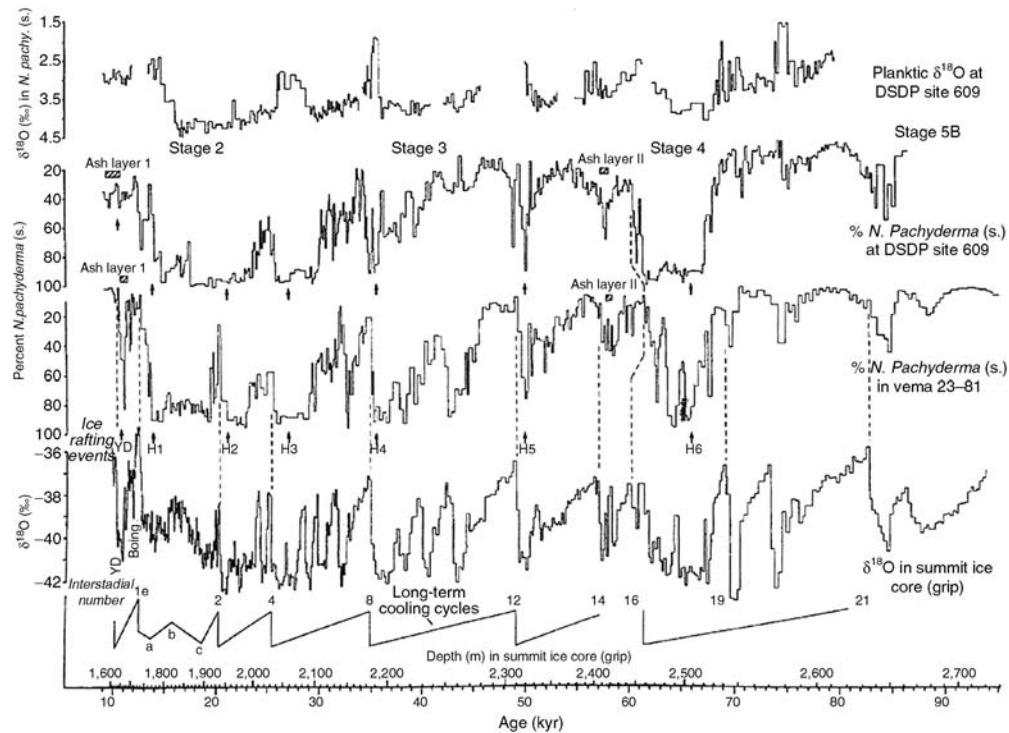


Figure T5 Sediment foraminiferal records from Bond et al. (1993) and ice core oxygen isotope records from Dansgaard et al. (1993) and GRIP (1993) as correlated by Bond et al. (1993). The Younger Dryas (YD) and six Heinrich events (H1–H6) are indicated. Also shown at the bottom is the saw tooth Bond Cycle pattern of successively weaker interstadials associated with a sequence of D-O oscillations following a Heinrich event (from Bond et al., 1993).

cycle consists of two phases. In the growth phase, the Laurentide Ice Sheet grew through snow accumulation while remaining attached to the bedrock. In the purge phase, the high pressures caused by the deep ice sheet caused thawing near the base of the ice sheet thereby allowing the ice sheet to surge seaward over a lubricated base through Hudson Strait. The resulting freshwater discharge into the North Atlantic would be of the order of 0.1–0.2 Sv over a period as short as 250–500 years.

Heinrich events, appearing about every 10,000 years, occur at the end of a sequence of D-O cycles during a prolonged cold period. Bond et al. (1993) noted that the sequences of D-O oscillations tend to follow a saw-tooth cycle (now termed a Bond Cycle) with successive D-O oscillations involving progressively cooler interstadials (Figure T5). They argued that this Bond Cycle was terminated by a Heinrich event, after which a rapid warming occurred and the process began anew.

The last cold event, known as the Younger Dryas (YD) (also known as Heinrich event zero, H0) took place between 12,700 and 11,650 years BP and terminated abruptly within a few decades. Proxy data suggest that during the YD, even the AMO was weakened. Further analysis of the proxy record indicates that the YD was preceded by a warm period in the North Atlantic climate, known as the Bølling-Allerød (B-A) warm interval (Figure T5). The B-A interval was accompanied by a strong global sea-level rise, apparently due to the melting of continental ice sheets. Until recently, it was not clear how to reconcile the warm North Atlantic climate during the B-A with melting of adjacent ice sheets. The latter would have caused a reduction of AMO, leading to a cooling, rather than warming of the North Atlantic. A possible explanation lies in the hypothesis that a significant portion of the observed rapid sea level rise during the B-A could have originated from the melting of Antarctic ice sheets, rather than solely from melting of the ice sheets surrounding the North Atlantic. A meltwater pulse into the Southern Ocean, originating from the partial collapse of an Antarctic ice sheet, could trigger an enhanced formation of NADW and an onset of warming in the North Atlantic (Weaver et al., 2003).

Despite these fundamental advances over the last few years, many challenges remain. In particular, a complete explanation including the essential role of the MOC, for the existence of millennial timescale (D-O) variability and its packaging into Bond Cycles in cold climates, its association with Heinrich events, and its dependence on the mean climatic state remains elusive to the paleoclimate community. Another major climate mystery is the cause of atmospheric CO₂ and CH₄ changes during the glacial cycles (Figure T4) and their possible connection to long-term changes of structure and strength of the GOC.

Andrew J. Weaver and Oleg A. Saenko

Bibliography

- Bond, G., Broecker, W., Johnsen, S., McManus, J., Labeyrie, L., Jouzel, J., and Bonani, G., 1993. Correlations between climate records from North Atlantic sediments and Greenland ice. *Nature*, **365**, 143–147.
- Dansgaard, W., Johnsen, S.J., Clausen, H.B., Dahl-Jensen, D., Gundestrup, N.S., Hammer, C.U., Hvidberg, C.S., Steffensen, J.P., Sveinbjörnsdóttir, A.E., Jouzel, J., and Bond, G., 1993. Evidence for general instability of past climate from a 250-kyr ice-core record. *Nature*, **364**, 218–220.
- GRIP Project Members, 1993. Climate instability during the last interglacial period recorded in the GRIP ice core. *Nature*, **364**, 203–207.

- Heinrich, H., 1988. Origin and consequences of cyclic ice rafting in the northeast Atlantic Ocean during the past 130,000 years. *Quaternary Res.*, **29**, 143–152.
- Killworth, P.D., 1983. Deep convection in the world ocean. *Rev. Geophys. Space Phys.*, **21**, 1–26.
- Petit, J.R., Jouzel, J., Raynaud, D., Barkov, N.I., Barnola, J.-M., Basile, I., Benders, M., Chappellaz, J., Davis, M., Delayque, G., Delmotte, M., Kotlyakov, V.M., Legrand, M., Lipenkov, V.Y., Lorius, C., Pépin, L., Ritz, C., Saltzman, E., and Stievenard, M., 1999. Climate and atmospheric history of the past 420,000 years from the Vostok ice core, Antarctica. *Nature*, **399**, 429–436.
- Rintoul, S.R., 1991. South Atlantic interbasin exchange. *J. Geophys. Res.*, **96**, 2675–2692.
- Saenko, O.A., Weaver, A.J., and Gregory, J.M., 2003. On the link between the two modes of the ocean thermohaline circulation and the formation of global-scale water masses. *J. Clim.*, **16**, 2797–2801.
- Schmitz, W.J. Jr., and McCartney, M.S., 1993. On the North Atlantic circulation. *Rev. Geophys.*, **31**, 29–49.
- Weaver, A.J., Eby, M., Wiebe, E.C., Bitz, C.M., Duffy, P.B., Ewen, T.L., Fanning, A.F., Holland, M.M., MacFadyen, A., Matthews, H.D., Meissner, K.J., Saenko, O., Schmittner, A., Wang, H., and Yoshimori, M., 2001. The UVic Earth System Climate Model: Model description, climatology and application to past, present and future climates. *Atmosphere-Ocean*, **39**, 361–428.
- Weaver, A.J., Saenko, O.A., Clark, P.U., and Mitrovica, J.X., 2003. Meltwater pulse 1A from Antarctica as a trigger of the Bølling-Allerød warm interval. *Science*, **299**, 1709–1713.
- Wunsch, C., 2002. What is the thermohaline circulation? *Science*, **298**, 1179–1181.

Cross-references

- [Antarctic Bottom Water and Climate Change](#)
[Binge-Purge Cycles of Ice Sheet Dynamics](#)
[Bølling-Allerød Interstadial](#)
[Dansgaard-Oeschger Cycles](#)
[Heinrich Events](#)
[Millennial Climate Variability](#)
[North Atlantic Deep Water and Climate Change](#)
[Ocean Paleocirculation](#)
[Younger Dryas](#)

TILLS AND TILLITES

Tills, and their lithified equivalents, tillites, are sediments deposited by glacier ice. In the past, this definition has been employed in a very broad sense, to include unsorted sediments deposited in subglacial, supraglacial, ice-marginal, and subaqueous environments. Such a broad definition is difficult to apply in practice, because it may hard to differentiate sediments deposited directly from ice and those later reworked by non-glacial processes. Many researchers now prefer to restrict the term *till* to sediments deposited directly by grounded glacier ice, in subglacial and supraglacial environments, and which have not undergone significant reworking by fluvial, gravitational, or other processes (Dreimanis, 1989; Benn and Evans, 1998). The non-genetic terms *diamict* and *diamictite* have now generally replaced the older, broad usage of till and tillite. The correct identification of tills and tillites is important, because they provide direct evidence for the former distribution of glaciers, and hence have wide-reaching paleoclimatic implications.

The main processes of formation of tills are: lodgement, deformation, melt-out, and sublimation. Lodgement refers to frictional retardation of clasts or slabs of debris below sliding

ice, and deformation is the re-molding of pre-existing sediments or debris in a subglacial deforming layer (Boulton, 1982). Melt-out and sublimation remove interstitial ice from englacial debris (Paul and Eyles, 1990). Tills rarely form by a single process (Hicock, 1990). Many tills exhibit evidence of subglacial deformation, indicating shear of unlithified sediments below glaciers and ice sheets although this is contested by some researchers. Unmodified melt-out tills are rare, because high pore-water pressures during de-icing encourage re-molding by gravitational processes. Sublimation tills are restricted to arid polar environments, where temperatures never exceed 0 °C and melting does not occur.

The identification of tills and tillites should be based on multiple criteria, including: (a) faceted and striated clasts, with stoss-lee forms; (b) far-traveled, erratic clasts; (c) moderate to strong a-axis fabrics, which show regional consistency; (d) evidence of shear (e.g., low-angle faults, attenuated stringers, and overfolds) at macro- and micro-scales; (e) tabular geometry; (f) massive, matrix-supported character; (g) multi-modal grain-size distributions, often with a significant silt fraction ('rock flour'); and (h) association with folded and thrust sediments (glacitectorites). Not all tills will exhibit all of these characteristics, and some non-glacial sediments may exhibit some of them. Tills form a very variable group of sediments, and their recognition requires careful study.

Douglas I. Benn

Bibliography

- Benn, D.I., and Evans, D.J.A., 1998. *Glaciers and Glaciation*. London: Arnold.
- Boulton, G.S., 1982. Subglacial processes and the development of glacial bedforms. In Davidson-Arnott, R., Nickling, W., and Fahey, B.D. (eds.), *Research in Glacial, Glacio-fluvial, and Glacio-lacustrine Systems*. Norwich: Geobooks, pp. 1–31.
- Dreimanis, A., 1989. Tills: Their genetic terminology and classification. In Goldthwait, R.P., and Matsch, C.L. (eds.), *Genetic Classification of Glacigenic Deposits*. Rotterdam: Balkema, pp. 17–84.
- Hicock, S.R., 1990. Genetic till prism. *Geology*, **18**, 517–519.
- Paul, M.A., and Eyles, N., 1990. Constraints on the preservation of diamict facies (melt-out tills) at the margins of stagnant glaciers. *Quaternary Sci. Rev.*, **9**, 51–69.

Cross-references

Diamicton
 Glacial Geomorphology
 Glacial Sediments
 Glaciomarine Sediments
 Ice-Rafted Debris (IRD)
 Moraines

TIME-SERIES ANALYSIS OF PALEOCLIMATE DATA

Introduction

This article is a brief synopsis of time-series analysis methods that have proven to be useful in the analysis of paleoclimate data. Space limitations precludes all but the briefest outline of the actual mathematics involved, but references are provided. The following sections define some basic functions such as spectrum and autocorrelations, outline the basic multitaper methods that are recommended to estimate them, describe

periodic components and Cramér–Rao bounds for frequency estimation, and coherence estimates. Other sections below discuss jackknife confidence limits for spectra and similar functions, spectrogram methods useful with nonstationary processes, discusses wavelets, Lomb–Scargle and Blackman–Tukey estimates which should be avoided for these applications. Finally, the last section summarizes the points made.

One should not expect the analysis of paleoclimate data to be easy. If one considers the effort that has been made over the last three or four decades in making general circulation models reproduce even fairly gross features of the climate system, one should not expect that the analysis of data produced by the real, and obviously far more complicated, climate system can be done simply. Added to this intrinsic difficulty, paleoclimate data is usually a proxy, the geographic distribution of samples is far from ideal, and from a data analysis viewpoint, the fact that the timescale is uncertain can be a major problem. Worse than these, however, is the problem that the climate system is nonstationary. *Stationarity* in this context implies that the *statistics* of the process do not depend on time.

Theoretical quantities

In this section we define some functions of a time series. Here we assume that the process $x(t)$ is stationary, that is its statistical properties do not vary with time; that the expected value of $x(t)$ is zero, denoted $\mathbf{E}\{x(t)\} = 0$; and that $x(t)$ has a Gaussian distribution. The samples are assumed to be equally spaced in time at a unit sampling rate. Thus the Nyquist frequency, $\frac{1}{2\Delta t}$ (where Δt is the time between samples) is $\frac{1}{2}$. Generally, the single most useful description of a time series is its power spectrum, also known as the power spectral density, or plain spectrum. The spectrum is a decomposition of the variance of the process as a function of frequency, and functionals of the spectrum give most of the interesting descriptive statistics of a time series. Thus, if we denote the spectrum at frequency f by $S(f)$, with $-\frac{1}{2} \leq f < \frac{1}{2}$, one has the process variance

$$\sigma^2 = \int_{-\frac{1}{2}}^{\frac{1}{2}} S(f) df \quad (1)$$

The units of the spectrum are $(data - units)^2$ per $(cycle/time-unit)$. As an example, if one has $\delta^{18}\text{O}$ data with samples measured at a rate of one per thousand years, the frequency range will be from $-\frac{1}{2 \times 1000}$ to $\frac{1}{2 \times 1000}$ and the spectrum will be in units of $(\delta^{18}\text{O})^2$ per $(cycle/1000\text{years})$. Most of the series encountered in paleoclimatology are real-valued so the spectrum is symmetric, that is the power at $-f$ is the same as the power at $+f$, so it is sufficient to plot the spectrum for positive frequencies only. However, if one has a series of directional data, say the north-south and east-west components of a magnetic field or flow, it makes sense to treat them as a complex-valued time-series, and in this case, the spectrum $S(-f)$ is different from $S(f)$.

Possibly as important as the variance, the one-step ahead prediction variance is given by:

$$\sigma_p^2 = \exp \left[\int_{-\frac{1}{2}}^{\frac{1}{2}} \ln S(f) df \right] \quad (2)$$

Climate studies are often associated with prediction and this formula shows that the overall shape of the spectrum on a logarithmic power scale is the critical parameter, not just the largest peak.

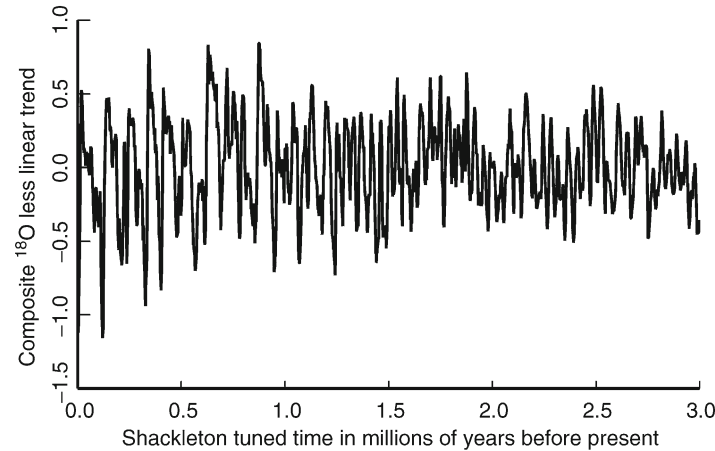


Figure T6 Shackleton's composite benthic $\delta^{18}\text{O}$ record, minus a linear trend, for the past 3 Myr.

Similarly, the single-sample interpolation variance given by

$$\sigma_I^2 = \frac{1}{\int_{-\frac{1}{2}}^{\frac{1}{2}} \frac{1}{S(f)} df} \quad (3)$$

shows that a missing sample may be interpolated with an accuracy approaching that of the measurement error. Together, equations (1), (2), and (3) are the arithmetic, geometric, and harmonic means of the spectrum, respectively.

The autocovariance function,

$$R(\tau) = E\{x(t)x(t+\tau)\} \quad (4)$$

is the Fourier transform of the spectrum

$$R(\tau) = \int_{-\frac{1}{2}}^{\frac{1}{2}} e^{i2\pi f\tau} S(f) df \quad (5)$$

so, comparing (1) and (5), $R(0) = \sigma^2$. The *autocorrelations*, $\rho(\tau)$ are just the autocovariances normalized by the variance $\rho(\tau) = R(\tau)/\sigma^2$ and are, as the name implies, the correlation of the process with delayed versions of itself. The Fourier transform of the autocovariance is the spectrum. Experience shows that the autocovariance is useful for prediction and interpolation. Even though the autocovariance and spectrum carry equivalent information, plots of the autocorrelation are usually remarkably uninformative. (John Tukey remarked that "I only knew one man who could look at an autocorrelation function and make sense of it, and he's dead.") One useful formula is that for the zero-crossing rate, the expected number of zeroes per sample (Kedem, 1994),

$$E\{R_z\} = \frac{1}{\pi} \arccos(\rho(1)) \quad (6)$$

As an example, the Lag-1 correlation of the data shown in Figure T6 is 0.978 with (6) evaluating to 0.0668, so one expects the curve to cross its average about every 15 samples or so.

Since the true spectrum is not known, the best estimate possible of a spectrum must be made. In estimating a spectrum, there are several competing criteria to optimize: bias, frequency resolution, variance, efficiency, ability to distinguish periodic from non-periodic components, minimum assumptions, and

robustness. The spectrum is, of course, not the only useful function and one should always plot the raw data and ancillary functions such as histograms, plots of $x(t)$ vs $x(t-1)$, Q-Q plots, as well as basic data checks such as histograms of bit and digit frequencies. Also, if the data is nonstationary (as much climate data is) one plots a *spectrogram*, see below, basically a sequence of spectrum estimates, usually computed on overlapping time segments and displayed as a function of both time and frequency.

Estimating the spectrum

As a data example, one can use the first 3 Myr of Shackleton's composite benthic $\delta^{18}\text{O}$ data from V19-30, ODP 677, and ODP 846 (see Shackleton et al., 1990, 1995a,b)¹. The time step was scaled by a factor of the ratio 41090.0/41234.9 to bring the strong obliquity line frequency into exact agreement with Laskar (1990). For the 3 Myr period being studied, this may be the most accurate orbital frequency available, see Laskar (1999). Assuming that a timescale has been established (see Pälike and Shackleton, 2000), and N data samples, $x(t)$, are available at a time-spacing of Δt years, the preferred method of estimating the power spectrum is the *multitaper* method. While the details of this method has been described in a series of papers (Thomson, 1982, 1990a,b, 2001; Thomson et al., 2007), and several books (Percival and Walden, 1993; Rao et al., 2003; Weedon, 2003), the basic idea is simple and consists of the following steps:

1. Choose the time-bandwidth product controlling frequency resolution and bias,

$$c_o = NW = BT = B \times N\Delta t \quad (7)$$

so, at unit sampling rate the bandwidth, W , is $W = c_o/N$ or, in physical units one has $B = c_o/T$ where T is the total duration of the data sample, $T = N\Delta t$. Usually one should choose $2 \leq c_o \leq 10$ and, for most paleoclimate data sets, a choice of 4 or 5 is a reasonable starting point. In this example $c_o = 5$ was used.

¹The data was obtained from [//delphi.esc.cam.ac.uk/coredata/v677846.html](http://delphi.esc.cam.ac.uk/coredata/v677846.html) and the few gaps interpolated; see Appendix A of Thomson et al. (2001).

The time–bandwidth product, c_o , is the dimension of the space of duration T and bandwidth T and to represent the information in such a space one needs c_o bases functions. It is convenient to work with real-valued bases functions, with the result that the true bandwidth spans the range from $-B$ to $+B$ and consequently one has a space of dimension $2BT$. Thus one has a set of $K \sim 2BT$ bases sequences that, in spectrum estimation problems, have historically been known as *data windows* or *data tapers*. A typical choice is $K = 2c_o - 2$, or $2NW - 2$ so if, takes $c_o = 5$ as we do here, one would use $K = 8$ windows.

The choice of c_o is fairly critical: if c_o is too small the estimate will have a high variance and relatively poor bias protection, but if c_o is too large, one will have poor frequency resolution. In this example values of the spectrum go from a minimum of ≈ 15 to a maximum of $\approx 4.7 \times 10^4$, a range of $\sim 3,000$, so extreme bias protection is not required.

2. Compute the first K lowest order *discrete prolate spheroidal sequences* or *Slepian sequences*, $v_t^{(k)}(N, W)$ where $0 \leq t \leq N - 1$. These sequences (Slepian, 1978), have the greatest possible energy concentration within the frequency band $(-W, W)$ of any time-limited sequence and, in sampled data, define the time–frequency uncertainty principle. They are defined by the algebraic eigenvalue equation

$$\lambda_k(N, W)v_t^{(k)}(N, W) = \sum_{m=0}^{N-1} \frac{\sin 2\pi W(t-m)}{\pi(t-m)} v_m^{(k)}(N, W) \quad (8)$$

The eigenvalues, $\lambda_k(N, W)$, define the energy concentration in $(-W, W)$. The first $K \approx \lfloor 2NW \rfloor$ are close to one and are the ones used in spectrum estimation. Although the Slepian sequences are defined by (8), this is emphatically *not* the way to compute them; see Appendix B of Thomson (1990a). For the rest of this article, the explicit dependence on N and W in the sequences and eigenvalues is dropped and λ_k and $v^{(k)}$ are used.

3. Subtract the mean, and possibly trend, from the data denoted $x(t)$.
4. For $k = 0, 1, \dots, K - 1$ compute the *eigencoefficients*

$$x_k(f) = \sum_{n=0}^{N-1} x(n)v_n^{(k)} e^{-i2\pi nf} \quad (9)$$

Normally the eigencoefficients are computed using a zero-padded fast Fourier transform (FFT). The procedure is:

- (a) Choose the number of transform points $M \geq N$ and usually $M \gg N$. The proper choice depends on how good the signal-to-noise ratio of your data is, with better data requiring larger M . It is generally unwise to choose $M < 2N$. For paleoclimate data, the choice $M = N$ is almost always a poor one as it implies circular correlations. (This means that the sample autocovariances obtained by taking the Fourier transform of the spectrum estimate, the sample equivalent of (5), would include both “legitimate” terms such as $x(n)x(n + \tau)$ and “illegitimate” ones such as $x(n)x(n + \tau - N)$ where the end of the sample wraps around and is correlated with the start.) The efficiency of the FFT algorithm depends on M being factorable into small primes, so choosing M as a product of 2’s, 3’s, 5’s, and other small primes up to 19 is necessary. Also note that, if one has a few hundred data points and the estimated spectrum differs noticeably between the choice of $M = 4000 = 2^5 \times 5^3$ and $M = 4096 = 2^{12}$, you are likely doing something wrong.

- (b) Multiply the data by the k^{th} taper. If one is using a standard (Singleton, 1969) FFT, say $\text{FFT}(M, X, Y)$ where X and Y are arrays of length M , X being the real part and Y the imaginary, one sets

$$X(n) = \begin{cases} x(n)v_n^{(k)} & 0 \leq n \leq N - 1, \\ 0 & N \leq n \leq M - 1 \end{cases} \quad (10)$$

$$Y(n) = 0 \quad 0 \leq n \leq M - 1 \quad (11)$$

The FFT computes

$$X_{out}(j) + iY_{out}(j) = \sum_{n=0}^{M-1} [X_{in}(n) + iY_{in}(n)] e^{-i2\pi \frac{nj}{M}} \quad (12)$$

for $j = 0, \dots, M - 1$. Because the data encountered in paleoclimate work is usually real-valued, it is only necessary to keep the outputs for positive frequencies, that is for $j = 0, 1, \dots, M/2$. Taking the time at the n^{th} sample to be $t_n = n\Delta t$ and the frequency at the j^{th} FFT bin as $f_j = j\delta f$ and comparing exponents it is evident that

$$\delta f = \frac{1}{M\Delta t} \quad (13)$$

so the effect of zero padding is simply to compute the frequencies on a finer grid. Note that one occasionally sees statements to the effect that “a FFT was not used and the Fourier transform was computed exactly.” This is a fallacy: not only is the FFT far quicker than naive evaluation of the formula, but it also computes exactly what it claims to compute and, because it uses far fewer operations to do it, suffers less from roundoff error than direct evaluation of the formula.

5. In practice one estimates the spectrum by solving (17) below, but to understand the properties of a multitaper estimate, it is easier to use the approximation

$$\bar{S}(f) = \frac{1}{K} \sum_{k=0}^{K-1} |x_k(f)|^2 \quad (14)$$

on the grid of frequencies $f_j = j\delta f$, $j = 0, 1, \dots, M/2$. This estimate has the following properties:

- (a) The bandwidth is

$$B = \pm \frac{c_o}{T} = \pm \frac{c_o}{N\Delta t} \quad (15)$$

Specifically, given a pure sinusoid at frequency f_o , one-half of the energy in the sinusoid would be distributed across the band $(f_o - W, f_o + W)$, and the other half of the energy across the symmetric band $(-f_o - W, -f_o + W)$. As will be described in the next section, when sinusoids are *known* to be present, one can estimate their frequencies much more accurately than B .

- (b) Under reasonable conditions the estimate (14) will have a chi-squared distribution with $2K$ degrees-of-freedom, written χ_{2K}^2 . At frequencies where there is a periodic, or other narrow-band component, the distribution will be a non-central chi-square, while at frequencies between such components *i.e.*, at frequencies where the signal is noise-like, the distribution is central chi-square. It is safer to

estimate the variance by using a jackknife than by relying on classical distribution theory. See below for details. As standard practice, both the classical and jackknife estimates are computed and compared.

- (c) The bias of the estimate, the energy leaking into the band $(f - W, f + W)$ through the sidelobes of the windows, can be bounded by

$$B(f) < \frac{1}{K} (1 - \lambda_{K-1}) \sigma^2 \tag{16}$$

where λ_k is the eigenvalue of the k^{th} Slepian sequence defined in (8), and σ^2 the process variance.

Finally, while (14) is easy to describe, in practice one uses an adaptively weighted estimate. Details are given in Thomson (1982) or on p 546 of Thomson (1990a), but the critical step is to solve

$$\sum_{k=0}^{K-1} \frac{\lambda_k (\hat{S}(f) - |x_k(f)|^2)}{[\lambda_k \hat{S}(f) + (1 - \lambda_k) \sigma^2]^2} = 0 \tag{17}$$

for $\hat{S}(f)$. It can be shown that this solution is between $\min_k \{|x_k(f)|^2\}$ and $\max_k \{|x_k(f)|^2\}$ and, in practice, an iterative solution starting at $\hat{S}(f) = (|x_0(f)|^2 + |x_1(f)|^2)/2$ usually converges in 2 or 3 iterations. The properties are very similar to those listed above except that, with (17), the effective degrees-of-freedom will be frequency dependent and usually lower near the minimum of the spectrum. This loss of degrees-of-freedom can be reduced by prewhitening.

Lines and Cramér–Rao bounds

A source of confusion in the analysis of paleoclimate data (and elsewhere) is the distinction between the continuous and line components of the spectrum. The lines are isolated periodic components such as those occurring in the familiar, e.g., Berger (1977, 1978), trigonometric expansions of eccentricity, obliquity, and precession, that is, sinusoids at discrete frequencies. The continuous part of the spectrum is basically everything else: measurement errors and related problems such as bioturbation, and non-deterministic parts of the climate process with a short prediction horizon.

The basic multitaper estimate for periodic components can be understood by considering the effects of a single sinusoid in noise. Define

$$y(t) = x(t) + A \cos(2\pi f_0 t + \phi) \tag{18}$$

which can be written

$$y(t) = x(t) + \frac{A}{2} e^{i\phi} e^{i2\pi f_0 t} + \frac{A}{2} e^{-i\phi} e^{-i2\pi f_0 t}, \tag{19}$$

where $A2e^{i\phi} = \mu$ is the complex amplitude and $x(t)$ is assumed to be non-periodic. The eigencoefficients of $y(t)$ are

$$y_k(f) = x_k(f) + \mu V_k(f - f_0) + \mu^* V_k(f + f_0) \tag{20}$$

where $V_k(f)$ is the Slepian function

$$V_k(f) = \sum_{n=0}^{N-1} v_n^{(k)} e^{-i2\pi f n} \tag{21}$$

Because of the energy concentration properties of the Slepian sequences, the term $\mu^* V_k(f + f_0)$ can usually be ignored if

$f_0 > W$. Because it is assumed that $x(t)$ is a zero-mean process, the expected value

$$E\{y_k(f)\} = \mu V_k(f - f_0) \tag{22}$$

One does a formal hypothesis test for the presence of a periodic component. The null hypothesis, \mathbf{H}_0 , is that the frequency band $(f - W, f + W)$ has an approximately flat (called “locally white”) spectrum of unknown power. The alternative hypothesis, \mathbf{H}_1 , is that in addition to the locally white noise, there is a sinusoid at frequency f . Estimate its amplitude μ by least-squares, that is minimize the error at frequency f between the data, the $y_k(f)$ ’s, and the model, (22). For an assumed complex amplitude $\hat{\mu}(f)$, the error is

$$E^2(f, \hat{\mu}(f)) = \sum_{k=0}^{K-1} |y_k(f) - \hat{\mu}(f) V_k(0)|^2, \tag{23}$$

where the assumption that the line frequency $f_0 = f$ results in the zero argument of the Slepian function. Taking the partial derivative of E with respect to $\hat{\mu}(f)^*$, one obtains

$$\hat{\mu}(f) = \frac{\sum_{k=0}^{K-1} y_k(f) V_k(0)}{\sum_{k=0}^{K-1} |V_k(0)|^2}, \tag{24}$$

the regression of the eigencoefficients on their expected values. One tests this regression in the usual way by using an F -test. This is the ratio of the energy explained by the assumed periodic component at frequency f to that remaining in the residuals,

$$F(f) = \frac{\frac{1}{2} |\hat{\mu}(f)|^2 \sum_{k=0}^{K-1} |V_k(0)|^2}{\frac{1}{2K-2} E^2(f, \hat{\mu}(f))}. \tag{25}$$

To understand this equation, recall that an F -statistic is defined as $(\chi_p^2/p)/(\chi_q^2/q)$ where χ_p^2 and χ_q^2 are independent chi-squared variables of p and q degrees-of-freedom, respectively. If there is no periodic component present, just “noise”, then, because $\hat{\mu}(f)$ is complex, $|\hat{\mu}(f)|^2$ is chi-squared with two degrees-of-freedom. The residual, E^2 , has $2K - 2$ degrees-of-freedom and is independent of the estimated mean, so $F(f)$ has a central F -distribution under \mathbf{H}_0 .

It can be shown by some tedious algebra that if one uses the frequency where $F(f)$ is maximized as an estimate of f_0 , it is usually within a few percent² of the Cramér–Rao bound on the achievable accuracy of a frequency estimate.

Notes on the harmonic F -test

When interpreting F -tests for lines, some precautions should be observed.

1. Because the F -test is computed as a function of frequency, there are approximately N independent tests in the frequency domain. Thus one should expect some false detections. For example, if one adopts a conventional 95% level, one should expect about $0.05N$ “detections” in cases when there are no lines present.
2. When there are strong lines present, the single-line F -test given above will suppress false detections within $\pm W$ of these lines.

²The actual factor is the estimate efficiency Ξ defined in Thomson (1982) §VII.

3. The test is sensitive to departures in assumptions. For example, an amplitude or phase modulated sinusoid will usually be rejected if the amplitude varies by a factor of two over the sample interval, or if the frequency, $\frac{1}{2\pi} \frac{d}{dt} \phi$, varies by about one-third of a Rayleigh resolution, that is, $1/(3T)$.
4. The test usually rejects multiple lines within the band.
5. When one observes a roughly rectangular peak of total width $\geq 2W$ in the spectrum without a peak in the F -test at the center frequency of the peak, one should test for multiple lines or for a modulated periodic component. (The lower precession band in Figure T8 is typical; this band, 42–45 c/Myr, contains four strong lines of which two are detected.) Tests are described in Thomson (1990a) and Johnson et al. (1996).
6. A peak in the F -test corresponding to a local minimum in the spectrum is usually a false detect. The line marked “20,850” in Figure T8 is almost certainly in this category. Similarly, the lines marked “13,397,” and “12,540” may be false detections, but could be a nonlinear interaction between obliquity and precession. Similarly, maxima in F on the sides of peaks, or on very steep slopes, are often false detections. The line marked “37,430” in Figure T8 is on the shoulder of the obliquity band. The reason for these false detections is that the “locally white” condition is violated, causing the y_k 's to be correlated.

7. When a sharp peak in the F -test occurs near the center of a roughly rectangular peak of total width $\approx 2W$, it is usually reliable. The 41,090-year obliquity line and 18,957-year precession line are prime examples, but again, the upper precession band contains lines at several closely-spaced periods.

The Cramér–Rao bound

The Cramér–Rao bound is a fundamental statistical inequality that gives lower limits on the accuracy with which various quantities can be estimated; here the frequency. For a single, isolated line, *i.e.*, one that is isolated from other lines by at least $\max(2, c_0)/T$, the bound is approximately

$$SD\{\hat{f}\} \geq \frac{1}{2\pi T} \sqrt{\frac{6}{\rho}} \tag{26}$$

where ρ is the effective signal-to-noise power ratio,

$$\rho = \frac{\frac{A^2}{4} T}{S_c(f)} \tag{27}$$

where $S_c(f)$ is the noise spectrum. This is the spectrum *without* the periodic components; in Figure T7 the noise spectrum near the 41,000 year obliquity line is about 500. Combining (26) and (27) it can be seen that, other things being equal, the variance of a frequency estimate decreases as T^{-3} . Thus, when a choice can be made, effort should be made obtaining longer series, not in making more precise measurements in a shorter series. As an example, if one wanted to double the accuracy of a frequency estimate one could consider either making more precise measurements or increasing the length of the series. The first choice, implies that σ^2 must be reduced by a factor of four, usually corresponding to a four-fold increase in measurement effort. The second requires increasing T by $\sqrt[3]{2}$, or

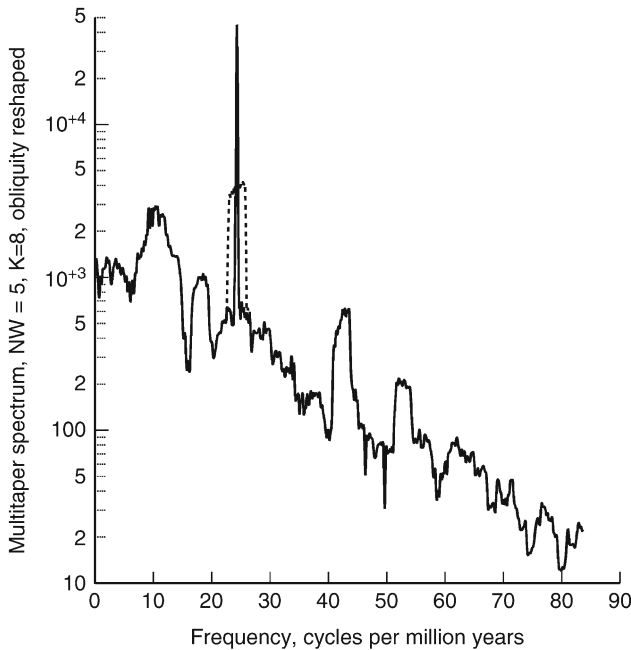


Figure T7 A multitaper estimate of the spectrum of the 3 Myr record shown in Figure T6. In making this estimate, $c_0 = NW = 5.0$ with $K = 8$ windows were used with adaptive weighting, (17). The dashed curve near 25 c/Myr (the 41090-year obliquity line) is the “raw” spectrum estimate, while the sharp black curve is the “reshaped” estimate. Because the significance level of the F -test exceeded the 99.999% level, the raw estimate was replaced with a peak at the estimated frequency. The width of the peak is given by the estimated frequency uncertainty, and the height is scaled to preserve power. The precession peaks (near 43 and 52 c/Myr) were not reshaped because they both consist of multiple lines and the eccentricity lines (7.8 – 10.5 c/Myr) are not resolved.

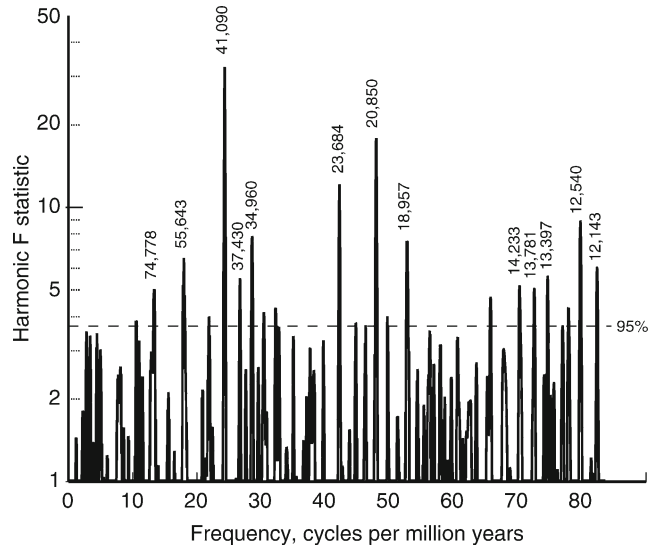


Figure T8 The single-line F -test for periodic components, (25). The data is the 3 Myr record shown in Figure T6, with parameters are as in Figure T7, so the test has 2 and 14 degrees-of-freedom. The low-frequency part is shown in Figure T10 and the horizontal dashed line shows the theoretical 95% level of the $F_{2,14}$ distribution.

about 26% more samples. Note that this calculation ignores the tuning problem.

If one is interested in estimating the *period* of a component, as is common in paleoclimate data, a Taylor's series argument shows that (26) becomes

$$SD\{\hat{P}\} \geq \frac{P^2}{2\pi T} \sqrt{\frac{6}{\rho}} \quad (28)$$

The F -test on the 41,000 year obliquity line was ~ 30 , and can be used as an estimate of ρ . Thus, if one oversimplifies things to ignore fine structure, possible frequency-modulation from changes in the earth's moments of inertia (see §11 of Thomson (1990a) and Figure T14 of Laskar et al., 1993) the accuracy of any estimate of the period from the 3 Myr record is bounded by

$$SD\{\hat{P}\} \approx \frac{41000^2}{2\pi \cdot 3 \times 10^6} \sqrt{\frac{6}{30}} \approx 38 \text{ years} \quad (29)$$

Because the period estimated from the original time scale was 41,234.9 years, 3.8 standard deviations from the nominal period of 41,090 years, the time was scaled by a factor of 41090.0/41234.9 to bring the two into agreement.

Equation (28) has further implications for data analysis. Because the Cramér–Rao bound is a fundamental statistical inequality, it does not apply to one particular estimation method or another, it simply says that one cannot estimate parameters with arbitrary accuracy. Arguments based on wavelet analysis of paleoclimate data claim that the precession line is frequency modulated. The usual trigonometric expansions used in celestial mechanics are, in fact, the Bessel function expansions of a frequency-modulated sinusoid. Since wavelets sequentially use data blocks half the length of the preceding one, the effective T in (28) at a given stage is much less than the length of the series. Thus (28) implies that the standard deviation will be proportionally larger, negating the argument.

Equation (26) also determines the amount of zero-padding necessary. A minimum requirement is that the frequency mesh, (13), should be less than about one-half the standard deviation implying

$$M \geq 4\pi \sqrt{\frac{\rho}{6}} N \quad (30)$$

For the 3 Myr series this implies that the 1,000 samples should be zero-padded to $2M \geq 28,000$ points and, in fact, these examples were zero-padded to $2M = 2^{17} = 131,072$.

When lines are *not* isolated and, in particular, when they are separated by less than twice the Rayleigh resolution, computing the bounds is more difficult. The bounds depend on the amplitudes and phases of the lines in addition to the frequency separation. Looking at the eccentricity expansions, there are four major lines with periods near 100,000 years. They are, explicitly, 94,782, 98,715, 123,818, and 130,615 years. Note that these come in two pairs; the frequency difference between the two frequencies in the first pair and those in the second both correspond to a period of 2.4 Myr. This means that estimating these frequencies with less than 4.8 Myr of data will be difficult even in utopian circumstances. Figure T9 shows the bounds for the four-line case computed using the frequencies, phases, and amplitudes from Berger (1977) as a function of the observation span. Note that, when the data span is less than 800,000 years, the *bound* on the standard deviation is 100,000 years, about the same as the period. Note also

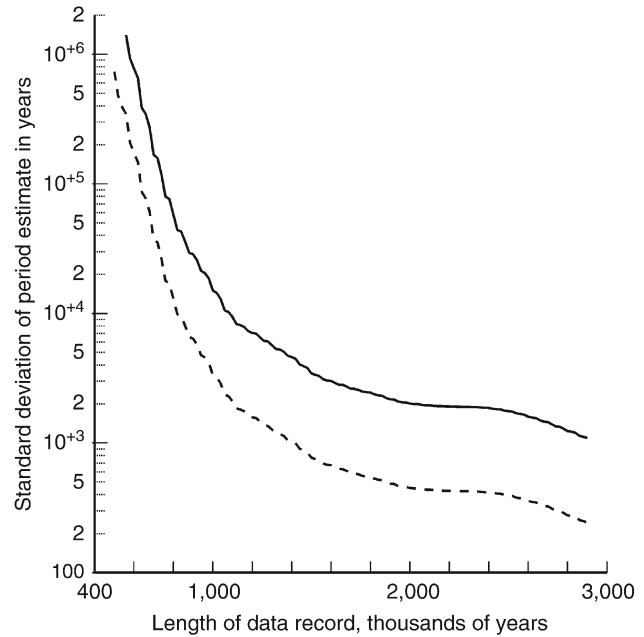


Figure T9 The Cramér–Rao *lower* bound for the standard deviation of the 123,000-year eccentricity line as a function of sample duration. A uniform sampling rate of $\Delta t = 1,000$ years is assumed. The upper curve corresponds to a signal-to-noise ratio $\rho = 5$, the lower to an unrealistically high value of 100. For a perfectly-tuned 800 Kyr record the standard deviation of the best period estimate is about the same as the period.

that these bounds are for Gaussian noise with a *known* timescale; when the timescale is estimated the bounds will be worse. Moreover, four pure sinusoids are assumed, whereas the eccentricity expansion includes dozens of lines in this band so, again, the bounds will be even worse than shown here. Thus, for example, attempts to discriminate between frequencies of 77,000 years and 95,000 lines with less than a few million years of data are futile. (It may be futile even with a few million years of data because 4.8 Myr is long enough for continental drift to significantly change climate dynamics.)

The multitaper setup for multiple lines is discussed in Thomson (1990a), and an example using the above data is shown here in Figure T10. The two-line test used here assumed a *known* frequency offset between the two lines, $1/2.2379 \times 10^6$ cycle/year, but even with this assumption, the test is only significant at about the 97% level.

Coherence

Many analysis problems in paleoclimate data involve studying several different series. The simplest case is the bivariate one, that is where one has two time series, $x(t)$ and $y(t)$. These are assumed to be on the same timescale, are sampled at the same time-step, and have the same number of samples³. Keeping the

³If the time-steps and number of samples are different one can still do the analysis as long as the total time span is the same and, obviously, one can always truncate a longer series. The frequencies used must be the same, so it may be necessary to use a “slow” Fourier transform (see e.g., Gentleman, 1969).

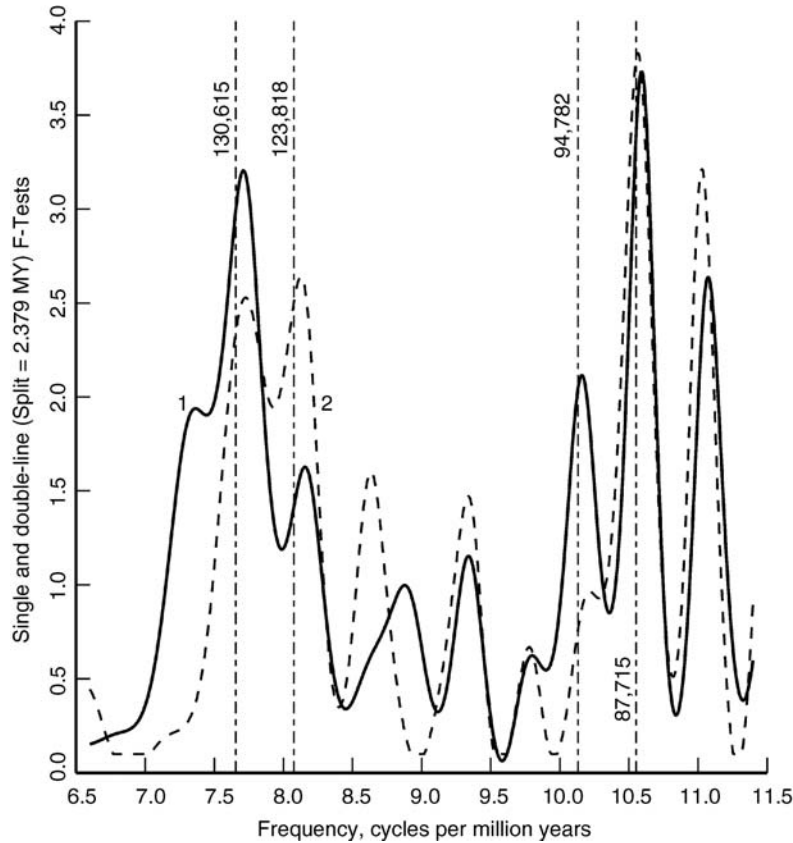


Figure T10 One (black) and two (dashed) line F-tests for periodic components in the eccentricity band. The two-line test assumed a frequency separation corresponding to a period of 2.379 Myr (this is the separation between each of the two pairs of lines).

definition of the eigencoefficients of $x(t)$ from (9), define those of $y(t)$ identically

$$y_k(f) = \sum_{n=0}^{N-1} y(n)v_n^{(k)} e^{-i2\pi n f} \quad (31)$$

and compute the *cross-spectrum*, $S_{xy}(f)$

$$S_{xy}(f) = \frac{1}{K} \sum_{k=0}^{K-1} x_k(f)y_k^*(f) \quad (32)$$

where, as before, the superscript “*” implies complex conjugate. It is usually more convenient to work with the complex quantity, *coherency*,

$$\gamma(f) = \frac{S_{xy}(f)}{[S_{xx}(f)S_{yy}(f)]^{1/2}} \quad (33)$$

where $S_{yy}(f)$ is the spectrum of $y(t)$. The absolute value $|\gamma(f)|$ is known as *coherence*; however, because usage in the literature has not been consistent, it is safer to use redundancy and refer to $\gamma(f)$ as “complex coherency.” In practice, use of *magnitude-squared coherence*, or MSC, defined as $|\gamma(f)|^2$ is preferable.

In common with correlation coefficients, one has $|\gamma(f)| \leq 1$ with $|\gamma(f)| = 1$ implying perfect correlation at frequency f , and $|\gamma(f)| \approx 0$ implying that the series are not related at that

frequency. One can, and often does, encounter both conditions in the same data, but usually, something in between occurs.

In data analysis one does not have the true coherence, but an estimate. The formal distribution of coherence estimates is complicated, but to answer the often-asked question “are these two series coherent, or can they be treated as independent?,” one can use a special case.

If the series are *independent* the probability distribution of an estimate of MSC, say \hat{C} , is

$$P\{\hat{C} < u\} = 1 - (1 - u)^{K-1} \quad (34)$$

so, if one has $K = 8$ windows, the probability that an estimate of coherence *at a given frequency* will be less than, say, 0.4 is $1 - (0.6)^7 = 0.972$. As with most frequency-domain statistics, the problem is that there are as many independent frequency estimates as there are data points with the result that, if one has 1,000 data samples, the odds are good that, at some frequency, an estimate will exceed the 99.9% significance level. This is where scientific judgement comes in; if such an event occurs at, for example, a period of 41,000 years in two long, well-dated ocean cores, one would be remiss in saying there is no evidence for coherence. If, however, it occurred at some “random” and otherwise unknown frequency, the most likely explanation is that it is a sampling fluctuation, not a new discovery. Here, looking at the two power spectra, $S_{xx}(f)$ and $S_{yy}(f)$ and the jackknife confidence intervals of these and coherence can help. If there are

pronounced peaks in both spectra, and the confidence intervals are tight, the peak is much more likely to be real than it is if the confidence bounds are wide and, particularly, if either or both of the spectra have local minima at f .

It is also useful to count the number of frequencies where the sample coherence is above the 10, 50, 80, and 90% significance levels. If one finds, for example, that the fraction of estimates above the nominal 90% level is 11% the series are probably independent. If, in contrast, 30% of the coherence estimates are above the nominal 90% point, one should assume that the series are related.

Coherency is a complex quantity, but thus far, we have only discussed its magnitude. Its phase is also important, primarily because it shows the delay characteristics between the series. One of the fundamental properties of the Fourier transform (see *e.g.*, Papoulis, 1962), is that a time-shifted function has the Fourier transform

$$\begin{aligned} F\{x(t - t_o); t \rightarrow f\} &= e^{-i2\pi f t_o} F\{x(t); t \rightarrow f\} \\ &= e^{-i2\pi f t_o} X(f) \end{aligned} \quad (35)$$

so that the phase $\theta(f) = 2\pi f t_o + \text{phase}\{X(f)\}$ has a linear frequency trend. In a coherence estimate between $x(t)$ and $x(t - t_o)$, the conjugate on $y_k(f)$ in (32) cancels the *phase* $\{X(f)\}$ term leaving $2\pi f t_o$. Thus, if $x(t)$ and $y(t)$ only differ in relative amplitude and a time delay, the phase of the coherency will be a linear slope in frequency. There are two things to remember about doing this in practice: first, a phase *estimate* is ambiguous to multiples of 2π radians or 360° , and these phase ambiguities need to be resolved. One way is to take at the difference between phases at adjacent frequencies and when the magnitude of the difference exceeds 180° , add or subtract 360° with the sign chosen to minimize the difference. Second, paleo-data is *not* noise-free, so that phase estimates are likely to be unreliable unless the coherence is high. One strategy for revealing phase trends is to pick frequencies where: (a) the MSC has a local maxima, and (b) is significant above, say, the 90% significance level. Then, at these frequencies, plot the uncorrected phase θ plus $\theta - 360^\circ$ and $\theta + 360^\circ$, and inspect.

Jackknife

The statistical *jackknife* was invented by Quenouille and named by Tukey after the boy scout's general purpose tool. It is a useful and reliable method to estimate variances of complicated statistics. The jackknife and the newer, and computationally more difficult, bootstrap are covered in several recent texts (see *e.g.*, Efron and Tibshirani, 1998; Davison and Hinkley, 1999). Lahiri (2003) describes resampling methods for dependent data, but the reliability of these for paleoclimate data has yet to be determined. Generally speaking, resampling schemes are intended for independent, identically-distributed data, and so cannot be applied naively to time series data. The eigencoeficients, $\{y_k(f)\}$ can be jackknifed (Thomson and Chave, 1991; Thomson 2007), and this has been a reliable method of assessing confidence limits on the various quantities. The basic rule is to delete each eigencoeficient in turn, then compute the mean and variance of the K "delete-one" estimates. To give a specific example, if one uses the frequency where the F -test is maximized as an estimate of location, one can write the sequence of operations (24) to (25) as

$$\hat{f}_{all} = \text{argmax}_f \{F(f) | x_0(f), x_1(f), \dots, x_{K-1}(f)\} \quad (36)$$

Now repeat these calculations for $0 \leq j \leq K - 1$ withholding the j^{th} eigencoeficient on each calculation

$$\begin{aligned} \hat{f}_{\setminus j} &= \text{argmax}_f \{F(f) | x_0, x_1, \dots, x_{j-1}, x_{j+1}(f), \\ &\quad \dots, x_{K-1}(f)\} \end{aligned} \quad (37)$$

where the subscript $\setminus j$ means that the j^{th} eigencoeficient has been omitted. One now computes the average,

$$\bar{f} = \frac{1}{K} \sum_{j=0}^{K-1} \hat{f}_{\setminus j} \quad (38)$$

and the variance,

$$\text{Var}\{\bar{f}\} = \frac{K-1}{K} \sum_{j=0}^{K-1} [\hat{f}_{\setminus j} - \bar{f}]^2 \quad (39)$$

where the extra factor of $K - 1$ in the variance formula occurs because the different delete-one estimates contain dependent data.

Nonstationarity and Holocene data

A major source of controversy in climate data is that the data is nonstationary, while the majority of papers appear to implicitly assume stationarity, at least when judged by the way they are analyzed. Such a dichotomy is almost guaranteed to cause problems on all timescales, but the higher time resolution of much Holocene data requires that the way the data is analyzed take nonstationarity into account.

In specific, lunar and solar influences on climate appear to be nonstationary. With the moon, the coupling is presumably tidal modulation of storm tracks while several mechanisms have been suggested for solar coupling. As specific examples, attempts to detect the 18.61 year period of the lunar node, the ordinary 11 year sunspot cycle, or the 22 year solar magnetic cycle in instrumental climate data usually either fail or else yield contradictory results. Both, however, appear to modulate the statistics of the climate system and are easily detectable in the central England temperature series as nonstationary features. Another family of periods that commonly occurs in climate data is the 104-year "Suess" cycle and harmonically related frequencies. While data from ocean and lake cores rarely have fine enough sampling to resolve these frequencies, the way they enter into instrumental data carries an important lesson for the analysis of paleo data. To put this idea into more definite form consider two oversimplified examples:

$$y_+(t) = x(t) + a \cos 2\pi f_o t, \quad (40)$$

and

$$y_{ns}(t) = (\alpha + \beta \cos 2\pi f_o t) y_{ns}(t-1) + x(t) \quad (41)$$

where $x(t)$ is an ordinary stationary process and a , α , and β constants. In the first example, $y_+(t)$, the sinusoid is easily detectable if a is sufficiently large and a long enough sample of the process is observed. This is what is usually assumed. Over a few years, the annual temperature cycle is of approximately this form. However, over longer time spans, the more complicated form of the annual cycle described in Thomson (1995) must be considered. In the second example, $y_{ns}(t)$ the periodic component only enters because it modulates the structure of the process. Thus, even though $y_{ns}(t)$ varies periodically,

it is not an additive periodicity and something more complicated than a simple spectrum is necessary to detect it.

As an example, Figures T11 and T12 show dynamic spectra and F -tests for the benthic $\delta^{13}\text{C}$ record from Core V19-30 (Shackleton and Pisias, 1985). The data was gap-filled and interpolated to be equally-spaced in time, then prewhitened using an AR-1 prediction error filter

$$y(t) = x(t) - \alpha x(t-1), \quad t = 1, \dots, N-1 \quad (42)$$

with $\alpha \approx 0.99878$, the one-step autocorrelation. Next, adaptively weighted multitaper spectra (17) and F -tests were computed on 399 overlapping 8,000 year blocks each offset

by 800 years. Because the prewhitening reduces the range of the spectrum, extreme bias protection was not as essential, so a time-bandwidth product of $c_o = 2.7$ and $K = 4$ tapers were used on each block. However, even with prewhitening, one notes that the range of the spectrogram, Figure T11, is $> 10^{10}$.

The corresponding F -test (Figure T12) shows a band of reasonably consistent maxima around 400 c/Myr ($\sim 2,500$ years) and another near the Bond period (Bond et al., 2001) of $\sim 1,500$ years, or 666 c/Myr. Because short windows were used in this example to highlight nonstationary aspects of the data, the fact that these are observed at all is rather surprising.

Turning again to the spectrogram (Figure T11), one of the more prominent features is the series of vertical “stripes” where

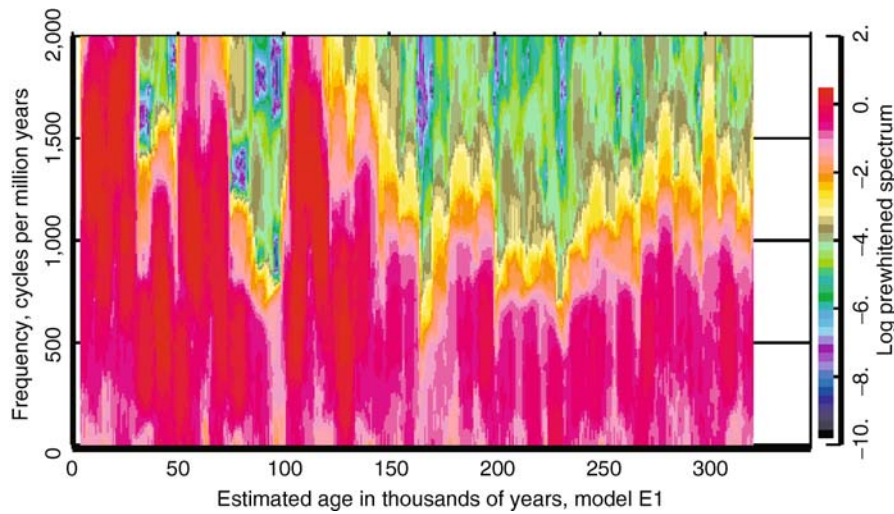


Figure T11 Log_{10} of a multitaper spectrogram for $\delta^{13}\text{C}$ in marine core V19-30. 8,000-year blocks, offset by 800-years were used with $c_o = WT = 2.7$ and $K = 4$ tapers on each block. The data was prewhitened using an autoregressive filter of order 1 (also known as a prediction error filter) and, even so, the range of the spectrum exceeds ten orders of magnitude. Much of the apparent structure appears to be systematic.

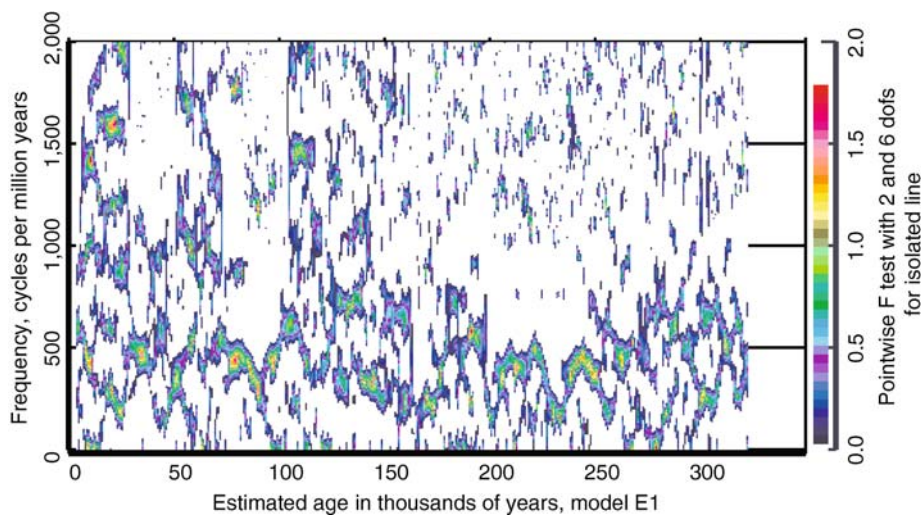


Figure T12 The single-line F -test, (25), for $\delta^{13}\text{C}$ in Core V19-30 with parameters as in Figure T11. The most unusual feature of this plot is the band of reasonably significant peaks visible near 440 c/Myr, corresponding to an average period of about 2,300 years.

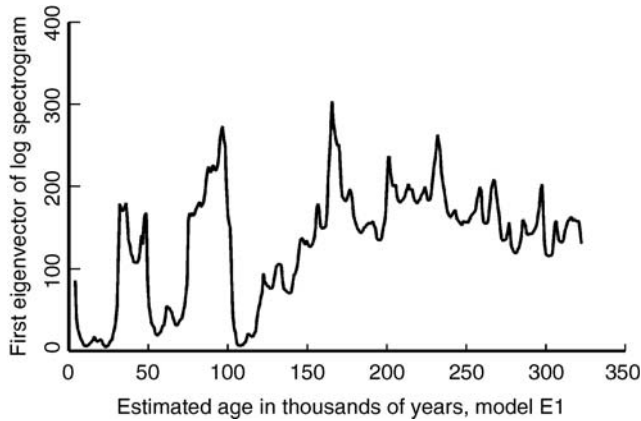


Figure 13 The first eigenvector in the time dimension of the SVD of $\ln S(t, f)$ of the core V19-30 $\delta^{13}\text{C}$ data shown in Figure T11. This is the eigenvector corresponding to the largest singular value.

one can count ~ 13 during the first 150,000 years. This corresponds to an approximate period of $\approx 11,500$ years, about one-half the 23,000 year precession cycle. More formally, on taking the singular value decomposition (SVD) of the log-spectrogram as described in Thomson (1990b), one finds that the *first* eigenvector accounts for more than 95 % of the variation on the log scale. This eigenvector is shown in Figure T13 where the most alarming features are the abrupt transitions.

Wavelets, Lomb–Scargle, Blackman–Tukey

There are several estimates that should be avoided when analyzing paleoclimate data. Some, including the periodogram and Blackman–Tukey estimates, are simply obsolete. It has been recognized for over a century (Rayleigh, 1903), that the periodogram is unreliable. Thomson (1977) has shown examples where the periodogram was in error by over a factor of 10^{12} over most of the frequency range. Examples where it is off by a factor of 10^3 and more, are common in geophysical problems.

The Blackman–Tukey estimate is a smoothed periodogram and inherits its bias problems, a fact that was recognized by Tukey himself. In Tukey (1967), John was recommending “direct” spectrum estimates with data tapering, basically the $k = 0$ term in (14).

Lomb–Scargle estimates (Lomb, 1976; Scargle, 1981) are simply least-squares fits to the data with a single sinusoid at a time, and reduce to the ordinary periodogram when the data is equally-spaced. They have their place, but are even more dangerous than the ordinary periodogram. For most of the problems considered here, it is safer to interpolate the data to an equally-spaced grid, then proceed as above. This is certainly the case if only a few samples are missing.

Wavelets, again, are dangerous for unskilled users. More than one example exists where a wavelet analysis was used to “prove” that precession was frequency modulated. The problem lies in (26); that is, when one makes the effective window length T shorter, as one does in a wavelet analysis, the variance of a frequency or period estimate increases as T^{-3} . Thus, if one uses a short window, line frequencies appear to be variable. This said, if wavelets are appropriate, read Daubechies (1992), Mallat (2001), and Percival and Walden (2000).

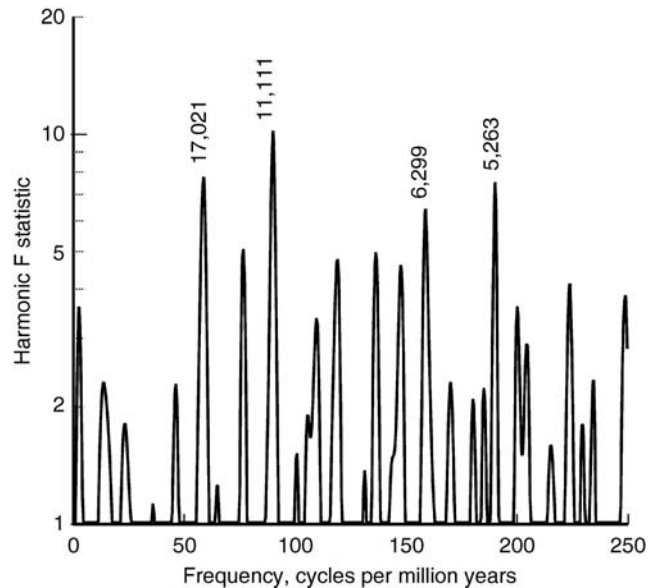


Figure T14 The F -test for periodic components from a multitaper of the eigenvector shown in Figure T13 using $c_0 = 4$ and $K = 5$. Periods of components with individual significance levels above the 97 % level are shown.

Summary and Recommendations

The major facts to remember in the analysis of paleoclimate data are as follows:

Analysis of paleoclimate data is difficult. Noting the efforts that have gone into getting general circulation models to reproduce even fairly gross features of the climate system, one should not expect that the analysis of data produced by the real (and obviously far more complicated) climate system to be simple.

The complexity of the data is not helped by the timing being uncertain. However, a carefully tuned series is preferable to an untuned one. While there is still some debate about whether the tuning process is a form of circular argument, my opinion is that the major remaining uncertainty is the change in precession and obliquity from glacial loading, and the earth’s response to this loading.

The power spectrum is almost always more informative than the autocovariance.

The best way to estimate a power spectrum from data is by multitaper methods.

Blackman–Tukey estimates are obsolete and should not be used. Parametric methods (ones based on autoregressive, moving average, and related models) rarely work well enough to bother computing them. Similarly, the periodogram should *never* be used as a spectrum estimate.

Paleoclimate data is almost certainly nonstationary, but much of the nonstationarity appears to be systematic. One should attempt to identify it.

As always, try several different methods to analyze data. It is recommended to choose the method that gives a good description of the observations with the simplest assumptions.

David J. Thomson

Bibliography

- Berger, A., 1977. Long-term variations of the earth's orbital elements. *Celestial Mech.*, **15**, 53–74.
- Berger, A., 1978. Long-term variations of daily insolation and quaternary climatic changes. *J. Atmos. Sci.*, **35**, 2362–2367.
- Bond, G., Kromer, B., Beer, J., Muscheler, R., Evans, M., Showers, W., Hoffmann, S., Lotti-Bond, R., Hajdas, I., and Bonani, G., 2001. Persistent solar influence on North Atlantic climate during the Holocene. *Science*, **294**, 2130–2136.
- Daubechies, I., (1992). *Ten Lectures on Wavelets*. Philadelphia: SIAM.
- Davison, A.C., and Hinkley, D.V., 1999. *Bootstrap Methods and their Application*. Cambridge: Cambridge University Press.
- Efron, B., and Tibshirani, R.J., 1998. *An Introduction to the Bootstrap*. Boca Raton, FL: Chapman & Hall/CRC.
- Gentleman, W.M., 1969. An error analysis of Goertzel's (Watt's) method for computing Fourier coefficients. *Comp. J.*, **12**, 160–165.
- Johnson, J., Thomson, D.J., Wu, E.X., and Williams, S.C.R., 1996. Multiple-window spectrum estimation applied to *in vivo* NMR spectroscopy. *J. Mag. Reson.*, **B110**, 138–149.
- Kedem, B., 1994. *Time Series Analysis by Higher Order Crossings*. New York: IEEE Press.
- Lahiri, S.N., 2003. *Resampling Methods for Dependent Data*. New York: Springer.
- Laskar, J., 1990. The chaotic motion of the solar system: A numerical estimate of the size of the chaotic zones. *Icarus*, **88**, 266–291.
- Laskar, J., 1999. The limits of earth orbital calculations for geological time-scale use. *Phil. Trans. R. Soc. Lond. A*, **357**, 1735–1759.
- Laskar, J., Joutel, F., and Boudin, F., 1993. Orbital, precessional, and insolation quantities for the earth from –20 myr to +10 myr. *Astron. Astrophys.*, **270**, 522–533.
- Lomb, N.R., 1976. Least-squares frequency analysis of unequally spaced data. *Astrophys. J. Suppl. Ser.*, **39**, 447–462.
- Mallat, S., (2001). *A Wavelet Tour of Signal Processing* (2nd edn.). San Diego: Academic Press.
- Pälike, H., and Shackleton, N.J., 2000. Constraints on astronomical parameters from the geological record for the last 25 Myr. *Earth Planet. Sci. Lett.*, **182**, 1–14.
- Papoulis, A., 1962. *The Fourier Integral and its Applications*. New York: McGraw-Hill.
- Percival, D.B., and Walden, A.T., 1993. *Spectral Analysis for Physical Applications; Multitaper and Conventional Univariate Techniques*. Cambridge: Cambridge University Press.
- Percival, D.B., and Walden, A.T., 2000. *Wavelet Methods for Time Series Analysis*. Cambridge: Cambridge University Press.
- Rao, A.R., Hamed, K.H., and Chen, H.-L., 2003. *Nonstationarities in Hydrologic and Environmental Time Series*. Dordrecht: Kluwer.
- Rayleigh, L., 1903. On the spectrum of an irregular disturbance. *Phil. Mag.*, **41**, 238–243. (In *Scientific Papers by Lord Rayleigh*, vol. V, Art. 285, New York: Dover Publications, 1964, pp. 98–102).
- Scargle, J.D., 1981. Studies in astronomical time series analysis. I. Modeling random processes in the time domain. *Astrophys. J. Suppl. Ser.*, **45**, 1–71.
- Shackleton, N.J., and Pisias, N.G., 1985. Atmospheric carbon dioxide, orbital forcing, and climate. In Sundquist E., and Broecker W. (eds.), *The Carbon Cycle and Atmospheric CO₂: Natural Variations Archaean to Present*. Washington: AGU, Geophysical Monograph 32, pp. 412–417.
- Shackleton, N.J., Berger, A., and Peltier, W.R., 1990. An alternative astronomical calibration of the lower Pleistocene timescale based on ODP site 677. *Trans. R. Soc. Edinburgh Earth Sci.*, **81**, 251–261.
- Shackleton, N.J., Crowhurst, S., Hageberg, T., Pisias, N.G., and Schneider, D.A., 1995a. A new late Neogene time scale: Application to leg 138 sites. *Proc. Ocean Drill. Program Sci. Results*, **138**, 73–101.
- Shackleton, N.J., Hall, M.A., and Pate, D., 1995b. Pliocene stable isotope stratigraphy of site 846. *Proc. Ocean Drill. Program Sci. Results*, **138**, 337–355.
- Singleton, R.A., 1969. An algorithm for computing the mixed radix fast Fourier transform. *IEEE Trans. Audio Electroacoust.*, **17**(2), 93–103.
- Slepian, D., 1978. Prolate spheroidal wave functions, Fourier analysis, and uncertainty V: The discrete case. *Bell Syst. Tech. J.*, **57**, 1371–1429.
- Thomson, D.J., 1977. Spectrum estimation techniques for characterization and development of WT4 waveguide. *Bell Syst. Tech. J.*, **56**, Part I 1769–1815, Part II, 1983–2005.
- Thomson, D.J., 1982. Spectrum estimation and harmonic analysis. *Proc. IEEE*, **70**, 1055–1096.
- Thomson, D.J., 1990a. Quadratic-inverse spectrum estimates: Applications to paleoclimatology. *Phil. Trans. R. Soc. Lond. A*, **332**, 539–597.
- Thomson, D.J., 1990b. Time series analysis of Holocene climate data. *Phil. Trans. R. Soc. Lond. A*, **330**, 601–616.
- Thomson, D.J., 1995. The seasons, global temperature, and precession. *Science*, **268**, 59–68.
- Thomson, D.J. 2001. Multitaper analysis of nonstationary and nonlinear time series data. In Fitzgerald, W., Smith, R., Walden, A., and Young, P. (eds.), *Nonlinear and Nonstationary Signal Processing*. Cambridge: Cambridge University Press, pp. 317–394.
- Thomson, D.J., and Chave, A.D., 1991. Jackknifed error estimates for spectra, coherences, and transfer functions. In Haykin, S. (ed.), *Advances in Spectrum Analysis and Array Processing*, vol. 1, chapter 2. Englewood Cliffs, NJ: Prentice-Hall, pp. 58–113.
- Thomson, D.J., Lanzerotti, L.J., and MacLennan, C.G., 2001. The interplanetary magnetic field: Statistical properties and discrete modes. *J. Geophys. Res.*, **106**, 15941–15962.
- Thomson, D.J., 2007. Jackknifing multitaper spectrum estimates. *IEEE Signal Processing Magazine*, **24**(7), 20–30.
- Thomson, D.J., Lanzerotti, L.J., Vernon, F.L., III, Lessard, M.R., and Smith, L.T.P., 2007. Solar modal structure of the engineering environment. *Proceedings of the IEEE*, **95**, 1085–1132.
- Tukey, J.W., 1967. An introduction to the calculations of numerical spectrum analysis. In Harris, B. (ed.), *Spectral Analysis of Time Series*. New York: Wiley, pp. 25–46.
- Weedon, G., 2003. *Time-Series Analysis and Cyclostratigraphy*. Cambridge: Cambridge University Press.

Cross-references

[Astronomical theory of climate change](#)
[Eccentricity](#)
[Obliquity](#)
[Ocean Drilling Program \(ODP\)](#)
[Precession, climatic](#)
[SPECMAP](#)

TRANSFER FUNCTIONS

Introduction

Paleoecologists use a number of different methods to reconstruct past changes in the Earth's climate and environment. One of the most useful is the analysis of the remains of microscopic plants and animals preserved in ocean, lake, and mire sediments. Interpretation of these biostratigraphic records is usually based on the principle of uniformitarianism: that is, knowledge of an organism's present-day ecology and climate preferences can be used to make inferences about past conditions. Transfer functions are mathematical response functions that allow paleoecologists to formalize this procedure by defining a series of equations that relate a set of biological species data to climate or other environmental parameters.

The transfer function methodology has developed rapidly since the early 1970s following the pioneering work of Imbrie and Kipp (1971) on sea surface temperature reconstruction from fossil foraminifera. Since then the approach has become one of the main tools for studying environmental change on a range of timescales, and has been used to derive quantitative paleoclimate and other environmental estimates from various

Table T2 The main biological proxies used in transfer functions and applications

Biological proxy	Archive	Application	Examples
Foraminifera, diatoms, coccoliths, dinoflagellates	Marine sediments	Sea surface temperature	Kucera et al. (2005); Andersen et al. (2004); Peyron and De Vernal (2001)
Terrestrial pollen	Marine, lake and mire sediments	Temperature, precipitation, growing degree days	Davis et al. (2003)
Coleoptera	Lake and mire sediments	Temperature	Coope (2002)
Diatoms, chironomids, Cladocera	Lake sediments	Temperature, salinity, pH, nutrients	Mackay et al. (2003); Larocque and Hall (2003)

biological proxies preserved in different sedimentary archives (Table T2).

Methods

The basic idea behind the transfer function approach to environmental reconstruction is that we can model a set of biological responses (Y) as a function of one or more environmental parameters (X) (Birks, 1995):

$$Y = f(x) + \text{error}$$

If we understood and could quantify the various physical, chemical and biological processes that determine the distribution and abundance of the taxa in question, we could derive the response functions $f(x)$ directly. Such detailed autoecological information is usually lacking, so instead we adopt an empirical approach and relate the modern distribution and abundance of taxa to contemporary environmental measurements. This usually involves a modern “training” or “calibration” dataset consisting of biological census counts extracted from surface sediments together with environmental measurements from the same sites. The relationship between the modern biological and environmental datasets is then used to solve $f(x)$ and the resulting transfer functions are applied to fossil assemblages in order to derive estimates of the environmental variable for times in the past (Figure T15).

The resulting accuracy and applicability of the transfer function depends in part on the size and quality of the training set from which it is derived. The training set is usually derived from the same type of sedimentary environment as the fossil material to minimize the influence of taphonomic effects. More important is that the training set includes the range of taxa present in the fossil assemblages and that it spans the range of environments likely to have occurred in the past. This requirement cannot always be met using small regional training sets so paleoecologists are increasingly collaborating to merge regional datasets into large continental or global training sets for some organisms (e.g., pollen: Davis et al., 2003; foraminifera: Kucera et al., 2005).

Modern training sets usually contain many taxa (20–300), have abundances expressed as percentages or proportions (i.e., have a constant-sum constraint), and individual taxa often exhibit a non-linear relationship with the environmental variable of interest. Such properties make the derivation of $f(x)$ a difficult statistical problem of multivariate calibration. Not surprisingly, a number of different numerical methods have been proposed, and some have a stronger ecological or statistical basis than others (see Birks, 1995; ter Braak, 1995).

Most methods can be classified into one of two groups. The first seeks to fit a single model to the training set data, providing a generalized description of the relationship between

taxa and environment. Examples of this approach are the principal component regression method of Imbrie and Kipp (1971), neural networks (Malmgren et al., 2001) used in paleoceanography, and the weighted averaging method and its extension – weighted averaging partial least squares – used in paleolimnology (e.g., Birks, 2003). The second group of methods includes the so-called modern analog technique (MAT) and its variants, known in the statistical literature as k -nearest neighbors. This is perhaps the most simple and intuitive method of calibration: rather than fitting a single model to the entire training set, MAT derives what is essentially a local model by searching the modern data for samples that most closely resemble the fossil assemblage. The dissimilarity between the modern and fossil assemblages is calculated by a numerical distance measure (e.g., squared chord distance), and a reconstruction is derived by averaging the environmental value of a small number (usually 10) of the closest analogs.

Differences in the properties of proxies in terms of training set size, taxonomic diversity, and complexity of the species-environment relationship make some numerical techniques more useful than others for particular biological groups. However, it is clear that there is no single mathematical technique that can be recommended as optimal, on either theoretical or empirical grounds. Because of this, many paleoecologists have moved away from the search for a single “best” method and recommend comparing results from several different techniques and combining them to derive a consensus reconstruction (e.g., Birks, 2003; Kucera et al., 2005).

How accurate are the reconstructions?

Given a modern training set and a series of fossil assemblages, all transfer function methods will produce some result. It is therefore important to evaluate the accuracy and reliability of the reconstructions. Direct comparison of the reconstructions with historical monitoring records provides perhaps the most powerful way of validating records for the recent past (e.g., Malmgren et al., 2001; Larocque and Hall, 2003). Over longer periods, independent environmental measurements are usually not available and some form of internal validation based on an analysis of the training set must be used. In this case, the prediction error of the transfer function is typically estimated by comparing the measured environmental variable with the predicted value across the training set samples. Since the same data is being used to both generate and test the model, some form of data splitting or computer-intensive resampling scheme is employed to better simulate the likely errors when the transfer function is applied to new data outside the training set (Birks, 1995).

One of the main assumptions of the transfer function approach is that the modern training set encompasses the range

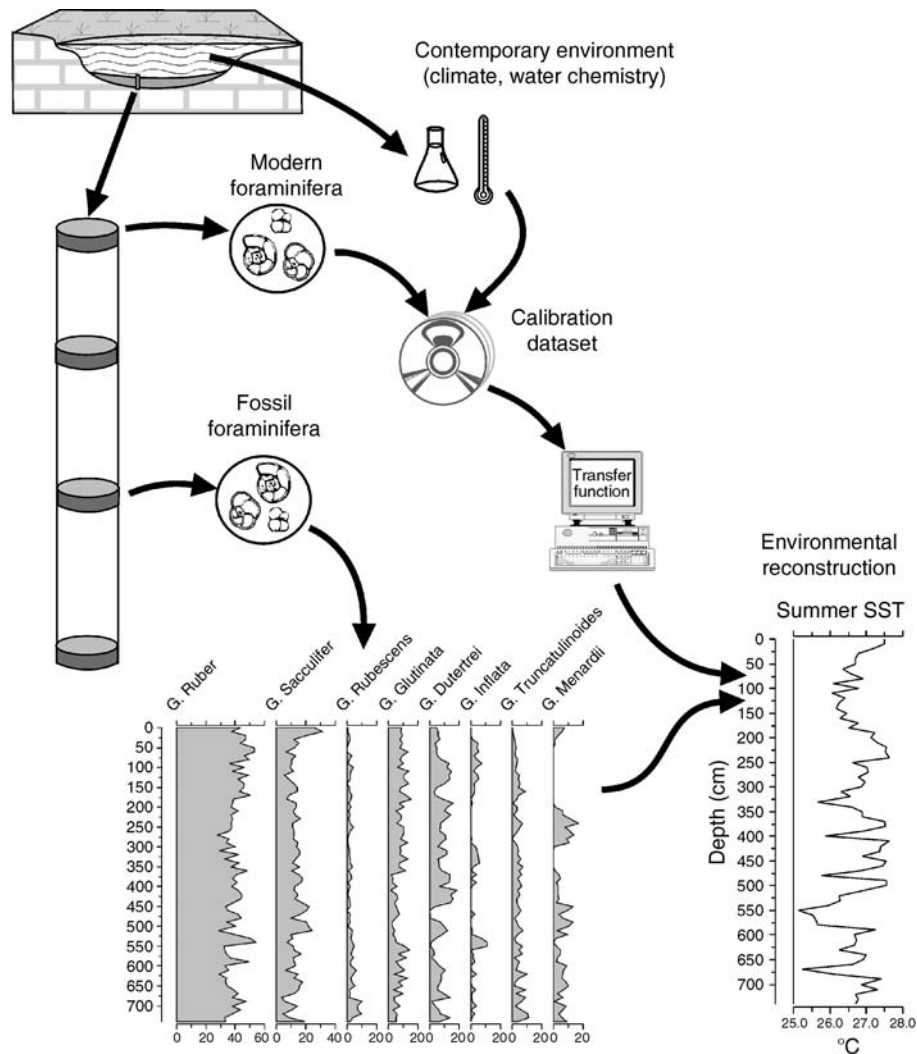


Figure T15 A schematic illustrating the transfer function approach to deriving a quantitative reconstruction of past sea-surface temperature from foraminifer biostratigraphic data using a modern training or calibration dataset.

of biological and environmental variability expressed by the fossil assemblages. This can be partially tested by calculating an analog measure between individual fossil samples and the training set: reconstructions for samples that lack good modern analogs are likely to be less reliable and should be treated with caution. Comparison of reconstructions obtained from the same fossil assemblages using different numerical procedures can highlight technique-specific bias, and together with analog measures, can be used to give a reliability rating to each reconstructed value (Kucera et al., 2005). In some cases, paleoecologists are able to compare reconstructions derived from independent biological or geochemical proxies measured on the same, or closely related, sedimentary sequences (e.g., Birks et al., 2000; Bard, 2001; Larocque and Bigler, 2004). Such comparisons are beginning to focus attention on the potential biases of individual proxies and on the need to understand the processes controlling organism distribution in the training set better.

An important corollary of the above assumption is that not only should the relationship between biota and the environmental variable of interest be invariant through time, but also that the joint distribution of other environmental factors controlling species distribution should have been the same in the past as it is today. This assumption is probably violated in many cases. Where the environmental variable is a strong determinant of species distribution and biological changes are large (e.g., in studies of recent lake acidification or eutrophication), such biases are likely to be small. Over longer timescales where the current training set does not encompass the past range of environmental conditions, or where the environmental variable being reconstructed is not a major determinant of species distribution, biases may be significant and are a focus of current research (e.g., Watkins and Mix, 1998; Anderson 2000).

Stephen Juggins

Bibliography

- Andersen, C., Koc, N., and Moros, M., 2004. A highly unstable Holocene climate in the subpolar North Atlantic: Evidence from diatoms. *Quaternary Sci. Rev.*, **23**, 2155–2166.
- Anderson, N.J., 2000. Diatoms, temperature and climate change. *Eur. J. Phycol.*, **35**, 307–314.
- Bard, E., 2001. Comparison of alkenone estimates with other paleotemperature proxies. *Geochim. Geophys. Geosyst.*, **2**, doi:10.1029/2000GC000050.
- Birks, H.H., Battarbee, R.W., and Birks, H.J.B., 2000. The development of the aquatic ecosystem at Kråkenes Lake, western Norway, during the late-glacial and early-Holocene - a synthesis. *J. Paleolimnol.*, **23**, 91–114.
- Birks, H.J.B., 1995. Quantitative palaeoenvironmental reconstructions. In Maddy, D., and Brew, J. (eds.), *Statistical Modelling of Quaternary Science Data*, Technical Guide 5. Cambridge, UK: Quaternary Research Association, pp. 161–254.
- Birks, H.J.B., 2003. Quantitative palaeoenvironmental reconstructions from Holocene biological data. In Mackay, A., Battarbee, R.W., Birks, H.J.B., and Oldfield, F. (eds.), *Global Change in the Holocene*. London: Arnold, pp. 107–123.
- Coope, G.R., 2002. Changes in the thermal climate in northwestern Europe during marine oxygen isotope stage 3, estimated from fossil insect assemblages. *Quaternary Sci. Rev.*, **57**, 401–408.
- Davis, B.A.S., Brewer, S., Stevenson, A.C., and Guiot, J., 2003. The temperature of Europe during the Holocene reconstructed from pollen data. *Quaternary Sci. Rev.*, **22**, 1701–1716.
- Imbrie, J., and Kipp, N.G., 1971. A new micropaleontological method for quantitative paleoclimatology: Application to a Late Pleistocene Caribbean core. In Turekian, K.K. (ed.), *The Late Cenozoic Glacial Ages*. New Haven: Yale University Press, pp. 77–181.
- Kucera, M., Weinelt, M., Kiefer, T., Pflaumann, U., Hayes, A., Weinelt, M., Chen, M.-T., Mix, A.C., Barrows, T.T., Cortijo, E., Duprat, J., Juggins, S., and Waelbroeck, C., 2005. Reconstruction of sea-surface temperatures from assemblages of planktonic foraminifera: Multi-technique approach based on geographically constrained calibration data sets and its application to glacial Atlantic and Pacific Oceans. *Quaternary Sci. Rev.*, **24**, 951–998.
- Larocque, I., and Bigler, C., 2004. Similarities and discrepancies between chironomid- and diatom-inferred temperature reconstructions through the Holocene at Lake 850, northern Sweden. *Quaternary Int.*, **122**, 109–121.
- Larocque, I., and Hall, R.I., 2003. Chironomids as quantitative indicators of mean July air temperature: Validation by comparison with century-long meteorological records from northern Sweden. *J. Paleolimnol.*, **29**, 475–493.
- Mackay, A.W., Jones, V.J., and Battarbee, R.W., 2003. Approaches to Holocene climate reconstruction using diatoms. In Mackay, A., Battarbee, R.W., Birks, H.J.B., and Oldfield, F. (eds.), *Global Change in the Holocene*. London: Arnold, pp. 294–309.
- Malmgren, B.A., Kucera, M., Nyberg, J., and Waelbroeck, C., 2001. Comparison of statistical and neural network techniques for estimating past sea-surface temperatures from planktonic foraminifer census data. *Paleoceanography*, **16**, 520–530.
- Peyron, O., and De Vernal, A., 2001. Application of artificial neural networks (ANN) to high-latitude dinocyst assemblages for the reconstruction of past sea-surface conditions in Arctic and sub-Arctic seas. *J. Quaternary Sci.*, **16**, 699–709.
- ter Braak, C.J.F., 1995. Non-linear methods for multivariate statistical calibration and their use in palaeoecology: A comparison of inverse (*k*-nearest neighbors, partial least squares and weighted averaging partial least squares) and classical approaches. *Chemometrics and Intelligent Lab. Syst.*, **28**, 165–180.
- Watkins, J.M., and Mix, A.C., 1998. Testing the effects of tropical temperature, productivity, and mixed-layer depth on foraminiferal transfer functions. *Paleoceanography*, **13**, 96–105.

Cross-references

Dendroclimatology
 Nearest-Living-Relative Method
 Ocean Paleotemperatures
 Paleobotany

TRIASSIC-JURASSIC CLIMATES

Ever since the late nineteenth century discovery of fossil conifers, ferns and cycadlike plants in Spitzbergen and Greenland, the Triassic and Jurassic periods of geological time (250–144 Ma) have been regarded as times of unusual global warmth. The twentieth century discovery of continental drift and plate tectonics did not explain paleoclimatic anomalies of forests at high latitudes, and even higher paleolatitude fossil forests were found in Antarctica. These observations, coupled with a likely role for carbon dioxide in global warming comparable with panes of a greenhouse, which was first suggested by nineteenth century physicists John Tyndall and Svanté Arrhenius, have led to the concept that “greenhouse paleoclimates” (as in Triassic and Jurassic) alternated with “icehouse paleoclimates” (such as Permian and modern) over the course of Earth history. In the current atmosphere of early twenty-first century global warming, the details and causes of such warm periods of the geological past remain of great interest.

Rock and fossil record

Especially obvious as evidence of greenhouse global warmth in the past are permineralized tree stumps and logs at high latitudes, well south or north of the modern treeline. Early Triassic fossil logs from Antarctica (Figure T16), for example, grew at paleomagnetically estimated paleolatitudes of 69–73°S, not very different from present paleolatitudes (76°S); however, at present there is a landscape of bare rock and ice with nothing larger than endolithic lichens growing. The fossil logs are up to 19 m long, and judging from their diameters compared with those of living pines, would have been trees 50 m high (Retallack, 1997a). Although these fossil logs are within ancient stream deposits and have been transported, they are associated with permineralized chunks of peaty soils that have not traveled far. Furthermore, untransported ancient soils containing large tree roots are found within the same sedimentary sequence (Figure T17).

The marked tree rings of Antarctic permineralized logs indicate strong climatic seasonality (Del Fueyo et al., 1995), presumably due to an annual snowy season. Fossil leaves of many high paleolatitude floras, such as the *Dicroidium* flora of Antarctica (Figure T18), show evidence of deciduous leaf shedding found in seasonally snowy climates today. The petioles of the fossil leaves have basal smooth callus tissue indicating that they were deliberately shed, rather than torn from their branches. Other fossils from the *Dicroidium* flora, presumably torn off during storms, show clustering of leaves in bundles (Anderson and Anderson, 1985), similar to short shoots and buds of cool temperate plants, such as oaks and pines.

Living relatives of high latitude fossil plants were the greatest surprise to pioneering paleobotanists. Jurassic floras of Greenland are dominated by leaves like those of living cycads and marattiaceous, matoniaceous, dipteridaceous and gleicheniaceous ferns, which are plants now found in warm temperate and tropical climates. Subsequently it was shown that the ferns belong to extinct species, and only a few of the cycadlike leaves were closely allied to modern cycads. Many of the cycadlike leaves belong to an extinct cycadlike group, the cycadeoids, with very different reproductive structures. Nevertheless, many of the fern and cycadlike leaves were large, too

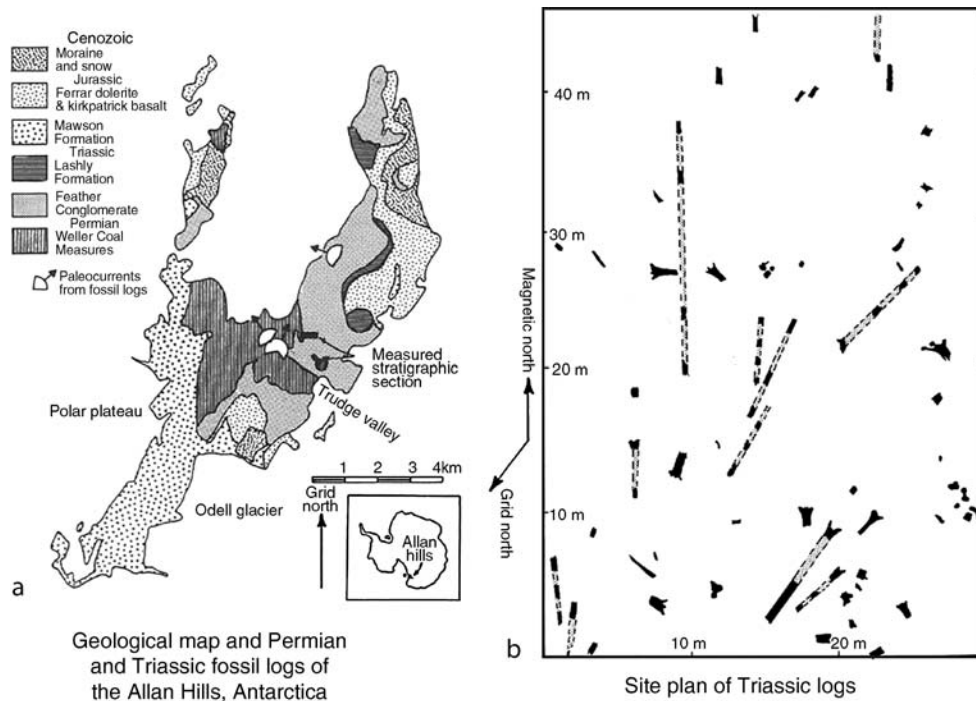


Figure T16 Geological map, paleocurrents (a) and site plan of fossil stumps and logs in Early Triassic sandstones (b) of the Feather Conglomerate in the Allan Hills, Victoria Land, Antarctica, currently at 76°S , and with estimated paleolatitude of $69\text{--}73^{\circ}\text{S}$ (after Retallack, 1997a).

large for polar tundra or taiga vegetation. Furthermore, some of the fossils had a palmlike growth form, with a large terminal meristem and a single parasol-like canopy of large spreading leaves. Frost sensitivity of such large terminal meristems is the main reason why palms, cycads and tree ferns fail to grow much further north or south of 30° latitude, unless in a greenhouse. This argument does not apply to fossil gleicheniaceae ferns, which today are mainly scrambling vines, or to all fossil cycadeoids and cycads, some of which differ from modern cycads in having slender and copiously branching twigs (Willis and McElwain, 2002). Nevertheless, the overall appearance of some high latitude Jurassic floras is more like a Malaysian jungle than taiga or tundra vegetation.

Fossil animals and their traces can also be evidence of global warmth. Large labyrinthodont amphibians from the early Triassic of Antarctica, for example, were probably “cold blooded” (ectothermic poikilotherms) like modern alligators of frost-free climates (Retallack and Krull, 1999). The paleoclimatic significance of dinosaurs is less clear, because their physiology (perhaps inertial or endothermic homeotherms) does not have modern analogues. Ground-dwelling termites are restricted to tropical and subtropical regions (Retallack, 2001a), and could be exploited as paleoclimatic indicators now that their distinctive nests have been recognized in paleosols (Hasiotis and Dubiel, 1995). Coral reefs spread to higher latitudes during global warming (Kiesling et al., 1999). However, some times of restricted reef distribution during the early (Pliensbachian) and middle Jurassic (Bajocian) and earliest Cretaceous (Berriasian), as well as prolonged disappearance of reefs during the earliest Triassic (Griesbachian), appear to have been due to mass extinctions, rather than paleoclimatic cooling (Hallam and Wignall, 1997).



Figure T17 An ancient soil of early Triassic age from the Feather Conglomerate in the Allan Hills, Antarctica. The clayey profile with large root traces and cracks was buried by a cross-bedded sandstone of an ancient river. Chemical analysis of this paleosol show that it was deeply weathered and depleted in common plant nutrients (Ca, Mg, K, Na), like modern Ultisols found no further south than 48° latitude (Retallack and Krull, 1999).

Fossil soils (paleosols) also present striking paleoclimatic anomalies indicative of unusually warm polar paleoclimates. Paleosols associated with early Triassic fossil logs in Antarctica (Figure T17) not only confirm that trees grew nearby, but show a degree of chemical leaching of common plant nutrients (Ca, Mg, K, Na) comparable to that found no further south than 48° latitude. These paleosols are enriched in clay and chemically weathered to the same extent as modern Ultisols, which

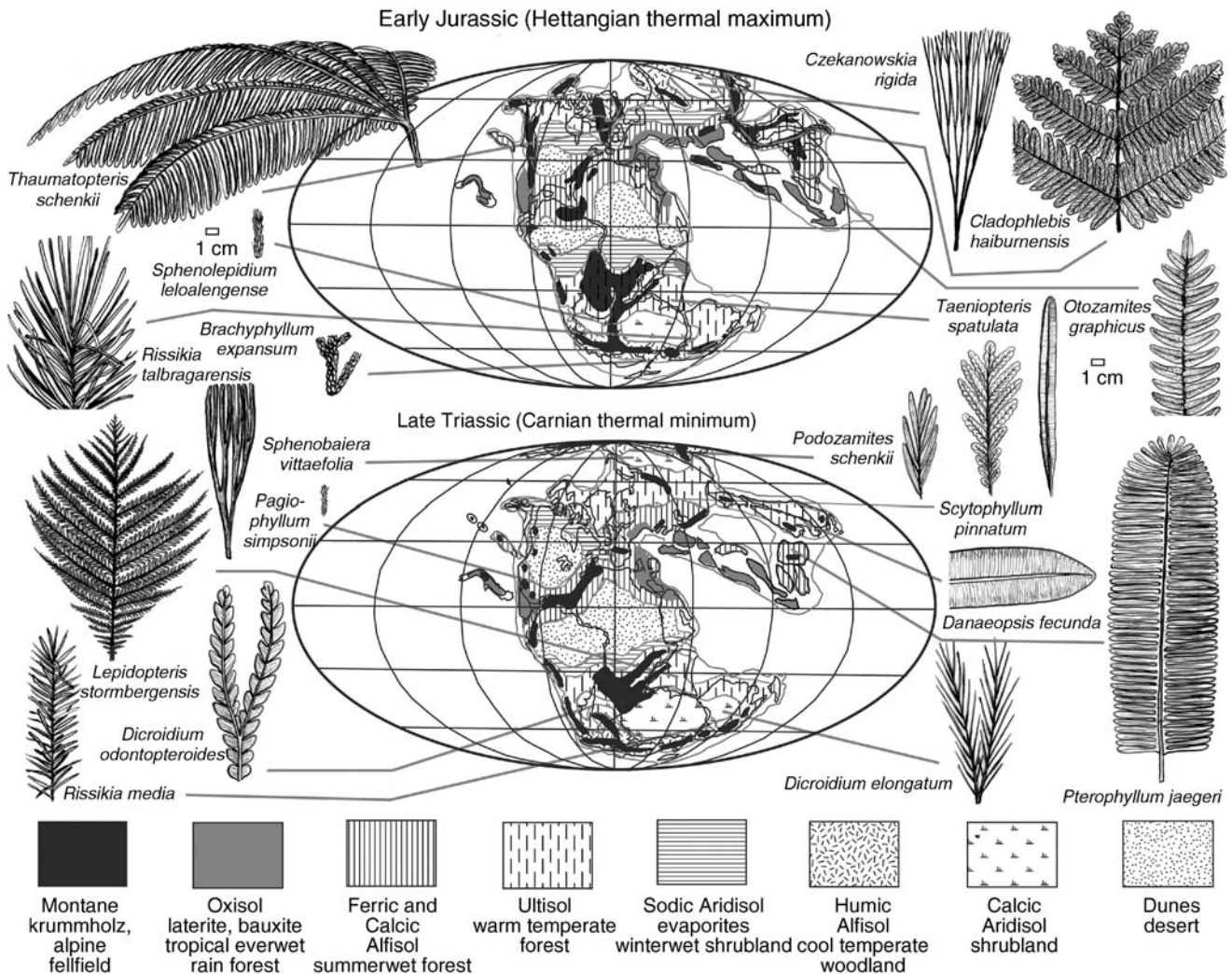


Figure T18 Late Triassic (Carnian) and early Jurassic (Hettangian) paleobiogeographic maps and world vegetation inferred from fossil soils and plants (after Retallack, 1997b, 2002; Willis and McElwain, 2002). Base maps © C. Scotese.

are a soil order found no further south than Tasmania and the North Island of New Zealand and no further north than the Chehalis lowlands of Washington State, USA (Retallack and Krull, 1999). These non-calcareous Antarctic paleosols are evidence of warm, as well as humid, paleoclimates.

Paleosols are especially useful paleoclimatic indicators because they are found in many places where fossil plants are not, as well as where conditions were suitably swampy, frequently flooded, or covered by volcanics, leading to fossil plant preservation (Retallack, 2001a). Paleosols thus provide a more comprehensive view of Triassic and Jurassic global paleoclimate and ecosystems than fossil plants. Fossil rain forest plants are not common, but rain forest paleosols (Oxisols) and their characteristic horizons (bauxites and laterites) can be locally common. Semiarid to subhumid shrubland and wooded shrubland, which can be inferred from fossil therapsids and dinosaurs, also have a very limited paleobotanical record, but can be inferred from sodic Aridisols and evaporites of winterwet subtropical regions and calcic Aridisols and calcretes of summer-wet tropical to temperate regions (Retallack, 1997b).

Fossil plants of summer-wet subtropical forests (such as the late Triassic flora of the Chinle Formation of Arizona) are associated with ferric and calcic Alfisol paleosols. Fossil plants of temperate broadleaf forests (such as the early Triassic flora of the Newport Formation of Australia) are associated with Ultisol paleosols. Fossil plants of cool temperate deciduous woodlands (such as the late Triassic flora of the Falla Formation of Antarctica) are associated with humic Alfisols. Provisional soil-vegetation maps of the late Triassic and early Jurassic (Figure T18) are in substantial agreement with such maps constructed from paleobotanical data alone, or from computer modeling of potential vegetation (Beerling and Woodward, 2001). Interpreted Triassic and Jurassic plant biomes reveal no indication of tundra or taiga, and temperate forests extend within both the Arctic and Antarctic Circles.

Paleosols are evidence not only of regional variation in climate and vegetation, but also of paleoclimatic changes through time. The Karoo Basin of South Africa, for example, had sodic-calcic paleosols (Aridisols) of desertic paleoclimates during the early Triassic (Scythian Katberg Formation), but by late

Triassic (Carnian Molteno Formation), the paleoclimate was humid with formation of non-calcareous red paleosols (Alfisol) and swamp paleosols (Histosols). By early Jurassic (Hettangian-Toarcian Elliot and Clarens Formation), paleosols were again calcareous and nodular, like dry climate soils (Aridisols).

Other indications of Triassic and Jurassic paleoclimates come from sedimentary indicators such as coals, evaporites, laterites, and bauxites (Parrish, 1998). These indicators of wet, dry and tropical climates, respectively, confirm paleoclimatic restorations based on plants and soils. Such linkage is not surprising considering that most coals form in Histosol soils, many evaporites in salid Aridisols, and many bauxites in Oxisols (Retallack, 2001a). One exception to the use of coal as a paleoclimatic indicator is a lack of coal anywhere in the world during the entire duration of the early Triassic. This multimillion-year coal gap may be due to extinction of coal-forming plants during the Permian-Triassic life crisis (Retallack, 1996), or to some continuing hazard such as methane degassing, which would have reduced oxygenation of already near-stagnant wetlands (Sheldon and Retallack, 2002).

Quantitative paleoclimatic proxies

Among a variety of proxies for the ups and downs of greenhouse paleoclimate, the best known is the oxygen isotopic composition of fossil seashells. This approach was first applied to the study of glacial versus interglacial benthic foraminifera by Cesare Emiliani, who found low isotopic values ($\delta^{18}\text{O}$) at times of warm oceans and high isotopic values at times of cold oceans. Such isotopic measurements have been extended to a variety of tropical fossil seashells ranging back in age by 550 million years (Veizer et al., 2000). The variation in isotopic value reflects increased temperature-dependent evaporation of the light isotope of oxygen (^{16}O) from the ocean relative to the heavier common isotope (^{18}O), and its sequestration in snow and ice of polar ice caps. There is also a salinity effect, because there is more evaporation of the light isotope than the heavy one from fresh waters. The net effect is that when the oxygen isotopic value ($\delta^{18}\text{O}$ in ‰ of standard notation) goes down, the ocean is warm, less saline and with small ice caps. Salinity and ice cap effects are generally disregarded in using a transfer function for the relationship between temperature and isotopic composition of modern foraminifera to estimate paleotemperatures of the past (Parrish, 1998). During the Triassic and Jurassic, however, there was a long-term increase in isotopic values, which is probably due to greater facility of the light isotope to emerge at the surface after subduction and crustal recycling in sedimentary pore water (Veizer et al., 2000). Nevertheless, the oxygen isotopic record is valuable because it is known in considerable detail, and because it indicates paleoclimatic volatility (Figure T19). This record suggests that tropical marine temperatures have varied considerably, perhaps by as much as 6 °C, between relatively cool periods that were nevertheless warmer than at present, and peaks of warmth during the earliest Triassic (Griesbachian), early-middle Triassic (Spathian), early Late Triassic (Carnian), earliest Jurassic (Hettangian), early-middle Jurassic (Toarcian), middle Jurassic (Bathonian-Callovian), and earliest Cretaceous (Berriasian).

These various peaks of warmth indicated by oxygen isotopic composition of tropical sea shells are also times of peak atmospheric carbon dioxide revealed by studies of the stomatal index of *Lepidopteris* and *Ginkgo* leaves (Figure T19), thus

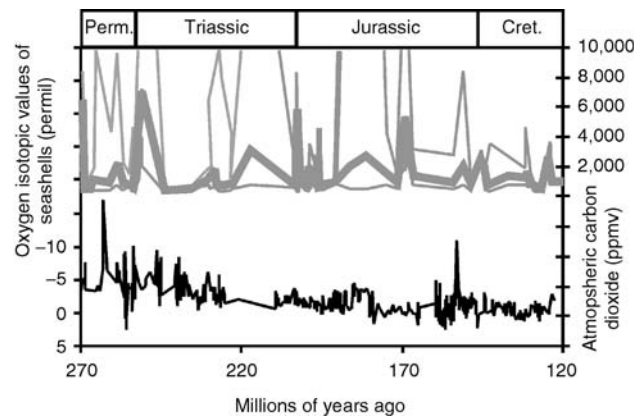


Figure T19 Ups and downs of the early Mesozoic greenhouse revealed by biogenic carbonate oxygen isotopic composition as a proxy for paleotemperature, and by stomatal index of fossil plants as a proxy for atmospheric carbon dioxide concentration (data from Veizer et al., 2000; Retallack, 2002). The oxygen isotopic data is plotted in reverse order so that peaks are warm and valleys are cold, and its long-term trend is in part an artefact of crustal recycling.

supporting a greenhouse mechanism for paleoclimatic change in the past. The stomatal index is a measure of the number of plant gas-intake pores (stomates) normalized to the total number of epidermal cells in well-preserved fossil leaves from which cuticles can be prepared and examined under the microscope. Plant leaves have fewer stomates when atmospheric carbon dioxide is high in order to conserve water transpired through the same stomatal pores. Quantification of this well-known plant response to rising atmospheric carbon dioxide has come from greenhouse studies of living *Ginkgo* plants, as well as of *Ginkgo* leaves conserved in herbaria during the past century of industrially generated increase in atmospheric carbon dioxide (Retallack, 2002). The amounts of atmospheric carbon dioxide revealed by this method are close to modern levels (280 ppmV) for Permian time, when glacial ice caps were as extensive as they are today. This result indicates that this quantification does not show long-term drift, as is apparent from the oxygen isotopic record (Figure T19). Earliest Triassic (Griesbachian), earliest (Hettangian) and middle Jurassic (Bathonian), and earliest Cretaceous (Berriasian) peaks of carbon dioxide abundance are startlingly high (>2,000 ppmV), and coincide with mass extinctions of life on land and in the ocean. There are other peaks of lesser magnitude, and intervening times of atmospheric carbon dioxide about twice modern levels (ca. 500 ppmV).

Paleosols also can provide proxies for paleoclimatic mean annual precipitation and mean annual temperature. Mean annual precipitation, for example, can be inferred from the relationship observed in modern calcareous soils of increased depth to the horizon of carbonate nodules in increasingly humid climates. For paleosols, compaction correction needs to be made to the depth of the calcic horizon in a paleosol in order to restore it to the original thickness before burial by overlying sediments (Retallack, 2001a). Mean annual precipitation and temperature also can be approximated by the degree to which non-calcareous, clayey, subsurface horizons of paleosols have been leached of alkaline earth (Ca, Mg) and alkali elements (K, Na). Both methods have been used to estimate paleoclimatic parameters of paleosols (Sheldon et al., 2002), but not

widely applied to Triassic and Jurassic paleosols. The Triassic and Jurassic paleosol record of the Colorado Plateau looks especially promising in this regard (Retallack, 1997b), because early middle Triassic paleosols (Anisian, Moenkopi Formation) are weakly calcareous, as are early late Triassic paleosols (Carnian Chinle Formation), but later Triassic paleosols (Carnian-Norian Chinle Formation) become increasingly calcareous with shallow calcic horizons. Earliest Jurassic paleosols (Hettangian Kayenta Formation) are weakly calcareous, but those few paleosols known from the early-middle Jurassic (Pliensbachian-Bajocian Navajo Sandstone – a desert dune sequence) are dolomitic and shallowly calcareous. Weakly calcareous paleosols are again found in the later middle Jurassic (Bathonian-Callovian Curtis and Summerville Formations), but calcareous paleosols are abundant in the late Jurassic (Tithonian-Kimmeridgian Morrison Formation). These observations suggest that global warm spikes were also wet spikes in the paleosol record. Warm-wet paleoclimatic spikes alternating with cold-dry paleoclimates can also be inferred from vegetation modeling (Beerling and Woodward, 2001) and biome reconstruction (Figure T18). Global thermal maxima of the Triassic and Jurassic were times when cool temperate vegetation retreated to higher latitudes and altitudes, temperate and tropical shrublands covered smaller areas, and summerwet subtropical and rain forests covered larger areas, compared with global thermal minima.

Yet another quantitative approach has been computer modeling of paleoclimate using modern general circulation models adjusted for ancient paleotopography, and for estimates of soil and vegetation albedo and other ecosystem properties. These models have predicted extreme seasonal paleoclimates for the continental interiors and megamonsoons for peritropical margins of the northern supercontinent Laurussia and the southern supercontinent Gondwana. Such paleoclimatic extremes are not compatible with the fossil plants, animals, and soils found there (Retallack, 1997b; Retallack and Krull, 1999). Some, but not all, of these problems are mitigated by running the computer models with elevated atmospheric carbon dioxide (Wilson et al., 1994), thus giving theoretical confirmation of the observed link between paleotemperature and greenhouse gases.

Causes of Triassic and Jurassic global paleoclimatic variation

Triassic and Jurassic records are effective tests for theories of global climatic variation because they allow exploration of greater paleoclimatic extremes than found during the Cenozoic, yet with animals and plants of more familiar kinds than found in the Paleozoic and Precambrian. The distinctive paleogeographic arrangement of a meridional supercontinent of Pangea, barely including the poles (Figure T18), is a striking difference from the scattered continents today, with one polar and several northern peripolar continents.

The supercontinent Pangea has been blamed for climatic cooling by virtue of its large size and drawdown of atmospheric carbon dioxide by soil formation and weathering, which proceeds by consumption of carbonic acid. In contrast, greenhouse pulses have been related to times of active sea floor spreading when mid-ocean ridges were high and displaced ocean water to form epicontinental seas. This idea was first advanced to explain long-term paleoclimatic change. The Permian icehouse

was caused by assembly of Pangea and the Mesozoic greenhouse by Pangean breakup and dispersal, followed by a Cenozoic ice-house initiated by Northern Hemisphere aggregation of Asia and North America (Fischer, 1984). Detailed paleoclimatic records now available (Figure T19) show paleoclimatic volatility on shorter timescales than continental drift, so this mechanism is not the whole answer.

Transient greenhouse warming has also been linked to volcanic activity, especially to continental flood basalts which coincide with observed warm spikes (Figure T19): earliest Triassic (Griesbachian Siberian Traps), earliest Jurassic (Hettangian Newark and Brito-Arctic volcanics), early-middle Jurassic (Toarcian Ferrar-Karoo basalts) and middle Jurassic (Bathonian Antarctic basalts), and earliest Cretaceous (Berriasian Parana-Etendeka traps). Global cooling, or “volcanic winter,” can be produced by eruptions of ashy particles and sulfate aerosols into the atmosphere, as first observed by Benjamin Franklin during Europe’s “year without a summer,” 1783, following the eruption of the Icelandic volcano Laki. Large flood basalts were not explosive eruptions like those of Laki, Pinatubo and Mt. Helens. Instead, flood basalts were low-viscosity lavas, which flowed without large explosions over large areas. Both kinds of eruptions also release enormous amounts of carbon dioxide and water vapor, which are potent greenhouse gases, their effects are felt after particles and aerosols are scrubbed from the atmosphere by rain. Unfortunately, the currently estimated gas release from even these enormous eruptions is too spread out in time and too small (Wignall, 2001) to have created the likely variation in atmospheric carbon dioxide (Figure T19).

Impact of large asteroids and comets also create global paleoclimatic havoc (Rampino, 2002), including short-term impact-winter from dust and aerosols cast aloft by crater excavation. This dust is more strongly acidic than for volcanic eruptions as it includes sulfur oxide gases that are rained out as sulfuric acid. Sulfuric acid may be very abundant if asteroids or comets vaporize gypsum or other sulfur-bearing rocks within the impact crater, as at the Chicxulub crater, Yucatan, Mexico. Another strong acid formed during impact is nitric acid, generated by impact shocking, and oxidation and hydration of atmospheric nitrogen. Both sulfuric and nitric acids are suspected to have created strongly leached boundary beds, and to have extinguished many shelled marine organisms at the Cretaceous-Tertiary boundary. These days to years of strong acid rain were followed by several tens of thousands of years of paleoclimatic warming, due to elevated greenhouse gases including water vapor and carbon dioxide. This carbon dioxide could have come from multiple sources including the death and decay of many kinds of organisms from the trauma of impact and impact winter, and the burning of forests browned by acid rain. Although scenarios for impact perturbation of life and paleoclimate have been most thoroughly explored for the Cretaceous-Tertiary boundary, large impacts coincide with other mass extinctions and global warm spikes during the Triassic and Jurassic (Rampino, 2002), including the early-late Triassic (Spathian) Araingahua Crater (40 km), the late Triassic (Norian) Manicougan (100 km) and Rochechouart (23 km) Craters, the middle Jurassic (Bajocian) Puchezh-Katunki Crater (80 km), and the earliest Cretaceous (Berriasian) Morokweng Crater (>70 km). Like flood basalts, however, the magnitude of the perturbations does not currently correlate closely with impact magnitude, as judged from crater size, or other evidence of impact (Rampino, 2002).

Another important cause of global paleoclimatic perturbation is methane hydrate destabilization, which could exacerbate impact and volcanic warming to truly catastrophic proportions. Methane created by microbial decay of organic matter deep within sediments and permafrost accumulates within subsurface heat traps maintained by geothermal gradients beneath cold oceans and permafrost. The methane is hydrated within ice crystals and is physically stable, but can be released by volcanic eruption, meteorite impact, submarine landslides, or general warming of overlying sediments or ice. This form of methane has a very distinctive isotopic composition, which has been used as a tracer for massive releases of methane, now well documented for the earliest Eocene (Ypresian), early Cretaceous (Aptian), early-middle Jurassic (Pliensbachian) and earliest Triassic (Griesbachian). The global warming and unusual abundance of ^{12}C at these times is attributed to thousands of gigatons of methane released to the atmosphere, where the isotopically light methane was oxidized to isotopically light carbon dioxide within 7–24 years, and this in turn fixed within isotopically light organic carbon and carbonate. Methane itself is a powerful greenhouse gas, 50 times more effective than carbon dioxide. Atmospheric pollution by methanogenic hydrocarbons has had catastrophic effects in the past, because some documented releases were also times of mass extinction (Hesselbo et al., 2000; Krull and Retallack, 2000).

If volcanoes, impacts, and methane release are the principal agents of global warming, the principal agent of global cooling is life itself, particularly its photosynthetic ability to reduce carbon within the bodies of organisms and to bury much carbon within sediments. Root respiration and soil animals also promote consumption of atmospheric carbon dioxide, as carbonic acid, the principal agent of silicate weathering that releases alkali (Na, K) and alkaline earth (Ca, Mg) elements, which fuel plant growth (Berner and Kothavala, 2001). Mountain uplift has also been proposed to cool the planet by means of silicate weathering (Raymo and Ruddiman, 1992). The mountains themselves do not promote cooling because silicate weathering is reduced under alpine meadows and ice fields compared with lowland forests and grasslands. Nevertheless, glacial loess from montane glaciers and desert dust from montane rain shadows are important sources of nutrients for soil formation and silicate weathering, which could have climatic ramifications. Changing ocean currents and thermohaline circulation also have been thought to have a cooling effect (Broecker, 1997), but these are also mechanisms for increasing biological productivity of surface waters and creating organic matter, which then sinks and is buried in oceanic sediments. Most marine productivity and carbon sequestration is nearshore and fueled by leakage of nutrients from soils and ecosystems on land. Transient global warming events caused by geological catastrophes were probably curtailed largely by biotic recovery and carbon sequestration in soils, lakes and nearshore marine environments.

Carbon sequestration by Triassic and Jurassic terrestrial ecosystems was probably different from that in both modern and Permian ecosystems for purely evolutionary reasons. Unlike modern ecosystems, there were no grasses or grasslands during the Triassic and Jurassic (Retallack, 2001b). Dry continental interiors supported dry shrublands of small-leaved cycadeoids, conifers and seed ferns in soils lacking the fine cracking and carbon-rich surface horizons of grassland soils. An array of rain forest, summerwet tropical forest, winterwet subtropical to

temperate woodland, warm temperate forest, and cool temperate woodlands formed similar soils to these plant formations today (Figure T18). No tundra and taiga vegetation was known in polar regions, but the montane equivalents alpine fellfield and krummholz were probably present, because there is evidence from fossil soils that plants had evolved into tundra and taiga vegetation as old as Carboniferous and Permian, respectively (Retallack, 2001a). Triassic and Jurassic ecosystems, unlike Permian ecosystems, had enormous herbivores and hordes of social insects. Early to middle Triassic therapsids were as large as rhinos, and late Triassic and Jurassic dinosaurs exceeded the bulk of large elephants. Ants and termites are known as body fossils only as old as Cretaceous, but fossil nests suggest comparable insects as old as Triassic (Hasiotis and Dubiel, 1995). Dinosaurs and social insects would have consumed large amounts of vegetation, and could have contributed to general global warmth during the colder and drier phases of early Mesozoic climatic oscillations (Retallack, 1997b). Climate and life on Earth have long been intimately interrelated because of their complimentary dependence on greenhouse gases.

Gregory J. Retallack

Bibliography

- Anderson, J.M., and Anderson, H.M., 1985. *Palaeoflora of Southern Africa. Prodrum of South African Megaflores: Devonian to Recent*. Rotterdam: Balkema, 423pp.
- Beerling, D.J., and Woodward F.I., 2001. *Vegetation and the Terrestrial Carbon Cycle*. Cambridge, UK: Cambridge University Press, 405 p.
- Berner, R.A., and Kothavala, Z., 2001. GEOCARBIII: A revised model of atmospheric CO_2 over Phanerozoic time. *Am. J. Sci.*, **301**, 182–204.
- Broecker, W.S., 1997. Thermohaline circulation, the Achilles heel of our climate systems: Will man-made CO_2 upset the current balance? *Science*, **278**, 1582–1588.
- Del Fueyo, G.M., Taylor, E.L., Taylor, T.N., and Cúneo, R., 1995. Triassic wood from the Gordon Valley, central Transantarctic Mountains, Antarctica. *IWA J.*, **16**, 111–126.
- Fischer, A.G., 1984. Biological innovations and the sedimentary record. In Holland, H.D., and Trendall, A.F. (eds.), *Patterns of Change in Earth evolution*. Berlin: Springer, pp. 145–157.
- Hallam, A., and Wignall, P.B., 1997. *Mass Extinctions and Their Aftermath*. Oxford: Oxford University Press, 320 p.
- Hasiotis, S.T., and Dubiel, D.C., 1995. Termite (Insecta, Isoptera) nest ichnofossils from the upper Triassic Chinle Formation, Petrified Forest National Monument, Arizona. *Ichnos*, **4**, 111–130.
- Hesselbo, S.P., Gröcke, D.R., Jenkyns, H.C., Bjerrum, C.J., Farrimond, P., Bell, H.S.M., and Green, O.R., 2000. Massive dissociation of gas hydrate during a Jurassic oceanic anoxic event. *Nature*, **406**, 392–395.
- Kiessling, W., Flügel, E., and Golonka, J., 1999. Paleoreef maps: Evaluation of a comprehensive database of Phanerozoic reefs. *Am. Assoc. Petrol. Geol. Bull.*, **83**, 1552–1587.
- Krull, E.S., and Rlack, G.J., 2000. $\delta^{13}\text{C}$ depth profiles from paleosols across the Permian-Triassic boundary: evidence for methane release. *Bull. Geol. Soc. Am.*, **112**, 1459–1472.
- Parrish, J.T., 1998. *Interpreting Pre-Quaternary Climate from the Geologic Record*. New York: Columbia University Press, 338pp.
- Rampino, M.R., 2002. Role of the galaxy in periodic impacts and mass extinctions on Earth. In Koeberl, C., and MacLeod, K.G. (eds.), *Catastrophic Events and Mass Extinctions: Impacts and Beyond*. Boulder, CO: Geological Society of America. GSA Special Paper 356, pp. 667–678.
- Raymo, M.E., and Ruddiman, W.F., 1992. Tectonic forcing of late Cenozoic climate. *Nature*, **359**, 117–122.
- Retallack, G.J., 1996. Global coal gap between Permian-Triassic extinction and Middle Triassic recovery of peat-forming plants. *Bull. Geol. Soc. Am.*, **108**, 195–207.

- Retallack, G.J., 1997a. Permian and Triassic driftwood from the Allan Hills, Antarctica. *US Antarct. J. for 1995*, **30**(5), 37–39.
- Retallack, G.J., 1997b. Dinosaurs and dirt. In Wolberg, D., and Stump, E. (eds.), *Dinofest*. Philadelphia, PA: Academy of Natural Sciences, pp. 345–359.
- Retallack, G.J., 2001a. *Soils of the Past*. Oxford: Blackwell, 404pp.
- Retallack, G.J., 2001b. Cenozoic expansion of grasslands and climatic cooling. *J. Geol.*, **109**, 407–426.
- Retallack, G.J., 2002. Carbon dioxide and climate over the past 300 Myr. *Phil. Trans. R. Soc. Lond.*, **A360**, 659–673.
- Retallack, G.J., and Krull, E.S., 1999. Ecosystem shift at the Permian-Triassic boundary in Antarctica. *Aust. J. Earth Sci.*, **46**, 785–812.
- Sheldon, N.D., and Retallack, G.J., 2002. Low oxygen levels in earliest Triassic soils. *Geology*, **30**, 919–922.
- Sheldon, N.D., Retallack, G.J., and Tanaka, S., 2002. Geochemical climofunctions from North American soils and applications to paleosols across the Eocene-Oligocene boundary in Oregon. *J. Geol.*, **110**, 687–696.
- Veizer, J., Godderis, Y., and François, L.M., 2000. Evidence for decoupling of atmospheric CO₂ and global climate during the Phanerozoic eon. *Nature*, **408**, 698–701.
- Wignall, P.B., 2001. Large igneous provinces and mass extinctions. *Earth Sci. Rev.*, **24**, 1–17.
- Willis, K.J., and McElwain, J.C., 2002. *The Evolution of Plants*. Oxford: Oxford University Press, 378pp.
- Wilson, K.M., Pollard, D., Hay, W.W., Thompson, S.L., and Wold, C.N., 1994. General circulation model simulations of Triassic climates: Preliminary results. In Klein, G.D. (ed.), *Pangea*. Boulder, CO: Geological Society of America. GSA Special Paper 288, pp. 91–116.

Cross-references

Arid Climates and Indicators
 Atmospheric Evolution, Earth
 Bolide Impacts and Climate
 Carbon Cycle
 Carbon Isotope Variations over Geologic Time
 Climate Change, Causes
 Coal Beds, Origin and Climate
 Continental Sediments
 Evaporites
 Flood Basalts, Climatic Implications
 “Greenhouse” (warm) Climates
 Laterite
 Mass Extinctions, Role of Climate
 Methane Hydrates, Carbon Cycling, and Environmental Change
 Mountain Uplift and Climate Change
 Monsoons, Pre-Quaternary
 Oxygen Isotopes
 Paleobotany
 Paleoclimate Modeling, Pre-Quaternary
 Paleotemperatures and Proxy Reconstructions
 Paleosols, Pre-Quaternary
 Paleo-Precipitation Indicators
 Plate Tectonics and Climate change
 Pre-Quaternary Milankovitch Cycles and Climate Variability
 Sedimentary Indicators of Climate Change
 Volcanic Eruptions and Climate Change
 Weathering and Climate

U

URANIUM-SERIES DATING

The discovery of natural radioactivity at the beginning of the twentieth century fundamentally changed our understanding of the physical and biological history of the Earth. Before then, the antiquity of the Earth was a very debatable issue and thus any process that required a long time, such as Darwin's theory of evolution, was very much in doubt. A number of clever approaches, based on estimates of time required for certain physical processes, were used to constrain the age of the Earth, such as Lord Kelvin's estimates based on the assumption of a molten Earth cooling to its present state. All of these estimates greatly underestimated the age of the Earth. The discovery of natural radioactivity (Becquerel, 1896) and the fact that the rate at which a particular radioactive nuclide decays is constant opened the way to obtaining absolute dates.

Many light elements, such as carbon and potassium have isotopes that decay in a single step to a stable isotope of another element. For example, ^{14}C decays to ^{14}N and ^{40}K decays to ^{40}Ar . All isotopes of elements heavier than bismuth are radioactive and have decay schemes that involve multiple stages of decay to intermediate isotopes. One of these elements, uranium, has two primary isotopes, ^{238}U and ^{235}U ; ^{234}U , is an intermediate daughter of ^{238}U . The decay of ^{238}U to ^{207}Pb involves 18 intermediate nuclides, while the decay of ^{235}U to ^{207}Pb involves 14 intermediate nuclides. U decay-series nuclides that are currently utilized for dating and their respective half-lives are shown in Figure U1.

Principle of radiometric dating

For a simple decay scheme, such as ^{87}Rb decaying to ^{87}Sr , where the radioactive isotope decays to a stable isotope, the amount of daughter isotopes, D , that is present after a time, t , has elapsed is related to the amount of parent isotope, P , at present as follows:

$$D = D_0 + P(e^{\lambda t} - 1) \quad (1)$$

where D is the total number of atoms of the daughter isotope at present, D_0 is the number of daughter isotopes present at

the beginning (since t time has passed, for example the age of a rock if one is dating a rock), P is the number of atoms of the parent isotope at present, λ is the decay constant and t is the age. As stated previously, the decay constant for a given radioactive isotope is constant and is related to the half-life (the amount of time required for a given number of atoms of a given radioactive isotope to be reduced by half due to decay) according to:

$$t_{1/2} = \frac{\ln 2}{\lambda} = \frac{0.693}{\lambda} \quad (2)$$

where $t_{1/2}$ is the half-life and λ is the decay constant for a particular radioactive isotope.

The range of events that are datable using a given parent-daughter isotope system depends on the half-life of the parent isotope. Typically, we cannot date events that are older than about seven half-lives of a given system. Conversely, to date young events we need to utilize isotope pairs with a short half-life parent. A number of the U-series nuclides have short half-lives that are useful to date recent events of human interest, such as past climate and environmental change and also, archeological and volcanic processes.

For radioactive isotopes that decay to another radioactive isotope, such as U-series nuclides, the number of an immediate daughter isotope that remains after time t is related to the number of atoms of the immediate parent:

$$D = \frac{\lambda_P}{\lambda_D - \lambda_P} P_0 (e^{-\lambda_P t} - e^{-\lambda_D t}) + D_0 e^{-\lambda_D t} \quad (3)$$

where D is the number of atoms of daughter isotope at present, D_0 is the number of atoms of the daughter isotope present initially, P_0 is the number of atoms of the parent isotope present initially and λ_P and λ_D are the decay constants of the parent isotope and the daughter isotope, respectively. The last term accounts for the decay of the daughter nuclide since time t . Expressions can be written describing the relationship between one nuclide and another nuclide at any stage in a given decay scheme.

After about seven half-lives of the shorter-lived nuclide of any two nuclides in a given series, the two nuclides reach

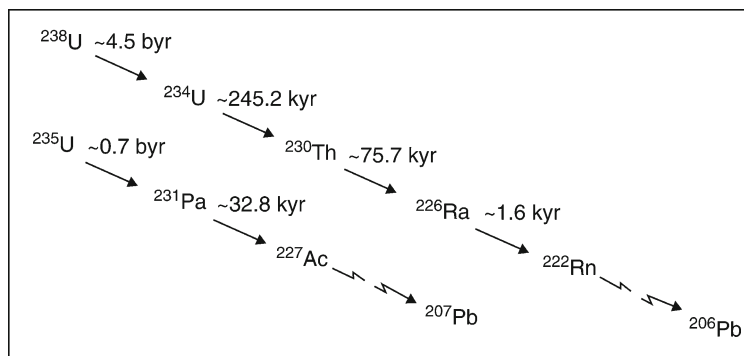


Figure U1 Schematic diagram of the U-series decay chain, showing some of the nuclides utilized in chronology and their approximate half lives. *byr*, Billions of years; *kyr*, thousands of years.

a state called “*secular equilibrium*.” When secular equilibrium is reached, the activity (the number of atoms of a nuclide multiplied by its decay constant) of both nuclides is equal, i.e.,

$$\frac{\lambda_1 N_1}{\lambda_2 N_2} = 1$$

In other words, their atomic ratio is constant from then on, equal to λ_1/λ_2 , and the age can no longer be determined.

Methods of U-series isotope analysis

The utility of U decay series isotopes for dating was recognized very early (Bateman, 1910) but the application was limited by technical difficulties related to separation chemistry and measurements of very small amounts of daughter nuclides. For example, in most rocks the abundance of ^{230}Th , the daughter of ^{238}U through ^{234}U (see Figure U1), is about one atom for every million atoms of uranium. Moreover, the ionization efficiency of Th in thermal ionization mass spectrometers (TIMS), the mass spectrometers used until recently for such measurements, is typically about 2×10^{-4} . In other words, about two ions (only ions are detected by TIMS) are produced for every 10,000 atoms loaded into the mass spectrometer.

The theoretical limit to precision of data (the counting statistics) is related to the number of ions detected as follows:

$$\text{Uncertainty } (1\sigma) = \frac{1}{\sqrt{N}}$$

where N is the number of atoms detected. Thus, the combined low abundance and low ion yield for many of the nuclides of interest made the application very difficult.

Early measurements, requiring large samples (thus low temporal resolution) were performed by alpha or gamma counting (e.g., Cherdynstev, 1956; Broecker, 1963; Ku, 1965). Advances in separation chemistry and mass spectrometry using TIMS (e.g., Chen et al., 1986; Edwards et al., 1987 for measurements of uranium and thorium isotopes, respectively; and Pickett et al., 1994 for measurement of protactinium by mass spectrometry) have made it possible to obtain high-precision U-series data for dating and isotope tracer application.

Application of U-series dating

A requirement for the application of U-series nuclides for tracer and dating purposes is that the process of interest has to fractionate one nuclide from another partially or completely.

The most widely used application of U-series dating has been for dating corals (Edwards et al., 1987) and speleothems (e.g., Polyak and Asmerom, 2001) for studying the timing of past climate change. These materials are ideal for dating because uranium under oxidizing conditions, which is the case in surface oceans and caves, is preferentially dissolved in water, while thorium is not soluble. Carbonate, calcite (CaCO_3) in speleothems and aragonite in corals (also CaCO_3 , but different crystal form), can contain up to 4 parts per million (ppm) U and negligible amounts of the daughter ^{230}Th nuclide, making them readily and precisely datable using the ^{238}U – ^{234}U – ^{230}Th series (Edwards et al., 1987). Assuming the sample did not contain ^{230}Th initially:

$$\left(\frac{^{230}\text{Th}}{^{238}\text{U}}\right) = (1 - e^{-\lambda_{230}t}) + \left(\frac{\lambda_{230}}{\lambda_{230} - \lambda_{234}}\right) \left(\frac{\delta^{234}\text{U}_m}{1,000}\right) (1 - e^{-(\lambda_{234} - \lambda_{230})t})$$

where

$$\left(\frac{^{230}\text{Th}}{^{238}\text{U}}\right)$$

is the activity ratio, t , is the age of the sample and $\delta^{234}\text{U}$ is equal to:

$$\left[\frac{^{234}\text{U}}{^{238}\text{U}} - 1\right] 1,000$$

$^{234}\text{U}/^{238}\text{U}$ is the atomic ratio. Uranium and thorium are chemically separated from carbonates and the ^{238}U , ^{234}U , and ^{230}Th are measured in a mass spectrometer. The age, t , is calculated iteratively. Any event or process that is associated with the formation of carbonate can be dated using this method.

Similar equations are written for dating volcanic rocks (Allègre, 1968), except that in the case of volcanic rocks, one cannot assume zero initial ^{230}Th . For volcanic rocks, the most versatile application of U-series nuclides has been in tracing sources of magma, constraining the time-scale of magma formation and evolution and providing relative timing of these events.

One of the novel applications for chronology using U-series nuclides has been combining ^{238}U – ^{234}U – ^{230}Th and ^{235}U – ^{231}Pa chronology on the same sample. If the ages are concordant (i.e., the two systems give the same age) it gives added validity

to the age (e.g., Edwards et al., 1997). In another approach, the presence of an excess or deficiency in daughter activity, i.e., daughter/parent ratio $\neq 1$, puts a maximum limit on the age of the material. For example, the presence of excess ^{210}Pb , which has a half-life of 22.3 years, indicates that an object is no older than around 150 years. ^{210}Pb is widely used for dating recent sediments in environmental research.

The utility of U-series isotopes for chronology and tracer work has been recognized for a long time, beginning after the discovery of radioactivity. However, implementation of the system was hindered by technical difficulties. Recent advances in mass spectrometry enable realization of the full potential of the system. One of the most exciting areas of application of this method that benefits from these technical gains is the study of past climate change, in particular dating annually banded speleothems (Asmerom and Polyak, 2004). These specimens often contain a variety of proxies of past climate change, including isotopic, chemical and physical proxies.

Recent advances in mass spectrometry, whereby a plasma source is combined with a magnetic analyzer and multiple detectors that consist of either a combination of Faraday cups and multiple electron multipliers, or Faraday cups and multiple channeltrons, stand to revolutionize the field. These high-resolution multi-collector inductively-coupled plasma mass spectrometers (MC-ICPMS) are capable of greater ion yields, up to an order of magnitude and greater, as compared with TIMS (Robinson et al., 2002), allowing for high spatial and temporal resolution.

Yemane Asmerom

Bibliography

Allègre, C.J., 1968. ^{230}Th dating of volcanic rocks: a comment: *Earth Planet. Sci. Lett.*, **5**, 209–210.

- Asmerom, Y., and Polyak, J.V., 2004. Comment on Betancourt et al. (2002): A test of annual resolution in stalagmites using tree rings. *Quaternary Res.*, **61**, 119–121.
- Bateman, H., 1910. The solution of a system of differential equations occurring in the theory of radioactive transformations. *Proc. Camb. Philos. Soc.*, **15**, 423.
- Becquerel, H., 1896. Sur les radiations invisibles émises par phosphorescence. *Comptes Rendus*, **122**, 420.
- Broecker, W.S., 1963. A preliminary evaluation of the uranium series in equilibrium as a tool for absolute age determination on marine carbonates. *J. Geophys. Res.*, **68**, 2817–2834.
- Chen, J.H., Edwards, R.L., and Wasserburg, G.L., 1986. ^{238}U , ^{234}U , and ^{232}Th in seawater. *Earth Planet. Sci. Lett.*, **80**, 241–251.
- Cherdyntsev, V.V., 1956. Determination of the absolute age of the Paleolithic. *Sovietski Arkheologi*, **25**, 64–86.
- Edwards, R.L., Chen, J.H., and Wasserburg, G.L., 1987. ^{238}U - ^{234}U - ^{230}Th - ^{232}Th systematics and the precise measurement of time over the past 500,000 y. *Earth Planet. Sci. Lett.*, **81**, 175–192.
- Edwards, R.L., Cheng, H., Murrell, M.T., and Goldstein, S.J., 1997. Protactinium-231 dating of carbonates by thermal ionization mass spectrometry: Implications for Quaternary climate change. *Science*, **276**, 782–786.
- Ku, T.-L., 1965. An evaluation of the $^{234}\text{U}/^{238}\text{U}$ method as a tool for dating pelagic sediments. *J. Geophys. Res.*, **70**, 3457–3474.
- Pickett, D.A., Murrell, M.T., and Williams, R.W., 1994. Determination of femtogram quantities of protactinium in geologic samples by thermal ionization mass spectrometry. *Anal. Chem.*, **66**, 1044–1049.
- Polyak, V.J., and Asmerom, Y., 2001. Late Holocene climate and cultural changes in the southwestern United States. *Science*, **294**, 148–151.
- Robinson, L.F., Henderson, G.M., and Slowey, N.C., 2002. U-Th dating of marine isotope stage 7 in Bahamas slope sediments. *Earth Planet. Sci. Lett.*, **196**, 175–187.

Cross-references

Coral and Coral Reefs
 Dating, Radiometric Methods
 Isotope Fractionation
 Speleothems

V

VARVED SEDIMENTS

Introduction

Varved sediments are sequences of sedimentary laminations deposited within a single year. A varve (Swedish: varv, layer) is a pair or set of laminae formed during different seasons within a year (varves – seasonal rhythmites – annually laminated sediments). Varves have been described in glacial, lacustrine and marine environments. Clastic varves in glacial lacustrine environments, i.e., glacial varves, are classic examples of varved sediments, but seasonal, rhythmic changes in biogenic production (e.g., diatoms) or water chemistry (e.g., carbonate content) also give rise to varve formation. In addition, annual layers in ice cores are varves, and chemical varves may be formed in precipitates and evaporates, such as stalagmites and gypsum beds.

Glacial varves

Varved clays are commonly found in Quaternary deposits in glaciated areas, but they have also been identified in deposits of older glaciations, such as the Carboniferous, Ordovician, and the late and early Proterozoic.

Glacial varves reflect the seasonal fluctuation of glacial meltwater flow from continental ice sheets or smaller glaciers (Figure V1). During the intensive melting period in spring and summer, coarse grained silt and sand is transported and deposited at the bottom of a water body, whereas finer particles settle out slowly, the finest clay particles only doing so during the next winter when the water bodies are frozen. The bedding in the coarse summer part of a varve is graded and the boundary between the fine winter layer and the next summer layer is sharp. Varves of this type are diatactic. They are formed in fresh water, whereas symmictic glacial varves that are formed in salt or brackish water are more complicated to identify because fine suspended particles group together into larger grains and settle rapidly with coarser grains. The varves that are formed close to a melting glacier may be up to several

tens of centimeters thick, whereas varves deposited distally may be less than a millimeter thick. Varve thickness also varies from year to year due to variations in climatic and local factors, e.g., the intensity of melting, the material supply and the velocity of meltwater flow. Variations in the thickness of varves within a sequence form a basis for correlating sequences, in addition to their color, grain size and chemical composition.

Nonglacial varves

A single annual unit – a varve – is composed of two or more layers (laminae) that can be distinguished on the basis of their thickness, composition and texture. In most cases, these individual layers are identified as representing certain seasons or even short-term events within seasons, e.g., spring flood allochthonous discharge or vernal precipitation of calcite crystals (Figure V2). The annual structure of the sediment is only preserved if there are no post-depositional disturbances of the sediment surface, such as bioturbation or water turbulence in the sediment-water interface.

In different lake environments worldwide, various characteristic limnological and hydrological processes govern the composition and structure of varves and the laminae they contain. They usually appear as calcareous (Brunskill, 1969), ferrogenic (Anthony, 1977; Renberg, 1981), biogenic (Saarnisto et al., 1977), clastic (Sturm, 1979) or clastic-organic (Renberg and Segerström, 1981; Ojala et al., 2000) (Figure V3) laminae couplets. The majority of identified varved lake records are located either in North America (Anderson et al., 1985; Lamoureux et al., 2001) or in Europe, particularly in the Alpine areas, in Fennoscandia, and in number of maar lakes (Pettersson, 1996; Zolitschka, 1998; Brauer et al., 2000; Ojala et al., 2000). However, they are also found in many other localities, such as Japan (Fukusawa, 1999) and Africa (Johnson et al., 2001).

Varved-clay chronology

Varved-clay chronology is based upon correlations between short varve series (50–200 years, but rarely as much as 1,000 years) from site to site in the general direction of ice-margin



Figure V1 Varved glacial clays in Tampere, southern Finland, which were deposited in the early Holocene Baltic basin. (Photo by J. J. Sederholm, 1907.)

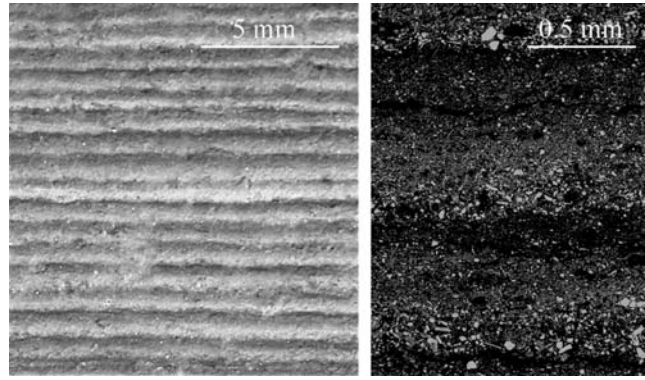


Figure V3 Images of Lake Nautajärvi (central Finland) clastic-organic nonglacial varves at ca. AD 200 taken from the fresh sediment surface (left) and thin-section using a back scattered mode of surface scanning electron microscope (right).

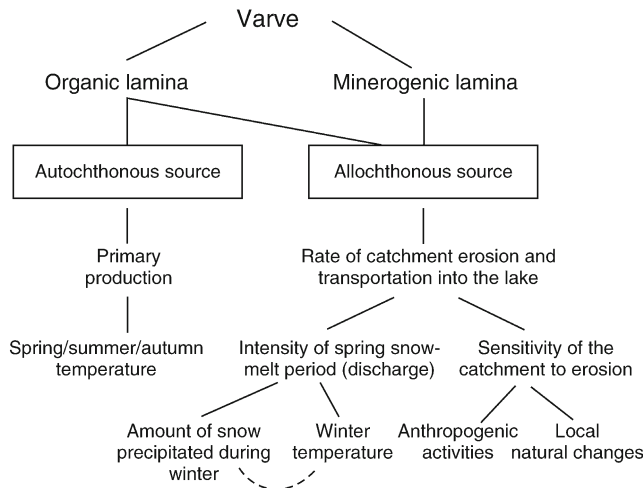


Figure V2 A simplified sketch of the formation of clastic-organic varves in temperate areas.

retreat. The original principle of De Geer (1884, 1940) was adopted in Finland by Sauramo (1918). The Swedish glacial varve chronology has been connected to the present-day through studies on postglacial and recent, varved deltaic sediments in

the Ångermanälven river in northern Sweden (Cato, 1998). The Swedish chronology covers 13,300 years, including the deglaciation from Scania to the Ångermanälven river area. The Swedish varve chronology has been constantly revised since De Geer's original work, and its correlation with the Greenland ice core records suggests that nearly 900 (875) varves have not been recognized in the Holocene part of the Swedish varve chronology (Andrén et al., 1999). The Finnish varve chronology covers nearly 2,800 years (Sauramo, 1929), 13,000–10,200 year, when the ice margin retreated from the Gulf of Finland to the Gulf of Bothnia. It is a floating chronology that has been connected to the calendar year time scale by reference to characteristic varves formed in connection with the drainage of the Baltic Ice Lake and the dating of this event (e.g., Strömberg, 1990).

Attempts to construct a regional deglaciation chronology using varved sediments outside Sweden and Finland have been rare. In North America, Antevs (1928) worked out a varve chronology based on 4,000 varves in Connecticut Valley, which was later extended by ca. 1,000 glacial varves by Ridge and Toll (1999). Glacial varves have also been investigated in a number of localities in Patagonia and other parts of northern Europe (Estonia, NW Russia).

Varved sediment sequences have been widely applied to reconstruct a continuous timescale of the sediment (varve chronology) and to determine the rates of annual accumulation of sediments and of any particular substance or organism in the sedimentary basin, as expressed in spatial and temporal units (influx). The longest known varved lake sediment sequence, Lago Grande di Monticchio (southern Italy) (Brauer et al., 2000), extends back to more than 100 ka interrupted by several tephra layers, but continuous records typically cover ca. 10,000 years or less. Among the most studied records in Europe are those from Lake Holzmaar (western Germany) covering 14,000 years (Zolitschka, 1998), Lake Gościąg (central Poland) covering 13,000 years (Goslar, 1998) and Lake Kassjön (northern Sweden) covering 6,500 years (Renberg and Segerström, 1981). However, some of these chronological sequences are floating in time (i.e., not fixed to the present day deposits). Moreover, even the best quality varves cannot provide a completely accurate chronology as they have been accumulated in a naturally variable environment. In most cases, and in the long-term, an acceptable margin

of varve counting error can be expected to be around $\pm 2\%$, and at best it yields an accuracy of $\pm 1\%$, as in Lakes Kassjön and Nautajärvi (central Finland) (Ojala and Saarinen, 2002). Corresponding chronological accuracy has been postulated for the Holocene part of Greenland ice core records (Alley, 2000).

Nonglacial Holocene varves have also been applied in assigning ages in relative sediment dating methods, such as paleomagnetic reference curves and widely distributed tephra layers. In Fennoscandia, Ojala and Saarinen (2002) and Snowball and Sandgren (2002) dated the features of paleomagnetic secular variation curves using the varve chronology of nearly 10,000-year-long sections of clastic-organic varves, whereas Zillén et al. (2002) assigned varve ages to several tephra layers deposited in southern Sweden in the Mid-Holocene.

Recently, the application of varve records has transformed from providing stratigraphical and chronological tools to being high-resolution indicators of the paleoenvironment, and in particular, they are being used as a tool to study the effects of climate forcing during the Holocene. Advancements in sediment sampling (e.g., epoxy-embedding, thin sectioning) combined with digital image analysis have provided an effective means to record and study the physical properties of varves with a high temporal resolution. Proglacial lakes in the Canadian Arctic are perhaps the most carefully studied environments (Hardy et al., 1996; Hughen et al., 2000; Lamoureux et al., 2001). Physical varve data (varve thickness, laminae thickness) have been shown to be strongly correlated with summer temperatures through their effects on the intensity of snowmelt runoff and the discharge of suspended sediment. In Fennoscandia, fluctuations of clastic-organic varves have been correlated with winter climate components, namely temperature and the amount of precipitated snow in the catchment. Based on such connections, it is possible to reconstruct past climatic conditions, thereby providing important knowledge about the global climate system in order to better predict the future.

Matti Saarnisto and Antti E. K. Ojala

Bibliography

- Alley, R.B., 2000. The Younger Dryas cold interval as viewed from central Greenland. *Quaternary Sci. Rev.*, **19**, 213–226.
- Anderson, R.Y., Dean, W.E., Bradbury, J.P., and Love, D., 1985. *Meromictic Lakes and Varved Lake Sediments in North America*. U.S. Geological Survey Bulletin 1607, 19pp.
- Andrén, T., Björck, J., and Johnsen, S., 1999. Correlation of the Swedish glacial varves with the Greenland (GRIP) oxygen isotope stratigraphy. *J. Quaternary Sci.*, **14**, 361–371.
- Antevs, E., 1928. *The Last Glaciation*. American Geographical Society Research Series 17. New York: American Geographical Society. pp. 1–292.
- Anthony, R.S., 1977. Iron-rich rhythmically laminated sediments in Lake of the Clouds, northeastern Minnesota. *Limnol. Oceanogr.*, **22**, 45–54.
- Brauer, A., Mingram, J., Frank, U., Günter, C., Schettler, G., Wulf, S., Zolitschka, B., and Negendank, J.F.W., 2000. Abrupt environmental oscillations during the Early Weichselian recorded at Lago Grande di Monticchio, southern Italy. *Quaternary Int.*, **73/74**, 79–90.
- Brunskill, G.J., 1969. Fayetteville Green Lake, New York. II. Precipitation and sedimentation of calcite in a meromictic lake with laminated sediments. *Limnol. Oceanogr.*, **14**, 830–847.
- Cato, I., 1998. Ragnar Lidéns post-glacial varve chronology from the Ångermanälven valley, northern Sweden. *Sveriges Geologisk Undersökning Ca*, **88**, 1–82.
- De Geer, G., 1884. Om möjligheten af att införa en kronologi för istiden. *Geol. För. i Stockholm Förhandl.*, **7**, 3.

- De Geer, G., 1940. *Geochronologia Suecica Principes*. *Kungliga Svenska Vetenskapsakademiens Handlingar, Tredje Serien, Bd*, **18**, 1–367.
- Fukusawa, H., 1999. Varved lacustrine sediments in Japan: Recent progress. *Quaternary Res.*, **38**, 237–243.
- Goslar, T., 1998. Floating varve chronology of Lake Gościąg. In Ralska-Jasiewiczowa, M., Goslar, T., Madeyska, T., and Starkel, L. (eds.), *Lake Gościąg, Central Poland, a Monographic Study*. Krakow: W. Szafer Institute of Botany, Polish Academy of Sciences., pp. 97–99.
- Hardy, D.R., Bradley, R.S., and Zolitschka, B., 1996. The climatic signal in varved sediments from Lake C2, northern Ellesmere Island, Canada. *J. Paleolimnol.*, **16**, 227–238.
- Hughen, K.A., Overpeck, J.T., Overpeck, J.T., and Anderson, R.F., 2000. Recent warming in a 500-year palaeotemperature record from varved sediments, Upper Soper Lake, Baffin Island, Canada. *The Holocene*, **10**, 9–19.
- Johnson, T.C., Barry, S.L., Chan, Y., Wilkinson, P., 2001. Decadal record of climate variability spanning the past 700 year in the southern tropics of East Africa. *Geology*, **29**, 83–86.
- Lamoureux, S.F., England, J.H., Sharp, M.J., Bush, A.B.G., 2001. A varve record of increased 'Little Ice Age' rainfall associated with volcanic activity, Arctic Archipelago, Canada. *The Holocene*, **11**, 243–249.
- Ojala, A.E.K., and Saarinen, T., 2002. Palaeosecular variation of Earth's magnetic field during the last 10,000 years based on the annually laminated sediment of Lake Nautajärvi, central Finland. *The Holocene*, **12**, 391–400.
- Ojala, A.E.K., Saarinen, T., and Salonen, V.-P., 2000. Preconditions for the formation of annually laminated lake sediments in southern and central Finland. *Boreal Env. Res.*, **5**, 243–255.
- Pettersson, G., 1996. Varved sediments in Sweden: A brief review. In Kemp, A.E.S. (ed.), *Palaeoclimatology and Palaeoceanography from Laminated Sediments*. Piccadilly, UK: Geological Society of London. pp. 73–77.
- Renberg, I., 1981. Formation, structure and visual appearance of iron-rich, varved lake sediments. *Verhandl. Internat. Verein. für Limnologie*, **21**, 94–101.
- Renberg, I., and Segerström, U., 1981. The initial points on a shoreline displacement curve for southern Västerbotten, dated by varve-counts of lake sediments. *Striae*, **14**, 174–176.
- Ridge, J., and Toll, N., 1999. Are late-glacial climate oscillations recorded in varves of the upper Connecticut Valley, northeastern United States? *GFF*, **121**, 187–193.
- Saarnisto, M., Huttunen, P., and Tolonen, K., 1977. Annual lamination of sediments in Lake Lovojärvi, southern Finland, during the past 600 years. *Ann. Bot. Fenn.*, **14**, 35–45.
- Sauramo, M., 1918. Geochronologische Studien über die spätglaziale Zeit in Südfinnland. *Bull. Comm. Géol. Finlande*, **50**, 1–44.
- Sauramo, M., 1929. The Quaternary Geology of Finland. *Bull. Comm. Géol. Finlande*, **86**, 1–110.
- Snowball, I.F., and Sandgren, P., 2002. Geomagnetic field variations in northern Sweden during the Holocene quantified from varved lake sediments and their implications for cosmogenic nuclide production rates. *The Holocene*, **12**, 517–530.
- Strömberg, B., 1990. A connection between the clay varve chronologies in Sweden and Finland. *Ann. Acad. Sci. Fennicae*, **154**, 1–32.
- Sturm, M., 1979. Origin and composition of clastic varves. In Schlüchter, C. (ed.), *Moraines and Varves*. Rotterdam: A. A. Balkema, pp. 281–285.
- Zillén, L.M., Wastegård, S., and Snowball, I.F., 2002. Calendar year ages of three mid-Holocene tephra layers identified in varved lake sediments in west central Sweden. *Quaternary Sci. Rev.*, **21**, 1583–1591.
- Zolitschka, B., 1998. A 14,000 year sediment yield record from western Germany based on annually laminated lake sediments. *Geomorphology*, **22**, 1–17.

Cross-references

- Continental Sediments
- Dating, Magnetostratigraphy
- Glacial Sediments
- Ice Cores, Antarctica and Greenland
- Lacustrine Sediments
- Tephrochronology

VOLCANIC ERUPTIONS AND CLIMATE CHANGE

Introduction

Volcanoes erupt fragmented mantle material into the upper atmosphere. Only the lightest particles remain suspended, however. These tiny supplements to the ordinary air, water vapor, and dust can strongly affect the chemical, radiative, and dynamical properties of the atmosphere. Critical to assessing the magnitude of these effects is knowledge of the sizes and chemical compositions of the volcanic particles, the total mass of particles injected, the vertical distribution of the injected particles, the geographical location of the volcano, and the prior state of the atmosphere. Detailed chronologies of modern volcanic eruptions and of their spreading particulate clouds (called “dust veils” or “dry fogs”) have been constructed in order to associate known volcanic eruptions with changes of long-term weather (“climate”). The volcano-climate connection can be studied either empirically, by using actual climate observations, or theoretically, by computing a general circulation model (GCM) of the atmosphere. Interest focuses on how global and regional climates respond to volcanic forcing on various timescales. Such an understanding of the consequences of historical eruptions can help to illuminate both the past and the future of the atmosphere of our planet, especially under different assumptions made about the frequency of large volcanic eruptions, the amount of solar variability, and the inputs of other natural and anthropogenic sources of atmospheric pollution.

History

On the day after the great eruption of Mount Vesuvius in the year 79, Pliny the Younger noted that the Sun appeared “lurid as if in eclipse,” but this atmospheric effect was probably only local. More widespread hazes after other eruptions during antiquity (e.g., Etna in 44 BC), although noted, were never associated with volcanoes by anybody at the time. Benjamin Franklin is the first person known to have inferred a relationship between the regional state of the atmosphere (North Atlantic dry haze in 1783 and a cold winter in 1784) and a large volcanic eruption (Laki, Iceland, 1783). Chemists at the time identified the dry tropospheric haze as being primarily what we would today call sulfuric acid (H_2SO_4). The ancient manifestations of it could now also be provisionally interpreted. However, it was the eruption of the Indonesian volcano Krakatau 100 years later that brought a volcano’s worldwide atmospheric effects to public attention: a fading and unusual coloration of the Sun, Moon, and stars, and an enhancement of the red twilight sky glow. A peculiar reddish ring seen around the Sun was named after its discoverer, Sereno Bishop, and the darkness of a total eclipse of the Moon in this period was traced to volcanic particles in the Earth’s upper atmosphere by Camille Flammarion. The particles were thought to be silicic ash and possibly sulfurous gases. The zonal circulation of the upper atmosphere (named the “stratosphere” by Teisserenc de Bort in 1900) was mapped by visually following the westward drift of the volcanic cloud. Only in hindsight were the unusual optical aftereffects of the even greater eruption of Tambora, Indonesia, in 1815 now associated with that event.

After a series of three large Caribbean eruptions in 1902 and Alaska’s Katmai (Novarupta) eruption in 1912, C. G. Abbot and W. J. Humphreys independently concluded that volcanic

eruptions produce temporary climate cooling, at least hemispherically. Many studies since 1913, with much impetus coming from Harry Wexler and H. H. Lamb, have confirmed this fundamental result. In 1961, C. E. Junge and his coworkers discovered an apparently permanent layer of sulfate particles in the lower stratosphere, which, in 1973, A. W. Castleman, Jr., and his coworkers conclusively demonstrated were volcanic in origin. Fresh stratospheric particles collected in situ by S. C. Mossop after the Agung, Indonesia eruption of 1963 had already shown most to be sulfuric acid aerosols. Numerous studies from the ground, air, and space were pursued after the eruptions of Mt. St. Helens, United States (1980); El Chichón, Mexico (1982); and Pinatubo, Philippines (1991). These results have enormously increased our detailed knowledge of volcanic aerosol clouds and their effects on climate.

Aerosol chemistry and physics

Although some small silicic ash particles remain suspended in the stratosphere for several weeks after a powerful volcanic eruption, the major constituents injected are gaseous: primarily CO_2 , H_2O , N_2 , SO_2 , and H_2S , and some HCl and HF. With both pre-existing and volcanically injected H_2O , the sulfur gases undergo a complicated series of heterogeneous chemical reactions in the presence of sunlight to form sulfuric acid aerosols (75% H_2SO_4 and 25% H_2O). These tiny droplets then grow by coagulation and mutual collisions over a period of weeks. Typically, their final mass density is 1.65 g cm^{-3} and their complex index of refraction in the visible is $m = 1.43 - 0i$, indicative of negligible light absorption at short wavelengths. Their shape appears roughly spherical and their size distribution can be described as approximately lognormal with an effective (area-weighted) radius of $r_{\text{eff}} = 0.3 \text{ }\mu\text{m}$, increasing with time to $0.5 \text{ }\mu\text{m}$, but this description is very crude and may be inaccurate for some eruptions and for some layers of the stratosphere. After the initial formation period, the size distribution continues to evolve owing to horizontal dispersion of the particles and to gravitational and convective sedimentation of the larger particles. The role of sulfate aerosols in destroying ozone (O_3) involves heterogeneous chemical reactions with primarily anthropogenic chlorine, and so would have been unimportant before the late twentieth century. Volcanic halogens are mostly scrubbed out of the eruption column before reaching the stratosphere.

Scattering of radiation by the aerosols leads to an attenuation of the incoming solar beam, whose incident intensity is I_0 . The optical depth of the light-scattering medium, defined as $\tau = -\ln(I/I_0)$, can be calculated by multiplying the cross-sectional scattering coefficient by the particle number density and integrating the product over the path length of the direct solar beam. Since τ is wavelength-dependent, a standard reference wavelength is taken to be $\lambda = 0.55 \text{ }\mu\text{m}$, which lies in the visible. Essentially, only the two quantities r_{eff} and τ_{vis} are needed, in practice, to compute the amount of radiative forcing by an aerosol cloud. Reflection of some incoming solar radiation back into space by the stratospheric aerosols reduces the total insolation in the troposphere, which in turn lowers the global-average surface air temperature. Absorption of long-wave radiation from the ground, troposphere, and Sun by the aerosols partially counters this effect, and manages to warm the stratosphere. However, the net result of the competition between the aerosols’ albedo and the greenhouse effect for the troposphere is always a cooling.

The total mass of the stratospheric aerosol veil, M_D , can be computed from the global-average stratospheric optical depth τ_D . It is given by $M_D = 150\tau_D$ megatons (Tg).

Records of volcanic eruptions

Catalogs of known volcanic eruptions during the Holocene epoch (the past 10,000 years) have been published by the Smithsonian Institution, making use of either eyewitness reports or geological studies of pyroclastic deposits around the volcano. Even earlier eruptions are known in a few cases from conspicuous eruptive deposits. These can be dated radiometrically or stratigraphically. They include the huge continental and oceanic flood basalt eruptions of the past 300 Myr, of which about a dozen have been recognized. The flood basalts were primarily effusive in style and sulfur-rich (like Hawaii's Kilauea), whereas most known volcanic eruptions have been of explosive type and silica-rich (like Indonesia's Krakatau).

All other methods of detecting volcanic eruptions are indirect. One method uses sulfate acidity and tephra fragments deposited from the stratosphere onto polar ice fields and incorporated in the annual layers of polar ice. Tephra found in sea, lake, and bog sediment cores (usually sited not far from the erupting volcano) can also be used. Documentary records of unusual atmospheric optical effects and even of abnormal regional cooling have proven especially valuable, because historically derived dates going back to 300 BC are typically accurate as to year and month. Ice-core dates are available for eruptions as far back as 100,000 years ago, but they begin to degrade in accuracy before AD 1000.

Quasi-periodicities in global volcanism occur on various timescales. A weak annual cycle exists, perhaps coupled to the hydrological cycle. Two other periods, 11 year and 80 year, are probably solar in origin, through the influence of solar variability on the atmosphere. Slower cycles of 10^4 – 10^5 year may be due to the influence of climate change on volcanism, arising from Milankovitch periodicities in the Earth's orbit that affect the amount of insolation and hence glaciation and sea level. Tectonic plate movements may also produce spurts of volcanism, at intervals of a few Myr. Flood basalt eruptions apparently follow a roughly 30-Myr cycle of uncertain origin. Even slower cycles may exist, e.g., a 300-Myr cycle of tectonism and associated volcanism.

Explosive strengths of volcanic eruptions have been estimated from such observable quantities as volume of pyroclastic ejecta and height of the eruption column. An example is the Volcanic Explosivity Index (*VEI*) of Newhall and Self (1982). The older Dust Veil Index (*DVI*) of Lamb (1970) includes solar-beam transmission data and surface air temperature decreases in addition to the near-source tephra volume. Robock and Free's (1995) newer Ice-core Volcanic Index (*IVI*) utilizes solely sulfate acidity in polar ice cores. The *VEI* of course does not take into account the variable sulfur content of volcanic tephra, while the *DVI* is an uneven and mixed indicator, and the *IVI* suffers from the special restrictions of the ice-core method, including the highly uncertain rates of aerosol deposition and the necessary corrections for non-stratospheric transport of aerosols and for the volcano's latitude (often unknown). Statistically, however, all indices are found to be correlated with τ_D whenever τ_D is available, and therefore they can be used to estimate τ_D when this is otherwise unknown.

Table V1 contains the stratospheric aerosol masses estimated for Pinatubo-class and larger volcanic eruptions of the past 75,000 years. The peak visual optical depth over Europe is also listed. The table is incomplete before 1883 and becomes more so the farther back in time one goes, especially for the Southern Hemisphere. Flood basalt eruptions, which are not listed, probably produced 10^4 Tg of aerosols; typical examples are the Columbia River Basalts (16 Myr ago) and the Deccan Traps (65 Myr ago). The cumulative effect of smaller, but more frequent, eruptions could have perturbed the Earth's radiative balance during some periods.

Movements of volcanic aerosol veils

Volcanoes are not distributed uniformly, or even randomly, over the globe. They are found in regions of exceptional geologic activity, e.g., along the "ring of fire" around the Pacific Ocean and along the Atlantic Mid-Ocean Ridge. Flood basalt eruptions occur over mantle plumes and hotspots. For purposes of climate studies, however, all volcanoes can be divided simply into extratropical (latitudes above 30°) volcanoes and tropical (or equatorial) volcanoes.

Stratospheric aerosol veils from tropical volcanoes are distributed by zonal winds very quickly so that they cover all longitudes in only 2–3 weeks. Their meridional dispersion is

Table V1 Major aerosol-producing volcanic eruptions of the past 75,000 years

Volcano	Latitude	Year	<i>DVI</i> / E_{\max}	<i>VEI</i>	<i>IVI</i>	European τ_{vis}	Aerosol M_D (Tg)
Pinatubo, Philippines	15° N	1991	1,000	6		0.2	30
Agung, Indonesia	8° S	1963	800	4	0.06	0.03	20
Santa Maria, Guatemala	15° N	1902	600	6	0.05	0.2	30
Krakatau, Indonesia	6° S	1883	1,000	6	0.12	0.2	44
Tambora, Indonesia	8° S	1815	3,000	7	0.50	1.3	200
Laki, Iceland	64° N	1783	2,300	4	0.19	~2	200
Huaynaputina, Peru	17° S	1600	>1,000	5			100
Unknown	Tropical	1258					400
Eldgjá, Iceland	64° N	934		4			130
Unknown	Northern?	797				~1	40?
Unknown		626					100?
Unknown		536				~2.5	300?
Etna, Italy	38° N	44 BC		3+			200
Unknown		145 BC					80?
Thera, Greece	36° N	1640? BC		6			200
Toba, Indonesia	3° N	74000? BC					3,000?

much slower (usually taking a few months), depending on the season of the year, the phase of the quasi-biennial oscillation (QBO) of the tropical stratospheric winds, and probably other factors. For unknown reasons, cross-equatorial spreading is occasionally inhibited, sometimes remarkably so (e.g., after El Chichón and especially after Agung). Almost complete halts of the poleward flow regularly occur at the Hadley cell circulation barrier (near 30°) in the summer and at the polar vortex edge (near 70°) in the winter. In this cyclical, seasonally dependent way, the equatorial reservoir of aerosols (discovered after the Agung eruption) replenishes the higher latitudes during the course of the year. Simultaneously, aerosols are constantly falling out of the stratosphere, the average time for depletion of the dust veil by a factor of e being 1 year. Once through the tropopause, aerosols are swept to the ground in a few days by either wet or dry deposition. In the wintertime polar vortex, too, they descend quickly in spite of a lower tropopause near the poles.

High-latitude volcanoes generate stratospheric aerosol veils that spread equatorward only as far as about 30°. Thus, they do not produce full hemispheric coverage (this was first realized after Laki and confirmed after Katmai). Using both Arctic and Antarctic ice cores, an unidentified volcano that erupted somewhere on the globe can usually be characterized at least as being tropical or extratropical, with always the possibility of error in an Agung-type situation.

Climatic effects (general)

Underneath the ash cloud in the volcano's vicinity, the surface air temperature initially rises but then falls precipitously as sunlight is blocked off. Such an extreme cooling happened noticeably after Laki, Tambora, and Krakatau. If the ash cloud either is very thin or resides at a high altitude, as was the case after Mt. St. Helens in 1980, the initial warming caused by the blanketing effect does not occur.

Feedback from the stratospheric aerosol veil on the global atmosphere is fairly complex. The simplest element in the feedback is a global-average cooling – as theoretically expected and observationally confirmed. Finer observational analysis, based mostly on compositing the effects of several modern eruptions, reveals more structural detail, both temporal and spatial. A prompt cooling (at least in the hemisphere of origin) lags the eruption by about 1 month and lasts 3–6 months. A rapid recovery is then followed by a prolonged cooling for 1–5 years, beginning with a comparable temperature drop in the year of the first post-eruption winter (but sometimes later). This first winter can be very cold for extratropical eruptions, but for tropical ones there occurs a slight winter warming over Northern Hemisphere continents at middle and high latitudes. This is caused by a faster zonal advection of warm (and wet) marine air that is associated with a strengthening of the stratospheric meridional temperature gradient and stratospheric polar vortex. The more rapid response of the land than the sea to radiative forcing is another factor that can explain the smaller winter warming in the land-starved Southern Hemisphere.

If the surface air temperature is arbitrarily assumed to have some power-law dependence on the transmitted intensity of the solar beam, say $T \propto F$, then $\Delta T \propto \tau$ for $\tau \ll 1$. In practice, the drop in hemispheric-average temperature amounts very roughly to $\Delta T (^{\circ}\text{C}) = 1.5 \tau_{\text{D}}$ for eruptions up to Pinatubo-class. However, average temperature is given by $\Delta T \propto \tau_{\text{D}}^{1/2}$ for significantly larger eruptions. The cooling is usually accompanied by increased cloudiness and precipitation.

Complications confuse this tidy picture, especially for very small eruptions whose climatic effects are easily masked. The El Niño-Southern Oscillation (ENSO) phenomenon, a quasi-cyclical warming of equatorial Pacific waters every 3–7 years, induces teleconnection effects elsewhere, notably an atmospheric warming over North America. Although its cause is uncertain, it is very doubtful that a sudden volcanic cooling is able to trigger an El Niño warming event. Outbreaks of cold polar air into mid-latitudes, on the other hand, certainly follow an eruption. The Icelandic pressure low and the northern jet stream move southward, for example; thus, the North Atlantic Oscillation (NAO), which is part of the overall Arctic Oscillation (AO), shows a disturbance of its normal modal pattern. The patterns of the NAO and SO consist of a cyclical shift in relative sea-level pressure (and other meteorological variables) between Iceland and the Azores (NAO) and between the Indian Ocean and the South Pacific Ocean (SO). Other climate forcing factors, however, can disturb these patterns. Natural variability of the climate system, characterized by chaotic, unpredictable behavior, also plays a role.

Climatic effects (specific eruptions)

Depending on the most characteristic method of dating or measuring the aerosol veil, six different periods in Earth history can be identified: geochemical, before 50,000 BC; ice-core, 50,000–300 BC; historical, 300 BC–AD 1880; pyrheliometric, 1881–1960; stellar-extinction, 1961–1978; and satellite, 1979–present. The pre-instrumental years (before 1881) have been divided into a prehistoric part (before 300 BC), for which indirect geological approaches are used, and a historical part, employing visual observations that can be calibrated by using modern techniques. If the total mass of sulfuric acid aerosols has been estimated by using either polar ice-core sulfate acidities or geochemical analyses of the sulfur content of local volcanic deposits, then the stratospheric turbidity can be computed from $\tau_{\text{D}} = M_{\text{D}}/150$. During the historical period, visual observations of solar dimming, of red twilight glows (dust-veil reflections), of Bishop's ring (aerosol diffraction pattern around the Sun), and of lunar-eclipse darkening (an inhibited refraction of sunlight into the shadow cone) can be used to obtain τ_{D} directly. The optical methods and the ice-core method in the historical period are about equally sensitive; the threshold aerosol mass for detecting a tropical eruption is a Pinatubo-class cloud of 30 Tg.

The largest known aerosol veils during the historical period occurred in 44 BC and AD 536, 626, 934, 1258, 1783, and 1815 (see Table VI), although the nature of the 536 veil is still controversial. Eruptions producing these veils are known to have been of explosive type in two cases (Etna and Tambora), and probably also in the 1258 case, but of effusive type in at least two other cases (Eldgjá and Laki). The crude climatic data available for these seven eruptions strongly indicate that their meteorological consequences followed the patterns for modern eruptions. However, these older eruptions were large enough to have had more severe impacts, including greater cold and raininess, extensive crop damage, famine, and serious disease outbreaks, as documented in written sources from the Mediterranean and Middle East. For still larger eruptions, the stratospheric residence time of climatically significant aerosols may be prolonged to 6 years or more. If so, tropospheric cooling could be augmented by positive feedbacks such as a larger planetary albedo arising from increased cloud, snow, and ice cover. It is not known, however, whether such large eruptions,

or even a long series of smaller eruptions, could cause an abrupt climate change that lasts for decades or longer, although this is thought to be theoretically possible in a metastable state of the climate system. Possibly, the long cold period known as the Little Ice Age (AD 1400–1900) was volcanically forced, at least in part, although a protracted solar minimum at this time is a more likely cause.

Less is known about prehistoric eruptions. The protohistorical eruption of Thera (Santorini), Greece, in the seventeenth (possibly sixteenth) century BC may have been of Tambora class. Toba, Indonesia, erupted about 74,000 years ago in a far greater paroxysm – a supereruption that exacerbated an existing climatic downturn and probably caused extensive loss of life, perhaps related to the human evolutionary “bottleneck” around this time. Pleistocene glacial fluctuations have also been attributed to volcanism.

At the top of the ladder are the flood basalt eruptions. These outflows must have led to massive pollution of air, land, and water, as well as to local darkness in the atmosphere for months at a time, regional wildfires, and global cooling for many years. Laki might represent a recent small-scale analogy. Flood basalt eruptions appear to have coincided with mass biotic extinctions, especially marine mass extinctions. Their release of heat-trapping CO₂ would have been sufficient to counteract, in part, the cooling brought on by the efficiently back-scattering sulfate aerosols. Very early in Earth’s history, and during periods of rapid ocean-floor subduction and accretion, when volcanism was more active, outgassing of CO₂ may even have been the predominant factor. Probably, outgassing supplied the atmosphere and oceans with their main constituents after the end of the massive early bombardment of Earth by comets and asteroids (3.9 Gyr ago).

Cultural impacts of the greatest volcanic eruptions should also be mentioned. Poetry has immortalized the atmospheric aftereffects of Thera, Etna, Laki, Tambora, and Krakatau in the Bible’s *Exodus*, Virgil’s *Georgics*, Cowper’s *Task*, Byron’s *Darkness*, and Tennyson’s *St. Telemachus*. A few memorable expressions have endured, such as “the year without a summer” in 1816. “Tambora skies” and “Krakatau sunsets” are possibly depicted in some paintings contemporary with those eruptions. However, the major cultural impacts were probably negative, reflecting the famines, epidemics, and social disorders that grew with the climate deterioration.

Richard B. Stothers

Bibliography

- Chester, D.K., 1988. Volcanoes and climate: Recent volcanological perspectives. *Prog. Phys. Geogr.*, **12**, 1–35.
- Clausen, H.B., Hammer, C.U., Hvidberg, C.S., Dahl-Jensen, D., Steffenson, J.P., Kipfstuhl, J., and Legrand, M., 1997. A comparison of the volcanic records over the past 4000 years from the Greenland Ice Core Project and Dye 3 Greenland ice cores. *J. Geophys. Res.*, **102**, 26707–26723.
- Crowley, T.J., 2000. Causes of climate change over the past 1000 years. *Science*, **289**, 270–277.
- D’Arrigo, R., Jacoby, G., Free, M., and Robock, A., 1999. Northern Hemisphere temperature variability for the past three centuries: Tree-ring and model estimates. *Clim. Change*, **42**, 663–675.
- D’Arrigo, R., Frank, D., Jacoby, G., and Pederson, N., 2001. Spatial response to major volcanic events in or about AD 536, 934 and 1258: Frost rings and other dendrochronological evidence from Mongolia and northern Siberia. *Clim. Change*, **49**, 239–246.
- Lacis, A.A., Hansen, J., and Sato, M., 1992. Climate forcing by stratospheric aerosols. *Geophys. Res. Lett.*, **19**, 1607–1610.
- Lamb, H.H., 1970. Volcanic dust in the atmosphere; with a chronology and assessment of its meteorological significance. *Philos. Trans. R. Soc. Lond. Ser. A*, **266**, 425–533.
- Newhall, C.G., and Self, S., 1982. The Volcanic Explosivity Index (VEI): An estimate of explosive magnitude for historical volcanism. *J. Geophys. Res.*, **87**, 1231–1238.
- Rampino, M.R., 2002. Supereruptions as a threat to civilizations on Earth-like planets. *Icarus*, **156**, 562–569.
- Rampino, M.R., Self, S., and Stothers, R.B., 1988. Volcanic winters. *Ann. Rev. Earth Planet. Sci.*, **16**, 73–99.
- Robock, A., 2000. Volcanic eruptions and climate. *Rev. Geophys.*, **38**, 191–219.
- Robock, A., and Free, M.P., 1995. Ice cores as an index of global volcanism from 1850 to the present. *J. Geophys. Res.*, **100**, 11549–11567.
- Stothers, R.B., 1999. Volcanic dry fogs, climate cooling, and plague pandemics in Europe and the Middle East. *Clim. Change*, **42**, 713–723.
- Stothers, R.B., 2002. Cloudy and clear stratospheres before AD 1000 inferred from written sources. *J. Geophys. Res.*, **107** (D23), Paper 4718.
- Zielinski, G.A., 2000. Use of paleo-records in determining variability within the volcanism-climate system. *Quaternary Sci. Rev.*, **19**, 417–438.

Cross-references

[Atmospheric Evolution, Earth](#)
[Bolide Impacts and Climate](#)
[Climate Change, Causes](#)
[Climate Forcing](#)
[Climate Variability and Change, Last 1,000 Years](#)
[Flood Basalts, Climatic Implications](#)
[Ice cores, Antarctica and Greenland](#)
[Paleotemperatures and Proxy Reconstructions](#)

W

WEATHERING AND CLIMATE

Weathering is an important biogeochemical process that is both influenced by and influences climate over the course of Earth history. Weathering processes control the flux of solutes and many nutrients to the oceans and the marine and terrestrial biospheres, and the transfer of carbon from the ocean-atmosphere system to sedimentary rocks. Weathering rates are dependent on climate, among several factors, and vary widely across the Earth's surface. In turn, weathering processes can alter the atmospheric concentrations of the important greenhouse gas, carbon dioxide. Weathering processes thus have the potential to act as a climate feedback, an idea that has been important in our understanding of the long-term evolution and stabilization of the Earth's climate for over 150 years.

"Weathering" refers to the chemical alteration of rock and sedimentary deposits under sub-aerial conditions at the Earth's surface. While some analogous processes occur in the oceanic crust during low temperature alteration by seawater, or during higher temperature hydrothermal alteration of the continental or oceanic crust, they fall outside the traditional definition of weathering. The kinds of geological materials that undergo weathering may be conveniently classified into silicates, carbonates, and organic matter. The types of weathering reactions, their products, and their dependence on and implications for climate differ between the three.

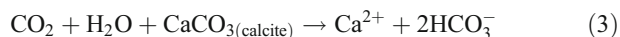
Weathering of both silicate and carbonate minerals can be described as an acid-base reaction, in which naturally occurring acids generated by volcanic gas emissions, weathering of sulfide minerals, dissolution of CO₂ in water, or decomposition of soil organic matter react with minerals phases to consume acidity and generate dissolved cations and, in most cases, alkalinity. One important difference between silicate mineral weathering and carbonate mineral weathering is that with silicates, an additional product of the weathering reaction is often a secondary alteration mineral ("clay"), whereas carbonate minerals generally dissolve completely. In both cases, weathering acts as a buffer to acidification, but the strength of the buffer depends on the mineral phase(s) involved.

Of the natural acids, carbonic acid (a "weak" acid, implying incomplete dissociation of the proton donor) and sulfuric acid are the most important. Sulfuric acid can be generated by the oxidation of sulfide minerals, volcanic gases (which commonly contain sulfur dioxide), or biogenic volatile compounds like carbonyl sulfide and dimethyl sulfide. These last reactions are important for atmospheric aerosol formation but are not significant sources of weathering acidity. Carbonic acid is generated by the dissolution of CO₂ in water:



Carbonic acid produced by the hydration of CO₂ (Reaction (1)) will partially dissociate to produce acidity and bicarbonate ion (Reaction (2)). At present atmospheric levels (PAL) for CO₂ (360 ppmv), the pH of water in equilibrium with the atmosphere is ca. 5.6. *p*CO₂ in soils can be much higher due to the decomposition of soil organic matter, and the pH of soil waters consequently lower. At *p*CO₂ = 10 PAL, pH = 5.1; at 100 PAL, pH = 4.6

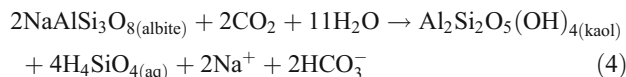
Carbonate rocks (primarily limestones and dolomites) play an important role in weathering fluxes at the Earth's surface because they are relatively soluble under typical conditions and act as a strong buffer to either natural or anthropogenic acidity. Natural acids react quickly with carbonate minerals, neutralizing the acidity and generating alkalinity in the form of bicarbonate and carbonate ions. An important reaction is:



in which CO₂ (from the atmospheric or from the decomposition of organic matter) reacts with calcite and water to produce dissolved calcium and bicarbonate ions. Under open system conditions and under present-day *p*CO₂, the pH at equilibrium with this reaction is near 8.6. Thus the hydrogen ion activity of the water-carbon dioxide system, with an ideal pH of ca. 5.6, is reduced by three orders of magnitude, illustrating the strong buffering effect that carbonate dissolution has on aqueous solutions. Bicarbonate ion is the dominant form of

dissolved inorganic carbon (DIC) at pHs between 5.7 and 10.2, which covers the range of most natural waters. Carbonate minerals are widely distributed, and most rivers have pHs that reflect their influence. The strong buffering effect ensures that waters in systems containing carbonate will generally be at neutral to slightly alkaline pH, which has important effects on the rates of other reactions involving aluminosilicate minerals and the solubility of many metals.

The weathering of aluminosilicate minerals is generally a more complicated process than for carbonates. Many reactions can be written depending on the phases involved. One important example is:



which illustrates a weathering reaction involving primary albite (Na-feldspar) and carbonic acid that yields a hydrated secondary clay mineral (kaolinite) which is depleted in cations and silica relative to the primary mineral. The other products are dissolved silicic acid, sodium ions, and bicarbonate. This type of weathering reaction, in which a new secondary phase is formed, is termed “incongruent” weathering, and is of fundamental importance for soil formation. Aluminosilicate mineral weathering rates depend strongly on pH, temperature, and reactive surface area, and are generally at a minimum at neutral pH. Thus, the presence of carbonate minerals in a soil may greatly reduce the rate of silicate mineral dissolution by buffering the pH to a range in which dissolution rates are slowest. Laboratory studies have documented that, under ideal conditions, reaction rates for aluminosilicate minerals increase by roughly a factor of three for each 10 °C temperature increase (Lasaga et al., 1994). Field studies have produced much more ambiguous results, probably in large part because of the difficulty in defining the effective surface area and also because of the inhibiting effects of ion sorption on some reactions (Drever and Clow, 1995).

Old organic carbon, stored in sedimentary rocks as “kerogen” also undergoes oxidative weathering reactions. These reactions are less well understood than those for mineral weathering, as they often involved the production of oxidized functional groups that may later serve as sites for bacterial attack. A schematic reaction may be written:



Reaction (5) illustrates that the weathering of organic matter consumes oxygen and produces carbon dioxide, although as written it provides little insight into the actual reaction pathways. Unlike carbonate and silicate weathering, organic carbon weathering is oxidative rather than fundamentally an acid-base reaction, although the production of organic acids ($\text{R-COOH} \rightarrow \text{R-COO}^- + \text{H}^+$) by partial oxidation may accompany kerogen degradation (Petch et al., 2000). Organic rich sediments such as shales and coals often contain pyrite, and the accompanying oxidation of FeS_2 results in the formation of sulfuric acid, which can lead to very low pHs. Sulfuric acid is a far stronger acid than carbonic acid, and may account for a significant fraction of the natural acidity even when pyrite is a minor component of the weathered rock.

In a classic work, Jenny (1941) laid out “state factors” that affect soil formation, and these generally apply to weathering

in natural systems. They include time, climate, topography and vegetation. Since most weathering reactions are strongly rate-limited, weathering can be slow even on a geologic time scale. Deeply weathered landscapes often have been stable for long times (10^6 – 10^8 years). Second, both temperature and rainfall are strong controls on natural weathering rates. Aluminosilicate reaction rates generally follow the Arrhenius relationship and can be strongly temperature dependent. Reaction rates can also depend on the degree of undersaturation of the solution in contact with the mineral and thus increased rainfall and more rapid flushing can enhance reaction rates and weathering reaction progress. “Wet” systems may leach out the available carbonate, removing the principal buffer, allowing pH to decrease and silicate weathering reaction rates to increase (Chadwick and Chorover, 2001). The decomposition of soil organic matter and production of organic and carbonic acids also depend positively on both temperature and (to the limit of saturation) moisture. Thus weathering rates can be expected to depend significantly on climate, and the global distribution of highly weathered soils supports this hypothesis. The removal of soil and regolith by erosion can expose fresh bedrock and enhance the overall weathering flux, although rapid removal will prevent weathering reactions from going toward completion. Two end member cases can be defined: “transport” limited systems, in which erosion removes regolith before it has a chance to undergo much chemical attack, and “weathering” limited systems, in which the development of a thick mantle of weathering products inhibits the introduction of water and acids to fresh mineral surface, thus slowing the overall weathering rate (Stallard and Edmond, 1983). A currently important area of study is the relationship between physical erosion, climate and weathering fluxes in difference environments, as it has been difficult to unambiguously point to a simple set of weathering rate controls across a variety of environments and spatial scales.

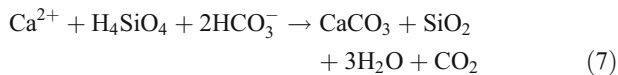
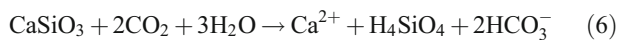
Interpretation of paleoclimate from paleoweathering studies

Paleosols are preserved weathering profiles found throughout most of the geological record. Their interpretation is complicated by a number of factors, including the state of preservation and the relationship of the regolith to the bedrock. For example, many soils have a significant (and in some cases like loessic soils, dominant) component of allochthonous transported material in them, transported by wind or other agents. Calculating the chemical weathering depletion of a soil by comparing its bulk chemistry to that of the underlying bedrock may not be meaningful in such cases, unless considerable care is taken to account for atmospheric deposition fluxes. Furthermore, it is often impossible to constrain the time scale of paleosol formation. However, some useful inferences can be drawn about paleoclimate from paleosol studies. These include qualitative data on precipitation and paleovegetation from isotopic studies of paleosol carbonates (Quade et al., 1989), and constraints on the composition of the atmosphere from models that use the differences in diffusivity of $^{13}\text{CO}_2$ and $^{12}\text{CO}_2$ to calculate $p\text{CO}_2$ in the overlying atmosphere (Cerling, 1992). The “paleosol $p\text{CO}_2$ barometer” has been widely applied to Phanerozoic sites, and gives a picture of the history of $p\text{CO}_2$ that is in broad agreement with modeling studies (Mora et al., 1996).

Influence of weathering processes on atmospheric $p\text{CO}_2$

The three basic weathering processes described above all involve CO_2 as a product or reactant. Recognition of the role of weathering process in controlling CO_2 , the role of climate in controlling weathering rates, and the role of CO_2 as a greenhouse gas led to the qualitative notion that a negative feedback existed in the geologic carbon cycle as early as the mid-nineteenth century (Ebelmen, 1845; Arrhenius, 1896; Chamberlin, 1899). The basic hypothesis is that increasing $p\text{CO}_2$, whether from volcanic emissions or some other source, would cause a warming of climate. The warm climate would enhance weathering reactions by a direct temperature effect, by increasing precipitation on land, or by increasing the activity of plants that would enhance weathering rates through increased soil $p\text{CO}_2$. The faster weathering reactions would result in enhanced consumption of CO_2 , eventually reducing the greenhouse effect and causing climate to cool. Conversely, an "externally" forced fall in $p\text{CO}_2$ would result in cooling and reduced weathering, gradually allowing natural sources of CO_2 to build up in the atmosphere and increase greenhouse warming. Beginning in the 1980s, these concepts were quantified with computer models, and the possibility of a viable climate stabilization with weathering-greenhouse feedback was demonstrated (Walker et al., 1981; Berner et al., 1983).

The three kinds of weathering processes have different impacts on the long-term carbon cycle. Carbonate weathering has no long-term effect – in the oceans, Reaction (1) is exactly reversible, and the formation of carbonate (biogenic or abiogenic) sediments in the ocean consumes the Ca^{2+} ion and the bicarbonate and returns the CO_2 to the ocean atmosphere system. In contrast, aluminosilicate weathering can be a net sink for CO_2 where Ca and/or Mg silicates are involved. A simple schematic pair of reactions illustrates the point:



Here a calcium (or equivalently magnesium) silicate undergoes attack by CO_2 and water to form Ca^{2+} ion, bicarbonate and silicic acid, consuming two moles of CO_2 per mole of mineral dissolved. In the ocean, the bicarbonate and calcium can precipitate to form sedimentary carbonate, releasing one mole of CO_2 back to the ocean-atmosphere system but with a net removal of one mole of CO_2 as carbonate. The net reaction is:



Because weathering of silicates is dependent on climate (temperature and rainfall), the weathering of Ca-Mg silicates can act as a feedback mechanism to stabilize atmospheric $p\text{CO}_2$ and thus climate. The weathering of K- and Na-silicates does not interact with the carbon cycle so simply, as K and Na do not form significant carbonate deposits. A fraction of K^+ and Na^+ released by mineral weathering undergoes ion exchange with Ca^{2+} , and thus can contribute to CO_2 consumption via this pathway, but the fraction is uncertain and probably not large, so weathering of alkali silicate minerals is an inefficient sink for CO_2 (France-Lanord and Derry, 1997). The direct role of Ca-Mg (alkaline earth) silicates in the carbon cycle and their generally faster weathering rates than K and Na

silicates indicate that weathering of mafic-intermediate rocks is the critical process by which silicate weathering can act as a climate feedback (Dessert et al., 2003).

Geochemical models that seek to investigate the global inter-dependence of climate and weathering have been used to estimate past atmospheric $p\text{CO}_2$, climate and weathering fluxes. Critical to these models is the formulation of the temperature dependence of weathering rate, typically according to the Arrhenius relationship:

$$k = A \exp(E_a/RT) \quad (9)$$

where k is the weathering reaction rate, A is a reaction-specific constant, R is the Universal Gas Constant, T is temperature (Kelvins), and E_a is the activation energy. This latter term determines the overall temperature sensitivity of the reaction. Two difficulties are immediately apparent with this approach. First, the Arrhenius "law" is most properly applied to a specific elementary reaction, but in practice the modeled reactions are composed of several (even many) elementary reactions, and it is not certain that the Arrhenius relationship holds under these circumstances, for which it was not originally determined. Second, determining an average temperature sensitivity (E_a) for silicate weathering reactions at a large scale is difficult. Most experimental data point toward values of E_a near 60 kJ per mole for the relevant silicate weathering reactions, which would imply about a factor of 5–6 increase in reaction rate between a cool climate (mean annual temperature 5 °C) and a warm climate (25 °C). Potentially more important than temperature changes are changes in precipitation that would result from global climate change. The primary driver for a weathering feedback to climate change may well be via global precipitation (White and Blum, 1995). Under warmer conditions, more water vapor should cycle through the atmosphere, resulting in greater rainfall and runoff. Complicating these relatively simple physico-chemical factors are the composition of exposed rock types, and the location of land masses in different climatic zones (Bluth and Kump, 1994). To illustrate the potential effects of these two factors, consider a paleogeography in which highly weatherable mafic-intermediate volcanic rocks were confined to high, cold and dry latitudes. The combination of low temperatures and low runoff should produce relatively low rates of CO_2 consumption. Alternatively, if these lithologies were primarily exposed in the warm and wet tropics, Ca-Mg silicate weathering should be enhanced, and CO_2 consumption maximized.

The weathering of organic matter has the opposite effect on the atmospheric CO_2 budget. Oxidation of kerogen releases CO_2 . This effect is, in the long term, nearly balanced by the burial of new organic matter in sediments, but sedimentary budget and carbon isotope studies indicate that there have been periods when the oxidation of old sedimentary carbon and burial of newly reduced carbon are not in balance. For example, changes in the net storage of organic carbon in sediments appear to have played a role in creating cool conditions in the Carboniferous (Canfield and Berner, 1989), but the impact of climate variability in creating suitable conditions for large burial fluxes of carbon as coal poses the problem of which came first. Glacially forced eustatic sea level variations appear to have been important in burying large quantities of terrestrial plant material in marginal swamps, while increasing this burial rate had the effect of further decreasing the quantity of carbon in the ocean-atmosphere system, which may have led to further

cooling. As in other intervals of Earth history, the feedback nature of the carbon-climate system can make it difficult to determine ultimate cause-effect relationships.

Mountain building episodes and weathering

The original quantitative models linking weathering, CO₂ and climate were essentially driven by the degassing fluxes from the Earth's interior, generally scaled to estimates of mid-ocean ridge crustal production rates. They did not take into account changes in "weatherability" of the mean continental surface, either by changes in the average composition of exposed rock types or by the enhancing effects of uplift and erosion on chemical weathering rates. The extent to which uplift affects regional or global scale weathering rates has been the focus of considerable debate in the geological literature in recent years (Raymo and Ruddiman, 1992). Fluxes of sediment are much higher from orogenic areas, particularly those located in wet climates (Milliman and Syvitski, 1992). Chemical weathering fluxes also are higher in streams that drain uplifted regions. Much of this enhanced flux is apparently due to carbonate dissolution, but silicate weathering fluxes have also been shown to be higher in regions of high relief (Sarin et al., 1989; Jacobson and Blum, 2003). More difficult is the question of how CO₂ consumption by weathering depends on uplift history, as both rock type and climate appear to play important roles as well. For example, the modern Himalaya do not appear to be a site of strongly enhanced CO₂ consumption by weathering, in part because rapid erosion limits the extent of completion of chemical alteration reactions, and in part because the alkali silicates common there are not efficient sinks for CO₂ (Galy and France-Lanord, 1999). The creation of large-scale topographic features may alter climate locally or regionally in ways that impact weathering. Perturbation of atmospheric circulation patterns by mountain uplift can create regional climates that are quite different from what would be expected in the absence of high topography. The current impact of the Tibetan plateau on monsoon circulation is the outstanding modern example (Prell et al., 1992). Many mountain ranges across the world strongly focus and intensify precipitation locally by orographic effects even if they are too small to drive major circulation patterns like the Indian monsoon. Increased precipitation is often associated with more rapid and/or complete weathering, but, conversely, rain shadow effects can result in significant areas of aridity and low weathering rates. The combination of regional circulation patterns, rain shadows, and low ocean surface temperatures results in low precipitation on the high Andean plateaus and on the west flank of the Andes, and very low weathering fluxes to the Pacific Ocean. On the east side of the Andes, high rainfall produces rapid erosion, and most of the solute fluxes in the large Amazon and Orinoco rivers are generated there (Stallard and Edmond, 1983). Thus, the effects of Andean uplift on weathering rates are highly asymmetric.

Mountain building can impact the organic part of the carbon cycle as well, through enhanced erosion and oxidation of old sedimentary kerogen, or through enhanced burial of "new" organic matter. Organic carbon sequestration rates are highest in areas of high sedimentation rates, and a large fraction of organic carbon burial takes place along continental shelves where productivity is high and sedimentation rates fast enough to ensure rapid burial and isolation. Currently, high sedimentation rates and a supply of refractory terrestrial organic matter make the Bengal Fan, the major sedimentary repository of the Himalaya, the largest site of organic carbon burial globally.

Because carbon-poor rocks are being eroded from the Himalayas, while carbon-rich sediments are deposited in the huge submarine fans, Himalayan erosion is a net sink for the organic carbon sub-cycle (France-Lanord and Derry, 1997).

The impact of the Himalayan (or any other) carbon sink on climate during the last 20 million years is not clear, as available paleoproxy data do not indicate any large shift in atmospheric *p*CO₂ since the early Miocene, a period during which large scale global cooling is well documented (Pagani and Freeman, 1999; Pearson and Palmer, 2000). The overall relationship between the carbon cycle and climate is not yet well understood, although there are a number of indications that the carbon cycle does play an important role in long-term climate change. The impact of weathering processes on the long-term carbon cycle, and the potential feedbacks involved remain one of the more interesting and complex features of the Earth system. The weathering-climate feedback is an attractive hypothesis for the stabilization of the Earth's climate over very long time scales (10⁸–10⁹ years). Changing solar output over those time scales could have forced drastic climatic changes in the absence of a stabilizing feedback, but for all but a few brief episodes of Earth history, surface temperatures appear to have been in the range of stability of liquid water. Gradually increasing solar luminosity may have been balanced by decreasing *p*CO₂, as weathering reactions gradually increased the storage of carbon in sediments at the expense of the ocean-atmosphere system. Such a transfer would be important from an atmospheric point of view, but quite small in terms of the sedimentary rock reservoir (a relative change on the order of 10⁻⁴).

Long term changes in global weathering rates: Sr isotope evidence

Available data from various sources, including paleo-sea level reconstructions, paleobotany, and oxygen isotopes in marine fossils, indicate that the Earth's climate has been considerably warmer at times in the geologic past. These "greenhouse" intervals, such as the Eocene warm period, or the mid-Cretaceous, should be associated with higher rates of weathering if the hypothesis of a long-term feedback between climate and weathering is valid. Conversely, "icehouse" intervals, with overall cool climates (such as the Pleistocene), should have lower globally averaged weathering rates. Model studies that incorporate a climate-weathering feedback do support this relationship, but that is clearly in part a function of the construction of the model around such a relationship (Berner, 1991). A reasonable question is whether there is good independent evidence of changes in global weathering rates that are correlated with climate on these long time scales. While paleosols do preserve information on weathering intensity from a particular location, they cannot be used to reconstruct global weathering rates reliably. Changes in ocean chemistry should result from long-term changes in weathering fluxes. Because the major element chemistry of seawater is, at best, imperfectly preserved in old sediments, attention has been given to isotopic tracers such as ⁸⁷Sr/⁸⁶Sr. Because strontium is a fairly abundant constituent of seawater and has a long residence time, it has a uniform isotopic composition in the world oceans at any one time. In a closed system (such as a given mineral phase), the ⁸⁷Sr/⁸⁶Sr ratio will increase over geologic time because of the decay of ⁸⁷Rb to ⁸⁷Sr, with a half life of 42 Ga. Minerals with a high parent-daughter ratio (high Rb/Sr) will evolve more rapidly than those with low Rb/Sr.

Analysis of many well-preserved marine carbonate samples has demonstrated that the ⁸⁷Sr/⁸⁶Sr ratio of seawater has varied

significantly over time (Burke et al., 1982; Veizer et al., 1999). Marine carbonates have very low levels of ^{87}Rb , and so should not evolve significant ^{87}Sr after their formation in the marine environment. The main causes of variation in the $^{87}\text{Sr}/^{86}\text{Sr}$ ratio of seawater (as recorded in marine carbonate sediments of various ages) must be changes in the fluxes of Sr to the oceans from sources with different characteristic $^{87}\text{Sr}/^{86}\text{Sr}$ ratios. The prime candidates are: (a) changes in the isotopic composition of Sr in the global river flux, and (b) changes in the relative contribution of Sr from submarine hydrothermal alteration and the river flux. The current value of $^{87}\text{Sr}/^{86}\text{Sr}$ in the oceans is 0.70917, while the global average river value is near 0.712. Mid-ocean ridge hydrothermal vents are near 0.7034, a value similar to the upper oceanic crust that they sample. In the simplest case, these input values imply that rivers supply two-third of the total Sr flux to the oceans, while hydrothermal systems supply the other third (Palmer and Edmond, 1992). Lower $^{87}\text{Sr}/^{86}\text{Sr}$ values of the oceans in the past would imply an increased hydrothermal flux, a reduced river (weathering) flux, or some combination. However, there are a number of important caveats to this simple approach. First, the estimate of the hydrothermal contribution to ocean chemistry based on Sr isotopes is higher than independent estimates from other chemical or isotopic tracers, and suggests that there are significant sources of non-radiogenic Sr to the oceans from crustal alteration of the oceanic crust at low temperature, away from ridge axes (Elderfield and Schultz, 1996). Second, the oceans are not now at steady state with respect to their Sr budget, and this disequilibrium results in an over-estimate of the hydrothermal contribution (Galy et al., 1999). Third, changes in the isotopic composition of the river flux with time can be large enough to confound attempts to extract the balance between hydrothermal and weathering fluxes through time. For example, Himalayan rivers have unusually high Sr concentrations as well as very high $^{87}\text{Sr}/^{86}\text{Sr}$, and the Neogene development of the Himalaya is at least in part responsible for the high average value of the global river flux to the present oceans (Edmond, 1992; Krishnaswami et al., 1992; Richter et al., 1992). Further, the $^{87}\text{Sr}/^{86}\text{Sr}$ of Himalayan rivers has changed significantly during the last 10 Ma (Derry and France-Lanord, 1996; Quade et al., 1997). The impact of Himalayan tectonic processes on the $^{87}\text{Sr}/^{86}\text{Sr}$ of the global river flux illustrates how changes in the types of rocks weathered at the Earth's surface can change the isotopic composition of one of the major contributors to the ocean Sr budget, and over time change the $^{87}\text{Sr}/^{86}\text{Sr}$ of the oceans, without necessarily implying large changes in globally averaged weathering rates or CO_2 consumption.

Finally, the fundamental interest in strontium isotope ratios as a measure of weathering fluxes is that strontium is chemically similar to calcium. Ideally, changes in the Sr mass balance of the oceans could be used to estimate changes in the global weathering calcium flux to the oceans. Carbonate sediments (limestones and dolomites) should record the $^{87}\text{Sr}/^{86}\text{Sr}$ of the ocean at the time they were deposited. Conversely, some silicate rocks, particularly those with granitic bulk compositions, can have high Rb/Sr ratios, and over time generate high $^{87}\text{Sr}/^{86}\text{Sr}$ ratios. The weathering of continental rocks should therefore yield high Sr isotope ratios in river waters, and the $^{87}\text{Sr}/^{86}\text{Sr}$ ratio of seawater should reflect increases in the weathering flux from old continental material on a million year time scale. Upon further consideration, an interesting conundrum appears. Granitic silicates have high Rb/Sr ratios and thus evolve to high $^{87}\text{Sr}/^{86}\text{Sr}$ values, but they also have relatively low Ca and Mg abundances.

Thus, their potential to act as weathering sinks for CO_2 via reactions like Reaction (8) is modest. Mafic silicates, including basalts and intermediate compositions generally have low Rb/Sr and low $^{87}\text{Sr}/^{86}\text{Sr}$ ratios, yet these compositions have abundant Ca and Mg, and can act as strong sinks for CO_2 (Dessert et al., 2003). The widely held view that increasing $^{87}\text{Sr}/^{86}\text{Sr}$ in the oceans should correlate with increased CO_2 consumption via silicate weathering is unlikely to be generally applicable (Raymo and Ruddiman, 1992).

A comparison of the available data on paleoclimate reconstructions with the $^{87}\text{Sr}/^{86}\text{Sr}$ ratio of past oceans suggests that at least some warm "greenhouse" periods of Earth history are associated with low $^{87}\text{Sr}/^{86}\text{Sr}$. This could reflect increased hydrothermal fluxes, but recent independent work strongly suggests that ocean crustal production rates have varied little since the Jurassic (Rowley, 2002). Instead, low $^{87}\text{Sr}/^{86}\text{Sr}$ during much of the Cretaceous and Paleogene may in part reflect enhanced alteration of mafic and intermediate silicate rocks, and thus relatively high rates of CO_2 consumption. The increase in marine $^{87}\text{Sr}/^{86}\text{Sr}$ since the Eocene is almost certainly in part due to changes in the types of rocks undergoing weathering, and may not reflect increased CO_2 consumption rates. It may reflect increased weathering rates of granitic materials, but as noted above, the associated CO_2 consumption can be modest.

Unfortunately, the question posed at the beginning of this section cannot be easily answered at present. While model results predict enhanced global weathering rates under warm "greenhouse" climates, there is no well-understood and fully independent data set that verifies this hypothesis. An increasingly well-documented set of laboratory and field experiments does support the general outlines of the hypothesis first posed by Ebelmen over 150 years ago, but we remain far from a complete understanding of weathering-climate relationships over geologic time.

Louis A. Derry

Bibliography

- Arrhenius, S., 1896. On the influence of carbonic acid in the air on the temperature on the ground. *Philos. Mag. J. Sci.*, **5**, 237–276.
- Berner, R.A., 1991. Atmospheric CO_2 levels over Phanerozoic time. *Science*, **249**, 1382–1386.
- Berner, R.A., Lasaga, A.C., and Garrels, R.M., 1983. The carbonate-silicate geochemical cycle and its effect on atmospheric carbon dioxide over the past 100 million years. *Am. J. Sci.*, **283**, 641–683.
- Bluth, G.J.S., and Kump, L.R., 1994. Lithologic and climatologic controls of river chemistry. *Geochim. Cosmochim. Acta*, **58**, 2341–2359.
- Burke, W.H., Denison, R.E., Hetherington, E.A., Keopnick, R.B., Nelson, H.F., and Otto, J.B., 1982. Variation of seawater $^{87}\text{Sr}/^{86}\text{Sr}$ throughout Phanerozoic time. *Geology*, **10**, 516–519.
- Canfield, D.E., and Berner, R.A., 1989. A new model for atmospheric oxygen over Phanerozoic time. *Am. J. Sci.*, **289**, 333–361.
- Cerling, E., 1992. Use of carbon isotopes in paleosols as an indicator of the $\text{P}(\text{CO}_2)$ of the paleoatmosphere. *Global Biogeochem. Cycles*, **6**, 307–314.
- Chadwick, O.A., and Chorover, J., 2001. The chemistry of pedogenic thresholds. *Geoderma*, **100**, 321–353.
- Chamberlin, T.C., 1899. An attempt to frame a working hypothesis of the cause of glacial periods on an atmospheric basis. *J. Geol.*, **7**, 545–584.
- Derry, L.A., and France-Lanord, C., 1996. Neogene Himalayan weathering history and river $^{87}\text{Sr}/^{86}\text{Sr}$: Impact on the marine Sr record. *Earth Planet. Sci. Lett.*, **142**, 59–74.
- Dessert, C., Dupre, B., Gaillardet, J., Francois, L.M., and Allegre, C.J., 2003. Basalt weathering laws and the impact of basalt weathering on the global carbon cycle. *Chem. Geol.*, **202**, 257–273.
- Drever, J.I., and Clow, D.W., 1995. Weathering rates in catchments. In White, A.F., and Brantley, S.L. (eds.), *Chemical weathering rates of*

- silicate minerals (Reviews in mineralogy, Vol. 31)*. Washington, D.C.: Mineralogical Society of America, pp. 463–483.
- Ebelmen, J.J., 1845. Sur les produits de la décomposition des espèces minérales de la famille des silicates. *Annales des Mines*, **7**, 3–66.
- Edmond, J.M., 1992. Himalayan tectonics, weathering processes, and the strontium isotope record in marine limestones. *Science*, **258**, 1594–1597.
- Elderfield, H., and Schultz, A., 1996. Mid-ocean ridge hydrothermal fluxes and the chemical composition of the ocean. *Annu. Rev. Earth Planet. Sci.*, **24**, 191–224.
- France-Lanord, C., and Derry, L.A., 1997. Organic carbon burial forcing of the carbon cycle from Himalayan erosion. *Nature*, **390**, 65–67.
- Galy, A., and France-Lanord, C., 1999. Weathering processes in the Ganges-Brahmaputra basin and the riverine alkalinity budget. *Chem. Geol.*, **159**, 31–60.
- Galy, A., France-Lanord, C., and Derry, L.A., 1999. The strontium isotopic budget of Himalayan rivers in Nepal and Bangladesh. *Geochim. Cosmochim. Acta*, **63**, 1905–1925.
- Jacobson, A.D., and Blum, J.D., 2003. Relationship between mechanical erosion and atmospheric CO₂ consumption in the New Zealand Southern Alps. *Geology*, **31**, 865–868.
- Jenny, H., 1941. *Factors of Soil Formation*. New York: McGraw-Hill, 281p.
- Krishnaswami, S., Trivedi, J.R., Sarin, M.M., Ramesh, R., and Sharma, K.K., 1992. Strontium isotopes and rubidium in the Ganga-Brahmaputra river system: Weathering in the Himalaya, fluxes to the Bay of Bengal and contributions to the evolution of oceanic ⁸⁷Sr/⁸⁶Sr. *Earth Planet. Sci. Lett.*, **109**, 243–253.
- Lasaga, A.C., Soler, J.M., Ganor, J., Burch, T.E., and Nagy, K.N., 1994. Chemical weathering rate laws and global geochemical cycles. *Geochim. Cosmochim. Acta*, **58**, 2361–2386.
- Milliman, J.D., and Syvitski, P.M., 1992. Geomorphic/tectonic control of sediment discharge to the ocean: the importance of small mountainous rivers. *J. Geol.*, **100**, 525–544.
- Mora, C.I., Driese, S.G., and Colarusso, L.A., 1996. Middle to Late Paleozoic atmospheric CO₂ levels from soil carbonate and organic matter. *Science*, **271**, 1105–1107.
- Pagani, M., and Freeman, K.H., 1999. Late Miocene atmospheric CO₂ concentrations and the expansion of C4 grasses. *Science*, **285**, 876–879.
- Palmer, M.R., and Edmond, J.M., 1992. Controls over the strontium isotope composition of river water. *Geochim. Cosmochim. Acta*, **56**, 2099–2111.
- Pearson, P.N., and Palmer, M.R., 2000. Atmospheric carbon dioxide concentrations over the past 60 million years. *Nature*, **406**, 695–699.
- Petch, S.T., Berner, R.A., and Eglinton, T.I., 2000. A field study of the chemical weathering of ancient sedimentary organic matter. *Org. Geochem.*, **31**, 475–487.
- Prell, W.L., Murray, D.W., and Clemens, S.C., 1992. Evolution and variability of the Indian Ocean summer monsoon: Evidence from the Western Arabian sea drilling program. In Duncan, R.A., Rea, D.K., Kidd, R.B., von Rad, U., and Weissel, J.K. (eds.), *Synthesis of Results from Scientific Drilling in the Indian Ocean*, Washington D.C.: American Geophysical Union, pp. 447–469.
- Quade, J., Cerling, T.E., and Bowman, J.R., 1989. Development of Asian monsoon revealed by marked ecological shift during the latest Miocene in northern Pakistan. *Nature*, **342**, 163–166.
- Quade, J., Roe, L., DeCelles, P.G., and Ojha, T.P., 1997. The late Neogene ⁸⁷Sr/⁸⁶Sr record of lowland Himalayan rivers. *Science*, **276**, 1828–1831.
- Raymo, M.E., and Ruddiman, W.F., 1992. Tectonic forcing of late Cenozoic climate. *Nature*, **359**, 117–122.
- Richter, F.M., Rowley, D.B., and DePaolo, D.J., 1992. Sr isotope evolution of seawater: The role of tectonics. *Earth Planet. Sci. Lett.*, **109**, 11–23.
- Rowley, D.B., 2002. Rate of plate creation and destruction: 180 Ma to present. *Geol. Soc. Am. Bull.*, **114**, 927–933.
- Sarin, M.M., Krishnaswami, S., Dilli, K., Omayajulu, B.I.K., and Moore, W.S., 1989. Major ion chemistry of the Ganga-Brahmaputra river system: Weathering processes and fluxes to the Bay of Bengal. *Geochim. Cosmochim. Acta*, **53**, 997–1009.
- Stallard, R.F., and Edmond, J.M., 1983. Geochemistry of the Amazon: 2. The influence of geology and weathering environment on the dissolved load. *J. Geophys. Res.*, **88**, 9671–9688.
- Veizer, J., Ala, D., Azmy, K., Bruckschen, P., Buhl, D., Bruhn, F., Carden, G.A.F., Diener, A., Ebner, S., Godderis, Y., Jasper, T., Korte,
- G., Pawellek, F., Podlaha, O.G. and Strauss, H., 1999. Sr-87/Sr-86, delta C-13 and delta O-18 evolution of Phanerozoic seawater. *Chem. Geol.*, **161**, 59–88.
- Walker, J.C.G., Hays, P.B., and Kasting, J.F., 1981. A negative feedback mechanism for the long-term stabilization of Earth's surface temperature. *J. Geophys. Res.*, **86**, 9776–9782.
- White, A.F., and Blum, A.E., 1995. Effects of climate on chemical weathering in watersheds. *Geochim. Cosmochim. Acta*, **59**, 1729–1747.

Cross-references

Carbon Cycle
 Marine Carbon Geochemistry
 Mineral Indicators of Past Climates
 Mountain Uplift and Climate Change
 Paleosols, Pre-Quaternary
 Strontium Isotopes

WISCONSINAN (WEICHSELIAN, WÜRM) GLACIATION

Introduction

The term “Wisconsinan Glaciation” refers to the last major glacial episode that affected North America, more properly referred to as the Wisconsinan Stage (Black et al., 1973; Fulton, 1989; Clark and Lea, 1992) (Figure W1). The term should be restricted to the deposits and events of the Laurentide Ice Sheet (LIS; see *Laurentide Ice Sheet*), which extended from the Canadian Arctic coast to the northern states in the USA, and across the Dakotas eastward to New England (Figure W2). In this sense, the term is not properly used to describe events of the Cordilleran Ice Sheet (see *Cordilleran Ice Sheet*), which extended from the Alberta foothills to the coast of British Columbia. Weichselian and Würm glaciations refer to the last glacial period in Fennoscandia and the Alps, respectively, although these terms, in addition to the “Wisconsinan,” are frequently applied to regions well-removed from the type areas.

The problem in nomenclature stems from efforts to integrate the mapping of glacial and other sediments associated with climatic variations into the standard American and International Stratigraphic Code (Hedberg, 1976). Terms such as Wisconsinan Glaciation or Sangamon Interglaciation are “Geologic-climate units” whereas Wisconsinan Stage is a time-stratigraphic unit that requires, by definition, upper and lower isochronous boundaries throughout the geographic area to which it is applied (Flint, 1971). By contrast, geologic-climate units are not constrained to be synchronous, which in reality agrees with the efforts to date the maximum limit of the LIS during its last major glacial advance (Dyke and Prest, 1987; Dyke et al., 2002). Such efforts indicate that the Last Glacial Maximum (LGM; Figure W1) is a global concept and the timing of the maximum of the late Wisconsinan Glaciation varies around its margins from around 22 to possibly as young as 13 cal ka BP (BP = Before Present with “present” equal to AD 1950). Frequently used terms such as the “late Wisconsin” generally refer to Marine Isotope Stage (MIS) 2 (Figure W1), but the definitions of middle and early Wisconsin are more varied in their usage and definitions (Fulton, 1989). The discussion gets convoluted in terms of definitions and semantics, leading to a lack of simplicity and uniformity in usage. For example, as a time-stratigraphic term, the Wisconsinan Stage ends at the Pleistocene/Holocene boundary, which

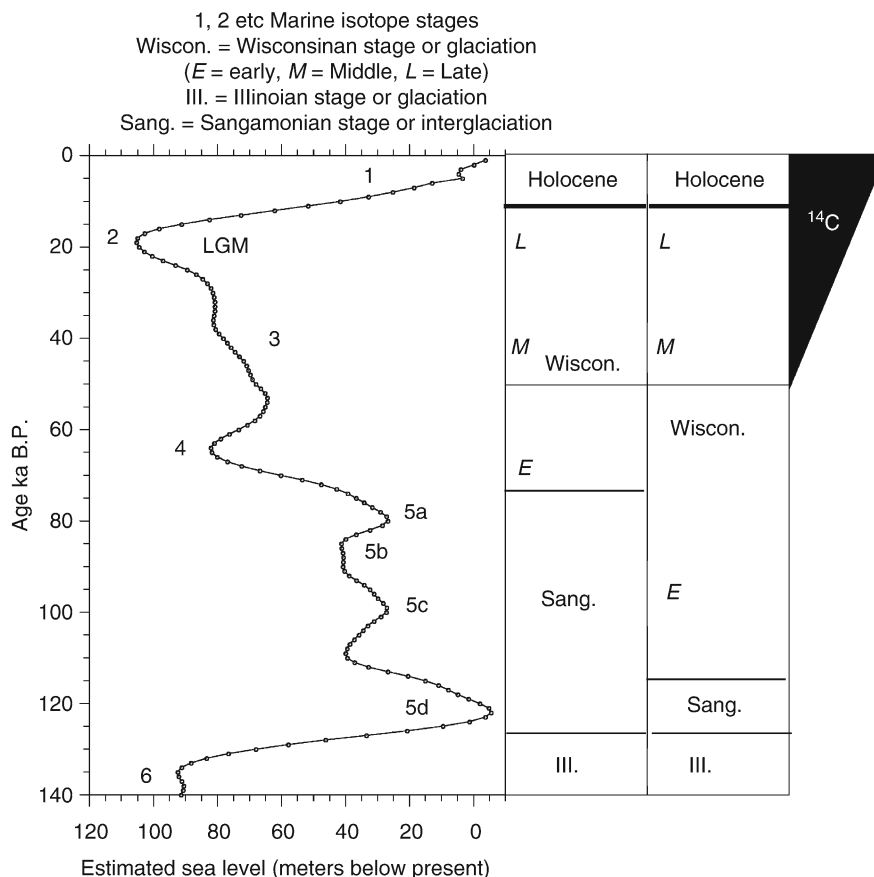


Figure W1 Estimated global changes in sea level over the last 140,000 years associated with the growth and retreat of the integrated global ice volume. The two columns to the right of the figure show alternative scenarios for Wisconsinan Glaciation and the boundary between the Pleistocene and Holocene. *E*, *M*, and *L* standard for early, middle and late Wisconsinan. *Sang.* is the Sangamonian Stage (Interglaciation), and *Ill.* is the penultimate Illinoian Stage (Glaciation). *LGM* is the late glacial (global) maximum. The final column shows the interval over which radiocarbon dating can be employed.

by international accord is 10,000 radiocarbon yBP or about 11,600 calendar yBP. However, the Wisconsinan Glaciation in the form of the LIS still covered vast areas of northern North America at this boundary time, and in fact, glacier ice associated with the geologic-climate unit still exists in the form of the Barnes Ice Cap on central Baffin Island, Nunuvit, Canada. The boundary for the transition between the last interglacial stage and the Wisconsinan Stage (Figure W1) can either be set to include the need for ice growth during MIS 5d and 5b, or the sustained interval of global ice expansion during MIS 4.

The Wisconsinan Glaciation is, however, of global importance because the LIS at its maximum at around 22,000 cal yBP (the Last Glacial Maximum or LGM, Figures W1 and W2) (see *Last Glacial Maximum*) was similar to the present Antarctic Ice Sheet in terms of area and volume. Hence, of the approximate 120 m of equivalent fall in global sea level (Figure W1), some ~70 m is attributed to the LIS (Denton and Hughes, 1981; Lambeck and Chappell, 2001). Actually, the terms Wisconsinan Glaciation or Weichselian Glaciation (NW Europe) are frequently used as general terms for the last glacial cycle *sensu lato*. However, this statement begs the question of when did the “Wisconsinan” Glaciation of North America really commence? The term “Wisconsinan” above is in quotations because

stratigraphic practice in North America variously defines the “Wisconsinan” Glaciation as beginning about 100 cal ka year ago or at the MIS 5/4 boundary ca. 75 cal ka (Figure W1). These temporal boundaries are not numerically dated but inferred from the stable oxygen isotope records preserved in deep sea sediments.

The Wisconsinan Glaciation and the marine isotope and sea level records

The overall structure of the last glaciation at a global scale is most frequently determined from a combination of studies of deep sea benthic foraminifera $\delta^{18}\text{O}$ variations (Shackleton, 1987), and evidence for past sea levels on tectonically active coastlines (Chappell et al., 1996). The chronology of these events is based on a combination of radiocarbon and U-series dating (see *Radiocarbon dating*), and fitting (tuning) the data to variations in orbital insolation (see *Astronomical theory of climate change*). Both methods explicitly track the global hydrological balance and seek to determine the volume (global) of ice located on land areas. Figure W1 illustrates the history of global ice sheet growth and melt from marine isotope stage (MIS) 5 to 1 (~130–10 cal ka).

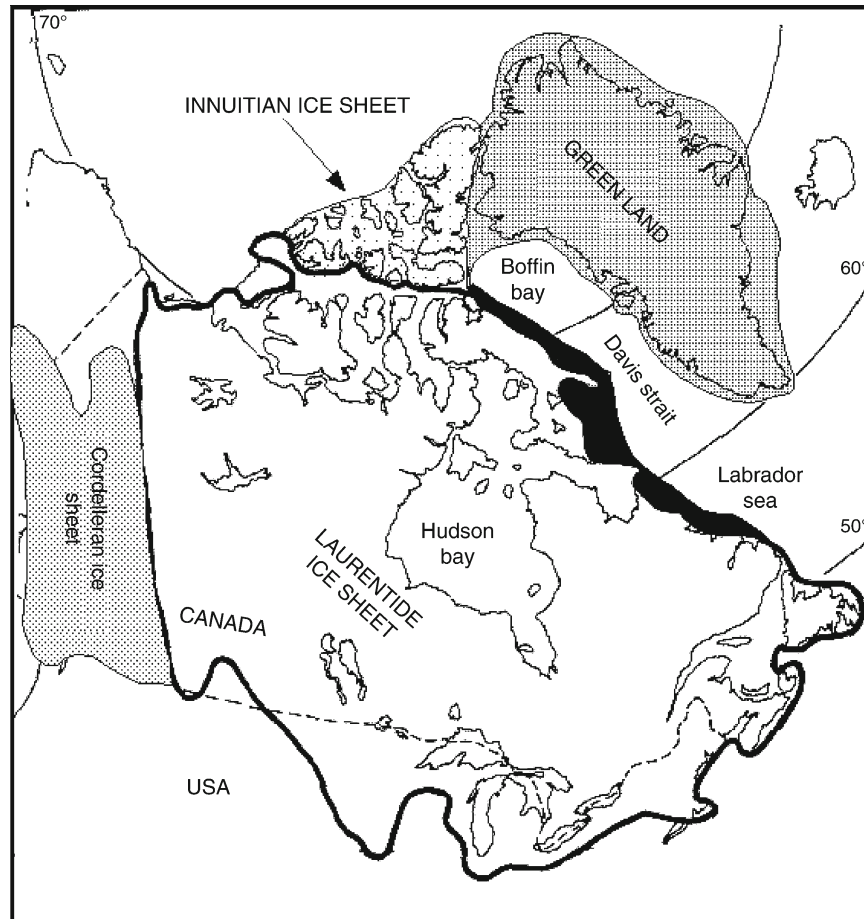


Figure W2 Extent of the ice sheets over North America and Greenland around 18,000 years ago. The regional glacial maxima vary around the ice sheet (see text). The *solid black area* represents the mapped extension of the Laurentide Ice Sheet during the late Wisconsinan Glaciation along the eastern margin of the ice sheet based on the 1987 compilations of Dyke and Prest (see Dyke et al., 2002).

Both approaches indicate that sea level was ~ 5 m above present during the last interglacial around 125 cal ka (MIS 5e) but then fell dramatically by 115 cal ka (MIS 5d), indicating that significant ice growth occurred somewhere on the planet. In terms of volume, this increase in glacier ice amounted to the equivalent of several present-day Greenland Ice Sheets. A Greenland Ice Sheet Unit (GISU) amounts to ~ 5 m of global sea level and the change in MIS 5d is in the range 4–10 GISU. Global sea level rose and hence ice sheets melted during MIS 5c and 5a, with an interval of growth during MIS 5b. It thus appears certain that significant ice sheets were present on the Earth's surface during MIS 5, but the exact location and individual sizes of these ice masses is uncertain at best and basically unknown.

Onset of glaciation in North America

The question of when the glaciation began is, at present, very difficult to answer because deposits associated with the early Wisconsinan Glaciation lie beyond the limits of radiocarbon dating, i.e., >45 ka BP (Figure W1). As noted above, a common approach is to examine the history of changes in global sea level since the last interglacial, the Sangamonian Interglaciation in North America. Because the LIS was the dominant factor in

changes of sea level on glacial timescales, the history of global sea level must therefore represent significant aspects of the volume history of the ice sheet, but it is probably not a 1:1 correspondence. It is possible that different sectors of this vast ice sheet experienced different chronologies because of the enormous range of glacial-climatic conditions that must have prevailed over such a massive ice sheet.

At present, the presumed centers of ice sheet growth and dispersal of the LIS are located in the vast uplands of the Eastern Canadian Arctic and Keewatin (Williams, 1979), which today have mean annual temperatures of between -13 and -5°C , with winter snowfalls ranging between 20 and 50 cm water equivalent. On Baffin Island, large areas of lichen/vegetation-free surfaces, caused by snow-kill, suggest that permanent snow/ice covered a large fraction on the region even as recently as the Little Ice Age, approximately 300–400 year ago. Significantly, the marine isotope data (Figure W1) indicate a very rapid increase in ice volume from MIS 5e to 5d. Such a rapid growth of ice sheets is incompatible with the slow growth associated with decreased temperatures (which would also decrease the precipitation) and therefore several authors have linked the onset of LIS glaciation with increased winter snowfall (Johnson and Andrews, 1979). These models

call for increased cyclonic activity in Baffin Bay, probably as the result of increased advection of warm modified Atlantic Water via the West Greenland Current. According to such a scenario, the development of ice over the islands and channels of the High Canadian Arctic would cut off the outflow of cold, “fresh” Polar Waters into Baffin Bay, resulting in a reduction in the extent and severity of sea-ice, in turn leading to increased fall precipitation over the uplands of Baffin Island and Labrador-Newfoundland. Such a paleoceanographic/climatic scenario is supported by the stratigraphy and molluscan faunas for glacial events along the eastern seaboard of Baffin Island that now lie beyond the limits of glaciation. Based on amino acid racemization constraints, these events are probably >75 cal ka and might be correlated with intervals of ice growth in MIS 5b and 5d (Figure W1).

However, even with such a “snowfall” model, Andrews and Mahaffy (1976) had great difficulty in driving a 3-D glaciological model to accommodate around 20 m of global sea level lowering in the 10,000 year required by the oxygen isotope data. However, this and later models all show the nucleation of ice sheets over the Canadian Arctic eastern uplands and growth across Hudson Strait. This must have resulted in the ponding of a large lake within Hudson Bay and the possibility of large outburst floods or subglacial release of water resulting from such a configuration.

The center of the Wisconsinan Ice Sheet – the record from Hudson Bay

The geographic center of the LIS during the Wisconsinan Stage was the area of Hudson Bay (Figure W2). Hence, the LIS is a marine-based ice sheet, defined as an ice sheet with a substantial fraction of its area located below sea level, with a major drainage directed through Hudson Strait into the Labrador Sea. Because of the density difference between ice (ca 900 kg m^{-3}) versus marine water (ca $1,028 \text{ kg m}^{-3}$), ice margins ending in the sea, or a lake, have the potential to “lift off,” resulting in a rapid increase in ice flow and the collapse of ice centers. The LIS thus had the potential to experience extensive deglaciation due to massive calving and collapse – this certainly occurred at the end of the glaciation some 8–9 cal ka but did it occur earlier in the last glacial cycle?

The late Quaternary stratigraphy of the Hudson Bay Lowlands (SW area of Hudson Bay) is beautifully preserved along hundreds of km of river section (Andrews et al., 1983; Thorleifson et al., 1992) (Figure W3). Although well preserved, the glaciological interpretation of the sequence is complicated by: (a) problems of assigning ages to materials at or beyond the limits of radiocarbon dating, and (b) differing interpretations of the genesis of rippled sands and laminated silts. Amino acid racemization data on marine mollusks, which are a product of both time and temperature, show that the presumed last interglacial marine sediments of the Bell Sea have ratios of around 0.24 compared with ratios of ~ 0.03 for the early Holocene Tyrrell Sea. Intermediate ratios of 0.12–0.14 were obtained from shells in sediments associated with the Prest Sea. Radiocarbon dates on the Prest Sea shells give finite dates between 35 and 40 ka BP and an age of ca. 40 cal ka is compatible with a reasonable thermal history for the site. It is possible that partial deglaciation occurred after Heinrich event 4 at around 38 cal ka (see below).

The glacial chronology of the Hudson Bay Lowlands is a critical but disputed element in our knowledge of the dynamics of the LIS.

Wisconsinan Ice Sheet instability – Heinrich events

Our understanding of ice sheet behavior during the Wisconsinan Glaciation has undergone substantial changes over the last few decades. In the 1970s and 1980s the focus was on the relationships between ice sheet mass balance, climate, and the Milankovitch orbital variations as the “pace maker” of the ice ages (Hays et al., 1976). Thus, thinking was restricted to cycles of ice sheet growth and retraction at 20, 40, or 100 ka insolation cycles. However, parallel with this paradigm was the realization (largely from theory) that marine-based ice sheets should be, or might be, unstable. This thinking was largely directed to the present and future history of the West Antarctic Ice Sheet. However, Heinrich (1988) presented a coherent argument for significant, but short-lived, ice-rafted detritus (IRD) events in the North Atlantic. This initial paper was followed by a deluge of studies that documented and tried to explain what are now universally referred to as Heinrich or H-events (Broecker et al., 1992; Andrews, 1998) (see *Heinrich events*).

Heinrich events represent 500–1,000-year intervals when the normal influx of IRD (see ice-rafted debris) into the North Atlantic was dramatically elevated. A key component of the Heinrich events is detrital carbonate. Using this as a tracer, plus studies of the isotopic composition and ages of the non-carbonate fraction, indicates that the primary source of the IRD in Heinrich-sediments is from Hudson Strait, demonstrating the inherent instability of marine-based ice sheets.

The elusive Middle Wisconsinan

The Middle Wisconsinan generally encompasses MIS3 or between 55 and 25 cal ka. Global sea level was higher than during the main global glacial intervals of MIS4 and 2, but still well below the interglacial levels of MIS5e and 1 (Figure W1). Ice sheet instability characterized some of this time (see above). A major problem is that these ages lie beyond 5 and 9 half-lives of the most-commonly used dating method, ^{14}C dating of wood, peats, mollusks, foraminifera, etc. (Figure W1). Contamination can frequently result in finite dates on material that show infinite ages, and temporal correlations are often unreliable as the stratigraphy of terrestrial deposits is difficult to trace unambiguously from outcrop to outcrop, often compounded by the absence of marker beds (such as tephra beds) around the margins of the LIS.

A survey of the glacial and non-glacial stratigraphy for northern North America (Andrews, 1987) indicated that middle Wisconsinan Glaciation (\sim MIS3) is absent from the mountains of Alberta and British Columbia (there appears to have been no middle Wisconsinan Cordilleran Ice Sheet), and moreover there is no evidence that the Prairie provinces were covered by an ice sheet (Figure W3). Similarly, in the Yukon Territory and the mountains of Alaska, the Boutellier non-glacial interval represents a long, middle Wisconsinan interval with reduced glacial cover when compared with the expansion of glaciers and ice sheets during MIS2. However, in the area of the Great Lakes, glacial and interstadial deposits exist, dated from >45 to ca. 25 cal ka. The Plum Point interstadial was followed by the LGM.

During MIS3, the LIS was restricted to the hard bed (glaciologically speaking) of the Canadian Shield, with limited advances and retreats along the southern margin (Figure W3). The location of the ice margin around two third of its perimeter during MIS3 is difficult to define at present. Cosmogenic dating and deep-sea sediment records suggest a series of rapid

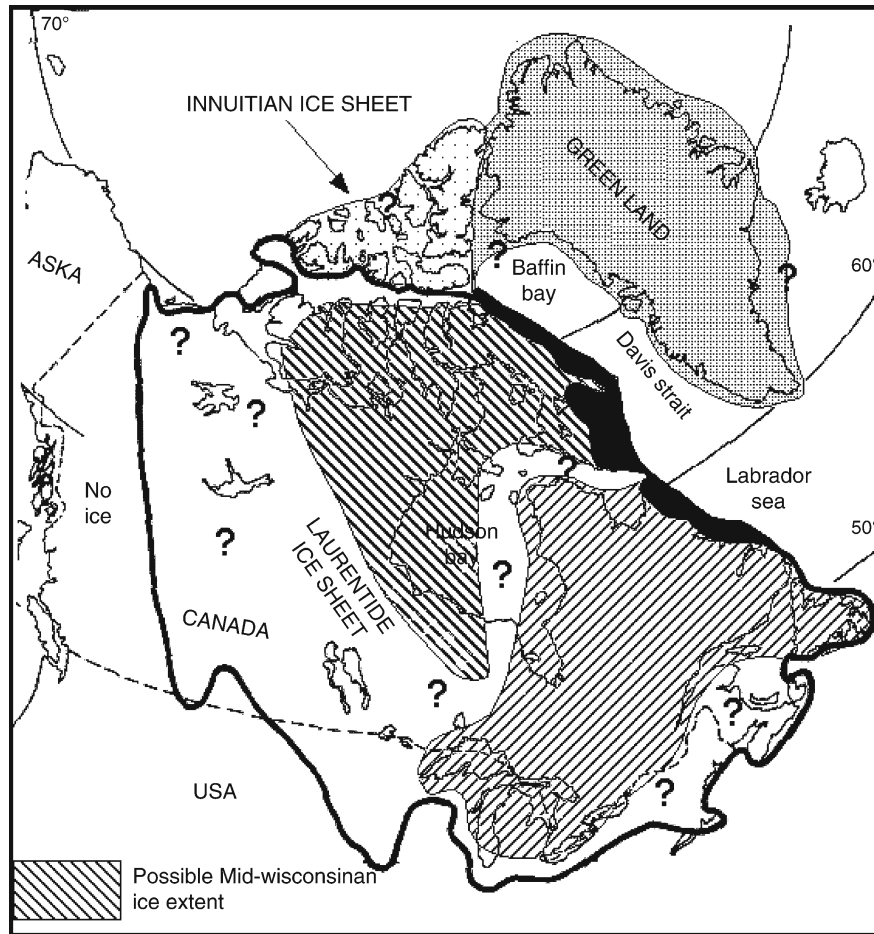


Figure W3 Extent of ice over northern North America and Greenland during the mid-Wisconsinan (Marine Isotope Stage 3) interval. Note the absence of ice over the Cordilleran region and over the western sector of the Laurentide Ice Sheet. The numerous question marks (?) indicate the major uncertainties in terms of timing and ice extent.

expansions and contractions especially as seen in Heinrich events 4 and 3, which occur within MIS3. In Baffin Bay, equivalent but possibly lagging IRD-rich units also are found, suggesting that the northern channels and ice streams in the Canadian Arctic Archipelago displayed a glaciological behavior similar to that of the Hudson Strait ice stream.

Big ice versus small ice at the LGM

There is a long-running dispute over the area and volume of the ice sheets during the LGM phase of the Wisconsin Glaciation. This was detailed in a global analysis by Denton and Hughes (1981), who highlighted the difference between a “big” ice sheet model, which placed large ice sheets and connecting ice shelves over vast areas of the Arctic and the Northern hemisphere, and a “small” ice world, where ice shelves were restricted and continental margins frequently terminated on land. In the last two decades, new tools, new insights into ice sheet behavior and basal conditions, and the exploration of new areas, have delineated ice margins that show a mosaic of “big ice” in some areas, whereas “small ice” appears necessary in other areas. Few papers deal with evidence for massive ice shelves across

the Arctic Ocean and marginal seas, and the implications for deep-water iceberg scouring at some sites is frequently ambiguous because of the inability to date the iceberg plough marks.

The ice sheet margin at the LGM has been extended seaward along the Labrador and Baffin Island coastline, largely on the basis of marine studies and cosmogenic dating (Steig et al., 1998). The consensus now maintains that an ice sheet extended across and drained through the Canadian High Arctic Channels and was contiguous with both the Greenland Ice Sheet along its eastern margin and the LIS along its southern limit (Dyke et al., 2002). A large ice sheet occupied the Barents Sea but the extent of LGM ice sheets further east along the arctic Eurasian margin is now restricted, and there is no evidence for such an ice sheet on the east Siberian shelf (Svendsen et al., 1999).

The concept of the Late Glacial Maximum (LGM) – is it useful?

The literature is now replete with the term “Late Glacial Maximum” or LGM (Figure W1). In a global sense, the term applies to the interval within MIS2 when ice volumes reached

a maximum and local sea levels at sites far removed from the ice sheet were at their lowest. However, the term should not be taken to imply that all ice sheets and glaciers experienced a synchronous interval of maximum extent around 22 cal ka. It is well known that various margins of the North American ice sheets reached their late glacial maxima at different times. As an example, the Puget Lobe of the Cordilleran Ice Sheet advanced south into the Puget Lowland at around 16 cal ka, which is also the date of the main advance across Des Moines, Iowa (Denton and Hughes, 1981). Hence the term “LGM” should not be used indiscriminantly and it should be made clear whether the term is being used in the global, integrated ice volume concept (Figure W1), or whether it is being used to refer to a regional glacial maximum limit that took place at a specific time within MIS2.

Pattern of deglaciation

The advent of radiocarbon dating in the late 1950s and 1960s rapidly led to the acquisition of data on the retreat of the Wisconsin Ice Sheet across the northern USA states and most of Canada (see *Laurentide Ice Sheet*). The first maps to show deglaciation isochrones were similar (Bryson et al., 1969). Subsequent maps show changes in important details, but not in the overall pattern and timing of retreat (Dyke and Prest, 1987). The isochrones are in 1,000s of radiocarbon years and hence underestimate the true ages by a few hundred to 1,000–2,000 years. Several authors used the maps to determine changes in area, and to derive estimates of volume changes over time.

The main pattern of retreat for the LIS can be summarized as follows:

1. Rapid deglaciation of the SW and W margins of the ice sheet. These margins lay on soft, deformable sediments.
2. During the time of rapid retreat of the SW and W margins, there was little change in the eastern margin facing Labrador and Baffin Bay.
3. Starting ca. 14 cal ka, the retreating S, SW, W, and NW margins frequently were adjacent to massive proglacial lakes which drained via several complex routes into the Gulf of Mexico, the shelf off the Hudson River, the St. Lawrence River, Hudson Strait, or the Mckenzie River in Arctic Canada (Dyke and Prest, 1987; Clark et al., 2001).
4. By 12 cal ka, the ice sheet had retreated across the St Lawrence Estuary and lay along the north shore of the Great Lakes.
5. Around 8–8.5 cal ka, a massive outburst flood linked the proglacial lakes in southern Hudson Bay and northern Quebec/Ontario with the encroaching sea in Hudson Strait. Earlier outburst floods had been directed via the other routes noted above.
6. By 7.5 cal ka, the last remnants of the LIS and the Wisconsin Glaciation were restricted to Baffin Island and other sites in eastern and northern Canada where modeling implied that the ice sheet had started its growth.
7. Technically speaking, the geologic-climate event of the Wisconsin Glaciation still persists in terms of deposits and climatic inferences that pertain to the Barnes Ice Cap, Nunavit, Canada, hence the obvious time-transgressive nature of this stratigraphic concept versus the chronostratigraphy embedded in the Wisconsin Stage and the Holocene.

The terms Wisconsin, Weichselian, and Würm glaciations

The application of the stratigraphic code (Hedberg, 1976) to issues of describing, naming, and correlating units within the Quaternary Era was a matter of considerable concern to terrestrial glacial stratigraphers from NW Europe, the northern USA, and Canadian researchers in the 1970s and early 1980s. However, the 1990s have seen the focus shift to the glacial impact on marine records, and the climatic significance and regional and global importance of abrupt climate “events,” such as the sequence of Heinrich IRD-rich sediment layers, the Younger Dryas cold event, and the impact of large freshwater outbursts on the regional to hemispheric climate. As a result, little attention has been paid to formal definitions and these terms are being largely used in an *ad hoc* manner.

Summary

The Wisconsin Stage and the Wisconsin Glaciation represent two different stratigraphic codes, although for many the differences are unclear. Radiocarbon dating of terrestrial and marine materials serves to define events and effect correlations over the last 30–40 ka (Figure W1), but correlations and events beyond the Middle Wisconsinian lie beyond the limits of radiocarbon dating and “dating” is frequently based on correlations to the marine isotope record (Figure W1) or relies on a range of new dating methods, including cosmogenic exposure ages, various luminescence methods, and amino acid racemization. Consequently, as yet there is little absolute knowledge about the timing of the onset of the last glaciation on North America or its history of expansion and retraction during MIS5, 4 and early stage 3 (Figure W1). However, it is known that the LIS suffered major catastrophic loss of mass during Heinrich events 4 through 1 (ca. 38 cal ka to 16 cal ka) as massive iceberg armadas carried sediments with provenance tracers indicative of sources in Hudson Strait and Hudson Bay into the North Atlantic to sites just west of Portugal and Ireland. How these events were manifest around the other sectors of the ice sheet is unclear, especially given the evidence for relative little ice in the Canadian Prairie provinces and even over the Cordilleran mountains during mid-Wisconsinian time (Figure W3).

John T. Andrews

Bibliography

- Andrews, J.T., 1987. The Late Wisconsin Glaciation and deglaciation of the Laurentide Ice Sheet. In Ruddiman, W.F., and Wright, H.E.J. (eds.), *North America and Adjacent Oceans During the Last Deglaciation*. Boulder, CO: Geological Society of America, pp. 13–37.
- Andrews, J.T., 1998. Abrupt changes (Heinrich events) in late Quaternary North Atlantic marine environments: A history and review of data and concepts. *J. Quaternary Sci.*, **13**, 3–16.
- Andrews, J.T., and Mahaffy, M.A., 1976. Growth rates of the Laurentide Ice Sheet and sea level lowering. *Quaternary Res.*, **6**, 167–183.
- Andrews, J.T., Shilts, W.W., and Miller, G.H., 1983. Multiple deglaciations in the Hudson Bay Lowland, Canada, since deposition of the Missinaibi (last-interglacial?). *Formation*, **19**, 18–37.
- Black, R.F., Goldthwait, R.P., and Willman, H.B., 1973. *The Wisconsin Stage*. Boulder, CO: Geological Society of America, 334pp.
- Broecker, W.S., Bond, G., McManus, J., Klas, M., and Clark, E., 1992. Origin of the Northern Atlantic's Heinrich events. *Clim. Dyn.*, **6**, 265–273.
- Bryson, R.A., Wendland, W.M., Ives, J.D., and Andrews, J.T., 1969. Radiocarbon isochrones on the disintegration of the Laurentide Ice Sheet. *Arct. Alp. Res.*, **1**, 1–14.
- Chappell, J., Omura, A., Esat, T., McCulloch, M., Pandolfi, J., Ota, Y., and Pillans, B., 1996. Reconciliation of late Quaternary sea levels derived

- from coral terraces at Huon Peninsula with deep sea oxygen isotope records. *Earth Planet. Sci. Lett.*, **141**, 227–236.
- Clark, P.U., and Lea, P.D., 1992. *The Last Interglacial – Glacial transition in North America*. Boulder, CO: Geological Society of America, 317pp.
- Clark, P.U., Marshall, S.J., Clarke, G.K.C., Hostetley, S.W., Licciardi, J.M., and Teller, J.T., 2001. Freshwater forcing of abrupt climate change during the last glaciation. *Science*, **293**, 283–287.
- Denton, G.H., and Hughes, T.J., 1981. *The Last Great Ice Sheets*. New York: Wiley, 484pp.
- Dyke, A.S., and Prest, V.K., 1987. Late Wisconsinan and Holocene history of the Laurentide Ice Sheet. *Geographie physique et Quaternaire*, **41**, 237–263.
- Dyke, A.S., Andrews, J.T., Clark, P.U., England, J.H., Miller, G.H., Shaw, J., and Veillette, J.J., 2002. The Laurentide and Innuitian Ice Sheets during the Last Glacial Maximum. *Quaternary Sci. Rev.*, **21**, 9–31.
- Flint, R.F., 1971. *Glacial and Quaternary Geology*. New York: Wiley, 892pp.
- Fulton, R.J.E., 1989. *Quaternary Geology of Canada and Greenland*. Boulder, CO: Geological Society of America, 839pp.
- Hays, J.D., Imbrie, J., and Shackleton, N.J., 1976. Variations in the Earth's Orbit: Pacemaker of the Ice Ages. *Science*, **194**, 112–1132.
- Hedberg, H.D., 1976. *International Stratigraphic Guide*. New York: Wiley, 200pp.
- Heinrich, H., 1988. Origin and consequences of cyclic ice rafting in the Northeast Atlantic Ocean during the past 130,000 years. *Quaternary Res.*, **29**, 143–152.
- Johnson, R.G., and Andrews, J.T., 1979. Rapid Ice-Sheet growth and initiation of the Last Glaciation. *Quaternary Res.*, **12**, 119–134.
- Lambeck, K., and Chappell, J., 2001. Sea level change through the Last Glacial Cycle. *Science*, **292**, 679–686.
- Shackleton, N.J., 1987. Oxygen isotopes, ice volume and sea level. *Quaternary Sci. Rev.*, **6**, 183–190.
- Steig, E.J., Wolfe, A.P., and Miller, G.H., 1998. Wisconsinan refugia and the glacial history of eastern Baffin Island, Arctic Canada: Coupled evidence from cosmogenic isotopes and lake sediments. *Geology*, **26**, 835–838.
- Svendsen, J.I., Astakhov, V.I., Bolshiyakov, D.Y., Demidov, I., Dowdeswell, J., Gataullin, V., Hjort, C., Hubberten, H.W., Larsen, E., Mangerud, J., Melles, M., Moller, P., Saarnisto, M., and Siegert, M.J., 1999. Maximum extent of the Eurasian Ice Sheets in the Barents and Kara Sea region during the Weichselian. *Boreas*, **28**, 234–242.
- Thorleifson, L.H., Wyatt, P.H., Shilts, W.W., and Nielsen, E., 1992. Hudson Bay Lowland Quaternary stratigraphy: Evidence for Early Wisconsinan Glaciation centered in Quebec. In Clark, P.U., and Lee, P.D. (eds.), *The Last Interglacial – Glacial Transition in North America*. Boulder, CO: Geological Society of America, pp. 207–222.
- Williams, L.D., 1979. An energy balance model of potential glacierization of northern Canada. *Arct. Alp. Res.*, **11**, 443–456.

Cross-references

- [Astronomical Theory of Climate Change](#)
- [Cordilleran Ice Sheet](#)
- [Glaciations, Quaternary](#)
- [Heinrich Events](#)
- [Ice-Rafted Debris \(IRD\)](#)
- [Last Glacial Maximum](#)
- [Last Glacial Termination](#)
- [Laurentide Ice Sheet](#)
- [Late Quaternary Megafloods](#)
- [Oxygen Isotopes](#)
- [Proglacial Lacustrine Sediments](#)
- [Radiocarbon Dating](#)
- [Scandinavian Ice Sheet](#)
- [SPECMAP](#)
- [Sea Level Change, Post-Glacial](#)
- [Sea Level Change, Quaternary](#)

Y

YOUNGER DRYAS

Introduction

Abrupt climate changes are events that have affected the Earth many times; it is not only possible but also likely that these will affect us in the future (Alley et al., 2002). While gradual climate changes allow time for those affected to adjust, rapid events often cause greater impact simply because of their rapidity. While we do not yet understand past rapid climate events enough to predict them, we can examine past data and use models to test our ideas about why they occur. One of the most useful ways to approach the data is to examine the occurrence, magnitude, timing, and distribution of these events, fitting together the pieces of a global puzzle.

Younger Dryas – prime example of abrupt climate change

The Younger Dryas (YD) is known as the best example of an abrupt climatic event recorded on land, in the oceans, and in ice cores (Alley et al., 2002, 2003). It was a cold event that occurred between 11,000 and 10,000 ¹⁴C years ago, (approximately 12,800 and 11,600 calendar years ago), and it lasted about 1,200 years. About 15,000 years ago, as Northern Europe ice sheets were retreating and trees were beginning to move northward replacing tundra, several brief returns to cold conditions suddenly took place. The most pronounced of these reversals, which could be correlated from place to place in Europe, was called the Younger Dryas. The name “Younger” was used because it was the last of these rapid cold events, while earlier events were called the Oldest Dryas and the Older Dryas (Jansen, 1938). The name *Dryas* was used because the layer contained fossil leaves and fruits of the *Dryas octopetala* plant, a member of the rose family (Rosaceae) that colonizes arctic-alpine regions. The layer just below the Younger Dryas that contained tree fossils was named Allerød for the Scandinavian locale.

After this striking reversal in macrofossils was noted by paleoecologists in Northern Europe in the late nineteenth and early part of the twentieth century, it was correlated from place to place using

palynology, the study of pollen and spores. Hundreds of pollen diagrams throughout Europe now show the effect that this event had on ecosystems and landscapes, causing the demise of forests and the increase of erosion and expansion of tundra (Watts, 1980) during this cold interval. Radiocarbon dating beginning in the 1950s secured the correlation of the reversal in Europe. However, more recent comparison of calendar ages to the radiocarbon scale indicates that plateaus exist in the radiocarbon scale, complicating the correlations somewhat.

Over the last twenty years, many scientists have studied the Younger Dryas in order to better understand rapid climatic events. The geographic range (Figure Y1), timing, and magnitude of this event are crucial to understanding its origin.

Europe

While the timing of the event in Europe was synchronous from place to place, each locale varied in the specific vegetational changes that took place. For example, while tundra herbs indicative of open, disturbed landscapes such as *Artemisia* (wormwood) and *Chenopodiaceae* replaced birch trees and conifers in the British Isles (Walker, 1994), in Scandinavia the change was more subtle, with colder tundra herbs replacing some that inhabited warmer environments. Some of the strongest effects of the Younger Dryas are noted in southern Europe, where summer temperatures may have been 8 °C lower than today. In Norway, Birks and Ammann (2000) estimated mean July temperature to be about 7–9 °C lower than today, and about 2–4 °C lower than the preceding Allerød warm interval. Substantial changes in vegetation characterized both coastal and inland areas all the way from northern Norway to the Mediterranean (Walker, 1994).

North America

While originally the Younger Dryas was thought to be solely a European phenomenon, the advent of accelerator mass spectrometry resulted in improved radiocarbon dating and the identification of plant macrofossils permitting identification of plants to the species level. Along with palynology, these vegetational changes resulted in proof of cooling that was correlative with the European YD. These results demonstrated the presence of a Younger Dryas event in the maritime provinces of Canada



Figure Y1 Global map of distribution of palynological evidence for the Younger Dryas cooling 11–10 ^{14}C kyBP (12,800–11,600 calendar years). Cooling is strongest in regions surrounding the N. Atlantic, including Greenland, Europe, and eastern North America. Cooling has also been identified in many places far from the N. Atlantic, such as N. Pacific Canada and Alaska, and East Asia. Tropical cooling has also been noted. Many sites are still controversial, where some evidence points to cooling and other evidence does not show the oscillation (i.e., New Zealand, Chile; after Peteet, 1995; Peteet et al., 1993).

(Mayle et al., 1993) and the northeastern coast of the United States (Peteet et al., 1993). Estimates of the cooling range from 3–4 °C in southern New England to 6–7 °C in eastern Canada. In the Maritime Provinces of Canada, shrub tundra was replaced by herb tundra in some places, while in others shrub tundra replaced spruce forest. In the mid Atlantic and southern New England regions, a mixed boreal and deciduous forest was replaced by boreal forest (spruce, fir, larch, alder, paper birch). Further investigations continue to document the YD event in the mid-Appalachian region, Midwestern USA, coastal British Columbia and Alaska, and Arctic Alaska. Documentation of the YD event in terrestrial locations as far west as Alaska revealed that the geographic extent of this cooling was not limited to the North Atlantic region, and that the forcing was possibly not limited to the North Atlantic Ocean (Figure Y1).

South America

Evidence for the YD event in South America is mixed. Evidence is most convincing in Colombia, where many sites show a late-glacial palynological oscillation but precise dating is lacking. In southern South America, while some data shows a prolonged YD which begins earlier than the North American event, some data suggests a correlation and some does not. In Peru, glacial advances do indicate a YD age advance.

Asia

North Pacific investigations now show that the YD was expressed in the Japan Sea as well as off coastal California (Behl and Kennett, 1996). While a cold interval on land in Japan has been linked to the YD, with indications of colder temperatures and declines in moisture, recent evidence from other annually laminated lakes suggests that the cooling event of about 3 °C lagged the European event by a few centuries (Nakagawa et al., 2003). The high-resolution speleothem monsoon record from coastal mid-latitude Hula Cave, China, also clearly shows a YD event (Wang et al., 2001), as do loess records in the region.

Marine evidence

In the 1980s, North Atlantic faunal changes concurrent with the terrestrial European signals led ocean paleoecologists to the conclusion that the North Atlantic polar front re-advanced to its glacial position at that time (Ruddiman and McIntyre, 1981). Subsequent geochemical analyses indicate that the production of North Atlantic Deep Water (NADW), which today is responsible for bringing heat to Europe, was greatly reduced at this time, as it was during the ice age (Broecker et al., 1985). The cause for the presence of this deep-water reduction is still in dispute, but it has been linked to diversions of Laurentide meltwater to specific locations in the North Atlantic. Convincing

marine evidence from the Atlantic for the YD shift comes from the Cariaco Basin, where sediment color and other data is interpreted as an increase in wind-induced upwelling off coastal Venezuela (Hughen et al., 1996) or decreased riverine runoff from adjacent countries.

North Pacific evidence for a YD event comes from the Santa Barbara Basin (Kennett and Ingram, 1995), the Gulf of California, the northwestern North Pacific, and even the eastern equatorial Pacific. An arid interval is correlated with the YD in the tropical Atlantic (Maslin and Burns, 2000) and off Africa.

Ice cores

The advent of ice core research was very important in demonstrating the importance of the Younger Dryas in the history of climate change. Camp Century, Dye 3, and Renland first illustrated this change, which was then confirmed in the GRIP and GISP-2 deep cores (Dansgaard et al., 1993). The signal is observed as a several per-mil shift in oxygen isotope ratios, corresponding to about 15 °C colder than today (Cuffey et al., 1995). What is unusual about the ice core shift as compared to pollen records is that the magnitude of the shift in the ice cores is almost equal to that of full-glacial conditions, while in pollen records throughout Europe, this shift is probably at most equal to half the shift in temperature represented by full-glacial conditions. Thus, the isotopes are complicated to interpret, either suggesting locally colder conditions than on continents adjacent to the North Atlantic, or a transport or source problem. In the ice cores, the YD is also marked by much higher dust levels and chemical concentrations than the previous Allerød or the subsequent Holocene. While the onset of the YD in the ice cores is gradual, the termination is very abrupt, occurring in as little as 1–3 years in some indicators. Snow accumulation rates during the YD were about half that of the Preboreal, and about one third of modern rates. The changes at the end of the YD were completed in three 5-yr steps spread over about 40 years (Taylor et al., 1993), and snow accumulation changed by about 90% in one year (Alley et al., 1993). The discovery of a YD methane signal in Antarctic ice was the first indication that this event made a global imprint. However, more recent ice core evidence for the YD event correlative with the European and Greenland ice cores is conflicting, suggesting that in some locations a YD is correlative but in others it precedes the northern hemisphere change. Ice cores from more temperate locations in Peru and Bolivia also show evidence of a late-glacial reversal, which probably is the YD but age control is problematic.

Mechanisms

The decreased NADW production during the YD is the chief hypothesis among those proposed as the reason for the cooling throughout the Northern Hemisphere (Broecker et al., 1985). Cold meltwater from the late-glacial release of Lake Agassiz to the North Atlantic would have been located in such a position that it could have slowed down the thermohaline circulation (THC). The 1,500-yr oscillations in marine, terrestrial and ice cores throughout the Holocene suggests that YD-type signals may be a complex recurring climate oscillation that was magnified during the YD by meltwater from receding ice sheets (Bond and Lotti, 1995). One potential problem with the THC hypothesis for YD and other similar events is that most atmospheric models show a restricted circum-North Atlantic response to the YD when a shutdown is forced (Rind et al., 1986; Renssen, 1997), although others show a muted cooling in the North Pacific (Mikolajewicz et al., 1997). Understanding how this mechanism could cause a

significant YD signal around the globe is a major challenge to modelers. Some recent research has focused on the tropics as a possible amplifier of abrupt climate change caused by shifts in the intertropical convergence zone (ITCZ) (Clement et al., 2001).

The impacts of the YD on human populations was probably extreme, and may have contributed to the beginnings of agriculture around the fertile crescent (Moore and Hillman, 1992). On the North Slope, Alaska, changes in human migration (Kunz and Reanier, 1996) during the YD are linked to a shift to major changes in moisture (Mann et al., 2002). Added to the human factor in North American mammal extinctions, it is possible that the YD pushed populations over the brink (Petee et al., 1990). Abrupt climate changes of lower magnitude than the YD occurred throughout the Holocene; these have been linked to reduced solar radiance (Bond et al., 2001). Much is still to be learned regarding the Younger Dryas event.

Dorothy M. Petee

Bibliography

- Alley, R.B., Meese, D.A., Shuman, C.A., et al., 1993. Abrupt increase in Greenland snow accumulation at the end of the Younger Dryas event. *Nature*, **362**, 527–529.
- Alley, R.B., Marotzke, J., Nordhaus, W.E., Overpeck, J.T., Petee, D.M., Pielke, R.A. Jr., Pierrehumbert, R.T., Rhines, P.B., Stocker, T.F., Talley, L.D., and Wallace, J.M., 2002. *Abrupt Climate Change: Inevitable Surprises*. Washington, DC: National Academy Press, National Research Council, 230pp.
- Alley, R.B., Marotzke, J., Nordhaus, W.E., Overpeck, J.T., Petee, D.M., Pielke, R.A. Jr., Pierrehumbert, R.T., Rhines, P.B., Stocker, T.F., Talley, L.D., and Wallace, J.M., 2003. Abrupt climate change. *Science*, **299**, 2005–2010.
- Behl, R.J., and Kennett, J.P., 1996. Brief interstadial events in the Santa Barbara basin, NE Pacific, during the past 60 kyr. *Nature*, **379**, 243–246.
- Birks, H.H., and Ammann, B., 2000. Two terrestrial records of rapid climate change during the glacial-Holocene transition (14,000 to 9,000 calendar years BP) from Europe. *Proc. Natl. Acad. Sci. USA*, **97**(4), 1390–1394.
- Bond, G., and Lotti, R., 1995. Iceberg discharges into the North Atlantic on millennial timescales during the last deglaciation. *Science*, **267**, 1005–1010.
- Bond, G.C., Kromer, B., Beer, J., Muscheler, R., Evans, M., Showers, W., Hoffmann, S., Lotti-Bond, R., Hajdas, I., and Bonani, G., 2001. Persistent solar influence on North Atlantic climate during the Holocene. *Science*, **294**, 2130–2136.
- Broecker, W., Petee, D., and Rind, D., 1985. Does the ocean-atmosphere have more than one stable mode of operation? *Nature*, **315**, 21–26.
- Clement, A.C., Cane, M.A., and Seager, R., 2001. An orbitally driven tropical source for abrupt climate change. *J. Clim.*, **14**, 2369–2375.
- Cuffey, K.M., Clow, G.D., Alley, R.B., Stuiver, M., Waddington, E.D., and Saltus, R.W., 1995. Large Arctic temperature change at the Wisconsin-Holocene glacial transition. *Science*, **270**, 455–458.
- Dansgaard, W., Johnsen, S.J., Clausen, H.B., et al., 1993. Evidence of instability of past climate from a 250-kyr ice core record. *Nature*, **364**, 143–147.
- Hughen, K., Overpeck, J., Peterson, L., and Trumbore, S., 1996. Rapid climate changes in the tropical Atlantic region during the deglaciation. *Nature*, **380**, 51–54.
- Jansen, K., 1938. Some west Baltic pollen diagrams. *Quartar*, **1**, 124–139.
- Kennett, J.P., and Ingram, B.L., 1995. A 20,000 year record of ocean circulation and climate change from the Santa Barbara basin. *Nature*, **377**, 510–513.
- Kunz, M., and Reanier, R., 1996. Paleoindians in Beringia. *Science*, **263**, 660–662.
- Mann, D.H., Petee, D.M., Reanier, R.E., and Kunz, M.L., 2002. Responses of an Arctic landscape to late-glacial and early Holocene climatic changes: The importance of moisture. *Quaternary Sci. Rev.*, **21**, 997–1021.

Author Index

A

Abbott, Mark B. 489
Almasi, Peter F. 929
Alverson, Keith 675
Anderson, Lesleigh 489
Andersson, Carin 609
Andrews, John T. 986
Archer, Allen W. 226
Archer, David 478, 533
Arnaud, Emmanuelle 384
Ashley, Gail M. 446
Asmerom, Yemane 916, 969
Avis, Chris 690

B

Baker, Paul A. 746
Baker, Victor R. 380, 504
Barker, Philip 738
Bassinot, Franck C. 911
Beer, Jürg 92, 211
Beltrami, Hugo 103
Benn, Douglas I. 382, 394, 948
Bennett, Matthew R. 768, 783, 873
Berger, André 51
Berger, Glenn W. 249
Berger, Wolfgang H. 525
Bickert, Torsten 136
Bjørklund, Kjell R. 869
Bond, Gerard 568, 929
Bosence, Dan 143
Boucot, Arthur J. 291
Bowen, David Q. 493, 798
Buckley, Brendan M. 239, 269
Burbank, Douglas W. 596

C

Catling, David C. 66
Cecil, C. Blaine 181
Chandler, Mark A. 566
Chappell, John M. 893
Choi, Kyungsik 183
Christensen, Phillip R. 540
Clague, John J. 206
Clarke, Jonathan 138

Colgan, Patrick M. 354
Coope, G. Russell 90
Cronin, Thomas M. 663, 757
Crosta, Xavier 31
Crowley, Thomas J. 164
Cullen, Heidi M. 619

D

Dalrymple, Robert W. 183
de Vernal, Anne 38, 280
DeConto, Robert M. 784
Delaygue, Gilles 278, 666
Derry, Louis A. 981
Dickens, Gerald R. 560
Dilcher, David 679
Dlussky, Konstantin G. 522
Donnelly, Jeffrey P. 763
Dorn, Ronald I. 275
Dowdeswell, Julian A. 471
Dowsett, Harry J. 338
Driese, Steven G. 748
Droser, Mary L. 10
Dugmore, Andrew J. 937
Dyke, Arthur S. 517

E

Emeis, Kay-Christian 875
Enters, Dirk 485

F

Fairbridge, Rhodes W. 294, 414, 428, 451, 551
Farquhar, James 61, 333
Fegley, Bruce, Jr. 75
Filippelli, Gabriel M. 780
Forswall, Clayton 560
Fowell, Sarah 766
Francois, Roger 634

G

Gagan, Michael K. 721
Gaines, Robert R. 10
Garver, John I. 247
Gasse, Françoise 733
Goodbred, Steven L. 265

Goodwin, Ian D. 89
Gornitz, Vivien 6, 294, 428, 573, 716, 813, 887
Goudie, Andrew 45
Gröcke, Darren R. 397
Gupta, Anil K. 589

H

Hall, Chris M. 255, 823
Harper, David A. T. 325
Hay, William W. 260
Hays, James D. 158
Haywood, Alan M. 804
Hemming, Sidney 409
Hendrix, Marc S. 192
Higginson, Matthew J. 341
Hoek, Wim Z. 100, 477
Hoffmann, Georg 282
Huber, Matthew 683
Huybrechts, Philippe 221

J

Jacobs, Stan 16
Johnson, Claudia C. 213
Juggins, Stephen 959

K

Kaplan, Jed O. 507
Karlén, Wibjörn 835
Kauffman, Erle G. 213
Kaufman, Alan J. 85
Kearney, Michael S. 899
Kneller, Margaret 766, 815
Knight, Peter G. 89, 155, 284, 320, 483, 594, 665
Kohfeld, Karen E. 286
Kolodny, Yehoshua 775
Kowalski, Elizabeth A. 679
Krijgsman, Wout 252
Kull, Christoph 675

L

Lacis, Andrew A. 2, 174
Lambeck, Kurt 374
Langereis, C. G. 252

Leavitt, Steven W. 133
LeGrande, Allegra N. 938
Lerman, Abraham 107
Leventer, Amy 279
Li, Qianyu 583
Licht, Kathy 24, 395
Link, Paul K. 463
Loope, David B. 319
Loutre, Marie-France 301, 625, 825
Lugli, Stefano 321, 559

M

Maasch, Kirk A. 709
Mangerud, Jan 877
Mann, Michael E. 178
Marchitto, Thomas M., Jr. 614
Marshall, Shawn J. 389
Martini, I. Peter 384
Maslin, Mark 841
Meissner, Katrin J. 690
Menzies, John 278, 361
Meyers, Philip A. 659
Miller, Gifford H. 233
Miller, Kenneth G. 879
Mogensen, Irene A. 229
Molina-Cruz, Adolfo 869
Montenegro, Alvaro 690
Mora, Germán 918
Morgan, Vincent I. 22
Morozova, Tatiana D. 752
Mosbrugger, Volker 607
Muhs, Daniel R. 312
Müller, Ulrich C. 302

N

Nash, David J. 284
Neuzil, Sandra G. 181
Newton, Anthony 937
Nitoiu, Daniela 103

O

Oglesby, Robert J. 709
Ojala, Antti E. K. 973
Olsen, Paul E. 826

P

Pagani, Mark 4
Paillard, Didier 495
Palmer, Martin R. 743
Parrenin, Frédéric 453
Paytan, Adina 644
Peck, William H. 34
Pekar, Stephen F. 354
Petee, Dorothy 993
Pierazzo, Elisabetta 217
Poulsen, Christopher J. 700
Price, Gregory D. 554
Prothero, Donald R. 728

R

Rampino, Michael R. 96
Raymond, Anne 498
Raynaud, Dominique 453
Rea, David K. 308
Reasoner, Mel A. 442
Retallack, Gregory J. 962
Reuss, Joanne C. 630
Rich, Thomas H. 13
Rind, David 57
Roberts, Neil 438
Ruffell, Alastair 539

S

Saarnisto, Matti 973
Sachs, Julian P. 612
Sadler, Peter M. 237
Saenko, Oleg A. 943
Sageman, Bradley 626
Saunders, Andrew D. 335
Schmidt, Gavin A. 696
Scotese, Christopher R. 498
Seidov, Dan 407
Sheldon, Nathan D. 871
Shindell, Drew T. 520, 550
Siegert, Martin J. 94
Simonson, Bruce M. 85
Smoot, Joseph P. 902
Spicer, Robert A. 156
Stauffer, Bernhard 118

Stothers, Richard B. 976
Strauss, Harald 926
Swainson, Ian P. 396

T

Talwani, Manik 473
Taylor, Kendrick 308
Taylor, R. Ervin 863
Tegen, Ina I, 286
Thompson, Lonnie G. 457, 595
Thomson, David J. 949
Tinner, Willy 442

U

Upchurch, Garland R., Jr. 547

V

Valley, John W. 34
Van Vliet-Lanoë, Brigitte 770
Veizer, Ján 128, 923, 926
Velichko, Andrei A. 752
Veron, John E. N. 198
Vickers-Rich, Patricia 13

W

Wang, Pinxian 583
Weaver, Andrew J. 943
Webb III, Thompson 188
Wefer, Gerold 525
Weinelt, Mara 651
Whiteside, Jessica H. 826
Widdowson, Michael 514
Williams, John Jack W. 856
Wolf-Gladrow, Dieter A. 123, 479
Wright, James D. 148

Y

Young, Grant M. 836, 907
Young, Jeremy R. 187

Z

Zeebe, Richard E. 123, 479
Zolitschka, Bernd 485

Subject Index

A

- AABW (*see* Antarctic Bottom Water)
- AAS (*see* Atomic Absorption Spectrophotometry)
- Aasivik Terrane (Greenland) 35
- Abakan Basin 506
- Abbot, Charles Greeley 428
- Abies* sp. 305, 822, 858
- ablation 395
- abrasion 364, 365
- Abu Dhabi 146, 147
- Acantharia 870
- Acanthocythereis* 665
- Acasta Gneiss Complex (Northwest Territories, Canada) 35
- ACC (*see* Antarctic Circumpolar Current)
- accelerated solvent extractor (ASE) 352
- accelerator mass spectrometry (AMS) 90, 92, 211, 259, 489, 493, 835, 865
- accretion
 - downstream 394
 - lateral 394
 - vertical 394
- ACD (*see* aragonite compensation depth)
- Acer*
 - saccharum* 241
 - sp. 817
- ACEX (*see* Arctic Coring Expedition)
- acid
 - alkanoic 660
 - alkenoic 660
 - carbonic 71, 124
 - fatty 660, 661
 - fulvic 112
 - humic 112
 - hydrochloric 124
 - n*-alkanoic 661
 - rain 97, 337, 420, 549, 736, 795, 836
 - mass extinction 549
 - nitric 98
 - sulfuric 76
 - sulfuric 76
- acidification 280
- ACR (*see* Antarctic Cold Reversal)
- acritarch 386
 - Inderites* 768
- Acropora* 205, 526
 - palmata* 145, 146, 355, 900
- acryogenic 433
- Actinaria 198
- activity
 - biological 62
 - cambial 240
 - chemical 365
 - human, record 459
 - hydrological 46
 - solar 212
 - volcanic 172, 464
- actualism 417
- adaptation, environmental 156
- Adelaide geosyncline (South Australia) 910
- Adèle Coast 944
- Adhémar, Joseph 428
- adjustment, isostatic 355
- Adriatic Sea 875
- Aegean Sea 505, 875
- aeolian flux 266
- aerosol 92, 174, 335, 511, 722, 794, 800, 937, 978
 - albedo 976
 - chemistry 976
 - formation 335
 - in ice cores 459
 - load 51
 - mineral 1
 - physics 976
 - scattering of radiation 976
 - stratospheric, total mass 977
 - sulfate 220, 548
 - sulfuric acid 335
 - veil 978
 - volcanic 423, 440
- Afar Desert (Ethiopia) 336, 735
- Africa 262, 267, 276, 285, 418, 425, 590, 732, 786, 858
 - aridification 450
 - onset 791
- Cambrian climate 292
 - cooling 449
 - drying 449
 - dune belt 424
 - endemic fauna 732
 - glacial period deserts 298
 - glaciation, Paleozoic 387
 - hominid speciation 798
 - ice cores 457
 - monsoon 736
 - tillites 469
- Aftonian interglacial 363
- Agassiz, Louis Jean Rodolphe 428, 519
- AGCM (*see* Atmospheric General Circulation Model)
- age
 - desert 48
 - radiometric 258
- aggradation 394
 - fluvial 46
- agriculture, onset 6
- Agung (Indonesia) 977, 978
 - eruption 1963 976
- air
 - analysis 118
 - composition, paleo-archive 456
 - in polar ice 118
 - mass, trajectories 597
- Airy model of isostasy 375
- Akaike Information Criterion 245
- Akilia Island 36
- Akkadian
 - collapse 7
 - empire 7, 8
- Akuyreyri (Iceland) 621
- alanine 234
- Alaska 207, 246, 274, 552, 553, 731
 - glaciation 206, 451
 - glacier ice 222
 - ice cores 457
 - loess cover 314
 - mountain glaciers 595
 - permafrost 222
 - warming 224

- Albatross (res. vessel) 529
albedo 2, 40, 51, 55, 99, 159–161, 297, 702, 710, 785, 789, 800, 838
 continental 160, 162
 Earth 24
 feedback 2–4, 465, 591
 global 2, 97, 422, 424
 planetary 2, 3, 55, 62
 sea ice 422
 spectral 2
 spherical 2
 surface 2, 440, 785
 annual mean 2, 3, 785
Alberta erratic trains 354
Albian stage 12
albite 982
alcohol, fatty 661
alcrete 285
Alcyonacea 198, 203
alder 816, 858
Ålesund interstadial 878
Aleutian Islands 296
alfalfa 134
algae 279, 527, 578, 739
 bloom 486, 740, 767
 colonial 766
 coralline, in cool-water carbonates 138
 green, calcareous 140
 red 140
 unicellular 40
alkalinity 125, 463, 467, 535, 536, 538
 definition 535
 oceans 98
 pelagic 98
 total (TA) 124–126
alkenones 4, 347–349, 351, 661, 719
 abundance 350
 diunsaturated 609
 long-chain 656
 thermometry 800
 unsaturation 5
 index 5, 348, 719
Alleghany Mountains 501
Allerød 100, 229, 995
 -Bølling interstadial 846
 -Younger Dryas oscillation 451
alluviation 524
Alnus 305, 858
Alpha Particle X-ray Spectrometer (APXS) 542
alpine
 belt 435
 glaciation 368
 glacier 457
Alps 116, 417, 434, 443, 520, 794, 986
 glacier
 complexes 225
 ice 222
 ice
 cap 439
 cores 457
 Riss/Würm 303
 Rotmoos Neoglacial 451
 temperature oscillations, Holocene 444
 treeline fluctuations, Holocene 444
Altai Mountains (Siberia) 381, 505
alteration, hydrothermal 35, 36
Alternate Drilling Platforms (APLACON) 474
Altiplano 8, 459
 basins 49
 lakes 49
althermal 451, 939
aluminosilicates 109, 539, 540
aluminum 285, 515, 580
 -26 212
 as proxy 344
 oxides 285, 575
 oxyhydroxides 575
 as climate indicator 573
 sesquioxides 196
Amazon 425, 499, 984
 Basin 1, 297, 459, 747, 921
 fan 747
 rainforest, dunes 298, 793
 Upper Devonian climate 293
 River 730
Amazonia 858
Amazonian 66, 74
 definition 66
 rain forest 860
amber 112
American
 isthmus 167
 beech 856
 Quaternary Association (AMQUA) 189
Amery
 Basin 25
 Ice Shelf 944
amino acid
 geochronology 233, 235
 racemization 233
 fossil 234
aminostratigraphy 235, 236
aminozone 235
ammonia (NH₃) 110, 613
ammonites 237, 239, 729
 extinction 328
ammonium ion (NH₄⁺) 613
ammonoids 238
amphibians 328, 330
amphiboles 80, 81, 574
AMQUA (*see* American Quaternary Association)
AMS (*see* accelerator mass spectrometry)
anaerobic oxidation of methane (AOM) 563
analcime 574, 582
analysis
 faunal assemblage 10
 functional 14
 petrographic 343
Anasazi settlement 9
Anatolia, high plateau formation 422
anchor ice 472
ancient
 climate 10
 glaciation, evidence 384
Andean 736
 uplift 984
Andes 46, 434, 793, 984
 ice cap 439
 ice core record 459
 mountain
 building 722
 glaciers 595
 permafrost 225
Andøya (Norway) 376, 378
Andros Island 184
anemones
 colonial 198
 tube 198
angiosperms 241, 330, 607, 682, 816
 fossil
 Cretaceous 679
 Paleogene 679
 leaves 680
Angkor (Cambodia) 553
Anglian glacial 363
Angola 49, 421
anhydrite 78, 98, 146, 147, 291, 321, 322, 324, 578, 579
 as climate indicator 573
 composition 321
 entherolithic 322
 Mars 69
 nodules 324
 paleo-environmental significance 574
animal 40
 mass 109
 proxy 13
 invertebrates 10
 remains 46, 47
ankerite 85, 109
ANN (*see* Artificial Neural Networks)
anomaly, geochemical 547
anoxic event (*see also* ocean anoxic event) 626
Anse aux Meadows (Newfoundland) 422, 552
Anshan Complex (China) 35
Antarctic 231, 262, 263, 275, 287, 609
 bathymetry 25
 bottom water (*see below*)
 Circumpolar Current (ACC) 25, 167, 687, 705, 791, 944
 climate
 spatial variability 677
 change 160
 Cold Reversal (ACR) 22–24, 120, 496
 continental margin 16
 T/S relationships 17
 core 162
 deglaciation 28
 Dome C 853
 dry valleys 27, 287, 425
 glacier 449
 Intermediate Water (AAIW) 944
 mountain glacier 417
 Oscillation 803
 Peninsula 24–28, 222, 225
 erosional unconformities 27
 peripheral sea-ice 422
 permafrost 770
 Plateau 222
 Polar Front 33
 sea ice
 extent 31, 721
 history 31
 Slope Front (ASF) 16, 17
 sub-ice topography 25
 temperature 119, 120
 evolution 496
 warming 231
Antarctic Bottom Water (AABW) 16, 31, 408, 610, 615, 635, 730, 944
 amount 16
 formation 498
 mechanisms 16
 rates 19
 regions 17
 past climate change 20
 production 16
 property variability 19

- temperature 19
 Antarctica 46, 48, 231, 283, 287, 418, 439, 496,
 705, 729, 730, 759, 814, 858, 944
 aridity 45
 CO₂ record 803
 deuterium record 120
 Early Ordovician climate 292
 evaporite minerals 322
 fossil forest 502
 glaciation
 history 24, 728
 Oligocene 791
 Paleogene 788
 Holocene, temperature 814
 ice cores 424, 434, 453, 455
 airborne debris 298
 chronology 453
 dust 309
 extent 28
 record 720
 ice sheet 21, 24, 118, 159, 168, 221, 222, 224,
 225, 493, 494, 731, 890, 893
 at Last Glacial Maximum 224
 collapse 356
 development 26, 705
 evolution 498
 first large 150
 growth 705
 radar mapping 381
 thickness 361
 values 222
 ice shelves 222
 ice streams, isotopic signatures 28
 Late Quaternary 31
 methane record 120
 Middle Devonian climate 293
 paleoenvironmental record 390
 sea ice 222
 formation 498
 temperature increase, Holocene transition 120
 thermal isolation 154
 tillites 469
 tree-rings 402
 wood samples 556
 antarcticite 574, 577
 composition 321
 Anthozoa 198
 anthracite 112
 anticyclone 57
 subtropical 425
 Antilles 263
 Antipatharia 198
 AO (*see* Arctic Oscillation)
 AOM (*see* anaerobic oxidation of methane)
 apatite 248, 777, 780
 Apennines, cool-water carbonates 141
 Apex chert (Australia) 37
 aphelion 54, 703
 apthitalite, composition 321
 APLACON (*see* Alternate Drilling Platforms)
 apogalacticon 294
 Apollinaris Patera 541
 Apollo missions 66
 Appalachian
 Ice Complex 518
 Plateau 782
 Appalachians 588, 800
 apparent sea-level change (ASL) 355
 Aptian 967
 oceanic anoxic event 402
 APXS (*see* Alpha Particle X-ray
 Spectrometer)
 aquifer 735
 Ar/Ar dating 824, 938
 Arab, expansion 8
 Arabia 49, 286, 418
 as dust source 308
 Cambrian climate 292
 Early Devonian climate 293
 Middle Ordovician climate 293
 Terra 66
 Arabian Peninsula 732
 dust 1
 glaciation, Paleozoic 387
 Arabian Gulf
 sediment distribution 147
 warm-water carbonate 146
 Arabian Sea 286, 412, 591, 786, 848
 core 351
 denitrification 613
 glacial dust deposition 286
 paleoproductivity 351
 surface sediment 343
 upwelling 743
 aragonite 89, 111, 127, 136, 467, 573, 577, 743,
 760, 970
 compensation depth (ACD) 136
 composition 321
 dissolution 140
 lysocline 127
 paleo-environmental significance 574
 sea 465, 578
 solubility product 127
 Aral Sea 381, 433, 505, 736
 Aral-Caspian Depression 49
 Arcadian Orogeny 401
 archaeomagnetic study 553
 Archean 34, 836
 atmosphere, reduced 63
 crust 35
 environment 37
 Eon, subdivision 34
 glaciation 385
 hydrosphere 36
 microbes 37
 ocean
 oxygen isotope ratios 36
 temperature 36
 rocks 34, 35
 Sun's luminosity 36
 zircon 36
 archive
 continental 51
 geological 389
 paleoceanographic 389
 arcitarchs 766
 Arctic 263, 274, 275, 424, 619
 Circle 39, 58, 419, 730
 Coring Expedition (ACEX) 475, 476
 European 233
 Front 44
 glaciation 611
 ice cap 39
 ice-sheet development 474
 Intermediate/Deep Water 614
 Ocean 38, 159, 296, 381, 422, 731,
 815, 890
 area 39
 map 39
 pack ice 39
 sea ice 221
 stratification 38
 Oscillation (AO) 42, 58, 60, 180, 619, 736,
 803, 933, 978
 Pliocene climate 811
 Russian 424
 sea ice
 Cenozoic development 43
 extent 223
 freshwater flux 41
 historical record 42
 temperature 41
Ardipithecus
 kadabba 447
 ramidus 447
 Arecaceae 607
 arenites, lithic 903
 arête 366
 Argentina 524
 glaciation, Silurian 387
 loess cover 314
 paleosol 402
 Argentine Precordillera
 Cambrian climate 292
 Early Ordovician climate 292
 argon 72, 211
 data 77
 degassing on Venus 77
 isochron diagram 824
 isotope (*see also* dating, Ar-Ar) 824
 Mars 72
 atmosphere 66
 isotopic ratio 72
 solar system abundance 79
 arid coast 186
 aridification 7, 266, 587, 590
 aridisol 903
 aridity 45, 46, 425
 causes 46
 definition 45
 degree 45
 evidence 46
 archaeological 48
 biological 46
 from the Oceans 48
 geomorphological 46
 historical 48
 sedimentological 46
 glacial-phase 298
 index 46
 indicators 46
 geomorphological 47
 Pleistocene accentuation 48
 Arizona 552
 arkose 903
 Arrhenius, Svante August 428
 arsiniotheres 732
Artemisia 822, 858, 993
 Artificial Neural Networks (ANN) 654
 artiodactyls 14
 Ascension eolianite 425
 ASE (*see* accelerated solvent extractor)
 ASF (*see* Antarctic Slope Front)
 ash 816
 cloud, cooling climate 415
 fall, Paleozoic 239
 particles, silicic 976
 Ashgillian Epoch 292
 Asia 387, 498, 590, 786
 deserts 46, 286

- Asia (*Continued*)
 ice cover 49
 monsoon 46, 587, 724, 786, 932
 belt 425
 circulation 589
 records 586
 tillites 469
 ASL (*see* apparent sea level)
 aspartic acid 234
 assemblage
 fossil 11, 13
 Heterozoan 140
 trilobite 11
 Cambro-Ordovician 11
 asteroid 96, 98
 collisions 420
 impact 174, 423
 Cretaceous 167
Asteromphalus sp. 280
 asthenosphere 468
 astrakanite, composition 321
 astrochronology 255, 553
 astronomical
 parameter 53
 long-term variation 53
 polarity time scale (APTS) 254
 theory of paleoclimates 51–53
 variations (*see also* Milankovitch cycles;
 orbital cycles) 163, 391
 asymmetry, climatic 297
 Atacama Desert (Chile) 46, 48, 195, 425, 793
 Athabasca Glacier (Canada) 445
 Atlantic 102, 609, 730
 aragonite lysocline 127
 Basin, heat transport 167
 biozone 451
 calcite lysocline 127
 carbonate ooze 137
 circulation 22
 climate variability 619
 Coastal Plain 805
 Conveyer 23, 24
 meridional overturning (AMO) 619, 944
 molluscan fauna 11
 Multidecadal Oscillation 9
 nutrient distribution 615
 Ocean 379, 387, 408, 409, 429, 439, 722
 air-sea interaction 619
 alkenones 350
 circulation 22, 634
 dusts blowing from Africa 308, 309
 eolian dust 308
 eolian record 310
 net ocean heat transport 614
 realm 291
 thermohaline circulation 802
 Atlas Mountains, permafrost 225
 atmosphere 87, 92, 231, 278, 342, 419, 716, 733
 accretionary 80
 ancient, $p\text{CO}_2$ level 131
 Archean, reduced 63
 carbon 113
 dioxide, concentration 109
 isotope ratio 638
 chemistry, model 63
 circulation 784, 798
 model 165
 composition 61
 Cambrian-Devonian 291
 variations 62
 dust 219
 early 85
 reduced state 63
 Earth's primordial 62
 Earth's secondary 62
 evolution, Earth 61
 feedbacks 62
 global 98
 history 87
 greenhouse gases 493
 heat transport 407
 infrared emission level 96
 impact erosion 70
 loss 70, 71
 volatile tracer 72
 methane 62, 231, 440, 511
 numerical model 160
 opacity 98
 oxygen content 87
 Phanerozoic
 greenhouse gases 62
 oxygen 64
 planetary waves 792
 pre-anthropogenic 123
 Precambrian
 greenhouse gases 62
 oxygen 63
 primordial 110
 Quaternary 190, 191
 solar 70
 sources and sinks 62
 Atmospheric General Circulation Model
 (AGCM) 586, 620, 684
 atoll 204
 Atomic Absorption Spectrophotometry (AAS) 655
 ATP 536
 attapulgite 580
 aurora 417, 429
 australis 417
 borealis 416
 cycle 296
 history 299
 periodicity 429
 Aurora Basin 25
 auroral oval 295, 299
 Australasia 858
 Australia 48, 235, 285, 286, 387, 418, 425, 590,
 730, 786, 884
 Antarctic Basin 17
 Cambrian climate 292
 Cenozoic northward movement 791
 climate
 Middle Devonian 293
 Middle Ordovician 293
 Silurian 293
 continental shelf 140
 cool-water carbonates 138
 deserts 309
 dust 1
 drought 721
 Early Devonian climate 293
 fauna 722
 endemic 732
 flora 722
 glacial period deserts 298
 glaciation
 Paleoproterozoic 385
 Paleozoic 387
 permafrost 225
 playas 323
 relict dunes 49
 sabkha 323
 salinas 323
 tillites 469
 zircons 35
 australopithecines 448
Australopithecus
 afarensis 448
 africanus 448
 anamensis 448
 autocompaction 901
 autotrophs 279
 Auvergne, volcanology 431
 Auversian Facies Shift 528–530
 auxin 240
 avalanche 835
 Axel Heiberg Island 13
Azolla spp. 476
 azooxanthellate 200
 Azores 297, 619
 High (AH) 314, 619
- B**
 Babbage, Charles 397
 Bacillariophyceae 280
 backstripping, flexural 357
 back-swamp-loessification 524
 bacteria 40, 112, 276
 chemolithoautotrophic 12
 methanotrophic 135
 nitrogen fixing 613
 soil 282
 sulfur-oxidizing 113
 swamp 423
 Baffin Island 519
 Bahamas 90, 262, 425, 451, 632, 884
 Baja California 261
 land snails 731
 playas (salinas) 323
 Bajocian 964
 Balashovskaya paleosol (Matuyama zone) 755
 Baldeggersee (Alps), varves 740
 Baltic 378
 Ice Lake 378–380, 974
 Sea 416, 423, 433, 875
 Eemian 305
 banded iron formations (BIFs) 63, 85, 574,
 575, 910
 Bangladesh 90
 Bar, gravel 394
 Barbados 377, 879, 890
 coral 506
 fossil reefs 900
 Barberton Greenstone Belt 579
 barchan 314
 Barents Sea 296, 424, 493, 505
 Ice Sheet 493, 890
 length of sea-ice 424
 Barents-Kara Ice Sheet 877
 barite 323, 579, 582, 927
 accumulation, ocean productivity
 reconstruction 645
 as climate indicator 573
 paleo-environmental significance 574
 barium 578, 636
 -calcium ratio 344
 barnacles, in cool-water carbonates 138
 Barnes Ice Cap 987
 baroclinicity 60

- Barremian-Aptian boundary, greenhouse mode 402
- barrier
island 183, 186
reef 204
- barycenter 295
- basal
ice 89
characteristics 89
debris 89
geomorphic potential 89
rheological properties 89
melting 20, 21
- basalt 985
eruption 335
flow
Hawaii 335
Iceland 335
Thulean 154
- basin
closed conditions 322
endoreic 734
evaporites 322
exoreic 734
formation 474
-to-basin fractionation 137
- Basin and Range Province (USA) 49
- basswood 816
- bat 729
- Bathonian-Callovian 965
- bauxite 196, 291, 433, 499, 575, 716
distribution 576
- Bay of Bengal 267, 590
- Bay of Fundy (Canada) 418
- Be-10, record 455
- beach
berm 89
deposits 89
erosion 90
face 89
internal stratigraphy 89
sand 89
subtropical 90
tropical 90
- beachrock 89, 578
age dating 90
cementation
mineralogy 89
origin 89
emerged 90
indicator of former sea level 90
sedimentology 89
submerged 90
- Beagle* 308
- bear 732
- Bear Island, Upper Devonian climate 293
- Beaufort
Group 388
Gyre 39, 40
- bedform, sandy 394
- bedrock, form 366
- beetle 90, 439, 742
climate indicator
late Tertiary 90
Quaternary 90
distribution, thermal constraints 91
fossil assemblage 91
Quaternary assemblages, North America 91
- beidellite, formula 574
- belemnites 12, 128, 130, 133
- Belgium 99
- Belingwe Greenstone Belt (Zimbabwe) 833
- Belize (Central America) 134
- Bellemnitella americana* 128
- Belukha, ice core 458
- Bengal Shelf 267
- Benguela Current 48, 422
- Bentley Trench 25
- bentonites 540
- Bering
Block rotation 791
Strait 409, 732, 771, 791, 844
deepening 611
first opening 811
link 296
- Beringia 518
- berm 900
- Bermuda 263, 425
High 764
Rise 305, 343, 617
- Berriasian 964, 965
- berthierine 574, 580, 582
as climate indicator 573
formula 574
paleo-environmental significance 574
- beryllium 92, 212, 213
applications 92
dating 93
production 92, 93
transport 93
fluxes 92
half-lives 92
neutron activation 92
- Betula* 100, 305, 817
- bicarbonate 71, 123, 129, 534
ion 113
- Bidar (India) 514
- BIFs (*see* banded iron formations)
- Big Badlands (South Dakota) 731
- Big Horn Basin (Wyoming) 15
- binge-purge cycles 95
- biochronology, foraminiferal 339
- biocomplexity 325, 326
- biodegradation, bacterial 4
- biodiversity 11, 325, 328, 768
- biofacies 11
foraminiferal 357
- biogeochemical cycles 98
- bioherm 139, 205, 465, 525
- biohorizon 237
cross-cutting 239
- biological
feedback 330
paleoproductivity 342
pump 111, 125, 127, 535–537, 790
- biomarker 43, 341, 343, 347, 742, 875
- molecules 660, 661
organic 719
ocean productivity reconstruction 649
- paleoenvironmental 350
paleoproductivity 351
sterol 347
- biomass
production 536
terrestrial, burning 98
- biome 46
- biomineral 128, 233, 234
carbonate 235
- biomineralization 128, 573
- bioproductivity 64
- biosphere 87, 684, 716
deep 474, 633
feedbacks with hydrosphere 463
marine 282
Quaternary 190, 191
terrestrial 282
- biostratigraphy 100, 237, 339, 528, 767
conodont 768
biostromes 139
- biota
Heterozoan 139
migration 325
Photozoan 139
terrestrial, model 330
- bioturbation 11, 266, 411, 487, 601, 740, 764
- biozone 237, 451
Atlantic 451
boreal 451
subboreal 451
- bipolar climate seesaw 496, 850
- birch 100, 816, 993
- Birch Lake (Alaska) 490
- bird, eggshell 235
- birdsfoot delta 184
- birnessite 576
paleo-environmental significance 574
- bischofite, composition 321
- bivalves 10–12, 747
benthic 12
dispersion patterns 213
rudist 203
- Bjerrum plot 124
- Black hole 295
- Black Sea 7, 263, 381, 414, 434, 505, 736, 875, 877
Basin, modeling 7
flooding 506
freshwater inundation, late Quaternary 506
New Euxine phase 381
- black shale 402, 580, 626
- blackbody, temperature 62
- Blake
Outer Ridge 263
Plateau 778
Ridge 561
- Blanco Fracture Zone 505
- Blanford, William Thomas 429
- bloedite, composition 321
- Blue Nile 415, 425
- blue-green algae 486
- boehmite 574–576
- bog oaks 440
- bolide
carbon dioxide release 219
climat 96
impact 213, 328, 548, 549
- Bolivia 8, 490, 499
glaciation, Silurian 387
high plateau formation 422
ice cores 457
- Bølling 229, 852
Transition 22–24
Sø (Denmark) 100
warming 889
- Bølling-Allerød (B-A) 853
-Dryas oscillation 51
interstadial 91, 100, 439, 852, 889
interval 496
warm interval 948
- Bona Churchill ice core 458

- Bonaparte Gulf (northern Australia) 140, 377
- Bond
 cycle 568–571, 802, 948
 shape 569
 temperatures 569
 event 592
- Bond, Gerard Clark 429
- bone
 histological cross-section 14
 isotopic composition 135
 phosphate of lime 775
- Bone Valley (Florida) 15
- Bonneville
 Depression (USA) 49
 Flood 380
- borate, evaporite 196
- Boreal Bio Province 99
- borehole climatology 103
- boron
 foraminiferan shells 744
 isotope
 seawater 743
 geochemistry 743
 total dissolved 124
- Bosporus Strait 7, 414, 434, 506
- Boston, glacial relief 361
- bottom water
 Antarctic 16, 31–944
 dysoxic 12
- bottom-simulating reflector (BSR) 561, 562
- boulder
 erratic 364
 pavement 384
 striated 364
 train 364
- Boutellier non-glacial interval 989
- brachiopods 11, 128, 130, 500
 in cool-water carbonates 138
 Ordovician 11
- Brahmaputra River 267, 590
- brain corals 900
- Bransfield Strait 16, 944
- brassicasterol 347, 351, 661
- Brazil 13, 418
 glaciation
 Carboniferous 384
 Silurian 387
 rift 421
- Brazilia, Silurian climate 293
- Brazos 267
- break-up, continental 474
- brine 41
- bristlecone pine, growth rings 440
- Bristol Channel 376
- Britain 100
 glaciations 363
 Medieval 552
- British
 Columbia 261
 glaciation 206
 late Tertiary landscape 210
 sea-level change 210
 Ice Sheet 494, 877
 Isles 91, 993
 glaciation 418
- bromide 735
- Brørup interstadial 878
- brown coal 433
- browsers, dietary preferences 15
- Brückner, Eduard 52
- Bruhnes-Matuyama
 boundary 425, 755
 magnetic reversal 911
- Bryansk (Farndale) epoch (interval) 754
- Bryansk interstadial 756
- bryozoans 129, 139, 143, 145
 in cool-water carbonates 138
- BSR (*see* bottom simulating reflector)
- buffer, carbonate 124
- buffering 124
- bulk forcing 684
- burial
 deep 130
 diagenetic alteration 749
- Bylot Island (Canada) 372
- Byrd ice core 23, 454
- Byzantine empire 8
- C**
- C_3
 $\delta^{13}C$ 130, 134
 / C_4 change 134
 pathway 130, 133
 plants 133
- C_4
 grass 48
 pathway 130, 134
 plant, $\delta^{13}C$ 130
- cadmium 636
 /calcium ratio 341, 344
- Cairo (Egypt) 425
- calcarenite 89, 90
- calcareous ooze 525, 527
 deep-sea 526
- calcification temperature 345
- calcisol 197, 903
- calcite 71, 76, 78, 89, 108, 111, 249, 291, 523, 573, 577, 578, 0, 735, 743, 758, 916, 970
 compensation 127
 composition 321
 crystals 487
 dissolution 615
 dominance period 578
 foraminiferal 574, 615, 745
 high-Mg 128
 low-Mg 128
 lysocline 127
 paleo-environmental significance 574
- precipitation
 autochthonous 486
 gametogenic 345
 temperature 148
 pseudomorph 578
 re-precipitation 140
 saturation 137
 horizon 127
 solubility product 127
 undersaturation 615
 vein 760
- calcium 98, 111, 580
 carbonate 87, 98, 285, 291, 338, 490, 528, 871, 916
 $^{13}C/^{12}C$ ratio 564
 compensation depth (CCD) (*see also* carbonate compensation depth) 127, 262, 537
 dissolution 113, 537
 precipitation 89, 125
 saturation 127
- solubility 126
 table, oxygen isotopic composition 746
 silicate, formation 112
 sulfate 291, 487
 calcrite 186, 285, 291, 320, 499, 578
 Early Devonian climate 293
 soil 580
- CALDRILL 261
- Caledonian Orogeny 401
- caliche (*see also* calcrite) 186, 285, 320, 578
- California
 margin 564
 Current 296
- Callimitra carolotae* 870
- Calvin
 Cycle 15
 pathway 130
 Calvin-Benson pathway 133
- calving 395
- CAM (crassulacean acid metabolism) plant 130
- cambisol 754
- cambium 240
 growth 240
- Cambrian 238, 338, 775, 836
 climate 291
 climatic evidence 292
 evaporite deposition 323
 explosion 328
 paleotemperatures 401
- camel 732
- Camp Century (Greenland) ice core 229, 453, 454
- Campanian, ocean 213
- Canaanite city-states, decline 8
- Canada 39, 41, 243, 273, 445, 858
 cool-water carbonates 141
 drumlins 369
 eskers 370
 geomagnetic fluctuations 416
 glaciation, Paleoproterozoic 385
 ice cores 457
 iceberg discharge 569
 permafrost 222
- Canadian
 Arctic Archipelago 41, 361, 518
 Basin 39
 Shield 518
 glacial landscape 368
- Canaries Current 296
- Canary Islands 49, 416
- Candona* 664
- CANOCO (*see* Canonical Correspondence Analysis)
- Canonical Correspondence Analysis (CANOCO) 156
- cap carbonates 467
- Cape Hatteras 161
- Cape of Good Hope 422
- Cape Roberts 28
 cores 27
 Project 25, 27
- caprock 285
- Caradocian epoch 292
- carbon 72, 107, 110, 265, 266, 277, 778
 -13
 C_3 plants 114
 C_4 plants 114
 CAM plants 114
 /carbon-12 ratio 114–116
 distribution 115

- 14 212
- activity 864
- calibration 865
- dating 160, 735
- half-life 863
- production 863, 864
- abundance 108
- atmosphere 113
- burial rate 466
- cycle 92, 107, 108, 116, 496, 508, 533, 560, 700, 710, 847
- capacitor 563
- deep 112
- endogenic 107
- exogenic 107
- glacial-interglacial 847
- global 96, 98, 133, 562, 794
- greenhouse pathways 400
- historical background 107
- marine 789
- model 549
- ocean 124
- past 686
- processes 112
- running 111
- structure 107
- DIC (*see* dissolved inorganic carbon)
- DOC (*see* dissolved organic carbon)
- dioxide (*see below*)
- elemental 108, 112
- fixation 5
- flux 114, 115
- fractionation 116
 - isotopic 5, 37, 114
 - factor 128
- hydrosphere 113
- in mantle 131
- incorporation into carbonates 128
- inorganic 108
 - chemistry 534
 - total dissolved 743
- isotope 14, 37, 109, 114, 434, 449
 - analysis 133, 135, 549, 742
 - composition 62, 116, 134, 567
 - excursion 549
 - fossil shells 800
 - fractionation 5, 37, 114
 - marine environment 135
 - marine geochemistry 533, 534
 - notation 133
 - ratio 63, 133, 463, 465, 659, 838
 - record 564, 647
 - stable 133
 - standard 128
 - terrestrial environment 133
 - variations 128
- loss 70
- mass
 - in land plants 107
 - in oceans 109
- monoxide 109, 113
 - reservoirs 109
- /nitrogen ratio 344, 659
- organic 98, 108, 262, 343, 351
 - accumulation 342
 - burial 626
 - $\delta^{13}\text{C}$ ratios 567
- oxidized 534
- particulate inorganic (PIC) 109, 115
- particulate organic (POC) 109
 - preservation 133
 - primordial Earth 110
 - pump
 - biological 125
 - physical 125
 - reduction 112
 - reservoirs 107–109, 130
 - residence time
 - oceanic 123
 - in seawater 128
 - sequestration 265
 - sinks 98
 - sputtering 71
 - storage 507
 - total dissolved inorganic 124, 125
 - carbon isotope ratio 127
 - distribution 125, 126
 - global inventory 126
 - measurement 125
 - trends 115
 - uptake 780
 - volatilization 115
- carbon dioxide 96, 110, 182, 334, 549, 560, 684, 711, 729, 746, 780, 798, 800, 836, 916
 - air-sea exchange 112
 - anthropogenic output 336
 - atmospheric 98, 109, 116, 117, 434
 - Last Glacial Maximum 55
 - Late Pliocene 55
 - long-term variation (over geologic time) 52, 467
 - mass 109
 - paleolevel 62, 63
 - recycling time 114
 - weathering lifetime 71
 - climate relationship 167
 - climatic effect 398
 - concentration
 - Eocene 154
 - Holocene 121, 122
 - Holocene transition 120
 - Last Glacial Maximum 51
 - paleoatmospheric 135
 - pre-industrial 107
 - Quaternary 391
 - variations 119, 166
 - Cretaceous level 214
 - data reliability 119
 - dissolution 109
 - in ocean 112, 123
 - in water 111
 - reactions 113
 - dissolved 109
 - forms 123
 - doubled 177
 - forcing 3
 - free 123
 - fugacity 124
 - hydration reaction 534
 - in icehouse climate 464
 - in Martian atmosphere 66
 - in primordial atmosphere 111
 - isotopic composition 118
 - measurement 119
 - metamorphic production 112
 - paleo-levels 567
 - partial pressure 113, 534, 743
 - Quaternary variations 118
 - reconstruction 390
 - record 119, 169
 - reservoirs 109
 - solubility 125
 - coefficient in seawater 124
 - volcanic production 466
 - on Venus 76
 - weathering
 - feedback loop 62
 - hypothesis 599
- Carbon Dioxide Information Analysis Center (CDIAC) 125
- carbonate 85, 98, 262, 322, 425, 534, 749, 775, 837, 970
 - $^{18}\text{O}/^{16}\text{O}$ ratio 564
 - alkalinity 535, 777
 - aragonite-dominated 138
 - buffer 124
 - calcite-dominated 138
 - cap 467
 - carbon
 - incorporation 128
 - isotopic composition 129
 - chemistry 124
 - processes 125
 - compensation depth (CCD) (*see also* calcium compensation depth) 136, 137, 466, 525, 527–529, 538
 - cool water 138, 144
 - deposition 140
 - diagenesis 139, 140
 - examples 141
 - lithification 140
 - deep sea 129, 525
 - deposits 134, 267, 525, 526
 - dissolution (*see also* carbon dioxide, dissolved) 140
 - depth 129
 - kinetics 136
 - eoianite 320
 - formation 267
 - ion 113, 123
 - isotopic fractionation 669
 - lysocline 136
 - marine 63, 87
 - distribution 140
 - recent 129
 - trace elements 578
 - mud 139
 - ocean productivity reconstruction 645
 - oolitic 578
 - ooze 136
 - oxygen, isotopic composition 129
 - paleoenvironmental significance 574
 - paleotemperature equation 778
 - pedogenic 62, 749
 - $\delta^{18}\text{O}$ 749
 - Paleozoic 749
 - U-Pb age-dating 751
 - Phanerozoic 87
 - platform 87, 499
 - post-depositional diagenetic overprint 129
 - precipitation 143, 322, 747
 - Eocene 731
 - inorganic 129
 - preservation, changes 137
 - production, biologic 140
 - productivity 99
 - ramp 146
 - reduction 129
 - rock 128, 130

- carbonate (*Continued*)
 carbon isotope study 128
 chemical weathering 98
 sand 425
 saturation, horizon 136
 sediment 110, 736
 distribution 143
 isotopic record 669
 oceanic 126
 shallow marine 128, 129
 shallow water 129
 skeletal 143
 species in seawater 534
 storage rates 115
 stromatolitic 837
 system, seawater 124
 tidal flat 184
 top of ramp 499
 warm water 143
 case studies 144
 geological past 144
 grains 144
- carbonatite 109
 magma 77
- carbonic acid 71, 124, 534, 916
 anhydrase 534
 pK^* values 124
- Carboniferous 115, 731
 coal 731, 784
 early climate 500
 glacial periods 358
 glaciation 463, 469
 carbon dioxide values 117
- carbonylsulfide 75, 78, 81, 82
- Cariaco Basin (Venezuela) 8, 725, 747, 802, 995
 millennial cycles 571
- Caribbean 8, 138, 297, 578, 619, 889
 Basin 263
 coral reefs 201, 205
 eolian dust 308
 plate 421
 Sea 261, 611
 deep-sea core 424
- Carlsbad Cave (New Mexico) 916
- camallite, composition 321
- carnivore 729
- carotenoid 347, 350
 pigment 350
- Carpinus* 305, 858
- Carya* 305
- Cascade Mountains 206, 597
- Cascadia Margin Gas Hydrates expedition 477
- Caspian Sea 381, 433, 505, 552, 734, 736
- Cassiar Mountains 207
- Castile Formation (New Mexico) 324, 831
- cataclastics 279
- catastrophic climatic cooling 548
- catchment
 area 734
 basin 268
 human influence 485
- cathodoluminescence 130
- Catskill Formation 401
- cattle 123, 732
- Caucasus, glacier complexes 225
- cave 47
 deposits, growth rate 747
 record 389
 sediment 800
- cavitation 95
- CCD (*see* calcium carbonate compensation depth)
- CDEX (*see* Center for Deep Earth Exploration)
- CDIAC (*see* Carbon Dioxide Information Analysis Center)
- CDW (*see* Circumpolar Deep Water)
- cedar 858
- cellulose 278, 741, 747
- Celtis* 305
- Cenomanian 886
- Cenomanian/Turonian
 boundary 132
 oceanic anoxic event 402
- Cenozoic 38, 148, 237, 239, 255, 261, 417, 449, 498, 607, 700, 728, 757, 928
 chemical weathering rate 811
 climate 148
 change 11, 149
 CO₂ level, reconstruction 794
 cooling 611, 705, 788
 coral reefs 203
 fossil 422
 assemblages 784
 glaciation 166, 386, 387, 463, 770
 ice age 470
 mountain building 794
 ocean circulation 790
 orbital variability 473
 paleoclimate reconstruction 608
 plate migration 421
 warm paleoclimate 417
- Center for Deep Earth Exploration (CDEX) 475
- Central America 8
- Central American Isthmus 205, 705, 790, 811
 closure 610, 611
 Neogene 791
- Central Asia
 Early Ordovician climate 292
 glacier ice 222
 loess cover 314
 Middle Devonian climate 293
 paleolake 381
- Central Atlantic Magmatic Province 336, 337, 402, 831
- Central Australia 47
- cephalopods 12, 338
- Ceriantharia 198
- Ceriantipatharia 198
- CFC (*see* chlorofluorocarbon)
- chabazite 582
 formula 574
 paleo-environmental significance 574
- Chaco Canyon 9
- Chad 447
 Upper Devonian climate 293
- Chad-Bodélé Depression 49
- chalcedony 580
- chalk, as climate indicator 573
- Challenger Expedition 338, 525
- Chamberlin, Thomas Chrowder 429
- Chambers, Robert 429
- champsosaurs 14
- change
 biotic 328
 climatic 49, 385
 context 49
 environmental 385, 474, 560
 extreme 564
 record 47
- eustatic 378
- faunal, glaciation-related 372
- floral, glaciation-related 372
- glacial-eustatic
 Holocene 356
 Pleistocene 356
 Pre-Pliocene 356
- tectonic 385
- channel 416
 fill 394
 steepness 602
 tidal 186
- Channeled Scabland (USA) 374, 504
- Chara* 491
- charcoal 46, 681, 741
 formation 682
- Charpentier, Jean de 429
- Chassigny 74
- chattermark, glacial 364
- cheirurids 11
- chelator 478
- chemical
 index of alteration (CIA) 750, 837
 remanent magnetization (CRM) 254
 weathering 365
- chemocline 87
- chemosynthesis 109, 534
- Chenopodiaceae 858, 993
- chemozem 754
- chert 85, 574, 575, 580, 778, 908
 as climate indicator 573
- Chesapeake Bay (USA) 99, 420
- chevron 323
 texture 577
- chicken wire (*see* anhydrite nodules)
- Chicxulub (Yucatan, Mexico) 99, 420, 966
 Crater 98, 174, 217
 impact 218, 219, 548
- Chikyu (drilling vessel) 475
- China 99, 414, 419, 553, 786, 848, 858
 climate 292, 293
 zones 587
 drought 8
 dust storms 308
 eolian deposits 48
 historical flood records 426
 ice cores 457
 loess 424
 deposits 48, 314, 425
 record 315
 Loess Plateau 286, 311, 315, 435, 587
 millennial cycles evidence 571
 permafrost 225
- Chinle Formation (Arizona) 585, 586, 964, 966
- chironomid 439, 488, 490
 temperature reconstruction 742
- chitin 766
- chitinozoans 766
- chloride 735, 836
- chlorine 110, 212, 350, 351, 613
- chlorite 309, 523, 539, 580, 581
 iron-rich 581
 paleo-environmental significance 574
 schists 539
- chlorofluorocarbon (CFC) 19, 78, 109
- chlorophyll 279, 350, 613, 661, 719
 $\delta^{15}\text{N}$ value 613
 production, biomarker 351
- cholesterol 347, 349, 661

- chondrite, carbonaceous 80, 109
 $^{36}\text{Ar}/^{38}\text{Ar}$ ratio 72
 Christmas Island, *Porites* microatoll 725
 chromatogram, gas 350
 chromatography 351
 chromium, extraterrestrial 36
 chromophore 350
 chron 253
 Brunhes 253
 Gauss 253
 Gilbert 253
 Matuyama 253
 nomenclature 253
 chronology
 high-resolution 474
 standardization 244
 index, normalized 244
 chronostratigraphy 100
 global 159
 Quaternary 875
 chronozone 238
 Chryse Basin (Mars) 68
 Chrysophyceae 280
 Chrysophyta 280
Chrysotila lamellosa 4
 Chuja River 505
 Chuja-Kuray Lake 505
 Chukchi Sea, sea ice decrease 42
Cibicidoides 345
 kullenbergi 646
 wuellerstorfi 646
 circulation
 abyssal 615
 Atlantic 22
 atmospheric 57, 174
 response to climate change 57
 change, theoretical considerations 60
 convective 420
 deep ocean 126, 530
 Hadley 59
 modeling, observational parameters 59
 modes 297
 monsoonal 49
 ocean 231, 422, 477
 global 421
 rate, proxies 638
 thermohaline 20, 22, 38, 41, 137, 229, 297,
 489, 506, 529, 610, 704, 790, 853, 943
 Atlantic 802
 North Atlantic Ocean 41
 stability modes 20
 Walker 59
 Circum-Antarctic Current 730, 731
 CircumArctic Paleo-Environments program
 (CAPE) 677
 Circumpolar Deep Water (CDW) 16, 17,
 615, 944
 cirque 155, 366
 formation 155
 glacier 155, 595
 lake 156
 palaeoclimatic information 156
 shape 155
 civilization
 ancient 7
 Maya 8
 Mochica 9
 pharaonic 7
 Tiwanaku 8
 clam 901
 CLAMP (*see* Climate Leaf Analysis Multivariate
 Program)
 Clark Fork River 504
Clarkeia 11
 Classical Wisconsin 493
 classification, eolian materials 313
Classopollis 549
 clast 382, 773, 907
 shape 384
 striated 467
 surface texture 384
 clastic
 contamination 85
 wedge 227
 clathrate 402, 790
 hydrate 560
 structures 560
 submarine 530
 Clausius-Clapeyron relationship 287
 clay 262, 278, 716, 749, 775
 detrital 539
 lacustrine 573
 marine 573
 Mars 69
 minerals 539, 580
 abundance 539, 540
 as climate indicator 573
 detrital 539
 diagenetic 539
 marine 539
 paleo-environmental significance 574
 structure 539
 mixed-layer 540
 red 136
 varves 552, 973
 claystone 837
 Clearwater spillway 381
 climate
 amplifier 391
 ancient 10
 archive 455, 462
 aridity 45, 439
 astronomic forcing 51, 449
 astronomical time scale 51
 Cambrian 292
 change 6, 16, 178, 265, 385, 399, 463, 560,
 566, 596, 599, 631, 684
 and evolution 325
 anthropogenic 178, 621
 astronomical theory 51
 atmospheric dust 801
 causes 154, 164
 Cenozoic 11, 148, 149, 154
 frequency 49
 global 188, 446
 ice-age 160
 iron 478
 long-term 325
 mass extinctions 547
 mountain uplift 599
 plate tectonics 784
 quasi-periodic 72
 Quaternary 853
 rapid 23, 474
 sedimentary indicators 902
 volcanism 794, 976
 cooling
 ash cloud 415
 dust cloud 415
 coupling, hemispheres 675
 Cretaceous 213, 214
 cycle (*see also* climate, oscillation) 415
 1,470-year 571
 millennial 568, 569, 848
 orbitally driven 532
 Quaternary 841
 threshold behavior 568
 definition 325
 Early Carboniferous 500
 Early Devonian 293
 Early Ordovician 292
 end-Cretaceous 219
 evolution 684
 external influences 294
 extreme 474
 feedback 22, 51, 175, 177, 391, 392, 567
 forcing 165, 173–175, 189, 567, 841
 anthropogenic 934
 catastrophic 174
 on geological time-scale 174
 radiative 176
 future 56
 global asymmetry 297
 gradient 292, 305
 history 528
 from ice cores 457
 millennial 179
 Holocene 6
 hominin evolution 447
 hot-house 498
 hyperarid 573
 indicator, Phanerozoic 132, 466
 influence on
 coasts 186
 tree growth 240, 269
 interglacial, cyclicity 303
 internal dynamics 391, 392
 Jurassic 962
 last interglacial 303
 late glacial 101
 Late Quaternary 495
 Martian 544
 mechanism 571
 Mesozoic 554
 Middle Devonian 293
 model 51, 53, 158, 171, 165, 572, 841
 numerical 568, 700
 modeling 43, 809, 814
 Pliocene 809
 monitoring 160
 Northern Hemisphere 335
 optimum 451, 303
 orbital forcing 189, 441
 Ordovician 293
 oscillation 42, 325
 causes 852
 mid-continent 425
 mid-ocean 425
 millennial scale 172
 orbitally-paced 856
 Paleogene 728
 paleo-vegetational 856
 Paleozoic 291
 Pangean 703
 peat/coal formation 182
 Pleistocene 798
 Pliocene 798
 polar, ocean circulation 789
 pre-Quaternary 700
 processes 391

- climate (*Continued*)
 Quaternary 495, 498, 504
 reconstruction 9, 148, 270, 856
 proxies 179, 273, 291, 459
 record, instrumental 179
 response 841
 to insolation 303
 short-term events 325
 Silurian 293
 system 40
 bifurcation 843
 greenhouse effect 398
 influences 392
 responses 177, 842
 time constants 165
 terrestrial 2
 time series 165, 188
 spikes 296
 transitions 841
 Quaternary 841
 treeless interstadials 91
 trends 6
 Triassic 962
 triggering mechanism 571
 Upper Devonian 293
 variability 325, 568
 interannual 764
 last 1,000 years 178
 millennial 51, 568
 past 53
 warming 461, 462
 zone (belt) 239
 ancient 10
 late Devonian 499
- Climate Leaf Analysis Multivariate
 Program (CLAMP) 156, 157,
 680, 719
 datasets 157
 limitations 158
 paleotemperatures 156
 reference datasets 156
- CLIMAP (*see* Climate Long-range
 Investigation Mapping And
 Prediction)
- Climate Long-Range Investigation Mapping
 and Prediction (CLIMAP) 51, 158, 160,
 339, 434, 711, 719, 800, 801, 813
 project 159, 224
 sea surface temperature 57
- Climate Variability and Predictability Program
 (CLIVAR) 676
- Climatic Optimum 551
 CLIMBER-2, climate model 572
- clinoptilolite 574, 582
 formula 574
- closed cell titration 125
- cloud 757, 785
 aqueous sulfuric acid 76
 coverage, global 702
 condensation nuclei 99
 motion 700
- Cnidaria 198, 200
- coal 109, 181, 195, 291, 387, 423, 499
 deposits 729
 formation 182
 paleoclimate 196
 precursors 182
 sulfur content 196
- Coal Age 401
 coalification 182
- coast 184–186
 climate 186
 geomorphology 184
 influence of glacial sea-level cycles 186
 Peruvian 7
- Coast Mountains (British Columbia) 206, 207
- coastline, migration 183
- coccoliths 43, 129, 136, 187, 526, 652, 743
 ooze 527
- coccolithophores 187, 645, 719, 732, 767
 fossil record 188
- coccolithophorids 4, 110, 527, 536, 719
 trace metal 344
- coccolithosphaerid 526
- Cocconeis* sp. 280
- coccosphere 187
- Coconino Sandstone 580, 716
- coefficient of efficiency (CE) 271
- Coelenterata 198
- coexistence
 approach 608, 679
 interval 608
- coherence 954
- COHMAP (*see* Cooperative Holocene
 Mapping Project)
- Col du Dôme ice core 458
- Coleoptera 90, 101, 439
 fossil 101
- collophane 579
- colluvium 47
- Colombia ice core 462
- Colorado 9, 267
 high plateau formation 422
 loess deposition 315
 Plateau 585
 sedimentary structures 195
 River 273
- Columbia
 Hills (Mars) 69
 River
 badlands 374
 basalts 977
 flood basalt 336
 mouth 505
 Province (USA) 336
- Columbian Andes 860
- comet 79, 96, 99, 174
 deuterium-hydrogen atomic ratio 80
 Shoemaker-Levy 9 219
 shower 99
- Community Climate Model (CCM0) 191
- COMPLEX (*see* Conference on Multiple
 Platform Exploration of the Ocean)
- composition
 atmospheric 455
 isotopic 480
 compound-specific 662
 compound, organic volatile 109
- CONCORD (*see* Conference on Cooperative
 Ocean Riser Drilling)
- condensation 175, 760
- condition
 glacial features 384
 paleoceanographic 12
 conductivity, electrical 308
- Conference on Cooperative Ocean Riser Drilling
 (CONCORD) 474
- Conference on Multiple Platform Exploration of
 the Ocean (COMPLEX) 474
- congelation 89
- Congo 418, 424
 Basin 49, 297
 ikaite 397
 River 298
- Coniacian 886
- conifer 240, 241, 269, 682, 758, 993
- conodonts 238, 239, 768
- continent
 crustal rifting 421, 795
 Pangaea 584
 rifting 421
- continental
 blocks 788
 drift 165, 296, 420, 429, 431, 432, 700
 fragments 788
 shelves 281
 slope 263
- continentality 46, 466, 598, 786
- convection 785
 deep 615
- convective mixing 705
- convergence 156, 786
- cooling 449, 495
 abrupt 449
 atmospheric 451
- climatic
 catastrophic 548, 549
 gradual 548
- feedback 41
- global 98, 99, 422, 424, 520, 788, 966
- terrestrial 421
- tropical 57
- tropospheric 978
- cool-water carbonate
 Austria 141
 deposition 140
 diagenesis 139, 140
 examples 141
 Greece 141
 lithification 140
- Cooperative Holocene Mapping Project
 (COHMAP) 188, 189
- copper
 Finland 354
 Lake Superior region 354
- corals 136, 143, 148, 281, 425, 441, 499, 525,
 527, 578, 622, 723, 746, 758, 970
 algae symbiosis 206
 aragonitic 129
 scleractinian 578
- black 198
- blue 202
- Cenozoic 200
- deep sea 616
- definition 198
- diversity 199
- fossil 723
- isotopes 135, 179
- Mesozoic 200
- organ-pipe 203
- Paleozoic 198
- records 672
- reef 143, 198, 389, 527
 Cenozoic 203
 classification 204
 distribution 205
 environment 205
 growth, Glacial Control Theory 429
 Mesozoic 203
 Paleozoic 199

- sea level 205
 symbiosis 206
 temperature 205
 types 204
 scleractinian 578
 stony 198
 zonation 205
 Corallimorpharia 198, 200
 corallite 200
 Cordillera (North America) 206, 444, 518, 800
 Cordillera Blanca ice cores 457
 Cordilleran Ice Sheet 206, 224, 372, 390, 493, 494, 504, 518, 519, 986
 growth and decay 207, 208
 maximum 207
 core
 Antarctic 162
 deep-sea 48
 dust deposition 311
 formation 34
 ice 89
 Coriolis
 acceleration 296, 639
 force 536, 639
 CORKs (long-term observatories in the ocean floor) 632
Corollina spp. 768
 corrasion 394
 corry (*see* cirque)
Corylus 305, 858
 sp. 822
Coscinodiscus nodulifer 644
 cosmic ray 92, 551
 galactic 211
 particle 92
 solar 211
 cosmogenic radionuclide, application 213
 Costa Rica Rift 632
 coupled general circulation model (CGCM) 685
 Coxcatlan Cave 868
 cracking
 desiccation 772
 thermal 771
 crag 385
 Cramér-Rao bounds 952, 953
Crassostera virginica 298, 901
 crassulacean acid metabolism (CAM) 114
 crater lakes 485
 craton, Slave 35
 creep 601
 Cretaceous 43, 238, 264, 280, 409, 554, 607, 609, 686, 719, 766, 880
 carbon dioxide levels 214
 carbonate compensation depth 137
 climate 11, 213, 214, 219, 557
 zones 213, 214
 early 262
 floras 557
 fossil 422
 gateways 704
 global warming 422
 greenhouse climate 703
 high-latitude warming 704
 hydrologic cycle 215
 late 253, 263
 greenhouse climate 516
 mass extinction 213, 729
 meridional thermal gradient 704
 ocean 557
 anoxic events 402, 789
 paleobiogeographic patterns 558
 paleoclimate data 558
 sea level 215
 sea-surface temperatures (SSTs) 701
 temperature, land 216
 -Tertiary boundary 262
 warm climates 213
 warmth 788
 Cretaceous/Tertiary (K/T) boundary 96, 98, 99, 149
 impact, climate effects 217
 iridium anomaly 217
 mass extinction 547, 558
 crisis, salinity 559
 cristobalite 580
 crocodilians 14, 729
 Croll, James 429
 Croll-Milankovitch cycle 439
 Cromerian interglacial 363
 crossdating 240, 430
 pine 438
 multiple tree ring 269
 cross-stratification 320
 Crusader period 8
 crust
 Archean 35
 continental 35
 emergence 35
 oldest 35
 growth model 35
 spreading, superfast 477
 upper, thermal history 247
 crustal rifting, continent 421
 Cryogenian
 climate, cycle 467
 glacial interval 467
 glaciation 468
 Period 463, 467
 cryogenic 433
 cryosphere 31, 221, 461, 574, 710
 before last glacial cycle 225
 components, extent 223
 definition 221
 elements, Last Glacial Maximum 224
 evolution 223
 ice distribution 221
 last glacial cycle 224
 mass balance 222
 residence times 222
 cryoturbation 771
 crystal 248, 249
 hoppered 576
 crystallization
 authigenic 573
 fractional 540
 Cubozoa 198
 cuirasse 575
 culture
 ancient 6
 Late Uruk 7
 Cupressaceae 858
 Curcubitaceae 817
 Curie temperature 252, 254
 cyanobacteria 285, 660, 876
 calcifying 200
 cycads 729
Cycladophora davisiana 160, 162
 cycle
 1,470-year 571
 biogeochemical 107
 Fischer 327
 galactic 294
 geochemical 107
 glacial-interglacial 56, 845
 periodicity 51
 Holocene 572
 last glacial 390
 lunar 296
 millennial 569
 multi-century 569
 nodal 299
 rock 126
 solar 296, 272, 299
 cyclicality, precessional 586
 cyclone 763, 790
 Atlantic 763
 formation 763
 intensity 763
 cyclothem 387, 502, 788, 893
 definition 226
 deposit 359
 driving mechanism 227
 glacio-eustatic 469
 Illinois-Basin 227
 Kansas 227
 model 227
 standard models 227
 Cyperaceae 817, 922
 cypress 858
 Cyprideis 665
 Czech Republic, Rocourt soil 307
D
 daily irradiation 54
 D-alloisoleucine 234
 Daly detector 259
 Daly, Reginald Aldworth 429
 Dang River (China) 735
 Danian 831
 Danish Bælts 378
 Dansgaard-Oeschger (D-O) event 23, 24, 49, 51, 120, 121, 229, 412, 433, 478, 498, 568–571, 590, 616, 710, 760, 801, 841, 843, 846, 848, 852, 946
 causes 849
 ocean sediment cores 230
 spacing of 1,470 years 572
 trigger 231
 Danube River 7, 26, 436, 756
 Dardanelles 434
 darkening, global 99
 Darkhat depression (Mongolia) 505
 Darwin, Charles 308
 Dasuopu
 ice core 458, 460
 Glacier (Tibetan Plateau) 726
 data
 geochemical 399
 geothermal 103
 ice core 8
 isotopic 34
 paleoclimate 949
 paleogeographic 10
 paleomagnetic 10, 11
 dating 213, 777, 800
 amino acid racemization 233
 Ar-Ar 824
 biostratigraphic methods 237
 diatreme eruption 249

- dating (*Continued*)
 Earth history 233
 electron-spin resonance (ESR) 235
 fission-track 247
 fossil wood 445
 incremental 487
 K-Ar 258
 lake sediments 741
 metal deposits 249
 meteoritic impacts 249
 methods 233, 735, 938
 tephrochronology 937
 Ne 257
 near-surface processes 255
 optical 249
 radiocarbon 100, 236, 249, 259, 438, 439,
 451, 489, 490, 493, 751, 822, 835, 863,
 938, 987
 calibrated 439
 radiometric techniques 233, 237, 247, 255,
 258, 260, 275, 969
 U-Pb, zircon 258
 U-series 760, 969, 970, 987
 U-Th-He 259
 volcanic
 ash deposition 249
 rocks 970
 tephra 824
- de Vries effect 865, 866
 Dead Sea 7, 49, 196, 324, 433, 490, 577
 evaporites 323
 lake levels 8
 Death Valley (California) 196, 277, 324
 debris 382
 basal ice 89
 cryoclastic 298
 distribution 472
 englacial 368
 flow 385, 395
 ice-rafted (IRD) (*see* ice rafted debris)
 release 472
 sources 472
 subglacial 368
 supraglacial 368
- decarbonation, thermocatalytic 129
 decarboxylation, thermocatalytic 130
 decay
 dating 213
 method 256
 radioactive 211
 uranium 247
- Deccan (India)
 deposit 429
 flood basalt lava 336, 337, 514, 549, 977
 volcanism 216
- deep
 biosphere 474, 633
 burial 130
- Deep Lake (Minnesota, USA) 940
 deep ocean
 acceleration 685
 carbonate deposition 137
 circulation 126
- deep sea
 carbonates 525
 corals
 dated 639
 core 48, 51, 160
 deposits 525
 gas clathrate 263
- oozes 128, 129
 petroleum 262
 sediment 126, 128, 260
 chronostratigraphy 159
 dating 159
 gas hydrates 560
 sedimentary record 261
 shale 871
- Deep Sea Drilling Project (DSDP) 26, 216,
 237, 260, 261, 338, 421, 431, 473,
 529, 630
- deep water
 circulation, thermohaline 651
 distribution 640
 flow rate 687
 formation 638, 705, 790, 844, 944
 location 687
 near-continent 944
 open ocean 944
 rate 616, 642, 687
 renewal rates 638
 temperature, reconstruction 652
- deer 732
- deflation 47, 49, 308
 flat 195
- deforestation 423
 natural 423
- deformation
 elastic 375
 till 193
- DeGeer (Baron) Gerhard Jacob 430
- deglaciation 439, 453, 479, 843, 846, 858, 887,
 890, 900
 late Pleistocene 508
- degradation, microbial 343
- degree of pyritization (DOP) 576
- Delaware (USA) 185
- Delaware Basin (Texas) 324
- delta
 birdsfoot 184
 Brazos 267
 climatic signals 266
 Colorado 267
 evolution 265
 formation 267
 impact of climate 265
 modeling 268
 morphological development 265
 Niger 268
 Rhine-Meuse 267
 sediment transport 266
 sequence development 265
 surface morphology 265
 Trinity 267
- delta notation 133
- demagnetization 254
- dendrochronology 239, 241, 246, 256, 269, 430,
 487, 553, 682, 835, 938
- dendroclimatology 241, 269–271, 438, 758
- dendrograph 273
- Denekamp interstadial 756
- denitrification 532
 microbial 613
 rate 613
- Denmark 415, 878
 Strait 791
 overflow water 614
- density, stomatal 567
- Dentoglobigerina altispira* 338
- denudation, landscape 893
- DEP (*see* dielectric property)
- depauperization, molluscan fauna 432
- deposit
 carbonate 267
 cave 735
 coal 729
 coastal 185
 colluvial 485
 continental margin 266
 dust 523
 early Pliocene 267
 eolian 320
 flood 266
 fluvial 485
 glacial 89, 386, 418, 469
 late Precambrian 702
 mid-Oligocene 731
 Permo-Carboniferous 418
 glaciofluvial 284
 glaciogenic 382
 hominin-bearing 446
 ice-distal 396
 lacustrine 740, 775
 stratigraphy 489
 late Miocene 267
 loess 286, 485
 glacio-eolian 420
 marine 385
 Neoproterozoic 323
 overwash 764
 petroleum 612
 pleniglacial 771
 shoreline 489
 slackwater 266
 storm-induced 764
 subglacial 365
- deposition 71
 colluvial 46
 dry 459, 523
 glacial 89, 210, 368
 landforms 369–371
 landscape systems 372
 processes 369
 wet 459
- depositional remanent magnetization (DRM) 254
- depression
 crustal 375
 frontal 553
 interdune 195
 isostatic 364
 mid-latitude 46
- desert 45, 46, 275
 age 48
 Australia 309
 biomes 440
 coastal 46, 48
 cold 771
 definition 194
 dune 439
 dust 449
 Mars 66
 orographic, evaporites 322
 Pleistocene 48
 climatic change 49
 polar 46
 red bed 196
 river 47
 sedimentary facies 195
 varnish 275
- desertification 423, 553

- desiccation 46
 cracks (fissures) 772
 glacial-phase 298
 theory 415
 thermally induced 772
- detritus
 Hudson Strait-derived 412
 ice-rafted (IRD) 150, 151, 286, 304, 409, 411–413
- deuterium 80, 278, 458, 759
 D/H ratio 278
 delta-deuterium (δD) record 119
 excess 278, 759
 temperature record 169
- Devensian glacial 363
- Devil's Hole (Nevada) 134, 760
 calcite vein 800
- Devon Island 43
- Devonian Period 113, 116, 238, 401, 499, 750
 carbon dioxide values 117
 climate 291
 Early 293
 Middle 293
 Upper 293
 extinction event 328
 glaciation 469
 Late
 climate zones 499
 equatorial cooling 499
 flora 499
 glaciation 501
 marine fauna 499
 sea-level rise 402
 sponge, diversity 499
- DeVries solar cycle 572
- dewatering 901
- diagenesis 129, 341
 burial 129
 cool-water carbonates 139
 meteoric 129
 overprint 343
- diamict 279, 948
 dropstone 383
- diamictite 87, 278, 384, 386, 419, 467, 836, 907, 948
 origin 384
 glacial marine 463
- diamicton 278, 284, 384, 395
 glacial 279, 368
 glaciomarine 395
 lithified 279
- diamond 108, 112
 western Great Lakes 354
- diapir 321
- diaspore 576
- diatom 40, 42, 238, 262, 279, 347, 351, 449, 486, 490, 526, 537, 580, 645, 732, 735, 746, 766
 assemblages 33
 fossil 31
 bloom 486, 740
 epitheca 279
 hypotheca 279
 Jurassic 280
 lower Cretaceous 280
 Paleocene 280
 salinity change 741
 taxonomy 280
- diatomites 559
- DIC (*see* dissolved inorganic carbon)
- dicotyledons, woody, CLAMP 719
- Dicroidium* flora 962
- dielectric property (DEP) method 308
- diffusion 133
- dimethyl sulfide 99
- dinitrogen 613
- dinocyst 281
 fossil 281
 hydrographical maps 281
- dinoflagellata 280
- dinoflagellate 43, 280, 347, 351, 652, 766
 bloom 730
 blooming 281
 calcareous 282
 tracer 282
 cyst 99, 281
 ecology 280
 life cycle 281
 neurotoxin 281
 photosynthesis 281
 red tides 281
- dinosaur 14, 213, 237, 330, 729, 967
 extinction 328
- dinosterol 347, 351, 661
- diplopterol, $\delta^{13}C$ analysis 135
- discoaster 187, 526, 527
- disease 8
- disequilibrium phenomena 128
- disk, galactic 295
- dissolution-reprecipitation 129, 130
 gradient 129
- dissolved inorganic carbon (DIC) 109, 615, 982
 in ocean 123
- dissolved organic carbon (DOC) 109, 115
- Distichopora* 198, 201
- distribution, faunal 399
- diversity, pelagic 465
- Dnieper
 River 7, 505
 glaciation 756
- Dniester River 7
- DOC (*see* dissolved organic carbon)
- dog 732
- Dole effect 282, 672
- dolomite 82, 108, 109, 113, 146, 436, 523, 577, 775, 981, 985
 composition 321
 ferroan 85
 paleo-environmental significance 574
- Dolomite Alps 436
- dolostone 909, 924
 $\delta^{13}C$ record 131
- Dome C ice core 27, 28, 118–121
- Dome Fuji ice core 453–455
- Don
 glaciation 755
 River 7, 381, 505
- Dongge Cave 592
- DOP (*see* degree of pyritization)
- Dorset (England) 415
- doubt house world 357, 730
- Douglass, Andrew Ellicott 430
- drainage
 basin 734, 738
 line 46, 49
 pattern
 glacial 320
- Drake Passage 19, 25, 154, 167, 409, 609, 705, 791
 opening 618, 687
- Drakensberg, permafrost 225
- Dreizack Seamount 569
- drift
 continental 420
 genetic 326
- drilling platform 475
- drillship 473, 475
- dripstone 916
- dropstone 383, 384, 464, 472, 476, 558, 837, 903, 908
 diamict 383
 facies 467
 mud 383
- drought 8, 97, 414, 424, 450, 734
 area index 273
 Mayan 8
 record 46
- drumlin 284, 364, 369, 383, 493, 506, 519
 field 284, 370
 origin 284
- dry deposition 459
- dry valley 805
- Dryas octopetala* 22, 100, 993
- DSDP (*see* Deep Sea Drilling Project)
- Dubai 146
- Dubois, Eugène 430
- Dumas, Jean Baptiste André 107
- dump moraine 383
- Dunde ice core 458, 460
- dune 47, 195, 319, 394
 barchan 314
 belt 424
 breaching 46
 classification 314
 development 47
 discordant trends 46
 fossil 46, 439
 linear 314
 mobility index 313
 parabolic 314
 relict 49
 rock 425
 sand 729
 stabilized 49
 past wind regime information 314
 stratigraphy 46
 type, dominant wind directions 314
- dung beetle 91
- Dunn, Edward John 430
- Durango 579
- duricrust 46, 284, 514, 576, 578
 formation 285
 climatic requirements 285
 lateritic 516, 575
 paleoenvironmental indicator 285
- dust 335, 684
 aerosol 1, 317
 atmospheric cycle 286
 size range 313
 atmospheric
 changing climate 801
 impact 219
 sources 308
- climate effects 2
- clouds 97
 cooling climate 415
 global 96
- composition 1, 309
- cosmic 419
- cycle 1
 modeling 288

- dust (*Continued*)
 deposition 48, 286, 310, 523
 Cenozoic record 310
 dry 1
 glacial 286
 history 309
 interglacial 286
 long-term change 309
 orbital timescale changes 311
 rate 286
 wet 1
 desert 449
 effects on climate 317
 indirect 318
 emission 1
 maxima 1
 volcanic 440
 eolian 308
 flux 507
 geochemistry 309
 global model 288
 grain size 309, 310
 gravitational settling 309
 impact on climate 288
 intergalactic 419
 lee-desert 424
 long-range-transported (LRT) 312, 317
 marine sediment 286
 mineralogy 309
 properties 1
 provenance 311, 341
 Quaternary 286
 radiative forcing 2
 Saharan 1, 309
 sources 1
 storm 308
 transport 1, 308
 ice core 286
 long-distance 424
 veil index (DVI) 977
 volcanic 178, 424
 dustiness, glacial 287
 Dwyka (South Africa) 432
 Conglomerate 430
 Group 388
 Dye 3 ice core 229, 454
 dysoxic bottom water 12
- E**
 EAC (*see* East Antarctic Continent)
 EAIS (*see* East Antarctic Ice Sheet)
 Early Cambrian, warm climate 401
 Early Carboniferous, warm climate 401
 Early Cenomanian, sea surface temperatures 215
 Early Cenozoic, warm climate 402
 Early Dryas 100
 Early Eocene Thermal Maximum (EETM)
 (*see also* Paleocene-Eocene Thermal
 Maximum) 476
 Early Paleozoic
 carbon dioxide concentration 117
 glacial features 386
 Early Pennsylvanian glacial event 359
 Early Proterozoic glaciation 359
 Early Toarcian oceanic anoxic event 402
 Early Triassic paleotemperatures 402
 Earth
 accretion 34, 35
 age 34
 albedo 24, 175, 176, 785
 as glacial planet 362
 atmosphere 78
 carbon dioxide content 78
 evolution 61
 isotopic composition 71
 nitrogen 63
 oxidation state 334
 oxygen content 78
 pressure 66
 primordial 62
 axis
 obliquity 168
 shift 415
 tilt 154
 climate system 446
 climatic controls 384
 collision with asteroid 217
 crustal
 carbon reservoir 78
 change 416
 cryosphere 461
 deformation 375
 deglaciation 504
 differentiation 294
 early 34
 atmosphere 334
 climate 399
 habitability 37
 energy balance 785
 equator 825
 evolution, records 128
 feedbacks 398
 geomagnetic field, fluctuations 429
 global mean temperature profile 176
 greenhouse effect 81
 heat loss 407
 history 34, 438, 788
 dating 233
 early 334
 hydrogen loss 81
 inclination 428
 internal
 heating 420
 temperature structure 255
 laws 294
 climatological consequences 294
 liquid water 36
 magnetic field 417
 reversal 160, 575
 magnetosphere 419
 mantle 261
 oxygen isotope ratio 35
 nitrogen inventory 70
 noble gases 79, 80
 obliquity 62, 334
 orbit 22, 53
 eccentricity 301, 391
 precession 64
 tilt 729, 758
 orbital
 changes 52, 303
 geometry 178
 parameters 51, 72, 175, 813
 plane 423
 origin of life 435
 oxygen 81
 paleoclimate history 463, 760
 physical evolution 294
 physiographic features 297
 planetary architecture 632
 polar radius 825
 prebiotic 110
 primordial carbon 110
 properties 76
 radiation budget 62
 rotational (spin) axis 22, 62, 468, 625
 solar orbit 159
 source of heat 407
 sulfur dioxide 78
 surface temperature 62
 system components 631
 temperature 78
 variability 758
 tide 424
 volatiles 70, 80
 volcanism 81, 82
 water
 deuterium-hydrogen ratio 80
 distribution 733
 origin 69
 Earth Models of Intermediate Complexity
 (EMIC) 710
 Earth-Sun distance 53
 Earth System Model (ESM) 710
 earthquake 217
 East Antarctic Ice Sheet 222
 regrowth 27
 East Africa 439
 continental rifts 421
 ice cores 457
 permafrost 225
 rift 296
 lakes 739
 salt lakes 741
 East Antarctic
 Continent (EAC) 356
 Ice Sheet (EAIS) 24, 224, 356, 361, 609,
 792, 804
 values 222
 East Asia, ice cap 439
 East European Plain 754
 East Indies 422, 424
 East Siberian Sea 39
 sea ice decrease 42
 easterlies 793
 eastern hemlock 856
 Ebro River 559
 eccentricity 53, 761, 798, 800, 803
 Earth orbit 301
 influence on incoming solar
 radiation 301
 long term variations 54, 302
 orbital 52, 391
 eccentricity 847
 echinoderms 146
 in cool-water carbonates 138
 echinoids 143, 146
 Eclipse Dome ice core 458
 ECM (*see* electrical conductivity method)
 ecological tolerance 679
 ECORD (*see* European Consortium for
 Research Drilling)
 ecosystem restructuring 326
 ecotone
 boreal-tundra 440
 timberline 445
 Ecuador 9
 ENSO 764
 Holocene lake records 571

- eddy 16, 407, 740
 mixing
 diapycnal 685
 isopycnal 685
 motion 702
- Ediacara fauna 328, 386
- Ediacaran (Vendian) Period 467
- Eemian 56, 303, 305, 307, 453, 493
 interglacial 51, 302, 303, 363, 752, 858
 temperature in France 762
 marine environment 304
 plant migration 302
 pollen record 305
 taxa composition 306
 time-transgressivity 305
 warming 225
 woodland 304
- EETM (*see* Early Eocene Thermal Maximum)
- effect, thermobaric 16
- Egypt 48, 50, 425, 438
 civilization 7
- Eiszeitvorbereitung 295
- Ekman pumping 686
- El Chichón (Mexico), eruption 1982 976
- El Niño/Southern Oscillation (ENSO) 7, 9,
 60, 134, 179, 194, 296, 346,
 423, 424, 441, 459, 460, 619,
 620, 721, 764, 789, 803, 891,
 933, 978
 behavior, last millennium 725
 cycle, quasi-periodicity 789
 frequency 721
 decadal variation 721
 history 297
 insolation forcing 724
 magnitude 721
 paleo-
 reconstruction 722
 record 724
 permanent 567
 teleconnection 724
 variability, reconstruction 764
 warming event 978
 weakening, glacial periods 724
- Elatina Formation (Australia) 386
- electrical conductivity method (ECM) 308
- electron trap 250
- electrostatic analyzer 258
- element, volatile 79
- elk
 fossil 100
 giant 363
 horn coral 145
- Ellesmere Island 148, 552
- Ellsworth Land 25
- elm 816
 pollen 451
- Elster glacial 363
- Elsterian 877
- Emiliana huxleyi* 4, 5, 188, 348, 349, 656,
 657, 719
- Emiliani, Cesaré 152, 430
- emission
 anthropogenic 62, 934
 solar 294
- empire
 Akkadian 8
 Byzantine 8
- empirical orthogonal function (EOF) 621
- emu eggshell 236
- enamel 14, 15
 chemical stability 14
- enantiomer 233
- end moraine (*see* moraine, end)
- end-Cretaceous
 climate 219
 extinction event 328
 mass extinction 217
- end-Ordovician extinction event 328
- endoreic 734
- end-Permian extinction event 328
- end-Triassic extinction event 328
- Endurance Crater (Mars) 543, 544
- energy
 balance 105 163, 700, 795
 model (EBM) 163, 700, 795
 received from Sun 301
 standing wave 58
- Enewetak Atoll 805
- englacial
 debris 368
 setting 193
- English
 Channel 298
 Eemian 305
 Lake District 661
- ENSO (*see* El Niño/Southern Oscillation)
- enthalpy 158
- environment
 Archean 34, 37
 coastal 183, 577
 climate impact 183
 deltaic 10
 depositional 382
 estuarine 15
 exaerobic 12
 glacial 298
 lacustrine 577
 marine, Eemian 304
 marine-phreatic 90
 meteoric-vadose 90
 periglacial 298
 terrestrial 305
- environmental change 560
- Environmental Processes of the Ice Age,
 Land, Oceans, Glaciers (EPILOG)
 program 677
- enzyme 241
- Eocambrian glaciation 434
- Eocene 248, 262, 611, 685, 728, 789, 884
 carbon dioxide concentration 154
 carbonate compensation depth 138
 foraminifera 745
 glacial-eustatic record 357
 glaciation 470
 global
 climate 745
 warmth 705
 Green River Formation 827
 meridional surface temperature gradient 705
 reptilian fauna 731
- eolian
 deposit, identification 320
 dust 308
 process 312
 sand 313
 deposits 903
 seas 903
 stratigraphy 314
 sediment 312
- eolianite 319, 425, 578
 carbonate 320
 definition 319
- colization 425
- Ephedra* sp. 822
- ephemeral river 194
- EPICA
 DML ice core 454
 Dome C ice core 453–455
- epidote 248
- epimerization 234
 isoleucine 234
- epithea 279
- epogalacticon 295
- EPR (*see* Exxon Production Research
 Company)
- epsomite, composition 321
- Epstein, Sam 148
- equator, celestial 825
- equilibrium
 condensation model 79
 dynamic 294
 isostatic 599
 radiative 176
 reaction 133
 thermodynamic 124
- equinox 52, 53, 449
 precession 53, 391
 vernal 825
- equivalent dose 251
- Era
 Hadean 34
 Priscoan 34
- erg 196
- Eric the Red 8, 552
- erionite 582
 formula 574
- erosion 724, 385
 by impact 70, 74
 fluvial 266
 glacial 89, 155, 210, 266, 364
 processes 364, 365
 isostatic response 600
 P-form 365
 processes 602
 proglacial 364
 rate 736
 subglacial 284
 supraglacial 364
- erosional system 600
- erratics 382, 417
 distribution 354
 drifting ice 418
 glacial 354
 northern Europe 417
 size 354
 transport by mudflow 418
- eruption (volcanism)
 basalt 335
 flood basalt 336, 979
 prehistoric 979
 volcanoes 424, 977
 explosive 335
 Krakatoa 424
 Tambora 424
- escape
 hydrodynamic 70, 72, 74
 nonthermal 70, 74
 thermal 74
 velocity 70

- esker 320, 321, 364, 369, 370, 372, 394, 493, 716, 903
 Eskimo cultures 552
 Esmark, Jens 430
 estuary 183
 definition 183
 ethane 560
 Ethiopia 49, 336, 418, 447
 monsoonal rain 425
 Ethiopian Plateau, volcanic eruptions 731
 ethyl ketones 4, 348
 Etna eruption 44 B.C 976
Eucommia 305
 euphotic zone 110, 536, 876
 Euphrates River 7
 Eurasia 91, 498, 703, 730, 858
 ice-sheet margins, late Quaternary 505
 Eurasian
 Arctic, warming 42
 Ice Sheet, flow type 392
 Plate 476
 Shelf 39
 Europe 229, 267, 285, 335, 736
 Cambrian climate 292
 climate
 Early Devonian 293
 Early Ordovician 292
 Middle Devonian 293
 Middle Ordovician 293
 Silurian 293
 Cretaceous chalk 141
 Danian chalk 141
 deglaciation 439
 diamictite 385
 flood of August 2002 733
 glaciation 363
 Ordovician 387
 glacier 451
 ice sheet 161, 378
 loess 424, 314
 Mikulinian 303
 permafrost 225
 Weichselian interstadials 478
 European Alps 598
 glaciations 363
 European Consortium for Research Drilling (ECORD) 475
 European-British land bridge 361
 eurythermal 420
 eustasy 355, 421, 434, 789, 884
 glacial 354, 421, 887
 history 356
 eustatic
 fluctuations 421
 movements 435
 sea level 439, 451
 eutrophication 280, 736, 740
 Euxine Abyssal Plain 505
 Euxinic freshwater lakes 414
 evaporation 22, 45, 175, 194, 263, 278, 489, 573, 710, 730, 746, 760
 rate 746
 seawater 322
 evaporite 85, 194, 196, 291, 321, 401, 465, 499, 559, 582, 716, 729, 775, 793, 926
 accumulation, supratidal 559
 ancient 323
 as climate indicator 573
 borate 196
 Cretaceous 98
 deep-water, ancient 324
 definition 321
 deposit 322, 323, 559
 diagenesis 321
 distribution 573
 Early Devonian climate 293
 formation 196, 321
 geochemistry 324
 marine 291
 Messinian 324
 mineral 579
 modern 322
 nonmarine 291
 precipitation sequence 322
 pseudomorphs 323
 pumping 322
 sediment with hydrocarbons 321
 shallow-water 323
 ancient 324
 supratidal 322
 evapotranspiration 45, 194, 266, 860
 actual 45
 potential 46, 313
 event
 8,200 year event 870, 938
 ice cores 940
 modeling 941
 anoxic 558, 626
 global 474
 climatic 168
 extinction 174, 203, 213, 217, 328, 329, 336, 463, 499, 503, 547–549, 558, 654, 729
 Heinrich 304
 macroevolutionary 329
 megaevolutionary 328
 Everglades 145
 evolution
 atmospheric 86
 oxygenic photosynthesis 64
 biological 294
 climate change 325
 Cuvier model 428
 Darwinian model 428
 factors 325
 Hominid 791
 hominin
 climate 447
 traits 448
 monsoon 588
 solar 62
 species level 326
 stellar 294
 evolutionary change, model 325
 Ewing, William Maurice 431
 Ewing-Donn theory of ice ages 422, 431
 exaerobic
 environment 12
 taxa 12
 zone 12
 exhumation 249, 794
 exoskeleton 91
 exosphere, Mars 71
 Experimental Mohole Project 630
 Export production 644
 extinction 326, 328, 547
 end-Cretaceous 201
 event 174, 203, 213, 217, 328, 329, 336, 463, 499, 503, 547–549, 558, 654, 729
 extratropics
 circulation change 60
 Last Glacial Maximum circulation 57
 observational circulation analysis 59
 Exxon Production Research Company (EPR) 355, 880
F
 Fabaceae 679
 factor
 analysis 159
 astronomical 52
 climatic 46
 fractionation 116, 128
 temperature dependency 128
 photosynthetic fractionation 127
 Revelle 124
 faeculae 930
Fagus 305, 858
 grandifolia 856
 faint young Sun paradox 333, 334, 399, 701, 836
 Fairbridge, Rhodes W. 431
 Falkland Islands 418
 Falla Formation (Antarctica)
 Triassic flora 964
 famine record 46
 fan, alluvial 194
 Fanning Island 527
 Faraday detector 259
 Faroe Islands 422
 fatty acids 660, 719
 fauna
 brachiopod 11
 cold climate 384
 disjunct 46
 Ediacara 330
 mammal
 Late Holocene 13
 Late Quaternary 13
 molluscan
 Atlantic 11
 Tertiary 10
 Tommotian 330
 feedback 51, 175, 177, 398, 847
 albedo 591
 biological 330
 climate 177
 cooling 41
 gain factor 177
 ice-albedo 392
 mechanisms 845
 positive 52
 feldspar 249, 409, 523, 539, 540, 837
 hematite-stained 575
 Fennoscandia 512
 paleogeographic reconstruction 379
 Fennoscandian
 Ice Sheet 22, 95, 225, 231, 380, 493, 495, 713, 850, 877, 899
 at Last Glacial Maximum 224
 Shield, glacial landscape 368
 rebound 378
 fermentation 129
 fern 816
 ferricretes 285, 514, 575, 576
 ferrihydrite 575
 ferromanganese 777
 ferruginization 755
 fertilization 780
 FID (*see* flame ionization detector)
 field, present geomagnetic 252

- Fiescherhorn ice core 458
 Filchner Trough 19
 filipodia 870
 Findeln Glacier (Switzerland) 373
 Findlinge (foundling – erratic block) 417, 430
 finger lake 366
 Finland
 drumlins 369
 glaciation, eoproterozoic 385
 kames 371
 millennial cycles evidence 571
 Finse Event 940
 fir (*see also* *Abies* sp.) 858
 firn 118
 porosity 454
 first appearance datum 238, 239
 Fischer
 cycles 327
 plot 826
 fish 739
 bone 777
 otolith 235
 fishery 619
 data, herring 299
 statistics 296
 fission track dating 247, 248
 decay rate 248
 fjord 366, 416
 flame ionization detector (FID) 352
 flare, solar 297
 flat, tidal 186
 Flint, Richard Foster 431
 floating ice 39
 flood 414, 724, 733, 734
 basalt 335
 Columbia River 336
 continental 335
 eruption 336, 979
 Miocene 336
 deposit 872
 Nile 426
 proglacial 484
 flooding
 cataclysmic 504
 surface 184
 floodplain 15, 780
 aggradation 898
 flora (*see also* paleobotany)
 cold climate 384
 diversification 402
 Florida 632
 Bay 145
 salinity 145
 eolian dust 308
 Keys 145
 Straits 616, 639, 642
 flow
 geostrophic, reconstruction 639
 hyperconcentrated 394
 till 279, 369, 382
 flowstone 916
 fluctuation
 climatic 325
 environmental 49
 eustatic 578
 fluid flow 156
 fluorapatite 14, 579
 flute 284, 383
 fluted moraine 369
 flyggsbergs 873
 folding 89, 95
 anticlinal 901
 synclinal 901
 food
 chain collapse 96
 web, oceanic 279
 foram (*see* foraminifera)
 foraminifera (foraminifers) 8, 43, 99,
 129, 130, 136, 143, 145, 146, 148,
 159, 235, 238, 239, 263, 267, 338,
 496, 499, 519, 525–527, 536, 551,
 578, 684, 722, 729, 758, 767, 800,
 880, 888
¹⁴C age differences 638
¹⁸O/¹⁶O ratio 159
 $\delta^{11}\text{B}$ 745
 $\delta^{18}\text{O}$ values 919
 benthic 25, 135, 338, 529, 578, 611, 616, 719,
 730, 876, 911
¹³C values 434
 barium 638
 $\delta^{13}\text{C}$ 636
 element ratios 636
 extinction 564
 geographic distribution 338
 oxygen isotopes 731
 spectral analysis 847
 zinc 638
 biochronological analyses 339
 calcitic, Cd/Ca concentrations 345
 carbonate 425
 cool-water carbonates 138
 dispersion patterns 213
 fossil 959
 geologic history 338
 isotopic analysis 135
 Jurassic 338
 oxygen isotope ratio 896
 pelagic 128
 planktonic 135, 338, 529, 606, 616, 719, 730,
 875, 911
 extinction 99
 geographic distribution 338
 zonation 339
 reduction 569
 shell 236, 0?
 size 338
 tests 338
 trace metal 344
 use in paleoclimatology 338
 Forbes, James David 431
 force, magnetic 252
 forcing 178
 anthropogenic 178
 external 850
 lunar 296
 luni-solar 299
 of climate change 165
 orbital 191, 845
 particulate 296
 radiative 121, 168, 175
 solar 172, 296
 tectonic 586
 forest 440, 449, 761
 as carbon reservoir 110
 evergreen 800
 montane 858
 podocarp 858
 formation, sapropel 875
Fortipecten 11
 fossil 607, 719, 777, 836
 assemblage 11, 13
 calcareous 529
 Cenozoic 422
 chironomid 439
 coleopteran 439
 Cretaceous 422
 elk 100
 flora 607
 climate estimates 608
 fuel 109
 burning 399
 reserves 109
 hominin 446, 447
 hydrocarbon burning 423
 indicator assemblage 607
 insect 436
 marine, oxygen isotopes 430
 material, chemical alteration 14
 paleoclimatic preferences 728
 plant, Mesozoic 431
 racemization of amino acids 234
 record, Tertiary 10
 reindeer 100
 sedimentary strata 237
 shoreline 740
 vertebrates 15
 foundling 417
 Fourier, Jean Baptiste Joseph 397
 fractionation
 basin-to-basin 137
 biogenic 128
 factor 116, 128, 480
 photosynthetic 127
 temperature dependency 128
 isotopic 72, 479, 480, 666
 carbon 114
 mass-independent 481
Fragilariopsis
curta 31
cylindrus 31
obliquecostata 31
 Fram Strait 40–42, 815, 890
 opening, Cenozoic 791
 France
 Ribains or Luhe 303
 temperature, Eemian interglacial 762
 francolite 574, 579, 775
 carbonate ion 778
 precipitation 778
 Sr content 777
 substitution 777
 unweathered seafloor 777
 Frasnian–Famnenian interval 402
Fraxinus 305
americanus 241
 frazil ice 39
 freeze-coring 740
 freeze-thaw process 365, 366
 freezing rate 783
 Fremont
 Glacier ice core 458
 paleoculture of Utah 135
 frequency 165
 freshwater flux 41
 fringing
 range 598
 reef 204
 Frisian Belt 552
 Frossnitz (Alps) 451

- Frost 46, 770–773
fruit 679
 ecological tolerance 679
 fossil 417
fucoxanthin 279, 350
Fuller's earths 540
fullerenes 549
fulvic acid 112, 754
fungi 275
Fungiina 201
- G**
- Gaia hypothesis 330
galactic cosmic radiation (GCR) 931
Galapagos Islands (Pacific), coral record 726
galaxy 295
 cycle 295
 Milky Way 419
Galileo Galilei 431
Gambier Limestone (Australia) 139
gametogenesis 345
Gamma Ray Spectrometer (GRS) 544
Ganges River 267, 590
garnet 248
gas
 atmospheric, anthropogenic modification 423
 chromatogram 350
 chromatography (GC) 119, 234, 351
 clathrate 263
 diffusion law 156
 greenhouse 333, 495, 888, 934
 hydrates 126, 263, 474, 560, 561, 564
 infrared active 62
 natural 109, 423
 noble 258
 solubility 534
 sulfur-bearing 219
 toxic 337
Gaskiers glaciation 467
gastropods 10, 11, 146, 338, 746
 dispersion patterns 213
gateway, oceanic 587
Gauss, Carl Friedrich 432
gaylussite, composition 321
GBR (*see* Great Barrier Reef)
GC (*see* gas chromatography)
GCM (*see* General Circulation Model)
GCR (*see* galactic cosmic radiation)
gelifluction 773
gelisol 903
General Circulation Model (GCM) 3, 57, 160, 189, 213, 507, 567, 700, 710, 941, 976
generalist, trophic 10
genetic drift 326
geochemical proxy, organic 659
Geochemical Ocean Sections Study (GEOSECS) 125
geochemistry
 evaporites 324
 inorganic 344
 organic 342
geochronology (*see also* dating) 234, 767, 800
 amino acid 233, 235
geolipid 347
geomagnetic field 92
 ancient 252, 254
 reversal 255
 polarity timescale (GPTS) 252
geomagnetism 416
geomorphology 312
 coastal environments 184
 deltaic environments
 deserts
 glacial
 definition 361
 lacustrine
 Mars 66
 mountains
 periglacial
GEOSECS (*see* Geochemical Ocean Sections Study)
geosol 752
geosphere 342
 Quaternary 190, 191
geothermal gradient 560
Gephyrocapsa oceanica 4, 348, 349
Gephyrocapsaceae 348
Germany 100, 877
Ghaub glaciation 467
GHSZ (*see* gas hydrate stability zone)
gibbsite 574–576
Gibraltar 621
Gilbert, William 432
ginger 679
Ginkgo 681
 stomatal index 965
giraffe 732
GIS (*see* Greenland interstadials)
GISP 2 isotopic record 43
 ice core, record 453, 454, 570, 850
glacial 51
 abrasion 873
 chattermark 364
 cycle 286, 443, 572
 last 6, 120, 390, 801
 deposition 210, 368, 386
 landforms 369–372
 processes 369
 desert 298
 diamicton 368
 dustiness 1
 environment 298
 erosion 210, 364
 fjord 430
 processes 364, 365
 erratic 354, 430
 eustasy 354, 421, 502, 887
 history 356
 evidence 158
 distribution 358
 features 384
 geomorphology 434
 definition 361
ice
 Late Wisconsinan distribution 362
 present distribution 362
inception 814
indicator 384
interglacial cycle 56, 845
isostasy 375, 392, 887
 analysis 375–378, 380
 definition 374
lake 194, 364, 381
landform 389
 orientation 369
 subdivision 366
landscape
 recent 363
 system 366
loading 376
mass balance 747
megaflood 381
megalake 380, 381
milk 365
outwash 193
quarrying 873
sediment 361, 364, 382
 deposition 368
 formation 382
 particle size distributions 382
 stratigraphy 361
stream 365
striae 364
system 192
theory 417, 425, 428, 430
till 193
transport 364, 368
 active 382
 passive 382
Glacial
 I 499
 II 501
 Lake Missoula 380
 glacier lake outburst flood 394
 North Atlantic Intermediate Water (GNAIW) 615, 641
glaciation 615, 716, 846
 alpine 368
 ancient
 evidence 193, 384
 records 467
 Antarctic 24
 Archean 385
 causes 361
 Cenozoic 387
 chronology 361
 continental 501
 major 166
 variance 167
 Cryogenian 468
 Early Carboniferous 469
 Early Silurian 468
 Eocambrian 419
 Eocene 470
 epeirogenic uplift 792
 extent 361
 recent 361
 global impact 361
 Gondwanan 469, 702
 high mountain 366
 impact beyond ice limits 372
 Late Devonian 469
 Late Ordovician 225, 468
 Laurentian 429
 low latitude 62, 468, 702
 Miocene 559
 Neoproterozoic 385
 Northern Hemisphere 286, 617, 788, 798
 onset 791
 numbers of 363
 orbital theory (*see also* astronomical theory of paleoclimates; Milankovitch cycles; orbital cycles) 168
 Ordovician 387, 702
 oxygen isotope record 363
 Paleoproterozoic 87, 385, 907
 Paleozoic 387
 periodicity 168
 Permo-Carboniferous, modeling 703

- Phanerozoic 387
Pleistocene, extent 361
Precambrian 385
pre-Quaternary 384
Quaternary 389, 429
Recent 470
snowball 909
glacier 89, 232, 457, 493, 758, 784
advance 296
alpine 193, 417
 archives 457
at Last Glacial Maximum 224
changes in size 835
cirque 595
distribution 222
flow physics 431
fluctuation 422
history 737
ice melting 746
 seasonal 740
lake outburst flood (GLOF) 394
last glacial cycle 224
mass balance 222
meltwater-dominated 395
mountain 595
 tropical 595
oscillations (*see* glacial cycles)
retreat 224, 461
sedimentation 89
snow lines 598
subpolar, model 395
tropical, paleoenvironmental record 390
valley 595
 landforms 361
 thickness 361
 Vatnajökull (Iceland) 422
 water residence time 734
glacioeustasy 421, 425, 884
 definition 354
glacio-hydro-isostasy 896
glacio-isostasy 899
glacioisostatic rebound 433
glaciology 221, 361
glaciomarine sediment 395
glaciotectonite (*also* glacitectonite) 383
glaserite, composition 321
Glasgow, glacial relief 361
glass, Icelandic 412, 572
glass/reference electrode cell 125
glauberite, composition 321
glaucanie 539
glaucanite 580, 582, 775, 778
 as climate indicator 573
 formula 574
 paleo-environmental significance 574
Gleissberg solar cycle 572
gleization 749
glendonite (*see also* ikaite) 396, 574, 578
 definition 396
gleyezem 754
gleysol, gelic 754
gleyzation 754
global
 climate model 96, 710
 cooling 420
 heat transport 489
 heating 97
 ice sheet volume 495
 ocean conveyor 791
 overturning circulation (GOC) 944
 temperature change 239
 tree ring 274
 vegetation model 508
 dynamic 508
 equilibrium 508
 warming 98, 274, 336, 716, 737
Global Network for Isotopes in Precipitation (GNIP) 677
Global Circulation Model (GCM) 441, 446, 736, 788
Globigerina
 bulloides 338, 345, 586, 587, 646
 ooze 526
 quinqueloba 646
Globigerinoides
 ruber 346, 348, 551, 722
 sacculifer 655, 744
Globobulimina sp. 646
Globorotalia
 tumida 646
 crassaformis 744
GLOF (*see* glacier lake outburst flood)
Glomar Challenger (res. vessel) 473, 529, 630
Glossopteris 420
 disappearance 402
glucose 113
Gluta usitata 241
glutamic acid 234
glycine 234
gneiss 35
 complex 35
Gobi 425
 Desert, dust 1
 goethite 62, 574–576
 paleo-environmental significance 574
Gondwana 25, 358, 418, 429, 432, 469, 498, 556, 557, 584, 702, 731, 786, 966
 glaciation 141, 225, 358, 469
 Carboniferous 788
 glacier 502, 548
 ice sheet 702, 703
 paleoglaciation 227
Goschener (Alps) 451
Gowganda
 Tillite 419
 Formation 385, 837, 909
 age 385
Grabau Amadeus William 432
gradient
 adiabatic 78
 climatic 292, 305
 geothermal 560
 latitudinal 10
 thermal, from North Pole to Equator 296
 vegetation 305
gradual climatic cooling 548
gradualism, phyletic 326
grain
 clastic 539
 size 266
 critical 254
 distribution 489
grainstone, bioclastic 146
Grand Canyon 580, 716
Grande Coupure 732
granite 248, 417
Granlund, Erik 432
graphite 108, 112
graptolite 238, 239
gravel
 bar 394
 glaciofluvial 394
 sheet 394
gravitation 252
gravity
 change 375
 wave 58
grazers 15
Great African Rift System 485
Great Australian Bight 138
Great Barrier Reef (GBR) 138, 205, 526, 528, 724, 884, 900
Great Basin (USA) 195
Great Britain, Ipswichian 303
Great Coal Age 423
Great Conveyor Belt (*see also* ocean circulation, thermohaline) 439, 634, 911
Great Ice Age 418
Great Lakes 306, 381, 860, 989
Great Plains (North America) 313, 314, 440
 loess record 315
Great Salinity Anomaly (North Atlantic) 20
Great Salt Lake 380
green algae 129, 486
 calcareous 143, 146
Green Bay Lobe (ice sheet) 372
Green River Formation 827
greenalite 62, 85, 87, 334
greenhouse 464, 687, 728
 biota, susceptibility 326
 climate 397
 Cretaceous 213, 703
 collapse 62
 definition 397
 effect 61, 62, 97–99, 333, 397, 398, 702, 788
 troposphere 976
 event 62
 gas 37, 88, 178, 333, 334, 336, 391, 398, 399, 423, 440, 493, 495, 507, 549, 563, 610, 621, 684, 687, 701, 729, 757, 790, 800, 836, 888, 934, 967
 analysis 118
 anthropogenic 434, 716, 764
 atmospheric evolution 62
 concentration 191
 early atmosphere 334
 forcing 334
 increase 174
 record 118
 Paleogene 213
 period 144
 runaway 81, 294
 warming 423
 anthropogenic 551
 world 148, 150
Greenland 8, 24, 37, 41–43, 120, 161, 168, 229, 282, 287, 422, 428, 552, 553, 731, 736, 759
 Camp Century drill hole 801
 climate records 24
 colonization 8, 552
 cooling events 412
 $\delta^{18}\text{O}$ record, CO_2 increase lag 121
 glaciation 611
 hematite-stained grains 575
 Holocene temperature 814
 ice cap 428
 ice core 101, 102, 424, 439, 451, 453, 455, 568, 569, 851
 airborne debris 298

- Greenland (*Continued*)
 chronology 453
 dust 309
 methane 496
 records 848
 ice sheet (*see also* glacier) 60, 118,
 159, 206, 221, 224, 225, 361,
 439, 850
 Last Glacial Maximum 224
 Last Interglacial 225
 mass balance 222
 melting 56
 thickness 361
 values 222
 icebergs 411
 interstadial (GIS) 102, 229, 849
 methane record 120, 803
 N₂O record 803
 paleoenvironmental record 390
 stadials 229
 super-tide 423
 Viking settlements 8, 42
 warming 231
 Greenland Ice Core Project (GRIP) 23, 120, 120,
 122, 229, 390, 453, 454, 760
 Greenland Ice Sheet 231, 390, 518, 611,
 811, 988
 Greenland Ice Sheet Project II 760, 802
 Greenland Sea 41, 614, 791
 Deep Water 614
 Greenland-Scotland Ridge 611, 844, 847
 Early Cenozoic 618
 greenschist 539
 Gregoriev ice core 458
 Grenzhorizont 432
 grèzes litées 298
 GRIP (*see* Greenland Icecore Project)
 Griquatown Iron Formation (South Africa) 86
 groundwater 45, 47, 733, 760, 783
 activity 46
 ancient 389
 flow paths 737
 isotopic
 composition 46, 747
 dating 47
 water residence time 734
 growth
 algal 140
 orogenic, climate impact 603
 GRS (*see* Gamma Ray Spectrometer)
 Guadalupe Island 261
 Guadix-Baza Basin (Spain) 14
 guano 775
 Gubbio (Italy) 217
 Gujarat, relict dunes 49
 Gulf Coast 764
 Gulf of Aden 421
 Gulf of Bothnia 416, 494, 974
 Gulf of California 995
 Gulf of Carpentaria 665
 Gulf of Eilat
 playas 323
 salinas 323
 Gulf of Finland 974
 Gulf of Lyons 875
 Gulf of Mexico 262, 267, 381, 392, 420, 764,
 793, 800, 900, 921
 storm activity 900
 Gulf of Oman 7
 marine core 460
 Gulf of St. Lawrence 39
 Gulf St. Vincent (South Australia) 140
 Gulf Stream 296, 422, 424, 506, 552, 554, 611,
 616, 639, 684, 706, 791, 809, 844, 847
 transport through the Florida Straits 616
 Guliya
 ice core 458–460
 Ice Cap 459
 Gulmarfjord (Gulmar Fjord) (Sweden) 423, 433
 Günz glacial 363
 Günz/Mindel interglacial 363
 Gusev Crater (Mars) 69, 542
 gymnosperm plant 328, 816
 gypcrete 285
 gypsisol 197
 gypsum 78, 146, 263, 291, 321, 322, 324, 487,
 578, 579, 762
 accumulation rate 322
 as climate indicator 573
 composition 321
 Mars 69
 paleo-environmental significance 574
 precipitation 322
 rose 579
 gyre 407
 circulation 567, 686
 subtropical 791
- H**
 H.M.S. Challenger 529
 habitation, human 46, 48
 Hadean 110, 294
 Era 34
 Hadley
 Cell 57, 59, 60, 801, 806
 circulation 59, 705, 721
 hafnium, tungsten dating 79
 Haida Gwaii (Queen Charlotte Islands) 210
 halides 576
 paleo-environmental significance 574
Halimeda 146, 527
 halite 291, 322, 487, 576, 577, 716
 accumulation rate 322
 as climate indicator 573
 composition 321
 paleo-environmental significance 574
 precipitation 322
 pseudomorphs 577
 halocarbons 63
 Hamersley Basin (Western Australia)
 385, 908
 Haney restoring 684
 Hangenberg Shale 499
 hanging valley 366
 hanksite, composition 321
 Haptophyta (haptophytes) 187, 188
 algae 4
 cultures 4
 populations 5
 Harappan civilization 7
 Hatch-Slack pathway 15, 130, 134
 Hawaii 336, 425
 Haze Famine 335
 hazel 816, 858
 nut 451
 head corals 900
 headwall 155
 heat
 balance 398
 capacity, specific 158
 diffusion, passive 255
 flow, geothermal 431
 latent 60, 158, 757
 production 34
 transport
 atmosphere 407
 cross-equatorial 409
 meridional 296, 407, 610
 oceanic 231, 407, 407, 789
 polar 167
 poleward 407, 785
 heating
 continental 786
 endogenic terrestrial 420
 interhemispheric 786
 internal 420
 Heer, Oswald 432
 Heinrich
 event 23, 24, 49, 51, 95, 231, 276, 303, 304,
 409, 412, 424, 429, 494, 498, 506,
 568–571, 590, 617, 710, 772, 802,
 841, 843, 846–848, 850, 946, 989
 decline of foraminifera 409
 layer 94, 95, 409
 chronology 411
 duration 411
 origin, causes 411, 413, 849
 provenance 409
 types I–IV 412
 Hekpoort Paleosol 872
Helicosphaera carteri 188
 heliocenter 295
Heliopora coerulea (Helioporacea) 198, 202
 heliosphere 92, 211
 helium 255
 Hellas impact basin 71
 Hellespont 505
 hematite 63, 81, 85, 87, 196, 543,
 574–576, 837
 Mars 69
 paleo-environmental significance 574
 spherules 69
Hemicythere villosa 664
 HEND (*see* High Energy Neutron Detector)
 Henry's law 124
 herbivores, mammalian 15
 herbivorous 729
 Hermit Formation 716
 herring 423, 433
 Herschel, Sir William 299
 Herzberg II nightglow 78
 Hesperian 66, 74
 definition 66
 heterococcoliths 188
Heterostegina 527
 Heterozoan
 assemblage 140
 association 138
 Hettangian 965
 Hexacorallia 198
 hexahydrite composition 321
 Hexi Corridor 603
 HI (*see* hydrogen index)
 High Energy Neutron Detector (HEND) 544
 High Plains (America) 49
 Highest Astronomical Tide 90
 high-pressure liquid chromatography (HPLC)
 234, 352
 hillslope angles 603

- Himalayan 49, 116, 154, 267, 424, 434, 493, 596, 786, 792, 984
erosion 984
Mountains 705
Plateau, uplift 611
rise 470
rivers, Sr concentrations 985
-Tibetan Plateau, uplift 794
uplift 138, 790, 811, 844
- Hirnantian 548
- histisol 197
- history
Earth 34
Martian 542
Moon 34
paleoclimatic 462
- histosol 903
- Hohokam people 552
- Hokkaido, permafrost 225
- Holden Crater (Mars) 67
- hollandite 576
- Holocene 51, 56, 229, 236, 267, 276, 286, 422, 424, 438, 451, 485, 496, 616, 709, 724, 736, 760, 768, 800, 814, 995
8,200-yr event 870
beginning 438
carbon dioxide concentration 121
pre-industrial 121
chronology 430
climatic
change 507
cooling 451
North Atlantic 736
optimum 225, 439, 590, 712, 771
orbital forcing 440
oscillation 425
reconstruction 679, 712, 795
variations 440
- cyclicality 572
- data sources 438
- de Vries effect 865
- deposit, fossil 442
- El Niño 764
- environmental history 438
- eruptions 440
- glacial-eustatic changes 356
- glaciers 835
- interglacial 51
- lake 439
salinity 440
- lake-level variation 490
- late, climatic variability 440
- methane concentration, pre-industrial 121
- mid, vegetation modeling 512
- sea level 506
- sediments 742
- soil cover 757
- solar radiation 440
- temperature oscillations 444
- thermal optimum (*see also* Holocene, climatic optimum) 43, 939
- timescale 441
- transition 120
- treeline fluctuations 443
- vegetation 438
distribution 860
history 507
warm phase (*see also* Holocene, climatic optimum) 451
- holococcoliths 188
- Holstein interglacial 363
- hominid speciation 798
- Hominidae 446
climate, evolutionary response 450
exodus from Africa 446
- hominins 449
bipedal locomotion 448
brain capacity 448
evolution 447
global climate 447
variability selection 449
- family tree 447
- fossil 447
- migration out of Africa 450
- phylogeny 447
- Homo* 448
age 448
erectus (Pithecanthropus) 430, 448
habilis 448
rudolfensis 448
sapiens 423, 448
stone tool 449, 449
- Hong Kong 425
- Hongyuan peat deposit 592
- Horn of Africa, as dust source 308
- hornbeam 858
- hornblende 81, 409
- horse, three-toed 732
- hothouse event 62
carbon dioxide concentration 62
- Hoti Cave 592
- Howchin, Reverend Walter 432
- Hoxnian interglacial 363
- HPLC (*see* high pressure liquid chromatography)
- Huascarán (Peru) 595, 722
ice core 458–460
- Huaynaputina (Peru) 977
- Hudson
Bay 299, 381, 424, 518, 907, 939, 989
beach series 299
Lowlands, glacial chronology 989
River 392, 991
Strait 94, 409, 505, 850, 948, 989, 991
Heinrich event 569
- Hula Cave (China) 994
- human (*see also Homo*) 446
bipedalism 446
brain development 446
evolution 449
habitation 46, 48
- humic, acid 112, 754
- humins 754
- humid climate, coast 186
- humidity 46
increased 46
specific 158
- hummocks 772
- hummocky moraine 369, 370
- humus 112, 754
- Huntington Principle 433
- Huntington, Ellsworth 432
- Huon Peninsula (Papua New Guinea) 434, 896
- Huron-Erie Lobe 372
- Huronian 385, 836
- Huronian Supergroup (Ontario) 385, 387, 907
CIA 837
- hurricane 60, 619, 763, 900
activity
changes 764
long-term record 764
- climate 764
frequency and intensity 764
historical record, North Atlantic 763
Last Glacial Maximum 59
prehistoric 765
- Hwang-Ho (Yellow River), flood 426
- hybridization 156
- hydrate, clathrate 560
- Hydrate Ridge 560, 561
seismic reflection profile 562
- hydrocarbon 98
gas 109
potential 344
quantification 344
trap 321
volatile 113
- hydrochloric acid 281, 420
- hydrodynamic escape 70, 72, 74
- hydrogen 72, 80, 97, 278, 759
chloride 78
fluoride 78
gas 278
index (HI) 344
isotopic ratio 457
loss 81
peroxide 63, 65, 67
sputtering 71
sulfide 110, 113, 576
- hydrogen-3 212
- hydrohalite 577, 582, 903
as climate indicator 573
paleo-environmental significance 574
- Hydroidea 198
- hydro-isostasy 887
- hydrolaccolith 774, 783
- hydrological
balance 46
cycle 286
global 97, 733
risk-assessment 736
system, human impact 736
variability, cause 734
- hydropower 619
- hydrosphere 87, 342, 733
Archean 36
carbon 113
thermal history 36
- hydroxyapatite 14
- hydroxyl radical 63, 65
- hydroxyoxides 574
- Hydrozoa (hydrozoans) 198, 201
- hypercane 549
mass extinction 549
- hyperfusibles 110
- hypersalinity 10
- hyposalinity 10
- hypotheca 279
- Hypsithermal 6, 451, 551, 939
- hystrichosphere 281
- I**
- IAEA (*see* International Atomic Energy Agency)
- Iapetus Ocean 777
- Iberian Portal (Spain) 610
- ice 574
ice age 51, 55, 158, 161, 354, 389, 450, 464
atmosphere, dust content 392
chronology 435

- ice (*Continued*)
 Ewing-Donn theory 422
 Late Cenozoic 438, 470
 Late Paleozoic 469
 loess deposition 801
 orbital theory 162
 phase, threshold tolerance 298
 Quaternary 421, 424
 wind 425
 albedo 392
 basal 89
 characteristics 89
 debris 89
 rheological properties 89
 berg 286
 cap 221
 at Last Glacial Maximum 224
 distribution 222
 polar 39
 cloud, mesospheric 97
 core 51, 89, 171, 179, 286, 304, 389, 453, 454, 457
 accumulation rate 622
 aerosols 459
 air bubbles 231
 annual layer 747
 Antarctic 231, 286, 453, 851
 Camp Century 229
 characteristics 308
 chronology 453
 correlations 458
 $\delta^{18}\text{O}$ fluctuations 231
 data 8
 dating 283
 Dye 3 229
 electrical measurements 308
 environmental information 456–458
 Greenland 453, 496, 519
 GRIP 390
 isotope ratios 622
 locations 454, 571
 melt layer 622
 Quelccaya 8, 9
 record 23, 65, 457, 570
 record of human activity 459
 research 457
 synchronization 455
 Vostok 168, 169, 390, 391
 crystal cloud 97
 deformation 94
 density 574
 drift velocity 40
 erratics 418
 floating 39, 418
 formation 118
 frazil 39
 glacial
 Late Wisconsinan distribution 362
 present distribution 362
 grease 39
 history 378
 house, Proterozoic 225
 lense 372, 772
 load 375
 mass, global 178
 melting 169
 movement 284
 multiyear 39
 new 39
 pack 39
 paleo-environmental significance 574
 pancake 39
 polar 453
 volume 578
 properties 456
 rafting 384
 sheet 51, 57, 89, 159, 193, 221, 232, 493, 758, 784
 albedo 58
 as internal climate factor 392
 Beringian 791
 binge-purge cycle, modeling 94
 build-up 94, 364
 climate influence 392
 continental 267, 710, 800
 Cordilleran 206
 cycles 709
 decay 94
 distribution 222
 early Wisconsinan 518
 elevation, threshold 713
 ephemeral 358
 equilibrium 160
 evolution 224
 failure 850
 Fennoscandian 22
 flow mechanisms 392
 fluctuations 22, 148
 former 284
 glaciation 210
 Greenland 56, 60, 206
 growth 728
 influences on water drainage 380
 internal dynamics 94
 internal instability 392
 landforms 361
 last glacial cycle 224
 Last Glacial Maximum 51
 late Pleistocene 518
 Laurentide 22, 24, 57, 58, 207
 mass balance 495, 706
 melting 364
 model 57, 94, 160, 165, 170
 North American 57
 Northern Hemisphere 495
 onset 151, 709
 oscillatory dynamics 94, 571, 572
 Pleistocene 170, 506
 polar 719
 reconstruction 27, 28, 191
 Scandinavian 57
 shrinkage 149
 size 191
 structure 711
 thickness 361
 topography 57
 volume 390
 waxing and waning 51
 shelf
 breakup 413
 water (ISW) 16, 17
 streams, paleo- 28
 thickness, Last Glacial Maximum 378
 trapping 169
 vein 771
 volume 564, 669
 global 12, 474
 periods 163
 wedge 372, 771
 Ice Stream B 27
 iceberg 38, 94, 230, 472, 728
 calving 94, 617, 728
 discharge 569
 dumping 384
 launching 423
 meltwater 16
 rafting 382
 residence time 395
 till 382
 ice-core volcanic index (IVI) 977
 icefield, Arctic, paleoenvironmental record 390
 icehouse 498, 687, 728
 characteristics 464
 climate 295, 463, 465, 466
 aragonite sea 465
 carbon burial 466
 carbon dioxide concentration 464, 465
 carbonate compensation depth 466
 oceans 464
 pelagic diversity 465
 sea level 465
 volcanic carbon dioxide production 466
 interval 295, 464
 sea level 464
 world 151
 Iceland 8, 42, 231, 261, 297, 422, 520, 553, 614, 619
 colonization 552
 crust 336
 Ice Sheet 231, 850
 icebergs 411
 jökulhlaups 939
 Lakagigar eruption 335
 Late Glacial eruptions 938
 Plateau 611
 Sea 412
 sea ice 422
 volcanic glass 569, 575
 Iceland-Faeroes passages 791
 Icelandic Low (IL) 619
 Iceland-Scotland Overflow Water 614
 ice-rafted debris (IRD) 26, 193, 230, 304, 409, 411–413, 464, 471, 472, 569, 575, 609, 611, 617, 802, 804, 877, 932, 989
 belt 569
 discharges 571
 high-resolution measurements 569
 increase 569
 long-distance correlation 473
 paleoenvironmental significance 472
 sedimentology 472
 ichthyolith 309
 ICP-ES (*see* inductively coupled plasma atomic emission spectrophotometry)
 ICP-MS (*see* inductively coupled plasma-mass spectrometry)
 Idaho 207
 glacier lake outburst flood 394
 IGBP (*see* International Geosphere Biosphere Programme)
 Ijssel Valley 552
 ikaite (*see also* glendonite) 396, 578, 903
 as climate indicator 573
 paleo-environmental significance 574
 pseudomorphs 397
 stabilization 396
 Ikka Fjord (Greenland) 396
 ilaenids 11
 Iles Formation (Colorado) 185

- Illinoian
deposits 52
glacial 363
- Illinois
Basin cyclothem model 227
end moraines 370
- illite 309, 523, 539, 580, 581, 749
formula 574
- Imbrie and Kipp (I&K) method 652
- IMF (*see* interplanetary magnetic field)
- impact (*see also* bolide; comet; meteorite, bombardment)
climatic effect 219
cooling 295
devolatilization 80
erosion 70, 74
glass 36
lunar 35
spherules 548
winter 548
- incandescence 249
- inclination, orbital 847
- Inderites* spp. 768
- index
alkenone unsaturation 348
stomatal 549
tree-ring 269
fossils 238
- India 46, 48, 285, 424, 425, 439, 498, 786
Cambrian climate 292
drought 8, 296, 721
Early Ordovician climate 292
famine 296
glacial period deserts 298
glaciation, Paleozoic 387
monsoon 59, 721, 984
records 588
system 590
- Ocean 58, 126, 146, 162, 263, 417, 422, 424, 609, 731, 786, 814, 932
carbonate compensation depth 136
carbonate ooze 137
cooling 791
current 786
colian record 310
upwelling 587
Walker-type circulation 814
- Silurian climate 293
tillites 469
Upper Devonian climate 293
- Indian Peninsula, desertification 553
- indicator 728
alkenones 347
geochemical, ocean productivity reconstruction 648
geomorphological 47
glacial 384
lithological 716
mineral 716
of past climate 573
paleoenvironmental 11
paleontological 719
pigments 350
sedimentary 716
sterol biomarker 347
taxa 607
terrestrial 729
- Indonesia 786
Archipelago 297
coral reefs 205
- drought 721
low 724
Passage 154
peat deposits 183
Seaway 789–791
throughflow 409
- indricotheres 732
- Inductively Coupled Plasma Atomic Emission Spectrophotometry (ICP-ES) 347
- Inductively Coupled Plasma Spectrometry (ICP-MS) 347, 655
- Indus Valley 7, 414
- industrialization 399
- Innuition, environmental 458
- Infra-Cambrian glaciation 434
- infrared
laser 119
nightglow 78
- inland water body 734
- inlet, tidal 186
- Inman Valley (Australia) 434
- Inuitian ice complex 390, 518
- insectivore 729
- insects 735
fossil 436
- insolation 53, 454, 495, 509, 611, 757, 845
caloric 55
changes 845
climate response 303
curve 53
daily 54, 55
feedback mechanisms 846
long-term variation 54
maximum 303
Northern Hemisphere 509
seasonal 191
- Integrated Ocean Drilling Program (IODP) 473
expeditions 475
science plan 474
structure 475
- interdune depression 195
- interflow 193
- interglacial 51, 774, 800
current 801
Eemian 51
Holocene 51
last 303, 305, 801
climate 303
soil development 801
temperature 119
- intermediate water 60
- International Atomic Energy Agency (IAEA) 667, 677
- International Geosphere-Biosphere Programme (IGBP) 813
- International Marine Past Global Changes Study (IMAGES) 676
- International Partnerships in Ice Core Sciences (IPICS) 456
- International Program of Ocean Drilling (IPOD) 263
- International Trans-Atlantic Scientific Expedition (ITASE) 677
- interplanetary magnetic field (IMF) 930
interstadial 22, 477, 774, 801
Allerød 100
Bølling 100
definition 477
Meiendorf 100
Weichselian 478
- intertidal
flat 147
zone 578
- Intertropical Convergence Zone (ITCZ) 8, 46, 59, 183, 267, 309, 501, 584, 703, 724, 725, 786, 801, 876, 940
shift 49, 786
- Inuit 8
- invertebrate 739
- bioturbation 11
marine 12
migration pattern 500
proxies 10
- Inzhavino epoch 755
- Io, volcanism 82
- Ioannina Basin (Pindus Mountain Range, Greece) 822
- IODP (*see* Integrated Ocean Drilling Program)
- ion microprobe technique 34, 258, 259
- ionization
in situ 258
potential 258
- IPICS (*see* International Partnerships in Ice Core Sciences)
- Ipswichian (*see* Eemian)
- Iran
Early Devonian climate 293
high plateau formation 422
permafrost 225
Silurian climate 293
Upper Devonian climate 293
- IRD (*see* ice-rafted debris)
- Ireland, speleothem record 760
- iridium 309
anomaly 99, 548
extraterrestrial 36
- Irminger Basin 412
- IRMS (*see* isotope ratio mass spectrometer)
- iron 275, 285, 537, 580
availability 478
banded 85
formations 63
climate change 478
complexed 478
dissolved 478
fertilization 318
formation 85, 87
Algoma-type 86
deposition 87
high-energy 86
low-energy 86
ore 291
Precambrian 87
sedimentary characteristics 85
Superior-type 86, 87
oxides 254, 285, 423, 574, 755, 908
sedimentary storage 423
oxyhydroxides 574
as climate indicator 573
formation 871
sesquioxides 196
sulfide 254, 576
- ironstone 85
oolitic 401
Phanerozoic 574
- irradiation 51
daily 54
solar 55, 572
variation 302, 626
- Irtys 505

- Irwin River (Australia) 431
 Isaq Gneiss Complex (Greenland) 35
 isoleucine 234, 235
 epimerization 234
 isopycnals 639
 isostasy 294, 599
 definition 374
 glacial 375, 392, 887
 analysis 375–378, 380
 definition 374
 local 375
 model 375
 isostatic response 599, 600
 isotope
 analysis 384
 sample selection 130
 teeth 135
 climate-sensitive 573
 cosmogenic 211, 551, 931
 dilution 260
 effect 479, 480
 kinetic 481
 fractionation 128, 133, 479, 480
 enzymatic 133
 equilibrium 480
 mass-independent 481
 nonequilibrium 481
 stomatal 133
 radioactive 969
 ratio 14, 133
 definitions 480
 delta notation 133
 mass spectrometer (IRMS) 133
 measuring 259
 relative abundance 128
 stable 14
 thermal interpretation 213
 standard 133
 NBS–21 graphite 133
 V-PDB (Vienna PDB) 133
 stratigraphy 476
 substage, marine 303
 thermometry 667
- Isotope
 Stage 1 152
 Stage 2 153
- Israel 425
 speleothem record 460
 speleothems 7
- Issyk-Kul 381
- isthmus, American 167
- Isthmus of Panama 296, 567
 closure 618, 722, 791
 oceanic circulation 449
- Isua
 Island 36
 metasediments (Greenland) 36
- ISW (*see* ice shelf water)
- Italy 415
 cool-water carbonates 141
 ice cores 457
- ITCZ (*see* Intertropical Convergence Zone)
- Itsaq Gneiss Complex 35, 36
- J**
- Jack Hills (Australia) 334
- Jackass Mountain Formation
 (British Columbia) 248
- Jackson Pond 782
- Jamieson, Thomas Francis 433
- Jan Mayen (*also* Juan Mayen), volcanic glass
 569, 575
- Japan 243
 Sea 994
- jarosite, Mars 69
- jasper 908
- Java, paleovegetation 722
- Jericho 8
- jet stream 58
- JOI Alliance 475
- JOIDES (*see* Joint Oceanographic Institutions
 for Deep Earth Sampling)
- Joides Resolution (res. vessel) 473–476, 526,
 529, 630, 633, 880
- Joint Oceanographic Institutions for Deep Earth
 Sampling (JOIDES) 630
- Jökulhlaups (Jökulhlaups) 372, 374, 394, 413, 939
- Juan de Fuca
 Hydrogeology Expedition 475
 Ridge 632
- Juan Mayen (*see* Jan Mayen)
- Junge Layer 335
- juniper 858
- Juniperus* 305, 858
- Jupiter 69, 424
 beat frequency 424
 impact of Shoemaker-Levy 9 219
- Jurassic 238, 280, 415, 554, 790
 atmospheric GCM 703
 climate 556, 557, 703
 General Circulation Model
 simulations 557
 diatoms 280
 evaporite deposition 557
 flora, Greenland 962
 foraminifers 338
 fungal spores 766
 late 253
 paleosols 966
 palynofloras 768
 warmth 703
- Jurassic-Cretaceous, evaporite deposition 323
- K**
- K/Ar dating 938
- K/T boundary 420
- Kaena subchron 253
- kaersutite 81
- Kaibab Limestone 716
- kainite, composition 321
- Kalahari Desert 298, 424
 dune activity 313
- Kallsjö bog (Sweden) 816
- kame (*see also* glacial geomorphology) 320,
 369, 371, 483, 716
 and kettle topography 394
 morphology 483
- Kamenka (Demnitz) interglacial 756
- Kansan glacial 363
- Kansas cyclothem model 227
- kaolin 291
- kaolinite 309, 499, 523, 539, 540, 575, 576,
 580–582, 716, 982
 abundances 581
 as climate indicator 573
 /chlorite ratio 574
 formula 574
 /illite ratio 581
 paleo-environmental significance 574
- K-Ar dating 823
- Kara Sea 225, 505
 Ice Sheet 493
 Last Glacial Maximum 378
- Karatau (Kazakhstan) 775
- Karelian 385
- Karoo Basin (South Africa) 964
- Karoo-Ferrar continental flood basalts 402
- karst 46, 47, 577
 vadose 898
- katathermal 451
- Katmai (Alaska)
 eruption 1912 976
- Katun River 505
- Kayenta Sandstone 580
- Kazakhstan 505, 768
 Middle Devonian climate 293
 Middle Ordovician climate 293
 Upper Devonian climate 293
- Kazantsevo (*see* Eemian)
- K-capture decay 256
- Keeling Curve 434
- Keewatin 518
- Kellwasser
 event bed 499
 Horizon 499
- Kelvin wave 789
- Kentucky, cool-water carbonates 141
- Kenya 447
- Keokuk geode 581
- Kepler's law 825
- Kerch Strait 505
- Kerguelen Plateau 337, 731
- Kerner-Marilaun, Fritz (von) 433
- kerogen 983
- kettle (*see also* kame) 483, 716
 hole 394
- K-feldspar 249
- Khubsugul (Mongolia) 775
- Khvalyn Paleolake 381, 505
- Kibo Crater (Kilimanjaro) 461
- kieserite
 composition 321
 Mars 69
- Kilauea (Hawaii) 977
- Kilimanjaro (Africa) 595
 ice core 458, 459, 940
 ice fields 461
- kimberlite pipe 108
- King, Lester C. 433
- Kitt Peak (Arizona) 276
- Kola Peninsula 578
- Kolyma River 38
- Köppen, Vladimir 52
- Korea 419
- Krakatau (Indonesia) 977
 eruption 1883 424, 459, 976
- Kranz pathway 130
- Krutitsa soil (Mezin complex) 754
- Krutitsy (Brorup) interstadial 756
- krypton 74
 on Mars 72
- Kunlun Shan 459
- Kurile Islands 243
- Kuroshio Current 296, 554
- Kuujjuarapik (Great Whale River) 299
- L**
- La Grande Pile (France) 762
- La Jolla (California) 261
- La Niña 60, 461, 462, 713, 721, 764

- Labrador 42
 last glacial cycle 390
 Sea 41, 43, 381, 409, 505, 569, 614, 940, 944
 icebergs 411
 sea ice cover 42
 sediments 412
 SST 620
 water 614, 944
 Lac Troie (Quebec, Canada) 367
 Lago Grande di Monticchio (Italy) 974
 Lago Mare 559
 lagoon 183
 coastal 573
 Laguna Pallcacocha (Ecuador) 724, 725
 Lahontan Depression (USA) 49
 Lakagigar (Iceland) eruption 335
 volatile budget 335
 lake 439
 acidification 280, 961
 allochthonous material 739
 annual laminations 835
 autochthonous material 739
 basin 47
 ancient 738
 hydrological status 46
 carbonate-rich 741
 climate change 738
 cycling of nitrogen 742
 $\delta^{18}\text{O}$ 741
 deposit 49
 depth variation 193
 ecosystem memory 738
 eutrophication 280, 490, 961
 evaporation 487
 former beds 740
 glacial 194, 364, 381
 hard water 487
 human influence 485
 ice 221
 evolution 224
 infill rate 193
 level 814
 changes 489, 746
 data 191
 fluctuations 49, 489
 radiocarbon data 188
 reconstruction 489, 490, 741
 variation 489, 490
 infill
 classification 193
 meltwater 505
 nutrient cycle
 reconstruction 742
 oligotrophic 490
 organic-rich 194
 oxygen
 depletion 487
 isotope analysis 741
 playa 194
 proglacial 193, 467, 835
 varve 837
 saline 578
 sediment 46, 299, 305, 519, 736, 738
 anerobic 741
 dating 741
 fossil chironomid larvae 742
 hydrocarbon potential 738
 radiocarbon measurement 741
 sedimentation rate 738
 shoreline 46
 subglacial 381
 tarn 366
 tectonic origin 485
 water residence time 734
 Lake Abhé (Afar Depression, Djibouti) 741
 Lake Agassiz (Canada) 381, 505, 814, 890, 939, 995
 Lake Ammersee (Germany) 762
 Lake Baikal 381, 553, 581, 739
 cataclysmic flooding 506
 pollen record 801
 Lake Bonneville (USA) 380, 493
 Lake Bosumtwi (Ghana) 490, 660, 742
 Lake Chad 424
 microfossil 424
 Lake Eyre Basin (Australia) 49
 Lake Gościąg (Poland) 974
 Lake Holzmaar (Germany) 974
 Lake Huron (Ontario, Canada) 907
 Lake Issyk-Kul (Kirgizstan) 505
 Lake Kassjön (Sweden) 974
 Lake Lahontan (America) 493
 Lake Mansi 505
 Lake Michigan Lobe 372
 Lake Missoula (Montana, USA) 374, 505
 Lake Missoula floods 374
 Lake Naivasha (Kenya) 582, 736
 Lake Nautajärvi (Finland) 975
 Lake Ojibway (Ontario) 381, 505, 890, 939
 Lake Poopo 380
 Lake Saki (Crimea), sediment core 552
 Lake Superior 381
 Lake Tanganyika 341
 Lake Titicaca (Bolivia/Peru) 8, 9, 380
 lake-level study 490, 491
 Lake Vostock 193, 381
 Lake Washington 246
 Laki (Iceland) 440, 966, 977
 laminite 267
 lamproite 108
 Lancashire (England) 890
 land
 animal
 demographic trends 619
 fertility 619
 bridge 361
 elevation 160
 heat capacity 786
 plant 109, 110
 migration 500
 record 51
 landform
 eolian 47
 erosional 365
 fluvio-glacial 369
 glacial (*see also* glacial geomorphology) 389, 361
 orientation 369
 subdivision 366
 glaciofluvial 483
 landscape (*see also* landform)
 glacial (*see also* glacial geomorphology),
 recent 363
 ice-marginal 373
 supraglacial 373
 system, glacial 366
 land-sea pattern 296
 landslide 835
 ancient 47
 shallow 601
 submarine 263
 land-use change 734
 Laptev Sea 38, 39
 large igneous provinces (LIPs) 335, 789, 795
 Laschamp event 93, 932
 laser absorption spectroscopy (infrared) 119
 last interglacial 307
 record 304
 sea level 303
 Last Glacial Maximum (LGM) 20, 33, 38, 49, 51, 55, 117, 148, 149, 188, 235, 267, 288, 339, 376, 381, 390, 408, 412, 439, 459, 477, 493, 495, 509, 518, 538, 615, 709, 711, 719, 722, 747, 757, 800, 813, 845, 846, 856, 858, 879, 888, 896, 898, 986
 air temperature 51
 atmospheric
 circulation 57
 dust concentration 511
 methane concentration 511
 carbon storage 511
 climate 493
 CO₂ concentration 51
 cryosphere 224
 extratropics circulation 57
 general circulation model (GCM) 57
 hurricanes 59
 ice sheet 51, 160, 161, 493
 extent 493
 global volume 390
 identification 160
 model 191
 sea ice cover 43
 sea level 51
 sea-surface temperatures 160, 711
 temperature 57, 736
 global mean 117
 vegetation 511
 modeling 510
 Last Glacial Termination 100, 495, 498
 history 498
 sequence of events 495
 last glacial-interglacial transition (LGIT) 100, 102, 841, 850
 last glaciation 6
 Last Interglacial (*see also* Eemian) 225, 305, 723
 sea level 225
 Late Albian, sea surface temperatures 215
 Late Devonian 99
 glacial event 359
 mass extinction 547, 548
 Late Dryas 100
 Late Glacial 485
 late glacial interstadial 100
 Late Glacial Maximum (LGM) (*see also* Last Glacial Maximum) 49, 771
 permafrost 771
 Late Holocene mammal fauna 13
 Late Mississippian glacial event 359
 Late Ordovician
 extinction 548
 glaciation 225, 359, 401
 mass extinction 547
 warm climate 401
 Late Paleocene Thermal Maximum (LPTM) (*see also* Early Eocene Thermal Maximum) 126, 730, 745
 Late Paleozoic glacial features 386
 Late Permian warm climate 402
 Late Quaternary mammal fauna 13
 Late Silurian warm climate 401

- Late Triassic
 bolide impacts 402
 climate 402
- Late Uruk culture 7
- Late Weichselian Ice Sheet 878
- Late Wisconsinan
 end moraines 372
 glacial landscapes 372
 glaciation 362
 ice-free corridors 372
- laterite 46, 197, 514, 716, 871
 formation 516, 871
 preservation 516
 profile
 formation 516
 Proterozoic
 South Africa 517
 weathering profile 514
- lateritization 514
- Lauraceae 607
- Laurasia 556, 584, 786
- Laurentian glaciation 429
- Laurentide Ice Sheet 22, 24, 57, 58, 94, 191, 207, 224, 225, 231, 315, 363, 372, 381, 390, 412–414, 493–495, 498, 505, 506, 509, 517, 611, 616, 703, 713, 793, 798, 814, 846–848, 850, 858, 890, 899, 939, 946, 986
 at Last Glacial Maximum 224
 Baffin Sector 518
 binge-purge cycles 94
 deglaciation 519
 destabilization 850
 discharge of freshwater 803
 flow type 392
 global sea-level change 518
 instabilities 850
 Keewatin Sector 518
 Labrador Sector 518
 melting 304
 retreat 381
 split-jet 58
 thickness 361
- Laurussia 498, 966
- lava (*see also* basalt; flood basalt; volcanism) 252
- law
 Henry's 124
 of superposition 294
- Law Dome (East Antarctica) 24
 ice core 23, 122
- layout, continental 175
- LCO (*see* Little Climatic Optimum)
- lead 277
 isotopes 309
- Leaellynasaura amicagraphica* 14
- leaf 99, 156, 679
 area 680
 index (LAI) 508
 character states 157
 density
 stomatal 610
 venation 680
 ecological tolerance 679
 efficiency 156
 fossil 417, 567
 margin, state 680
 morphology 507, 679
 physiognomy 680, 719
 inherent climatic signal 156
 shape 729, 762
- Lebanon 425
- Leif Ericsson 552
- Lena River 38, 756
- leonhardtite, composition 321
- leonite, composition 321
- Lepidobalanus 860
- lepidocrocite 574
- Lepidopteris*, stomatal index 965
- Les Echets (France) 762
- leucine 234, 235
- LGIT (*see* last glacial-interglacial transition)
- LGM (*see* Last Glacial Maximum)
- Libya 499
 Early Devonian climate 293
 Middle Devonian climate 293
- Libyan Desert 48, 49
- lichens 275
- life
 earliest evidence 37
 fossil 37
 early 37
 evolution 37
 fingerprint 37
 origin 37, 328
 Phanerozoic 330
 lifestyle, hunting-gathering 6
- light, polarized 233
- lignification 241
- lignin 719
 derivatives 662
- lignite 112
- Likhvin (Holstein) interglacial 755
- lime muds 146
- limestone 47, 108, 109, 113, 490, 499, 924, 981
 ancient 417
 debris 429
 $\delta^{13}\text{C}$ record 131
 diagenetically stabilized 129
 dissolution 140
 lithification 140
 marine 716
 phosphatic 775
 precipitates 47
- Limfjord (Denmark) 890
- Limitisporites monstrosus* 768
- lineation, glacial 28, 29
- lipid
 production conditions 347
 temperature-sensitive 347
- liquid chromatography 351
- Lisbon (Portugal) 621
- lithification 320
- Lithomelissa setosa* 871
- lithosphere 87, 342, 468, 716
- Little Bahama Bank 345
- Little Climatic Optimum (LCO) 422, 551
- Little Ice Age 38, 171, 174, 180, 224, 246, 419, 422, 441, 443, 451, 460, 520, 551, 552, 621, 725, 736, 747, 764, 843, 931, 979
 climate anomalies, NAO 621
 cooling, causes 521
 dike-break 432
 European temperature 520
 flooding 432
 Iceland 521
 Maunder Minimum 419
 volcanism 521
 wind 521
- living fossil 681
- Livingstone corer 740
- lizards 14
- Llanos 49
- loading, glacial 376
- Löbben (Alps) 451
- Locusta migratoria* 551
- lodestone 252
- lodgement 383
 subglacial 382
 till 193, 279, 383
- loess 311, 312, 314, 372, 424, 523, 575, 746, 754
 altered 523
 carbonate content 523
 China, sources 315
 compression strength 523
 cover 314
 deposit 298, 389, 425
 extension 314
 glacio-eolian 420
 deposition 286, 801
 conditions 523
 rate 286
 distance-decay function 316
 distribution 524
 eolian 435
 glacial 523
 grain size 286
 magnetic properties 575
 New Zealand 424
 origin 523
 Patagonia 424
 peridesert 523
 periglacial 523
 primary 523
 profile 46
 red paleosol 425
 secondary 523
 sediment 374, 523
 sheet 47
 steppe 800
 thermoluminescence ages 316
 transport distance 313
 water-laid 435
- Loess Plateau (China) 347, 524, 575
 dust history 588
 Quaternary record of climate change 311
- Lofer cycle 826
- Lomonosov Ridge 476
- lonestone (*see* dropstone)
- loss, atmospheric 70, 71
 volatile tracer 72
- Loxocochoa* 665
- LRT dust (*see* dust, long-range-transported)
- luminescence 266, 735
 dating methods 249, 938
 geochronology 249
 photon-stimulated 249
 thermally stimulated 249
- luminosity, solar 62, 174
 as evolutionary factor 325
- Mars 69
- lunar
 cycle 296, 416, 423
 nodal 416, 424
 forcing 296
 perihelion 424
 phase, syzygy 299
- lunette 46, 47
- Luochuan (China) 316
 loess section, stratigraphy 315

- Lusitanian shells 305
 luvisol 754
 lycophytes 816
 lysocline 527
 aragonite 127
 calcite 127
 chemical 136
 definition 529
- M**
- Mackenzie
 Delta (Canada) 783
 Mountains 206, 207
 River 38, 381, 505
 Mackereth corer 740
 macroevolution 327
 macrofossil 442, 490, 741, 814, 835
 plant 519, 856
 macrophyte 110, 489, 491, 747
 Madagascar 425
 Madre de Dios 499
 Maestrichtian stage 12
 Magellan mission 75, 76
 radar images 77
 maghemite 574, 575
 magma 252
 Archean 35
 eruption 335
 magnesite 71, 82
 magnesium 111, 578
 /calcium ratio 345, 655
 magnet 252
 magnetic
 field, reversals 159
 sector analyzer 259
 storm 297
 magnetism 252
 magnetite 81, 85, 575
 formation 575
 paleo-environmental significance 574
 magnetization 261
 chemical remanent 254
 depositional remanent 254
 natural remanent 254
 oceanic crust 252
 thermoremanent 254
 magnetometer 252
 magnetosphere 297
 magnetostratigraphy 252, 339, 432, 559, 882
 application 255
 dating, sedimentary sequences 255
 maize 134, 868
 Makganyene 385
 Malan ice core 458
 Malaysia, peat deposits 183
 Malvinokaffric realm 291
 mammal 237, 729
 Asian 732
 bone 519
 early Pleistocene NLR 607
 evolutionary radiation 730
 teeth, carbon isotope 730
 mammoth 363
 fossil bone 415
 manganese 275
 /calcium ratio 341
 nodules 576
 oxides 576
 oxyhydroxides 576
 manganite 576
 mangrove 145, 267
 Manitoba glacial lake 381
 mantle
 behavior 375
 carbon 131
 $\delta^{13}\text{C}$ 130
 deformation 376
 elastic 375
 displacement rate 375
 plume 335
 rheology 378
 viscosity 380
 Manych
 Paleochannel 381
 spillway 505
 maple (*see also Acer*) 679, 817
 marcasite 576
 Marcella Lake (Yukon Territory) 490
 mareograph 899
 Marguerite Bay, glacial lineations 29
 marialite 76
 Mariana subduction zone 632
 Marie Byrd Land 25
 Marindan 434
 marine
 environment, Eemian 304
 invertebrates 12
 isotope substage 303
 magnetic anomaly record 252
 oxygen isotope stages 722
 sediment 308
 tillites 468
 Marine Isotopic Stage 11, 32, 56, 504
 Marinoan 467, 838
 glaciation 386
 Marion Plateau 884
 marl 146
 hemipelagic 267
 lake 490
 Marmara Sea 7, 875
 Mars
 anhydrite 69
 argon 71
 isotopic fractionation 72
 asteroid bombardment 66, 69
 atmosphere
 composition 66
 dust content 66
 evolution 66, 74
 isotopic composition 71
 loss 71, 72
 methane 67
 O₂ content 78
 present-day 66
 pressure 66
 sedimentation 66
 volatiles 69
 carbon dioxide
 ice 66
 inventory 70
 loss 70, 71
 photochemical cycle 78
 carbonates 542
 channels, genesis 68
 clays 69
 climate 541
 quasi-periodic 72
 hypothesis 69
 orbital-driven change 73
 past 67, 540, 542
 dust 73
 eccentricity 73
 exosphere 71
 Exploration Rover B 69
 Express
 OMEGA experiment 540
 spacecraft 69
 fluvial activity 541
 geologic timescale 66
 geomorphology 66
 Global Surveyor orbiter 67, 69, 540
 greenhouse effect 69
 gullies 68, 545, 546
 gypsum 69
 Hellas impact basin 71
 hematite 69
 abundances 543
 history 74
 hydrodynamic escape 70
 hydrogen 66
 peroxide 67
 ice ages 66
 impact craters 66
 insolation 72
 ionosphere 71
 isotopic ratio
 hydrogen 71
 oxygen 71
 jarosite 69
 kieserite 69
 krypton 72
 landforms 544
 liquid water 67
 loss of volatiles 66
 magnetic field 70
 magnetization, remnant 71
 mass 66
 meteorites 66, 71
 isotopic composition 71
 methane 69
 Milankovitch cycle 72
 minerals 540
 neon isotopic fractionation 72
 nitrogen
 inventory 70
 loss 70
 noble gases 71, 79
 depletion 69
 nonthermal escape 70
 obliquity 72, 73
 fluctuation 72
 Odyssey 544
 orbital elements 72, 73
 eccentricity 72
 Orbiter Camera 67
 oxygen loss 71
 past ocean 68
 Pathfinder 69
 planetary parameters 66
 polar layered terrain (deposits) 73
 possibility of life 66
 pressure 66
 radius 66
 rotation 72
 season of perihelion 73
 snow and ice 544
 snowmelt model 545
 solar luminosity 69
 sputtering 70
 sulfates 69

- Mars (*Continued*)
 sulfur 69
 dioxide 69
 surface 66
 temperature 66
 ultraviolet light 66
 valleys 67, 74
 formation 67
 Viking landers 69
 volatile
 fraction 70
 isotopic composition 71
 origin 69
 volcanism 70, 540
 water 66, 540, 543, 544
 ice 545
 liquid 69
 polar 544
 wind erosion 66
 xenon 71
 isotopic fractionation 72
- Marsh, coastal 901
- mass extinction 174, 213, 336, 463, 499, 503, 547–549
 end-Cretaceous 217
 end-Permian 203
 end-Triassic 203
 late Devonian 499
 mechanisms 548
 role of climate 547
 spectrometer 128
- mass spectrometer 128, 258
 gas source 258
 thermal ionization (TIMS) 258
 negative (NTIMS) 258
- Massachusetts, glacial relief 361
- Massignano Section (Italy) 99
- master chronologies 240
- Maastrichtian 831
- MAT (*see* Modern Analog Technique)
- material
 eolian, classification 313
 fossil, chemical alteration 14
 terrestrial, submerged 376
- matter
 inorganic, evolution of $\delta^{13}\text{C}$ 130
 organic 341
 $^{13}\text{C}/^{12}\text{C}$ ratio 564
 C/N ratios 659
 evolution of $\delta^{13}\text{C}$ 130
 in sediment 130
 oxidation 129
 sources 344
 stable isotopic compositions 659
- Matuyama-Brunhes reversal 575, 800
- Maud Rise 731
- Mauna Loa (Hawaii) 434
- Maunder Minimum 93, 174, 419, 440, 521, 550, 931
 climate 933
 Sun, reduced brightness 521
 sunspot abundance 550
- Mauritania, dune 314
- Mayan
 cities 8
 civilization 8
 downfall 553
 drought 8
 population 8
- Mckenzie River 991
- McMurdo Sound 28, 29
- Mean Annual Air Temperature (MAAT) 770
- mean annual precipitation (MAP) 750
- Mean Annual Soil Temperature (MAST) 770
- Mean High Water Spring Tide 90
- measurement
 electrical, categories 308
 microthermometric 324
- mechanics, celestial 53
- mechanism, climate-centered 571
- Medieval (Mediaeval) Warm Period
 (MWP) 8, 9, 38, 180, 246, 273, 422, 441, 521, 551–553, 725, 764
 frontal depression 553
 North Magnetic Pole 553
 Northern Hemisphere climate 553
 peaks 553
 polar jet 553
 sea ice coverage 554
 sea level 552
 westerlies 554
- Medieval warming 460
- Mediterranean 154, 203, 233, 559, 736, 790, 800, 814, 978
 Basin 559, 790
 cool-water carbonates 138
 evaporite formation 559
 catchment 876
 cool-water carbonates 141
 evaporites 324, 559
 giant evaporites 559
 isolation 559
 precipitation 59
 Salinity Crisis (*see also* Messinian Salinity Crisis) 263, 387, 610
 sapropel formation 876
 Sea 263, 387, 412, 421, 424, 435, 505, 610, 875
 coring 263
 deep convection 944
 nitrogen fixation 613
 shells 305
 SST 620
- medithermal 451
- megacontinent 583, 588
- mega-cyclothem 227
- mega-evolution 328
- mega-flood (*see also* flooding, cataclysmic)
 glacial 381
 landscape 504
 late Quaternary 504
 subglacial 284, 506
- megaflood 284
- megafossil 442
- Mega-Kalahari 49
- mega-lake 380
 glacial 380, 381
 ice-marginal lowland 380
 intermontane, ice-dammed 380
 structural/tectonic basin 380
 types 380
 subglacial 381
- mega-monsoon (*see also* monsoon) 583, 584, 588, 788
- mega-spore 766
- Mega-Thar 49
- mega-thermal 451
- Mehler reaction 282
- Meiendorf interstadial 100
- meionite 76
- melissopalynology 767
- melt-out 279, 284, 948
 supraglacial 484
 till 193, 279
- meltwater 519, 835, 837, 910
 action 365
 debris-laden 395
 glacial 20, 835
 high pressure 365, 371
 input 395
 pulse (MWP) 477, 939
 sources 890
 stream 835
- Mercenaria mercenaria* 901
- Mercury 294
- Meridiani Planum (Mars) 69, 543
 geologic history 69
 hematite 543
- Meridional Overturning Circulation (MOC) 619, 634, 684, 944
 Quaternary climate change 946
- Mesa Verde 9
- mesofossil 682
- mesopause 97
- Mesopotamia 7, 50, 414
 desertification 553
- Mesoproterozoic 384, 836, 837
- Mesozoic 237, 239, 253, 281, 384, 554, 679, 700, 703, 728, 749, 750
 climates 11, 554
 Pangean 555
 coral reefs 203
 carbon dioxide values 117
 cyclothem 788
 fossil assemblages 784
 glacial-eustatic record 358
 glacial sediments 554
 ocean temperatures 556
 paleoatmosphere 750
 plant fossil 431
 sea level 555
 trans-Africa seaway 421
 trans-America seaway 421
- Messinian 559
 evaporites 324
 salinity crisis (*see also* Mediterranean salinity crisis) 387, 559, 610
 stage 610
- metamorphism 182, 254
- Metasequoia* 681
- metazoan 328
- meteoric water
 stable isotope ratio 920
 line 278
- meteorite 34
 bombardment 35
 late heavy 35
 chondritic 80
 dating 79
 deuterium-hydrogen atomic ratio 80
 flux, terrestrial 35
 four component model 80
 impact 34
 isotopic composition 71
 Martian 66
 shergottite 71
- methane 62, 109, 110, 113, 182, 263, 399, 423, 549, 560, 729, 803, 836, 967
 ^{13}C -depleted 562
 abrupt release 126
 atmospheric 231, 440

- concentration 62
 Greenland ice cores 496
 clathrate 168
 hydrate 560
 release 135
 concentration
 last millennium 122
 Quaternary 391
 variations 119
 cycling 562
 data reliability 119
 emission 507
 fluxes 563
 hydrate (gas) 337, 402, 560, 730
 release 135
 reserves 109
 hydration 967
 isotopic composition 118
 latitudinal distribution 118
 measurement 119
 microbial oxidation 563
 on Mars 67
 Quaternary variations 118
 record 119, 455
 release 135, 563
 ancient 564
 climatic effects 563
 reservoirs 109, 473
 significant minimum 122
 sources 423
 pre-industrial 123
 method
 analytical 118
 CLAMP 156
 Imbrie and Kipp (I&K) 652
 potassium-argon 580
 rubidium-strontium 580
 methyl
 chloride 78
 ketone 4, 348
 Meuse 267
 Mexico 10, 273
 monsoon 786
 Mezin complex 756
 Mg/Ca paleothermometry 722
 MGS (*see* Mars Global Surveyor)
 MI (*see* IODP Management International (IOD))
 Michigan
 Basin 324
 end moraines 370
 micrite 130, 139
 microalgae 4
 microbe, Archean 37
 microbial activity 89
 microbialite 200
 microevolution 326
 microfossil 90, 187, 237, 239, 266, 282, 424,
 449, 728, 736, 875
 acid-resistant 766
 assemblage, ocean productivity
 reconstruction 646
 benthic 800
 calcareous 162
 carbon isotope composition 609
 Lake Chad 424
 planktic 800
 siliceous 162, 747
 species 652
 microorganism 747
 photosynthetic, bloom 838
 micropaleontology 338
 microsampling technique 12
 microspherules 549
 microtektites 99
 Mid-Atlantic Ridge 262, 633
 Mid-Cretaceous warm climate 402
 Middle Devonian paleotemperature 401
 Middle East 7
 drought 8
 precipitation 59
 Middle Jurassic warm climate 402
 Mid-Pleistocene Revolution (MPR) 841, 843,
 847, 848
 Mid-Pliocene warming, interpretation 567
 migration 325
 Mikankovich-Croll cycles 516
 Mikulinian (*see* Eemian)
 Mikulino (Eemian, Sangamon) interglacial 752,
 754, 756
 Milankovitch
 cycle (*see also* orbital cycle) 22, 194, 295,
 325, 359, 420, 449, 502, 710, 804, 900
 Mars 72
 debate 52
 forcing 49, 175
 frequencies 911
 hypothesis (*see* Milankovitch (orbital) theory)
 orbital parameters 423
 periodicity 977
 pre-Quaternary 826, 830
 radiation curve 451
 scale 268
 summer radiation curve 53
 theory 168, 175, 375, 431, 433, 434, 495, 498,
 760, 826
 variation 391
 Milankovitch, Milutin 52, 433
 Milky Way Galaxy 294
 millennial
 climate cycles 801
 description 569
 evidence 571
 history 569
 mechanisms 571
 modes 568
 variations, global distribution 570
 Millepora (Milleporina) 198, 201
 millisite 777
 Mindel
 glacial 363
 /Riss interglacial 363
 mineral 284
 aerosol 1
 as paleoclimate indicators 573, 574
 as provenance marker 574
 climate-sensitive 716
 definition 573
 diagenetic 539
 evaporite 579
 as climate indicator 573
 formation 35
 glendonite-type 138
 hydrothermal 539
 hydrous 80
 magnetic 254
 oxidation sensitive 573
 saline 321
 mineralization, authigenic 0
 Minnesota River (Superior Province, USA)
 35, 381
 Miocene 38, 263, 267, 609, 686, 768, 770, 790
 carbonate compensation depth 138
 climate
 change 609
 optimum 609
 cooling 609
 evolution of
 grasslands 706
 tundra 706
 fauna 91
 flood basalt 336
 glaciation 559
 global cooling event 336
 icehouse conditions 609
 late, divergence between apes and human 448
 pCO₂ 609
 warming event 10
 mirabilite 574, 579, 903
 composition 321
 mire 774
 raised 195
 Mississippi River 381, 425, 505, 889
 basin 392
 delta 184, 432, 879
 loess 524
 millennial cycles evidence 571
 Mississippian 499
 glacial deposits 499
 paleoclimate 499
 Mistassini (Quebec) 369
 MOC (*see* meridional overturning circulation)
 Moche 9
 Mochica civilization 9
 model (*see also* modeling) 57
 atmospheric
 chemistry 63
 circulation 53, 213
 general circulation 219
 binge-purge 571
 carbon cycle 549
 climate 158, 709
 change 171
 Community Climate Model (CCM0) 191
 cosmochemical 75
 cyclothem 227
 depositional system 373
 drumlin 370
 dune activity 313
 energy balance 163
 equilibrium condensation 79
 four component meteorite 80
 general circulation climate model (GCM) 3
 GEOCARB III 401
 geochemical 75, 166
 hydrological 191
 ice
 flow 455
 sheet 57, 170
 trapping 169
 Illinois-Basin cyclothem 227
 Kansas cyclothem 227
 landscape system 373
 mantle deformation 376
 Mintz-Arakawa GCM 161
 numerical 160
 ocean 167
 paleoclimatic 33
 planetary accretion 79
 radiative transfer 3
 solar

- model (*see also* modeling) (*Continued*)
 evolution 62
 nebula 79
 standard cyclothem 227
 stratospheric dust-layer 219
 terrestrial biota 330
 topography 57
- modeling
 circulation 59
 glaciological 454
 numerical 586
 ocean-atmosphere 99
 paleo-hydrometeorological 7
 paleoclimate 568
 vegetation 507
- Modern Analog Technique (MAT) 31, 653, 761, 960
- Mohole
 21st Century 474
 Project 630
- Mohorovicic discontinuity 260
- Mohr, Friedrich 107
- moisture 158
- molecule
 achiral 233
 biomarker 660, 661
 chiral 233
- mollisol 872
- mollusk 11, 12, 129, 143, 146, 148, 233, 235, 425, 487, 525, 527, 729
 armored 527
 in cool-water carbonates 138
 marine 519
 Mediterranean 7
 Pliocene 327
 shell 236, 491
- Mongolia loess 424
- monkey 732
- monsoon 266, 267, 449, 459, 598
 Asian 46, 425, 459, 587
 circulation 589
 records 586
- belt 424
- change, centennial to millennial-scale 590
- circulation systems 439, 786
 Indian 590
 modern 586
- climate 189
 definition 589
 Earth's rotation 786
 evolution 588
 forcing, mechanisms 590
 Holocene variability 590
 Indian 59
 records 588
- Late Triassic 585
- pre-Quaternary 583
- proxy 591
- Quaternary 589
 changes 590
 SW Asian 267
- Mont Blanc 459
 ice core 458
- Mont Miné Glacier (Valais, Switzerland) 364
- Montana 207
- Montastrea* 900
- Monterey Formation 609, 778
- montmorillonite 523, 540
 formula 574
- Moon 423, 625, 825
 climate effect 423
- declination 424
 formation 34
 history 34
 impact cratering 66
 meteorite bombardment 35
 nodal cycle 423
 orbital plane 423
 oxygen isotope ratio 35
 physical evolution 294
 rocks 34
 role in weather cycle 416
 tide-raising force 423
 zenith shift 296
- moosehorn coral 900
- moraine 364, 493, 519, 594, 716
 dump 383
 end 369, 370, 372, 430
 fluted 369, 371, 383
 hummocky 369–371
 marginal 594
 morphology 594
 recessional 370
 ribbed (*see* rogen moraine)
 rogen 369, 506
 sedimentology 594
 subglacial 594
 supraglacial 594
 terminal (*see* end moraine)
- Moravia (Czech Republic), loess/paleosol cycles 425
- mordenite 582
 formula 574
- Morita-Dole effect 282
- Morocco 425
- morphotype 680
- Morwell (Australia) lake deposit 14
- Moscow Basin 502
- moss 816
- mound
 palsa 774
 pingo 774
- Mount Billingen (Sweden) 380
- Mount Everest 596
- Mount Kenya 742
- Mount Kilimanjaro 838, 908
- Mount Logan, ice core 457, 458
- Mount Pinutubo (Philippines) 795
- Mount Roe 334
 paleosol 62
- Mount St. Helens (USA) 246, 966, 978
 eruption 1980 976
- Mount Taupo (New Zealand) 246
- Mount Vesuvius eruption 79 976
- mountain
 building, climate implications active 599
 elevation 705
 glacier 221, 457, 595
 advance 734
 climate record 459
 climate warming 461
 ice cores 457–459
 retreat 734
 tropical 595
 values 222
- impact on precipitation 793
- range as barrier 597
- topography, climate impact 601
- uplift 421, 596, 599, 792, 794
 climate 596
 drivers 599
- mouth bar 184
- movement, isostatic (*see also* isostasy) 210
- MPR (*see* Mid-Pleistocene Revolution)
- MS (*see* Inductively Coupled Plasma Spectrometry (IC))
- mud flow 773
- mudstone 716, 872
- multiple regression analysis 270
- multiyear ice 39
- Murmansk Current 296
- mutation 156
- Mutual Climatic Range (MCR) method 91
- MWP (*see* Medieval Warm Period)
- Mycorrhizae 781
- Myodocopa 663
- Myriophyllum* 491
- Mytilus edulis* 607, 901
- N**
- NADW (*see* North Atlantic Deep Water)
- nahcolite, composition 321
- nahklites 74
- n*-alkanes 347, 661, 747
- n*-alkanoic acid 347
- n*-alkanols 347, 661
- Namib Desert 46, 48, 195
 dune activity 313
- Namibia 421, 425
- Namurian 502
 stage 11
- Nanedi Vallis (Mars) 67
- Nankai subduction zone 632
- Nankai Trough (Japan) ikaite 397
- nannoconid 187
- nannofossil 4, 238, 239, 262, 280
 calcareous 187, 527
 ooze 525
- nannoplankton, calcareous 99
- Nansen Fjord 8
- NAO (*see* North Atlantic Oscillation)
- Napier Complex (Antarctica) 35
- Narryer Gneiss Complex (Western Australia) 34, 35
- Naskal (India) 14
- Nassellaria 870
- Natal (Zululand) 430
- natron 903
 composition 321
- Natufian groups 7
- natural
 decay rate 256
 gas 109
 remanent magnetization (NRM) 254
- Navajo
 Country 313
 Sandstone 580
- NBS–21 graphite isotope standard 133
- Neandertals 303
- Near East 8
 Cambrian climate 292
 paleoprecipitation 8
- nearest-living-relative (NLR) method 13, 607, 679, 719
 qualitative indicator
 assemblage approach 607
 taxon approach 607
- Nebraskan glacial 363
- nebula, solar 69
 elemental abundances 79
- needle ice 772

- Negev Desert 8, 276
 Neoproterozoic Era 88, 463, 836, 837, 907, 924
 carbonate 467
 climatic convulsions 837
 glaciation 62, 385, 434, 467, 468, 838
 seawater 928
Neotoma 48
 Neptune 52, 294
 net primary production (productivity) (NPP) 113, 114, 508, 644
 network, hydrological 46
 neurotoxine 281
 neutron 211
 activation 251
 irradiation 248
 Nevada-Utah, orographic desert 322
 New Jersey Coastal Plain 356, 880
 margin 880
 New Jersey Sea Level Expedition 476, 477
 New Mexico 9, 324, 552
 New Red Sandstone 580
 New York Harbor, frozen 520
 New York State
 drumlins 369
 fluted moraines 370
 New Zealand 287, 493, 524, 731, 858
 Alps, glacier complexes 224, 225
 cool-water carbonates 138, 141
 Last Glacial Maximum (LGM) 390
 loess 314, 424
 mountain glaciers 595
 permafrost 225
 Newark Basin (NE America) 253, 585, 831
 Supergroup 585
 Newfoundland 422, 518, 522
 ice cover 518
 Newport Formation (Australia), Triassic flora 964
 NGRIP ice core 453
n-hexacosan-1-ol 348
 Nicaragua Rise 261
 sediment
 late Tertiary 261
 Quaternary 261
 Nigardsbreen (Norway) 366
 Niger 268
 Nile River 415, 425, 559
 delta 267, 432
 sediments 574
 flood 414, 426, 434, 721, 725
 cycles 415
 valley 7, 414
 Nileids 11
 nimravids 732
 Niobrara Formation 215
 Nippewalla Group 577
 nitrate 342, 613, 615, 735, 876
 production 98
 reduction 129
 nitric acid 98, 217, 420, 549
 nitrification 613
 nitrite 613
 nitrogen 62, 72, 74, 92, 107, 110, 211, 419, 536, 612, 659, 780, 876
 atmosphere 613
 cycle 612
 global 613
 marine 613
 dinitrogen gas (N₂) 613
 fixation 63, 98, 613, 742
 bacteria 613
 biological 61
 rate 613
 in Martian atmosphere 66
 in photosynthesis 113
 in primordial atmosphere 111
 isotope 742, 800
 ratio 613
 limiting nutrient primary production 612
 loss 70
 molecular 110
 ocean
 sinks 613
 sources 613
 on Earth 70
 on Mars 70
 on Venus 70
 organic 613
 oxide 98, 217
 oxides on Venus 78
 solar system abundance 79
 sputtering 71
 stable isotopes 612
 total amount, plants and animals 613
 nitrogenase 478
 nitrous oxide 399
 NLR (*see* nearest-living-relative (NLR) method)
n-nonacosane 348
 Noachian 66, 72, 74
 craters 67
 definition 66
 erosion rates 67
 highlands 67
 noble gas 80, 258
 fractionation 70
 Mars 69
 Venus 79
 nodal cycle 299
 Noelaerhabdaceae 4
 non-sea salt calcium deposition (nssCa) 120
 nonstationarity 956
 nonthermal escape 70
 nontronite 580
 formula 574
 Norfolk Broads 552
 Normanian 553
 Norse settlements (*see* Viking settlement)
 Norsemen 552
 North Africa 276, 425
 climate
 Early Ordovician 292
 Middle Devonian 293
 Middle Ordovician 293
 Silurian 293
 glaciation, Paleozoic 387
 sabkha 323
 North America 48, 99, 286, 336, 425, 451, 590, 730, 800
 Atlantic coast 376
 carbonate eolianites 320
 climate
 Cambrian 292
 Early Devonian 293
 Middle Devonian 293
 Middle Ordovician 293
 Silurian 293
 deglaciation 439, 519
 diamictite 385
 glacial megalake 381
 glaciation 363
 onset 988
 Ordovician 387
 Paleoproterozoic 385
 ice margins, Last Glacial Maximum 378
 ice sheet 57, 897
 late Wisconsinan 517
 limits 378
 loess cover 314
 mountain building 449
 permafrost 225
 plant record 219
 plate 421
 pollen record 519
 Sangamonian 303
 temperature gradient 58
 North Atlantic 38, 41–43, 94, 121, 126, 231, 261, 281, 286, 296, 409, 411, 520, 620, 705, 731, 743, 791, 932
 carbonate compensation depth 136
 circulation 169
 climate 476
 change 160
 predictability 622
 cool-water carbonates 138
 Current 408, 413, 706, 791
 Deep Water (*see below*)
 deep-sea sediments 568, 569
 density of surface water 41
 glacial 616
 Great Salinity Anomaly 20
 hurricane 763
 LGM 161
 lunar modulation 296
 Oscillation (*see below*)
 phosphate 345
 salinity 616
 sea ice, reconstruction 44
 sea surface
 salinity 615
 temperature (SST) 615, 620
 Subtropical Gyre 791
 temperature gradient, Eemian 305
 thermohaline circulation 41, 42, 381, 392
 warming 496
 wind-driven circulation 615
 North Atlantic Deep Water (NADW) 16, 20, 21, 60, 171, 392, 408, 610, 614, 634, 635, 714, 731, 791, 811, 850, 939, 944, 994
 formation 137, 138, 640, 814, 843
 model 571
 oscillations 171
 tectonics 617

- North Atlantic Oscillation (NAO) 42, 58, 60, 179, 180, 194, 297–299, 305, 460, 521, 553, 590, 619, 764, 803, 815, 978
- Arctic ice cores 620
- climate impact 620
- global warming 621
- impact on agriculture 619
- index 620, 621
- Little Ice Age 621
- negative state 619
- paleoproxy reconstruction 622
- positive state 619
- predictability 622
- temperature variability 621
- tree ring records 620
- tropospheric 623
- zonal index cycle 621
- North Dakota, glacial lake 381
- North GRIP ice core 454
- North Magnetic Polar oval 296
- North Magnetic Pole, asymmetry 297
- North Pacific 38, 286, 296, 791, 848
- climate change 160
- dust deposition 48
- Intermediate Water (NPIW) 944
- Oscillation 620
- Pliocene gyre strengthening 567
- North Pole 498
- North Sea 267, 423, 877
- Eemian 305
- ice sheet 378
- SST 620
- North West India 49
- Northeast Monsoon 786
- Northern Component Water 609
- Northern Hemisphere
- climate
- change, millennial 180
- oscillations 42
- continental ice volume 52
- glacial-interglacial cycles 389
- Glaciation (NHG) 48, 168, 609, 611, 841, 843, 844
- onset 611
- trigger 391
- Hadley Cell 57, 59
- ice-sheet extent, Last Glacial Maximum 224
- ice volume 163, 170
- jet streams 297
- landmass asymmetry 298
- last glacial cycle 390
- Last Glacial Maximum 51
- plant
- environmental adaption 156
- record 219
- Pleistocene glaciation 53
- sea ice 224
- cover 38
- extent 40
- values 222
- snow cover, values 222
- species migration, glaciation-related 372
- summer
- insolation 52
- rainfall 49
- temperature
- change 180
- increase, Holocene transition 120
- reconstruction 274
- records 458
- winter 52, 54
- Northwest India 49, 50
- Norway 8, 416, 424, 429
- coast erosion 416
- crustal uplift 416
- glaciers 224
- Norwegian Sea 408, 791, 870, 877
- alkenones 350
- Greenland Sea 263
- Nothofagus* 860
- Novaya Zemlya 225
- NPP (*see* net primary production)
- NSF (*see* U.S. National Science Foundation)
- nssCa (*see* non-sea salt calcium deposition)
- Nubian Desert 49
- nuclear winter 219, 295
- nucleus 256
- nuclide
- anthropogenic sources 211
- cosmogenic 592, 638
- lifetime 211
- main species 212
- production rate 211, 212
- detection limits 211
- Nummulites gizehensis* 338
- nutrient
- availability 341, 342
- biolimiting 87
- content, ocean productivity reconstruction 648
- cycle 341
- distribution 687
- inorganic, indicator 344
- loading 266
- NADW 615
- transport 342
- upwelling 464
- O**
- oak (*see also Quercus*) 679, 816, 858, 860
- oats 134
- Ob River 38, 505
- Obik Sea 732
- oblateness 175
- obliquity 53, 295, 625, 798, 800
- fluctuation 72
- long-term variation 54
- variations 625
- OCC (*see* Oceanic Core Complex)
- ocean
- anoxic event (OAE) 36, 558, 626, 733, 789
- mechanisms 627
- Mesozoic 628
- types 627
- Archean
- oxygen isotope ratios 36
- temperature 36
- Arctic 38
- area 39
- map 39
- pack ice 39
- basin change 693
- carbon
- balance 112
- cycle 124, 533
- dioxide (*see below*)
- flux 536
- mass 109
- carbon dioxide
- content 533
- dissolution 112, 123
- uptake 135
- circulation 60, 165, 178, 341, 392, 567, 573, 616, 685, 730
- bottom 800
- changes 474
- global system 407, 616
- meridional 20
- model 165, 616
- past changes 640
- proxy 578
- rate 687
- threshold 571
- climate history 528
- colder 464
- composition, Cambrian-Devonian 291
- core 46
- crust 261
- current 239, 784
- current
- velocities 684
- Drilling Program (ODP) 26, 168, 265, 309, 338, 363, 526, 744, 880
- contributions 631
- history 630
- organization 634
- research objectives 630
- technology 633
- export production 644
- floor 473
- drilling 261
- rebound 375
- formation 110
- gateway 789
- changes 687
- closing 789
- opening 789
- general circulation model (OGCM) 685
- heat transport 407, 616, 684, 789
- history 421
- inorganic carbon concentration 123
- load 375
- model 167
- North Atlantic 38, 41
- overturning 790
- oxic 478
- oxygen isotopic evolution 401
- paleocirculation 634
- paleomagnetic anomalies 421
- paleo-pH 746
- paleoproductivity 644
- paleotemperatures 651
- pH 537
- past variation 743, 764
- phosphogenesis 777
- photosynthesis 536
- plateau 335
- productivity 644, 800
- net primary 644
- primary 790
- reconstruction 647
- ridge 685
- subseafloor 474
- surface
- cooling 569
- salinity 571
- temperatures 117
- Mesozoic 556
- past 556
- total alkalinity, vertical profile 125
- vertical diffusion 685
- oceanic

- Core Complex (OCC) 476
 plants 110
 state, transition 326
 oceanicity 297
 Octocorallia 198
 Oden (diesel-electric icebreaker) 475
 ODP (*see* Ocean Drilling Program)
 Oeschger, Hans 433
 Oetzal ice man 224
 Ohio, end moraines 370
 OI (*see* oxygen index)
 oil 423
 atmospheric role 423
 Ojibway 519
 Phase 939
 Okatovo interglacial 755
 Old Red Sandstone 401
 Older Dryas 229
 Olduvai
 Gorge (Tanzania) 446
 subchron 253
Olea 305
 olenids 11
 Olenitsa River 578
 Oligocene 10, 99, 728, 880
 Antarctic glaciation 791
 onset 789
 carbonate compensation depth 138
 cooling 732
 extinctions 731
 glacial-eustatic record 356
 global cooling 731
 Grande Coupure 732
 vegetation 732
 olivine 540
 Ologesailie (Kenya) 446
 Oloy Ridge 557
 Olympic Mountains 206
 OM (*see* organic matter)
 Oman 786
 OMZ (*see* oxygen minimum zone)
 Onset of Northern Hemisphere
 Glaciation (ONHG) 844,
 845, 847
 Ontario, glacial lake 381
 Ontong-Java Plateau (Pacific) 337, 345, 402,
 744, 795
 ooid 129, 139, 143, 147, 465
 barrier
 beach 146
 island 146
 carbonate 266
 high magnesium calcite 144
 low magnesium calcite 144
 Oort Cloud 174
 ooze
 calcareous 525–527
 carbonate 136
 coccolith 527
 deep-sea 128, 129
 foraminifer 525
 Globigerina 526
 nannofossil 525
 pteropod 528
 siliceous 136, 526
 opal 580
 -A 580
 -CT 580
 ocean productivity reconstruction 645
 paleo-environmental significance 574
 Opportunity rover (Mars) 69
 optical
 dating 249
 depth 97
 atmospheric 96
 optically stimulated luminescence (OSL)
 314, 894
 dating 249
 Orangeburg Scarp 805
 orbital cycles (*see also* Milankovitch cycles) 800
 orbital theory (*see also* Milankovitch theory)
 162, 163, 168
Orbulina universa 345
 Ordovician 238, 239, 750, 784
 climate 11, 293
 Early 292
 glaciation 387, 463, 468
 hot-house 502
 ice age 418
 paleogeography 702
 paleotemperatures 401
 phosphatic limestone 775
 ore, metallic 552
 Oregon 560
 glacier lake outburst flood 394
 organic
 carbon 98, 743
 accumulation 342
 burial 626
 oxidation 745
 total 344
 fraction, eolian 343
 matter (OM) 98, 109, 278, 341, 489,
 615, 687, 719, 736, 740, 743, 777,
 780, 794
 abundance 341
 allochthonous 343
 analysis 341
 analytical methods 754
 autochthonous 343
 bulk 343
 C/N ratios 343, 344
 carbon isotopes 922
 composition 341
 degradation 266
 degradation rate 342
 marine, carbon isotopic composition 610
 marine, oxidation 99
 microbial decay 967
 oxidation 129
 respiration 112
 soil 781
 terrestrial, oxidation 99
 types 341, 344
 signal 342
 organism
 marine
 diversity 10
 pelagic 129, 239
 non-photosynthetic 138
 photosynthetic 138
 zoanthellate 138
 organ-pipe, coral 203
 Orinoco 984
 ornithomimosaur 14
 orogen, steady-state 603
 orogeny 384, 421, 599
 orography 792
 Orpheus Island (Australia) 377
Orrorin tugenensis 447, 448
 osbornite 79
 oscillation
 Arctic 58, 60
 Atlantic multidecadal 9
 North Atlantic 58, 60
 Pacific decadal 9
 quasi-biennial (QBO) 295, 299
 OSL (*see* optically-stimulated luminescence)
 osmium 258
 ratio 216
 thermal ionization 258
 ostracod 146, 235, 487, 490, 663, 719, 735, 741,
 746, 921
 ecology 663
 fossil 762
 morphology 663
 salinity reconstruction 741
 Ottawa River 381
 Ottoman 553
 Ouachita Mountains 501
 outburst, flood 372
 outflow channel 68
 output, solar 53, 159, 178
 outwash 903
 glacial 193
 head 394
 pitted 394
 plain 484, 665
 proglacial 483
 overbank, fine 394
 overflow 193
 Oxford Clay 12
 oxidation 129
 benthic 343
 photochemical 78
 oxides 85
 paleo-environmental significance 574
 oxisol 197, 872
 oxygen 62, 72, 92, 211, 265, 419, 687, 759, 778
 -18 depletion 569
 atmospheric evolution 62, 64
 dissolved 282
 foraminiferal 434
 fractionation 760
 gas 110
 in the Phanerozoic atmosphere 64
 in the Precambrian atmosphere 63
 index (OI) 344
 infrared nightglow 78
 ionized 71
 Isotope Stages 363
 isotopic
 composition 64, 282, 571, 762
 fractionation 778
 ratio 457, 838
 isotope 15, 101, 449, 654, 666, 729, 764,
 794, 896
 analysis 102, 148, 741
 atmospheric fractionation 666
 chronology 434
 data 711
 equation 148
 isotope ratios 12, 36, 879
 marine fossils 430
 measurements 800
 natural 666
 paleothermomete 148
 Pleistocene variations 152
 ratio 14, 36, 159, 389
 record 36, 148, 229, 304

- oxygen (*Continued*)
 stratigraphy 493
 variability 801
 level, ancient benthic 11
 minimum zone (OMZ) 343
 molecular, photosynthetic production 113
 paleoatmospheric 64
 paleolevel 11
 photosynthetic production 87
 seawater 12
 sink reactions 63
 sputtering 71
 stress 532
 oxygenation 87
 benthic 687
 oxyhydroxide 582, 781
 binding capacity, phosphate 781
 oysters 12, 901
 ozone 63, 65, 399, 521, 757, 933
 stratospheric 98, 109, 295
 Last Glacial Maximum 58
 reduction 97, 623
 troposphere 98, 109
- P**
 Pacific 126, 261, 417, 422, 505, 557, 609, 613, 705, 722, 731, 764, 789, 803, 814
 aragonite lysocline 127
 calcite lysocline 127
 carbonate
 compensation depth 136, 137
 ooze 137
 -Caribbean gateway, closure 844
 corals 201
 Decadal Oscillation 9, 460
 denitrification 613
 dust deposition, record 311
 jet stream 58
 Plate 263
 movement 263
 subduction 791
 Rim, mollusks 732
 sea ice cover 43
 Walker-type circulation 814
 pack ice 39
 packstone, bioclastic 146
 PAGES
 data archives 678
 NEWS 678
 website 678
 Pakistan 48
 drought 8
 paleoaltimetry 599
 paleoaltitude, determination 158
 paleo-archive, air composition 456
 paleobathymetry 11, 357, 684
 paleocean
 modeling 683
 predictions 685
 pH 746
 paleoceanography 473, 525, 528, 651, 690
 dinocyst 281
 Paleocene 43, 280, 728
 climate, early 219
 /Eocene boundary
 $^{18}\text{O}/^{16}\text{O}$ ratios 564
 drop in the $^{13}\text{C}/^{12}\text{C}$ ratio 564
 methane release 564
 -Eocene Thermal Maximum (PETM) 168, 402, 476, 696–699, 790
 modeling 698
 glacial-eustatic record 358
 paleochannel 47, 735
 paleocirculation 634
 reconstruction 635
 paleoclimate (*see also* paleoclimatology) 11–13, 91, 132, 133, 539, 790, 949
 and Environments of the Northern and Southern Hemispheres (PANASH) 675
 data 558
 determination 156
 dynamical model (PDM) 710
 fossil plants 679
 geologic record 399
 indicators 192
 latitudinal gradients 11
 modeling 431, 567, 568
 pre-Quaternary 700
 Modeling Intercomparison Project (PIMP) 813
 proxy 12, 576, 578
 data 485
 reconstruction 12, 679
 record 7–9, 192, 651
 system, variations 157, 166
 paleoclimatology 294, 312, 361, 399, 525, 607, 663
 dinocyst 281
 popularization 417
 roots 414
 vegetation model 508
 paleoecology 361, 525, 607, 675
 dinocyst 281
 Paleo-El Niño-Southern Oscillation (ENSO) 9
 paleoenvironment 11, 13, 133, 663
 reconstruction 14
 paleoenvironmental biomarker 350
 paleoequator 499
 coal belt 501
 paleoflood (*see also* megafloods) 505
 Tuva 505
 Paleogene 264, 607, 679, 719, 728, 788
 climate 728
 paleogeography 296
 data 10
 planetary, plate tectonic controlled 296
 paleogeostrophy 616
 paleohydrological modeling 737
 paleohydrology 733
 aims 733
 applications 736
 chemical waste 737
 fluvial 734
 human societies 736
 landscape evolution 736
 paleoclimatology 736
 radioactive waste 737
 water resource management 737
 paleo-ice streams 28
 paleointensity, geomagnetic intercalibration 476
 paleolake 47, 380, 381, 736
 Central Asian 381
 Khvalyn 505
 Paleolake Abhè, Afar desert (Ethiopia) 735
 paleolatitute 10, 11, 836
 paleolimnology 734, 738
 chronology, counting of annual varves 740
 climate change 741
 radiometric methods 741
 paleomagnetic
 data 10, 11
 reversals 239, 800
 paleomagnetism 735, 741
 Paleo-Mediterranean desiccation (*see also* Messinian salinity crisis) 610
 paleometallurgy 456
 paleomonsoon 422
 paleonutrient, tracer 616
 paleopalynology 767
 paleopedology 748
 paleoprecipitation 489, 720, 735
 lacustrine indicators 746
 marine sedimentary indicators 747
 natural archive 746
 Near East 8
 speleothems 747
 tropical ice core 747
 paleoproductivity 344, 644
 biological 342
 biomarker 351
 equation 343
 proxy 578
 Paleoproterozoic 87, 836, 837, 907
 glacial deposits 837
 glaciation 62, 385
 paleoredox conditions 341
 paleoseawater 128
 paleoshoreline 376
 paleosol 46, 47, 63, 196, 306, 313, 514, 523, 575, 716, 752, 758, 762, 800, 871, 903
 chronostratigraphy 752
 classification 197
 Devonian 750
 formation
 forest 754
 steppe 754
 time scale 982
 genesis 753
 interglacial 429
 loess deposits 752
 occurrence 752
 Ordovician 750
 organic matter 749
 plant root traces 748
 pre-Quaternary 748
 Silurian 750
 paleotemperature 27, 46, 99, 132, 144, 341, 401, 556, 558, 573, 652
 data 557
 equation 152
 gradients 12
 indicator 651
 late Quaternary 760
 ocean 651
 oscillations 425
 proxy 12, 578, 652
 racemization-derived 235
 reconstruction 171, 654, 657, 778
 concepts 652
 methods 758
 record 651
 paleotemperature 765
 paleothermometer 148, 235, 435, 919
 isotopic 668
 TEX₈₆ 215
 uk37 alkenone 188
 paleotide 693
 paleovegetation 511, 680, 982
 simulation 508
 paleowater 278
 paleowind direction 195, 580

- Paleozoic Era 116, 237, 498, 700, 703, 749, 750, 766, 788
 carbon fractionation 116
 corals 198
 glacial-eustatic record 358
 glaciation 387, 465, 469
 Great Coal Age 423
 paleoatmosphere 750
 paleoclimate 11, 499
- Palestine 425
- palm 679, 729
- Palmer drought severity index 273
- palmitic acid 747
- Palmyra (Syria) 553
- Palo Duro Basin (Texas) 324
- Palos Verde Hills (Los Angeles, California) 901
- palsa 774
- palygorskite 540, 580, 775
 formula 574
 paleo-environmental significance 574
- palynoflora
 Jurassic 768
 Triassic 768
- palynology 100, 281, 478, 487, 490, 746, 766
- palynomorph 766
- Pampa 49
- Pan African orogeny 926
- Panama Isthmus (gateway) 154, 611, 844
 closing 687, 790
- Panama Strait
 closing 422
 late Pliocene 422
 opening 422
- Panamanian Seaway 791
- Pangea 296, 498, 502, 555, 556, 583, 584, 588, 703, 786, 872, 884, 966
 climate 556, 703
 simulation 788
 circulation pattern 872
- evaporation 786
- glaciation 387
- megamonsoon 584
- precipitation 786
- red bed 872
- rifting 703
- surface temperatures 703
- Panthalassa Ocean 201, 203, 421, 584, 777, 786
- Papua New Guinea 438, 791, 900
 Cenozoic northward movement 791
 mountain glaciers 595
 paleovegetation 722
- PAR (*see* photosynthetically available radiation)
- parameter
 astronomical 53
 long-term variations 53, 54
 environmental 456
- Paranthropus boisei* 448
- parasequence 186
- Paratethys Sea 586, 790
- Paris Basin 425
 sandstone 425
- Parnaíba Basin, Upper Devonian climate 293
- parrot-fish 146
- partial annealing zone (PAZ) 248
- particle
 ionized 294, 295
 rounding 394
- particulate
 inorganic carbon (PIC) 109
 organic carbon (POC) 109
- Patagonia 46, 161, 418, 479
 glacier
 complexes 225
 ice 222
 ice core 462
 Last Glacial Maximum (LGM) 390
 loess 424
 permafrost 225
- Patagonian Desert 322, 793
- pathway, photosynthetic 133
 Hatch-Slack 15
- pattern matching 240
- patterned ground 768, 772
- pavement, abraded 384
- PDB (*see* Pee Dee Belemnite)
- Pearson product-moment correlation (R_p) 271
- peat 387, 762
 accumulation 195
 blanket 183
 bogs 485
 deposit 182, 183
 domed 183
 formation 181, 182
 climate controls 182, 183
 environment 182
 mineral content 182
- pebble 425
- peccaries 732
- pedocomplex 523
- pedogenesis 285, 752
 duration 751
- pedostratigraphic units 752
- Pee Dee Belemnite (PDB) isotope standard
 133, 654
- Peedee Formation (South Carolina) 128, 133
- pelecypods 901
- peloids 129, 146
- Penck, Albrecht 52
- Pend Oreille Lake (Idaho, USA) 504
- Penicillus* 146, 527
- Pennales 280
- Pennatulacea* 198
- Pennsylvanian 238, 498
 cyclothem 226
- Pensacola (Florida) 184
- Pensacola Basin 25, 27
- pentahydrate, composition 321
- PEP-carboxylase 134
- percolation 285
- perennial river 194
- perigalacticon 294, 295
- periglacial 372, 770
 environment 298
 landscape, present-day 770
 mounds 774
 solifluction 772
- perihelion 53, 54, 175, 391, 423, 424, 703
 longitude 825
- periodicities
 of glacial-interglacial cycles 51
 orbital 847
- permafrost 221, 756, 769, 770, 774, 783
 Antarctic 770
 distribution 222
 interglacial-glacial extent 771
 Last Glacial Maximum 224, 225, 771
 melting 567
 present extent 770
 table 770
 thickness 770
- values 222
- Verkoyansk Mountains 770
- warming 224
- Permian 498, 502, 686, 716
 evaporite deposition 323
 glacial periods 358
 Phosphoria Formation 775
 -Triassic boundary
 greenhouse interval 402
- Permo-Carboniferous 64
 glacial deposit 418
 glaciation 166
 Ice Age 418
- Permo-Triassic boundary 548
 mass extinction 547, 549
- Persian Gulf 111, 138, 578, 944
 sabkha 323
- Peru 8, 9, 490
 coast 235
 erosion 724
 flood 724
 ice cores 457
 Middle Ordovician climate 293
- Peruvian Margin 561
- PETM (*see* Paleocene-Eocene Thermal Maximum)
- petroleum 109
 deposits 612
- Pettersson, Otto (Sven Otto) 433
- P-form (erosion type) 365, 366
- pH
 measurement 125
 ocean 537
 past variation (*see also* paleocean pH) 743
 seawater 537, 743
- Phaeocystis* 187
- Phaeodaria 870
- phaeozems 754
- Phanerozoic Eon 86, 99, 239, 266, 384, 702, 790, 836, 925, 928
 atmosphere
 greenhouse gases 62
 oxygen 64
 biotic change 330
 carbon dioxide changes 117
 carbonate rocks 111
 climate
 indicators 466, 555
 modes 399
 $\delta^{13}\text{C}$ trend 131
 evaporite deposits 793
 glaciation 387, 463
 ironstone 574
 isotopic ratios 465
 life 330
 $p\text{CO}_2$ reconstruction 131, 750
 solar luminosity 117
 time scale 237
- pheophorbide 350
- pheophytin 350
- phillipsite 582
 as climate indicator 573
 formula 574
 paleo-environmental significance 574
- Phillyrea* 305
- phloem 240
- phosphatase 780
- phosphate 342, 579, 615, 781, 837
 accumulation 402
 deposit 291

- phosphate (*Continued*)
 giants 779
 marine
 sedimentation 781
 surface weathering 775
 paleo-environmental significance 574
 rock 775
 soluble 5
 phosphogenesis 775
 Neogene 777
 ocean 777
 phosphogypsum 777
 phospholipid 781
 Phosphoria Formation 402, 775, 777
 phosphorite 85, 579, 580, 775
 accumulation 401
 as climate indicator 573
 classification 776
 $\delta^{18}\text{O}$ 778
 deposition 464, 779
 distribution 775
 formation, dating 777
 REE 777
 sulfate ion 778
 Tethys 775
 trace elements 777
 uranium 777
 phosphorus 107, 780
 accumulation, sediment 781
 availability 780
 biolimiting element 778
 biologically available, residence time 781
 cycle 780
 human impact 780
 impact of climate change 782
 lake sediment approach 782
 soil 780
 dissolved 781
 in photosynthesis 113
 limiting nutrient 780
 particulate 781
 riverine transport 781
 photodissociation 64
 photorespiration 134, 282, 858
 photosynthate 626
 photosynthesis 61, 63, 64, 96, 107, 109, 112, 114, 125, 127, 243, 282, 487, 534, 923
 development 328
 energy 113
 marine, uptake of ^{12}C 615
 nutrients 113
 oceanic 536
 origin 328
 oxygen-generating 131
 reaction 112, 130
 photosynthetic pathway 133
 as paleoenvironmental indicator 134
 Hatch-Slack 15
 rate 508
 photosynthetically available radiation (PAR) 536
 photozoan 138
 assemblage 138
 association 138
 phyllosilicate 580
 Physg3ar dataset 157
 Physg3br dataset 157
 physical carbon pump 125
 physiology, floral 399
 phytane 661
 phytogeography 500
 phytomass 109
 phytoplankton 110, 111, 127, 279, 478, 479, 487, 536, 649, 743, 781
 community 341
 fossil 800
 marine 99
 extinction 99
 productivity 612
 PIC (*see* particulate inorganic carbon)
Picea 305, 856
 pig 732
 pigments 347, 350, 661, 719
 pillow lava, oldest 36
 Pinatubo (Philippines), 977
 eruption 1991 98, 335, 966, 976
 Pindus Mountains 823
 pine 816, 858
 cross-dating 438
 Pine Island 224
 Pingo 372, 774, 783, 784, 903
Pinus
 merkusii 241
 siberica 243
 sp. 305, 817, 822, 858
 Pioneer Venus 75, 76
 pirssonite, composition 321
Pistacia 305
Pithecanthropus erectus 430
 plagioclase 309
 planetary
 accretion 80
 vorticity 792
 wave
 atmospheric 792
 wind 70
 planetesimal 79, 80
 hypothesis 429
 plankton
 calcareous 98
 pelagic 98
 photosynthetic, extinction 96
 plant 282, 679
 anemophilous 817
 aquatic and subaerial 735
 autogamous 817
 C₃ 14, 922
 C₄ 14, 922
 extinction, global 858
 fossil 417, 679, 762
 Mesozoic 431
 paleoclimate 679
 genetic determination 156
 growth 679
 gymnosperm 328
 hyp-hydrogamous 817
 land 109, 110
 leaf 156
 macrofossils 134, 519
 matter, isotopic composition 133
 morphology 156
 oceanic 110
 organs 679
 paleoclimatic information 683
 Paleozoic 679
 pathology 767
 pteridophyte 328
 remains 46, 47
 root traces 748
 taxonomy 767
 tissue, isotopic ratios 679
 treeless communities 442
 woody dicotyledonous 156
 zoophilous 817
 Plant Functional Type (PFT) 507, 856
 plasma, solar 211
 plate
 boundary, convergent 794
 Caribbean 421
 migration, Cenozoic 421
 North America 421
 pair, spreading rates 254
 tectonics 262, 296, 420, 429, 432, 434, 449, 466, 730, 784
 climate 784
 global carbon cycle 794
 orographic response 421
 plateau
 growth 598
 uplift 296, 586
 platform reef 204
 playa lake 323, 194, 195, 322
 Pleistocene 10, 51, 266, 339, 422, 425, 439, 617, 709, 0, 722, 800, 860
 angiosperms 607
 climate 798, 946
 classification 800
 cold landscapes 770
 millennial variability 798
 desert 48
 environmental
 fluctuations 49
 reconstruction 800
 Epoch 159
 fauna 860
 glacial
 -eustatic changes 356
 -interglacial cycles 408
 glaciation 53
 extent 361
 -Holocene boundary 438, 439
 ice ages 481, 431, 449, 705, 711, 800
 theory 52
 ice sheets 170, 506, 703
 last cold period 485
 late deglaciation 508
 palynology 817
 sea level 434
 thermal oscillation 439
 varve 908
 vegetation pattern 801
 Pliensbachian 964, 967
 Pliocene 263, 267, 425, 609, 768, 770, 804
 atmospheric CO₂ 610, 809
 climate 798, 804
 Arctic 811
 change, causes 809
 models 805
 climatic deterioration 811
 Hadley Cell 806
 ice sheet
 Antarctica 804
 Greenland 804
 late, glacial-interglacial cycles 617
 marine diatoms 804
 mean annual temperature 804
 Northern Hemisphere Glaciation 609, 789, 804
 oceanic heat transport 809
 pressure systems 807
 Research, Interpretations and Synoptic Mapping (PRISM) 568

- sea
 ice 804
 level 567, 804, 805
 surface temperatures (SSTs) 567, 806
 surface air temperatures 566
 total precipitation 806
 warm period 339
 warming 566, 610, 706
 cause 809
 future climate change 567
 wind
 directions 806
 speed 807
- Plio-Pleistocene transition 858
 plucking 365
 Plum Point interstadial 989
 plumes, iron-rich 87
 Pluto 294
 pluvial, Saharan 298
 Po River 559
 Poaceae 817, 858, 922
 POC (*see* particulate organic carbon)
Podocarpus neriifolius 246
 Podocopa 663
 podzol 754
 podzoluvisol 756
 Point Culver (Western Australia) 139
 Poland 878
 drumlins 369
 polar
 animals 729
 bear 40
 coast 186
 Front 20, 60, 161, 183
 ice cap 39
 growth 730
 jet 335, 553
 plants 729
 vortex 58, 297
 warmth 790
 Polar Frontal Zone 791
 polarity
 chron
 nomenclature 253
 geomagnetic 252
 history, geomagnetic 252
 intervals 252
 normal 252
 reversed 252
 pole
 north magnetic, asymmetry 297
 paleomagnetic 468
 Pole-Equator-Pole (PEP) terrestrial transects 675
 pollen 179, 238, 281, 442, 489, 507, 679, 719,
 724, 739, 766, 814, 816, 858
 accumulation rate 819
 analysis 46, 47, 91, 438, 451, 487, 741, 746,
 800, 815
 historical development 815
 Holocene 817
 Pleistocene 817
 sampling methods 818
 theory 816
 arboreal 101, 746
 assemblages
 fossil 816
 interpretation 822
 calibration data set 189
 collection basin 817
 concentration 819
Corollina spp. 768
 data 189
 radiocarbon-dated 188
 deposition rate 819
 diagram 100, 816, 820
 dispersal 817
 fossil 189, 389, 761, 768, 817
 grain 281, 680, 817
 influx 819
 lake 424
Limitisporites monstrosus 768
 non-arboreal 746
 production 817
 variation 817
 radiocarbon dating 189
 rain 816
 record 304, 820
 Eemian 305, 306
 examples 822
 Gröbern 304
 Tenaghi Philippon 304
 spectrum 820
 sum 819
Vittatina 768
 zone 451
 boundaries 101
 pollutant, industrial airborne 739
 pollution, atmospheric 736
 polyhalite, composition 321
 polynya 17, 21, 40
 biological production 40
 extent 40
 pond tortoise 439
 Ponderosa pine 273, 430
 tree rings 430
 Pongola Basin, diamictite 385
 Ponta Delgados (Azores) 621
 Popigai 99
 Porcupine Bank (North Atlantic) 140
 Porcupine Basin Carbonate Mounds Expedition 476
Porites 145, 200, 204, 527
 growth bands 204
 Portlandian
 ammonite 415
 turtle 415
 positive feedback 52
Potamogeton 491
 potassium 111, 580, 823
 -argon method (*see also* dating, Ar-Ar) 580
 as proxy 344
 Pratt model of isostasy 375
 Preboreal 995
 Precambrian 86, 384, 700
 atmosphere, oxygen 63
 biotic change 328
 glacial features 386
 glaciation 166, 385
 oxygen threshold 423
 precession 52, 53, 168, 295, 770, 800, 848
 astronomical 825
 axial 53
 climatic 825
 effect 428
 long-term variation 54
 cycle 303
 precipitate
 chemical 573
 marine 129
 precipitation 45, 194, 240, 266, 278, 489, 667, 0,
 746, 758, 835
 Anatolian 7
 convective 786
 history 746
 impact of mountains 793
 mean annual prediction 680
 orographic 596, 597
 rate 193
 variability 746
 Pre-Pliocene glacial-eustatic changes 356
 pre-Quaternary glaciation 384
 pressure
 dissolution 141
 -solution 130
 primary
 production 281
 limiting nutrient, nitrogen 612
 ocean 780
 oceanic, history 743
 rate 342
 productivity 88, 266, 686, 743, 800
 influence on climate 612
 ocean, reduction 98
 primates 732
 evolution 449
 Prince Charles Mountains 27
 Princess Louise Inlet (British Columbia, Canada)
 367
 principal component (PC) 621
 principle of
 ecological amplitude 242
 homeostasis 294, 298
 limiting factors 242
 uniformitarianism 959
 Priscoan Era 34
 PRISM (*see* Pliocene, Research, Interpretations
 and Synoptic Mapping)
 pristane 661
 process
 biological 342
 eolian 312
 evolutionary 325
 freeze-thaw 365, 366
 product means test (PM) 271
 production
 biogenic 395
 export 644
 net primary (NPP) 113, 114, 644
 planktonic photosynthetic 342
 productivity (*see also* primary production;
 production) 573
 biogenic 40
 global 672
 biological 62
 ocean 98, 786
 organic 486
 reconstruction 644, 645
 proglacial
 lake 193, 837
 sediment 368
 setting 193
 propagule 856
 propane 560
 Proterozoic 87, 766, 768, 836
 glacial strata 467
 glaciation 836
 ice
 age 418
 house 225
 paleoclimate, interpretation 836
 paleoclimatology 836

- Proterozoic (*Continued*)
 Snowball Earth 359
 Protista 766
 protists 280
 protolith 515
 proton 211
 provenance 573
 marker 574
 province
 igneous 474
 molluscan 10
 proxy 128, 485, 716, 735, 746
 animal 10, 13
 biological 488
 chronology, high-resolution 299
 circulation rates 638
 climate 291, 495, 622
 concepts 341
 data 179, 489, 521, 690
 environmental 14
 geochemical 341, 342, 659
 indicators 179
 inorganic 341
 metal ratios 341
 monsoon 591
 multiple 720
 ocean circulation 578
 organic, analytical techniques 351
 paleoclimate 12, 567, 576, 578
 paleoenvironmental 347
 paleoproductivity 578
 paleotemperature 12, 578, 652
 physicochemical 488
 sedimentary 488
 sequences 299
 shell chemistry 12
 significance 341
 temperature 758
 terms 341
 time series, spikes 296
 vegetation 679
 water mass 635
 Prydz Bay 26–28
 cores 27
 sediments record 27
 prymnesiophyte 351, 657
Prymnesium 187
Pseudodictyophimus gracilipes 871
 pseudogleys 754
 pseudomorphs 323, 397
 PSL dating 249
 pteridophyte plant 328
Pterocarya 305
 pteropod 136
 aragonitic 129
 ooze 528
 pterosaurs 330
 Puget Lowland (Washington State) 207, 519
 Pulsation Theory 432
 pump, biological 111, 127, 535–537
 Purbeck group 557
 Puruogangri ice core 458
 Pyrenees 598
 geology 429
 glacier complexes 225
 tectonics 429
 pyrite 63, 78, 85, 487, 576, 582, 0
 as climate indicator 573
 paleo-environmental significance 574
 pyritization 576
 pyrolusite 576
 pyrolysis, Rock-Eval 341, 344
 pyrotoxin 217
 pyroxene 248, 540, 574
- Q**
 Qatar 146
 QBO (*see* quasi-biennial oscillation)
 Qianxi Complex (China) 35
 Qinan 588
 Qomolangma ice core 458
 Qori Kalis Glacier (Peru) 595
 quadropole 258
 quarrying 365
 quartz 93, 249, 309, 523, 580, 0, 837
 hematite-stained 575
 paleo-environmental significance 574
 quasi-biennial oscillation (QBO) 295, 424, 978
 peak 296
 Quaternary 38, 236, 252, 261, 267, 276, 281, 286, 425, 428, 485, 608, 719, 734, 804, 826, 893
 Antarctic sea ice extent 31, 33
 chronostratigraphy 875
 climate 188, 495, 498, 504, 710, 843
 cycle 841
 orbital forcing 191
 processes 391
 simulation 710
 transitions 841
 variations 266
 Environment of the Eurasian North project (QUEEN) 677
 glacial
 -interglacial cycles 389
 lakes 485
 periods 51, 389, 421, 424, 429, 517
 Great Ice Age 418
 ice volume 389
 changes 498
 interglacials 770
 late 722
 climate change 507
 megafloods 504
 vegetation history 507
 macroevolutionary change 860
 methane venting 564
 monsoon 589
 paleoclimate modeling 709
 historical development 711
 soil formation 752
 vegetation change 860
 consequences 860
 warming event 564
 Quebec 416
 cool-water carbonates 141
 last glacial cycle 390
 Quebrada de los Burros (Peru) 724
 Quebrada Tacahuay (Peru) 724
 Queen Elizabeth Islands, last glacial cycle 390
 Quelccaya Ice Cap (Andes, Peru) 8, 726
 ice core 8, 9, 457, 458, 460
Quercus 305, 681, 858
 crispula 243
 sp. 822, 860
 Qunf Cave 592
- R**
 rabbit 732
 raccoon 732
 racemization 233, 236
 activation energy 235
 amino acid 233, 894, 989
 fossil 234
 rate 233, 235
 radar, ice-penetrating 381
 radiation 46, 328, 693
 adaptive 327
 balance 398
 budget 398
 dose rate 257
 dosimetry 249
 electromagnetic 294, 295
 infrared 97, 407
 absorption 757
 solar 22, 55, 61, 219, 333, 407, 419, 422
 variation 62
 ultraviolet 61, 70, 295
 radiative forcing 168
 radioactive
 decay 211, 255
 waste 737
 radioactivity 255
 radiocarbon age
 conversion into calendar age 213
 dating 489, 490, 752, 863, 938
 model 863
 plateaux 102
 radioisotopes 178
 radiolarian 238, 239, 262, 526, 580, 652, 719, 766, 869
 biostratigraphy
 Quaternary 870
 Tertiary 870
 distribution 869
 DNA 870
 evolution 869
 polycystine 870
 taxonomy 870
 radioluminescence 249
 radionuclide 93, 211
 cosmogenic 211, 266
 source 211
 radon 251
 rainfall
 as evolutionary factor 325
 tropical 489
 rainforest 421
 rainshadow 46, 793
 raised mire 195
 Rajang River Delta 184
 RAM (*see* Revised Analog Technique)
 Ramsay, Wilhelm 434
 Rapakavi granites 354, 430
 Rapitan Group (northern Cordilleran region, North America) 910
 rare-earth elements 777
 Rarotonga 346
 rate
 evapotranspiration 266
 soil erosion 266
 Ravi Vallis (Mars) 68
 Ravinement surface 185
 Rayleigh
 distillation 481
 scattering 3
 reaction
 kinetic 133
 Urey 112
 rebound

- Fennoscandian 378
 isostatic 378
 Recent 238
 glaciation 470
 recharge rate 46
 recirculation, gyre 639
 recombination, dissociative 71
 reconstruction
 climate 9
 environmental 48
 paleoenvironmental 15, 46, 341
 paleogeographic 297
 record 128
 cave 389
 deep sea 341
 fossil 328
 Tertiary 10
 geological 587
 paleoclimate 399
 lacustrine 341
 paleoclimate 8
 paleoenvironmental
 age 341
 geochemical composition 341
 terrestrial 341
 pollen, Eemian 305
 sedimentary
 mass 115
 resolution 193
 terrestrial 192
 stratigraphic, evaluation of eustatic changes 355
 recrystallization front 130
 red algae 140
 red bed 196, 401, 837, 871
 desert 196
 formation 871
 geologic record 872
 identification of paleosol 872
 Pangea 872
 savannah 196
 red clay 136, 587
 red kangaroo 722
 red noise spectrum 165
 Red Sea 263, 323, 421, 875, 944
 coral reefs 205
 opening 296
 playas 323
 sabkha 323
 red tides 281, 767
 Redfield ratio 113, 536
 land plants 113
 reduction of error test (RE) 271
 Redwall Formation 716
 redwood 858
 REE, heavy 777
 reef 89, 111, 186
 ancient 900
 barrier 204
 classification 204
 distribution 205
 environment 205
 Holocene age 900
 platform 204
 Pleistocene age 900
 types 204
 refugia theory 459
 regional
 climate models (RCM) 711
 models of isostasy 375
 regolith 467, 982
 regression 183
 forced 184
 reindeer, fossil 100
 relative sea-level 355
 relic cryogenic microrelief (RCM) 757
 relief theory 434
 remains
 faunal 46, 47
 floral 47
 remineralization, organic material 282
 remote sensing 735
 reptiles 328, 330, 727
 Republic of Georgia 449
 respiration 63, 112, 125
 autotrophic 282
 dark 282
 heterotrophic 282
 ocean 282
 response function analysis 270
 retardation 298
 reticulate ice 772
 Reusch, Hans Henrik 434
 Revelle factor 124
 Revelle, Roger Randall Dougan 434
 reversal
 geomagnetic 297
 periodicity 297
 paleomagnetic 425
 reverse-phase liquid chromatography (RPLC) 234
 Revised Analog Technique (RAM) 654
 rheology 376
 mantle 378
 Rhine 267, 426, 522, 756
 Valley, loess 524
 Rhinoceros, woolly 363
 rhizoliths 320
 rhizopodia 870
 Rhode Island, washover 764
 rhodochrosite 487
 Rhone River 559
 rhythmites 384
 glacial-lacustrine 193
 Ribains (*see* Eemian)
 ribulose biphosphate carboxylase (Rubisco) 134
 rice cultivation 123
 Rice, Ramsperger, Kassel, Marcus (RRKM)
 theory 481
 Richmond Gulf (Canada) 376
 ridge, submarine, geological activity 422
 riegel 366
 Rifian Corridor (Morocco) 610
 Rift Valley 461, 573
 rifting 421
 ring width 240
 Rio
 Basin 8
 Moquegua 9
 Río Desaguadero 490
 ripple 394
 Riss
 glacial 363
 /Würm (*see* Eemian)
 river
 bed geometry 394
 ephemeral 194
 ice 221
 evolution 224
 incision rate 736
 metal ions 111
 network, proglacial 394
 perennial 194
 planforms 266
 system
 glacially influenced 372
 inactive 46
 water residence time 734
 roche moutonnée 365, 366, 383, 385, 873
 rock
 Archean 34, 35
 channel 385
 coating 277
 cycle 126
 dune 425
 flour 365, 382
 generation 129
 igneous 35
 Martian 540
 metamorphic 115
 paleomagnetic signal 254
 Phanerozoic 36
 phosphate 775
 polished 365
 salt 716
 step 366
 varnish 275
 weathering 285
 Rock-Eval pyrolysis 341, 344
 Rockhall Bank (North Atlantic) 140
 Rocknest Formation 832
 Rocky Mountains 206, 207, 286, 434, 792
 ice
 cores 457
 sheet 224
 pluvial 298
 lakes 298
 Rocourt soil 307
 rodents 732
 arvicolid 13
 Rodinia 786
 continental breakup 795
 Rogen moraine 369, 506
 Romny interval 756
 root
 depth distribution 508
 hairs 780
 pore space 780
 Rosaceae 993
 Rosetta Stone 879
 Ross Embayment 28, 29
 Ross Sea 16, 17, 26, 27, 263, 610, 944
 glaciation 27
 record 27
 salinity 17
 temperature 17
 till 28
 Rossby waves 789, 792
 rotation velocity, Earth 702
 Rotliegend Formation 581
 Rotmoos (Alps) 451
 Rotmoos Neoglacial 451
 Rottneist
 Island 552
 Stage 552
 Route, colonization 856
 Roza eruption 336
 rubefication 755
 rubidium-strontium method 580
 rubisco (ribulose biphosphate carboxylase) 134
 Ruddimann IRD belt 569
 rudist bivalves 203

- Rugosa 198, 199
 corallites 199
 runaway greenhouse 81
 Russia 879
 Arctic islands, last glacial cycle 390
 climate 293
 glaciation, Paleoproterozoic 385
 loess 314, 424
 permafrost 222
 Salyn Soil 307
 Russian
 Plain 757
 Platform 502
 Rzhaksa soil 755
- S**
 Saale glacial 363
 Saalian 877
 sabkhas 146, 322, 573, 578
 ancient 324
 coastal 322
 continental 323
 sagebrush 858
 Sahara 46–49, 194, 286, 298, 347, 418, 424,
 425, 432, 439, 509, 512, 733, 736,
 747, 876
 dune orientation 315
 duricrusts 47
 dust 1, 308, 309
 record 317
 storms 308
 groundwater recharge 47
 lake levels 59
 migration 736
 Saharan
 air layer 317
 pluvial 298
 region
 Sahel
 as dust source 1, 308
 drought 733
Sahelanthropus tchadensis 447
 Sahul Shelf 297
 Sajama 460
 ice core 458–460
 Salair climate
 Early Devonian 293
 Upper Devonian 293
 salina (*see also* playa) 323
 desiccated 323
 ephemeral 323
 perennial 323
 Salina Formation 324
 Saline mineral 321
 salinity 16, 46, 124, 730, 746
 crisis (*see also* Messinian salinity crisis;
 Mediterranean salinity crisis) 559
 effect 356
 lake water, diatom-inferred 735
 reconstruction, ostracodes 741
 sink, global 422
 surface 684
 salinization 7
Salix 858
 Salpuasselkä 371
 salt
 dome 262
 industry 552
 pan 323
 Phanerozoic 128
 pillow 321
 tectonics 321
 saltation 1
 Salyn soil 307
 sample 130
 geological, analysis 341
 preservation 130
 San Andres Formation 324
 San Clemente Island (California) 901
 San Marcos Cave 868
 sand 425
 body, fluvial 194
 carbonate 89
 creeping population 195
 deposit, eolian 573
 dune 46, 313
 eolian 195, 313
 boundary-layer zone of transport 313
 stratigraphy 314
 glaciofluvial 394
 sea 49
 sheet 313
 laminated 394
 wedge 771
 windblown 312
 sandstone 89, 425, 716, 871
 iron-stained 574
 wedge 385
 sandur 394
 plane 484
 Sangamon County (Illinois) 306
 Sangamon Geosol 303, 306, 307
 Sangamonian 901
 interglacial (*see also* Eemian interglacial) 302,
 303, 305, 363, 986
 Stage 307
 Santa Barbara Basin (California) 135, 565, 724,
 848, 901
 Santa Catarina (Brazil) 421
 Santa Maria (Guatemala) 977
 Santorini (Greece) 440
 saponite, formula 574
 sapropel 266, 487, 875
 deposition 876
 formation 875
 Mediterranean 876
Sarcobatus sp. 822
 Sardinia
 Cambrian climate 292
 cool-water carbonates 141
 Sargasso Sea 521, 551
 SST 620
 Saros 299
 Saskatchewan 370
 Saturn 334, 424
 Saudi Arabia 8, 418
 savannah 449
 red bed 196
 scabland, bedrock erosion 504
 Scandinavia 100, 296, 416, 520, 877
 isostatic rebound 378
 last glacial cycle 390
 Scandinavian Ice Sheet 57, 231, 378, 494, 519,
 757, 793, 877
 melting 304
 scapolite 76
 Scarborough Formation 518
 scarps 900
 scenario, darkness-at-noon 219
 Schimper, Karl Friedrich 434
Schoenoplectus tatora 491
 Schove series 296
 Scientific Committee for Ocean Research
 (SCOR) 676
 Scientific Committee on Antarctic Research
 (SCAR) 677
 Scleractinia 198–200
 evolutionary history 200
 family tree 202
 structure 200
 scolecodonts 766
 Scotland 520
 drumlins 369
 geomorphology 431
 Scott Coast 29
 Scripps Institution of Oceanography 473
 Scyphozoa 198
 Scythian Katberg Formation 964
 sea
 anemones 198
 epeiric 579
 fans 198
 ice 31, 40, 221, 222, 232, 694, 710, 789, 804
 air temperature 40
 albedo 40, 422
 arctic 38
 at mid-latitudes 464
 Cenozoic development 43
 change 42
 climate oscillations 42, 43
 cooling feedback 41
 decrease 42
 definition 38
 diatoms 31
 distribution 221
 drift 40–42
 extent 31, 38–42, 160
 fluctuation 38
 food web 40
 formation 38, 39
 influence on climate system 40, 41
 influence on thermohaline circulation 41
 instrumental record 41
 phytoplankton 42
 proxies 42
 Quaternary record 43
 records 31, 42, 43
 sediment transport 472
 sedimentary tracer 42
 time series 43
 water reservoir 41
 land, distribution 586
 level (*see below*)
 pens 198
 proglacial 467
 surface salinity (SSS) 346
 surface temperature (SST) 57, 159, 160,
 269, 346, 348, 551, 567, 611, 620,
 651, 684, 701, 721, 764, 786, 800,
 813, 844
 change 304
 Last Glacial Maximum 719
 Pliocene 806
 tropical 149
 wasps 198
 water
 density 407
 heat capacity 407
 supersaturation 463

- sea level 149, 160
 apparent, change 355
 at last interglacial 303
 causes 884
 change 210, 266, 326, 375, 474
 eustatic 307
 last 250 million years 879
 local 355
 pre-Quaternary 879
 Quaternary 893
 relative 377
 controlling factor 354
 Cretaceous 215
 definition 354
 eustatic 266, 303, 884
 fluctuation 421
 fluctuation 227
 glacial 361
 global 879
 effect of glaciation 421
 history 183
 icehouse climate 465
 indicators 552, 578, 899
 isostatic signal 376
 Last Glacial Cycle 896
 Last Glacial Maximum 224, 898
 Last Interglacial 225
 lowering 161, 559
 lunar modulation 296
 mean
 actual 421
 universal shift 421
 mid-Cretaceous 884
 middle to late Holocene 890
 minimum 390
 oscillations, Holocene 887
 Pliocene 898
 post-glacial 887
 pressure (SLP) 269, 620
 field 57
 reconstruction 389
 relative 266, 355
 rise 224, 296, 567
 after last glaciation 888
 Recent 891
 transect, New Jersey 880
 Sea of Azov 505
 Sea of Japan 848
 Sea of Marmara 505
 Sea of Okhotsk 944
 seafloor
 cementation 140
 hydrothermal systems 37
 methane
 release 563
 venting 563
 spreading 111, 252, 262, 296, 421, 528,
 578, 789
 chronology 431
 subduction 528
 temperatures 563
 venting 560
 seagrass 145
 seal 40
 seasonality 296
 effects 10
 seawater 534
 cadmium concentration 636
 carbon, isotopic composition 128
 carbonate
 alkalinity 535
 buffer 124
 species 534
 $\delta^{13}\text{C}$ 131
 glaciations 131
 evaporation 89, 322
 isotopic
 composition of past 128
 evolution 130
 neodymium 638
 oxygen 12
 pH 537
 Phanerozoic 577
 recording media of isotopic composition 128
 sediment 128
 thermal compressibility 16
 seaway 798
 Central American 205
 Indonesian 587
 Tethys 205
 sediment 278
 accumulation 355
 rate 395, 686
 aeolian luminescence date 49
 age 252
 allochthonous 486
 analysis of pollen 746
 annually laminated 740
 Archean 35, 63
 as paleoclimate indicator 192
 Atlantic radionuclides 639
 autochthonous 486
 biogenic 525, 526, 528
 calcareous 527
 biostratigraphic dating 527
 carbonate 110
 marine 138
 chemical 36
 clastic 486
 climate-sensitive 399
 compaction 355
 continental 192
 core 179
 deep-sea 389
 laminated 179
 deep-sea 51, 126, 128, 253, 389
 evidence for glacials 159
 deltaic 265
 deposition 265
 diagenetic modification 129
 eolian 47, 312
 Famennian 499
 fine 396
 fluvial discharge 266
 freshwater 90
 glacial 193, 361, 364, 368, 369, 382, 483
 glacioaeolian 374
 glaciofluvial 394
 glaciogenic 138, 279
 glaciolacustrine 369, 383
 glaciomarine 361, 369, 383, 395, 396
 gravity flow 394
 hypersaline 559
 lacustrine 364, 389, 485–488, 835
 clastic 486
 law of superposition 739
 limit 489
 littoral 489
 loess 374
 marine 231, 286, 308, 364, 389, 525, 539
 marl 490
 oceanic, as carbon reservoir 108
 opaline 530
 organic
 carbon, distribution 343
 matter 644
 over-consolidated 389
 particle rounding 394
 phosphorus 644
 proglacial 368
 redeposition 395
 redox state 576
 remobilization 193, 740
 sea floor, eolian dust-dominated 308
 seawater 128
 size sorting 394
 subglacial 284
 deformation 94
 supply 355
 surface
 alkenones 350
 U_{37}^{K} index 349
 trap 343
 types 115
 varved 890, 973
 sedimentation 128, 421
 cyclic 226
 glacial 89
 lacustrine 485
 modification 487
 rate 255
 sedimentoecstasy 421
 sedimentology 312
 seed 679
 ecological tolerance 679
 SEH (*see* Snowball Earth Hypothesis)
 Selwyn Mountains 207
 Selwyn, Alfred Richard Cecil 434
 semi-arid 46
 sepiolite 540, 574, 580
 formula 574
 Sepukhovian 500
 Sequence boundary
 glacioecstasy-controlled 357
 glacial to interglacial 295
 Sequoia 305, 608
 serine 234
 serpentine 580
 Serpukhovian glaciation 501
 biotic response 501
 South Polar cooling 500
 sesquioxide 516
 Shackleton, Nicholas J. 434
 shale
 black 580, 626
 iron-stained 574
 shallow ocean carbonate deposition 137
 Shan-Thai Terrane, Early Ordovician
 climate 292
 Shark Bay 138
 Shatsky Rise 311
 shearing 89
 sheet silicates 580
 shelf
 Arctic 614
 Bengal 267
 Bering 791
 Chukcki 791
 continental, flooding 499
 Texas 267

- shell 128, 901
 aragonite 743
 aragonitic 12
 calcareous 159
 oxygen isotopes 159
 calcite 743
 calcitic 12
 chemistry 12
 fossil 148
 sample 130
 Lusitanian 305
 molluscan 425
 ostracod 921
 shellfish 281
 shergottites (type of martian meteorite) 71, 74
 Shiva Hypothesis 419
 shoreface, upper 89
 shoreline 47
 ancient 46
 movement 183
 Shropshire (England) 362
 Siberia 263, 419, 500, 553, 619, 877
 climate
 Cambrian 292
 Early Devonian 293
 Middle Devonian 293
 Middle Ordovician 293
 Upper Devonian 293
 glacier complexes 225
 Kazantsevo 303
 Last Glacial Maximum 378
 permafrost 225
 Tunguska event 420
 Siberian
 -Alaskan land bridge 361
 High 786
 Platform, climate
 Early Ordovician 292
 Middle Ordovician 293
 Upper Devonian 293
 Sea 38
 Traps 336, 337, 402
 Sicily 553
 siderite 62, 71, 85, 334, 487, 574, 575, 578, 0
 paleo-environmental significance 574
 precipitation 87
 siderophores 478
 Sierra Leone
 glaciomarine deposits 387
 Rise 345
 Sierra Nevada (California) 196, 597, 598
 Sierran-Coloradan region, uplift 844
 sign test (ST) 271
 Sigsbee Abyssal Plain 262
 silcrete 285
 silica 71, 76, 285, 741
 biogenic 31, 736
 minerals 580
 paleo-environmental significance 574
 opaline 279
 valves 279
 varieties 580
 silicates 85, 837
 chemical weathering 98, 112
 siliceous ooze 136
 deep-sea 526
 silicoflagellates 280, 580
 silicon-32 212
 silicon/aluminum ratio 344
 silt 424
 glacial 835
 glaciofluvial 394
 siltation, fluvial 46
 siltstone 716, 837, 871
 iron-stained 574
 Silurian 238, 239, 750
 climate 11, 293
 glaciation 468
 similarity maximum (SIMMAX) 654
 Simpson Desert (Australia) 871
 Sinai-Red Sea link 296
 single-aliquot-regeneration (SAR) 251
 sink
 -holes 773
 cold-water 422
 surface 70, 71
 Sioux Quartzite (South Dakota/Minnesota) 354
 Siple
 Coast ice stream 224
 Dome core 27
 site, archeological, distribution 46
 Siwalik Foothills 48
 skeleton plotting 240
 Slave Craton 35
 slickenside 385
 Smalfjord Formation 386
 Small Ice Cap Instability (SICI) 703
 smectites 540, 574, 580, 581, 716, 749
 smectite/illite ratio 581
 smog, photochemical 98
 SMOW (*see* Vienna Standard Mean Ocean Water)
 SMT (*see* sulfate/methane transition)
 Snail, land 729
 Snake River 380
 snow 746
 accumulation 148, 747
 compaction 118
 cover 710
 seasonal 221, 222
 densification 453, 454
 -firm transition 453
 recrystallization 453
 seasonal 221, 223
 Snowball Earth Hypothesis (SEH) 62, 131, 225, 294, 359, 434, 468, 702, 795, 838, 907
 events 62
 hypothesis 330
 problems 838, 909
 snowfall 835
 snowline 762
 instability 168
 past 598
 shift 601
 sodium 111, 580
 chloride 291, 487
 Sognefjorden 877
 SOI (*see* Southern Oscillation Index)
 soil
 aggregates 748
 animal traces 749
 arid 577
 bacteria 282
 biota 423
 buried 313
 calcrete 580
 carbonate 134, 449
 carbon isotopic composition 62
 chronosequence 751
 classification
 International (FAO) system 754
 Russian system 754
 deflation 287
 dust 1
 erosion 8
 formation 752-754
 fossil 46, 748
 genesis 753
 micromorphological method 754
 fossilization 754
 freezing 768
 horizons 748
 humus
 content 754
 mass 109
 interglacial 752
 lateritic 575, 576
 microbes 781
 mineral components, analytical methods 753
 moisture 45
 organic
 carbon 134
 matter 115, 749, 754
 plasma
 iron oxide accumulation 755
 redox state 576
 residual, as climate indicator 573
 Rocourt 307
 Salyn 307
 stratigraphic units 752
 wedge 771
 Solar
 activity 92, 212, 428
 atmosphere 70
 constant 53, 54, 93, 428, 467
 cycles 296, 299, 572, 930
 emission 294, 424, 428
 quasibiennial oscillation 424
 energy 96, 428, 785
 evolution 333, 700
 model 174, 333
 flare 297
 average 298
 forcing 172, 296, 934
 changes 168
 irradiation 55, 93, 572
 changes 802
 luminosity 62, 174, 333, 836
 early Precambrian 701
 magnetic activity 930
 nebula 69, 79
 output 53, 159, 178, 180
 perturbation 452
 plasma 211
 radiation 55, 96, 333, 407, 419, 422, 449, 521, 700, 736, 757, 785
 absorber 219
 delayed response to 298
 fluctuation 451
 forcing 298
 type 295
 variation 62
 System 35, 294
 abundances 79
 barycenter 294
 evolution 429
 meteorite bombardment 35
 origin 435
 passage through galactic arms 295
 perigalactic and apogalactic phases 297

- variability 172, 930
 and climate 931
 and Paleoclimate 932
 wind 70, 71, 74, 211, 294, 417, 419
 solifluction 298, 372, 774, 903
 periglacial 772
 solvent extraction 352
 Somali Current 786
 Somalia 786
 soot 217
 Sorachi Plateau (Japan) 337
 sorghum 134
 source, molecular indicators 347
 South Africa 90, 387, 425, 448
 Archean glaciation 385
 glaciation
 Ordovician 387
 Paleoproterozoic 385
 Middle Ordovician climate 293
 pseudomorphs 323
 Upper Carboniferous to Triassic succession 388
 South America 262, 287, 387, 415, 418, 609, 722, 730, 786, 848
 Altiplano 49
 Cambrian climate 292
 climate
 Early Ordovician 292
 Middle Devonian 293
 Middle Ordovician 293
 endemic fauna 732
 glaciation
 Devonian 387
 Ordovician 387
 Paleozoic 387
 Silurian 387
 ice cores 457
 Last Glacial Maximum 747
 Little Ice Age 747
 relict dunes 49
 tillites 469
 Younger Dryas 747
 South American Seaway 611
 South Asia-Indonesian land bridge 361
 South Atlantic 261, 412
 carbonate compensation depth 136
 South China Sea 586, 588, 848
 core 348
 South Florida
 sediments 145
 warm-water carbonate 145
 South Pacific 791
 South Pole 48
 glaciation 498
 South Tasman Rise 357
 Southeast Faroes Drift 618
 Southeast Trades 786
 southern beech 860
 Southern California 578
 Southern Component Water 609
 Southern Hemisphere 59, 219
 Cambrian climate 292
 climatic system 31
 Last Glacial Maximum circulation 58
 rainfall 49
 sea ice
 at Last Glacial Maximum 224
 values 222
 snow cover, values 222
 water circulation 21
 Southern Ocean 16, 19, 20, 48, 120, 126, 224, 263, 280, 349, 408, 421, 422, 496, 687, 730, 944
 circulation 609
 cool-water carbonates 138
 deep water production 169
 diatoms 31
 gateways 687, 790, 791
 heat transport 791
 iron fertilization 120
 LGM 616
 salinity 20
 sea ice 31
 temperature 791
 warming 496
 wind-driven upwelling 687
 Southern Oscillation Index (SOI) 297, 620, 721, 725, 726
 Southwest Monsoon 786
 Sovetskiy Soyuz (nuclear icebreaker) 475
 Spathian 965
 Speciation, allopatric 326
 species
 abundances 652
 evolution 326
 extinction 200
 SPECMAP project (SPECTral Mapping Project)
 163, 434, 911
 astronomically derived timescale 911
 spectroscopy, laser absorption 119
 speleothem 7, 46, 47, 134, 341, 485, 578, 0, 735, 746, 758, 814, 898, 916, 970
 carbon isotopic composition 917
 growth 916
 Italian 8
 oxygen isotope variation 917
 records 460, 578, 672
 Spencer Gulf (South Australia) 140
 sphaeroidal carbonaceous particles (SCPs) 741
 sphaerosiderite 578
Sphagnum 662
 spherules 548
 spiral arm (galaxy) 295
 Spirit Rover (Mars) 69, 542
Spiritus silvestris 107
 Spiro sandstone 581
Spirocyrtis scalaris 870
 Spitsbergen (Greenland) 553, 877
 hematite-stained grains 575
 flora 422
 split-jet 58
 spodosol 197, 903
 sponges 146, 200
 aragonitic 578
 Devonian diversity 499
 in cool-water carbonates 138
 spicules 901
 spore 238, 281, 719, 816
 embryophyte 766
 fungal 766
 sporopollenin 281, 766, 817
 degradation 817
 spreading rate (*see* seafloor spreading;
 plate tectonics)
 spruce 856
 Spumellaria 870
 sputtering 70
 Sr-isotopic stratigraphy 882
 SSS (*see* sea-surface salinity)
 SST (*see* sea-surface temperature)
 St. Elias Mountains 207
 St. Helena, eolianite 425
 St. Lawrence River 381, 392, 505, 518, 616, 991
 stable isotopes
 paleothermometry 435, 919
 ratios in meteoric water 920
 stadials 801
 cold 875
 stalactite 747, 578, 760
 growth 299
 stalagmite 134, 578, 622, 760, 747
 Standard Light Antarctic Precipitation (SLAP) 278
 standard mean ocean water (SMOW) 80
 standing wave energy 58
 statistical dynamical model (SDM) 710
 steam, atmosphere 80
 Steingletscher (Switzerland) 364
 stem growth, daily change 273
 stenothermal 420
 Stephan Boltzman Law 333
 Stephanian 502
 steppe vegetation 858
 steroid 661
 sterol 347, 349, 661, 719
 4-methyl 661
 biomarker 347
 derivatives 661
 steryl chlorin ester 350
 Stevns Klint (Denmark) 217
 stomata 442
 stomatal
 density 680, 719
 index 549, 679
 stomatopoid 200
 stone tool making 449
 Stone Age 423
 Storbreen Glacier 371
 storm 60, 763
 cyclonic 549
 frequency 186
 generation 60
 intensity 186
 magnetic 297
 Stormberg Group 388
 Strait of Florida 145
 Strait of Georgia 207, 210
 Strait of Gibraltar 296
 Strait of Hormuz (*see also* Panama isthmus;
 Panama gateway) 146
 Strait of Panama, closure 798
 strandflat 416
 strandplain 183, 184
 Strangelove Ocean 98
 stratification 266
 stratigraphy 165
 stratosphere 96, 97, 282, 335, 424
 ozone changes 521
 stratospheric aerosol layer 335
 stream
 bedload-dominated 193
 ephemeral 194
 glacial, milky 365
 perennial 194
 supraglacial 483
 stromatolites 37, 146, 147, 199, 837
 stromatoporoids 200, 578
 strontium 578
 /calcium ratio 341, 345
 isotopes 309, 777, 923
 evolution of seawater 924

- strontium (*Continued*)
 isotopic ratios 463
 Phanerozoic 465
 Sturtian 434, 467, 838
 glaciation 386
 Stykkisholmur (Iceland) 621
Stylaster 198, 201
Stylasterina 198, 201
Styloclytia validispina 871
 Sua Pan (Botswana) 285
 sub-Antarctic islands, permafrost 225
 subchron 253
 Kaena 253
 Olduvai 253
 subduction 111, 296, 422
 seafloor 528
 zone 421, 794
 subglacial
 debris 368
 setting 193
 sliding 94
 zone 89
 sub-humid 46
 sublimation 395, 746, 949
 till 949
 subseafloor
 biosphere 474
 microbiota 474
 subsidence 355, 378
 rate 193
 subtropical coast 186
 subtropics
 circulation change 60
 Last Glacial Maximum circulation 59
 observational circulation analysis 59
 sea surface temperature 59
 succession, transgressive 184
 Succotash Marsh (Rhode Island) 765
 Sudan, Middle Ordovician climate 293
 Suess, Eduard 435
 sugar
 cane 134
 maple 241
 sulfate 98, 579, 778, 836
 aerosol 220, 548
 /methane transition (SMT) 563
 paleo-environmental significance 574
 porewater 927
 reduction 129
 bacterial 927
 seawater 926
 sulfide 85, 927
 paleo-environmental significance 574
 sulfite 927
 sulfur 98, 110, 927
 aerosol 795
 dioxide 110, 220, 399
 conversion to anhydrite 78
 biological cycling, evolution 928
 global cycle 96, 927
 isotope 63, 926
 anomalous signature 63
 evolution of seawater 927
 isotopic ratios 463
 Phanerozoic 465
 magmatic
 $\delta^{34}\text{S}$ value 927
 solar system abundance 79
 trioxide 76
 vapor 82
 sulfuric acid 420, 794
 aerosol 96, 98
 fallout 98
 summer
 pack ice 39
 wetness index 551
 Summit
 drillings
 GISP2 229
 GRIP 229
 region (Greenland) 760
 Sun 51, 294, 449, 625, 825
 aerosol diffraction pattern 978
 -climate connections 929
 coronal holes 92
 dimming 336
 history 294
 magnetic activity 929
 spin rate 294
 Sunda Shelf (Indonesia) 297, 377, 890
 sunlight 52, 684
 reduction 98
 Sun-like stars 931
 Sunnybrook Drift (Toronto) 518
 sunspot 416, 419, 428, 930
 abundance 550
 cycle 295, 296, 417, 424, 426, 440, 521
 formation, influence of planets 416
 Supai Group 716
 supercontinent 555–557
 climate persistence 466
 cycle 466, 467
 supercycle, tectonic 467
 super-greenhouse 79, 82
 supernova explosion 92
 super-tide 423
 Greenland 423
 herring 423
 supraglacial
 debris 368
 setting 193
 surface
 sink 70, 71
 striated 469
 temperature 165
 variation 467
 Susceptibility 295
 suturing, Variscan 555
 Svalbard, Upper Devonian climate 293
 Sverdrup Basin 141
 Swedenborg, Emanuel 435
 Swedish Deep-Sea Expedition 529
 Swiss
 Alps 102
 ice cores 457
 sylvite 577
 as climate indicator 573
 composition 321
 paleo-environmental significance 574
 Syria, desertification 553
 Syrtis Major 541
 system
 aquatic, organic matter 342
 depositional 192
 alluvial fan 194
 climate indicator 195
 continental 192
 desert 194
 eolian 194
 glacial 192, 373
 lakes 193
 rivers 194
 eolian 195
 erosional 600
 landscape 368
 geomorphic, climate impact 601
 hydrothermal 37
 monsoon 589
 syzygy phase, lunar 299
- T**
 TA (*see* total alkalinity)
 Tabulata 198
 Tadjikistan loess 524
 Tahiti 879
 Sea Level Expedition 476, 477
 tail 385
 Taimyr Peninsula 877
 Takla Makan (Taklamakan) and Inner Mongolian
 deserts of northern China 287
 dust 1
 Talchir (India) 432
 Boulder Beds 362
 Tillite 418
 TAM (*see* Transantarctic Mountains)
 Tambora (Indonesia) 977
 eruption 1815 335, 424, 459, 976
 taphonomy 14, 527, 607
 taphrogenesis 296
 Tarim
 Basin 603
 Early Devonian climate 293
 tarn lake 366
 Tasman Rise 154
 Tasmania
 permafrost 225
 Permian limestones 141
 Tasmanian
 Passage 791
 Seaway 25
 Taucu Lake 380
 taxa
 exaerobic 12
 thermophilous 858
 Taxaceae 858
 Taxodiaceae 858
Taxus 305
 Taylor Dome ice core 120, 121
 TDC (*see* total dissolved carbon)
 te Kuiti Limestone (New Zealand) 141
 teak 241
 technique, microsampling 12
 tectomict 279, 369
Tectona grandis 241
 tectonic reconstruction
 uncertainties 784
 uplift 792
 tectonics 254, 265, 0
 local 355
 tectonism 421, 599, 603, 773
 cycle 977
 tectono-eustasy 421, 887
 teeth, isotopic analysis 135
 teleconnections 721
 temperature 46, 51, 158, 326, 669
 air, Pliocene 566
 anomalies, global 759
 Antarctic 119, 120
 Archean ocean 36
 as evolutionary factor 325

- atmospheric 758
 feedbacks 177
 blackbody 62
 catchment-integrated 266
 depth profile 104
 Earth
 history 758
 surface 62
 forcing 3
 global 757
 mean surface 117, 176, 461
 gradient 58
 equator-to-pole 3
 latitudinal 57, 58
 oceanic 149
 history 103
 ice history 759
 indicator, inorganic 345
 interglacial 119
 lake records 761
 Last Glacial Maximum 117
 marine, Cretaceous 215
 mean annual 157
 prediction 680
 oceanic 758
 proxy 853
 reconstruction 349, 390
 Northern Hemisphere 274
 techniques 347
 tree ring 758
 rise, IPCC projections 566
 sea surface 477, 567
 tropical 149
 tropospheric 792
 variability 758, 467
 Tenaghi Philippon (Greece) 304
 tephra 977
 composition 937
 deposits 937, 938
 characterization 938
 dating 938
 destruction of
 Herculaneum 937
 Pompeii 937
 dispersal 938
 particle 459
 production 938
 properties 937
 Toba, distribution across India 938
 tephrochronology 247, 487, 735, 741, 937
 application 938
 countries 938
 terminal moraine (*see* moraine, end)
 termination 495
 carbon cycle 496
 definition 495
 III 495
 last, chronology 495
 V 495
 termites 423
 terraces 394
 marine 900
 terrestrial environment 305
 Tertiary 10, 261, 281, 499, 680, 719, 804, 860
 carbon dioxide values 117
 carbonate compensation depth 137
 fauna 860
 late glaciation 501
 thermal maxima 516
 Tertiary Tsondab Sandstone 48
 TES (*see* Thermal Emission Spectrometer)
 Tethyan
 current regime 686
 monsoonal systems 703
 Tethys 99, 201, 203, 295, 296, 417, 421, 422, 531, 609
 circumglobal current 704
 Ocean 154, 557, 610, 705, 790
 Sea 789
 Seaway 205
 TEX₈₆ paleothermometer 215
 Texas 267, 306
 A&M University 473
 shelf 267
 Thailand 246
 Early Ordovician climate 292
Thalassia 145
Thalassiosira antarctica 280
 Thames 441
 frozen 441
 Thar Desert 440
 THC (*see* thermohaline circulation)
 The Netherlands 100
 theca 281
 thenardite, composition 321
 Theory of Continental Drift (*see also* plate tectonics) 418
 Thera (Santorini, Greece) 977, 979
 thermal maximum 451
 Thermal Emission Spectrometer (TES) 540
 thermal ionization mass spectrometry (TIMS) 90, 347
 thermal noise 259
 thermobaricity 16
 thermocline 140, 531
 equatorial 788
 thermohaline circulation (THC) 229, 567, 610, 790, 931, 933, 943, 995
 Atlantic 802, 939
 early Pliocene 611
 thermokarst 772
 activity 774
 generation 774
 thermoluminescence (TL) 249, 257, 894
 thermoremanent magnetization (TRM) 254
 thiosulfate 927
 thorium 211, 248, 970
 threonine 234
 threshold
 climatic 303, 568
 effects 298
Thuja 305
 occidentalis 243
 Thule Culture 552
 Thulean basalt 154
 Thunder Bay 381
 Tian Shan (Asia) 736
 Tiber 441
 frozen 441
 Tibet 48, 49, 91, 162, 422, 792
 drought 8
 millennial cycles evidence 571
 Tibetan Plateau 48, 154, 434, 461, 587, 603, 705, 783, 844, 932, 984
 Asian monsoon 598
 ice cores 457, 459, 460
 Ice Sheet 225
 mountain building 449
 mountain glaciers 595
 permafrost 225
 uplift 422, 286, 296, 310, 474, 611, 705, 790, 811
 Tibetan-Himalayan Plateau (*see* Tibetan Plateau)
 uplift (*see* Tibetan Plateau, uplift)
 tidal
 channel 186
 flat 89, 183, 186
 inlet 186
 pumping 89
 wave 423
 tide
 current velocity 424
 luni-solar 423
 Tien Shan, Upper Devonian climate 293
 Tigris River 7
 till 279, 284, 368, 382, 384, 518, 716, 948
 classification 369
 deformation 193
 diamict 383
 flow 279, 369, 382
 formation 948
 glacial 193
 iceberg 382
 identification 949
 lodgement 193, 279, 383
 lowered 382
 melt-out 193, 279
 types 193
 waterlain 382
 tillite 291, 384, 430, 434, 469, 558, 716, 948
 identification 949
 marine 468
 Permian 431
 Precambrian 419
 Silurian climate 293
 tilt, axial 52
 Timan, Upper Devonian climate 293
 timberline 442
 ecotone 445
 time of flight mass analyzer 259
 timescale
 biostratigraphically based 239
 centennial-millennial 171
 climate system 165
 glacial-interglacial 168
 tectonic 166
 TIMS (*see* thermal ionization mass spectrometry)
 Tiquina Strait 490
 Titan 334
 titanite 248
 titanium 8
 Tithonian-Kimmeridgian Morrison Formation 966
 Titius-Bode Law 432
 titration
 closed cell 125
 potentiometric 125
 Tiwanaku (*see also* civilization, ancient) 8
 abandonment 8
 civilization 8
 collapse 9
 TL (*see* thermoluminescence)
 Toarcian 965
 Toba (Indonesia) 977, 979
 eruption 98
 TOC (*see* total organic carbon)
 todorokite 576
 Tommotian Fauna 330

- tooth enamel 14, 15
topography 603
 effective 57
 model 57
Toroweap Formation 716
tortoises 731
total alkalinity (TA) 124, 125
 distribution 125
 global inventory 126
 measurement 125
total dissolved boron 124
total dissolved carbon (TDC)
 seawater 130
total dissolved inorganic carbon (*see also*
 dissolved, inorganic carbon) 124, 125, 743
 carbon isotope ratio 127
 distribution 125, 126
 global inventory 126
 measurement 125
total organic carbon (TOC) 344
total solar irradiance (TSI) 930
Tournaisian 499
 flora, phytogeography 500
tracer 213, 687
 geochemical 569, 635
 kinematic 635
 lithological 33
 paleonutrient 616
 petrological 569
 Sedimentary 42
 water mass 635
trade winds 46, 60, 764, 786, 794, 801
 velocity 48
Trans Polar Drift 39–42
Transantarctic Mountain Range 25, 27, 222,
 792, 804
 uplift 25
transfer function 719, 735, 741, 800, 813, 959
 accuracy 960
 applicability 960
 development 959
 reconstruction 960
 training set 960
transgression 183
Transient Tracers in the Oceans (TTO) 125
transition state theory 481
transpiration 45
Transpolar Drift 476
transport
 eolian 46
 fluvial 46
 glacial 364, 368
 glaciofluvial, effects 394
 spasmodical 364
travertine 47
tree 239
 annual growth ring 269
 C–14 flux 299
 cellulose 278
 climatically sensitive 242
 $\delta^{13}\text{C}$ 134
 growth 241, 243, 269
 anomalies 270
 boundary 442
 conceptual model 242
 height 442
 microclimate 269
 multiple-banding 241
 ring 171, 179, 269, 299, 424, 429, 442, 451,
 485, 520, 679, 681, 720, 735, 746, 758
 dating 246
 dating of glacial fluctuations 246
 density 622
 global warming 246, 274
 identification of solar cycles 430
 Irish bog oaks 440
 reconstruction of climate 273
 standardization 245
 width 622
 analysis 682
 NAO 620
 tropical 682
 stumps, fossil 901
treeline 442, 762, 858
 drought-caused 442
 fluctuations 442
 reconstruction 442
 mountain 442
 temperature-controlled 443
 polar 442
 reconstruction 442
 records, chronology 442
 spatial position 442
tremolite 80
Triassic 238, 554
 climate 556
 climatic history 556
 flora
 Chinle Formation 964
 Falla Formation 964
 Newport Formation 964
 fossil logs, Antarctica 962
 General Circulation Model
 simulations 556
 -Jurassic boundary
 mass extinction 547
 labyrinthodont amphibians 963
 late 253
 Latemar Formation 827
 life crisis 965
 Newark Supergroup 831
 paleosols 966
 palynofloras 768
tricalcium phosphate 775
tridymite 580
trilobite 237
 assemblage 11
 Cambro-Ordovician 11
 Ordovician 327
Trinidad 263
Trinity 267
troilite 79
trona, composition 321
tropical
 coast 186
 rain forest 858
 seasonal forest 858
 treeline, depression 858
tropics
 circulation change 60
 Last Glacial Maximum circulation 59
 observational circulation analysis 59
 sea surface temperature 59
tropopause 335
 Last Glacial Maximum 58
 tropical 78
troposphere 96
 dust aerosol, residence time 335
 lapse rate 792
 Northern Hemisphere 336
 sulfate, residence time 335
 temperature 792
trough 366
TSI (*see* total solar irradiance)
Tsuga 305
Tsuga canadensis 856
tsunami 217, 420, 423
TTO (*see* Transient Tracers in the Oceans)
tube, anemones 198
tubeworms, intertidal 891
Tubiphytes 203
Tubipora 198, 203
 musica 203
tufa 46, 47, 49
Tuktoyaktuk Peninsula (Canada)
 pingo 783
tundra 100, 451, 792, 800
 forb 511
 graminoid 511
 vegetation 729
tungsten, extraterrestrial 36
Tunguska-scale impact (*see also* bolide impact)
 98
turbidite 286
 deposit 395
 glaciolacustrine 383
 sedimentation 412
turbidity 140, 487
 current 557
Turgai
 divide 381
 Strait 732
Turk Atoll 296
Turkana (Kenya) 446
Turkey 7, 440
 glaciation, Ordovician 387
 lacustrine sediments 7
 permafrost 225
 Upper Devonian climate 293
Turonian 886
 seaway 686
turtle 415, 729
Tuva 505
Twelve Apostles (Australia) 139
Tyndall, John 398
Tyrrell Sea 299, 939, 989
- U**
U.S. National Science Foundation (NSF) 475
Udotea 146
Uivak gneisses (Labrador) 35
uk37 alkenone paleothermometer 188
Ukraine 877
Ulmus sp. (elms) 305, 822
 decline 451
ultisol 872, 903
ultraviolet
 flux 334
 light 66
 photolysis 76, 78
 radiation 61, 70, 295
underflow 193
underthrusting 599
Uniformitarian Principle 270
uniformitarianism 417, 816
unit
 chronostratigraphic 303
 terrestrial biostratigraphic 302
Unitas 598
 ice cores 457

- uplift (*see also* mountain uplift) 355, 449, 600
 Cenozoic 794
 definition 599
 epeirogenic 792
 Himalayan 844
 Himalayan/Tibetan 267
 hydro-isostatic 431
 late Cenozoic 610
 mountain 421
 orogenic 422
 tectonic 420, 524, 792
 Tibet 422
 Tibetan Plateau 286
 Upper Riphean 434
 upwelling 12, 422, 479, 525, 536, 609, 646, 685, 686, 722, 730, 778, 786
 coastal 531
 equatorial 531
 mapping, phosphorite distribution 778
 polar regions 422
 prediction 686
 regions 529
 velocity 686
 wind-driven 687
 zone 703
 equatorial 136
 Ural Mountains 768
 Urals 502
 Early Devonian climate 293
 Upper Devonian climate 293
 uraninite 63, 576, 582
 as climate indicator 573
 detrital 63
 uranium 211, 435, 777, 970
 dating 969
 decay 247, 255
 series 777, 800
 Uranus 52, 424
 beat frequency 424
 Urey reaction 76, 112
 Urey, Harold C. 148, 435
 U-series, isotope analysis
 methods 970
 Uthusslön (Sweden) 369
 Uvigerina peregrina 646
 Uyuni Salt Pan 380
 Uzboi Channel 381
- V**
 Valdai glaciation 757
 Valles Marineris (Mars) 66, 541, 544
 valley
 glaciation 155
 glacier 361, 595
 geometry 224
 thickness 361
 hanging 366
 tunnel 366
 van Helmont, Jan Baptista 107
 van Krevelen plot 344
 Vancouver Island 207, 210
 vapor
 meteoroid 97
 water 97
 vaporization 158
 Varangerfjorden (Varanger Fjord), Norway 419, 434
 Varangian 418
 glaciation 386, 467
 Neoproterozoic 385
- variability, climate, millennium-scale 51
 variation, astronomical (*see also* astronomical
 theory of paleoclimates; orbital cycles)
 astronomical 391
 orbital 163, 391
 varnish (desert) 275
 development 275
 Negev Desert 276
 trace element XE "trace element"
 geochemistry 277
 Tunisian 276
 varve 383, 384, 430, 451, 835, 837, 908
 annual 740
 clay chronology 973
 glacial 193, 973
 chronology 974
 lake sediment 974
 nonglacial 973
 Pleistocene 908
 sediment 890, 973
 thickness 973
 vaterite 577
 Vatnajökull (Iceland) 422
 Vega 2 landing site 77
 vegetation 51, 733
 change 449
 conditions, past 47
 cover 46
 reconstruction 746
 reduced 46
 distribution, quaternary 856
 fossil, physiognomy 794
 global, devastation 97
 gradient 305
 history 341, 856
 reconstruction 856
 Holocene 438
 late glacial 101
 LGM 511
 limit 442
 mapping 189
 Quaternary 507
 modeling 507
 asynchronous coupled 511
 Holocene 507
 interactive coupled 511
 inverse 512
 LGM 510
 mid-Holocene 512
 Quaternary 507
 Quaternary 720, 856
 rain forest 747
 Recent 720
 shift 134
 species composition 156
 vein calcite 760
 Vema Channel 19
 Vendian Period (*see* Ediacaran Period) 434, 467
 Venediger (Alps) 451
 Venera 13 (Venus) landing site 77
 Venera 14 (Venus) landing site 77
 Venezuela 8, 263
 Venus 424
 accretion 79
 argon-40, degassing 77
 atmosphere
 accretionary 80
 composition 75-78
 evolution 75, 81, 82
 present 75
 beat frequency 424
 climate 76
 change 81
 dry formation 79
 global cloud layer 76
 hydrous minerals 80
 lithosphere, sulfur content 81
 Magellan mission 75
 nitrogen inventory 70, 78
 noble gases 79, 80
 oxidation 81
 oxygen loss (*see* atmosphere, composition,
 evolution)
 Pioneer Venus 75
 properties 75, 76
 runaway greenhouse 81
 Soviet missions (*see also* Venera 13, 14) 75
 steam atmosphere 81
 sulfur dioxide (*see also* atmosphere,
 composition, evolution) 78
 super-greenhouse 79, 82
 temperature 75
 tremolite 80
 volatile inventory 79, 80
 volcanism 81, 82
 water 79-81
 deuterium-hydrogen atomic ratio 80
 loss 81
 wet formation 80
 Verkoyansk Mountains (Siberia) 770
 vermiculite 523
 formula 574
 vernadite 576
 vertebrates
 fossil 15
 functional interpretation 14
 proxy 13
 vertisol 197, 871, 903
 Vesterålen (Norway) 378
 Vestfold Hills (Antarctica) 376
 Vesuvius, A.D. 79 eruption 937
 Victoria 425
 Vidar Viking (drilling vessel) 475
 Vienna Standard Mean Ocean Water (V-SMOW)
 278, 282, 667
 Vienna-Pee-Dee Belemnite 480
 Vietnam, Upper Devonian climate 293
 Viking (Mars)
 lander 71
 measurements 71
 mission 77
 Orbiter, images 68
 probes 66
 Stage 552
 Viking/Rottneast 553
 Vikings 8, 42
 colonization voyages 422
 settlements, 42, 520
 Virginia oyster 298
 Viridophytae 816
 viruses 40
 Visean 499
 flora, phytogeography 500
 stage 11
 Vistula River (Poland) 756, 877
 visual microlaminations (VML) 275
 vital effect 128, 131
 viticulture 552
Vittatina spp. 768
 vivianite 487

- volatile hydrocarbons 113
 volatiles 110
 atmospheric loss 70
 excess 110
 hydrodynamic escape 70
 impact erosion 70
 on Mars 69
 primordial 110
 reactive 80
 sputtering 70
 surface sinks 70
 volcanic
 activity 172
 aerosol 440
 movements 977
 ash 739, 835
 crater 740
 dust 424
 eruption (*see also* Krakatau, Mt. St. Helens, Thera, Toba, Vesuvius) 174, 521
 chronology 976
 climate change 976
 frequency 976
 heat-shielding effect 440
 history 976
 Holocene 977
 records 977
 explosivity index (VEI) 977
 halogen 976
 outgassing 789
 tephra layer 741
 winter 336, 548
 volcanism (*see also* volcanic) 326, 402, 421, 794
 climatic effect 784
 cycle 977
 volcano (*see also* volcanism, volcanic) 415, 423, 976
 Volga
 Delta 552
 River 7, 381, 505
 Von Richthofen, Baron Ferdinand 435
 Vøring Plateau 611
 Vorona (Muchkap) interglacial 755
 Vortex, polar 58
 vorticity 792
 Vosges 52
 Vostok (Antarctica) 46, 761
 ice core 56, 118, 119, 168, 169, 286, 304, 390, 391, 453–455
 glacial-interglacial cycles 318
 V-PDB (Vienna PDB) isotope standard 133
- W**
 Wärm glaciation 986
 Wah Wah range (Utah) 832
 WAIS (*see* West Antarctic Ice Sheet)
 Wake Island 553
 Wales 52
 Walker circulation 59, 721, 788, 841, 843, 844
 intensification 844
 Walker, Sir Gilbert 297, 299
 walrus 8
 Walvis Ridge 348
 warming 495
 Antarctic 231
 climatic 99
 global 446, 737, 774, 967
 anthropogenic 763
 Cretaceous 422
 Keeling Curve 434
 long-term 549
 NAO 621
 role of ocean carbonates 434
 greenhouse 423
 Greenland 231
 late 20th century 423
 mid-Pliocene 566
 post-Heinrich event 569
 Warrego Valles (Mars) 542
 Warthe Glaciation (Germany) 493
 Washington 207, 261
 glacier lake outburst flood 394
 washover 764
 Rhode Island 764
 water 110, 182
 Antarctic bottom 16
 availability 46
 balance, concept 45
 fossil 735
 gas reaction 80
 ice
 melting 736
 shelf 16
 interstitial 777
 liquid, stability field 62
 marine
 freezing 38
 thermohaline characteristics 41
 mass, proxies 635
 on Mars 66
 quality trend 738
 renewal 734
 residence time 734
 resource management 619
 -rock interaction 36
 specific heat 785
 storage 45
 UV decomposition 81
 vapor 51, 55, 97, 399
 coagulation time 97
 injection, effects on atmosphere 97
 photolysis 71
 stratospheric, increase 97
 watershed 734
 wave
 base 146
 -cut notches 400
 energy 58, 60
 height 619
 wavellite 777
 weasel 732
 weather forecasting 710
 weathering 71, 254, 266, 284, 981
 alumino-silicate minerals 982
 atmospheric $p\text{CO}_2$ 983
 biological 748
 carbon cycle 983
 carbonate minerals 981
 chemical 46, 365, 486, 573, 716, 748, 780, 794, 800, 837, 872
 continental 779
 crust 47
 mountain building 984
 physical 748, 780
 product 514
 rate 981, 984
 rock 285
 silicate and carbonate minerals 981
 silicate rocks 794
 Webster soil 581
 Weddell
 Gyre 19, 32
 Polynya 16, 18, 20
 -Scotia Confluence 16
 Sea 16–20, 28, 222, 610, 944
 bottom water 19
 circulation patterns 17
 dissolved oxygen 18
 T/S diagram 16
 Wegener, Alfred 52, 296
 Weichsel glacial 363
 Weichselian 877
 glaciation (Wisconsin) 91, 493, 986
 interstadials 478
 late glacial 100, 102
 West Africa 49, 424
 West Antarctic Ice Sheet (WAIS) 24, 222, 361, 392
 West Sayan Mountains 506
 westerlies 792
 circumpolar 46
 western hemisphere 8
 Western Interior Coal Basin 227
 Western Interior Seaway (North America) 557, 704
 Western Pacific Warm Pool (WPWP) 788, 791
 Westphalian glaciation 502
 wet deposition 459
 whale 40, 729
 wheat 134
 Whillans Ice Stream 27
 white ash 241
 White Nile 425
 flood 425
 White Sea
 Eemian 305
 whitebark pine 860
 whittings 129
 Wien's Law 333
 wildfires 98, 295
 global 98, 217, 220
 Wilkes Basin 25, 27
 William of Malmesbury 552
 William of Normandy 552
 willow 858
 wind 46
 as evolutionary factor 325
 direction 46, 314
 erosion 746
 katabatic 21, 374
 planetary 70
 ripple 195
 solar 70
 speed 746
 stratospheric 623
 strength, reconstructions 459
 stress fields 567
 Windermere interstadial 100
 windthrow 856
 winter
 impact 548
 severity index 551
 volcanic 548
 wireline coring 262
 Wisconsinan 361, 901
 glacial 306
 late
 glacial history 518
 glacial limit 519

- glacial 229, 231, 363
Glaciation 517, 986
Ice Sheet
 center 989
 instability 989
 sea level records 987
 Stage 986
Witwatersrand Basin, diamictite 385
WOCE (*see* World Ocean Circulation Experiment) 125
wollastonite 76
Wolstonian glacial 363
wood 679
 anatomy 681
 determination of paleoclimate 682
 cellulose 682
 density 240
 isotopic composition 622
 nitrite 682
 physiognomy 680
 volume 240
woodland, Eemian 304
Wopmay Orogen 832
World Climate Research Program (WCRP) 676, 813
World Ocean 43
 Circulation Experiment (WOCE) 125
worms 145, 146
Wright corer 740
Würm glacial 363
Wyoming Province (USA) 35
- X**
Xanthophyceae 280
xanthophylls 279, 350
xenon 34, 560
 Mars, isotopic ratio 72
- xerothermal 451
X-ray fluorescence (XRF) 77
xylem 240
- Y**
Yamal Peninsula 756
Yangtsi flood 426
Yarmouth interglacial 363
Yaroslavl¹ cryogenic stage 757
yedoma loess-ice complex 524
Yellow River (China) 890
 delta, marining 432
Yellow Sands 580
Yemen, millennial cycles evidence 571
Yenesei (Yenessei) River 38, 505, 557
Younger Dryas 7, 22–24, 49, 91, 191, 229, 276, 314, 378, 381, 392, 496, 498, 506, 616, 710, 747, 814, 841, 843, 846, 852, 853, 858, 890, 896, 948, 993
 abrupt cooling 815
 Asia 994
 Canada 993
 Chronozone 858
 climatic reversal 439
 cooling 519
 Europe 993
 Fennoscandia 379
 methane signal, Antarctic ice 995
 NADW 616
 South America 994
 stadial 100, 439
 Stadial 850
Ypresian 967
Yucatan (Texas) 420, 553
Yucatan Peninsula (Mexico) 8, 174, 217, 632
Yukon
 River (Alaska) 207, 424, 524
- Territory 207
 glaciation 206
 late Tertiary landscape 210
- Z**
Zambia 49
Zea mays 868
Zechstein evaporites 324
zeolite minerals 574, 582
 authigenic 582
Zeuner, Frederick Everard 436
Zijderveld diagram 254
Zimbabwe 49
zinc 636
zircon 248, 249
 crystallization 35
 detrital 34
 Archean 36
 Jack Hills 35
 oldest 35
 grain 334
 isotopic analysis 35
 oxygen isotopes 35, 36
 Western Australia 35
Zoanthidia 198
zone
 euphotic 110, 536
 exaerobic 12
 intertidal 89
 seismogenic 475
 subglacial 89
 supratidal 89
zooplankton 40, 109, 111, 536, 649
zooxanthellae 281, 672
zooxanthellate 200
 diversity 204
Zuider Zee 552

EARTH HISTORY TABLE

Table 1 Major Events in Earth's Climate History

PHANEROZOIC EON

Cenozoic Era

Quaternary Period (1.8 my–present)

Holocene (Recent) Epoch (12 ky–present) Maunder Minimum (~1645–1715 AD). Little Ice Age (~1400–1850 AD). Medieval Warm Period (~900–1200 AD). Rise of cities and irrigation (~5 ky). Hypsithermal (~9–5 ky). The 8,200-year cold event. Sea level meltwater pulse 1B (11,500–11,000 ky). Megafaunal extinctions.

Pleistocene Epoch (1.8 my–12 ky)

Younger Dryas cold spell (12.8–11.6 ky). Antarctic Cold Reversal (14.5–13.0 ky). Bølling-Allerød interstadial (14.5–12.7 ky). Sea level meltwater pulse 1A (~14.6–14.3 ky). Onset of post-glacial sea level rise (22–20 ky). Last Glacial Termination (20–14.7 ky). Last Glacial Maximum (23–19 ky). Last (Eemian) interglacial (126 ky, equivalent to base marine isotope stage 5e). Earliest *Homo sapiens* (<200 ky). Brunhes-Matuyama magnetic reversal (781 ky). Mid-Pleistocene Revolution: transition from 41 to 100 ky ice age cycles (1–0.8 my).

Neogene Period (1.8–23.0 my)

Pliocene Epoch (5.3–1.8 my)

Earliest *Homo* (~1.9–1.8 my). Intensification of the Walker circulation (~1.9 my). Onset of Northern Hemisphere glaciation (~2.5 my). Intensification of Asian monsoon (2.6 my). Oldest stone tools (2.6–2.5 my). Closure of Isthmus of Panama (4.25–3.4 my). Mid-Pliocene warm period (3.15–2.85 my). Earliest australopithecines (4 my). Progressive narrowing of Indonesian gateway and drying of East Africa (5–2 my).

Miocene Epoch (23.0–5.3 my)

Messinian salinity crisis (5.33–5.96my). Earliest hominins (7–6 my). Development of Indian and east Asian monsoon (9–8 my; possibly at 22 my). Accelerated phase of eastern Himalayan uplift (13–9 my). East African rifting (12–1.5 my). Deep-water cooling and east Antarctic ice sheet expansion (15 my).

Paleogene Period

Oligocene Epoch (33.9–23.0 my)

Initiation of Antarctic Circumpolar Current (~25–23 my). Initiation of North Atlantic Deep Water current. Opening of Tasmanian Passage (~33.5 my). Onset of ice build-up, Antarctica (34 my).

Eocene Epoch (55.8–33.9 my)

Opening of Drake Passage (~44–22 my). Onset of Himalayan uplift (~40 my). Gradual cooling trend (49–37 my). Early Eocene climatic optimum (55–50 my). Paleocene–Eocene Thermal maximum (55.5 my) – warm episode, large negative $\delta^{13}\text{C}$ anomaly.

Paleocene Epoch (65.5–55.8 my)

Late Paleocene – India collides with Asia.

Mesozoic Era

Cretaceous Period (145.5–65.5 my)

Cretaceous–Tertiary impact. Major mass extinction. Last dinosaurs, ammonites, and others. Massive eruption of Deccan Traps (~65 my). Some short-lived cold episodes. Ocean anoxic events. Starting ~125 mya, generally warm. Elevated sea level. Massive flood basalts – southwest Pacific Ocean. Increased CO₂ outgassing.

Jurassic Period (199.6–145.5 my)

Break-up of Gondwanaland; separation of India, Australia, Antarctica, Early Cretaceous. Temperate climate.

Triassic Period (251.0–199.6 my)

Rifting – eastern North America. Sea floor spreading and sea level rise. Generally warm. Ocean anoxic event. Mass extinction – end Triassic. Onset of Pangean break-up, Late Triassic. Generally warm. Monsoonal climate. Extensive evaporites – hot and dry – interior Pangea.

Paleozoic Era

Permian Period (299.0–251.0 my)

End-Permian mass extinction. Onset of warm climate. Ocean anoxic event. Massive eruption of Siberian Traps (flood basalts) (249.4 my). Glaciation persists to Middle–Late Permian. Final assembly of Pangea. First mammals.

Carboniferous Period (345–299.0 my)

“The Coal Age”.

Pennsylvanian (318.1–299.0 my)

Onset of Southern Hemisphere glaciation (320 my). Extensive paleoequatorial coal deposition. Cyclothem.

Mississippian (359.2–318.1 my)

Warming trend. First land vertebrates.

Devonian Period (416.0–359.2 my)

Mass extinction. Late Devonian to early Carboniferous glaciation (~374.5 my). Early-mid Devonian, warm, and dry.

Silurian Period (443.7–416.0 my)

Moderate climate, high sea levels, shallow continental seas.

Ordovician Period (488–443.7 my)

Mass extinction – end Ordovician. Late Ordovician to early Silurian high latitude, Southern Hemisphere glaciation. First land plants. Early Ordovician – warm, arid climate.

Cambrian Period (542.0–488.3 my)

Generally warm and arid. First exoskeletal invertebrates. “Cambrian explosion.” Ocean anoxia at Precambrian–Cambrian boundary.

PROTEROZOIC EON (2,500–542 my)

Neoproterozoic Era (1,000–542 my)

First preserved macroscopic soft-bodied fossils (Ediacaran fauna ~600 my). Neoproterozoic glaciations (~725–635 my).

Mesoproterozoic Era (1,600–1,000 my)

Paleoproterozoic Era (2,500–1,600 my)

Huronian glaciation (2400–2200 my). Early increase in O₂; massive banded iron and manganese formations during the Huronian.

ARCHAEAN EON (~4,000–2,500 my)

Earliest fossil evidence for life, Apex Chert Australia (~3.5 by). Oldest water-deposited rocks, Isua Supracrustal sequence, Greenland (3.7–3.8 by). “Late heavy bombardment” by meteorites (~3.9 by), by analogy to the Moon.

HADEAN EON (~4,650–4,000 my)

Oldest minerals/rocks: zircon crystals, Narryer Gneiss Complex, Western Australia (4.4–4.0 by); Acasta Gneiss, Great Slave Lake, NW Canada (4.03 by). Low surface temperature (4.4–4.0 by), based on oxygen isotope ratios in zircon.

Age of Earth (4.54 by)

Age of Solar System (4.57 by)

Dates for geologic periods are taken from *International Commission on Stratigraphy* (2004) Overview of Global Boundary Stratotype Sections and Points (GSSP's) (<http://www.stratigraphy.org/gssp.htm>). Major events listed in the table are described in the individual articles in this volume unless otherwise indicated.